Springer Handbook of Surface Science

Rocca
Rahman
Vattuone
Editors

Springer

Springer Handbook of Surface Science

Springer Handbooks provide a concise compilation of approved key information on methods of research, general principles, and functional relationships in physical and applied sciences. The world's leading experts in the fields of physics and engineering will be assigned by one or several renowned editors to write the chapters comprising each volume. The content is selected by these experts from Springer sources (books, journals, online content) and other systematic and approved recent publications of scientific and technical information.

The volumes are designed to be useful as readable desk book to give a fast and comprehensive overview and easy retrieval of essential reliable key information, including tables, graphs, and bibliographies. References to extensive sources are provided.

Springer Handbook of Surface Science

Mario Rocca, Talat S. Rahman, Luca Vattuone (Eds.)

With 840 Figures and 66 Tables

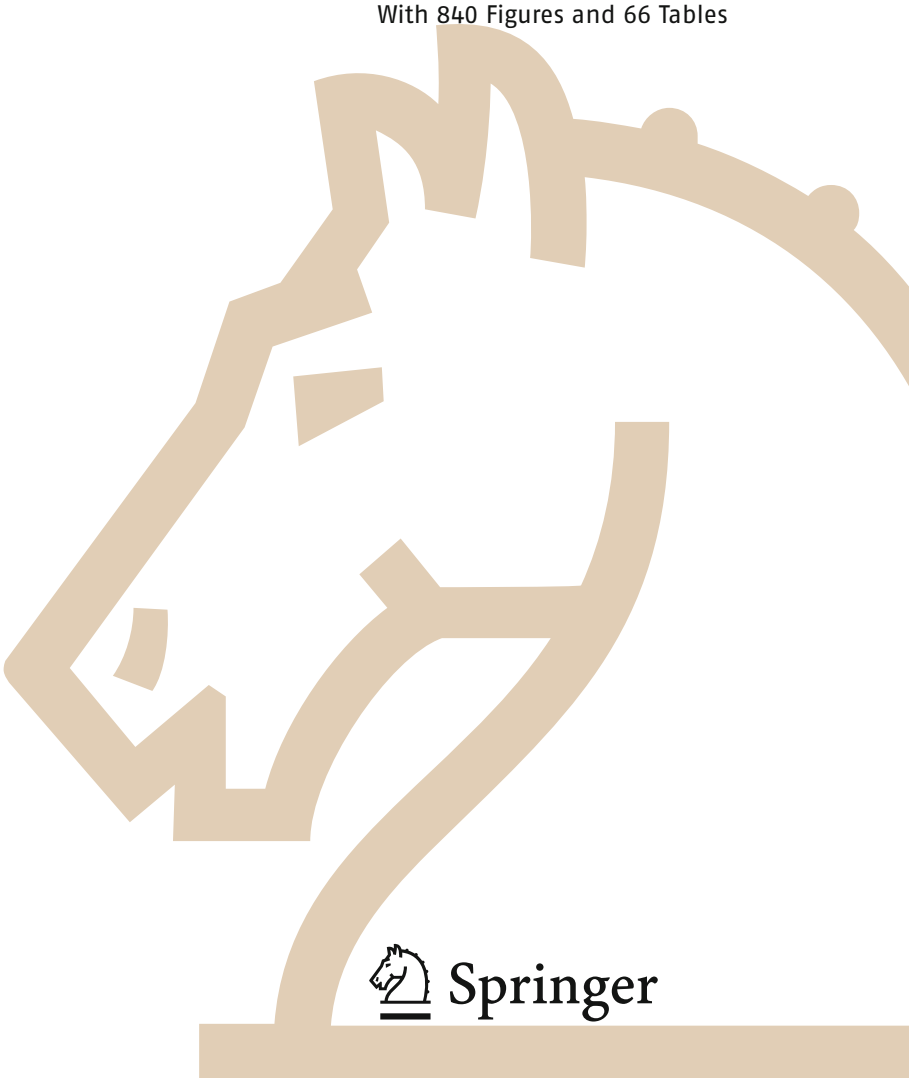

Springer

Editors
Mario Rocca
Dipt. di Fisica
Università di Genova
Genova, Italy

Talat S. Rahman
Department of Physics
University of Central Florida
Orlando, FL, USA

Luca Vattuone
Dipt. di Fisica
Università di Genova and IMEM-CNR Unità di Genova
Genova, Italy

ISBN 978-3-030-46904-7 e-ISBN 978-3-030-46906-1
https://doi.org/10.1007/978-3-030-46906-1

Dedicated to the memory of Gian Paolo Brivio

Foreword

The study of processes on well-defined solid surfaces is a relatively young discipline. It first gained prominence during the 1960s, when the advent of ultrahigh vacuum technology enabled the production and maintenance of clean and well-defined ordered single-crystal surfaces of solids. The first issue of the journal *Surface Science* appeared in 1964; by the end of 2018, around 680 volumes of this journal had been published, reflecting the enormous growth of this field. This period also saw the development of a wide variety of experimental techniques enabling the investigation of different aspects of the energetic, kinetic, structural, electronic, magnetic, and dynamic properties of surfaces with great accuracy. The advent of scanning probe methods allowed atomic processes to be studied in unprecedented detail.

More recently, the study of "real" surfaces at elevated pressures became possible, which has since developed into a mature field of research ranging from phenomena associated with nanotechnology and thin-film formation to the heterogeneous catalysis of industrial processes.

The present handbook consists of contributions written by numerous experts in this field and covers the main aspects of this fascinating branch of science. It should prove invaluable to all those interested in this discipline.

Gerhard Ertl

Gerhard Ertl, recipient of the 2007 Nobel Prize in Chemistry for his studies of chemical processes on solid surfaces

Preface

Surfaces have always attracted the attention and curiosity of humans, since they define the outer limits of objects—those that we can see with our eyes and feel with our hands. One of the earliest mentions of surfaces in the literature was a comment by Pliny the Elder, who reported that choppy waves at the surface of the sea could be calmed by pouring oil on the water. This observation was later also made by Benjamin Franklin, who mentioned that a spoonful of oil could cover a lake. Unfortunately, he did not perform the easy calculation which would have told him that the sea would then have been covered by a film one molecule thick. When studying earthquakes, Thomas Strutt—also known as Sir Rayleigh—noticed that the greatest destruction was caused by surface waves, because they shake buildings laterally. At the beginning of the nineteenth century, Berzelius became fascinated by surfaces because they are the sites for chemical reactions and useful catalytic processes. Later on, electronic surface states came to the forefront when an understanding of the junctions between differently doped semiconductors was needed to realize the transistor. However, it was only after the Second World War that scientists began to comprehend the behavior of surfaces at the atomic scale, due to the development of clean vacuum systems that allowed well-defined surfaces to be prepared and kept clean for long enough to permit their characterization. It soon became clear that surfaces are not simply discontinuations of crystals; they can include rather complicated structural reconstructions. Catalytic activity is often facilitated by these reconstructions, as well as defects in the outermost atomic layers of a body. On the other hand, a theoretical understanding of surfaces at the atomistic limit also became possible during this period due to the availability of inexpensive computing power that allowed the simulation of more and more atoms, thus loosening the restrictions imposed by the application of periodic boundary conditions, which—by definition—do not hold at surfaces and interfaces.

Nowadays, there is a vast community of surface scientists comprising physicists, chemists, and materials scientists and engineers. The wide range of backgrounds of surface scientists is advantageous, as it means that different surface scientists will approach the same problem in different ways. Once the simple systems were understood, more complex and thus more realistic situations could be addressed on a knowledge basis.

Indeed, it is difficult to imagine how nanotechnology could have developed as it has without a background knowledge of surface science. Surfaces are used as templates to grow films just one or a few monolayers thick, as well as nanoparticles and nanowires that are used for catalytic and electronic applications. Issues as complex as biofouling and biocompatibility, involving adsorbates consisting of millions of atoms, can be tackled using surface science. Lately, interest has focused on the fantastic properties of purely two-dimensional materials: sheets of atoms without any underlying volume. Their properties were found to be different from those of a surface of the same material in bulk form (e.g., graphene versus a graphite surface). This led to the discovery of new phenomena with the potential for novel applications.

There are approximately 40 chapters in this Handbook, to which over a hundred scientists, physicists, chemists, and engineers have contributed. The authors are distributed across different countries and continents and belong to strongly interdisciplinary groups. The Editors embarked on this adventure in 2015, sending out the first invitations in 2016. This work constitutes a milestone in the field of surface science. It should help young people who are entering the field while also providing a useful base that allows expert colleagues to assess the state of the art. We hope that this Handbook will stimulate further interest in surface science and that its readers will find it as useful as we believe it to be.

This Handbook is dedicated to Professor Gian Paolo Brivio, who wrote one of its chapters together with Guido Fratesi, and who unfortunately passed away on May 25th, 2020.

Gian Paolo graduated with a PhD in physics in 1973 under the supervision of Professor Giorgio Benedek at the University of Milano. After performing postdoctoral research at the University of Liverpool with Professor T.B. Grimley, he returned to Milano and started his academic career at the University of Milano. In 1986 he became Associate Professor in Condensed Matter Physics, after which he moved to the Department of Materials Science at the University of Milano-Bicocca, where he was promoted to Full Professor in 2000.

All three Editors of the present Handbook met him for the last time at the workshop on Atoms and Molecules on Solid Surfaces (AMOSS) in Milano, on his 70th birthday.

His contributions to surface science focused on the theoretical treatment of the dynamics of gas–surface in-

teractions (sticking, scattering, desorption), and more recently on the application of density functional theory to more realistic adsorption conditions. To this end, he investigated magnetic effects in the interactions of molecules with graphene and the adsorption of organic molecules on solid surfaces, concentrating on the role played by excited states and the timescales over which the molecule–surface interaction takes place.

He published around 120 papers in peer-reviewed journals, and reported his results in over 130 contributions and invitations to conferences and seminars at research institutions all over the world. He always prized scientific collaborations, and served as a Visiting Professor in Germany, Canada, and USA. He also prided himself on nurturing the next generation of scientists. For this reason, in 2006 he promoted the foundation of a European network for doctorates in the physics and chemistry of advanced materials—a network that currently includes fifteen universities from nine different countries and promotes internationalization through the exchange of students and teachers.

Gian Paolo took pleasure in organizing thematic conferences and workshops, paying tremendous attention to scientific, cultural, and artistic details that made the events memorable for all participants. The Editors of this Handbook fondly remember the 4th Vibration and Surfaces Meeting in Santa Margherita that Gian Paolo organized with Mario Rocca in 1992, the Summer School in Erice that he organized with Luca Vattuone in 2008, and the 17th Workshop on Dynamical Phenomena at Surfaces that he organized with Talat Rahman in Milan in 2016. In his true form as a scientist, a scholar, and a man of art, Gian Paolo also served as the external evaluator for the doctorate thesis of Luca Vattuone in 1995. Gian Paolo's passion for science, his warm personality, his thoughtful nature, and his desire to touch the lives of others made moments with him memorable.

We will miss his enlightened way of thinking and his humanity.

Summer 2020

Mario Agostino Rocca
(Editor-in-Chief)
Talat Shahnaz Rahman
(Co-Editor)
Luca Vattuone (Co-Editor)

About the Editors

Mario Rocca is an experimental physicist, working on the experimental measurement of surface phonon spectra, conventional and acoustic surface plasmon dispersion, and gas surface interaction. He graduated in Physics from the University of Genova. He received his PhD from RWTH Aachen. He was a research staff member at the University of Genoa from 1984 to 1992. In 2001, he became a Full Professor for Condensed Matter Physics. Mario Rocca is Vice Chair of the Surface Science Division of the International Union for Vacuum Science, Techniques, and Application (IUVSTA) and a member of the scientific board of the Italian Union of Scientists for Disarmament. He was Editor of the journal Surface Science Reports until 2018 and is currently Editor of Applied Surface Science and of the Springer Series in Surface Science.

Talat S. Rahman is Pegasus Professor at the Department of Physics at the University of Central Florida. She received her PhD from the University of Rochester and has held various academic positions, among which were positions at UC Irvine and Kansas State University, where she was the first female faculty member in the Physics Department. Her impressive list of visiting appointments includes stays at the MPI for Solid-State Research in Stuttgart, Germany, EPFL Lausanne, Switzerland, and the Brook Haven National Laboratory, USA. Talat Rahman has received numerous fellowships, including an Alexander von Humboldt Research Fellowship. Her research focus is multiscale modeling of chemical reactions and related phenomena at surfaces. She contributes actively to reforming STEM education, supporting women and minorities in STEM. She serves on the editorial board of Journal of Physics Condensed Matter.

Luca Vattuone has been Associate Professor of Condensed Matter Physics at the University of Genova since 2012. After graduating in physics from the University of Genoa, he received his PhD in Physics for his work on the sticking probability of oxygen on silver surfaces employing a molecular beam and for the EEL spectrometer he designed. He was a researcher in the group of D.A. King at the University of Cambridge, as well as the University of Genoa and INFM. His research activity focussed on the investigation of gas-surface interaction by high-resolution electron energy loss spectroscopy, supersonic molecular beams, and single-crystal calorimetry. He is currently Coordinator for the Material Science Courses of the University of Genova.

About the Authors

Maite Alducin
Centro de Física de Materiales CFM/MPC
(CSIC-UPV/EHU)
Donostia-San Sebastián, Spain
maite.alducin@ehu.eus

Matteo Amati
Elettra – Sincrotrone Trieste SCpA
Trieste, Italy

Thierry Angot
CNRS, PIIM, Campus de Saint-Jérôme
Aix-Marseille Université
Marseille, France
thierry.angot@univ-amu.fr

Alexei Barinov
Elettra – Sincrotrone Trieste SCpA
Trieste, Italy
alexey.barinov@elettra.eu

Daniel Beato-Medina
CNRS, PIIM, Campus de Saint-Jérôme
Aix-Marseille Université
Marseille, France

Giorgio Benedek
Department of Materials Science – U5
University of Milano-Bicocca
Milano, Italy
and
Donostia International Physics Center (DIPC)
Donostia/San Sebastián, Spain
giorgio.benedek@unimib.it

Marco Bernasconi
Department of Materials Science
University of Milano-Bicocca
Milano, Italy
marco.bernasconi@unimib.it

Carlo Maria Bertoni
Dept. of Physics, Informatics and Mathematics
University of Modena and Reggio Emilia
Modena, Italy
carlo.m.bertoni@gmail.com

Luca Giacomo Bettini
CIMaINa and Dipartimento di Fisica
"Aldo Pontremoli"
Università degli Studi di Milano
Milano, Italy
lucagiacomo.bettini@gmail.com

Stefan Blügel
Peter Grünberg Institute and Institute for
Advanced Simulation
Forschungszentrum Jülich
Jülich, Germany
s.bluegel@fz-juelich.de

Gianangelo Bracco
Dipartimento di Fisica
Università di Genova
Genova, Italy
bracco@fisica.unige.it

Alberto Brambilla
Dipartimento di Fisica
Politecnico di Milano
Milano, Italy

Gian Paolo Brivio
Dept. of Materials Science
University of Milano-Bicocca
Milano, Italy
gianpaolo.brivio@unimib.it

Guido Busca
Università di Genova
Genova, Italy
guido.busca@unige.it

Arrigo Calzolari
Centro NANO-S3
CNR-Istituto Nanoscienze
Modena, Italy
arrigo.calzolari@nano.cnr.it

Davide Campi
Theory and Simulation of Materials and National
Centre for Computational Design and Discovery of
Novel Materials
Ecole Polytechnique Fédérale de Lausanne
Lausanne, Switzerland
davide.campi@epfl.ch

Alessandra Catellani
Centro NANO-S3
CNR-Istituto Nanoscienze
Modena, Italy
alessandra.catellani@nano.cnr.it

Yves J. Chabal
Dept. of Materials Science and Engineering
University of Texas at Dallas
Dallas, TX, USA
chabal@utdallas.edu

Evgueni V. Chulkov
Faculty of Chemical Sciences,
Materials Physics Department
University of the Basque Country, UPV/EHU
Donostia-San Sebastián, Spain
and
Departamento de Física de Materiales
Universidad del País Vasco, UPV/EHU, Facultad de Ciencias Químicas
San Sebastián/Donostia, Spain
evguenivladimirovich.tchoulkov@ehu.eus

Franco Ciccacci
Dipartimento di Fisica
Politecnico di Milano
Milano, Italy

Giancarlo Cicero
Dipt. di Scienza Applicata e Tecnologia
Politecnico di Torino
Torino, Italy
and
Centro NANO-S3
CNR-Istituto Nanoscienze
Modena, Italy
giancarlo.cicero@polito.it

Victor Climent
Instituto Universitario de Electroquímica
Universidad de Alicante
San Vicente del Raspeig, Alicante, Spain
victor.climent@ua.es

Martina Corso
Centro de Física de Materiales
CSIC/UPV-EHU-Materials Physics Center
San Sebastian, Spain

Paola De Padova
Istituto di Struttura della Materia
Consiglio Nazionale delle Ricerche
Roma, Italy
paola.depadova@ism.cnr.it

Ricardo Díez Muiño
Centro de Física de Materiales CFM/MPC
(CSIC-UPV/EHU)
Donostia-San Sebastián, Spain
rdm@ehu.eus

Shixuan Du
Institute of Physics and University of Chinese Academy of Sciences
Chinese Academy of Sciences
Beijing, China
sxdu@iphy.ac.cn

Lamberto Duò
Dipartimento di Fisica
Politecnico di Milano
Milano, Italy

S. V. Eremeev
Laboratory of Surface Phenomena Physics
Institute of strength Physics and Materials Science
Tomsk, Russian Federation
eremeev@ispms.tsc.ru

Prescott E. Evans
Lincoln, NE, USA
prescott.evans@huskers.unl.edu

Riccardo Ferrando
Physics Department
University of Genoa
Genoa, Italy
ferrando@fisica.unige.it

Marco Finazzi
Dipartimento di Fisica
Politecnico di Milano
Milano, Italy

Guido Fratesi
Physics Department
University of Milano
Milano, Italy
guido.fratesi@unimi.it

Hans-Joachim Freund
Chemical Physics Dept.
Fritz Haber Institute of the Max Planck Society
Berlin, Germany
freund@fhi-berlin.mpg.de

Massimiliano Galluzzi
Shenzhen Institutes of Advanced Technology,
Chinese Academy of Sciences
Materials Interfaces Center
Shenzhen, China
galluzzi@siat.ac.cn

Pietro Gambardella
Laboratory for Magnetism and Interface Physics,
Department of Materials
ETH Zurich
Zurich, Switzerland
pietro.gambardella@mat.ethz.ch

Hong-Jun Gao
Institute of Physics and University of Chinese
Academy of Sciences
Chinese Academy of Sciences
Beijing, China
hjgao@iphy.ac.cn

Qingfeng Ge
qge@chem.siu.edu

Simeon Gilbert
Lincoln, NE, USA
simeon.gilbert@outlook.com

Enrico Gnecco
Otto Schott Institute of Materials Research
Friedrich Schiller University Jena
Jena, Germany
enrico.gnecco@uni-jena.de

Luca Gregoratti
Elettra – Sincrotrone Trieste SCpA
Trieste, Italy
luca.gregoratti@elettra.eu

Guanhua Hao
Lincoln, NE, USA
guanhuahao@huskers.unl.edu

Rolf Heid
Institute for Quantum Materials and Technologies
Karlsruhe Institute of Technology
Karlsruhe, Germany
rolf.heid@kit.edu

Georg Held
Dept. of Chemistry
University of Reading
Reading, UK
and
Diamond Light Source Ltd
Didcot, UK
georg.held@diamond.ac.uk

Enrique Herrero
Instituto Universitario de Electroquímica
Universidad de Alicante
San Vicente del Raspeig, Alicante, Spain
herrero@ua.es

Markus Heyde
Chemical Physics Dept.
Fritz Haber Institute of the Max Planck Society
Berlin, Germany
heyde@fhi-berlin.mpg.de

Conor Hogan
Institute of Structure of Matter (ISM-CNR)
National Research Council of Italy
Rome, Italy
conor.hogan@ism.cnr.it

Peijun Hu
p.hu@qub.ac.uk

Andrew P. Jardine
Cavendish Laboratory
University of Cambridge
Cambridge, UK
apj24@cam.ac.uk

Stephen J. Jenkins
Dept. of Chemistry
University of Cambridge
Cambridge, UK
sjj24@cam.ac.uk

Ado Jorio
Departamento de Física
Universidade Federal de Minas Gerais
Belo Horizonte, Brazil
adojorio@gmail.com

J. Iñaki Juaristi
Depto de Física de Materiales
Facultad de Químicas UPV/EHU
Donostia-San Sebastián, Spain
josebainaki.juaristi@ehu.eus

Jacques Jupille
Institute of Nanosciences of Paris
Sorbonne University
Paris, France
jacques.jupille@insp.jussieu.fr

David A. King
The Foreign and Commonwealth Office
London, UK
dk@camkas.co.uk

Maya Kiskinova
Elettra – Sincrotrone Trieste SCpA
Trieste, Italy
maya.kiskinova@elettra.eu

Tadahiro Komeda
Institute of Multidisciplinary Research for Advanced Materials (IMRAM)
Tohoku University
Sendai, Japan
tadahiro.komeda.a1@tohoku.ac.jp

Takashi Komesu
Lincoln, NE, USA
tkomesu2@unl.edu

Eugene E. Krasovskii
Dept. of Materials Physics
University of the Basque Country, Donostia International Physics Center, and IKERBASQUE, Basque Foundation for Science
Donostia-San Sebastián, Spain
eugene.krasovskii@ehu.eus

H. Jürgen Kreuzer
Department of Physics and Atmospheric Science
Dalhousie University
Halifax, Canada
h.j.kreuzer@dal.ca

Helmut Kuhlenbeck
Chemical Physics Dept.
Fritz Haber Institute of the Max Planck Society
Berlin, Germany
kuhlenbeck@fhi-berlin.mpg.de

Guy Le Lay
PIIM CNRS Campus de Saint-Jérôme
Aix-Marseille University
Marseille, France
guy.lelay@univ-amu.fr

Andrea Claudio Levi
Dipartimento di Fisica
Università di Genova
Genova, Italy
andrealevi.genova@yahoo.com

Jorge Lobo-Checa
Instituto de Ciencia de Materiales de Aragón (ICMA)
CSIC-Universidad de Zaragoza
Zaragoza, Spain
and
Departamento de Física de la Materia Condensada
Universidad de Zaragoza
Zaragoza, Spain

Eric C. Mattson
Dept. of Materials Science and Engineering
University of Texas at Dallas
Dallas, TX, USA

Paolo Milani
CIMaINa and Dipartimento di Fisica "Aldo Pontremoli"
Università degli Studi di Milano
Milano, Italy
paolo.milani@mi.infn.it

Francesca Moresco
Center for Advancing Electronics Dresden
TU Dresden
Dresden, Germany
francesca.moresco@tu-dresden.de

Aitor Mugarza
Institut Catalá de Nanociencia i Nanotecnologia (ICN2)
Bellaterra-Barcelona, Spain

Vladimir U. Nazarov
National Research University (MIPT NRU)
Moscow Institute of Physics and Technology
Dolgoprudny, Russian Federation
nazarov@gate.sinica.edu.tw

Niklas Nilius
Institut für Physik
Carl von Ossietzky Universität Oldenburg
Oldenburg, Germany
niklas.nilius@uni-oldenburg.de

Norio Okabayashi
School of Mathematics and Physics
Kanazawa University
Kanazawa, Japan
okabayashi@staff.kanazawa-u.ac.jp

Michio Okada
Institute for Radiation Sciences and Department of Chemistry, Graduate School of Science
Osaka University
Osaka, Japan
okada@chem.sci.osaka-u.ac.jp

J. Enrique Ortega
Departamento Física Aplicada I
Universidad del País Vasco
San Sebastian, Spain
and
Centro de Física de Materiales
CSIC/UPV-EHU-Materials Physics Center
San Sebastian, Spain
enrique.ortega@ehu.es

Maurizia Palummo
Dept. of Physics and INFN
University of Rome "Tor Vergata"
Rome, Italy
maurizia.palummo@roma2.infn.it

Jinbo Pan
Institute of Physics and University of Chinese Academy of Sciences
Chinese Academy of Sciences
Beijing, China
jbpan@iphy.ac.cn

Roberto Paniago
Departamento de Física
Universidade Federal de Minas Gerais
Belo Horizonte, Brazil
paniago@fisica.ufmg.br

Herbert Pfnür
Festkörperphysik (Solid State Physics), ATMOS
Leibniz Universität Hannover
Hannover, Germany
pfnuer@fkp.uni-hannover.de

Andrea Picone
Dipartimento di Fisica
Politecnico di Milano
Milano, Italy
andrea.picone@polimi.it

Paolo Piseri
CIMaINa and Dipartimento di Fisica "Aldo Pontremoli"
Università degli Studi di Milano
Milano, Italy
paolo.piseri@fisica.unimi.it

Alessandro Podestà
CIMaINa and Dipartimento di Fisica "Aldo Pontremoli"
Università degli Studi di Milano
Milano, Italy
alessandro.podesta@mi.infn.it

Olivia Pulci
Dept. of Physics, and INFN
University of Rome "Tor Vergata"
Rome, Italy
olivia.pulci@roma2.infn.it

Talat S. Rahman
Department of Physics
University of Central Florida
Orlando, FL, USA
talat.rahman@ucf.edu

Thomas Risse
Institute of Chemistry and Biochemistry – Physical and Theoretical Chemistry
Freie Universität Berlin
Berlin, Germany
risse@chemie.fu-berlin.de

Mario Rocca
Dipt. di Fisica
Università di Genova
Genova, Italy
rocca@fisica.unige.it

Igor P. Rusinov
Laboratory of Nanostructured Surfaces and Coatings
Tomsk State University
Tomsk, Russian Federation
rusinovip@gmail.com

Alessandro Sala
University of Trieste
Trieste, Italy
and
CNR – Istituto Officina dei Materiali
Trieste, Italy
sala@iom.cnr.it

Eric Salomon
Physics Department, Campus de Saint-Jérôme
Aix-Marseille Université
Marseille, France
eric.salomon@univ-amu.fr

Letizia Savio
Istituto dei Materiali per l'Elettronica ed il Magnetismo
Consiglio Nazionale delle Ricerche
Genova, Italy
letizia.savio@imem.cnr.it

Swetlana Schauermann
Institut für Physikalische Chemie
Christian-Albrechts-Universität zu Kiel
Kiel, Germany

Frederik Schiller
Centro de Física de Materiales
CSIC/UPV-EHU-Materials Physics Center
San Sebastian, Spain
and
Donostia International Physics Centre
San Sebastian, Spain

Thomas Schmidt
Chemical Physics Dept.
Fritz Haber Institute of the Max Planck Society
Berlin, Germany
thomas.schmidt@fhi-berlin.mpg.de

Daiichiro Sekiba
Institute of Applied Physics
The University of Tsukuba
Tsukuba, Japan
sekiba@tac.tsukuba.ac.jp

Hikmet Sezen
Elettra – Sincrotrone Trieste SCpA
Trieste, Italy
and
Institute for Methods and Instrumentation for Synchrotron Radiation Research FG-ISRR
Helmholtz-Zentrum Berlin für Materialien und Energie GmbH
Berlin, Germany

Shamil Shaikhutdinov
Chemical Physics Dept.
Fritz Haber Institute of the Max Planck Society
Berlin, Germany
shaikhutdinov@fhi-berlin.mpg.de

Vyacheslav M. Silkin
Dept. of Materials Physics
University of the Basque Country, Donostia International Physics Center, and IKERBASQUE, Basque Foundation for Science
Donostia-San Sebastián, Spain
waxslavas@ehu.es

Irina Y. Sklyadneva
Donostia International Physics Center (DIPC)
Donostia/San Sebastián, Spain
swxskski@ehu.eus

Marco Smerieri
Istituto dei Materiali per l'Elettronica ed il Magnetismo
Consiglio Nazionale delle Ricerche
Genova, Italy

Edmar Avellar Soares
Departamento de Física
Universidade Federal de Minas Gerais
Belo Horizonte, Brazil
edmar@fisica.ufmg.br

Martin Sterrer
Institute of Physics
University of Graz
Graz, Austria
martin.sterrer@uni-graz.at

Iori Tanabe
Lincoln, NE, USA
iori.tanabe@ni.edu

Christoph Tegenkamp
Institut für Physik
Technische Universität Chemnitz
Chemnitz, Germany
christoph.tegenkamp@physik.tu-chemnitz.de

J. Peter Toennies
Max-Planck-Institut fuer Dynamik und Selbstorganisation
Goettingen, Germany

Luca Vattuone
Dipt. di Fisica
Università di Genova and IMEM-CNR Unità di Genova
Genova, Italy
vattuone@fisica.unige.it

Matthieu J. Verstraete
Nanomat/Q-Mat/CESAM, ETSF – Institut de Physique, Bat. B5a 3/7
Université de Liège
Liège, Belgium
matthieu.verstraete@uliege.be

Ziyun Wang
University of Toronto
Toronto, Canada
ziyunwang.wang@utoronto.ca

Andrew J. Yost
Oklahoma State University
Stillwater, OK, USA
andrew.yost@okstate.edu

Yu-Yang Zhang
Institute of Physics and University of Chinese Academy of Sciences
Chinese Academy of Sciences
Beijing, China
zhangyuyang@ucas.ac.cn

Contents

Part F Lattice Dynamics

Part G Gas Surface Interaction

List of Abbreviations

2-DBZ	2-D Brillouin zone
2DEG	two-dimensional electron gas

A

ADF	annular dark-field
AES	Auger electron spectroscopy
AFM	atomic force microscopy
AIMD	ab-initio molecular dynamics
ALDA	adiabatic local density approximation
ARPES	angle-resolved photoemission spectroscopy
ASP	acoustic surface plasmon

B

bcc	body-centered cubic
BCCF	bond-counting contribution factor
BCM	bond charge model
BCSOS	body-centered solid-on-solid
BEP	beam equivalent pressure
BNN	bulk nearest neighbor
BOA	Born–Oppenheimer approximation
BZ	Brillouin zone

C

CAGR	compounded average growth rate
CAICISS	coaxial-impact-collision ion scattering spectroscopy
CARS	coherent anti-Stokes Raman scattering
ccp	cubic close packed
CDW	charge-density wave
CMOS	complementary metal–oxide–semiconductor
CMSA	corrugation-mediated selective adsorption
CNT	carbon nanotube
CPM	Car–Parrinello method
CPO	catalytic partial oxidation
CTF	contrast transfer function
CVD	chemical vapor deposition

D

DEF	disordered even flat
DEMS	differential electrochemical mass spectrometry
DFT	density functional theory
DLC	diamond-like carbon
DOS	density of states
DRRS	double-resonance Raman scattering
DRS	differential reflectance spectroscopy
DW	Debye–Waller

E

EAM	embedded-atom method
ED-GIXRD	energy-dispersive grazing incidence x-ray diffraction
EDX	energy-dispersive x-ray analysis
EELS	electron energy-loss spectroscopy
ELS-LEED	electron energy-loss-low-energy electron diffraction
EMT	effective medium theory
EPI	electron–phonon interaction
EPR	electron paramagnetic resonance
ERDA	elastic recoil detection analysis
ESR	electron spin resonance
EXAFS	x-ray absorption fine structure

F

FBZ	first Brillouin zone
fcc	face-centered cubic
FESEM	field-emission scanning electron microscopy
FET	field-effect transistor
FFT	fast Fourier transform
FLAPW	full-potential linearized augmented plane wave
FM	ferromagnetic
FMR	ferromagnetic resonance
FTIR	Fourier transform infrared
FWHM	full width at half maximum

G

GGA	generalized gradient approximation
GIXD	grazing incidence x-ray diffraction
GNR	graphene nanoribbon

H

h-BN	hexagonal boron nitride
HAS	helium atom scattering
hcp	hexagonal close-packed
HF	Hartree–Fock
HOMO	highest occupied molecular orbital
HOPG	highly oriented pyrolytic graphite
HREELS	high-resolution electron energy-loss spectroscopy
HRLEED	high-resolution low-energy electron diffraction
HRSEM	high-resolution secondary-electron microscopy
HRTEM	high-resolution transmission electron microscopy

I

ICISS	impact-collision ion scattering spectroscopy
ICP	inductively coupled plasma
IETS	inelastic electron tunneling spectroscopy
IMFP	inelastic mean free path
IPES	inverse photoemission spectroscopy
IRAS	infrared reflection absorption spectroscopy
ISS	ion scattering spectroscopy
IXS	inelastic x-ray spectroscopy

J

JDOS	joint density of states

K

KS	Kohn–Sham

L

LDA	local density approximation
LDOS	local density of states
LEED	low-energy electron diffraction
LEEM	low-energy electron microscopy
LEIS	low-energy ion scattering
LSDA	local spin density approximation
LUMO	lowest unoccupied molecular orbital

M

MAS NMR	magic-angle spinning nuclear magnetic resonance
MBE	molecular beam epitaxy
MCA	magnetocrystalline anisotropy
MCD	magnetic circular dichroism
MD	molecular dynamics
MDC	momentum distribution curve
MEIS	medium-energy ion scattering
MEMS	microelectromechanical system
MFA	mean-field approximation
MFM	magnetic force microscopy
ML	monolayer
MOF	metal–organic framework
MOKE	magneto-optic Kerr effect
MOSFET	metal–oxide–semiconductor field-effect transistor
MPA	magnetic prism array
MSHD	mean square height difference
MSHG	magnetic second harmonic generation
MTJ	magnetic tunnel junction

N

NAP	near-ambient pressure
NC-AFM	noncontact atomic force microscopy
NEXAFS	near-edge x-ray absorption fine structure spectroscopy
NIS	neutron inelastic scattering
NP	nanoparticle
NRA	nuclear reaction analysis
NW	nanowire

O

OLED	organic light-emitting diode
ORR	oxygen reduction reaction
OSA	order-sorting aperture

P

PAW	projector-augmented wave
PBE	Perdew–Burke–Ernzerhof
PCM	phase-change material
PDOS	projected density of states
PED	photoelectron diffraction
PEEM	photoelectron emission microscopy
PES	photoemission spectroscopy
PES	potential energy surface
PIXE	particle-induced x-ray emission
PLD	pulsed laser deposition
PMCS	pulsed microplasma cluster source
PPP	pseudopotential perturbation
PSD	position-sensitive detector
PSF	point spread function
PVD	physical vapor deposition

Q

Q2-D	quasi two-dimensional
QAH	quantum anomalous Hall
QC	quasiclassical
QENS	quasielastic neutron scattering
QHAS	quasielastic helium atom scattering
QP	quasiparticle
QSHE	quantum spin Hall effect
QW	quantum well
QWS	quantum well states

R

RAIRS	reflection-absorption infrared spectroscopy
RAS	reflection anisotropy spectroscopy
RBS	Rutherford backscattering spectrometry
REELS	reflection electron energy-loss spectroscopy
REMPI	resonance-enhanced multiphoton ionization
RHEED	reflection high-energy electron diffraction
RKKY	Ruderman–Kittel–Kasuya–Yosida
RPA	random phase approximation
RT	room temperature

S

SAM	self-assembled monolayer
sc	simple-cubic
SCAC	single-crystal adsorption calorimetry
SCBD	supersonic cluster beam deposition
SDRS	surface differential reflectance spectroscopy

SEM	scanning electron microscopy
SEXAFS	surface-extended x-ray absorption fine structure
SFG	sum frequency generation
SHG	second-harmonic generation
SIMS	secondary ion mass spectroscopy
SiND	Si nanodot
SiNR	Si nanoribbon
SMB	supersonic molecular beam
SMSI	strong metal-support interaction
SNR	signal-to-noise ratio
SOC	spin–orbit coupling
SP	surface plasmon
SP-STM	spin-polarized scanning transmission microscopy
SPALEED	LEED spot profile analysis
SPELEEM	spectroscopic photoemission and low-energy electron microscope
SPEM	scanning photoelectron microscopes
SPLEEM	spin-polarized LEEM
SPP	surface plasmon polariton
SPPES	spin-polarized photoemission spectroscopy
SPSTM	spin-polarized scanning tunneling microscopy
SQUID	superconducting quantum interference device
SRPES	spin-resolved photoemission spectroscopy
STEM	scanning transmission electron microscopy
STM	scanning tunneling microscopy
STS	scanning tunneling spectroscopy
SXRD	surface x-ray diffraction

T

TB	tight-binding
TDDFT	time-dependent density functional theory
TDS	thermal desorption spectroscopy
TEM	transmission electron microscopy
TI	topological insulator
TMO	transition-metal oxide
TMR	tunnel magnetoresistance
TO	transverse optical
TOF	time-of-flight
TPD	temperature-programmed desorption
TST	transition state theory

U

UHV	ultrahigh vacuum
UPS	ultraviolet photoemission spectroscopy

V

VASP	Vienna Ab Initio Simulation Package
VB	valence band
vdW	van der Waals
VFF	valence force field
VOC	volatile organic compound

W

WF	Wilson–Frenkel

X

XANES	x-ray absorption near-edge spectroscopy
XAS	x-ray absorption spectroscopy
XMCD	x-ray magnetic circular dichroism
XMLD	x-ray magnetic linear dichroism
XPD	x-ray photoelectron diffraction
XPEEM	x-ray photoemission electron microscopy
XPS	x-ray photoelectron spectroscopy
XRD	x-ray diffraction
XRF	x-ray fluorescence
XSW	x-ray standing wave

Part A Kinetics a

Part A Kinetics and Thermodynamics at Surfaces

Part A deals with surface thermodynamics and kinetics. These are the phenomena that lead to the equilibrium configuration of the surface and imply additional degrees of freedom as compared to bulk thermodynamics; e.g., the surface area may vary, affecting the crystal shape, and the broken symmetry in the direction normal to the surface may lead to new excitations and surface-localized phenomena. Indeed, the structure of a real surface, as imaged by scanning tunneling microscopy or inferred from diffraction experiments, can be quite different from that expected from the ideal truncation of the solid. These features may not be surprising if the system is out of equilibrium, but could be unexpected under equilibrium conditions.

If we want a faithful and not oversimplified picture, we must think of the surface as a dynamic entity in which the positions of the atoms are neither constant in time nor perfectly periodic in space, even under equilibrium conditions. The former phenomenon may be due to the diffusion of atoms, while the latter corresponds to the formation of a rough surface (atoms at the lattice positions parallel to the surface plane but displaced randomly in height) or surface melting (atoms at random positions with respect to all directions), which are frequent phenomena at temperatures close to the melting point of the solid. The surface is also home to a variety of localized excitations that have their own manifestations in the physical and chemical properties of surfaces, as will be seen.

The theoretical framework is provided by equilibrium surface thermodynamics. The surface free energy is therefore the main thermodynamic potential to consider when seeking deeper insights into the overall phenomenology.

Chapter 1 describes the roughening transition from both theoretical and experimental points of view. Although solid surfaces often seem to be rougher at low than at high temperatures, this observation corresponds to nonequilibrium situations in which the surface atoms did not have sufficient time to reach the minimum energy configuration. The opposite holds true under equilibrium conditions, and surfaces may undergo a roughening transition at high temperatures that is characterized by the onset of divergence in the height-height correlation of the lattice positions. The same happens for steps: above the roughening transition they will not be straight but wavy, and they appear frizzy to scanning tunneling microscopy inspections. The first part of the chapter provides a theoretical description of the roughening phase transition, while the second part exploits the sensitivity of diffraction to disorder and provides examples of such transitions for low and high Miller index surfaces.

Chapter 2 is devoted to diffusion and the latest theoretical as well as experimental techniques that are used to study it. The chapter first describes elementary diffusion processes on flat and stepped surfaces, and then discusses the long-term behavior resulting from the combination of elementary steps. Two main approaches are used: those based on single particle motion and collective diffusion. The former approach concentrates on the motions of single adatoms or adsorbates, while the latter focuses on the decay of long-wavelength density fluctuations over time. An overview of available experimental techniques for surface diffusion measurements is also provided; in particular, the recently developed helium spin-echo technique is described.

Chapter 3 provides an overview of surface thermodynamics. First, a summary of bulk thermodynamics is provided and the main surface thermodynamic functions are introduced. Then the chapter anticipates the surface nomenclature and reviews some of the most widely used theoretical approaches. The key quantity here is the surface free energy, which includes the contributions from vibrational and configurational entropy. In the second part of the chapter, many examples of the vibrational density of states and the thermodynamic functions for both low and high Miller index surfaces are provided.

1. Roughening Transition: Theories and Experiments

Gianangelo Bracco, Andrea Claudio Levi

This chapter deals with the thermal phenomenon of equilibrium roughening, which is a genuine phase transition, with no counterpart in the bulk. Although the transition is a weak (infinite order) transition, it affects the growth of crystals and their equilibrium shape: a facet disappears above T_R.

The first part of the chapter is devoted to the description of the theories of roughening, starting with the BCF article and reviewing the work of many research groups that contributed to the foundation of the theory, and refering the reader to recent review articles for more advanced contributions. The second part of the chapter contains a review of the experimental investigations showing results that support the existence of a roughening transition and introducing the reader to the experimental problems of these studies.

1.1 Overview

Thermal roughening is a phase transition occurring on the surface of a crystal. Usually, the surface considered separates the solid from a gas (or vacuum) phase. An exception is helium, where the solid exists only at elevated pressures and the surface separates it from a liquid phase (we will briefly deal with the helium case in Sect. 1.10.1). As was shown already in 1951 by *Burton*, *Cabrera*, and *Frank* in their famous article (BCF) [1.1], a clean surface can exist in two different states: smooth and rough. At low temperatures the surface is smooth, and goes over to the rough state at a well-defined roughening temperature T_R. There is immediately here an apparent paradox. Experimentally, solid surfaces very often seem to be rougher at low T than at high T; but this is a nonequilibrium effect: disorder is frozen at low T. In equilibrium the opposite happens, and roughening occurs with rising temperature. The present chapter deals only with the latter phenomenon, equilibrium roughening, which is a genuine phase transition, with no counterpart in the bulk. Recently, an interesting theoretical overview of roughening was presented by *Akutsu* and *Yamamoto* [1.2]. For the somehow related subject of the equilibrium shape of crystals we refer the reader to the exhaustive review article by *T. Einstein* [1.3]. Many interesting contributions to the theory of roughening were presented at the Erice School in 1990 and are contained in the book by *Taub* et al. [1.4]. An up-to-date, advanced theoretical review of surfaces, both in equilibrium and out of equilibrium, was recently published by *Misbah* et al. [1.5]. This goes, however, beyond the limited scope of the present chapter, and many interesting topics presented there will not be discussed here.

M. Rocca, T.S. Rahman, L. Vattuone (Eds.), *Springer Handbook of Surface Science*, Springer Handbooks,
https://doi.org/10.1007/978-3-030-46906-1_1

1.2 Theoretical Considerations

Probably the most famous article on the theory of crystal growth was the above-mentioned BCF, recently reanalyzed by *Woodruff* [1.6]. But BCF's paper has an unusual structure: it is composed, actually, of two different articles. The first part, written by Frank, and known as a Bible to the students of crystal growth (as much as BCS's paper to those of superconductivity), contains the model of spiral growth around a screw dislocation, which solved the paradox, then quite puzzling, of layer-by-layer growth (which takes place even under such low disequilibria that the growth rate would be impossibly slow in terms of classical nucleation theories). The second part, written by Burton and Cabrera, discusses in detail the hypothesis of a roughening transition. Burton and Cabrera's starting point is a fundamental difference between two $(1+1)$ and three $(2+1)$ dimensions. In two dimensions, the separation element between two phases is a line. At $T=0$ it would be a straight line; but as the temperature increases point defects accumulate along the line, in the form of kinks, so that at any $T>0$ the line wanders away from the straight line and has a rough appearance. Not so in three dimensions. Here the separation element between two phases is a surface, reducing to a plane for $T=0$. But the defects that might roughen the surface are not point defects like the kinks along a line; they are steps, essentially infinitely long steps. And step creation is an energetically costly process, virtually impossible at low T, where, indeed, the most likely defects are point defects (adatoms, vacancies), irrelevant from the point of view of roughness. Thus, the surface remains smooth until T becomes so high that dangerous defects (i.e., steps) can form. At a certain point the steps multiply and the surface roughens, but this can only happen at a well-defined transition temperature T_{R}, the roughening temperature.

Roughening can be seen in the perspective of the γ-plot, i.e., of the orientational dependence of the surface free energy. The γ-plot is a polar representation of that dependence, where a surface is constructed in an abstract space by drawing vectors from the origin such that the length of a vector is proportional to the surface free energy γ per unit area for a surface perpendicular to that vector. The γ-plot is a highly singular object, since it is in principle nowhere differentiable; it has an inward cusp at every orientation characterized by a set of integer Miller indices: such orientations are dense on the solid angle. The strength of the cusp, however, decreases rapidly with increasing Miller indices (according to a fourth-power law), so that the only relevant cusps are those corresponding to low Miller indices (singular surfaces). Thus, the γ-plot resembles a raspberry, with inward cusps at the high-symmetry directions (Frank's raspberry) [1.6, 7]. In the equilibrium shape of a little crystal, corresponding to the strong inward cusps of the γ-plot, plane facets appear, whose angular extension is a monotonically increasing function of the strength of the cusps. As the temperature is increased, the inward cusps become less pronounced, until they disappear altogether and are replaced by rounded minima. The disappearance of a cusp in the γ-plot implies the disappearance of the corresponding face in the equilibrium shape of a little crystal. It also implies roughening of the corresponding surface of a large crystal. It should be mentioned that, for many purposes, the important quantity is not γ, but the *stiffness* $\tilde{\gamma}$, where

$$\tilde{\gamma} = \gamma + \frac{\mathrm{d}^2\gamma}{\mathrm{d}\phi^2}\,, \tag{1.1}$$

with ϕ being the azimuth [1.8]. In fact, the surface curvature is determined by the local stiffness, as was shown in 1951 by *Herring* [1.9]. Important contributions to the physics of roughening were presented by *Bienfait* [1.10], *Wortis* [1.11], *van Beijeren* and *Nolden* [1.12], *Lapujoulade* and *Salanon* [1.13], and others.

Burton and Cabrera's theory was convincing as a matter of principle, but in detail was not correct. They assumed a finite number of surface levels (in the case of two levels, they could use the well-known results of the two-dimensional Ising model), while in fact for a correct theory an infinite number of levels is essential. This advancement was obtained in the 1970s. Even before the formulation of an exact model, a number of mathematical theorems clarified the situation:

1. Dobrushin's theorem proved Burton and Cabrera's basic assumption for the Ising model in 3 $(2+1)$ dimensions: there exists a temperature $\hat{T}$ such that the surface is smooth for $T<\hat{T}$ [1.14].
2. Gallavotti's theorem proved the contrary in 2 $(1+1)$ dimensions: the separation line between two phases of the Ising model is always rough for any $T>0$ [1.15].
3. Van Beijeren's theorem showed that Dobrushin's temperature $\hat{T}$ is not less than the transition temperature of the corresponding two-dimensional Ising model [1.16].

Then a decisive step forward was made by *van Beijeren* himself in 1977 [1.17]. He succeeded in mapping a surface model (the body-centered solid-on-solid or BCSOS model) onto a special, antiferroelectric case of

the 6-vertex model, whose phase diagram was known. This proved explicitly the existence of the roughening transition in an exactly solvable statistical-mechanical model and, moreover, gave the mathematical properties of the transition. These properties are very interesting. Roughening, indeed, belongs to the class (studied by *Kosterlitz* and *Thouless* [1.18], who have just received the Nobel prize, to a large extent for this discovery) of topological, two-dimensional transitions whose free energy, although nonanalytical, is continuous at the transition with all its derivatives. Kosterlitz and Thouless discuss a number of extremely weak, infinite-order phase transitions in two dimensions (the Coulomb gas, a system of dislocations, the magnetic XY model, the two-dimensional crystal, the neutral superfluid). In most of these cases (notwithstanding the differences among the different systems) there is a transition from an ordered state below T_c to a disordered situation above; but the ordering below T_c is very different and weaker than the conventional ordering typically occurring in three dimensions. The two-dimensional, topological ordering is related, not to a two-point correlation function, but to the behavior at long distances. A general review of statistical mechanics involving Kosterlitz–Thouless (KT) transitions has recently been presented in an illuminating article by *Kosterlitz* himself [1.19]. Roughening belongs to this class of transitions.

For a general surface, it is not very easy to give a rigorous definition of roughness. Indeed, when a solid is in equilibrium with its vapor, an atom may belong to either phase, and the surface is not perfectly sharp. A simple approximation, where the surface is perfectly sharp and where the roughness may be easily defined, is the so-called solid-on-solid (SOS) model. This model in (x, y, z) space is such that the atoms are arranged in columns defined by x and y coordinates: in each column atoms belong to the solid up to a maximum $z = \zeta(x, y)$, while for $z > \zeta$ they belong to the vapor (solid-on-solid, indeed, means that below every solid atom there are only solid atoms, thus the model neglects vacancies in the crystal, as well as overhangs in the surface and flying atoms in the vapor). The difference between smooth and rough can be written in terms of $\zeta(x, y)$.

Considering two points with coordinates (x_1, y_1) and (x_2, y_2), the mean square height difference (MSHD) $\langle[\zeta(x_2, y_2) - \zeta(x_1, y_1)]^2\rangle = g(x_1, y_1, x_2, y_2) > 0$ depends on the difference of coordinates between the two points (in particular on their distance R on the surface). Now, when R tends to infinity, two cases are possible: either g tends to a finite limit g^* (it is easy to see that $g^* = 2\sigma^2$, where σ is the root mean square fluctuation of surface levels) in which case the surface is smooth and characterized by moderate oscillations around a mean plane; or g tends to infinity, and the surface is rough: for a rough surface no mean plane can be defined. It is thus clear that the distinction between smooth and rough is an asymptotic property.

For a surface or an interface which does not possess the SOS property, the concepts of smooth and rough may still be defined, but more caution is necessary. Let S be an infinite set (the solid) whose points fill most of the half-space $z < 0$, but are present sporadically also for $z > 0$. Let P_0 be a point in the plane $z = 0$, with coordinates $(x_0, y_0, 0)$; then for any radius R and level h the number of points of S, with coordinates (x, y, z), such that $(x - x_0)^2 + (y - y_0)^2 < R^2$ and $z > h$, will be a finite number $N(R, h)$, tending to 0 as h tends to infinity. Then for any small number ϵ and for any R there will be a level $\hat{h}$ such that, if $h > \hat{h}$, $N(R, h) < \pi R^2 \epsilon$. If this behavior is uniform (i.e., if $\hat{h}$ may be chosen to depend only on ϵ but not on R) the surface or the set S will be called smooth (at least at P_0). Otherwise we will be forced to allow $\hat{h}$ to increase and to diverge with R: then we will say that the surface is rough, and the nature of the roughness will be characterized mathematically by the diverging behavior of $\hat{h}$.

These geometrical definitions of roughness and roughening have an energetic counterpart. The creation of a step is energetically costly. This is true at $T = 0$, and remains true as long as the steps are few. But when they become really numerous (i.e., when the surface roughens), adding one more step makes no difference, so that the step free energy per unit length (i.e., the work necessary to nucleate it) vanishes at T_R. It is energetically favorable for a vicinal surface (i.e., for a surface forming a small angle θ with a high-symmetry surface) to form terraces of the high-symmetry surface, separated by regularly spaced steps. Then, if the surface free energy (per unit area) of the high-symmetry surface is γ_0, that of the vicinal surface is given by $\gamma = \gamma_0 \cos\theta + (\beta/a)|\sin\theta|$ where a is the step height and $a/|\sin\theta|$ the spacing between steps, and where β is the step free energy per unit length. The presence of the absolute value $|\sin\theta|$ determines a slope discontinuity in the γ-plot. At T_R, β vanishes and the slope becomes continuous. This determines both a continuity of the free energy derivative (actually, also of all higher order derivatives), and the disappearance of the corresponding facet in the equilibrium shape of a little crystal.

Much theoretical work on roughening has been done for the SOS surface models. *Chui* and *Weeks* introduced in 1976 [1.20] an important (and partly solvable) model, the DGSOS model and showed that the DGSOS partition function is a version of the SOS Hamiltonian in the form

$$H = J \sum_j \sum_\delta [m_{(j+\delta)} - m_j]^2 + J' \sum_j [m_j]^2 \qquad (1.2)$$

(this version, because of the Gaussian dependence of the Boltzmann factor, is called the Discrete Gaussian SOS model, or DGSOS), where the integer m_j defines the height of the SOS column j. The first term describes the interaction between the columns (i.e., the cost of steps), while the second term has merely the effect of anchoring the surface in the neighborhood of $m = 0$. In the DGSOS model, of course, the levels m are discrete, corresponding to crystallographic positions. If all real values of m were allowed and the sums were replaced by integrals, the so-called Continuous Gaussian (CG) would be obtained: the CG model had been solved by *Berlin* and *Kac* [1.21] as early as 1952, but the CG model is always rough at any positive T and has no transition. Now Chui and Weeks were able to prove that the DGSOS partition function is the product of the CG partition function (which has no singularities) times the partition function of the two-dimensional Coulomb gas, studied, e.g., by Kosterlitz and Thouless, so that the roughening transition of the DG model turns out to be isomorphic to the dielectric-plasma transition of the latter (with, however, a reversal of temperatures: the low-T dielectric corresponds to the high-T rough surface and the high-T plasma to the low-T smooth state). Then the critical properties of the Coulomb gas carry over to the surface case: the transition is extremely weak (infinite order); the maximum in the specific heat, which for the Coulomb gas took place after the transition, while the system was already a plasma, now takes place before the transition, while the surface is still smooth. But probably the most relevant result that Chui and Weeks drew from their mapping on the Coulomb gas refers to the asymptotic behavior of the correlations. The MSHD (bounded in the smooth state) diverges in the rough state, but only logarithmically: this very weak divergence, basically due to topology, is characteristic of two dimensions and contrasts sharply with the linear (Markovian) divergence of the mean square displacement in one dimension.

Chui and Weeks' roughening theory was a major step forward. But, since the two-dimensional Coulomb gas had not been solved completely, so neither was their DGSOS model: in particular, T_R was not known. Therefore van Beijeren's achievement, who (as mentioned above) mapped a somewhat similar roughening model, which he called the body-centered solid-on-solid (BCSOS) model, onto a completely solved model of statistical mechanics, the 6-vertex model [1.22], was important. Van Beijeren considered the (100) surface of a body-centered cubic lattice, where two sets of atoms forming two sublattices, corner atoms and center atoms, appear. By construction the projection of every corner atom onto the surface plane has only projections of center atoms as two-dimensional nearest neighbors, and vice versa. Thus the (100) surface is identified as

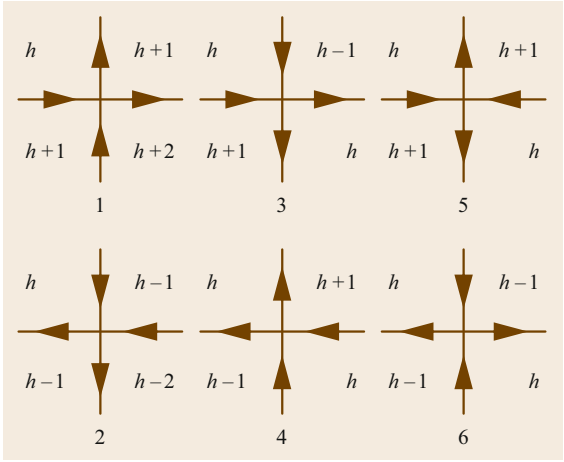

Fig. 1.1 The six vertices. For each vertex the corresponding height configuration that obeys van Beijeren's mapping is indicated

a square lattice, turned 45° with respect to the cube sides. Moreover, the level difference between two nearest neighbors is always exactly half a cube side (this can be used as height unit). Then it is possible to apply van Beijeren's mapping, where across the bond connecting the projections onto the surface plane of two surface nearest neighbors an arrow is drawn such that the higher atom lies, e.g., to the right of the arrow. At each point of the dual lattice four arrows meet, obeying the so-called *ice rule* that two arrows are pointing in and two out. But these are exactly the conditions defining the 6-vertex model of statistical mechanics (describing *two-dimensional ice* and two-dimensional ferroelectrics; this electrostatic interpretation has nothing to do with the Coulomb gas).

About the latter model, solved in the 1960s by the *Yangs* [1.23–25], *Lieb* [1.26–28], *Wu* [1.29] and *Sutherland* [1.30], nearly everything is known [1.22]. The six vertices, shown in Fig. 1.1, describe the six possible arrangements at the meeting of four arrows obeying the *ice rule*. To the arrows energies ϵ_j are associated, where j varies from 1−6. The simplest and most important situation is that of the symmetric 6-vertex model, where $\epsilon_2 = \epsilon_1, \epsilon_4 = \epsilon_3, \epsilon_6 = \epsilon_5$; in this case three Boltzmann factors $a_j = \exp(-\epsilon_j/(kT))$ suffice and, in fact, all physical properties are determined by the parameter

$$\Delta = \frac{a_1^2 + a_3^2 - a_5^2}{2a_1a_3} \,. \tag{1.3}$$

In the surface interpretation a smooth surface corresponds to Δ strongly negative (in the electrostatic interpretation, to antiferroelectricity); the ideal situation at $T = 0$ implies that all vertices are 5 and 6, hence Δ is $-\infty$; increasing T Δ increases, and roughening cor-

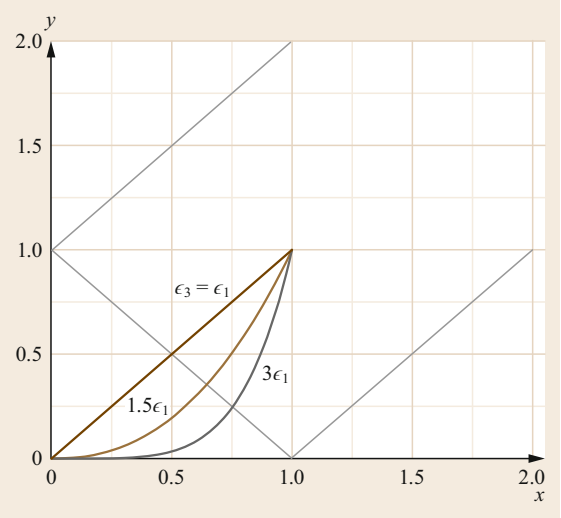

Fig. 1.2 The phase diagram of the six-vertex model, as interpreted for the smooth and rough phases, in the (x, y)-plane, where $x = a_1/a_5$ and $y = a_3/a_5$. The area for $x + y < 1$ corresponds to the smooth phase, the area for $x - 1 < y < x + 1$ to the rough phase. The areas for $y < x - 1$ and for $y > x + 1$ have no meaning for surfaces (although they are important in the ferroelectric interpretation). Roughening takes place on the line $x + y = 1$. Three temperature trajectories are drawn (for $\epsilon_3 = \epsilon_1$, for $\epsilon_3 = 1.5\epsilon_1$, and for $\epsilon_3 = 3\epsilon_1$). The point $(0, 0)$ corresponds to zero temperature, the point $(1, 1)$ to infinite temperature, and the straight line $(x + y = 1)$ to roughening

responds to

$$\Delta = -1 \tag{1.4}$$

(in the electrostatic interpretation, to the transition from the antiferroelectric to the paraelectric state). The BCSOS model is isomorphic to the special case where $\epsilon_1 = \epsilon_3 = \epsilon$, $\epsilon_5 = 0$, for which the very simple result $kT_R = \epsilon / \ln 2$ holds.

Other important results of the 6-vertex model (written of course in surface language) are:

1. *Sutherland*'s result [1.31] for the correlation of steps at the high temperature $2T_R$ (at this temperature the solution is particularly simple). If the correlations are sought in the direction perpendicular to the steps, the correlation at the distance l vanishes if l is even and is given by $-4/(\pi l)^2$ if l is odd: this correlation thus decays very slowly, hence it extends to large distances between steps.
2. *Forrester*'s result [1.32] giving the probability P_m of being at level m in the smooth phase. In such phase $\Delta < -1$, and defining λ from $\Delta = -\cosh\lambda$ the probability is $P_m = A \exp[-\lambda(m - 1/2)^2]$. From Forrester's result *Levi* et al. [1.33] obtained the probability B_m of stepping down from level m to level $m-1$ (if $m > 0$): $B_m = \sum_n (-1)^n \exp[-\lambda n(n + 2m - 1)]$.

The roughness is asymptotically described in terms of the logarithmic behavior of the mean square height difference

$$g = \langle |m(L) - m(0)|^2 \rangle \approx 2K \ln |L| \,. \tag{1.5}$$

Here $K(T)$ is a function of temperature (defined above T_R), which was calculated by *Youngblood* et al. [1.34] as

$$K(T) = (\pi \arccos \Delta)^{-1} \,, \tag{1.6}$$

for $T = 2T_R$, $K = 2/\pi^2$, which agrees with the above result of Sutherland. The phase diagram of the six-vertex model, in the form appropriate for surface roughening, is shown in Fig. 1.2.

1.3 Renormalization Group Analysis

These results of the 6-vertex model, although interesting, are rather model specific. Conversely, the most important properties of the roughening transition are universal and depend only on what happens at very long distances. As such, they can be expected to be obtainable from renormalization procedures, where the short distance behavior, depending on the details of the interaction, disappears from the picture. This is in fact the case, as was shown first by *Ohta* and *Kawasaki* [1.35]. We sketch briefly here such renormalization group analysis (which turns out to be essentially that of *Kosterlitz* [1.36]). We follow here the treatment of *Lapujoulade* and *Salanon* [1.13].

1.3.1 Continuous Solid

If layering is neglected, the surface is always rough, and the fluctuations have a logarithmic behavior. Indeed, if such fluctuations are small, the surface free energy can be written to first order

$$F = \gamma_0 S + W = \gamma_0 S + \frac{1}{2} \int_S \bar{\gamma} (\nabla z)^2 \mathrm{d}^2 \boldsymbol{R} \,, \tag{1.7}$$

where $S = L^2$ and $\tilde{\gamma}$ is the surface stiffness, i.e., for a slope θ, $\tilde{\gamma} = \gamma + \mathrm{d}^2\gamma/\mathrm{d}\theta^2$, and where W is the adiabatic work needed to create the fluctuations.

Going over to $\boldsymbol{q}$-space, $z = \sum_{\boldsymbol{Q}} z_{\boldsymbol{Q}} \exp(\mathrm{i}\boldsymbol{Q}\cdot\boldsymbol{R})$ and

$$W = \sum_{\boldsymbol{Q}} \frac{1}{2}\tilde{\gamma}L^2Q^2\langle z_{\boldsymbol{Q}}\rangle \,. \tag{1.8}$$

In the free fluctuating regime the modes are not coupled and each of them contributes $(1/2)k_\mathrm{B}T$ (there is no kinetic energy!) to the surface energy. The work W can be identified with the fluctuation contribution to the surface energy, so that

$$\langle z_{\boldsymbol{Q}}\rangle = \frac{k_\mathrm{B}T}{L^2\tilde{\gamma}Q^2} \,, \tag{1.9}$$

and the mean square deviation is

$$\langle(\Delta h)^2\rangle = \sum_{\boldsymbol{Q}}\langle z_{\boldsymbol{Q}}^2\rangle \tag{1.10}$$

$$= \frac{k_\mathrm{B}T}{L^2\tilde{\gamma}}\sum_{\boldsymbol{Q}} Q^{-2} \tag{1.11}$$

$$= \frac{k_\mathrm{B}T}{4\pi^2\tilde{\gamma}}\int_{\pi/L}^{\pi/a}\frac{2\pi Q}{Q^{-2}}\mathrm{d}Q \tag{1.12}$$

$$= \frac{k_\mathrm{B}T}{2\pi\tilde{\gamma}}\ln\left(\frac{L}{a}\right), \tag{1.13}$$

where a is an appropriate atomic scale.

Similarly, it is easy to show that the MSHD behaves asymptotically as

$$g(R) = \langle[z(R) - z(0)]^2\rangle = \frac{k_\mathrm{B}T}{\pi\tilde{\gamma}}\ln\left(\frac{R}{a}\right). \tag{1.14}$$

The fact that the coefficient of the logarithm in $g(R)$ is twice that in $\langle(\Delta h)^2\rangle$ is rather obvious, since if $\boldsymbol{R} = \boldsymbol{R}_2 - \boldsymbol{R}_1$, then

$$\begin{aligned} g(R) &= \langle[z(\boldsymbol{R}_2) - z(\boldsymbol{R}_1)]^2\rangle \\ &= \langle[z(\boldsymbol{R}_2) - z(\boldsymbol{R}_0) - z(\boldsymbol{R}_1) + z(\boldsymbol{R}_0)]^2\rangle \end{aligned}$$

(where $\boldsymbol{R}_0$ is an arbitrary point on the surface)

$$\begin{aligned} &= \langle[z(\boldsymbol{R}_2) - z(\boldsymbol{R}_0)]^2\rangle + \langle[z(\boldsymbol{R}_1) - z(\boldsymbol{R}_0)]^2\rangle \\ &\quad - 2\langle[z(\boldsymbol{R}_2) - z(\boldsymbol{R}_0)][z(\boldsymbol{R}_1) - z(\boldsymbol{R}_0)]\rangle \\ &\approx \langle[z(\boldsymbol{R}_2) - z(\boldsymbol{R}_0)]^2\rangle + \langle[z(\boldsymbol{R}_1) - z(\boldsymbol{R}_0)]^2\rangle \end{aligned}$$

(because of the asymptotic decay of correlations) and, since $\boldsymbol{R}_0$ is arbitrary, each of the two terms equals $(\Delta h)^2$.

1.3.2 Crystal

In order to simulate the crystallographic structure a periodic potential $V(z)$, forcing the surface to be preferentially located on equidistant parallel planes, is introduced.

The surface free energy becomes

$$F = \int_S \left(\gamma + \frac{1}{2}\tilde{\gamma}(\nabla z)^2 + V(z)\right)\mathrm{d}^2\boldsymbol{R} \,. \tag{1.15}$$

$V(z)$ may be taken to be

$$V(z) = V_0\left[l\cos\left(2\pi\frac{z}{a_z}\right)\right]. \tag{1.16}$$

In $\boldsymbol{q}$-space the energy E still depends on the set of the $z_{\boldsymbol{Q}}$'s; the potential, however, introduces a coupling between the modes. In the calculation of the partition function Z, integrals have to be performed over the variables

$$Z = \int\cdots\int_{\pi/L<Q<\pi/a} \mathrm{d}z_{\boldsymbol{Q}}\mathrm{e}^{E[z_{\boldsymbol{Q}}]/(k_\mathrm{B}T)} \,. \tag{1.17}$$

Since the interesting things happen asymptotically (i.e., at small Q), a new (smaller) cut-off $\bar{Q}$ is introduced, such that $\pi/L << \bar{Q} < \pi/a$. The *short-wavelength modes* (with $\bar{Q} < q < \pi/a$) are integrated away, and Z becomes a functional integral over the long-wavelength modes only

$$\int\cdots\int_{\pi/L<Q<\bar{Q}} \mathrm{d}z_{\boldsymbol{Q}}\mathrm{e}^{\bar{E}[z_{\boldsymbol{Q}}]/(k_\mathrm{B}T)} \,, \tag{1.18}$$

where $\bar{E}$ is a new functional of the $z_{\boldsymbol{Q}}$'s. It can be shown, by an expansion in powers of V up to second order, that $\bar{E}$ retains the same functional form as E provided that $\tilde{\gamma}$ and V are replaced by new, *renormalized* parameters $\bar{\gamma}$ and $\bar{V}$. The renormalization procedure can be iterated, and, in fact, can be made *differential* by varying the cut-off infinitesimally from $\bar{Q}$ to $\bar{Q} - \mathrm{d}\bar{Q}$.

Letting

$$\lambda = \ln\frac{\pi}{a\bar{Q}} \qquad x = \frac{2a^2\tilde{\gamma}}{\pi k_\mathrm{B}T} \qquad y = \frac{4\pi\bar{V}}{k_\mathrm{B}T\bar{Q}^2} \tag{1.19}$$

the dimensionless renormalized parameters x and y are seen to evolve as the renormalization variable, λ, changes from 0 to ∞, according to the following system of differential equations, first obtained by *Kosterlitz* and

Thouless [1.18, 36]

$$\frac{\mathrm{d}x}{\mathrm{d}\lambda} = \frac{y^2}{2x} A\left(\frac{2}{x}\right) \tag{1.20}$$

$$\frac{\mathrm{d}y}{\mathrm{d}\lambda} = 2y\left(1 - \frac{1}{x}\right), \tag{1.21}$$

$A(\xi)$ being a slowly varying function calculated exactly by *Nozières* and *Gallet* [1.37].

It is often sufficient, ignoring λ, to study the *renormalization trajectories* in the (x, y)-plane. The pair of equations (1.20) and (1.21) are then replaced by a single differential equation for $y(x)$

$$\frac{\mathrm{d}y}{\mathrm{d}x} = 4\frac{1 - \frac{1}{x}}{a(x)y}, \tag{1.22}$$

where $a(x) = A(2/x)$.

This differential equation is easy to solve (it is a separate variables equation), but it is interesting to approximate it further by replacing $A(x)$ by its maximum, which is the number of Nozières and Gallet $A(2) = 4\exp(-4\gamma) = 0.3975$ (where γ is Euler's constant 0.5772).

In this case the solution is represented by the hyperbolas shown in Fig. 1.3. The most important point about these equations is that $\mathrm{d}y/\mathrm{d}\lambda$ (and $\mathrm{d}y/\mathrm{d}x$) vanish for $x = 1$. Moreover $\mathrm{d}x/\mathrm{d}\lambda > 0$ always, and, for small λ (i.e., at the initial stages of the renormalization), $\mathrm{d}y/\mathrm{d}\lambda < 0$, $\mathrm{d}y/\mathrm{d}x < 0$. Hence two cases are possible:

a) If the initial value of y is large (i.e., at low temperatures), a minimum of y is reached for $x = 1$. Subsequently y increases and *diverges* as $\lambda \to \infty$. This divergence of the effective potential $\bar{V}/\bar{Q}^2$ implies that the surface is *pinned* at some crystallographic level:, i.e., it is *smooth*.
b) At high T the initial value of y is small. Then the renormalization trajectory bends down and meets the x-axis at some point $x^* \leq 1$. The effective potential becomes infinitely weak and is unable to hold the surface at a given level. The surface is then *rough*, and resembles closely the surface of a continuous solid, with, however, a renormalized value

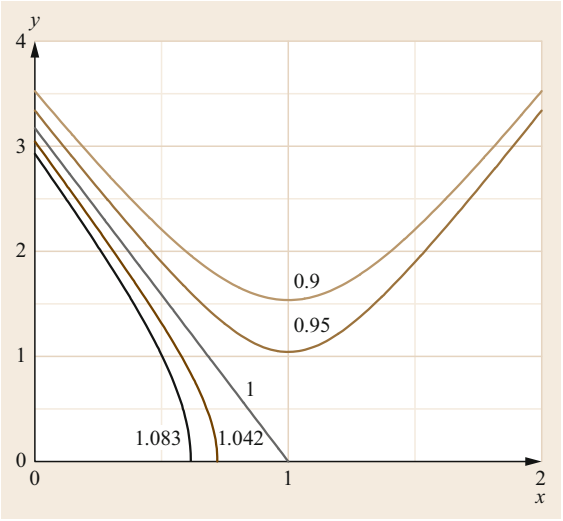

Fig. 1.3 Hyperbolas solving (1.22) for different temperatures. Curve 1: $T/T_\mathrm{R} = 0.9$; curve 2: $T/T_\mathrm{R} = 0.95$; curve 3: $T = T_\mathrm{R}$ (roughening); curve 4: $T/T_\mathrm{R} = 25/24$; curve 5: $T/T_\mathrm{R} = 13/12$

γ^* for the stiffness. Thus, the MSHD behaves again as

$$g(R) = 2a^2 K \ln R \tag{1.23}$$

with

$$K = K(T) = \frac{k_\mathrm{B} T}{2\pi a^2 \gamma^*}. \tag{1.24}$$

Of special interest is the limiting case, where y vanishes *exactly* at $x^* = 1$: this case corresponds to the roughening temperature. Then we have

$$\gamma^* = \frac{\pi k_\mathrm{B} T_\mathrm{R}}{2a^2} \tag{1.25}$$

and substituting into (1.24) the important result

$$K(T_\mathrm{R}) = \pi^{-2} \tag{1.26}$$

is obtained. This is again in agreement with the results obtained above by *Sutherland* [1.31] and by *Youngblood* et al. [1.34].

1.4 (110) Surfaces

As can be seen, the theoretical activity on roughening has been quite extensive. Conversely, the first experiments involved rather unusual systems, such as organic crystals [1.38, 39] or the helium solid–superfluid interface [1.40–43]. In the following, after a few words on the more classical roughening of *singular* surfaces, we shall discuss *missing-row roughening*.

For a long time not much was known about the roughening transition of low-Miller-index metal surfaces (except for the beautiful experiments of *Heyraud* and *Métois* on small Pb [1.44] and In clusters [1.45]).

Outside the realm of metals, the most interesting case is of course ^{4}He (Sect. 1.10.1), where the melting line is nearly horizontal in the (p versus T)-plot (rather than nearly vertical as for all other substances). As a consequence, the roughening of the different faces in the equilibrium shape (starting from the less stable) can be studied by simply increasing the temperature along the solid–superfluid coexistence curve [1.40–43]. From the theoretical point of view, an interesting study was presented by *Touzani* and *Wortis* [1.46].

The Trieste group proposed, however [1.47], that a notable exception to the relative lack of realizations of the roughening phenomenon on low-index metal surfaces may be the (110) faces of nonreconstructed noble (Cu, Ag) or near-noble (Ni, Rh, Pd) metals. For these surfaces, we expect roughening to occur well below T_M, where surface melting plays no role, and this is experimentally confirmed as we shall show in the experimental part. Such surfaces are good candidates for roughening because of the nondirectional nature of the cohesive forces in these metals. For a filled or nearly filled d-shell a large contribution to the cohesive energy can be obtained simply with a high coordination, irrespective of bond angles. In first approximation the cohesive energy may be written as the sum of a conventional two-body contribution, plus a many-body *glue* term [1.48, 49] $V_{\text{glue}} = \sum_i U(n_i)$. Here n_i, the number of neighbors of atom i, is given by $n_i = \sum_{j\neq i} \rho(\boldsymbol{r}_j - \boldsymbol{r}_i)$; $U(n)$ can be so chosen as to be minimal for $n = 12$, the number of nearest neighbors in the ideal fcc lattice, while $\rho(\boldsymbol{r})$ is some decreasing function of distance. For a surface, the effect of the glue at $T = 0$ is to reduce all surface energies, but more drastically so the energy of well-packed faces, in particular the (111) face. When the ratio $\gamma_{(111)}/\gamma_{(110)}$ decreases below the critical value $\sqrt{2/3} = 0.8165$, the (110) surface spontaneously reconstructs missing-rows, forming grooves whose flanks are (111) microfacets: this is what happens to gold and platinum (iridium appears to show more complex reconstructions). Noble metals (Cu, Ag, and Au) have a filled d-band; near-noble metals (Ni, Rh, Pd, Ir, Pt) are fcc transition metals with a nearly filled d-band (however, Co, although belonging to the same column in Mendeleev's table as Rh and Ir, has a different crystal structure). In the lighter noble (Cu, Ag) and near-noble metals (Ni, Rh, Pd) the above ratio remains slightly higher than the critical value, so that they do not reconstruct at $T = 0$; they are, however, on the verge of reconstruction (as shown, e.g., by the fact that Cu, Ag, and Pd do reconstruct in the presence of a small coverage of alkali atoms [1.50–53]) and, therefore, the missing rows are dominant defects at $T > 0$. When such defects proliferate, *missing-row roughening* ensues [1.47]. As first shown by *Jayaprakash* and *Saam* [1.54], van Beijeren's BCSOS model can also describe the (110) surface of the fcc lattice (the case of the (100) surface had been considered earlier by *Shugard* et al. [1.55]). It suffices to expand the lattice along the $\langle 1\bar{1}0\rangle$ rows by a factor $\sqrt{2}$, and then turn by 45°. The resulting surface becomes then very similar to the (100) surface of a bcc lattice. The only difference is that in the case of an (ideal) fcc lattice it is not really appropriate to consider as nearest neighbors of a surface atom only atoms in the second layer, since there are nearest neighbors in the surface itself. For noble and near-noble metals, however, a considerable inward relaxation takes place, so that the use of the BCSOS model is more justified [1.47].

An important characteristic of the (110) surface of fcc crystals is its anisotropy. The unit cell is a rectangle with sides a in the $\langle 001\rangle$ direction, but only $a/\sqrt{2}$ in the $\langle 1\bar{1}0\rangle$ direction (a being the cube side), so that *rows* of atoms are formed in the $\langle 1\bar{1}0\rangle$ direction: the forces keeping the atoms together within a row are much stronger than the forces between different rows. The (110) surface is rather open and has a high surface energy in comparison to the much stabler (111) surface. The missing-row reconstruction is a (2×1) reconstruction where alternate rows are suppressed, thereby uncovering atoms of the *third* layer. This reconstruction (and, for the unreconstructed metals, missing-row roughening at high temperatures [1.56]) is favored because the flanks of the grooves thus generated are rather stable (111) microfacets while, at the same time, very little energy is spent in the reconstruction because of the loose nature of the surface in the $\langle 001\rangle$ direction.

The missing-row reconstruction is destroyed by extended defects at high temperature, by a *deconstruction transition*. The interplay between deconstruction and roughening in Au and Pt is a very interesting and complicated problem, to which a wealth of experimental and theoretical work was devoted. We will discuss briefly some of the relevant concepts and results here

(relying heavily on *Mazzeo* et al. and *Bernasconi*'s work [1.57–61]). Similar, although less evident, phenomena occur in the unreconstructed case, where a *preroughening transition* is expected.

First of all, it is convenient to consider the (110) surface as a rectangular chequerboard composed of two two-dimensional sublattices, whose sites, following *Mazzeo* et al. [1.57], will be called here *white* and *black* sites. White and black sites not only alternate in the plane, but also in level, the height difference between a white and a black layer being one unit (i.e., $a/2\sqrt{2}$): white layers are at odd levels, black layers at even levels. At $T = 0$ the top layer is formed solely by white atoms (at level $m = 1$), while the second layer (at level $m = 0$) is black. But at higher temperatures there will be patches of black atoms on the top layer (formed either by adding atoms ($m = 2$) or by taking atoms away ($m = 0$)). It is then possible to define an *order parameter* P_{BW}, equal to the fraction of the surface top layer occupied by white atoms minus the fraction occupied by black atoms. $P_{BW} = 1$ at $T = 0$, but at a certain temperature T_{BW} a phase transition is expected where the sublattice ordering is destroyed and P_{BW} vanishes.

It may happen that T_{BW} coincides with T_R (this is the case, e.g., of the simple BCSOS model [1.58]), but it may also happen that $T_{BW} < T_R$. In the latter case, in the temperature range $T_{BW} < T < T_R$, the surface is still smooth but is inherently disordered. Such situations were first considered by *Rommelse* and *den Nijs* [1.62, 63], who introduced the concept of a disordered flat (DOF) phase. In their model the sign of a step is taken into account, and it is shown that, mostly for entropic reasons, two steps of the same sign repel while two steps of opposite sign attract each other. As a consequence, the steps tend to organize themselves in pairs of opposite sign, and although they become numerous at relatively high T, their cumulative effect on the level difference between two distant points is still negligible, i.e., the surface finds itself in a DOF phase. This can be represented as a backbone of steps, whose signs alternate, reproducing an antiferroelectric 6-vertex model on a *mesoscopic* scale. At still higher temperatures the backbone (or at least its antiferroelectric ordering) is destroyed by thermal fluctuations, and roughening ensues.

Rommelse and den Nijs' model, however, is only one of many models that have been proposed for the high-T behavior of (110) surfaces. Most of these models were aimed at describing the intriguing situation of the reconstructed gold and platinum surfaces, where the simple (but anisotropic) 6-vertex model, which was sufficient, at least in first approximation, for the unreconstructed surfaces of Ni, Cu, Pd and Ag, did not work. The point is that the (110) surface of the latter is mapped by *van Beijeren*'s construction [1.17], onto an

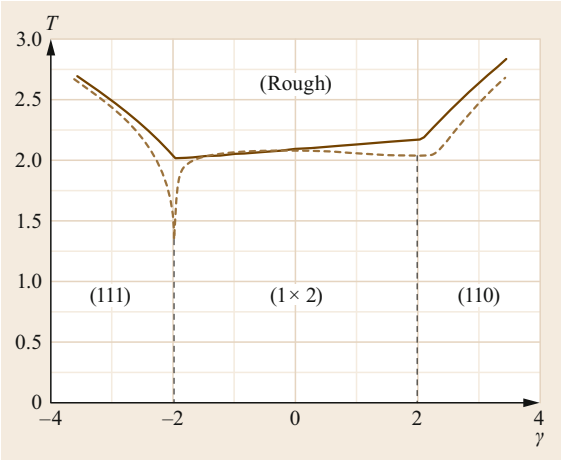

Fig. 1.4 Phase diagram of one of the models computed by Levi and Touzani with the ribbon transfer matrix method, as a function of the parameter $\gamma = (\epsilon_1 - \epsilon_3)/\epsilon_{56}$, where ϵ_1 and ϵ_3 are the energies of vertices 1 and 3 and ϵ_{56} is the repulsive energy involving adjacent vertices 5 and 6 (van Beijeren's mapping is used). (111) and (110) indicate faceting, while (1×2) indicates the missing-row reconstruction. Redrawn from data of [1.64]

antiferroelectric version of the 6-vertex model, where $\epsilon_5 < \epsilon_1 < \epsilon_3$. Since, in the reconstructed case, the flanks of the missing-row grooves are (111) microfacets corresponding to vertices 1 and 2, one might be tempted to try to mimic the reconstructs by lowering ϵ_1, going over to a 6-vertex model where $\epsilon_1 < \epsilon_5 < \epsilon_3$. Unfortunately this version of the model is *ferroelectric*, which, in the surface case, means not (2×1)-reconstruction but rather *faceting*, with the formation of macroscopic grooves whose flanks are extended (111) facets. In order to obtain a (2×1), missing-row reconstructed ground state the model has to be modified.

The simplest modification was proposed by *Levi* and *Touzani* [1.64] who introduced a 6-vertex model with nearest-neighbor interactions *between vertices*. Such interactions prevent the formation of extended areas occupied by vertices of type 1 (or 2) only, i.e., prevent faceting. The model cannot be solved exactly in the thermodynamic limit, but can be solved easily in the case where the system is a *ribbon* whose width is kept finite (and rather small) and whose length goes to ∞, by the *ribbon transfer matrix method*, well known in statistical mechanics (see, e.g., [1.65]), provided the interactions act only *across* the ribbon. The Levi–Touzani model leads to a simple phase diagram for (110) surfaces (including both the reconstructed and the unreconstructed case), reproduced in Fig. 1.4.

A model very similar to that of Levi and Touzani was proposed by *Kohanoff* et al. [1.66, 67] and studied,

by Monte Carlo simulations, by *Mazzeo* et al. [1.57]. The only difference is that the model of Kohanoff et al. is written in SOS language instead of in vertex language. In the most elementary case there is complete isomorphism. Introducing vertex–vertex interactions, however, corresponds, in SOS language, to introducing interactions between more distant neighboring atoms on the surface, but the correspondence is not perfect: there are small differences, so that the two models are not perfectly equivalent. More importantly, the model of Kohanoff et al. has been studied in complete detail by simulation, and this has yielded very interesting results [1.57] that the ribbon transfer matrix could not give. The most important result is that there are *two* distinct phase transitions, not one. In the reconstructed case the first transition is a *deconstruction transition*, while in the unreconstructed case it can be described as *preroughening*. In both cases, the second transition (at a temperature about 10% higher than the first) is the roughening transition. Deconstruction has critical exponents very near those of the 2-D Ising model. Conversely, preroughening has a new set of critical exponents (e.g., α is negative, about -0.23, i.e., the specific heat remains finite). Finally, roughening seems to be a transition of the *Kosterlitz–Thouless* type [1.18], but this is less certain.

The models proposed by *Villain* and *Vilfan* [1.68–74] are somewhat different. They compare two kinds of defects: domain walls and steps. A domain wall can be thought of as a bound pair of steps of opposite signs. If the binding energy is large enough, the domain walls are so energetically cheap in comparison to steps that a phase transition occurs, ahead of roughening, by proliferation of domain walls. The phase present between this kind of preroughening and roughening, however, is rather different from den Nijs' DOF phase: P_{BW} indeed, does not vanish in this phase, since a domain wall of the above kind does not invert the sublattice ordering. Such a phase was called by *Bernasconi* disordered even flat (DEF) [1.61, 75].

Then several *scenarios* are possible (Fig. 1.5) for the deconstruction and roughening of surfaces such as Au(110) and Pt(110) (the present classification is slightly modified with respect to [1.61, 75]):

a) First deconstruction takes place (by proliferation of domain walls) at some temperature T_D and the surface goes over from a low-temperature reconstructed phase to a DEF phase. At some higher temperature T_{BW} the steps proliferate, but their backbone preserves an antiferroelectric ordering: P_{BW} vanishes and the surface goes over from a DEF phase to a DOF phase. Finally, at a still higher temperature T_R, roughening takes place.

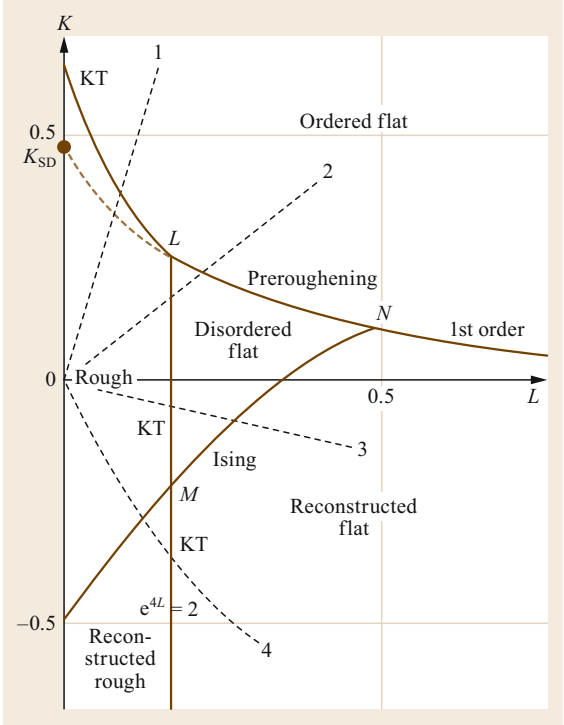

Fig. 1.5 Schematic phase diagram of the RSOS model. K and L are the nearest and next-nearest neighbor interactions. Both are in units of k_BT. Infinite temperature corresponds to $(K, L) = (0, 0)$. The *dashed lines* represent characteristic experimental paths. Reproduced from data of [1.76]

b) Deconstruction takes place by proliferation of domain walls at T_D. A DEF phase is formed and persists up to T_R.
c) Deconstruction takes place by step proliferation. The surface goes directly from the low-temperature reconstructed phase to den Nijs' DOF phase: T_{BW} coincides with T_D, but T_R is higher.
d) $T_D = T_{BW} = T_R$: there is only one transition, i.e., deconstruction and roughening occur together.

Scenario c) is one of the possibilities in *den Nijs*' theory [1.77–79], while scenario b) corresponds to the description of *Villain* and *Vilfan* [1.68–70] (both theories predict the possibility of scenario d)). The more complex scenario a), with three transitions, has been considered for the first time by *Bernasconi* [1.61]. *Mazzeo*'s thorough study [1.60], based on the Hamiltonian of Kohanoff et al., shows two transitions, between which the surface is in a state well described by den Nijs' DOF phase (scenario c)). Experiments on gold (Sect. 1.10.3) clearly showed two transitions. The intermediate phase cannot be DOF, since there is no broadening of the spec-

ular peak in antiphase, which would be a hallmark of the DOF phase [1.61]. Thus, the scenario for gold appears to be b). The case of platinum may be different. At first it seemed that there was only one transition (scenario d)) [1.80, 81], but more recent experiments showed two transitions, indicating scenarios b) or c) as described in the experimental section of this chapter.

An illuminating study of the competition between reconstruction and roughening was presented by *den Nijs* ([1.77], also on p. 247 of [1.4]), who considered deconstruction transitions (*preroughening*) which behave according to some typical properties of the Ising model, together with true roughening, which is, as we have seen, a transition belonging to the Kosterlitz–Thouless class. All this in the Reduced (RSOS) model. In this model, the level difference between two neighboring atoms is restricted to be 1, 0, or −1: the model is thus, by construction, smoother than DGSOS or ASOS, where in ASOS (absolute SOS) the squares appearing in (1.2) are replaced by absolute values.

1.5 Vicinal Surfaces

A vicinal surface is a crystal surface near to a high-symmetry, or *singular* surface. The singular surfaces correspond to the minima of free energy, i.e., to the inward singularities in the shape of Frank's raspberry. The vicinals show a first-order singularity (i.e., a first-order increase of free energy with respect to the singular surface, whatever is the sign of the deviation angle). But when analyzed in more detail the free energy increase usually contains a third-order term, as shown by *Gruber* and *Mullins* [1.82] while the second-order term is usually absent for high-symmetry surfaces. (A notable exception is the work by *Carlon* and *van Beijeren* [1.83], describing a model in which crossing steps form a network: in this model the second-order term is present and, for small deviation angles, is much more relevant than the usual third-order term.) This is the situation at low-temperatures.

Very different is the situation at roughening. Here there is no discontinuity in the derivative, i.e., no first-order term. On the contrary, the second-order term is present and dominant. Just above T_R, the vicinal surface free energy per unit area [1.2] is given by

$$f(p) = f(0) + \frac{\pi k_B T_R}{4a_z^2}|p|^2 + \dots , \qquad (1.27)$$

where a_z is the appropriate step height and p is the appropriate deviation angle.

Vicinal surfaces are liable to show roughening, very often at temperatures much lower than those appropriate to singular surfaces and farther down from melting. A general discussion of the roughening transition of high-index crystal faces was given by *Villain* et al. [1.84]. In more detail, vicinal surfaces can be conveniently (although not exactly) described in terms of the traditional TSK picture: the surface is characterized by terraces alternating with steps; there is a statistical distribution of steps; such steps are not straight, but are rather perturbed by atomistic irregularities (kinks). Hence the Terrace–Step–Kink (TSK) description. Such description is old, going back to *Kossel* and *Stranski* [1.85, 86], but is still very useful nowadays. Steps repel each other, and this allows the stability of terraces at low temperatures, until some sort of roughening occurs. It is clear, therefore, that the step–step interactions are essential; but, at the same time, there may be kink–kink interactions, which are also relevant for the properties of a vicinal surface at different temperatures. The statistical-mechanical problem of the roughening of vicinals depends thus on step–step and kink–kink interactions, and defines the nature of the phase corresponding to the different temperatures. Since the melting temperature T_M is typically much higher than the temperatures considered, the atomic positions can safely be assumed to remain the discrete positions dictated by crystallography, and only the occupation of the different crystal positions need be studied. Below the roughening temperature T_R, the steps remain sufficiently ordered; above T_R, the steps meander freely and kinks abound, giving rise to divergent fluctuations in the surface height profile. However, even below T_R there may in principle be disorder, related to the repulsion of parallel kinks. If such repulsion is strong enough, it could be possible to stabilize a disordered flat (DOF) phase: this would be disordered, because kinks are present in large amount along the steps, but flat, because of the limited step lateral excursion. A new phase transition, preroughening (PR) would occur in this case, whereas true roughening would be shifted to a higher temperature. Preroughening had been proposed (in a somewhat different context) by den Nijs and Rommelse who showed that long-range interactions favor the formation of a DOF phase, while a thorough discussion of the present problem has been given by *Prestipino* and *Tosatti* [1.63, 87]. Previously, a simpler theory had been given by Villain et al., in their discussion of the roughening transition of vicinals, where only the interaction among steps had been taken into

account: and the work of Prestipino and Tosatti is a modification of the theory of Villain et al. Such modification was necessary, because of the refined experimental work of *Hoogeman* et al. [1.88], who studied in depth, by scanning tunneling microscopy, the behavior of the (115) surface of silver. There had been indications of roughening at 490 K, and also indications of a previous roughening at a lower temperature, 440 K, with an average value of 465 K. One possibility, however, was that between 440 K and 490 K the surface is DOF. The very detailed and complex analysis by Prestipino and Tosatti affords much information, but some of the main doubts remain unsettled.

In parallel to their experiment, *Hoogeman* and *Frenken* performed a numerical simulation of the roughening of the (115) surface of silver [1.89]. Their Monte Carlo simulation was based on the TSK (also called TLK: Terrace–Ledge–Kink) model. The relevant energies are the kink formation energy and the interaction between steps: such parameters are extracted from previous experimental work by the authors [1.88]. The height correlation function diverges logarithmically with a prefactor $K(T)$ at high temperatures; $K(T_R)$ must equal π^{-2}, and this allows them to determine $T_R = 423 \pm 6$ K, in reasonable agreement with their experimental value of 465 ± 25 K.

1.6 Kinetic Roughening

An important issue is that of kinetic roughening, related to the process of surface growth under smooth or respectively rough conditions. For a discussion of the basic concepts of the theory of crystal growth we refer to *Weeks* and *Gilmer* [1.90] and also partly to *Levi* et al. [1.91], and *Levi* and *Kotrla* [1.92].

The process is usefully described by stochastic, partial differential equations such as *Edwards–Wilkinson* (EW) [1.93], *Chui–Weeks* (CW) [1.94], and *Kardar–Parisi–Zhang* (KPZ) [1.95].

Actually, kinetic roughness is an enormously vast subject, described in the excellent review by *Halpin-Healy* and *Zhang* [1.96]. In the present chapter, we limit ourselves to the most elementary aspects, which not only are simplest, but also are physically most relevant for the roughening transition of crystals.

The simplest time-dependent description of a stochastic surface is afforded by the EW equation [1.93]

$$\frac{\partial h}{\partial t} = \nu \nabla^2 h + \eta \tag{1.28}$$

where ν has the dimensions of a diffusion coefficient, and η is a noise term. This Edwards–Wilkinson equation was originally proposed for sedimentation, but can also describe a growing surface. In the present form, it is considered as written in the comoving frame. In $2+1$ dimensions the solutions of the EW equation give rise to a mean square height (h) difference

$$g(r) = \langle [h(r) - h(0)]^2 \rangle \tag{1.29}$$

behaving asymptotically as $\ln r$. This logarithmic roughness is quite similar to that of a surface in equilibrium (above T_R).

If the crystal structure is taken into account, the equation is modified by a periodic force favoring the integer levels, e.g.,

$$\frac{\partial h}{\partial t} = \nu \nabla^2 h + \frac{y \sin 2\pi h}{a + \eta} \,. \tag{1.30}$$

This is the *Chui–Weeks* equation [1.94]. The additional term tends to make the surface smoother: a surface obeying the CW equation either is smooth, or if it is rough cannot be more than logarithmically rough.

Another nonlinear modification of the EW equation was introduced by *Kardar*, *Parisi*, and *Zhang* [1.95]

$$\frac{\partial h}{\partial t} = \nu \nabla^2 h + \lambda (\nabla h)^2 + \eta \,. \tag{1.31}$$

This KPZ equation generates surfaces whose roughness may be stronger than logarithmic, i.e., power-law. Situations where such power-law roughness occurs are relevant in many situations [1.96] (the microbic growth on a substrate is a well-known example in biophysics: see for example the experiment by *Matsushita* and *Fujikawa* [1.97]. Conversely, in the present solid-state problem the same happens when the disequilibrium is very strong [1.98]).

Crystal growth modes vary widely, ranging from the fast *Wilson–Frenkel* mode (WF) (upper velocity limit) [1.99, 100] to slow nucleation, described in particular by *Becker* and *Döring* [1.101]. The EW equation describes a situation belonging to the most elementary mode of growth [1.102] often called the Volmer–Weber mode in the literature and similar to Wilson–Frenkel. Conversely, the CW equation at low temperatures is related to Becker and Döring (BD).

This discussion has a strong bearing on the roughening transition. In fact a smooth surface grows ac-

cording to something similar to the CW equation (with parameters determined by the physical details, e.g., by two-dimensional nucleation, see below), but after roughening the mode of growth degenerates to a simple EW behavior (actually, however, this change occurs already at a temperature somewhat lower than T_R, by an effect discovered by *Nozières* and *Gallet* [1.37]; we shall discuss this Nozières–Gallet effect below).

An interesting feature of growth conditions is a nontrivial scaling behavior. We have already mentioned the power-law roughness that may arise from the KPZ equation. More generally, the width w of the surface (i.e., the mean square height difference, given by $w^2 = \langle\langle h^2\rangle - \langle h\rangle^2\rangle$), very often obeys, as numerical simulations of simple models of crystal growth show, a scaling law with increasing time t and system size N [1.96, 103]

$$w(t,N) = N^{\zeta} f\frac{t}{N^z}\,, \tag{1.32}$$

i.e., a power-law roughness. Notice the very different (logarithmic) behavior occurring in equilibrium (in the rough phase)

$$w^2 = K(T)\ln N\,, \tag{1.33}$$

where, e.g., in the BCSOS model

$$K(T) = \frac{1}{\pi \arccos \Delta} \tag{1.34}$$

while in the smooth phase w remains finite. Simulations show that such logarithmic roughness still holds under growth conditions, provided the disequilibrium $\Delta\mu$ is small; there is a progressive change from logarithmic to power-law roughness with increasing disequilibrium [1.98].

The CW equation lends itself to a renormalization procedure similar to that used in the equilibrium case (Sect. 1.3). Both in equilibrium and off equilibrium the form of the surface is sharply different (at small q, i.e., at large distances) between a smooth and a rough surface.

This is characteristically related to the mode of growth. Typically, a smooth surface grows via nucleation of two-dimensional clusters on the surface: the classical theory of *Becker* and *Döring* [1.101] holds, and the growth velocity is proportional to the exponential

$$\exp\left(\frac{-\epsilon^2}{3kT\Delta\mu}\right) \tag{1.35}$$

(where $\Delta\mu$ is the chemical potential difference between fluid and solid, measuring the disequilibrium, and ϵ is the energy needed to increase the length of the border of a two-dimensional cluster by an atom): such velocity can be extremely slow if $\Delta\mu$ is small. Conversely, a rough surface, where steps and two-dimensional clusters are already present, grows at a much faster rate. Measuring the growth velocity in the smooth regime a measure of ϵ is obtained: this is the energetic cost of island border per atom, decreases steadily when roughening is approached (following the characteristic KT behavior), and vanishes at roughening. As an example, in the experimental part of the chapter we will show the data obtained by *Gallet* et al. [1.104] on the solid–superfluid interface of ^{4}He, where ϵ, the nucleation energy per atom, decreases, following precisely the KT law, in the range 1.13−1.22 K (above 1.22 K, however, the Nozières–Gallet effect takes over, see below, and the growth resembles closely that of a rough surface).

1.7 Nozières–Gallet Effect

In their important article of 1987, *Nozières* and *Gallet* [1.37] introduced an interesting effect, which refers to the behavior of a surface just below the roughening transition, under growth conditions.

In the nonequilibrium case Nozières and Gallet discovered that the rough behavior manifests itself already at a temperature a little less than T_R. They showed that, under growth conditions, the roughening transition becomes gradual and no longer sharp. Just below roughening the growth mode becomes Volmer–Weber and everything happens as if the surface were already rough. Moreover, the phenomena described become progressively stronger as the disequilibrium is increased.

Nozières and Gallet obtained their effect as a consequence of renormalization, stopping it in a similar way, for a growing surface (just below T_R) and for an equilibrium rough surface. Here, we give a more physical interpretation of the effect.

As discussed by *Levi* and *Kotrla*, this effect can be described as follows [1.105]. The (equilibrium) correlation length ξ diverges at roughening. For example, for the 6-vertex model characterized by the parameter Δ

(which is negative and less than -1 in the smooth phase and equal to -1 at T_R), ξ behaves as

$$\xi \approx a \exp\left[\frac{\pi^2}{2\sqrt{-2(\Delta+1)}}\right], \qquad (1.36)$$

another function with a typical KT behavior. As soon as ξ becomes larger than the size λ of the average terrace, everything happens as if ξ was infinite, i.e., as if the surface was rough, and the mode of growth appears as a simple Edwards–Wilkinson behavior, even though we are still below T_R.

A more detailed physical interpretation of this effect was given by *Levi* and *Kotrla* [1.92] (Fig. 1.6).

Let us briefly describe the physical situation near the roughening transition. In the Chui–Weeks equation the term $\nu\nabla^2 h$ describes the propagation over the surface of the information concerning the local level h. A new layer is completed in the time $\tau = a/v$ (where a is the vertical lattice spacing and v is the growth velocity), and in this time the information is propagated to a distance $L = \sqrt{2\nu\tau}$. As long as this distance is large enough—in fact, as long as it is larger than ξ, the equilibrium correlation length on the surface—, the surface grows layer-by-layer, in the nucleation mode, according to the same Becker–Döring laws as hold at lower temperatures. But near roughening ξ diverges and, as soon as it is larger than L, the information can no longer travel as far as ξ before a new layer is created. Everything occurs as if ξ were infinite: the surface roughens and the growth law becomes trivial: in particular, the growth velocity becomes linear in the disequilibrium $\Delta\mu$. The result is an effective lowering of the roughening temperature with increasing $\Delta\mu$.

Following [1.92], it is possible to attempt a more detailed discussion. According to classical nucleation theory (as applied to crystal growth by *Becker* and *Döring* [1.101]), a growth island of N atoms has a Gibbs free energy G made up of two terms: a negative term $-N\Delta\mu$ and a positive term, related to the energy cost of building the step that serves as island boundary, given by $B\epsilon$, where B is the number of boundary atoms and ϵ is the step free energy per atom.

If the island is convex, B is given by $B = b\sqrt{N}$, where, e.g., $b = 4$ for a square island. G is maximal for the critical nucleus, i.e., for $N = N^* = b^2\epsilon^2/(4\Delta\mu)$. If, however, L is relatively small, the surface behaves as if it had a finite size L and, in particular, if L is less than the size of the critical nucleus, the latter does not form: the area of the largest islands is of the order of L^2, which also implies a lowering of the nucleation barrier.

This is irrelevant at low temperatures, where $\xi \ll L$, but becomes important just below T_R. It should be recalled that ξ and ϵ are inversely proportional to each other: ξ long corresponds to ϵ small. The relevant quantities in our problem are $x = \beta\epsilon$, $y = \beta\Delta\mu$. The growth velocity v may be written as the *rough* (or *Wilson–Frenkel*) growth velocity v_0 divided by a factor ω, related to the nucleation barrier, which is not fixed but depends, in turn, on the size of the effective critical nucleus, i.e., on the growth velocity: thus the problem is self-consistent. The characteristic length L (which may be identified with the size of the relevant islands) can be found from the Chui–Weeks equation as $L = \sqrt{2\nu\tau}$, where ν, the coefficient of the Laplacian term in the stochastic equation, is of the order of av_0, and τ is the time for growing one layer, i.e., a/v. Then $L = a\sqrt{2\omega}$.

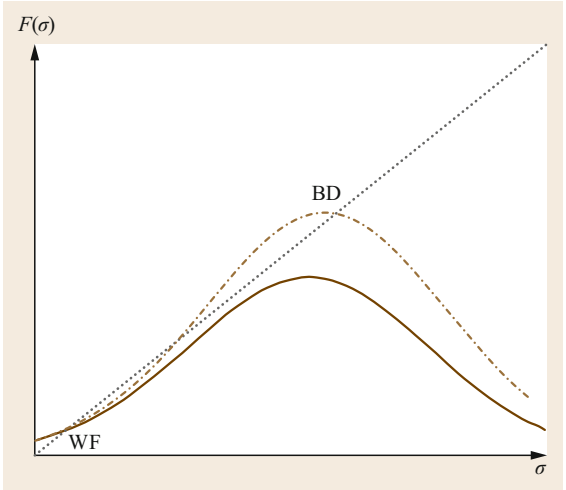

Fig. 1.6 Kinetic roughening as a first-order transition described by (1.37), for a dimensionless disequilibrium $y = 0.03$. *Dot-dashed curve* ($x = 0.36$): the equation has three solutions, of which the physical one, marked BD, corresponds to slow, Becker–Döring-like growth. *Solid curve* ($x = 0.34$): the slow solution has disappeared altogether and the growth takes place according to a small σ-value, i.e., to fast growth, corresponding to the point marked WF. Reproduced from data of [1.92]

Letting $\varpi = \sigma^2$, this leads to a self-consistency equation of the type

$$\sigma = \exp(px\sigma - qy\sigma^2)\,. \qquad (1.37)$$

In a simple description, the numbers p and q are given by $p = 2\sqrt{2}/3$, $q = 1/3$ (where the famous *Kolmogorov's cubic root* for two-dimensional nucleation has been used [1.90, 106]).

Let us consider the solutions of (1.37), and let us fix y (i.e., essentially the disequilibrium). Then for large x (i.e., far from roughening) there is only one, Becker–Döring-like, solution, but below a certain value of x (provided that y is less than a critical value $y_c =$

0.0747) there are two more solutions, corresponding to faster growth. Beyond another x-value, the slow mode disappears altogether and a jump is unavoidable to a faster growth mode. This appears as an indication that the Nozières–Gallet effect has set in. Conversely, if $y > y_c$, the growth should go to a faster regime smoothly, *supercritically*: this is understandable since at such strong disequilibria the critical nucleus is small anyway and even the Becker–Döring growth is fast anyway. The possibility of genuine critical phenomena in the neighborhood of such growth is an important point worth investigating (although *Tartaglino* and *Levi* did not find evidence for them in simulations [1.107]).

The relation between roughening and adsorption was first studied theoretically by *Suhl* and collaborators [1.108, 109]. More recently, the interesting problem of roughening on a surface covered with adsorbed molecules has been addressed by *Zhdanov* and *Kasemo* [1.110]. They showed that the adsorbate may lower the roughening temperature by several mechanisms:

a) Indirect next-nearest neighbor adsorbate–substrate repulsion
b) Attractive nearest-neighbor adsorbate–substrate lateral interaction
c) Repulsive adsorbate–adsorbate lateral interaction.

Vakarin and *Badiali* [1.111] showed, however, the situation to be more complicated: as a function of increasing coverage, T_R may first decrease, then increase again.

Finally, a possible relationship between roughening and surface melting was considered by *Levi* and *Tosatti* [1.112], who studied the roughening of molten surfaces. A step on the solid–liquid interface induces the formation, at the free liquid surface, of a corresponding feature whose shape and free energy cost are evaluated from the interplay between surface tension, attraction to the crystal, and layering. This cost prevents roughening until, just below bulk melting, the molten layer becomes so thick that the two interfaces decouple.

More recently, the relationship between roughening and surface melting has been studied in depth by Tosatti and coworkers, who have shown that surface melting may induce a sort of preroughening with a different mechanism from that considered by *den Nijs* and *Rommelse* [1.63]. From the point of view of the SOS model, assuming surface melting to be only incipient and therefore limited to a single layer, the surface may be covered by locally wet microareas in such a way that its symmetry plane is a half atom above the nominal level: this is indeed a description of a preroughened, or DOF, phase. To prove that this scenario is real, they use the Potts model of statistical mechanics. The latter involves a variable s_i, varying over N states, and is a generalization of the Ising model (reducing to the latter when $N = 2$). For $N > 2$ the Potts model has three different phases, which may be used to represent solid, liquid, and vapor [1.113]. In the present case the interesting values of N are very large. *Jagla* et al. show that for $N > 50$ the model shows a clear preroughening, which for $N > 80$ becomes first order [1.114–116].

Such a preroughening transition is confirmed by experiments concerning the high-temperature behavior of rare gas crystals [1.117] (we shall refer to such evidence in the experimental part), as well as, although not so easily, by Monte Carlo simulations of Lennard-Jones systems, describing with considerable precision the properties of such crystals [1.118].

These theories also afford a possible explanation of the surprising phenomenon of reentrant layering, where layering steps in adsorption isotherms first disappear, then reappear again [1.119].

1.8 Experimental Considerations

As shown in the above theoretical sections, the roughening transition is characterized at T_R by two related facts: the logarithmic divergence of the MSHD g and the disappearance of the corresponding facet from the equilibrium crystal shape. The occurrence of these two facts can be exploited to investigate experimentally the roughening transition: the observation of crystal shape in the macroscopic approach or the investigation of g in the microscopic approach. Other approaches based on the study of thermodynamic quantities are not feasible since the roughening transition, as we have shown, belongs to the Kosterlitz–Thouless universality class, hence is extremely weak (an infinite-order transition), and no discontinuities can be observed in thermodynamic functions that could provide the experimental evidence of the transition and could fix T_R.

The crystal shape can be observed on a crystal kept in equilibrium conditions at different increasing temperatures and the size of a facet can be followed up to its disappearance (or its appearance for decreasing temperatures starting above T_R). The crystal size must be visible (using an optical microscope or even an electron microscope), but big sizes hamper the possibility of a very uniform temperature of the sample and of a fast

response to approach equilibrium, while the behavior of too small crystals might be influenced by the interaction with the solid support underneath.

In the microscopic approach, the logarithmic behavior of g is asymptotic, therefore a large (on the atomic scale) exposed surface is required to average the experimentally determined g at long distances, and this poses several limitations both on experimental techniques and on samples. Real single crystals always present domains limiting the size of the perfect crystal under investigation and the exposed surface is cut within limited precision from the wanted crystal surface, involving the so-called miscut angle. Sensitivity to microscopic quantities on large atomic scale and at different temperatures can be obtained by using diffraction techniques sensitive to surface properties, i.e., diffraction techniques based on x-rays [1.120], electrons (low-energy electron diffraction, LEED) [1.121, 122]) or atom beams [1.123, 124], which perform the average of microscopic quantities on the size of the incident beam spot on the sample. In fact, measured diffraction patterns are analyzed in the reciprocal space and long distances are translated into small ranges of momentum exchange. Therefore a study of the shape of diffraction peaks, generally of the specular peak, contains information on g. Conversely, the experimental peak width is finite due to limitations of the experimental setup, such as divergence of the incident beam and acceptance angle of the detector, and all this is generally synthesized in the so-called transfer width on the sample [1.125, 126], i.e., the maximum size on the sample visible with the technique that corresponds to minimum peak width obtained by the setup. Hence the study of surface properties is limited to distances smaller than the transfer width, since larger distances are mapped within the minimum peak width. For an experimental setup, in particular for atomic beams, the presence of inelastic intensities means that also the energy resolution of the detector could be an important factor in order to reject inelastic contributions, accepting truly elastic (coherent or incoherent) intensities, such separation being important for the peak shape analysis. Moreover, a knowledge of defect density, in order to estimate the temperature where defect proliferation occurs, although not directly related to T_R, can be useful to understand the roughening mechanism and to correct the diffraction intensities: this can also be investigated with other techniques, sensitive to defects at short distances, to complement the diffraction ones, such as ion scattering techniques [1.127, 128] or scanning probe techniques [1.129, 130]. In fact structural information obtained in reciprocal space through diffraction is not unequivocally transformed into real space information at atomic level to distinguish the processes involved in a transition.

The microscopic approach could present a drawback for what concerns the equilibrium conditions. In fact the probe used in the experimental setup (e.g., in the case of electron or atom scattering) may require vacuum conditions, so that the crystal is not surrounded by its vapor at the proper equilibrium pressure. Instead this condition can be more easily obtained by working in a cell, which is generally the case for the macroscopic approach, and x-ray techniques could be suitable in this case.

Scanning probe techniques, e.g., scanning tunneling microscope (STM) in case of conductive samples, can reach atomic resolution; therefore the acquired images can show adatoms, vacancies and steps and a statistical analysis of their height distribution is feasible with the nuisance that many images are necessary to perform the necessary statistical average. The acquisition time is large compared to the diffusion at atomic scale, therefore mobile defects such as adatoms at high temperatures could contribute to some artifacts in images, the surface itself evolves during the acquisition time and the tip–surface interaction can modify the appearance of steps [1.131–134]. The development of high-speed instruments has partially mitigated all these problems [1.135].

Finally, another point is the presence of impurities in the crystal and their effect on the roughening transition. This point is usually neglected because the impurity density in crystals relevant for the present studies is generally low, but for solids with high melting temperature and high roughening temperatures, the necessity to keep the crystal at high temperature for long periods of time to perform measurements favors the segregation of impurities from the bulk. The contamination, even at very low coverage below the sensitive limit of conventional techniques to test surface cleaning such as Auger spectroscopy, has been shown to change the thermal behavior of surfaces, as will be described in the section about experimental results. As we have seen, the related topic of adsorbate effects on rough surfaces was theoretically investigated by *Resnyanskii* et al. [1.136], *Zhdanov* and *Kasemo* [1.110], and by *Vakarin* and *Badiali* [1.111]. For small coverage of the adsorbate, the results showed that T_R is a decreasing function of the coverage. Conversely, those studies were based on SOS models and Monte Carlo simulations or the lattice gas model and did not take into account the dynamics of the steps. Therefore, the pinning of steps due to contaminants is not treated, although pinning is probably very important for changing T_R and roughening mechanism (see for instance the case of Ag(110) or Au(110)).

1.9 Diffraction Techniques

As observed above, diffraction techniques are among the best options to study the roughening transition. In fact those techniques are sensitive to defects such as steps and the diffraction peak shape contains information about the distribution of those defects performing in real time the necessary statistical average on a macroscopic region corresponding to the beam spot size on the sample. In the following we will give a brief introduction, further information on diffraction techniques to study roughening can be found in reviews by *Conrad* [1.137], *Kern* [1.138], and *Lapujoulade* [1.139].

In general, diffraction requires the treatment of multiple scattering [1.140–145] and the analysis of a diffraction pattern can become very difficult. A single-scattering approximation greatly simplifies this analysis and this is generally a good approximation for x-rays [1.120], while electrons and atoms strongly interact with atoms in the crystal and this approximation is questionable, in particular for atoms [1.146]. Conversely, this so-called kinematical theory allows one to draw some general conclusions on the shape of diffraction peaks for all the probes useful to extract information on roughening.

In the single-scattering approximation, the intensity can be separated into two factors

$$I(\boldsymbol{Q}, q_z) = I_0(\boldsymbol{Q}) \sum_{\boldsymbol{R}} \exp(\mathrm{i}\boldsymbol{Q}\cdot\boldsymbol{R}) \times \langle \exp(\mathrm{i}q_z[h(\boldsymbol{R}) - h(\boldsymbol{0})]) \rangle \,, \tag{1.38}$$

where $\boldsymbol{q} = (\Delta\boldsymbol{K}, q_z)$ is the momentum exchange, $\Delta\boldsymbol{K}$ is its component parallel to the surface while the component perpendicular to the surface is q_z. We note that the experimental intensities contain also other contributions which are related to the atomic lattice vibrations: a brief discussion will be given below. The first factor, $I_0(\boldsymbol{Q})$, depends on the arrangement of atoms in the unit cell but does not depend on the roughness, it is related to the Bragg intensity for a perfect lattice. The second factor depends on the statistical properties of the surface. To further proceed, the so-called Gaussian approximation may be assumed in order to simplify this term

$$\begin{aligned} &\langle \exp(\mathrm{i}q_z[h(\boldsymbol{R}) - h(\boldsymbol{0})]) \rangle \\ &\quad \approx \exp(-p(q_z)\langle (h(\boldsymbol{R}) - h(\boldsymbol{0}))^2 \rangle) \\ &\quad = \exp(-p(q_z) g(\boldsymbol{R})) \,, \end{aligned} \tag{1.39}$$

where

$$p(q_z) = \frac{1}{2}\{q_z a_z \mod 2\pi\}^2 \,. \tag{1.40}$$

When p is an even multiple of π the scattering is in in-phase condition, i.e., constructive interference for scattered waves, the diffraction pattern is insensitive to surface defects, while for odd multiples of π the scattering is in out-of-phase condition, i.e., destructive interference, where the diffraction presents the highest sensitivity to surface defects.

In this approximation, the diffraction pattern is therefore related to the Fourier transform of the exponential of the MSHD. Below T_R, the MSHD asymptotically tends to a constant value so that its Fourier transform contains a Dirac δ-function, i.e., a diffraction peak which is the coherent part of the elastic intensity. At short distance, the MSHD will increase from a small value to the asymptotic value; assuming a linear increase, the Fourier transform is a Lorentzian function which is the incoherent part of the elastic intensity. Of course, the simple shape given by the δ function plus the Lorentzian function must be convoluted with the experimental resolution (transfer width) discussed in the previous section.

At and above T_R, the MSHD diverges in a logarithmical way. The lack of an asymptote means that the coherent part of the diffraction vanishes and only the incoherent part is present, and its shape is a power law

$$(a_x^2 Q_x^2 + \eta a_y^2 Q_y^2)^{(\tau/2-1)} \,, \tag{1.41}$$

where η accounts for the anisotropy, a_x and a_y are the lattice parameters of the surface cell, and the exponent τ depends on the temperature and the scattering conditions (p of (1.39)): in out-of-phase conditions for $T = T_R$

$$\tau(T_R, (2n+1)\pi) = 1 \,. \tag{1.42}$$

Moreover, this expression for the peak shape is valid when the roughening exponent is $\tau < 2$.

As shown in the theoretical part, steps are an important ingredient of roughening. They separate regions (terraces) with different height and the waves scattered by terraces interfere depending on the $p(q_z)$ value, therefore their presence can be inferred from the periodic oscillation in the peak profiles changing the scattering conditions from in-phase to out-of-phase [1.147–151].

To account for lattice vibrations that destroy the order of a lattice and in turn reduce elastic intensities, a Debye–Waller factor F_{DW} is introduced. For atom scattering, the related theory can be very complicated [1.152], but in the philosophy of the kinematical approximation, a simple expression valid for all the probes is an exponential decay $F_{DW} = \exp(-\langle(\boldsymbol{q}\cdot\boldsymbol{u})^2\rangle)$ where $\langle \ldots \rangle$ is a thermal average and $\langle \boldsymbol{u}^2 \rangle$ are the mean

square atomic displacements. For relatively small values of T, lattice vibrations can be treated in harmonic approximation and the mean square displacement increases linearly with T. Conversely, for higher temperatures the vibrations become anharmonic, therefore $\langle u^2 \rangle$ increases faster with T. Since T_R could be a sizable fraction of T_M, measurements can see anharmonic effects close to the transition.

Point defects, such as isolated adatoms and vacancies, produce a diffuse background: this further reduces the intensity I of those peaks but without a change of their shape [1.153]

$$I = I_0 \exp[-\langle (\boldsymbol{q} \cdot \boldsymbol{u})^2 \rangle](1-\theta)^{n_s \Sigma} \quad (1.43)$$

where Σ is the cross section for diffuse scattering of a single isolated defect, θ the point defect concentration, and n_s the number of lattice sites. We note that Σ for atom scattering can be larger than the surface unit cell. At low temperature, the concentration of single defects is generally small but increasing the temperature, especially when the vibrations become anharmonic, the excitation of adatoms/vacancies pair becomes more probable.

To set T_R, two criteria can be employed:

1. The vanishing of the coherent intensity
2. The peak shape analysis to get the exponent τ and measure the temperature for which $\tau = 1$.

The former approach is hampered by the finite acceptance angle of the detector that cannot distinguish between coherent and incoherent intensity at small Q and by the onset of anharmonic effects and point defect proliferation. The latter approach is more reliable although the peak shape requires a deconvolution to take into account the experimental resolution in particular for atom scattering. Examples are the results on Ag(110) and Cu(115).

1.10 Experimental Results

In this section, we will briefly describe the results of experimental investigations obtained on different systems and, in case also theoretical studies are available, the comparison with specific theoretical results. Other results will be included to describe also the onset of the transition with vibrational anharmonic effects and defect proliferation.

One of the first observations of roughening was obtained in 1977 by *Jackson* and *Miller* [1.38] who studied the growth from the vapor phase for both C_2Cl_6 and NH_4Cl which are crystals with cubic structures that sublime at atmospheric pressure rather than melting. The materials were sealed in a capsule and heated up in a two-zone furnace, the two capsule ends were kept with a temperature difference of about 10 K. The material at the hot end was the vapor source for the growth of crystals at the cold end. If the cold end is below the roughening temperature, the crystal grows with a faceted morphology, while its morphology is rounded for a temperature of the cold end higher than the roughening one as shown in Fig. 1.7. In this way the authors were able to set $T_R = 373$ K for C_2Cl_6 and $T_R = 638$ K for NH_4Cl.

Other pioneering studies on the equilibrium crystal shape at different temperatures, in particular on the morphology of included vapor in crystals (negative crystals) of tetrabromomethane, were performed by *Nenow* and coworkers who observed transitions from facets to rounded regions [1.154].

In the following review, we will present more detailed studies starting with the helium case and then passing to metal surfaces with an emphasis on the (110) surfaces of fcc metals.

1.10.1 Roughening in Helium

The study of roughening of helium surfaces is very important, in particular because helium shows surface phenomena in the cleanest form, without a number of perturbations that other systems have [1.155].

We shall discuss briefly here ^{4}He, by far the most important isotopic species (^{3}He of course is different in many ways). Helium differs from all other substances because it does not solidify at low temperatures, except at relatively high pressures. The solid and the liquid, in fact, are in equilibrium at a pressure p (for ^{4}He near to 25 bars and almost independent of temperature at low T). The helium surfaces are thus solid–liquid interfaces. The interesting temperature range is below 2.5 K: at such temperatures liquid ^{4}He is a superfluid. The most important roughening phenomenon takes place at 1.28 K, as can be seen in Fig. 1.8 [1.155]. Crystals of ^{4}He are hexagonal close-packed (except for a very small area of the (p, T) plane where bcc crystals form). For such an hcp crystal the most visible surface is the (0001) surface, in this case in equilibrium with the superfluid. The surface displays the properties predicted by theory, in particular it is smooth at low temperatures

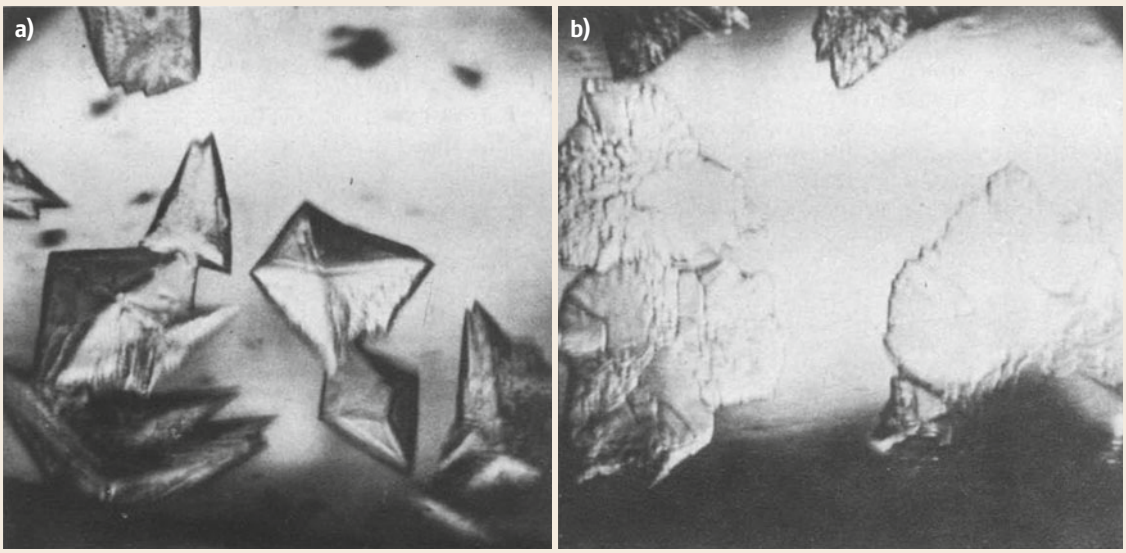

Fig. 1.7a,b Growth morphologies of vapor-transported C_2Cl_6, just below and just above the surface roughening transition. **(a)** Hot end 378 K, cold end 368 K; **(b)** Hot end 388 K, cold end 378 K. Reprinted from [1.38] with permission from Elsevier

and rough at higher temperatures. *Wolf* et al. [1.156] and *Gallet* et al. [1.104] measured the step free energy as a function of temperature: the step free energy decreases in the smooth situation, vanishes at roughening, and is zero in the rough situation as shown in Fig. 1.9. The step free energy is measured via the growth velocity, since, when a crystal grows by two-dimensional nucleation, the classical *Becker–Döring* theory holds [1.101] and gives the growth velocity in terms of an exponential dependence on the step free energy. The experimental results are shown in Fig. 1.9, where the step free energy is shown to decrease from $T = 1.15$ to $T = 1.23$ and to vanish at higher temperatures. This decrease is exponential, accordingly to a *Kosterlitz–Thouless* law [1.18] (in fact, this is presumably the case where the KT behavior is displayed most clearly). The roughening temperature can be evaluated to be $T_R = 1.28$ K. As expected for a KT transition, the step free energy vanishes at T_R with all its derivatives. But between 1.23 and 1.28 K the *Nozières–Gallet* effect [1.37] manifests itself: the step free energy is already effectively zero, although we are still below roughening.

1.10.2 Unreconstructed (110) Surfaces

In this part we will describe the results for the (110) surfaces of Cu, Ag, Ni, Pd, Pb, and Al. As mentioned in the theoretical part, the (110) surface of those fcc metals is unreconstructed but a missing-row reconstruction is observed upon deposition of a small amount of alkali metals. Hence the theory for (110) surfaces is suitable to describe their behavior.

Cu(110)

The first evidence of roughening on (110) surfaces was observed in 1976 by *Stock* and *Menzel* on crystals of 2 mm size of Cu supported on graphite stripes heated by direct current [1.157]. Photographs of those crystals close to melting showed only (111) and (100) facets. One year later, the study of photoemission data on Cu(110) showed an anomalous behavior with temperature [1.158]. The normal photoemission spectrum at a photon energy of $h\nu = 45$ eV was measured in the range between 300 and 1073 K. The spectrum significantly changes with temperature and, at high temperature, the d-band peak becomes asymmetric resembling that of polycrystalline copper. The authors ascribed this behavior to thermal disorder.

Several years later, *Gorse* and *Lapujoulade* using He atom scattering [1.159] obtained similar results. The authors carried out a comparative study on Cu(100) and Cu(110). They measured the specular peak for different kinematical conditions and, for the analysis, the peak was separated into two components: a Gaussian function, which fits the elastic coherent part of the signal, and a Lorentzian function, which could fit either the elastic incoherent or the inelastic contributions, since their apparatus did not perform energy analysis of the scattered beams. Up to 573 K the two copper surfaces behave in a similar way with a small Lorentzian compo-

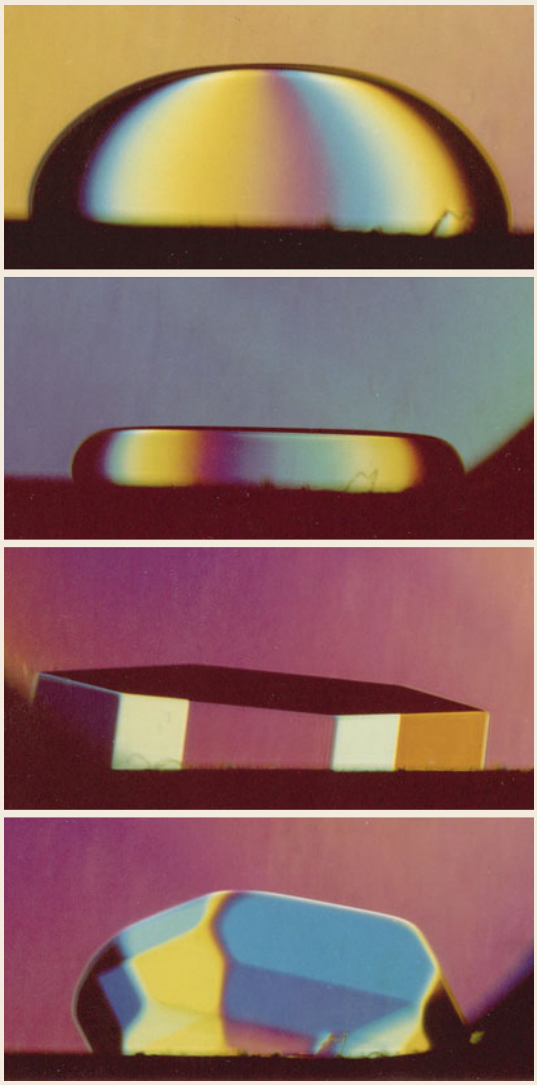

Fig. 1.8 Faceting of ^{4}He crystals during the cooling of the system. From *top* to *bottom panel*, the temperature is 1.4, 1, 0.4, and 0.1 K, respectively. The size of the facets is larger than on equilibrium shapes, because of the slow growth from the surrounding superfluid. Reprinted from [1.155]. Copyright 2005 by the American Physical Society

nent. Above this temperature, the Lorentzian intensity starts to increase but, for Cu(100), the Gaussian one is measurable up to 1273 K (melting temperature 1373 K) indicating that this surface retains some order up to temperatures close to melting. Instead, for Cu(110), the intensity starts to decrease faster than for Cu(100) and the authors were not able to perform measurements above 973 K since the signal dropped below the noise of the instrument. The strong decrease of the scattered

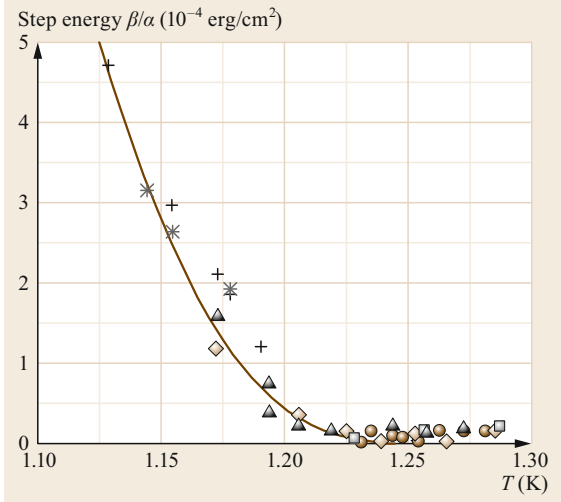

Fig. 1.9 Step free energy for ^{4}He. Drawn from data of [1.104]

intensity was ascribed to thermal excitation of point defects.

Two years later, the interpretation suggested by He atom scattering data was modified by *Fauster* et al. with ion scattering [1.160]. In fact the scattering at 50° of 500 eV Na^+ clearly showed that above 400 K there is a decrease of the scattered intensity and this can be related to huge vibration amplitudes and/or other atomic rearrangements. To gain further information, the authors also performed measurements on 5-keV Ne^+ in quasiback-scattering configuration (deflection angle 164°), i.e., they performed impact-collision ion scattering spectroscopy (ICISS). The angular position of the focusing peak depends on the nearest neighbors distance and its width is sensitive to atomic displacements from equilibrium positions, i.e., to vibration amplitudes. Moreover, a missing nearest neighbor means that the focusing peak shifts to the angular position corresponding to the next-nearest neighbor one, hence ICISS can discriminate between enhanced vibrational amplitude and point defect excitation. The analysis of ICISS data, although not completely conclusive, showed that point defects alone cannot explain all the features of the spectra, and large amplitudes of atomic vibrations in the surface were invoked without excluding the possibility of an atomic rearrangement for $T >$ 500 K.

In the meantime *Mochrie* [1.161] carried out an x-ray diffraction experiment which was consistent with an increase of the mean square roughness of the surface. He considered a reversible vanishing of the Bragg intensity and estimated a roughening temperature of $T_R = 873$ K, but he did not perform any peak shape

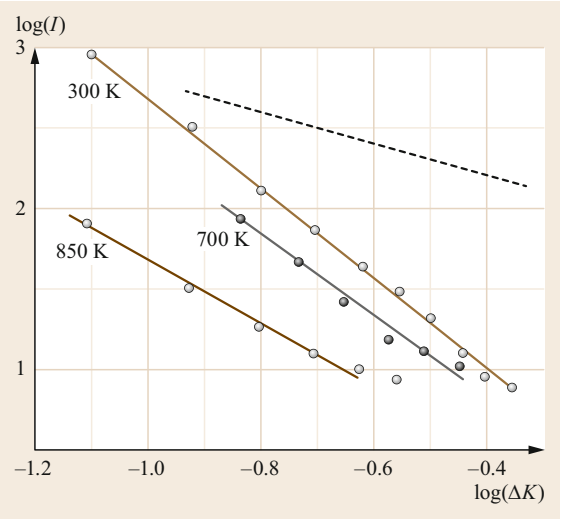

Fig. 1.10 Log–log plot of specular peak profiles in an extended region of the first Brillouin zone for different temperatures. The *dashed line* has a slope of 1 as expected for a peak measured from a surface at its roughening temperature while the experimental points show a much steeper slope. Redrawn from data of [1.163]

analysis to detect a power-law behavior. Conversely, experiments on slightly miscut Cu(110) surfaces performed by surface x-ray diffraction [1.162] showed that the surface can undergo a faceting transition, and some doubts were raised on conclusions about roughening obtained by previous x-ray data.

Zeppenfeld et al. [1.163], analyzing He scattering data obtained with time-of-flight detection, showed that above 550 K the decrease of the intensity is not accompanied by a substantial change of the specular profile, as shown in Fig. 1.10, so that steps are not thermally excited on Cu(110) up to 900 K. In this case, the increase of the mean square displacement measured by Mochrie was due to enhanced surface anharmonicity and not to roughening. In fact, this anharmonicity was directly measured later by *Baddorf* and *Plummer* [1.164] who studied phonon energies and lifetimes between 21 and 766 K by using high-resolution electron-energy-loss spectroscopy, observing a substantial change of the surface phonon lifetime above 450 K. Conversely, Zeppenfeld et al. also measured the diffuse (incoherent) elastic peak as a function of temperature and for various scattering geometries, observing that this intensity decreases with increasing temperature. Therefore, they also excluded the increase of point defect density as the main cause for the observed anomalous thermal behavior for $T > 550$ K. This second point is questionable, however, since both coherent and incoherent contributions decrease with temperature due to the increasing inelastic contributions. To reduce the inelastic effects, the ratio between coherent and incoherent intensity has to be considered; the ratio increases as can be inferred from their data, and this is a sign of defect formation. In fact, analysis of new Ne^+ ion scattering data in ICISS configuration in the energy range 4–5 keV [1.165] supports the enhanced surface anharmonicity for $T > 550$ K, but some observed features can only be explained by the presence of adatoms on top of flat terraces for $T > 455$ K. Moreover, above 1000 K an increase of the broadening of the spectra, not completely described by anharmonic atom vibrations, suggested a rearrangement of surface atoms which could be due to a roughening transition.

The data by *Kern* [1.138] obtained by means of He scattering with energy selection set the roughening temperature at $T_R = 1070$ K (about the value which was obtained by extrapolation of the data of [1.163]).

Comparing experiments with the results on the theoretical side, molecular dynamic simulations based on interaction potentials obtained from the embedded-atom method by *Yang* and *Rahman* [1.166] supported an enhancement of vibrations for surface atoms starting at 600 K (with the further indication that, around 900 K, adatoms and vacancies are created on the surface), but they excluded any roughening of the surface. *Häkkinen* et al. [1.167], using a combination of lattice-gas Monte Carlo and molecular dynamics methods based on the same many-atom interactions derived from the effective-medium theory, estimated the height–height correlation function, which presents a logarithmic divergence that sets the roughening temperature around 1000 K.

Further experimental evidence of the roughening transition for Cu(110) was found in measurements performed for instance by directional elastic peak electron spectroscopy [1.168] where the contrast in logarithmic scale shows a clear change of slope at about 1000 K, and more recently by reflection anisotropy spectroscopy (RAS) and scanning tunneling microscopy [1.169] which also set the transition around 1000 K.

Instead, other measurements performed by means of reflection anisotropy spectroscopy [1.170, 171] set the transition at a lower value around 900 K. The studies are based on the disappearance of the peak at 2.1 eV and on the observation of an energy shift of a feature of the spectrum from 4.2 to 4.3 eV. We can observe that previous results have shown that 900 K is the temperature at which adatoms and vacancies are created and it can be considered to be the onset of the process that will bring the surface to the transition: therefore, the claim of these RAS works on the roughening transition sets only a lower limit to the transition; they have demonstrated the sensitivity of the electronic transitions to surface disorder.

Finally, we would like to mention that in [1.169] the authors did not observe irreversible changes in the results treating the sample up to 850 K. Instead, with higher annealing temperatures, after cooling the sample to room temperature, they observed a permanent change and the previous situation was recovered by ion bombardment. No further analysis was done to relate this irreversible change to segregation of contaminants from bulk, but this effect might be a possible explanation.

Ag(110)

The (110) surface of Ag was the second metal surface extensively (and more successfully) studied to determine the presence and the mechanism of a roughening transition. The first study was performed by *Held* et al. with surface x-ray diffraction [1.172] on a surface having a miscut of 0.3° in the temperature range 373–823 K. The authors carried out radial and transverse scans that clearly showed the evolution of the shape of a bulk-forbidden diffracted peak with the temperature. At 373 K they observed a sharp peak; increasing the temperature to 648 K, the shape slightly changed and at higher temperatures it started to develop substantial tails with an appreciable decrease of the intensity. The radial peak shape was fitted by the sum of a Gaussian function and a Lorentzian one, which represent the coherent (Bragg) diffraction and diffuse scattering from steps, respectively. Above 723 K, the coherent part vanishes and even the tails showed a power-law shape with an exponent consistent with the roughening transition. Moreover, the observed transition was reversible with temperature, indicating that it is indeed an equilibrium phase transition and not a nonequilibrium microfaceting process. Instead, up to 773 K, the integrated intensity of the bulk Ag(111) peak decreases only by 20%, as expected by the Debye–Waller factor, without a change in line shape. The different behavior between surface and bulk peaks demonstrated that the observed changes are exclusively related to those in the surface morphology and T_R was estimated as (723 ± 25) K.

Several years later, *Robinson* et al. [1.173, 175] using x-ray diffraction investigated along the $\langle 1\bar{1}0 \rangle$ direction the peak shape as a function of the momentum exchange q_z perpendicular to the surface and found a behavior that did not agree with the prediction of the roughening theories. For temperatures well below T_R, the peak shape in out-of-phase condition, i.e., in the condition of *Held* et al. [1.172], could be described by a single component. However, when increasing q_z, the diffracted peaks showed an asymmetry and two scattering components were necessary to improve the fit. The authors interpreted this as the coexistence of two phases on the surface, i.e., a faceting. This faceting was explained by the authors as due to the existence

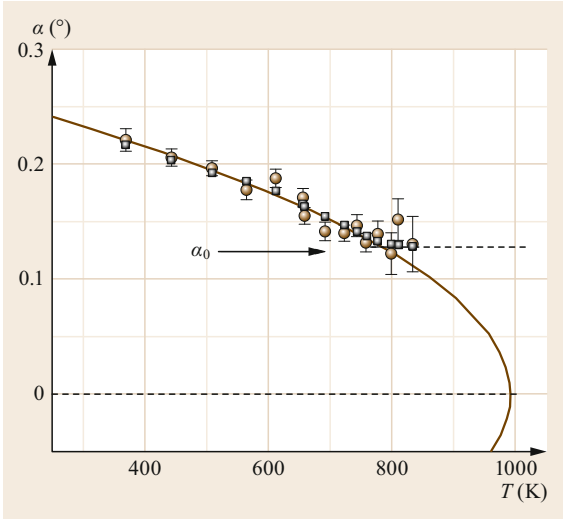

Fig. 1.11 Angle of tilt between the two surface phases, as measured from the separation of the two components of the peak (*brown circles*) or from their relative intensities (*black squares*) using (1.44). Redrawn from data of [1.173]

of forbidden directions in the equilibrium crystal shape around the (110) facet. Since real crystals are cut along the (110) plane within a miscut angle α_0, in the case this angle corresponds to a forbidden direction [1.176, 177], the surface free energy can be lowered separating the surface into regions corresponding to the (110) facet (A) and stepped (rough) regions (B), the so called hill-and-valley configuration. The angular separation between the two scattering components, related to the tilt angle between the (110) facet and rough regions, and their relative intensities, related to the surface area, supported this hypothesis. In fact, at room temperature, the data showed that the tilt angle α was greater than α_0 in order to preserve the macroscopic miscut and decreased until it leveled off at the value corresponding to α_0, as shown in Fig. 1.11. At the same temperature, the scattering intensity associated with the (110) facet vanished namely the (110) facet disappeared from the equilibrium crystal shape. The authors, by using the lever rule [1.178] made a second independent estimate of the tilt angle α' based on the surface areas of the A and B phases, and since the integrated intensities of the two fitting components, I_A and I_B, are proportional to areas, they obtained the following relationship

$$\alpha' = \frac{\alpha_0 (I_A + I_B)}{I_B} \qquad (1.44)$$

and the results are plotted in Fig. 1.11a. Cooling the sample, the surface phase separated once again into flat A and tilted rough B regions, but only a few points were measured for temperatures above 650 K.

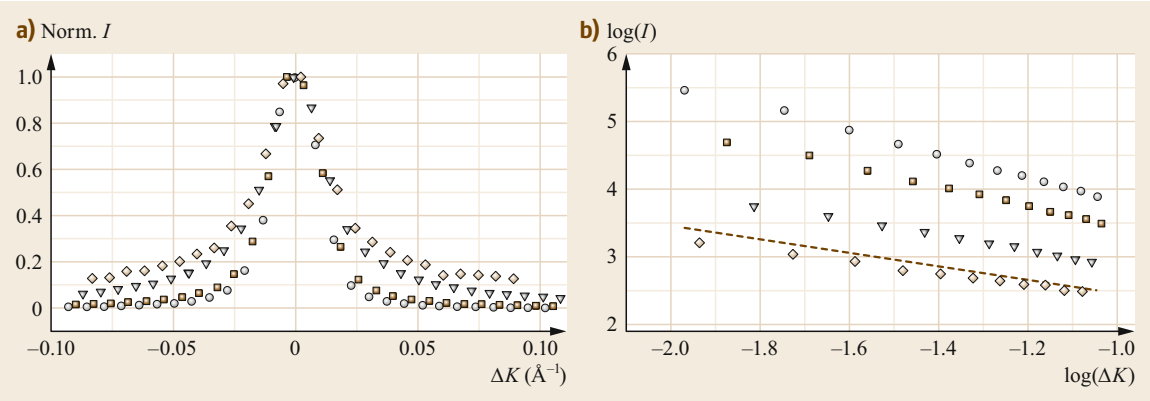

Fig. 1.12 **(a)** Normalized intensity of the specular peak measured from Ag(110) along ⟨001⟩ at 643 K (*circles*), 766 K (*squares*), 861 K (*triangles*), 951 K (*diamonds*). A constant background has been subtracted from all of the data shown. **(b)** Log–log plots of the tails of specular He profiles of **(a)**. Estimated values for the roughening exponent τ: 0.22 at 643 K, 0.49 at 766 K, 0.91 at 861 K, 1.17 at 951 K. The *dashed line* has the slope expected for a surface at its roughening temperature: $\tau = 1$. Redrawn from data of [1.174]

This behavior suggested a mechanism to roughen the surface different from that described in the theoretical part. On real surfaces (110) facets are coexistent with rough regions. Increasing the temperature results in new excited steps on the facets. These steps migrate toward the stepped regions which expand at the expense of the (110) facets. At the temperature T^*, which thus depends on the miscut angle, all the surface is covered by stepped regions and the surface becomes rough. Hence T^* corresponds to T_R and the roughening mechanism, which for classical theories is the proliferation of steps on a flat surface, must be replaced by the redistribution between flat and rough regions. In particular, Robinson et al. found $T^* = 790$ K for their crystal having $\alpha_0 \approx 0.14°$ and the discrepancy with the previous estimate of T_R [1.172] was ascribed to the large miscut angle, 0.3°, of the crystal used in the previous experiment. Moreover, they also extrapolated their results to estimate the roughening temperature of a perfect (110) surface ($\alpha_0 = 0°$) obtaining an approximate value of 990 K. These conclusions were drawn for the $\langle 1\bar{1}0 \rangle$ direction and Robinson et al. left open the possibility that the classical mechanism can act along ⟨001⟩.

The ⟨001⟩ direction was investigated by *Bracco* et al. [1.174] by means of He scattering with time-of-flight detection. There was no evidence, however, of a double component in the specular peak profile and all the data agreed with the classical picture of roughening. In fact, up to ≈ 700 K the intensity of the specular peak decreased following the prediction of the Debye–Waller factor and the incoherent to coherent ratio was almost constant, while for $T > 700$ K, the intensity decreased more rapidly along with the increase of the ratio, a clear sign of the proliferation of point defects. The analysis of the specular peak shape in out-of-phase scattering conditions showed that the onset of the transition happens for $T \approx 700$ K and a roughening temperature of 910 ± 15 K was estimated (Fig. 1.12). Moreover, the crystal used in the experiment had a miscut of $\approx 0.15°$ and this last estimate of the roughening temperature could not be explained by the hill-and-valley mechanism of *Robinson* et al. [1.175] without invoking two different roughening temperatures on the same surface. Other studies performed by means of STM and x-ray scattering [1.179, 180] showed that the faceting transition observed by Robinson is due to segregation of contaminants from the bulk, very probably sulfur. In fact, prolonged heating of the crystal at temperatures higher than 850 K determines the segregation of sulfur and even an estimated coverage of 0.001 of a monolayer was able to change the surface morphology. STM images showed clusters containing 10–20 sulfur atoms which act as pinning sites for steps. Studies performed with He scattering [1.181] showed the evolution of the surface morphology with prolonged Ar^+ sputtering. By using ions at low energies (100 eV), that are not effective to sputter Ag atoms but enough to remove low mass contaminants, and starting from a faceted surface the specular peak shape gradually lost the satellite peaks due to tilted areas. After 24 h the shape did not show additional components; therefore, the surface had recovered a morphology with uniformly distributed steps across the surface. The crystal treated in this way showed sufficient stability to allow the completion of experiments also at a temperature higher than 900 K before a new treatment was required. New x-ray results [1.182] on a sample, treated under ultra-high vacuum (UHV) conditions by several hours Ar^+-ion

sputtering at 500 eV and subsequent annealing up to 1000 K, gave an estimate of T_R of (900 ± 50) K. A few years later, another study carried out with He scattering [1.181, 183] performed a careful investigation of the effects that can affect the estimation of the roughening temperature through peak shape analysis. In fact, since He scattering is very sensitive to surface atomic vibrations, truly elastic intensities should be considered and collecting some inelastic intensities reduces the estimated values: for instance a deconvolution of the peak in elastic and inelastic phonon contribution increases T_R of 4% with respect to the case in which the intensity of each point of the peak profile is obtained by integrating the scattered signal within an energy window of 0.8 meV around the elastic intensity. Moreover, the short-range behavior of the MSHD can obscure the asymptotic evolution towards a power-law shape (see for instance the Cu(115) case) and taking into account that this effect increases T_R by about 10%. Including all these effects, the first estimated T_R at 910 ± 15 K increased up to 1000 ± 30 K.

Other experiments [1.184] showed that surface phonon anharmonicity is similar to Cu(110) and above 600 K frequency shifts increase due to proliferation of defects. A direct measurement of self-diffusion of Ag adatoms [1.185, 186] showed that silver adatoms migrate with a strong anisotropy. Diffusion limited to the $\langle 1\bar{1}0 \rangle$ direction started at a crystal temperature above 600 K, in agreement with theoretical simulations [1.187]. The analysis of an ion scattering investigation [1.188] showed that the $\langle 1\bar{1}0 \rangle$ atomic rows remain defect free up to 700 K while along $\langle 001 \rangle$ the defect percentage increases rapidly above 600 K. All the data indicated the presence of missing rows confirming the theoretical prediction about the proliferation of missing rows at the onset of the transition [1.47].

Molecular dynamic simulation on Ag(110) [1.189] showed that up to 700 K the mean square vibrational amplitudes of the surface atoms are very similar both in the surface plane and perpendicular to the plane, while above 700 K the amplitudes along the in-plane directions begin to become the larger ones, in particular along $\langle 001 \rangle$, and above 750 K, the surface begins to disorder due to the creation of adatom–vacancy pairs with adatoms that diffuse preferentially along the close-packed rows, i.e., along $\langle 1\bar{1}0 \rangle$. The roughening temperature was estimated to be 930 K with a statistical error of 20 K. More recent calculations [1.190] found a surface roughening at 950 K, essentially in agreement with previous simulations and with the experimental results.

Ni(110)

The roughening transition of Ni(110) was investigated by *Cao* and *Conrad* [1.191] using high-resolution low-energy electron diffraction. The sample was initially heated to 1120 K in O_2 at 10^{-6} Torr for 24 h to remove excess subsurface carbon. Then the sample was sputtered with 500 eV Ar^+ at a sample temperature of 1070 K to remove any remaining oxygen and sulfur contamination. Although the Auger signal showed no detectable contamination, the authors observed a non-reversible peak splitting of diffraction peaks when the sample was heated above 750 K. The sample was further treated with three weeks of repeated sputtering at 1070 K followed by annealing up to 1170 K and cooling down to 670 K with a slow rate of 0.4 K/s. After these prolonged treatments the splitting was no longer observed. On this clean sample, the measurements showed that, up to 900 K, the logarithm of the diffraction peak intensities linearly decayed; therefore the temperature dependence of specular and diffracted beams could be accounted for by a Debye–Waller factor. Instead, for temperatures up to 1200 K, the decay was faster with no change in the peak shape both for in-phase or for out-of-phase conditions so the anomalous decrease of the intensity was interpreted as due to anharmonic effects. This was also consistent with the trend of the background to peak intensity ratio which started to increase at 1150 K indicating vacancy formation at this temperature. For the analysis, the specular peak was fitted by a Gaussian central peak (G) and a Lorentzian function (L). Between 1200 and 1400 K the width of the L component in out-of-phase condition broadened and the ratio between G and L which was constant up to 1150 K started to decrease and before reaching 1400 K the ratio almost vanished. From these results, Cao and Conrad estimated a roughening temperature $T_R \geq 1300$ K.

Other experimental evidence of the roughening transition was found by *Mróz* studying the contrast in Auger signal versus sample temperature [1.192]. Above 740 K, the contrast showed a change of the slope with an increase in the decay followed by another increase for temperatures higher than 1300 K. The low temperature change was interpreted as due to anharmonic effects that set in above 740 K and the second change to a lateral disorder in the first atomic layers consistent with a roughening transition at 1300 K.

Molecular dynamics simulations performed by *Beaudet* et al. [1.193] and based on a semiempirical embedded-atom method gave results in substantial agreement with the Cao and Conrad results. In fact, Cao and Conrad estimated a vacancy density of the order of 4% at 1000 K, and between 5% and 15% at 1200 K to be compared with calculated values of 4% and 13%, respectively. The logarithmic divergence of the MSHD was not estimated to precisely set T_R due to the small scale of the simulations, however, at approximately 1300 K, the calculations showed that out-of-plane dis-

order reached the second layer. *Chen* et al. performed similar investigations [1.194] in which the embedded-atom theory is used to describe interatomic interactions. Although the main interest was the study of surface melting of Ni(110), they found that up to 1250 K the density profile showed a gradual change and, only at 1450 K, they observed the formation of an adlayer absent at lower temperatures. Since they did not perform simulations between 1250 and 1450 K, this temperature range is in agreement with the lower limit experimentally determined by Cao and Conrad for T_R at 1300 K.

The behavior for $T < T_R$ of the diffracted peaks, fitted by means of a broad Lorentzian plus a Gaussian central peak, was also consistent with the occurrence of a preroughening transition, even if no conclusive evidence for that was obtained [1.137].

Pd(110)

Hörnis et al. investigated the structure of Pd(110) with high-resolution low-energy electron diffraction [1.195]. The sample presented a miscut angle of 0.1° and was cleaned in situ by thousands of cycles of argon-ion sputtering at 500 eV for 10 min, followed by annealing at 1273 K for 10 min. After this cleaning procedure, Auger spectra did not show C, S, or O contaminations and it was possible to keep the sample at 1473 K for 30 min and then cool it to room temperature without a change in the diffraction intensity. The authors observed that a well-ordered (110) surface could only be obtained with slow cooling of the sample from 1273 to 673 K in no less than 3 min.

The width of the specular peak was measured for different scattering conditions and was found to oscillate with a period $2\pi/h$, where h is the height of a monatomic step on the Pd(110) surface ($h = 2.75$ Å) indicating that monatomic steps are present on the Pd(110) surface even at room temperature.

For temperatures below 1273 K, the authors observed the presence of satellite peaks near the specular peaks as shown in Fig. 1.13 along the direction perpendicular to the atomic rows, i.e., ⟨001⟩, as well as in the $\langle 1\bar{1}0\rangle$ parallel to the atomic rows. These satellite peaks were consistent with a large-scale 80×45 reconstruction of the Pd(110) surface [1.196]. This reconstruction was very stable since it was observed up to 1273 K.

We note that this long-range reconstruction for bare Pd(110) was not reproduced in subsequent investigations in real space with scanning tunneling microscopy carried out by *Niehus* and *Achete* [1.197], and long-range superstructures were observed only with oxygen adsorption.

Conversely, it is interesting to consider the results by *Hörnis* et al. [1.195] concerning the high-

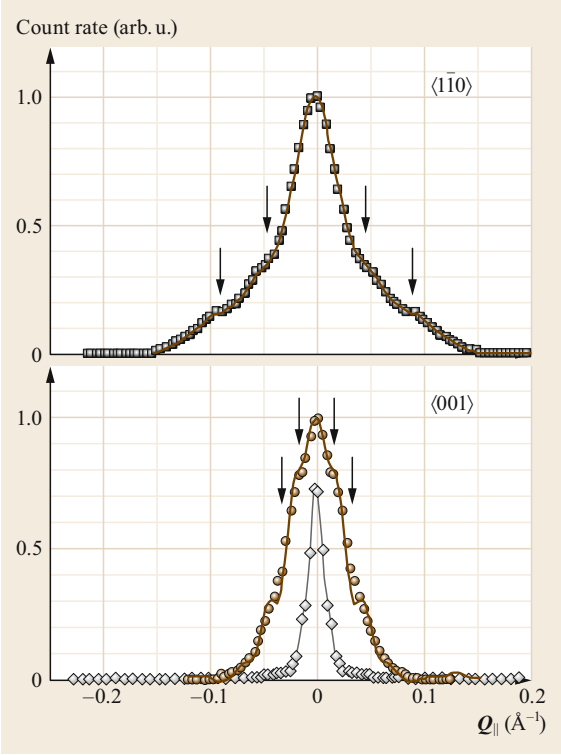

Fig. 1.13 Parallel momentum $Q_{||}$ scans through the (110) point taken both perpendicular to the atom rows, ⟨001⟩ (*circles*) and along the rows, $\langle 1\bar{1}0\rangle$ (*squares*). For comparison, the (220) in-phase peak is shown (*diamonds*). Measurements were carried out at 523 K with an electron energy of 307 eV, and an incident angle (relative to the sample normal) of 82.7°. *Arrows* indicate the positions of the satellite peaks. The *solid line* for the (001) azimuth is a fit assuming islands of 59 atoms, separated by 20 atomic spacings forming a system with periodicity of 79 atomic spacings. Reproduced with permission from [1.195]

temperature behavior of Pd(110). Their analysis showed that the width of the diffraction peaks shows three temperature regions as shown in Fig. 1.14. In fact, the line shapes were essentially constant up to 773 K. In the interval between 773 and 1173 K, the FWHM in the ⟨001⟩ direction, perpendicular to the atom rows, decreases, while in the $\langle 1\bar{1}0\rangle$ directions the FWHM increase is due mostly to an increase in the broad background component of the line shape. Since the separation distance between satellite peaks does not change in this interval the superlattice period remains constant. Therefore, the changes in the FWHM indicate a rearrangement of the structure of the superlattice cell.

Above 1373 K, the line shapes changed suggesting a transformation in the surface morphology since the satellite peaks disappear and the entire line shape be-

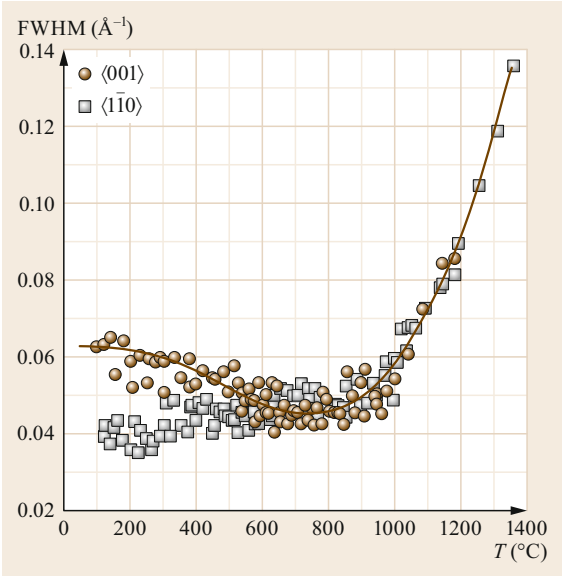

Fig. 1.14 FWHM of the (110) peak of Pd(110) versus temperature for scans along ⟨001⟩ (*circles*) and along ⟨1$\bar{1}$0⟩ (*squares*) directions. The *solid line* is a guide to the eye for the (001) data. Measurements performed at an electron energy of 307 eV, and with an incident angle (relative to the sample normal) of 82.7° for all scans. Reproduced with permission from [1.195]

gins to broaden and the broadening was observed for peaks in out-of-phase scattering condition. This could be assigned to a roughening transition at a temperature of 1373 K. However, the authors took with caution this line-shape broadening as due entirely to a thermal roughening transition. In fact, Pd's vapor pressure between 1073 and 1273 K, increase from 1.2×10^{-9} to 8.4×10^{-7} Torr. At an even higher temperature of 1373 K, the evaporation rate from the surface is about one ML/s therefore the origin of this Pd(110) roughness cannot not be completely due to thermal equilibrium in the surface alone but even the kinetic of the evaporation, that could be considered as a negative growth process, can contribute to it.

Pb(110)

Heyraud and *Métois* studied the equilibrium shape of lead microcrystals lying on a graphite cleavage plane [1.44, 199]. In the first step, they condensed a 1000 Å-thick film on a cleaved graphite monocrystal in UHV, then, heating the film above the Pb melting temperature, the films broke in droplets of $\approx 5\,\mu$m size. The second step was the lowering of the temperature at the chosen value and a further Pb condensation of 1000 Å yielded the growth of flat crystallites. Finally, the sample, removed from the UHV preparation chamber, was observed by scanning electron microscopy. For growth temperatures above 393 K, only the (111) and (100) facets were observed. Below this temperature, the (110) was also observed.

Yang et al. measured the roughening transition of Pb(110) by means of high-resolution LEED (HRLEED) [1.198] on a sample whose miscut was estimated to be 0.1°. The authors measured the specular peak as well as another two diffracted peaks, (10) and (01). At low temperature, the peak profiles were smooth and without shoulders or peak splitting. Moreover, changing the incident energy, the FWHM of the peaks did not show any oscillatory behavior. However, an oscillatory behavior was observed upon raising the temperature, a clear sign that steps were generated on the surface, as shown in Fig. 1.15. From the

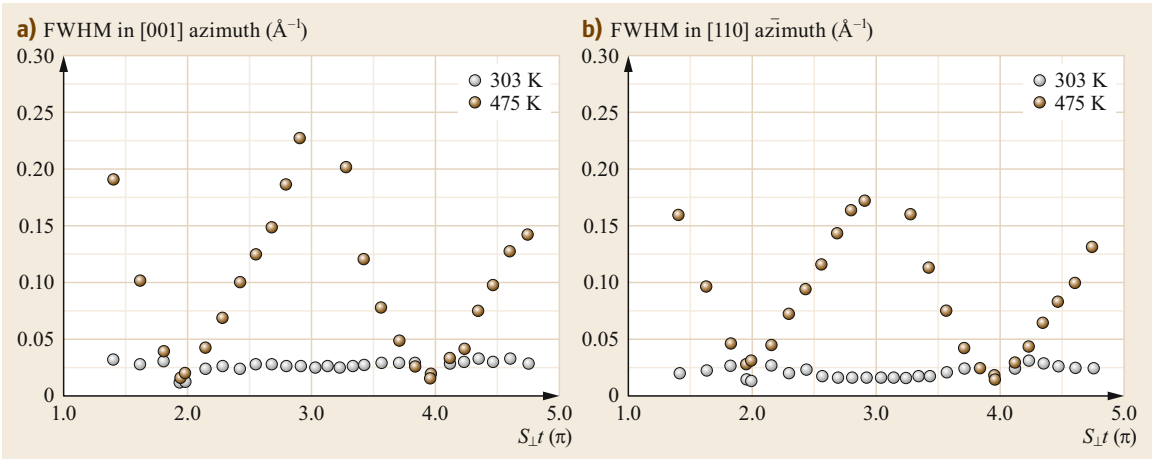

Fig. 1.15a,b FWHM of the (00) beam versus the perpendicular momentum exchange $S_\perp$ measured along **(a)** [001] and **(b)** [1$\bar{1}$0] directions. Measurements were performed at 303 and 475 K, t is the step height. Reproduced with permission from [1.198]

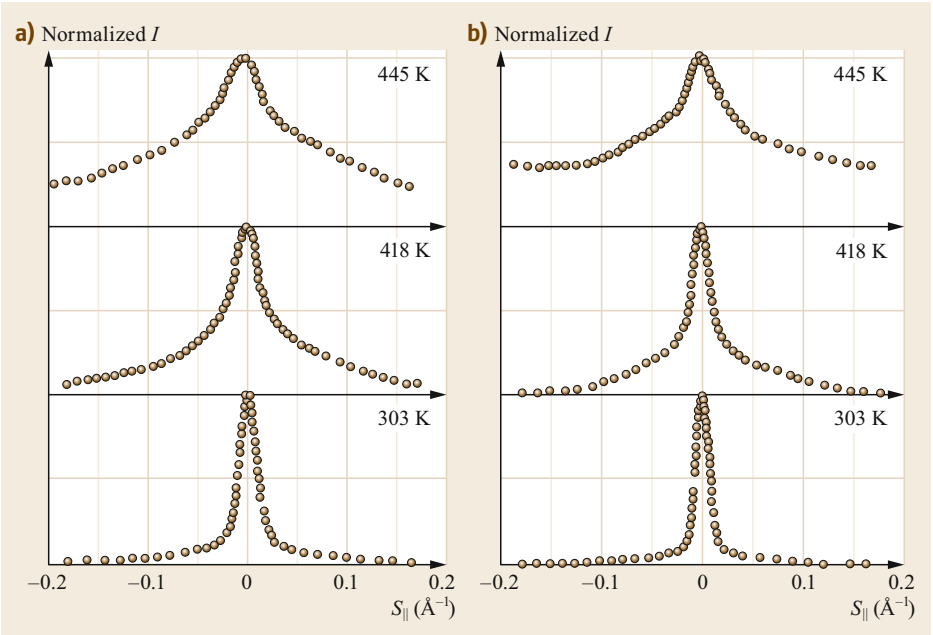

Fig. 1.16a,b Angular profiles of the (00) beam at 303, 418, and 445 K are plotted as a function of the parallel momentum transfer $S_{\|}$ and in out-of-phase condition ($S_{\perp}t = 3\pi$) at an incident energy $E = 27.0$ eV. **(a)** In [001] azimuth; **(b)** in $[1\bar{1}0]$ azimuth. Reproduced with permission from [1.198]

period of oscillation, the authors deduced that the surface contains single atomic steps with a step height of 1.75 ± 0.05 Å, a value consistent with the bulk value.

The authors also observed the evolution of the peak profiles measured along both the [001] and $[1\bar{1}0]$ directions at different temperatures in the out-of-phase condition shown in Fig. 1.16.

At low temperature the peak shape is sharp; substantial tails were instead observed at 418 K. Since close to the roughening transition, the peak shape is a power law due to the logarithmic behavior of the MSHD, the authors performed an analysis of tails as shown in Fig. 1.17 where the intensity is plotted as a function of the momentum exchange. The slope $\tau = -1$ is reached at about 415 K, hence they set $T_R \approx 415$ K.

Landa et al. performed a molecular dynamics simulation of Pb(110). They considered a semi-infinite system modeled by means of a slab of Pb atoms interacting through a many-body glue potential [1.48]. The simulations showed that the Pb(110) surface started to disorder through the excitation of adatom–vacancy pairs in the temperature range between 320 and 360 K. Up to 400 K, adatoms were isolated, but just above 400 K they formed small clusters of 2–3 atoms. With a further increase to 450 K, the authors observed clusters formed by 10–20 atoms and they identified this type of behavior with the roughening transition. With further increases in temperature, the Pb(110) surface disorders by step formation, first along the $[1\bar{1}0]$ direction and then along [001] direction. The exact transition temperature was estimated by the authors mapping their solid–gas interface model to an anisotropic 6-vertex solid-on-solid BCSOS model. As shown in Sect. 1.2, by using (1.4), the authors estimated $T_R = 436$ K, not far from the experimental value.

Al(110)

Schwarz et al. studied the dependence of Al(110) structure on the temperature by means of low-energy electron diffraction [1.200]. The study was performed between 100 and almost 900 K. The authors observed a sinusoidal variation of the FWHM at 300 K due to the presence of steps but this variation deviated from a sinusoid above 500 K. At the same temperature, the ratio of the background to the specular peak intensity showed a gradual increase. Analyzing the peak shape in out-of-phase condition, at low temperature it was well described by a Lorentzian function; instead, closer to the roughening transition, the shape was better represented by a power law whose exponent indicated a roughening temperature at about 550 K along $\langle 1\bar{1}0 \rangle$ and about 650 K along $\langle 001 \rangle$. On average a roughening transition at about 600 K was estimated.

A previous investigation by *Pavlovska* et al. [1.201], although not precisely fixing a value for T_R, concluded that in the range 420–750 K the surface is in a roughening state, accompanied by anharmonic vibrations not only parallel but also normal to the surface. An investigation carried out by *Pedemonte* et al. with ion scattering in backscattering mode provided another indication that supports the roughening transition for Al(110) at about 600 K [1.202].

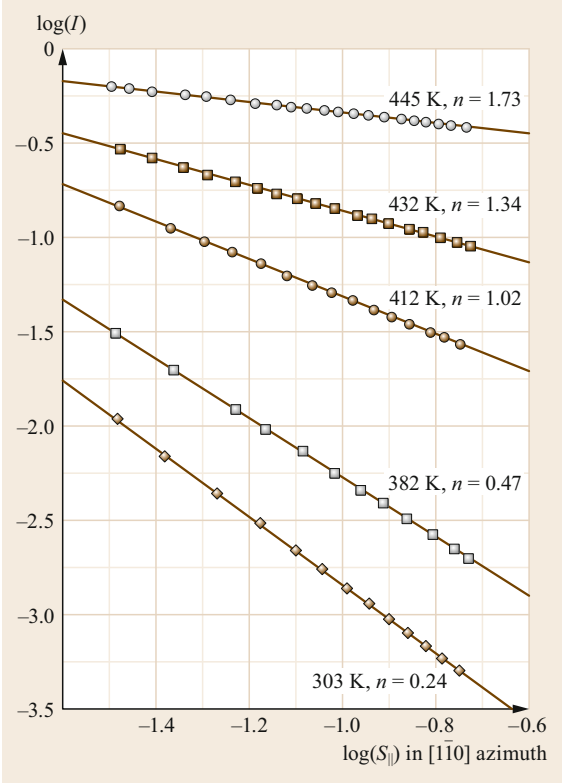

Fig. 1.17 The log–log plots of the tail part of the (00) beam profiles, measured in the $[1\bar{1}0]$ direction and in out-of-phase condition ($S_\perp t = 3\pi$), are shown at different temperatures. The data were taken from 2% to 10% of the Brillouin zone away from the center of the Bragg peak. The slope of the plots is equal to $(2-n)$ and, at roughening, $n = 1$. Similar plots were obtained for profiles measured in the [001] direction. Reproduced with permission from [1.198]

1.10.3 Reconstructed (110) Surfaces

As described in the theoretical part, in these systems two different transitions can be present, deconstruction and roughening, and it was interesting to study the coupling between them, to establish whether they occur at different temperatures, and to determine the universality class to which they belong.

Au(110)

Wolf et al. observed the deconstruction transition between the low-temperature missing-row reconstructed (1×2) to the unreconstructed (1×1) (110) surface of gold Au(110) with LEED at $T_D = 693 \pm 15$ K [1.203]. A few years later, *Campuzano* et al. carried out a detailed study of the deconstruction transition [1.204] investigating the dependence on the temperature half-order peaks related to the reconstructed phase. The sample presented a miscut angle of 0.5° and was carefully prepared. At room temperature the diffraction pattern presented the double periodicity but, for temperatures greater than 700 K, the half-order peaks disappeared and a diffraction pattern related to a primitive (1×1) structure was observed and the peak intensities did not show hysteresis as a function of temperature. Since near a second-order transition, the diffraction peak shape can be separated into two contributions [1.205]

$$I(\delta K, t) = \rho(t)^2 \delta\left(\Delta\boldsymbol{K} - \boldsymbol{G}_{\frac{1}{2}}\right) + \chi\left(\Delta\boldsymbol{K} - \boldsymbol{G}_{\frac{1}{2}}, t\right), \tag{1.45}$$

where $\boldsymbol{G}_{1/2}$ is the reciprocal vector of a half-order diffraction peak for the Au(110)(2×1) and $t = (T - T_D)/T_D$ is the reduced temperature. The first term, related to the long-range order parameter of the transition ρ, mainly contributes to the peak for $T < T_D$ and tends to zero at the transition as $|t|^{2\beta}$, the second term is the only term present above T_D and is related to the susceptibility χ which depends on the order parameter correlation function that diverges at T_D as $t^{-\gamma}$ and whose correlation length diverges as $|t|^{-\nu}$ contributing to the peak width above T_D as $|t|^{\nu}$: β, γ, and ν are the critical exponents of the transition and, through the investigation of the peak shape around T_D, their values can be estimated. In particular, for the two-dimensional Ising universality class of interest for the deconstruction transition, the exponents are $\beta = 1/8$, $\gamma = 7/4$, and $\nu = 1$. The analysis of the half-order peak shape based on (1.45) suggested that the transition indeed belonged to the 2-D Ising class with a deconstruction temperature $T_D = (649.2 \pm 1.5)$ K as shown in Fig. 1.18.

An ion scattering study was performed by *van de Riet* et al. [1.208] in the temperature range 300–900 K. They observed that single vacancy formation started at 530 K and up to 750 K double vacancy contribution was negligible. Above 650 K a background contribution due to the number of steps on the surface also started. The results of an x-ray study performed by *Keane* et al. [1.209] on the temperature dependence of the in-plane superlattice and integral-order surface peaks as well as on the specular reflectivity showed that the deconstruction transition happens at $T_D = 735$ K without an increase of step density and with estimated critical exponents close to 2-D Ising values. Above 784 K there was a significant increase in the density of surface steps that could be related to surface roughening and they estimated the onset in the range 752–784 K. They also observed a systematic shift in the deconstruction temperature: a decrease of 1 K for every four hours the sample temperature was above 700 K. This was interpreted as being caused by contaminants with

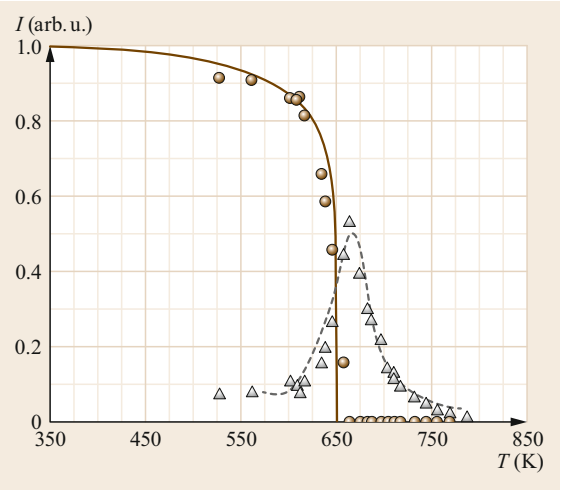

Fig. 1.18 Plot of the diffracted peak intensity measured from Au(110) (*circles*) related to long-range order and *Onsager*'s theoretical result [1.206] (*solid curve*); the fluctuations (*triangles*) and theoretical results by *Fisher* and *Burford* [1.207] (*dashed curve*) are also shown. Reproduced with permission from [1.204]

a coverage below the level of detectability of their Auger analyzer. Sprösser et al. investigated Au(110) with He atom diffraction. The deconstruction temperature was estimated at 650 K and, through a peak shape analysis and assuming the roughening exponent $\tau = 1$, T_R was estimated 740 K. Conversely, since the steps were observed not to be simply monatomic but instead presented a multiple-height distribution, and simulations performed by the authors [1.210] showed that T_R should be about 10% lower than the estimation obtained through the roughening exponent, they assigned T_R at 690 K, the onset temperature for specular broadening. An ion scattering investigation by *Hoss* et al. on the roughening and melting of Au(110) [1.211] reported an anomalous behavior at 680 K and a possible interpretation was the occurrence of a roughening transition. Another ion scattering study was carried out by *Höfner* and *Rabalais* [1.212] to investigate the deconstruction transition. Measurements were performed in the range of 298–720 K and the results of the data analysis showed that features related to the (1×2) reconstruction could still be observed at 720 K, reflecting the unusually high stability of the reconstruction. Another He beam scattering experiment was performed by *Cvetko* et al. [1.213]. The deconstruction was Ising-like and its temperature was estimated at 700 ± 5. An analysis of the peak shape was carried out up to 723 K where the power law shape showed a negative exponent -1.55. Unfortunately, the authors were not able to perform measurements at higher temperatures: in fact the segregation of Ca determined a relatively fast decay of the specular intensity; instead measurements below 725 K were reproducible. Since the exponent was smaller than the expected value at the roughening transition, the authors estimated $T_R > 723$ K.

A study on the specific heat anomalies by *Clark* et al. [1.214] showed that the critical exponents for the deconstruction were consistent with an Ising transition and the estimated critical temperature was $T_D = 695 \pm 3$ K.

Sturmat, *Koch*, and *Rieder* performed an STM investigation of Au(110) in the temperature range 300–700 K [1.215]. Since any real surface presents a miscut, terraces have a finite extension and are separated by steps and the authors observed that those steps became more jagged on increasing the temperature up to T_D. Instead the (1×2) reconstruction was stable above T_D as observed with ion scattering. Therefore, the authors proposed that the Ising transition observed with diffraction techniques was due to the 2-D roughening of the step edges, at higher temperature the (1×2) reconstruction is still present and only at the 3-D roughening transition (≈ 700 K) the surface deconstructs. These results confirmed that there are two transitions at different temperatures but the details of the step evolution involved in the deconstruction are in contrast with the theoretical models. Although some doubts were raised by *Rost* and *Frenken* [1.216] about possible artifacts due to the limited scan speed, the observation of jagged step edges was confirmed by *Koch* and *Schulz* [1.217].

It is interesting to consider the investigation by *McRae* et al. [1.218] on Sn segregation to the (110) surface of a nominally pure Au crystal. The authors carried out experiments with low-energy electron diffraction, Auger electron spectroscopy, and low-energy ion scattering and observed a change of the deconstruction temperature which depended on the Sn coverage. Sn segregated for $T > 675$ K and for a coverage of 0.002 ML T_D decreased by 15 K, while for 0.13 ML the decrease was 200 K. This sensitivity to contamination could be a possible explanation of the spread in the estimated transition temperatures among different experiments, since different samples can contain different amounts of contaminants.

Pt(110)

Robinson, *Vlieg*, and *Kern* investigated Pt(110) with x-ray diffraction [1.81]. The Pt crystal presented a miscut angle of 0.1° and was prepared with treatments in O_2 and annealing to 1200 K to remove C impurities. The peak shape analysis showed that the coherent intensity related to (1×2) reconstruction vanished at 1020 ± 1 K and within 5 K from this transition, the width and position of those peaks started to increase, as shown in

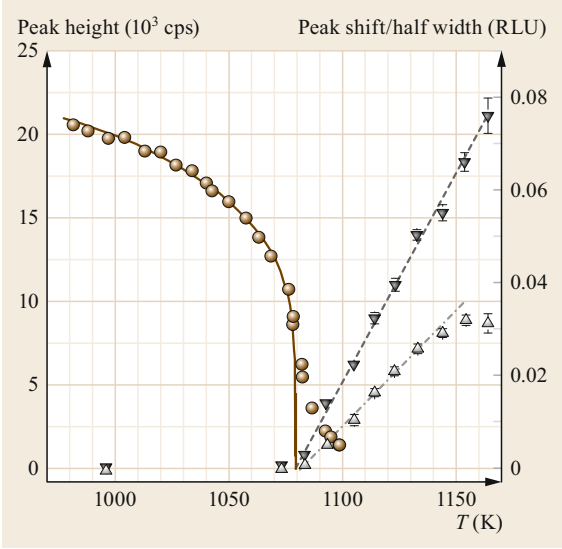

Fig. 1.19 Temperature dependence of the Lorentzian fitting parameters of the Pt(110) radial lineshape measured at $(1.5, 0, 0.06)$: peak height (*circles*) and fit (*solid line*) obtained with $T_D = 1080\,K$ and $\beta = 0.11$. Half-width (*black down triangles*) and its linear fit (*dashed line*); shift (*gray up triangles*) and its linear fit (*dot-dashed line*). Shifts and widths are in reciprocal lattice units (RLU). Drawn from data of [1.81]

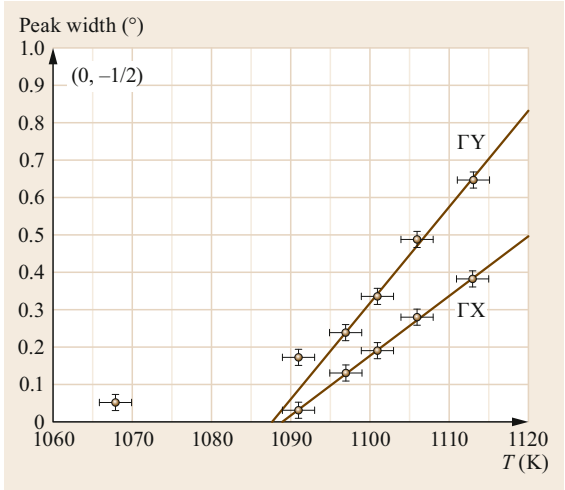

Fig. 1.20 Deconvoluted $(0, -1/2)$ peak width (FWHM) along $\langle 001 \rangle$ (ΓY) and $\langle 1\bar{1}0 \rangle$ (ΓX) directions versus surface temperature. *Full lines* are best fits line with $T_D = 1087 \pm 5\,K$. Reproduced with permission from [1.219]

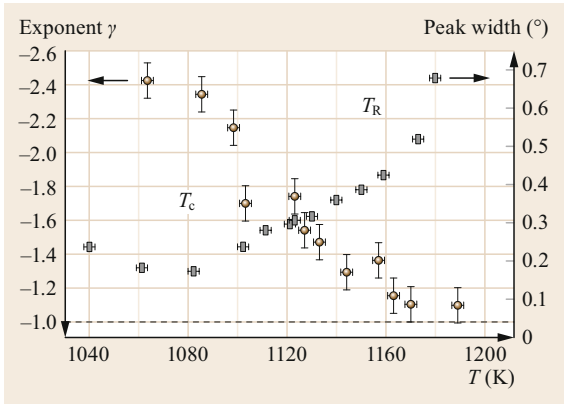

Fig. 1.21 Deconvoluted specular peak width (FWHM) (*gray rectangles*) versus temperature. *Brown circles*: exponent γ from the best fit of the specular tails to the power law, $|\Delta Q|^{-\gamma}$. T_c deconstruction temperature, T_R roughening temperature. Reproduced with permission from [1.219]

Fig. 1.19. Since the shift is in contrast with the expected behavior for an Ising system the authors interpreted this fact as due to spontaneous step formation above the deconstruction transition and hence assumed that the surface is in a rough phase, although they did not perform a fit for establishing that the peak shape is a power-law.

A He scattering study performed by *Cvetko* et al. [1.219] found a different behavior. The deconstruction temperature was estimated at $1087 \pm 5\,K$ and the behavior is consistent with an Ising transition. The broadening of half-integer order peaks (shown in Fig. 1.20) is similar to x-ray results. Conversely, above this temperature, the specular peak broadening is less pronounced than that of the half-integer order peaks and the authors interpreted this difference as due to a density of single steps that increased at a much slower rate than the density of domain walls, therefore single steps are only partially involved in the deconstruction. Moreover, a peak shape analysis up to 1250 K separating elastic from inelastic contributions showed that the specular peak in out-of-phase condition evolved to a power-law shape and the roughening exponent was close to -1 at $1160 \pm 10\,K$, as shown in Fig. 1.21. *Krzyzowski* et al. studied Pt(110)(1×2) with He scattering and electron diffraction [1.220]. They found that the deconstruction transition at $1025 \pm 10\,K$ is consistent with an Ising transition. At higher temperature the analysis of the peak evolution to a power-law shape allowed them to evaluate $T_R = 1095 \pm 20\,K$.

Koch et al. also performed a comparative study of Au(110) and Pt(110) with STM [1.221]. The two surfaces showed a similar behavior for what concerned the presence of the (2×1) reconstruction above the transition at lower temperature due to 2-D roughening of preexisting steps, but with the difference that for Pt there is also a simultaneous formation of islands and holes in the flat terraces.

1.10.4 Vicinal Surfaces

The roughening on metal singular-faces, as (110), requires step formation on a flat step-free surface and a lot of energy is involved in the process, therefore it is foreseen that singular faces roughen at high temperatures close to the melting one. Instead on vicinal metal surfaces a step array is already present and its disordering due to kink formation costs less in energy, therefore the roughening temperature is much lower than the melting temperature: for this reason, experimental studies on vicinal surfaces were in some way easier to perform, but if the temperatures are really low this can impede the attainment of equilibrium conditions.

Cu(113) was investigated by *Salanon* et al. with helium atom diffraction [1.222]. The authors performed a peak shape analysis and estimated $T_R = 720 \pm 50$ K. A previous x-ray study by *Liang* et al. [1.223] estimated a step-roughening transition temperature at (620 ± 10) K only analyzing the vanishing of diffraction peaks. The discrepancy between the two values was explained by the different analysis procedure.

Cu(113) was also investigated by *Wollschläger* et al. with electron diffraction [1.224]. They found a vanishing of the coherent scattering intensity at 750 K but the peak shape was consistent with a linear divergence of MSHD. This linear trend for the correlation function was found also by *Fabre* et al. studying Cu(1 1 11) with He atom diffraction [1.225].

Cu(115) was investigated by *Fabre* et al. with helium atom diffraction [1.226, 227] and through a peak shape analysis roughening was estimated to occur at $T_R = 380$ K. Several years later, *Ernst* et al. [1.228] investigated the thermal roughening with energy-resolved atom diffraction and questioned the previous results for the following points. The first is related to the energy window of the experiment, in fact without energy resolution they obtained results compatible with those of Fabre et al. with a $T_R = 420$ K, but reducing the inelastic contributions the estimated temperature became $T_R > 700$ K. The second point is related to the form of the MSHD, which is logarithmically divergent at long range, but at short range must present a lower cutoff to regularize its behavior, therefore two different lengths must be compared: the transfer width of the experiment and the length where there is the crossover between short- and long-range behavior. In order to observe the logarithmic behavior, the transfer width must be larger than the crossover position. Moreover, the position of the crossover poses also the requirement on a third length: the linear size of domains on the surface must be larger than the crossover position. A more recent study was carried out by *Le Goff* et al. with STM and x-ray diffraction on Cu(115) and copper alloys [1.229]. For bare Cu(115), through a comparison with Monte Carlo simulations a roughening temperature was estimated at 380 K, a value supported also by the analysis of x-ray data, confirming the first estimate.

Ni(113) was investigated by *Conrad* et al. with energy-resolved He scattering [1.230, 231] and through a lineshape analysis the estimated temperature value was $T_R = 750 \pm 50$ K. These results were also confirmed by *Robinson* et al. with x-ray diffraction [1.232]. The authors performed a detailed analysis of the peak shape and found $T_R = 770 \pm 30$ K.

Ni(115) was investigated by *Conrad* et al. and a roughening temperature of 450 ± 50 K was estimated [1.233].

Ni(117) was investigated by *Blanchard* et al. and they estimated $T_R = 400 \pm 50$ K [1.234].

Ag(115) was investigated by *Hoogeman* et al. with STM [1.88, 235, 236]. The authors performed a direct measurement of the height correlation function on the acquired images and initially found a linear behavior of MSHD which was in agreement with the results on other vicinal surfaces described above. Conversely, the authors observed that the MSHD did not rise monotonically with temperature. A detailed study showed that on a large scale the surface was not perfectly flat, therefore the supposed (115) surface had an orientation that varied around (115) and the authors estimated a temperature-independent root-mean-square deviation of 0.20°. These residual variations in surface orientation are the main contributions to the estimated MSHD masking the true temperature-dependent roughness involved in the roughening transition. They developed a pattern recognition procedure based on the crystallographic information of the possible step heights and step distances on Ag(115): the algorithm selected small regions of the full image and was demonstrated to be insensitive to statistical noise and to bad resolution of the STM tip. The procedure used one-dimensional windows, smaller than that of the full image, and accepted only positions where the scan line had the same height at the beginning and at the end of the window. By employing this procedure the expected logarithmic behavior was recovered. The authors also commented that the equal-height condition was similar to periodic boundary conditions in computer simulations. To further support their procedure, the authors performed Monte Carlo simulations to mimic the selection procedure [1.89] and the results showed that deviations of T_R were less than 2% from the prediction of the TLK model [1.88]. The estimate roughening temperature was $T_R = 465 \pm 25$ K from the analysis of STM images and 423 ± 6 K from the simulations.

1.10.5 Other Systems

The (111) surfaces of fcc metals are very stable [1.237]: calculations show that the roughening does not happen below the melting of the crystal [1.238] and in fact they have not been observed to roughen. An investigation performed by *Pluis* et al. on Pb with ion scattering showed that the (111) surface retains its order up to the melting [1.239]. The single exception is Al(111) for which calculations performed by *Trudu* et al. and based on embedded-atom interactions [1.240] set the roughening at 890 K, well below the bulk melting value of 933 K.

For the (100) surface of fcc metals the situation is not so clear and could depend on the system. For Cu(100), the observation on 2-mm size crystals supported on graphite stripes [1.157] suggests that in this case (100) is stable up to melting. Moreover, as noted before for the Cu(110) case, He diffraction experiments [1.159] showed that the specular peak from Cu(100) is measurable up to 1273 K ($\approx 0.93 T_M$) and the authors commented that the surface retains some order up to the highest temperature measured.

Yang et al. studied Pb(100) using high-resolution low-energy electron diffraction [1.241]. They observed an anomalous surface expansion below 480 K and a sudden proliferation of vacancies between 480 and 540 K, with an increase of $(20 \pm 5)\%$ from room temperature to 530 K. For both the out-of-phase and in-phase diffraction conditions, the peak shape analysis did not show changes or broadening due to steps up to 5 K from T_M. Hence Pb(100) was not observed to roughen.

Conversely, *Abernathy* et al. [1.242] performed an x-ray scattering study on Pt(001) which shows a hexagonal reconstruction. The sample was a Pt disk with a mosaic of 0.01° full-width at half-maximum (FWHM) and a miscut angle of 0.06° away from the crystallographic (001) plane. The sample was treated with procedures yielding a surface that remained clean at elevated temperatures for extended periods of time. The authors observed that the surface morphology below 1820 K is atomically smooth. However, above 1820 K, the Pt(001) surface is unreconstructed and rough. The coherent x-ray scattering experiments by *Pierce* et al. [1.243] on Pt(001) provide a further support to previous results and the analysis of the data showed that $T_R = 1834$ K similarly to the previous estimation.

Au(001) presents a reconstruction similar, but not identical, to Pt(001) [1.244, 245]. Even for what concerns roughening, the x-ray reflectivity investigation by *Gibbs* et al. [1.246] and coherent x-ray scattering study by *Pierce* et al. [1.243, 247] did not support the occurrence of a roughening transition on Au(001).

Roughening of In, which presents a face-centered tetragonal structure, i.e., a distorted fcc structure, was investigated by *Métois* and *Heyraud* [1.248] and by *Pavlovska* et al. [1.249]. Both groups observed microcrystals with electron microscopy and T_R was determined for a few faces. The temperature determined by the two groups agrees within a few K for {113} ($T_R = 373$ K [1.248], $T_R = 375$ K [1.249]), in reasonable agreement for {110} ($T_R = 283$ K [1.248], $T_R < 305$ K [1.249]), with a larger discrepancy for {311} ($T_R = 317$ K [1.248], $T_R = 355$ K [1.249]) and {011} ($T_R = 293$ K [1.248], $T_R = 345$ K [1.249]). One year later, *Georgiev* et al. [1.250] performed low-energy electron diffraction studies of In(100) and In(110) surfaces. For (100), as expected from the results on microcrystals, the specular peak shape did not change almost up to T_M. In the case of (110) the specular peak shape behaves in a way similar to (100); hence, in contrast with the results based on the macroscopic disappearance of (110), the results of microscopic observations of the (110) disordering show that this occurs without any evidence of roughening. The authors suggested that this behavior is due to anharmonic vibrations and a high density of adatoms and vacancies. In a study of In(111), *Lin* et al. [1.251] observed creation of vacancies and adatoms but no step roughness was detected up to 426 K.

Pavlovska et al. also investigated Sn microcrystals [1.249] and for several surfaces a roughening temperature was estimated below the melting temperature.

Roughening of Ta was investigated by *Vanselow* and *Li* [1.252] on vicinal areas of (110) and (100) surfaces with field-emission microscopy. They carried out growth studies on Ta crystallites at different temperatures and observed a transition with an increase in growth rate, as predicted by roughening theories.

Systems different from metals were also studied, including He and the systems mentioned in the introduction, C_2Cl_6, NH_4Cl, and tetrabromomethane.

Ohachi and *Taniguchi* investigated the roughening of bcc α-Ag_2S [1.253]. The observation of the sample in a transparent furnace allowed them to follow the evolution of the faceting of the crystal at different temperatures. For (110) surfaces T_R was estimated at 853 K and, for (100), at 753 K.

The roughening in rare gas crystals different from He was also investigated. *Maruyama* investigated Xe and Kr [1.254] by an apparatus that worked in a constant-temperature cryostat. A vacuum jacket surrounded the cell and this part was immersed in liquid nitrogen. The cell, inside the jacket, was made of two copper parts: an upper copper block and a lower copper substrate with the substrate thermally insulated by the copper block. At the beginning of the experiment, the cell was pumped and when the required temperature was reached, the cell was filled with the sample gas. The crystals were grown decreasing the temperature of the

substrate below the block temperature: crystals grown on the block sublimated behaving as a source of gas for those grown on the substrate, with a supersaturation given by $s = P_B(T_B)/P_S(T_S) - 1$, where P_B is the vapor pressure at the temperature of the block T_B and P_S is the vapor pressure at temperature of the substrate T_S. For Xe at 114 K and $s = 0.4°$, facet crystals grew and both the (111) and (100) facets were observed. At 125 K and $s = 0.7°$, both facets and curved surfaces appeared. At an estimated temperature of 129 K, all the crystals are bounded by curved surfaces. Since this shape could be related to supercooled liquid droplets, the author described some facts that indicated that those curved samples actually were solid. For Kr, the behavior was similar to that of Xe and the estimated temperature, at which the crystal was observed bounded by curved surfaces, was 93 K. Of course this investigation, although semiquantitative since it did not give an estimate of the roughening temperature for each facet separately, suggests that, on these rare gas systems, (111) facets do not survive up to the melting of crystal.

Pontikis and *Rosato* performed a molecular dynamics study of the (110) surface of Ar [1.255, 256]. They observed an increase of the vacancy-adatoms pairs above $0.7T_M$ and by using this value they estimated a roughening transition at about 58 K for Ar(110).

More recent experiments on multilayer films of Ar, Kr, and Xe on graphite [1.117, 119, 257] showed intriguing behaviors related to preroughening and its connections with surface melting (this will be briefly commented upon at the end of this section). The film growth proceeds layer-by-layer and a first-order transition is present as observed in adsorption isotherms, where at each completion of a layer steps appear: this layering transition terminates at a layering critical temperature $T_c(n)$ which depends on the number of layers n. Above this critical temperature, the film grows in a continuous way and atoms are present at layer $n+1$, $n+2$ etc. a situation similar to the rough phase, in fact it was suggested that the limit of $T_c(n)$ for increasing n is the roughening temperature of the exposed face of the 3-D crystal [1.258]. *Youn* and *Hess* [1.119] performed ellipsometric adsorption isotherm measurements to investigate the layering transitions of Ar films on graphite and found $T_c(2) = 69.4 \pm 0.2$ K, $T_c(3) = 67.6 \pm 0.2$ K while, at higher temperatures, the layering steps disappeared. This first part was consistent with results already present in the literature [1.259, 260] with an estimate for the roughening of Ar(111) at $T_R = 68$ K, but, for a further increase of the temperature, Youn and Hess observed that the steps reappeared for $T > 70$ K and persisted up to 77 K and they named this phenomenon *reentrant layering*. Moreover, the reentrant steps in isotherms were not aligned with the previous steps but happened in between, in a position corresponding to half of a layer. Of course this finding poses the question about the nature of the second transition. Other measurements by *Day* et al. [1.261] and by *Larese* and *Zhang* [1.262] confirmed these results. From the analysis of the phase diagram, on one hand the transition was interpreted as a signature of a preroughening transition with the surface layer in a disordered flat phase, while on the other hand it pointed to a possible relationship of this transition with a liquid phase at the outermost layer.

The growth of Ar thick films on single-crystal MgO was investigated with x-ray reflection by *Rieutord* et al. [1.263]. At 70 K, in a reproducible way, they observed a jump in the total thickness which corresponded to half a layer, consistent with Youn and Hess' results for films grown on graphite, therefore this is a property of the film. Moreover, the authors performed measurements of the peak shape and no evidence for a divergent MSHD was found therefore the transition was not a roughening transition. Finally, reflectivity data could not be fitted at every temperature with a one-layer description but with a two-layer description which the authors assigned to correspond to the liquid and solid parts of the film. These results therefore supported the idea that the surface melting starts with a preroughening transition.

Si(100) was investigated by *Bartelt* et al. with low-energy electron microscopy (LEEM) [1.264]. The authors studied in real-time equilibrium step fluctuations at different temperatures obtaining an estimate of the step free energy that vanishes at 1473 K. Since at 1443 K, the sublimation rate is about 0.12 ML/s, the transition could be a kinetic roughening but the authors observed an increase of step fluctuations already at 1373 K, where sublimation is very small, supporting a thermodynamic origin of the surface roughening observed at higher temperature.

The equilibrium crystal shape of silicon was investigated by *Bermond* et al. with electron microscopy [1.266]. The (111) surface was present up to $T = 1673$ K, 13 K lower than T_M. The roughening temperatures in equilibrium experiments were evaluated as 1643 K for (110) and 1613 K for (113). Similar studies were performed by *Suzuki* et al. [1.267] on high-index surfaces. A study of Si(331) was performed by *Noh* et al. with x-ray scattering experiments [1.268]. The analysis of diffraction peaks indicated the occurrence of roughening at (1075 ± 10) K in good agreement with the estimated value by *Suzuki* et al. [1.267], but these results were not completely confirmed by an STM study performed by *Hibino* and *Ogino* [1.269].

Roughening of H_2O ice was studied by *Elbaum* [1.270] who observed the transition on the prism facet $\{10\bar{1}0\}$ at 271 K while the basal facet {0001} per-

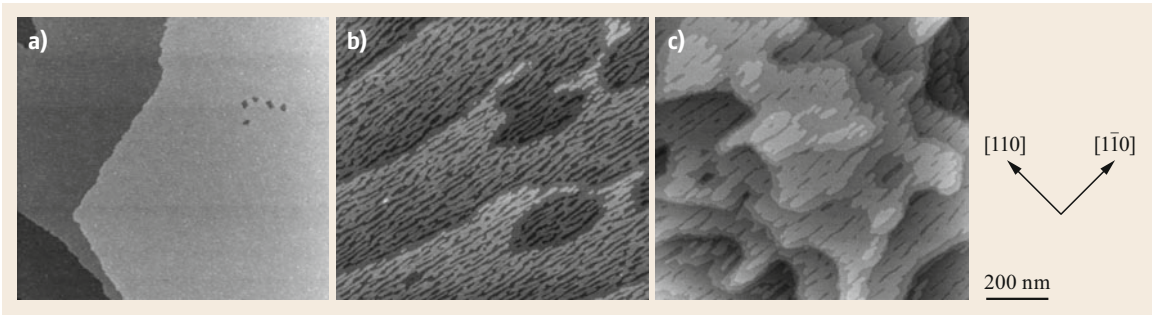

Fig. 1.22a–c Three 1 μm × 1 μm filled-state STM images of the GaAs(001) surface prepared under different annealing conditions. **(a)** Ordered flat (783 K and 0.03 μTorr As_4), **(b)** disordered flat (838 K and 0.03 μTorr As_4) showing single level islands, **(c)** rough (878 K and 0.03 μTorr As_4) showing multilevel islands. Reprinted figure with permission from [1.265]. Copyright 2003 by the American Physical Society

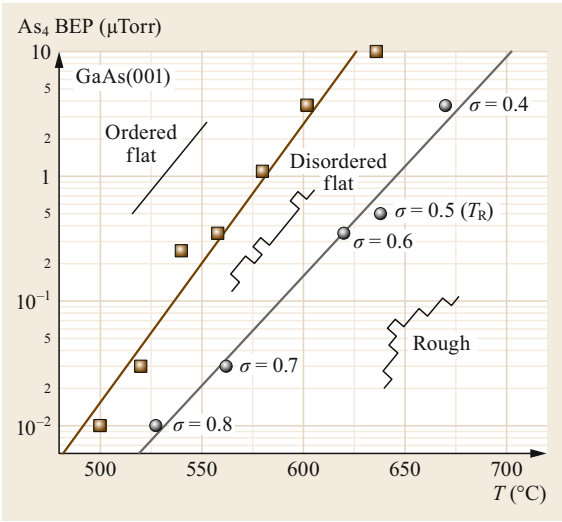

Fig. 1.23 Phase diagram of a GaAs(001) (2 × 4) reconstructed surface prepared under different annealing conditions and As_4 beam equivalent pressures (BEP). The *brown line* with *squares* is the boundary of ordered flat and disordered flat phases. To the left of this line, the coverage of islands is zero. The *brown line* with *circles* is the transition boundary between disordered flat and rough phases. For this line the data points are also labeled with the island coverage reached just prior to roughening. Notice that the coverage just before roughening varies from 80–40% as the substrate temperature is increased. Reproduced with permission from [1.265]

sisted until melting. *Maruyama* performed a study at high pressure [1.271] and measured the roughening of the prism facet at $T_R = 257$ K for H_2O at 160 MPa and $T_R = 259$ K for D_2O at 180 MPa; even in this case, the basal plane was stable up to 273 K.

Ionic crystals of NaCl were studied by *Lampert* and *Reichelt* [1.272] and a roughening temperature was estimated between 898 and 948 K. *Heyraud* and *Métois* [1.273] showed that for $T \leq 923$ K the NaCl crystal is bounded by sharp facets, while above 923 K the facets started to become rounded. *Arsic* et al. studied cesium halide crystals in saturated aqueous solution droplets and in the temperature range from 275 to 344 K [1.274]. For cesium bromide, a roughening temperature $T_R = 278 \pm 1$ K was estimated.

Finally, although outside the scope of the present chapter, we would also like to mention the roughening of grain boundaries which are important for technological applications. For example, roughening influences the mobility of grain boundaries in the process of their removal [1.275]. More information on this topic can be found in the review by *Straumal* et al. [1.276].

To conclude this experimental section, we briefly consider again the preroughening transition. A striking evidence of this transition was obtained in real space for GaAs(001) by *Ding* et al. with STM [1.265]. The samples were prepared by annealing at fixed temperature in the range 773–973 K for a time that assured equilibrium conditions and in a fixed As_4 flux. Then the samples were cooled to room temperature following by a procedure that froze-in the surface morphology present at higher temperatures and images acquired at three different annealing temperatures are shown in Fig. 1.22 where the different morphologies of the surface are clear. Modifying the annealing temperatures and the As_4 flux a phase diagram was determined and is shown in Fig. 1.23.

The surface at low temperature and high flux is in the flat phase, increasing the temperature (and/or decreasing the flux) the surface undergoes a preroughening transition to a disordered flat phase and, then, for higher temperatures, to a rough phase.

In the study of the various systems, a roughening transition was not always observed but sometimes there was only an increase of adatom–vacancy pairs. This

could be a signature of a preroughening transition as observed by *Tosatti* and coworkers [1.114, 115] who discussed a relationship between surface melting and preroughening, where initial melting phenomena determine a preroughening behavior, thus explaining the results of experiments on multilayer films of rare gases on graphite. They also suggested a similar interpretation for the behavior of Pb(100) and Au(100).

1.11 Conclusions: Growth

As we have discussed in the present chapter, roughening was an interesting application of statistical mechanics to solids. The roughening transition is an infinite-order phase transition, and is one of the most evident examples of a Kosterlitz–Thouless transition. Most of the theoretical predictions have been satisfactorily verified experimentally. An equally important point (and more relevant, even today, for practical applications) is the relation between roughening and the surface growth mode. Indeed, the bulk of the experimental work on the roughening transition to study mechanism and temperatures was done in the 1990s, but the results are still important today for the growth of bulk or nanostructured materials. For an extensive discussion of growth modes, see the classical work of *Weeks* and *Gilmer* [1.90]; see also *Levi* et al. [1.91, 92]. Although the distinction is not sharp, it is clear that a smooth surface tends preferentially to grow in the layer growth mode, where a layer is completed locally before a new layer is started above it, and there is a bottleneck: the nucleation of 2-D islands. Conversely, a rough surface tends to grow in the continuous, or 3-dimensional growth mode, where atoms may stick anywhere, forming hillocks. These two modes are completely different, with the consequence that the transition, which in equilibrium is an extremely weak, Kosterlitz–Thouless transition, dynamically involves a dramatic change. In Sect. 1.6 we have briefly discussed the problems of kinetic roughening, which appear to be very relevant from the present point of view and may give rise to the vast set of phenomena discussed in the reviews by *Halpin-Healy* and *Zhang* [1.96] and by *Misbah* et al. [1.5].

References

1.1 W.K. Burton, N. Cabrera, F.C. Frank: The growth of crystals and the equilibrium structure of their surfaces, Philos. Trans. R. Soc. A **243**(866), 299 (1951)

1.2 N. Akutsu, T. Yamamoto: Rough–smooth transition of step and surface. In: *Handbook of Crystal Growth*, 2nd edn., ed. by T. Nishinaga (Elsevier, Amsterdam 2015) p. 265

1.3 T.L. Einstein: Equilibrium shape of crystals. In: *Handbook of Crystal Growth*, 2nd edn., ed. by T. Nishinaga (Elsevier, Amsterdam 2015) p. 215

1.4 H. Taub, G. Torzo, H.J. Lauter, S.C. Fain Jr. (Eds.): *Phase Transitions in Surface Films 2* (Plenum, New York 1990)

1.5 C. Misbah, O. Pierre-Louis, Y. Saito: Crystal surfaces in and out of equilibrium: A modern view, Rev. Mod. Phys. **82**, 981 (2010)

1.6 D.P. Woodruff: How does your crystal grow? A commentary on Burton, Cabrera and Frank (1951) 'The growth of crystals and the equilibrium structure of their surfaces', Philos. Trans. R. Soc. A **373**, 20140230 (2015)

1.7 F.C. Frank: The geometrical thermodynamics of surfaces. In: *Metal Surfaces: Structure, Energetics And Kinetics* (American Society for Metals, Metals Park 1963) p. 1

1.8 A. Zangwill: *Physics at Surfaces* (Cambridge Univ. Press, Cambridge 1988)

1.9 C. Herring: The use of classical macroscopic concepts in surface-energy problems. In: *Structure and Properties of Solid Surfaces*, ed. by R. Gomer, C.S. Smith (Univ. of Chicago Press, Chicago 1953) pp. 5–18

1.10 M. Bienfait: Roughening and surface melting transitions: Consequences on crystal growth, Surf. Sci. **272**(1), 1 (1992)

1.11 M. Wortis: Conference summary: Where from? Where to? In: *Phase Transitions in Surface Films 2*, ed. by H.J. Lauter, H. Taub, G. Torzo, S.C. Fain (Plenum, New York 1990) p. 471

1.12 H. van Beijeren, I. Nolden: The roughening transition. In: *Structure and Dynamics of Surfaces II: Phenomena, Models, and Methods*, Topics in Current Physics, ed. by W. Schommers, P. von Blanckenhagen (Springer, Berlin, Heidelberg 1987) p. 259

1.13 J. Lapujoulade, B. Salanon: The roughening transition on surfaces. In: *Phase Transitions in Surface Films 2*, ed. by H.J. Lauter, H. Taub, G. Torzo, S.C. Fain (Plenum, New York 1990) p. 217

1.14 R.L. Dobrusin: Gibbs states describing a coexistence of phases for the three-dimensional Ising model, Theor. Probl. Appl. (USSR) **17**(4), 582–600 (1972)

1.15 G. Gallavotti: The phase separation line in the two-dimensional Ising model, Commun. Math. Phys. **27**(2), 103 (1972)

1.16 H. van Beijeren: Interface sharpness in the Ising system, Commun. Math. Phys. **40**(1), 1 (1975)

1.17 H. van Beijeren: Exactly solvable model for the roughening transition of a crystal surface, Phys. Rev. Lett. **38**, 993 (1977)

1.18 J.M. Kosterlitz, D.J. Thouless: Ordering, metastability and phase transitions in two-dimensional systems, J. Phys. C **6**(7), 1181 (1973)

1.19 J.M. Kosterlitz: Kosterlitz–Thouless physics: A review of key issues, Rep. Prog. Phys. **79**(2), 026001 (2016)
1.20 S.T. Chui, J.D. Weeks: Phase transition in the two-dimensional Coulomb gas, and the interfacial roughening transition, Phys. Rev. B **14**, 4978 (1976)
1.21 T.H. Berlin, M. Kac: The spherical model of a ferromagnet, Phys. Rev. **86**, 821 (1952)
1.22 R.J. Baxter: *Exactly Solved Models in Statistical Mechanics* (Academic Press, London 1953)
1.23 C.N. Yang, C.P. Yang: One-dimensional chain of anisotropic spin–spin interactions. I. Proof of Bethe's hypothesis for ground state in a finite system, Phys. Rev. **150**, 321 (1966)
1.24 C.N. Yang, C.P. Yang: One-dimensional chain of anisotropic spin–spin interactions. II. Properties of the ground-state energy per lattice site for an infinite system, Phys. Rev. **150**, 327 (1966)
1.25 C.N. Yang, C.P. Yang: One-dimensional chain of anisotropic spin–spin interactions. III. Applications, Phys. Rev. **151**, 258 (1966)
1.26 E.H. Lieb: Residual entropy of square ice, Phys. Rev. **162**, 162 (1967)
1.27 E.H. Lieb: Exact solution of the *F* model of an antiferroelectric, Phys. Rev. Lett. **18**, 1046 (1967)
1.28 E.H. Lieb: Exact solution of the two-dimensional slater KDP model of a ferroelectric, Phys. Rev. Lett. **19**, 108 (1967)
1.29 F.Y. Wu: Exactly soluble model of the ferroelectric phase transition in two dimensions, Phys. Rev. Lett. **18**, 605 (1967)
1.30 B. Sutherland: Exact solution of a two-dimensional model for hydrogen-bonded crystals, Phys. Rev. Lett. **19**, 103 (1967)
1.31 B. Sutherland: Correlation functions for two-dimensional ferroelectrics, Phys. Lett. A **26**(11), 532 (1968)
1.32 P.J. Forrester: Exact calculation of the local height probabilities in the body-centred SOS model, J. Phys. A **19**(3), L143 (1986)
1.33 A.C. Levi, R. Spadacini, G.E. Tommei: Atom scattering from a Markovian bcc(001) surface. In: *The Structure of Surfaces II*, ed. by J.F. van der Veen, M.A. van Hove (Springer, Berlin, Heidelberg 1988) p. 530
1.34 R. Youngblood, J.D. Axe, B.M. McCoy: Correlations in ice-rule ferroelectrics, Phys. Rev. B **21**, 5212 (1980)
1.35 T. Ohta, K. Kawasaki: Renormalization group theory of the interfacial roughening transition, Prog. Theor. Phys. **60**(2), 365 (1978)
1.36 J.M. Kosterlitz: The critical properties of the two-dimensional xy model, J. Phys. C **7**, 1046 (1974)
1.37 P. Nozières, F. Gallet: The roughening transition of crystal surfaces. I. Static and dynamic renormalization theory, crystal shape and facet growth, J. Phys. France **48**(3), 353 (1987)
1.38 K.A. Jackson, C.E. Miller: Experimental observation of the surface roughening transition in vapor phase growth, J. Cryst. Growth **40**(2), 169 (1977)
1.39 D. Nenow: Surface premelting, Prog. Cryst. Growth Charact. **9**(3), 185 (1984)
1.40 J.E. Avron, L.S. Balfour, C.G. Kuper, J. Landau, S.G. Lipson, L.S. Schulman: Roughening transition in the ^{4}He solid–superfluid interface, Phys. Rev. Lett. **45**, 814 (1980)
1.41 S. Balibar, B. Castaing: Possible observation of the roughening transition in helium, J. Phys. Lett. **41**(14), 329 (1980)
1.42 S. Balibar, B. Castaing: Helium: Solid–liquid interfaces, Surf. Sci. Rep. **5**(3), 87 (1985)
1.43 K.O. Keshishev, A.Y. Parshin, A.B. Babkin: Crystallization waves in He^4, Sov. Phys. JETP **53**(2), 362 (1981)
1.44 J.C. Heyraud, J.J. Métois: Equilibrium shape and temperature; Lead on graphite, Surf. Sci. **128**(2–3), 334 (1983)
1.45 J.C. Heyraud, J.J. Métois: Surface free energy anisotropy measurement of indium, Surf. Sci. **177**(1), 213 (1986)
1.46 M. Touzani, M. Wortis: Simple model for the equilibrium shape of ^{4}He crystals, Phys. Rev. B **36**, 3598 (1987)
1.47 A. Trayanov, A.C. Levi, E. Tosatti: Missing-row roughening of (110) surfaces, Europhys. Lett. **8**(7), 657 (1989)
1.48 F. Ercolessi, E. Tosatti, M. Parrinello: Au (100) surface reconstruction, Phys. Rev. Lett. **57**, 719 (1986)
1.49 F. Ercolessi, M. Parrinello, E. Tosatti: Simulation of gold in the glue model, Philos. Mag. A **58**(1), 213 (1988)
1.50 B.E. Hayden, K.C. Prince, P.J. Davie, G. Paolucci, A.M. Bradshaw: Alkali metal-induced reconstruction of Ag(110), Solid State Commun. **48**(4), 325 (1983)
1.51 M. Copel, W.R. Graham, T. Gustafsson, S. Yalisove: Ion scattering study of the lithium induced reconstruction of Cu(110), Solid State Commun. **54**(8), 695 (1985)
1.52 C.J. Barnes, M.Q. Ding, M. Lindroos, R.D. Diehl, D.A. King: A LEED structural study of the Pd110-(1×1) surface and an alkali-metal-induced (1×2) surface reconstruction, Surf. Sci. **162**(1), 59 (1985)
1.53 Z.P. Hu, B.C. Pan, W.C. Fan, A. Ignatiev: Structure analysis of the Cu(110)-(1×2) surface reconstruction induced by alkali-metal adsorption, Phys. Rev. B **41**, 9692 (1990)
1.54 C. Jayaprakash, W.F. Saam: Thermal evolution of crystal shapes: The fcc crystal, Phys. Rev. B **30**, 3916 (1984)
1.55 W.J. Shugard, J.D. Weeks, G.H. Gilmer: Monte Carlo test of theories for the planar model, the *F* model, and related systems, Phys. Rev. Lett. **41**, 1399 (1978)
1.56 A. Trayanov, A.C. Levi, E. Tosatti: Anisotropic roughening theory of the (110) faces of Cu, Ni, Pd, and Ag, Surf. Sci. **233**(1), 184 (1990)
1.57 G. Mazzeo, G. Jug, A.C. Levi, E. Tosatti: Monte Carlo study of phase transitions and scattering intensities in a model of Au(110), Surf. Sci. **273**(1), 237 (1992)
1.58 G. Mazzeo, G. Jug, A.C. Levi, E. Tosatti: Sublattice order parameter in the BCSOS model: A finite-size Monte Carlo study, J. Phys. A **25**(15), L967 (1992)
1.59 G. Mazzeo: *A Model of Surface Reconstruction and Roughening: A Monte Carlo Study*, Magister Thesis (SISSA, Trieste 1990)

1.60 G. Mazzeo: *Interplay Between Surface In-Plane Ordering and Roughening*, Ph.D. Thesis (SISSA, Trieste 1992)

1.61 M. Bernasconi: *On Deconstruction and Roughening Phase Transitions on Au(110) and Pt(110) Surfaces*, Magister Thesis (SISSA, Trieste 1991)

1.62 K. Rommelse, M. den Nijs: Preroughening transitions in surfaces, Phys. Rev. Lett. **59**, 2578 (1987)

1.63 M. den Nijs, K. Rommelse: Preroughening transitions in crystal surfaces and valence-bond phases in quantum spin chains, Phys. Rev. B **40**, 4709 (1989)

1.64 A.C. Levi, M. Touzani: The Au(110) surface described by interacting 6-vertex models, Surf. Sci. **218**(1), 223 (1989)

1.65 J.M. Luck: Finite-size lattice method and the roughening transition, J. Phys. Lett. **42**, 275 (1981)

1.66 J. Kohanoff, G. Jug, E. Tosatti: Interplay between Ising and six-vertex symmetries in a model for the roughening of reconstructing surfaces, J. Phys. A **23**(23), 5625 (1990)

1.67 J. Kohanoff, G. Jug, E. Tosatti: A model for the roughening of reconstructed surfaces: Finite-size study and phase diagram, J. Phys. A **23**, L209 (1990)

1.68 J. Villain, I. Vilfan: Surface deconstruction of Au(110), Surf. Sci. **199**(1), 165 (1988)

1.69 I. Vilfan, J. Villain: Phase transitions on reconstructed (110) surfaces, Surf. Sci. **257**(1), 368 (1991)

1.70 I. Vilfan, J. Villain: Comment on "Non-Ising behavior of the Pt(110) surface phase transition", Phys. Rev. Lett. **65**, 1830 (1990)

1.71 J. Villain, I. Vilfan: A roughening transition with $a = 1/2$ and upper critical dimension 4, Europhys. Lett. **12**(6), 523 (1990)

1.72 J. Villain, I. Vilfan: A roughening transition with $\alpha = 1/2$ and upper critical dimension 4, Europhys. Lett. **12**(8), 741 (1990)

1.73 J. Villain, I. Vilfan: A roughening transition with $\alpha = 1/2$ and upper critical dimension 4, Europhys. Lett. **13**(3), 285 (1990)

1.74 J. Villain, J.L. Rouviere, I. Vilfan: Phenomenology of surface reconstruction. In: *Phase Transitions in Surface Films 2*, ed. by H. Taub, G. Torzo, H.J. Lauter, S.C. Fain (Plenum, New York 1990) p. 201

1.75 M. Bernasconi, E. Tosatti: Reconstruction, disordering and roughening of metal surfaces, Surf. Sci. Rep. **17**(7), 363 (1993)

1.76 M. den Nijs: Preroughening of crystal surfaces and energy differences between inside and outside corners, Phys. Rev. Lett. **64**, 435 (1990)

1.77 M. den Nijs: Preroughening of crystal surfaces and energy differences between inside and outside corners, Phys. Rev. Lett. **64**, 435 (1990)

1.78 M. den Nijs: Roughening-induced deconstruction in (110) facets of fcc crystals, Phys. Rev. Lett. **66**, 907 (1991)

1.79 M. den Nijs: Interplay between surface roughening, preroughening, and reconstruction. In: *Phase Transitions in Surface Films 2*, ed. by H.J. Lauter, H. Taub, G. Torzo, S.C. Fain (Plenum, New York 1990) p. 247

1.80 K. Kern, I.K. Robinson, E. Vlieg: The high temperature phase transition of Pt(110) (1×2), Vacuum **41**(1), 318 (1990)

1.81 I.K. Robinson, E. Vlieg, K. Kern: Structure and roughening of the Pt(110) surface, Faraday Discuss. Chem. Soc. **89**, 159 (1990)

1.82 E.E. Gruber, W.W. Mullins: On the theory of anisotropy of crystalline surface tension, J. Phys. Chem. Solids **28**(5), 875 (1967)

1.83 E. Carlon, H. van Beijeren: Networks of steps on crystal surfaces, Phys. Rev. Lett. **76**, 4191 (1996)

1.84 J. Villain, D.R. Grempel, J. Lapujoulade: Roughening transition of high-index crystal faces: The case of copper, J. Phys. F **15**(4), 809 (1985)

1.85 W. Kossel: Zur Theorie des Kristallwachstums, Nachr. Ges. Wiss. Göttingen Math.-Phys. Kl. **1927**, 135 (1927)

1.86 I.N. Stranski: Zur Theorie des Kristallwachstums, Z. Phys. Chem. **136**, 259 (1928)

1.87 S. Prestipino, E. Tosatti: Kink–kink interactions and pre-roughening of vicinal surfaces, Philos. Mag. B **81**(7), 637 (2001)

1.88 M.S. Hoogeman, D.C. Schlößer, J.B. Sanders, L. Kuipers, J.W.M. Frenken: Surface energetics and thermal roughening of Ag(115) studied with STM movies, Phys. Rev. B **53**, R13299 (1996)

1.89 M.S. Hoogeman, J.W.M. Frenken: Monte Carlo simulation on the roughening of vicinal surfaces, Surf. Sci. **448**(2), 155 (2000)

1.90 J.D. Weeks, G.H. Gilmer: Dynamics of crystal growth. In: *Advances in Chemical Physics*, Vol. 40, ed. by I. Prigogine, S.A. Rice (Wiley, New York 1979) pp. 157–228

1.91 A.C. Levi, C. Garrod, M. Kotrla, M. Touzani: Growth modes and models for smooth and rough surfaces, Phys. Scr. **T49**, 593 (1993)

1.92 A.C. Levi, M. Kotrla: Theory and simulation of crystal growth, J. Phys. Condens. Matter **9**(2), 299 (1997)

1.93 S.F. Edwards, D.R. Wilkinson: The surface statistics of a granular aggregate, Proc. R. Soc. A **381**(1780), 17 (1982)

1.94 S.T. Chui, J.D. Weeks: Dynamics of the roughening transition, Phys. Rev. Lett. **40**, 733 (1978)

1.95 M. Kardar, G. Parisi, Y.-C. Zhang: Dynamic scaling of growing interfaces, Phys. Rev. Lett. **56**, 889 (1986)

1.96 T. Halpin-Healy, Y.-C. Zhang: Kinetic roughening phenomena, stochastic growth, directed polymers and all that. Aspects of multidisciplinary statistical mechanics, Phys. Rep. **254**(4), 215 (1995)

1.97 M. Matsushita, H. Fujikawa: Diffusion-limited growth in bacterial colony formation, Physica A **168**(1), 498 (1990)

1.98 M. Kotrla, A.C. Levi: Kinetic roughness in the BCSOS model, J. Phys. A **25**(11), 3121 (1992)

1.99 H.A. Wilson: On the velocity of solidification and viscosity of supercooled liquids, Philos. Mag. **50**, 238 (1900)

1.100 J. Frenkel: Note on a relation between the speed of crystallization and viscosity, Phys. Z. Sowjetunion **1**, 498 (1932)

1.101 R. Becker, W. Döring: Kinetische Behandlung der Keimbildung in übersättigten Dämpfen, Ann. Phys. **416**(8), 719 (1935)

1.102 M. Volmer, W. Schultze: Kondensation an Kristallen, Z. Phys. Chem. A **156**, 1 (1931)
1.103 F. Family, T. Vicsek: Scaling of the active zone in the Eden process on percolation networks and the ballistic deposition model, J. Phys. A **18**(2), L75 (1985)
1.104 F. Gallet, S. Balibar, E. Rolley: The roughening transition of crystal surfaces. II. Experiments on static and dynamic properties near the first roughening transition of hcp ^{4}He, J. Phys. France **48**(3), 369 (1987)
1.105 A.C. Levi, M. Kotrla: Poor man's interpretation of the Nozières–Gallet effect, Nuovo Cimento D **15**, 485 (1993)
1.106 A.N. Kolmogorov: On the statistical theory of the crystallization of metals, Bull. Acad. Sci. USSR Math. Ser. **1**(3), 355–359 (1937)
1.107 U. Tartaglino, A.C. Levi: Dynamic roughening: Nucleation and stochastic equations, Physica A **277**(1–2), 83 (2000)
1.108 B. Yang, H. Suhl: Energetics of surface roughness and adsorption, Phys. Rev. B **31**, 614 (1985)
1.109 R. Kariotis, H. Suhl, B. Yang: Roughening transition temperature in the presence of an adsorbing fluid, Phys. Rev. B **32**, 4551 (1985)
1.110 V.P. Zhdanov, B. Kasemo: Effect of adsorption on surface roughening, Phys. Rev. B **56**, R10067 (1997)
1.111 E.V. Vakarin, J.P. Badiali: Roughening transition in the presence of adsorbates, Phys. Rev. B **60**, 2064 (1999)
1.112 A.C. Levi, E. Tosatti: On the roughening of molten surfaces, Surf. Sci. **178**(1), 425 (1986)
1.113 C.S. Jayanthi: Surface melting in a Potts lattice-gas model, Phys. Rev. B **44**, 427 (1991)
1.114 E.A. Jagla, S. Prestipino, E. Tosatti: Phase transitions at the early stages of surface melting, Surf. Sci. **454/456**(Suppl. C), 608 (2000)
1.115 E.A. Jagla, S. Prestipino, E. Tosatti: Surface-melting-induced preroughening, Phys. Rev. Lett. **83**, 2753 (1999)
1.116 E.A. Jagla, E. Tosatti: Interplay of surface preroughening, roughening, and melting in three-dimensional lattice models, Phys. Rev. B **62**, 16146 (2000)
1.117 H.S. Youn, X.F. Meng, G.B. Hess: Multilayer adsorption of xenon, krypton, and argon on graphite: An ellipsometric study, Phys. Rev. B **48**, 14556 (1993)
1.118 C.S. Jayanthi, F. Celestini, F. Ercolessi, E. Tosatti: Disordered flat phase separation of the Lennard-Jones fcc(111) surface, Surf. Sci. **460**(1), L503 (2000)
1.119 H.S. Youn, G.B. Hess: Reentrant first-order layering transitions in multilayer argon films on graphite, Phys. Rev. Lett. **64**, 918 (1990)
1.120 I.K. Robinson, D.J. Tweet: Surface X-ray diffraction, Rep. Prog. Phys. **55**(5), 599 (1992)
1.121 M.A. VanHove, W.H. Weinberg, C.-M. Chan: *Low-Energy Electron Diffraction*, Springer Series in Surface Sciences, Vol. 6 (Springer, Berlin, Heidelberg 1986)
1.122 K. Heinz: LEED and DLEED as modern tools for quantitative surface structure determination, Rep. Prog. Phys. **58**(6), 637 (1995)
1.123 E. Hulpke: *Helium Atom Scattering from Surfaces*, Springer Series in Surface Sciences, Vol. 27 (Springer, Berlin, Heidelberg 1992)
1.124 D. Farias, K.-H. Rieder: Atomic beam diffraction from solid surfaces, Rep. Prog. Phys. **61**(12), 1575 (1998)
1.125 R.L. Park, J.E. Houston, D.G. Schreiner: The LEED instrument response function, Rev. Sci. Instrum. **42**(1), 60 (1971)
1.126 G. Comsa: The coherence length in molecular and electron beam diffraction. In: *Dyn. Gas-Surf. Interact., Proc. Int. Sch. Mater. Sci. Technol. 1981, Erice*, ed. by G. Benedek, U. Valbusa (Springer, Berlin, Heidelberg 1982) p. 79
1.127 J.W. Rabalais: Time-of-flight scattering and recoiling spectrometry (TOF-SARS) for surface structure determinations. In: *Fundamental Aspects of Heterogeneous Catalysis Studied by Particle Beams*, ed. by H.H. Brongersma, R.A. van Santen (Springer, Boston 1991) p. 313
1.128 V.A. Esaulov: Low energy ion scattering and recoiling spectroscopy in surface science. In: *Surface Science Techniques*, ed. by G. Bracco, B. Holst (Springer, Berlin, Heidelberg 2013) p. 423
1.129 A. Della Pia, G. Costantini: Scanning tunneling microscopy. In: *Surface Science Techniques*, ed. by G. Bracco, B. Holst (Springer, Berlin, Heidelberg 2013) p. 565
1.130 H.P. Bonzel: 3D equilibrium crystal shapes in the new light of STM and AFM, Phys. Rep. **385**(1), 1 (2003)
1.131 J. Li, R. Berndt, W.-D. Schneider: Tip-assisted diffusion on Ag(110) in scanning tunneling microscopy, Phys. Rev. Lett. **76**, 1888 (1996)
1.132 F. Mugele, A. Rettenberger, J. Boneberg, P. Leiderer: The influence of tip-sample interaction on step fluctuations on Ag(111), Surf. Sci. **400**(1), 80 (1998)
1.133 S. Speller, W. Heiland, A. Biedermann, E. Platzgummer, C. Nagl, M. Schmid, P. Varga: An STM study of the step structure of Pb(110) and Pb(111), Surf. Sci. **331–333**, 1056 (1995)
1.134 R. Koch, J.J. Schulz, K.H. Rieder: Scanning tunneling microscopy artifact and real structure: Steps of Ag(110), Europhys. Lett. **48**(5), 554 (1999)
1.135 L. Kuipers, M.S. Hoogeman, J.W.M. Frenken: Step dynamics on Au(110) studied with a high-temperature, high-speed scanning tunneling microscope, Phys. Rev. Lett. **71**, 3517 (1993)
1.136 E.D. Resnyanskii, E.I. Latkin, A.V. Myshlyavtsev, V.I. Elokhin: Monomolecular adsorption on rough surfaces with dynamically changing morphology, Chem. Phys. Lett. **248**(3–4), 136 (1996)
1.137 E.H. Conrad: Surface roughening, melting, and faceting, Prog. Surf. Sci. **39**(1), 65 (1992)
1.138 K. Kern: Thermal roughening of surfaces: Experimental aspects. In: *Phase Transitions and Adsorbate Restructuring at Metal Surface*, The Chemical Physics of Solid Surfaces, Vol. 7, ed. by D.A. King, D.P. Woodruff (Elsevier, Amsterdam 1994) p. 291
1.139 J. Lapujoulade: The roughening of metal surfaces, Surf. Sci. Rep. **20**(4), 195 (1994)
1.140 G.A. Somorjai, P.J. Rous: John Pendry: his contributions to the development of low energy electron diffraction surface crystallography, J. Phys. Condens. Matter **20**(30), 304210 (2008)
1.141 D. Sébilleau, C. Natoli, G.M. Gavaza, H. Zhao, F. Da Pieve, K. Hatada: MsSpec-1.0: A multiple scatter-

ing package for electron spectroscopies in material science, Comput. Phys. Commun. **182**(12), 2567 (2011)
1.142 H. Chow, E.D. Thompson: Diffraction and selective adsorption in the corrugated hard wall model, Surf. Sci. **54**(2), 269 (1976)
1.143 V. Bortolani, A.C. Levi: Atom surface scattering theory, Riv. Nuovo Cimento **9**(11), 1 (1986)
1.144 J.R. Manson: Theoretical aspects of atom-surface scattering. In: *Helium Atom Scattering from Surfaces*, Springer Series in Surface Sciences, Vol. 27, ed. by E. Hulpke (Springer, Berlin 1992) p. 173
1.145 A. Bellman, A. Morgante, M. Polli, F. Tommasini, D. Cvetko, V.R. Dhanak, A. Lausi, K.C. Prince, R. Rosei: Quantitative structure determination of (1 × 2)-Rh(110) by helium scattering, Surf. Sci. **298**(1), 1 (1993)
1.146 A. Šiber, B. Gumhalter: Diffraction of He atoms from Xe monolayer adsorbed on the graphite (0001) revisited: The importance of multiple scattering processes, Surf. Sci. **529**(3), L269 (2003)
1.147 T.-M. Lu, M.G. Lagally: Diffraction from surfaces with randomly distributed steps, Surf. Sci. **120**(1), 47 (1982)
1.148 M.G. Lagally: The present status of low-energy electron diffraction, Appl. Surf. Sci. **13**(1), 260 (1982)
1.149 M. Henzler: LEED studies of surface imperfections, Appl. Surf. Sci. **11/12**(Suppl. C), 450 (1982)
1.150 B. Poelsema, R.L. Palmer, G. Mechtersheimer, G. Comsa: Helium scattering as a probe of the clean and adsorbate covered Pt(111) surface, Surf. Sci. **117**(1), 60 (1982)
1.151 P. Fenter, T.-M. Lu: Diffraction from a surface with incommensurate domain walls, Surf. Sci. **154**(1), 15 (1985)
1.152 A.C. Levi, H. Suhl: Quantum theory of atom-surface scattering: Debye-Waller factor, Surf. Sci. **88**(1), 221 (1979)
1.153 B. Poelsema, G. Comsa: *Scattering of Thermal Energy Atoms from Disordered Surfaces*, Springer Tracts in Modern Physics, Vol. 115 (Springer, Berlin, Heidelberg 1989) p. 1
1.154 A. Pavlovska, D. Nenow: Experimental study of the surface melting of tetrabrommethane, J. Cryst. Growth **39**(2), 346 (1977)
1.155 S. Balibar, H. Alles, A.Y. Parshin: The surface of helium crystals, Rev. Mod. Phys. **77**, 317 (2005)
1.156 P.E. Wolf, F. Gallet, S. Balibar, E. Rolley, P. Nozières: Crystal growth and crystal curvature near roughening transitions in hcp 4He, J. Phys. France **46**(11), 1987 (1985)
1.157 K.D. Stock, E. Menzel: Surface melting on spherically shaped copper crystals, Surf. Sci. **61**(1), 272 (1976)
1.158 R.S. Williams, P.S. Wehner, J. Stöhr, D.A. Shirley: Thermally induced breakdown of the direct-transition model in copper, Phys. Rev. Lett. **39**, 302 (1977)
1.159 D. Gorse, J. Lapujoulade: A study of the high temperature stability of low index planes of copper by atomic beam diffraction, Surf. Sci. **162**(1–3), 847 (1985)
1.160 T. Fauster, R. Schneider, H. Dürr, G. Engelmann, E. Taglauer: Thermally induced disorder on a Cu(110) surface studied by low-energy ion scattering and inverse photoemission, Surf. Sci. **189/190**, 610 (1987)
1.161 S.G.J. Mochrie: Thermal roughening of the copper (110) surface: An x-ray diffraction experiment, Phys. Rev. Lett. **59**, 304 (1987)
1.162 B.M. Ocko, S.G.J. Mochrie: Reversible faceting of the copper (110) surface: X-ray Fresnel reflectivity, Phys. Rev. B **38**, 7378 (1988)
1.163 P. Zeppenfeld, K. Kern, R. David, G. Comsa: No thermal roughening on Cu(110) up to 900 K, Phys. Rev. Lett. **62**, 63 (1989)
1.164 A.P. Baddorf, E.W. Plummer: Enhanced surface anharmonicity observed in vibrations on Cu(110), Phys. Rev. Lett. **66**, 2770 (1991)
1.165 H. Dürr, R. Schneider, T. Fauster: Anomalous dynamical behavior of the Cu(110) surface, Phys. Rev. B **43**, 12187 (1991)
1.166 L. Yang, T.S. Rahman: Enhanced anharmonicity on Cu(110), Phys. Rev. Lett. **67**, 2327 (1991)
1.167 H. Häkkinen, J. Merikoski, M. Manninen, J. Timonen, K. Kaski: Roughening of the Cu(110) surface, Phys. Rev. Lett. **70**, 2451 (1993)
1.168 A. Mróz, S. Mróz: Temperature effects in directional elastic peak electron spectroscopy for the Cu(011) face: Observation of the surface roughening transition, Surf. Sci. **320**(3), 307 (1994)
1.169 D.S. Martin, A. Maunder, P. Weightman: Thermal behavior of the Cu(110) surface studied by reflection anisotropy spectroscopy and scanning tunneling microscopy, Phys. Rev. B **63**, 155403 (2001)
1.170 O. Zeybek: Thermal behavior of the roughened Cu(110) surface, Solid State Commun. **139**(7), 339 (2006)
1.171 O. Zeybek, A.M. Davarpanah, D.S. Martin, S.D. Barrett: Surface resonance transition of roughened Cu(110), Surf. Sci. **601**(9), 2012 (2007)
1.172 G.A. Held, J.L. Jordan-Sweet, P.M. Horn, A. Mak, R.J. Birgeneau: X-ray scattering study of the thermal roughening of Ag(110), Phys. Rev. Lett. **59**, 2075 (1987)
1.173 I.K. Robinson, E. Vlieg, H. Hornis, E.H. Conrad: Surface morphology of Ag(110) close to its roughening transition, Phys. Rev. Lett. **67**, 1890 (1991)
1.174 G. Bracco, C. Malò, C.J. Moses, R. Tatarek: On the primary mechanism of surface roughening: The Ag(110) case, Surf. Sci. **287**, 871 (1993)
1.175 H. Hornis, E.H. Conrad, E. Vlieg, I.K. Robinson: Facet coexistence in the roughening transition of Ag(110). In: *Surface X-Ray and Neutron Scattering*, Springer Proceedings in Physics, Vol. 61, ed. by H. Zabel, I.K. Robinson (Springer, Heidelberg 1992) p. 73
1.176 C. Herring: Some theorems on the free energies of crystal surfaces, Phys. Rev. **82**, 87 (1951)
1.177 E.D. Williams: Surface steps and surface morphology: Understanding macroscopic phenomena from atomic observations, Surf. Sci. **299**, 502 (1994)
1.178 M. Wortis: Equilibrium crystal shapes and interfacial phase transitions. In: *Chemistry and Physics of Solid Surfaces VII*, ed. by R.F. Howe, R. Vanselow (Springer, Heidelberg 1988) p. 367
1.179 G.A. Held, D.M. Goodstein, R.M. Feenstra, M.J. Ramstad, D.Y. Noh, R.J. Birgeneau: Pinned

and unpinned step dynamics on vicinal silver (110) surfaces, Phys. Rev. B **48**, 8458 (1993)
1.180 J.S. Ozcomert, W.W. Pai, N.C. Bartelt, J.E. Reutt-Robey: Kinetics of oxygen-induced faceting of vicinal Ag(110), Phys. Rev. Lett. **72**, 258 (1994)
1.181 G. Bracco, L. Pedemonte, R. Tatarek: Equilibrium morphology of the Ag(110) surface, Surf. Sci. **352**, 968 (1996)
1.182 S. Pflanz, H.L. Meyerheim, W. Moritz, I.K. Robinson, H. Hoernis, E.H. Conrad: Anisotropic roughening of vicinally miscut Ag(110): X-ray-reflection profile analysis using the domain-matrix method, Phys. Rev. B **52**, 2914 (1995)
1.183 G. Bracco, L. Pedemonte, R. Tatarek: Energy-resolved He-atom-scattering study of Ag(110) up to 900 K, Phys. Rev. B **54**, 10385 (1996)
1.184 G. Bracco, L. Bruschi, L. Pedemonte, R. Tatarek: Temperature dependence of the Ag(110) surface phonons, Surf. Sci. **377**, 325 (1997)
1.185 L. Pedemonte, R. Tatarek, G. Bracco: Self-diffusion on Ag(110) studied by quasielastic He-atom scattering, Surf. Sci. **502**, 341 (2002)
1.186 L. Pedemonte, R. Tatarek, M. Vladiskovic, G. Bracco: Anisotropic self-diffusion on Ag(110), Surf. Sci. **507**, 129 (2002)
1.187 R. Ferrando: Correlated jump-exchange processes in the diffusion of Ag on Ag(110), Phys. Rev. Lett. **76**, 4195 (1996)
1.188 L. Pedemonte, G. Bracco, R. Tatarek, M. Aschoff, K. Brüning, W. Heiland: The Ag(110) thermal disordering mechanism studied by low-energy ion scattering, Surf. Sci. **482**, 1457 (2001)
1.189 T.S. Rahman, Z. Tian, J.E. Black: Surface disordering, roughening and premelting of Ag(110), Surf. Sci. **374**(1–3), 9 (1997)
1.190 C. van der Walt, J.J. Terblans, H.C. Swart: Molecular dynamics study of the temperature dependence and surface orientation dependence of the calculated vacancy formation energies of Al, Ni, Cu, Pd, Ag, and Pt, Comput. Mater. Sci. **83**, 70 (2014)
1.191 Y. Cao, E.H. Conrad: Approach to thermal roughening of Ni(110): A study by high-resolution low-energy electron diffraction, Phys. Rev. Lett. **64**, 447 (1990)
1.192 A. Mróz: High-temperature crystalline effects in Auger electron spectroscopy: The possibility of observation of the surface roughening transition on the Ni(110) face, Surf. Sci. **294**(1), 78 (1993)
1.193 Y. Beaudet, L.J. Lewis, M. Persson: Surface anharmonicities and disordering on Ni(100) and Ni(110), Phys. Rev. B **50**, 12084 (1994)
1.194 E.T. Chen, R.N. Barnett, U. Landman: Surface melting of Ni(110), Phys. Rev. B **41**, 439 (1990)
1.195 H. Hörnis, J.D. West, E.H. Conrad, R. Ellialtioğlu: Temperature-dependent order of clean Pd(110), Phys. Rev. B **48**, 14577 (1993)
1.196 H. Hörnis, J.R. West, E.H. Conrad, R. Ellialtioğlu: Island ordering on clean Pd(110), Phys. Rev. B **47**, 13055 (1993)
1.197 H. Niehus, C. Achete: Oxygen-induced mesoscopic island formation at Pd(110), Surf. Sci. **369**(1), 9 (1996)
1.198 H.-N. Yang, T.-M. Lu, G.-C. Wang: High-resolution low-energy electron diffraction study of Pb(110) surface roughening transition, Phys. Rev. Lett. **63**, 1621 (1989)
1.199 J.C. Heyraud, J.J. Métois: Growth shapes of metallic crystals and roughening transition, J. Cryst. Growth **82**(3), 269 (1987)
1.200 M. Schwarz, C. Mayer, P. von Blanckenhagen, W. Schommers: Temperature dependence of the strucutre of Al(110) and Au(110) surfaces, Surf. Rev. Lett. **04**(06), 1095 (1997)
1.201 A. Pavlovska, M. Tikhov, Y. Gu, E. Bauer: Thermal disordering of the Al(110) surface, Surf. Sci. **278**(3), 303 (1992)
1.202 L. Pedemonte, G. Bracco, A. Robin, W. Heiland: Residual order within the molten Al(110) surface layer, Phys. Rev. B **65**, 245406 (2002)
1.203 D. Wolf, H. Jagodzinski, W. Moritz: Diffuse LEED intensities of disordered crystal surfaces: III. LEED investigation of the disordered (110) surface of gold, Surf. Sci. **77**(2), 265 (1978)
1.204 J.C. Campuzano, M.S. Foster, G. Jennings, R.F. Willis, W. Unertl: Au(110) (1×2)-to-(1×1) phase transition: A physical realization of the two-dimensional Ising model, Phys. Rev. Lett. **54**, 2684 (1985)
1.205 R.F. Willis: Surface reconstruction phase transfonnations. In: *Dynamical Phenomena at Surfaces, Interfaces and Superiattices*, Vol. 3, ed. by R.F. Willis, F. Nizzoli, K.-H. Rieder (Springer, Berlin 1992) p. 126
1.206 L. Onsager: Crystal statistics. I. A two-dimensional model with an order-disorder transition, Phys. Rev. **65**, 117 (1944)
1.207 M.E. Fisher, R.J. Burford: Theory of critical-point scattering and correlations. I. The Ising model, Phys. Rev. **156**, 583 (1967)
1.208 E. van de Riet, H. Derks, W. Heiland: Observation of pre-phase transitional phenomena on an Au(110) surface, Surf. Sci. **234**(1), 53 (1990)
1.209 D.T. Keane, P.A. Bancel, J.L. Jordan-Sweet, G.A. Held, A. Mak, R.J. Birgeneau: Evidence for two-step disordering of the Au(110)-(1×2) reconstructed surface, Surf. Sci. **250**(1), 8 (1991)
1.210 B. Salanon, J. Lapujoulade: A generalization of the gaussian approximation for the analysis of diffraction data from rough surfaces, Vacuum **41**(1), 748 (1990)
1.211 A. Hoss, M. Nold, P. von Blanckenhagen, O. Meyer: Roughening and melting of Au(110) surfaces, Phys. Rev. B **45**, 8714 (1992)
1.212 C. Höfner, J.W. Rabalais: Deconstruction of the Au{110}-(1×2) surface, Phys. Rev. B **58**, 9990 (1998)
1.213 D. Cvetko, A. Lausi, A. Morgante, F. Tommasini, K.C. Prince: He beam study of deconstruction and roughening of Au(110)(1×2), Surf. Sci. **269**, 68 (1992)
1.214 D.E. Clark, W.N. Unertl, P.H. Kleban: Specific-heat anomaly of Au(110) (1×2) studied by low-energy electron diffraction, Phys. Rev. B **34**, 4379 (1986)
1.215 M. Sturmat, R. Koch, K.H. Rieder: Real space investigation of the roughening and deconstruction transitions of Au(110), Phys. Rev. Lett. **77**, 5071 (1996)
1.216 M.J. Rost, J.W.M. Frenken: Comment on "Real space investigation of the roughening and deconstruc-

tion transitions of Au(110)", Phys. Rev. Lett. **87**, 039603 (2001)
1.217 R. Koch, J.J. Schulz: Koch and Schulz reply:, Phys. Rev. Lett. **87**, 039604 (2001)
1.218 E.G. McRae, T.M. Buck, R.A. Malic, G.H. Wheatley: Segregation of Sn at the Au(110) surface and its effect on the $1 \times 2 \leftrightarrow 1 \times 1$ phase transition, Phys. Rev. B **36**, 2341 (1987)
1.219 D. Cvetko, V. De Renzi, L. Floreano, A. Morgante, F. Tommasini: Deconstruction and roughening transitions on (1x2)Pt(110), Solid State Commun. **91**(7), 539 (1994)
1.220 M.A. Krzyzowski, P. Zeppenfeld, C. Romainczyk, R. David, G. Comsa, K.E. Kuhnke, K. Kern: Thermal disordering of the Pt(110)-(1×2) surface, Phys. Rev. B **50**, 18505 (1994)
1.221 R. Koch, M. Sturmat, J.J. Schulz: High-temperature STM investigation of Au(110), Pt(110) and Ag(110), Surf. Sci. **454–456**(Suppl. C), 543 (2000)
1.222 B. Salanon, F. Fabre, J. Lapujoulade, W. Selke: Roughening transition on Cu(113): A quantitative analysis of new experimental results, Phys. Rev. B **38**, 7385 (1988)
1.223 K.S. Liang, E.B. Sirota, K.L. D'Amico, G.J. Hughes, S.K. Sinha: Roughening transition of a stepped Cu(113) surface: A synchrotron x-ray-scattering study, Phys. Rev. Lett. **59**, 2447 (1987)
1.224 J. Wollschläger, E.Z. Luo, M. Henzler: Thermal roughness of the homogeneous and inhomogeneous Cu(311) surface studied by high-resolution low-energy electron diffraction, Phys. Rev. B **44**, 13031 (1991)
1.225 F. Fabre, B. Salanon, J. Lapujoulade: Roughness of Cu(1,1,11): A very anisotropic face, Solid State Commun. **64**(8), 1125 (1987)
1.226 F. Fabre, D. Gorse, J. Lapujoulade, B. Salanon: An experimental study of the roughening transition on a stepped surface: Cu(115), Europhys. Lett. **3**(6), 737 (1987)
1.227 F. Fabre, D. Gorse, B. Salanon, J. Lapujoulade: Observation of surface roughening on Cu(1, 1, 5), J. Phys. France **48**(6), 1017 (1987)
1.228 H.-J. Ernst, R. Folkerts, L. Schwenger: Thermal roughening of Cu(115): An energy-resolved helium-atom-beam scattering study, Phys. Rev. B **52**, 8461 (1995)
1.229 E. Le Goff, L. Barbier, Y. Garreau, M. Sauvage: Thermal roughening restrained by bulk chemical order: Cu–Pd(17%)(115) versus Cu(115) and Cu_3Au(1112) surfaces, Surf. Sci. **522**(1), 143 (2003)
1.230 E.H. Conrad, L.R. Allen, D.L. Blanchard, T. Engel: Kosterlitz-Thouless roughening at the Ni(113) surface, Surf. Sci. **187**(2), 265 (1987)
1.231 E.H. Conrad, L.R. Allen, D.L. Blanchard, T. Engel: Energy resolved measurements of the diffuse scattering near the roughening transition of Ni(113), Surf. Sci. **198**(1), 207 (1988)
1.232 I.K. Robinson, E.H. Conrad, D.S. Reed: X-ray study of the roughening transition of the Ni(113) surface, J. Phys. France **51**, 103 (1990)
1.233 E.H. Conrad, R.M. Aten, D.S. Kaufman, L.R. Allen, T. Engel, M. den Nijs, E.K. Riedel: Erratum: Observations of surface roughening on Ni(115) [J. Chem. Phys. 84, 1015 (1986)], J. Chem. Phys. **85**, 4756 (1986)
1.234 D.L. Blanchard, D.F. Thomas, H. Xu, T. Engel: Observation of the surface roughening transition on Ni(117), Surf. Sci. **222**(2), 477 (1989)
1.235 M.S. Hoogeman, M.A.J. Klik, D.C. Schlößer, L. Kuipers, J.W.M. Frenken: Real-space measurement of surface roughening, Phys. Rev. Lett. **82**, 1728 (1999)
1.236 M.S. Hoogeman, M.A.J. Klik, D.C. Schlößer, L. Kuipers, J.W.M. Frenken: An experimental verification of the theory of surface roughening from a quantitative STM study, Surf. Sci. **448**(2–3), 142 (2000)
1.237 T.D. Daff, I. Saadoune, I. Lisiecki, N.H. de Leeuw: Computer simulations of the effect of atomic structure and coordination on the stabilities and melting behaviour of copper surfaces and nano-particles, Surf. Sci. **603**(3), 445 (2009)
1.238 R. Freitas, T. Frolov, M. Asta: Step free energies at faceted solid surfaces: Theory and atomistic calculations for steps on the Cu(111) surface, Phys. Rev. B **95**, 155444 (2017)
1.239 B. Pluis, A.W. Denier van der Gon, J.F. van der Veen, A.J. Riemersma: Surface-induced melting and freezing I. Medium-energy ion scattering investigation of the melting of Pb{hkl} crystal faces, Surf. Sci. **239**(3), 265 (1990)
1.240 F. Trudu, V. Fiorentini, P. Ruggerone, U. Hansen: Roughening of close-packed singular surfaces, Phys. Rev. B **63**, 153402 (2001)
1.241 H.-N. Yang, K. Fang, G.-C. Wang, T.-M. Lu: Vacancy-induced disordering in the Pb(100) surface, Phys. Rev. B **44**, 1306 (1991)
1.242 D.L. Abernathy, S.G.J. Mochrie, D.M. Zehner, G. Grübel, D. Gibbs: Thermal roughness of a close-packed metal surface: Pt(001), Phys. Rev. Lett. **69**, 941 (1992)
1.243 M.S. Pierce, A. Barbour, V. Komanicky, D. Hennessy, H. You: Coherent x-ray scattering experiments of Pt(001) surface dynamics near a roughening transition, Phys. Rev. B **86**, 184108 (2012)
1.244 D.L. Abernathy, D. Gibbs, G. Grübel, K.G. Huang, S.G.J. Mochrie, A.R. Sandy, D.M. Zehner: Reconstruction of the (111) and (001) surfaces of Au and Pt: Thermal behavior, Surf. Sci. **283**(1), 260 (1993)
1.245 D.L. Abernathy, S.G.J. Mochrie, D.M. Zehner, G. Grübel, D. Gibbs: Orientational epitaxy and lateral structure of the hexagonally reconstructed Pt(001) and Au(001) surfaces, Phys. Rev. B **45**, 9272 (1992)
1.246 D. Gibbs, B.M. Ocko, D.M. Zehner, S.G.J. Mochrie: Absolute x-ray reflectivity study of the Au(100) surface, Phys. Rev. B **38**, 7303 (1988)
1.247 M.S. Pierce, K.C. Chang, D. Hennessy, V. Komanicky, M. Sprung, A. Sandy, H. You: Surface x-ray speckles: Coherent surface diffraction from Au(001), Phys. Rev. Lett. **103**, 165501 (2009)
1.248 J.J. Métois, J.C. Heyraud: SEM studies of equilibrium forms: Roughening transition and surface melting of indium and lead crystals, Ultramicroscopy **31**(1), 73 (1989)

1.249 A. Pavlovska, D. Dobrev, E. Bauer: Roughening transition of tetragonal metals: An initial growth shape study, Surf. Sci. **314**(3), 331 (1994)

1.250 N. Georgiev, A. Pavlovska, E. Bauer: Surface disordering without surface roughening, Phys. Rev. B **52**, 2878 (1995)

1.251 B. Lin, H.E. Elsayed-Ali: Temperature dependent reflection electron diffraction study of In(111) and observation of laser-induced transient surface superheating, Surf. Sci. **498**(3), 275 (2002)

1.252 R. Vanselow, X.Q.D. Li: Roughening transitions in the vicinal areas of Ta110 and Ta100 observed during vapour growth on clean, thermally rounded Ta crystallites, Surf. Sci. Lett. **281**(1), 326 (1993)

1.253 T. Ohachi, I. Taniguchi: Roughening transition for the ionic-electronic mixed superionic conductor α-Ag_2S, J. Cryst. Growth **65**(1), 84 (1983)

1.254 M. Maruyama: Growth and roughening transition of rare gas crystals, J. Cryst. Growth **89**(4), 415 (1988)

1.255 V. Pontikis, V. Rosato: Roughening transition on the (110) face of argon: A molecular dynamics study, Surf. Sci. **162**(1), 150 (1985)

1.256 V. Rosato, G. Ciccotti, V. Pontikis: Molecular-dynamics study of surface premelting effects, Phys. Rev. B **33**, 1860 (1986)

1.257 J.M. Phillips, J.Z. Larese: Microscopic structure and transitions in xenon multilayer films, Phys. Rev. B **56**, 15938 (1997)

1.258 R. Pandit, M. Schick, M. Wortis: Systematics of multilayer adsorption phenomena on attractive substrates, Phys. Rev. B **26**, 5112 (1982)

1.259 D.-M. Zhu, J.G. Dash: Surface melting and roughening of adsorbed argon films, Phys. Rev. Lett. **57**, 2959 (1986)

1.260 D.-M. Zhu, J.G. Dash: Evolution of multilayer Ar and Ne films from two-dimensional to bulk behavior, Phys. Rev. B **38**, 11673 (1988)

1.261 P. Day, M. Lysek, M. LaMadrid, D. Goodstein: Phase transitions in argon films, Phys. Rev. B **47**, 10716 (1993)

1.262 J.Z. Larese, Q.M. Zhang: Phase transitions of argon multilayer films on graphite: Evolution from multilayer film to bulk solid, Phys. Rev. B **51**, 17023 (1995)

1.263 F. Rieutord, R. Simon, R. Conradt, P. Müller-Buschbaum: Surface melting and preroughening of argon: An x-ray reflection study, Europhys. Lett. **37**(8), 565 (1997)

1.264 N.C. Bartelt, R.M. Tromp, E.D. Williams: Step capillary waves and equilibrium island shapes on Si(001), Phys. Rev. Lett. **73**, 1656 (1994)

1.265 Z. Ding, D.W. Bullock, P.M. Thibado, V.P. LaBella, K. Mullen: Atomic-scale observation of temperature and pressure driven preroughening and roughening, Phys. Rev. Lett. **90**, 216109 (2003)

1.266 J.M. Bermond, J.J. Métois, X. Egéa, F. Floret: The equilibrium shape of silicon, Surf. Sci. **330**(1), 48 (1995)

1.267 T. Suzuki, H. Minoda, Y. Tanishiro, K. Yagi: REM studies of the roughening transitions of Si high index surfaces, Thin Solid Films **343/344**(Suppl. C), 423 (1999)

1.268 D.Y. Noh, K.S. Liang, Y. Hwu, S. Chandavarkar: Thermal roughness of a Si(331) surface, Surf. Sci. **326**(1), L455 (1995)

1.269 H. Hibino, T. Ogino: Two-stage phase transition of 12×1 reconstruction on Si(331), Phys. Rev. B **53**, 15682 (1996)

1.270 M. Elbaum: Roughening transition observed on the prism facet of ice, Phys. Rev. Lett. **67**, 2982 (1991)

1.271 M. Maruyama: Roughening transition of prism faces of ice crystals grown from melt under pressure, J. Cryst. Growth **275**(3), 598 (2005)

1.272 B. Lampert, K. Reichelt: Anisotropy of round evaporation spirals on rocksalt surfaces, J. Cryst. Growth **47**(1), 77 (1979)

1.273 J.C. Heyraud, J.J. Métois: Equilibrium shape of an ionic crystal in equilibrium with its vapour (NaCl), J. Cryst. Growth **84**(3), 503 (1987)

1.274 J. Arsic, I.C. Reynhout, W.J.P. van Enckevort, E. Vlieg: Equilibrium morphologies and thermal roughening of cesium halides, J. Cryst. Growth **245**(1), 171 (2002)

1.275 P. Rajak, S.B. Lee, S. Bhattacharyya: Indication of thermal roughening in the retrieved mean inner potential across a $\Sigma 5$ grain boundary in $SrTiO_3$ annealed at different temperatures, J. Mater. Sci. **51**(3), 1484 (2016)

1.276 B.B. Straumal, O.A. Kogtenkova, A.S. Gornakova, V.G. Sursaeva, B. Baretzky: Review: Grain boundary faceting–roughening phenomena, J. Mater. Sci. **51**(1), 382 (2016)

Gianangelo Bracco

Dipartimento di Fisica
Università di Genova
Genova, Italy
bracco@fisica.unige.it

Gianangelo Bracco received his PhD in Physics from the University of Genoa (1987). In 2015, he was appointed Associate Professor of Experimental Physics in the Department of Physics at the University of Genoa, where is currently continuing his activity on the study of surface properties and molecular beams. The results of his scientific activity have been published in more than 110 publications in journals and books.

Andrea C. Levi

Dipartimento di Fisica
Università di Genova
Genova, Italy
andrealevi.genova@yahoo.com

Andrea Claudio Levi graduated in physics in 1960 from Genoa University. Levi became a full professor and was called to Naples in 1981. In 1987, and again between 1989 and 1992, Levi stayed at the SISSA in Trieste. He has published 112 scientific papers and is the author of 3 books of collections of tales and essays.

2. Surface Diffusion

Riccardo Ferrando, Andrew P. Jardine

Surface diffusion is a key step in several phenomena occurring on crystal surfaces, for example in thin-film growth and in chemical reactions. Here, we review the basic concepts of surface diffusion. The elementary diffusion mechanisms on flat and stepped surfaces, such as jumps and exchanges are treated first. Then, the long-time result of the combination of such elementary diffusion moves is considered, both from the point of view of single-particle (or tracer) diffusion and of collective diffusion. Finally, an overview of the experimental techniques to measure surface diffusion is given, with special attention being paid to the helium spin-echo technique.

Adatom mobility is extremely important in a series of processes of technological relevance, such as thin-film growth and heterogeneous catalysis. In fact, smooth thin films can be grown only if the deposited atoms are able to move around on terraces and between different terraces. On the other hand, surface chemical reactions are possible only if the reactants, which usually impinge on the surface in random positions, can move around to meet each other. In this chapter, we review the basic aspects of adatom mobility on surfaces, first focusing on the elementary atomic moves and then on the combination of these moves in determining the long-time stochastic motion of the adatoms. Literature on this subject is vast, and, therefore, we refer to a narrower domain, metal-on-metal diffusion, as regards the specific examples. The interested reader may refer to books and review articles for more complete overviews [2.1–6]. Moreover, we focus on single-adatom mobility, recalling, however, that mobility on surfaces may involve also atomic aggregates [2.7–24].

2.1 Elementary Mechanism of Surface Diffusion

Let us consider an atom that is deposited on an otherwise empty crystal surface. The adsorbed atom can exchange energy with the substrate, which acts as a thermostat at temperature T. For simplicity, we assume now that the substrate does not participate actively in mass transport, i.e., that substrate atoms simply oscillate around their lattice positions. This assumption will be relaxed when dealing with exchange diffusion. After deposition, a series of different processes may take place in sequence for the adatom. These processes may be schematically described as follows:

- *Transient mobility*. When the incoming atom hits the surface, it may have a significant amount of kinetic energy, coming from the kinetic energy of the beam and from the condensation energy on the sub-

M. Rocca, T.S. Rahman, L. Vattuone (Eds.), *Springer Handbook of Surface Science*, Springer Handbooks,
https://doi.org/10.1007/978-3-030-46906-1_2

strate (which is of the order of few eV for transition metals), or from the dissociation energy in the case in which molecules, such as O_2, are deposited. This excess energy may cause some transient mobility of the adatom before the initial nonthermal energy is dissipated to the substrate [2.25, 26]. Dissipation may take place either by exciting phonons or by creating electron–hole pairs in the substrate [2.27]. The former mechanism contributes to the phononic part of the friction, whereas the latter contributes to the electronic part of the friction. Recent estimates for diffusion of Na on Cu(111) [2.28] show that dissipation to phonons and to electron–hole pairs account for $\approx 80\%$ and 20% of the total friction, respectively.

- *Thermalization*. After the initial excess energy is dissipated, the atom equilibrates with the substrate in some adsorption site, where it stays for some time by making small oscillations of frequency ν_{osc} at the potential well bottom. This is possible if the potential energy well associated with the adsorption site is much deeper than $k_{\mathrm{B}}T$, where T is the temperature of the substrate. If adsorption sites are very shallow, the adatom equilibrates on the substrate but keeps on moving in a quasicontinuous way. This type of motion is, however, rather uncommon. An example is the case of adatom diffusion on fcc(111) surfaces, as discussed.
- *Activated escape*. Even if deeper than $k_{\mathrm{B}}T$, an adsorption site is not infinitely deep, so that the adatom can escape from it through a saddle point, by surmounting an energy barrier E_{b}. Here, we consider only diffusion by thermal activation, since quantum tunneling is relevant only at low temperatures (< 100 K for hydrogen and at even lower temperatures for other atoms [2.1, 29]). The escape rate ν_j is given by an expression known as the *Arrhenius law*

$$\nu_j = \nu_{0j} \mathrm{e}^{-\frac{E_{\mathrm{b}}}{k_{\mathrm{B}}T}} , \tag{2.1}$$

where ν_{0j} is the *rate prefactor*. Since $\nu_{0j} \approx \nu_{\mathrm{osc}}$ [2.5] one has

$$\nu_j \ll \nu_{\mathrm{osc}} . \tag{2.2}$$

Energy barriers for diffusion depend on many factors. For a given type of substrate and adatom, the barrier depends on the surface orientation. For example, for Au, Ag, and Cu adatom diffusion on the surfaces of these metals, the barrier for hopping diffusion is of a few tens of meV for diffusion on the (111) surface, and of a few hundred meV on the (100) surface [2.30–35]. The very low barriers on the (111) surface cause a quasicontinuous diffusive motion in the network on fcc and hcp adsorption sites, which can take place already at room temperature. As discussed in Sect. 2.1.2, E_{b} is different in the vicinity of steps and other defects than on the flat, perfect surface. For diffusion of metal atoms on insulating surfaces, E_{b} may also depend on the charge state of the adatom [2.36]. Diffusion barriers may depend on the direction on anisotropic surfaces, to the extent that diffusion may become essentially one-dimensional in some cases [2.37–41].

- *Jump diffusion*. After jumping out from an adsorption site, the adatom will finally thermalize in another adsorption site, which may be either a nearest/neighbor site or a more distant site [2.5, 42]. In the latter case, a *long jump* has taken place. For deep potential wells, the time of flight τ_{fl} between escaping from the first site and thermalizing in the new site is much shorter than the average residence time in the well τ_j

$$\tau_{\mathrm{fl}} \ll \tau_j = \frac{1}{\nu_j} . \tag{2.3}$$

The residence time is, therefore, sufficiently long to eliminate correlations between subsequent jumps, so that the overall adatom motion will be a sequence of uncorrelated events, which produces a random walk in the lattice of adsorption sites.

A schematic representation of the trajectory of a diffusion event of an adatom is given in Fig. 2.1. The adatom oscillates in an adsorption site, then it jumps to a nearest-neighbor site and, finally, thermalizes there and keeps on oscillating.

The occurrence of long jumps indicates a weak energy exchange between the adatom and the substrate. This can be qualitatively discussed in the framework of the Langevin model, in which the energy exchange between adatom and substrate is described in terms of friction and white noise. In the Langevin model, the motion of the adatom obeys a stochastic differential equation. For simplicity, we discuss the one-dimensional case, which is relevant, for example, in diffusion along channels or steps. Let us assume that the adatom is diffusing in a spatially periodic system of period a, which corresponds to the lattice distance between nearest-neighbor adsorption sites of our system. The displacement $x(t)$ of the adatom of mass m is ruled by

$$m\frac{\mathrm{d}^2x}{\mathrm{d}t^2} = -m\gamma v + F(x) + \Gamma(t) , \tag{2.4}$$

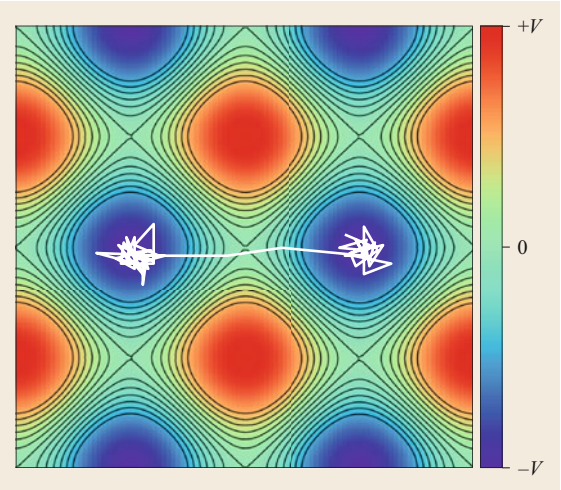

Fig. 2.1 Trajectory (projected in the surface plane) of an adatom jumping between two adsorption sites (of energy $-V$ at the well bottom) through a saddle point of energy 0 (the saddle point is at the *center*). The energy barrier E_b is given by the energy difference between the saddle point and the minimum, $E_b = V$

where v is the velocity of the adatom, $F(x) = -\mathrm{d}V/\mathrm{d}x$ is a spatially periodic force derived from the *adiabatic potential*, which describes the average interaction with the substrate, and γ is the friction per unit mass; $\Gamma(t)$ is a δ-correlated white noise, whose intensity is related to the friction by the fluctuation-dissipation theorem [2.43]. While the friction term can only subtract energy to the adatom, the noise term can give and subtract energy to insure thermal equilibrium with the substrate.

In order to discuss the occurrence of long jumps [2.44, 45], let us calculate the energy dissipated by the adatom that crosses a lattice cell assuming that the amplitude $A = E_b/2$ of $V(x)$ is much larger than $k_B T$. We can assume that the adatom starts from the top of the barrier with a kinetic energy of $k_B T$ and then dissipates the energy Δ while crossing the cell to reach the next barrier top

$$\Delta = \int_0^a m\gamma v(x)\mathrm{d}x \,. \tag{2.5}$$

Since long jumps can occur only when dissipation is small, we can estimate $v(x)$ as if the motion of the adatom would be conservative, i.e., assuming that

$$\frac{1}{2}mv^2(x) + V(x) = E_b + k_B T \,, \tag{2.6}$$

so that

$$\Delta = \gamma \int_0^a \sqrt{2m[E_b + k_B T - V(x)]}$$

$$\simeq \gamma \int_0^a \sqrt{2m[E_b - V(x)]} \,, \tag{2.7}$$

because $E_b \gg k_B T$. In this limit, the main contribution to the integral comes from x close to the well bottom, so that the integral itself can be approximated by E_b/ν_{osc}. The condition for the occurrence of long jumps thus becomes

$$\frac{\Delta}{k_B T} \ll 1 \quad \longrightarrow \quad \frac{\gamma}{\nu_{osc}} \ll \frac{k_B T}{E_b} \,. \tag{2.8}$$

Long jumps have been observed in different experiments [2.37, 38, 46–50] and in many simulations and calculations [2.16, 31, 32, 51–56].

Mass transport on surfaces can take place by several different mechanisms besides jumps. Below we describe the most important ones.

2.1.1 Exchange Diffusion

In exchange diffusion, an adatom enters the substrate taking the place of a substrate atom, which is pushed up on the surface and becomes the new adatom. Even though this mechanism implies an active role of the substrate, for homoepitaxial systems it can be treated by the same line of reasoning as the jumps, since the final result of the process is the same as in a jump between the appropriate initial and final sites. For heteroepitaxial systems, after the exchange process, the new diffusing adatom may, of course, be of a different species.

There are several systems in which the exchange mechanism is favored over the simple jump. The first example is the diffusion of adatoms on the (110) surface of fcc metals. This is a channeled surface, with atomic rows running along the $[1\bar{1}0]$ direction (Fig. 2.2). Diffusion across these channels, i.e., in the [001] direction, can hardly take place by jumps. In fact, in the adsorption site, the adatom has five nearest neighbors, which reduce to two at the saddle point for the jump process, with a corresponding huge amount of energy which is of the order of 1 eV and more for transition and noble metals. On the contrary, diffusion by exchange requires surmounting much smaller barriers, often well < 0.5 eV.

Exchange diffusion has been observed also on surfaces with square symmetry, such as the (100) surface of fcc crystals. As shown in Fig. 2.2b, the adatom enters the substrate taking the place of one of its four

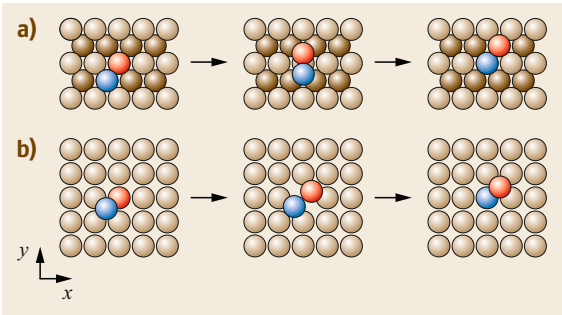

Fig. 2.2 **(a)** Exchange process on a (100) surface of an fcc metal. This channeled surface, with atom rows along the [1$\bar{1}$0] direction (*x*-direction) is shown in a top view. The atom rows are very difficult to surmount by a jump process to reach the adjacent channel. In the *middle panel* the typical symmetric *dumbbell configuration* is shown. This is either the saddle point or a short-lifetime metastable configuration corresponding to a very shallow local minimum. **(b)** Exchange process on a (100) surface of an fcc metal. The adatom enters the substrate and substitutes an atom that becomes the new adatom. The process causes mass transport along the diagonal, in the [011] direction. A single jump process would cause mass transport either along the *x* or the *y*-direction

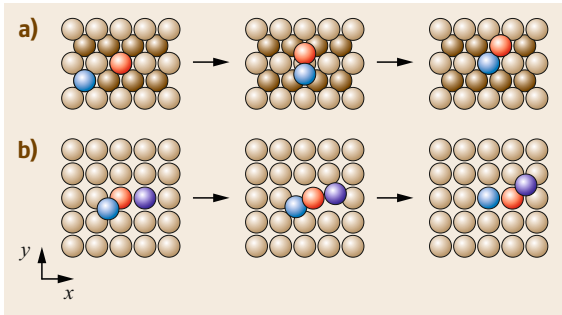

Fig. 2.3 **(a)** A correlated jump-exchange process [2.51] on an fcc(110) surface. The original adatom (*blue color*) makes a jump along the a channel in the [1$\bar{1}$0] direction, but, instead of stopping in the next well, it pushes a substrate atom of an adjacent row (*red color*) to the next channel and takes its place in the row. **(b)** A multiple exchange process on an fcc(100) surface [2.67] in which the adatom is incorporated into the substrate by pushing two atoms. One of them (*violet color*) becomes the new adatom

nearest neighbors. This process produces a net displacement in a diagonal direction (such as the [011] direction), i.e., the same displacement that would be obtained by a jump to a second-neighbor site. Therefore, if diffusion on this surface takes place exclusively by exchange, the adsorption sites of a single sublattice can be visited by a series of subsequent exchanges, while the other sublattice is never visited. This sublattice is rotated by 45°, like the network of white squares on a checkerboard. On the other hand, if diffusion takes place by jumps or by a combination of jumps and exchanges, all sites can be visited. This allows us to single out pure exchange diffusion in experiments [2.57, 58]. There are also systems in which both exchanges and jumps occur at comparable frequencies, for example, in W/W(100) [2.59].

In simulations, exchange diffusion has been observed for a large variety of metal-on-metal homoepitaxial and heteroepitaxial systems [2.31, 51, 60–66].

Exchange processes may also take complex pathways involving the displacement of more than two atoms. Evidence in favor of these multiatom processes essentially comes from simulations [2.51, 67–75]. In some cases, also correlated processes involving a jump and an exchange part have been seen [2.31, 51]. Schematic representations of a correlated jump-exchange process and of a three-atom exchange are given in Fig. 2.3.

2.1.2 Diffusion Across and Along Steps

Surface diffusion in the presence of defects is also an important research topic. Steps are the most common extended defects on a surface, and both diffusion along and across steps play an important role in the evolution of the surface during thin-film growth [2.76, 77].

Adatom diffusion across a step (Fig. 2.4) is an asymmetric process. In metal-on-metal diffusion, descending from the upper to the lower terrace is usually easier than the reverse process (upward diffusion). This happens because the site reached by the adatom on the lower terrace is more coordinated than sites on the upper terrace, so that there is an energy gain in the downward move. For other systems, the behavior may

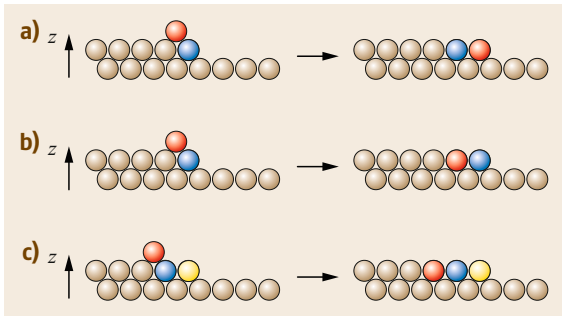

Fig. 2.4 **(a)** An adatom jumps down at a step. **(b)** The adatom is incorporated in the step riser after an exchange, whereas a former step atom is the new adatom that can diffuse either along the step or on the bottom terrace. **(c)** The adatom is incorporated in an inner position of the terrace by a multiple-exchange process

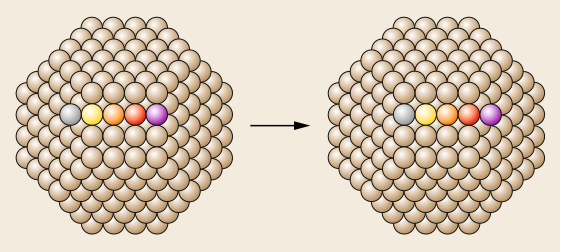

Fig. 2.5 An adatom on the border between a (111) and a (100) facet on an fcc truncated octahedral cluster pushes a row of atoms of the (100) facet, so that finally an adatom appears on the opposite (111) facet

be different—for example, simulations of the diffusion of oxygen on Cu(001) by reactive force fields [2.78] have shown that in this case, upward diffusion is easier than downward diffusion. In the following, we focus on metal-on-metal diffusion, in which downward diffusion between terraces is the easier process.

Diffusion across steps can take place by jumps and by exchange, the latter being possible also from sites that are not in the close vicinity of the terrace border, as is shown in Fig. 2.4. Even though there is a final energy gain in the downward diffusion processes, the intermediate configurations of these processes often contain severely undercoordinated atoms, as is schematically shown in Fig. 2.4. For this reason, the activation barrier for downward diffusion can be higher than the barrier for diffusion on the upper terrace. The additional barrier for crossing the step is known as the Ehrlich–Schwoebel (ES) barrier [2.79, 80]. In Fig. 2.6, we sketch a typical energy profile of the diffusion pathway across a step. If the diffusion on the upper terrace, far away from the step, has a barrier E_{ut}, and the downward diffusion across the step has a barrier $E^{\perp}_{\mathrm{step}}$, then the ES barrier is defined by $E^{\perp}_{\mathrm{step}} = E_{\mathrm{ut}} + E_{\mathrm{ES}}$. The ES barrier is a crucial factor in determining the thin-film growth mode. Small or nonexistent ES barriers favor layer-by-layer growth, while large ES barrier favor three-dimensional growth because they hinder the mobility between terraces at different levels [2.76]. There are even cases in which the barrier for downward step crossing may be lower than the barrier on the flat terrace, as was found in calculations for exchange crossing on Ag(100) [2.81]. In these cases, the ES barrier is negative. Zero or even negative ES barriers may be found also for downward crossing at step kinks [2.7, 82, 83].

Also the diffusion of adatoms between adjacent facets on a nanoparticle [2.84, 85] takes place by similar types of mechanisms to the diffusion between terraces of high-index crystal surfaces. Interfacet diffusion processes, therefore, have their own ES barriers [2.68, 86]. In nanoparticles, there is also the possibility of chain diffusion mechanisms that allow the displacement of atoms between opposite sides of the nanoparticle [2.68, 87], as shown in Fig. 2.5.

The diffusion of adatoms across steps has been studied in many cases, especially by simulations. For metal-on-metal diffusion, these studies considered both homoepitaxial [2.88–92] and heteroepitaxial systems [2.92–94]

Diffusion along steps may take place on the lower and on the upper side of the step. Since the sites on the lower side have higher coordination, they act as traps of adatoms. On the other hand, the adsorption energy in sites on the upper side of the step is usually very close to that of inner terrace sites. For these reasons, most studies have focused on diffusion along the lower sides of steps. Diffusion along steps is quite difficult to measure directly in experiments, but it has important experimental consequences as far as the shape of

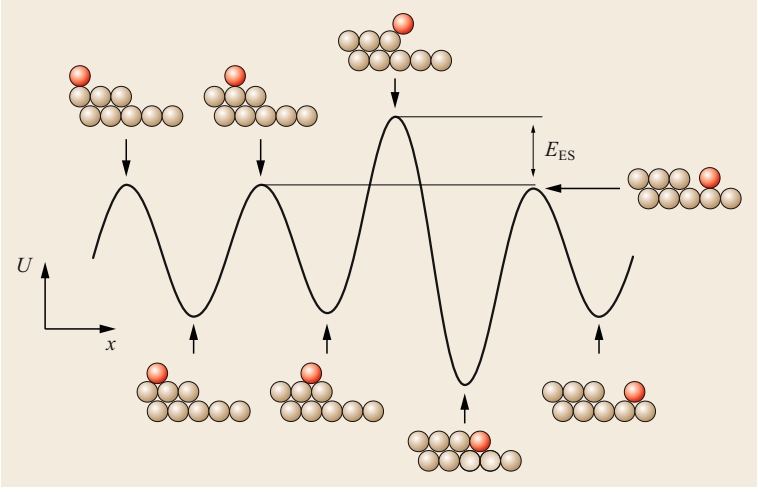

Fig. 2.6 Potential energy profile along the diffusion pathway of an atom crossing a step to descend to the lower terrace. The additional ES barrier E_{ES} for crossing the step is indicated

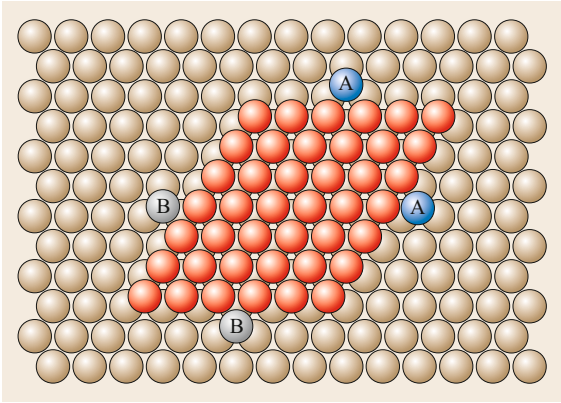

Fig. 2.7 An island on a (111) surface of an fcc crystal. The island is limited by straight steps, and there are four adatoms diffusing on the lower edges of the steps. There are two different types of steps. The steps of type A (those of the adatoms marked by A) have square facets on the step riser. The steps of type B (those of the adatoms marked by B) have triangular facets on the step riser

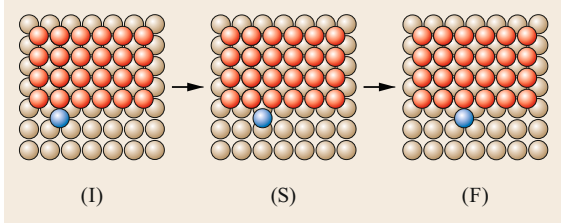

Fig. 2.8 Diffusion of an adatom along a straight step on an fcc(100) surface. From the initial position (I), the adatom passes through the saddle point (S) and then moves to the final site (F). In (I) and (F), the adatom has five first neighbors, while in (S) it has four first neighbors

growing islands is concerned [2.76, 95, 96], especially if diffusion around corners is also considered. The presence of steps is also important because it can alter the interaction between adsorbed molecules on the terraces, thus influencing their diffusion coefficient [2.97].

Due to the difficulty of measuring the diffusion of adatoms along steps, most studies in the literature are simulation studies. For metal-on-metal diffusion, one may refer to, for example, [2.93, 98–102].

The diffusion barriers for adatoms diffusing along steps strongly depend on the symmetry of the surface and on the type of step. This can be exemplified by considering straight steps on two high-index surfaces of fcc crystals, the (111) and the (100) surfaces.

Let us consider first the (111) surface. In Fig. 2.7, a schematic representation of an island on a (111) surface is shown. This island is limited by four straight steps, which, however, are not equivalent, because two of them present square facets on the step riser (steps of type A), and two of them present triangular facets on the step riser (steps of type B). If there is an A step on one side of the island, on the opposite side there will be a B step. Rhombic and hexagonal islands must, therefore, present both step types, while triangular islands (of orientations differing by 60°) present a single type of step [2.76]. Diffusion of adatoms along these steps may be characterized by different energy barriers [2.98]. Also the diffusion pathway along A and B steps may be somewhat different. In fact, calculations for Au(111) and Ag(111) showed that the preferential diffusion pathway is a straight line along step B, whereas it has a cosine-like shape along step A [2.98]. However, the most important point is that on this surface, diffusion along steps has much higher barriers than diffusion on the flat terrace. In Ag and Au(111), the former has barriers of a few tenths of eV, while the latter has barriers of ≤ 0.1 eV [2.30, 98]. This means that there is a temperature range in which terrace diffusion is activated while diffusion along steps is not, allowing the growth of fractal-like islands [2.76].

On the (100) surface, the situation is quite different. In fact, referring again to Ag and Au as examples, diffusion on the flat terrace is characterized by barriers of a few tenths of eV [2.31]. In the jump mechanism, terrace diffusion takes place by passing through a saddle point, where coordination is decreased from four to two. For diffusion along a straight step, the decrease in coordination at the saddle point is only from five to four, as shown in Fig. 2.8. This indicates that the barrier for diffusion along straight steps may be lower than that on the terrace, as is, indeed, verified by several calculations ([2.101] and references therein). Therefore, on these (100) surfaces, there is no temperature interval in which terrace diffusion is activated while diffusion along steps is not. This causes the growth of islands limited by straight steps, which are much more compact than the island grown on the on the (111) surface of the same metals.

2.2 Single-Particle and Collective Diffusion Coefficients

In the previous section, we focused on the elementary moves by which an adatom can displace from one site to another on a crystal surface. Now we focus on the long-time result of the combination of such elementary moves, assuming that they are statistically independent of each other. This amounts to assuming that each time the diffusing atom reaches a new adsorption site on the surface, it stays there for a sufficiently long time to equilibrate with the substrate.

As we will show in the following, the combination of statistically independent elementary moves leads to a long-time behavior in which the mean square displacement of the adatom increases (apart from a numerical constant related to the dimensionality of the system) linearly as $D_s t$, where D_s is the single-particle (or tracer) diffusion coefficient; D_s is, thus, related to the average behavior of each individual diffusing particle. However, this is not the only diffusion coefficient that can be defined. In fact, there is also the collective diffusion coefficient D_c, which describes how density gradients relax to equilibrium in the system; D_s and D_c may both depend on the density of the adsorbate, but, as we will see in the following, in quite different ways.

2.2.1 Single-Particle (Tracer) Diffusion

Let us consider an isotropic surface and a single diffusing adatom whose position as a function of time t is $\boldsymbol{r}(t)$. The diffusing adatom is in contact with the substrate, which exchanges energy with the adatom, thus acting as a thermostat at a temperature T. For sufficiently long times, the motion of the diffusing adatom can be described as a random walk. The net mean displacement of the adatom is

$$\langle \Delta \boldsymbol{r}(t) \rangle = \langle [\boldsymbol{r}(t) - \boldsymbol{r}(0)] \rangle = 0 \tag{2.9}$$

due to left-right symmetry. On the contrary, the mean square displacement

$$\langle \Delta \boldsymbol{r}^2(t) \rangle = \langle [\boldsymbol{r}(t) - \boldsymbol{r}(0)]^2 \rangle \tag{2.10}$$

is different from zero and tends to increase as t^α, with the exponent $\alpha > 0$, for sufficiently long times. This allows us to define the single-particle (or tracer) diffusion coefficient D_s

$$D_s = \lim_{t\to\infty} \frac{\langle \Delta \boldsymbol{r}^2(t) \rangle}{2dt} , \tag{2.11}$$

where d is the dimensionality of the system, $d = 2$. The limit in (2.11) converges to a finite value if asymptotically $\langle \Delta \boldsymbol{r}^2(t) \rangle \propto t$, i.e., $\alpha = 1$. If this does not happen, i.e., if the asymptotic behavior is proportional to t^α with $\alpha \neq 1$, one has the so-called *anomalous diffusion*, of which there are some examples also in the case of surfaces [2.103, 104]. It can be easily shown that (2.11) is equivalent to [2.43]

$$D_s = \frac{1}{d} \int_0^\infty \langle \boldsymbol{v}(t) \cdot \boldsymbol{v}(0) \rangle \mathrm{d}t , \tag{2.12}$$

where $\boldsymbol{v}$ is the velocity of the adatom.

In the general case, the surface can be anisotropic, so that one has to consider the diffusion tensor $\mathbf{D}_s$

$$\mathbf{D}_s = \begin{pmatrix} D_s^{xx} & D_s^{xy} \\ D_s^{yx} & D_s^{yy} \end{pmatrix} , \tag{2.13}$$

where

$$\begin{aligned} D_s^{xx} &= \lim_{t\to\infty} \frac{\langle [x(t) - x(0)]^2 \rangle}{2t} , \\ D_s^{yy} &= \lim_{t\to\infty} \frac{\langle [y(t) - y(0)]^2 \rangle}{2t} , \\ D_s^{xy} &= D_s^{yx} = \lim_{t\to\infty} \frac{\langle [x(t) - x(0)][y(t) - y(0)] \rangle}{2t} ; \end{aligned} \tag{2.14}$$

$\mathbf{D}_s$ is, thus, symmetric by definition, so that it can be diagonalized. This allows us to find two principal diffusion directions x_p and y_p for which

$$\begin{aligned} D_s^x &= \lim_{t\to\infty} \frac{\langle [x_p(t) - x_p(0)]^2 \rangle}{2t} , \\ D_s^y &= \lim_{t\to\infty} \frac{\langle [y_p(t) - y_p(0)]^2 \rangle}{2t} . \end{aligned} \tag{2.15}$$

If x_p and y_p are equivalent, one recovers the isotropic case, i.e., $D_s^x = D_s^y$.

Let us consider jump diffusion. We first restrict ourselves to the case of isotropic lattices in which only jumps to nearest neighbor sites are allowed. There are n_{pv} nearest neighbors ($n_{pv} = 4$, 6, and 3 for the square, the triangular, and the honeycomb lattices, respectively). The adatom starts from the origin of the coordinates and jumps on average at intervals δt, which means that its total jump rate (or frequency) is $\nu_j = 1/\delta t$. At the i-th jump, the adatom displacement from its previous position is

$$\delta \boldsymbol{r}_i = (\delta x_i, \delta y_i) , \tag{2.16}$$

while its total displacement after n jumps is

$$\boldsymbol{r}^{(n)}(t) = \sum_{i=1}^{n} \delta \boldsymbol{r}_i \,, \tag{2.17}$$

with $t = n\delta t$. Taking into account that for $i \neq j$ jumps are statistically independent and that all jumps are equivalent, the mean square displacement is given by

$$\begin{aligned} \langle \Delta \boldsymbol{r}^2(t) \rangle &= \langle \boldsymbol{r}^{(n)}(t) \cdot \boldsymbol{r}^{(n)}(t) \rangle \\ &= \left\langle \sum_{i=1}^{n} \delta \boldsymbol{r}_i \cdot \sum_{j=1}^{n} \delta \boldsymbol{r}_j \right\rangle \\ &= \left\langle \sum_{i=1}^{n} \delta \boldsymbol{r}_i \cdot \delta \boldsymbol{r}_i \right\rangle = n \langle \delta \boldsymbol{r}_1^2 \rangle \,. \end{aligned} \tag{2.18}$$

The tracer diffusion coefficient is, thus, given by

$$D_\mathrm{s} = \lim_{t\to\infty} \frac{\langle \Delta \boldsymbol{r}^2(t) \rangle}{4t} = \lim_{t\to\infty} \frac{n \langle \delta \boldsymbol{r}_1^2 \rangle}{4n\delta t} = \frac{1}{4} \nu_j \langle \delta \boldsymbol{r}_1^2 \rangle \,. \tag{2.19}$$

If the distance of first neighbors is a, whatever direction is taken for the jump, the square displacement is a^2, so that

$$\langle \delta \boldsymbol{r}_1^2 \rangle = a^2 \,, \tag{2.20}$$

which leads to the final expression of the tracer diffusion coefficient in a jump model with nearest-neighbor jumps

$$D_\mathrm{s} = \frac{1}{4} \nu_j a^2 \,. \tag{2.21}$$

For anisotropic lattices, we have

$$D_\mathrm{s}^x = \frac{1}{2} \nu_j^x a^2 \quad D_\mathrm{s}^y = \frac{1}{2} \nu_j^y b^2 \,, \tag{2.22}$$

where ν_j^x, ν_j^y are the total jump rates in x and y directions, respectively, and a, b are the nearest-neighbor distances in the directions x and y.

As we saw in the previous section, there are several examples of surface diffusion in which jumps to more distant neighbors than the first ones are possible. Let us consider the contribution of these long jumps to diffusion. We consider the isotropic case and calculate $\langle \delta \boldsymbol{r}_1^2 \rangle$. From the site of departure (in $\boldsymbol{r} = 0$ for simplicity), the adatom can jump to any other site $\boldsymbol{l}$ of the lattice with probability $\pi_{\boldsymbol{l}}$, with the normalization condition

$$\sum_{\boldsymbol{l}\neq 0} \pi_{\boldsymbol{l}} = 1 \,. \tag{2.23}$$

We have that $\langle \delta \boldsymbol{r}_1^2 \rangle$ equals the mean-square jump length $\langle l^2 \rangle$

$$\langle \delta \boldsymbol{r}_1^2 \rangle = \sum_{\boldsymbol{l}\neq 0} \pi_{\boldsymbol{l}} (\boldsymbol{l} \cdot \boldsymbol{l}) = \langle l^2 \rangle \,, \tag{2.24}$$

giving

$$D_\mathrm{s} = \frac{1}{4} \nu_j \langle l^2 \rangle \,. \tag{2.25}$$

If long jumps occur in one dimension, for example, on channeled surfaces such as the (1×2) missing-row reconstructed surface, the expression for $\langle l^2 \rangle$ is

$$\langle l^2 \rangle = \sum_{l\neq 0} \pi_l (la)^2 \,, \tag{2.26}$$

with l an integer. Since $\pi_l = \pi_{-l}$, we can define $p_l = 2\pi_l$ for $l > 0$ and write

$$\langle l^2 \rangle = \sum_{l=1}^{\infty} p_l l^2 a^2 \,. \tag{2.27}$$

The diffusion coefficient is

$$D_\mathrm{s} = \frac{1}{2} \nu_j a^2 \sum_{l=1}^{\infty} p_l l^2 \,. \tag{2.28}$$

Single-particle diffusion is not limited to isolated adatoms. In fact, in general, D_s can be defined for a dense adsorbate. For N diffusing adatoms (which are here assumed to be identical), D_s is defined exactly in the same way as for an isolated adatom, with the advantage (quite important in simulations) of averaging on all adatoms. The definition for the isotropic case is

$$D_\mathrm{s} = \lim_{t\to\infty} \frac{1}{2dt} \sum_{i=1}^{N} \langle \Delta \boldsymbol{r}_i^2(t) \rangle \,. \tag{2.29}$$

Lattice models are very often used to treat diffusion in dense adsorbates, because they allow a simplified treatment. Here, we consider a specific two-dimensional lattice model, which is known as the *Langmuir gas*. This model allows us to easily understand the main differences between tracer and collective diffusion. Our discrete lattice contains M equivalent adsorption sites, and it is filled by N adatoms. Each site can be occupied by no more than one adatom, so that the fraction of occupied sites, usually called coverage, is $\theta = N/M$; D_s will depend on θ, generally in a quite complex way. The adatoms diffuse by jumping between nearest-neighbor sites on the lattice and are assumed

to interact only by *site blocking*. Site blocking mimics the short-distance hard-sphere repulsion between the adatoms forbidding multiple occupancy of sites. Even for this simple model, the exact analytical expression for $D_s(\theta)$ is not known. In the limit $\theta \to 0$, D_s must tend to the expression of (2.21). Then, due to site blocking, $D_s(\theta)$ decreases with θ. As a first approximation, we note that, on average, the jump rate is decreased proportionally to the average fraction of occupied nearest-neighbor sites, which is given by θ is this simple model. Therefore, a mean-field expression for $D_s(\theta)$ is

$$D_s(\theta) = \frac{1}{4}\nu_j a^2(1-\theta)\,. \tag{2.30}$$

This expression is exact for both limits $\theta = 0$ and $\theta = 1$ (for $\theta = 1$, no adatom can move), but it overestimates the true D_s for intermediate θ. This is due to neglecting *memory effects*, which correlate sequences of subsequent jumps. To understand why memory effects lower D_s compared to the mean-field expression of (2.30), one may note that after a jump, the adatom leaves a free site behind, so that a jump back is more likely than a jump to another site, whose probability of being empty is $1-\theta$. In order to take into account memory effects, a *tracer correlation factor* $f_t(\theta)$ is introduced, so that

$$D_s(\theta) = \frac{1}{4}\nu_j a^2(1-\theta) f_t(\theta)\,. \tag{2.31}$$

Evaluating $f_t(\theta)$ by analytical means is quite complicated, so that numerical evaluations by Monte Carlo simulations are often used [2.105]. Anyway, very accurate analytical formulas have been produced [2.106–108], mostly by using projection-operator techniques. For example, for a square lattice, one may use

$$f_t(\theta) = 1 - \frac{2\theta}{6-\theta-\xi(2-\theta)}\,, \tag{2.32}$$

with $\xi = 10\,440/9443$. The behavior of $D_s(\theta)$ according to the different approximations is reported in Fig. 2.9.

Further interactions between the adatoms besides site blocking are usually called *lateral interactions*. In general, attractive lateral interactions slow down tracer diffusion, because each adatom has to break the bonds with its neighbors to make a jump. On the other hand, repulsive lateral interactions may enhance diffusion, unless they are so strong (compared to $k_B T$) as to cause the formation of ordered phases, whose rigid framework leads to a decrease in adatom mobility.

2.2.2 Collective Diffusion

While tracer diffusion describes the long-time motion of each adatom individually, collective diffusion describes the time decay of long-wavelength density fluctuations of the whole adsorbate [2.1, 2, 5, 109]. Let us consider an isotropic adsorbate with average density $\overline{\rho}$. At a given point $\boldsymbol{r}$ on the surface and time t, the density is $\rho(\boldsymbol{r}, t)$, so that the density fluctuation $\delta\rho$ is

$$\delta\rho(\boldsymbol{r}, t) = \rho(\boldsymbol{r}, t) - \overline{\rho}\,. \tag{2.33}$$

We assume that the flux of matter in the adsorbate is proportional to the density gradient according to Fick's law

$$\boldsymbol{J}(\boldsymbol{r}, t) = -D_c \nabla\rho(\boldsymbol{r}, t) = -D_c \nabla\delta\rho(\boldsymbol{r}, t)\,, \tag{2.34}$$

where $\boldsymbol{J}$ is the current density, and D_c is the collective diffusion coefficient. Combining this equation with the

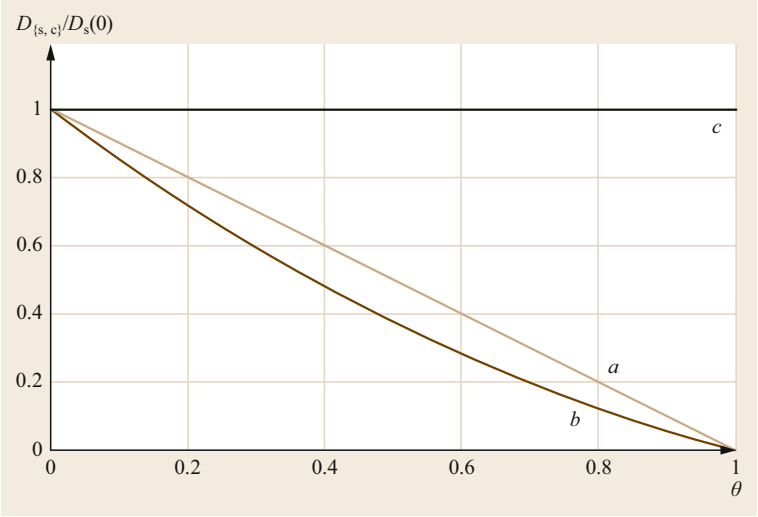

Fig. 2.9 Normalized diffusion coefficients $D_{\{s,c\}}/D_s(0)$ as functions of the coverage θ in a Langmuir gas: *a* mean-field approximation for D_s (2.30), *b* D_s with memory effects taken into account (2.31) and (2.32), *c* D_c (Sect. 2.2.2), which, in the Langmuir gas, does not depend on coverage

continuity equation we obtain the diffusion equation

$$\frac{\partial \delta\rho}{\partial t} = D_c \nabla^2 \delta\rho \,. \tag{2.35}$$

Let us consider a periodic density fluctuation and calculate how it decays with time according to (2.35). The fluctuation at time $t = 0$ is

$$\delta\rho(\boldsymbol{r}, 0) = \delta\rho_0 \cos(\boldsymbol{q}_0 \cdot \boldsymbol{r}) = \delta\rho_0 \frac{\mathrm{e}^{\mathrm{i}\boldsymbol{q}_0\cdot\boldsymbol{r}} + \mathrm{e}^{-\mathrm{i}\boldsymbol{q}_0\cdot\boldsymbol{r}}}{2} \,. \tag{2.36}$$

We define

$$S(\boldsymbol{q}, t) = \int \mathrm{d}\boldsymbol{r} \mathrm{e}^{\mathrm{i}\boldsymbol{q}\cdot\boldsymbol{r}} \delta\rho(\boldsymbol{r}, t) \,, \tag{2.37}$$

with the inversion formula

$$\delta\rho(\boldsymbol{r}, t) = \frac{1}{(2\pi)^d} \int \mathrm{d}\boldsymbol{q} \mathrm{e}^{-\mathrm{i}\boldsymbol{q}\cdot\boldsymbol{r}} S(\boldsymbol{q}, t) \,. \tag{2.38}$$

Substituting in (2.35) we find an equation for the evolution of S

$$\frac{\partial S}{\partial t} = -D_c q^2 S(\boldsymbol{q}, t) \,, \tag{2.39}$$

with solution

$$S(\boldsymbol{q}, t) = S(\boldsymbol{q}, 0) \mathrm{e}^{-D_c q^2 t} \,, \tag{2.40}$$

with

$$S(\boldsymbol{q}, 0) = (2\pi)^d \frac{\delta\rho_0}{2} \left[\delta(\boldsymbol{q} - \boldsymbol{q}_0) + \delta(\boldsymbol{q} + \boldsymbol{q}_0)\right] . \tag{2.41}$$

Substituting in (2.38)

$$\delta\rho(\boldsymbol{r}, t) = \delta\rho_0 \cos(\boldsymbol{q}_0 \cdot \boldsymbol{r}) \mathrm{e}^{-D_c q_0^2 t} \,, \tag{2.42}$$

which gives that the fluctuation decays exponentially with time constant

$$\tau_c(\boldsymbol{q}_0) = \frac{1}{D_c q_0^2} \,. \tag{2.43}$$

Now, we treat collective diffusion in a Langmuir gas. We consider fluctuations in the coverage, by considering the evolution of $\theta_{\boldsymbol{l}}(t)$, which represents the probability that at time t site $\boldsymbol{l}$ is occupied, from an initial periodic configuration. This evolution is described by a *master equation*

$$\frac{\mathrm{d}\theta_{\boldsymbol{l}}}{\mathrm{d}t} = \alpha \sum_{\boldsymbol{a}} (\theta_{\boldsymbol{l}+\boldsymbol{a}} - \theta_{\boldsymbol{l}}) \,, \tag{2.44}$$

where $\boldsymbol{l} + \boldsymbol{a}$ are the positions of the first neighbors of site $\boldsymbol{l}$ of the two-dimensional Bravais lattice (noting that the only isotropic two-dimensional Bravais lattices are the square and the hexagonal lattices). The coefficient $\alpha = \nu_j / n_{\mathrm{pv}}$ is the directional jump rate from $\boldsymbol{l}$ to $\boldsymbol{l} + \boldsymbol{a}$. The equilibrium probability is the average coverage θ, so that the fluctuation of the coverage is given by

$$\delta\theta_{\boldsymbol{l}}(t) = \theta_{\boldsymbol{l}}(t) - \theta \,. \tag{2.45}$$

The master equation for $\delta\theta_{\boldsymbol{l}}(t)$ is, thus,

$$\frac{\mathrm{d}\delta\theta_{\boldsymbol{l}}}{\mathrm{d}t} = \alpha \sum_{\boldsymbol{a}} (\delta\theta_{\boldsymbol{l}+\boldsymbol{a}} - \delta\theta_{\boldsymbol{l}}) \,. \tag{2.46}$$

which has to be solved with the initial condition

$$\delta\theta_{\boldsymbol{l}}(0) = \delta\theta_0 \cos(\boldsymbol{q}_0 \cdot \boldsymbol{l}) \,; \tag{2.47}$$

$S(\boldsymbol{q}, t)$, in this case, is defined as

$$S(\boldsymbol{q}, t) = \sum_{\boldsymbol{l}} \mathrm{e}^{\mathrm{i}\boldsymbol{q}\cdot\boldsymbol{l}} \delta\theta_{\boldsymbol{l}}(t) \,, \tag{2.48}$$

with the inversion formula

$$\delta\theta_{\boldsymbol{l}}(t) = A_c \int \mathrm{d}\boldsymbol{q} \mathrm{e}^{-\mathrm{i}\boldsymbol{q}\cdot\boldsymbol{l}} S(\boldsymbol{q}, t) \,, \tag{2.49}$$

where A_c is the area of the primitive unit cell of the Bravais lattice. Inserting (2.49) in (2.46), one obtains

$$\frac{\mathrm{d}S}{\mathrm{d}t} = -f(\boldsymbol{q}) S(\boldsymbol{q}, t) \,, \tag{2.50}$$

with

$$f(\boldsymbol{q}) = \alpha \sum_{\boldsymbol{a}} (1 - \mathrm{e}^{-\mathrm{i}\boldsymbol{q}\cdot\boldsymbol{a}}) = \alpha \sum_{\boldsymbol{a}} [1 - \cos(\boldsymbol{q} \cdot \boldsymbol{a})] \,. \tag{2.51}$$

For long-wavelength fluctuations $q \ll 1/a$,

$$f(\boldsymbol{q}) = \alpha \sum_{\boldsymbol{a}} \frac{1}{2} (\boldsymbol{q} \cdot \boldsymbol{a})^2 = \frac{\nu_j}{4} a^2 q^2 \,, \tag{2.52}$$

recalling that $\alpha = \nu_j / n_{\mathrm{pv}}$ and verifying the equation for the square and hexagonal lattices. However, from (2.30) $\nu_j a^2 / 4 = D_s(0)$, so that

$$f(\boldsymbol{q}) = D_s(0) q^2 \,. \tag{2.53}$$

Therefore,

$$S(\boldsymbol{q}, t) = S(\boldsymbol{q}, 0) \mathrm{e}^{-D_s(0) q^2 t} \,, \tag{2.54}$$

with

$$S(\boldsymbol{q}, 0) = \frac{\delta\theta_0}{2A_c} [\delta(\boldsymbol{q} - \boldsymbol{q_0}) + \delta(\boldsymbol{q} + \boldsymbol{q_0})] \tag{2.55}$$

and, finally,

$$\delta\theta_{\boldsymbol{l}}(t) = \delta\theta_0 \cos(\boldsymbol{q}_0 \cdot \boldsymbol{l}) \mathrm{e}^{-D_s(0) q_0^2 t} \,, \tag{2.56}$$

which shows that the fluctuation decays with a time constant

$$\tau_c(\boldsymbol{q}_0) = \frac{1}{D_s(0)q_0^2} \,. \tag{2.57}$$

Comparing this with (2.43), one obtains

$$D_c(\theta) = D_s(0) \,, \tag{2.58}$$

which means that in a Langmuir gas, the collective diffusion coefficient does not depend on coverage, and its value is equal to the zero-coverage tracer diffusion coefficient, as shown in Fig. 2.9. Therefore, collective diffusion in the Langmuir gas is as fast in the limit of full coverage as in the limit of zero coverage. This seemingly counterintuitive result can be explained by recalling that D_c always measures the mobility of density fluctuations. In the limit of $\theta \to 1$, density fluctuations are a few isolated atomic vacancies in the adsorbate, which diffuse as fast as isolated adatoms in the limit $\theta \to 0$.

An equivalent definition of D_c can be given in terms of the asymptotic behavior of the displacement of the center of mass of the adsorbate $\boldsymbol{R} = \sum_{i=1}^{N} \boldsymbol{r}_i$

$$D_c = \lim_{t\to\infty} \frac{1}{2dNS_0 t} \langle [\boldsymbol{R}(t) - \boldsymbol{R}(0)]^2 \rangle \,, \tag{2.59}$$

where S_0 is the *static structure factor*, which can be related to the isothermal compressibility of the adsorbate χ_T by

$$S_0 = \overline{\rho} k_B T \chi_T \,, \tag{2.60}$$

where the average density $\overline{\rho}$ is given by $\overline{\rho} = \theta/a^2$. The equivalence of the definitions of D_c by (2.59) and by Fick's law can be demonstrated in a straightforward but lengthy way. The interested reader is referred to [2.111]. From the computational point of view, the comparison of (2.11) and (2.59) shows that D_s is much easier to calculate than D_c, because in a single simulation box, there are N independent samples for calculating D_s, while there is a single sample (the coordinate of the center of mass) for calculating D_c.

The calculation of D_c in interacting systems turns out to be quite difficult. However, at variance with D_s, we note that for D_c memory effects are absent in the Langmuir gas, so that we may assume that they are somewhat less important even in the presence of lateral interactions besides site blocking. If memory effects are neglected, D_c in a lattice gas of coverage θ turns out to be given by the following expression [2.112, 113]

$$D_c = \frac{a^2 \langle \nu_j \rangle}{4 k_B T \theta \chi_T} \,, \tag{2.61}$$

where $\langle \nu_j \rangle$ is the thermally averaged jump rate.

Results about the dependence of D_c in a triangular lattice gas with repulsive interactions are given in Fig. 2.10. These results [2.110] have been obtained

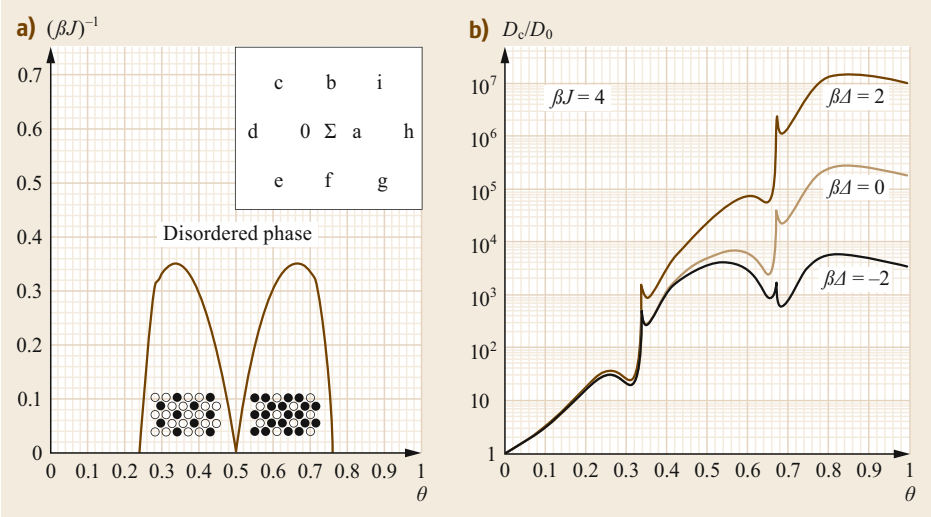

Fig. 2.10 **(a)** Phase diagram of the repulsive lattice gas on a triangular lattice. Nearest-neighbor interactions are assumed. The *inset* considers an adatom that jumps from the adsorption site 0 to the adsorption site a, passing through the saddle point Σ. In 0, the adatom feels the repulsion of other adatoms which may occupy sites b, c, d, e, and f. This repulsion has intensity $J > 0$. At the saddle point, the adatom feels the interaction with other adatoms in sites b and f, with intensity J_Σ, which may be either positive or negative. Putting $\Delta = J - J_\Sigma$, the energy barrier E_b for this jump is given by $E_b = E_0 - J(n_c + n_d + n_e) - \Delta(n_b + n_f)$, where E_0 is the energy barrier for an isolated adatom, and the variables n are either 0 or 1, depending on the corresponding site being free or occupied by an adatom. **(b)** Behavior of D_c depending on the coverage θ for $\beta J = 4$ and different values of $\beta\Delta$, with $\beta = 1/(k_B T)$ (adapted from [2.110])

by the approximation of (2.61), in which the thermally averaged quantities $\langle \nu_j \rangle$ and χ_T were calculated by the cluster variation method [2.114]. The results of Fig. 2.10 are representative of the complex dependence of D_c on coverage in systems in which there is the formation of ordered phases. This complex behavior results from the competition between the decrease of both $\langle \nu_j \rangle$ and of χ_T in the ordered phases. Outside the region of the phase diagram corresponding to the ordered phases, D_c shows a tendency to increase with θ because of the repulsive character of the interactions.

However, it must be noted that the approximation of (2.61) may be insufficient in the vicinity of phase transitions in the adsorbate, where memory effects may become important also for collective diffusion [2.115]. More sophisticated analytical approaches have been developed in more recent times [2.116, 117], also for heterogeneous and anisotropic lattices [2.118–120].

2.3 Experimental Measurements of Diffusion

Various techniques have been established to measure diffusion of atoms and molecules at surfaces experimentally. Again, the literature is vast, and there have been a number of comprehensive reviews on experimental progress [2.1, 4, 121–123]. There is a broad distinction between experimental techniques that either measure the evolution of an initially imposed concentration profile of a surface species, and those that follow the motion of individual particles moving in equilibrium. The former generally measures diffusion over relatively large length scales and interprets the motion within Fick's law and usually provides chemical diffusion constants and their temperature dependence. Once the concentration profile has been established, its evolution can be measured by various methods [2.1], including work function probes, photoelectron microscopy, and scanning Auger microscopy. Similarly, laser-induced thermal desorption has been used to repeatedly desorb species from a particular region of the surface and to subsequently monitor the rate of refilling by diffusion. All these methods rely on being able to generate a suitable initial configuration and, more fundamentally, are only indirectly related to the underlying microscopic characteristics of the system.

Equilibrium methods generally follow the motion of individual particles or fluctuations in the equilibrium configuration of an assembly of particles. Equilibrium methods, therefore, provide more direct microscopic information; specifically, local correlations in individual particle motion can be understood in detail, along with the transition between localized microscopic interactions and dynamics that follow Fick's law in the macroscopic limit. Equilibrium diffusion measurements can be routinely performed using time-lapse imaging, typically based on scanning tunneling microscopy (STM) or field ion microscopy (FIM) [2.121, 124]. However, because of the limited framing rate (interframe times are at least milliseconds [2.124]) they can only distinguish the *before* and *after* states associated with jumps between adsorption sites—the detail of, for example, long jumps cannot be captured. Similarly, to limit the extent of motion between frames, low temperatures are usually required (i.e., thermal energy, $k_B T \ll$ activation energy, E_a), which means such data is often from a different regime than to many physical processes of practical interest, such as catalysis or epitaxial growth. Fluctuation correlation methods such as fluorescence correlation spectroscopy (FCS) [2.125] and x-ray photon correlation spectroscopy (XPCS) [2.126] are equilibrium methods that provide more extensive information, as they yield correlation information on specific length scales, using optical and x-ray scattering, respectively. However, as they are sensitive to mesoscopic length scales and relatively long timescales, they still cannot provide a complete atomic-scale description of motion.

The technique of helium spin-echo (HeSE) [2.127–130] is a relatively recent equilibrium approach to measuring surface diffusion. The method provides perhaps the most comprehensive surface transport data available—giving access to both diffusion and other forms of surface motion. The technique is the surface analogue of quasielastic neutron scattering (QENS) [2.131] and involves scattering a beam of *neutral* thermal energy helium atoms from mobile species on a surface. The scattered atom distribution is directly related to a pair correlation function that provides a comprehensive statistical description of the motion, with information spanning timescales between picoseconds and nanoseconds and length scales from ångströms up to tens of nanometers. Since HeSE provides such comprehensive data, we will focus on that method here and provide a series of examples.

2.3.1 Helium Scattering and the Spin–Echo Technique

The broad technique of helium atom scattering has been used routinely in a number of specialist laboratories around the world since the 1970s. The method involves producing a nearly monochromatic, collimated,

beam of thermal energy helium atoms (typically 10 to 100 meV), then scattering the atomic beam from a surface in order to study the surface properties [2.132–135]. Since the incident energy of helium is so low, the atoms scatter from the outermost valence electrons at the surface. Through that interaction, the helium atoms can, in general, exchange momentum, $\hbar\Delta\boldsymbol{k}$, and energy, $\hbar\omega$, with the surface, where $\boldsymbol{k}$ and ω relate to wavevector and frequency, respectively. Both elastic and inelastic scattering are possible, enabling surface structure and dynamical processes to be studied, respectively.

In the case of elastic scattering, when the helium atoms experience no energy exchange with the surface, the main processes are diffraction and diffuse scattering. These have been used to study surface structure and growth, often in relation to thin films and delicate adsorbed species [2.133, 134]. During inelastic scattering, helium atoms generally interact with surface phonons or adsorbate vibrations. If the interaction is with a single mode, the well-defined energy transfer condition corresponding to the vibrational frequency of the mode means surface dispersion curves can be mapped out [2.135]. Multiphonon interactions are also possible.

If helium atoms interact with an aperiodically moving species (i.e., a diffusing atom), energy changes are still possible, but are now centered around zero energy transfer, i.e., around the elastic peak. These *quasielastic* energy changes are characteristic of that aperiodic diffusive motion and, hence, enable the motion to be studied—the phenomenon is known as *quasielastic helium atom scattering* (QHAS) and underpins the HeSE method. Note that these quasielastic energy changes are very small, usually in the μeV range, or even smaller.

In general, quantitative interpretation of helium scattering data can be complex, and various approximations have been developed [2.132]. Fortunately, for helium atoms scattered from mobile adsorbates on a surface, the kinematic approximation can be used to simplify analysis by decomposing the overall scattered intensity, $A(\Delta\boldsymbol{K},\omega)$, into the product of an intensity structure factor, S, and an amplitude form factor, F,

$$A(\Delta\boldsymbol{K},\omega) = S(\Delta\boldsymbol{K},\omega)\cdot|F(\Delta\boldsymbol{K},\omega)|^2 \ ; \qquad (2.62)$$

$S(\Delta\boldsymbol{K},\omega)$ is determined by the position of the scatterers on the surface, and $F(\Delta\boldsymbol{K},\omega)$ is a result of the shape of each scatterer. For analysis of adsorbate dynamics, the approximation works very well [2.136]; $\Delta\boldsymbol{K}$ represents the change in wavevector of the helium atoms during scattering, projected into the surface plane and is given by the scattering geometry according to

$$\Delta K = k_\mathrm{f}\sin(\theta_\mathrm{SD}-\theta_\mathrm{i}) - k_\mathrm{i}\sin(\theta_\mathrm{i}); \qquad (2.63)$$

k_i and k_f are the incident and final helium wavevectors, and θ_SD and θ_i are the total scattering angle and incident angles, respectively; $S(\Delta\boldsymbol{K},\omega)$ is known as the dynamic structure factor, a quantity used extensively in neutron scattering [2.131], and which was shown by *Van Hove* [2.137] to be related to a pair correlation function, $G(\boldsymbol{R},t)$, by a double Fourier transform in both space and time, through the intermediate scattering function, $I(\Delta\boldsymbol{K},t)$,

$$S(\Delta\boldsymbol{K},\omega) \overset{\text{Temporal FT}}{\rightleftharpoons} I(\Delta\boldsymbol{K},t) \overset{\text{Spatial FT}}{\rightleftharpoons} G(\boldsymbol{R},t). \qquad (2.64)$$

The pair correlation function $G(\boldsymbol{R},t)$ provides a complete statistical description of the motion of the scatterers.

In most energy-resolved helium scattering experiments, the scattering angles are controlled by the experimental setup, and the *absolute* energy distribution of the scattered beam is measured using time-of-flight methods [2.134]. Hence, providing F can be accounted for or ignored, $S(\Delta\boldsymbol{K},\omega)$ is obtained directly from the experiment, which then provides information about diffusion and vibration through the relationship with $G(\boldsymbol{R},t)$. For QHAS experiments of surface diffusion, the finite velocity spread in the initial helium beam is a serious limit on time-of-flight measurements. The velocity spread masks the tiny quasielastic energy changes that relate to surface diffusion in all but a very few physical systems [2.138, 139]. In contrast, HeSE experiments only measure the energy *changes* during scattering, and so are not limited by the spread of energies in the incident helium beam, and, thus, the HeSE method can be applied much more widely. As we will describe below, HeSE experiments obtain the intermediate scattering function, $I(\Delta\boldsymbol{K},t)$, directly, hence providing a more direct link to the information about diffusion that is encoded in $G(\boldsymbol{R},t)$. By measuring $I(\Delta\boldsymbol{K},t)$ under a sufficiently wide range of conditions, analysis can reveal the full detail of surface transport, including diffusion, vibration, energy exchange, and collective motion, in a regime that is not accessible to any other experimental technique.

2.3.2 Measuring the Intermediate Scattering Function with HeSE

Before proceeding to discuss HeSE measurements of diffusion, we give a brief overview of the technique, following the semiclassical description by *Gähler* et al. [2.140]; for more details, the reader is directed to [2.130]. The basic principle of HeSE is shown schematically in Fig. 2.11. An HeSE instrument con-

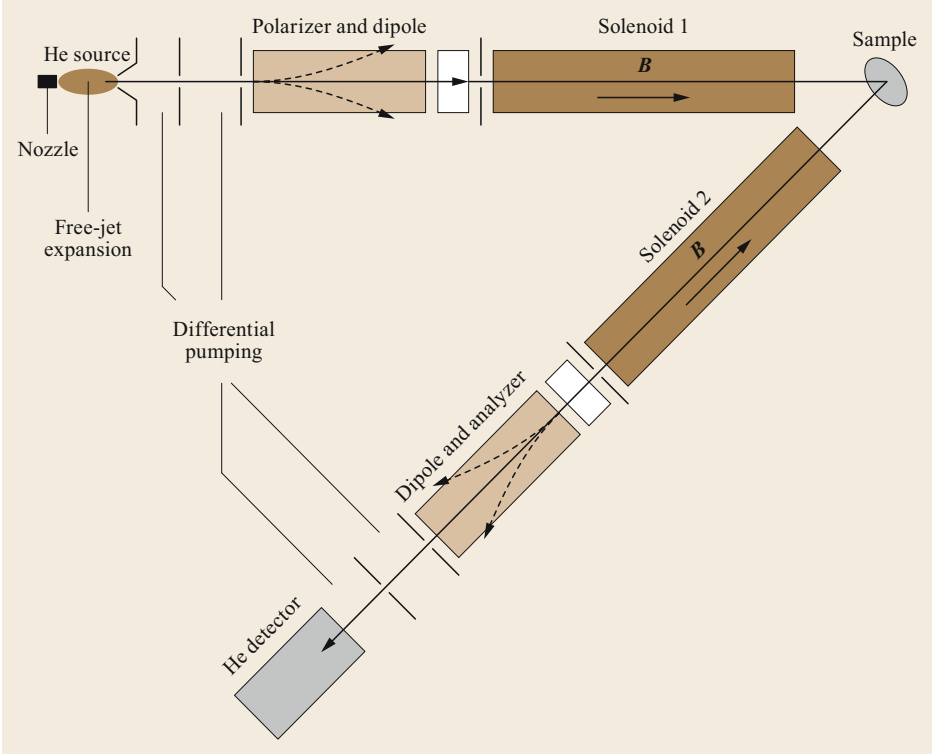

Fig. 2.11 The HeSE technique. Atoms produced in the helium source are polarized in a hexapole magnet, spin-aligned in a dipole field, and then passed through a solenoid magnet. The solenoid splits the helium wavepacket into two spin components, which reach the sample separated by a short time delay t_{SE}. Along the second arm of the instrument, the spin components are recombined and passed through a further dipole and hexapole to spin-analyze the beam. The beam-averaged polarization is proportional to the intermediate scattering function $I(\Delta \boldsymbol{K}, t)$.

sists of an extended series of vacuum chambers to convey a beam of helium atoms from the beam source to the sample and then to transfer atoms scattered in a particular direction, to the detector. Along the two beamlines, a series of magnetic components are used to measure the intermediate scattering function, by making use of the nuclear spin of ^{3}He.

Working along the beamlines shown in Fig. 2.11, the beam of ^{3}He atoms is first produced in a standard free-jet supersonic expansion, followed by several stages of differential pumping to reduce the background helium pressure diffusing along the beamline from the source chamber. Next, the beam is passed through an intense hexapole magnetic field, where the ^{3}He nuclear spins must align either parallel or antiparallel to the local-field direction. The hexapole field is highly inhomogeneous and has a magnitude B_h, which varies quadratically with the radius. Consequently, the field applies a force to each spin, given by $\boldsymbol{F} = \pm\mu\nabla B_h$, which focusses one polarization of atoms onto the sample, while the other is defocused and removed for recycling. The focused component of the beam is then passed through a dipole field, which aligns the spins in a particular direction perpendicular to the beamline, which we denote as the state $|+\rangle_x$. The focused atoms then continue into a solenoidal field B_s oriented along the beamline. Inside the solenoid, the helium wavepacket can be represented as a superposition of two spin eigenstates, aligned either parallel or antiparallel to the field,

$$|+\rangle_x = \frac{1}{\sqrt{2}}(|+\rangle_z + |-\rangle_z), \tag{2.65}$$

whose energies are split by $\pm\mu B_s$, respectively. Since the energies are split, the two spin components, $|\pm\rangle_z$, travel at different velocities and so separate as they travel towards the sample. It can be shown [2.130] that the two components reach the sample with a time delay, t_{SE}, given by

$$t_{SE} = \frac{\gamma\hbar}{mv^3}\int_0^L B_s \mathrm{d}l\,, \tag{2.66}$$

where γ, m and v are the gyromagnetic ratio, mass, and velocity of the ^{3}He atoms, respectively, and the integral is through the solenoid field of length L. In practice, t_{SE} is controlled by adjusting the current in the solenoid windings, and can range from a fraction of a picosecond to the nanosecond range.

After interacting with the surface, atoms scattered in a particular outgoing direction pass along the second beamline, through an identical but reversed solenoid field, where the separated components, $|\pm\rangle_z$, are recombined. If the surface remains unchanged over t_{SE}, both spin components will scatter from the surface in exactly the same way, so the original polarized form, $|+\rangle_x$, will be recovered. However, if the surface has changed, for example, if an atom has jumped between adsorption sites, the recovered spin direction will be changed, and, on average, there will be a reduction in the overall polarization of the beam.

The recovered spins then pass through an analyzer dipole and hexapole, which selects the x component of the polarization, and focuses that proportion of atoms into a mass-spectrometer detector. Quadrature methods, which involve adding an extra $\pi/4$, $\pi/2$, and $3\pi/2$ of spin rotation near the first dipole field, enable the full polarization to be determined [2.141]. The measured polarization, $P(\Delta\boldsymbol{K}, t_{SE})$, is usually a good approximation to the normalized intermediate scattering function, $I(\Delta\boldsymbol{K}, t)$, given by

$$P(\Delta\boldsymbol{K}, t_{SE}) = \frac{I(\Delta\boldsymbol{K}, t_{SE})}{I(\Delta\boldsymbol{K}, 0)} \,. \tag{2.67}$$

In other words, by measuring polarization, we make a direct measurement of the surface correlation over time t_{SE} and on the length scale and in the direction determined by the wavevector $\Delta\boldsymbol{K}$. Note that to measure certain properties, such as phonon linewidths, a more sophisticated *wavelength transfer matrix* approach is helpful [2.130, 142, 143], but this is beyond the scope of the present chapter.

The HeSE measurement principle is very general and thus can be applied to a wide variety of experiments, including measuring surface diffusion, surface and adsorbate vibrations, and for probing energy exchange rates. To date, experiments have usually been carried out on single crystal samples under ultra-high vacuum conditions. Samples are mounted on a six axis manipulator to enable $\Delta\boldsymbol{K}$ to be aligned along any surface direction. The vacuum systems include standard surface preparation and characterization tools, as well as sample transfer for rapid-exchange into the measurement facility.

2.3.3 Measuring Diffusion with HeSE

Studying diffusion, or other surface properties, with HeSE involves interpreting the measured intermediate scattering function. Although, in principle, $G(\boldsymbol{R}, t)$ contains a complete description of all the surface dynamics and is related to $I(\Delta\boldsymbol{K}, t_{SE})$ by a spatial Fourier transform, it is usually not possible to obtain sufficient data to perform an inverse transform directly. Hence, HeSE analysis is generally based on examining changes in the shape of $I(\Delta\boldsymbol{K}, t_{SE})$ across a range of values of $\Delta\boldsymbol{K}$.

Figure 2.12 shows a cartoon of the typical form of $I(\Delta\boldsymbol{K}, t_{SE})$ for a measurement of an adsorbed species on a surface. The function takes a decaying form as the surface correlation, as seen by the helium beam over the length scale and direction determined by $\Delta\boldsymbol{K}$, reduces with time. Oscillations in $I(\Delta\boldsymbol{K}, t_{SE})$ relate to surface vibrations, such as phonons, and generally die away quickly at a rate that is characteristic of energy exchange with the substrate. The overall decay relates to aperiodic processes such as the dephasing of vibrations [2.144], where the characteristic time is usually less than a few picoseconds, or surface diffusion, where the characteristic time can be much longer. Surface dif-

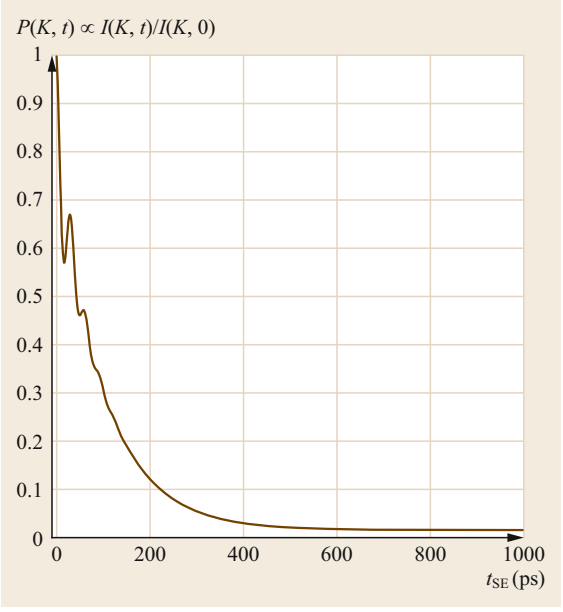

Fig. 2.12 The typical form of $I(\Delta\boldsymbol{K}, t_{SE})$ as measured by HeSE. The general form is a decaying function, as the surface correlation, as seen by the helium beam over the length scale and direction determined by $\Delta\boldsymbol{K}$ reduces with spin echo time t_{SE}. Periodic surface processes, such as phonons, result in oscillations, while aperiodic processes such as diffusion generally result in an exponential decay

fusion generally results in an exponentially decaying form

$$I(\Delta \boldsymbol{K}, t_{\mathrm{SE}}) = A \exp(-\alpha t) \,, \tag{2.68}$$

as correlations in the surface configuration, measured at a particular value of $\Delta \boldsymbol{K}$, decay with a well-defined rate $\alpha(\Delta \boldsymbol{K})$, known as the *dephasing rate*. Different analytic models for surface transport, such as simple hopping, long jumping, or continuous Brownian motion, each give rise to a characteristic variation of α with $\Delta \boldsymbol{K}$. Hence, by measuring $\alpha(\Delta \boldsymbol{K})$, the microscopic mechanism of motion can be determined. Once the mechanism is understood, parameters describing that motion can be obtained by fitting a suitable model to the empirical data, and from those model parameters, macroscopic quantities, such as diffusion constants or energy barriers, can be determined [2.130].

Jump Diffusion

Jump diffusion was first analyzed by *Chudley* and *Elliott* [2.145] in order to interpret quasielastic neutron scattering data. The same principles were applied to HeSE [2.146] and resulted in $I(\Delta \boldsymbol{K}, t_{\mathrm{SE}})$ taking the general form in (2.68), with $\alpha(\Delta \boldsymbol{K})$ varying sinusoidally,

$$\alpha(\Delta \boldsymbol{K}) = 2 \sum_j \nu_j \sin^2 \left(\frac{\Delta \boldsymbol{K} \cdot \boldsymbol{j}}{2} \right) . \tag{2.69}$$

The summation is over all the possible adsorbate jumps $\boldsymbol{j}$ within the unit cell, and ν_j are the associated jump frequencies—in other words, each possible jump type contributes a sinusoidal component to the overall dependence. The tracer diffusion constant may then be estimated using [2.147]

$$D_{\Delta K} = \frac{1}{2} \nu \left\langle j^2_{\Delta K} \right\rangle \,,$$

where the parameters are projected along a particular $\Delta \boldsymbol{K}$ direction.

As an example, Fig. 2.13 shows measured HeSE data for the jump diffusion of H and D atoms on a Pt(111) surface, from [2.148]. Here, the mechanism of motion almost conforms perfectly to a single jump model, in excellent agreement with the form in (2.69). More widely, measurements have established that show that most systems exhibit jump characteristics, although the precise mechanism often contains a distribution of different jump lengths, elements of continuous motion (e.g., intracell diffusive motion [2.144]), and more complex processes (see later). In the case of different jump lengths, these can be distinguished by fitting a series of Fourier components to the measured $\alpha(\Delta \boldsymbol{K})$ dependence, one for each type of jump, using (2.69).

Other examples where good approximations to jump diffusion have been observed include alkali metals atoms on transition metals [2.149–152] (although in many situations the motion can be further complicated by lateral interactions, leading to correlated motion) and many small molecules [2.153–160]. Note that (2.69) applies to jumps between adsorption sites that form a Bravais lattice directly. For other networks of adsorption sites, such as the hexagonal lattice that can be formed from the two types of hollow sites on a (111) surface, a more complex model applies [2.161].

Continuous Brownian Motion

If the lateral variation in the potential between adsorbates and substrate is weak, or if the coupling between adsorbate and substrate is very strong, then rather than hopping, continuous Brownian motion can result, even on the atomic scale. Analysis of such motion [2.147] also results in $I(\Delta \boldsymbol{K}, t_{\mathrm{SE}})$ decaying exponentially with t_{SE}, but this time, α varies quadratically with $\Delta \boldsymbol{K}$,

$$\alpha(\Delta \boldsymbol{K}) = D \Delta \boldsymbol{K}^2 \,, \tag{2.70}$$

scaled by the diffusion constant. Note that in the limit of large length scales (small $\Delta \boldsymbol{K}$), all microscopic mechanisms approach this form, including the limiting case of the previous jump model. An example of perfect Brownian motion at an atomic level is the case of benzene adsorbed on graphite [2.162], as shown in Fig. 2.14. The behavior is a result of the extended nature of the molecule averaging over multiple atomic interactions, combined with a high rate of energy exchange between the molecule and the substrate.

Activation Energies

At a particular $\Delta \boldsymbol{K}$, the dephasing rate, α, usually varies with temperature T according to the well-known Arrhenius law

$$\alpha = \alpha_0 \exp \left(-\frac{E_{\mathrm{a}}}{k_{\mathrm{B}} T} \right) , \tag{2.71}$$

where E_{a} is an activation energy for motion, and k_{B} is the Boltzmann constant. Hence, activation energies can be routinely determined from measurements of $I(\Delta \boldsymbol{K}, t_{\mathrm{SE}})$ at different temperatures. However, it is important to approach such analysis with care. Depending on the mechanism of motion, values of $I(\Delta \boldsymbol{K}, t_{\mathrm{SE}})$ at a particular value of ΔK may contain contributions from multiple processes, each with different temperature dependencies. For example, at the sinusoidal minima in Fig. 2.13, at $\Delta \boldsymbol{K} \approx 2.5\,\text{Å}^{-1}$, measurements of $I(\Delta \boldsymbol{K}, t_{\mathrm{SE}})$ contain a vanishing amount of information about the jump mechanism. Similarly, it is also

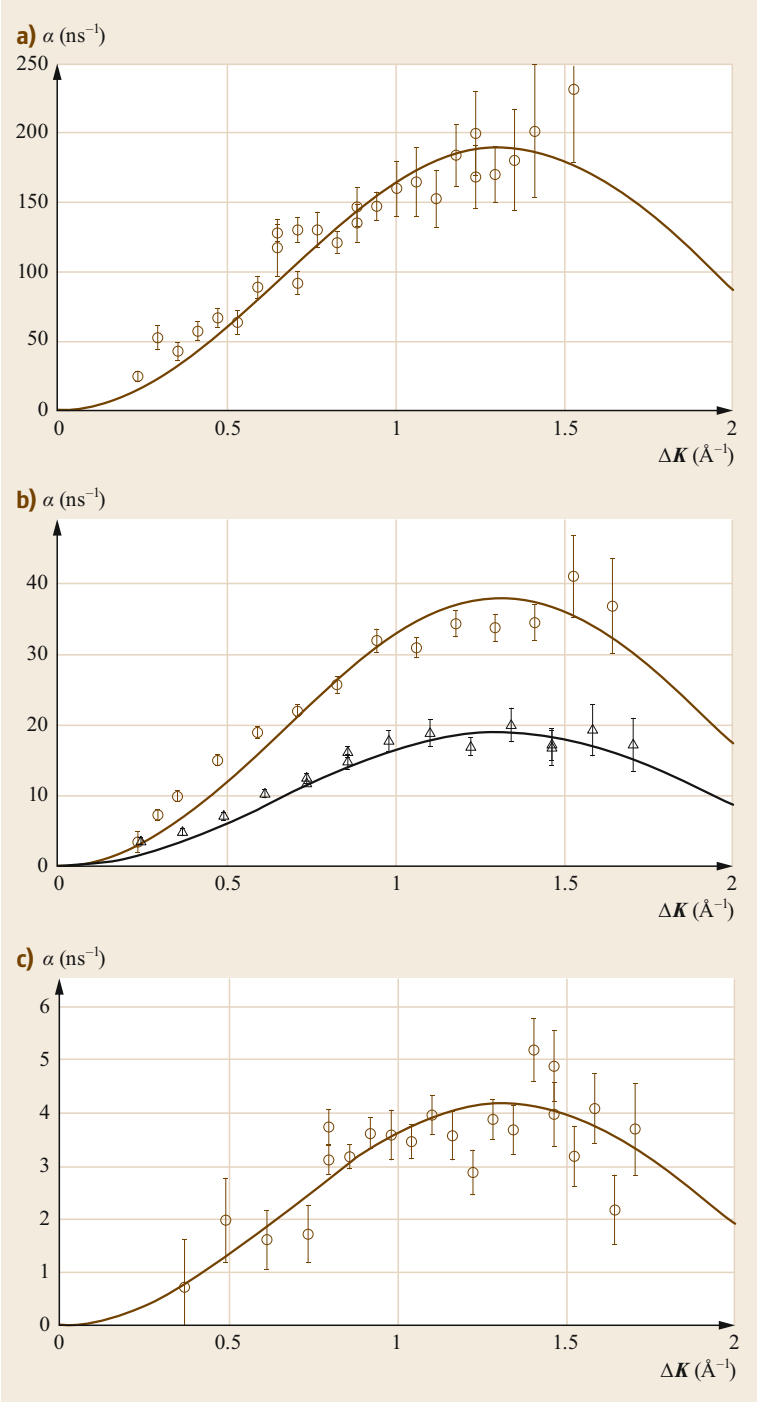

Fig. 2.13a–c HeSE measurements (dephasing angle α versus momentum transfer $\Delta\boldsymbol{K}$) of H (*brown circles*) and D (*black triangles*) diffusion on a Pt(111) surface at three temperatures: **(a)** 220 K, **(b)** 140 K, and **(c)** 90 K. The measurements are in excellent agreement with a single jump model for hopping between adjacent fcc hollow sites (adapted with permission from [2.148], Copyright 2012 by the American Physical Society)

possible for the mechanism of motion to change with temperature, further affecting the analysis. Figure 2.15 illustrates Arrhenius plots for ethanethiol adsorbed on Cu(111) [2.163]; at low temperatures the data is dominated by localized rotation of the molecule (see below), whereas as higher temperatures it is overtaken by translation. The mechanism in each regime was determined from the form of $\alpha(\Delta\boldsymbol{K})$, which subsequently enabled the Arrhenius behavior to be understood and accurate activation energies to be extracted.

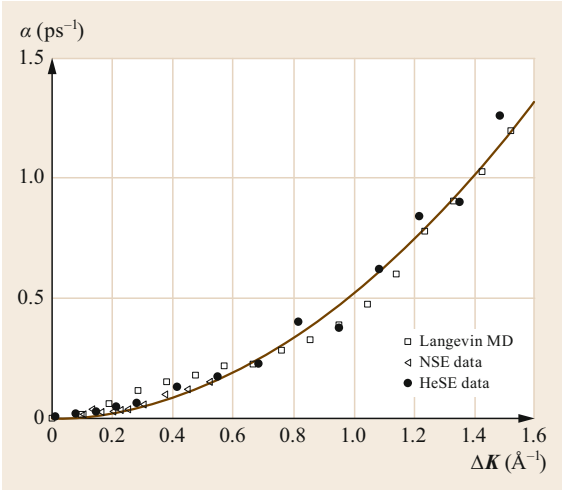

Fig. 2.14 HeSE measurements of the diffusion of benzene molecules on a graphite surface, showing continuous Brownian motion on the atomic scale. The *solid line* is a quadratic fit, as per (2.70), resulting in a diffusion constant of $D = 5.39 \pm 0.13 \times 10^{-9}$ m^2 s^{-1}. HeSE experiments (*circles*) were also shown to be in good agreement with neutron spin-echo measurements (*triangles*) performed at low coverages and Langevin MD simulations described in [2.162]

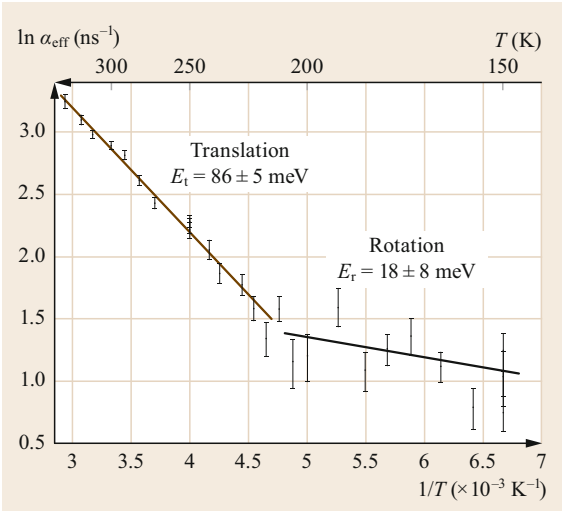

Fig. 2.15 Arrhenius plots of the dephasing rate, α, extracted from the rotational and translationally dominated measurement regimes for ethanethiol on Cu(111) (adapted with permission from [2.163], Copyright 2012 by the American Physical Society)

Diffusion measurements are often used to estimate the adiabatic potential energy barrier to diffusion, and it is possible to use HeSE data to estimate these barriers. The activation energy obtained from Arrhenius analysis alone usually underestimates the adiabatic barrier, and currently, the most accurate way to obtain the true barrier is to use Langevin molecular dynamics simulations to refine a trial potential, including adjustment of the adiabatic barrier heights, to best fit the experimental data (see below).

2.3.4 Beyond Diffusion Constants

Most real systems do not conform fully to the simple analytic models of diffusion discussed so far. For example, when alkali metals are adsorbed onto metal surfaces, electron transfer sets up a strong dipole. Consequently, there is strong dipole–dipole repulsion between adsorbed atoms and, thus, strong correlations in the motion result [2.149–152]. In order to interpret such systems, more sophisticated methods are required and, in general, analytic expressions are insufficient. Simulations are routinely used to predict adsorbate motion given a specific model, from which simulated HeSE data can be produced and subsequently compared with experiment. Free parameters within the model can then be refined to best fit the experimental data. Molecular dynamics simulations that treat all the atoms in the substrate individually can be used but are computationally intensive. For computational speed, the Langevin framework has been used widely, within which only the adsorbed atoms are treated explicitly. The adsorbate–substrate interaction is described by a *frozen* adiabatic potential, $V(\boldsymbol{R})$, and a frictional coupling parameter, η, is used to describe energy exchange. The equation of motion for the i-th adsorbate atom then becomes

$$m\ddot{\boldsymbol{R}}_i = -\nabla V(\boldsymbol{R}_i) - \eta m\dot{\boldsymbol{R}}_i + \xi_i(t) + \sum_{j\neq i} F(|\boldsymbol{R}_j - \boldsymbol{R}_i|), \tag{2.72}$$

where the second and third terms are drag and stochastic excitation, respectively, describing interaction with the substrate heat bath in terms of η, which is scaled according to the fluctuation dissipation theorem [2.164]. The final term can be added to include pairwise interaction forces F between adsorbed atoms. The Langevin framework thus provides a much more sophisticated and general description of the dynamical adsorbate–substrate interaction than is possible using diffusion constants alone.

Interaction Potentials

In general, since adsorbate motion explores the entire surface, HeSE data enables the complete shape of the potential energy surface for diffusion to be determined, not just the rate-limiting adiabatic barri-

ers. The Langevin molecular dynamics approach has thus been used to determine many experimental potentials [2.149–152, 154–160, 165]. Usually such a determination can be performed to a level of better than 10 meV, depending on the complexity of the system and the quantity of HeSE data available.

Figure 2.16a shows a typical experimental potential energy surface, in this case determined for CO molecules on Cu(111) [2.156]. The cross section in Fig. 2.16b shows the potential along the high-symmetry directions within the unit cell. Various features are clearly evident, including the adsorption minima (top site), the overall maximum (hollow site), as well as intermediate minima and maxima, the latter which forms the principal rate-limiting barrier for diffusion. In this case, as the coverage of CO is increased, CO interactions were not found to be described by pairwise interactions, but to result in *nonpairwise* changes in the form of the potential, as shown by the dashed brown line in the figure. Despite being clearly observed, at present, the theoretical origin of this effect is not well understood.

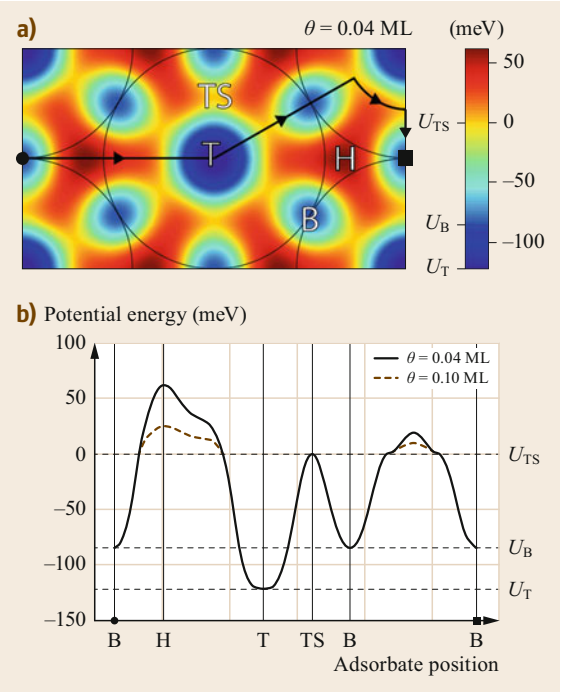

Fig. 2.16a,b Experimental adsorbate–substrate potential energy surface determined for the center of mass motion of CO molecules on a Cu(111) surface (adapted from [2.156]). T, H, B, and TS represent the top site (adsorption site), hollow site (potential maximum), bridge site (local minimum), and the transition state (rate limiting maximum), respectively. **(a)** shows the lateral variation, while **(b)** shows cross sections along the directions indicated in **(a)**. Increasing the CO coverage results in changes to the potential energy surface rather than localized interaction effects (adapted from [2.156], © IOP Publishing. Reproduced with permission. All rights reserved)

As well as providing a detailed fundamental description of the surface interaction, such interaction potentials have been used as a sensitive test of the validity of first-principles theory for predicting potentials—recent advances in dispersion-corrected density functional theory have been tested [2.160]. Similarly, as more complex molecular systems are beginning to be studied using HeSE, it is becoming possible to explore how higher degrees of freedom can be included in the potential. For example, the coupling between diffusion and molecular orientation has been examined for pentacene molecules [2.166].

Energy Transfer and Rate Theory

Transition state theory (TST) can be used to estimate transition rates across a barrier (i.e., hopping, in the present context), by using the energy barrier and partition functions in both the transition and well states [2.5]. More sophisticated rate theory models [2.167] also take account of the rate of energy exchange between the substrate and adsorbate, parameterized by the friction, η. Friction has a significant effect on both the mechanism and rate of diffusion. At a simple level, if the friction is weak, the rate of activation to jumping is low, as it takes a long time for fluctuations to provide sufficient energy to overcome the limiting barrier. However, once activated, it also takes a long time for motion to deactivate, so adsorbates subsequently take long jumps over the surface. Conversely, if the friction is very high, adsorbates are turned around before they actually cross the barrier, and so the rate of jumping is also low, but with well-defined single jumps. In the intermediate regime, the highest rates of transport are achieved.

Through these effects on adsorbate dynamics the different frictional regimes can be identified clearly in HeSE data—using the combined effect on the mechanism and the absolute rate of motion. In general, low-friction regimes can be identified by the presence of long jumps, evident through flattened sinusoidal $\alpha(\Delta \boldsymbol{K})$ curves containing many Fourier components (2.69), such as in the case of Cs/Cu(111) [2.150]. High-friction regimes result in single jumps on a corrugated surface, as is the case for H on Pt(111) [2.148], or Brownian motion on an uncorrugated surface, which is the situation seen for benzene on graphite [2.162]. Langevin molecular dynamics simulations are, again, used to obtain quantitative values of η, and, thus, most

systems where HeSE data has been analyzed in detail have provided precise values of the frictional energy exchange rate.

Adsorbate Interactions and Correlated Motion

Repulsive adsorbate interactions have been studied extensively using HeSE [2.149, 152, 154, 156]. In general, pairwise repulsion between adsorbates leads to the formation of a quasihexagonal overstructure to maximize their separation. These repulsive interactions are superimposed upon the usual adsorbate–substrate interaction potential and can at low coverages lead to a series of larger-scale structures forming. Thermal excitation still leads to motion, which is then determined by both the substrate potential and interactions between adsorbates. The effect on HeSE measurements is the introduction of a *peak and dip* structure superimposed on the $\alpha(\Delta \boldsymbol{K})$ curve. The peak corresponds to jumping within the preferred hexagonal structure, as in (2.69). The dip corresponds to the *preferred* length scale of greatest stability, i.e., at the momentum transfer of the diffraction ring associated with the quasihexagonal structure.

In general, the form of such interactions can be tested by adjusting the form of the pairwise interaction, $F(R)$ in (2.72), and comparing simulations with experiment as usual. For alkali metal atoms moving on transition metal substrates, good agreement has been found with a dipole–dipole repulsion model based on the Topping model for the coverage dependence of the dipole moment [2.149–152]. Conversely, in other systems, it has been possible to rule out the presence of pairwise forces altogether, such as in the case of CO on Pt(111) [2.154]. Here, the signatures for pairwise repulsion between adsorbates were found to be completely absent from the experimental HeSE data. In the existing literature, pairwise forces have been widely invoked to explain changes in the heat of adsorption. The HeSE dynamics data leads to the conclusion that changes in the CO dynamics must be due to more complex longer-scale mean-field changes in the CO/substrate interaction, which cannot be described in a pairwise manner. Such effects cannot be observed with simpler techniques and require direct observation of the dynamical correlations in order to be distinguished.

2.4 Perspectives—Towards Complex Surface Motion

The examples above have illustrated the rich variety of diffusion information that can be accessed experimentally, which motivate new theory. We can clearly see that real systems exhibit complex diffusive behavior, which is related to both the substrate and to the mobile species. Looking forwards, we can highlight a few representative examples of areas where HeSE methods are just beginning to be applied and where further new and interesting phenomena can be expected.

One of the most obvious issues is the fact that real surfaces are much more complex than the flat surfaces generally studied so far. Complex surface structure can modulate and confine diffusion, fundamentally altering the nature of transport at the atomic scale. Signatures of confined diffusion in HeSE measurements have been established [2.130] and essentially involve $I(\Delta \boldsymbol{K}, t_{\mathrm{SE}})$ decaying to a finite level at large t_{SE}—since confinement means the adsorbate always retains some correlation in its position. However, to date, there have been few studies of any form of confined diffusion. Existing work either relates to motion perpendicular to the surface during lateral diffusion [2.149] or diffusion that is confined to narrow stepped terraces of atoms [2.152], where highly anisotropic motion has been observed. In the latter case, anisotropy in the correlations between atoms has also been seen, indicating effective screening of interactions between adsorbates on different terraces.

As molecules become more structurally complex, it becomes crucial to distinguish between many possible dynamical processes. These could include, for example, changes in conformation or motion of a side chain, as well as center of mass motion. To date, HeSE has generally been applied to point particles or rigid molecules with rotation. Specifically, analytic forms of the HeSE signatures for rotational motion have been identified [2.168] and used to distinguish ongoing rotational motion of adsorbed thiols from the onset of translational motion [2.163]. Similarly, jumping, rotating, and flapping motion has been distinguished for thiophene on Cu(111) [2.158], and the contribution of rotational modes in boosting the overall rate of diffusion has been established [2.159]. The next steps are likely to involve decoupling and, thus, an understanding of nonrigid species.

So far, we have only discussed classical mechanisms of diffusion. However, for sufficiently small species and low temperatures, quantum processes can be dominant. The transition towards a quantum diffusion-dominated regime has been observed for H and D atoms on Pt(111) [2.148] and more extensively on Ru(0001) [2.169]. As well as the direct technological relevance of such results to the *hydrogen economy*, HeSE also provides an ideal opportunity for fundamental testing of quantum-rate theory models, and in

particular models for the transition between coherent and incoherent modes of propagation.

All of these areas suggest that a much greater wealth of fundamental information on diffusion is available, which can be accessed experimentally through HeSE, given the method's unique sensitivity to dynamics on the combination of picosecond time and nanometer length scales. Further development of HeSE instrumentation will be important in measuring these increasingly complex forms of motion—for example, to enable better separation of processes by timescales. Fortunately, further increases in resolution and signal level are both realistic prospects [2.170]. We look forward to a next generation of spin-echo measurement facility, and subsequent uptake by the user community, to take forward our scientific understanding in this exciting and unique regime.

References

2.1 R. Gomer: Diffusion of adsorbates on metal surfaces, Rep. Prog. Phys. **53**(7), 917–1002 (1990)

2.2 A. Danani, R. Ferrando, E. Scalas, M. Torri: Lattice–gas theory of collective diffusion in adsorbed layers, Int. J. Mod. Phys. B **11**(19), 2217–2279 (1997)

2.3 H. Brune: Microscopic view of epitaxial metal growth: Nucleation and aggregation, Surf. Sci. Rep. **31**(4), 125–229 (1998)

2.4 J.V. Barth: Transport of adsorbates at metal surfaces: From thermal migration to hot precursors, Surf. Sci. Rep. **40**(3), 75–149 (2000)

2.5 T. Ala-Nissila, R. Ferrando, S.C. Ying: Collective and single particle diffusion on surfaces, Adv. Phys. **51**(3), 949–1078 (2002)

2.6 G. Ehrlich, G. Antczak: *Surface Diffusion – Metals, Metal Atoms, and Clusters* (Cambridge Univ. Press, Cambridge 2010)

2.7 J. Merikoski, I. Vattulainen, J. Heinonen, T. Ala-Nissila: Effect of kinks and concerted diffusion mechanisms on mass transport and growth on stepped metal surfaces, Surf. Sci. **387**(1), 167–182 (1997)

2.8 T.R. Linderoth, S. Horch, L. Petersen, S. Helveg, E. Lægsgaard, I. Stensgaard, F. Besenbacher: Novel mechanism for diffusion of one-dimensional clusters: Pt/Pt(110)-(1 × 2), Phys. Rev. Lett. **82**, 1494–1497 (1999)

2.9 F. Montalenti, R. Ferrando: Leapfrog diffusion mechanism for one-dimensional chains on missing-row reconstructed surfaces, Phys. Rev. Lett. **82**, 1498–1501 (1999)

2.10 J. Heinonen, I. Koponen, J. Merikoski, T. Ala-Nissila: Island diffusion on metal fcc (100) surfaces, Phys. Rev. Lett. **82**, 2733–2736 (1999)

2.11 O.S. Trushin, P. Salo, T. Ala-Nissila: Energetics and many-particle mechanisms of two-dimensional cluster diffusion on Cu(100) surfaces, Phys. Rev. B **62**, 1611–1614 (2000)

2.12 P. Salo, J. Hirvonen, I.T. Koponen, O.S. Trushin, J. Heinonen, T. Ala-Nissila: Role of concerted atomic movements on the diffusion of small islands on fcc(100) metal surfaces, Phys. Rev. B **64**, 161405 (2001)

2.13 L. Xu, G. Henkelman, C.T. Campbell, H. Jónsson: Small Pd clusters, up to the tetramer at least, are highly mobile on the MgO(100) surface, Phys. Rev. Lett. **95**, 146103 (2005)

2.14 G. Barcaro, A. Fortunelli, F. Nita, R. Ferrando: Diffusion of palladium clusters on magnesium oxide, Phys. Rev. Lett. **95**, 246103 (2005)

2.15 E. Pijper, A. Fasolino: Quantum surface diffusion of vibrationally excited molecular dimers, J. Chem. Phys. **126**(1), 014708 (2007)

2.16 R. Ferrando, A. Fortunelli: Diffusion of adatoms and small clusters on magnesium oxide surfaces, J. Phys. Condens. Matter **21**(26), 264001 (2009)

2.17 A. Karim, A. Kara, O. Trushin, T.S. Rahman: The crossover from collective motion to periphery diffusion for two-dimensional adatom-islands on Cu(111), J. Phys. Condens. Matter **23**(46), 462201 (2011)

2.18 S.I. Shah, G. Nandipati, A. Kara, T.S. Rahman: Self-diffusion of small Ni clusters on the Ni(111) surface: A self-learning kinetic Monte Carlo study, Phys. Rev. B **88**, 035414 (2013)

2.19 K. Nakao, T. Ishimoto, M. Koyama: Density functional theory study for Ni diffusion on Ni(111) surface under solid oxide fuel cell operating condition, J. Phys. Chem. C **120**(30), 16641–16648 (2016)

2.20 X. Dai, J. Yang, W. Hu, Y. Liu: Diffusion of Al dimers on the surface of Mg clusters, Eur. Phys. J. B **90**(6), 113 (2017)

2.21 S.I. Shah, G. Nandipati, A. Karim, T.S. Rahman: Self-learning kinetic Monte Carlo simulations of self-diffusion of small Ag islands on the Ag(111) surface, J. Phys. Condens. Matter **28**(2), 025001 (2016)

2.22 S.R. Acharya, S.I. Shah, T.S. Rahman: Diffusion of small Cu islands on the Ni(111) surface: A self-learning kinetic Monte Carlo study, Surf. Sci. **662**(Suppl C), 42–58 (2017)

2.23 K.C. Lai, J.W. Evans, D.-J. Liu: Communication: Diverse nanoscale cluster dynamics: Diffusion of 2D epitaxial clusters, J. Chem. Phys. **147**(20), 201101 (2017)

2.24 D.I. Rogilo, L.I. Fedina, S.S. Kosolobov, A.V. Latyshev: On the role of mobile nanoclusters in 2D island nucleation on Si(111)-(7 × 7) surface, Surf. Sci. **667**(Suppl C), 1–7 (2018)

2.25 D.Z. Gao, M.B. Watkins, A.L. Shluger: Transient mobility mechanisms of deposited metal atoms on insulating surfaces: Pd on MgO (100), J. Phys. Chem. C **116**(27), 14471–14479 (2012)

2.26 V.J. Bukas, K. Reuter: Hot adatom diffusion following oxygen dissociation on Pd(100) and Pd(111): A first-principles study of the equilibration dynam-

ics of exothermic surface reactions, Phys. Rev. Lett. **117**, 146101 (2016)
2.27 B.N.J. Persson: *Sliding Friction – Physical Principles and Applications* (Springer, Berlin 2000)
2.28 S.P. Rittmeyer, D.J. Ward, P. Gütlein, J. Ellis, W. Allison, K. Reuter: Energy dissipation during diffusion at metal surfaces: Disentangling the role of phonons versus electron–hole pairs, Phys. Rev. Lett. **117**, 196001 (2016)
2.29 W. Fang, J.O. Richardson, J. Chen, X.-Z. Li, A. Michaelides: Simultaneous deep tunneling and classical hopping for hydrogen diffusion on metals, Phys. Rev. Lett. **119**, 126001 (2017)
2.30 R. Ferrando, G. Tréglia: Tight-binding molecular dynamics study of diffusion on Au and Ag(111), Surf. Sci. **331–333**, 920–924 (1995)
2.31 F. Montalenti, R. Ferrando: Jumps and concerted moves in Cu, Ag, and Au(110) adatom self-diffusion, Phys. Rev. B **59**, 5881–5891 (1999)
2.32 J. Ferrón, L. Gómez, J.J. de Miguel, R. Miranda: Nonstochastic behavior of atomic surface diffusion on Cu(111) down to low temperatures, Phys. Rev. Lett. **93**, 166107 (2004)
2.33 S.S. Hayat, M. Alcántara Ortigoza, M.A. Choudhry, T.S. Rahman: Diffusion of the Cu monomer and dimer on Ag(111): Molecular dynamics simulations and density functional theory calculations, Phys. Rev. B **82**, 085405 (2010)
2.34 M. Mińkowski, M.A. Zaluska-Kotur: Diffusion of Cu adatoms and dimers on Cu(111) and Ag(111) surfaces, Surf. Sci. **642**(Suppl C), 22–32 (2015)
2.35 A. Kotri, E. El Koraychy, M. Mazroui, Y. Boughaleb: Static investigation of adsorption and hetero-diffusion of copper, silver, and gold adatoms on the (111) surface, Surf. Interface Anal. **49**(8), 705–711 (2017)
2.36 J. Repp, W. Steurer, I. Scivetti, M. Persson, L. Gross, G. Meyer: Charge–state-dependent diffusion of individual gold adatoms on ionic thin NaCl films, Phys. Rev. Lett. **117**, 146102 (2016)
2.37 D. Cowell Senft, G. Ehrlich: Long jumps in surface diffusion: One-dimensional migration of isolated adatoms, Phys. Rev. Lett. **74**, 294–297 (1995)
2.38 T.R. Linderoth, S. Horch, E. Lægsgaard, I. Stensgaard, F. Besenbacher: Surface diffusion of Pt on Pt(110): Arrhenius behavior of long jumps, Phys. Rev. Lett. **78**, 4978–4981 (1997)
2.39 M. Aminpour, O. Trushin, T.S. Rahman: Effect of misfit dislocation on surface diffusion, Phys. Rev. B **84**, 035455 (2011)
2.40 P. Nita, K. Palotás, M. Jałochowski, M. Krawiec: Surface diffusion of Pb atoms on the Si(553)-Au surface in narrow quasi-one-dimensional channels, Phys. Rev. B **89**, 165426 (2014)
2.41 W. Du, J. Yang: One-dimensional diffusion of Sr atoms on Sr/Si(111)-3×2 reconstruction surface, Surf. Sci. **653**(Suppl C), 222–225 (2016)
2.42 G. Antczak, G. Ehrlich: Jump processes in surface diffusion, Surf. Sci. Rep. **62**(2), 39–61 (2007)
2.43 H. Risken: *The Fokker–Planck Equation: Methods of Solution and Applications* (Springer, Berlin, Heidelberg 1989)
2.44 R. Ferrando, R. Spadacini, G.E. Tommei: Kramers problem in periodic potentials: Jump rate and jump lengths, Phys. Rev. E **48**, 2437–2451 (1993)
2.45 R. Ferrando, R. Spadacini, G.E. Tommei, G. Caratti: Correlation functions in surface diffusion: The multiple-jump regime, Surf. Sci. **311**(3), 411–421 (1994)
2.46 J.W.M. Frenken, B.J. Hinch, J.P. Toennies, C. Wöll: Anisotropic diffusion at a melting surface studied with He-atom scattering, Phys. Rev. B **41**, 938–946 (1990)
2.47 J. Ellis, J.P. Toennies: Observation of jump diffusion of isolated sodium atoms on a Cu(001) surface by helium atom scattering, Phys. Rev. Lett. **70**, 2118–2121 (1993)
2.48 M. Schunack, T.R. Linderoth, F. Rosei, E. Lægsgaard, I. Stensgaard, F. Besenbacher: Long jumps in the surface diffusion of large molecules, Phys. Rev. Lett. **88**, 156102 (2002)
2.49 D.G. Sangiovanni, D. Edström, L. Hultman, V. Chirita, I. Petrov, J.E. Greene: Dynamics of Ti, N, and TiN_x (x = 1–3) admolecule transport on TiN(001) surfaces, Phys. Rev. B **86**, 155443 (2012)
2.50 A. Tamtögl, M. Sacchi, I. Calvo-Almazán, M. Zbiri, M.M. Koza, W.E. Ernst, P. Fouquet: Ultrafast molecular transport on carbon surfaces: The diffusion of ammonia on graphite, Carbon **126**(Suppl C), 23–30 (2018)
2.51 R. Ferrando: Correlated jump–exchange processes in the diffusion of Ag on Ag(110), Phys. Rev. Lett. **76**, 4195–4198 (1996)
2.52 O.M. Braun, R. Ferrando: Role of long jumps in surface diffusion, Phys. Rev. E **65**, 061107 (2002)
2.53 R. Guantes, J.L. Vega, S. Miret-Artés, E. Pollak: Kramers' turnover theory for diffusion of Na atoms on a Cu(001) surface measured by He scattering, J. Chem. Phys. **119**(5), 2780–2791 (2003)
2.54 J.L. Bentz, J.J. Kozak, G. Nicolis: Efficiency of encounter-controlled reaction between diffusing reactants in a finite lattice: Non-nearest-neighbor effects, Physica A **353**(Suppl C), 73–84 (2005)
2.55 J. Ferrón, R. Miranda, J.J. de Miguel: Atomic jumps during surface diffusion, Phys. Rev. B **79**, 245407 (2009)
2.56 S. Hallerberg, A.S. de Wijn: Understanding and controlling regime switching in molecular diffusion, Phys. Rev. E **90**, 062901 (2014)
2.57 G.L. Kellogg, P.J. Feibelman: Surface self-diffusion on Pt(001) by an atomic exchange mechanism, Phys. Rev. Lett. **64**, 3143–3146 (1990)
2.58 C. Chen, T.T. Tsong: Displacement distribution and atomic jump direction in diffusion of Ir atoms on the Ir(001) surface, Phys. Rev. Lett. **64**, 3147–3150 (1990)
2.59 T. Olewicz, G. Antczak, L. Jurczyszyn, J.W. Lyding, G. Ehrlich: Coexistence of two diffusion mechanisms: W on W(100), Phys. Rev. B **89**, 235408 (2014)
2.60 P.J. Feibelman: Diffusion path for an Al adatom on Al(001), Phys. Rev. Lett. **65**, 729–732 (1990)
2.61 H. Bulou, C. Massobrio: Mechanisms of exchange diffusion on fcc(111) transition metal surfaces, Phys. Rev. B **72**, 205427 (2005)

2.62 O.A. Oviedo, E.P.M. Leiva, M.M. Mariscal: Diffusion mechanisms taking place at the early stages of cobalt deposition on Au(111), J. Phys. Condens. Matter **20**(26), 265010 (2008)

2.63 J.Y. Yang, W.Y. Hu, J.F. Tang: Surface self-diffusion of a Pt adatom on cuboctahedral and truncated decahedral clusters, size dependence, Eur. Phys. J. B **78**(3), 315–321 (2010)

2.64 H. Jónsson: Simulation of surface processes, Proc. Natl. Acad. Sci. U. S. A. **108**(3), 944–949 (2011)

2.65 X. Lin, A. Dasgupta, F. Xie, T. Schimmel, F. Evers, A. Groß: Exchange processes in the contact formation of Pb electrodes, Electrochim. Acta **140**, 505–510 (2014)

2.66 D.G. Sangiovanni, A.B. Mei, D. Edström, L. Hultman, V. Chirita, I. Petrov, J.E. Greene: Effects of surface vibrations on interlayer mass transport: Ab initio molecular dynamics investigation of Ti adatom descent pathways and rates from TiN/TiN(001) islands, Phys. Rev. B **97**, 035406 (2018)

2.67 J.E. Black, Z.-J. Tian: Complicated exchange-mediated diffusion mechanisms in and on a Cu(100) substrate at high temperatures, Phys. Rev. Lett. **71**, 2445–2448 (1993)

2.68 F. Baletto, C. Mottet, R. Ferrando: Molecular dynamics simulations of surface diffusion and growth on silver and gold clusters, Surf. Sci. **446**(1), 31–45 (2000)

2.69 M. Labayen, C. Ramirez, W. Schattke, O.M. Magnussen: Quasi-collective motion of nanoscale metal strings in metal surfaces, Nat. Mater. **2**, 783–787 (2003)

2.70 M. Labayen, C. Haak, O.M. Magnussen: Surface dynamics of nanoscale hex strings on Au(100) electrodes, Phys. Rev. B **71**, 241409 (2005)

2.71 H. Bulou, J.-P. Bucher: Long range substrate mediated mass transport on metal surfaces induced by adatom clusters, Phys. Rev. Lett. **96**, 076102 (2006)

2.72 K.L. Man, M.C. Tringides, M.M.T. Loy, M.S. Altman: Superdiffusive motion of the Pb wetting layer on the Si(111) surface, Phys. Rev. Lett. **110**, 036104 (2013)

2.73 E. Granato, S.C. Ying, K.R. Elder, T. Ala-Nissila: Anomalous fast dynamics of adsorbate overlayers near an incommensurate structural transition, Phys. Rev. Lett. **111**, 126102 (2013)

2.74 H. Zhang, Y. Yang, J.F. Douglas: Influence of string-like cooperative atomic motion on surface diffusion in the (110) interfacial region of crystalline Ni, J. Chem. Phys. **142**(8), 084704 (2015)

2.75 C. Urban, R. Otero, D. Ecija, M. Trelka, N. Martin, J.M. Gallego, R. Miranda: Collective concerted motion in a molecular adlayer visualized through the surface diffusion of isolated vacancies, J. Chem. Phys. **145**(15), 154706 (2016)

2.76 T. Michely, J. Krug: *Islands, Mounds and Atoms* (Springer, Berlin, Heidelberg 2004)

2.77 A.L. Barabasi, H.E. Stanley: *Fractal Concepts in Surface Growth* (Cambridge Univ. Press, Cambridge 1995)

2.78 Q. Zhu, W.A. Saidi, J.C. Yang: Step-induced oxygen upward diffusion on stepped Cu(100) surface, J. Phys. Chem. C **119**(1), 251–261 (2015)

2.79 G. Ehrlich, F.G. Hudda: Atomic view of surface self-diffusion: Tungsten on tungsten, J. Chem. Phys. **44**(3), 1039–1049 (1966)

2.80 R.L. Schwoebel: Step motion on crystal surfaces II, J. Appl. Phys. **40**(2), 614–618 (1969)

2.81 U. Kürpick, T.S. Rahman: Diffusion processes relevant to homoepitaxial growth on Ag(100), Phys. Rev. B **57**, 2482–2492 (1998)

2.82 F. Liu, W. Hu, Y. Chen, H. Deng, H. Chen, X. Yang, W. Luo: Atomic self-diffusion behaviors relevant to 2D homoepitaxy growth on stepped Pd(001) surface, Surf. Sci. **624**, 89–94 (2014)

2.83 D. Cai, Y. Mo, X. Feng, Y. He, S. Jiang: Simulation study of temperature-dependent diffusion behaviors of Ag/Ag(001) at low substrate temperature, Appl. Surf. Sci. **406**, 277–284 (2017)

2.84 A. Surrey, D. Pohl, L. Schultz, B. Rellinghaus: Quantitative measurement of the surface self-diffusion on Au nanoparticles by aberration-corrected transmission electron microscopy, Nano Lett. **12**(12), 6071–6077 (2012)

2.85 G. Peng, M. Mavrikakis: Adsorbate diffusion on transition metal nanoparticles, Nano Lett. **15**(1), 629–634 (2015)

2.86 F. Baletto, C. Mottet, R. Ferrando: Microscopic mechanisms of the growth of metastable silver icosahedra, Phys. Rev. B **63**, 155408 (2001)

2.87 S. Valkealahti, M. Manninen: Diffusion on aluminum-cluster surfaces and the cluster growth, Phys. Rev. B **57**, 15533–15540 (1998)

2.88 R. Ferrando, G. Tréglia: High-temperature study of the Schwoebel effect in Au(111), Phys. Rev. Lett. **76**, 2109–2112 (1996)

2.89 R. Ferrando, G. Tréglia: Step-descent mechanisms on Ag and Au(111), Surf. Sci. **377–379**, 843–846 (1997)

2.90 O.V. Lysenko, V.S. Stepanyuk, W. Hergert, J. Kirschner: Interlayer mass transport in homoepitaxy on the atomic scale, Phys. Rev. B **68**, 033409 (2003)

2.91 U. Kürpick: Self-diffusion on stepped Ir(111) surfaces, Phys. Rev. B **69**, 205410 (2004)

2.92 H. Yildirim, T.S. Rahman: Diffusion barriers for Ag and Cu adatoms on the terraces and step edges on Cu(100) and Ag(100): An ab initio study, Phys. Rev. B **80**, 235413 (2009)

2.93 K. Sbiaai, Y. Boughaleb, M. Mazroui, A. Hajjaji, A. Kara: Energy barriers for diffusion on heterogeneous stepped metal surfaces: Ag/Cu(110), Thin Solid Films **548**, 331–335 (2013)

2.94 M. Benlattar, E. Elkoraychy, K. Sbiaai, M. Mazroui, Y. Boughaleb: Ehrlich–Schwöbel barriers and adsorption of Au, Cu and Ag stepped (100) surfaces, Mod. Phys. Lett. B **31**(05), 1750037 (2017)

2.95 M. Einax, W. Dieterich, P. Maass: Colloquium: Cluster growth on surfaces: Densities, size distributions, and morphologies, Rev. Mod. Phys. **85**, 921–939 (2013)

2.96 T. Michely, M. Hohage, M. Bott, G. Comsa: Inversion of growth speed anisotropy in two dimensions, Phys. Rev. Lett. **70**, 3943–3946 (1993)

2.97 O. Godsi, G. Corem, T. Kravchuk, C. Bertram, K. Morgenstern, H. Hedgeland, A.P. Jardine, W. Allison,

J. Ellis, G. Alexandrowicz: How atomic steps modify diffusion and inter-adsorbate forces: Empirical evidence from hopping dynamics in Na/Cu(115), J. Phys. Chem. Lett. **6**(20), 4165–4170 (2015)

2.98 R. Ferrando, G. Tréglia: Anisotropy of diffusion along steps on the (111) faces of gold and silver, Phys. Rev. B **50**, 12104–12117 (1994)

2.99 M.-C. Marinica, C. Barreteau, D. Spanjaard, M.-C. Desjonquères: Diffusion rates of Cu adatoms on Cu(111) in the presence of an adisland nucleated at fcc or hcp sites, Phys. Rev. B **72**, 115402 (2005)

2.100 C. Goyhenex, K. Farah, A. Taobane: Lattice mismatch effect in atomic migration along steps during heteroepitaxial metal growth, Surf. Sci. **601**(23), L132–L135 (2007)

2.101 K. Pötting, W. Schmickler, T. Jacob: Self-diffusion on Au(100): A density functional theory study, ChemPhysChem **11**(7), 1395–1404 (2010)

2.102 K. Sbiaai, Y. Boughaleb, A. Kara, S. Touhtouh, B. Sahraoui: Long jumps contribution to the adatom diffusion process near the step edge: The case of Ag/Cu(110), Phys. Status Solidi (b) **251**(4), 838–844 (2014)

2.103 N. Sändig, E. Bakalis, F. Zerbetto: Stochastic analysis of movements on surfaces: The case of C60 on Au(111), Chem. Phys. Lett. **633**(Suppl C), 163–168 (2015)

2.104 T. Furnival, R.K. Leary, E.C. Tyo, S. Vajda, Q.M. Ramasse, J. Meurig Thomas, P.D. Bristowe, P.A. Midgley: Anomalous diffusion of single metal atoms on a graphene oxide support, Chem. Phys. Lett. **683**(Suppl C), 370–374 (2017)

2.105 R. Ferrando, E. Scalas: Self-diffusion in a 2D lattice gas with lateral interactions, Surf. Sci. **281**(1), 178–190 (1993)

2.106 D.K. Chaturvedi: Tracer diffusion in cubic lattices, Phys. Rev. B **28**, 6868–6872 (1983)

2.107 R.A. Tahir-Kheli, R.J. Elliott: Correlated random walk in lattices: Tracer diffusion at general concentration, Phys. Rev. B **27**, 844–857 (1983)

2.108 D.K. Chaturvedi: Exact solution of continued fraction for tracer diffusion in solids, J. Phys. C **17**(18), L449 (1984)

2.109 S.C. Ying, I. Vattulainen, J. Merikoski, T. Hjelt, T. Ala-Nissila: Memory expansion for diffusion coefficients, Phys. Rev. B **58**, 2170–2178 (1998)

2.110 A. Danani, R. Ferrando, E. Scalas, M. Torri: Collective surface diffusion on triangular and square interacting lattice gases, Surf. Sci. **409**(1), 117–129 (1998)

2.111 G.F. Mazenko: Statistical mechanical models and surface diffusion. In: *Surface Mobilities on Solid Materials*, ed. by V.T. Bihn (Plenum, New York 1983) pp. 27–62

2.112 R. Ferrando, E. Scalas, M. Torri: Projection-operator route to the generalized Darken equation, Phys. Lett. A **186**(5), 415–418 (1994)

2.113 T. Hjelt, I. Vattulainen, J. Merikoski, T. Ala-Nissila, S.C. Ying: A dynamical mean field theory for the study of surface diffusion constants, Surf. Sci. **380**(2), L501–L505 (1997)

2.114 R. Kikuchi: A theory of cooperative phenomena, Phys. Rev. **81**, 988–1003 (1951)

2.115 I. Vattulainen, S.C. Ying, T. Ala-Nissila, J. Merikoski: Memory effects and coverage dependence of surface diffusion in a model adsorption system, Phys. Rev. B **59**, 7697–7707 (1999)

2.116 A.A. Tarasenko, L. Jastrabik, F. Nieto, C. Uebing: Adatom diffusion on a square lattice: Comparison of real-space renormalization group and Monte Carlo approaches, Phys. Rev. B **59**, 8252–8261 (1999)

2.117 A.A. Tarasenko, F. Nieto, L. Jastrabik, C. Uebing: Collective surface diffusion of repulsively interacting particles on a triangular lattice: Comparison of real-space renormalization group and Monte Carlo approaches, Phys. Rev. B **64**, 075413 (2001)

2.118 A. Tarasenko, L. Jastrabik, T. Müller: Modeling diffusion on heterogeneous lattices: Derivation of general analytical expressions and verification for a two-dimensional square lattice, Phys. Rev. B **75**, 085401 (2007)

2.119 A. Tarasenko, L. Jastrabik: Diffusion in heterogeneous lattices, Appl. Surf. Sci. **256**(17), 5137–5144 (2010)

2.120 A. Tarasenko, L. Jastrabik: Diffusion of particles over anisotropic heterogeneous lattices, Physica A **391**(4), 1048–1061 (2012)

2.121 A.G. Naumovets, Y.S. Vedula: Surface diffusion of adsorbates, Surf. Sci. Rep. **4**, 365 (1985)

2.122 G.L. Kellogg: Field ion microscope studies of single-atom surface diffusion and cluster nucleation on metal surfaces, Surf. Sci. Rep. **21**(1/2), 1–88 (1994)

2.123 G. Ehrlich: Diffusion of individual adatoms, Surf. Sci. **299/300**, 628–642 (1994)

2.124 M.J. Rost, D.A. Quist, J.W.M. Frenken: Grains, growth, and grooving, Phys. Rev. Lett. **91**(2), 026101 (2003)

2.125 J. Zhao, S. Granick: How polymer surface diffusion depends on surface coverage, Macromolecules **40**(4), 1243–1247 (2007)

2.126 S.K. Sinha, Z. Jiang, L.B. Lurio: X-ray photon correlation spectroscopy studies of surfaces and thin films, Adv. Mater. **26**(46), 7764–7785 (2014)

2.127 M. DeKieviet, D. Dubbers, C. Schmidt, D. Scholz, U. Spinola: ^{3}He spin echo: New atomic beam technique for probing phenomena in the neV range, Phys. Rev. Lett. **75**, 1919–1922 (1995)

2.128 A.P. Jardine, S. Dworski, P. Fouquet, G. Alexandrowicz, D.J. Riley, G.Y.H. Lee, J. Ellis, W. Allison: Ultrahigh-resolution spin-echo measurement of surface potential energy landscapes, Science **304**, 1790–1793 (2004)

2.129 P. Fouquet, A.P. Jardine, S. Dworski, G. Alexandrowicz, W. Allison, J. Ellis: Thermal energy 3He spin-echo spectrometer for ultrahigh resolution surface dynamics measurements, Rev. Sci. Instrum. **76**(5), 053109 (2005)

2.130 A.P. Jardine, H. Hedgeland, G. Alexandrowicz, W. Allison, J. Ellis: Helium-3 spin-echo: Principles and application to dynamics at surfaces, Prog. Surf. Sci. **84**, 323–379 (2009)

2.131 M. Bee: *Quasielastic Neutron Scattering* (IOP, Bristol 1988)

2.132 D. Farias, K.-H. Rieder: Atomic beam diffraction from solid surfaces, Rep. Prog. Phys. **61**, 1575–1664 (1998)

2.133 B. Poelsema, G. Comsa: *Scattering of Thermal Energy Atoms* (Springer, Berlin, Heidelberg 1989)

2.134 E. Hulpke (Ed.): *Helium Atom Scattering from Surfaces* (Springer, Berlin, Heidelberg 1992)

2.135 G. Benedek, J.P. Toennies: *Atomic Scale Dynamics at Surfaces: Theory and Experimental Studies with Helium Atom Scattering* (Springer, Berlin, Heidelberg 2018)

2.136 A.R. Alderwick, A.P. Jardine, W. Allison, J. Ellis: An evaluation of the kinematic approximation in helium atom scattering using wavepacket calculations, Surf. Sci. **678**, 65–71 (2018)

2.137 L. Van Hove: Correlations in space and time and born approximation scattering in systems of interacting particles, Phys. Rev. **95**(1), 249–262 (1954)

2.138 J. Ellis, J.P. Toennies: Observation of jump diffusion of isolated sodium atoms on a Cu(001) surface by helium atom scattering, Phys. Rev. Lett. **70**, 2118–2121 (1993)

2.139 J. Ellis, A.P. Graham, J.P. Toennies: Quasielastic helium atom scattering from a two-dimensional gas of Xe atoms on Pt(111), Phys. Rev. Lett. **82**(25), 5072–5075 (1999)

2.140 R. Gähler, R. Golub, K. Habicht, T. Keller, J. Felber: Space-time description of neutron spin echo spectrometry, Physica B **229**(1), 1–17 (1996)

2.141 A. Tamtögl, B. Davey, D.J. Ward, A.P. Jardine, J. Ellis, W. Allison: Polarisation in spin-echo experiments: Multi-point and lock-in measurements, Rev. Sci. Instrum. **89**, 023902 (2018)

2.142 G. Alexandrowicz, A.P. Jardine: Helium spin-echo spectroscopy: Studying surface dynamics with ultra-high-energy resolution, J. Phys. Condens. Matter **19**(30), 305001 (2007)

2.143 P.R. Kole, A.P. Jardine, H. Hedgeland, G. Alexandrowicz: Measuring surface phonons with a ^{3}He spin echo spectrometer: A two-dimensional approach, J. Phys. Condens. Matter **22**, 304018 (2010)

2.144 A.P. Jardine, J. Ellis, W. Allison: Effects of resolution and friction in the interpretation of QHAS measurements, J. Chem. Phys. **120**, 8724–8733 (2004)

2.145 C.T. Chudley, R.J. Elliot: Neutron scattering from a liquid on a jump diffusion model, Proc. Phys. Soc. **77**, 353–361 (1961)

2.146 J.W.M. Frenken, B.J. Hinch, J.P. Toennies, C. Wöll: Anisotropic diffusion at a melting surface studied with He-atom scattering, Phys. Rev. B **41**, 938–946 (1990)

2.147 J.W.M. Frenken, B.J. Hinch: Quasielastic helium scattering studies of adatom diffusion on surfaces. In: *Helium Atom Scattering from Surfaces*, Springer Series in Surface Sciences, Vol. 27, ed. by E. Hulpke (Springer, Berlin, Heidelberg 1992) pp. 287–313

2.148 A.P. Jardine, E.Y.M. Lee, D.J. Ward, G. Alexandrowicz, H. Hedgeland, W. Allison, J. Ellis, E. Pollak: Determination of the quantum contribution to the activated motion of hydrogen on a metal surface: H/Pt(111), Phys. Rev. Lett. **105**, 136101 (2010)

2.149 G. Alexandrowicz, A.P. Jardine, H. Hedgeland, W. Allison, J. Ellis: Onset of 3D collective surface diffusion in the prescence of lateral interactions: Na/Cu(001), Phys. Rev. Lett. **97**, 156103 (2006)

2.150 A.P. Jardine, G. Alexandrowicz, H. Hedgeland, R.D. Diehl, W. Allison, J. Ellis: Vibration and diffusion of Cs atoms on Cu(001), J. Phys. Condens. Matter **19**(30), 305010 (2007)

2.151 H. Hedgeland, P.R. Kole, H.R. Davies, A.P. Jardine, G. Alexandrowicz, W. Allison, J. Ellis: Surface dynamics and friction of K/Cu(001) characterized by helium-3 spin-echo and density functional theory, Phys. Rev. B **80**, 125426 (2009)

2.152 O. Godsi, G. Corem, T. Kravchuk, C. Bertram, K. Morgenstern, H. Hedgeland, A.P. Jardine, W. Allison, J. Ellis, G. Alexandrowicz: How atomic steps modify diffusion and inter-adsorbate forces: Empirical evidence from hopping dynamics in Na/Cu(115), J. Phys. Chem. Lett. **6**, 4165–4170 (2015)

2.153 G. Alexandrowicz, A.P. Jardine, P. Fouquet, S. Dworski, W. Allison, J. Ellis: Observation of microscopic CO dynamics on Cu(001) using 3He spin-echo spectroscopy, Phys. Rev. Lett. **93**(15), 156103 (2004)

2.154 G. Alexandrowicz, P. Kole, E. Lee, H. Hedgeland, R. Ferrando, A.P. Jardine, W. Allison, J. Ellis: Observation of uncorrelated microscopic motion in a strongly interacting adsorbate system, J. Am. Chem. Soc. **130**, 6789–6794 (2008)

2.155 A.P. Jardine, H. Hedgeland, D. Ward, Y. Xiaoqing, W. Allison, J. Ellis, G. Alexandrowicz: Probing molecule-surface interactions through ultra-fast adsorbate dynamics: Propane/Pt(111), New J. Phys. **10**, 125026 (2008)

2.156 P.R. Kole, H. Hedgeland, A.P. Jardine, W. Allison, J. Ellis, G. Alexandrowicz: Probing the non-pairwise interactions between CO molecules moving on a Cu(111) surface, J. Phys. Condens. Matter **24**, 104016 (2012)

2.157 H. Hedgeland, B.A.J. Lechner, F.E. Tuddenham, A.P. Jardine, W. Allison, J. Ellis, M. Sacchi, S.J. Jenkins, B.J. Hinch: Weak intermolecular interactions in an ionically bound molecular adsorbate: Cyclopentadienyl/Cu(111), Phys. Rev. Lett. **106**, 186101 (2011)

2.158 B.A.J. Lechner, M. Sacchi, A.P. Jardine, H. Hedgeland, W. Allison, J. Ellis, S.J. Jenkins, P.C. Dastoor, B.J. Hinch: Jumping, rotating, and flapping: The atomic-scale motion of thiophene on Cu(111), J. Phys. Chem. Lett. **4**, 1953–1958 (2013)

2.159 H. Hedgeland, M. Sacchi, P. Singh, A.J. McIntosh, A.P. Jardine, G. Alexandrowicz, D.J. Ward, S.J. Jenkins, W. Allison, J. Ellis: Mass transport in surface diffusion of van der Waals bonded systems: Boosted by rotations?, J. Phys. Chem. Lett. **7**, 4819–4824 (2016)

2.160 M. Sacchi, P. Singh, D.M. Chisnall, D.J. Ward, A.P. Jardine, W. Allison, J. Ellis, H. Hedgeland: The dynamics of benzene on Cu(111): A combined helium spin echo and dispersion-corrected DFT study into the diffusion of physisorbed aromatics on metal surfaces, Faraday Discuss. **204**, 471–485 (2017)

2.161 F.E. Tuddenham, H. Hedgeland, A.P. Jardine, B.A.J. Lechner, B.J. Hinch, W. Allison: Lineshapes in quasi-elastic scattering from species hopping between non-equivalent surface sites, Surf. Sci. **604**, 1459–1475 (2010)

2.162 H. Hedgeland, P. Fouquet, A.P. Jardine, G. Alexandrowicz, W. Allison, J. Ellis: Measurement of single-molecule frictional dissipation in a prototypical nanoscale system, Nat. Phys. **5**, 561–564 (2009)

2.163 S. Paterson, W. Allison, H. Hedgeland, J. Ellis, A.P. Jardine: Rotation and translational motion prior to self-assembly: Dynamics of ethanethiolate on Cu(111), Phys. Rev. Lett. **106**, 256101 (2011)

2.164 R. Kubo: The fluctuation-dissipation theorem, Rep. Prog. Phys. **29**, 255–284 (1966)

2.165 B.A.J. Lechner, A.S. de Wijn, H. Hedgeland, A.P. Jardine, B.J. Hinch, W. Allison, J. Ellis: Atomic scale friction of molecular adsorbates during diffusion, J. Chem. Phys. **138**, 194710 (2013)

2.166 P. Rotter, B.A.J. Lechner, A. Morherr, D.M. Chisnall, D.J. Ward, A.P. Jardine, J. Ellis, W. Allison, B. Eckhardt, G. Witte: Coupling between diusion and orientation of pentacene molecules on an organic surface, Nat. Mater. **15**, 397–400 (2016)

2.167 P. Hänggi, P. Talkner, M. Borkovec: Reaction-rate theory: Fifty years after Kramers, Rev. Mod. Phys. **62**, 251–341 (1990)

2.168 S. Paterson, C.J. Aas, A.P. Jardine: Quasi-elastic lineshapes for atoms and simple molecules undergoing jump rotation on surfaces, Surf. Sci. **606**, 426–434 (2012)

2.169 E.M. McIntosh, K.T. Wikfeldt, J. Ellis, A. Michaelides, W. Allison: Quantum effects in the diffusion of hydrogen on Ru(0001), J. Phys. Chem. Lett. **4**, 1565–1569 (2013)

2.170 A.R. Alderwick, A.P. Jardine, H. Hedgeland, D.A. MacLaren, W. Allison, J. Ellis: Simulation and analysis of solenoidal ion sources, Rev. Sci. Instrum. **79**, 123301 (2008)

Riccardo Ferrando

Physics Department
University of Genoa
Genoa, Italy
ferrando@fisica.unige.it

Riccardo Ferrando is currently Professor of Theoretical Condensed Matter Physics at the University of Genoa, Italy. He is the author of about 230 articles in peer-reviewed international journals. His research activity lies in the field of computational modeling of nanosystems, interfaces, and colloids.

Andrew Jardine

Cavendish Laboratory
University of Cambridge
Cambridge, UK
apj24@cam.ac.uk

Dr Andrew Jardine is University Lecturer in Physics at the Cavendish Laboratory, University of Cambridge, and a Fellow and Director of Studies at Fitzwilliam College within the University. He received his PhD from the University of Cambridge (2002). His research interests include developing new experimental techniques and instrumentation for condensed matter research, studying picosecond dynamics of atoms and molecules on surfaces, and understanding the mechanical and constitutive properties of materials.

3. Surface Thermodynamics and Vibrational Entropy

Talat S. Rahman

As with bulk material, a few thermodynamic variables determine the stability and equilibrium properties of solid surfaces. Since the environment at the surface is typically very different from that in the bulk, as a result of the lack of symmetry created by the presence of the surface, thermodynamics plays an important role in determining surface structure and dynamics. The quantity of interest here is the surface free energy, which inherently includes the contribution of vibrational (and configurational) entropy. Given the existence of surfaces vibrational modes whose features are distinct from those in the bulk, and dependent on local surface geometry and electronic structure, the emphasis in this chapter is on the characteristics of vibrational entropy, which, in turn, affect surface thermodynamical quantities that are in excess of values in the bulk. Special attention is paid to characteristics of vibrational density of states of low and high Miller index surfaces and their contribution to vibrational entropy, and, hence, to thermodynamical functions. In fact, it is argued that the distinguishing features in the vibrational density of states, namely enhancement of the number of modes at low frequencies and appearance of modes above the bulk band, highlight the impact of the undercoordinated atoms at surfaces, steps, and kink sites and lead to variations in the local surface electronic structure. The characteristics found on high Miller index surfaces in particular pave the way for understanding vibrational dynamics of nanoparticles. Contact is made with experimental data where available.

In this chapter, after presenting a summary of bulk thermodynamics in Sect. 3.1, the stage is set for summarizing the essentials of surface thermodynamical functions in Sect. 3.2. Surface nomenclature is discussed in Sect. 3.3 and details of theoretical techniques are presented in Sect. 3.4. A sampling of results obtained on a few surfaces is provided in Sect. 3.5 and a summary is presented in Sect. 3.6.

Over four decades of experimental and theoretical research in surface science has brought us to the point where we can probe the subtle role played by thermodynamics in determining unique features of solid surfaces and nanostructures. The lack of symmetry created by removal of the top half-atoms to create a surface inherently leads to a heterogeneous environment with nonuniform local geometric and modified electronic structure that can promote a plethora of surface phenomena, which continue to be revealed at length scales ranging from the microscopic (localized surface states and vibrational modes), to the macroscopic (surface tension, surface acoustic wave) and at time scales going down to femtoseconds. In this Handbook, a number of chapters address the experimental and theoretical findings of a multitude of surface phenomena, allowing this chapter to concentrate only on the peculiarities of surface thermodynamics that make the surface an interesting playground for realization of physical and chemical properties than that in the bulk.

M. Rocca, T.S. Rahman, L. Vattuone (Eds.), *Springer Handbook of Surface Science*, Springer Handbooks,
https://doi.org/10.1007/978-3-030-46906-1_3

In considerations of relative stability of surfaces, nanostructures, as well as bulk phases of different crystallographic orientations, the quantity of interest is the free energy, which includes contributions from the structural potential energy and the system's vibrational and configurational entropy. Assuming the structural potential energy to be insensitive to temperature variations, it is the entropic contributions that control the surface phase diagram and structural stability. In this regard, configurational entropy is an important constituent for any system containing more than one type of element (for example, alloys), but for surfaces and nanostructures of single elements, it is vibrational entropy that accounts for the temperature dependencies of surface free energy, mean-square vibrational amplitudes of surface atoms, the surface Debye temperature, and the surface heat capacity, albeit within the harmonic and quasiharmonic approximation of lattice dynamics. It is also the quantity that may determine the equilibrium shape of crystal surfaces and its possible structural phase transitions and surface reconstructions. These comments are not to disregard the role of configurational entropy for single-element surfaces at temperatures that accompany structural disorder. Such considerations are beyond the scope of this chapter. Knowledge of surface free energy, together with that of the step and kink free energy, is also essential for considerations of surface faceting, bunching, and roughening. The extraction of free energy from experimental data is, however, nontrivial [3.1]. The lattice contribution, which can be critical for determining structural transitions, is nonzero, albeit a small fraction of the structural energy. It is, thus, encouraging to see the flurry of activity in analyzing the contribution of vibrational entropy [3.2] to the thermodynamic functions for several surface systems [3.3–5]. These calculations have already provided a qualitative measure of the effect of vibrational entropy on surface stability and structure and have set the stage for a systematic evaluation of the local vibrational contribution to the free energy. Since these calculations were based on the usage of many-body interaction potentials [3.6], questions have been asked about their accuracy, particularly for 5d metals Pt, Ir, and Au, for which these potentials are not expected to work as well as they do for Ag, Cu, and Ni. With the availability of ab-initio electronic structure methods based on the density functional perturbation theory [3.7, 8], surface phonon dispersion curves can be calculated with remarkable accuracy [3.9]. These dispersion curves further lend themselves to the extraction of vibrational density of states and, thus, of the vibrational contribution to surface free energy and entropy. Efforts have thus been made to analyze surface thermodynamic properties of the several metals using ab-initio methods and to compare the findings with those obtained using semiempirical approaches [3.10].

3.1 Some Essentials of Bulk Thermodynamics

In this section, some background information is provided on thermodynamic functions to provide context and facilitate discussion, greater details of which can be found in textbooks [3.11, 12]. With the entropy already mentioned above, two extensive thermodynamic variables need to be introduced: the Helmholtz free energy F equivalent to the maximum amount of work a system can do at constant volume and temperature and the Gibbs free energy G, which is the maximum amount of work a system can do at constant pressure and temperature; G is a minimum for closed systems at equilibrium with a well-defined temperature and pressure. Both Helmholtz and Gibbs free energies are known as thermodynamic potential. Furthermore, the first law of thermodynamics states that the increase in energy $\mathrm{d}U$ of a system is equal to the difference of the heat absorbed by the system δQ and the amount of work done by the system δW as quantified by

$$\mathrm{d}U = \delta Q - \delta W \,. \tag{3.1}$$

Equation (3.1) implies that there is a quantity U called the internal energy which is a function of the state of the system (temperature and pressure) and that the difference between two values of U is independent of the path of getting from one state to the other. In other words, U is the integral of an exact differential $\mathrm{d}U$. If the energy of the system can be described by the thermodynamic variables' pressure, temperature, and volume, then for an infinitesimal quasistatic reversible process, the work done by the system is $P\mathrm{d}V$, and the heat absorbed is $T\mathrm{d}S$. Thus,

$$\mathrm{d}U = T\mathrm{d}S - P\mathrm{d}V \,, \tag{3.2}$$

from which temperature and pressure follow as respective derivatives of the internal energy U. Since S and V are often inconvenient independent variables [3.13], it is more usual to work with T and P. The thermodynamic potentials, F and G introduced before and the enthalpy H are then defined by

$$F = U - TS = U - S\left(\frac{\delta U}{\delta S}\right)_v \,, \tag{3.3}$$

$$H = U + PV \,, \tag{3.4}$$

$$G = U - TS + PV = H - TS \,. \tag{3.5}$$

While the quantities form the basis of thermodynamical description of bulk material with an infinite sea of particles, Gibbs' introduction [3.14] of the explicit dependence of U on the number of particles N and their related chemical potential μ allows us to extend these thermodynamic concepts to solid surfaces. There is, thus, a consensus that in equilibrium, a one-component system can be fully defined by its internal energy (U), which is a unique function of the entropy (S), volume (V), and number of particles (N), such that

$$U = U(S, V, N) \,, \tag{3.6}$$

$$\mathrm{d}U = T\mathrm{d}S - P\mathrm{d}V + \mu\mathrm{d}N \,. \tag{3.7}$$

The reader is referred to more detailed analysis in *Zangwill* [3.11] from where some of the description has been extracted.

3.2 Surface Thermodynamic Functions

When it comes to surfaces, in addition to volume V, area (A) should also play a role, since we need energy to create a surface with a particular *surface energy*. The creation of a surface should inherently involve an increase in the total internal energy proportional to the area. Thus, the internal energy equation should include an additional term

$$U = TS - PV + \mu N + \gamma A \,, \tag{3.8}$$

where γ is the surface tension. Of course, the introduction of the surface brings in an ambiguity, as the boundary of the surface is not well defined. For example, the density of the electrons in a one-component system will not fall off sharply at the surface. Rather, it would tail off as one moves away from the surface, in a manner characteristic of the material. Additionally, surface thermodynamical quantities would follow from those calculated for the bulk with the inclusion of one term that accounts for excesses from the bulk value needed to create the surface. Equation (3.8) has also introduced another observable, surface tension, which is a macroscopic property of a material.

Surface internal energy may, thus, be defined as an excess over the bulk value in the manner described very nicely by *Somorjai* and *Li* [3.12], assuming that a crystalline solid is bound by two surfaces and denoting the energy and entropy of each bulk atom by U^{b} and S^{b}, respectively, and the surface energy per unit area as U^{s}. The total internal energy of the solid is then

$$U = NU^{\mathrm{b}} + AU^{\mathrm{s}} \,. \tag{3.9}$$

Here, AU^{s} is the excess from the bulk. In the same way, the total entropy of the system can be written as

$$S = NS^{\mathrm{b}} + AS^{\mathrm{s}} \,. \tag{3.10}$$

Note that the surface term (with the suffix s) is with respect to per unit surface area. Bearing in mind that the surface terms are excess over the bulk value in the manner described above, we can write the expressions for the surface Helmholtz and Gibbs free energies (per unit area) and the enthalpy (per unit area) in terms of the corresponding expressions for the bulk

$$F^{\mathrm{s}} = U^{\mathrm{s}} - TS^{\mathrm{s}} \,, \tag{3.11}$$

$$G^{\mathrm{s}} = H^{\mathrm{s}} - TS^{\mathrm{s}} \,. \tag{3.12}$$

Here, H^{s} is the specific surface enthalpy, which is the excess heat absorbed by the system per unit surface area created under constant external force, i.e., pressure. By the same token, the total Gibbs free energy of the system can be written in terms of G^{b}, the Gibbs free energy per bulk atom and G^{s}, and the Gibbs free energy per unit surface area

$$G = NG^{\mathrm{b}} + AG^{\mathrm{s}} \,. \tag{3.13}$$

We next move on to considerations of some of the thermodynamic functions for surfaces and other reduced dimensional materials. However, before we do so we need to establish the nomenclature, the calculation methodology, and provide some background information.

3.3 Surface Nomenclature and Geometry

Bulk solids exist in a number of crystallographic structures, details of which can be found in standard textbooks [3.15]. The fundamental property of a solid is its inherent periodic structure, which is defined by a lattice containing an infinite array of points generated by a primitive lattice translation vector

$$\boldsymbol{T}_m = m_1\boldsymbol{a} + m_2\boldsymbol{b} + m_3\boldsymbol{c} \,, \tag{3.14}$$

where m_i is an integer (positive, negative, or zero) and $\boldsymbol{a}$, $\boldsymbol{b}$, and $\boldsymbol{c}$ are three mutually perpendicular vectors,

generally taken to be along the Cartesian x, y, and z coordinates. A lattice point $m_1\boldsymbol{a} + m_2\boldsymbol{b} + m_3\boldsymbol{c}$ lies in the direction $[m_1, m_2, m_3]$. Generally, the values of m_i are divided by their greatest common divisor, so as to have the smallest integer set. For example, the body diagonal of a unit cell is denoted by the direction [111] (rather than [333], etc.). Furthermore, a set of directions, such as [100], [010], [001], $[\bar{1}00]$, $[0\bar{1}0]$, $[00\bar{1}]$, which may be related by symmetry, are denoted by the bracket $\langle 100\rangle$.

The planes containing the lattice point define the crystal structure and the ensuing symmetry and other geometrical characteristics of the surface. These planes are usually defined in terms of Miller indices (hkl), where the values of h, k, and l follow from the following. If a plane intersects the axes ($m_1\boldsymbol{a}$, $m_2\boldsymbol{b}$, and $m_3\boldsymbol{c}$), the Miller indices of the plane are the set of integers, without a common multiple, that are inversely proportional to the intercept of the axes with the plane. That is, $h : k : l = 1/m_1 : 1/m_2 : 1/m_3$. Thus, in a cubic lattice, the direction $\langle hkl\rangle$ is perpendicular to the plane (hkl). Here, too, a family of planes that are equivalent by symmetry are denoted by curly brackets { }. These Miller indices provide a convenient way to classify surfaces with respect to the extent of their terraces and regularly present steps and kinks. As will be seen below and was already presented in [3.5], the low and high Miller index surfaces provide two sets of surfaces with distinct crystallography.

3.3.1 Low Miller Index Surfaces

The low Miller index surfaces are those for which h, k, and l have the values 0 or 1. These are extended surfaces without any step or kink [3.16]. A simple example is that of a cube with its six faces $\langle 100\rangle$, $\langle 010\rangle$, etc., represented collectively by {100}. The low Miller index surfaces (100), (110), and (111) of both fcc and bcc cubic crystals are shown in Fig. 3.1. Note that the (111) surface is the most close-packed, while the least so is the (110) surface. In the early days of surface science, the majority of investigations were carried out on the three low Miller index surfaces for obvious reasons. They were relatively easy to characterize experimentally with techniques such as low-energy electron diffraction (LEED) and were amenable to theoretical calculations, both analytical and numerical with the then available computational power. However, the larger number of low-coordinated sites offered by surfaces containing steps and kinks compared to those without them, led both experimentalists and theorists to venture into the more complex, and intriguing, local environment offered by the high-Miller index surfaces, also called vicinal surfaces. These surfaces can now be created and characterized with a variety of techniques, as summarized in several other chapters in this Springer Handbook. Their well-defined periodic arrangement of steps and kinks provides regions of low coordination with interesting implications for their physics and chemistry, as we shall see in this book. They also serve as benchmarks for understanding properties of nanoparticles while offering sites with a range of low coordination that lack the periodicity of vicinal surfaces.

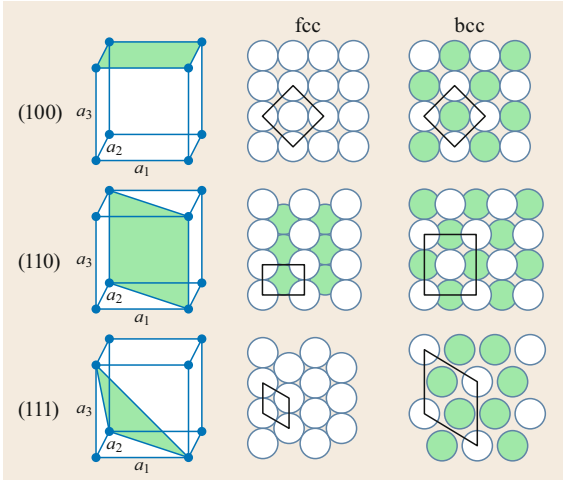

Fig. 3.1 Low Miller index surfaces

3.3.2 High Miller Index Surfaces

The simplest vicinal surfaces consist of regularly-spaced low Miller index terraces separated by monatomic steps. A slight miscut of the crystal at an angle slightly off the low Miller index ((100), (111), and (110)) planes will give rise to a vicinal surface. In Fig. 3.2, we depict a hard sphere diagram of an fcc(977) surface showing the geometry of the terrace and the step face. On this surface, the terrace has fcc(111) orientation and is eight-atom wide, while the step face has a (100) microfacet. This vicinal is created by cutting the crystal at 7° away from the (111) plane towards the $[2\bar{1}\bar{1}]$ direction, which results in monatomic steps along the $[0\bar{1}1]$ direction. Note that on the fcc(111) surface, the $\langle 110\rangle$ direction is not parallel to any plane of symmetry, and there exist two different ways of generating monatomic stepped surfaces: by directing the miscut angle towards either the $[2\bar{1}\bar{1}]$ or the $[\bar{2}11]$ direction. In the case of the former, as we can see in Fig. 3.1, the step face has a (100) microfacet (the so-called A type), while in the case of the latter, it would yield a (111) microfacet (the so-called B type). Such a surface with an eight-atom wide fcc(111) terrace and a (111) microfacet is the fcc(997) surface for which

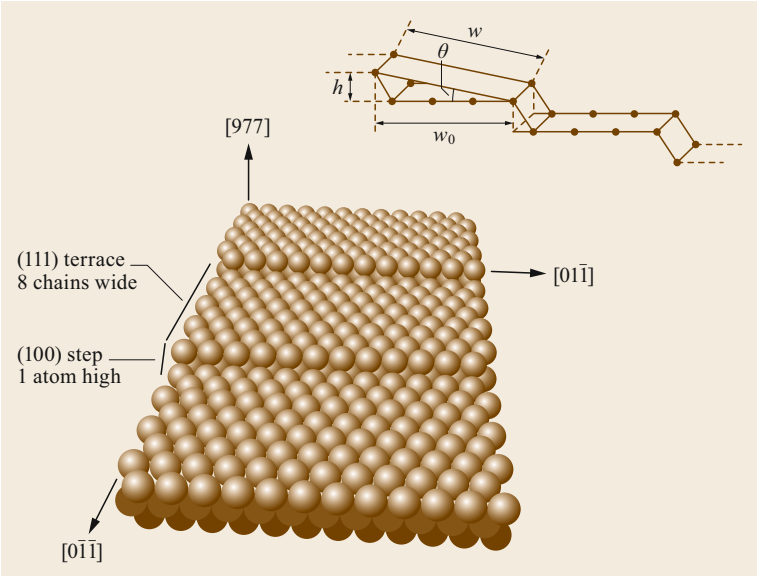

Fig. 3.2 Hard sphere model of the fcc(977) surface that is a vicinal of fcc(111) with an eight-atom wide terrace and a monatomic (100) microfaceted step face. The miscut angle θ and the terrace width w are shown in the *inset*. (Adapted from [3.17], © IOP Publishing. Reproduced with permission. All rights reserved)

the miscut angle is 6.5°. It is complementary to the fcc(977) surface shown in Fig. 3.2. Since a monoatomic stepped surface may have a (100) or (111) microfacet, a more self-contained notation for the surface structure was introduced by *Lang* et al. [3.18] in the general form $S(h_t k_t l_t) \times (n_s k_s l_s)$, where $(h_t k_t l_t)$ represents the Miller indices of the terrace plane and $(n_s k_s l_s)$ that of the step face, and S is the atomic width of the terrace. In Table 3.1, we summarize the notation for the various vicinal surfaces that are discussed in this chapter, together with their miscut angles θ and the interatomic separations for ideal (bulk terminated) geometry. Here, w is the width of the terrace (Fig. 3.2) and $f..r$ is the registry (Fig. 3.5).

This relationship of the vicinal surface to the low Miller index mother surface is also nicely captured in Fig. 3.3, which presents a stereographic view of stepped surfaces of varying terrace widths and geometries, drawn around the pole at fcc(100) and converging on the other two low Miller index surfaces (111) and (100). As already mentioned, the two equal terrace-width vicinals of fcc(111), fcc(997), and fcc(977) fall on the two sides of the graph around (111) separated by 60°. Similar to the (997) surface, the (331) and (551) surfaces have a B-type step face but only three-atom wide terraces.

For fcc(100) surfaces, the stereograph map neatly separates the two types of step face of its vicinals: those with a close-packed (111) microfacet lie along the line joining the (100) pole to (111) and those with the (110) microfacet along the other line. An angle of 45° separates the in-plane orientation of these steps. Similarly, the set of loosely and close-packed step faces of vicinals of fcc(110) flank the location of (110) on the stere-

Table 3.1 Structural notation and geometric features for several fcc vicinals. Here, d_b is the bulk interlayer separation, Δr is the surface registry and w is the terrace width (all in units of a, the lattice constant). (Adapted from [3.17], © 2003 IOP Publishing)

Miller index *hkl*	Compact step notation $S(h_t k_t l_t) \times (n_s k_s l_s)$	Miscut angle (deg)	d_b (a)	Δr (a)	w (a)
311	2(100)×(111)	25.24	0.3015	0.6396	1.1726
511	3(100)×(111)	15.8	0.1924	0.680	1.8368
310	3(100)×(110)	18.44	0.1581	0.4743	1.581
410	4(100)×(110)	14.04	0.1212	0.4849	2.0616
211	3(111)×(100)	19.5	0.2041	0.5773	1.7319
977	8(111)×(100)	7.01	0.0747	0.6078	4.730
331	3(111)×(111)	22.0	0.2294	0.5677	1.5408
210	2(110)×(100)	26.56	0.2236	0.4472	1.118
320	3(110)×(100)	11.3	0.1387	0.6933	1.8026
551	3(110)×(111)	8.05	0.1400	0.9901	2.5247

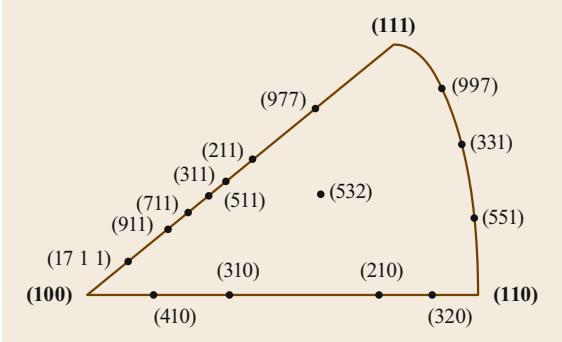

Fig. 3.3 A stereographic projection for fcc crystals around the (100) pole showing several vicinal surfaces in relation to the low Miller index surfaces from which they are derived. (Adapted from [3.17], © IOP Publishing. Reproduced with permission. All rights reserved)

ograph with a separation of 90° between them. Thus, along each side of the stereograph the terrace geometry and width change logically while maintaining the same geometry for the step face. In the Miller index notation, vicinals lying along the (100)–(110) side of the stereograph have indices ($hk0$), while those along (110)–(111) have (hhk) and those along (111)–(100) are denoted by (hkk).

To examine the finer details of the local atomic environment, we take the example of a set of vicinal surfaces whose terraces are approximately three-atom wide with either (100), (111), or (110) crystallographic orientation and two types of step microfacets. These six surfaces are shown in Fig. 3.4.

Here, (511) and (310) are vicinals of fcc(100), with (111) and (100) microfaceted step faces, respectively. As is noticeable in Fig. 3.4, the (310) surface has an open-step arrangement, akin to a regularly kinked step edge. The coordination of the step atoms on the fcc(310) is also 6, which is typical of atoms at a kink site. Similarly, the (211) and (331) surfaces in Fig. 3.4 are corresponding vicinals of the fcc(111) surfaces with the A and B types of step microfacet, respectively. Finally, the corresponding vicinals of the fcc(110) surface are the (551) and (320) surfaces, the former with a close-packed (111) step face and the latter with a kinked (100) microfacet. The structural parameters of the above six surfaces, given in terms of the lattice

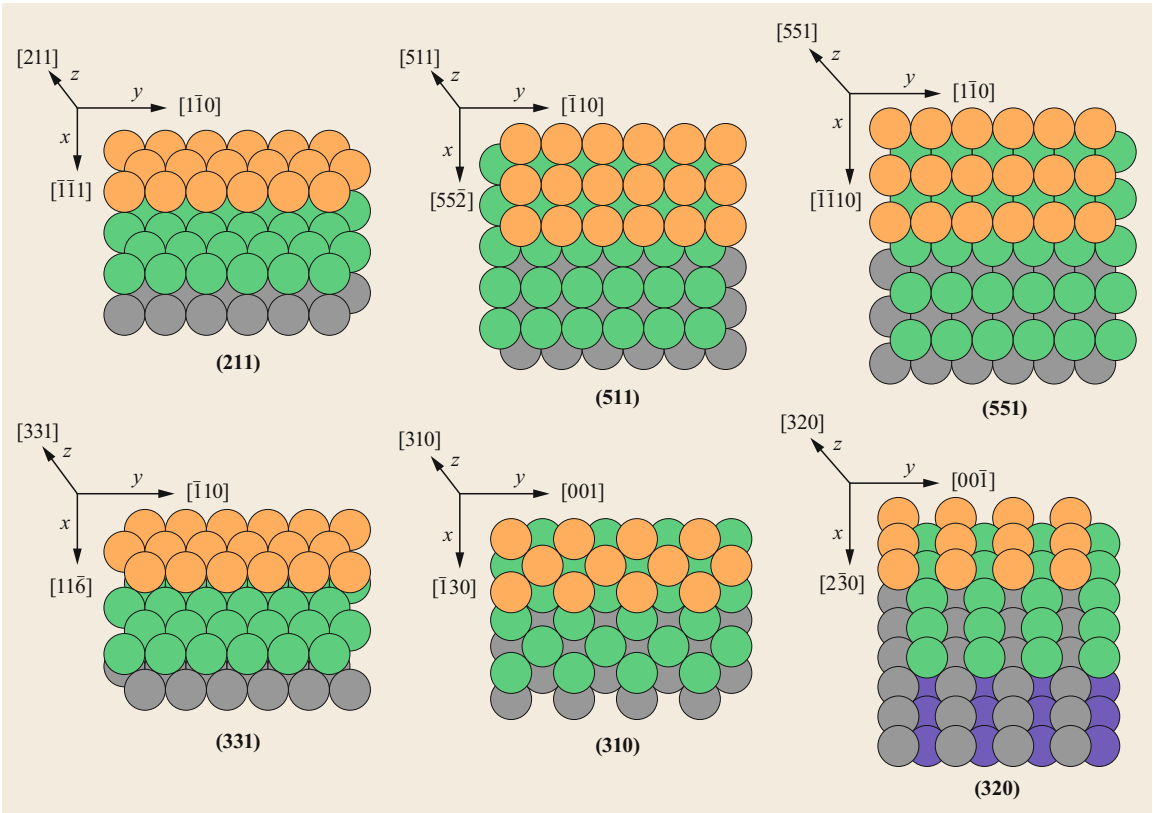

Fig. 3.4 A top view of six vicinals of three-atom wide terraces. (Adapted from [3.17], © IOP Publishing. Reproduced with permission. All rights reserved)

constant, in Table 3.1, together with those of few other related vicinal surfaces, show that the fcc(977) surface is just a broader terrace version of the fcc(211) surface, while the fcc(410) surface is related to the fcc(310) surface, except for the difference in terrace width.

As in several previous studies [3.4, 11, 12, 14] we will use the following notation for the surface atoms, as illustrated in Fig. 3.5: SC for atoms in the step chain; TC for atoms in the terrace chain (if there are more than one, we label them as TC1, TC2, etc.), and CC for atoms in the corner chain. For the three surfaces (310), (320), and (551), there are actually five undercoordinated sites—three in the top terrace and two underneath. On the other hand, on the (511), (211), and (331) surfaces, there are only three undercoordinated sites. Together, these six surfaces provide atoms with the range of coordination extending from 6 to 11. As we shall see the atom labeled BNN in Fig. 3.5, a bulk nearest neighbor of the corner atom contributes interestingly to the vibrational density of states of these surfaces. Note that in the calculations, the x and y-axes are taken to lie in the surface plane, the x-axis being perpendicular to the step and the y-axis along the step. The z-axis is along the normal to the surface.

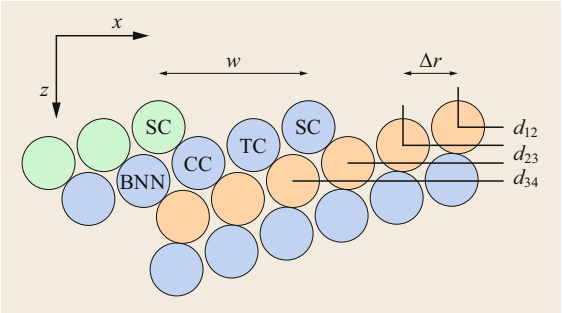

Fig. 3.5 A side view of the vicinal surface showing the step (SC), terrace (TC), corner (CC) and BNN atoms, interlayer separations d_{ij}, and surface registry (Δr). (Adapted from [3.17], © IOP Publishing. Reproduced with permission. All rights reserved)

3.4 Theoretical Techniques

The goal in this section is to provide the reader with some details of theoretical techniques that have been used to calculate the ingredients mentioned above that are needed to determine surface thermodynamical functions such as vibrational entropy, heat capacity, mean-square vibrational amplitudes, and, subsequently, the *Debye* temperature for the surface in question. We put Debye in italics here as the concept of Debye temperature, which is based on the Debye model for the vibrational density of states, is not valid for surfaces and nanostructures for which, as we shall see, the vibrational density of states does not follow the same dependence on energy as the atoms in the bulk [3.19]. Of course, the quantity of prime importance is the vibrational density of states to calculate which one needs to first evaluate the system minimum energy configuration, followed by a calculation of the system vibrational dynamics and, thence, that of the thermodynamical functions. Calculations for details of the electronic structure, charge redistributions, and local electronic densities of states are also of interest, but as they are included in other chapters in this book, they will not be discussed here in any detail. In this section, we provide some of the essentials for the calculations of:

a) Geometrical structure
b) Vibrational dynamics
c) Vibrational free energy.

3.4.1 Determination of Surface Structure and Energetics

Once the coordinates of atoms for the system with the surface geometry discussed in Table 3.1 are generated, it is necessary to allow the system to relax so that atoms find their equilibrium positions in their undercoordinated sites. As is well known, atoms in the surface layers of a solid relax away from their bulk terminated positions, as a result of the bonds that were severed in the creation of the surface. These relaxations can be inwards or outwards with respect to the surface plane. To obtain the relaxed position standard algorithms, such as simulated annealing, steepest descent, and conjugate gradient methods, are used for minimizing the total energy of the system [3.20]. A critical input for all such calculations is the form of the interaction between the atoms/ion cores/electrons, which, not surprisingly, has been the subject of decades of research.

A simple way to proceed is to assume an analytical form of the interaction, such as a Lennard-Jones or Morse potential. However, extensive studies have shown that pair potentials fail to capture some of the main features of solids and their surfaces. A very practical alternative was introduced some years ago in the form of semiempirical many-body potentials, such as those from the embedded atom method (EAM) [3.6, 21] and effective medium theory (EMT) [3.22], which

continue to be widely applied. Although based on fitting of parameters from experiments (and sometimes from more sophisticated theoretical methods) these interaction potentials have had tremendous success in predicting/explaining the characteristics of surfaces and nanostructures of six transition metals (Ni, Cu, Ag, Pd, Pt, Au). Of course, their reliability needs to be checked by comparison with more accurate methods, such as those based on ab-initio density functional theory. Below, we give some general details of ab-initio electronic structure calculations that we and others have used. We follow this up with a short description of the EAM potentials that have been used to calculate structural properties of vicinal surfaces.

Ab-initio Electronic Structure Calculations

Since this topic is covered in detail in several other chapters, only a summary of calculational details is provided here. Ab-initio electronic structure calculations based on density functional theory (DFT) are performed either within a pseudopotential or an all-electron approach using either the local-density approximation (LDA) [3.23] or the generalized gradient approximation (GGA) [3.24]. Of the variety of DFT based codes that are available, two that are frequently used here are the Vienna ab-initio simulation package (VASP) [3.25] and the Quantum ESPRESSO [3.26]. For example, to model the charge density distribution and structural relaxation of nanoparticles, *Shafai* et al. [3.27] adopted the pseudopotential approach [3.25] to describe the interaction of the electrons and the nucleus employing projector-augmented wave (PAW) [3.28, 29] pseudopotentials. For systems in which relativistic effects are significant, as in gold, scalar relativistic pseudopotentials are used [3.30–33]. The Kohn–Sham orbitals are expanded as plane waves with a reasonable kinetic energy cutoff (for example, 720 eV for Au). The exchange-correlation functional proposed by *Perdew*, *Burke*, and *Ernzerhof* (PBE) [3.34] was used. The ion cores in the system are allowed to relax using a conjugate gradient algorithm until the Hellman–Feynman forces acting on each atom are less than 1×10^{-3} eV/Å. Similarly, the total energy is taken to be converged if the changes in the energy in the self-consistent loop are below 10^{-6} eV. Since we use periodic boundary conditions, the supercell for the system of interest is taken to be large enough such that the interactions between the model system and its periodic images are negligible. That is in addition to a specific number of layers of atoms, the model system contains about 12−15 Å of vacuum. The resulting supercells, thus, have dimensions that depend on the size/shape of the system under study. Further details of these calculations may be found elsewhere [3.10].

Many-Body Interaction Potentials

To describe the interactions between the atoms in model systems, several types of many-body, semiempirical potentials [3.6, 21, 22, 35, 36] have been proposed. Without doing justice to others, some details of the semiempirical, many-body potential, EAM, developed by *Foiles*, *Baskes*, and *Daw* [3.6, 21] are presented. Although the EAM potentials neglect the large gradient in the charge density near the surface and use atomic (elemental) charge densities to describe those for the corresponding solid, for the six fcc metals Ag, Au, Cu, Ni, Pd, and Pt, and their alloys, these interatomic potentials have done a good job of reproducing many of the characteristics of bulk and surface systems [3.6, 21]. We have also found EAM potentials to be reliable for examining the temperature-dependent structure and dynamics of the low Miller index surfaces of Ag and Cu [3.37–41] and also for describing the energetics of vicinal surfaces of Cu and self-diffusion processes on the (100) surfaces of Ag, Cu, and Ni [3.42]. This method exploits the findings that the ground state of an interacting electron gas is a unique functional of the total electron charge density [3.23]. It further assumes that the energy of an impurity in a host is a functional of the electron density of the unperturbed host electron density [3.43].

The many-body term in the total energy has the form $E = F_{Z,R}(\rho_{\mathrm{h}}(r))$, where $\rho_{\mathrm{h}}(r)$ is the electron density of the host without impurity at R, the position at which the impurity is to be replaced, and Z is the type of impurity. Each atom in a solid is, thus, viewed as an impurity embedded in a host consisting of all other atoms, and its energy is given by

$$E_{\mathrm{tot}} = \sum_i F_{i,j}(\rho_{\mathrm{h},i}) + \frac{1}{2}\sum_{\substack{i,j \\ (i\neq j)}} \varnothing_{i,j}(R_{i,j}) \,, \tag{3.15}$$

where $\varnothing_{i,j}$ is the short-range pair potential ($\varnothing_{i,j} = Z_i(r)Z_j(r)/r$) and $R_{i,j}$ is the distance between atoms i and j. Further simplification is introduced by assuming that the host density ($\rho_{\mathrm{h},i}$) is a sum of the atomic densities (ρ_j^{a}) and given by

$$\rho_{\mathrm{h},i} = \sum_{j(\neq i)} \rho_j^{\mathrm{a}}(R_{ij}) \,, \tag{3.16}$$

where ρ_j^{a} is the contribution to the electron density from atom j. Connection to the atomic densities makes the total energy to be a function of the atomic positions in electron density ρ_i, and $\varnothing$ is a short-range electrostatic pair potential between atoms i and j.

It is further assumed that the electron density ρ_i is given by a linear superposition of the electron densities of the constituent atoms, which is taken to be spherically symmetric. The EAM functions for the six fcc metals, Ag, Au, Cu, Ni, Pd, and Pt, and their alloys were developed by numerically fitting the functions to the bulk lattice constants, cohesive energy, elastic constants, vacancy formation energy, and alloy heats of mixing. Using these interactions for a model system constructed in its bulk terminated positions, the conjugate gradient method is used to relax the system to 0 K equilibrium configuration. The dynamical matrix needed to calculate the vibrational (or phonon) density of states for a system of interest is then obtained from analytical expressions for the partial second derivatives of the EAM potentials [3.6, 21].

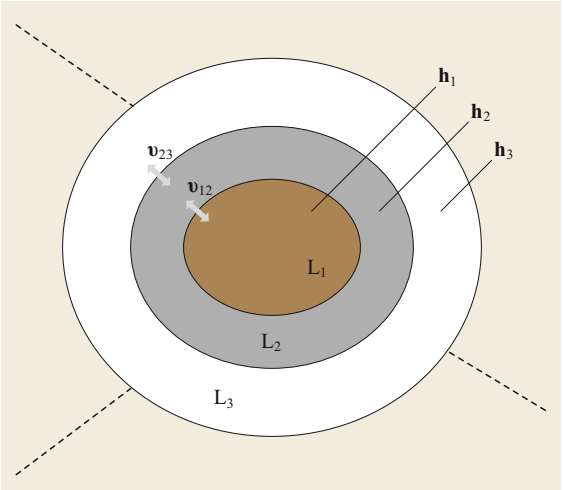

Fig. 3.6 Localities and submatrices. (Adapted with permission from H. Yildirim, Dissertation, UCF 2010)

3.4.2 Determination of the Vibrational Density of States

There are several theoretical techniques for calculations for surface and bulk phonons in crystals, ranging from those based on DFT to those that rely on some form of interatomic potentials. Ab-initio methods based on density functional perturbation theory and their applications are covered elsewhere in this Handbook and, hence, will not be covered here. Instead, we will focus here on methods that typically employ semiempirical interaction potentials. In these cases, the most commonly used is the slab method in which one needs to diagonalize the dynamical matrix portraying the interactions between the particles in N layers of the slab [3.44]. In the case of high Miller index surfaces, in particular those with large terraces, representative of large surface periodicities, slab calculations are hampered by the need for model systems with an extraordinarily large number of layers to describe the inhomogeneities of the surface structure. Furthermore, our interest is in calculating the phonon density of states, rather than phonon dispersion curves, of systems that lack long-range order, because of the presence of steps, kinks, etc. For such purposes, the continued fraction method [3.45] using a real space Green's function developed by *Wu* and coworkers [3.46] is especially suitable, since it determines the local densities of states (LDOS) directly. In fact, the total phonon density of states is calculated as a sum of the contributions from the individual regions of interest. For example, the regions of interest could be the surface layer, the second layer, and so on. Or it could be the kink sites, the steps, the terraces, and so forth. The approach is based on constructing the resolvent matrix of an infinite block-tridiagonal matrix [3.45]. Green's function is defined as the matrix representation of the resolvent operator that yields the LDOS via its matrix elements. Such a matrix must be constructed in a block-tridiagonal form, and the range of the interactions must be finite, which is fortunately the case for the transition metals named above. The system Hamiltonian is then written in a block-tridiagonal matrix as

$$\mathbf{H} = \begin{pmatrix} \ddots & & & \\ \boldsymbol{v}_{i,i-1} & \mathbf{h}_i & \boldsymbol{v}_{i,i+1} & \\ & \boldsymbol{v}_{i+1,i} & \mathbf{h}_{i+1} & \boldsymbol{v}_{i+1,i+2} \\ & & & \ddots \end{pmatrix} , \quad (3.17)$$

where $\mathbf{h}_i$ submatrices along the diagonal are $3n_i \times 3n_{i+1}$ square matrices, $\boldsymbol{v}_{i,i+1}$ matrices along the off-diagonals have dimension $3n_i \times 3n_{i+1}$, and n_i is the number of particles in the chosen locality. Figure 3.6 shows such a system divided into three regions (localities labeled L_1 to L_3). For each locality, there is a submatrix ($\mathbf{h}_1$, $\mathbf{h}_2$ and $\mathbf{h}_3$) describing the interactions within the associated locality. The submatrices ($\boldsymbol{v}_{12}$ and $\boldsymbol{v}_{23}$) describe the interactions between localities. The interactions beyond these localities are assumed to be bulk-like.

Note that in our calculations, the system Hamiltonian is described by the force constant matrix, which is obtained from the second derivative of the interaction potential. The eigenvalue can be derived by means of the Green's function that is associated with the matrix $\mathbf{H}$ and is given by

$$\mathbf{G}(z) = (z\mathbf{I} - \mathbf{H})^{-1} , \quad (3.18)$$

where $z = \omega^2 + \mathrm{i}\varepsilon$, ε is the width of the Lorentzian representing the delta function at ω^2, and $\mathbf{I}$ is a unit matrix

of the same dimension as that of **H**. The diagonal element of the Green's function matrix corresponding to a chosen locality is expressed as

$$\mathbf{G}_{ii} = [(z\mathbf{I} - \mathbf{h}_i) - \boldsymbol{v}_{i,i+1}\Delta_{i+1}^{+}\boldsymbol{v}_{i+1,i} - \boldsymbol{v}_{i,i-1}\Delta_{i-1}^{-}\boldsymbol{v}_{i-1,i}]^{-1} . \quad (3.19)$$

Δ_i^+ and Δ_i^- are defined as forward and backward partial Green's functions and described by

$$\Delta_i^{+} = (z\mathbf{I} - \mathbf{h}_i - \boldsymbol{v}_{i,i+1}\Delta_{i+1}^{+}\boldsymbol{v}_{i+1,i})^{-1} , \quad (3.20)$$

$$\Delta_i^{-} = (z\mathbf{I} - \mathbf{h}_i - \boldsymbol{v}_{i,i-1}\Delta_{i-1}^{-}\boldsymbol{v}_{i-1,i})^{-1} . \quad (3.21)$$

The relation between the successive diagonal elements of the Green's function matrix **G** is obtained by

$$\mathbf{G}_{ii} = \Delta_i^{\pm} + \Delta_i^{\pm}\boldsymbol{v}_{i,i\pm1}\mathbf{G}_{i\pm1,i\pm1}\boldsymbol{v}_{i\pm1,i}\Delta_i^{\pm} . \quad (3.22)$$

As can be seen the calculation of Green's function mainly depends on the forward and backward Green's functions ($\Delta_i^{\pm}$), which are the inverses of matrices with the dimensions same as that of $\mathbf{h}_i$. The convergence procedure for the calculation of $\Delta_i^{\pm}$ for an infinite system starts with the condition as

$$\Delta_1^{+(1)} = \lim_{\substack{m\to\infty,\\ \varepsilon\to 0}} \Delta_1^{+(m)}(z) , \quad (3.23)$$

where

$$\Delta_1^{+(m)} = \{(zI_1 - h_1) - v_{12}[(zI_2 - h_2) - \ldots[v_{m-1,m} \times (zI_m - h_m)^{-1}v_{m,m-1}]^{-1}\ldots]^{-1}v_{21}\}^{-1} . \quad (3.24)$$

From this equation, one can define the forward Green's function for any chosen regime as

$$\Delta_1^{+(1)} = (zI_1 - h_1)^{-1} , \quad (3.25)$$

$$\Delta_1^{+(2)} = [(zI_1 - h_1) - v_{12}(zI_2 - h_2)^{-1}v_{21}]^{-1} , \quad (3.26)$$

$$\Delta_1^{+(3)} = \{zI_1 - h_1 - v_{12}[(zI_2 - h_2) - v_{23}(zI_3 - h_3)^{-1}v_{32}]^{-1}v_{21}\}^{-1} , \quad (3.27)$$

$$\vdots$$

$$\Delta_1^{+(m)} . \quad (3.28)$$

The convergence procedure shows that the information obtained in previous steps cannot be used to calculate $\Delta_1^{+(m)}$ for the current step; hence, for each step, the sequence must be repeated independently. This requires excessive computing time. In order to make use of the information obtained at the previous step ($\Delta_1^{+(m-1)}$) and the current one ($\Delta_1^{+(m)}$), a recursive method is introduced that defines the forward Green's function for the localities ($\Delta_1^{+(1)}$, $\Delta_1^{+(2)}$, $\Delta_1^{+(3)}$, …, $\Delta_1^{+(m)}$) for a finite system as

$$\begin{aligned}
\Delta_1^{+(1)} &= (zI_1 - h_1)^{-1} \equiv \Delta_1^{-} , \\
\Delta_1^{+(2)} &\equiv G_{11}^{(2)} , \\
\Delta_1^{+(3)} &\equiv G_{11}^{(3)} , \\
&\vdots , \\
&\vdots , \\
\Delta_1^{+(m)} &\equiv G_{11}^{(m)} ,
\end{aligned} \quad (3.29)$$

where $G_{11}^{(m)}$ is the (1, 1) diagonal block of Green's function corresponding to the matrix $H^{(m)}$. Using (3.22), $\Delta_1^{+(2)}$ and $G_{22}^{(2)}$ are given by

$$\Delta_1^{+(2)} = G_{11}^{(2)} = \Delta_1^{-} + \Delta_1^{-}v_{12}G_{22}^{(2)}v_{21}\Delta_1^{-} , \quad (3.30)$$

$$G_{22}^{(2)} = \Delta_2^{-} = [(zI_2 - h_2) - v_{12}\Delta_1^{-}v_{21}]^{-1} . \quad (3.31)$$

So, the relation between the successive forward Green's functions is obtained as

$$\Delta_1^{+(2)} = \Delta_1^{+(1)} + A_1\Delta_2^{-}B_1 , \quad (3.32)$$

where $A_1 = \Delta_1^{-}v_{12}$ and $B_1 = v_{12}\Delta_1^{-}$. Repeating the same steps, general recursive relation can be obtained

$$\Delta_1^{+(m)} = \Delta_1^{+(m-1)} + A_{m-1}\Delta_m^{-}B_{m-1} , \quad (3.33)$$

$$A_{m-1} = A_{m-2}\Delta_{m-1}^{-}v_{m-1,m} , \quad (3.34)$$

$$B_{m-1} = v_{m,m-1}\Delta_{m-1}^{-}B_{m-2} . \quad (3.35)$$

This method, thus, simplifies the calculation of Green's functions to inversion and multiplication of matrices whose dimensions are much smaller than the total number of degrees of freedom of the system. The diagonal element of Green's function represents the entire system. The method ensures that Green's function associated with a particular locality in the system can be reasonably calculated. Further details may be found in [3.46–49].

In calculating the LDOS for the surfaces of interest, we take each system to consist of an infinite number of layers with in-plane periodicity and specify a certain number of layers to constitute a locality. The submatrix elements of the block-tridiagonal matrix represent the

force constants between the atoms, within and between the chosen localities. We then determine the normalized LDOS from the trace of Green's function by employing

$$g(\nu^2) = \frac{-1}{3n\pi} \lim_{\varepsilon \to 0} \mathrm{Im}\{\mathrm{tr}[G(\nu^2 + \mathrm{i}\varepsilon)]\} , \tag{3.36}$$

$$N(\nu) = 2\nu g(\nu^2) , \tag{3.37}$$

where ε is the width of the Gaussian and frequency-dependent LDOS ($N(\nu)$) is related to the normalized local LDOS ($g(\nu^2)$).

The method has been applied successfully to both high and low-symmetry systems [3.47–52] such as bulk, low and high Miller index surfaces, and single-element [3.53, 54] and bimetallic NPs [3.55]. These studies have proved that it can accurately reveal the vibrational properties, especially for low-symmetric systems. Applications of the method have provided insights into the effect of coordination and alloying on vibrational and thermodynamical properties of such low-symmetry systems [3.49].

3.4.3 Determination of Surface Thermodynamics

Having calculated the vibrational density of states, as described above, the task is to determine the surface thermodynamical functions, which includes vibrational entropy. Since the harmonic approximation of lattice dynamics was invoked in the above section, in what follows, the same approximation will be implicit. We expect the results summarized here to be valid for low temperatures. Molecular dynamics simulations for Cu and Ag surfaces [3.37, 39, 40], using EAM potentials, show the atomic mean-square displacements to vary linearly with temperature even beyond half the melting temperature, implying the validity of the harmonic approximation for that temperature range. Below, we provide some details of the calculations of the local and excess vibrational free energy for surfaces. The main quantity of interest here is the vibrational contribution to surface free energy. While details may be found in [3.17], we include the main points here.

As discussed before, the free energy of a system is given by the standard definition $F = U - TS$, where U is the internal energy, S is the entropy, and T is the temperature. Both U and S have contributions from atomic configurations and vibrations, such that $F = F_{\mathrm{conf}} + F_{\mathrm{vib}}$. That is, for each atomic configuration of the system, there is a specific vibrational contribution, which can be further written as $F_{\mathrm{vib}} = U_{\mathrm{vib}} - TS_{\mathrm{vib}}$. It is this latter quantity that we calculate here for the surface systems of interest for their relaxed atomic configurations (of minimum energy) at 0 K. In the harmonic approximation, the vibrational free energy, the vibrational internal energy, and the vibrational entropy are given by

$$F^{\mathrm{vib}} = k_{\mathrm{B}}T \int_0^\infty N(\nu) \ln\left[2 \sinh\left(\frac{x}{2}\right)\right] \mathrm{d}\nu , \tag{3.38}$$

$$U_{\mathrm{vib}} = k_{\mathrm{B}}T \int_0^\infty N(\nu) \left(\frac{1}{2}x + \frac{x}{\mathrm{e}^x - 1}\right) \mathrm{d}\nu , \tag{3.39}$$

$$S_{\mathrm{vib}} = k_{\mathrm{B}} \int_0^\infty N(\nu) \left[-\ln(1 - \mathrm{e}^{-x}) + \frac{x}{\mathrm{e}^x - 1}\right] \mathrm{d}\nu , \tag{3.40}$$

where k_{B} is the Boltzmann constant, T is the temperature, $x = h\nu/(k_{\mathrm{B}}T)$, and h is the Planck constant. The vibrational density of states can, in turn, be written as $N(\nu) = \sum_l n_l(\upsilon)$, where $n_l(\upsilon)$ is the local density of states of the region of interest, the layer, the step, the kink, or any other locality.

To calculate the vibrational contribution to the free energy of a surface (flat, stepped, kinked, ...) we consider a slab of N atoms, arranged such that the top and bottom surfaces consist of the Miller index planes. The surface free energy, which is defined as the excess over the values associated with the bulk system, is evaluated using the expression

$$F^{\mathrm{vib}}_{\mathrm{SURF}} = \frac{F^{\mathrm{vib}}_{\mathrm{SLAB}} - NF^{\mathrm{vib}}_{\mathrm{BULK}}}{2A} . \tag{3.41}$$

In (3.41), $F^{\mathrm{vib}}_{\mathrm{SLAB}}$ and $F^{\mathrm{vib}}_{\mathrm{BULK}}$ are, respectively, the vibrational free energy calculated for a finite slab representing the surface system and a single bulk atom, and A is the surface area of the system. The factor 2 arises from the fact that the system contains two free surfaces. In the same vein, the step vibrational free energy is defined as the excess energy over that for a low Miller index surface of the same geometry as the terrace. The vibrational contribution to the step free energy is then calculated using [3.3]

$$F^{\mathrm{vib}}_{\mathrm{STEP}} = F^{\mathrm{vib}}_{\mathrm{S}}(\theta) - (p - 1 + f)F^{\mathrm{vib}}_{\mathrm{S}}(\infty) , \tag{3.42}$$

where $F^{\mathrm{vib}}_{\mathrm{STEP}}$ is the vibrational step free energy, $F^{\mathrm{vib}}_{\mathrm{S}}(\theta)$ and $F^{\mathrm{vib}}_{\mathrm{S}}(\infty)$ are the vibrational surface energies of the corresponding high and low Miller index surfaces forming the terraces of the vicinal surface, p is the number of atomic chains on the terrace, and f is a geometrical factor determined by the projection of the ledge on the terrace. According to this definition f is 2/3 for (211), 1/3 for (331), and 1/2 for (511).

3.5 Results

In this section, we present examples of vibrational density of states for some prototype low and high Miller index surfaces. For the former, we consider the (100) surfaces of Pd, Pt, and Au, for which an extensive study was carried out in [3.10] to compare the results obtained from application of the EAM potentials with those from DFT, while for the latter we focus on Ni(977).

3.5.1 Local Vibrational Density of States

The layer-resolved vibrational density of states for the first four layers of Pd(100), Pt(100), and Au(100) are presented in Fig. 3.7. We note from the figure that the LDOS for the atoms in the first layer is remarkably different from that for the atoms in the second, third, and fourth layers. It, thus, suffices to focus our analysis of the LDOS only for atoms in the first layer. The reader is reminded that the first-layer atoms on the fcc(100) surface have coordination 8, since they have lost four neighbors. As a result, there is a loosening of bonds and a softening of the in-plane force constants in the first layer. The softening of the force constants, in turn, yields a shift towards lower frequencies that is reflected in Fig. 3.7. Note that this red shift in the density of states is a characteristic of all the five elements discussed in this chapter. This is not a global red shift of the density of states, which would have had drastic consequences for the stability of the surfaces. Rather, it is depletion of the high-frequency band accompanying an enhancement of the low-frequency band. We can also conclude from Fig. 3.7 that these effects are marginal for the second-layer atoms and are absent for the third and fourth layers. Though not presented in Fig. 3.7, the LDOS for Cu(100) and Ag(100) show the same trend as the three surfaces shown therein.

Turning next to high Miller index surfaces, we present the calculated local density of states for the step and the terrace atoms of Ni(977) and compare them with those for the Ni(111) surface atoms in Fig. 3.8. We have chosen here Ni(977), since this surface displays a step localized vibrational mode at a frequency [3.52] that is close to that of one that was observed experimentally using the He-atom surface scattering method [3.56, 57]. Note that the terrace of Ni(977) contains eight atoms, seven of which have the same coordination (9) as that of the atoms in the top layer of Ni(111), and the eighth is at the step with coordination 7. Because of the reasonably large terrace width, the LDOS of the Ni(977) terrace atoms is similar to that of the atoms in the top layer of Ni(111).

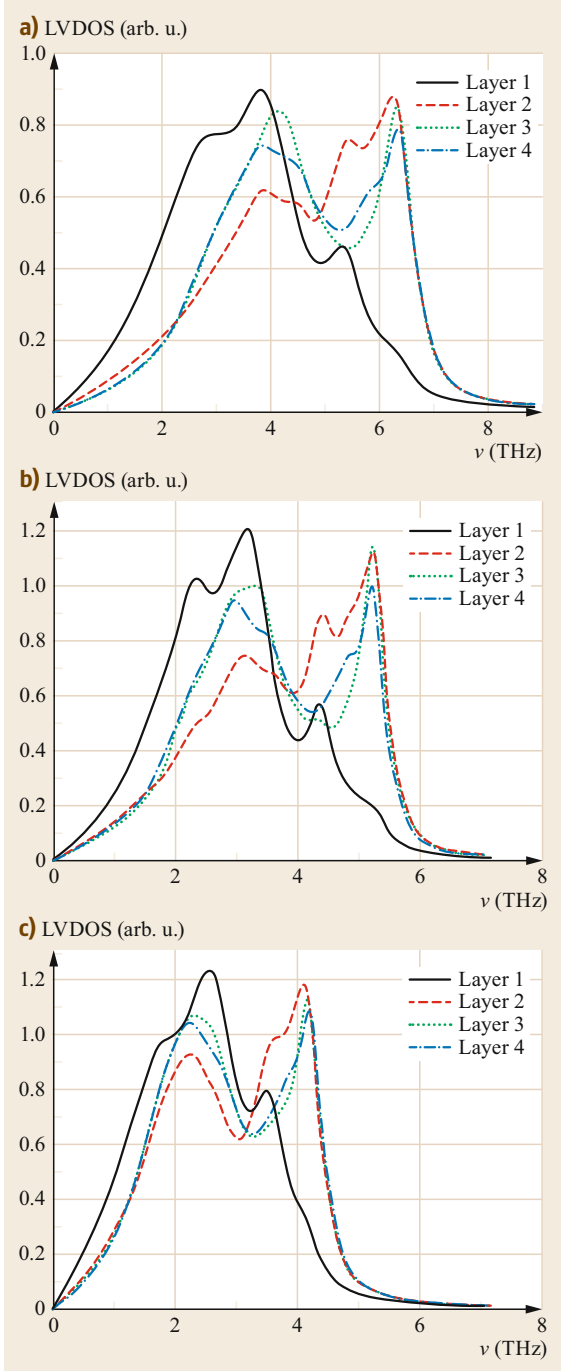

Fig. 3.7a–c Layer-resolved vibrational densities of states for **(a)** Pd(100), **(b)** Pt(100), and **(c)** Au(100). (Reprinted from [3.10], with permission from Elsevier)

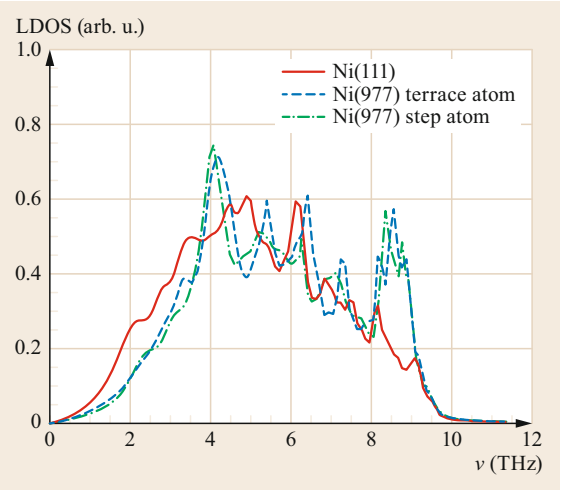

Fig. 3.8 Projected vibrational densities of states for the Ni(977) step, terrace, and Ni(111) surface atoms. (Reprinted from [3.52], with permission of AIP Publishing)

This result suggests that in studies of phonons of vicinal surfaces with relatively large terraces, as in (977), or on realistic surfaces with nonregularly distributed steps, it is feasible to use a local approach to determine the phonons of the step and its surrounding atoms, while resorting to standard techniques (diagonalizing a force constant-based dynamical matrix for a slab with a large number of layers) for calculating phonons of the close-packed flat surface for the terrace. Another interesting feature in Fig. 3.8 is that the low-frequency modes associated with the step atoms display a global shift to lower frequencies, to the modes associated with the terrace (and Ni(111) surface atoms), thereby pointing to an extra softening of relevant force constants, in agreement with suggestions of *Niu* et al. [3.56, 57]. As shown in Table 3.2, the force constants between the surface atoms, calculated using EAM interaction potentials, undergo both softening and stiffening.

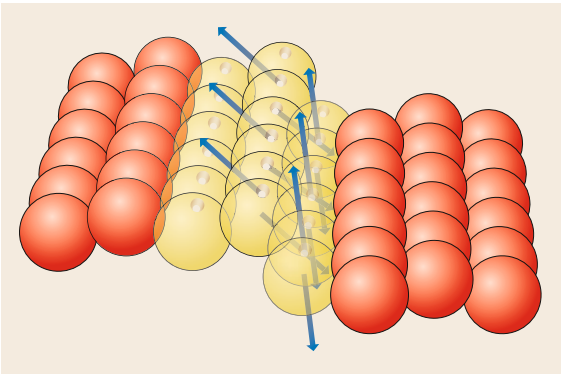

Fig. 3.9 The displacement pattern of the step-localized vibrational mode on Ni(977). (Adapted from [3.18], © IOP Publishing. Reproduced with permission. All rights reserved)

A detailed examination of the LDOS of Ni(977) [3.52] shows that the most prominent low-frequency mode is at 3.3 THz with maximum displacement along the x-direction. The displacement vectors of the atoms contributing to this mode, found from the imaginary part of the Green function, is shown in Fig. 3.9. Note that this mode is quasi-one dimensional: it involves only the concerted motion of the SC and CC atoms in conjunction with that of the TC atoms. The step atoms alternate with displacement vectors $(+1, 0, -0.67)$ and $(-1, 0, +0.67)$, the corner atoms with vectors $(+0.27, 0, -1)$ and $(-0.27, 0, +1)$, and the TC atoms with vectors $(0, +0.24, 0)$ and $(0, -0.24, 0)$. Thus, the step and the corner atoms move in the xz-plane, while the TC atoms move along the y-direction to accommodate the propagation of this mode along the direction parallel to the step. The rest of the atoms are at rest. The wavelength of the mode is $2\times$ *nearest-neighbor distance* or 4.978 Å, and its wavevector $q = (0.0, 1.262\,\text{Å}^{-1}, 0.0)$. This is a *super*localized mode, since the motion is restricted to the step atoms and their immediate neighbors on the

Table 3.2 Force constant matrices (in eV Å^{-2}/unit mass) between the step atom and it neighbors on Ni(977). (Adapted from [3.17], © 2003 IOP Publishing)

Atoms		Surface			Bulk		
		x	*Y*	*z*	*x*	*y*	*Z*
SC–SC	*x*	0.0236	0.1489	0.0044	0.0816	0.0000	0.0058
	y	−0.1489	−2.6386	−0.2796	0.0000	−3.0568	0.0000
	z	0.0044	0.2796	−0.0050	0.0058	0.0000	0.0805
SC–CC	*x*	−1.5876	0.0000	1.7094	−1.3359	0.0000	1.5649
	y	0.0000	0.0966	0.0000	0.0000	0.0753	0.0000
	z	2.0976	0.0000	−2.0658	1.5649	0.0000	−1.6342
SC–BNN	*x*	−0.0411	−0.3809	−0.6780	−0.0314	0.2890	−0.4983
	y	−0.3225	−0.7339	−1.5004	0.2890	−0.7026	1.3300
	z	−0.6080	−1.5720	−2.5342	−0.4983	1.3300	−2.1632

Table 3.3 Observed (Exp.) and calculated (Th.) vibrational modes on metal vicinal surfaces, in THz. (Adapted from [3.17], © IOP Publishing)

Surface	Method[a]	Modes
Cu(511)	Exp. HAS	1.51, 2.76, 3.24, 3.84
Cu(511)	Exp. EELS	3.41
Cu(511)	Th. EAM-LD	7.51, 7.80
Cu(511)	Th. EAM-RSGF	2.25
Cu(511)	Th. EAM-LD	1.1, 1.2, 1.6, 2.3, 2.8, 3.0, 3.25, 3.35, 6.4
Cu(211)	Exp. HAS	1.32, 1.82, 2.52, 2.62, 2.66, 3.36
Cu(211)	Exp. EELS	3.24, 8.16
Cu(211)	Th. EAM-LD	2.35, 6.22, 7.51, 7.80
Cu(211)	Th. EAM-RSGF	2.52
Cu(211)	Th. TB-LD	2.50, 2.78, 3.25, 3.59, 6.20
Cu(211)	Th. DFT-PW	2.76, 2.98, 5.93
Cu(211)	Th. EAM-LD	1.2, 1.6, 2.3, 2.5, 2.8, 2.9, 3.3, 4.0, 4.2, 5.7, 6.3, 6.8
Cu(331)	Th. EAM-RSGF	2.92, 5.26, 6.12
Cu(1 1 17)	Exp. EELS	2.69, 3.14, 6.72
Cu(1 1 17)	Th. EAM-LD	7.46, 7.92
Ni(977)	Exp. HAS	3.55, 3.60
Ni(977)	Th. EAM-RSGF	3.3, 3.9, 4.9, 9.1
Pt(775)	Exp. EELS	6.15

[a] See [3.17] for references

surface. Modes such as the one displayed in Fig. 3.9 exist on a number of vicinal surfaces. Similarly, along the y and z-directions there are noticeable peaks, at low frequencies, at 3.9, and 4.9 THz, respectively. There is also a prominent high-frequency peak at 9.1 THz, close to the top of the bulk band. In Table 3.3, we present a summary of the frequencies of the observed modes and refer the reader to discussions in related publications.

3.5.2 Surface Vibrational Free Energies

An important conclusion from the calculated LDOS of the (100) surfaces of Pd, Pt, and Au presented in Fig. 3.7 is that we should expect deviations in surface thermodynamics from the bulk values, and that this difference will be mainly for the top-layer atoms. This inference (obtained using DFT) is in accord with what was reported in earlier publications on the vibrational dynamics and thermodynamics of vicinal and kinked fcc metal surfaces using EAM potentials [3.6, 21]. The quantities of interest here are the lattice heat capacity (local and excess), the contribution of the vibrational dynamics to the free energy (local and excess), and the atomic mean-square displacements. As shown in Figs. 3.10a, 3.11a and 3.12a, the local lattice heat capacity (C_V) of the first-layer atoms of Pd(100), Pt(100), and Au(100) differs from that of the other atoms in the system, and that this difference is temperature dependent. These deviations from the bulk values are better described by the local excess from the bulk as illustrated in Figs. 3.10b, 3.11b, and 3.12b. Indeed, for Pd and Pt(100), the maximum deviation was found to be 3.4 and 2.8 J/(K mol), respectively, both occurring at a temperature of 50 K. However, the first-layer atoms of Au(100) behave differently; with a maximum deviation of only 2.2 J/(K mol) occurring at a lower temperature (30 K).

Let us now turn our attention to the local and excess vibrational free energy. The results are presented in Figs. 3.10, 3.11, and 3.12, for Pd, Pt, and Au(100), respectively. Here again, only the first-layer atoms show differences from the atoms in the other layers. As shown in the figures, the local contributions to the vibrational free energies for the layers beyond the second converge to the corresponding bulk values. For the atoms in the first layer, the local contribution to the vibrational free energy decreases with temperature and reaches −48, −64, and −79 meV/atom for Pd, Pt, and Au(100), respectively, at 300 K. The excess vibrational free energies are significantly different for the first-layer atoms, as can be seen in Figs. 3.10d, 3.11d, and 3.12d, with the contribution amounting to 19, 17, and 14 meV/atom at 300 K. Our DFT calculations for Cu and Ag(100) show 15 meV/atom, which is in good agreement with the EAM results (about 18 meV/atom for both surfaces at 300 K).

In the harmonic approximation, the mean-square vibrational amplitude (MSVA) is expected to vary linearly with temperature. Note that at 0 K, the MSVA does not go to zero due to the zero-point motion. In Figs. 3.10e, 3.11e, and 3.12e, we present our DFT results for the MSVA of Pd, Pt, and Au(100), respectively. The MSVA of the atoms in the third and fourth layers are bulk-like (0.008, 0.0075, and 0.0130 Å^2 at 300 K for Pd, Pt, and Au(100), respectively). Though MSVA of the second-layer atoms is close to the bulk values, that corresponding to the first-layer atoms shows large deviations. The ratio between the first-layer and the bulk MSVA is 2.06, 1.73, and 1.73 for Pd, Pt, and Au(100), respectively. This deviation is due to the decrease of coordination at the surface as compared to the bulk. Note that the ratio is the same for Pt and Au(100) and the highest for Pd(100), reflecting the mass effect.

We now turn to a summary of the impact of further undercoordination on the vibrational contribution to the thermodynamic properties as presented by vicinal surfaces with a few specific examples. In Fig. 3.13, we show the vibrational LDOS for the step (SC), terrace (TC), and corner (CC) atoms of Cu(511), Cu(211), and Cu(331). The shift towards low frequencies, in each

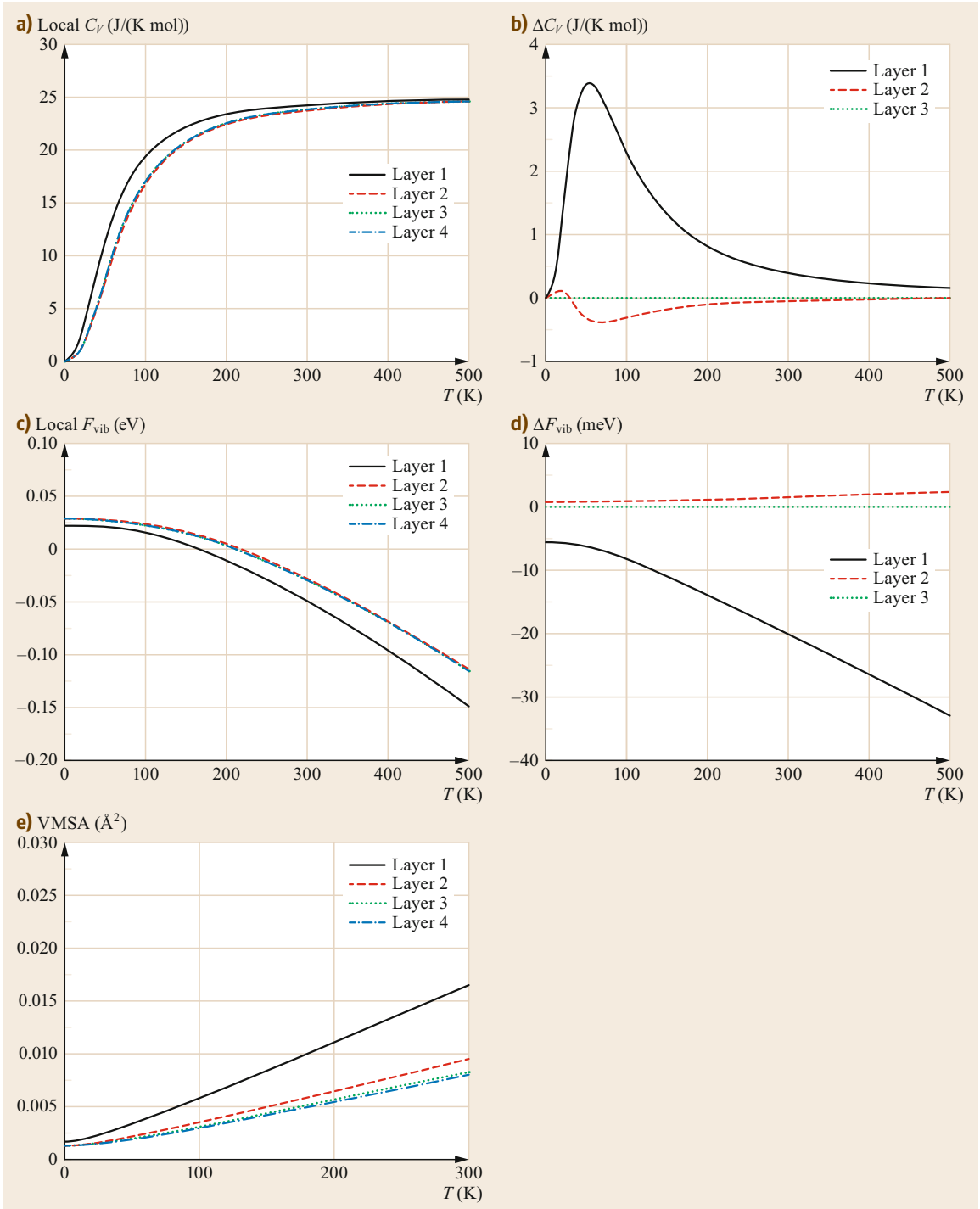

Fig. 3.10a–e The thermodynamic functions for Pd(100): **(a)** lattice heat capacity; **(b)** excess lattice heat capacity; **(c)** vibrational contribution to the free energy; **(d)** excess vibrational contribution to the free energy; **(e)** vibrational mean-square amplitude. (Reprinted from [3.10], with permission from Elsevier)

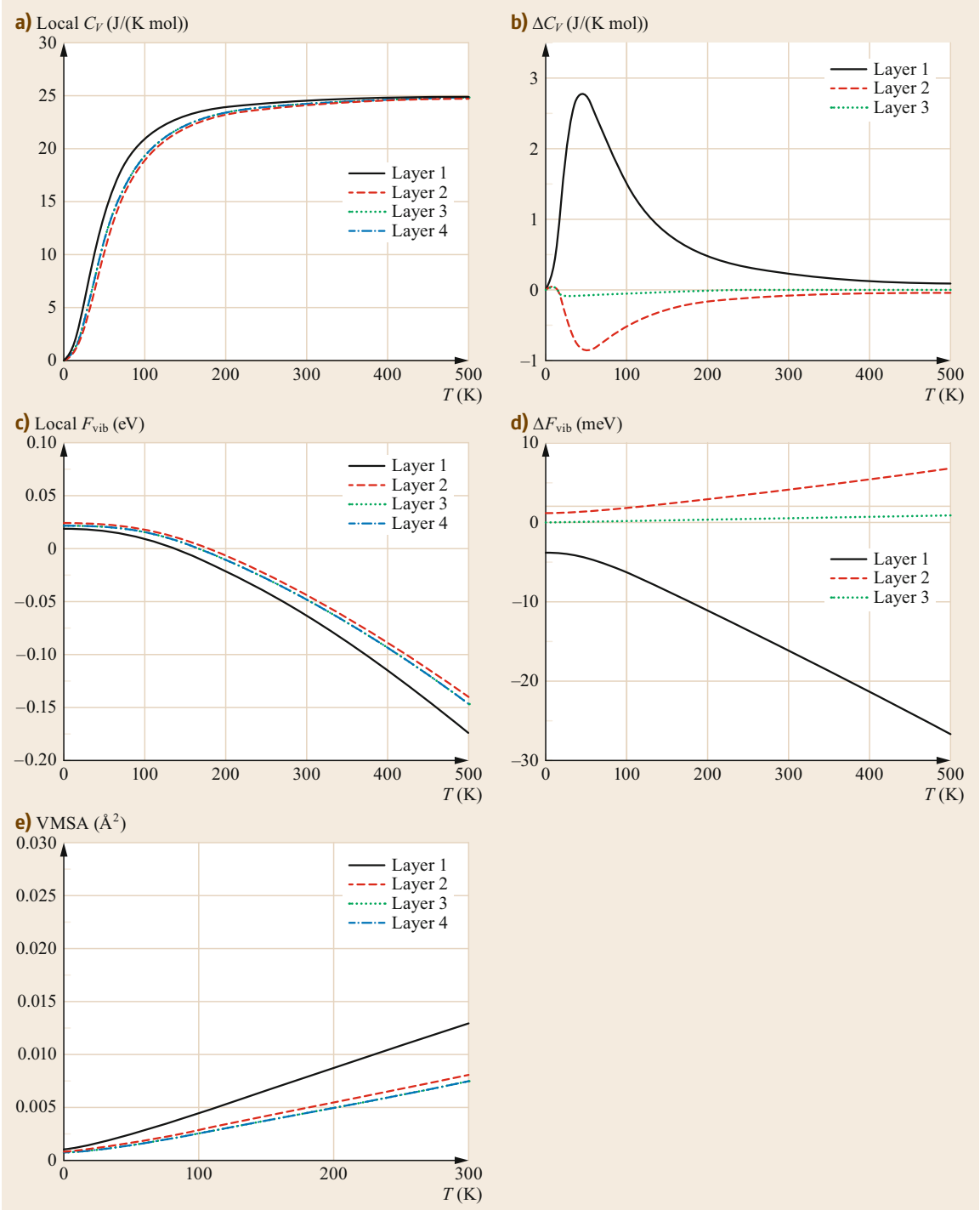

Fig. 3.11a–e The thermodynamic functions for Pt(100): **(a)** lattice heat capacity; **(b)** excess lattice heat capacity; **(c)** vibrational contribution to the free energy; **(d)** excess vibrational contribution to the free energy; **(e)** vibrational mean-square amplitude. (Reprinted from [3.10], with permission from Elsevier)

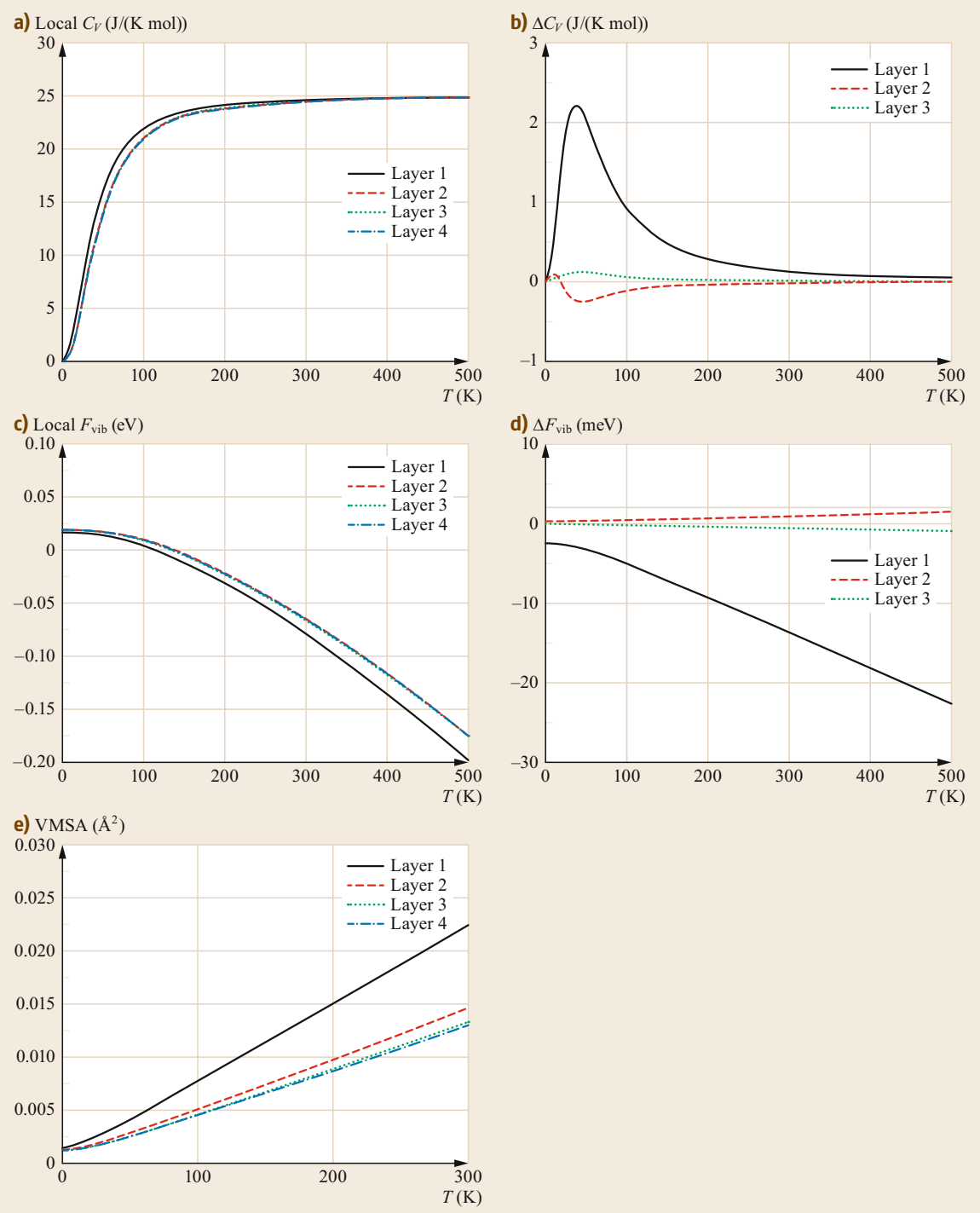

Fig. 3.12a–e The thermodynamic functions for Au(100): **(a)** lattice heat capacity; **(b)** excess lattice heat capacity; **(c)** vibrational contribution to the free energy; **(d)** excess vibrational contribution to the free energy; **(e)** vibrational mean-square amplitude. (Reprinted from [3.10], with permission from Elsevier)

case, reflects the lower coordination of these atoms. There are some differences in LDOS between the sets of atoms on the three surfaces. On Cu(331), for example, the corner atom is almost bulk-like, while the other two atoms contribute more to the lower-frequency modes than the atoms in the bulk. As noted in previous publications [3.3, 11], the LDOS of the (211) and the (511) surfaces are similar to each other and different from those of the (331). These similarities and differences are related to trends in the multilayer relaxation patterns on these surfaces, as discussed above. Furthermore, the plots in Fig. 3.13 suggest complexity in the way the different surface localities differ from those of the atoms in the bulk. We also find that the LDOS of the BNN atoms (in the layer adjacent to the corner atoms) show an enhancement in the *high*-frequency region over bulk values [3.3]. This enhancement at the high-frequency end is very prominent in the LDOS of the surface atoms on Cu(532), which has a regular array of kinks, as can be seen in Fig. 3.14.

The effect of new features in the vibrational dynamics is reflected in the calculated local vibrational free energy illustrated in Fig. 3.15 for the top layers of (511), (211), and (331). On Cu(511) and Cu(211), the local contribution to vibrational entropy from atoms in the three surface chains (SC, TC, CC) is distinct from that of the atoms in the bulk. On Cu(331), however, layer 3, which corresponds to CC atoms on the terrace, shows characteristics more akin to those of atoms in the bulk than those on the surface. This interesting behavior can, again, be traced to the effective coordination number. As we know from Table 3.2, the coordination number for a CC atom of (511) and (211) is 10, while that of a (331) surface is 11, close to the value 12 for a bulk atom. In the equilibrium configuration obtained after ionic relaxation of the model system [3.3, 11], while the CC atom of (211) and (511) moves upward, away from the bulk, that of (331) moves toward the rest of the bulk, increasing its effective coordination number. Note that the difference in coordination between the terrace atoms on (511) and (211) (8 and 9, respectively) is also displayed in the local free energies in Fig. 3.15. The terrace atoms on (511) have contributions closer to those of their step atoms, while on (211), they are closer to those of the corner atoms. The reader is referred to [3.3] for details of the effects of varying coordination and complex relaxation patterns on the vibrational thermodynamic properties of the vicinal surfaces. We summarize the essential points below.

For convenience, we focus the discussion on local thermodynamical quantities calculated at 300 K. Interestingly, the contributions of the step atoms (SC) are about the same on all three vicinal surfaces. On the Cu surfaces, it is almost 41 meV/atom, while on

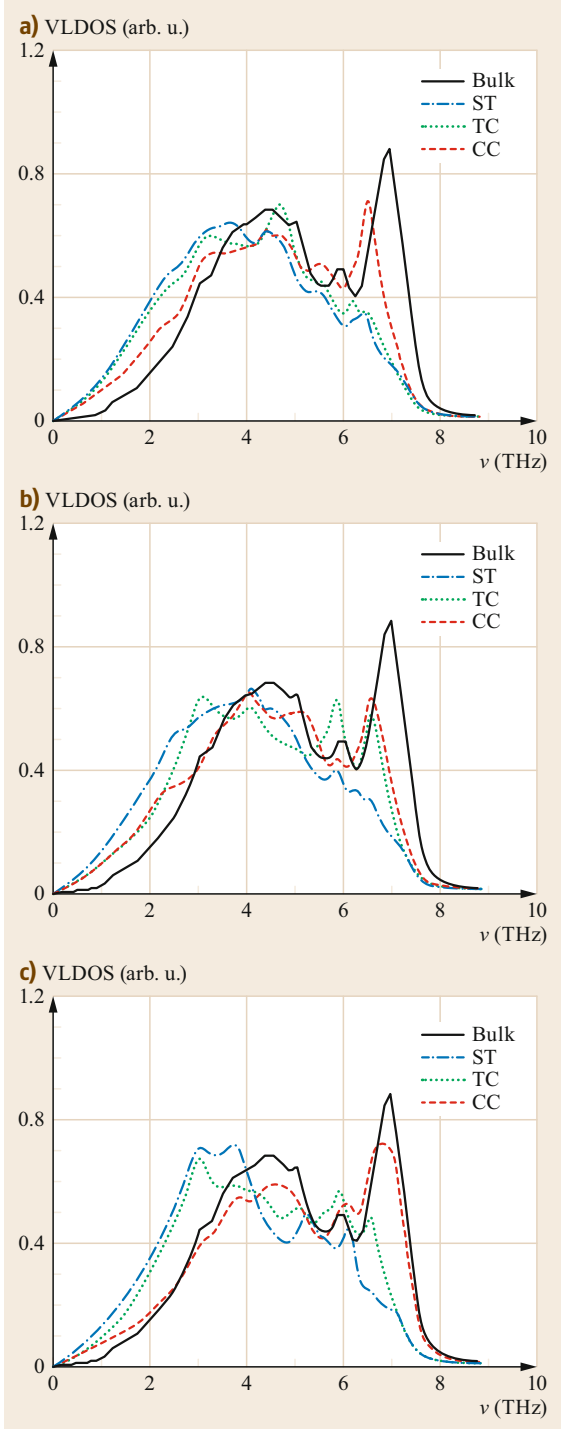

Fig. 3.13a–c Projected vibrational densities of states of the step (SC), terrace (TC), and corner (CC) atoms on **(a)** Cu(511), **(b)** Cu(211), and **(c)** Cu(311) compared to that of a bulk atom. (Adapted from [3.17], © IOP Publishing. Reproduced with permission. All rights reserved)

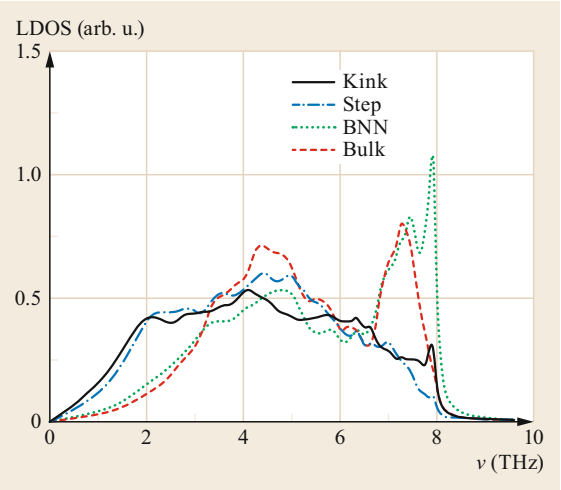

Fig. 3.14 The projected vibrational density of states of kink sites on Cu(532). (Adapted from [3.17], © IOP Publishing. Reproduced with permission. All rights reserved)

the Ag surfaces, it is about 68 meV/atom. Although the percentage enhancement over the bulk value is larger on Cu surfaces than on Ag, in each case, it is in excess of about 19 meV/atom over that in the bulk. Turning to the contributions of the TC atoms, we find a good correspondence with their respective coordination number. On (511), on which their coordination is 8, they contribute about 17 meV/atom more than the bulk atoms, similarly to the value for the atoms on (100) surface with the same coordination. On (211) and (331), their contribution over the bulk is about 13–11 meV/atom, resembling that of the surface atoms on (111), which also have a coordination of 9. The largest difference in contribution for the atoms on the three types of vicinal surface comes from the corner atoms, which contribute only 2–3 meV/atom more than the atoms in the bulk on Cu(331), while on Cu(511) and Cu(211) the corresponding amount is 9 meV/atom. This is, again, understandable from previous arguments based on atomic coordination. The atoms in the other layers in the tables have similar contributions to the bulk, and small variations can, again, be linked to their ionic relaxation and nonbulk-like contribution to the vibrational DOS. The above findings regarding the differential, local vibrational free energy contribution of atoms in undercoordinated sites show that the vibrational free energy does not scale with the coordination number in a simple manner, although its dependence on atomic coordination is remarkable. This is not surprising, as other factors also impact the characteristics of the surface atoms. Ionic relaxations of the individual atoms and their bond lengths with the surrounding atoms are also expected to play

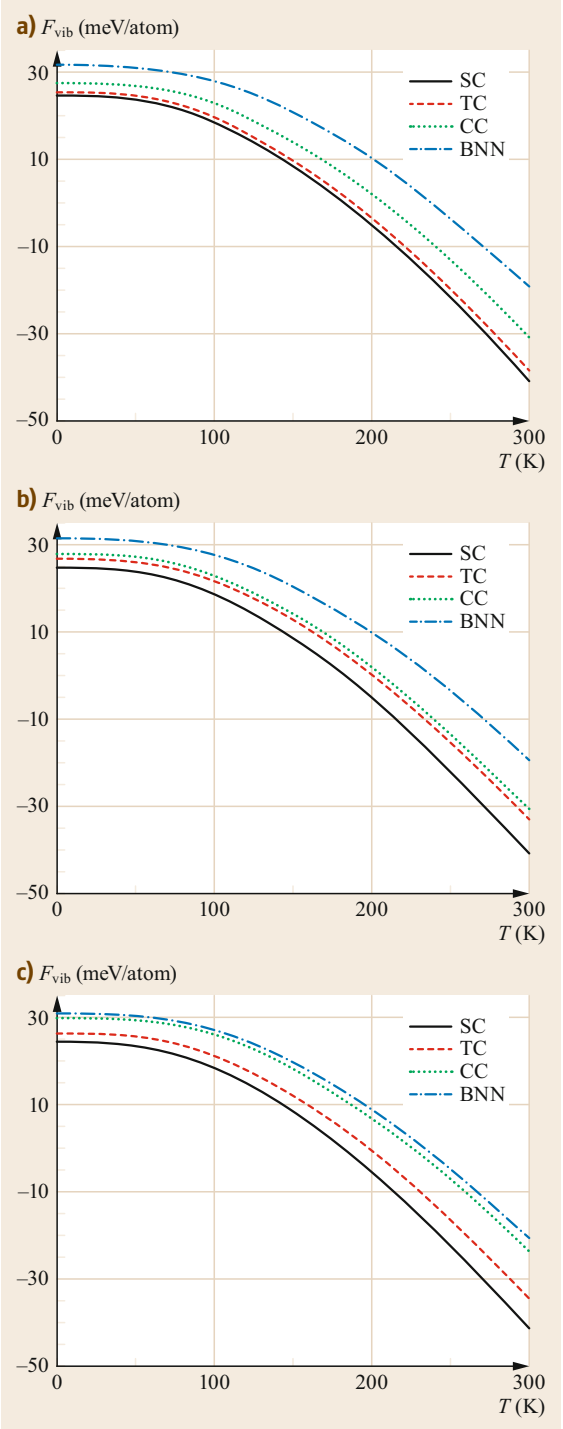

Fig. 3.15a–c The dependence of the local contribution on the vibrational free energy F_{vib} of vicinal surfaces on the local coordination for **(a)** Cu(511), **(b)** Cu(211), and **(c)** Cu(331). (Adapted from [3.17], © IOP Publishing. Reproduced with permission. All rights reserved)

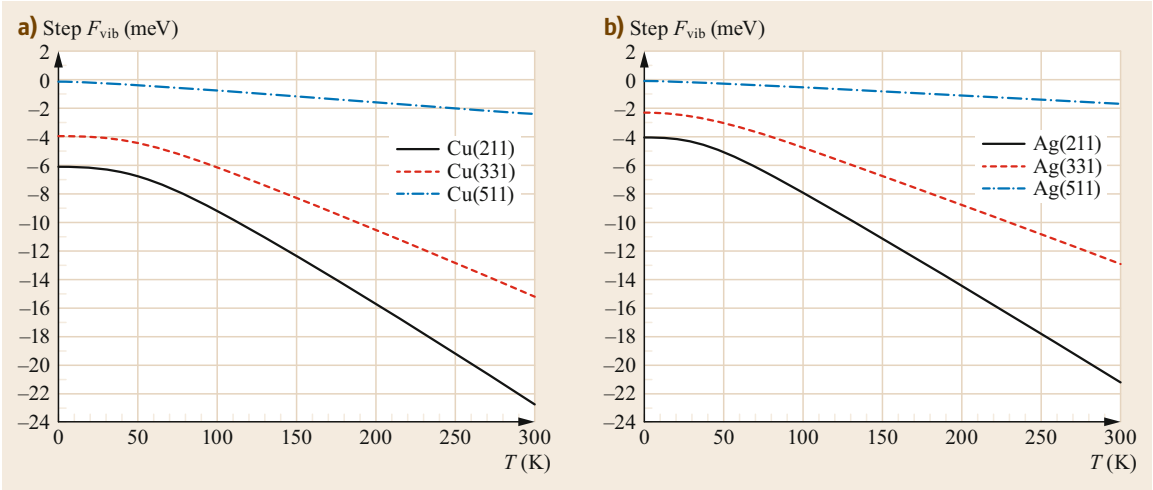

Fig. 3.16a,b The dependence of the excess step free energy (vibrational part) on the surface geometry. (Adapted from [3.17], © IOP Publishing. Reproduced with permission. All rights reserved)

a role in defining the local characteristics of a surface. While atoms on low Miller index surfaces lose symmetry in the direction perpendicular to the surface, the atoms forming the terraces of vicinal surfaces experience a lack of symmetry along the direction perpendicular to the step edge, in the terrace plane, in addition to the direction normal to it. This, in turn, leads to complex relaxation patterns and bond lengths for the surface atoms, as shown in previous studies [3.11, 22], resulting in distinctive characteristics of the local regions on the surface. Note that in this chapter, relaxation patterns of the surfaces considered are not presented, to keep the focus on vibrational contributions. However, there is a direct link between frequencies of surface (and step) localized modes, the changes in force constants from the values in the bulk, and the manner in which atoms in undercoordinated sites relax to configurations away from their bulk terminated positions. The reader is encouraged to refer to previous studies that summarize these interesting and complex relaxation patterns.

Using the local contributions to the vibrational entropy we can calculate the surface and step excess free energies, following the procedure discussed earlier; we find the calculated surface excess vibrational free energies for Cu and Ag vicinals at 0, 100, and 300 K to be quite small. The calculation of the excess step free energies, however, shows a remarkable effect of the vibrational component. The temperature variation of the step vibrational free energy for the three surface geometries is plotted in Fig. 3.16. It is remarkable that the excess vibrational contribution is almost nonexistent for both Ag(511) and Cu(511). From 0 to 300 K, it shows a variation of only about 1 meV/atom. On the other hand, the contribution is remarkable for both Ag(211) and Cu(211) and constitutes about 10% of the total free energy [3.3, 58] in the case of Cu. The case of the (331) surfaces lies in between the other two geometries. Since the step free energy is relevant to the roughening temperature of a surface, we expect vibrational contributions to play an important role, particularly for Cu(211) and Ag(211).

3.6 Summary

This chapter contains some details of the calculation of local vibrational contributions of surface atoms to selected dynamical properties and thermodynamic quantities. Already published results obtained by the author and her coworkers (A. Kara, S. Durkanoglu, M. Alcantara Ortigoza, and H. Yildirim) are used as examples of the novel vibrational characteristics that impact the thermodynamical properties of a set of low and high Miller index surfaces of several transition metals. Calculations were performed using either ab-initio electronic structure calculations or many-body interaction potentials. Comparisons of results are made with experimental data where available. The main conclusion to be drawn is that of the important role of the local coordination and geometry in determining the structural, dynamical, and, ultimately, thermodynamical proper-

ties of these surface nanostructures. Of the large list of vicinals of varying surface geometry, terrace width, step-face orientation, and elemental metal summarized here, the striking feature in the multilayer relaxation is the large outward relaxation of the corner atom (actually, the least undercoordinated atom) coupled with the inward relaxation of its neighboring surface atom. At least for Cu, Pd, Al, and selected vicinals of Ni, Ag, and Pt, the trends in the calculated multilayer relaxations point to this enhanced local effect at the step and near the corner site, in accordance with principles of charge smoothing. The reduced coordination of the surface atoms leads to electronic densities of states that are narrower and shifted towards the Fermi level. Furthermore, changes in the bond lengths of the surface atoms from their neighbors are reflected in corresponding softening and stiffening of force constants with respect to those in the bulk. As a result, localized modes appear on stepped surfaces whose existence has been verified experimentally. Moreover, projected vibrational densities of states of surface atoms show enhancements of modes at the low-frequency end, as well as near (and sometimes above) the top of the bulk modes. The vibrational entropies of these surfaces are thereby impacted on by their local geometry and coordination. The local contributions scale with coordination in a complex manner. While the surface free energies of a set of vicinals of Ag and Cu show very little sensitivity to the vibrational contribution, the excess step free energy could have a vibrational contribution of about 25%.

In considerations of growth and surface stability, vibrational contributions cannot be ignored. Needless to say, surface relaxations are an inherent component of the novel features of vicinal surfaces and should not be ignored in any serious examination of these surfaces. Last but not least, the modifications in the structural, dynamical, and subsequently thermodynamical, properties introduced by the presence of steps on surfaces are local in nature, thereby allowing an extension of the knowledge gained from systematic studies of stepped surfaces to more complex environments such as those on nanocrystals.

References

3.1 C. Bombis, A. Emundts, M. Nowicki, H.P. Bonzel: Absolute surface free energies of Pb, Surf. Sci. **511**(1), 83–96 (2002), https://doi.org/10.1016/S0039-6028(02)01554-6

3.2 H.P. Bonzel, A. Emundts: Absolute values of surface and step free energies from equilibrium crystal shapes, Phys. Rev. Lett. **84**(25), 5804–5807 (2000), https://doi.org/10.1103/PhysRevLett.84.5804

3.3 S. Durukanoğlu, A. Kara, T.S. Rahman: Local and excess vibrational free energies of stepped metal surfaces, Phys. Rev. B **67**(23), 235405 (2003), https://doi.org/10.1103/PhysRevB.67.235405

3.4 J.W.M. Frenken, P. Stoltze: Are vicinal metal surfaces stable?, Phys. Rev. Lett. **82**(17), 3500–3503 (1999), https://doi.org/10.1103/PhysRevLett.82.3500

3.5 A. Kara, T.S. Rahman: Vibrational dynamics and thermodynamics of surfaces and nanostructures, Surf. Sci. Rep. **56**(5), 159–187 (2005), https://doi.org/10.1016/j.surfrep.2004.09.003

3.6 S.M. Foiles, M.I. Baskes, M.S. Daw: Embedded-atom-method functions for the fcc metals Cu, Ag, Au, Ni, Pd, Pt, and their alloys, Phys. Rev. B **33**(12), 7983–7991 (1986), https://doi.org/10.1103/PhysRevB.33.7983

3.7 S. Baroni, P. Giannozzi, A. Testa: Green's-function approach to linear response in solids, Phys. Rev. Lett. **58**(18), 1861–1864 (1987), https://doi.org/10.1103/PhysRevLett.58.1861

3.8 P. Giannozzi, S. de Gironcoli, P. Pavone, S. Baroni: Ab initio calculation of phonon dispersions in semiconductors, Phys. Rev. B **43**(9), 7231–7242 (1991), https://doi.org/10.1103/PhysRevB.43.7231

3.9 R. Heid, K.P. Bohnen: Ab initio lattice dynamics of metal surfaces, Phys. Rep. **387**(5), 151–213 (2003), https://doi.org/10.1016/j.physrep.2003.07.003

3.10 H. Yildirim, A. Kara, T.S. Rahman, R. Heid, K.-P. Bohnen: Surface vibrational thermodynamics from ab initio calculations for fcc(100), Surf. Sci. **604**(3), 308–317 (2010), https://doi.org/10.1016/j.susc.2009.11.022

3.11 A. Zangwill: *Physics at Surfaces* (Cambridge Univ. Press, Cambridge 1988)

3.12 G.A. Somorjai, Y. Li: *Introduction to Surface Chemistry and Catalysis* (Wiley, Hoboken 2010)

3.13 C. Kittel: *Introduction to Solid State Physics*, 6th edn. (Wiley, Hoboken 1995)

3.14 J.W. Gibbs: *Collected Works*, Vol. 1 (Yale, New Haven 1948)

3.15 G. Burns: *Solid State Physics* (Academic Press, Orlando 1985)

3.16 L. Vattuone, L. Savio, M. Rocca: Bridging the structure gap: Chemistry of nanostructured surfaces at well-defined defects, Surf. Sci. Rep. **63**(3), 101–168 (2008), https://doi.org/10.1016/j.surfrep.2007.11.001

3.17 T.S. Rahman, A. Kara, S. Durukanoğlu: Structural relaxations, vibrational dynamics and thermodynamics of vicinal surfaces, J. Phys. Condens. Matter **15**(47), S3197–S3226 (2003), https://doi.org/10.1088/0953-8984/15/47/002

3.18 B. Lang, R.W. Joyner, G.A. Somorjai: Low energy electron diffraction studies of chemisorbed gases on stepped surfaces of platinum, Surf. Sci. **30**(2), 454–474 (1972), https://doi.org/10.1016/0039-6028(72)90012-X

3.19 G. Shafai, M.A. Ortigoza, T.S. Rahman: Vibrations of Au_{13} and $FeAu_{12}$ nanoparticles and the limits of the Debye temperature concept, J. Phys. Condens. Matter **24**(10), 104026 (2012), https://doi.org/10.1088/0953-8984/24/10/104026

3.20 W.H. Press, B.P. Flannery, S.A. Teukolsky, W.T. Vetterling: *Numerical Recipes in Fortran 77: The Art of Scientific Computing*, 2nd edn. (Cambridge Univ. Press, Cambridge 1992)

3.21 M.S. Daw, S.M. Foiles, M.I. Baskes: The embedded-atom method: A review of theory and applications, Mater. Sci. Rep. **9**(7), 251–310 (1993), https://doi.org/10.1016/0920-2307(93)90001-U

3.22 K.W. Jacobsen, J.K. Norskov, M.J. Puska: Interatomic interactions in the effective-medium theory, Phys. Rev. B **35**(14), 7423–7442 (1987), https://doi.org/10.1103/PhysRevB.35.7423

3.23 P. Hohenberg, W. Kohn: Inhomogeneous electron gas, Phys. Rev. **136**(3B), B864–B871 (1964), https://doi.org/10.1103/PhysRev.136.B864

3.24 J. Perdew: Unified theory of exchange and correlation beyond the local density approximation. In: *Electronic Structure of Solids '91*, Physical Research, Vol. 17 (Akademie Verlag, Berlin 1991) pp. 11–20

3.25 G. Kresse, J. Furthmüller: Efficient iterative schemes for ab initio total-energy calculations using a plane-wave basis set, Phys. Rev. B **54**(16), 11169–11186 (1996), https://doi.org/10.1103/PhysRevB.54.11169

3.26 P. Giannozzi, S. Baroni, N. Bonini, M. Calandra, R. Car, C. Cavazzoni, D. Ceresoli, G.L. Chiarotti, M. Cococcioni, I. Dabo, A. Dal Corso, S. de Gironcoli, S. Fabris, G. Fratesi, R. Gebauer, U. Gerstmann, C. Gougoussis, A. Kokalj, M. Lazzeri, L. Martin-Samos, N. Marzari, F. Mauri, R. Mazzarello, S. Paolini, A. Pasquarello, L. Paulatto, C. Sbraccia, S. Scandolo, G. Sclauzero, A.P. Seitsonen, A. Smogunov, P. Umari, R.M. Wentzcovitch: QUANTUM ESPRESSO: A modular and open-source software project for quantum simulations of materials, J. Phys. Condens. Matter **21**(39), 395502 (2009), https://doi.org/10.1088/0953-8984/21/39/395502

3.27 G. Shafai, S. Hong, M. Bertino, T.S. Rahman: Effect of ligands on the geometric and electronic structure of Au_{13} clusters, J. Phys. Chem. C **113**(28), 12072–12078 (2009), https://doi.org/10.1021/jp811200e

3.28 P.E. Blöchl: Projector augmented-wave method, Phys. Rev. B **50**(24), 17953–17979 (1994), https://doi.org/10.1103/PhysRevB.50.17953

3.29 G. Kresse, D. Joubert: From ultrasoft pseudopotentials to the projector augmented-wave method, Phys. Rev. B **59**(3), 1758–1775 (1999), https://doi.org/10.1103/PhysRevB.59.1758

3.30 R.D. Cowan, D.C. Griffin: Approximate relativistic corrections to atomic radial wave-functions, J. Opt. Soc. Am. **66**(10), 1010–1014 (1976), https://doi.org/10.1364/Josa.66.001010

3.31 D.D. Koelling, B.N. Harmon: A technique for relativistic spin-polarised calculations, J. Phys. C **10**(16), 3107–3114 (1977), https://doi.org/10.1088/0022-3719/10/16/019

3.32 M. Nejjar, A. Qachaou: Extended relativistic norm-conserving pseudopotentials, C. R. Acad. Sci. IV **1**(10), 1303–1308 (2000), https://doi.org/10.1016/S1296-2147(00)01122-7

3.33 G.B. Bachelet, M. Schluter: Relativistic norm-conserving pseudopotentials, Phys. Rev. B **25**(4), 2103–2108 (1982), https://doi.org/10.1103/PhysRevB.25.2103

3.34 J.P. Perdew, K. Burke, M. Ernzerhof: Generalized gradient approximation made simple, Phys. Rev. Lett. **77**(18), 3865–3868 (1996), https://doi.org/10.1103/PhysRevLett.77.3865

3.35 F. Ercolessi, M. Parrinello, E. Tosatti: Simulation of gold in the glue model, Philos. Mag. A **58**(1), 213–226 (1988), https://doi.org/10.1080/01418618808205184

3.36 M.W. Finnis, J.E. Sinclair: A simple empirical n-body potential for transition-metals, Philos. Mag. A **50**(1), 45–55 (1984), https://doi.org/10.1080/01418618408244210

3.37 L.Q. Yang, T.S. Rahman: Enhanced anharmonicity on Cu(110), Phys. Rev. Lett. **67**(17), 2327–2330 (1991), https://doi.org/10.1103/PhysRevLett.67.2327

3.38 L.Q. Yang, T.S. Rahman, M.S. Daw: Surface vibrations of Ag(100) and Cu(100) – A molecular-dynamics study, Phys. Rev. B **44**(24), 13725–13733 (1991), https://doi.org/10.1103/PhysRevB.44.13725

3.39 T.S. Rahman: Dynamics and structure at metal surfaces – A molecular dynamics study. In: *Condensed Matter Theories* (Nova Science, New York 1994) p. 299

3.40 A.N. Al-Rawi, A. Kara, T.S. Rahman: Anharmonic effects on Ag(111): A molecular dynamics study, Surf. Sci. **446**(1–2), 17–30 (2000), https://doi.org/10.1016/S0039-6028(99)01071-7

3.41 Z.J. Tian, T.S. Rahman: Energetics of stepped Cu surfaces, Phys. Rev. B **47**(15), 9751–9759 (1993), https://doi.org/10.1103/PhysRevB.47.9751

3.42 U. Kurpick, T.S. Rahman: Vibrational free energy contribution to self-diffusion on Ni(100), Cu(100) and Ag(100), Surf. Sci. **383**(2–3), 137–148 (1997), https://doi.org/10.1016/S0039-6028(97)00105-2

3.43 M.J. Stott, E. Zaremba: Quasiatoms – An approach to atoms in nonuniform electronic systems, Phys. Rev. B **22**(4), 1564–1583 (1980), https://doi.org/10.1103/PhysRevB.22.1564

3.44 R.E. Allen, G.P. Alldredge, F.W.D. Wette: Studies of vibrational surface modes. 1. General formulation, Phys. Rev. B **4**(6), 1648 (1971), https://doi.org/10.1103/PhysRevB.4.1648

3.45 R. Haydock, V. Heine, M.J. Kelly: Electronic structure based on the local atomic environment for tight-binding bands, J. Phys. C **5**(20), 2845–2858 (1972), https://doi.org/10.1088/0022-3719/5/20/004

3.46 S.Y. Wu, J. Cocks, C.S. Jayanthi: General recursive relation for the calculation of the local green-function in the resolvent-matrix approach, Phys. Rev. B **49**(12), 7957–7963 (1994), https://doi.org/10.1103/PhysRevB.49.7957

3.47 A. Kara, C.S. Jayanthi, S.Y. Wu, F. Ercolessi: Local analysis of the dynamics of the relaxed and reconstructed Au(511) surface using the real-space greens-function method, Phys. Rev. Lett. **72**(14), 2223–2226 (1994), https://doi.org/10.1103/PhysRevLett.72.2223

3.48 A. Kara, C.S. Jayanthi, S.Y. Wu, F. Ercolessi: Structure and dynamics of the reconstructed Au(511)

surface, Phys. Rev. B **51**(23), 17046–17062 (1995), https://doi.org/10.1103/PhysRevB.51.17046
3.49 S. Durukanoğlu, T.S. Rahman: Structure of Ag(410) and Cu(320), Phys. Rev. B **67**(20), 205406 (2003), https://doi.org/10.1103/PhysRevB.67.205406
3.50 A. Kara, S. Durukanoglu, T.S. Rahman: Local thermodynamic properties of a stepped metal surface: Cu(711), Phys. Rev. B **53**(23), 15489–15492 (1996), https://doi.org/10.1103/PhysRevB.53.15489
3.51 S. Durukanoğlu, A. Kara, T.S. Rahman: Local structural and vibrational properties of stepped surfaces: Cu(211), Cu(511), and Cu(331), Phys. Rev. B **55**(20), 13894–13903 (1997), https://doi.org/10.1103/PhysRevB.55.13894
3.52 A. Kara, S. Durukanoglu, T.S. Rahman: Vibrational dynamics and thermodynamics of Ni(977), J. Chem. Phys. **106**(5), 2031–2037 (1997), https://doi.org/10.1063/1.473309
3.53 A. Kara, T.S. Rahman: Vibrational properties of metallic nanocrystals, Phys. Rev. Lett. **81**(7), 1453–1456 (1998), https://doi.org/10.1103/PhysRevLett.81.1453
3.54 A. Kara, A.N. Al-Rawi, T.S. Rahman: Vibrational dynamics and excess entropy of multi-grain nanoparticles, J. Comput. Theor. Nanosci. **1**(2), 216–220 (2004), https://doi.org/10.1166/jctn.2004.019
3.55 H. Yildirim, A. Kara, T.S. Rahman: Structural, vibrational and thermodynamic properties of Ag_nCu_{34} nanoparticles, J. Phys. Condens. Matter **21**(8), 084220 (2009), https://doi.org/10.1088/0953-8984/21/8/084220
3.56 L. Niu, D.D. Koleske, D.J. Gaspar, S.J. Sibener: Vibrational dynamics of a stepped metallic surface – Step-edge phonons and terrace softening on Ni(977), J. Chem. Phys. **102**(22), 9077–9089 (1995), https://doi.org/10.1063/1.468856
3.57 L. Niu, D.J. Gaspar, S.J. Sibener: Phonons localized at step edges – A route to understanding forces at extended surface-defects, Science **268**(5212), 847–850 (1995), https://doi.org/10.1126/science.268.5212.847
3.58 P.J. Feibelman: First-principles step- and kink-formation energies on Cu(111), Phys. Rev. B **60**(15), 11118–11122 (1999), https://doi.org/10.1103/PhysRevB.60.11118

Talat S. Rahman

Department of Physics
University of Central Florida
Orlando, FL, USA
talat.rahman@ucf.edu

Talat S. Rahman is a Pegasus Professor of Physics at University of Central Florida. Her research interests are in computational design of functional nanomaterials through microscopic understanding of their physical and chemical properties. A related interest is in multiscale modeling of chemical reactions and thin film growth processes. She is engaged in implementing evidence-based teaching strategies and in efforts that enhance the participation of women and underrepresented minority groups in physics.

Surface C Part B

Part B Surface Crystallography

Part B deals with surface crystallography. When the solid—which ideally fills the entire space—is cut to create a surface, translational invariance in the direction perpendicular to the surface plane is lost. This generates unsaturated chemical bonds (also called dangling bonds), affecting not only the structure but potentially all properties of the material in the surface region—in particular the vibrational spectrum, the electronic and magnetic structure, and the chemical reactivity. Minimization of the free energy of the system may then lead to relaxation (i.e., a change in the distance between the outermost atomic planes) and/or potentially extensive and complex surface reconstruction (i.e., the rearrangement of atoms in the surface plane). Possibly the most famous reconstruction is the (7×7) rearrangement of Si(111), which involves three atomic planes and 49 surface unit cells. Interestingly, since the number of dangling bonds (one per atom) is odd, the resulting surface is metallic, albeit with a very low density of states at the Fermi energy. Work to determine the atomic positions took decades and involved dozens of laboratories worldwide. Determining the structures of other materials can be as challenging (e.g., the many phases of SiC surfaces). The presence of supported adsorbate layers, ultrathin films, and two-dimensional (2-D) materials at surfaces makes surface systems even more complex, but they are important since they have properties that are not present in 3-D systems. An example is provided by Dirac fermions in graphene: their effective mass of zero gives electrons an extremely high mobility that is not attained in graphite.

Chapter 4 provides a brief but general introduction to surface crystallography. Starting from an overview of bulk crystallography, the chapter presents point and space group symmetries in 2-D. The concept of a reciprocal lattice is introduced and Bloch's theorem is formulated. The chapter also addresses low-energy electron diffraction and Ewald sphere construction to describe the scattering process. In its final part, stereographic projection is introduced and several examples are given. The chapter also provides a useful compilation of the different notations used in surface crystallography.

Chapter 5 addresses the theoretical ab initio methods that are used to determine the surface structures of semiconductors. Such methods have advanced tremendously in recent years and now have the ability to make reliable predictions, especially for low-dimensional systems. The chapter first introduces the theoretical framework and the most suitable protocols for solving problems ranging from the microscopic characterization of interfaces (mandatory when, for example, designing contacts) to functionalization and sensing. The chapter also covers recent developments in contacts and heterojunctions, with an emphasis on ohmic versus Schottky barriers, core–shell nanowires, and alternative plasmonic systems. Finally, it explores the semiconductor/water interface and compares the characteristics of this interface with those of a metal/water interface.

Chapter 6 first briefly reviews the structures of the surfaces of a variety of oxides and then focuses on rock salt oxides and perovskites. For ionic solids, surface relaxation involves the rumpling of anions and cations, which undergo significant displacements. Rock salt oxide surfaces are therefore particularly intriguing since they form a series of compounds with identical structures in which only the cations change. Ternary oxides are used for applications in which the exact surface structure must be known. As an example, the surface terminations and reconstructions of $SrTiO_3(100)$ are discussed in detail, with special attention paid to the roles of Sr stoichiometry and defects that make it challenging to prepare a single-phase terminated surface.

Chapter 7 is devoted to the crystallography of metallic surfaces that are clean and covered with adsorbates. In the first part, details of the main experimental techniques used to determine surface structures are presented (LEED, XPD, SXRD, and XSW) and critically compared. Further analysis is presented to show that these techniques allow the determination of atomic positions with an accuracy of up to 0.01 Å. In the second part of the chapter, common trends in the surface structures of metals are presented, and the chemisorption characteristics of several inorganic and organic adsorbate layers are enumerated and compared.

Chapter 8 deals with the imaging, spectroscopy, and manipulation performed in scanning tunneling microscopy. This technique is shown to provide not only images of the surface at the subnanoscale, but also spectroscopic information on the local density of states. A large part of the chapter is devoted to the use of the tip to manipulate adatoms and admolecules, thus establishing a bridge to nanotechnology in a bottom-up approach. Lateral manipulation as well as the use of electric fields and the inelastic tunneling of electrons are explored. Possible directions for future research include single-molecule motors and ultraminiaturized circuits, and the factors limiting such fascinating developments are discussed in the final part of the chapter.

Chapter 9 presents an overall summary of the synthesis and growth of 2-D materials of the 'ene' family (graphene, silicene, germanene, stanene, hafnene) on transition metal surfaces in a controlled ultrahigh-vacuum environment. Calculations based on density functional theory are provided to explain the observed structures, in particular their Moiré patterns. Recent progress in device building suggests that these materi-

als will begin to be used in applications in the very near future. Given their importance, some of these materials will also be addressed in greater detail in the last section of this Handbook.

Chapter 10 reviews the properties of ultrathin oxide thin films. These systems were initially investigated to simulate bulk oxide surfaces as they allow the application of electron-based techniques, but they were soon recognized to offer their own exotic phases and to exhibit intriguing chemical and physical properties that differ from those of the surfaces of the corresponding bulk oxides, with the additional advantage of tunability. These differences ultimately arise from their intrinsic reduced dimensionality and, at the monolayer limit, the influence of the substrate. The first part of the chapter describes the structures of various films, including those of MgO, CaO, silica, iron oxide, and other transition metal oxides. In the second part, the effects of charge transfer and doping with impurities and adatoms are discussed. In the final part of the chapter, practical applications of thin oxide films are described, with particular attention paid to catalysis, since these films can be used as active supports for metal nanoparticles (e.g., Pt deposited on FeO is used to catalyze CO oxidation) or directly as catalysts themselves (e.g., the partial oxidation of methanol on vanadium oxide).

4. Crystallography of Surfaces

Stephen J. Jenkins

In no aspect is the two-dimensional nature of the surface more readily apparent than in its crystallography. Concepts familiar from the three-dimensional crystallography of bulk materials must be modified to suit the surface subspace, with important consequences for the symmetries and structural forms that may occur. The lowering of symmetry at the surface affords scope for relaxations and reconstructions that are not seen in the parent material, and these phenomena can be of crucial importance in dictating the physical and chemical properties of the surface region. Here, we shall review the basics of three-dimensional crystallography (lattices, unit cells, reciprocal space, etc.) and demonstrate how they carry over into the two-dimensional realm of the surface. We shall also focus upon consequences for point and space symmetries, relating these to surface structural features (e.g., steps, kinks, etc.) via a stereographic representation developed to place vicinal surfaces within a unified conceptual framework. Finally, we introduce and comment upon standard notational schemes for referencing symmetry-breaking reconstruction and/or adsorbate superstructure.

4.1 Context

The application of crystallographic techniques to three-dimensional materials has a long and illustrious history, dating back at least to early experiments by pioneers such as the Braggs in the first decades of the twentieth century. Investigation of the two-dimensional crystallography of surfaces followed somewhat later, but by now is no less developed, albeit the practical difficulties faced by its proponents unavoidably limits the information that may be gleaned. Nevertheless, the parallels between three- and two-dimensional crystallography are sufficiently strong that both may usefully be presented side-by-side, the former shedding light upon the latter (or vice versa, depending upon one's viewpoint). Let us begin our discussion, therefore, by defining some fundamental terms that are common to both situations.

4.2 Bravais Lattices and Crystal Structure

We shall take as our definition of a crystalline material one in possession of long-range spatial periodicity. That is, a crystal must have a structure in which the same local arrangement of atoms recurs repetitively across large length scales. Within this definition, amorphous materials are clearly excluded, since any short-range

M. Rocca, T.S. Rahman, L. Vattuone (Eds.), *Springer Handbook of Surface Science*, Springer Handbooks,
https://doi.org/10.1007/978-3-030-46906-1_4

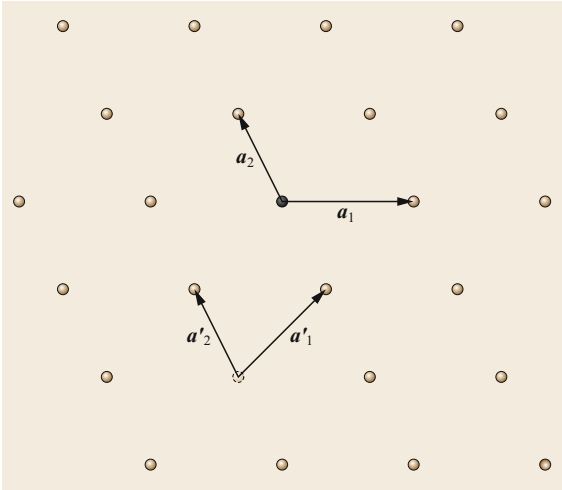

Fig. 4.1 A two-dimensional Bravais lattice, generated by the primitive lattice vectors $\boldsymbol{a}_1$ and $\boldsymbol{a}_2$. General lattice points are small light-brown balls; the dark-gray ball represents the origin. Note that vectors $\boldsymbol{a}'_1$ and $\boldsymbol{a}'_2$, together with a different origin, would define precisely the same lattice equally well

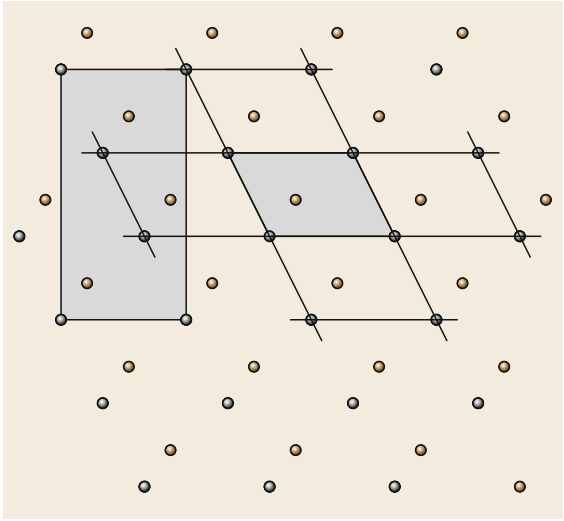

Fig. 4.2 A two-dimensional crystal generated by adding a two-atom motif to the Bravais lattice depicted in Fig. 4.1. The primitive unit cell corresponding to vectors $\boldsymbol{a}_1$ and $\boldsymbol{a}_2$ in that figure is *shaded*, and its tessellation indicated with *construction lines*; an alternative, nonprimitive, unit cell of higher symmetry is also *shaded*

structures that *may* recur throughout the material do not do so according to a repetitive pattern. Furthermore, quasicrystalline materials are also excluded, since the recurrence of short-range structures in these cases, whilst conforming to a well-defined pattern, is again not truly periodic.

From a mathematical standpoint, perhaps the simplest way to define a prototypical crystal is by specifying a set of so-called primitive lattice vectors, which we shall denote $\boldsymbol{a}_i$. In the three-dimensional case, this allows us to write a general lattice vector as

$$\boldsymbol{R} = \alpha_1\boldsymbol{a}_1 + \alpha_2\boldsymbol{a}_2 + \alpha_3\boldsymbol{a}_3 \tag{4.1}$$

in which α_1, α_2 and α_3 are integer coefficients (of either sign). In two dimensions, the linear combination is, of course, restricted to the form

$$\boldsymbol{R} = \alpha_1\boldsymbol{a}_1 + \alpha_2\boldsymbol{a}_2 \tag{4.2}$$

but the cases are otherwise analogous. Each lattice vector may be viewed as terminating at a well-defined location in either three- or two-dimensional space, which we shall describe as a lattice point, with the case corresponding to $\alpha_1 = \alpha_2(= \alpha_3) = 0$ constituting the origin of our system. Three-dimensional crystallography is, of course, covered in far greater detail within many textbooks, for example the classic work of *Ashcroft* and *Mermin* [4.1]; our intent in briefly summarizing it here is merely to highlight the similarities between three- and two-dimensional situations.

Taking the complete (infinite) set of lattice points obtained by essaying all possible combinations of α_1, α_2 and (if appropriate) α_3, one obtains the mathematical entity known as a Bravais lattice (Fig. 4.1). Placing a single atom (of some particular species) at each and every lattice point will necessarily generate a crystalline material, whose structure conforms identically to that of its parent Bravais lattice. Evidently, such a structure exhibits long-range spatial periodicity by construction, satisfying that definition of a crystal introduced above. Note, however, that the same Bravais lattice may be defined in terms of infinitely many sets of primitive lattice vectors, each of which is equally satisfactory. In contrast, as we shall shortly quantify, the number of symmetrically distinct crystalline structures that may be described simply by placing an atom at each lattice point within a Bravais lattice is rather limited. For a start, no crystalline structure containing more than a single element could be thus described, and even many common single-element crystal structures (diamond, for example) would remain out of reach. Fortunately, of course, one may retain the long-range periodicity whilst introducing considerable structural flexibility by placing a well-defined atomic motif at each lattice point (Fig. 4.2) rather than a single atom (such motifs are sometimes described as the atomic basis). In this manner, the number of symmetrically distinct crystalline structures expands to encompass *all* possible cases within our working definition.

Conveniently, one may now consider the region spanned by the primitive lattice vectors (an area in the two-dimensional case, but a volume in the three-dimensional case) to constitute the primitive unit cell of the crystal. It contains precisely one lattice point, and correspondingly just one repeat of the atomic motif; moreover, it tessellates (by translation through the primitive lattice vectors) to fill space and reproduce the entire crystal structure. On occasion, it may prove convenient to eschew the primitive unit cell in favor of a larger cell of higher symmetry, which may be termed (if it is frequently employed) the conventional unit cell. There is much to be said for working with the highest-symmetry unit cell possible for any given structure, although the advantage of the primitive unit cell in containing the fewest atoms is also compelling. Certainly, when making use of a primitive unit cell, one should prefer (out of the many possible choices) that which exhibits maximum symmetry. Let us, therefore, proceed by considering the symmetry properties of atomic systems in general, and of two- and three-dimensional cases in particular.

4.3 Point and Space Group Symmetries

It is evident that two crystalline structures differing only by a uniform scaling are only trivially distinct from one another. Similarly, changing the elemental identity of atoms within a structure does not fundamentally imply an entirely distinct structure, so long as spatial arrangements remain generically the same. Diamond and silicon, for example, may both be said to share the same crystal structure, despite the obvious substitution of carbon atoms for silicon, and the consequent difference in lattice spacing. Gallium arsenide, on the other hand, is generally held to adopt a distinctly different structure, because atoms of its two constituent elements alternate (albeit their positions match those of diamond and silicon, to within a trivial scaling). In order to classify crystal structures, therefore, it will be desirable to focus only upon nontrivial differences, and it has become standard to do so by prioritizing intrinsic symmetry properties over contingent details.

To be clear, we should first state what is meant by a symmetry of the system. In essence, a symmetry operation may be considered to be any operation that, when enacted upon an entity, leaves that entity indistinguishable from its original state. The simplest symmetry operation is merely that of identity, which consists of doing nothing whatsoever; clearly this must, by definition, leave the entity unchanged. Other symmetry operations, however, include reflection (across a plane), rotation (around an axis) and inversion (through a point). The planes, axes and/or points associated with these symmetry operations are known generically as symmetry elements, which a particular entity may or may not possess. All such symmetry elements imply at least one point that remains literally unmoved under the corresponding symmetry operation, and collectively they are known as the point symmetry elements and point symmetry operations.

For any entity, whether localized (e.g., an atom or molecule) or extended (e.g., a solid or surface), it is possible to collate the set of all point symmetry operations that it exhibits. This set is known as the point group of that entity, and in the case of a localized entity this fully describes the entirety of its spatial symmetry. Point groups in localized cases are typically labeled within either the Schönflies or the Hermann–Mauguin convention. For reasons of brevity, we shall merely summarize the main features of these two conventions here; the reader is referred to standard texts on symmetry for a more complete explanation.

In the Schönflies notation, point groups are assigned labels comprising a capital letter and a subscript: the letters C, S, D, T, O and I indicate symmetries of cyclic, spiegel, dihedral, tetrahedral, octahedral and icosahedral type, respectively. The *cyclic* symmetry groups feature only an n-fold rotational axis. The term *spiegel* is taken from the German, literally meaning mirror, but here noting the existence of a so-called rotoreflection axis—the symmetry element combining both rotation and reflection. The *dihedral* symmetry groups contain not only an n-fold rotational axis, but also n two-fold axes at right angles to it. The *tetrahedral*, *octahedral* and *icosahedral* symmetry groups are characterized by the rotational axes pertaining to the corresponding platonic solids. In the Schönflies notation, subscripts may be numeric and/or include the lowercase letters v, h or d, indicating the nature of any special axes and/or the orientation of any special planes. Thus, by way of example, the water, methane and benzene molecules display C_{2v}, T_d and D_{6h} symmetries, respectively, each symbol fully specifying the symmetry elements that are present.

Turning to the Hermann–Mauguin notation, in contrast, the defining symmetries of the point group (i.e., those symmetries that collectively serve to distinguish the point group from all other point groups) are simply listed, employing an italic letter m to indicate the presence of a mirror plane and/or a number to indi-

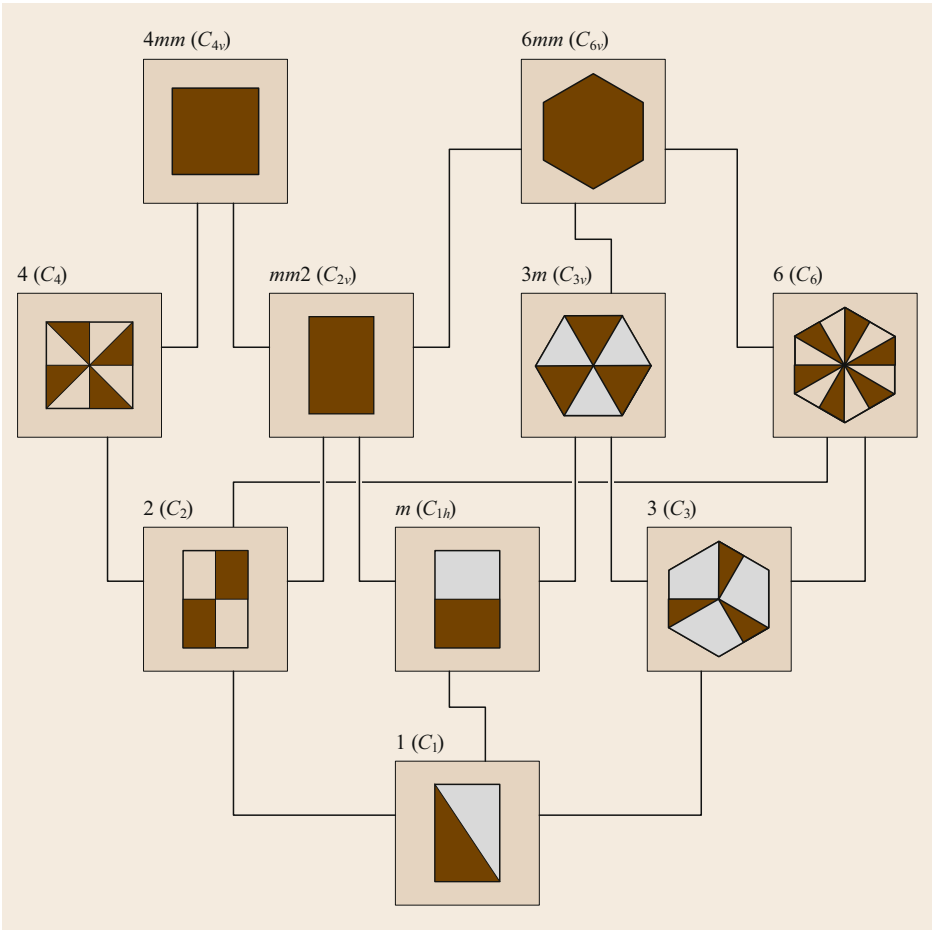

Fig. 4.3 The ten point groups compatible with two-dimensional translational periodicity. Illustrative shapes in each case should be understood as lacking any symmetry operations involving the dimension perpendicular to the page. Connections between different point groups indicate when those lower down the page are subgroups of those higher up the page

cate the presence of a rotational axis (a number with an overline indicates a rotoinversion axis, combining both rotation and inversion). Thus, the point groups C_{2v}, T_d and D_{6h} mentioned above are represented as *mm*2, $\overline{4}3m$ and 6/*mmm*, respectively; the way in which the individual components of these symbols are combined provides information about the geometric relationship of the various symmetry elements, but the details of this need not concern us unduly here.

In the case of extended systems, matters are a little more complicated, since the possibility of translation as a symmetry operation now arises; displacement of a crystalline entity through any of the primitive lattice vectors (and, by extension, through any integer linear combination of them) results in a crystal indistinguishable from the original. There is no corresponding symmetry element (unless one considers the relevant lattice vector to play this role) and the operation is certainly not a point one. Moreover, the translation operation may be combined with either reflection (yielding the operation known as glide) or rotation (giving rise to the screw operation); the former is associated with the symmetry element known as the glide plane, and the latter with a so-called screw axis. The complete set of symmetry operations displayed by such an extended system, including pure translation, together with glide and screw operations if present, is then known as the space group.

In light of the foregoing discussion, it is clear that we need to take some care in describing the symmetry of crystalline materials. We may, for instance, wish to describe the point group of the lattice, or the point group of the crystal; equally, one may speak of the space group of the lattice, as distinct from the space group of the crystal. To make matters yet more complicated, we must also recognize the existence of the so-called point group of the space group, which is obtained from the space group of the crystal by converting all glide operations to reflection operations and all screw operations to rotation operations; it is *this* point group that determines the symmetry of macroscopically observable crystalline phenomena, including morphological, electronic, magnetic and optical properties. Note that the point group of

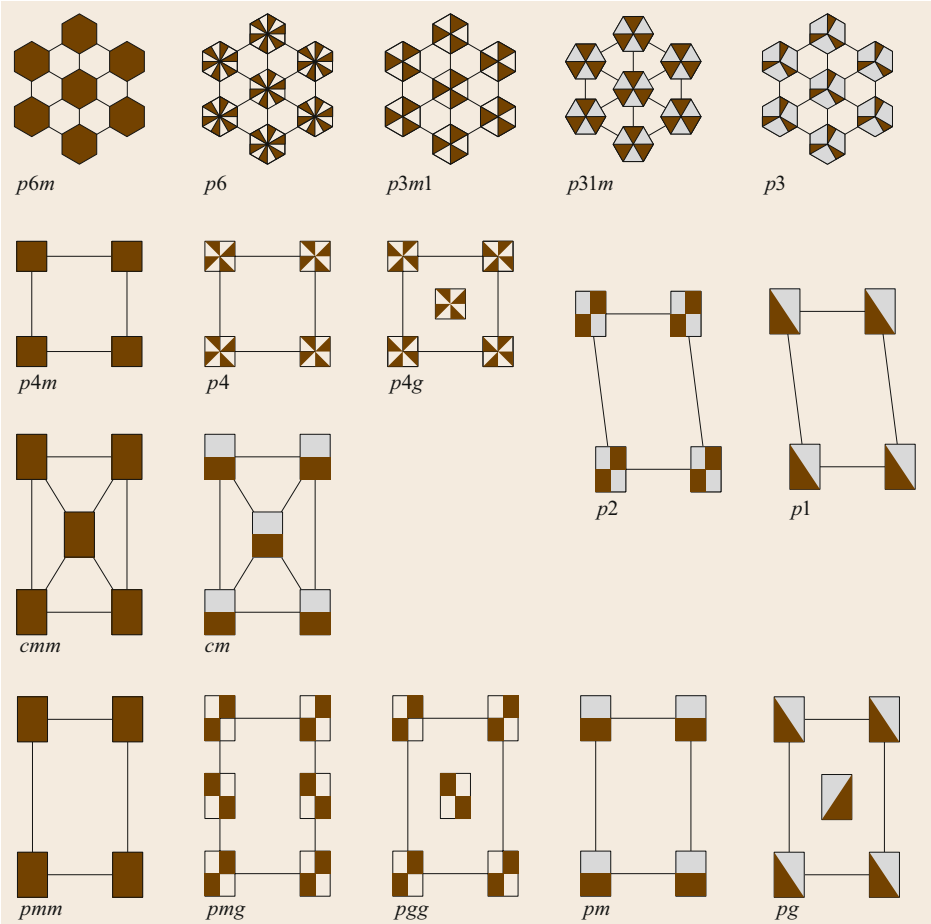

Fig. 4.4 The 17 space groups compatible with two-dimensional translational periodicity. Illustrative shapes in each case should be understood as repeating ad infinitum within the plane of the page, whilst lacking any symmetry operations involving the dimension perpendicular to that plane

the space group is *not* generally synonymous with the point group of the crystal, although it is quite common for the latter term to be used when strictly the former would be more accurate.

In three dimensions, it turns out that only 32 point groups are compatible with translational periodicity, and these are known as the crystallographic point groups. The point group of a crystalline space group must fall within this set, and accordingly there exist only 230 possible space groups that may be adopted by three-dimensional crystals. As for the parent Bravais lattices, only 14 different types may be envisioned, once categorized in terms of the their space groups, consisting of four within the orthorhombic system, three within the cubic system, two each within the tetragonal and monoclinic systems, and one each within the hexagonal, rhombohedral and triclinic systems. Note that the seven lattice systems mentioned here differ from the seven crystal systems or six crystal families whose definitions are based on the space group of the crystal rather than that of the lattice. Confusingly, whilst the three different categorization schemes conform to one another in most cases, the hexagonal and rhombohedral lattice systems are conjoined to form the hexagonal crystal family, and jumbled to form the hexagonal and trigonal crystal systems.

Moving to two dimensions, matters are drastically simplified. Now, only ten crystallographic point groups are compatible with translational periodicity (Fig. 4.3) giving rise to a total of only 17 distinct space groups for two-dimensional crystals (Fig. 4.4). Moreover, only five distinct Bravais lattice types exist, categorized according to *their* space groups; two of these fall within the rectangular two-dimensional lattice system, with one each in the oblique, triangular and square two-dimensional lattice systems; examples are shown in Fig. 4.5. It follows from this discussion that the symmetries exhibited by surfaces are strictly limited, and the two-dimensional lattices upon which their structures are based even more so. The diversity of surface structure (as opposed to the paucity of surface symmetry) derives from the range of observed motifs rather than of lattices.

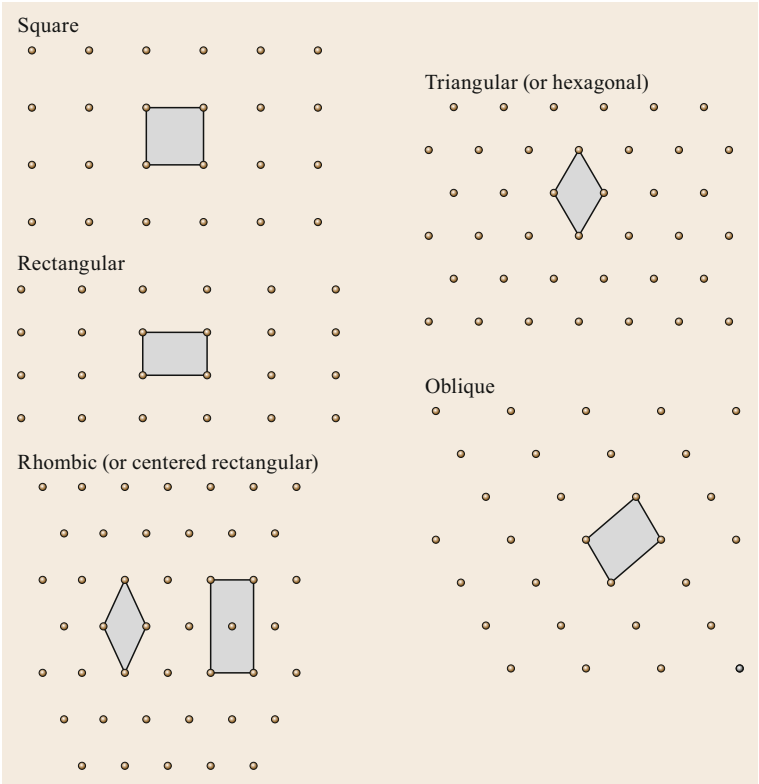

Fig. 4.5 Two-dimensional Bravais lattices of square, triangular, rectangular, rhombic and oblique symmetry. In each case, the primitive unit cell of maximum symmetry is *shaded*; in the rhombic case, a conventional (nonprimitive) rectangular unit cell is also depicted, justifying the alternative name of centered rectangular. Internal angles for the square and rectangular cells are, of course, right angles; those for the cell in the triangular (or hexagonal) case are 60° and 120°

Considering the surface to be a semi-infinite object, the motif attached to each two-dimensional lattice point consists of an infinite stack of atoms descending into the bulk from the uppermost atomic layer. The nature of both the two-dimensional lattice and the associated motif will depend upon both the three-dimensional crystalline structure of the bulk material and the relative orientation of the surface plane.

4.4 The Reciprocal Lattice and Its Implications

Whenever wavelike phenomena occur within crystalline materials, instances that are commensurate with the periodicity of the parent Bravais lattice (i.e., repeat precisely from one primitive unit cell to the next) take on a special significance. Writing the general mathematical form of a sinusoidal wave as

$$f(\boldsymbol{r}) = F\mathrm{e}^{\mathrm{i}(\boldsymbol{k}\cdot\boldsymbol{r}-\omega t)} \tag{4.3}$$

with amplitude F, wavevector $\boldsymbol{k}$ and frequency ω, the property we seek may be captured in the constraint that

$$f(\boldsymbol{r}) = f(\boldsymbol{r}+\boldsymbol{R}) \tag{4.4}$$

with $\boldsymbol{R}$ being any lattice vector of the crystal's parent Bravais lattice. Clearly this implies

$$\mathrm{e}^{\mathrm{i}\boldsymbol{k}\cdot\boldsymbol{r}} = \mathrm{e}^{\mathrm{i}\boldsymbol{k}\cdot(\boldsymbol{r}+\boldsymbol{R})} \tag{4.5}$$

from which we may infer that commensurate waves are simply those for which $\boldsymbol{k}\cdot\boldsymbol{R} = 2\pi n$, with integer n. Given that there exist infinitely many lattice vectors, $\boldsymbol{R}$, it follows that there must be infinitely many wavevectors satisfying this condition, collectively forming a mathematical entity that we may describe as the reciprocal lattice (in recognition that the spacing of its points scales inversely with the spacing of points within what we shall henceforth call the real-space lattice).

Specifying general points within the reciprocal lattice (i.e., reciprocal lattice points) by means of reciprocal lattice vectors, denoted $\boldsymbol{G}$, we may write

$$\boldsymbol{G} = \beta_1\boldsymbol{b}_1 + \beta_2\boldsymbol{b}_2 + \beta_3\boldsymbol{b}_3 \tag{4.6}$$

in three dimensions, or

$$\boldsymbol{G} = \beta_1\boldsymbol{b}_1 + \beta_2\boldsymbol{b}_2 \tag{4.7}$$

in two, where β_1, β_2 and (if appropriate) β_3 are integer coefficients (of either sign) and the vectors $\boldsymbol{b}_i$ are primitive reciprocal lattice vectors.

Furthermore, given a set of primitive lattice vectors, $\boldsymbol{a}_i$, for a particular three-dimensional crystal, the corresponding set of primitive reciprocal lattice vectors, $\boldsymbol{b}_i$, may readily be obtained as

$$\boldsymbol{b}_1 = 2\pi \frac{\boldsymbol{a}_2 \times \boldsymbol{a}_3}{\boldsymbol{a}_1 \cdot (\boldsymbol{a}_2 \times \boldsymbol{a}_3)} \tag{4.8}$$

$$\boldsymbol{b}_2 = 2\pi \frac{\boldsymbol{a}_3 \times \boldsymbol{a}_1}{\boldsymbol{a}_2 \cdot (\boldsymbol{a}_3 \times \boldsymbol{a}_1)} \tag{4.9}$$

$$\boldsymbol{b}_3 = 2\pi \frac{\boldsymbol{a}_1 \times \boldsymbol{a}_2}{\boldsymbol{a}_3 \cdot (\boldsymbol{a}_1 \times \boldsymbol{a}_2)} \tag{4.10}$$

in which a cyclic pattern is clearly discernible. That this construction ensures conformity with the necessary condition $\boldsymbol{G} \cdot \boldsymbol{R} = 2\pi n$ should be similarly evident, from the fact that we have engineered a situation where $\boldsymbol{a}_i \cdot \boldsymbol{b}_j = 2\pi\delta_{ij}$ (with δ_{ij} the Kronecker delta).

The same convenient construction may be retained in the two-dimensional case by the simple expedient of supplementing the two *real* primitive lattice vectors, $\boldsymbol{a}_1$ and $\boldsymbol{a}_2$, with a third *dummy* primitive lattice vector of arbitrary length pointing in the surface normal direction; that is, we set $\boldsymbol{a}_3 = |\boldsymbol{a}_3|\hat{\boldsymbol{n}}$ with $\hat{\boldsymbol{n}}$ the surface normal unit vector. We then obtain

$$\boldsymbol{b}_1 = 2\pi \frac{\boldsymbol{a}_2 \times \hat{\boldsymbol{n}}}{\boldsymbol{a}_1 \cdot (\boldsymbol{a}_2 \times \hat{\boldsymbol{n}})} \tag{4.11}$$

$$\boldsymbol{b}_2 = 2\pi \frac{\hat{\boldsymbol{n}} \times \boldsymbol{a}_1}{\boldsymbol{a}_1 \cdot (\hat{\boldsymbol{n}} \times \boldsymbol{a}_1)} \tag{4.12}$$

$$\boldsymbol{b}_3 = \frac{2\pi\hat{\boldsymbol{n}}}{|\boldsymbol{a}_3|} \tag{4.13}$$

in which the third primitive reciprocal lattice vector may itself be taken as a *dummy* vector. Alternatively, we can think of our two-dimensional system as a pseudo-three-dimensional system, by allowing the magnitude of $\boldsymbol{a}_3$ to tend towards infinity, implying that the two-dimensional reciprocal lattice points become pseudo-three-dimensional reciprocal lattice rods (i.e., the two-dimensional points are extruded in the surface-normal direction).

Whether in two or three dimensions, the significance of the reciprocal lattice lies in its utility in representing arbitrary sinusoidal waves, not only those that happen to be commensurate with the parent Bravais lattice. This role can, perhaps, be seen most clearly in the description of electronic wavefunctions by means of Bloch's theorem. Here, we note that an electron within a crystal may possess a wavefunction, $\psi(\boldsymbol{r})$, whose periodicity need not correspond to that of the crystal itself. Nevertheless, this wavefunction may always be written (following Bloch) in the form

$$\psi_{n,\boldsymbol{k}}(\boldsymbol{r}) = \mathrm{e}^{\mathrm{i}\boldsymbol{k}\cdot\boldsymbol{r}} u_{n,\boldsymbol{k}}(\boldsymbol{r}) \tag{4.14}$$

where the function $u_{n,\boldsymbol{k}}(\boldsymbol{r})$ (the Bloch function) *does* exhibit identical periodicity to the crystalline structure. The subscript $\boldsymbol{k}$ is introduced to keep track of which Bloch function goes with which exponential function, whereas the subscript n recognizes that, in general, many different wavefunctions may be possible for each value of $\boldsymbol{k}$. Clearly, the implication is that electronic wavefunctions in crystalline materials may be conceived of as the product of a simple plane wave (of wavevector $\boldsymbol{k}$) with a commensurately periodic function (tied to that same wavevector $\boldsymbol{k}$). Moreover, it turns out that one may restrict the values of $\boldsymbol{k}$ to extend only within that region of reciprocal space lying closer to the origin than to any other reciprocal lattice point, without loss of generality. In some sense, this region, known as the Brillouin zone, may be viewed as fulfilling an equivalent function to the primitive unit cell in real-space lattices (Fig. 4.6).

A corollary of applying this (voluntary) restriction is that one may think of the plane wave factor as controlling the long-range behavior of the wavefunction (repeating at length scales beyond that of the primitive unit cell) whilst the Bloch function controls its short-range behavior (showing structure within each primitive unit cell, but simply repeating that structure from one to the next).

One further consequence of Bloch's theorem, which will be of particular interest to us, is most readily seen by defining Bloch functions associated with wavevectors lying *outside* the Brillouin zone in terms of those lying *within* it. There being no constraint upon their functional form other than the requirement of lattice periodicity, we are free to do this in the following manner

$$u_{n,\boldsymbol{k}+\boldsymbol{G}}(\boldsymbol{r}) = \mathrm{e}^{-\mathrm{i}\boldsymbol{G}\cdot\boldsymbol{r}} u_{n,\boldsymbol{k}}(\boldsymbol{r}) \tag{4.15}$$

whereupon one finds

$$\psi_{n,\boldsymbol{k}+\boldsymbol{G}}(\boldsymbol{r}) = \mathrm{e}^{\mathrm{i}(\boldsymbol{k}+\boldsymbol{G})\cdot\boldsymbol{r}} u_{n,\boldsymbol{k}+\boldsymbol{G}}(\boldsymbol{r}) \tag{4.16}$$

$$= \mathrm{e}^{\mathrm{i}\boldsymbol{k}\cdot\boldsymbol{r}} u_{n,\boldsymbol{k}}(\boldsymbol{r}) = \psi_{n,\boldsymbol{k}}(\boldsymbol{r})\,, \tag{4.17}$$

which is to say that the wavefunctions associated with two wavevectors differing by a reciprocal lattice vector are identical with one another, or equivalently that the wavevector associated with a particular wavefunction is well defined only to within the addition or subtraction of an arbitrary reciprocal lattice vector. Identifying $\hbar\boldsymbol{k}$ with the linear momentum of a quantum particle, we hence conclude that the electron's crystal momentum (i.e., the momentum associated with the plane wave factor in its Bloch form) is well defined only to within the

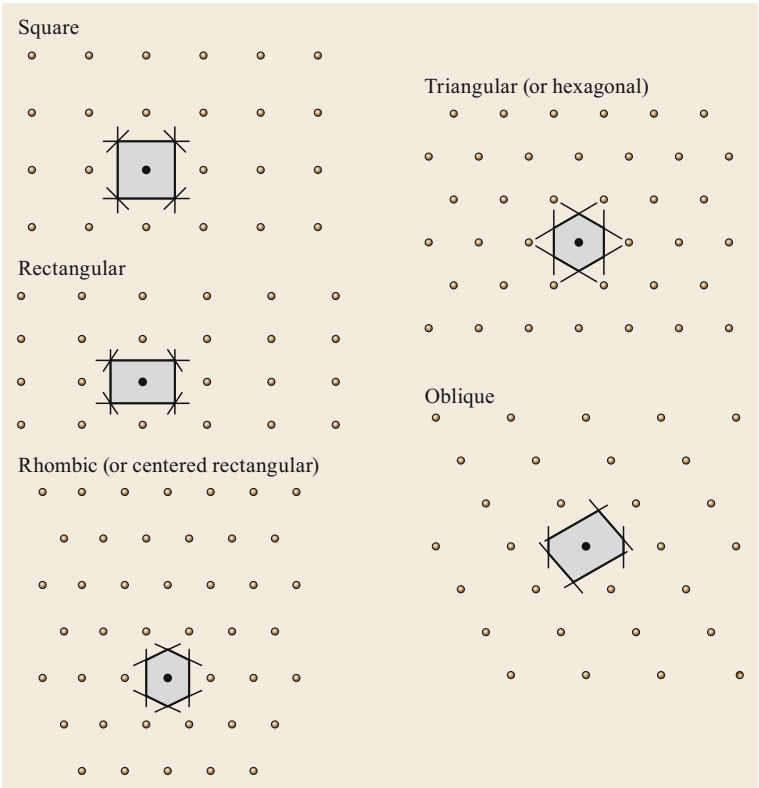

Fig. 4.6 Two-dimensional reciprocal lattices, with the origin *marked* and the first Brillouin zone *shaded* in each case; *construction lines* are perpendicular bisectors of reciprocal lattice vectors, included to demonstrate that these regions lie closer to the origin than to any other reciprocal lattice point

addition or subtraction of a discrete (but essentially arbitrary) offset, $\hbar \boldsymbol{G}$. In the context of electrons scattering from a crystalline surface, we must therefore anticipate that linear momentum within the plane of the surface must be conserved only to within a similarly defined offset, and it is this fact that accounts for the observed diffraction patterns that typically result, as we shall shortly see.

4.5 Low-Energy Electron Diffraction (LEED)

The ubiquity of x-ray diffraction in *bulk* crystallographic studies rests upon two important (and related) factors: firstly, that the relatively weak interaction of such short-wavelength light with matter ensures a penetration depth sufficient that surface effects may largely be ignored in the subsequent analysis; and secondly that the same weak interaction allows that analysis to be conducted on the assumption that each photon scatters only once. In efforts to elucidate the structure and symmetry of the *surface*, in contrast, it is natural to turn for one's probe to wavelike phenomena whose strong interaction with matter restricts the penetration depth to the selvedge region, even though this typically implies that multiple scattering will complicate the process of data analysis. One candidate for this role is the helium atom, whose light mass is consistent with a quantum wavelength comparable with the spacing of atoms in solids. In view of the dominance of electron-based techniques over helium scattering, however, we shall eschew any further discussion of detail in this chapter; from a mathematical perspective, the helium scattering problem differs little from the brief treatment of electron scattering offered below, despite obvious divergence in terms of the practical experimental details. Here, then, we shall focus upon the diffraction of low-energy electrons, whose quantum wavelength is again comparable with interatomic spacings in solids, and whose penetration depth rarely exceeds a few nanometres. An excellent dedicated textbook on this subject, covering experimental details and methods of analysis, is the work by *Van Hove*, *Weinberg* and *Chan* [4.2], so for our present purposes we merely summarize the basic principles of the technique and its relationship with the concept of the reciprocal lattice.

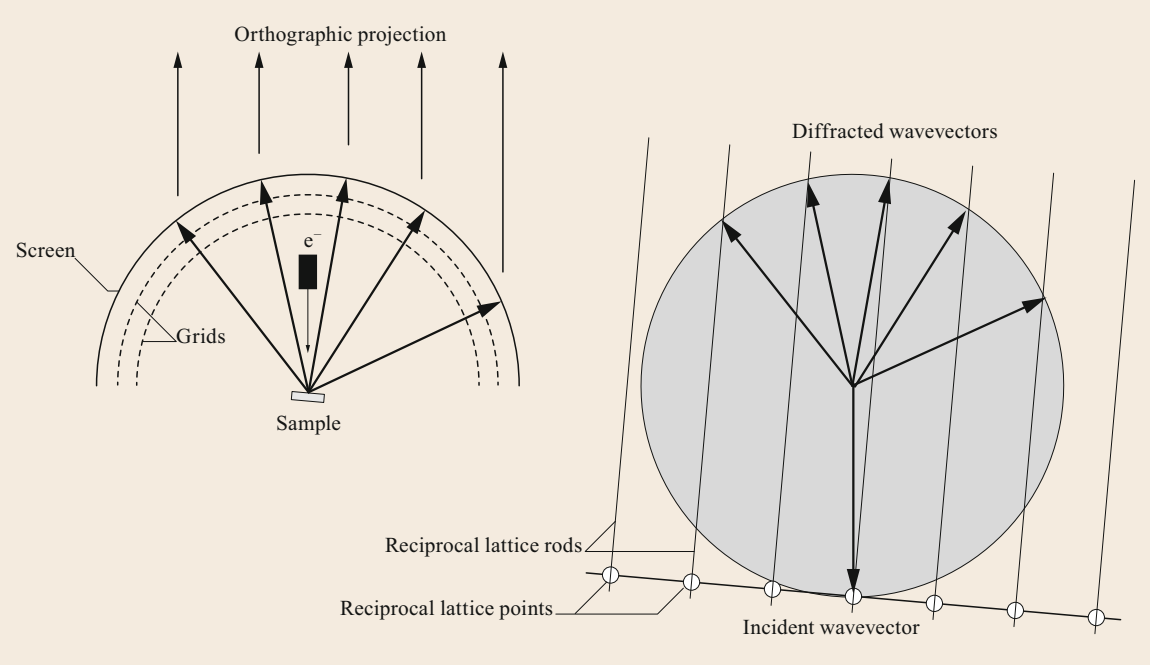

Fig. 4.7 LEED geometry and the Ewald sphere construction; reciprocal lattice rods are oriented perpendicular to the sample surface, and pass through reciprocal lattice points whose two-dimensional wavevectors differ from the surface-parallel component of the incident wavevector by surface reciprocal lattice vectors

At the simplest level, a prototypical LEED experiment involves the impingement of a monoenergetic electron beam upon a crystalline surface, and the collection of scattered electrons by means of some position-sensitive detector. In the vast majority of cases, this detector comprises little more than a phosphor-coated hemispherical screen that glows in response to the impact of electrons. It is usual to interpose two or three fine wire grids between the screen and the sample, which is situated at the focal point of the screen; the role of these grids, which are held at carefully chosen potentials during the experiment, is first to screen out any inelastically scattered electrons that may confuse the interpretation of elastic scattering events, and then to accelerate the remaining electrons towards the screen in order to maximize the electron-induced glow and hence the sensitivity. The diffraction pattern may then be observed upon the screen, from either the same or the opposite side as the sample (the latter option requiring a transparent screen, of course). The incident beam is generated by an electron gun, situated either between the sample and the screen, or more usually on the far side of the screen (the latter option requiring a small hole to be present in the center of the screen). Although normal incidence of electrons onto the sample is by no means an absolute necessity, it is nevertheless the norm.

Considering the general case of nonnormal incidence, we can predict the diffraction pattern due to electron scattering by means of a simple geometric construction known as the Ewald sphere (Fig. 4.7). We start with a vector in reciprocal space, representing the wavevector of the incident electron, and imagine a sphere of radius equal to the magnitude of this vector and centered on the origin. Conservation of energy implies that elastically scattered electrons must leave the surface with wavevectors whose tips lie somewhere on this sphere. Conservation of linear momentum, on the other hand, implies that the surface-parallel component of any outgoing wavevector must equal that of the incoming wavevector, to within an offsetting reciprocal lattice vector $\boldsymbol{G}$. We can include this in the construction by adding reciprocal lattice rods, positioned so that one rod passes through the tip of the incident wavevector and the orientation is perpendicular to the surface. Points where these rods intersect the sphere become, therefore, the only points at which outgoing wavevectors may terminate. The complete set of outgoing wavevectors satisfying the demands of the Ewald construction thus defines the pattern of outgoing electron beams constituting the diffraction pattern. In the standard geometry, with the sample lying at the focal point of a hemispherical screen and electrons imping-

ing at normal incidence, the orthographic projection of the bright spots in the pattern corresponds perfectly to the reciprocal lattice of the sample. Varying the energy of the incoming electron beam (by varying the accelerating voltage in the electron gun) causes a scaling of the observed pattern, due to a change in the incident wavevector, but no change in its qualitative features. The intensity of different outgoing beams does change with incoming beam energy, however, so that some LEED spots may become imperceptible under certain circumstances. Scanning the incoming beam energy is advisable, therefore, to ensure that patterns are correctly identified. Moreover, the intensity of individual LEED spots may be plotted as a function of the accelerating voltage, yielding so-called *I–V* curves. In just the same way that intensity variation with wavelength carries detailed structural information in x-ray diffraction experiments, here too the *I–V* curves carry similar detail embedded in their peaks and troughs. Analysis of LEED *I–V* curves is considerably more difficult than the comparatively simple extraction of structural detail by direct inversion of x-ray diffraction data, due to the multiple scattering of electrons, but nevertheless a trial and error approach works well.

4.6 Stereographic Representation of Surface Symmetry and Structure

Surfaces may be considered high-energy defects, relative to an idealized defect-free bulk material. Indeed, we can assign a specific surface energy (i.e., excess energy per unit area of surface) to any exposed facet, and one should expect the system as a whole to adopt a morphology that minimizes the total surface energy (i.e., the summed product of specific surface energies for different facets with the corresponding surface areas of those facets). To a first approximation, the specific surface energy may be expected to be roughly proportional to the number of nearest-neighbor interatomic bonds that are severed in creating the surface by cleavage of the bulk material, and hence it is no surprise that the lowest specific surface energies are typically found for the most close-packed structures. In crystals of face-centered cubic structure (Fig. 4.8) the most stable surface facet is of {111} type (coordination number of nine in the outermost layer) while the second most stable is of {100} type (coordination number of eight in the outermost layer). In crystals of body-centered cubic structure, on the other hand, the most stable surface is of {110} type (coordination number of six in the outermost layer), whereas this combination of Miller indices yields only the third most stable surface of face-centered cubic materials (coordination number of seven in the outermost layer). It is worth bearing in mind that the bulk coordination number in the body-centered cubic structure is only eight, compared to 12 in the face-centered cubic case. Notwithstanding this viewpoint, however, it is certainly the case that real surfaces will themselves play host to a variety of defects. The most stable (and hence most prolific) defective structure on an otherwise close-packed surface may most simply be described as a step, separating two terraces of nondefective material. Next, in order of stability, comes the kink, in which an otherwise straight-edged step suffers a lateral dislocation. Isolated adatoms and/or vacancies are also possible, of course, but these are typically so much higher in energy that their existence may be ignored at first blush. Accordingly, the TSK (terrace-step-kink) model of surface structure (Fig. 4.9) is widely taken as the basis for morphological discussions.

We should stress, at this point, that the occurrence of steps and kinks on close-packed surfaces is essentially random, depending in its precise detail upon the (unknown and unknowable) microscopic history of our sample's preparation. Granted, a systematic miscut of the sample may bias its surface towards a particular type and/or frequency of steps and/or kinks, but other preparational aspects (e.g., polishing, sputtering, etc.)

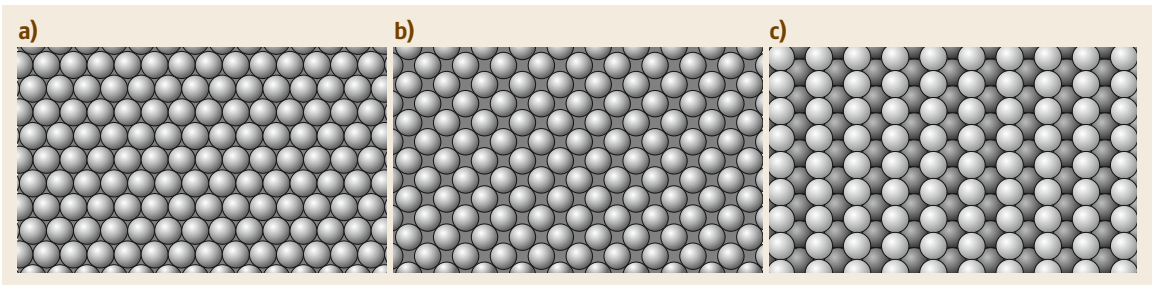

Fig. 4.8a–c Models of the (**a**) {111}, (**b**) {100} and (**c**) {110} surfaces of the face-centered cubic crystal structure

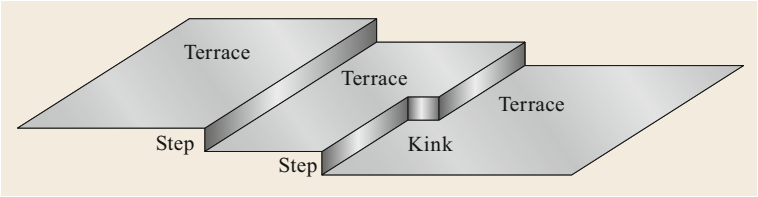

Fig. 4.9 Schematic view of the terrace-step-kink (TSK) model of surface morphology

will typically ensure that considerable heterogeneity and contingency characterizes their actual manifestation. Moving away from the close-packed surfaces, however, increasing attention is now paid to surfaces cut at some considerable angle from the low-index {111}, {100} and {110} planes. These high-index (sometimes described as vicinal) surfaces are distinguished in displaying more-or-less regular arrays of steps and/or kinks, presenting an opportunity to study what can be rather important low-coordination sites in a controlled manner. It is, therefore, to the classification of symmetry and structure in high-index surfaces that we now turn. Note the etymology of the word vicinal implies a degree of proximity (vicar, vicarious, etc.) and indeed the correct usage ought to describe certain high-index surfaces as *vicinal to* {111} or *vicinal to* {100} and so forth. That is, the term should indicate the low-index surface to which the high-index surface most closely approximates. Perhaps unfortunately, however, there is a tendency in modern usage to employ the word vicinal without qualification, simply as a synonym for *not low-index*.

4.6.1 The Surface Symmetry Stereogram

Let us begin with a focus on symmetry, taking the face-centered and body-centered cubic crystal structures as our case studies. Together, these two structures account for nearly all of the transition and coinage metals commonly used in catalytic applications. The concepts outlined here may readily be extended to other, more complicated, crystal structures; for a full introduction to the philosophy behind this approach, and an application to the hexagonal close-packed crystal structure, see the work by *Jenkins* and *Pratt* [4.3]. Our first task will be to represent graphically those surfaces possessing mirror symmetry, and we shall achieve this by means of either a spherical or a stereographic representation. Here, one must first imagine a vast single crystal in the shape of a sphere, the significance of which is that a microscopic examination of any sufficiently small region of its surface would reveal atoms arranged in accordance with a tiny patch of planar surface. Different points on the sphere necessarily correspond to different surface orientations, with eight points giving rise to patches of {111} type, six yielding patches of {100} type, and 12 revealing patches of {110} type; elsewhere on the sphere, one would find all possible high-index surface orientations represented at well-defined locations.

In order to highlight *surfaces* possessing mirror symmetry, it will prove helpful first to consider the mirror symmetries of the parent *bulk* material. In both face-centered *and* body-centered cubic crystals, mirror planes exist in the orientations perpendicular to the ⟨100⟩ and ⟨110⟩ crystallographic directions. Imagining the complete set of these mirror planes converging at the center of the sphere, one can confirm that all surface orientations corresponding to points on the surface of the sphere cut by one of these planes must necessarily exhibit that particular mirror symmetry. Marking the great circles of intersection between sphere and mirror planes with lines (which we shall henceforth describe as zones) one obtains the construction shown in Fig. 4.10a. More commonly, this spherical representation is subjected to a stereographic projection in order to render it onto a flat plane, as in Fig. 4.10b. Here, we can state immediately that any surface orientation corresponding to a point on the sphere lying at the junction between four of the marked zones must possess four distinct mirror symmetries; only the surfaces of {100} type satisfy this condition, and indeed they *are* the only surfaces of face- or body-centered cubic crystals that support so many mirror planes. Similarly, any surface orientation corresponding to a point on the sphere lying at the junction between three of the marked zones must possess three distinct mirror symmetries, and this time it is the surfaces of {111} type that uniquely exhibit this property. Likewise, the surfaces of {110} type are the only ones that lie at the junction between two of the marked zones, implying that they are the only examples that possess precisely two mirror planes. The low-index surfaces we have discussed above in the context of the TSK model, without ever presenting a firm dividing line between the epithets *low* and *high*, thus turn out to correspond precisely to the subset of face- or body-centered cubic surfaces possessing multiple mirror symmetries. On the other hand, an infinite number of surfaces may be envisioned that lie upon just a single marked zone, and *all* of these possess just one mirror plane within their space group.

Turning now to those surfaces whose orientations correspond to a point on the sphere that does *not* co-

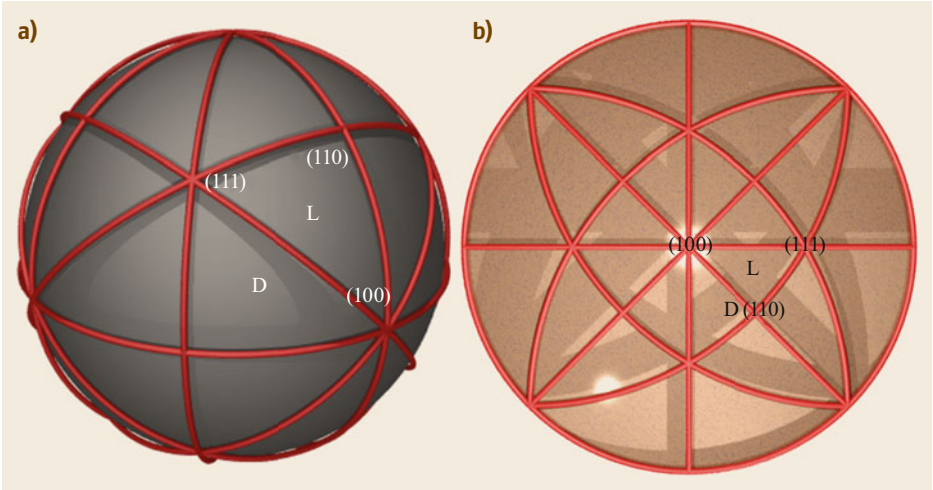

Fig. 4.10a,b Representation of surface symmetry for face-centered and body-centered cubic materials, with highlighted zones indicating surfaces displaying at least one mirror symmetry. In **(a)** these mirror zones are shown on the surface of a notional single-crystalline sphere, while in **(b)** the same information is stereographically projected onto a two-dimensional plane. Selected high-symmetry surfaces are indicated in each case, and two stereographic triangles in which chiral surfaces (lying off the mirror zones) labeled D or L are marked

incide with any of the marked zones, it follows that these must necessarily be devoid of any mirror symmetry. In the absence of any possible inversion symmetry (incompatible with all surface geometries) it further follows that all such surfaces are actually chiral—that is to say, the mirror image of such a surface would not be superimposable upon the original surface itself. The consequences of such a state of affairs for asymmetric synthesis, separation or sensing applications are, needless to say, potentially profound, and these surfaces have drawn quite a bit of attention in this regard over the last couple of decades.

Just as chiral molecules are typically labeled to distinguish their two nonsuperimposable mirror images (or, more properly, their enantiomers) so too it has proved useful to agree upon a convention for labeling the two nonsuperimposable mirror images of a chiral surface (which we shall call its enantiomorphs). Certainly the most popular scheme (proposed originally by *Attard* [4.4]) is one based upon the Cahn–Ingold–Prelog rules, whereby groups attached to a central carbon atom within a chiral molecule are assigned (arbitrary, but well-defined) priorities and the chiral label *R* or *S* is determined by the sense of rotation in going from high to low priority when viewed from a particular direction. (The labels *R* and *S* derive from the Latin words *rectus* and *sinister*, meaning right and left; there is, however, nothing objectively right-handed about one structure and left-handed about the other, even though they are often colloquially described in these terms once their labels have been assigned.) In the surface-modified version, one first examines the surface structure and identifies microfacets of {111}, {100} and {110} type in the vicinity of a kink, assigning them priority in order of their degree of close packing. If, when viewed from above the surface and visited in this order, these microfacets are arranged in the clockwise sense, the surface is labeled *R*, but if the arrangement is anticlockwise the label must be *S*. The method is simple, requiring nothing more than a structural model of the surface for its application, and has been adopted by most authors in this field. It does, however, suffer from a serious drawback when dealing with chiral surfaces that do not display kinks and hence do not possess microfacets of all three types. Fortunately, in the case of face-centered cubic crystals, all chiral surfaces *do* possess kinks (as we shall confirm in the next subsection) and so this problem does not arise. For surfaces of body-centered cubic crystals, however, the issue is very real and an alternative approach to labeling enantiomorphs is required.

Amongst the surfaces of face-centered cubic materials, the Attard convention may, in fact be simplified thus: a surface whose Miller indices are all positive and arranged in descending order of magnitude (e.g., the (531) surface) will acquire the label *S*, as will any surface whose Miller indices may be obtained from this instance via cyclic permutation and/or change of sign in any two indices. If the Miller indices are all positive but arranged in ascending order of magnitude (e.g., the (135) surface) or may be obtained from *this* instance by cyclic permutation and/or change of sign in any two indices, the appropriate label will be *R*. Finally, we note

that noncyclic permutations, or a change of sign in any one or all three indices will swap chirality labels between *S* and *R*.

One alternative approach (proposed by *Pratt et al.* [4.5]) emerges directly from the stereographic philosophy. Here, one first identifies the stereographic triangle within which a particular surface orientation lies, and then visits the vertices of this triangle in order of increasing symmetry (i.e., {110} followed by {111} followed by {100}); if, in so doing, the itinerary proceeds in a clockwise sense, one assigns the chirality label D, but if it proceeds anticlockwise then L must be the correct label. (The labels D and L once again derive from Latin, but in this case the words *dexter* and *laevo* are used as synonyms for right and left. In molecular chemistry, the assignment of D and L as chiral labels is made on the basis of similarities in structure with the compound glyceraldehyde, for which labeling is essentially arbitrary.) When applied to the surfaces of face-centered cubic crystals, the equivalences $R \equiv$ D and $S \equiv$ L hold true in all cases; for body-centered cubic crystals, the same is true where both labeling systems apply, but the D/L system continues to hold even when the *R*/*S* system fails.

4.6.2 The Surface Structure Stereogram

Having rendered the mirror symmetries of crystalline surfaces in stereographic form, it is an interesting and illuminating exercise to perform the same trick with aspects of their structure. One might, in principle, achieve this in various ways, but for the face- and body-centered cubic systems discussed above, the most natural approach is arguably to focus upon the crystallographic directions within the bulk material that correspond with atomic close-packing. In face-centered crystals, close packing of atoms occurs only along the ⟨110⟩ axes, whereas in body-centered crystals the same role is played by the ⟨111⟩ axes. Highlighting, on a sphere or stereogram, those surfaces for which one or other of these axes lies parallel to the surface plane, one arrives at the constructions shown in Fig. 4.11.

The significance of the newly marked zones in these diagrams is that they tell us specifically about the disposition of steps and kinks on the surface. A surface orientation corresponding to a point lying on precisely one of these zones necessarily features one, and only one, in-plane direction in which close-packed chains of atoms can be found; this state of affairs may be most reasonably described as indicating a regularly stepped surface (as opposed to one that merely happens to possess a low concentration of randomly distributed steps). Surface orientations corresponding to points that do not lie on any of these zones do not feature close-packed atomic chains at all, and are best described as regularly kinked (as distinct from merely possessing a low concentration of randomly distributed kinks). Finally, surface orientations corresponding to points lying at the junction of two or more of these zones necessarily feature the appropriate number of distinct directions within which close-packed chains of atoms are found, and hence must be considered atomically flat (in the sense of possessing neither regular steps nor regular kinks). In the case of face-centered cubic crystals, flat surfaces comprise those of {111} and {100} type, with three or two distinct close-packed directions respec-

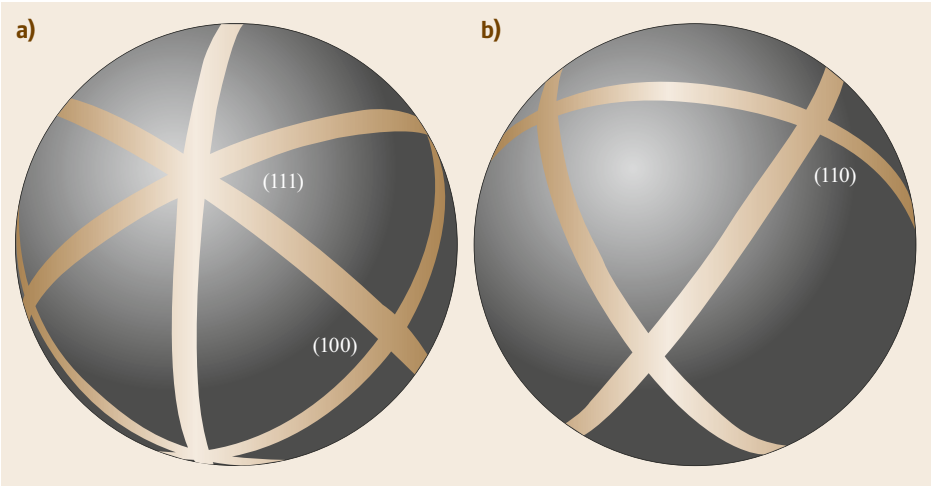

Fig. 4.11a,b Representation of surface structure for **(a)** face-centered cubic and **(b)** body-centered cubic materials. The highlighted zones indicate surfaces displaying close-packed atoms in at least one surface-parallel direction, described as regularly stepped; intersections correspond to atomically flat surfaces, while off-zone surfaces are regularly kinked

tively, whereas in the case of body-centered crystals only the surfaces of {110} type, with two distinct close-packed directions, may be considered to be flat within this scheme.

Importantly, the definitions of flat, stepped and kinked surfaces described here do actually correspond to physically measurable and significant features. Indeed, strong support for the meaningfulness of these categories is provided by a series of experiments from the *Gellman* group, in which propylene oxide and 3-methylcyclohexanone have been used as probe molecules to gauge the strength of binding at different surface sites on a variety of flat, stepped and kinked surfaces [4.6–12]. Results conform very closely to expectations based on the model described here. Specifically, it may be noted that the presently discussed definitions relate especially closely to the coordination number of atoms in the outermost layer, with consequences in turn for surface energy and stability against roughening. In the case of face-centered cubic crystals, the flat surfaces have the highest coordination number in the outermost layer (nine for the {111} type and eight for the {100} type), while the stepped surfaces all have the same slightly lower coordination number (seven) and the kinked surfaces all share the lowest coordination number (six). Unsurprisingly, the specific surface energies of the kinked surfaces are always higher than those of the stepped surfaces, which in turn are higher than those of the flat surfaces. Moreover, one may also make secure statements about the propensity for roughening based upon the concept of creating an adatom/vacancy pair by removing an atom from the outermost layer and redepositing it elsewhere on an otherwise pristine region of the surface. For the {111} surface, this process would involve first breaking nine nearest-neighbor bonds, and then making just three; the overall cost of six bonds implies that adatom/vacancy pair creation is enthalpically unfavorable, and that roughening would only occur at sufficiently elevated temperature so that entropic effects dominate. Similarly, for the {100} surface the formation of a vacancy would require the breaking of eight nearest-neighbor bonds, while the redeposition of an adatom would make only four; the overall cost of four bonds, whilst less than in the previous case, would still prohibit roughening at moderate temperatures. Turning to the stepped surfaces, however, removal of an atom from the step itself involves the breaking of only seven nearest-neighbor bonds, while redeposition would involve making five, for an overall cost of just two bonds; accordingly, roughening of stepped surfaces is expected to occur at lower temperature than for otherwise similar flat surfaces, and indeed this is generally found to be true. On kinked surfaces, in contrast, the removal of an atom to form a vacancy requires only six nearest-neighbor bonds to be broken, while redeposition elsewhere to form an adatom would create precisely the same number of new bonds; as a consequence, there will be very little enthalpic cost involved in adatom/vacancy pair creation, meaning that it can happen repeatedly at low temperature, implying that kinked surfaces will always be atomically rough. Very similar arguments apply to surfaces of body-centered cubic crystals, where the cost of adatom/vacancy pair creation amounts to four nearest-neighbor bonds on flat {110} surfaces, two such bonds on stepped surfaces, and zero on kinked surfaces; once again the flat surfaces are most stable against roughening, the stepped surfaces slightly less so, and the kinked surfaces not at all. It is worth mentioning, at this juncture, that simplistic energetic arguments based upon nearest-neighbour bonds work reasonably well for close-packed metals (i.e., face-centered cubic or hexagonal close-packed) but rather less well for more open structures (e.g., body-centered cubic). In large part, this is because interactions between next-nearest neighbors play a much larger role in the latter cases. Nevertheless, to a first approximation, conclusions drawn from these arguments do serve to frame the results of more detailed examination (e.g., through density functional calculations), which tend to concur in their essentials with the simpler picture.

4.6.3 Synthesis of Symmetry and Structure

Whilst the analysis presented above provides a framework for discussion of flat, stepped and kinked surfaces, it is possible to extend the idea based upon structural features of the parent bulk material other than just close-packed chains of atoms. One might, for example, seek out other extended motifs like zig-zag chains of atoms, plotting the zones corresponding to these onto stereograms to define additional families of surface orientations. A roadmap summarizing the structural connections between different surfaces, as revealed by this kind of approach, has been presented by *Jenkins* and *Pratt* [4.3] and the interested reader is directed to that work. For the present purpose, we shall focus on structure only at the most basic level. Nevertheless, important observations may be made by combining the spherical or stereographic representation of surface structure with that of surface symmetry. The resulting constructions for face-centered and body-centered cubic materials are presented in Fig. 4.12, with permissible combinations of symmetry and structure derived from these summarized in Fig. 4.13.

Considering first the representation for the face-centered cubic structure, we see immediately that whilst the zones indicating stepped surfaces all coincide with

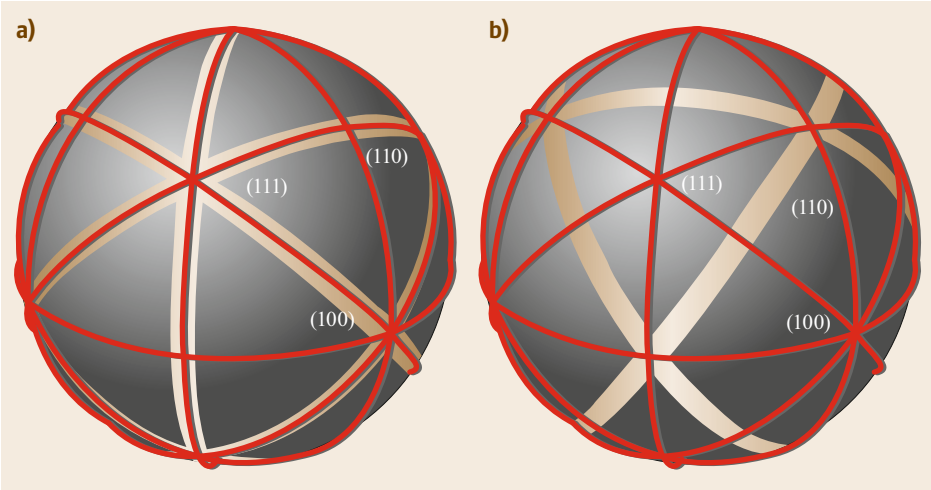

Fig. 4.12a,b Representation of surface symmetry and structure for **(a)** face-centered cubic and **(b)** body-centered cubic materials, showing mirror zones *and* structural zones together

zones indicating mirror symmetries, the reverse is not the case. Not only, therefore, does the diagram confirm that only the flat surfaces (those of {111} and {100} type) are of high symmetry (exhibiting three or four mirror planes) but it also reveals that *all* stepped surfaces of face-centered cubic structure necessarily display mirror symmetry, although not all mirror-symmetric surfaces are stepped. Specifically, we can see that surfaces with precisely two Miller indices of the same magnitude generally possess both a stepped structure and a single mirror plane; the only exceptions are surfaces of {110} type, which are the most highly symmetric stepped surfaces, having two mirror planes. At the same time, we can observe that all chiral surfaces are kinked, though not all kinked surfaces are chiral. That is, surfaces with three nonzero Miller indices of inequivalent magnitude possess no mirror symmetry and display no surface-parallel chains of close-packed atoms; surfaces with a single zero Miller index, other than the {110} surface, are also kinked in their structure, but do possess a single mirror plane. It follows, from the the discussion of surface stability offered in the preceding subsection, that the intrinsically chiral surfaces of face-centered cubic materials are necessarily always going to be prone to significant surface roughening. This propensity has indeed been observed in the

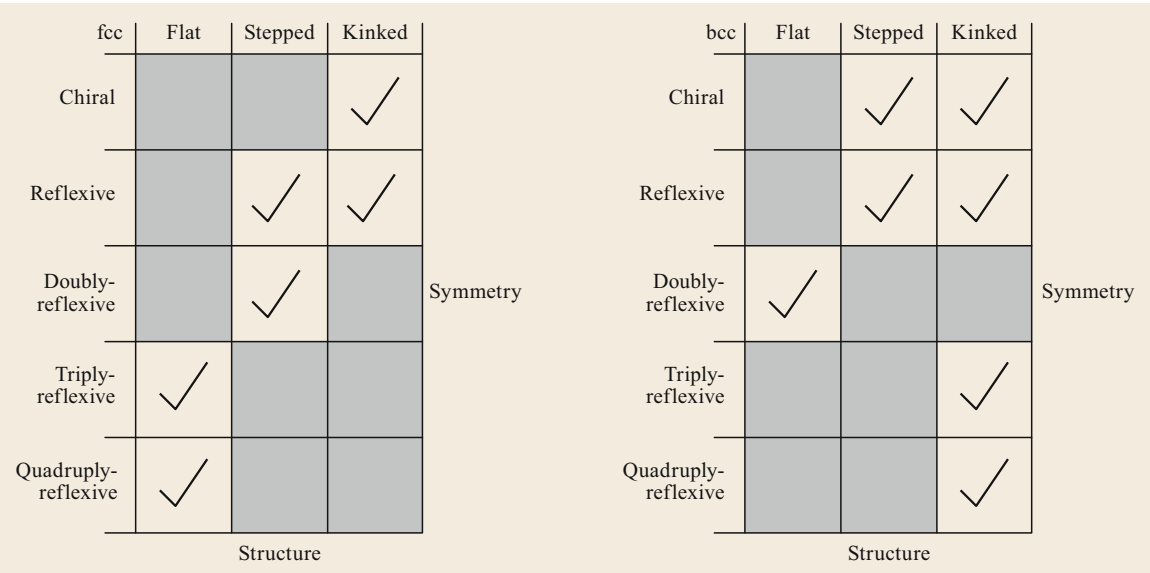

Fig. 4.13 Permitted combinations of symmetry and structure categories for face-centered and body-centered cubic materials

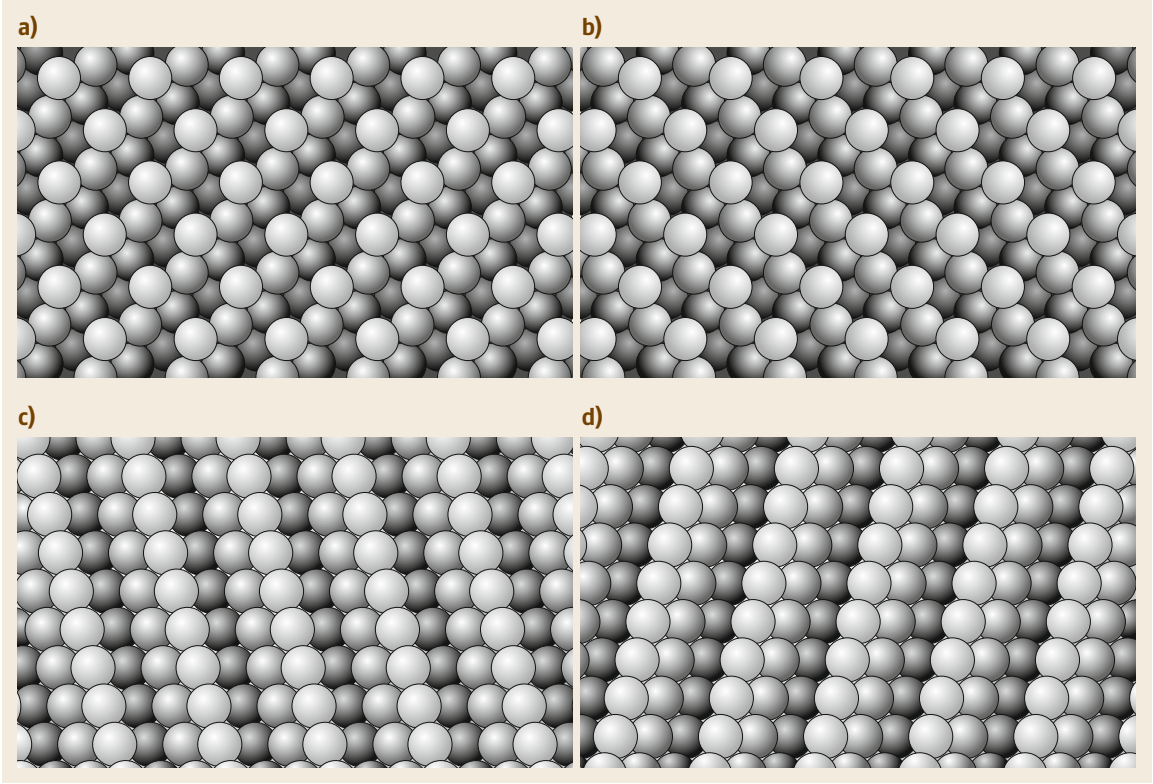

Fig. 4.14a–d Examples of chiral surfaces. As with all chiral surfaces of face-centered cubic materials, those of {531} type are kinked **(a)** fcc-{531}-L; **(b)** fcc-{531}-D. Materials taking the body-centered cubic crystal structure, in contrast, have not only kinked chiral surfaces, but also stepped chiral surfaces, as illustrated here by the examples of {321} type: **(c)** fcc-{321}-L; **(d)** fcc-{321}-D

case of Cu{531} [4.13] and is likely to be generally true, although it seems also that some degree of ordering may be imposed by the action of certain adsorbates.

In the body-centered cubic case, the picture is radically altered. Here, we immediately see that the zones indicating stepped surfaces do not, in general, coincide with those indicating mirror symmetries. Once again, the only flat surfaces (those of {110} type) are confirmed to display relatively high symmetry (exhibiting two mirror planes) but the very highest symmetry surfaces are, in fact, of the kinked variety (those of {100} and {111} type, with four or three mirror planes respectively). Surfaces having either two Miller indices of the same magnitude, or one zero Miller index, display a single mirror plane and are generally also kinked; the only exceptions are surfaces of {211} type, which are merely stepped. Indeed, the {211} surfaces are the most highly symmetric of the stepped surfaces for body-centered cubic materials (occupying a similar role to that of the {110} surfaces in the face-centered cubic case) and *all* other stepped surfaces are found to be chiral; these stepped surfaces may be identified from their Miller indices by the fact that two of the index magnitudes can be summed to give the magnitude of the remaining index (Fig. 4.14). There are, of course, as the spherical/stereographic representation also makes clear, many chiral kinked surfaces in addition to the stepped ones, but these will suffer a similar degree of instability against roughening as is expected of their face-centered cubic counterparts. The stepped chiral surfaces, on the other hand, are anticipated to be significantly more stable against roughening, and hence eminently suitable for studies of asymmetric surface phenomena.

4.7 Notational Conventions for Surface Superstructure

Our discussion thus far has focused upon idealized clean surfaces, whose structure is simply that of a bulk crystal terminated on a two-dimensional plane. In reality, of course, any such termination lowers the symmetry at the surface, implying unbalanced forces on the selvedge atoms, and opens the possibility of surface relaxation and potentially surface reconstruction. Here, we define surface reconstruction as any change in atomic positions resulting in a surface structure that either (a) is of lower symmetry than the ideal bulk-terminated surface, or (b) cannot be obtained through a continuous deformation of the bulk-terminated surface without passing through a lower-symmetry intermediate state. The first situation may be described as a *real* lowering of symmetry, and the second as a *virtual* one. Any displacement of atoms that falls short of this definition will be described as a surface relaxation. In general, one or other of these phenomena must occur at all surfaces, although in the absence of surface reconstruction the atomic displacements associated with surface relaxation may range from significant to barely perceptible. The change in symmetry involved in surface reconstruction (whether real or virtual) may occur within the point group of the surface, but equally may be limited only to translational symmetry elements; either way, it is convenient to define a notational standard to specify how the periodicity of a reconstructed surface relates to that of the ideal bulk-terminated surface. Similarly, when surface adsorption occurs, the adsorbed atoms and/or molecules may arrange themselves in an orderly periodic fashion, and the same notational convention will serve to keep track of this phenomenon equally well.

4.7.1 Wood's Notation

Since we aim to describe surface adsorption *and* surface reconstruction by means of the same notation, we shall refrain from drawing figures showing either type of situation explicitly. Instead, we will simply indicate, on a diagram of the ideal bulk-terminated surface, a unit cell (usually primitive) corresponding to the reconstructed and/or adsorbate-covered surface. We also depict an appropriate primitive unit cell of the clean unreconstructed surface for reference. The essence of our notational approach will be to define the former in terms of the latter.

In what is known as Wood's notation, the primitive unit cell of the surface superstructure is indicated by means of two multiplying factors to be applied to the primitive lattice vectors spanning the ideal surface's primitive unit cell. Wood's notation $(m \times n)$ is therefore to be interpreted as referring to a unit cell spanned by the vectors $m\boldsymbol{a}_1$ and $n\boldsymbol{a}_2$ (where $\boldsymbol{a}_1$ and $\boldsymbol{a}_2$ are primitive lattice vectors for the clean unreconstructed surface). The primitive unit cell of the ideal surface is, in this notation, simply the (1×1) cell, and the area of any general unit cell is precisely mn times greater than this. In certain cases, it may be necessary not only to scale the (1×1) cell in order to represent the superstructure, but also to rotate it, in which circumstance the notation may be augmented to read $(m \times n)\mathrm{R}\theta$, where θ is the necessary rotation (anticlockwise) about the surface normal. Examples are depicted in Fig. 4.15.

A special case arises where the primitive unit cell of the surface superstructure cannot simply be represented as a scaled and rotated version of the (1×1) cell, but where the addition of an additional lattice point at the center of each $(m \times n)$ will suffice to achieve the desired mapping. In such circumstances, the proper notation takes the form $\mathrm{c}(m \times n)$, where the prefix indicates a *centered* cell; on occasion, ordinary *noncentered* cells may be written in the form $\mathrm{p}(m \times n)$, where the prefix indicates *primitive*, but this is essentially redundant and not a universal practice. Centered cells may, of course, be rotated relative to the (1×1) cell, if necessary, and again a postfixed $\mathrm{R}\theta$ serves to indicate such an eventuality. An example of such a centered cell is again provided in Fig. 4.15.

Alert readers will, by now, have spotted two critical flaws in an otherwise convenient and concise notational scheme: firstly, that there can certainly exist superstructures whose periodicity does not happen to conform to

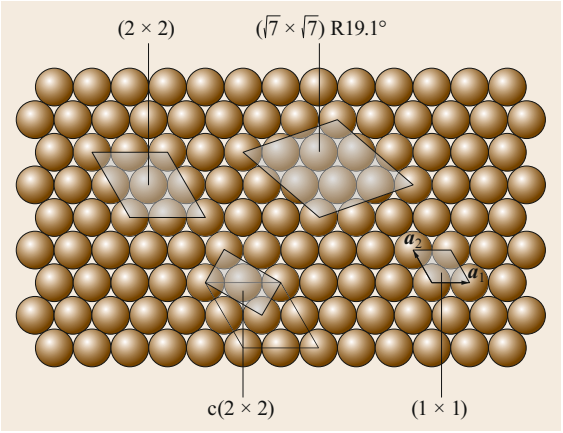

Fig. 4.15 Examples of Wood's notation at the {111} surface of a face-centered cubic material, with the relevant primitive lattice vectors (and corresponding primitive unit cell) of the unreconstructed clean surface shown for reference

a simple scaling and/or rotation of the ideal surface's primitive unit cell; and secondly, that the definition of the ideal surface's primitive unit cell is, in itself, not well defined. The first problem may be addressed by adopting the so-called matrix notation described in the next subsection, but the second is fundamentally an issue for *both* notational approaches. Unfortunately, although some attempts have been made to standardize the choice of primitive unit cells, none of these have yet been universally adopted within the surface science community. We shall discuss the matter further below, but for the moment it is worth emphasizing that neither notational scheme is adequate to describe the periodicity of surface superstructures unless the choice of primitive lattice vectors for the ideal surface is first explicitly defined.

4.7.2 Matrix Notation

As alluded to above, one can readily conceive of surface superstructures whose periodicity cannot be represented as a simple scaling and/or rotation of the ideal surface's lattice. In these cases, Wood's notation proves inadequate, and the more general matrix notation must be adopted. Here, the primitive lattice vectors of the superstructure, which we shall denote $\boldsymbol{a}'_1$ and $\boldsymbol{a}'_2$, are written in terms of those defining the ideal surface lattice, denoted $\boldsymbol{a}_1$ and $\boldsymbol{a}_2$, by means of a matrix multiplication. Thus,

$$\begin{pmatrix} \boldsymbol{a}'_1 \\ \boldsymbol{a}'_2 \end{pmatrix} = \begin{pmatrix} m_{11} & m_{12} \\ m_{21} & m_{22} \end{pmatrix} \begin{pmatrix} \boldsymbol{a}_1 \\ \boldsymbol{a}_2 \end{pmatrix} \tag{4.18}$$

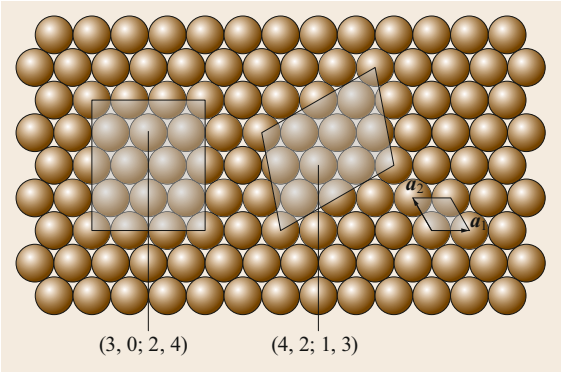

Fig. 4.16 Examples of matrix notation at the {111} surface of a face-centered cubic material, with the relevant primitive lattice vectors (and corresponding primitive unit cell) of the unreconstructed clean surface shown for reference

with integer matrix coefficients. The superstructure may then conveniently be referred to by the in-line form of the matrix, i.e., $(m_{11}, m_{12}; m_{21}, m_{22})$. Examples are shown in Fig. 4.16.

Just as Wood's notation provided a simple check on the area of the superstructure's primitive unit cell, relative to that of the unreconstructed clean surface, so the determinant of the matrix (i.e., $m_{11}m_{22} - m_{12}m_{21}$) performs the same function here, or rather its magnitude does; the *sign* of the determinant indicates whether the trio of vectors $\boldsymbol{a}'_1$, $\boldsymbol{a}'_2$ and $\hat{\boldsymbol{n}}$ form a coordinate system whose handedness matches (positive) or opposes (negative) that adopted for the $\boldsymbol{a}_1$, $\boldsymbol{a}_2$ and $\hat{\boldsymbol{n}}$ vectors.

4.8 On the Choice of the (1×1) Cell

Since both notational schemes discussed above define superstructure periodicity relative to that of the unreconstructed clean surface, it is clear that they each become meaningless when there remains any doubt as to how that reference periodicity is defined. Specifically, different choices for the primitive (1×1) unit cell of the unreconstructed clean surface will, in general, yield different notations for the same superstructure periodicity, and indeed different superstructure periodicities for the same notation. Figure 4.17, for example, shows three different potential choices for the (1×1) cell of a surface having a rectangular two-dimensional Brillouin zone, each of which yields differently shaped cells corresponding to (1×2) periodicity in Wood's notation. Similar ambiguity also arises in matrix notation, for precisely the same reason.

Unsurprisingly, surface scientists have adopted a number of (largely unspoken) conventions when choosing the (1×1) cell, in order that some degree of agreement between different workers may generally be anticipated. In cases with square, triangular and rectangular lattices, for example, such cells are almost invariably chosen to reflect the maximum possible symmetry, as per Fig. 4.5 and the associated discussion. Sadly the same cannot always be said of cases with rhombic lattices, where symmetry is often ignored in choosing the reference cell. For rectangular cells, the standard choice is that $\boldsymbol{a}_1$ should be shorter than $\boldsymbol{a}_2$, while for nonorthogonal cells (of the triangular, rhombic or oblique lattices) the angle between $\boldsymbol{a}_1$ and $\boldsymbol{a}_2$ is chosen to be obtuse. Finally, the trio of vectors $\boldsymbol{a}_1$, $\boldsymbol{a}_2$ and $\hat{\boldsymbol{n}}$ is most often chosen to form a right-handed set of axes. Widespread adherence to these conventions eliminates much confusion, but it should be stressed that it is certainly best practice to explicitly state the choice of reference cell and the disposition of the

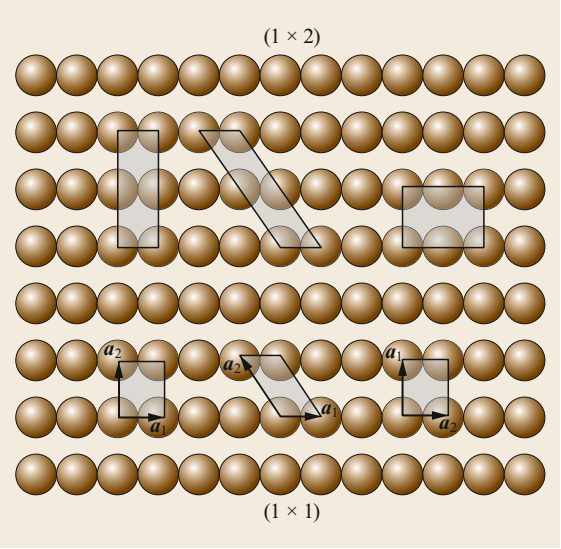

Fig. 4.17 Illustrating the ambiguity of notation when different choices are made for the (1×1) unit cell, in the case of a face-centered cubic {110} surface (only top-layer atoms depicted, for clarity). Each of the superstructure cells can be described as having (2×1) periodicity, relative to the (1×1) cells shown beneath

associated primitive lattices vectors whenever any doubt may arise.

It is worth mentioning, at this point, that these conventions do break down somewhat when dealing with chiral surfaces. Here, it is not always possible to satisfy the requirements pertaining to the length of, and angle between, the primitive lattice vectors, whilst also retaining a right-handed coordinate system with the surface normal vector. It seems to the present author that adoption of a left-handed coordinate system for surfaces bearing the chirality label *S* (or L) would avoid this problem, with a right-handed system used for those bearing the chirality label *R* (or D) and as a default for those surfaces that are achiral. This is not, however, standard practice. Nevertheless, it is true that attempts have been made to promote standard conventions to deal with these problematic cases and to resolve any possible ambiguities that may remain. One proposal, originating with *Barlow* and *Raval* [4.14], turned out not to resolve fully all possible ambiguous situations, but a more recent scheme, proposed by *Merz* and *Ernst* [4.15], does appear to be watertight; nonetheless, neither proposal has garnered sufficient support to be considered settled, and scope for proposal of alternative conventions remains.

References

4.1 N.W. Ashcroft, N.D. Mermin: *Solid State Physics* (Harcourt Brace Jovanovich, New York 1976)

4.2 M.A. Van Hove, W.H. Weinberg, C.-M. Chan: *Low-Energy Electron Diffraction: Experiment, Theory and Structure Determination* (Springer, Berlin, Heidelberg 1986)

4.3 S.J. Jenkins, S.J. Pratt: Beyond the surface atlas: A roadmap and gazetteer for surface symmetry and structure, Surf. Sci. Rep. **62**, 373–429 (2007)

4.4 G.A. Attard: Electrochemical studies of enantioselectivity at chiral metal surfaces, J. Phys. Chem. B **105**, 3158–3167 (2001)

4.5 S.J. Pratt, S.J. Jenkins, D.A. King: The symmetry and structure of crystalline surfaces, Surf. Sci. **585**, L159–L165 (2005)

4.6 J.D. Horvath, A.J. Gellman: Enantiospecific desorption of *R*- and *S*-propylene oxide from a chiral Cu(643) surface, J. Am. Chem. Soc. **123**, 7953–7954 (2001)

4.7 A.J. Gellman, J.D. Horvath, M.T. Buelow: Chiral single crystal surface chemistry, J. Mol. Catal. A Chem. **167**, 3–11 (2001)

4.8 J.D. Horvath, A.J. Gellman: Enantiospecific desorption of chiral compounds from chiral Cu(643) and achiral Cu(111) surfaces, J. Am. Chem. Soc. **124**, 2384–2392 (2002)

4.9 J.D. Horvath, A. Koritnik, P. Kamakoti, D. Sholl, A.J. Gellman: Enantioselective separation on a naturally chiral surface, J. Am. Chem. Soc. **126**, 14988–14994 (2004)

4.10 P. Kamakoti, J. Horvath, A.J. Gellman, D.S. Sholl: Titration of chiral kink sites on Cu(643) using iodine adsorption, Surf. Sci. **563**, 206–216 (2004)

4.11 Y. Huang, A.J. Gellman: Enantiospecific adsorption of (*R*)-3-methylcyclohexanone on naturally chiral Cu(531)$^{R\&S}$ surfaces, Catal. Lett. **125**, 177–182 (2008)

4.12 Y. Huang, A.J. Gellman: Enantiospecific adsorption of (*R*)-3-methylcyclohexanone on naturally chiral surfaces vicinal to Cu(110), Top. Catal. **54**, 1403–1413 (2011)

4.13 M.L. Clegg, S.M. Driver, M. Blanco-Rey, D.A. King: Atomic roughness of an intrinsically chiral surface orientation of an fcc metal: Cu{531, J. Phys. Chem. C **114**, 4114–4117 (2010)

4.14 S. Barlow, R. Raval: Complex organic molecules at metal surfaces: Bonding, organisation and chirality, Surf. Sci. Rep. **50**, 201–341 (2003)

4.15 L. Merz, K.-H. Ernst: Unification of the matrix notation in molecular surface science, Surf. Sci. **604**, 1049–1054 (2010)

Stephen J. Jenkins

Dept. of Chemistry
University of Cambridge
Cambridge, UK
sjj24@cam.ac.uk

Stephen J. Jenkins is Professor of Physical & Computational Surface Chemistry at the University of Cambridge, where he conducts research within the Department of Chemistry. His core interests include the dynamics of surface processes, hydrogen- and/or halogen-bonded overlayers, and the manifestation of chirality at surfaces. His book on the latter topic was published by Wiley in 2018.

5. Ab Initio Simulations of Semiconductor Surfaces and Interfaces

Arrigo Calzolari, Giancarlo Cicero, Alessandra Catellani

Calculations of the electronic properties of solids and surfaces span years of research activity and have produced an enormous amount of publications over the last decades. However, only recently have quantum simulations reached the degree of accuracy to be predictable against experimental data, and this is particularly true for systems with reduced periodicity, such as surfaces, interfaces, and nanostructures. In this review, we present a survey about the characterization of low-dimensional semiconductor-based systems by ab initio density functional methods and compare them with the experimental data available.

Several computational issues afflict the description of the different systems; we will not enter into the details of the theoretical approach and of the very many refinements, which cover a broad chapter by themselves. Rather, a discriminating analysis of the single computational protocols to describe and complement specific experimental problems is presented. Prototypical examples that can be considered as templates for the specific problem, with particular emphasis on surface and interface effects, will be addressed.

5.1 Overview

The ability to manipulate semiconductor surfaces and interfaces has gained significant attention in the past few years, in particular to design novel routes for the development of sensors and new materials, like smart tissues for biophysics applications, but also nanostructures with tailored electronic and optical properties that can be used for enhanced data control and communications or optical filters and intelligent (meta)materials. Most efforts could be avoided if predictive tools in the design were available. We are, thus, interested in a predictive theory of solids. Although no single theory exists that gives all observables for every material or issue, a suitable combination of different approximations and approaches allows us to characterize the electronic properties of solids and related phenomena, such as surface reconstruction, surface reactivity, chemisorption, polarization, etc.

Here, we stick to simulations based on ab initio density functional theory (DFT) [5.1, 2] and we emphasize the essential approximations and point out successes and failures with the aid of selected prototypical examples. DFT is the most popular, robust, and successful theory for the description of the ground-state properties of solids, including surfaces and nanostructures; it provides a solid methodology that can be rather simply implemented, with controlled accuracy, and the codes can be usually sophisticatedly tuned and optimized for the specific hardware parallel architecture, so as to de-

M. Rocca, T.S. Rahman, L. Vattuone (Eds.), *Springer Handbook of Surface Science*, Springer Handbooks,
https://doi.org/10.1007/978-3-030-46906-1_5

scribe complex problems with hundreds of atoms and thousands of electrons. Furthermore, implementations of hybrid functionals [5.3] or Hubbard corrections [5.4–6] allow us to study the effects of a strongly correlated electron gas, which are difficult to describe in the pure, in principle exact, DFT formulation, based on a nearly homogeneous electron-gas treatment of the electron density, without severe trade-offs in computational cost.

In this review, by capitalizing on our experience in this field, we will show the capabilities of first principles approaches in studying complex physical effects (e.g., reconstruction, molecular adsorption, chemical and optical sensitization, wettability, mechanical response, etc.) that take place at the surface and interfaces of semiconductors. To this aim, we present a few selected examples—taken from our own group's results, with no presumption of completeness—with an eye to the final application. Besides the description of the physical aspects of the single presented scientific cases, we will focus on the main advantages and challenges of ab initio techniques in treating such realistic systems and how the simulated results can be compared with experimental data.

The work is organized as follows: In Sect. 5.2 we briefly revise the main computational approach that is generally adopted as the standard frame for these sorts of simulations; Sections 5.3 and 5.4 are devoted to the study of surface functionalization, with particular emphasis on the description of photovoltaic, bio, and gas sensing applications; a route to engineering nanocantilevers via a suitable control of the surface chemistry of the substrate is provided. Section 5.5 is devoted to the study of bulk interfaces between semiconductors, or metals and semiconductors, such as those required to obtain contacts; here we stick to a wide-gap metal oxide, zinc oxide (ZnO), whose popularity is rapidly increasing as its optoelectronic properties can be suitably modified to find applications in a wide frequency range of operation, from IR plasmonics (with metal doping) up to UV devices. Water being ubiquitous, one may wonder how the interaction with liquid or molecular water can alter the surface properties, and how these effects can be theoretically described; we conclude this review by describing in Sect. 5.6 the water/surface interaction in two specific cases: a semiconductor, namely silicon carbide (SiC) and a metal (gold) substrate.

5.2 Theoretical Framework

This paper is devoted to the ab initio study of semiconductor surfaces and interfaces.

In general, solid-state DFT codes take advantage of periodic boundary conditions. The loss of translational symmetry perpendicular to the surface/interface can be accounted for within the supercell approach, i.e., by a periodic repetition of supercells along the surface perpendicular direction. The supercell contains a sufficiently thick slab of substrate layers and a thick vacuum spacer that separates the material slabs in neighboring supercells to electronically decouple them from one another. Indeed, although creating a surface generally involves local changes that vanish within few layers, recovery of bulk behavior in the inner part of the slab is mandatory, both from a numerical point of view, as a test, and also to prevent interaction of surfaces across the slab itself. We describe this situation in Fig. 5.1, where we schematize the oscillating behavior of dipoles in a polar compound, ZnO: at least three bilayers (L1) are required to damp oscillations and recover the bulk dipole value. Similarly, a reconstructed surface, with reduced two-dimensional (2-D) periodicity (Fig. 5.2), or impinging molecules on the surface, impose the minimum value of lateral cell size (L2, Fig. 5.1c). This means that the bulk and vacuum depths are chosen as at least twice a specific decay length, which is characteristic of the property to be analyzed. This length, in turn, defines the number of layers to be included to regain bulk behavior (L1 in Fig. 5.1) and/or the number of unit cell replicas in the surface plane to have noninteracting adsorbates in the surface plane (L2 in Fig. 5.1). In order to improve efficiency and convergence, symmetric slabs are generally preferred [5.7]. This is, however, not a strong requirement, and sometimes asymmetric slabs are considered, with one surface possibly *passivated* by hydrogen atoms.

Depending on the actual code, special k-points [5.9] are eventually used for Brillouin zone summations. If this is not possible, as in the case of ab-initio molecular dynamics (AIMD) [5.10–12], where better performances are obtained by sampling only the Γ point of the supercell, a large enough number of atoms per layer should be considered, in order to sample the surface unit cell; in this latter case, typical calculations are done with few (e.g., four) replicas of the number of atoms/layer necessary to describe the surface reconstruction [5.13–15]. This is, thus, equivalent to considering a set of some (accordingly $\simeq 4$ for the example above) symmetry points sampling.

Although not an explicit requirement, in general the interaction between electrons and ionic cores is evaluated via pseudopotentials [5.16], which allow us to use a reduced number of basis functions than that which would be required to describe the rapidly oscillating atomic-like core wavefunctions. Generally,

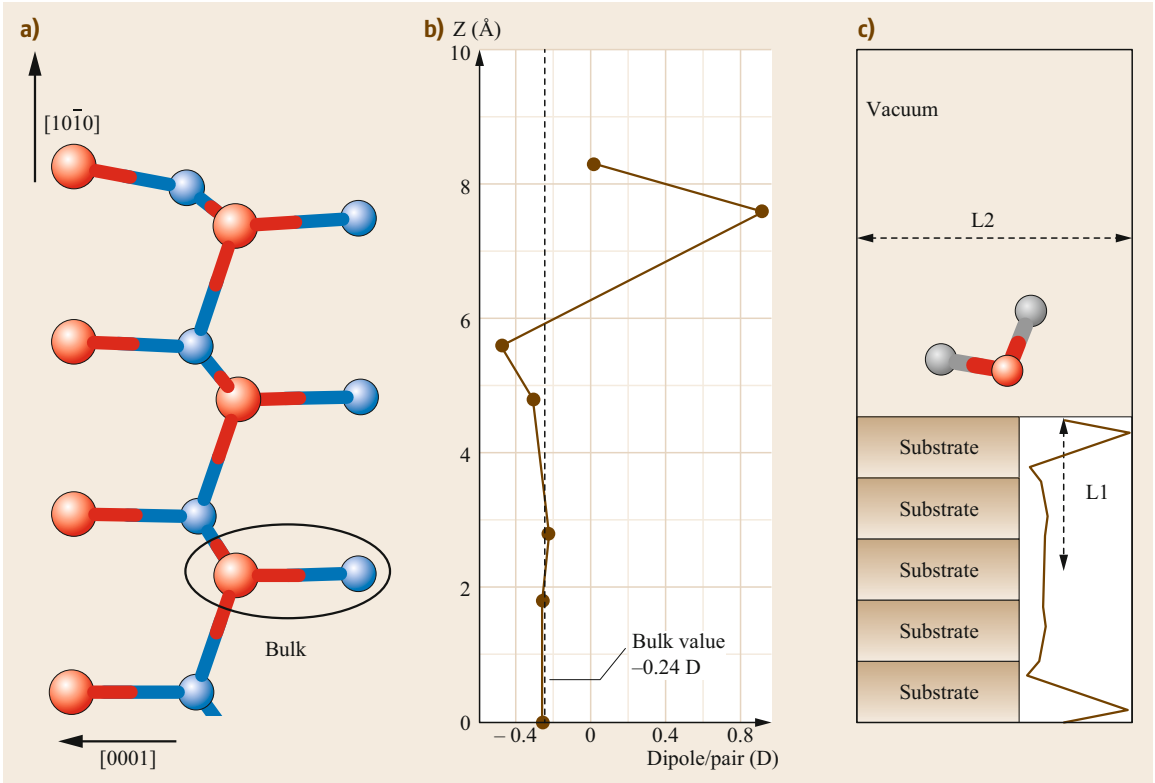

Fig. 5.1a–c Defining the optimal lengths for a supercell. **(a,b)** The size of the slab portion must be large enough to reproduce bulk values: here the local dipole values at the surface and underlayer are remarkably different from the bulk one and several (at least 3–4) bilayers are required to reproduce the bulk value and allow defining the polarization of a ZnO surface [5.8]. **(c)** A sketch of the final supercell, namely the minimal unit that will be used. A different example useful to define lengths in the surface plane is offered instead, e.g., in Fig. 5.2. (Adapted with permission from [5.8]. Copyright (2009) by the American Physical Society)

a plane wave expansion of the electronic wavefunctions and charge density is implemented. Accurate state-of-the-art calculations have also been performed, however, with Gaussian basis sets [5.17]. Alternatively, all-electron description are sometimes used [5.18]; in this case, however, the system size (i.e., number of atoms) that can be numerically treated is much smaller. Whenever possible, we adopt ultrasoft pseudopotentials [5.19], which may contain computational costs, further reducing the cutoff energy of plane waves in the charge density and wavefunction expansion, without a severe compromise in the description of the electronic properties of the system. In most cases, we describe the electronic structure at the PBE-GGA (Perdew–Burke–Ernzerhof generalized gradient approximation) [5.20] level of approximation for the exchange and correlation functional, V_{xc}. This parametrization was proved to be an accurate tool, more suited to describe broken bonds and rehybridization [5.21–23].

Being a ground-state theory, DFT will, in general, fail in describing energy gaps, optical transitions, but also weakly bonded or strongly correlated systems. While band gap underestimation is usually recovered by merely applying a scissor operator for simple systems, different approximations have been developed to cure more complex problems (e.g., hybrid functionals, *GW*, etc.). Various semiempirical schemes have been implemented to include weak van der Waals forces, dispersive interactions relevant in physisorption and closed shell systems [5.26]; here, a few examples of this sort of approximation are discussed to describe the wettability of a gold surface [5.27] and the functionalization of a SiC surface with benzene and porphyrin [5.28]. A different problem where DFT will eventually fail is the description of strongly correlated electron systems, where both delocalized s and p states must be treated along with highly localized atomic-like d/f states, such as in the cases presented here for Zn compounds. Among the different schemes imple-

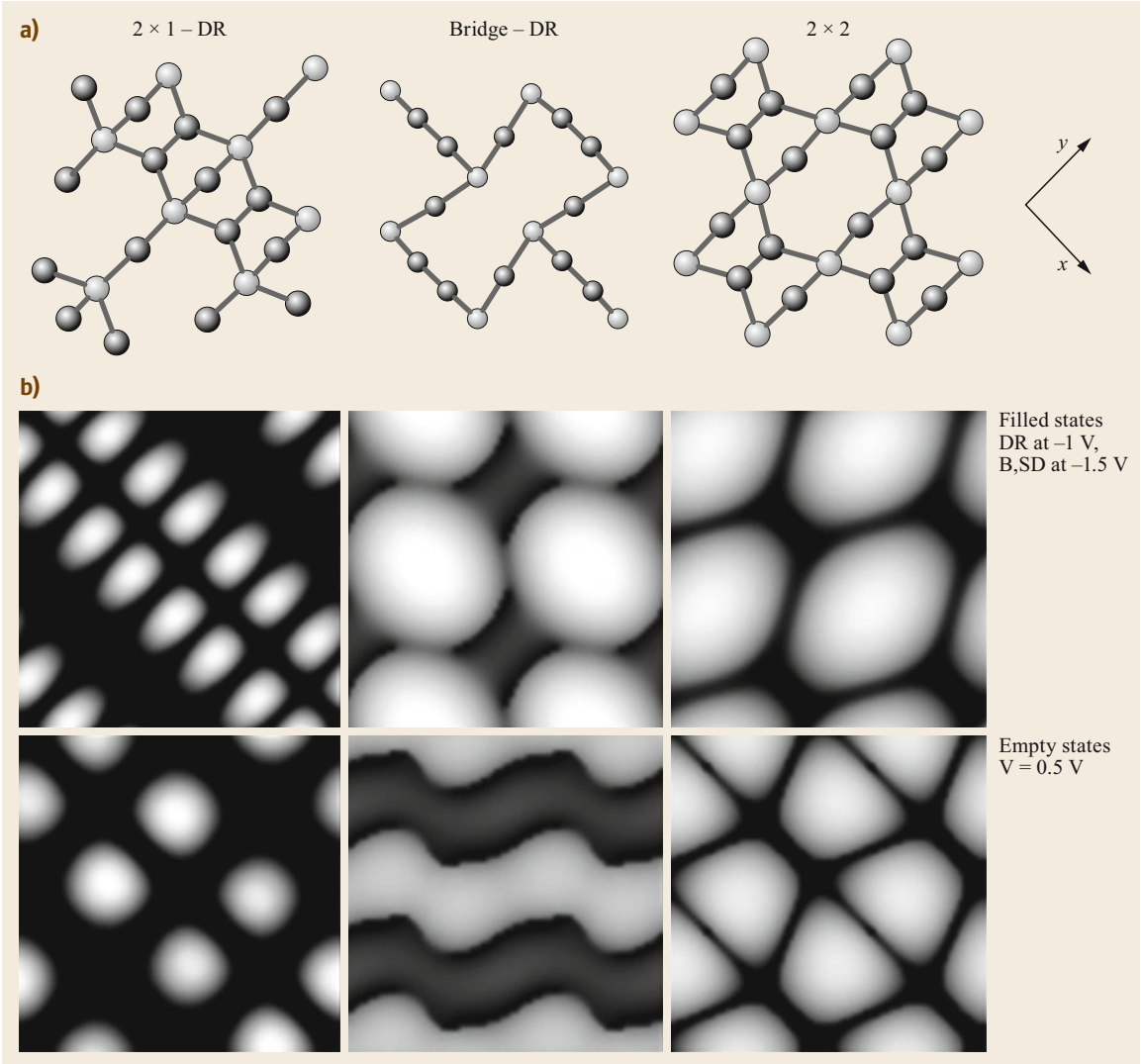

Fig. 5.2a,b An example of different predicted surface reconstructions for the carbon-terminated (001) stoichiometric surface of cubic SiC [5.14]. **(a)** Panels reproduce the atomic geometry of the two outermost layers: *black* (*gray*) *dots* represent C (Si) atoms. The strong atomic rearrangement for each different reconstruction is evident and reveals the reduced two-dimensional periodicity associated with the reconstruction, with respect to the original bulk face centered cubic (fcc) plane. Below each panel, the corresponding predicted STM images [5.24] for filled and empty states are reproduced **(b)**, which allow us to recognize at a glance the original surface reconstruction. Note that different preparation methods can lead to one or the other configuration, as well as different choices of the exchange-correlation functional (V_{xc}) will stabilize a different reconstruction [5.14]. However, extremely clean experimental conditions and refined V_{xc} will lead to the same optimal Bridge geometry, in agreement with [5.25]. Results are in agreement with a number of experimental investigations on both C and Si-terminated surfaces ([5.14] and references therein). (Reprinted with permission from [5.14]. Copyright (1996) by the American Physical Society)

mented, we choose to correct the DFT band structure including a Coulomb repulsion term U as a Hubbard-like correction, as described in [5.5, 29, 30]. This approach is relatively simple to implement and computationally cheap.

Upon relaxation of all the degrees of freedom, namely all ionic and electronics coordinates, up to a desired convergence level (on Hellman–Feynman forces and total energy) a ground-state electronic and geometrical structure is obtained. This rather simple protocol

allows us to obtain the correct crystal structure as the lowest energy configuration, bond lengths, bulk moduli, and so on, are accurate within a few percent with respect to experiments. This leads to information such as:

- Surface reconstruction or relaxation
- Presence of surface states, as induced by broken/wrong bonds at variance with the bulk ones
- Energetics, electronics, and structural properties of different adsorbates in the case of surface functionalization
- Schottky barriers and band offsets in the case of heterojunctions

More refined information that requires higher convergence levels can lead to phonon dispersions, elastic constants for the surface, and polarization decay, to quote only few examples. This frame, as implemented in the Quantum ESPRESSO package [5.31], is the standard along which we obtain our results, as described below.

Some definitions that are generally used when dealing with simulations of surfaces and interfaces will be given in the sections where they are addressed.

5.2.1 Surface Relaxation and Reconstruction

Creating a surface by truncating a bulk is accompanied by formation of highly energetic, charged, and unstable dangling bonds. In order to reduce the free energy, atoms in the outermost layers will be subjected to rearrangements, which are more relevant the higher the number of dangling bonds created per atom, the polarity and directionality of the bond in the compound and the surface direction. Metals and nonpolar surfaces of semiconductors generally present a simple relaxation, that is, a tiny rearrangement of surface layers, with small adjustments in the coordinates perpendicular to the surface plane, with no change in surface periodicity. This is what occurs for the nonpolar surface of SiC and ZnO, which will be subject of the following sections. On the other hand, a cut along polar directions of directional bonds promotes large geometric rearrangements and bond rehybridization possibly accompanied by the presence of surface states in the pristine bulk band gap of the material; this is the case for cubic and hexagonal SiC, as described below. An example of surface reconstruction of cubic SiC to create a (001) surface is presented in Fig. 5.2.

Among several possible choices to illustrate the methodology described above and the role of surface reconstruction, we choose as an example the first principles simulation of cubic silicon carbide (β-SiC) growth [5.15, 32].

Silicon carbide (SiC) is a unique compound semiconductor, with appealing properties for high-power electronics and biological sensors. The material appears in nature in a number of tetrahedral polytypes [5.32–35], thus the potential energy surface which determines the relative stability of these different bulk phases has several almost degenerate local minima; the largest difference of only few meV occurs between the zincblende 3C (*ABC* stacking sequence) and the wurtzite lattice 2H (*AB* stacking sequence), which is characterized by a reduced symmetry compatible with a spontaneous polarization field that lowers the formation energy with respect to the more symmetric zincblende phase [5.35, 36], optimizing the internal atomic coordinates in the unit cell. The two crystal structures are identical up to third neighbors. The polytypes, however, sensibly differ in (opto)electronic properties, e.g., the electron mobility of the 6H polytype is less than half the cubic one [5.33]. Thus, particular attention must be paid to convergence tests, k-point sampling, and the accuracy of the pseudopotential and exchange correlation functional adopted [5.7, 21, 32].

SiC Growth

In order to provide some basic understanding of experimental studies about homoepitaxy of SiC [5.37], we proposed an ab initio simulation of the initial stages of β-SiC(111) growth which highlights the role of surface reconstruction of the underlying SiC substrate [5.38]. The SiC(111) surface presents a hexagonal lattice, with C_{3v} symmetry, and is thus fully compatible with the surfaces of both zincblende and wurtzite lattices, along the polar direction. Furthermore, experimental results [5.39] revealed that a cubic phase is grown by homoepitaxy on the Si-terminated $(\sqrt{3}\times\sqrt{3})$ SiC(0001) polar surface, despite the hexagonal topology of the underlying substrate. If this were to be confirmed by independent theoretical or experimental analysis, it could be argued that a surface-controlled growth procedure may affect the stacking sequence of the grown material, favoring one polytype among all the others when performing homoepitaxy of SiC. This information would be relevant from the technological point of view, since it would open the possibility to determine the stacking of newly attached bilayers, and thus the optoelectronic properties of the compound. From the fundamental point of view it would also assign a leading role to the surface properties, like order, stoichiometry, energetics to control formation, and order of adlayers. With this in mind, our simulation was performed in a rather large simulation supercell, includ-

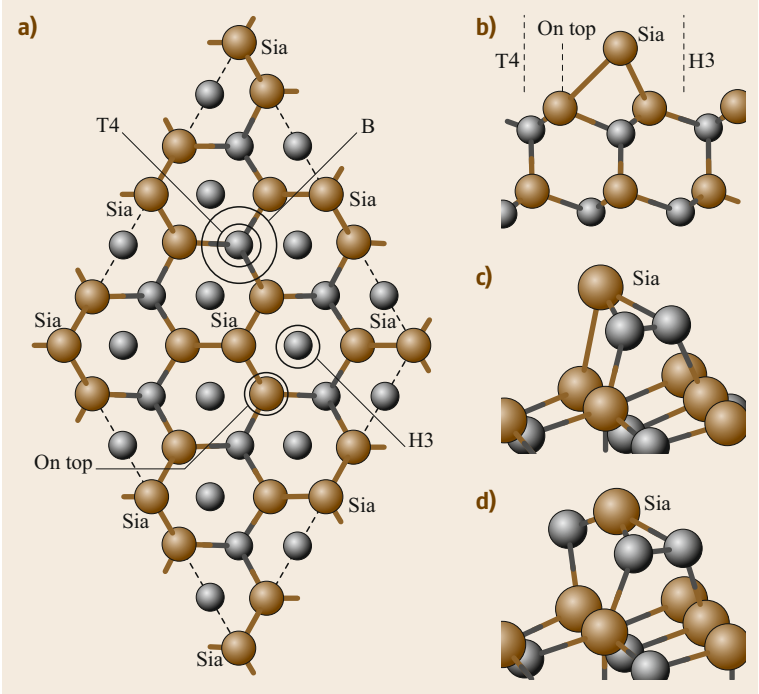

Fig. 5.3a–d The role played by the surface reconstruction. Here we utilize our theoretical prediction to describe the initial stages of a layer-by-layer growth of SiC(111) and predict the diffusion coefficient for C adatoms on the silicon terminated SiC surface. In the theoretical experiment, a C adatom is positioned at the most likely sites upon the Si−SiC(111) surface, and then the whole system is relaxed. The surface reconstruction shapes a multilevel potential energy surface that favors the occupation of the correct sites (on top) for bulk continuation, along with the formation of strong C−Si bonds at the expenses of weaker Si−Si bonds breaking, which restores the local order and layer stoichiometry. (Adapted with permission from [5.15] Copyright (2003) by the American Physical Society)

ing four replicas of the atoms required to describe the surface reconstruction, leading to a $(2\sqrt{3}\times 2\sqrt{3})$ 2-D periodicity; this means 12 atoms per layer, and 4 SiC bilayers (Fig. 5.3). The large in-plane size was chosen with two purposes: (i) At low coverages, it allows for the study of isolated adatoms, avoiding the interaction of an adatom with its periodic replicas; (ii) it provides a reasonable sampling of the $(\sqrt{3}\times\sqrt{3})$ surfaces, when the sole Γ point is included in the Brillouin zone summations. Tests on the cutoff energy of the plane-waves expansion, but also on different choices of V_{xc} were considered [5.32]. First, a fine description of the adsorption sites on the surface was obtained by evaluating the potential energy surface (PES). Then, a nudged elastic band method [5.40] was adopted to compute energy barriers for adatom diffusion, which were then employed in a kinetic Monte Carlo simulation of the growth [5.38]. This allows us to follow the adatom diffusion at realistic growth temperatures and mesoscopic time scales.

Our results showed that the specific stoichiometry of the surface outermost layer and its reconstruction are responsible for the attainment of high-quality films, when suitable growth conditions are selected; the reconstruction geometry is associated with a multivalley PES that models the adatom kinetics and incorporation. The surface reconstruction along with the most favorable adsorption sites for C adatoms, as result from the simulation process, are depicted in Fig. 5.3.

We also identified a further important role played by the surface reconstruction in reducing the adatom mobility on the surface; Si adatoms in the substrate act as nucleation centers for the newly deposited impinging C atoms (Fig. 5.3). This may favor layer-by-layer growth, as observed, e.g., for metallic surfaces. The strong energy gain upon surface stabilization is responsible for the reorganization of disordered atoms into the ordered crystal structure. Our results provide some understanding of processes, such as atomic layer epitaxy, that allow for surface superstructures to be stabilized during growth and for the formation of defect-free layers in SiC homoepitaxy.

Hydrogen at SiC

Another relevant example where a proper description of surface details is mandatory for comparison with the experiment is the study of SiC surface metallization induced by hydrogen adsorption under extremely controlled and clean conditions [5.41, 42]. Recent studies performed both on the theoretical [5.42–45] and the experimental [5.41, 42] side have surprisingly revealed that adsorption of atomic H on one of the possible reconstructions of cubic SiC surfaces (namely the SiC(100)-(3×2)) actually promotes the appearance of surface states (Fig. 5.4), in dramatic contrast with the common experience that surface states are removed (*quenched*) by chemisorbed atoms or molecules. These H-induced dangling bonds result in a nanotunnel open-

ing at the semiconductor subsurface that offer a promising template to capturing atoms or molecules promoting novel nanofunctionalization approaches. Furthermore, depending on H coverage and surface treatment, this can lead to surface metallicity, an important result for the nanofabrication of conducting channels. Such nanotunnels have also been recently predicted for the C-terminated 3C-SiC(001)-c(2×2) surface [5.46].

5.3 Surface/Molecule Interaction

Low-dimensional electronic systems have attracted much interest, because of fundamental problems as well as for technological reasons. Modifying the electronic properties of a material by modifying its surface, either chemically, via adsorption and functionalization reactions, or via geometric patterning, is a possible route to enhance its sensitivity and reactivity to environmental agents. Depending on the specific field of applications, ranging from plasmonics, to photovoltaics, catalysis and (bio)sensors, experimental and theoretical studies of different systems were presented, including self-organized arrays of atomic metal chains [5.47, 48], covalent binding of organic molecules [5.28, 30, 49, 50], and protein docking [5.51–53]. In the following, we discuss some examples devoted to surface functionalization for understanding the role of surface states in charge transfer processes towards photovoltaic (PV) applications in dye-sensitized solar cell (DSSC) design [5.30, 54, 55] and in biosensors [5.28, 56]. Similar concepts, and the same computational frame, help to shed light on other sensing mechanisms, which are described in the subsequent specific sections.

5.3.1 Surface Functionalization

The adsorption of organic molecules on solid substrates is a fundamental step in many important processes and is also becoming an increasingly significant aspect of surface modification in microelectronics and sensing technology. A precise control of the electronic properties of the new system thus obtained could improve versatility and widen applicability in (opto)electronics and sensing [5.57, 58]. Computer simulations based on a quantum-mechanical description of the interactions between adsorbates and the substrate are a fundamental tool to shed light on the intimate nature of the functionalized system; in recent years, these have gained an increasingly important impact on solid-state physics and chemistry and on material science, promoting a deeper understanding, and thus offering a relevant contribution to material design for future technologies.

In particular, a refined description of the electronic properties of the semiconductor substrate in the band gap region, with respect to the distribution of the states of the molecule, provides a rigorous instrument to tailor the optoelectronic properties of the functionalized hybrid system and select suitable ligands.

Catechol at Semiconductor Surfaces

Among the wide-gap semiconductors, oxides are experiencing a renewed interest in different fields because of their stability, high quality, and low production costs [5.30, 59]. ZnO in particular has a wide range of applications, including optoelectronics, plasmonics, nanowire lasers, gas and bio-sensing, catalysis, advanced material for solar cells, and transparent conductors (TC). Indeed, adsorption of molecular dyes can tailor the optical response of the metal oxide, making it photoactive in the visible range and thus useful as photoanodes in dye-sensitized solar cells or contaminant detectors in photocatalytic sensors. The catechol unit (1,2-dihydroxybenzene) has emerged as a very attractive ligand for the functionalization of a wide range of substrates by providing effective, stable, and versatile surface modification, also in wet conditions [5.60]. In particular, catechol is a prototype sensitizer and molecular binder for solar cells. In this sense, catechol on a ZnO surface can be considered as a paradigmatic example.

As both ZnO and catechol exhibit the fundamental transition between edge states in the UV range, in order to understand the sensitization process that enables operation in the visible energy range for the hybrid catechol/ZnO interface, as required for PV cells, the study of the energy level alignment of the functionalized system is mandatory. Indeed, upon adsorption the establishment of molecular levels in the substrate energy gap and the formation of a staggered *type-II* interface are necessary (for a thorough description of band offset and band alignment, see Fig. 5.11). Only this specific band distribution allows for absorption of visible light and separation of electrons and holes across the interface and fast injecting photoelectrons from dye to metal oxide. The formation of a *type-I* interface, could, in principle, be possible, as it happens in the case of similar small molecules (e.g., water, formic acidic) on metal oxide surfaces (e.g., TiO_2, ZnO, MgO) or organic molecules (e.g., benzene, styrene) on Si surfaces. However, only favoring splitting and quick

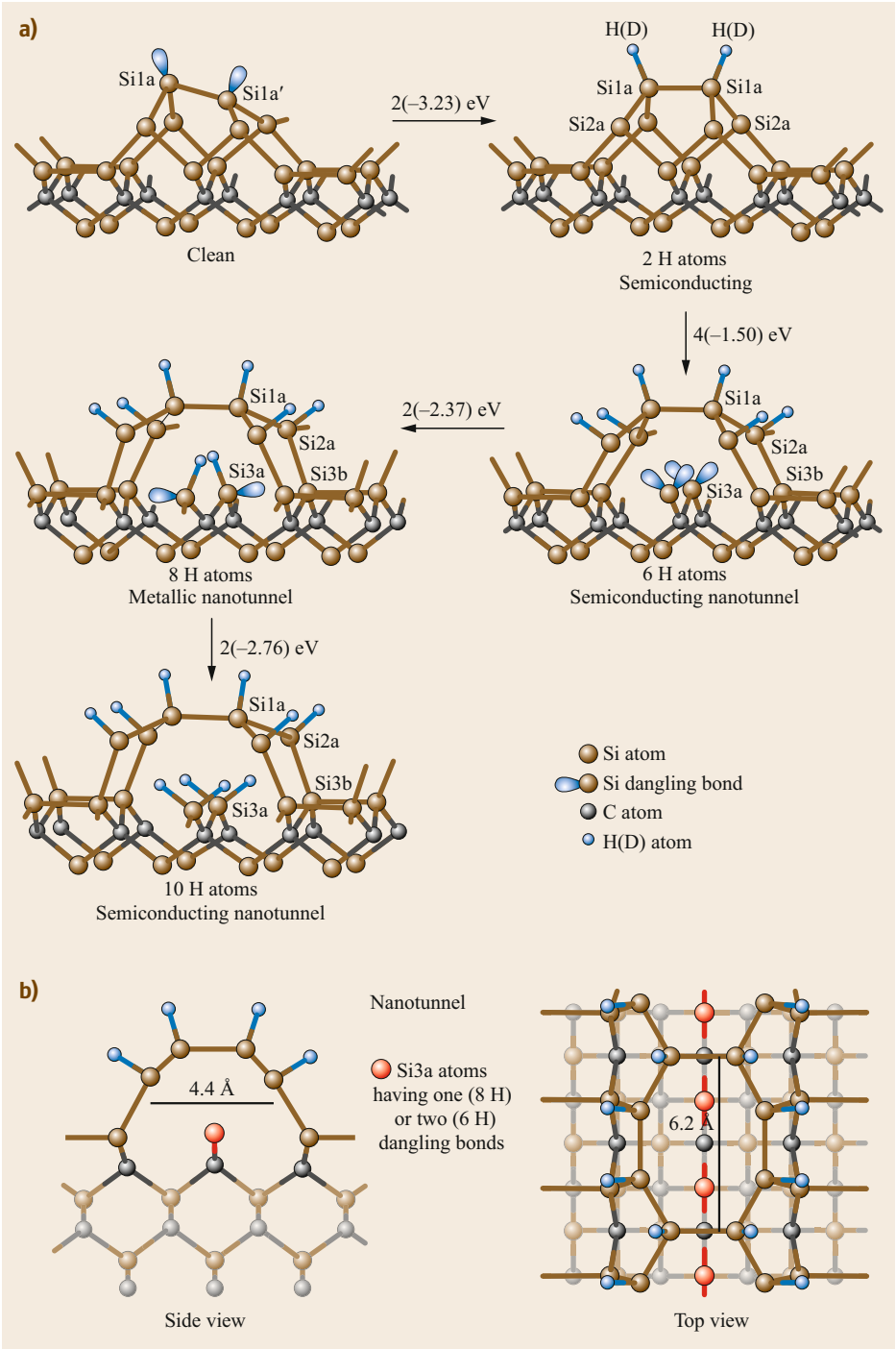

Fig. 5.4a,b Structures of the clean and H/3C-SiC(100)-(3×2) surfaces and views of a nanotunnel. **(a)** The 2H, 6H, 8H, and 10H structures refer to the number of H atoms per surface unit cell. Nanotunnel opening is seen for 6H, 8H and 10H. The energy release per H atom for each step is indicated. Si1a(b), Si2a, and Si3a(b) refer to Si atoms in the first, second, and third plane, respectively. Si dangling bonds are depicted in *blue*. **(b)** The nanotunnel has a size of 6.2 × 4.4 Å (at the level of the second layer). The *red* atoms within the nanotunnel mark Si atoms with one or two dangling bonds corresponding to the 8H (metallic) and 6H (insulating) structures, respectively. (Adapted from [5.42])

charge separation can lead to obtaining charge flow and open-circuit conditions, as required for PV cells.

We have thus studied catechol adsorption on the nonpolar $(10\bar{1}0)$ ZnO surface via ab initio DFT simulations. As it happens for most compound semiconductors [5.59], the acknowledged description of the clean ZnO surface presents ordered rows of buckled dimers lying along the polar (0001) direction, with a net electron accumulation on the exposed oxygen atoms, and no reconstruction but a mere relaxation of the outermost

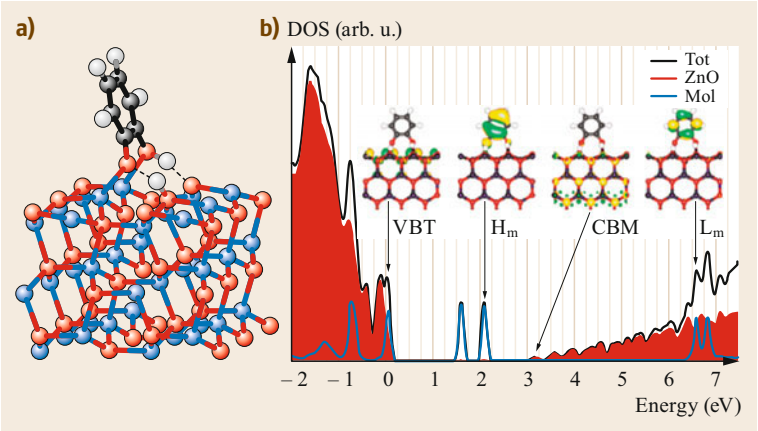

Fig. 5.5a,b Catechol at ZnO. **(a)** Side view of the relaxed atomic structure of catechol adsorbed on ZnO($10\bar{1}0$). **(b)** Portion around the pristine ZnO bandgap of the total DOS (*black line*) and projected contributions on ZnO substrate (*shaded area*) and catechol (*blue line*) for the molecule/surface interface. *Inner panels* show representative single-particle states, at the DFT+U level. The zero of the energy scale is aligned to the top of the valence band (VBT) of the clean ZnO surface. Here, CBM stands for the substrate conduction band minimum, and H_m (L_m) for the catechol highest occupied (lowest unoccupied) molecular orbital. (Reprinted with permission from [5.30]. Copyright 2011 American Chemical Society)

layers [5.30, 61, 62]. On the electronic side, surface relaxation introduces a surface state per dimer at the top of the valence band (VB) in the 2-D band structure, which reduces the gap to 2.9 eV. The bottom of the conduction band (CB) instead maintains its sp bulk-like behavior. It is here relevant to note that to obtain this correct description, in particular of the system band structure around the bandgap, the introduction of specific corrections to V_{xc} are mandatory to cure the fictitiously large hybridization between Zn-3d and O-2p states, induced by the incorrect treatment of correlated d states within DFT. We here chose to use ad hoc Hubbard correction both on d orbitals of Zn ($U = 12.0$ eV) and 2p orbitals of O ($U = 6.5$ eV) [5.63]. This strategy recovers correct bandgap and energy position of d levels (Sect. 5.2).

Our results show that catechol adsorbs on the nonpolar ($10\bar{1}0$)ZnO surface, forming two chemical bonds with the substrate through the hydroxyl terminations of the molecule; namely we observe partial dissociation of these terminations with formation of two Zn−O bonds and two H bonds to the substrate (an H-donating and an accepting one, see Fig. 5.5a). Bond formation induces molecular states in the ZnO bandgap that efficiently reduce the optical gap and allow for an ultrafast dye-to-substrate electron injection (Fig. 5.5). We demonstrate that the origin of this staggered band alignment is due to the specific lone pair interaction between the oxygen atoms along with the aromatic nature of the phenyl ring. Furthermore, taking catechol as the reference structure, we studied how it is possible to modify the interface properties varying the band alignment by inserting different end groups or aromatic rings in the adsorbing molecule [5.30].

This study led us to compare different semiconductor substrates, namely SiC, GaN, InN, CdS, and CdSe [5.59]. We selected wurtzite substrates presenting different ionicities, reactivities, and band properties and concentrated on flat periodic nonpolar ($10\bar{1}0$) surfaces, which are among the most frequently exposed faces in hexagonal nanostructures [5.64]. We demonstrated how the geometrical and electrostatic modifications in the substrate surfaces affect the catechol adsorption and the bonding path; surface effects, such as bond distortion, surface stress and surface states in the bandgap, must be fully taken into account, especially for the most reactive substrates. In particular, for the case of SiC, and only in this case in view of the peculiar indirect gap and bond lengths, we observe a full deprotonation of the impinging catechol, which dissociates when approaching the SiC surface to form tight Si−O bonds with the substrate, while the dissociated H atoms bind to the C atoms of the broken SiC surface dimer, revealing charge transfer and structural reorganization at the interface.

Biosensors: Porphyrin at SiC

A different application that we have considered in view of possible routes for the design of biosensors is the functionalization of SiC surfaces via deposition of aromatic fragments, up to a full porphyrin molecule [5.28].

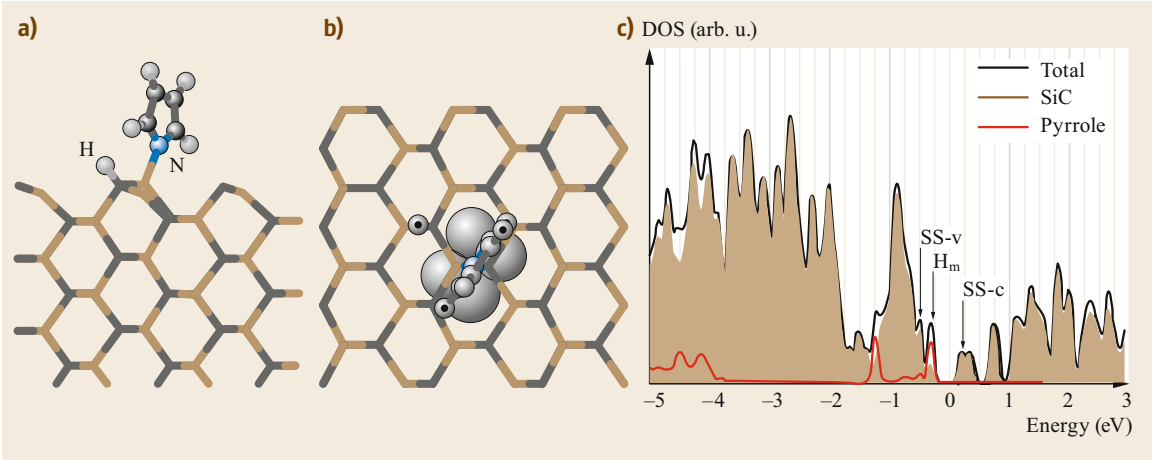

Fig. 5.6a–c Pyrrole on SiC(110) clean surface. **(a)** Side view of functionalized surface. **(b)** Simulated STM image of filled states ($V_{tip} = 0.5\,eV$); here the structural pattern is superimposed to help reading. **(c)** Total and projected density of state. Zero energy is referred to the Fermi level. SS-v and SS-c are, respectively, occupied and empty surface states in the energy gap. (Reprinted with permission from [5.28]. Copyright 2011 American Chemical Society)

The functionalization of SiC surfaces by means of specific organic molecules is strategic for the realization of biosensors based on molecular recognition. However, although they are extensively used, operating devices that adopt macrocycles as functional groups are not easily achievable, mainly because of a poor control on chemical/physical processes occurring at the interface between molecule and substrate. The porphyrin macrocycle itself, beyond offering the interesting characteristic coordination properties of the carbon rings, does not allow for the formation of strong chemical bonds but rather leads to π–π interaction.

Also in this case we studied a nonpolar surface, namely SiC(110) of the cubic polytype. Again, as described before (Sect. 5.2) this can also be representative of hexagonal nonpolar surfaces, since the two crystal structures are equivalent up to third neighbors. Moreover, β-SiC is expected to present better electronic properties than the most common and stable hexagonal phases [5.33]; it is expected to present better biocompatibility [5.56] and it is fully compatible with Si technology. As discussed above, the surface simply relaxes, with Si moving inward, which gives rise to modest ($\simeq 9^\circ$) buckling; correspondingly, the electronic distribution presents one dangling bond per Si and C atoms, respectively [5.7, 17]. The surface can be easily hydroxylated via dissociative adsorption of water molecules, with H atoms bonding to C and −OH groups to Si atoms [5.65].

We demonstrated that among the various fragments considered, only pyrrole can form covalent bonds to the clean β-SiC substrate, with strong modifications of its electronic properties around the Fermi level. This is illustrated in Fig. 5.6, where we report the structural details of the functionalized surface (Fig. 5.6a), along with the corresponding density of states in the bandgap region that presents several charge transfer states induced by molecular dissociation and bonding to the surface (Fig. 5.6c). A simulated STM image for the filled state is also reproduced [5.13, 24].

Benzene, fluorinated-benzene and the full porphyrin do not chemically bind to SiC, even including London corrections [5.26] in the exchange correlation potential to account for van der Waals interactions. Furthermore, a comparative study of absorption on the hydroxylated SiC surface reveals minor modifications to the present picture, in view of the increased inertness of the surface that impedes bond formation. Similarly, first principles molecular dynamics at finite temperature reveals that the impinging molecules float over the surface, without drastic inter-unit bending distortions that would allow to expose reactive units to the substrate and favor bonding. Our results thus rule out the possibility of forming stable hybrids obtained via porphyrin adsorption on the clean SiC(110), as observed for other wide-gap materials such as TiO_2 [5.66]. Modification of the surface may, however, take advantage of grafting through pyrrole groups, as linker for further functionalization.

5.4 DFT for Sensing

A deep understanding of the sensing mechanism is often required to improve the sensor efficiency in terms of sensitivity and selectivity and to further engineer the sensing element for tailored applications. Surfaces of materials are often involved in the sensing mechanism, although the actual role played by the surfaces is not always known in detail. DFT studies have been employed to unravel the role of surfaces in determining the sensing mechanism of different types of sensors. In the following, we will comment on two theoretical key studies based on DFT calculations that were recently reported in the literature. The first study is related to understanding the effect of surface functionalization on the mechanical properties of vibrating cantilevers, often employed as mechanical sensors. The second study regards the study of the mechanism leading to gas sensing in ZnO nanostructures and, in particular, focuses on understanding the origin of the changes in the electrical properties of the nanostructures upon interaction with gases.

5.4.1 Mechanical Properties of Functionalized Silicon Surfaces

Introduction to Cantilever-Based Detection Mechanism

The ability to realize micro and nanoelectronics with controlled dimensions and tailored surface chemistry has opened up the opportunity to create hybrid devices exploiting the properties and features of both organic and inorganic materials. One of the most promising approaches consists of combining organic materials with more conventional semiconductors, like silicon, with the aim of engineering semiconductor surfaces to induce specific properties useful for a given sensing application. In particular, in the last decades, microcantilever-based sensors have gained large attention since they can be employed to detect specific molecules with a very high sensitivity. When the surface of a beam comes into contact with an analyte, it responds with a mechanical transduction signal directly related to the concentration of the molecule in the environment. The mechanism on which these kinds of sensors are based is the following: upon interaction of the analyte with the surface of the cantilever that has been chemically modified, the surface stress varies and, as a consequence, the cantilever bends; correspondingly, the resonance frequency of the beam changes. The amount of bending (static detection mode) and the change in resonance frequency (dynamical detection mode) following molecule/surface interaction can be measured with high accuracy and can be related to the amount of the adsorbed species (Fig. 5.7).

Although many cantilever sensors exploit adsorption induced bending, the transduction detection based on resonance frequency shifts can potentially provide ultimate sensitivity for unravelling the presence of a single molecule on the cantilever surface [5.67]. The resonance frequency of a beam depends on the effective spring constant, K, and on the effective mass, m^*, of the cantilever as follows: $f = 1/(2\pi)\sqrt{K/m^*}$. Upon attachment of an analyte to the cantilever surface the observed frequency shift, Δf, depends both on change of the adsorbed mass (variation of m^*) and on variations of the surface elastic constants (variation of K). As such, performing an accurate quantitative analysis of the analyte concentration would require knowledge of the amount of the shift which can be ascribed to the change in m^* and which to the change in K. Unfortunately, this estimate is not easily achieved and, during experimental analysis, the frequency shift is usually fully ascribed to absorbed mass leading to an overestimation of the detected amount of analyte. Ab initio atomistic simulations provide a powerful predictive tool to access these quantities as detailed in the following.

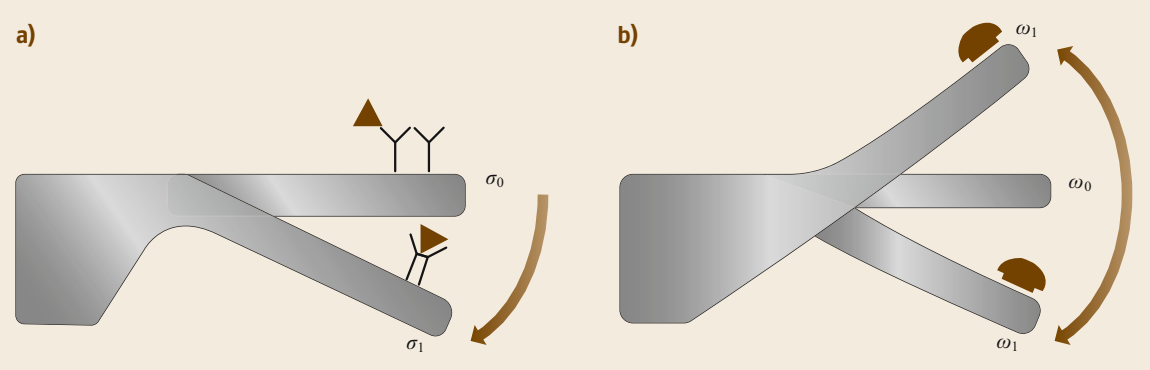

Fig. 5.7a,b Cantilever sensor operation in the static deflection mode **(a)** and in the dynamic resonant frequency mode **(b)**

Calculations of Surface Strain and Surface Elastic Constants

Both surface stress and surface elastic constants can be calculated with high accuracy by employing first principles simulations. For a given material surface, simulated with a finite slab of atomic layers, surface stresses, σ_i^{surf}, can be estimated by computing the stress tensor of the simulation supercell, σ_i^{bulk}. This is done, within ab initio calculations by applying the Nielson–Martin stress theorem [5.68], according to which the stress can be expressed as a functional of the ground-state density. In particular, the above-mentioned two quantities are linked through the equation

$$\sigma_i^{\text{surf}} = \frac{1}{2}\sigma_i^{\text{bulk}} c \,, \tag{5.1}$$

where c is the length of the supercell along the surface normal, and the coefficient $1/2$ takes into account the presence of two equivalent surfaces in a slab calculation. As pointed out in [5.69], the stress values estimated at a given plane waves' energy cutoff have to be corrected because of a fictitious stress contribution arising from the use of a finite basis set.

The surface elastic constants of a given material can, instead, be calculated by exploiting the relationship between the second-order derivative of the energy of the system (E^{Tot}) and the strain, ϵ_i, imposed on the slab

$$\left.\frac{\partial^2 E^{\text{Tot}}}{\partial\epsilon_i \partial\epsilon_j}\right|_{\epsilon=0} = V_0 D_{ij} \,. \tag{5.2}$$

In this equation, D_{ij} represents the plate (slab) elastic response when an axial strain is applied along one of the surface primitive cell directions, while V_0 is the slab equilibrium volume. The elastic response is usually divided in two contributions [5.70]: one arises from the inner atomic layers and is related to the *bulk-like* response of the system, and the other is associated to the two identical surfaces corresponding to the outer atomic layers. Within this approach, (5.2) can be rewritten as

$$V_0 D_{ij} = 2A_0 S_{ij} + V_0 C'_{ij} \,, \tag{5.3}$$

where the above-mentioned contributions are explicitly represented by the surface elastic constants, S_{ij}, and the bulk elastic constants C'_{ij}; A_0 is the equilibrium surface area. The bulk term also takes into account that, once strained along a surface direction, a material plate is free to contract in the direction perpendicular to the surface. We recall that, if S_{ii} (with $i = j$) yields positive values, the surface layer is mechanically stiffer than the inner bulk layers, while negative values would indicate that surface bond breaking gives rise to local bond weakening and, correspondingly, to softer surfaces. On the other hand, negative S_{ij} (with $i \neq j$) values correspond to a softening of the surface and imply that the surface stress in the i direction has an opposite behavior with respect to the j surface stress component, similarly to a negative Poisson's ratio in the case of a bulk system; positive S_{ij} can be thought as the equivalent of a positive Poisson's ratio in a bulk material.

Mechanical Properties of Propyl–Urea Functionalized Silicon Surfaces

The method described above has been employed to predict the mechanical properties on Si(111) surface functionalized with propyl-urea molecules [5.71]. Such molecules have been chosen because they are able to form intermolecular hydrogen bonds and thus give rise to stiffer and more stable self-assembled monolayers (SAM). This feature would not only render a device more durable in time but would also increase the performance of a sensor. Indeed, in micro and nanomechanical resonators with surfaces functionalizated able to respond to specific chemical stimuli, larger values of the surface elastic constant imply larger resonance frequencies and, thus, larger sensitivity [5.72]. Moreover, the study of a propyl-urea SAM was proposed as a test case to tailor surface properties by changing the lateral intermolecular interactions.

The structure of the propyl-urea SAM on the Si(111) was predicted by employing DFT calculations by taking into account the ability of propyl-urea to form periodic H-bonded chains and considering the periodicity of the silicon(111) surface [5.73]. Several SAM configurations were initially built trying to maximize the intermolecular H-bond interaction by at the same time keeping the periodicity constraints imposed by the surface binding sites. It was found that propyl-urea can form stable SAM at the Si surface at a maximum coverage of half of a monolayer. Larger coverage would give rise to endothermic hydrosilation reaction. Indeed, at high coverages, the molecules in the SAM would be too densely packed and would repel each other, yielding positive formation and cohesive (about 1 eV) energies. The most favorable Si(111)/propyl-urea structure is represented in Fig. 5.8. In this configuration, H-bonded molecular chains form at the surface, as indicated by the dashed lines. The H bonds are optimized along the molecular chains and, consequently, the molecules are folded with respect to the axis perpendicular to the surface. In particular, each propyl-urea molecule forms two kinds of H bonds (2.06 and 2.22 Å long) responsible for a quite large SAM cohesive energy of $-0.44\,\text{eV/molecule}$.

The surface stress of the functionalized surface has one tensile component, $\sigma_1 = 0.89\,\text{J/m}^2$, along the

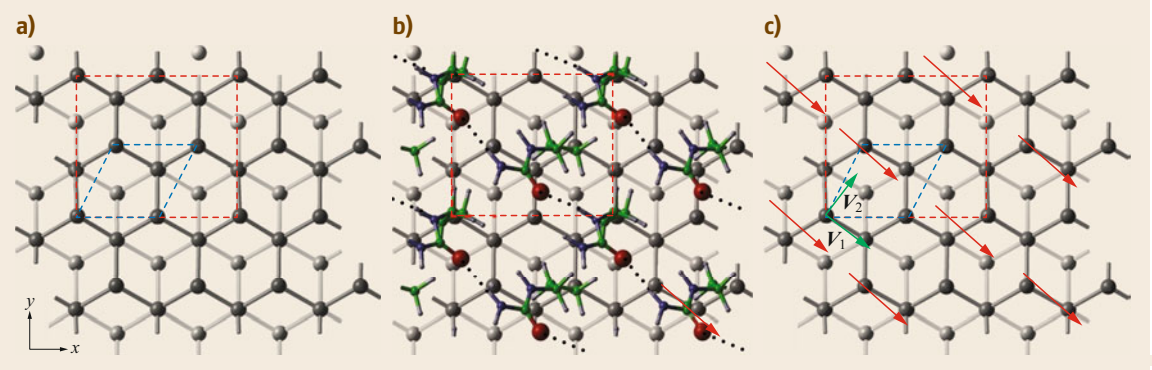

Fig. 5.8a–c Ball and stick representation (*top view*) of the clean **(a)** and propyl-urea functionalized **(b,c)** Si(111) surfaces. The *darker gray balls* correspond to Si atoms of the outermost layer, the *lighter gray* to Si atoms of the inner layers. *Red balls* represent O atoms, *green ones* C atoms, *blue ones* N atoms, and *smaller gray ones* H atoms. The *dashed lines* correspond to the surface supercells; the *blue* (*red*) *line* indicates the primitive cell of the clean (functionalized) Si(111). The *black dotted lines* in **(b)** show the hydrogen bonds between the molecules of the SAM. The dipole molecule orientation is represented by *red arrows* **(b,c)** while the *green arrows* **(c)** represent the direction of the principal axis of the surface stress. Reprinted from [5.71] with permission from Elsevier

molecular chain direction, and one compressive, $\sigma_2 = -0.04\,\mathrm{J/m^2}$ in the perpendicular direction, as indicated by the green arrows in Fig. 5.8. The tensile stress component is due to the H-bond interaction between propyl-urea molecules that would pull the molecules and shorten the intermolecular distance, whereas the weak compressive stress can be associated with the repulsion between dipoles of parallel molecular chains. The surface elastic constants of the functionalized surface were found to be larger than those of the clean and hydrogenated Si(111) surfaces, indicating an increase of surface stiffness due to H-bond network formation (Tab. 5.1). Although propyl-urea attachment renders the surface structurally anisotropic, the two surface elastic constants, S_{11} and S_{22}, are similar. This is due to the fact that the H bonds are oriented along the diagonal of the surface cell, as a consequence $S_{12} \simeq S_{21}$. H-bond network optimization is also responsible for the change in sign of the S_{12} elastic constant.

The values of surface elastic constants estimated via ab initio simulations have been used as input parameters to a finite element (FE) model that allows us to assign mechanical constitutive relations to the surfaces of a three-dimensional (3-D) object [5.74] representing a microcantilever. The latter has been modeled as a rectangular-shaped silicon beam with typical micrometric dimensions $l = 100\,\mu\mathrm{m}$ (length), $w = 20\,\mu\mathrm{m}$ (width), and $t = 0.9\,\mu\mathrm{m}$ (depth) [5.75]. It was found that the frequency shift due to the functionalization with a propyl-urea SAM is mainly due to the inertial effect rather than to changes of surface elastic constants. On the other hand, if all the shift is erroneously ascribed to the inertial contribution, the mass of the SAM is overestimated by more than two times.

In conclusion, for the model systems of Si(111)/propyl-urea it was proved that both the change in surface elastic constants and the amount of loaded mass at the cantilever surfaces are important contributions to the resonance frequency shift. In particular, ignoring the change in surface elastic constants would lead to a large overestimation of the attached mass, invalidating the analysis of the adsorbed mass.

Table 5.1 Surface stress and surface elastic constants for the clean Si(111), hydrogenated Si(111)-H and functionalized silicon surfaces. σ_i^{surf} corresponds to the surface stress along the principal axis of the stress tensor and $\bar{\sigma}^{\mathrm{surf}}$ is the trace of the same tensor. In the clean and hydrogenated Si(111), the principal axis coincides with the Cartesian directions of the supercell surface ($i = x, y$, see the red dashed line of Fig. 5.8), whereas in the functionalized surface, the principal axes are indicated by the vectors v_1 and v_2 reported as green arrows in Fig. 5.8c

Surface	σ_1^{surf} (J/m^2)	σ_2^{surf} (J/m^2)	$\bar{\sigma}^{\mathrm{surf}}$ (J/m^2)	S_{11} (eV/Å^2)	S_{22} (eV/Å^2)	S_{12} (eV/Å^2)
Clean-Si(111)	−0.41	−0.41	−0.41	0.151	0.151	−0.138
H-Si(111)	−0.10	−0.10	−0.10	0.258	0.258	−0.104
SAM-Si(111)	0.89	−0.04	0.42	0.305	0.306	2.441

5.4.2 Understanding the Gas Sensing Mechanism of Oxide Nanostructures

ZnO Nanowire–Based Chemoresistors

Due to their large surface to volume ratio, metal oxide nanostructures have showed great potential in chemical sensing applications [5.76]. The mechanism leading to detection of specific chemical species was discussed in recent publications [5.77, 78]. Among the type of sensors employing nanowires proposed in literature, chemoresistors are the most easily realized. These are based on the measurement of changes in conductance of the sensing element (i.e., single or collection of NWs) upon interaction with target molecules. Typically, resistance versus time plots of the sensor are recorded, and increases or drops in resistance values are directly related to the concentration of target molecules. The response of a chemoresistor can be defined as follows

$$\text{Response} = \frac{R_a - R_b}{R_a} \times 100\,, \tag{5.4}$$

where R_a and R_b are the electric resistance of the sensor measured in air and in the presence of the target molecule, respectively. Ideal gas sensors should show a high response and should be characterized by complete recovery of the electric conductance when back in air. For example, a response of 1850% was obtained for 0.5 ppm of NO_2 concentration at 200 °C in [5.78]. Typically, gas species are divided in two classes: reducing and oxidizing species. When a reducing gas (such as ethanol) is introduced to a chemical sensor, the interaction of the molecules with the nanowire surface results in an overall increase of the electrical conductance of metal oxide nanowires; on the other hand, if a chemical sensor is exposed to an oxidant gas (such as NO_2), the gas molecules serve as charge acceptor, withdrawing electrons from the nanowire and inducing a reduction of the electrical conductance.

Among the nanostructured oxides that have recently been proposed for the realization of chemoresistors with excellent properties, ZnO nanowires have attracted a lot of attention in the literature because they can be used for detection of a wide class of chemicals. ZnO gas sensing capabilities have been exploited both for reducing and oxidizing species, thanks also to the superior properties of this material, such as enhanced sensitivity, stability, and low cost [5.79]. DFT calculations have been recently employed to understand the mechanism leading to sensing phase in ZnO for two gas species, ethanol and NO_2 [5.77, 78], which are prototype molecules for reducing and oxidant gases, respectively. In particular, the studies presented in the literature highlight the role played by oxygen molecules pre-adsorbed over the ZnO surfaces. We now present the results on the modification of a ZnO surface when gas molecules are adsorbed on it and discuss how sensing is achieved.

Ethanol and the NO_2 Gas Sensing Mechanism

Chemical sensors based on oxide structure usually work in ambient atmosphere and, as such, it is expected that the ZnO surfaces will already be covered with gas species before being exposed to an analyte. In particular, one of the most reactive and abundant gases known to be adsorbed on the surface of metal oxides [5.80, 81] is molecular oxygen. For this reason, when analyzing gas sensing mechanisms, before studying the interaction of ZnO with the gas that is to be sensed, it is mandatory to understand whether oxygen has effects on the electronic features of the pristine ZnO nanostructures. Experimental evidence shows that ZnO presents intrinsic n-type conductivity, both in the form of bulk and nanostructures. Although the origin of this behavior has been the subject of debate in the literature, it was recently ruled out that neutral oxygen vacancies are responsible for the unintentional n-type character of the compound, which is rather ascribed to hydrogen interstitial impurities [5.82–84] and/or to Zn vacancies [5.85]. While the clean surface is semiconducting (Sect. 5.3), the presence of hydrogen impurities shifts the Fermi level (E_F) in the conduction band of ZnO, in an otherwise barely modified DOS. Hence, the ZnO surface becomes conductive (Fig. 5.9).

DFT calculations have shown that O_2 absorbs at the clean ZnO surface in two stable configurations which are characterized by an elongation of the O=O bond that appears to be weakened by the interaction with the surface. The most stable adsorption geometry corresponds to a bridging configuration in which both the oxygen atoms of O_2 bind to two neighboring Zn atoms on the surface (Zn_{surf}–O distance of 2.13 Å) and, correspondingly, the oxygen molecule bond length increases by about 5% (Fig. 5.10a); the adsorption energy (E_b) is −0.35 eV per molecule.

Oxygen adsorption at the H-doped ZnO $(10\bar{1}0)$ face induces a shift of the Fermi level from the CB into the pristine energy gap of the oxide. In particular, O_2 generates both occupied and empty states in the gap, which are responsible for a shift of the E_F position that is brought to coincide with one of these states (Fig. 5.9b). The state at the Fermi level derives from the lowest unoccupied state of the oxygen molecule, which becomes filled upon oxygen/surface interaction, due to an electron transfer from the H-ZnO conduction band to the adsorbed O_2. This electron trapping pins the Fermi level of the system within the ZnO energy gap. These results show that when n-type ZnO is exposed to ambient atmosphere, the concentrations of free carri-

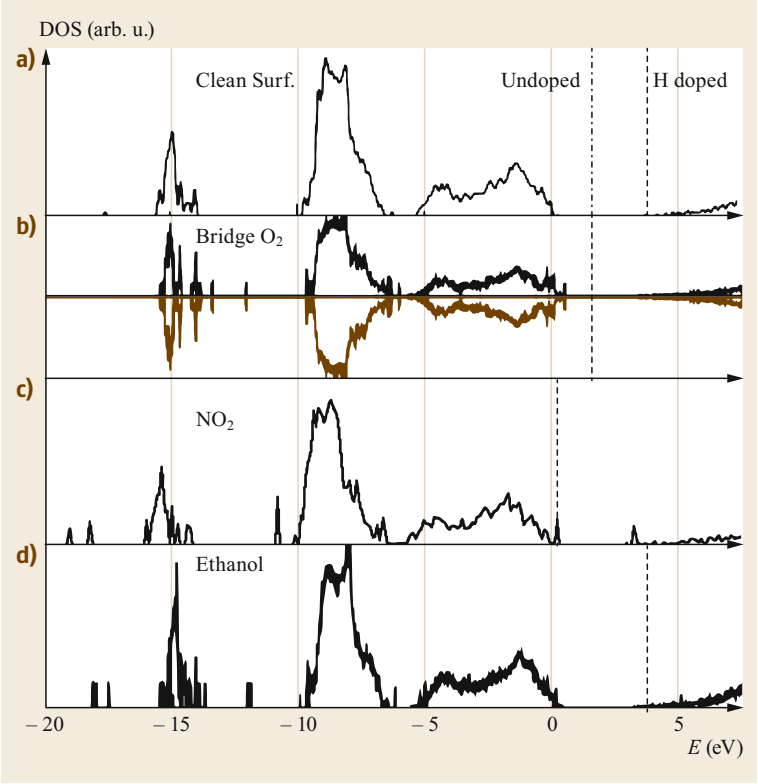

Fig. 5.9a–c Density of state (DOS) for the ZnO($10\bar{1}0$) surface **(a)**, oxygen molecule **(b)**, NO_2 molecule **(c)**, and ethanol molecule **(d)** adsorbed on the H-doped ZnO($10\bar{1}0$) surfaces. In **(a)** the Fermi level is indicated by the *dotted* (*dotted-dashed line*) for the H-doped (undoped) system. In **(b)** the spin-up and spin-down DOS are represented by the *black* and *brown curves*, respectively. The presence of hydrogen was accounted for by introducing an isolated hydrogen atom in the vacuum buffer of the supercell. The H-interstitial impurity was located in a deep inner (the fifth) layer away from the outermost surface plane with concentration of about 0.70 at.%. in the simulation supercell representing the ZnO surface. This way, we could avoid possible structural deformations induced by the impurity on the ZnO surface structure. When located in an interstitial ZnO site, H forms a strong O–H bond 0.98 Å long with one of the closest oxygen atoms of the crystal, consequently a local distortion of the lattice network occurs characterized by an out of plane shift ($\simeq 1$ Å) of the Zn atom initially bonded to the H-bonded oxygen. The presence of hydrogen below the surface does not alter the structural properties of the outer layer (the one exposed to air during gas sensing experiments), but it strongly modifies the electronic properties of the surface. Figure adapted with permission from [5.77, 78]. Copyright 2014 and 2016 American Chemical Society

ers in the conduction band of the oxide decreases and, consequently, the conductivity of the nanowire sample decreases, due to oxygen adsorption at surfaces.

The above condition is the one presented by the ZnO sensing elements before being exposed to gas species. We now analyze the changes induced at the surface when NWs are exposed to ethanol and NO_2, the first representing a reducing species and the second an oxidant one. In particular, DFT calculations have been used to predict the adsorption geometries and energies of these gases and to understand the modification in the electronic properties of oxygen covered H-ZnO when sensing is achieved [5.77, 78].

Results of the interaction of ethanol with the ZnO($10\bar{1}0$) surface show that adsorption of this species occurs in a geometry in which the hydroxyl group (–OH) binds to the two surface atoms in a bridge configuration (Fig. 5.10b). In particular, ethanol forms a Zn_{surf}–O bond 2.05 Å long and an O_{surf}–H bond 1.56 Å long, with an energy gain of –0.96 eV, which is much larger than that occurring for O_2. As for the electronic properties of the ZnO/ethanol adsorbed system, an analysis of the DOS highlights features that are very similar to those of the clean n-doped surface. In particular, at variance with the case of oxygen adsorption, the position of E_F is very close to that of the pristine

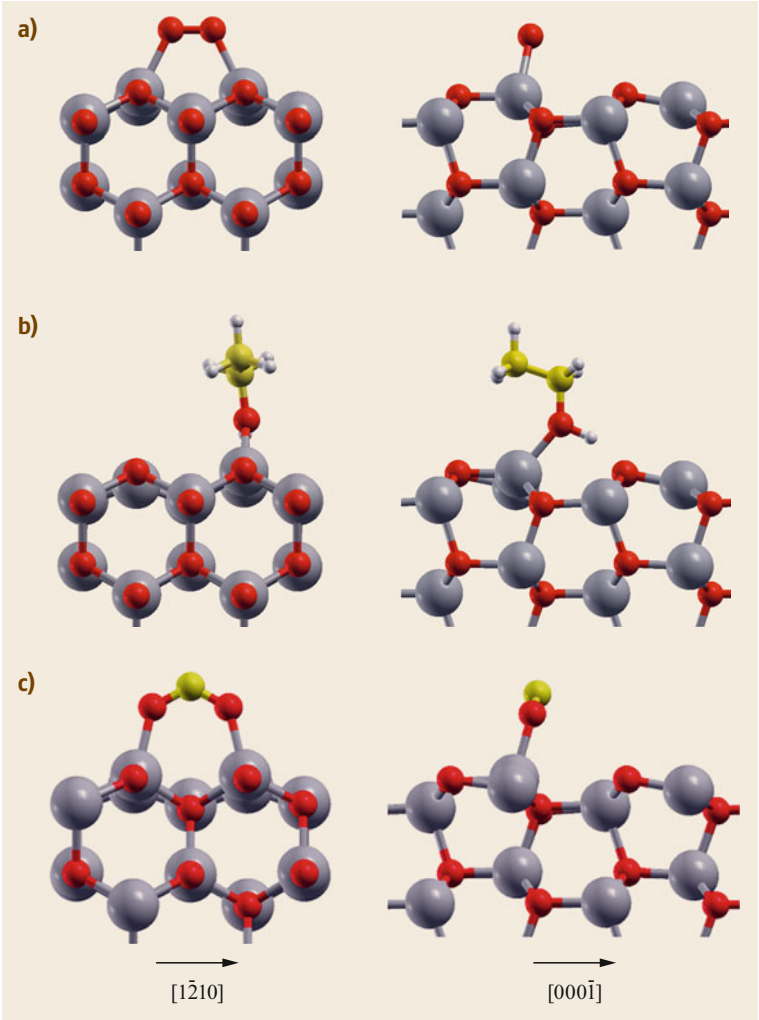

Fig. 5.10a–c Side view of the optimized O_2/ZnO(10$\bar{1}$0) interface **(a)** ethanol/ZnO(10$\bar{1}$0) interface **(b)** and NO_2/ZnO(10$\bar{1}$0) interface **(c)** represented along the [1$\bar{2}$10] (*left structures*) and [000$\bar{1}$] (*right structures*) directions. Only two bilayers of the ZnO slab are represented beside the adsorbate molecules. *Gray*, *red*, and *white spheres* represent zinc, oxygen, and hydrogen atoms, respectively. *Yellow spheres* represent carbon and nitrogen atoms in **(b,c)**. Figure adapted with permission from [5.77, 78]. Copyright 2014 and 2016 American Chemical Society

n-type clean surface (Fig. 5.9d). Thus, when ZnO wires are covered with ethanol, they are found in a low resistance state, and conductivity is due to the free electrons in the CB due to intrinsic doping.

Similarly to the oxygen and ethanol molecules, NO_2 chemisorbs to the ZnO nonpolar surface. The lowest energy configurationcorresponds to a bidentate geometry in which the oxygen atoms of NO_2 bind to two neighboring Zn surface ions, while the nitrogen atom points outwards (Fig. 5.10c). In this adsorption configuration the N–O bond elongated by 0.05 Å and the bond angle contracted by 12°, correspondingly; the adsorption energy is –0.59 eV. As in the case of ethanol, it is predicted that NO_2 binds to the ZnO(10$\bar{1}$0) surface more strongly than O_2. When a chemical sensor based on ZnO NWs is exposed to NO_2, the nanostructure surfaces would be readily covered with NO_2 molecules that may either occupy free binding sites or may displace some of the chemisorbed oxygen molecules. The DOS for the H-doped ZnO surface after adsorption of NO_2 is reported in Fig. 5.9c. This figure shows that when NO_2 interacts with the H-ZnO(10$\bar{1}$0) surface the Fermi level shifts down in energy with respect to the condition in which the NWs are found in air, and it is found right at the top of the valence band. This occurs because NO_2 generates surface levels deeper than those generated by O_2, which trap free electrons from the H-ZnO conduction band more strongly. Such trapping induces an increase in sensor resistance as has been found experimentally [5.78].

From the results obtained for the interaction of O_2, ethanol, and NO_2 with H-ZnO (10$\bar{1}$0), the sensing mechanism of ZnO NWs has been drawn. When n-type conducting ZnO NWs are exposed to an ambient condition, which is normally rich in oxygen gas, their surfaces will immediately be covered by O_2 species

($E_b = -0.35$ eV). The adsorbed oxygen captures electrons from CB, hence the substrate will be forced back to the semiconducting configuration. When ethanol or NO_2 are introduced into the atmosphere, increases and decreases in conductivity are observed, respectively. This effect is attributed to phenomena occurring at the surface: (i) since both ethanol and NO_2 have a higher adsorption energy compared to oxygen, they are able to remove oxygen from the surface; (ii) this is accompanied by a change in the surface conductivity of the ZnO NWs. In particular, when ethanol replaces adsorbed O_2, electrons trapped in mid gap states are injected back to CB and conductivity increases. For each ethanol molecule that replaces an oxygen molecule on the ZnO surface, one electron is restored to CB. Therefore, surface carrier density will be closely linked to the concentration of ethanol in the atmosphere, and higher conductivities should be attained when O_2 molecules are completely removed from the surface. In the case of NO_2 adsorption, deep acceptor levels are generated close to the top of the ZnO valence band, which are responsible for further electron trapping and for the resistance increase observed experimentally.

In conclusion, for simple gas molecules such as ethanol and NO_2, ab initio simulations revealed that it is the competitive adsorption between the pre-adsorbed oxygen molecules and the target molecules on the surface of n-type ZnO that is responsible for sensing. These findings give insights on the detection mechanism of ZnO NWs, which may provide crucial details essential for improving the performance of ZnO-based devices for gas detection and other related applications.

5.5 DFT for Interfaces

5.5.1 Contact and Heterojunctions

One of the most studied problems with respect to semiconductors is the optoelectronic characterization of interfaces and heterojunctions, when paired with other semiconductors or with metals [5.86]. Semiconductor/semiconductor interfaces are at the basis of most electronic (e.g., diodes, field effect transistors (FETs), rectifiers, etc.) and optical (e.g., LEDs, lasers, etc.) devices, while metal/semiconductor systems are the building blocks of most electrical contacts. The specific operation of such different devices is mainly related to the peculiar electronic properties of the semiconductor in the bandgap region. Hence, control of gap states is fundamental for the final application, since their presence can produce disruptive effects or be of primary importance in devices that involve light coupling for very different purposes (e.g., absorption, emission, photochemical reactions, plasmon excitations).

In the case of semiconductor/semiconductor interfaces three kinds of possible band alignments may exist (Fig. 5.11), depending on the relative energy position of the valence band top (VBT) and the conduction band minimum (CBM) of the two systems [5.87]. In straddling interfaces (*type-I*, left panel) both VBT and CBM of the materials with the smaller bandgap lie in the bandgap region of the other semiconductor. The discontinuities of the bands are such that both types of carriers, electrons (el) and holes (h), need energy to change from the material with the smaller bandgap to the one with the larger gap; vice versa, carriers from the other side gain the same energy. *Type-I* interfaces favor energy transfer, and fluorescence decays are thus used for biological tagging [5.88] and in light-emitting diodes [5.89, 90]. In staggered interfaces (namely *type-II*), the bandgaps of the two sides partially overlap with the VBT of one semiconductor that lies in the bandgap of the other. The interface is energetically asymmetric, thus carriers gain energy moving in opposite directions. Following Fig. 5.11a (central panel), electrons (holes) gain energy moving from left (right) to right (left), respectively. This specific band distribution is particularly suited for absorption of light and separation of el–h pairs across the interface (i.e., exciton splitting), and thus it is useful for devices that produce photocurrent and/or voltage drop, such as photovoltaic solar cells [5.91–94]. Furthermore, once a *type-II* interface is formed, the energy position of VBT inside the other bandgap, i.e., closer to the valence rather than to the conduction band, affects some characteristic properties of the final device, such as the direct/inverse polarization offset of photodiodes or the open-circuit voltage in excitonic solar cells. The broken-gap heterojunction (*type-III*) is a special case of type-II, where the CBM of one side is lower than the VBT of the other. Thus, the conduction band of the former overlaps the valence band of the latter, while the bandgaps do not overlap at all. The situation for carrier transfer is like *type-II*, just more pronounced. These band alignments may be also realized in hybrid organic/inorganic interfaces, where semiconductor surfaces are coupled to molecular adsorbates. For example, the catechol/ZnO interface shown in Sect. 5.3 realizes a *type-II* junction that has been proposed for excitonic light harvesting applications [5.30, 59], as described above (Sect. 5.3).

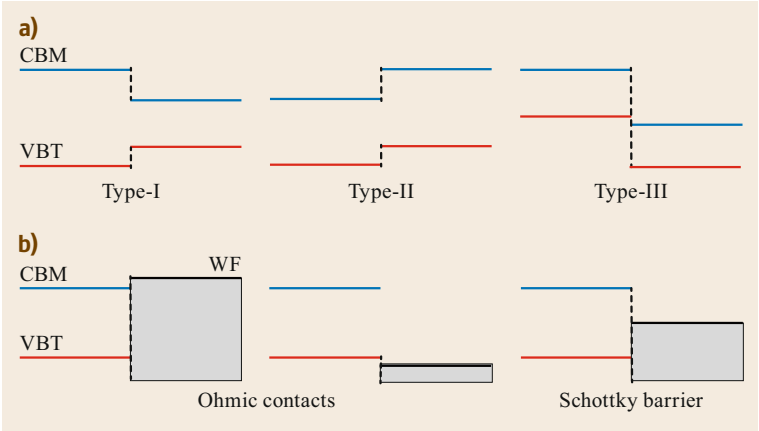

Fig. 5.11a,b Semiconductor heterojunctions organized by band alignments: **(a)** semiconductor/semiconductor interface; **(b)** semiconductor/metal interface. Here, VBT (CBM) is the valence band top (conduction band minimum) and WF the work function

In the presence of a metal-semiconductor interface, the electrical character of the heterojunction is dictated by the position of the metal Fermi level and work function (WF) value, with respect to the semiconductor bandgap (Fig. 5.11b). If metal E_F is degenerate with the conduction (left panel) or valence band (central panel) of the semiconductor, an Ohmic (non-rectifying) junction is established. This causes a free charge transfer (electrons in the left, holes in the central scheme) across the interface, until the charge neutrality is achieved. Ohmic junctions are the archetype of the optimal low-loss electrical contacts, necessary to drive the current from the active part of the device to the external circuitry. When, instead, the metal E_F lies in the semiconductor gap, a Schottky barrier (right panel) is formed. In the case of n-type semiconductors, an electron can be freely injected from the conduction band of the semiconductor into the metal contact, while an energy barrier has to be overcome to excite an electron from the metal contact into the semiconductor. The opposite holds for p-type systems. A Schottky barrier acts as a rectifier and typically results in both a low forward voltage drop and very fast switching. Schottky diodes are useful in voltage clamping applications and prevention of transistor saturation due to the higher current density in the Schottky diode. Also, because of the low forward voltage drop, less energy is wasted as heat, therefore making them a good choice for applications that are sensitive to efficiency [5.87]. Other relevant physical effects can take place at the metal/semiconductor interface in the presence of an external electromagnetic field. This is the case, for instance, of the excitation of surface plasmon polaritons (SPP). SPPs are mixed oscillatory modes, generated by the coupling between the incident light radiation and the surface charge fluctuations that can propagate on the metal/dielectric interfaces that are exploited as waveguides and telecommunication applications [5.95].

The electrical and optical character of both semiconductor/semiconductors and metal/semiconductor interfaces results from the balance between different effects; a few (such as the bandgap, the work function, the energy level distribution) are intrinsic to the materials that compose the junction, others derive from the details of the specific interface that is formed (such as surface states, surface reconstruction, defects, traps etc.). In this light, a rationale to predict lineups between the two materials, starting from local properties of the isolated systems, and the comparison with the properties of the actual heterojunction is of paramount importance for the improvement of the final application.

In the following, we present three prototypical examples based on ZnO interfaces that clearly show the large capability of first principles techniques in predicting both electrical and optical and plasmonic properties of heterojunctions, giving deep insights about the microscopic mechanisms that regulate the charge transfer and the band alignment at the interface.

Since the optoelectronic properties mostly depend on the region around the Fermi level, a proper treatment of the bandgap is an unavoidable point that must be carefully taken into account. As mentioned above, standard DFT fails in the quantitative description of the bandgap. In all the examples, a pseudohybrid implementation of DFT+U approach (namely ACBN0 [5.5]) is adopted in order to correct the severe DFT gap underestimation. As described in Sect. 5.2, this approach profitably corrects also the dielectric [5.63] and vibrational [5.96] properties of semiconductors. The band alignment resulting from the formation of semiconductor heterostructures has an important effect also on the optical properties of the system. The direct evaluation of the absorption spectrum of surfaces and interfaces, also at the single-particle level, is usually computationally very expensive for systems as large as the ones proposed in the next sections. In the following

examples, a novel first principles tight-binding (TB) approach [5.97] was used to simulate the optical properties of bulks and interfaces through the solution of the generalized Drude–Lorentz expression of the macroscopic complex dielectric function $\hat{\epsilon} = \epsilon_1 + i\epsilon_2$, where both intraband (Drude-like) and interband (Lorentz-like) contributions are explicitly taken into account. This procedure combines the accuracy and the predictive value of first principles approaches with the low computational cost of TB techniques. Furthermore, it is particularly useful for the evaluation of properties such as the optical absorption spectra that require a precise and ultrafine reciprocal space integration, which is too computationally expensive.

Ohmic Versus Schottky Barrier: The Al/ZnO Interface

In its simplest approximation, the barrier Φ between a metal (m) and a semiconductor (s) is predicted to be proportional to the difference of the metal-vacuum work function (WF) and the semiconductor-vacuum electron affinity (EA) in the case of n-doped semiconductors [5.86]. For p-doped materials, a similar expression holds, with the ionization potential (IP) in place of the electron affinity. However, in principle, the quantities WF, AE, and IP are ill defined in supercell approaches where the absolute value of the vacuum level is not univocally defined, due to the periodic boundary conditions. In order to overcome this problem, it is useful to adopt an approach originally proposed by M. Peressi and coworkers [5.98], which consists in the evaluation of Φ as the sum of two separate contributions

$$\Phi = \Delta\epsilon + \Delta\bar{\bar{V}}\,, \tag{5.5}$$

where the first term

$$\Delta\epsilon = (E_F - \bar{\bar{V}}_m) - (\mathrm{VBT} - \bar{\bar{V}}_s) \tag{5.6}$$

derives from bulk calculations and gives the difference between the Fermi energy (E_F) of the metal and the VBT of the semiconductor, each measured with respect to the *macroscopic average* of the electrostatic potential of the corresponding crystal $\bar{\bar{V}}_{m,s}$. The macroscopic average of the electrostatic potential $\bar{\bar{V}}(z)$ is related to the charge distribution by a one-dimensional Poisson equation, and it is defined as [5.98, 99]

$$\bar{\bar{V}}(z) = \frac{1}{a}\int_{-a/2}^{+a/2} \bar{V}(z')\mathrm{d}z'\,, \tag{5.7}$$

where a is the characteristic length along the direction (z) perpendicular to the surface, and $\bar{V}$ is the planar average of the electrostatic potential over the xy plane. The second term in (5.5) ($\Delta\bar{\bar{V}}$) is an interface-specific property and must be extracted from supercell calculations by using the same macroscopic average technique; $\Delta\bar{\bar{V}}$ is related through the Poisson equation to dipole formation at the interface, and it is strictly dependent on the atomic details of the surface reconstruction at the interface. The intermediate step of referring E_F and VBT to the bulk average potential $\bar{\bar{V}}$, allows for the definition of an accessible energy reference, alternatively to the vacuum level; provided that the supercell calculation includes a metal and a semiconductor layer thick enough to reproduce the corresponding bulk in their central section (see also Sect. 5.2). The energy level scheme for a generic semiconductor/metal is described in Fig. 5.12a.

The formation of good contacts with external metals is a necessary step for the realization of efficient electronic devices. Due to its low work function [5.100, 101], aluminum has been used in the formation of Ohmic contacts with n-doped ZnO. Furthermore, it has been proposed that the Al/ZnO contact witnesses out-diffusion of oxygen atoms from ZnO to participate in the formation of Al_2O_3 at the interface, with accumulation of oxygen vacancies close to the ZnO surface. In spite of its strategic relevance in view of applications, the Al/ZnO junction is a debated system; a number of different metallization schemes have been proposed, ranging from the deposition of the single metal to alloys and sandwiches of different metal layers to optimize the electrical characteristics and block inter/outer diffusion and degradation of the contact ([5.102] and references therein), and eventually the possibility to obtain a Schottky-like electric behavior was reported [5.103]. Here, we characterize the formation of the electrical contact at the Al/ZnO interface built along the polar ZnO(0001) axis, which is the most common direction of growth. The interface (Fig. 5.12b) is composed of a layer of Al(111) metal and a layer of ZnO semiconductor, exposing the polar (0001)-Zn terminated face. Further details on the (000$\bar{1}$)-O terminated surface are reported in the original paper [5.104]. From the computational point of view, particular attention must be devoted to the potential drop inside the slab, which stems from the internal polarization field along the polar c-axis of the wurtzite structure and the surface charge rearrangement [5.105]. Depending on the growth techniques, the ZnO(0001) surface is stabilized by either surface vacancies (as in the present case) or by surfactants (such as −OH groups), which compensate the internal polarization field.

Upon exposing the vacancy-reconstructed ZnO (0001) [5.105] surface to Al deposition, we observe intermixing at the interface layer (Fig. 5.12b). The formation of the contact causes an aluminum atom

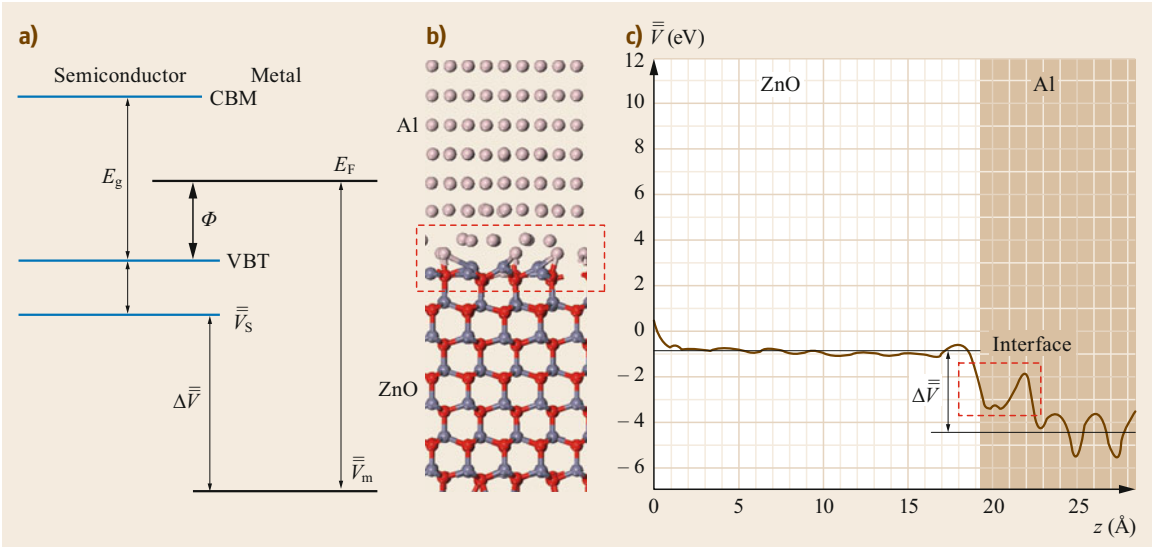

Fig. 5.12a–c **(a)** Energy level scheme corresponding to Φ as defined in (5.5). **(b)** Side view of the Al/ZnO(0001) relaxed heterojunction. The *dashed line* marks the atomic readjustment at the interface. **(c)** Average potential profile for the simulated Al/ZnO interface

to penetrate into the site that was left empty by one of the (three) Zn vacancies and became involved in bonding with the surrounding oxygen atoms. This result is also in agreement with the observation of the Zn-substitutional behavior of Al dopants in formation of Al-doped ZnO (AZO) [5.106, 107]. The complex surface relaxation imparts a net charge dipole at the interface, which can be quantified in terms of $\Delta\bar{\bar{V}}$, as shown in Fig. 5.12c.

The application of the potential-dipole model mentioned above would give a negative Φ barrier, with the Fermi level of the metal higher in energy than the conduction band minimum of the semiconductor [5.102]. Clearly, such band alignment would correspond to a thermodynamically unstable system; the equilibrium condition is restored upon a metal-to-semiconductor charge transfer that zeroes the barrier. This is the fingerprint of an Ohmic contact. The analysis of the electronic structure (e.g., DOS) reveals that the Fermi level of the interface is located within the ZnO conduction band, which is consistent with an occupation of bulk-like ZnO states. Further, the energy region close to the Fermi level is occupied by Al-ZnO states. These interface states, which lie in the pristine bandgap of ZnO, derive from the natural charge spilling from the Al surface. The charge piles up at the interface and decays within the very first ZnO interface layers. The charge transfer that accompanies the Fermi level realignment is the dominant effect, and it is related to the Ohmic character of the Al/ZnO junction, in agreement with most experimental results.

On the other hand, the intercalation of a single gold monolayer between ZnO and Al compounds is sufficient to change the electrical behavior of the barrier, moving from an Ohmic to a Schottky contact, as for the ZnO/Au interface [5.108]. This remarkable difference reflects the fact that the Schottky barrier is very sensitive to interfacial details, in agreement with the experimental observation. In this case, the Fermi level of the interface lies in the projected ZnO bandgap and a bunch of Au-derived states, responsible for interface dipoles, fills the forbidden energy region also in this case, while the CBM of ZnO remains empty.

We further note that this kind of analysis is possible only because the atomistic details of the interfaces (and the corresponding charge transfer) are treated explicitly from first principles. The pivotal role of charge redistribution at the interface is often neglected in simplified models, such as the Schottky–Mott rule, where the Schottky barrier is evaluated as the difference between the metal work function and the semiconductor electron affinity of the separated bulk systems. Despite the crude approximations, the present approach has been proved to give realistic results on both the electrical character (i.e., Ohmic versus Schottky) and the barrier heights in most metal/semiconductor junctions. The results are usually accurate enough to be directly compared with the experiment. On the other hand, other effects such as the quantification of band-bending and of the charge depletion region, which have a mesoscopic spatial extent, are not caught by atomistic approaches that have access

only to a restricted region (a few nanometers) around the interface.

One Dimensional Type-II Alignment: ZnO/ZnS Core/Shell Nanowires

As seen before, semiconductor nanostructures have received much attention for their potential use in a wide range of technological applications, including solar cells [5.54], UV detectors [5.109], light emitters and lasers [5.110], bioimaging [5.111], and gas sensors [5.112]. In particular, the use of quasi-one-dimensional (1-D), vertically aligned nanostructures to construct three-dimensional architectures as building blocks for optoelectronic (e.g., photovoltaic, LEDs) devices, boosting charge transport and collection, and/or enhancing light absorption, has demonstrated advantages over conventional planar devices [5.113, 114].

However, intrinsic problems in 1-D nanowires, such as the high number of defects and surface states, due to the presence of surface atoms with reduced coordination, along with the high electron–hole recombination rate upon light absorption, reduce the device performances and limit their large-scale commercial application for optoelectronic devices. For example, to facilitate efficient charge separation, great efforts have been made to impart a p-n junction functionality to nanowires [5.115], through selective doping [5.116]. However, doping small nanosystems is a tremendous experimental challenge, and if such p-n junctions can be formed, due to the small size of the system the junction can have a large device-to-device fluctuation.

The optoelectronic properties of 1-D wires can be adjusted as desired not only by impurity doping but also through surface modification [5.117–120]. Beyond the functionalization processes of semiconductor surfaces addressed in the previous Sect. 5.3, further modification with inorganic adlayers can be a suitable tool to passivate surface defects and design novel nanocomposites with different properties. By changing the band alignment at the interface, it is possible to tailor the bandgap of the resulting material [5.64]. Previous attempts in the formation of fully inorganic heterostructures dealt mainly with quantum dots or extended superlattices, while the synthesis of one-dimensional heterostructures is a much more recent achievement. In general, two types of one-dimensional heterostructures can be formed: stacked longitudinal (SL) and coaxial core-shell (CCS) heterostructures.

Here, we focus on the latter [5.121, 122], which are nanowires with different core and shell compositions. In contrast to the bulk situation, the carrier localization profile relies on the core diameter and the shell thickness. Because of quantum confinement, the growth of a shell of a higher bandgap material on a core of another lower bandgap material is expected to form a *type-II* heterostructure, while the opposite would realize a *type-I* interface. Despite the fact that, in principle, the formation of 1-D nanoscale heterostructures is conceptually simple, their synthesis, control, and characterization are a formidable task for both experiments and theory. Indeed, the first unambiguous experimental reports on such 1-D component-modulated materials appeared mainly in the last years.

On the theoretical side, the simulation of CCS heterostructures is a tremendous challenge, as it requires the explicit treatment of very large systems that are hardly accessible even with the parallel supercomputers that are available nowadays. Here, we present the prototypical case of a CCS nanowire of ZnO (core) and ZnS (shell), which was experimentally synthesized [5.123–127]. The system has 588 atoms and ≈ 5300 electrons. The core is made of ZnO, and it has an internal radius $r_c = 1.1\,\text{nm}$, which is large enough to correctly reproduce a realistic ZnO wire [5.8, 128]. The shell is made of ZnS, the total radius of the heterostructure is $r_s = 1.9\,\text{nm}$, close to that of experimental samples [5.123]. The wire is aligned along the polar c-axis of the wurtzite ZnO crystal. The CCS structure has a hexagonal symmetry and exposes only nonpolar $(10\bar{1}0)$ faces. Due to the huge dimension of the system, only two bilayers of ZnS-ZnO wurtzite material are included along the wire direction, i.e., the minimum to obtain a periodic wire.

In the optimized structure (Fig. 5.13a) the inner ZnO core almost maintains its ideal geometry, while the external ZnS shell undergoes remarkable distortion due to the relaxation of the mismatch at the interface. Nonetheless, the outermost layer exhibits a buckled dimer arrangement, typical of the ZnS$(10\bar{1}0)$ surface. The resulting electronic structure is summarized in Fig. 5.13b. Albeit ZnO and ZnS have similar bandgap $\left(E_g^{\text{ZnO}} = 3.1\,\text{eV} \text{ and } E_g^{\text{ZnS}} = 2.8\,\text{eV}\right)$, the different ionization potential causes the formation of a staggered *type-II* band alignment at the interface, with the top of ZnS valence band lying in the pristine gap of ZnO. This implies a reduction of the bandgap of the overall structure $E_g = 1.2\,\text{eV}$ that lies in the near-IR range (NIR). Accordingly, the highest occupied molecular orbital (HOMO) state is localized in the ZnO core, while lowest unoccupied molecular orbital (LUMO) is confined in the external ZnS shell. This also gives information on the charge transport mechanisms along the wire; hole carriers flow in the external ZnS crown, while electrons move in the internal ZnO core, confirming the intrinsic charge separation observed experimentally [5.127].

Simulated optical properties are summarized in Fig. 5.13c. The peaks in the imaginary part of the dielectric function ϵ_2 correspond to single-particle valence-to-conduction transitions. As expected, it is

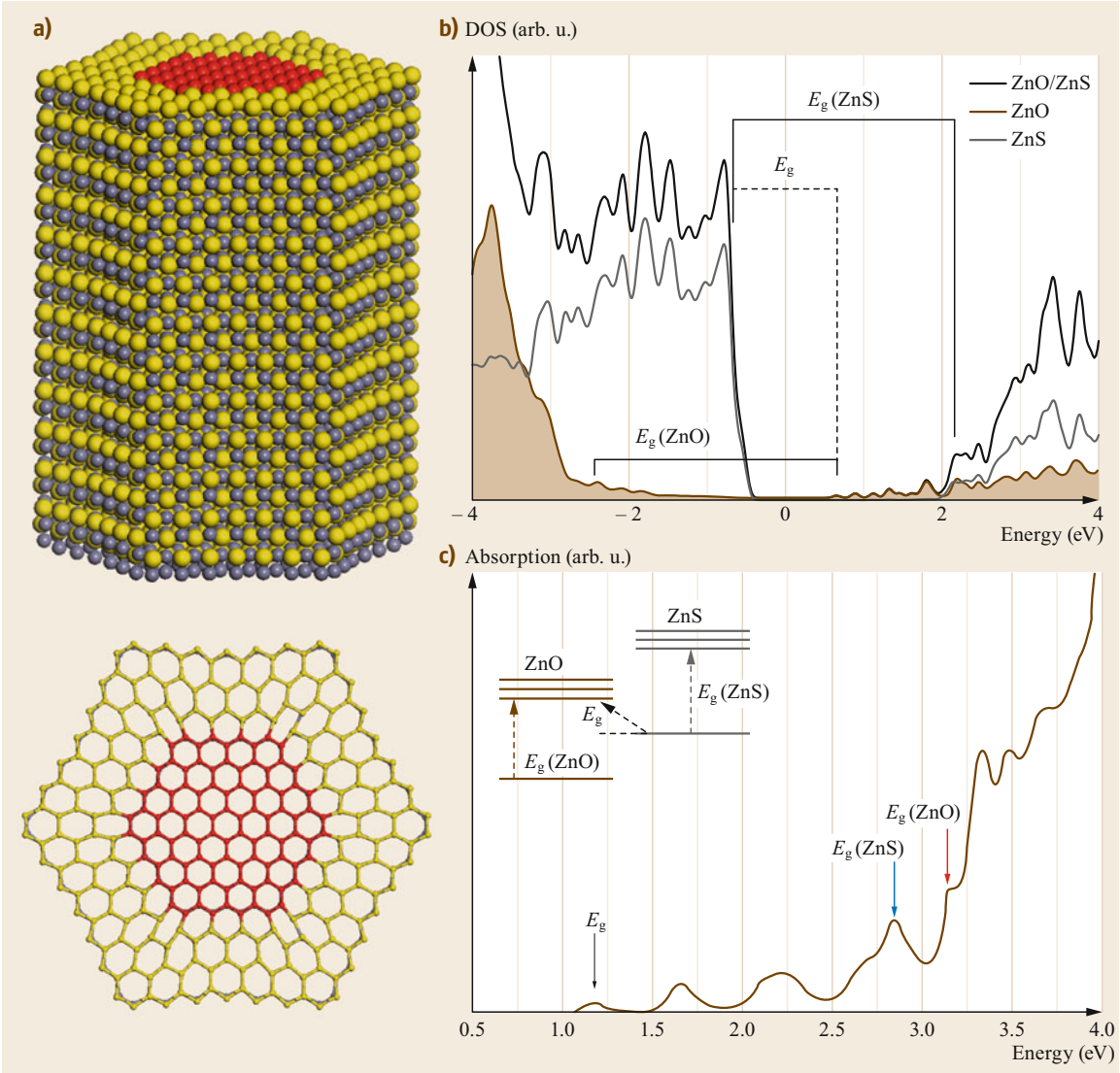

Fig. 5.13a–c **(a)** Side and top view of the CCS ZnO/ZnS nanowire. **(b)** Total and material-projected DOS plot. **(c)** Imaginary part of dielectric function of ZnS/ZnO nanowires. The *inset* highlights the band-alignment scheme and lowest-energy vertical transitions. Figure adapted with permission from [5.97]. Copyright 2016 by the American Physical Society

easy to recognize the valence-to-conduction absorption edges in the external ZnS shell (2.8 eV, blue arrow) and in the inner ZnO (3.1 eV, red arrow), which correspond to the E_g values of each material. However, other lower-energy transitions are present in the range 1.2–2.8 eV, which correspond to intermaterial ZnO-to-ZnS transitions, as depicted in the inset of the figure. Although the frontier's orbitals are mostly localized in the core (electrons) and in the shell (hole), the overlap and the symmetry of the wave functions give low but not negligible oscillator strength to the first four transitions. This agrees well with the dramatic red shift of the absorption edge (i.e., from UV to near-IR) observed experimentally [5.125, 126].

Alternative Plasmonic Systems: AZO/ZnO Interface

Surface plasmons are the normal modes of charge fluctuation at a metallic surface that govern the long-range interaction between the metal and the external environment [5.129]. Surface plasmons may be induced on both nanoparticles and planar surfaces. In the former

case, they are referred to as *localized surface plasmons* (LSP), in the latter case as *surface plasmon polariton* (SPP) modes [5.130]. SPPs, in particular, involve the excitation of an electric field which propagates a metal/dielectric interface and provide the opportunity of confining light in very small dimensions (Fig. 5.14a). This allows one to conjugate the compactness of electronic devices and the speed of photonic systems, opening up a wide range of applications from energy conversion [5.131, 132] to telecommunications [5.133, 134].

The polarization induced by an electromagnetic radiation on a sample can be described by the material's complex dielectric function, denoted by $\hat{\epsilon} = \epsilon_1 + i\epsilon_2$. While the real part of the dielectric function (ϵ_1) describes the strength of the polarization induced by an external electric field; the imaginary part (ϵ_2) describes the losses encountered in polarizing the material. Following Drude theory, it is easy to demonstrate that efficient plasmonic materials present negative ϵ_1 for energy lower than the plasma frequency $\omega_p^2 = ne^2/(\epsilon_0 m^*)$, which must be higher than the desired frequency of application. Because noble metals (e.g., Au, Ag) tend to have large plasma frequencies and high electrical conductivity, they have traditionally been the materials of choice for plasmonics [5.136]. However, they are plagued by large losses (i.e., large ϵ_2), especially in the visible and UV spectral ranges, arising in part from interband electronic transitions and in part from dissipative scattering events (e.g., el-el, el-ph). These losses are detrimental to the performance of plasmonic devices, seriously limiting the feasibility of many plasmonic applications.

Because these losses are inherent to the constituent materials, the research/design of alternative plasmonic materials with lower losses are required to develop robust plasmonic devices [5.137]. As an alternative to metals, semiconductors are conventionally regarded as dielectric materials for frequencies above several hundred THz. However, semiconductors can actually exhibit a negative real permittivity in this spectral region when heavily doped. Due to the ease of fabrication and flexibility in tuning their properties, such as carrier concentration, semiconductors are also potential materials for plasmonics. In order to qualify as a low-loss plasmonic material, both the bandgap and plasma frequency of the semiconductor must be larger than the frequency range of interest. While a large plasma frequency ensures a negative real part of dielectric function, a large bandgap ensures almost no interband transition losses.

Heavy doping ($\approx 10^{21}\,\mathrm{cm}^{-3}$) with Al and Ga elements is possible in oxide semiconductors such as zinc oxide and indium oxide. These semiconductors have wide bandgaps, and their ϵ_2 values are moderately low. In addition, relatively high mobilities of charge carriers can be achieved with polycrystalline microstructures and very high mobilities are typically observed in single crystals. In particular, AZO can have losses as low as four times smaller than that of silver in the NIR. Together with indium tin oxide (ITO) these compounds were recently proposed also as low-loss plasmonic materials in the NIR/visible range [5.133, 135, 138–140]. Furthermore, they are qualified as transparent conductive oxide (TCO) materials [5.141], i.e., they show an unusual coexistence of high conductivity and high transparency in the visible region. This makes these materials very appealing for optoelectronic applications, such as solar cells and liquid crystal displays, and opens new alternatives for plasmonic applications in the optical spectrum, with the further advantage of a relatively low production cost, with respect to noble metals. In the following, we will focus on the characteristics of SPP at the AZO/ZnO interfaces, where AZO is the metal part and ZnO the dielectric component of the system.

The properties of SPP derive from the combination of the dielectric properties of the two components. In general, SSP can propagate along a metal/dielectric interface when the condition

$$\hat{\boldsymbol{k}}_{\parallel} = \frac{\omega}{c}\left(\sqrt{\frac{\hat{\epsilon}_m \hat{\epsilon}_d}{\hat{\epsilon}_m + \hat{\epsilon}_d}}\right), \tag{5.8}$$

is satisfied; $\hat{\boldsymbol{k}}_{\parallel}$ is the complex wavevector parallel to metal surface, along the propagation direction, $\hat{\epsilon}_{m,d}$ are the complex dielectric functions of the metal and the dielectric bulks, and c is the light velocity in vacuum. The real part of $\hat{\boldsymbol{k}}_{\parallel}(\omega)$ completely defines the dispersion relation of the excitation. For a pure Drude-like metal it exhibits a divergence for $\omega = \omega_p$, giving rise to high and low-energy branches, separated by a forbidden gap for $\omega_{sp} \le \omega \le \omega_p$, where ω_{sp} is the surface plasmon frequency, which for simple Drude metals is $\omega_{sp} = \omega_p/\sqrt{2}$. Within the forbidden gap, $\hat{\boldsymbol{k}}_{\parallel}(\omega)$ is a purely imaginary number, prohibiting wave propagation. The high-energy branch ($\omega > \omega_p$) does not describe a surface wave (Fig. 5.14). This corresponds to the fact that for $\omega > \omega_p$ the metal is no longer reflecting, becoming transparent to the incoming radiation. The nonradiative character of SPP in the low-energy branch ($\omega < \omega_{sp}$) follows from the fact that the surface plasmon polariton propagates with a momentum larger than that of an electromagnetic wave traveling in the dielectric part with the same angular frequency. As a consequence, SSP cannot couple with light in the de-excitation process, and only nonradiative inelastic scattering effects (e.g., el-ph) can take place. At large wavevectors SPP approaches the nonpropagating surface plasmon limit (ω_{sp}).

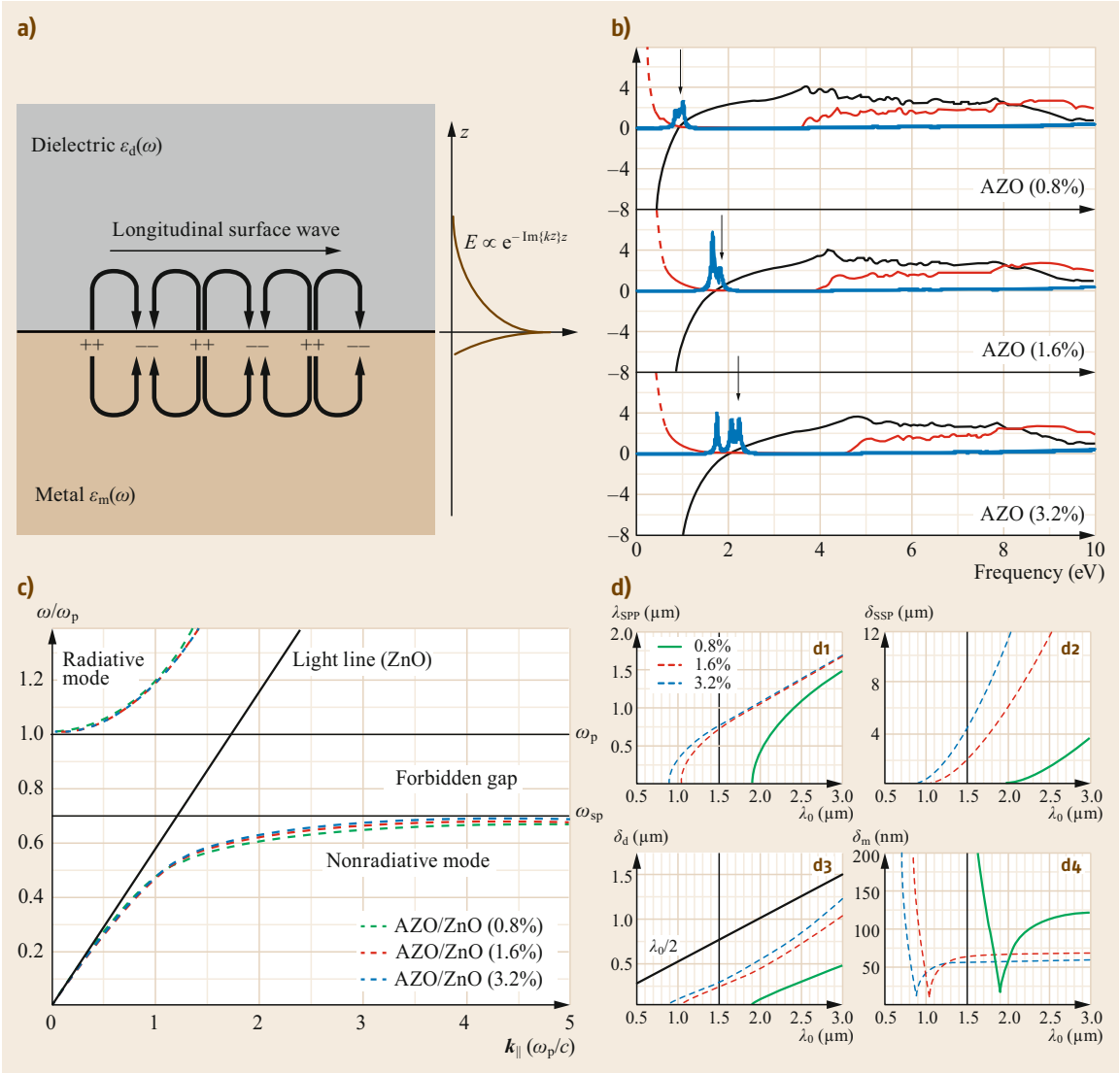

Fig. 5.14a–d **(a)** Localized SPP propagating on the metal surface at the metal/dielectric interface. **(b)** Real (*black line*) and imaginary (*red line*) parts of the complex dielectric function and the electron energy-loss function (*blue line*) of AZO at different Al concentrations. *Vertical arrows* mark the plasma frequency. **(c)** Dispersion relation of the real part of the SPP wavevector $\boldsymbol{k}_\parallel$ of AZO/ZnO interfaces at different Al concentrations. The *thick black line* marks the dispersion relation for light in the ZnO region. *Horizontal gray lines* define the forbidden gap. **(d)** Characteristic lengths of SPP (λ_{SPP}) in AZO/ZnO interfaces at different Al concentrations. *Vertical black lines* mark the characteristic wavelength for telecommunications. The *dashed line* in *panel* (d_3) corresponds to the upper compactness limit $\delta_d = \lambda/2$. Figure adapted with permission from [5.135]. Copyright 2014 American Chemical Society

In order to apply the matching condition of (5.8), it is necessary to know the dielectric function of the two separate materials over the frequency range of interest. However, while for noble metals the plasma frequency and the other plasmonic properties can be extracted once and for all from experimental data, in the case of TCOs this is not possible because of the doping-induced modifications in the optoelectronic properties of the host material. First principles simulations provide a very useful tool for the evaluation of the optical and electronic properties of materials and their interfaces, also in the case of dopants and impurities as in AZO, where semiempirical values for the dielectric function are not univocally defined. Here, for the description of

the optical properties of bulk-like systems, we adopted the TB approach described above [5.97], which has its foundation on the DFT characterization of the ground-state electronic structure. Once the complete dielectric function is known, the electron energy-loss function can also be easily obtained as $L(\omega) = \mathrm{Im}\{-1/\hat{\epsilon}\}$.

As doping may change the optoelectronic properties of AZO, we investigated different doped systems, as obtained by varying the number of substitutional Al atoms in the range 0–3.2%, in the virtual crystal approximation [5.84, 106]. Within the solubility limit (3.5%), Al dopants mostly assume Zn-substitutional sites, and the crystalline order of the ZnO host is only slightly perturbed, as results from complete relaxation of the atomic structure. This has two main effects on the electronic structure of AZO: (i) Al does not induce the formation of defect states in the ZnO bandgap, and (ii) Al donates its 3p electron to the ZnO conduction band, without remarkably changing the shape and the curvature of the conduction band minimum. This is the typical fingerprint of an intrinsic n-type conductor. Increasing the doping percentage forces an upward energy shift of the Fermi energy in the pristine ZnO conduction band. The simultaneous presence of point defects (e.g., Zn or O vacancies) or other impurities (e.g., H) may change the details of the resulting electronic structure, introducing further charge-compensation effects [5.85, 142]. However, this does not change the general picture described above. In virtue of the single quasi-parabolic band at the ZnO bottom of the conduction band, the effect of Al doping is the formation of a free electron gas in the metal oxide. This is the fundamental prerequisite for a plasmonic material. The results of the optical properties are summarized in Fig. 5.14b. For all the dopant ratios, we distinguish two energy regions. In the UV range, the imaginary part of the dielectric function has a net peak, whose energy position depends on the doping level. This corresponds to the interband valence-to-conduction absorption edge. In all cases, there is a blue shift of the absorption edge, which may be explained in terms of the Burnstein–Moss effect [5.143]. At lower frequencies, the optical properties of AZO completely differ from the original ZnO ones, being similar to an ideal simple metal. The rapid decay of ϵ_2 (red line) expresses viscous electron damping due to scattering processes associated with the electrical resistivity. The real part of the dielectric function (black line) is negative and diverges for $\omega \to 0$, in agreement with the formation of a free electron gas upon Al doping. Where $\epsilon_1 = 0$ and $\epsilon_2 \ll 1$, the loss function (blue line) has a peak corresponding to the plasma frequency ω_p of the system. The presence of Al dopants imparts a drastic shift of the plasma frequency that moves from the far-UV ($\approx 17\,\mathrm{eV}$, not shown) in the case of ZnO to the NIR and the visible range in the case of AZO, in agreement with recent experimental results [5.138]. This proves that in the case of TCOs ω_p can be tuned by controlling the electron density, i.e., by changing doping content. Even in the heavy doping regime (e.g., 3.2%), the plasma frequency does not overlap with the interband transition energy region. This assures low losses in the NIR-VIS range, reducing one of the most challenging problems that plagues standard metallic materials. This, along with the agreement with the experimental results, confirms the validity of the Drude model for this compound, which actually acts a low-loss plasmonic metal.

Once the dielectric functions of AZO and ZnO are known, the SPP properties can be investigated. The dispersion relations (5.8) for the AZO/ZnO interface at different Al concentrations are shown in Fig. 5.14c. At low frequencies, the surface mode asymptotically approaches the light line for ZnO (black line). As the frequency increases, the SPP mode separates from the light line and approaches the surface plasmon frequency (ω_sp) of the conductor (AZO). From $\hat{\boldsymbol{k}}_\parallel(\omega)$ we can derive the length scales that characterize the spatial profile of the SPP mode for the AZO/ZnO ideal interface as a function of the incoming radiation (λ_0) and of Al doping, as is shown in Fig. 5.14d. For the potential application of these materials in telecommunication devices, we mark the corresponding characteristic wavelength ($1.5\,\mu\mathrm{m}$) with a vertical line. The SPP profile can be described in terms of wavelength (λ_SPP), propagation length (δ_SPP), and dielectric (δ_d) and metal (δ_m) penetration depths. In the case of the AZO/ZnO interface, λ_SPP (panel d_1) is of the order of $1.0\,\mu\mathrm{m}$. Since λ_SPP defines the periodicity of the SPP wave, it also defines the scale of optical structures (e.g., Bragg scatterers) typically used to control the SPP. The propagation length (δ_SPP) is the distance over which the intensity of the SPP mode falls to $1/\mathrm{e}$ of its initial value. For any real application, it is necessary that $\delta_\mathrm{SPP} > \lambda_\mathrm{SPP}$; i.e., SPP should propagate as a straight ray in geometrical optics. This is the case for the AZO/ZnO interface, where the SPP can propagate up to a few microns also at the telecom wavelength (panel d_2), if the doping level is sufficiently high. The penetration lengths into the dielectric and metallic layers determine the compactness of the SPP, giving a measure of the minimum thickness required for the dielectric and metal layers. The need for high localization at interfaces imposes that the penetration depths be as small as possible. The penetration length inside the ZnO layer δ_d (panel d_3) is very short ($\approx 200\,\mathrm{nm}$ depending on the Al content) at $\lambda = 1.5\,\mu\mathrm{m}$, giving rise to a high compact optical system. In order to highlight this feature, we reported (black dashed line, panel d_3) the so-called *upper compactness* limit

$\delta_d = \lambda_0/2$, which corresponds to the minimal diameter spot of a dielectric photonic device. The fact that for the AZO/ZnO interface δ_d is always below the $\lambda_0/2$ line indicates that the SPP mode has electromagnetic field enhancement properties typical of photonic systems and the subwavelength confinement of electronic devices. Notably, standard plasmonic materials such as Au and Ag do not fulfill this requirement, crossing the compactness limit in the range 300–500 nm. The skin-depth properties of the metallic layer are quantified in terms of the penetration length inside the metal δ_m (panel d_4). In the present case, δ_m is at least two orders of magnitude smaller than the corresponding δ_d for each doping considered.

The good agreement with the experimental results confirms, on the one hand, the validity of the Drude–Lorentz model in the description of this class of materials, and on the other hand, the capability of DFT approaches to characterize and predict the optoelectronic properties of complex materials and interfaces.

5.6 Exploring Water/Solid Interfaces via DFT Simulations

One of the most compelling tasks when dealing with atomistic ab initio approaches is the description of the physical properties of solid/water interfaces. Understanding at an atomistic level how liquid water wets a solid surface is of fundamental relevance both at a basic and an applied research level. On the one hand, it would be desirable to understand how concepts such as hydrophobicity/hydrophilicity are revealed at the molecular level and to identify the fingerprints of the resulting wetting layer; whereas, from a macroscopic point of view, it would be important to predict how the presence of the hydration layer influences the physical properties of the material when employed in devices or applications occurring in liquid environment. In the following, we summarize the results of two of the few examples reported in the literature dealing with the microscopic description of the interface between liquid water and a solid surface obtained by ab initio molecular dynamics simulations. In particular, we will focus on the hydroxylated Si-SiC(001) surface [5.144] and the gold(111) surface [5.27]; we will give an insight into the perturbation induced in water at the surface layer both under the structural and electronic point of view. A detailed analysis of the interaction of water molecules with the atoms at the surface reveals the hydrophilic character of these two surfaces, but the mechanism leading to such behavior is different when comparing a clean metal surface like gold and a hydroxylated semiconductor surface such as that of Si-SiC(001).

5.6.1 How to Build a Solid/Liquid Interface?

Contrary to all the previously presented cases, here we cannot assume a single static configuration for the solid/liquid interface. In fact, at room temperature the molecules that form the liquid continuously fluctuate, changing their position in space and the bonding path with both the other molecules of the solvent and the solid surface. Therefore, a molecular dynamics (MD) approach is needed. Before presenting the results on the wetting behavior of water obtained by means of ab initio molecular dynamics, we first discuss an important step along the computational strategy for the simulation of a solid/liquid interface: the preparation of the initial MD configuration. Performing an ab initio molecular dynamic simulation of a solid/liquid interface requires a good initial starting configuration, which is not straightforward to achieve. The main difficulty derives from the fact that the majority of computer codes employed to perform ab initio molecular dynamics use plane waves to expand the system wavefunction and, as such, are coded to deal with simulation cells that are periodic in three directions, as discussed in Sect. 5.2. In the case of simulations involving a disordered system, and in particular a polar solvent like water, this poses a further difficulty. When placing the liquid slab on top of the surface, one has to select the number of molecules needed to represent the correct density of the liquid phase, and, in this respect, some attention must be paid due to the existence of an exclusion volume at a solid surface that is due to steric effects. Neglecting the exclusion volume present at the surface would lead to an overestimation of the volume occupied by the liquid and, consequently, to studying an interface with a less dense liquid.

Typically, two alternative methods have been used to cope with this problem and to prepare a realistic interface. In the first approach, the starting configuration for the first principles simulations is obtained by performing preliminary classical MD simulations employing a classical force field for water–water and water–surface interaction, if available. In the water/solid system the supercell dimensions in the (x, y) plane are fixed and determined by the size of a solid surface periodicity. To obtain an estimate of the surface exclusion volume, which is connected to the supercell lattice

parameter in the direction perpendicular to the interface (z), the cell dimension is varied, until the stress along this direction yields a pressure equal to the atmospheric one. Alternatively, one can fix the supercell size in the z-direction and change (increase or decrease) the number of water molecules in the supercell until the stress on the simulation cell corresponds to atmospheric pressure.

The second approach consists in a short (few ps) ab initio molecular dynamics of the solid/liquid interface at low coverage regime (for example, one monolayer of molecules). The result of this simulation allows estimating the average distance between the interfacial water molecules and the surface, and thus the thickness of the exclusion volume. In the two solid/water interface examples described below both approaches were used and, in particular, a preliminary classical molecular dynamics run has been used for the gold/water surface. Once the initial configuration is obtained, the first principles calculation typically starts with an initial thermalization of the system at $T = 400$ K for a few picoseconds, employing a thermostat to keep the temperature constant. The equilibration is then followed by 10–20 ps of production run (microcanonical ensemble, NVE) and, finally, the trajectories are analyzed. The ab initio molecular dynamics that we present here are performed at the temperature (400 K) at which DFT using PBE and Car–Parrinello dynamics yields results in good agreement with experiments for structural and diffusion properties of liquid water at ambient conditions [5.145, 146]. This thus allows us to compare bulk and interface water properties, to enhance the effect of interfaces.

5.6.2 The Cases of Si-SiC/Water and Gold/Water Interfaces

The interface between water and two hydrophilic interfaces, namely hydroxylated Si-SiC(001) and clean gold(111) surfaces, as discussed in [5.27, 144] are represented in Fig. 5.15. For both systems, the structural properties of interfacial water was first investigated by analyzing how the average water density and the number of hydrogen bonds change as a function of the distance from the interface. As shown in Fig. 5.16, at both Si-SiC and gold surfaces, water density presents a high peak when in contact with the solid surface. This enhanced density at the interface was observed in other simulations of solid/water interfaces [5.147, 148], and it is determined by packing forces, and by the tendency of water to maximize hydrogen bonds. The observed interfacial peak is expected to be at a closer distance to the outermost atomic layer in the case of hydrophilic surfaces if compared to hydrophobic surfaces. In particular, in the case of the hydroxylated Si-SiC surface, the water density presents a single intense peak at 2.2 Å from the surface hydroxyl groups (Fig. 5.16b), while in the case of gold, the first high-density maximum is a structured peak that has a maximum at 3.2 Å from the surface atoms and presents a prominent shoulder (the red arrow and the inset in Fig. 5.16a) at a shorter distance of about 2.6 Å. A detailed analysis of the restructuring of the water network occurring at this interfacial water layer reveals that the mechanism leading to the hydrophilic behavior is different for these two surfaces.

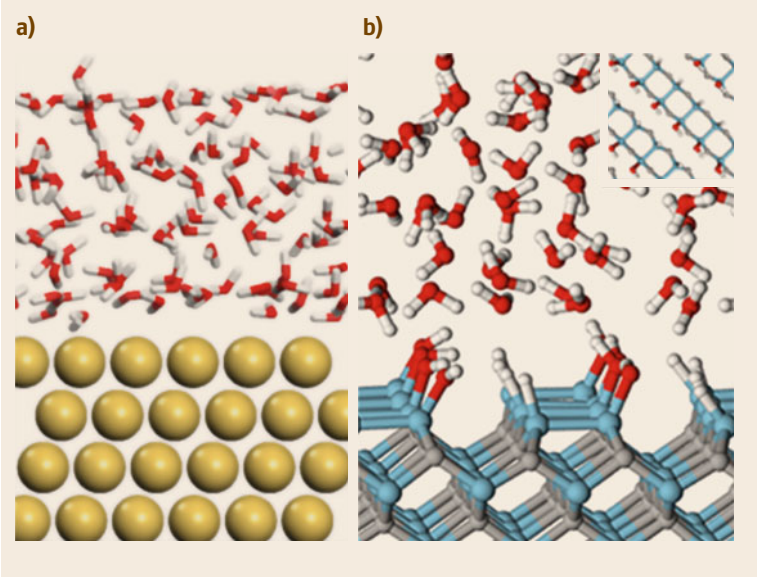

Fig. 5.15 **(a)** Side view of the starting configuration for the liquid water/gold system in the simulated unit cell. Large golden spheres represent Au atoms, while red and white sticks represent oxygen and hydrogen atoms, respectively. **(b)** Ball-and-stick rendering of a representative configuration for the interface between the hydroxylated Si-SiC surface and liquid water. *Inset* Top view of the hydroxylated Si-SiC surface. *Red*, *white*, *gray*, and *light blue spheres* represent oxygen, hydrogen, carbon, and silicon atoms, respectively. Figure adapted with permission from [5.27, 144]. Copyright 2005 and 2011 American Chemical Society

In the case of Si-SiC, water molecules at the surface form a smaller number of hydrogen bonds than in the bulk; at a distance of about 3 Å from the surface atoms, the bulk value of 3.6 H bond/water is recovered; see Fig. 5.16d, where the H bonds connecting water molecules to the surface hydroxyl groups were not included. As shown by the blue and red curves in Fig. 5.16d, the water molecules at the surface do not show any preference in accepting or donating H bonds. A deeper structural analysis also shows that the water molecules close to the surface do not adopt a tetrahedral-like coordination but rather are arranged so as to optimize their H-bonding network in a manner compatible with the orientation and periodicity of the surface hydroxyl groups. In particular, a study of the spatial distribution of the interfacial water molecules proves that water molecules do not wet the surface uniformly, preferring the direction parallel to the hydroxylated surface dimer rows. In other words, in such a hydroxylated surface, it is the geometry of the surface −OH groups [5.65] that plays a determinant role in the restructuring of the interfacial water layer. These induce a directionality in the filling space properties of water and ultimately determine the presence of chains of hydrogen bonded molecules bridging over hydrophilic surface groups. To assess more specifically the nature of the water/surface interaction in this case, the total electron density of the interface, ρ_{int}, was compared to that of the isolated hydroxylated surface, ρ_{SiC} and water, ρ_{water}, for a given snapshot of the molecular dynamics run. The changes in electronic charge induced by the water surface interaction is expressed as: $\rho_{diff} = \rho_{int} - [\rho_{SiC} + \rho_{water}]$. The quantity ρ_{diff} is positive when there is an addition of charge to the system with respect to the isolated fragments, and negative in the opposite case. In Fig. 5.17a ρ_{diff} is represented for a particular snapshot of the simulation run. The depletion and accumulation of charge, with respect to the isolated water and surface systems, are represented by blue and yellow iso-surfaces, respectively. The main changes in the charge density are localized directly at the interface, and in particular they are located along the directions of the hydrogen bonds established between the surface −OH groups and water molecules. The projection of ρ_{diff} on two clip planes containing two different surface −OH groups is represented in Fig. 5.17b, which shows one −OH group donating (left panel) and the other accepting (right panel) a hydrogen bond. In both cases, it is

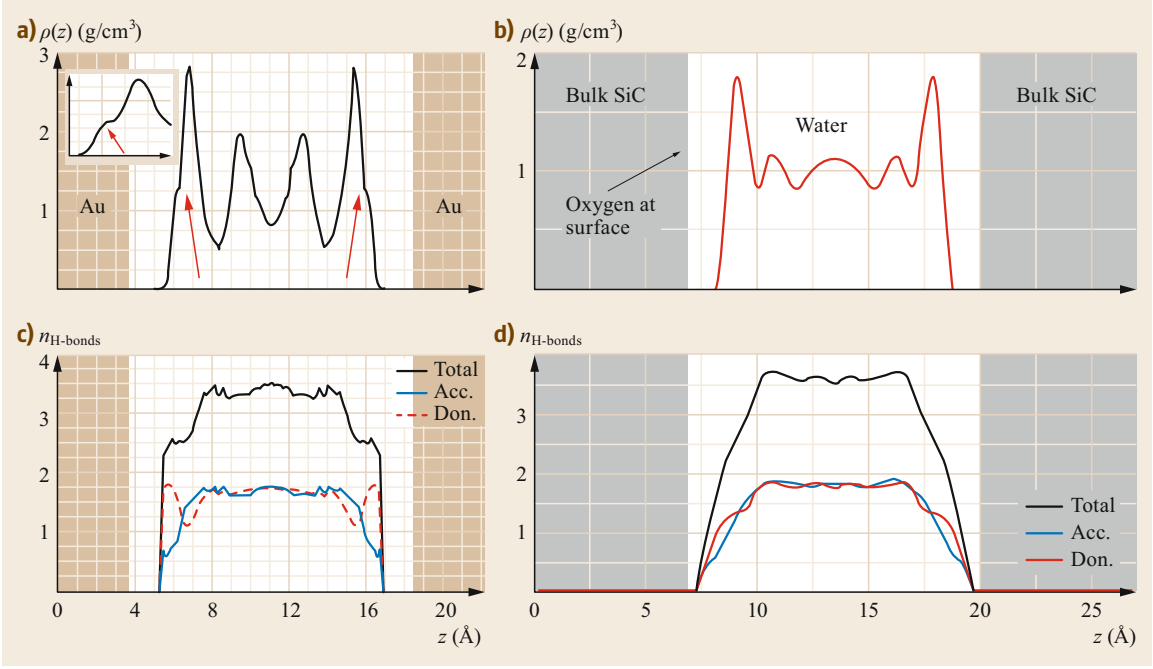

Fig. 5.16a–d Average oxygen density (**a**,**b**) and average number of water–water H bonds (**c**,**d**) as a function of the distance from the interface between liquid water and the Au(111) surface (**a**,**c**) and the hydroxylated Si-SiC(001) surface (**b**,**d**). The curves in (**c**) and (**d**) were obtained by counting the number of H-bond donors (*red curve*) or acceptors (*blue curve*) for each water molecule; the sum of the two curves is also reported (*black line*). The following geometric criterion to define a H bond was chosen: O−O distance < 3.5 Å and O−HO angle > 140°. Figure adapted with permission from [5.27, 144]. Copyright 2005 and 2011 American Chemical Society

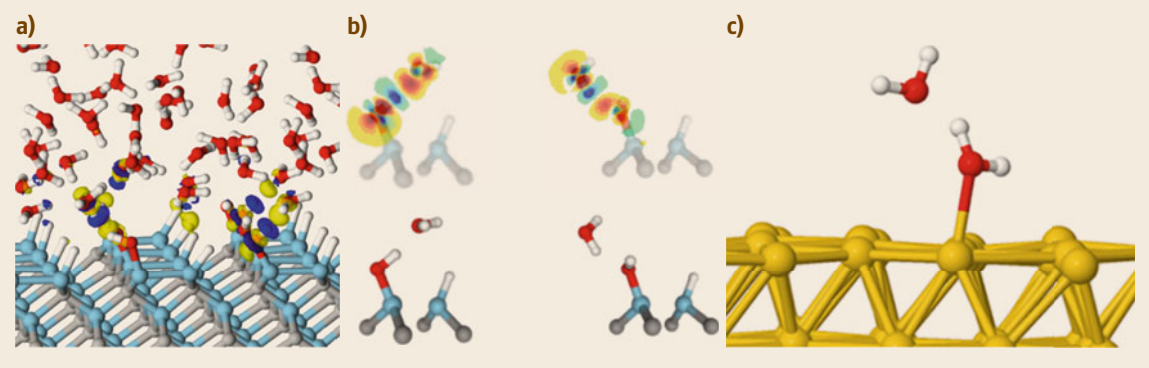

Fig. 5.17 **(a)** Isosurfaces of the electron density difference, ρ_{diff}, at the interface between the hydroxylated surface and liquid water. *Yellow* (*blue*) isosurfaces represent charge density increase (decrease) with respect to isolated surfaces. *Red*, *white*, *gray*, and *light blue spheres* represent oxygen, hydrogen, carbon, and silicon atoms, respectively. **(b)** Projection of the isosurface of the electron density difference onto a clip plane passing through an −OH surface group acting as a H-bond donor (*left panel*) and acceptor (*right panel*). **(c)** Representative snapshot (side view) along the molecular dynamics simulation run for the Au(111) surface exposed to 1 ML of water molecules. One water molecule interacts through its lone pair with a surface gold atom (Au−O = 2.5 Å) and at the same time it is involved in a hydrogen bond interaction with a water molecule in the gas phase (O−O = 2.6 Å). The other water molecules have been removed for a clearer rendering. Figure adapted with permission from [5.27, 144]. Copyright 2005 and 2001 American Chemical Society

found that upon H-bond formation the −OH group polarity is enhanced, and the H atom resides in a positive charge basin (blue spot). At the same time, the electron density in the region of the lone pair of the oxygen accepting the hydrogen bond increases. These results confirm that most of the surface/water interaction is local and strongly related to the capability of the hydroxyl groups at the surface to establish H bonds.

In the case of gold, the surface atoms are not able to directly form strong hydrogen bonds with surrounding water molecules, yet the interaction with the first liquid layer with the exposed gold atoms strongly affects the ability of these water molecules to establish hydrogen bonds. This is evidenced by an analysis of Fig. 5.16c, where the average number of hydrogen bonds per water molecule is reported as a function of the distance from the surface. Although, similarly to Si-SiC(001) far from the surface (beyond 4 Å) the average number of H bonds is the one observed for water in the liquid phase (with an equivalent number of H-bond acceptors and donors), the situation is different for the molecules of the surface hydration layer. These molecules have only one half of their hydration shell and, for this reason, form a smaller number of H bonds, yet, it is surprising to notice that at distances < 2.8 Å from the surface water molecules persistently behave as H-bond donors; their average number of donated H bonds is even slightly larger than that found far from the surface (i.e., for liquid water). This feature has not been observed for the hydroxylated SiC. By inspection of the spatial distribution of the water molecules in contact with the gold surface, i.e., the molecules of the density shoulder located at the 2.6 Å distance, it is revealed that the oxygen atoms preferentially reside at on-top Au(111) sites while the hydrogen atoms are uniformly distributed around them. This orientation is due to the formation of a dative-like bond between the lone pair at the oxygen atom of water and the gold atoms at the surface (Fig. 5.17c). This type of interaction is responsible for an oxygen-to-gold charge transfer, which favors a dynamical attractive coupling between the metal and the first wetting layer. Moreover, this interaction is responsible for the enhanced H-bond formation of the interfacial water. In fact, a detailed analysis of the hydrogen bond strength of interfacial water indicates that the intermolecular H bond is stronger in the presence of the gold surface by about 0.2 eV. In other words, interfacial water molecules, due to their interaction with the gold surface, appear more acidic and keener on donating H and forming H bonds that are stronger than those in the liquid phase, rendering the surface "hydrophilic-like."

The hydrophilic behavior of both gold and Si-SiC surfaces has also been addressed by calculating the average water dipole moment in the liquid sample in contact with the two surfaces. The dipole of a water molecule is strongly influenced by the number of hydrogen bonds that the molecule forms. In particular, the dipole increases passing from the gas phase 1.87 D (no H bonds) to the liquid 2.88 D (about 3.6 H bonds) and to the solid phase 3.00 D (4 H bonds). Interfacial water molecules would present different dipole values depending on the

hydrophobicity/hydrophilicity of the surface. In particular, at hydrophobic surfaces molecules have a number of H bonds typically smaller than in liquid and, for this reason, have smaller dipoles, while in the case of a hydrophilic surface, the molecules have dipoles similar to those found in liquid water [5.148]. Both in the case of the hydroxylated Si-SiC and in the case of the Au surface, it was found that the average dipole moments of the interfacial water molecules are unchanged with respect to the liquid value, and it is thus consistent with a surface of hydrophilic character.

In conclusion, the results presented above show for two sample surfaces how it is possible to achieve detailed atomistic models for solid/liquid interfaces together with insight into the electronic and bonding properties, by using predictive and accurate ab initio simulations. A detailed analysis of water restructuring at the surface shows that only the molecules in the first water layer are perturbed by the surface and that the interaction is local. The local nature of the water/solid interaction is confirmed by electronic structure analyses, indicating that all major changes in the charge density of the isolated liquid and the material slabs are localized at the interface. While in the case of Si-SiC, the hydrophilic character of the surface and the water rearrangements are guided by the presence of −OH groups at the surface, in the case of gold, it is rather the surface together with its hydration layer that has a hydrophilic character. This latter conclusion can be drawn based on the observation that the water molecules interacting with the gold atoms form H bonds that are stronger than the average hydrogen bond strength in liquid water.

5.7 Conclusions

In this short review, without presumption of completeness, we have presented a number of test cases where ab initio DFT simulations are found to be fundamental in the understanding and predictivity of specific issues relevant to parallel experiments in surface science. We chose to describe the protocols most suited to complement some experimental problems that range from the microscopic characterization of interfaces, mandatory for, e.g., the design of contacts, to functionalization and sensing. This has been done at the expense of a detailed formal description of the advances in theory, which are beyond the present scope. Yet, the field is continuously evolving, with the inclusions of many different approximations that allow us to study more complex systems, and eventually at the expense of simplicity, efficacy, and speed. For these issues we refer the reader to specific reviews, such as [5.149].

References

5.1 R.G. Parr, W. Yang: *Density-Functional Theory of Atoms and Molecules* (Oxford Univ. Press, New York 1989)

5.2 A.D. Becke: Perspective: Fifty years of density-functional theory in chemical physics, J. Chem. Phys. **140**, 18A301 (2014)

5.3 W. Chen, A. Pasquarello: First-principles determination of defect energy levels through hybrid density functionals and GW, J. Phys.: Condens. Matter **27**, 133202 (2015)

5.4 V.I. Anisimov, F. Aryasetiawan, A.I. Lichtenstein: First-principles calculations of the electronic structure and spectra of strongly correlated systems: The LDA + U method, J. Phys.: Condens. Matter **9**(4), 767 (1997)

5.5 L.A. Agapito, S. Curtarolo, M. Buongiorno Nardelli: Reformulation of DFT+U as a pseudohybrid Hubbard density functional for accelerated materials discovery, Phys. Rev. X **5**, 011006 (2015)

5.6 A. Janotti, D. Segev, C.G. Van de Walle: Effects of cation *d* states on the structural and electronic properties of III-nitride and II-oxide wide-band-gap semiconductors, Phys. Rev. B **74**, 045202 (2006)

5.7 A. Catellani, A. Galli: Theoretical studies of silicon carbide surfaces, Prog. Surf. Sci. **69**, 101–124 (2002)

5.8 G. Cicero, A. Ferretti, A. Catellani: Surface-induced polarity inversion in ZnO nanowires, Phys. Rev. B **201304**(R), 80 (2009)

5.9 H.J. Monkhorst, J.D. Pack: Special points for Brillouin-zone integrations, Phys. Rev. B **13**, 5188–5192 (1976)

5.10 R. Car, M. Parrinello: Unified approach for molecular dynamics and density-functional theory, Phys. Rev. Lett. **55**, 2471–2474 (1995)

5.11 M.C. Payne, M.P. Teter, D.C. Allan, T.A. Arias, J.D. Joannopoulos: Iterative minimization techniques for ab initio total-energy calculations: Molecular dynamics and conjugate gradients, Rev. Mod. Phys. **64**, 1045–1097 (1993)

5.12 D. Marx, J. Hutter: Ab initio molecular dynamics: theory and implementation. In: *NIC Series Vol. 3: Modern Methods and Algorithms of Quantum Chemistry – Proceedings*, 2nd edn., ed. by J. Gro-

tendorst (Forschungszentrum Juelich, Juelich 2000) pp. 329–478, NIC-Directors Ed.
5.13 A. Catellani, G. Galli, F. Gygi, F. Pellacini: Influence of stress and defects on the silicon-terminated SiC(001) surface structure, Phys. Rev. B **57**, 12255–12261 (1998)
5.14 A. Catellani, G. Galli, F. Gygi: Reconstruction and thermal stability of the cubic SiC (001) surfaces, Phys. Rev. Lett. **77**, 5090–5093 (1996)
5.15 M.C. Righi, C.A. Pignedoli, R. Di Felice, C.M. Bertoni, A. Catellani: Ab initio simulations of homoepitaxial SiC growth, Phys. Rev. Lett. **91**, 136101 (2003)
5.16 D. Hamann: Generalized norm-conserving pseudopotentials, Phys. Rev. B **40**, 2980–2987 (1989)
5.17 J. Pollmann, P. Krüger, M. Sabisch: Atomic and electronic structure of SiC surfaces from ab-initio calculations, Phys. Status Solidi (b) **202**, 421–445 (1997)
5.18 C. Stampfl, W. Mannstadt, R. Asahi, A.J. Freeman: Electronic structure and physical properties of early transition metal mononitrides: Density-functional theory LDA, GGA, and screened-exchange LDA FLAPW calculations, Phys. Rev. B **63**, 155106 (2001)
5.19 D. Vanderbilt: Soft self-consistent pseudopotentials in a generalized eigenvalue formalism, Phys. Rev. B **41**, 7892–7895 (1990)
5.20 J.P. Perdew, K. Burke, M. Ernzerhof: Generalized gradient approximation made simple, Phys. Rev. Lett. **77**, 3865–3868 (1996)
5.21 A. Catellani, G. Galli, P.L. Rigolli: Carbon lines on the cubic SiC(001) surface, Phys. Rev. B **62**, 4794–4797 (2000)
5.22 F. Bernardini, V. Fiorentini, D. Vanderbilt: Accurate calculation of polarization-related quantities in semiconductors, Phys. Rev. B **63**, 193201 (2001)
5.23 R.O. Jones, G. Seifert: Structure and bonding in carbon clusters C_{14} to C_{24}: Chains, rings, bowls, plates, and cages, Phys. Rev. Lett. **79**, 443–446 (1997)
5.24 J. Tersoff, D.R. Hamman: Theory of the scanning tunneling microscope, Phys. Rev. B **31**, 805–813 (1985)
5.25 V. Bermudez, J. Long: Characterization of reconstructed SiC(100) surfaces using soft-x-ray photoemission spectroscopy, Appl. Phys. Lett. **66**, 475–478 (1995)
5.26 S. Grimme: Semiempirical GGA-type density functional constructed with a long-range dispersion correction, J. Comput. Chem. **27**, 1787–1799 (2006)
5.27 G. Cicero, A. Calzolari, S. Corni, A. Catellani: Anomalous wetting layer at the Au(111) surface, J. Phys. Chem. Lett. **2**, 2582–2586 (2011)
5.28 A. Catellani, A. Calzolari: Functionalization of SiC(110) surfaces via porphyrin adsorption: Ab initio results, J. Phys. Chem. C **116**, 886–892 (2012)
5.29 A. Terentjevs, A. Catellani, D. Pendergast, G. Cicero: Importance of on-site corrections to the electronic and structural properties of InN in crystalline solid, nonpolar surface, and nanowire forms, Phys. Rev. B **82**, 165307 (2010)
5.30 A. Calzolari, A. Ruini, A. Catellani: Anchor group versus conjugation: Toward the gap-state engineering of functionalized ZnO(10-10) surface for optoelectronic applications, J. Am. Chem. Soc. **133**, 5893–5899 (2011)
5.31 P. Giannozzi, S. Baroni, N. Bonini, M. Calandra, R. Car, C. Cavazzoni, D. Ceresoli, G.L. Chiarotti, M. Cococcioni, I. Dabo: QUANTUM ESPRESSO: A modular and open-source software project for quantum simulations of materials, J. Phys.: Condens. Matter **21**, 395502 (2009), http://www.quantum-espresso.org
5.32 M.C. Righi, C.A. Pignedoli, G. Borghi, R. Di Felice, C.M. Bertoni, A. Catellani: Surface-induced stacking transition at SiC(0001), Phys. Rev. B **66**, 045320 (2002)
5.33 O. Madelung, U. Rössler, M. Schulz (Eds.): *Landolt-Boernstein: Numerical Data and Functional Relationship in Science and Technology*, New Series (Springer, Berlin 1982)
5.34 F. Bechstedt, P. Kaeckell, A. Zywietz, K. Karch, B. Adolph, K. Tenelsen, J. Furthmueller: Polytypism and properties of silicon carbide, Phys. Status Solidi (b) **202**, 35–62 (1997)
5.35 G.P. Brandino, G. Cicero, B. Bonferroni, A. Ferretti, A. Calzolari, C.M. Bertoni, A. Catellani: Polarization properties of (1-100) and (11-20) SiC surfaces from first principles, Phys. Rev. B **76**(8), 085322 (2007)
5.36 A. Dal Corso, M. Posternak, R. Resta, A. Baldereschi: *Ab initio* study of piezoelectricity and spontaneous polarization in ZnO, Phys. Rev. B **50**, 10715–10721 (1994)
5.37 A. Fissel, U. Kaiser, K. Pfennighaus, B. Schroeter, W. Richter: Growth of 6HSiC on 6H-SiC(0001) by migration enhanced epitaxy controlled to an atomic level using surface superstructures, Appl. Phys. Lett. **68**, 1204–1206 (1996)
5.38 M.C. Righi, C.A. Pignedoli, R. Di Felice, C.M. Bertoni, A. Catellani: Combined ab initio and kinetic Monte Carlo simulations of C diffusion on the $(\sqrt{3}\times\sqrt{3})\beta$-SiC(111) surface, Phys. Rev. B **71**, 075303 (2005)
5.39 U. Starke, J. Schardt, J. Bernhardt, M. Franke, K. Heinz: Stacking transformation from hexagonal to cubic SiC induced by surface reconstruction: A seed for heterostructure growth, Phys. Rev. Lett. **82**, 2107–2110 (1999)
5.40 G. Henkelman, H. Jonsson: Improved tangent estimate in the nudged elastic band method for finding minimum energy paths and saddle points, J. Chem. Phys. **113**, 9901 (2000)
5.41 V. Derycke, P. Soukiassian, F. Amy, Y. Chabal, M. D'Angelo, H. Enriquez, M. Silly: Nanochemistry at the atomic scale revealed in hydrogen-induced semiconductor surface metallization, Nat. Mater. **2**, 253–258 (2003)
5.42 P. Soukiassian, E. Wimmer, E. Celasco, C. Giallombardo, S. Bonanni, L. Vattuone, L. Savio, A. Tejeda, M. Silly, M. D'Angelo, F. Sirotti, M. Rocca: Hydrogen-induced nanotunnel opening within semiconductor subsurface, Nat. Commun. **4**, 1–10 (2013)
5.43 R.D. Felice, C.M. Bertoni, C.A. Pignedoli, A. Catellani: Hydrogen-induced surface metallization of b-SiC(100)-(3×2) revisited by density functional theory calculations, Phys. Rev. Lett. **94**, 116103 (2005)

5.44 X. Peng, P. Krueger, J. Pollmann: Metallization of the 3C-SiC(001)-(3x2) surface induced by hydrogen adsorption: A first-principles investigation, Phys. Rev. B **72**, 245320 (2005)

5.45 H. Chang, J. Wu, B. Gu, F. Liu, W. Duan: Physical origin of hydrogen-adsorption-induced metallization of the SiC surface: n-Type doping via formation of hydrogen bridge bond, Phys. Rev. Lett. **95**, 196803 (2005)

5.46 E. Rosso, R. Baierle, W. Orellana, R. Miwa: Hydrogen-induced nanotunnel structure on the C-terminated beta-SiC(001)-c(2 x 2) surface investigated by ab-initio calculations, Appl. Surf. Sci. **357**, 1753–1757 (2015)

5.47 F. Hoetzel, K. Seino, S. Chandola, E. Speiser, N. Esser, F. Bechstedt, A. Pucci: Metal-to-insulator transition in Au chains on Si(111)-5x2-Au by band filling: Infrared plasmonic signal and ab initio band structure calculation, J. Phys. Chem. Lett. **6**, 3615–3620 (2015)

5.48 J.N. Crain, M.D. Stiles, J.A. Stroscio, D.T. Pierce: Electronic effects in the length distribution of atom chains, Phys. Rev. Lett. **96**, 156801 (2006)

5.49 H.J. Snaith, L. Schmidt-Mende: Advances in liquid-electrolyte and solid-state dye-sensitized solar cells, Adv. Mater. **19**, 3187–3200 (2007)

5.50 M. Nunez, M. Buongiorno Nardelli: First-principles theory of metal-alkaline earth oxide interfaces, Phys. Rev. B **73**, 235422 (2006)

5.51 J.H. Harding, D.M. Duffy, M.L. Sushko, P.M. Rodger, D. Quigley, J.A. Elliot: Computational techniques at the organic-inorganic interface in biomineralization, Chem. Rev. **108**, 4823–4854 (2008)

5.52 S.R. Whaley, D.S. English, E.L. Hu, P.F. Barbara, A.M. Belcher: Selection of peptides with semiconductor binding specificity for directed nanocrystal assembly, Nature **405**, 665–668 (2000)

5.53 A. Calzolari, G. Cicero, C. Cavazzoni, R. Di Felice, A. Catellani, S. Corni: Hydroxyl-rich β-sheet adhesion to the gold surface in water by first-principle simulations, J. Am. Chem. Soc. **132**, 4790–4795 (2010)

5.54 B.R. O', M. Graetzel: A low-cost, high-efficiency solar cell based on dye-sensitized colloidal TiO_2 films, Nature **353**, 737–740 (1991)

5.55 B.E. Hardin, H.J. Snaith, M.D. McGehee: The renaissance of dye-sensitized solar cells, Nat. Photonics **6**, 162–169 (2012)

5.56 S. Schoell, M. Sachsenhauser, A. Oliveros, J. Howgate, M. Stutzmann, M. Brandt, C. Frewin, S. Saddow, I. Sharp: Organic functionalization of 3C-SiC surfaces, ACS Appl. Mater. Interfaces **5**, 1393–1399 (2013)

5.57 Y. Yin, A.P. Alivisatos: Colloidal nanocrystal synthesis and the organic-inorganic interface, Nature **437**, 664–670 (2005)

5.58 D. Belanger, J. Pinson: Electrografting: A powerful method for surface modification, Chem. Soc. Rev. **40**, 3995–4048 (2011)

5.59 A. Calzolari, A. Ruini, A. Catellani: Surface effects on catechol/semiconductor interfaces, J. Phys. Chem. C **116**, 17158–17163 (2012)

5.60 T. Gillich, E.M. Benetti, E. Rakhmatullina, R. Konradi, W. Li, A. Zhang, A.D. Schlater, M. Textor: Self-assembly of focal point oligo-catechol ethylene glycol dendrons on titanium oxide surfaces: Adsorption kinetics, surface characterization, and nonfouling properties, J. Am. Chem. Soc. **133**(28), 10940–10950 (2011)

5.61 D. Vogel, P. Krüger, J. Pollmann: Self-interaction and relaxation-corrected pseudopotentials for II-VI semiconductors, Phys. Rev. B **54**, 5495–5511 (1996)

5.62 O. Dulub, L.A. Boatner, U. Diebold: STM study of the geometric and electronic structure of ZnO(0001)-Zn, (0001)-O, (1010), and (1120) surfaces, Surf. Sci. **519**(3), 201–217 (2002)

5.63 P. Gopal, M. Fornari, S. Curtarolo, L.A. Agapito, L.S.I. Liyanage, M. Buongiorno Nardelli: Improved predictions of the physical properties of Zn- and Cd-based wide band-gap semiconductors: A validation of the ACBN0 functional, Phys. Rev. B **91**(24), 245202–245209 (2015)

5.64 M. Law, L.E. Greene, J.C. Johnson, R. Saykally, P. Yang: Nanowire dye-sensitized solar cells, Nat. Mater. **4**, 455–459 (2005)

5.65 A. Catellani, G. Cicero, G. Galli: Wetting behavior of low-index cubic SiC surfaces, J. Chem. Phys. **124**(2), 024707 (2006)

5.66 G.F. Moore, J.D. Blakemore, R.L. Milot, J.F. Hull, H. Song, L. Cai, C.A. Schmuttenmaer, R.H. Crabtree, G.W. Brudvig: A visible light water-splitting cell with a photoanode formed by codeposition of a high-potential porphyrin and an iridium water-oxidation catalyst, Energy Environ. Sci. **4**, 2389–2392 (2011)

5.67 P.G. Datskos, T. Thundat, N.V. Lavrik: *Micro and Nanocantilever Sensors, Enciclopedia of Nanoscience and Nanotechnology*, Vol. 5 (American Scientific Publishers, Stevenson Ranch 2004) pp. 551–560

5.68 O.H. Nielsen, R.M. Martin: Stresses in semiconductors: Ab initio calculations on Si, Ge, and GaAs, Phys. Rev. B **32**, 3792–3805 (1985)

5.69 P.G. Dacosta, O.H. Nielsen, K. Kunc: Stress theorem in the determination of static equilibrium by the density functional method, J. Phys. C **19**(17), 3163 (1986)

5.70 R.E. Miller, V.B. Shenoy: Size-dependent elastic properties of nanosized structural elements, Nanotechnology **11**(3), 139 (2000)

5.71 F. Risplendi, A. Ricci, G. Cicero: Functionalization layer effect on the mechanical properties of silicon based micro-cantilever mass sensors: A theoretical study, Sens. Actuators B **195**, 177–180 (2014)

5.72 C. Ziegler: Cantilever-based biosensors, Anal. Bioanal. Chem. **379**(7), 946–959 (2004)

5.73 F. Risplendi, G. Cicero: Si(111) surface functionalized with H-bonded SAM: A theoretical study, Appl. Surf. Sci. **267**, 17–20 (2013)

5.74 A. Ricci, C. Ricciardi: A new finite element approach for studying the effect of surface stress on microstructures, Sens. Actuators A **159**(2), 141–148 (2010)

5.75 S. Kim, K.D. Kihm: Effect of adsorption-induced surface stress change on the stiffness of a microcantilever used as a salinity detection sensor, Appl. Phys. Lett. **93**(8), 081911 (2008)

5.76 Y.-F. Sun, S.-B. Liu, F.-L. Meng, J.-Y. Liu, Z. Jin, L.-T. Kong, J.-H. Liu: Metal oxide nanostructures and their gas sensing properties: A review, Sensors **12**(3), 2610 (2012)

5.77 K.K. Korir, A. Catellani, G. Cicero: Ethanol gas sensing mechanism in ZnO nanowires: An ab initio study, J. Phys. Chem. C **118**(42), 24533–24537 (2014)

5.78 A. Tamvakos, K. Korir, D. Tamvakos, D. Calestani, G. Cicero, D. Pullini: NO_2 Gas sensing mechanism of ZnO thin-film transducers: Physical experiment and theoretical correlation study, ACS Sensors **1**(4), 406–412 (2016)

5.79 N. Tiwale: Zinc oxide nanowire gas sensors: Fabrication, functionalisation and devices, Mater. Sci. Technol. **31**(14), 1681–1697 (2015)

5.80 G. Korotcenkov: Metal oxides for solid-state gas sensors: What determines our choice?, Mater. Sci. Eng.: B **139**(1), 1–23 (2007)

5.81 M. Batzill, U. Diebold: The surface and materials science of tin oxide, Prog. Surf. Sci. **79**(2–4), 47–154 (2005)

5.82 E.V. Lavrov, F. Börrnert, J. Weber: Dominant hydrogen-oxygen complex in hydrothermally grown ZnO, Phys. Rev. B **71**, 035205 (2005)

5.83 G.A. Shi, M. Stavola, S.J. Pearton, M. Thieme, E.V. Lavrov, J. Weber: Hydrogen local modes and shallow donors in ZnO, Phys. Rev. B **72**, 195211 (2005)

5.84 A. Catellani, A. Ruini, G. Cicero, A. Calzolari: First principles description of the electronic properties of doped ZnO, Phys. Status Solidi (b) **250**(10), 2106–2109 (2013)

5.85 F. Fabbri, M. Villani, A. Catellani, A. Calzolari, G. Cicero, D. Calestani, G. Calestani, A. Zappettini, B. Dierre, T. Sekiguchi, G. Salviati: Zn vacancy induced green luminescence on non-polar surfaces in ZnO nanostructures, Sci. Rep. **4**, 5158 (2014)

5.86 H. Lüth: *Solid Surfaces, Interfaces and Thin Films* (Springer, Berlin Heidelberg 2001)

5.87 S.M. Sze, K.K. Ng: *Physics of Semiconductor Devices* (Wiley, New York 2006)

5.88 A.P. Alivisatos: The use of nanocrystals in biological detection, Nat. Biotechnol. **22**, 47–52 (2004)

5.89 N. Tessler, V. Medvedev, M. Kazes, S.-H. Kan, U. Banin: Light-emitting diodes efficient near-infrared polymer nanocrystal, Science **295**, 1506–1508 (2002)

5.90 S. Coe, W.-K. Woo, M. Bawendi, V. Bulović: Electroluminescence from single monolayers of nanocrystals in molecular organic devices, Nature **420**, 800–803 (2002)

5.91 I. Gur, N. Fromer, M.L. Geier, A.P. Alivisatos: Air-stable all-inorganic nanocrystal solar cells processed from solution, Science **310**, 462–465 (2005)

5.92 J. Schrier, D.O. Demchenko, L.-W. Wang: Optical properties of ZnO/ZnS and ZnO/ZnTe heterostructures for photovoltaic applications, Nano Lett. **7**, 2377–2382 (2007)

5.93 D. Gross, A.S. Susha, T.A. Klar, E. Da Como, A.L. Rogach, J. Feldmann: Charge separation in type-II tunneling structures of closed-packed CdTe and CdSe nanocrystals, Nano Lett. **8**, 1482–1485 (2008)

5.94 N.N. Hewa-Kasakarage, P.Z. El-Khoury, A.N. Tarnovsky, M. Kirsanova, I. Nemitz, A. Nemchinov, M. Zamkov: Ultrafast carrier dynamics in type II ZnSe/CdS/ZnSe nanobarbells, ACS Nano **4**, 1837–1844 (2010)

5.95 M. Rocca: Low-energy EELS investigation of surface electronic excitations on metals, Surf. Sci. Rep. **22**, 1–71 (1995)

5.96 A. Calzolari, M. Buongiorno Nardelli: Dielectric properties and Raman spectra of ZnO from a first principles finite-differences/finite-fields approach, Sci. Rep. **3**, 2999 (2013)

5.97 P. D'Amico, L. Agapito, A. Catellani, A. Ruini, S. Curtarolo, M. Fornari, M. Buongiorno Nardelli, A. Calzolari: Accurate ab initio tight-binding Hamiltonians: Effective tools for electronic transport and optical spectroscopy from first principles, Phys. Rev. B **94**, 165166 (2016)

5.98 M. Peressi, N. Binggeli, A. Baldereschi: Band engineering at interfaces: Theory and numerical experiments, J. Phys. D: Appl. Phys. **31**(11), 1273 (1998)

5.99 A. Baldereschi, S. Baroni, R. Resta: Band offsets in lattice-matched heterojunctions: A model and first-principles calculations for GaAs/AlAs, Phys. Rev. Lett. **61**, 734–737 (1988)

5.100 H. von Wenckstern, H. Schmidt, M. Brandt, A. Lajn, R. Pickenhain, M. Lorenz, M. Grundmann, D. Hofmann, A. Polity, B. Meyer, H. Saal, M. Binnewies, A. Borger, K.-D. Becker, V. Tikhomirov, K. Jug: Anionic and cationic substitution in ZnO, Progr. Solid State Chem. **37**(2–3), 153–172 (2009)

5.101 S. Kim, B.S. Kang, F. Ren, Y.W. Heo, K. Ip, D.P. Norton, S.J. Pearton: Contacts to p-type ZnMgO, Appl. Phys. Lett. **84**(11), 1904–1906 (2004)

5.102 L.J. Brillson, Y. Lu: ZnO Schottky barriers and Ohmic contacts, J. Appl. Phys. **109**(12), 121301 (2011)

5.103 N.K. Reddy, Q. Ahsanulhaq, J.H. Kim, M. Devika, Y.B. Hahn: Selection of non-alloyed ohmic contacts for ZnO nanostructure based devices, Nanotechnology **18**(44), 445710 (2007)

5.104 A. Catellani, A. Calzolari, A. Ruini: Effect of ultrathin gold on the Ohmic-to-Schottky transition in Al/ZnO contacts: A first-principles investigation, J. Appl. Phys. **115**, 043711–043715 (2014)

5.105 A. Calzolari, M. Bazzani, A. Catellani: Dipolar and charge transfer effects on the atomic stabilization of ZnO polar surfaces, Surf. Sci. **607**, 181–186 (2013)

5.106 M. Bazzani, A. Neroni, A. Calzolari, A. Catellani: Optoelectronic properties of Al:ZnO: Critical dosage for an optimal transparent conductive oxide, Appl. Phys. Lett. **98**(12), 121907 (2011)

5.107 H. Mondragón-Suárez, A. Maldonado, M. la L Olvera, A. Reyes, R. Castanedo-Pérez, G. Torres-Delgado, R. Asomoza: ZnO:Al thin films obtained by chemical spray: Effect of the Al concentration, Appl. Phys. Lett. **193**, 52–59 (2002)

5.108 C.S. Lao, J. Liu, P. Gao, L. Zhang, D. Davidovic, R. Tummala, Z.L. Wang: ZnO Nanobelt/nanowire

Schottky diodes formed by dielectrophoresis alignment across Au electrodes, Nano Lett. **6**(2), 263–266 (2006)

5.109 C. Soci, A. Zhang, B. Xiang, S.A. Dayeh, D.P.R. Aplin, J. Park, X.Y. Bao, Y.H. Lo, D. Wang: ZnO nanowire UV photodetectors with high internal gain, Nano Lett. **7**(4), 1003–1009 (2007)

5.110 V.I. Klimov, S.A. Ivanov, J. Nanda, M. Achermann, I. Bezel, J.A. McGuire, A. Piryatinski: Single-exciton optical gain in semiconductor nanocrystals, Nature **447**, 441–446 (2007)

5.111 X. Michalet, F.F. Pinaud, L.A. Bentolila, J.M. Tsay, S. Doose, J.J. Li, G. Sundaresan, A.M. Wu, S.S. Gambhir, S. Weiss: Quantum dots for live cells, in vivo imaging, and diagnostics, Science **307**, 538–544 (2005)

5.112 J. Chen, L. Xu, W. Li, X. Gou: α-Fe_2O_3 nanotubes in gas sensor and lithium-ion battery applications, Adv. Mater. **17**, 582–586 (2005)

5.113 R. Yan, D. Gargas, P. Yang: Nanowire photonics, Nat. Photonics **3**, 569–576 (2009)

5.114 Y. Su, C. Liu, S. Brittman, J. Tang, A. Fu, N. Kornienko, Q. Kong, P. Yang: Single-nanowire photoelectrochemistry, Nat. Nanotechnol. **11**, 609–612 (2016)

5.115 E.C. Garnett, P. Yang: Silicon nanowire radial p-n junction solar cells, J. Am. Chem. Soc. **130**(29), 9224–9225 (2008)

5.116 X. Duan, Y. Huang, Y. Cui, J. Wang, C.M. Lieber: Indium phosphide nanowires as building blocks for nanoscale electronic and optoelectronic devices, Nature **409**, 66–69 (2001)

5.117 M. Zhou, H. Zhu, Y. Jiao, Y. Rao, S. Hark, Y. Liu, L. Peng, Q. Li: Optical and Electrical properties of Ga-doped ZnO nanowire arrays on conducting substrates, J. Phys. Chem. C **113**(20), 8945–8947 (2009)

5.118 Q. Xu, H. Schmidt, S. Zhou, K. Potzger, M. Helm, H. Hochmuth, M. Lorenz, A. Setzer, P. Esquinaz, C. Meinecke, M. Grundmann: Room temperature ferromagnetism in ZnO films due to defects, Appl. Phys. Lett. **92**, 082508 (2008)

5.119 K. Tomioka, J. Motohisa, S. Hara, K. Hiruma, T. Fukui: GaAs/AlGaAs core multishell nanowire-based light-emitting diodes on Si, Nano Lett. **10**(5), 1639–1644 (2010)

5.120 Y. Tak, S.J. Hong, J.S. Lee, K. Yong: Fabrication of ZnO/CdS core/shell nanowire arrays for efficient solar energy conversion, J. Mater. Chem. **19**, 5945–5951 (2009)

5.121 L.J. Lauhon, M.S. Gudiksen, D. Wang, C.M. Lieber: Epitaxial core-shell and core-multishell nanowire heterostructures, Nature **420**, 57–61 (2002)

5.122 J. Xiang, W. Lu, Y. Hu, Y. Wu, H. Yan, C.M. Lieber: Ge/Si nanowire heterostructures as high-performance field-effect transistors, Nature **441**, 489–493 (2006)

5.123 J. Li, D. Zhao, X. Meng, Z. Zhang, J. Zhang, D. Shen, Y. Lu, X. Fan: Enhanced ultraviolet emission from ZnS-coated ZnO nanowires fabricated by self-assembling method, J. Phys. Chem. B **110**(30), 14685–14687 (2006)

5.124 X.Q. Meng, H. Peng, Y.Q. Gai, J. Li: Influence of ZnS and MgO shell on the photoluminescence properties of ZnO core/shell nanowires, J. Phys. Chem. C **114**, 1467–1471 (2010)

5.125 X. Fang, Z. Wei, R. Chen, J. Tang, H. Zhao, L. Zhang, D. Zhao, D. Fang, J. Li, F. Fang, X. Chu, X. Wang: Influence of exciton localization on the emission and ultraviolet photoresponse of ZnO/ZnS core–shell nanowires, ACS Appl. Mater. Interfaces **7**(19), 10331–10336 (2015)

5.126 X. Fang, Z. Wei, Y. Yang, R. Chen, Y. Li, J. Tang, D. Fang, H. Jia, D. Wang, J. Fan, X. Ma, B. Yao, X. Wang: Ultraviolet electroluminescence from ZnS@ZnO core–shell nanowires/p-GaN introduced by exciton localization, ACS Appl. Mater. Interfaces **8**(3), 1661–1666 (2016)

5.127 S. Jeong, M. Choe, J.-W. Kang, M.W. Kim, W.G. Jung, Y.-C. Leem, J. Chun, B.-J. Kim, S.-J. Park: High-performance photoconductivity and electrical transport of ZnO/ZnS core/shell nanowires for multifunctional nanodevice applications, ACS Appl. Mater. Interfaces **6**(9), 6170–6176 (2014)

5.128 A. Catellani, A. Ruini, M. Buongiorno Nardelli, A. Calzolari: Unconventional co-existence of plasmon and thermoelectric activity in In:ZnO nanowires, RSC Advances **5**(56), 44865–44872 (2015)

5.129 S.A. Maier: *Plasmonics: Fundamentals and Applications* (Springer Science-Business Media, New York 2007)

5.130 W.A. Andrew, W.L. Barnes: Plasmonic materials, Adv. Mater. **19**, 3771–3782 (2007)

5.131 J. Li, S.K. Cushing, F. Meng, T.R. Senty, A.D. Bristow, N. Wu: Plasmon-induced resonance energy transfer for solar energy conversion, Nat. Photonics **9**(9), 601–607 (2015)

5.132 H.A. Atwater, A. Polman: Plasmonics for improved photovoltaic devices, Nat. Mater. **9**, 205–213 (2010)

5.133 H. Kim, M. Osofsky, S.M. Prokes, O.J. Glembocki, A. Piqué: Optimization of Al-doped ZnO films for low loss plasmonic materials at telecommunication wavelengths, Appl. Phys. Lett. **102**(17), 171103 (2013)

5.134 H. Lu, B.P. Cumming, M. Gu: Highly efficient plasmonic enhancement of graphene absorption at telecommunication wavelengths, Opt. Lett. **40**(15), 3647–3650 (2015)

5.135 A. Calzolari, A. Ruini, A. Catellani: Transparent conductive oxides as near-IR plasmonic materials: The case of Al-doped ZnO derivatives, ACS Photonics **1**(8), 703–709 (2014)

5.136 M. Pelton, J. Aizpurua, G. Bryant: Metal-nanoparticle plasmonics, Laser Photonics Rev. **2**(3), 136–159 (2008)

5.137 G.V. Naik, V.M. Shalaev, A. Boltasseva: Alternative plasmonic materials: Beyond gold and silver, Adv. Mater. **25**(24), 3264–3294 (2013)

5.138 G.V. Naik, J. Liu, A. Kildishev, V.M. Shalaev, A. Boltasseva: Demonstration of Al:ZnO as plasmonic component for near infrared metamaterials, Proc. Natl. Am. Soc. **109**(23), 8834–8838 (2012)

5.139 J.H. Noh, H.S. Jung, J.-K. Lee, J.Y. Kim, C.M. Cho, J. An, K.S. Hong: Reversible change in electrical and

optical properties in epitaxially grown Al-doped ZnO thin films, J. Appl. Phys. **104**(7), 073706 (2008)
5.140 A. Frölich, M. Wegener: Spectroscopic characterization of highly doped ZnO films grown by atomic-layer deposition for three dimensional infrared metamaterials, Opt. Mater. Expr. **1**(5), 883–889 (2011)
5.141 K. Ellmer: Past achievements and future challanges in the development of optically transparent electrodes, Nat. Photonics **6**(12), 809–817 (2012)
5.142 A. Catellani, A. Ruini, A. Calzolari: Optoelectronic properties and color chemistry of native point defects in Al:ZnO transparent conductive oxide, J. Mater. Chem. C **3**(32), 8419–8424 (2015)
5.143 T.S. Moss: The interpretation of the properties of indium antimonide, Proc. Phys. Soc. Sec. B **67**(10), 775 (1954)
5.144 G. Cicero, J.C. Grossman, A. Catellani, G. Galli: Water at a hydrophilic solid surface probed by ab initio molecular dynamics: inhomogeneous thin layers of dense fluid, J. Am. Chem. Soc. **127**(18), 6830–6835 (2005)
5.145 J.C. Grossman, E. Schwegler, E.W. Draeger, F. Gygi, G. Galli: Towards an assessment of the accuracy of density functional theory for first principles simulations of water, J. Chem. Phys. **120**(1), 300–311 (2004)
5.146 E. Schwegler, J.C. Grossman, F. Gygi, G. Galli: Towards an assessment of the accuracy of density functional theory for first principles simulations of water. II, J. Chem. Phys. **121**(11), 5400–5409 (2004)
5.147 S.H. Lee, P.J. Rossky: A comparison of the structure and dynamics of liquid water at hydrophobic and hydrophilic surfaces: A molecular dynamics simulation study, J. Chem. Phys. **100**(4), 3334–3345 (1994)
5.148 G. Cicero, J.C. Grossman, E. Schwegler, F. Gygi, G. Galli: Water confined in nanotubes and between graphene sheets: A first principle study, J. Am. Chem. Soc. **130**(6), 1871–1878 (2008)
5.149 K. Lejaeghere, G. Bihlmayer, T. Björkman, P. Blaha, S. Blügel, V. Blum, D. Caliste, I.E. Castelli, S.J. Clark, A. Dal Corso, S. de Gironcoli, T. Deutsch, J.K. Dewhurst, I. Di Marco, C. Draxl, M. Dułak, O. Eriksson, J.A. Flores-Livas, K.F. Garrity, L. Genovese, P. Giannozzi, M. Giantomassi, S. Goedecker, X. Gonze, O. Grånäs, E.K.U. Gross, A. Gulans, F. Gygi, D.R. Hamann, P.J. Hasnip, N.A.W. Holzwarth, D. Iuşan, D.B. Jochym, F. Jollet, D. Jones, G. Kresse, K. Koepernik, E. Küçükbenli, Y.O. Kvashnin, I.L.M. Locht, S. Lubeck, M. Marsman, N. Marzari, U. Nitzsche, L. Nordström, T. Ozaki, L. Paulatto, C.J. Pickard, W. Poelmans, M.I.J. Probert, K. Refson, M. Richter, G.-M. Rignanese, S. Saha, M. Scheffler, M. Schlipf, K. Schwarz, S. Sharma, F. Tavazza, P. Thunström, A. Tkatchenko, M. Torrent, D. Vanderbilt, M.J. van Setten, V. Van Speybroeck, J.M. Wills, J.R. Yates, G.-X. Zhang, S. Cottenier: Reproducibility in density functional theory calculations of solids, Science **351**(6280), aad3000 (2016)

Arrigo Calzolari

Centro NANO-S3
CNR-Istituto Nanoscienze
Modena, Italy
arrigo.calzolari@nano.cnr.it

Arrigo Calzolari graduated in physics in 2003 at University of Modena and Reggio Emilia in Modena, Italy. He has been a researcher at the Istituto Nanoscienze of the National Research Council of Italy (CNR-NANO) since 2010. His research activity is focuses on the ab-initio study of the structural, electronic, optical, vibrational, and transport properties of nanostructures, molecules, surfaces, and interfaces, for energy conversion, molecular electronics, and nanotechnology applications.

Giancarlo Cicero

Centro NANO-S3
CNR-Istituto Nanoscienze
Modena, Italy
Dipt. di Scienza Applicata e Tecnologia

Politecnico di Torino
Torino, Italy
giancarlo.cicero@polito.it

Giancarlo Cicero received his PhD in Physics in 2003 from the University of Torino. He is currently at the Politecnico di Torino as Associate Professor in the Materials Science and Chemical Engineering Department. His main expertise is the atomistic simulations of surfaces and nanostructures to be employed in nanoscale devices and, in particular, third generation solar cells.

Alessandra Catellani

Centro NANO-S3
CNR-Istituto Nanoscienze
Modena, Italy
alessandra.catellani@nano.cnr.it

Alessandra Catellani is Senior Researcher at the Istituto Nanoscienze of the National Research Council of Italy (CNR-NANO). Her main research interests are related to the ab-initio simulation of structural and electronic properties of low-dimensional systems, such as nanostructures and interfaces, for energy conversion and (nano)sensor applications.

6. Surfaces of Bulk Oxides

Jacques Jupille

Following a brief overview that illustrates the strong research activity dealing with the surface structures of binary oxide, two issues are addressed herein: the relaxation at oxide surfaces and the surface structure of ternary oxides. As a quite general phenomenon, the compensation of the stress generated by the creation of a surface results in relaxation of interlayer spacings and, in the case of ionic solids, in difference in displacement between anions and cations, the so-called rumpling. Rocksalt oxides are of particular interest in this context because they form a series of compounds of identical structure of which only the cations change. Due to the gradual variation they present over the series, they offer a unique playground for the critical analysis of relaxation and rumpling at ionic surfaces.

The many applications of the oxides of perovskite structure require the control of terminations at the atomic scale. Despite puzzling discrepancies in preparation conditions, many $SrTiO_3$(100) surface reconstructions—c(4 × 2), c(6 × 2), ($\sqrt{5} \times \sqrt{5}$)-R26.6°, ($\sqrt{13} \times \sqrt{13}$)-R33.7°—are reproducibly obtained, leading to a set of structural models. However, the demonstration that strontium and stoichiometry defects play a direct role in reconstructions questions the present models and challenges the goal of preparation of single-terminated $SrTiO_3$(100) surfaces of uniform structure.

6.1 Overview

Oxides are ubiquitous in natural and industrial environments, whether in the form of bulk compounds or corrosion layers covering metals and alloys. In the many circumstances in which oxides or oxidized objects come into chemical or mechanical contact with foreign media, the knowledge of surface structures is essential to understanding surface chemistry [6.1, 2]. Surface structures are key ingredients of the behavior of oxides in catalysis [6.3, 4], photochemistry [6.5–7], gas sensing [6.8, 9], microelectronics [6.10], and adhesion [6.11]. They are also central in geochemistry, in the context of minerals in the environment [6.12–16]. In surface science of oxides, the study of thin films fruitfully completes the analysis of single crystals [6.17–22]. The primary incentive for synthesis of thin films was to escape the limitations imposed by the insulating character of most oxide substrates and to enable imaging of surfaces at the atomic scale by scanning tunneling microscopy (STM). However, the field quickly turned out to be a prodigious source of original structures that do not exist in bulk [6.17–21]. Synthesis of thin films offered a versatile approach for the study of oxide nanostructures in reduced dimensions [6.18, 19] and microscopic characterization of interfaces [6.18, 22]. The important role played by defects is another aspect specific to oxide surfaces. As detailed in a book dedicated to defects on oxide surfaces [6.23] and in a number of review articles, defects are strongly involved in the chemistry and physics of metal oxide surfaces. Defects can be classified according to topological features that include terraces, steps, kinks and corners [6.24–26], and point defects, which

M. Rocca, T.S. Rahman, L. Vattuone (Eds.), *Springer Handbook of Surface Science*, Springer Handbooks,
https://doi.org/10.1007/978-3-030-46906-1_6

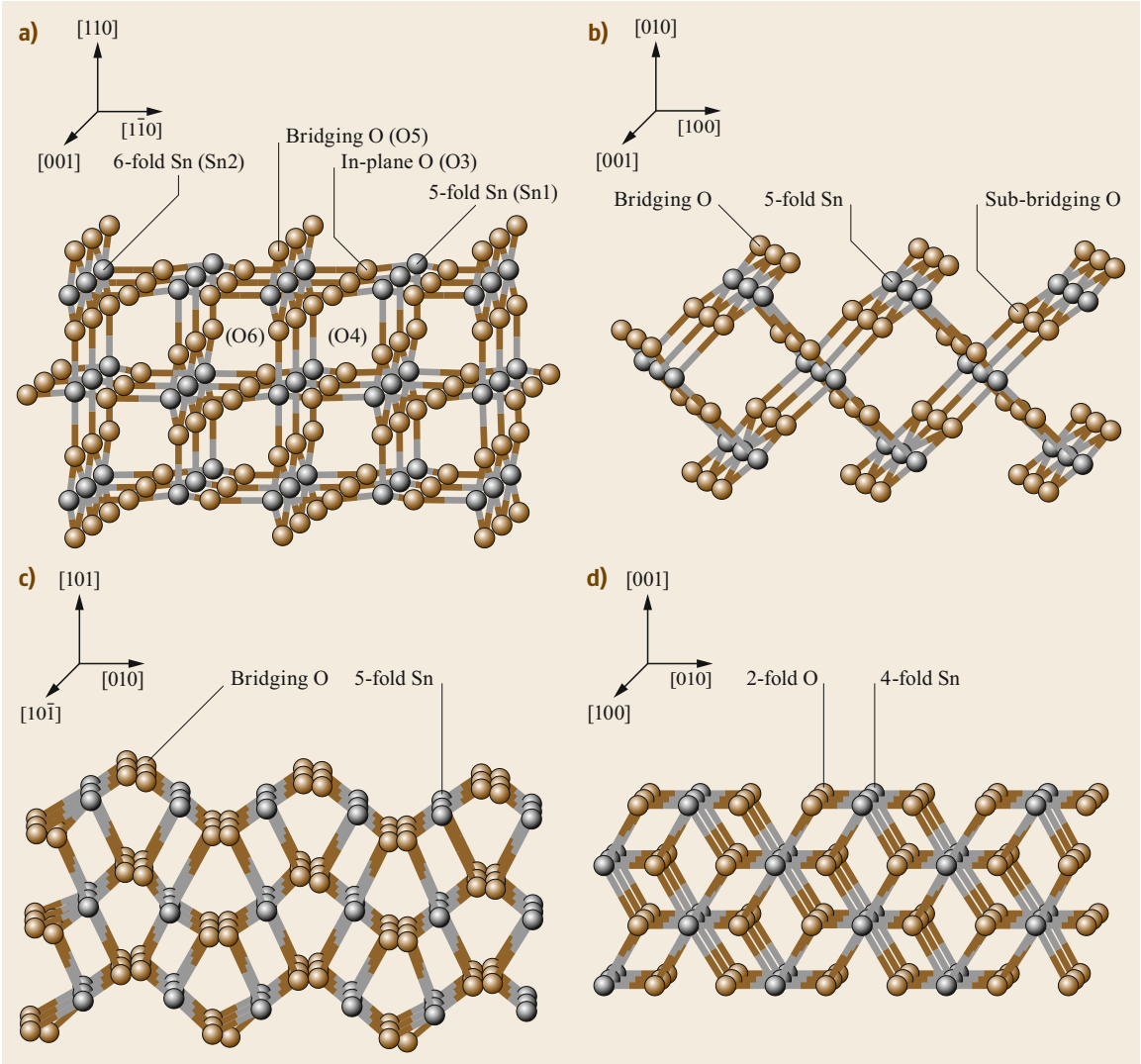

Fig. 6.1a–d The low-index surfaces of SnO_2: **(a)** (110); **(b)** (100); **(c)** (101); **(d)** (001), with ions shown in unrelaxed positions. Sn and O atoms are represented by *gray* and *brown spheres*, respectively. Coordinations of surface and subsurface ions are indicated (Reprinted from [6.27], with permission from Elsevier)

involve vacancies, adatoms, and interstitial and substitutional atoms. Many efforts have been devoted to the formation of these at the surface of metal oxides, either reducible [6.28, 29] or irreducible [6.28], and of rare earth oxides [6.29]. The main related issues are the identification of defects [6.30–34] and the localization of defective states [6.35–37], the impact of the defects created on the crystallographic [6.38, 39] and electronic structure [6.9], and their role in surface chemistry and photochemistry [6.5, 6] and electronic transport [6.40]. The omnipresence of thin films, nanoparticles, and extended or point defects explains the growing role of near-field microscopy in the study of the surface crystallography of oxides, since the flexibility of the method allows for the combination of structural and spectroscopic analysis at different scales. In support of the experiment or in parallel with it, numerical simulations have increasing importance. To better describe localized states, density functional theory approaches are complemented by hybrid functionals, which involve Fock and DFT (density functional theory) exchange energy, and the so-called DFT + U method in which the Coulomb interaction is partially screened.

Oxide surfaces are made very complex by changes in stoichiometry, reconstructions, stabilization processes required by polar terminations [6.41–43], and

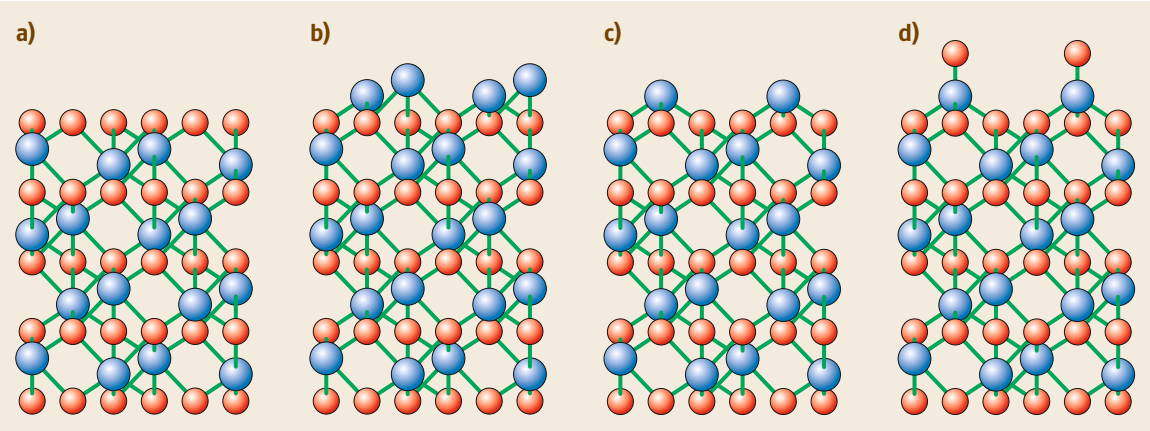

Fig. 6.2a–d Side view of the four possible (0001) terminations of the corundum structure (see text) **(a)** O_3; **(b)** full-metal; **(c)** half-metal; **(d)** Me=O (Reprinted with permission from [6.44]. Copyright 2013 American Chemical Society)

the sometimes uncontrolled reactivity with hydrogen or water. As a result, since the 2000s, where structures of oxide surfaces have been reviewed extensively, most of the dedicated articles focus on a limited selection of compounds, often only one. In this introductory part of the chapter, we discuss recent advances regarding the main oxide families—titanium oxide, SnO_2 and transparent conductive oxides, corundum-phase oxides, oxides of rocksalt structure, vanadium oxides, iron oxides, ceria, and zinc oxide—and the reasons that prompted us to focus the present review on oxides of rocksalt and perovskite structure.

TiO_2 surfaces have attracted much attention due to their direct involvement in many applications, such as solar energy conversion, self-cleaning coatings, biocompatible materials, photochemistry, and (photo)catalysis, as highlighted in the seminal review by *Diebold* [6.45]. Recent experimental and theoretical reviews have been dedicated to low-index rutile [6.46] and anatase [6.47] surfaces. A comprehensive issue of *Chemical Reviews* dedicated to titanium dioxide nanomaterials [6.48, 49] includes in particular papers on structure–property relationships [6.47] and on the synthesis of titania nanocrystals (anatase, rutile, and brookite) with tailored facets [6.50]. Finally, through surface science, approaches for TiO_2 photocatalysis provide molecular-level insights into photon-initiated events occurring at TiO_2 surfaces [6.5, 6]. The low activity relative to thin films of titanium oxide is likely explained by the availability of high-quality single crystals of that compound and the ease with which they are made conductive by reduction [6.46].

Among the several polymorphs of SnO_2, the most important naturally occurring form is cassiterite, a phase with a tetragonal rutile structure [6.8, 27, 51]. The hierarchy of the surface energies of the crystallographic orientations shown in Fig. 6.1 ((110) < (100) < (101) < (001) [6.27]) drives the growth and shape of the nanoparticles and controls the physicochemical activity. SnO_2 is widely used as oxidation catalyst, gas sensor, and transparent conductor. Those properties rely on the natural nonstoichiometry of the oxide that results from the low formation energies of tin interstitials and oxygen vacancies and on the multivalence of tin that easily switches from Sn(IV) as in SnO_2 and Sn(II) as in SnO. In particular, electrons donated by defects to the conduction band without increasing optical interband absorption explain the coexistence of conductivity and transparency, a unique property among the column-IV oxides [6.52]. However, the market for transparent conductive oxides is dominated by the tin-doped indium oxide (labeled ITO), as the material offers a better combination of conductivity and transparency than doped ZnO or SnO_2 [6.9]. This property was a strong motivation for the study of the structure of In_2O_3 surfaces. Under ambient conditions, In_2O_3 adopts a body-centered cubic bixbyite structure which is close to the parent fluorite structure, while alternative rhombohedral (corundum-like) and orthorhombic phases have been identified [6.9].

Besides the popular α-Al_2O_3, the corundum-phase oxides currently studied are V_2O_3, Cr_2O_3, and hematite α-Fe_2O_3 [6.44]. With respect to the most studied basal (0001) orientation, the rhombohedral structure can be represented by flat oxygen layers in hexagonal arrangement that sandwich double planes of aluminum atoms occupying two of three octahedral oxygen sites. By cleaving the bulk lattice, the obtained termination can be oxygen O_3−Me−Me, full-metal Me−Me−O_3, or half-metal Me−O_3−Me (Fig. 6.2). The latter is the expected nonpolar termination for that orientation which belongs to Tasker's type II classification. However, in

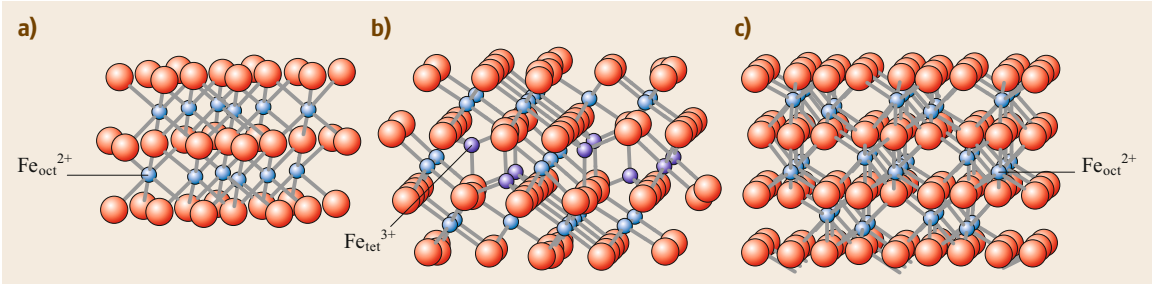

Fig. 6.3a–c The close-packed O^{2-} anion sublattice (*red spheres*) that is common to **(a)** wüstite, $Fe_{1-x}O$ (fcc oxygen lattice), **(b)** magnetite, Fe_3O_4 (fcc oxygen lattice), **(c)** hematite, α-Fe_2O_3 (hcp oxygen lattice), and maghemite (not shown) is clearly observed. The Fe cations in octahedral (*light blue*) and tetrahedral (*dark blue*) sites are indicated (Reprinted from [6.53], with permission from Elsevier)

all four cases, the issue is debated. Although the existence of the Al-terminated α-$Al_2O_3(0001)$ surface is postulated on the basis of measurements supported by atomistic simulations, some experiments suggest a partial termination of the surface by hydroxyl groups, even after annealing in ultrahigh vacuum. The presence of these groups could explain the discrepancy between the relaxation calculated by DFT for the Al-terminated surface and experimental measurements. Both experimental and theoretical approaches for $V_2O_3(0001)$, $Cr_2O_3(0001)$, and α-$Fe_2O_3(0001)$ suggest terminations in which the half-metal surface atoms are capped with oxygen atoms to give rise to Me=O termination (Fig. 6.2). Those terminations, which are not derived from bulk structure, are labeled vanadyl, chromyl, and ferryl, respectively. The O_3 and vanadyl terminations are alternatively suggested for $V_2O_3(0001)$ thin films [6.21]. Fe-, O_3-, and Fe=O terminations are identified on both α-$Fe_2O_3(0001)$ films and single crystals. However, the surface phase diagram remains controversial, in part because, since the conditions required to prepare stoichiometric surfaces are far different from those of common surface science studies, well-identified monophase surface terminations are lacking [6.21, 53]. Different Cr-terminations $Cr_2O_3(0001)$ are evidenced at low oxygen chemical potential, while chromyl groups are formed upon exposure to oxygen.

The vanadium–oxygen system is characterized by different oxidation states from V^{2+} to V^{5+} and various oxygen coordination geometries that are at the origin of the unique catalytic performance. Vanadium is the most important metal used in supported metal oxide catalysis [6.54]. Vanadium oxides involve binary compounds from VO (V^{2+}) to V_2O_5 (V^{5+}), and mixed-valence compounds such as Magnéli phases V_nO_{2n-1} and Wadsley phases $V_{2n}O_{5n-1}$ [6.21, 55]. Beyond studies dedicated to single crystals such as $V_2O_5(001)$, $VO_2(011)$, $V_2O_3(0001)$, and $V_2O_3(10\bar{1}2)$ [6.55], investigations of films supported on either oxides or metals became dominant because they offer a much wider choice of orientations and composition and are easily analyzed by electronic probes [6.17–19, 21, 55].

Iron oxides can be considered as a class since they have in common a close-packed layer of oxygen atoms (Fig. 6.3) [6.21, 53]. Wüstite FeO crystallizes in the rocksalt structure. Fe^{2+} ions are in octahedral positions. Wüstite is often nonstoichiometric because of cation deficiency. Magnetite Fe_3O_4 has an inverse spinel structure with tetrahedrally coordinated Fe^{3+} and a 50 : 50 mixture of Fe^{2+} and Fe^{3+} in octahedral position. (Spinels have the general formula AB_2O_4. In so-called normal spinels, such as $MgAl_2O_4$, the A^{2+} and B^{3+} cations occupy tetrahedral and octahedral positions, respectively. However, if A^{2+} cations have a large crystal field stabilization energy [6.53], as in the case of Fe_3O_4, they occupy half of the octahedral sites, while the displaced B^{3+} cations are in tetrahedral sites; such materials are known as *inverse spinel*.) Magnetite is the most studied iron oxide because at 125 K it undergoes the so-called Verwey transition from a monoclinic to an inverse spinel structure that leads to profound changes in conductivity and magnetic properties. In hematite α-Fe_2O_3, the most stable phase, Fe^{3+} ions occupy octahedral sites. Direct oxidation of Fe_3O_4 leads to maghemite γ-Fe_2O_3, in which Fe^{2+} is converted into Fe^{3+}, while the spinel structure, with Fe vacancies in octahedral positions, is preserved. Although the spinel structure is metastable with respect to the corundum structure, the transformation requires the difficult transition of the O^{2-} lattice from fcc to hcp. Conversely, transitions from wüstite to magnetite to maghemite are easy because they only require cation rearrangement while keeping the fcc oxygen lattice.

Ceria CeO_2 has the fluorite (CaF_2) crystal structure, with a face-centered cubic sublattice of Ce cations and a simple cubic arrangement of O anions. Although ceria single crystal surfaces are used, surface science studies of ceria are generally performed on thin films that

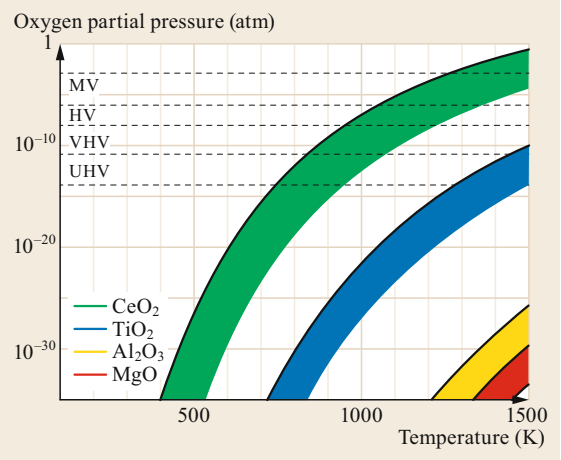

Fig. 6.4 Comparison of so-called reducible (here, CeO_2 and TiO_2) and irreducible oxides (Al_2O_3 and MgO): A $P(O_2)$ versus T phase diagram, as determined by density functional theory approaches, shows transition curves from pristine to defective surfaces in thermodynamic equilibrium. *Colored areas* give estimates of errors. *Dashed horizontal lines* indicate residual pressures encountered in various vacuum regimes. The reducible character of ceria is highlighted (Reprinted with permission from [6.20]. Copyright 2013 American Chemical Society)

are prepared either by direct deposition of the oxide or via precursors or, most often, by oxidation of cerium films [6.56]. The catalytic applications of ceria, a material of which a particular property is the ability to pass rapidly through redox cycles (Fig. 6.4) [6.20], are the focus of much attention [6.3, 20, 29, 56, 57].

Zinc oxide is commonly used as catalyst, especially in the industrially important production of methanol, and as pigment. ZnO powders of wurtzite structure reveal nonpolar facets, $(10\bar{1}0)$ and $(11\bar{2}0)$, and polar zinc- and oxygen-terminated facets, $(000\bar{1})$-Zn and $(000\bar{1})$-O [6.58, 59]. As regards the $(10\bar{1}0)$ surface, overall consistency is observed between experimental approaches and between these approaches and the theoretical modeling. Conversely, little is known about the polar $(000\bar{1})$-O surface that is stressed as being the most catalytically active ZnO termination. Neither the compensation of the electrostatic instability of that surface nor its hydrogen termination is understood [6.58].

This brief overview illustrates the strong research activity relating to the surface structures of binary oxides. I propose herein to address two important issues from angles that seem to avoid redundancies: (i) the quite general question of surface relaxation, and (ii) the surface of strontium titanate, whose structure/property relations are strongly debated [6.10, 60–67].

In the first part, special attention is paid to rumpling, an issue common to all ionic surfaces [6.68, 69]. The rocksalt oxide surfaces, recently reviewed by *Woodruff* [6.44], are chosen in this context because, given the gradual variation they present over the series, they offer a unique playground for the critical analysis of relaxation and rumpling mechanisms. Whatever the material, the creation of a surface generates a stress that is compensated by atomic rearrangements whose energetically dominant contribution is the relaxation of the surface and subsurface interlayer spacings [6.70–75]. Within a given atomic layer, cations and anions show different displacements in the direction normal to the surface because of their specific polarizability and bonding. The difference between these displacements is the so-called rumpling. With an energy of two orders of magnitude lower than relaxation [6.70], rumpling has, however, attracted continual interest because its mechanism relies on the nature of the atomic interactions in the surface region. In this context, oxides of rocksalt structure are of particular interest because they form a series of compounds of identical structure, of which only the cations change. After the examination of MgO(100), one of the oxide surfaces having accumulated the greatest number of studies, the data related to the series of the (100) nonpolar orientation of the alkaline earth oxides (CaO, SrO, BaO) and the oxides of the transition metals of Group III (MnO, FeO, CoO, NiO) are considered, respectively.

The second part of the review turns toward a reflection on ternary oxides. Many applications require surfaces with precisely defined structures [6.10, 60–67], although their composition reflects the bulk complexity. In the global movement that has focused on oxide surfaces and interfaces over the past few decades, the early discovery of catalytic [6.76], sensing [6.77], ferroelectric [6.78], and dielectric [6.79] properties of oxides of perovskite structure has prompted intense investigations, with particular interest in the crystallographic orientation (100) of strontium titanate $SrTiO_3$, which is the subject of this review. The surface structures of $SrTiO_3(110)$ and $SrTiO_3(111)$ (polar) and those of the other oxides of perovskite structure have been much less investigated [6.10, 80–82]. The story began with the early use of $SrTiO_3$ for growing epitaxial high-temperature superconducting oxide films [6.83]. The need for atomically defined substrate prompted *Kawasaki* et al. to prepare single-terminated $SrTiO_3(100)$ surfaces [6.84] that subsequently inspired many other studies. Epitaxial growth on $SrTiO_3(001)$ depends intimately on the surface structure. The $(\sqrt{13} \times \sqrt{13})$-R33.7° reconstruction favors homoepitaxy [6.85], while heteroepitaxy is easier on

the $(\sqrt{13}\times\sqrt{13})$-R33.7° [6.86] and (2×1) [6.87] structures. The nucleation of perovskite is forbidden on $SrTiO_3(001)$-c(6×2) [6.87] but allows pseudomorphic CdTe(211) growth [6.88]. High-quality epitaxy [6.89] and lower critical temperature [6.90] are obtained for $YBa_2Cu_3O_{7-x}$ on smooth single-terminated terminations. Unusual transport properties are observed on $SrTiO_3(106)$ stepped surfaces [6.91]. Such a close matching of many oxides and semiconductors on $SrTiO_3(100)$ surfaces was the source of an impressive series of new findings. Examples are provided by the crystalline gate dielectric in silicon-based devices [6.92], channels for field-effect transistors [6.93, 94], two-dimensional electron gases (2DEGs) [6.61]—later observed at cleaved STO surfaces [6.66]—ferroelectric superlattices [6.62], and superconducting and magnetic interfaces [6.65], which have paved the way for atomically fabricated innovative heterostructures. Referred to as the "gold standard" [6.95] for its ability to act as a photocatalyst in promoting water splitting without bias [6.76], strontium titanate became a workhorse [6.10, 67] for the emerging oxide nanoelectronics, similar to what silicon is for the field of semiconductors [6.10, 64, 66, 67]. In relation to these developments, the control of the structure and composition of the $SrTiO_3(100)$ surface is of crucial importance. The second part of the review examines the TiO_2 and SrO terminations of $SrTiO_3(100)$ and describes the reconstructions of that surface, before discussing the limits of the current state of the art.

6.2 Oxides of Rocksalt Structure

MgO(100) is a reference for the surface science of oxides. The simple rocksalt cubic structure of the oxide is tractable for calculations, while the easy cleavage along the low-energy (100) face allows for the preparation of well-defined surfaces in a reproducible manner. Magnesium oxide is also obtained in the form of cubic nanoparticles closed by (100) facets by various methods ranging from decomposition of hydroxides or carbonates in vacuum [6.96, 97], burning metallic magnesium in oxygen [6.98], or gas-phase reaction of magnesium with oxygen [6.99]. Those nanocrystalline powders exhibit a variety of low-coordinated ions that were used as a model for catalytic reactions [6.96] and water [6.97, 100] or hydrogen [6.99] dissociation. CaO and BaO powders contribute many applications such as bioactive glass ceramics [6.101, 102] and dye-sensitized core–shell nanocrystals [6.103]. BaO allows the storage of NO_x emissions in three-way catalysts [6.104]. MgO is the basic component of catalysts for the activation of methane [6.105]. Single-crystalline Fe/MgO/Fe magnetic tunnel junctions show giant tunneling magnetoresistance [6.106]. Although CaO has attracted fewer experimental surface studies than MgO, and SrO and BaO none, the numerous applications, especially those related to catalysis, have stimulated the development of theoretical approaches [6.107–110]. The (100) surfaces of the transition-metal oxide series MnO, CoO, FeO, and NiO also became quite popular because they are cleavage planes of oxides that are antiferromagnets below Néel temperatures of 116, 198, 291, and 525 K, respectively [6.111], used as catalysts [6.112–114] and commonly encountered as corrosion products [6.115].

6.2.1 Surface Geometry

Relaxation and rumpling are currently defined in two different ways. A first approach is based on the relative position of the atoms of the i-th layer compared with those of the $(i+1)$-th layer. Another description uses the absolute positions of the atomic layers with respect to the first undistorted deep layer, which is more appropriate when the relaxation involves more than one surface layer [6.72, 73]. If the first undistorted atomic layer is the third one, the distances d_O and d_{Me} of the oxygen and metallic ions, respectively, are defined with respect to this layer (Fig. 6.5). Relaxation δ_{rel} and rumpling δ_{rump} are expressed as a percentage of the bulk interlayer spacing d_{bulk} [6.72]

$$\delta_{rel} = \frac{d_O + d_{Me} - 4d_{bulk}}{2d_{bulk}} , \tag{6.1}$$

$$\delta_{rump} = \frac{d_O - d_{Me}}{d_{bulk}} . \tag{6.2}$$

A positive (negative) value of the relaxation means that the first interlayer spacing is expanded (contracted). A positive (negative) value of the rumpling indicates that the anion (cation) shifts outward with respect to the cation (anion).

6.2.2 MgO(100)

MgO is the first in the series of alkaline earth oxides classified by increasing molecular weight. The crystallographic structures of MgO, CaO, SrO, and BaO all belong to the $Fm\bar{3}m$ space group. The lattice param-

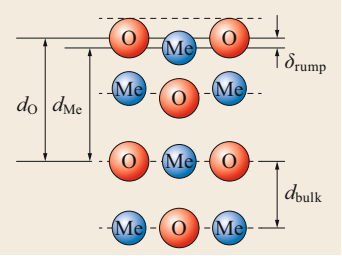

Fig. 6.5 Schematic representation of a nonpolar oxide surface with an inward relaxation and a positive rumpling in which anions shift outward with respect to cations. *Dashed lines* represent the position of layers separated by the bulk interlayer distance d_{bulk} (After [6.72])

eters are 4.21, 4.81, 5.16, and 5.52 Å for MgO, CaO, SrO, and BaO, respectively [6.116]. Similarly to the decrease in the bulk modulus, the surface energy decrease along the MgO–BaO series indicates a weakening of the interatomic interactions [6.71–75]. The trend in ionic character is a decrease from MgO to BaO [6.73, 74, 117–119].

Many experimental and theoretical studies have been dedicated to the determination of relaxation and rumpling at the MgO(100) surface. Data are summarized in Fig. 6.6 [6.71–75, 120–153]. The experimental methods used by the cited authors include low-energy electron diffraction (LEED), impact-collision ion scattering spectroscopy (ICISS), electron energy loss fine structure (EELFS), medium-energy ion scattering (MEIS), grazing incidence x-ray scattering (GIXS), fast-atom diffraction (FAD), transmission electron microscopy (TEM), and helium diffraction. The calculations quoted were performed by shell methods, density functional theory (DFT) by calculating exchange–correlation density and potential within both the local density approximation (LDA) and the generalized gradient approximation (GGA), Hartree–Fock (HF) approaches, and hybrid functional (B3LYP). Overall, the MgO(100) surface is close to bulk-terminated, with surface relaxation and rumpling which essentially go from −1 to +3% and 0 to 6%, respectively. Rumpling appears systematically positive, while the sign of the relaxation seems indeterminate, since positive and negative values are found by both theory and experiment (Fig. 6.6). Before analyzing the data set in more detail, it is worth examining the surface preparation methods.

Surface Preparation

The strong hydrophilicity of MgO [6.97, 98, 100] prompted the preparation of clean surfaces dedicated to ultrahigh vacuum (UHV) analysis via vacuum cleavage, as in most of the structural studies of MgO(100) by electron diffraction [6.120–123, 125]. Indeed, very large relaxations observed on air-cleaved or polished surfaces [6.126, 127] could be suspected to come from adsorbates [6.127, 154], although nothing systematic can be proven [6.121]. The drawback of cleavage is the generation of rather rough surfaces involving steps, slip lines, adstuctures, and holes, as shown by atomic force microscopy (AFM) [6.155] and noncontact atomic force microscopy (NC-AFM) [6.156] (Fig. 6.7a,b). Next to fairly flat areas where terraces are separated by monatomic steps (Fig. 6.7b, left), the cleaved surfaces present very chaotic zones with series of multiatomic steps (Fig. 6.7b, right) whose distribution, which is beyond control, can lead to unreproducible measurements. Moreover, defects generate complex relaxations. For example, relaxations tend to smoothen steps by shifting footstep atoms outward and terrace atoms away from step edges, as nicely shown by TEM [6.128] (Fig. 6.7c), in agreement with simulations [6.129, 130, 157, 158]. Therefore, cleaved surfaces are poor candidates for diffraction studies requiring large coherence length [6.131]. To solve this issue, several groups have combined annealing at high temperature and ion bombardment [6.131, 132]. Ion bombardment alone leads to disordered surfaces [6.124], but annealing to 1640−1870 K in UHV enables surface diffusion that restores the crystallinity [6.124, 126, 131, 132]. Appropriate combinations of bombardment by ions or atoms, annealing, and exposure to oxygen lead to flat defect-free MgO surfaces with wide (100) terraces, as demonstrated by x-ray diffraction (XRD) [6.132] and FAD [6.131].

Relaxation and Rumpling

Measurements performed on those defect-free surfaces [6.131, 132] lead to values of $(-0.56 \pm 0.35)\%$ [6.132] for relaxation and $(1.07 \pm 0.5)\%$ [6.132] or $(1.6 \pm 1.5)\%$ [6.131] for rumpling, which can be considered the most reliable experimental data. The mostly negative experimental estimates of relaxation (Fig. 6.6) support the inward relaxation evidenced by XRD measurement. Conversely, the outward relaxation of $(3 \pm 4)\%$ determined by TEM [6.128] deviates significantly from all other measurements. This singular value is probably due to the very defective nature of the surfaces on which the measurements have been made, as shown by the fact that in TEM images, the displacements of the surface atoms are all influenced by the vicinity of the steps (Fig. 6.7c, middle). Unlike experiments, calculations favor an expansion of the first interlayer spacing. In particular, the DFT calculations performed on the thicker slabs [6.72–75, 133], which are expected to be the most reliable, lead systematically to positive values of the relaxation (Fig. 6.6).

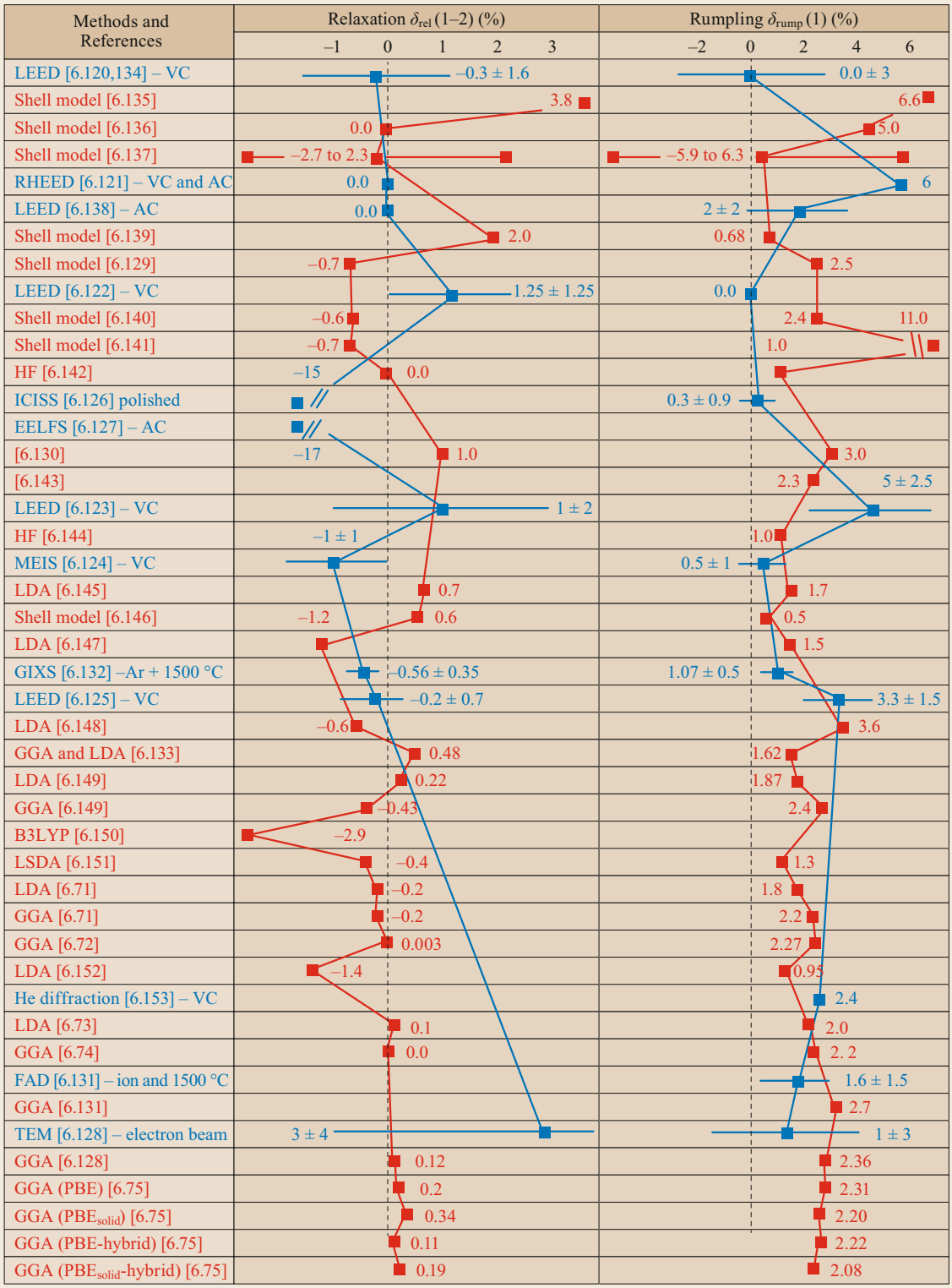
Methods and References
Relaxation δ_{rel} (1–2) (%)
–1 0 1 2 3
Rumpling δ_{rump} (1) (%)
–2 0 2 4 6
LEED [6.120,134] – VC
–0.3 ± 1.6
0.0 ± 3
Shell model [6.135]
3.8
6.6
Shell model [6.136]
0.0
5.0
Shell model [6.137]
–2.7 to 2.3
–5.9 to 6.3
RHEED [6.121] – VC and AC
0.0
6
LEED [6.138] – AC
0.0
2 ± 2
Shell model [6.139]
2.0
0.68
Shell model [6.129]
–0.7
2.5
LEED [6.122] – VC
1.25 ± 1.25
0.0
Shell model [6.140]
–0.6
2.4
11.0
Shell model [6.141]
–0.7
1.0
HF [6.142]
–15
0.0
ICISS [6.126] polished
0.3 ± 0.9
EELFS [6.127] – AC
[6.130]
–17
1.0
3.0
[6.143]
2.3
5 ± 2.5
LEED [6.123] – VC
1 ± 2
HF [6.144]
–1 ± 1
1.0
MEIS [6.124] – VC
0.5 ± 1
LDA [6.145]
0.7
1.7
Shell model [6.146]
–1.2
0.6
0.5
LDA [6.147]
1.5
GIXS [6.132] –Ar + 1500 °C
–0.56 ± 0.35
1.07 ± 0.5
LEED [6.125] – VC
–0.2 ± 0.7
3.3 ± 1.5
LDA [6.148]
–0.6
3.6
GGA and LDA [6.133]
0.48
1.62
LDA [6.149]
0.22
1.87
GGA [6.149]
–0.43
2.4
B3LYP [6.150]
–2.9
LSDA [6.151]
–0.4
1.3
LDA [6.71]
–0.2
1.8
GGA [6.71]
–0.2
2.2
GGA [6.72]
0.003
2.27
LDA [6.152]
–1.4
0.95
He diffraction [6.153] – VC
2.4
LDA [6.73]
0.1
2.0
GGA [6.74]
0.0
2. 2
FAD [6.131] – ion and 1500 °C
1.6 ± 1.5
GGA [6.131]
2.7
TEM [6.128] – electron beam
3 ± 4
1 ± 3
GGA [6.128]
0.12
2.36
GGA (PBE) [6.75]
0.2
2.31
GGA (PBE_{solid}) [6.75]
0.34
2.20
GGA (PBE-hybrid) [6.75]
0.11
2.22
GGA (PBE_{solid}-hybrid) [6.75]
0.19
2.08

Fig. 6.6 Experimental (*blue*) and theoretical (*red*) values of the relaxation δ_{rel} (1−2) of the topmost spacing and surface rumpling δ_{rump} (1) for MgO(100). Methods and sample preparation are indicated (VC, AC: vacuum- and air-cleaved). The classification by year is based on Fig. 18 of *Schüller* et al. [6.131], which presents data of the same type. A similar classification is used in Figs. 6.8, 6.11 and 6.16 ◄

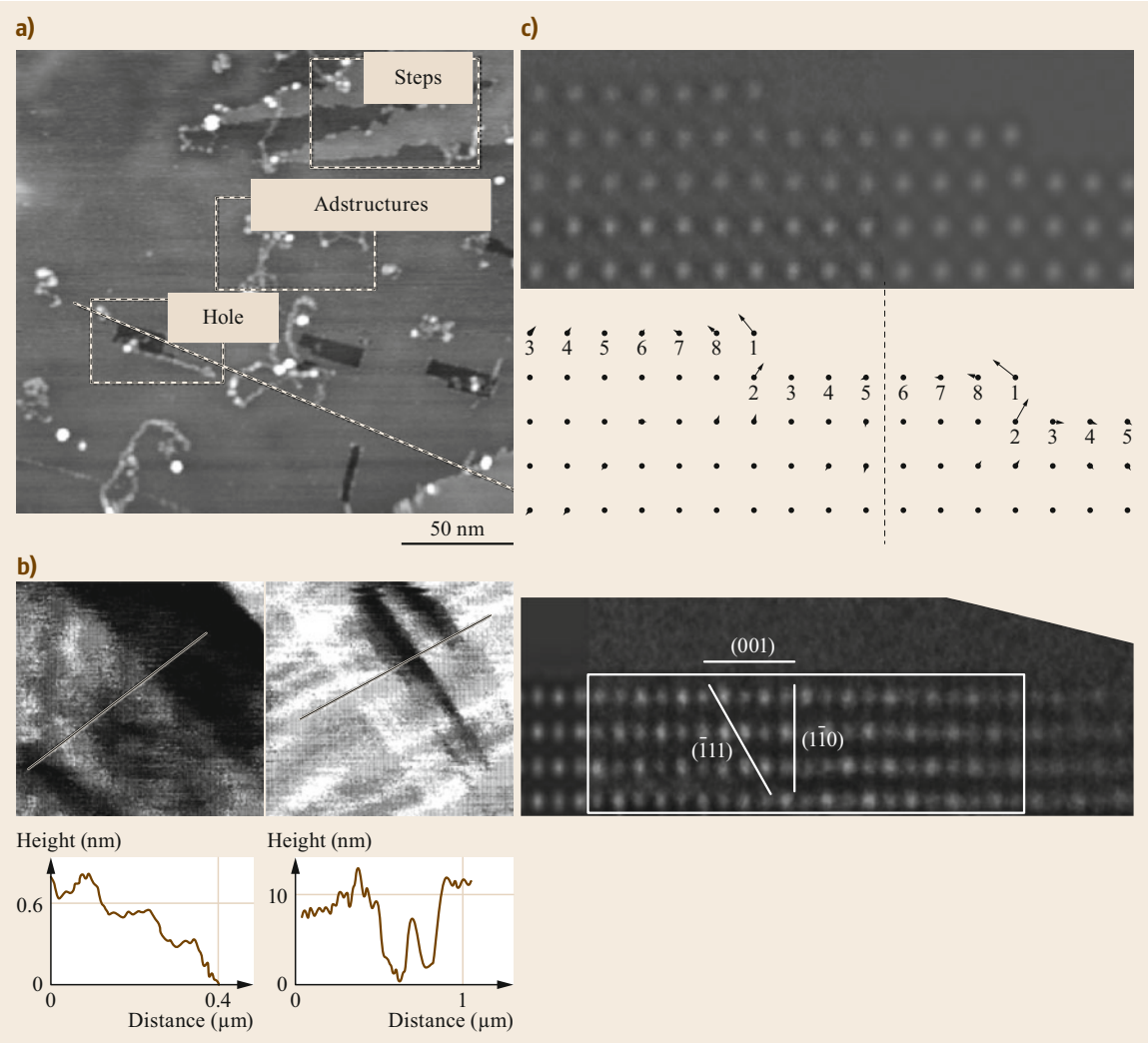

Fig. 6.7a–c MgO(100) surfaces: **(a)** NC-AFM image of a cleaved MgO surface (Adapted with permission from [6.156]. Copyright 2003 by the American Physical Society); **(b)** AFM images of an air-cleaved MgO(100) surface: Areas with multiatomic steps (*left*) and series of monatomic steps (*right*) (Adapted with permission from [6.155]. Copyright 1996 Elsevier); **(c)** High-resolution transmission electron microscopy (HRTEM) image of MgO high-Miller-index surface faceted into small (100) surfaces; *top left* with respect to *dashed line*: Experimental image around the step; *top right*: Simulated image using DFT calculation result as input; *middle*: Visualization of atomic displacements corresponding to the image from the top. All *arrows* are magnified five times; *bottom*: HRTEM image of a (001) surface in the [110] zone axis (Reprinted with permission from [6.128]. Copyright 2013 by the American Physical Society)

Rumpling data show much clearer trends. The systematically positive values of the rumpling (Fig. 6.6) demonstrate that the oxygen ions protrude above the magnesium ions at the MgO(100) surface. Theoretical estimates from shell models that are based on empirical parameters and LEED measurements are somewhat scattered (Fig. 6.6). It is logical to compare the values measured on surfaces with large and well-defined

terraces by XRD ($1.07 \pm 0.5\%$ [6.132]) and FAD ($1.6 \pm 1.5\%$ [6.131]) to DFT calculations performed on the thicker slabs (≥ 6 layers), i.e., 2.31% [6.133], 2.2% [6.72], 2.22% [6.73], 2.08% [6.74], and 2.2% [6.75], the latter value corresponding to four averaged values from [6.75]. (In the case of the rumpling determined by FAD [6.131], the value of the atomic displacement of oxygen with respect to magnesium (0.033 ± 0.03 Å) is sometimes confused with the percentage of the bulk interlayer spacing—$\delta_{\mathrm{rump}}(1)$ in Fig. 6.6—that defines the rumpling [6.44, 75].) The DFT values of the rumpling are remarkably similar. The scatter due to the difference between the exchange–correlation functionals that are used in the various calculations appears quite marginal [6.75, 131].

The average values obtained by the calculations performed on the thickest slabs [6.72–75, 133] (taking only average values from the four values calculated in [6.75]) are $+0.16\%$ for relaxation and 2.1% for rumpling. Therefore, theoretical estimates for relaxation and rumpling are a little less than 1% above the XRD and FAD experimental values (Fig. 6.6). These discrepancies are comparable to those observed on metal surfaces, although metals are believed to involve a simpler approach than oxide surfaces. For example, theoretical and experimental relaxation values differ significantly for low-index Al, Pd, Pt, Au, and Ti surfaces [6.159].

6.2.3 Alkaline Earth Metal Oxides

The calculated values of surface relaxation and rumpling in the CaO(100), SrO(100), and BaO(100) series are summarized in Fig. 6.8 [6.71–75, 149, 151]. Trends are comparable, but numbers differ widely. The surface relaxation of the (100) orientation, which is close to zero in the case of MgO, is predicted by calculations to be increasingly negative along the series of alkaline earth metal oxides from CaO to BaO [6.71–75, 149]. (It should be noted, however, that the rather low relaxation values found by *Skorodumova* et al. [6.72] (Fig. 6.8) with respect to the other groups comes in part from the use of (6.1). According to these authors, the subsurface layer relaxes outward. Therefore, a relaxation defined as the variation in the distance between the first and second layers leads to higher values than a calculation that considers the absolute positions [6.72].) In parallel, the rumpling which is positive on MgO(100) is the opposite for the rest of the series. It is increasingly negative for CaO(100), SrO(100), and BaO(100), which means that cations are expected to protrude from the surface. Measurements were performed on CaO(100) [6.160, 161]. The relaxation of -1% found by LEED agrees with the simulation, but the value of 2% found for the rumpling is at odds with the theoretical predictions. The authors have suggested that a negative rumpling could lead to a better fit of the data, but did not explore this possibility [6.160]. A standing wave analysis concluded that the relaxation was too small to be observed [6.161].

Most studies report negative electron affinity for MgO(100) [6.73, 162–164] and also for CaO(100) and SrO(100), but not for BaO [6.73]. Conversely, *Logsdail* et al. find positive electron affinity along the MgO–BaO series [6.75], in agreement with thermionic measurements performed on MgO [6.165]. However, a confirmation would be required [6.166], since those measurements were conducted under conditions that do not totally exclude the presence of adsorbates, especially given the very hydrophilic nature of MgO (Sect 6.2.1).

Surface Relaxation

In fully covalent systems, surface relaxation results from the competition between band energy and short-range repulsion terms that in simple models vary as $\sqrt{Z}$ and Z, respectively, if Z is the coordination number [6.69, 70]. Surfaces are therefore expected to relax inward. In fully ionic systems, atomistic approaches relying on electrostatic and short-range interactions result in interatomic distances that vary as Z/α (where α is the Madelung constant), which again leads to inward relaxation [6.69, 70]. Iono-covalent systems are shown to behave in a way which depends on the variations in the three terms (covalent, electrostatic, and repulsion) as a function of environment [6.69, 70]. Beyond the debate on the relative importance of the ionic [6.73] or covalent [6.69, 70] character of the alkaline earth metal oxide surfaces, it appears that the delocalization of the electrons plays an important role in the surface relaxation of these oxides [6.70–73, 149].

Cleavage results in a downward shift of the semicore p-state of surface cations [6.72, 73]. This has little effect on MgO, since the Mg p-state lies very low in energy. At CaO, SrO, and BaO(100) surfaces, the upward shift of the cation p-state would result in wider p-O bands in the absence of relaxation. The effect of relaxation is to narrow those bands. The electron localization around oxygen atoms then increases the Coulomb interaction between cations and anions, which causes a contraction of the surface and subsurface interlayer spacings. *Skorodumova et al.* divide the relaxation energy into a band energy term that represents the occupied one-electron states and a term corresponding to the sum of electron–electron Coulomb interaction (Hartree term), electron–core interaction, electronic exchange and correlation, and core–core Coulomb energy [6.72]. The MgO(100) relaxation mostly stems from the first contribution, while SrO(100) and BaO(100) relaxations are dominated by electrostatic interactions. CaO(100) is a border case [6.72].

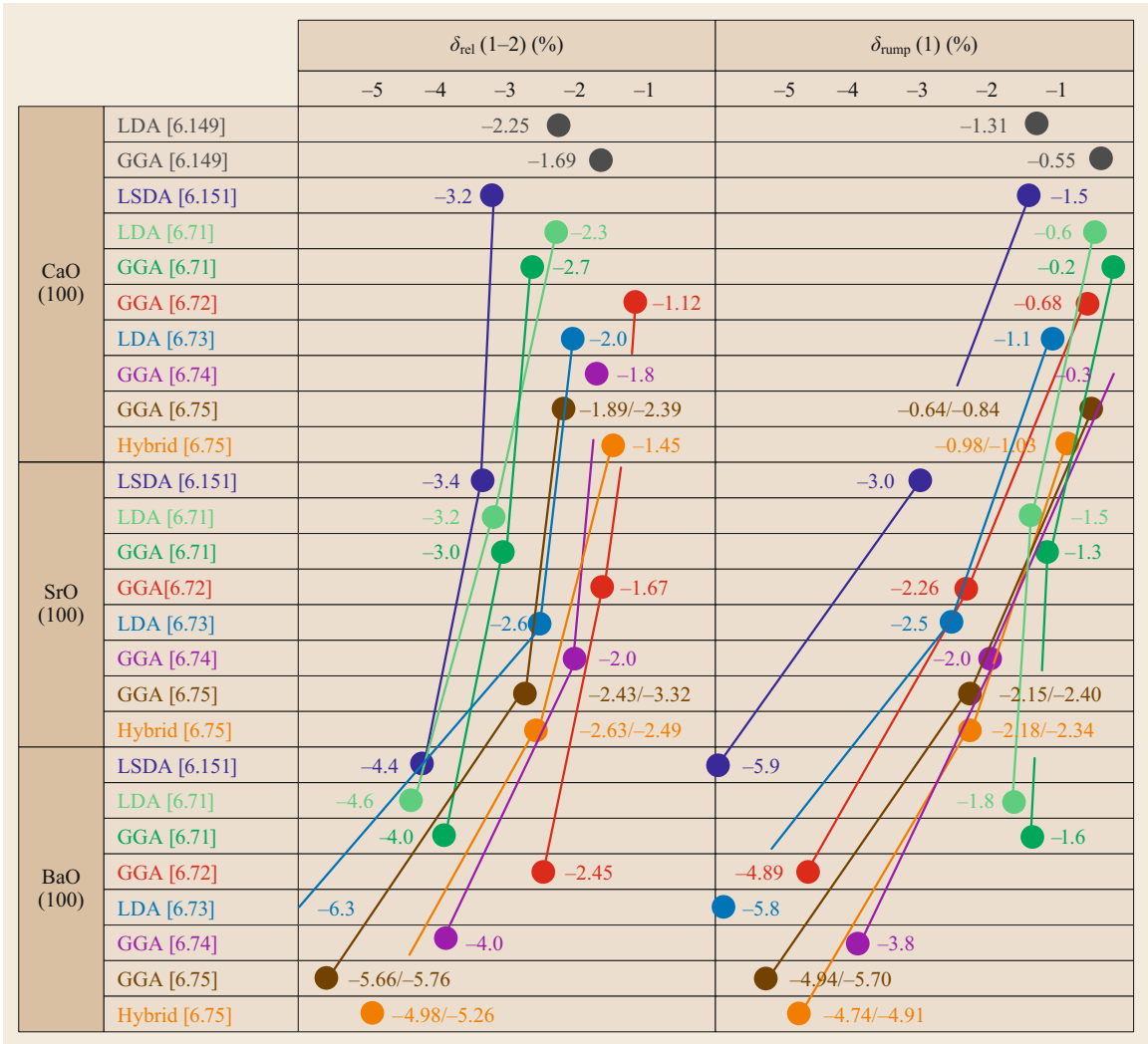

Fig. 6.8 Calculated values of the relaxation δ_{rel} (1−2) of the topmost interplanar spacing and of the surface rumpling δ_{rump} (1) for CaO(100), SrO(100), and BaO(100)

Role of Electron Delocalization

Rumpling is due to an asymmetric response of cations and anions to bulk cleavage that can originate from differences in either polarizability or bond characteristics [6.70, 71]. In the earlier model of *Verwey* [6.167], the rumpling stems from the difference in anion and cation polarizabilities. Having the highest polarizability, the oxygen ion protrudes outward, as observed on MgO(100) (Sect. 6.2.2). However, if the difference in polarizability were the only driving force for rumpling, all oxides in the alkaline earth metal oxide series should exhibit a positive rumpling [6.71, 149], since the Pauling polarizabilities of Mg^{2+}, Ca^{2+}, Sr^{2+}, Ba^{2+}, and O^{2-} are 0.094, 0.47, 0.86, 1.55, and 3.88, respectively [6.71]. In addition to the Verwey model, which still holds even if it is not dominant, driving forces that stem from atomic bonds were suggested [6.71–74, 149]. On the basis of contracted and expanded unit cells in which ionicity is preserved, the opposite rumpling of MgO(100) and CaO(100) was suggested by *Alfonso* et al. to come from valence repulsion effects, or in other words, steric effects [6.149]. *Broqvist* et al. [6.71] distinguished two types of differences in bond characteristics: metal–oxygen covalence, and bonds between oxygen next-nearest neighbors that rely on electron delocalization. The authors observed that the O(2p)–O(2p) overlap decreases from MgO to BaO. At the MgO(100) surface, they suggest that the positive rumpling results from next-nearest-neighbor interaction via the strong

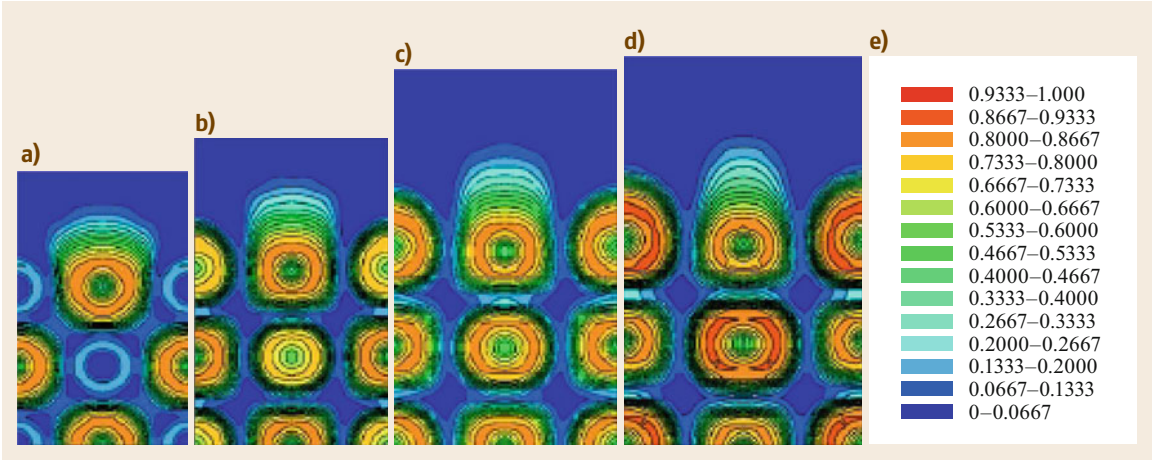

Fig. 6.9a–e Electron localization function for the (100) surfaces of **(a)** MgO, **(b)** CaO, **(c)** SrO, and **(d)** BaO. The values 0.5 and 1 **(e)** correspond to complete delocalization and localization, respectively. The delocalized oxygen electrons that protrude in vacuum appear to noticeably shrink from MgO(100) to BaO(100). The increasing electron localization around oxygen accompanies the band narrowing (Reprinted with permission from [6.72]. Copyright 2005 by the American Physical Society)

O(2p)–O(2p) overlap. Conversely, the electron delocalization progressively reduces along the CaO, SrO, and BaO series, while the contribution of the nearest-neighbor interactions (Me−O bond) increases [6.71]. To increase cohesion, the surface ions tend to relax toward the subsurface layer. However, because of differences in polarizability, the covalence of the bonds between surface anions and subsurface cations is higher than that of the bonds between surface cations and subsurface anions. This effect favors a negative rumpling. Therefore, the increasingly negative values of rumpling that are predicted in the CaO, SrO, and BaO series for both (100) and (110) orientations have been attributed to a balance between the effect of electron delocalization (anion–anion repulsion) and the metal–oxygen bond [6.71].

At cleaved oxide surfaces, *Skorodumova* et al. [6.72] and *Baumeier* et al. [6.73] observed a downward shift of the semicore p-states of surface cations which they link to the surface and subsurface relaxation and rumpling. (As noted in [6.72], the interaction between the metal p-M and oxygen states has already been shown to stabilize ABO_3 perovskite structures [6.168].) The electronic structure of the oxides is characterized by a narrowing of the valence band, consisting mostly of the p-O states, along the alkaline earth metal oxide series: 4.44 eV (MgO), 2.57 eV (CaO), 2.08 eV (SrO), and 1.83 eV (BaO) [6.71, 72]). The spill-out of the oxygen electrons is predicted to narrow that surface p-O band and to cause semicore s oxygen states to shift outward [6.72] (Fig. 6.9). The low-lying p-Mg state hardly affects the oxygen p band at the MgO(100) surface. In contrast, the width of the semicore p-O states associated with CaO, SrO, and BaO surfaces correlates strongly with the energy position of p-M [6.71, 72]. It becomes wider than in bulk as the p-M states shift toward lower energy. The increasing localization of oxygen electrons increases Coulomb interactions. The anions are pushed downward by the surrounding cations, which leads to negative rumpling on the (100) surfaces of CaO, SrO, and BaO. The role of the semicore states is highlighted by calculation of slabs involving artificially expanded or contracted surface in-plane lattices [6.72]. Relaxations change in amplitude but keep their sign, except in the border case of CaO. Upon lattice expansion, the neighboring cations of the surface anions move away, which causes the p-M band to shift downward and the oxygen electron to delocalize. Therefore, the expansion of the in-plane lattice parameter promotes positive rumpling. Compression has the opposite effect [6.72].

Rumpling is suggested to be of local origin [6.71], since the change in rumpling between MgO and the CaO, SrO, and BaO series has been previously reported for small $(MeO)_{12}$ clusters [6.169, 170]. In the case of MgO(100), the local origin of the rumpling might explain the relevance of TEM measurements made on highly defective samples [6.128] (Fig. 6.7c). They lead to a value of rumpling of $(1 \pm 3)\%$, in fair agreement with values determined by diffraction on high-quality surfaces [6.131, 132], while the relaxation analyzed in the context of the same TEM measurements strongly deviates from the bulk of the other data (Fig. 6.6).

6.2.4 Transition-Metal Oxides

The transition-metal oxides (TMOs) MnO, FeO, CoO, and NiO crystallize in the rocksalt structure in the paramagnetic phase with lattice parameters of 4.44, 4.30, 4.27, and 4.17 Å, respectively. They become antiferromagnetically ordered below Néel temperatures of 116 K (MnO), 198 K (FeO), 291 K (CoO), and 525 K (NiO) [6.171] with rhombohedral (MnO and NiO) or monoclinic (FeO and CoO) distortions. Not observed by STM [6.172, 173] (Fig. 6.10a), the (2×1) ferromagnetic surface over-structure is evidenced by LEED on Ni(100) in normal conditions [6.174]. By DFT approaches, *Schrön* et al. predict the observation of pronounced spin contrasts by spin-polarized STM (using ferromagnetic tips) in the (2×1) structure along the MnO(100), FeO(100), CoO(100), and NiO(100) series [6.175] (Fig. 6.10b).

As in the case with alkaline earth metal oxide surfaces, the relaxations of the (100) faces of the paramagnetic phases of the TMOs are bulk-like terminated with interlayer spacing relaxation and intra-layer rumpling that minimize the surface energy. The related results are summarized in Fig. 6.11. From the reported data, the superficial relaxation of NiO(100) is the only case which appears indisputable. The eight values obtained by measurement or calculation, which range from −1.4 to −2%, are in fair agreement in indicating an outward displacement of surface oxygen atoms with respect to surface nickel atoms. Data on the other, most studied TMO surface, MnO(100), are inconclusive. DFT and MD predict a contraction of the first interlayer spacing. Conversely, measurements favor an expansion, although with large error bars (Fig. 6.11).

As a trend, the values found for rumpling are positive for the four surfaces, except for two DFT calculations [6.151] and two MEIS measurements [6.180, 181] on MnO(100) and NiO(100) surfaces (Fig. 6.11). Data on thin films are presented in Fig. 6.11 [6.179, 183, 185, 187]. Are they meaningful with respect to bulk samples? Supported films may offer better crystalline surface quality than cleaved crystals, and are often preferred for structural studies [6.183, 185], as highlighted in the introduction for oxide surfaces in general. In the case of FeO, the disproportionation of the bulk oxide into Fe and Fe_3O_4 below 840 K [6.53] encourages the preparation of thin films, although care must be taken to avoid mixtures of $Fe_{1-x}O$, Fe, and Fe_3O_4 [6.53, 185]. Surface interlayer relaxations of supported films partly compensate the in-plane interface

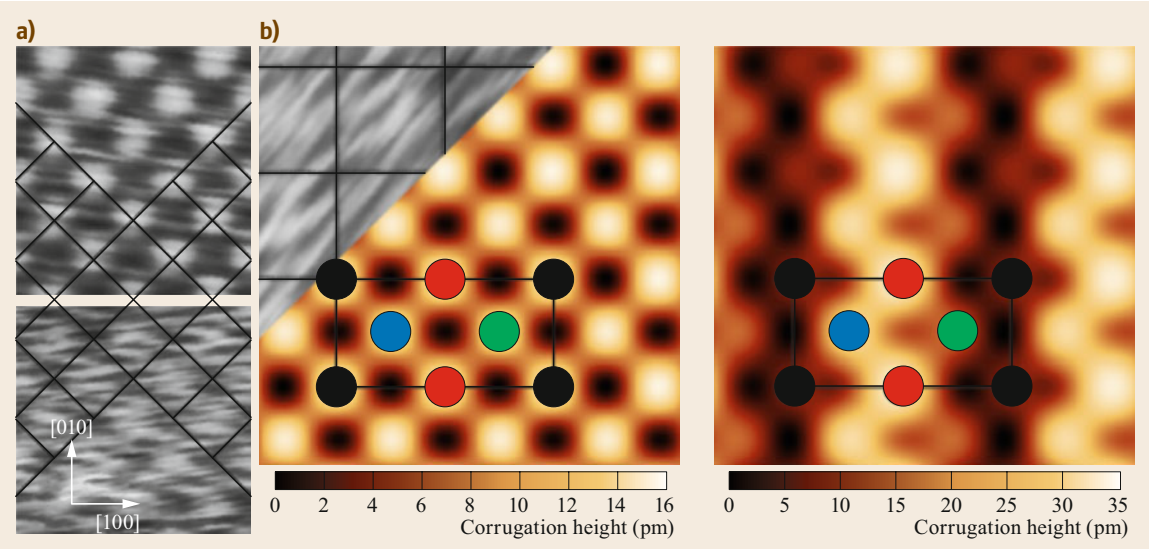

Fig. 6.10a,b The NiO(100) surface **(a)** (1×1) structure seen by STM: Images of empty states, where bright spots correspond to Ni sites (*top*) and filled states (*bottom*) where oxygen dominates (Reprinted with permission from [6.172]. Copyright 1997 by the American Physical Society); **(b)** simulation of the (1×1) STM image (*left*) and of the (2×1) SP-STM (*right*) of the filled states with an integration up to −1.5 eV below the VBM; *black* (*red*) *spheres* indicate TM↑ (TM↓) ions, and *blue* (*green*) *spheres* indicate O↑ (O↓); the simulated (1×1) STM image that shows O and Ni as bright spots is compared with the experimental image (*bottom* **(a)** [6.172] in *inset*). On the simulated (2×1) SP-STM image, the Ni^{2+} ions with magnetic moments aligned antiparallel to the tip magnetization become brighter due to tunneling from the minority-spin t_{2g} states, which increases the contrast between Ni^{2+} (Reprinted with permission from [6.175]. Copyright 2015 by the American Physical Society)

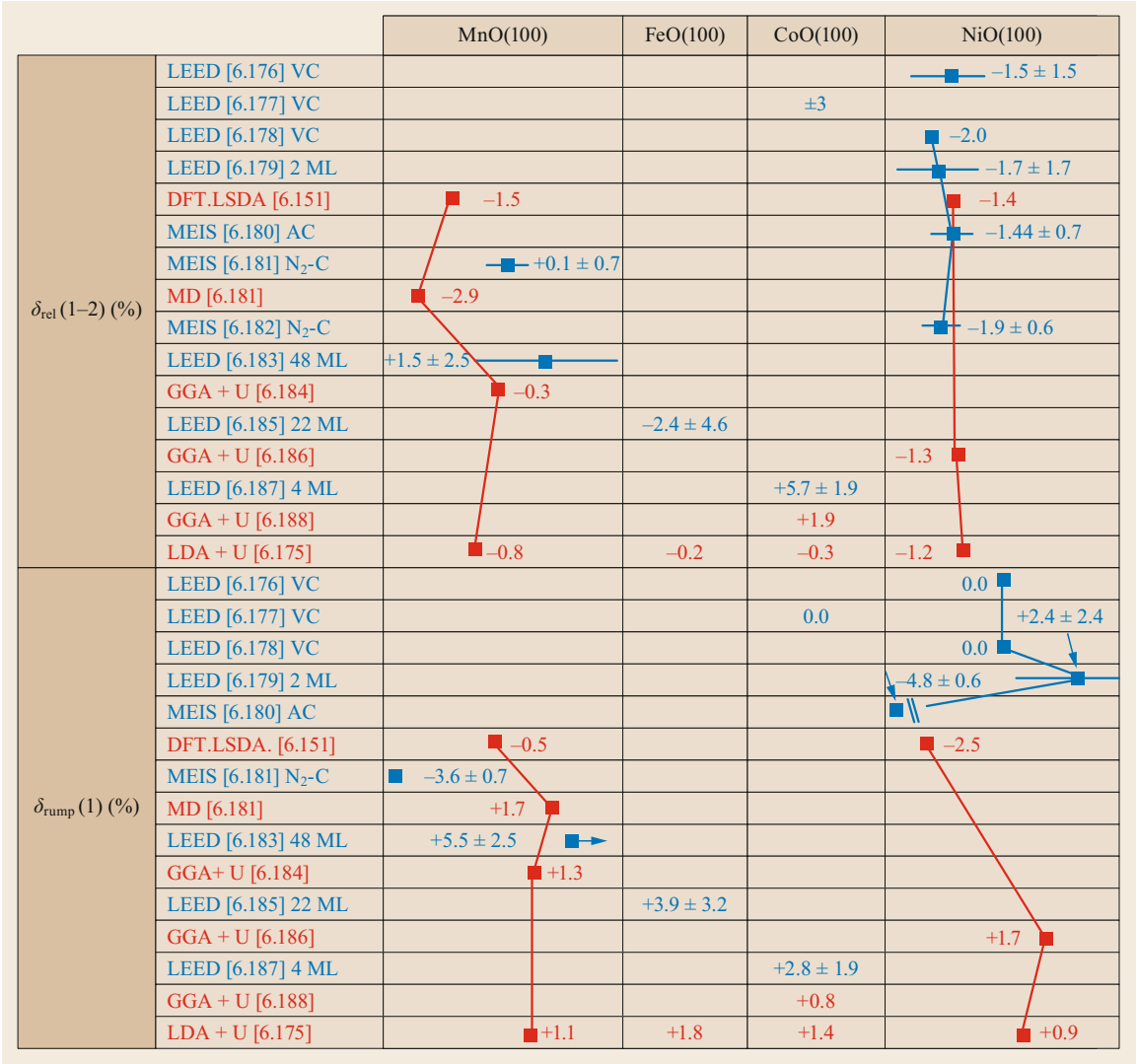

Fig. 6.11 Experimental and theoretical values of the relaxation of the topmost interplanar spacing δ_{rel} (1−2) and surface rumpling δ_{rump} (1) for MnO(100), FeO(100), CoO(100), and NiO(100). Methods and preparation are indicated (VC, AC, N_2-C for vacuum-, air-, and N_2-cleaved)

strain [6.187], which likely results in an expansion of the 4 ML CoO(100) film [6.187] with respect to bulk, while the 48 ML MnO(100) film [6.183] and the 22 ML FeO(100) film [6.185] are contracted. Therefore, the comparison of the relaxation of thin films with that of bulk samples is not straightforward. The case of rumpling is different. The rumpling at the surface of metal-supported films depends on the interface oxide–metal bond [6.189, 190]. An estimate of the film thickness for which the surface geometry escapes the influence of the substrate is given by DFT calculations relative to three-layer MgO(100) and BaO(100) films deposited on Al, Mo, Ag, Au (MgO) and on Pt, Pd, Ag, Au (BaO) [6.189]. Positive surface rumpling of 2.3−2.8% (MgO) and 3.3−5.8% (BaO) is reported [6.189], in agreement with predictions related to the (100) surface of bulk oxides (Fig. 6.8). This validates the values of rumpling determined on the MnO(100) (48 ML) [6.183], FeO(100) (22 ML) [6.185], CoO(100) (4 ML) [6.187], and NiO(100) (2 ML) [6.179] films (Fig. 6.11). All those values support the above suggestion that, as a trend, rumpling is positive along the series MnO(100)–NiO(100). Surprisingly, both surface relaxation (-1.7 ± 1.7)% and rumpling (-2.4 ± 2.4)% of the 2 ML-thick NiO(100)/Ag(100) film [6.179] agree with the other results obtained on NiO(100) surfaces

(Fig. 6.11). Finally, the rumpling at the (100) surface of oxides of rocksalt structure was suggested to be proportional to the lattice spacing, with an increase through the series NiO, MgO, CoO, FeO, MnO [6.185]. However, the absence of a clear trend through the whole MnO–NiO data set reported in Fig. 6.11 questions the suggested rule. Moreover, it does not apply to the negative CaO–BaO rumpling (Fig. 6.8).

In Fig. 6.11, the extreme experimental values are separated by significant differences ($\approx 9\%$ and $\approx 7\%$ for the rumpling of MnO(100) and NiO(100), respectively) that are far beyond the estimated errors. They can have different origins: (i) DFT calculations were carried out on the ferromagnetic phase, whereas, except in the case of NiO(100), measurements were performed on the paramagnetic phase. Indeed, a series of MEIS measurements shows a strong increase in the interlayer spacing and an inversion of the rumpling in the 300–600 K temperature range, i.e., through the antiferromagnetic–ferromagnetic transition [6.182]; (ii) in a manner comparable to that observed on MgO surfaces (Sect. 6.2.2, Fig. 6.7a,b [6.155, 156]), the NiO(100) surfaces obtained by cleavage exhibit very disturbed areas [6.191, 192].

6.3 The $SrTiO_3$(100) Surface

The mineral of $CaTiO_3$ composition was named perovskite by the geologist Gustav Rose in the 1830s, after the Russian mineralogist Lev Aleksevich von Perovski [6.193]. The ideal perovskite has an ABO_3 stoichiometry and a cubic crystal structure (space group $Pm\bar{3}m$) in which the A ion is often an alkaline earth or rare earth element and the B ion is a transition-metal element. The cell consists of a height corner-sharing network of BO_6 octahedra with, at its center, the A ion that is coordinated to 12 oxygen atoms (Fig. 6.12). However, in the real ABO_3 perovskites, the difference in radii between cations causes lattice distortions that tilt BO_6 octahedra in a way which is predicted by the Goldschmidt tolerance factor. The resulting changes in lattice symmetry lead to orthogonal, rhombohedral, tetragonal, monoclinic, and triclinic phases that are at the origin of the immense diversity of the physical and chemical properties of perovskite-type oxides [6.80, 193–196].

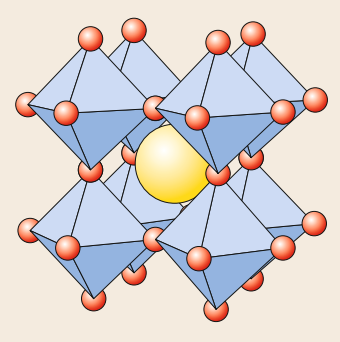

Fig. 6.12 Unit cell of the ideal cubic perovskite structure ABO_3: BO_6 tetrahedra (*blue*) with oxygen ions (*red*); central A ion (*yellow*) (Reprinted with permission from [6.195]. Copyright 2012 American Chemical Society)

6.3.1 Single Terminations

Along ⟨100⟩ directions, as all the ABO_3 oxides of perovskite structure, $SrTiO_3$ consists of alternating stacks of AO and BO_2 atomic layers that can be terminated by either of these. Because those mixed terminations are unsuited to most applications, an early concern was the preparation of atomically smooth single-terminated crystals of either composition.

Coexistence of TiO_2 and SrO Terminations

As first evidenced by electron diffraction [6.197] and consistently confirmed since, SrO and TiO_2 domains coexist systematically on as-received $SrTiO_3$(100) surfaces. The $SrTiO_3$(100) surface was first modeled with this double termination [6.198, 199]. Reliable estimates of the relative Sr/Ti surface coverage are given by ion scattering techniques, including low-energy ion scattering (LEIS) [6.84, 200, 201], medium-energy ion scattering (MEIS) [6.202, 203], and coaxial-impact-collision ion scattering spectroscopy (CAICISS) [6.204–206]. Although electron spectroscopies are quite flexible probes, they hardly characterize the composition of the extreme surface in an unambiguous way. By using ion scattering, the SrO coverage was found to range from ≈ 5 to 25% at the (100) surface of commercial $SrTiO_3$ crystals [6.84, 204], to $\approx 66\%$ on a fractured surface [6.207].

The coexistence of terraces of different chemical composition is also evidenced by the observation of non-integer unit-cell-high steps by STM or atomic force microscopy (AFM) [6.10, 89, 207–211]. These techniques motivated the search for methods to characterize the nature of the terminations. Direct imaging of the two types of termination is provided by friction force microscopy [6.205, 212–215] and phase-lag analysis [6.216], which can be used to distinguish

the different domains on a local scale. The chemical composition profoundly influences the morphology of the steps. It has been suggested that TiO_2-terminated terrace edges meander along the [100] and [010] directions, while the SrO-terminated terrace edges are curved [6.212], this under the assumption—which has since been questioned [6.213]—that the friction forces are lower on TiO_2 than on SrO [6.205, 212]. However, the geometry of the step edges of the SrO and TiO_2 terraces is sometimes the opposite of that suggested by [6.212], with the former following a broken line and the latter being rounded [6.216]. The dependence of the friction force on tip termination [6.215] and on the environment may explain these discrepancies. The friction force in particular is greatly increased on SrO terminations (not on TiO_2 terminations) by exposure to water vapor [6.217].

TiO_2 Termination

Kawasaki et al. took advantage of the opposite acid–base character of the two terminations to develop a method that eliminates one of the two [6.84]. Buffered NH_4F-HF (BHF) solutions with a pH at a critical value of 4.5 allowed full dissolution of the basic SrO surface domains. Ion scattering spectroscopy measurements demonstrated the uniformity of the BHF-etched TiO_2 termination [6.84]. The preparation leads to flat surfaces that involve wide single-terminated terraces with one-bulk-unit-cell-high steps that are suitable for film growth [6.84, 89, 209, 211, 213], as shown by the AFM image presented in Fig. 6.13. Nevertheless, the etching process does not completely eliminate the SrO domains, which still cover around 10% of the surface, as shown by MEIS analysis [6.202, 203].

The risk of hole formation during acid treatment [6.218] has inspired an evolution of the preparation method—the addition of a water immersion step to the process—based on the propensity of SrO to form hydroxides that are more prone to dissolution in acid and make the preparation less sensitive to the pH of the solution [6.89, 213] (Fig. 6.13). The treatment proved to be quite reproducible [6.219]. CAICISS analysis showed that annealing in vacuum above 570 K results in segregation of Sr, which forms SrO microclusters that cover between 15 and 20% of the surface [6.206]. The observation was confirmed by high-resolution synchrotron photoemission spectroscopy [6.220]. After removal of Sr by re-etching treatments, the TiO_2 termination is stable up to 970 K [6.206]. The segregated Sr can also be eliminated in vacuum [6.221]. In line with this, the BHF-prepared $SrTiO_3(100)$ surface was made smoother by sonication in deionized water [6.222]. Subsequently, the etching by water was rationalized to avoid the use of acids, which raises a safety issue [6.210]. In addition, the contact with the BHF solution results in unintentional F-doping of the $SrTiO_3(100)$ surface [6.223]. Motivated by those concerns, two groups have developed acid-free etchant methods [6.210, 223]. Processes combining only rinsing in deionized water and annealing at 1220–1270 K in air were shown to be effective in preparing TiO_2-terminated flat $SrTiO_3(100)$ surfaces [6.210, 223].

SrO Terminations

So far, it has been shown that the $SrTiO_3(100)$ surfaces are almost always partially covered with SrO. However, obtaining single SrO-terminated surfaces is not easy. A first strategy relies on the deposition of an SrO monolayer on TiO_2-terminated $SrTiO_3(100)$ [6.84, 224] or on other substrates [6.225]. Oxygen plasma was also used to prepare SrO-terminated surfaces to enable the deposition of high-quality YBaCuO films [6.226]. However, the treatment could not be reproduced [6.219], possibly because of the role of adventitious fluorine in the etching of strontium titanate [6.226]. Annealing $SrTiO_3(100)$ surfaces in oxygen has long been observed to activate the diffusion of strontium toward the surface, although the SrO surface coverage obtained remains fractional [6.202, 205, 206, 227–233]. High-temperature treatments can even lead the oxide to dismantle to form Ruddlesden–Popper phases [6.228]. Nevertheless, *Bachelet* et al. succeeded in controlling the enrichment in SrO of the surface at high temperature [6.216]. By annealing an initially TiO_2-terminated

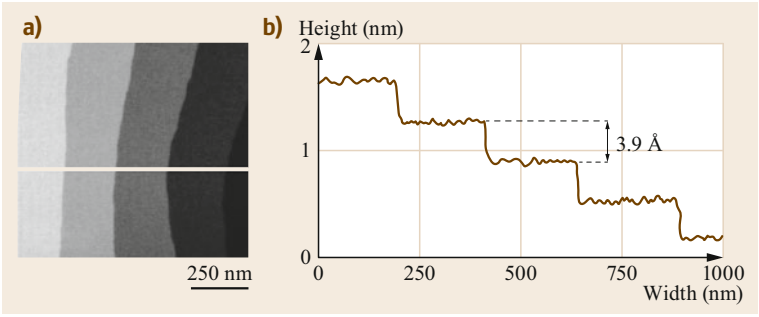

Fig. 6.13a,b TiO_2-terminated $SrTiO_3(100)$ surface **(a)** AFM image with flat terraces; **(b)** height profile along the *line* drawn in **(a)**, with 0.39 nm-high steps which correspond to a single bulk unit cell (Reprinted from [6.213], with the permission of AIP Publishing)

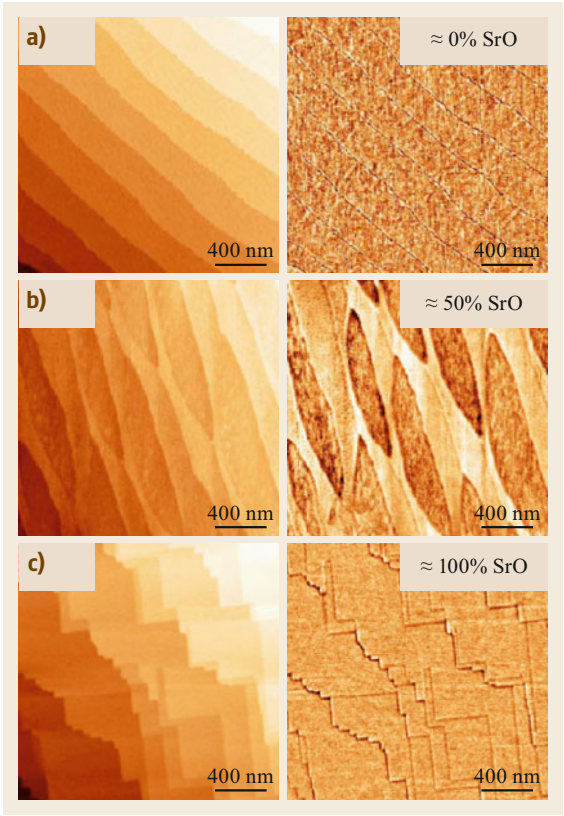

Fig. 6.14a–c Formation of an SrO-terminated surface from a TiO_2-terminated $SrTiO_3$(100) surface, as evidenced by comparing AFM topographic (*left*) to phase-lag AFM (*right*) after annealing at 1570 K in air for: **(a)** 2 h: Atomically flat surface with sharp steps of one unit cell in height and smooth step edges. The absence of contrast in the phase-lag image characterizes a single TiO_2 termination; **(b)** 12 h: Narrow terraces edging with oval regions separated by half-unit-cell-high steps indicate the appearance of a second type of chemical termination (SrO); **(c)** 72 h: The uniformity of the phase-lag image supports the formation of a single SrO-terminated surface (Reprinted from [6.216], with the permission of AIP Publishing)

$SrTiO_3$(100) crystal in air at 1570 K for 72 h, they obtained a fully SrO-terminated surface while avoiding the formation of Ruddlesden–Popper phases. Surface terminations were also characterized by combining [6.216] amplitude-modulation AFM with phase-lag analysis [6.234] (Fig. 6.14) and x-ray photoelectron spectroscopy (XPS). *Ogawa* et al. obtained an SrO-terminated surface that shows a $(\sqrt{2}\times\sqrt{2})$-R45° structure, which was assigned to a periodically SrO-deficient surface on the basis of first-principles calculations [6.235]. This structure is suggested to correspond to the c(2×2) reconstruction that was described by other groups [6.225, 236] on the SrO-terminated $SrTiO_3$(100) surface [6.235]. The ability to prepare terminations comprising simultaneous SrO and TiO_2 terminations in the form of nanostructured domains [6.216] was subsequently monitored using chemically nanopatterned substrates [6.237].

Fractured and Vicinal Surfaces

As mixed-terminated surfaces, fractured and vicinal surfaces deserve particular attention since they are required for specific applications. In particular, it is at cleaved $SrTiO_3$(100) surfaces that 2DEGs are observed [6.66]. Vicinal $SrTiO_3$(106) surfaces show an "astonishing degree of long-range order" [6.238]. Straight steps arranged in a perfectly regular way are shown to involve alternating SrO and TiO_2 rows (Fig. 6.15a). By fracturing $SrTiO_3$ crystals [6.207, 239], in the absence of a natural cleavage plane, rather smooth steps were obtained at the nanometer scale at room temperature, by scribing the sample by means of a high-precision dicing saw prior to fracturing it [6.207]. Conductance maps recorded by scanning tunneling spectroscopy reveal two types of striped domains with characteristic widths ranging from 10 to 30 nm. Comparison of the conductance maps with the topography analyzed by STM shows that the long-range order of the stripes is independent of the directions of the step edges (Fig. 6.15b). TiO_2 domains are narrower (≈ 12 nm) than SrO (≈ 24 nm) domains. The rough appearance of SrO stripes was judged to be consistent with the lower stability of SrO surfaces (Fig. 6.15b) [6.207]. Similar to layered oxides [6.240], less defective surfaces with larger terraces were obtained by fracturing at lower temperature [6.241]. Significantly, 2DEGs are only observed on surfaces fractured at low temperature [6.66].

Surface Structures

The strong dependence of the $SrTiO_3$(100) surface structure on the preparation conditions was noted [6.197, 227, 242–244] prior to the development in the mid-1990s of surface preparations that reproducibly lead to well-defined terminations [6.84]. The control of the chemical termination of $SrTiO_3$(100) was the starting point for the systematic exploration of its surface structure, with a main focus on TiO_2-terminated surfaces. After a few years, in the early 2000s, a number of $SrTiO_3$(100) surface structures were identified: (1 × 1), (2 × 1), (2 × 2), c(4 × 2), (4 × 4), c(4 × 4), c(6 × 2), (6 × 2), $(\sqrt{5}\times\sqrt{5})$-R26.6°, and $(\sqrt{13}\times\sqrt{13})$-R33.7° (the latter two are hereafter referred to as $(\sqrt{5}\times\sqrt{5})$ and $(\sqrt{13}\times\sqrt{13})$ for simplicity). The reconstruction of $SrTiO_3$(100) were first attributed to ordered □−Ti−O vacancy complexes (□ stands for an oxygen vacancy) [6.245–247] before two models were proposed, one based on a double-

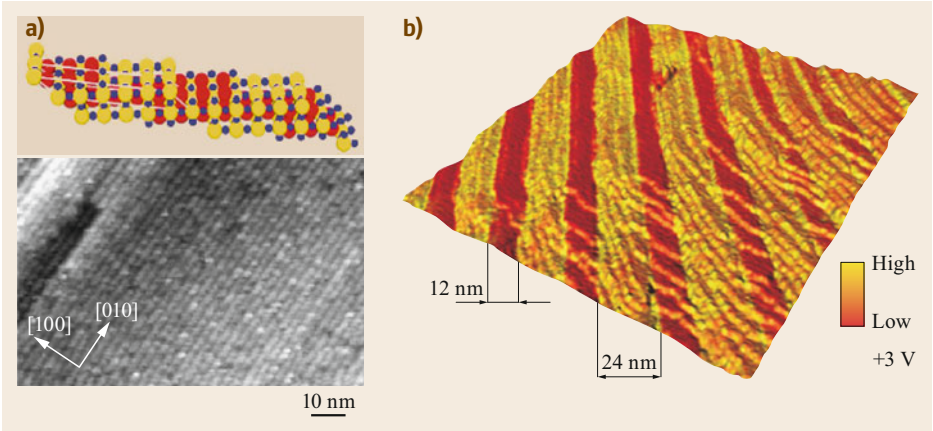

Fig. 6.15a,b Vicinal and fractured $SrTiO_3$ surfaces: **(a)** *Bottom*: $SrTiO_3(106)$ recorded by scanning tunneling microscopy (STM)—*Top*: Model of the surface as determined by grazing incidence x-ray diffraction: Sr, Ti, and O atoms are represented by *red*, *yellow*, and *blue spheres*, respectively (Reprinted with permission from [6.238]. Copyright 2005 Elsevier); **(b)** Conductance map of a fractured $SrTiO_3$ surface overlaid with the topographic AFM image. *Dark* (12 nm) and *bright* (24 nm) *areas*, assigned to SrO and TiO_2 terminations, respectively, reveal a long-range order of the local density of states that escapes the surface geometry (Reprinted with permission from [6.207]. Copyright 2009 American Chemical Society)

layer TiO_2-terminated surface [6.248] and the other on the enrichment of the TiO_2 surface layer by segregating strontium atoms [6.249]. In the following description of the $SrTiO_3(100)$ reconstructions, the (1×1) termination and the associated structures, (2×1) and (2×2), are presented first, because they give rise to a particular problem [6.200, 250]. Figure 6.16 summarizes the preparation conditions for the various reconstructions and the experimental observations by LEED, reflection high-energy electron diffraction (RHEED), STM, HRTEM, XRD, MEIS, and NC-AFM [6.85–87, 197, 200, 202, 203, 208, 221, 244, 245, 248–277].

6.3.2 $SrTiO_3(100)$-(1×1) Surfaces

Sharp (1×1) diffraction patterns have long been observed on $SrTiO_3(100)$, independent of the control of the surface termination [6.84]. They were obtained early by ion bombardment followed by annealing either in UHV (1100–1200 K [6.251, 252] or 870–1070 K [6.208, 245, 253]) or in oxygen (1020–1170 K [6.208, 253, 254] or 1100–1200 K [6.255]), or successively in oxygen, hydrogen, and UHV at 1300–1400 K [6.78]. A sharp (1×1) LEED pattern allowed the first structural study of $SrTiO_3(100)$ that was shown to combine SrO and TiO_2 domains [6.78]. The two domains then proved to coexist quite systematically on pristine surfaces. The same structure was observed on fractured surfaces, although the LEED pattern was slightly diffuse [6.251]. RHEED patterns were obtained after annealing in vacuum at 1020–1070 K [6.244]. Most importantly, similar (1×1) patterns were observed on smooth $SrTiO_3(100)$ substrates pretreated in buffered NH_4-HF solution [6.84], after annealing in vacuum or under oxygen partial pressure [6.86, 200, 202, 250, 256, 266], either by LEED [6.86, 256, 266], RHEED [6.86, 202, 203, 279], or XRD [6.200, 250].

However, the occurrence of extremely sharp (1×1) diffraction patterns contrasts astonishingly with the absence of structurally ordered surfaces at the atomic scale in STM analysis [6.86, 211, 245, 256, 266, 278]. A way to tackle the contradiction is to invoke a carbon contamination that blurs the surface imaging by STM of an otherwise well-defined structure. The (1×1) LEED pattern is suggested to originate from the ordered $SrTiO_3$ layers beneath the carbon adlayer [6.256]. Another suggestion is the occurrence of randomly distributed charges that perturb the imaging process. The NC-AFM reveals that well-defined surface structures can involve localized defect charges [6.266], thus leading to both fairly sharp diffraction patterns and blurred imaging by near-field microscopies operated at the atomic level.

An alternative explanation came from the x-ray diffraction study of *Herger* et al. [6.200, 250], who combined the XRD analysis of the $SrTiO_3(100)$ surface performed at room temperature with measurements at 1023 K under 10^{-5} mbar O_2, in typical conditions for growth of perovskite films. At 300 K, the (2×2), (2×1), and (1×1) domains are stable, at least over the measurement time. Conversely, at 1023 K, the (2×2) and (2×1) rapidly vanish, and the (1×1) structure dom-

Struct.	Sample	Temperature (K) 800 900 1000 1100 1200 1300 1400 1500 1600 1700	Time (min/h)	Method	References
(1×1)	Fractured	1200 K UHV		LEED	[6.251]
	Ar^+	1100 K UHV	60	LEED	[6.252]
	Ar^+	1400 K O_2H_2 + 1300 K UHV		LEED	[6.197]
	Polished	870–1070 K UHV	2–120	LEED, STM	[6.208, 245, 253, 254]
	Polished	1020–1170 K 10^{-5}/0.15 mbar O_2	10	LEED, STM	[6.253]
	Ar^+ Bt	900 K (UHV + 1×10^{-6} O_2)		LEED, SXRD	[6.255]
	BHF	870–1270 K 5×10^{-6}/1×10^{-5} mbar O_2	30–60	LEED, RHEED, MEIS	[6.86, 202, 203]
	BHF	870 K UHV	30	LEED	[6.256]
	BHF	1220 K UHV (2×1 + 2×2 + 1×1)	60	XRD	[6.200, 250]
(2×1)	Ar^+	1100 K 10^{-5}mbar O_2 and UHV (2×1 + 2×2 + 1×1)	60	LEED	[6.252]
	Polished	1020–1170 K UHV	20–120	LEED, RHEED, STM	[6.208, 244, 253, 254]
	(1×1)	1220 K 5×10^{-7} mbar H_2	120	LEED, STM	[6.208]
	BHF	870–1070 K UHV	30	LEED, STM	[6.257]
	BHF	1220 K UHV (2×1 + 2×2 + 1×1)	60	XRD	[6.200, 250]
	BHF	1170 K 1×10^{-2} mbar O_2	30	RHEED	[6.87]
	Ion milling	1220–1270 K O_2 flow	0.5–5 h	HRTEM	[6.248]
(2×2) *p2mg* > *p4mm* {	Ar^+	1100 K 1×10^{-5} mbar O_2 and UHV (2×1 + 2×2 + 1×1)	60	LEED	[6.252]
	Polished	1270–1470 K UHV	2–20	LEED, STM	[6.253]
	Polished	970 K 1×10^{-7} mbar O_2	Hours	LEED	[6.258]
	BHF	1270 K UHV [2×2 + c(4×4)]	20	STM	[6.259]
	BHF	1220 K UHV (2×1 + 2×2 + 1×1)	60	XRD	[6.200, 250]
	Ar^+ Bt	1070 K UHV	5 h	STM	[6.259]
	BHF	870–1270 K UHV	20–120	STM, LEED	[6.260, 261]
c(4×2)	Polished	1220 K UHV + H_2 5×10^{-7} and 10^{-5} mbar	120	LEED, STM	[6.208]
	BHF + Ar^+	1470 K UHV	15	LEED, STM	[6.256]
	BHF + Ar^+	1130 K UHV	5	LEED, STM	[6.257]
	Ion milling	1100–1200 K flowing O_2	0.5–5 h	TEM	[6.262, 263]
	BHF + Ar^+	1470 K UHV	15	STM	[6.264]
	Ar^+	1120 K 10^{-6} O_2	Cycle	LEED, STM	[6.265]
	BHF	1270 K flowing O_2	30	LEED	[6.266]
(4×4)	BHF	c(4×4) to 1450 K = 4×4 + √5×√5	Flash	STM	[6.259]
c(4×4)	BHF	1170–1670 K [+(2×1)]	> 30	LEED, STM	[6.256]
UHV dots	BHF	1370 K	20	STM	[6.259]
	BHF	2×2 to 1300 K = c(4×4)	120	STM	[6.260]
	Polished	1270 K	60	STM	[6.267]
c(6×2)	Polished	1070–1370 K flow O_2 Traces c(6×2) in √13×√13	15 h		[6.244]
O_2 flow	Polished	1220–1370K, 3 – 5 h, Fl. O_2 1220 K 5×10^{-7} H_2 or UHV	3–5 h	LEED, STM	[6.208, 254]
	Ion milled	1320–1370 K O_2 flow	2–5 h	TEM, XRD, STM	[6.268]
	Ion milled	1320 K or 1320–1470 K O_2 flow	10 h	TEM	[6.269, 270]
√5 ×√5	Polished	1470 K	2	RHEED, STM	[6.245, 271]
	Polished,	15 h 1170 K 2 min 1470 K	2	RHEED, STM	[6.272]
		1455 K	2	STM	[6.273]
		1100 K	120	LEED	[6.274]
UHV	BHF	1470 K	2	STM, NC-AFM	[6.249]
	BHF	1470 K	Flash	STM	[6.259]
	Polished	1670 K	80	LEED, STM	[6.267]
		1470–1670 K	Hours	STM	[6.275]
√13 ×√13	Polished	1070–1370 K flow O_2 (traces c(6×2))	15 h	RHEED	[6.244]
	BHF	1320 K O_2 flow – air stable	5 h	TEM	[6.276]
	BHF	1270 K flowing O_2	10 h	LEED	[6.266]
	BHF	1520 K (after √5 × √5)	Flash	STM	[6.259]
	BHF	1120 K 10^{-5}mbar O_2	40	RHEED, STM	[6.85, 221, 277]

Fig. 6.16 Reconstructions of the $SrTiO_3$(100) surface. Treatments are given. Annealing temperature ranges are shown as *horizontal red bars*. Annealing times are indicated (numbers without indication are minutes)

inates. It is necessary [6.200, 250] to understand the (2×2) and (2×1) reconstructions before examining the (1×1) structure, hence the order of the following paragraphs.

(2×1) Reconstruction

The $SrTiO_3(100)$-(2×1) structure is commonly observed by annealing in UHV [6.208, 244, 253, 256, 266] or moderate oxygen pressure (10^{-5} mbar [6.200, 250]) at temperatures ranging from 1020 to 1220 K.

Erdman et al. [6.248] examined the $SrTiO_3(100)$-(2×1) by high-resolution transmission electron microscopy (HRTEM) on an electron-transparent $SrTiO_3$ (100) sample prepared by ion milling and then annealed at 1220–1270 K in oxygen. The treatment proved efficient to both cure the damage caused by ion bombardment and promote the (2×1) surface reconstruction. The resulting model is a double-layer TiO_2-terminated surface (Fig. 6.17). The z position of atoms was determined by plane-wave pseudo-potential DFT calculations. The top layer has a TiO_2 stoichiometry. It involves zigzag rows of 5-coordinated TiO_5 units (giving rise to $p2mg$ symmetry) that share edges between them as well as with the layer underneath, which is made of slightly tilted bulk-like TiO_6 octahedra. In the surface layer, oxygen atoms that belong to shared edges (O1, O2) are bulk-like. In contrast, those not shared by neighboring octahedra bear a significantly reduced charge. More covalent Ti–O bonding compensates for the lower coordination number, particularly in the case of the surface oxygen atom O4 which is double-bonded to the surface titanium atom Ti1. The edge-shared TiO_5 units yield a charge-neutral reconstructed surface with the stoichiometry TiO_2. The authors suggest that edge-shared assembly of TiO_x units, analogous to creation of a *block structure* in Nb_2O_{5-x} and ReO_3-type bulk-like structures, controls the surface structure of $SrTiO_3(100)$ [6.248].

The (2×1) structure of the $SrTiO_3(100)$ surface was also studied by surface x-ray diffraction (SXRD) measurements by *Herger* et al. [6.200, 250]. The analysis was performed on a BHF-treated $SrTiO_3(100)$ substrate annealed eventually to 1220 K in UHV [6.84, 213]. Three different domain types were identified. At room temperature, the best fit of the SXRD data led to a combination of (2×2) (43%) and (2×1) (37%) reconstructions and a contribution of (1×1) termination (20%). The fit procedure included R-factor but also the physical reasonableness of the models. Surface energies determined by DFT calculations were also considered [6.200, 250]. As regards the (2×1) structure, test models included terminations previously proposed by other groups, i.e., oxygen-deficient surfaces [6.256] and Sr- or SrO-rich substrates [6.206, 259]. The obtained model, terminated by a double TiO_2 layer [6.200, 250], is in perfect agreement with that proposed by *Erdman* et al. [6.248].

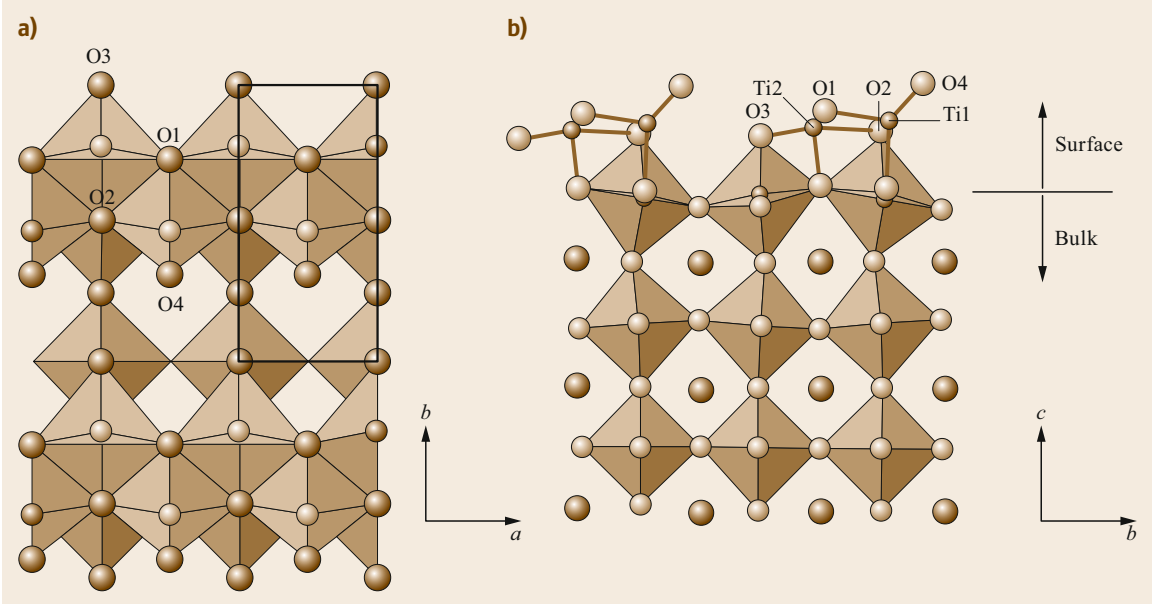

Fig. 6.17a,b Schematic representation of the (2×1) surface structure of $SrTiO_3(100)$. **(a)** Top view, which makes visible the zigzag rows of edge-sharing 5-coordinated TiO_5 units. **(b)** Side view, which shows the tilted bulk-like TiO_6 octahedra of the first subsurface layer (Reprinted with permission from [6.248]. Copyright 2002 Nature)

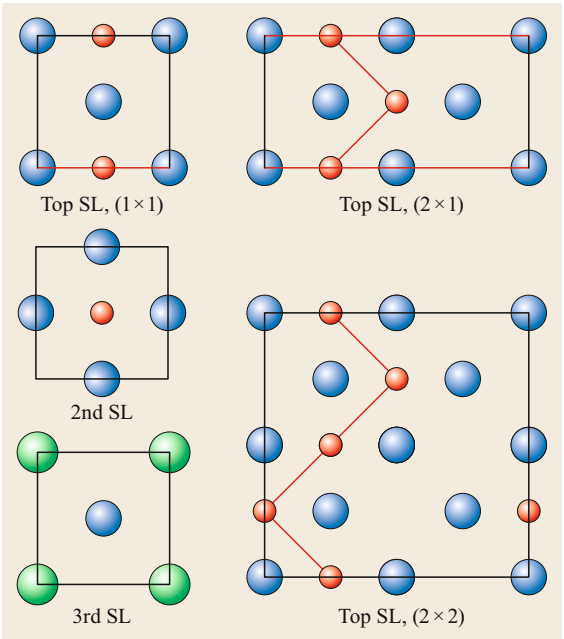

Fig. 6.18 Top surface layer (SL) of the (2×1) and *p2mg* (2×2) structure of the TiO_2-terminated $SrTiO_3(100)$ surface as determined by SXRD. The *zigzag motifs* in the two reconstructions are shown by a *red line*; Ti, Sr, and O atoms are represented by *red*, *green*, and *blue spheres*, respectively (Reprinted with permission from [6.250]. Copyright 2007 by the American Physical Society) ►

(2×2) Reconstruction

p2mg Symmetry. Two different symmetries were observed for the $SrTiO_3(100)$-(2×2) surface structure (Fig. 6.16). *Herger* et al. assigned the (2×2) reconstruction that they observed to a double-layer TiO_2-terminated structure of *p2mg* symmetry [6.200, 250] (Fig. 6.18) which had been found to be energetically favorable by *Warschkow* et al. (the (2×2)A structure in [6.279]). The (2×2) structure can be viewed as a juxtaposition of the (2×1) structure with its mirror image (Fig. 6.18) [6.250].

p4mm Symmetry. Another (2×2) reconstruction of the $SrTiO_3(100)$ surface, but this time of fourfold *p4mm* symmetry, was observed by annealing in UHV at 1220–1270 K [6.259, 260, 280]. It was obtained on a BHF-etched $SrTiO_3(100)$ by repeated annealing at 870 K [6.261]. Several models were tested, including an Sr-terminated surface [6.259], by comparing experimental STM images to DFT simulations [6.261]. The TiO_{2-x} terminated surfaces were modeled using a repeated slab configuration. The proposed (2×2) model corresponds to the (2×2) C structure of *p4mm* space symmetry previously suggested by *Warschkow* et al. [6.279]. It does not correspond to a reduced configuration. The structural model includes two types of surface oxygen atoms represented in Fig. 6.19 by light blue and dark blue spheres, respectively. The former correspond to bulk-like oxygen atoms. The

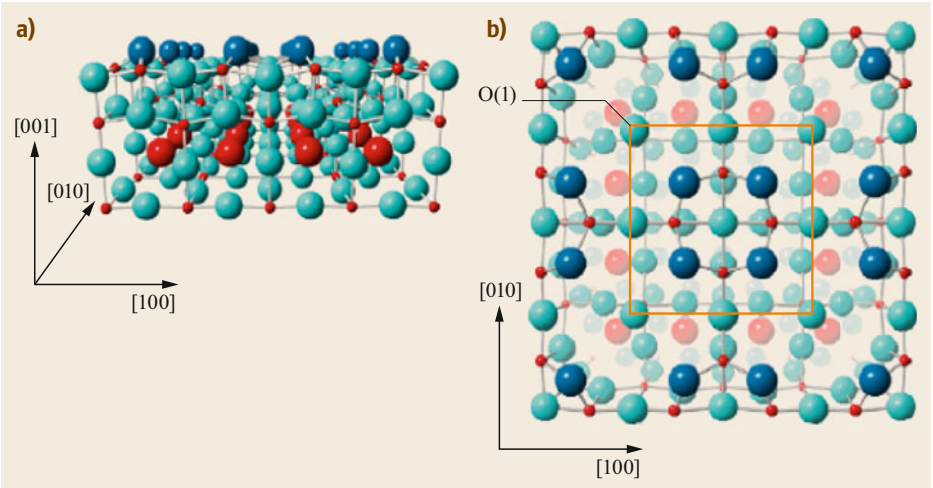

Fig. 6.19 **(a)** Side and **(b)** top views of the double-layer TiO_2-terminated $SrTiO_3(100)$-(2×2) surface with a fourfold rotational *p4mm* symmetry as determined by STM and DFT. Ti and Sr atoms are represented by *small* and *large red spheres*, respectively. O atoms are colored *light blue* and *dark blue*. The *dark blue* O atoms are *floating* atoms without bonding to the subsurface. An *orange square* features the surface unit cell. Note the onefold-coordinated surface oxygen atoms O(1) at the corner of the unit cell (Reprinted from [6.261], with permission from Elsevier)

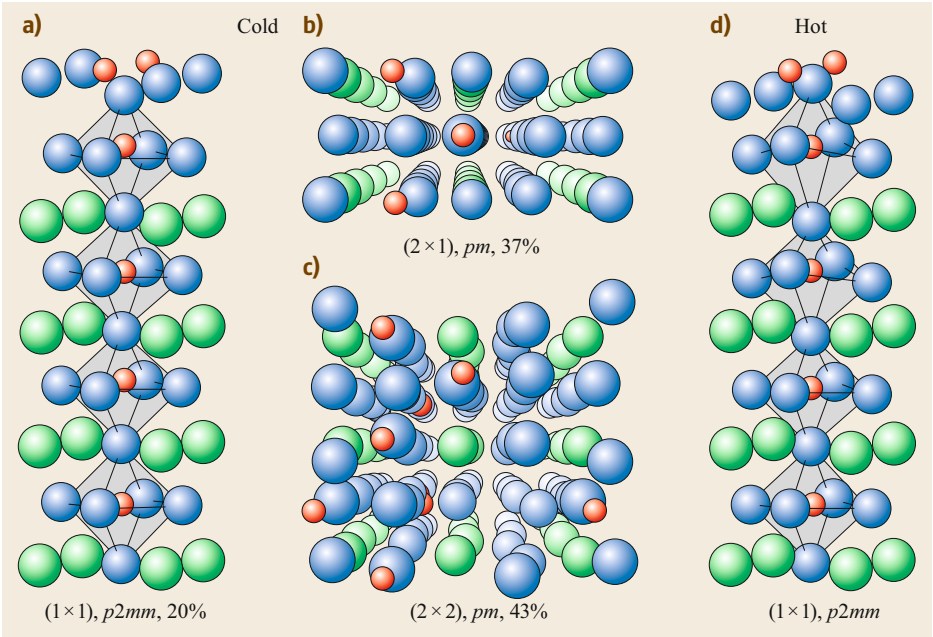

Fig. 6.20a–c Structural models for the cold **(a–c)** and the hot **(d)** $SrTiO_3(100)$ surface. Symmetries and coverages are indicated. Side views are given for the (1×1) structure **(a,d)**, top views for the (2×1) and (2×2) terminations **(b,c)**. Colors are as in Fig. 6.18 (Reprinted with permission from [6.250]. Copyright 2007 by the American Physical Society)

latter correspond to atoms bound to two surface Ti atoms but to none of the subsurface Ti atoms. Similar *floating* oxygen atoms were found in structural models related to the (2×1) [6.248] (Sect. 6.3.2 and Fig. 6.17) and the $c(4 \times 2)$ (Sect. 6.3.1) [6.263] reconstructions. In addition, there are onefold-coordinated surface oxygen atoms at the corners of the surface unit cell (O(1) in Fig. 6.19) that are only bonded to the subsurface Ti atoms lying underneath. They form Ti=O double bonds whose bond length is about 0.3 Å less than that of the typical Ti−O single bond in $SrTiO_3$ bulk [6.263]. The $SrTiO_3(100)$-(2×1) structural model involves a similar Ti=O bond, but in this case, both titanium and oxygen are surface atoms [6.248] (Sect. 6.3.2 and Fig. 6.17). Onefold-coordinated oxygen atoms are also found at the surface of the (2×1)-reconstructed rutile $TiO_2(011)$ surface [6.281] and are rather commonly encountered at surfaces of oxides of corundum structure. Chromyl (Cr=O), ferryl (Fe=O), and vanadyl (V=O) species have been revealed at the surface of α-$Cr_2O_3(0001)$ [6.282] and α-$Fe_2O_3(0001)$ [6.283] single crystals and $V_2O_3(0001)$ thin films [6.284], respectively. Lin et al. observed that shifting every second reconstructed cell row in the (2×2) structure (Fig. 6.19) by one bulk lattice constant results in the $c(4 \times 2)$ configuration (Sect. 6.3.3). The geometrical similarity led them to suggest that the (2×2) surface is transformed from the $c(4 \times 2)$ surface by using different sample preparation conditions [6.261].

(1×1) Termination

Herger et al. noted that the double-layer (1×1) termination seems to be unlikely for its much too high surface energy, while poor fits discard the *ideal* bulk (1×1) termination [6.200, 250], in line with the suggestion that this termination does not exist [6.285]. In the same way as for the (2×1) and (2×2) reconstructions, fits of (1×1) data significantly favored the configurations involving a double-layer TiO_2 termination and a zigzag motif of the top Ti atoms [6.200, 250]. Surface energy considerations suggested that the (1×1) structure results from a mixture of (2×1) and (2×2) reconstructions with a disordered combination of the zigzag motifs. Such origin is consistent with the unique occurrence of the (1×1) structure at high temperature. The surface vibrational energy might exceed the difference in surface energy between the (2×1) and (2×2) domains, resulting in their complete mixing [6.200, 250] in an order–disorder transition [6.286] similar to what was observed for the W(100) clean surface phase transition [6.287]. The best fit of the *hot* (1×1) leads to a structure similar to the (1×1) found at room temperature [6.200, 250], but with more puckering of the top TiO_2 surface layer via protruding surface Ti atoms (Fig. 6.20).

Comparison Between Models

The (1×1) [6.200, 250, 279, 285, 288], (2×1) [6.200, 250, 279, 285, 288], (2×2) [6.200, 250, 279], and $c(4 \times 2)$ [6.279] reconstructions of the $SrTiO_3(100)$ surface

have been studied using ab initio approaches. Many tests have been carried out for each structure, by removing atomic rows, changing the surface terminations, or creating vacancies [6.200, 250, 285], or using different symmetry groups [6.279]. Overall, the results of the calculations support the experimental results, in particular the double-layer (DL) TiO_2-terminated (1×1) [6.200, 250], (2×1) [6.200, 248, 250], and *p2mg* (2×2) [6.200, 250] models. DFT calculations predict the (1×1) DL to be unstable [6.250, 288]. They confirm the very low surface energies of the (2×1)-DL and (2×2)-DL reconstructions, the latter having the lowest energy [6.250, 279]. However, the (2×1)-DL is not clearly favored with respect to the bulk-terminated (1×1) [6.250, 285].

Calculations relative to the geometry of the $SrTiO_3$ (001)-(2×1) structure are in good agreement [6.200, 248, 250, 279, 285, 288]. In all models, the predicted reconstruction extends over three atomic layers, and the featured trends appear very similar. A puckering [6.200, 250] of the surface Ti atoms is evidenced [6.248, 285]. However, the out-of-plane relaxation of a surface oxygen atom (O4 in Fig. 6.17 [6.248]), which is modeled in [6.248, 285], does not appear in the model proposed in [6.200, 250] (Figs. 6.18 and 6.20).

Finally, in the absence of assignment to a defined structure, the measurements performed on the surface relaxation of $SrTiO_3$ by LEED, RHEED, and MEIS [6.78, 197, 203, 229] can hardly be reconciled with an atomistic description of the surface. As a trend, however, they indicate systematically a small positive rumpling [6.78, 197, 203, 229], which might correspond to the protrusion of some surface oxygen atoms in the (2×1) [6.248, 279, 285] and (2×2) [6.200, 250] structures which are the dominant contributions of the $SrTiO_3$(001)-(1×1) termination [6.200, 250].

6.3.3 $SrTiO_3$(100) Reconstructions

c(4 × 2)

Observed by annealing at 1220 K under hydrogen at a partial pressure of 5×10^{-5} mbar [6.208], the c(4 × 2) structure can be obtained after sputtering with Ar^+ ions and annealing either to 1470 K in UHV [6.256, 264] or to 1120 K under oxygen at 1×10^{-6} mbar [6.265]. However, *Dagdeviren* et al. prepared it by annealing the (1×1) at 1270 K under flowing oxygen for 30 min, which evidences a totally different origin of the reconstruction [6.266]. The reconstructed c(4 × 2) surface involves domains rotated by 90° with respect to each other, as analyzed by LEED [6.208, 256, 266]. STM images show straight step edges aligned with the [001] and [010] directions [6.208, 256, 257, 265]. The reproducible observation that steps are one bulk unit cell high implies a unique termination which is assumed to be TiO_2 [6.208, 256, 266]. Auger electron spectroscopy (AES) analysis rules out the possibility that impurities could be the driving force for the reconstruction [6.208].

Erdman et al. [6.263] analyzed the c(4 × 2) reconstruction by the same HRTEM technique as the (2×1) structure [6.248]. Samples are prepared by ion milling and then annealing under flowing oxygen (Fig. 6.16). Measurements made by HRTEM on the electron-transparent samples were complemented by plane-wave pseudo-potential DFT calculations to determine z positions. The surface structure consists of a periodic pattern of clustered quartets of edge-sharing TiO_5 polyhedra. The subsurface is a bulk-like TiO_2 layer (Fig. 6.21) [6.263, 264]. The c(4 × 2) and (2×1) models are close to each other. However, the c(4 × 2) termination is more stable than the (2×1) reconstruction, as determined by DFT. Consistently, the c(4 × 2) is obtained by annealing in flowing oxygen at a lower

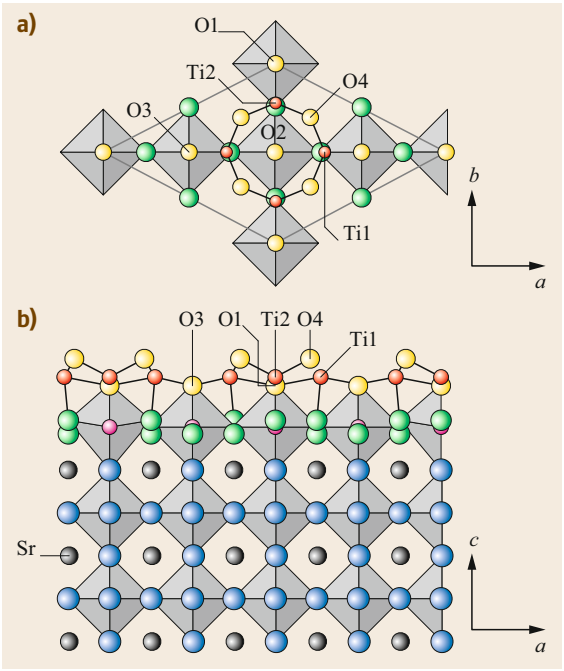

Fig. 6.21 **(a)** Top and **(b)** side view of the $SrTiO_3$(100)-c(4 × 2) reconstruction. Note the oxygen atoms (O4) in flexible positions (not bonded to subsurface Ti atoms). The Ti, Sr, surface O, and subsurface O atoms are represented by *red*, *black*, *yellow*, and *green spheres*, respectively. Bulk TiO_6 octahedra are shown in *blue*. Floating oxygen O4 are similar to those found in the $SrTiO_3$(100)-(2×1) (Fig. 6.17) [6.248] and in $SrTiO_3$(100)-(2 × 2) of *p4mm* symmetry (Fig. 6.19) [6.261] (Reprinted with permission from [6.263]. Copyright 2003 American Chemical Society)

temperature than the (2 × 1) structure (1100–1200 and 1220–1270 K, for the c(4 × 2) [6.262] and the (2 × 1) [6.248], respectively). In the proposed c(4 × 2) structure [6.263], half of the surface oxygen atoms occupy a flexible position (oxygen atoms with no Ti atom positioned directly underneath, O4 in Fig. 6.21), while there are only one-quarter of such atoms in the (2 × 1) structure proposed by the same group [6.248].

c(6 × 2)

After annealing an $SrTiO_3$(100) crystal at 1270 K in flowing oxygen, faint spots assigned to the c(6 × 2) structure were observed to coexist with the ($\sqrt{13} \times \sqrt{13}$) RHEED pattern [6.244]. *Jiang* and *Zegenhagen* observed the c(6 × 2) reconstruction by heating the crystal to 1220–1370 K for 4–5 h in pure oxygen at atmospheric pressure and then at 1220 K for 2 h in the UHV system [6.208, 254]. LEED and STM characterize a (6 × 2) surface structure whose twofold symmetry is at odds with the fourfold symmetry of the $SrTiO_3$(100) surface. The accommodation of the reconstruction by the substrate explains that the surface is tiled randomly by equivalent (6 × 2) domains rotated by 90° with respect to each other and aligned in ⟨100⟩ directions. However, a slight miscut favors a single-domain superstructure [6.254]. The unit-cell-high steps indicate a unique termination, assumed to be Ti-rich on the basis of AES analysis. As in the case of the c(4 × 2), the possibility that the reconstruction is induced by impurities is discarded. Interestingly, the c(6 × 2) reconstruction, which is always obtained upon annealing in flowing oxygen, proves to be extremely stable. It is even hardly affected by exposure to oxygen or ambient air [6.208, 254].

A first model for the atomic structure for the c(6 × 2) was proposed by combining transmission electron diffraction, surface x-ray diffraction, and density functional theory [6.268]. Samples were prepared in conditions similar to those used previously [6.208, 244, 254]. The TEM and x-ray analyses were performed on electron-transparent samples and $SrTiO_3$(001) crystals, respectively, annealed for 2–5 h at 1320–1370 K under a flow of high-purity oxygen at atmospheric pressure. The surface was suggested to involve four related structures, either stoichiometric or slightly reduced, and nonperiodic surface TiO_2 units [6.268]. However, a recent study by the same group questioned this view [6.269, 270]. High-resolution secondary-electron microscopy (HRSEM) coupled with annular dark-field (ADF) TEM allowed for simultaneous measurement of both the atomically resolved bulk (ADF) and surface crystal structure (HRSEM) [6.269, 270]. The analysis revealed that the previous model [6.268] involves a shift of the surface $SrTiO_3$ layers with respect to the bulk. The DFT approach used to reconcile the complete data set led to a c(6 × 2) structure (also belonging to the *c2mm* space group) consisting of a triple TiO_2 overlayer terminated by TiO_5 octahedrally coordinated titanium similar to those found on (2 × 1) [6.248] and c(4 × 2) [6.262, 263] surfaces. In addition, in each c(6 × 2) unit, two Sr atoms with sevenfold coordination to oxygen are substitutionally exchanged for Ti in the uppermost surface layer (Fig. 6.22) [6.269, 270].

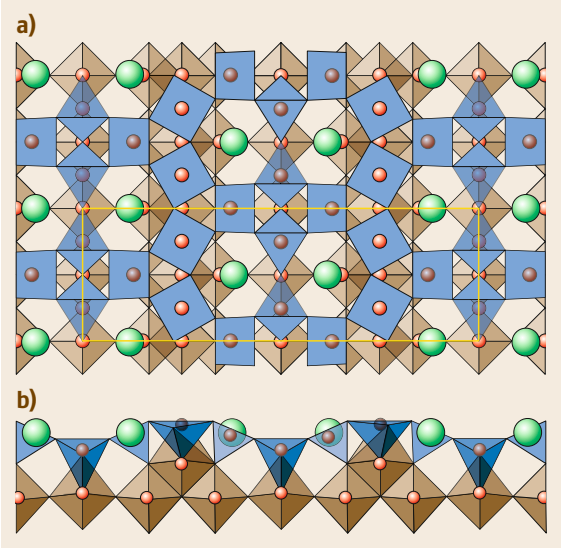

Fig. 6.22 **(a)** Top and **(b)** side view of the $SrTiO_3$(001)-c(6 × 2) reconstruction as suggested by *Ciston* et al. [6.269]. Ti atoms, Sr atoms, surface TiO_5 truncated octahedra, and bulk-like subsurface TiO_6 octahedra are in *red*, *green*, *blue*, and *brown*, respectively. The unit cell is shown in *yellow* (Adapted with permission from [6.269])

($\sqrt{13} \times \sqrt{13}$)-R33.7°

The air-stable [6.276] $SrTiO_3$(100)-($\sqrt{13} \times \sqrt{13}$) reconstruction has been observed by RHEED [6.244], TEM [6.276], and LEED [6.266] after annealing at 1070–1370 K in flowing oxygen for 5–15 h [6.244, 266, 276] (Fig. 6.16). The ($\sqrt{13} \times \sqrt{13}$) RHEED pattern was also observed following a treatment at similar temperatures under much lower oxygen partial pressure (Fig. 6.16), either at 1120–1270 K under (i) 3×10^{-5} mbar O_2 for 40 min [6.85, 221, 277], or (ii) at 900 K under 1×10^{-6} mbar O_2 for 16 h [6.266]. In the latter case, however, the ($\sqrt{13} \times \sqrt{13}$) phase was mixed to traces of the initial c(4 × 2) structure [6.266]. What distinguishes the formation conditions of c(6 × 2) from those of ($\sqrt{13} \times \sqrt{13}$) is unclear. Both are obtained under flowing oxygen at similar temperature, to the point that they can coexist [6.244] (Fig. 6.16). However, they differ strongly. In particular, the c(6 × 2)

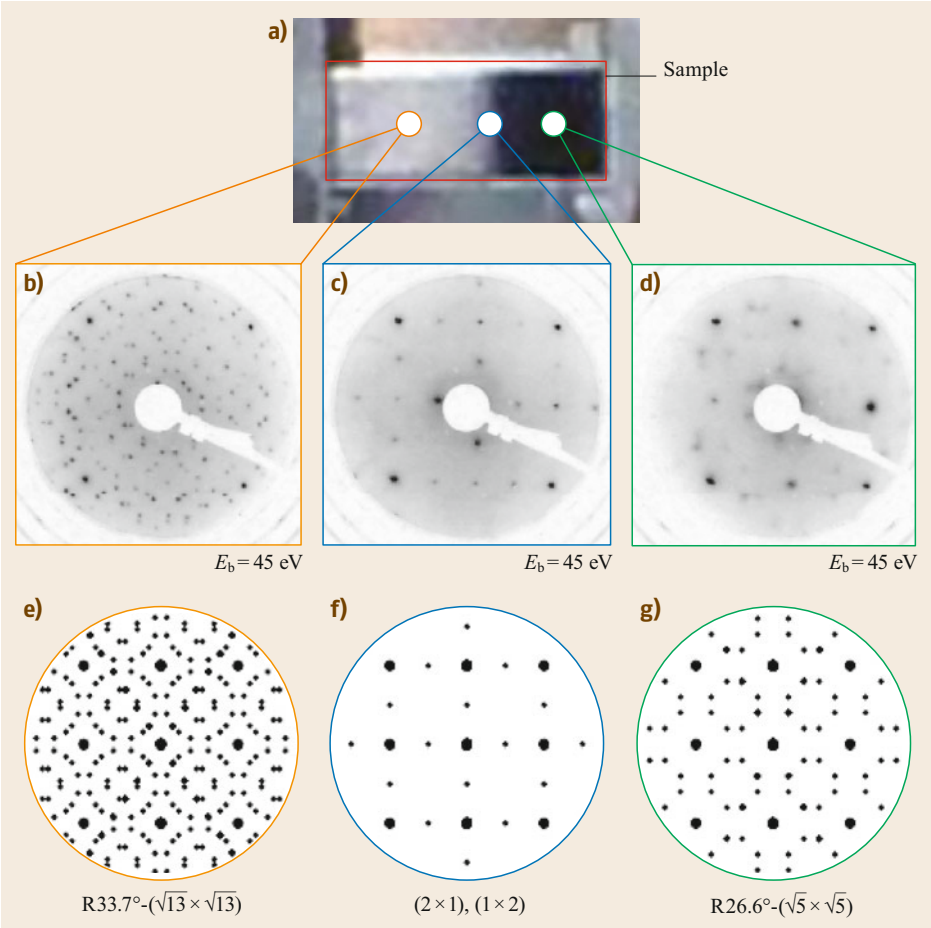

Fig. 6.23a–g $SrTiO_3$(100) structural surface reconstruction versus the reduction state of the crystal. **(a)** Photograph of the crystal annealed at 1070 K for 24 h while being subjected to a dc voltage; **(b–d)** LEED patterns from $(\sqrt{13} \times \sqrt{13})$, (2×1)-(1×2), and $(\sqrt{5} \times \sqrt{5})$ reconstructions that are unambiguously associated with **(b)** the transparent zone (positive electrode), **(c)** the intermediate zone, and **(d)** the dark zone (negative electrode), respectively; **(e–g)** schematic representation of the LEED patterns (Reprinted from [6.289], with the permission of AIP Publishing)

structure includes surface Sr atoms [6.269], while the $(\sqrt{13} \times \sqrt{13})$ reconstruction is TiO_2-terminated [6.276, 277], with a marginal Sr segregation at steps [6.221] (see later in chapter).

A Reconstruction of Highly Oxidized $SrTiO_3$(100) Surfaces. The diversity of the preparation conditions for the $(\sqrt{13} \times \sqrt{13})$ structure makes it impossible to determine whether it is associated with a precise oxidation state of the substrate. The experiments of *Shimizu* et al. [6.289] help remove the ambiguity. These authors resistively annealed an $SrTiO_3$(100) crystal to $\approx$ 970–1070 K in UHV by a dc current via a thick Pt film deposited on the back of the sample. Upon annealing, defective sites migrate close to the negative electrode, as shown by the spatial color gradation of the $SrTiO_3$ crystal from transparent to black (Fig. 6.23a). LEED patterns associated with the $(\sqrt{13} \times \sqrt{13})$, (2×1), and $(\sqrt{5} \times \sqrt{5})$ reconstructions appear in the transparent area, the intermediate blue part, and the strongly reduced black zone, respectively (Fig. 6.23b–g). In accordance with the colors, the Ti 2p levels shift from Ti^{4+} to Ti^{3+} states. STM images of the three reconstructions were recorded in preparation conditions similar to those of the LEED. The oxidized and reduced zones are generated by the diffusion of the species under the effects of the electric field, but are not generated by either the gaseous environment or the elevation in temperature. Therefore, the spontaneous $(\sqrt{13} \times \sqrt{13})$ reconstruction of the transparent part of the crystal indicates that $(\sqrt{13} \times \sqrt{13})$ is the stable structure of the fully oxidized $SrTiO_3$(100) surface [6.289]. This is in

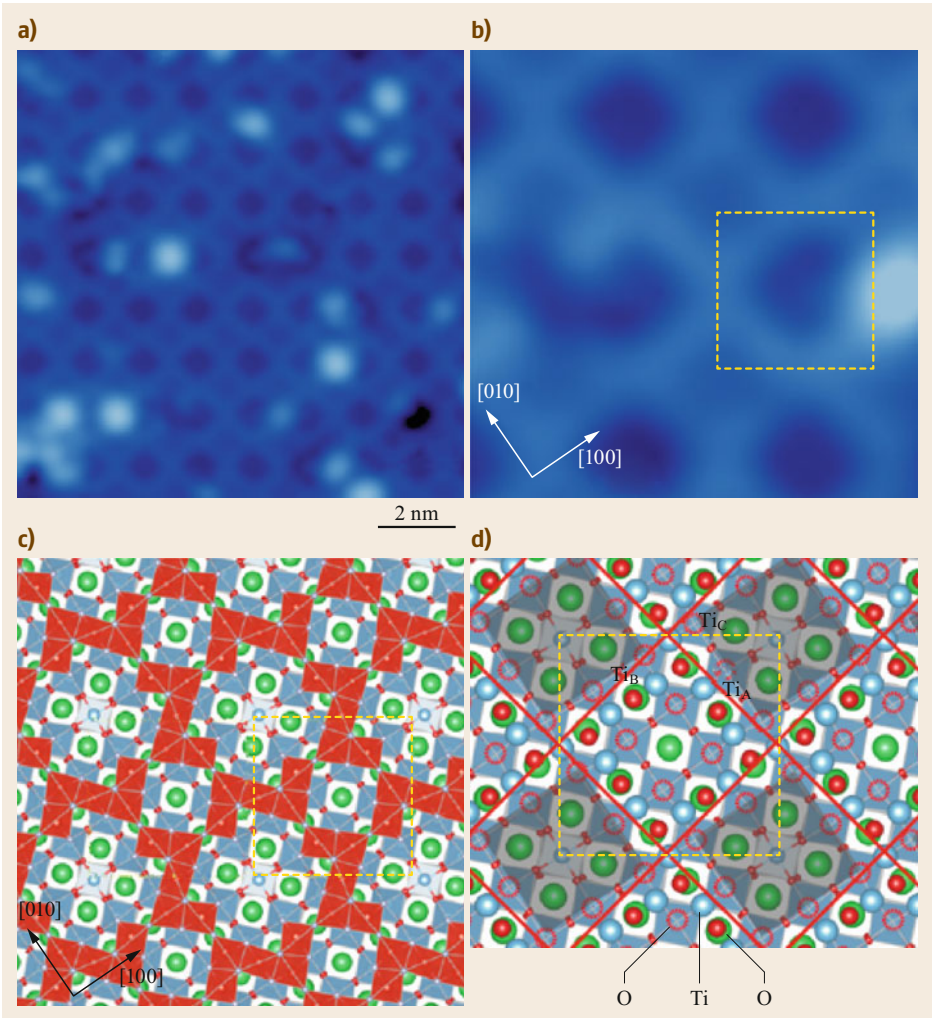

Fig. 6.24a–d STM analysis of the $(\sqrt{13}\times\sqrt{13})$ reconstruction of the $SrTiO_3(100)$ surface. **(a)** Topographic image; **(b)** $3.7\times3.7\,nm^2$ topographic image; the *dashed squares* correspond to the $(\sqrt{13}\times\sqrt{13})$ unit cell; **(c)** $(\sqrt{13}\times\sqrt{13})$ surface structure: Sr, Ti, and O atoms correspond to *green*, *blue*, and *red spheres*, respectively; *blue* and *red polyhedra* indicate TiO_6 octahedra in bulk and truncated octahedra TiO_5 at the surface, respectively. **(d)** Other representation of the $(\sqrt{13}\times\sqrt{13})$ structure on the bulk-like TiO_2-terminated surface (Sr, Ti, and O atoms correspond to *green*, *blue*, and *red* (*filled* or *empty*) *spheres*, respectively); dark and faint-dark zones seen in STM images **(a)** and **(b)** are indicated, as well as the three inequivalent surface Ti atoms (Ti_A, Ti_B, Ti_C) (Adapted with permission from [6.277]. Copyright 2014 American Chemical Society)

line with the formation of the structure upon annealing at 1070–1370 K in flowing oxygen for 5–15 h [6.244, 266, 276], under conditions of time and pressure that likely bring the system close to equilibrium. This does not contradict the formation of the $(\sqrt{13}\times\sqrt{13})$ structure at 1120 K under lower O_2 pressures [6.85, 221, 277], since it has been shown that the reconstructed surface obtained in such conditions is almost perfectly stoichiometric, with no detectable contribution of Ti^{3+} [6.221]. The puzzling $(\sqrt{13}\times\sqrt{13})$ structure obtained by annealing an $SrTiO_3(100)$-$(\sqrt{5}\times\sqrt{5})$ surface at 1520 K for a few seconds [6.259] likely stems from kinetic effects.

The TiO_2 Termination. The topographic STM image of the $(\sqrt{13}\times\sqrt{13})$ exhibits dark and faint-dark tiles separated by a bright lattice [6.221, 259, 277, 289] (Fig. 6.24a,b). Two very close geometries have been proposed. One is based on HRTEM [6.276]. The other, which is derived from STM imaging [6.277], is pre-

sented here because it also accounts for the distribution of the surface d states. To model the reconstruction from the STM data, dark and faint-dark tiles were assigned to vacant sites in the TiO_x adlayer. This adlayer was then arranged to fulfill the periodicity and the fourfold symmetry of the $(\sqrt{13}\times\sqrt{13})$ reconstruction. The stoichiometric surface TiO_2 layer consists of Z-shaped units involving five edge-sharing TiO_5 truncated octahedra that form a two-dimensional network with small and large vacant sites. The model derived from the STM analysis is shown in Fig. 6.24c. Its relevance was tested by DFT calculation [6.277]. The geometry is very close to that determined by HRTEM [6.276]. The model also accounts for marked changes in the differential conductance dI/dV obtained from differentiation of the tunneling current (I) at each point, as a function of the sample bias voltage (V) [6.277]. It is assumed that the degeneracy of the t_{2g} levels (d_{xy}, d_{yz}, d_{zx}) is lifted upon reconstruction. However, the energy levels and localizations of the orbitals differ for each of the three types of Ti atoms that belong to the surface TiO_2 lattice: Ti_A and Ti_B have corner sharing in addition to edge sharing, while Ti_C has only edge sharing (Fig. 6.24d). The marked energy dependence of the spectroscopic image is attributed to changes in the d orbitals probed with STS, which are suggested to be d_{xy} at lower bias (≤ 1.2 eV) and $d_\pi(d_{yz} + d_{zx})$ at higher bias (≥ 1.3 eV). The proposed structural model satisfactorily accounts for the observed dI/dV profile [6.277].

Therefore, the atomistic description of the double-layer TiO_2-terminated model of the $SrTiO_3$(100)-$(\sqrt{13}\times\sqrt{13})$ reconstruction [6.276, 277] is consistent with the macroscopic analysis. The structure appears on a highly oxidized surface close to stoichiometry [6.221, 289], on which one-unit-cell-high steps are indicative of a single-terminated surface [6.85]. The Sr coverage at the $(\sqrt{13}\times\sqrt{13})$ surface was estimated at only 1% and was attributed to segregation at steps [6.221]. The apparent contradiction of this situation with the constant observation that Sr segregates upon annealing in vacuum of BHF-treated $SrTiO_3$(100) substrate [6.202, 205, 206, 230–233] is not explained.

$(\sqrt{5}\times\sqrt{5})$-R26.6°

All preparations of the $SrTiO_3$(100)-$(\sqrt{5}\times\sqrt{5})$ reconstruction consist in annealing the $SrTiO_3$ crystal to 1455−1670 K in UHV [6.242, 245, 249, 259, 267, 271–273, 275, 290] (Fig. 6.16). The $(\sqrt{5}\times\sqrt{5})$ reconstruction was first obtained by annealing an $SrTiO_3$(100) crystal to 1470 K for 2 min in UHV, possibly after degassing at 1070−1170 K, and initially attributed to reducing conditions [6.242, 245, 249, 259, 271–273]. The c(4 × 4)-dot and $(\sqrt{5}\times\sqrt{5})$ reconstructions both result from annealing in UHV. However, the former shows up at slightly lower temperature. It actually coexists with the $(\sqrt{5}\times\sqrt{5})$ structure [6.259] which covers the whole surface after further annealing [6.259, 267]. In greater reducing conditions, by heating an $SrTiO_3$ crystal to 1470−1680 K for many hours, a crystal conductivity jump was observed to parallel the $(\sqrt{5}\times\sqrt{5})$ reconstruction, which means that the reconstruction is due to a significant reduction of the crystal [6.267, 275]. On the annealed $SrTiO_3$ crystal under polarization (Fig. 6.23), the structure $(\sqrt{5}\times\sqrt{5})$ is formed at the strongly reduced end, on the side opposite the one where the structure $(\sqrt{13}\times\sqrt{13})$ is seen [6.289]. Therefore, the preparations which rest on prolonged heating times that tend probably to equilibrium [6.267, 275, 289] all indicate that the $(\sqrt{5}\times\sqrt{5})$ structure is the reconstruction of reduced $SrTiO_3$(100) surfaces.

The STM image corresponding to the $SrTiO_3$(100)-$(\sqrt{5}\times\sqrt{5})$ reconstruction was initially described as a (2 × 2) structure [6.242] before being properly assigned [6.245, 271, 272]. The bright spots on the STM images were first assigned to oxygen vacancies, and the reconstruction was assumed to be a $\square-Ti^{3+}-O$ complex [6.245, 271, 272], as supported by simulations [6.246, 291]. The model was later questioned by the prediction that the bright spots should be split into two spots [6.247].

Kubo and *Nozoye* investigated the $SrTiO_3$(100)-$(\sqrt{5}\times\sqrt{5})$ structure by means of STM (Fig. 6.25a) and NC-AFM (Fig. 6.25b) imaging, supported by ab initio calculations [6.249, 259, 290]. In particular, images at the atomic scale of the $(\sqrt{5}\times\sqrt{5})$ lattice cell recorded by NC-AFM were assumed to reflect a surface corrugation (Fig. 6.25b). The bright spots at the corner of the lattice were assigned to Sr atoms, and the dark spots aligned along the [001] and [010] directions (inset of Fig. 6.25b) were suggested to be related to the oxygen atoms of the TiO_2 plane. In this way, the $(\sqrt{5}\times\sqrt{5})$ structure was viewed as an ordered array of Sr adatoms sitting at oxygen fourfold hollow sites on a TiO_2-terminated surface [6.249, 259, 290] (Fig. 6.25d). The interpretation of the STM and NC-AFM images was supported by first-principles total energy calculations. Subsequent studies confirmed these results. A cross-shaped protrusion observed by STM at the center of the $(\sqrt{5}\times\sqrt{5})$ unit cell was attributed to Ti−O−Ti bridges [6.275] by comparison with [6.199]. The $(\sqrt{5}\times\sqrt{5})$ was shown by Auger spectroscopy [6.267] and photoemission [6.292] to correspond to a Ti enrichment, a strong O depletion, and a clear reduction of Sr [6.292] over the UHV cleaved sample taken as representative of the bulk composition [6.267]. The lack of sensitivity of STM to sample bias (from $+3.5$ to -3.5 eV) was judged to be indicative of the metallicity of the reconstructed

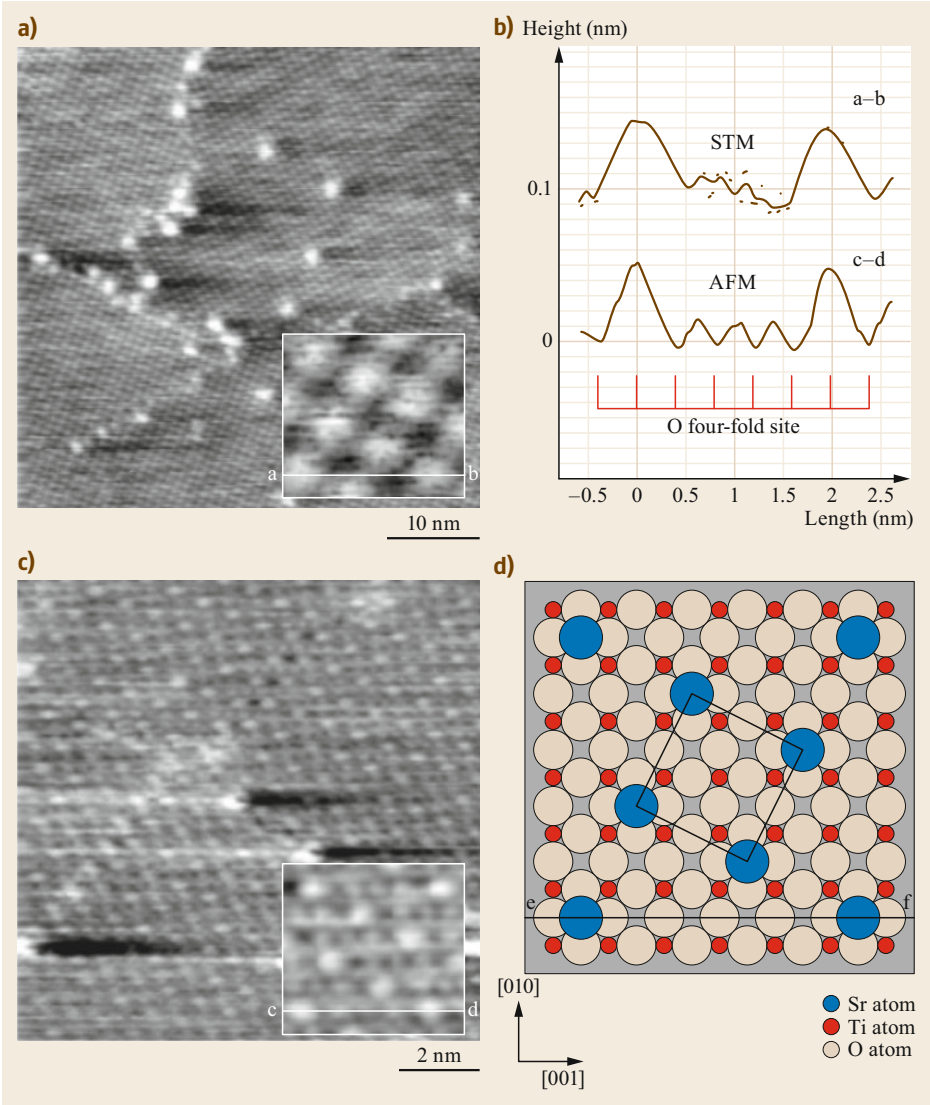

Fig. 6.25a–d Analysis of the $SrTiO_3(100)$-$(\sqrt{5}\times\sqrt{5})$ reconstruction. **(a)** STM image 50×50 nm^2 and **(c)** NC-AFM image 12×12 nm^2; **(b)** vertical profiles along the *lines* a–b and c–d drawn in *insets* in **(a)** and **(c)**; **(d)** suggested model for the $(\sqrt{5}\times\sqrt{5})$ structure; the *line* e–f corresponds to both the *lines* a–b and c–d in **(a)** and **(c)**, respectively (Reprinted with permission from [6.249]. Copyright 2001 by the American Physical Society)

surface [6.267]. A phase separation occurring on the strongly reduced surface was suggested by *Newell* et al. to give rise, on the one hand, to the Sr adatoms of the $(\sqrt{5}\times\sqrt{5})$ structure and, on the other hand, to islands whose composition was assumed to be TiO [6.293] (corresponding to Ti^{2+}) on the basis of the Ti LMV Auger line shape [6.267]. (The observation that the shape of the Ti LMV line reflects the stoichiometry in compounds containing reduced titanium [6.251, 294, 295] was substantiated by the identification of the components of the Ti LMV transition [6.296, 297].) Despite the relatively poor overall Sr content of the surface region of the $(\sqrt{5}\times\sqrt{5})$ reconstruction, *Newell* et al. support the Sr-terminated model [6.267]. Interestingly, doping affects the $(\sqrt{5}\times\sqrt{5})$ reconstruction in a way that seems compatible with that model. The structure is observed on Nb-doped but not La-doped STO(100). Nb^{5+} ions that are located substitutionally on Ti sites do not segregate, while La^{3+} ions located on Sr sites do segregate and presumably prevent the segregation of Sr and the formation of the $(\sqrt{5}\times\sqrt{5})$ reconstruction [6.298].

Kubo et al. further extended the Sr-terminated model [6.249] to the c(2 × 2), c(4 × 4), (2 × 2), (4 × 4), $(\sqrt{5}\times\sqrt{5})$, and $(\sqrt{13}\times\sqrt{13})$ reconstructions that they achieved by a succession of short annealing cycles (a few seconds) separated by small temperature increments, from 1270 to 1520 K [6.249, 259]. They assumed that the reconstructions so obtained consist of phase transitions rather than composition changes [6.259,

290]. However, first-principles total energy calculations of Sr-terminated $SrTiO_3$(100) reconstructions [6.299] led to the conclusion that the only stable structures for the temperature and pressure ranges indicated by *Kubo* and *Nozoye* and *Kubo* et al. [6.249, 259, 290] are the (2×2) and $(\sqrt{5}\times\sqrt{5})$ reconstructions.

A different model came from an STM study supported by DFT calculations of the $BaTiO_3$(001)-$(\sqrt{5}\times\sqrt{5})$-R26.6° surface reconstruction [6.300]. By comparing the surface phase diagram of $BaTiO_3$(001) determined by DFT calculations to STM and STS investigations, Martirez et al. favored TiO_2-$Ti_{3/5}$ or TiO_2-$Ti_{4/5}$ terminations in which Ti adatoms occupy hollow sites of the TiO_2 surface. These atoms, whose density of states strongly contributes to the conduction band, are expected to be observed mostly in empty-state images. Conversely, Ti atoms belonging to the TiO_2 layer, of which the density of states involves bandgap states, are predicted to appear in filled-state images. The model includes three different Ti atoms. *Martirez* et al. suggested that it could apply to the $(\sqrt{5}\times\sqrt{5})$ reconstruction of the $SrTiO_3$(001) surface [6.300]. Leaving aside that suggestion, which is not supported by any $SrTiO_3$ modeling, the Sr-terminated model of the $SrTiO_3$(001)-$(\sqrt{5}\times\sqrt{5})$ from Kubo and Nozoye is concordant [6.267, 275, 292], but its extension to other surfaces is not recognized.

(4×4) and $c(4\times4)$ Reconstructions

Other structures—(4×4) and $c(4\times4)$—have been observed on $SrTiO_3$(100) surfaces. Also, nanostructured $SrTiO_3$(100) surfaces and defective structures can be obtained by annealing in UHV, as recently reviewed by *Marshall* et al. [6.38]. Annealing a (2×1) structure at 1170−1670 K in UHV after BHF etching gave rise to a $c(4\times4)$ reconstruction that consists of broken lines running in the [100] direction [6.256]. The periodicity of the breaks (four bulk unit cells) and the offset of the line result in a $c(4\times4)$ structure suggested to evolve from the (2×1) areas through ordering of defects. The two reconstructions coexist even after annealing at 1670 K [6.256].

A different $c(4\times4)$ reconstruction was obtained by annealing an $SrTiO_3$(100)-(2×2) surface at 1300 K in UHV [6.260] or, alternatively, by annealing a BHF-etched $SrTiO_3$(001) surface in UHV at 1270 K [6.267]. The structure now consists of ordered bright spots oriented in ⟨110⟩ directions (for that reason, it is labeled $c(4\times4)$ dots in Fig. 6.16). Eventually, after 80 min at 1350 °C, the formation of the $(\sqrt{5}\times\sqrt{5})$ reconstruction follows a significant increase in conductivity of the crystal [6.267]. *Kubo* and *Nozoye* [6.259] observed small (2×2) and $c(4\times4)$ domains after annealing at 1270 K for 20 min. By successive annealing for several seconds at 1370, 1420, 1450, and 1470 K, they observed a series of reconstructed surfaces, i.e., $c(4\times4)$, (4×4), a mixture of (4×4) and $(\sqrt{5}\times\sqrt{5})$, and $(\sqrt{5}\times\sqrt{5})$, that were all assigned to ordered arrays of surface Sr atoms [6.259]. The $c(4\times4)$ structures obtained in [6.259, 267] are apparently similar. Both result from heating an $SrTiO_3$(100)-(2×2) surface in UHV. Both lead by further annealing to the $(\sqrt{5}\times\sqrt{5})$ reconstruction, but with extremely different annealing times, a few seconds in one case [6.259] and 80 min in the other investigation [6.267].

6.3.4 Open Issues

A vast corpus of experiments shows that the chemistry of the bulk, near-surface, and surface of an $SrTiO_3$(100) crystal depends on its temperature and environment. Upon annealing in vacuum, the $SrTiO_3$(100) surface loses oxygen while the Sr content increases relative to titanium [6.202, 208, 227, 266]. But it is unclear [6.266, 267] whether such enrichment is proof of the surface segregation of strontium [6.249, 259, 290]. The oxygen deficiencies induced by annealing in UHV leave two electrons behind that reduce the transition-metal cations [6.267]. However, it is not easy to distinguish the effects of annealing from those resulting from the presence of vacancies [6.289]. Although the complex formed by oxygen vacancies and reduced titanium was suggested in early works [6.242, 245, 246, 271, 291] to drive the $(\sqrt{5}\times\sqrt{5})$ reconstruction prior to being discarded [6.247, 249], little attention has since been paid to the influence of the degree of reduction of the solid on the surface reconstruction [6.289]. Defective sites and charge transfers complicate the configurations formed by the three elements involved in the oxide, to the point that the analysis is hardly tractable.

Stoichiometry-Driven Reconstructions

From this point of view, insights can be gained by experiments that favor one particular parameter, all other parameters being unaffected. The above-described experiment by *Shimizu* et al. (Sect. 6.3.3 and Fig. 6.23) follows such an approach [6.289]. Three structures appear in the UHV-annealed and polarized $SrTiO_3$ crystal: $(\sqrt{13}\times\sqrt{13})$, (2×1), and $(\sqrt{5}\times\sqrt{5})$. They clearly rely on the oxidation state of the substrate lying underneath, either fully oxidized, partially reduced, or fully reduced. Similar ideas come from *Newell* et al.'s observation on annealed $SrTiO_3$ crystal that the onset of the formation of the $(\sqrt{5}\times\sqrt{5})$ LEED pattern correlates with a jump in conductivity, i.e., a sudden increase in bulk concentration of reduced species [6.267]. However, while the colors of the polarized $SrTiO_3$ crystal could be reversibly reversed by switching the polarity of the bias

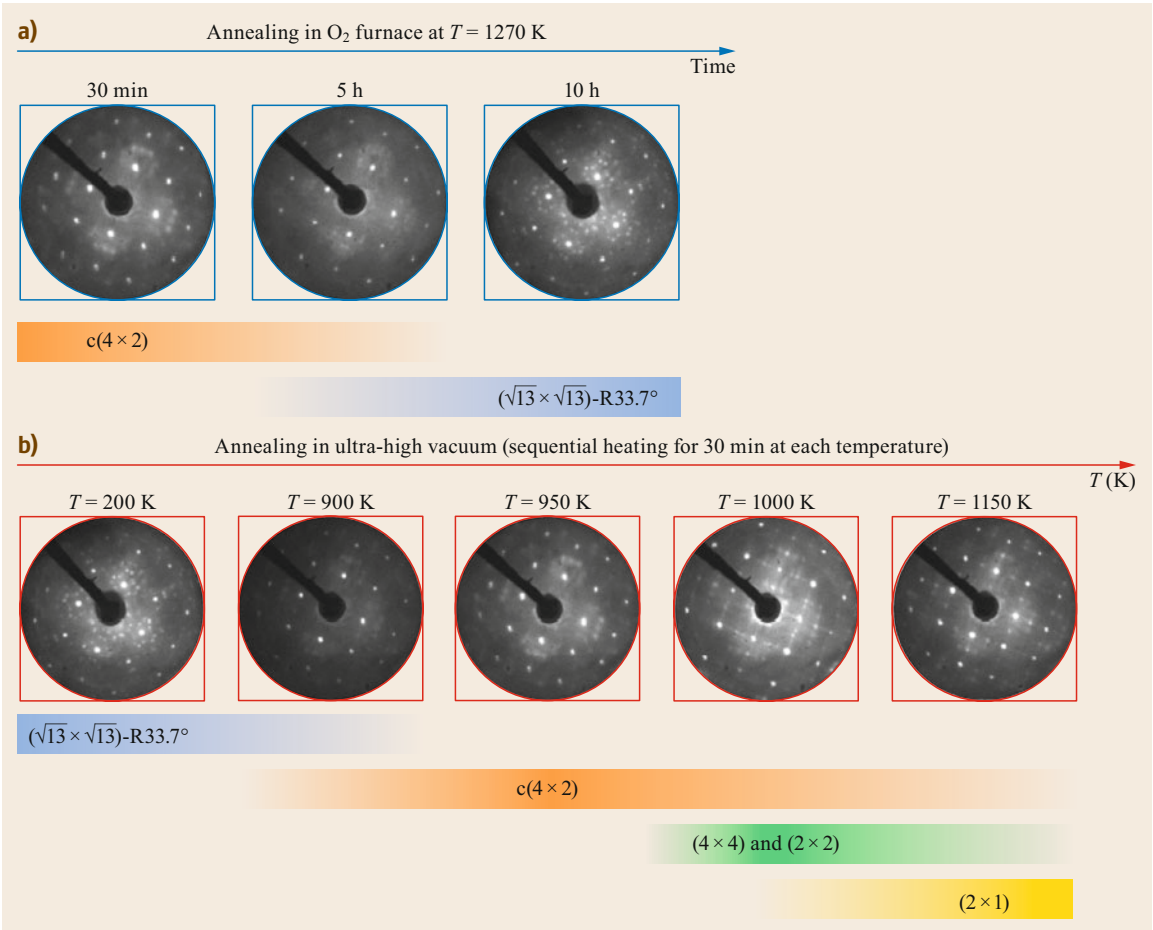

Fig. 6.26a,b Structural transition on $SrTiO_3(100)$ as a function of temperature and environment. **(a)** Annealing of $SrTiO_3(100)$-(1×1) at 1270 K in flowing oxygen; the $c(4 \times 2)$ structure that first appears is progressively replaced by the $(\sqrt{13} \times \sqrt{13})$ reconstruction; **(b)** annealing the $(\sqrt{13} \times \sqrt{13})$ termination in UHV, the reverse transformation results in the recovery of the $c(4 \times 2)$ structure and then in combinations of (4×4), (2×2), and (2×1) structure (Reprinted with permission from [6.266]. Copyright 2016 by the American Physical Society)

voltage, it was not possible to modify the reconstructions by this means [6.289]. Such behavior is indicative of a reconstruction process that does not stem from the bulk defect concentration alone. It likely involves more complex correlations between Sr, Ti, O, and vacancies that depend on the redox status of the $SrTiO_3$ substrate. In particular, for thermodynamic reasons, the concentration of defective sites at reducible oxide surfaces can strongly differ from that in bulk, as observed in the case of the rutile TiO_2 (110) [6.301, 302].

Dagdeviren et al. reported a series of $SrTiO_3(100)$ reconstructions obtained by varying the temperature and/or the annealing time under given environments, including oxygen at normal pressure (Fig. 6.26) [6.266]. They pay particular attention to transitions and reverse transitions between reconstructions. Annealed in a furnace at 1270 K under flowing oxygen, the original (1×1) surface structure transforms first into a $c(4 \times 2)$ reconstruction and then, after 10 h, into a $(\sqrt{13} \times \sqrt{13})$ structure. A similar transformation is observed when the sample is removed from the O_2 furnace after 30 min and then annealed at 900 K in a UHV chamber in 10^{-6} mbar O_2, although traces of the $c(4 \times 2)$ phase are still visible after 16 h. Conversely, the $(\sqrt{13} \times \sqrt{13})$ structure could be switched into the $c(4 \times 2)$ reconstruction by annealing the crystal at 950 K in UHV. Further annealing at 1000 and 1150 K gives rise to (4×4), (2×2), and (2×1) reconstructions. As discussed earlier, the $(\sqrt{13} \times \sqrt{13})$ reconstruction appears as the favored surface structure under oxidizing conditions. The $c(4 \times 2)$, (4×4), (2×2), and (2×1) are likely comparatively increasingly oxygen-deficient [6.266].

On the $SrTiO_3(100)$-c(4 × 2) substrate, the systematic observation of terraces separated by unit-cell step height [6.266] proves the uniform coverage of the surface by a single termination. Upon annealing the c(4 × 2) surface in UHV at increasing temperatures, AES analysis shows that Sr and Ti segregate at the $SrTiO_3(100)$ surface while the Sr/Ti ratio increases, in agreement with the commonly accepted behavior. A chemical surface and subsurface disorder is evidenced by temperature- and bias-induced changes in surface roughness. In parallel, steps and holes of fractional unit-cell step heights (770−1170 K) evidenced by NC-AFM reveal the progressive emergence of surface terminations of various natures (Sect. 6.3.1 *Coexistence of TiO_2 and SrO*). Therefore, the transition from the $SrTiO_3(100)$-c(4 × 2) to (4 × 4), (2 × 2), and (2 × 1) by annealing in UHV is accompanied by changes in chemical composition and appearance of various terminations, although the c(4 × 2) [6.263], (2 × 2) [6.200, 250, 261], and (2 × 1) [6.200, 248, 250, 261] reconstructions are modeled by similar double-layer TiO_2 structures.

Surface Chemistry

The changes in the surface structure of $SrTiO_3(100)$ that are caused by deposition of strontium and titanium [6.265] follow the same direction as the above findings. In a similar way as on the $SrTiO_3(110)$ [6.303] and $SrTiO_3(111)$ [6.304] surfaces, *Gerhold* et al. transformed the surface reconstructions of the $SrTiO_3(100)$ surface by Sr and Ti deposition [6.265]. A two-domain c(4 × 2) reconstruction was transformed into a (2 × 2) structure by deposition of strontium and annealing to 1120 K in 10^{-6} mbar O_2. The inverse transformation can be performed by titanium deposition and annealing in oxygen. The operation can be repeated more than ten times without visible degradation. For the two structures, unit-cell step heights characterize a single-terminated surface, and the Ti core-level profiles are indicative of fully oxidized surfaces. However, the steps aligned with ⟨100⟩ directions observed on the c(4 × 2) reconstructed surface and the curved steps seen on the (2 × 2) surface [6.265] are reminiscent of the TiO_2 and SrO terrace edges [6.212], respectively. This and the higher Sr/Ti ratio found by LEIS on the (2 × 2) surface question the prediction of a similar double-layer TiO_2 termination for the two reconstructions. *Gerhold* et al. suggest that the building blocks of the two surfaces should be different and that the surface stoichiometry is at the origin of the formation of the different reconstructions of the $SrTiO_3(100)$ surface [6.265]. This conclusion is in line with the suggestion by *Dagdeviren* et al. that the c(4 × 2) and (2 × 2) terminations exhibit different terminations [6.266].

6.4 Outlook

The always positive values of the rumpling at MgO(100), as determined by both experiment and theory, demonstrate that the oxygen ions protrude above the magnesium ions at that surface. As a trend, rumpling is also positive along the series of (100) surfaces of transition-metal oxides MnO, FeO, CoO, and NiO. Conversely, the rumpling is predicted to switch from positive on MgO(100) to increasingly negative along the CaO(100), SrO(100), and BaO(100) series, with cations protruding outward. Because the earlier model of Verwey, which relies on differences in ion polarizability, cannot account for that trend, these predictions suggest a relaxation mechanism that includes the metal and oxygen semicore state interactions and the overlap O(2p)−O(2p) between next-nearest neighbors. As regards relaxation, x-ray diffraction performed on high-quality MgO(100) single crystal shows that the first interlayer spacing is slightly contracted, while atomistic simulations predict a weak expansion, leading to the qualitative conclusion that the MgO(100) surface relaxation is close to zero. An increasing negative relaxation is predicted along the CaO(100)–BaO(100) series, in agreement with the only existing measurement, which was carried out on CaO(100). There is complete consensus on the contraction of the first interlayer spacing of NiO(100), but nothing is clear about the MnO, FeO, CoO series. Overall, the support of experimental data by numerical simulations reinforces the reliability of the conclusions. However, in the case of the much-studied relaxation and rumpling of MgO(100), the theory puts forward estimates that are about 1% higher than experimental values. These small but systematic discrepancies indicate that the issue escapes complete understanding.

The c(4 × 2), c(6 × 2), $(\sqrt{5} \times \sqrt{5})$, and $(\sqrt{13} \times \sqrt{13})$ surface reconstructions of $SrTiO_3(100)$ are reproducibly prepared. However, the temperature and pressure conditions observed from one group to another for the formation of given reconstructions often escape rationality and sometimes seem contradictory. A crucial concern is the preparation of single-terminated surfaces with unambiguous surface composition. As shown by the formation of specific reconstructions as a function of the degree of reduction of the material, species associated with the reduction of the oxide, oxy-

gen vacancies, or reduced cations are definitely active in driving reconstructions. In addition, the involvement of surface strontium in reconstructions is underestimated. Nevertheless, the existing structural models of $SrTiO_3(100)$ reconstructions hardly take those species into account.

References

6.1 C.T. Campbell, J. Sauer: Introduction: surface chemistry of oxides, Chem. Rev. **113**, 3859–3862 (2013)

6.2 C.T. Campbell, J. Sauer (Eds.): *Surface Chemistry of Oxides Reviews (Special Issue)*, Chemical Reviews, Vol. 113 (ACS Publications, Washington 2013)

6.3 R.A. van Santen, I. Tranca, E.J.M. Hensen: Theory of surface chemistry and reactivity of reducible oxides, Catal. Today **244**, 63–84 (2015)

6.4 Y. Li, W. Shen: Morphology-dependent nanocatalysts: rod-shaped oxides, Chem. Soc. Rev. **43**, 1543–1574 (2014)

6.5 M.A. Henderson: A surface science perspective on TiO_2 photocatalysis, Surf. Sci. Rep. **66**, 185–297 (2011)

6.6 Z. Zhang, J.T. Yates Jr.: Defects on TiO_2—key pathways to important surface processes, Springer Ser. Surf. Sci. **58**, 81–121 (2015)

6.7 Z. Zhang, J.T. Yates Jr.: Band bending in semiconductors: chemical and physical consequences at surfaces and interfaces, Chem. Rev. **112**, 5520–5551 (2012)

6.8 S. Das, V. Jayaraman: SnO_2: a comprehensive review on structures and gas sensors, Prog. Mater. Sci. **66**, 112–255 (2014)

6.9 R.G. Egdell: Dopant and defect induced electronic states at In_2O_3 surfaces, Springer Ser. Surf. Sci. **58**, 351–400 (2015)

6.10 F. Sanchez, C. Ocal, J. Fontcuberta: Tailored surfaces of perovskite oxide substrates for conducted growth of thin films, Chem. Soc. Rev. **43**, 2272–2285 (2014)

6.11 J. Lutzenkirchen, G.V. Franks, M. Plaschke, R. Zimmermann, F. Heberling, A. Abdelmonem, G.K. Darbha, D. Schild, A. Filby, P. Eng, J.G. Catalano, J. Rosenqvist, T. Preocanin, T. Aytug, D. Zhang, Y. Gan, B. Braunschweig: The surface chemistry of sapphire-c: a literature review and a study on various factors influencing its IEP, Adv. Colloid Interface Sci. **251**, 1–25 (2018)

6.12 H.A. Al-Abadleh, V.H. Grassian: Oxide surfaces as environmental interfaces, Surf. Sci. Rep. **52**, 63–161 (2003)

6.13 G.E. Brown, G. Calas: Mineral-aqueous solution interfaces and their impact on the environment, Geochem. Perspect. **1**, 483–742 (2012)

6.14 C. Fischer, I. Kurganskaya, T. Schäfer, A. Lüttge: Variability of crystal surface reactivity: What do we know?, Appl. Geochem. **43**, 132–157 (2014)

6.15 J. Jupille: Analysis of mineral surfaces by atomic force microscopy. In: *Spectroscopic Methods in Mineralogy and Materials Sciences*, Reviews in Mineralogy Geochemistry, Vol. 78, ed. by G.S. Henderson, D.R. Neuville, R.T. Downs (2014) pp. 331–369

6.16 G.J. Qian, Y.B. Li, A.R. Gerson: Applications of surface analytical techniques in Earth Sciences, Surf. Sci. Rep. **70**, 86–133 (2015)

6.17 N. Nilius: Properties of oxide thin films and their adsorption behavior studied by scanning tunneling microscopy and conductance spectroscopy, Surf. Sci. Rep. **64**, 595–659 (2009)

6.18 F.P. Netzer, F. Allegretti, S. Surnev: Low-dimensional oxide nanostructures on metals: hybrid systems with novel properties, J. Vac. Sci. Technol. B **28**, 1–16 (2010)

6.19 S. Surnev, A. Fortunelli, F.P. Netzer: Structure–property relationship and chemical aspects of oxide–metal hybrid nanostructures, Chem. Rev. **113**, 4314–4372 (2013)

6.20 J. Paier, C. Penschke, J. Sauer: Oxygen defects and surface chemistry of ceria: quantum chemical studies compared to experiment, Chem. Rev. **113**, 3949–3985 (2013)

6.21 H. Kuhlenbeck, S. Shaikhutdinov, H.-J. Freund: Well-ordered transition metal oxide layers in model catalysis—a series of case studies, Chem. Rev. **113**, 3986–4034 (2013)

6.22 A. Picone, M. Riva, A. Brambilla, A. Calloni, G. Bussetti, M. Finazzi, F. Ciccacci, L. Duò: Reactive metal–oxide interfaces: a microscopic view, Surf. Sci. Rep. **71**, 32–76 (2016)

6.23 J. Jupille, G. Thornton (Eds.): *Defects at Oxide Surfaces*, Springer Series in Surface Sciences, Vol. 58 (Springer, Berlin, Heidelberg 2015)

6.24 M.J. Wolf, A.L. Shluger: The structure and properties of clean steps at oxide surfaces, Springer Ser. Surf. Sci. **58**, 191–214 (2015)

6.25 C. Barth: Defects on Bulk Mg0(001) imaged by nc-AFM, Springer Ser. Surf. Sci. **58**, 215–239 (2015)

6.26 T. Berger, O. Diwald: Defects in metal oxide nanoparticle powders, Springer Ser. Surf. Sci. **58**, 273–301 (2015)

6.27 J. Oviedo, M.J. Gillan: Energetics and structure of stoichiometric SnO_2 surfaces studied by first-principles calculations, Surf. Sci. **463**, 93–101 (2000)

6.28 G. Pacchioni: Numerical simulations of defective structures: the nature of oxygen vacancy in non-reducible (MgO, SiO_2, ZrO_2) and reducible (TiO_2, NiO, WO_3) oxides, Springer Ser. Surf. Sci. **58**, 1–28 (2015)

6.29 M.V. Ganduglia-Pirovano, A. Hofmann, J. Sauer: Oxygen vacancies in transition metal and rare earth oxides: current state of understanding and remaining challenges, Surf. Sci. Rep. **62**, 219–270 (2007)

6.30 N. Nilius, M. Sterrer, M. Heyde, H.-J. Freund: Atomic scale characterization of defects on oxide surfaces, Springer Ser. Surf. Sci. **58**, 29–80 (2015)

6.31 M.V. Ganduglia-Pirovano: Oxygen defects at reducible oxide surfaces: the example of ceria and vanadia, Springer Ser. Surf. Sci. **58**, 149–190 (2015)

6.32 J.V. Lauritsen: Noncontact AFM imaging of atomic defects on the rutile TiO_2(110) surface, Springer Ser. Surf. Sci. **58**, 241–272 (2015)

6.33 E. Giamello, M. Chiesa, M.C. Paganini: Point defects in electron paramagnetic resonance, Springer Ser. Surf. Sci. **58**, 303–326 (2015)

6.34 C.L. Pang, G. Thornton: Photon-, electron-, and scanning tunneling microscopy-induced defects on oxide surfaces, Springer Ser. Surf. Sci. **58**, 429–451 (2015)

6.35 Z. Dohnálek, I. Lyubinetsky, R. Rousseau: Thermally-driven processes on rutile TiO_2(110)-(1×1): a direct view at the atomic scale, Prog. Surf. Sci. **85**, 161–205 (2010)

6.36 S. Bourgeois, B. Domenichini, J. Jupille: Excess electrons at oxide surfaces, Springer Ser. Surf. Sci. **58**, 123–147 (2015)

6.37 W.-J. Yin, B. Wen, C. Zhou, A. Selloni, L.-M. Liu: Excess electrons in reduced rutile and anatase TiO_2, Surf. Sci. Rep. **73**, 58–82 (2018)

6.38 M.S.J. Marshall, A.E. Becerra-Toledo, L.D. Marks, M.R. Castell: Defects on strontium titanate, Springer Ser. Surf. Sci. **58**, 327–349 (2015)

6.39 M. Setvín, M. Wagner, M. Schmid, G.S. Parkinson, U. Diebold: Surface point defects on bulk oxides: atomically-resolved scanning probe microscopy, Chem. Soc. Rev. **46**, 1772–1784 (2017)

6.40 A. Mehonic, A.J. Kenyon: Resistive switching in oxides, Springer Ser. Surf. Sci. **58**, 401–428 (2015)

6.41 C. Noguera: Polar oxide surfaces, J. Phys. Condens. Matter **12**, R367–R410 (2000)

6.42 J. Goniakowski, F. Finocchi, C. Noguera: Polarity of oxide surfaces and nanostructures, Rep. Prog. Phys. **71**, 016501 (2008)

6.43 C. Noguera, J. Goniakowski: Polarity in oxide Nanoobjects, Chem. Rev. **113**, 4073–4105 (2013)

6.44 D.P. Woodruff: Quantitative structural studies of corundum and rocksalt oxide surfaces, Chem. Rev. **113**, 3863–3886 (2013)

6.45 U. Diebold: The surface science of titanium dioxide, Surf. Sci. Rep. **48**, 53–229 (2003)

6.46 C.L. Pang, R. Lindsay, G. Thornton: Structure of clean and adsorbate-covered single-crystal rutile TiO_2 surfaces, Chem. Rev. **113**, 3887–3948 (2013)

6.47 F. De Angelis, C. Di Valentin, S. Fantacci, A. Vittadini, A. Selloni: Theoretical studies on anatase and less common TiO_2 phases: bulk, surfaces, and nanomaterials, Chem. Rev. **114**, 9708–9753 (2014)

6.48 X. Chen, A. Selloni: Introduction: titanium dioxide (TiO_2) nanomaterials, Chem. Rev. **114**, 9281–9282 (2014)

6.49 X. Chen, A. Selloni (Eds.): *Titanium Dioxide Nanomaterials Reviews (Special Issue)*, Chemical Reviews, Vol. 114 (ACS Publications, Washington 2014)

6.50 G. Liu, H.G. Yang, J. Pan, Y.Q. Yang, G.Q. Lu, H.-M. Cheng: Titanium dioxide crystals with tailored facets, Chem. Rev. **114**, 9559–9612 (2014)

6.51 M. Batzill, U. Diebold: The surface and materials science of tin oxide, Prog. Surf. Sci. **79**, 47–154 (2005)

6.52 Ç. Kılıç, A. Zunger: Origins of coexistence of conductivity and transparency in SnO_2, Phys. Rev. Lett. **88**, 095501 (2002)

6.53 G.S. Parkinson: Iron oxide surfaces, Surf. Sci. Rep. **71**, 272–365 (2016)

6.54 B.M. Weckhuysen, D.E. Keller: Chemistry, spectroscopy and the role of supported vanadium oxides in heterogeneous catalysis, Catal. Today **78**, 25–46 (2003)

6.55 S. Surnev, M. Ramsey, F. Netzer: Vanadium oxide surface studies, Prog. Surf. Sci. **73**, 117–165 (2003)

6.56 D.R. Mullins: The surface chemistry of cerium oxide, Surf. Sci. Rep. **70**, 42–85 (2015)

6.57 D.R. Mullins, P.M. Albrecht, F. Calaza: Variations in reactivity on different crystallographic orientations of cerium oxide, Top. Catal. **56**, 1345–1362 (2013)

6.58 C. Woell: The chemistry and physics of zinc oxide surfaces, Prog. Surf. Sci. **82**, 55–120 (2007)

6.59 S.G. Kumar, K.S.R. Koteswara Rao: Zinc oxide based photocatalysis: tailoring surface-bulk structure and related interfacial charge carrier dynamics for better environmental applications, RSC Advances **5**, 3306–3351 (2015)

6.60 D. Grosso, C. Boissiere, B. Smarsly, T. Brezesinski, N. Pinna, P.A. Albouy, H. Amenitsch, M. Antonietti, C. Sanchez: Periodically ordered nanoscale islands and mesoporous films composed of nanocrystalline multimetallic oxides, Nat. Mater. **3**, 787–792 (2004)

6.61 A. Ohtomo, H.Y. Hwang: A high-mobility electron gas at the $LaAlO_3/SrTiO_3$ heterointerface, Nature **427**, 423–426 (2004)

6.62 H.N. Lee, H.M. Christen, M.F. Chisholm, C.M. Rouleau, D.H. Lowndes: Strong polarization enhancement in asymmetric three-component ferroelectric superlattices, Nature **433**, 395–400 (2005)

6.63 K. Szot, W. Speier, G. Bihlmayer, R. Waser: Switching the electrical resistance of individual dislocations in single-crystalline $SrTiO_3$, Nat. Mater. **5**, 312–320 (2006)

6.64 C. Cen, S. Thiel, J. Mannhart, J. Levy: Oxide nanoelectronics on demand, Science **323**, 1026–1030 (2009)

6.65 L. Li, C. Richter, J. Mannhart, R.C. Ashoori: Coexistence of magnetic order and two-dimensional superconductivity at $LaAlO_3$=$SrTiO_3$ interfaces, Nat. Phys. **7**, 762–766 (2011)

6.66 A.F. Santander-Syro, O. Copie, T. Kondo, F. Fortuna, S. Pailhès, R. Weht, X.G. Qiu, F. Bertran, A. Nicolaou, A. Taleb-Ibrahimi, P. Le Fèvre, G. Herranz, M. Bibes, N. Reyren, Y. Apertet, P. Lecoeur, A. Barthélémy, M.J. Rozenberg: Two-dimensional electron gas with universal subbands at the surface of $SrTiO_3$, Nature **469**, 189–193 (2011)

6.67 A. Brinkman: Streaks of conduction, Nat. Mater. **12**, 1085–1086 (2013)

6.68 C. Noguera: Insulating oxides in low dimensionality, a theoretical review, Surf. Rev. Lett. **8**, 121–167 (2001)

6.69 C. Noguera: *Physics and Chemistry at Oxide Surfaces* (Cambridge Univ. Press, Cambridge 1996)

6.70 J. Goniakowski, C. Noguera: Relaxation and rumpling mechanisms on oxide surfaces, Surf. Sci. **323**, 129–141 (1995)

6.71 P. Broqvist, H. Grönbeck, I. Panas: Surface properties of alkaline earth metal oxides, Surf. Sci. **554**, 262–271 (2004)

6.72 N.V. Skorodumova, K. Hermansson, B. Johansson: Structural and electronic properties of the (100) surface and bulk of alkaline-earth metal oxides, Phys. Rev. B **72**, 125414 (2005)

6.73 B. Baumeier, P. Krüger, J. Pollmann: Bulk and surface electronic structures of alkaline earth metal oxides: bound surface and image-potential states from first principles, Phys. Rev. B **76**, 205404 (2007)

6.74 C. Cárdenas, F. De Proft, E. Chamorro, P. Fuentealba, P. Geerlings: Theoretical study of the surface reactivity of alkaline earth oxides: local density of states evaluation of the local softness, J. Chem. Phys. **128**, 034708 (2008)

6.75 A.J. Logsdail, D. Mora-Fonz, D.O. Scanlon, C.R.A. Catlow, A.A. Sokol: Structural, energetic and electronic properties of (100) surfaces for alkaline earth metal oxides as calculated with hybrid density functional theory, Surf. Sci. **642**, 58–65 (2015)

6.76 M.S. Wrighton, A.B. Ellis, P.T. Wolczanski, D.L. Morse, H.B. Abrahamson, D.S. Ginley: Strontium titanate photoelectrodes. Efficient photoassisted electrolysis of water at zero applied potential, J. Am. Chem. Soc. **98**, 2774–2779 (1976)

6.77 T. Bieger, J. Maier, R. Waser: Kinetics of oxygen incorporation in $SrTiO_3$ (Fe-doped)—an optical investigation, Sens. Actuators B **7**, 763–768 (1992)

6.78 N. Bickel, G. Schmidt, K. Heinz, K. Müller: Ferroelectric relaxation of the $SrTiO_3$(100) surface, Phys. Rev. Lett. **62**, 2009–2011 (1989)

6.79 A. Walkenhorst, C. Doughty, X.X. Xi, S.N. Mao, Q. Li, T. Venkatesan, R. Ramesh: Dielectric properties of $SrTiO_3$ thin films used in high superconducting field-effect devices, Appl. Phys. Lett. **60**, 1744–1746 (1992)

6.80 E. Grabowska: Selected perovskite oxides: characterization, preparation and photocatalytic properties—a review, Appl. Catal. B **186**, 97–126 (2016)

6.81 A. Biswas, C.-H. Yang, R. Ramesh, Y.H. Jeong: Atomically flat single terminated oxide substrate surfaces, Prog. Surf. Sci. **92**, 117–141 (2017)

6.82 T.K. Andersen, D.D. Fong, L.D. Marks: Pauling's rules for oxide surfaces, Surf. Sci. Rep. **73**, 213–232 (2018)

6.83 P. Chaudhari, R.H. Koch, R.B. Laibowitz, T.R. McGuire, R.J. Gambino: Critical-current measurements in epitaxial-films of $YBa_2Cu_3O_{7-x}$ compound, Phys. Rev. Lett. **58**, 2684–2686 (1987)

6.84 M. Kawasaki, K. Takahashi, T. Maeda, R. Tsuchiya, M. Shinohara, O. Ishiyama, T. Yonezawa, M. Yoshimoto, H. Koinuma: Atomic control of the $SrTiO_3$ crystal surface, Science **266**, 1540–1542 (1994)

6.85 R. Shimizu, K. Iwaya, T. Ohsawa, S. Shiraki, T. Hasegawa, T. Hashizume, T. Hitosugi: Atomic-scale visualization of initial growth of homoepitaxial $SrTiO_3$ thin film on an atomically ordered substrate, ACS Nano **5**, 7967–7971 (2011)

6.86 T. Hitosugi, R. Shimizu, T. Ohsawa, K. Iwaya: Scanning tunneling microscopy/spectroscopy on perovskite oxide thin films deposited in situ, Chem. Rec. **14**, 935–943 (2014)

6.87 S.-H. Phark, Y.J. Chang, T.W. Noh: Selective growth of perovskite oxides on (001) by control of surface reconstructions, Appl. Phys. Lett. **98**, 161908 (2011)

6.88 S. Neretina, R.A. Hughes, G.A. Devenyi, N.V. Sochinskii, J.S. Preston, P. Mascher: Atypical grain growth for (211) CdTe films deposited on surface reconstructed (100) $SrTiO_3$ substrates, Appl. Surf. Sci. **255**, 5674–5681 (2009)

6.89 G. Koster, G. Rijnders, D.H.A. Blank, H. Rogalla: Surface morphology determined by (001) single-crystal $SrTiO_3$ termination, Physica C **339**, 215–230 (2000)

6.90 T. Nakamura, H. Inada, M. Iiyama: In situ surface characterization of $SrTiO_3$(001) substrates for well-defined $SrTiO_3$ and $YBa_2Cu_3O_{7-x}$ thin film growth, Jpn. J. Appl. Phys. **36**, 90–93 (1997)

6.91 C. Jooss, R. Warthmann, H. Kronmüller, T. Haage, H.-U. Habermeier, J. Zegenhagen: Vortex pinning due to strong quasiparticle scattering at antiphase boundaries in $YBa_2Cu_3O_{7-x}$, Phys. Rev. Lett. **82**, 632–635 (1999)

6.92 R.A. McKee, F.J. Walker, M.F. Chisholm: Crystalline oxides on silicon: the first five monolayers, Phys. Rev. Lett. **81**, 3014–3017 (1998)

6.93 J.A. Misewich, A.G. Schrott: Room-temperature oxide field-effect transistor with buried channel, Appl. Phys. Lett. **76**, 3632–3634 (2000)

6.94 K. Ueno, I.H. Inoue, H. Akoh, M. Kawasaki, Y. Tokura, H. Takagi: Field-effect transistor on $SrTiO_3$ with sputtered Al_2O_3 gate insulator, Appl. Phys. Lett. **83**, 1755–1757 (2003)

6.95 M. Plaza, X. Huang, J.Y.P. Ko, M. Shen, B.H. Simpson, J. Rodríguez-López, N.L. Ritzert, K. Letchworth-Weaver, D. Gunceler, D.G. Schlom, T.A. Arias, J.D. Brock, H.D. Abruña: Structure of the photo-catalytically active surface of $SrTiO_3$, J. Am. Chem. Soc. **138**, 7816–7819 (2016)

6.96 M. Boudart, A. Delbouille, E.G. Derouane, V. Indovina, A.B. Walters: Activation of hydrogen at 78 K on paramagnetic centers of magnesium oxide, J. Am. Chem. Soc. **94**, 6622–6630 (1972)

6.97 S. Coluccia, A.J. Tench, R.L. Segall: Surface structure and surface states in magnesium oxide powders, J. Chem. Soc. Faraday Trans. I **75**, 1769–1779 (1979)

6.98 A.F. Moodie, C.E. Warble: Electron microscopic investigations of MgO morphology and surfaces, J. Cryst. Growth **10**, 26–38 (1970)

6.99 E. Knözinger, K.-H. Jacob, S. Singh, P. Hofmann: Hydroxyl groups as IR active surface probes on MgO crystallites, Surf. Sci. **290**, 388–402 (1993)

6.100 P.J. Anderson, P.L. Morgan: Effects of water vapour on sintering of MgO, Trans. Faraday Soc. **60**, 930–937 (1964)
6.101 T. Kokubo: Bioactive glass-ceramics—properties and applications, Biomaterials **12**, 155–163 (1991)
6.102 J.R. Jones, L.M. Ehrenfried, L.L. Hench: Optimising bioactive glass scaffolds for bone tissue engineering, Biomaterials **27**, 964–973 (2006)
6.103 A. Kay, M. Gratzel: Dye-sensitized core-shell nanocrystals: improved efficiency of mesoporous tin oxide electrodes coated with a thin layer of an insulating oxide, Chem. Mater. **14**, 2930–2935 (2002)
6.104 E. Fridell, M. Skoglundh, B. Westerberg, S. Johansson, G. Smedler: NO_x storage in barium-containing catalysts, J. Catal. **183**, 196–209 (1999)
6.105 K. Kwapien, J. Paier, J. Sauer, M. Geske, U. Zavyalova, R. Horn, P. Schwach, A. Trunschke, R. Schloegl: Sites for methane activation of lithium-doped magnesium oxide surfaces, Angew. Chem. Int. Ed. **53**, 8774–8778 (2014)
6.106 S.S.P. Parkin, C. Kaiser, A. Panchula, P.M. Rice, B. Hughes, M. Samant, S.H. Yang: Giant tunnelling magnetoresistance at room temperature with MgO(100) tunnel barriers, Nat. Mater. **3**, 862–867 (2004)
6.107 K.J. Klabunde, J. Stark, O. Koper, C. Mohs, D.G. Park, S. Decker, Y. Jiang, I. Lagadic, D.J. Zhang: Nanocrystals as stoichiometric reagents with unique surface chemistry, J. Phys. Chem. **100**, 12142–12153 (1996)
6.108 P. Broqvist, I. Panas, E. Fridell, H. Persson: NO_x storage on BaO(100) surface from first principles: a two channel scenario, J. Phys. Chem. B **106**, 137–145 (2002)
6.109 H. Gronbeck, P. Broqvist, I. Panas: Fundamental aspects of NO_x adsorption on BaO, Surf. Sci. **600**, 403–408 (2006)
6.110 M. Tutuianu, O.R. Inderwildi, W.G. Bessler, J. Warnatz: Competitive adsorption of NO, NO_2, CO_2, and H_2O on BaO(100): a quantum chemical study, J. Phys. Chem. B **110**, 17484–17492 (2006)
6.111 A. Schrön, M. Granovskij, F. Bechstedt: Influence of on-site Coulomb interaction U on properties of MnO(001)2×1 and NiO(001)2×1 surfaces, J. Phys. Condens. Matter **25**, 094006 (2013)
6.112 M.J. Girgis, B.C. Gates: Reactivities, reaction networks, and kinetics in high-pressure catalytic hydroprocessing, Ind. Eng. Chem. Res. **30**, 2021–2058 (1991)
6.113 J. Park, E. Kang, S.U. Son, H.M. Park, M.K. Lee, J. Kim, K.W. Kim, H.J. Noh, J.H. Park, C.J. Bae, J.G. Park, T. Hyeon: Monodisperse nanoparticles of Ni and NiO: synthesis, characterization, self-assembled superlattices, and catalytic applications in the Suzuki coupling reaction, Adv. Mater. **17**, 429–434 (2005)
6.114 A. Debart, A.J. Paterson, J. Bao, P.G. Bruce: Alpha-MnO_2 nanowires: a catalyst for the O_2 electrode in rechargeable lithium batteries, Angew. Chem. Int. Ed. **47**, 4521–4524 (2008)
6.115 J. Robertson: The mechanism of high-temperature aqueous corrosion of stainless-steels, Corros. Sci. **32**, 443–465 (1991)
6.116 R. Wyckoff: *Crystal Structures* (Wiley, New York 1963)
6.117 G. Pacchioni, P.S. Bagus: Theoretical analysis of the O(1s) binding-energy shifts in alkaline-earth oxides: chemical or electrostatic contributions, Phys. Rev. B **50**, 2576–2581 (1994)
6.118 J.B. Torrance: The relation between conductivity, optical absorption, and ionicity in oxides and organic compounds. J. Solid State Chem. **96**, 59–66 (1992)
6.119 R.L. Nelson, J.W. Hale: Electronic-spectra of surfaces of alkaline-earth oxides. Discuss. Faraday Soc. **52**, 77–88 (1971)
6.120 K.O. Legg, M. Prutton, C. Kinniburgh: A LEED study of MgO(100). I. Experiment, J. Phys. C **7**, 4236–4246 (1974)
6.121 T. Gotoh, S. Murakami, K. Kinosita, Y. Murata: Surface rumpling of MgO(100) deduced from changes in RHEED Kikuchi pattern. I. Experimental, J. Phys. Soc. Jpn. **50**, 2063–2068 (1981)
6.122 T. Urano, T. Kanaji, M. Kaburagi: Surface structure of MgO(100) surface studied by LEED, Surf. Sci. **134**, 109–121 (1983)
6.123 D.L. Blanchard, D.L. Lessor, J.P. LaFemina, D.R. Baer, W.K. Ford, T. Guo: A low-energy electron-diffraction study of the MgO(100) surface-structure, J. Vac. Sci. Technol. A **9**, 1814–1819 (1991)
6.124 J.B. Zhou, H.C. Lu, T. Gustafsson, P. Häberle: Surface structure of MgO(001): a medium energy ion scattering study, Surf. Sci. **302**, 350–362 (1994)
6.125 D. Ferry, J. Suzanne, V. Panella, A. Barbieri, M. Van Hove, J.-P. Bibérian: MgO(100) surface relaxation by symmetrized automated tensor low energy electron diffraction analysis, J. Vac. Sci. Technol. A **16**, 2261–2266 (1998)
6.126 H. Nakamatsu, A. Sudo, S. Kawai: Relaxation of the MgO(100) surface studied by ICISS, Surf. Sci. **194**, 265–274 (1988)
6.127 A. Santoni, D.B. Tran Thoaif, J. Urban: MgO(100) surface topology determination by surface extended energy loss fine structure, Solid State Commun. **68**, 1039–1041 (1988)
6.128 S.R. Lu, R. Yu, J. Zhu: Atomic steps on the MgO(100) surface, Phys. Rev. B **87**, 165436 (2013)
6.129 P.W. Tasker, D.M. Duffy: The structure and properties of the stepped surfaces of MgO and NiO, Surf. Sci. **137**, 91–102 (1984)
6.130 W.C. Mackrodt: Atomistic simulation of the surfaces of oxides, I. Chem. Soc. Faraday Trans. **2**(85), 541–554 (1989)
6.131 A. Schüller, D. Blauth, J. Seifert, M. Busch, H. Winter, K. Gärtner, R. Włodarczyk, J. Sauer, M. Sierka: Fast atom diffraction during grazing scattering from a MgO(001), Surf. Sci. **606**, 161–173 (2012)
6.132 O. Robach, G. Renaud, A. Barbier: Very-high-quality MgO(001) surfaces: roughness, rumpling and relaxation, Surf. Sci. **401**, 227–235 (1998)
6.133 Y. Yan, M.F. Chisholm, S.J. Pennycook, S.T. Pantelides: Structures of pure and Ca-segregated MgO(001) surfaces, Surf. Sci. **442**, 251–255 (1999)
6.134 C.G. Kinniburgh: A LEED study of MgO(100). III. Theory at off-normal incidence, J. Phys. C **9**, 2695–2708 (1976)

6.135 R.N. Barnett, R. Bass: Calculation of strain and polarization fields at the surface of MgO crystals. Breathing shell model, J. Chem. Phys. **67**, 4620–4625 (1977)

6.136 M.R. Welton-Cook, M. Prutton: A simple shell model calculation of the differential ionic relaxation of the MgO(100) surface, Surf. Sci. **74**, 276–284 (1978)

6.137 A.J. Martin, H. Bilz: Charge deformation and geometric relaxation at the (001) MgO surface, Phys. Rev. B **19**, 6593–6600 (1979)

6.138 M.R. Welton-Cook, W. Berndt: A LEED study of the MgO(100) surface: identification of a finite rumple, J. Phys. C **15**, 5691–5710 (1982)

6.139 E.A. Colburn, W.C. Mackrodt: Irregularities at the (001) surface of MgO: topography and other aspects, Solid State Ion. **8**, 221–231 (1983)

6.140 F.W. de Wette, W. Kress, U. Schröder: Relaxation of the rocksalt (001) surface: alkali halides, MgO, and PbS, Phys. Rev. B **32**, 4143–4157 (1985)

6.141 G.V. Lewis, C.R.A. Catlow: Potential models for ionic oxides, J. Phys. C **18**, 1149–1161 (1985)

6.142 M. Causà, R. Dovesi, C. Pisani, C. Roetti: Ab initio Hartree–Fock study of the MgO(100) surface, Surf. Sci. **175**, 551–560 (1986)

6.143 J.P. LaFemina, C.B. Duke: Dependence of oxide surface structure on surface topology and local chemical bonding, J. Vac. Sci. Technol. A **9**, 1847–1855 (1991)

6.144 G. Pacchioni, T. Minerva, P.S. Bagus: Chemisorption of CO on defect sites of MgO, Surf. Sci. **275**, 450–458 (1992)

6.145 S. Pugh, M.J. Gillan: The energetics of NH_3 adsorption at the MgO(001) surface, Surf. Sci. **320**, 331–343 (1994)

6.146 Y. Li, D.C. Langreth, M.R. Pederson: Surface structure of MgO(001): ab initio versus shell model, Phys. Rev. B **55**, 16456–16465 (1997)

6.147 V. Musolino, A. Selloni, R. Car: First principles study of adsorbed Cu_n (n=1–4) microclusters on MgO(100): structural and electronic properties, J. Chem. Phys. **108**, 5044–5054 (1998)

6.148 F. Finocchi, J. Goniakowski, C. Noguera: Interaction between oxygen vacancies on MgO(100), Phys. Rev. B **59**, 5178–5188 (1999)

6.149 D.R. Alfonso, J.A. Snyder, J.E. Jaffe, A.C. Hess, M. Gutowski: Opposite rumpling of the MgO and CaO(100) surfaces: a density-functional theory study, Phys. Rev. B **62**, 8318–8322 (2000)

6.150 Y. Xu, J. Li, Y. Zhang, W. Chen: CO adsorption on MgO(001) surface with oxygen vacancy and its low-coordinated surface sites: embedded cluster model density functional study employing charge self-consistent technique, Surf. Sci. **525**, 13–23 (2003)

6.151 H. Momida, T. Oguchi: First-principles studies of antiferromagnetic MnO and NiO surfaces, J. Phys. Soc. Jpn. **72**, 588–593 (2003)

6.152 C. Quintanar, R. Caballero, V.M. Castan: Adsorption of CO on the rumpled MgO(100), MgO(100):Ni, and MgO(100):Cr surfaces: a density functional approach, Int. J. Quantum Chem. **102**, 820–828 (2005)

6.153 R. Martinez-Casado, B. Meyer, S. Miret-Artés, F. Traeger, C. Woell: Diffraction patterns of He atoms from the MgO(100) surface calculated by the close-coupling method, J. Phys. Condens. Matter **19**, 305006 (2007)

6.154 A.R. Gerson, T. Bredow: MgO(100) surface relaxation and vacancy defects: a semi-empirical quantum-chemical study, Phys. Chem. Chem. Phys. **1**, 4889–4896 (1999)

6.155 D. Abriou, F. Creuzet, J. Jupille: Characterization of cleaved MgO(100) surfaces, Surf. Sci. **352–354**, 499–503 (1996)

6.156 C. Barth, C.R. Henry: Atomic resolution imaging of the (001) surface of UHV cleaved MgO by dynamic scanning force microscopy, Phys. Rev. Lett. **91**, 196102 (2003)

6.157 J. Goniakowski, C. Noguera: Atomic and electronic structure of steps and kinks on MgO(100) and MgO(110), Surf. Sci. **340**, 191–204 (1995)

6.158 L.N. Kantorovich, J.M. Holender, M.J. Gillan: The energetics and electronic structure of defective and irregular surfaces on MgO, Surf. Sci. **343**, 221–239 (1995)

6.159 N.E. Singh-Miller, N. Marzari: Surface energies, work functions, and surface relaxations of low-index metallic surfaces from first principles, Phys. Rev. B **80**, 235407 (2009)

6.160 M. Prutton, J.A. Ramsey, J.A. Walker, M.R. Welton-Cook: A LEED study of the structure of the (100) surface of CaO, J. Phys. C **12**, 5271–5280 (1979)

6.161 T. Kendelewicz, P. Liu, W.B. Labiosa, G.E. Brown Jr.: Surface EXAFS and x-ray standing wave study of the cleaved CaO(100) surface, Physica B **441**, 208–209 (1995)

6.162 P.V. Sushko, A.L. Shluger, C.A. Catlow: Relative energies of surface and defect states: ab initio calculations for the MgO(001) surface, Surf. Sci. **450**, 153–170 (2000)

6.163 D. Ricci, G. Pacchioni, P.V. Sushko, A.L. Shluger: Electron trapping at neutral divacancy sites on the MgO surface, J. Chem. Phys. **117**, 2844–2851 (2002)

6.164 T. Jaouen, G. Jézéquel, G. Delhaye, B. Lépine, P. Turban, P. Schieffer: Work function shifts, Schottky barrier height, and ionization potential determination of thin MgO films on Ag(001), Appl. Phys. Lett. **97**, 232104 (2010)

6.165 J.R. Stevenson, E.B. Hensley: Thermionic and photoelectric emission from magnesium oxide, J. Appl. Phys. **32**, 166–172 (1961)

6.166 F. Illas, G. Pacchioni: Surfaces are different: a perspective on structural, energetic and electronic properties of (001) surfaces of alkaline earth metal oxides as calculated with hybrid density functional theory by Andrew J. Logsdail, David Mora-Fonz, David O. Scanlon, C. Richard A. Catlow, Alexey A. Sokol, Surf. Sci. **642**, 66–67 (2015)

6.167 E.J.W. Verwey: Lattice structure of the free surface of alkali halide crystals, Recl. Trav. Chim. Pays-Bas **65**, 521 (1946)

6.168 B. Magyari-Köpe, L. Vitos, B. Johansson, J. Kollar: Origin of octahedral tilting in orthorhombic perovskites, Phys. Rev. B **66**, 092103 (2002)

6.169 F. Bawa, I. Panas: Limiting properties of $(MgO)_n$ and $(CaO)_n$ clusters, Phys. Chem. Chem. Phys. **3**, 3042–3047 (2001)

6.170 F. Bawa, I. Panas: Competing pathways for MgO, CaO, SrO, and BaO nanocluster growth, Phys. Chem. Chem. Phys. **4**, 103–108 (2002)

6.171 A. Schrön, C. Rödl, F. Bechstedt: Crystalline and magnetic anisotropy of the 3d-transition metal monoxides MnO, FeO, CoO, and NiO, Phys. Rev. B **86**, 115134 (2012)

6.172 S.L. Dudarev, A.I. Liechtenstein, M.R. Castell, G.A.D. Briggs, A.P. Sutton: Surface states on NiO(100) and the origin of the contrast reversal in atomically resolved scanning tunneling microscope images, Phys. Rev. B **56**, 4900–4908 (1997)

6.173 M.R. Castell, S.L. Dudarev, G.A.D. Briggs, A.P. Sutton: Unexpected differences in the surface electronic structure of NiO and CoO observed by STM and explained by first-principles theory, Phys. Rev. B **59**, 7342–7345 (1999)

6.174 F.P. Netzer, M. Prutton: LEED and electron spectroscopic observations on NiO(100), J. Phys. C **8**, 2401–2412 (1975)

6.175 A. Schrön, F. Bechstedt: Spin-dependent properties and images of MnO, FeO, CoO, and NiO(001) surfaces, Phys. Rev. B **92**, 165112 (2015)

6.176 C.G. Kinniburgh, J.A. Walker: LEED calculations for the NiO(100) surface, Surf. Sci. **63**, 274–282 (1977)

6.177 R.C. Felton, M. Prutton, S.P. Tear, M.R. Welton-Cook: A LEED analysis of the CoO(100) surface, Surf. Sci. **88**, 474–478 (1979)

6.178 M.R. Welton-Cook, M. Prutton: LEED calculations for the NiO(100) surface: extension to lower energies, J. Phys. C **13**, 3993–4000 (1980)

6.179 M. Caffio, B. Cortigiani, G. Rovida, A. Atrei, C. Giovanardi, A. di Bona, S. Valeri: Ultrathin nickel oxide films grown on Ag(001): a study by XPS, LEIS and LEED intensity analysis, Surf. Sci. **531**, 368–374 (2003)

6.180 T. Okazawa, Y. Yagi, Y. Kido: Rumpled surface structure and lattice dynamics of NiO(001), Phys. Rev. B **67**, 195406 (2003)

6.181 T. Okazawa, Y. Kido: Surface structure and lattice vibrations of MnO(001) analyzed by high-resolution medium energy ion scattering spectroscopy, Surf. Sci. **556**, 101–108 (2004)

6.182 T. Okazawa, Y. Nakagawa, Y. Kido: Temperature-dependent surface structure and lattice dynamics of NiO(001), Phys. Rev. B **69**, 125412 (2004)

6.183 E.A. Soares, R. Paniago, V.E. de Carvalho, E.L. Lopes, G.J.P. Abreu, H.-D. Pfannes: Quantitative low-energy electron diffraction analysis of MnO(100) films grown on Ag(100), Phys. Rev. B **73**, 035419 (2005)

6.184 V. Bayer, C. Franchini, R. Podloucky: Ab initio study of the structural, electronic, and magnetic properties of MnO(100) and MnO(110), Phys. Rev. B **75**, 035404 (2007)

6.185 E.L. Lopes, G.J.P. Abreu, R. Paniago, E.A. Soares, V.E. de Carvalho, H.-D. Pfannes: Atomic geometry determination of FeO(001) grown on Ag(001) by low energy electron diffraction, Surf. Sci. **601**, 1239–1245 (2007)

6.186 N. Yu, W.-B. Zhang, N. Wang, Y.-F. Wang, B.-Y. Tang: Water adsorption on a NiO(100) surface: a GGA+U study, J. Phys. Chem. C **112**, 452–457 (2008)

6.187 K.-M. Schindler, J. Wang, A. Chassé, H. Neddermeyer, W. Widdra: Low-energy electron diffraction structure determination of an ultrathin CoO film on Ag(001), Surf. Sci. **603**, 2658–2663 (2009)

6.188 B.S. Youmbi, F. Calvayrac: Structure of CoO(001) surface from DFT+U calculations, Surf. Sci. **621**, 1–6 (2014)

6.189 S. Prada, U. Martinez, G. Pacchioni: Work function changes induced by deposition of ultrathin dielectric films on metals: a theoretical analysis, Phys. Rev. B **78**, 23542 (2008)

6.190 J. Goniakowski, C. Noguera: Polarization and rumpling in oxide monolayers deposited on metallic substrates, Phys. Rev. B **79**, 155433 (2009)

6.191 H. Hosoi, K. Sueoka, K. Hayakawa, K. Mukasa: Atomic resolved imaging of cleaved NiO(100) surfaces by NC-AFM, Appl. Surf. Sci. **157**, 218–221 (2000)

6.192 S.C. Petitto, C.L. Berrie, M. Langell: Novel mesoscale defect structure on NiO(100) surfaces by atomic force microscopy, Surf. Sci. **600**, L229–L235 (2006)

6.193 H. Tanaka, M. Misono: Advances in designing perovskite catalysts, Curr. Opin. Solid State Mater. Sci. **5**, 381–387 (2001)

6.194 J.B. Goodenough: Electronic and ionic transport properties and other physical aspects of perovskites, Rep. Prog. Phys. **67**, 1915–1993 (2004)

6.195 A. Kubacka, M. Fernandez-Garcia, G. Colon: Advanced nanoarchitectures for solar photocatalytic applications, Chem. Rev. **112**, 1555–1614 (2012)

6.196 J. Shi, L. Guo: ABO_3-based photocatalysts for water splitting, Proc. Nat. Sci. Mater. **22**, 592–615 (2012)

6.197 N. Bickel, G. Schmidt, K. Heinz, K. Müller: Structure determination of the $SrTiO_3$(100) surface, Vacuum **41**, 46–48 (1990)

6.198 J. Padilla, D. Vanderbilt: Ab initio study of $SrTiO_3$ surfaces, Surf. Sci. **418**, 64–70 (1998)

6.199 E. Heifets, R.I. Eglitis, E.A. Kotomin, J. Maier, G. Borstel: First-principles calculations for $SrTiO_3$(100) surface structure, Surf. Sci. **513**, 211–220 (2002)

6.200 R. Herger, P.R. Willmott, O. Bunk, C.M. Schlepütz, B.D. Patterson, B. Delley: Surface of strontium titanate, Phys. Rev. Lett. **98**, 076102 (2007)

6.201 V. Khvostov, O. Sokol, V. Babaev, M. Guseva: Resonance charge-exchange in ion scattering and sputtering at the $SrTiO_3$ surface, Surf. Sci. **340**, L993–L996 (1995)

6.202 T. Nishimura, A. Ikeda, H. Namba, T. Morishita, Y. Kido: Structure change of TiO_2-terminated $SrTiO_3$(001) surfaces by annealing in O_2 atmosphere and ultrahigh vacuum, Surf. Sci. **421**, 273–278 (1999)

6.203 A. Ikeda, T. Nishimura, T. Morishita, Y. Kido: Surface relaxation and rumpling of TiO_2-terminated $SrTiO_3$(001) determined by medium energy ion scattering, Surf. Sci. **433–435**, 520–524 (1999)

6.204 M. Kawai, Z.Y. Liu, T. Hanada, M. Katayama, M. Aono, C.F. McConville: Layer controlled growth of oxide superconductors, Appl. Surf. Sci. **82**, 487–493 (1994)

6.205 K. Iwahori, S. Watanabe, M. Kawai, K. Mizuno, K. Sasaki, M. Yoshimoto: Nanoscale composition analysis of atomically flat by friction force microscopy, J. Appl. Phys. **88**, 7099–7103 (2000)

6.206 T. Ohnishi, K. Shibuya, M. Lippmaa, D. Kobayashi, H. Kumigashira, M. Oshima, H. Koinuma: Preparation of thermally stable TiO_2-terminated $SrTiO_3$(100) substrate surfaces, Appl. Phys. Lett. **85**, 272–274 (2004)

6.207 N.P. Guisinger, T.S. Santos, J.R. Guest, T.-Y. Chien, A. Bhattacharya, J.W. Freeland, M. Bode: Nanometer-scale striped surface terminations on fractured $SrTiO_3$ surfaces, ACS Nano **3**, 4132–4136 (2009)

6.208 Q.D. Jiang, J. Zegenhagen: c(6 × 2) and c(4 × 2) reconstruction of $SrTiO_3$(001), Surf. Sci. **425**, 343–354 (1999)

6.209 J. Mannhart, D.H.A. Blank, H.Y. Hwang, A.J. Millis, J.-M. Triscone: Two-dimensional electron gases at oxide interfaces, MRS Bulletin **33**, 1027–1034 (2008)

6.210 J.G. Connell, B.J. Isaac, G.B. Ekanayake, D.R. Strachan, S.S.A. Seo: Preparation of atomically flat $SrTiO_3$ surfaces using a deionized-water leaching and thermal annealing procedure, Appl. Phys. Lett. **101**, 251607 (2012)

6.211 Y.J. Chang, S.-H. Phark: Atomic-scale visualization of initial growth of perovskites on $SrTiO_3$(001) using scanning tunneling microscope, Curr. Appl. Phys. **17**, 640–656 (2017)

6.212 J. Fompeyrine, R. Berger, H.P. Lang, J. Perret, E. Mächler, C. Gerber, J.-P. Locquet: Local determination of the stacking sequence of layered materials, Appl. Phys. Lett. **72**, 1697–1699 (1998)

6.213 G. Koster, B.L. Kropman, G.J.H.M. Rijnders, D.H.A. Blank, H. Rogalla: Quasi-ideal strontium titanate crystal surfaces through formation of strontium hydroxide, Appl. Phys. Lett. **73**, 2920–2922 (1998)

6.214 K. Iwahori, S. Watanabe, T. Komeda, M. Kawai, A. Saito, Y. Kuwahara, M. Aono: Force microscopy study of $SrTiO_3$(001) surfaces with single atomic-layer steps, Jpn. J. Appl. Phys. **38**, 3946–3948 (1999)

6.215 H. Tanaka, H. Tabata, T. Kawai: Probing the surface forces of atomic layered $SrTiO_3$ films by atomic force microscopy, Thin Solid Films **342**, 4–7 (1999)

6.216 R. Bachelet, F. Sánchez, F.J. Palomares, C. Ocal, J. Fontcuberta: Atomically flat Sr0-terminated substrate, Appl. Phys. Lett. **95**, 141915 (2009)

6.217 K. Iwahori, S. Watanabe, M. Kawai, K. Kobayashi, H. Yamada, K. Matsushige: Effect of water adsorption on microscopic friction force on $SrTiO_3$(001), J. Appl. Phys. **93**, 3223–3227 (2003)

6.218 G. Koster, B.L. Kropman, G.J.H.M. Rijnders, D.H.A. Blank, H. Rogalla: Influence of the surface treatment on the homoepitaxial growth of $SrTiO_3$, Mat. Sci. Eng. B **56**, 209–212 (1998)

6.219 R. Gunnarsson, A.S. Kalabukhov, D. Winkler: Evaluation of recipes for obtaining single terminated perovskite oxide substrates, Surf. Sci. **603**, 151–157 (2009)

6.220 D. Kobayashi, H. Kumigashira, M. Oshima, T. Ohnishi, M. Lippma, K. Ono, M. Kawasaki, H. Koinuma: High-resolution synchrotron-radiation photoemission characterization for atomically-controlled $SrTiO_3$(001) substrate surfaces subjected to various surface treatments, J. Appl. Phys. **96**, 7183 (2004)

6.221 T. Ohsawa, R. Shimizu, K. Iwaya, S. Shiraki, T. Hitosugi: Negligible Sr segregation on $SrTiO_3$(001)-$(\sqrt{13} \times \sqrt{13})$R33.7° reconstructed surfaces, Appl. Phys. Lett. **108**, 161603 (2016)

6.222 J.E. Boschker, T. Tybell: Qualitative determination of surface roughness by in situ reflection high energy electron diffraction, Appl. Phys. Lett. **100**, 151604 (2012)

6.223 S.A. Chambers, T.C. Droubay, C. Capan, G.Y. Sun: Unintentional F doping of $SrTiO_3$(001) etched in HF acid-structure and electronic properties, Surf. Sci. **606**, 554–558 (2012)

6.224 A. Hirata, K. Saiki, A. Koma, A. Ando: Electronic structure of a Sr0-terminated $SrTiO_3$(100) surface, Surf. Sci. **319**, 267–271 (1994)

6.225 M. Radovic, N. Lampis, F. Miletto Granozio, P. Perna, Z. Ristic, M. Salluzzo, C.M. Schlepütz, U. Scotti di Uccio: Growth and characterization of stable Sr0-terminated surfaces, Appl. Phys. Lett. **94**, 022901 (2009)

6.226 A.G. Schrott, J.A. Misewich, M. Copel, D.W. Abraham, Y. Zhang: A-site surface termination in strontium titanate single crystals, Appl. Phys. Lett. **79**, 1786–1788 (2001)

6.227 Y. Liang, D.A. Bonnell: Structures and chemistry of the annealed $SrTiO_3$(001) surface, Surf. Sci. **310**, 128–134 (1994)

6.228 K. Szot, W. Speier: Surfaces of reduced and oxidized $SrTiO_3$ from atomic force microscopy, Phys. Rev. B **60**, 5909–5926 (1999)

6.229 P.A.W. van der Heide, Q.D. Jiang, Y.S. Kim, J.W. Rabalais: X-ray photoelectron spectroscopic and ion scattering study of the $SrTiO_3$(001) surface, Surf. Sci. **473**, 59–70 (2001)

6.230 H. Wei, L. Beuermann, J. Helmbold, G. Borchardt, V. Kempter, G. Lilienkamp, W. Maus-Friedrichs: Study of Sr0 segregation on $SrTiO_3$(001) surfaces, J. Eur. Ceram. Soc. **21**, 1677–1680 (2001)

6.231 J.M. Huijbregtse, J.H. Rector, B. Dam: Effect of the two (100) $SrTiO_3$ substrate terminations on the nucleation and growth of $YBa_2Cu_3O_{7-\delta}$ thin films, Physica C **351**, 183–199 (2001)

6.232 R. Bachelet, F. Sánchez, J. Santiso, C. Munuera, C. Ocal, J. Fontcuberta: Self-assembly of $SrTiO_3$(001) chemical-terminations: a route for oxide-nanostructure fabrication by selective growth, Chem. Mater. **21**, 2494–2249 (2009)

6.233 S. Shiraki, M. Nantoh, S. Katano, M. Kawai: Nanoscale structural variation observed on the vicinal surface, Appl. Phys. Lett. **96**, 231901 (2010)

6.234 R. García, R. Magerle, R. Pérez: Nanoscale compositional mapping with gentle forces, Nat. Mater. **6**, 405–411 (2007)

6.235 S. Ogawa, K. Kato, N. Nagatsuka, S. Ogura, K. Fukutani: $\sqrt{2} \times \sqrt{2}$R45° reconstruction and electron doping at the Sr0-terminated $SrTiO_3$(001) surface, Phys. Rev. B **96**, 085303 (2017)

6.236 K. Iwaya, R. Shimizu, T. Ohsawa, T. Hashizume, T. Hitosugi: Stripe charge ordering in SrO-terminated $SrTiO_3$(001) surfaces, Phys. Rev. B **83**, 125117 (2011)

6.237 M. Paradinas, L. Garzon, F. Sanchez, R. Bachelet, D.B. Amabilino, J. Fontcuberta, C. Ocal: Tuning the local frictional and electrostatic responses of nanostructured $SrTiO_3$–surfaces by self-assembled molecular monolayers, Phys. Chem. Chem. Phys. **12**, 4452–4458 (2010)

6.238 X. Torrelles, J. Zegenhagen, J. Rius, T. Gloege, L.X. Cao, W. Moritz: Atomic structure of a long-range ordered vicinal surface of $SrTiO_3$, Surf. Sci. **589**, 184–191 (2005)

6.239 W. Sitaputra, N. Sivadas, M. Skowronski, D. Xiao, R.M. Feenstra: Oxygen vacancies on SrO-terminated $SrTiO_3$(001) surfaces studied by scanning tunneling spectroscopy, Phys. Rev. B **91**, 205408 (2015)

6.240 Y. Pennec, N.J.C. Ingle, I.S. Elfimov, E. Varene, Y. Maeno, A. Damascelli, J.V. Barth: Cleaving-temperature dependence of layered-oxide surfaces, Phys. Rev. Lett. **101**, 216103 (2008)

6.241 T.Y. Chien, N.P. Guisinger, J.W. Freeland: Survey of fractured surfaces: from the micrometer to nanometer scale, J. Vac. Sci. Technol. B **28**, C5A11–C5A13 (2010)

6.242 T. Matsumoto, H. Tanaka, T. Kawai, S. Kawai: STM-imaging of a $SrTiO_3$(100) surface with atomic-scale resolution, Surf. Sci. Lett. **278**, L153–L158 (1992)

6.243 T. Hikita, T. Hanada, M. Kudo, M. Kawai: Structure and electronic state of the TiO, and SrO terminated $SrTiO_3$(100) surfaces, Surf. Sci. **287/288**, 377–381 (1993)

6.244 M. Naito, H. Sato: Reflection high-energy electron diffraction study on the $SrTiO_3$, Physica C **229**, 1–11 (1994)

6.245 H. Tanaka, T. Matsumoto, T. Kawai, S. Kawai: Surface structure and electronic properties of $SrTiO_3$(001) surface observed by scanning tunnelling microscopy/spectroscopy, Jpn. J. Appl. Phys. **32**, 1405–1409 (1993)

6.246 S. Kimura, J. Yamauchi, M. Tsukada: First-principles study on electronic structure of the (001) surface of $SrTiO_3$, Phys. Rev. B **51**, 11049–11054 (1995)

6.247 D.-K. Seo, K. Perdue, J. Ren, M.-H. Whangbo: Study of scanning tunneling microscopy images and probable relaxations of the $SrTiO_3$(100) surface by electronic structure calculations, Surf. Sci. **370**, 245–251 (1997)

6.248 N. Erdman, K.R. Poeppelmeier, M. Asta, O. Warschkow, D.E. Ellis, L.D. Marks: The structure and chemistry of the TiO_2-rich surface of $SrTiO_3$(001), Nature **419**, 55–58 (2002)

6.249 T. Kubo, H. Nozoye: Surface structure of $SrTiO_3$(100)-$\sqrt{5}\times\sqrt{5}$-R26.6°, Phys. Rev. Lett. **86**, 1801–1804 (2001)

6.250 R. Herger, P.R. Willmott, O. Bunk, C.M. Schlepütz, B.D. Patterson, B. Delley: Surface structure of $SrTiO_3$(001), Phys. Rev. B. **76**, 195435 (2007)

6.251 V.E. Henrich, G. Dresselhaus, H.J. Zeiger: Surface defects and the electronic structure of $SrTiO_3$ surfaces, Phys. Rev. B **17**, 4908–4921 (1978)

6.252 B. Cord, R. Courths: Electronic study of $SrTiO_3$(001) surfaces by photoemission, Surf. Sci. **162**, 34–38 (1985)

6.253 Q.D. Jiang, J. Zegenhagen: $SrTiO_3$(001) surfaces and growth of ultra-thin $GdBa_2Cu_{7-x}$ films studied by LEED/AES and UHV-STM, Surf. Sci. **338**, L882–L888 (1995)

6.254 Q.D. Jiang, J. Zegenhagen: $SrTiO_3$(001)-c(6×2): a long-range, atomically ordered surface stable in oxygen and ambient air, Surf. Sci. **367**, L42–L46 (1996)

6.255 G. Charlton, S. Brennan, C.A. Muryn, R. McGrath, D. Norman, T.S. Turner, G. Thornton: Surface relaxation of $SrTiO_3$(001), Surf. Sci. **457**, L376–L380 (2000)

6.256 M.R. Castell: Scanning tunneling microscopy of reconstructions on the $SrTiO_3$(001) surface, Surf. Sci. **505**, 1–13 (2002)

6.257 M.R. Castell: Nanostructures on the $SrTiO_3$(001) surface studied by STM, Surf. Sci. **516**, 33–42 (2002)

6.258 P.J. Møller, S.A. Komolov, E.F. Lazneva: Selective growth of a MgO(100)-c(2×2) superstructure on a $SrTiO_3$(100)-(2×2) substrate, Surf. Sci. **425**, 15–21 (1999)

6.259 T. Kubo, H. Nozoye: Surface structure of $SrTiO_3$(100), Surf. Sci. **542**, 177–191 (2003)

6.260 F. Silly, D.T. Newell, M.R. Castell: $SrTiO_3$(001) reconstructions: the (2×2) to c(4×4) transition, Surf. Sci. **600**, L219–L223 (2006)

6.261 Y. Lin, A.E. Becerra-Toledo, F. Silly, K.R. Poeppelmeier, M.R. Castell, L.D. Marks: The (2×2) reconstructions on the $SrTiO_3$ (001) surface: a combined scanning tunneling microscopy and density functional theory study, Surf. Sci. **605**, L51–L55 (2011)

6.262 N. Erdman, L.D. Marks: $SrTiO_3$(001) surface structures under oxidizing conditions, Surf. Sci. **526**, 107–114 (2003)

6.263 N. Erdman, O. Warschkow, M. Asta, K.R. Poeppelmeier, D.E. Ellis, L.D. Marks: Surface structures of $SrTiO_3$(001): a TiO_2-rich reconstruction with a c(4×2) unit cell, J. Am. Chem. Soc. **125**, 10050–10056 (2003)

6.264 A.E. Becerra-Toledo, M.S.J. Marshall, M.R. Castell, L.D. Marks: c(4×2) and related structural units on the $SrTiO_3$(001) surface: scanning tunneling microscopy, density functional theory, and atomic structure, J. Chem. Phys. **136**, 214701 (2012)

6.265 S. Gerhold, Z. Wang, M. Schmid, U. Diebold: Stoichiometry-driven switching between surface reconstructions on $SrTiO_3$(001), Surf. Sci. **621**, L1–L4 (2014)

6.266 O.E. Dagdeviren, G.H. Simon, K. Zou, F.J. Walker, C. Ahn, E.I. Altman, U.D. Schwarz: Surface phase, morphology, and charge distribution transitions on vacuum and ambient annealed $SrTiO_3$(100), Phys. Rev. B **93**, 195303 (2016)

6.267 D.T. Newell, A. Harrison, F. Silly, M.R. Castell: $SrTiO_3$(001)-($\sqrt{5}\times\sqrt{5}$)-R26.6° reconstruction: A surface resulting from phase separation in a reducing environment, Phys. Rev. B **75**, 205429 (2007)

6.268 C.H. Lanier, A. van de Walle, N. Erdman, E. Landree, O. Warschkow, A. Kazimirov, K.R. Poeppelmeier,

J. Zegenhagen, M. Asta, L.D. Marks: Atomic-scale structure of the $SrTiO_3(001)$-c(6×2) reconstruction: experiments and first-principles calculations, Phys. Rev. B **76**, 045421 (2007)

6.269 J. Ciston, H.G. Brown, A.J. D'Alfonso, P. Koirala, C. Ophus, Y. Lin, Y. Suzuki, H. Inada, Y. Zhu, L.J. Allen, L.D. Marks: Surface determination through atomically resolved secondary-electron imaging, Nat. Commun. **6**, 7358 (2015)

6.270 P. Koirala, Y. Lin, J. Ciston, L.D. Marks: When does atomic resolution plan view imaging of surfaces work?, Ultramicroscopy **170**, 35–42 (2016)

6.271 H. Tanaka, T. Matsumoto, T. Kawai, S. Kawai: Interaction of oxygen vacancies with O_2 on a reduced $SrTiO_3(001)\left(\sqrt{5}\times\sqrt{5}\right)$R26.6° surface observed by STM, Surf. Sci. **318**, 29–38 (1994)

6.272 T. Matsumoto, H. Tanaka, K. Kouguchi, T. Kawai, S. Kawai: A scanning tunneling microscopy study of laser molecular beam epitaxy on $SrTiO_3(100)$ surface, Surf. Sci. **312**, 21–30 (1994)

6.273 R. Akiyama, T. Matsumoto, H. Tanaka, T. Kawai: Electric field and contact interactions of tip with adenine molecules on $SrTiO_3(100)$-$\sqrt{5}\times\sqrt{5}$ surfaces, Jpn. J. Appl. Phys. **36**, 3881–3886 (1997)

6.274 M.S. Martín Gonzalez, M.H. Aguirre, E. Morán, M.A. Alario-Franco, V. Perez-Dieste, J. Avila, M.C. Asensio: In situ reduction of (100) $SrTiO_3$, Solid State Sci. **2**, 579–524 (2000)

6.275 I. Shiraki, K. Miki: $SrTiO_3(100)$-$\sqrt{5}\times\sqrt{5}$-R26.6 surface observed by high-resolution scanning tunneling microscopy, Surf. Sci. **605**, 1304–1307 (2011)

6.276 D.M. Kienzle, A.E. Becerra-Toledo, L.D. Marks: Vacant-site octahedral tilings on $SrTiO_3$ (001), the $\sqrt{13}\times\sqrt{13}$-R33.7° surface, and related structures, Phys. Rev. Lett. **106**, 176102 (2011)

6.277 I. Hamada, R. Shimizu, T. Ohsawa, K. Iwaya, T. Hashizume, M. Tsukada, K. Akagi, T. Hitosugi: Imaging the evolution of d states at a strontium titanate surface, J. Am. Chem. Soc. **136**, 17201–17206 (2014)

6.278 T. Ohsawa, K. Iwaya, R. Shimizu, T. Hashizume, T. Hitosugi: Thickness-dependent local surface electronic structures of homoepitaxial $SrTiO_3$ thin films, J. Appl. Phys. **108**, 073710 (2010)

6.279 O. Warschkow, M. Asta, N. Erdman, K.R. Poeppelmeier, D.E. Ellis, L.D. Marks: TiO_2-rich reconstructions of $SrTiO_3(001)$: a theoretical study of structural patterns, Surf. Sci. **573**, 446–456 (2004)

6.280 F. Silly, M.R. Castell: Self-assembled supported Co nanocrystals: the adhesion energy of face-centered cubic Co on $SrTiO_3(100)$-(2×2), Appl. Phys. Lett. **87**, 053106 (2005)

6.281 T.J. Beck, A. Klust, M. Batzill, U. Diebold, C. Di Valentin, A. Selloni: Surface structure of $TiO_2(011)$-(2×1), Phys. Rev. Lett. **93**, 036104 (2004)

6.282 O. Bikondoa, W. Moritz, X. Torrelles, H.J. Kim, G. Thornton, R. Lindsay: Impact of ambient oxygen on the surface structure of α-$Cr_2O_3(0001)$, Phys. Rev. B **81**, 205439 (2010)

6.283 A. Barbier, A. Stierle, N. Kasper, M.-J. Guittet, J. Jupille: Surface termination of hematite at environmental oxygen pressure: experimental surface phase diagram, Phys. Rev. B **75**, 233406 (2007)

6.284 C. Kolczewski, K. Hermann, S. Guimond, H. Kuhlenbeck, H.-J. Freund: Identification of the vanadyl terminated $V_2O_3(0001)$ surface by NEXAFS spectroscopy: a combined theoretical and experimental study, Surf. Sci. **601**, 5394–5402 (2007)

6.285 K. Johnston, M.R. Castell, A.T. Paxton, M.W. Finnis: $SrTiO_3(001)(2\times1)$ reconstructions: first-principles calculations of surface energy and atomic structure compared with scanning tunneling microscopy images, Phys. Rev. B **70**, 085415 (2004)

6.286 L.D. Roelofs, G.Y. Hu, S.C. Ying: Monte-Carlo and renormalization-group studies of surface structural phase-transition, Phys. Rev. B **28**, 6369–6376 (1983)

6.287 J. Jupille, K.G. Purcell, D.A. King: W(100) clean surface phase transition studied by core-level-shift spectroscopy: order-order or order-disorder transition, Phys. Rev. B **39**, 6871–6879 (1989)

6.288 E. Heifets, S. Piskunov, E.A. Kotomin, Y.F. Zhukovskii, D.E. Ellis: Electronic structure and thermodynamic stability of double-layered $SrTiO_3(100)$ surfaces: ab initio simulations, Phys. Rev. B **75**, 115417 (2007)

6.289 R. Shimizu, K. Iwaya, T. Ohsawa, S. Shiraki, T. Hasegawa, T. Hashizume, T. Hitosugi: Effect of oxygen deficiency on $SrTiO_3(001)$ surface reconstructions, Appl. Phys. Lett. **100**, 263106 (2012)

6.290 T. Kubo, H. Orita, H. Nozoye: Atomic structures of the defective $SrTiO_3(001)$ surface, Phys. Chem. Chem. Phys. **13**, 16516–16519 (2011)

6.291 Z. Fang, K. Terakura: Spin and orbital polarizations around oxygen vacancies on the (001) surfaces of $SrTiO_3$, Surf. Sci. **470**, L75–L80 (2000)

6.292 D. Wrana, C. Rodenbücher, W. Bełza, K. Szot, F. Krok: In situ study of redox processes on the surface of $SrTiO_3$ single crystals, Appl. Surf. Sci. **432**, 46–52 (2018)

6.293 S.B. Lee, F. Phillipp, W. Sigle, M. Rühle: Nanoscale TiO island formation on the $SrTiO_3(001)$ surface studied by in situ high-resolution transmission electron microscopy, Ultramicroscopy **104**, 30–38 (2005)

6.294 J. Lo, G.A. Sormorjai: Temperature-dependent surface structure, composition, and electronic properties of the clean $SrTiO_3(111)$ crystal face: low-energy-electron diffraction, Auger-electron spectroscopy, electron energy loss, and ultraviolet-photoelectron spectroscopy studies, Phys. Rev. B **17**, 4942–4950 (1978)

6.295 C.N. Rao, D.D. Sarma: Interatomic Auger transitions in transition-metal oxides, Phys. Rev. B **25**, 2927–2929 (1982)

6.296 J. Danger, H. Magnan, D. Chandesris, P. Le Fèvre, S. Bourgeois, J. Jupille, R. Gotter, A. Verdini, A. Morgante: Intra-atomic versus interatomic process in resonant Auger spectra at the Ti 2p egdes in rutile, Phys. Rev. B **64**, 045110 (2001)

6.297 P. Le Fèvre, J. Danger, H. Magnan, D. Chandesris, J. Jupille, S. Bourgeois, M.A. Arrio, R. Gotter, A. Verdini, A. Morgante: Stoichiometry-related Auger lineshapes in titanium oxides: influence of va-

lence-band profile and of Coster-Kronig processes, Phys. Rev. B **69**, 155421 (2004)
6.298 M.S.J. Marshall, D.T. Newell, D.J. Payne, R.G. Egdell, M.R. Castell: Atomic and electronic surface structures of dopants in oxides: STM and XPS of Nb- and La-doped $SrTiO_3$(001), Phys. Rev. B **83**, 035410 (2011)
6.299 L.M. Liborio, C.G. Sánchez, A.T. Paxton, M.W. Finnis: Stability of Sr adatom model structures for $SrTiO_3$(001) surface reconstructions, J. Phys. Condens. Matter **17**, L223–L230 (2005)
6.300 J.M.P. Martirez, E.H. Morales, W.A. Saidi, D.A. Bonnell, A.M. Rappe: Atomic and electronic structure of the $BaTiO_3$(001) ($\sqrt{5} \times \sqrt{5}$)R26.6° surface reconstruction, Phys. Rev. Lett. **109**, 256802 (2012)
6.301 P. Krüger, J. Jupille, S. Bourgeois, B. Domenichini, A. Verdini, L. Floreano, A. Morgante: Intrinsic nature of the excess electron distribution at the TiO_2(110) surface, Phys. Rev. Lett. **108**, 126803 (2012)
6.302 J. Li, R. Lazzari, S. Chenot, J. Jupille: Contributions of oxygen vacancies and titanium interstitials to the band gap states of reduced titania, Phys. Rev. B **97**, 041403 (2018)
6.303 Z. Wang, F. Yang, Z. Zhang, Y. Tang, J. Feng, K. Wu, Q. Guo, J. Guo: Evolution of the surface structures on $SrTiO_3$(110) tuned by Ti or Sr concentration, Phys. Rev. B **83**, 155453 (2011)
6.304 J. Feng, X. Zhu, J. Guo: Reconstructions on $SrTiO_3$(111) surface tuned by Ti/Sr deposition, Surf. Sci. **614**, 38–45 (2013)

Jacques Jupille

Institute of Nanosciences of Paris
Sorbonne University
Paris, France
jacques.jupille@insp.jussieu.fr

Jacques Jupille is an Emeritus CNRS Senior Scientist at the Institute of Nanosciences of Paris (INSP). He received his PhD from the University of Nancy. In 1990, he moved to the joint CNRS–Saint-Gobain laboratory Glass Surfaces and Interfaces. In 2002, he moved to INSP to create the Low-Dimensional Oxides group. His research activity focuses on the physical chemistry of oxide surfaces and interfaces, from ultra-high vacuum to ambient conditions. In 2019, he has been awarded the "Grande Médaille" of the French Society of Metallurgy and Materials (SF2M).

7. Crystallography of Metal Surfaces and Adsorbed Layers

Georg Held

Crystallography involves the determination of atom positions with accuracy better than a few percent of interatomic bond lengths. The first part of this chapter describes the main experimental techniques that are used for surface crystallography on metal surfaces: low-energy electron diffraction, photoelectron diffraction, surface x-ray diffraction, and the x-ray standing wave technique. The second part discusses common features and trends found in the structures of metal surfaces with and without adsorbates, and presents representative examples of experimentally determined surface structures. These examples illustrate how the interplay between vertical (adsorbate–substrate) and lateral (adsorbate–adsorbate) interactions of different strengths determines the arrangement of atoms at the surface.

7.1 Experimental Surface Crystallographic Techniques

Since the 1960s, single-crystal surfaces have been used routinely for surface science studies, which has also enabled the development of techniques for characterizing these crystals. The availability of reliable laboratory instruments and synchrotron radiation and a massive increase in computer power over the past five decades have made a number of surface crystallographic techniques readily available today. The choice of technique depends on the type of surface under investigation and the type of information that is required. The most accurate structural information is obtained from diffraction techniques, such as low-energy electron diffraction (LEED), surface x-ray diffraction (SXRD), x-ray photoelectron diffraction (XPD), photoelectron diffraction (PhD), or the x-ray standing wave technique (XSW). These techniques yield the positions of surface atoms with an accuracy of typically 0.01–0.1 Å, depending on their contribution to the overall diffraction signal. They do, however, rely on a homogeneous surface, with either long-range order (LEED, SXRD) or at least identical adsorption sites (XPD, PhD, XSW). We will concentrate on these techniques in the following section. Scanning probe microscopy techniques such as scanning tunneling microscopy (STM) or atomic force microscopy (AFM) (discussed in Chap. 8) do not have the same restriction in terms of surface homogeneity, but their lateral resolution in terms of atomic positions is typically poor at the atomic level (≈ 0.5 Å). Spectroscopic techniques, such as x-ray photoelectron spectroscopy (XPS), near-edge x-ray absorption fine structure spectroscopy (NEXAFS), or vibrational spectroscopy (high-resolution electron energy loss spectroscopy HREELS, reflection-absorption infrared spectroscopy RAIRS) (discussed in Chap. 25), require identical adsorption sites but no long-range order. They will only yield a subset of structural parameters, such as coordination of atoms or bond angles, which can be very useful in cases where the full crystallographic data set cannot be acquired. For further details on surface characterization methods, we refer to recent general

M. Rocca, T.S. Rahman, L. Vattuone (Eds.), *Springer Handbook of Surface Science*, Springer Handbooks,
https://doi.org/10.1007/978-3-030-46906-1_7

textbooks [7.1, 2] and review articles on specific techniques, as cited below.

7.1.1 Basic Concepts of Surface Diffraction Techniques

As a surface breaks the translational symmetry of a crystal in the direction perpendicular to the surface plane, there is only two-dimensional periodicity within this plane. The surface sensitivity or penetration depth of the probe used in an experiment (e.g., electrons, x-rays) determines to what extent the periodicity perpendicular to the surface affects the diffraction pattern.

Surface Lattice

The two-dimensional periodicity is described by two lattice vectors, $\boldsymbol{a}_1, \boldsymbol{a}_2$, and reciprocal lattice vectors $\boldsymbol{b}_1, \boldsymbol{b}_2$, which are parallel to the surface plane, as discussed in Chap. 4. The vector $\boldsymbol{R}$ between two equivalent lattice points of a periodic surface is an integer multiple of these lattice vectors

$$\boldsymbol{R} = n_1\boldsymbol{a}_1 + n_2\boldsymbol{a}_2 \,. \tag{7.1}$$

The two-dimensional Laue condition leads to the following relationship between $\boldsymbol{a}_1, \boldsymbol{a}_2$ and the reciprocal lattice vectors $\boldsymbol{b}_1, \boldsymbol{b}_2$

$$\begin{aligned} \boldsymbol{a}_1\boldsymbol{b}_1 &= \boldsymbol{a}_2\boldsymbol{b}_2 = 2\pi \,, \\ \boldsymbol{a}_1\boldsymbol{b}_2 &= \boldsymbol{a}_2\boldsymbol{b}_1 = 0 \,, \end{aligned} \tag{7.2}$$

and explicit expressions

$$\boldsymbol{b_1} = \frac{2\pi}{a_{1x}a_{2y} - a_{1y}a_{2x}} \begin{pmatrix} a_{2y} \\ -a_{2x} \end{pmatrix}, \tag{7.3}$$

$$\boldsymbol{b_2} = \frac{2\pi}{a_{1x}a_{2y} - a_{1y}a_{2x}} \begin{pmatrix} -a_{1y} \\ a_{1x} \end{pmatrix}, \tag{7.4}$$

where $a_{1x}, a_{1y}, a_{2x}, a_{2y}$ are the coordinates of the real-space lattice vectors. The reciprocal lattice vectors have units of Å^{-1} and are also parallel to the surface, as mentioned earlier. In analogy to the real lattice vectors, they define the diffraction pattern in reciprocal space. Each diffraction spot corresponds to the sum of integer multiples of $\boldsymbol{b}_1$ and $\boldsymbol{b}_2$,

$$\boldsymbol{g}(n_1, n_2) = n_1\boldsymbol{b}_1 + n_2\boldsymbol{b}_2 \,. \tag{7.5}$$

The pair of integer numbers (n_1, n_2) are used as indices to label the respective spots. Examples of real-space and reciprocal-space lattices are shown in Fig. 7.1.

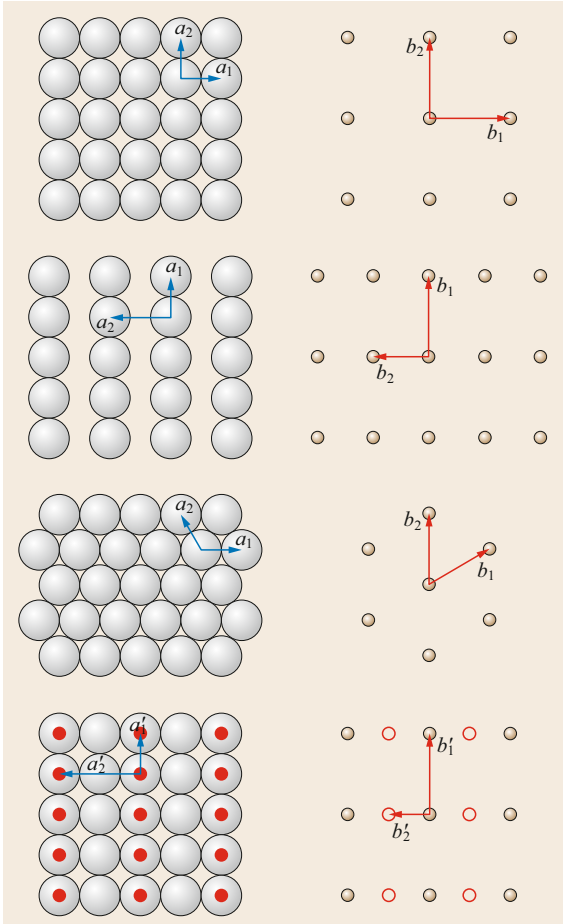

Fig. 7.1 Examples of diffraction patterns for common surfaces: fcc{100}, fcc{110}, fcc{111}, fcc{100}-p(2 × 1)

Superstructures

In many cases, the periodicity of the surface lattice is larger than expected for the bulk-truncated surface of a given crystal due to adsorption or reconstruction. This leads to additional (superstructure) spots in the diffraction pattern, for which fractional indices are used. There are two nomenclatures commonly used to describe such superstructures, the matrix notation [7.3] and the Wood notation [7.4], which are also described in Chap. 4. Here we concentrate on the matrix notation, as this is the most general way of describing a superstructure.

The lattice vectors $\boldsymbol{a}_1'$ and $\boldsymbol{a}_2'$ of such superstructures can be expressed as multiples of the (1 × 1) lattice vectors $\boldsymbol{a}_1$ and $\boldsymbol{a}_2$

$$\begin{aligned} \boldsymbol{a}_1' &= m_{11}\boldsymbol{a}_1 + m_{12}\boldsymbol{a}_2 \,, \\ \boldsymbol{a}_2' &= m_{21}\boldsymbol{a}_1 + m_{22}\boldsymbol{a}_2 \,, \end{aligned} \tag{7.6}$$

where the numbers m_{ij} are the coefficients of the superstructure matrix $\mathbf{M}$

$$\mathbf{M} = \begin{pmatrix} m_{11} & m_{12} \\ m_{21} & m_{22} \end{pmatrix} = (m_{11}\, m_{12}; m_{21}\, m_{22})\,. \tag{7.7}$$

The area of the superstructure unit cell, A', is given by

$$A' = \det \mathbf{M}\, A\,, \tag{7.8}$$

where A is the area of the (1×1) unit cell and $\det \mathbf{M} = m_{11}m_{22} - m_{12}m_{21}$.

Also, the positions and indices of the additional diffraction spots can be calculated directly from the superstructure matrix. The reciprocal lattice vectors $\boldsymbol{b}'_1, \boldsymbol{b}'_2$ which correspond to the superstructure vectors $\boldsymbol{a}'_1$ and $\boldsymbol{a}'_2$ are given by

$$\begin{aligned} \boldsymbol{b}'_1 &= +\frac{m_{22}}{\det \mathbf{M}}\boldsymbol{b}_1 - \frac{m_{21}}{\det \mathbf{M}}\boldsymbol{b}_2\,, \\ \boldsymbol{b}'_2 &= -\frac{m_{12}}{\det \mathbf{M}}\boldsymbol{b}_1 - \frac{m_{11}}{\det \mathbf{M}}\boldsymbol{b}_2\,. \end{aligned} \tag{7.9}$$

The reciprocal lattice, and hence the diffraction pattern of the superstructure, can be constructed by integer multiples of $\boldsymbol{b}'_1$ and $\boldsymbol{b}'_2$ in the same way as in (7.5),

$$\begin{aligned} \boldsymbol{g}(n'_1, n'_2) &= n'_1\boldsymbol{b}'_1 + n'_2\boldsymbol{b}'_2 \\ &= \frac{n'_1 m_{22} - n'_2 m_{12}}{\det \mathbf{M}}\,\boldsymbol{b}_1 \\ &\quad + \frac{-n'_1 m_{21} - n'_2 m_{11}}{\det \mathbf{M}}\,\boldsymbol{b}_2\,. \end{aligned} \tag{7.10}$$

As $\det \mathbf{M}$ is greater than 1, the prefactors of $\boldsymbol{b}_1$ and $\boldsymbol{b}_2$ in (7.10) are fractions, and therefore the superstructure spots have fractional indices.

Often, the actual diffraction pattern contains more superstructure spots than one would get from constructing the reciprocal lattice according to (7.10). This is the case when the symmetry of the superstructure lattice is lower than the symmetry of the substrate and the adsorption complex. In this case, the domains of all symmetry-equivalent superstructure orientations are present at the surface covering equal areas. These orientations are found by applying the missing symmetry operations to the superstructure lattice.

As the diameter of an electron or x-ray beam in a conventional diffraction experiment is orders of magnitude larger than the typical domain size (100–1000 Å), the observed diffraction pattern is normally a superposition of all rotational and/or mirror domains. Hence, the diffraction pattern usually shows the same symmetry as the substrate, even if the superlattice symmetry is lower. Important exceptions are the superstructures of enantiopure chiral molecules, which themselves do not have any mirror symmetry. For these structures, mirror domains are not observed, since applying a mirror operation would turn the molecule into the opposite enantiomer. For the same enantiomer, applying a mirror operation to the lattice would alter the adsorption site geometry of the molecule [7.5].

The left-hand column of Fig. 7.2 shows three examples of LEED patterns observed for different amounts of CO adsorbed on Ni{111} [7.6], $\mathrm{p}(\sqrt{3}\times\sqrt{3})\mathrm{R30°}/(1\,2;-1\,1)$ at 0.33 ML; $\mathrm{c}(2\times4)/(2\,0;1\,2)$ at 0.33 ML, and $\mathrm{p}(\sqrt{7}\times\sqrt{7})\mathrm{R19°}/(3\,1;-1\,2)$ at 0.57 ML. The white arrows indicate the reciprocal lattice vectors for one domain. The column on the right shows the superstructure unit cells of all domains observed in the patterns. The Ni{111} surface has a $p3m1$ symmetry, i.e., threefold rotation symmetry and three mirror planes. The $\mathrm{p}(\sqrt{3}\times\sqrt{3})\mathrm{R30°}$ superstructure has the same symmetry; therefore, only one domain is observed. The $\mathrm{c}(2\times4)$ superstructure has a rectangular unit cell with pm symmetry, which shares a mirror plane with the substrate, but not the rotational symmetry; therefore, three domains, rotated by 120° and 240° with respect to each other, are observed in the LEED pattern. The $\mathrm{p}(\sqrt{7}\times\sqrt{7})\mathrm{R19°}$ unit cell has a threefold $p3$ symmetry without the mirror plane; therefore, two domains are observed, which are related by a mirror operation.

7.1.2 Low-Energy Electron Diffraction (LEED)

Low-energy electron diffraction (LEED) is the diffraction technique most commonly used to study surfaces. A number of textbooks describe the technique in great detail [7.1, 7–9]. As shown in Fig. 7.3, the surface is exposed to a monoenergetic collimated beam of electrons, and the diffraction pattern of the backscattered electrons is detected on a transparent fluorescent screen. Between the screen and sample there is an assembly of suppressor grids, which filter out inelastically scattered electrons and only allow electrons with the same energy as the incoming beam to be detected. The de Broglie wavelength of an electron of kinetic energy E_{kin} is

$$\lambda_{\mathrm{e}} = \sqrt{\frac{h^2}{2m_{\mathrm{e}}E_{\mathrm{kin}}}} = \sqrt{\frac{150.41\,\mathrm{eV}}{E_{\mathrm{kin}}}}\,\text{Å}\,, \tag{7.11}$$

where h is Planck's constant and m_{e} the electron mass. The corresponding wave vector is

$$k_{\mathrm{e}} = \frac{2\pi}{\lambda_{\mathrm{e}}} = \sqrt{\frac{E_{\mathrm{kin}}}{3.8099\,\mathrm{eV}}}\,\text{Å}^{-1}\,. \tag{7.12}$$

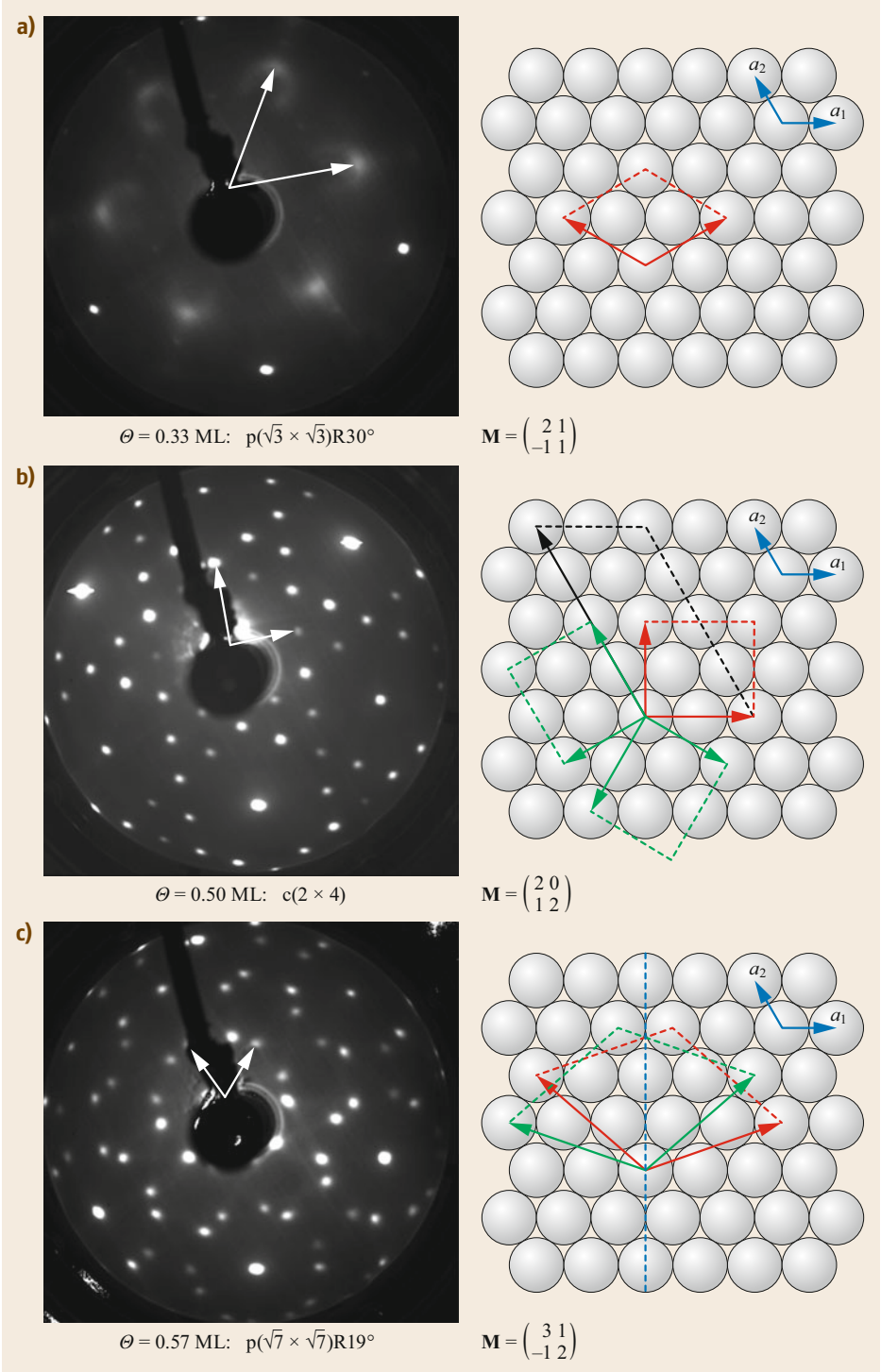

Fig. 7.2a–c Experimental LEED patterns for CO adsorbed on Ni{111} (*left*) and corresponding real-space unit cells (*right*): p($\sqrt{3} \times \sqrt{3}$)R30° (**(a)**, only one domain), c(2 × 4) (**(b)**, 3 rotational domains), and p($\sqrt{7} \times \sqrt{7}$)R19° (**(c)**, 2 mirror domains) [7.6]. Note that real-space diagrams are rotated by about 30° with respect to the crystal orientation of the experiment

For low kinetic energies between 40 and 600 eV, the electron wavelength ranges from 2 to 0.5 Å, which is the same range as the wavelengths used in x-ray crystallography. *Davisson* and *Germer* were the first to observe diffraction patterns for low-energy electrons in 1927 [7.10], and realized already then that the

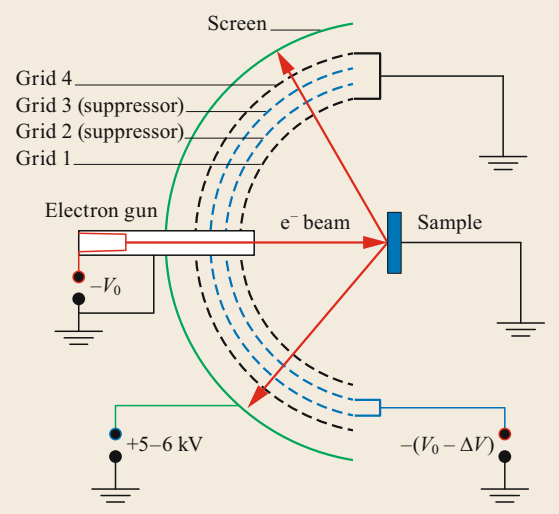

Fig. 7.3 Schematic of a typical LEED experiment. The incident electron beam, accelerated by the potential V_0, is emitted from a small electron gun behind a transparent hemispherical fluorescent screen and hits the sample through a hole in the screen. The surface is in the center of the hemisphere, so that all back-diffracted electrons travel toward the LEED screen on radial trajectories. Before the electrons hit the screen, they have to pass a retarding field energy analyzer (RFA). It consists of four (sometimes three) hemispherical grids concentric with the screen. The first grid (nearest the sample) is connected to earth, as is the sample, in order to provide a field-free region between the sample and this grid. A negative potential $-(V_0 - \Delta V)$ is applied to the second and third grid, the so-called suppressor grids. These repel all electrons that have undergone inelastic scattering processes and have lost more than $e\Delta V$ (typically $\approx 5\,\mathrm{eV}$) of their original kinetic energy. Thus, only elastically scattered electrons and those with small energy losses can pass through to the fluorescent screen. The fourth grid is usually on ground potential in order to reduce field penetration of the screen voltage to the suppressor grids. The screen is at a potential of around 5–6 kV; it provides the electrons with enough energy to cause bright fluorescence on the screen. The pattern can be observed through a viewport from behind the screen

diffraction of low-energy electrons (LEED) could be used to determine the structure of single-crystal surfaces. Because of their small inelastic mean free path (IMFP) of typically $< 10\,\text{Å}$, electrons in this energy range probe only the topmost atomic layers of a surface and are, therefore, better suited for the analysis of surface geometries than x-rays which have a much larger mean free path (typically a few micrometers). As a consequence, low-energy electrons do not sample the periodicity perpendicular to the surface plane, and only a two-dimensional Laue condition must be satisfied for a diffraction spot to be observed

$$\boldsymbol{k}(n_1, n_2) = \boldsymbol{k}_{\text{in}} + \boldsymbol{g}(n_1, n_2)\,, \tag{7.13}$$

where $\boldsymbol{k}_{\text{in}}$ and $\boldsymbol{k}(n_1, n_2)$ are the wave vectors of the incoming and outgoing electron beams, $\boldsymbol{g}(n_1, n_2)$ is a reciprocal lattice vector, as defined by (7.5), and n_1, n_2 are the spot indices. The parallel component of the outgoing wave vector is

$$\boldsymbol{k}_{\parallel}(n_1, n_2) = \boldsymbol{k}_{\parallel,in} + \boldsymbol{g}(n_1, n_2)\,. \tag{7.14}$$

Diffraction is only observed for elastically scattered electrons. Therefore, the lengths of the incoming and outgoing wave vectors are the same, $|\boldsymbol{k}| = \sqrt{2m_{\text{e}}E_{\text{kin}}/\hbar^2}$. The vertical component, $k_{\perp}$, of the electrons back-diffracted into spot (n_1, n_2) is defined by energy conservation

$$k_{\perp}(n_1, n_2) = \sqrt{\frac{2m_{\text{e}}E_{\text{kin}}}{\hbar^2} - |\boldsymbol{k}_{\parallel}(n_1, n_2)|^2}\,. \tag{7.15}$$

Equation (7.15) also limits the number of observable LEED spots, since the expression under the square root must be greater than zero. With increasing electron energy, the number of LEED spots increases, while the polar emission angle with respect to the specular spot $(0, 0)$ decreases for each spot. The specular spot does not change its position if the angle of incidence is kept constant. This is often visualized in terms of an Ewald construction, as illustrated in Fig. 7.4. The incoming and outgoing wave vectors start from the center of the Ewald sphere. Unlike for x-rays, for electrons only the incoming vector needs to point to a reciprocal lattice point. The two-dimensional Laue condition is already fulfilled when the outgoing vector points at the intersect of the Ewald sphere and a reciprocal lattice rod. These reciprocal lattice rods pass through a reciprocal lattice point and are perpendicular to the surface plane. Figure 7.4 shows Ewald constructions for the same angle of incidence but two different energies. The specular $(0, 0)$ vectors emerge at the same angle in both cases, but the angles of the other vectors are different: the higher the energy, the smaller the angles between the vectors. As a result, the diffraction pattern is more compressed at higher energies (i.e., shorter wavelengths). There are also more rods intersecting the larger Ewald sphere at the higher energy; hence more diffraction spots are observed.

Multiple scattering plays an important role in the diffraction process of electrons at solid surfaces. This does not affect the positions of diffraction spots; hence the surface periodicity (size and orientation of the surface lattice) can be determined using the equations

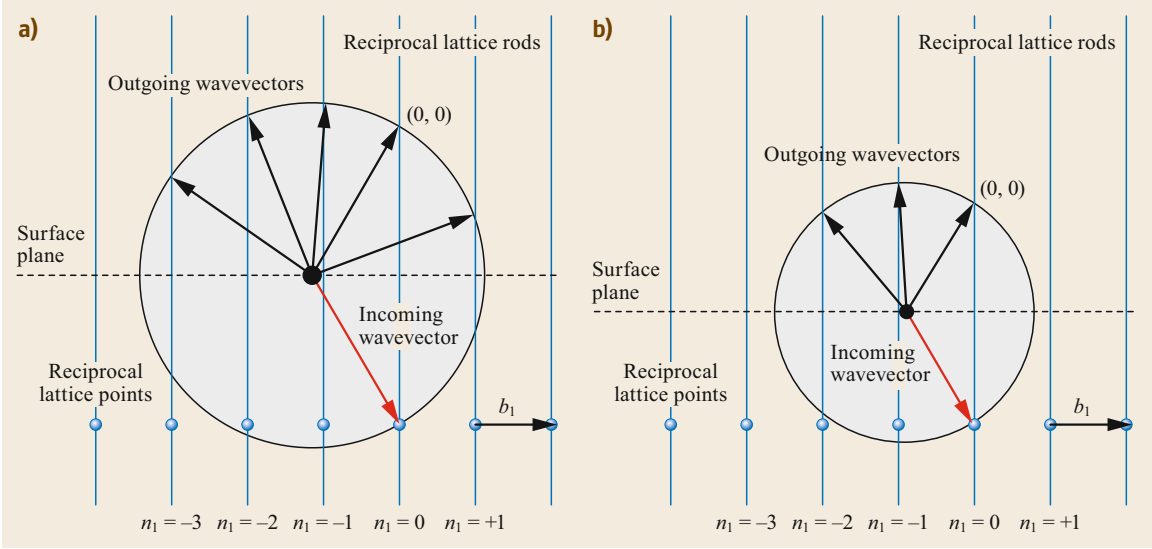

Fig. 7.4a,b Ewald sphere for LEED. **(a)** High energy; **(b)** low energy

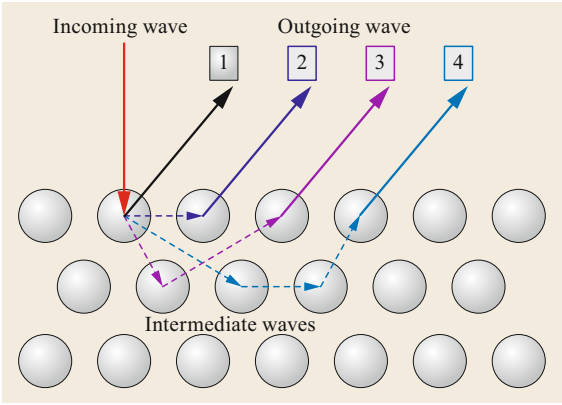

Fig. 7.5 Schematic illustration of single- and multiple-scattering events. The numbers indicate the number of atoms involved in each scattering path

above. The intensities of the diffraction spots, however, are determined by the interference of electron partial waves scattered from the different surface atoms within the unit cell. Figure 7.5 schematically illustrates single- and multiple-scattering events. In the latter, the electron wave interacts with more than one atom before it leaves the surface toward the detector. As a consequence, the phase differences between partial waves depend on the relative positions of all the atoms along the scattering paths and the phase shifts imposed onto the electron wave due to the interaction with the potential of the atoms. The amplitude, and hence the intensity, of the outgoing wave in the direction of a diffraction spot is determined by the superposition of an infinite number of partial waves from all possible (single and multiple) scattering paths, which contain information about the relative positions of atoms within the surface. The amplitudes of each partial electron wave Ψ_k decay exponentially while propagating through the solid, with an energy-dependent decay length, $l(E)$, typically of a few angstroms

$$|\Psi(\boldsymbol{r}+\boldsymbol{s})| = \mathrm{e}^{-\frac{|\boldsymbol{s}|}{2l(E)}}|\Psi(\boldsymbol{r})|\,, \tag{7.16}$$

($|\boldsymbol{s}|$ is the path length of travel). Therefore, the number of multiple scattering paths that need to be considered in practice is limited.

The positions of the atoms can be extracted from the energy dependence of the spot intensities, the so-called LEED I–V, or $I(E)$, curves. Examples are shown in Fig. 7.6. By comparing experimental I–V curves with calculated curves for different test geometries the surface geometry can be identified and refined. The agreement between experimental and theoretical data is quantified using so-called reliability factors (R factors), of which Pendry's R factor is the most common [7.11]. This way, the process of optimizing the atom positions reduces to a minimization problem which can be automated easily. The relative importance of multiple scattering requires fully dynamical quantum mechanical calculations in order to produce I–V curves for the test geometries. A standard approach for calculating LEED I–V curves has been developed in the 1970s through the 1990s by *Pendry*, *Tong*, *Van Hove*, and others [7.7, 9, 12, 13].

To date, structure analysis by LEED I–V is the most accurate and reliable means of determining the atomic positions at surfaces. In particular, the fact that

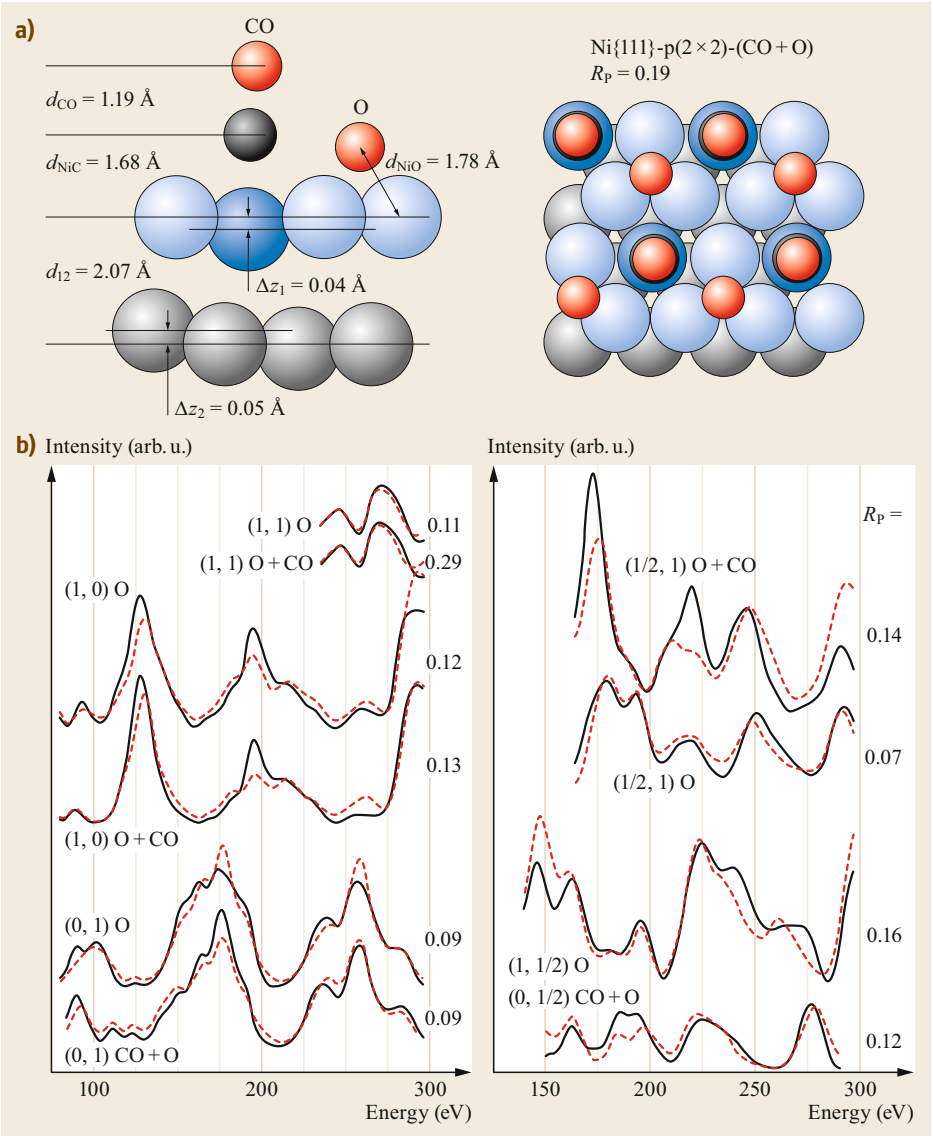

Fig. 7.6
(a) Adsorption geometry for the p(2 × 2) superstructure of co-adsorbed CO and O on Ni{111} according to [7.14] and **(b)** selected LEED *I–V* curves for this structure (CO + O) and the p(2 × 2) superstructure of oxygen only (O). The *black solid lines* are experimental; the *red dashed lines* are calculated *I–V* curves

LEED is sensitive to the atomic positions not only in the topmost layer but down to several layers below the surface makes it an ideal tool for studying intrinsic or adsorbate-induced surface reconstructions. General restrictions are that LEED usually requires ordered and conducting surfaces; otherwise charging would distort the LEED pattern. The time needed for calculating the *I–V* curves and the number of trial geometries are factors limiting the complexity of accessible surface structures on the computational side; the density of LEED spots on the fluorescent screen is an experimental factor limiting the size of unit cells that can be studied.

Since LEED theory was initially developed for close-packed clean metal surfaces, these are the most reliably determined surface structures with theory–experiment agreement comparable to that between two experimental sets of *I–V* curves and error bars for the atomic coordinates as small as 0.01 Å. A good overview of state-of-the-art LEED structure determinations of clean metal surfaces and further references are found in a series of articles by *Heinz* et al. [7.13, 15, 16]. For more open adsorbate-covered and/or reconstructed surfaces, certain approximations used in the standard programs are less accurate, which leads to higher R_P factor values. For simple superstructures of monatomic adsorbates or small molecules on metal, the agreement is usually not as good, and is worse for large molecules, which often adsorb in complex super-

structures and semiconductor surfaces. Since the error margins scale with the agreement between experimental data and theoretical calculations, the accuracy of atomic coordinates in these latter cases is smaller, with error bars up to 0.1 Å. A review of structure determinations of molecular adsorbates was published by *Over* [7.17]; the structure determination of semiconductor surfaces was reviewed by *Kahn* [7.18]. In general, the accuracy is higher for coordinates perpendicular to the surface than for lateral coordinates. For further details about the history, experimental setup, and theoretical approaches of LEED, refer to the books by *Pendry* [7.7], *Van Hove* and *Tong* [7.12], *Van Hove* et al. [7.9], and *Clarke* [7.8].

7.1.3 X-ray Photoelectron Diffraction (PhD, XPD)

Diffraction effects are also observed when an electron is emitted from an atom due to the photoelectric effect. In this case, the energy of a photon, $h\nu$, is transferred onto a valence or core electron, which leaves the emitter atom with a kinetic energy of

$$E_{\mathrm{el}} = h\nu - E_{\mathrm{B}} - \Phi \,, \tag{7.17}$$

where E_{B} is the binding energy of the emitted electron, and Φ the work function of the sample. For x-rays in the energy range from a few hundred to a few thousand electron volts (*soft x-rays*) and binding energies in a similar range, the kinetic energies of the photoelectrons are similar to those in LEED with de Broglie wavelengths of the order of 1 Å. Therefore, the propagation of photoelectrons from an atom which is embedded in a solid is governed by very similar effects as the propagation of LEED electrons. The part of the photoelectron wave function that is scattered by atoms surrounding the emitter atom interferes with the directly emitted electron wave, which leads to significant intensity variations as a function of the detection angle and kinetic (photon) energy. These photoelectron diffraction effects strongly depend on the position of the scattering atoms with respect to the emitter, and can thus be used as a tool to determine the surface structure [7.19–21]. As with LEED, the fact that electrons of relatively low energies are detected makes photoelectron diffraction a surface-sensitive technique. However, there are several important differences between LEED and photoelectron diffraction:

- The wave function of the primary photoelectron is described by a spherical wave, whereas in LEED the incoming electron is described as a plane wave.
- The primary, unscattered part of the photoelectron wave function is always detected alongside the diffracted part, which leads to smaller variations in the recorded intensities compared with LEED.
- The emitter atom is a specific element, and only the environment of this atom is probed. The type of emitter atom can be selected by choosing the kinetic/binding energy of the photoelectron, according to (7.17). In practice, of course, the signal measured is the superposition of signals from all atoms emitting electrons with the respective energy.
- Only the immediate vicinity of the emitter atom contributes to the photoelectron scattering. Therefore, the long-range arrangement of atoms (beyond the inelastic mean free path) does not affect the signal, and no sharp diffraction spots are observed.

In order to measure a photoelectron diffraction signal, one needs a monochromatic photon source and an energy-resolving electron detector. Photon sources are either an x-ray anode with fixed photon energy (typically Al K_α with $h\nu = 1486.7\,\mathrm{eV}$ or Mg K_α with $h\nu = 1253.6\,\mathrm{eV}$) or a synchrotron radiation source, which provides tunable photon energy. The most common detectors are hemispherical electron energy analyzers. For a more detailed description of the experimental setup see [7.19–22]. The current state of the technique and its applications were recently reviewed by *Woodruff* [7.23]. The particular advantage of photoelectron diffraction over other surface-sensitive diffraction methods, such as LEED and surface x-ray diffraction (SXRD), is that it is element-specific and does not require long-range order; the only condition is that the local environment be the same for all atoms that emit electrons of the same binding energy.

Figure 7.7 shows the angular dependence of the scattering factor for electrons of different kinetic energies on a Cu atom, which is representative of most atoms. The scattering factor is proportional to the probability of the electron being scattered in the a direction of polar angle θ. From Fig. 7.7 it is clear that the highest probability is always for scattering in the forward direction ($\theta = 0°$), but at low energies, about 300 eV and below, scattering sideways ($40° < \theta < 120°$) and backward ($\theta \approx 180°$) is also strong, whereas $> 500\,\mathrm{eV}$ the scattering factor is strongly peaked in the forward direction. Therefore, the crystallographic information extracted from photoelectron diffraction is strongly dependent on the kinetic energy of the electrons detected. At high kinetic energies, the signal is affected predominantly by atoms which are between the emitter atom and the detector (*forward focusing*); at low energies, the signal has strong contributions from all atoms surrounding the emitter (*backscattering*).

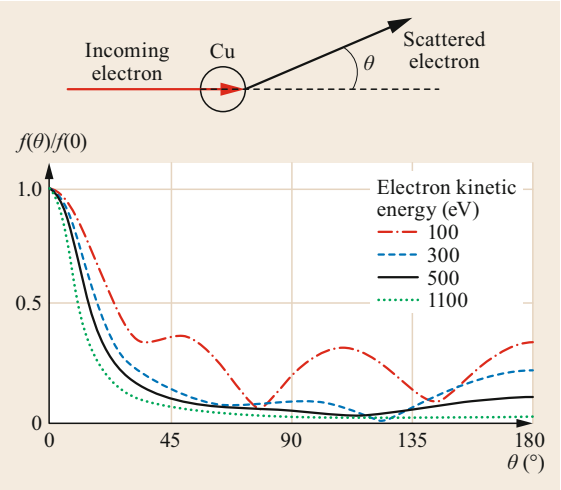

Fig. 7.7 Angular dependence of the modulus of the atomic scattering factor for electrons by a copper atom at several different electron energies (Reprinted with permission from [7.23] with permission from Elsevier)

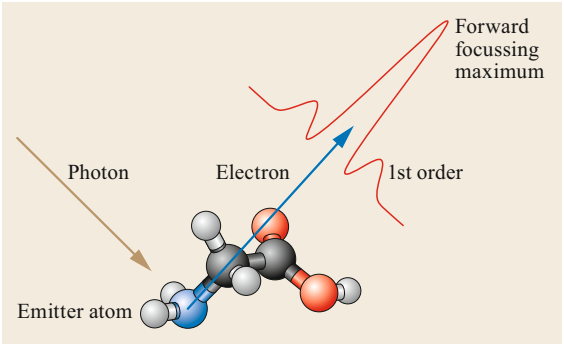

Fig. 7.8 Basic principle of forward focusing. A maximum of the photoelectron signal is observed when a *focusing atom* is between the emitter atom and detector. In this example, the N 1s signal from the N atom in glycine is focused by the neighboring C atom

Forward Focusing (XPD)

For kinetic energies above $\approx 500\,\text{eV}$, electrons are predominantly scattered in the forward direction [7.20, 24]. This leads to the so-called *forward-focusing effect* when another atom is between the emitter and the detector. In this direction, the intensity is amplified; in addition, small-intensity minima are observed at angles 10°–20° from this direction, as indicated in Fig. 7.8. The magnitude of these x-ray photoelectron diffraction (XPD) intensity variations decreases with increasing distance between emitter and scatterer such that effectively only atoms within the same molecule or close neighbors in solids need to be considered. The maxima in the angular distribution of the photoelectron intensity, therefore, correspond directly to the connecting lines between the emitter and neighboring atoms. This makes the data analysis straightforward such that even the adsorption geometry of molecules as large as C_{60} can be determined [7.25]. XPD studies have most commonly been carried out using conventional x-ray sources, often equipped with purpose-built automated in-vacuum goniometers to scan the entire hemisphere above the surface [7.26, 27]. Until recently, synchrotron beamlines did not offer great advantages, since high-energy resolution is usually not required, and the total photon flux at the high end of the soft x-ray range which is required for these measurements is often comparable with un-monochromated Al K_α sources. The higher stability of laboratory sources in terms of flux is an additional advantage over synchrotron radiation, since scanning the entire hemisphere requires long data acquisition times. Recently, however, synchrotron radiation has been used very successfully for this type of experiment [7.28, 29]. Tunable photon energies and polarization enable contrast enhancement by exploiting resonance effects [7.30]. XPD has been applied mostly to studying the structures of thin films and adsorption geometries of molecules, including enantiomeric differences in the adsorption geometries of chiral molecules [7.28, 29].

Backscattering (PhD)

For kinetic energies $< 300\,\text{eV}$, elastic scattering away from the forward direction is very significant, whereby backscattering is a particularly important scattering path. The photoelectron signal emitted from adsorbate atoms is therefore the superposition of the direct wave and the electron wave backscattered from the substrate atoms. The interference of these two waves carries information about the registry between adsorbate and substrate, i.e., adsorption sites and adsorbate–substrate bond lengths, which is not accessible through XPD. In order to make a distinction between the forward and backward scattering regimes in photoelectron diffraction, crystallographic studies using the low kinetic energy range have been termed *PhD* (for *photoelectron diffraction*). Scanning the photon energy with the detector recording the photoemission signal at a fixed angle has become the standard means of data acquisition for this technique. This procedure is repeated for several angles [7.23]. The photon energy range is chosen such that the kinetic energy of the photoelectrons typically varies between 20 and 300 eV. Therefore, these measurements can only be performed at synchrotron beamlines with tunable monochromators. Both hard ($> 2\,\text{keV}$) and soft x-ray ($< 2\,\text{keV}$) beamlines have been used to access core levels of different adsorbates, depending on the binding energies of the relevant core

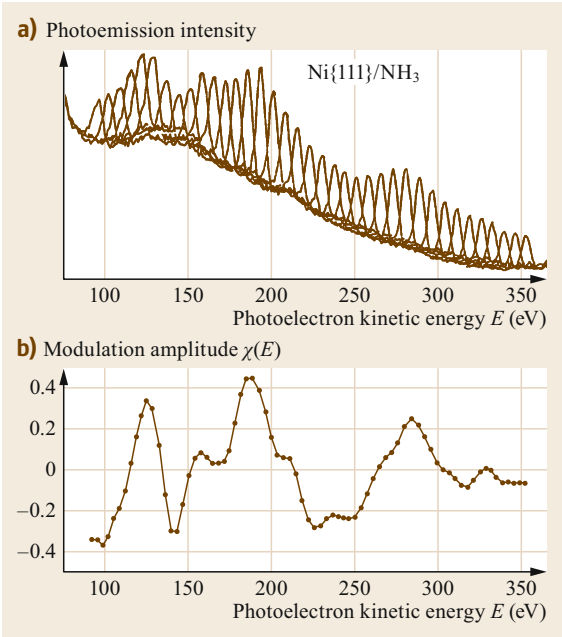

Fig. 7.9a,b Experimental PhD data for NH_3 adsorption on Ni{111} [7.31]. **(a)** Individual N 1s photoelectron spectra as a function of kinetic energy. **(b)** PhD modulation spectrum (relative deviation of the integrated N 1s peak intensities from the sliding average) as a function of the kinetic energy. See text for details (Reprinted with permission from [7.23] with permission from Elsevier)

levels. For most molecular adsorbates, soft x-rays are required to access the core levels of C (1s ≈ 285 eV), N (1s ≈ 400 eV), and O atoms (1s ≈ 530 eV).

As the electron wavelength changes when the kinetic energy is varied, the interference conditions between the direct and the backscattered electron wave change, and intensity variations are observed as a function of photon/kinetic energy, which is illustrated in Fig. 7.9 for the N 1s photoelectrons emitted from NH_3 on Ni{111} [7.31]. The data analysis is not as straightforward as in XPD, and involves multiple-electron scattering theory, similar to LEED. The intensity variations (relative deviation from the unperturbed intensity, see lower panel of Fig. 7.9) are calculated for model geometries and compared with the experimental data. Optimization of the model geometries to improve the agreement eventually leads to the adsorption geometry. A large number of adsorption geometries have been determined to date using PhD, mostly for atomic adsorbates and small molecules adsorbed on metal or metal oxide surfaces (see [7.23] for a complete review up to 2007).

The high energy resolution of third-generation synchrotron beamlines makes it possible to separate the intensity variations for different chemical shifts, i.e., different chemical environments of emitter atoms of the same element. Their positions with respect to the substrate can thus be determined separately, which is particularly important for oxide surfaces, when the signal of molecular oxygen atoms needs to be separated from the substrate [7.32, 33].

7.1.4 Surface X-ray Diffraction (SXRD)

The principle of surface x-ray diffraction (SXRD) is very similar to that of low-energy electron diffraction (LEED). The wavelength of x-rays is related to the photon energy E_{ph} as

$$\lambda_X = \frac{hc}{E_{ph}} = \frac{12\,398\,\text{eV}}{E_{ph}}\text{Å}\,, \tag{7.18}$$

the wave vector of a photon is

$$k_X = \frac{2\pi}{\lambda_X} = \frac{E_{ph}}{1974.2\,\text{eV}}\text{Å}^{-1}\,. \tag{7.19}$$

Therefore, *hard x-rays* of energies ≈ 12 keV (i.e., 1 Å) are best suited for probing atomic positions. Since the groundbreaking work of *Bragg* and *Bragg*, *von Laue*, and others [7.34–36], x-ray diffraction has been successfully used to determine countless crystal structures, from simple atomic solids to complex biomolecules, by analyzing the intensities of Bragg reflections. The relatively low scattering cross section and large penetration depth of x-rays, which is about three to four orders of magnitude larger than that of low-energy electrons, means that the signal recorded from x-ray diffraction is usually dominated by bulk contributions. Intense x-ray sources, such as synchrotrons, and grazing scattering geometries make it possible, however, to extract crystallographic information about the surface geometry as well [7.37–40].

Because of the large penetration depth of x-rays, they, unlike electrons, probe the periodicity of a single crystal normal to the surface, which leads to sharp Laue conditions not only in the surface plane but also in the perpendicular direction. However, the fact that the periodic stacking of layers abruptly ends at the surface causes a relaxation of the Laue condition normal to the surface. As a consequence, some intensity is scattered into the momentum space between the Bragg spots along lines perpendicular to the surface, as indicated in Fig. 7.10. These lines are referred to as *crystal truncation rods*, or *CTRs*. The intensity along the CTRs can be measured by varying the angles of the incident x-ray beam and/or the detector with respect to the surface. This signal contains very useful information about the surface geometry due to the interference between bulk and surface scattering. By convention, in surface x-ray crystallography, two of the real-space lattice vectors, $\boldsymbol{a}_1$ and $\boldsymbol{a}_2$, are chosen as described in (7.1). The

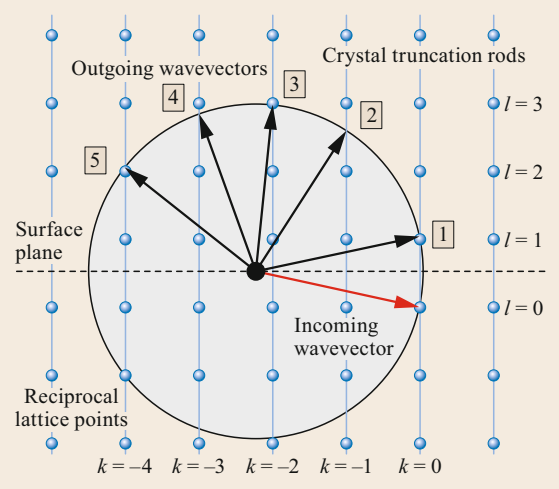

Fig. 7.10 Ewald construction for SXRD

third lattice vector, $\boldsymbol{a}_3$, is perpendicular to the surface. Consequently, the corresponding reciprocal lattice vectors are also parallel ($\boldsymbol{b}_1, \boldsymbol{b}_2$) and perpendicular ($\boldsymbol{b}_3$) to the surface plane. For details regarding the choice of lattice vectors see [7.38, 41].

In general, the intensity diffracted from a single crystal into a Bragg peak is proportional to the square of the structure factor $|F|^2$

$$I(h\boldsymbol{b}_1, k\boldsymbol{b}_2, l\boldsymbol{b}_3) = I_0 \frac{e^4}{m^2 c^4 R^2} P |F(h\boldsymbol{b}_1, k\boldsymbol{b}_2, l\boldsymbol{b}_3)|^2 , \tag{7.20}$$

where I_0 is a constant depending on material properties (e.g., scattering cross section), e the charge and m the mass of an electron, and R the distance between sample and detector. The polarization factor P is unity if the polarization of the incoming wave is normal to the scattering plane (i.e., the plane containing the incoming and diffracted beams), and $P = \cos^2(2\theta)$ if it is within this plane, whereby 2θ is the angle between the incoming and diffracted beams.

For a finite bulk-terminated crystal, the structure factor can be calculated using single-scattering theory [7.37]

$$\begin{aligned} &|F(\boldsymbol{q}_1, \boldsymbol{q}_2, \boldsymbol{q}_3)|^2 \\ &= \left| \sum_{n_1=0}^{N_1-1} \sum_{n_2=0}^{N_2-1} \sum_{n_3=0}^{N_3-1} \exp[\mathrm{i}(n_1 \boldsymbol{q}_1 \boldsymbol{a}_1 + n_2 \boldsymbol{q}_2 \boldsymbol{a}_2 + n_3 \boldsymbol{q}_3 \boldsymbol{a}_3)] \right|^2 \\ &= \frac{\sin^2(\frac{1}{2} N_1 \boldsymbol{q}_1 \boldsymbol{a}_1)}{\sin^2(\frac{1}{2} \boldsymbol{q}_1 \boldsymbol{a}_1)} \frac{\sin^2(\frac{1}{2} N_2 \boldsymbol{q}_2 \boldsymbol{a}_2)}{\sin^2(\frac{1}{2} \boldsymbol{q}_2 \boldsymbol{a}_2)} \frac{\sin^2(\frac{1}{2} N_3 \boldsymbol{q}_3 \boldsymbol{a}_3)}{\sin^2(\frac{1}{2} \boldsymbol{q}_3 \boldsymbol{a}_3)} , \end{aligned} \tag{7.21}$$

where N_1, N_2, N_3 are the (large) numbers of unit cells along the directions of the three real lattice vectors, and $\boldsymbol{q}_1, \boldsymbol{q}_2, \boldsymbol{q}_3$ are vectors in reciprocal space pointing in the directions of the reciprocal lattice vectors. If $\boldsymbol{q}_1$ and $\boldsymbol{q}_2$ are integer multiples of $\boldsymbol{b}_1$ and $\boldsymbol{b}_2$, respectively, such that $\boldsymbol{q}_1 \boldsymbol{a}_1 = 2\pi h; \boldsymbol{q}_2 \boldsymbol{a}_2 = 2\pi k$, the respective terms in (7.21) reduce to $N_1^2 N_2^2$. Hence, the intensity along the truncation rods (i.e., along the continuous variable $\boldsymbol{q}_3$ perpendicular to the surface) is proportional to

$$|F(h\boldsymbol{b}_1, k\boldsymbol{b}_2, \boldsymbol{q}_3)|^2 = N_1^2 N_2^2 \frac{\sin^2(\frac{1}{2} N_3 \boldsymbol{q}_3 \boldsymbol{a}_3)}{\sin^2(\frac{1}{2} \boldsymbol{q}_3 \boldsymbol{a}_3)} . \tag{7.22}$$

For $N_3 \to \infty$ and $\boldsymbol{q}_3 \boldsymbol{a}_3 \neq 2\pi l$ we get

$$|F(h\boldsymbol{b}_1, k\boldsymbol{b}_2, \boldsymbol{q}_3)|^2 \to N_1^2 N_2^2 \frac{1}{\sin^2(\frac{1}{2} \boldsymbol{q}_3 \boldsymbol{a}_3)} . \tag{7.23}$$

The shape of this function for a perfectly flat surface is plotted as a solid black line in Fig. 7.11. The intensity distribution along the crystal truncation rods is strongly dependent on the arrangement of atoms near the surface. Surface roughness at the atomic level, i.e., partial occupation of the layer or several of the layers nearest the surface, leads to deeper minima between the Bragg peaks. This is described by the structure factor

$$\begin{aligned} &|F(h\boldsymbol{b}_1, k\boldsymbol{b}_2, \boldsymbol{q}_3)|^2 \\ &= N_1^2 N_2^2 \frac{(1-\beta)^2}{[1 + \beta^2 - 2\beta \cos(\boldsymbol{q}_3 \boldsymbol{a}_3)]} \frac{1}{4 \sin^2(\frac{1}{2} \boldsymbol{q}_3 \boldsymbol{a}_3)} , \\ &\text{for } \boldsymbol{q}_3 \boldsymbol{a}_3 \neq 2\pi l , \end{aligned} \tag{7.24}$$

where the parameter β describes the partial occupation of the surface layers (for details see [7.37]). The corresponding intensity distribution along the truncation rod is plotted as a dashed line in Fig. 7.11.

Expansion or compression of interlayer distances near the surface leads to asymmetric intensity distributions, as in the red curve plotted in Fig. 7.11. In this case, the distance between the first and the second layer is expanded by 10% with respect to the bulk interlayer distance $|\boldsymbol{a}_3|$. If (7.21) is modified accordingly, this leads to a structure factor

$$\begin{aligned} &|F(h\boldsymbol{b}_1, k\boldsymbol{b}_2, \boldsymbol{q}_3)|^2 \\ &= N_1^2 N_2^2 \left(\frac{\left\{ 2 \sin\left(\frac{1}{2} \boldsymbol{q}_3 \boldsymbol{a}_3\right) - \sin\left[\frac{1}{2} \boldsymbol{q}_3 (2\boldsymbol{d} - \boldsymbol{a}_3)\right] \right\}^2}{4 \sin^2\left(\frac{1}{2} \boldsymbol{q}_3 \boldsymbol{a}_3\right)} \right. \\ &\qquad \left. + \frac{\cos^2\left[\frac{1}{2} \boldsymbol{q}_3 (2\boldsymbol{d} - \boldsymbol{a}_3)\right]}{4 \sin^2\left(\frac{1}{2} \boldsymbol{q}_3 \boldsymbol{a}_3\right)} \right) \\ &\text{for } \boldsymbol{q}_3 \boldsymbol{a}_3 \neq 2\pi l , \end{aligned} \tag{7.25}$$

where $\boldsymbol{d}$ is the vector pointing from the second to the first layer.

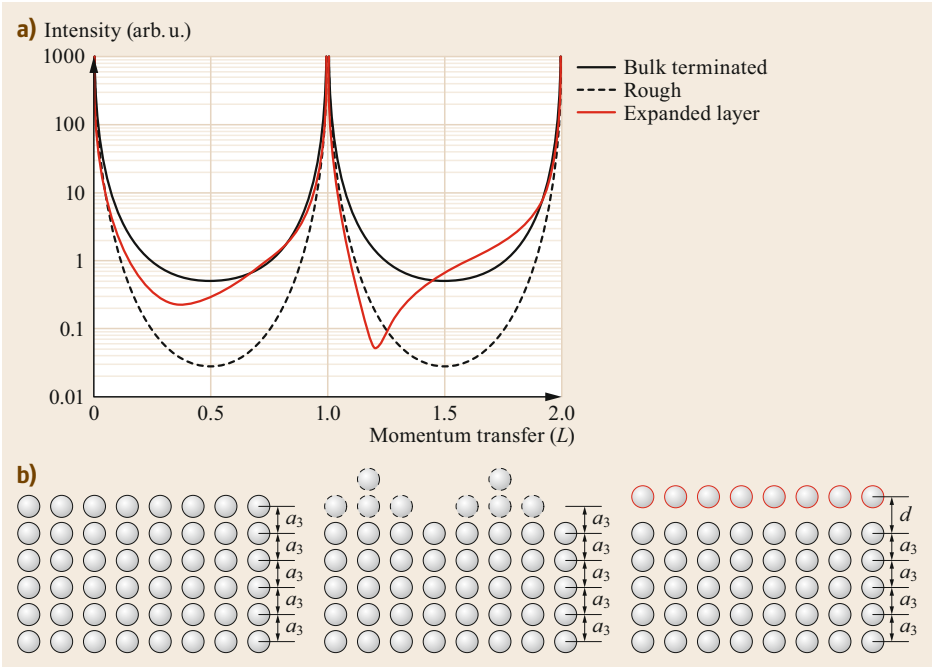

Fig. 7.11
(a) Calculated crystal truncation rods for a bulk-terminated surface (*solid black line*), a rough surface (*dashed black line*), and a surface where the interlayer distance of the topmost layer d is expanded by 10% with respect to a_3 (*solid red line*). **(b)** Corresponding schematic models; (*left*) bulk-terminated; (*middle*) atomically rough surface; (*right*) expanded first layer

The intensity variations between the maximum of the Bragg peaks and the minimum of the CTR span about five orders of magnitude. Therefore, an intense x-ray source is needed, such as a third-generation synchrotron source, to be able to measure the entire profile of the rod. The data analysis determining the surface structure is based on a trial-and-error approach similar to LEED I–V structure determination. Intensity (structure factor) distributions along the CTRs are calculated for different trial geometries and compared with the experimental data. The atom positions within the trial geometries are optimized until the best possible agreement is achieved.

Reflectivity scans measure the intensity of the specularly reflected x-ray beam as a function of incidence angle. This is a special case of CTR with $h = k = 0$. As no lateral momentum transfer is involved, the signal contains no information about the lateral distortions near the surface. The reflectivity signal can thus be used for an independent determination of only the vertical interlayer distances. Lateral parameters can be determined from CTRs with $h, k \neq 0$.

When an ordered superstructure is present at the surface, additional weak rods are observed at fractional h, k values, as discussed in Sect. 7.1.1. As superstructures are located at the surface, the intensities of these spots show very little variation as a function of $\boldsymbol{q}_3$ and predominantly contain information about the lateral positions and electron densities of atoms within the surface unit cell. These can be extracted by means of the two-dimensional Patterson function [7.39, 42]

$$P(x,y) = \frac{1}{A}\sum_{hk} |F(h\boldsymbol{b}_1, k\boldsymbol{b}_2)|^2_{\text{exp}} \cos\left[(h\boldsymbol{b}_1 + k\boldsymbol{b}_2)\begin{pmatrix}x\\y\end{pmatrix}\right], \quad (7.26)$$

where A is the area of the surface unit cell, $\binom{x}{y}$ is a vector parallel to the surface within the superstructure unit cell, and $|F(h\boldsymbol{b}_1, k\boldsymbol{b}_2)|^2_{\text{exp}}$ are proportional to the experimentally determined intensities at the h, k superstructure spot positions. The latter are extracted from the spot intensities measured at constant $\boldsymbol{q}_3$ and using (7.20).

The Patterson function can be interpreted as a real-space map of interatomic distances, i.e., the vectors from the origin of the Patterson map to each maximum correspond to vectors between atoms. Figure 7.12 shows an early example of a Patterson function constructed from the fractional-order Bragg peaks by *Robinson* [7.43], together with a schematic structure model for the missing-row reconstruction. The map clearly shows a main maximum for the vector connecting the lateral coordinates of the first- and second-layer atom. It also clearly shows the absence of maxima corresponding to the atoms of the missing row.

Because of the low scattering cross section of x-rays compared with electrons, and because the cross section scales roughly with the square of the atomic num-

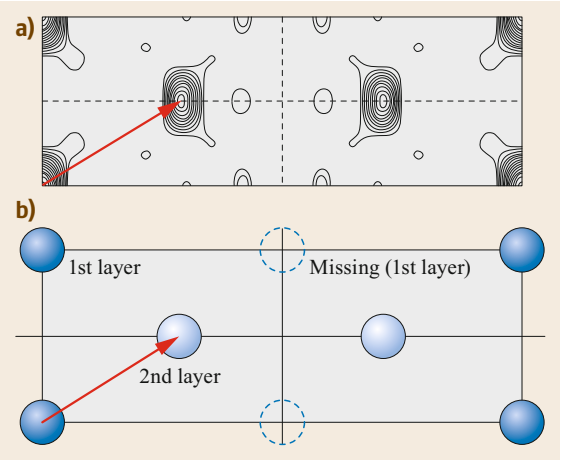

Fig. 7.12 **(a)** Patterson function of the p(2×1) missing-row reconstruction of Au{110}. (Note that the map of the full unit cell was constructed from the bottom left quadrant by applying mirror operations with respect to the indicated mirror planes.) **(b)** Geometry model compatible with the Patterson function [7.43] (**(a)** reprinted with permission from [7.43] Copyright 1983 by the American Physical Society)

ber Z, the positions of light atoms such as hydrogen, carbon, nitrogen, or oxygen are difficult to determine with surface x-ray diffraction. To date, the method has largely been applied to determine the structures of complex metal, oxide, and semiconductor surface reconstructions. Recently, the fact that hard x-rays can penetrate matter, and therefore x-ray diffraction experiments do not necessarily require vacuum conditions, has been used extensively to study model catalyst surfaces in reactive gas-phase environments [7.40, 44] and even electrochemical interfaces under reaction conditions [7.45].

7.1.5 X-ray Standing Waves (XSW)

The x-ray standing wave (XSW) technique is another crystallographic method that makes use of the photoelectric effect. In contrast to photoelectron diffraction, however, the crystallographic information is derived from the interference of the incoming and outgoing x-ray waves [7.46–49]. As a consequence, hard x-rays (typically $h\nu > 3\,\mathrm{keV}$) are used in order to match the wavelengths with interatomic distances. The principle is illustrated in Fig. 7.13. Photoelectron spectra from a single-crystal sample are measured over a range of photon energies near the Bragg condition for x-ray diffraction from a set of crystallographic planes. When the Laue condition is fulfilled, the superposition of the incoming x-ray beam and the outgoing beam of the Bragg refection results in a standing wave field parallel to the Bragg planes with well-defined periodic maxima and minima. Depending on where an atom sits with respect to the standing wave, the cross section for photoemission will be different. If the atom is near a maximum of the wave field, the photoemission probability will be high; near a minimum it will be low. The relative intensity I of the standing wave field is given by

$$I = \left|1 + \left(\frac{E_\mathrm{h}}{E_0}\right) \exp\left(\frac{-2\pi \mathrm{i} z}{d_\mathrm{h}}\right)\right|^2 , \qquad (7.27)$$

where z is the vertical distance above the Bragg plane corresponding to the reflection used, and d_h the distance between these planes. E_h/E_0 is the ratio of amplitudes of the reflected and incident x-ray beams, given by

$$\frac{E_\mathrm{h}}{E_0} = -\sqrt{\frac{F_\mathrm{h}}{F_{\bar{\mathrm{h}}}}} \left(\eta \pm \sqrt{\eta^2 - 1}\right) , \qquad (7.28)$$

where F_h and $F_{\bar{\mathrm{h}}}$ are the structure factors corresponding to the incident and reflected beams, and η is a quantity that depends on the deviation from the actual Laue condition in terms of angle or photon energy (for an exact definition and a complete description see [7.47]). With the latter expression (7.28), (7.27) can be rewritten as

$$I = 1 + R + 2\sqrt{R}\, \cos\left(\Phi - \frac{2\pi z}{d_\mathrm{h}}\right) , \qquad (7.29)$$

whereby R and the phase angle Φ depend only on the crystal structure and the x-ray properties, and can be easily calculated. By either rocking the sample or varying the photon energy around the Laue condition (within the natural width of the Bragg peak), Φ and hence the positions of the maxima can be moved with respect to the crystal lattice in the direction perpendicular to the Bragg planes. Thus, positions of the emitter atoms can be determined from fits to the intensity variations of the photoemission signal versus rocking angle or photon energy, respectively. In cases where the emitter atoms are in identical well-defined z positions above the Bragg planes, the experimental data will yield their vertical position. If this is not the case, the parameters determined by the fits are the so-called coherent fraction f_co and position d_co. They are defined through

$$f_\mathrm{co} \exp\left(\frac{2\pi \mathrm{i} d_\mathrm{co}}{d_\mathrm{h}}\right) = \int_0^{d_\mathrm{h}} f(z) \exp\left(\frac{2\pi \mathrm{i} z}{d_\mathrm{h}}\right) \mathrm{d}z , \qquad (7.30)$$

and can be seen as weighted average values of positions z and occupancies $f(z)$ of all emitter atoms, which also

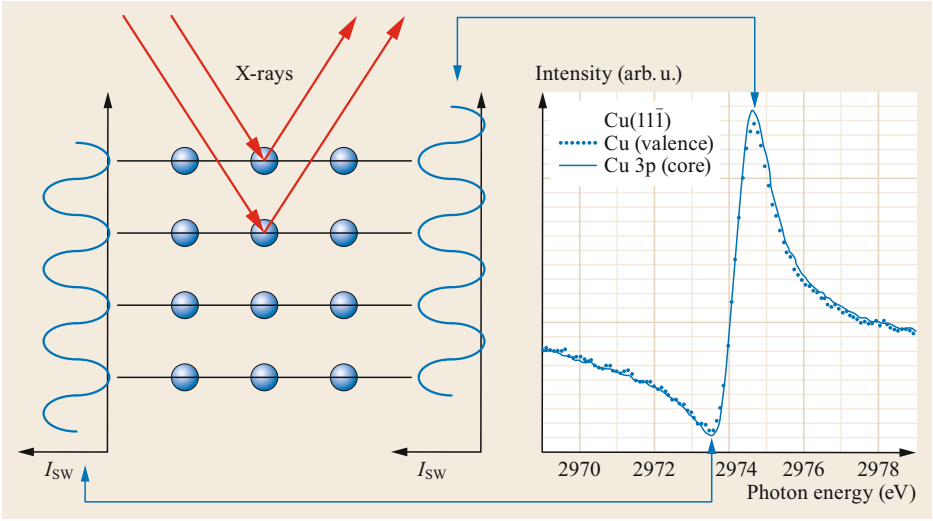

Fig. 7.13 The principle of the x-ray standing wave (XSW) technique. At the low-energy side of the Bragg maximum, the maxima of the standing wave field are between the atomic planes of the bulk crystal (*left*), and at the high-energy side, the maxima are on the atomic planes (*middle*). This leads to a minimum followed by a maximum of the integrated XPS signal from the atoms within the atomic planes. The spectrum on the *right* shows the integrated Cu 3p and valence band signal from a Cu single crystal (Right part of the figure reprinted from [7.48] with permission from Elsevier)

Table 7.1 Key properties of techniques with examples (UHV = ultra-high vacuum)

Technique	LEED	XPD/PhD	SXRD	XSW
Incoming beam	Electrons	X-rays	X-rays	X-rays
Typical energy (eV)	50–500	< 1500	≈ 10 000	3000–10 000
Detected signal	Electrons	Electrons	X-rays	Electrons (fluorescence)
Order necessary	Long-range	Identical sites	Long-range	Identical sites
Element-specific	No	Yes	No	Yes
Information obtained	Complete surface structure	Relative position of emitter atom w/r to neighbors	Complete surface structure	Position of emitter atom w/r to bulk lattice
Typical application	Adsorbate superstructures; surface reconstruction; medium-sized unit cell	Small adsorbates (atoms, small molecules) with identical adsorption sites; ordered or lattice gas disorder	Complex surface reconstructions; medium-sized unit cell	Adsorbates (atoms, molecules) with identical adsorption sites or height above surface
Vacuum requirements	UHV	UHV	UHV to bar	UHV to mbar
Laboratory/synchrotron	Laboratory	XPD: laboratory; PhD: synchrotron	Synchrotron	Synchrotron

take into account static and dynamic (thermal) disorder within the sample.

Photoelectrons provide the signal that is normally detected, but other secondary signals, such as Auger electrons or fluorescence, can also be used to determine changes in the photoemission cross section, as long as the measured signal is element-specific.

The standing wave technique has been used very successfully for studying the adsorption geometries of large organic molecules and self-assembled monolayers [7.50, 51]. A very recent new application of XSW is the study of electrochemical interfaces in combination with ambient-pressure XPS analyzers [7.52].

7.1.6 Comparison of Surface Crystallographic Techniques

Table 7.1 summarizes the key properties of the surface crystallographic techniques discussed in the previous sections, together with examples of applications.

7.1.7 Non-Crystallographic Techniques

Scanning probe microscopy and a number of surface spectroscopies are non-crystallographic techniques which provide valuable information about the coordination and orientation of atoms and molecules on surfaces. This information is often used as a starting point to inform the choice of model geometries for crystallographic trial-and-error optimization. Some of the most relevant non-crystallographic techniques are briefly discussed below; details can be found in other chapters of this handbook.

Scanning Probe Microscopy

Scanning probe microscopy techniques such as scanning tunneling microscopy (STM) and atomic force microscopy (AFM) have become standard tools of surface science [7.1]. STM typically reaches lateral resolutions of the order of 1 Å, while the vertical resolution is typically better than 0.1 Å. As STM interacts predominantly with valence electrons, the positions of the atom nuclei are not directly accessible. It is therefore a very useful tool for qualitative surface structure determination and for assessing the degree of long-range order; however, it is difficult to extract accurate crystallographic data, especially for the layers below the uppermost surface layers. Despite this, modeling STM images for structures predicted by density functional theory (DFT) can, to some extent, help in discriminating between different low-energy structures.

Spectroscopic Techniques

The chemical environment of atoms will always affect their electronic and vibrational properties. Therefore, spectroscopies which probe these properties will, in many cases, yield indirect information about the coordination and orientation of atoms and molecules. Chemical shifts in x-ray photoelectron spectroscopy (XPS) and vibrational spectroscopy, as well as selection rules and angular dependencies in infrared (IR), ultraviolet/visible (UV/Vis), and x-ray absorption spectroscopies, are common examples of how spectroscopy can be used to extract crystallographic information. Spectroscopies have the particular advantage that they do not depend on long-range order, in contrast to most diffraction techniques.

7.2 Examples of Surface Geometries

In the following we will discuss some common trends in surface structures of metals with and without adsorbates, and present examples to illustrate these. A full discussion of all surface structures that have been characterized using surface crystallographic methods would far exceed the scope of this chapter. The most complete compilation of crystallographically characterized surface structures is the National Institute of Standards and Technology (NIST) Surface Structure Database (SSD) [7.53]; other compilations are included in [7.17, 54, 55].

7.2.1 Clean Metal Surfaces

The majority of solid elemental metals have either hexagonal close-packed (hcp), cubic close-packed/face-centered cubic (fcc), or body-centered cubic (bcc) crystal structures. For these, the equilibrium crystal shapes are terminated by close-packed facets with low Miller indices: {0001} and $\{10\bar{1}0\}$ for hcp; {111}, {100}, and {110} for fcc; {110} and {100} facets for bcc. Therefore, single-crystal surfaces with these terminations have received most of the attention over the past few decades. Practically all close-packed surfaces of metals which can be prepared and cleaned under ultrahigh vacuum conditions have been characterized in some way with surface crystallographic techniques, mostly LEED *I–V* [7.9, 54, 55]. Some examples are listed in Table 7.2. Most of the clean close-packed metal surfaces show the same two-dimensional periodicity parallel to the surface as the bulk-terminated surface geometry. However, in many cases, the vertical distance between the first few atomic layers (d_{12}, d_{23}, etc.) shows significant deviations from the bulk interlayer distance. Generally, the topmost layer moves closer to the second layer as a means of partially compensating for the missing neighbors at the surface. For the closest-packed surfaces, such as fcc {111} and {100}, hcp {0001}, and bcc {110}, these vertical relaxations are very small, typically less than 2% of the bulk interlayer distance; some metals, such as Al and Pt, even show a slight expansion. The more open fcc {110}, hcp $\{10\bar{1}0\}$, and bcc {100} display significantly larger deviations in the interlayer distances near the surface. Typically they show an oscillatory behavior, with d_{12} contracted by around -10%, d_{23} expanded, and d_{34} contracted again, by a few percent each.

Large-scale lateral reconstructions are found for the late 5d transition metals Ir, Pt, and Au. These include the p(23×1) *herringbone reconstruction* of Au{111} [7.68, 76], the p$(5\times N)$ quasi-hexagonal reconstructions of Au{100} ($N\geq1$) [7.69], Pt{100} ($N=1$) [7.67], and Ir{100} ($N=1$) [7.63, 64], and

Table 7.2 Key geometry parameters for examples of close-packed clean metal surfaces. – indicates that the parameter was not determined (mr = missing-row reconstruction; hb = herringbone reconstruction; hex = quasi-hexagonal reconstruction)

Surface	Superstructure	Δd_{12} (%)	Δd_{23} (%)	Δd_{34} (%)	Method [Ref.]
fcc					
Al{111}	p(1 × 1)	+ 0.8	–	–	LEED [7.56]
Al{110}	p(1 × 1)	− 8.6	+ 5.0	− 1.6	LEED [7.57]
Ni{111}	p(1 × 1)	0.0	–	–	LEED [7.58]
Ni{100}	p(1 × 1)	− 1.0	+ 0.0	–	LEED [7.59]
Ni{110}	p(1 × 1)	− 8.7	+ 3.0	− 0.5	LEED [7.60]
Cu{111}	p(1 × 1)	− 0.3	–	–	LEED [7.61]
Cu{100}	p(1 × 1)	− 1.1	+ 1.7	–	LEED [7.62]
Cu{110}	p(1 × 1)	− 9.1	+ 2.3	–	LEED [7.62]
Ag{110}	p(1 × 1)	− 5.7	+ 2.2	–	LEED [7.62]
Ir{100}	p(5 × 1) (hex)	− 3.6/ − 4.5	+ 1.0/ + 1.3	0.0/ − 0.3	LEED [7.63, 64]
Ir{110}	p(2 × 1) (mr)	− 12.3	− 11.6	− 6.0	LEED [7.65]
Pt{111}	p(1 × 1)	+ 1.0	–	–	LEED [7.66]
Pt{110}	p(2 × 1) (mr)	− 18.4	− 12.6	− 8.4	LEED [7.67]
Au{111}	p(23 × 1) (hb)	–	–	–	SXRD [7.68]
Au{100}	p(5 × 20) (hex)	+20	−1	–	SXRD [7.69]
Au{110}	p(2 × 1) (mr)	− 20.0	+ 2.1	+ 2.1	LEED [7.70]
hcp					
Ru{0001}	p(1 × 1)	− 2.3	–	–	LEED [7.71]
Re{0001}	p(1 × 1)	− 4.3	+ 2.3	− 1.7	LEED [7.72]
Re{10$\bar{1}$0}	p(1 × 1)	− 17.0	+ 1.5	–	LEED [7.73]
bcc					
W{110}	p(1 × 1)	0.0	–	–	LEED [7.74]
W{100}	p(1 × 1)	− 6.0/ − 8.0	–	–	LEED [7.74, 75]

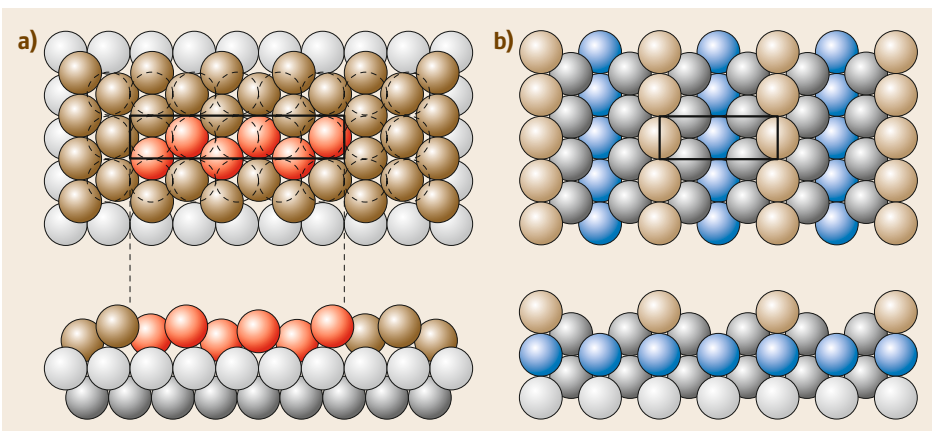

Fig. 7.14a,b Schematic structures of the Ir{100}-p(5 × 1) quasi-hexagonal reconstruction **(a)** and the Ir{110}-2 × 1 missing-row reconstruction **(b)**. *Top*: top view; *bottom*: side view; the *rectangles* indicate the surface unit cells

p(2 × 1) *missing-row* reconstructions of Ir{110} [7.65], Pt{110} [7.67], and Au{110} [7.43, 77]. Both the herringbone reconstruction and the quasi-hexagonal reconstruction lead to a denser packing of atoms within the topmost layer, at the expense of some of the coordination with atoms in the layer below. In the p(5 × 1) superstructure, six first-layer atoms are arranged in the space that would be occupied by five atoms in a bulk-terminated arrangement, as shown in the left panel of Fig. 7.14. In the herringbone reconstruction of gold, the compression is 22 : 23. The missing-row reconstruction (Fig. 7.14b) is also driven by the surface atoms, maximizing their overall lateral coordination, if one considers the slopes as the actual surface rather than the nominal surface plane. All three types of reconstruction show interesting structural changes and roughening

transitions at higher temperatures, which have been studied by SXRD [7.68, 69, 78].

More open single-crystal surfaces of metals with large numbers of low-coordinated atoms are characterized by high surface energies and are therefore normally not exposed in equilibrium-shaped crystals. Nevertheless, they are frequently studied as model systems for low-coordinated sites of nanoparticles [7.79, 80] and/or for chirally modified catalyst surfaces [7.81–84]. Combined quantitative LEED *I–V* and DFT studies of the {531} surfaces of Pt and Cu [7.85–87] showed that these surfaces do not reconstruct, and have lateral arrangements of atoms very similar to bulk termination, except for very strong inward relaxations of the low-coordinated atoms in the topmost layer. On the other hand, theoretical and experimental studies have also shown that Pt{531} is thermally relatively unstable [7.85, 88] and tends to roughen. The structures of several other open Cu, Pd, and Pt surfaces have been studied by LEED *I–V* and DFT, including Cu{211} [7.89], Cu{210} [7.90, 91], Pt{210} [7.92], Cu{311} [7.93], Cu{320} [7.94], Pd{320} [7.95], and Cu{532} [7.96]. Again, these studies report no indications of large-scale lateral reconstructions, which indicates that there is enough space for rearrangement of atoms within the larger unit cells of these open surfaces and no need for expanding the periodicity of the surface. In all these surfaces, however, one finds large relaxations of the under-coordinated atoms, as predicted theoretically [7.97]. STM studies of the clean Cu{643}, Cu{610}, and Cu{5 8 90} surfaces [7.98–100] show high mobility of the Cu surface atoms but, on average, a regular arrangement of kinks and steps.

7.2.2 Small Single-Site Bonded Adsorbates on Metal Surfaces

Atomic adsorbates and small diatomic molecules such as CO, NO, and N_2 only bind to one adsorption site of a metal surface, which can involve one (atop sites) or multiple metal atoms (hollow or bridge sites). The (vertical) bond with the surface is usually covalent for these adsorbates and causes some degree of charge transfer; therefore, (through space) electrostatic interactions and (surface-mediated) charge depletion dominate the lateral forces between the adsorbates, and no direct chemical bonds are formed between them, except when a surface reaction occurs, upon which the reaction product is usually desorbed from the surface.

On close-packed metal surfaces, pure layers of these atoms and molecules typically form well-ordered superstructures with small unit cells, which are often driven by the competition for the most favorable adsorption sites and by maximizing the adsorbate–adsorbate distance. In co-adsorbed systems, lateral interactions are more complicated, but mutual site-blocking is still a factor in the formation of ordered structures. In cases where clean metal surfaces reconstruct, strongly chemisorbed adsorbates tend to lift these reconstructions. Examples are the missing-row reconstruction of Pt{110}, which is lifted by the adsorption of CO [7.101–103], and the herringbone reconstruction of Au{111}, which is lifted by the adsorption of halogens in favor of a much simpler p($\sqrt{3}\times\sqrt{3}$) superstructure [7.104]. Unreconstructed open and stepped metal surfaces, on the other hand, can show large-scale reconstructions and etching, in particular upon adsorption of oxygen. Examples of such oxygen-induced effects are large-scale nanofaceting of open Cu [7.99, 105, 106] and Ir surfaces [7.107], step-bunching of Ni [7.108], Rh [7.109], and Ru surfaces [7.110], and adatom extraction on Ag{110} [7.111, 112].

As the surfaces are well ordered, the unit cells are small, and the adsorbates normally occupy identical adsorption sites, such structures can be easily determined by LEED or PhD. Reference [7.17] provides an excellent critical overview of surface structures of pure and co-adsorbed layers of atoms (e.g., oxygen, nitrogen, sulfur) and small molecules (e.g., CO, NO, NH_3) relevant to heterogeneous catalysis which had been determined before 1998.

More recent examples are the co-adsorption structures of CO and oxygen or hydrogen on Ni{111} [7.14, 113]. The former is shown in Fig. 7.6 of the previous section. It shows that both adsorbates lead to an expansion of the first substrate layer distance, d_{12}, which depends on the strength of the chemisorption bond (greater for O than for CO). In the clean surface, the first layer of the metal substrate is bulk-terminated with an interlayer distance of $d_{12} = 2.04$ Å (Table 7.2).

7.2.3 Chemisorbed Molecular Adsorbates with Strong Intermolecular Interaction

Larger molecules, in particular those with relevance to biology, often show attractive lateral interactions on surfaces, which are due to hydrogen or ionic bonds. This leads to an interesting competition between the vertical molecule–substrate and the lateral molecule–molecule bonds, which affects the complexity of the adsorption geometry (size of unit cell, adsorption sites) as well as the strength and chemical composition of the adsorbate layer. In the following sections we will concentrate on two groups of molecular adsorption systems which have been covered relatively well by surface crystallographic methods, water and amino acids.

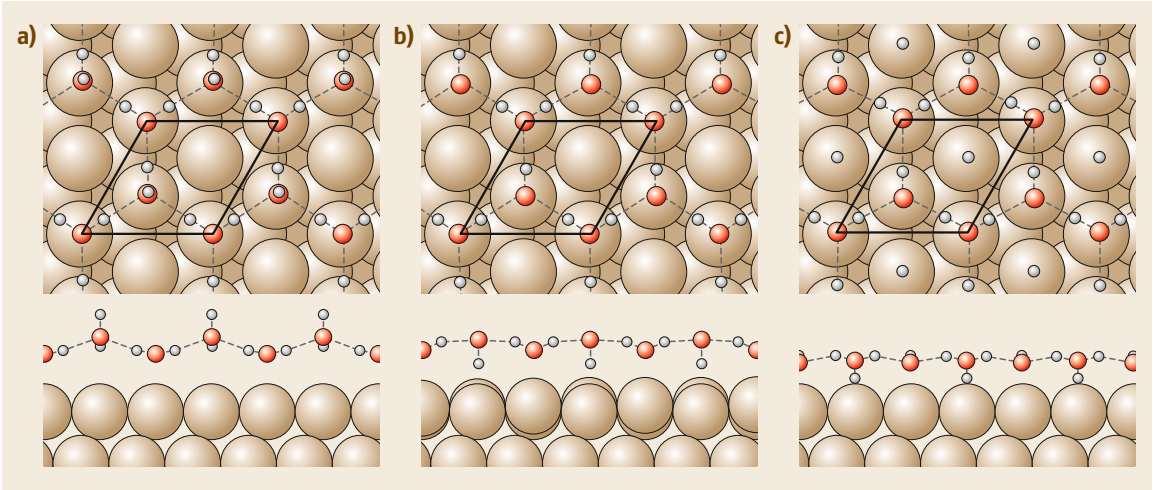

Fig. 7.15a–c Structures of two variants of water bilayers, H-up **(a)** and H-down **(b)**, and an H_2O-OH-H overlayer **(c)** on a hexagonal metal surface. The parallelogram indicates the surface p($\sqrt{3}\times\sqrt{3}$)R30° unit cell (Reprinted with permission from [7.114] Copyright 2004 by the American Physical Society)

Water

The adsorption of water on metal surfaces has been studied extensively since the early days of surface science, owing to its relevance to many fields ranging from catalysis and corrosion to bio-inorganic interfaces [7.115–117]. As water molecules form strong hydrogen bonds in liquid water and ice, it was at first assumed that the observed superstructures on hexagonal close-packed metal surfaces were essentially two-dimensional ice layers, consisting of a bilayer of H_2O molecules arranged in puckered hexagons, as shown in Fig. 7.15a,b. A combination of surface crystallography (LEED), spectroscopy (XPS, RAIRS), and DFT modeling revealed, however, that in many cases, water partially dissociates. In the dissociated layer, the oxygen atoms have a similar arrangement as in the water bilayer, but the chemical composition of the adsorbed layer is a mixture of H_2O, OH, and H [7.114, 118–121].

The simplest of these structures has a p($\sqrt{3}\times\sqrt{3}$)R30° superstructure, as observed on Ru{0001} [7.118, 120] (Fig. 7.15c), but larger unit cells with more complicated structures, such as p(3 × 3) on Pt{111} [7.121] or p($\sqrt{7}\times\sqrt{7}$)R19° on Ni{111} [7.122], have also been observed. The lateral hydrogen bonds and the water–substrate bond are of similar magnitude. As a consequence, the chemical composition and arrangement of atoms at the surface are determined by the details of the molecule–substrate interaction and can be very different even for metal surfaces, which otherwise behave very similarly, such as the Pt group metals [7.123].

Amino Acids and Other Biomolecules

The adsorption of amino acids has been studied in great detail over the past two decades, for two reasons. First, they can be used as chiral modifiers for metal catalysts, and second, they are model systems for bio-inorganic interfaces. All proteins consist of macromolecular chains of amino acids. Therefore, the protein–metal interaction ultimately comes down to the interaction of individual amino acids with a metal surface. Adsorption structures of amino acids have been discussed in several recent reviews [7.5, 84, 124–126]. All amino acids, except glycine, are chiral. The lack of mirror symmetry in the adsorption complex and lateral interactions is usually reflected in the unit cell and the lattice symmetry of ordered superstructures formed by these amino acids. As a consequence, the superstructures of adsorbed layers depend on the chirality (*handedness*) of the molecules [7.5, 126]. Adsorption of amino acids or other organic molecules on copper surfaces can even cause large-scale reconstructions with facets that expose surface termination with chiral symmetry when the adsorbed molecules are chiral [7.127–131].

Despite the relevance of chiral amino acids for the modification of catalyst surfaces, the best-studied amino acid in terms of surface crystallography is the non-chiral glycine. It has been extensively studied by PhD [7.133–136], STM [7.137], and LEED [7.132]. The structure of the ordered p(3 × 2)pg superstructure of glycine on Cu{110}, as determined by LEED *I–V*, is shown in Fig. 7.16. Although the gas-phase molecule is non-chiral, it still forms a chiral adsorption com-

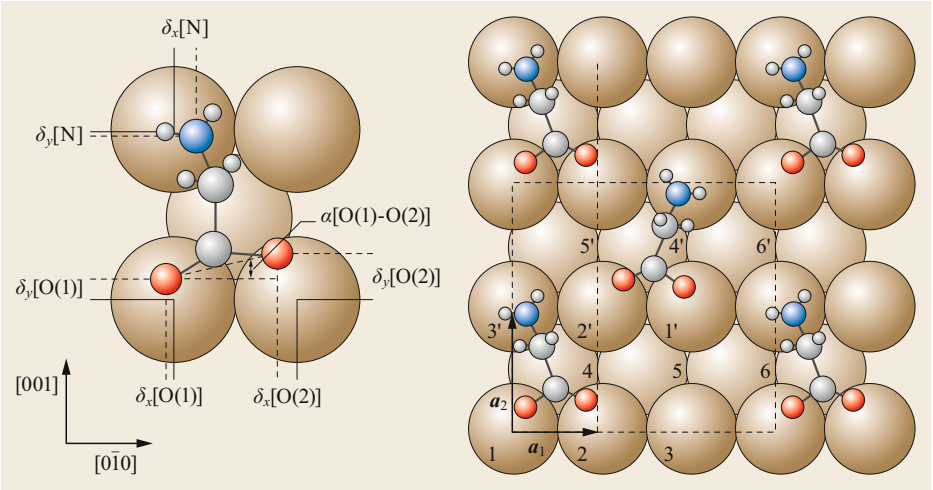

Fig. 7.16 Structure of the p(3 × 2) overlayer of glycine on Cu{110} (Reprinted with permission from [7.132] Copyright 2011 American Chemical Society)

plex, breaking the mirror symmetries of the Cu{110} surface, parallel to the [100] and [1$\bar{1}$0] directions. The unit cell contains two molecules with opposite handedness, resulting in an overall glide-line symmetry of the adsorbate layer. The latter leads to missing spots in the LEED pattern, which enables a very accurate determination of the structure [7.132, 135]. The adsorption geometry is prototypical for amino acid adsorption. The molecules are deprotonated and form a total of three bonds each with Cu atoms through the two oxygens of the carboxylate group and the nitrogen of the amino group. Their arrangement on the surface is such that each molecule is involved in four hydrogen bonds between the amino and carboxylate groups of neighboring molecules, which account for about one third of the adsorption energy [7.138]. Similar adsorption geometries with respect to the substrate are expected for other amino acids on Cu and Ag surfaces, based on crystallographic and spectroscopic data and theoretical predictions. The superstructures do, however, vary due to different sizes of the molecules and different hydrogen bonding configurations [7.5, 126].

Besides amino acids, the adsorption complexes of a small number of other bio-related molecules adsorbed on Cu surfaces have also been studied by PhD and XPD. These include the nucleobases cytosine [7.139], thymine [7.140], and uracil [7.136], which only adsorb with no or poor long-range order, thus making LEED analysis difficult, and tartaric acid [7.28], which does show good long-range order but has not been studied with any other crystallographic method. The latter work, alongside other XPD studies of chiral molecules [7.29], demonstrated that XPD is a very straightforward method for determining the absolute chirality of adsorbed molecules.

On most metal surfaces other than those of group 11, even small organic molecules like glycine do not form long-range ordered structures, nor do they assume identical adsorption sites, which has prevented detailed crystallographic studies on these systems up to now. The adsorption of numerous amino acids and other small biomolecules, in particular on Ni, Pd, and Pt surfaces, has been characterized by means of STM and various spectroscopic techniques [7.141].

7.2.4 Carbon Materials

The adsorption geometries of large aromatic carbon systems are dominated by the interaction of π-electrons with strong contributions of van der Waals interaction. We will discuss three examples here: aromatic molecules, graphene, and C_{60}.

Aromatic Molecules: Benzene and PTCDA

The adsorption of benzene on close-packed metal surfaces is dominated by the interaction between the aromatic π-system and the d-electrons of the metal, which causes the molecules to adsorb parallel to the surface. The late transition metals provide a strong vertical interaction and allow enough mobility for chemisorbed benzene layers to arrange in ordered structures with unit cells that are essentially determined by the repulsive interaction between the molecules. Many ordered overlayer structures of benzene adsorbed on transition metals have been studied by LEED I–V [7.143]. The example of the p($\sqrt{7} \times \sqrt{7}$)R19° structure of benzene on Ru{0001} [7.142] shown in Fig. 7.17 includes the determination of the hydrogen positions, which are usually difficult to determine because of their low scattering cross section. The upward bending of the C–H

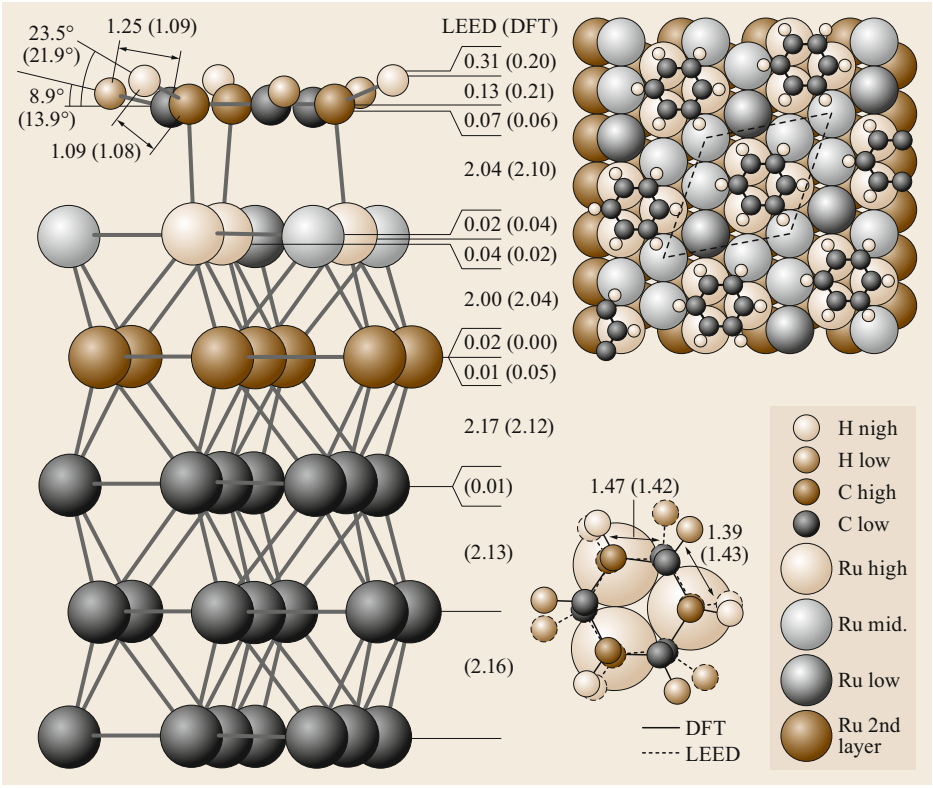

Fig. 7.17 Structure of the $p(\sqrt{7} \times \sqrt{7})R19°$ structure of benzene on Ru{0001} (Figure reprinted with permission from [7.142] Copyright (2001) by the American Physical Society)

bonds agrees well with predictions from DFT modeling, which are also indicated in the figure.

The adsorption of a number of larger aromatic molecules has been studied with surface crystallographic methods as well. The most complete body of work concerns 3,4,9,10-perylene tetracarboxylic dianhydride (PTCDA), which tends to adsorb with its perylene core parallel to the surfaces of weakly bonding metal surfaces [7.144]. On coinage metal surfaces, these molecules form very well long-range ordered structures with unit cells that are generally too large to be analyzed by LEED *I–V*. The adsorption heights of PTCDA above several Au, Ag, and Cu surfaces have been determined by XSW [7.51, 145–151] in combination with DFT modeling and other experimental techniques. It was shown that differences in adsorption heights and bending of the peripheral oxygen atoms correlate with the work function of the bare metal surfaces and, hence, with the charge transfer between substrate and PTCDA [7.51, 151, 152].

Graphene

Graphene could be considered as an infinitely large aromatic molecule. It is certainly one of the most interesting materials that has been discovered in recent years. As a consequence, a large number of surface science studies exist. Graphene can be synthesized relatively easily on close-packed surfaces of the transition metals [7.153, 154]. Depending on the lattice (mis)match between graphene and the substrate surface and on the nature of the graphene–substrate bond, three types of structures are observed on hexagonal surfaces:

- If the lattices of substrate and graphene match (i.e., two-dimensional lattice constants ≈ 2.46 Å), a strong covalent interaction can be expected and a commensurate $p(1 \times 1)$ overlayer is formed. This is the case for Ni{111} [7.155] and Co{0001} [7.156]. The structure of the $p(1 \times 1)$ overlayer of graphene on Ni{111}, as determined by LEED *I–V*, is shown in Fig. 7.18a. The vertical C–Ni distances are 2.11 and 2.16 Å, which indicates strong covalent bonds.
- For metals with larger lattice constants, more complex moire-like superstructures are formed, which manifest themselves through satellite spots around the integer-order spots in LEED. A weak interaction leads to flat graphene layers (Fig. 7.18b) at a vertical distance of ≈ 3.35 Å from the substrate, which is close to the interlayer distance in graphite and indicates that the substrate bond is van der Waals-like. Examples are Pt{111} [7.157] and Ir{111} [7.160], which have been studied by LEED *I–V* and SXRD, respectively.

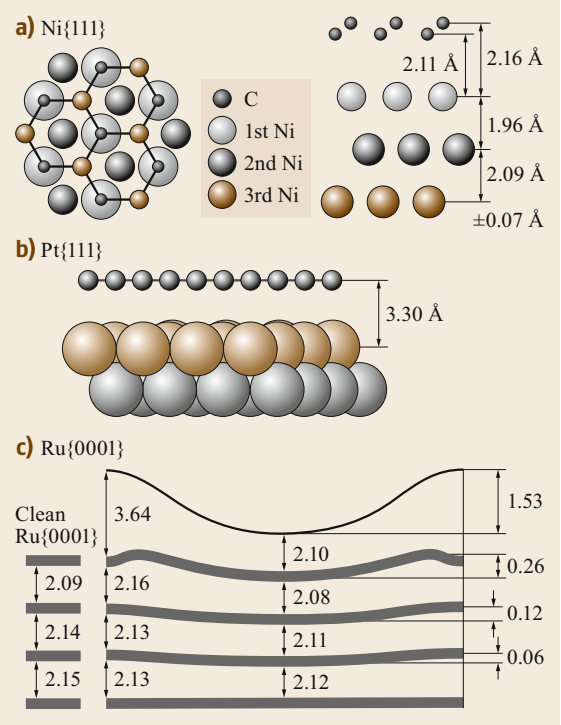

Fig. 7.18 **(a)** Adsorption geometry of the p(1 × 1) structure of graphene on Ni{111} (Reprinted with permission from [7.155] Copyright (1997) of Elsevier). **(b)** Schematic adsorption geometry of graphene on Pt{111} (Reprinted with permission from [7.157] Copyright (2009) of the American Physical Society). **(c)** Adsorption geometry of the p(22 × 22) structure of graphene on Ru{0001}; the numbers indicate the vertical distances at the maxima and minima, as determined by LEED (Reprinted with permission from [7.158] Copyright (2010) by the American Physical Society)

- For metals with larger lattice constants and strong graphene–substrate interaction, the overlayer is strongly corrugated. Examples are the p(9 × 9) overlayer on Re{0001} [7.161] and the p(22 × 22) overlayer on Ru{0001} [7.158]. Within the latter unit cell, the positions of the carbon atoms with respect to the first Ru layer change from hollow to atop sites. The structure, as determined by LEED *I–V* [7.158], is shown in Fig. 7.18c. The graphene layer is strongly corrugated, which is also reflected in the heights of the Ru atoms in the first and second substrate layers, albeit to a lesser degree. The vertical C–Ru distances oscillate between 2.10 (atop sites) and 3.64 Å (hollow sites). This indicates that the bonding varies between covalent and van der Waals, depending on the relative position of the carbon atoms with respect to the Ru layer.

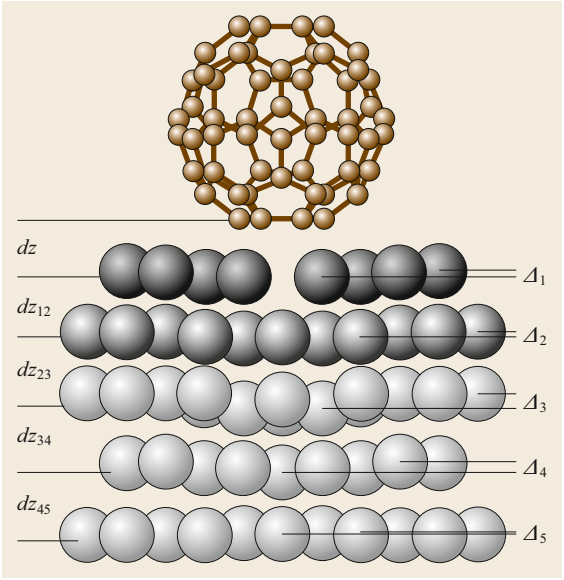

Fig. 7.19 Adsorption geometry of the p($2\sqrt{3} \times 2\sqrt{3}$)R30° superstructure of C_{60} on Ag{111} (Reprinted with permission from [7.159] Copyright (2009) by the American Physical Society)

Thus the growth of graphene on transition-metal surfaces provides an excellent example of how the interplay between lateral interaction (within the adsorbate layer) and adsorbate–substrate bond shapes the structure of the overlayer. In the case of graphene, the lateral C–C bonds are strongly covalent, whereas the substrate bond varies from strongly covalent to relatively weak van der Waals bonding.

Fullerene (C_{60})

The perfect symmetry, the cage structure, and the high stability of fullerenes have attracted significant attention over the past three decades since their discovery. The interaction of C_{60} and other carbon-cage molecules with metal surfaces has been studied extensively as well. On many surfaces, well-ordered superstructures are formed. In terms of surface crystallography, the large size of the molecules certainly poses a challenge; however, the high symmetry helps to reduce the number of independent structural parameters that have to be determined. Adsorption structures of C_{60} on several metal surfaces have been determined at different levels of completeness by XPD [7.25], SXRD [7.162], and LEED *I–V* [7.159, 163]. Figure 7.19 shows the result of a LEED *I–V* structure determination of the p($2\sqrt{3} \times 2\sqrt{3}$)R30° superstructure of C_{60} on Ag{111} [7.159]. The most remarkable finding is that there is an atom missing in the topmost Ag layer, just below the molecule. A similar

substrate vacancy underneath the molecule was found in an SXRD study of the p($\sqrt{13} \times \sqrt{13}$)R13.9° superstructure of C_{60} on Pt{111} [7.162]. For C_{60} on Cu{111}, a structure with as many as seven substrate vacancy sites was recently found by LEED *I–V* study [7.163].
C_{60} is probably the largest adsorbate molecule for which complete structure determinations have been performed to date. The structures clearly demonstrate that even molecules which are generally regarded as weakly interacting with metal surfaces can induce very significant surface reconstructions.

7.3 Conclusion

The accurate determination of atom positions near the surface usually relies on diffraction of either electrons or x-rays with wavelengths of typically ≈ 1 Å. While direct diffraction techniques such as low-energy electron diffraction and surface x-ray diffraction are capable of determining the complete surface structure, these techniques usually require long-range order, and the data analysis can be complicated and ambiguous if the data set is not large enough. Photoelectron diffraction and the x-ray standing wave technique are based on electron and x-ray diffraction, respectively, combined with photoemission (x-ray-induced emission of electrons). As a consequence, these techniques are element-specific and enable the determination of the structural parameters of specific atoms only, which makes them less dependent on long-range order. All the above techniques allow for the determination of atom positions with accuracies at the 0.01–0.1 Å level. The greatest problem in surface crystallography is often the relatively small size of the available data set, which can lead to ambiguities in the resulting structures.

References

7.1 D.P. Woodruff: *Modern Techniques of Surface Science* (Cambridge Univ. Press, Cambridge 2016)
7.2 G. Friedbacher, H. Bubert: *Surface and Thin Film Analysis—A Compendium of Principles, Instrumentation, and Applications* (Wiley-VCH, Weinheim 2011)
7.3 R.L. Park, H.H. Madden: Annealing changes on the (100) surface of palladium and their effect on CO adsorption, Surf. Sci. **11**, 188 (1968)
7.4 E.A. Wood: Vocabulary of surface crystallography, J. Appl. Phys. **35**, 1306 (1964)
7.5 S.M. Barlow, R. Raval: Complex organic molecules at metal surfaces: Bonding, organisation and chirality, Surf. Sci. Rep. **50**, 201–341 (2003)
7.6 G. Held, J. Schuler, W. Sklarek, H.-P. Steinrück: Determination of adsorption sites of pure and coadsorbed CO on Ni(111) by high resolution x-ray photoelectron spectroscopy, Surf. Sci. **398**, 154–171 (1998)
7.7 J.B. Pendry: *Low Energy Electron Diffraction* (Academic Press, New York 1974)
7.8 L.J. Clarke: *Surface Crystallography—An Introduction to Low Energy Electron Diffraction* (Wiley, New York 1985)
7.9 M.A. Van Hove, W.H. Weinberg, C.-M. Chan (Eds.): *Low-Energy Electron Diffraction* (Springer, Berlin, Heidelberg 1986)
7.10 C.J. Davisson, L.H. Germer: Diffraction of electrons by a crystal of nickel, Phys. Rev. **30**, 705 (1927)
7.11 J.B. Pendry: Reliability factors for LEED calculations, J. Phys. C Solid State Phys. **13**, 937–944 (1980)
7.12 M.A. Van Hove, S.Y. Tong (Eds.): *Surface Crystallography by LEED* (Springer, Berlin, Heidelberg 1979)
7.13 K. Heinz, S. Müller, L. Hammer: Crystallography of ultrathin iron, cobalt and nickel films grown epitaxially on copper, J. Phys. Condens. Matter **11**, 9437 (1999)
7.14 W. Braun, H.-P. Steinrück, G. Held: The surface geometry of carbon monoxide and oxygen co-adsorbed on Ni{111}, Z. Phys. Chem. **218**, 915 (2004)
7.15 K. Heinz: Geometrical and chemical restructuring of clean metal surfaces as retrieved by LEED, Surf. Sci. **299/300**, 433 (1994)
7.16 K. Heinz, L. Hammer, S. Müller: The power of joint application of LEED and DFT in quantitative surface structure determination, J. Phys. Condens. Matter **20**, 304204 (2008)
7.17 H. Over: Crystallographic study of interaction between adspecies on metal surfaces, Prog. Surf. Sci. **58**, 249–376 (1998)
7.18 A. Kahn: 30 years of atomic and electronic-structure determination of surfaces of tetrahedrally coordinated compound semiconductors, Surf. Sci. **299/300**, 469 (1994)
7.19 C.S. Fadley: The study of surface structures by photoelectron diffraction and Auger electron diffraction. In: *Synchrotron Radiation Research. Advances in Surface and Interface Science Techniques*, ed. by R.Z. Bachrach (Plenum, New York 1992) pp. 421–518
7.20 H.P. Bonzel: Studies of adsorbed molecules by x-ray photoelectron diffraction (XPD), Prog. Surf. Sci. **42**, 219–229 (1993)

7.21 D.P. Woodruff, A.M. Bradshaw: Adsorbate structure determination on surfaces using photoelectron diffraction, Rep. Prog. Phys. **57**, 1029–1080 (1994)

7.22 G. Held: Photoelectron spectroscopy of metal surfaces for potential heterogeneous catalysis. In: *Techniques, Materials and Applications*, Spectroscopic Properties of Inorganic and Organometallic Compounds, Vol. 42, ed. by J. Yarwood, R. Douthwaite, S. Duckett (Royal Society of Chemistry, London 2011) pp. 1–33

7.23 D.P. Woodruff: Adsorbate structure determination using photoelectron diffraction: Methods and applications, Surf. Sci. Rep. **62**, 1–38 (2007)

7.24 T. Greber, J. Wider, E. Wetli, J. Osterwalder: X-Ray photoelectron diffraction in the backscattering geometry: A key to adsorption sites and bond lengths at surfaces, Phys. Rev. Lett. **81**, 1654–1657 (1998)

7.25 R. Fasel, P. Aebi, R.G. Agostino, D. Naumović, J. Osterwalder, A. Santaniello, L. Schlapbach: Orientation of adsorbed C_{60} molecules determined via x-ray photoelectron diffraction, Phys. Rev. Lett. **76**, 4733 (1996)

7.26 T. Greber, O. Raetzo, T.J. Kreutz, P. Schwaller, W. Deichmann, E. Wetli, J. Osterwalder: A photoelectron spectrometer for k-space mapping above the Fermi level, Rev. Sci. Intrum. **68**, 4549–4554 (1997)

7.27 Y.J. Kim, C. Westphal, R.X. Ynzunza, Z. Wang, H.C. Galloway, M. Salmeron, M.A. Van Hove, C.S. Fadley: The growth of iron oxide films on Pt(111): A combined XPD, STM, and LEED study, Surf. Sci. **416**, 68–111 (1998)

7.28 R. Fasel, J. Wider, C. Quitmann, K.-H. Ernst, T. Greber: Determination of the absolute chirality of adsorbed molecules, Angew. Chem. Int. Ed. **43**, 2853–2856 (2004)

7.29 T. Greber, Z. Sljivancanin, J. Wider, B. Hammer: Chiral recognition of organic molecules by atomic kinks on surfaces, Phys. Rev. Lett. **96**, 56103 (2006)

7.30 M. Treier, P. Ruffieux, R. Fasel, F. Nolting, S. Yang, L. Dunsch, T. Greber: Looking inside an endohedral fullerene: Inter- and intramolecular ordering of Dy3N@C80 (I_h) on Cu(111), Phys. Rev. B **80**, 81403 (2009)

7.31 K.-M. Schindler, V. Fritzsche, M.C. Asensio, P. Gardner, D.E. Ricken, A.W. Robinson, A.M. Bradshaw, D.P. Woodruff, J.C. Conesa, A.R. González-Elipe: Structural determination of a molecular adsorbate by photoelectron diffraction: Ammonia on Ni{111}, Phys. Rev. B **46**, 4836–4843 (1992)

7.32 F. Allegretti, S. O'Brien, M. Polcik, D.I. Sayago, D.P. Woodruff: Adsorption bond length for H_2O on TiO_2(110): A key parameter for theoretical understanding, Phys. Rev. Lett. **95**(22), 226104 (2005)

7.33 F. Allegretti, S. O'Brien, M. Polcik, D.I. Sayago, D.P. Woodruff: Quantitative determination of the local structure of H_{20} on TiO_2(1 1 0) using scanned-energy mode photoelectron diffraction, Surf. Sci. **600**, 1487–1496 (2006)

7.34 W.H. Bragg, W.L. Bragg: The reflection of x-rays by crystals, Proc. R. Soc. A **88**, 428–438 (1913)

7.35 M. von Laue: Zur Optik der Raumgitter, Phys. Z. **14**, 1040–1041 (1913)

7.36 M. von Laue: Zur Optik der Raumgitter, Phys. Z. **14**, 1286–1287 (1913)

7.37 I.K. Robinson: Crystal truncation rods and surface roughness, Phys. Rev. B **33**, 3830–3836 (1986)

7.38 I.K. Robinson: X-ray crystallography of surfaces and interfaces, Acta Crystallogr. A **54**, 772–778 (1998)

7.39 R. Feidenhans'l: Surface structure determination by x-ray diffraction, Surf. Sci. Rep. **10**, 105–188 (1989)

7.40 A. Stierle, J. Gustafson, E. Lundgren: Surface-sensitive x-ray diffraction across the pressure gap. In: *Operando Research in Heterogeneous Catalysis*, Springer Series in Chemical Physics, Vol. 114, ed. by J. Frenken, I. Groot (Springer, Cham 2017) pp. 59–87

7.41 I.K. Robinson: Surface crystallography. In: *Handbook of Synchrotron Radiation*, ed. by D.E. Moncton, G.S. Brown (Elsevier, Amsterdam 1990)

7.42 A.L. Patterson: A direct method for the determination of the components of interatomic distances in crystals, Z. Kristallogr. **90**, 517 (1935)

7.43 I.K. Robinson: Direct determination of the Au(110) reconstructed surface by x-ray diffraction, Phys. Rev. Lett. **50**, 1145–1148 (1983)

7.44 E. Lundgren, C. Zhang, L.R. Merte, M. Shipilin, S. Blomberg, U. Hejral, J. Zhou, J. Zetterberg, J. Gustafson: Novel in situ techniques for studies of model catalysts, Acc. Chem. Res. **50**, 2326–2333 (2017)

7.45 Y. Gründer, C.A. Lucas: Surface x-ray diffraction studies of single crystal electrocatalysts, Nano Energy **29**, 378–393 (2016)

7.46 J. Zegenhagen: Surface structure determination with x-ray standing waves, Surf. Sci. Rep. **18**, 199 (1993)

7.47 D.P. Woodruff: Surface structure determination using x-ray standing waves, Rep. Prog. Phys. **68**, 743 (2005)

7.48 J.C. Woicik: Site-specific x-ray photoelectron spectroscopy using x-ray standing waves, Nucl. Instrum. Methods Phys. Res. A **547**, 227–234 (2005)

7.49 J. Zegenhagen, A. Kazimirov: *The X-Ray Standing Wave Technique—Principles and Applications* (World Scientific, Singapore 2013)

7.50 M. Yu, N. Bovet, C.J. Satterley, S. Bengió, K.R.J. Lovelock, P.K. Milligan, R.G. Jones, D.P. Woodruff, V. Dhanak: True nature of an archetypal self-assembly system: Mobile Au-thiolate species on Au(111), Phys. Rev. Lett. **97**(16), 166102 (2006)

7.51 A. Hauschild, R. Temirov, S. Soubatch, O. Bauer, A. Schöll, B.C.C. Cowie, T.-L. Lee, F.S. Tautz, M. Sokolowski: Normal-incidence x-ray standing-wave determination of the adsorption geometry of PTCDA on Ag(111): Comparison of the ordered room-temperature and disordered low-temperature phases, Phys. Rev. B **81**, 125432 (2010)

7.52 S. Nemsak, A. Shavorskiy, O. Karslioglu, I. Zegkinoglou, A. Rattanachata, C.S. Conlon, A. Keqi, P.K. Greene, E.C. Burks, F. Salmassi, E.M. Gullikson, S.-H. Yang, K. Liu, H. Bluhm,

C.S. Fadley: Concentration and chemical-state profiles at heterogeneous interfaces with sub-nm accuracy from standing-wave ambient-pressure photoemission, Nat. Commun. **5**, 5441 (2014)
7.53 M.A. Van Hove, K. Hermann, P.R. Watson: The *NIST* surface structure database—SSD version 4, Acta Crystallogr. B **58**, 338–342 (2002)
7.54 H. Ohtani, C.-T. Kao, M.A. Van Hove, G.A. Somorjai: A tabulation and classification of the structures of clean solid surfaces and of adsorbed atomic and molecular monolayers as determined from low energy electron diffraction patterns, Prog. Surf. Sci. **23**, 155–316 (1986)
7.55 P.R. Watson: Critical compilation of surface structures determined by low-energy electron diffraction crystallography, J. Phys. Chem. Ref. Data **16**, 953–992 (1987)
7.56 H.B. Nielsen, D.L. Adams: R-factor analysis of the effect of non-structural parameters in LEED, applied to Al(111), J. Phys. C Solid State Phys. **15**, 615–632 (1982)
7.57 J.N. Andersen, H.B. Nielsen, L. Petersen, D.L. Adams: Oscillatory relaxation of the Al(110) surface, J. Phys. C **17**(1), 173 (1984)
7.58 P. Kaukasoina, M. Lindroos, R.D. Diehl, D. Fisher, S. Chandavarkar, I.R. Collins: LEED determination of the structures of Ni(111) and the p(2*2) overlayer of potassium on Ni(111), J. Phys. Condens. Matter **5**, 2875–2886 (1993)
7.59 W. Oed, H. Lindner, U. Starke, K. Heinz, K. Müller: Adsorbate-induced relaxation and reconstruction of c(2x2)O/Ni(100): A reinvestigation by LEED structure analysis, Surf. Sci. **224**, 179–194 (1989)
7.60 D.L. Adams, L.E. Petersen, C.S. Sorensen: Oscillatory relaxation of the Ni(110) surface: A LEED study, J. Phys. C Solid State Phys. **18**, 1753–1766 (1985)
7.61 S.P. Tear, K. Röll, M. Prutton: A comparison of reliability (R) factors in a LEED structural analysis of the copper (111) surface, J. Phys. C Solid State Phys. **14**, 3297–3311 (1981)
7.62 H.L. Davis, J.R. Noonan: Multilayer relaxation in metallic surfaces as demonstrated by LEED analysis, Surf. Sci. **126**, 245–252 (1983)
7.63 A. Schmidt, W. Meier, L. Hammer, K. Heinz: Deep-going reconstruction of Ir(100)-5×1, J. Phys. Condens. Matter **14**, 12353–12365 (2002)
7.64 K. Johnson, Q. Ge, S. Titmuss, D.A. King: Unusual bridged site for adsorbed oxygen adatoms: Theory and experiment of Ir{100}-1×2-O, J. Chem. Phys. **112**, 10460 (2000)
7.65 C.-M. Chan, M.A. Van Hove: Confirmation of the missing-row model with three-layer relaxations for the reconstructed Ir(110)-1×2 surface, Surf. Sci. **171**, 226–238 (1986)
7.66 D.L. Adams, H.B. Nielsen, M.A. Van Hove: Quantitative analysis of low-energy-electron diffraction: Application to Pt(111), Phys. Rev. B **20**, 4789–4806 (1979)
7.67 E.C. Sowa, M.A. Van Hove, D.L. Adams: The missing-row model for the reconstructed Pt(110)-1×2 surface: A leed intensity analysis showing multilayer distortions, Surf. Sci. **199**, 174–182 (1988)
7.68 D.L. Abernathy, D. Gibbs, G. Grübel, K.G. Huang, S.G.J. Mochrie, A.R. Sandy, D.M. Zehner: Reconstruction of the (111) and (001) surfaces of Au and Pt: Thermal behavior, Surf. Sci. **283**, 260–276 (1993)
7.69 B.M. Ocko, D. Gibbs, K.G. Huang, D.M. Zehner, S.G.J. Mochrie: Structure and phases of the Au(001) surface: Absolute x-ray reflectivity, Phys. Rev. B **44**, 6429–6443 (1991)
7.70 W. Moritz, D. Wolf: Multilayer distortion in the reconstructed (110) surface of Au, Surf. Sci. **163**, L655–L665 (1985)
7.71 G. Michalk, W. Moritz, H. Pfnür, D. Menzel: A LEED determination of the structures of Ru(001) and of CO Ru(001)($\sqrt{3}\times\sqrt{3}$)R30°, Surf. Sci. **129**, 92–106 (1983)
7.72 H.A. Etman, Z.V. Zheleva, G. Held, R.A. Bennett: Epitaxial growth of ultrathin palladium films on Re{0001}, J. Phys. Chem. C **115**, 4191–4199 (2011)
7.73 H.L. Davis, D.M. Zehner: Structure of the clean Re(1010) surface, J. Vac. Sci. Technol. **18**, 190–193 (1980)
7.74 M.A. Van Hove, S.Y. Tong: Surface structures of W(110) and W(100) faces by the dynamical LEED approach, Surf. Sci. **54**, 91–100 (1976)
7.75 F.S. Marsh, M.K. Debe, D.A. King: W(001) 1×1 surface structure: Pseudo-relativistic LEED calculations and R-factor analysis, J. Phys. C **13**, 2799–2805 (1980)
7.76 J.V. Barth, H. Brune, R.J. Behm, G. Ertl: Scanning tunneling microscopy observations on the reconstructed Au(111) surface—atomic-atructure, long-range superstructure, rotational domains, and surface-defects, Phys. Rev. B **42**, 9307–9318 (1990)
7.77 D.L. Adams, H.B. Nielsen, M.A. Van Hove, A. Ignatiev: LEED study of the Pt(110)-1×2 surface, Surf. Sci. **104**, 47 (1981)
7.78 D.L. Abernathy, S.G.J. Mochrie, D.M. Zehner, G. Grübel, D. Gibbs: Orientational epitaxy and lateral structure of the hexagonally reconstructed Pt(001) and Au(001) surfaces, Phys. Rev. B **45**, 9272–9291 (1992)
7.79 L. Vattuone, L. Savioa, M. Rocca: Bridging the structure gap: Chemistry of nanostructured surfaces at well-defined defects, Surf. Sci. Rep. **63**, 101 (2008)
7.80 G.A. Somorjai, C. Aliaga: Molecular studies of model surfaces of metals from single crystals to nanoparticles under catalytic reaction conditions. Evolution from prenatal and postmortem studies of catalysts, Langmuir **26**, 16190–16203 (2010)
7.81 C.F. McFadden, P.S. Cremer, A.J. Gellman: Adsorption of chiral alcohols on chiral metal surfaces, Langmuir **12**, 2483 (1996)
7.82 S. Pratt, S.J. Jenkins, D.A. King: The symmetry and structure of crystalline surfaces, Surf. Sci. **585**, L159 (1997)
7.83 S.J. Jenkins, S. Pratt: Beyond the surface atlas: A roadmap and gazetteer for surface symmetry and structure, Surf. Sci. Rep. **62**, 373–429 (2007)
7.84 G. Held, M.J. Gladys: The chemistry of intrinsically chiral surfaces, Top. Catal. **48**, 128–136 (2008)
7.85 S.R. Puisto, G. Held, D.A. King: Energy-dependent cancellation of diffraction spots due to surface roughening, Phys. Rev. Lett. **95**, 036102 (2005)

7.86 S.R. Puisto, G. Held, V. Ranea, S.J. Jenkins, E.E. Mola, D.A. King: The structure of the chiral Pt{531} surface: A combined LEED and DFT study, J. Phys. Chem. B **109**, 22456–22462 (2005)

7.87 G. Jones, M. Gladys, J. Ottal, S.J. Jenkins, G. Held: Surface geometry of Cu{531}, Phys. Rev. B **79**, 165420 (2009)

7.88 T.D. Power, A. Asthagiri, D.S. Sholl: Atomically detailed models of the effect of thermal roughening on the enantiospecificity of naturally chiral platinum surfaces, Langmuir **18**, 3737 (2002)

7.89 T. Seyller, R.D. Diehl, F. Jona: Low-energy electron diffraction study of the multilayer relaxation of Cu(211), J. Vac. Sci. Technol. A **17**, 1635–1638 (1999)

7.90 Ismail, S. Chandravakar, D.M. Zehne: Multilayer relaxation of the Cu(2 1 0) surface, Surf. Sci. **504**, L201–L207 (2002)

7.91 Y.Y. Sun, H. Xu, J.C. Zheng, J.Y. Zhou, Y.P. Feng, A.C.H. Huan, A.T.S. Wee: Multilayer relaxation of Cu(210) studied by layer-doubling LEED analysis and pseudopotential density functional theory calculations, Phys. Rev. B **68**, 115420–115425 (2003)

7.92 X.-G. Zhang, M.A. Van Hove, G.A. Somorjai, P.J. Rous, D. Tobin, A. Gonis, J.M. MacLaren, K. Heinz, M. Michl, H. Lindner, K. Müller, M. Ehsasi, J.H. Block: Efficient determiniation of multilayer relaxation in the Pt(210) stepped and densely kinked surface, Phys. Rev. Lett. **67**, 1298–1301 (1991)

7.93 S.R. Parkin, P.R. Watson, R.A. McFarline, K.A.R. Mitchell: A revised LEED determination of the relaxations present at the (311) surface of copper, Solid State Commun. **78**, 841–843 (1991)

7.94 Y. Tian, J. Quinn, K.-W. Lin, F. Jona: Structure of stepped surfaces: Cu{320}, Phys. Rev. B **61**, 4904–4909 (2000)

7.95 M. Hirsimäki, T. Pitkänen, M. Valden, M. Lindroos, C.J. Barnes: Multilayer relaxation of the Pd(320) surface, Surf. Sci. **454–456**, 6–10 (2000)

7.96 F. Mehmood, A. Kara, T.S. Rahman: First principles study of the electronic and geometric structure of Cu(532), Surf. Sci. **600**, 4501–4507 (2006)

7.97 Y.Y. Sun, H. Xu, Y.P. Feng, A.C.H. Huan, A.T.S. Wee: Multilayer relaxations of (3 1 1), (3 3 1) and (2 1 0) fcc transition metal surfaces studied by pseudopotential DFT calculations, Surf. Sci. **548**, 309–316 (2004)

7.98 X. Zhao, S.S. Perry: Ordered adsorption of ketones on Cu(6 4 3) revealed by scanning tunneling microscopy, J. Mol. Catal. A **216**, 257 (2004)

7.99 P.J. Knight, S.M. Driver, D.P. Woodruff: Scanning tunnelling microscopy investigation of the oxygen induced faceting and "nano-faceting" of a vicinal copper surface, Surf. Sci. **376**, 374 (1997)

7.100 M. Giesen, S. Dieluweit: Step dynamics and step-step interactions on the chiral Cu(5 8 90) surface, J. Mol. Catal. A **216**, 263–274 (2004)

7.101 N. Freyer, M. Kiskinova, G. Pirug, H.P. Bonzel: Site-specific core level spectroscopy of CO and NO adsorption on Pt(110)(1×2) and (1×1) surfaces, Appl. Phys. A **39**, 209–219 (1986)

7.102 N. Freyer, M. Kiskinova, G. Pirug, H.P. Bonzel: Oxygen adsorption on Pt(110)-1×1 and Pt(110)-1×1, Surf. Sci. **166**, 206–220 (1986)

7.103 S. Karakatsani, Q. Ge, M.J. Gladys, G. Held, D.A. King: Coverage-dependent molecular tilt of carbon monoxide chemisorbed on Pt{110}: A combined LEED and DFT structural analysis calculations, Surf. Sci. **606**, 383–393 (2012)

7.104 Z.V. Zheleva, V.R. Dhanak, G. Held: Experimental structure determination of the chemisorbed overlayers of chlorine and iodine on Au{111}, Phys. Chem. Chem. Phys. **12**, 10754–10758 (2010)

7.105 P.J. Knight, S.M. Driver, D.P. Woodruff: Oxygen-induced step-edge faceting; a precursor to (410) planar faceting of Cu(100) vicinal surfaces, Chem. Phys. Lett. **259**, 503–507 (1996)

7.106 P.J. Knight, S.M. Driver, D.P. Woodruff: Missing rows on oxygen-covered Cu(100) vicinal surfaces: A scanning tunnelling microscopy investigation, J. Phys. Condens. Matter **9**, 21–31 (1997)

7.107 I. Ermanoski, K. Pelhos, W. Chen, J.S. Quinton, T.E. Madey: Oxygen-induced nano-faceting of Ir(2 1 0), Surf. Sci. **549**, 1 (2004)

7.108 R. Koch, O. Haase, M. Borbonus, K.H. Rieder: Can oxygen modify step arrangements? STM and LEED investigations on Ni(771), Surf. Sci. **272**, 17–26 (1992)

7.109 G. Hoogers, D.A. King: Adsorbate-induced step-doubling reconstruction of a vicinal metal surface: Oxygen on Rh{332}, Surf. Sci. **286**, 306–316 (1993)

7.110 G. Held, S. Uremovic, D. Menzel: Rearrangement of stepped Ru(001) surfaces upon oxygen adsorption, Surf. Sci. **331–333**, 1122–1128 (1995)

7.111 J. Pal, T.B. Rawal, M. Smerieri, S. Hong, M. Alatalo, L. Savio, L. Vattuone, T.S. Rahman, M. Rocca: Adatom extraction from pristine metal terraces by dissociative oxygen adsorption: Combined STM and density functional theory investigation of O/Ag(110), Phys. Rev. Lett. **118**, 226101 (2017)

7.112 T.B. Rawal, M. Smerieri, J. Pal, S. Hong, M. Alatalo, L. Savio, L. Vattuone, T.S. Rahman, M. Rocca: Deciphering complex features in STM images of O adatoms on Ag(110), Phys. Rev. B **98**, 035405 (2018)

7.113 W. Braun, H.-P. Steinrück, G. Held: The surface geometry of carbonmonoxide and hydrogen coadsorbed on Ni{111}, Surf. Sci. **574**, 193–204 (2005)

7.114 A. Michaelides, A. Alavi, D.A. King: Insight into H_2O-ice adsorption and dissociation on metal surfaces from first-principles calculations, Phys. Rev. B **69**(11), 113404 (2004)

7.115 P.A. Thiel, T.E. Madey: The interaction of water with solid surfaces: Fundamental aspects, Surf. Sci. Rep. **7**, 221 (1987)

7.116 M.A. Henderson: The interaction of water with solid surfaces: Fundamental aspects revisited, Surf. Sci. Rep. **46**, 1 (2002)

7.117 A. Hodgson, S. Haq: Water adsorption and the wetting of metal surfaces, Surf. Sci. Rep. **64**, 381 (2009)

7.118 G. Held, D. Menzel: The structure of the p($\sqrt{3}\times\sqrt{3}$)R30° bilayer of D_2O on Ru(001), Surf. Sci. **316**, 92 (1994)

7.119 P.J. Feibelman: Partial dissociation of water on Ru(0001), Science **295**, 99–102 (2002)

7.120 S.R. Puisto, T.J. Lerotholi, G. Held, D. Menzel: A refined LEED analysis of water on Ru(0001): An exper-

imental test of the partial dissociation model, Surf. Rev. Lett. **10**, 487–492 (2003)
7.121 G. Held, C. Clay, S.D. Barrett, S. Haq, A. Hodgson: The structure of the mixed OH+H_2O overlayer on Pt{111}, J. Chem. Phys. **123**, 64711 (2005)
7.122 M.E. Gallagher, S. Haq, A. Omer, A. Hodgson: Water monolayer and multilayer adsorption on Ni(111), Surf. Sci. **601**, 268–273 (2007)
7.123 A. Shavorskiy, M. Gladys, G. Held: Chemical composition and reactivity of water on hexagonal Pt-group metal surfaces, Phys. Chem. Chem. Phys. **10**, 6150 (2008)
7.124 F. Rosei, M. Schunack, Y. Naitoh, P. Jiang, A. Gourdon, E. Lægsgaard, I. Stensgaard, C. Joachim, F. Besenbacher: Properties of large organic molecules on metal surfaces, Prog. Surf. Sci. **71**, 95 (2003)
7.125 C.J. Baddeley, G. Held: Chiral molecules on surfaces. In: *Comprehensive Nanoscience and Technology*, ed. by D. Andrews, G. Scholes, G. Wiederrecht (Elsevier, Amsterdam 2010) pp. 105–133
7.126 D. Costa, C.-M. Pradier, F. Tielens, L. Savio: Adsorption and self-assembly of bio-organic molecules at model surfaces: A route towards increased complexity, Surf. Sci. Rep. **70**, 449–553 (2015)
7.127 X. Zhao, Z. Gai, R.G. Zhao, W.S. Yang, T. Sakurai: Adsorption of glycine on Cu(001) and related step faceting and bunching, Surf. Sci. **424**, L347–L351 (1999)
7.128 X. Zhao, R.G. Zhao, W.S. Yang: Adsorption of alanine on Cu(001) studied by scanning tunneling microscopy, Surf. Sci. **442**, L995–L1000 (1999)
7.129 X. Zhao: Fabricating homochiral facets on Cu(001) with L-lysine, J. Am. Chem. Soc. **122**, 12584–12585 (2000)
7.130 X. Zhao, R.G. Zhao, W.S. Yang: Scanning tunneling microscopy investigation of L-lysine adsorbed on Cu(001), Langmuir **16**, 9812–9818 (2000)
7.131 Q. Chen, N.V. Richardson: Surface facetting induced by adsorbates, Prog. Surf. Sci. **73**, 59–77 (2003)
7.132 Z.V. Zheleva, T. Eralp, G. Held: Complete experimental structure determination of the p(3×2)pg phase of glycine on Cu110, J. Phys. Chem. C **116**, 618–625 (2012)
7.133 N.A. Booth, D.P. Woodruff, O. Schaff, T. Gießel, R. Lindsay, P. Baumgärtel, A.M. Bradshaw: Determination of the local structure of glycine adsorbed on Cu(110), Surf. Sci. **397**, 258–264 (1998)
7.134 J.-H. Kang, R.L. Toomes, M. Polcik, M. Kittel, J.-T. Hoeft, V. Efstathiou, D.P. Woodruff, A.M. Bradshaw: Structural investigation of glycine on Cu(100) and comparison to glycine on Cu(110), J. Chem. Phys. **118**(13), 6059–6071 (2003)
7.135 R.L. Toomes, J.-H. Kang, D.P. Woodruff, M. Polcik, M. Kittel, J.-T. Hoeft: Can glycine form homochiral structural domains on low-index copper surfaces, Surf. Sci. Lett. **522**, L9–L14 (2003)
7.136 D.A. Duncan, K.M. Bradley, W. Unterberger, D. Kreikemeyer-Lorenzo, J. Robinson, D.P. Woodruff: Deprotonated glycine on Cu(111): Quantitative structure determination by energy-scanned photoelectron diffraction, J. Phys. Chem. C **116**, 9985–9995 (2012)
7.137 Q. Chen, D.J. Frankel, N.V. Richardson: Chemisorption induced chirality: Glycine on Cu {110}, Surf. Sci. **497**, 37–46 (2002)
7.138 G. Jones, S.J. Jenkins, D.A. King: Hydrogen bonds at metal surfaces: Universal scaling and quantification of substrate effects, Surf. Sci. **600**, L224–L228 (2006)
7.139 D.C. Jackson, D.A. Duncan, W. Unterberger, T.J. Lerotholi, D. Kreikemeyer Lorenzo, M.K. Bradley, D.P. Woodruff: Structure of cytosine on Cu(110): A scanned-energy mode photoelectron diffraction study, J. Phys. Chem. C **114**, 15454–15463 (2010)
7.140 F. Allegretti, M. Polcik, D.P. Woodruff: Quantitative determination of the local structure of thymine on Cu(110) using scanned-energy mode photoelectron diffraction, Surf. Sci. **601**, 3611–3622 (2007)
7.141 C.J. Baddeley, T.E. Jones, A.G. Trant, K.E. Wilson: Fundamental investigations of enantioselective heterogeneous catalysis, Top. Catal. **54**, 1348–1356 (2011)
7.142 G. Held, W. Braun, H.-P. Steinrück, S. Yamagishi, S.J. Jenkins, D.A. King: Light-atom location in adsorbed benzene by experiment and theory, Phys. Rev. Lett. **87**, 216102 (2001)
7.143 G. Held, H.-P. Steinrück: Cyclic Hydrocarbons (3.8.7). In: *Physics of Covered Surfaces, A. Adsorbed Layers on Surfaces*, Landolt-Börnstein, New Series III, Vol. 42, ed. by H.P. Bonzel (Springer, Berlin, Heidelberg 2005), Chap. 3.8.7
7.144 F.S. Tautz: Structure and bonding of large aromatic molecules on noble metal surfaces: The example of PTCDA, Prog. Surf. Sci. **82**, 479–520 (2007)
7.145 A. Hauschild, K. Karki, B.C.C. Cowie, M. Rohlfing, F.S. Tautz, M. Sokolowski: Molecular distortions and chemical bonding of a large π-conjugated molecule on a metal surface, Phys. Rev. Lett. **94**, 036106 (2005)
7.146 A. Gerlach, S. Sellner, F. Schreiber, N. Koch, J. Zegenhagen: Substrate-dependent bonding distances of PTCDA: A comparative x-ray standing-wave study on Cu(111) and Ag(111), Phys. Rev. B **75**, 045401 (2005)
7.147 S.K.M. Henze, O. Bauer, T.-L. Lee, M. Sokolowski, F.S. Tautz: Vertical bonding distances of PTCDA on Au(111) and Ag(111): Relation to the bonding type, Surf. Sci. **601**, 1566–1573 (2007)
7.148 M. Rohlfing, R. Temirov, F.S. Tautz: Adsorption structure and scanning tunneling data of a prototype organic-inorganic interface: PTCDA on Ag(111), Phys. Rev. B **76**, 115421 (2007)
7.149 O. Bauer, G. Mercurio, M. Willenbockel, W. Reckien, C.H. Schmitz, B. Fiedler, S. Soubatch, T. Bredow, F.S. Tautz, M. Sokolowski: Role of functional groups in surface bonding of planar π-conjugated molecules, Phys. Rev. B **86**, 235431 (2012)
7.150 G. Mercurio, O. Bauer, M. Willenbockel, N. Fairley, W. Reckien, C.H. Schmitz, B. Fiedler, S. Soubatch, T. Bredow, M. Sokolowski, F.S. Tautz: Adsorption height determination of nonequivalent C and O species of PTCDA on Ag(110) using x-ray standing waves, Phys. Rev. B **87**, 045421 (2013)

7.151 S. Weiß, I. Krieger, T. Heepenstrick, S. Soubatch, M. Sokolowski, F.S. Tautz: Determination of the adsorption geometry of PTCDA on the Cu(100) surface, Phys. Rev. B **96**, 075414 (2017)
7.152 M. Willenbockel, D. Lüftner, B. Stadtmüller, G. Koller, C. Kumpf, S. Soubatch, P. Puschnig, M.G. Ramsey, F.S. Tautz: The interplay between interface structure, energy level alignment and chemical bonding strength at organic–metal interfaces, Phys. Chem. Chem. Phys. **17**, 1530–1548 (2015)
7.153 J. Wintterlin, M.-L. Bocquet: Graphene on metal surfaces, Surf. Sci. **603**, 1841–1852 (2009)
7.154 M. Batzill: The surface science of graphene: Metal interfaces, CVD synthesis, nanoribbons, chemical modifications, and defects, Surf. Sci. Rep. **67**, 83–115 (2012)
7.155 Y. Gamo, A. Nagashima, M. Wakabayashi, M. Terai, C. Oshima: Atomic structure of monolayer graphite formed on Ni(111), Surf. Sci. **374**, 61–64 (1997)
7.156 D. Eom: Structure and electronic properties of graphene nanoislands on Co(0001), Nano Lett. **9**, 2844–2848 (2009)
7.157 P. Sutter, J.T. Sadowski, E. Sutter: Graphene on Pt(111): Growth and substrate interaction, Phys. Rev. B **80**, 245411 (2009)
7.158 W. Moritz, B. Wang, M.-L. Bocquet, T. Brugger, T. Greber, J. Wintterlin, S. Günther: Structure determination of the coincidence phase of graphene on Ru(0001), Phys. Rev. Lett. **104**, 136102 (2010)
7.159 H.I. Li, K. Pussi, K.J. Hanna, L.-L. Wang, D.D. Johnson, H.-P. Cheng, H. Shin, S. Curtarolo, W. Moritz, J.A. Smerdon, R. McGrath, R.D. Diehl: Surface geometry of C60 on Ag(111), Phys. Rev. Lett. **103**, 056101 (2009)
7.160 C. Busse, P. Lazić, R. Djemour, J. Coraux, T. Gerber, N. Atodiresei, V. Caciuc, R. Brako, A.T. N'Diaye, S. Blügel, J. Zegenhagen, T. Michely: Graphene on Ir(111): Physisorption with chemical modulation, Phys. Rev. Lett. **107**, 036101 (2011)
7.161 E. Miniussi, M. Pozzo, A. Baraldi, E. Vesselli, R.R. Zhan, G. Comelli, T.O. Menteş, M.A. Niño, A. Locatelli, S. Lizzit, D. Alfè: Thermal stability of corrugated epitaxial graphene grown on Re(0001), Phys. Rev. Lett. **106**, 216101 (2011)
7.162 R. Felici, M. Pedio, F. Borgatti, S. Iannotta, M. Capozi, G. Ciullo, A. Stierle: X-ray-diffraction characterization of Pt(111) surface nanopatterning induced by C_{60} adsorption, Nat. Mater. **4**, 688–692 (2005)
7.163 G. Xu, X.-Q. Shi, R.Q. Zhang, W.W. Pai, H.T. Jeng, M.A. Van Hove: Detailed low-energy electron diffraction analysis of the (4×4) surface structure of C_{60} on Cu(111): Seven-atom-vacancy reconstruction, Phys. Rev. B **86**, 075419 (2012)

Georg Held

Dept. of Chemistry
University of Reading
Reading, UK

Diamond Light Source Ltd
Didcot, UK
georg.held@diamond.ac.uk

Georg Held is Principal Beamline Scientist at Diamond Light Source and Visiting Professor at the University of Reading. His research interests concentrate on fundamental aspects of heterogeneous catalysis, in particular structure-functionality relationships at surfaces. Key activities are experimental studies of surface geometries and adsorbate-substrate. His current research focuses on the surface chemistry of small bio-relevant molecules and water on metal surfaces, and fundamental aspects of chiral modification of metal catalysts.

8. Local Information with Scanning Tunneling Microscopy

Francesca Moresco

This chapter reviews the main concepts of imaging, spectroscopy, and manipulation by scanning tunneling microscopy, an experimental technique that, since its invention in 1981, has strongly changed surface science and has proven to be much more than an imaging technique. After a historical introduction, we will describe the working principle of scanning tunneling microscopy and the role of tunneling electrons for performing local electron spectroscopy. In the second part of the chapter, we present the different possible manipulation methods that allow us to build structures atom by atom or molecule by molecule. Manipulation with the tip of a scanning tunneling microscope allows us to obtain precise local information about mechanical properties and interactions, and opens the way to applications in atomic-scale technologies.

8.1 Short History

The invention of scanning tunneling microscopy (STM) in 1981 dramatically changed the field of surface science, making it possible for the first time to image conducting surfaces and adsorbates with very high resolution in real space [8.1]. This revolutionary technique for imaging provided in a short time after its invention the first image of atoms of a surface [8.2], the first image of adatoms [8.3], and the first image of a molecule adsorbed at a surface [8.4, 5]. Since that time, STM has become a standard imaging technique, able to solve many problems in surface science and crystallography. The use of tunneling electrons to obtain high-resolution images is accompanied by the possibility of using tunneling electrons in spectroscopy. Scanning tunneling spectroscopy (STS) has proven to be a very useful technique for studying electronic properties of materials and adsorbates locally and with high spatial resolution. STM is presently used in modern surface science in many laboratories worldwide to solve problems related to the structure of conducting and semiconducting surfaces, adsorption processes, excitations at the atomic and molecular scale, on-surface chemistry, and several others [8.6].

The history of STM started in the late 1970s at IBM's research Laboratory in Zürich. Heinrich Rohrer was studying nanometer-size defects on ultrathin insulating films deposited on metal or semiconducting surfaces, important for electronic applications and the development of semiconductor technologies. Looking for an experimental technique able to resolve such defects, he came together with Gerard Binnig to the idea of using the tunnel effect to do microscopy [8.7]. They understood that the exponentially vanishing tunnel current between a very fine metal tip and a conducting surface can give rise to a very powerful tool for imaging nanometer structures with high spatial resolution. With the help of Christoph Gerber, they constructed a simple instrument constructed of a very thin metallic tip that can scan the surface at a few atomic distances. In 1981, the first prototype was working [8.8]. By apply-

M. Rocca, T.S. Rahman, L. Vattuone (Eds.), *Springer Handbook of Surface Science*, Springer Handbooks,
https://doi.org/10.1007/978-3-030-46906-1_8

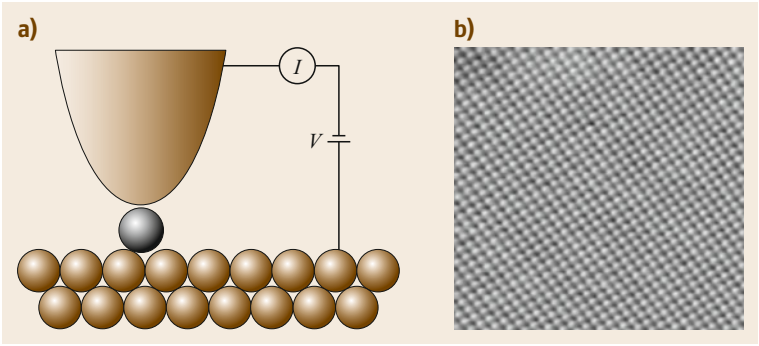

Fig. 8.1 (**a**) Principle of scanning tunneling microscopy. A bias voltage V is applied between metallic tip and conducting sample kept at a few atomic distances, measuring a tunneling current I. (**b**) STM image of the Ag(100) surface with atomic resolution

ing a bias voltage of the order of magnitude of 1 V between tip and surface, a tunneling current of a few nA could be measured, which is strongly dependent on the tip–surface distance, showing an increase of the current of a factor 10 when the tip moves 0.1 nm towards the surface. A schematic view of the working principle of a scanning tunneling microscope is shown in Fig. 8.1a. Soon after, in 1982, the first atomic-resolution images were recorded [8.2]. Karl-Heinz Rieder provided the first samples and experienced with all the inventors the first exciting atomic-resolution images of a surface [8.9]. The scanning tunneling microscope had been invented, opening up a completely new way of doing surface science. Figure 8.1b shows an example of an STM image of the Ag(100) surface with atomic resolution. Heinrich Rohrer and Gerard Binnig won for this invention the Nobel Prize in Physics in 1986.

Besides atomic-resolution imaging, STM also offers the opportunity to use tunneling electrons for spectroscopic investigations. The bias voltage defines not only the direction of electron tunneling, but also the energy of the tunneling electrons. Hence, the different electronic states of the sample can be probed by ramping the bias voltage over the desired energy range. STS was already used in 1986 to probe the electronic density of states around the Fermi level and is now a standard technique in many laboratories [8.10].

Crucial for STM to work is the precise control of the tip position in the three spatial directions. In the first prototypes, the movement of the tip was driven by three piezoelectric elements, as schematically shown in Fig. 8.2. In the following decades, several other geometries were proposed to optimize the tip approach and the scanning over the surface. However, the principle of the instrument did not change and modern STMs are still based on piezoelectric elements driving a thin metal tip.

With the invention of STM, a new adventure could begin, impossible with other microscopy techniques: for the first time it was possible to position exactly a thin metallic tip on a surface with atomic-scale precision, and to be therefore able to touch an atom or a molecule with its tip apex. In this way, the tip apex can be imagined to be the extension of the researcher's finger, touching and modifying atoms and molecules on a surface [8.7]. The invention of STM therefore revolutionized our relationship to matter, not only because it allows us to see matter down to the atomic scale, but also because it opens up a completely new way to build structures atom by atom in a bottom-up approach. With this microscope as a tool, a novel scientific and technological approach began, where molecular structures could be assembled artificially atom by atom. Equipped with STM, scientists have the opportunity to design new molecules and to produce tiny nanomachines.

Extraordinary results have been obtained in the last two decades in imaging individual molecules adsorbed at surfaces and the ultimate spatial resolution of STM [8.11] and atomic force microscopy (AFM) [8.12] has allowed us to gain an exceptional insight into the structure and the intra- and intermolecular bonding of a large number of molecules [8.13, 14]. Besides imaging, STM permits us to probe the electronic, vibrational,

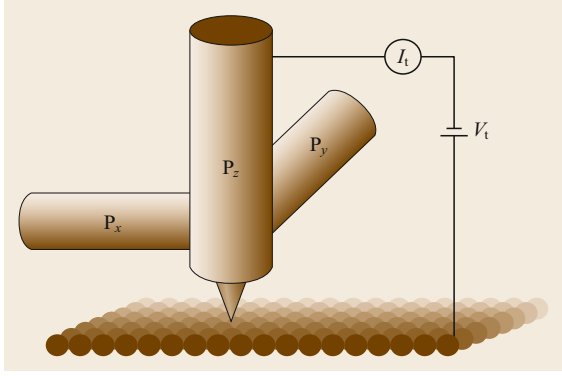

Fig. 8.2 Schematic principle of a STM scanner: A metallic tip is fixed to three piezocrystals (P_x, P_y, P_z). The piezoelectric elements allow a precise positioning of the tip

and optical properties of single atoms and molecules by means of STS and inelastic electron tunneling spectroscopy (IETS) [8.15]. These exceptional advances generate a remarkable improvement in our fundamental understanding of processes occurring at the nanoscale and can now be applied to the controlled fabrication of atomic and molecular devices and to investigate signal transport at the atomic and molecular scale.

Many books [8.16, 17] and reviews [8.1, 6, 18] have been written on STM development, theory, and applications. In this chapter we do not aim at covering the vast range of technical developments and applications that have occurred in STM to make it one of the most important experimental methods in surface science. Instead we want to focus on the basics of imaging, spectroscopy, and manipulation done by STM at low temperature and consider a few examples that can open up new ways for the development of nanoscale electronics and to study mechanics at the molecular level.

8.2 Principles of Scanning Tunneling Microscopy

The working principle of STM is based on the quantum-mechanical tunnel effect, where electrons are able to overcome a potential barrier that would be classically forbidden. The exponential dependence of the transmission coefficient with the barrier width leads to the same dependence of the tunneling current with the tip–surface distance, and is the main reason for the high spatial resolution of this instrument.

A schematic representation of the tunneling process in one dimension (1-D) is shown in Fig. 8.3. If the two electrodes are at the same potential, the tunneling probability would be the same in both directions and the resulting current would vanish. Therefore, a bias voltage must be applied to the tunnel junction to favor one tunneling direction with respect to the other and thereby to induce a measurable tunneling current [8.17]. In Sect. 8.3, the basic principle of the tunneling effect will be explained in more detail, discussing STM imaging, and further details will be given in Sect. 8.4, discussing STS.

To create a two-dimensional image of a surface, a sharp metallic tip is kept at a controlled distance and scanned with a distance of a few tenths of a nanometer over a conductive surface and a bias voltage in the order of 1 V is applied. A tunneling current in the order of nA will be detected in each point, amplified and visualized on a computer display. A feedback loop allows us to control the position of the tip on the surface with respect to the tunneling current. The STM is normally used in one of two different imaging modes: constant

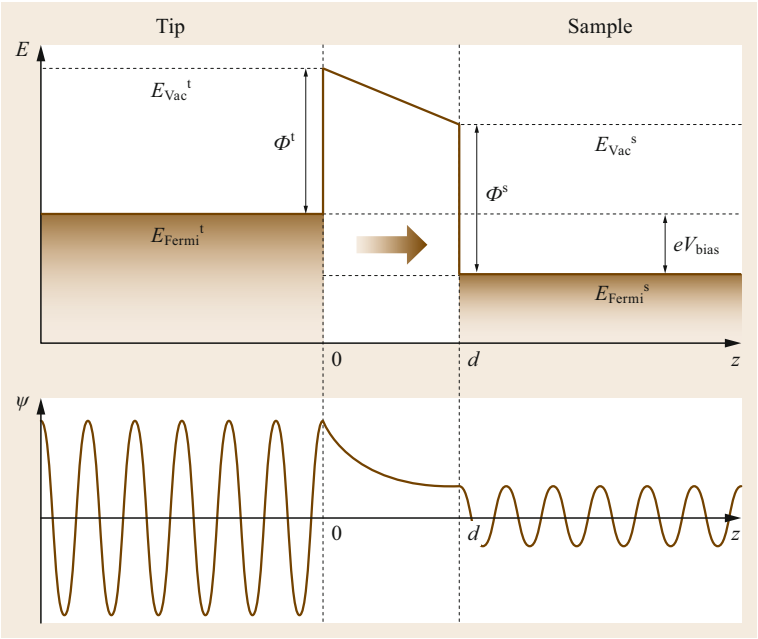

Fig. 8.3 Schematic energy diagram and wave function ψ in one dimension: only the real part of the wave function is imaged. Electrons tunneling from the tip to the sample ($E_{Fermi}^{t/s}$ Fermi energies, $E_{Vac}^{t/s}$ vacuum levels, $\phi^{t/s}$ work functions for tip/sample respectively, V_{bias} bias voltage)

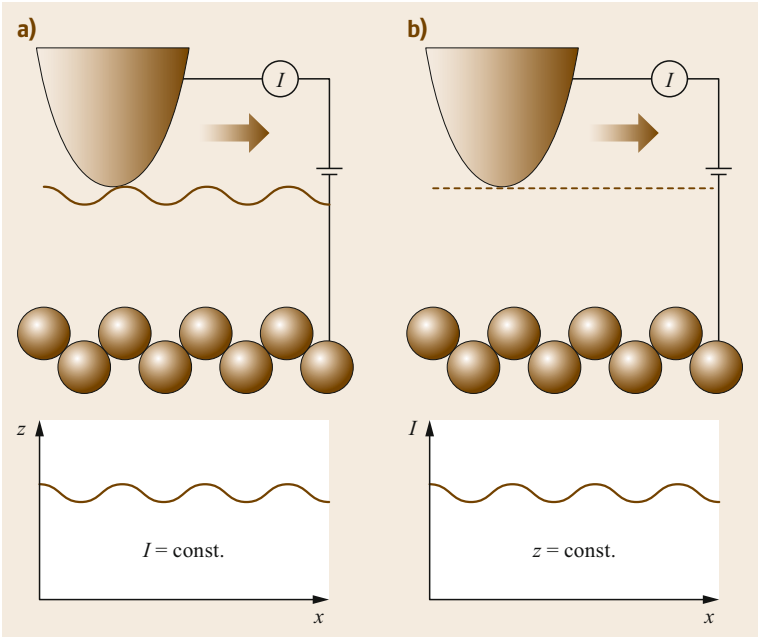

Fig. 8.4a,b Schematic of STM imaging modes: the measurement principles of constant current mode are shown in **(a)**, while constant height mode is depicted in **(b)**. The corresponding measurement signals are shown underneath

current mode and constant height mode, as schematically shown in Fig. 8.4.

In the constant current mode, the tunneling current between the sample and the tip is held constant by the feedback loop. Therefore, the distance between tip and sample remains the same for every point of the image. According to the variations of the sample's topography, the tip height is varied by the feedback loop to keep the current constant and the z-displacement of tip is imaged. In the constant height mode, in contrast, the absolute height of the tip is held constant. In this case the distance between sample and tip changes according to the sample's topography. The resulting changes in tunneling current are imaged. In general, the constant height mode is rarely used and normally only when it is necessary to image the surface very fast, like for example when dynamic processes are studied. The image acquisition time in constant height mode can be in fact considerably lower than in constant current mode, since no feedback related tip height adjustments need to be made. On the other hand, the absence of a feedback loop might easily cause tip crushes into step edges or other defects present on the surface while scanning with constant height. Accordingly, constant height mode is normally applied to small or very flat surface areas [8.17].

Since STM is a surface-sensitive measurement technique, as is common in surface science it is crucial to have an extremely clean surface. Even a very low amount of adsorbed gas molecules strongly influences the STM measurements. At a pressure of 10^{-6} mbar one gas molecule hits each surface unit cell once per second. Even if not every contact leads to surface contamination, these numbers give a rough estimate of the base pressure needed to investigate single molecules on clean metal surfaces. The STM measurements presented in this chapter have been therefore performed in ultrahigh vacuum (UHV) conditions, at a basis pressure $P \approx 10^{-10}$ mbar.

A further problem, especially for experiments with single atoms and molecules, is the diffusion of the investigated adsorbates on the substrate, also considering that STM is a quite slow experimental technique (one needs several minutes for a high-resolution image of a few square nm). Since the diffusion is temperature dependent, STM experiments on single atoms and molecules are mostly conducted at low temperatures (e.g., liquid helium (5 K)). The low temperature has some other beneficial influences on the experiments: the drift of the piezodriven tip is lowered, the base pressure is reduced because of the increased adsorption on the cryostat walls, and the thermal noise is also reduced. Low-temperature STM (LT-STM) at cryogenic temperatures and in UHV conditions allows us to investigate and manipulate single molecules and atomic adsorbates on surfaces with atomic precision, showing moreover a stability of the tip position at the picometer scale.

8.3 Local Imaging

To understand the high spatial resolution of STM, we have to start from the basics of the tunnel effect. Quantum mechanically, electrons are able to tunnel across the barrier given by the surface–tip separation.

In general, the wave function of an electron in a one-dimensional junction with a rectangular barrier (Fig. 8.5) is

$$\psi(z) = \Psi(0)\mathrm{e}^{-kz}\,, \tag{8.1}$$

where

$$k = \frac{\sqrt{2m(V-E)}}{\hbar} \tag{8.2}$$

ψ is the electronic wavefunction, z the tip–sample separation, m the electron mass, V the potential of the barrier, E the energy of the tunneling electron, and $\hbar$ the Planck constant.

The tunneling current I is proportional to the probability distribution of the electron and therefore to the square of the wavefunction

$$I(z) \propto |\Psi(x)|^2 \propto \mathrm{e}^{-kz}\,. \tag{8.3}$$

For small biases, the quantity $(V-E)$ can be approximated as the work function of the metal (≈ 5 eV) [8.19] and therefore the tunneling current changes by about an order of magnitude for every 1 Å change in z. The atomic-scale precision of STM is enabled by this exponential current decay. In other words, this means that the tunneling current is extremely localized under the tip apex, making STM sensitive to both lateral and vertical changes in topography and allowing for atomic resolution. It is also important to note that the macroscopic form of the tip has in STM a secondary importance, being the tunneling current localized under the last atom (or the few last atoms) of the tip.

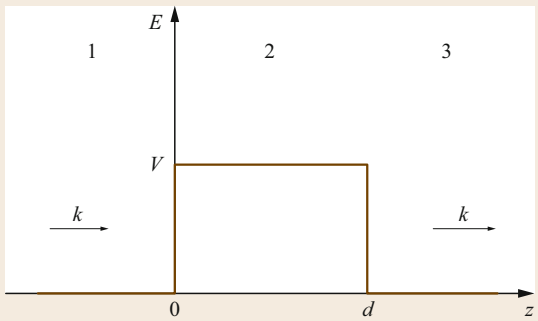

Fig. 8.5 One-dimensional rectangular potential barrier of height V and thickness d

In Fig. 8.6 some examples of STM images on metals and semiconductors are shown. Further examples include molecules adsorbed on metals [8.20], thin insulating films [8.11], or nanostructures adsorbed on oxide thin films [8.21].

To theoretically describe the STM tunneling current in the three-dimensional case and to be able to extract the topographic information from a STM image, further theoretical considerations are needed.

The extension from the one-dimensional to the three-dimensional case can be done following the approach of *Bardeen* [8.22] already published in 1961 and initially applied to the case of two metal plates. He calculated the tunneling matrix element for the electrons tunneling between two weakly coupled electrodes using

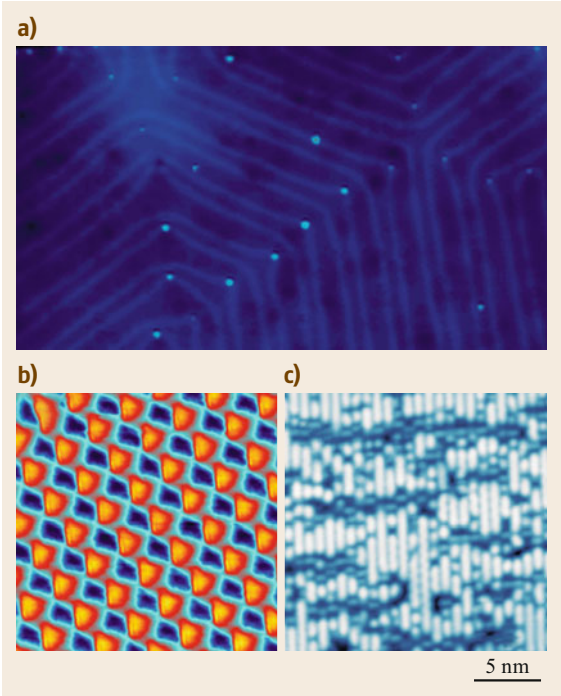

Fig. 8.6a–c Examples of STM images of clean metallic and semiconducting surfaces. **(a)** Au(111) with herringbone reconstruction (image size: 80 nm × 45 nm); **(b)** Ag(100) surface (image size: 2.5 nm × 2.5 nm); **(c)** Si(001)2×1 surface, where dangling bond rows and several defects are visible (image size: 20 nm × 20 nm, I = 30 pA; $V = -2.0$ V)

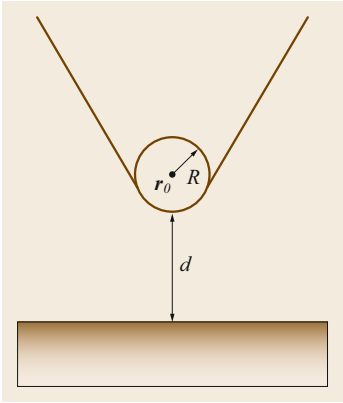

Fig. 8.7 Schematic representation of the geometry of the tunneling junction for a tip with apex radius R in position $\boldsymbol{r}_0$

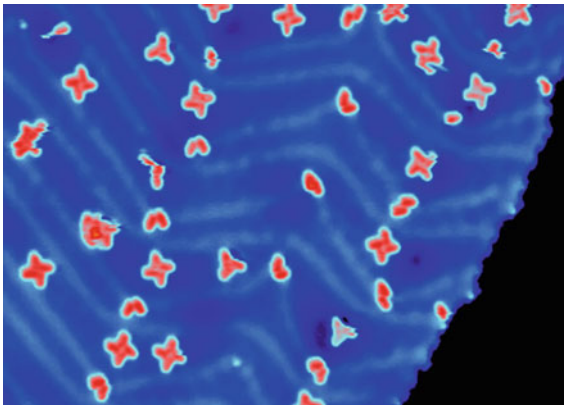

Fig. 8.8 Example of STM image of molecular adsorbates. Acetylbiphenyl molecules adsorbed on Au(111) and forming H-bonded nanostructures (image size 80 nm × 50 nm)

the time-dependent perturbation theory. The resulting tunneling matrix depends on the wave functions of both electrodes (in our case tip and sample).

To calculate the matrix element and consequently the tunneling current we would therefore need to know the wave functions of tip and sample at every point in space. In the case of STM this turns out to be nontrivial, since the atomic structure of the tip is generally unknown. In 1983, *Tersoff* and *Hamann* developed an approximated calculation of the tunneling current in a STM junction [8.23, 24]. They represented the tip by a s-wave function, practically considering only the radial symmetric atomic s-states and a plane sample. The modeled tip has an apex of radius R and the position of the apex is $\boldsymbol{r}_0$ (Fig. 8.7).

Moreover, they assumed a small bias voltage and low temperature. In such an approach, one can rewrite the Bardeen tunneling matrix element and obtain the following expression for the tunneling current I in a three-dimensional STM junction

$$I(z) \propto D_\mathrm{t}(E_\mathrm{Fermi})\rho_\mathrm{s}(\boldsymbol{r}_0, E_\mathrm{Fermi}) \,, \tag{8.4}$$

where $D_\mathrm{t}(E_\mathrm{Fermi})$ is the density of states of the tip per unit volume and $\rho_\mathrm{s}(\boldsymbol{r}_0, E_\mathrm{Fermi})$ is expressed by

$$\rho_\mathrm{s}(\boldsymbol{r}_0, E_\mathrm{Fermi}) = \sum_\mathrm{s} |\psi_\mathrm{s}(\boldsymbol{r}_0)|^2 \delta(E_\mathrm{s} - E_\mathrm{Fermi}) \,, \tag{8.5}$$

which represents the local density of states (LDOS) of the surface at the Fermi energy, at the position of the tip apex, where the sum runs over all involved states.

In other words, the Tersoff–Hamann approximation formally demonstrates that the tunneling current depends on the local electronic density of states of the surface, and not only on the tip–surface distance. This result opens up the way for using STM to study the electronic properties of surfaces and adsorbed molecules (as discussed in detail in Sect. 8.4). In semiconductors and molecules, the tunneling current results from electrons tunneling from the occupied states of the tip through the vacuum barrier into unoccupied states of the surface or vice versa (Fig. 8.3).

The local density of states is normally calculated by density functional theory (DFT) [8.25, 26] and then the tunneling current is determined from it using the Tersoff–Hamann approach. This is a quite simple method that is therefore largely applied. The role of the tip is however completely neglected, limiting the agreement between theory and experiments. For example, the Tersoff–Hamann approach is not able to describe atomic resolution on metal surfaces, the STM images of many atomic and molecular adsorbates, as well as high-resolution STM images with functionalized tips. For a precise theoretical determination of STM images, image charge effects, van der Waals forces, and chemical forces between tip and sample have to be included and demands that we treat the surface–adsorbate–tip system as an entity [8.6].

More sophisticated methods to calculate STM images have been developed that are, however, much more time consuming. In such cases, the tip–adsorbate–surface system is not anymore separated into tip and sample. A total wave function is calculated, where the tunnel junction is considered as a defect in which the electrons are scattered. In this way a scattering matrix can be calculated, which allows us to determine the transmission coefficient, the conductance, and finally the STM images point by point. Some examples of such approaches have been proposed [8.27–29] that are able to precisely determine the tunneling current.

An example of an STM image of molecular adsorbates is shown in Fig. 8.8. As one can see, no intramolecular details are normally visible. The resolution of adsorbed molecules in STM images is normally limited by the strong contribution of the electronic resonances to the tunneling current. This is one of the reasons why the best spatial resolution of molecular adsorbates is obtained by noncontact AFM with a functionalized tip [8.13, 14]. However, as shown in Fig. 8.9, STM images at very low bias voltage and with a tip functionalized with CO can also show submolecular resolution with the possibility to precisely image the molecular structure [8.30, 31]. Similar to the case of AFM, high-resolution molecular images are possible with flat molecules but more difficult with three-dimensional geometrical arrangements.

To conclude this section, the recorded topography STM image is dependent on both the geometric structure and the local density of states of tip and sample. Especially for the case of molecular adsorbates and semiconducting surfaces, the influence of the local density of states on the STM images plays a relevant role. As described in Sect. 8.4, this fundamental property of the STM current signal allows us to use this instrument not only to determine a topographic structure, but also to record the electronic density of states at the position of the tip, thus performing local spectroscopy.

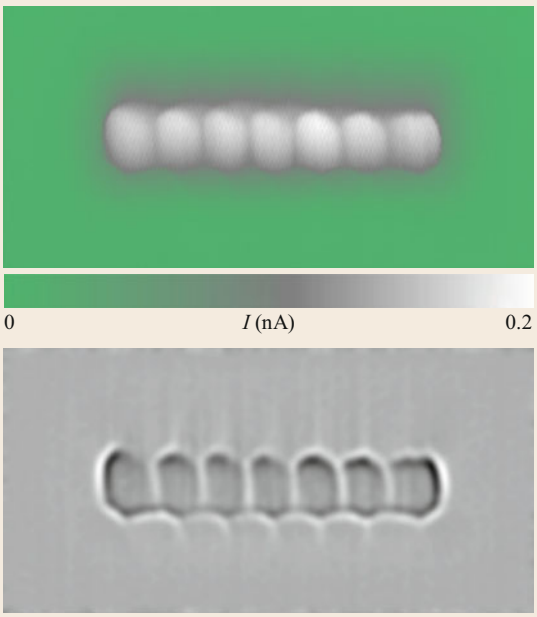

Fig. 8.9 Example of a high-resolution image of a molecular adsorbate, recorded in constant height mode with a CO-functionalized tip. Hexacene on Au(111). The *bottom panel* shows the same image after a Laplace filtering (image size: 1.5 nm × 3.0 nm)

8.4 Local Spectroscopy

A very important aspect of STM is the dependence of the tunneling current on the local density of states. This fundamental property can be applied to locally study the electronic properties of surfaces and adsorbates. Already observed in 1986 [8.10], scanning tunneling spectroscopy (STS) has developed in the last decade as an experimental technique that is commonly applied in many laboratories.

Starting from (8.4) and further following the Tersoff–Hamann approximation, one can conclude that the tunneling current at a small voltage V is obtained by integrating over the electron energy, giving the final result

$$I(\boldsymbol{r}_0, V) = \frac{2\pi}{\hbar} \int_{E_{\mathrm{Fermi}}}^{E_{\mathrm{Fermi}}+eV} \rho_{\mathrm{t}}(\boldsymbol{r}_0, E-eV) \times T(\boldsymbol{r}_0, E-eV)\rho_{\mathrm{s}}(\boldsymbol{r}_0, E)\mathrm{d}E\,, \tag{8.6}$$

where ρ_{t} is the density of states of the tip, ρ_{s} the density of states of the sample, and T the transmission coefficient that depends on the energy of the electrons and on the applied voltage.

From this relation it is straightforward to conclude that the first derivative of the tunneling current is directly proportional to the electronic local density of states of sample and tip at the position of the tip, assuming that the transmission coefficient T varies very slowly with energy. By extracting the first derivative of the tunneling current it is therefore possible to perform local electronic spectroscopy [8.17].

To experimentally obtain the first derivative of the tunneling current, a lock-in amplifier is commonly used, allowing us to measure not only the electronic local density of states at the Fermi energy but also at any other (low) energy. To do this, the bias voltage, defining the energy level, is modulated with a small sinusoidal voltage of a given frequency. This modulation is consequently also superposed onto the tunneling current. The lock-in amplifier can now act as a band pass filter for this frequency and gives the amplitude of the signal related to the modulation. If the modulation is small compared to the bias voltage, the measured amplitude is equal to the derivative of the tunneling current at the bias voltage.

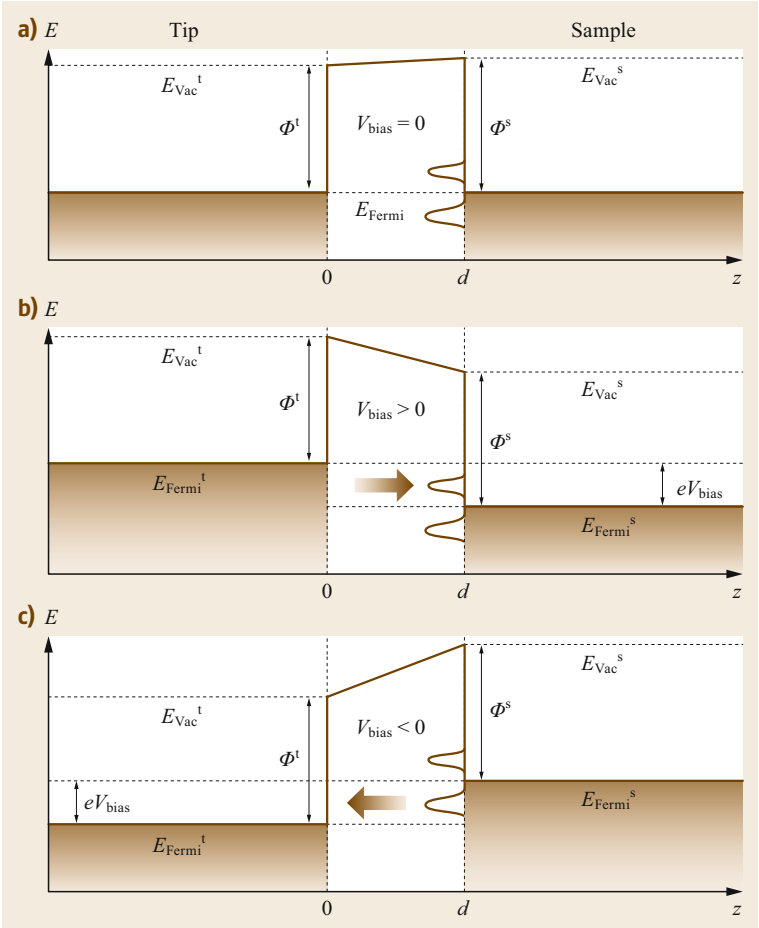

Fig. 8.10a–c Schematic representation of scanning tunneling spectroscopy (STS) **(a)** without bias voltage, **(b)** with positive bias voltage (unoccupied states), **(c)** with negative bias voltage (occupied states)

In more detail, if we consider a modulated bias voltage V_{bias} applied between tip and sample

$$V_{bias} = V_0 + V_{mod}\cos(\omega t)\,, \tag{8.7}$$

where the sinusoidal modulation voltage V_{mod} is typically a few mV, this modulation leads to a corresponding modulation of the tunneling current I with the same frequency. The tunneling current I can be therefore expressed in terms of its Fourier components, with respect to the applied modulation frequency ω,

$$\begin{aligned} &I\left[V_0 + V_{mod}\cos(\omega t)\right] \\ &= I_0 + V_{mod}\frac{\mathrm{d}I(V_0)}{\mathrm{d}V}\cos(\omega t) \\ &\quad + \frac{1}{2}V_{mod}^2\frac{\mathrm{d}^2I(V_0)}{\mathrm{d}V^2}\cos^2(\omega t) + \ldots\,. \end{aligned} \tag{8.8}$$

The first summand I_0 corresponds to the tunneling current in the unmodulated case. The second summand, proportional to $\mathrm{d}I/\mathrm{d}V$, is related to the LDOS of the sample. Its amplitude can be recorded with the aid of a lock-in amplifier tuned to V_0. For small modulation voltages this amplitude is in first approximation proportional to the slope in I/V and consequently to the first derivative of the current, $\mathrm{d}I/\mathrm{d}V$.

In a similar way, it is possible to record the second-derivative signal, obtaining information about the vibrational excitations of a molecule adsorbed on the surface. This kind of spectroscopy is called inelastic electron tunneling spectroscopy (IETS) and was first applied by the group of *Wilson Ho* in 1998 [8.32]. In IETS, the small increase in conductance given by the opening of an inelastic channel due to a molecular vibrational mode can be recorded. Details and applications of IFTS are presented in Chap. 25.

Figure 8.10 shows a schematic of STS for the case of a molecule adsorbed on a metallic surface. At zero bias (Fig. 8.10a), the Fermi levels of substrate and tip are in equilibrium and no tunneling current is measured. The two peaks at the substrate side of the gap symbolize hybridized states related to the highest

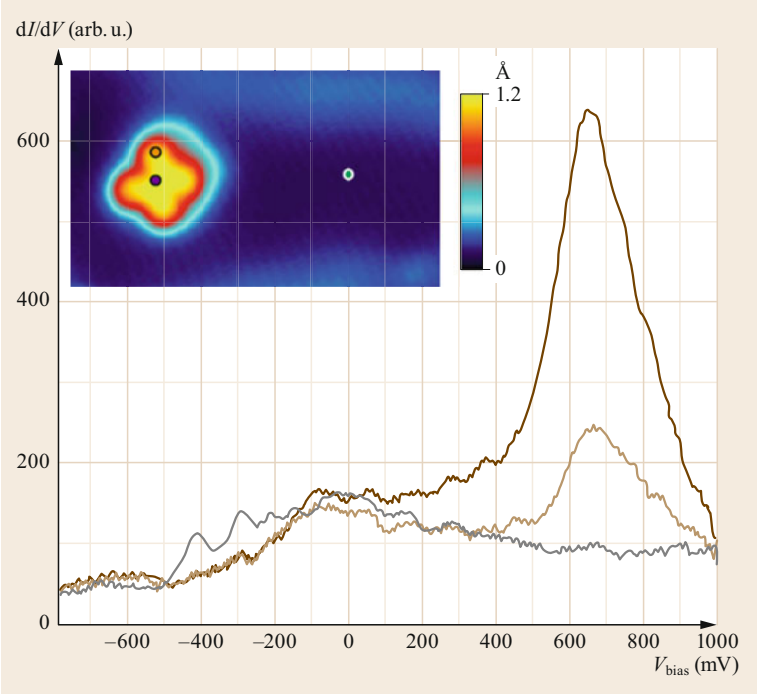

Fig. 8.11 STS spectrum of an aza-BODIPY molecule on Au(111): spectral positions are marked in the STM topography image according to the color code used in the STS graphs (image size: $8 \times 5\,\mathrm{nm}^2$)

occupied molecular orbital (HOMO) and lowest unoccupied molecular orbital (LUMO) of an adsorbed molecule. For positive bias (Fig. 8.10b), the Fermi level of the tip is shifted upward by $|eV_{\mathrm{bias}}|$ and electrons can tunnel from the tip into the unoccupied states of the substrate (including the LUMO of the adsorbate). The tunneling current is determined by the density of unoccupied states of the substrate–adsorbate system within the energy range $|eV_{\mathrm{bias}}|$. For negative bias (Fig. 8.10c), the Fermi level of the substrate is increased by $|eV_{\mathrm{bias}}|$ and hence electrons can tunnel from the occupied states of the sample (including the HOMO of the adsorbate) to the tip. In this case, the tunneling current is determined by the density of occupied states of the substrate–adsorbate system within the energy range $|eV_{\mathrm{bias}}|$.

It is important to note that the electronic resonances of a molecule on a metallic surface are not exactly the HOMO and LUMO orbitals on the molecule in the gas phase, but are slightly shifted in energy and broadened by the interaction with the metallic surface electron continuum and with the tip. Moreover, a mutual electronic coupling of different molecular states through the surface can influence the energy resonances. It is also important to note that it is difficult to compare the HOMO–LUMO gap measured by STS with an optical measured gap, because in the case of STM there is no direct transition of electrons from one orbital to the next [8.11, 33].

Figure 8.11 shows an example of STS spectra recorded on a single aza-BODIPY molecule and on the bare Au(111) surface [8.34]. The spectra recorded on the molecule show a single broad and intense peak centered approximately at $V = 0.7\,\mathrm{V}$ corresponding to unoccupied electronic states. The amplitude of this peak is maximal at the center of the molecule and decreases to the edge. This can be seen by comparing the orange to the violet graph in Fig. 8.11 (see inset for spectra positions). The two spectra are almost identical on the occupied states ($V_{\mathrm{bias}} < 0$), indicating that these states are delocalized over the whole molecule. Furthermore, the absence of peaks and the small difference to the spectrum acquired over bare Au(111) point to a strong hybridization between metal substrate and adsorbate for these states.

In STM experiments, it is also possible to combine the measuring principles of topography and spectroscopy. In this way, one can image the spatial distribution of distinct electronic resonances of surfaces and molecular adsorbates with high spatial resolution. To create such a map of distinct states, the bias voltage is set at the energy of a distinct state (previously determined by $\mathrm{d}I/\mathrm{d}V$ spectroscopy) and the modulation of the bias is switched on. Then the $\mathrm{d}I/\mathrm{d}V$ signal is recorded point by point in parallel to the STM topography signal while scanning the area of interest. Note that due to the modulation period and the limited speed of the feedback loop, the time to measure a $\mathrm{d}I/\mathrm{d}V$ map

is far longer than the time needed for a STM topography image. While a constant current image can be acquired in about 5 min, a dI/dV map takes about 3–6 h. The measurement time strongly depends on the feedback loop and lock-in amplifier parameters. It is common to directly measure the tunneling current during dI/dV maps to be able to detect small changes in the current signal, which indicate a too-high scanning speed.

An example of a dI/dV map of the molecular resonances of a single hexacene molecule adsorbed on Au(111) is shown in Fig. 8.12. The molecule was obtained by surface-assisted reduction of specially designed precursors [8.35, 36]. As one can see, and as similarly observed for several acenes to the length of hexacene [8.37], the interaction of the molecules with the gold surface is weak enough to observe the electronic structure of the molecules with high precision.

Furthermore, it is possible to take a grid of spectra of the desired area. In these measurements a dI/dV spectrum is recorded for each image point. This leads to a data cube where two axes are the coordinates on the sample surface and the third one is given by the applied bias and represents the energy. A dI/dV signal is available at each point of this cube. Being very time consuming however, this technique is only applied if the spectral information is essential for the experiment. Note that this method also provides a dI/dV map at every energy in the range of the spectrum (dependent on spectral resolution) [8.38].

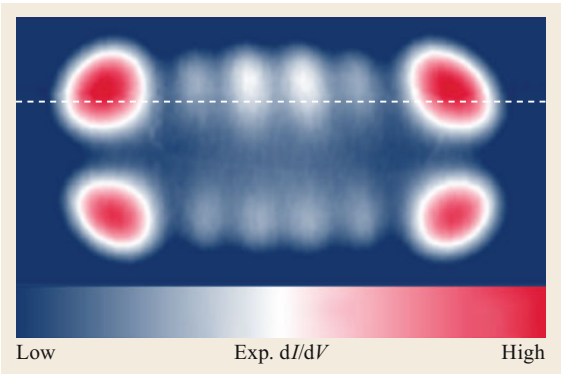

Fig. 8.12 dI/dV map of a single hexacene molecule on Au(111) recorded at a voltage of −0.65 V. The map shows the molecular orbital resonances of hexacene of the molecule on Au(111) (corresponding to the HOMO). Image size: 1.3 nm × 2.6 nm

8.5 Manipulation

STM was invented to image surfaces and adsorbates in real space with an unprecedented resolution and it is successfully used to resolve several problems of surface structure and electronic contrast. However, for many scientists daily working with LT-STM, the most fascinating property of this instrument is the concrete possibility to touch atoms and molecules by means of the STM tip and to modify matter at the nanoscale, constructing new functional structures and new molecules. Already in 1990 the first manipulation experiments were performed [8.39], opening up a completely new way to relate with matter at the atomic and molecular scale. In the following decades, STM was proven to be a versatile tool for atomic-scale manipulation and the construction of nanostructures [8.6, 39–43]. Single atoms and molecules have been precisely positioned by lateral [8.43] or vertical manipulation [8.44]. Different mechanisms of manipulation were developed on metals [8.43], ultrathin insulators [8.45], and semiconductors [8.46]. Voltage pulses are used to desorb [8.47] or dissociate [8.48] molecules, and to induce conformational changes [8.49, 50] or chemical reactions [8.36, 48, 51].

If we consider the kind of tip–sample interaction inducing the manipulation, three different manipulation mechanisms can be distinguished that are schematically shown in Fig. 8.13. In all these cases, it is first of all necessary to exactly position the tip on the adsorbate. Then, different parameters can be varied by selecting the physical principle driving the manipulation. In the first case (Fig. 8.13a) the height of the tip on the surface is reduced and the tip moved over the adsorbate, activating chemical and van der Waals forces [8.43]. In the second case (Fig. 8.13b) an electric field is ap-

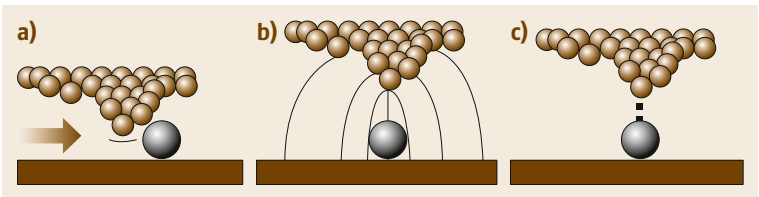

Fig. 8.13a–c Schematic representation of the different mechanisms of manipulation: **(a)** lateral manipulation induced by van der Waals interaction; **(b)** electric-field-induced manipulation; **(c)** manipulation driven by inelastic tunneling electrons

plied by tuning the tunneling current and the applied bias voltage [8.52, 53]. Due to the close distance between tip and surface, electric fields in the range of 10^7 V/cm can be normally applied under the STM tip. Finally, as shown in Fig. 8.13c, the energy of the electrons can be varied, allowing the electrons to perform an inelastic electron-induced manipulation, where the tunneling electrons can lose energy, exciting vibrational, rotational, or electronic resonances that can result in motion. The tunneling current determines the number of electrons tunneling through the tunnel barrier formed by adsorbate and surrounding substrate [8.53]. Using these different mechanisms of interaction, it is possible to perform lateral or vertical manipulation, and to induce chemical reactions, dissociation, or desorption. Vertical manipulation, in particular, is the case of an adsorbate picked up from the surface. The tip is then moved to the desired place and the adsorbate is released. A first case of vertical manipulation in 1991 showed the possibility of reversibly transferring a Xe atom between the tip and the surface [8.44]. However, as vertical manipulation strongly modifies the tip apex and is not always controllable and reversible, it is mostly used to functionalize the STM tip with selected atoms or small molecules, in order to change or increase the tip resolution.

8.5.1 Lateral Manipulation with the STM Tip

Lateral manipulation is commonly considered the lateral displacement of a molecule or an atom adsorbed on a surface, taking advantage of the van der Waals interaction between the adsorbate and the STM tip [8.43]. By lateral manipulation it is possible to controllably move small molecules and single atoms, as well to induce translation and conformational changes in larger molecules.

The standard method for lateral manipulation of single atoms [8.43], single molecules [8.40], or small groups of molecules [8.54] is to use short-range forces between tip and sample, bringing the tip of the STM close to the adsorbate and thereby increasing the tip adsorbate interaction, and then moving the tip to the desired final location on the surface [8.42, 43], as schematically shown in Fig. 8.14. In the first example of a single-atom STM lateral manipulation, Xe atoms were moved one at a time on a metal surface [8.39].

In general, the forces between adsorbate and tip can be attractive or repulsive and this results in different manipulation modes. In all cases, for the manipulation the distance between the tip and the adsorbate is varied in order to tune the force. Typical distances are between 3 and 5 Å. With lateral manipulation exper-

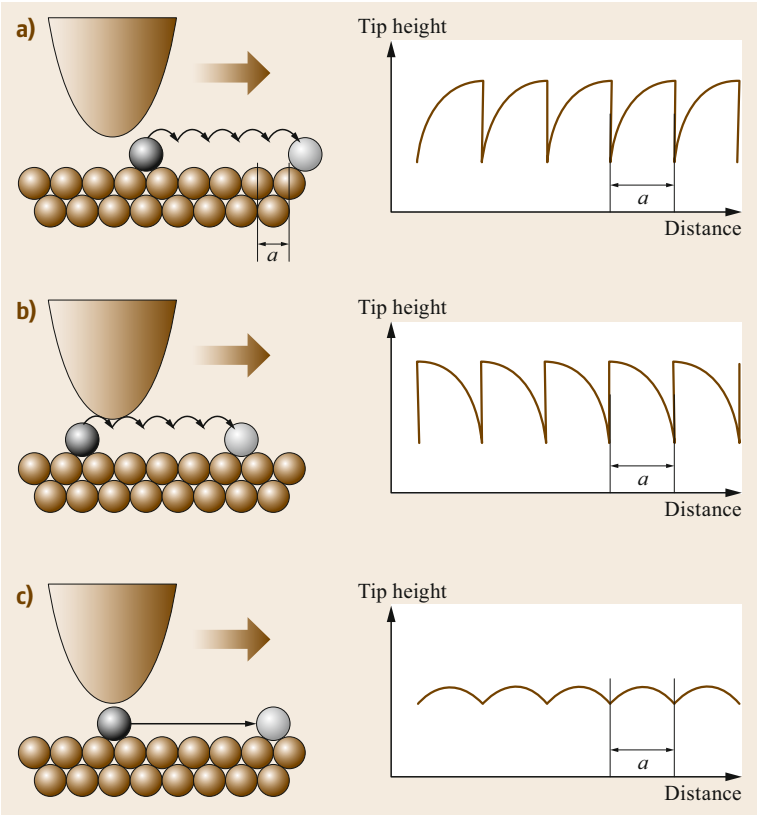

Fig. 8.14a–c The different modes of lateral manipulation: **(a)** pushing, **(b)** pulling, **(c)** sliding

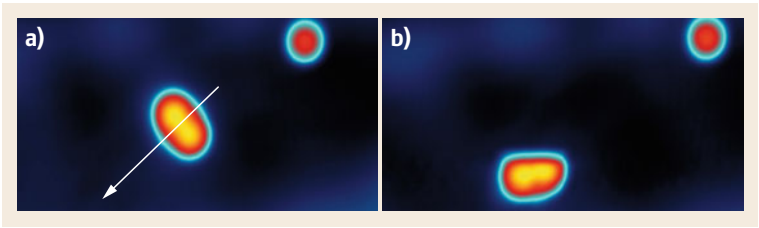

Fig. 8.15a,b Examples of lateral manipulation of a double-wheel molecule. **(a)** STM images before the manipulation; **(b)** STM images after the manipulation. $V = 0.08$ V; $I = 35$ pA; tunneling resistance by lateral manipulation $R = 6$ MW. Image size: $6 \times 3.6\,\mathrm{nm}^2$

iments on single atoms or small molecules, different modes of manipulation such as pushing, pulling, and sliding can be distinguished by measuring the feedback signal during manipulation [8.43]. In particular, by manipulation in constant current mode, detailed information on the process is obtained from the tip height signal, which reflects the interaction between the tip apex and the adsorbate [8.55]. The common procedure includes moving the tip to the desired particle in imaging distance (about 10 Å), then decreasing the distance and moving the tip with the adsorbate to the desired place and subsequently increasing the distance to lose contact. During the process the tip height is recorded. From these curves, different modes of manipulation can be distinguished. Such modes and the corresponding curves are illustrated in Fig. 8.14 [8.43]. In the pushing mode, repulsive forces are used to push the adsorbate in front of the tip across the surface. The tip is moved over the adsorbed particle until a threshold is reached, which induces hopping of the adsorbate away from the tip. In this moment the tip height decreases, before it increases again and the process is repeated. Most of the time, a jumping distance that corresponds to the lattice parameter of the substrate surface can be observed. The pulling and sliding modes make use of attractive forces between tip and adsorbate to perform the manipulation. In the pulling mode the adsorbed particle jumps to the tip, which is why the tip height increases. When the tip is moved further the height decreases until a threshold is reached and the adsorbate jumps below the tip, increasing the height again. In the sliding mode adsorbates are moved continuously across the surface. To achieve this mode, the force between tip and adsorbed particle has to be significantly higher than in the pulling mode. The adsorbate can stay under the tip and does not jump to the energetically favored positions on the surface. The corrugation in the corresponding tip-height trace is due to the atoms on the surface.

A similar procedure can be used to manipulate complex molecules, most of the time also inducing conformational changes [8.40]. In these cases, the manipulation signal that is recorded is normally more complex than for single atoms or small molecules like CO, especially when the molecule presents internal mechanical degrees of freedom. For example, intramolecular conformation changes can be induced during the manipulation of porphyrine-based molecules [8.56]. This type of movement is added to a rigid-like lateral-type motion on the surface, as one can observe from the manipulation signal. Manipulation signals for complex molecules therefore normally do not show the regular periodic modes over long periods observed for single atoms and small molecules. Changes from one mode to another during manipulation are often observed [8.57]. In some cases, manipulation signals do not present any periodicity and the peaks are irregular in intensity, length and shape [8.58]. Molecular flexure and reorientation of the internal conformations play a major role, as well as the reorientation of the molecule relative to the surface. In Fig. 8.15 an example of lateral manipulation of a subphthalocyanine double-wheel molecule is shown. Even if in particular cases the molecular wheels rotate on the Au(111) surface, they are normally pushed by the tip in the same way as smaller adsorbates [8.57].

8.5.2 Manipulation by Electric Field

If the adsorbate is charged or has a dipole moment, electric-field-assisted diffusion is possible. In general, every time a bias voltage is applied between the STM tip and the surface, a static electric field is created. This field can be used to manipulate atoms or molecules. The strength of such an electric field is relatively large, due to the close proximity of the tip to the surface. In a common STM experiment where a bias voltage of about 1 V is applied with a tunneling current of about 1 nA, the electric field between tip and surface has a typical value of 10^8 V/cm and is comparable with the fields experienced by electrons in atoms or molecules. Depending on the tip shape, such an electric field is concentrated in an inhomogeneous way near the tip apex, but its extension can reach hundreds of nanometers. The interaction of an adsorbate with such a strong electric field in the STM junction was first used to position Cs atoms on a semiconductor surface [8.59]. In this case, the inter-

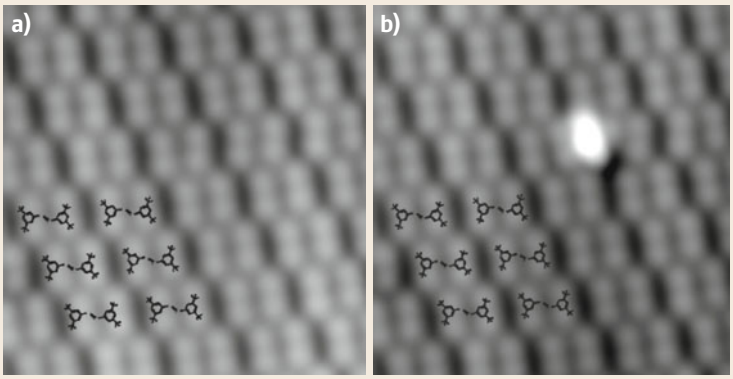

Fig. 8.16a,b **(a)** STM image of a molecular island of *trans*-tetra-*tert*-butylazobenzene molecules on Au(111). **(b)** By applying an electric field, a molecule has been switched to the *cis*-configuration (*bright lobe*)

action between the dipole moment of a Cs atom and the electric field induces a potential energy gradient along the surface, which allows the lateral positioning of single atoms.

Atoms and molecules can be manipulated by electric field even in the limit of zero tunneling current. In such a case, no tunneling current can be measured between tip and sample, but an electric field is present, which is able to manipulate molecules showing a dipole moment. Another kind of electric-field-induced manipulation is possible when the applied voltage overcomes the value of the work function of the tip or the surface and electrons are therefore field emitted [8.60].

The reversible isomerization of azobenzene derivatives by means of the electric field has been demonstrated [8.61]. A detail of that experiment is shown in Fig. 8.16. The *trans–cis* isomerization of 3,3′,5,5-tetra-*tert*-butylazobenzene, an azobenzene molecule carrying four lateral *tert*-butyl groups, can be reversibly induced on Au(111). The relationship between the applied bias voltage necessary for switching and the tip height shows that the process is caused by the electric field between the STM tip and the sample surface.

8.5.3 Manipulation by Inelastic Tunneling Electrons

Inelastic electron-tunneling-induced manipulation is a process where tunneling electrons are injected from the tip positioned above the adsorbed molecule, thus moving it. The electron energy is normally transferred through an excited state, leading to excitation (rotational, vibrational, or electronic), the rate of which is controlled by the applied bias and the tunneling current [8.18].

Experimentally, electron-tunneling-induced manipulation is realized by positioning the STM tip above the molecule at a fixed height. The feedback loop is switched off and tunneling current and/or voltage are increased from imaging to manipulation parameters. The electrons can be injected either from the tip or from the substrate depending on the bias polarity. The moment where a change happens is determined by monitoring the tunneling current versus time. A sudden change in current is indicative of the success of the manipulation. These sudden changes are caused by changes in the apparent height of the molecule either

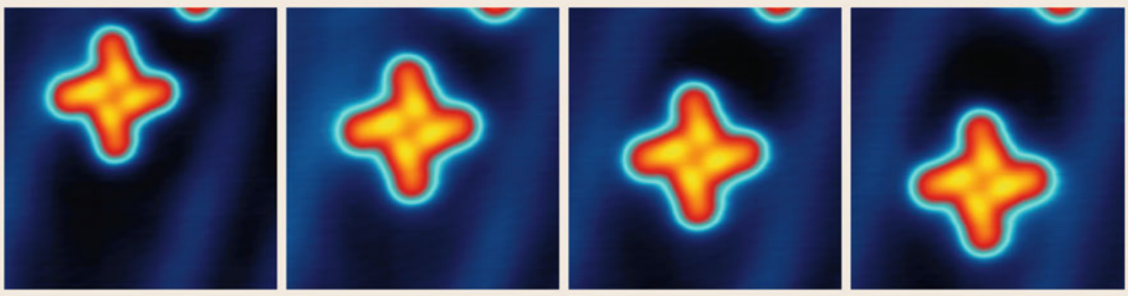

Fig. 8.17 Electronically controlled manipulation by inelastic tunneling electrons. The structure composed of four molecules can be translated by voltage pulses. Series of images after voltage pulses of 2.3 V, 1.7 nA, 10 s. Image size $7 \times 7\,\mathrm{nm}^2$

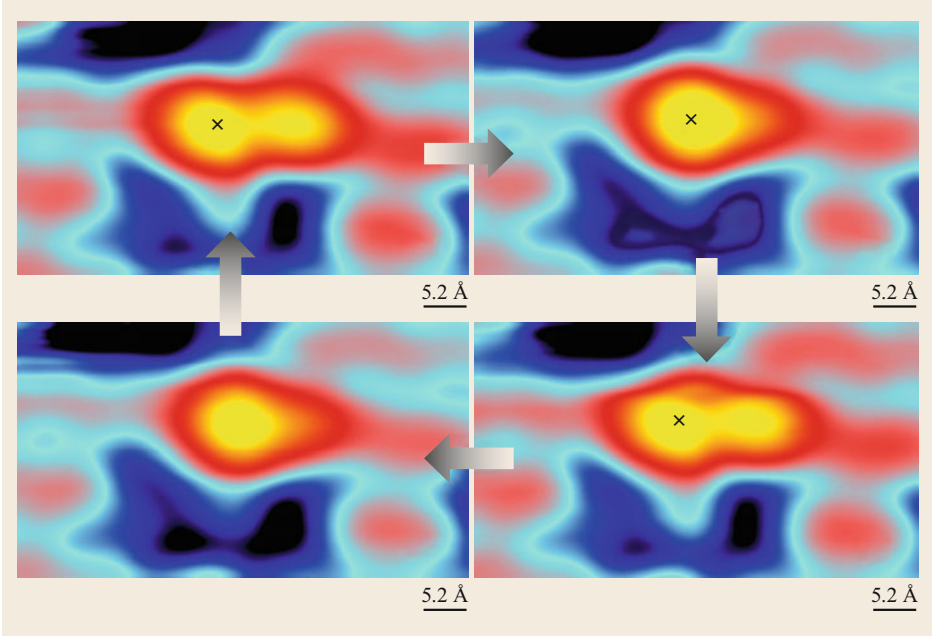

Fig. 8.18 Reversible switching of an acetylbiphenyl molecule anchored on a Si(100) dangling bond. The *crosses* indicate the position of the tip during voltage pulses of −2.6 V

through the motion of the molecule or through a modification of this electronic structure [8.62].

Electron tunneling can be used for example to induce the controlled rotational switching of a molecular motor [8.63]. A molecular motor adsorbed on a gold surface can be rotated in a clockwise or anticlockwise direction by selective inelastic electron tunneling through different subunits of the motor.

Recently, it was demonstrated that by electron-tunneling-induced manipulation it is possible to move in a controlled way supramolecular structures [8.64]. By applying voltage pulses just on one selected molecule of the structure, the complete supramolecular assembly moves to a chosen position on the surface without being destroyed (Fig. 8.17). Moreover, by moving the same nanostructure it is possible to collect a gold adatom and to rotate or translate it by manipulating the molecular structure [8.65]. With the help of theoretical calculations one can determine the work done by the nanostructure to move the atom.

The reversible switching of an acetylbiphenyl molecule on the Si(100) surface can be induced by inelastic tunneling electrons, proving the principle of an electrically driven molecular latch, able to passivate and depassivate Si dangling bonds. As one can see in Fig. 8.18, the molecule can be switched from its native surface conformation with two lobes to a one-lobe conformation and back by applying voltage pulses.

8.6 Outlook

As described in this chapter, extraordinary results have been obtained in the last decades in imaging individual molecules adsorbed on surfaces, and the high spatial control and resolution of STM has allowed us to gain an exceptional insight into the structure and the intra- and intermolecular bonding of a large number of molecules. Since the pioneering works of D. Eigler, many different methods to control the manipulation of atoms and molecules with a STM tip have been developed. Mechanical interaction, tunneling current, bias voltage, and enhanced electric field are the main means to modify the position or the conformation state of a molecule. Tip height and current signal recorded during the manipulation process provide detailed information on the molecular movement, and conformational molecular switches can be operated by manipulation [8.40].

The mechanics of single molecules have been investigated extensively in the last years. In particular, atomic and molecular manipulation allows us today to create new molecules and nanostructures on a surface, and to investigate mechanics at the molecular scale. The next step is now to construct complex mechanical machines molecule by molecule [8.66]. Single-molecule motors working collectively in a synchronous manner

will represent a milestone for nanotechnology. To this aim, a deep understanding of processes and laws governing transmission of motion from molecular motors to molecules and from molecule to molecule is demanded and will be the focus of research in the next years.

Additionally, besides imaging, STM permits us to probe the electronic, vibrational, and optical properties of single atoms and molecules by studying the details of the tunneling current of its derivatives. These exceptional advances generate a remarkable improvement in our fundamental understanding of processes occurring at the nanoscale and can now be applied to the controlled fabrication of atomic and molecular devices and to investigate signal transport at the atomic and molecular scale. The possibility to replace solid-state transistors with molecular electronic devices in ultraminiaturized circuits is a fascinating perspective. Serious limitations of this approach are the low conductance and low power gain of a molecular device, together with the problem of tunneling leakage currents that can exist between the devices and between the interconnections. An alternative approach is to develop an atomic-scale technology, where surface electronic circuits are constructed by manipulating atoms of a passivated semiconductor surface, opening up the way to new approaches to quantum computation [8.67]. In this framework, STM will be a fundamental tool for the development of new electronic technologies at the atomic scale, building structures one by one and addressing them with tunneling electrons.

References

8.1 G. Binnig, H. Rohrer: Scanning tunneling microscopy – From birth to adolescence, Rev. Mod. Phys. **59**, 615–625 (1987)

8.2 G. Binnig, H. Rohrer, C. Gerber, E. Weibel: 7 × 7 reconstruction on Si(111) resolved in real space, Phys. Rev. Lett. **50**, 120–123 (1983)

8.3 D.M. Eigler, P.S. Weiss, E.K. Schweizer, N.D. Lang: Imaging Xe with a low-temperature scanning tunneling microscope, Phys. Rev. Lett. **66**, 1189–1192 (1991)

8.4 J.K. Spong, H.A. Mizes, L.J. LaComb Jr, M.M. Dovek, J.E. Frommer, J.S. Foster: Contrast mechanism for resolving organic molecules with tunnelling microscopy, Nature **338**, 137–139 (1989)

8.5 J.K. Gimzewski, E. Stoll, R.R. Schlittler: Scanning tunneling microscopy of individual molecules of copper phthalocyanine adsorbed on polycrystalline silver surfaces, Surf. Sci. **181**, 267–277 (1987)

8.6 K. Morgenstern, N. Lorente, K.-H. Rieder: Controlled manipulation of single atoms and small molecules using the scanning tunnelling microscope, Phys. Status Solidi (b) **250**, 1–81 (2013)

8.7 C. Joachim, L. Plévert: *Nanosciences: The Invisible Revolution* (World Scientific, Singapore 2009)

8.8 G. Binnig, H. Rohrer, C. Gerber, E. Weibel: Surface studies by scanning tunneling microscopy, Phys. Rev. Lett. **49**, 57–61 (1982)

8.9 K.-H. Rieder: "Oh yes, oh yes, these are the atoms!" A personal recollection from the times of the invention of the STM, Chimia **66**, 8–9 (2012)

8.10 J.A. Stroscio, R.M. Feenstra, A.P. Fein: Electronic structure of the Si(111)2×1 surface by scanning-tunneling microscopy, Phys. Rev. Lett. **57**, 2579–2582 (1986)

8.11 J. Repp, G. Meyer, S.M. Stojković, A. Gourdon, C. Joachim: Molecules on insulating films: Scanning-tunneling microscopy imaging of individual molecular orbitals, Phys. Rev. Lett. **94**, 026803 (2005)

8.12 F.J. Giessibl: Advances in atomic force microscopy, Rev. Mod. Phys. **75**, 949–983 (2003)

8.13 N. Pavliček, L. Gross: Generation, manipulation and characterization of molecules by atomic force microscopy, Nat. Rev. Chem. **1**, 0005 (2017)

8.14 L. Gross, F. Mohn, N. Moll, P. Liljeroth, G. Meyer: The chemical structure of a molecule resolved by atomic force microscopy, Science **325**, 1110–1114 (2009)

8.15 N. Lorente, M. Persson, L.J. Lauhon, W. Ho: Symmetry selection rules for vibrationally inelastic tunneling, Phys. Rev. Lett. **86**, 2593–2596 (2001)

8.16 C.J. Chen: *Introduction to Scanning Tunneling Microsopy* (Oxford Univ. Press, New York 1993)

8.17 R. Wiesendanger: *Scanning Probe Microscopy and Spectroscopy: Methods and Applications* (Cambridge Univ. Press, Cambridge 1994)

8.18 A.M. Moore, P.S. Weiss: Functional and spectroscopic measurements with scanning tunneling microscopy, Annu. Rev. Anal. Chem. **1**, 857–882 (2008)

8.19 J.H. Coombs, M.E. Welland, J.B. Pethica: Experimental barrier heights and the image potential in scanning tunneling microscopy, Surf. Sci. **198**, L353–L358 (1988)

8.20 J. Krüger, F. García, F. Eisenhut, D. Skidin, J.M. Alonso, E. Guitián, D. Pérez, G. Cuniberti, F. Moresco, D. Peña: Decacene: On-surface generation, Angew. Chem. Int. Ed. **56**, 11945–11948 (2017)

8.21 M. Smerieri, J. Pal, L. Savio, L. Vattuone, R. Ferrando, S. Tosoni, L. Giordano, G. Pacchioni, M. Rocca: Spontaneous oxidation of Ni nanoclusters on MgO monolayers induced by segregation of interfacial oxygen, J. Phys. Chem. Lett. **6**, 3104–3109 (2015)

8.22 J. Bardeen: Tunnelling from a many-particle point of view, Phys. Rev. Lett. **6**, 57–59 (1961)

8.23 J. Tersoff, D.R. Hamann: Theory and application for the scanning tunneling microscope, Phys. Rev. Lett. **50**, 1998–2001 (1983)

8.24 J. Tersoff, D.R. Hamann: Theory of the scanning tunneling microscope, Phys. Rev. B **31**, 805–813 (1985)

8.25 W. Kohn, L.J. Sham: Self-consistent equations including exchange and correlation effects, Phys. Rev. **140**, A1133–A1138 (1965)

8.26 P. Hohenberg, W. Kohn: Inhomogeneous electron gas, Phys. Rev. **136**, B864–B871 (1964)
8.27 P. Sautet, C. Joachim: Electronic interference produced by a benzene embedded in a polyacetylene chain, Chem. Phys. Lett. **153**, 511–516 (1988)
8.28 P. Sautet: Images of adsorbates with the scanning tunneling microscope: Theoretical approaches to the contrast mechanism, Chem. Rev. **97**, 1097–1116 (1997)
8.29 P. Sautet, C. Joachim: Calculation of the benzene on rhodium STM images, Chem. Phys. Lett. **185**, 23–30 (1991)
8.30 L. Gross, N. Moll, F. Mohn, A. Curioni, G. Meyer, F. Hanke, M. Persson: High-resolution molecular orbital imaging using a *p*-wave STM Tip, Phys. Rev. Lett. **107**, 086101 (2011)
8.31 P. Hapala, G. Kichin, C. Wagner, F.S. Tautz, R. Temirov, P. Jelínek: Mechanism of high-resolution STM/AFM imaging with functionalized tips, Phys. Rev. B **90**, 085421 (2014)
8.32 B.C. Stipe, M.A. Rezaei, W. Ho: Localization of inelastic tunneling and the determination of atomic-scale structure with chemical specificity, Phys. Rev. Lett. **82**, 1724 (1999)
8.33 J.-L. Bredas: Mind the gap!, Mater. Horiz. **1**, 17–19 (2014)
8.34 J. Meyer, A. Wadewitz, Lokamani, C. Toher, R. Gresser, K. Leo, M. Riede, F. Moresco, G. Cuniberti: Molecules for organic electronics studied one by one, Phys. Chem. Chem. Phys. **13**, 14421–14426 (2011)
8.35 J. Krüger, F. Eisenhut, J.M. Alonso, T. Lehmann, E. Guitián, D. Pérez, D. Skidin, F. Gamaleja, D.A. Ryndyk, C. Joachim, D. Peña, F. Moresco, G. Cuniberti: Imaging the electronic structure of on-surface generated hexacene, Chem. Comm. **53**, 1583–1586 (2017)
8.36 J. Krüger, N. Pavliček, J.M. Alonso, D. Pérez, E. Guitián, T. Lehmann, G. Cuniberti, A. Gourdon, G. Meyer, L. Gross, F. Moresco, D. Peña: Tetracene formation by on-surface reduction, ACS Nano **10**, 4538–4542 (2016)
8.37 W.H. Soe, C. Manzano, A. De Sarkar, N. Chandrasekhar, C. Joachim: Direct observation of molecular orbitals of pentacene physisorbed on Au(111) by scanning tunneling microscope, Phys. Rev. Lett. **102**, 176102 (2009)
8.38 J. Meyer, R. Ohmann, A. Nickel, C. Toher, R. Gresser, K. Leo, D.A. Ryndyk, F. Moresco, G. Cuniberti: Influence of organic ligands on the line shape of the Kondo resonance, Phys. Rev. B **93**, 155118 (2016)
8.39 D.M. Eigler, E.K. Schweizer: Positioning single atoms with a scanning tunnneling microscope, Nature **344**, 524–526 (1990)
8.40 F. Moresco: Manipulation of large molecules by low-temperature STM: Model systems for molecular electronics, Phys. Rep. **399**, 175–225 (2004)
8.41 J.A. Stroscio, D.M. Eigler: Atomic and molecular manipulation with the scanning tunneling microscope, Science **254**, 1319 (1991)
8.42 T.A. Jung, R.R. Schlittler, J.K. Gimzewski, H. Tang, C. Joachim: Controlled room-temperature positioning of individual molecules: Molecular flexure and motion, Science **217**, 181–184 (1996)
8.43 L. Bartels, G. Meyer, K.-H. Rieder: Basic steps of lateral manipulation of single atoms and diatomic clusters with a scanning tunneling microscope tip, Phys. Rev. Lett. **79**, 697–700 (1997)
8.44 D.M. Eigler, C.P. Lutz, W.E. Rudge: An atomic switch realized with the scanning tunnelling microscope, Nature **352**, 600–603 (1991)
8.45 I. Swart, T. Sonnleitner, J. Niedenführ, J. Repp: Controlled lateral manipulation of molecules on insulating films by STM, Nano Lett. **12**, 1070–1074 (2012)
8.46 M. Lastapis, M. Martin, D. Riedel, L. Hellner, G. Comtet, G. Dujardin: Picometer-scale electronic control of molecular dynamics inside a single molecule, Science **308**, 1000–1003 (2005)
8.47 P.A. Sloan, S. Sakulsermsuk, R.E. Palmer: Nonlocal desorption of chlorobenzene molecules from the Si(111)–(7×7) surface by charge injection from the tip of a scanning tunneling microscope: Remote control of atomic manipulation, Phys. Rev. Lett. **105**, 048301 (2010)
8.48 S.W. Hla, L. Bartels, G. Meyer, K.-H. Rieder: Inducing all steps of a chemical reaction with the scanning tunneling microscope tip: Towards single molecule engeneering, Phys. Rev. Lett. **85**, 2777–2780 (2000)
8.49 J. Henzl, M. Mehlhorn, H. Gawronski, K.-H. Rieder, K. Morgenstern: Reversible cis–trans isomerization of a single azobenzene molecule, Angew. Chem. Int. Ed. **45**, 603–606 (2006)
8.50 A. Nickel, T. Lehmann, J. Meyer, F. Eisenhut, R. Ohmann, D.A. Ryndyk, C. Joachim, F. Moresco, G. Cuniberti: Electronically driven single-molecule switch on silicon dangling bonds, J. Phys. Chem. C **120**, 27027–27032 (2016)
8.51 Y. Kim, K. Motobayashi, T. Frederiksen, H. Ueba, M. Kawai: Action spectroscopy for single-molecule reactions – Experiments and theory, Prog. Surf. Sci. **90**, 85–143 (2015)
8.52 Y.-Q. Xu, Z. Jun, B.-K. Yuan, K. Deng, R. Yang, X.-H. Qiu: Electric field assisted hopping of tert-butylamine on Cu(111) surface, Acta Phys. Chim. Sin. **26**, 2686–2690 (2010)
8.53 B.C. Stipe, M.A. Rezaei, W. Ho: Inducing and viewing the rotational motion of a single molecule, Science **279**, 1907–1909 (1998)
8.54 M. Böhringer, K. Morgenstern, W.D. Schneider, R. Berndt: Separation of a racemic mixture of two-dimensional molecular clusters by scanning tunneling microscopy, Angew. Chem. Int. Ed. **38**, 821–823 (1999)
8.55 X. Bouju, C. Joachim, C. Girard: Single-atom motion during a lateral STM manipulation, Phys. Rev. B **59**, R7845–R7848 (1999)
8.56 F. Moresco, G. Meyer, K.-H. Rieder, H. Tang, A. Gourdon, C. Joachim: Recording intramolecular mechanics during the manipulation of a large molecule, Phys. Rev. Lett. **87**, 088302 (2001)
8.57 A. Nickel, J. Meyer, R. Ohmann, H.-P. Jacquot de Rouville, G. Rapenne, F. Ample, C. Joachim, G. Cuniberti, F. Moresco: STM manipulation of a subphthalocyanine double-wheel molecule on Au(111), J. Phys. Condens. Matter **24**, 404001 (2012)
8.58 M. Alemani, L. Gross, F. Moresco, K.-H. Rieder, C. Wang, X. Bouju, A. Gourdon, C. Joachim: Recording the intramolecular deformation of a 4-legs molecule

during its STM manipulation on a Cu(211) surface, Chem. Phys. Lett. **402**, 180–185 (2005)
8.59 L.J. Whitman, J.A. Stroscio, R.A. Dragoset, R.J. Celotta: Manipulation of adsorbed atoms and creation of new structures on room-temperature surfaces with a scanning tunneling microscope, Science **251**, 1206–1210 (1991)
8.60 R. Martel, P. Avouris, I.-W. Lyo: Molecularly adsorbed oxygen species on Si(111)–(7×7): STM-induced dissociative attachment studies, Science **272**, 385–388 (1996)
8.61 M. Alemani, M.V. Peters, S. Hecht, K.-H. Rieder, F. Moresco, L. Grill: Electric field-induced isomerization of azobenzene by STM, J. Am. Chem. Soc. **128**, 14446–14447 (2006)
8.62 R.A. van Delden, M.K.J. ter Wiel, M.M. Pollard, J. Vicario, N. Koumura, B.L. Feringa: Unidirectional molecular motor on a gold surface, Nature **437**, 1337–1340 (2005)
8.63 U.G.E. Perera, F. Ample, H. Kersell, Y. Zhang, G. Vives, J. Echeverria, M. Grisolia, G. Rapenne, C. Joachim, S.-W. Hla: Controlled clockwise and anticlockwise rotational switching of a molecular motor, Nat. Nanotechnol. **8**, 46–51 (2013)
8.64 A. Nickel, R. Ohmann, J. Meyer, M. Grisolia, C. Joachim, F. Moresco, G. Cuniberti: Moving nanostructures: Pulse-induced positioning of supramolecular assemblies, ACS Nano **7**, 191–197 (2013)
8.65 R. Ohmann, J. Meyer, A. Nickel, J. Echeverria, M. Grisolia, C. Joachim, F. Moresco, G. Cuniberti: Supramolecular rotor and translator at work: On-surface movement of single atoms, ACS Nano **9**, 8394–8400 (2015)
8.66 C. Joachim, G. Rapenne (Eds.): *Single Molecular Machines and Motors* (Springer, Cham 2015)
8.67 M. Kolmer, C. Joachim (Eds.): *On-Surface Atomic Wires and Logic Gates* (Springer, Cham 2017)

Francesca Moresco

Center for Advancing Electronics Dresden
TU Dresden
Dresden, Germany
francesca.moresco@tu-dresden.de

Francesca Moresco studied physics at the University of Genova and received her PhD at the University of Hannover (1998). Her habilitation work at FU Berlin was awarded with the Karl-Scheel Prize of the German Physical Society in Berlin (2003). She joined the Institute of Materials Science at TU Dresden at the end of 2009. Since October 2017 Francesca Moresco leads the Single Molecule Machines research group at the Center for Advancing Electronics Dresden (cfaed).

9. Two-Dimensional Crystals: Graphene, Silicene, Germanene, and Stanene

Yu-Yang Zhang, Jinbo Pan, Shixuan Du, Hong-Jun Gao

Since the successful exfoliation of graphene from graphite in 2004, research on two-dimensional crystals has attracted significant attention. An increasing number of new two-dimensional materials have been synthesized, ranging from graphene-like crystals such as hexagonal boron nitride (h-BN) and germanene, to three-atom-thick transition-metal dichalcogenides, and to layered oxides and hydroxides. A wide spectrum of electronic and magnetic properties of great interest have been discovered in these new two-dimensional materials. In this chapter, we review the history and current status of research on group IVA two-dimensional crystals, i.e., graphene, silicene, germanene, and stanene. We give an overall summary of the syntheses of these two-dimensional crystals, especially epitaxial growth in an ultrahigh-vacuum environment. We hope that the knowledge gained from the reviewed systems will guide the design and synthesis of other two-dimensional crystals.

In this chapter, we give a brief review on the epitaxial growth of group IVA two-dimensional (2-D) monolayers on transition-metal substrates in ultrahigh-vacuum (UHV) environments. In Sect. 9.1, we discuss the epitaxial growth of graphene on a Ru(0001) and other transition-metal substrates. In Sects. 9.2 and 9.3, we review the synthesis of silicene and germanene. Stanene and several other monolayers made with metallic elements are discussed in Sect. 9.4.

Part B | 9

The family of 2-D materials containing one to several layers of atoms has been widely investigated in recent decades. They are not only important for fundamental physics but also show great potential for future applications; for example, taking advantage of its high carrier mobility, graphene (Gr) has been used in transistors that can work at extremely high frequencies [9.1, 2]. MoS_2 has been used in the smallest transistors, only 1 nm in size [9.3]. Due to their extremely high surface-to-volume ratio, some 2-D materials are also good catalysts [9.4–8]. Scientists have also shown interest in putting several 2-D materials together to build both lateral and vertical heterostructures [9.9–13].

Recent research regarding 2-D materials started from the exfoliation of graphene from graphite in 2004 [9.14]. Then, it quickly expanded to h-BN and boron carbon nitride (BCN), which have honeycomb structures and satisfy the same electron counting rule [9.15–17]. Monolayers of silicon and germanium, other group IVA elements that also have four valence electrons, are also theoretically predicted to be stable [9.18–20]. Experimental evidence of these two

M. Rocca, T.S. Rahman, L. Vattuone (Eds.), *Springer Handbook of Surface Science*, Springer Handbooks,
https://doi.org/10.1007/978-3-030-46906-1_9

monolayers has been found, although some debate remains regarding the names of these two materials [9.21, 22]. Recently, stanene, a monolayer of Sn, was synthesized, enriching the family of group IVA 2-D materials [9.23].

Another major class of 2-D materials is transition-metal chalcogenides (TMCs) [9.24, 25]. Some of these are also star materials; for example, MoS_2, a traditional solid lubricant, was used to fabricate the smallest transistors [9.3]. Monolayer FeSe has attracted substantial attention as a superconductor [9.26]. $NbSe_2$ shows an abnormal incommensurate charge density wave (CDW) [9.27, 28]. As most chalcogenides/dichalcogenides have a layered structure, exfoliation from bulk materials has been used to produce monolayer dichalcogenides [9.29]. Large-scale and high-quality molecular beam epitaxy (MBE) and chemical vapor deposition (CVD) methods have also been applied to produce monolayer dichalcogenides [9.30, 31].

Monolayer oxide materials constitute another booming research direction in 2-D materials. Though most bulk oxide materials are not layered structures, several-atomic-layer thick oxides in 2-D form have been synthesized in various ways [9.32]; for example, a perovskite-type $LaNb_2O_7$ monolayer was formed via a nanosheet deposition process [9.33], TiO_2 monolayers were grown on Ag(100) substrates [9.34], and recently, single-atom-thick CuO and ZnO membranes were synthesized in graphene pores and on a graphene substrate, opening a new window for research into monolayer oxide materials [9.35, 36].

Exfoliation from layered bulk parents has been demonstrated to be an effective way to fabricate 2-D materials [9.16, 37, 38]. In addition to graphene, which was historically exfoliated from graphite using Scotch tape, there are plenty of other examples of 2-D materials that can be mechanically exfoliated from their three-dimensional parent, such as MoS_2, $MoSe_2$, and $NbSeO_2$. Chemical exfoliation methods are then typically used to break the van der Waals (vdW) interactions inside the layered structures to obtain 2-D materials.

Epitaxial growth of 2-D materials is another synthesis strategy. CVD and physical vapor deposition (PVD) have been successfully demonstrated for the fabrication of many 2-D materials on a large scale [9.39–41]. The as-fabricated 2-D materials are then generally transferred to another substrate, such as a silicon wafer. Direct selenization of a Pt substrate to fabricate a $PtSe_2$ monolayer and the synthesis of graphene on a transition-metal (TM) substrate by chemical reactions are other examples of epitaxial growth of 2-D materials [9.42, 43]. The advantage of the epitaxial growth method is that the fabricated 2-D materials have high quality for further applications. Another advantage of the epitaxial growth method is that it can be used to synthesize 2-D materials without relying on layered 3-D (three-dimensional) parents, e.g., silicene and germanene.

9.1 Graphene on Transition-Metal Substrates

In the 1960s, graphene was found to form on transition-metal surfaces [9.44, 45]. Indeed, it required considerable effort from scientists to get rid of these carbon films to obtain a clean transition-metal surface. However, since its successful exfoliation [9.14, 46], graphene on transition-metal surfaces has again attracted attention from scientists. Due to the convenient synthesis process and the high quality of the fabricated graphene, systems formed of graphene on a transition-metal substrate have been comprehensively investigated [9.47]. For certain transition-metal substrates, the strong interaction between the graphene adlayer and the transition-metal substrate reduces the carrier mobility of the graphene and makes it difficult to open an energy gap [9.48, 49]. These obstacles can now be overcome in several ways, such as intercalation techniques [9.50, 51]. It has also been reported that the interaction of Au or Si can restore graphene nanoislands (GNIs) and graphene nanoribbons (GNRs) to a pristine state [9.52, 53]. The as-prepared epitaxial graphene can also be decoupled from the substrate by etching [9.54]. Thus, the epitaxial growth of graphene on a transition-metal substrate is still a promising method for industrial production of graphene in the future.

9.1.1 Epitaxial Growth of Graphene on Ru(0001)

Large-scale and highly ordered graphene can be synthesized by annealing a ruthenium single-crystal substrate containing a small amount of carbon [9.48, 49, 55] or using precursors containing carbon atoms [9.56]. During the annealing process, the carbon atoms segregate from the bulk ruthenium, and graphene grows on the Ru(0001) surface. The annealing process is described in the literature [9.48, 55]. A brief description of the sequence is as follows: the temperature of the ruthenium substrate is slowly increased to 1000 K and held for 20 min, then the substrate is cooled to room temperature. Comparison of the Auger electron spectroscopy

(AES) and x-ray photoemission spectroscopy (XPS) results before and after the annealing process confirmed the segregation of carbon. XPS and AES also helped to confirm that no other new elements were present.

Taking the above work as an example, the quality of the as-fabricated graphene on an 8-mm-diameter Ru(0001) substrate was examined from edge to edge by low-energy electron diffraction (LEED). As shown in Fig. 9.1a, LEED patterns were collected at each pink spot. Compared with bare Ru(0001), which generates a simple hexagonal pattern, extra spots due to epitaxial graphene can be clearly identified in Fig. 9.1d–f. The spots in the graphene pattern show the same orientation, indicating that the whole sample was covered by a homogeneous, high-quality epitaxial graphene layer. It is only at the edge of the sample (Fig. 9.1b,c) that the spots related to graphene become weak.

Based on many high-quality atomic-resolution STM images and density functional theory (DFT) calculations [9.57–60], the atomic structure of graphene on Ru(0001) has been fully revealed. It is now believed that the moiré pattern is due to the lattice mismatch between graphene and the Ru substrate. As shown in Fig. 9.2a, in a relaxed configuration of a (12×12) graphene lattice sitting on a (11×11) Ru(0001) lattice, there are three typical regions. For the higher region, C atoms of both sublattices in graphene are located in (or close to) the face-centered cubic (fcc) and hexagonal close-packed (hcp) hollow site of the Ru substrate. The centers of the honeycomb lie above (or close to) the top of a top-layer Ru atom. This upper region is thus commonly called the top or atop region. For the lower region, the center of the honeycomb is above (or close to) second- or third-layer Ru atoms. These regions are commonly named the hcp (above a second-layer Ru atom) or fcc (above a third-layer Ru atom) regions. For the region with intermediate height, close inspection of the atomic structure reveals that the centers of the honeycomb are located above the centers of two top-layer Ru atoms. This region is called the bridge region. Sometimes, this region is further divided into several different regions depending on the neighbors; for example, the bridge region between the atop and fcc regions can be referred to as the atop–fcc region.

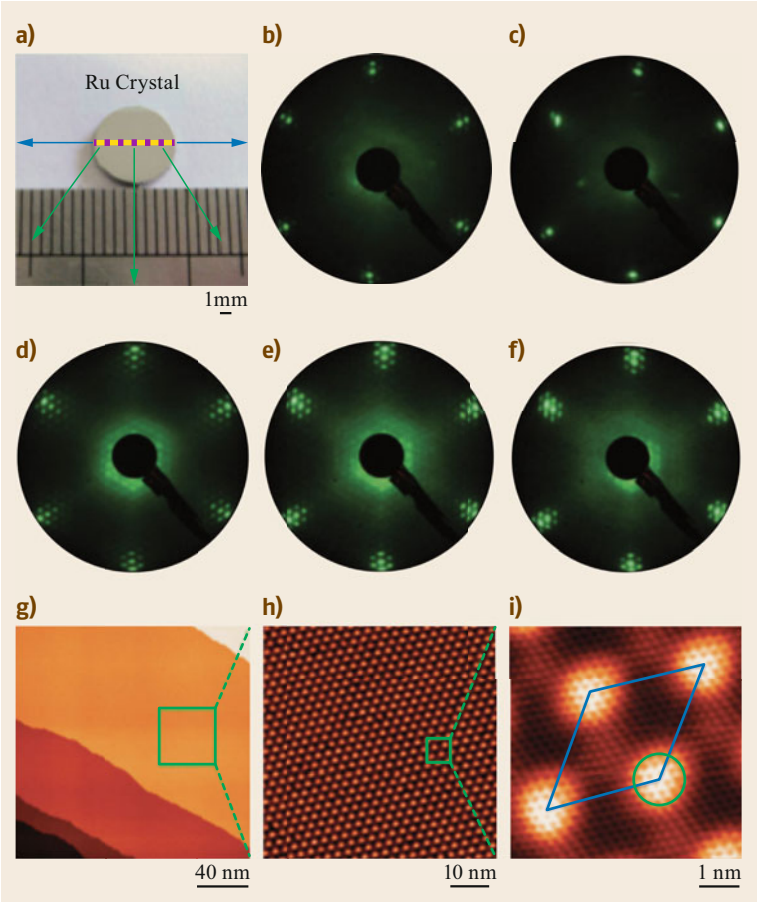

Fig. 9.1a–i LEED patterns and STM images confirming the high quality of graphene on Ru(0001). **(a)** A sample 8 mm in diameter. The electron beam was moved along the *yellow line* to obtain the different LEED patterns. The *pink spots* are the locations where the photographs shown in **(b–f)** were taken. **(b,c)** At the edge of the sample, the additional spots are weak. **(d–f)** In other parts of the sample, the additional spots are sharp and have the same arrangement. Scanning tunneling microscopy (STM) images at large scale **(g)**, zoomed in **(h)**, and at atomic resolution **(i)** show that a flat graphene flake extended over entire Ru terraces (reprinted by permission from [9.48], © Wiley 2009)

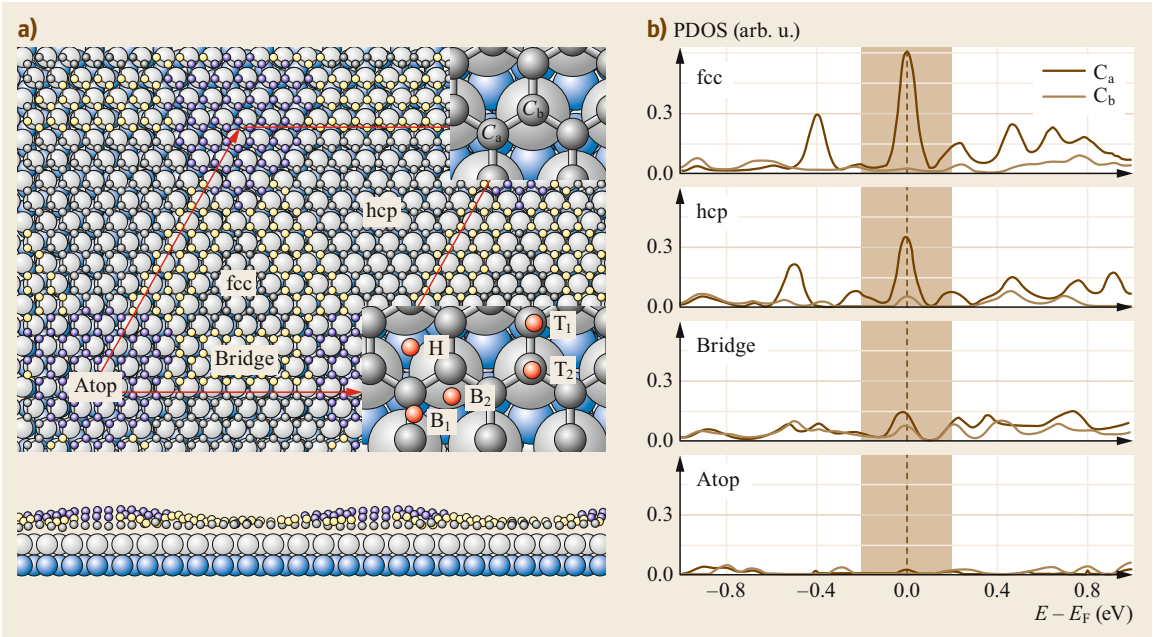

Fig. 9.2a,b Atomic structure and electronic properties of a (12×12) graphene lattice on a (11×11) Ru(0001) substrate. **(a)** Top view (*top panel*) and side view (*lower panel*) of the atomic structure. **(b)** Density of states projected (PDOS) to p_z orbits for different C atoms at different locations (reprinted by permission from [9.60], © Wiley 2014)

Although debate continues on whether this represents a (12×12) graphene lattice sitting on a (11×11) Ru(0001) substrate or a (25×25) graphene lattice sitting on a (23×23) Ru(0001) surface [9.56], most quantum-mechanical calculations based on DFT have adopted the former atomic model, which is much smaller in size than the second. The atomic structure and electronic properties of the graphene-on-Ru(0001) system have been investigated [9.57–59]. The choice of the exchange-correlation function, how to treat the van der Waals interactions, the number of Ru layers in a slab model, the energy cutoff on the wavefunction expansion, and other numerical parameters generally affect the details of the resulting atomic structure and electronic properties. It is widely accepted that the large ripple revealed in STM images is not only caused by the electronic structure but also a real atomic corrugation.

Carbon atoms within one period of the moiré pattern at different locations have different electronic structures. The projected density of states (PDOS) on p_z orbitals of different carbon atoms is shown in Fig. 9.2b, where C_a and C_b denote atoms located on hollow and top sites of Ru(0001) in the fcc and hcp regions, respectively [9.60]. The intensity of the PDOS of C atoms at the Fermi level in fcc regions is much higher than that in the other regions, implying stronger sp^3 hybridization and higher activity of C_a atoms in the fcc region. This difference further affects the physical and chemical properties of graphene; for example, at low coverage, many transition-metal atoms selectively adsorb on the fcc region of graphene/Ru(0001) and form ordered dispersed metal nanoclusters [9.61–63].

As one of the earliest systems comprising high-quality epitaxial graphene on a transition-metal substrate, Gr/Ru(0001) has attracted significant attention. Many fundamental studies and potential applications have been explored in this system; for example, quantum-dot and quantum-well effects have been investigated [9.64–66]. This system is also used as a template for selective adsorption and self-assembly patterns [9.67, 68]. Many intercalations between graphene and the Ru substrate have also been achieved for future applications [9.50, 69–71].

9.1.2 Epitaxial Growth of Graphene on Other Transition-Metal Substrates

Graphene has also been epitaxially grown on other transition-metal substrates, including Pt [9.72, 73], Ir [9.74, 75], Rh [9.76, 77], Ni [9.7, 76], and Cu [9.78]. Various sizes of moiré patterns have been observed. Figure 9.3 shows moiré patterns of graphene on several widely investigated transition-metal substrates with a typical periodicity of 1–2 nm.

For all such samples, the epitaxial growth method and kinetic factors during the growth process strongly

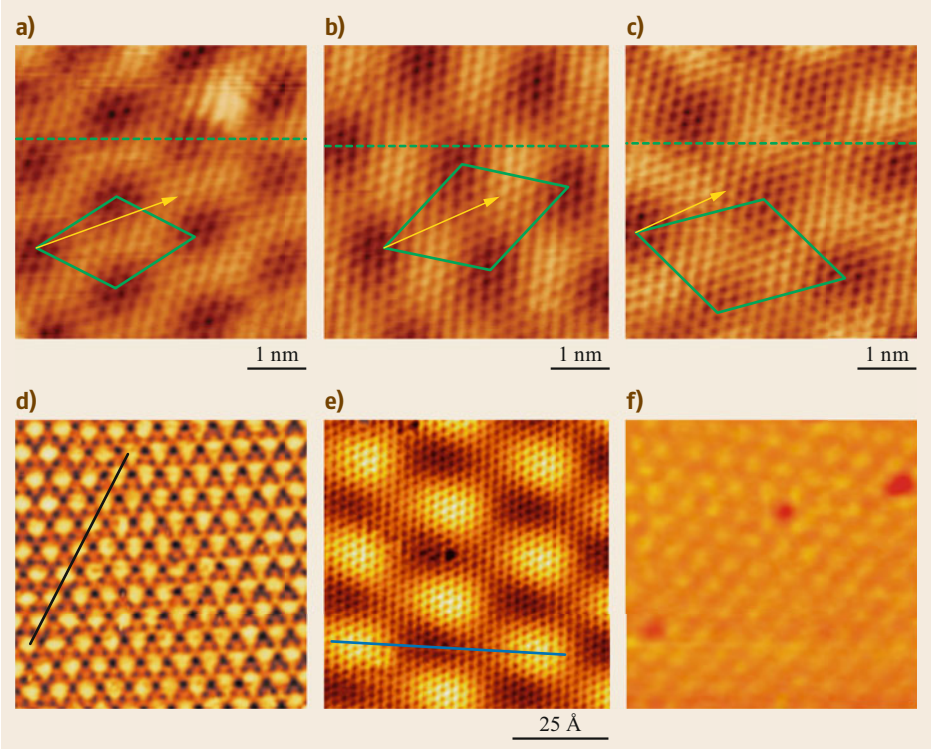

Fig. 9.3a–f STM images of graphene epitaxially grown on transition-metal substrates. **(a–c)** Graphene grown on a Pt(111) surface, showing domains with different orientations [9.72]. **(a)** is for $(\sqrt{37}\times\sqrt{37})$R21°. **(b)** is for $(\sqrt{61}\times\sqrt{61})$R26°. **(c)** is for $(\sqrt{67}\times\sqrt{67})$R12°. **(d)** Graphene on a Rh(111) $10\times10\,\mathrm{nm}^2$ surface [9.76]. **(e)** Graphene on an Ir(111) $6\times6\,\mathrm{nm}^2$ surface [9.75]. **(f)** Graphene on a Cu(111) $20\times20\,\mathrm{nm}^2$ surface [9.78] (reprinted by permission from [9.72, 75, 76, 78], © American Institute of Physics, Institute of Physics, American Chemical Society)

affect the quality of the resulting graphene [9.79, 80], as do a high-quality transition-metal substrate, suitable precursor partial pressure, and controlled annealing temperature.

The lattice mismatch between the graphene and transition-metal substrate affects not only the size of the moiré pattern [9.81] but also the quality of the graphene. *Preobrajenski* and collaborators showed that, with a larger lattice mismatch, the graphene film corrugated more because of the inhomogeneous interaction between the graphene and substrate [9.82]. XPS measurements confirmed this effect.

The quality of the graphene on a transition-metal substrate prepared by the epitaxial growth method is also affected by the interaction between them. For strongly interacting systems, at the initial stage of growth, the graphene islands have the same orientation and thus connect to each other seamlessly during growth. The as-fabricated graphene thus contains fewer defects. However, if the graphene–substrate interaction is weak, the initial islands have different orientations and the as-fabricated graphene may thus show many domains. Grain boundaries may also affect the electronic properties of the graphene [9.83–86].

An example of a strongly interacting graphene–substrate system is Gr/Ru(0001), described above. The moiré pattern is well defined. In contrast, graphene on Pt(111) is an example of a weakly interacting graphene–substrate system. In contrast to the case of a unique (12×12) graphene lattice sitting on a (11×11) Ru(0001) substrate, graphene on Pt(111) forms different moiré patterns that may rotate to different orientations. Figure 9.3a–c shows typical STM images of Gr/Pt(111), indicating $(\sqrt{37}\times\sqrt{37})$R21°, $(\sqrt{61}\times\sqrt{61})$R26°, and $(\sqrt{67}\times\sqrt{67})$R12° orientations. Compared with Gr/Ru(0001), Gr/Pt(111) shows lesser corrugation.

In scanning tunneling spectroscopy (STS), the $\mathrm{d}I/\mathrm{d}V$ curve of the sample is measured, thus when the tip is carefully treated, it reflects the local density of states (LDOS) of the sample. This method is widely used to investigate the electronic structure of epitaxial graphene on transition-metal substrates with high spatial resolution. Taking the Gr/Ru(0001) system as an

example, STS results show that the graphene retains some of its physical properties after being placed on the metal surface but with a shift of the Dirac point by −0.3 eV [9.48, 49].

Epitaxial graphene on an Ir(111) substrate is another system that has been well investigated by STM/STS, especially regarding the effect of silicon intercalation [9.87]. Figure 9.4a shows STS measurements of Gr/Ir(111) on both an intercalated area (black curve) and an un-intercalated area (red curve). It is clear that, after silicon intercalation: (i) the surface state of the Ir substrate disappears and (ii) the occupied states and unoccupied states become symmetric. After silicon intercalation, the two prominent features of graphene, viz. the G and 2-D peaks, become visible (Fig. 9.4c). These results indicate that the coupling between graphene and Ir(111) is weakened by silicon intercalation [9.87].

Taking advantage of its high spatial resolution, STS has also been used to reveal the edge states of graphene

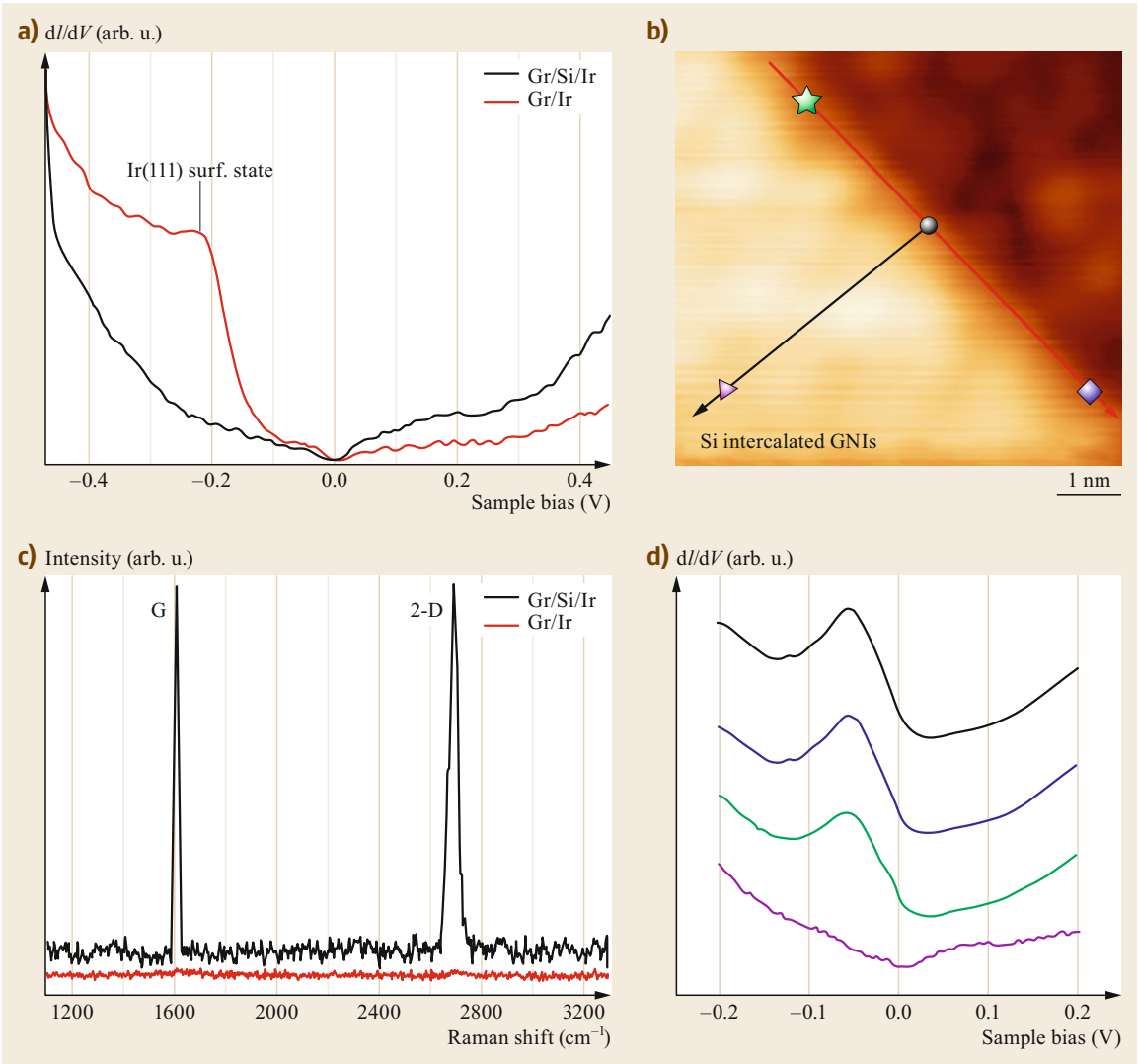

Fig. 9.4a–d STS measurements on Gr/Ir(111). **(a)** dI/dV spectra measured on both an intercalated (*black line*) and an un-intercalated area (*red line*) [9.87]. **(c)** Comparison of Raman spectra at 532 nm for graphene grown on Ir(111) before and after silicon intercalation, denoted by *red* and *black lines*, respectively [9.87]. **(b)** STM image showing a straight edge of a Si-intercalated graphene nanoisland [9.88]. **(d)** dI/dV spectra collected at different points along the line perpendicular to the edge marked by *black dots* in **(b)** [9.88] (reprinted by permission from [9.87, 88], © AIP 2012, Springer Nature 2017)

nanoribbons (GNRs) and nanoislands (GNIs) [9.88, 89]. Figure 9.4b is an STM image showing a straight edge of a GNI on Ir(111). The dI/dV spectra collected at different points around the edge (Fig. 9.4d), marked by different dots in Fig. 9.4b, indicate that a pronounced peak appears at -50 mV in the dI/dV spectra acquired at this straight edge. This pronounced peak is not the surface state of the Ir(111) substrate, which is located at ≈ -0.2 eV, and is attributed to the edge state of the graphene nanoisland [9.88].

The electronic properties of graphene on transition-metal substrates have also been investigated using theoretical calculations. Some use a more realistic model, which contains the full moiré pattern. However, because of the size of the supercell, these calculations usually adopt the local density approximation (LDA) and generalized gradient approximation (GGA) with or without van der Waals interactions [9.90–94]. Higher-level calculations based on a more accurate approach, such as the random phase approximation (RPA) or *GW* approach, can only handle tens of atoms. In these high-level calculations, a (1×1) or $(\sqrt{3}\times\sqrt{3})$ graphene lattice is often used, which neglects the lattice mismatch between graphene and the transition-metal substrate [9.95, 96]. There are also theoretical calculations to address the growth process and mechanism [9.97].

9.2 Epitaxial Silicene on Transition-Metal Substrates

Silicene, made up of silicon atoms rather than carbon atoms, is a 2-D atomic crystal with a honeycomb structure similar to graphene. It has attracted considerable attention due to its peculiar properties [9.19, 20, 98–101], e.g., compatibility with current silicon-based technology and the quantum spin Hall effect. Due to the long Si−Si bond length and the partial sp^3 hybridization, freestanding silicene is a low-buckled structure. Recently, silicene has been successfully synthesized on several transition-metal substrates, e.g., Ag(110) [9.102], Ag(111) [9.98, 103–107], Ir(111) [9.21], and ZrB_2 thin films [9.108]. In this section, we discuss in detail the epitaxial growth and characterization of silicene on Ir(111) and Ag(111) surfaces.

9.2.1 Silicene on Ir(111)

Epitaxial silicene on an Ir(111) surface, as shown in Fig. 9.5, was synthesized by depositing silicon atoms on the Ir(111) surface at room temperature followed by annealing at 670 K for 30 min [9.21]. The LEED pattern of the sample is shown in Fig. 9.5a. The spots highlighted by the yellow dashed circles are assigned to the (1×1) Ir(111) substrate. The other diffraction spots originate from the silicon superstructure on the Ir(111) substrate. The diffraction spots can be separated into two identical patterns with different orientations, as shown in the sketch map in Fig. 9.5b, in which two different spots highlighted by different colors correspond to two domains. Each domain can be identified as a $(\sqrt{7}\times\sqrt{7})$ superstructure with respect to the Ir(111) substrate. The corresponding angles between Ir[110] and the high-symmetry direction of $(\sqrt{7}\times\sqrt{7})$ of the two silicene domains are 40.9° and 19.1°, respectively.

Figure 9.5c,d shows large-area and zoomed-in STM images of one silicene domain. The angle between the orientation of the silicene superstructure and the Ir[110] direction is 40.9°, consistent with the result detected in the $(\sqrt{7}\times\sqrt{7})$ LEED patterns in Fig. 9.5a. The overview STM image shows a long-range ordered hexagonal lattice of protrusions. Figure 9.5e shows the line profile along the black line in Fig. 9.5d. The periodicity of the bright protrusions in the STM image is approximately 0.72 nm, which is $\sqrt{7}$ times the Ir(111) lattice constant (0.271 nm). The height of the protrusions in the silicene overlayer is approximately 0.6 Å, indicating that silicene on Ir(111) is buckled.

In the high-resolution STM image shown in the upper part of Fig. 9.5f, the different regions of a unit cell are marked by upward and downward triangles. The middle and bottom parts are the STM simulation and the optimized geometric structure of silicene on Ir(111) based on DFT calculations, respectively [9.19, 20]. The protruding silicon atoms are yellow, while the other silicon atoms are orange. The unit cell of the $(\sqrt{7}\times\sqrt{7})$ superstructure is indicated by a black rhombus. There are six silicon atoms in the unit cell: one (yellow) sits on the top site, two are located at the hcp hollow and fcc hollow sites, and the other three are located at the bridge sites. The silicon atoms at different sites exhibit different silicon–substrate interactions and thus have different heights and electron density distributions. The simulated STM image shown in the middle part of Fig. 9.5f is highly consistent with the experimental STM image.

A further electron localization function calculation implies that the interaction between silicon atoms is via covalent bonding, while the interaction between silicon and iridium is mainly electrostatic. This electrostatic in-

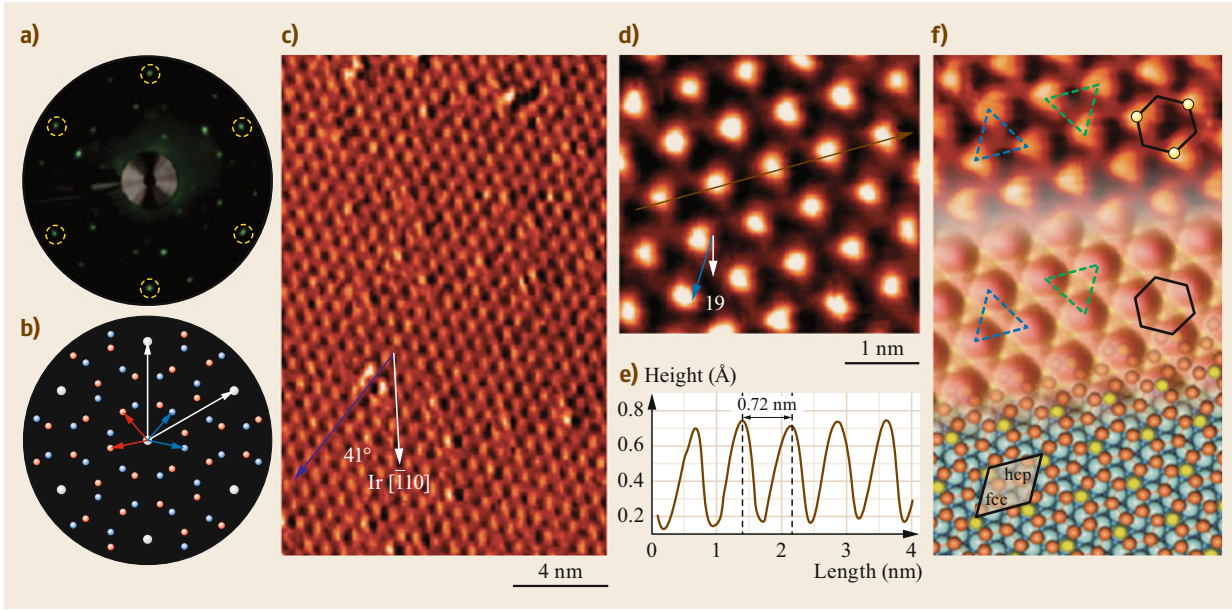

Fig. 9.5a–f Silicene on Ir(111). **(a)** LEED patterns and **(b)** corresponding schematic diagrams of the silicon superstructure formed on Ir(111). **(c)** and **(d)** STM images showing two different $(\sqrt{7}\times\sqrt{7})$ superstructure domains of silicene on Ir(111). ($U = -1.5$ V; $I = 0.25$ nA) **(e)** Line profile along the *black line* in **(d)**, revealing the periodicity of the protrusions (0.72 nm) and a corrugation of approximately 0.4 Å for the silicene. **(f)** STM image (*upper*), simulated STM image (*middle*), and atomic model (*lower*) of buckled silicene on Ir(111). The *rhombus* indicates the unit cell. The *triangles* indicate the two different regions in a unit cell. The honeycomb feature is indicated by the *black hexagon* (reprinted by permission from [9.21], © ACS 2013)

teraction is not strong enough to affect the formation of Si–Si bonds or the extension of the silicon sheet; two-dimensional continuous silicene has indeed been successfully fabricated on Ir(111).

9.2.2 Silicene on Ag(111) and Other Transition-Metal Substrates

Epitaxial silicene on Ag(111) is synthesized by directly depositing silicon atoms onto the Ag(111) surface and then annealing in UHV [9.103–105, 107]. A variety of silicene superstructures can be formed depending on the substrate temperature, deposition rate, and silicon coverage. At lower substrate temperature, below 400 K, silicon atoms deposited on Ag(111) tend to form silicon clusters or disordered structures. When the substrate temperature is above 400 K during deposition, the resulting silicene sheet typically exhibits five ordered phases: from the T phase to (4×4), $(\sqrt{13}\times\sqrt{13})$ R $\pm$ 13.9°, $(2\sqrt{3}\times 2\sqrt{3})$, and finally to a $(\sqrt{3}\times\sqrt{3})$ phase with increasing substrate temperature, while other ordered structures can also be observed. The deposition rate also plays an important role because it can affect the nucleation rate and growth rate of silicene. A recent DFT calculation by *Shu* et al. revealed that the silicene nucleation rate on Ag(111) is very high compared with the rate of graphene nucleation on TM surfaces due to the low diffusion barrier of Si atoms and the low nucleation barrier [9.109]. Such higher deposition rates would lead to silicene samples that have smaller domains and more defects. In addition, the coverage of silicon is also important, since an inappropriate value will lead to other silicon phases.

The structure and properties of silicene on Ag(111) remain under debate, although the silicene/Ag(111) system has been intensively studied in the past few years. Synthesis of monolayer silicene was first reported by *Lalmi* et al. on an Ag(111) surface [9.107]. However, based on their experimental measurements, the reported lattice parameter of silicene was approximately 17% smaller than that of bulk silicon. *Lay* et al. later argued that such a small lattice actually corresponds to a clean Ag(111) (1×1) surface rather than silicene [9.111]. *Vogt* et al. claimed to have synthesized monolayer silicene on Ag(111) for the first time, revealing a superstructure of (3×3) silicene on a (4×4) Ag(111) surface in STM images, as shown in Fig. 9.6a [9.98]. This phase was also observed by Feng et al. However, *Feng* et al. proposed it to be incomplete silicene stabilized by hydrogen with ordered holes (Fig. 9.6b) [9.103]. In-

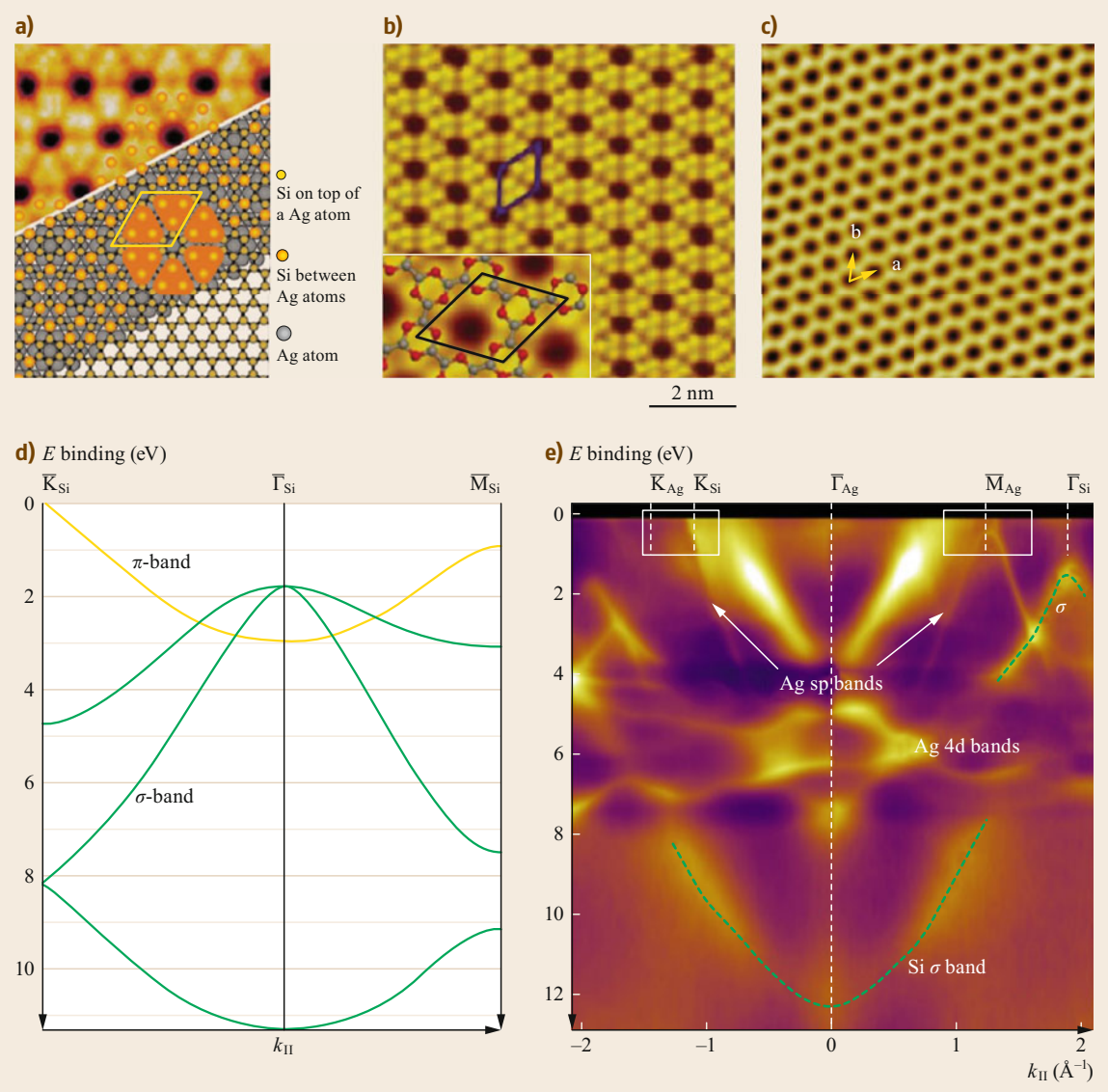

Fig. 9.6a–e Silicene on Ag(111). **(a)** STM image, atomic structure, and simulated STM image of silicene on Ag(111) [9.98]. **(b)** STM image of (3×3) superstructure of silicene on Ag(111) with one-potential atomic models [9.103]. **(c)** STM image of silicene monolayer showing the $(\sqrt{3}\times\sqrt{3})$ R30° honeycomb superstructure ($U = 1.2$ V, measurement temperature 77 K [9.103]). **(d)** Calculated band dispersion of σ (*green*) and π (*yellow*) states of a free-standing (1×1) silicene layer [9.110]. **(e)** Angle-resolved photoemission spectra of (4×4) silicene grown on Ag(111) using photon energy of 135 eV. *Dashed green lines* follow the dispersion of the Si-σ state [9.110] (reprinted by permission from [9.98, 103, 110], © APS 2012, ACS 2012, and Elsevier 2017)

stead, true monolayer silicene is in another phase with a honeycomb-like $(\sqrt{3}\times\sqrt{3})$ R30° superstructure, as shown in Fig. 9.6c. Later, *Resta* et al. and other groups reported their observation of the same phase as shown in Fig. 9.6b; they found that the $(\sqrt{3}\times\sqrt{3})$ R30° phase is always found on the thicker patch of the sample, indicating that it may possibly be multilayer silicene [9.112]. Later, *Chen* et al. found a phase transition of silicene on Ag(111) [9.113]. At temperatures above 40 K, silicene on Ag(111) has a $(\sqrt{3}\times\sqrt{3})$ R30° honeycomb structure; however, below 40 K, it transforms into two mirror-symmetric rhombic structures that are boundary

separated but energy degenerate. DFT calculations on monolayer silicene structures have indicated that the energy barrier between these two configurations is very small (no more than 38 meV). This enables a dynamic flip–flop motion that cannot be followed by STM at sample temperatures higher than 40 K, resulting in the $(\sqrt{3}\times\sqrt{3})$ R30° honeycomb structure observed in STM images.

The electronic properties of silicene on Ag(111) have also been investigated. It has been reported that silicene on Ag(111) exhibits linear electronic dispersion resembling that of relativistic Dirac fermions at the K points of the Brillouin zone based on angle-resolved photoemission spectroscopy measurements [9.98], and STS measurements [9.105]. *Feng* et al. also provided direct evidence for the existence of Dirac cones in the monolayer silicene (3×3)/Ag(111) system by observing that the Dirac cones evolve with increasing binding energy around both the M and K points [9.114]. However, their arguments were questioned later because the influence of the Ag substrate was shown to be nonnegligible. *Lin* et al. argued that silicene would lose its Dirac fermion characteristic due to substrate-induced symmetry breaking and that the linear dispersion characteristic originates from the Ag bulk sp-band along the Γ-K direction [9.115]. Moreover, *Carbone* et al. investigated (4×4) silicene on Ag(111) and mixed (4×4) and $(\sqrt{13}\times\sqrt{13})$ R13.9° silicene on Ag(111) [9.110, 116, 117]. They found that the Ag(111) substrate modified the π band of freestanding silicene (Fig. 9.6d) and that the reported Dirac fermion feature derives from the Ag interface state (Fig. 9.6e) rather than silicene. Further experimental and theoretical studies are thus needed to clarify this phenomenon.

9.3 Germanene Growth on Transition-Metal Surfaces

Freestanding germanene is also a low-buckled structure similar to silicene. The spin-orbital effect can open a bandgap of 23.9 meV, much wider than those of graphene and silicene (1.55 and 2.9 meV, respectively) [9.20]. The quantum spin Hall effect can thus be observed in germanene. Germanene has been fabricated on several substrates by an epitaxial growth method, e.g., on Pt(111) [9.22], Au(111) [9.118], Al(111) [9.119], and MoS_2 [9.120] surfaces. In this section, we discuss in detail the epitaxial growth and characterization of germanene on Pt(111), Au(111), and MoS_2 surfaces.

9.3.1 Germanene Growth on a Pt(111) Surface

Epitaxial germanene on Pt(111) has been synthesized by depositing germanium atoms on a clean Pt(111) surface at room temperature under UHV conditions and then annealing in the temperature range of 600–750 K for 30 min [9.22]. The annealing temperature was kept below 800 K to avoid the formation of Ge-Pt surface alloy. Germanene was then fabricated, as shown in Fig. 9.7. LEED was used to characterize the superstructure, as shown in Fig. 9.7a. The six outer bright spots correspond to the (1×1) diffraction spots of the Pt(111) surface. The additional distinct diffraction spots originate from the germanium superstructure. These diffraction spots can be divided into two groups, identified by red and blue spots in Fig. 9.7b, originating from two different germanium superstructures with rotation of 23.4° and 36.6° relative to the Pt[$1\bar{1}0$] direction, respectively. From the LEED pattern, a $(\sqrt{19}\times\sqrt{19})$ superstructure with respect to the Pt(111) surface can be identified.

The long-range order of the germanium superstructure formed on a Pt(111) surface can be seen in Fig. 9.7c. The small rhombus indicates the supercell of the superstructure. The orientation of the supercell is rotated by approximately 23° relative to the Pt[$1\bar{1}0$] direction, which is consistent with the LEED results. Figure 9.7d shows a zoomed-in STM image of Fig. 9.7c. There are three bright spots in the supercell; one spot is at the corner of the rhombus, while two lie inside the rhombus. Figure 9.7e shows the line profile along the dashed line in Fig. 9.7d, revealing that the periodicity of the superlattice in the STM image is approximately 1.2 nm. The corrugation of the germanium layer is approximately 0.6 Å. Previous theoretical studies predicted the lattice constant of free-standing germanene to be approximately 3.97–4.02 Å. In that case, a (3×3) superlattice of germanene has a lattice spacing of approximately 11.91–21.06 Å, matching well with the periodicity of the superlattice obtained from the STM measurements.

DFT calculations were performed to obtain the detailed structure and properties of the germanium adlayer on Pt(111). Several models with (3×3) germanene on Pt(111) surface were considered, in which the germanium atoms have different locations with respect to the substrate. Figure 9.7f shows the most stable configuration; the binding energy per germanium atom

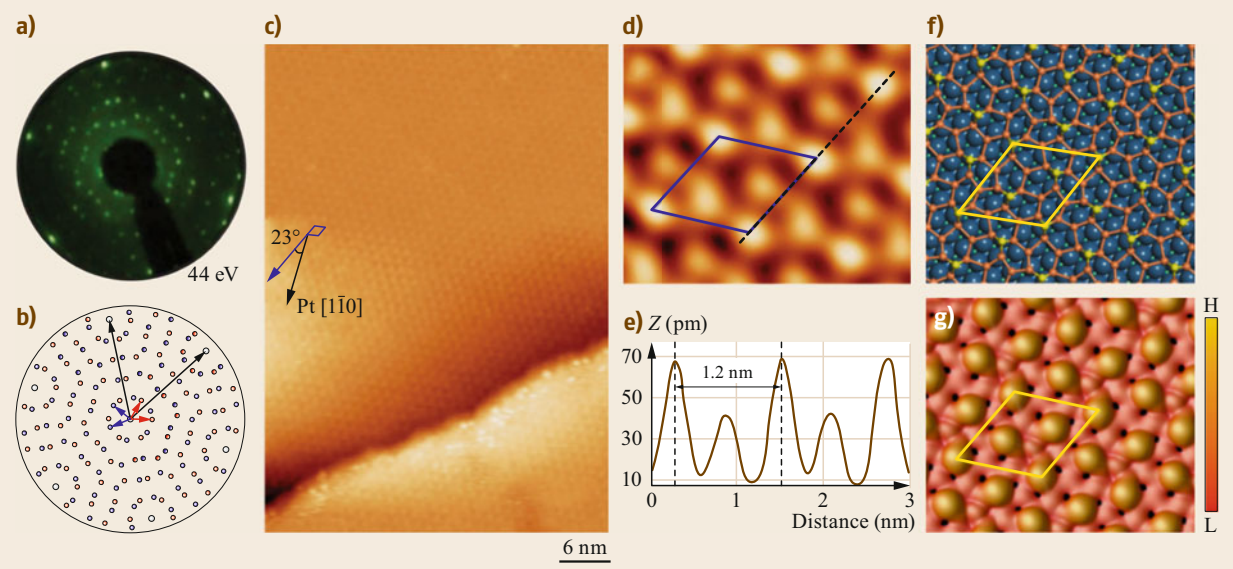

Fig. 9.7a–g Germanene on a Pt(111) surface. **(a)** LEED patterns and **(b)** corresponding diagram of germanene on a Pt(111) surface. **(c)** Large-area STM image ($U = -1.45$ V, $I = 0.25$ nA), showing a $(\sqrt{19} \times \sqrt{19})$ superstructure of the germanium adlayer formed on the Pt(111) surface. The close-packed direction of Pt[110] is indicated by the *black arrow*. The angle between the *blue* and *black arrows* is approximately 23°. **(d)** Zoomed-in STM image ($U = 1$ V, $I = 0.05$ nA) of germanene on the Pt(111) surface. **(e)** Line profile along the *dashed line* in panel **(d)**, revealing the periodicity of the germanium superstructure (1.2 nm). **(f)** Optimized geometric structure of germanene on the Pt(111) surface; the *yellow rhombus* indicates the unit cell. *Blue*, *yellow*, and *orange spheres* represent Pt, protruding Ge, and other Ge atoms, respectively. **(g)** Simulated STM image of germanene on Pt(111) surface, showing similar features to the STM image (reprinted by permission from [9.22], © Wiley 2014)

is approximately 1.39 eV. After relaxation, the honeycomb structure of the germanium adlayer becomes distorted; however, the six-membered rings structure is maintained. There are four protrusions labeled in yellow at the vertices of the rhombus and two at the centers of the two triangular regions in a supercell. These features match well with the STM observations in Fig. 9.7d. STM simulations were performed using the Tersoff–Hamann approach for comparison with the STM observations. The simulated STM image is shown in Fig. 9.7g; it has the same features as the STM image, namely four bright spots at the vertices of the rhombus and two at the center. This STM simulation further confirms that the superstructure observed by STM is a distorted germanium adlayer (germanene) on the Pt(111) surface.

Although the germanene layer has a distorted and buckled structure, it is a continuous layer rather than a germanium adatom array, according to electron localization function (ELF) calculations [9.22]. The charge localization between any two neighboring germanium atoms is very strong, indicating strong covalent bonding between neighboring germanium atoms. The charge localizations between germanium atoms and the underlying Pt atoms are all very weak; the interactions between germanium and the underlying Pt atoms are mainly electrostatic. The interactions are not strong enough to affect the formation of Ge−Ge bonds and the extension of the germanium sheet. STM measurements and DFT calculations demonstrate that a continuous 2-D germanene layer was successfully fabricated on Pt(111).

It is worth noting that Ge-Pt surface alloys have also been reported previously. *Ho* et al. prepared their samples by annealing at 900–1200 K to form a Ge-Pt surface alloy [9.121]; this annealing temperature is much higher than that used when preparing germanene samples [9.22]. In STM images of the Ge-Pt alloys, only four bright protrusions were located at the corners of each $(\sqrt{19} \times \sqrt{19})$ supercell with respect to the (1×1) Pt(111) surface. It has fewer features per unit cell than the present high-resolution STM image shown in Fig. 9.7d. *Švec* et al. also proposed a $(\sqrt{19} \times \sqrt{19})$ Ge-Pt surface alloy tetramer model [9.122]. In their simulated STM image, there are also only four bright spots at the corner of each $(\sqrt{19} \times \sqrt{19})$ supercell. At the center of the supercell, the brightness is much lower. One bright and one dark triangular-shaped feature can

be found at the centers of the supercell. Thus, these two Ge-Pt surface alloy models are not applicable to the germanene case.

9.3.2 Germanene Growth on a Au(111) Surface

An atomically thin, two-dimensional multiphase germanene film was fabricated using germanium molecular beam epitaxy on a Au(111) surface as the substrate [9.118]. Several different substrate temperatures were used to anneal the film. A combination of LEED and STM observations was performed at room temperature at different growth stages. The reason for choosing Au(111) as the substrate is that the inverse system, viz. gold grown on a Ge(111) surface, was confirmed in a recent study to form atomically sharp interfaces, without intermixing [9.123].

Figure 9.8 shows an STM image of a monolayer germanium adlayer on a Au(111) surface obtained at a growth temperature of $\approx 200\,^{\circ}\mathrm{C}$. The size of the germanium adlayer on the Au(111) surface is greater than $50 \times 50\,\mathrm{nm}^2$ with a honeycomb appearance and a very small corrugation of only 0.01 nm. Here, the cell size of the honeycomb arrangement is much larger than that of a freestanding monolayer germanene. The cell size of the honeycomb structure in the bottom left corner fits to a $(\sqrt{7} \times \sqrt{7})$ R19.1° superstructure in terms of Au(111). Figure 9.8b shows the LEED pattern of the germanium adlayer superstructures on the Au(111) surface. Figure 9.8c shows a schematic diagram of the diffraction spots in Fig. 9.8b. Diffraction spots from different phases can be observed, namely those from the $(\sqrt{19} \times \sqrt{19})$ R23.4°, (5×5), and $(\sqrt{7} \times \sqrt{7})$ R19.1° phases.

Although the unit cell of the superstructures with respect to the Au(111) surface is confirmed by the STM image and LEED pattern, detailed information regarding the surface adlayer is still difficult to obtain due to the lack of atomic-resolution STM images. According to the previous study, the distance between neighboring germanium atoms is $d_{\mathrm{Ge-Ge}} = 0.238\,\mathrm{nm}$. For the $(\sqrt{7} \times \sqrt{7})$ superstructure, both (2×2) and $(\sqrt{3} \times \sqrt{3})$ R30° germanene adlayers could be possible structures of the unit cell due to the small lattice mismatch. The Ge−Ge distances are 0.221 and 0.255 nm (projected in-plane Ge−Ge distance) for (2×2) and $(\sqrt{3} \times \sqrt{3})$ R30° germanene, respectively.

DFT calculations were performed to optimize the possible geometric structures and simulate the STM images. Figure 9.9 shows several optimized structures and their STM simulations. Due to the lattice mismatch of (2×2) freestanding germanene on the $(\sqrt{7} \times \sqrt{7})$ Au(111) surface, the 4.2% compression strain distorts the germanene lattices and induces considerable buckling in the structure. The atomic structures and simulated STM images of the two lowest-energy structures for (2×2) germanene on top of the $(\sqrt{7} \times \sqrt{7})$ Au(111) supercell are shown in Fig. 9.9a,b. The average height variations in structures 1 and 2 are 0.150 and

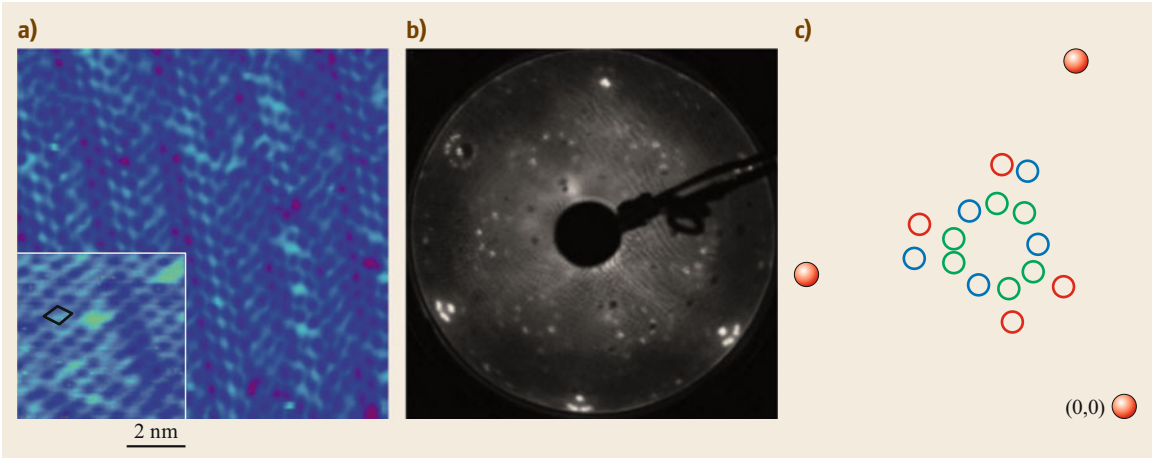

Fig. 9.8a–c STM image and LEED pattern of germanene/Au(111) superstructure. **(a)** STM image of germanium honeycomb structure on a Au(111) surface, where the modulated honeycomb $(\sqrt{7} \times \sqrt{7})$ superstructure is in the *bottom left corner* ($U = -1.12\,\mathrm{V}$, $I = 1.58\,\mathrm{nA}$; the $(\sqrt{7} \times \sqrt{7})$ unit cell is drawn in *black*). **(b)** LEED pattern taken at 59 V; **(c)** schematic illustration of one-sixth of the pattern, with *filled dots*: hidden (0,0) spot and integer order spots, *open circles*: *red*, *blue*, and *green spots* corresponding to the $(\sqrt{7} \times \sqrt{7})$, $(\sqrt{19} \times \sqrt{19})$ and (5×5) superstructure, respectively (reprinted by permission from [9.118], © Institute of Physics 2014)

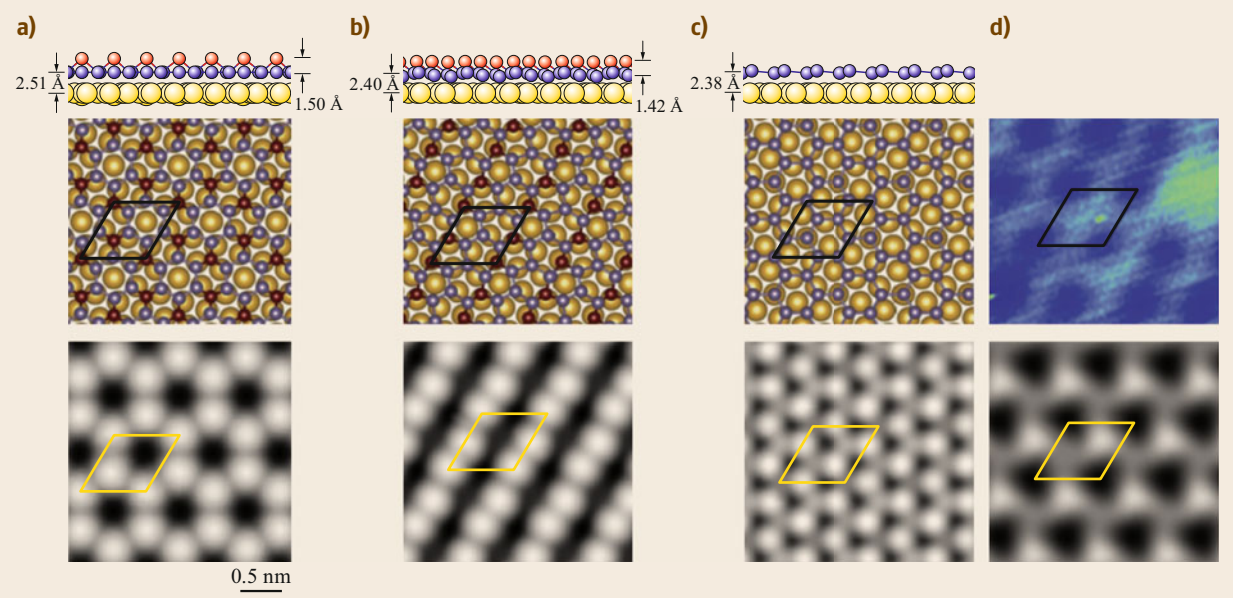

Fig. 9.9a–d Atomic structures and corresponding STM simulations of germanene/Au(111). **(a–c)** Atomic structures (*side* and *top views*) and simulated STM images of three different models of germanene on the $(\sqrt{7}\times\sqrt{7})$ Au(111) surface. Structures 1 **(a)** and 2 **(b)** have (2×2) periodicity, while structure 3 **(c)** has $(\sqrt{3}\times\sqrt{3})$ periodicity with respect to germanene. Protruding Ge atoms are highlighted in *dark red*. The *yellow rhombus* in the STM image indicates the supercells. **(d)** Comparison between STM image (*upper panel*) and simulated STM image for structure 3 after smearing (*lower panel*) (reprinted by permission from [9.118], © Institute of Physics 2014)

0.142 nm, respectively, much larger than what is measured in experiments. In contrast, for the $(\sqrt{3}\times\sqrt{3})$ germanene structure on the $(\sqrt{7}\times\sqrt{7})$ Au(111) surface, the surface adlayer is much flatter (with buckling of less than 0.05 nm). Figure 9.9d shows a comparison between the STM image and the smeared STM simulation image in Fig. 9.9c; their bright spot features match well. DFT calculations also found that structure 3 is more stable than structures 1 and 2. The absorption energy per germanium atom of structure 3 is approximately 10 meV lower than that of structures 1 and 2. In addition, the Au-Ge alloy was also considered. However, the 3d core-level spectra of Ge does not match the experimental observations. The possibility of a Au-Ge alloy can thus be excluded. Finally, a $(\sqrt{3}\times\sqrt{3})$ reconstructed germanene layer on top of a $(\sqrt{7}\times\sqrt{7})$ Au(111) surface can be identified.

9.3.3 Germanene Growth on a MoS_2 Surface

When a germanene epitaxial layer forms on a transition-metal substrate, the pristine Dirac nature of germanene will be destroyed due to the hybridization effect between the epitaxial germanene and the transition-metal substrate [9.22, 118, 119]. Therefore, it is of vital importance to fabricate germanene on a semiconductor (or insulator) with a weak germanene–substrate interaction. Recently, *Zhang* et al. reported the growth and electronic properties of germanene on MoS_2 [9.120].

The MoS_2 samples were cleaved from synthesized 2H-MoS_2 and mounted on a Mo sample holder then introduced into an ultrahigh-vacuum system. Ge was deposited onto the MoS_2 substrate at room temperature and annealed at 1100 K. After the deposition of germanium, the MoS_2 sample was immediately inserted into the STM chamber. The deposition rate was estimated by analyzing several STM images.

Figure 9.10a shows a small-scale STM image of the MoS_2-germanium system. The much brighter STM image of germanium islands on the substrate can be observed clearly. Figure 9.10b,c shows zoomed-in images of the bare MoS_2 substrate and germanium island part, respectively. Differential conductivity (dI/dV) spectra for a germanium island and the bare MoS_2 substrate are depicted in Fig. 9.10d. On the bare MoS_2 region, the dI/dV curve shows a gap near zero bias, which can be explained by the semiconductor properties of MoS_2. In contrast, the dI/dV curve shows a well-defined V shape around zero bias on the germanium island. Un-

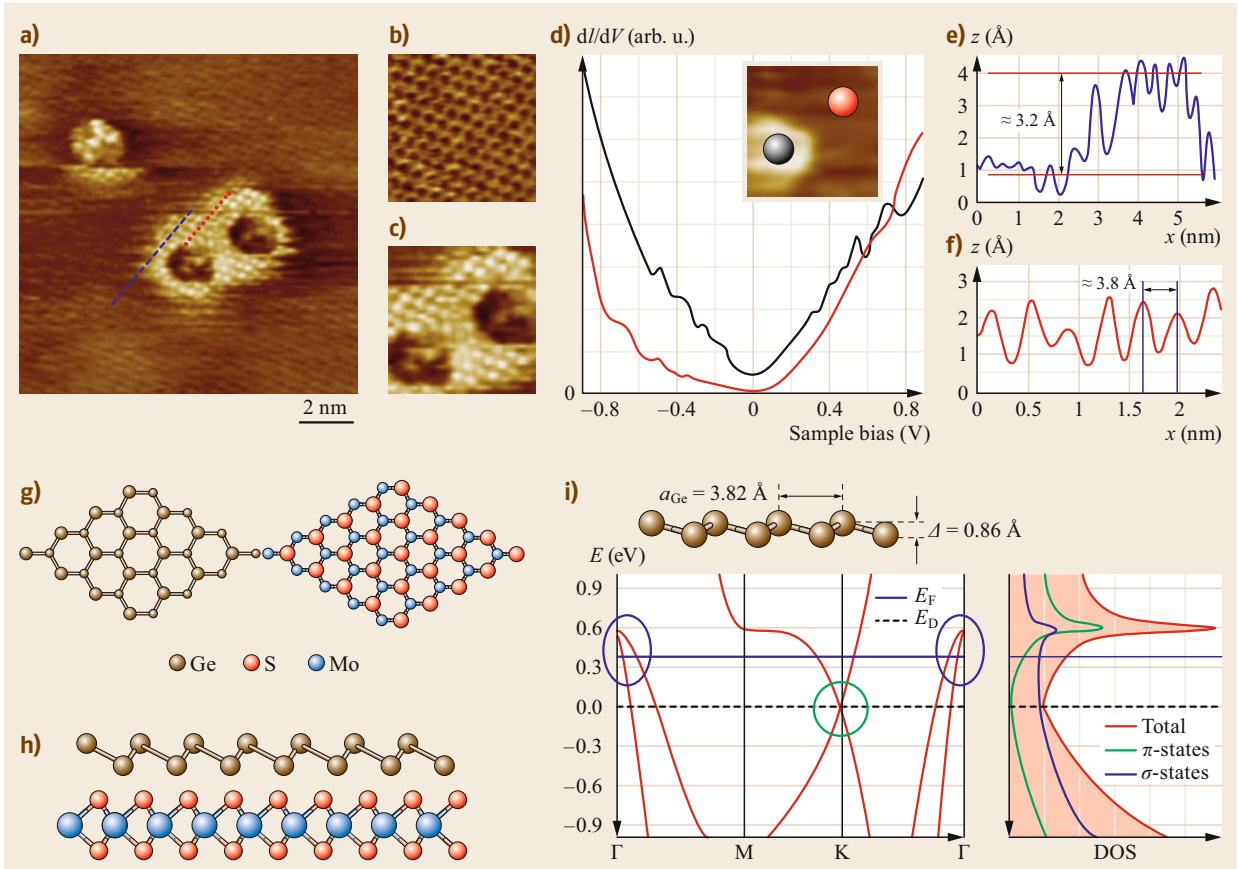

Fig. 9.10a–i Germanium structure on MoS_2. **(a)** STM image of germanium island on MoS_2 substrate ($U = 0.5$ V and $I = 0.3$ nA). **(b)** Zoomed-in STM image on a bare MoS_2 area. **(c)** Zoomed-in STM image on the germanene island of panel **(a)**. **(d)** dI/dV curves on a germanene island (*black curve*) and bare MoS_2 surface (*red curve*). **(e)** Line profile taken across the germanene island indicated by the *blue dashed line* in **(a)**. The apparent height of the germanene islands is ≈ 3.2 Å. **(f)** Line scan taken on top of the germanene island indicated by the *red dashed line* in **(a)**. The measured lattice constant of the germanene island corresponds to 3.8 ± 0.2 Å. **(g)** *Top* and **(h)** *side view*, respectively, of the schematic model of germanene on MoS_2. **(i)** Band structure and projected density of states of the contracted germanene with lattice constant of 3.8 ± 0.2 Å (reprinted by permission from [9.120], © American Physical Society 2016)

der a small bias voltage, the differential conductivity is proportional to the density of states; the density of states of the germanium islands should thus also exhibit a V shape, which is one of the hallmarks of a 2-D Dirac system. Based on the dI/dV measurements, it was concluded that the germanium islands are actually germanene islands. Figure 9.10e,f shows the line profiles across the germanene island as labeled by blue and red dashed lines in Fig. 9.10a. The height of the germanene island is ≈ 3.2 Å, and the periodicity is ≈ 3.8 Å. After increasing the deposition of germanium, the germanium islands become much larger, and a near-monolayer island can be obtained. Figure 9.10g,h shows the top view and side view, respectively, of the schematic model of germanene on MoS_2. The germanium island and the underlying MoS_2 substrate have the same threefold symmetry.

DFT calculations were performed to elucidate the STM observations. Figure 9.10i shows the band structure and projected density of states of contracted germanene with a lattice constant of 3.8 ± 0.2 Å. The germanene is metallic since there are two σ bands close to the Γ point crossing the Fermi energy, while the π bands lead to the formation of a Dirac cone in the vicinity of the K point. The contribution of the σ states to the density of states (DOS) is weakly dependent on energy, as the corresponding dispersion is nearly quadratic [$E_\sigma(k) \propto k^2$]. Therefore, the observed V shape of the total DOS originates predominantly from the π states of germanene.

9.4 Synthesis of Stanene and Other Related Monolayers

In comparison with the first three elements in group IVA (carbon, silicon, and germanium), tin behaves differently. The element tin is usually classified as a post-transition metal. Thus, it is not natural for tin to form a honeycomb monolayer.

9.4.1 Epitaxial Stanene on a Bi_2Te_3 Surface

Stanene is also an important member of the two-dimensional group IVA materials. Theoretical studies have predicted that two-dimensional stanene has a larger bandgap [9.124, 125] and could support a near-room-temperature quantum anomalous Hall (QAH) effect [9.126]. Thermoelectricity enhancement and topological superconductivity of stanene have also been reported [9.127, 128]. Two-dimensional stanene was first synthesized on a $Bi_2Te_3(111)$ surface by using the MBE method [9.23]. High-purity (99.999%) Sn was evaporated from effusion cells onto a flat and well-ordered Bi_2Te_3 surface. The deposition rate was approximately 0.4 ML/min, while the substrate was kept at room temperature. The thickness and growth mode of the Sn film were monitored by reflection high-energy electron diffraction (RHEED) and STM. The STM images were acquired at 77 and 4 K.

Figure 9.11 shows the atomic structure of freestanding stanene and stanene on a Bi_2Te_3 surface. Freestanding stanene has a two-dimensional structure similar to that of silicene and germanene, with a buckled honeycomb lattice as shown in Fig. 9.11a. The height difference between the upper and lower Sn atoms is approximately 0.1 nm. Figure 9.11b shows the RHEED pattern after deposition of an ultrathin Sn film. According to the distance between adjacent diffraction lines in the RHEED patterns obtained before and after deposition of stanene, the in-plane lattice constant of the Sn film matches the substrate within the experimental uncertainty. Figure 9.11c shows the RHEED intensity as a function of deposition time, revealing an obvious variation of the RHEED intensity. The stanene film was formed when deposition was stopped near the peak position of the RHEED intensity, as marked by the blue arrow. STM was also used to investigate the structure of stanene on the $Bi_2Te_3(111)$ surface. Figure 9.11d,e shows large terraces and steps of single quintuple-layer height of the $Bi_2Te_3(111)$ surface and STM topography of Sn films of more than single biatomic layer coverage. Under this coverage, several layers of Sn are observed. According to the measured height line profile in Fig. 9.11f (corresponding to the black line in Fig. 9.11e), the height between the first, second, and third layers of Sn is the same, viz. approximately 0.35 ± 0.02 nm, consistent with the spatial distance between the biatomic layers along the $\langle 111 \rangle$ direction in α-Sn. This indicates that the observed Sn film is a biatomic-layer structure. The large-scale STM topography of the stanene film in Fig. 9.11g indicates that the stanene film is unperturbed after stanene growth. Sharp Bi_2Te_3 steps with a height of 1 nm were still observed, as shown in Fig. 9.11j. Figure 9.11h shows a zoom-in STM image of the stanene film, revealing that it covers about 90% of the substrate and that about 10–15% of the Sn atoms stay on top of it as small islands. From the atomic-resolution STM image in Fig. 9.11i, a (2×2) reconstruction of the surface Sn atoms was observed. The stanene film is not perfectly flat, showing a random height modulation of approximately 0.06 nm, which can be observed from the height line profile in Fig. 9.11k. The biatomic-layer structure of the stanene film is further confirmed by Fig. 9.11l, m. The height difference between the upper and lower atoms is approximately 0.12 ± 0.02 nm, which matches well with the distance between Sn atomic layers in the biatomic-layer structure of stanene.

9.4.2 Epitaxial Hafnene Growth on an Ir(111) Surface

Studies on graphene, silicene, germanene, and other 2-D atomic crystals have been highly successful. However, all these materials are made of group IVA elements, in which the atoms are bonded through sp^2-hybridized orbitals. Meanwhile, two-dimensional atomic crystals made of elements with d electrons are still rare. The questions of whether transition-metal atoms can form monolayer atomic crystals and whether such structures will exhibit novel properties have attracted tremendous interest. Recently, the first pure transition-metal epitaxial honeycomb lattice of hafnium, so-called hafnene, was reported by *Li* et al. [9.129].

Experiments were performed in an UHV system with base pressure in the range of 10^{-10} mbar. Epitaxial hafnene was synthesized by depositing Hf on a clean Ir(111) surface at room temperature and then annealing at 673 K. The sample was subsequently annealed until a well-ordered structure was observed. STM and LEED were performed to characterize the structure and electronic properties of the sample.

Figure 9.12a shows an STM image of a continuous two-dimensional lattice with a honeycomb structure. The orientation of the honeycomb structure is parallel

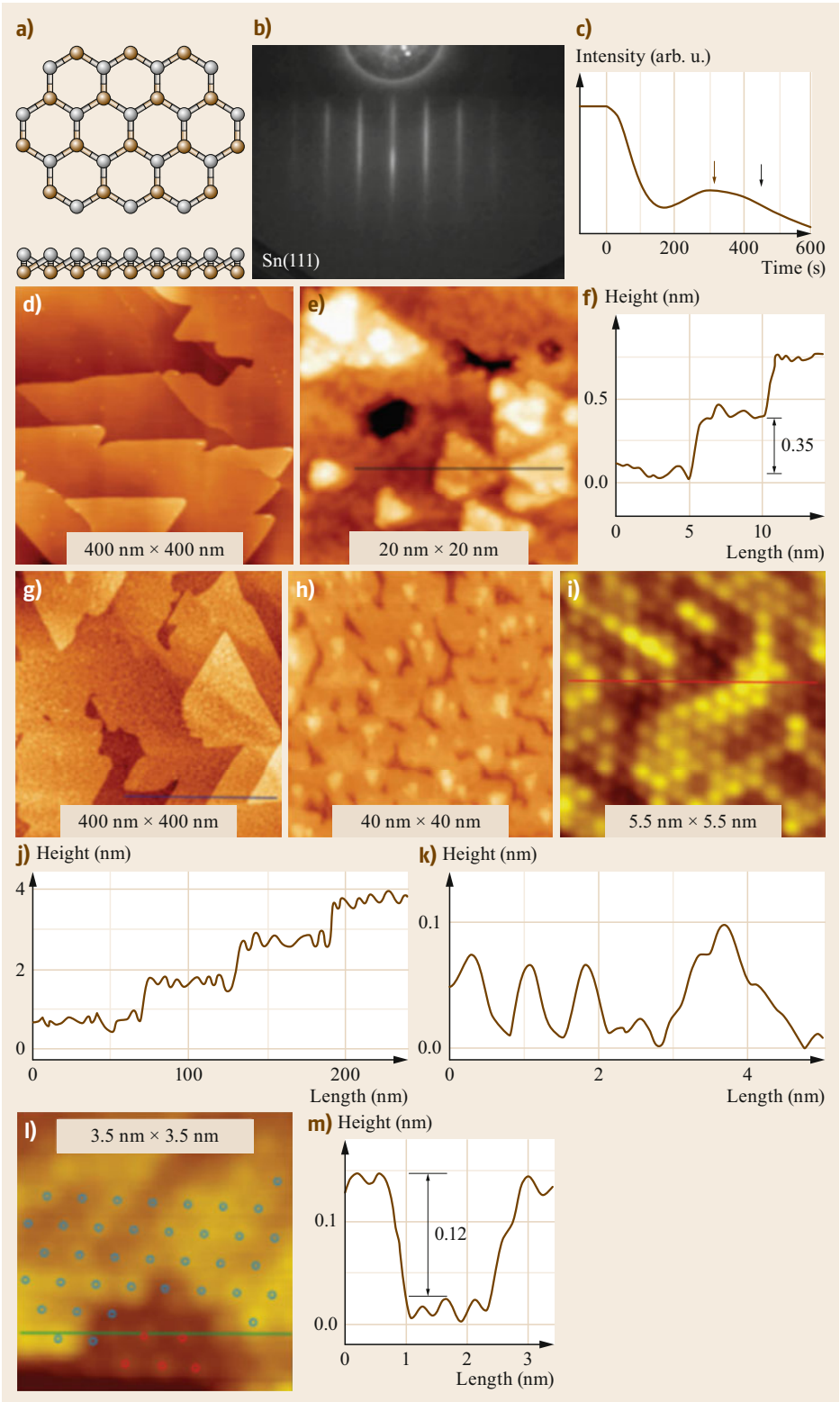
a)
b)
Sn(111)
c)
Intensity (arb. u.)
0
200
400
600
Time (s)
d)
400 nm × 400 nm
e)
20 nm × 20 nm
f) Height (nm)
0.5
0.0
0.35
0
5
10
Length (nm)
g)
400 nm × 400 nm
h)
40 nm × 40 nm
i)
5.5 nm × 5.5 nm
j) Height (nm)
4
2
0
0
100
200
Length (nm)
k) Height (nm)
0.1
0.0
0
2
4
Length (nm)
l)
3.5 nm × 3.5 nm
m) Height (nm)
0.1
0.0
0.12
0
1
2
3
Length (nm)

Fig. 9.11a–m Atomic structure of stanene on Bi_2Te_3 surface. **(a)** Top and side view of freestanding stanene. **(b)** RHEED pattern of stanene film. **(c)** The intensity of a single RHEED point (the *center of the middle strip*) as a function of growth time. The *brown arrow* marks the deposition time for stanene. **(d)** and **(e)** Large-scale STM image of $Bi_2Te_3(111)$ and Sn films of more than biatomic-layer coverage. The corresponding deposition time is marked by the *black arrow* in **(c)**. **(f)** Height line profile of Sn film in **(e)**. **(g)** Large-scale STM image of the stanene film. **(h)** Zoomed-in STM image of stanene. **(i)** Atomically resolved STM image of stanene. **(j)** and **(k)** Height line profiles in **(g)** and **(i)**. **(l)** Atomically resolved STM image of top and bottom atomic layers of stanene. *Blue dots* mark the upper Sn atoms. *Red dots* mark the lower Sn atoms. The two lattices do not coincide. **(m)** Height line profile recorded along the *green line* in panel **(l)** (reprinted by permission from [9.23], © Springer Nature 2015) ◄

to the close-packed $[1\bar{1}0]$ direction of the Ir(111) lattice. The inset LEED pattern reveals that the hafnium honeycomb structure on Ir(111) is a (2×2) superstructure with respect to the Ir(111) lattice. Figure 9.12b shows a zoom of the image in Fig. 9.12a; a perfect honeycomb lattice can be observed. The height profile curve in Fig. 9.12c indicates that the periodicity of the honeycomb lattice is 5.4 Å, consistent with the (2×2) superstructure implied by the LEED pattern. The distance between neighboring hafnium atoms can thus be estimated to be approximately 3.12 Å, very close to the hafnium–hafnium bond length in the bulk material. This suggests that the honeycomb structure is a compact graphene-like structure rather than a hafnium adatom array on the Ir(111) surface.

DFT calculations were also conducted to confirm the experimental observations. To determine the most likely structure on the Ir(111) surface, several different geometric structures thereon were considered. The pure Hf honeycomb lattice on the Ir(111) surface was found to be the most stable structure. Figure 9.12d shows the STM images (top panel), STM simulations (middle panel), and optimized geometry of a hafnium layer on the Ir(111) surface deduced from STM images (lower panel). The simulated STM image shows perfect honeycomb electronic states, consistent with the STM image, further confirming that the hafnium honeycomb structure was successfully fabricated on the Ir(111) surface. Since the hafnium monolayer structure is made of only hafnium atoms and has a similar honeycomb structure to graphene, it can thus be called *hafnene*. Apart from the Ir(111) surface, hafnene can also form on a Rh(111) surface, indicating that hafnene has a very stable honeycomb structure and can be easily synthesized [9.129].

Because hafnium is a transition metal, unlike carbon, silicon, germanium, and other group IVA atoms, monolayer hafnene exhibits its own peculiar properties. Figure 9.12e shows the spin-polarized band structure and density of states of freestanding monolayer hafnene. The density of states of hafnene reveals that d-orbitals are the major contributors to the electronic states around the Fermi energy. This honeycomb structure is metallic, and an obvious spin-polarized density of states can be observed. Further calculations showed that hafnene is ferromagnetic with a magnetic moment of $1.46\,\mu_B$ per Hf atom. Band structure calculations also suggest that Dirac cones exist at the Fermi energy near the K and K′ points of the Brillouin zone for spin-up states. The Fermi velocity at the Dirac cone is approximately 25% of that in graphene. The spin–orbit coupling effect can open a gap of 0.05 eV at the Dirac point. Due to the exchange coupling effect between electrons, the Dirac cone for the spin-down states is about 1.0 eV higher than that for the spin-up states. Such a spin-polarized density of states with d-dominated orbitals around the Fermi energy opens up potential applications for hafnene in spintronics and catalysis.

Although hafnene can be formed on different metal surfaces, the nature of the bonding still needs to be uncovered. This would be helpful for the future construction of transition-metal and other atomic honeycomb structures. These honeycomb structures could provide new platforms to investigate hitherto-unknown quantum phenomena and electronic behaviors in 2-D systems, which may have broad potential applications in future nanotechnology and related areas.

In addition to stanene and hafnene, there has also been progress in synthesizing other metallic element monolayer structures. One such advance is the formation of unsupported iron membranes in graphene nanopores [9.130]. Zhao et al. noticed that, when transferring graphene to TEM grids using $FeCl_3$ etching solution, remnant Fe species from decomposed $FeCl_3$ formed in graphene nanopores. Comprehensive experimental observations and theoretical calculations showed that 2-D crystalline Fe membranes formed in graphene nanopores. Theoretical calculations also predict that a Au membrane can exist in graphene nanopores [9.131]. Meanwhile, recent experiments have shown that a monolayer oxide membrane can form as well [9.35, 36].

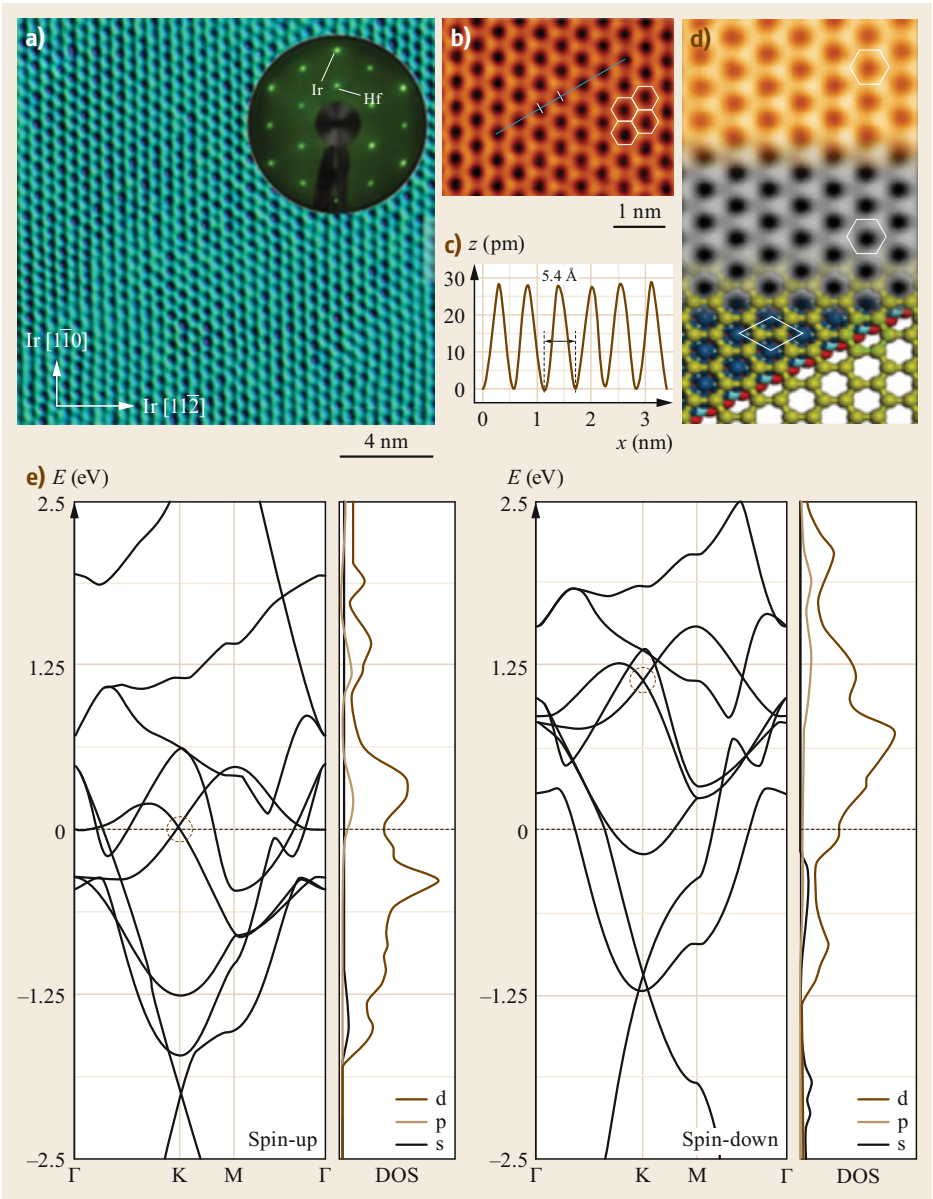

Fig. 9.12a–e Monolayer hafnene on Ir(111) surface. **(a)** STM image of monolayer hafnium structures ($U = -1.0$ V, $I = 0.8$ nA), with *inset* LEED pattern. **(b)** High-resolution STM image ($U = -0.7$ V, $I = 0.16$ nA) and **(c)** height profile taken along the *blue line* in **(b)**. **(d)** Geometric structure (*bottom*), simulated STM image (*middle*), and STM image (*top*) of the monolayer hafnium lattice. The *rhombus* indicates the unit cell of monolayer hafnium atoms. **(e)** Band structure and DOS of free-standing monolayer hafnene for spin-up and spin-down states (reprinted by permission from [9.129], © American Chemical Society 2013)

9.5 Outlook

As an effective method for synthesizing various types of 2-D material, epitaxial growth on transition-metal substrates has made significant advantages. The growth process is well controlled. The fabricated materials are of extremely high quality. However, challenges remain. To take advantage of the as-fabricated high-quality 2-D materials for devices, scientists either need to develop easy and reliable transfer techniques that do not cause too much damage, or fabricate devices in situ. There has been significant progress in both directions in recent years. We can expect an increasing number of high-quality group IVA monolayer materials to be synthesized on more transition-metal surfaces, ultimately leading to the construction of devices.

References

9.1 Y. Wu, Y.-M. Lin, A.A. Bol, K.A. Jenkins, F. Xia, D.B. Farmer, Y. Zhu, P. Avouris: High-frequency, scaled graphene transistors on diamond-like carbon, Nature **472**, 74 (2011)

9.2 R. Cheng, J. Bai, L. Liao, H. Zhou, Y. Chen, L. Liu, Y.-C. Lin, S. Jiang, Y. Huang, X. Duan: High-frequency self-aligned graphene transistors with transferred gate stacks, Proc. Natl. Acad. Sci. **109**, 11588 (2012)

9.3 S.B. Desai, S.R. Madhvapathy, A.B. Sachid, J.P. Llinas, Q. Wang, G.H. Ahn, G. Pitner, M.J. Kim, J. Bokor, C. Hu, H.S.P. Wong, A. Javey: MoS_2 transistors with 1-nanometer gate lengths, Science **354**, 99 (2016)

9.4 H. Li, C. Tsai, A.L. Koh, L. Cai, A.W. Contryman, A.H. Fragapane, J. Zhao, H.S. Han, H.C. Manoharan, F. Abild-Pedersen, J.K. Norskov, X. Zheng: Activating and optimizing MoS_2 basal planes for hydrogen evolution through the formation of strained sulphur vacancies, Nat. Mater. **15**, 48 (2016)

9.5 Q. Tang, D.-E. Jiang: Mechanism of hydrogen evolution reaction on 1T-MoS_2 from first principles, ACS Catalysis **6**, 4953 (2016)

9.6 X.-L. Fan, Y. Yang, P. Xiao: W.-M. Lau. Site-specific catalytic activity in exfoliated MoS_2 single-layer polytypes for hydrogen evolution: basal plane and edges, J. Mater. Chem. A **2**, 20545 (2014)

9.7 Y. Huang, R.J. Nielsen, W.A. Goddard, M.P. Soriaga: The reaction mechanism with free energy barriers for electrochemical dihydrogen evolution on MoS_2, J. Am. Chem. Soc. **137**, 6692 (2015)

9.8 X. Zhao, D. Fu, Z. Ding, Y.-Y. Zhang, D. Wan, S.J.R. Tan, Z. Chen, K. Leng, J. Dan, W. Fu, D. Geng, P. Song, Y. Du, T. Venkatesan, S.T. Pantelides, S.J. Pennycook, W. Zhou, K.P. Loh: Mo-terminated edge reconstructions in nanoporous molybdenum disulfide film, Nano Lett. **18**, 482 (2018)

9.9 A.K. Geim, I.V. Grigorieva: Van der Waals heterostructures, Nature **499**, 419 (2013)

9.10 L. Lu, J. Velasco, E. Huang, S. Kahn, C. Nosiglia, H.-Z. Tsai, W. Yang, T. Taniguchi, K. Watanabe, Y. Zhang, G. Zhang, M. Crommie, A. Zettl, F. Wang: Photoinduced doping in heterostructures of graphene and boron nitride, Nat. Nanotech. **9**, 348 (2014)

9.11 M. Lee, J.R. Wallbank, P. Gallagher, K. Watanabe, T. Taniguchi, V.I. Fal'ko, D. Goldhaber-Gordon: Ballistic miniband conduction in a graphene superlattice, Science **353**, 1526 (2016)

9.12 S. Chen, Z. Han, M.M. Elahi, K.M.M. Habib, L. Wang, B. Wen, Y. Gao, T. Taniguchi, K. Watanabe, J. Hone, A.W. Ghosh, C.R. Dean: Electron optics with p-n junctions in ballistic graphene, Science **353**, 1522 (2016)

9.13 W. Zhou, Y.-Y. Zhang, J. Chen, D. Li, J. Zhou, Z. Liu, M.F. Chisholm, S.T. Pantelides, K.P. Loh: Dislocation-driven growth of two-dimensional lateral quantum-well superlattices, Sci. Adv. **4**, eaap9096 (2018)

9.14 K.S. Novoselov, A.K. Geim, S.V. Morozov, D. Jiang, Y. Zhang, S.V. Dubonos, I.V. Grigorieva, A.A. Firsov: Electric field effect in atomically thin carbon films, Science **306**, 666 (2004)

9.15 Y. Lin, J.W. Connell: Advances in 2D boron nitride nanostructures: nanosheets, nanoribbons, nanomeshes, and hybrids with graphene, Nanoscale **4**, 6908 (2012)

9.16 S. Stankovich, D.A. Dikin, G.H.B. Dommett, K.M. Kohlhaas, E.J. Zimney, E.A. Stach, R.D. Piner, S.T. Nguyen, R.S. Ruoff: Graphene-based composite materials, Nature **442**, 282 (2006)

9.17 K. Raidongia, A. Nag, K.P.S.S. Hembram, U.V. Waghmare, R. Datta, C.N.R. Rao: BCN: a graphene analogue with remarkable adsorptive properties, Chem. Eur. J. **16**, 149 (2010)

9.18 K. Takeda, K. Shiraishi: Theoretical possibility of stage corrugation in Si and Ge analogs of graphite, Phys. Rev. B **50**, 14916 (1994)

9.19 S. Cahangirov, M. Topsakal, E. Aktürk, H. Şahin, S. Ciraci: Two- and one-dimensional honeycomb structures of silicon and germanium, Phys. Rev. Lett. **102**, 236804 (2009)

9.20 C.-C. Liu, W. Feng, Y. Yao: Quantum spin Hall effect in silicene and two-dimensional germanium, Phys. Rev. Lett. **107**, 076802 (2011)

9.21 L. Meng, Y. Wang, L. Zhang, S. Du, R. Wu, L. Li, Y. Zhang, G. Li, H. Zhou, W.A. Hofer: Buckled silicene formation on Ir(111), Nano Lett. **13**, 685 (2013)

9.22 L. Li, S. Lu, J. Pan, Z. Qin, Y. Wang, Y. Wang, G. Cao, H. Gao: Buckled germanene formation on Pt(111), Adv. Mater. **26**, 4820 (2014)

9.23 F.F. Zhu, W.J. Chen, Y. Xu, C.L. Gao, D.D. Guan, C.H. Liu, D. Qian, S.C. Zhang, J.F. Jia: Epitaxial growth of two-dimensional stanene, Nat. Mater. **14**, 1020 (2015)

9.24 X. Duan, C. Wang, A. Pan, R. Yu, X. Duan: Two-dimensional transition metal dichalcogenides as atomically thin semiconductors: opportunities and challenges, Chem. Soc. Rev. **44**, 8859 (2015)

9.25 A.A. Tedstone, D.J. Lewis, P. O'Brien: Synthesis, properties, and applications of transition metal-doped layered transition metal dichalcogenides, Chem. Mater. **28**, 1965 (2016)

9.26 J.-F. Ge, Z.-L. Liu, C. Liu, C.-L. Gao, D. Qian, Q.-K. Xue, Y. Liu, J.-F. Jia: Superconductivity above 100 K in single-layer FeSe films on doped $SrTiO_3$, Nat. Mater. **14**, 285 (2015)

9.27 M. Langer, M. Kisiel, R. Pawlak, F. Pellegrini, G.E. Santoro, R. Buzio, A. Gerbi, G. Balakrishnan, A. Baratoff, E. Tosatti, E. Meyer: Giant frictional dissipation peaks and charge-density-wave slips at the $NbSe_2$ surface, Nat. Mater. **13**, 173 (2014)

9.28 X. Xi, L. Zhao, Z. Wang, H. Berger, L. Forró, J. Shan, K.F. Mak: Strongly enhanced charge-density-wave order in monolayer $NbSe_2$, Nat. Nanotech. **10**, 765 (2015)

9.29 G. Cunningham, M. Lotya, C.S. Cucinotta, S. Sanvito, S.D. Bergin, R. Menzel, M.S.P. Shaffer, J.N. Coleman: Solvent exfoliation of transition metal dichalco-

genides: dispersibility of exfoliated nanosheets varies only weakly between compounds, ACS Nano **6**, 3468 (2012)
9.30 D. Fu, X. Zhao, Y.-Y. Zhang, L. Li, H. Xu, A.R. Jang, S.I. Yoon, P. Song, S.M. Poh, T. Ren, Z. Ding, W. Fu, T.J. Shin, H.S. Shin, S.T. Pantelides, W. Zhou, K.P. Loh: Molecular beam epitaxy of highly crystalline monolayer molybdenum disulfide on hexagonal boron nitride, J. Am. Chem. Soc. **139**, 9392 (2017)
9.31 J. Zhou, J. Lin, X. Huang, Y. Zhou, Y. Chen, J. Xia, H. Wang, Y. Xie, H. Yu, J. Lei, D. Wu, F. Liu, Q. Fu, Q. Zeng, C.-H. Hsu, C. Yang, L. Lu, T. Yu, Z. Shen, H. Lin, B.I. Yakobson, Q. Liu, K. Suenaga, G. Liu, Z. Liu: A library of atomically thin metal chalcogenides, Nature **556**, 355 (2018)
9.32 M. Osada, T. Sasaki: Two-dimensional dielectric nanosheets: novel nanoelectronics from nanocrystal building blocks, Adv. Mater. **24**, 210 (2012)
9.33 B.-W. Li, M. Osada, T.C. Ozawa, Y. Ebina, K. Akatsuka, R. Ma, H. Funakubo, T. Sasaki: Engineered interfaces of artificial perovskite oxide superlattices via nanosheet deposition process, ACS Nano **4**, 6673 (2010)
9.34 A. Atrei, A.M. Ferrari, D. Szieberth, B. Cortigiani, G. Rovida: Lepidocrocite-like structure of the TiO_2 monolayer grown on Ag(100), Phys. Chem. Chem. Phys. **12**, 11587 (2010)
9.35 K. Yin, Y.-Y. Zhang, Y. Zhou, L. Sun, M.F. Chisholm, S.T. Pantelides, W. Zhou: Unsupported single-atom-thick copper oxide monolayers, 2D Mater. **4**, 011001 (2017)
9.36 H.T. Quang, A. Bachmatiuk, A. Dianat, F. Ortmann, J. Zhao, J.H. Warner, J. Eckert, G. Cunniberti, M.H. Rümmeli: In situ observations of free-standing graphene-like mono- and bilayer ZnO membranes, ACS Nano **9**, 11408 (2015)
9.37 Y. Wang, C. Zhou, W. Wang, Y. Zhao: Preparation of two dimensional atomic crystals BN, WS_2, and MoS_2 by supercritical CO_2 assisted with ultrasound, Ind. Eng. Chem. Res. **52**, 4379 (2013)
9.38 Q.H. Wang, K. Kalantar-Zadeh, A. Kis, J.N. Coleman, M.S. Strano: Electronics and optoelectronics of two-dimensional transition metal dichalcogenides, Nat. Nanotech. **7**, 699 (2012)
9.39 C. Berger, Z. Song, T. Li, X. Li, A.Y. Ogbazghi, R. Feng, Z. Dai, A.N. Marchenkov, E.H. Conrad, P.N. First, W.A. de Heer: Ultrathin epitaxial graphite: 2D electron gas properties and a route toward graphene-based nanoelectronics, J. Phys. Chem. B **108**, 19912 (2004)
9.40 G.M. Rutter, J.N. Crain, N.P. Guisinger, T. Li, P.N. First, J.A. Stroscio: Scattering and interference in epitaxial graphene, Science **317**, 219 (2007)
9.41 A. Reina, X. Jia, J. Ho, D. Nezich, H. Son, V. Bulovic, M.S. Dresselhaus, J. Kong: Large area, few-layer graphene films on arbitrary substrates by chemical vapor deposition, Nano Lett. **9**, 30 (2009)
9.42 Y. Wang, L. Li, W. Yao, S. Song, J.T. Sun, J. Pan, X. Ren, C. Li, E. Okunishi, Y.-Q. Wang, E. Wang, Y. Shao, Y.Y. Zhang, H. Yang, E.F. Schwier, H. Iwasawa, K. Shimada, M. Taniguchi, Z. Cheng, S. Zhou, S. Du, S.J. Pennycook, S.T. Pantelides, H.-J. Gao: Monolayer $PtSe_2$, a new semiconducting transition-metal-dichalcogenide, epitaxially grown by direct selenization of Pt, Nano Lett. **15**, 4013 (2015)
9.43 X. Lin, J.C. Lu, Y. Shao, Y.Y. Zhang, X. Wu, J.B. Pan, L. Gao, S.Y. Zhu, K. Qian, Y.F. Zhang, D.L. Bao, L.F. Li, Y.Q. Wang, Z.L. Liu, J.T. Sun, T. Lei, C. Liu, J.O. Wang, K. Ibrahim, D.N. Leonard, W. Zhou, H.M. Guo, Y.L. Wang, S.X. Du, S.T. Pantelides, H.J. Gao: Intrinsically patterned two-dimensional materials for selective adsorption of molecules and nanoclusters, Nat. Mater. **16**, 717 (2017)
9.44 S. Hagstrom, H.B. Lyon, G.A. Somorjai: Surface structures on the clean platinum(100) surface, Phys. Rev. Lett. **15**, 491 (1965)
9.45 S.D. Robertson: Carbon formation from methane pyrolysis over some transition metal surfaces—I. Nature and properties of the carbons formed, Carbon **8**, 365 (1970)
9.46 Y. Zhang, Y.-W. Tan, H.L. Stormer, P. Kim: Experimental observation of the quantum Hall effect and Berry's phase in graphene, Nature **438**, 201 (2005)
9.47 Y. Pan, L. Zhang, L. Huang, L. Li, L. Meng, M. Gao, Q. Huan, X. Lin, Y. Wang, S. Du, H.-J. Freund, H.-J. Gao: Construction of 2D atomic crystals on transition metal surfaces: graphene, silicene, and hafnene, Small **10**, 2215 (2014)
9.48 Y. Pan, H.G. Zhang, D.X. Shi, J.T. Sun, S.X. Du, F. Liu, H.-J. Gao: Highly ordered, millimeter-scale, continuous, single-crystalline graphene monolayers formed on Ru(0001), Adv. Mater. **21**, 2777 (2009)
9.49 A.L. Vázquez de Parga, F. Calleja, B. Borca, M.C.G. Passeggi, J.J. Hinarejos, F. Guinea, R. Miranda: Periodically rippled graphene: growth and spatially resolved electronic structure, Phys. Rev. Lett. **100**, 056807 (2008)
9.50 J. Mao, L. Huang, Y. Pan, M. Gao, J. He, H. Zhou, H. Guo, Y. Tian, Q. Zou, L. Zhang, H. Zhang, Y. Wang, S. Du, X. Zhou, A.H. Castro Neto, H.-J. Gao: Silicon layer intercalation of centimeter-scale, epitaxially grown monolayer graphene on Ru(0001), Appl. Phys. Lett. **100**, 093101 (2012)
9.51 S. Lizzit, R. Larciprete, P. Lacovig, M. Dalmiglio, F. Orlando, A. Baraldi, L. Gammelgaard, L. Barreto, M. Bianchi, E. Perkins, P. Hofmann: Transfer-free electrical insulation of epitaxial graphene from its metal substrate, Nano Lett. **12**, 4503 (2012)
9.52 P. Leicht, L. Zielke, S. Bouvron, R. Moroni, E. Voloshina, L. Hammerschmidt, Y.S. Dedkov, M. Fonin: In situ fabrication of quasi-free-standing epitaxial graphene nanoflakes on gold, ACS Nano **8**, 3735 (2014)
9.53 O. Deniz, C. Sánchez-Sánchez, T. Dumslaff, X. Feng, A. Narita, K. Müllen, N. Kharche, V. Meunier, R. Fasel, P. Ruffieux: Revealing the electronic structure of silicon intercalated armchair graphene nanoribbons by scanning tunneling spectroscopy, Nano Lett. **17**, 2197 (2017)
9.54 L. Gao, W. Ren, H. Xu, L. Jin, Z. Wang, T. Ma, L.-P. Ma, Z. Zhang, Q. Fu, L.-M. Peng, X. Bao, H.-M. Cheng: Repeated growth and bubbling transfer of graphene with millimetre-size single-

crystal grains using platinum, Nat. Commun. **3**, 699 (2012)
9.55 Y. Pan, D.-X. Shi, H.-J. Gao: Formation of graphene on Ru(0001) surface, Chin. Phys. **16**, 3151 (2007)
9.56 D. Martoccia, P.R. Willmott, T. Brugger, M. Björck, S. Günther, C.M. Schlepütz, A. Cervellino, S.A. Pauli, B.D. Patterson, S. Marchini, J. Wintterlin, W. Moritz, T. Greber: Graphene on Ru(0001): a 25 × 25 supercell, Phys. Rev. Lett. **101**, 126102 (2008)
9.57 J.-T. Sun, S.-X. Du, W.-D. Xiao, H. Hu, Y.-Y. Zhang, G. Li, H.-J. Gao: Effect of strain on geometric and electronic structures of graphene on Ru(0001) surface, Chin. Phys. B **18**, 3008 (2009)
9.58 D.-E. Jiang, M.-H. Du, S. Dai: First principles study of the graphene/Ru(0001) interface, J. Chem. Phys. **130**, 074705 (2009)
9.59 B. Wang, M.L. Bocquet, S. Marchini, S. Gunther, J. Wintterlin: Chemical origin of a graphene moire overlayer on Ru(0001), Phys. Chem. Chem. Phys. **10**, 3530 (2008)
9.60 L.Z. Zhang, S.X. Du, J.T. Sun, L. Huang, L. Meng, W.Y. Xu, L.D. Pan, Y. Pan, Y.L. Wang, W.A. Hofer, H.J. Gao: Growth mechanism of metal clusters on a graphene/Ru(0001) template, Adv. Mater. Interfaces **1**, 1300104 (2014)
9.61 Y. Pan, M. Gao, L. Huang, F. Liu, H.J. Gao: Directed self-assembly of monodispersed platinum nanoclusters on graphene moiré template, Appl. Phys. Lett. **95**, 093106 (2009)
9.62 K. Donner, P. Jakob: Structural properties and site specific interactions of Pt with the graphene–Ru(0001) moiré overlayer, J. Chem. Phys. **131**, 164701 (2009)
9.63 B. Wang, B. Yoon, M. König, Y. Fukamori, F. Esch, U. Heiz, U. Landman: Size-selected monodisperse nanoclusters on supported graphene: bonding, isomerism, and mobility, Nano Lett. **12**, 5907 (2012)
9.64 B. Borca, S. Barja, M. Garnica, D. Sánchez-Portal, V.M. Silkin, E.V. Chulkov, C.F. Hermanns, J.J. Hinarejos, A.L. Vázquez de Parga, A. Arnau, P.M. Echenique, R. Miranda: Potential energy landscape for hot electrons in periodically nanostructured graphene, Phys. Rev. Lett. **105**, 036804 (2010)
9.65 H.G. Zhang, T. Greber: Comment on "potential energy landscape for hot electrons in periodically nanostructured graphene", Phys. Rev. Lett. **105**, 219701 (2010)
9.66 H.G. Zhang, H. Hu, Y. Pan, J.H. Mao, M. Gao, H.M. Guo, S.X. Du, T. Greber, H.J. Gao: Graphene based quantum dots, J. Phys. Condens. Matter **22**, 302001 (2010)
9.67 G. Li, H.T. Zhou, L.D. Pan, Y. Zhang, J.H. Mao, Q. Zou, H.M. Guo, Y.L. Wang, S.X. Du, H.-J. Gao: Self-assembly of C_{60} monolayer on epitaxially grown, nanostructured graphene on Ru(0001) surface, Appl. Phys. Lett. **100**, 013304 (2012)
9.68 K. Yang, W.D. Xiao, Y.H. Jiang, H.G. Zhang, L.W. Liu, J.H. Mao, H.T. Zhou, S.X. Du, H.J. Gao: Molecule–substrate coupling between metal phthalocyanines and epitaxial graphene grown on Ru(0001) and Pt(111), J. Phys. Chem. C **116**, 14052 (2012)
9.69 X. Fei, L. Zhang, W. Xiao, H. Chen, Y. Que, L. Liu, K. Yang, S. Du, H.-J. Gao: Structural and electronic properties of Pb-intercalated graphene on Ru(0001), J. Phys. Chem. C **119**, 9839 (2015)
9.70 A. Dong, Q. Fu, M. Wei, Y. Liu, Y. Ning, F. Yang, H. Bluhm, X. Bao: Facile oxygen intercalation between full layer graphene and Ru(0001) under ambient conditions, Surf. Sci. **634**, 37 (2015)
9.71 E. Voloshina, N. Berdunov, Y. Dedkov: Restoring a nearly free-standing character of graphene on Ru(0001) by oxygen intercalation, Sci. Rep. **6**, 20285 (2016)
9.72 M. Gao, Y. Pan, L. Huang, H. Hu, L.Z. Zhang, H.M. Guo, S.X. Du, H.J. Gao: Epitaxial growth and structural property of graphene on Pt(111), Appl. Phys. Lett. **98**, 033101 (2011)
9.73 P. Sutter, J.T. Sadowski, E. Sutter: Graphene on Pt(111): growth and substrate interaction, Phys. Rev. B **80**, 245411 (2009)
9.74 J. Coraux, A.T. N'Diaye, M. Engler, C. Busse, D. Wall, N. Buckanie, F.-J.M. zu Heringdorf, R. van Gastel, B. Poelsema, T. Michely: Growth of graphene on Ir(111), New J. Phys. **11**, 023006 (2009)
9.75 A.T. N'Diaye, J. Coraux, T.N. Plasa, C. Busse, T. Michely: Structure of epitaxial graphene on Ir(111), New J. Phys. **10**, 043033 (2008)
9.76 M. Sicot, S. Bouvron, O. Zander, U. Rüdiger, Y.S. Dedkov, M. Fonin: Nucleation and growth of nickel nanoclusters on graphene moiré on Rh(111), Appl. Phys. Lett. **96**, 093115 (2010)
9.77 E.N. Voloshina, Y.S. Dedkov, S. Torbrügge, A. Thissen, M. Fonin: Graphene on Rh(111): scanning tunneling and atomic force microscopies studies, Appl. Phys. Lett. **100**, 241606 (2012)
9.78 L. Gao, J.R. Guest, N.P. Guisinger: Epitaxial graphene on Cu(111), Nano Lett. **10**, 3512 (2010)
9.79 E. Loginova, N.C. Bartelt, P.J. Feibelman, K.F. McCarty: Factors influencing graphene growth on metal surfaces, New J. Phys. **11**, 063046 (2009)
9.80 P.W. Sutter, J.-I. Flege, E.A. Sutter: Epitaxial graphene on ruthenium, Nat. Mater. **7**, 406 (2008)
9.81 P. Zeller, X. Ma, S. Günther: Indexing moiré patterns of metal-supported graphene and related systems: strategies and pitfalls, New J. Phys. **19**, 013015 (2017)
9.82 A.B. Preobrajenski, M.L. Ng, A.S. Vinogradov, N. Mårtensson: Controlling graphene corrugation on lattice-mismatched substrates, Phys. Rev. B **78**, 073401 (2008)
9.83 J.C. Koepke, J.D. Wood, D. Estrada, Z.-Y. Ong, K.T. He, E. Pop, J.W. Lyding: Atomic-scale evidence for potential barriers and strong carrier scattering at graphene grain boundaries: a scanning tunneling microscopy study, ACS Nano **7**, 75 (2013)
9.84 K.W. Clark, X.G. Zhang, I.V. Vlassiouk, G. He, R.M. Feenstra, A.-P. Li: Spatially resolved mapping of electrical conductivity across individual domain (grain) boundaries in graphene, ACS Nano **7**, 7956 (2013)
9.85 R.-S. Ma, Q. Huan, L.-M. Wu, J.-H. Yan, Y.-Y. Zhang, L.-H. Bao, Y.-Q. Liu, S.-X. Du, H.-J. Gao: Direct measurements of conductivity and mobility in mil-

limeter-sized single-crystalline graphene via van der Pauw geometry, Chin. Phys. B **26**, 066801 (2017)
9.86 R. Ma, Q. Huan, L. Wu, J. Yan, W. Guo, Y.-Y. Zhang, S. Wang, L. Bao, Y. Liu, S.-X. Du, S.T. Pantelides, H.-J. Gao: Direct four-probe measurement of grain-boundary resistivity and mobility in millimeter-sized graphene, Nano Lett. **17**, 5291 (2017)
9.87 L. Meng, R. Wu, H. Zhou, G. Li, Y. Zhang, L. Li, Y. Wang, H.J. Gao: Silicon intercalation at the interface of graphene and Ir(111), Appl. Phys. Lett. **100**, 083101 (2012)
9.88 H. Chen, Y. Que, L. Tao, Y.-Y. Zhang, X. Lin, W. Xiao, D. Wang, S. Du, S.T. Pantelides, H.-J. Gao: Recovery of edge states of graphene nanoislands on an iridium substrate by silicon intercalation, Nano Res. **11**, 3722 (2017)
9.89 Y. Li, D. Subramaniam, N. Atodiresei, P. Lazić, V. Caciuc, C. Pauly, A. Georgi, C. Busse, M. Liebmann, S. Blügel, M. Pratzer, M. Morgenstern, R. Mazzarello: Absence of edge states in covalently bonded zigzag edges of graphene on Ir(111), Adv. Mater. **25**, 1967 (2013)
9.90 R. Brako, D. Šokčević, P. Lazić, N. Atodiresei: Graphene on the Ir(111) surface: from van der Waals to strong bonding, New J. Phys. **12**, 113016 (2010)
9.91 M. Fuentes-Cabrera, M.I. Baskes, A.V. Melechko, M.L. Simpson: Bridge structure for the graphene/Ni(111) system: a first principles study, Phys. Rev. B **77**, 035405 (2008)
9.92 X. Peng, R. Ahuja: Epitaxial graphene monolayer and bilayers on Ru(0001): *ab initio* calculations, Phys. Rev. B **82**, 045425 (2010)
9.93 M. Iannuzzi, J. Hutter: Comparative study of the nature of chemical bonding of corrugated graphene on Ru(0001) and Rh(111) by electronic structure calculations, Surf. Sci. **605**, 1360 (2011)
9.94 M. Lei, W. Rongting, Z. Lizhi, L. Linfei, D. Shixuan, W. Yeliang, H.J. Gao: Multi-oriented moiré superstructures of graphene on Ir(111): experimental observations and theoretical models, J. Phys. Condens. Matter **24**, 314214 (2012)
9.95 F. Mittendorfer, A. Garhofer, J. Redinger, J. Klimeš, J. Harl, G. Kresse: Graphene on Ni(111): strong interaction and weak adsorption, Phys. Rev. B **84**, 201401 (2011)
9.96 T. Olsen, K.S. Thygesen: Random phase approximation applied to solids, molecules, and graphene–metal interfaces: From van der Waals to covalent bonding, Phys. Rev. B **87**, 075111 (2013)
9.97 R.G.V. Wesep, H. Chen, W. Zhu, Z. Zhang: Communication: Stable carbon nanoarches in the initial stages of epitaxial growth of graphene on Cu(111), J. Chem. Phys. **134**, 171105 (2011)
9.98 P. Vogt, P. De Padova, C. Quaresima, J. Avila, E. Frantzeskakis, M.C. Asensio, A. Resta, B. Ealet, G. Le Lay: Silicene: compelling experimental evidence for graphenelike two-dimensional silicon, Phys. Rev. Lett. **108**, 155501 (2012)
9.99 M. Ezawa: Valley-polarized metals and quantum anomalous Hall effect in silicene, Phys. Rev. Lett. **109**, 055502 (2012)
9.100 N. Drummond, V. Zolyomi, V. Fal'Ko: Electrically tunable band gap in silicene, Phys. Rev. B **85**, 075423 (2012)
9.101 L. Huang, Y.-F. Zhang, Y.-Y. Zhang, W. Xu, Y. Que, E. Li, J.-B. Pan, Y.-L. Wang, Y. Liu, S.-X. Du, S.T. Pantelides, H.-J. Gao: Sequence of silicon monolayer structures grown on a Ru surface: from a herringbone structure to silicene, Nano Lett. **17**, 1161 (2017)
9.102 B. Aufray, A. Kara, S. Vizzini, H. Oughaddou, C. Leandri, B. Ealet, G. Le Lay: Graphene-like silicon nanoribbons on Ag(110): a possible formation of silicene, Appl. Phys. Lett. **96**, 183102 (2010)
9.103 B. Feng, Z. Ding, S. Meng, Y. Yao, X. He, P. Cheng, L. Chen, K. Wu: Evidence of silicene in honeycomb structures of silicon on Ag(111), Nano Lett. **12**, 3507 (2012)
9.104 C.-L. Lin, R. Arafune, K. Kawahara, N. Tsukahara, E. Minamitani, Y. Kim, N. Takagi, M. Kawai: Structure of silicene grown on Ag(111), Appl. Phys. Express **5**, 045802 (2012)
9.105 L. Chen, C.-C. Liu, B. Feng, X. He, P. Cheng, Z. Ding, S. Meng, Y. Yao, K. Wu: Evidence for dirac fermions in a honeycomb lattice based on silicon, Phys. Rev. Lett. **109**, 056804 (2012)
9.106 P. De Padova, C. Quaresima, C. Ottaviani, P.M. Sheverdyaeva, P. Moras, C. Carbone, D. Topwal, B. Olivieri, A. Kara, H. Oughaddou, B. Aufray, G. Le Lay: Evidence of graphene-like electronic signature in silicene nanoribbons, Appl. Phys. Lett. **96**, 261905 (2010)
9.107 B. Lalmi, H. Oughaddou, H. Enriquez, A. Kara, S. Vizzini, B. Ealet, B. Aufray: Epitaxial growth of a silicene sheet, Appl. Phys. Lett. **97**, 223109 (2010)
9.108 A. Fleurence, R. Friedlein, T. Ozaki, H. Kawai, Y. Wang, Y. Yamada-Takamura: Experimental evidence for epitaxial silicene on diboride thin films, Phys. Rev. Lett. **108**, 245501 (2012)
9.109 H. Shu, D. Cao, P. Liang, X. Wang, X. Chen, W. Lu: Two-dimensional silicene nucleation on a Ag(111) surface: structural evolution and the role of surface diffusion, Phys. Chem. Chem. Phys. **16**, 304 (2014)
9.110 S.K. Mahatha, P. Moras, P.M. Sheverdyaeva, V. Bellini, T.O. Menteş, A. Locatelli, R. Flammini, K. Horn, C. Carbone: Absence of Dirac cones in monolayer silicene and multilayer Si films on Ag(111), J. Electron. Spectrosc. Relat. Phenom. **219**, 2 (2017)
9.111 G.L. Lay, P.D. Padova, A. Resta, T. Bruhn, P. Vogt: Epitaxial silicene: can it be strongly strained?, J. Phys. D Appl. Phys. **45**, 392001 (2012)
9.112 A. Resta, T. Leoni, C. Barth, A. Ranguis, C. Becker, T. Bruhn, P. Vogt, G. Le Lay: Atomic structures of silicene layers grown on Ag(111): scanning tunneling microscopy and noncontact atomic force microscopy observations, Sci. Rep. **3**, 2399 (2013)
9.113 L. Chen, H. Li, B. Feng, Z. Ding, J. Qiu, P. Cheng, K. Wu, S. Meng: Spontaneous symmetry breaking and dynamic phase transition in monolayer silicene, Phys. Rev. Lett. **110**, 085504 (2013)
9.114 Y. Feng, D. Liu, B. Feng, X. Liu, L. Zhao, Z. Xie, Y. Liu, A. Liang, C. Hu, Y. Hu, S. He, G. Liu, J. Zhang, C. Chen,

Z. Xu, L. Chen, K. Wu, Y.-T. Liu, H. Lin, Z.-Q. Huang, C.-H. Hsu, F.-C. Chuang, A. Bansil, X.J. Zhou: Direct evidence of interaction-induced Dirac cones in a monolayer silicene/Ag(111) system, Proc. Natl. Acad. Sci. **113**, 14656 (2016)

9.115 C.-L. Lin, R. Arafune, K. Kawahara, M. Kanno, N. Tsukahara, E. Minamitani, Y. Kim, M. Kawai, N. Takagi: Substrate-induced symmetry breaking in silicene, Phys. Rev. Lett. **110**, 076801 (2013)

9.116 S.K. Mahatha, P. Moras, V. Bellini, P.M. Sheverdyaeva, C. Struzzi, L. Petaccia, C. Carbone: Silicene on Ag(111): a honeycomb lattice without Dirac bands, Phys. Rev. B **89**, 201416 (2014)

9.117 P.M. Sheverdyaeva, S.K. Mahatha, P. Moras, L. Petaccia, G. Fratesi, G. Onida, C. Carbone: Electronic states of silicene allotropes on Ag(111), ACS Nano **11**, 975 (2017)

9.118 M.E. Davila, A. Rubio, G.L. Lay: Germanene: a novel two-dimensional germanium allotrope akin to graphene and silicene, New J. Phys. **16**, 95002 (2014)

9.119 M. Derivaz, D. Dentel, R. Stephan, M.-C. Hanf, A. Mehdaoui, P. Sonnet, C. Pirri: Continuous germanene layer on Al(111), Nano Lett. **15**, 2510 (2015)

9.120 L. Zhang, P. Bampoulis, A.N. Rudenko, Q. Yao, A. van Houselt, B. Poelsema, M.I. Katsnelson, H.J.W. Zandvliet: Structural and electronic properties of germanene on MoS_2, Phys. Rev. Lett. **116**, 256804 (2016)

9.121 C.-S. Ho, S. Banerjee, M. Batzill, D.E. Beck, B.E. Koel: Formation and structure of a $(\sqrt{19}\times\sqrt{19})$ R23.4°-Ge/Pt(111) surface alloy, Surf. Sci. **603**, 1161 (2009)

9.122 M. Švec, P. Hapala, M. Ondráček, P. Merino, M. Blanco-Rey, P. Mutombo, M. Vondráček, Y. Polyak, V. Cháb, J.A. Martín Gago, P. Jelínek: Silicene versus two-dimensional ordered silicide: Atomic and electronic structure of Si-$(\sqrt{19}\times\sqrt{19})$ R23.4°/Pt(111), Phys. Rev. B **89**, 201412 (2014)

9.123 S. Hajjar, G. Garreau, L. Josien, J.L. Bubendorff, D. Berling, A. Mehdaoui, C. Pirri, T. Maroutian, C. Renard, D. Bouchier, M. Petit, A. Spiesser, M.T. Dau, L. Michez, V. Le Thanh, T.O. Mentes, M.A. Nino, A. Locatelli: Morphology and composition of Au catalysts on Ge(111) obtained by thermal dewetting, Phys. Rev. B **84**, 125325 (2011)

9.124 Y. Xu, B. Yan, H.-J. Zhang, J. Wang, G. Xu, P. Tang, W. Duan, S.-C. Zhang: Large-gap quantum spin Hall insulators in tin films, Phys. Rev. Lett. **111**, 136804 (2013)

9.125 G.-F. Zhang, Y. Li, C. Wu: Honeycomb lattice with multiorbital structure: topological and quantum anomalous Hall insulators with large gaps, Phys. Rev. B **90**, 075114 (2014)

9.126 S.-C. Wu, G. Shan, B. Yan: Prediction of near-room-temperature quantum anomalous Hall effect on honeycomb materials, Phys. Rev. Lett. **113**, 256401 (2014)

9.127 Y. Xu, Z. Gan, S.-C. Zhang: Enhanced thermoelectric performance and anomalous Seebeck effects in topological insulators, Phys. Rev. Lett. **112**, 226801 (2014)

9.128 J. Wang, Y. Xu, S.-C. Zhang: Two-dimensional time-reversal-invariant topological superconductivity in a doped quantum spin-Hall insulator, Phys. Rev. B **90**, 054503 (2014)

9.129 L. Li, Y. Wang, S. Xie, X.-B. Li, Y.-Q. Wang, R. Wu, H. Sun, S. Zhang, H.-J. Gao: Two-dimensional transition metal honeycomb realized: Hf on Ir(111), Nano Lett. **13**, 4671 (2013)

9.130 J. Zhao, Q. Deng, A. Bachmatiuk, G. Sandeep, A. Popov, J. Eckert, M.H. Rümmeli: Free-standing single-atom-thick iron membranes suspended in graphene pores, Science **343**, 1228 (2014)

9.131 P. Koskinen, T. Korhonen: Plenty of motion at the bottom: atomically thin liquid gold membrane, Nanoscale **7**, 10140 (2015)

Yu-Yang Zhang

Institute of Physics and University of Chinese Academy of Sciences
Chinese Academy of Sciences
Beijing, China
zhangyuyang@ucas.ac.cn

Yu-Yang Zhang is associate professor at the School of Physical Sciences, University of Chinese Academy of Sciences. He obtained his PhD degree from the Institute of Physics, Chinese Academy of Sciences and completed two terms as a postdoc at Rensselaer Polytechnic Institute and Vanderbilt University. His research includes quantum-mechanical DFT calculations to understand the fundamental physics of materials and devices for future nanoelectronics and energy-related applications.

Jinbo Pan

Institute of Physics and University of Chinese Academy of Sciences
Chinese Academy of Sciences
Beijing, China
jbpan@iphy.ac.cn

Jinbo Pan received his PhD in physics from the Institute of Physics, Chinese Academy of Sciences in 2016. He subsequently held a postdoctoral position at Temple University. He became an associate professor at the Institute of Physics, Chinese Academy of Sciences in 2019. His research interests focus on the construction of a two-dimensional materials database, and their applications in electronics and catalysis.

Shixuan Du

Institute of Physics and University of Chinese Academy of Sciences
Chinese Academy of Sciences
Beijing, China
sxdu@iphy.ac.cn

Shixuan Du studied at Peking University (B.S.), and received her PhD in physical chemistry from Beijing Normal University in 2002. She was appointed as associate professor in 2002 and became a professor at the Institute of Physics, Chinese Academy of Sciences in 2009. Her research interests focus on DFT calculations of the structural, physical, and dynamic properties of low-dimensional materials.

Hong-Jun Gao

Institute of Physics and University of Chinese Academy of Sciences
Chinese Academy of Sciences
Beijing, China
hjgao@iphy.ac.cn

Hong-Jun Gao received his PhD in physics from Peking University in 1994. He became a professor at the Institute of Physics, Chinese Academy of Sciences in 1995. He is an academician of the Chinese Academy of Sciences and of the Developing-Country Academy of Sciences (TWAS). His research interests include the construction and physical properties of quantum nanostructures, including two-dimensional atomic/molecular crystals, and scanning tunneling microscopy/spectroscopy.

10. Thin Oxide Films as Model Systems for Heterogeneous Catalysts

Hans-Joachim Freund, Markus Heyde, Helmut Kuhlenbeck, Niklas Nilius, Thomas Risse, Swetlana Schauermann, Thomas Schmidt, Shamil Shaikhutdinov, Martin Sterrer

This chapter summarizes efforts to use thin oxide films as model supports for heterogeneous catalysts. We demonstrate that the oxide film route provides a useful platform to study oxide surfaces, per se its interaction with species from the gas phase, supported metal and oxide nanoparticles using the entire tool box of surfaces science under ultrahigh vacuum conditions. The extension to use thin oxide films as template also under ambient conditions or under water, is discussed and the potential to use oxide films as genuine two-dimensional materials is exemplified with vitreous and crystalline silica films.

10.1 Preamble

Reprinted with permission from [10.1], © 2016 American Chemical Society.

> "A detailed understanding of processes at surfaces requires knowledge of the surface structure at the atomic scale. Unraveling this knowledge for metal surfaces caused the success of surface science and its application to chemical reactions at surfaces and heterogeneous catalysis culminating in the 2007 Nobel Prize for *Gerhard Ertl* [10.2]. The surface science approach was limited for quite a while to metal single crystal surfaces. Only in the mid-nineties, the books by *Cox* [10.3], by *Henrich* and *Cox* [10.4] as well as by *Noguera* [10.5] on oxide surfaces alerted the broader community that this important class of materials should also be included into consideration of surface scientists. The field of oxide surface science has been developed since. The oxide single crystal surface for which most of the data have been published is $TiO_2(110)$ [10.6, 7]. *Henrich* and *Cox* [10.3, 4] also pointed out that reproducible preparation is at the heart of studies on oxide surfaces, specifically bulk single crystal surfaces. Based on this comment researchers started to think about alternative routes to reproducibly prepare oxide surfaces, which led to the birth of thin oxide film surface science [10.8–17]. The idea was to grow oxide films on metal single crystals using the rules of epitaxial growth. If made sufficiently thin, surface charg-

M. Rocca, T.S. Rahman, L. Vattuone (Eds.), *Springer Handbook of Surface Science*, Springer Handbooks,
https://doi.org/10.1007/978-3-030-46906-1_10

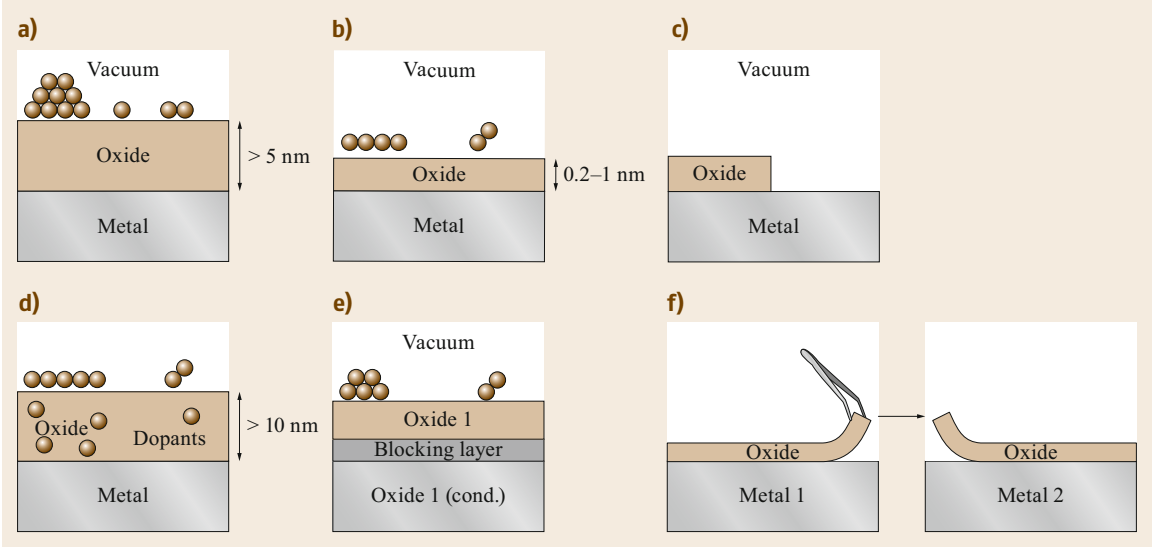

Fig. 10.1a–f Schematic illustration of various thin film systems and scenarios. Reprinted (adapted) with permission from [10.1] Copyright (2016) American Chemical Society

ing, which hampers the investigation of insulating bulk oxides when using charged information carriers, such as electrons or ions, does not occur. The field has further developed tremendously in recent years. Two books [10.18, 19] and a number of review articles have been published on the subject [10.8–17] providing the reader with an impression of what has been achieved. A wide variety of techniques has been applied to study oxide thin films, as collected therein. The present chapter will discuss a number of examples, mainly from the laboratories of the authors, to demonstrate how the field has developed and to highlight interesting avenues for future research in this area.

Before we discuss specific examples, we would like to address a few general scenarios, as schematically indicated in Fig. 10.1. Figure 10.1a shows an oxide film of a thickness chosen in such a way that the buried interface between oxide film and metal support does not influence the surface properties of the oxide film. Molecules, metal or compound (for example another oxide) nanoparticles, deposited and adsorbed on the surface, would experience the same geometric and electronic environment as on a bulk single crystal surface. A different situation is depicted in Fig. 10.1b. Here, the film is so thin that the buried interface influences the properties of the oxide surface, at least electronically, even if the geometric structure were the same as on a bulk single crystal surface, or, instead, it radically changes structure and properties. These ultrathin films are used to create novel materials or grow films that are hard to prepare as thicker samples [10.19]. Examples are silica films [10.20–22], aluminosilicate films [10.23], modeling zeolites or films of quasi crystals [10.24]. However, it may also be used to develop and test general concepts by controlling certain parameters via the presence of the oxide–metal support interface. Consider, for example, charge transfer processes. If the energy to remove an electron from the buried oxide–metal interface is smaller than the energy released by attaching this electron to an adsorbate, then this process is favorable and will occur if an appropriate electron transport mechanism is available in the system under consideration [10.25–27]. Such systems may be of interest for studying electron transfer to adsorbed metal nanoparticles, in order to investigate the general influence of electron transfer on the chemistry on supported particles and on the interface between the metal nanoparticle and the oxide film. Another option is to create a film, which does not fully cover the metal support, so that there is an open oxide metal interface between the oxide film and the metal single crystal (Fig. 10.1c) [10.28]. This is often called an inverse catalyst (inverse with respect to metal particles on oxides) which allows the interrogation of the oxide–metal interface [10.29–31]. The nomenclature is, however, somewhat misleading, as it implies that for the interface it does not matter whether one investigates metals on oxides or oxides on metals. Obviously, this is incorrect, because the surface will be different.

Still, those investigations may be useful in their own right. A situation, schematically represented in Fig. 10.1c may be encountered when dealing with the so-called *strong metal support interaction* (SMSI) [10.32–41]. The scenarios sketched in Fig. 10.1b and Fig. 10.1c are, of course, relevant to model catalysts and conceptually such studies also offer the possibility to combine them with approaches modeling the bulk situation based on the scheme depicted in Fig. 10.1a. Figure 10.1d, again, shows an oxide film of sufficient thickness to model the bulk without interference of the buried metal–oxide interface. However, in this case, dopants have been implanted into the oxide film [10.42–48]. If the appropriate combination between host material and dopant is chosen then one might envision that those dopants serve as sources for electron transfer to induce a situation, which is similar to the one encountered for ultra-thin films, described above. Within limits, such an approach may be compared with the standard approach in semiconductor physics, where n- and p-doped semiconductors are used to engineer the band structure and, thus, the electronic properties of those materials [10.49, 50]. Realizing that dopants control the electronic properties of oxides offers yet another possibility for studying ultra-thin films. Imagine the situation depicted in Fig. 10.1e: Here, an ultrathin oxide film is grown homoepitaxially on a specially prepared substrate of the same oxide [10.51–53]. In this substrate oxygen vacancies have been created in the oxide by reduction, which renders the substrate conductive. Given the envisioned homo-epitaxial growth on top, those oxygen vacancies would diffuse into the film grown on top upon thermal treatment. However, if a so-called *blocking layer* is introduced, the ultrathin film, grown on top will not be influenced by the exchange of vacancies with the underlying substrate and will behave, as if it was grown on a conductive substrate. Yet the entire system would represent a bulk material. This might be a procedure to approach the situation encountered for bulk single crystals, using, however, the advantages of thin film preparations. There is one aspect, which needs to be included conceptually in this introduction. This aspect is concerned with the possibility to remove ultrathin films from their substrate to create truly two-dimensional materials (Fig. 10.1f), similar to graphene [10.54–56], but based on oxides [10.57, 58]. Those films may, of course, be used to create stacks of two-dimensional materials of varying stoichiometry and varying electronic properties [10.59]."

Reprinted with permission from [10.1], © 2016 American Chemical Society.

The paper is organized in four sections: We first report on structural properties of epitaxial oxide films, then we turn to tuning the structural and electronic properties of oxide films, before we discuss their chemical reactivity. While in those sections we report on properties characterized mainly under UHV (ultra-high vacuum) conditions, in the final section we attempt to look at oxide films beyond UHV in an ambient.

10.2 Structural Properties of Epitaxial Oxide Films

Reprinted with permission from [10.60]. © 2019 Materials Research Society.

"The number of thin-film model systems that have been prepared and characterized in the past is enormous and covers almost all binary oxides existing in the bulk [10.8, 11, 19, 61]. In fact, the variability of thin-film oxides is even larger than that of their bulk counterparts. The reason can be found in the much higher structural and compositional flexibility of oxide films of few-monolayer thickness, giving rise to a plethora of nonstoichiometric, strained and polar structures that would be unstable in the bulk limit [10.8, 62]. Moreover, the geometric template effect of the substrate combined with different electronic coupling schemes is able to stabilize various unusual thin-film configurations [10.19, 63]. In the following, we will introduce the oxide films explored in our group starting with binary ionic alkaline earth oxide surfaces with simple rock salt structure towards transition metal oxides, which can pose considerable challenges with respect to possible surface terminations. The structural properties provide the necessary basis for the subsequent discussion of the electronic as well as chemical properties discussed in Sect. 10.3 to 10.5.

10.2.1 MgO and CaO(100) Films

The two rocksalt oxides MgO and CaO are probably the most prominent model systems for chemically and catalytically-driven surface science stud-

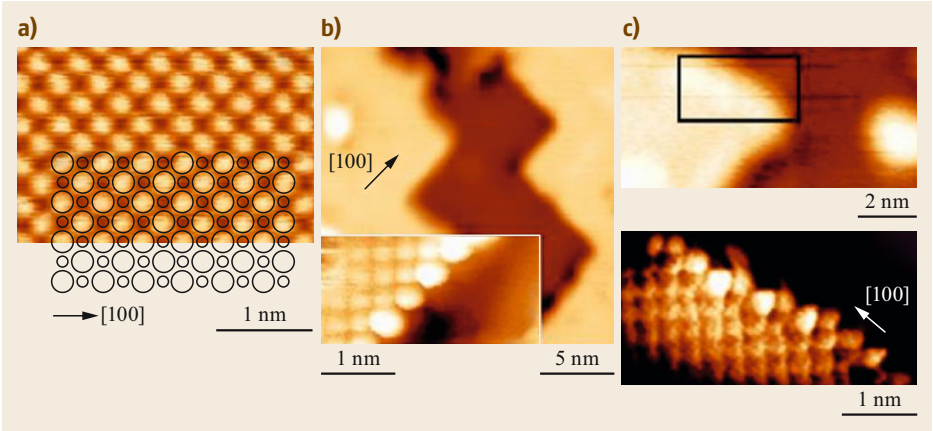

Fig. 10.2a–c Low-temperature STM (scanning tunneling microscopy) images of a 4 ML (monolayer) MgO(100) film on Ag(001), showing an atomically resolved terrace region **(a)**, overview and atomically resolved images of a regular step edge **(b)** and an irregular step edge **(c)**. Only one ionic sublattice of the MgO is resolved in the measurement. Reproduced with permission from [10.60], © Materials Research Society 2019

ies [10.10]. Their importance relies on several aspects. The rocksalt oxides are characterized by particularly simple structural and electronic properties, i.e., a cubic unit cell with two atoms in the base and a wide, electronic band gap, respectively. As a consequence, they are highly accessible to theoretical calculations, but can also be prepared on a variety of squared atomic lattices with matching dimensions. Suitable supports for MgO (lattice parameter 4.2 Å) are Ag(001) [10.64], Fe(001) [10.65] and Mo(001) [10.66, 67], while CaO (lattice parameter 4.8 Å) is typically grown on Mo(001) [10.68]. Given the symmetry of the support, the rocksalt layers develop their thermodynamically preferred (100) termination that is both structurally compact and charge compensated (Fig. 10.2). Attempts to stabilize alternative rocksalt surfaces, e.g., the (111) termination, turned out to be challenging at least in an UHV environment [10.69]. This can be explained with the polar nature of the hexagonal rocksalt plane, which needs to be compensated for either by surface reconstruction or adsorption of charged adspecies [10.70, 71].

The structural quality of MgO and CaO(100) films is largely governed by a nonperfect lattice match with the support, which induces interfacial lattice strain and needs to be released by structural distortions in the film. Not surprisingly, relatively smooth and homogenous MgO films has been grown on Ag(001) that features only 3° lattice mismatch with bulk MgO (Fig. 10.2) [10.64]. The film quality can be further improved by post-annealing these layers at 773 K, followed by a slow cooling-down procedure [10.72, 73]. The lattice mismatch due to Mo(001) is considerably larger (5.3°) and results in the development of a dense dislocation network to compensate the strain [10.67]. These line defects share a number of properties with the grain boundaries in realistic, polycrystalline MgO, and shall thus been discussed in more detail [10.74].

The dislocation network has a periodicity of 55–60 Å with straight defect lines running parallel to the MgO[110] direction, as revealed with STM and grazing incidence x-ray diffraction (GIXD) in real and reciprocal space, respectively [10.75]. Along these directions, an extra Mg–O row that has no counterpart in the Mo support is introduced for 18 regular oxide rows. The result is a (19×19) MgO on (18×18) Mo coincidence lattice with square symmetry (Fig. 10.3). On the atomic scale, the dislocation network is associated with periodic switches of the interface registry, changing from O to Mg ions sitting atop the Mo atoms of the support. Energetically, the O–Mo registry is preferred, as reflected in a shorter interface binding length (2.3 Å) as compared to the Mg–Mo domains (3.5 Å) [10.76]. As the O–Mo and Mg–Mo regions lie on different height levels, the MgO films develops a considerable mosaicity, being reflected in a prominent splitting of the fundamental MgO spots in low-energy electron diffraction data [10.75]. The modulated interface distance also produces a work function pattern on the MgO film, in which high work function values are found for the Mg–Mo registry, while values for the O–Mo domains are 1.5 eV lower. The differ-

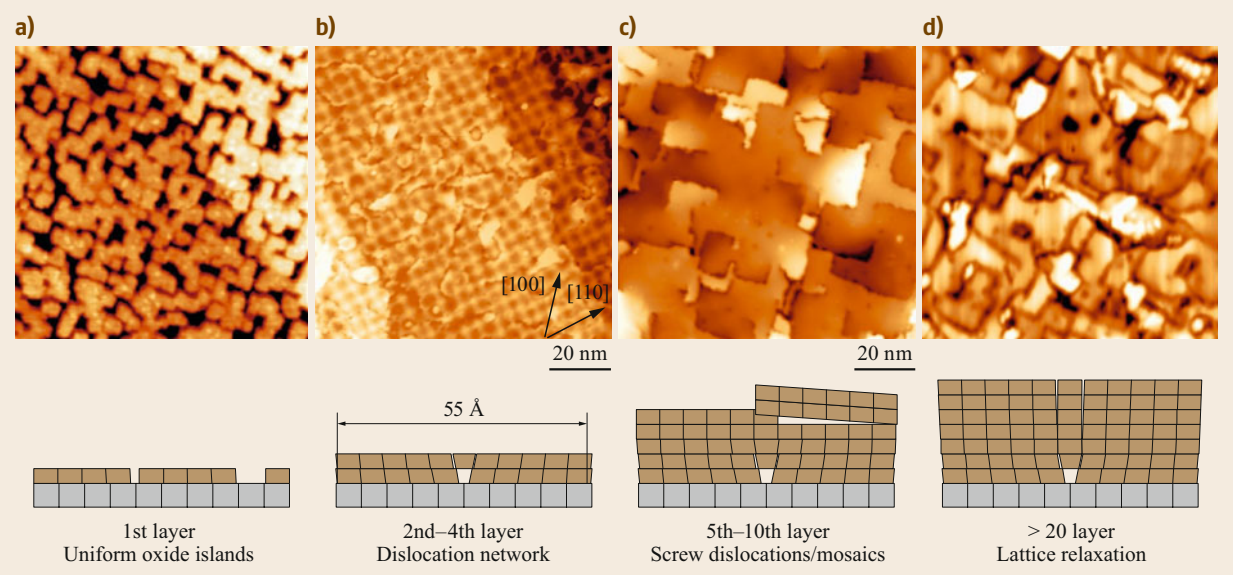

Fig. 10.3a–d STM images showing several states of strain relaxation in MgO thin films on a Mo(001) support ($100 \times 100\,nm^2$, $V_S = 4.0\,V$). **(a)** Submonolayer coverage with square shaped MgO islands. Their size is controlled by the interfacial lattice strain. **(b)** 3 ML thick film displaying a squared coincidence lattice. **(c)** 7 ML thick film characterized by wide, atomically flat terraces, separated by edge and screw dislocations. **(d)** 18 ML film with bulk-like lattice parameter. The image quality in **(d)** is degraded due to the vanishing conductivity of thick MgO layers. Reproduced with permission from [10.60], © Materials Research Society 2019

ence can be explained with the suppressed electron spill-out from the Mo support at the compact O–Mo interface [10.77]. The reduced thermodynamic stability of the Mg–Mo registry finally leads to a higher concentration of point defects in these domains [10.78]. The strain-induced dislocation network on MgO/Mo thin films gives rise to a spatially modulated adsorption behavior that can be exploited as template for the preparation of well-ordered ensembles of metal particles [10.76].

With increasing oxide thickness, additional defect types develop next to the dislocation network (Fig. 10.3). Prominent defects at 10 ML film thickness are screw and edge dislocations the latter being aligned with the nonpolar MgO[100] direction [10.75]. Also point defects, in particular oxygen vacancies, become more abundant. They mostly locate along step edges, where the atomic coordination is reduced with respect to atoms embedded in a compact terrace. The lattice position of oxygen vacancies has been thoroughly characterized by angle-dependent EPR (electron paramagnetic resonance) measurements in combination with scanning probe techniques [10.79, 80]."

Reprinted with permission from [10.60]. © 2019 Materials Research Society.

Oxygen vacancies can be stabilized in three charge states on the oxide surface that is as neutral (F^0), singly (F^+) and doubly charged color centers (F^{2+}). The latter turned out to be energetically unfavorable in thin films given the quasi infinite electron reservoir of the metal support just below the film. Recent STM and AFM (atomic force microscopy) experiments have proven that the precise charge state of the color centers can be determined on the single-defect level (Fig. 10.4). Whereas STM conductance spectroscopy evaluates the energy position of defect-induced gap states in MgO [10.81], AFM probes the electrostatic interactions between the charged defect and the probe tip [10.82].

Charge trapping is not only observed for point defects, but plays an even larger role for extended line defects in MgO thin films. Several experimental and theoretical evidences have been accumulated that show the enormous ability of line defects to trap excess electrons [10.74]. Quantitative data comes from EPR spectroscopy, where a pronounced bulk-like resonance at $g = 2.003$ shows up after filling the electron traps by exposure to atomic hydrogen [10.83]. From the disappearance of the signal after annealing to 500 K, the depth of the trap states was estimated to ≈ 1.0 eV below the conduction band onset, in good agreement with DFT (density functional theory) models of the MgO grain boundaries [10.84]. Local information on the po-

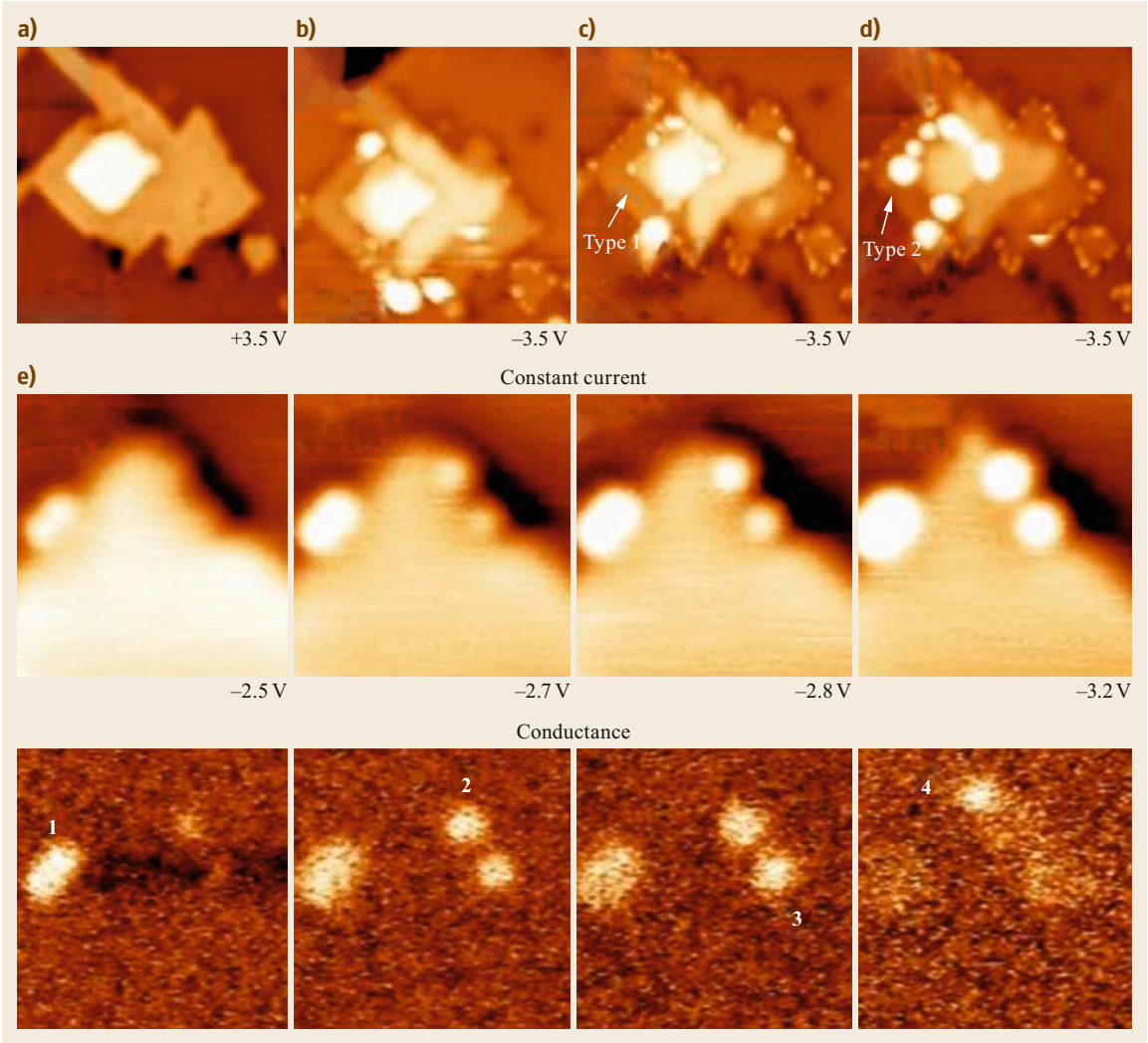

Fig. 10.4 **(a,b)** STM images ($25 \times 25\,nm^2$) of a MgO island on 4 ML MgO/Ag(001) imaged at $V_S = +3.5$ and -3.5 V. **(c,d)** Continuous scanning of the same surface region at high positive bias produces distinct defects that can be assigned to F^+ (type 1) and F^0 (type 2) color centers. **(e)** Constant current and conductance images of type 1 defects located at an MgO step edge taken at different bias voltages ($5 \times 5\,nm^2$) [10.81]

sition of the electron traps inside the MgO film comes from STM topographic and luminescence data [10.85]. In high-bias STM images, the MgO line defects appear with negative contrast as compared to the regular film (Fig. 10.5a). As the true geometric corrugation is small, the dark appearance of the dislocations network is interpreted as an electronic effect. In fact, the high number of electrons trapped in the defects leads to a local increase of the electron potential, which in turn reduces the transmissibility for tunneling electrons and forces the STM tip to approach the surface. The shift of the local electron potential due to excess electrons can be quantified by probing the vacuum states above the MgO surface via tunneling spectroscopy [10.86]. The spectra reveal an upshift of the lowest resonance from 3.7 eV on defect-free oxide patches to 4.4 eV above the dislocation lines, in agreement with the anticipated presence of excess charges in the defects [10.83].

Similar information is obtained from STM luminescence maps taken on MgO/Mo films. The oxide's optical response is governed by radiative electron transitions from higher vacuum states to the ground state, and defect-related potential shifts thus produce a contrast in the luminescence pattern (Fig. 10.5b) [10.85]. On regular MgO, the emission channel opens up already at 5.1 V excitation bias and oxide terraces con-

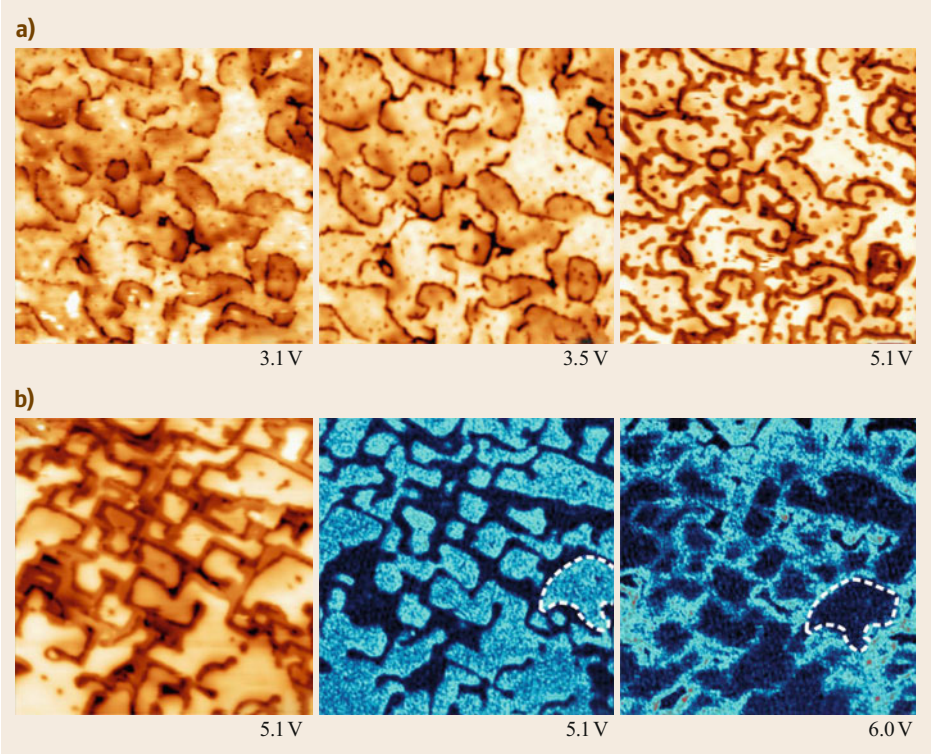

Fig. 10.5 **(a)** STM image of 12 ML MgO/Mo(001) ($100 \times 100\,nm^2$) taken as a function of bias voltage. The line defects appear as deep grooves in the oxide surface as the bias increases. **(b)** Topographic image and photon maps ($75 \times 75\,nm^2$) taken at the bias position of the second vacuum state on MgO terraces (*middle*) and line defects (*right*). The contrast reversal between both images reflects work function modulations in the film. Reprinted with permission from [10.83]. Copyright (2010) by the American Physical Society

sequently appear bright in those images. Conversely, the optical channel becomes available only at 6.0 V in defect regions, due to the upward shift of the vacuum states, which results in a contrast reversal with respect to the low-bias luminescence maps [10.83].

Charge trapping is a unique behavior of both, point and line defects in MgO thin films. The often weakly bound electrons are susceptible to be transferred into adsorbates, making defects indispensable for the redox chemistry of oxide materials [10.87, 88]. This interrelation has been verified in a number of adsorption and reaction experiments on MgO films, demonstrating for instance low-temperature CO-oxidation over defective MgO/Mo(001) [10.89].

10.2.2 The Silica Film

Reprinted with permission from [10.60]. © 2019 Materials Research Society.

> "The alkaline earth oxides discussed above represent a class of oxides, which tends to crystallize in a well-defined simple lattice driven by the Madelung potential of the highly ionic system. As discussed above even such prototypical ionic systems exhibit considerable structural complexity in particular with respect to the defect structure. Another level of complexity arises if the system under consideration tends to form amorphous structures.
>
> The prototype for amorphous network structures is silicon dioxide. This material is the simplest and most common type of glass. Many elements and compounds can form glasses and some of the oldest man-made objects found are made from glass materials [10.90–92]. Glass materials and especially silicates are relevant in nature and various branches of modern technologies, e.g., in semiconductor devices, optical fibers and as a support in industrial catalysis [10.93]. In order to push this material class forward and to understand chemical reaction at surfaces in the context of heterogeneous catalysts, we should characterize their structures and properties at the atomic scale.

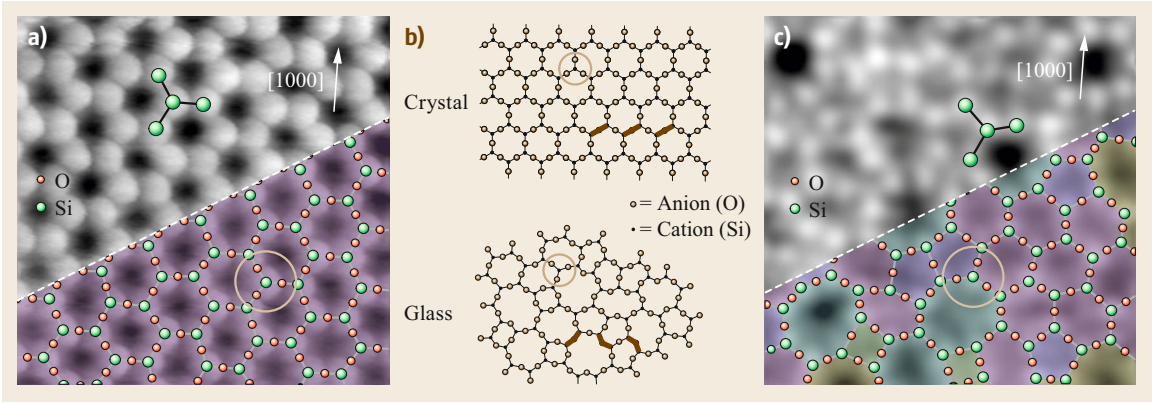

Fig. 10.6a–c Atomically resolved crystalline and vitreous regions of the thin silica film by STM (the scan area of image **(a,c)** is 3.5 nm × 3.5 nm). Reprinted (adapted) with permission from [10.21]. Copyright (2012) American Chemical Society. An atomic model of the topmost layer of the silica film is superimposed onto the lower section of the images in **(a,c)** (*green balls*: Si atoms, *red balls*: O atoms). *Zachariasen*'s scheme of crystalline and glass network structures is given in **(b)** for comparison [10.94]. Reprinted (adapted) with permission from [10.94]. Copyright (1932) American Chemical Society

W.H. Zachariasen postulates laid the foundation to the so-called *Random Network Theory* 80 years ago to explain the structure of amorphous materials [10.94]. Due to the comparable mechanical properties of amorphous and crystalline materials he assumed that the bonding forces between the atoms in the two phases should be essentially identical. The lack of periodicity and symmetry are the main features that distinguish a glass from a crystal. Early on, it had been suggested that tetrahedral atomic configurations were required to form glasses. Zachariasen used these predictions to sketch an atomic picture of a glass. In his paper he reduced the three-dimensional (3-D) picture into a two dimensions (2-D) analogy (Fig. 10.6b). For silicon dioxide, the simplest structural unit in the 3-D case is a SiO_4 tetrahedron. If the complexity of the system is reduced from 3-D to 2-D, the simplest structural unit for silicon dioxide changes from the SiO_4 tetrahedron to a SiO_3 triangle. The brown circle in Fig. 10.6 marks the SiO_3 building unit. The SiO_3 triangles are linked to each other as individual building blocks at fixed 180° angles, corresponding to a crystalline material. This creates long-range order and periodicity. If the angle between these structural units varies, the building blocks can develop an extended network with rings of different sizes. As can be seen in Fig. 10.6b (bottom) the uniform structural units are linked to each other at apparently random angles. Zachariasen drew a 2-D diagram in which trigonal units are linked together to create the amorphous network. Due to the large variety of Si–O–Si angles which bridge two neighboring building units, the glass structure lacks periodicity and long range order.

In our department we have developed a recipe to grow thin silica bilayer films on Ru(0001). This film system nicely verifies the complex atomic arrangement of the Random Network Theory with a striking similarity. The observed protrusions at atomic separations in the STM images shown in Fig. 10.6a,c. are arranged in propeller shaped structures. By comparing to Zachariasen's model and based on this propeller symmetry the protrusions can be assigned to Si atoms (green balls in Fig. 10.6a,c). Such propeller shaped units have been separately marked in Fig. 10.6. Here, a Si sensitive contrast is observed and the position of the O atoms has been calculated based on the Si coordinates. In this way the 2-D model of the topmost O and Si atoms has been completed. Please note that a modified tip termination can make the O instead of the Si positions visible [10.21]. This silica film system corroborates crystalline structures [10.20], but also verifies Zachariasen's predictions of a vitreous random network for a glass [10.22].

Besides the separate characterization of each phase, also interface structures between crystalline and amorphous phases have been addressed [10.95]. In the glass community, there has always been a controversy about how crystalline and vitreous phases are connected to one another. From the experimental point of view, a real-time observation at the atomic scale of an active front during a glass transition process is not currently feasible. But a static image of such an interface region can be gained. For further details see [10.95].

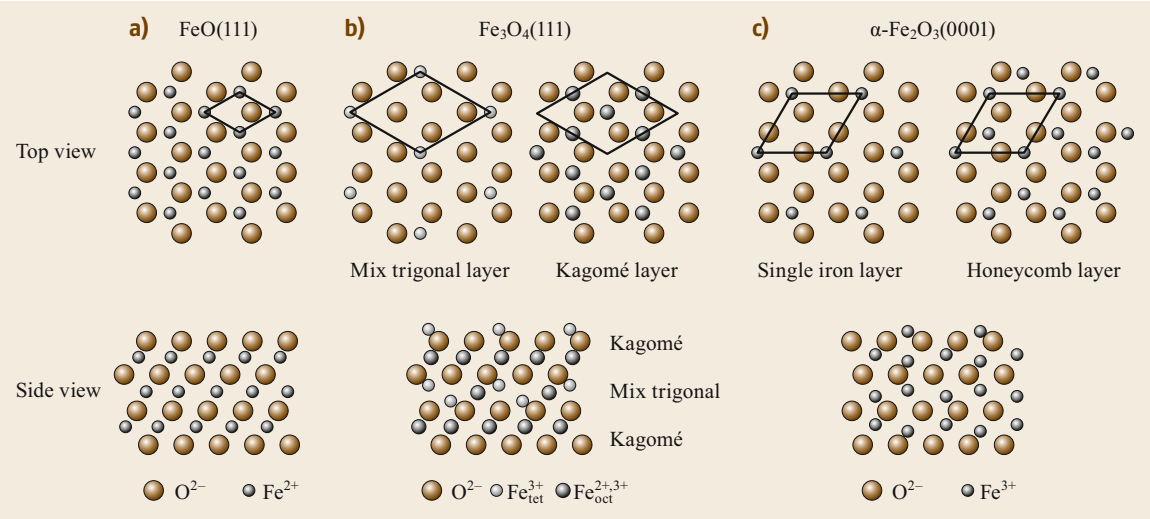

Fig. 10.7a–c Models of iron oxides structure for (a) wustite (FeO), (b) magnetite (Fe_3O_4), and (c) hematite (α-Fe_2O_3)

Furthermore, it should be mentioned that silica bilayer films can be grown on a number of substrates [10.22, 96–98], which leaves room for tuning the properties of these films, but also shows that these films resemble a completely new materials class of its own.

With these experiments, a clear image of an amorphous material has been obtained which allowed for the first time the derivation of atomic sites and a detailed analysis from real space coordinates. The text book example of the amorphous silica structure proposed by Zachariasen in 1932 has thereby finally been verified. Also Mo(112) and Pt(111) substrates have been used to prepare thin silica films.

10.2.3 Iron Oxide Films

The oxide films discussed so far were simple in the sense that the oxidation state of the constituents is well-defined. This restriction is lifted if transition metal oxides are considered. In addition, the ability to form oxides with different formal oxidation states of the metal ion is associated with changes in the bulk crystal structures. With respect to the atomic structure of the surfaces observed for different oxides the surface termination becomes a central aspect. To illustrate these aspects we will present results on iron oxide films.

Iron oxides films have a wide field of technological applications, ranging from magnetic devices to heterogeneous catalysis [10.99, 100]. This class of material exhibits rather different magnetic or conducting properties [10.101] depending on their crystal structures, which is strongly determined by the way of preparation. The morphology and termination of the oxide film have a strong influence on the chemical properties and are, therefore, subject of intense studies [10.102–105]."

Reprinted with permission from [10.60]. © 2019 Materials Research Society.

Figure 10.7 briefly sketches the crystal structures of iron oxide phases discussed in the following, the main ones being FeO (wustite), Fe_3O_4 (magnetite) and α-Fe_2O_3 (hematite). For a more detailed overview of these different crystalline structures see *Weiss* and *Ranke* [10.102] α-Fe_2O_3 crystallizes in the corundum structure with a hexagonal unit cell. Along the [0001] direction the O anions form a close-packed hcp sublattice with ABAB stacking. The Fe^{3+} species between these layers are arranged in honeycomb $(\sqrt{3}\times\sqrt{3})R30°$ like layers. Fe_3O_4 crystallizes in the inverse spinel structure. The O anions form a close-packed fcc sublattice (ABC stacking along the [111] axis of the lattice) with Fe^{2+} and Fe^{3+} cations located in the interstitial sites. The O planes are similar to those in α-Fe_2O_3. Between the close-packed planes of oxygen ions either one Kagomé or three hexagonal (mixtrigonal) Fe layers alternate. Both ion sublattices are arranged in a (2×2) like fashion on the close-packed oxygen layer. FeO crystallizes in the rock salt structure, hence the O and Fe (111) planes form ideal two-dimensional hexagonal lattices with a cubic ABC stacking sequence along the [111] direction. FeO films in (111) termination are intrinsically unstable as they develop a polar dipole that increases with film thickness. The impact of the polarity on the

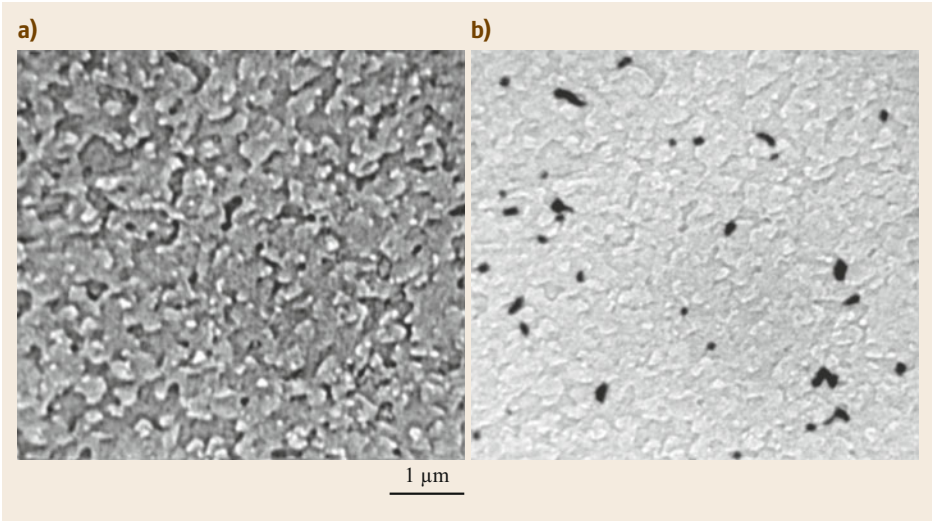

Fig. 10.8a,b Morphology of a well-prepared Fe_3O_4 film, completely covering the Pt(111) support. Both LEEM images show the identical surface area in **(a)** bright- and **(b)** dark-field imaging mode, utilizing the (0;0) and the (1/2;0) diffraction spots, respectively. The contrast is caused by the morphology. Additionally, domains rotated by 180° become visible as dark areas in the dark-field image. Reprinted with permission from [10.106]. Copyright (2012) by the American Physical Society

local surface potential largely governs the adsorption behavior of the film, and can be probed with STM, for example [10.107].

Morphology of Thin Fe_3O_4(111) Films

Fe_3O_4(111) films of about 10 nm thickness were grown on a Pt(111) single crystal support by repeated cycles of Fe deposition at room temperature (RT) and oxidation at elevated temperatures, after one complete FeO layer was formed initially [10.102]. In each cycle, between 5 and 10 ML of Fe was deposited, and oxidized at 1×10^{-6} mbar of O_2, starting at RT, followed by annealing to 900 K, which was kept for 5 min. Upon cooling, the oxygen pressure was reduced only after cooling to 500 K. By following this procedure, the Pt(111) crystal is completely covered by an Fe_3O_4 film (Fig. 10.8a). The LEED (low energy electron diffraction) pattern of the film matches perfectly the one described in literature [10.108]. The film consists of terraces up to a width of 100 nm, most of them with polygonal shape. As seen in LEEM (low energy electron microscopy), the step density increased after every cycle, especially > 20 nm of film thickness. However, the film could be smoothed if the final oxidation treatment was done at an elevated temperature of ≈ 1000 K. Here, it was necessary that the film was completely closed and thicker than 7 nm, otherwise the annealing up to 1000 K led to a de-wetting (see the following section). A subsequent thermal flash in UHV did not produce further morphological changes, but improved the homogeneity of the surface structure (see Sect. 10.2.3).

Magnetite crystallizes in an inverse spinel structure with space group *Fd*3*m*, while the Pt substrate exhibits a fcc structure with space group *Fm*3*m*. Therefore, the Fe_3O_4

Reprinted with permission from [10.60]. © 2019 Materials Research Society.

> "islands created by initial nucleation on a clean Pt(111) surface may coalesce with improper stacking [10.109, 110] and form a complete film with two twin domains rotated by 180°. Dark field LEEM studies using the (1/2;0) and (0;1/2) spots showed a predominance of one rotational domain; coverage ratio for these rotational domains ranged between 75°/25° and 98°/2°, depending on the preparation condition. Figure 10.8b shows a dark-field LEEM image visualizing the two rotational domains as dominating bright and small black areas. This preponderance is maintained even after subsequent cycles of Fe deposition and oxidation. On average, the rotational domain size is larger than the terrace width; some of the domains were even several µm wide. A comparison between dark field and bright field LEEM images shows that the rotational domains are preferentially placed in correspondence of the step bunches of the substrate, providing a partial correlation be-

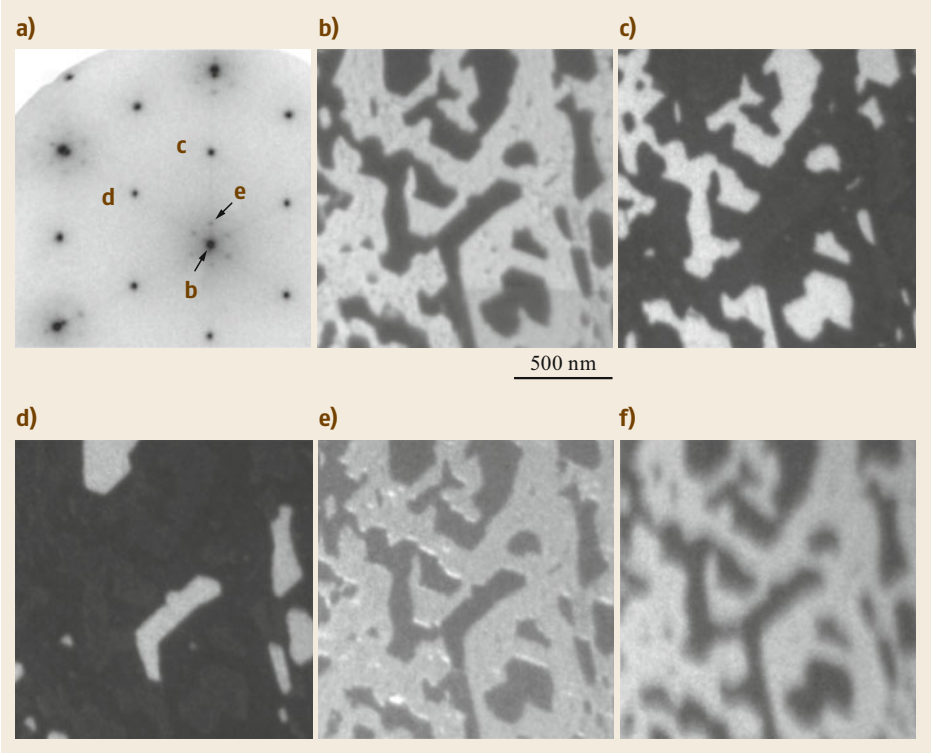

Fig. 10.9a–f Dewetted Fe_3O_4 film, studied by **(a)** LEED, **(b–e)** LEEM and **(f)** XPEEM. The LEED pattern shows a superposition of the Fe_3O_4 and FeO structures. The LEEM images use selected LEED spots as labelled in **(a)**. In the bright-field LEEM image **(b)** the Fe_3O_4 and FeO surface areas appear dark and bright, respectively. The dark-field images **(c,d)** identify the Fe_3O_4 area with rotational domains, whereas in **(e)** only the FeO layer appears bright. **(f)** XPEEM image using the Pt $4f_{7/2}$ photoemission line. Adapted from [10.106]

tween substrate morphology and crystallographic inhomogeneities."

Reprinted with permission from [10.60]. © 2019 Materials Research Society.

Morphological Inhomogeneities

The oxidation temperature plays a crucial role for the uniformity of the thin film.

Reprinted excerpt with permission from [10.106] © 2012 by the American Physical Society.

> "On the one hand it should be high enough to enable the oxidation process, but on the other hand not too high, especially during the first deposition cycles, to avoid a de-wetting of the Fe_3O_4 film. The latter was observed for a film thickness of 7 nm at oxidation temperatures above 900 K, as FeO areas became clearly visible in the *holes* of the $Fe_3O_4(111)$ film. The width of these FeO domains increased dramatically at further increase of the temperature, from approximately 100 nm to several μm for an oxidation temperature of 1000 K. The FeO areas could be identified by various experiments: bright and dark field LEEM (Fig. 10.9b–e), LEED (Fig. 10.9a) and XPEEM (x-ray photoelectron emission microscopy) (Fig. 10.9f). In the de-wetted case bright field LEEM images (Fig. 10.9b), Fe_3O_4 (dark) and FeO (white) areas are visible with different contrast, while the corresponding LEED pattern shows the superposition of the $Fe_3O_4(111)$ pattern and the Moiré pattern (six satellite spots surrounding the central (0;0) spot) typical for the FeO(111)/Pt(111) interface. By dark field imaging using the Fe_3O_4 (1/2;0) and (0;1/2) spots (Fig. 10.9c,d) the FeO areas appear dark, while the Fe_3O_4 areas show a contrast between rotational domains due to the three-fold symmetry of the $Fe_3O_4(111)$ crystal structure. On the contrary, the FeO domains can be unambiguously identified as brighter areas if one of the satellite spots around (0;0) is selected (Fig. 10.9e). XPEEM images obtained with Pt $4f_{7/2}$ core level

emission line (Fig. 10.9f) additionally reveal that the FeO domains formed by de-wetting are indeed deep holes in the Fe_3O_4 film."

Reprinted excerpt with permission from [10.106] © 2012 by the American Physical Society.

The FeO areas are so thin that the electrons photoemitted in the Pt substrate can still pass through, while the Fe_3O_4 film is thick enough to completely damp the Pt signal. Considering the electron mean free path length of ≈ 0.5 nm at the used kinetic electron energy (104.2 eV), one can estimate the thickness of the FeO areas as a few Angstroms. Once the Fe_3O_4 film had de-wetted and FeO holes were formed, it was not possible to recover a closed Fe_3O_4 film by several additional cycles of Fe deposition and oxidation. Obviously, the Fe atoms adsorbed on the FeO areas at room temperature migrated onto the Fe_3O_4 areas during the oxidation process at 900 K. Consequently, only the Fe_3O_4 grew in thickness, while the FeO zones remained unchanged. Furthermore, wide-range LEEM images of an almost closed Fe_3O_4 film show that FeO domains are formed preferentially at the step bunches of the Pt(111) substrate, where the Fe_3O_4 is unstable, most likely due to the strain induced by the steps and step bunches [10.106].

Surface Termination

Besides the two inhomogenities in the rotational domains and in the morphology, a third type related to the surface termination was found and was investigated using four techniques:

(i) SPALEED (spot profile analysis low energy electron diffraction (profile analysis of LEED spots)) studying the profile of the LEED spots in-real-time during oxidation and flash in UHV yielding the domain sizes for different preparations
(ii) XPS (x-ray photoelectron spectroscopy) of the surface before and after the final annealing, determining the chemical composition of the surface, excluding contaminations of carbon, nitrogen or molybdenum containing species
(iii) STM of the *as prepared* surface, visualizing about 2 nm wide objects and therefore smaller than the LEEM resolution
(iv) Dynamical LEED analysis of the spot intensities for differently prepared surfaces, studying the surface unit cell structure and therefore the termination [10.106].

In the special LEEM set-up, we collected *I*/*V*-LEED (intensity/voltage low energy electron diffraction (intensity analysis of LEED spots)) spectra of the Fe_3O_4 thin film at room temperature before and after the flash at 900 K. The intensity of six different diffraction spots, (0;0), (1/2;0), (0;1/2), (1;0), (0;1) and (1/2;1/2), were analyzed within an energy range between 40 and 300 eV, equivalent to an overall dataset of 1560 eV. In contrast to a standard back-view LEED, the operation condition of the electron gun and the image columns of our system are not altered during the energy scan, but solely the sample potential is changed. Consequently, the beam current on the sample is constant during the scan, for all experiments. Additionally, due to the special LEEM optics the investigated diffraction spots do not move in position on the detector during the energy scan and the (0;0) spot is visible even at full perpendicular illumination. It is also possible to directly inspect the probed surface region from where the diffracted electrons are collected. Combining this with a dark field image, which gives the portions of the two possible rotational domains, one can easily disentangle the contributions of the two rotational domains and extract the real spectra of (1/2;0), (0;1/2), (1;0) and (0;1) spots of a single rotational domain. This is not possible with a standard back-view LEED set-up because of the superposition of two threefold pattern with unknown relative abundance. Therefore, one is usually forced to average the spectra of spots of the same diffraction order, with consequent loss of information.

The resulting disentangled I/V-LEED spectra for the *as prepared* and *after flash* surfaces differ strongly in some energy ranges (see arrows in Fig. 10.10). This can be interpreted as a change in the surface termination. Additionally, we found that the spectra of the *as prepared* surface do not change significantly for different cooling rates. For a full I/V-LEED analysis different models for the surface atomic structure were assumed, from simple truncation of the bulk crystal unit cell along the (111) plane, yielding six different terminations, up to more complex structure models, i.e., with incomplete site occupation and/or changed coordination sites. Every configuration was optimized until the change in each atomic coordinate in a single iteration loop was < 0.1 Å. The most reliable model with a resulting Pendry reliability (R) factor of $R = 0.14$ is 1/4 ML Fe atom belonging to the MixTrigonal layer on a closed-packed oxygen layer resting upon a Kagomé iron layer. The surface after the flash presents the expected atomic termination and confirms the results obtained first by *Barbieri* et al. [10.104] and then by *Ritter* and *Weiss* [10.111].

The fit of the I/V curves measured for *as prepared* films gave no clear resulting structure because all R-factors were much larger with respect to the values obtained for the flashed surface. The most reliable model

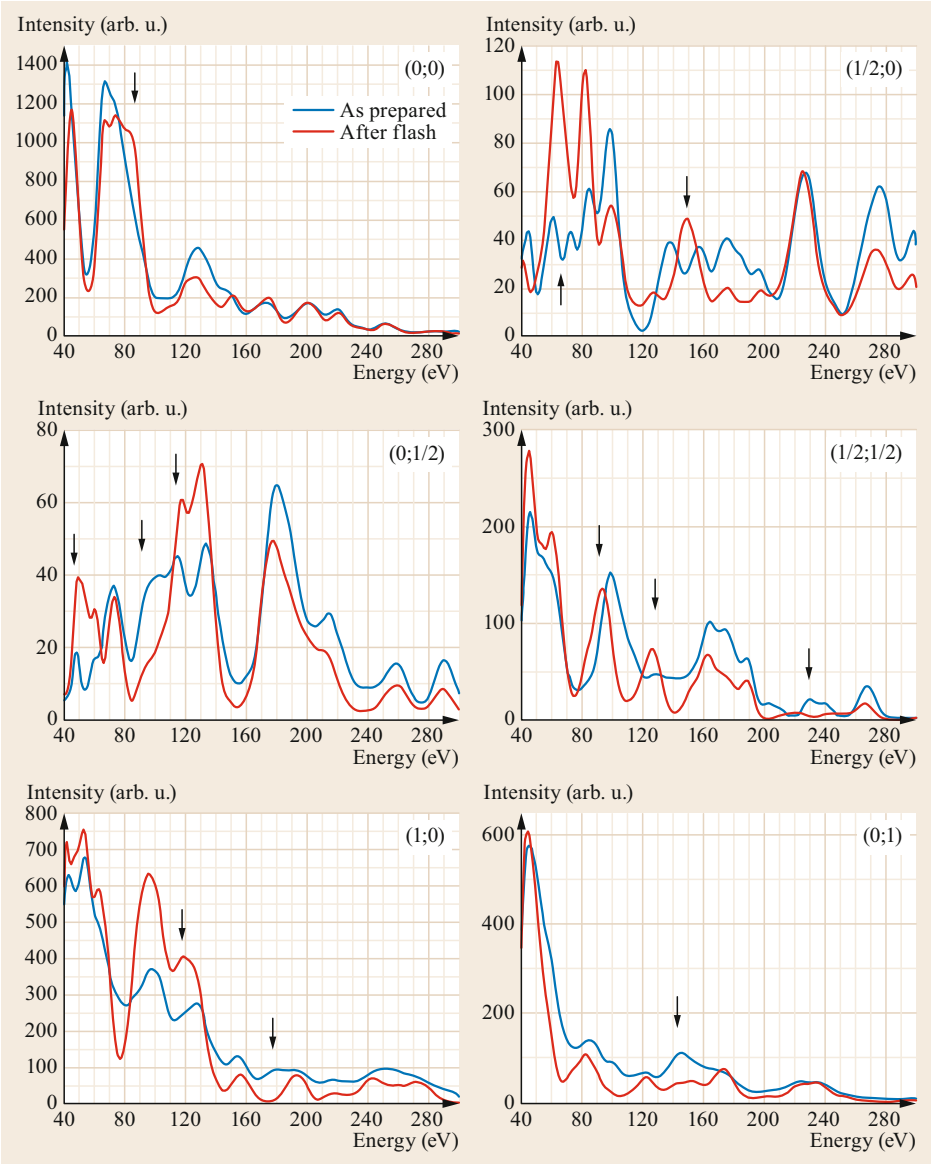

Fig. 10.10 Surface termination of the Fe_3O_4 films at different preparation steps. IV-LEED curves of the first six diffraction spots for the as-prepared film (in *blue*) and after annealing at 900 K in UHV (in *red*). The major changes due to this flash are indicated by *arrows*. Reprinted with permission from [10.106]. Copyright (2012) by the American Physical Society

was still the one described above for the flashed surface, but with a *R*-factor of 0.33 much worse than before. One can assume that, as shown by STM, part of the *as prepared* surface exposes the termination dominant after the annealing. Therefore, the spectra were also fitted with a linear combination of the *after flash* surface and the unknown structure. Even with this extra parameter, the analysis did not result in structures with acceptable *R*-factor. Simple explanations, that the IV-LEED method fails in this case, are (i) the low atomic order of the objects, as seen in STM, and (ii) the small object size of 2 nm (i.e., $\approx$ 7 atomic distances), not suitable for the method, which assumes infinite periodic conditions.

The nature and the origin of these *extra objects* could be studied indirectly. In the (0;0) LEED spot profiles they exhibit a significant shoulder like broadening, corresponding to an average domain size of 2 nm, as also observed in STM. Real time SPALEED measurements clearly show, that the extra objects were not present during the oxidation process at temperatures > 900 K, but were formed during the cooling down at temperatures < 750 K. Furthermore, if the oxygen exposure was cut off during the cooling process > 750 K, no extra object was detected. Therefore, the formation of extra objects on the surface must be directly related to the O_2 exposure at lower temperature.

Once formed, the extra objects can be completely removed by annealing up to 900 K in UHV. As shown in LEEM and SPALEED, this flash in UHV transforms the *as prepared* surface with a rough morphology and small objects of less-ordered and highly oxygen containing domains into a smooth surface with a homogeneous 1/4 Fe termination. Therefore, this final flash determines the morphology and termination of the prepared Fe_3O_4 film. Recent studies indicate that the extra objects may be due to water adsorption from the background.

Interconversion of Fe_3O_4(111) and α-Fe_2O_3(111) Thin Films

An additional inhomogeneity observed in oxide films are domains of different bulk structures. Under our preparation conditions iron oxide films grown on the Pt(111) or Ag(111) surfaces were composed of the Fe_3O_4 phase and of a few microns large domains of α-Fe_2O_3, covering a few percent of the entire surface. The two phases coexist for intermediate preparation parameters [10.112], often also showing small FeO domains due to partial dewetting (Fig. 10.11a). The annealing of the film in 3×10^{-5} mbar O_2 pressure (i.e., a higher pressure than used for the initial preparation) starting at RT up to 700 K, leads to an oxidation of the Fe_3O_4 area into α-Fe_2O_3 as monitored in LEEM (Fig. 10.11b–i). The conversion starts at 670 K (Fig. 10.11c) as a growth front of dendritical shape. The process becomes faster when the temperature is increased, indicating that the transformation process is thermally activated [10.113].

The conversion can be inverted by extra Fe deposition, which leads to a shrinkage of the α-Fe_2O_3 upon annealing in UHV. Here, the Fe is incorporated into the hematite area, causing a change in stoichiometry and crystal structure [10.112]. Without Fe deposition, annealing in UHV can also lead to a reduction of the α-Fe_2O_3 by desorption of oxygen. This was observed when Ag(111) was used as support [10.112, 114]. However, on a Pt(111) support, the UHV annealing yields the opposite result: the Fe_3O_4 is converted into α-Fe_2O_3. The reason for this unexpected behavior is the special ability of the Pt(111) support to dissolve Fe. Therefore, Fe from the Fe_3O_4 phase can diffuse into the bulk, producing an intermediate nonstoichiometric Fe_3O_4 phase or even α-Fe_2O_3, which subsequently is structurally transformed into hematite.

The preparation of $\approx$ 10 nm thin iron oxide films on metal supports is determined by various parameters like growth temperature, oxidation temperature and pressure but also kind and morphology of the supporting substrate. These parameters may have a crucial influence on e.g., the film morphology, the film roughness, surface termination and crystal structures. Therefore, the control of the preparation is essential for the proper characterization of the chemical properties of oxide films.

10.2.4 Other Transition Metal Oxide Surfaces

Surface Structure of V_2O_5(001) and V_2O_3(0001)

Vanadium oxides are catalytically active for a number of reactions, most of them involve the transfer of oxygen atoms [10.115] which triggered a number of studies in the areas of basic and applied research. Some aspects are summed up in recent review papers [10.14, 62, 116–120]. Vanadium catalysts are often based on V^{5+} but lower oxidation states are likely to play a role during catalytic processes. The relevance of vanadium oxides in catalysis has motivated scientists to perform model catalytic studies for which well-characterized high-quality crystalline oxide surfaces are required.

Ordered V_2O_5(001) layers have been prepared on Au(111) only [10.121, 122], while V_2O_3(0001) layers have been grown on a number of substrates: Au(111) [10.123, 124], W(110) [10.125], Rh(111) [10.126], Pd(111) [10.127], and Cu_3Au(100) [10.128]. There have also been reports of VO_2(110) growth on TiO_2(110) [10.129] and SnO_2(110) [10.130, 131] but extended adsorption/reaction studies have not been reported.

The main difference between the preparation recipes for V_2O_5(001) and V_2O_3(0001) is that the preparation of V_2O_5(001) layers requires higher oxygen pressures than the preparation of V_2O_3(0001) layers: the former is prepared in an oxygen pressure in the 50 mbar range [10.121, 122] while for the latter UHV compatible pressures in the 10^{-6} mbar range suffice [10.123–125]. The preparation recipe for V_2O_5(001) on Au(111) is described in detail in [10.122]: well defined layers with a very low density of point defects may be produced as shown in Fig. 10.12. The bonding of the V_2O_5(001) layers to the Au(111) substrate is so weak that the islands in in the left panel of Fig. 10.12 exhibit different azimuthal lattice directions which leads to ring-type intensity patterns in the LEED images [10.122]. When enough material is deposited to close the layers then the islands grow together which leads to the lines in the center panel where azimuthally differently oriented areas meet. V_2O_5(001) is terminated with vanadyl double rows which are clearly recognizable in the right panel of Fig. 10.12.

V_2O_3(0001) layers may also be grown on Au(111) [10.123–125]. These layers are also well ordered but with a somewhat higher density of point defects, see Fig. 10.13. The surface structure of a model

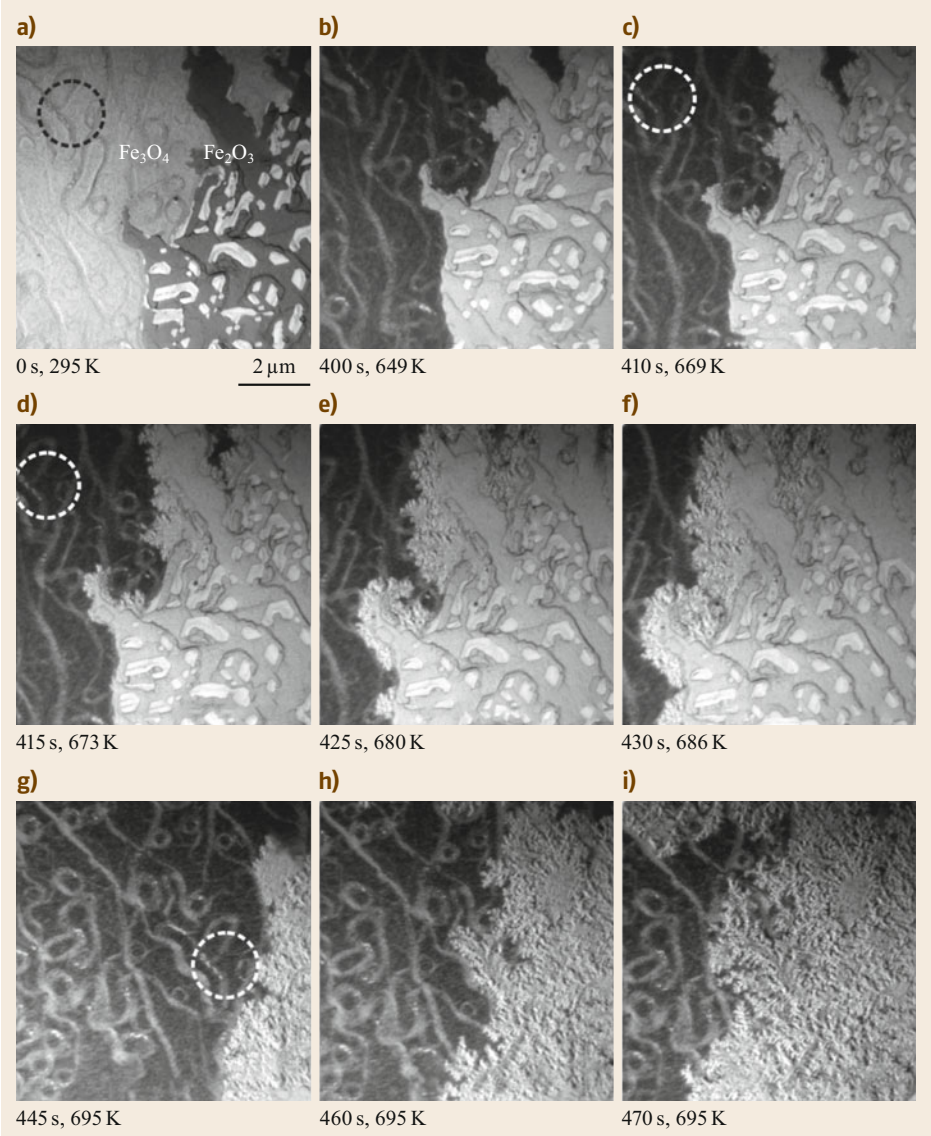

Fig. 10.11a–i Conversion of Fe_3O_4 into α-Fe_2O_3 by oxidation at $p_{O_2} = 3 \times 10^{-5}$ mbar in a temperature range between RT and 700 K. Images are taken in the sequence from **(a)** to **(i)** whereas the conversion time and temperature are indicated at the respective image. **(a)** The initial surface consists of α-Fe_2O_3 (*dark*) and Fe_3O_4 (*bright*) areas and FeO holes (*bright*). Between **(f)** and **(g)** the sample was shifted to follow the conversion front. As a help for the eye, the *circle* marks the identical surface spot. Reprinted (adapted) with permission from [10.112]. Copyright (2014) American Chemical Society

catalyst is a relevant parameter for its catalytic activity and therefore this aspect was investigated in detail in the first stages of the V_2O_3(0001) related studies.

V_2O_3 has a corundum lattice and the (0001) surface is a basal plane of this hexagonal lattice. Seen from the side, this lattice consists of alternating quasi-hexagonal oxygen layers and vanadium double layers. Three different surface terminations may be obtained by cutting the structure parallel to (0001): DM, SM, and bulk O_3, see Fig. 10.14. The stability of such surfaces from an electrostatic point of view has been initially analyzed by *Tasker* [10.133] who could show that polar structures, i.e., structures with electrically nonneutral layers parallel to the surface may energetically be stable only under certain conditions. The consequences have been discussed for a large variety of systems and the interested reader may be referred to the current literature [10.8, 70] Among the V_2O_3 terminations shown in Fig. 10.14 only SM is electrostatically stable according to the *Tasker* criteria [10.133]. However, the vanadium atoms at the SM terminated surface are chemically rather active and therefore it was assumed that the surface might actually be terminated by vanadyl groups, V=O in Fig. 10.14. This assumption was later supported by infrared spectroscopy and HREELS (high resolution electron energy loss spec-

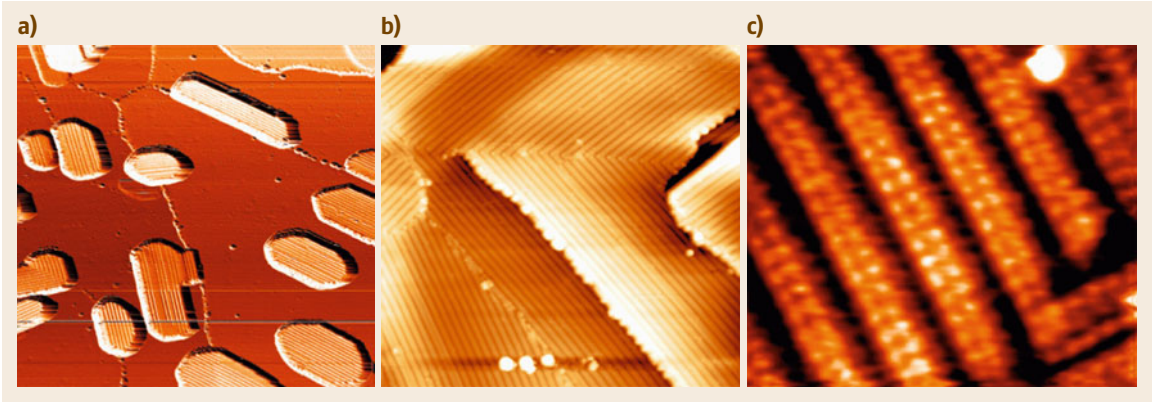

Fig. 10.12a–c STM images of $V_2O_5(001)/Au(111)$. **(a)** $V_2O_5(001)$ islands on Au(111), $100 \times 100\,nm^2$, $U = 3\,V$, $I = 0.2\,nA$. **(b)** Closed $V_2O_5(001)$ layer, $50 \times 50\,nm^2$, $U = 2\,V$, $I = 0.2\,nA$. **(c)** Small area scan, $5.8 \times 6.4\,nm^2$, $U = 3.5\,V$, $I = 0.2\,nA$. For details see [10.121, 121]

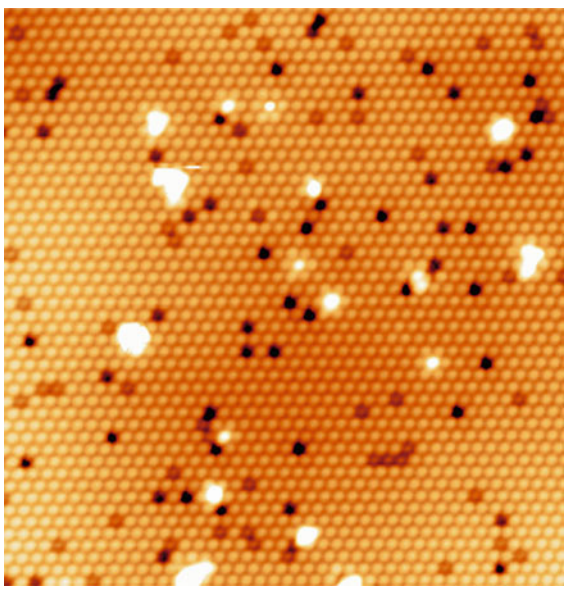

Fig. 10.13 STM image of vanadyl terminated $V_2O_3(0001)$ on Au(111), $20 \times 20\,nm^2$, $U = 1.5\,V$, $I = 0.2\,nA$. After [10.132]

troscopy) data which feature intense structures related to the vanadyl V=O vibration and by STM data like the one shown in Fig. 10.13 [10.125, 126]. This model was later challenged by studies featuring ion scattering experiments and DFT calculations which came to the conclusion that the surface termination should be the one named rec. O_3 in Fig. 10.14 [10.127, 134, 135]. This structure is similar to the bulk O_3 termination with the difference that a vanadium atom from the second double layer below the surface moves into the first vanadium double layer below the surface. This view was recently refuted by a detailed combined I/V-LEED + STM + ion scattering study which could conclusively show that the surface is terminated by vanadyl groups under standard UHV conditions [10.123, 124].

Preparation of Rutile $TiO_2(110)$ Layers on Rutile $TiO_2(110)$ Single Crystals with a Diffusion Blocking Layer

Mixed or doped oxides may offer additional catalytic reaction paths due to the presence of the additional component which may play a role for a specific reaction. This issue was studied with the example of vanadium mixed into rutile $TiO_2(110)$. The first step of that project was the preparation of a suitable sample. Several tries were made to prepare ordered $TiO_2(110)$ layers on different gold and platinum surfaces but suitable layers could not be obtained (see *Sedona* et al. [10.136] for TiO_x on Pt(111)). Interface stress due to overlayer-substrate lattice mismatch was assumed to be the reason for this failure and therefore it was tried to prepare $TiO_2(110)$ layers on rutile $TiO_2(110)$ single crystals [10.51] since in this case the lattice parameters of the overlayer and the substrate would be identical. High-quality layers could be prepared in this way, but when vanadium was mixed into the layers it turned out that the vanadium diffused into the substrate at temperatures required for the preparation of the films, so that vanadium doped oxide layers could not be prepared. In the next step a layer between the overlayer and the substrate was introduced with the aim of blocking vanadium diffusion. The blocking layer was a $TiO_2(110)$ layer with ions of another metal mixed into it. The admixed metal was chosen such that the ionic diameter of its 4+ ions was somewhat larger than that of the Ti^{4+}

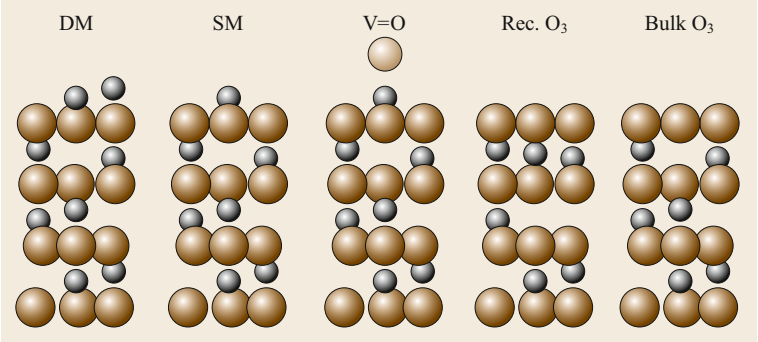

Fig. 10.14 Different possible $V_2O_3(0001)$ surface terminations (DM: double metal termination; SM: single metal termination). For details see text. *Brown*: bulk oxygen, *beige*: vanadyl oxygen, *gray*: vanadium. Reprinted (adapted) with permission from [10.123]. Copyright (2015) American Chemical Society

ions in $TiO_2(110)$. This stresses the rutile lattice of the TiO_2 host oxide, thereby increasing the diffusion barrier. A relevant property of the blocking layer is that it is a good support for the growth of rutile $TiO_2(110)$ overlayers, with and without vanadium doping. Therefore the structure and the lattice parameters of the blocking layer had to be very similar to the corresponding rutile TiO_2 properties. For this reason the metal ions mixed into the blocking layer were chosen among metals having oxides with rutile structure. Another relevant property is the thermal stability with respect to diffusion of the admixed metal ions, which should be high to prevent diffusion of the admixed ions into the overlayer and finally to the surface. Lead, tungsten and tantalum were tested as admixed components in the blocking layer. Lead appeared to segregate and was therefore discarded. Tungsten ions turned out to be thermally less stable than tantalum ions and therefore tantalum was selected to be the metal admixed to the TiO_2 in the blocking layer [10.51]. The prepared blocking layers were usually ≈ 3 nm thick and had an approximate composition of $Ti_{0.8}Ta_{0.2}O_2$. The thermal stability of the layers was such that with XPS weak tantalum signals could only be detected in surface-near regions of the top layer after 10 h of annealing at 800 K or 2 h at 900 K.

It was demonstrated that the blocking layer does not only impede vanadium diffusion but also the diffusion of Ti^{3+} ions resulting from the reduction of $TiO_2(110)$ [10.51]. This is illustrated in Fig. 10.15 which shows UPS (ultra-violet photoelectron spectroscopy) spectra of the $TiO_2(110)$ band gap state which is known to be related to Ti^{3+} ions [10.137–139]. The spectra have been measured at a grazing electron detection angle which means that most of the intensity in the spectra stems from just the topmost layer of the respective sample. Spectrum (b) was recorded from a sputtered single crystal after annealing at 800 K in vacuum for 10 min while spectrum (d) is the spectrum of a $TiO_2(110)$ layer subjected to the same procedure. Both, sputtering and annealing produce Ti^{3+} ions. However, the Ti^{3+} related feature at ≈ 0.75 eV is much

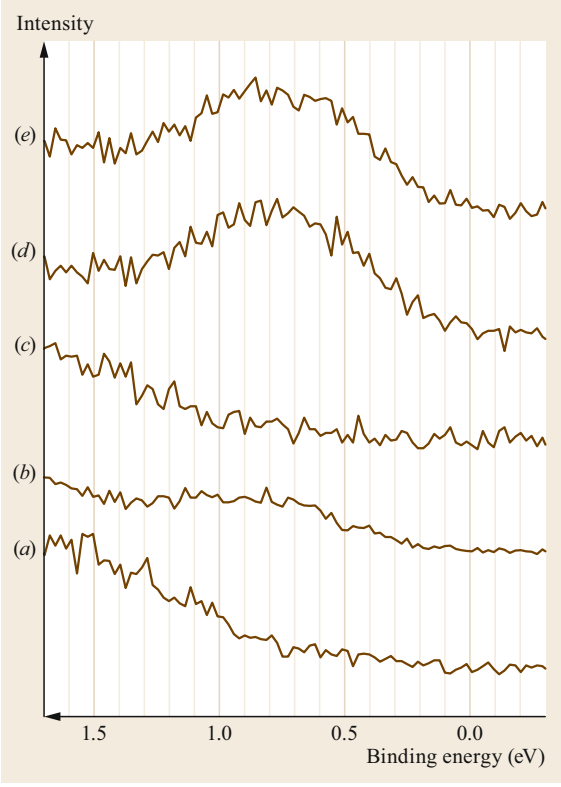

Fig. 10.15 HeI UPS spectra of differently prepared $TiO_2(110)$ surfaces recorded at an electron detection angle of 70° with respect to the crystal surface normal. The spectra show the energy range of the $TiO_2(110)$ band gap region. (*a*) Single crystal annealed at 800 K in 10^{-6} mbar O_2 for 10 min. (*b*) Single crystal reduced by sputtering at RT and annealing at 800 K in vacuum for 10 min. (*c*) $TiO_2(110)$ thin film annealed at 800 K in 10^{-6} mbar O_2 for 10 min. (*d*) $TiO_2(110)$ thin film reduced by sputtering at RT and annealing at 800 K in vacuum for 10 min. (*e*) The layer produced in step (*d*) annealed for 10 more min at 800 K in vacuum. Reprinted (adapted) with permission from [10.51]. Copyright (2016) American Chemical Society

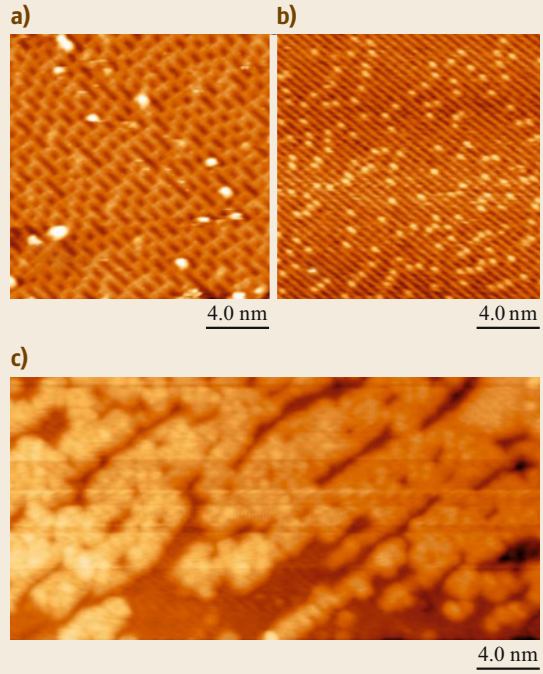

Fig. 10.16a–c STM images (2.0 V, 0.1 nA) of differently prepared TiO_2(110) surfaces. **(a)** A TiO_2(110) thin film annealed in vacuum at 900 K for 20 min. **(b)** A TiO_2(110) thin film annealed in 10^{-6} mbar O_2 at 600 K for 10 min. **(c)** A TiO_2(110) single crystal surface annealed in 10^{-6} mbar O_2 at 600 K for 10 min. For the images shown in **(b,c)** the samples were annealed at 800 K in vacuum prior to oxidation which resulted in flat surfaces with large terraces. Reprinted (adapted) with permission from [10.51]. Copyright (2016) American Chemical Society

more intense in the spectrum of the thin film. This would not be the case if the Ti^{3+} ions could pass the blocking layer since in this case the Ti^{3+} ions would have diffused into the substrate, which happened in the case of the single crystal substrate (spectrum (b)) and led to the smaller intensity in the spectrum. Further annealing of the thin film did not change the intensity of the band gap state since the Ti^{3+} ions could not diffuse into the substrate (spectrum (e)).

TiO_2(110) single crystals studied with electrons (using electron spectroscopy, electron scattering, STM, ...) have to be electrically conductive which is usually achieved by a mild reduction which produces Ti^{3+} ions. In addition to vacancies in the bulk this leads to oxygen vacancies at the surface (*bridging oxygen vacancies*) which may and often do play a role in catalytic surface reactions. The introduction of blocking layers offers a way to prepare surfaces without bridging oxygen vacancies which do not charge and can therefore be studied with charged particles, provided that the layers are not too thick. Also strongly reduced layers may be prepared without reducing the substrate notably.

Figure 10.16a displays a STM image of a TiO_2(110) film ($\approx$ 10 nm thick, on a blocking layer) after annealing in vacuum. A high density of bridging oxygen vacancies (the links between the continuous rows) is observed as expected from the discussion above. After annealing in oxygen (Fig. 10.16b) the bridging oxygen vacancies are not visible anymore and some bright features on the rows show up, which are attributed to oxygen adatoms, resulting from oxygen dissociation [10.138, 140]. The result is different if the single crystal is exposed to oxygen (Fig. 10.16c). In this case extended structures form which result from the diffusion of Ti^{3+} ions to the surface where they are oxidized [10.141]. Since there is no blocking layer in the case of the single crystal, Ti^{3+} ions from far below the surface can diffuse to the surface which the reason for the formation of the extended protrusion in Fig. 10.16c.

It could be shown that vanadium admixed to TiO_2(110) prefers subsurface locations under reducing conditions [10.53]. The vanadium has the effect that the host oxide becomes more reducible, which was traced back to the lower binding energy of vanadium to oxygen [10.53]. This has the effect that layers containing vanadium are usually more reduced than layers without vanadium, which affects the surface reactivity: bridging oxygen vacancies and extended reduction induced defects like the strands known for heavily reduced (1×2) reconstructed TiO_2(110) appear in elevated concentrations at the surface, where they may interact with adsorbates, modifying reactions rates, selectivities and reaction paths.

10.3 Tuning the Properties of Oxide Films

Apart from the structural properties of oxide films, which have been addressed in the previous section, it is important to elucidate the physical and chemical properties of these systems in more detail. Within this section we would like to elucidate the possibilities to tune the properties of the oxide films. A variety of strategies have been reported in literature on how the properties of these systems can be modified. We will

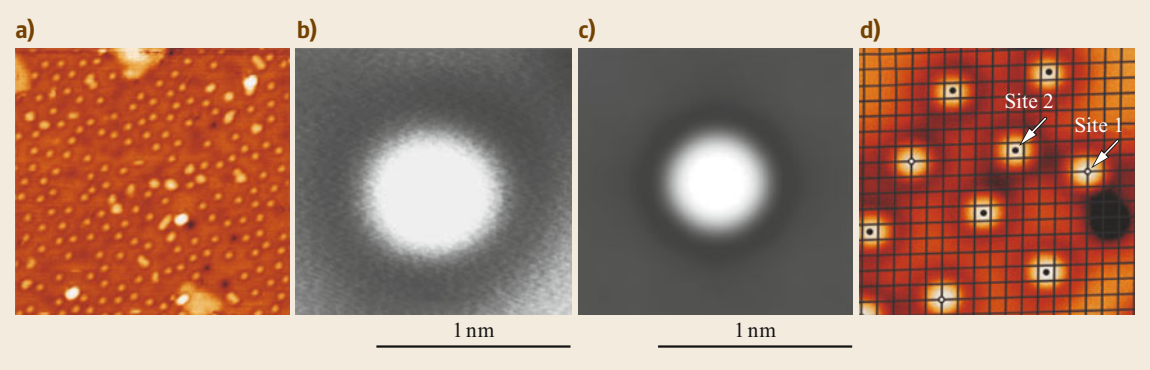

Fig. 10.17 **(a)** STM image (30 nm × 30 nm) of Au atoms adsorbed on a 3 ML thin MgO film. **(b)** Experimental STM image and **(c)** calculated STM image of Au atoms on 3 ML MgO/Ag(001). **(d)** STM image (5 nm × 5 nm) of Au atoms on 3 ML MgO/Ag(001); the *grey lattice* is the ionic sublattice extracted from a high resolution image of the clean MgO film

restrict the discussion to two aspects. First we would like to discuss the effect of film thickness. We will refrain from discussing the complex structural variability of several ultrathin oxide film systems, which have been reviewed recently, but we will focus on charge transfer processes and their impact on the properties of molecular adsorbates as well as metal atoms and particles. While a discussion of ultrathin oxide films may sound like an academic curiosity it is important to note that the concepts observed for the ultrathin films can largely be transferred to bulk oxides if suitable electron donors or acceptors are provided. We will use CaO as an exploratory example to show how suitable doping of a bulk, wide-band gap oxide can modify the properties of the system, which is very comparable to the observations made for the ultrathin MgO film.

10.3.1 Charge Transfer Effects on Thin Oxide Films

MgO as the prototype of an ionic oxide is a good starting point for the discussion of charge transfer effects on thin oxide films. The interaction of molecules as well as metal atoms with the stoichiometric (001)-plane of the rock salt lattice is rather weak resulting in a low stability of individual metal atoms and growth of 3-dimensional metal particles at ambient temperature. Gold atoms adsorbed on bulk like 30 ML MgO(001) films were shown to be neutral entities [10.142]. However, the binding of the atoms on-top of the oxygen ions of the MgO lattice leads to a polarization of the valence electrons of the Au atom, which enables charge transfer to molecular adsorbates such as CO [10.143]. Theory had proposed that Au atoms deposited onto ultrathin MgO films get negatively charged due to a charge transfer from the metal substrate to the Au atom [10.25, 144, 145]. This is due to the fact that the unoccupied part of the Au 6 s level found in the band gap on thick films is located below the Fermi-energy of the support for the thin film system. There are different contributions to this effect. First, the deposition of MgO onto the metal substrate reduces the work function of the system, which has been confirmed both theoretically as well as experimentally [10.64, 77, 146]. Second, charged Au atoms adsorbed on the surface of the ultrathin MgO film are stabilized by polaronic distortions of the oxide lattice [10.144, 147].

Experimental evidence for the charging of Au atoms on ultrathin MgO(001) films comes from low-temperature STM experiments. As seen from the STM image (Fig. 10.17a) Au atoms deposited on a 3 ML MgO film ($T = 5-10$ K) form an ordered structure indicating significant repulsion between them [10.27]. In contrast to that adsorption of Pd atoms (3 ML thick MgO film, $T = 5-10$ K) is in perfect agreement with expectations based on a statistical distribution of the atoms [10.27]. Further evidence for a charged state of the Au atoms can be found from the STM signatures of single Au in comparison with simulated ones applying the Tersoff–Hamann approximation (Fig. 10.17b,c) [10.149]. The experimental appearance of the Au atoms showing a *sombrerolike* protrusion surrounded by a depression is nicely reproduced theoretically, however, it is absent in the simulated STM images of neutral atoms [10.150]. Similar observations were found for other systems such as Au on ultrathin NaCl films [10.151]. To elucidate this question in more detail it is interesting to note that on bulk MgO or thick films Au atoms were found to nucleate on top of oxygen ions [10.142], while theory predicts charged Au atoms on thin films to adsorb preferably on Mg sites or hollow sites [10.25, 144, 152]. STM can provide evidence for the change in the distribution of the adsorption sites by superimposing the

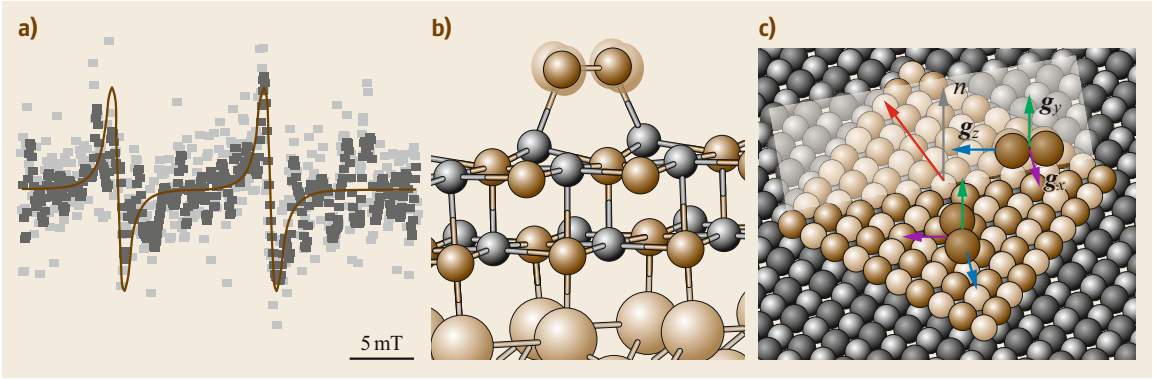

Fig. 10.18 **(a)** EPR spectrum of 20 L O_2 adsorbed at 40 K on a 4 ML thick MgO(001) film on Mo(001) with the magnetic field in the surface plane along a [110] equivalent direction. **(b)** Result of a DFT calculation of O_2 on a 2 ML thin MgO(001) film on Mo(001) showing the polaronic distortion of the MgO lattice. **(c)** Sketch of oxygen molecules adsorbed on 2 ML MgO films as predicted by theory. The *transparent area* indicates the plane in which the magnetic field was lying in **(a)**. The orientation of the three principal components of the $\boldsymbol{g}$-matrix of the two symmetry equivalent molecules are shown as *color coded arrows*. As an EPR experiment probes the $\boldsymbol{g}$-value oriented along the static magnetic field it is readily clear that both molecules are not identical for the magnetic field lying in the surface plane. Adapted from [10.148]

MgO lattice on the STM images of Au atoms. For an 8 ML film > 80% of the atoms occupy one adsorption site, while at least two different adsorption sites are populated with almost equal probability on 3 ML films (Fig. 10.17d), which clearly shows the change in adsorption site [10.27].

Charge transfer is not restricted to metal atoms with sufficiently high electron affinity, but was theoretically predicted for molecules with high electron affinities such as NO_2 or O_2 adsorbed on ultrathin MgO(001) films grown on Ag(001) or Mo(001) [10.147, 153, 154]. From an experimental point of view the characterization of the superoxide anion (O_2^-) can be approached using EPR spectroscopy [10.155] as the superoxide anion is a radical with a doublet ground state. Figure 10.18a shows an EPR spectrum of molecular oxygen adsorbed at 40 K on a 4 ML thick MgO(001) film grown on Mo(001) [10.148]. The spectrum consists of a doublet of lines at $\boldsymbol{g}$-values of 2.072 and 2.002, which are well in line with expectations based on O_2^- radicals observed on MgO powder [10.156–158]. In line with theoretical predictions the radicals show significant stability ($T_{\mathrm{des}} \approx 350$ K) and disappear for thicker MgO films (> 15 ML). A detailed analysis of angle dependent spectra reveals that the O_2^- radicals are adsorbed on the terraces of the MgO(001) surface aligned with [110] equivalent directions as predicted theoretically (Fig. 10.18b). A comparison of the $\boldsymbol{g}_{zz}$ component (for an alignment of the $\boldsymbol{g}$-matrix with the molecular framework see Fig. 10.18c) of the $\boldsymbol{g}$-matrix ($\boldsymbol{g}_{zz} = 2.072$) with values observed for O_2^- radicals on terraces of MgO powders ($\boldsymbol{g}_{zz} = 2.091$) [10.157] provides additional physical insight into the interaction between the molecule and the surface as the observed value depends critically on the local electric field experienced by the radical. The reduction of the $\boldsymbol{g}_{zz}$ component on the film as compared to bulk MgO is associated with an increase of the local electric field, which is due to the polaronic distortion of the MgO lattice in case of the ultrathin film (Fig. 10.18b) as revealed by quantum chemical calculations [10.148].

We have already shown that single Au atoms become charged upon adsorption on very thin MgO(001) films. Hence, it is interesting to explore the consequences of charge transfer on the growth mode of Au particles. Theory predicted that charge transfer onto the gold particles leads to the formation of 2-dimensional structures on ultrathin MgO films in contrast to expectations on bulk MgO, where 3-dimensional particles are expected [10.9, 10, 26]. The reduced stability of the 2-dimensional structure with film thickness is due to a decreasing stabilization due to the image charge as well as the increasing cost for the polaronic distortion with increasing film thickness. The latter is caused by a stiffening of the MgO lattice due to the long-range nature of the Coulomb interaction. A low temperature STM study provided experimental evidence for the predicted crossover in growth mode. For an 8 ML MgO/Ag(001)-film 3-dimensional particles are observed after annealing to room temperature, whereas the Au-structures on 3 ML MgO/Ag(001) stay 2-dimensional after the corresponding annealing step (Fig. 10.19) [10.27].

An increase of the contact area between metal and oxide film allows to optimize the charge transfer. For a close-packed Au layer on an ultrathin MgO(001)/Ag(001) an average charge transfer of about

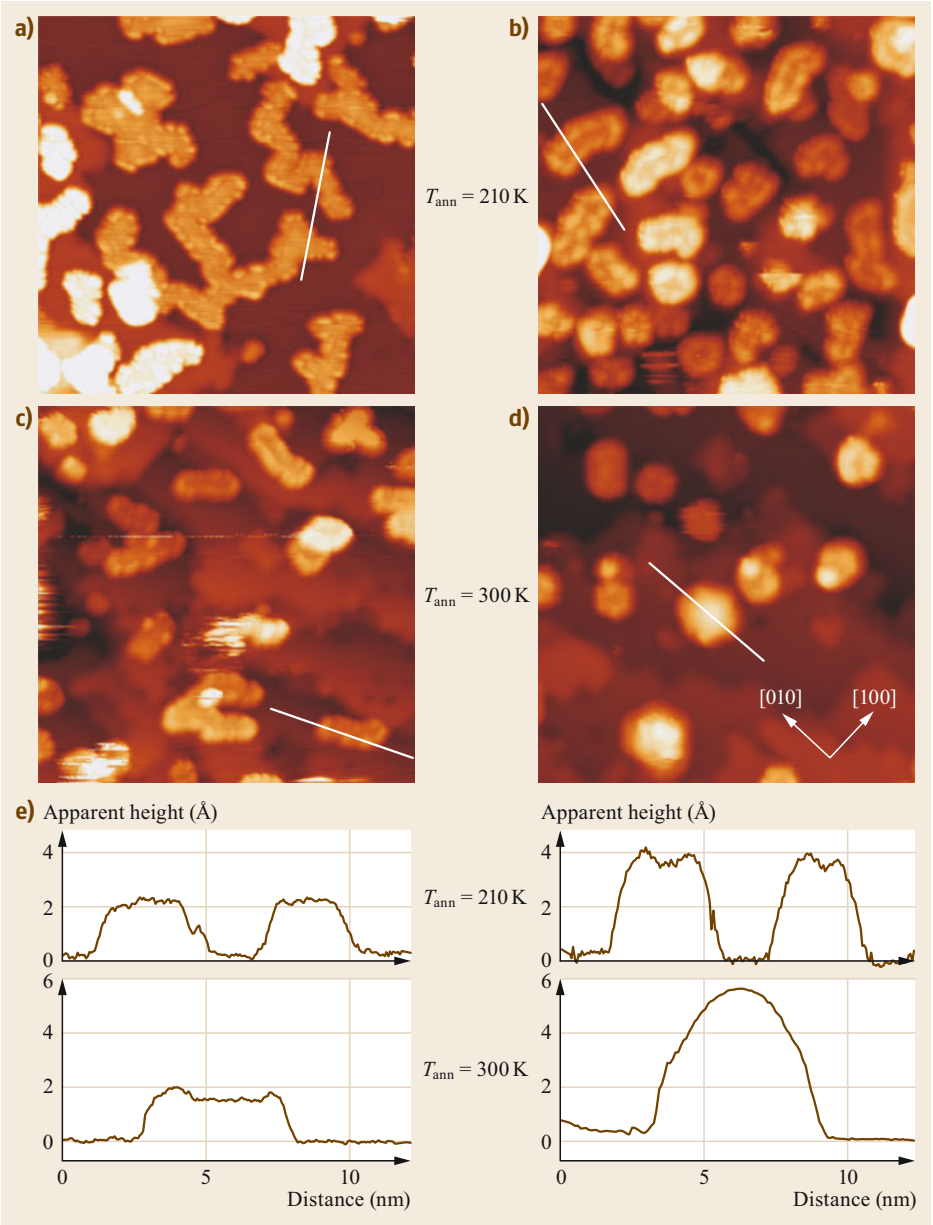

Fig. 10.19a–e STM images of Au deposits on 3 ML **(a,c)** and 8 ML **(b,d)** MgO(001)/Ag(001) ($30 \times 30\,nm^2$) after annealing of Au deposits to 210 K and 300 K, respectively. **(e)** Line profiles of characteristic clusters found in **(a–d)** [10.27]

$-0.2|e|$ per adatom has been calculated [10.159]. As shown for Au chains on alumina/NiAl(110) it is not expected that the charge distribution within Au islands is homogeneous [10.160]. Experimentally, this distribution can be interrogated by so-called conduction maps, which show an enhanced dI/dV contrast around the Fermi level at the island edges indicating a higher density of states at these sites [10.161]. This observation is nicely reproduced by semi-empirical tight-binding DFT calculations, which reveal an increase of charges at the perimeter of the particles [10.161].

A more detailed picture of the electronic structure of the adsorbed Au particles can be obtained by exploring so called quantum well states (QWS), which are derived from the 6 s levels of the Au atoms and hence allow for an analysis in a 2-dimensional electron gas model [10.162]. Figure 10.20a,b shows three STM images providing information on topography as well as electronic structure of occupied as well as unoccupied states of a small Au cluster with about 10 Å diameter grown on a 2 ML MgO/Ag(001) film [10.159]. The image taken around the Fermi energy reveals mainly the

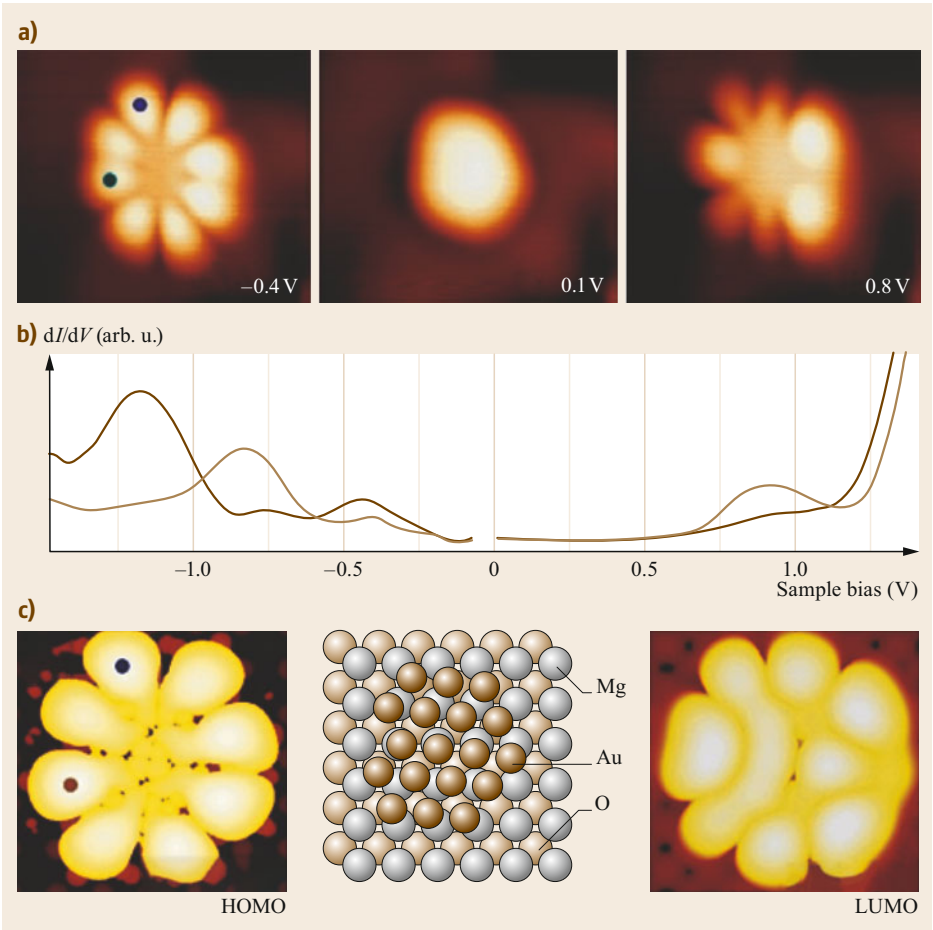

Fig. 10.20 **(a)** STM images of a symmetric Au cluster on 2 ML MgO/Ag(001) taken at the given sample bias. **(b)** dI/dV spectra of top (*dark brown*) and left part (*light brown*) of the Au cluster in panel **(a)**. **(c)** Calculated images of the HOMO (highest occupied molecular orbital) and LUMO (lowest unoccupied molecular orbital) as well as structure model of an Au_{18} cluster on MgO/Ag(001). Reprinted with permission from [10.161]. Copyright (2009) by the American Physical Society

cluster morphology as no states are available in the energy range probed by the STM experiment. At higher bias the appearance of the cluster changes to flowerlike protrusions. The bias-dependent contrast is clear evidence for tunneling governed by electronic and not topographic properties of the island. Both observed QWS probed by STM resemble the eigenstates of a free-electron gas in a 2-dimensional parabolic potential, which can be characterized by an angular momentum quantum number j [10.163]. Both states, observed at −0.4 and +0.8 V, respectively, exhibit four nodal planes ($j = 4$), which corresponds to G-symmetry. The next two lower lying occupied states, found at −0.8 and −1.2 V, exhibit P-symmetry (not shown). A detailed analysis of the electronic structure of this Au cluster including its charge state was achieved by comparing the experimental results to DFT calculations [10.159]. However, an extensive search of the parameter space is required to determine the number of atoms, the geometric structure as well as the charge state of the cluster. The degree to which theory is able to reproduce the experimental results is nicely shown in Fig. 10.20c assuming a planar Au_{18} cluster lacking one corner atom of a Au_{19} cluster, the latter being a so-called magic-size. In agreement with the experiment, the highest occupied as well as the lowest unoccupied state are of G-symmetry being located in the 5th level of the harmonic potential, whereas the highest states of the 4th shell of this potential are of P-symmetry in line with the experimental results. Once this has been established, the charge state is readily determined by counting the filled states in the potential. There are 11 doubly occupied orbitals,

hence, 22 electrons. The 18 Au atoms contribute 18 electrons, which leads to a 4-fold negatively charged cluster being provided by charge transfer from the support. A Bader analysis of the DFT calculation yields a value of $-3.54|e|$ for the Au_{18} cluster. Please note that this amounts to an average transfer of almost $0.2|e|$ per atom as calculated for closed-packed Au layers on the MgO thin film [10.161].

In this chapter we have discussed charge transfer effects on ultrathin oxide films using MgO as an exploratory example. We have shown how microscopy as well as spectroscopy can be used to provide experimental evidence for charge transfer between the substrate and adsorbed species such as metal atoms or molecular adsorbates with appropriate properties. The tools and concepts used here are, however, not limited to the ultrathin films, but it is possible to transfer some of them to bulk like oxide films if suitable electron donors or acceptors are provided. Such species can be introduced into oxide films by doping, which will be discussed in more detail in following section.

10.3.2 Modifying the Properties of Oxide Materials via Doping

The former paragraphs have illustrated that spontaneous electron transfer through oxide thin films has an enormous impact on the equilibrium shape of metal particles and even enables molecular activation [10.27, 148]. So the question arises, whether the concept of charge-mediated control of the oxide properties is restricted to ultrathin films, or can be extended to thicker layers or even bulk materials, as used in heterogeneous catalysis [10.29, 164]. A possible route might be the insertion of suitable charge sources directly into the oxide material, preferentially into a near-surface region to allow for charge exchange with adsorbates [10.165]. By this means, all advantages of charge control could be maintained for oxide slabs of arbitrary thickness. Although the fundamental concepts of doping were introduced and brought to perfection in the semiconductor technology already decades ago, a direct transfer to oxide materials is challenging due to several structural and electronic peculiarities [10.166]. Oxides are subject to self-doping by native defects and unwanted impurities, the concentration of which is difficult to control experimentally [10.138]. Both lattice defects and impurity ions may adopt different charge states in the oxide matrix [10.167], a variability that leads to pronounced compensation effects and is less common in semiconductors. And finally, the dopants may be electrically inactive in wide-gap oxides, as thermal excitation is insufficient to promote electrons from the defect states to the bulk bands. The excess charges thus remain trapped at the host ions and are unavailable for charge transfer. However, the following examples demonstrate that doping is a versatile approach to tailor the properties of bulk-like oxides as well.

In general, doping is carried out with impurity ions that adopt either a higher or a lower valence state than the native oxide ions [10.165]. Whereas high-valence dopants may serve as charge donors and provide extra electrons, low-valent dopants have acceptor character and may accommodate electrons from suitable adsorbates. In rare cases, charge-preserving doping is realized where geometric and strain effects take the role of the charge transfer [10.168]. Based on the above considerations, we expect that charge donors inserted in an oxide lattice may resume the role of the metal support in the case of ultrathin oxide films. This assumption has first been verified in studies of the growth morphology of gold on crystalline CaO(100) doped with trace amounts of Mo (Fig. 10.21) [10.47]. On the doped oxide, gold was found to spread out into extended monolayer islands, while the conventional 3-D growth prevailed on the nondoped material. Evidently, the donor character of the Mo ions is responsible for the 2-D growth morphology, while the metal–oxide adhesion on pristine CaO(100) is negligible.

According to DFT calculations, Mo dopants in CaO mainly occupy Ca substitutional sites and adopt the typical 2+ charge state of the rock salt lattice. In the 2+ configuration, four Mo 4d electrons are localized in the dopant, three of them occupying (t_{2g}-α) crystal field states and one sitting in a (t_{2g}-β) level close to the conduction band onset (Fig. 10.21c) [10.169]. Especially, the latter is in an energetically unfavorable position and thus susceptible to be transferred into an acceptor state with lower energy. Such states are provided by the Au ad-atoms that exhibit a half-filled Au 6s affinity level, being ready to take the topmost Mo 4d electron. The result is an Au^- anion that, as discussed before, experiences reinforced bonding to the CaO surface [10.25]. DFT calculations find an increase of the binding energy from ≈ 1.5 to ≈ 3.5 eV upon doping, whereby the electrically-active Mo ion may be located up to ten layers below the CaO surface [10.47]. Moreover, not only Mo^{2+} ions are susceptible to electron transfer into gold, but also Mo^{3+} and Mo^{4+} are active donors as their topmost occupied d states are still higher in energy than the Au 6s affinity level [10.169]. Mo impurities in the CaO lattice are therefore robust electron donors, and as such directly responsible for the 2-D growth of gold found experimentally [10.47].

The presence of suitable dopants is, however, not the only requirement for a stable donor characteristic and also the interplay between dopants and the host oxide governs the redox activity, as shown for Cr-

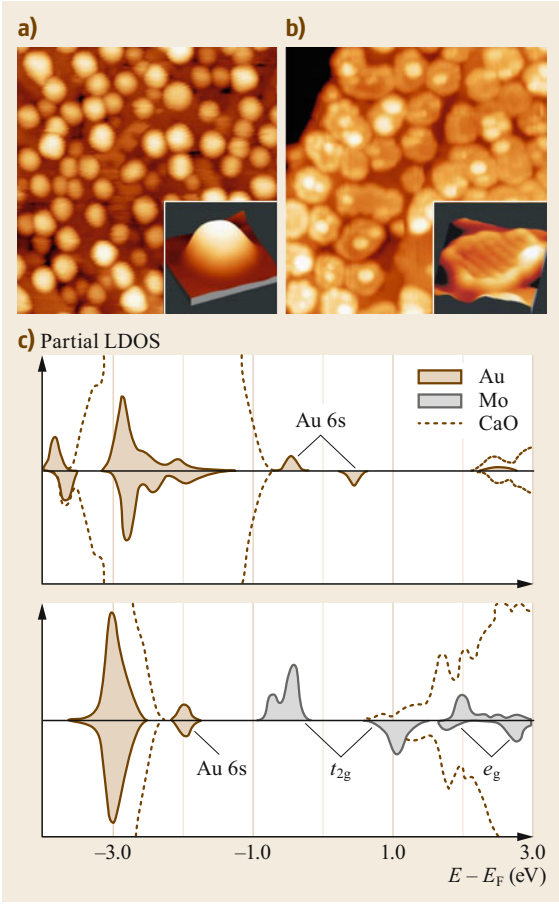

Fig. 10.21a–c STM images of 0.7 ML Au deposited onto **(a)** pristine and **(b)** doped CaO films (4.5 V, $50 \times 50\,nm^2$). The *insets* display close-up images of two characteristic particles (−5.0 V, $10 \times 10\,nm^2$). **(c)** PBE (Perdew–Burke-Ernzerhof (DFT functional)) projected state-density calculated for nondoped (*top*) and doped (*bottom*) CaO films in presence of an Au adatom. Reprinted with permission from [10.47]

doped MgO films next [10.170]. Although chromium has a similar electronic structure as Mo, i.e., the same number of d electrons, it is unable to influence the Au growth on MgO supports (Fig. 10.22). Even at high Cr concentration, gold adopts 3-D shapes and hardly any 2-D islands are found on the surface [10.44]. The reason is the low energy position of the Cr t_{2g} levels in the MgO band-gap, reflecting the large stabilization effect of the MgO crystal field on the Cr electrons. Note that the crystal field in MgO is much stronger than in CaO given the larger lattice parameter of the latter [10.171]. In addition, the Cr ionization energies are higher than those for Mo, and formation of Cr^{4+} and Cr^{5+} ions is energetically costive. As a result, Cr is able to donate only a single electron to gold, which compares to three in the case of Mo ions in CaO [10.169, 170]. More critically, not even this electron may reach the ad-metal, but is likely captured by parasitic electron traps in the oxides, such as cationic defects or grain boundaries. Cation vacancies or *V*-centers are the preferred compensating defects for high-valance dopants, as they are able to neutralize the extra charges released by the impurity ions (Fig. 10.22e) [10.166]. According to DFT calculations, the formation energy of a *V*-center decreases from 8 eV in bare CaO or MgO to 1.0−1.5 eV in the presence of high-valence dopants [10.44]. Accordingly, an effective compensation mechanism becomes available that fully annihilates the donor character of the Cr ions. Because Mo impurities in CaO are able to release more electrons, full charge compensation is impossible and the impact of the donors prevails in that case.

Low-valence dopants generate hole-states in the electronic structure of rocksalt oxides and are able to trap excess electrons as well [10.172, 173]. Their response is therefore similar to the one of compensating lattice defects, as shown in a codoping experiment on CaO using both, Mo donors and Li acceptors [10.46]. At low Li concentration with respect to Mo, most of the Au particles still adopt 2-D shapes, indicating that the charge transfer into the gold is maintained. With increasing Li doping level, more and more charges get trapped in the Li-induced defects until the charge flow into the ad-gold breaks down completely and the Au particles turn 3-D. In fact, monovalent Li^+ substituting a Ca^{2+} ion produces a deep hole in the O 2p states of adjacent oxygen that effectively traps all available free carriers and neutralizes the Mo donors. Let's note that Li doping alone did not result in any observable change in the Au growth characteristic on the CaO surface. This finding suggests an effective intrinsic compensation mechanism to be active also in the case of low-valence dopants [10.174]. Hereby, oxygen vacancies play the role of the compensating defect, as they are able to release electrons according to

$$F^0 \rightarrow F^+ + e^- \rightarrow F^{2+} + 2\,e^-$$

which then fill up the hole states produced by the Li ions. Hole-doping of oxides, as a means to tailor the properties of metal ad-particles, is therefore more difficult to realize than electron-doping with donor-type impurities [10.175].

So far, electron-transfer processes induced by dopants in the oxide lattice have been shown to modify the growth behavior of ad-metals on oxide surfaces. However, charge exchange is also a promising route for molecular activation, as demonstrated before for oxy-

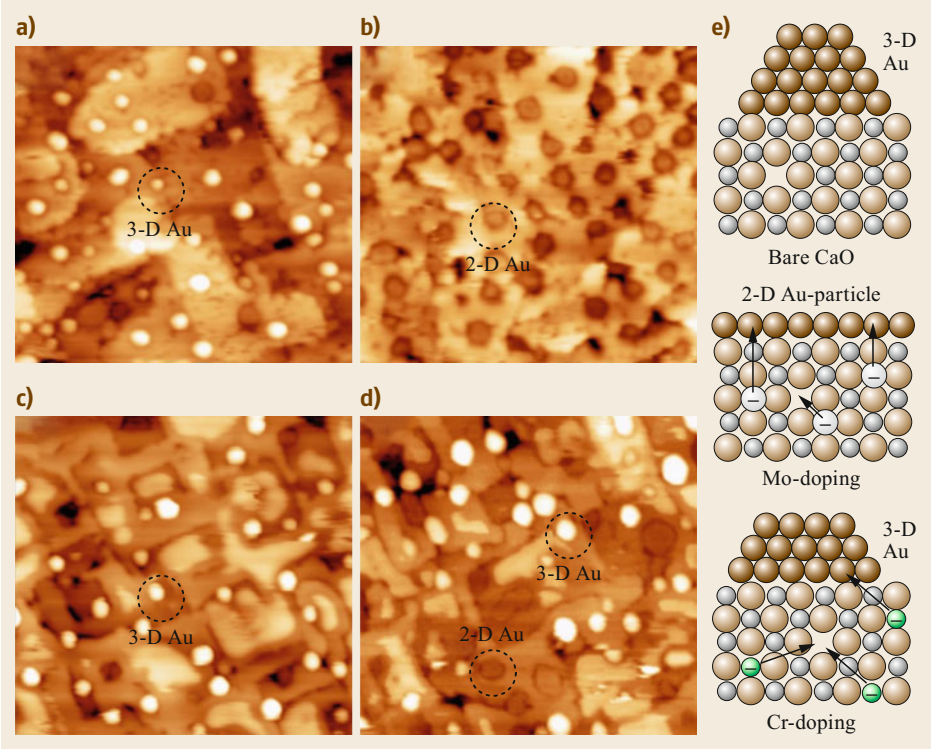

Fig. 10.22a–e STM images of **(a)** bare and **(b)** Mo-doped CaO(100) films of 60 ML thickness after dosing 0.5 ML of Au ($60 \times 50\,nm^2$, $V_S = 6.0\,V$). The 2-D Au islands appear as depressions on the insulting oxide, because electron transport through the gold is inhibited at high positive bias. Similar measurements on **(c)** bare and **(d)** Cr-doped MgO(100) films of 20 ML thickness. The particle shape is not affected by the dopants in this case. **(e)** Ball models visualizing charge-transfer processes between the doped oxide and the ad-metal and their effect on the particle shape

gen exposed to thin MgO/Mo films [10.148]. In the following section, we will show that a similar scheme holds for bulk-like oxides, in which high-valence dopants have been inserted as intrinsic charge source.

Not unexpectedly, stoichiometric CaO(100) as a chemically inert, wide gap insulator shows little activity toward adsorption and dissociation of oxygen (Fig. 10.23a) [10.176]. Neither at room nor low temperature (20 K) is the oxide able to bind oxygen, apart from some trace amounts attached to low-coordinated edge and corner sites. This situation changes considerably for a material doped with Mo ions [10.43]. The STM images now reveal a high concentration of depressions on the CaO surface after oxygen exposure, both at 20 and 300 K (Fig. 10.23b). In fact, two oxygen species are distinguished on the surface. The first one shows up as 0.6 Å deep and 10 Å wide depression and is assigned to an oxygen molecule (Fig. 10.23c). Exposing it to electrons from the tip, it can be converted into a pair of shallow dents surrounded by a bright halo. Apparently, the molecule gets dissociated into its atomic constituents via electron injection [10.177]. Whereas a mean O–O separation of 10−15 Å is observed directly after dissociation, the distance increases over time, indicating the repulsive character of the O–O interaction on the surface (Fig. 10.23c).

The ability of the CaO(100) surface to adsorb oxygen is apparently triggered by the presence of high valence Mo ions in the lattice. The underlying interaction mechanism relies again on an electron transfer between the high-lying Mo 4d states and the LUMO of the oxygen molecule, as revealed by DFT calculations performed at the B3LYP (Becke, three-parameter, Lee–Yang–Parr (DFT functional)) +D level [10.43]. On nondoped CaO(100), the oxygen physisorbs with ≈ 0.13 eV to a Ca–Ca bridge position. On doped CaO, an O_2^- species develops due to charge transfer from the Mo dopants, which strongly interacts with a surface Ca^{2+} ion. The calculated binding energy amounts to 0.87 eV if the associated donor is a Mo^{3+} ion located in the third subsurface plane. Even larger adsorption energies are found for Mo^{2+} species serving as donor, as well as

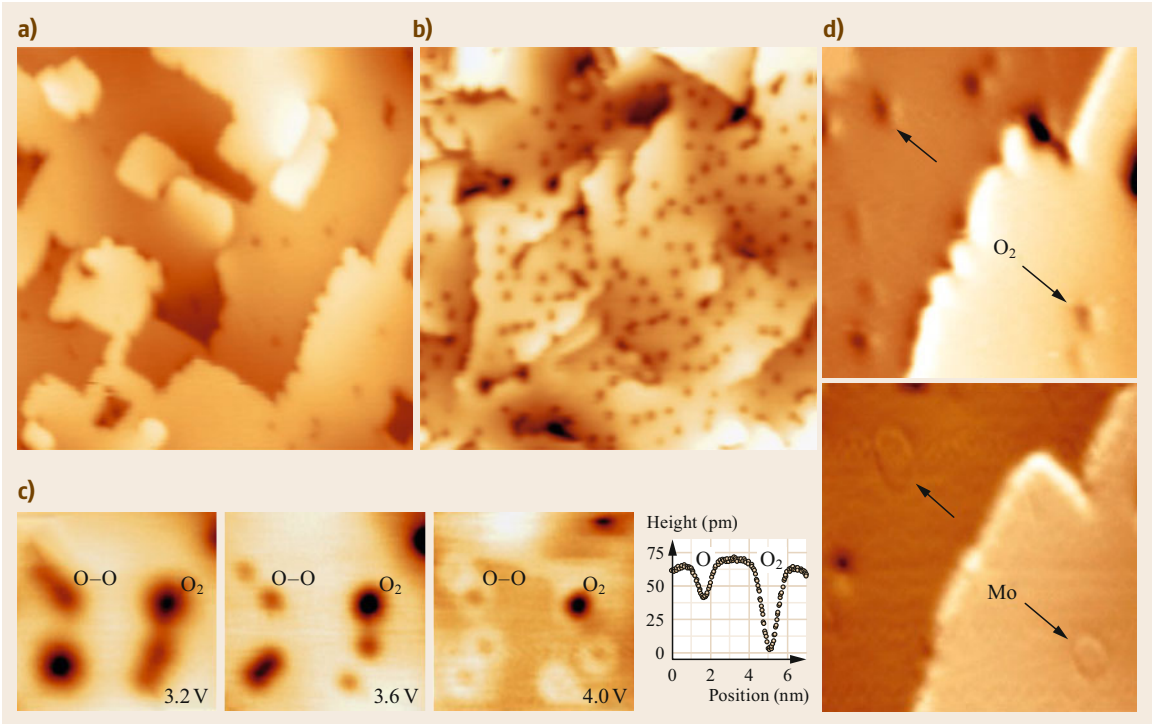

Fig. 10.23 **(a,b)** STM images of bare and Mo-doped CaO after dosing 5 Langmuir O_2 at 20 K ($40 \times 40\,nm^2$). **(c)** Bias-dependent contrast and height profile of oxygen molecules (deep minima) and atoms (faint double dents). Note the dissociation of an O_2 in the *lower left part* of the image during scanning. **(d)** Appearance of charging rings, characteristic for subsurface Mo dopants, after desorbing two O_2 molecules from the surface ($17 \times 17\,nm^2$). Reprinted with permission from [10.43]

for dopant positions closer to the surface [10.43]. Further evidence for the formation of O_2^- species comes from the bond elongation (121−133 pm) and the reduced stretching frequency (1537−1200 cm^{-1}) of the oxygen molecule after charge transfer. In addition, a decreasing total spin of the system has been calculated, evolving from 5/2 (3/2 for Mo^{3+} plus 2/2 for neutral O_2) to 3/2 (2/2 for Mo^{4+} plus 1/2 for the O_2) due to the electron exchange. The superoxo species formed on the doped CaO surface exhibits, finally, a two times lower barrier for dissociation, if compared with a neutral O_2 on pristine CaO. This theoretical finding is in good agreement with the observation that oxygen adspecies can be effectively dissociated via electron injection from the tip. The DFT calculations therefore clearly corroborate the idea that electron transfer from Mo dopants is responsible for the adsorption, activation and finally dissociation of O_2 molecules on the CaO surface [10.43].

Further experimental evidence supports the above mechanism. If single oxygen molecules are removed from the surface by means of a controlled bias pulse given to the STM tip, a Mo donor shows up via a characteristic ring structure on the CaO surface, arising from a temporal change of the Mo charge state as the tip scans this oxide region (Fig. 10.24d). The spatial correlation between the impurity position in the oxide and the preferred O_2 adsorption site underlines that the dopant indeed mediates the binding of oxygen. Interestingly, the active dopant never occupies a position directly in the CaO top layer, but sits in subsurface planes as deduced from the diameter of characteristic charging rings emerging in the STM images [10.178]. The charge transfer to adsorbates hereby occurs via electron tunneling over distances as large as 1 nm. A last experimental hint for O_2^- formation on doped CaO films comes from the evaluation of the vacuum states above the oxide surface (Fig. 10.24). As mentioned already in Sect. 10.2.1, the vacuum states are a sensitive probe of the local surface potential [10.86] and up-shift in energy if negatively charged species accumulate at the surface but downshift on surfaces holding a positive net-charge. This provides a direct probe of the direction of charge transfer in the CaO/Mo(001) system. An oxide region densely covered with O_2^- species exhibits a series of vacuum states, the lowest of which being located

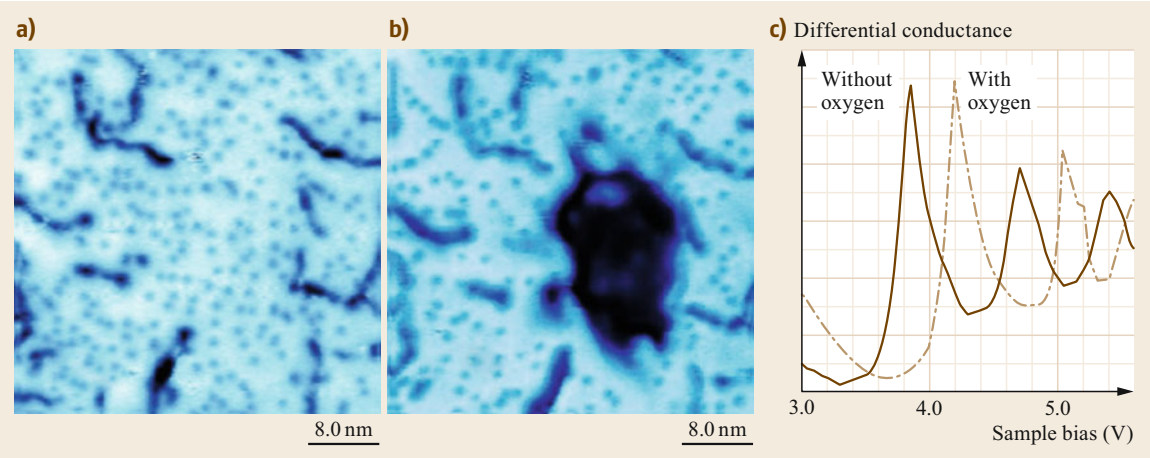

Fig. 10.24 (a,b) Conductance images of CaO/Mo(001) before and after desorbing O_2 molecules from the central region with a tip voltage pulse ($40 \times 40\,nm^2$). The bias voltage for imaging has been tuned to the first vacuum state of the oxygen-covered surface (4.0 eV), which consequently appears with bright contrast. After oxygen removal, the local surface potential, and hence the vacuum states, downshift and the affected surface region shows lower conductance and appears dark. (c) STM conductance spectra showing the energy shift of CaO vacuum states after O_2 desorption from the surface. Reprinted with permission from [10.43]

at 4.2 V above the Fermi level (Fig. 10.24c) [10.43]. After desorbing the molecules with a tip pulse, the vacuum states experience a clear downshift, reflecting the decreasing electron density after removing the negatively charged superoxo species. The excess electrons released during desorption return to their Mo host-ions located in subsurface CaO planes, where they do not perturb the surface potential anymore. The effect of a decreasing surface potential after oxygen desorption can best be visualized in work function maps, plotting the contribution of selected vacuum states to the electron transport between tip and sample (Fig. 10.24a,b). Whereas the overall electron transmissibility is high on the oxygen covered surface, with the exception of certain CaO line defects, a localized patch of low contrast emerges after removal of the O_2^- species from this region. The measurement reflects the local drop of the surface potential after oxygen desorption, which suddenly makes the lowest vacuum state unavailable for electron transport and explains the low contrast in this region. Also this data cannot be explained without taking the effect of charge transfer between the doped oxide and the O_2 molecules into account.

In summary, doped bulk oxides display in many respects similar adsorption properties as ultrathin oxide films [10.179]. In both systems, excess electrons are transferred into the ad-species and open up specific charge-mediated interaction schemes. Whereas for ultrathin films, the extra electrons are provided by the metal substrate below the film, doped oxides contain intrinsic charge sources in the form of aliovalent impurity ions. As shown here, high-valence dopants in the CaO lattice are able to alter the equilibrium shape of metal particles from 3-D to 2-D, which is expected to change the reactivity pattern of the metal–oxide system as well. Moreover, the charge transfer opens a suitable pathway to activate small molecules, such as oxygen or carbon dioxide, even on smooth, defect-free surfaces of a nonreducible, but doped oxide. Whereas thin oxide films on metal single crystals are of large academic interest, as they provide easy access to the properties of oxide materials via conventional surface science methods, doped oxides are of direct, practical relevance for heterogeneous catalysis.

10.3.3 Metal Deposits on Silica Films

In order to make use of the silica film system in the context of heterogeneous catalysts and to further characterize its chemical and physical properties, the adsorption behavior of

> "Au and Pd over bilayer SiO_2/Ru has been investigated by using scanning-probe microscopy, XPS, and density functional theory (DFT) [10.180]. Low temperature (≈ 5 K) AFM and STM measurements reveal the presence of small adsorption features after exposing the samples to small doses of either metal (Fig. 10.25a,b). In the case of

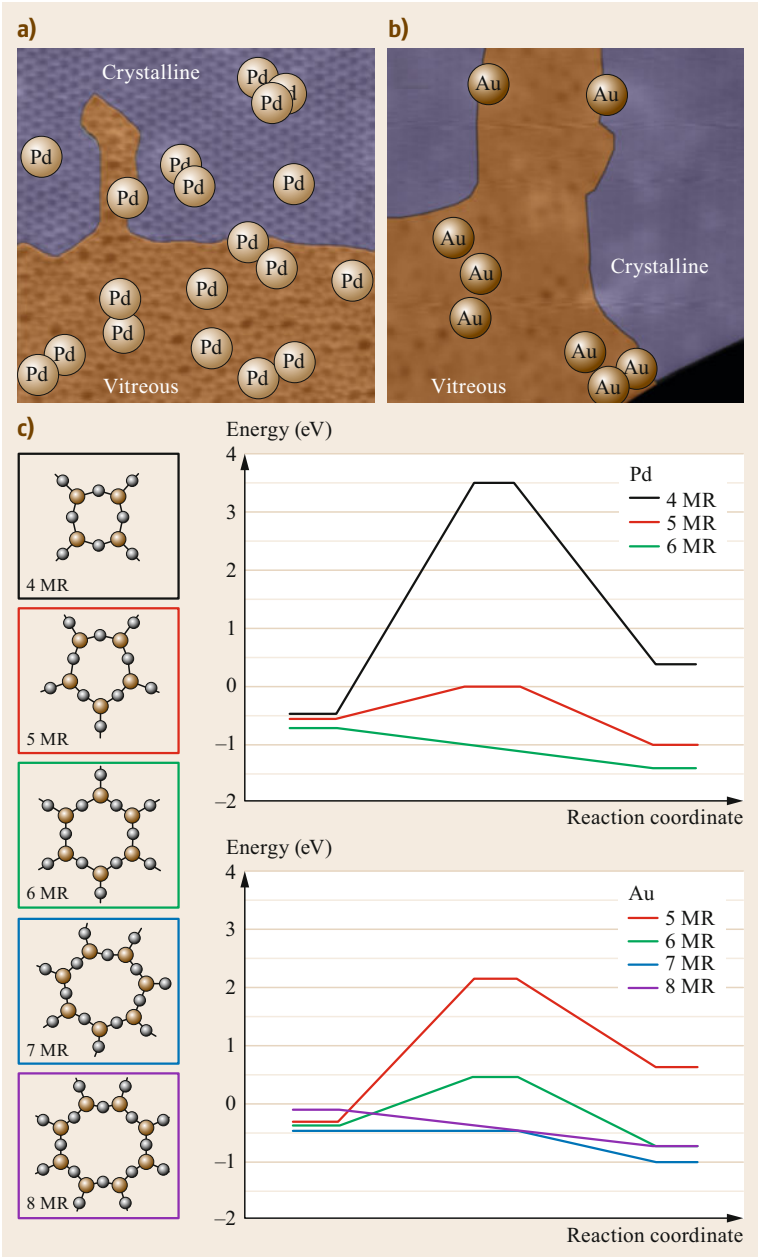

Fig. 10.25a–c STM images showing Pd and Au adsorption over silica. **(a)** Pd on SiO_2; **(b)** Au on SiO_2. Crystalline regions are colored *purple* and amorphous regions are colored *brown*. Note: The nonregular dimmer features throughout the crystalline portions of both samples likely result from native SiO_2/Ru species, as they are present both before and after metal adsorption. All images: 15 nm × 15 nm, $V_S = 2$ V, $I_T = 100$ pA. **(c)** Penetration profiles for Pd and Au through rings of different size. Energies are computed with respect to the metal atom in the gas phase. In the *left panels* the *n* membered SiO_2 rings (MR) are reported ($n = 4–8$; *brown* and *gray* represent Si and O atoms, respectively). Reprinted (adapted) with permission from [10.180]. Copyright (2014) American Chemical Society

Pd, we note a homogeneous distribution of adsorbates across the entire surface, marked by circles and elemental symbols (Fig. 10.25a), which consists of both amorphous and crystalline phases. Au, however, adsorbs only over amorphous areas and domain boundaries, which possess larger pores than can be found in the ordered portions of the film (Fig. 10.25b). DFT calculations reveal that this difference is rooted in the pore-size-dependent barriers for diffusion of the two metals into the film, where they can then bind stably at the Ru interface (Fig. 10.25c). Auger parameter analysis of the Pd 3d and Au 4f core-levels from atoms binding in this manner show upward orbital-energy shifts, which, according to the results of theoretical calculations, originate from effects similar to those causing surface core-level-shifts for such metals [10.181]. Further analysis of the computational results shows that such atoms donate electron density to the Ru support, which is consistent with

> XPS results that show band-bending effects related to decreases in the work function of the sample after adsorbing either metal. Additional features in the XPS studies suggest that a secondary binding mechanism, mediated by cluster formation over the SiO_2 film, becomes increasingly favorable as temperature and loading increase."

Reprinted with permission from [10.180] © 2014 American Chemical Society.

For the crystalline SiO_2 film on Mo(112), a similar size-dependent adsorption behavior has been observed. Whereas Pd and Ag atoms were found to penetrate the six-membered –Si–O– rings with little barrier, Au atoms can pass the silica over-layer along domain boundaries only, which contain larger, i.e., eight-membered rings [10.182]. However, it is not the size of the atoms that governs the penetration behavior, but their electronic structure. Both, Pd and Ag atoms deplete their spatially expanded 5s orbital before passing the film, while the highly electronegative Au cannot strip off its 6s-electron and is thus unable to penetrate the regular SiO_2. Inserting metal atoms at the interface between ordered silica films and the Mo support opens a number of other fascinating functionalities. Addition of interfacial Li, for example, gives rise to a dramatic decrease of the work function of the thin film system, controlled by the highly electropositive character of the Li-ions [10.183]. Iron deposition, on the other hand, leads to the formation of single-ion magnetic units at the metal–oxide interface [10.184].

10.4 Chemical Reactivity of Oxide Surfaces

Chemical reactions at oxide surfaces play a pivotal role in a variety of technological processes in particular in heterogeneous catalysis. Therefore, it is of great interest to understand these processes at the atomic level. Tremendous efforts have been made for powdered materials to get to this point, but the complexity of these systems usually hampers an atomistic characterization. In this section we will exemplify the level of understanding that can be achieved by discussing first the interaction of water with oxide surfaces as well as the impact of hydroxylation on the growth of metal nanoparticles using the systems introduced above. Subsequently, we will focus on chemical transformations of gas phase molecules on oxide surfaces using vanadium oxide as an exploratory example and will finally show results on CO oxidation on an thin FeO(111) film grown on Pt(111) at elevated pressures and molecular beam studies on alkene hydrogenation as well as the H_2/D_2 exchange reaction using a model catalyst consisting of oxide supported metal nanoparticles.

10.4.1 Interaction of Gas-Phase Water with Well-Defined Oxide Surfaces

The interaction of water with oxide surfaces is of major interest in surface science because of the strong impact of hydroxyl groups on the surface properties, in particular, the reactivity of solid surfaces, which is important in diverse fields such as biology, materials science, environmental science, geochemistry, and heterogeneous catalysis. Depending on the chemical potential of water (and oxygen) and the chemical properties of the oxide surface, the adsorption state of water is either molecular or dissociated, or a combination of the two.

Reprinted with permission from [10.60]. © 2019 Materials Research Society.

> "In this section, we review some of the results obtained with the thin oxide films introduced in Sect. 10.2 with regard to water interaction, showing how a combination of different methods allows to gain atomistic insight into the energetics of adsorption processes as well as the nature of the surface species.

Water on Alkaline Earth Oxide and Silica Surfaces: Monolayer Structures and Hydroxylation

A comparison of water adsorption on the (100) surfaces of the alkaline earth oxides is interesting because they all have the same structure (fcc, rocksalt), but different lattice constants and basicity, which is expected to strongly influence the water adsorption (molecular or dissociative) and the ability to form long-range ordered 2-dimensional structures. While monolayer water adsorption on MgO has extensively been studied in the past both experimentally and theoretically and is now well-understood, details about the higher alkaline earth oxides such as CaO and SrO have only recently become available. It is well established that a single water molecule adsorbs molecularly on the MgO(100) surface, but may dissociate, even under UHV conditions, on defects such as low-coordinated cation-anion pairs on step edges. By contrast, single molecule adsorption is dissociative on CaO and SrO and involves considerably higher adsorption energies, as shown in

Fig. 10.26a, which displays the computed E_{ads} for water on the various oxides [10.185]. The dissociated monomer consists of a dynamic ion pair with the hydroxyl group (*free* OD, OD_f) adsorbed in bridge position between two cations and the proton transferred to a nearby oxygen ion (*surface* OD, O_sD, Fig. 10.26c) [10.186]. An interesting trend is seen for increasing water coverage, i.e., for increasing the number of water molecules per (3×4) unit cell used in the calculations: While the adsorption energy increases with increasing coverage for MgO and 2-dimensional monolayer structures are found to be the most stable water adsorption states, the calculated adsorption energy for water on CaO(001), although very similar in the entire coverage range, is highest for 1-dimensional structures. For SrO, isolated and dissociated monomer and dimer species are expected to be more stable than the oligomer species. Experimentally, evidence for the 2-dimensional ordered arrangement of the water monolayer on MgO has been provided by diffraction and scattering methods more than 20 years ago [10.187, 188]. More recently, the stability of 1-dimensional water structures was proven by STM upon water adsorption on thick CaO(001) films at room temperature (Fig. 10.26b) [10.185, 189], and the confirmation of the dynamic ion pair nature of a single, dissociated water molecule, as well as the stability of dimer species, on SrO has been obtained by STM on SrO-terminated $Sr_3Ru_2O_7$ [10.190].

Generally, diffraction methods and STM do not allow the positions of the individual water species and their chemical nature (molecular or dissociated) within the 1- and 2-dimensional water structures found on MgO(001) and CaO(001) to be determined, and one has to resort to high-level computations and spectroscopic methods to learn more about the molecular-scale details of these structures. Whereas electron spectroscopies can provide information about the presence of dissociated and molecular water, which, for example, has provided first experimental proof for the existence of mixed molecular/dissociated water molecules in the water monolayer on MgO(001) [10.192], comparison of experimentally measured and computationally obtained frequencies of water and hydroxyl vibrations is considered to provide additional information about the structural details.

The latter approach has been used to identify and confirm the structural models of the 2-dimensional water monolayer on MgO(001) [10.191], and of the 1-dimensional chain structures found by STM on CaO(001) [10.185, 189]. Figure 10.26d shows the experimental IRAS (infrared reflection absorption spectroscopy) spectra (top panel) for the water monolayer prepared on MgO (left panel) at low temperature (160 K), and for the water chain structures prepared on CaO(001) at room temperature (right panel), and the corresponding calculated anharmonic vibrational spectra (lower panel). (Note that the experiments and calculations were performed with D_2O instead of H_2O). The experimental spectra are qualitatively similar and exhibit reasonably narrow bands in the range $2600-2750\,cm^{-1}$ and broad absorption between 2000 and $2500\,cm^{-1}$. The individual spectral contributions can be assigned based on the good agreement between the experimental spectra and the calculated spectra of the most stable structures shown in Fig. 10.26. For both, the MgO(001) and CaO(001) surface, the ordered water structures are comprised of dissociatively and molecularly adsorbed water. In the case of MgO, two ordered structures with different water coverage, the high coverage $c(4 \times 2)$ and the low-coverage $pg(3 \times 2)$ structure, coexist at 160 K and can be distinguished based on the different frequencies of the O_sD groups [10.191]. Note that, due to the metal surface selection rule, the molecular water species, which are oriented almost parallel to the surface in both structures, give rise to only weak absorption signals. In fact, they do not contribute to the IR spectrum of the $pg(3 \times 2)$ structure. In the case of the $c(4 \times 2)$ structure, the molecular water species stabilize the protruding OH_f group, and combinations of their symmetric and anti-symmetric stretch vibrations lead to signal contributions in the $2100-2400\,cm^{-1}$ spectral range, which are detected in the experiment as a broad featureless absorption. Molecular water species in the 1-dimensional chain structure on CaO(001) are also oriented parallel to the surface and contribute only little to the IR signal on the thin film sample. The more defined signals for water on CaO(001) originate from OH_f (at highest wavenumber) and O_sD groups from dissociated water. Note that the O_sD groups in the 1-dimensional chain structure on CaO(001) are spectrally much more separated than in the 2-dimensional structures on MgO because the strength of hydrogen bonding between O_sD groups and OD_f groups is markedly different in the tetramer unit and in the linker unit [10.185].

The combined experimental and computational analysis of water adsorption on the alkaline earth oxides has not only contributed to a better understanding of the molecular details of wa-

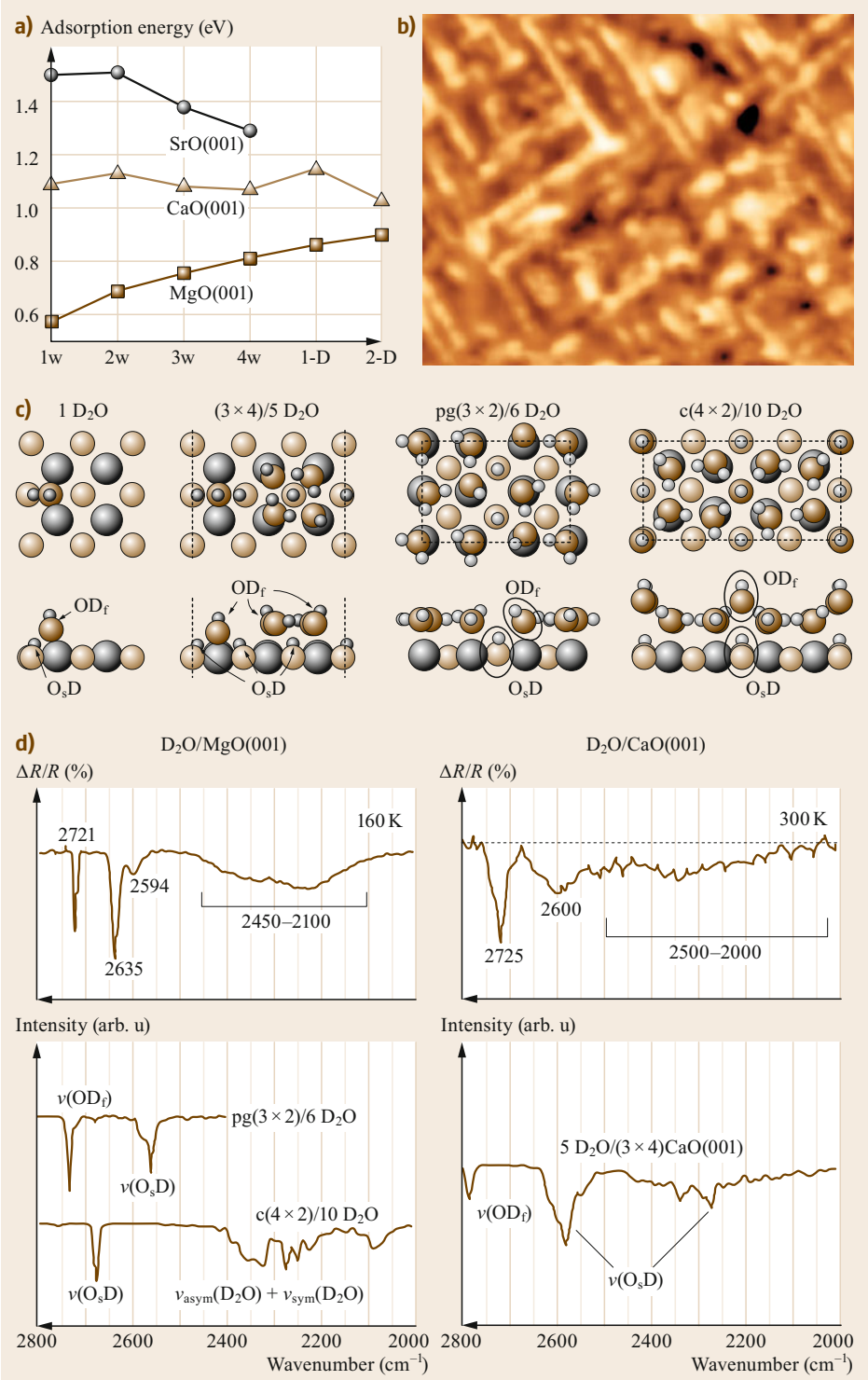

Fig. 10.26
(a) Calculated adsorption energy per water molecule on CaO(001), MgO(001), and SrO(001) for increasing water coverage (1w, etc.: 1 water molecule per (3×4) unit cell; 1-D, etc.: 1-dimensional water/hydroxyl structures). **(b)** RT-STM image ($30 \times 25\,nm^2$) of 1-dimensional water chains formed on CaO(001). **(c)** Most stable structures of the dissociated water monomer on CaO(001), the 1-D chain structure on CaO(001), and the two most stable ordered 2-D water phases (pg(3×2) and c(4×2)) on MgO(001). **(d)** Experimental (*top*) and computed (*bottom*) IR (infrared) spectra of the 2-D (D_2O) structures on MgO(001) (*left*) and the 1-D (D_2O) chain structure on CaO(001) (*right*). After [10.185, 189, 191]

ter structures, but additionally allows conclusions about the evolution of different structures on the surfaces to be drawn. Dissociation of a single water molecule is favored and involves larger adsorption energies when going from MgO to SrO. This can be explained by the increasing lattice constant and substrate flexibility when descending the AEO series [10.193]. Additionally, the subtle balance between intermolecular and molecule-surface interactions determines also the stability of higher coverage structures: Two-dimensional ordered structures are stabilized on MgO(001) because of the weak interaction between water and the MgO surface and the favorable dimension of the MgO lattice parameter, which allows a strong hydrogen bonding network between adsorbed water and hydroxyl species to be established. The CaO lattice is slightly too large to enable the formation of a hydrogen-bonded network, and the water structures therefore collapse into a 1-D configuration at low coverage. Similar 1-D assemblies become stable also on MgO(001) when its lattice parameter is artificially increased to reduce the effect of intermolecular coupling. In contrast on SrO(001), the water residuals are always too far away to form uniaxial or 2-dimensional hydrogen-bonded arrangements [10.185].

The results presented for the alkaline earth oxides demonstrate that not only the acid-base properties of the oxide surface, but also the lattice parameter and hence, the ability to form hydrogen-bonds between neighboring hydroxyl groups, has a major impact on the adsorbed water structures.

The examples discussed so far refer to water adsorption on bulk-like thin films (i.e., films of reasonable thickness and structurally similar as the corresponding bulk oxides) at UHV conditions, where no structural modifications of the oxide lattice take place during adsorption. For complete hydroxylation of the oxide surfaces, which is expected to occur when environmentally more realistic water partial pressure conditions (mbar range) or higher water coverages are approached, reactions between water and the oxide surfaces have to be considered as well. For the more ionic oxides in particular, this may involve hydrolysis of cation-anion bonds and strong structural modifications. The hydroxylation of MgO and CaO single crystal surfaces and the partial transformation into the corresponding hydroxide as a function of relative humidity have been studied by ambient pressure XPS. Those studies revealed that the CaO(001) surface gets fully hydroxylated even under UHV conditions and transforms into the hydroxide, involving hydroxylation of the subsurface regions, at elevated water partial pressure [10.194]. On the other hand, a certain threshold water pressure in the sub-mbar range has to be applied to achieve sufficient surface hydroxylation of MgO(001) [10.195]. Studies on the corresponding thin film surfaces confirmed these results. Figure 10.27a compares STM images of the surface of a clean CaO(001) film (top) and after a saturation dose of water under UHV conditions at room temperature (bottom) [10.185, 189]. Clearly, water adsorption leads to strong structural modification of the surface, which is due to complete surface hydroxylation and partial solvation of Ca^{2+} ions. The latter can in part be explained by the sufficiently large structural flexibility of the CaO lattice, which allows easy rupture of cation–anion bonds.

By contrast, hydroxylation of thick, bulk-like MgO(001) films at room temperature and in UHV conditions is limited to defect sites, and in order to obtain complete hydroxylation a threshold water partial pressure of about 0.01 mbar has to be applied (Fig. 10.27b) [10.196]. Titration of Mg^{2+} sites with CO has shown that the number of low-coordinated Mg^{2+} sites gets strongly enhanced upon hydroxylation, suggesting the occurrence of similar structural modifications as in the case of CaO(001). Interestingly, the threshold pressure for hydroxylation decreases by 3 orders of magnitude as the film thickness is reduced from 12 to 2 ML (Fig. 10.27b) [10.196]. This effect is not related to an increased abundance of defects on the ultrathin film, but can be explained by a decreased energetic barrier for the rupture of $Mg^{2+}-O^{2-}$ bonds, which is related to the greater structural flexibility of the MgO lattice in the ultrathin regime [10.197].

Polar oxide surfaces are intrinsically reactive towards water because surface hydroxyls provide compensating charges necessary to remove polarity. Similarly, in polar oxide films grown on metal substrates, while the compensating charge density at the metal–oxide interface is readily provided by the metal, the free film surface needs to be compensated by conventional mechanisms, e.g., surface hydroxylation. Conversely, the thinnest oxide films (monolayers) are intrinsically non-polar, thus reducing their activity towards water. In fact, the FeO(111) monolayer film is stable in pure water vapor environment, as shown by the O 1s XP spectrum obtained after exposure to 1 mbar water vapor, which exhibits only one component attributable to the lattice oxygen

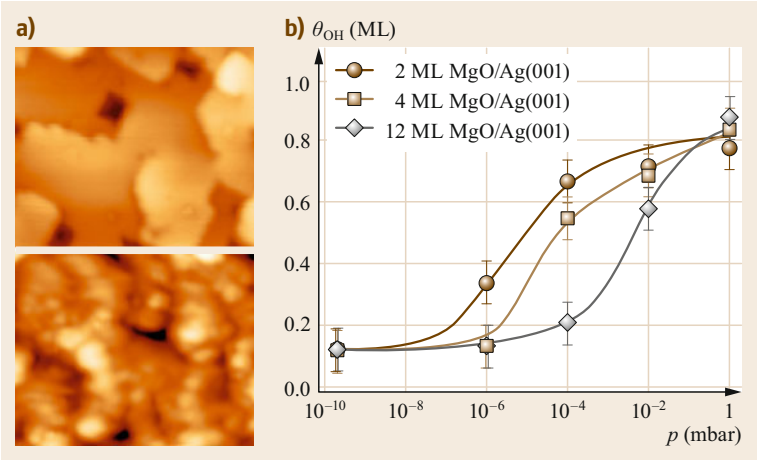

Fig. 10.27 **(a)** STM images ($30 \times 25\,nm^2$) of 10 ML CaO(001)/Mo(001) (*top*) and of the same surface exposed to a saturation dose of water at RT (*bottom*). Reprinted with permission from [10.189], © ACS (2016). **(b)** H_2O pressure dependent surface hydroxyl coverage on Ag(001)-supported MgO(001) films of different thickness obtained from fits of the O 1s XP spectra. Reprinted (adapted) with permission from [10.196]. Copyright (2010) American Chemical Society

species, and no further contribution from hydroxyls (Fig. 10.28a) [10.198]. In addition, the structural integrity of the FeO(111) monolayer appears to be maintained upon exposure to air ambient and even liquid water, as shown by the STM images presented in Fig. 10.28c, where the long-range ordered Moiré superlattice characteristic of FeO(111)/Pt(111) is proven to persist in the corresponding environment.

As will be discussed in more detail below (Sect. 10.4.3), exposure of FeO(111) to a high-pressure oxygen atmosphere leads to a transformation of the FeO bilayer to a O–Fe–O trilayer [10.35, 37, 39]. Both, the additional oxygen incorporated in the film, which shows up in XPS as a shoulder on the high binding energy side of the main O 1s component (Fig. 10.28a), and the similarity of the STM appearance suggest that this transformation occurs also upon exposure of the FeO film to air. In addition, the IRA spectrum of an air-exposed film reveals the presence of hydroxyl species with characteristic vibrations at $3650\,cm^{-1}$. It can, therefore, be concluded that the trilayer structure is not only highly active in the catalytic oxidation of CO, but also in water dissociation. As a result, an O–Fe–OH trilayer is formed (Fig. 10.28d) and the additional O 1s signal in XPS can be attributed to hydroxyl species [10.198]. XPS quantification reveals a maximum hydroxyl coverage of 0.45 ML. Together with the ordered appearance in STM this suggests that the hydroxylation activity is restricted to the most reactive region within the Moiré unit cell, which, according to DFT calculations, is the Fe-hcp region [10.37]. Note that also the hydroxylated FeO layer is highly active in CO oxidation [10.198].

All UHV-based, well-defined silica models have a common structural motif, which consists of corner-sharing [SiO_4] tetrahedra arranged in a honeycomb structure (Sect. 10.2.2) [10.202]. The fact that the surfaces are terminated by siloxane bonds renders the regular parts of the films hydrophobic and, thus, unreactive towards water. Indeed, the silica bilayer on Ru(0001) can be exposed to air and pH neutral aqueous solutions without any noticeable accompanying chemical and structural modifications to the film (see also Sect. 10.5.1). Hydroxylation of these model systems occurs only at defect sites, which, on well-prepared films, are scarce [10.203]. Since hydroxyl groups on silica (silanol groups) are of enormous importance for several technological applications, their creation and further utilization on well-defined model systems may help obtain more fundamental insight into specific interfacial reactions where silanols are involved. Hydroxylation of the films could be achieved with the help of electron bombardment of the water (ice) layer [10.199]. This is exemplified by the TPD spectra shown in Fig. 10.28e, which have been obtained after dosing water (D_2O) at a substrate temperature of 100 K and followed by heating to RT (normal route, black curve), or with an additional electron bombardment prior to heating (electron-assisted route, red curve). The strong

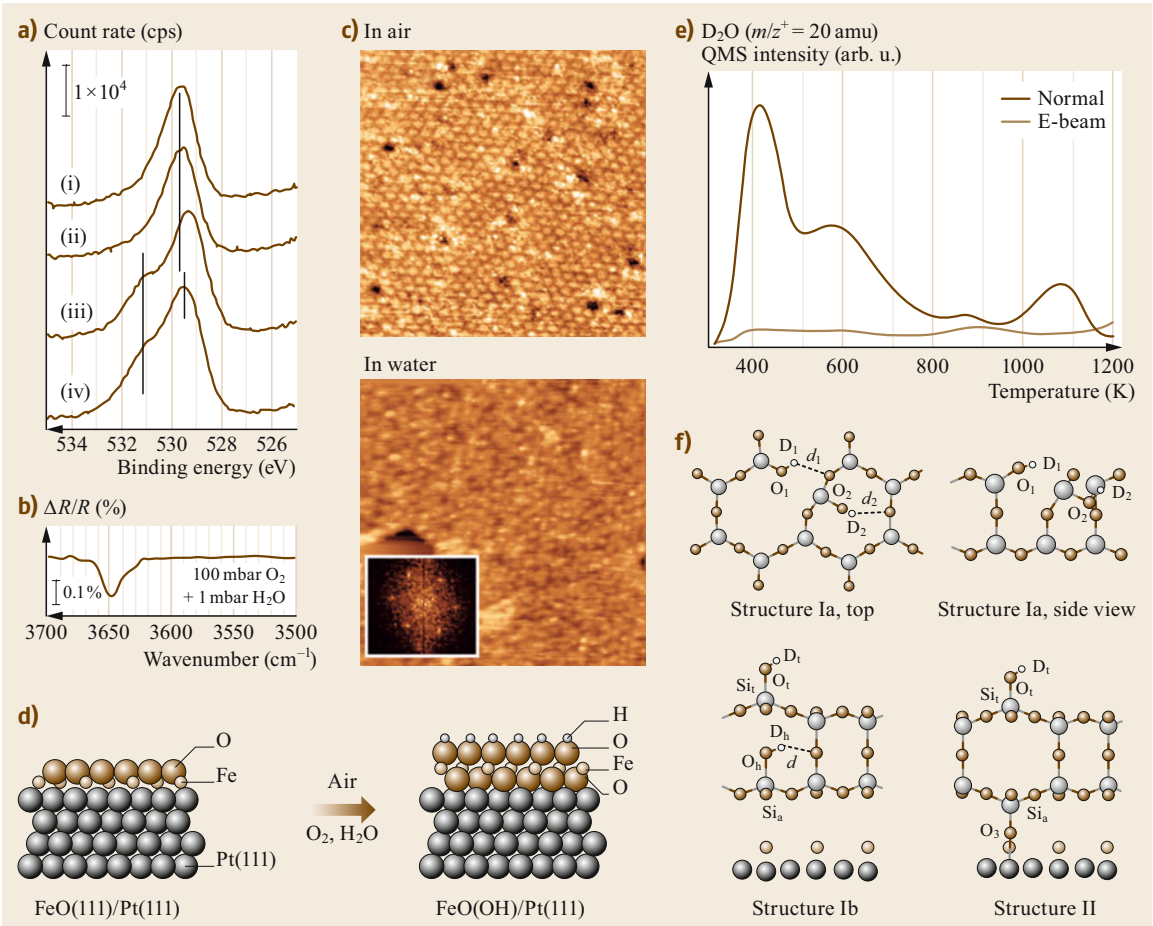

Fig. 10.28 **(a)** O 1s XP spectra, from *top* to *bottom*, of (i) clean FeO(111)/Pt(111), the film exposed to (ii) 1 mbar D_2O, (iii) air, and (iv) 100 mbar O_2 and 1 mbar H_2O. **(b)** IR spectrum of the FeO(111)/Pt(111) film exposed to 100 mbar O_2 and 1 mbar H_2O. **(c)** Ambient-STM images ($60 \times 60\,nm^2$) of the FeO(111)/Pt(111) film in air (*top*) and in liquid water (*bottom*). Reprinted with permission from [10.198], © (2011) American Chemical Society. **(d)** Model of the FeO(111)/Pt(111) film (*left*) and of the Pt–O–Fe–OH film (*right*) formed by exposure to air. **(e)** TPD (temperature programmed desorption) spectra ($m/z^+ = 20$ amu) of SiO_x samples exposed to 5 Langmuir D_2O at 100 K and then exposed (*e-beam*, *light brown* trace) or not exposed (*normal*, *dark brown* trace) to an electron beam (0.05 mA, 200 eV, 60 s). **(f)** Hydroxylation structures for silica films involving breaking of in-plane (structure Ia, *top*) and vertical (structures Ib and II, *bottom*) siloxane bridges, obtained from DFT calculations. Reprinted (adapted) with permission from [10.199]. Copyright (2011) American Chemical Society

enhancement of water desorption from the electron-bombarded sample in this region is related to a significantly increased abundance of D_2O and OD's on the silica surface. More specifically, the thermal route leads to the formation of isolated hydroxyl groups at defect sites within the film, which recombine at elevated temperature and desorb as molecular water at 900 K, and some additional hydrogen-bonded physisorbed water, which desorbs at lower temperatures (< 500 K). The small amount of water desorbing from this sample supports the idea of the inert nature of the silica bilayer film surface. By contrast, enhanced hydroxylation of the electron-bombarded sample gives rise to much larger and more clearly defined water desorption peaks with maxima at 450 and 600 K, as well as an additional high temperature desorption feature at ≈ 1070 K [10.199, 204]. It is interesting to see that in terms of peak temperatures associated with individual desorption states, there is general agreement with analogous TPD spectra collected from hydroxylated bulk silica samples,

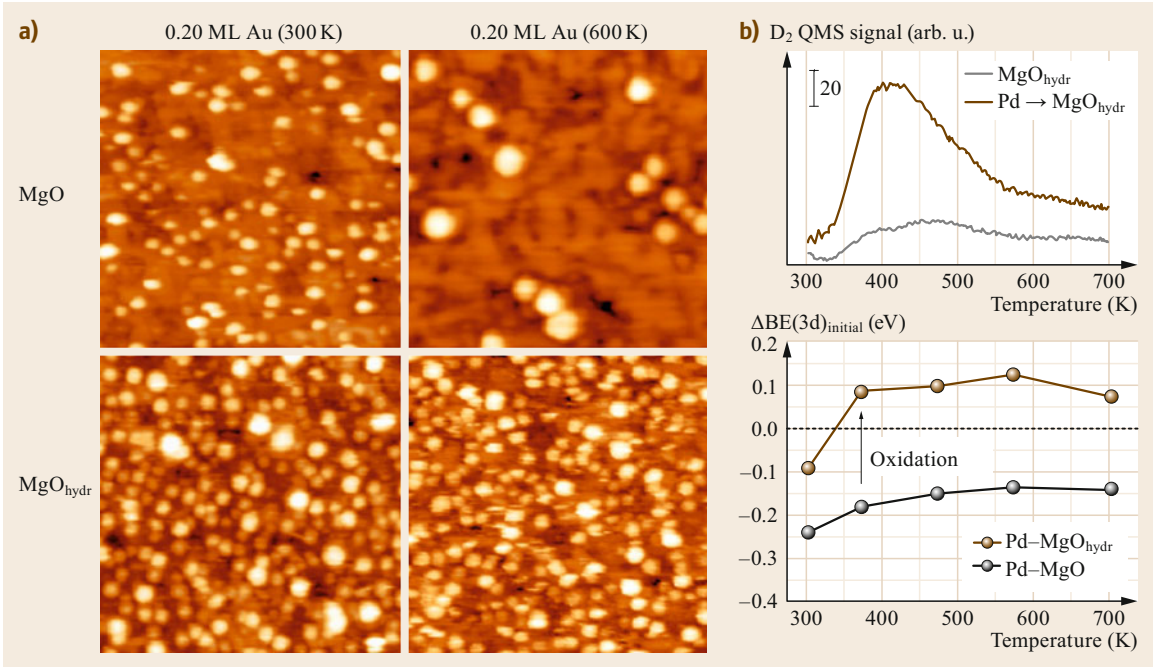

Fig. 10.29 **(a)** STM topographs (50 nm × 50 nm) of 0.2 ML of Au deposited on clean (*top*) and hydroxylated MgO(001)/Mo(001) (*bottom*) at RT (*left*) and after annealing at 600 K (*right*) [10.200]. **(b)** *Top*: TPD spectra tracking the $m/z^+ = 4$ (D_2) evolution from hydroxylated MgO (*gray*) and hydroxylated MgO with 0.4 ML Pd (*brown*) deposited at RT. Reprinted (adapted) with permission from [10.200]. Copyright (2011) American Chemical Society. **(b)** *Bottom*: Temperature-dependent Pd 3d electron binding energy variations relative to Pd(111) due to changes in the initial states of the photoemission process for Pd–MgO (*black*) and Pd–MgO$_{hydr}$ (*brown*). Reprinted (adapted) with permission from [10.201]. Copyright (2014) American Chemical Society

which suggests the presence of similar water and hydroxyl species on the hydroxylated silica film. According to the *Zhuravlev* model [10.205], the desorptions are attributed to the following adsorption states and processes: Chemisorbed molecular water gives rise to desorption at 400 K, whereas the high temperature peaks are assigned to recombinative water desorption originating from vicinal (at 600 K) and isolated hydroxyls (above 800 K). The creation of silanols requires the rupture of siloxane bridges and several possibilities how this could be achieved have been modeled by DFT [10.199]. As shown by the structural models presented in Fig. 10.28f, rupture of an in-plane siloxane bridge results in two silanol groups, which are both engaged as donor groups in hydrogen bonds (structure Ia). On the other hand, breaking the Si–O–Si linkage between the two silicate layers results in one hydrogen-bonded silanol and one terminal silanol species (structure Ib). In addition to these processes, which are basically the same as assumed for bulk silica surfaces, the presence of the metallic substrate underneath the silica film opens the possibility for another mechanism, which involves hydrogen release and Ru oxidation (structure II). According to the computed hydroxylation energies and further experimental observations (D_2 desorption observed in TPD and infrared signals of terminal OD groups) [10.199], all three proposed structures are likely to be formed initially during electron bombardment or are created via transformation of one structure into the other during heating to elevated temperature. Further experimental studies into the mechanism of electron-assisted hydroxylation of the silica films support the idea that the primary effect of electron irradiation is not the creation of defects (i.e., rupture of siloxane bridges) in the films, but the formation of reactive water radiolysis products (e.g., hydroxyl radicals) in the ice layer, which diffuse to the silica-ice interface and attack the siloxane bridges [10.204]."

Reprinted with permission from [10.60]. © 2019 Materials Research Society.

Metal Nucleation on Hydroxylated MgO Surfaces

Controlled creation of hydroxylated oxide thin film surfaces allows the influence of the hydroxyl groups on surface processes to be studied. As an example, the effect of hydroxyls on metal nucleation on hydroxylated MgO is presented. A most conspicuous evidence for the influence of hydroxyls on nucleation and sintering of Au on MgO(100) is provided by STM. The images displayed in Fig. 10.29a present the surface morphology for gold deposited at 300 K and after subsequent heating to 600 K on clean MgO(100) and hydroxylated MgO, respectively [10.200]. Two main conclusions can be drawn from these results: (i) the density of nucleation sites is much higher on MgO_{hydr}, and (ii) the stability of Au particles towards sintering is greatly enhanced on MgO_{hydr}. This latter point is essential for catalysis because it basically means that the high Au dispersion is maintained at elevated temperature, a result that is corroborated by related CO-TPD studies showing a higher CO adsorption capacity for Au/MgO_{hydr} as compared to Au/MgO(100) [10.206]. With the help of additional XPS and IRAS measurements the enhanced Au sinter stability could partly be explained by the stronger adhesion of Au to the hydroxylated surface, which is a result of the chemical modification (oxidation) of interfacial Au because of the interaction with hydroxyls [10.200]. In addition, one has to take into account that the microscopic roughness of MgO increases upon hydroxylation [10.196], which might also contribute to limited diffusion of Au clusters on the surface.

Similar experiments have also been performed with Pd instead of Au, and in this case more details about the chemical interaction between the metal atoms and the surface hydroxyl groups could be obtained [10.201]. The interaction of metal atoms with hydroxyls is expected to follow a redox reaction

$$\mathrm{Me} + -\mathrm{OH}^- \rightarrow -\mathrm{O}_2^- - \mathrm{Me}^+ + \frac{1}{2}\mathrm{H}_2 \,,$$

resulting in the simultaneous oxidation of the metal and evolution of H_2. This could indeed be observed with Pd atoms deposited on MgO_{hydr} (hydroxylation was performed with D_2O) as shown in Fig. 10.29b. The top panel displays D_2-TPD spectra taken from MgO_{hydr} and Pd deposited on MgO_{hydr}, which shows that the presence of Pd leads to a strong enhancement of D_2 evolution from MgO_{hydr} at elevated temperature (> 350 K). To correlate D_2 evolution with electronic structure changes of Pd, Pd 3d spectra and in particular, a deconvolution of the Pd 3d binding energy shift in initial-state and final-state contributions using Auger parameter analysis was performed. The bottom panel of Fig. 10.29b compares the initial-state binding energy shift relative to the Pd 3d binding energy of bulk Pd (352.1 eV) for Pd on clean MgO(001) (black data points) and Pd on MgO_{hydr} (blue data points). The shift from negative to positive ΔBE values for $Pd-MgO_{hydr}$ at 373 K, which correlates with the onset of D_2 evolution from the $Pd-MgO_{hydr}$ sample, indicates that Pd gets oxidized at this temperature. Thus, the interrelation of these processes provides direct evidence of the redox reaction between Pd and hydroxyls, which results in Pd oxidation and hydrogen (deuterium) evolution [10.201].

10.4.2 Methanol Partial Oxidation on $V_2O_3(0001)$ and $V_2O_5(001)$

An often studied reaction in model catalysis is the partial oxidation of methanol. This can be readily investigated under low pressure conditions since the educt (methanol) as well as the common precursor (methoxy) are reasonably strongly bound to the surface and do not desorb at low pressure and not too high temperature. $V_2O_5(001)$ and $V_2O_3(0001)$ were studied with respect to their catalytic performance using the partial oxidation of methanol as a test reaction [10.132, 207, 208]. It turned out that the vanadyl terminated surfaces are not reactive with respect to this reaction since methanol just binds molecularly to the surface without forming the methoxy intermediate [10.132, 208]. Therefore, the surfaces were reduced prior to methanol exposure by electron irradiation. For small electron doses the electron beam leads to the removal of vanadyl oxygen atoms resulting in isolated or aggregated point defects, see Fig. 10.30a,b. The surface structure after irradiation with a high electron dose was studied with I/V-LEED in the case of $V_2O_3(0001)$ [10.209]. An STM image is displayed in the right panel of Fig. 10.30. It could be shown that this surface exposes the SM termination as schematically depicted in Fig. 10.14. The dark areas exhibit the same surface structure as the more elevated areas.

The following will discuss methanol adsorption for the case of a low degree of reduction where isolated vacancies or small groups of them prevail. Figure 10.31 shows STM images of a $V_2O_3(0001)$ surface before electron irradiation, after electron irradiation and after dosage of methanol onto the reduced surface. The point defects found at the surface of a freshly prepared oxide layer (Fig. 10.31a) are not active for methoxy formation, but the vacancies produced by electron irradiation are [10.132]. Therefore, only part of the surface defects is covered by methoxy groups (seen as bright protrusions) in Fig. 10.31c.

STM data of the type shown in Fig. 10.31 were recorded for two different energies of the reducing electrons (50 and 500 eV) and different electron doses

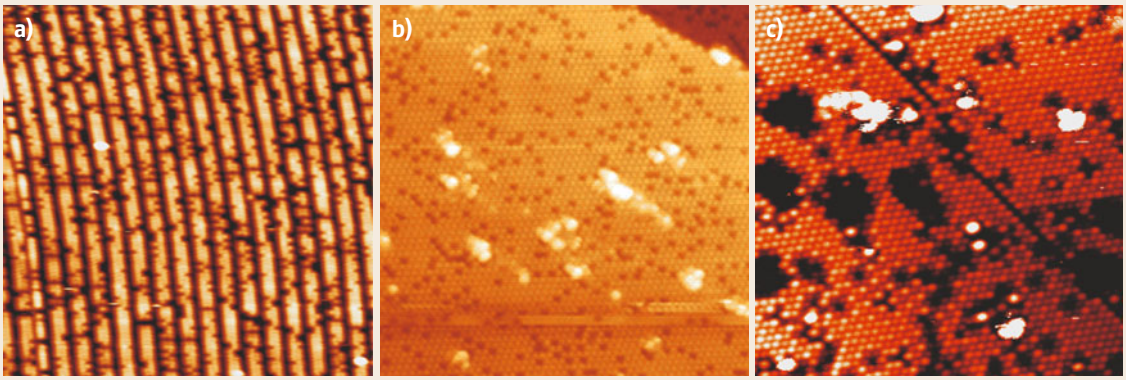

Fig. 10.30a–c STM images on vanadium oxide layers on Au(111) reduced by electron irradiation. **(a)** Weakly reduced $V_2O_5(001)$, $20 \times 20\,nm^2$, $U = 2\,V$, $I = 0.2\,nA$. **(b)** Weakly reduced $V_2O_3(0001)$, $25 \times 25\,nm^2$, $U = -1.5\,V$, $I = 0.2\,nm$. **(c)** Fully reduced $V_2O_3(0001)$, $20 \times 20\,nm^2$, $U = -1\,eV$, $I = 0.2\,nA$. The electron doses (energies) used for reduction are **(a)** 3 mC (50 eV), **(b)** 1.5 mC (50 eV), **(c)** 80 mC (500 eV)

< 0.8 mC (500 eV) and 1.6 mC (50 eV), respectively. In each series the number of defects before and after electron irradiation and the number of methoxy groups after exposure of the surface to methanol were counted. The methanol layer was prepared by dosing multilayer amounts of methanol at 90 K and the STM images of the methoxy-covered surfaces were recorded after a flash to 400 K in order to desorb the molecularly adsorbed methanol.

Figure 10.32 displays the results of the evaluation. The main outcome is that the number of methoxy groups is approximately twice as large as the number of surface defects which is the consequence of a self-limiting chain reaction at the surface [10.132]. In the initial step, which occurs already when methanol is adsorbed at 90 K all electron induced defects carry one methoxy group

$$n\,CH_3OH + n\,V + n\,VO \rightarrow n\,CH_3OV + n\,VOH \quad (10.1)$$

V denotes a vanadium site produced by electron irradiation, VO is a surface vanadyl group, and n is the number of surface vanadyl oxygen vacancies.

If the sample is warmed up water forms at 270 K due to the recombination of hydroxyl groups as shown by TPD [10.132]. This reaction consumes substrate oxygen which is the signature of *Mars–van Krevelen* type reactions [10.210]

$$n\,VOH \rightarrow \tfrac{1}{2}n\,H_2O + \tfrac{1}{2}n\,VO + \tfrac{1}{2}n\,V \quad (10.2)$$

This step occurs at a temperature where molecular methanol is still at the surface. Therefore, the surface

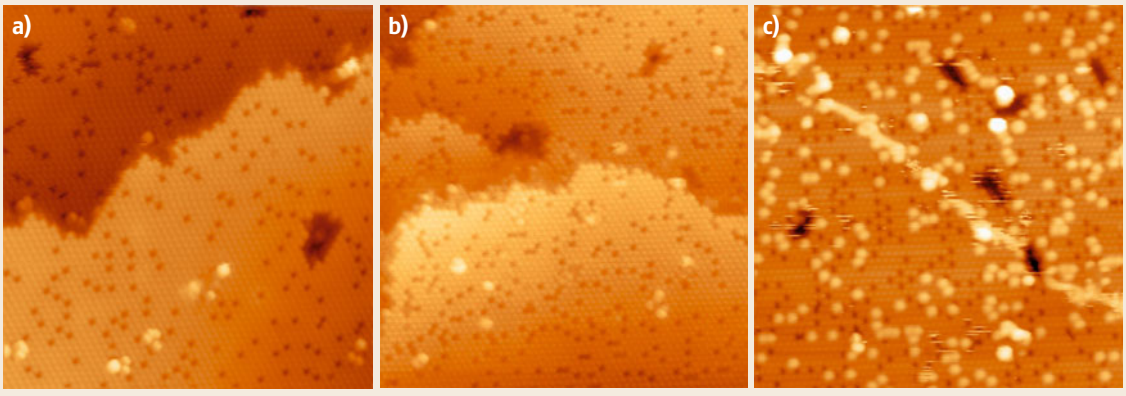

Fig. 10.31a–c STM data of freshly prepared **(a)**, reduced **(b)**, and methoxy covered reduced **(c)** $V_2O_3(0001)$. Vanadyl oxygen vacancies were prepared by irradiation with 1.5 mC of 50 eV electrons. $25 \times 25\,nm^2$, $U = -1.5\,V$, $I = 0.2\,nA$. After [10.132]

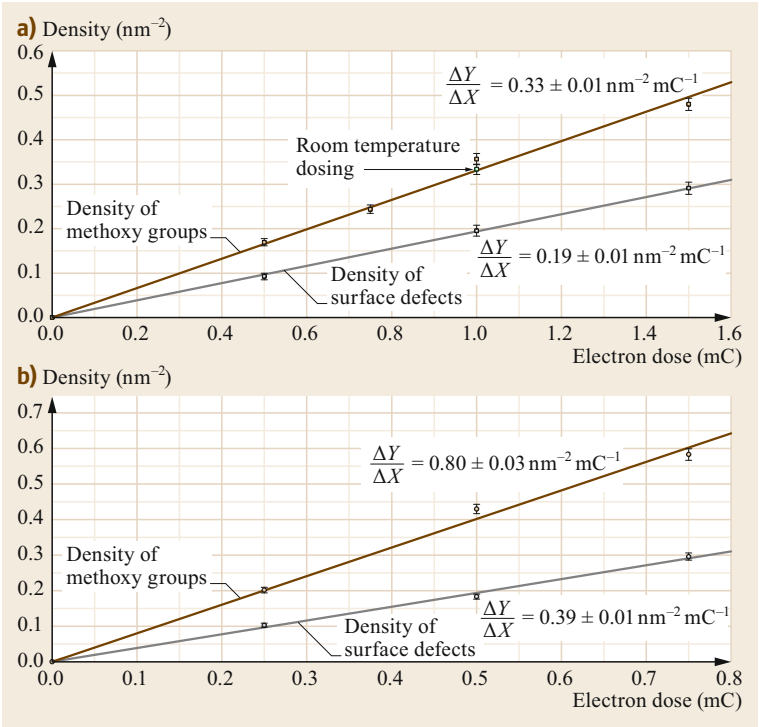

Fig. 10.32a,b Density of defects induced by electron irradiation and the number of methoxy groups as a function of the electron dose for two electron energies **(a)** $E = 50\,\text{eV}$ and **(b)** $E = 500\,\text{eV}$. The data were obtained from STM images like the ones shown in Fig. 10.27 (CH_3OH/weakly reduced $V_2O_3(0001)$). The number of surface defects in this figure is the number of surface defects in images recorded after electron irradiation minus the number of defects already present at the surface before exposure to the reducing electron beam. After [10.132]

with its $n/2$ V sites can split $n/2$ methanol molecules into $n/2$ methoxy groups and $n/2$ hydroxyl groups

$$\tfrac{1}{2}n\,CH_3OH + \tfrac{1}{2}n\,V + \tfrac{1}{2}n\,VO \rightarrow \tfrac{1}{2}n\,CH_3OV + \tfrac{1}{2}n\,VOH \quad (10.3)$$

The $n/2$ hydroxyl groups produced in this step can again form water

$$\tfrac{1}{2}n\,VOH \rightarrow \tfrac{1}{4}n\,H_2O + \tfrac{1}{4}n\,VO + \tfrac{1}{4}n\,V \quad (10.4)$$

With this reaction the cycle goes on. The overall number of methoxy groups produced in this reaction is

$$N_{\text{methoxy}} = n + \tfrac{1}{2}n + \tfrac{1}{4}n + \ldots = 2n \quad (10.5)$$

This is in full agreement with the data in Fig. 10.32.

Figure 10.33 shows the effect of this self-limiting chain reaction on IRAS spectra. The intensity increase of the methoxy C–O vibration at $\approx 1040\,\text{cm}^{-1}$ can be attributed to the chain reaction occurring at $\approx 270\,\text{K}$ where the hydroxyl groups at the surface react to form water: the methoxy coverage doubles and so does (approximately) the intensity of the C–O vibrational band. The band labelled V=^{18}O and V=^{16}O are due to vibrations of vanadyl groups with ^{18}O and ^{16}O. The presence of both isotopes is a result of the preparation history of the $V_2O_3(0001)$ sample.

The case of methanol on $V_2O_5(001)$ is different from the case of methanol on the case for methanol on $V_2O_3(0001)$ due to somewhat different activation energies [10.132, 207]. The reaction kinetics of methanol on $V_2O_5(001)$ has been studied in some detail with TPD [10.208]. Figure 10.34 displays the amount of formaldehyde formed by methanol partial oxidation at the surface of slightly reduced $V_2O_5(001)$ as a function of the methanol dose. This quantity was estimated from the area of the formaldehyde mass 29 desorption peak in TPD spectra. At elevated temperature the methoxy groups react on the surface, forming formaldehyde and therefore the mass 29 peak area is a good measure for the methoxy coverage. The red line in Fig. 10.34 shows the best fit to the data assuming a sticking coefficient proportional to the number of unoccupied adsorption sites. It is clear that this simple model is not correct which means that the reality must be more complex.

Therefore a model considering water formation from hydroxyl groups and methanol formation from methoxy and hydroxyl groups was formulated, i.e., the following two reaction step were incorporated

$$VOH + VOH \rightarrow VO + V + H_2O \quad \text{(water formation)} \quad (10.6)$$

$$VOH + CH_3OV \rightarrow VO + V + CH_3OH \quad \text{(methanol formation)} \quad (10.7)$$

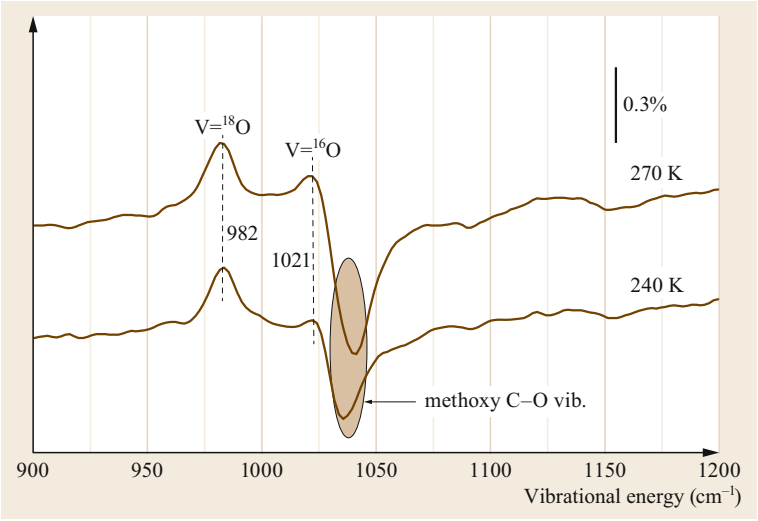

Fig. 10.33 IRAS spectra of methanol-dosed moderately reduced $V_2O_3(0001)$ after annealing at 240 and 270 K, respectively. Methanol was dosed at 90 K and the surface was reduced with an electron dose of 8 mC. After [10.132]

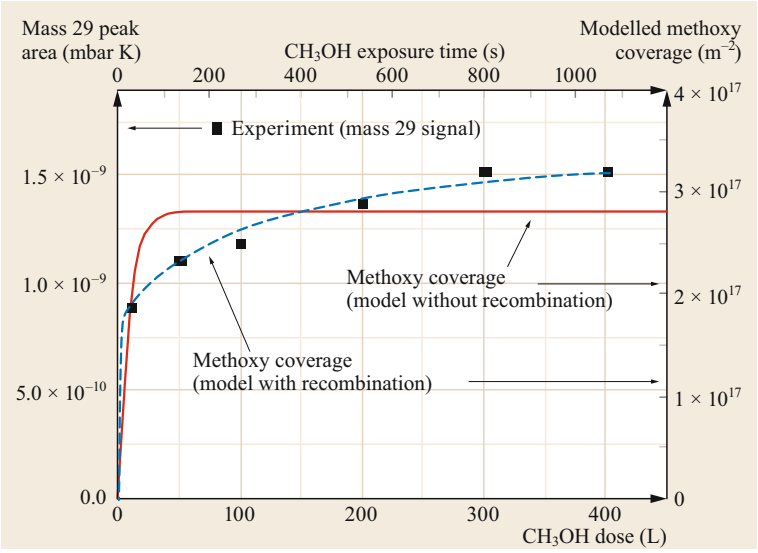

Fig. 10.34 TPD formaldehyde peak area (*solid black squares*) as a function of methanol dose for methanol on weakly reduced $V_2O_5(001)$ in comparison with surface methoxy coverages calculated according to two different models (*solid red* and *dashed blue line*, see text). The sample was reduced by irradiation with electrons with a kinetic energy of 50 eV, dose: 1 mC. Dosing was performed at room temperature to prevent the formation of a molecularly adsorbed methanol layer. Reproduced from [10.208] with permission of The Royal Society of Chemistry

Herewith the following differential equation system was set up for the time-derivative of the methoxy coverage θ_M and the hydroxyl coverage θ_{OH} [10.208]

$$N_{tot}\frac{d\theta_M}{dt} = S(\theta)\Phi_M - N_{tot}\theta_M\theta_{OH}\nu\exp\left(-\frac{E_1}{kT}\right) \quad (10.8)$$

$$N_{tot}\frac{d\theta_{OH}}{dt} = S(\theta)\Phi_M - 2N_{tot}\theta_{OH}^2\nu\exp\left(-\frac{E_2}{kT}\right) - N_{tot}\theta_M\theta_{OH}\nu\exp\left(-\frac{E_1}{kT}\right) \quad (10.9)$$

$S(\theta)$ is a coverage-dependent sticking coefficient, t is the time, N_{tot} is the number of vanadyl lattice sites (4.8×10^{18} m^{-2}), ν is the attempt frequency (set to 10^{13} s^{-1}), E_1 and E_2 are the energy barriers for methoxy–OH recombination and OH–OH combination, respectively, θ_M is the flux of methanol molecules per unit area and time, k is Boltzmann's constant and T is the adsorption temperature ($T = 298$ K). It is assumed that there are no further reaction paths and that diffusion can be neglected which is reasonable if it is much quicker than the water and methanol formation reactions. The sticking coefficient $S(\theta)$ is assumed to be coverage-dependent

$$S(\theta) = \frac{N_0 - N_M}{N_{tot}} \quad (10.10)$$

with N_0 and N_M being the number of possible adsorption sites per unit area and the number of methoxy groups per unit area, respectively ($N_M = \theta_M N_{tot}$). Methanol molecules that hit the surface at an unoccupied defect site do stick, while molecules that hit a nonreduced or occupied surface site do not. We note that the calculated water and methanol formation rates are three orders of magnitude smaller than the rate at which methanol molecules impinge onto the surface. Therefore the reactive defect sites are nearly fully covered and details of the sticking coefficient equation do not play a relevant role.

The set of differential equations was solved numerically with E_1 and E_2 as parameters to fit the experimental data in Fig. 10.34. N_0 was set to 7.5% which is approximately the density of surface oxygen vacancies after exposing the surface to 1 mC of electrons with a kinetic energy of 50 eV. The best fit was obtained for $E_1 = E_2 = 0.85$ eV (blue curve in Fig. 10.34). The blue curve reproduces the experimental data quite well and the activation energies for water and methanol formation are indeed identical within the error range of the fit. Somewhat similar activation energies ($E_1 = E_2 = 0.75$ eV) could be obtained from a fit of TPD data [10.208].

These studies highlight the role of hydroxyl groups in the methanol partial oxidation reaction. Hydroxyl groups are not just spectators in this reaction (with the side effect that they reduce the substrate when they react to form water), they can affect the kinetics and therefore the reaction rate. They may also affect the selectivity as observed for $V_2O_3(0001)$ [10.132] (not discussed here).

10.4.3 Strong Metal Support Interaction Effects on Reactivity: FeO/Pt in CO Oxidation

> "The reactivity of ultrathin transition metal oxide (TMO) films is closely related to so called *strong metal-support interaction* (SMSI) [10.212], which is mostly discussed in terms of a full or partial encapsulation of metal particles by a thin oxide layer stemming from a support.
>
> A number of studies have addressed this problem. In particular, our own studies [10.33, 38, 40] of Pt nanoparticles deposited onto well-defined iron oxide surfaces showed encapsulation of the Pt surface by an iron oxide layer identified as FeO(111) monolayer film that is virtually identical to the one grown on a Pt(111) single crystal [10.213]. However, the FeO(111) film, initially stacked as an O–Fe bilayer, transforms at elevated oxygen pressures to an O-rich, FeO_{2-x} film with a trilayer (O–Fe–O) structure [10.37, 39]. Although the film stoichiometry implies Fe cations in the formal oxidation state 4+, i.e., unusual for iron compounds, DFT results showed that Fe ions in the trilayer structure are in the oxidation state 3+ due to a substantial electron transfer from the Pt(111) substrate. However, for brevity, we will use FeO and FeO_2 for the bi-layer and tri-layer structures, respectively. The CO oxidation reaction has been used as a probe reaction.
>
> The reaction mechanism of CO oxidation, addressed by DFT using the model of a continuous FeO_2 film, suggested CO reacting with the weakly bound, topmost oxygen atom in the O–Fe–O trilayer, thus forming CO_2 that desorbs leaving an oxygen vacancy behind [10.39]. The vacancy must be replenished by the reaction with molecular oxygen to complete the catalytic cycle. Our systematic study of reactivity of ultrathin oxide films formed from a number of different transition metals, such as Ru, Zn, Fe, and Mn, suggested the oxygen binding energy as a good descriptor for reactivity of the ultrathin oxide films [10.214] which may also be present at the rim of oxide islands.
>
> *Bao* and coworkers have addressed the reactivity of FeO(111) and other TMO(111) monolayer structures on Pt(111) exposing the oxide/metal boundary [10.215–218]. On the basis of DFT calculations [10.216, 218], a Pt–cation ensemble was proposed, where coordinatively unsaturated TMO cations at the edges of TMO islands are highly active for O_2 adsorption and dissociation. Dissociated oxygen binds to Pt at the TMO/Pt interface and is responsible for the facile CO oxidation. Note, however, that the calculations employed a simplified model, using a TMO ribbon, which does not account for the experimentally observed epitaxial relationships of oxide and Pt and related lattice mismatches, in turn resulting in various edge structures as observed [10.219]. More importantly, the oxide phase was modelled by the bilayer, i.e., O–TM–Pt(111), structure, which is not the structure relevant for technological CO oxidation reaction conditions, neither for FeO(111) nor for ZnO(0001) films on Pt(111) [10.28, 39]. Nonetheless, following these studies, the highest reactivity is expected to be on the rim of the FeO(111) islands, which are oxygen deficient and expose the unsaturated Fe^{2+} cations [10.215, 217, 218].
>
> Recently, *Huang* and coworkers [10.220] have addressed the reactivity of FeO(111)/Pt(111) sur-

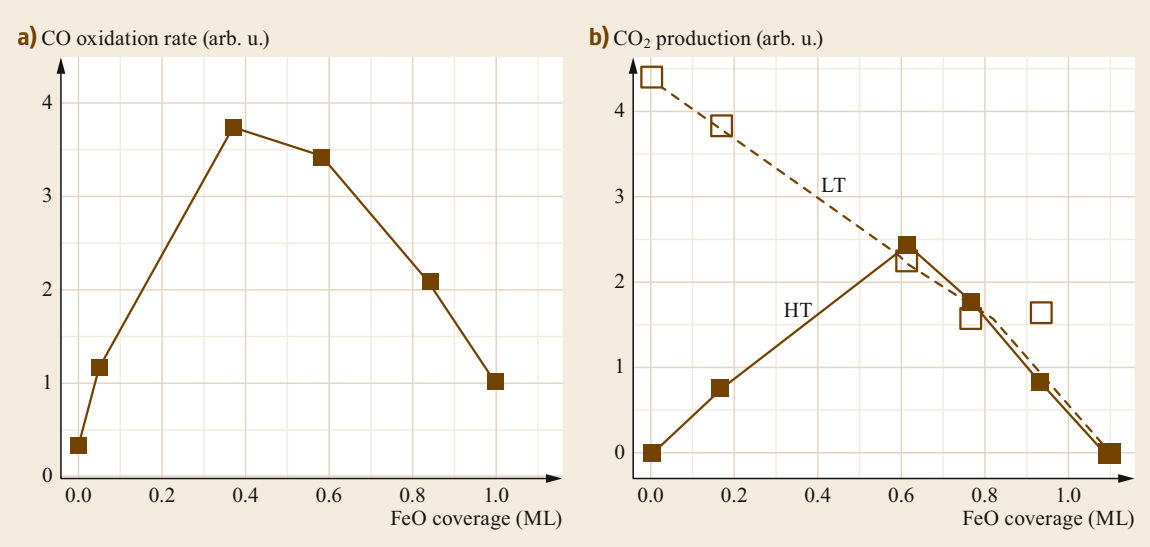

Fig. 10.35 **(a)** CO oxidation rate as a function of the FeO(111) coverage on Pt(111). Reaction conditions: 10 mbar CO and 50 mbar O_2, balanced by He to 1 bar; 450 K. **(b)** Total CO_2 production measured by TPD in low and high temperature (LT, HT) regions as a function of FeO coverage in original films

faces in the water gas shift reaction and preferential oxidation of CO in excess of H_2 using temperature programmed desorption (TPD) technique. It appears that the oxide structure is strongly affected via the reaction with water and hydrogen. A DFT study [10.221] performed on a more realistic model of FeO_x/Pt(111), showed that, beyond terraces of the oxygen-rich FeO_{2-x} phase, considered for a close film [10.39], also FeO_2/FeO and FeO_2/Pt boundaries may be involved in reactions. Finally, the metal–oxide synergy effect may also result from oxygen spillover from the oxide to the metal support.

We also studied the reactivity of FeO(111)/Pt(111) films at submonolayer coverage both under near atmospheric and UHV-compatible pressures in order to bridge the *pressure gap* that may cause some controversy in results obtained by different groups [10.211]. We have shown that a much higher reactivity is, indeed, achieved by exposing an interface between the Pt support and the oxygen-rich FeO_{2-x} phase. Two synergetic effects concur: a low oxygen extraction energy at the FeO_2/Pt interface and a strong adsorption of CO on Pt(111) in its direct vicinity. Weak adsorption of CO on oxide surfaces levels out the (negligible) role of CO adsorption characteristics in the reaction over the closed oxide films, thus rendering the oxygen binding energy as the decisive parameter for reactivity of ultrathin oxide films [10.214].

Figure 10.35a shows the CO oxidation rate (measured by gas chromatography) over FeO(111)/Pt(111) films at 450 K in the reaction mixture of 10 mbar CO and 50 mbar O_2 (balanced by He to 1 bar) for different oxide coverages. (Note, that the initial rate was solely measured in order to neglect any deactivation effects). In the course of the reaction the initially grown FeO(111) islands transformed into the FeO_{2-x} islands in agreement with STM results of *Fu* et al. [10.217] The rate vs coverage plot revealed a maximum at ≈ 0.4 ML coverage. The rate is substantially (by a factor of 3.5) higher than obtained for a closed, monolayer film, which is, in turn, more active than the pristine Pt(111) surface, in full agreement with our previous studies [10.39]. Obviously, the oxide/metal interface provides reaction sites more active than those on the (interior) surface of FeO_2 islands.

More detailed experiments on FeO(111)/Pt(111) films at sub-ML coverages using CO TPD as a function of oxide coverage, exposure, and preparation conditions revealed that CO_2 production from CO oxidation came in two temperature regimes. The one at low temperature (LT, below 350 K) is very similar to that obtained on pristine Pt(111), whereas the reaction at high temperature (HT, 350−550 K) originates only on oxide covered surface.

Figure 10.35b depicts the total amounts of CO_2 measured in six consecutive CO TPD spectra in

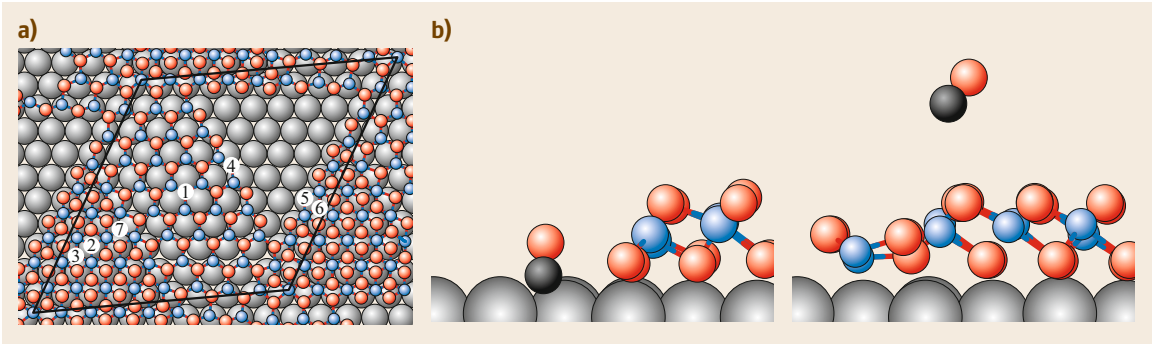

Fig. 10.36 **(a)** Computational model of a sub-monolayer FeO_x film on the Pt(111) surface. The nonequivalent oxygen sites are labeled 1–7: T–FeO (1), T_I-FeO_2 (2), T_S-FeO_2 (3), E-FeO/Pt (4), E_I-FeO_2/Pt (5), E_S-FeO_2/Pt (6), E-FeO_2/FeO (7). Pt, O and Fe atoms are represented by *gray*, *red* and *blue spheres*, respectively. **(b)** Most stable CO adsorption configurations at the FeO_2/Pt (*left*) and FeO_2/FeO (*right*) boundaries depicted in panel **(a)**. Pt, O, C and Fe atoms are represented by *gray*, *red*, *black*, and *blue spheres*, respectively. Reprinted with permission from [10.211]

the LT and HT regions, respectively, as a function of oxide coverage. The LT signal reversely scales with the oxide coverage, in full agreement with reaction taking place on uncovered areas of Pt(111). The observed linear relationship also suggests no (or negligible) oxygen spillover from FeO_2 islands onto the Pt(111) surface. In contrast, CO_2 production in the HT state goes through the maximum in the same manner as observed for the CO oxidation rate at near atmospheric pressures (Fig. 10.35a), thus providing compelling evidence that the enhanced activity must be attributed to the reaction at the interface between Pt(111) and FeO_2 trilayer.

Also, DFT calculations have been performed to estimate the thermodynamic stability of oxygen at a variety of alternative terrace and boundary sites, characteristic of Pt-supported FeO_x film at sub-ML coverage. The computational model depicted in Fig. 10.36a represents an oxide coverage of 0.6 ML, with an equal proportion of FeO and FeO_2, accounting for the case of large FeO_x islands on the Pt(111) surface. It consists of embedded FeO_2 islands, with trilayer O–Fe–O structure, located primarily in the region of the so-called *hcp* lattice registry (O ions on-top of surface Pt atoms, Fe ions in the hollow sites), where the oxygen-rich film forms the most easily [10.37]. Conversely, bare FeO(111) is most stable in regions of *fcc* registry (both O and Fe ions in three-fold hollow sites of a Pt(111) substrate). The large unit cell contains also the region of a bare Pt(111) surface created by removing the oxide from regions of *top* registry (O ions in the hollow sites, Fe ions on-top of a surface Pt), where the stability of a FeO_x film is the lowest [10.37, 222].

While the oxygen extraction thermodynamics identified edge (E-FeO_2/Pt and E-FeO_2/FeO) sites as the most plausible candidates to react with CO (with a small preference for the latter), the very different characteristics of CO adsorption (2.05 vs 0.05 eV, respectively) clearly indicates that these two sites have a different efficiency for CO oxidation. Since CO binds only weakly to the FeO_2/FeO boundary, the Eley–Rideal reaction mechanism is anticipated on these sites. Conversely, strong CO binding in the direct vicinity of the FeO_2/Pt boundaries makes the Langmuir–Hinshelwood mechanism operative. Although in the latter case CO and O binding characteristics are close to those obtained on the bare Pt(111) surface, the FeO_2 oxide phase provides O atoms which do not suffer from the CO blocking effect which, otherwise, poisons the CO oxidation reaction on the bare Pt surface.

Certainly, for the rate enhancement to occur CO must adsorb sufficiently strongly, otherwise it desorbs intact before reaction with oxygen. Therefore, weakly adsorbing metal surfaces, such as Ag(111), do not show such effect as previously reported for ZnO(0001) films [10.223]. Accordingly, using oxygen binding energy as a principal descriptor for CO oxidation over ultrathin oxide films seems to be valid only for the systems exhibiting relatively weak CO adsorption which does not compete for oxygen adsorption sites. In the case of systems exposing a metal/oxide interface, the reactivity may be considerably enhanced by metals strongly adsorbing CO like Pt. In such cases, the model of overlapping states [10.224] seems to be fairly predictive, suggesting high activity when the

desorption profiles for each individual molecule reacting at the surface overlap.

10.4.4 Olefin Hydrogenation over $Pd/Fe_3O_4(111)$

Real catalytic processes often require small amounts of some additives (promoters), such as e.g., alkali metals or halogens [10.100], that ensure high catalytic activity and selectivity. The role that these compounds play at a microscopic level remains unclear for most of the known catalytic systems in operation. One of the most important coadsorbates, particularly in hydrocarbon chemistry, is carbon resulting from decomposition of the reactants. Accumulation of carbon was recognized to considerably affect the activity and the selectivity in hydrocarbon conversions promoted by transition metals [10.226]. In our studies, by comparing the hydrogenation activity of clean and C-containing Pd nanoparticles we addressed the underlying microscopic mechanisms of C-induced changes in the catalytic performance for hydrogenation of olefins [10.227–229].

Hydrogenation rates of *cis*-2-butene over clean and C-containing Pd nanoparticles supported on $Fe_3O_4(111)/Pt(111)$ film are shown in Fig. 10.37a. Pd nanoparticles were saturated first with deuterium to form both surface and subsurface D species [10.230] and then short pulses of *cis*-2-butene were applied. Clean Pd nanoparticles exhibit high hydrogenation activity for an initial short period of time (a few butene pulses), after which it drops to zero. In contrast, if carbon was deposited on Pd nanoparticles before the reaction, a sustained hydrogenation rate was observed. Using CO as a probe molecule for different adsorption sites, it can be shown that deposited carbon modifies the low-coordinated site such as edges and corners [10.230]. However, it is not clear whether carbon resides on the surface or might penetrate into the subsurface region as predicted theoretically [10.231]. This effect demonstrates the exceptional importance of carbon for olefin hydrogenation, which can be carried out in a truly catalytic fashion for many turnovers, only on C-containing Pd nanoparticles.

The role of carbon in promotion of sustained hydrogenation was rationalized by employing transient molecular beam experiments and resonant nuclear reaction analysis (rNRA) for hydrogen depth profiling. First, we obtained the first direct experimental evidence that the presence of H(D) absorbed in the Pd particle volume is required for olefin hydrogenation, particularly for the second half-hydrogenation step [10.227], in agreement with previous experimental evidences [10.232]. This result explains the high initial hydrogenation rates, observed on the clean particles fully saturated with D, and vanishing hydrogenation activity in steady state because of the depletion of the subsurface D reservoir (Fig. 10.37a). Apparently, the inability to populate subsurface D sites arises from hindered D subsurface diffusion through the surface covered with hydrocarbons. Further, it was shown that even a submonolayer coverage of carbon significantly affects the H(D) depth distribution in Pd particles [10.227]. Based on these observations, and on the analysis of the hydrogenation kinetics [10.229], we attribute the sustained hydrogenation activity to facilitation of H(D) diffusion into the particle volume by deposited carbon.

The proposed mechanism was confirmed both theoretically and experimentally [10.233, 234]. Computational studies on Pd nanoclusters demonstrated that deposited carbon dramatically enhances the hydrogen diffusion rate into subsurface, mainly due to a local elongation of Pd–Pd bonds and a concomitant lowering of the activation barrier [10.233]. This dramatic reduction of the activation barrier can account for the experimentally observed unusual promotion of sustained hydrogenation activity by carbon. In contrast, the lateral rigidity of the extended Pd(111) surface was predicted to hinder this effect, in agreement with experimental observations [10.228]. The results demonstrate the conceptual importance of atomic flexibility of sites near particle edges, which, in contrast to intrinsically rigid regular single crystal surfaces, play a crucial role in H subsurface diffusion on Pd.

Finally, we provided direct experimental evidence for a faster subsurface H diffusion through C-modified low-coordinated surface sites on Pd nanoparticles by probing the diffusion rate via $H_2 + D_2 \rightarrow HD$ exchange in different temperature regimes [10.234]. It was previously shown [10.230] that the formation of HD can occur either via recombination of two surface H and D species or an involvement of subsurface H or D species. The latter pathway dominates at low

temperatures between 200 and 300 K. Our experimental results are consistent with the scenario implying that one subsurface atom (H or D) recombines with a surface-adsorbed atom to form HD. In the case of slow subsurface H(D) diffusion, the formation rate of subsurface species will be the limiting step in HD production, and can, therefore, be addressed by probing the rate of isotopic scrambling.

Figure 10.37c shows the steady state HD formation rates at 260 and 320 K on clean and C-modified Pd nanoparticles. C–modification of the particles edges was found to affect the HD formation rate in a dramatically different way for two reaction temperatures: whereas at 320 K preadsorbed C *reduces* the overall reaction rate by about 30°, the reaction rate *increases* by about 100° at 260 K on the C-modified particles. The decreased HD formation rate at 320 K, where HD formation is dominated by the recombination of the surface H and D species [10.230], can be rationalized as a consequence of the blocking of surface adsorption sites by carbon. Interestingly, even though a part of the surface is blocked by carbon, the HD formation rate is significantly increased at 260 K, where desorption involves at least one subsurface H(D) species. This effect can be explained only by the higher formation rate of the subsurface H(D) species on the C-modified particles, resulting in a higher steady state concentration.

Such insight allowed us to identify an exceptionally important role of carbon in hydrogenation chemistry on nanostructured catalysts that was previously not clearly appreciated. According to our model, small amounts of carbon modify the low-coordinated surface site of Pd nanoclusters (edges, corners), thus allowing for effective replenishment of subsurface H in steady state and enabling sustained hydrogenation. These results also highlight the crucial role of subsurface H diffusion, which is a strongly structure-sensitive process on Pd surfaces, in hydrogenation of the olefinic bond. Computational studies suggest that the atomic flexibility of the low-coordinated surface sites is an important structural feature that is responsible for easy subsurface diffusion of H under operation condition."

Reprinted with permission from [10.225], © 2013 American Chemical Society.

10.5 Oxide Films Beyond UHV

Reprinted with permission from [10.60]. © 2019 Materials Research Society.

"The investigations discussed so far were limited to systems studied under UHV conditions which immediately poses the question how these results relate to oxide systems at ambient conditions such as an aqueous environment. In the following we illustrate how such well-defined systems prepared under UHV conditions can be used to study the properties of the oxide surfaces under ambient conditions.

10.5.1 Alkaline Earth Oxides, Iron Oxides and Silica Out of UHV into Solution

Stability and Dissolution of Thin Oxide Films in Aqueous Environment

A variety of technologically important processes, such as catalyst preparation by wet impregnation, involve processes at the liquid/oxide interface. Aiming at the investigation of such processes using well-defined thin oxide films the system has to be stable under the specific environmental conditions of interest. For surface science investigations in particular, it is desirable that the structural order is maintained. Since the chemical properties of (most) oxide thin films are similar as those of the corresponding bulk analogues, their stability and dissolution behavior is expected to follow the same trends. Dissolution rates for oxide thin film samples can be derived from the measured decrease of film thickness upon exposure to aqueous solution, which can straightforwardly be determined from the intensities of the oxide and substrate XPS or AES (Auger electron spectroscopy) emissions.

XP spectra (O 1s and Si 2p regions) taken after exposing bilayer SiO_2/Ru to deionized water at 90 °C, and NaOH(aq) at 25 °C for various times are displayed in Fig. 10.38a [10.204]. Clearly, deionized water (pH 7) does not affect the film structure to any significant extent, even at elevated temperature. While a small shift of all silica-related XP peaks to higher BE, which reflects a slight change in the electronic structure of the system (band bending), is noted, neither the Si 2p nor the O 1s peaks suffer any loss of intensity. In

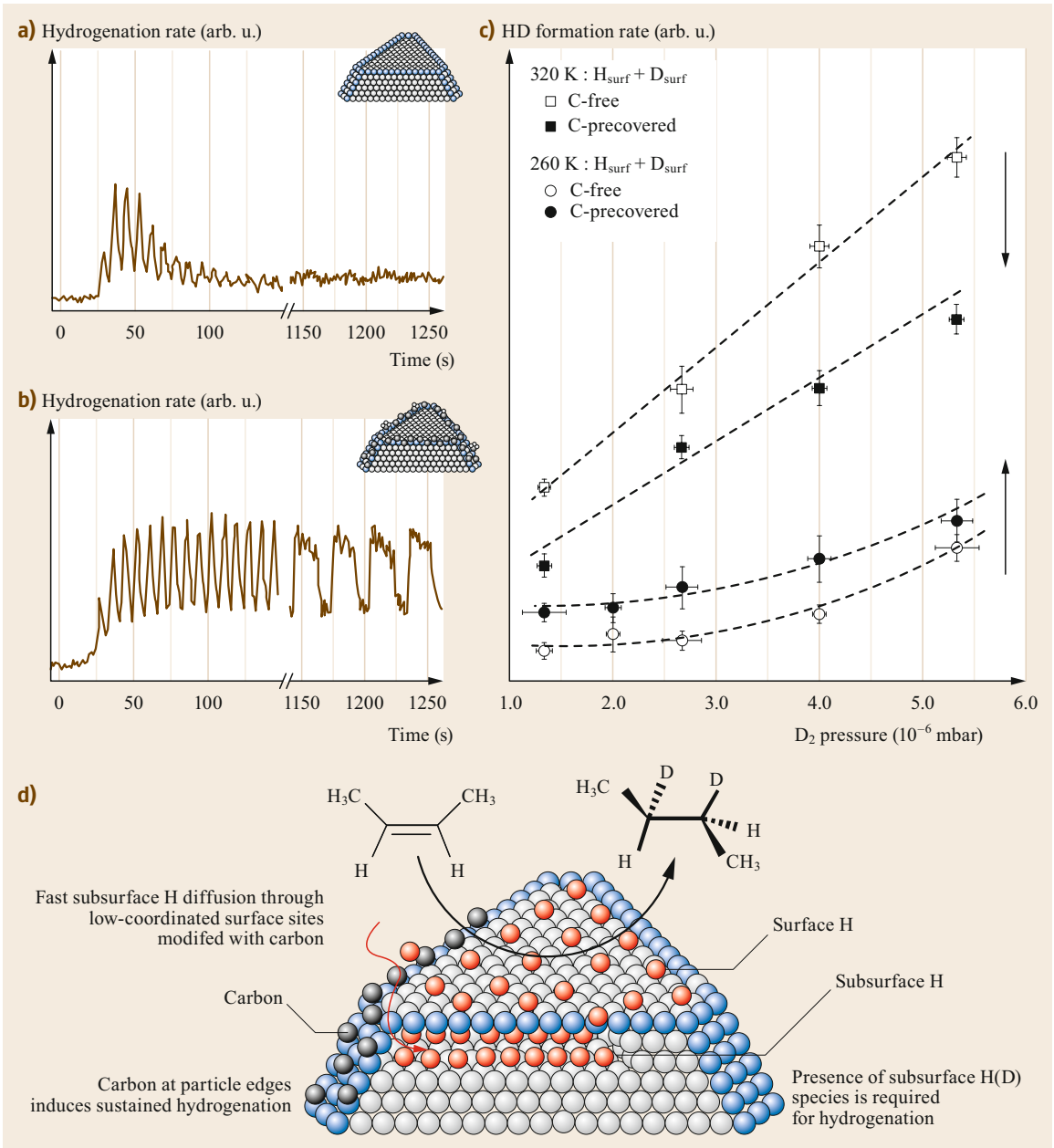

Fig. 10.37a,b Hydrogenation rate of *cis*-2-butene at 260 K over clean **(a)** and C-precovered (carbon adsorbed at Pd nanoparticle edges) **(b)** model catalysts $Pd/Fe_3O_4/Pt(111)$. **(c)** The steady state HD formation ($H_2 + D_2 \rightarrow 2HD$) rates obtained on the pristine and C-precovered Pd nanoparticles supported on $Fe_3O_4/Pt(111)$ at 260 and 320 K. Reprinted (adapted) with permission from [10.234]. Copyright (2011) American Chemical Society. **(d)** Proposed reaction mechanism of olefin hydrogenation on Pd nanoparticles

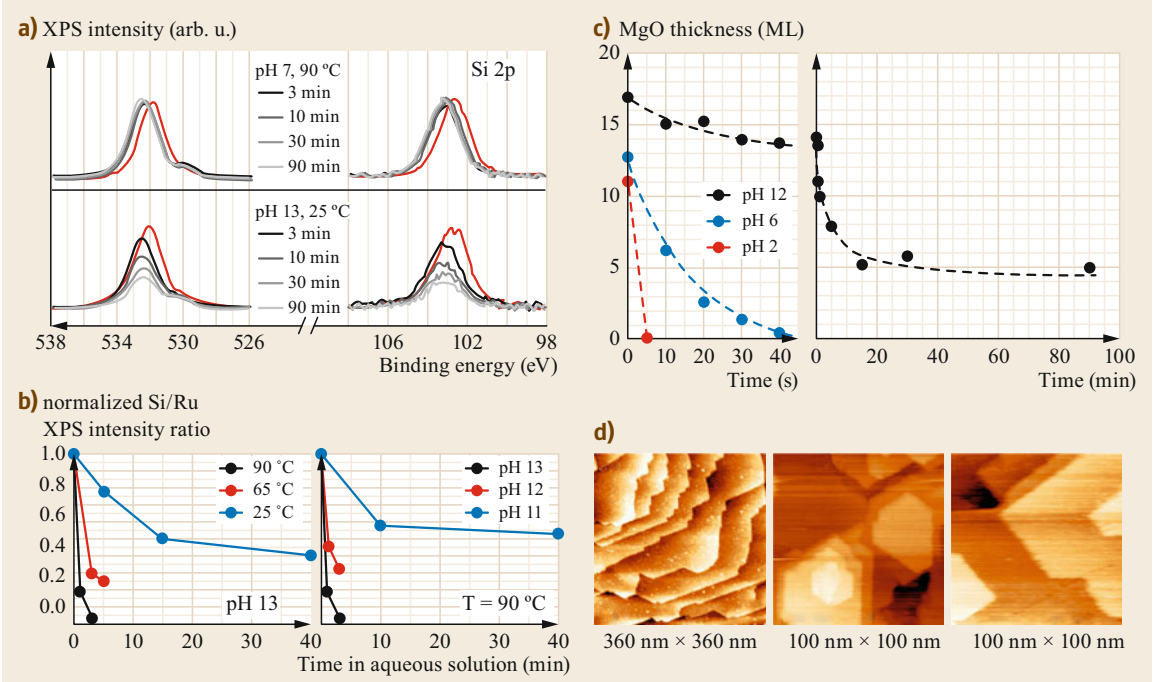

Fig. 10.38 **(a)** Evolution of O 1s (*left*) and Si 2p (*right*) XP spectra of SiO_2/Ru(0001) samples as a function of time of exposure to (*top*) deionized water at 90 °C, and (*bottom*) 0.1 M NaOH at 25 °C. **(b)** Peak intensity ratios of Si 2p relative to Ru 3d for bilayer SiO_2/Ru samples exposed to aqueous NaOH solutions at pH 13 and various temperatures (*left*) and varying pH at 90 °C (*right*) as a function of time spent within the aqueous environments. Reprinted from [10.204], with permission from Elsevier. **(c)** *Left*: Dissolution of MgO(001)/Ag(001) films (initial thicknesses corresponding to the values at time = 0 s) in various environments plotted as MgO film thickness vs. time of exposure to solutions; *black*: 0.01 M NaOH solution (pH 12), *blue*: Millipore water (pH 6), *red*: 0.01 M HCl solution (pH 2). **(c)** *Right*: Dissolution of MgO(001)/Ag(001) in 0.01 M NaOH. Reprinted from [10.235], with permission from Elsevier. **(d)** Air-STM images of Fe_3O_4(111)/Pt(111) taken after transfer from UHV to air (*left*), after 60 min exposure to 0.1 M HCl, pH 1 (*middle*) and after 60 min exposure to $NaOH_{aq}$, pH 10 (*right*)

contrast, the intensity of both peaks decreases significantly, even at 25 °C, when the silica bilayer is exposed to alkaline media (NaOH, pH 13). The equal relative signal intensity loss of Si and O peaks observed with time of exposure allows to conclude that, in accordance with general experience, the dissolution process in alkaline media can be described as the OH^- catalyzed hydrolysis of SiO_2 ($SiO_2 + 2\,H_2O \rightarrow H_4SiO_4$). One can further state that the bilayer SiO_2/Ru films resemble the dissolution behavior of other, more abundant forms of silica (quartz, amorphous silica), which are found to be practically insoluble in the neutral pH range, and more strongly soluble in alkaline conditions. From more systematic studies of dissolution as a function of temperature and pH (Fig. 10.38a, lower part) it is clear that removal of SiO_2 from the sample shows a preference for larger values of both parameters, which is also qualitatively consistent with the behavior noted from bulk-phase silica analogues [10.236]. The dissolution rates for the thin film sample can be modeled by the general silica dissolution rate model derived by *Bickmore* et al. [10.236], which accounts for variations in pH, temperature, and the coverage of neutral (θ_{Si-OH}) and deprotonated (θ_{Si-O-}) silanols. Because the silica film is hydrophobic and lacks significant initial silanol coverage, the latter two contributions can be neglected and the rate equation simplifies to

$$\frac{\mathrm{dSi}}{\mathrm{d}t}\frac{\mathrm{mol}}{\mathrm{s}} = \mathrm{e}^{6.7\pm1.8}\,T\mathrm{e}^{\frac{-77.5\pm6.0}{RT}}[\mathrm{OH}^-].$$

A comparison of the dissolution rates predicted from that relation to those estimated on the basis of the initial rates of Si XPS peak attenuations from the thin films shows good agreement between the model and the experiment [10.204]. From this, it

is concluded that dissolution of the film in alkaline media is initiated by OH^- attack at Si centers. Note that this leads to rupture of siloxane bonds. Thus, the initial step in the dissolution process can qualitatively be described by models that are similar to those used to explain electron-assisted hydroxylation of the silica film (Fig. 10.28f). In general, the silica bilayer films were found to be stable (i.e., negligible dissolution rates observed) at room temperature in acidic and neutral aqueous solutions, and in alkaline media up to pH 10 [10.204].

MgO is a basic oxide (point of zero charge (PZC) in the pH 10 range) and therefore expected to be more stable in alkaline media than in neutral and acidic environment [10.237]. Results of dissolution experiments performed with MgO(001)/Ag(001) thin films are presented in Fig. 10.38b, where the variation of MgO film thickness as a function of time is displayed for exposure to acidic (pH 2, 0.01 M HCl), alkaline (pH 12, 0.01 M NaOH) and close to neutral (pH 6, Millipore water) environments, respectively [10.235]. The data shown in Fig. 10.38b is consistent with the expected faster dissolution of MgO in acidic media. In fact, in 0.01 M HCl solution the dissolution is so fast that a 11 ML thick film was completely dissolved within the first 5 s of exposure. The dissolution rate is smaller at pH 6; however, even under these conditions a 13 ML thin MgO film was completely dissolved within 5 s of exposure. During the same period, only 3 ML MgO were dissolved from the MgO sample upon exposure to alkaline (pH 12) solutions. For the latter, the dissolution behavior was studied for prolonged exposures (up to 90 min), the results of which show that the dissolution is initially fast and considerably slows down with time, until a stable surface state is obtained after 20–30 min of exposure. This suggests the formation of a brucite ($Mg(OH)_2$)-like passivating surface layer during exposure to alkaline solution, for which dissolution rates are considerably smaller than for MgO [10.238]. Because of the partial dissolution, and transformation of the surface layers into a hydroxide, MgO films exposed to alkaline media are subject to strong restructuring. Even if the crystallinity of the films can partially be recovered by annealing at elevated temperature, the initial structure of the MgO(001) films cannot be restored [10.235].

Iron oxides are, according to the corresponding Fe-water Pourbaix diagram, stable in aqueous solutions in a wide range of pH. Thus, it is not surprising that also thin iron oxide films are very stable in aqueous solutions. As an example, STM images taken in air from $Fe_3O_4(111)/Pt(111)$ films, which have been prepared in UHV and subsequently transferred to air ambient and exposed to aqueous solutions (pH 1, 0.1 M HCl and pH 10, $NaOH_{aq}$) for 1 h, are shown in Fig. 10.40c [10.239, 240]. These images reveal that the island-terrace-step structure of the thin film remains intact. Furthermore, the step edges run straight along the crystallographically preferred directions and the terraces are atomically flat. XPS taken from the exposed films indicates a slight oxidation of the surface, but this does obviously not lead to structural modifications. Both, $Fe_3O_4(111)/Pt(111)$ and bilayer silica films (and to a limited extent also MgO(001)/Ag(001)) are therefore well suited for further investigations of processes involving oxide-liquid interfaces."

Reprinted with permission from [10.60]. © 2019 Materials Research Society.

Surface Science Approach to Catalyst Preparation: Pd–Fe_3O_4 as an Example

In Sect. 10.4.4 we have already shown that Pd nanoparticles deposited on a $Fe_3O_4(111)$ surface are good catalysts for hydrogenation reactions. The system discussed above was prepared by physical vapor deposition of Pd atoms onto the oxide surface under UHV conditions. However, almost all supported catalysts employed industrially are prepared by wet-chemical methods such as impregnation, deposition–precipitation, spreading, and ion exchange [10.74]. The first step in a commonly applied wet-chemical catalyst preparation procedure consists of the interaction of the support with precursor solutions that contain the metal component in the form of salts or complexes. This is followed by drying, calcination and reduction steps, which are necessary to transform the adsorbed metal precursor into the catalytically active phase. Among other approaches, thin oxide films have recently been used to model typical catalyst preparation procedures with flat, single-crystalline substrates [10.235, 239–242].

With $Fe_3O_4(111)/Pt(111)$ as support, the preparation of supported Pd nanoparticles using $PdCl_2$ as a precursor has been studied [10.239, 240]. The speciation of $PdCl_2$ in aqueous solutions has been the subject of intense research in the past. In strongly acidic conditions, the tetrachloro complex $PdCl_4^{2-}$ is the most abundant species (Fig. 10.39a). Upon hydrolysis, the chlorine ligands are gradually replaced by aqua or hydroxo ligands, leading finally to $Pd(OH)_4^{2-}$ species in strongly basic medium [10.243, 244]. Neutral Pd complexes of the kind $[PdCl_2(H_2O)_2]$ are formed at an intermediate stage of hydrolysis. These complexes

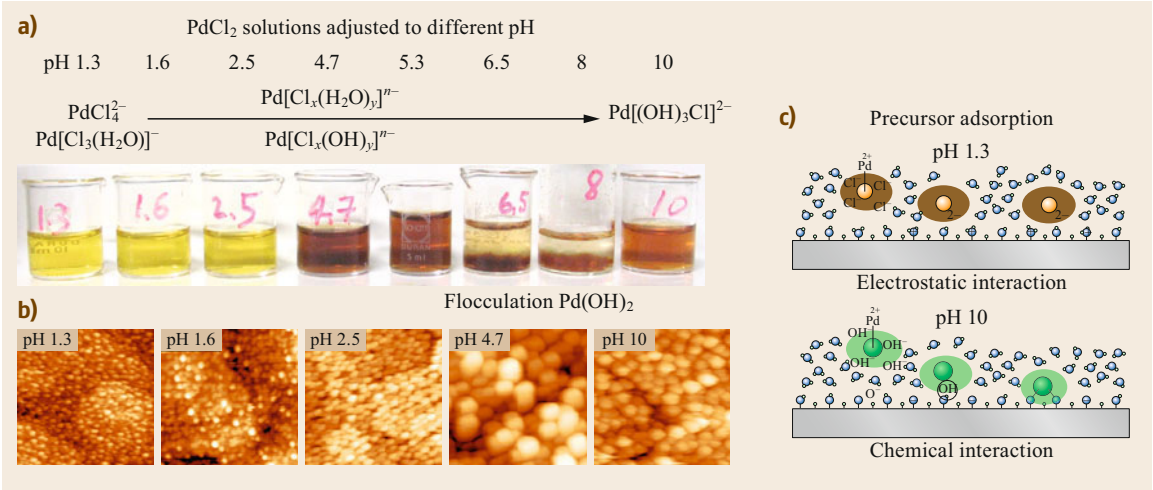

Fig. 10.39 **(a)** pH-dependent speciation of $PdCl_2$ in aqueous solution. **(b)** STM images ($75 \times 75\,nm^2$) of Pd nanoparticles on $Fe_3O_4(111)$ obtained by exposure of freshly prepared $Fe_3O_4(111)/Pt(111)$ to $PdCl_2$ solutions of different pH followed by drying and annealing at 600 K in UHV. **(c)** Schematic representation of the adsorption of Pd-complexes on oxide surfaces in acidic (pH below the PZC of the oxide) and alkaline media (pH above the PZC of the oxide)

are most probably responsible, because of their tendency for polymerization (→ polynuclear Pd-hydroxo complexes, PHC), for the formation of colloidal particles [10.245], seen with the appearance of the dark brown color of the Pd solution (Fig. 10.39a). The pH at which formation of PHC's sets in can be slightly varied by changing the Pd^{2+} and Cl^- concentration. The strong influence of the solution pH on the Pd loading and the particle morphology is demonstrated by means of the STM images displayed in Fig. 10.39b. These images were obtained following exposure of the $Fe_3O_4(111)$ films to precursor solutions (5 mM $PdCl_2$) exhibiting different pH (as indicated in Fig. 10.39b), and subsequent thermal treatment at 600 K in UHV, which transforms the adsorbed Pd precursor into Pd particles. First, the samples prepared with the low pH solutions (pH 1.3–2.5), where the influence of PHC's can be excluded, are considered. The trend toward higher Pd loading and slightly increasing Pd particle size with increasing pH is obvious and in agreement with results obtained for similar preparations carried out with powder samples [10.246]. Within the *strong electrostatic adsorption* model (Fig. 10.39c, top), which seems to be applicable for the given conditions (negatively charged precursor and positively charge support surface, PZC of Fe_3O_4 is ≈ pH 6.5) the suppression of Pd precursor adsorption at low pH, which results in low Pd loading, is typically explained by the lowering of the equilibrium adsorption constant as an effect of the higher ionic strength of the strongly acidified precursor solution [10.247].

While small and homogeneously distributed Pd particles are formed following exposure to the low pH solutions, a high Pd loading and large Pd particles are obtained if the pH 4.7 precursor solution is applied (Fig. 10.39b). At first glance, this result might be related to the adsorption of colloidal particles present in the precursor solution. However, deposited particles could not be identified by STM directly after deposition. Therefore, a different adsorption mechanism for the Pd precursor needs to be considered at this pH conditions. Since at pH 4.7 the Fe_3O_4 surface is essentially uncharged and a considerable fraction of the solution species is charge-neutral, a strong chemical interaction via hydrolytic adsorption of the precursor complexes could be the reason for the high Pd loading. With the basic pH 10 precursor solution the Pd loading decreased again and a particle size distribution that is more homogeneous as compared to the one obtained with the pH 4.7 precursor solution was obtained. Since both the oxide surface and the solution complexes are negatively charged in this case, electrostatic adsorption is believed to play a negligible role and the adsorption of Pd occurs mainly via hydrolytic adsorption of the Pd-hydroxo complexes on the surface hydroxyl groups (Fig. 10.39c, bottom). Copyright Springer [10.242].

More detailed studies regarding the stepwise decomposition of the adsorbed precursors into metallic nanoparticles were conducted with samples prepared by exposure to pH 1.3 and pH 10 precursor solutions, respectively [10.239, 240]. As an example, the results obtained with the alkaline precursor solution

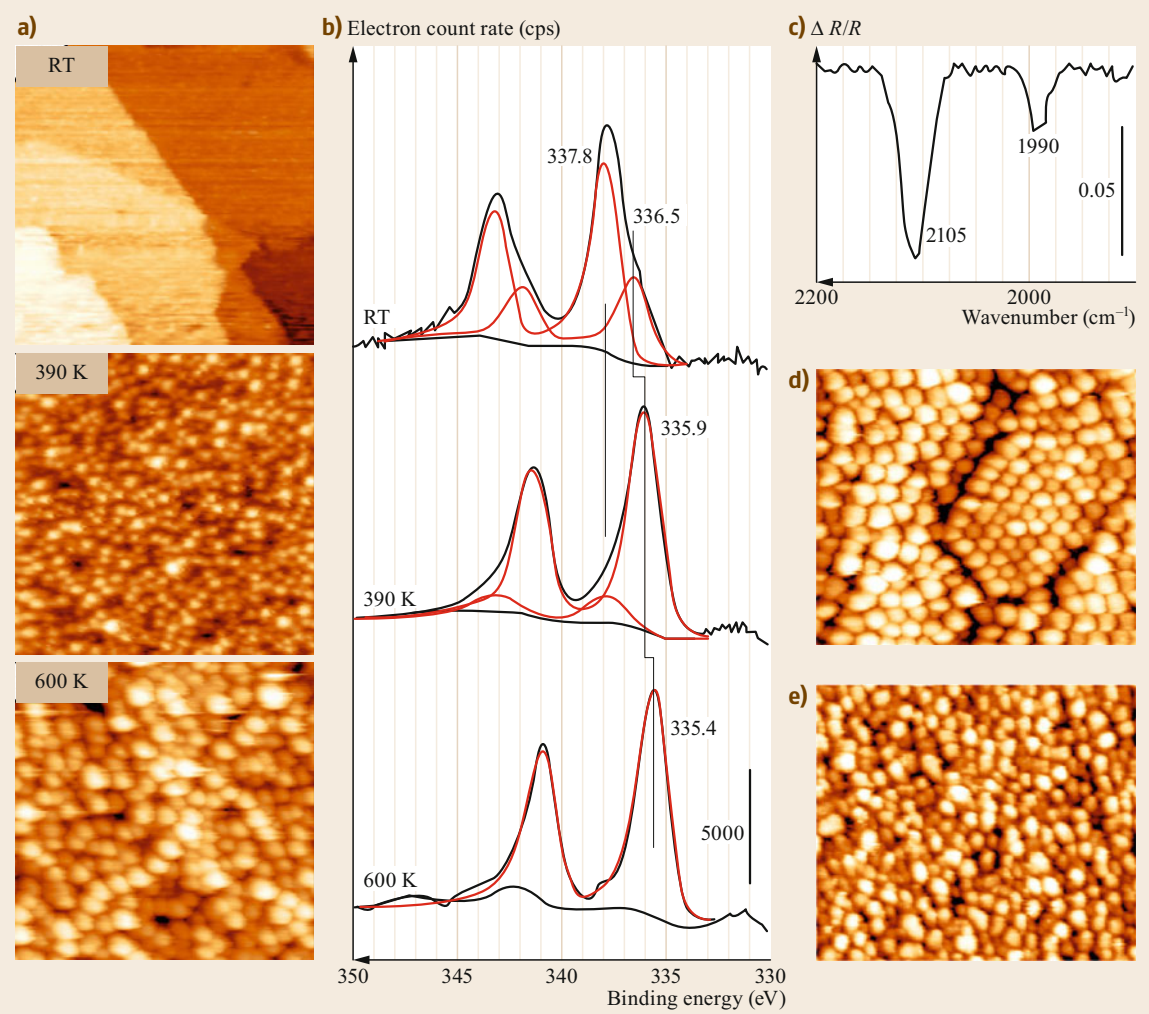

Fig. 10.40 **(a)** STM images ($100 \times 100\,nm^2$) and **(b)** corresponding Pd 3d XP spectra of a $Fe_3O_4(111)$/Pt(111) thin film surface acquired after exposure to Pd precursor solution (5 mM $PdCl_2$, pH 10) and subsequent drying (RT, *top*), after drying at 390 K (*middle*), and subsequent heating to 600 K (*bottom*). **(c)** IRA spectrum taken after adsorption of CO at 80 K on a Pd/$Fe_3O_4(111)$ model catalyst prepared by exposure to pH 10 $PdCl_2$ precursor solution. **(d)** STM image ($100 \times 100\,nm^2$) of Pd/$Fe_3O_4(111)$ prepared by physical vapor deposition of Pd onto a $Fe_3O_4(111)$ surface modified by treatment with NaOH solution. After [10.242]

are reproduced in Fig. 10.40a (STM) and Fig. 10.40b (XPS) [10.240]. An STM image of the $Fe_3O_4(111)$ surface following exposure to the precursor solution (2 mM $PdCl_2$, pH 10) and subsequent water rinsing and drying shows an apparently *clean* oxide surface with the typical morphological features of $Fe_3O_4(111)$ (Fig. 10.40a, top). However, the corresponding XPS spectrum confirms the presence of Pd on this surface (Fig. 10.40b, top). Obviously, the adsorbed precursor complexes are homogeneously distributed across the surface and cannot be individually resolved in STM. The two Pd $3d_{5/2}$ photoemission signals identified at 337.8 and 336.5 eV BE can be assigned to Pd-hydroxo and PdO species, respectively. It has to be mentioned that the high BE component was found to be sensitive to x-ray irradiation, and the PdO component identified at this stage of the preparation results most probably from x-ray induced decomposition of the Pd-hydroxide into PdO. Only mild drying at 390 K completely changes the surface morphology, which displays small particles with an average diameter of 2.5–3 nm (Fig. 10.40a, middle). This morphological change is accompanied by an almost complete transformation of the adsorbed Pd-hydroxide precursor into PdO, as deduced from the loss

of the high BE component in XPS and the concurrent increase of the 335.9 eV feature (Fig. 10.40b, middle). Finally, fully reduced Pd particles (particle diameter: 3–7 nm) are found after further thermal treatment at 600 K (Fig. 10.40a,b, bottom). These particles contain some carbon contamination remaining from the preparation process, which can be eliminated by oxidation at 500 K in 1×10^{-6} mbar O_2. Subsequent reduction in CO atmosphere restores the metallic state, which then presents CO-IRAS signatures typical for supported Pd nanoparticles (Fig. 10.40c) with two bands arising, respectively, from on-top bound (2105 cm^{-1}) and bridge-bonded CO (1990 cm^{-1}) [10.248]. Alternatively, the final reduction step was performed in H_2 instead of CO atmosphere, which led to the formation of bimetallic Pd–Fe particles due to strong metal support interaction (SMSI). This modification can be easily understood on the basis of the catalytic action of Pd in providing H atoms for reduction of the Fe_3O_4 support via H_2 dissociation and H spill-over. Iron atoms from the reduced support then migrate into the Pd particles.

An important question to ask at this point is whether or not the morphology of a model catalyst prepared by wet-chemical procedures as described above differs from that of a corresponding model catalyst prepared exclusively in UHV. In other words, does the nature of the precursor (single atoms in UHV vs. metal complexes in solution) or the support properties (clean surface in UHV vs. a surface modified by exposure to precursor solution) affect the properties of the activated model catalyst? In order to answer this question two additional $Pd/Fe_3O_4(111)$ model catalysts were prepared: One, where Pd was deposited onto a clean $Fe_3O_4(111)$ support in UHV by vapor deposition (Pd/Fe_3O_4(UHV), Fig. 10.40d), and another one, where Pd was deposited by vapor deposition onto a $Fe_3O_4(111)$ surface following a treatment with NaOH (pH 12) solution (Pd/Fe_3O_4(hydr), Fig. 10.42b,e). The NaOH treatment was applied in order to achieve a surface functionality comparable to the solution deposition experiment. Inspection of the corresponding STM images (Fig. 10.40d,e) reveals differences between the two samples with respect to the arrangement of the Pd particles and the particle size distribution. While the Pd particles are uniform in size and arranged in an almost perfect hexagonal array on the clean $Fe_3O_4(111)$ surface, the surface order is lost on the pretreated Fe_3O_4 surface and a deviation from the normal particle size distribution is apparent. Most notably, the morphology of the Pd/Fe_3O_4(hydr) sample (Fig. 10.40e) closely resembles that of the model catalyst prepared by deposition of Pd from the pH 10 precursor solution (Fig. 10.40a, bottom). This finding suggests that in the present case the morphology of the activated model catalyst is mainly governed by the interfacial properties, and not by the nature of the precursor. The more heterogeneous sintering of Pd particles on the modified surfaces is attributed to the presence of hydroxyl groups and the existence of a variety of adsorption sites with differing Pd adhesion properties [10.240], Copyright Springer [10.249].

10.5.2 Water/Silica Interface

To date, most of the research on silica bilayers has been performed in idealized ultra-high vacuum environments. These conditions provide a high degree of experimental control which enables unambiguous structural assessment. Yet real world applications of silica and its derivatives demand higher pressures and temperatures and occur under ambient condition. Recent research on silica bilayers beyond ultra-high vacuum addresses these practical considerations by bridging the gap between UHV and ambient.

In order to bridge such gap, the structure of silica has been investigated with high-resolution liquid atomic force microscopy (AFM). Silica films are grown in UHV and subsequently transferred through ambient to the liquid environment (400 mM NaCl solution). Figure 10.41 shows images of the bilayer silica structure attained with ultra-high vacuum STM and high resolution liquid-AFM [10.250]. The low-temperature UHV STM images exhibit atomic resolution of the silica structure while the resolution of the room temperature liquid-AFM images allows to identify the ring structures. The structures appear remarkably similar as confirmed quantitatively from pair distribution functions of the ring center positions. These results show that the silica film is structurally robust against ambient and aqueous conditions; this result is consistent with the conclusions of the previous study which found the silica bilayer film to be exceptionally stable against hydroxylation [10.199]. In contrast, many UHV surface structures are not stable under ambient conditions due to unsaturated bonds [10.198, 235]. The stability of the silica bilayer makes it an optimal playground to test the resolution of liquid AFM as the amorphous structure circumvents the common challenge of distinguishing between true atomic resolution and lattice resolution [10.251]. Furthermore, establishing the stability of the silica bilayer under ambient conditions opens the door to future device applications.

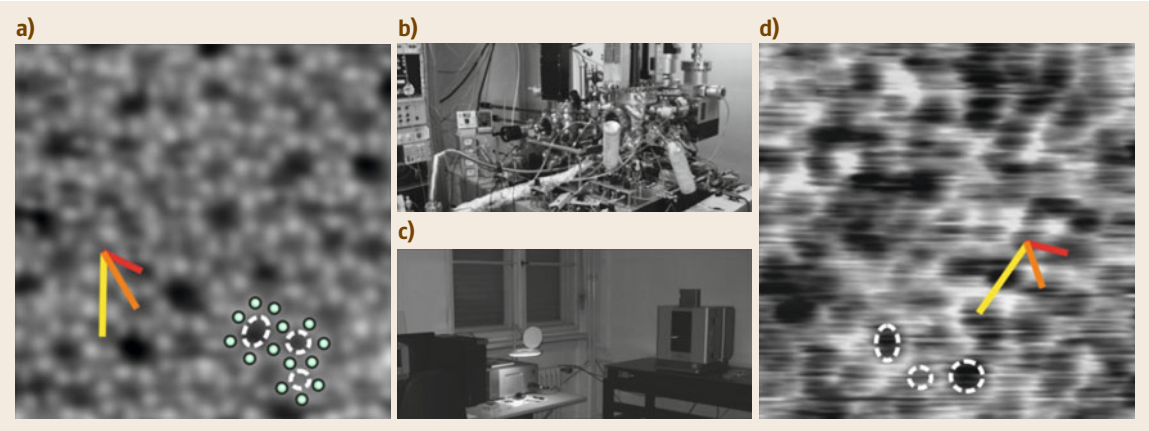

Fig. 10.41a–d An amorphous silica bilayer film with atomic resolution of silicon atoms by STM in UHV **(a)** and ring resolution by liquid-AFM in **(d)**. Both images have a scan frame of 5 nm × 5 nm. *Red*, *orange*, and *yellow measurement bars* show examples of ring center–center distances for the first three families of ring neighbors identified in the amorphous silica bilayer. Several individual rings are marked in each image. **(d)** Reprinted from [10.250], with the permission of AIP Publishing. The measurement in **(a)** has been obtained with a custom-made low temperature ultra-high vacuum STM shown in **(b)** while **(d)** has been taken with a commercial liquid-AFM photographed in **(c)**

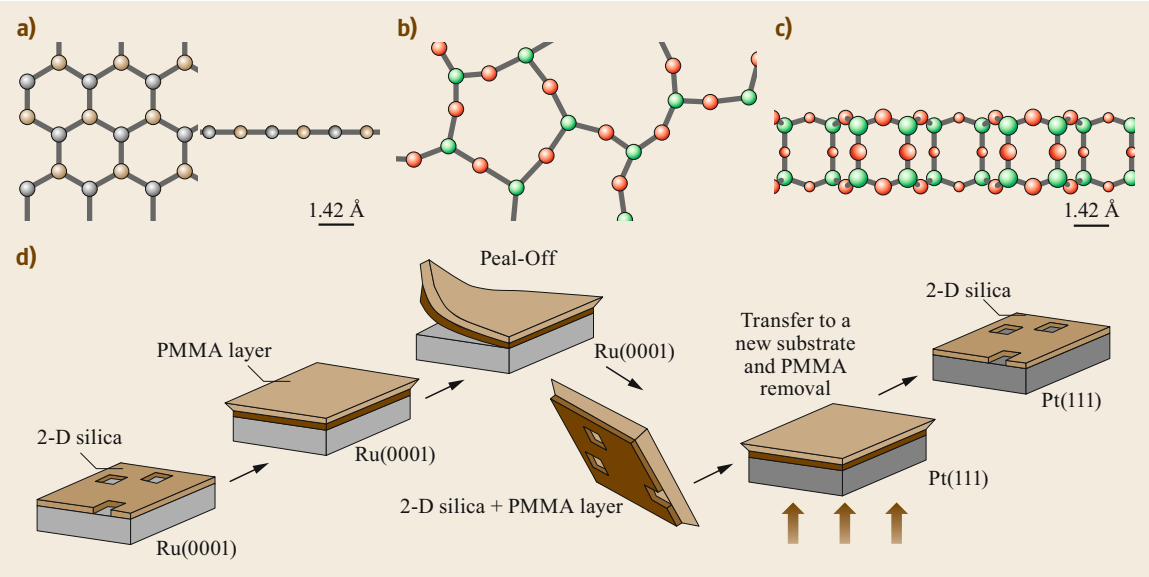

Fig. 10.42 **(a)** Top and side view of a boron nitride layer in comparison to the silica bilayer **(b)** and **(c)**. In contrast to graphene both shown 2-D materials are wide band-gap insulators. **(d)** Schematic of the transfer procedure: silica bilayer on ruthenium substrate, spin coating of system with polymethyl methacrylate (PMMA) layer, mechanical exfoliation of PMMA, silica adheres to PMMA layer, silica supported on PMMA layer, placing the PMMA-supported silica layer on clean Pt(111) substrate, subsequent heat treatment, after PMMA removal, silica is supported on Pt(111) substrate. Reprinted (adapted) with permission from [10.57]. Copyright (2016) American Chemical Society

10.5.3 Peal-Off Experiments with Silica Films

Silica bilayers are an ideal candidate material for inclusion in two-dimensional nanoelectronic heterostructures due to its insulating character and high degree of structural integrity under ambient conditions [10.252]. Novel nanoelectronic heterostructure devices are designed with tailored properties by bottom-up production which combines two-dimensional insulating, semi-

conducting, and conducting materials. Numerous options exist for two-dimensional semiconductors, yet to date hexagonal boron nitride is the most widely used two-dimensional insulator. Silica bilayers are wide band-gap insulators with band gaps on the order of 6.5–7.3 eV [10.253, 254] and provide a two-dimensional analog of the SiO_x insulating layer used in the semi-conductor industry. In order to use bilayer silica for nanoelectronic devices, transfer of the bilayer from the growth substrate is necessary. This procedure has been sketched in Fig. 10.42. Silica bilayers are grown on Ru(0001) in vacuum and subsequently moved to ambient [10.57]. The silica bilayer has been successfully transferred to a new Pt(111) substrate via polymer assisted mechanical exfoliation. The transferred sample is heated to remove polymer residue and the structural integrity of the silica film is maintained throughout the process. With this achievement, silica has been added to the toolbox of two-dimensional materials for nanoelectronics, bridging the gap between fundamental structural studies and technological applications.

10.6 Conclusions

In this chapter we have compiled a range of experimental results to address some of the important questions that need to be understood if aiming at an atomistic understanding of chemical processes at oxide surfaces. The experiments described here use well-defined, single crystalline oxide films as model systems, which were proven to be suitable to address the properties of oxide surfaces and allow for their characterization with the rigor of modern surface science methodology. The basis for the atomistic understanding is a detailed knowledge of the structural properties of the system at hand. Using some selected systems, we have shown how the machinery of modern surface science can be used to determine the structural properties of oxide surfaces. It is important to emphasize the increased complexity of oxide surface structures in comparison to metals and we have addressed some of these such as surface termination and defect structures, among others. Oxides cover a wide range of chemical and physical materials properties from wide band-gap insulators to metallic systems. We provide some examples how the properties of the oxides can be tuned focusing on the ability to control charge transfer processes at the surface of oxides using the film thickness or appropriate doping of the system as exemplified for alkaline earth oxide surfaces. Oxide surfaces play a pivotal role in heterogeneous catalysis not only as support for transition metal nanoparticles but also as catalytically active phases. In addition, alterations of the surface structure may occur by reaction of the surface with gas phase species not necessarily being educts of the chemical reaction. To this end as well as because of its great importance for a variety of technological and natural processes, the interaction of water with oxide surfaces is of great interest. We have compiled a variety of experimental results to indicate the level of information that may be obtained. Furthermore, as an example for transition metal oxide surfaces we allude to vanadia in order to show how a detailed characterization of surface species on model systems can help to gain insight that may also be transferred onto more complex powder systems. Apart from these studies we demonstrate the ability to study the kinetics of chemical reactions on such model systems in great detail using molecular beam techniques. The model systems also lend themselves to studies at elevated pressures to learn about modifications of the surface under those conditions, which may have direct consequences for the chemical reactivity of the system. Finally, we discuss the possibility to transfer these systems prepared under UHV conditions into the ambient, exemplifying this by discussing the growth of metal nanoparticles from solution as well as the ability to peal silica films off the supporting metal surface.

References

10.1 H.-J. Freund: The surface science of catalysis and more, using ultrathin oxide films as templates: A perspective, J. Am. Chem. Soc. **138**, 8985–8996 (2016)

10.2 G. Ertl: Reactions at surfaces: From atoms to complexity (Nobel lecture), Angew. Chem. Int. Ed. **47**, 3524–3535 (2008)

10.3 P.A. Cox: *Transition Metal Oxides. An Introduction to Their Electronic Structure and Properties* (Clarendon, Oxford 1992)

10.4 V.E. Henrich, P.A. Cox: *The Surface Science of Metal Oxides* (Cambridge Univ. Press, Cambridge 1994)

10.5 C. Noguera: *Physics and Chemistry at Oxide Surfaces* (Cambridge Univ. Press, Cambridge 1996)

10.6 U. Diebold: The surface science of titanium dioxide, Surf. Sci. Rep. **48**, 53–229 (2003)

10.7 C.L. Pang, R. Lindsay, G. Thornton: Structure of clean and adsorbate-covered single-crystal rutile TiO_2 surfaces, Chem. Rev. **113**, 3887–3948 (2013)

10.8 H.J. Freund, H. Kuhlenbeck, V. Staemmler: Oxide surfaces, Rep. Prog. Phys. **59**, 283–347 (1996)

10.9 M. Bäumer, H.-J. Freund: Metal deposits on well-ordered oxide films, Prog. Surf. Sci. **61**, 127–198 (1999)

10.10 C.R. Henry: Surface studies of supported model catalysts, Surf. Sci. Rep. **31**, 231–326 (1998)

10.11 C.T. Campbell: Ultrathin metal films and particles on oxide surfaces: Structural, electronic and chemisorption properties, Surf. Sci. Rep. **27**, 1–111 (1997)

10.12 D.W. Goodman: Model catalysts: From extended single crystals to supported particles, Surf. Rev. Lett. **2**, 9–24 (1995)

10.13 J. Libuda, H.-J. Freund: Reaction kinetics on complex model catalysts under single scattering conditions, J. Phys. Chem. **B106**, 4901–4915 (2002)

10.14 H. Kuhlenbeck, S. Shaikhutdinov, H.-J. Freund: Well-ordered transition metal oxide layers in model catalysis: A series of case studies, Chem. Rev. **113**, 3986–4034 (2013)

10.15 G. Pacchioni, H.-J. Freund: Electron transfer at oxide surfaces. The MgO paradigm: From defects to ultrathin films, Chem. Rev. **113**, 4035–4072 (2013)

10.16 H.-J. Freund, G. Pacchioni: Oxide ultra-thin films on metals: New materials for the design of supported metal catalysts, Chem. Soc. Rev. **37**, 2224–2242 (2008)

10.17 H.J. Freund, N. Nilius, T. Risse, S. Schauermann: A fresh look at an old nano-technology: Catalysis, Phys. Chem. Chem. Phys. **16**, 8148–8167 (2014)

10.18 H.-J. Freund: Oxide films as catalytic materials and models of real catalysts. In: *Oxide Ultrathin Films: Science and Technology*, ed. by G. Pacchioni, S. Valeri (Wiley-VCH, Weinheim 2012) pp. 145–179

10.19 F.P. Netzer, A. Fortunelli: *Oxide Materials at the Two-Dimensional Limit*, Springer Series in Materials Science (Springer, Cham 2016)

10.20 D. Löffler, J.J. Uhlrich, M. Baron, B. Yang, X. Yu, L. Lichtenstein, L. Heinke, C. Büchner, M. Heyde, S. Shaikhutdinov, H.-J. Freund, R. Włodarczyk, M. Sierka, J. Sauer: Growth and structure of crystalline silica sheet on Ru(0001), Phys. Rev. Lett. **105**, 146104 (2010)

10.21 L. Lichtenstein, M. Heyde, H.-J. Freund: Atomic arrangement in two-dimensional silica: From crystalline to vitreous structures, J. Phys. Chem. C **116**, 20426–20432 (2012)

10.22 L. Lichtenstein, C. Büchner, B. Yang, S. Shaikhutdinov, M. Heyde, M. Sierka, R. Włodarczyk, J. Sauer, H.-J. Freund: The atomic structure of a metal-supported vitreous thin silica film, Angew. Chem. Int. Ed. **51**, 404–407 (2012)

10.23 J.A. Boscoboinik, X. Yu, B. Yang, F.D. Fischer, R. Włodarczyk, M. Sierka, S. Shaikhutdinov, J. Sauer, H.-J. Freund: Modeling zeolites with metal-supported two-dimensional aluminosilicate films, Angew. Chem. Int. Ed. **51**, 6005–6008 (2012)

10.24 S. Foerster, K. Meinel, R. Hammer, M. Trautmann, W. Widdra: Quasicrystalline structure formation in a classical crystalline thin-film system, Nature **502**, 215–218 (2013)

10.25 G. Pacchioni, L. Giordano, M. Baistrocchi: Charging of metal atoms on ultrathin MgO/Mo(100) films, Phys. Rev. Lett. **94**, 226104 (2005)

10.26 D. Ricci, A. Bongiorno, G. Pacchioni, U. Landman: Bonding trends and dimensionality crossover of gold nanoclusters on metal-supported MgO thin films, Phys. Rev. Lett. **97**, 036106 (2006)

10.27 M. Sterrer, T. Risse, M. Heyde, H.-P. Rust, H.-J. Freund: Crossover from three-dimensional to two-dimensional geometries of Au nanostructures on thin MgO(001) films: A confirmation of theoretical predictions, Phys. Rev. Lett. **98**, 206103 (2007)

10.28 Y. Martynova, B.H. Liu, M.E. McBriarty, I.M.N. Groot, M.J. Bedzyk, S. Shaikhutdinov, H.J. Freund: CO oxidation over ZnO films on Pt(111) at near-atmospheric pressures, J. Catal. **301**, 227–232 (2013)

10.29 I.X. Green, W.J. Tang, M. Neurock, J.T. Yates: Spectroscopic observation of dual catalytic sites during oxidation of CO on a Au/TiO_2 catalyst, Science **333**, 736–739 (2011)

10.30 J.A. Rodriguez, S. Ma, P. Liu, J. Hrbek, J. Evans, M. Pérez: Activity of CeO_x and TiO_x nanoparticles grown on Au(111) in the water-gas shift reaction, Science **318**, 1757–1760 (2007)

10.31 K. Hayek, M. Fuchs, B. Klötzer, W. Reichl, G. Rupprechter: Studies of metal–support interactions with "real" and "inverted" model systems: Reactions of CO and small hydrocarbons with hydrogen on noble metals in contact with oxides, Top. Catal. **13**, 55–66 (2000)

10.32 M. Bowker, P. Stone, P. Morrall, R. Smith, R. Bennett, N. Perkins, R. Kvon, C. Pang, E. Fourre, M. Hall: Model catalyst studies of the strong metal–support interaction: Surface structure identified by STM on Pd nanoparticles on TiO_2(110), J. Catal. **234**, 172–181 (2005)

10.33 Z.H. Qin, M. Lewandowski, Y.N. Sun, S. Shaikhutdinov, H.J. Freund: Encapsulation of Pt nanoparticles as a result of strong metal-support interaction with Fe_3O_4(111), J. Phys. Chem. C **112**, 10209–10213 (2008)

10.34 Y.-N. Sun, Z.-H. Qin, M. Lewandowski, S. Kaya, S. Shaikhutdinov, H.-J. Freund: When an encapsulating oxide layer promotes reaction on noble metals: Dewetting and in situ formation of an "inverted" FeO_x/Pt catalyst, Catal. Lett. **126**, 31–35 (2008)

10.35 Y.N. Sun, Z.H. Qin, M. Lewandowski, E. Carrasco, M. Sterrer, S. Shaikhutdinov, H.J. Freund: Monolayer iron oxide film on platinum promotes low temperature CO oxidation, J. Catal. **266**, 359–368 (2009)

10.36 Y. Lei, M. Lewandowski, Y.-N. Sun, Y. Fujimori, Y. Martynova, I.M.N. Groot, R.J. Meyer, L. Giordano, G. Pacchioni, J. Goniakowski, C. Noguera, S. Shaikhutdinov, H.-J. Freund: CO+NO versus $CO+O_2$ reaction on monolayer FeO(111) films on Pt(111), ChemCatChem **3**, 671–674 (2011)

10.37 L. Giordano, M. Lewandowski, I.M.N. Groot, Y.N. Sun, J. Goniakowski, C. Noguera, S. Shaikhutdinov, G. Pacchioni, H.J. Freund: Oxygen-induced transformations of an FeO(111) film on Pt(111): A combined DFT and STM study, J. Phys. Chem. C **114**, 21504–21509 (2010)

10.38 M. Lewandowski, Y.N. Sun, Z.H. Qin, S. Shaikhutdinov, H.J. Freund: Promotional effect of metal encapsulation on reactivity of iron oxide supported Pt catalysts, Appl. Catal. A **391**, 407–410 (2011)

10.39 Y.N. Sun, L. Giordano, J. Goniakowski, M. Lewandowski, Z.H. Qin, C. Noguera, S. Shaikhutdinov, G. Pacchioni, H.J. Freund: The interplay between structure and CO oxidation catalysis on metal-supported ultrathin oxide films, Angew. Chem. Int. Ed. **49**, 4418–4421 (2010)

10.40 M.G. Willinger, W. Zhang, O. Bondarchuk, S. Shaikhutdinov, H.-J. Freund, R. Schlögl: A case of strong metal–support interactions: Combining advanced microscopy and model systems to elucidate the atomic structure of interfaces, Angew. Chem. Int. Ed. **53**, 5998–6001 (2014)

10.41 O. Dulub, W. Hebenstreit, U. Diebold: Imaging cluster surfaces with atomic resolution: The strong metal-support interaction state of Pt supported on TiO_2(110), Phys. Rev. Lett. **84**, 3646–3649 (2000)

10.42 Y. Cui, X. Shao, S. Prada, L. Giordano, G. Pacchioni, H.-J. Freund, N. Nilius: Surface defects and their impact on the electronic structure of Mo-doped CaO films: An STM and DFT study, Phys. Chem. Chem. Phys. **16**, 12764–12772 (2014)

10.43 Y. Cui, X. Shao, M. Baldofski, J. Sauer, N. Nilius, H.-J. Freund: Adsorption, activation, and dissociation of oxygen on doped oxides, Angew. Chem. Int. Ed. **52**, 11385–11387 (2013)

10.44 F. Stavale, X. Shao, N. Nilius, H.-J. Freund, S. Prada, L. Giordano, G. Pacchioni: Donor characteristics of transition-metal-doped oxides: Cr-doped MgO versus Mo-doped CaO, J. Am. Chem. Soc. **134**, 11380–11383 (2012)

10.45 X. Shao, N. Nilius, H.-J. Freund: Crossover from two- to three-dimensional gold particle shapes on CaO films of different thicknesses, Phys. Rev. B **85**, 115444 (2012)

10.46 X. Shao, N. Nilius, H.-J. Freund: Li/Mo codoping of CaO films: A means to tailor the equilibrium shape of Au deposits, J. Am. Chem. Soc. **134**, 2532–2534 (2012)

10.47 X. Shao, S. Prada, L. Giordano, G. Pacchioni, N. Nilius, H.-J. Freund: Tailoring the shape of metal ad-particles by doping the oxide support, Angew. Chem. Int. Ed. **50**, 11525–11527 (2011)

10.48 R.A. Bennett, P. Stone, M. Bowker: Scanning tunnelling microscopy studies of the reactivity of the TiO_2(110) surface: Re-oxidation and the thermal treatment of metal nanoparticles, Faraday Discuss. **114**, 267–277 (1999)

10.49 W. Mönch: *Electronic Properties of Semiconductor Interfaces* (Springer, Berlin, Heidelberg 2004)

10.50 S. Schäfer, S.A. Wyrzgol, R. Caterino, A. Jentys, S.J. Schoell, M. Hävecker, A. Knop-Gericke, J.A. Lercher, I.D. Sharp, M. Stutzmann: Platinum nanoparticles on gallium nitride surfaces: Effect of semiconductor doping on nanoparticle reactivity, J. Am. Chem. Soc. **134**, 12528–12535 (2012)

10.51 X. Song, E. Primorac, H. Kuhlenbeck, H.-J. Freund: Decoupling a thin well-ordered TiO_2(110) layer from a TiO_2(110) substrate with a Ti+Ta mixed oxide interlayer, J. Phys. Chem. C **120**, 8185–8190 (2016)

10.52 O. Karslioуglu, X. Song, H. Kuhlenbeck, H.-J. Freund: Mo+TiO_2(110) mixed oxide layer: Structure and reactivity, Top. Catal. **56**, 1389–1403 (2013)

10.53 X. Song, H. Kuhlenbeck, H.-J. Freund: Effect of vanadium admixing on the surface structure of TiO_2(110) under non-oxidizing conditions, Surf. Sci. **653**, 181–186 (2016)

10.54 H.P. Boehm, A. Clauss, G.O. Fischer, U. Hofmann: Das Adsorptionsverhalten sehr dünner Kohlenstoff-Folien, Z. Anorg. Allg. Chem. **316**, 119–127 (1962)

10.55 H.P. Boehm, R. Setton, E. Stumpp: Nomenclature and terminology of graphite intercalation compounds (IUPAC recommendations 1994), Pure Appl. Chem. **66**, 1893–1901 (1994)

10.56 K.S. Novoselov, A.K. Geim, S.V. Morozov, D. Jiang, Y. Zhang, S.V. Dubonos, I.V. Grigorieva, A.A. Firsov: Electric field effect in atomically thin carbon films, Science **306**, 666–669 (2004)

10.57 C. Büchner, Z.-J. Wang, K.M. Burson, M.-G. Willinger, M. Heyde, R. Schlögl, H.-J. Freund: A large-area transferable wide band gap 2D silicon dioxide layer, ACS Nano **10**, 7982–7989 (2016)

10.58 H.-J. Freund, M. Heyde, C. Büchner: *Transferable Silica Bilayer Film*, EP3217423A1 (EPO, Munich 2016)

10.59 P. Zhao, S. Desai, M. Tosun, T. Roy, H. Fang, A. Sachid, M. Amani, C. Hu, A. Javey: 2D layered materials: From materials properties to device applications. In: *IEEE Int. Electron Devices Meet. (IEDM)* (2015) pp. 27.23.21–27.23.24

10.60 M. Sterrer, N. Nilius, S. Shaikhutdinov, M. Heyde, T. Schmidt, H. Freund: Interaction of water with oxide thin film model systems, J. Mater. Res. **34**(3), 360–378 (2019)

10.61 N. Nilius: Properties of oxide thin films and their adsorption behavior studied by scanning tunneling microscopy and conductance spectroscopy, Surf. Sci. Rep. **64**, 595–659 (2009)

10.62 S. Surnev, M.G. Ramsey, F.P. Netzer: Vanadium oxide surface studies, Prog. Surf. Sci. **73**, 117–165 (2003)

10.63 G. Kresse, M. Schmid, E. Napetschnig, M. Shishkin, L. Köhler, P. Varga: Structure of the ultrathin aluminum oxide film on NiAl(110), Science **308**, 1440–1442 (2005)

10.64 S. Schintke, S. Messerli, M. Pivetta, F. Patthey, L. Libioulle, M. Stengel, A. De Vita, W.-D. Schneider: Insulator at the ultrathin limit: MgO on Ag(001), Phys. Rev. Lett. **87**, 2768011–2768014 (2001)

10.65 M. Klaua, D. Ullmann, J. Barthel, W. Wulfhekel, J. Kirschner, R. Urban, T.L. Monchesky, A. Enders, J.F. Cochran, B. Heinrich: Growth, structure, electronic, and magnetic properties of MgO/Fe(001) bilayers and Fe/MgO/Fe(001) trilayers, Phys. Rev. B **64**, 134411 (2001)

10.66 M.C. Wu, J.S. Corneille, C.A. Estrada, J.W. He, D.W. Goodman: Synthesis and characterization of ultra-thin MgO films on Mo(100), Chem. Phys. Lett. **182**, 472–478 (1991)

10.67 S. Benedetti, H.M. Benia, N. Nilius, S. Valeri, H.J. Freund: Morphology and optical properties of MgO thin films on Mo(001), Chem. Phys. Lett. **430**, 330–335 (2006)

10.68 X. Shao, P. Myrach, N. Nilius, H.J. Freund: Growth and morphology of calcium-oxide films grown on Mo(001), J. Phys. Chem. C **115**, 8784–8789 (2011)

10.69 N. Nilius, S. Benedetti, Y. Pan, P. Myrach, C. Noguera, L. Giordano, J. Goniakowski: Electronic and electrostatic properties of polar oxide nanostructures: MgO(111) islands on Au(111), Phys. Rev. B **86**, 205410 (2012)

10.70 J. Goniakowski, C. Finocchi, C. Noguera: Polarity of oxide surfaces and nanostructures, Rep. Prog. Phys. **71**, 016501–016555 (2008)

10.71 F. Finocchi, A. Barbier, J. Jupille, C. Noguera: Stability of rocksalt (111) polar surfaces: Beyond the octopole, Phys. Rev. Lett. **92**, 136101 (2004)

10.72 J. Pal, M. Smerieri, E. Celasco, L. Savio, L. Vattuone, M. Rocca: Morphology of monolayer MgO films on Ag(100): Switching from corrugated islands to extended flat terraces, Phys. Rev. Lett. **112**, 126102 (2014)

10.73 J. Pal, M. Smerieri, E. Celasco, L. Savio, L. Vattuone, R. Ferrando, S. Tosoni, L. Giordano, G. Pacchioni, M. Rocca: How growing conditions and interfacial oxygen affect the final morphology of MgO/Ag(100) films, J. Phys. Chem. C **118**, 26091–26102 (2014)

10.74 K.P. McKenna, A.L. Shluger: Electron-trapping polycrystalline materials with negative electron affinity, Nat. Mater. **7**, 859–862 (2008)

10.75 S. Benedetti, P. Torelli, S. Valeri, H.M. Benia, N. Nilius, G. Renaud: Structure and morphology of thin MgO films on Mo(001), Phys. Rev. B **78**, 195411–195418 (2008)

10.76 S. Benedetti, F. Stavale, S. Valeri, C. Noguera, H.J. Freund, J. Goniakowski, N. Nilius: Steering the growth of metal ad-particles via interface interactions between a MgO thin film and a Mo support, Adv. Funct. Mater. **23**, 75–80 (2013)

10.77 L. Giordano, F. Cinquini, G. Pacchioni: Tuning the surface metal work function by deposition of ultrathin oxide films: Density functional calculations, Phys. Rev. B **73**, 045414 (2006)

10.78 H.M. Benia, P. Myrach, N. Nilius, H.J. Freund: Structural and electronic characterization of the MgO/Mo(001) interface using STM, Surf. Sci. **604**, 435–441 (2010)

10.79 M. Sterrer, E. Fischbach, T. Risse, H.-J. Freund: Geometric characterization of a singly charged oxygen vacancy on a single-crystalline MgO(001) film by electron paramagnetic resonance spectroscopy, Phys. Rev. Lett. **94**, 186101 (2005)

10.80 M. Sterrer, E. Fischbach, M. Heyde, N. Nilius, H.P. Rust, T. Risse, H.J. Freund: Electron paramagnetic resonance and scanning tunneling microscopy investigations on the formation of F^+ and F^0 color centers on the surface of thin MgO(001) films, J. Phys. Chem. B **110**, 8665–8669 (2006)

10.81 M. Sterrer, M. Heyde, M. Novicki, N. Nilius, T. Risse, H.P. Rust, G. Pacchioni, H.J. Freund: Identification of color centers on MgO(001) thin films with scanning tunneling microscopy, J. Phys. Chem. B **110**, 46–49 (2006)

10.82 T. König, G.H. Simon, H.P. Rust, G. Pacchioni, M. Heyde, H.J. Freund: Measuring the charge state of point defects on MgO/Ag(001), J. Am. Chem. Soc. **131**, 17544–17545 (2009)

10.83 H.M. Benia, P. Myrach, A. Gonchar, T. Risse, M. Nilius, H.J. Freund: Electron trapping in misfit dislocations of MgO thin films, Phys. Rev. B **81**, 241415 (2010)

10.84 K.P. McKenna, A.L. Shluger: First-principles calculations of defects near a grain boundary in MgO, Phys. Rev. B **79**, 224116 (2009)

10.85 H.M. Benia, P. Myrach, N. Nilius: Photon emission spectroscopy of thin MgO films with the STM: From a tip-mediated to an intrinsic emission characteristic, New J. Phys. **10**, 013010 (2008)

10.86 E.D.L. Rienks, N. Nilius, H.P. Rust, H.J. Freund: Surface potential of a polar oxide film: FeO on Pt(111), Phys. Rev. B **71**, 2414041–2414044 (2005)

10.87 M. Sterrer, T. Risse, H.J. Freund: CO adsorption on the surface of MgO(001) thin films, Appl. Catal. A **307**, 58–61 (2006)

10.88 L.M. Molina, B. Hammer: Some recent theoretical advances in the understanding of the catalytic activity of Au, Appl. Catal. A **291**, 21–31 (2005)

10.89 B. Yoon, H. Häkkinen, U. Landman, A.S. Wörz, J.M. Antonietti, S. Abbet, K. Judai, U. Heiz: Charging effects on bonding and catalyzed oxidation of CO on Au-8 clusters on MgO, Science **307**, 403–407 (2005)

10.90 S. Sastry, P.G. Debenedetti, F.H. Stillinger: Signatures of distinct dynamical regimes in the energy landscape of a glass-forming liquid, Nature **393**, 554–557 (1998)

10.91 R. Zallen: *The Physics of Amorphous Solids* (Wiley-VCH, Weinheim 2004)

10.92 L. Berthier, G. Biroli: Theoretical perspective on the glass transition and amorphous materials, Rev. Mod. Phys. **83**, 587–645 (2011)

10.93 J.C. Mauro, E.D. Zanotto: Two centuries of glass research: Historical trends, current status, and grand challenges for the future, Int. J. Appl. Glass Sci. **5**, 313–327 (2014)

10.94 W.H. Zachariasen: The atomic arrangement in glass, J. Am. Chem. Soc. **54**, 3841–3851 (1932)

10.95 L. Lichtenstein, M. Heyde, H.-J. Freund: Crystalline-vitreous interface in two dimensional silica, Phys. Rev. Lett. **109**, 106101 (2012)

10.96 X. Yu, B. Yang, J.A. Boscoboinik, S. Shaikhutdinov, H.-J. Freund: Support effects on the atomic structure of ultrathin silica films on metals, Appl. Phys. Lett. **100**, 151608 (2012)

10.97 P.Y. Huang, S. Kurasch, A. Srivastava, V. Skakalova, J. Kotakoski, A.V. Krasheninnikov, R. Hovden, Q. Mao, J.C. Meyer, J. Smet, D.A. Muller, U. Kaiser: Direct imaging of a two-dimensional silica glass on graphene, Nano Lett. **12**, 1081–1086 (2012)

10.98 E.I. Altman, U.D. Schwarz: Structural and electronic heterogeniety of two dimensional amorphous silica layers, Adv. Mater. Interfaces **1**, 1400108 (2014)

10.99 R.M. Cornell, U. Schwertmann: *The Iron Oxides* (Wiley-VCH, Weinheim 2004)

10.100 G. Ertl, H. Knözinger, F. Schueth, J. Weitkamp: *Handbook of Heterogeneous Catalysis* (VCH, Weinheim 2008)

10.101 R. Zboril, M. Mashlan, D. Petridis: Iron(III) oxides from thermal processessynthesis, structural and magnetic properties, Mössbauer spectroscopy characterization, and applications, Chem. Mater. **14**, 969–982 (2002)

10.102 W. Weiss, W. Ranke: Surface chemistry and catalysis on well-defined epitaxial iron-oxide layers, Prog. Surf. Sci. **70**, 1–151 (2002)

10.103 N.G. Condon, F.M. Leibsle, T. Parker, A.R. Lennie, D.J. Vaughan, G. Thornton: Biphase ordering on Fe_3O_4(111), Phys. Rev. B **55**, 15885–15894 (1997)

10.104 A. Barbieri, W. Weiss, M.A.V. Hove, G.A. Somorjai: Magnetite Fe_3O_4(111): Surface structure by LEED crystallography and energetics, Surf. Sci. **302**, 259–279 (1994)

10.105 G.S. Parkinson: Iron oxide surfaces, Surf. Sci. Rep. **71**, 272–365 (2016)

10.106 A. Sala, H. Marchetto, Z.H. Qin, S. Shaikhutdinov, T. Schmidt, H.-J. Freund: Defects and inhomogeneities in Fe_3O_4(111) thin film growth on Pt(111), Phys. Rev. B **86**, 155430 (2012)

10.107 N. Nilius, E.D.L. Rienks, H.-P. Rust, H.-J. Freund: Self-organization of gold atoms on a polar FeO(111) surface, Phys. Rev. Lett. **95**, 066101 (2005)

10.108 M. Melzer, J. Urban, H. Sack-Kongehl, K. Weiss, H.-J. Freund, R. Schlögl: Preparation of vanadium and vanadium oxide clusters by means of inert gas aggregation, Catal. Lett. **81**, 219–221 (2002)

10.109 W. Weiss, M. Ritter: Metal oxide heteroepitaxy: Stranski–Krastanov growth of iron oxides on Pt(111), Phys. Rev. B **59**, 5201–5213 (1999)

10.110 D.T. Margulies, F.T. Parker, M.L. Rudee, F.E. Spada, J.N. Chapman, P.R. Aitchison, A.E. Berkowitz: Origin of the anomalous magnetic behavior in single crystal Fe_3O_4 films, Phys. Rev. Lett. **79**, 5201–5165 (1997)

10.111 M. Ritter, W. Weiss: Fe_3O_4(111) surface structure determined by LEED crystallography, Surf. Sci. **432**, 81–94 (1999)

10.112 F. Genuzio, A. Sala, T. Schmidt, D. Menzel, H.-J. Freund: Interconversion of α-Fe_2O_3 and Fe_3O_4 thin films: Mechanisms, morphology, and evidence for unexpected substrate participation, J. Phys. Chem. C **118**, 29068–29076 (2014)

10.113 F. Genuzio, A. Sala, T. Schmidt, D. Menzel, H.-J. Freund: Phase transformations in thin iron oxide films: Spectromicroscopic study of velocity and shape of the reactions fronts, Surf. Sci. **648**, 177–187 (2016)

10.114 C. Schlueter, M. Lubbe, A.M. Gigler, W. Moritz: Growth of iron oxides on Ag(111)—Reversible Fe_2O_3/Fe_3O_4 transformation, Surf. Sci. **605**, 1986–1993 (2011)

10.115 B. Grzybowska-Swierkosz, F. Trifiro, J.C. Vedrine: Vanadia catalysts for selective oxidation of hydrocarbons and their derivatives, Appl. Catal. A **157**(1–2), 1–425 (1997)

10.116 A. Chieregato, J.M.L. Nieto, F. Cavani: Mixed-oxide catalysts with vanadium as the key element for gas-phase reactions, Coord. Chem. Rev. **301**, 3–23 (2015)

10.117 B.B. Jiang, S.L. Yuan, N. Chen, H.B. Wang, J.D. Wang, Z.L. Huang: Reaction kinetics of n-butane oxidation on VPO catalyst, Prog. Chem. **27**, 1679–1688 (2015)

10.118 M. Sutradhar, L. Martins, M. da Silva, A.J.L. Pombeiro: Vanadium complexes: Recent progress in oxidation catalysis, Coord. Chem. Rev. **301**, 200–239 (2015)

10.119 L. Artiglia, S. Agnoli, G. Granozzi: Vanadium oxide nanostructures on another oxide: The viewpoint from model catalysts studies, Coord. Chem. Rev. **301**, 106–122 (2015)

10.120 C.A. Carrero, R. Schloegl, I.E. Wachs, R. Schomaecker: Critical literature review of the kinetics for the oxidative dehydrogenation of propane over well-defined supported vanadium oxide catalysts, ACS Catalysis **4**, 3357–3380 (2014)

10.121 S. Guimond, D. Göbke, Y. Romanyshyn, J.M. Sturm, M. Naschitzki, H. Kuhlenbeck, H.-J. Freund: Growth and characterization of ultrathin V_2O_y($y \approx 5$) films on Au(111), J. Phys. Chem. C **112**, 12363–12373 (2008)

10.122 S. Guimond, J.M. Sturm, D. Göbke, Y. Romanyshyn, M. Naschitzki, H. Kuhlenbeck, H.J. Freund: Well-ordered V_2O_5(001) thin films on Au(111): Growth and thermal stability, J. Phys. Chem. C **112**, 11835–11846 (2008)

10.123 F.E. Feiten, H. Kuhlenbeck, H.J. Freund: Surface structure of V_2O_3(0001): A combined I/V-LEED and STM study, J. Phys. Chem. C **119**, 22961–22969 (2015)

10.124 F.E. Feiten, J. Seifert, J. Paier, H. Kuhlenbeck, H. Winter, J. Sauer, H.J. Freund: Surface structure of V_2O_3(0001) revisited, Phys. Rev. Lett. **114**, 216101 (2015)

10.125 A.C. Dupuis, M. Abu Haija, B. Richter, H. Kuhlenbeck, H.J. Freund: V_2O_3(0001) on Au(111) and W(110): Growth, termination and electronic structure, Surf. Sci. **539**, 99–112 (2003)

10.126 J. Schoiswohl, M. Sock, S. Surnev, M.G. Ramsey, F.P. Netzer, G. Kresse, J.N. Andersen: V_2O_3(0001)

surface terminations: From oxygen- to vanadium-rich, Surf. Sci. **555**, 101 (2004)
10.127 A.J. Window, A. Hentz, D.C. Sheppard, G.S. Parkinson, H. Niehus, D. Ahlbehrendt, T.C.Q. Noakes, P. Bailey, D.P. Woodruff: V_2O_3(0001) surface termination: Phase equilibrium, Phys. Rev. Lett. **107**, 016105 (2011)
10.128 H. Niehus, R.P. Blum, D. Ahlbehrendt: Structure of vanadium oxide (V_2O_3) grown on Cu_3Au(100), Surf. Rev. Lett. **10**, 353–359 (2003)
10.129 B. Tepper, B. Richter, A.C. Dupuis, H. Kuhlenbeck, C. Hucho, P. Schilbe, M.A. bin Yarmo, H.J. Freund: Adsorption of molecular and atomic hydrogen on vacuum-cleaved V_2O_5(001), Surf. Sci. **496**, 64–72 (2002)
10.130 A. Atrei, U. Bardi, C. Tarducci, G. Rovida: Growth, composition, and structure of ultrathin vanadium films deposited on the SnO_2(110) surface, J. Phys. Chem. B **104**, 3121–3129 (2000)
10.131 A. Atrei, U. Bardib, B. Cortigiani, G. Rovida: XPD study of vanadium oxide films grown on the SnO_2(110) surface, Surf. Rev. Lett. **6**, 1187–1193 (1999)
10.132 Y. Romanyshyn, S. Guimond, D. Göbke, J.M. Sturm, H. Kuhlenbeck, J. Döbler, M.V. Ganduglia-Pirovano, J. Sauer, H.J. Freund: Methanol adsorption on V_2O_3(0001), Top. Catal. **54**, 669–684 (2011)
10.133 P.W. Tasker: Stability of ionic-crystal surfaces, J. Phys. C **12**, 4977–4984 (1979)
10.134 A.J. Window, A. Hentz, D.C. Sheppard, G.S. Parkinson, D.P. Woodruff, W. Unterberger, T.C.Q. Noakes, P. Bailey, M.V. Ganduglia-Pirovano, J. Sauer: The structure of epitaxial V_2O_3 films and their surfaces: A medium energy ion scattering study, Surf. Sci. **606**, 1716–1727 (2012)
10.135 J. Seifert, E. Meyer, H. Winter, H. Kuhlenbeck: Surface termination of an ultrathin V_2O_3-film on Au(111) studied via ion beam triangulation, Surf. Sci. **606**, L41–L44 (2012)
10.136 F. Sedona, G.A. Rizzi, S. Agnoli, F. Xamena, A. Papageorgiou, D. Ostermann, M. Sambi, P. Finetti, K. Schierbaum, G. Granozzi: Ultrathin TiOx films on Pt(111): A LEED, XPS, and STM investigation, J. Phys. Chem. B **109**, 24411–24426 (2005)
10.137 C.M. Yim, C.L. Pang, G. Thornton: Oxygen vacancy origin of the surface band-gap state of TiO_2(110), Phys. Rev. Lett. **104**, 036806 (2010)
10.138 S. Wendt, P.T. Sprunger, E. Lira, G.K.H. Madsen, Z. Li, J.Ø. Hansen, J. Matthiesen, A. Blekinge-Rasmussen, E. Lægsgaard, B. Hammer, F. Besenbacher: The role of interstitial sites in the Ti3d defect state in the band gap of titania, Science **320**, 1755–1759 (2008)
10.139 C. Di Valentin, G. Pacchioni, A. Selloni: Reduced and n-type doped TiO_2: Nature of Ti^{3+} species, J. Phys. Chem. C **113**, 20543–20552 (2009)
10.140 S. Wendt, R. Schaub, J. Matthiesen, E.K. Vestergaard, E. Wahlstrom, M.D. Rasmussen, P. Thostrup, L.M. Molina, E. Laegsgaard, I. Stensgaard, B. Hammer, F. Besenbacher: Oxygen vacancies on TiO_2(110) and their interaction with H_2O and O_2: A combined high-resolution STM and DFT study, Surf. Sci. **598**, 226–245 (2005)
10.141 M. Li, W. Hebenstreit, U. Diebold, A.M. Tyryshkin, M.K. Bowman, G.G. Dunham, M.A. Henderson: The influence of the bulk reduction state on the surface structure and morphology of rutile TiO_2(110) single crystals, J. Phys. Chem. B **104**, 4944–4950 (2000)
10.142 M. Yulikov, M. Sterrer, M. Heyde, H.P. Rust, T. Risse, H.-J. Freund, G. Pacchioni, A. Scagnelli: Binding of single gold atoms on thin MgO(001) films, Phys. Rev. Lett. **96**, 146804 (2006)
10.143 M. Sterrer, M. Yulikov, T. Risse, H.-J. Freund, J. Carrasco, F. Illas, C. Di Valentin, L. Giordano, G. Pacchioni: When the reporter induces the effect: Unusual IR spectra of CO on Au_1/MgO(001)/Mo(001), Angew. Chem. Int. Ed. **45**, 2633–2635 (2006)
10.144 L. Giordano, G. Pacchioni: Charge transfers at metal/oxide interfaces: A DFT study of formation of K^+ and Au^- species on MgO/Ag(100) ultra-thin films from deposition of neutral atoms, Phys. Chem. Chem. Phys. **8**, 3335–3341 (2006)
10.145 P. Frondelius, A. Hellman, K. Honkala, H. Häkkinen, H. Grönbeck: Charging of atoms, clusters, and molecules on metal-supported oxides: A general and long-ranged phenomenon, Phys. Rev. B **78**, 085426–085427 (2008)
10.146 J. Goniakowski, C. Noguera: Electronic states and schottky barrier height at metal/MgO(100) interfaces, Interface Sci. **12**, 93–103 (2004)
10.147 H. Grönbeck: Mechanism for NO_2 charging on metal supported MgO, J. Phys. Chem. B **110**, 11977–11981 (2006)
10.148 A. Gonchar, T. Risse, H.-J. Freund, L. Giordano, C. Di Valentin, G. Pacchioni: Activation of oxygen on MgO: O_2^- radical ion formation on thin, metal-supported MgO(001) films, Angew. Chem. Int. Ed. **50**, 2635–2638 (2011)
10.149 J. Tersoff, D.R. Hamann: Theory of the scanning tunneling microscope, Phys. Rev. B **31**, 805 (1985)
10.150 M. Sterrer, T. Risse, U. Martinez Pozzoni, L. Giordano, M. Heyde, H.-P. Rust, G. Pacchioni, H.-J. Freund: Control of the charge state of metal atoms on thin MgO films, Phys. Rev. Lett. **98**, 096107 (2007)
10.151 J. Repp, G. Meyer, F.E. Olsson, M. Persson: Controlling the charge state of individual gold adatoms, Science **305**, 493–495 (2004)
10.152 K. Honkala, H. Häkkinen: Au adsorption on regular and defected thin MgO(100) films supported by Mo, J. Phys. Chem. C **111**, 4319–4327 (2007)
10.153 A. Hellman, S. Klacar, H. Grönbeck: Low temperature CO oxidation over supported ultrathin MgO films, J. Am. Chem. Soc. **131**, 16636–16637 (2009)
10.154 P. Frondelius, H. Häkkinen, K. Honkala: Adsorption and activation of O_2 at Au chains on MgO/Mo thin films, Phys. Chem. Chem. Phys. **12**, 1483–1492 (2010)
10.155 H. Schlienz, M. Beckendorf, U.J. Katter, T. Risse, H.-J. Freund: Electron-spin-resonance investigations of the molecular-motion of NO_2 on

Al_2O_3(111) under ultrahigh-vacuum conditions, Phys. Rev. Lett. **74**, 761–764 (1995)
10.156 M. Chiesa, E. Giamello, M.C. Paganini, Z. Sojka, D.M. Murphy: Continuous wave electron paramagnetic resonance investigation of the hyperfine structure of $^{17}O_2^-$ adsorbed on the MgO surface, J. Chem. Phys. **116**, 4266–4274 (2002)
10.157 G. Pacchioni, A.M. Ferrari, E. Giamello: Cluster model of O_2^- adsorption on regular and defect sites and F_s centers of the MgO(100) surface, Chem. Phys. Lett. **255**, 58–64 (1996)
10.158 M. Sterrer, O. Diwald, E. Knözinger: Vacancies and electron deficient surface anions on the surface of MgO nanoparticles, J. Phys. Chem. B **104**, 3601–3607 (2000)
10.159 X. Lin, N. Nilius, H.J. Freund, M. Walter, P. Frondelius, K. Honkala, H. Häkkinen: Quantum well states in two-dimensional gold clusters on MgO thin films, Phys. Rev. Lett. **102**, 206801 (2009)
10.160 N. Nilius, M.V. Ganduglia-Pirovano, V. Brazdova, M. Kulawik, J. Sauer, H.J. Freund: Counting electrons transferred through a thin alumina film into Au chains, Phys. Rev. Lett. **100**, 096802 (2008)
10.161 X. Lin, N. Nilius, M. Sterrer, P. Koskinen, H. Häkkinen, H.-J. Freund: Characterizing low-coordinated atoms at the periphery of MgO-supported Au islands using scanning tunneling microscopy and electronic structure calculations, Phys. Rev. B **81**, 153406 (2010)
10.162 M. Walter, P. Frondelius, K. Honkala, H. Häkkinen: Electronic structure of MgO-supported Au clusters: Quantum dots probed by scanning tunneling microscopy, Phys. Rev. Lett. **99**, 096102 (2007)
10.163 C. Kittel: *Introduction to Solid State Physics* (Wiley, New York 2005)
10.164 A.A. Herzing, C.J. Kiely, A.F. Carley, P. Landon, G.J. Hutchings: Identification of active gold nanoclusters on iron oxide supports for CO oxidation, Science **321**, 1331–1335 (2008)
10.165 E.W. McFarland, H. Metiu: Catalysis by doped oxides, Chem. Rev. **113**, 4391–4427 (2013)
10.166 J. Robertson, S.J. Clark: Limits to doping in oxides, Phys. Rev. B **83**, 075303 (2011)
10.167 H.Y. Kim, H.M. Lee, R.G.S. Pala, V. Shapovalov, H. Metiu: CO oxidation by rutile TiO_2(110) doped with V, W, Cr, Mo, and Mn, J. Phys. Chem. C **112**, 12398–12408 (2008)
10.168 E.N. Sgourou, D. Timerkaeva, C.A. Londos, D. Aliprantis, A. Chroneos, D. Caliste, P. Pochet: Impact of isovalent doping on the trapping of vacancy and interstitial related defects in Si, J. Appl. Phys. **113**, 113506 (2013)
10.169 S. Prada, L. Giordano, G. Pacchioni: Charging of gold atoms on doped MgO and CaO: Identifying the key parameters by DFT calculations, J. Phys. Chem. C **117**, 9943–9951 (2013)
10.170 F. Stavale, N. Nilius, H.J. Freund: Cathodoluminescence of near-surface centres in Cr-doped MgO(001) thin films probed by scanning tunnelling microscopy, New J. Phys. **14**, 033006 (2012)
10.171 G. Pacchioni, J.M. Ricart, F. Illas: Ab-initio cluster model-calculations on the chemisorption of CO_2 and SO_2 probe molecules on MgO and CaO(100) surfaces—A theoretical measure of oxide basicity, J. Am. Chem. Soc. **116**, 10152–10158 (1994)
10.172 Z. Hu, B. Li, X. Sun, H. Metiu: Chemistry of doped oxides: The activation of surface oxygen and the chemical compensation effect, J. Phys. Chem. C **115**, 3065–3074 (2011)
10.173 B. Li, H. Metiu: DFT studies of oxygen vacancies on undoped and doped La_2O_3 surfaces, J. Phys. Chem. C **114**, 12234–12244 (2010)
10.174 P. Myrach, N. Nilius, S.V. Levchenko, A. Gonchar, T. Risse, K.P. Dinse, L.A. Boatner, W. Frandsen, R. Horn, H.J. Freund, R. Schlögl, M. Scheffler: Temperature-dependent morphology, magnetic and optical properties of Li-doped MgO, ChemCatChem **2**, 854–862 (2010)
10.175 S. Lany, J. Osorio-Guillén, A. Zunger: Origins of the doping asymmetry in oxides: Hole doping in NiO versus electron doping in ZnO, Phys. Rev. B **75**, 241203(R) (2007)
10.176 F. Bebensee, V. Voigts, W. Maus-Friedrichs: The adsorption of oxygen and water on Ca and CaO films studied with MIES, UPS and XPS, Surf. Sci. **602**, 1622–1630 (2008)
10.177 B.C. Stipe, M.A. Rezaei, W. Ho, S. Gao, M. Persson, B.I. Lundqvist: Single-molecule dissociation by tunneling electrons, Phys. Rev. Lett. **78**, 4410–4413 (1997)
10.178 Y. Cui, N. Nilius, H.-J. Freund, S. Prada, L. Giordano, G. Pacchioni: Controlling the charge state of single Mo dopants in a CaO film, Phys. Rev. B **88**, 205421 (2013)
10.179 Y. Cui, C. Stiehler, N. Nilius, H.-J. Freund: Probing the electronic properties and charge state of gold nanoparticles on ultrathin MgO versus thick doped CaO films, Phys. Rev. B **92**, 075444 (2015)
10.180 C. Büchner, L. Lichtenstein, S. Stuckenholz, M. Heyde, F. Ringleb, M. Sterrer, W.E. Kaden, L. Giordano, G. Pacchioni, H.-J. Freund: Adsorption of Au and Pd on ruthenium-supported bilayer silica, J. Phys. Chem. C **118**, 20959–20969 (2014)
10.181 W.E. Kaden, C. Büchner, L. Lichtenstein, S. Stuckenholz, F. Ringleb, M. Heyde, M. Sterrer, H.-J. Freund, L. Giordano, G. Pacchioni, C.J. Nelin, P.S. Bagus: Understanding surface core-level shifts using the Auger parameter: A study of Pd atoms adsorbed on ultrathin SiO_2 films, Phys. Rev. B **89**, 115436 (2014)
10.182 S. Ulrich, N. Nilius, H.-J. Freund, U. Martinez, L. Giordano, G. Pacchioni: Realization of an atomic sieve: Silica on Mo(112), Surf. Sci. **603**, 1145–1149 (2009)
10.183 S. Ulrich, N. Nilius, H.-J. Freund, U. Martinez, L. Giordano, G. Pacchioni: Tailoring adsorption properties of inert oxide films by inserting anchor sites, Phys. Rev. Lett. **102**, 016102 (2009)
10.184 J.-F. Jerratsch, N. Nilius, D. Topwal, U. Martinez, L. Giordano, G. Pacchioni, H.-J. Freund: Stabilizing monomeric iron species in a porous silica/Mo(112) film, ACS Nano **4**, 863–868 (2010)

10.185 X. Zhao, X. Shao, Y. Fujimori, S. Bhattacharya, L.M. Ghiringhelli, H.-J. Freund, M. Sterrer, N. Nilius, S.V. Levchenko: Formation of water chains on CaO(001): What drives the 1D growth?, J. Phys. Chem. Lett. **6**, 1204–1208 (2015)

10.186 J. Carrasco, F. Illas, N. Lopez: Dynamic ion pairs in the adsorption of isolated water molecules on alkaline-earth oxide (001) surfaces, Phys. Rev. Lett. **100**, 016101 (2008)

10.187 D. Ferry, A. Glebov, V. Senz, J. Suzanne, J.P. Toennies, H. Weiss: Observation of the second ordered phase of water on the MgO(100) surface: Low energy electron diffraction and helium atom scattering studies, J. Chem. Phys. **105**, 1697–1701 (1996)

10.188 J. Heidberg, B. Redlich, D. Wetter: Adsorption of water vapor on the MgO(100) single-crystal surface, Ber. Bunsenges. Phys. Chem. **99**, 1333–1337 (1995)

10.189 Y. Fujimori, X. Zhao, X. Shao, S.V. Levchenko, N. Nilius, M. Sterrer, H.-J. Freund: Interaction of water with the CaO(001) surface, J. Phys. Chem. C **120**, 5565–5576 (2016)

10.190 D. Halwidl, B. Stöger, W. Mayr-Schmölzer, J. Pavelec, D. Fobes, J. Peng, Z.Q. Mao, G.S. Parkinson, M. Schmid, F. Mittendorfer, J. Redinger, U. Diebold: Adsorption of water at the SrO surface of ruthenates, Nat. Mater. **15**, 450–455 (2016)

10.191 R. Włodarczyk, M. Sierka, K. Kwapień, J. Sauer, E. Carrasco, A. Aumer, J.F. Gomes, M. Sterrer, H.-J. Freund: Structures of the ordered water monolayer on MgO(001), J. Phys. Chem. C **115**, 6764–6774 (2011)

10.192 Y.D. Kim, R.M. Lynden-Bell, A. Alavi, J. Stulz, D.W. Goodman: Evidence for partial dissociation of water on flat MgO(100) surfaces, Chem. Phys. Lett. **352**, 318–322 (2002)

10.193 X.L. Hu, J. Carrasco, J. Klimes, A. Michaelides: Trends in water monomer adsorption and dissociation on flat insulating surfaces, Phys. Chem. Chem. Phys. **13**, 12447–12453 (2011)

10.194 P. Liu, T. Kendelewicz, G.E. Brown, G.A. Parks, P. Pianetta: Reaction of water with vacuum-cleaved CaO(100) surfaces: An x-ray photoemission spectroscopy study, Surf. Sci. **416**, 326–340 (1998)

10.195 P. Liu, T. Kendelewicz, G.E. Gordon, G.A. Parks: Reaction of water with MgO(100) surfaces. Part I: Synchrotron x-ray photoemission studies of low-defect surfaces, Surf. Sci. **412/413**, 287–314 (1998)

10.196 E. Carrasco, M.A. Brown, M. Sterrer, H.-J. Freund, K. Kwapien, M. Sierka, J. Sauer: Thickness-dependent hydroxylation of MgO(001) thin films, J. Phys. Chem. C **114**, 18207–18214 (2010)

10.197 L. Savio, E. Celasco, L. Vattuone, M. Rocca, P. Senet: MgO/Ag(100): Confined vibrational modes in the limit of ultrathin films, Phys. Rev. B **67**, 075420 (2003)

10.198 F. Ringleb, Y. Fujimori, H.F. Wang, H. Ariga, E. Carrasco, M. Sterrer, H.J. Freund, L. Giordano, G. Pacchioni, J. Goniakowski: Interaction of water with FeO(111)/Pt(111): Environmental effects and influence of oxygen, J. Phys. Chem. C **115**, 19328–19335 (2011)

10.199 X. Yu, E. Emmez, Q. Pan, B. Yang, S. Pomp, W.E. Kaden, M. Sterrer, S. Shaikhutdinov, H.-J. Freund, I. Goikoetxea, R. Wlodarczyk, J. Sauer: Electron stimulated hydroxylation of a metal supported silicate film, Phys. Chem. Chem. Phys. **18**, 3755–3764 (2016)

10.200 M.A. Brown, Y. Fujimori, F. Ringleb, X. Shao, F. Stavale, N. Nilius, M. Sterrer, H.-J. Freund: Oxidation of Au by surface OH: Nucleation and electronic structure of gold on hydrohylated MgO(001), J. Am. Chem. Soc. **133**, 10668–10676 (2011)

10.201 Y. Fujimori, W.E. Kaden, M.A. Brown, B. Roldan Cuenya, M. Sterrer, H.-J. Freund: Hydrogen evolution from metal–surface hydroxyl interaction, J. Phys. Chem. C **118**, 17717–17723 (2014)

10.202 S. Shaikhutdinov, H.J. Freund: Ultrathin silica films on metals: The long and winding road to understanding the atomic structure, Adv. Mater. **25**, 49–67 (2013)

10.203 B. Yang, E. Emmez, W.E. Kaden, X. Yu, J.A. Boscoboinik, M. Sterrer, S. Shaikhutdinov, H.-J. Freund: Hydroxylation of metal-supported sheet-like silica films, J. Phys. Chem. C **117**, 8336–8344 (2013)

10.204 W.E. Kaden, S. Pomp, M. Sterrer, H.-J. Freund: Insights into silica bilayer hydroxylation and dissolution, Top. Catal. **60**, 471–480 (2016)

10.205 L.T. Zhuravlev: The surface chemistry of amorphous silica. Zhuravlev model, Colloids Surf. A **173**, 1–38 (2000)

10.206 M.A. Brown, E. Carrasco, M. Sterrer, H.J. Freund: Enhanced stability of gold clusters supported on hydroxylated MgO(001) surfaces, J. Am. Chem. Soc. **132**, 4064–4065 (2010)

10.207 D. Göbke, Y. Romanyshyn, S. Guimond, J.M. Sturm, H. Kuhlenbeck, J. Döbler, U. Reinhardt, M.V. Ganduglia-Pirovano, J. Sauer, H.J. Freund: Formaldehyde formation on vanadium oxide surfaces V_2O_3(0001) and V_2O_5(001): How does the stable methoxy intermediate form?, Angew. Chem. Int. Ed. **48**, 3695–3698 (2009)

10.208 J.M. Sturm, D. Göbke, H. Kuhlenbeck, J. Döbler, U. Reinhardt, M.V. Ganduglia-Pirovano, J. Sauer, H.J. Freund: Partial oxidation of methanol on well-ordered V_2O_5(001)/Au(111) thin films, Phys. Chem. Chem. Phys. **11**, 3290–3299 (2009)

10.209 F.E. Feiten, H. Kuhlenbeck, H.J. Freund: Reducing the V_2O_3(0001) surface through electron bombardment–A quantitative structure determination with I/V-LEED, Phys. Chem. Chem. Phys. **18**, 3124–3130 (2016)

10.210 P. Mars, D.W. van Krevelen: Oxidations carried out by means of vanadium oxide catalysts, Chem. Eng. Sci. **3**, 41 (1954)

10.211 Q. Pan, X. Weng, M.S. Chen, L. Giordano, G. Pacchioni, C. Noguera, J. Goniakowski, S. Shaikhutdinov, H.-J. Freund: Enhanced CO oxidation on oxide/metal interface: From ultra-high vacuum

to near-atmospheric pressures, ChemCatChem **7**, 2620–2627 (2015)
10.212 S.J. Tauster: Strong metal-support interactions, Acc. Chem. Res. **20**, 389–394 (1987)
10.213 G.H. Vurens, M. Salmeron, G.A. Somorjai: Structure, composition and chemisorption studies of thin ordered iron oxide films on platinum (111), Surf. Sci. **201**, 129–144 (1988)
10.214 Y. Martynova, S. Shaikhutdinov, H.-J. Freund: CO oxidation on metal-supported ultrathin oxide films: What makes them active?, ChemCatChem **5**, 2162–2166 (2013)
10.215 Q. Fu, F. Yang, X. Bao: Interface-confined oxide nanostructures for catalytic oxidation reactions, Acc. Chem. Res. **46**, 1692–1701 (2013)
10.216 D. Sun, X.-K. Gu, R. Ouyang, H.-Y. Su, Q. Fu, X. Bao, W.-X. Li: Theoretical study of the role of a metal-cation ensemble at the oxide-metal boundary on CO oxidation, J. Phys. Chem. C **116**, 7491–7498 (2012)
10.217 Q. Fu, Y. Yao, X. Guo, M. Wei, Y. Ning, H. Liu, F. Yang, Z. Liu, X. Bao: Reversible structural transformation of FeO_x nanostructures on Pt under cycling redox conditions and its effect on oxidation catalysis, Phys. Chem. Chem. Phys. **15**, 147408–114714 (2013)
10.218 Q. Fu, W.-X. Li, Y. Yao, L. Hongyang, Q. Fu, H.-Y. Su, D. Ma, X.-K. Gu, L. Chen, Z. Wang, H. Zhang, B. Wang, X. Bao: Interface-confined ferrous centers for catalytic oxidation, Science **328**, 1141–1144 (2010)
10.219 H. Zeuthen, W. Kudernatsch, L.R. Merte, L.K. Ono, L. Lammich, F. Besenbacher, S. Wendt: Fe oxides on Ag surfaces: Structure and reactivity, ACS Nano **9**, 573–583 (2015)
10.220 L. Xu, Z. Wu, Y. Jin, Y. Ma, W. Huang: Reaction mechanism of WGS and PROX reactions catalyzed by Pt/oxide catalysts revealed by an FeO(111)/Pt(111) inverse model catalyst, Phys. Chem. Chem. Phys. **15**, 12068–12074 (2013)
10.221 L. Giordano, G. Pacchioni, C. Noguera, J. Goniakowski: Identification of active sites in a realistic model of strong metal–support interaction catalysts: The case of platinum (1 1 1)-supported iron oxide film, ChemCatChem **6**, 185–190 (2014)
10.222 L. Giordano, G. Pacchioni, J. Goniakowski, N. Nilius, E.D.L. Rienks, H.-J. Freund: Interplay between structural, magnetic, and electronic properties in a FeO/Pt (111) ultrathin film, Phys. Rev. B **76**, 075416 (2007)
10.223 Q. Pan, B.H. Liu, M.E. McBriarty, Y. Martynova, I.M.N. Groot, S. Wang, M.J. Bedzyk, S. Shaikhutdinov, H.-J. Freund: Reactivity of ultra-thin ZnO films supported by Ag(111) and Cu(111): A comparison to ZnO/Pt(111), Catal. Lett. **144**, 648–655 (2014)
10.224 A.M. Doyle, S.K. Shaikhutdinov, H.J. Freund: Alkene chemistry on the palladium surface: Nanoparticles vs single crystals, J. Catal. **223**, 444–453 (2004)
10.225 S. Schauermann, N. Nilius, S. Shaikhutdinov, H.-J. Freund: Nanoparticles for heterogeneous catalysis: New mechanistic insights, Acc. Chem. Res. **46**, 1673–1681 (2013)
10.226 G.C. Bond: *Metal-Catalysed Reactions of Hydrocarbons* (Springer, New York 2005)
10.227 M. Wilde, K. Fukutani, W. Ludwig, B. Brandt, J.-H. Fischer, S. Schauermann, H.J. Freund: Influence of carbon deposition on the hydrogen distribution in Pd nanoparticles and their reactivity in olefin hydrogenation, Angew. Chem. Int. Ed. **47**, 9289–9293 (2008)
10.228 W. Ludwig, A. Savara, S. Schauermann, H.-J. Freund: Role of low-coordinated surface sites in olefin hydrogenation: A molecular beam study on Pd nanoparticles and Pd(111), ChemPhysChem **11**, 2319–2322 (2010)
10.229 W. Ludwig, A. Savara, K.-H. Dostert, S. Schauermann: Olefin hydrogenation on Pd model supported catalysts: New mechanistic insights, J. Catal. **284**, 148–156 (2011)
10.230 M. Wilde, K. Fukutani, M. Naschitzki, H.J. Freund: Hydrogen absorption in oxide-supported palladium nanocrystals, Phys. Rev. B **77**, 113412 (2008)
10.231 F. Viñes, C. Loschen, F. Illas, K.M. Neymann: Edge sites as a gate for subsurface carbon in palladium nanoparticles, J. Catal. **266**, 59–63 (2009)
10.232 A.M. Doyle, S.K. Shaikhutdinov, S.D. Jackson, H.-J. Freund: Hydrogenation on metal surfaces: Why are nanoparticles more active than single crystals?, Angew. Chem. Int. Ed. **42**, 5240–5243 (2003)
10.233 K.M. Neymann, S. Schauermann: Hydrogen diffusion into palladium nanoparticles: Pivotal promotion by carbon, Angew. Chem. Int. Ed. **49**, 4743–4746 (2010)
10.234 W. Ludwig, A. Savara, R.J. Madix, S. Schauermann, H.-J. Freund: Subsurface hydrogen diffusion into Pd nanoparticles: Role of low-coordinated surface sites and facilitation by carbon, J. Phys. Chem. C **116**, 3539–3544 (2012)
10.235 F. Ringleb, M. Sterrer, H.-J. Freund: Preparation of Pd–MgO model catalysts by deposition of Pd from aqueous precursor solutions onto Ag(001)-supported MgO(001) thin films, Appl. Catal. A **474**, 186–193 (2014)
10.236 B.R. Bickmore, J.C. Wheeler, B. Bates, K.L. Nagy, D.L. Eggett: Reaction pathways for quartz dissolution determined by statistical and graphical analysis of macroscopic experimental data, Geochim. Cosmochim. Acta **72**, 4521–4536 (2008)
10.237 D.A. Vermilyea: Dissolution of MgO and $Mg(OH)_2$ in aqueous solutions, J. Electrochem. Soc. **116**, 1179–1183 (1969)
10.238 O.S. Pokrovsky, J. Schott: Experimental study of brucite dissolution and precipitation in aqueous solutions: Surface speciation and chemical affinity control, Geochim. Cosmochim. Acta **68**, 31–45 (2004)
10.239 H.F. Wang, H. Ariga, R. Dowler, M. Sterrer, H.J. Freund: Surface science approach to catalyst preparation—Pd deposition onto thin Fe_3O_4(111) films from $PdCl_2$ precursor, J. Catal. **286**, 1–5 (2012)

10.240 H.F. Wang, W.E. Kaden, R. Dowler, M. Sterrer, H.J. Freund: Model oxide-supported metal catalysts—Comparison of ultrahigh vacuum and solution based preparation of Pd nanoparticles on a single-crystalline oxide substrate, Phys. Chem. Chem. Phys. **14**, 11525–11533 (2012)

10.241 S. Pomp, W.E. Kaden, M. Sterrer, H.J. Freund: Exploring Pd adsorption, diffusion, permeation, and nucleation on bilayer SiO_2/Ru as a function of hydroxylation and precursor environment: From UHV to catalyst preparation, Surf. Sci. **652**, 286–293 (2016)

10.242 M. Sterrer, H.-J. Freund: Towards realistic surface science models of heterogeneous catalysts: Influence of support hydroxylation and catalyst preparation method, Catal. Lett. **143**, 375–385 (2013)

10.243 N.B. Milić, Z.D. Bugarčić: Hydrolysis of the palladium(II) ion in a sodium-chloride medium, Transit. Met. Chem. **9**, 173–176 (1984)

10.244 J.M. van Middlesworth, S.A. Wood: The stability of palladium(II) hydroxide and hydroxy-chloride complexes: An experimental solubility study at 25–85 °C and 1 bar, Geochim. Cosmochim. Acta **63**, 1751–1765 (1999)

10.245 B. Didillon, E. Merlen, T. Pages, D. Uzio: From colloidal particles to supported catalysts: A comprehensive study of palladium oxide hydrosols deposited on alumina, Stud. Surf. Sci. Catal. **118**, 41–54 (1998)

10.246 L. Jiao, J.R. Regalbuto: The synthesis of highly dispersed noble and base metals on silica via strong electrostatic adsorption: I. Amorphous silica, J. Catal. **260**, 329–341 (2008)

10.247 A.M. Shah, J.R. Regalbuto: Retardation of Pt adsorption over oxide supports at pH extremes—Oxide dissolution or high ionic-strength, Langmuir **10**, 500–504 (1994)

10.248 K. Wolter, O. Seiferth, H. Kuhlenbeck, M. Bäumer, H.-J. Freund: Infrared spectroscopic investigation of CO adsorbed on Pd aggregates deposited on an alumina model support, Surf. Sci. **399**, 190–198 (1998)

10.249 C. Büchner, L. Lichtenstein, M. Heyde, H.-J. Freund: The atomic structure of two-dimensional silica. In: *Noncontact Atomic Force Microscopy*, ed. by S. Morita, F.J. Giessibl, E. Meyer, R. Wiesendanger (Springer, Cham 2015)

10.250 K.M. Burson, L. Gura, B. Kell, C. Büchner, A.L. Lewandowski, M. Heyde, H.-J. Freund: Resolving amorphous solid-liquid interfaces by atomic force microscopy, Appl. Phys. Lett. **108**, 201602 (2016)

10.251 F.F. Abraham, I.P. Batra: Theoretical interpretation of atomic-force-microscope images of graphite, Surf. Sci. Lett. **209**, L125–L132 (1989)

10.252 M. Osada, T. Sasaki: Two-dimensional dielectric nanosheets: Novel nanoelectronics from nanocrystal building blocks, Adv. Mater. **24**, 210–228 (2012)

10.253 E. Gao, B. Xie, Z. Xu: Two-dimensional silica: Structural, mechanical properties, and strain-induced band gap tuning, J. Appl. Phys. **119**, 014301 (2016)

10.254 L. Lichtenstein, M. Heyde, S. Ulrich, N. Nilius, H.-J. Freund: Probing the properties of metal-oxide interfaces: Silica films on Mo and Ru supports, Phys. Condens. Matter **24**, 354010–354017 (2012)

Hans-Joachim Freund

Chemical Physics Dept.
Fritz Haber Institute of the Max Planck Society
Berlin, Germany
freund@fhi-berlin.mpg.de

Hans-Joachim Freund received his PhD (1978) and his habilitation (1983) from the University of Cologne. 1983, he became Associate Professor at Erlangen University and in 1987 Professor at Bochum University. In 1995, he accepted a position as scientific member and director of the Department of Chemical Physics at the Fritz-Haber-Institut der Max-Planck-Gesellschaft in Berlin. He serves as Honorary Professor of five universities. He received several national and international awards.

Markus Heyde

Chemical Physics Dept.
Fritz Haber Institute of the Max Planck Society
Berlin, Germany
heyde@fhi-berlin.mpg.de

Markus Heyde heads the Scanning Probe Microscopy group in the Department of Chemical Physics at the Fritz-Haber-Institute. His research is focused on high-resolution local structure measurements on model systems for heterogeneous catalysis. Well-defined crystalline and amorphous oxide thin film systems are characterized by atomic resolution microscopy to gain insight into the chemical reactions taking place at these surfaces.

Helmut Kuhlenbeck

Chemical Physics Dept.
Fritz Haber Institute of the Max Planck Society
Berlin, Germany
kuhlenbeck@fhi-berlin.mpg.de

Helmut Kuhlenbeck studied physics at the University of Osnabrück. In 1995, he finished the habilitation procedure at the University of Bochum. He has been a work group leader at the Chemical Physics department of the Fritz Haber Institute in Berlin since 1996. His activities are focused on areas related to structural studies and spectroscopy of chemical processes on well-ordered oxide surfaces.

Niklas Nilius

Institut für Physik
Carl von Ossietzky Universität Oldenburg
Oldenburg, Germany
niklas.nilius@uni-oldenburg.de

Niklas Nilius studied physics and received his PhD in the group of H.-J. Freund for investigating the optical properties of individual nanoparticles. In 2002/2003, he worked as a postdoc with W. Ho on monatomic chains artificially assembled from single metal atoms. He has held a professorship at Oldenburg University since 2013, where he develops oxide model systems for photovoltaic and photochemical applications.

Thomas Risse

Institute of Chemistry and Biochemistry – Physical and Theoretical Chemistry
Freie Universität Berlin
Berlin, Germany
risse@chemie.fu-berlin.de

Thomas Risse received his Doctorate in Physical Chemistry from Ruhr-Universität Bochum. From 1997 until 2010 he was staff scientist at the Fritz Haber Institute, with an interlude of 1 year as a postdoc at UCLA. In 2010 he became Professor of Physical Chemistry at Freie Universität Berlin. He is interested in ESR spectroscopy and its application to surfaces and spin labeled proteins.

Swetlana Schauermann

Institut für Physikalische Chemie
Christian-Albrechts-Universität zu Kiel
Kiel, Germany

Swetlana Schauermann studied chemistry and received her PhD (2005) in the group of H.-J. Freund investigating heterogeneously catalyzed reactions at the atomistic level. Between 2006 and 2007, she was a postdoctoral fellow with R.M. Lambert (Cambridge University) and C.T. Campbell (University of Washington).She has been a professor at Kiel University since 2015. Her current research is focused on the kinetics of complex surface reactions and thermodynamics of gas–surface interactions.

Thomas Schmidt

Chemical Physics Dept.
Fritz Haber Institute of the Max Planck Society
Berlin, Germany
(BESSY II)

Helmholtz-Zentrum Berlin für Materialien und Energie
Berlin, Germany
thomas.schmidt@fhi-berlin.mpg.de

Thomas Schmidt studied physics at the University of Hanover, where he received his PhD in 1994. After postdoc positions in Clausthal, ELETTRA (Trieste), and Würzburg, he became a group leader at the FHI in 2008. Using XPEEM, XPS, XEXAFS, LEEM, and LEED he investigates the growth and properties of ultrathin oxide films supported by metal single crystals.

Shamil Shaikhutdinov

Chemical Physics Dept.
Fritz Haber Institute of the Max Planck Society
Berlin, Germany
shaikhutdinov@fhi-berlin.mpg.de

Shamil Shaikhutdinov has received his PhD (1986) from the Moscow Institute of Physics and Technology. He has worked at the Boreskov Institute of Catalysis (Novosibirsk) and as a postdoctoral fellow in Germany and France. Since 2004, he has been leading the group Structure and Reactivity in the Fritz-Haber Institute (Berlin). His research interest is focused on understanding of the atomic structure and surface chemistry of functional materials.

Martin Sterrer

Institute of Physics
University of Graz
Graz, Austria
martin.sterrer@uni-graz.at

Martin Sterrer received his PhD in Physical Chemistry from TU Vienna. In 2003 he joined Professor Freund's department as a postdoc and later headed the Catalysis and Laser Spectroscopy group in the department. In 2014, he moved to University of Graz, where he is now Professor of Experimental Physics and Head of the Surface Science group, working on model catalysis, solid–liquid interfaces and adsorption structures of large organic molecules.

Part C Electronic Structure Of Surfaces

Part C encompasses six chapters devoted to surface electronic structure, presenting both experimental and theoretical points of view. A number of experimental techniques and related state-of-the-art theoretical methods are described. This field is characterized by a strong interaction between experiment and theory, since the latter is required to interpret the complexities often encountered in experimental findings. A lack of correspondence between theoretical and experimental results also points to the need to refine the theory of surface electronic structure to make it accurate enough to use for reliable predictions in the future.

Chapter 11 initially describes the experimental methods of photoemission and inverse photoemission spectroscopy, which are widely used to investigate filled and empty electronic states, respectively. Group theory, dipolar theory, and the relevant selection rules are then applied to explain the observed spectra of CO in the gas phase and when adsorbed on metal surfaces. In the second part of the chapter, x-ray photoelectron spectroscopy and core-level shifts are introduced, and examples are given of the possible effects that may be observed and identified from the changes in the chemical environments of adsorbates on both metallic and organic substrates.

Chapter 12 describes electronic states at vicinal surfaces of metals. The presence of ordered sequences of terraces and steps generates a high density of step-based atoms with identical coordination numbers that are lower than and relaxations that differ from those of the atoms on the terrace, causing well-defined core-level shifts. Moreover, the presence of atomic steps leads to a periodic modulation of the surface potential, which in turn results in scattering and ultimately the confinement of the surface electronic states. Interestingly, one-dimensional quantization across the steps is also observed. Therefore, all of the electronic levels of the atoms in the steps are affected, from deep core levels to surface states. This influences physical and chemical phenomena at the surface/vacuum interface, such as chemical reactions and epitaxial growth. Detailed studies are performed either with samples cut at a specific miscut angle, which produces a vicinal surface with specified high Miller indices, or using curved surfaces through which a number of vicinal surfaces with varying high Miller indices can be accessed. At least in principle, stepped surfaces allow the surface electronic structure to be tailored almost at will.

Chapter 13 reviews the use of low-energy and photoemission electron microscopes and their application to the investigation of model systems of interest for nanotechnology, nanomagnetism, materials science, catalysis, energy storage, thin films, and 2-D materials. After an historical overview of these techniques, the chapter describes their basic operating principles, procedures for extracting spectroscopic information, and the origin of contrast in the images. A number of examples are presented to illustrate state-of-the-art capabilities, such as the identification of graphene domains with different thicknesses and the magnetic imaging of Fe nanowires.

Chapter 14 is devoted to scanning photoelectron microscopy. In order to achieve the desired lateral resolution without losing spectral resolution, it is necessary to use third-generation synchrotron light sources. High spatial resolution can be achieved by either magnifying the image of the irradiated surface area using a suitable electron optical system, as described in Chap. 13 (LEEM and PEEM), or—as explained here—by demagnifying the incident photon beam to a very small spot using x-ray photon optics and scanning the beam over the crystal surface. Under realistic conditions, subnanometer spatial resolution can be attained. The advantage over optical microscopy is the contrast achieved with x-ray photoelectron spectroscopy or x-ray absorption spectroscopy. Many examples are given, including those illustrating the surface reactivities of metals used as catalysts and the degradation mechanism of light-emitting diodes, as well as images of different nano- and microstructures.

The section ends with two theoretical chapters.

Chapter 15 focuses on topological insulators—materials which are insulating in the bulk but host topologically protected metallic states at the surface. Interest in these materials arises from their possible use in spintronics and quantum computing. This chapter is devoted to natural topological heterostructures composed of different sublattices, at least one of which is a topological insulator, and demonstrates that they all support Dirac surface states.

Chapter 16 covers methods of calculating the energetic ground state and electronic band structure of a surface. First, DFT methods utilizing the local density and general gradient approximations are introduced. Hybrid functionals are also discussed. Then the issue of van der Waals interactions is tackled. Several examples are presented, ranging from clean single-crystal surfaces to the adsorption of simple molecules at different surfaces and recent results on organic adsorbates. The theoretical results are compared with state-of-the-art experimental findings showing that the interplay of theory and experiments has led to the successfully determination of adsorption sites, geometries, possible surface reconstructions, molecular orientations, potential energy barriers, wavefunctions, and vibrational frequencies.

11. Integrated Experimental Methods for the Investigation of the Electronic Structure of Molecules on Surfaces

Andrew J. Yost, Prescott E. Evans, Iori Tanabe, Guanhua Hao, Simeon Gilbert, Takashi Komesu

In this chapter, we introduce the efficacy of photoemission and inverse photoemission in determining the interactions of adsorbates with a substrate, with an emphasis on simple adsorbates on various metallic and oxide surfaces. We cover symmetry and selection rules, and how hybridization, bonding, and molecular orientation affect x-ray photoemission (XPS), angle resolved photoemission (ARPES), and angle resolved inverse photoemission (ARIPES). The application of ARPES and ARIPES in the determination of the orientation of molecular adsorbates and the wave vector dependence of the adsorbate molecular orbitals is addressed. We also address some of the difficulties associated with photoemission data interpretation as they relate to initial states and screened and unscreened final states, surface-to-bulk core level shifts, and core level satellites. This chapter is intended to help those new to photoemission spectroscopy with a basic understanding of the photoemission phenomenon and the associated intricacies that will be encountered in an experimental setting.

11.1 Photoemission Spectroscopy

11.1.1 Introduction to Photoemission

Photoemission spectroscopy is an extremely powerful technique in the identification and investigation of materials with reference to their electronic environment and band structure. This process is also appropriate for molecular adlayers on materials which can additionally show bonding structure and orientation. Essential to in-depth studies of materials are ARPES techniques, which exploit the use of highly plane-polarized incident light. The combination of highly plane-polarized incident light and angular resolution means that photoemission selection rules can be applied. This means more than simply atomic angular momentum conservation, which restricts resonant photoemission to a change in ℓ, (orbital angular momentum quantum number), such that $\Delta\ell = \pm 1$, but also symmetry selection rules. For a highly symmetric molecule (as opposed to a molecule which lacks invariance under applied symmetry operations), the molecular orbitals will have a photoemission cross-section that varies with the photoemission geometry and the symmetry of the molecular orbital. This has a profound consequence for a molecule aligned along the surface normal, or parallel to the surface and aligned along a high-symmetry crystallographic axis of the substrate, as the molecular orientation can be determined. Similarly, overlapping molecular orbitals within a material or molecular adlayer can sometimes be isolated through changing photoemission geometry. Here, one molecular orbital will have greater intensity in the photoemission spectra than other closely lying photoemission features based on selection rules. Varying photon energy can also be of great benefit, allowing access to a wider portion of a material's electronic states. However, changing photon energy and exploiting highly-polarized light generally implies the need for a synchrotron light source, although bright laboratory light sources with polarization capabilities are becoming available. The details of the photoemission process and the symmetry selection rules follow.

M. Rocca, T.S. Rahman, L. Vattuone (Eds.), *Springer Handbook of Surface Science*, Springer Handbooks,
https://doi.org/10.1007/978-3-030-46906-1_11

11.1.2 Symmetry and Selection Rules in Electron Spectroscopy

Photoemission Spectroscopy and Inverse Photoemission Spectroscopy

In the past several decades, photoemission spectroscopy has proven to be a powerful tool to study the band structure and electronic structure of various types of materials, including molecular adlayers. There are several types of photoemission spectroscopies, dependent upon the light source, such as a ultraviolet (UV) lamps, x-rays, or synchrotron radiation. UV photoemission spectroscopy, which uses ultraviolet photons with energy below 200 eV, has been a fundamental experimental method to probe the occupied band (valence band) structure of materials [11.1–11]. When a photon impinges on a sample, the electrons excited by the photoelectric effect are ejected into the vacuum with a kinetic energy, E_{kin}. From the principle of conservation of energy, one can write the following equation describing the photoemission process as

$$E_{\mathrm{kin}} = h\nu - E_{\mathrm{b}} - \Phi \,, \tag{11.1}$$

where $h\nu$ is the incident photon energy, $E_{\mathrm{b}}$is the binding energy of the electrons in the sample, and Φ is the work function (Fig. 11.1b). An electron energy analyzer detects the photoelectron kinetic energy, E_{kin}, and its angle with respect to the incident light $(\theta_{\mathrm{i}} + \theta_{\mathrm{f}})$ and the surface $(\theta_{\mathrm{f}}, \phi)$ as schematically shown in Fig. 11.1a, where θ_{f} and ϕ are the polar and azimuthal angles of the photoelectrons, respectively. The momentum of the photoelectrons is given as

$$E_{\mathrm{kin}} = \frac{p^2}{2m} \;\Rightarrow\; p = \sqrt{2mE_{\mathrm{kin}}} \tag{11.2}$$

and the direction of $\boldsymbol{p}/\hbar$ is determined from θ_{f} and ϕ [11.12].

Inverse photoemission spectroscopy (IPES) [11.14–23] has been utilized to study the unoccupied electronic structure of solids (conduction band). In the case of IPES, an electron with energy E_{i} impinges the sample surface, and the electron loses its energy and decays to an unoccupied bound state with energy E_{f}, while emitting a photon with the energy $h\nu = E_{\mathrm{i}} - E_{\mathrm{f}}$, as shown in Fig. 11.2. A Geiger–Müller detector can be used to measure the photon counts while the e-gun sweeps a range of energy to elicit the photon energy emitted. If the kinetic energy of the incoming electron, E_{i}, and momentum are well defined from the experimental conditions, then the energy of the unoccupied state, E_{f}, is determined by the conservation of energy, as seen in (11.3) below,

$$E_{\mathrm{i}} - E_{\mathrm{f}} - h\nu = 0 \,. \tag{11.3}$$

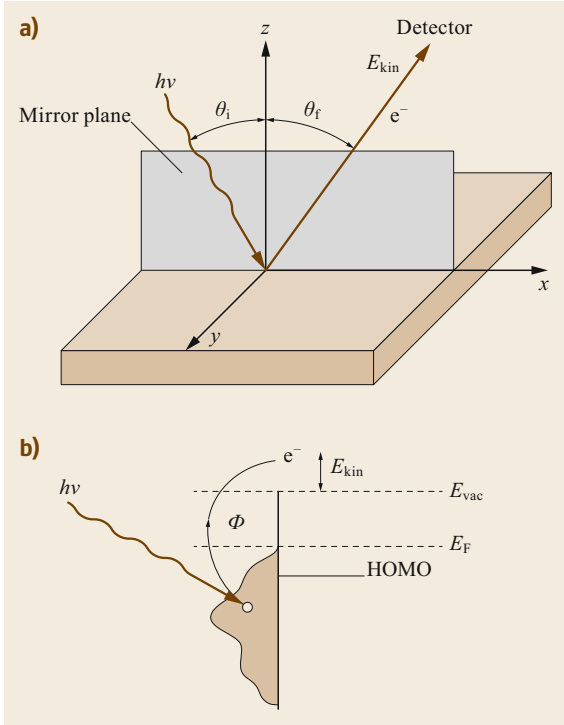

Fig. 11.1a,b Ultraviolet photoemission spectroscopy. **(a)** The photon with energy $h\nu$ with the incident angle θ_{i} with respect to the surface normal impinges on the surface of the sample. Then, the photoelectron with kinetic energy E_{kin} is emitted with an angle θ_{f}. **(b)** Sketch of the photoemission process (Reprinted from [11.13], with permission from Elsevier)

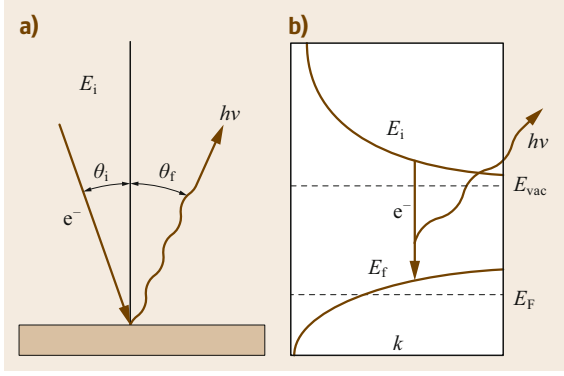

Fig. 11.2a,b Inverse photoemission spectroscopy. **(a)** An electron with energy E_{i} with the incident angle θ_{i} with respect to the surface normal impinges on the surface of the sample. Then, a photon with energy $h\nu$ is emitted with an angle θ_{f}. **(b)** Sketch of the inverse photoemission process (Reprinted from [11.13], with permission from Elsevier)

The Theory of Photoemission

Let us consider the transition probability per unit time between the initial state, Ψ_i, and the final state, Ψ_f, given by time-dependent perturbation theory, both for the photoemission process and the inverse photoemission process. Recall that the transition probability rate describes the likelihood of transitioning from one energy eigenstate to another under the influence of some perturbation. Assuming a small perturbation $H'(t)$ due to the incident photon, the photoemission transition rate ω is calculated by Fermi's golden rule

$$\omega \propto \frac{2\pi}{\hbar} \left|\langle \Psi_\mathrm{f} \left| H' \right| \Psi_\mathrm{i} \rangle\right|^2 \delta\left(E_\mathrm{f} - E_\mathrm{i} - \hbar\nu\right) . \tag{11.4}$$

The Hamiltonian of an electron in an external electromagnetic field is

$$H = H_0 + H' = \frac{1}{2m}\left(\boldsymbol{p} + \frac{e\boldsymbol{A}}{c}\right)^2 - eU - e\phi \ , \tag{11.5}$$

where $\boldsymbol{A}$ and ϕ are the vector and scalar potentials, respectively, and $\boldsymbol{p}$ is the momentum operator where $\boldsymbol{p} = \mathrm{i}\hbar\nabla$. Thus, the perturbation Hamiltonian $H'(t)$ is given as

$$\begin{aligned} H'(t) = {} & \frac{e}{2mc}\left(\boldsymbol{A}\cdot\boldsymbol{p} + \boldsymbol{p}\cdot\boldsymbol{A}\right) \\ & + \frac{e^2}{2mc^2}\boldsymbol{A}\cdot\boldsymbol{A} - e\phi \ . \end{aligned} \tag{11.6}$$

By choosing the appropriate condition such that the scalar potential is zero, $\phi = 0$, and neglecting $\boldsymbol{A}\cdot\boldsymbol{A}$, which represents the two photon process, which is unlikely and complicated, and is usually small compared to $\boldsymbol{p}\cdot\boldsymbol{A}$ terms, i.e., $\boldsymbol{A}\cdot\boldsymbol{A} \ll \boldsymbol{p}\cdot\boldsymbol{A}$, (11.6) becomes

$$H'(t) = \frac{e}{2mc}\left(\boldsymbol{A}\cdot\boldsymbol{p} + \boldsymbol{p}\cdot\boldsymbol{A}\right) . \tag{11.7}$$

Now, using the commutation relation, $\boldsymbol{A}\cdot\boldsymbol{p} + \boldsymbol{p}\cdot\boldsymbol{A} = 2\boldsymbol{A}\cdot\boldsymbol{p} + \mathrm{i}\hbar\left(\nabla\cdot\boldsymbol{A}\right)$ and setting $\nabla\cdot\boldsymbol{A} = \boldsymbol{0}$, because the photon wavelength is much larger than the atomic dimensions, we have

$$H'(t) = \frac{e}{mc}\boldsymbol{A}\cdot\boldsymbol{p} \ . \tag{11.8}$$

In ultraviolet photoemission spectroscopy, one can adopt the dipole approximation to treat the vector potential $\boldsymbol{A}$ as a constant $\boldsymbol{A_0}$, because the wavelength of the incident photon is much larger than the radius of the atom. Therefore, the perturbation Hamiltonian $H'(t)$ is finally written as

$$H'(t) = \frac{e}{mc}\boldsymbol{A_0}\cdot\boldsymbol{p} \ . \tag{11.9}$$

Now, we should make some approximation to analyze the transition matrix elements $\langle \Psi_\mathrm{f} \left| H' \right| \Psi_\mathrm{i} \rangle$. In the photoemission process, the irreducible representation of the initial state, Ψ_i, is considerably different from that of the final state, Ψ_f, after one electron is ejected by a photon. Unless it is a hydrogen atom, the systems under study have many electrons with many degrees of freedom mutually interacting with each other. However, we can adopt an assumption of a one-electron view for the initial and final wavefunctions instead of the complicated many-body theory to deal with the photoemission analysis [11.3, 24–29]. When photoelectrons are created by photoionization of the various orbitals the initial wavefunction, $\Psi_\mathrm{i}(N)$, is described as the product of a wavefunction of a single electron which is to be photoemitted, $\varphi_{\mathrm{i},k}$, and the wavefunction of the remaining $(N-1)$-electrons, $\Psi_\mathrm{i}^k\,(N-1)$, provided that the system has N number of electrons. Thus, the N-electron initial state, $|\Psi_\mathrm{i}(N)\rangle$, is

$$|\Psi_\mathrm{i}(N)\rangle = |\varphi_{\mathrm{i},k}\rangle |\Psi_\mathrm{i}^k(N-1)\rangle \ . \tag{11.10}$$

Similarly, the final wavefunction, $\Psi_\mathrm{f}(N)$, is written as the product of a wavefunction of the emitted electron, $\varphi_{\mathrm{f},E_\mathrm{kin}}$, with kinetic energy equal to E_kin and the wavefunction of the rest of the electrons, $\Psi_{\mathrm{f},s}^k\,(N-1)$. Here, s denotes the number of excited states the remaining $(N-1)$-electrons have, since the final $(N-1)$-electron states should, in general, be different from the initial one due to energy relaxation. Thus, the N-electron final state $|\Psi_\mathrm{f}(N)\rangle$ is

$$|\Psi_\mathrm{f}(N)\rangle = |\varphi_{\mathrm{f},E_\mathrm{kin}}\rangle |\Psi_{\mathrm{f},s}^k\,(N-1)\rangle \ . \tag{11.11}$$

Then, the transition matrix element becomes

$$\begin{aligned} \langle \Psi_\mathrm{f} | H' | \Psi_\mathrm{i} \rangle = {} & \langle \varphi_{\mathrm{f},E_\mathrm{kin}} \left| H' \right| \varphi_{\mathrm{i},k} \rangle \\ & \times \left\langle \Psi_{\mathrm{f},s}\,(N-1) \left| \Psi_\mathrm{i}^k\,(N-1) \right\rangle \right. . \end{aligned} \tag{11.12}$$

Therefore, the photoemission transition rate ω finally yields

$$\begin{aligned} \omega \propto {} & \frac{2\pi}{\hbar} \left|\langle \varphi_{\mathrm{f},E_\mathrm{kin}} \left| H' \right| \varphi_{\mathrm{i},k} \rangle\right|^2 \\ & \times \sum_s \left|\left\langle \Psi_{\mathrm{f},s}\,(N-1) \left| \Psi_\mathrm{i}^k\,(N-1) \right\rangle \right.\right|^2 \\ & \times \delta\left(E_\mathrm{kin} + E_s\,(N-1) - E_0(N) - h\nu\right) , \end{aligned} \tag{11.13}$$

where $E_0(N)$ is the ground state energy of the N-electron system.

While the classical vector potential $\boldsymbol{A}$ for the photoemission process generates mostly the same results,

as it is treated quantum mechanically, the inverse photoemission process requires the vector potential $\boldsymbol{A}$ to be quantized as

$$\boldsymbol{A}(\boldsymbol{x},t) = \sum_{\boldsymbol{q}}\sum_{r}\left(\frac{\hbar c^2}{2V\omega_{\boldsymbol{q}}}\right)^{\frac{1}{2}} \times \boldsymbol{\varepsilon}_r(\boldsymbol{q})\left[a_r(\boldsymbol{q},t)\,\mathrm{e}^{\mathrm{i}\boldsymbol{q}\cdot\boldsymbol{x}} + a_r^{\dagger}(\boldsymbol{q},t)\,\mathrm{e}^{-\mathrm{i}\boldsymbol{q}\cdot\boldsymbol{x}}\right], \tag{11.14}$$

where $\omega_{\boldsymbol{q}} = c|\boldsymbol{q}|$ [11.30, 31]. This is due to the fact that the inverse photoemission process is an excited electron system without an electromagnetic field, which causes the transition matrix elements of the dipole operator to become zero in the semiclassical expression [11.13]. Similar to the initial and final states of photoemission, for inverse photoemission, the initial state comprises an electron within a continuum state with no photons and is expressed as $|\psi_{\mathrm{i}}, n_{h\nu} = 0\rangle$, and the final state comprises an electron in a bound state and a photon with wave vector $\boldsymbol{q}$ and is expressed as $|\psi_{\mathrm{f}}, n_{h\nu}(\boldsymbol{q}) = 1\rangle$ [11.13].

Symmetry and Dipole Selection Rules

Exploiting symmetry and dipole selection rules gives us a very useful insight to analyze the transition matrix element presented as (11.12). Table 11.1 shows the character table for the C_{2v} point group which consists of the four symmetry operations, E, C_2, σ_v, σ_v'. The left column lists the name of the irreducible representations A_1, A_2, B_1, B_2, known as Mulliken symbols, and the two columns on the right-hand side of the table comprise basis functions for the irreducible representations. Since these basis functions also correspond to the symmetry of the atomic or molecular orbitals, dipole selection rules predict, without the direct calculation of the transition matrix element, which transition is allowed or not allowed using the symmetry properties of the initial and final states in solids and the electric dipole operator of the perturbed Hamiltonian described in (11.9), especially if polarized light is used. In photoemission experiments, one can use p- and s-polarized light from a synchrotron radiation source, which is highly plane (linearly)-polarized. p-polarized light has its vector potential $\boldsymbol{A}$ parallel to the plane of the sample surface (the incident beam is perpendicular to sample surface), and s-polarized light has its vector potential $\boldsymbol{A}$ normal to the plane of the sample surface (the incident beam is parallel to the sample surface, at a shallow angle of incidence). As an integral for an odd function will necessarily be zero, the transition matrix element vanishes if the product of the functions in $\langle\Psi_{\mathrm{f}}|\,\boldsymbol{A}\cdot\boldsymbol{p}\,|\Psi_{\mathrm{i}}\rangle$ is orthogonal, which occurs when functions belong to different irreducible representations of a group. In other words, the direct product of the representations of the initial and final state wavefunctions should contain the representation of the dipole operator $\boldsymbol{A}\cdot\boldsymbol{p}$ [11.13, 32]. The initial state must be symmetric (even) if the vector potential $\boldsymbol{A}$ is parallel to the mirror plane, and the initial state must be antisymmetric (odd) if the vector potential $\boldsymbol{A}$ is normal to the mirror plane.

If we consider a face-centered-cubic (fcc) metal as an example, then the normal emission along the Σ direction of the Brillouin zone (the principal direction [110] at $k_{||} = 0$), as depicted in Fig. 11.3, has C_{2v} symmetry. Table 11.2 is a result of implementing group theory to the dipole matrix element [11.32]. For p-polarized light, parallel to the Σ direction, the allowed transitions are of the type $\Sigma_1 \rightarrow \Sigma_1$. For s-polarized light, perpendicular to the Σ direction and also parallel to the x direction, the allowed transitions are of the type $\Sigma_1 \rightarrow \Sigma_3$, whereas for s-polarized light, they are perpendicular to the Σ direction and also parallel to

Table 11.1 C_{2v} character table. The Mulliken symbols A_1, A_2, B_1, B_2, are the irreducible representations of the C_{2v} point group, the row with E, C_2, σ_v, σ_v' represents the symmetry operations of the group, and the two columns on the right-hand side of the table represent the basis functions of the irreducible representations

C_{2v}	E	C_2	$\sigma_v(xz)$	$\sigma_v'(yz)$		
A_1	1	1	1	1	z	x^2, y^2, z^2
A_2	1	1	−1	−1	R_z	xy
B_1	1	−1	1	−1	x, R_y	xz
B_2	1	−1	−1	1	y, R_x	yz

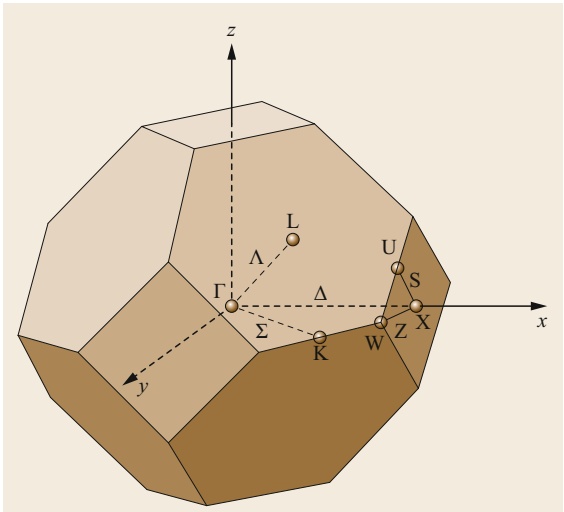

Fig. 11.3 Brillouin zone of the face-centered-cubic (fcc) lattice. The high-symmetry points and lines are indicated (Reprinted with permission from [11.32] Copyright (1980) by the American Physical Society)

Table 11.2 C_{2v} dipole transitions along the Σ line of the Brillouin zone of the fcc crystal. (+) stands for the vector potential $\boldsymbol{A} \parallel \Sigma$, (0) stands for $\boldsymbol{A} \perp \Sigma$ and $\boldsymbol{A} \parallel x$, and ($X$) stands for $\boldsymbol{A} \perp \Sigma$ and $\boldsymbol{A} \parallel y$

C_{2v}	Σ_1	Σ_2	Σ_3	Σ_4
Σ_1	+	⋯	0	X
Σ_2	⋯	+	X	0
Σ_3	0	X	+	⋯
Σ_4	X	0	⋯	+

the y direction; the allowed transitions are of the type $\Sigma_1 \rightarrow \Sigma_4$. Here, Σ_1, Σ_2, Σ_3, and Σ_4 correspond to the irreducible representation A_1, A_2, B_1, and B_2, respectively. Therefore, A_1 (includes atomic orbitals s, p_z, $d_{z^2-r^2}$), B_1 (this includes atomic orbitals p_x, d_{xz}), and B_2 (this includes atomic orbitals p_y, d_{yz}) atomic or molecular orbitals can be observed depending on the light polarization, but orbitals with A_2 symmetry cannot be observed.

The derivations above are obtained by nonrelativistic dipole selection rules. Taking into account the effect of spin–orbit coupling suggests the use of relativistic dipole selection rules [11.33, 34].

As can be seen from the previous example, assignment of the irreducible representation can be done easily once the point group of the system is determined by looking at how the state in question behaves physically under the symmetry operations of the group. Consider (11.13), as mentioned above, if the direct product of the irreducible representation of $\boldsymbol{A} \cdot \boldsymbol{p}$ on the irreducible representation of ψ_i does not cast the initial state into the same irreducible representation of the final state, there will be no intensity as $|\langle \psi_f | \psi_i \rangle|^2 = 0$. Again, it is important to understand that the final state in all photoemission is that of the free electron being measured by the energy analyzer, which has the irreducible representation $\boldsymbol{A}_1$. Thinking of the electron as a geometric sphere, the free electron is fully symmetric under all symmetry operators of *any* point group which, in general, are forms of mirror and rotation operations (C_n, σ_v, σ_h, i, etc.). The forms of these symmetry operators can be found elsewhere [11.37, 38]. In terms of the vector potential for the geometries of diatomic molecules bonded upright from the surface, if the vector potential $\boldsymbol{A}$ is parallel to the molecular axis (along z in Fig. 11.4), $\boldsymbol{A} \cdot \boldsymbol{p}$ typically belongs to the A_1 representation [11.13]. If the vector potential $\boldsymbol{A}$ is perpendicular to the molecular axis (parallel to x–y plane in Fig. 11.4), $\boldsymbol{A} \cdot \boldsymbol{p}$, depending on surface geometry, belongs to the irreducible representations B_1, B_2, E_1, or E_2 [11.13]. While the final state is well defined in general, it is the initial state which is complicated; here we turn to molecular orbital theory.

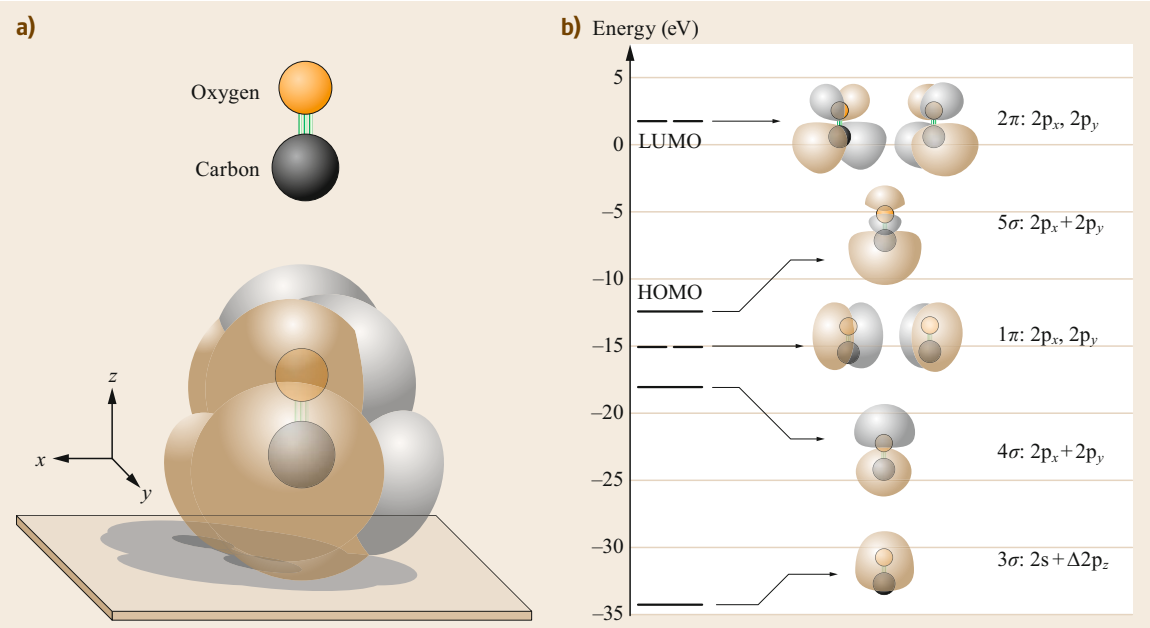

Fig. 11.4a,b Schematic of the CO molecule. **(a)** CO molecule without molecular orbitals (*top* of **(a)**) and with molecular orbitals (*bottom*); **(b)** 3σ, 4σ, 1π, 5σ, and 2π orbitals and corresponding energy levels calculated using a density functional calculation based on the global hybrid generalized gradient approximation, with the B3LYP functional, and the 6-31G* polarization basis set in the Spartan 16′ software package [11.35, 36]

In molecular orbital theory, we gain the structure of the molecular orbitals in terms of energy and contributions from atomic orbitals, and from this we can form the wavefunction of the orbitals and assign symmetry. As with homonuclear molecules (N_2) the equal energy atomic orbitals produce molecular orbitals that have *vertical* mirror symmetry, as each atomic orbital equally contributes to each molecular orbital, and this feature is clearly lacking in the CO molecule. As is shown in Fig. 11.4, the molecular orbitals of CO all have some apparent symmetry; however before the assignment of irreducible representation of each we must know which symmetry group the system belongs to, and interestingly this is different for gas phase and adsorbate phase, as we will see in the following examples.

Gas Phase Carbon Monoxide. Gas phase carbon monoxide belongs to the symmetry group $C_{\infty v}$, due to the molecule containing infinite rotational symmetry (C_∞) about the molecular axis in addition to infinite planes of mirror symmetry (σ_v) parallel to the rotational axis while lacking a dihedral mirror plane, as illustrated in Fig. 11.5. The assignment of symmetry groups quickly becomes complicated for larger molecules and systems, and the methodology of this assignment can be found elsewhere [11.37]. Now that the gas phase carbon monoxide system has been assigned a symmetry group, we may allot irreducible representations to the molecular orbitals, as shown in Fig. 11.4, by using the character table for the symmetry group shown in Table 11.3.

From the character table, we can note that the 3σ, 4σ, and 5σ occupied molecular orbitals (Fig. 11.4) belong to the A_1 irreducible representation, as they are symmetric under the identity operator (E), have infinite rotation (C_∞), and have infinite mirror planes $(\sigma_v) : (1,\ 1,\ \ldots,\ 1)$. We also note that the 1π occupied orbital belongs to the E_1 irreducible representation due to a lack of infinite mirror plane symmetry: $(2,\ 2\cos(\varphi),\ \ldots,\ 0)$. While assignment of symmetry and irreducible representations can be done by using a mathematical representation of the state in question, it is far easier to think of or use a physical model and apply the symmetry operations. Once the irreducible representation is known, one can determine the necessary configuration of the vector potential $\boldsymbol{A}$ from the direct product table for the symmetry group, as provided in Table 11.4. Using (11.13) together with the knowledge that the final state free electron is of representation A_1, in order to access the 3σ, 4σ, and 5σ occupied molecular orbitals requires $\boldsymbol{A}\cdot\boldsymbol{p}$ to be of the form A_1 (along z), as given by $|\langle A_1|A_1|A_1\rangle|^2 = |\langle A_1|A_1\rangle|^2 \neq 0$. Similarly, to access the 1π occupied orbital requires $\boldsymbol{A}\cdot\boldsymbol{p}$ to be of form of E_1 (parallel to x–y plane), as the resulting direct product has some A_1 characteristic $|\langle A_1|E_1|E_1\rangle|^2 = |\langle A_1|A_1\rangle|^2 + \cdots \neq 0$. Hence, the problem of gas phase carbon monoxide is seemingly solved; if we pick the appropriate polarization of light, we access different molecular orbitals. Overall, this process is more easily done without consideration of mathematical complexity; it is simply a short and easy tool to find selection rules. However, so far, we have only considered a single molecule of carbon monoxide. In the real gas phase, the orientation of the carbon monoxide molecules is random, such that there are portions of the gas that are perpendicular to one another; hence there is no polarization dependence for photoemission in the free gas phase. Regardless of polarization, we will have some portion of the gas in which the vector potential falls along A_1 or E_1 in relation to the molecules, enabling access to all molecular orbitals given the correct incident energy.

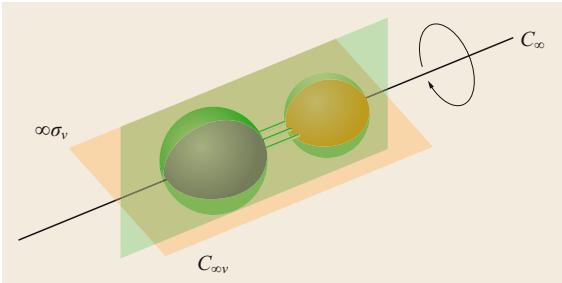

Fig. 11.5 Depiction of the rotation operation, C_∞, and mirror operation symmetries, $\infty\sigma_v$ of the $C_{\infty v}$ point group for the carbon monoxide molecule

Table 11.3 Character table for the $C_{\infty v}$ point group. The Mulliken symbols A_1, A_2, and E_1 are the irreducible representations of the $C_{\infty v}$ point group, the row with E, $2C_\infty$, $\infty\sigma_v$ represents the symmetry operations of the group, and the two columns on the right-hand side of the table represent the basis functions of the irreducible representations

$C_{\infty v}$	E	$2C_\infty$	$\cdots$	$\infty\sigma_v$	Linear	Quadratic
A_1	1	1	$\cdots$	1	z	x^2+y^2, z^2
A_2	1	1	$\cdots$	-1	R_z	
E_1	2	$2\cos(\varphi)$	$\cdots$	0	x, y, R_x, R_y	xz, yz
$\cdots$	$\cdots$	$\cdots$	$\cdots$	$\cdots$	$\cdots$	$\cdots$

Table 11.4 Direct product table for the $C_{\infty v}$ point group. The Mulliken symbols A_1, A_2, and E_1 represent the irreducible representations of the point group

$C_{\infty v}$	A_1	A_2	E_1	$\cdots$
A_1	A_1	A_2	E_1	$\cdots$
A_2		A_1	E_1	$\cdots$
E_1			$A_1+A_2+\ldots$	$\cdots$
$\cdots$	$\cdots$	$\cdots$	$\cdots$	$\cdots$

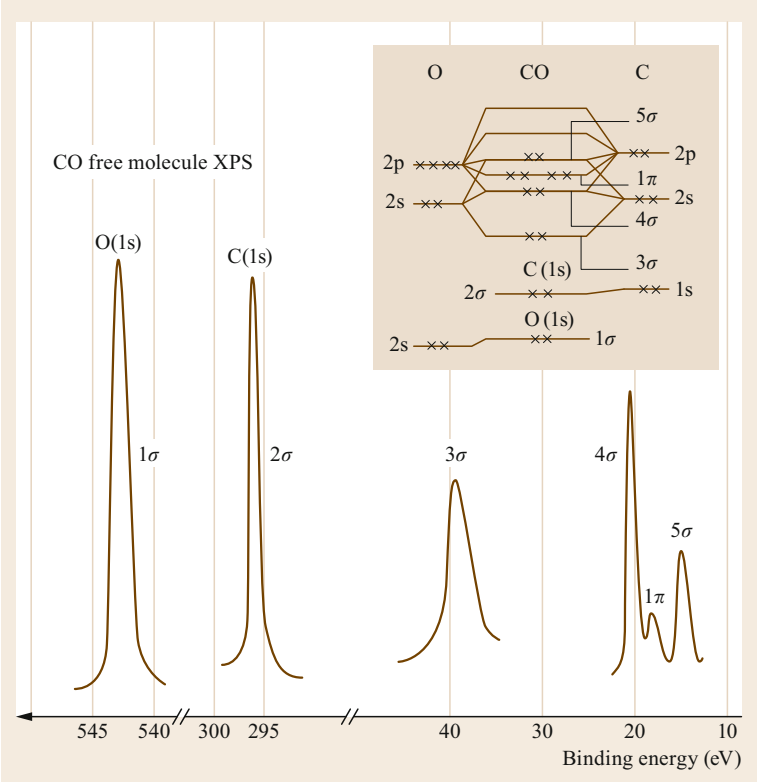

Fig. 11.6 Photoemission spectra of gas phase carbon monoxide; all molecular orbitals are accessed with the same polarization of light (From [11.39])

The phenomenon of polarization independence is evident from Fig. 11.6 for a free carbon monoxide molecule where there is no indication of light source polarization, in comparison to Fig. 11.7 which shows polarization dependent photoemission spectra of carbon monoxide on Ni(100). When the molecules are all oriented in the same direction, we will have polarization dependence, as is the case with carbon monoxide on metal surfaces, which is also the next example.

Adsorbate Phase Carbon Monoxide. As discussed with gas phase carbon monoxide, the symmetry group of the system is vital when determining the irreducible representations of the molecular orbital. The polarization dependence of the molecular orbital will develop a framework for polarization-dependent photoemission selection rules. Recall that we determined that gas phase carbon monoxide is of $C_{\infty v}$ symmetry. Adsorbate phase carbon monoxide is slightly different in that with the adherence of an adsorbate to a substrate, the system takes on the symmetry of the lowest symmetry component. Understandably, $C_{\infty v}$ has a very high degree of symmetry, thus in the interaction of CO with surfaces, the system symmetry is based on that of the surface. A good example of this is the difference in symmetry from different planes of fcc nickel where Ni(100) is C_{4v} or fourfold rotationally symmetric with four corresponding planes of vertical mirror symmetry, or Ni(111), which is C_{6v} or sixfold rotationally symmetric with six corresponding planes of vertical mirror symmetry, as shown in Fig. 11.8.

There must now be a quick discussion of the effects of the bonding of the carbon monoxide onto the surface. While the symmetry reduction is purely geometrical, the chemical process of bonding must have influence on the molecular orbitals. Interestingly, as can be seen in Fig. 11.9, the process of bonding with the surface pushes the 5σ to higher binding energy through electron donation to the metal, while also making 2π the highest occupied molecular orbital of the CO through backbonding and electron contribution of the metal to the $2\pi^*$ orbital [11.39].

If a CO molecule is adsorbed on Ni(100), we know that the system follows the symmetry operations of the C_{4v} group. If the molecular axis of the CO is along z, from Fig. 11.9 and Table 11.5, the 3σ, 4σ, and 5σ occupied molecular orbitals are of A_1 representation, as they are fully symmetric about the z-axis, both rotationally and along mirror planes: (1, 1, 1, 1, 1). Hence to access the 3σ, 4σ, and 5σ orbitals in photoemission, following Table 11.6, we need $\boldsymbol{A}\cdot\boldsymbol{p}$ to be of the form A_1 (along z), as (11.13) allows $|\langle A_1|A_1|A_1\rangle|^2 =$

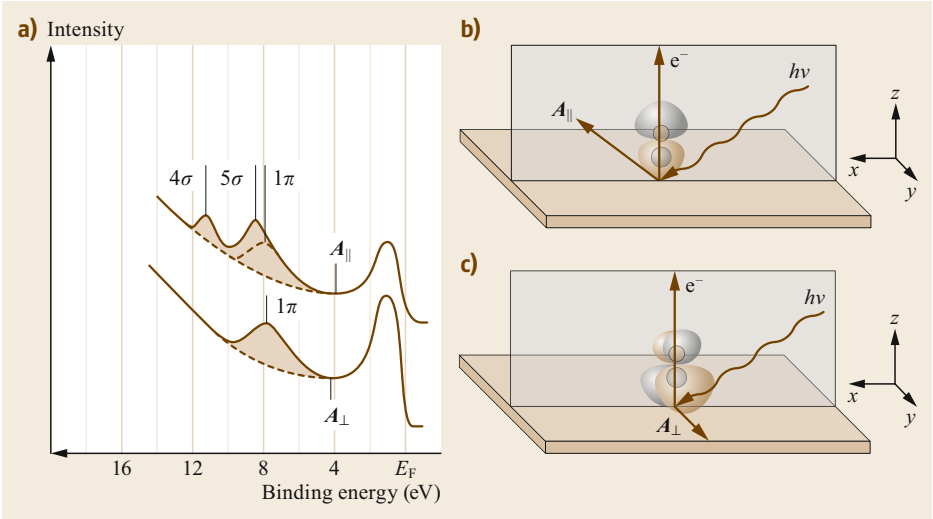

Fig. 11.7a–c **(a)** Photoemission spectra of carbon monoxide on Ni(100), geometry of the experiment indicating in **(b)** the 4σ molecular orbital of carbon monoxide with the polarization vector parallel to the molecular axis (z axis) and in **(c)** the 1π molecular orbital of carbon monoxide with the polarization vector perpendicular to the molecular axis (parallel to x–y plane) (**(a)** from [11.39])

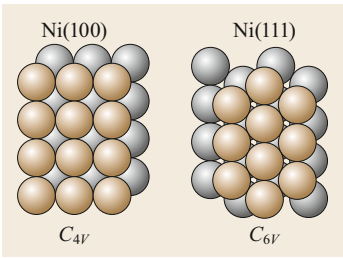

Fig. 11.8 Ni(100) and Ni(111) surfaces with C_{4v} and C_{6v} symmetry, respectively

$|\langle A_1|A_1\rangle|^2 \neq 0$. Likewise, the 1π occupied orbital belongs to the E representation due to the lack of C_4 rotational symmetry about the z-axis. This implies that to access the 1π state $\boldsymbol{A}\cdot\boldsymbol{p}$ needs to be of the form E (parallel to the x–y plane), as again from Table 11.4, $|\langle A_1|E|E\rangle|^2 = |\langle A_1|A_1\rangle|^2 + \ldots \neq 0$. Subsequent application of this methodology can be applied to the C_{6v} case of Ni(111). Here, we find that the 3σ, 4σ, and 5σ occupied molecular orbitals are again of A_1 representation (Table 11.7) due to being fully symmetric about the z-axis for rotational and mirror operations, which according to Table 11.8 would require $\boldsymbol{A}\cdot\boldsymbol{p}$ to be of the form A_1 (along z) to observe photoemission. Assignment of the 1π occupied orbital falls under the E_1 representation in Table 11.7, due to loss of C_6 rotational symmetry about the z-axis, requiring $\boldsymbol{A}\cdot\boldsymbol{p}$ to be of the form E_1 (parallel to x–y plane) for photoemission (Table 11.8). Unlike the gas phase carbon monoxide, the adsorbate phase has ordering and alignment of carbon monoxide on particular metal surfaces. Due to this ordering, we observe polarization-dependent photoemission (Fig. 11.7) for the C_{4v} Ni(100) case, where we do not for the gas phase (Fig. 11.6). The 4σ and 5σ of the CO/Ni(100) are accessed through parallel polarized light, and 1π is accessed through perpendicular polarized light as predicted from symmetry arguments (Fig. 11.7b,c).

Table 11.5 Character table for the C_{4v} point group. The Mulliken symbols A_1, A_2, B_1, B_2, and E are the irreducible representations of the C_{4v} point group, the row with E, $2C_4$, C_2, and $2\sigma_v$, $2\sigma_d$ represents the symmetry operations of the group, and the two columns on the right-hand side of the table represent the basis functions of the irreducible representations

C_{4v}	E	$2C_4$	C_2	$2\sigma_v$	$2\sigma_d$	Linear	Quadratic
A_1	1	1	1	1	1	z	x^2+y^2, z^2
A_2	1	1	1	−1	−1	R_z	
B_1	1	−1	1	1	−1		x^2-y^2
B_2	1	−1	1	−1	1		xy
E	2	0	−2	0	0	x, y, R_x, R_y	xz, yz

Table 11.6 Direct product table for the C_{4v} point group. The Mulliken symbols A_1, A_2, B_1, B_2, and E, represent the irreducible representations of the point group

C_{4v}	A_1	A_2	B_1	B_2	E
A_1	A_1	A_2	B_1	B_2	E
A_2		A_1	B_2	B_1	E
B_1			A_1	A_2	E
B_2				A_1	E
E					$A_1+A_2+B_1+B_2$

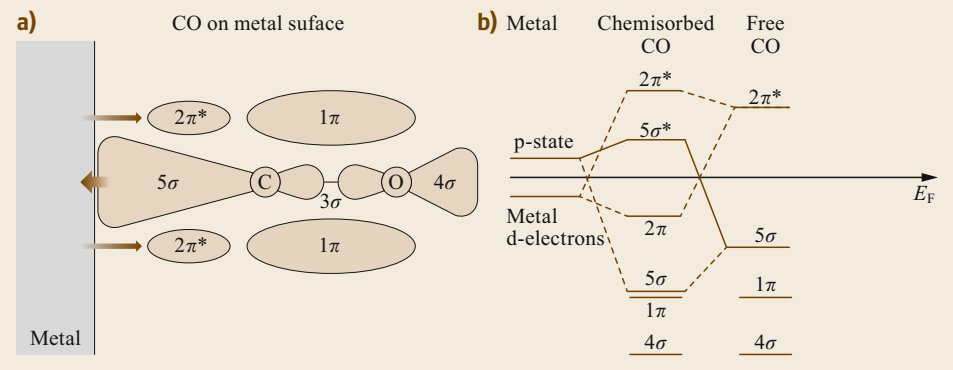

Fig. 11.9a,b Bonding geometry of carbon monoxide to the metal surface **(a)**, electron donation indicated by *arrows*, and molecular orbital diagram of adsorbed carbon monoxide **(b)** (From [11.39])

Table 11.7 Character table for the C_{6v} point group. The Mulliken symbols A_1, A_2, B_1, B_2, E_1, and E_2 are the irreducible representations of the C_{6v} point group, the row with E, $2C_6$, $2C_3$, C_2, and $3\sigma_v$, $3\sigma_d$ represents the symmetry operations of the group, and the two columns on the right-hand side of the table represent the basis functions of the irreducible representations

C_{6v}	E	$2C_6$	$2C_3$	C_2	$3\sigma_v$	$3\sigma_d$	Linear	Quadratic
A_1	1	1	1	1	1	1	z	x^2+y^2, z^2
A_2	1	1	1	1	−1	−1	R_z	
B_1	1	−1	1	−1	1	−1		
B_2	1	−1	1	−1	−1	1		
E_1	2	1	−1	−2	0	0	x, y, R_x, R_y	xz, yz
E_2	2	−1	−1	2	0	0		x^2-y^2, xy

Table 11.8 Direct product table for the C_{6v} point group. The Mulliken symbols A_1, A_2, B_1, B_2, E_1, and E_2 represent the irreducible representations of the point group

C_{6v}	A_1	A_2	B_1	B_2	E_1	E_2
A_1	A_1	A_2	B_1	B_2	E_1	E_2
A_2		A_1	B_2	B_1	E_1	E_2
B_1			A_1	A_2	E_2	E_1
B_2				A_1	E_2	E_1
E_1					$A_1+A_2+E_2$	$B_1+B_2+E_1$
E_2						$A_1+A_2+E_2$

ARPES and ARIPES at a Glance

ARPES can be used to explore the occupied molecular orbital band structure of molecular crystals and ordered molecular adlayers, while ARIPES can be used to explore the unoccupied molecular orbital band structure. The band structure can be defined as the energy dependence of the electron states as a function of the wave vector [11.13]. The measured band structure is resolved in reciprocal space, i.e., momentum space, and as such is useful for investigating the wave-like nature of the electron. As the band structure is represented in reciprocal space, it helps to define the Brillouin zone (BZ) of the material under study. Before diving into experimental examples, it is instructive to briefly discuss band dispersion.

Electronic band dispersion in the case of ARPES (ARIPES) refers to the relationship between the kinetic energy of the emitted electron (photon) and the wave vector $\boldsymbol{k}$. As the kinetic energy is directly related to the binding energy, the band dispersion can be viewed as a variation of the molecular orbital binding energy as a function of the wave vector [11.8–11, 13, 40–45]. It is important to note that the wave vector also heavily influences the allowed irreducible representation, and any changes in the wave vector could change the symmetry of the point group [11.13].

We can follow the derivation from *Dowben* et al. [11.13] where the one-dimensional periodic wavefunction is just a linear combination of wavefunctions at each lattice site m, which can be represented by the following equation

$$\psi_{\boldsymbol{k}} = \sum_m \mathrm{e}^{\mathrm{i}\boldsymbol{k}ma}\xi_m \,. \tag{11.15}$$

When $\boldsymbol{k}=0$ the wavefunction becomes,

$$\psi_{\boldsymbol{k}=0} = \sum_m \xi_m \,. \tag{11.16}$$

When $\boldsymbol{k}=\pi/a$, at the BZ boundary the wavefunction becomes,

$$\psi_{\boldsymbol{k}=\pi/a} = \sum_m (-1)^m \xi_m \,. \tag{11.17}$$

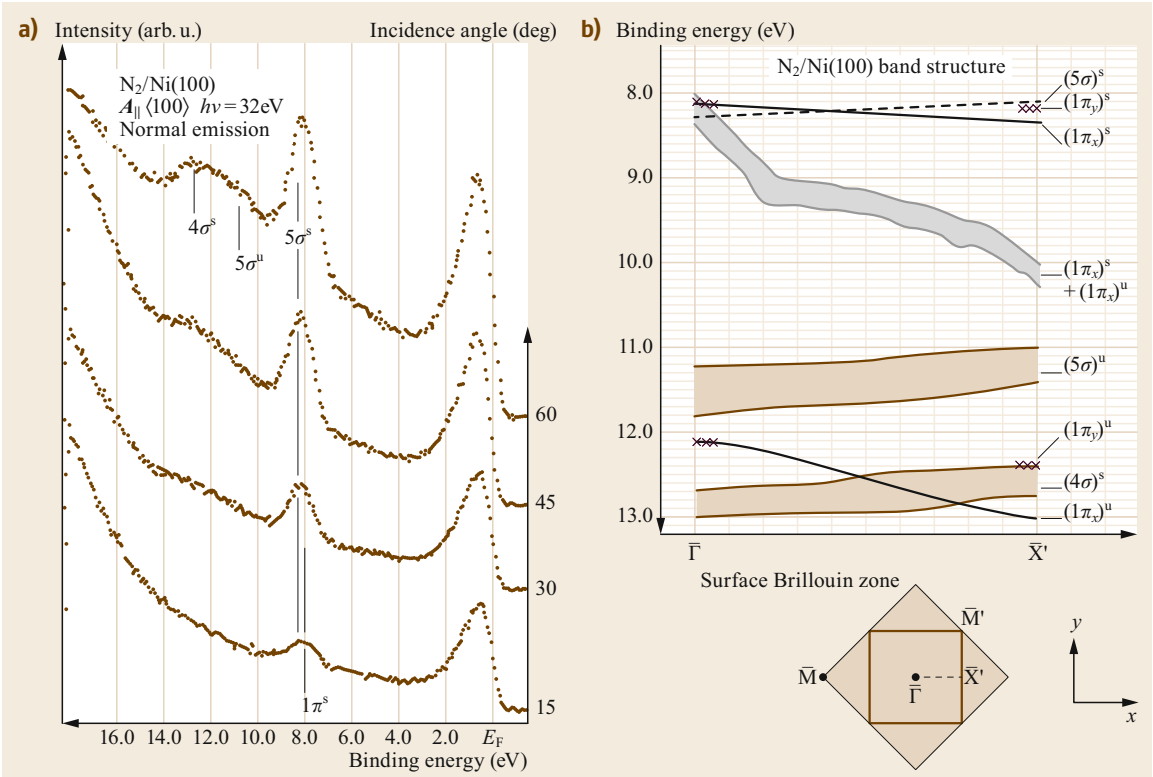

Fig. 11.10 **(a)** Incidence angle dependence of the photoemission spectra for Ni(100)c(2×2)-N_2. The features are assigned with orbital contributions using dipole selection rules and **(b)** the band dispersion of the N_2 molecular orbital taken from $\overline{\Gamma}$ to $\overline{X}'$ (Reprinted from [11.46], with permission from Elsevier)

The dependence on the wave vector influences the overall wavefunction and the observed binding energy [11.8, 9, 11, 13, 41, 43]. If we apply the law of conservation of momentum to the physical process of ARPES (ARIPES), then the energy band dispersion relation, as it relates to the wave vector $\boldsymbol{k}$, can be determined. Consider the process of ARPES (ARIPES): in the UV energy range, an incident photon (electron) strikes the surface of the ordered material and emits an electron (photon). The momentum of the incident (emitted) photon is negligible compared to the emitted (incident) electron, thus we can neglect the momentum of the incident (emitted) photon [11.47]. The momentum is conserved in the direction parallel to the surface, and as such the wave vector component parallel to the surface, $k_{\parallel}$, is conserved. On the other hand, the momentum is not conserved in the direction perpendicular to the surface, and as such the wave vector component perpendicular to the surface, $k_{\perp}$, is not conserved. The momentum is not conserved in the perpendicular direction because of the cutoff at the crystal surface [11.13]. The kinetic energy can be written as,

$$E_{\mathrm{kin}} = \frac{\hbar^2}{2m}\left(k_{\parallel}^2 + k_{\perp}^2\right). \tag{11.18}$$

This leads to the following expression for the parallel component of the wave vector,

$$k_{\parallel} = \sqrt{\frac{2m}{\hbar^2}E_{\mathrm{kin}}}\sin\theta\,, \tag{11.19}$$

where θ is the emission angle of the photoelectron with respect to the surface normal or the incident angle of the electron in IPES.

Now that we have discussed the electronic energy band dispersion in terms of the wave vector we can take a closer look at an experimental example, specifically the study performed by *Dowben* et al. on molecular N_2 on Ni(100) [11.46]. In this experiment, molecular nitrogen adsorbs onto the surface of clean Ni(100) in an ordered overlayer. Following N_2 deposition, ARPES was performed using an s-polarized ultraviolet light

source, where $\boldsymbol{A}$ is parallel to the surface. The incidence angle dependent photoemission spectra are shown in Fig. 11.10a, which indicates two features: one at 8 eV and the second at 12 eV binding energy. As N_2 has $C_{\infty v}$ symmetry (although, realistically, the symmetry is reduced to the C_{4v} symmetry of the Ni(100) surface), the feature observed at 8 eV is generally attributed to the 1π and 5σ orbitals, while the broad feature around 12 eV is considered the 4σ orbital contribution [11.48–51]. If one considers screened and unscreened final state effects, the details of which will be discussed later in the chapter,then there are six possible features that may show up in the final state photoemission spectrum for N_2 due to the screened and unscreened 4σ, 5σ, and 1π orbitals [11.50, 52]. *Dowben* et al. [11.46] argue that the N_2 molecule is oriented on Ni(100) with the molecular axis perpendicular to the Ni(100) surface, as there are only two features observed with s-polarized light at the $\overline{\Gamma}$ point of the BZ. The two features observed at $\overline{\Gamma}$ are assigned as $1\pi^{s}$ and $1\pi^{u}$ at 12.1 and 8.1 eV, respectively. Here, the superscripts s and u stand for screened and unscreened, respectively. At higher incidence angles, 45° and 60°, the σ features have the same orientation as the N_2 molecule, such that the molecular axis of N_2 is perpendicular to the Ni(100) surface. Dowben et al. use *Messmer*'s [11.52] cluster calculations to assign the features at 8.3, 11.4, and 12.8 eV to the $5\sigma^{s}$, $5\sigma^{u}$, and $4\sigma^{s}$ orbitals of N_2, respectively.

Dowben et al. [11.46] also measured dispersion curves from $\overline{\Gamma}$ to $\overline{X'}$ in the BZ for N_2 on Ni(100), which are shown in Fig. 11.10b. The main point to take away from the dispersion curves is that at $\overline{\Gamma}$ the σ orbitals are in bonding configurations, while the π orbitals are in antibonding configurations. As the dispersion moves from $\overline{\Gamma}$ to $\overline{X'}$, we can see that the bonding configuration changes, rather at $\overline{X'}$ the σ orbitals are now in antibonding configurations, while the π orbitals have changed to bonding configurations.

11.2 Chemical Shifts in XPS

11.2.1 Initial and Final State Effects and Screened and Unscreened Final States

This section will deal with the possible effects that may be observed and identified from photoemission and inverse-photoemission spectra due to changes in the chemical environment of adsorbates on both metallic and organic substrates. To describe screened and unscreened final states we must first discuss initial and final state effects in general, and the influence these play in spectroscopic data.

To begin with, initial state effects within the combined inverse and photoemission spectra arise from changes in the electrostatic potential of the core associated with the Madelung energy, charge transfer, and chemical bonding [11.53]. On the other hand, final state effects arise from screening via charge transfer from the bulk material to the adsorbate or vice versa. Another way to phrase this difference is that in the XPS process, our incident x-ray is absorbed by the material, whereby the latter is ionized; the characteristics of the ionization process are dependent on the chemical environment of the material as stated above, and this is our initial state effect. Once in the ionized state, the relaxation of a core-hole from the excited state produces an Auger photoelectron whose kinetic energy is measured and, in turn, provides the binding energy of states within the material. However, if during this relaxation process there is charge transfer from the bulk, as contributed by final state effects, then there exists a partial charge that screens the hole produced from the ionization. Depending on the direction of the charge transfer, the binding energy of the state moves accordingly.

Now we should discuss how initial and final state effects can shift spectral features. As is apparent from studies on gadolinium thin films [11.53], the shifting of the HOMO (highest occupied states of the molecular orbital) and the LUMO (lowest unoccupied states of the molecular orbital) structures within valence band (occupied states) and conduction band (unoccupied states) spectra for initial and final states appears vastly different. The central point introduced by *Ortega* et al. is that changes in spectra from initial state effects result in a shifting of the band gap, more so that both the HOMO and LUMO are rigidly shifted higher or lower in binding energy [11.53]. This is obvious when considering a change in chemical environment surrounding atoms within the substrate; the addition of an adsorbate with higher electronegativity will have a tendency to remove electron density from the substrate. This depletion of electrons forces the HOMO and LUMO to lower energy as the filling of the energy levels within the substrate with less electron density results in the highest occupied state to be a lower bound state than before, and similarly the lowest unoccupied state shifts to lower energy in response. If these states are shifted to lower values, for photoemission spectroscopy PES this requires a greater photon energy to ionize and, thus, results in a higher (more negative) binding energy. Similarly, for IPES, an incident electron of lower kinetic energy may absorb into the LUMO and, thus, we would observe both the HOMO and LUMO to have greater binding energy.

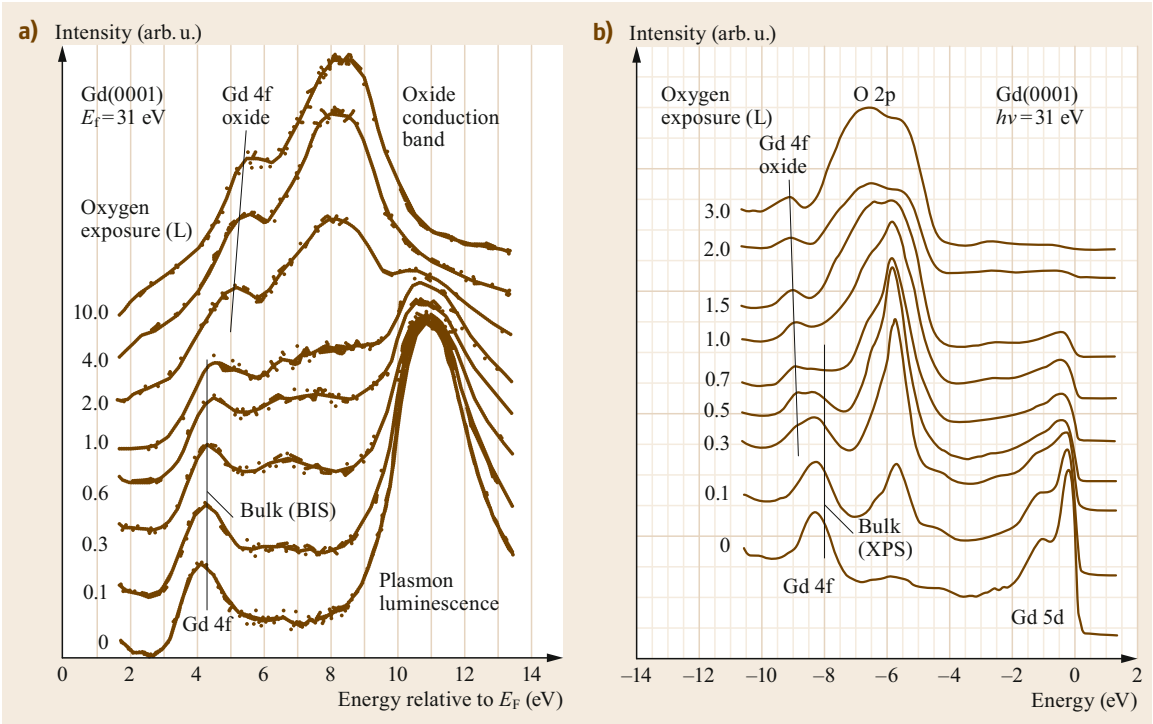

Fig. 11.11 **(a)** IPES and **(b)** PES plots of Gd(0001) with increasing levels of oxygen exposure (Reprinted from [11.53], with permission from Elsevier)

In contrast to these observed initial state effects, there are the final state effects wherein the HOMO and LUMO shift toward or away from one another. This phenomenon can be visualized on the basis of screened and unscreened final states or charge transfer where there exists a sign change in the induced charge when transitioning from a hole in the occupied core level to an extra electron in the empty core level [11.53]. Thus, for a system where there is charge transfer of electron density from an adsorbate to the substrate (screened final state), this appears as a decrease in binding energy of the HOMO within PES due to electron transfer screening the core-hole and producing a repulsive potential with respect to the photoelectron and, hence, increasing the kinetic energy of the ejected photoelectron. Screening effects also produce an increase in the LUMO binding energy within IPES, as the incident electron experiences an attractive potential due to the sign change in the charge transfer from the adsorbate requiring an electron with less kinetic energy for the absorption process and, thus, in turn produces a higher (more negative) binding energy of the LUMO. Hence, screened final states overall reduce the HOMO–LUMO gap found within spectra. On the other hand, it is in unscreened final states where there is a lack of net charge transfer. In this case, within PES the photoelectron experiences only the attractive potential of the core-hole with no reduction from screening and, hence, the photoelectron will have less kinetic energy, forcing the HOMO to have higher binding energy. Within IPES, the absorbed electron does not experience the attractive potential seen within screening and, hence, requires an incident electron with greater kinetic energy, producing a LUMO with lower (less negative) binding energy than in the presence of screening. Hence, unscreened final states lacking a net charge transfer act in such a way to increase the HOMO–LUMO gap.

Central to understanding the differences between the aforementioned effects, we should discuss the case of *Ortega* et al.'s oxygen coverage-dependent spectroscopy of Gd(0001) [11.53]. For the situation where screened final states are dominant, as seen in Fig. 11.11, at lower oxygen coverages, the Gd 4f peak in both PES and IPES shifts to lower binding energy due to the adsorbed oxygen pulling electron density away from the Gd and, thus, reducing the binding energy of both (initial state effect). At higher oxygen coverages it is apparent that unscreened final state effects dominate as the Gd 4f peaks move farther apart. In this situation the strong electronic pull of the oxygen does not allow for screening or results in reduced screening of the core-hole.

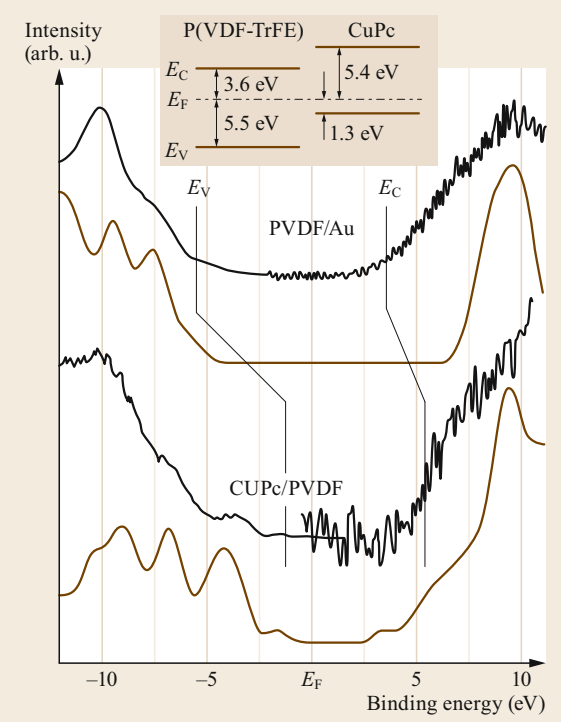

Fig. 11.12 IPES and PES band structure of CuPc/PVDF and PVDF/Au with theoretical band structure given in *brown* (P(VDF-TrFE)—poly(vinylidenefluoride-co-trifluoroethylene)) (Reprinted from [11.54], with the permission of AIP Publishing)

We may also observe systems where both initial and final state effects are congruent, as in the systems of PVDF/Au and CuPc/PVDF [11.54]. PVDF stands for polyvinylidene fluoride, which is a type of fluoropolymer, and Pc stands for phthalocyanine, which is a type of organic compound. Initial state effects can be observed in the two PVDF-based systems, for example as can be seen in Fig. 11.12, in the PVDF/Au system with the addition of Au, the band structure becomes n-type, as HOMO and LUMO rigidly shift to higher (more negative) binding energy. However, in the CuPC/PVDF system with the addition of the CuPc on PVDF, the system becomes p-type as HOMO and LUMO rigidly shift to lower (more positive) binding energy. Both of the shifts in the Au/PVDF and CuPc/PVDF systems are in response to a change in the chemical environment. Additionally, some final state effects are present as the HOMO–LUMO gap has widened or compressed due to an adlayer, as can be seen in the insert of Fig. 11.12. Although final state effects can be observed in both the PVDF/Au and CuPc/PVDF systems, *Xiao* et al. conclude that final state effects are negligible as the rigid shift in the band edges are far greater than the change in the HOMO–LUMO gap [11.54]. Thus, in a system where both effects are present, it is clear that the initial state effects are dominating, and the final state effects are not large enough to change either system from insulating to conductive in character, in other words, changing a large band gap to a small band gap.

It is instructive to consider another example where *Xiao* and *Dowben* studied CoPc, NiPc, and CuPc on PVDF [11.55]. In these systems Co, Ni, or Cu, serve as the metal centers of a phthalocyanine organic compound. Again, within each system variable coverages of the phthalocyanines produce small changes in the size of the band gaps. However, the more interesting comparison is the change in band gaps when comparing phthalocyanines with different metal centers. As illustrated in Fig. 11.13, the simple change in chemi-

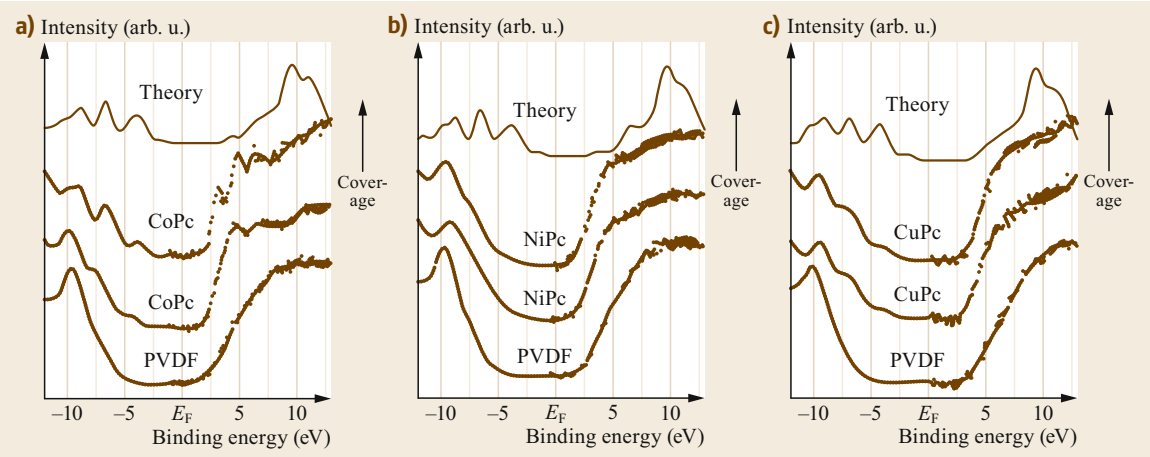

Fig. 11.13a–c PES and IPES spectra showing the band structure for different systems of **(a)** CoPc, **(b)** NiPc, and **(c)** CuPc on PVDF (Reproduced from [11.55] with permission of The Royal Society of Chemistry)

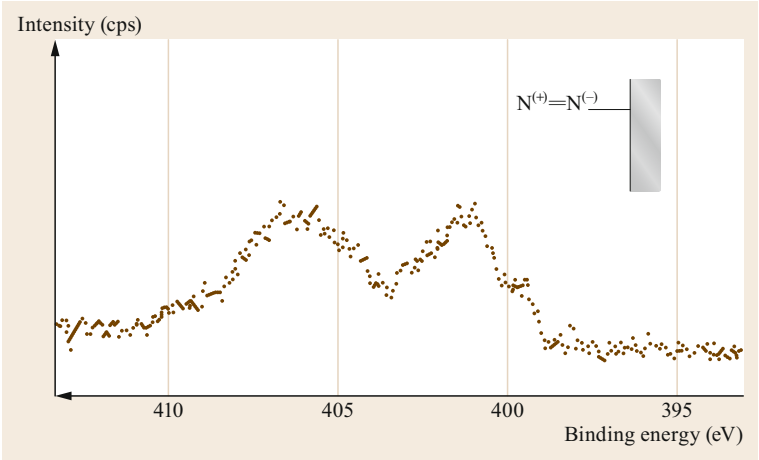

Fig. 11.14 N 1s spectra of N_2 on Ni(110) (Reprinted from [11.56], with permission from Elsevier)

cal environment from the contribution of the Co^{2+} $3d^7$, Ni^{2+} $3d^8$, and Cu^{2+} $3d^9$ orbitals within these phthalocyanines vastly changes the characteristics of the valence band [11.55]. Still, the initial state effects from varying the metal II centers greatly overshadow any final state effects present.

While the previous cases show initial state effects dominating the final state effects, we may also observe initial state effects causing splitting of final state spectra peaks as is the case with N_2 on Ni [11.46, 56]. As illustrated in Fig. 11.14, the higher binding energy peak within the N 1s spectrum is that of the unscreened final states, and the lower binding energy peak belonging to that of screened final states is further split by the separate chemical states of the nitrogen adsorbed on the surface [11.56].

The initial state effects and screened and unscreened final states effects may be further described in terms of bonding and antibonding orbitals and in conjunction with photoemission selection rules as well as the HOMO–LUMO position to determine adsorbate orientation [11.46, 54]. Such further analysis and identification is, indeed, complicated and better suited to be described in more detail elsewhere. However, understanding how initial state and final state processes affect spectroscopic data creates a good foundation for deeper investigation.

11.2.2 Surface-to-Bulk Core Level Shift

It is apparent from the above discussion that the core level binding energies are heavily influenced by the chemical environment of the atom from which the electron is emitted. The core level binding energies can experience a shift to either higher or lower binding energies for several reasons. One type of peak shift observed in XPS spectra is a core-level shift known as a surface-to-bulk core level shift, which has an extensive experimental history [11.57, 58] and is supported by many theoretical studies [11.59–63]. The surface-to-bulk core level shift is observed because surface atoms have different chemical environments than their bulk atom counterparts. If we consider how the neighboring atoms differ for a bulk atom versus a surface atom, it is apparent that the coordination number (number of bonds) of surface atoms is reduced compared to that of bulk atoms. The reduced coordination number leads to a narrowing of the valence band due to charge redistribution, which causes a change in potential and effectively results in a shift of the surface state as observed in the XPS spectra [11.58, 64]. The shift can be toward higher or lower binding energy, depending on the degree of filling of the valence band.

As is appropriate when introducing any new concept, an example of the surface-to-bulk core level shift will help to illustrate what is observed in an experimental setting. As the first example let us consider the study performed by *Wooten* et al. on $Li_2B_4O_7(110)$ [11.65]. The Li atom can exist in only one oxidation state, which suggests that the observation of a surface-to-bulk core level shift can be attributed to a large difference in the electronic structure of surface versus bulk positions. Wooten et al. used ARPES to identify the Li 1s surface-to-bulk core level shift. As shown in Fig. 11.15, the bulk Li 1s core level binding energy was measured at -56.5 ± 0.4 eV for a geometry where the electron undergoes normal photoelectron emission. Furthermore, note there is a broad bump at lower binding energy, -53.7 ± 0.5 eV, which is attributed to a surface component. By increasing the emission angle from 0° to 20°, the intensity of the lower binding energy component increases, as is expected for a surface component of the core level [11.57, 58]. The large separation in binding energy between the bulk and surface peaks suggests that

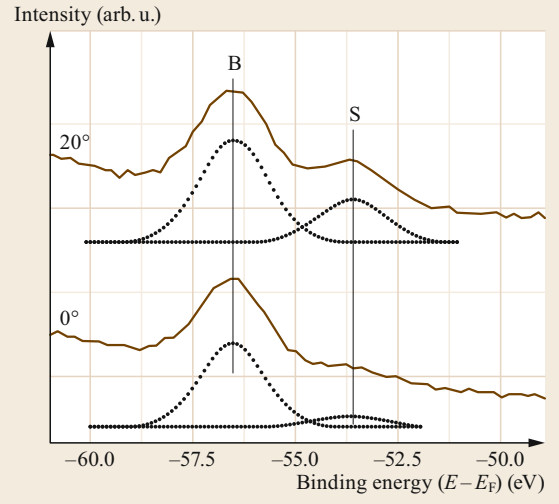

Fig. 11.15 ARPES spectra of $Li_2B_4O_7(110)$ in the region of the Li 1s core level, for photoelectron emission angles 20° and 0°. B denotes the bulk component and S the surface component (Reprinted from [11.65], with permission from Elsevier)

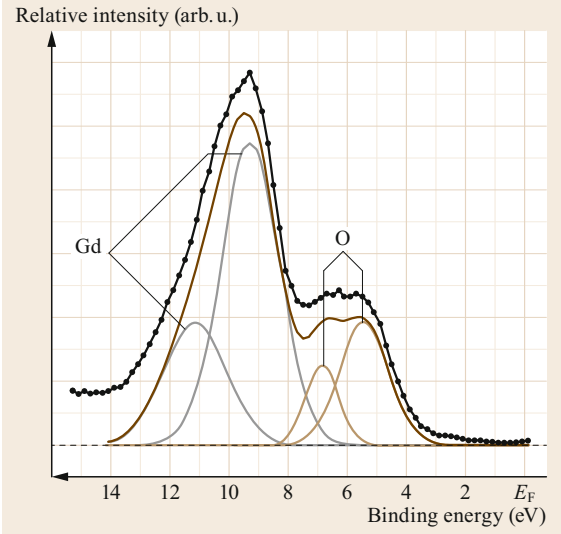

Fig. 11.16 The photoemission spectrum of the valence band of $Gd_2O_3(\bar{4}02)$ with Gd and O contributions labeled (Reprinted from [11.66]. © IOP Publishing. Reproduced with permission. All rights reserved)

the surface electronic structure is vastly different from the bulk [11.65].

As an additional example let us consider the n-type Gd_2O_3 studied by *Losovyj* et al. [11.66]. In their study, the x-ray emission spectroscopy spectra of Gd-doped HfO_2 and Gd_2O_3 are compared to one another with respect to the Gd 4f states. Here, we focus on the observed surface-to-bulk core level shift of Gd_2O_3, as it is absent in the Gd-doped HfO_2 system. It is apparent from the photoemission spectrum of the valence band, as is shown in Fig. 11.16, that there are two major contributions to the band structure, one due to Gd and the other due to O. The Gd contribution can be fit with two peaks roughly centered at 9.5 and 11.5 eV. Using resonant photoemission at various energies, *Losovyj* et al. [11.66] observe a change in intensity of the Gd contribution, as shown in Fig. 11.17a. The intensity of the resonant photoemission spectra is plotted versus the photon energy in Fig. 11.17b, taking into consideration the two peaks located at 9.5 and 11.5 eV. *Losovyj* et al. [11.66] determine that the two Gd 4f contributions at binding energies of 9.5 and 11.5 eV are due to bulk and surface states, respectively. Their separation is roughly 2 eV and may be ascribed to the oxide environment.

The two examples considered above show how the surface state can appear at higher or lower binding energy, depending on the system under investigation. The physics behind the surface-to-core level shift is rich and complicated, and for interested readers a more thorough review and analysis of surface core level spectroscopy can be found in a perspective by *Spanjaard* et al. [11.57].

11.2.3 Core Level Satellites

In XPS spectroscopy, there are sometimes additional signals or peaks at higher binding energy (lower kinetic energy), besides the main peak(s). These additional higher binding energy peaks are called satellite peaks. In principle, there are two types of processes that can cause satellite structures. The first source of satellite peaks can be understood if we consider the photoemission process. When an electron is excited from a core level as it travels to the surface, it will have a tendency to interact with the other electrons due to Coulomb and exchange interactions. These excited electrons, in turn, provide excitation to others in the systems, and these interactions cause the system to make a transition from the ground state to an excited state. Since extra energy is needed in this process, the corresponding signal will be at lower kinetic energy and as such appear as a peak at a higher binding energy in the spectrum with respect to the main peak. The second source of satellite features can be attributed to inelastic collisions. As the photoexcited electron makes its way to the surface it passes through the space that is occupied by the other electrons, so the likelihood of experiencing an inelastic collision and thus exciting the system is large. Since this excitation energy affects the kinetic energy of the outgoing electron, this means the signal will appear at

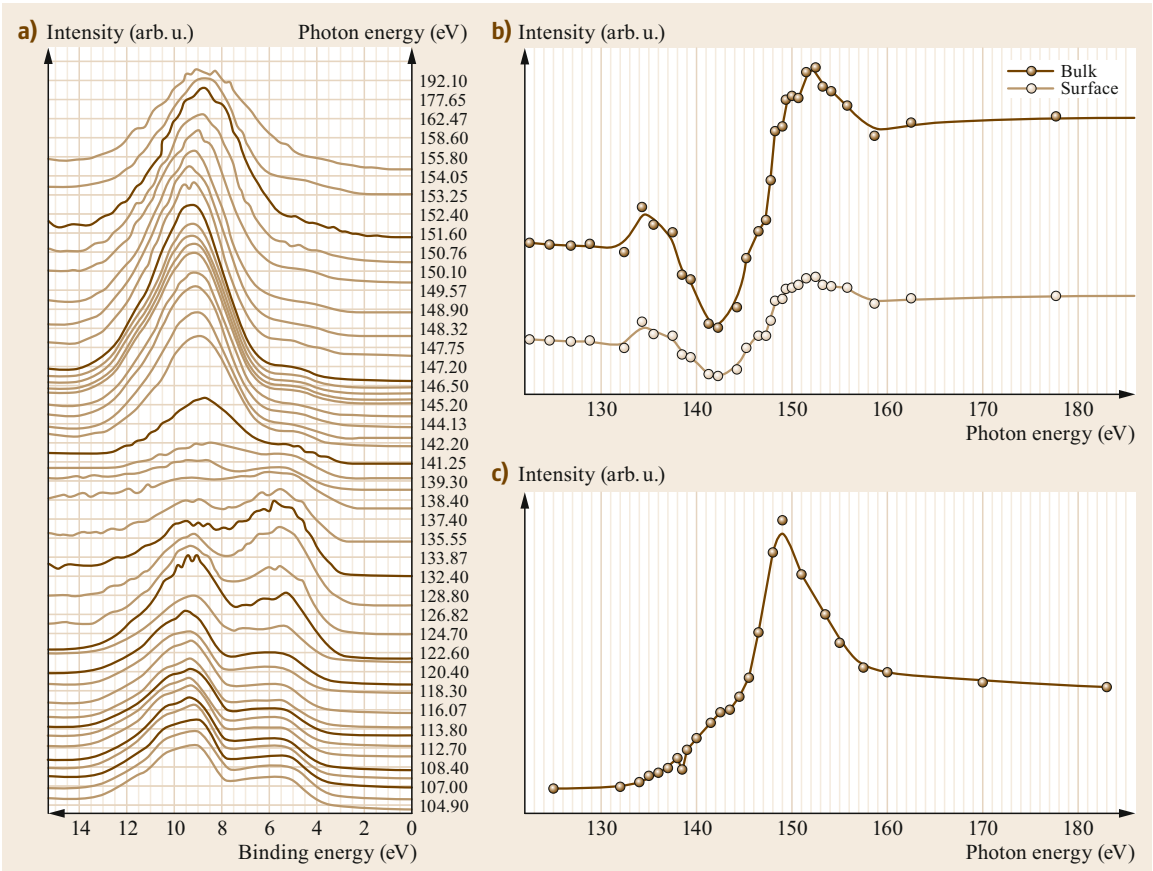

Fig. 11.17 **(a)** The resonant photoemission spectra for photon energies through the 4d → 4f resonance for Gd_2O_3 and the resonant photon intensity of the bulk versus the surface contributions plotted against photon energy for **(b)** Gd_2O_3 and **(c)** Hf-doped Gd_2O_3 (Reprinted from [11.66]. © IOP Publishing. Reproduced with permission. All rights reserved)

higher binding energy in the spectrum. No matter which case occurs, the system will have excited states that are close to the ground state. The ground state appears as the main peak, and the excited states appear as satellite peaks slightly higher in binding energy with respect to the main peaks. The intensity of these peaks is proportional to the overlap integral of their initial and final state wavefunctions [11.39].

Generally, a satellite will occur if there exist more than one final state during the photoemission process. The main peaks and satellite peaks contain different screening situations in the final state, but the analysis of those satellite features still remains difficult in most cases. Let us consider a simple case as a first example.

Transition metals possess the ability to exist in a number of different oxidation states. Furthermore, they experience what is known as multiplet splitting, a type of satellite-like feature. Multiplet splitting is caused by a coupling between the core level vacancy left behind by the photoemitted electron and the unpaired electrons in the valence state. This coupling also results in an excited state and is quite difficult to interpret. The energy separation and the shape of the multiplet peaks in combination with the main peaks can be used to determine the oxidation state of transition metals [11.67–74]. In particular, Fe compounds have been heavily investigated using XPS techniques [11.67–72, 74]. The Fe cation can take on a 2^+ oxidation state, ferrous (Fe^{2+}), or a 3^+ oxidation state, ferric (Fe^{3+}). The position of the satellite peaks in core level Fe $2p_{1/2}$ and Fe $2p_{3/2}$ spectra are sensitive to the oxidation states, and this, in turn, allows for a way to qualitatively analyze the chemical states of Fe. It has been shown that the $Fe^{2+}(2p_{3/2})$ and $Fe^{3+}(2p_{3/2})$ shake-up satellites are found at 714.5 and 719 eV, respectively, about 5–8 eV higher in binding energy than the main core $2p_{1/2}$ and $2p_{3/2}$ lines, as shown in Fig. 11.18 [11.68]. This effect, along with the separation between the multiplet splitting peaks allows one to determine the oxidation state of Fe [11.70].

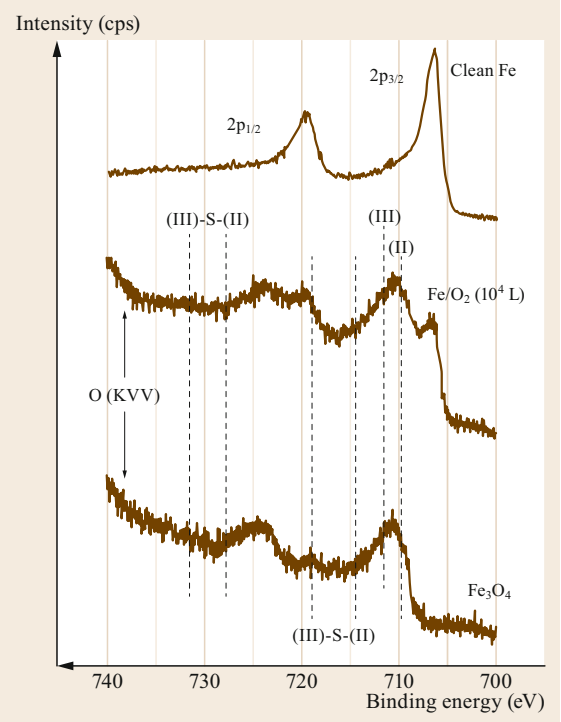

Fig. 11.18 XPS of Fe(2p) spectra for clean Fe, oxidized Fe by 10^4 L of O_2 exposure and Fe_3O_4 powder sample. (S = shake-up satellite, II and III indicate the oxidation state of Fe.) (Reprinted from [11.68], with permission from Elsevier)

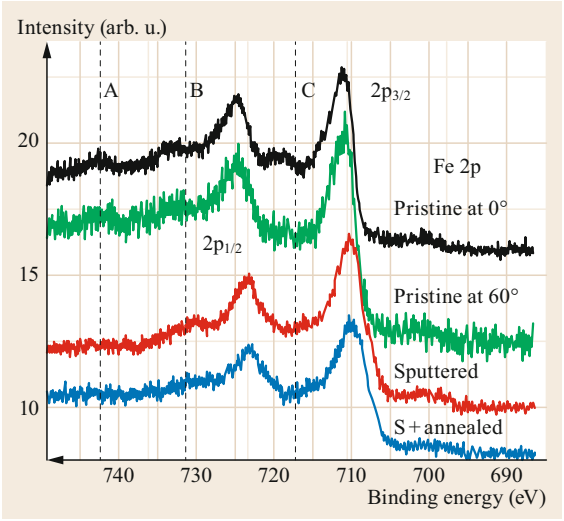

Fig. 11.19 XPS spectra for the Fe 2p core level electron structure in h-$LuFeO_3$ for pristine (both at 0° and 60° take-off angle), sputtered only, and sputtered and annealed samples taken at 0° take-off angle (Reprinted from [11.70]. © IOP Publishing. Reproduced with permission. All rights reserved)

As a second example let us take a look at the Fe 2p spectra of h-$LuFeO_3$ shown in Fig. 11.19 [11.70]. There are two main peaks ($2p_{3/2}$ and $2p_{1/2}$) with three satellites labeled by A, B, and C in Fig. 11.19. In the pristine sample, satellite C is located at 719 eV, which indicates an Fe^{3+} valance character. This feature does not change when the sample angle is changed with respect to the normal along the detector optical path, so both the surface and the bulk Fe correspond to Fe^{3+} states. However, after sputtering and annealing, the satellite moves to a lower binding energy, and the separation of energy between the satellite and the main $2p_{3/2}$ peak becomes smaller. This indicates that the oxidation state changes from Fe^{3+} to Fe^{2+}, so the local environment of Fe changes after sputtering and annealing, and it is due to the decrease of electron density around Fe by oxygen deficiencies [11.70].

The previous examples are just a couple well-studied cases of satellite features, and they are by no means exhaustive. Obtaining a thorough understanding of all the information involved with satellite transitions is still challenging and requires precise measurements coupled with extensive modeling.

11.3 Concluding Remarks

While photoemission is often used as a method to *fingerprint* molecules adsorbed on surfaces, this valuable tool has much more to offer for the understanding of the complicated nature of these systems. Photoemission can be used to identify molecular orientation, and in this sense it is complementary to near edge x-ray absorption spectroscopy. For ordered molecular adlayers, photoemission and inverse photoemission (if angle resolved) can be used to determine the extent of intermolecular interaction from the dispersion of the occupied (photoemission) and unoccupied (inverse photoemission) molecular orbitals. The often complex interactions between adsorbate and substrate can be probed through study of the photoemission spectra and asking questions such as: are there satellite features? Are screening effects present and which ones? The insight that one should gain from this brief overview is to be aware that photoemission is multifaceted and often quite complex. This means that interpreting photoemission spectra often needs caution and diligence to understand all the subtlety and value that photoemission and related spectroscopies have to show. This

chapter has shown how powerful a tool photoemission can be when used together with appropriate physical principles. It is hoped that the above discussions will provide assistance to those beginning their journey in photoemission measurement techniques and help to divulge some of the deeper physics hidden in our world.

Acknowledgments. We would like to thank the Department of Energy for supporting this research, specifically; DOE Grant DE-FG02-07ER15842. We would also like to thank Professor Peter A. Dowben for his long discussions about the physics of photoemission and his guidance with our interpretations. Prof. Dowben is truly a source of inspiration and we are eternally grateful.

References

11.1 D.W. Turner, C. Baker, A.D. Baker, C.R. Brundle: *Molecular Photoelectron Spectroscopy* (Wiley, New York 1970)
11.2 N.V. Richardson, A.M. Bradshaw: Symmetry and the electron spectroscopy of surfaces. In: *Electron Spectroscopy: Theory, Techniques and Applications*, Vol. 4, ed. by C.R. Brundle, A.D. Baker (Academic Press, San Diego 1984) p. 153
11.3 J. Braun: The theory of angle-resolved ultraviolet photoemission and its applications to ordered materials, Rep. Prog. Phys. **59**, 1267–1338 (1996)
11.4 M. Cardona, L. Ley: *Photoemission in Solids I* (Springer, Berlin, Heidelberg 1978)
11.5 R.E. Ballard: *Photoelectron spectroscopy and molecular orbital theory* (A. Hilger, Bristol 1978)
11.6 J. Hermanson: Final-state symmetry and polarization effects in angle-resolved photoemission spectroscopy, Solid State Commun. **22**, 9–11 (1977)
11.7 L. Ley, M. Cardona: *Photoemission in Solids II* (Springer, Berlin, Heidelberg 1979)
11.8 E.W. Plummer, W. Eberhardt: Angle-resolved photoemission as a tool for the study of surfaces, Adv. Chem. Phys. **49**, 533–656 (1982)
11.9 H.P. Steinrück: Angle-resolved UV-photoelectron spectroscopy, Vacuum **45**, 715–731 (1994)
11.10 W. Eberhardt: *Applications of Synchrotron Radiation: High-Resolution Studies of Molecules and Molecular Adsorbates on Surfaces* (Springer, Berlin, Heidelberg 1994)
11.11 S.D. Kevan: *Angle Resolved Photoemission* (Elsevier, Amsterdam 1992)
11.12 S. Hufner: *Photoelectron Spectroscopy* (Springer, Berlin, Heidelberg 1970)
11.13 P.A. Dowben, B. Xu, J. Choi, E. Morikawa: Band structure and orientation of molecular adsorbates on surfaces by angle-resolved electron spectroscopies. In: *Handbook of Thin Films*, Vol. 2, ed. by H.S. Nalwa (Academic Press, Burlington 2002) pp. 61–114
11.14 P.M.G. Allen, P.J. Dobson, R.G. Egdell: Empty electronic states in the sodium tungsten bronzes: A study by inverse photoemission spectroscopy, Solid State Commun. **55**, 701–704 (1985)
11.15 D. Funnemann, H. Merz: 10 eV photon detector for inverse photoemission, J. Phys. E **19**, 554–557 (1986)
11.16 P.O. Gartland, B.J. Slagsvold: Transitions conserving parallel momentum in photoemission from the (111) face of copper, Phys. Rev. B **12**, 4047–4058 (1975)
11.17 N.V. Smith: Inverse photoemission, Rep. Prog. Phys. **51**, 1227–1294 (1988)
11.18 F.J. Himpsel: Inverse photoemission from semiconductors, Surf. Sci. Rep. **12**, 3–48 (1990)
11.19 N. Memmel: Spectroscopy of metal surface states by inverse photoemission, Prog. Surf. Sci. **42**, 75–88 (1993)
11.20 P.M. Echenique, M.E. Uranga: Image potential states at surfaces, Surf. Sci. **247**, 125–132 (1991)
11.21 V. Dose: VUV isochromat spectroscopy, Appl. Phys. **14**, 117–118 (1977)
11.22 J.C. Fuggle, J.E. Inglesfield (Eds.): *Unoccupied Electronic States* (Springer, Berlin, Heidelberg 1992)
11.23 B. Reihl, R.R. Schlittler, H. Neff: Unoccupied surface state on Ag(110) as revealed by inverse photoemission, Phys. Rev. Lett. **52**, 1826–1829 (1984)
11.24 L. Hedin: On correlation effects in electron spectroscopies and the *GW* approximation, J. Phys. Condens. Matter **11**, R489 (1999)
11.25 L. Hedin, S. Lundqvist: Effects of electron-electron and electron-phonon interactions on the one-electron states of solids, Solid State Phys. **23**, 1–181 (1970)
11.26 L. Hedin, J. Michiels, J. Inglesfield: Transition from the adiabatic to the sudden limit in core-electron photoemission, Phys. Rev. B **58**, 15565–15582 (1998)
11.27 W. Bardyszewski, L. Hedin: My IOPscience a new approach to the theory of photoemission from solids, Phys. Scr. **32**, 439–450 (1985)
11.28 A. Kotani, T. Jo, J.C. Parlebas: Many-body effects in core-level spectroscopy of rare-earth compounds, Adv. Phys. **37**, 37–85 (1988)
11.29 C.S. Fadley: Basic concepts of x-ray photoelectron spectroscopy. In: *Electron Spectroscopy: Theory, Techniques and Applications*, 2nd edn., ed. by C.R. Brundle, A.D. Baker (Academic Press, New York 1978)
11.30 J.J. Sakurai: *Advanced Quantum Mechanics* (Pearson Education and Dorling Kindersley, Delhi 1967)
11.31 F. Mandl, G. Shaw: *Quantum Field Theory*, 2nd edn. (Wiley, West Sussex 2010)
11.32 W. Eberhardt, F.J. Himpsel: Dipole selection rules for optical transitions in the fcc and bcc lattices, Phys. Rev. B **21**, 5572–5576 (1980)
11.33 G. Borstel, W. Braun, M. Neumann, G. Seitz: Band structure of rhodium and photoemission from its low index surfaces, Phys. Status Solidi (b) **95**, 453–460 (1979)
11.34 G. Borstel, M. Neumann, M. Wohlecke: Necessity of relativistic dipole selection rules in photoemission, Phys. Rev. B **23**, 3121–3124 (1981)
11.35 Y. Shao, Z. Gan, E. Epifanovsky, et al.: Advances in molecular quantum chemistry contained in the Q-

Chem 4 program package, Mol. Phys. **113**, 184–215 (2015)
11.36 D.C. Young: Appendix A: Software Packages. In: *Computational Chemistry: A Practical Guide for Applying Techniques to Real World Problems*, ed. by D.C. Young (Wiley, New York 2002) pp. 330–331
11.37 D. Harris, M. Bertolucci: Symmetry and spectroscopy; an introduction to vibrational and electronic spectroscopy, J. Mol. Struct. **62**, 301 (1980)
11.38 M. Tinkham: *Group Theory and Quantum Mechanics* (McGraw-Hill, New York 1964)
11.39 S. Hüfner: *Photoelectron spectroscopy. Principles and applications*, 3rd edn. (Springer, Heidelberg, Berlin 2003)
11.40 C.R. Brundle, A.D. Baker: *Electron Spectroscopy: Theory, Experiments and Applications* (Academic Press, New York 1978)
11.41 R. Hoffmann: A chemical and theoretical approach to bonding at surfaces, J. Phys. Condens. Matter (1993), https://doi.org/10.1088/0953-8984/5/33A/001
11.42 J.E. Inglesfield, E.W. Plummer: The physics of photoemission. In: *Angle Resolved Photoemission*, ed. by S.D. Kevan (Elsevier, Amsterdam 1992)
11.43 G.J. Miller: Solids and surfaces: A chemist's view of bonding in extended structures, Angew. Chem. **101**, 1570–1571 (1989)
11.44 W.R. Salaneck, S. Stafström, J.L. Brédas: *Conjugated Polymer Surfaces and Interfaces: Electronic and Chemical Structure of Interfaces for Polymer Light Emitting Devices* (Cambridge Univ. Press, Cambridge 1996)
11.45 J.J. Sakurai: *Advanced Quantum Mechanics* (Addison-Wesley, Reading 1980)
11.46 P.A. Dowben, Y. Sakisaka, T.N. Rhodin: Angle-resolved photoemission from molecular N_2 adsorbed on Ni(100), Surf. Sci. **147**, 89–102 (1984)
11.47 H.A. Bethe, E.E. Salpeter: *Quantum Mechnanics of One and Two Electron Atoms*, 1st edn. (Springer, Berlin, Heidelberg, New York 1957)
11.48 C.R. Brundle, P.S. Bagus, D. Menzel, K. Herman: Adsorption of molecular nitrogen on nickel. II. Comparison of photoemission for N_2/Ni(100) to CO/Ni(100) and to theory, Phys. Rev. B **24**, 7041 (1981)
11.49 K. Herman, P.S. Bagus, C.R. Brundle, D. Menzel: Adsorption of molecular nitrogen on nickel. I. Cluster-model theoretical studies, Phys. Rev. B **24**, 7025 (1981)
11.50 K. Horn, J. Dinardo, W. Eberhardt, H.-J. Freund, E.W. Plummer: The adsorption of N_2: Chemisorbed on Ni(110) and physisorbed on Pd(111), Surf. Sci. **118**, 465–495 (1982)
11.51 P.S. Bagus, K. Hermann, M. Steel: Bonding and photoemission of chemisorbed molecules: Molecular orbital cluster model theory, J. Vac. Sci. Technol. **18**, 435–452 (1981)
11.52 R.P. Messmer: Theoretical studies of metal clusters and of chemisorption on metals, J. Vac. Sci. Technol. A **2**, 899–904 (1984)
11.53 J.E. Ortega, F.J. Himpsel, D. Li, P.A. Dowben: Initial and final state contributions of the core level shifts for Gd(0001), Solid State Commun. **91**, 807–811 (1994)
11.54 J. Xiao, A. Sokolov, P.A. Dowben: Changing band offsets in copper phthalocyanine to copolymer poly(vinylidene fluoride with trifluoroethylene) heterojunctions, Appl. Phys. Lett. (2007), https://doi.org/10.1063/1.2747672
11.55 J. Xiao, P.A. Dowben: The role of the interface in the electronic structure of adsorbed metal(II) (Co, Ni, Cu) phthalocyanines, J. Mater. Chem. **19**, 2172–2178 (2009)
11.56 M. Golze, M. Grunze, R.K. Driscoll, W. Hirsch: XPS as a tool to study the kinetics and thermodynamics of molecular adsorption: N_2 on Ni(110), Appl. Surf. Sci. **6**, 464–472 (1980)
11.57 D. Spanjaard, C. Guillot, M.-C. Desjonquères, G. Tréglia, J. Lecante: Surface core level spectroscopy of transition metals: A new tool for the determination of their surface structure, Surf. Sci. Rep. **5**, 1–85 (1985)
11.58 P.H. Citrin, G.K. Wertheim, Y. Baer: Core-level binding energy and density of states from the surface atoms of gold, Phys. Rev. Lett. **41**, 1425–1428 (1978)
11.59 J.A. Appelbaum, D.R. Hamann: Electronic structure of the Cu(111) surface, Solid State Commun. **27**, 881–883 (1978)
11.60 B. Johansson, N. Mårtensson: Core-level binding-energy shifts for the metallic elements, Phys. Rev. B **21**, 4427–4457 (1980)
11.61 A. Rosengren, B. Johansson: Calculated transition-metal surface core-level binding-energy shifts, Phys. Rev. B **22**, 3706–3709 (1980)
11.62 P.J. Feibelman, D.R. Hamann: Surface states of Sc(0001) and Ti(0001), Solid State Commun. **31**, 413–417 (1979)
11.63 P.J. Feibelman, J.A. Appelbaum, D.R. Hamann: Electronic-structure of a Ti(0001) film, Phys. Rev. B **20**, 1433–1443 (1978)
11.64 F. Cyrot-Lackmann: On the electronic structure of liquid transitional metals, Adv. Phys. **16**, 393–400 (1967)
11.65 D. Wooten, I. Ketsman, J. Xiao, Y.B. Losovyj, J. Petrosky, J. McClory, Y.V. Burak, V.T. Adamiv, P.A. Dowben: The surface core level shift for lithium at the surface of lithium borate, Phys. B Condens. Matter **405**, 461–464 (2010)
11.66 Y.B. Losovyj, D. Wooten, J.C. Santana, J.M. An, K.D. Belashchenko, N. Lozova, J. Petrosky, A. Sokolov, J. Tang, W. Wang, N. Arulsamy, P.A. Dowben: Comparison of n-type Gd_2O_3 and Gd-doped HfO_2, J. Phys. Condens. Matter (2009), https://doi.org/10.1088/0953-8984/21/4/045602
11.67 A.P. Grosvenor, B.A. Kobe, M.C. Biesinger, N.S. McIntyre: Investigation of multiplet splitting of Fe 2p XPS spectra and bonding in iron compounds, Surf. Interface Anal. **36**, 1564–1574 (2004)
11.68 T.C. Lin, G. Seshadri, J.A. Kelber: A consistent method for quantitative XPS peak analysis of thin oxide films on clean polycrystalline iron surfaces, Appl. Surf. Sci. **119**, 83–92 (1997)

11.69 T. Yamashita, P. Hayes: Analysis of XPS spectra of Fe^{2+} and Fe^{3+} ions in oxide materials, Appl. Surf. Sci. **254**, 2441–2449 (2008)

11.70 S. Cao, T.R. Paudel, K. Sinha, X. Jiang, W. Wang, E.Y. Tsymbal, X. Xu, P.A. Dowben: The stability and surface termination of hexagonal $LuFeO_3$, J. Phys. Condens. Matter (2015), https://doi.org/10.1088/0953-8984/27/17/175004

11.71 S. Cao, X. Zhang, K. Sinha, W. Wang, P.A. Dowben, X. Xu: Phase separation in $LuFeO_3$ films, Appl. Phys. Lett. (2016), https://doi.org/10.1063/1.4950991

11.72 S. Beniwal, X. Zhang, S. Mu, A. Naim, P. Rosa, G. Chastanet, J.-F. Létard, J. Liu, G.E. Sterbinsky, D.A. Arena, P.A. Dowben, A. Enders: Surface-induced spin state locking of the $[Fe(H_2B(pz)_2)_2(bipy)]$ spin crossover complex, J. Phys. Condens. Matter (2016), https://doi.org/10.1088/0953-8984/28/20/206002

11.73 B.T. Thole, X.D. Wang, B.N. Harmon, D. Li, P.A. Dowben: Multiplet fine structure in the photoemission of the gadolinium and terbium 5p levels, Phys. Rev. B **47**, 9098–9101 (1993)

11.74 N.S. McIntyre, D.G. Zetaruk: X-ray photoelectron spectroscopic studies of iron oxides, Anal. Chem. **49**, 1521–1529 (1977)

Andrew J. Yost

Oklahoma State University
Stillwater, OK, USA
andrew.yost@okstate.edu

Dr Yost received his PhD in Condensed Matter Physics from the University of Wyoming in 2017. He was a Postdoctoral Research Associate at the University of Nebraska-Lincoln from 2017 to 2019. Dr Yost is currently an Assistant Professor at Oklahoma State University. Dr Yost has expertise in scanning tunneling microscopy and angle resolved photoemission spectroscopy. His research interests involve multiferroic oxides, 2-D materials, organic and inorganic solar cell materials, nanoparticle solar cell materials, spin crossover molecules on molecular ferroelectric thin films, and topological materials.

Prescott E. Evans

Lincoln, NE, USA
prescott.evans@huskers.unl.edu

Prescott received his PhD in Physics from the University of Nebraska-Lincoln in 2020 under the guidance of Professor Peter A. Dowben. His research focuses on heterogeneous catalyst systems with an emphasis on surface chemistry tunability.

Iori Tanabe

Lincoln, NE, USA
iori.tanabe@ni.edu

Dr Tanabe studied the electronic structures of two-dimensional semiconducting materials with Professor Peter A. Dowben and received his PhD in Physics at the University of Nebraska-Lincoln in May 2017. Dr Tanabe is currently working as an application engineer for National Instruments Japan.

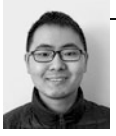

Guanhua Hao

Lincoln, NE, USA
guanhuahao@huskers.unl.edu

Guanhua received his MSc in Physics from the University of Nebraska-Lincoln in 2017 and is currently in Professor Peter A. Dowben's group in Physics at the University of Nebraska-Lincoln. His research area includes spin crossover molecules and surface science.

Simeon Gilbert

Lincoln, NE, USA
simeon.gilbert@outlook.com

Simeon received his BSc in Physics from South Dakota State University in 2015. He is currently studying the electronic structure of two-dimensional materials and pursing his PhD at the University of Nebraska-Lincoln under the guidance of Professor Peter A. Dowben.

Takashi Komesu

Lincoln, NE, USA
tkomesu2@unl.edu

Dr Komesu received his PhD in Physics from the University of Nebraska-Lincoln (UNL) in 2002. Dr Komesu is currently Research Associate Professor. Dr Komesu has been working in solid-state physics, especially electronic structure measurements on magnetic thin films, 2D materials, and organo-metal compounds. Dr Komesu has expertise in spin polarized inverse photoemission spectroscopy (SPIPES), investigating the spin-polarized unoccupied electronic structure, which can only be done at UNL.

12. Electronic States of Vicinal Surfaces

J. Enrique Ortega, Aitor Mugarza, Frederik Schiller, Jorge Lobo-Checa, Martina Corso

Vicinal surfaces are crystal planes oriented a few degrees off from a high symmetry direction. Such a small deviation (called miscut) from a high symmetry axis leads to a characteristic periodic roughness at the nanoscale, namely atom-height step arrays that separate atomically-flat terraces. The alternating series of "terraces" and "steps" makes electronic properties of vicinal surfaces very peculiar, distinct from those of atomically-flat surfaces. On the one hand, terraces and steps feature atoms with distinct coordination and complex and varied elastic relaxations, influencing their core-level energies. We show how core levels at a vicinal surface exhibit a miscut-dependent stress release, as well as fine structural relaxations, such as faceting. On the other hand, atomic steps create a periodic modulation of the crystal potential, affecting two-dimensional (2-D) surface states of metals. This leads to Bloch scattering of surface electrons by the step lattice, and eventually, to one-dimensional (1-D) quantization by confinement at terraces or step edges. We discuss the occurrence and observation of superlattice scattering and 1-D confinement at a vicinal surface, the importance of the atomic nature of the surface state wave function, the dependence on the lattice constant of the step array, and the rich scattering phenomenon that arises in faceted structures and spin-textured bands.

12.1 General Considerations About Vicinal Surfaces

Vicinal surfaces have been always fundamental in technologically relevant fields, such as catalysis [12.1] and crystal growth [12.2], and are more recently becoming very attractive as growth templates for nanostructure research [12.3]. Cutting a crystal at a vicinal angle results in a regular pattern of atomic steps that delimit high-symmetry mini-facets called *terraces*. Such an ideal, periodic monatomic step-terrace structure is sketched in Fig. 12.1a. The surface plane is defined by the (high index) crystallographic orientation (e.g., (557) in Fig. 12.1a), or simply by its macroscopic deviation (miscut α) from the high-symmetry plane of the terrace ((111) in Fig. 12.1a). Beyond the periodic atomic discontinuities at steps, the vicinal surface is characterized by varied atomic coordination. For the face centered cubic (fcc) crystal shown in Fig. 12.1a, the atomic coordination varies from bulk $B = 12$, to terrace $T = 9$ and step $S = 7$, whereas the corner C depends on the orientation of the miscut, as depicted in Fig. 12.1b. For A-type steps with {100}-like pack-

M. Rocca, T.S. Rahman, L. Vattuone (Eds.), *Springer Handbook of Surface Science*, Springer Handbooks,
https://doi.org/10.1007/978-3-030-46906-1_12

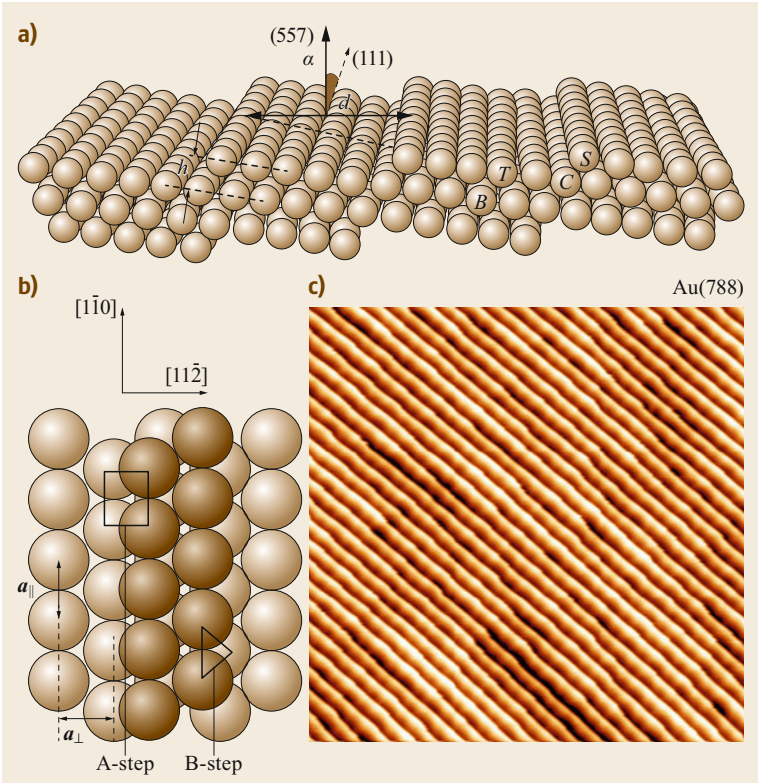

Fig. 12.1a–c Atomic structure of a vicinal surface: **(a)** the (557) surface ($\alpha = 9.5°$), which is vicinal to the (111) high-symmetry surface. Miscut angle α, terrace size d, and monatomic step height h are the characteristic magnitudes describing these step arrays. B, C, T, and S indicate the atomic sites with different coordinations. **(b)** Top-view description of the different A-type and B-type steps found in (111) vicinals of fcc crystals. **(c)** STM image ($100\,\mathrm{nm}^2$) of a Au(788) surface ($\alpha = 3.5°$), featuring straight monoatomic steps with a low density of kinks and reconstructed terraces

ing at step edges (Fig. 12.1b, square), we find $C = 10$, whereas for B-type with {111}-like packing (Fig. 12.1b, triangle), $C = 11$. Changing the miscut α will change the periodicity of the step lattice, i.e., the step modulation of the surface potential, but also the relative abundance of T, S, and C atoms, and consequently, all physical and chemical properties of the surface.

Real vicinal surfaces deviate from perfect step arrays. Ideal step and terrace networks exhibit fine structural properties that influence the electronic states. Such characteristic features are best observed in scanning tunneling microscopy (STM) images. In Fig. 12.1c, we show the case of the Au(788) vicinal plane, imaged by STM at 300 K. Terraces show atomic reconstructions, whereas monatomic steps occasionally contain kinks, i.e., step edge atoms with a missing neighbor, and hence with the coordination further reduced to 6. The terrace reconstruction may substantially vary as a function of the miscut angle α [12.4], whereas the density of kinks depends on the *in-plane* orientation (azimuth) of the step array. However, the most important property observed in Fig. 12.1c is the randomly varying width of the terraces around the nominal d value. Such a phenomenon affects any vicinal surface irrespectively of the miscut or azimuth. It is linked to the thermal excitation of kinks that leads to a temperature-dependent terrace width distribution (TWD). As we shall see in this chapter, the shape of the TWD reflects the elastic equilibrium of the vicinal surface, which in turn is fundamental to understanding subtle variations in its spectrum of electronic states.

Due to the step corrugation and the varied atomic coordination, electron energy levels at a vicinal surface are different from those of the high symmetry plane. In Fig. 12.2a, we sketch the fundamental features that can be expected at two different energy ranges, i.e., near the Fermi energy in 2-D surface states and at the deeply lying core levels. Delocalized surface electrons will sense the periodic perturbation of the crystal potential at step edges, affecting their in-plane, 2-D dispersion. Such step-edge potential is connected to the spill-out charge or charge smoothing around step atoms that leads to a net step dipole [12.7]. Figure 12.2b shows the case of Au(788). Due to the step dipole potential, the vicinal surface effectively becomes a periodic superlattice, at which the 2-D Shockley state scatters. As a result, the otherwise free-electron-like parabolic dispersion is broken up into subbands separated by mini-gaps, whose size determines the step dipole barrier strength [12.5, 8]. The step dipole also leads to a local reduction of the

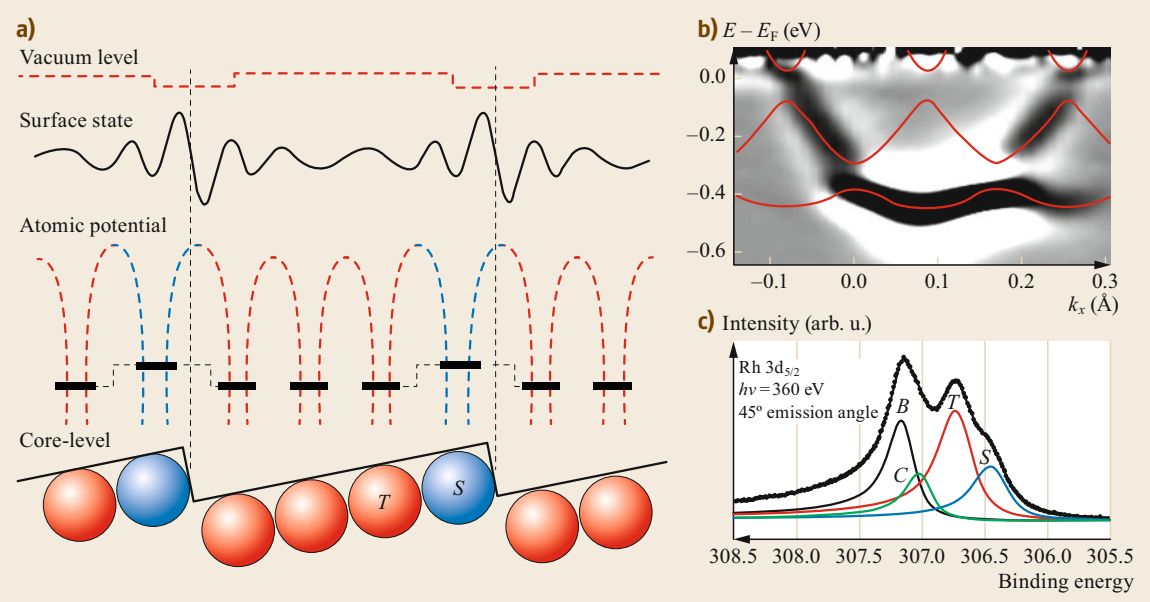

Fig. 12.2a–c Electronic states at a vicinal surface: **(a)** the surface potential (*dashed lines*) at a vicinal surface. Core levels exhibit energy shifts due to different coordinations of surface atoms at step (*S*) and terraces (*T*). Surface states scatter at step edges modulating their wave functions. **(b)** The Shockley state in Au(788), showing step superlattice bands and gaps [12.5]. **(c)** 3-D core-level emission from Rh(335), showing distinct *B*, *C*, *T*, and *S* features. (Figure reprinted with permission from [12.6]. Copyright 2003 by the American Physical Society)

work function in the proximity of the step edge. This has been shown to affect 2-D image states of vicinal surfaces, which also become superlattice states, where a 1-D step-edge state may eventually split off [12.9, 10]. On the other hand, changes in surface atomic coordination, e.g., from *S* to *T* will influence core-level energies. This is shown in Fig. 12.2c for the vicinal Rh(335) surface, where the Rh $3d_{5/2}$ core-level peak appears split into four different contributions, i.e., at the highest binding energy, the peak of bulk atoms in subsurface layers, followed by the small contribution from corner atoms below step edges, and by the terrace and step atom emission from the vicinal surface plane [12.6].

Step density, type, azimuthal orientation, as well as terrace reconstructions can be readily selected through the macroscopic miscut, allowing one to tune surface bands and core-level energies. Step type and azimuthal orientation (kink density) lead to different average dipole potentials, and hence to different scattering strengths for 2-D surface states. The step density changes the superlattice parameter, but also the relative abundance of *T* and *S* atoms, and hence the physical–chemical response of the vicinal surface. The miscut angle can be chosen to modify reconstruction patterns in terraces or to achieve complex hill-and-valley step superlattices. As a result, the electronic states are modified. In the case of Au(111) vicinal surfaces, the electronic properties at the surface are even more perturbed by the tendency to form herring-bone patterns at (111) terraces. In Au(21 23 23), monatomic steps and fcc/hexagonal close packed (hcp) patches of (111) terraces define a square pattern of quantum wells that confines surface electrons, as shown in Fig. 12.3a,b [12.11]. In contrast, the Au(9 9 11) vicinal surface undergoes a faceting transition, resulting in a periodic superstructure formed by one wide (reconstructed) and two narrow (unreconstructed) (111) terraces, which, respectively, bind the $n = 1$ (confined) and $n = 2$ (propagating) superlattice states (Fig. 12.3c), as probed by angle-resolved photoemission (ARPES, Fig. 12.3d [12.5], see also Sect. 12.2).

The rich variety of structures and electronic states that arise as a function of miscut and azimuth can be systematically explored with curved crystal samples. Although distinct macroscopic shapes have been historically tested, the $\alpha = 30°$ cylindrical sections shown in Fig. 12.4a are gaining popularity, since they are compatible with standard techniques and setups utilized in surface science [12.4, 8, 12–16]. On such surfaces, steps are aligned parallel to the cylinder axis, whereas the step density smoothly varies across the perpendicular,

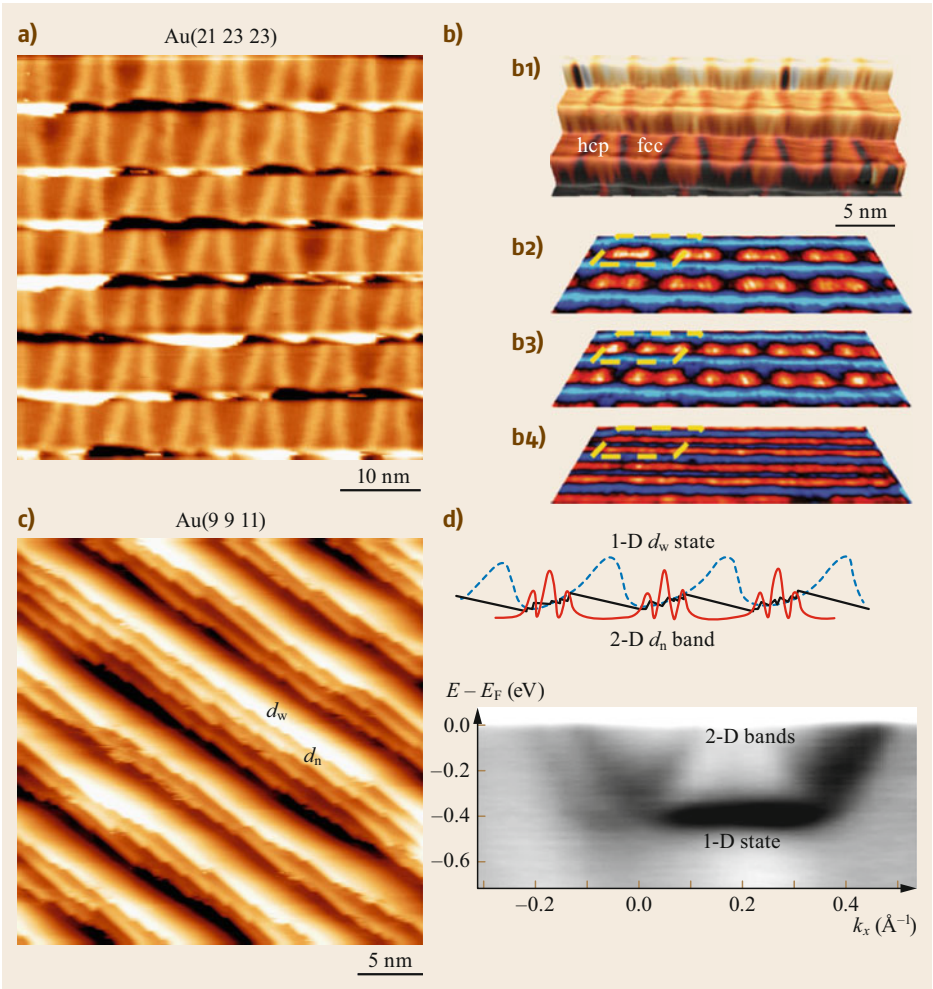

Fig. 12.3a–d Surface states at vicinal Au(111) surfaces: **(a)** STM image of Au(21 23 23) showing fcc/hcp patches in terraces separated by discommensuration lines (*bright horizontal*) that run practically perpendicular to step edges (*vertical*). The resulting square pattern of potential wells leads to the surface state wave function modulation shown in **(b)**. (Reprinted by permission from MacMillan Publishers Ltd.: [12.11]). **(c)** Faceted structure in Au(9 9 11), defined by bunches of unreconstructed $d_n = 13$ Å terraces separated by a single reconstructed $d_w = 39$ Å terrace. **(d)** Schematic wave functions (*top*) and measured Shockley bands (*bottom*) of Au(9 9 11); d_w-related 1-D quantum-wells appear under the d_n-modulated 2-D superlattice state [12.5]

curved direction. For example, the Au, Cu, and Ag samples of Fig. 12.4a were designed to have both A-type and B-type steps separated by the (111) high-symmetry plane at its center, as sketched in Fig. 12.4b. The use of small ($< 100\,\mu$m) size probes allows one to scan the different crystallographic orientations, such as to test, e.g., the characteristic miscut-dependent Shockley state shift (terrace shift) shown in Fig. 12.4c. In the latter, the presence of the reference (111) plane in the same sample and the smooth variation of the miscut with the surface position allows us to accurately determine the strength of the dipole potential at step edges [12.8].

In this chapter, we review the state-of-the-art in experiments and theory of electronic states at vicinal surfaces. Much general understanding has been gained through recent experiments performed on curved surfaces [12.4, 8, 13–16]. These have neatly demonstrated the subtle, but important variations in the spectrum of surface electronic states as the miscut is varied. Such an understanding will pave the way towards the rational choice of vicinal surface planes for technology and research applications, namely for catalysis, electron scattering problems, and nanostructure growth.

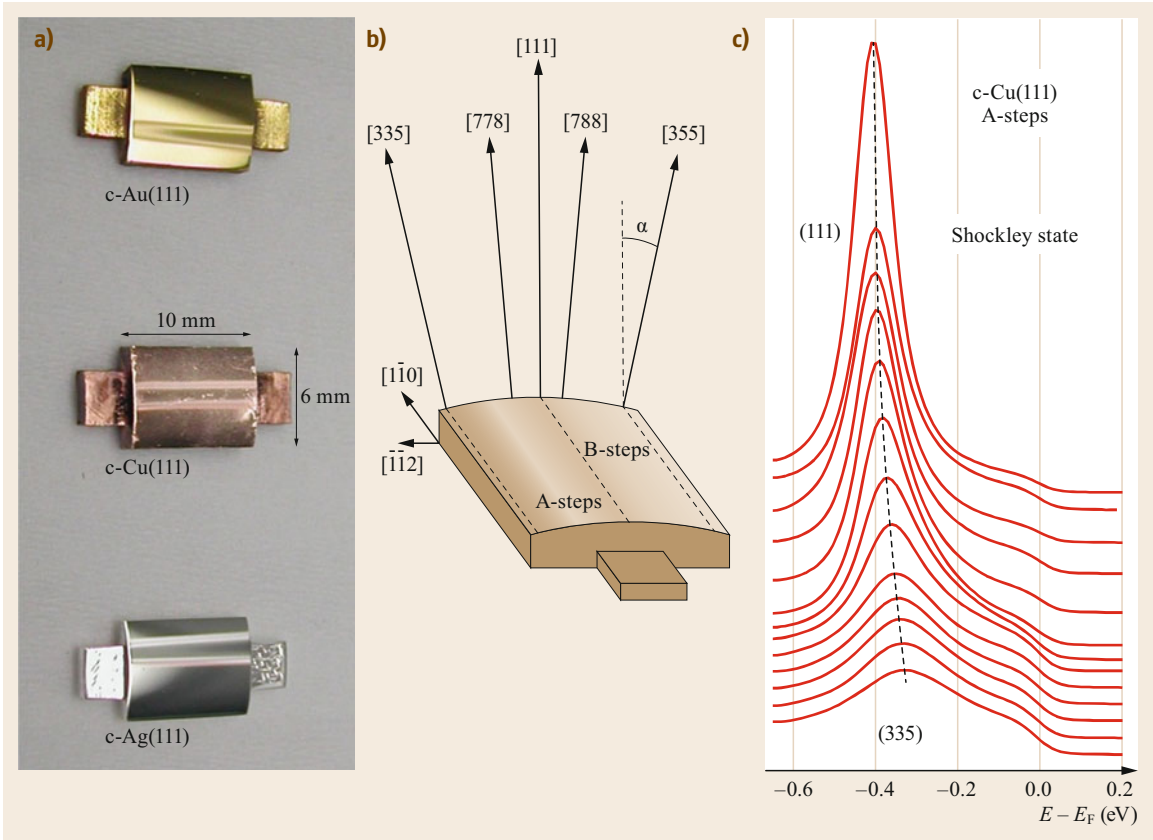

Fig. 12.4a–c Tunable vicinal surfaces using curved crystals in the form of cylindrical sections: **(a)** photography of Au, Cu, and Ag single crystal samples curved around the (111) direction. **(b)** Sketch description of a curved c-(111) single crystal sample with the different surface crystallographic orientations indicated. **(c)** ARPES scan of the Shockley band minimum probed from the (111) to the (335) plane in the c-Cu(111) crystal exhibiting the characteristic terrace-dependent energy shift

12.2 Structural Properties of Vicinal Surfaces

The electronic properties of a vicinal surface are connected not only to the local atomic structure of terraces and steps, but also to the particular way steps self-arrange at the nanoscale level. At the local scale, the fundamental feature is the variety of atomic coordinations and their corresponding core-level energies, although one will need to be aware of relaxation effects, which lead to subtle core-level energy shifts as a function of the miscut. Elastic relaxation also explains the shape of the TWD at thermal equilibrium, and the occurrence of step bunching and faceting, i.e., the rearrangement of the step lattice at the nanoscale that further shapes surface electronic bands.

12.2.1 Atomic Relaxations Around Surface Steps

After bond breaking and creation of the surface, tensile stress appears at the topmost crystal plane. Such surface stress can be relieved through local atomic rearrangement, i.e., by terrace reconstructions, but also through a characteristic crystal lattice relaxation in the vicinity of steps. Ab-initio density functional theory (DFT) calculations performed for slabs with vicinal orientations reveal the displacement of surface atoms with respect to the expected position in the bulk lattice. This is shown in Fig. 12.5 for the case of the Au(233)

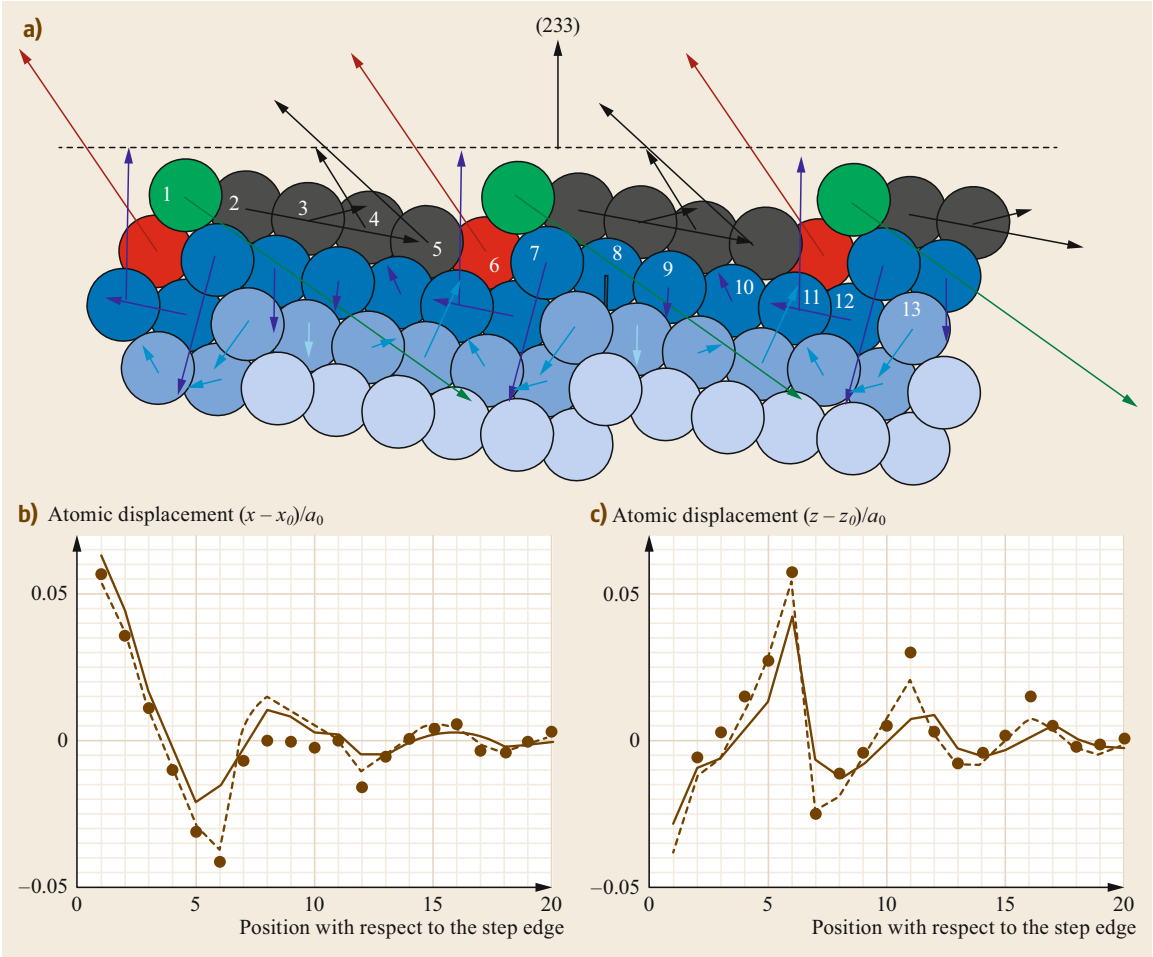

Fig. 12.5a–c Crystal lattice relaxation at a vicinal surface: **(a)** DFT calculations of atomic displacements at the Au(233) surface. *Arrows* indicate the relative magnitude and direction of the atomic relaxation with respect to the fcc bulk crystal position. **(b,c)** Damping of the atomic relaxation away from the steps, parallel (see atom numbering in **(a)**) and perpendicular to the surface, respectively. *Solid lines* fit the DFT data (*dots*) assuming a force-dipole potential model to calculate atomic relaxations. *Dashed lines* fit x-ray diffraction data (not shown) using the same force-dipole model. (Figures reprinted with permission from [12.17]. Copyright 2010 by the American Physical Society)

crystal [12.17], and analogous results are obtained for other surfaces [12.18, 19]. In the side-view sketch of Fig. 12.5a, the arrows indicate the direction in which atoms relax with respect to the ideal fcc lattice, and their length represents the relative magnitude of such atomic displacement, affecting all atoms at several outer layers. The maximum displacement corresponds to the top and the bottom atom at the step edge (*S* and *C* in Fig. 12.1), which effectively move inwards and outwards of the nominal fcc lattice. The relaxation effect damps away from the step in both the surface and the bulk direction with a similar decay constant, as shown in Fig. 12.5b,c. In particular, when looking at all *T* atoms as a whole in Fig. 12.5a, we note that they move away from the step edge and against one another, i.e., the terrace becomes laterally compressed. This leads to the characteristic core-level shift that will be discussed in Sect. 12.3.

The individual atomic relaxations of the vicinal surface obtained from first-principles DFT can be well reproduced assuming lines of force dipoles at step edges and then calculating the linear elastic response of the atomic lattice. Note that a net torque is exerted at the step edge, which explains the opposite displacements shown for *S* and *C* atoms in Fig. 12.5a. Solid and dotted lines in Fig. 12.5b,c, respectively, fit DFT results (dots) and grazing incidence x-ray diffraction (GIXD) data from vicinal crystals, using the step-force dipole as a fitting parameter. The latter allows one to experimentally

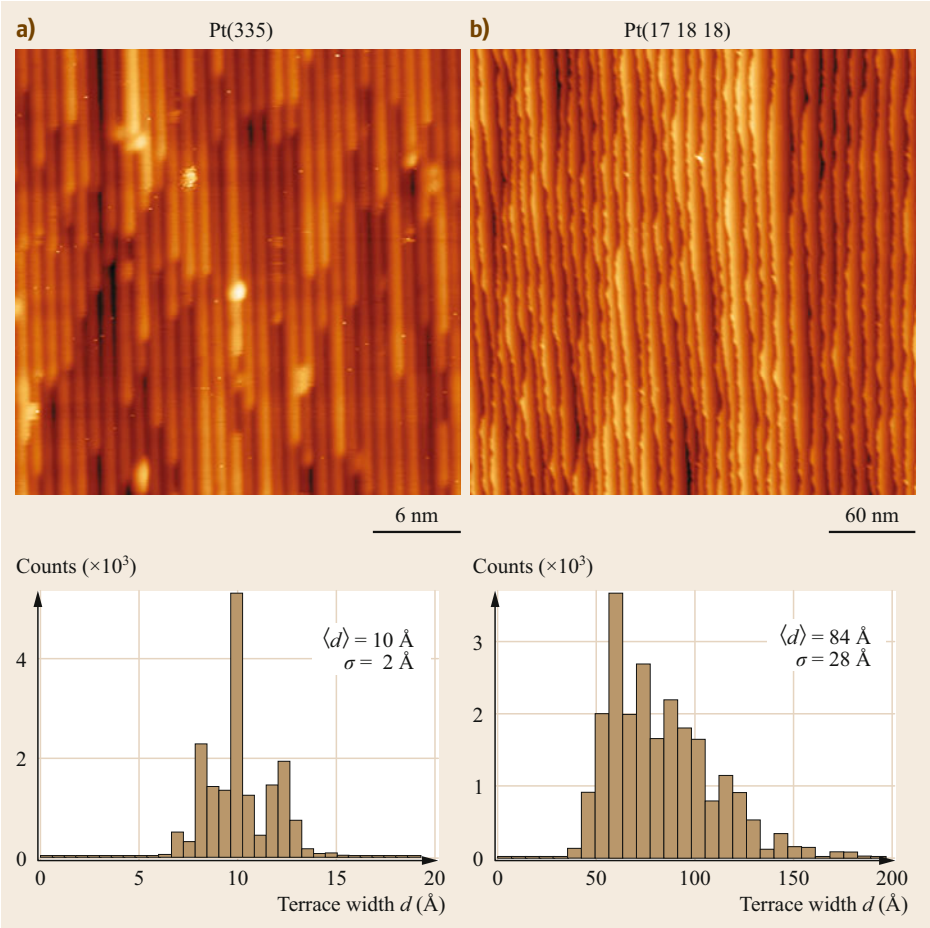

Fig. 12.6a,b Terrace width distribution (TWD) for vicinal Pt(111): characteristic STM images of **(a)** Pt(335) and **(b)** Pt(17 18 18), with their respective histogram analysis of the TWD. The TWD is symmetric for narrow, $\langle d\rangle = 10$ Å terraces in Pt(335) and broad and asymmetric for wide $\langle d\rangle = 84$ Å terraces in Pt(17 18 18) [12.14]

estimate the strength $\tilde{A}$ of the repulsive step–step elastic interaction $U(d) = \tilde{A}/d^2$, which arises in the classical elastic approach of the vicinal surface [12.20, 21].

12.2.2 Step–Step Interactions and Terrace Width Distribution

In the continuum model, the equilibrium shape of the surface is driven by the minimum free energy γ. In the case of vicinal planes with monatomic steps, γ can be expressed in terms of the miscut α and as a function of the temperature T as [12.21, 22]

$$\gamma(\alpha) = \gamma_0 + \beta\frac{|\tan\alpha|}{h} + \frac{B(T)}{a_{\|}h^3}|\tan\alpha|^3\,, \qquad (12.1)$$

where γ_0 represents the surface energy per unit area of the terraces, β the step energy per unit length, h the step height, $a_{\|}$ the lattice constant at the surface (Fig. 12.7b), and $B(T)$ the step interaction term. The latter includes the so-called entropic interaction $g(T)$ and the elastic step–step interaction. The entropic term $g(T)$ arises due to the inability of two contiguous steps to cross as they *meander* on the surface. Step wandering is activated through thermal excitation of kinks, and hence it is the key ingredient to explain the TWD that characterizes all vicinal surfaces at thermal equilibrium. In Fig. 12.6, we show the case of Pt(335) and Pt(17 18 18), namely two Pt(111) vicinals with A and B-type steps, respectively, and different α angles. The bottom panels show the TWD in each case, resulting from the statistical analysis performed over a number of STM images such as those shown on the top panels. Such analysis immediately renders the average terrace size $\langle d\rangle$ and the standard deviation σ indicated in each panel. The TWD peaks close to the expected value for the respective ideal plane, but it shows a sizeable width and a characteristic asymmetry, which is more pronounced for the wider $\langle d\rangle = 8.4$ nm terraces of Pt(17 18 18) [12.14].

On the grounds of the elastic theory described by (12.1) and assuming step meandering through

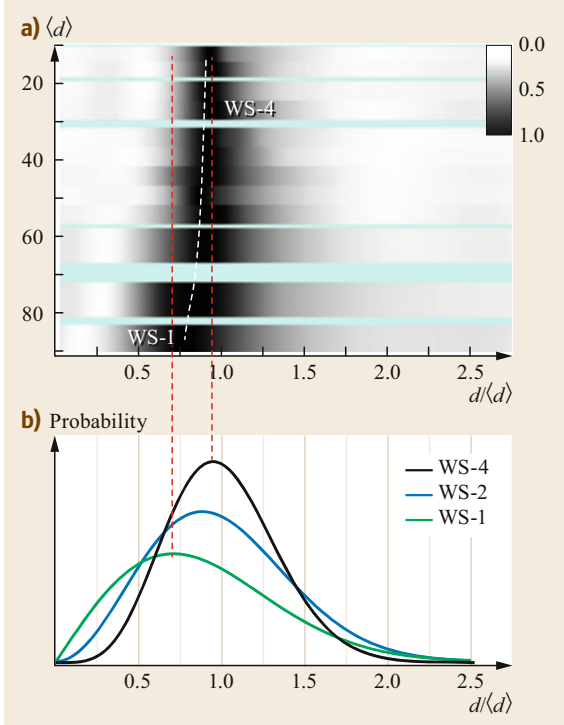

Fig. 12.7a,b Terrace width distribution variation in a curved crystal: **(a)** evolution of the TWD histogram as a function of the mean terrace width $\langle d\rangle$ measured in the A-side of a curved Pt(111) sample. *Horizontal stripes* correspond to individual histograms with the probability shown in *gray scale*. The *white dotted line* tracks histogram maxima, suggesting a gradual change of the statistical function from WS-1 at small $\langle d\rangle$ to WS-4 at large $\langle d\rangle$. The diverse WS functions are represented in **(b)** [12.14] ►

thermally activated kinks, TWDs are expressed through mathematical functions called "Wigner surmise" [12.23]. The specific d-dependent Wigner surmise is defined by the *order* parameter ϱ, depending on the nature of the step–step interactions. For elastic-like step repulsions following $U(d) = \tilde{A}/d^2$, the $\varrho = 4$ Wigner surmise should explain the TWD at all miscuts [12.23]. However, the latest experiments performed on curved crystals point to a smooth variation from $\varrho = 1$ (attractive step interaction) to $\varrho = 4$ (repulsive elastic), as a function of the miscut α [12.14–16]. In Fig. 12.7, we show the TWD for vicinal Pt(111) surfaces with A-type steps, measured by STM on a curved crystal sample [12.14]. Horizontal stripes represent the individual TWDs obtained at the indicated mean terrace width $\langle d\rangle = h/\sin\alpha$, plotted against the normalized coordinate $d/\langle d\rangle$. A clear shift of the TWD maximum from $d/\langle d\rangle \approx 0.8$ to $d/\langle d\rangle \approx 0.94$ is observed when moving from large to small $\langle d\rangle$ values. Such a shift can only be accounted for by assuming a Wigner surmise of variable ϱ. This points to the α-dependence of the step interaction term $B(T)$ in (12.1), which in turn suggests the nonlinear character of the elastic relaxation around the surface steps.

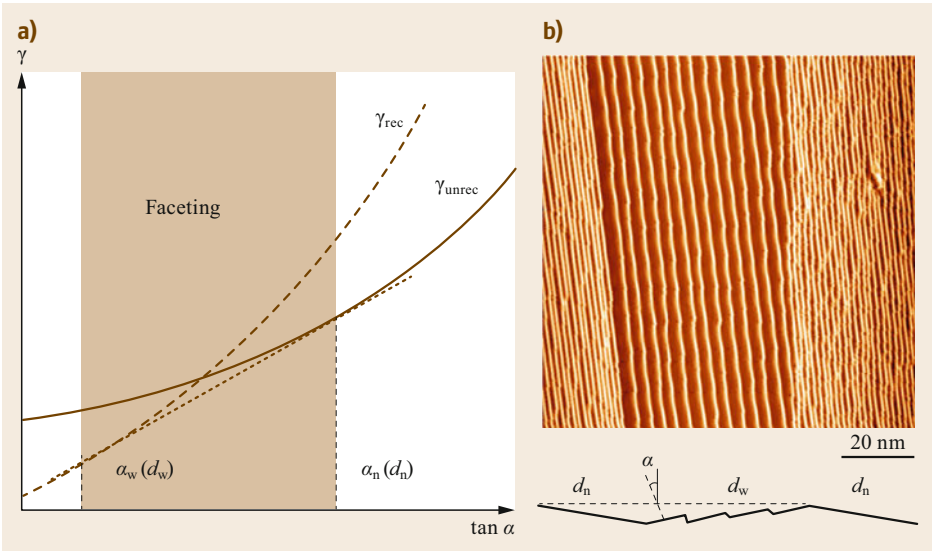

Fig. 12.8a,b Phase-competing structural model of faceting in vicinal Au(111): **(a)** the surface free energy for reconstructed and unreconstructed Au(111) surfaces. The *dotted line* joins inflexion points in both curves, defining a region (*shaded area*) at which phase segregation into d_w and d_n phases is energetically optimal. **(b)** STM image of the Au(566) surface showing large d_w and d_n phases [12.4]

12.2.3 Faceting

Vicinal surfaces with terrace reconstructions, such as the herringbone in Au(111), generally exhibit faceting or step bunching instabilities at critical miscuts [12.20, 22]. This can also be explained through (12.1), by assuming the existence of two competing phases, i.e., vicinal surfaces with reconstructed terraces of γ_0^{rec} and step-formation energy β^{rec}, versus a second phase defined by strained, unreconstructed terraces with $\gamma_0^{\mathrm{unrec}} > \gamma_0^{\mathrm{rec}}$ and low step energy $\beta^{\mathrm{unrec}} < \beta^{\mathrm{rec}}$. As is schematically represented in Fig. 12.8a, the surface free energy in each case will generally exhibit a local minimum, or inflection point at distinct α_{w} (corresponding to reconstructed d_{w}-wide terraces) and α_{n} (corresponding to unreconstructed d_{n} terraces). Therefore, for a macroscopic $\alpha_{\mathrm{w}} < \alpha < \alpha_{\mathrm{n}}$, the minimum free energy is achieved through a weighted sum of d_{w} and d_{n} phases (facets), as is schematically depicted in the bottom of Fig. 12.8b, and, in fact, observed in Au(566) (Fig. 12.8b, top). This phenomenon, which strongly affects vicinal Au(111) surfaces with both A and B type steps, will dramatically influence the electronic states, as discussed below.

12.3 Surface Core-Level Shifts at a Vicinal Surface

Core-level spectroscopy is widely utilized to assess changes in the chemical environment of atoms through energy shifts. The simplest case is that of the crystal surface, where the reduced atomic coordination with respect to the bulk manifests in its characteristic surface core-level shift (SCLS). Although many-body (also called final state) effects are also important [12.24], the SCLS is generally explained by the different filling of electron bands at the surface with respect to the bulk, which in turn is caused by the band narrowing associated to the lower atomic coordination. If the band is nearly filled, its center of gravity is below the Fermi energy. Therefore, band narrowing leads to further electron filling (reduction), and the surface core level will shift to a lower binding energy. If the band is nearly empty, band narrowing will lead to electron depletion (oxidation), and hence to a SCLS towards higher binding energy. The central panel of Fig. 12.9 displays the Pt 4f core-level spectrum measured from Pt(111) with high-resolution photoemission. Pt possesses an almost filled d-shell, and hence band narrowing leads to the observed surface peak (T) shifted by ≈ 0.4 eV to lower binding energy with respect to the bulk peak (B).

At a vicinal surface, new atomic coordinations appear at step sites, namely the corner C and step S (Fig. 12.1b), which are thus expected to lead to distinct SCLSs. In practice, core-level emission from both C and S atoms has been resolved in W and Rh vicinals only [12.6, 25]. Both W and Rh have the d-band center below E_{F}, and hence a progressive shift to a higher binding energy is consistently observed from B to C, T, and S (Fig. 12.2c). A notable feature that is common to all vicinal surfaces examined so far is the subtle shift observed in the surface T peak when going from flat

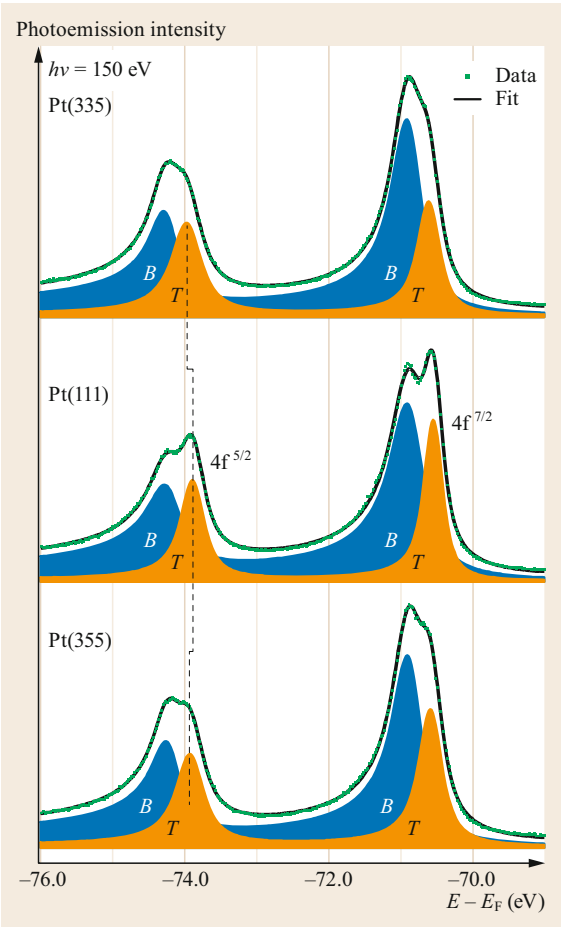

Fig. 12.9 Surface core-level shift in flat and vicinal Pt(111) surfaces: Pt 4f core-level photoemission spectra from Pt(111) (*center*), as compared to spectra measured from Pt(335) (*top*) and Pt(355) (*bottom*). *Dotted lines* mark the emission from T surface atoms, which shifts towards the bulk B line at the vicinal surface [12.14] ►

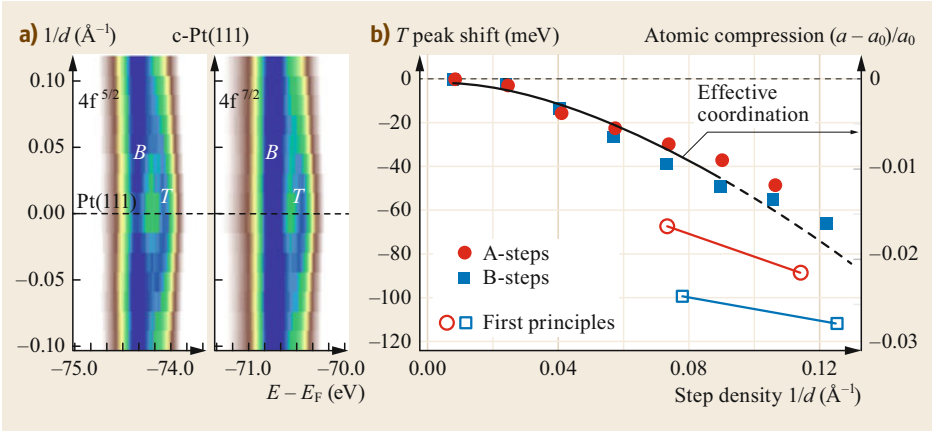

Fig. 12.10a,b Pt 4f peak scan across curved Pt(111) (α-scan): **(a)** Pt 4f core-level emission intensity plot represented against the step density $1/d$, as measured in a c-Pt(111) crystal. The surface peak shows a characteristic $1/d$-dependent shift to higher binding energy (positive T-shift), reflecting that the tensile stress at the vicinal surface, in average, is being relieved. **(b)** Average compressive strain of surface atoms as deduced from the T peak shift (*filled symbols*) and using an effective coordination model (*solid-dashed line*). Results are compared to DFT calculations (*open symbols*) [12.14]

to vicinal surfaces [12.6, 14, 25]. The case of Pt(111) vicinals is shown in Fig. 12.9. The Pt 4f T emission of Pt(335) and Pt(355) reveals a ≈ 50 meV shift with respect to the T peak in the Pt(111) surface. This small effect has been investigated in more detail using a curved Pt(111) crystal, in which the density of steps is smoothly varied. The result is shown in the core-level scan of Fig. 12.10a. The image is made of 15 different spectra, systematically recorded across the curved surface (α-scan). Taking the center of the crystal as a reference, the α-scan allows one to visualize a consistent and symmetric shift to a higher binding energy in both Pt $4f^{5/2}$ and Pt $4f^{7/2}$ surface core-level lines as a function of the step density $1/d$. Since the main contribution to this peak originated from terrace T atoms, this $1/d$-dependent shift is called a terrace shift.

The terrace shift is the spectroscopic signature of the surface layer relaxation of the vicinal surface sketched in Fig. 12.5. Such relaxation becomes more pronounced as the density of steps $1/d$ increases, such that the T peak shifts towards the bulk B peak. This connection between core-level energy and relaxation has been proven in first-principles calculations [12.14]. Substantial core-level energy variations appear in the terrace T atoms depending on the local degree of strain with respect to the fcc lattice. The T peak in Figs. 12.9 and 12.10 is thus made by contributions from the differently-relaxed T atoms of Fig. 12.5. As discussed earlier, steps allow terrace T atoms to partially relieve their tensile stress by compressing against each other. Such compression results in the larger overlap of wave functions with neighboring atoms, and hence to an effectively enhanced coordination [12.26]. Since the compression is larger for T atoms closer to step edges (Fig. 12.5), this explains the shift of the T peak towards the B peak as the step spacing d decreases. Moreover, an effective coordination model can be utilized to directly determine the average compressive strain of T atoms from the measured T core-level energy [12.14, 26]. The result is shown in Fig. 12.10b. It agrees with the lattice strain determined in both first-principles calculations and surface x-ray diffraction experiments (Fig. 12.5b,c).

The evidence that surface core-level energies mirror lattice strain variations at the surface can be of great help to investigate relevant processes in which substrate stress is a key parameter, such as catalytic reactions [12.27]. Although the expected core-level energy shifts are small, experiments on curved crystals may facilitate their accurate determination. In Fig. 12.11a, we show the α-scan of the C 1s for the CO-saturated c-Pt(111) surface. The T_{top} C 1s line for CO adsorbed on top of terrace atoms exhibits a terrace shift, although it goes in the opposite direction to that of the Pt 4f in Fig. 12.10, i.e., toward low binding energy. In reality, both shifts originate from the same stress-relief effect of surface steps, but their opposite direction indicates that the Pt(111) surface stress has changed sign upon CO saturation, that is, the negative shift of Fig. 12.11a indicates that the CO saturated Pt(111) terrace is submitted to compressive stress [12.28], in contrast to the tensile stress of the clean Pt(111) surface.

Changes in the lattice strain also occur during the spontaneous relaxation of high symmetry planes, e.g., in Au(111), where the (111) surface atomic plane forms a herring-bone reconstruction, characterized by a 4%

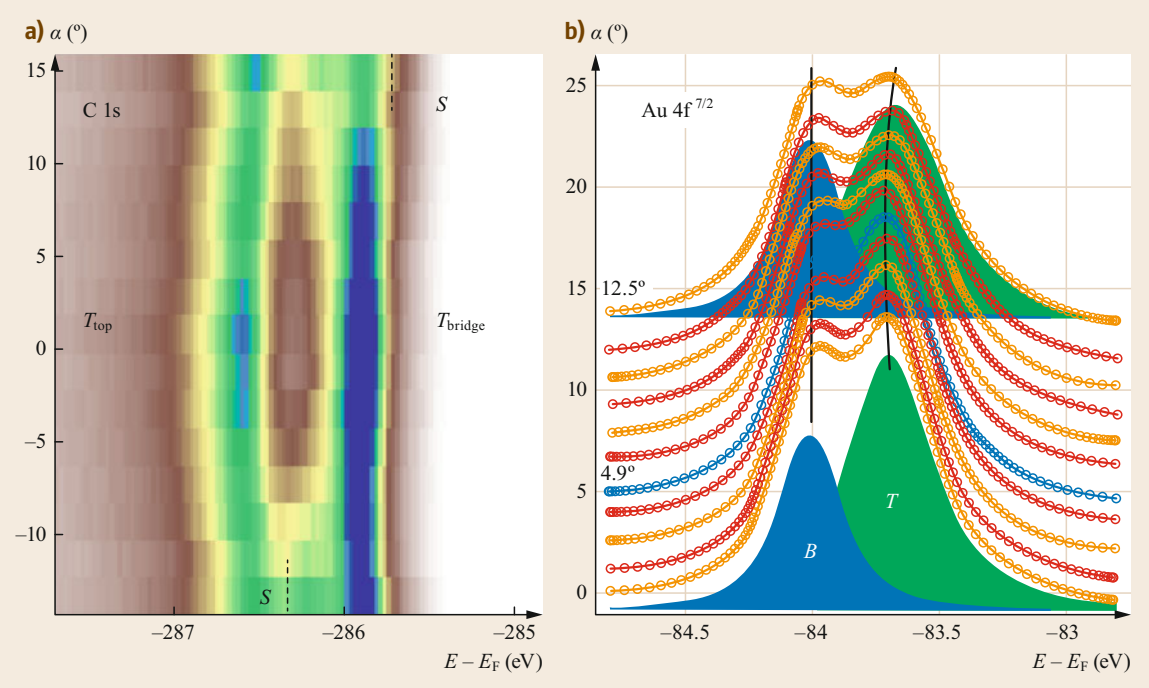

Fig. 12.11a,b Core-level α-scans for CO-covered c-Pt(111) and faceted c-Au(111): **(a)** α-scan of the C 1s level for a c-Pt(111) crystal saturated with CO. The negative T_{top} shift suggests that compressive stress diminishes from the CO-covered (111) plane to the CO-covered vicinal surface [12.14]. **(b)** Negative T shift in the Au $4f^{7/2}$ α-scan performed on a c-Au(111) surface. This is explained by the reduction of the atomic density in unreconstructed (111) terraces that progressively appear beyond $\approx 4°$

larger atomic density with respect to the bulk (111) plane. In vicinal Au(111), (111) terraces exhibit herringbone-like patterns at low miscut angles, but the reconstruction is progressively suppressed across the 4–10° faceting transition. In Fig. 12.11b, we show the α-scan of Au $4f^{7/2}$ performed on the B-step side of the c-Au(111) surface (Fig. 12.8b). From the high-symmetry (111) surface and for small miscuts, the T peak exhibits a subtle shift to higher binding energies as a function of α, similar to c-Pt(111), due to the stress-relief effect of the steps. However, the terrace shift is reversed around 3.5–5° at the threshold of the faceting transition shown in Fig. 12.8b. In fact, beyond $\approx 4°$, wide, densely-packed reconstructed terraces are smoothly replaced by narrow, unreconstructed Au(111) terraces with lower atomic density. The lower binding energy T shift is mostly due to the increasing presence of this second phase featured with terraces of higher tensile stress.

12.4 Surface States at Vicinal Noble Metal Surfaces

The (111) surface of noble metals is characterized by a projected bulk band gap that binds 2-D surface electronic states. These can be derived in a very intuitive, yet accurate way assuming a 1-D quantum well (QW) in the bulk z-direction [12.29]. As depicted in Fig. 12.12, such a 1-D QW is defined by the bulk band gap on one side and the vacuum potential barrier on the other. QW energy levels correspond to a series of 2-D electronic states located, according to their expected value $\langle z \rangle$, at an increasing distance from the surface, which makes them sensitive to surface scatterers at a different degree [12.30]. The $n = 0$ QW level, also called the intrinsic or Shockley state, is located close to the outermost atomic layer, and hence it is highly sensitive to surface impurities or structural defects such as atomic steps. As we move to higher lying states of the series, the so-called image potential states ($n \geq 1$) are located farther away from the surface, being perturbed only by the possible distortion of the vacuum level around such defects (Fig. 12.2a [12.31, 32]).

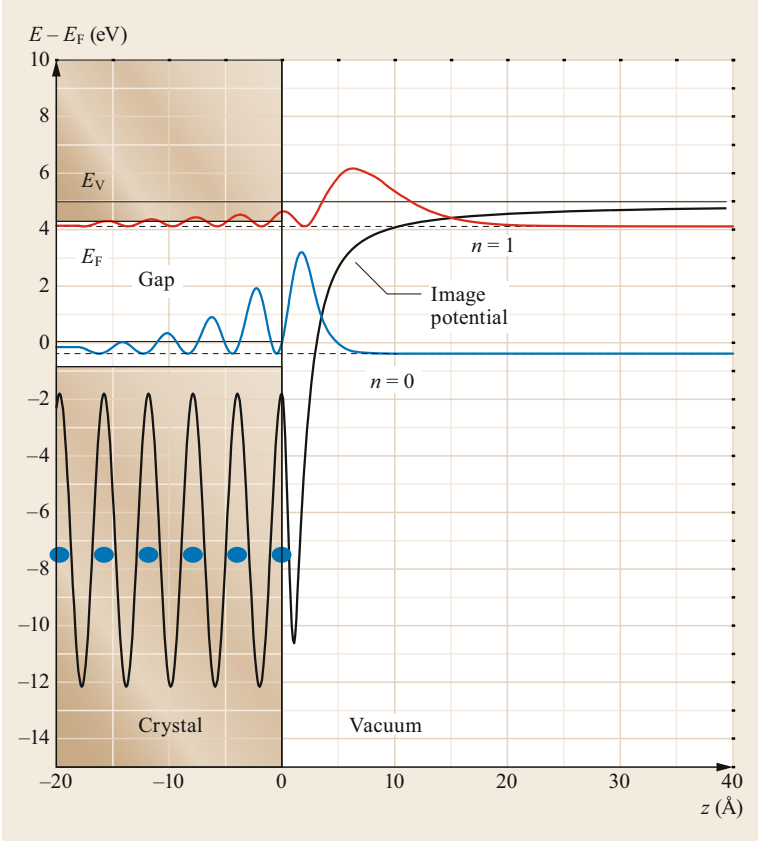

Fig. 12.12 Surface and image states: potential and probability density for the surface ($n = 0$) and image states ($n = 1$) in Cu(111). Surface electrons are trapped between the vacuum barrier (image potential) and the crystal projected bulk band gap [12.29]

The step superlattice in a vicinal surface represents an additional nanoscale potential that adds to that of the atomically flat surface. The dipolar fields originated at the undercoordinated edge atoms give rise to fully anisotropic, 1-D rows of periodic potential barriers. Understanding the effect of such periodic potential barriers on surface electrons is relevant from two different perspectives: on the one hand, it will affect electron-mediated phenomena such as adsorbate interactions, [12.33, 34] self-assembly, [12.35, 36] and chemical reactions [12.37–39]. Even the superlattice stability itself can be entangled to the final electronic structure either via electronic step–step interactions, [12.40, 41] or the induction of energy gaps at the Fermi level [12.42]. On the other hand, the combination of a 2-D nearly free electron gas in the presence of a 1-D superlattice potential grid provides a perfect scenario for modeling electronic confinement and superlattice band engineering.

The following subsections are focused on the interaction of Shockley states of (111) noble metal surfaces with monatomic steps, gradually increasing complexity from isolated pairs of steps, to simple step arrays, faceted vicinals, and, finally, to heterogeneous superlattices.

12.4.1 Electron Confinement in Isolated Step Resonators

Quantum electron confinement on metallic surfaces was elegantly demonstrated in pioneering atomic manipulation experiments performed by STM [12.43, 44]. The possibility of fabricating quantum corrals of different geometry and chemical nature by moving atoms one by one boosted research on electron confinement phenomena, providing simple model cases for quantitative studies of the QW resonator parameters, [12.44, 45] and for the exploration of more exotic phenomena such as the quantum mirage and invisibility [12.46, 47].

Similar quantum resonators can also be fabricated in a pristine surface using the intrinsic potential barriers of monatomic steps. Indeed, atomic and vacancy islands constitute effective 2-D resonators, similar to atomic quantum corrals, as shown in Fig. 12.13 [12.48]. An advantage of using steps instead of adatoms is that one can build simple 1-D resonators out of parallel steps, which can be simulated with analytical multiple scattering models. *Bürgi* and coworkers exploited this concept by artificially inducing straight parallel steps by controlled tip crashes and using the Fabry–Pérot model

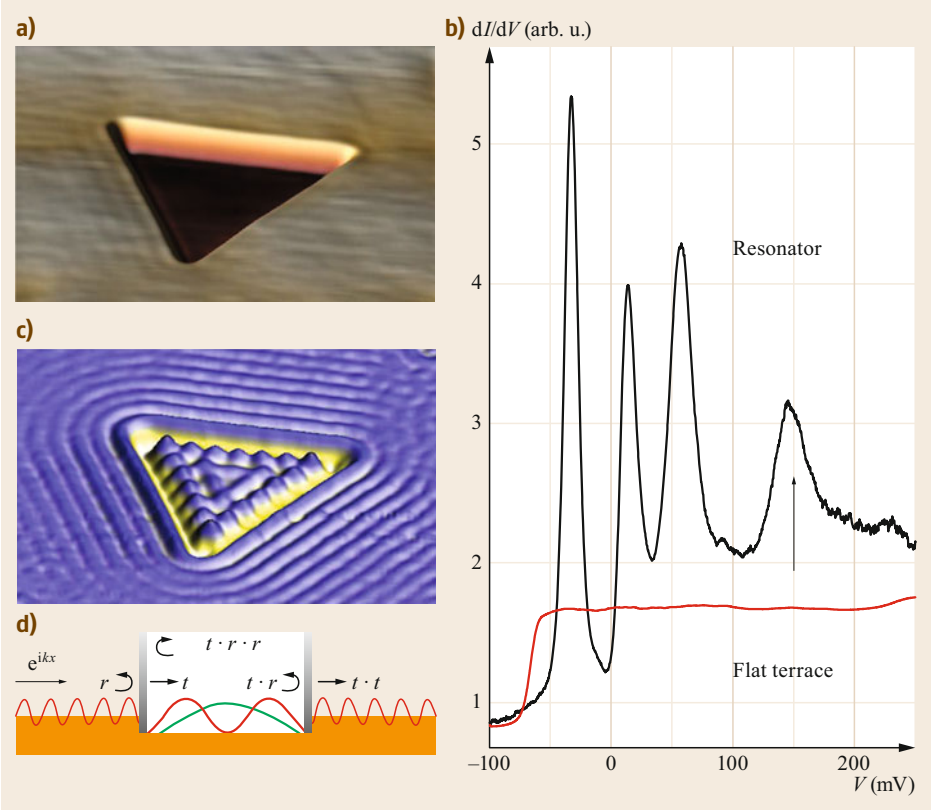

Fig. 12.13a–d Electron confinement inside a step resonator: **(a)** topographic STM image of a triangular, monatomic vacancy island on an Ag(111) surface. The length of the edges is 20 nm. **(b)** $\mathrm{d}I/\mathrm{d}V$ spectra acquired on the flat terrace (*red*) and at the center of the island (*black*). Quantization of the Shockley band gives rise to sharp peaks in the latter. **(c)** $\mathrm{d}I/\mathrm{d}V$ map acquired at the energy of the quantum-well state at +172 mV, marked with an *arrow* in **(b)**. **(d)** Multiple scattering that gives rise to quantum-well states inside the resonator

to analyze resonances [12.49]. The scattering coefficients extracted from this analysis indicated that steps in isolated resonators behave as quasi-infinite hard walls with negligible transmission. Reflection was shown to be significantly reduced by scattering into bulk states, which in the model appeared as an effective absorption. The results also revealed strongly asymmetric potential barriers that led to larger reflection coefficients for the step descending direction.

A weakness of the Fabry–Pérot model is that transmission depends on the wave function phase shift at the resonator barriers. This is determined by fitting the tail of the resonance in this region, which can be hindered by step-related local-density-of-states (LDOS) features and uncertainties in the precise barrier position. In order to directly address transmission coefficients, *Yazdani* and co-workers designed a different experiment consisting in measuring the energy-dependent LDOS modulation of the continuum electron gas outside the resonator [12.50]. For leaky barriers, transmission antiresonates at the QW energies, resulting in dips in the LDOS outside the resonator. Then, an analytical multiple scattering model can be applied to relate the energy modulation of the LDOS with the transmission coefficient [12.50].

In Fig. 12.14, this method is applied to investigate the transmission of Shockley states across steps on the Ag(111) surface [12.13]. The topographic image shows a step resonator that consists of a $d = 57$ Å wide terrace, surrounded by two larger terraces. Transmission measurements are carried out on the right terrace. Its width, $d = 1220$ Å, is well above the coherence length of Shockley states near the Fermi level, [12.51] the maximum distance where phase coherence of incoming and scattered waves permits quantum interference. Quantization effects can, therefore, be excluded here. Conductance ($\mathrm{d}I/\mathrm{d}V$) spectra acquired along a line that crosses the resonator reveal the different LDOS corresponding to the resonator and the semi-infinite terrace: coherent scattering at the two steps results in discrete

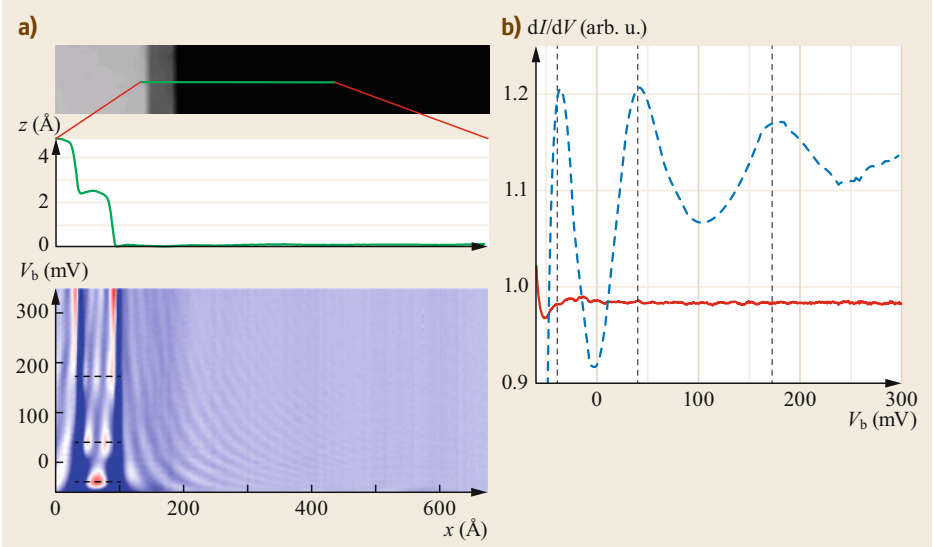

Fig. 12.14a,b Transmission across isolated steps: **(a)** topographic image of a step resonator of $d = 57.5$ Å (*top*), profile along the *green line* (*center*), and color scale dI/dV spectra acquired along the *same line* (*bottom*). **(b)** dI/dV spectra spatially averaged over the resonator (*blue*) and over the large terrace on the *right* (*red*). A background spectrum acquired at the center of a large terrace has been subtracted to all spectra in order to remove features related to the DOS of the infinite terrace and the tip [12.13]

electronic levels (dashed lines) separated by forbidden energy gaps in the resonator terrace. Outside the resonator, scattering at a single step gives rise to quasiparticle interferences that spatially modulate the LDOS over the continuum of energy. Energy modulations due to such interferences are best detected by getting rid of spatial modulations, either averaging spectra in real space or by performing the Fourier transform. Figure 12.14b shows the spatial average on the resonator (dashed lines) and on the right terrace (solid lines). The curves have been normalized by subtraction of a reference spectrum obtained far away from scatterers, in order to remove the density-of-states (DOS) onset of the noninteracting surface state and any contribution from the tip DOS. The normalized dI/dV curve is flat, without any sizeable dip at the resonant energies of the QW states (dashed vertical lines), indicating that transmission of Shockley states across isolated steps is negligible, in agreement with the Fabry–Pérot analysis [12.49]. An upper limit of $T < 0.3$ (i.e., $|T|^2 < 0.1$) can be estimated by fitting the normalized fast Fourier transform (FFT) intensity with the analytical function developed in [12.50] (not shown here).

In summary, STM studies of surface electron confinement within isolated step resonators on Ag(111) reveal that monatomic steps lead to asymmetric upwards/downwards scattering with negligible lateral transmission and significant absorption via coupling to bulk states. Similar studies on quantum corrals built by adatoms of different nature on other noble metal surfaces suggest that this is a general behavior, i.e., insensitive to the type of scatterer [12.52–54].

12.4.2 Superlattice Bands in Coupled Step Resonators

A vicinal surface can be conceived as a self-assembled periodic array of step resonators. Depending on the electron coupling strength between contiguous resonators, the resulting surface electronic structure will consist of either an array of noninteracting QW states or of propagating superlattice bands. Both cases are schematically depicted in Fig. 12.15a.

In strong contrast to the total electron confinement probed by STM on isolated step resonators, a vast number of studies demonstrate that surface electrons on vicinal surfaces propagate across steps and behave as superlattice states [12.4, 5, 8, 13, 42, 55–66]. These are mainly based on the analysis of ARPES measurements, where band perturbations such as energy shifts, backfolding and gap opening can be readily observed. Such parameters can be related to the step-barrier strength, periodicity, and scattering coefficients by fitting the bands, e.g., with the periodic Kronig–Penney potential model (Fig. 12.15b) [12.5, 64, 67]. Figure 12.15c is an illustrative example of the electronic structure of a vicinal Au surface, Au(788), where the free electron-like parabola of the flat (111) terrace is split into subbands

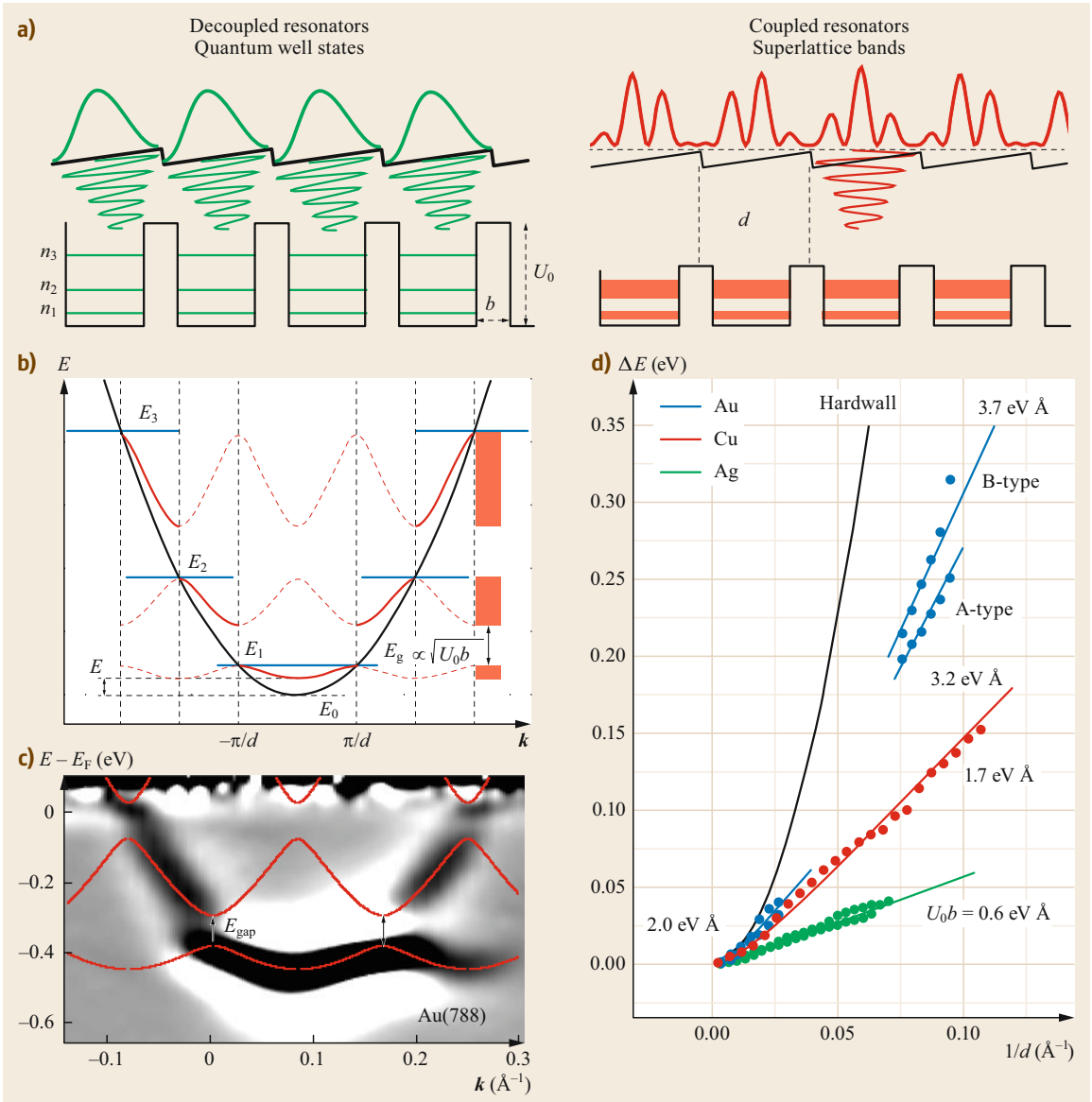

Fig. 12.15a–d Surface states at vicinal surfaces: **(a)** decoupled and coupled resonators confining QW states and giving rise to superlattice bands, respectively. Kronig–Penney potentials with barrier strength $U_0\,b$ and periodicity d are depicted below each case. **(b)** 1-D band structure of a free electron gas (*black*), superlattice states (*red*), and QW states (*blue*). **(c)** ARPES data of a Au(788) vicinal surface, with $d = 39$ Å, exhibiting superlattice bands, in inverted gray scale. The second derivative of the photoemission intensity is used to enhance the peak maxima, which explains the (bright) depression around the band. **(d)** Energy shift of the band bottom as a function of superlattice periodicity obtained from the ARPES data measured on curved Au, Cu, and Ag crystals [12.8]. *Colored lines* are fits of the data with the Kronig–Penney model (12.2), and the *black line* represents the hard-wall case

separated by small gaps. The red curves are a fit of the Kronig–Penney bands, from which the step-barrier strength $U_0\,b$ and periodicity d can be derived. The spectral weight of each subband is dominated by the zero-order Bloch component that follows the nonperturbed parabolic dispersion, minimizing the contribution of the $n = 2$ and $n = 3$ folded subbands in the first Brillouin zone [12.68].

A more reliable way of obtaining $U_0\,b$ resides on varying the miscut angle of the vicinal surface to ana-

Fig. 12.16a–c Analysis of the Fourier components of the surface states through k_x–k_z diffraction plots: **(a)** The *bottom part* sketches the exponential decay of the surface state wave function towards the bulk for QW states confined in (111) terraces (*green*) and superlattice states propagating along the macroscopic plane (*red*). In the k_x–k_z plot on the *top*, corresponding rods represent the momentum distribution of the decaying waves, peaking at the L points. For QW states, Fourier components spread along the [111] direction, whereas for superlattice states, vertical rods locate at $k_x = (2n+1)\pi/d$ (n integer), i.e., the superlattice zone edge boundaries. **(b)** Photon-energy-dependent band dispersions for a curved crystal at a position where $d = 71$ Å. *Vertical lines* mark zone-boundary edges of the step superlattice. Free-electron-like dispersion curves (*red*) that fit data are included. **(c)** k_x–k_z diffraction plots for several points of a curved Au crystal. *Red* data belong to lattices that exhibit split bands, where band minima are determined by parabolic fitting and the point size correlates with the ARPES intensity. *Blue data points* correspond to lattices where a double band cannot be resolved, and k_x data are determined from intensity maxima. In this case, split rods are not perfectly resolved around the intermediate k_z values, although alignment along the [111] direction never occurs [12.13] ►

lyze the band bottom energy shift with respect to that of the flat surface, namely the terrace shift as a function of d: $\Delta E(d) = E(d, k = 0) - E_0$. For that purpose, the continuous tunability of d offered by curved surfaces turns out to be extremely useful, enabling the acquisition of systematic, high data density plots such as the one shown in Fig. 12.15d [12.8]. Here, $\Delta E(d)$ obtained for the Shockley state on curved Au(111), Cu(111), and Ag(111) crystals are plotted and fitted to the Kronig–Penney relation [12.8]

$$\Delta E = \frac{2\hbar^2}{m^*}\frac{1}{d^2}\left[\tan^{-1}\left(\frac{q_0}{q}\right)\right]^2 , \qquad (12.2)$$

where $q_0 = (m^*/\hbar^2)U_0\, b$ and $q = \sqrt{(2m^*/\hbar^2)(E - E_0)}$. Both E_0 and m^* are obtained from fitting the parabolic dispersion on the flat region of the crystal, whereas $U_0\, b$ is left as the only fitting parameter in (12.2). A single value $U_0\, b$ holds for each crystal at all d regimes, except in Au, where the interplay between steps and the surface reconstruction results in complex relaxations and faceted regions (Sect. 12.2.3). The largest barrier strengths correspond to Au, ranging from 2.0 to 3.7 eV Å depending on step density and type, then Cu with 1.7 eV Å, and Ag presents barriers as low as 0.6 eV Å. Such differences can be scaled with variations in the step dipole moment of each crystal, as suggested by partial comparative measurements in surface-vacuum [12.63] or surface-electrolyte interfaces, [12.69] supporting the electrostatic origin of the step barrier.

An alternative proof of the superlattice nature of the wave functions in the whole energy region explored with curved crystals is provided by the direction of the plane that defines its 2-D character, also called modulation plane. QW states are terrace modulated, i.e., with the bulk decaying tail perpendicular to the (111) direction, whereas superlattice bands are step modulated, i.e., propagating along the macroscopic surface plane and hence exhibiting a decaying tail perpendicular to it (Fig. 12.15a). In reciprocal space the oscillatory damping towards the bulk, with fundamental frequency $k_L = \sqrt{3}\pi/a$, gives rise to a broad spectral momentum distribution along the decaying direction that peaks at the L points [12.13]. Taking the parallel direction to the vicinal surface plane and perpendicular to the steps as the x-direction, the two cases are represented as cigar-shaped rods in the k_x–k_z cut of Fig. 12.16a, also called k_x–k_z diffraction plot for its resemblance with the low-energy electron diffraction (LEED) analysis of vicinal surfaces [12.70]. The spectral rods of terrace-modulated states spread along the [111] direction, whereas those of step-modulated states appear vertically aligned at $k_x = (2n+1)\pi/d$ (integer n), the superlattice zone edges. This spectral distribution can be elegantly probed by scanning the photon energy in ARPES measurements, i.e., by sweeping the Ewald sphere across the reciprocal space. The latter is shown in Fig. 12.16b for the curved Au crystal at a position of $d = 71$ Å. By a parabolic fitting of the data, disregarding superlattice minigaps for simplicity, one can extract the position and intensity of the band bottom. These are represented in the diffraction plots of Fig. 12.16c, the dot size being proportional to the intensity. The vertical umklapp rods indicate that the Shockley state is clearly step modulated for periodicities as large as $d = 108$ Å, and similar results are obtained with the curved Ag crystal for values of d up to 180 Å [12.13]. The slight deviations found for some points at the largest d values (blue points) appear to be a consequence of the terrace width distribution (TWD, see Sect. 12.2.2), which is expected to lead, in analogy to LEED, to broadening and effective overlap of contiguous reciprocal lattice rods $(2n+1)\pi/d$. One can, therefore, conclude that Shockley states on vicinal surfaces behave as propagating superlattice states all the way from rather small periodicities ($d \approx 10$ Å) up to the largest values that can be reliably probed in ARPES ($d = 100$–200 Å), i.e., up to the limit set by natural TWD broadening in step arrays.

The above scenario is not compatible with the transitions from superlattice to QW states proposed in previous studies on single-miscut vicinals. Those were

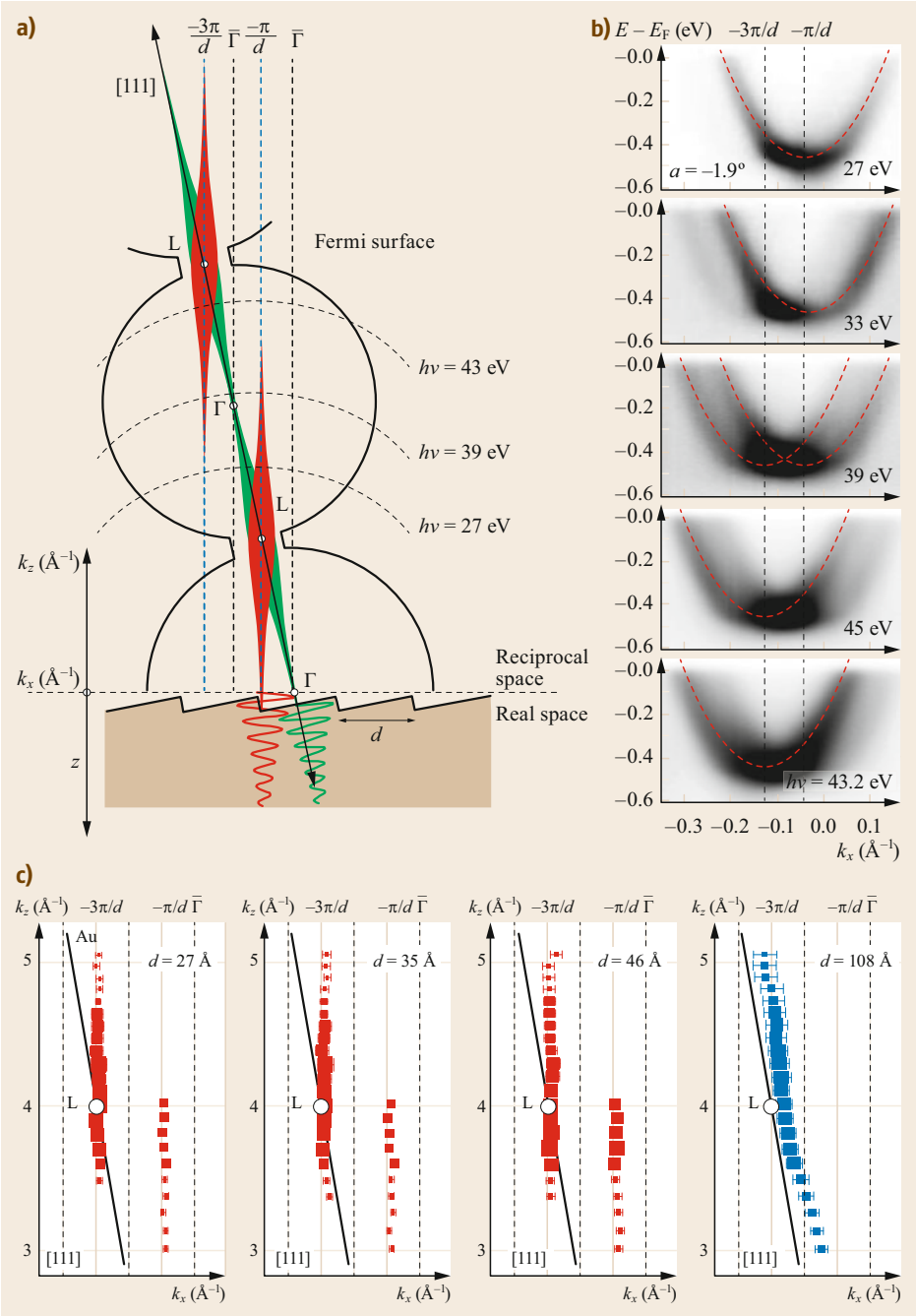

attributed to different mechanisms, such as a transition from deeper lying surface resonances to true surface states, [12.5] the depopulation of surface states, [12.72] or lattice disorder at the proximity of the Fermi nesting period $d = \lambda_F/2$ [12.42]. The fundamental role of lattice disorder in the induction of confined states was recently confirmed at the local scale by STM measurements in regions with significant disorder, revealing the coexistence of 1-D QW states and superlattice 2-D bands, as can be seen in Fig. 12.17 [12.71, 73]. In general, as we vary the miscut angle, complex electronic phenomena may emerge, in parallel to the also complex structural variations that real vicinal surfaces exhibit. However, all experiments in curved

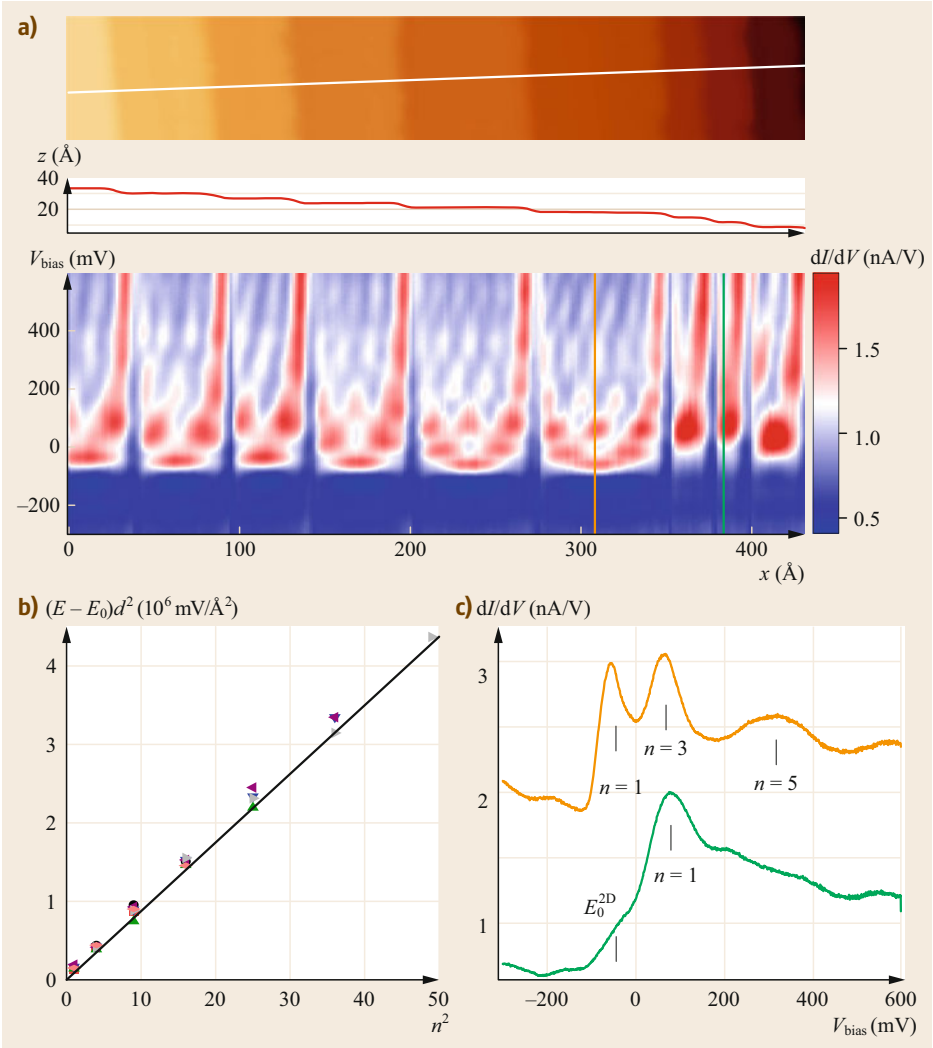

Fig. 12.17a–c Coexistence of 1-D QW states and 2-D superlattice bands: **(a)** dI/dV spectra acquired by STM along the *white line* indicated in the topographic image displayed at the *top* (the topographic profile is added right below it). **(b)** Energy shift (normalized by d^2) of the lateral 1-D resonances, obtained by fitting the spectra in **(a)** with Lorentzian peaks. Data are compared to the 1-D hard-wall potential expectation (*line*). Values obtained at different terraces are plotted in *different color*. **(c)** Individual dI/dV spectra extracted from the set of **(a)** (*vertical lines*). Both spectra exhibit clear 1-D resonant peaks. The onset of the dispersing 2-D state (E_0^{2D}) is only visible in the spectra of the smaller terrace (*green curve*), where it does not overlap with the 1-D resonant peaks [12.71]

crystals with reasonably ordered, coherent step lattices exhibit Shockley bands that can be interpreted within a simple Kronig–Penney model, using a single value of the step barrier for all miscut angles at experimental reach. Interestingly, this step barrier can be manipulated by decorating the step superlattice with metallic and molecular wires and stripes. One can tune the step-barrier strength and even invert the sign from repulsive, [12.74] switch from macroscopic to (111) terrace modulation plane [12.75], or passivate the dipole to make the step transparent [12.76].

12.4.3 Electronic States in Faceted Surfaces

The surface electronic structure becomes rather complex at vicinal surfaces that exhibit periodic faceting. As discussed above, faceting is triggered by the reconstruction of the high-symmetry plane of the terraces. This is the case of vicinal Au(111) surfaces with miscut

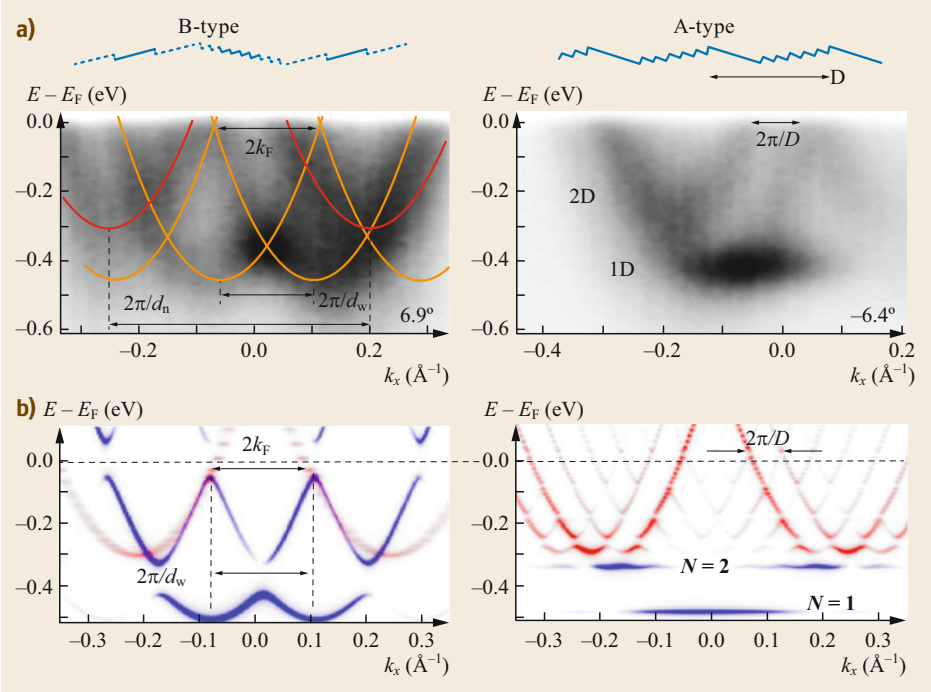

Fig. 12.18a,b Shockley bands in faceted Au(111) surfaces: **(a)** photoemission intensity maps measured with 43 eV photon energy in the B-type side (*left panel*) of the c-Au(111) surface at 6.9° miscut angle; d_w and d_n surface bands appear superimposed. *Solid lines* are guide-to-the-eye parabolic functions that agree to the periodic faceting. The *right panel* corresponds to bands at the A-side of the crystal measured at 6.4° miscut angle. The surface band splits into a quasi-1-D state (low energy) and a 2-D band (high energy). **(b)** Calculated photoemission intensity maps for B- and A-type faceted surfaces (*left* and *right panels*). For the B-side we assume 30 small $d_n = 14$ Å terraces embedded between two facets made up of 30 large $d_w = 30$ Å terraces. For the A-side we consider a periodic succession of six small $d_n = 14$ Å terraces and a single $d_w = 40$ Å terrace [12.4]

angles between $\approx 4°$ and $\approx 10°$, which exhibit periodic faceting that results in a hill-and-valley structure of wide ($d_w = 31–41$ Å) and narrow ($d_n = 13–14$ Å) terraces. As shown in Fig. 12.3c, for A-type steps, the d_w phase is characterized by a single terrace, while the d_n phase consists of several steps [12.4, 5, 77]. Therefore, a periodic superstructure with lattice constant $D = d_w + m \times d_n$ arises, where m depends on the local miscut angle. For B-type steps, bunches of terraces are formed in both d_w and d_n phases, resulting in much larger D periodicity (Fig. 12.8b). Due to faceting, Au(111) Shockley states split into low ($E_B = 0.45$ eV) and high ($E_B = 0.29$ eV) energy bands for d_w and d_n phases, respectively. For B-type steps, with large d_w and d_n phases, d_w and d_n states are decoupled, whereas the single d_w terrace in A-type faceting allows d_w and d_n bands to hybridize, leading to a complex band structure [12.5]. Such A/B faceting differences are readily observed when monitoring the evolution of the Shockley state on the curved Au(111) sample [12.4, 12]. At the upper and lower onsets of faceting, both A and B exhibit free-electron-like bands folded with $g_w = 2\pi/d_w$ (as in Fig. 12.2b) and $g_n = 2\pi/d_n$ umklapp vectors, respectively. In Fig. 12.18a, we show the characteristic spectra taken at α miscuts within the faceting region in both A and B sides (−6.4° and 6.9°). At the B side, with no d_w–d_n interactions, independent d_w and d_n bands appear superimposed. In contrast, on the A-side the d_w–d_n interaction leads to a coherent band structure, made of 2-D (dispersing) band features with the characteristic 2-D $\Delta k_x = 2\pi/D$ umklapps near E_F, plus a (weakly dispersing) 1-D quantum-well-like state split-off at $E_B = 0.4$ eV [12.4, 5].

Despite the apparent complexity of band structures of Fig. 12.18, these can be well reproduced within the same free-electron-like plus step-barrier-potential framework discussed for simple step lattices. However, the photoemission matrix element must be accounted for in order to disentangle experimental observations [12.4]. The simulated photoemission intensity maps shown in Fig. 12.18b were calculated within the dipolar approach, assuming free-electron waves as final

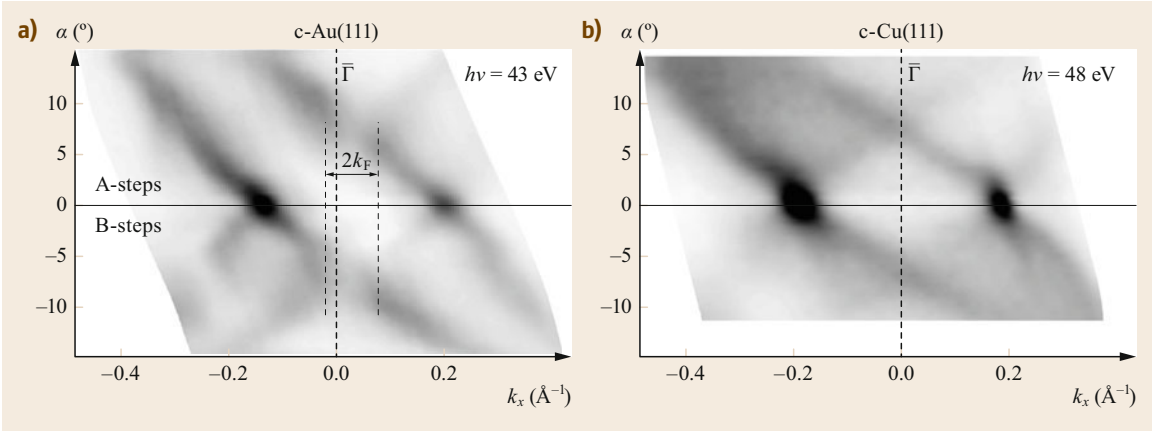

Fig. 12.19a,b ARPES α-scan at the Fermi level on c-Au(111) and c-Cu(111) surfaces: photoemission intensity map measured at E_F for the curved Au(111) surface as a function of the miscut angle α and the wave vector k_x perpendicular to the step array on the local surface plane for **(a)** c-Au(111) and **(b)** c-Cu(111) surfaces. Differences stand out at a critical $\approx 5-7^\circ$ miscut range. In c-Au(111), faceting occurs with a characteristic k_F oscillation in both d_w and d_n phases. In c-Cu(111), no apparent instabilities are observed at E_F

states and Shockley states as initial states [12.78]. The latter are free-electron-like parallel to the steps, while in the k_x-direction they scatter with a periodic 1-D step potential that mimics the faceted superstructure. Using the step-barrier potential width $U_0 = 2$ Å and height $b = 1$ eV (in agreement with Fig. 12.15d), effective mass $m^* = 0.27\,m_e$, and reference energies of terraces $E_0(d_w) = -0.53$ eV and $E_0(d_n) = -0.42$ eV, the model fits the experimental bands in the top panels for both A and B-like superlattices. Blue and red colors are assigned to electronic states with higher probability at d_w and d_n facets, respectively. The simulation validates the wave function model for the A-type superstructure sketched in Fig. 12.3. The weakly dispersing quantum well state at $E_B = 0.4$ eV appears connected to electron confinement into single d_w terraces, whereas the higher-lying 2-D band manifold corresponds to wave functions that are strongly modulated within d_n nanofacets [12.4, 5].

A closer look at ARPES experiments and simulations of Fig. 12.18 reveals the existence of peculiar Shockley state modulations near E_F. At the lower $\approx 4^\circ$ onset, we notice that d_w bands nest at the Fermi energy with $k_F = \pi/d_w$ vectors. In fact, a superlattice gap opens up for d_w bands around E_F, as shown in the model calculation for B-type steps. In this panel, we also observe that, despite their different energy and periodicity, Shockley bands of both d_n and d_w phases exhibit the same Fermi wave vector $k_F = \pi/d_w$. Such k_F coincidence for d_n and d_w phases appears as a characteristic property for Au faceting, since it is also present in the more coherent A-type faceted superstructure. This can be readily visualized in the α-scan of the Shockley state for the c-Au(111) crystal, which is compared with the corresponding α-scan of the c-Cu(111) crystal in Fig. 12.19. Each image represents the photoemission intensity at E_F, at fixed $k_y = 0$, along k_x (perpendicular to the steps), and across the curved surface. The two dark spots at $\alpha = 0$ mark $\pm k_F$ values of the Shockley state in the (111) surface, which are similar for both Au(111) and Cu(111). The pair of oblique k_F-lines that split from each $\alpha = 0$ point are superlattice umklapps. For a regular step array with a linearly-dependent step density $1/d$, such as that of c-Cu(111), opposite k_F lines cross at a critical ($\approx 7^\circ$) miscut, where the 1-D Fermi surface is nested with step-lattice vectors. On Au(111), however, the faceting transition prevents the k_F line crossing, i.e., the nesting of the Fermi surface in the k_x-direction. Instead, a $2k_F$-wide neck-like feature opens up at $\bar{\Gamma}$ and across the faceting region, for both steps A and B.

Although it is clear that the herringbone reconstruction of the Au(111) plane is the driving force in faceting, specific d_w and d_n values might be partly explained by the interplay with the electronic states [12.4]. The $2k_F$ neck of Fig. 12.19 indicates that both d_w and d_n phases share a characteristic Fermi wavelength. This property appears to be rather intriguing. In reality, the photoemission data and the model shown in Fig. 12.18 indicate that the step superlattice gap lies at the Fermi energy for the d_w phase in B-type faceting. This may, in fact, suggest that a charge-density wave-like instability with critical π/d_w wavelength may occur around d_w, as discussed long ago [12.81]. Such a possibility has been evaluated by comparing elastic (12.1) and electronic energy variations in vicinal noble metal surfaces as a function of miscut [12.8]. The size of the step su-

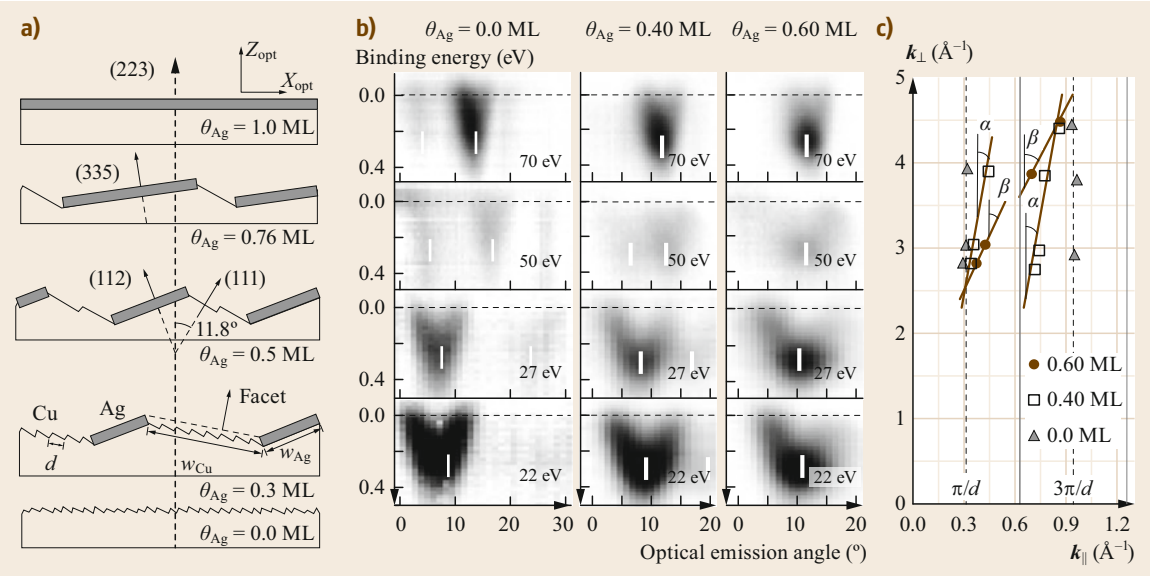

Fig. 12.20a–c Electronic structure modification of the Ag/Cu(223) system: **(a)** graphical representation of the evolution of Ag/Cu(223) with increasing Ag coverage (θ_{Ag}). Ag stripes (gray overlayers on the Cu substrate) grow in width (w_{Ag}), creating a step-bunching effect underneath them. The depletion of steps at neighboring clean Cu stripes increases the average terrace size inside the stripe, changing the local nanofacet orientation. **(b)** Photoemission gray scale plots (*darker color* corresponds to more intense features) of the surface states as a function of photon energy for pristine Cu(223) (*left*), 0.40 ML Ag (*middle*), and 0.60 ML Ag (*right*). The *white vertical lines* mark the center minima of the states. For best visualization, the Fermi step has been removed from the data and the photoemission intensity scaled to a common range. **(c)** k_x–k_z diffraction plots for the three cases shown in **(b)**. Data points line up at different angles, α and β, which correspond to the average direction in the respective Ag-free Cu nanofacet (α for 0.4 ML and β for 0.6 ML) [12.79, 80]

perlattice gap, i.e., the strength of the step dipole barrier becomes a key property. For Ag(111), where the barrier is too small, electronic energy variations are not significant, but for Au(111) and Cu(111), electronic energy instabilities are much larger. On Au(111), these can stabilize a particular lattice spacing (d_w) around the faceting transition. On Cu(111), nesting and gapping of the Shockley state could, in fact, explain the TWD instabilities observed around the $\approx 7°$ critical miscut [12.8].

Surface reconstructions can generally be induced by small amounts of adsorbates. Therefore, adsorption on a vicinal surface may also lead to a faceting transition, i.e., to the segregation of adsorbate-covered (reconstructed) and adsorbate-free facets. This option opens the way to the observation of complex surface electronic states with potential tunability, by simply modifying the coverage of the adsorbate in the submonolayer range. This is the case of Ag on vicinal Cu(111) [12.5, 65, 79, 80, 82]. By varying the Ag coverage, the surface morphology presents structural tunability due to Ag-induced periodic faceting of the Cu substrate. In particular, Ag close-packed stripes have a preference for the (112) orientation, since this allows substrate/adsorbate lattice matching, providing an efficient way to relieve the surface stress. Ag-covered and clean Cu self-assembled nanostripes appear aligned along the step directions, generating coverage-dependent hill-and-valley structures (Fig. 12.20a). By increasing the Ag coverage the clean Cu facets are progressively depleted of steps, until Ag-free Cu areas become (111)-oriented nanostripes. Consequently, the Ag coverage has a direct influence on both the Ag and Cu stripe widths and on the local, vicinal angle of the clean Cu facet.

Laterally-modulated Ag and Cu phases are both featured with Shockley states. However, in contrast to the electronic coupling between phases observed in faceted Au(111), in the Ag/Cu nanostripe system, the Shockley state appears confined within each nanofacet. However, Shockley states still reflect the coverage-dependent changes of the structure (Fig. 12.20b). In particular, the binding energy as well as the photoelectron emission angle from Ag and Cu nanostripes mirror both the nanostripe size [12.5, 65] and its local surface orientation [12.5, 65, 79, 80]. Figure 12.20b shows that for Ag/Cu(223) the emission angle of the Cu nanostripe state varies strongly with Ag coverage and photon energy. The white lines that mark the mini-

mum position of the Cu-like surface state show smaller separations between umklapps (two are visible for pristine and $\theta_{Ag} = 0.4$ ML). Indeed, the angular separation between the parabolas decreases with increasing coverage, as expected from the progressive increase in terrace size inside the Ag-free Cu nanofacet. Indeed, when the coverage approaches $\theta_{Ag} = 0.6$ monolayers (ML) only (111) terraces remain, so no splitting is observed. The photon-energy dependence allows a quantitative k_x–k_z diffraction plot analysis of the Fourier space for each superstructure (Ag coverage), in a similar way as performed for curved crystals (Fig. 12.16). This plot is shown in Fig. 12.20c. The average (223) direction is taken as the common k_x reference for all the data, i.e., for the band minima of the selected coverages in Fig. 12.20b. Separate pairs of lines fit each set of data, showing different line spacings and inclinations. Spacing and inclination angle correspond, respectively, to the step density and orientation of the local Cu nanostripe, evidencing that electrons photoemitted from the Cu facets are referred to its local facet direction [12.79].

12.5 Quantum Well States in Stepped Thin Films

In past decades, QW states of metal thin films became widely popular, due to their connection to quantum size effects in heterostructures, such as magnetic coupling in multilayers [12.83]. Such *vertical* QWs arise when a strong reflection of electron waves at the substrate interface is produced, resulting in electron confinement in the perpendicular direction of the film, in contrast to the *lateral* confinement of Shockley QWs discussed in Sect. 12.4.1. Therefore, the basic requirement for a metallic QW to exist is the presence of an electronic band gap in the crystal substrate at the right energy and momentum, whereas the film thickness (Θ) is the fundamental structural parameter that defines its energy spectrum [12.83, 84]. Laterally nanostructured thin-film/substrate systems that exhibit vertical QWs, such as those that can be grown on vicinal surfaces, may have potential interest in technology applications [12.2, 3]. Although QWs are bulk-like, their electron wave function may have an important weight at the surface or the interface, and hence be influenced by the presence of surface scatterers such as steps. Thus, the question arises whether and to which extent vertical QWs undergo, as Shockley states do, lateral scattering by a surface/interface step potential.

The Ag/Au(111) thin-film system exhibits smooth layer by-layer growth and abrupt Ag/Au interface, both resulting in sharp QW spectra in ARPES [12.85]. This is the perfect scenario to test the existence of (potentially small) lateral quantum size effects on vertical QWs. The spectrum of QWs of Ag films grown on vicinal Au(111) surfaces is thoroughly probed in ARPES experiments using a curved Au(111) sample (ϑ-axis) and a Ag wedge (Θ-axis, 7–12 ML) grown on top, as sketched in Fig. 12.21a. Figure 12.21b shows the $n = 1$ QW spectrum evolution by scanning the Ag wedge at the Au(111) surface, in the center of the curve. In a Θ-scan, one can observe the characteristic upward energy shift as a function of the Ag layer thickness in the $n = 1$ QW state. Figure 12.21c shows the in-plane 2-D band dispersion of the $n = 1$ QW state at 11.4 ML thickness, together with the Shockley band emission from the surface of the film and near E_F. Both the upward shift and the dispersion undergo strong variations at the stepped part of the film, as is shown in Fig. 12.22.

The Shockley band of the clean Au(788) surface ($\alpha = 3.5°$) is again displayed in Fig. 12.22a, in order to be directly compared with the electronic states for the 15 ML Ag film at the same α miscut. In the latter, the intense emission at ≈ 50 meV below E_F corresponds to the Shockley state at the surface of the vicinal Ag(111) film. At higher binding energies, one can observe the entire dispersion of two QW states ($n = 1$ and $n = 2$) and traces of $n = 3$. The momentum scale is referred to the local surface normal $\alpha = 3.5°$ away from the [111] direction. The dashed lines mark the minima of QW bands, which coincide with those of surface states of both the Au(788) substrate and the Ag film surface. Umklapp bands for both surface and QWs have minimum energies at π/d and $3\pi/d$ zone centers, suggesting that both undergo a similar process of scattering by the step lattice.

To qualitatively assess the strength of the step scattering in the Ag QW, constant energy cuts are compared for surface states of the Au(788) substrate and the $n = 1$ QW in a 9 ML film in Fig. 12.22c,d. The k_y–k_x intensity maps displayed were acquired at $E - E_F = -0.36$ eV for the surface state and at 120 meV above the $n = 1$ band minimum for the QW, i.e., the energies at which surface state and $n = 1$ QW umklapps, respectively, nest. Constant energy surfaces in both cases consist of a double ring structure (dashed lines are added as a guide for the eye) with a depleted intensity around the $\bar{\Gamma}$-points, indicating the presence of a superlattice gap. Figure 12.22e illustrates a typical α-scan (equivalent to the ϑ-scan in Fig. 12.21a) for a 7 ML film. For the sake of comparison, the zero in the momentum scale refers to the normal emission with respect to the local surface plane in each case. A single $n = 1$ QW band is observed,

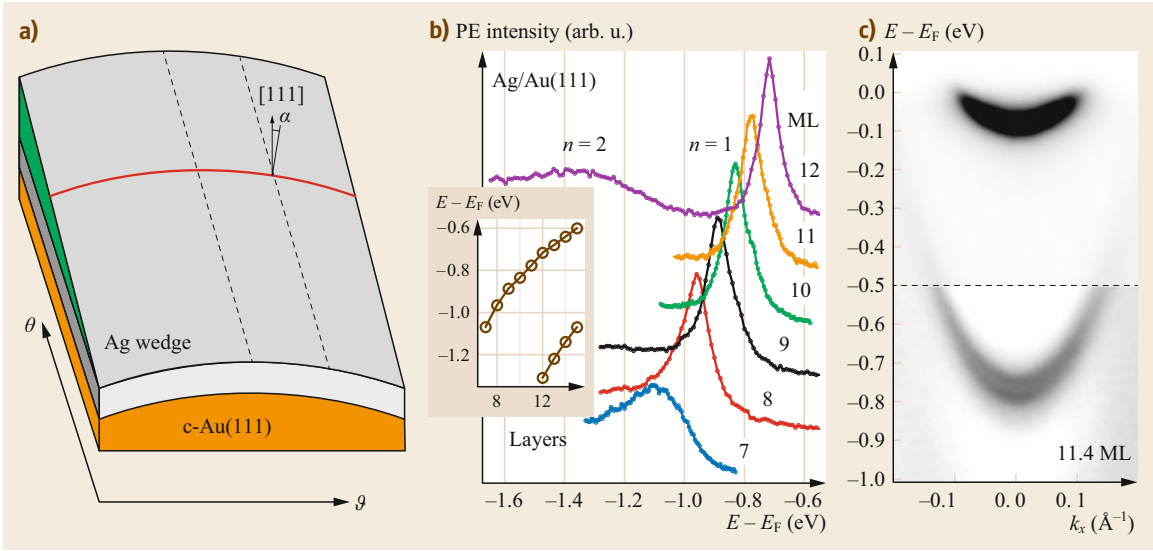

Fig. 12.21a,b Quantum well states on thin Ag films on c-Au(111): angle-resolved photoemission from Ag QWs on vicinal Au(111) surfaces, after creating a Ag wedge over a curved Au(111) surface ($h\nu = 21$ eV). **(a)** The thickness of the film is selected along the grown wedge in the Θ direction, whereas the miscut α varies along the ϑ direction. **(b)** Film thickness-dependent shift of QWs for a 7–12 ML wedge at $\alpha = 0$. **(c)** 2-D band dispersion of the $n = 1$ and the Shockley state for the 11.4 ML film at $\alpha = 0$ [12.71]

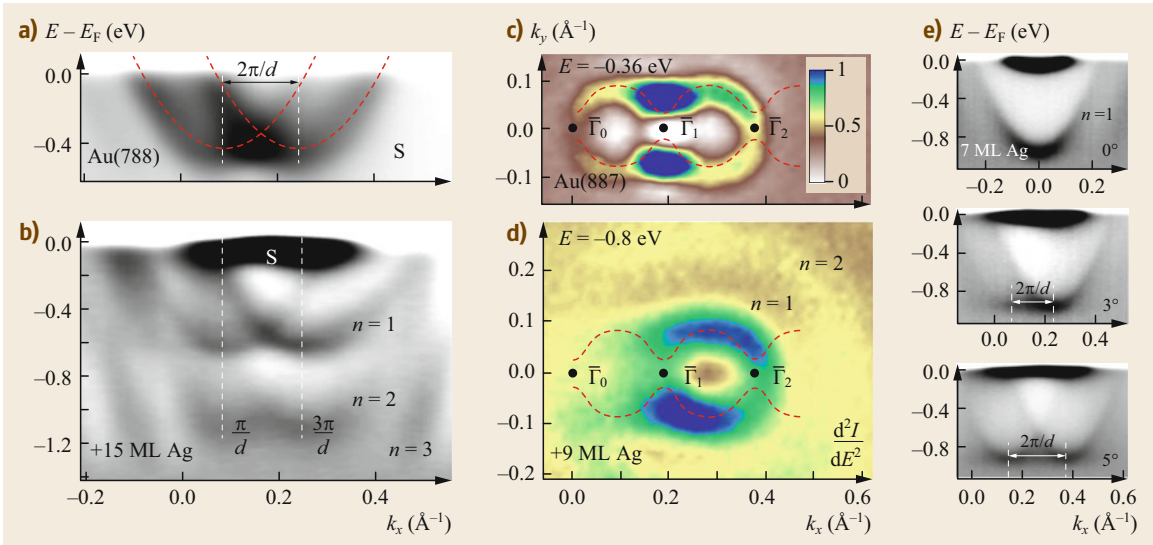

Fig. 12.22a–e Photoemission intensity plots of Ag films on c-Au(111) ($h\nu = 41$ eV): **(a)** clean c-Au(111), showing the surface state and **(b)** 15 ML Ag/c-Au(111), both at $\alpha = 3.5°$. This miscut corresponds to the (788) surface orientation. Three QW bands with step-lattice umklapps appear in the latter, which are aligned with the surface state at zone boundaries π/d and $3\pi/d$. **(c,d)** Constant energy surfaces (second derivative) at –0.36 eV, for the surface state of the Au substrate, and at 0.12 eV above the $n = 1$ QW band minimum (at 0.8 eV), for the 9 ML film, both at $\alpha = 3.5°$. The crossing of the two umklapp rings at $\bar{\Gamma}$ defines a region of lower intensity, revealing a similar gap in both surface and QW states. **(e)** 7 ML Ag/c-Au(111) QW bands in a ϑ-scan, showing the d-dependent splitting of the $n = 1$ QW bands [12.71]

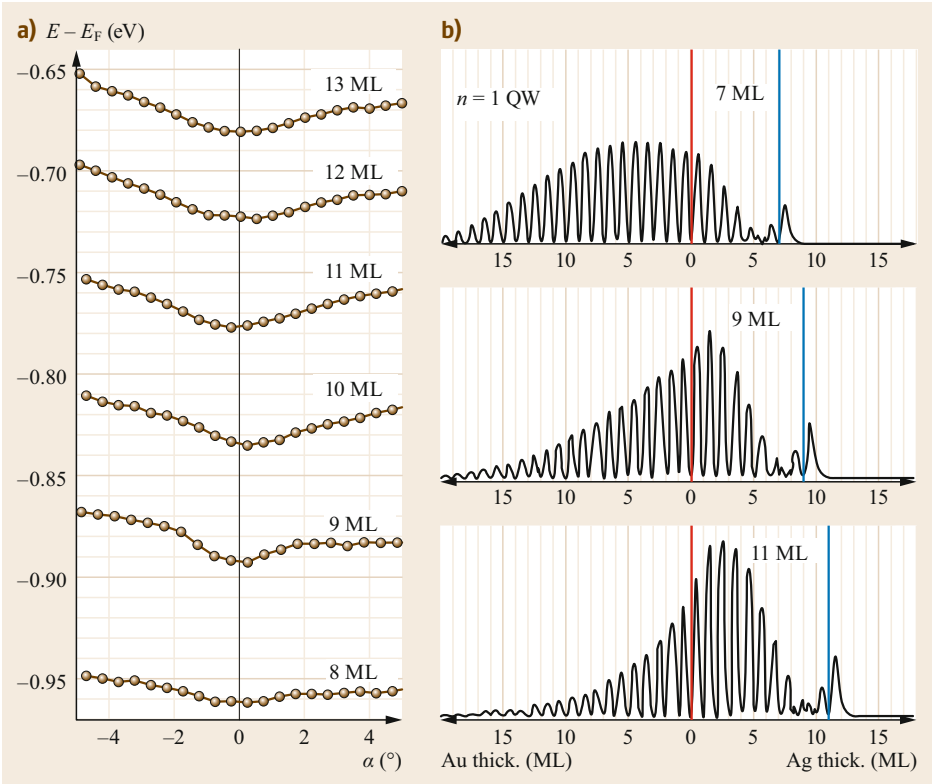

Fig. 12.23a,b Terrace size effect in QW states of stepped films: **(a)** $n = 1$ QW state energy (band minimum) measured in a full θ–ϑ-scan from a 8–13 ML wedge. The upwards shift from $\alpha = 0$ demonstrates a lateral quantum size effect. **(b)** QW wave functions in Ag films of different thicknesses grown on Au(111). *Blue* and *red lines* mark the surface and the interface position, respectively [12.71]

which exhibits the miscut-dependent $2\pi/d$ umklapp characteristic of curved surfaces [12.8]. The quantitative analysis of the step-scattering effect in QWs of the Ag/Au(111) system is shown in Fig. 12.23a. The series represents the energy minimum of the $n = 1$ QW band at different Ag film thickness and as a function of the miscut in the A (negative miscut) and B (positive miscut) sides of the curved crystal. Only small α angles below the faceting transition in the Au substrate are considered. We observe the characteristic upward (≈ 20 meV at $\alpha = 5°$) terrace energy shift, which barely depends of the film thickness in the whole 8–13 ML range.

The terrace shift and the superlattice effects (umklapp and gaps) shown in Figs. 12.22 and 12.23 prove the existence of lateral step scattering in metallic (vertical) QWs, quantitatively and qualitatively similar to that observed in surface states. This is a surprising result, since QW states are expected to have a much smaller probability in the surface plane compared to surface states, and hence are unlikely to sense the surface step dipole. However, it has been discussed that the terrace shift in QWs could result from an equally intense double contribution, i.e., a pure step-scattering effect, due to the sizeable probability density located at the surface/interface, plus a topological effect, arising from the tilt in the bulk-band quantization axis of the film, which is observed to switch from the [111] direction in flat films to the vicinal crystal direction in stepped Ag layers [12.71].

12.6 Spin-Textured Surface Bands at Vicinal Surfaces

In the absence of spin–orbit interaction (SOI), electron bands are spin degenerated and, hence, any scattering vector can connect a pair of states with the same spin and give rise to the quasiparticle interferences observed by STM (Fig. 12.24a). A very different scenario arises when the spin–orbit interaction lifts the spin degeneracy, resulting in nonconventional spin-textured bands. These occur in metals where the 2-D electron gas is affected by a sizable Rashba interaction, [12.86] or in the surfaces of topological insulators, [12.87] both depicted in Fig. 12.24b.

The Rashba effect is a consequence of the breaking of the 3-D translational symmetry at the surface or at the interface of materials with different atomic lattices.

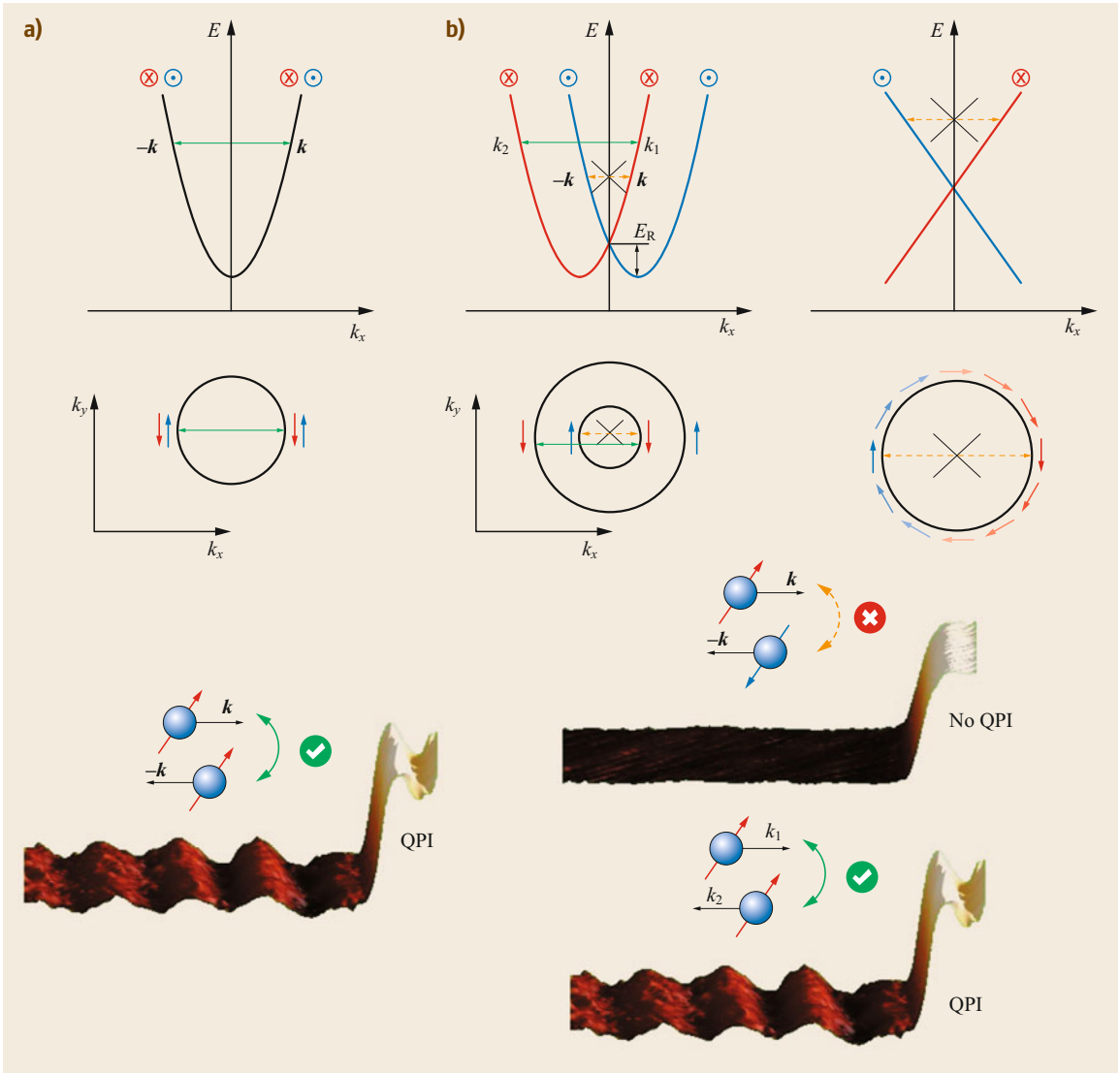

Fig. 12.24a,b Scattering within spin-textured bands: spin-polarized 1-D band structure (*top*) and 2-D constant energy cut (*bottom*) of **(a)** a free electron gas with no SOI and **(b)** an ideal Rashba system (*left*) and topological insulator (*right*). The spin polarization is represented in *blue/red* color code. Examples of forbidden/allowed scattering transitions are illustrated by *orange/green arrows*. *Bottom images* show a pictorial description of incoming and outgoing electrons scattering from a step, with their *red/blue arrows* representing their spin. In the absence of SOI, backward scattering between k and $-k$ give rise to quasiparticle interferences (QPI). In the presence of SOI, the orthogonal spins of k and $-k$ states cannot give rise to QPIs. These, however, can be formed by intraband scattering between k_1 and k_2 states

In the presence of SOI, this symmetry rupture lifts the degeneracy of a 2-D electron gas by a momentum splitting of bands with opposite spin. In an ideal Rashba system, the SOI locks the spin to the momentum of the 2-D electron gas, confining it at the surface plane, always at 90° with respect to the momentum. This particular entanglement gives rise to the helical spin texture depicted in Fig. 12.24b. In this scenario, the scattering between k and $-k$ states is forbidden by the lifting of Kramers degeneracy (only orthogonal states with opposite spin exist at k and $-k$). Other scattering events, such as the intraband transition highlighted in Fig. 12.24b by a green arrow, can still be allowed by spin conservation rules.

A more exotic spin texture is that of topological surface states, characterized in the ideal case by a spin-

polarized Dirac cone dispersion. In one dimension, the only scattering events connect orthogonal Kramers pairs, i.e., states with opposite momentum and spin, leading to an effective quenching of backscattering. Signatures of reduction of backscattering have indeed been detected by several STM quasiparticle interference experiments using randomly distributed impurities, [12.88, 89] and also monatomic steps [12.50].

In the field of spintronics, spin-momentum locking that is responsible of the unconventional spin textures of these materials represents a novel and effective strategy for controlling spins with charge currents [12.90]. It is, therefore, crucial to understand spin-dependent scattering mechanisms, and how steps may act as structural defects that filter or enhance the spin signal, or even trigger new spin textures. In this respect, vicinal surfaces might pave an exciting route towards spin-texture engineering, spin-polarized confinement, or anisotropic charge and spin transport.

A model example of a nondegenerated spin texture is that of the Shockley state in Au(111). A sizeable Rashba-type interaction in this surface gives rise to the splitting of the spin-degenerated band into two parabolic 100% spin-polarized subbands, shifted in momentum by $0.026\,\text{Å}^{-1}$ with respect to each other, as measured in high-resolution ARPES [12.91–93]. The resulting momentum distribution close to the Fermi level consists of two concentric rings with spin polarization vectors lying in-plane and tangential to the circular shape (Fig. 12.25). According to ab-initio calculations, the largest contribution to spin-splitting on Au(111) originates from its topmost atomic layer [12.94], making it susceptible to modifications in the presence of steps.

Vicinal Au(111) surfaces may, therefore, be utilized to investigate the interplay between spin–orbit coupling and scattering. This is done in Fig. 12.25 for Au(788) and Au(223). High-resolution ARPES measurements reveal an intact pair of Rashba-split Shockley bands propagating parallel to the steps, [12.96], but the broadening induced by both the reduced lifetime and the TWD hinders the observation of any split bands perpendicular to the steps (Fig. 12.25b) [12.60]. Only dedicated experimental techniques, such as spin-resolved ARPES (SR-ARPES) are able to detect the subtlety of the expected changes [12.95, 97]. The top panels of Fig. 12.25c, corresponding to a momentum distribution curve (MDC) perpendicular to the steps (direction marked with dashed lines in the top sketch in Fig. 12.25a), are obtained using SR-ARPES [12.95]. They show that spin textures persist in the presence of different step densities, indicating that neither scattering within the step superlattice nor the disorder introduced by the TWD destroy the overall spin structure. The number of peaks used for the data fitting match the expected components from the top sketch, each presenting its own spin vector. In consequence, the main and umklapp subbands still exhibit 100% polarization and maintain the spin helicity of the Au(111) surface. The spin textures observed closely relate to the flat case independently of the presence of the herringbone reconstruction. The main difference is found in the high step density Au(233) surface, where an increase of spin splitting, Δk, is observed. The cause of this has been interpreted in terms of an effective increase of one of the parameters that determine the strength of Rashba interaction, namely the out-of-plane potential gradient that the electron wave functions experience, as also illustrated by the dependence observed on the Miller indices of the surface, [12.98] the presence of adsorbates, [12.99] or the buckling of the surface layer [12.100].

Rashba interaction on vicinal Au surfaces does not seem to lead to qualitatively different electron scattering behavior due to an efficient spin-conserving intraband transition (Fig. 12.24b) [12.101, 102]. This is reflected on the value of its step-barrier, even higher than for Ag, with negligible SOI, and the endurance of the helical spin texture. Such an analogy of spin-degenerated systems is expected in model Rashba systems, where each Shockley subband is 100% spin polarized and, hence, momentum conserving intraband scattering is allowed. However, the scenario becomes more entangled in other materials with mixed orbital and spin texture. This is the case of the monolayer-thick $BiAg_2$ surface alloy grown on Ag(111), which is characterized by surface bands with record-high Rashba splitting [12.103, 104].

Highly-perfect $BiAg_2$ surface alloy domains can be grown by simply depositing 0.33 ML of Bi on Ag(111), followed by a soft annealing. The electronic structure of the surface alloy near the Fermi level consists of various sets of split parabola, all with negative effective mass, and each one with different spin and orbital composition (Fig. 12.26b) [12.100, 105]. The hybrid p_x–p_y band above the Fermi level is particularly interesting, since its spin–orbital texture is far from the 100% of ideal Rashba systems. In fact, the pair of initial and final states that leads to the spin-conserving intraband scattering observed in Au(111), exhibit spin polarization of opposite sign in $BiAg_2$ (dashed line on the right panel of Fig. 12.26a). Such a scattering process would not be allowed in a spin-conserving process. However, quasiparticle interference measurements performed near an individual step reveal strong interference patterns related to such intraband scattering transitions, as can be seen in Fig. 12.26a [12.100, 105]. Here, we show $\mathrm{d}I/\mathrm{d}V$ spectra acquired along a line perpendicular to

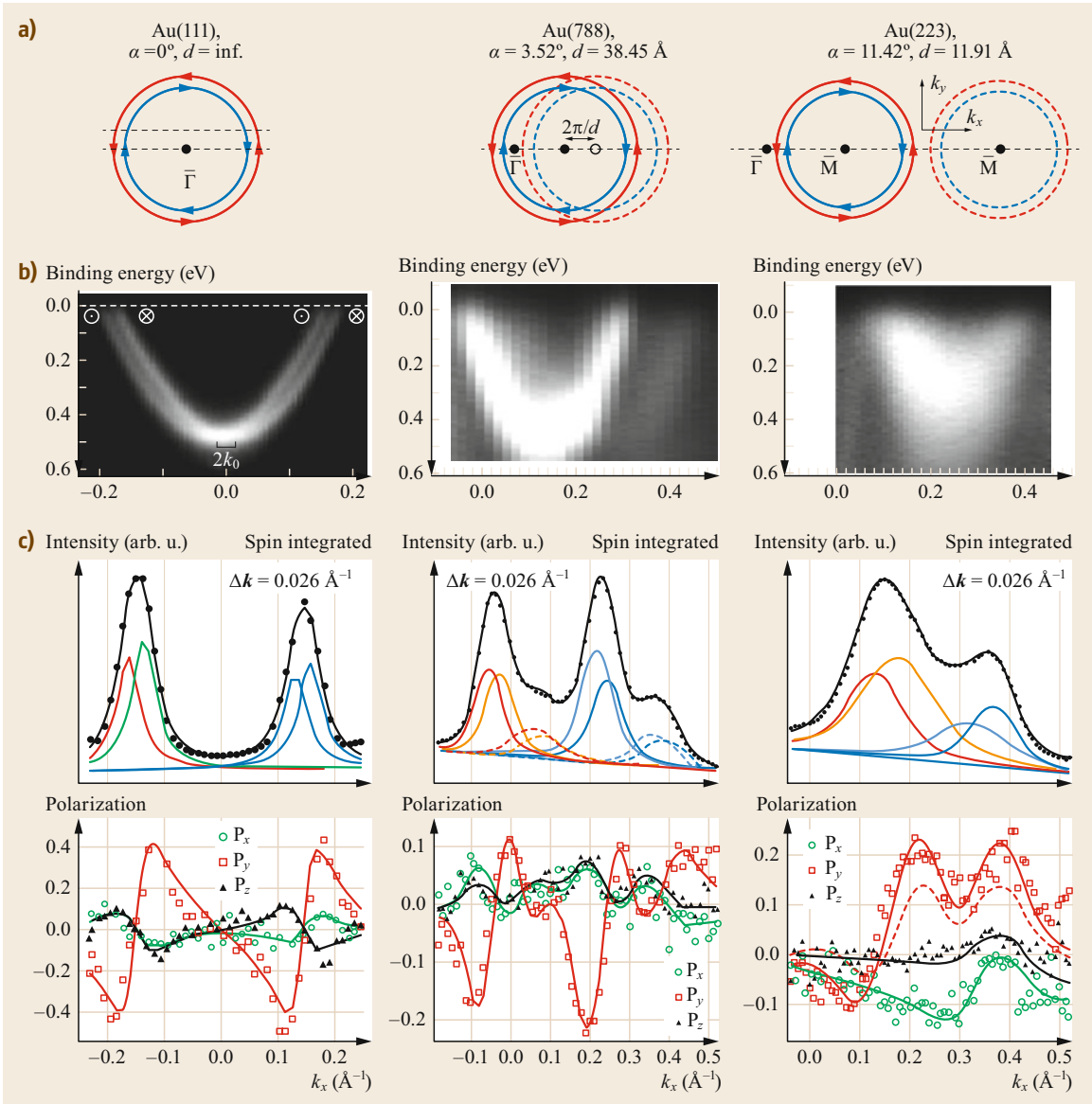

Fig. 12.25a–c Spin-resolved ARPES for Au(111), Au(788) and Au(223). For each surface, rows from *top* to *bottom* consist of: **(a)** graphical representation of the Fermi surface maps for the different miscuts indicating main (*solid circles*) and umklapp states (*dotted circles*); **(b)** spin-integrated band dispersions perpendicular to the steps, taken with $h\nu =$ 21 eV photon energy. Rashba splitting is resolved in the Au(111) surface, but in step arrays of Au(788) and Au(223) TWD broadening effects masks spin splitting; **(c)** spin-resolved MDCs acquired at $E - E_F = -50$ meV with $h\nu = 23$ eV. The *upper graphs* show the spin-integrated intensities that include the necessary peaks to fit the data and directly below the corresponding spin polarization curves for the three spatial directions [12.95]

several steps. The energy-dependent quasiparticle interferences found in real space are converted into scattering wavevectors by an FFT transformation along the x-axis (central panel), resulting in two clear branches labeled $\boldsymbol{D}_1$ and $\boldsymbol{D}_2$.

We focus on the $\boldsymbol{D}_1$ branch, which very nicely fits intraband transitions of the unoccupied split bands, as is shown in the right panel of Fig. 12.26a, by making use of the band structure obtained by ab-initio calculations. This can only be explained by considering

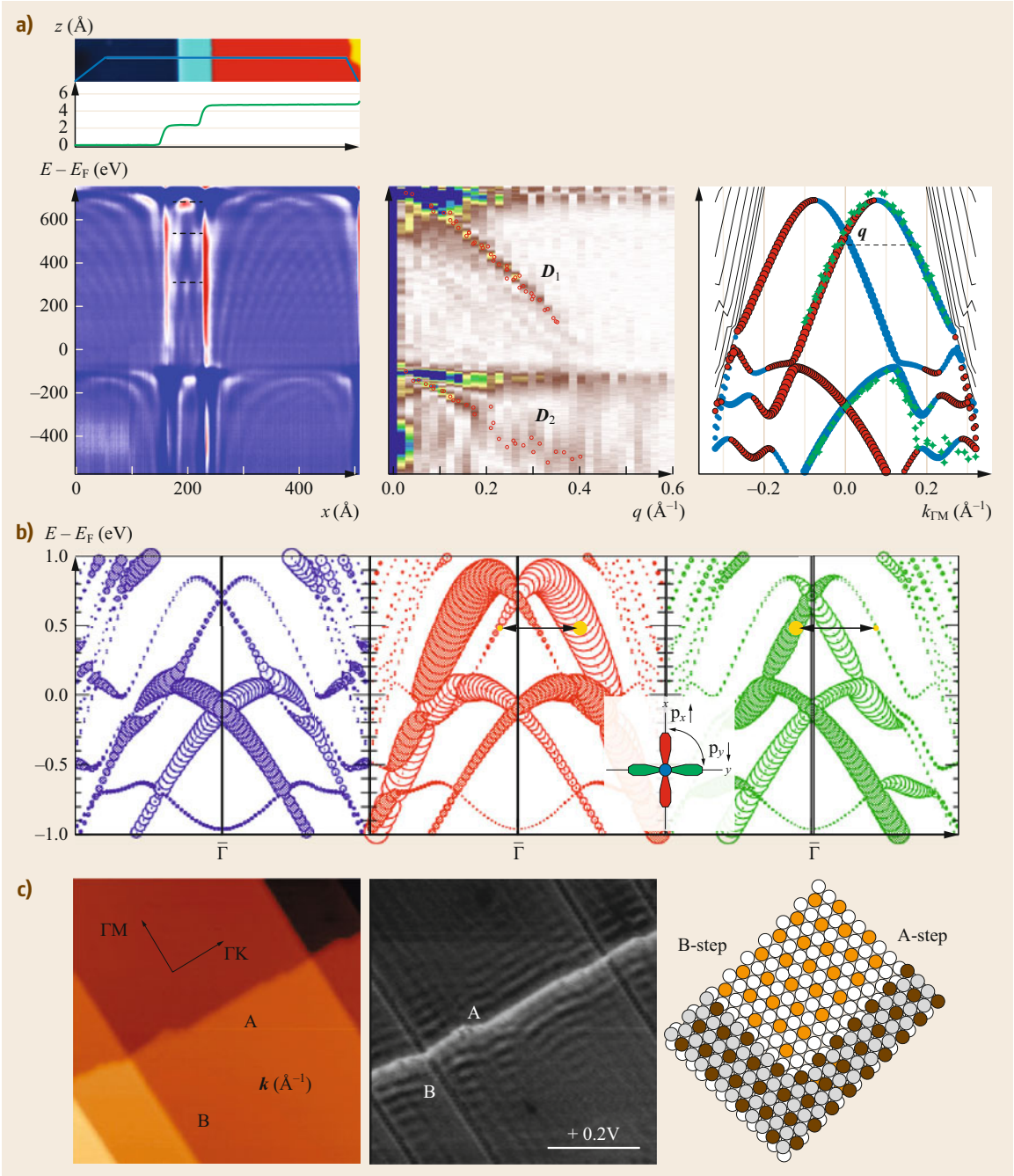

that the spin–orbit interaction in the scattering enables combined orbital and spin flips that conserve the total momentum. That is, p_x orbitals of a given spin scatter into p_y orbitals of opposite spin and vice versa (see the inset in Fig. 12.26b). Electron confinement studies on step resonators built on the surface alloy demonstrate that this spin-flip scattering mechanism can be as effective as the conventional spin conserving one in noble metals, leading to negligible transmission [12.105]. The effectiveness of this spin–orbit-dependent scattering mechanism, nevertheless, depends on the presence of Bi, and hence varies with the chemical composition of the step (Fig. 12.26c). The different scattering properties of each step type can be visualized in the

Fig. 12.26a–c Electronic scattering on the $BiAg_2$ surface alloy. **(a)** *Left*: a series of dI/dV spectra acquired along a line crossing a pair of A-steps (see **(c)**). The line is displayed in the topographic image on top. QW states can be observed in the small terrace, whereas larger terraces show oscillations in the continuum DOS. *Center*: Fourier transform of the spectra along the x-coordinate, showing two different branches of scattering vectors $\boldsymbol{D}_1$ and $\boldsymbol{D}_2$. *Right*: ab-initio calculation of the Rashba split bands, with initial and final scattering states resulting from vectors $\boldsymbol{D}_1$ and $\boldsymbol{D}_2$ superimposed as *green diamonds*. The color and size of the points in the band structure correspond to the sign and magnitude of spin polarization in the $\boldsymbol{k}_\parallel \times \boldsymbol{z}$-direction [12.105]. **(b)** Orbital and spin decomposition of the ab-initio band structure. The size of the symbols indicates the Bi p_z (*left*), p_x (*middle*), and p_y (*right*) contribution to the state. Opposite spin directions are shown by *full* and *empty symbols*. *Inset*: combined spin and orbital flip occurring in the scattering between the states marked by the *yellow dots* in the graph (same as the *green arrows* in **(a)**) [12.105]. **(c)** Topography (*left*) of a region with different step types and simultaneously acquired dI/dV map (*right*) displaying interference patterns from scattering at steps. The standing waves parallel to A-steps are clearly more pronounced. The chemical composition of each step type is illustrated on the *right schematics* ◄

spectroscopic map of Fig. 12.26c, where A-type steps induce significantly more pronounced standing waves than B-type steps, where the Bi concentration is more dilute.

The experiment discussed above was carried out utilizing individual steps on the flat $BiAg_2$ surface grown on Ag(111). However, in contrast to the more challenging case of topological insulators, the growth of stepped $BiAg_2$ alloys can be envisioned by deposition of Bi on vicinal Ag(111) surfaces. In fact, exciting phenomena may arise when combining spin–orbit interaction with real stepped surfaces, as experimentally demonstrated for several high Miller index bismuth surfaces, namely Bi(441) and Bi(114). With, respectively, 45° and 56° of miscut, they cannot be considered vicinal to the (111) surface, and thus their electronic structure cannot be described in terms of the 2-D states of the (111) surface under a periodic step potential. In fact, the STM to-

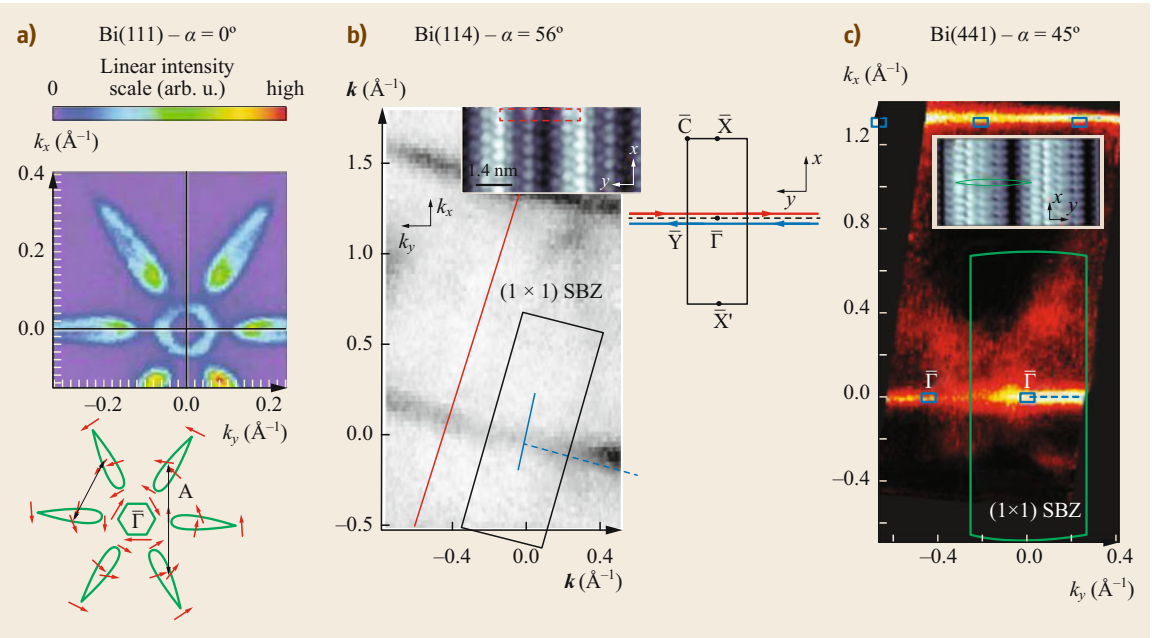

Fig. 12.27a–c Fermi surface of Bi(111), Bi(114), and Bi(441): the **(a)** Bi(111) flower-like contour presents a definite spin texture (sketched at the *bottom*) that transforms into dominant 1-D-like streaks in the direction perpendicular to the steps for both vicinal surfaces. Adapted from [12.106], with permission from Elsevier. **(b)** Bi(114) [12.107] and **(c)** Bi(441). Adapted from [12.108], with permission from the American Physical Society. These 1-D states are nondegenerate and give rise to Fermi contours consisting of two narrowly separated parallel lines with mainly in-plane opposite spin vectors, as schematically shown in the Bi(114) and Bi(441) graphs. Such small spin splitting cannot be resolved with spin-integrated ARPES. The complex atomic structure of these vicinal surfaces is shown in the STM images of the *insets* (**(a)** and **(c)** adapted from [12.106, 108])

pographic images show strong surface reconstructions where the terraces lack single (111) planes separated by monatomic steps. Figure 12.27 compares the Bi(111) surface states with those of Bi(114) and Bi(441). The flat surface exhibits a flower-like Fermi contour with oppositely rotating in-plane spin directions, a signature of the spin–orbit interaction in this material (Fig. 12.27a). In the stepped surfaces, the 2-D contour is replaced by extended 1-D streaks in the direction perpendicular to the steps, a signature of 1-D localization in such directions (Fig. 12.27b,c). Interestingly, the 1-D states are also spin-split, as demonstrated by SR-ARPES measurements [12.107, 108]. Constant energy surfaces in the vicinal planes consist of two narrowly separated parallel lines mainly featuring in-plane opposite spin vectors, as shown in the sketch in Fig. 12.27b,c. These, together with the Dirac-like dispersion along the steps, make these spin-polarized states analogous to the quantum spin Hall states of topological insulators [12.108]. Similar one-dimensional topological states have also been observed at the edges of bulk Bi islands [12.109] and isolated Bi bilayers [12.110].

12.7 Summary and Outlook

Vicinal surfaces are characterized by a varied atomic coordination and by a nanoscale step-edge corrugation, both leading to significant changes in surface electronic states. All electron wavefunctions are affected, from deep core levels to surface states, thereby influencing the variety of physical-chemical phenomena that occur at the surface–vacuum interface, such as chemical reactions and epitaxial growth. From this perspective, selecting different vicinal planes by simply changing miscut angle and azimuthal orientation, opens vast possibilities. To this aim, the use of curved surfaces with a smooth variation of the miscut are crucial, not only to choose the optimal vicinal plane for practical applications, but also, as shown in this chapter, to understand the subtle electronic effects that characterize vicinal surfaces and their relation to its structural properties, such as the atomic relaxation occurring around surface steps.

Future research based on curved crystals will surely be aimed at three different directions: nanostructure growth, chemical reactions and catalysis, and electron scattering. The growth of low-dimensional structures using vicinal surfaces, such as nanowires and nanoribbons [12.111], can notably gain from the use of curved surfaces, since they can speed up the choice of the appropriate surface template. The combined use of curved crystals and surface-sensitive techniques that operate in real conditions, such as ambient-pressure core-level photoemission, may considerably help the advance in heterogeneous catalysis research [12.112]. For example, to investigate the balance between more active (step) to less active (terrace) sites, which determines the optimal mass flow of reactants, or to directly visualize different active sites (steps and kinks) on the same sample, i.e., under the same reaction conditions [12.15].

An important amount of research is still necessary to shed light upon the fundamental scattering processes at single steps and vicinal surfaces. Crucial spectroscopic magnitudes connected to the very nature of the step-potential barrier, such as the lifetime, have barely been investigated. In this sense, pump–probe techniques, such as two-photon photoemission are best suited. Early results on image potential states of Cu vicinals validated key properties, such as the existence of quasi-elastic intraband and interband decay channels [12.113], the asymmetric inelastic decay for electrons moving up and down the steps [12.63], and the change in the modulation plane across the image-state series [12.55]. The use of curved surfaces could foster more systematic, accurate investigations. This also applies to research on spin-dependent scattering at steps, in both single-crystal and epitaxial systems [12.114], in combination with spatially averaging spectroscopic techniques, such as SR-ARPES. The early experiments on vicinal Au(111) and stepped Bi surfaces discussed in this chapter reveal complex and intriguing spin-dependent properties. In this particular field, as demonstrated by the impact of quantum well research on magnetic recordings in past decades [12.115], the knowledge obtained has the prospect of becoming key to future devices in the field of spintronics.

References

12.1 G. Somorjai, Y. Li: *Introduction to Surface Chemistry and Catalysis* (John Wiley & Sons, New York 2010)

12.2 I. Markov: *Crystal Growth for Beginners: Fundamentals of Nucleation, Crystal Growth and Epitaxy* (World Scientific, Singapore 2003)

12.3 V. Shchukin, N. Ledentsov, D. Bimberg: *Epitaxy of Nanostructures*, NanoScience and Technology (Springer, Berlin Heidelberg 2013)

12.4 M. Corso, F. Schiller, L. Fernández, J. Cordón, J.E. Ortega: Electronic states in faceted Au(111) studied with curved crystal surfaces, J. Phys. Condens. Matter **21**, 353001 (2009)

12.5 A. Mugarza, F. Schiller, J. Kuntze, J. Cordón, M. Ruiz-Osés, J.E. Ortega: Modelling nanostructures with vicinal surfaces, J. Phys. Condens. Matter **18**, S27 (2006)

12.6 J. Gustafson, M. Borg, A. Mikkelsen, S. Gorovikov, E. Lundgren, J.N. Andersen: Identification of step atoms by high resolution core level spectroscopy, Phys. Rev. Lett. **91**, 056102 (2003)

12.7 R. Smoluchowski: Anisotropy of the electronic work function of metals, Phys. Rev. **60**, 661–674 (1941)

12.8 J.E. Ortega, M. Corso, Z.M. Abd El-Fattah, E.A. Goiri, F. Schiller: Interplay between structure and electronic states in step arrays explored with curved surfaces, Phys. Rev. B **83**, 085411 (2011)

12.9 J.E. Ortega, F.J. Himpsel, R. Haight, D.R. Peale: One-dimensional image state on stepped Cu(100), Phys. Rev. B **49**, 13859–13862 (1994)

12.10 X.J. Shen, H. Kwak, D. Mocuta, A.M. Radojevic, S. Smadici, R.M. Osgood: Observation of a one-dimensional state on stepped Cu(775), Phys. Rev. B **63**, 165403 (2001)

12.11 C. Didiot, S. Pons, B. Kierren, Y. Fagot-Revurat, D. Malterre: Nanopatterning the electronic properties of gold surfaces with self-organized superlattices of metallic nanostructures, Nat. Nanotechnol. **2**, 617–621 (2007)

12.12 F. Schiller, M. Corso, J. Cordón, F.J.G. de Abajo, J.E. Ortega: Interplay between electronic states and structure during Au faceting, New J. Phys. **10**, 113017 (2008)

12.13 J.E. Ortega, J. Lobo-Checa, G. Peschel, S. Schirone, Z.M. Abd El-Fattah, M. Matena, F. Schiller, P. Borghetti, P. Gambardella, A. Mugarza: Scattering of surface electrons by isolated steps versus periodic step arrays, Phys. Rev. B **87**, 115425 (2013)

12.14 A.L. Walter, F. Schiller, M. Corso, L.R. Merte, F. Bertram, J. Lobo-Checa, M. Shipilin, J. Gustafson, E. Lundgren, A.X. Brión-Ríos, P. Cabrera-Sanfelix, D. Sánchez-Portal, J.E. Ortega: X-ray photoemission analysis of clean and carbon monoxide-chemisorbed platinum(111) stepped surfaces using a curved crystal, Nat. Commun. **6**, 8903 (2015)

12.15 S. Blomberg, J. Zetterberg, J. Zhou, L.R. Merte, J. Gustafson, M. Shipilin, A. Trinchero, L.A. Miccio, A. Magaña, M. Ilyn, F. Schiller, J.E. Ortega, F. Bertram, H. Grönbeck, E. Lundgren: Strain dependent light-off temperature in catalysis revealed by planar laser-induced fluorescence, ACS Catalysis **7**, 110–114 (2017)

12.16 M. Ilyn, A. Magaña, A.L. Walter, J. Lobo-Checa, D.G. de Oteyza, F. Schiller, J.E. Ortega: Step-doubling at vicinal Ni(111) surfaces investigated with a curved crystal, J. Phys. Chem. C **121**, 3880–3886 (2017)

12.17 G. Prévot, Y. Girard, V. Repain, S. Rousset, A. Coati, Y. Garreau, J. Paul, N. Mammen, S. Narasimhan: Elastic displacements and step interactions on metallic surfaces: grazing-incidence x-ray diffraction and *ab initio* study of Au(332), Phys. Rev. B **81**, 075415 (2010)

12.18 G. Prévot, P. Steadman, S. Ferrer: Determination of the elastic dipole at the atomic steps of Pt(977) from surface x-ray diffraction, Phys. Rev. B **67**, 245409 (2003)

12.19 G. Prévot, A. Coati, Y. Garreau: Grazing-incidence x-ray diffraction measurement of the relaxations and elastic step interactions on Cu(211) and Cu(322), Phys. Rev. B **70**, 205406 (2004)

12.20 V.I. Marchenko, A.Y. Parshin: Elastic properties of crystal surfaces, Sov. J. Exp. Theor. Phys. **52**, 129 (1980)

12.21 E.D. Williams, N.C. Bartelt: Thermodynamics of surface morphology, Science **251**, 393–400 (1991)

12.22 H.-C. Jeong, E.D. Williams: Steps on surfaces: experiment and theory, Surf. Sci. Rep. **34**, 171–294 (1999)

12.23 T. Einstein: Using the Wigner–Ibach surmise to analyze terrace-width distributions: history, user's guide, and advances, Appl. Phys. A **87**, 375–384 (2007)

12.24 W. Egelhoff: Core-level binding-energy shifts at surfaces and in solids, Surf. Sci. Rep. **6**, 253–415 (1987)

12.25 X. Zhou, J.L. Erskine: Surface core-level shifts at vicinal tungsten surfaces, Phys. Rev. B **79**, 155422 (2009)

12.26 A. Baraldi, L. Bianchettin, E. Vesselli, S. de Gironcoli, S. Lizzit, L. Petaccia, G. Zampieri, G. Comelli, R. Rosei: Highly under-coordinated atoms at Rh surfaces: interplay of strain and coordination effects on core level shift, New J. Phys. **9**, 143 (2007)

12.27 M. Gsell, P. Jakob, D. Menzel: Effect of substrate strain on adsorption, Science **280**, 717–720 (1998)

12.28 H. Ibach: The role of surface stress in reconstruction, epitaxial growth and stabilization of mesoscopic structures, Surf. Sci. Rep. **29**, 195–263 (1997)

12.29 P.M. Echenique, J.B. Pendry: The existence and detection of Rydberg states at surfaces, J. Phys. C **11**, 2065–2075 (1978)

12.30 M. Machado, E. Chulkov, V. Silkin, U. Höfer, P. Echenique: Electron lifetimes in image-potential states at metal–dielectric interfaces, Prog. Surf. Sci. **74**, 219–237 (2003)

12.31 S. Stepanow, A. Mugarza, G. Ceballos, P. Gambardella, I. Aldazabal, A.G. Borisov, A. Arnau: Localization, splitting, and mixing of field emission resonances induced by alkali metal clusters on Cu(100), Phys. Rev. B **83**, 115101 (2011)

12.32 F. Craes, S. Runte, J. Klinkhammer, M. Kralj, T. Michely, C. Busse: Mapping image potential states on graphene quantum dots, Phys. Rev. Lett. **111**, 1–5 (2013)

12.33 N. Knorr, H. Brune, M. Epple, A. Hirstein, M. Schneider, K. Kern: Long-range adsorbate interactions mediated by a two-dimensional electron gas, Phys. Rev. B **65**, 1–5 (2002)

12.34 J. Repp, F. Moresco, G. Meyer, K.H. Rieder, P. Hyldgaard, M. Persson: Substrate mediated long-range oscillatory interaction between adatoms: Cu/Cu(111), Phys. Rev. Lett. **85**, 2981–2984 (2000)

12.35 S. Lukas, G. Witte, C. Wöll: Novel mechanism for molecular self-assembly on metal substrates: Unidirectional rows of pentacene on Cu(110) produced by a substrate-mediated repulsion, Phys. Rev. Lett. **88**, 283011–283014 (2002)

12.36 F. Silly, M. Pivetta, M. Ternes, F. Patthey, J.P. Pelz, W.-D. Schneider: Creation of an atomic superlattice by immersing metallic adatoms in a two-dimensional electron sea, Phys. Rev. Lett. **92**, 016101 (2004)

12.37 W. Wurth, D. Menzel: Ultrafast electron dynamics at surfaces probed by resonant Auger spectroscopy, Chem. Phys. **251**, 141–149 (2000)

12.38 H. Petek, M.J. Weida, H. Nagano, S. Ogawa: Real-time observation of adsorbate atom motion above a metal surface, Science **288**, 1402–1404 (2000)

12.39 H. Chen, W. Zhu, D. Xiao, Z. Zhang: CO oxidation facilitated by robust surface states on Au-covered topological insulators, Phys. Rev. Lett. **107**, 056804 (2011)

12.40 J. Frohn, M. Giesen, M. Poensgen, J.F. Wolf, H. Ibach: Attractive interaction between steps, Phys. Rev. Lett. **67**, 3543–3546 (1991)

12.41 W.W. Pai, J.S. Ozcomert, N.C. Bartelt, T.L. Einstein, J.E. Reutt-Robey: Terrace-width distributions on vicinal Ag(110): Evidence of oscillatory interactions, Surf. Sci. **307–309**, 747–754 (1994)

12.42 F. Baumberger, M. Hengsberger, M. Muntwiler, M. Shi, J. Krempasky, L. Patthey, J. Osterwalder, T. Greber: Step-lattice-induced band-gap opening at the Fermi level, Phys. Rev. Lett. **92**, 1–4 (2004)

12.43 M.F. Crommie, C.P. Lutz, D.M. Eigler: Confinement of electrons to quantum corrals on a metal surface, Science **262**, 218–220 (1993)

12.44 E.J. Heller, M.F. Crommie, C.P. Lutz, D.M. Eigler: Scattering and absorption of surface electron waves in quantum corrals, Nature **369**, 464–466 (1994)

12.45 S. Crampin, H. Jensen, J. Kröger, L. Limot, R. Berndt: Resonator design for use in scanning tunneling spectroscopy studies of surface electron lifetimes, Phys. Rev. B **72**, 35443 (2005)

12.46 H. Manoharan, C. Lutz, D. Eigler: Quantum mirages formed by coherent projection of electronic structure, Nature **403**, 512–515 (2000)

12.47 J. Fransson, H.C. Manoharan, A.V. Balatsky: Detection and cloaking of molecular objects in coherent nanostructures using inelastic electron tunneling spectroscopy, Nano Lett. **10**, 1600–1604 (2010)

12.48 H. Jensen, J. Kröger, R. Berndt, S. Crampin: Electron dynamics in vacancy islands: Scanning tunneling spectroscopy on Ag(111), Phys. Rev. B **71**, 1–5 (2005)

12.49 L. Bürgi, O. Jeandupeux, A. Hirstein, H. Brune, K. Kern: Confinement of surface state electrons in Fabry–Pérot resonators, Phys. Rev. Lett. **81**, 5370–5373 (1998)

12.50 J. Seo, P. Roushan, H. Beidenkopf, Y.S. Hor, R.J. Cava, A. Yazdani: Transmission of topological surface states through surface barriers, Nature **466**, 343–346 (2010)

12.51 H. Brune, O. Jeandupeux, K. Kern, L. Bürgi: Quantum coherence and lifetimes of surface-state electrons, J. Electron Spectrosc. Relat. Phenom. **109**, 33–49 (2000)

12.52 M. Crommie: Observing electronic scattering in atomic-scale structures on metals, J. Electron Spectrosc. Relat. Phenom. **109**, 1–17 (2000)

12.53 S. Crampin, M.H. Boon, J.E. Inglesfield: Influence of bulk states on laterally confined surface state electrons, Phys. Rev. Lett. **73**, 922–925 (1994)

12.54 S. Crampin, O. Bryant: Fully three-dimensional scattering calculations of standing electron waves in quantum nanostructures: The importance of quasiparticle interactions, Phys. Rev. B **54**, R17367–R17370 (1996)

12.55 X. Wang, X. Shen, R.M. Osgood, R. Haight, F.J. Himpsel: Observation of lateral superlattice effects on stepped Cu(001), Phys. Rev. B **53**, 15738–15742 (1996)

12.56 X.Y. Wang, X.J. Shen, R.M. Osgood: Surface electron motion near monatomic steps: two-photon photoemission studies on stepped Cu(111), Phys. Rev. B **56**, 7665–7674 (1997)

12.57 J.E. Ortega, S. Speller, A.R. Bachmann, A. Mascaraque, E.G. Michel, A. Närmann, A. Mugarza, A. Rubio, F.J. Himpsel: Electron wave function at a vicinal surface: Switch from terrace to step modulation, Phys. Rev. Lett. **84**, 6110–6113 (2000)

12.58 A. Mugarza, A. Mascaraque, V. Pérez-Dieste, V. Repain, S. Rousset, F. García de Abajo, J. Ortega: Electron confinement in surface states on a stepped gold surface revealed by angle-resolved photoemission, Phys. Rev. Lett. **87**, 3–6 (2001)

12.59 F. Baumberger, T. Greber, J. Osterwalder: Fermi surfaces of the two-dimensional surface states on vicinal Cu(111), Phys. Rev. **64**, 1–8 (2001)

12.60 A. Mugarza, A. Mascaraque, V. Repain, S. Rousset, K. Altmann, F. Himpsel, Y. Koroteev, E. Chulkov, F. García de Abajo, J. Ortega: Lateral quantum wells at vicinal Au(111) studied with angle-resolved photoemission, Phys. Rev. B **66**, 1–10 (2002)

12.61 J.E. Ortega, A. Mugarza, V. Pe, V. Repain, S. Rousset, A. Mascaraque: Probing wave functions at step superlattices: Confined versus propagating electrons, Mater. Sci. Eng. B **96**, 154–158 (2002)

12.62 J.E. Ortega, A. Mugarza, V. Repain, S. Rousset, V. Pérez-Dieste, A. Mascaraque: One-dimen-

sional versus two-dimensional surface states on stepped Au(111), Phys. Rev. B **65**, 1–7 (2002)
12.63 M. Roth, M. Pickel, J. Wang, M. Weinelt, T. Fauster: Image-potential states on stepped Cu(001) surfaces, Appl. Phys. B **74**, 661–664 (2002)
12.64 A. Mugarza, J.E. Ortega: Electronic states at vicinal surfaces, J. Phys. Condens. Matter **15**, S3281 (2003)
12.65 J.E. Ortega, M. Ruiz-Osés, J. Kuntze: Finite size effects in surface states of stepped Cu nanostripes, Phys. Rev. B **72**, 195416 (2005)
12.66 N. Zaki, K. Knox, P.D. Johnson, J. Fujii, I. Vobornik, G. Panaccione, R.M. Osgood: Surface states on vicinal Cu(775): STM and photoemission study, Phys. Rev. B **83**, 205420 (2011)
12.67 R. de L. Kronig, W.G. Penney: Quantum mechanics of electrons in crystal lattices, Proc. Royal Soc. A **130**, 499–513 (1931)
12.68 D. Malterre, B. Kierren, Y. Fagot-Revurat, S. Pons, A. Tejeda, C. Didiot, H. Cercellier, A. Bendounan: ARPES and STS investigation of Shockley states in thin metallic films and periodic nanostructures, New J. Phys. **9**, 391–391 (2007)
12.69 G. Beltramo, H. Ibach, U. Linke, M. Giesen: Determination of the step dipole moment and the step line tension on Ag(001) electrodes, Electrochim. Acta **53**, 6818–6823 (2008)
12.70 M. Henzler: Atomic steps on single crystals: Experimental methods and properties, Appl. Phys. **9**, 11–17 (1976)
12.71 F. Schiller, Z.M.A. El-Fattah, S. Schirone, J. Lobo-Checa, M. Urdanpilleta, M. Ruiz-Osés, J. Cordón, M. Corso, D. Sánchez-Portal, A. Mugarza, J.E. Ortega: Metallic thin films on stepped surfaces: lateral scattering of quantum well states, New J. Phys. **16**, 123025 (2014)
12.72 K. Morgenstern, K.-F. Braun, K.-H. Rieder: Surface-state depopulation on small Ag(111) terraces, Phys. Rev. Lett. **89**, 20–23 (2002)
12.73 M. Hansmann, J.I. Pascual, G. Ceballos, H. Rust, K. Horn: Scanning tunneling spectroscopy study of Cu(554): Confinement and dimensionality at a stepped surface, Phys. Rev. B **67**, 121409 (2003), R)
12.74 F. Baumberger, T. Greber, B. Delley, J. Osterwalder: Tailoring confining barriers for surface states by step decoration: CO/vicinal Cu(111), Phys. Rev. Lett. **88**, 237601 (2002)
12.75 S. Wang, M.B. Yilmaz, K.R. Knox, N. Zaki, J.I. Dadap, T. Valla, P.D. Johnson, R.M. Osgood: Electronic structure of a Co-decorated vicinal Cu(775) surface: High-resolution photoemission spectroscopy, Phys. Rev. B **77**, 115448 (2008)
12.76 F. Schiller, M. Ruiz-Osés, J. Cordón, J.E. Ortega: Scattering of surface states at step edges in nanostripe arrays, Phys. Rev. Lett. **95**, 1–4 (2005)
12.77 S. Rousset, V. Repain, G. Baudot, Y. Garreau, J. Lecoeur: Self-ordering of Au(111) vicinal surfaces and application to nanostructure organized growth, J. Phys. Condens. Matter **15**, S3363 (2003)
12.78 A. Mugarza, J.E. Ortega, F.J. Himpsel, F.J. García de Abajo: Measurement of electron wave functions and confining potentials via photoemission, Phys. Rev. B **67**, 081404 (2003)
12.79 J. Lobo-Checa, A. Mugarza, J.E. Ortega, E.G. Michel: Determination of the photoelectron reference plane in nanostructured surfaces, New J. Phys. **13**, 103013 (2011)
12.80 J. Lobo, E.G. Michel, A.R. Bachmann, S. Speller, J. Kuntze, J.E. Ortega: Tuning the surface state dimensionality of Cu nanostripes, Phys. Rev. Lett. **93**, 137602 (2004)
12.81 E. Bertel, M. Donath (Eds.): *Electronic Surface and Interface States on Metallic Systems: Proceedings of the 134th WE-Heraeus Seminar, Physikzentrum, Bad Honnef, Germany, October 17–20, 1994* (World Scientific, Singapore 1995) p. 63
12.82 A.R. Bachmann, S. Speller, A. Mugarza, J.E. Ortega: Driving forces for Ag-induced periodic faceting of vicinal Cu(111), Surf. Sci. **526**, L143 (2003)
12.83 J.E. Ortega, F.J. Himpsel: Quantum well states as mediators of magnetic coupling in superlattices, Phys. Rev. Lett. **69**, 844–847 (1992)
12.84 T.-C. Chiang: Photoemission studies of quantum well states in thin films, Surf. Sci. Rep. **39**, 181 (2000)
12.85 F. Forster, E. Gergert, A. Nuber, H. Bentmann, L. Huang, X.G. Gong, Z. Zhang, F. Reinert: Electronic localization of quantum-well states in Ag/Au(111) metallic heterostructures, Phys. Rev. B **84**, 075412 (2011)
12.86 Y.A. Bychkov, E.I. Rashba: Properties of a 2D electron gas with lifted spectral degeneracy, JETP Letters **39**, 66–69 (1984)
12.87 M. Hasan, C. Kane: Colloquium: Topological insulators, Rev. Mod. Phys. **82**, 3045–3067 (2010)
12.88 P. Roushan, J. Seo, C.V. Parker, Y.S. Hor, D. Hsieh, D. Qian, A. Richardella, M.Z. Hasan, R.J. Cava, A. Yazdani: Topological surface states protected from backscattering by chiral spin texture, Nature **460**, 1106–1109 (2009)
12.89 T. Zhang, P. Cheng, X. Chen, J.F. Jia, X. Ma, K. He, L. Wang, H. Zhang, X. Dai, Z. Fang, X. Xie, Q.K. Xue: Experimental demonstration of topological surface states protected by time-reversal symmetry, Phys. Rev. Lett. **103**, 1–4 (2009)
12.90 D. Pesin, A.H. MacDonald: Spintronics and pseudospintronics in graphene and topological insulators, Nat. Mater. **11**, 409–416 (2012)
12.91 S. Lashell, B.A. Mcdougall, E. Jensen: Spin splitting of a Au(111) surface state band observed with angle resolved photoelectron spectroscopy, Phys. Rev. Lett. **77**, 3419–3422 (1996)
12.92 G. Nicolay, F. Reinert, S. Hüfner, P. Blaha: Spin-orbit splitting of the L-gap surface state on Au(111) and Ag(111), Phys. Rev. B **65**, 033407 (2001)
12.93 M. Hoesch, M. Muntwiler, V.N. Petrov, M. Hengsberger, L. Patthey, M. Shi, M. Falub, T. Greber, J. Osterwalder: Spin structure of the Shockley surface state on Au(111), Phys. Rev. B **69**, 241401 (2004)
12.94 G. Bihlmayer, Y. Koroteev, P. Echenique, E. Chulkov, S. Blügel: The Rashba-effect at metallic surfaces, Surf. Sci. **600**, 3888–3891 (2006)

12.95 J. Lobo-Checa, F. Meier, J.H. Dil, T. Okuda, M. Corso, V.N. Petrov, M. Hengsberger, L. Patthey, J. Osterwalder: Robust spin polarization and spin textures on stepped Au(111) surfaces, Phys. Rev. Lett. **104**, 187602 (2010)

12.96 C. Didiot, Y. Fagot-Revurat, S. Pons, B. Kierren, C. Chatelain, D. Malterre: Reconstruction-induced multiple gaps in the weak coupling limit: The surface bands of Au(111) vicinal surfaces, Phys. Rev. B **74**, 081404 (2006)

12.97 J.H. Dil: Spin and angle resolved photoemission on non-magnetic low-dimensional systems, J. Phys. Condens. Matter **21**, 403001 (2009)

12.98 Y.M. Koroteev, G. Bihlmayer, J.E. Gayone, E.V. Chulkov, S. Blügel, P.M. Echenique, P. Hofmann: Strong spin-orbit splitting on Bi surfaces, Phys. Rev. Lett. **93**, 046403 (2004)

12.99 F. Forster, S. Hu: Rare gases on noble-metal surfaces: An angle-resolved photoemission study with high energy resolution, J. Phys. Chem. B **108**, 14692–14698 (2004)

12.100 G. Bihlmayer, S. Blügel, E. Chulkov: Enhanced Rashba spin-orbit splitting in Bi/Ag(111) and Pb/Ag(111) surface alloys from first principles, Phys. Rev. B **75**, 1–6 (2007)

12.101 L. Petersen, P. Laitenberger, E. Lægsgaard, F. Besenbacher: Screening waves from steps and defects on Cu(111) and Au(111) imaged with STM: Contribution from bulk electrons, Phys. Rev. B **58**, 7361–7366 (1998)

12.102 K. Schouteden, P. Lievens, C. Van Haesendonck: Fourier-transform scanning tunneling microscopy investigation of the energy versus wave vector dispersion of electrons at the Au(111) surface, Phys. Rev. B **79**, 195409 (2009)

12.103 C.R. Ast, J. Henk, A. Ernst, L. Moreschini, M.C. Falub, D. Pacile, P. Bruno, K. Kern, M. Grioni: Giant spin splitting through surface alloying, Phys. Rev. Lett. **98**, 186807 (2007)

12.104 H. Bentmann, F. Forster, G. Bihlmayer, E.V. Chulkov, L. Moreschini, M. Grioni, F. Reinert: Origin and manipulation of the Rashba splitting in surface alloys, Eur. Lett. **87**, 3703 (2009)

12.105 S. Schirone, E.E. Krasovskii, G. Bihlmayer, R. Piquerel, P. Gambardella, A. Mugarza: Spin-flip and element-sensitive electron scattering in the $BiAg_2$ surface alloy, Phys. Rev. Lett. **12**, 066802 (2015)

12.106 P. Hofmann: The surfaces of bismuth: structural and electronic properties, Prog. Surf. Sci. **81**, 191–245 (2006)

12.107 J.W. Wells, J.H. Dil, F. Meier, J. Lobo-Checa, V.N. Petrov, J. Osterwalder, M.M. Ugeda, I. Fernandez-Torrente, J.I. Pascual, E.D.L. Rienks, M.F. Jensen, P. Hofmann: Nondegenerate metallic states on Bi(114): A one-dimensional topological metal, Phys. Rev. Lett. **102**, 096802 (2009)

12.108 M. Bianchi, F. Song, S. Cooil, Å.F. Monsen, E. Wahlström, J.A. Miwa, E.D.L. Rienks, D.A. Evans, A. Strozecka, J.I. Pascual, M. Leandersson, T. Balasubramanian, P. Hofmann, J.W. Wells: One-dimensional spin texture of Bi(441): Quantum spin Hall properties without a topological insulator, Phys. Rev. B **91**, 165307 (2015)

12.109 I.K. Drozdov, A. Alexandradinata, S. Jeon, S. Nadj-Perge, H. Ji, R.J. Cava, B.A. Bernevig, A. Yazdani: One-dimensional topological edge states of bismuth bilayers, Nat. Phys. **10**, 664–669 (2014)

12.110 A. Takayama, T. Sato, S. Souma, T. Oguchi, T. Takahashi: One-dimensional edge states with giant spin splitting in a bismuth thin film, Phys. Rev. Lett. **114**, 066402 (2015)

12.111 J. Cai, P. Ruffieux, R. Jaafar, M. Bieri, T. Braun, S. Blankenburg, M. Muoth, A.P. Seitsonen, M. Saleh, X. Feng, K. Müllen, R. Fasel: Atomically precise bottom-up fabrication of graphene nanoribbons, Nature **466**, 470–473 (2010)

12.112 L. Vattuone, L. Savio, M. Rocca: Bridging the structure gap: chemistry of nanostructured surfaces at well-defined defects, Surf. Sci. Rep. **63**, 101–168 (2008)

12.113 M. Roth, M. Pickel, M. Weinelt, T. Fauster: Dynamics of image-potential states on stepped Cu(001) surfaces, Appl. Phys. A **78**, 149–153 (2004)

12.114 J.E. Ortega, G. Vasseur, F. Schiller, I. Piquero-Zulaica, A.P. Weber, J. Rault, M.A. Valbuena, S. Schirone, S. Matencio, L.A. Sviatkin, Y.M. Koroteev, E.V. Chulkov, A. Mugarza, J. Lobo-Checa: Atomically precise step grids for the engineering of helical states, arXiv:1902.05777 (2019)

12.115 F.J. Himpsel, J.E. Ortega, G.J. Mankey, R.F. Willis: Magnetic nanostructures, Adv. Phys. **47**, 511–597 (1998)

J. Enrique Ortega

Departamento Física Aplicada I
Universidad del País Vasco
San Sebastian, Spain

Centro de Física de Materiales
CSIC/UPV-EHU-Materials Physics Center
San Sebastian, Spain
enrique.ortega@ehu.es

J. Enrique Ortega received his PhD (1990) in Physics at the Autonomous University of Madrid. Ortega became known during the 1990s for his seminal works on metallic quantum wells. He later pioneered the study of electronic states of stepped metal surfaces. He has been paving the way to the use of curved crystals on physical-chemical research of surface phenomena linked to atomic steps. He has coauthored over 140 peer-reviewed publications.

Aitor Mugarza

Institut Catalá de Nanociencia i Nanotecnologia (ICN2)
Bellaterra–Barcelona, Spain

Aitor Mugarza received his PhD in Physics at the University of the Basque Country (2002). He was appointed Group Leader of the Atomic Manipulation and Spectroscopy Group (2013) and ICREA Research Professor (2015) at ICN2. He has carried out pioneering studies on the use of stepped surfaces for electron confinement and band engineering. He has coauthored over 50 peer-reviewed publications.

Frederik Schiller

Centro de Física de Materiales
CSIC/UPV–EHU–Materials Physics Center
San Sebastian, Spain

Donostia International Physics Centre
San Sebastian, Spain
frederikmichael.schiller@ehu.eus

Frederik Schiller (Zwickau, Germany, 1971) received his PhD in Physics at the Technische Universität Dresden. He moved to Spain in 2003 and became a permanent staff member of the Spanish Research Council in San Sebastian. He has coauthored more than 50 peer-reviewed publications. His research is focused on the magnetic and electronic structure of low-dimensional systems and catalytic reactions at stepped surfaces and curved crystals with varying density of steps.

Jorge Lobo-Checa

Instituto de Ciencia de Materiales de Aragón (ICMA)
CSIC–Universidad de Zaragoza
Zaragoza, Spain
Departamento de Física de la Materia Condensada

Universidad de Zaragoza
Zaragoza, Spain

Jorge Lobo-Checa obtained his Doctoral Degree in Physics in 2004 from the Autonomous University of Madrid. He moved to CFM (San Sebastian, 2012–2015) and established at the Material Science Center of Aragon (Zaragoza, Spain) in 2015. He has coauthored more than 50 publications. His research interests lie in the investigation of the electronic and physical-chemical properties of low dimensional systems, focusing on projects related to curved crystals, porous organometallic networks, and on-surface synthesis reactions.

Martina Corso

Centro de Física de Materiales
CSIC/UPV–EHU–Materials Physics Center
San Sebastian, Spain

Martina Corso received her PhD from the University of Zürich (Switzerland 2006). She occupies a Tenured Scientist position at the Spanish Research Council CSIC in the Centro de Física de Materiales in San Sebastián. Her research has been devoted to the study of physical-chemical properties of low-dimensional nanostructures grown in-situ on crystal surfaces. She has contributed to 41 publications in peer-reviewed scientific journals.

13. Imaging at the Mesoscale (LEEM, PEEM)

Alessandro Sala

The capability to display images containing chemical, magnetic, and structural information and to perform spectroscopy and diffraction from a μm-sized area makes cathode lens electron microscopy one of the most used and reliable techniques to analyze surfaces at the mesoscale. Thanks to its versatility, LEEM/PEEM systems are currently employed to study model systems in the fields of nanotechnology, nanomagnetism, material science, catalysis, energy storage, thin films, and 2-D (two-dimensional) materials. In this chapter, we will present a brief but complete review of this class of instruments. After a historical digression in the introductory section, we will first show the basic operating principles of a simple setup and then the elements that can be added to improve performance. Later, two sections will be dedicated to LEEM and PEEM, respectively. In both cases, a theoretical discussion on the contrast mechanisms will prelude to a showcase of the operating modes of the instrument, with clear examples that will show the best performance available today. Finally, a brief discussion about the future developments of cathode lens electron microscopy will close the chapter.

Cathode lens electron microscopy is a technique that uses slow electrons as information carriers [13.1]. Differently to the case of scanning or transition electron microscopy, in this system electrons interact with the probe at very low kinetic energy, below a few hundred electronvolts (eV). In such a range, the inelastic mean free path (IMFP) ensures a probing depth of just a few atomic layers, making cathode lens microscopy a surface-sensitive technique. It is therefore not surprising that its history parallels the history of surface science since the early years. The first example of an emission microscope with slow electrons goes back to 1932, a few years after the *Davisson* and *Germer* experiment [13.2], when *Brüche* and *Johansson* produced the first thermionic emission microscope [13.3, 4]. They used coils as magnetic lenses to produce magnified images of a hot cathode's surface on a fluorescent screen. Glass enclosures and diffusion pumps provided the vacuum system, necessary to avoid dispersion of the electrons. One year later, *Brüche* built the first prototype of the photoemission electron microscope (PEEM) [13.5], using a cold cathode illuminated by UV light (Fig. 13.1a). These milestones and the rise of theoretical electron optics gave birth to a flourishing scientific community. Several theoretical calculations concerning magnification, chromatic and spherical aberration of magnetic lenses, electrostatic mirrors and einzel lenses, were made available [13.6–9]. It was soon understood [13.10] that resolution performance could be enhanced well above that of light microscopy if electrons travel through the lens system at relatively high energies—tens of keV. The suggested setup was then to place the sample on a negative bias, i.e., using it as a cathode, in order to accelerate electrons after take-

M. Rocca, T.S. Rahman, L. Vattuone (Eds.), *Springer Handbook of Surface Science*, Springer Handbooks,
https://doi.org/10.1007/978-3-030-46906-1_13

off. This basic principle is still used today for modern microscopy. The development of electron optics then suffered a sudden pause during the 1940s, not only because of World War II, but also because of the technological limitations of that age.

The *renaissance* period of the 1960s coincides with the development of UHV technology: several new solutions, such as ion pumps, Cu gaskets, valves and sample transfer systems, boosted surface science and hence the creation of more sophisticated instruments. In 1962, *Ernst Bauer* conceived the low-energy electron microscope (LEEM) [13.12, 13], which uses elastically backscattered electrons as a probe (Fig. 13.1b). In this system, electrons generated by a gun are decelerated to a few eV before interaction with the surface. Once backscattered, the outgoing electron beam is separated from the incoming one by a magnetic field, and then processed by the lens system. In the same period, emission electron microscopy reached a period of maturity, when the demonstrated resolution of $\approx 10\,\text{nm}$ made explicit new limitations, such as lens aberration and astigmatism, energy dispersion, electron detection, surface stability and cleanness. The attention of the microscopy community was then gradually driven away by the success of transmission electron microscopy (TEM); during the 1970s the LEEM project was frozen, while the few PEEM systems were mainly dedicated to investigation of biologic systems [13.14] and test additional light sources, such as lasers and synchrotron radiation [13.15]. Only in the following decade did cathode lens electron microscopy manifest itself as one of the principal surface science tools. Many up-

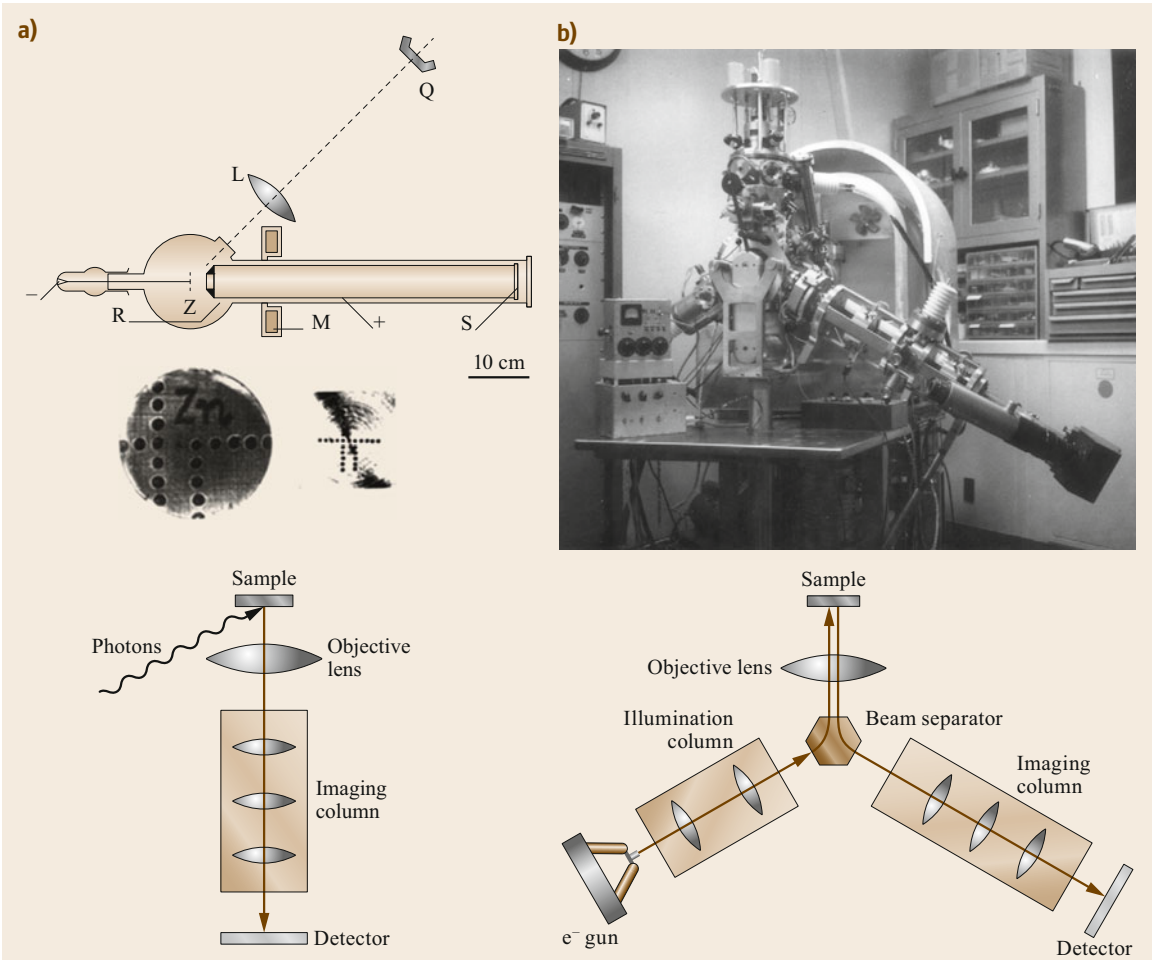

Fig. 13.1 (**a**) *Top*: schematic of Brüche's first PEEM system and the first PEEM image of a scraped Zn plate with holes (Reproduced from [13.5] with permission, copyright 1933 Springer Science + Business Media). *Bottom*: scheme of an ideal PEEM system. (**b**) *Top*: picture of the original LEEM instrument in the 1960s (Reproduced from [13.11] with permission, copyright 2012 Elsevier). *Bottom*: scheme of an ideal LEEM system with 120° deflection

grades were introduced, enhancing the versatility and the power of such systems in the investigation of surfaces at the mesoscale. The microscopy approach was combined with other investigation methods such as spectroscopy and diffraction, already known for their successful application in surface science. In 1981, low-energy electron diffraction (LEED) patterns were displayed in LEEM systems using the backfocal plane of the objective lens [13.16–18], giving the possibility to spatially select the probing area. *Tonner* et al. demonstrated the feasibility of PEEM with synchrotron radiation in the late 1980s [13.19], while *Ertl*'s group at the Fritz Haber Institute increased interest in the chemistry community for PEEM showing the oscillatory behavior of gas adsorption on active surfaces during catalytic reactions [13.20]. A few years later, the first cathode lens system equipped with a hemispherical energy analyzer (spectroscopic photoemission and low-energy electron microscope, SPELEEM) was planned and later hosted at BESSY and Elettra synchrotrons. The first x-ray PEEM (XPEEM) image, i.e., made with core-level electrons photoemitted by x-rays, was published in 1998 [13.21]. In the same years, two LEEM systems were equipped with a spin-polarized electron gun [13.22, 23], pioneering magnetic imaging. Magnetic contrast was achieved also in PEEM using circular and linear dichroism of polarized light [13.24]. The development of new operation modes continues today, with the construction of aberration-free systems towards the ultimate spatial resolution [13.25–27], the use of pulsed light to enable time-resolved dynamic microscopy [13.28], and the design of special sample holders to modify the mechanic, electric, and magnetic properties of the probe in operando [13.29]. Moreover, firms started to create commercial versions of LEEM and PEEM systems. The most notable examples are Elmitec GmbH in 1995 (based on Ernst Bauer's design) and SPECS GmbH (based on Ruud Tromp's design) [13.30, 31].

Although the cost of such systems is relatively high compared to other microscopes, the openness of the labs to external users, e.g., at the synchrotron endstations, helped to create a vast and heterogeneous user community. Nowadays, cathode lens microscopy is widely appreciated by surface scientists. Thanks to its multidisciplinarity and to the interplay between microscopy, spectroscopy and diffraction, it has become an essential technique for the overall comprehension of surface phenomena.

13.1 Cathode Lens Microscopy

13.1.1 Operating Principles

The first optical element electrons run into after takeoff from the sample surface is also the most important. The cathode lens, often integrated with other refocusing elements and called the objective lens, must both accelerate the electrons emitted from the sample and form a first magnified image. To do so, the sample is placed at negative potential V of about 10−50 kV to act as a cathode. The first electrode is grounded and attracts the electrons towards its central aperture, where they pass through the other magnetic or electrostatic elements of the objective lens. An equipotential plot of a lens is displayed in Fig. 13.2a. The overall focal length is determined by two opposite contributions, one divergent generated by the anode aperture and one convergent generated by the other elements of the lens [13.32, 33]. Figure 13.2b helps to explain the relevant physics in detail.

When electrons are emitted from the surface at a distance L from the entrance aperture of the microscope with kinetic energy E_0 and angle θ_0, the acceleration in the quasihomogeneous electric field in the cathode lens imposes a parabolic traj>ectory (in blue). This real situation can be converted to a virtual frame, in which electrons assume a linear trajectory and appear to have originated from a virtual image plane located at a distance $2L$ from the anode (green trajectory). Since in the real case the anode aperture distorts the electric field, the optical effect is to create a thin diverging lens with focal length $-4L$, called the *aperture lens* [13.35]. The final virtual image is then placed at a distance $4L/3$ from the anode (red trajectory), magnified by a factor $2/3$. After the aperture, the field of the other elements of the objective lens magnifies the electron beam by a factor of M_M.

This conversion can be defined as a change of relative coordinates, from real spatial and angular coordinates at takeoff (x_0, θ_0,) to virtual coordinates (x, θ) [13.36]. Given the overall lateral magnification of the objective lens M and defining the immersion factor as $k = E/E_0$, one has the following relations

$$M = \frac{2}{3} M_M \,, \qquad M_A = \left(k^{\frac{1}{2}} M\right)^{-1} \,,$$

$$\frac{x}{x_0} = M \,, \qquad \frac{\theta}{\theta_0} = M_A \,, \quad \frac{q_0}{q} = M \,,$$

where $q_0 = \theta_0/\lambda_0$ and $q = \theta/\lambda$ are the spatial frequencies parallel to the surface in the real and virtual plane respectively, and M_A is the angular magnification. In the case of low-energy electrons, i.e., if E_0 is just a few eV,

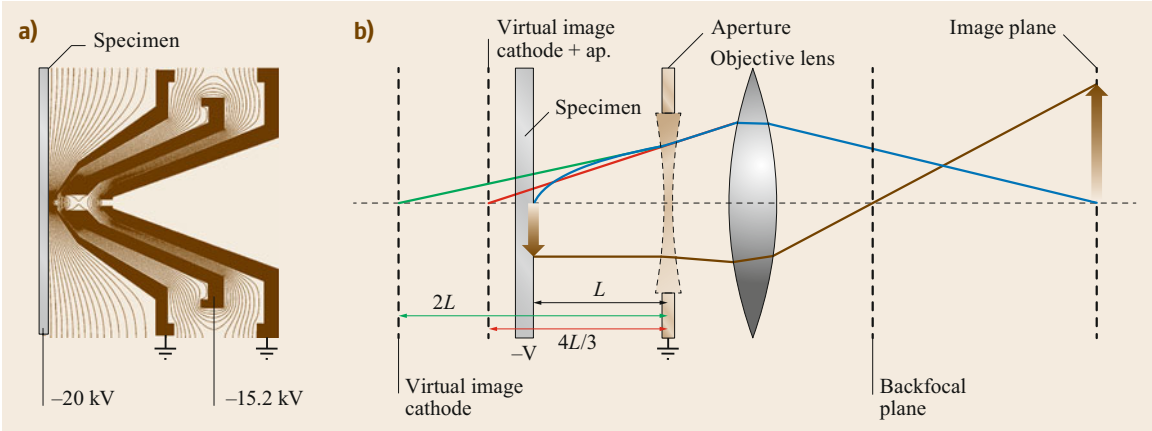

Fig. 13.2 (a) Field contour plot of a tetrode objective lens. The equipotential lines are 1250 V apart (Reproduced from [13.34] with permission, copyright 2002 AIP Publishing). subfigref Scheme of the cathode immersion lens

the application of a potential of a few tens of kV guarantees a large immersion factor.

In the simplest configuration, the objective lens displays the magnified image to the electron detector, e.g., a phosphorescent screen. In this case, only a limited magnification can be reached: the overall lateral magnification of the modern objective lens ranges typically between 15 and 40. To increase the performance of the microscope, a series of magnetic and electrostatic lenses can be added, to constitute the so-called *imaging column*. The focal length of the lenses can be controlled by changing the current of magnetic lenses, or the potential of electrostatic lenses. Electrons travel through the imaging column with kinetic energy equal to $E = E_0 + eV$. Since usually electrons can escape from a surface with different E_0 simultaneously, their trajectory in the imaging column can differ considerably from the optimum one. To guarantee that electrons with a selected initial kinetic energy pass through the lenses along the optimal trajectory, a tunable bias must be subtracted from the potential V between sample and aperture. The bias value, also called *start voltage* (V_0), imposes the optimal trajectory and speed to only the electrons with initial kinetic energy $E_0 = eV_0$. For them, the final kinetic energy will be $E = eV$. Electrons with different kinetic energy still pass through the objective lens, but can be easily filtered at a later stage due to their different trajectories. Moreover, the fixed trajectory and speed of the electrons allow the lenses of the imaging column to be set once and for all. This not only improves the usability of the instrument, but permits apertures and slits to be placed to mold the image in a convenient plane.

The advantage of having an imaging column is twofold. Besides the improved magnification, it gives access to the angular distribution of the emitted electrons. In optics, for objects a finite distance away, rays that leave the object with a given angle (Fig. 13.2b, brown trajectory) cross at a precise point in the backfocal plane of the objective lens. There, the image maps the distribution of electrons as a function of their emission angle, i.e., in the reciprocal space. In the case of electrons backscattered or photoemitted from a crystalline surface, this plane contains the diffraction pattern. The imaging column can then be set to display a magnification of the backfocal plane on the screen instead of the image plane.

At the end of the imaging column, it is possible to place an *energy filter* that excludes electrons with different kinetic energy. By knowing the displacement as a function of energy, one can filter out the electrons by placing a slit of given size. Typically, the energy analyzer is optically neutral, i.e., the entrance plane is displayed in the dispersive plane at the exit with unit magnification. Finally, another series of lenses project the desired plane onto the detector.

In conclusion, three different operation modes can be defined:

- In the *Microscopy* mode (Fig. 13.3a) the image plane is displayed on the screen. In the imaging column, the backfocal plane is reproduced and an aperture (called *contrast aperture*) can be inserted to limit the acceptance angle of the electrons. If an energy analyzer is installed, the imaging column is set to display the reciprocal plane at its entrance. The energy slit is placed at the dispersive plane and only lets electrons with a selected kinetic energy pass. The projector displays the image plane back onto the detector. Since the apertures are inserted on diffraction planes, the real image is still fully available.

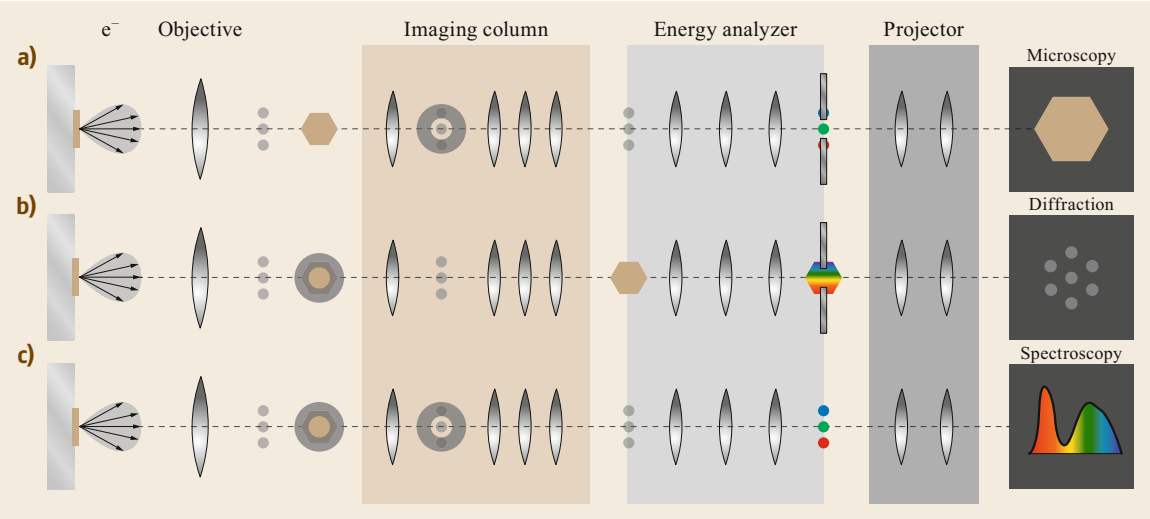

Fig. 13.3a–c Scheme of PEEM optics with energy filtering. Three main operational modes are presented: **(a)** microscopy mode, **(b)** diffraction mode, **(c)** spectroscopy mode. The *hexagon* represents the image plane, while the *gray dots* represent the diffraction plane. *Rainbow colors* symbolize the dispersive plane. The *gray ring* indicates the presence of an aperture

- The *Diffraction* mode (Fig. 13.3b) displays the distribution of electrons in the reciprocal space. In this case, no contrast aperture has to be placed. Nonetheless, an aperture in the image plane of the objective lens, called the *field limiting aperture*, can filter the electrons in the real space: the diffraction image is then made only from electrons emitted in a particular area. The imaging column transfers the image plane to the entrance of the energy filter: the slit at the dispersive plane does not influence the reciprocal image. The projector converts the image plane at the exit of the analyzer to the diffraction plane.
- In the *Spectroscopy* mode (Fig. 13.3c) the projector magnifies the dispersive plane at the end of the energy filter. In this case, both the contrast aperture and the field-limiting aperture can be inserted, to limit conveniently the acceptance angle and the probed area. The reciprocal plane is usually displayed at the entrance of the energy analyzer. The dispersive plane then looks like a line with modulated intensity. The intensity line profile over the spread electron beam reveals the energy distribution of the electrons.

The easy switch between the three operational modes is at the origin of the versatility of cathode lens microscopy. In addition, the insertion of apertures and slits in the convenient planes allows microscopic, spectroscopic, and diffraction information to be combined in a single experiment: the active filtering in real space, reciprocal space, and kinetic energy can be simultaneously activated to obtain a unique characterization of the probed surface.

13.1.2 Instrumentation

The simplest setup, with objective lens, imaging column and electron detector, is already capable of performing microscopy and diffraction measurements on surfaces. Over the years, cathode lens microscopes have become more sophisticated, with the addition of multiple optical elements. This section will show the most common components available today, with a brief discussion on the working principles and the experimental advantages introduced.

Beam Separator

The beam separator is a magnetic element that imposes different trajectories to electron beams with opposite direction by using the Lorentz force. While in standard PEEM it has no practical use, it is an essential element in LEEM and in aberration-corrected instruments equipped with an electrostatic mirror. The decoupling between incident and reflected electrons allows a separate treatment of the two beams, i.e., in LEEM a full-field detection of the illuminated area, with no shadows cast by the electron gun (like for standard LEED optics). The beam splitter is usually placed after the objective lens, so apertures and slits can be introduced along the incident or the reflected path separately.

The first separator installed in the original LEEM was a simple *Archard–Mulvey* type with 10° deflection [13.39]. Very soon it became clear that the magnetic field strongly impacts the image quality [13.16], therefore more sophisticated and multipolar MPAs were developed. Over the years, two geometries emerged as standard: 120° deflection (Bauer/Elmitec) and 90° de-

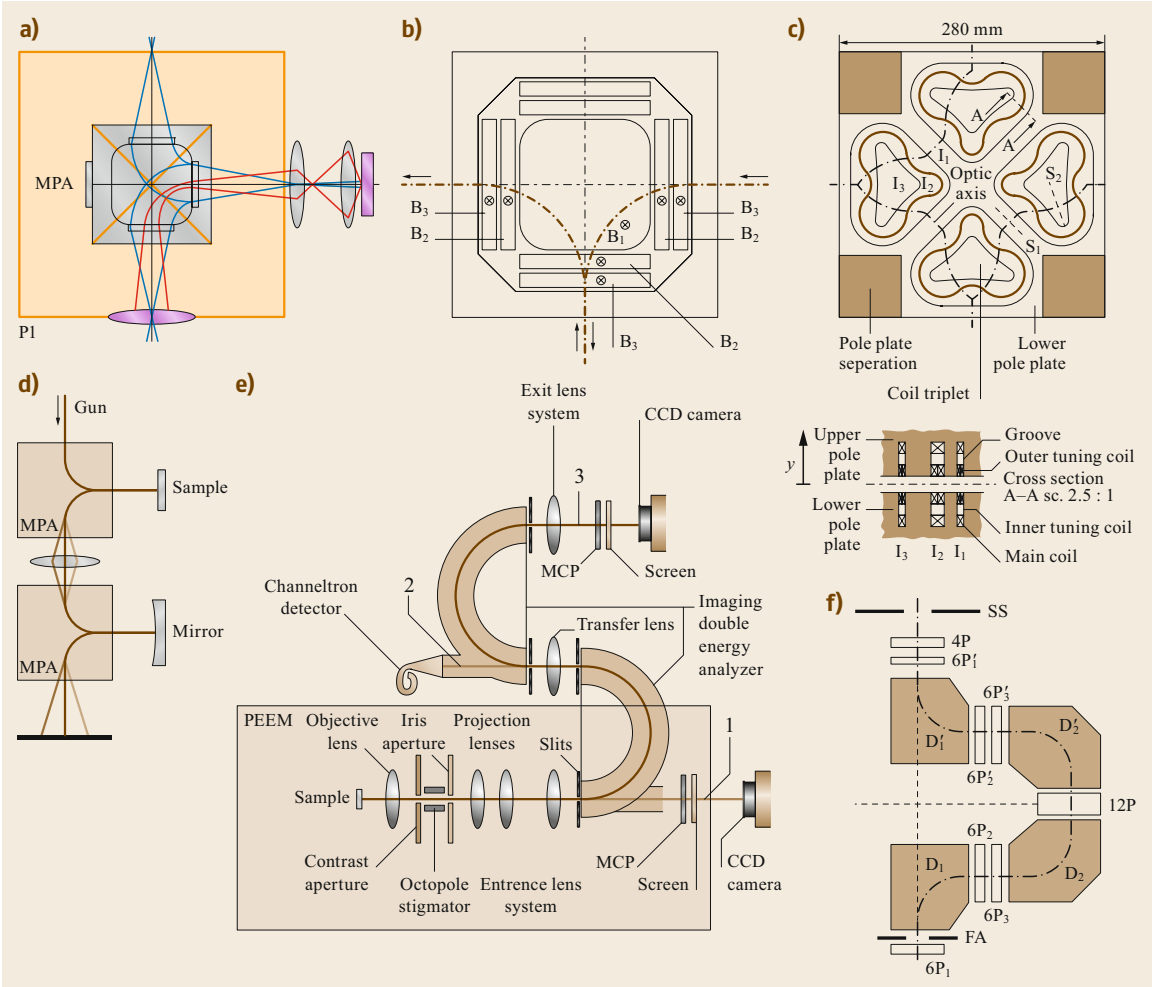

Fig. 13.4a–f Scheme of beam separators **(a–c)** and energy filters **(d–f)** used in cathode lens microscopy. **(a)** Diagram of the magnetic prism array (MPA) used in Tromp's IBM LEEM-II system. The *orange boxes* around the MPA indicate the position of diffraction planes. Intermediate image planes are located on the MPA diagonals (Reproduced from [13.26] with permission, copyright 2010 Elsevier). **(b)** Layout of Mankos' magnetic prism array with four pairs of rectangular sectors (Reproduced from [13.37] with permission, copyright 2007 Elsevier). **(c)** Midsection view of the twofold-symmetric beam separator that equips SMART microscope. Vertical cross section along A–A is represented below. Symmetry plane S_1 and S_2 are highlighted (Reproduced from [13.25] with permission, copyright 1997 Elsevier). **(d)** Diagrams of energy filtering with a double MPA. The induced dispersion is depicted with *light brown lines* (Reproduced from [13.26] with permission, copyright 2010 Elsevier). **(e)** Schematic layout of the NanoESCA instrument equipped with the imaging double energy analyzer. The three electron paths are indicated: (1) PEEM mode, (2) selected-area spectroscopy, and (3) energy-filtered imaging (Reproduced from [13.38] with permission, copyright 2005 IOP Science). **(f)** Schematic layout of the Omega filter equipping SMART. Dipoles (D), quadrupoles (4P), hexapoles (6P), and dodecapoles (12P) are highlighted. The introduction of a field aperture (FA) and a selection slit (SS) enables the filtering (Reproduced from [13.25] with permission, copyright 1997 Elsevier)

flection (Tromp/SPECS, SMART, PEEM3, and others). For the first case, unfortunately no detailed information has been published. In the other case, several solutions have been employed. In the square MPA used by *Tromp* (Fig. 13.4a) a large central squared and four rectangular magnetic field segments provide the deflection and a stigmatic refocus of the electron beam [13.26, 40], so that the images produced at the entrance and exit plane are equivalent. The lenses of the microscope are set to display the focused incoming electron beam and the

outgoing diffraction plane at the entrance planes. With this geometry, the image plane is created on the diagonal plane of the MPA. The contrast aperture is then displaced in the exit plane of the MPA, together with the first projective lens. A similar design, but with more elements, is used in a LEEM with dedicated optics for high-throughput performance (Fig. 13.4b; [13.37]). In this case, four pairs of smaller rectangular sectors, in which the magnetic field is about three times stronger, surround the central squared magnetic field. The advantage to have a pair of independent coils per side is that the same 90° deflection can be achieved with different pairs of flux density values, favoring a more precise alignment of the device and allowing a larger field of view without significant distortions.

It is worth noting that the Lorentz force imposes different deflection to electrons with different kinetic energy, i.e., the MPA displays a chromatic dispersion on the exit plane. As will be discussed in Sect. 13.1.2, *Energy Analyzers*, the beam deflector can be used as an energy filter. Moreover, the four sectors can be independently set to deploy different magnetic field strengths, so as to deflect electron beams when the incoming and outgoing electrons have different kinetic energy. This is the case of secondary electron microscopy (SEM) and Auger electron microscopy (AEM), which use slow secondary electrons or Auger electrons as information carriers. In both cases, the kinetic energy of the emitted electrons is lower than the one of the electrons used for illumination: the beam separator must then be set to deflect properly both beams along the optimum trajectory.

The performance of beam separators became more crucial with the advent of aberration-corrected instruments. In LEEM/PEEM systems, the compensation of aberrations is made with the introduction of a particular electrostatic mirror along the electron path (Sect. 13.1.2, *Aberration Correctors*). Its application requires a second deflection that separates entering and reflected beams. The beam separator used for this purpose needs not only to be stigmatic and distortion-free, but also with no chromatic dispersion. To do so, two solutions have been employed. The first is to use two identical deflectors, one in front of the objective lens and one for the electrostatic mirror, connected by transfer optics. In this case, most of aberrations and the chromatic dispersion are canceled out by symmetry. Rose and Preikszas proposed a second solution with the development of a highly symmetric four-quadrant beam separator (Fig. 13.4c; [13.41]), used successfully by SMART and PEEM3 instruments [13.25, 27, 42]. Each quadrant contains a coil triplet that produces two regions with opposite magnetic field. Electrons pass through the field of two coils for every 90° deflection. The shape of the triplet is such that the fields are axially symmetric and point symmetric about the diagonal planes of the beam separator (S_1) and the bisector plane of the coil triplet (S_2). This double symmetry ensures automatic compensation of deviations and dispersion up to second order. Since the Rose deflector has four quadrants, it can be used for both deflections required by the objective lens and the mirror.

Energy Analyzers

As seen in Sect. 13.1.1, the energy filtering of electrons activates a third, scientifically very important operating mode of cathode lens microscopy. The most logical way to filter electrons with different kinetic energy is to exploit their different trajectories along the optical path and to cut them out with an aperture. The energy window ΔE around the pass energy E required to perform active spectroscopy of photoemitted electrons is typically below 200 meV; since E is some tens of keV, the order of magnitude of the resolving power $E/\Delta E$ must be considerable, about 10^5. The simplest device that acts as an energy filter is the beam separator. The brightest example of this kind is the aberration-corrected LEEM developed by *Tromp*, equipped with two identical deflectors (Fig. 13.4d; [13.26]). In this setup, the MPAs are connected by a transfer lens, which resends the dispersed image at the exit of MPA1 to MPA2. This double pass guarantees an achromatic image on the electrostatic mirror. After a second pass through MPA2, the newly formed dispersive plane is used to filter electrons on a narrow energy window with a slit. The low dispersion of the beam separator, 6 µm/eV, allows a proved energy resolution of 250 meV.

To achieve better resolution performance, a dedicated energy analyzer with larger dispersion is necessary. The fact of having a separate device to filter electrons has a few further advantages. In fact, despite the more complicated setup, it allows full control over the energy window and the pass energy. Moreover, it enables active filtering in the *diffraction* mode if the image plane is projected at its entrance, as mentioned in Sect. 13.1.1. The first spectroscopic instrument, the SPELEEM [13.21, 43], was equipped with an electrostatic hemispherical deflector analyzer (HDA), a common solution for filtering in photoelectron spectroscopy. In the analyzer electrons travel through the space between two concentric hemispheres held at different potentials. The electrostatic field disperses the electrons depending on their kinetic energy around an optimal trajectory, given by particles with a well-defined *pass energy*. The resolving power $E/\Delta E$ of an HDA is typically 10^3–10^4; therefore for cathode lens microscopy it is necessary to slow down electrons with a dedicated retarding lens from E (few tens of keV) to a pass energy of 1 keV or less. Such deceleration

is a critical parameter, since the resulting immersion factor expands the angular spreading of the electron beam and degrades the lateral and the energy resolution via spherical aberrations. In the first version of SPELEEM the pass energy in HDA was 1800 eV and the demonstrated energy resolution was 0.5 eV. The optimized commercial version by Elmitec lowered the pass energy to 900 eV to obtain a reported energy resolution of 110 meV in *spectroscopic* mode and about 150–200 meV in the other modes [13.44]. The passage through an HDA induces second-order aberrations at the exit plane. Their correction can be achieved with the introduction of a second twin HDA (Fig. 13.4e). This configuration, called the imaging double energy analyzer (IDEA), equips the NanoESCA PEEM [13.38, 45]. The path symmetry forces the electron trajectories to coincide after the double passage, thus generating an achromatic image at the exit plane. The energy filtering in *imaging* and *diffraction* mode is obtained with the introduction of a slit in the dispersive plane placed between the HDAs. This system is capable of a demonstrated energy resolution of 12 meV with pass energy 15 eV. Higher pass energies, more suited for core-level spectroscopy and imaging, degrades the resolution to 50–100 meV. Remarkably, NanoESCA can also work as a single-pass photoelectron energy analyzer and as a classic PEEM with no energy filtering.

Another filtering solution with large dispersion factors is the so-called *Omega filter* that was originally developed for TEM [13.46] and that now equips the SMART instrument (Fig. 13.4f; [13.25, 42]). It is made by four magnetic 90° deflectors, arranged in a way that the resulting optic axis resembles the Greek capital letter Omega. The symmetry of the path and the placement of a quadrupole, six hexapoles, and a dodecapole on convenient planes allow correction of all second-rank aberrations. The pass energy of this instrument is 15 keV, i.e., no retarding field is required, and the designed resolving power is 150 000. The calculated dispersion at the exit plane, 35 μm/eV, is large enough to display a window of ≈ 10 eV in *spectroscopy* mode with a demonstrated energy resolution better than 180 meV [13.47].

Aberration Correctors

In optics, aberration is the deviation from the nominal image raised by defects of the optical system. Such deviation can depend on geometrical factors (rays with different initial trajectories can be refocused on different planes—*spherical aberration*) or physical factors (the refraction index of the lens changes with the wavelength of the ray—*chromatic aberration*). In light optics, an easy way to correct aberrations is to combine convex and concave lenses conveniently, since the two types produce aberrations of opposite sign and the overall effect can cancel out. In electron optics, this circumstance is prohibited by *Scherzer*'s theorem [13.48]:

> The chromatic and spherical aberrations of an electron microscope with round lenses, real images, static fields, no space charge and a potential and its derivative without discontinuities, are always positive.

The resolution of a cathode lens microscope is then dominated by chromatic and spherical aberrations, mainly resulting from the objective lens. In the ideal case of an aberration-free system, the image of a point-like source is again a point. The blur induced by aberrations transforms the point image into a disk with a width d_0. Since effects like coma and field distortion are negligible in a LEEM/PEEM system, d_0 can be expressed as a Gaussian convolution of the contributions given by chromatic aberration, spherical aberration, and the diffraction limit [13.49, 50]. Given the acceptance angle α, the energy width ΔE, and the start energy E_0, one has that

$$d_0 = \sqrt{d_\mathrm{d}^2 + d_\mathrm{s}^2 + d_\mathrm{c}^2}\,,$$

with

$$d_\mathrm{d} = \frac{0.61\sqrt{\frac{1.5}{E_0}}}{\sin\alpha}\,,$$

$$d_\mathrm{s} = C_0 \sin\alpha + C_\mathrm{s}\sin^3\alpha + C_\mathrm{ss}\sin^5\alpha\,,$$

$$d_\mathrm{c} = C_\mathrm{c}\frac{\Delta E}{E_0}\sin\alpha + C_\mathrm{cc}\left(\frac{\Delta E}{E_0}\right)^2\sin\alpha + C_\mathrm{sc}\frac{\Delta E}{E_0}\sin^3\alpha\,.$$

Here, d_d is the radius of the confusion spot due to diffraction at the smallest aperture. The other components d_s and d_c are the radii of the confusion disc due to spherical and chromatic aberration, expressed to the lowest orders of a Taylor series. In standard experimental conditions d_d is less than 1 nm, thus the resolution is mainly determined by spherical and chromatic aberrations. The effect of the first one is predominant at higher kinetic energy, while the second is more significant at lower kinetic energy.

The constraints of Scherzer's theorem can be circumvented in many ways: some solutions were already known in the early years of theoretical electron optics, but were not implemented before the 1970s [13.51, 52]. Historically, the field of aberration correction was pioneered by the TEM community [13.53, 54], while its

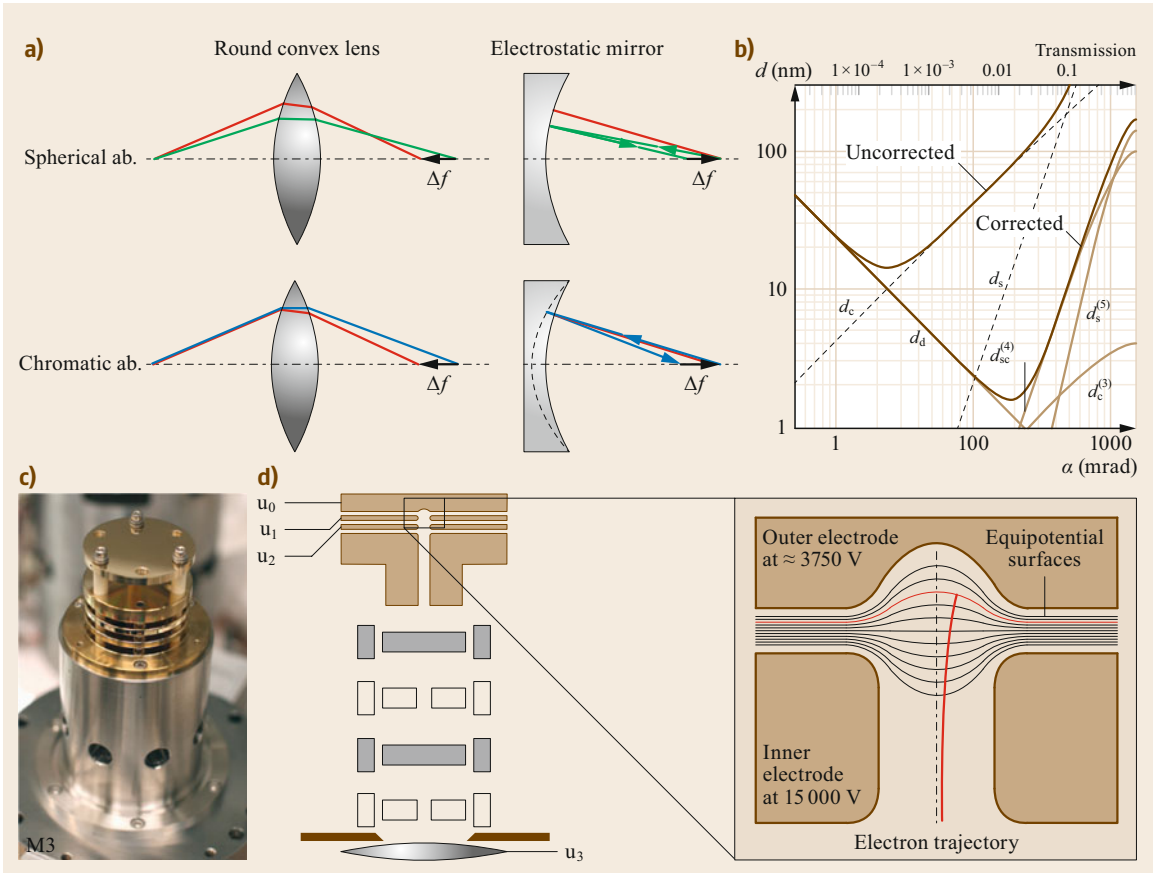

Fig. 13.5 **(a)** Schematics of the effect of spherical and chromatic aberration on a round convex lens and on an electrostatic mirror. **(b)** Resolution limit as a function of the acceptance angle α for uncorrected and corrected SMART in the case $E_0 = 10\,\text{eV}$ and $\Delta E = 2\,\text{eV}$. The dominating aberration components are added: *dashed line* for the uncorrected and *thin solid lines* for the corrected case (Reproduced from [13.49] with permission, copyright 2002 World Scientific). **(c)** Photograph of the electron tetrode mirror assembly used in IBM LEEM-II and **(d)** scheme of the tetrode mirror that equips SMART. The equipotential surfaces in the latter mirror stage are highlighted (Reproduced from [13.26] and [13.25] with permission, copyright 2010 and 1997 Elsevier)

development in cathode lens microscopy started much later. Among the multiple methods already tested in TEM, the most convincing one for cathode lens microscopy is the use of an electrostatic mirror [13.41, 55–57]. The principle how a mirror can compensate spherical and chromatic aberrations is shown in Fig. 13.5a. In the first case, an electrostatic mirror and a round convex lens with the same radius produce focal displacements ΔF of equal magnitude and opposite of sign. In the second case, the electrostatic mirror deflects more the trajectory electrons with higher kinetic energy, compensating the focal displacement ΔF induced in the round convex lens. The electrostatic tetrode mirror can compensate the aberration effect by reducing simultaneously the lower order coefficients C_s and C_c to zero. The effect on resolution and transmission calculated for the SMART instrument is presented in Fig. 13.5b. The cancelation of low-order aberration coefficients can improve the resolution by an order of magnitude. Moreover, since the acceptance angle can now be broadened without loss of resolution, the transmission of the microscope results are enhanced as well, with sensible reduction of the acquisition time.

The mirror is currently employed in several aberration-corrected systems. The first in chronological order is a pure PEEM microscope equipped with a hyperbolic mirror with only two electrodes, capable of compensating simultaneously spherical and chromatic aberrations only for one magnification and one energy [13.58, 59]. The maximum flexibility is obtained with a tetrode mirror (Fig. 13.5c), currently employed in several instruments (SMART, PEEM3,

Tromp/SPECS, Elmitec) [13.25–27]. While the first electrode is at ground potential, the potential of the three others can be varied. They modify the shape of the equipotential surfaces that act as a mirror for the incoming electrons, thus determining the focal length, the chromatic aberration, and the spherical aberration. The mirror is then set conveniently with the operation mode and kinetic energy to cancel out the primary aberration coefficients induced by the lens system. The C_s and C_c coefficients of the mirror can be calculated in a reasonable amount of time for a given E_0, so that standard values of the electrodes can be easily set. Furthermore, the aberration coefficients of the system can be directly evaluated with a series of routine measurements, thus enabling fine correction. PEEM3 reported a lateral resolution of 5.4 nm for PEEM images of biological samples with a 233-nm laser as photon source [13.59]. The first aberration-corrected LEEM image of SMART visualized nanometer surface structures such as the herringbone reconstruction of the Au(111) surface with a lateral resolution of 2.6 nm [13.60]. Both the Tromp/SPECS and Elmitec systems report now an ultimate lateral resolution below 2 nm in LEEM [13.26]. Better results are still theoretically possible, but are very difficult to achieve for long periods of time due to the intrinsic instability of the corrected state, which constrains the lifetime of the corrected state to just a few minutes [13.61]. Nonetheless, it should be remarked that the gain in transmission guaranteed by the aberration corrector is of great help for measurements, e.g., with x-ray photoemitted electrons, where the exposure time and the weakness of the photon source can be a crucial issue for the success of the experiment [13.62].

Electron and Photon Sources

The electron source in LEEM is an electron gun capable of emitting electrons with high brilliance and narrow energy distribution. Over the years, several kinds of emitters have been used. The most frequent electron source is a LaB_6 or CeB_6 crystal with conical shape showing the (100) surface on the flat tip. Once heated by a filament, electrons leave the crystal via thermionic emission from the tip, because of the low work function of the (100) surface. A Wehnelt aperture placed in front of the tip with negative potential suppresses the emission from other faces of the crystal [13.63]. These thermionic emitters have a long lifetime and can draw a very high current with an energy width larger than 0.7 eV [13.64]. The use of thermionic emitters is not recommended for high-resolution microscopes: cold field emitters and Schottky emitters can generate electron beams with a narrower energy spread (0.3 eV), thus reducing the influence of chromatic aberrations, at the cost of lower brilliance and shorter lifetime [13.65–67]. Rarer, but with very interesting applications, are the spin-polarized electron sources. The interaction between spin-polarized electrons and the specimen in LEEM systems provides unique information on magnetic phenomena with lateral resolution (Sect. 13.2.3, *Spin-Polarized LEEM*). The most common one uses the photoemission of electrons from III–V semiconductors with circularly polarized light [13.68–71]. Under particular conditions of strain, the photocathode can generate an electron beam with polarization ≈ 0.9, while the selection of the light polarization switches easily the polarization vector of the beam.

The photon sources employed in PEEM span over a broad range of photon wavelengths and time duration of the pulses, enabling a wide variety of surface science experiments. The easiest way to produce photoemission is with continuous UV illumination by discharging lamps. The first PEEM systems used a Hg short-arc lamp emitting UV light at 4.9 eV (254 nm). The low energy of the photons restricted its application to samples with low work function and low electron affinity. Higher photon energy can be provided by a He gas discharge lamp: the HeI emission mode (21.6 eV) is still used for energy-filtered angle-resolved photoemission diffraction measurements of valence band electrons.

Laser sources have been used to stimulate photoemission in PEEM since the 1970s [13.72]. Pulsed lasers can provide very short flashes of light along a wide wavelength spectrum and are currently used for time-resolved studies in pump-probe mode and for multiphoton photoemission. Several systems are suited for LEEM, such as Nd:YAG and Ti:sapphire, and are often used with higher harmonic photon generation [13.73–75]. The high throughput of lasers concentrated in a single pulse is the major limitation to their employment in PEEM measurement. The dense bunch of photoemitted electrons experience a reciprocal Coulomb repulsion while they travel to the detector, causing a general degradation of the carried information (the so-called *space-charge* effect—Sect. 13.3.2). This phenomenon can be mitigated with a high pulse repetition rate and with a low energy per pulse, so that PEEM experiments with a dynamic timescale of some tens of fs and good lateral resolution are now possible [13.76].

The most successful photoelectron source for PEEM is synchrotron radiation. Since the first installation of SPELEEM in Elettra, Italy, it was clear that the tunable, intense light provided by insertion devices in the third-generation synchrotron is the most versatile and powerful complement to cathode lens systems [13.21]. For example, the SPELEEM beam-

line [13.44, 81] is equipped with two Sasaki Apple II undulators that provide elliptically polarized light (circular left and right, linear horizontal and vertical) in a spectral range between 40 and 1000 eV. The light is monochromatized by two variable line space plane gratings with a resolving power $E/\Delta E = 4000$ at 400 eV. The beamline flux exceeds 10^{13} photons at 150 eV and is above 10^{12} photons in an energy range between 50 and 600 eV. These numbers permit to develop a great variety of experiments with valence band and core-level photoemitted electrons and with state-of-the-art lateral and energy resolution. The only technical limitation arises through the pulsed structure of the synchrotron radiation: space-charge effects limit again the lateral resolution of XPEEM images with core-level electrons to about 20 nm [13.62, 82]. This restriction could be overcome not only with photon intensity reduction, but also with an intelligent placement of apertures to cut away electrons not used for imaging. Nowadays, about 20 synchrotron endstations are equipped with a PEEM, with energies ranging from near-UV to hard x-rays (HAXPEEM), supplying the greatest contribution to the growth of the cathode lens microscopy user community.

13.1.3 Performance

At this point it is useful to summarize the performance of the various imaging techniques of cathode lens microscopy, highlighting the advantages and underlining the limitations. The list in Table 13.1 incorporates some of the state-of-the-art results, as well as routine performance achievable with good quality samples. The purpose of this section is to help the nonexpert reader in choosing the technique that correctly fits their needs, with no claim to being exhaustive. It must be remarked that the state-of-the-art results are obtained in very controlled and stable environmental conditions, with flat and conductive samples and cannot be achieved in every measurement of that kind. A charging and nonatomically flat sample can degrade performance easily by an order of magnitude. In this sense, the routine values are more significant, as they give a more realistic expectation for a generic experiment.

Table 13.1 Performance for the various operating modes of cathode lens microscopy

Resolution	Operation mode	Performance	References
Lateral resolution	LEEM		
	Nonaberration corrected	Routine: 20 nm Best: 4.1 nm (LEEM) (SPLEEM)	[13.26]
	Aberration corrected	Routine: 5–10 nm Best: 2.6 nm 2.0 nm 2.0 nm	[13.26, 30, 60]
	PEEM		
	Nonaberration corrected	Routine: 40–100 nm Best: 7.0 nm	[13.33]
	Aberration corrected	Routine: 40 nm Best 5.4 nm (UVPEEM) 18 nm (XPEEM) 2.6 nm (laser)	[13.59, 62, 77]
Energy resolution	PEEM		
	With MPA energy filter	Routine: 1–2 eV Best: 0.25 eV (spectroscopy) 1.7 eV (imaging)	[13.31]
	With HDA energy filter	Routine: 0.7 eV Best: 0.11 eV (spectroscopy) 0.2 eV (imaging)	[13.30, 44]
	With double HDA	Routine: 0.1 eV Best: 0.01–0.05 eV	[13.78]
Angular resolution	With HDA	Best: 0.047 A^{-1}	[13.44]
	With double HDA	Best: 0.005 A^{-1}	[13.78]
Time resolution	Laser	Routine: tens of fs (lateral resolution 20–50 nm) Best: 200 as (lateral resolution 200 nm)	[13.79, 80]
	Synchrotron	Few ps (single bunch width)	

13.2 Low-Energy Electron Microscopy

LEEM uses backscattered electrons as information carriers. Unlike scanning microscopy, electrons are collected simultaneously from an illuminated area of several tens of μm. The image formed by the magnification lenses can then be acquired even in video-rate (down to 1 ms/frame), depending on the detector quality and the signal intensity. The image contrast depends on how electrons interact with the surface: the higher or lower reflectivity can depend on several factors, e.g., morphology, crystallinity, and quantum effects. It is therefore important to understand how electrons interact with the surface and how the image is formed. Elastic and inelastic scattering of electrons on solids is a well-studied subject in condensed matter physics. Herein, only the most important concepts will be presented, leaving a more complete description to other textbooks [13.83].

13.2.1 Basic Image Contrast

The simplest conceptual case from where to start is the *single scattering* frame, i.e., an electron scattered only once by a surface atom. Here, the scattering amplitude is given by the atomic scattering factor $f_n(\boldsymbol{s})$, where $\boldsymbol{s} = \boldsymbol{k}_{\text{out}} - \boldsymbol{k}_{\text{in}}$ is the momentum transfer between incident and diffracted plane wave with wave vectors $\boldsymbol{k}_{\text{in}}$ and $\boldsymbol{k}_{\text{out}}$, respectively. Considering now a monoenergetic electron beam, represented by a plane wave with amplitude

$$\psi_{\text{in}} = \psi_0 \mathrm{e}^{\mathrm{i}\boldsymbol{k}_{\text{in}}\cdot\boldsymbol{R}} ,$$

the amplitude of a diffracted beam is represented by

$$\psi_{\text{out}} = \psi_0 \left[\sum_n \alpha f_n(\boldsymbol{s}) \mathrm{e}^{\mathrm{i}\boldsymbol{s}\cdot\boldsymbol{R}_n} \right] \mathrm{e}^{\mathrm{i}\boldsymbol{k}_{\text{out}}\cdot\boldsymbol{R}} .$$

Here $f_n(\boldsymbol{s})$ is the atomic scattering factor for the n-th atom at position $\boldsymbol{R}_n$. For an elastic scattering, the kinetic energy E_0 must be preserved, i.e.,

$$E_0 = \frac{\hbar^2}{2m} |\boldsymbol{k}_{\text{in}}|^2 = \frac{\hbar^2}{2m} |\boldsymbol{k}_{\text{out}}|^2 .$$

The contribution of atomic scattering factor and the diffraction effects generate image contrast in LEEM. In fact, areas with different composition, stoichiometry, and crystal structure will have a different electron reflectivity and will appear in LEEM as brighter and darker areas.

For a complete description of electron reflection, inelastic effects and multiple scattering must be taken into account. When traveling inside solids, electrons have a certain probability to experience an inelastic event. Therefore, their probability to be reflected with no losses depends on how deep the scattering center is placed into the bulk. To model this behavior, one can introduce a mean free path expressed by an imaginary component of the electron–surface interaction potential, such that the scattering amplitude decays exponentially in the direction of wave propagation. In general, the electron mean free path is energy dependent and relatively independent of the material, so that its value follows a *universal curve*. Such a universal curve has a V-shape, i.e., presents a minimum for energies around 30–100 eV: in this range the mean free path is so small (few Å) that elastic electrons come from only the top-most atomic layers. LEEM and PEEM performed in this range are then surface sensitive. Electrons with higher kinetic energy can probe the sample in more depth, while at very low energy (≈ 10 eV) the IMFP can show large deviations in accordance with the density of states of the material: at a few eV, organic thin films with very low density of states can show a mean free path of 10 nm, while transition metals with dense d or f bands above the Fermi energy can damp scattered electrons already at a depth of 0.5 nm. The surface sensitivity can be used in LEEM to achieve image contrast even between samples with the same stoichiometry and different surface reconstruction.

At very low kinetic energy, another quantum phenomenon can affect the elastic backscattering of electrons from thin films. When electron wavelength and penetration depth are comparable to film thickness, i.e., at very low kinetic energy, the confinement imposed by the vacuum boundary and the film-substrate interface induces a one-dimensional quantum well condition [13.84]. This so-called quantum size effect (QSE) rises from the interference between electron waves reflected at the surface and at the film-substrate interface. In first approximation, for a film of thickness d, the phase shift induced by the different path length is

$$\phi = \frac{2d}{\hbar} \sqrt{2m(E_0 + V_{\text{i}})} , \tag{13.1}$$

where V_{i} is the inner potential of the thin film. The electron reflectivity is then subject to periodic oscillations as a function of electron kinetic energy and film thickness. QSE is extensively used to measure directly the thickness of thin films: significant examples will be given in Sect. 13.2.3.

13.2.2 Image Formation

The reflection of plane waves is also influenced by the morphology of the surface: atomic steps, kinks, domain boundaries, and defects create interference and modulate the electron reflectivity. To better understand how to interpret the features in a LEEM image, it is necessary to address the theory of image formation. Over the last two decades, several approaches have been used to calculate the image formation in LEEM. The first is from *Chung* and *Altman* [13.22, 85], who developed a wave-optical model to describe the step contrast in ideal and real conditions, i.e., taking into account instrumental broadening and beam coherence. Later the model was improved by a Fourier optics formalism [13.36], which elucidates the image formation for objects with different scattering amplitude and phase and incorporates aberration effects of the objective lens, diffraction cut-off by a contrast aperture, lens defocus, energy spread of the electron beam, and instabilities in lens current and voltage. In parallel, *Jesson* and coworkers [13.86, 87] proposed an alternative approach, based on the definition of a contrast transfer function (CTF), into which flow all the effects of the imaging system on the transfer from real object to image. *Schramm* et al. [13.88] integrated this method with fifth-order aberrations, making it suitable for aberration-corrected instruments. The CTF formalism is attractive for its low computational cost and its universal treatment of arbitrary phase, amplitude, or mixed amplitude-phase objects. In the following, a brief excursus on the CTF formalism is depicted.

Consider having an object illuminated by a monoenergetic plane wave, as in Sect. 13.2.1. It has been shown that the reflection causes variation of wave amplitude and phase. In general, the reflected wave is given by

$$\psi_{\text{out}} = \psi_{\text{in}}\psi_{\text{obj}}$$

with

$$\psi_{\text{obj}}(\boldsymbol{R}) = \sigma(\boldsymbol{R})\mathrm{e}^{\mathrm{i}(\boldsymbol{k}_{\text{out}}-\boldsymbol{k}_{\text{in}})\cdot\boldsymbol{R}}\mathrm{e}^{\mathrm{i}\phi(\boldsymbol{R})} .$$

Here $\sigma(\boldsymbol{R})$ is the amplitude modification factor, while the phase modification factor $\phi(\boldsymbol{R})$ incorporates the phase difference between outgoing and incoming waves induced by the surface morphology. Supposing that the surface is the plane xy at $z = 0$, its morphology can be modeled by a surface height function $h(\boldsymbol{R}_0)$ expressed in unit of step height a_0. $\boldsymbol{R}_0$ is then a two-dimensional position vector spanning over the surface plane. In case of normal incidence, only the vertical component of the wave vector matters, i.e., $\boldsymbol{k} = |\boldsymbol{k}|\hat{z}$. Given $|\boldsymbol{k}| = 2\pi/\lambda_0$, the phase shift defining the surface is given by

$$\phi(\boldsymbol{R}_0) = 2\frac{2\pi}{\lambda_0}a_0 h(\boldsymbol{R}_0) .$$

The phase object function includes the effects of surface morphology on the reflected wave, assuming no significant modification of the accelerating electric field.

The reflected wave is then modified by the cathode immersion lens. First of all, the acceleration from kinetic energy E_0 to E imposes the change of coordinates as in Sect. 13.1.1, from takeoff coordinates in real ($\boldsymbol{R}_0$) and reciprocal space (q_0) to respective virtual coordinates ($\boldsymbol{R}$ and $\boldsymbol{q}$). The transfer from virtual object to magnified image can be described in real or reciprocal space. In real space, the response of the system is described by the point spread function (PSF) $T(\boldsymbol{R})$, which models the blurring of an ideal point object. The final image $\psi(\boldsymbol{R})$ is then the convolution of the outgoing wave ψ_{out} and the PSF,

$$\psi(\boldsymbol{R}) = (\psi_{\text{out}} * T)(\boldsymbol{R}) .$$

Using the fact that convolution in real space corresponds to multiplication in the Fourier space,

$$\psi(\boldsymbol{R}) = \mathcal{F}^{-1}\{\mathcal{F}[\psi_{\text{out}}(\boldsymbol{R})]\,\mathcal{F}[T(\boldsymbol{R})]\} .$$

$T(\boldsymbol{q}) = \mathcal{F}[T(\boldsymbol{R})]$ is the CTF of the LEEM imaging system and it is modeled as the product of all relevant contributions imposed by the optical system, i.e., the frequency cutoff imposed by the contrast aperture, chromatic and spherical aberration, defocus, and instrument-related instabilities. One can model $T(\boldsymbol{q})$ as follows

$$T(\boldsymbol{q}) = M(\boldsymbol{q})W(\boldsymbol{q}, \Delta f)\mathcal{E}(\boldsymbol{q}, \Delta E) .$$

Here, $M(\boldsymbol{q})$ incorporates the effect of a round contrast aperture placed in the backfocal plane, where the reciprocal space is displayed. Its effect is to filter high spatial frequencies

$$M(\boldsymbol{q}) = \begin{cases} 1 & \text{if } |\boldsymbol{q}| < q_{\max} \\ 0 & \text{if } |\boldsymbol{q}| \geq q_{\max} . \end{cases}$$

$q_{\max}$ corresponds to the maximum spatial frequency imposed by the aperture size and it is equal to $\alpha_{\max}/\lambda$, with $\alpha_{\max}$ being the maximum angle accepted. It should be noted that the contrast aperture acts downline of the acceleration stage, therefore the electron wavelength is calculated from the final kinetic energy E.

The wave-aberration contribution $W(\boldsymbol{q})$ refers to deviations of the wave path from the ideal one, induced

by defocus Δf and by spherical aberrations, which may be expressed by Taylor series coefficients as in Sect. 13.1.2, *Aberration Correctors*

$$W(\boldsymbol{q}, \Delta f) = \exp\left[\frac{\mathrm{i}\pi}{2}\left(C_\mathrm{s}\lambda^3 q^4 + \frac{C_{\mathrm{ss}}}{3}\lambda^5 q^6 - 2\Delta f \lambda q^2\right)\right].$$

The defocus Δf also takes into account the unintentional focus oscillations caused by voltage and current fluctuations in lenses and high-voltage supplies.

Finally, the chromatic aberration damping envelope $\mathcal{E}(\boldsymbol{q}, \Delta E)$ comes from an integration over the weighted contribution of the different energies within the Gaussian energy distribution with FWHM ΔE. Limiting the expression of chromatic aberration to the first-order coefficient, one has that

$$\mathcal{E}(\boldsymbol{q}, \Delta E) = \exp\left[-\frac{\left(\pi C_\mathrm{c}\lambda q^2\right)^2}{16\ln 2}\left(\frac{\Delta E}{E}\right)^2\right].$$

The final LEEM image is an intensity distribution of the reflected wave modified by the lens system, so it can be calculated as

$$I(\boldsymbol{R}') = \frac{1}{M^2}\left|\psi(\boldsymbol{R})\right|^2,$$

with $\boldsymbol{R}'$ being the two-dimensional coordinates at the detector plane.

The CTF approach is currently used to produce simulation of LEEM images for a surface with arbitrary height map $h(\boldsymbol{R}_0)$ and given scattering amplitude. It has been used not only to prove well-known surface features, like atomic steps [13.86], but also to construct valuable morphology models of peculiar surfaces, as in the case of corrugated MnAs layers on GaAs(001) [13.89] or sub-surface line dislocations in magnetite thin films [13.90]. Moreover, the CTF algebra helps to figure out how to achieve the best performances from a cathode lens microscope. It is now clear the effect of the contrast aperture, which on one side deteriorates the image by acting as a low-pass filter and on the other side limits the acceptance angle and therefore the blurring induced by spherical aberration. The energy distribution of electrons coming, e.g., from the electron source, act together with the chromatic aberration, while the voltage and current instability can be modeled as an additional defocus. This knowledge has proven to be crucial in the case of aberration-corrected systems, where the lifetime of fully-corrected state has observed to be just a few minutes. After a correct estimation of every contribution, *Schramm* et al. [13.61] concluded that the stability of power supplies, the active damping of vibrations, good electromagnetic shielding and improved detectors are the crucial factors for maintaining the corrected state, and that more accurate monitor and correction systems must be developed to prolong its lifetime and make it usable for complex experiments.

13.2.3 Imaging Mode

LEEM and LEEM-IV

The first operating mode of LEEM corresponds to the magnified image plane displayed on the detector. Typically, the camera interconnects with the microscope software to capture single images or videos on varying the start voltage, the sample temperature, the lens settings, and so on. In this way, several in situ experiments and diagnostic procedures can be performed. In principle, the LEEM image is the intensity distribution of electrons on the image plane. The local intensity is then converted to a gray-scale image, where the contrast depends on how the objects modify the reflected electron plane wave in phase and amplitude. In the following, we will show topical examples of how phase and amplitude objects are displayed in LEEM.

The simplest phase object giving contrast in LEEM is an atomic step on an elsewhere flat, crystalline surface. The uniform, regular distribution of atoms, as in the case of a terrace, gives no contrast in LEEM, since the electron beam is backscattered everywhere in the same way. Plane waves coming from two adjacent terraces have different phases, so that at the terrace edges the interference between them degrades the reflected intensity. Figure 13.6a shows a LEEM image of a clean, stepped Si(111) surface with (7×7) reconstruction: monoatomic steps are displayed as dark lines with a faint, brighter decoration on one side [13.85]. This appearance is confirmed by simulation performed with CTF formalism [13.86]. In this case, the surface height function $h(\boldsymbol{R}_0)$ is expressed as a simple step function of height $a_0 = 0.31$ nm (Fig. 13.6b, brown line). The simulated intensity line profile (Fig. 13.6b, black line) displays a minimum in the vicinity of the step and a maximum on one side. In general, the presence of minima and maxima is related to the phase shift, i.e., the electron kinetic energy and the step height: For $\phi(\boldsymbol{R}_0) = 2n\pi$ the contrast is almost absent, while in the complete out-of-phase condition $\phi(\boldsymbol{R}_0) = (2n+1)\pi$ the line profile is symmetric (no bright decoration). The asymmetric maximum is observed at the intermediate phase conditions and is most pronounced at $\phi(\boldsymbol{R}_0) = (2n+1)\pi/2$. The relative position of maxima and minima can be inverted periodically as a function of the phase shift. CTF formalism can be readily extended to

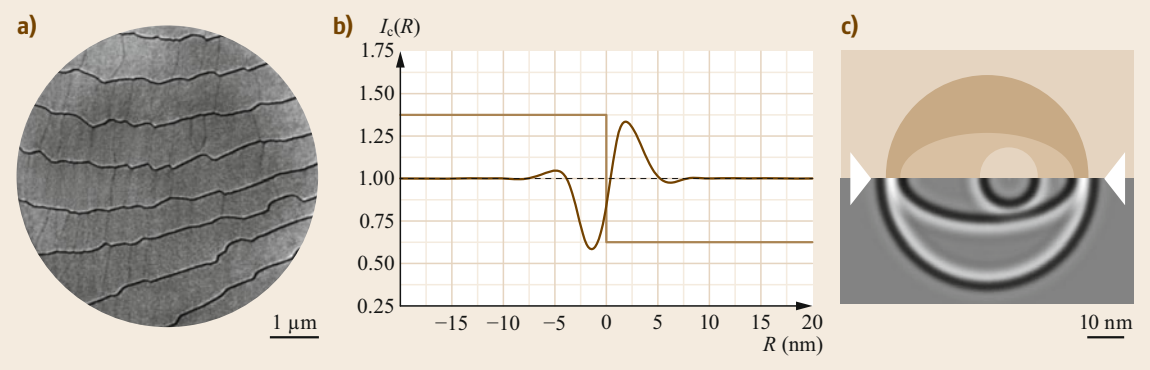

Fig. 13.6a–c Imaging with phase contrast. **(a)** Underfocus LEEM image of monoatomic steps on the Si(111)-(7×7) surface. Imaging energy $E_0 = 45$ eV (Reproduced from [13.85] with permission, copyright 1998 Elsevier). **(b)** Intensity line profile (*black line*) calculated for the superimposed step profile (*brown line*) with the inclusion of chromatic damping. **(c)** Plane view schematic (*top*) and simulated LEEM image (*bottom*) of an arrangement of terraces separated by a single atomic step. Bright regions of constructive interferences, where the steps are in close proximity, are *arrowed*. **(b)** and **(c)** reproduced from [13.86] with permission, copyright 2009 World Scientific

two spatial dimensions: Fig. 13.6c shows the simulation of how an ideal Si(111) surface with monolayer-step-height circular and elliptical terraces (top) appear in LEEM for a given phase shift. It should be noted that more complicated interference patterns could be produced when steps were closer together, e.g., in the region highlighted with white arrows. The correct interpretation in such cases must pass through an extensive simulation of model surfaces in different conditions of focus, electron kinetic energy, and morphology.

The amplitude contrast is produced between two adjacent areas that have different scattering amplitude. This case is quite common during an experiment: any area with a different composition, stoichiometry, crystal structure, and even surface reconstruction gives amplitude contrast. The exact calculation from first principles of how crystalline surfaces diffract electron beams in LEEM is derived from kinematic and dynamic LEED theory developed already in the late 1960s [13.83] and will not be discussed here in detail. An example of amplitude contrast is given in Fig. 13.7a, displaying a LEEM image of a Pt(111) surface covered with a graphene (Gr) layer of variable thickness [13.91]. In this particular case, the contrast is given not only by changes in amplitude, as between monolayer and bilayer Gr, but also by the quantum size effect. The difference is more evident by looking at the *I–V* characteristics obtained from a stack of LEEM images with increasing start voltage (Fig. 13.7b). The *I–V* curve for ML Gr reflects the particular morphology of the system, where the carbon sheet rests 3.30 Å upon the Pt substrate. The other reflectivity curves appear quite similar to one another at kinetic energies above 20 eV, since the Gr thickness becomes bigger than the IMFP and no contribution from substrate atoms is present. Nonetheless, pronounced oscillations due to quantum size effects can be observed at lower kinetic energies (Fig. 13.7c). In particular, the number of minima of these oscillations scales with the number of layers. This characteristic has been observed not only on 2-D materials, but also on epitaxial thin films on metal substrates, and therefore can be used as a universal fingerprint to estimate the film thickness. Moreover, one can plot the phase shift from (13.1) as a function of the energies at which interference maxima or minima are observed (Fig. 13.7d) and determine accurately the film thickness and the inner potential with a fit. In this particular case, the analysis confirms that Gr stacks thicker than three layers have identical layer separation to graphite.

Brightfield and Darkfield LEEM

Up to now, we have only considered the case in which incoming and reflected electron beams are perpendicular to the sample surface. Even with a perpendicular incoming beam, the outgoing electrons distribute over the solid angle to form a diffraction pattern in the back-focal plane of the objective lens. Then, the contrast aperture limits the acceptance angle in order to only let electrons pass that are emitted in the neighborhood of the zero-order diffraction spot. This configuration is called *brightfield* and is schematized in Fig. 13.8a. However, it would be interesting to build the LEEM image also with nonperpendicular electrons, i.e., with higher or fractional order diffraction spots; in this way the crystallographic information contained in the diffraction pattern can be transferred to the real space and generate a crystallographic map of the sample. This case is called *darkfield* and can be achieved in

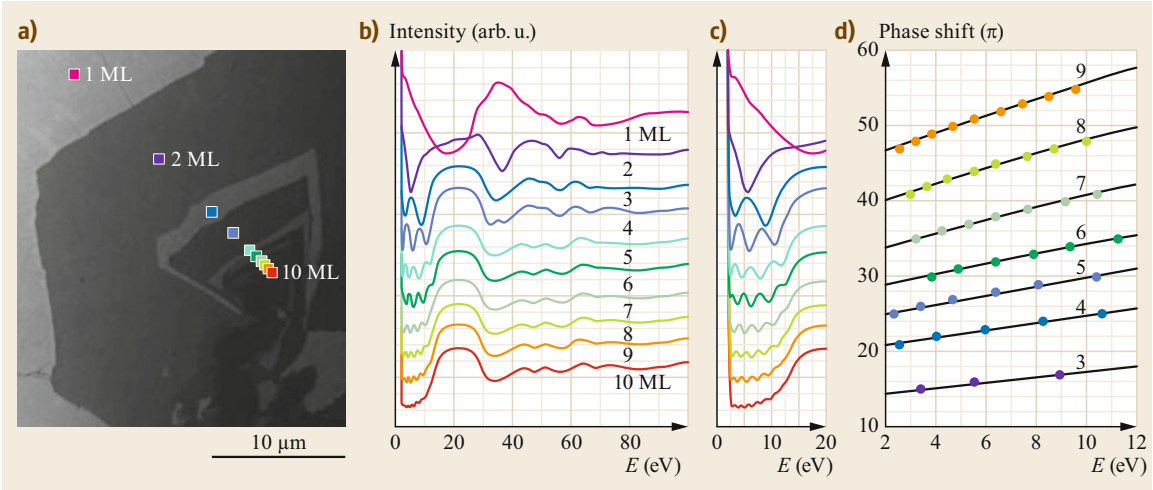

Fig. 13.7a–d Imaging amplitude objects. **(a)** LEEM image (electron energy 4.4 eV) of a few-layer Gr stack nucleated at a boundary between rotationally misaligned ML Gr domains. *Markers* denote areas with coverage between one and ten Gr layers. **(b)** *I–V* characteristics obtained from a stack of LEEM images with electron energy from 2 to 100 eV at the locations marked in **(a)**. **(c)** Higher magnification of the same data set at electron energies below 20 eV, showing fringes due to interference of electrons backscattered from the Gr surface and Gr/Pt interface. **(d)** Phase shifts for constructive and destructive interference (fringe maxima and minima in **(c)**) as a function of electron energy. *Black lines* are theoretical fits calculated assuming a free-electron propagation model. (Reproduced from [13.91] with permission, copyright 2009 American Physical Society)

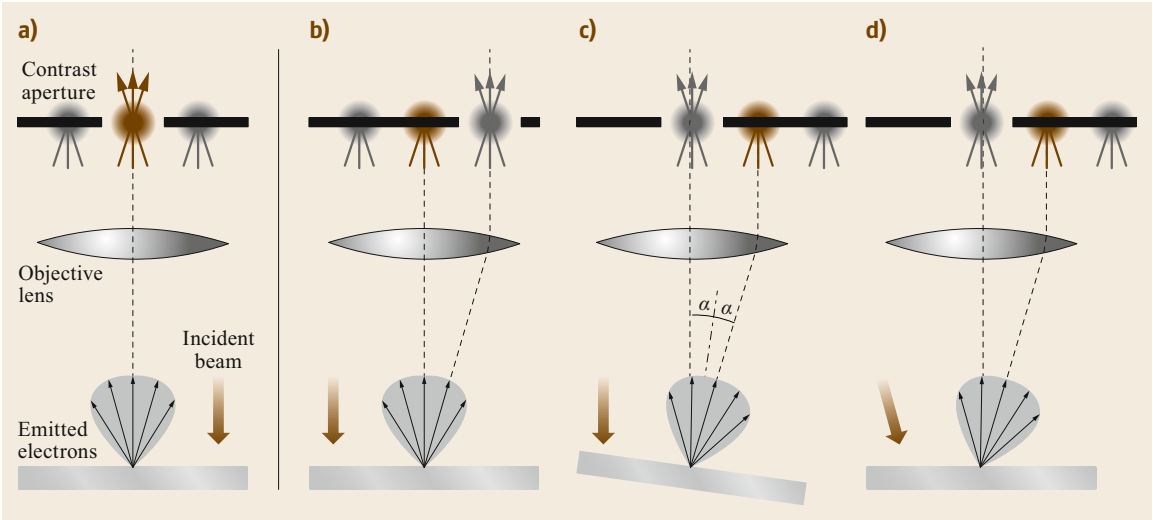

Fig. 13.8a–d Scheme of brightfield **(a)** and darkfield **(b–d)** LEEM operation. Darkfield can be performed by displacing the contrast aperture **(b)**, tilting the sample **(c)**, and deflecting the incident electron beam **(d)**. The zero-order diffraction spot is depicted in *brown*, while the higher order ones are in *gray*

different ways. The simplest way is (i) to move the contrast aperture and accept electrons with a nonzero emission angle, e.g., from a first-order diffraction spot (Fig. 13.8b). This method has the disadvantage that the selected electron trajectory is far from the optical axis and therefore the spherical aberrations may blur the image. A way to overcome this limitation is (ii) to incline the sample tilt by a certain angle α to let the selected diffraction feature with emission angle 2α pass through the contrast aperture along the optical axis (Fig. 13.8c). In this case the incident electron beam is not perpendicular to the surface, so one should take into account

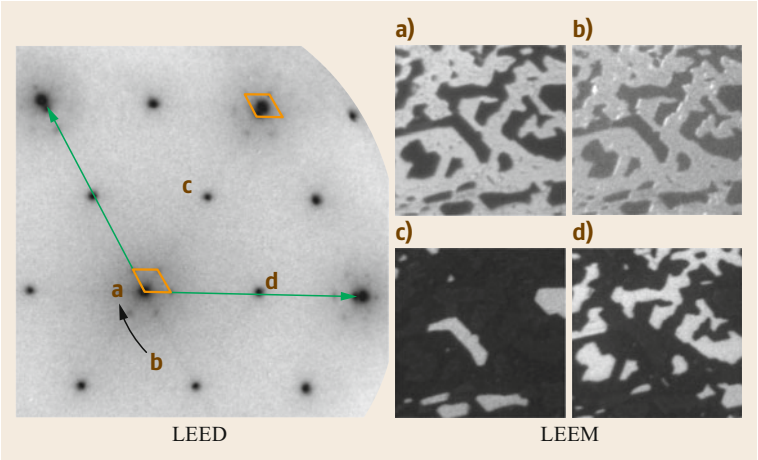

Fig. 13.9a–d LEED (*left*) and LEEM (*right*) images of a strongly dewetted $Fe_3O_4(111)$ thin film. In LEED ($E_0 = 88\,eV$) the reciprocal vectors of a $Fe_3O_4(111)$ unit cell and FeO(111) moiré pattern are highlighted in *green* and *orange*, respectively. The labels in LEED mark the selected diffraction spots used for LEEM ($E_0 = 24\,eV$): **(a)** brightfield, **(b)** darkfield with FeO(111) moiré, **(c)** and **(d)** darkfield with (2×2) inequivalent spots of $Fe_3O_4(111)$ (Reproduced from [13.92] with permission, copyright 2012 American Physical Society)

the different atomic scattering factor $f(\boldsymbol{s})$, as it depends on the momentum transfer $\boldsymbol{s} = \boldsymbol{k}_{out} - \boldsymbol{k}_{in}$. This approach does not need a dedicated alignment of the lens system, but lacks accuracy and reliability due to mechanical limitations of the sample manipulator. The most convenient method to produce darkfield LEEM is (iii) to leave the sample untouched and tilt the incoming electron beam with deflectors placed in the illumination column (Fig. 13.8d). It is optically equivalent to the previous case, but with the advantage that the sample holder and the lens system are untouched, and deflectors can be remotely controlled and accurately calibrated, enabling fast switching between brightfield and darkfield.

The contrast mechanism in darkfield LEEM measurement adds substantial information on the crystal structure of the sample. Electrons forming a particular spot in the diffraction pattern are emitted only from areas with a certain crystal structure. Thus, a LEEM image produced with these electrons shows as bright the area from where they were emitted, and as dark the areas with another structure. By studying the area distribution in darkfield LEEM for several diffraction spots, one can reveal if a LEED pattern is produced from a single phase over the entire surface or is a superposition of two or more contributions. Images over a large field of view offer a direct measurement of the relative coverage of the phases. Moreover, domains with the same crystal structure but rotated orientation can be distinguished. Even if the domains give the same LEED pattern geometry, the intensity of same-order spots differs, thus resulting in an amplitude contrast among rotational domains. An example of both occurrences is given in Fig. 13.9. The system is a dewetted $Fe_3O_4(111)$ thin film of thickness larger than 7 nm, grown on a Pt(111) surface [13.92]. The film holes do not expose a clean Pt surface, but are decorated by a single bilayer of FeO(111) [13.93, 94]. The corresponding LEED pattern, obtained with illumination over a large area, is a superposition of two distinct patterns: the (2×2) superstructure over the $Fe_3O_4(111)$ spots (unit cell in green) and the moiré pattern of FeO(111) surrounding the Pt(111) spots. Brightfield LEEM (Fig. 13.9a) shows areas with different reflectivity, but at a first glance one cannot distinguish which is Fe_3O_4 and which is FeO/Pt. Darkfield LEEM performed with electrons from the moiré (Fig. 13.9b) shows as bright the FeO(111) areas, leaving the rest as dark. The contrast inverts when one of the $Fe_3O_4(111)$ (2×2) spots is used, but while the FeO patches appear dark, only one rotational domain of Fe_3O_4 enlightens (Fig. 13.9c). The other rotational domain, rotated by 180°, emerges on darkfield LEEM by using the inequivalent (2×2) spot (Fig. 13.9d). It should be noted that the FeO darkfield image corresponds to the sum of the two Fe_3O_4 darkfield images when the contrast is inverted, thus excluding the presence of a third crystalline phase. Moreover, the amplitude contrast between rotational domains is achieved only at some kinetic energies, for which two inequivalent LEED spots with the same order have a different intensity. Other energies can eliminate or invert the contrast.

Mirror Electron Microscopy

It has been shown that in LEEM the reflectivity of electrons changes with the momentum transfer $\boldsymbol{s}$ occurring during backscattering. Such reflectivity is always less than unitary, i.e., part of the electrons is lost due to inelastic scattering, bulk absorption, surface and quantum effects. The only way to achieve total reflection is to decrease the start voltage until all electrons are reflected above the sample surface, turning the cathode immersion lens into an electrostatic mirror. However, the equipotential surface in front of the specimen is still influenced by field inhomogeneities determined by the surface morphology, work function changes,

contact potentials, and magnetic fields. As electrons decrease speed and reverse direction, their trajectories are deviated by such perturbations, thus giving contrast to the electron image. This imaging technique is called mirror electron microscopy (MEM) and has the advantage of probing surfaces without direct impact, giving access to nonconductive specimens and imaging phenomena in a nonperturbative way. The contrast mechanism in MEM has been discussed and modelized over the years [13.95–97], in order to extract quantitative information regarding morphology and microfields. Although the algebra is in some cases quite similar to the CTF approach described in Sect. 13.2.2, it will not be discussed here. In general, the lateral resolution in MEM is worse than standard LEEM imaging on the same surface, ranging around several tens of nm. Nonetheless, the high sensitivity to height variations and equivalent surface potentials gives a remarkable depth resolution of about 1 nm. Like in LEEM, the intensity line profile of features in different focus conditions can be simulated and reverted to quantitative real-space models. $I(V)$ spectra of different areas through the LEEM-MEM threshold can be used to extrapolate a map of the local potential, owed to work function changes, charge states, or application of external fields.

Spin-Polarized LEEM

Spin is a degree of freedom of the incident electron beam that can be used to achieve imaging of magnetic states of the specimen surface. As shown in Sect. 13.1.2, *Aberration Correctors*, spin-polarized sources such as III–V semiconductor photocathodes can provide beams with a high degree of polarization $\boldsymbol{P}$. In SPLEEM, the usual image contrast is augmented by magnetic contrast generated by the exchange interaction between incident spin-polarized electrons and spin-polarized electrons in the magnetic material [13.98–101]. This exchange contribution to the scattering is proportional to $\boldsymbol{P}\cdot\boldsymbol{M}$, with $\boldsymbol{M}$ being the magnetization vector of the target material. In a magnetic material $\boldsymbol{M}$ results from the difference between the number of electrons with parallel and antiparallel spin contained in the occupied states of majority and minority bands, respectively (Fig. 13.10a; [13.102]). The two electronic populations produce nonequivalent exchange-correlation potentials, so that electron beams with different polarization are scattered differently. Moreover, the minority spin band offers more unoccupied states for an inelastic event, thus minority electrons are more effectively scattered than majority electrons and the IMFP decreases. This leads to a larger reflectivity for majority electrons. The intensity difference between parallel ($I_{1\uparrow}$) and antiparallel ($I_{1\downarrow}$) configurations, normalized to the sum of the intensities, i.e.,

$$A = \frac{I_{1\uparrow} - I_{1\downarrow}}{I_{1\uparrow} + I_{1\downarrow}} ,$$

is called exchange asymmetry and is proportional to $\boldsymbol{P}\cdot\boldsymbol{M}$, weighted with the damping caused by the different IMFP. It should be noticed that the difference at the numerator cleans the resulting image from nonmagnetic diffraction and topological features resulting from conventional LEEM imaging, leaving only contrast from magnetic features. The effect of spin on exchange correlation potential and IMFP decreases rapidly as the kinetic energy of incident electrons increases. For this reason, the best magnetic contrast in SPLEEM is obtained at energy typically below 20 eV.

The photocathode electron gun delivers electron beams with a fixed spin polarization vector that can be eventually flipped by changing the sense of the circular polarized light. The spin polarization vector can be subsequently changed with a spin manipulator, where electrostatic and magnetic deflectors and a magnetic rotator lens give three degrees of freedom on the spin orientation. This allows complete characterization of the sample magnetization direction in both in- and out-of-plane geometry, and tilted directions in between. An example of SPLEEM asymmetry images with different polarization orientation is given in Fig. 13.10b. Here, two epitaxial Fe ribbons produced by deposition of 5 ML of Fe on a W(110) surface and annealing at 650 K are displayed with the polarization vector in-plane and parallel to [001] (1) and [1$\bar{1}$0] (2) crystallographic direction, respectively [13.103]. The magnetic state of the ribbons is primarily determined by the interplay between exchange and stray-field energy, which prefers magnetization along the [001] axis, and the surface/-magnetoelastic energy, whose minimization produces states with magnetization along [1$\bar{1}$0]. The consequent multidomain state can be extracted by the intensity pattern in the SPLEEM asymmetry image: brightest areas have a parallel magnetization vector, darkest have an antiparallel one, while neutral gray are oriented perpendicularly. By combining images with different polarization vectors one can construct a consistent domain model, as presented on the sides for the marked regions.

SPLEEM has been used to address phenomena such as domain wall structures in thin magnetic films, micromagnetic configurations in surface-supported nanostructures, spin reorientation transition, magnetic coupling in multilayers, phase transitions, and finite-size effects. Its application has several advantages, such as real-time observation and the possibility to combine crystallographic and magnetic information. The surface

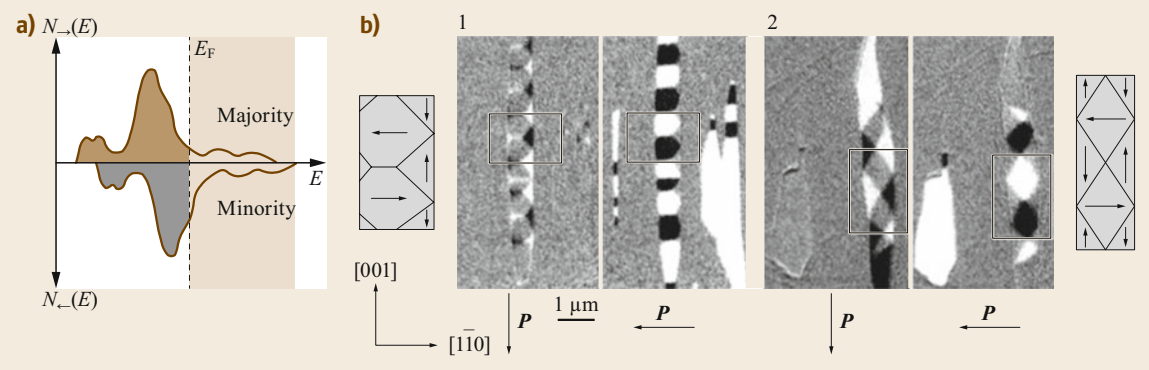

Fig. 13.10 **(a)** Density of states in a ferromagnetic metal. Because of the spin interaction, the electronic band can be conceived as a superposition of a majority (*brown*) and minority (*gray*) population. **(b)** Domain structure of epitaxial Fe ribbon crystals on W(110). The image pairs were taken with the polarization vector of the electrons parallel to the [001] (1) and [1$\bar{1}$0] (2) directions, respectively. The magnetization distribution in the *marked regions* is indicated on the sides (Reproduced from [13.103] with permission, copyright 2006 John Wiley & Sons)

sensitivity limits its usefulness to samples prepared in situ or grown elsewhere and protected by a removable capping layer. The main disadvantage in the use of SPLEEM is its strong sensitivity to applied magnetic fields, which distress the trajectory of electrons and degrade the image quality. Modest fields of few hundred gauss can be applied only in the surface normal direction, so that the Lorentz force is geometrically minimized. This limitation affects important fields of research, such as dynamics on domain walls and exotic magnetic states of matter.

Electron Energy Loss Microscopy

LEEM systems equipped with an energy filter have the possibility to use inelastic electrons for imaging with opportune detuning of the energy analyzer [13.81, 105]. Electrons can lose some kinetic energy during the scattering process and the energy distribution of all inelastically scattered electrons provides information about the local physical and chemical properties of the specimen. The low-loss region (< 50 eV) of this energy spectrum contains valuable information about the band structure and the dielectric properties of the material, e.g., electron–phonon interaction, band gaps, and surface plasmons [13.106, 107]. Such inelastic electrons can pass through the energy analyzer with optimal trajectory if a supplementary bias is applied. The usual slit at the exit plane selects only electrons with a certain energy loss. Electron energy loss microscopy (EELM) images typically have very low intensity and contrast, but can be used to display the surface distribution of plasmons and to distinguish between surface areas with different phononic and plasmonic properties [13.108]. For example, this is the case when Gr and hexagonal boron nitride (h-BN) patches rest one aside the other upon a surface [13.104]. Figure 13.11a shows

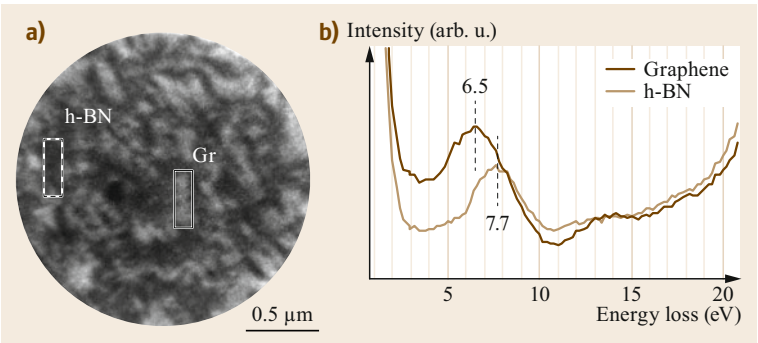

Fig. 13.11 **(a)** EELM image of Gr and h-BN coplanar flakes on Pt(111) collected with electron energy $E_0 = 32$ eV and a loss of 6.5 eV. Graphene (Gr) patches appear brighter than h-BN due to the plasmonic excitation. **(b)** Electron energy loss spectra of Gr and h-BN extracted from a stack of EELM images at different energy losses. The spectrum measured in region Gr shows a π-plasmon loss at 6.5 eV; the spectrum measured in region h-BN shows a π-plasmon loss at 7.7 eV (Reproduced from [13.104] with permission, copyright 2015 Wiley-VCH Verlag)

an EELM image of adjacent Gr and h-BN flakes grown on a Pt(111) surface from a single molecular precursor, dimethylamine borane (DMAB). The simultaneous presence of B, C, and N atoms obtained from dissociation of DMAB at 1000 K is a very efficient way to obtain a continuous, almost free-standing layer mostly made of Gr and h-BN, with only a low percentage of impurities. Gr and h-BN flakes have a different plasmon energy loss and therefore display a contrast for particular electron loss energies. Local integration over a stack of EELM images allows the collection of size-selected electron energy loss spectra (Fig. 13.11b). It is shown that in the bright areas in EELM the collective excitation of the electrons is found at 6.5 eV, whereas in the dark areas a peak centered at 7.7 eV is found. These spectroscopic features are assigned to π-plasmon energy loss in slightly doped Gr and h-BN, respectively [13.109, 110].

The use of energy loss microscopy in LEEM systems can provide additional information on the dielectric nature of surfaces and thin films. However, its accuracy cannot be compared to a dedicated apparatus. In LEEM the monochromaticity of the incident electron beam, a few tenths of eV, is not enough to resolve vibrational states of molecules and adatoms. Despite this aspect, EELM is ideal to characterize inhomogeneous surfaces, showing the lateral extent of every species with different plasmonic signature with a resolution of some tens of nm.

13.2.4 Diffraction Mode

μ-LEED

The second operating mode in LEEM is the so-called diffraction mode, i.e., when the backfocal plane of the objective lens is displaced on the detector. This mode gives access to the angular distribution of backscattered electrons, which forms a diffraction pattern in the case of crystalline surfaces. The use of LEEM systems for diffraction studies has many advantages with respect to standard LEED optics:

- The operation conditions of the electron gun and the illumination angle are fixed, while the kinetic energy at the interaction is governed by the start voltage. This ensures beam stability and constant current, even for dynamic measurements.
- The backfocal plane is displayed for electrons traveling at a kinetic energy E, independently of their takeoff energy E_0. This means that the displayed reciprocal space has the same lateral extent for every start voltage, so the diffraction spots do not move during an energy scan. The calibration of the reciprocal space can be calculated by looking at the linear expansion of the Ewald sphere with increasing start voltage, or through the position of the diffraction spots for a known surface, e.g., Gr, Si(111)-7×7 or oxidized W(110).
- The probed region can be inspected in LEEM and selected by placing an opportune aperture in the image plane. Commercial LEEM systems can reduce the illuminated area to a diameter of 250 nm [13.30].
- The electrons can be filtered in energy and the background of secondary electrons can be removed.
- The zero-order diffraction spot can be easily detected, as the magnetic beam splitter separates the incoming and outgoing electron beams.

The collection of LEED measurements from a selected region is often referred to as micro-LEED or μ-LEED. Figure 13.12 shows how microscopy and diffraction can be combined to obtain structural information on surfaces and nanostructures under particular conditions. The LEEM image in Fig. 13.12a presents cerium oxide microparticles grown on a Ru(0001) surface saturated with oxygen [13.111, 112]. This system is a model catalyst, used to study the interplay between oxide and metal under reaction conditions. A 500-nm wide illumination aperture can be introduced and placed on a large CeO_2 particle (as indicated by the red circle), so that electrons are backscattered from only this single object. The transfer lens setup is then changed to display the LEED pattern. The real-time observation of the diffraction pattern was used to investigate how the reduction of ceria particles influences their atomic surface structure. LEED patterns were acquired in real time while dosing up to 4800 L of molecular hydrogen at a substrate temperature of 700 K (Fig. 13.12b). Before hydrogen exposure, only the (1×1) integer spots of CeO_2 are visible. After dosing 500 L of H_2 at 5×10^{-7} mbar, additional spots emerge as a consequence of the local ordering of oxygen vacancies induced by H_2 dissociation and surface reduction. At this moment, the superstructure spots exhibit a periodicity of 2.6 with respect to the integer spots of CeO_2. A further dose of H_2 at higher pressure leads to larger periodicities in the diffraction pattern, notably (3×3) at 1900 L and (4×4) at 4800 L, as well as slight in-plane lattice expansion, detectable from the contraction of first-order spots. The structural changes observed in LEED, together with other LEEM analysis not shown here [13.111], helped the authors to conclude that under reducing conditions three stable phases of reduced ceria exist, which coexist for intermediate oxidation states.

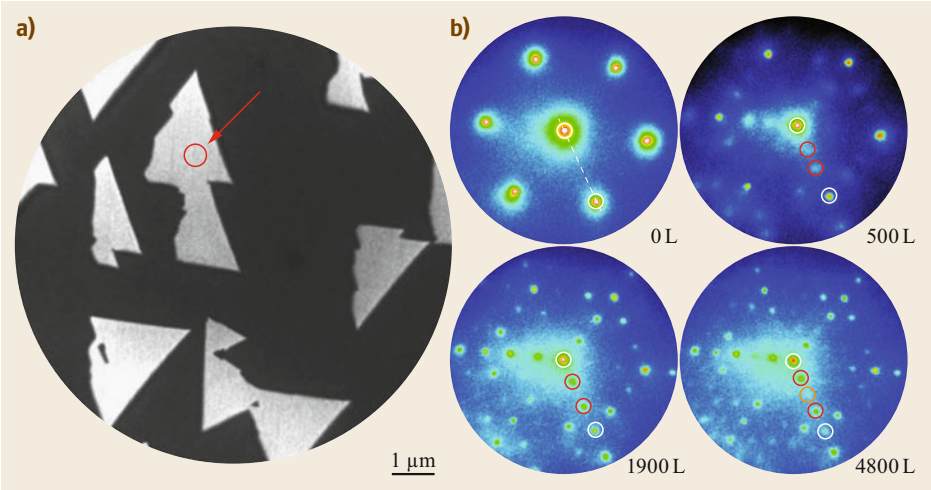

Fig. 13.12 **(a)** LEEM image recorded at 16.3 eV of ceria microparticles (*bright*) on the Ru(0001) support (*dark*). The *red circle* highlighted with an *arrow* illustrates the electron beam spot size and position during µ-LEED. **(b)** µ-LEED image series obtained during reduction of a single ceria microparticle in hydrogen at 700 K. *White circles* indicate the reflections of CeO_2. *Red* and *orange circles* indicate the positions of the superstructure spots (Reproduced from [13.111] with permission, copyright 2015 Wiley-VCH Verlag)

Spot Profile Analysis and LEED-IV

The real-time observation of an energy-filtered, stable LEED pattern is a valuable tool to investigate inhomogeneous surfaces under changing conditions. The quality of LEED images taken in LEEM is such that other analysis methods are made available. For example, the intensity line profile of a particular diffraction spot along a selected crystallographic direction can reveal many details in relation to surface morphology and roughness, such as step distribution and the presence of defects and ordered superstructures [13.113]. The sampling frequency of the profile is determined by the magnification of the backfocal plane and the number of pixels of the detector. The sharpness limit for LEED spots is determined by the transfer width of the electron beam at the surface and depends on the type of electron source and other instrumental effects of the LEEM apparatus.

Figure 13.13a gives an example of a LEED spot profile analysis (SPALEED) performed with LEEM optics on an $Fe_3O_4(111)$ thin film grown on a Pt(111) substrate [13.92]. Magnetite films are used both as a model catalyst and a support for catalytically active nanoparticles. Its surface termination, deeply connected with its functional and catalytic properties, changes with the preparation conditions. In this case, the film was grown with subsequent cycles of Fe deposition and oxidation at 900 K. After the last oxidation performed at 1000 K, if the sample is cooled in an oxygen atmosphere, the zero-order diffraction spot presents a shoulder-like broadening. Such broadening disappears after flashing at 900 K in UHV. The (0,0) spot profile can be fitted with a superposition of a Gaussian peak, accounting for the instrumental broadening, and a shoulder that can be described as a sum of three Lorentz$_{3/2}$-like functions of different half-widths [13.114].

$$I(\boldsymbol{k}) = I_{\mathrm{Gauss}}(\boldsymbol{k}) + I^{(1)}_{\mathrm{Lor3/2}}(\boldsymbol{k}) + I^{(2)}_{\mathrm{Lor3/2}}(\boldsymbol{k}) + I^{(3)}_{\mathrm{Lor3/2}}(\boldsymbol{k}) \,.$$

The prominent broadening is described by the first part, $I^{(1)}_{\mathrm{Lor3/2}}(\boldsymbol{k})$. The weakly modulated background, ascribable to small clusters or adsorbates on the surface, is described by $I^{(2)}_{\mathrm{Lor3/2}}(\boldsymbol{k})$ with a FWHM as large as the first Brillouin zone (FBZ). The third component, $I^{(3)}_{\mathrm{Lor3/2}}(\boldsymbol{k})$, has a FWHM slightly larger than the Gaussian one and can be related to the presence of atomic steps. The spot profile has then been collected over an energy range between 40 and 200 eV, in order to highlight the changes in the relative intensities of the components. It has been found that the FWHM of the components increased linearly with the perpendicular component of $\boldsymbol{k}$, indicating that the surface has a mosaic structure with a calculated angular spread of 0.2°. Moreover, the ratio G between integral intensities of $I_{\mathrm{Gauss}}(\boldsymbol{k})$ and $I^{(3)}_{\mathrm{Lor3/2}}(\boldsymbol{k})$ spot components,

$$G = \frac{I_{\mathrm{Gauss}}}{I_{\mathrm{Gauss}} + I^{(3)}_{\mathrm{Lor3/2}}} \,,$$

revealed a periodic exchange between the two intensities with a period linearly related to the perpendicular

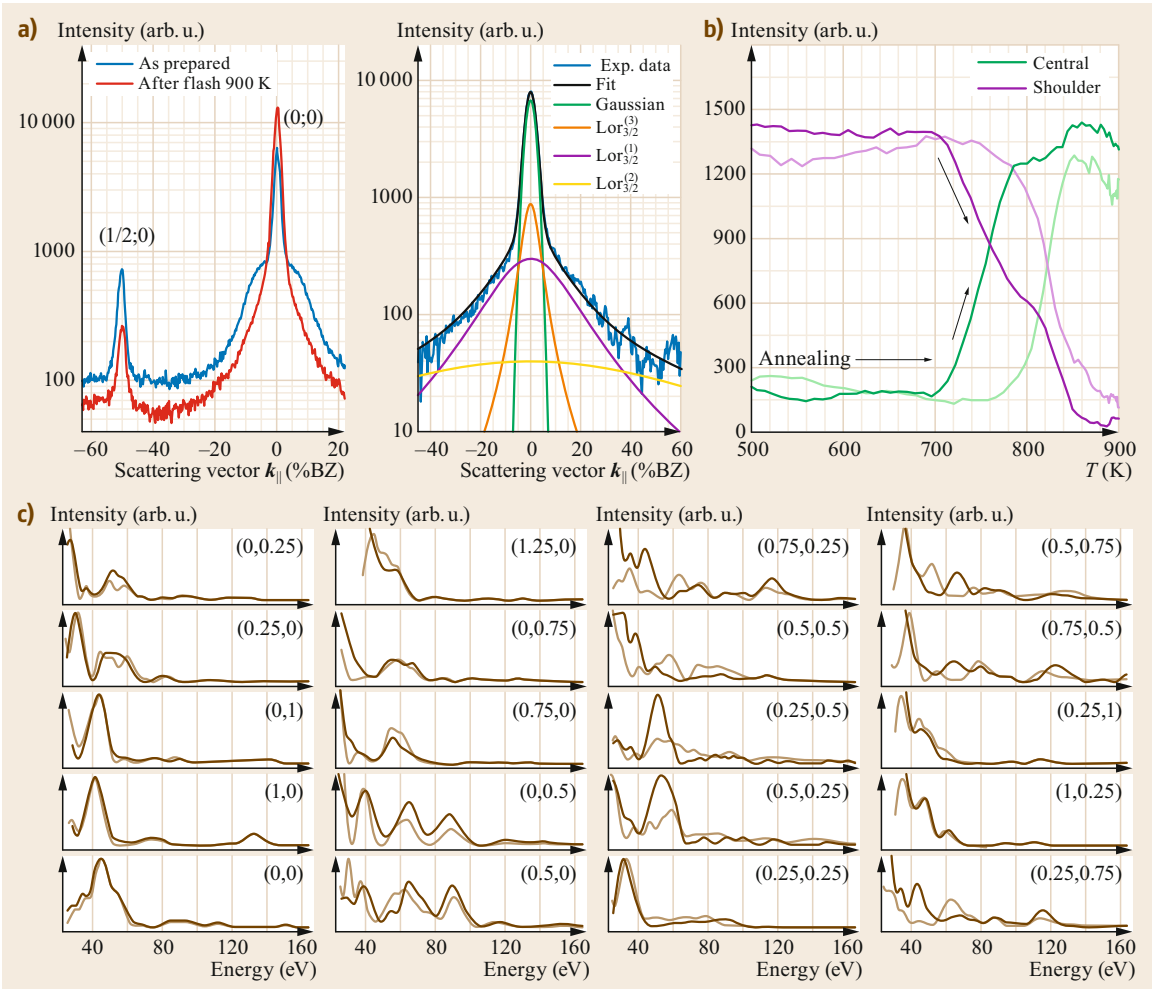

Fig. 13.13 **(a)** Spot profile analysis of $Fe_3O_4(111)$ LEED pattern along the (1,0) vector for the as-prepared surface and after a final annealing at 900 K. The preparation conditions for the $Fe_3O_4(111)$ thin film are described in the main text. The fit of the (0,0) LEED spot profile on the *right* shows a narrow central Gaussian peak in green, two $Lorentz_{3/2}$ peaks in *orange* and *purple* for the shoulder-like broadening, and a very broad $Lorentz_{3/2}$ peak in *dark yellow*. **(b)** Integral intensity of the central Gaussian and the shoulder during cooling in oxidation conditions. The formation of surface inhomogeneities is influenced by the cooling rate, $\approx 4\,K/s$ for *dark lines* and $\approx 1\,K/s$ for *light lines* (**(a)** and **(b)** reproduced from [13.92] with permission, copyright 2012 American Physical Society). **(c)** Comparison of experimental *I–V* curves (*dark brown*) taken with μ-LEED and best-fit calculated curves (*light brown*) for the (4×4) diffraction structure of oxidized Ag(111) (Reproduced from [13.115] with permission, copyright 2007 American Institute of Physics)

component of $\boldsymbol{k}$. Such behavior is consequent to the periodic constructive and destructive interference between two adjacent terraces separated by an atomic step [13.113]. By fitting this periodicity one can calculate the step height: in this case, it was found to be 4.79 ± 0.09 Å, in fair agreement with the height of the magnetite unit cell (4.84 Å).

The nature of the objects giving the shoulder-like broadening was then clarified with real-time acquisition of the LEED pattern under dynamic conditions. Figure 13.13b shows the intensities of the Gaussian and the first $Lorentz_{3/2}$-like spot components during formation under cooling in an oxygen atmosphere for two different cooling rates. The broadening in the zero-order diffraction spot and its behavior during cooling under oxidation conditions suggest that the prepared surface is roughened by oxygen-related objects smaller than the lateral resolution in LEEM [13.92]. Such objects can

expose atoms with different coordination and charge states with respect to the ideal surface and therefore influence the catalytic behavior of the system [13.116].

As in the case of LEEM, the collection of LEED patterns over a broad energy range gives access to structural information. The intensity modulation of diffraction peaks can be simulated with full dynamic calculations. The calculation packages available today allow the comparison of calculated and experimental *I–V* curves to find the most probable atomic configuration of the surface. The acquisition of LEED-IV spectra in a LEEM system starts with the collection of a stack of LEED images with variable start voltage. The intensity of a single peak can be extracted with proper fitting of the line profile, as in the case of SPALEED, or with direct integration over a rounded region of interest of the image. In both cases, a background subtraction is required. To perform a reliable dynamic analysis, the data set, calculated as the sum of the energy widths for every inequivalent diffraction spot, must be in the range of thousands of eV [13.83, 117]. The *I–V* curves must then be smoothed by a convolution with a Lorentzian curve of width 1−2 eV to reduce the noise [13.118]. The first successful *I–V* analysis performed with LEEM optics related to the (4×4) superstructure created by surface oxidation of Ag(111) [13.115]. The comparison of experimental *I–V* curves and calculated ones for the best fit model is shown in Fig. 13.13c. In this experiment, the data set was compared with one recorded with a conventional LEED system. It is shown that LEED acquisition with LEEM optics offers a much better signal-to-noise ratio (some faint diffraction spots were visible in LEED/LEEM and undistinguishable from background in conventional LEED) and a larger energy range for every spot.

The combination of LEED and LEEM gives another advantage with respect to conventional LEED optics [13.90, 92]. In the latter one, the illuminated area is very large, of the order of several hundreds of μm. In the case of a surface with rotational domains, some inequivalent spots from different domains of unknown relative abundance can superpose which forces the researcher to average spectra of spots of the same diffraction order and makes the detection of separated spectra impossible. In LEED/LEEM systems the active selection of the illuminated area can solve this problem. The probed region can be inspected with darkfield LEEM using an inequivalent diffraction spot and the relative abundance p of the domains can be calculated. Then, the disentangled *I–V* spectra can be extracted as follows. Assuming that the experimental LEED pattern is a weighted, incoherent superposition of the rotated LEED patterns, in the case of two rotational domains one can write that

$$I_{\text{total}}(\boldsymbol{k}_{xy}, k_z) = (1-p)I_+(\boldsymbol{k}_{xy}, k_z) + pI_-(\boldsymbol{k}_{xy}, k_z) \,,$$

where $I_+(\boldsymbol{k})$ and $I_-(\boldsymbol{k})$ are the intensity of two inequivalent spots of the same order, produced by two domains with abundance $(1-p)$ and p, respectively. The symmetry condition between rotational domains imposes an equivalency between same-order spots. In the case of two domains with 180° symmetry,

$$I_+(\boldsymbol{k}_{xy}, k_z) = I_-(-\boldsymbol{k}_{xy}, k_z) \,.$$

As a consequence, one can separate the two contributions

$$I_+(\boldsymbol{k}_{xy}, k_z) = \frac{1-p}{1-2p} I_{\text{total}}(\boldsymbol{k}_{xy}, k_z) - \frac{p}{1-2p} I_{\text{total}}(-\boldsymbol{k}_{xy}, k_z) \,.$$

With this method, *I–V* spectra of inequivalent spots become accessible, thus improving the data set quality and the reliability of its dynamic analysis.

13.2.5 Spectroscopy Mode

μ-EELS

If the LEEM apparatus is equipped with an energy filter, its dispersive plane can be displayed on the detector and spectroscopy over a selected area can be performed. The energy spectrum of reflected low-energy electrons presents a very intense peak of elastically scattered electrons, a weaker tail due to inelastic events and the secondary yield. In a region close to the elastic peak, one can perform electron energy loss spectroscopy from a micrometer-sized area (μ-EELS) and detect the electrons that interact with the specimen via creation of plasmons and phonons, in the same fashion as Fig. 13.11b. Although the direct measurement of the dispersive plane offers a better energy resolution and signal-to-noise ratio than the spectrum extrapolation from EELM images, the performance is still too low compared to a dedicated EELS apparatus [13.106, 107]. Other loss features at higher energies, such as ionization edges of core-level electrons, are poorly visible from an apparatus optimized for low-energy electrons. For these reasons, the spectroscopy mode in a LEEM system is used marginally and only as a complement to other investigation techniques. Its counterpart with emitted electrons is much more scientifically valuable, therefore a more complete technical review of the mode can be found in Sect. 13.3.5.

13.3 Photoemission Electron Microscopy

PEEM is equipped with a photon source that illuminates the specimen with ultraviolet and x-ray photons. Electrons emitted via photoelectric effect are collected by the cathode immersion lens and used as information carriers. The image formed on the detector can be acquired in real time as in LEEM, but the acquisition time of a single frame can vary considerably as a consequence of the electron beam intensity: while video-rate is still possible with secondary electrons for intermediate magnification, the collection of a single XPEEM image with core-level electrons requires minutes. The nature of image contrast in PEEM is different from the case of LEEM and is governed mainly by the physics behind the photoemission process and the chemical state of the probed matter. Here only a general discussion will be presented, followed by a more detailed examination of space-charge phenomena that affect PEEM with pulsed light sources.

13.3.1 Basic Image Contrast

The main difference in image formation between PEEM and LEEM is the electron coherence. The photoemitted electrons are in general incoherent in time and space, although for delocalized valence-band electrons some coherence can be seen in reciprocal space. As a consequence, the intensity distribution of the image is the convolution of the intensities of the phase object and the CTF (while in LEEM, i.e., under coherent conditions, the intensity is the square modulus of the convolution) [13.88]. Following the definitions given in Sects. 13.2.1 and 13.2.2 leads to

$$I(\boldsymbol{R}) = \left|\psi_{\mathrm{obj}}(\boldsymbol{R})\right|^2 * \left|T_{\mathrm{inco}}(\boldsymbol{R})\right|^2 \ .$$

The incoherent process modifies the definition of the CTF. In the coherent case, the chromatic damping envelope $\mathcal{E}(\boldsymbol{q}, \Delta E)$ comes from an integration over the weighted contribution of the different energies within the Gaussian energy distribution of the incoming beam. For PEEM, the temporal incoherence imposes a different algebra. *Schramm* et al. [13.88] have modeled the square modulus of the PSF $|T_{\mathrm{inco}}(\boldsymbol{R})|^2$ as the Fourier transform of the square modulus of the CTF for the monochromatic case weighted over the energy distribution $N(E)$,

$$\left|T_{\mathrm{inco}}(\boldsymbol{R})\right|^2 = \mathcal{F}^{-1}\left[\int_{-\infty}^{\infty} \left|H_{\mathrm{mono}}(\boldsymbol{q}, E)\right|^2 N(E)\mathrm{d}E\right] \ .$$

The electron incoherence implies that only amplitude objects give contrast: in PEEM phase objects like atomic steps and other morphologic features are generally invisible. Figure 13.14a reports one of the first images taken in 1934 with an improved version of Brüche's first PEEM [13.119, 120] and shows a polycrystalline Pt foil annealed at high temperature. The contrast is given by the work function difference among the facets and the grain boundaries. The lateral resolution for amplitude objects depends on the kinetic energy of the electrons and their energy and angular distribution. In UVPEEM, a standard Hg short-arc lamp induces photoemission of valence band electrons with a $\cos\theta$ angular distribution over an energy window ΔE larger than 1 eV. In this case, it has been calculated that the best lateral resolution should be about 7 nm for noncorrected instruments and less than 4 nm for the aberration-corrected case [13.88]. Similar values can be expected also in energy-filtered XPEEM

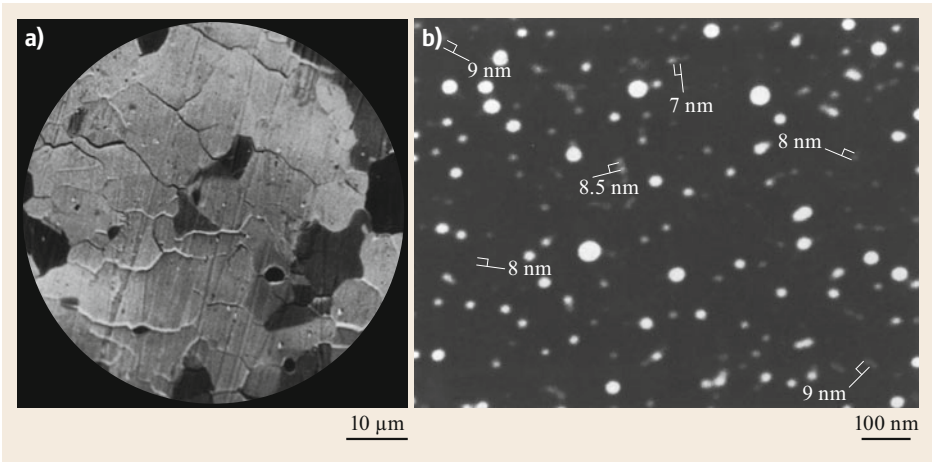

Fig. 13.14
(a) Brüche's PEEM image of a polycrystalline Pt foil after annealing at high temperature (Reproduced from [13.119]). **(b)** PEEM image of colloidal silver demonstrating 7-nm resolution (Reproduced from [13.33] with permission, copyright 1992 Elsevier)

for low start voltages [13.49], while for higher take-off energies the performance gets worse. Such limits were partially reached when PEEM systems with UHV technology were made available. *Gertrude Rempfer* and coworkers demonstrated in the late 1980s a lateral resolution of 7 nm with a nonaberration-corrected UVPEEM [13.33]. Figure 13.14b shows a photoelectron micrograph of colloidal silver particles taken with her instrument. Aberration-corrected instruments lowered the limit for UVPEEM to about 5 nm.

13.3.2 Space-Charge Effects

The lateral resolution in XPEEM is a particular case that deserves a dedicated discussion. The use of monochromatic synchrotron radiation to excite core-level electrons and employ them for imaging has brought huge advantages in terms of flux and versatility, but its pulsed time structure has a worsening effect on both lateral and energy resolution. When a pulsed light beam illuminates the sample, the photoemitted electrons are packed in a small volume. During the flight the cloud density is such that electrons experience reciprocal Coulomb repulsion, thus degrading the transported information [13.121]. This effect, called space charge, has been broadly studied for electron sources and influences both the energy distribution (Börsch effect [13.122]) and the trajectory displacement (Löffer effect [13.123]). Fewer studies addressed the problem in x-ray photoelectron spectroscopy (XPS) [13.124] and specifically in PEEM, not only using synchrotron radiation [13.62, 82] but also fs-laser [13.75, 125].

In the specific case of synchrotron radiation, the photon beam used for XPEEM delivers typically $\approx 10^{13}$ photons/s of variable energy on a small area of a few tens of μm^2. The photon flux is not constant in time, but is organized in pulses. Every pulse has a duration of a few tens of ps and hosts about 20 000 photons. The number of photoelectrons emitted during a single pulse depends on the total photoionization quantum yield: in the case of photoemission from transition metals, this can be estimated as about 400–600 electrons. However, just a few of them are core-level electrons used directly in XPEEM, while the overwhelming majority ($\approx 97\%$) are secondary electrons emitted by inelastic events and filtered away in a second moment by the energy analyzer. In order to understand the magnitude of the space-charge effect, *Locatelli* et al. [13.82] showed LEEM and XPEEM images of the same surface at different photon flux. In LEEM the continuous flow of incident electrons ensures a photocurrent density three orders of magnitude lower than the one in XPEEM, producing a space-charge free image. The latter was then compared to secondary electron ($E_0 = 4$ eV) XPEEM images acquired with the same alignment and configuration of the microscope, but for different photon fluxes (Fig. 13.15a). The lateral resolution in secondary XPEEM increases linearly with the photon flux, from 35 nm with 2.0×10^{12} photons/s to 180 nm with 5.5×10^{13} photons/s. Such degradation is visible also in imaging with core-level electrons. Figure 13.15b shows LEEM and XPEEM images of the same surface, using backscattered electrons and W $4f_{7/2}$ core-level electrons at a kinetic energy of 147 eV, respectively. Again, the XPEEM image blurs as the photon flux rises. The lateral resolution ranges from 31 nm with 2.0×10^{12} photons/s to 82 nm with 5.9×10^{13} photons/s, a degradation smaller than the case of secondary PEEM. An analogous effect can be seen on the energy resolution. *Locatelli* et al. reported a broadening of the Fermi level on a Au(100)-hex surface in a series of spectroscopy measurements with increasing photon flux. At high fluences, the broadening induced by the space-charge effect dominated over the contribution of the energy analyzer.

Space-charge effects occur also when PEEM is performed with a femtosecond laser. *Nakagawa* et al. [13.75] proved that the laser light from a Ti:sapphire laser with pulses of 100 fs produces blurred PEEM images with worse resolution than using a non-pulsed, continuous wave (CW) laser. Figure 13.15c shows images of the same surface acquired with photons of energy 3.1 eV and increasing incident laser power, from 0.2 to 7.8 mW. In this case, the photon flux is much higher than the one with synchrotron light, 8×10^{10} photons per pulse. Again, the lateral resolution is inversely proportional to the laser power, forcing the power output to be greatly reduced and the integration time to be increased to obtain good lateral resolution. Similar results were found by *Buckanie* et al. [13.125] using a Ti:sapphire laser with comparable pulse length and lower photon flux. Such evidence demonstrates how space-charge effects are the biggest restriction for the implementation of pump-probe experiments in PEEM, forcing users to work at low power output, with high repetition rates and long acquisition times.

In order to overcome the resolution limitation induced by space-charge effects, it is important to understand in more detail the evolution of the electron beam from emission to detection. From observation, it is clear that the space-charge effect is determined by the number of photons per time per emitting surface. X-ray photoemission with pulsed light produces a large majority of low-energy secondary photoelectrons and a small amount of core-level electrons with high energy, all taking off from the sample surface in a time range equal to the pulse length. Then, the high volt-

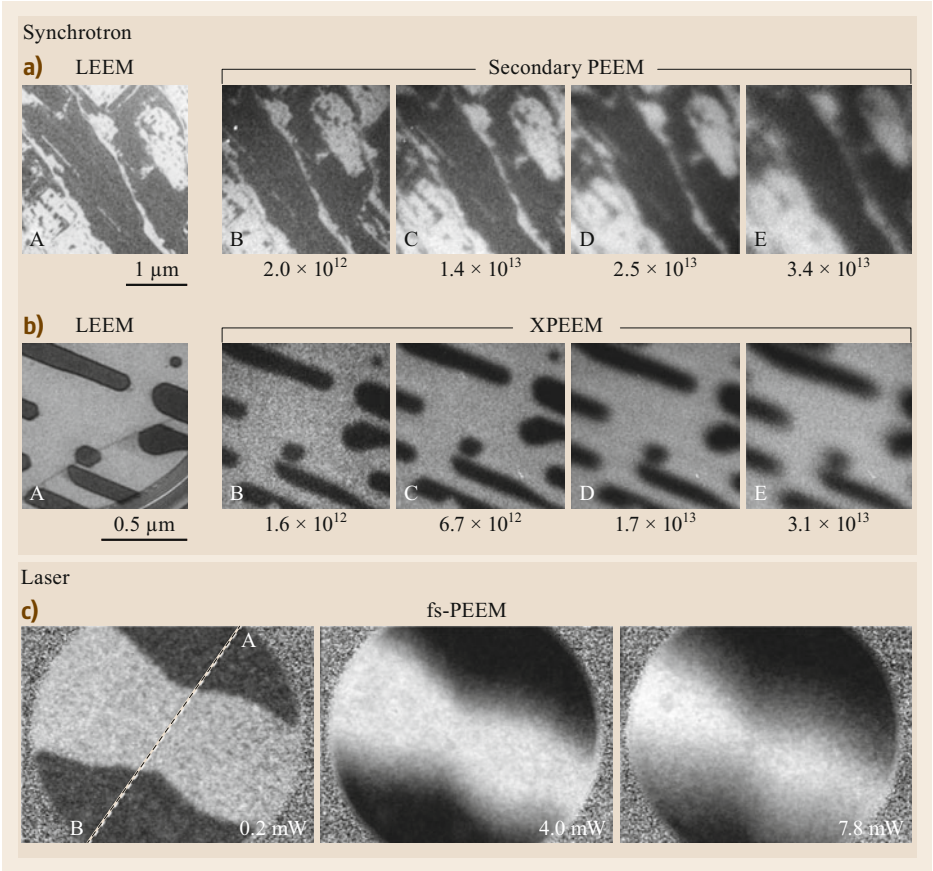

Fig. 13.15 **(a)** LEEM and secondary XPEEM images of 1-ML-thick Au islands on Ir(001). $E_0 = 4\,\text{eV}$. **(b)** LEEM and W $4f_{7/2}$ XPEEM images of thick Fe islands on W(110). $E_0 = 147\,\text{eV}$. Both series of XPEEM images illustrate the degradation of the microscope lateral resolution with increasing photon flux, which is indicated below each image (in photons/s). Photon energy: 182 eV. The operating conditions of the microscope were the same in LEEM and XPEEM (Reproduced from [13.82] with permission, copyright 2010 Elsevier). **(c)** Magnetic circular dichroism fs-PEEM images at increasing laser power of 12 ML Ni deposited on Cu(001) and covered by Cs to reduce the work function. The photon source was a femtosecond laser with a photon energy of 3.1 eV. The lateral resolution was evaluated along the A–B cross section (Reproduced from [13.75] with permission, copyright 2009 IOP Science)

age between sample and objective lens accelerates the electron cloud. The lens system of the microscope induces several crossovers of the electron beam along the path, i.e., where the diffraction and image planes are placed. The first crossover is located in the back-focal plane of the objective lens, while the second is the first intermediate image plane. The magnification induced by the objective lens implies that the lateral size of the crossovers is larger than the initial size of the electron cloud at takeoff. Therefore, no special point with significantly large space-charge density may cause local image blurring, i.e., the blurring occurs along the entire electron path. Moreover, simple kinematic calculations show that the strong overlap between secondary and core-level electrons within one single pulse decays with time due to their different flight speeds. For the SMART microscope, core-level electrons with a takeoff energy of 100 eV are separated from the secondary electron bunch after 70 cm of flight. Behind this point the electron–electron interaction can be neglected for XPEEM measurements. The best strategy to reduce space-charge blurring is then to remove non-necessary electrons as soon as possible along the electron path. In particular, *Schmidt* et al. demonstrated that the insertion of a small field-limiting aperture that cuts away electrons emitted outside the field of view reduces the electron beam intensity behind that point and improves the lateral resolution. This, together with accurate photon flux reduction, led to a demonstrated lateral resolution of 18 nm in XPEEM [13.62]. This

limit is still far from the analogue result in LEEM, but there are reasons to think that a future, dedicated instrument could bridge the gap, at least partially. In particular, such an instrument should be equipped with apertures at the backfocal plane in order to cut non-necessary electrons with different emission angles, and at the first dispersive plane inside the beam separator, to roughly filter away secondary electrons. Highly efficient detectors and improved illumination optics would also help to obtain good quality images with lower photon flux. These measures to reduce the space-charge effect will result in higher resolution.

13.3.3 Imaging Mode

PEEM and XPEEM

The imaging mode with photoemitted electrons displays a magnified real-space image of the probed surface. Such an image contains valuable information on the physical and chemical state of the specimen. The contrast mechanism in PEEM has already been discussed: in the case of low-energy photons, areas can emit a different number of electrons as a function of the local work function and of the local density of states of the valence band. In the case of energy-filtered XPEEM with core-level electrons, the amplitude contrast can also be given, in first approximation, by the relative local abundance of the particular element. The photon energy is often selected in order to maximize the image intensity, in agreement with the atomic cross section of the selected emission line and the brilliance of the photon source. The resulting kinetic energy of the photoemitted electrons typically ranges between 50 and 200 eV, so that the small probing depth due to the IMFP influences the contrast. Figure 13.16 shows a direct example of XPEEM images with chemical contrast. In this case, an Ir(100) surface is partially covered by single and multilayer Gr [13.126]. XPEEM images using Ir $4f_{7/2}$ photoemitted electrons (Fig. 13.16a) shows areas with different intensity. The attenuation of the signal is due to the screening from Gr layers of different thickness. This is confirmed by XPEEM images taken with C 1s electrons (Fig. 13.16b), where the intensity is proportional to the Gr thickness.

The screening effect can be evaluated quantitatively by changing the start voltage and extracting the I–V curve, with the same procedure seen for LEEM. In this case, the collected intensity curve is the local spectro-

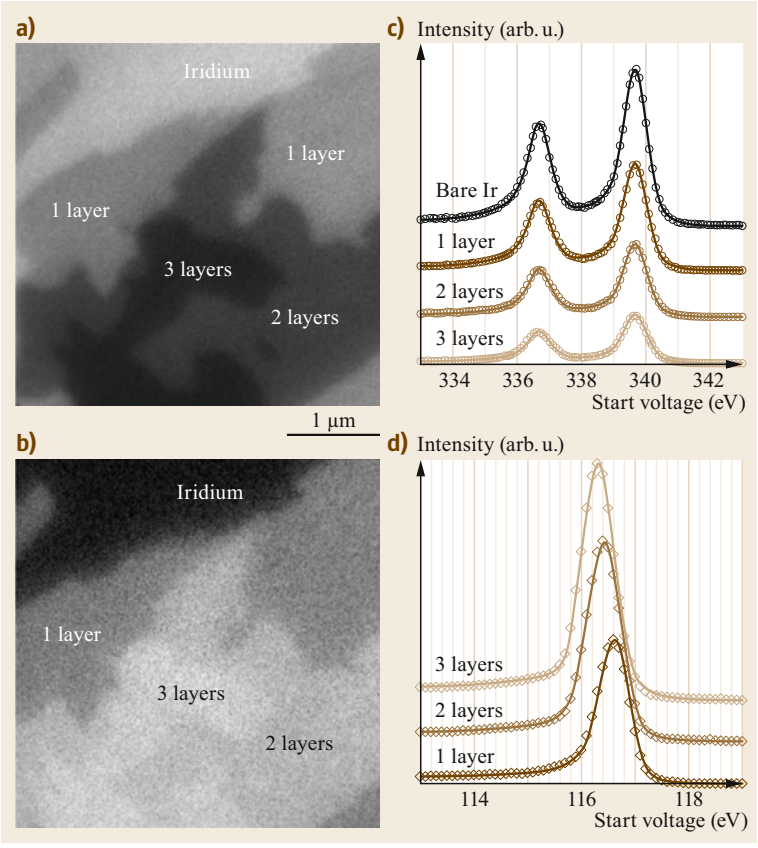

Fig. 13.16 **(a)** XPEEM Ir $4f_{7/2}$ image of a multithickness Gr island. The bare iridium surface is visible on the *top*; **(b)** XPEEM C 1s image of the same surface region; **(c)** Ir 4f and **(d)** C 1s XPS spectra measured in the regions indicated by the labels. The start voltage corresponds to the kinetic energy of the photoemitted electrons. A photon energy of 400 eV was used in the experiment (Reproduced from [13.126] with permission, copyright 2014 Elsevier)

scopic photoemission peak, i.e., a stack of XPEEM images gives access to local XPS spectra. Figure 13.16c,d displays, respectively, the Ir 4f and C 1s core-level emission spectra, obtained by integration over selected regions of interest over a stack of XPEEM images at different start voltages. The intensity drop in the Ir 4f photoemission line follows the exponential damping factor $e^{-d/\lambda_{gr}(E_0)}$, where d is the layer separation and $\lambda_{gr}(E_0)$ is the kinetic-energy-dependent effective attenuation length [13.127]. The intensity growth of the C 1s core-level shows a similar behavior, although it does not increase linearly with thickness. This deviation is given by the screen effect of the outermost Gr layers that diffract the photoelectrons emitted from buried C atoms. This example demonstrates how the intensity evaluation of XPEEM imaging provides an alternative method of assigning thin film thickness.

Brightfield and Darkfield PEEM

The ordinary microscope setup in PEEM includes the insertion of a contrast aperture to limit the acceptance angle in order to reduce spherical aberration and enhance contrast and resolution. Usually, the aperture selects only electrons with normal emission, i.e., limits the diffraction pattern to a neighborhood of the Γ point of the FBZ. As in the case of LEEM, it would be convenient to build PEEM images with electrons coming from other regions of the FBZ [13.129, 130]. The methods for implementing darkfield measurement have already been reviewed in Sect. 13.2.3, *Brightfield and Darkfield LEEM* and schematized in Fig. 13.8. In the case of emitted electrons, only the first two are available, i.e., (i) to position the contrast aperture around the desired k-point of the reciprocal space and (ii) to incline the sample tilt by a certain angle. In addition, it is possible to deflect the emitted beam after the objective lens. Among the three, the second offers the best advantages in terms of PEEM image quality, since it is the one that lets the electrons travel along the optical axis. It should be remarked that the required tilt inclination is reduced by the change of coordinates due to the accelerating field of the cathode immersion lens. It is sufficient to incline the tilt angle by less than 2° to obtain a consistent shift of the reciprocal image in the backfocal plane of the objective lens and to get to the edge of the FBZ of most materials. The best procedure to select the desired diffraction feature for imaging is to display the backfocal plane and to modify the sample tilt mechanically until the selected point is positioned at the center. Once the contrast aperture is placed, the microscope can be shifted to imaging mode, whereas the intensity is proportional to the local density of states at the selected k-point.

Darkfield PEEM is very powerful tool for probing the local electronic properties of heterogeneous surfaces. For example, it has been employed on Gr grown on Ni(111), a model case for the study of interfacial interactions that can play a key role in tailoring the magnetic [13.131] and chemical [13.132] properties of 2-D materials. In particular, darkfield PEEM has been used to determine the lateral extension of epitaxial and rotated monolayer Gr grown on Ni(111), and to identify particular areas in which the rotated Gr is metallic due to the formation of an interstitial carbide layer [13.128]. Brightfield LEEM image of the system (Fig. 13.17a) reveals the presence of three coexisting phases with different gray levels. Characteristic I–V reflectivity curve and μ-LEED measurements (not shown here) assigned the brighter area in the upper right side to epitaxial Gr (labeled EG), while the neutral gray area and the dark gray patches are rotated Gr (labeled RG). Local XPS measurement on the C 1s core-level performed with the method addressed in the previous Section proved that the dark patches are small areas in which the monolayer Gr rests upon a Ni-carbidic interface layer (labeled RGC) [13.133]. Darkfield PEEM was then performed with electrons photoemitted from Gr's π-band. When the reciprocal space K-point of the epitaxial Gr is selected, only the upper right area becomes bright (Fig. 13.17b). When the equivalent point of the rotated Gr is used, the contrast shows a dependence on the selected start voltage. The RGC phase

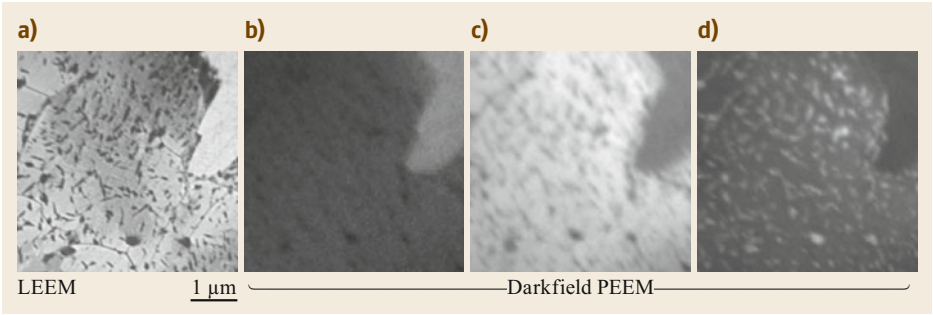

Fig. 13.17 **(a)** LEEM and **(b–d)** darkfield PEEM of: **(b)** EG on Ni(111); **(c)** RG flakes grown on Ni(111); **(d)** RGC patches on a Ni-carbide interstitial layer (Reproduced from [13.128])

exhibits a high density of states at a binding energy of 0.2 eV (Fig. 13.17c), while the RG phase shows the same behavior only at 2.2 eV (Fig. 13.17d; [13.134]). This demonstrated that the π-band of RGC Gr has the Dirac point very close to the Fermi energy, i.e., shows an almost metallic state, while in EG and RG it undergoes a severe hybridization with the substrate states. This result, together with the angular-resolved photoelectron spectroscopy measurement, demonstrated that the presence of the interstitial carbide layer decoupled the monolayer Gr from the substrate.

XAS–PEEM and Magnetic PEEM Imaging

It has been shown that when x-rays illuminate a sample, the displayed intensity of slow secondary electrons exceeds by orders of magnitude the one of photoemitted electrons. It is therefore convenient to use them for imaging, enabling even video-rate acquisition. Moreover, imaging with secondary electrons is particularly useful in the presence of tunable x-ray sources such as synchrotron beamlines. Direct secondary PEEM imaging during photon energy scans reveals intensity variations due to the x-ray absorption process, i.e., the characteristic curve for a selected region of interest corresponds to the local x-ray absorption spectrum (XAS) [13.135, 136]. Compared to XPS, the XAS has a bigger signal-to-noise ratio and uses electrons with a larger IMFP, thus enabling a larger probing depth. Moreover, it can be performed even without active energy filtering, as the photoemitted electrons give a negligible contribution to the overall intensity. The possibility to select a desired photon polarization also gives access to magnetic characterization of materials [13.102]. In the case of circular polarized light, one can use the x-ray magnetic circular dichroism (XMCD) to obtain magnetic contrast in PEEM. In XMCD the angular momentum of circular polarized light is used to impose selection rules over the photon absorption process [13.137]. In ferromagnetic materials, the valence and the conduction band are split in two electron populations, a majority with spin parallel to the magnetization vector and a minority with spin antiparallel. In the photon absorption process, Fermi's Golden Rule imposes that the transition probability of an electron from the initial core-level to an unoccupied state depends on their density of states. Therefore, the different final density of unoccupied states in the majority and minority population determines two distinct absorption probabilities for left and right circular polarized light. The magnetic dichroism is defined by convention as the intensity difference between the two absorption spectra, $I_{\mathrm{XMCD}} = I_{\uparrow\downarrow} - I_{\uparrow\uparrow}$ and is directly proportional to the scalar product between the magnetic moment of the sample and the photon polarization vector. XMCD can be performed in PEEM by taking two images with opposed circular polarization at the absorption photon energy and subtracting one from the other, thus extracting the exchange asymmetry image, as in the case of SPLEEM,

$$I_{\mathrm{XMCD}} = \frac{I_{\uparrow\downarrow} - I_{\uparrow\uparrow}}{I_{\uparrow\downarrow} + I_{\uparrow\uparrow}} \,.$$

The XAS-PEEM imaging process is illustrated in Fig. 13.18a, where Fe nanowires on a W(110) surface

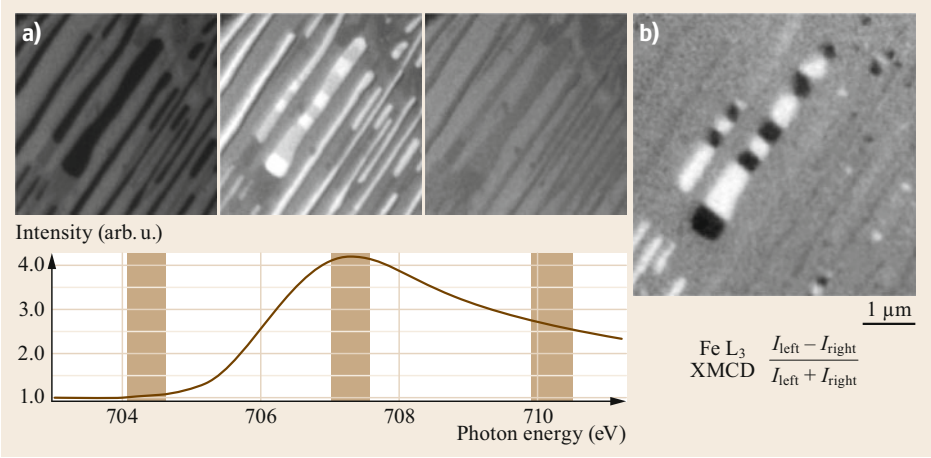

Fig. 13.18 **(a)** Illustration of imaging spectroscopy in XAS mode. Fe nanowires on W(110) appear dark on the *left panel* at a photon energy of 704.5 eV. At the Fe L_3 threshold, the wires become much brighter (*middle panel*). The XAS spectrum *below* is extracted from the largest nanowire in the center. **(b)** Illustration of XMCD-PEEM imaging. The photon energy is tuned to the L_3 maximum. The field of view is 5 µm. The start voltage is 3 eV in order to collect secondary electrons. Within the image plane, the x-ray direction is perpendicular to the nanowire axis (Reproduced from [13.44])

are displayed [13.44]. When the photon energy is set to be off-resonance (left), the contrast is given simply by the different secondary yield. Once the photon energy is set to the Fe absorption L_3 edge (center), the nanowires become brighter whereas the clean W(110) surface in between shows no change. The contrast reduces again for higher, above-resonance photon energies (right), although it is changed also as the new Fe $2p_{3/2}$ photoemission channel enhances the Fe secondary yield. The entire absorption spectrum of an individual nanowire (below) can be extracted from local integration over a stack of PEEM images at different photon energy. Then, XMCD imaging is obtained by tuning the photon energy to the Fe L_3 adsorption edge and taking the difference between two secondary PEEM images with opposed circular polarization (Fig. 13.18b). The wires with magnetization perpendicular to the polarization direction appear gray as the scalar product reduces the XMCD signal to zero. The black and white regions in the central wires are dipolar domains with magnetization parallel and antiparallel to the beam direction, respectively. Note that the strong magnetic contrast in the case of highly magnetic materials is visible even at the single XAS image acquired with one circular polarization. The most advanced PEEM systems are then capable of acquiring magnetic images at video rate, thus enabling dynamic studies of the magnetic domain evolution in nonequilibrium conditions.

In particular samples, magnetic imaging can also be performed using x-ray magnetic linear dichroism (XMLD). The sum rules are similar to those for XMCD [13.102], so the technical implementation mimics the one already discussed. Its main application field is the study of antiferromagnetic materials and their interfaces with ferromagnetic materials, as well as multiferroics. In conclusion, it should be noted that in a synchrotron beamline equipped with insertion devices, the polarization vector could be varied only in the plane perpendicular to the photon beam propagation direction. Therefore, XMCD-XMLD contrast can be achieved only for selected geometries. PEEM systems with perpendicular illumination can characterize only out-of-plane magnetization states, while grazing photon incidence gives its best with in-plane states.

13.3.4 Diffraction Mode

μ-ARPES and μ-XPD

As in the case of μ-LEED, the diffraction operation mode of a PEEM system gives access to the angular distribution of energy-filtered photoemitted electrons. The convenient placement of a field-limiting aperture on an intermediate image plane selects a probed region down to 1 μm in size. ARPES is one of the most important methods to study the band structure of solids [13.138, 139]. The direct display of the entire angular spectrum in a single image gives PEEM systems the possibility to acquire ARPES spectra over a large energy range in a very short amount of time without any mechanical movement of the sample. The same operation mode is then capable of detecting XPD spectra, when the angular distribution of photoemitted core-level electrons is displayed. Although the energy resolution is not comparable to a dedicated ARPES machine, its fast acquisition and the possibility to conjugate it with microscopy measurement makes PEEM systems ideal for studies on dynamic and/or heterogeneous systems [13.140].

ARPES spectra are usually collected at relatively low photon energy. Typical photon sources are lasers under high harmonic generation (the fourth harmonic of a Ti:sapphire laser delivers 6 eV photons), He discharging lamps (HeI emission line at 21.2 eV) and synchrotrons (10−100 eV). The latter is more indicated to highlight surface states, because of the smaller IMFP of photoemitted electrons. Among others, μ-ARPES has been employed to access the π-band of Gr and to quantify the local doping induced by foreign species and/or interaction with the substrate [13.142]. In particular, the local probing in diffraction mode was crucial to determine the doping level of 2-D heterojunctions created with selected-area low-energy irradiation of a monolayer Gr with N_2^+ ions at room temperature [13.141]. Figure 13.19a shows a LEEM image of the boundary region between irradiated and nonirradiated Gr grown on an Ir(111) surface. The first appears notably darker than the second due to the development of corrugations and defects. Microprobe ARPES measurements were performed separately on the two areas (Fig. 13.19b). The reciprocal space image, taken with photon energy of 40.5 eV and at a binding energy of 0.45 eV, displays a large density of states around the *K*-point due to the Gr band structure, while the background modulation resembles the surface states of the Ir(111) substrate. While in the nonirradiated area the circular feature around the *K*-point corresponds to a slice of the Dirac cone, the irradiated area showed no band splitting at this point. The entire band structure can be depicted if one extracts the intensity line profile along a high-symmetry direction over a stack of ARPES images at different kinetic energy. Figure 13.19c shows the momentum distribution curve (MDC) along the normal to Γ-K direction on the *K*-point for both areas. The nonirradiated Gr presented a linear dispersion of the π-band centered at the Dirac point $E_D = 0.08 \pm 0.03$ eV, corresponding to a slight p-doping due to the interaction with the substrate. The irradiated Gr showed a large shift of the Dirac point towards higher binding energies, quantified as $E_D = -0.45 \pm 0.07$ eV. This n-doping was induced by the implantation of N atoms in the C mesh

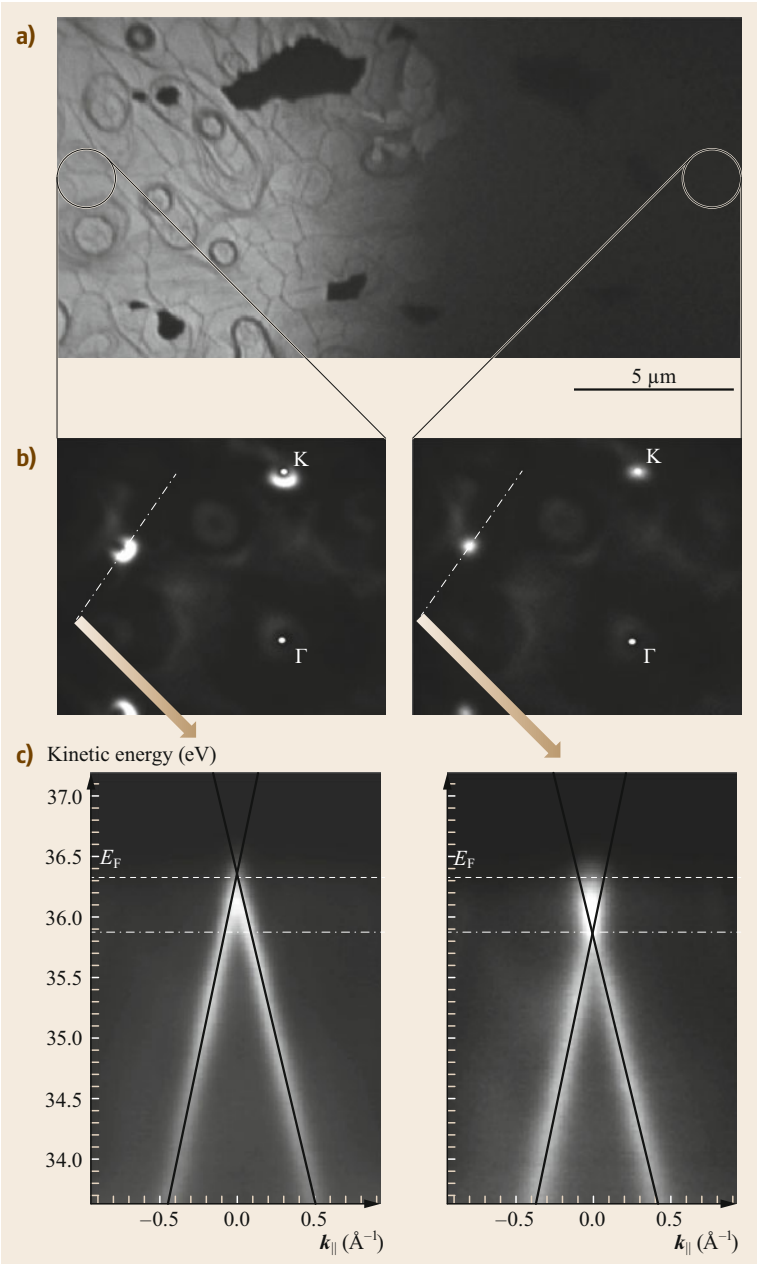

Fig. 13.19 **(a)** LEEM image ($E_0 =$ 7 eV) of the boundary between N_2^+ irradiated (*dark*) and nonirradiated graphene (*bright*) grown on Ir(111). **(b)** μ-ARPES patterns of nonirradiated (*left*) and irradiated (*right*) epitaxial graphene on Ir(111) before annealing. The image was acquired 0.45 eV below the Fermi level. The *dash-dot line* passing through the *K*-point identifies the high symmetry direction perpendicular to ΓK; $h\nu = 40.5$ eV. **(c)** Intensity cut in the plane passing through K along ΓM. The MDCs demonstrate linear dispersion of the π-band close to the Fermi energy E_F (*left*). On the *right*, the same intensity cut for an N_2^+ irradiated sample (3 min at $p_{N_2} = 2 \times 10^{-5}$ mbar, ion current 0.14 μA). The Dirac energy was estimated by fitting the MDC and determining the intersection of the resulting *solid lines*. $E_D = -0.45 \pm 0.07$ eV. The Fermi energy E_F is highlighted by the *dashed line*, while the *dash-dot line* represents the energy of the images in **(b)** (Reproduced from [13.141] with permission, copyright 2015 Wiley-VCH Verlag)

of Gr [13.143]. This example shows clearly how microprobe ARPES in PEEM systems has the power to characterize the electronic states of micrometer-sized regions.

The SPELEEM microscope used in these measurements is an energy-filtered LEEM/PEEM station dedicated to the probe of surfaces with backscattered electrons and synchrotron radiation. The lens setup is designed to guarantee good performance overall, but is not devised for state-of-the-art measurement in every single operational mode. The provided energy resolution, 330 meV, was adequate to accurately detect the shift of the Gr π-band, but was insufficient to determine whether a small band gap has been opened by the substitutional implantation of N [13.142]. PEEM stations specifically designed for high performance in ARPES, e.g., NanoESCA [13.45, 140], forgoes the lateral resolution for a better energy and angular resolution. Such systems are often labeled as momentum microscopes or *k*-PEEM.

13.3.5 Spectroscopy Mode

μ-XPS

The spectroscopy analysis of photoemitted electrons is a major tool in surface science. Since its first development by Kai Siegbahn in 1957, Electron Spectroscopy for Chemical Analysis showed how the accurate measurement of photoemitted core-level electrons allows the retrieval of information on the chemical structure and bonding, the elemental composition, and the surface state of atoms [13.144]. PEEM systems equipped with an energy analyzer are capable of performing photoemission spectroscopy (PES) from a selected area of the sample, much smaller in size than a standard PES machine [13.145]. The probed area can be selected by strong demagnification of the illuminating photon beam and insertion of a field-limiting aperture in the first intermediate image plane. The best PEEM systems available worldwide for PES measurements make use of synchrotron radiation and take advantage of its high brilliance and energy tunability. The access to the dispersive plane in PEEM enables direct measurement of the photoemission spectrum from a localized area and is often called microprobe XPS (μ-XPS).

The standard setup for a PEEM in dispersive mode includes the insertion of the field-limiting aperture at the intermediate image plane and the contrast aperture at the diffraction plane (Fig. 13.3), limiting conveniently the probed area and the acceptance angle. The dispersive plane is then projected on the detector and appears as a thin line with modulated intensity. Electrons with initial kinetic energy equal to the bias value eV_0 are projected at the center. The width of the energy window depends on the final magnification of the dispersive plane and the construction constraints, and can be as wide as $\pm 5\,\mathrm{eV}$. The energy spectrum around the bias value is then revealed with an intensity line profile after opportune background subtraction and response function division. The photoemission spectrum collected in dispersive mode has a better energy resolution and a more favorable signal-to-noise ratio than the one extracted from a stack of XPEEM images over a start voltage range. In several cases the signal-to-noise ratio is sufficiently high to enable fast image acquisition up to video rate. This opens the gates to the microprobing of dynamic processes in real time, such as catalytic reactions, thin film growth, deposition of atoms and molecules on surfaces, and testing in changing conditions of temperature and pressure. The data quality is well visible in the XPS data measured for the heterogeneous system already presented in Sect. 13.3.4. In Fig. 13.20a,b N 1s and C 1s core-level photoemission spectra are depicted, respectively, of a monolayer Gr grown on Ir(111) and locally irradiated with low-energy N_2^+ ions at room temperature [13.141]. It has already been shown with μ-ARPES that the ion irradiation induces a negative doping on the Gr sheet. The XPS N 1s spectrum of the irradiated Gr describes in great detail the film stoichiometry and the atomic arrangement of N atoms in the C mesh. The photoemission peak can be fitted with four Doniach–Šunjic line profiles [13.142, 143, 146], later assigned to pyridine-like, twofold coordinated nitrogen (N1), pyrrole-like, threefold coordinated nitrogen (N2) and substitutional nitrogen (N3 graphitic and N4 secondary graphitic) on the basis of their binding energy. By evaluating the areas of the various components, one can establish the relative abundance of the defects and obtain that 43% of the N is in substitutional configuration. The N 1s spectrum of nonirradiated graphene confirms that no N atoms are detected few μm aside. The analysis of the C 1s spectra shows a notable broadening for the irradiated area at higher binding energies with respect to the main emission line (the only component in the nonirradiated area). This is consistent with the picture of Gr functionalized with N. The irradiated spectrum was fitted considering the different contributions of sp^2 and sp^3 carbon, vacancies and carbon species bonded with nitrogen [13.147, 148]. The evaluation of peak areas allows a vacancy abundance of 1.7% of a ML to be estimated, evidencing the little damage suffered by Gr. Moreover, from the comparison of N 1s and C 1s peak areas one can estimate the overall N coverage. Since both core-levels have the same number of electrons and were measured at the same photon energy ($h\nu = 500\,\mathrm{eV}$), the N/C peak area A ratio can be normalized with the *Yeh* and *Lindau* photoionization cross section σ [13.149] and the energy-dependent transmission of the microscope, which in the case of SPELEEM is proportional to the kinetic energy E_0 of the photoemitted electrons. In the case of coplanar species, no IMFP correction is needed (as in Sect. 13.3.3), therefore the nitrogen abundance is equal to

$$\theta_\mathrm{N} = \frac{A_\mathrm{N1s}}{A_\mathrm{C1s}} \frac{\sigma_\mathrm{C1s}}{\sigma_\mathrm{N1s}} \frac{E_0^\mathrm{N1s}}{E_0^\mathrm{C1s}} \,.$$

The stability test of locally implanted nitrogen took full advantage of the real-time capability of μ-XPS. Annealing in UHV up to a temperature of 800 °C followed probing the N 1s photoemission line every 2 s. The intensity of the various components, as determined in a fit, is presented in Fig. 13.20c. As can be seen, both N2 and N4 components decrease steadily with increasing temperature, reaching negligible intensity at high temperature. The N1 component, associated with in-

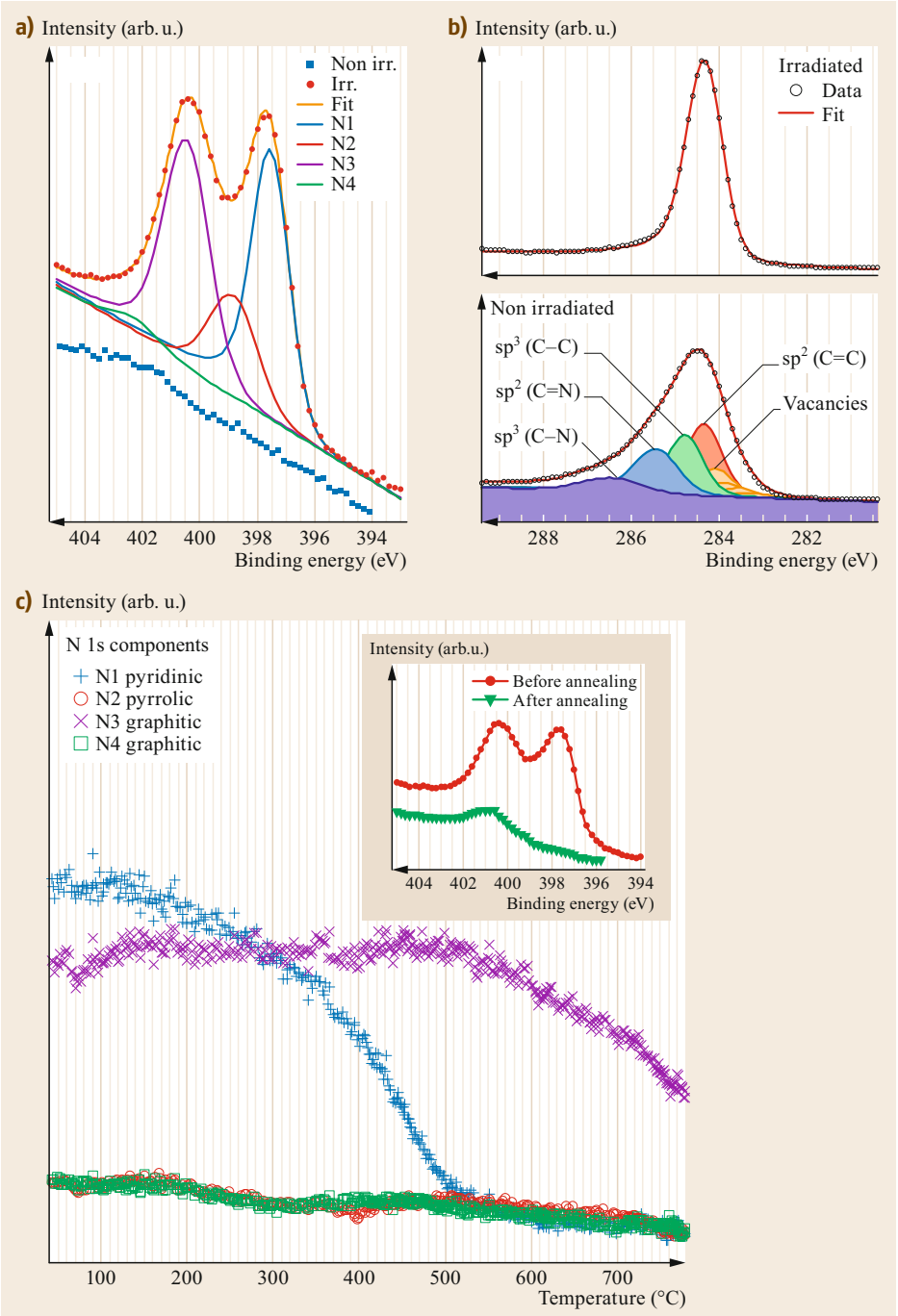

Fig. 13.20 **(a)** N 1s spectra and **(b)** C 1s spectra obtained from the nonirradiated and N_2^+ irradiated graphene on Ir(111). The best fit to the experimental data is also shown: the simulated curve for the irradiated Gr is shown as the sum of different components, each with a Doniach–Šunjic line profile. **(c)** Evolution of the intensity of the N 1s components, N1–N4, plotted as a function of the annealing temperature. In the *inset* the N 1s spectra of ion-irradiated Gr before and after annealing at 800 °C are compared; $h\nu = 500$ eV (Reproduced from [13.141] with permission, copyright 2014 Wiley-VCH Verlag)

tercalated, pyridine-like nitrogen, decreases moderately up to 430 °C and suddenly decays above this temperature. The N3 component, related to graphitic nitrogen, remains constant up to 500 °C and decays moderately with annealing temperature. After annealing, the overall nitrogen coverage decreased from 0.07 to 0.04 ML. The real-time μ-XPS highlighted the different evolution of each defect species during annealing, giving highly valuable information on the stability of doping level for annealed heterostructures embedded in a single Gr sheet.

The dispersion mode can probe photoemitted electrons at any given start voltage. Therefore, it is suitable to probe not only core-level electrons, but also valence band electrons and even secondary electrons. It should be noted that the size of the contrast aperture determines the angular acceptance, i.e., the probed region in the reciprocal space. Usually the neighborhood of Γ in the FBZ is selected, but one can use the methods introduced for darkfield measurement (Sect. 13.3.3) to filter another region of *k*-space. Very often, core-level XPS measurement is combined with valence band measurement up to the Fermi edge, in order to use it as reference for zero binding energy. The Fermi edge of conductive surfaces at low temperature is frequently used to test on the go the energy resolution of the instrument. The edge of the secondary yield can also be probed to measure the work function differences among separate areas.

13.4 Perspectives

More than 80 years after the first PEEM image, cathode lens microscopy continues to be one of the most used techniques in surface science. The ability to conjugate microscopy, spectroscopy, and diffraction in a single instrument is the key to its successful application in several fields. The increasingly high level of sophistication led to the construction of systems with many specializations, such as magnetic imaging, pump-probe photoemission, synchrotron endstations, momentum microscopes, and more. The growing user community shares its findings and perspectives in many dedicated workshops; among others, the LEEM-PEEM biennial gathering reviews the status of LEEM, PEEM, SPLEEM, XPEEM and related techniques, promotes applications of cathode lens microscopy to a broader audience and highlights the most recent scientific advances and instrumental developments.

After the advent of synchrotron radiation, spin-polarized electron guns and pulsed laser in the attosecond domain, cathode lens microscopy can be defined as a mature and well-established technique. In more recent years, much of the technical effort has been spent addressing three main problems, here reviewed briefly:

- *Reduction of space-charge effect:* its inevitability imposes the creation of a system expressly designed to circumvent it. Such apparatus must have particular filters in the backfocal plane, in the first intermediate image plane and in the first dispersive plane, all of them placed very close to the objective lens. Moreover, it must be equipped with a state-of-the-art detection system. The new generation of SMART microscope, called SMART 2, is currently (2017) under construction and implements most of the strategies discussed to give full advantage of aberration correction in XPEEM. This development is needed for advances in pump-probe experiments.
- *Resolution improvement:* in principle, aberration correction via an electrostatic mirror pushes LEEM towards the ultimate resolution, i.e., the diffraction limit. Several groups, with particular mention of Ruud Tromp's team, have investigated theoretical and experimental aspects of aberration correction. They discovered that the correct state is intrinsically unstable due to the performance of electronics. The creation of more stable devices and a dynamic feedback system that prolongs the lifetime of the correct state remains a serious challenge.
- *Pressure gap:* in a standard cathode lens microscope, the high electrostatic field of the accelerating stage limits the pressure in the main chamber so that it is lower than $\approx 10^{-5}$ mbar. The direct observation of surfaces under near-ambient pressures is highly desirable, e.g., in the field of catalysis. In principle, the implementation of high-pressure cathode lens microscopy can take profit from the technical development of near-ambient pressure XPS systems, which have been available since the late 2000s. These systems are equipped with a pressure cell that maintains high pressure in a small volume in front of the sample and lets photoemitted electrons escape through nozzles and membranes towards the detector placed under UHV conditions. The design of a high-pressure cell that works with the strong electrostatic fields required in cathode lens microscopy is a very difficult task that may require years of research and development. A successful breakthrough in the pressure problem can breathe new life into the cathode lens microscopy user community and ensure a bright future for this technique.

References

13.1 E. Bauer: *Surface Microscopy with Low Energy Electrons* (Springer, New York 2014)

13.2 C.J. Davisson, L.H. Germer: Diffraction of electrons by a crystal of nickel, Phys. Rev. **30**, 705–740 (1927)

13.3 E. Brüche: Elektronenmikroskop, Naturwissenschaften **20**, 49 (1932)

13.4 E. Brüche, H. Johansson: Elektronenoptik und Elektronenmikroskopie, Naturwissenschaften **20**, 353–358 (1932)

13.5 E. Brüche: Elektronenmikroscopische Abbildung mit lichtelektrischen Elektronen, Z. Phys. **86**, 448–450 (1933)

13.6 E. Brüche, O. Scherzer: *Geometrische Elektronenoptik* (Springer, Berlin, Heidelberg 1934)

13.7 W. Henneberg, A. Recknagel: Der chromatische Fehler bei elektronenoptischen Anwendungen, insbesondere beim Bildwandler, Z. Tech. Phys. **16**, 230–235 (1935)

13.8 H. Boersch: Über die primäre and sekundäre Bild im Elektronenmikroskop. I. Eingriffe in das Beugungsbild und ihr Einfluss auf die Abbildung, Ann. Phys. **26**, 631–644 (1936)

13.9 A. Recknagel: Zur Theorie des Elektronenspiegels, Z. Tech. Phys. **17**, 643–645 (1936)

13.10 A. Recknagel: Theorie des elektrisches Elektronenmikroskops für Selbststrahler, Z. Phys. **117**, 689–708 (1941)

13.11 E. Bauer: LEEM and UHV-PEEM: A retrospective, Ultramicroscopy **119**, 18–23 (2012)

13.12 E. Bauer: Electron microscopy. In: *Proc. Fifth Int. Congr. Electron Microsc.*, ed. by S.S.J. Breese (Academic Press, New York 1962) p. D-11

13.13 G. Turner, E. Bauer: Design features of an ultrahigh-vacuum electron microscope, J. Appl. Phys. **35**(10), 3080 (1964)

13.14 O.H. Griffith, G.H. Lesch, G.F. Rempfer, G.B. Birrell, C.A. Burke, D.W. Schlosser, M.H. Mallon, G.B. Lee, R.G. Stafford, P.C. Jost, T.B. Marriot: Photoelectron microscopy: A new approach to mapping organic and biological surfaces, Proc. Nat. Acad. Sci. U.S.A. **69**, 561–565 (1972)

13.15 G. Pfefferkorn, K. Schur: Beiträge zur elektronenmikroskopischen Direktabbildung von Oberflächen. In: *Proc. First Int. Conf. Emiss. Electron Microsc.* (R.A. Remy, Münster 1979) pp. 205–233

13.16 W. Telieps: Ph.D. Thesis, TU Clausthal (1983)

13.17 W. Telieps, E. Bauer: An analytical reflection and emission UHV surface electron microscope, Ultramicroscopy **17**, 57–65 (1985)

13.18 W. Telieps, E. Bauer: The (7×7) ↔ (1×1) phase transition on Si(111), Surf. Sci. **162**, 163–168 (1985)

13.19 B.P. Tonner, G.R. Harp: Photoelectron microscopy with synchrotron radiation, Rev. Sci. Instrum. **59**, 853 (1988)

13.20 H.H. Rotermund, W. Engel, M. Kordesch, G. Ertl: Imaging of spatio-temporal pattern evolution during carbon monoxide oxidation on platinum, Nature **343**, 355–357 (1990)

13.21 T. Schmidt, S. Heun, J. Slezak, J. Diaz, K.C. Prince, G. Lilienkamp, E. Bauer: SPELEEM: Combining LEEM and spectroscopic imaging, Surf. Rev. Lett. **5**, 1287–1296 (1998)

13.22 M.S. Altman, W.F. Chung, C.H. Liu: LEEM phase contrast, Surf. Rev. Lett. **5**, 1129–1141 (1998)

13.23 T. Duden, E. Bauer: A compact electron-spin-polarization manipulator, Rev. Sci. Instrum. **66**, 2861 (1995)

13.24 J. Stöhr, Y. Wu, B.D. Hermsmeier, M.G. Samant, G.R. Harp, S. Koranda, D. Dunham, B.P. Tonner: Element-specific magnetic microscopy with circularly polarized x-rays, Science **259**, 658–661 (1993)

13.25 R. Fink, M.R. Weiss, E. Umbach, D. Preikszas, H. Rose, R. Spehr, P. Hartel, W. Engel, R. Degenhardt, R. Wichtendahl, H. Kuhlenbeck, W. Erlebach, K. Ihmann, R. Schlögl, H.-J. Freund, A.M. Bradshaw, G. Lilienkamp, T. Schmidt, E. Bauer, G. Benner: SMART: A planned ultrahigh-resolution spectromicroscope for BESSY II, J. Electron Spectrosc. Relat. Phenom. **84**, 231–250 (1997)

13.26 R.M. Tromp, J.B. Hannon, A.W. Ellis, W. Wan, A. Berghaus, O. Schaff: A new aberration-corrected, energy-filtered LEEM/PEEM instrument. I. Principles and design, Ultramicroscopy **110**, 852–861 (2010)

13.27 W. Wan, J. Feng, H.A. Padmore, D.S. Robin: Simulation of a mirror corrector for PEEM3, Nucl. Instrum. Methods Phys. Res. A **519**, 222–229 (2004)

13.28 J. Vogel, W. Kuch, M. Bonfim, J. Camarero, Y. Pennec, F. Offi, K. Fukumoto, J. Kirschner, A. Fontaine, S. Pizzini: Time-resolved magnetic domain imaging by x-ray photoemission electron microscopy, Appl. Phys. Lett. **82**, 2299 (2003)

13.29 M. Foerster, J. Prat, V. Massana, N. Gonzalez, A. Fontsere, B. Molas, O. Matilla, E. Pellegrin, L. Aballe: Custom sample environments at the ALBA XPEEM, Ultramicroscopy **171**, 63–69 (2016)

13.30 Elmitec: http://www.elmitec-gmbh.com

13.31 SPECS Surface Nano Analysis: http://www.specs.de

13.32 E. Bauer: The resolution of the low energy electron reflection microscope, Ultramicroscopy **17**, 51–56 (1985)

13.33 G.F. Rempfer, O.H. Griffith: Emission microscopy and related techniques – Resolution in photoelectron microscopy, low-energy electron-microscopy and mirror electron-microscopy, Ultramicroscopy **47**, 35–54 (1992)

13.34 J. Feng, H. Padmore, D.H. Wei, S. Anders, Y. Wu, A. Scholl, D. Robin: Modeling the acceleration field and objective lens for an aberration corrected photoemission electron microscope, Rev. Sci. Instrum. **73**, 1514 (2002)

13.35 C.J. Davisson, C.J. Calbick: Electron lenses, Phys. Rev. **42**, 580 (1932)

13.36 A.B. Pang, T. Müller, M.S. Altman, E. Bauer: Fourier optics of image formation in LEEM, J. Phys. Condens. Matter **21**, 314006 (2009)

13.37 M. Mankos, D. Adler, L. Veneklasen, E. Munro: Electron optics for high throughput low energy electron microscopy, Surf. Sci. **601**, 4733–4741 (2007)

13.38 M. Escher, N. Weber, M. Merkel, C. Ziethen, P. Bernhard, G. Schönhense, S. Schmidt, F. Forster, F. Reinert, B. Krömker, D. Funnemann: Nanoelectron spectroscopy for chemical analysis: A novel energy filter for imaging x-ray photoemission spectroscopy, J. Phys. Condens. Matter **17**, S1329–S1338 (2005)

13.39 G.D. Archard, T. Mulvey: Magnetic deflexion of electron beams without astigmatism, J. Sci. Instrum. **35**, 279–283 (1958)

13.40 V. Kolarik, M. Mankos, L.H. Veneklasen: Close packed prism arrays for electron microscopy, Optik (Stuttg) **87**, 1–12 (1991)

13.41 H. Rose, D. Preikszas: Outline of a versatile corrected LEEM, Optik (Stuttg) **92**, 31–44 (1992)

13.42 R. Wichtendahl, R. Fink, H. Kuhlenbeck, D. Preikszas, H. Rose, R. Spehr, P. Hartel, W. Engel, R. Schlögl, H.-J. Freund, A.M. Bradshaw, G. Lilienkamp, T. Schmidt, E. Bauer, G. Benner, E. Umbach: SMART: An aberration-corrected XPEEM/LEEM with energy filter, Surf. Rev. Lett. **5**, 1249–1256 (1998)

13.43 A. Locatelli, L. Aballe, T.O. Menteş, M. Kiskinova, E. Bauer: Photoemission electron microscopy with chemical sensitivity: SPELEEM methods and applications, Surf. Interface Anal. **38**, 1554–1557 (2006)

13.44 T.O. Menteş, G. Zamborlini, A. Sala, A. Locatelli: Cathode lens spectromicroscopy: Methodology and applications, Beilstein J. Nanotechnol. **5**, 1873–1886 (2014)

13.45 M. Escher, N. Weber, M. Merkel, B. Krömker, D. Funnemann, S. Schmidt, F. Reinert, F. Forster, S. Hüfner, P. Bernhard, C. Ziethen, H.J. Elmers, G. Schönhense: NanoESCA: Imaging UPS and XPS with high energy resolution, J. Electron Spectrosc. Relat. Phenom. **144**, 1179–1182 (2005)

13.46 S. Lanio, H. Rose, D. Krahl: Test and improved design of a corrected imaging magnetic energy filter, Optik (Stuttg) **73**, 56–68 (1986)

13.47 H. Marchetto: Ph.D. Thesis, FU Berlin (2006)

13.48 O. Scherzer: Über einige Fehler von Elektronenlinsen, Z. Phys. **101**, 593–603 (1936)

13.49 T. Schmidt, U. Groh, R. Fink, E. Umbach, O. Schaff, W. Engel, B. Richter, H. Kuhlenbeck, R. Schlögl, H.-J. Freund, A.M. Bradshaw, D. Preikszas, P. Hartel, R. Spehr, H. Rose, G. Lilienkamp, E. Bauer, G. Benner: XPEEM with energy-filtering: Advantages and first results from the smart project, Surf. Rev. Lett. **9**, 223–232 (2002)

13.50 R.M. Tromp: Measuring and correcting aberrations of a cathode objective lens, Ultramicroscopy **111**, 273–281 (2011)

13.51 I. Dietrich, K.H. Herrmann, C. Passow: Proposal for a high-voltage electron microscope with superconducting microwave linear accelerator and superconducting lenses, Optik (Stuttg) **42**, 439–462 (1975)

13.52 M. Hibino, S. Maruse: Correction of the spherical aberration of a magnetic lens with a foil lens, J. Electron Microsc. (Tokyo) **25**, 229–236 (1976)

13.53 M. Haider, S. Uhlemann, E. Schwan, H. Rose, B. Kabius, K. Urban: Electron microscopy image enhanced, Nature **392**, 768–769 (1998)

13.54 O.L. Krivanek, N. Dellby, A.R. Lupini: Towards sub-Å electron beams, Ultramicroscopy **78**, 1–11 (1999)

13.55 G.F. Rempfer, M.S. Mauch: Correction of chromatic aberration with an electron mirror, Optik (Stuttg) **92**, 3–8 (1992)

13.56 H. Rose, D. Preikszas: Time-dependent perturbation formalism for calculating the aberrations of systems with large ray gradients, Nucl. Instrum. Methods Phys. Res. A **363**, 201 (1995)

13.57 P.W. Hawkes: Aberration correction past and present, Philos. Trans. A **367**, 3637–3664 (2009)

13.58 R. Könenkamp, T. Jones, J. Elstner, R. Word, G. Rempfer, T. Dixon, L. Almaraz, W. Skoczylas: Image properties in an aberration-corrected photoemission electron microscope, Phys. Procedia **1**, 505–511 (2008)

13.59 R. Könenkamp, R.C. Word, G.F. Rempfer, T. Dixon, L. Almaraz, T. Jones: 5.4 nm spatial resolution in biological photoemission electron microscopy, Ultramicroscopy **110**, 899–902 (2010)

13.60 T. Schmidt, H. Marchetto, P.L. Lévesque, U. Groh, F. Maier, D. Preikszas, P. Hartel, R. Spehr, G. Lilienkamp, W. Engel, R. Fink, E. Bauer, H. Rose, E. Umbach, H.J. Freund: Double aberration correction in a low-energy electron microscope, Ultramicroscopy **110**, 1358–1361 (2010)

13.61 S.M. Schramm, S.J. van der Molen, R.M. Tromp: Intrinsic instability of aberration-corrected electron microscopes, Phys. Rev. Lett. **109**, 163901 (2012)

13.62 T. Schmidt, A. Sala, H. Marchetto, E. Umbach, H.-J. Freund: First experimental proof for aberration correction in XPEEM: Resolution, transmission enhancement, and limitation by space charge effects, Ultramicroscopy **126**, 23–32 (2013)

13.63 L. Reimer: *Transmission Electron Microscopy* (Springer, Berlin, Heidelberg 1997)

13.64 W.A. Mackie, G.G. Magera: Defined emission area and custom thermal electron sources, J. Vac. Sci. Technol. B **29**, 06F601 (2011)

13.65 R.M. Tromp, M. Mankos, M.C. Reuter, A.W. Ellis, M. Copel: A new low energy electron microscope, Surf. Rev. Lett. **5**, 1189–1197 (1998)

13.66 L.W. Swanson, G.A. Schwind: A review of the cold-field electron cathode, Adv. Imaging Electron Phys. **159**, 63–100 (2009)

13.67 L.W. Swanson, G.A. Schwind: A review of the ZrO/W Schottky cathode. In: *Handbook of Charged Particle Optics*, ed. by J. Orloff (CRC Press, Boca Raton 1997) pp. 77–102

13.68 X. Jin, N. Yamamoto, Y. Nakagawa, A. Mano, T. Kato, M. Tanioku, T. Ujihara, Y. Takeda, S. Okumi, M. Yamamoto, T. Nakanishi, T. Saka, H. Horinaka, T. Kato, T. Yasue, T. Koshikawa: Super-high brightness and high-spin-polarization photocathode, Appl. Phys. Express **1**, 45002 (2008)

13.69 X. Jin, F. Ichihashi, A. Mano, N. Yamamoto, Y. Takeda: Fourfold increase in quantum efficiency in highly spin-polarized transmission-type photocathode, Jpn. J. Appl. Phys. **51**, 108004 (2012)

13.70 X. Jin, S. Matsuba, Y. Honda, T. Miyajima, M. Yamamoto, T. Utiyama, Y. Takeda: Picosecond electron bunches from GaAs/GaAsP strained superlattice photocathode, Ultramicroscopy **130**, 44–48 (2013)

13.71 X. Jin, A. Mano, F. Ichihashi, N. Yamamoto, Y. Takeda: High-performance spin-polarized photocathodes using a GaAs/GaAsP strain-compensated superlattice, Appl. Phys. Express **6**, 15801 (2013)

13.72 L. Wegmann, R. Buhl, H.D. Dannohl, R. Graber, E. Grauer-Carstensen, M. Gribi: Über einige neue Ergebnisse aus der Photoemissions-Elektronenmikroskopie. In: *Ergebnisse der Hochvakuumtechnik und der Physik dünner Schichten*, Vol. II, ed. by M. Auwärter (Wissenschaftliche Verlagsgesellschaft, Stuttgart 1971) pp. 111–130

13.73 G. Massey, M. Jones, J. Johnson: Nonlinear photoemission for viewing guided or evanescent waves, IEEE J. Quantum Electron. **17**, 1035–1041 (1981)

13.74 F.-J. Meyer zu Heringdorf, L.I. Chelaru, S. Möllenbeck, D. Thien, M. Horn-von Hoegen: Femtosecond photoemission microscopy, Surf. Sci. **601**, 4700–4705 (2007)

13.75 T. Nakagawa, K. Watanabe, Y. Matsumoto, T. Yokoyama: Magnetic circular dichroism photoemission electron microscopy using laser and threshold photoemission, J. Phys. Condens. Matter **21**, 314010 (2009)

13.76 T. Nakagawa, T. Yokoyama: Laser induced threshold photoemission magnetic circular dichroism and its application to photoelectron microscope, J. Electron Spectrosc. Relat. Phenom. **185**, 356–364 (2012)

13.77 T. Taniuchi, Y. Kotani, S. Shin: Ultrahigh-spatial-resolution chemical and magnetic imaging by laser-based photoemission electron microscopy, Rev. Sci. Instrum. **86**, 23701 (2015)

13.78 C. Tusche, A. Krasyuk, J. Kirschner: Spin resolved bandstructure imaging with a high resolution momentum microscope, Ultramicroscopy **159**, 520–529 (2015)

13.79 O. Schmidt, M. Bauer, C. Wiemann, R. Porath, M. Scharte, O. Andreyev, G. Schönhense, M. Aeschlimann: Time-resolved two photon photoemission electron microscopy, Appl. Phys. B **74**, 223–227 (2002)

13.80 A. Mikkelsen, J. Schwenke, T. Fordell, G. Luo, K. Klünder, E. Hilner, N. Anttu, A.A. Zakharov, E. Lundgren, J. Mauritsson, J.N. Andersen, H.Q. Xu, A. L'Huillier: Photoemission electron microscopy using extreme ultraviolet attosecond pulse trains, Rev. Sci. Instrum. **80**, 123703 (2009)

13.81 T.O. Menteş, M.A. Niño, A. Locatelli: Spectromicroscopy with low-energy electrons: LEEM and XPEEM studies at the nanoscale, e-J. Surf. Sci. Nanotechnol. **9**, 72–79 (2011)

13.82 A. Locatelli, T.O. Menteş, M.Á. Niño, E. Bauer: Image blur and energy broadening effects in XPEEM, Ultramicroscopy **111**, 1447–1454 (2011)

13.83 M.A. Van Hove, W.H. Weinberg, C.-M. Chan: *Low-Energy Electron Diffraction* (Springer, Berlin, Heidelberg 1986)

13.84 M.S. Altman, W.F. Chung, Z.Q. He, H.C. Poon, S.Y. Tong: Quantum size effect in low energy electron diffraction of thin films, Appl. Surf. Sci. **169–170**, 82–87 (2001)

13.85 W.F. Chung, M.S. Altman: Step contrast in low energy electron microscopy, Ultramicroscopy **74**, 237–246 (1998)

13.86 S.M. Kennedy, N.E. Schofield, D.M. Paganin, D.E. Jesson: Wave optical treatment of surface step contrast in low-energy electron microscopy, Surf. Rev. Lett. **16**, 855–867 (2009)

13.87 R.P. Yu, S.M. Kennedy, D.M. Paganin, D.E. Jesson: Phase retrieval low energy electron microscopy, Micron **41**, 232–238 (2010)

13.88 S.M. Schramm, A.B. Pang, M.S. Altman, R.M. Tromp: A contrast transfer function approach for image calculations in standard and aberration-corrected LEEM and PEEM, Ultramicroscopy **115**, 88–108 (2012)

13.89 A.B. Pang, A. Pavlovska, L. Däweritz, A. Locatelli, E. Bauer, M.S. Altman: LEEM image phase contrast of MnAs stripes, Ultramicroscopy **130**, 7–12 (2013)

13.90 A. Sala: Ph.D. Thesis, FU Berlin (2013)

13.91 P. Sutter, J.T. Sadowski, E. Sutter: Graphene on Pt(111): Growth and substrate interaction, Phys. Rev. B **80**, 1–10 (2009)

13.92 A. Sala, H. Marchetto, Z.H. Qin, S. Shaikhutdinov, T. Schmidt, H.J. Freund: Defects and inhomogeneities in Fe_3O_4(111) thin film growth on Pt(111), Phys. Rev. B **86**, 1–10 (2012)

13.93 W. Weiss, W. Ranke: Surface chemistry and catalysis on well-defined epitaxial iron-oxide layers, Prog. Surf. Sci. **70**, 1–151 (2002)

13.94 F. Genuzio, A. Sala, T. Schmidt, D. Menzel, H.-J. Freund: Interconversion of α-Fe_2O_3 and Fe_3O_4 thin films: Mechanisms, morphology, and evidence for unexpected substrate participation, J. Phys. Chem. C **118**, 29068–29076 (2014)

13.95 S.M. Kennedy, C.X. Zheng, W.X. Tang, D.M. Paganin, D.E. Jesson: Laplacian image contrast in mirror electron microscopy, Proc. R. Soc. A (2010), https://doi.org/10.1098/rspa.2010.0093

13.96 S.M. Kennedy, C.X. Zheng, W.X. Tang, D.M. Paganin, D.E. Jesson: Caustic imaging of gallium droplets using mirror electron microscopy, Ultramicroscopy **111**, 356–363 (2011)

13.97 S.M. Kennedy, D.E. Jesson, D.M. Paganin: Laplacian and caustic imaging theories of MEM work-function contrast, IBM J. Res. Dev. **55**, 3:1–3:8 (2011)

13.98 M.S. Altman, H. Pinkvos, J. Hurst, H. Poppa, G. Marx, E. Bauer: Spin polarized low energy electron microscopy of surface magnetic structure, MRS Proc. **232**, 125 (1991)

13.99 T. Duden, E. Bauer: Spin-polarized low energy electron microscopy of ferromagnetic layers, J. Electron Microsc. (Tokyo) **47**, 379–385 (1998)

13.100 E. Bauer: Spin-polarized low energy electron microscopy. In: *Handbook of Magnetism and Advanced Magnetic Materials*, ed. by H. Kronmüller, S. Parkin, R. Wiesendanger, G. Guntherodt (Wiley, Chichester 2007), https://doi.org/10.1002/9780470022184.hmm308

13.101 N. Rougemaille, A.K. Schmid: Magnetic imaging with spin-polarized low-energy electron microscopy, Eur. Phys. J. Appl. Phys. **50**, 20101 (2010)

13.102 J. Stöhr, H.C. Siegmann: *Magnetism* (Springer, Berlin, Heidelberg 2006)

13.103 E. Bauer, R. Belkhou, S. Cherifi, R. Hertel, S. Heun, A. Locatelli, A. Pavlovska, R. Zdyb, N. Agarwal, H. Wang: Microscopy of mesoscopic ferromagnetic systems with slow electrons, Surf. Interface Anal. **38**, 1622–1627 (2006)

13.104 S. Nappini, I. Píš, T.O. Menteş, A. Sala, M. Cattelan, S. Agnoli, F. Bondino, E. Magnano: Formation of a quasi-free-standing single layer of graphene and hexagonal boron nitride on Pt(111) by a single molecular precursor, Adv. Funct. Mater. **26**, 1120–1126 (2016)

13.105 R.M. Tromp, Y. Fujikawa, J.B. Hannon, A.W. Ellis, A. Berghaus, O. Schaff: A simple energy filter for low energy electron microscopy/photoelectron emission microscopy instruments, J. Phys. Condens. Matter **21**, 314007 (2009)

13.106 H. Ibach, D.L. Mills: *Electron Energy Loss Spectroscopy and Surface Vibrations* (Academic Press, New York 2013)

13.107 L. Vattuone, L. Savio, M. Rocca: High resolution electron energy loss spectroscopy (HREELS): A sensitive and versatile surface tool. In: *Surface Science Techniques*, ed. by G. Bracco, B. Holst (Springer, Berlin, Heidelberg 2013) pp. 499–529

13.108 J. Sun, J.B. Hannon, R.M. Tromp, P. Johari, A.A. Bol, V.B. Shenoy, K. Pohl: Spatially-resolved structure and electronic properties of graphene on polycrystalline Ni, ACS Nano **4**, 7073–7077 (2010)

13.109 A. Politano, A.R. Marino, V. Formoso, D. Farías, R. Miranda, G. Chiarello: Quadratic dispersion and damping processes of π plasmon in monolayer graphene on Pt(111), Plasmonics **7**, 369–376 (2012)

13.110 C.T. Pan, R.R. Nair, U. Bangert, Q. Ramasse, R. Jalil, R. Zan, C.R. Seabourne, A.J. Scott: Nanoscale electron diffraction and plasmon spectroscopy of single- and few-layer boron nitride, Phys. Rev. B **85**, 45440 (2012)

13.111 J. Höcker, T.O. Menteş, A. Sala, A. Locatelli, T. Schmidt, J. Falta, S.D. Senanayake, J.I. Flege: Unraveling the dynamic nanoscale reducibility ($Ce^{4+} \rightarrow Ce^{3+}$) of CeO_x–Ru in hydrogen activation, Adv. Mater. Interfaces **2**, 1500314 (2015)

13.112 J.I. Flege, J. Höcker, B. Kaemena, T.O. Menteş, A. Sala, A. Locatelli, S. Gangopadhyay, J.T. Sadowski, S.D. Senanayake, J. Falta: Growth and characterization of epitaxially stabilized ceria(001) nanostructures on Ru(0001), Nanoscale **8**, 10849 (2016)

13.113 J. Wollschläger, M. Henzler: Defects at the Si(111)/SiO_2 interface investigated with low-energy electron diffraction, Phys. Rev. B **39**, 6052 (1989)

13.114 T. Schmidt: Ph.D. Thesis, University of Hannover (1994)

13.115 R. Reichelt, S. Günther, J. Wintterlin, W. Moritz, L. Aballe, T.O. Menteş: Low energy electron diffraction and low energy electron microscopy microspot I/V analysis of the (4×4)0 structure on Ag(111): Surface oxide or reconstruction?, J. Chem. Phys. **127**, 134706 (2007)

13.116 S. Shaikhutdinov, M. Ritter, X. Wang, H. Over, W. Weiss: Defect structures on epitaxial Fe_3O_4(111) films, Phys. Rev. B **60**, 62–69 (1999)

13.117 A. Barbieri, W. Weiss, M.A. Van Hove, G.A. Somorjai: Magnetite Fe_3O_4(111): Surface structure by LEED crystallography and energetics, Surf. Sci. **302**, 259–279 (1994)

13.118 J.B. Pendry: Reliability factors for LEED calculations, J. Phys. C **13**, 937–944 (2000)

13.119 E. Bauer: A brief history of PEEM, J. Electron Spectrosc. Relat. Phenom. **185**, 314–322 (2012)

13.120 J. Pohl: Formation of electron-optical image with photoelectrons (PEEM and THEEM of Pt), Z. Tech. Phys. **15**, 579–581 (1934)

13.121 P.W. Hawkes, E. Kasper: *Principles of Electron Optics* (Academic Press, London 1996)

13.122 H. Boersch: Experimentelle Bestimmung der Energieverteilung in thermisch ausgelösten Elektronenstrahlen, Z. Phys. **139**, 115–146 (1954)

13.123 J. Orloff: *Handbook of Charged Particle Optics* (CRC, New York 1997)

13.124 X.J. Zhou, B. Wannberg, W.L. Yang, V. Brouet, Z. Sun, J.F. Douglas, D. Dessau, Z. Hussain, Z.X. Shen: Space charge effect and mirror charge effect in photoemission spectroscopy, J. Electron Spectrosc. Relat. Phenom. **142**, 27–38 (2005)

13.125 N.M. Buckanie, J. Göhre, P. Zhou, D. von der Linde, M. Horn-von Hoegen, F.-J. Meyer zu Heringdorf: Space charge effects in photoemission electron microscopy using amplified femtosecond laser pulses, J. Phys. Condens. Matter **21**, 314003 (2009)

13.126 A. Locatelli, G. Zamborlini, T.O. Menteş: Growth of single and multi-layer graphene on Ir(100), Carbon N. Y. **74**, 237–248 (2014)

13.127 C.J. Powell, A. Jablonski: Surface sensitivity of x-ray photoelectron spectroscopy, Nucl. Instrum. Methods Phys. Res. A **601**, 54–65 (2009)

13.128 C. Africh, C. Cepek, L.L. Patera, G. Zamborlini, P. Genoni, T.O. Menteş, A. Sala, A. Locatelli, G. Comelli: Switchable graphene-substrate coupling through formation/dissolution of an intercalated Ni-carbide layer, Sci. Rep. **6**, 19734 (2016)

13.129 T.O. Menteş, A. Locatelli: Angle-resolved x-ray photoemission electron microscopy, J. Electron Spectrosc. Relat. Phenom. **185**, 323–329 (2012)

13.130 N. Barrett, E. Conrad, K. Winkler, B. Krömker: Dark field photoelectron emission microscopy of micron scale few layer graphene, Rev. Sci. Instrum. **83**, 83706 (2012)

13.131 V.M. Karpan, G. Giovannetti, P.A. Khomyakov, M. Talanana, A.A. Starikov, M. Zwierzycki, J. van den Brink, G. Brocks, P.J. Kelly: Graphite and graphene as perfect spin filters, Phys. Rev. Lett. **99**, 176602 (2007)
13.132 E. Celasco, G. Carraro, M. Smerieri, L. Savio, M. Rocca, L. Vattuone: Influence of growing conditions on the reactivity of Ni supported graphene towards CO, J. Chem. Phys. **146**, 104704 (2017)
13.133 L.L. Patera, C. Africh, R.S. Weatherup, R. Blume, S. Bhardwaj, C. Castellarin-Cudia, A. Knop-Gericke, R. Schloegl, G. Comelli, S. Hofmann, C. Cepek: In situ observations of the atomistic mechanisms of Ni catalyzed low temperature graphene growth, ACS Nano **7**, 7901–7912 (2013)
13.134 Y.S. Dedkov, M. Fonin, U. Rüdiger, C. Laubschat: Rashba effect in the graphene/Ni(111) system, Phys. Rev. Lett. **100**, 107602 (2008)
13.135 F.M.F. de Groot: X-ray absorption and dichroism of transition metals and their compounds, J. Electron Spectrosc. Relat. Phenom. **67**, 529–622 (1994)
13.136 J. Stöhr: *NEXAFS Spectroscopy* (Springer, Berlin, Heidelberg 1992)
13.137 J. Stöhr: Exploring the microscopic origin of magnetic anisotropies with x-ray magnetic circular dichroism (XMCD) spectroscopy, J. Magn. Magn. Mater. **200**, 470–497 (1999)
13.138 E.W. Plummer, W. Eberhardt: Angle-resolved photoemission as a tool for the study of surfaces. In: *Advances in Chemical Physics*, Vol. 49, ed. by I. Prigogine, S.A. Rice (Wiley, Hoboken 2007) pp. 533–656
13.139 P. Hofmann: *Solid State Physics: An Introduction* (Wiley, New York 2015)
13.140 C.M. Schneider, C. Wiemann, M. Patt, V. Feyer, L. Plucinski, I.P. Krug, M. Escher, N. Weber, M. Merkel, O. Renault, N. Barrett: Expanding the view into complex material systems: From micro-ARPES to nanoscale HAXPES, J. Electron Spectrosc. Relat. Phenom. **185**, 330–339 (2012)
13.141 A. Sala, G. Zamborlini, T.O. Menteş, A. Locatelli: Fabrication of 2D heterojunction in graphene via low energy N_2^+ irradiation, Small **11**, 5927 (2015)
13.142 D. Usachov, O. Vilkov, A. Grüneis, D. Haberer, A. Fedorov, V.K. Adamchuk, A.B. Preobrajenski, P. Dudin, A. Barinov, M. Oehzelt, C. Laubschat, D.V. Vyalikh: Nitrogen-doped graphene: Efficient growth, structure, and electronic properties, Nano Lett. **11**, 5401–5407 (2011)
13.143 M. Scardamaglia, B. Aleman, M. Amati, C. Ewels, P. Pochet, N. Reckinger, J.F. Colomer, T. Skaltsas, N. Tagmatarchis, R. Snyders, L. Gregoratti, C. Bittencourt: Nitrogen implantation of suspended graphene flakes: Annealing effects and selectivity of sp2 nitrogen species, Carbon N. Y. **73**, 371–381 (2014)
13.144 J.B. Pendry: Theory of photoemission, Surf. Sci. **57**, 679–705 (1976)
13.145 S. Hüfner: *Photoelectron Spectroscopy* (Springer, Berlin, Heidelberg 1996)
13.146 K. Kim, S. Yang, Y. Park, M. Lee, B. Kim, H. Lee: Annealing effects after nitrogen ion casting on monolayer and multilayer graphene, J. Phys. Chem. C **117**, 2129–2134 (2013)
13.147 A. Barinov, L. Gregoratti, P. Dudin, S. La Rosa, M. Kiskinova: Imaging and spectroscopy of multiwalled carbon nanotubes during oxidation: Defects and oxygen bonding, Adv. Mater. **21**, 1916–1920 (2009)
13.148 T. Susi, M. Kaukonen, P. Havu, M.P. Ljungberg, P. Ayala, E.I. Kauppinen: Core level binding energies of functionalized and defective graphene, Beilstein J. Nanotechnol. **5**, 121–132 (2014)
13.149 J.J. Yeh, I. Lindau: Atomic subshell photoionization cross sections and asymmetry parameters: $1 \leqslant Z \leqslant 103$, At. Data Nucl. Data Tables **32**, 1–155 (1985)

Alessandro Sala

University of Trieste
Trieste, Italy

CNR – Istituto Officina dei Materiali
Trieste, Italy
sala@iom.cnr.it

Dr Alessandro Sala is currently Research Fellow at the University of Trieste and CNR-IOM, Trieste, Italy. His research fields in surface science are low-dimensional materials, biomimetic molecules, and model catalysis. He has worked with LEEM/PEEM systems since 2008, first on the SMART project at the Fritz-Haber-Institute, Berlin, Germany, then at the SPELEEM equipping Nanospectroscopy Beamline at Elettra Sincrotrone Trieste, Italy.

14. Scanning Photoelectron Microscopy: Past, Present and Future

Matteo Amati, Alexei Barinov, Luca Gregoratti, Hikmet Sezen, Maya Kiskinova

Adding submicrometer lateral resolution to the analytic capabilities of photoelectron spectroscopy was a milestone that opened up new opportunities to access lateral fluctuations in the chemical composition and electronic and magnetic structure of surfaces and interfaces and to explore exotic properties of nanostructured matter. To achieve a high spatial resolution while preserving the spectral resolution of this technique requires the very intense photon flux that has become available with the advent of third-generation synchrotron storage rings. The high spatial resolution of x-ray photoelectron microscopes, operated at synchrotron facilities, is achieved by either: (i) magnifying the image of the irradiated surface area using a suitable electron optical imaging system; or (ii) demagnifying the incident photon beam using x-ray photon optics. The contrast mechanisms in both instruments are based on photon absorption and the photon-induced electron emission is used to obtain spectroscopic information encoding the composition and electronic structure of the sample under investigation.

This paper offers a brief overview of the history, operational principles and potential of scanning photoelectron microscopes where the imaging is performed by scanning the sample with respect to the focused beam.

14.1 X-Ray Microscopy—A Brief Overview

The trend of modern nanotechnology is to fabricate nanostructured and composite materials with improved structural, chemical, electric, magnetic and optical properties that relate directly to the performance of energy harvesting, storage media, catalysts and a variety of electronic devices and applications. It is also well known that the nanoscale confinement leads to new properties, feeding vanguard technologies to improve device functionalities, for example in the fields of communications, chemical sensing and biomedical appliances. Understanding the properties of such exotic functional materials requires experimental techniques that allow access to their structure and composition at proper length and depth scales. Much progress in nanoscience and nanotechnology has been made thanks to the availability of sophisticated methods such as electron microscopy and scanning probe microscopy, in addition to standard techniques such as x-ray and neutron diffraction, x-ray scattering, and other spectroscopies. Other techniques that have flourished in the recent three decades with the construction of third-generation synchrotron light sources are encompassed in so-called x-ray microscopy [14.1, 2]. The contrast mechanisms in the x-ray microscopes are based on photon absorption,

M. Rocca, T.S. Rahman, L. Vattuone (Eds.), *Springer Handbook of Surface Science*, Springer Handbooks,
https://doi.org/10.1007/978-3-030-46906-1_14

phase shift and photon-induced x-ray or electron emission. Depending on the detection mode, the chemically specific information is provided by x-ray absorption spectroscopy (XAS) [14.3], fluorescence spectroscopy (FS) or photoelectron spectroscopy (PES) [14.4].

Many of the complex functional materials playing an essential role in technology advancements involve interfaces that call for understanding and control at submicron length scales, in particular for the correlation between the surface and near-surface properties and elementary processes such as adsorption, chemical reactions, growth and processing. When these phenomena are investigated, the advantage of the electron detection mode in x-ray microscopes is the limited escape depth the emitted electrons that provides high surface sensitivity. Using PES the energy filtered electrons emitted from atomic core and valence levels as a result of interaction with monochromatic photons provide the most straightforward quantitative compositional information and are also excellent fingerprints for the chemical state and the structural and chemical environment of the emitting atoms. More specific electronic and structural information can be obtained by angle-resolved measurements of the valence band and through photoelectron diffraction. Angle-resolved photoelectron spectroscopy (ARPES), is a direct experimental technique to observe the distribution of the electrons (more precisely, the density of single-particle electronic excitations) in the reciprocal space of solids. The technique is a refinement of ordinary photoemission spectroscopy, studying photoemission of electrons from a sample achieved usually by illumination with soft x-rays. ARPES gives information on the direction, speed and scattering process of valence electrons in the sample being studied (usually a solid). This means that information can be gained on both the energy and momentum of an electron, providing detailed information on band dispersion and the Fermi surface. This technique is also known as angle-resolved ultraviolet photoelectron spectroscopy (ARUPS) since ultraviolet light is more commonly used to generate photoemission. The XAS spectra exhibit resonant electronic transitions from core levels into unfilled valence states, governed by well-established selection rules. Using circularly or linearly polarized photon beams the element specific XAS can also provide information on the average magnetic moment and symmetry of the chemical bonds, called x-ray magnetic circular or linear dichroism (XMCD or XMLD).

The sample probing depth in PES-related techniques is determined by the kinetic energy of the photoemitted electrons and can be varied from less than ten to hundred angstrom. In XAS, measured by detecting low-energy secondary electrons, the information can originate from a sample depth up to a few hundred angstroms.

There are two distinct approaches to x-ray microscopy using synchrotron radiation, called full-field imaging and scanning. In the full-field imaging method a magnified image of the irradiated sample area is obtained by tailoring the transmitted photons or photoemitted electrons using appropriate photon or electron optical elements. In the scanning method photon optics demagnify the monochromatized photon beam to a small spot onto the sample, and an image is acquired by collecting emitted or transmitted photons or emitted electrons while scanning the sample with respect to the microprobe provided by the focused beam.

In the scanning approach the spatial resolution is achieved by reflective, glancing or near-normal-incidence mirror systems or diffractive circular grating optical elements, called zone plate (ZP) lenses [14.5]. Today ZPs can cover the wide photon energy range 100–15 000 eV [14.6, 7]. The grazing geometry (generally defined as Kirkpatrick–Baez (K–B)) system consists of two crossed mirrors for separated focusing in the vertical and horizontal planes. Only in the recent decade has advanced K–B fabrication technology reached sub-100 nm microprobes [14.8] but this is still not easily achievable using soft x-rays. The advantage of K–B optics is that they are achromatic and allow for easy x-ray absorption near edge spectroscopy (XANES) measurements keeping the optics–sample distance invariant. Another optical system optimized for the focalization of low-energy photons is based on a set of two spherical multilayer mirrors with a normal incidence (Schwarzschild objective, SO), which have been demonstrated to provide submicrometer resolution, but since the reflectivity drops very rapidly with increasing photon energy this optical system works well only at very soft x-rays (< 200 eV) [14.9].

The full-field imaging microscopes based on detection of photoelectron emission are a special class of microscopes. They were called photoelectron emission microscopes (PEEM) and date from the early 1930s when they used a laboratory UV photon source. They use a suitable electrostatic or magnetostatic electron optical imaging system for a magnified projection of the emitted electrons and dispersive elements for their energy discrimination. It was decades before synchrotron sources provided sufficiently high x-ray fluxes to operate PEEMs as XPEEMs; it happened in mid-1990s and today at least one instrument operates at each main synchrotron facility. The great potential of the XPEEM direct imaging approach is that one can follow dynamics with temporal resolution down to nanoseconds, depending on the signal level. Today XPEEMs are very popular instruments for the characterization of antifer-

romagnetic and ferromagnetic samples using XMLD and XMCD, taking advantage of the time structure of the synchrotrons for applying dynamic pump-probe measurements as well. Another notable advantage of XPEEM is that by adding an electron source it can become a multifunctional instrument providing complementary structural information at the same time via low-energy electron microscopy (LEEM). Details of the working modes and the applications capabilities of XPEEM, and XPEEM combined with LEEM, can be found in [14.10–13].

The present review article is intended to introduce the reader to the capabilities of the scanning photoelectron microscopes (SPEM) for characterization of matter, which is either laterally inhomogeneous at micro-to-nano length scales or consists of nanostructures that need to be probed individually. The major strength of SPEM is for exploiting processes occurring at solid surfaces in contact with gas and recently also ambient liquid, relevant to operation of technologically important materials where issues of complexity at microscopic length scales, such as lateral inhomogeneity in the stoichiometry and/or morphology, should be faced and understood. It should be noted that SPEM dedicated to μ-ARPES became very attractive more recently, when the discovery of graphene and other appealing two-dimensional (2-D) materials, as semiconductors with direct gap, topological insulators, Weyl semimetals etc. have opened up new unexplored scientific fields. These exotic materials have called for adequate characterization methods of small devices demanding sophisticated microscopic tools capable of harvesting important information about their electronic structure as well. In this respect μ-ARPES is becoming a unique tool for band structure determination especially for 2-D materials since the interpretation of results is rather straightforward with precisions of the order of few meV and below $0.01\,\text{Å}^{-1}$ in k-space [14.14–16]. If compared to full-field instruments, the scanning instruments, where the x-ray beam is focused to a microprobe, provide a flexible and adaptable sample environment and an optimal performance in terms of spectral, spatial and variable depth information.

Here we will present in more details the recent achievements with SPEMs using SO and ZP optical systems, referred as SO-SPEM and ZP-SPEM respectively. The review is divided in three sections: the first part illustrates the construction principles of SPEM including focusing optical elements, which determine the microprobe, detectors and possible operation modes. The second part uses selected results obtained with the microscopes operated at the Elettra Laboratory to demonstrate the new information provided by combining chemical sensitivity with submicron spatial resolution. The third section reports on the most recent developments of experimental setups in ZP-SPEM for breaking the pressure gap and studying materials near to the realistic operation conditions.

14.2 Operation Principle of SPEM

The general setup of a SPEM instrument operated at a synchrotron light source is schematically shown in Fig. 14.1. The drawing is for ZP-based SPEMs but, except for the optics providing the microprobe, all x-ray beamlines hosting SPEM include the following components: a photon source (usually an undulator) and suitable photon transport and tailoring optics (mirrors, gratings and slits) in order to meet the requirements of the focusing optics (ZP, SO or K–Bs) providing the microprobe onto the sample.

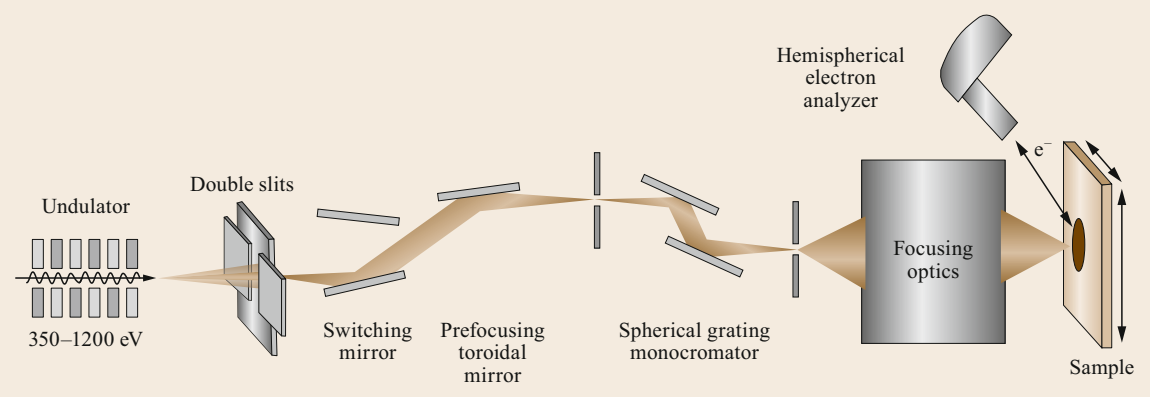

Fig. 14.1 General setup of a SPEM instrument operated at a synchrotron light source

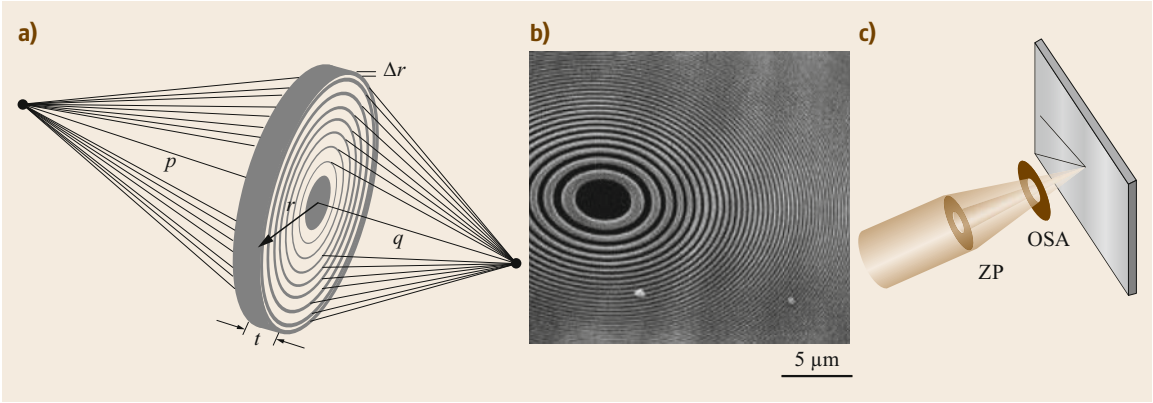

Fig. 14.2 **(a)** Schematic drawing of a ZP used to form an image of a source point onto the image plane with p and q as object and image widths respectively. The ZP has radius r, outermost zone width Δr, and thickness t. **(b)** Scanning electron microscopy (SEM) image of the inner structures of a ZP used for focusing soft x-rays [14.2]. **(c)** Typical arrangement of the ZP and OSA in front of the sample

As noted above the microprobe in the SPEMs hosted at the ESCAmicroscopy and Spectromicroscopy beamlines at Elettra is provided by a zone plate (ZP) and normal incident Schwarzschild objectives (SOs), respectively [14.17, 18].

14.2.1 Zone Plate Optics

The high-resolution ZPs that today can reach 10 nm resolution in the soft x-ray range are circular diffraction gratings with a radially increasing line density (Fig. 14.2). They obey the visible light lens rule $1/f = 1/p + 1/q$ [14.6], where f denotes the focal length, p the source distance and q the image width. The basic relation between the focal length in the m-th diffracted order, f_m, photon wavelength, λ (or energy, E, in eV), ZP radius, r, and the outermost zone width, Δr, is expressed as [14.5]

$$f_m = \frac{2r\Delta r}{m\lambda} \approx \frac{2r\Delta r}{1240m}E\ (\mathrm{eV})\,. \qquad (14.1)$$

This equation shows that, as with any diffraction gratings, the ZPs are highly chromatic optics with an infinite number of diffraction orders. The first-order diffraction is the most commonly used one in SPEM and, as shown in Fig. 14.2, a central stop and order-sorting aperture (OSA) are needed to cut the undesired orders. For a ZP with a numerical aperture $\mathrm{NA} \approx \lambda/(2\Delta r)$ the depth of focus (DOF) is described by the following (14.2)

$$\mathrm{DOF} = \pm\frac{\lambda}{2(\mathrm{NA})^2} \approx \pm\frac{\Delta r}{\mathrm{NA}} \approx \pm\frac{2(\Delta r)^2}{\lambda}\,. \qquad (14.2)$$

The spatial resolution is not only a function of the diffraction-limited resolution $\delta_i = 1.22\Delta r/m$ (applying the Rayleigh criterion), but also of the light monochromaticity. In order to avoid chromatic aberrations, δ_m, which reduce the spatial resolution the source monochromaticity has to exceed $E/\Delta E \geq Nm$, where N is the number of zones [14.19].

Another important parameter of the ZP is the diffraction efficiency ϵ_m, which is the fraction of the incident light focused in the m-th diffraction order. It can be calculated using the scalar diffraction theory introduced by *J. Kirz* [14.20] and the complex refractive index $\eta = 1 - \delta - \mathrm{i}\beta$, tabulated for most elements by *Henke* and coworkers [14.21], which are at the base of (14.3)

$$\varepsilon_m = \frac{1}{(m\pi)^2}(1 + \mathrm{e}^{-2k\phi} - 2\mathrm{e}^{-k\phi}\cos\phi)\,, \qquad (14.3)$$

where $k = \beta/\delta$, and $\Phi = 2\pi\delta t/\lambda$ denotes the phase shift of diffracting structures with height t. Equation (14.3) is valid for rectangular zone shapes and not too high aspect ratios of the zone structures [14.22]. In the case of $k \to 0$, i.e., dominating phase shift, the maximum first-order diffraction efficiency of $4/\pi^2 \approx 40\%$ can be achieved, while for $k \to \infty$ or high absorption, the first-order efficiency is limited to $1/\pi^2 \approx 10\%$. An important and limiting factor in the fabrication process is the aspect ratio (height/width of zone structures), which lowers the diffraction efficiency to real values below 20%.

The ZPs used in the ZP-SPEM at Elettra have diameters ranging from 200–250 μm and minimum outermost zone width of 50 nm. They are selected to have good compromise between spatial resolution in microspectroscopy and sufficient signal to get good spec-

tral resolution. Depending on the photon energy used for the experiments for these ZP parameters the typical focal distances in the first-order diffraction range should be from 4 to 15 mm and one should consider that also there is the OSA (a pinhole) placed between the sample and the ZP. It has to be noted that, although the size of the focused beam becomes smaller using higher diffraction orders ($\delta_i \approx 1/m$), it is almost not applicable for SPEM because the diffraction efficiency scales with $1/m^2$ and when using soft x-rays the sample–OSA/ZP distance becomes very short, obstructing the emitted electrons.

The monochromaticity of the ZP optics imposes the requirement for moving the sample when scanning the photon energy in order to preserve the spot size since the focal distance varies with the photon energy. This requirement impedes easy implementation of micro-XAS in total electron yield but recently interferometer controlled sample movements have been implemented in ZP-SPEMs to solve the problem [14.23]. The optical system ZP/OSA generating the x-ray microprobe is mounted on appropriate stages, which enable independent positioning of the ZP and OSA in x-, y- and z-directions.

14.2.2 Schwarzschild Objectives

SO with multilayered primary and secondary spherical mirrors is the final focusing element of the SO-SPEM hosted at the Spectromicroscopy beamline used to provide the microprobe on the sample. The high reflectivity ($\approx 50\%$ per mirror) for the selected energy by multilayer spacing on the energy line secures a high photon flux in the microprobe, which is essential to satisfy the requirements of the photon-hungry μ-ARPES. Compared to the soft x-ray ZP described in the previous subsection the SO has a much longer working distance (12.5 cm), which eases the movements of the internal electron analyzer around the sample in order to perform angular resolved measurements. In fact, for photon energies less than 100 eV used for ARUPS the ZPs are not suitable due to the reduced focal distance and transmission. A SO system is schematically shown in Fig. 14.3.

The major disadvantage of the SO is the constraint imposed by using multilayer pairs of mirrors that perform only at a preselected photon energy. Currently two SOs are installed at the SO-SPEM at Elettra; they can be easily selected without vacuum break. They work at photon energies of 27 and 74 eV that fit well to the ARUPS measurements. Indeed, compared to ZPs the spatial resolution achievable with SO are ≈ 250 nm considering that the diffraction limit for such types of optics is 120 nm. However, due to aberrations caused by figure errors of the objective's mirrors, the realistic spatial resolution in microspectroscopy is ≈ 500 nm.

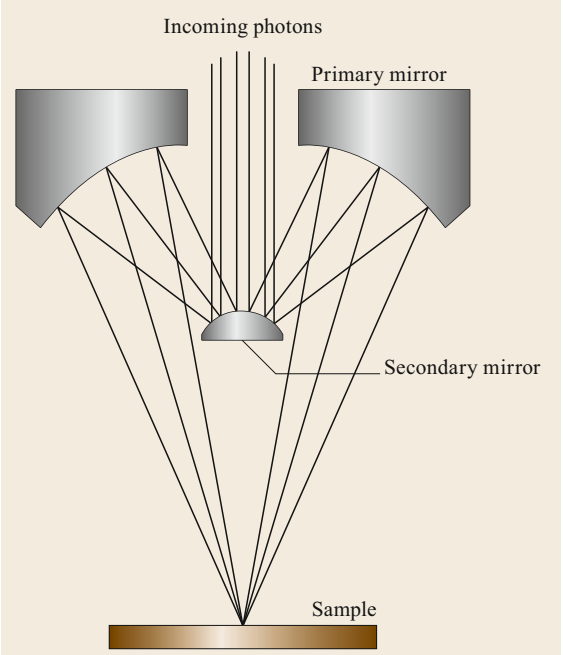

Fig. 14.3 Schematic view of a SO system. The incoming photons are first focused by the secondary mirror onto the primary mirror and then projected to the focal spot at the sample surface

14.2.3 Sample Environment and Detection Systems

The SPEM optics-sample-analyzer setup is sketched in Fig. 14.4. The samples are mounted on a scanning stage manipulator, which allows for quick XYZ positioning, controlled by stepper motors and a fine $X-Y$ piezoelectric stage that holds and scans the sample with respect to the microprobe for obtaining two-dimensional images. In the ZP-SPEM the sample temperature can be varied between 150 and 1300 K and also there are possibilities for applying potentials in the range of several volt that have been used for in situ studies of electrochemical energy devices [14.24]. The research performed using SO-SPEM also requires cooling so the sample temperature can be varied within the range of 35–400 K by combination of liquid helium or liquid nitrogen cooling and a sample heater.

Since in both types of SPEM the microprobe hits normal to the sample surface the emitted photoelectrons are detected and energy filtered by an electron analyzer positioned at a grazing angle. The ZP-SPEM working in the 400–1200 eV photon energy range is dedicated

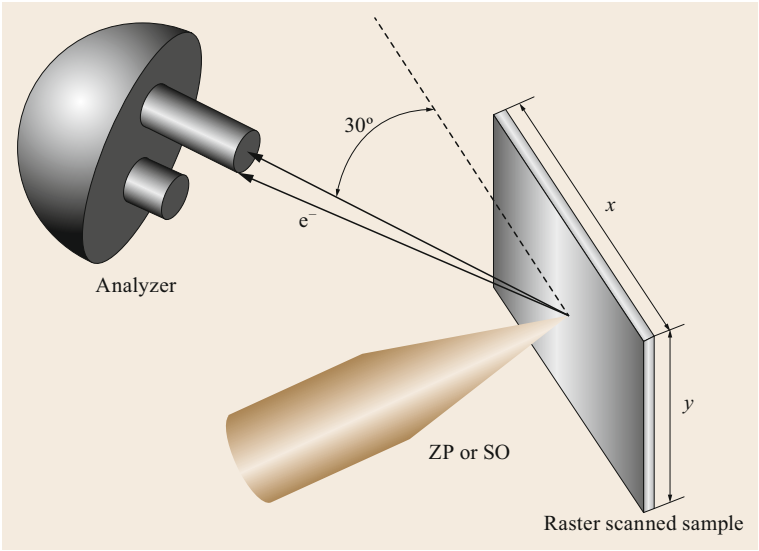

Fig. 14.4 Typical optics-sample-analyzer setup of a SPEM

exclusively to core-level spectroscopy and uses a classical type hemispherical electron analyzer (HEA) where the electron detection is based on a delay-line technology developed at Elettra [14.25]. The SO-SPEM for μ-ARUPS has a movable HEA designed and constructed in-house. It is mounted on a goniometer inside the vacuum chamber that can face the sample from different directions within a section of sphere covering $50° \times 50°$ [14.18]. The relatively long distance between the sample and the analyzer entrance slit (73 mm) has allowed the placing of a five-element electrostatic lens system designed to transform the cone of photoelectrons up to 16° to an entrance slit preserving their angular dispersion. The photoelectrons are further dispersed in energy between the hemispheres of the analyzer and detected by multichannel plates mounted on a delay-line setup, where the X–Y position of the electron pulse is monitored. By combining stacks of 2-D k–E (E being the energy) dispersion images from the detector while rotating the goniometer one can obtain the three-dimensional (3-D) band structure of a considerable part of the Brillouin zone. We would like to note that thanks to the high reflectivity of SO this electron analyzer, although small, operates at low pass energies reaching spectral and angular resolutions better than 50 meV and ±0.3° maintaining reasonable count rates.

Both SO-SPEM and ZP-SPEM at Elettra use in-house designed detectors based on the delay-line technology. The detector of the ZP-SPEM is a one-dimensional (1-D) array configured as a multichannel sensor, which reduces substantially the time necessary for getting chemically specific information and handles topography effects as well. In multichannel detection, the number of images collected simultaneously is equal to the number of the channels, where each channel corresponds to a specific kinetic energy, defined by the selected energy window. The multichannel imaging allows not only mapping of different chemical states and the background with a single scan of the sample, but also reconstruction of the spectrum corresponding to the energy window, so-called spectra imaging, as described in the next section. The SO-SPEM uses a 2-D array with working area $20 \times 20\,\mathrm{mm}^2$.

14.2.4 Imaging and Spectroscopy Acquisition Modes

The main advantage of the scanning photoemission microscopes is that imaging and microspot spectroscopy are independent modes. This allows optimization of each mode accounting for the required spectral and lateral resolution and acquisition time. In the imaging mode, one can map element concentration, element chemical state, Fermi band structure etc. by scanning the sample and simultaneously collecting the photoelectrons within a selected kinetic energy window that defines the property under investigation. The microspot spectroscopy (termed μ-spectroscopy) uses the whole analytical power of PES, providing detailed information on the composition and local electronic structure of the probed microscopic area. However, as illustrated below the imaging mode can also offer sufficient spectral information when the multichannel detection system is properly exploited.

In imaging mode the contrast map visualizes the lateral distribution of a particular sample constituent. Figure 14.5 illustrates the advantages of mapping, including spectral imaging by using a 48-channel detector

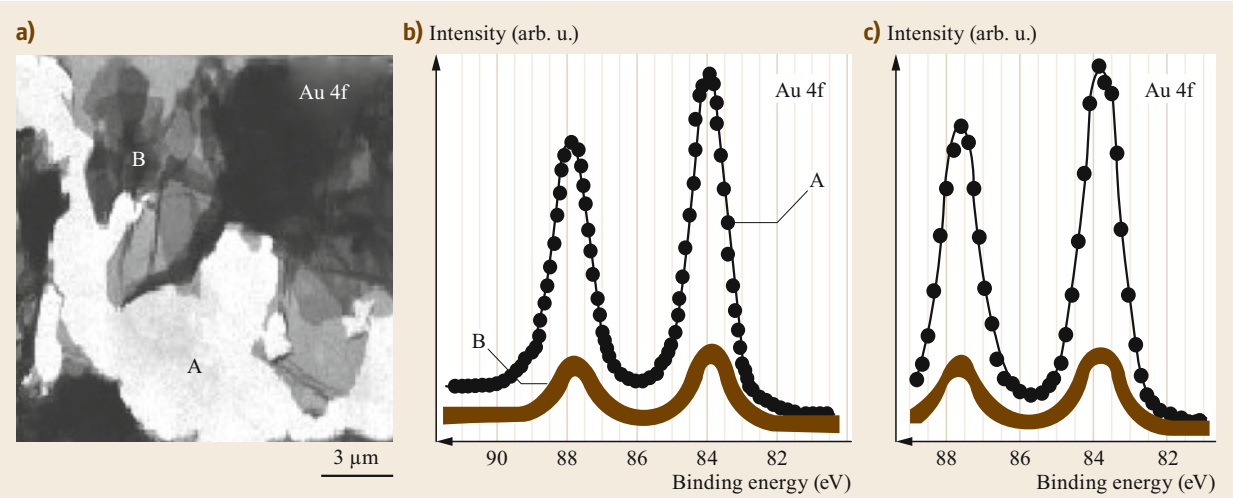

Fig. 14.5 **(a)** Au $4f_{7/2}$ map ($15 \times 15\,\mu m^2$) illustrating areas partially covered by graphene flakes. **(b)** Au 4f spectra measured in µ-spectroscopy mode from the positions, marked as A and B in **(a)**. **(c)** Reconstructed Au 4f spectra from the same A and B areas. The similarity with conventional µ-spectra is evident

in the ZP-SPEM. The example is an Au surface partially covered by graphene flakes, where the Au 4f signal shows significant intensity variations as a function of the local graphene thickness. The contrast level in the Au 4f map (Fig. 14.5a), obtained by summing the signal from all 48 channels covering the Au $4f_{7/2}$ energy window, reflects the lateral variations of the graphene thickness. This is confirmed by comparing the intensity of the high-resolution Au 4f spectra taken in $0.01\,\mu m^2$ spots A and B (Fig. 14.5b) indicating thicker graphene overlayer in position B that strongly attenuates the signal. From the Au map we reconstructed the Au 4f spectra corresponding to the indicated selected areas (Fig. 14.5c). One can clearly see striking similarity achieved using spectral imaging, despite the lower spectral resolution due to the higher pass energy used in the imaging mode. Furthermore, by selecting a few channels corresponding to a specific photoelectron energy that is a fingerprint of a chemical or electronic state one can visualize its lateral distribution or can account for the topographic contributions, as described below. It should be noted that by increasing the number of parallel counting channels the pass energy of the analyzer can be increased accordingly, accepting a much wider energy range of the emitted photoelectrons while maintaining the same energy resolution on each channel.

Since SPEM operates with a grazing angle detection this enhances the topography contributions to the signal intensity. Topography affects the intensity of the detected signal in each pixel and its contribution depends on the angle between the sample surface and the axis of the HEA lenses. This contribution can be expressed by the following equation:

$$I = I_0 e^{\frac{-d}{\lambda \cos\theta}} , \tag{14.4}$$

where I_0 is the photoelectron yield from the top atomic layer, d is the probing depth, λ is the inelastic mean free path for the specific material and θ is the angle between the surface normal and the HEA lenses axis. For the ZP-SPEM at Elettra θ is 60° with respect to the surface normal, a geometry that increases the surface sensitivity, as evidenced by (14.4), but also favors stronger topographic effects, represented by an enhancement of the signal from the side of the feature facing the HEA due to locally smaller θ and attenuation from the opposite side due to shadowing of the emitted electrons.

Although the topography contribution obscures the quantitative information, in many cases it is also useful to look for possible correlations between topography and chemical or electronic properties. However, in order to get quantitative information the topographical contribution should be removed using proper processing approaches [14.26]. The most common one is based on the application of rather simple algorithms such as

$$I = \frac{I_{pk}}{I_{bg}} ,$$
$$I = \frac{(I_{pk} - I_{bg})}{I_{bg}} , \tag{14.5}$$

where I_{pk} is the intensity recorded at the maximum of a photoemission core level, while I_{bg} is the measured background signal at the lower binding energy region of the core level.

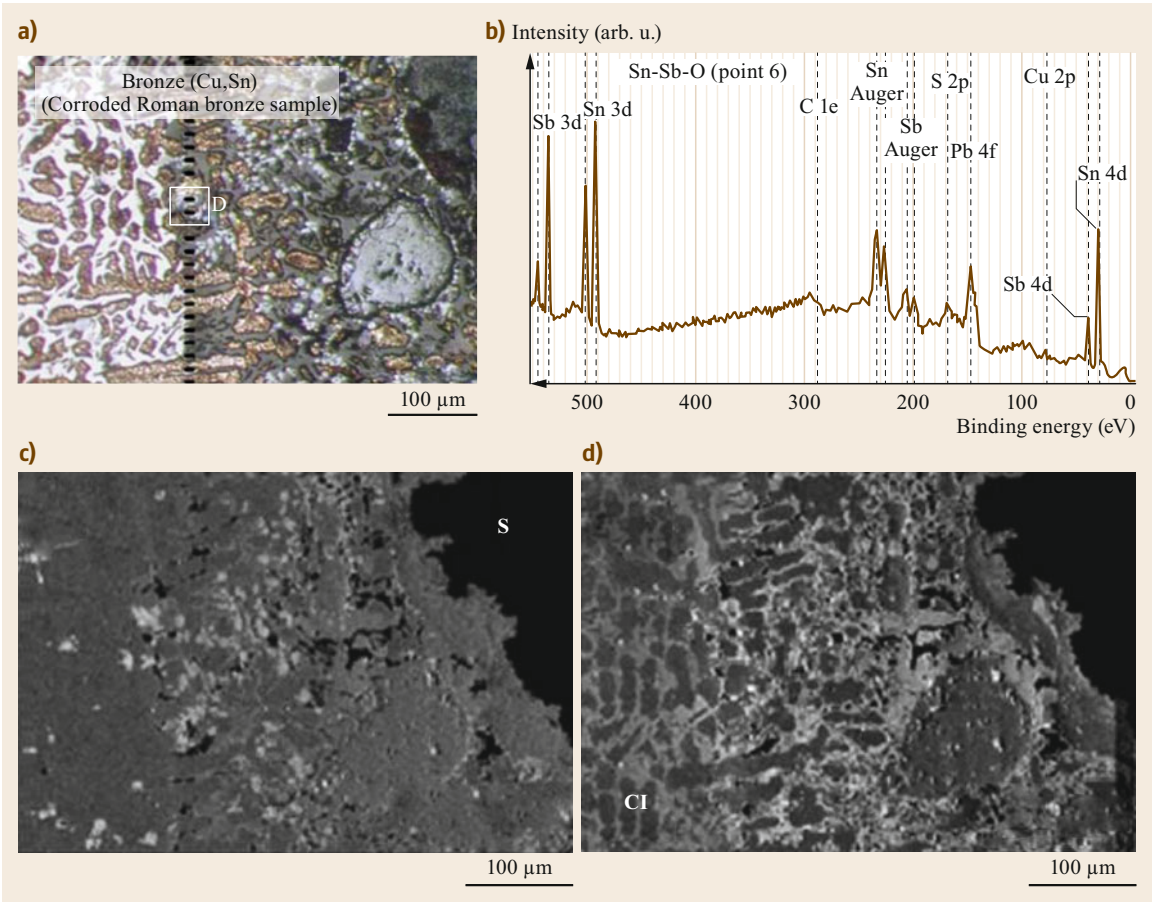

Fig. 14.6 **(a)** Optical image of an ancient bronze coin after thousands of years of environmental degradation. **(b)** Survey XPS spectrum revealing the main coin constituents: Sb, Sn, S, Cl, C and Cu. **(c,d)** Processed S 2p and Cl 2p images after applying (14.5) where the topographic contribution to the contrast is removed, leaving the pure lateral variations of the S and Cl content

An example of the processing procedures for getting quantitative information from the SPEM images is reported in Fig. 14.6 using results obtained in studies of an ancient bronze coin after thousands of years of exposure to environmental degradation. The optical image in Fig. 14.6a clearly reveals the surface topography with colored regions of different heights. The survey XPS spectrum in Fig. 14.6b shows the average elemental content, namely Sb, Sn, S, Cl, C and Cu. By applying (14.5) we were able to visualize the lateral elemental distribution quantitatively. This is illustrated by the S 2p and Cl 2p maps in Fig. 14.6c,d showing that S is generally homogeneously distributed with few microscopic areas where the S concentration appears higher (bright) or lower (dark), while Cl appears concentrated in specific confined regions that correlate with the topographic features of the optical map.

A detailed analysis of the ancient coin Sn chemistry is reported in Fig. 14.7 where the high resolution XPS spectra in Fig. 14.7a taken in different regions contain components characteristic of different Sn chemical states: the yellow vertical band represents the energetic position of the metallic Sn while the light blue one covers the energy position of Sn oxides. The images in Fig. 14.7b–d are obtained by selecting channels covering different energy windows. The variations in the entire Sn surface content are represented by Fig. 14.7b, obtained by integrating the whole Sn energy window. By selecting the specific energy ranges as indicated by the two bands in Fig. 14.7a and removing the topographical contribution we get the images shown in Fig. 14.7c,d, which reveal the distribution of the metallic and oxidized tin. More details about the characterization of the ancient coin can be found in [14.27].

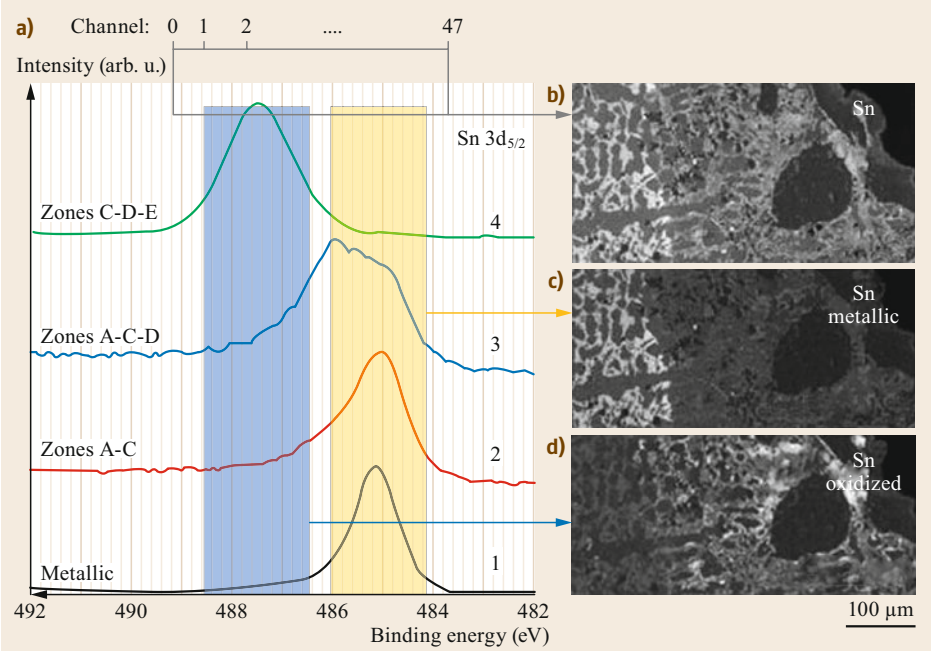

Fig. 14.7 **(a)** Sn $3d_{5/2}$ core-level spectra acquired in different regions of the coin shown in Fig. 14.6a; the *yellow vertical band* represents the energetic position of the metallic Sn while the *light blue* one covers the energy position of Sn oxides. **(b)** SPEM Sn image obtained by integrating the whole Sn 3d energy window where the contrast indicates variations in the Sn surface content. **(c,d)** Sn metallic and oxide maps obtained by selecting the corresponding energy widows components after removal of topographic contribution showing inhomogeneous oxidation

14.3 Some Representative Examples of Systems Studied with SPEMs

14.3.1 Surface Reactivity of Metals Used as Catalysts

Several early SPEM studies were focused on the lateral variation in the surface reactivity that has been well evidenced in exploiting the initial oxidation states of single-crystal transition metals, such as Ru and Rh [14.28–31]. In both cases a distinct feature of the initial oxidation is a laterally nonuniform oxide growth, which was evidenced by the SPEM images tuned to the selected transition metal core level and the O 1s spectra. From both spectra we were able to follow the evolution of oxidation based on the core-level shifts and relative intensities of oxide and metallic components. A representative example of such experiments is reported in Fig. 14.8 where the lateral variations in the contrast of the O 1s and Rh_{ox} $3d_{5/2}$ (Rh_{ox} means that the oxidized related energy window is selected to produce the map) images and the spectra taken in selected spots clearly evidence inhomogeneity in the Rh oxidation state. Close inspection of the two images shows that there is no correlation between the bright and dark regions, as one expects considering single stoichiometry of the oxidation state. On the contrary, most of the brighter areas in the O image appear darker in the Rh_{ox} image, with some exceptions, e.g., region (3). This can only be explained supposing that the inhomogeneity is due to spatial variations in the local density of the Rh and O atoms in the oxide film. In fact, we obtained numbers corresponding to the existing two Rh bulk oxides, the rutile RhO_2 and the corundum Rh_2O_3 from the Rh_{ox}(dark)/Rh_{ox}(bright) and O(bright)/O(dark) and Rh/O intensity ratios, evaluated from the maps and the spectra. The appearance of regions type (1) (dark in Rh_{ox} and bright on O maps) resembles the step bunches observed often on the Rh(110) surface that indicates that structural defects and irregular structures may act as more effective centers for O_2 dissociation that stabilize the RhO_2-like film, which requires a higher O density. Similar nonuniform ox-

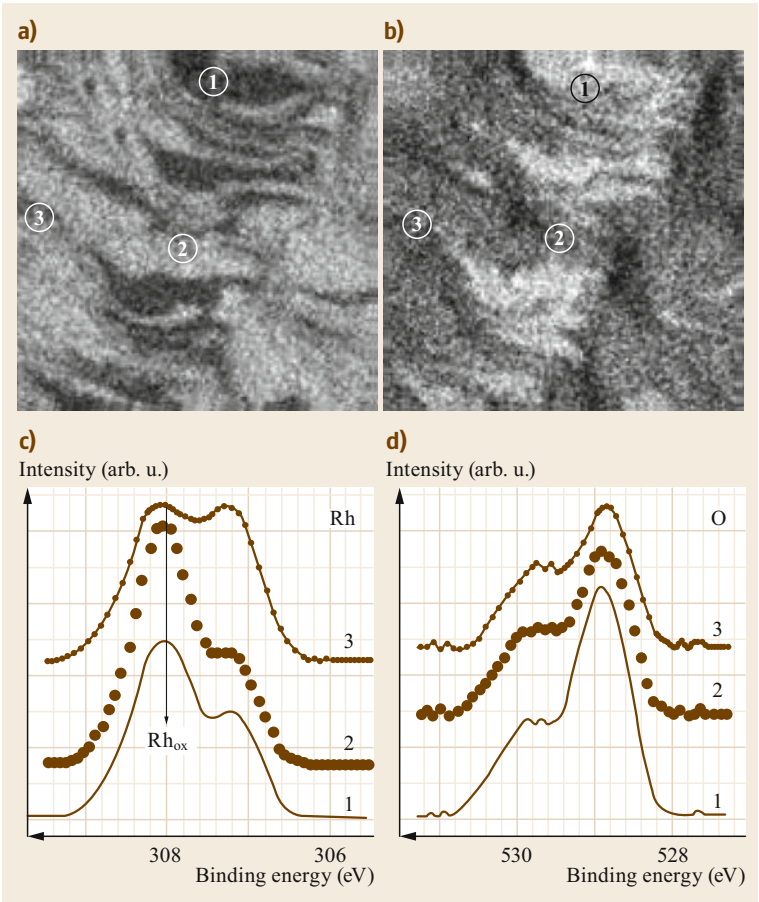

Fig. 14.8 **(a,b)** Rh_{ox} and O 1s images ($12.8 \times 12.8\,\mu m^2$) taken after exposure of Rh(110) to 1.2×10^5 L O_2 at 750 K. **(c,d)** Rh $3d_{5/2}$ and O 1s spectra reconstructed from the regions marked as 1, 2, and 3 in the images, where the component corresponding to the Rh oxides and used for taking the Rh_{ox} map in **(a)** is indicated by an *arrow*. The lower energy Rh components contain contributions from the metallic and interfacial Rh below the thin oxide film

ide growth is observed during the initial oxidation of Ru(0001) carried out under comparable oxidation conditions where not only the stable bulk oxide, RuO_2, can exist; the coexistence of ordered oxide and disordered precursor phases were evidenced in the transient oxidation stages [14.28, 29].

14.3.2 Degradation Mechanism of Light-emitting Diodes

The simultaneous information about the surface topology and chemical composition at local microscales provided by SPEM has made it possible to shed light on degradation mechanisms in organic light-emitting diodes (OLEDs) consisting of InSn oxide (ITO) anode organic emitters, electron transport layers and Al cathodes [14.32–34]. Comparing the results obtained from the characterization of the degraded microscopic areas of the Al cathode, occurring in OLEDs operated and exposed to different ambient conditions, has revealed that in all cases the final degradation state is similar. Degraded surfaces show small fractures usually with swollen regions in the vicinity. As illustrated in Fig. 14.9 these morphology changes are apparently created by eruptions and are clearly encoded as a distinct dark hole in the Al 2p map where the swollen regions are outlined by the topography-related enhancement.

The morphology highlighted by the In 3d map is very similar to that of Al, but distinct features comparing both images are the hole areas and those in the vicinity of the hole: (i) there is some In 3d emission from the hole and (ii) the surrounding regions appear brighter in the In maps and darker in the Al maps. Since the contrast level is a measurement of the element presence and concentration this indicates removal of the organic layers in the hole location and deposition of In on top of the Al surface around it. This is confirmed by the spectra in Fig. 14.9b, measured within the hole and in the areas in the hole vicinity. The spectra from the dark hole, created by the eruption, are very similar to the ITO spectra, with the exception of the presence of very weak C 1s and small Si 2p peaks, originating from organic film residues and from the ITO glass support. Consider-

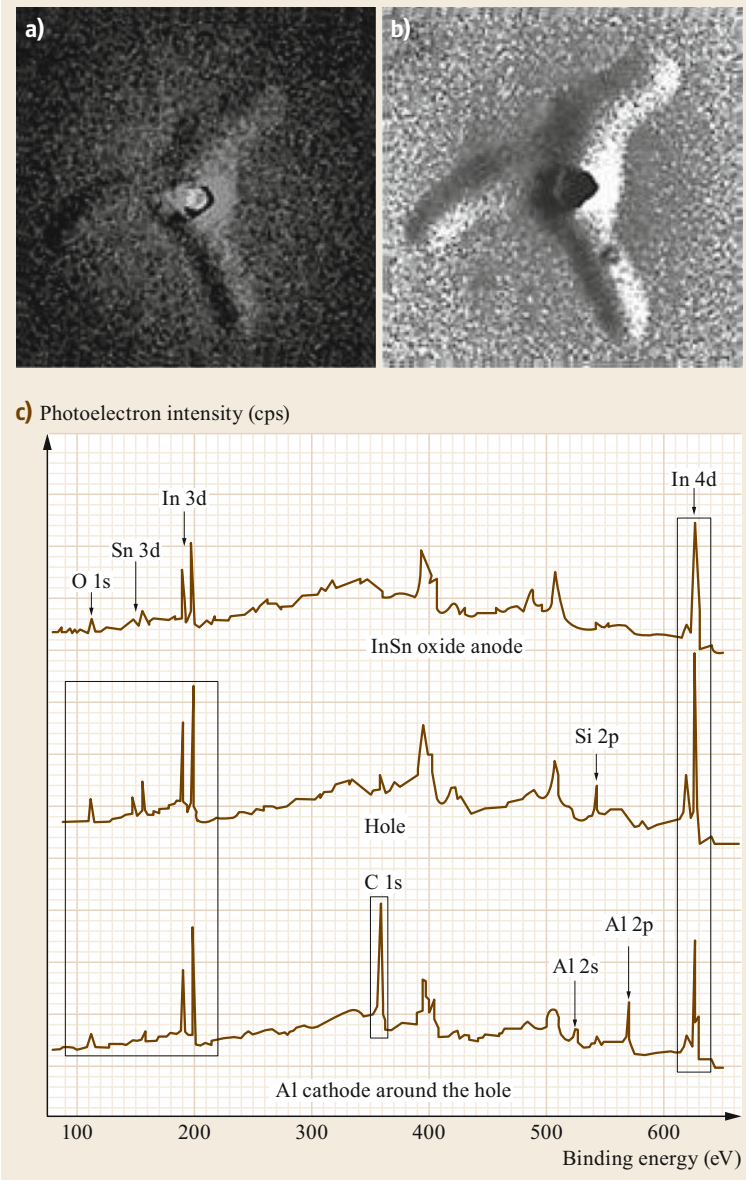

Fig. 14.9 **(a)** In 3d and **(b)** Al 2p maps centered in the hole created after operating the device in UHV and increasing the voltage to 32 V. **(c)** XPS survey spectra taken in the hole and in the vicinity of the hole. For the sake of comparison the ITO spectrum is shown as well

ing the small photoelectron probing depth the presence of Si 2p indicates that the ITO film thickness below the hole has been dramatically reduced due to material loss. The presence of In and C in the spectrum taken from the areas surrounding the hole point to local decomposition of the ITO anode and organic layer, resulting in deposition of volatile products on the Al surface, including In_xO_y and organic fragments. Since this final state of fractured OLEDs was observed even when they were fabricated and operated under ultrahigh vacuum (UHV) [14.32, 33], this suggests that the degradation is due to spikes resulting in local temperature rises sufficiently high to decompose the organic layers and ITO film. The pressure burst of the released volatile products causes delamination and fracture of the Al cathode. The conclusion was that the main reason for such local electrical shorts is intrinsic imperfections in structure, topography or chemical composition at ITO electrode surfaces and that the environment where the OLED is assembled only promotes the degradation. This feedback has pushed for improvements in the technology for fabrication of more perfect defect-free ITO films.

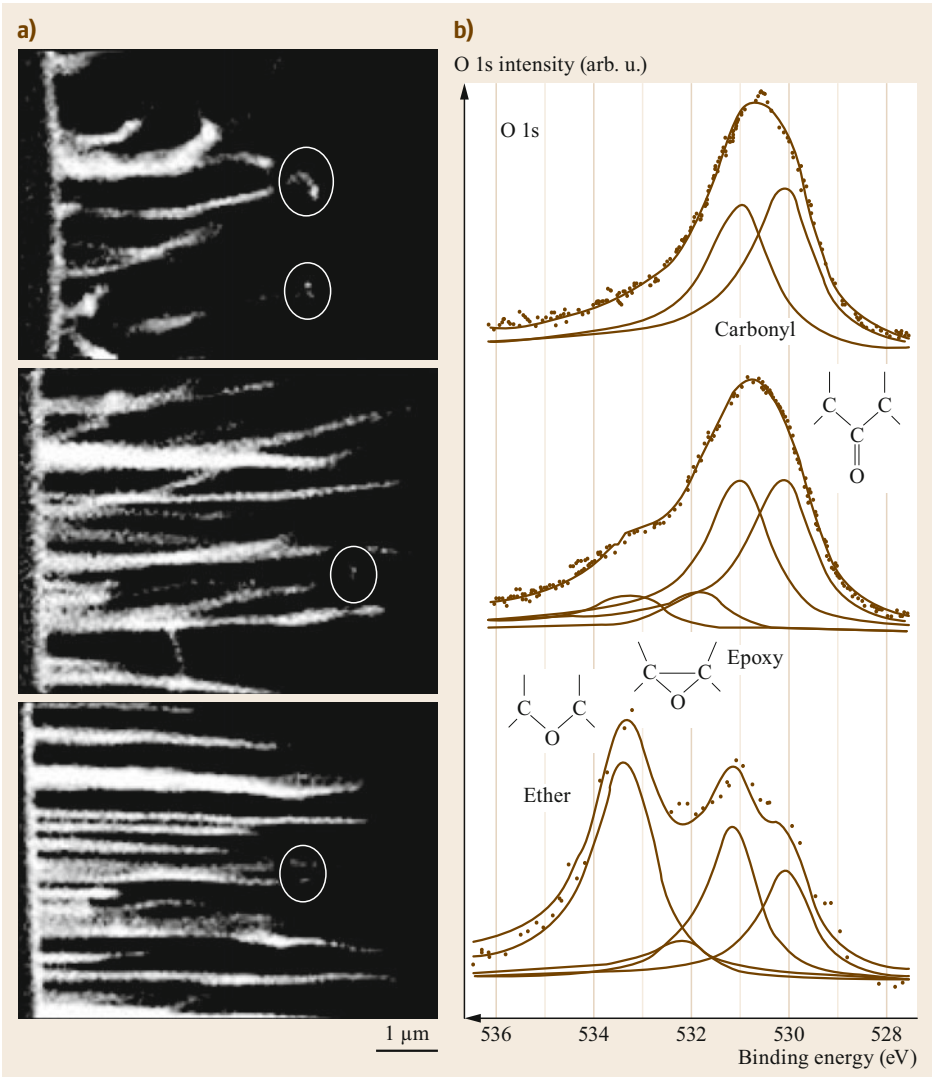

Fig. 14.10
(a) Sequence of C 1s images of a CNT array grown on Si substrate taken after exposure to increasing oxygen doses at 500 K. The silicon substrate on the *left* appears *dark gray* (secondary photoelectron emission), whereas the vacuum around the CNTs appears *dark*. **(b)** O 1s spectra taken in the spots indicated in the C 1s images. For this experiment atomic oxygen was used. Oxygen doses for the three images in **(a)** are from bottom to top: 0.5×10^{17}, 2.7×10^{17}, 8.1×10^{17} atoms/cm^2

14.3.3 Free-standing Nanostructures

Using SPEM we were able to explore the properties of individual free-standing nanotubes, nanowires and nanostructures [14.35–42]. In one of the studies we followed and compared the evolution of multiwall carbon nanotubes (CNT) during oxidation, one of the most common methods used for purification and tailoring their properties by introducing oxygenated groups in the C cage [14.36]. The C 1s images of the aligned CNT and the O 1s spectra, taken at selected microspots, are reported in Fig. 14.10a. Comparing the initial and advanced stages of CNT oxidation one can clearly see the morphological and chemical changes occurring as a result of the interaction of carbon with oxygen. It is clear that the oxidation and consumption via gasification starts from the more reactive tips of the CNTs and also that the oxidation rate varies when comparing the evolution of the individual CNTs. The different oxidation rate was attributed to the fact that it depends on the density of defects in the C cage, a characteristic property for each single CNT. The O 1s spectra contain features corresponding to different oxygenated groups, ether epoxy and carbonyl, which evolve with advancement of oxidation, and the carbonyls, which are those preceding gasification. It has been revealed that the major reason for the different oxidation rate of single CNTs is that the type and abundance of the oxygenated functional groups is controlled by the presence and type of the vacancy defects in the C cage, which is encoded in the C 1s spectrum of each CNT [14.35]. Since the introduction of a selected oxygenated func-

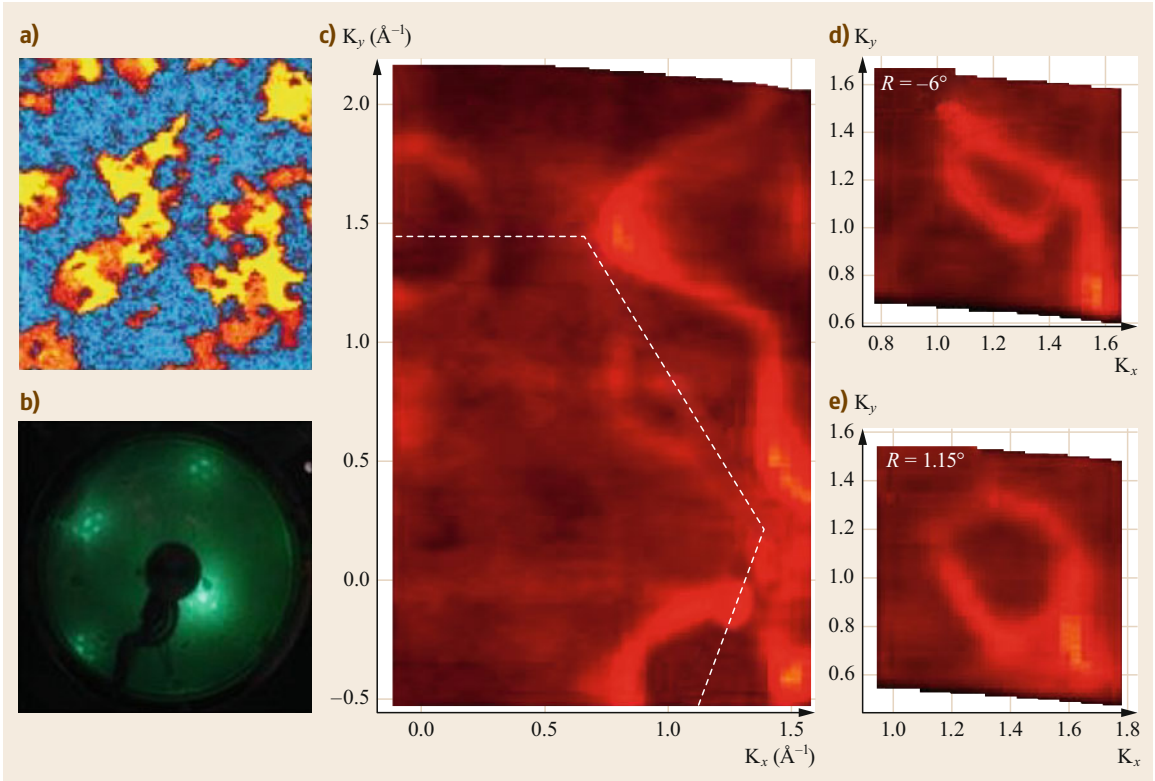

Fig. 14.11 **(a)** Scanning μ-ARPES of graphene bilayer flakes grown on Ir(111) $100 \times 100\,\mu m^2$ and **(b)** corresponding LEED pattern. **(c)** Measured Ir(111) Fermi surface and graphene Brillouin zone aligned along the main directions of Ir schematically shown as a *dashed hexagon* with K points at its vertexes. **(d,e)** Constant energy slices 400 meV below E_f through the graphene Dirac cones indicated by a *dashed line* in **(d)** taken from two different domains rotated differently at an angle R with respect to the Ir substrate

tional group can be used to tailor the physical, chemical or electronic properties of the CNTs, the obtained results suggest that controlled introduction of defects can be used to favor a desired modification. In this respect SPEM can be used as an excellent characterization tool.

14.3.4 Graphene Microstructures

This last example demonstrates the potential of μ-ARPES in mapping the band structure of graphene grown on an Ir(111) single crystal by vapor deposition (few cycles of methanol exposure and annealing to ≈ 1270 K). This growth procedure results in the formation of microsized flakes with different rotations. Apparently, such samples cannot be characterized with the traditional ARPES instruments since they require not only high spectral and angular resolution but also a sub-micrometer spatial resolution. The image of the graphene rotational domains taken with SO-SPEM is shown in Fig. 14.11, where the contrast variations are provided by different rotations of the flakes on the Ir surface. In order to obtain this image the analyzer was set to exclusively collect electrons emitted from the domains appearing brighter while the photoelectrons from other domain bands were only partially collected and these domains appear darker.

A standard low-energy electron diffraction pattern (Fig. 14.11b) demonstrates the diffraction peaks from such incommensurate domains. However, incommensurability and concomitant rotations complicate considerably interpretation of such space-averaging measurements. The constant energy slice at the Fermi level (E_f) shows the Fermi surface of Ir(111) and in blue the Brillouin zone of graphene is schematically shown for the case in which graphene orientation coincides with the substrate. Analysis of the ARPES measured for each individual domain allows clear interpretation of domain rotations, understanding their thickness and electronic structure. The rotation angles of particular domains, i.e., position of their K points with respect to the aligned graphene Brillouin zone (Fig. 14.11c) can be evaluated from constant energy slices below E_f, at which the

graphene π bands have a truncated triangular profile, as indicated by dashed lines in Fig. 14.11d centered at the K point. In Fig. 14.11d,e, showing fragments of Brillouin zones around the K point, such profiles are shown for two types of domains, rotated by $R = -6°$ and 1.2° with respect to the Ir substrate. Analysis of the angle-energy dispersions k–E (not shown) has also indicated that the domains are graphene bilayers with only the top layer rotationally misaligned and nondoped while the first layer exhibits p-type doping and has the same orientation as the substrate.

However, it should be recognized that the μ-ARPES technique although promising has limits to shedding light on new physics at the nanoscale; spatial resolution better than 50 nm is still a desire for the future. The main advantage and applicability of μ-ARPES today is in exploiting the physics of operative microsized devices, i.e., for the samples produced ex situ. However, also here the application is not trivial and many aspects should be considered for rational sample design, i.e., beam-induced effects, cleanness of the transfer of 2-D materials of interest and the choice of the substrate. For example, historically the graphene flakes were placed on thick SiO_2 substrate allowing them to be aligned in an optical microscope. Therefore, for several years these were also the first-choice samples studied with ARUPS. There have been a few attempts to measure the electronic structure of ex situ prepared devices as well but the obtained band widths were large, i.e., with quite modest resolution not allowing the use of the full potential of our μ-ARPES because of intrinsic complications in the sample design and sample degradation under the photon beam. For example, in the works reported in [14.43, 44] the bands of MoS_2 monolayer on Si oxide are broad, while for a bilayer they look better and the bulk one is comparable to other average ARPES measurements. A real breakthrough for such types of measurements was achieved only recently with proper device design combining dry transfer of monolayers, right choice of the substrate and encapsulation by an inert monolayer i.e., by graphene [14.45] or boron nitride (BN). In this case, the spectral resolutions we obtained are comparable to standard ARPES measurements and hence can provide quantitative access to many important parameters such as small spin orbit couplings, band alignments between different monolayers etc. This first achievement opens up further new possibilities, e.g., for exploiting the electronic structure of contacted devices, including applications exploring the gate potentials as well.

14.4 Near-ambient Pressure (NAP) Experiments with SPEM

Overcoming the pressure gap limits can be considered as the most significant recent development opening up the route for in operando SPEM experiments. We would like to note that soft x-ray SPEM cannot use the classical near-ambient pressure XPS approach with a differentially pumped analyzer, since the geometrical arrangement with ZP focusing optics in front of the sample does not allow for placing of the sample very close to the entrance aperture of the analyzer.

In this section, which can also be considered as an outlook, we will present the current state of different approaches developed in recent years aimed at exploiting with submicron spatial resolution the functional materials in their natural ambient environment. At present many of the obtained results are still a proof of principle for the performance of developed setups. Nevertheless, the implementation of new technical solutions is moving ahead extremely rapidly making these methods more reliable and user friendly.

14.4.1 The Dynamic High-pressure Setup

The dynamic high pressure (DHP) system developed at Elettra uses a highly collimated gas jet, as a supersonic jet expansion into a vacuum chamber, to confine the gases into a narrow beam pointing to the sample surface illuminated by x-rays. By using a pulsed jet instead of a continuous one the space volume containing the high-pressure gas is limited to a small region near the sample. This particular setup is also adopted in other research fields to control the amount of injected gas [14.46]. The schematic view of the DHP setup is reported in Fig. 14.12a: a gas jet is generated in the region around a sample by a thin needle oriented to avoid any interference with the x-ray optic system and the electron analyzer. It should be noted that to run the DHP no particular upgrades were necessary for the SPEM chamber pumping system, except for an additional differential pumping of the HEA electron detector section. The plot of the pressure time profile on the sample is shown in Fig. 14.12b. A pulsed valve produces a series of gas jet shots at a fixed repetition time. Each shot generates a short burst of pressure in a small and confined volume near the sample, which, expanding through the entire volume of the vacuum chamber, induces an increase of the background pressure. If the duration of shots is properly tuned, the injected gas is efficiently diluted into the large chamber volume to keep the back-

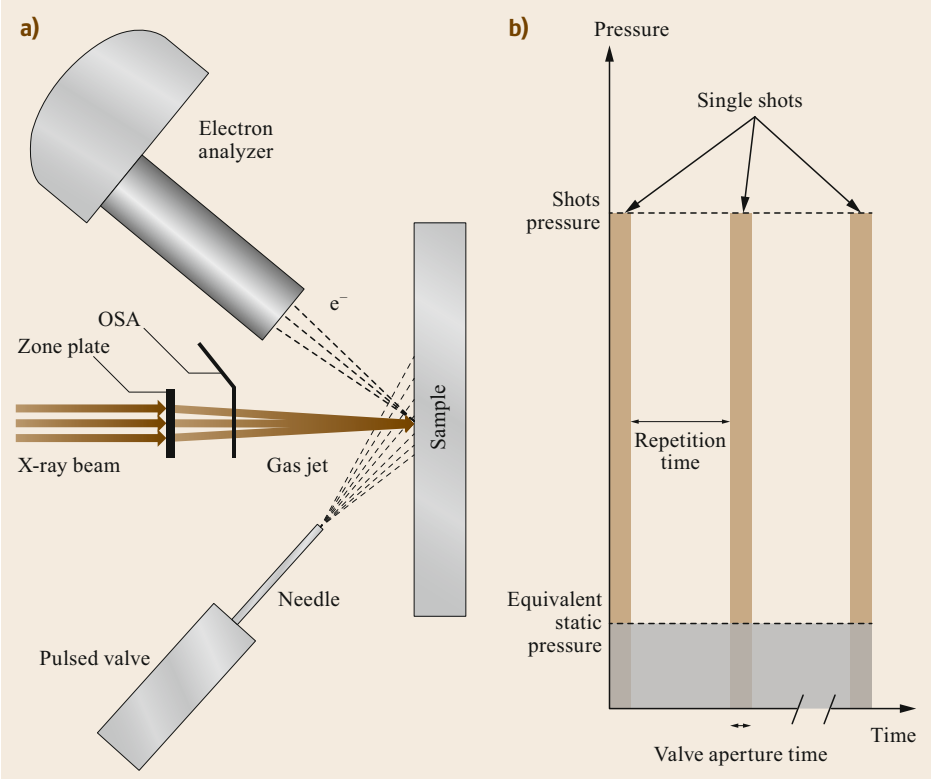

Fig. 14.12
(a) Schematic view of the DHP setup; a commercial pulsed valve has been used. This valve, which can operate in a UHV environment, provides high repeatability and response operation as fast as 160 μs and the peculiar design of the valve outlet gas section avoids dead volumes as well. **(b)** Plot of the pressure time profile on the sample with time

ground pressure low enough to not exceed the limits for XPS measurement, set to 1×10^{-5} mbar in the electron detector region. After each shot the background pressure rapidly recovers to the initial UHV condition.

Due to the geometrical constraints existing in the SPEM chamber (sample and optics stages, HEA) the DHP system is mounted with a grazing angle geometry as shown in Fig. 14.12a. Both the pulsed valve and the needle are mounted inside the SPEM vacuum chamber while the gases are supplied through a feedthrough from the air side of the chamber. The whole DHP system is mounted on a precision three-axis manipulation stage to allow a fine alignment of the gas jet with the focused x-ray beam and electron analyzer focal position. More details about the setup are given in [14.46].

The single shot pressure time profiles at the sample surface as a function of the pulsed valve aperture time are shown in Fig. 14.13. The distance between the sample and the needle tip were fixed to 2 mm while the valve inlet gas pressure was set to 3.5 bar. An aperture time of the valve ranging from 3.2 to 3.8 ms produces a burst of pressure at the sample surface in the range of few tenths of mbar; small changes of the aperture time generate significant variations of the outgoing jet pressure as clearly visible in the figure. The inset in Fig. 14.13 shows the time evolution of the pressure in the electron detector region of the HEA for a 3.2 ms-long pulse corresponding to a 10 mbar shot at the sample; the pressure in the most critical zone of the SPEM chamber does not overcome the pressure limit ($\approx 1\times10^{-5}$ mbar) and can be considered the upper limit for the valve aperture. The injected amount of gas by each jet corresponds to an equivalent dosage of 10^3-10^4 mbar s. As shown in Fig. 14.13, the time needed to recover a UHV condition in the SPEM chamber is a couple of seconds. For a prolonged use of the DHP we have found that pulses repeated with a frequency of 0.35 Hz with a 3.2 ms aperture time never exceed the background pressure limit. The system has demonstrated a high level of reproducibility of the parameters over long periods (> 7 h) of operation.

No significant changes in the performance of the system have been observed by changing the valve inlet gas pressure by ±0.5 bar. Due to the gas jet profile an alignment between the x-ray beam and the gas jet with a precision of 0.5 mm is required to maximize the shot pressure in the analyzed area of the sample surface.

The DHP setup was first used in the in operando study of a self-driven MnO_2 cathode/YSZ/NiO anode cell exposed to H_2 and CH_4+O_2 reactant mixture, where we were able to detect the current generated by

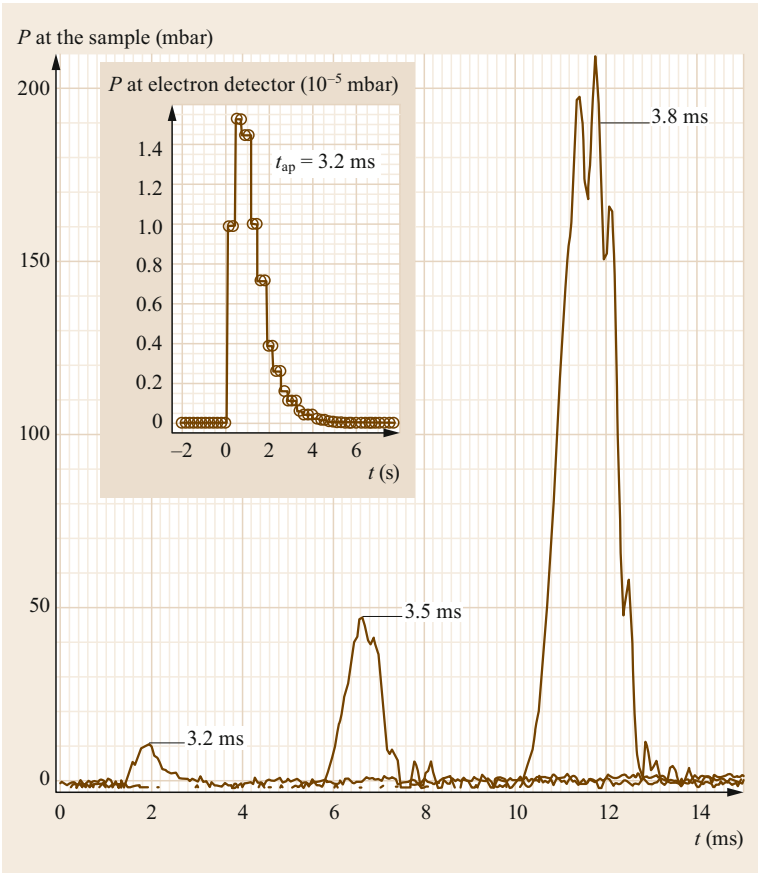

Fig. 14.13 Single shot pressure time profiles at the sample surface as a function of the pulsed valve aperture time. The *inset* shows the time evolution of the pressure in the electron detector region of the HEA for a 3.2 ms-long pulse corresponding to a 10 mbar shot at the sample

the electrochemical processes [14.24, 47]. By collecting Ni 2p maps of the electrode in the vicinity of the electrolyte we took advantage of the lateral and spectral resolution of SPEM to monitor both the evolution of the chemical state of the anode and the current-induced spectral shift that is a direct measure of the created local overpotential. Using the Ni $2p_{3/2}$ energy window both for imaging and microspot spectroscopy covering the oxide and metallic Ni components we were also able to follow the evolution after starting the reaction. The duration of each vertical scan and the time required for collecting a microspot spectrum determined the time resolution (better than 60 s), which allowed us to follow the growth of the metallic Ni^0 component at the expense of the oxide Ni^{2+} one and the overpotential shift (Fig. 14.14a).

The time evolution of the oxidation state and local potential of the working Ni anode are exemplified by the Ni $2p_{2/3}$ spectra in Fig. 14.14a, measured close to the Ni/YSZ interface (three-phase boundary), i.e., the most electrochemically active region. Immediately after switching to $H_2 + O_2$ the Ni $2p_{2/3}$ spectrum undergoes a rigid energy shift. Since in the initial state the Ni electrode is oxidized, the shift is better evidenced by the Ni^{2+} component that is present in all spectra. The energy shift of the spectra is a measure of the overpotential resulting from the current flow generated by the hydrogen oxidation that starts on the NiO electrode; this process is anodic so the shift is to higher binding energy (lower kinetic energy). As illustrated by the plots in Fig. 14.14b and c under the applied reaction conditions, starting from a NiO, the steady chemical state resulting from the concurrence between anodic oxidation and chemical reduction is achieved after 30 min; the same time is needed to reach the steady-state overpotential of 0.8 eV. These results have shed light on competing electrochemical and chemical processes occurring in real electrochemical devices generating electrical current. They demonstrate the great potential of the used advanced experimental approach to gain insight into electrochemical and chemical processes taking place in energy conversion systems, which could guide the design of next-generation devices with improved performance.

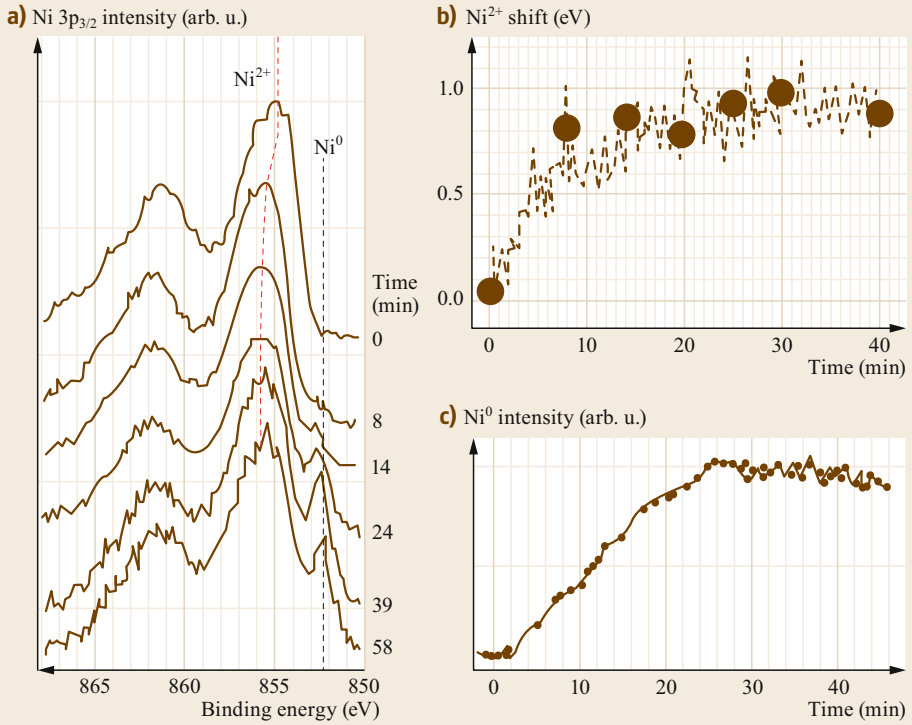

Fig. 14.14 **(a)** Ni $2p_{3/2}$ spectra (the positions of the Ni^{2+} and Ni^0 are indicated by *dashed lines*) taken in a selected microspot in the vicinity on Ni-electrolyte interface illustrating the time evolution after exposing the cell to $H_2 + O_2$ ambient air at 920 K. **(b)** The shift of the Ni^{2+} as a function of exposure time that encodes the electrochemical reaction; **(c)** the increase of Ni^0 intensity as a function of exposure that results from the chemical reaction

14.4.2 Compact Near-ambient Pressure Cells

The development of compact cells to enable PES at near-ambient pressure started several years ago [14.48]; to tackle the problem of replacing samples in UHV systems it is necessary to have retractable cells versatile enough to offer the desired reaction conditions (e.g., a sample heating system). Moreover, in order to achieve a certain flexibility to attain nearly realistic in operando conditions a sophisticated design of the differentially pumped HEA is required. However, to date the possibility to use these cells for laterally resolved photoemission studies has remained a dream; the main obstacle in the case of ZP-based SPEMs is the severely constrained space available around the sample where focusing optics, HEA nose, and sample scanners are located.

The cell designs for SPEM have exploited the advantage of using a focused x-ray beam. The first SPEM reaction cell had a small pinhole of 2 μm diameter on the front plate and was vacuum sealed using electron transparent graphene or graphene oxide membranes to separate the sample environment from the UHV without requiring any differential pumping. The graphene sealed setups have already been described in detail in several reports [14.49–51]. Indeed, the great advantage of the sealed cells is that they can also be used for studies of reaction in liquids, but this requires fabrication of very high quality defect-free membranes, very well-developed and reliable sealing technology and a long-term resistance of the graphene membranes to intense x-ray radiation. The graphene-sealed cells have already found wide applications in electron microscopes as well and are really the only means to study events in ambient gas pressures and liquid environments using electron detection. Attempts to design electrochemical cells where the graphene window can also act as a working electrode have already been made and the first results demonstrating electrochemical deposition from an electrolyte are promising [14.51].

Recently, the team of the Escamicroscopy beamline at Elettra succeeded in developing a retractable near ambient pressure cell (NAPCell) capable of performing XPS sample analysis with the typical spatial resolution of the ZP-SPEM (≈ 100 nm) at pressures as high as 0.1 mbar without using a sealing membrane. Indeed, this novel approach works only in gas ambient environments but it does use membranes that also attenuate the intensity of the emitted photoelectron signal. As noted above the x-ray microprobe used in SPEM allows the use of small-dimension pinholes as photon in/photoelectron out apertures. Since the gas leak through such pinholes is very weak this avoids the use of differ-

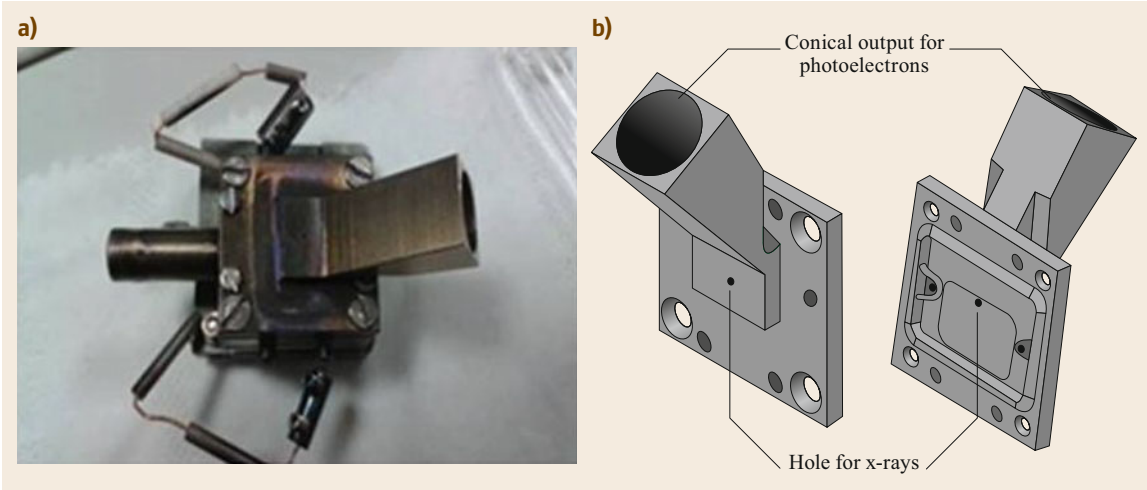

Fig. 14.15 **(a)** Picture of the compact NAPCell. The material used to build the current version is stainless steel. **(b)** CAD drawings showing the top plate (front and back side); the holes for the incoming x-rays in the center and the conical output for the photoelectrons have been indicated

entially pumped HEA, barely adaptable in a SPEM. As described below this much simplified approach has made SPEM a unique microscope for both UHV and near-ambient pressure experiments.

The SPEM NAPCell, illustrated in Fig. 14.15, is vacuum sealed. It is provided with two pinholes: one of 500 μm diameter on the front plate providing an entrance port of the focus x-ray beam and a second one of the same size that laterally extends in a conical shape pointing to the HEA (i.e., with an angle of 60° with respect to the x-ray beam) through which the photoelectrons generated on the surface sample will escape and reach the HEA. The dimension of the first pinhole defines also the accessible area of samples while the size of the lateral pinhole with the outer cone has been selected to provide the same maximum acceptance angle of the HEA.

The reactive gases are delivered into the cell via a mechanically flexible part of the dosing line inside the SPEM chamber and a complimentary external part connecting to the atmosphere side. The gas pressure can be adjusted by means of dosing valves and a Pirani pressure gage. An external pumping stage is attached to the NAPCell to pump the dosing line and the cell. The NAPCell is also constantly pumped through the pinhole by the vacuum provided by the main chamber pumping system. The pumping power of the SPEM chamber and the size of pinholes enable pressures up to 0.1 mbar to be achieved inside the cell and below 10^{-5} mbar inside the SPEM chamber, which is the upper safe pressure limit for performing photoelectron spectroscopy without any failure on the electron detection system and the beamline. An encapsulated heater, placed on the back of the sample, allows varying of the sample temperature in the range 300–720 K. Additional electrical contacts are available for the thermocouple connection and/or biasing of sample. All parts of the cell, including the heater and the thermocouple feedthroughs, were made of UHV-compatible materials to avoid undesirable degassing especially at elevated temperatures.

The following example reports on the oxidation and reduction of a Rh metal surface. It represents the first experiment performed with the NAPCell in the mbar pressure range. The evolution of Rh 3d and O 1s core levels acquired from an unpolished polycrystalline Rh foil under successive exposures of oxygen and hydrogen at 670 K was characterized by acquiring core-level photoemission spectra and maps.

Figure 14.16a shows a small-scale Rh $3d_{5/2}$ map of the foil inside the NAPCell. The image represents the lateral variations of the selected photoelectron emission signal, including the background as well. These well-resolved structures prove that the typical submicron resolution of the ZP-SPEM instrument is preserved, i.e., the cell setup does not deteriorate the SPEM spatial resolution. The performance of the high-pressure cell was examined by investigating the oxidation and reduction of the Rh metal surface.

The lineshape of the top Rh $3d_{5/2}$ spectrum A in Fig. 14.16b is typical for a sample being exposed to air before being introduced into the cell, where it was annealed at 570 K in the ambient air of 0.1 mbar of $H_2(g)$ for 60 min in order to recover its metallic state. The spectrum, which has been deconvoluted by using Doniach–Sunjich functions (colored solid lines), reveals a dominant metallic Rh component centered

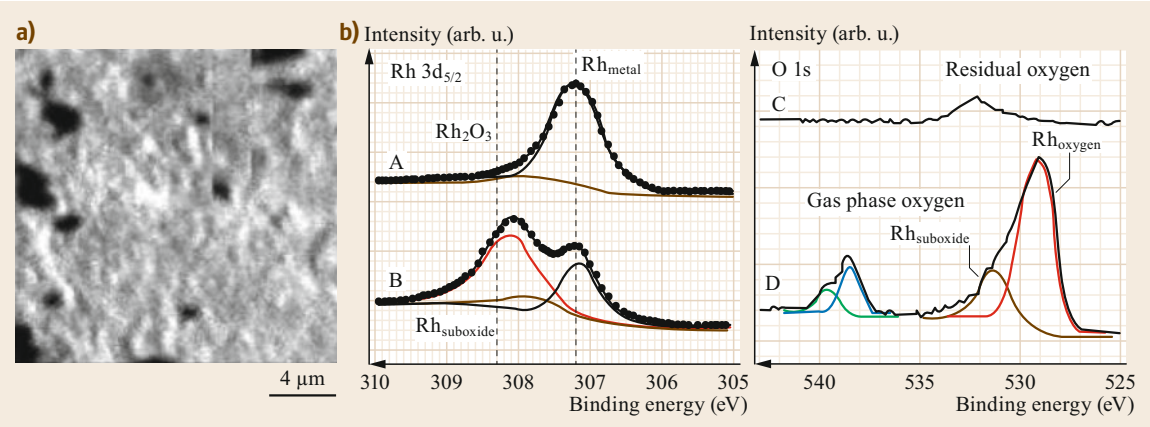

Fig. 14.16 **(a)** $20 \times 20\,\mu m^2$ Rh map acquired with the ZP-SPEM during the exposure to 0.1 mbar O_2. As it is visible the characteristic spatial resolution of the ZP-SPEM is kept also in this environment. **(b)** Rh $3d_{5/2}$ and O 1s core-level XPS spectra acquired before and after the oxidation. The presence of the gas phase O 1s peak should be noted in spectrum D

at 307.2 eV binding energy (eV) and a minor additional contribution at 307.8 eV, indicative for the presence of residual substoichiometric surface oxides. These values are in fair agreement with previous experiments [14.52]. This result provides clear evidence that the annealing at 0.1 mbar H_2 exposure had effectively reduced the surface and also removed the C contaminants (not shown), which is not possible for H_2 exposures of maximum allowable pressure level of 1×10^{-5} mbar by backfilling of the SPEM chamber. The same surface was then exposed to 0.1 mbar O_2 for 30 min, keeping the temperature of the sample at 670 K. After the oxygen treatment the measured Rh $3d_{5/2}$ spectrum (B in the Rh $3d_{5/2}$ panel of Fig. 14.16b) is dominated by a new peak situated at 308.2 eV BE, corresponding to Rh_2O_3 [14.52, 53]. These results show an uneven reactivity of the Rh surface at the length scale reachable with the SPEM.

The observed changes in the Rh 3d and O 1s spectra after oxidation are in good agreement with previous results for oxidized Rh films and Rh polycrystalline foils at ambient pressures, where the observed two components were attributed to Rh_2O_3 and RhO_2/RhOOH species [14.54, 55].

A clear proof that the sample inside the cell is exposed to O_2 pressure at the mbar level are the O 1s core-level spectra, recorded before and during exposure of the Rh foil to O_2. The spectrum C, measured after the initial treatment in H_2, appears as a broad feature peaked at $\approx$ 532–533 eV, well matching residual suboxides reported in literature [14.52]. The presence of this residual oxygen component is also in agreement with the existence of a small high BE component of the Rh $3d_{5/2}$ in the spectrum A. As for the Rh $3d_{5/2}$ also the O 1s spectrum undergoes an evident change during the 0.1 mbar O_2 exposure. In spectrum D two new distinct O 1s doublet spectral features appear. The most intense doublet is dominated by a component located at $\approx$ 529.3 eV and the second weaker one at $\approx$ 531.3 eV belonging to O 1s of Rh_2O_3 and $Rh_{suboxide}$ phases respectively. The second nicely resolved doublet within the $\approx$ 538.5–539.6 eV range corresponds to the gas phase oxygen molecules inside the cell, directly ionized by the x-ray photon beam. The presence of a well-resolved O 1s spectral feature from the gas phase oxygen also validates that the high-pressure cell allows mbar pressure levels to be reached, so the Rh undergoes oxidation that cannot occur under high vacuum conditions.

14.5 Conclusions

In this short review we hope that we were able to introduce the reader to the growing ability of SPEM in the last decade to characterize the surface and interfacial properties and the events occurring at gas-surface interfaces, where the microprobe added the missing lateral resolution. Looking to the future, we expect further advances to fully overcome the material and in operando gaps, which means pushing further lateral resolution, time resolution and the performance of real in operando studies. These are the only viable routes in the attempt to optimize the fabrication processes or reveal the chemical states and all possible desired and undesired events that determine the performance of the complex functional materials.

References

14.1 J. Kirz, C. Jacobsen: The history and future of X-ray microscopy, J. Phys.: Conf. Ser. **186**, 12001 (2009), https://doi.org/10.1088/1742-6596/186/1/012001

14.2 R. Falcone, C. Jacobsen, J. Kirz, S. Marchesini, D. Shapiro, J. Spence: New directions in X-ray microscopy, Contemp. Phys. **52**, 293–318 (2011), https://doi.org/10.1080/00107514.2011.589662

14.3 J. Stöhr: *NEXAFS Spectroscopy* (Springer, Berlin 1992)

14.4 K. Siegbahn: From x-ray to electron spectroscopy and new trends, J. Electron Spectrosc. Relat. Phenom. **51**, 11–36 (1990)

14.5 D. Attwood: *Soft X-rays and Extreme Ultraviolet Radiation: Principles and Application* (Cambridge Univ. Press, Cambridge 1999)

14.6 A.G. Michette: *Optical Systems for Soft X-rays* (Plenum, New York 1986)

14.7 I. Mohacsi, P. Karvinen, I. Vartiainen, V.A. Guzenko, A. Somogyi, C.M. Kewish, P. Mercere, C. David: High-efficiency zone-plate optics for multi-keV x-ray focusing, J. Synchrotron Radiat. **21**, 497–501 (2014)

14.8 K. Yamauchi, M. Yabashi, H. Ohashi, T. Koyama, T. Ishikawa: Nanofocusing of x-ray free-electron lasers by grazing-incidence reflective optics, J. Synchrotron Radiat. **22**, 592–598 (2015), and references therein

14.9 G. Margaritondo, F. Cerrina: Overview of soft-x-ray photoemission spectromicroscopy, Nucl. Instrum. Methods Phys. Res. A **291**, 26–35 (1990)

14.10 E. Bauer: *Surface Microscopy with Low Energy Electrons* (Springer, New York 2014)

14.11 C.M. Schneider, G. Schönhense: Investigating surface magnetism by means of photoexcitation electron emission microscopy, Rep. Prog. Phys. **65**, R1785–R1839 (2002)

14.12 M. Amati, A. Barinov, V. Feyer, L. Gregoratti, M. Al-Hada, A. Locatelli, T.O. Mentes, H. Sezen, C.M. Schneider, M. Kiskinova: Photoelectron microscopy at Elettra: Recent advances and perspectives, J. Electron Spectrosc. Relat. Phenom. **224**, 59–67 (2018)

14.13 C. Tusche, M. Ellguth, A. Krasyuk, A. Winkelmann, D. Kutnyakhov, P. Lushchyk, K. Medjanik, G. Schönhense, J. Kirschner: Quantitative spin polarization analysis in photoelectron emission microscopy with an imaging spin filter, Ultramicroscopy **130**, 70–76 (2013)

14.14 P. Dudin, P. Lacovig, C. Fava, E. Nicolini, A. Bianco, G. Cautero, A. Barinov: Angle-resolved photoemission spectroscopy and imaging with a sub-micrometre probe at the SPECTROMICROSCOPY-3.2L beamline of Elettra, J. Synchrotron Radiat. **17**, 445–450 (2010)

14.15 J. Avila, I. Razado-Colambo, S. Lorcy, B. Lagarde, J. Giorgetta, F. Polack, M.C. Asensio: ANTARES, a scanning photoemission microscopy beamline at SOLEIL, J. Phys. Conf. Ser. **425**, 192023 (2013)

14.16 E. Rotenberg, A. Bostwick: microARPES and nanoARPES at diffraction-limited light sources: Opportunities and performance gains, J. Synchrotron Radiat. **21**, 1048–1056 (2014)

14.17 Elettra Sincrotrone Trieste: ESCA Microscopy, https://www.elettra.eu/elettra-beamlines/escamicroscopy.html

14.18 Elettra Sincrotrone Trieste: Spectromicroscopy, https://www.elettra.eu/elettra-beamlines/spectromicroscopy.html

14.19 W. Yun, B. Lai, Z. Cai, J. Maser, D. Legnini, E. Gluskin, Z. Chen, A.A. Krasnoperova, Y. Vladimirsky, F. Cerrina, E. Di Fabrizio, M. Gentili: Nanometer focusing of hard x-rays by phase zone plates, Rev. Sci. Instrum. **70**, 2238 (1999)

14.20 J. Kirz: Phase zone plates for x-rays and the extreme uv, J. Opt. Soc. Am. **64**, 301–309 (1974)

14.21 B.L. Henke, E.M. Gullikson, J.C. Davis: X-ray interactions: Photoabsorption, scattering, transmission and reflection at $E = 50–30\,000$ eV, $E = 1–92$, At. Data Nucl. Data Tables **54**(2), 181–342 (1993)

14.22 J. Maser, G. Schmahl: Coupled wave description of the diffraction by zone plates with high aspect ratios, Opt. Commun. **89**, 355–362 (1992)

14.23 Synchrotron SOLEIL: ANTARES, https://www.synchrotron-soleil.fr/en/beamlines/antares

14.24 B. Bozzini, M. Amati, L. Gregoratti, M. Kiskinova: In-situ photoelectron microspectroscopy and imaging of electrochemical processes at the electrodes of a self-driven cell, Sci. Rep. **3**, 2848 (2013)

14.25 G. Cautero, R. Sergo, L. Stebel, P. Lacovig, P. Pittana, M. Predonzani, S. Carrato: A two-dimensional detector for pump-and-probe and time resolved experiments, Nucl. Instrum. Methods Phys. Res. A **595**, 447–459 (2008)

14.26 S. Gunther, A. Kolmakov, J. Kovac, M. Kiskinova: Artefact formation in scanning photoelectron emission microscopy, Ultramicroscopy **75**, 35–51 (1998)

14.27 B. Bozzini, B. Alemán, M. Amati, M. Boniardi, V. Caramia, G. Giovannelli, L. Gregoratti, M. Abyaneh Kazemian: Novel insight into bronze disease gained by synchrotron-based photoelectron spectro-microscopy, in support of electrochemical treatment strategies, Stud. Conserv. **9**, 465–473 (2016)

14.28 A. Böttcher, U. Starke, H. Conrad, R. Blume, H. Niehus, L. Gregoratti, B. Kaulich, A. Barinov, M. Kiskinova: Spectral and spatial anisotropy of the oxide growth on Ru(0001), J Chem. Phys. **117**, 8104 (2002)

14.29 R. Blume, H. Niehus, H. Conrad, A. Böttcher, L. Aballe, L. Gregoriatti, A. Barinov, M. Kiskinova: Identification of subsurface oxygen species created during oxidation of Ru(0001), J. Phys. Chem. B **109**, 14052–14058 (2005)

14.30 P. Dudin, A. Barinov, L. Gregoratti, M. Kiskinova, F. Esch, C. Dri, C. Africh, G. Comelli: Initial oxidation of a Rh(110) surface using atomic or molecular oxygen and reduction of the surface oxide by hydrogen, J. Phys. Chem. B **109**, 13649–13655 (2005)

14.31 P. Dudin, A. Barinov, M. Dalmiglio, L. Gregoratti, M. Kiskinova, A. Goriachko, H. Over: Nanoscale morphology and oxidation of ion-sputtered Rh(110) and Ru(0001), J. Electron Spectrosc. Relat. Phenom. **166**, 89–93 (2008)

14.32 P. Melpignano, A. Baron-Toaldo, V. Biondo, S. Priante, R. Zamboni, M. Murgia, S. Caria, L. Gregoratti, A. Barinov, M. Kiskinova: Mechanism of dark-spot degradation of organic light-emitting devices, Appl. Phys. Lett. **86**, 41105 (2005)

14.33 S. Gardonio, L. Gregoratti, P. Melpignano, L. Aballe, V. Biondo, R.M. Murgia, S. Caria, M. Kiskinova: Degradation of organic light-emitting diodes under different environment at high drive conditions, Org. Electron. **8**, 37–43 (2007)

14.34 S. Gardonio, L. Gregoratti, D. Scaini, C. Castellarin-Cudia, P. Dudin, P. Melpignano, V. Biondo, R. Zamboni, S. Caria, M. Kiskinova: Characterization of indium tin oxide surfaces after KOH and HCl treatments, Org. Electron. **8**, 253–261 (2008)

14.35 A. Barinov, H. Üstünel, S. Fabris, L. Gregoratti, L. Aballe, P. Dudin, S. Baroni, M. Kiskinova: Defect-controlled transport properties of metallic atoms along carbon nanotube surfaces, Phys. Rev. Lett. **99**, 046803 (2007)

14.36 A. Barinov, L. Gregoratti, P. Dudin, S. La Rosa, M. Kiskinova: Imaging and spectroscopy of multi-walled carbon nanotubes during oxidation: Defects and oxygen bonding, Adv. Mater. **21**, 1916–1920 (2009)

14.37 F. Jabeen, S. Rubini, F. Martelli, A. Franciosi, A. Kolmakov, L. Gregoratti, M. Amati, A. Barinov, A. Goldoni, M. Kiskinova: Contactless monitoring of the diameter-dependent conductivity of GaAs nanowires, Nano Res. **3**, 706–713 (2010)

14.38 C. Struzzi, D. Erbahar, M. Scardamaglia, M. Amati, L. Gregoratti, M.J. Lagos, G. Tendeloo, R. Snyders, C. Ewels, C. Bittencourt: Selective decoration of isolated carbon nanotubes by potassium evaporation: Scanning photoemission microscopy and density functional theory, J. Mater. Chem. C **3**(11), 2518–2527 (2015)

14.39 M. Scardamaglia, C. Struzzi, F.J. Aparicio Rebollo, P. De Marco, P.R. Mudimela, J. Colomer, M. Amati, L. Gregoratti, L. Petaccia, R. Snyders, C. Bittencourt: Tuning electronic properties of carbon nanotubes by nitrogen grafting: Chemistry and chemical stability, Carbon **83**, 118–127 (2015)

14.40 M. Scardamaglia, B. Aleman, M. Amati, C. Ewels, P. Pochet, N. Reckinger, J. Colomer, T. Skaltsas, N. Tagmatarchis, R. Snyders, L. Gregoratti, C. Bittencourt: Nitrogen implantation of suspended graphene flakes: Annealing effects and selectivity of sp2 nitrogen species, Carbon **73**, 371–381 (2014)

14.41 M. Scardamaglia, M. Amati, B. Llorente, P. Mudimela, J. Colomer, J. Ghijsen, C. Ewels, R. Snyders, L. Gregoratti, C. Bittencourt: Nitrogen ion casting on vertically aligned carbon nanotubes: Tip and sidewall chemical modification, Carbon **77**, 319–328 (2014)

14.42 P. Gondoni, P. Mazzolini, V. Russo, M. Diani, M. Amati, L. Gregoratti, V. De Renzi, G.C. Gazzadi, J. Martí-Rujas, A. Li Bassi, C.S. Casari: Tuning electrical properties of hierarchically assembled Al-doped ZnO nanoforests by room temperature pulsed laser deposition, Thin Solid Films **594**(Part A), 12–17 (2015)

14.43 H. Yuan, Z. Liu, G. Xu, B. Zhou, S. Wu, D. Dumcenco, K. Yan, Y. Zhang, S. Mo, P. Dudin, V. Kandyba, M. Yablonskikh, A. Barinov, Z. Shen, S. Zhang, Y. Huang, X. Xu, Z. Hussain, H.Y. Hwang, Y. Cui, Y. Chen: Evolution of the valley position in bulk transition-metal chalcogenides and their monolayer limit, Nano Lett. **16**, 4738–4745 (2016)

14.44 W. Jin, P. Yeh, N. Zaki, D. Zhang, J.T. Liou, J.T. Sadowski, A. Barinov, M. Yablonskikh, J.I. Dadap, P. Sutter, I.P. Herman, R.M. Osgood Jr.: Substrate interactions with suspended and supported monolayer MoS_2: Angle-resolved photoemission spectroscopy, Phys. Rev. B **91**, 121409(R) (2015)

14.45 N.R. Wilson, P.V. Nguyen, K. Seyler, P. Rivera, A.J. Marsden, Z.P.L. Laker, G.C. Constantinescu, V. Kandyba, A. Barinov, N.D.M. Hine, X. Xu, D.H. Cobden: Determination of band offsets, hybridization, and exciton binding in 2-D semiconductor heterostructures, Sci. Adv. **8**, e1601832 (2017)

14.46 M. Amati, M. Kazemian Abyaneh, L. Gregoratti: Dynamic high pressure: A novel approach toward near ambient pressure photoemission spectroscopy and spectromicroscopy, J. Instrum. **8**, T05001 (2013), and references therein

14.47 B. Bozzini, M. Amati, L. Gregoratti, C. Mele, M. Abyaneh, M. Prasciolu, M. Kiskinova: In-situ photoelectron microspectroscopy during the operation of a single-chamber SOFC, Electrochem. Commun. **24**, 104–107 (2012)

14.48 S.K. Eriksson, M. Hahlin, J.M. Kahk, I.J. Villar-Garcia, M.J. Webb, H. Grennberg, R. Yakimova, H. Rensmo, K. Edström, A. Hagfeldt, H. Siegbahn, M.O.M. Edwards, P.G. Karlsson, K. Backlund, J. Åhlund, D.J. Payne: A versatile photoelectron spectrometer for pressures up to 30 mbar, Rev. Sci. Instrum. **85**, 075119 (2014)

14.49 A. Kolmakov, D.A. Dikin, L.J. Cote, J. Huang, M.K. Abyaneh, M. Amati, L. Gregoratti, S. Gunther, M. Kiskinova: Graphene oxide windows for in situ environmental cell photoelectron spectroscopy, Nat. Nanotechnol. **6**, 651–657 (2011)

14.50 J. Kraus, R. Reichelt, S. Günther, L. Gregoratti, M. Amati, M. Kiskinova, A. Yulaev, I. Vlassiouk, A. Kolmakov: Photoelectron spectroscopy of wet and gaseous samples through graphene membranes, Nanoscale **6**, 14394 (2014)

14.51 A. Kolmakov, L. Gregoratti, M. Kiskinova, S. Günther: Recent approaches for bridging the pressure gap in photoelectron microspectroscopy, Top. Catal. **59**, 448–468 (2016)

14.52 M. Dalmiglio, M. Amati, L. Gregoratti, T.O. Menteş, M.A. Niño, L. Felisari, M. Kiskinova: Oxidation of supported PtRh particles: Size and morphology effects, J. Phys. Chem. C **114**, 16885–16891 (2010)

14.53 P. Dudin, A. Barinov, L. Gregoratti, D. Scaini, Y.B. He, H. Over, M. Kiskinova: MgO-supported rhodium particles and films: Size, morphology, and reactivity, J. Phys. Chem. C **112**, 9040–9044 (2008)
14.54 T.L. Barr: An ESCA study of the termination of the passivation of elemental metals, J. Phys. Chem. **82**, 1801–1810 (1978)
14.55 M. Peuckert: A comparison of thermally and electrochemically prepared oxidation adlayers on rhodium: Chemical nature and thermal stability, Surf. Sci. **141**, 500–514 (1984)

Matteo Amati

Elettra – Sincrotrone Trieste SCpA
Trieste, Italy
matteo.amati@elettra.eu

Matteo Amati received his PhD in Physics, Astrophysics, and Applied Physics in 2006 from the University of Milano (Italy), where he worked as a postdoc until 2008. Since 2008 he has been a beamline scientist at the ESCAmicroscopy beamline, operated at the Elettra Laboratory. He is a coauthor of 75 articles in peer-reviewed scientific journals in various domains of materials science.

Alexei Barinov

Elettra – Sincrotrone Trieste SCpA
Trieste, Italy
alexey.barinov@elettra.eu

Alexei Barinov graduated at Moscow Institute of Physics and Technology in 1998 and received his PhD in Solid-State Physics from RRC Kurchatov Institute in 2003. Since 2004 he has been employed as a supporting beamline scientist at Elettra and since 2008 he has been coordinating the angle-resolved photoemission spectromicroscopy beamline at Elettra. He is co-author of about 110 articles in peer-reviewed scientific journals.

Luca Gregoratti

Elettra – Sincrotrone Trieste SCpA
Trieste, Italy
luca.gregoratti@elettra.eu

Luca Gregoratti received his PhD in 2003 at King's College, London. Since 2001 he has held a permanent research position at Elettra–Sincrotrone, Trieste, where his activity has mainly focused on the field of photoemission spectromicroscopy and its application in various domains of materials science. He is coauthor of more than 170 articles in peer-reviewed scientific journals.

Hikmet Sezen

Elettra – Sincrotrone Trieste SCpA
Trieste, Italy
Institute for Methods and
Instrumentation for Synchrotron
Radiation Research FG-ISRR

Helmholtz-Zentrum Berlin für Materialien
und Energie GmbH
Berlin, Germany

Hikmet Sezen received his PhD (2012) in Chemistry from Bilkent University (Ankara, Turkey). He worked as a postdoc at Karlsruhe Institute of Technology (Germany) between 2012 and 2014 and at Elettra, ESCAmicroscopy beamline (Italy) between 2014 and 2017. He currently has a scientist position at Helmholtz-Zentrum Berlin, at the Slicing Femtospex Molecules and Surface Endstation and High Harmonic Laser Laboratory (Germany).

Maya Kiskinova

Elettra – Sincrotrone Trieste SCpA
Trieste, Italy
maya.kiskinova@elettra.eu

Maya Kiskinova received her PhD in 1977 and her ScD in 1989 in Physical Chemistry. She has worked at research centers and universities in Bulgaria, USA, and Germany and, since 1991, at Elettra, where she is presently Research Coordinator. She received Italian citizenship for scientific merits in 2002 and the Distinguished Humboldt Grant in 2005. Her research focuses on properties and transient states of functional materials. http://www.elettra.eu/PEOPLE/index.php?n=MayaKiskinova.HomePage

15. Natural Topological Insulator Heterostructures

S. V. Eremeev, Igor P. Rusinov, Evgueni V. Chulkov

A topological insulator is a state of quantum matter that, while being an insulator in the bulk, hosts metallic topologically protected electronic states at the surface. These states open the way for realizing a number of new applications in spintronics and quantum computing. In order to take advantage of their unique properties, topological insulators should be tuned in such a way that isolated Dirac cones are located within the topological transport regime, without any scattering channels.

This chapter is devoted to natural topological heterostructures composed of different sublattices, at least one of which is a topological insulator. We demonstrate that these systems show diverse electronic properties and, depending on the structure and composition, can be topological insulators supporting Dirac surface states whose dispersion essentially depends on the surface termination, topological Weyl semimetals, or trivial band insulators.

The chapter is organized in five sections. Section 15.1 provides computational details. In Sect. 15.2, we discuss the crystal structure and electronic states in the $(C^{IV}B^{VI})_{n=1}(A^{V}_2B^{VI}_3)_{m>1}$ superlattices. Section 15.3 is devoted to the peculiarities of the topologically protected electronic states in the $(C^{IV}B^{VI})_{n>1}(A^{V}_2B^{VI}_3)_{m=1}$ compounds. Temperature-driven topological phase transitions in the $Ge_2Sb_2Te_5$ phase-change materials are addressed in Sect. 15.4. Finally, we end with a summary and conclusions in Sect. 15.5.

Part C | 15

Over the past decade, the strong impact of topology on the electronic structure of numerous materials and related properties such as novel spin textures, surface and edge Dirac states, magnetic properties in two- and three-dimensional topological insulators, spin and charge transport, and exotic superconducting states have been actively discussed [15.1–4]. This research work resulted in the introduction of a topological classification based on topological order parameters. The most decisive contribution in this context is the definition of a class of topological insulators (TIs) based on $\mathbb{Z}_2$ classification. A topological insulator differs from a conventional band insulator (semiconductor) in that it features a nontrivial topological invariant in its bulk electronic wave functions.

Among the various formulations for the computation of the $\mathbb{Z}_2$ topological invariants, the Fu–Kane approach [15.5] is most suitable for analyzing band structures of crystals with inversion symmetry. In this approach, $\mathbb{Z}_2$ invariants can be determined from the matrix elements of Bloch wave functions at time-reversal invariant momentum (TRIM) points in the Brillouin zone (BZ). The three-dimensional (3-D) materials with inversion symmetry are classified according to four $\mathbb{Z}_2$ topological invariants, ν_0; $(\nu_1\nu_2\nu_3)$, which can be determined by the parity $\xi_m(\Gamma_i)$ of occupied bands at eight TRIM $\Gamma_{i=(n_1,n_2,n_3)} = (n_1\boldsymbol{b}_1 + n_2\boldsymbol{b}_2 + n_3\boldsymbol{b}_3)/2$ of the 3-D Brillouin zone, where $\boldsymbol{b}_1, \boldsymbol{b}_2, \boldsymbol{b}_3$ are primitive reciprocal lattice vectors, and $n_j = 0$ or 1 [15.5, 6]. The $\mathbb{Z}_2$ invariants are determined by

$$(-1)^{\nu_0} = \prod_{i=1}^{8} \delta_i$$

and

$$(-1)^{\nu_k} = \prod_{n_k=1;n_{j\neq k}=0,1} \delta_{i=(n_1n_2n_3)} ,$$

M. Rocca, T.S. Rahman, L. Vattuone (Eds.), *Springer Handbook of Surface Science*, Springer Handbooks,
https://doi.org/10.1007/978-3-030-46906-1_15

where $\delta_i = \prod_{m=1}^{N} \xi_{2m}(\Gamma_i)$ [15.6]. The strong time-reversal symmetry-driven topological insulators, which we will deal with in this chapter, are determined by a nontrivial topological invariant $\nu_0 = 1$. In the case of $\nu_0 = 1$, the topological invariants ν_1, ν_2, ν_3, provided that at least one of them is nonzero, indicate weak topological insulators.

The 3-D topological insulators are characterized by an inverted energy gap at an odd number of symmetry points of the bulk Brillouin zone due to strong spin–orbit coupling (SOC). The intriguing property of topological insulators is the formation of unique topologically protected metallic surface/edge states in spite of bulk insulating behavior [15.1, 6–11]. The surface state protection is provided by a combination of time-reversal symmetry and spin–orbit coupling [15.1, 6, 8, 9]. As a result, any nonmagnetic surface perturbation, such as surface passivation or doping, does not eliminate this surface state [15.5, 12–15].

The topological surface states (TSS) possess a range of properties that allow us to employ topological insulators in spin-based electronics (spintronics) [15.6, 8–10, 16]. First, these states demonstrate a linear dispersion forming a Dirac cone with a crossing (Dirac) point at/close to the Fermi level, which leads to high charge carrier mobility, similar to the case of graphene. Also, these carriers are spin-polarized, and a manipulation of spin-currents is an essential requirement for spintronics. In the search for efficient materials for spintronics, some studies have proposed topological insulators [15.7, 17–19] that possess a surface state for which the effects of spin–orbit coupling are maximal in the sense that an electron spin orientation is fixed relative to its propagation direction. Additionally, there are several exotic effects that exist on the surfaces of topological insulators that are based on half-quantized conductivity. A half-quantum Hall effect can be observed in TI surfaces with an odd number of Dirac cones and with time-reversal symmetry breaking induced by out-of-plane magnetization, as well as in thin films under external magnetic perturbation or magnetic doping [15.20]. Such an effect is a common feature for massless states like Dirac cones in TIs or graphene [15.9, 21–23]. The topological magnetoelectric effect is also the consequence of the half-quantization and results in an increase in the Hall current along the surface. This current is directed perpendicular to the applied electric field and is an intrinsic property of TIs that is independent of the system details [15.21, 24]. A related scenario has been found when the TI surfaces are radiated by linearly polarized light [15.25]. The possible existence of an image magnetic monopole in the proximity of the charge close to the surface of the topological insulator has also been reported. In this case, the system can be considered with additional charge both inside the topological insulator and in the imaginary magnetic monopole [15.26].

Among the currently known strong TIs, the layered binary compounds Bi_2Te_3, Bi_2Se_3, and Sb_2Te_3 have been widely investigated both experimentally [15.16, 27–29] and theoretically [15.30–33]. Realization of many of the predicted topological phenomena requires tuning of the conduction properties of topological insulators when they are in contact with magnetic semiconductors or superconductors and modification of the topological state by doping [15.14, 15, 26, 34–42]. The realization of topological properties also necessitates the search for new families of topological insulators. A particularly promising method for designing new TI materials with tunable surface electronic properties relies on the fact that pseudo-binary systems $(C^{IV}B^{VI})_n(A_2^VB_3^{VI})_m$, where A^V are elements of group V = Bi, Sb; B^{VI} are elements of group VI = Te, Se; and group IV elements C^{IV} = Ge, Sn, Pb, contain homologous series of ternary compounds. These include a wide variety of mixed-layer materials that have a more complex crystal structure than their parent TIs and can be characterized as natural topological insulator heterostructures.

The structurally simplest systems $(n = 1, m = 1)$, i.e., $C^{IV}A_2^VB_4^{VI}$ compounds, are composed of septuple-layer (SL) hexagonally ordered blocks stacked along the c-axis and separated by van der Waals (vdW) spacings. The SL building block can be obtained from the original quintuple-layer (QL) block of $A_2^VB_3^{VI}$ compounds by introducing the $C^{IV}B^{VI}$ bilayer in the middle part of the QL. These compounds, $PbBi_2Te_4$, $SnBi_2Te_4$, $SnSb_2Te_4$ and others, were predicted to be 3-D $\mathbb{Z}_2$ TI [15.43] with a single Dirac cone in the bulk energy gap, which was subsequently confirmed experimentally [15.29, 44].

The $(C^{IV}B^{VI})_n(A_2^VB_3^{VI})_m$ compounds, where $n = 1$ and $m > 1$, have tetradymite-like layered structures but with distinct many-layered slabs stacked along the c-axis of the hexagonal unit cell. The bonding within the slabs is ionic-covalent, whereas the slabs are linked by weak van der Waals forces. In contrast to $A_2^VB_3^{VI}$ and $C^{IV}A_2^VB_4^{VI}$ topological insulators, the structures of which are formed by quintuple and septuple layers, respectively, the $(n = 1, m > 1)$ compounds are built of alternating QLs and SLs; in other words, they are natural superlattices consisting of blocks of different topological insulators.

Another type of $(C^{IV}B^{VI})_n(A_2^VB_3^{VI})_m$ system is that with $n > 1$ and $m = 1$. Unlike the previous structures in these compounds for C^{IV} = Sn, Pb, the $(C^{IV}B^{VI})_n$ sublattice is built in the middle part of the $A_2^VB_3^{VI}$ QL, and thus their crystal structure is formed by unique, nonalternating building blocks composed of two different

sublattices. As we will later show, the surface spectrum strongly depends on the material of the $C^{IV}B^{VI}$ sublattice, e.g., SnTe, which is topological crystalline insulator, or PbTe—the trivial insulator.

A special case of ($n > 1$, $m = 1$) systems corresponds to compounds with C^{IV} = Ge, which belong to the class of phase-change materials. An example is $Ge_2Sb_2Te_5$, i.e., the $(GeTe)_{n=2}(Sb_2Te_3)_{m=1}$ system, which can adopt four different hexagonal layered structures. At low temperature, it has a nonuple-layer (NL) structure similar to the related compounds with Sn and Pb, while in other phases, GeTe and Sb_2Te_3 sublattices are separated and alternate along the c-axis as in ($n = 1$, $m > 1$) structures. We later show that stable crystal structures of $Ge_2Sb_2Te_5$ possess different topological quantum phases: a topological insulator phase, realized in its low-temperature structures, and a Weyl semimetal phase, characteristic of the stable high-temperature structure. Since the structural phase transitions are caused by the temperature factor, the switching between different topologically nontrivial phases can be driven by variations in temperature.

15.1 Computational Methods

For structural optimization and electronic calculations, for most of the compounds we use the Vienna Ab Initio Simulation Package (VASP) [15.45, 46] with a generalized gradient approximation (GGA) [15.47] for the exchange correlation potential. The interaction between the ion cores and valence electrons is described by the projector-augmented wave method [15.48, 49]. Relativistic effects, including SOC, are taken into account. The atomic positions of bulk compounds are optimized. DFT-D3 van der Waals corrections [15.50] are applied for accurate structure optimization. For slab calculations, we use over 40 atomic layers, and a vacuum space of ≈ 20 Å is included to ensure negligible interaction between opposite surfaces. The k-point meshes of $7 \times 7 \times 7$ and $11 \times 11 \times 1$ are used for the bulk and slab calculations, respectively. Total-energy convergence of better than 1.0×10^{-6} eV is obtained.

To treat the disordered phase in the case of a $Ge_2Sb_2Te_5$ phase-change material, we employ a virtual crystal approximation (VCA) as implemented in the ABINIT code [15.51], where the averaged potential of a virtual atom occupying a site in the Ge/Sb sublattice is defined as a mixture $V_{VCA} = xV_{Ge} + (1-x)V_{Sb}$ of Ge (V_{Ge}) and Sb (V_{Sb}) pseudopotentials. In ABINIT calculations, we use GGA-PBE (Perdew–Burke–Ernzerhof) Hartwigsen–Goedecker–Hutter (HGH) relativistic norm-conserving pseudopotentials, which include the SOC [15.52]. For surface electronic structure calculations, first, the results of DFT calculations are used in the WANNIER90 code [15.53] to construct a tight-binding model. The chosen basis consists of six spinor p-type orbitals for each atom: $|p_x^{\uparrow}\rangle$, $|p_y^{\uparrow}\rangle$, $|p_z^{\uparrow}\rangle$, $|p_x^{\downarrow}\rangle$, $|p_y^{\downarrow}\rangle$, $|p_z^{\downarrow}\rangle$. The low-lying s orbitals are not taken into consideration. The surface tight-binding model is derived from the bulk model with inclusion of band-bending effects obtained from direct surface calculations within DFT. The surface spectrum is calculated using the surface Green function approach [15.54, 55].

The $\mathbb{Z}_2$ invariant is calculated from the parity of occupied electronic states at the time-reversal invariant points of the bulk Brillouin zone [15.6].

15.2 $(C^{IV}B^{VI})_n(A_2^VB_3^{VI})_m$ Superlattices ($n = 1$, $m > 1$)

The crystal structure of the $(C^{IV}B^{VI})_{n=1}(A_2^VB_3^{VI})_{m=2}$ compounds belongs to the hexagonal group $P3m1$, and the unit cell contains alternating QL and SL blocks formed by alternating anion and cation layers, B^{VI}-A^V-B^{VI}-A^V-B^{VI} and B^{VI}-A^V-B^{VI}-C^{IV}-B^{VI}-A^V-B^{VI}, respectively [15.56]. Each block consists of strongly bonded ionic-covalent atoms, whereas the bonding between blocks is determined by vdW forces. Ternary compounds of this series with $m = 3$ also have a hexagonal crystal structure, but it differs from that with $m = 2$ in that it is built of alternating SL and *two* QL blocks along the hexagonal c-axis. As an example, the crystal structures of parent Bi_2Te_3 (QL-structured) and $PbBi_2Te_4$ (SL-structured) compounds and of the superlattices based on them, $PbBi_4Te_7$ ($m = 2$) and $PbBi_6Te_{10}$ ($m = 3$), are shown in Fig. 15.1. Compounds such as $SnBi_4Te_7$, $SnSb_4Te_7$ ($m = 2$) and $SnBi_6Te_{10}$, $SnSb_6Te_{10}$ ($m = 3$) have similar crystal structures.

The Dirac cone in binary TIs such as Bi_2Te_3, Sb_2Te_3, and Bi_2Se_3 originates from the inversion of the bands forming the gap edges: the conventional sequence of the energy levels is inverted by strong spin–orbit coupling [15.6, 13]. In binary compounds, the bottom of the conduction band in the vicinity of

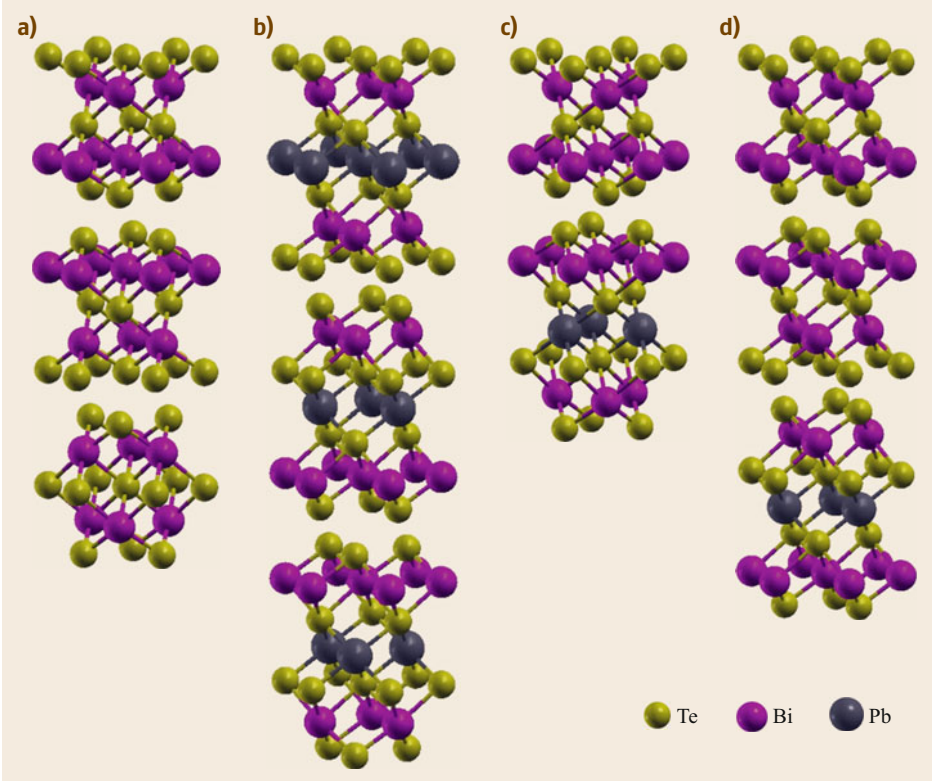

Fig. 15.1a–d Atomic structure of Bi_2Te_3 and Pb-based ternary compounds $(C^{IV}B^{VI})_{n=1}(A_2^VB_3^{VI})_{m\geq 1}$: **(a)** Bi_2Te_3; **(b)** $PbBi_2Te_4$ ($m = 1$); **(c)** $PbBi_4Te_7$ ($m = 2$); and **(d)** $PbBi_6Te_{10}$ ($m = 3$)

the Γ point is derived predominantly from the states localized at the outermost QL chalcogen atoms, whereas the top of the valence band is formed by the pnictogen atoms. A similar band inversion is found in ternary SL-structured TIs, with the only difference being that the top of the valence band is occupied by both A^V and C^{IV} [15.57].

A more complicated SOC-induced band structure is found in compounds with alternating QL and SL slabs. For example, the $SnSb_4Te_7$ compound is a narrow-bandgap semiconductor that demonstrates a direct gap of ≈ 70 meV at the A point (Fig. 15.2a). As can be seen in Fig. 15.2b, left-hand side, the bands forming the gap edges have a *normal* band order, i.e., the valence band edge is predominantly formed by the anionic (Te) orbitals, while the conduction band minimum is mainly determined by the cationic (Sb, Sn) orbitals. The inclusion of the SOC in the calculation leads to a significant modification of the gap (Fig. 15.2a), which becomes indirect, with a width of ≈ 100 meV. At the A point, the SOC induces a complicated inversion of the gap edge states (Fig. 15.2b, right-hand side): the Te states reveal themselves in the conduction band, whereas the top valence band is basically formed by Sb and Sn orbitals of the SL block, while Sb states of the QL block appear in the second top band (Fig. 15.2b, right-hand side). A similar band inversion is characteristic of isostructural compounds $SnBi_4Te_7$ and $PbBi_4Te_7$.

Another feature of band-inverted insulators $C^{IV}A_4^VB_7^{VI}$, whose crystal structure consists of alternating SL and QL building blocks, is that the surface can be formed by SL or QL building blocks, which we define as 7L and 5L terminations, respectively.

The surface band structures of the 7L and 5L terminations of $SnSb_4Te_7$ and $SnBi_4Te_7$ compounds are shown in Fig. 15.3. The spectrum of 7L-terminated $SnSb_4Te_7$ demonstrates a strictly linear dispersion of the Dirac state, which is spatially localized within both surface SL and subsurface QL building blocks. The dispersion of the Dirac state on the 5L termination in the vicinity of the Dirac point (DP), where it is also localized within two building blocks (surface QL and subsurface SL) is also linear. However, at higher energies, above the Fermi level, the state changes its spatial distribution, which becomes predominantly localized in the surface QL block, and the dispersion of the TSS changes. The Dirac cone at the 7L termination of $SnBi_4Te_7$ is warped near the conduction band simi-

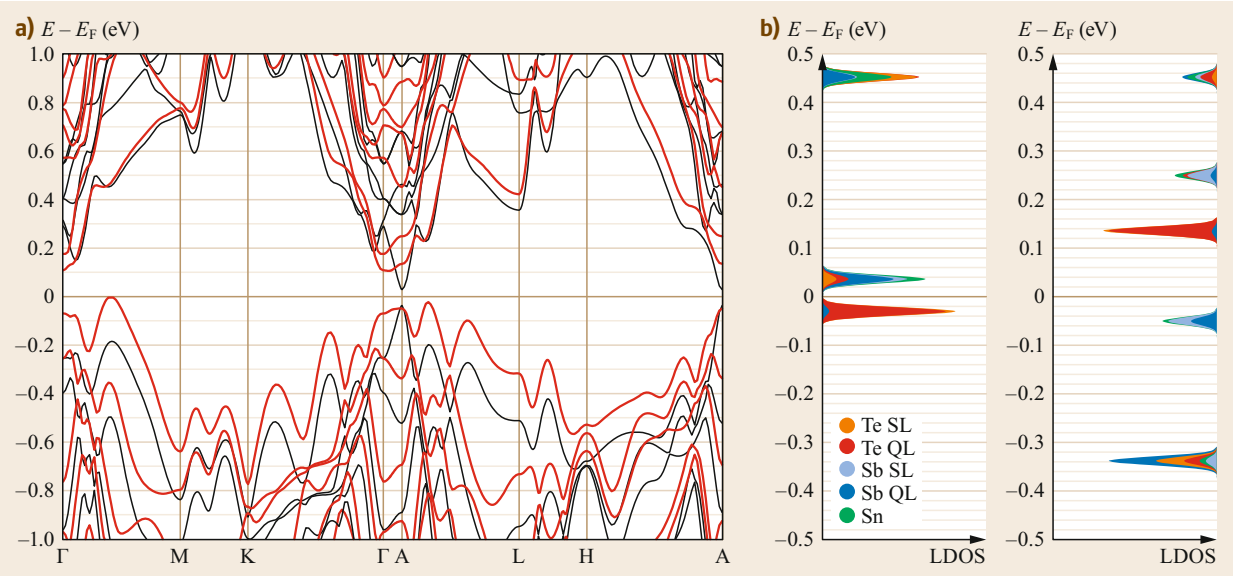

Fig. 15.2 **(a)** Bulk band spectra of $SnSb_4Te_7$ along the high symmetry lines in the Brillouin zone. *Red/black lines* correspond to results with/without SOC included. **(b)** Local density of states (LDOS) calculated without (*left-hand side*) and with (*right-hand side*) SOC included at the vicinity of the A point. *Colors* in the LDOS correspond to different atomic contributions

lar to that in the parent Bi_2Te_3. In contrast to $SnSb_4Te_7$, the TSS at the 7L-terminated $SnBi_4Te_7$ surface is completely localized within the surface SL block, as in the case of $PbBi_4Te_7$ [15.43]. The Dirac state at the 5L termination of $SnBi_4Te_7$ also demonstrates a change in the dispersion above the DP, which is attributed to its inhomogeneous spatial localization.

Another feature of the 5L-terminated surface spectra of both $SnSb_4Te_7$ and $SnBi_4Te_7$ compounds is the occupied Dirac state that lies in the valence bandgap at the $\overline{\Gamma}$ point at −0.15 eV (−0.25 eV). The dispersion and localization of this Dirac state is similar to that of the parent $Sb(Bi)_2Te_3$ compounds and is associated with complicated bulk bandgap inversion in $C^{IV}A_4^VB_7^{VI}$ crystals when the inverted QL states appear inside the valence band, which in turn allows the original TSS of the parent binary TI to survive in the $C^{IV}A_4^VB_7^{VI}$ heterostructure.

It should be noted that at the real crystal surface, owing to the presence of both QL- and SL-surface terminations, both Dirac states should appear simultaneously at the $\overline{\Gamma}$ point, as shown in the example of the $PbBi_4Te_7$ compound in Fig. 15.4. These two Dirac cones have been successfully resolved in the angle-resolved photoemission spectroscopy (ARPES) spectrum [15.58].

Ternary compounds SnX_6Te_{10} (X = Sb, Bi) differ from SnX_4Te_7 in that they are built of alternating SL and *two* QL blocks along the hexagonal *c*-axis. Calculations of the $\mathbb{Z}_2$ topological invariant have shown that it is nonzero for $SnBi_6Te_{10}$, whereas it is zero for $SnSb_6Te_{10}$. The nonzero $\mathbb{Z}_2$ in $SnBi_6Te_{10}$ is provided by the band gap inversion at the Z point of the bulk Brillouin zone. In the calculation with SOC excluded, the Z point gap is above > 300 meV. The switching on of the SOC leads to substantial narrowing of the gap at Z. Similar to the $C^{IV}A_4^VB_7^{VI}$ systems, the band inversion has a complicated character when the orbitals of the atoms constituting different building blocks contribute to the gap edges. However, because of the more complicated crystal structure of $SnBi_6Te_{10}$, the gap inversion is more complicated as well. The lowest conduction band is formed by the orbitals of Te atoms faced to each other at the vdW spacing between neighboring QLs (marked as Te QL/QL in Fig. 15.5b, right-hand panel), whereas two upper bands are composed of orbitals of Te atoms lying at the van der Waals spacing between neighboring QL and SL blocks (marked as Te QL/SL and Te SL). The top valence band, as in the case of $C^{IV}A_4^VB_7^{VI}$, is formed in the main part by the states of the SL building block, and the next two, deeper, bulk valence bands are determined by the orbitals of Bi atoms of the QL blocks.

The $C^{IV}A_6^VB_{10}^{VI}$ crystals, and in particular $SnBi_6Te_{10}$, have two nonequivalent cleavage planes: between SL and QL blocks, and between two neighboring QLs. Such cleavages give rise to three different surface terminations. Two of these, 5L with surface QL and subsurface SL blocks, and 7L with the opposite sequence of the surface and subsurface building blocks,

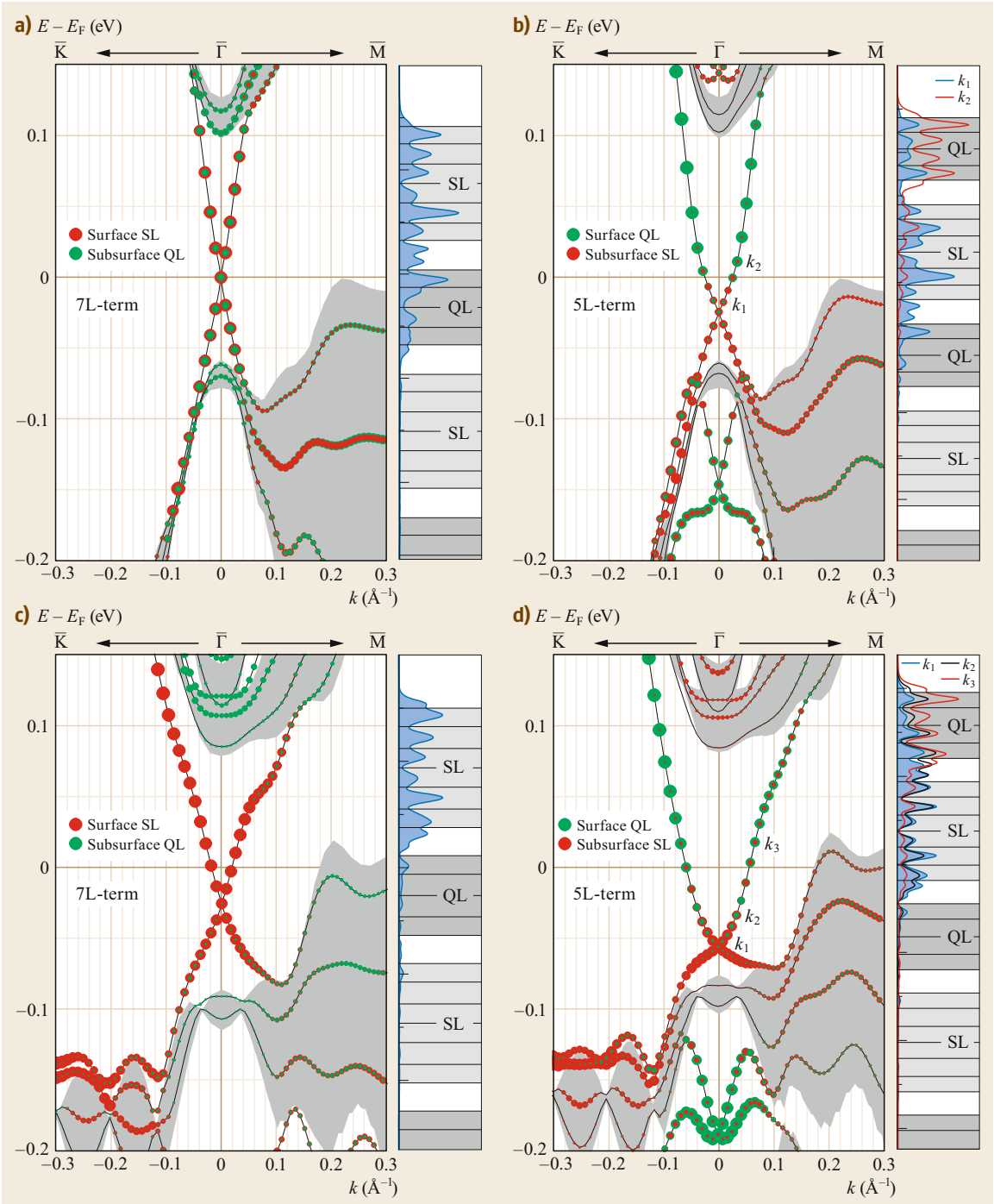

Fig. 15.3a–d Band spectra and charge-density profiles for the 7L **(a)** and 5L **(b)** surfaces of $SnSb_4Te_7$ and for the 7L **(c)** and 5L **(d)** surfaces of $SnBi_4Te_7$

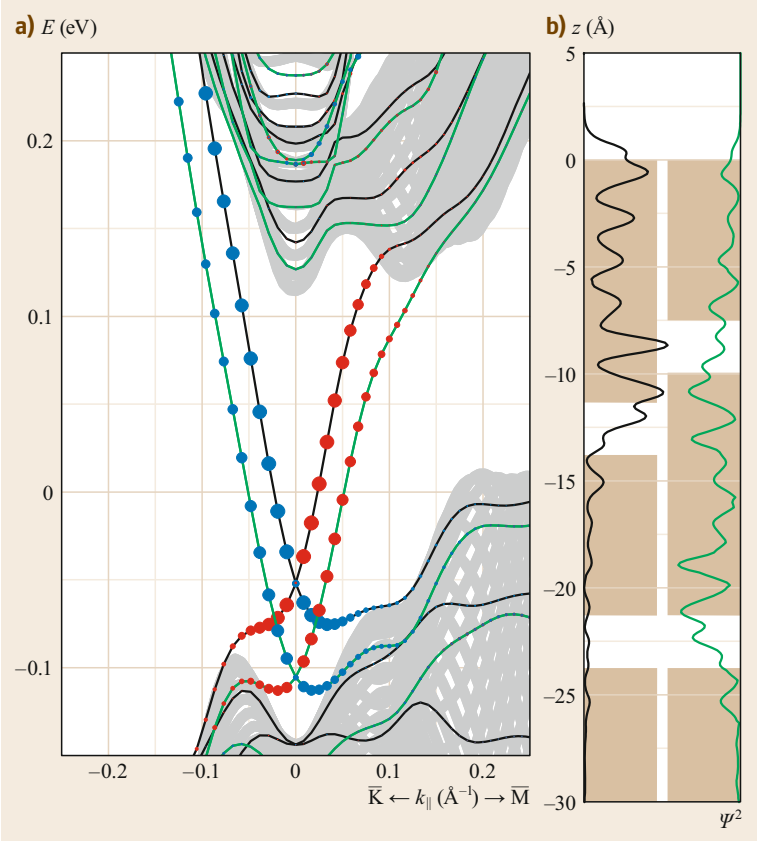

Fig. 15.4 **(a)** Calculated surface band structure of $PbBi_4Te_7$ with the 7L and 5L terminations (*black* and *green curves*, respectively); *circles* represent weights of the states in the two outermost blocks multiplied by the value of in-plane spin components (*red* and *blue circles* denote positive and negative values of spin, respectively). The *shaded area* corresponds to the projection of bulk bands, and the bulk bandgap is ≈ 100 meV. **(b)** Depth profile of the charge density of the topological surface state for the 5L- (*green line*) and 7L-terminated (*black line*) surface

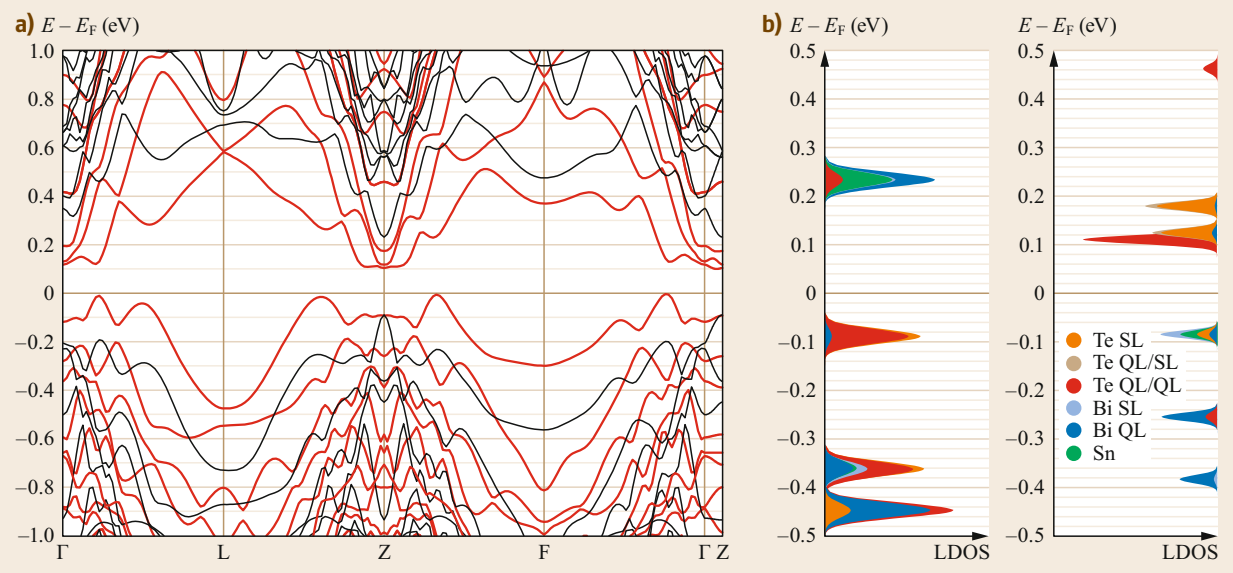

Fig. 15.5 Same as in Fig. 15.2 but for $SnBi_6Te_{10}$

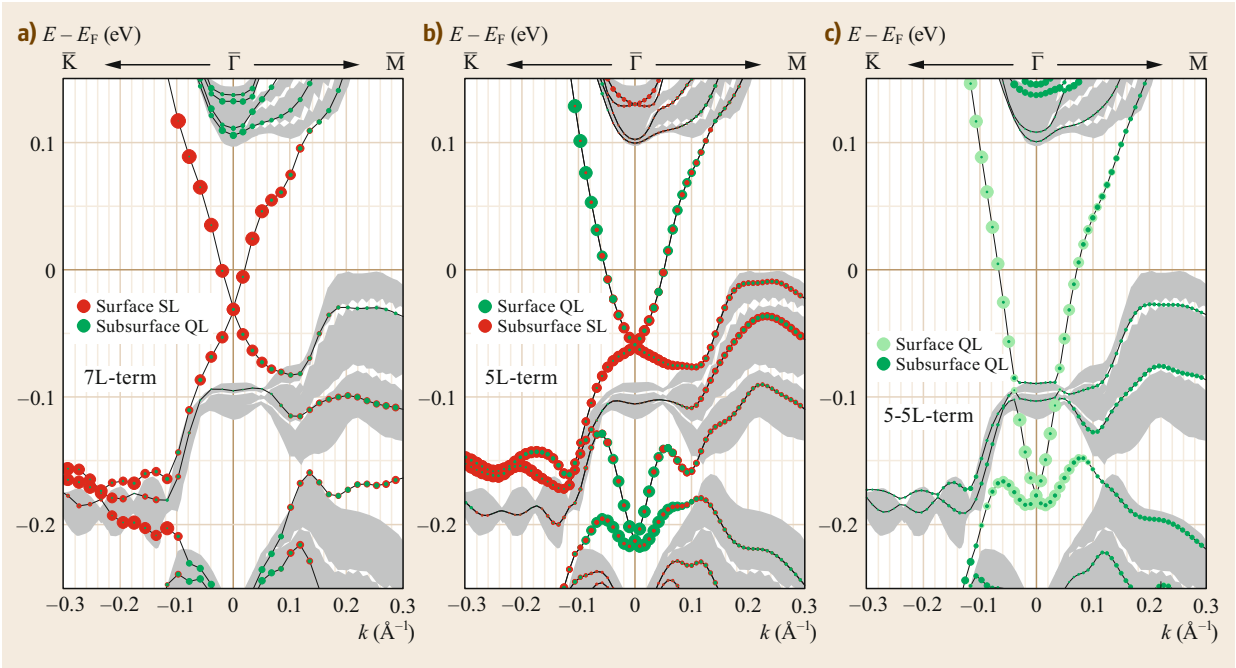

Fig. 15.6a–c Band spectrum of the $SnBi_6Te_{10}$ surface terminated by the SL (**a**), QL (**b**), and double-QL (**c**) blocks, respectively. The size of the *colored circles* reflects the weight of the state in the surface and subsurface blocks

are the same as in the $SnSb(Bi)_4Te_7$ crystals discussed earlier. The third termination that can be obtained by the cleavage of the $SnBi_6Te_{10}$ crystal is the surface in which both the surface and subsurface blocks are QLs. We will call this surface termination the 5-5L termination.

Figure 15.6 shows the surface band spectra of $SnBi_6Te_{10}$ with all types of terminations. The dispersion of the Dirac state at the 7L- and 5L-terminated surfaces is similar to that at the respective terminations of $SnBi_4Te_7$. The spatial charge distributions of the TSS on these terminations are also akin those in $SnBi_4Te_7$.

However, on the 5-5L termination, the TSS forms an exotic cone with a Dirac point in the local gap of the valence bulk band. This unusual behavior can be understood from the fact that the occupied states localized at the Bi atoms of the QL block are not at the gap edge, but below the Bi and Sn states of the SL block, which for this termination lies deep in the bulk and forms the top of the bulk valence band. In particular, the Dirac point is located in the local gap of the bulk valence band. As a result, this Dirac cone possesses two segments: located in the local and in the fundamental bandgap. However, the charge density of the TSS in both segments is mostly localized in the surface QL block.

The dispersion of the Dirac cones at the 7L, 5L and 5-5L surfaces of $SnBi_6Te_{10}$ is similar to

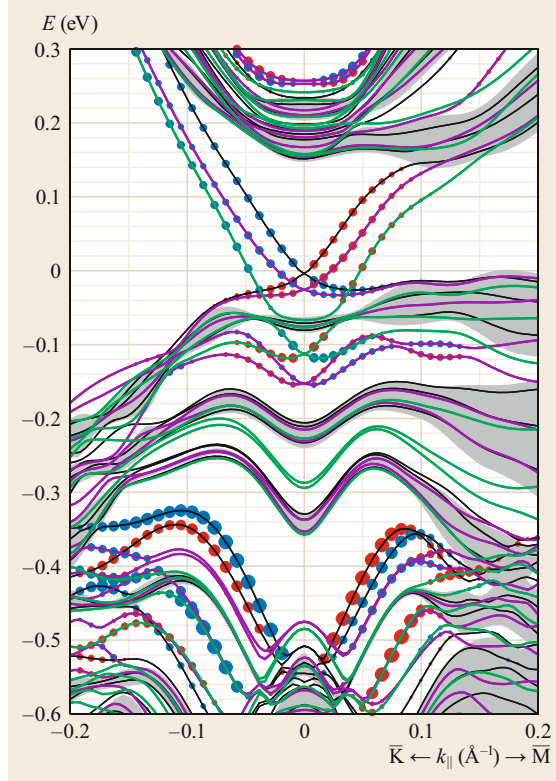

the respective surfaces of $PbBi_6Te_{10}$ [15.43]. As in the case of compounds with simpler structure $(C^{IV}B^{VI})_{n=1}(A_2^VB_3^{VI})_{m=2}$, here different surface terminations, which should be present inevitably in a real crystal due to the stepped morphology of the surface, result in the presence of multiple coexisting Dirac states, as shown in the example of the $PbBi_6Te_{10}$ compound in Fig. 15.7, where spectra for three surface terminations are superposed. Three Dirac cones have been found in this material experimentally [15.59], in accord with the prediction. In particular, as can be seen in Fig. 15.7, the 7L surface shows a rather linear dispersion close to its DP_{7L}, which lies ≈ 60 meV above the $\overline{\Gamma}$ valence band edge, in agreement with the experimental value of ≈ 80 meV [15.59]. The Dirac point of the 5L TSS lies at ≈ 40 meV lower than DP_{7L}, closer to the bulk valence states, consistent with the estimated experimental value of 120 meV. At the same time, the 5L TSS deviates markedly from the linear dispersion, approaching the Dirac point. The Dirac point of the 5-5L termination ($DP_{5\text{-}5L}$) emerges below (≈ 15 meV) the first valence band, so that the Dirac cone loses its localized character passing through the narrow energy region of the first valence band and becomes localized (and spin-polarized) again in the local gap between the first and second bulk valence bands.

15.3 $(C^{IV}B^{VI})_n(A_2^VB_3^{VI})_m$ Compounds ($n > 1$, $m = 1$)

Different $(C^{IV}B^{VI})_n(A_2^VB_3^{VI})_m$ systems, containing layers of $A_2^VB_3^{VI}$ topological insulators and $C^{IV}B^{VI}$ materials like SnTe and PbTe, are formed when $n > 1$ and $m = 1$. In contrast to the compounds of the $(n = 1, m > 1)$ series containing alternating QL and SL structural units, the $(n \geq 1, m = 1)$ compounds are formed of unique, nonalternating building blocks. The simplest system ($n = 1$, $m = 1$), e.g., $SnBi_2Te_4$, is composed of SL hexagonally ordered blocks stacked along the c-axis and separated by van der Waals spacings. The SL building block (Fig. 15.8b) can be obtained from the original QL block of Bi_2Te_3 (Fig. 15.8a) by introducing the SnTe bilayer in the middle part of the QL. The $SnBi_2Te_4$ compound was earlier predicted to be 3-D $\mathbb{Z}_2$ TI [15.43]. The heterostructure with a larger n index, $Sn_2Bi_2Te_5$ ($n = 2, m = 1$), is formed by NL building blocks [15.60]. The NL block (Fig. 15.8c) can be obtained from the SL block by the introduction of an additional SnTe bilayer in the middle of the SL. Another experimentally confirmed structure $(SnTe)_n(Bi_2Te_3)_m$, which is also built from the ionic-covalent bonded Bi_2Te_3 and SnTe atomic layers, is $Sn_3Bi_2Te_6$ ($n = 3, m = 1$), see Fig. 15.8d [15.60]. The compounds with C^{IV}=Pb have similar crystal structures. However, it should be noted that PbTe is a trivial insulator, while SnTe [15.61, 62] belongs to the class of topological materials in which the topological surface states are protected by the crystal mirror symmetry [15.63]—so-called topological crystalline insulators (TCI).

The bulk band structures of $Sn_2Bi_2Te_5$ have been calculated without (Fig. 15.9a) and with (Fig. 15.9b) SOC included. In the calculated spectrum without SOC, a direct energy gap of 0.32 eV exists at Γ. The switching on the SOC transforms it into an indirect gap of 0.11 eV (Fig. 15.9b). This value is in good agreement with the experimental gap of 0.09 eV [15.60].

The time-reversal invariant momenta in the bulk Brillouin zone are the Γ, A, and triply degenerate M and L points. We found that the parity inversion of bulk bands occurs at the Γ point, which leads to $\mathbb{Z}_2$ invariants 1;(000) as in the parent TI Bi_2Te_3. In spite of this similarity, the band inversion at Γ is an entanglement of two different inversions corresponding to each sublattice, Bi_2Te_3 and SnTe. Thus, in Bi_2Te_3, the SOC inverts the top valence band state (predominantly of p_z character) of Te atoms lying in the outer layers of the QL (Te_o) and the Bi p_z-state of the bottom conduction band. A similar band inversion occurs in the bulk SnTe, where Sn and Te orbitals are inverted in the L point of the cubic Brillouin zone. In the case of the $Sn_2Bi_2Te_5$ heterostructure, both Bi and Sn states form the bottom of the conduction band, while the states of the Te_o atoms and Te atoms of the central layer of the NL (Te_c) lie in the top valence band of the spectrum calculated without SOC (Fig. 15.9c,d). Switching on the SOC results in an inversion of Bi and Te_o states and Sn and Te_c states. However, in contrast to the parent systems, this inversion has a more complex character. As can be seen in Fig. 15.9e, after switching on the SOC, the Te_o states become dominant in the conduction band while the Bi states occupy the second valence band. The SOC-inverted Sn states lie in the highest valence band, and Te_c states appear in the second conduction

Fig. 15.7 Calculated band structure of $PbBi_6Te_{10}$ surfaces along the $\overline{K}$-$\overline{\Gamma}$-$\overline{M}$ direction with the 7L, 5L, and 5-5L terminations (*black*, *violet*, and *green lines*, respectively); the size of the *colored circles* represents the weights of the states in the surface layers; *red* and *blue colors* denote the sign of in-plane spin components (positive and negative, respectively), and the *shaded area* identifies the bulk-projected bands ◄

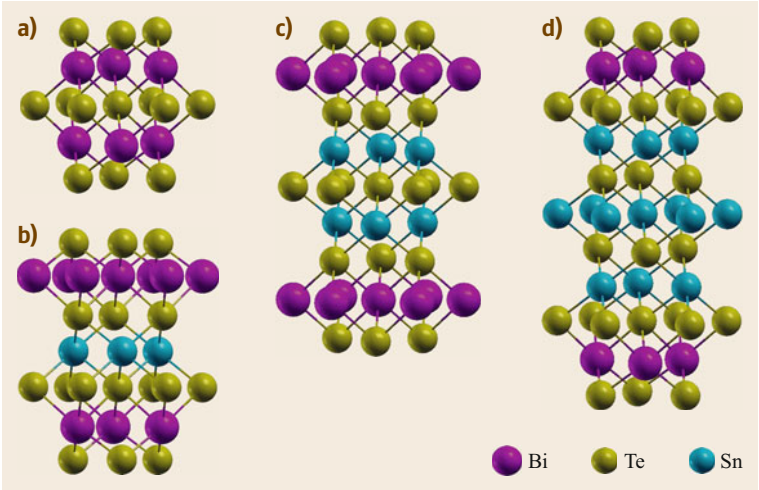

Fig. 15.8a–d Building blocks of Bi_2Te_3 **(a)**, $SnBi_2Te_4$ **(b)**, $Sn_2Bi_2Te_5$ **(c)**, and $Sn_3Bi_2Te_6$ **(d)**

band (Fig. 15.9f). Additionally, the SOC-inverted Sn states (with smaller weight) appear in the second valence band. Thus, the $Sn_2Bi_2Te_5$ TI has a competitive bulk band inversion, which comprises the inversion of the states belonging to different sublattices, SnTe and Bi_2Te_3, so that the valence band edge is formed mainly by Sn states and the conduction band edge occupied by Te_o states, i.e., inverted gap edges are formed by the orbitals of atoms belonging to different sublattices.

The superposition of the SOC-induced bulk band inversions in the SnTe and Bi_2Te_3 sublattices of the $(SnTe)_2(Bi_2Te_3)_1$ heterostructure results in the formation of two topological surface states at the $\overline{\Gamma}$ point. The upper TSS lies in the bandgap (see light pink rectangle in Fig. 15.10a), while the lower TSS (light green rectangle in Fig. 15.10a) resides in the valence band (hereafter referred to as bandgap and valence band TSSs, respectively). The valence band TSS, residing in the local valence bandgap, has typical Dirac dispersion, similar to that in Bi_2Te_3. In contrast, the bandgap TSS displays nonlinear dog-leg dispersion. It has two linear sections, near the band crossing (Dirac point) and below the conduction band, which connect to each other in the middle part of the gap with the formation of shoulders in the spectrum. As in other TIs, the TSSs in $Sn_2Bi_2Te_5$ are localized within the surface building block. However, in this case, the building block has SnTe and Bi_2Te_3 sublattices, and the localization of the TSS is affected by the peculiarities in the bulk band inversion. The Bi and Sn orbital weights are shown in Fig. 15.10b,c for the band gap and valence band topological surface states, respectively. As can be seen, the valence band TSS has dominant Bi weights that reflect its dominant localization in the outer Bi-Te layers of NL, i.e., in the Bi_2Te_3 sublattice. Comparing the dispersion of this state with the dispersion of the Dirac cone in Bi_2Te_3 [15.33] (Fig. 15.10e), one can conclude that the two bands are almost identical. In the lower linear section near the band crossing of the bandgap TSS (Fig. 15.10b), the Sn contribution dominates, and thus the state is mainly localized in the SnTe sublattice. Approaching the shoulders, the Sn contribution disappears rather quickly, and above the band shoulders the TSS becomes mostly localized in the Bi-Te layers. Thus, the band shoulders in the TSS spectrum are associated with the change in the TSS localization from the SnTe to Bi_2Te_3 sublattice. It is worth noting that the dispersion of the upper linear section of the bandgap TSS (at $k_\parallel > 0.1\,\text{Å}^{-1}$) is comparable to the slope of the Bi_2Te_3 Dirac cone (Fig. 15.10d), while that of the lower linear section ($k_\parallel < 0.05\,\text{Å}^{-1}$) differs notably from both Bi_2Te_3 and SnTe(111) [15.64] Dirac states.

The linear fitting of the lower and upper sections in the bandgap TSS gives $E/k_\parallel$ slopes of 2.22 and 1.13 eV Å, respectively. Between these linear sections, at $0.05 < k_\parallel < 0.1\,\text{Å}^{-1}$, two inflection points exist that limit the almost flat section in the TSS spectrum. Owing to slightly negative dispersion of the TSS in the shoulder region, the system can pass from one velocity mode in the lower linear section to the other velocity mode in the upper linear section through the three surface Fermi pockets at energy of ≈ 50 meV (Fig. 15.10f).

The spin texture of the bandgap TSS is demonstrated in Fig. 15.10g,h. Figure 15.10g shows spin-resolved constant energy contours (CECs) for the lower (inner contour) and upper (outer contour) linear sections of the TSS, at energies of 25 meV below and above the shoulders, respectively. Both contours demonstrate the in-plane clockwise spin polarization. In addition, the outer contour indicates the presence of the out-of-plane spin component S_z, which is zero along $\overline{\Gamma}$-$\overline{M}$ and reaches a minimum (maximum) value in the $\overline{\Gamma}$-$\overline{K}$ di-

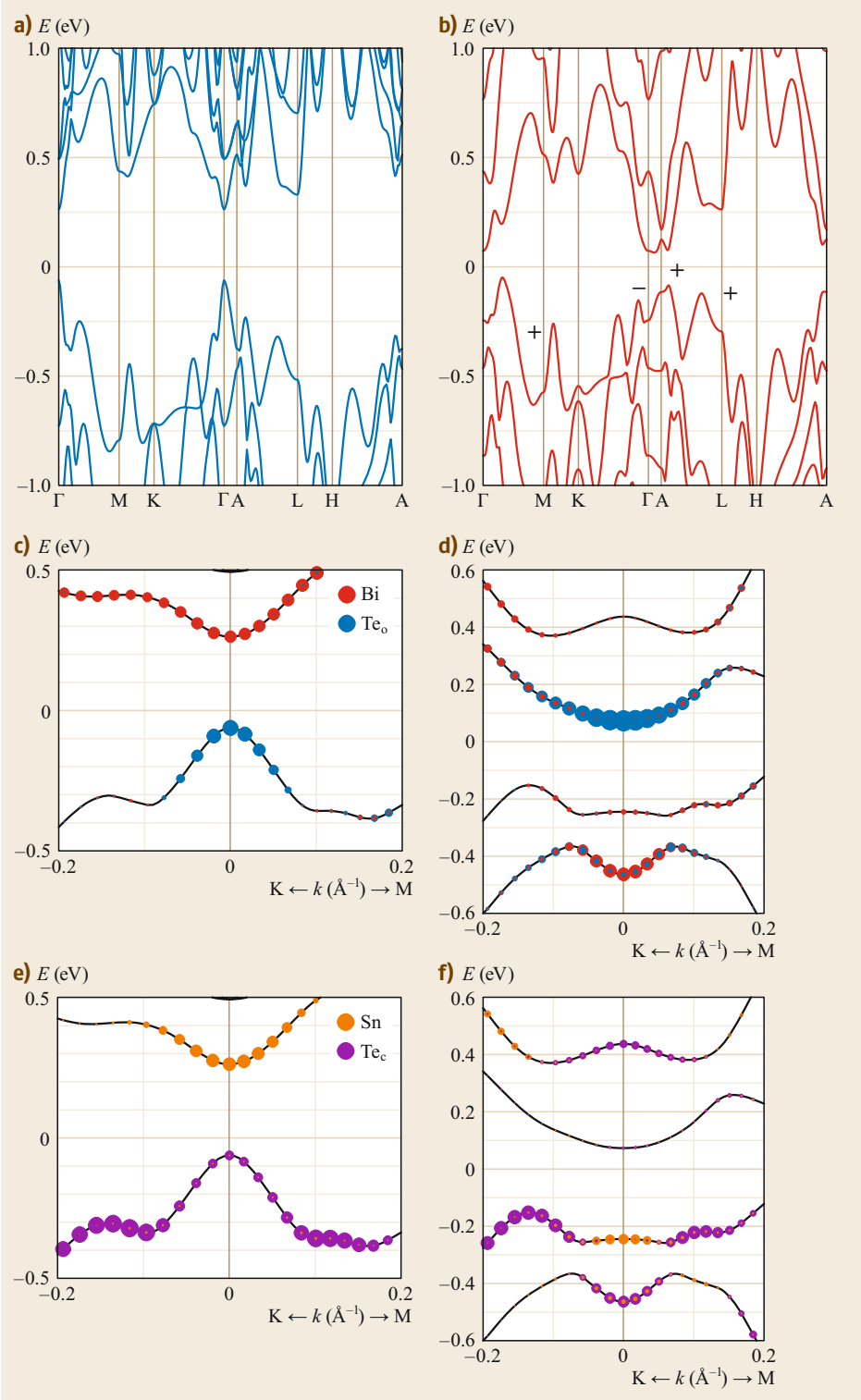

Fig. 15.9a–f Bulk electronic structure of $Sn_2Bi_2Te_5$ calculated without **(a)** and with **(b)** SOC included (signs of band parities at the TRIM are also shown). Atomic composition of the near-gap states in bulk $Sn_2Bi_2Te_5$ calculated without **(c,e)** and with **(d,f)** SOC included

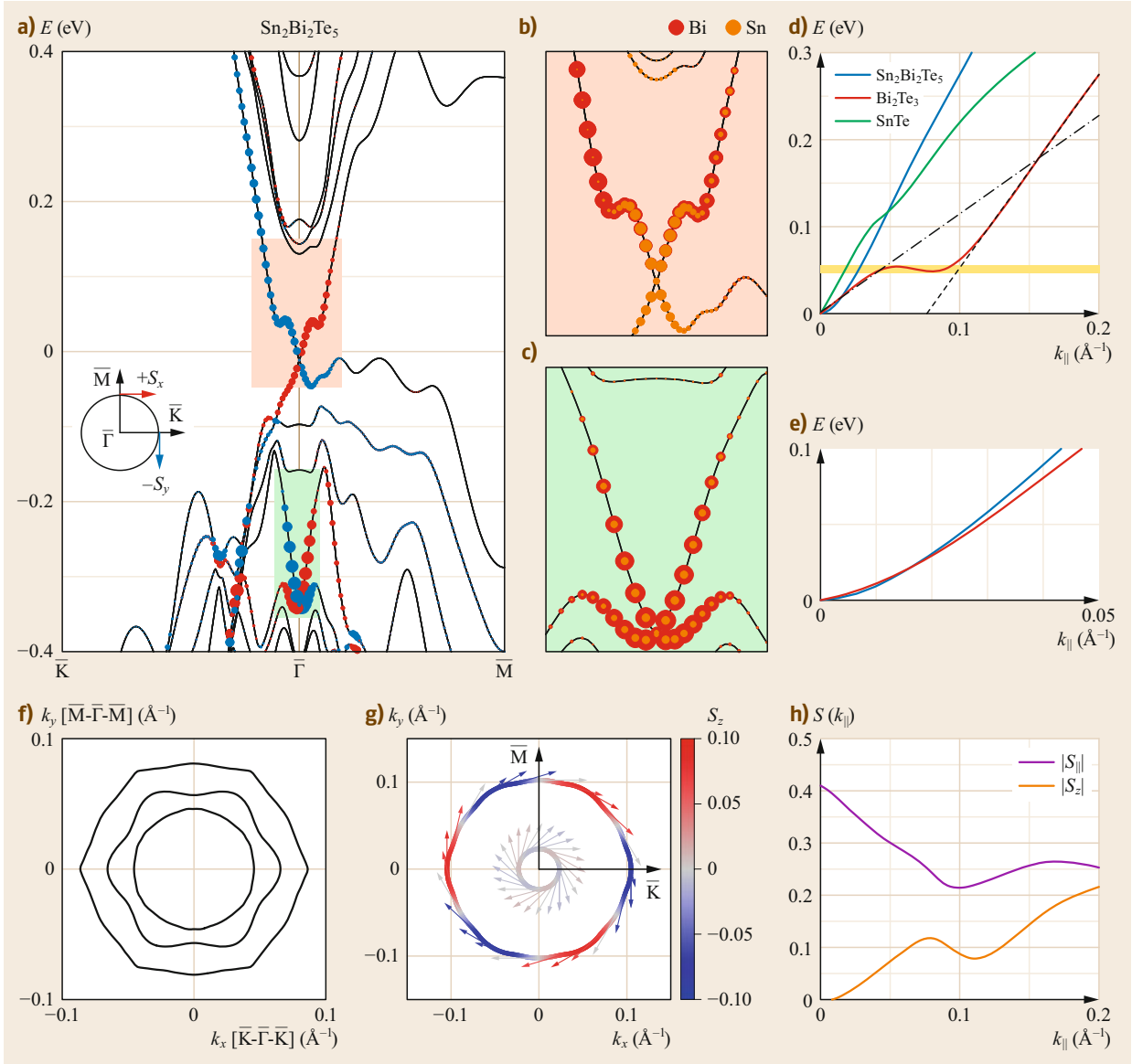

Fig. 15.10 **(a)** Surface electronic structure of $Sn_2Bi_2Te_5$; the size of the *colored circles* represents the weight of the states in the outermost building block (NL) of the slab; *red* and *blue colors* show the sign of the in-plane (S_x and S_y) spin components; *light pink* and *light green rectangles* mark the areas of the bandgap and valence band topological surface states, respectively. Atomic weights of Bi and Sn in the bandgap **(b)** and valence band **(c)** TSSs. **(d)** Energy dispersion of the bandgap TSS compared with Bi_2Te_3 and SnTe $\overline{\Gamma}$ Dirac cones. *Dashed* and *dot-dashed lines* are linear fits for the TSS above and below the shoulder, respectively. **(e)** Dispersion of the valence band TSS compared with Bi_2Te_3. **(f)** Constant energy contours in the shoulder region (*yellow stripe* in **(d)**). **(g)** Spin-resolved constant energy contours for bandgap TSS at energies of 25 meV below and above the shoulders. *Arrows* adjacent to the contours denote the in-plane spin component $S_\parallel$. The out-of-plane spin component S_z is indicated by the *red* and *blue color* corresponding to positive and negative values, respectively. **(h)** The spin components $S_\parallel$ and S_z for bandgap TSS as functions of $k_\parallel$ along the $\overline{\Gamma}$-$\overline{K}$ direction

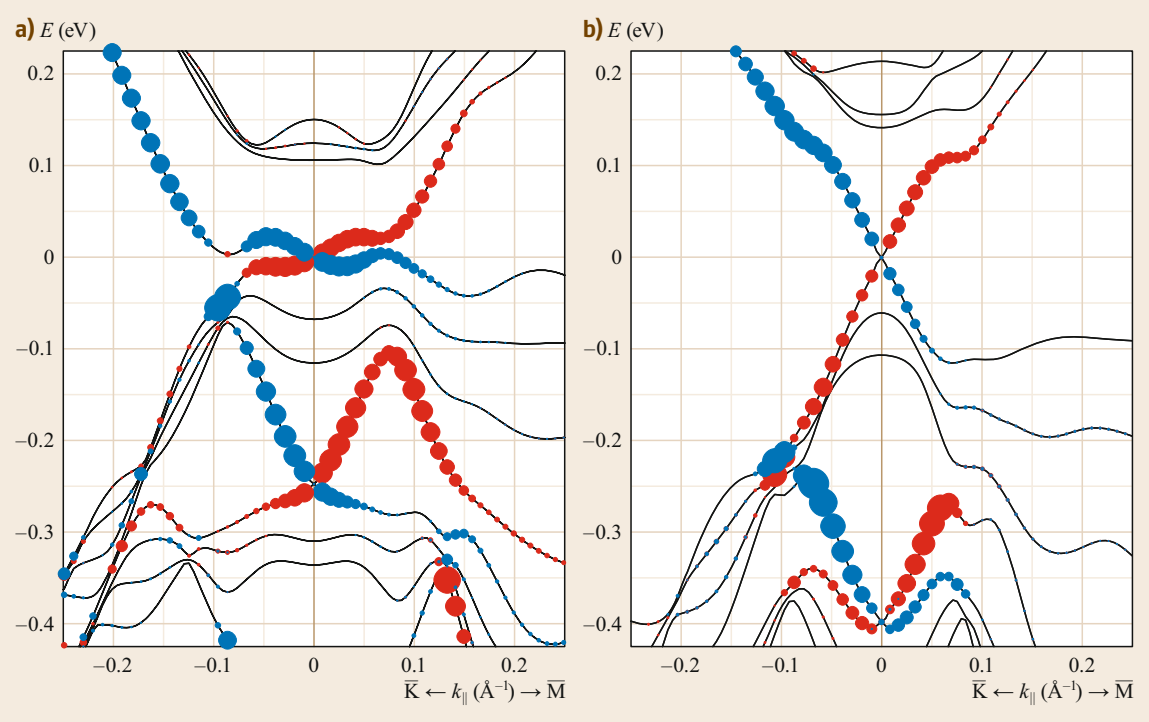

Fig. 15.11a,b Spin-resolved surface electronic structure of **(a)** $Sn_3Bi_2Te_6$ and **(b)** $Sn_2Sb_2Te_5$

rections. Such a spin texture is an intrinsic feature of the spin-polarized states at hexagonal surfaces. At the same time, S_z for the inner contour is very small. The dependence of absolute values for $S_\parallel$ and S_z on $k_\parallel$ along $\overline{\Gamma}$-$\overline{K}$ is shown in Fig. 15.10h. The in-plane spin polarization having a maximum near the Dirac point rapidly decreases approaching the shoulder. At $k_\parallel > 0.1$ Å^{-1}, i.e., in the upper linear section, it increases with $k_\parallel$ until it reaches the region of the bulk states. In contrast, the out-of-plane spin polarization increases with $k_\parallel$ in both linear sections of the TSS, having a kink at the band shoulder.

Let us consider the $(C^{IV}B^{VI})_{n>1}(A_2^VB_3^{VI})_{m=1}$ heterostructure with a larger n index. The increase in the index up to $n = 3$ corresponds to the addition of a SnTe bilayer in the building block and leads to the formation of the $Sn_3Bi_2Te_6$ compound. As can be seen in Fig. 15.11a, in this case two TSSs are also present in the surface spectrum, and a dog-leg dispersion is the feature of the bandgap surface state. The difference from the $Sn_2Bi_2Te_5$ case is that the band shoulders lie closer to the bulk valence band, making the lower section of the TSS very short and half as steep.

Another system of the $(C^{IV}B^{VI})_{n=2}(A_2^VB_3^{VI})_{m=1}$ series is a heterostructure, where the $A_2^VB_3^{VI}$ sublattice is Sb_2Te_3. As can be seen in Fig. 15.11b, the surface spectrum of $Sn_2Sb_2Te_5$ also holds two TSSs with dog-leg dispersion in the bandgap TSS. However, in contrast to the case of $Sn_2Bi_2Te_5$, the band shoulders arise near the conduction band.

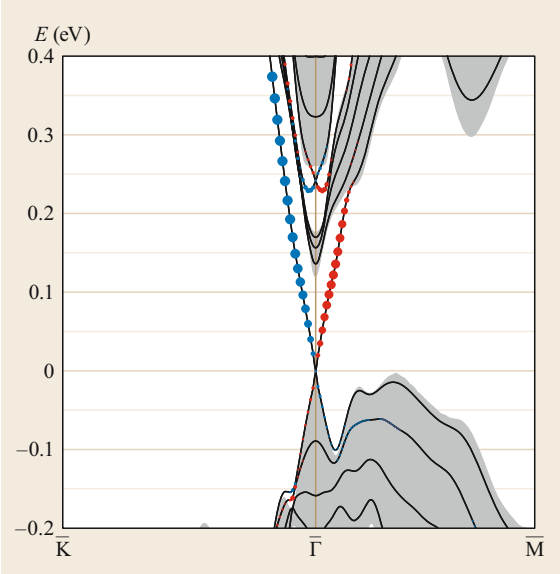

Fig. 15.12 Spin-resolved surface electronic structure of $Pb_2Bi_2Te_5$

On the other hand, if the $(C^{IV}B^{VI})_{n>1}(A_2^VB_3^{VI})_{m=1}$ heterostructure is built of a Bi_2Te_3 topological insulator and trivial insulator sublattices, as in the case of the $Pb_2Bi_2Te_5$ compound, the only one band inversion, provided by the Bi_2Te_3 sublattice, occurs in the bulk spectrum. As a result, in this case a single Dirac state with linear dispersion arises in the surface spectrum (Fig. 15.12).

15.4 Phase-Change Materials

The $Ge_2Sb_2Te_5$ compound is regarded as a prototype conventional phase-change material (PCM) [15.65–67]. It is known that this compound, i.e., $(GeTe)_{n=2}(Sb_2Te_3)_{m=1}$ heterostructure, can adopt four different hexagonal layered structures [15.68]. Experimentally, the most stable phase of $Ge_2Sb_2Te_5$ is the so-called Kooi structure [15.69], which is formed by nonuple-layer building blocks, where GeTe bilayers are incorporated into the Sb_2Te_3 QL, i.e., it has the same structure as in $(C^{IV}B^{VI})_{n=2}(A_2^VB_3^{VI})_{m=1}$ systems with C^{IV} = Pb, Sn. Other crystal phases are the Petrov structure [15.70], in which the $(GeTe)_2$ blocks are sandwiched between Sb_2Te_3 QLs with a Ge-Te-Te-Ge sequence within the block; the inverted-Petrov structure, with a Te-Ge-Ge-Te sequence; and the so-called Ferro structure, in which the atomic layer sequence in the $(GeTe)_2$ block has the order Ge-Te-Ge-Te, i.e., as in ferroelectric bulk GeTe.

The stability of these four structures is dependent on temperature. It was shown by means of calculations of enthalpy as a function of temperature [15.71] that the Kooi phase has the lowest enthalpy at 0 K, in agreement with earlier DFT results [15.68] and experiments [15.69]. However, upon raising the temperature, the enthalpy of the Kooi structure increases, and above $\approx$ 125 K the Ferro phase becomes the most stable structure [15.71]. It has been established that the metastable Petrov and inverted Petrov phases are involved in the atomic mechanism of the crystal phase transformation from the Kooi to Ferro structure [15.71].

For the low-temperature Kooi structure, the narrow-gap band insulator phase has been obtained theoretically [15.68, 72, 73]. This is in contrast to the related compounds $Ge_2Bi_2Te_5$ and $Sn_2Sb(Bi)_2Te_5$, which were shown to be topological insulators [15.73, 74]. The $(GeTe)_n(Sb_2Te_3)_m$ compound with indices $n = 1$ and $m = 2$ has also been predicted to be TI [15.43]. At the same time, the DFT calculations for Ferro and Petrov structures predicted the trivial band insulator phase, while another metastable structure, the inverted Petrov structure, was shown to possess the Dirac semimetal phase [15.68]. We will deal with the electronic structure of stable low-temperature Kooi and high-temperature Ferro structures, whose equilibrium crystal structures are shown in Fig. 15.13.

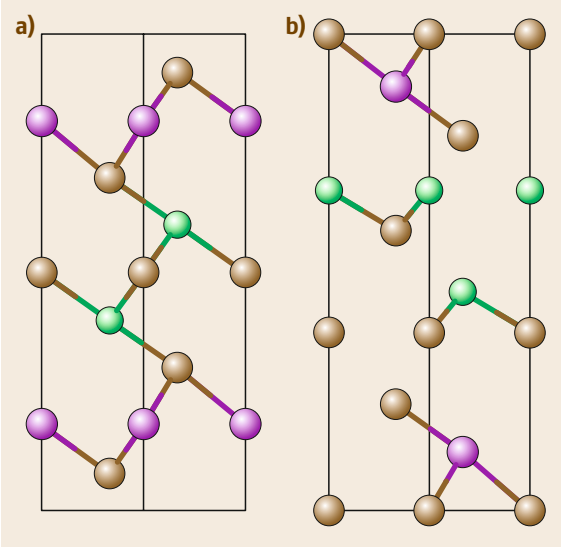

Fig. 15.13a,b Unit cells of the (a) low-temperature Kooi and (b) high-temperature Ferro phases of $Ge_2Sb_2Te_5$

The calculated bulk band structure of the Kooi phase demonstrates the insulating state with a gap of 25.2 meV in the middle of the Γ-A direction (Fig. 15.14a, red lines), which gives a trivial band insulator according to the $\mathbb{Z}_2$ topological invariant calculation. This result is in agreement with earlier calculation data [15.68, 72, 73]. The small bandgap value obtained may be an indication that the system is close to the topological quantum phase transition (TQPT) and can be converted into the topological phase by applying hydrostatic pressure, as was shown for the Sb_2Se_3 band insulator [15.75, 76], or by increasing the spin–orbit interaction strength. We checked the possibilities and found that, with the increase in the hydrostatic pressure (contraction of the cell volume), the gap gradually shifts toward the A point, decreasing in magnitude, and at $\approx$ 10% volume contraction (corresponding to pressure of 6.3 GPa), the A-gap closes and a bulk Dirac cone with linear dispersion is formed. With a further increase in the pressure, when the system has gone through the critical point of the TQPT, the A-point gap reopens with inverted order of the bands; however, under these conditions, the spectrum is metallic, and

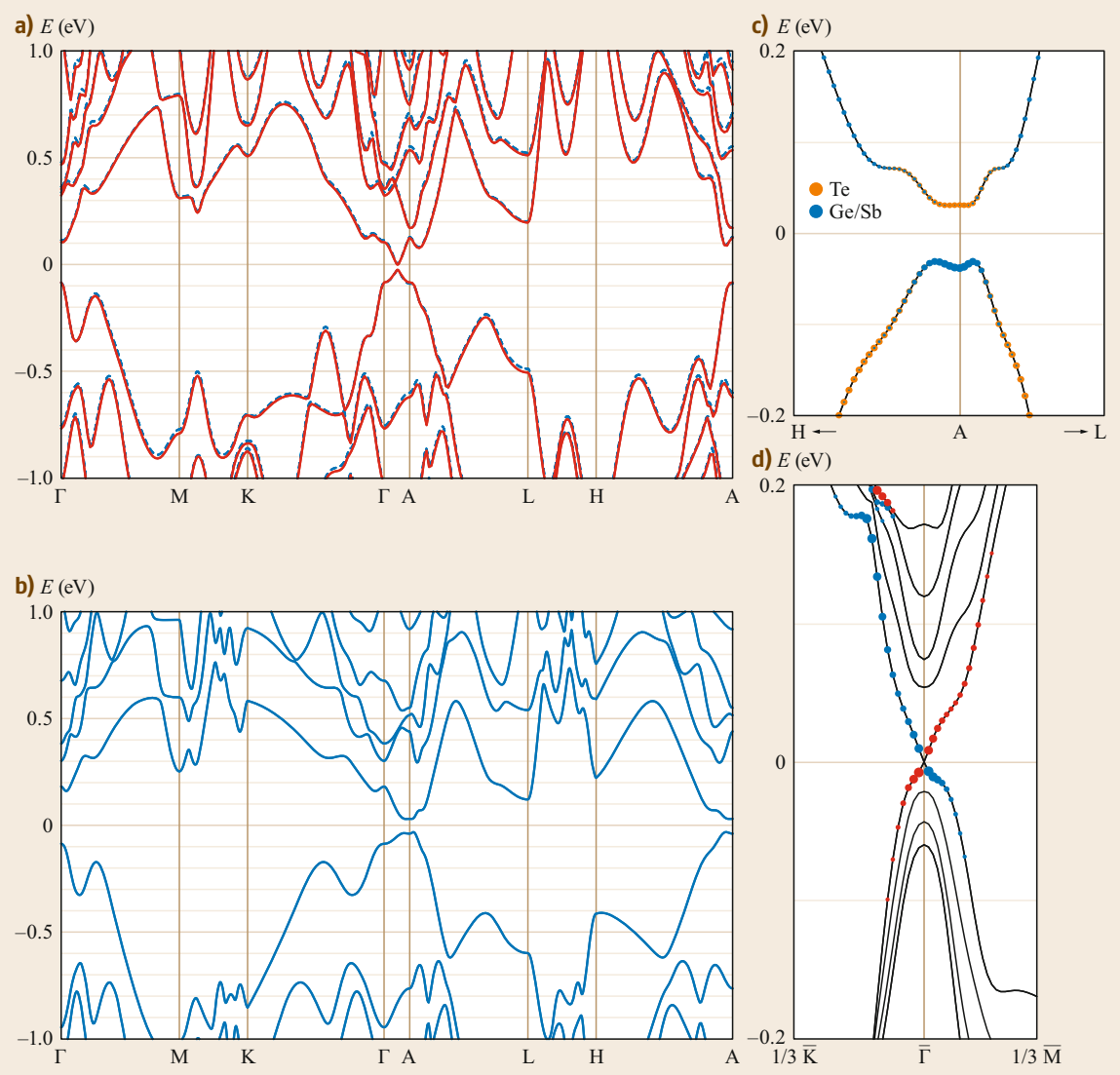

Fig. 15.14 **(a)** Bulk band structure of ordered Kooi phase with equilibrium crystal structure parameters (*red solid lines*, VASP calculation; *blue dashed lines*, ABINIT calculation). **(b)** Band structure of Kooi-$Ge_2Sb_2Te_5$ with Ge/Sb mixing (VCA-ABINIT calculation) and **(c)** its magnified view near the A-gap, with indication of the weights of Te and Ge/Sb p_z orbitals (VCA-ABINIT calculation). **(d)** Surface electronic spectrum for Kooi-$Ge_2Sb_2Te_5$ with Ge/Sb mixing. *Red* and *blue circles* denote the positive and negative sign of the in-plane spin, respectively

hence the system can be characterized as a topological metal. We also artificially increased the spin–orbit interaction strength λ in the ordered equilibrium structure and found that, as in the case of hydrostatic pressure, it leads to a shift of the gap toward the A point, along with its narrowing. Upon a further increase in the spin–orbit interaction strength, the gap becomes inverted, achieving at $\lambda/\lambda_0 = 1.4$ a width of 76 meV at the A point. This result is in line with the fact that the TI phase was predicted for $Ge_2Bi_2Te_5$ [15.73], in which the atomic spin–orbit coupling strength is larger owing to the larger atomic mass of Bi as compared with Sb.

However, it is known from experiments that the stable $Ge_2Sb_2Te_5$ contains mixed Ge/Sb atomic layers [15.77]. This mixing has been taken into account in the calculations within the virtual crystal approximation using the ABINIT code. The band structure for the ordered phase with ABINIT code is in good agreement with the VASP result (Fig. 15.14a, dashed blue lines). The calculated spectrum has a gap of 29.5 meV

in the middle of the Γ-A direction. Next, according to the experiment [15.77], we constructed $Ge_{0.56}/Sb_{0.44}$ and $Ge_{0.44}/Sb_{0.56}$ virtual atoms for the outer and inner Ge/Sb layers of NL, respectively. We find that in the case of the mixed Ge/Sb atomic layers, a minimum gap of 61 meV appears at the A point (Fig. 15.14b) and, being inverted (Fig. 15.14c), results in the nontrivial topological invariant $\mathbb{Z}_2 = 1$. This signifies that the Kooi structure possesses the TI quantum phase. Therefore, Ge/Sb mixing in the $Ge_2Sb_2Te_5$ Kooi structure effectively increases the spin–orbit interaction. The surface band structure for $Ge_2Sb_2Te_5$ with mixed Ge/Sb layers is shown in Fig. 15.14d. As can be seen, the surface spectrum of the Kooi structure holds the topological surface state with the Dirac point at the Fermi level.

The distinctive feature of the Ferro structure of $Ge_2Sb_2Te_5$ (Fig. 15.13b) is the lack of inversion symmetry. It results in the spin–orbit splitting of the bulk energy spectrum (Fig. 15.15a), which resembles the Rashba-like band splitting in the bulk GeTe [15.78]. The presented spectrum has a small gap of 11 meV in the A-H direction at $k_x \approx 0.1\,\text{Å}^{-1}$ away from the A point. Near the gap, the spin texture differs from the Rashba spin-helical picture and demonstrates almost collinear spin alignment perpendicular to the A-H (k_x) direction, with a sizable S_z component of the same sign both below and above the gap (Fig. 15.15b). Away from the H-A-L plane at $k_z = \pi/c \pm 0.015\,\text{Å}^{-1}$ (where $k_z = \pi/c$ is the H-A-L plane), the gap closes, forming a pair of Weyl nodes (Fig. 15.15c), which is a distinctive feature of the topological Weyl semimetal (TWS) phase.

The TWS can be realized by breaking either time-reversal or inversion symmetry in a topological Dirac semimetal [15.17]. In this regard, the appearance of the TWS quantum phase in the $Ge_2Sb_2Te_5$ with Ferro structure can be understood from the comparison with the intermediate inverted Petrov structure. The inverted Petrov structure predicted to be a Dirac semimetal differs from the Ferro structure only in the atomic layer sequence within the $(GeTe)_2$ block, so that the latter is inversion-asymmetric.

The Weyl topological phase is predicted to provide a realization of the chiral anomaly, giving rise to a negative magnetoresistance under parallel electric and magnetic fields, the semi-quantized anomalous Hall effect, unusual optical conductivity, and nonlocal transport and local nonconservation of the current [15.79–85]. At the surface, the bulk band topology should result in the formation of unusual surface states that form disjoint Fermi arcs connecting the projections of the Weyl nodes onto the surface Brillouin zone [15.86, 87]. The Fermi arcs are predicted to show unconventional quantum oscillations in magneto-transport, as well as unusual quantum interference effects in tunneling spectroscopy [15.87–90].

The $Ge_2Sb_2Te_5$ compound with a Ferro structure can adopt six different surface terminations depending on the Sb_2Te_3 QL and GeTe bilayer sequence near the cleavage plane. The geometries of the terminations are shown schematically in the insets in Fig. 15.16. The calculated surface electronic spectra (Fig. 15.16, odd columns) demonstrate that all surface terminations hold the trivial Rashba-split surface states resulting from splitting off from bulk bands due to the band-bending effect, which is negative for QL-GeTe-GeTe, GeTe-GeTe-QL, and GeTe-QL-GeTe terminations (first column in Fig. 15.16) and positive for terminations shown in the third column. Besides these states, as can be seen in the Fermi surface maps (Fig. 15.16, even columns), each surface termination holds the Fermi arcs connecting the Weyl pairs. In most cases, the arcs connect the Weyl nodes within each $\overline{\Gamma}$-$\overline{K}$ pair, while in the case of the TeGe-QL-TeGe termination, the arcs connect points of neighboring pairs via the hole-like Rashba surface state, which crosses the Fermi level twice in the $\overline{\Gamma}$-$\overline{M}$ direction, but once in $\overline{\Gamma}$-$\overline{K}$, and touches the Weyl nodes on the conduction band side. A similar effect of Weyl node reconnection was recently observed in the TWS phase arising in BiTeI under pressure [15.91].

15.5 Conclusions

In this chapter we have demonstrated the diversity of electronic states in natural topological heterostructures. These ternary compounds, with the general formula $(C^{IV}B^{VI})_n(A_2^VB_3^{VI})_m$, where A^V are elements of group V = Bi, Sb; B^{VI} are elements of group VI = Te, Se; and group IV elements C^{IV} = Ge, Sn, Pb, have layered hexagonal crystal structures with two distinct sublattices, one of which is the well-known topological insulator $A_2^VB_3^{VI}$ such as Bi_2Te_3, and another sublattice can be a strong topological insulator, topological crystalline insulator, or trivial insulator. Depending on the elemental composition and stoichiometry, these heterostructures can possess a van der Waals superlattice structure, may take the form of built-in sublattices within unique structural blocks, or can demonstrate phase-change behavior with temperature. Such a wealth of structures results in a wide variety of topological surface states in these materials.

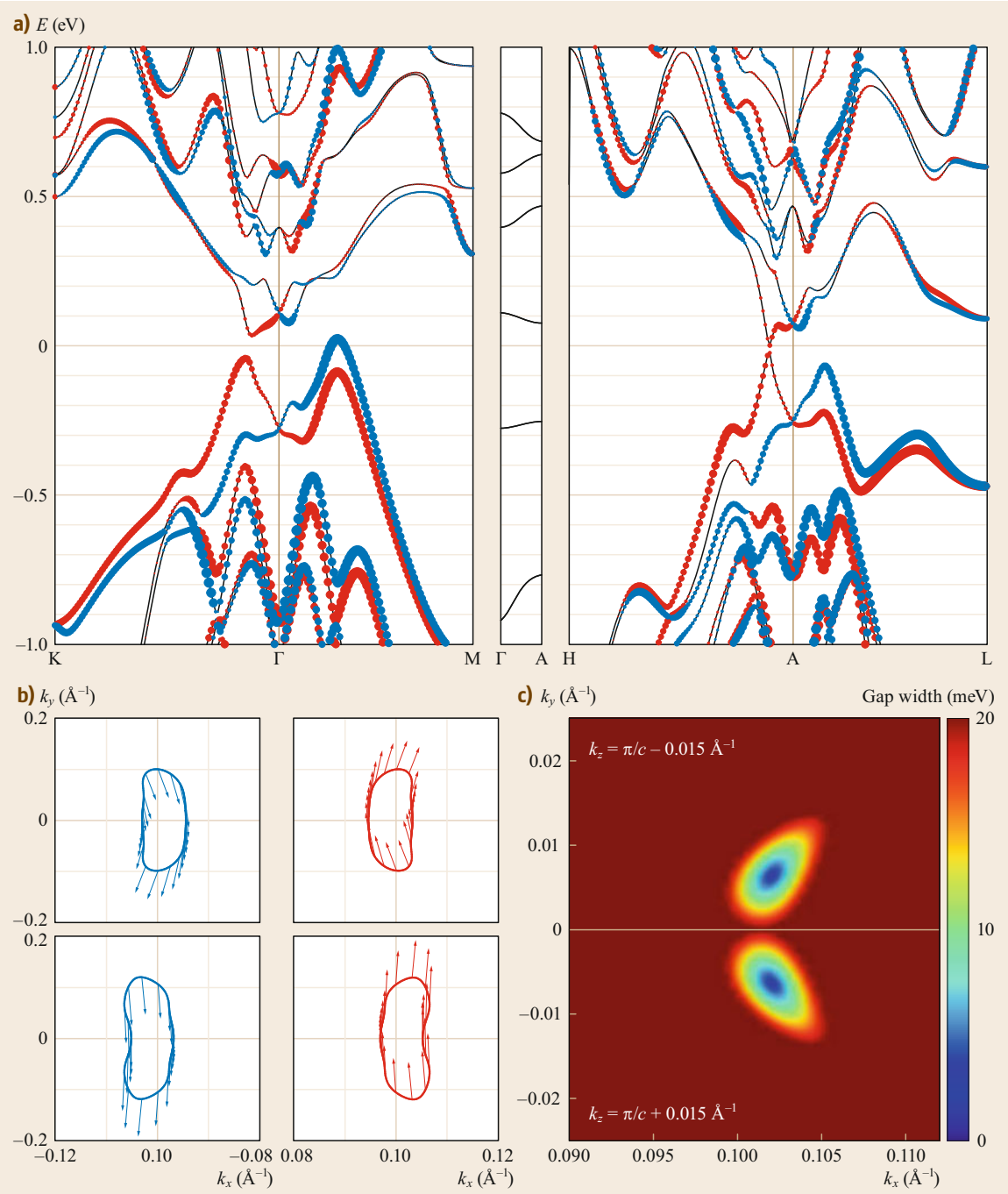

Fig. 15.15 **(a)** Bulk band spectrum of the high-temperature Ferro-$Ge_2Sb_2Te_5$ structure; *red/blue circles* indicate the positive/negative sign of the in-plane $S_\parallel$ spin components. **(b)** Spin-resolved constant energy contours taken below and above the gap (*left-* and *right-hand panels* for the H-A and A-H directions, respectively); here, *arrows* show the in-plane spin direction, and the *red/blue color* corresponds to the positive/negative sign of S_z. **(c)** The dependence of the gap width on $k_\parallel$ at $k_z = \pi/c - 0.015$ and $k_z = \pi/c + 0.015$ Å^{-1}; the zero-gap points correspond to the Weyl nodes

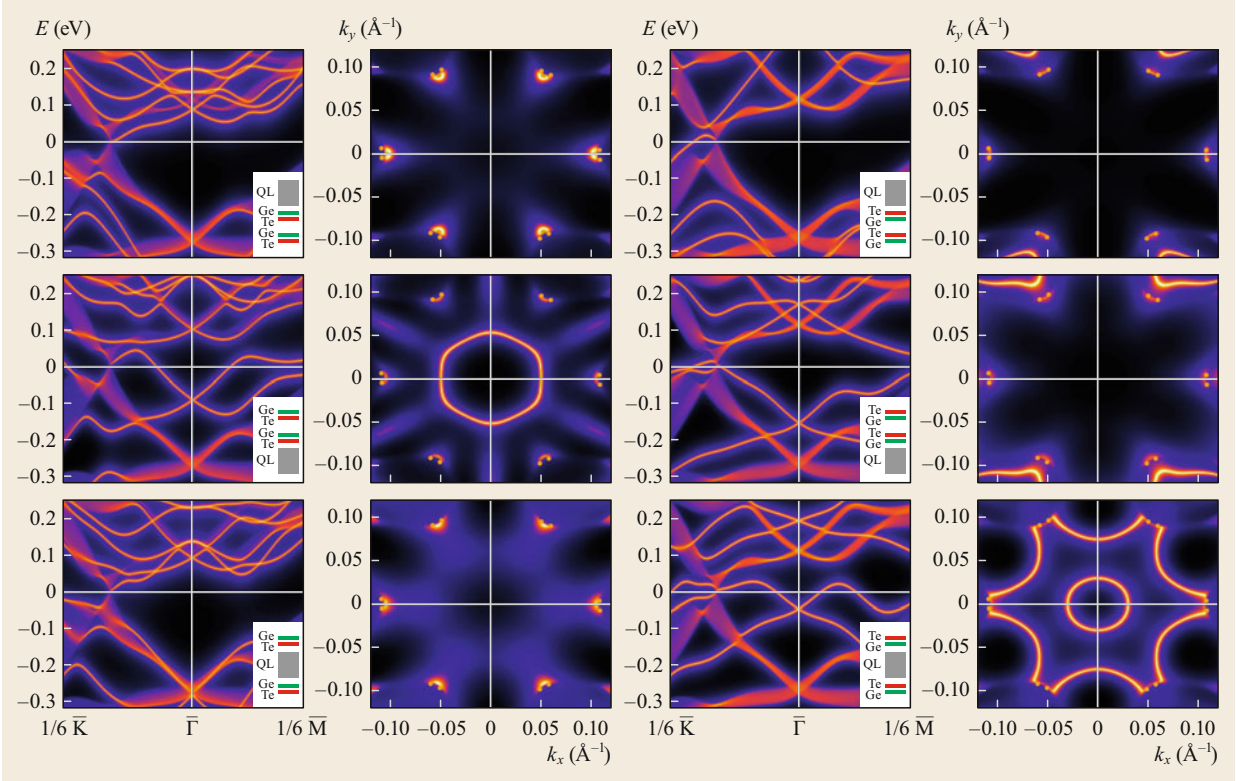

Fig. 15.16 Surface electronic structure for different Ferro-$Ge_2Sb_2Te_5$ surface terminations (*odd columns*), whose structure is shown in the insets, and corresponding Fermi surfaces (*even columns*). *Small red points* on the Fermi surfaces mark positions of the Weyl nodes. k_x- and k_y-axis directed along $\overline{\Gamma}$-$\overline{K}$ and $\overline{\Gamma}$-$\overline{M}$, respectively

In particular, most of the $(C^{IV}B^{VI})_{n=1}(A_2^VB_3^{VI})_{m>1}$ superlattices, including $PbBi_4Te_7$, $PbSb_4Te_7$, $PbBi_6Te_{10}$, $SnBi_4Te_7$, and $SnBi_6Te_{10}$ and others, are 3-D $\mathbb{Z}_2$ topological insulators [15.43], while some of them, like $SnSb_6Te_{10}$, are trivial insulators. The topological insulator superlattices exhibit a more complicated surface electronic structure and spin behavior than their parents, thus providing an efficient way to manipulate both the spin structure and the spatial localization of the conducting state. They demonstrate strong differences in the dispersion of the topological surface state and its spin polarization depending on the cleavage surface. Since in a real cleavage surface the different surface terminations are present due to the stepped morphology of the surface, the multiple coexisting Dirac cones centered at the $\overline{\Gamma}$ point of the reciprocal space arise in the ARPES spectra [15.58, 59]. These findings aid in understanding the diversity of topological surface states in TI superlattices and may pave the way for the application of topological insulators to real spintronic devices.

The $(C^{IV}B^{VI})_{n>1}(A_2^VB_3^{VI})_{m=1}$ heterostructures contain layers of $A_2^VB_3^{VI}$ topological insulator and $C^{IV}B^{VI}$ materials like SnTe and PbTe. The compounds with the trivial band insulator sublattice PbTe, such as $Pb_2Bi_2Te_5$, demonstrate a linear Dirac state in the surface spectrum similar to that in the parent binary TI. On the other hand, heterostructures with a SnTe sublattice (a material that is a topological crystalline insulator in bulk phase), such as $(SnTe)_{n=2,3}(Bi(Sb)_2Te_3)_{m=1}$ compounds, are $\mathbb{Z}_2$ topological insulators. In these TIs, two spin-helical topological surface states arise at the $\overline{\Gamma}$ point. These states reside in the bandgap and in the local gap of the valence band. The latter TSS, lying deep below the Fermi level, has a dispersion similar to that in the Bi_2Te_3 TI, while the bandgap TSS demonstrates an exotic dog-leg dispersion with two linear sections of different slope and a very low-velocity shoulder section between them. In $Sn_2Bi_2Te_5$, the shoulders are located in the middle of the gap, and the velocities of carriers in the lower and upper linear sections differ by a factor of two. Thus, in contrast to all hitherto known TIs, where the slope of the spin-helical TSS is linear or varies smoothly with energy, the bandgap TSS in the $(SnTe)_{n=2,3}(Bi_2Te_3)_{m=1}$ compounds shows an abrupt switch of the velocity of topological carriers

with a change in the Fermi surface topology in the narrow energy range (shoulder section), where the spin and charge current should be blocked. This novel finding paves a way for the efficient control of the group velocity with sufficiently large spin-current density by tuning the chemical potential.

Another type of $(C^{IV}B^{VI})_{n>1}(A_2^VB_3^{VI})_{m=1}$ heterostructures comprises materials with a GeTe sublattice, like the $Ge_2Sb_2Te_5$ compound, which is a phase-change material. The $(GeTe)_{n=2}(Sb_2Te_3)_{m=1}$ system can adopt four different hexagonal layered structures. At low temperatures it has a nonuple-layer structure similar to the related compounds with Sn and Pb, while in other phases the GeTe and Sb_2Te_3 sublattices are separated and alternate along a c-axis as in ($n = 1$, $m > 1$) structures. Thus, the temperature-induced structural phase transformation is accompanied by a quantum topological phase transition from the TI phase in the low-temperature Kooi crystal structure to the topological Weyl semimetal phase in the high-temperature Ferro structure. Together with the earlier predicted Dirac semimetal phase for the intermediate metastable inverted Petrov structure, the TI and Weyl semimetal phases form a rich topological family realized in the same material. The Dirac surface states of TI, with potential for spintronic applications, and the exotic bulk and surface electronic states of TWS, providing an ideal platform for many novel physical phenomena including negative magnetoresistance, anomalous quantum Hall effect, and chiral magnetic effect, can be realized in $Ge_2Sb_2Te_5$, substantially expanding the application potential of this material.

References

15.1 M.Z. Hasan, C.L. Kane: Colloquium: Topological insulators, Rev. Mod. Phys. **82**, 3045–3067 (2010)

15.2 J.E. Moore: The birth of topological insulators, Nature **464**, 194 (2010)

15.3 M.Z. Hasan, J.E. Moore: Three-dimensional topological insulators, Ann. Rev. Condens. Matter Phys. **2**(1), 55–78 (2011)

15.4 A. Bansil, H. Lin, T. Das: Colloquium: Topological band theory, Rev. Mod. Phys. **88**, 021004 (2016)

15.5 L. Fu, C.L. Kane, E.J. Mele: Topological insulators in three dimensions, Phys. Rev. Lett. **98**, 106803 (2007)

15.6 L. Fu, C.L. Kane: Topological insulators with inversion symmetry, Phys. Rev. B **76**, 045302 (2007)

15.7 D. Pesin, A.H. MacDonald: Spintronics and pseudospintronics in graphene and topological insulators, Nat. Mater. **11**, 409 (2012)

15.8 J.C.Y. Teo, L. Fu, C.L. Kane: Surface states and topological invariants in three-dimensional topological insulators: Application to $Bi_{1-x}Sb_x$, Phys. Rev. B **78**, 045426 (2008)

15.9 X.-L. Qi, T.L. Hughes, S.-C. Zhang: Topological field theory of time-reversal invariant insulators, Phys. Rev. B **78**, 195424 (2008)

15.10 H. Zhang, C.-X. Liu, X.-L. Qi, X. Dai, Z. Fang, S.-C. Zhang: Topological insulators in Bi_2Se_3, Bi_2Te_3 and Sb_2Te_3 with a single Dirac cone on the surface, Nat. Phys. **5**, 438 (2009)

15.11 S.V. Eremeev, G. Bihlmayer, M. Vergniory, Y.M. Koroteev, T.V. Menshchikova, J. Henk, A. Ernst, E.V. Chulkov: Ab initio electronic structure of thallium-based topological insulators, Phys. Rev. B **83**, 205129 (2011)

15.12 J.E. Moore, L. Balents: Topological invariants of time-reversal-invariant band structures, Phys. Rev. B **75**, 121306 (2007)

15.13 C.L. Kane: An insulator with a twist, Nat. Phys. **4**, 348 (2008)

15.14 L. Fu, C.L. Kane: Probing neutral Majorana fermion edge modes with charge transport, Phys. Rev. Lett. **102**, 216403 (2009)

15.15 R. Roy: Topological phases and the quantum spin Hall effect in three dimensions, Phys. Rev. B **79**, 195322 (2009)

15.16 Y. Xia, D. Qian, D. Hsieh, L. Wray, A. Pal, H. Lin, A. Bansil, D. Grauer, Y.S. Hor, R.J. Cava, M.Z. Hasan: Observation of a large-gap topological-insulator class with a single Dirac cone on the surface, Nat. Phys. **5**, 398–402 (2009)

15.17 A.A. Burkov, D.G. Hawthorn: Spin and charge transport on the surface of a topological insulator, Phys. Rev. Lett. **105**, 066802 (2010)

15.18 D. Culcer, E.H. Hwang, T.D. Stanescu, S. Das Sarma: Two-dimensional surface charge transport in topological insulators, Phys. Rev. B **82**, 155457 (2010)

15.19 M.H. Fischer, A. Vaezi, A. Manchon, E.-A. Kim: Spin-torque generation in topological insulator based heterostructures, Phys. Rev. B **93**, 125303 (2016)

15.20 T. Morimoto, A. Furusaki, N. Nagaosa: Topological magnetoelectric effects in thin films of topological insulators, Phys. Rev. B **92**, 085113 (2015)

15.21 X.-L. Qi, T.L. Hughes, S.-C. Zhang: Fractional charge and quantized current in the quantum spin Hall state, Nat. Phys. **4**, 273 (2008)

15.22 R. Yoshimi, A. Tsukazaki, Y. Kozuka, J. Falson, K.S. Takahashi, J.G. Checkelsky, N. Nagaosa, M. Kawasaki, Y. Tokura: Quantum Hall effect on top and bottom surface states of topological insulator $(Bi_{1-x}Sb_x)_2Te_3$ films, Nat. Commun. **6**, 6627 (2015)

15.23 X. Wu, Y. Hu, M. Ruan, N.K. Madiomanana, J. Hankinson, M. Sprinkle, C. Berger, W.A. de Heer: Half integer quantum Hall effect in high mobility single layer epitaxial graphene, Appl. Phys. Lett. **95**(22), 223108 (2009)

15.24 V. Dziom, A. Shuvaev, A. Pimenov, G.V. Astakhov, C. Ames, K. Bendias, J. Böttcher, G. Tkachov, E.M. Hankiewicz, C. Brüne, H. Buhmann,

L.W. Molenkamp: Observation of the universal magnetoelectric effect in a 3D topological insulator, Nat. Commun. **8**, 15197 (2017)
15.25 G.S. Jenkins, A.B. Sushkov, D.C. Schmadel, N.P. Butch, P. Syers, J. Paglione, H.D. Drew: Terahertz Kerr and reflectivity measurements on the topological insulator Bi_2Se_3, Phys. Rev. B **82**, 125120 (2010)
15.26 X.-L. Qi, R. Li, J. Zang, S.-C. Zhang: Inducing a magnetic monopole with topological surface states, Science **323**(5918), 1184–1187 (2009)
15.27 Y.L. Chen, J.G. Analytis, J.-H. Chu, Z.K. Liu, S.-K. Mo, X.L. Qi, H.J. Zhang, D.H. Lu, X. Dai, Z. Fang, S.C. Zhang, I.R. Fisher, Z. Hussain, Z.-X. Shen: Experimental realization of a three-dimensional topological insulator, Bi_2Te}Te3, Science **325**(5937), 178–181 (2009)
15.28 T. Zhang, P. Cheng, X. Chen, J.-F. Jia, X. Ma, K. He, L. Wang, H. Zhang, X. Dai, Z. Fang, X. Xie, Q.-K. Xue: Experimental demonstration of topological surface states protected by time-reversal symmetry, Phys. Rev. Lett. **103**, 266803 (2009)
15.29 K. Kuroda, M. Arita, K. Miyamoto, M. Ye, J. Jiang, A. Kimura, E.E. Krasovskii, E.V. Chulkov, H. Iwasawa, T. Okuda, K. Shimada, Y. Ueda, H. Namatame, M. Taniguchi: Hexagonally deformed Fermi surface of the 3D topological insulator Bi_2Se_3, Phys. Rev. Lett. **105**, 076802 (2010)
15.30 Y. Zhang, K. He, C.-Z. Chang, C.-L. Song, L.-L. Wang, X. Chen, J.-F. Jia, Z. Fang, X. Dai, W.-Y. Shan, S.-Q. Shen, Q. Niu, X.-L. Qi, S.-C. Zhang, X.-C. Ma, Q.-K. Xue: Crossover of the three-dimensional topological insulator Bi_2Se_3 to the two-dimensional limit, Nat. Phys. **6**, 584 (2010)
15.31 J.-H. Song, H. Jin, A.J. Freeman: Interfacial Dirac cones from alternating topological invariant superlattice structures of Bi_2Se_3, Phys. Rev. Lett. **105**, 096403 (2010)
15.32 W. Zhang, R. Yu, H.-J. Zhang, X. Dai, Z. Fang: First-principles studies of the three-dimensional strong topological insulators Bi_2Te_3, Bi_2Se_3 and Sb_2Te_3, New J. Phys. **12**(6), 065013 (2010)
15.33 S.V. Eremeev, Y.M. Koroteev, E.V. Chulkov: Effect of the atomic composition of the surface on the electron surface states in topological insulators $A^V{}_2B_3{}^{VI}$, JETP Letters **91**(8), 387–391 (2010)
15.34 D. Hsieh, Y. Xia, D. Qian, L. Wray, J.H. Dil, F. Meier, J. Osterwalder, L. Patthey, J.G. Checkelsky, N.P. Ong, A.V. Fedorov, H. Lin, A. Bansil, D. Grauer, Y.S. Hor, R.J. Cava, M.Z. Hasan: A tunable topological insulator in the spin helical Dirac transport regime, Nature **460**, 1101 (2009)
15.35 L.A. Wray, S.-Y. Xu, Y. Xia, D. Hsieh, A.V. Fedorov, Y.S. Hor, R.J. Cava, A. Bansil, H. Lin, M.Z. Hasan: A topological insulator surface under strong Coulomb, magnetic and disorder perturbations, Nat. Phys. **7**, 32 (2011)
15.36 Y.S. Hor, P. Roushan, H. Beidenkopf, J. Seo, D. Qu, J.G. Checkelsky, L.A. Wray, D. Hsieh, Y. Xia, S.-Y. Xu, D. Qian, M.Z. Hasan, N.P. Ong, A. Yazdani, R.J. Cava: Development of ferromagnetism in the doped topological insulator $Bi_{2-x}Mn_xTe_3$, Phys. Rev. B **81**, 195203 (2010)
15.37 A.M. Essin, J.E. Moore, D. Vanderbilt: Magnetoelectric polarizability and axion electrodynamics in crystalline insulators, Phys. Rev. Lett. **102**, 146805 (2009)
15.38 M. Dzero, K. Sun, V. Galitski, P. Coleman: Topological Kondo insulators, Phys. Rev. Lett. **104**, 106408 (2010)
15.39 J. Linder, Y. Tanaka, T. Yokoyama, A. Sudbø, N. Nagaosa: Unconventional superconductivity on a topological insulator, Phys. Rev. Lett. **104**, 067001 (2010)
15.40 M. Franz: Starting a new family, Nat. Mater. **9**, 536 (2010)
15.41 J. Henk, A. Ernst, S.V. Eremeev, E.V. Chulkov, I.V. Maznichenko, I. Mertig: Complex spin texture in the pure and Mn-doped topological insulator Bi_2Te_3, Phys. Rev. Lett. **108**, 206801 (2012)
15.42 S.V. Eremeev, V.N. Men'shov, V.V. Tugushev, P.M. Echenique, E.V. Chulkov: Magnetic proximity effect at the three-dimensional topological insulator/magnetic insulator interface, Phys. Rev. B **88**, 144430 (2013)
15.43 S.V. Eremeev, G. Landolt, T.V. Menshchikova, B. Slomski, Y.M. Koroteev, Z.S. Aliev, M.B. Babanly, J. Henk, A. Ernst, L. Patthey, A. Eich, A.A. Khajetoorians, J. Hagemeister, O. Pietzsch, J. Wiebe, R. Wiesendanger, P.M. Echenique, S.S. Tsirkin, I.R. Amiraslanov, J.H. Dil, E.V. Chulkov: Atom-specific spin mapping and buried topological states in a homologous series of topological insulators, Nat. Commun. **3**, 635 (2012)
15.44 D. Niesner, S. Otto, V. Hermann, T. Fauster, T.V. Menshchikova, S.V. Eremeev, Z.S. Aliev, I.R. Amiraslanov, M.B. Babanly, P.M. Echenique, E.V. Chulkov: Bulk and surface electron dynamics in a *p*-type topological insulator $SnSb_2Te_4$, Phys. Rev. B **89**, 081404 (2014)
15.45 G. Kresse, J. Hafner: Ab initio molecular dynamics for open-shell transition metals, Phys. Rev. B **48**, 13115–13118 (1993)
15.46 G. Kresse, J. Furthmüller: Efficient iterative schemes for ab initio total-energy calculations using a plane-wave basis set, Phys. Rev. B **54**, 11169–11186 (1996)
15.47 J.P. Perdew, K. Burke, M. Ernzerhof: Generalized gradient approximation made simple, Phys. Rev. Lett. **77**, 3865–3868 (1996)
15.48 P.E. Blöchl: Projector augmented-wave method, Phys. Rev. B **50**, 17953–17979 (1994)
15.49 G. Kresse, D. Joubert: From ultrasoft pseudopotentials to the projector augmented-wave method, Phys. Rev. B **59**, 1758–1775 (1999)
15.50 S. Grimme, J. Antony, S. Ehrlich, H. Krieg: A consistent and accurate ab initio parametrization of density functional dispersion correction (DFT-D) for the 94 elements H-Pu, J. Chem. Phys. **132**(15), 154104 (2010)
15.51 X. Gonze, B. Amadon, P.-M. Anglade, J.-M. Beuken, F. Bottin, P. Boulanger, F. Bruneval, D. Caliste, R. Caracas, M. Côté, T. Deutsch, L. Gen-

ovese, P. Ghosez, M. Giantomassi, S. Goedecker, D. Hamann, P. Hermet, F. Jollet, G. Jomard, S. Leroux, M. Mancini, S. Mazevet, M. Oliveira, G. Onida, Y. Pouillon, T. Rangel, G.-M. Rignanese, D. Sangalli, R. Shaltaf, M. Torrent, M. Verstraete, G. Zerah, J. Zwanziger: ABINIT: First-principles approach to material and nanosystem properties, Comput. Phys. Commun. **180**(12), 2582–2615 (2009)

15.52 M. Krack: Pseudopotentials for H to Kr optimized for gradient-corrected exchange-correlation functionals, Theor. Chem. Acc. **114**(1), 145–152 (2005)

15.53 N. Marzari, D. Vanderbilt: Maximally localized generalized Wannier functions for composite energy bands, Phys. Rev. B **56**, 12847–12865 (1997)

15.54 M.P. Lopez Sancho, J.M. Lopez Sancho, J.M.L. Sancho, J. Rubio: Highly convergent schemes for the calculation of bulk and surface Green functions, J. Phys. F **15**(4), 851–858 (1985)

15.55 J. Henk, W. Schattke: A subroutine package for computing Green's functions of relaxed surfaces by the renormalization method, Comput. Phys. Commun. **77**(1), 69–83 (1993)

15.56 L.E. Shelimova, O.G. Karpinskii, M.A. Kretova, V.I. Kosyakov, V.A. Shestakov, V.S. Zemskov, F.A. Kuznetsov: Homologous series of layered tetradymite-like compounds in the Sb-Te and $GeTe$-Sb_2Te_3 systems, Inorg. Mater. **36**(8), 768–775 (2000)

15.57 T.V. Menshchikova, S.V. Eremeev, Y.M. Koroteev, V.M. Kuznetsov, E.V. Chulkov: Ternary compounds based on binary topological insulators as an efficient way for modifying the Dirac cone, JETP Letters **93**(1), 15 (2011)

15.58 T. Okuda, T. Maegawa, M. Ye, K. Shirai, T. Warashina, K. Miyamoto, K. Kuroda, M. Arita, Z.S. Aliev, I.R. Amiraslanov, M.B. Babanly, E.V. Chulkov, S.V. Eremeev, A. Kimura, H. Namatame, M. Taniguchi: Experimental evidence of hidden topological surface states in $PbBi_4Te_7$, Phys. Rev. Lett. **111**, 206803 (2013)

15.59 M. Papagno, S.V. Eremeev, J. Fujii, Z.S. Aliev, M.B. Babanly, S.K. Mahatha, I. Vobornik, N.T. Mamedov, D. Pacilé, E.V. Chulkov: Multiple coexisting Dirac surface states in three-dimensional topological insulator $PbBi_6Te_{10}$, ACS Nano **10**(3), 3518–3524 (2016)

15.60 B.A. Kuropatwa, H. Kleinke: Thermoelectric properties of stoichiometric compounds in the $(SnTe)_x(Bi_2Te_3)_y$ system, Z. Anorg. Allg. Chem. **638**(15), 2640–2647 (2012)

15.61 T.H. Hsieh, H. Lin, J. Liu, W. Duan, A. Bansil, L. Fu: Topological crystalline insulators in the SnTe material class, Nat. Commun. **3**, 982 (2012)

15.62 Y. Tanaka, Z. Ren, T. Sato, K. Nakayama, S. Souma, T. Takahashi, K. Segawa, Y. Ando: Experimental realization of a topological crystalline insulator in SnTe, Nat. Phys. **8**, 800 (2012)

15.63 L. Fu: Topological crystalline insulators, Phys. Rev. Lett. **106**, 106802 (2011)

15.64 S.V. Eremeev, Y.M. Koroteev, I.A. Nechaev, E.V. Chulkov: Role of surface passivation in the formation of Dirac states at polar surfaces of topological crystalline insulators: The case of SnTe(111), Phys. Rev. B **89**, 165424 (2014)

15.65 R.E. Simpson, P. Fons, A.V. Kolobov, T. Fukaya, M. Krbal, T. Yagi, J. Tominaga: Interfacial phase-change memory, Nat. Nanotechnol. **6**, 501 (2011)

15.66 T.C. Chong, L.P. Shi, R. Zhao, P.K. Tan, J.M. Li, H.K. Lee, X.S. Miao, A.Y. Du, C.H. Tung: Phase change random access memory cell with superlattice-like structure, Appl. Phys. Lett. **88**(12), 122114 (2006)

15.67 T.C. Chong, L.P. Shi, X.Q. Wei, R. Zhao, H.K. Lee, P. Yang, A.Y. Du: Crystalline amorphous semiconductor superlattice, Phys. Rev. Lett. **100**, 136101 (2008)

15.68 J. Tominaga, A.V. Kolobov, P. Fons, T. Nakano, S. Murakami: Ferroelectric order control of the Dirac-semimetal phase in $GeTe$-Sb_2Te_3 superlattices, Adv. Mater. Interfaces **1**(1), 1300027 (2014)

15.69 B.J. Kooi, J.T.M. De Hosson: Electron diffraction and high-resolution transmission electron microscopy of the high temperature crystal structures of $Ge_xSb_2Te_{3+x}(x = 1, 2, 3)$ phase change material, J. Appl. Phys. **92**(7), 3584–3590 (2002)

15.70 I.I. Petrov, R.M. Imamov, Z.G. Pinsker: Electron-diffraction determination of the structures of $Ge_2Sb_2Te_5$ and $GeSb_4Te_7$, Sov. Phys. Crystallogr. **13**, 339–342 (1968)

15.71 X. Yu, J. Robertson: Modeling of switching mechanism in GeSbTe chalcogenide superlattices, Sci. Rep. **5**, 12612 (2015)

15.72 I.V. Silkin, Y.M. Koroteev, G. Bihlmayer, E.V. Chulkov: Influence of the Ge–Sb sublattice atomic composition on the topological electronic properties of $Ge_2Sb_2Te_5$, Appl. Surf. Sci. **267**, 169–172 (2013)

15.73 J. Kim, J. Kim, K.-S. Kim, S.-H. Jhi: Topological phase transition in the interaction of surface Dirac fermions in heterostructures, Phys. Rev. Lett. **109**, 146601 (2012)

15.74 S.V. Eremeev, T.V. Menshchikova, I.V. Silkin, M.G. Vergniory, P.M. Echenique, E.V. Chulkov: Sublattice effect on topological surface states in complex $(SnTe_{n>1})(Bi_2Te_3)_{m=1}$ compounds, Phys. Rev. B **91**, 245145 (2015)

15.75 A. Bera, K. Pal, D.V.S. Muthu, S. Sen, P. Guptasarma, U.V. Waghmare, A.K. Sood: Sharp Raman anomalies and broken adiabaticity at a pressure induced transition from band to topological insulator in Sb_2Se_3, Phys. Rev. Lett. **110**, 107401 (2013)

15.76 W. Li, X.-Y. Wei, J.-X. Zhu, C.S. Ting, Y. Chen: Pressure-induced topological quantum phase transition in Sb_2Se_3, Phys. Rev. B **89**, 035101 (2014)

15.77 T. Matsunaga, N. Yamada, Y. Kubota: Structures of stable and metastable $Ge_2Sb_2Te_5$, an intermetallic compound in $GeTe$-Sb_2Te_3 pseudobinary systems, Acta Crystallogr. B **60**(6), 685–691 (2004)

15.78 D. Di Sante, P. Barone, R. Bertacco, S. Picozzi: Electric control of the giant Rashba effect in bulk GeTe, Adv. Mater. **25**(4), 509–513 (2013)

15.79 A.A. Zyuzin, A.A. Burkov: Topological response in Weyl semimetals and the chiral anomaly, Phys. Rev. B **86**, 115133 (2012)

15.80 K.-Y. Yang, Y.-M. Lu, Y. Ran: Quantum Hall effects in a Weyl semimetal: P ossible application in pyrochlore iridates, Phys. Rev. B **84**, 075129 (2011)
15.81 D.T. Son, B.Z. Spivak: Chiral anomaly and classical negative magnetoresistance of Weyl metals, Phys. Rev. B **88**, 104412 (2013)
15.82 C.-X. Liu, P. Ye, X.-L. Qi: Chiral gauge field and axial anomaly in a Weyl semimetal, Phys. Rev. B **87**, 235306 (2013)
15.83 H. Wei, S.-P. Chao, V. Aji: Excitonic phases from Weyl semimetals, Phys. Rev. Lett. **109**, 196403 (2012)
15.84 P.E.C. Ashby, J.P. Carbotte: Magneto-optical conductivity of Weyl semimetals, Phys. Rev. B **87**, 245131 (2013)
15.85 K. Landsteiner: Anomalous transport of Weyl fermions in Weyl semimetals, Phys. Rev. B **89**, 075124 (2014)
15.86 X. Wan, A.M. Turner, A. Vishwanath, S.Y. Savrasov: Topological semimetal and Fermi-arc surface states in the electronic structure of pyrochlore iridates, Phys. Rev. B **83**, 205101 (2011)
15.87 P. Hosur: Friedel oscillations due to Fermi arcs in Weyl semimetals, Phys. Rev. B **86**, 195102 (2012)
15.88 T. Ojanen: Helical Fermi arcs and surface states in time-reversal invariant Weyl semimetals, Phys. Rev. B **87**, 245112 (2013)
15.89 A.C. Potter, I. Kimchi, A. Vishwanath: Quantum oscillations from surface Fermi arcs in Weyl and Dirac semimetals, Nat. Commun. **5**, 5161 (2014)
15.90 Y. Zhang, D. Bulmash, P. Hosur, A.C. Potter, A. Vishwanath: Quantum oscillations from generic surface Fermi arcs and bulk chiral modes in Weyl semimetals, Sci. Rep. **6**, 23741 (2016)
15.91 I.P. Rusinov, T.V. Menshchikova, I.Y. Sklyadneva, R. Heid, K.-P. Bohnen, E.V. Chulkov: Pressure effects on crystal and electronic structure of bismuth tellurohalides, New J. Phys. **18**(11), 113003 (2016)

Sergey Eremeev

Laboratory of Surface Phenomena Physics
Institute of strength Physics and Materials Science
Tomsk, Russian Federation
eremeev@ispms.tsc.ru

Sergey Eremeev received a PhD degree from Tomsk State University in 1997. In 1998 he began work in the Institute of Strength Physics and Materials Science, Siberian Branch of the Russian Academy of Sciences, Tomsk. He now works on computational materials science, focused on the electronic structure of low-dimensional systems and topological insulators.

Igor Rusinov

Laboratory of Nanostructured Surfaces and Coatings
Tomsk State University
Tomsk, Russian Federation
rusinovip@gmail.com

Igor Rusinov graduated from Kostroma State University, Kostroma, Russian Federation, in 2010, and received the PhD degree from Tomsk State University in 2013. Since 2011, he has worked in the laboratory for nanostructured surfaces and coatings of Tomsk State University. He now investigates electronic structures and topological properties of materials with strong spin-orbit coupling.

Evgueni Chulkov

Departamento de Física de Materiales
Universidad del País Vasco, UPV/EHU,
Facultad de Ciencias Químicas
San Sebastián/Donostia, Spain
evguenivladimirovich.tchoulkov@ehu.eus

Evgueni Chulkov is Professor at the University of the Basque Country, San Sebastian, Spain, and a head of the laboratory of electronic and spin structure of nanosystems at Saint Petersburg University. He received his PhD from Tomsk State University in 1980. His work focuses on electronic structures in materials with strong spin-orbit interactions and electronic properties of topological insulators.

16. Energetic Ground State Calculations, Electronic Band Structure at Surfaces

Gian Paolo Brivio, Guido Fratesi

Ground-state properties and electronic band structures at surfaces are a very important field of research in surface science not only for catalysis, but more recently for organic electronics where several sensitive experimental techniques have been developed. Nowadays, a joint theoretical and experimental effort based on exceptionally improved computer power/algorithms and experimental advances is successful in describing adsorption sites, geometry, reconstruction, and many-body properties. In the first section, we focus on density functional theory (DFT) including its historical improvements: generalized gradient approximation, self-interaction correction, hybrid functionals (orbital-dependent functional), and phenomenological treatments of van der Waals (vdW) interaction. After examining the methods to compute band structures, we present organic classes of molecules. Polycyclic aromatic hydrocarbons have attracted significant interest for organic electronic devices, and are presented through examples of pentacene on silicon, noble metals, and aluminum. Charge rearrangement/dipoles/spin distributions induced by adsorption complete this chapter.

16.1 Preliminary Remarks

Energetic ground-state calculations and electronic band structure at surfaces have been important fields of research in surface science since crystallographic surfaces were grown under ultrahigh vacuum conditions and several surface-sensitive techniques were developed. Currently clean, almost two-dimensional (2-D) periodic surfaces can be obtained even after adsorbing complex organic molecules.

Adsorption is a very relevant phenomenon and well known are its implications for corrosion, heterogeneous catalysis, and more recently for organic electronics. But the understanding of such processes requires an understanding of bonding of atoms and molecules at solid surfaces. Nowadays, a joint experimental and theoretical effort, based on first-principles calculations, strongly propelled by the enormously increased computer power, is often successful in determining adsorption sites, geometry, possible surface reconstruction, orientation of molecules, potential energy barriers, wavefunctions, vibrations, and more recently in a few cases many-body properties such as plasmon, polariton on metals, magnons, etc. The density of states of the clean surface and of the surface bands projected onto the molecular eigenstates now enjoy clearer pictures.

M. Rocca, T.S. Rahman, L. Vattuone (Eds.), *Springer Handbook of Surface Science*, Springer Handbooks,
https://doi.org/10.1007/978-3-030-46906-1_16

We can distinguish surface-projected bulk states, resonant surface ones, and also localized surface electronic states. Refined two-photon photoemission experiments or inverse photoemission experiments have detected image potential states determined by the long-range Coulomb tails of the surface potential. Quantum well states localized between an adsorbate overlayer and the surface are also important. Surface states can be used as a tool to monitor adsorption but may also occur as a consequence of such phenomena.

The study of molecule–surface interaction boasts a great variety of systems and of physical and chemical properties. Large binding energy implies chemisorption. This is often the case of open-shell atoms, while inorganic molecules may form strong bonds or dissociate by unsaturated states on the surface. In this respect, alkali adatoms are benchmark systems of which the state of knowledge is not only remarkable but reveals unexpected phenomena such as the *vertical diffusion* probed by ^{3}He scattering. Physisorption is relevant in the simpler noble gas–solid interaction but often also dictates coupling both in an overlayer or in a thin film of organic molecules. Adsorption of organic molecules has opened up new research perspectives. In fact, such moieties display an almost infinite possibility of combining atoms to the required functionalization. Studies have in particular focused on hybrid interfaces in which an organic overlayer is adsorbed on an inorganic one, in view of applications to photovoltaics and electronic devices. Here molecular π and σ states may couple to the substrate and the vdW interaction often plays a crucial role.

16.2 Density Functional Theory at Surfaces

Reliable theoretical models of the electronic properties of surfaces are paramount to interpreting measurements, to account for the molecule surface interaction, and to suggest new routes to the experimental activity. In this respect, density functional theory (DFT) is currently the most popular method because, first, it is an ab initio approach and second, on the basis of Hohenberg–Kohn–Sham theorems, it provides a quantum description capable of handling several hundreds of atoms. Its main limitation is related to an approximate treatment of the exchange-correlation functional which is essentially semilocal in common implementations. A pairwise vdW interaction damped at shorter distances, is usually added to remedy such an incomplete correlation. Apart from the computationally very expensive methods of theoretical chemistry, the study of ground states by DFT is sometimes implemented by many-body perturbation theory. However, the size of the system to be treated limits most of calculation to density functional theory (plus a phenomenological addition of the vdW coupling). Kohn–Sham (KS) eigenstates are found to provide an approximate yet useful description of electronic bands even though these lie outside the realm of DFT being a ground-state theory.

16.2.1 Theoretical Framework

Density functional theory currently constitutes the only practical ab initio method for calculating the electronic properties of condensed matter systems that allow one to deal with a few thousand electrons (hundreds of atoms) [16.1]. Consequently, it is the best approach to deal with a realistic description of adsorbate systems where the interaction between molecules and the surface requires consideration of several layers. The DFT formalism is based on the Hohenberg–Kohn theorem which states that there is a one-to-one correspondence between the charge density $n(\boldsymbol{r})$ of an N interacting electron system and an external potential (up to a constant) $v_{\text{ext}}(\boldsymbol{r})$ [16.2]. In practice, a condensed matter system is fully identified by the electron–nuclei potential

$$v_{\text{ext}}(\boldsymbol{r}) = -\sum_a \frac{Z_a}{|\boldsymbol{r}-\boldsymbol{R}_a|}\,, \tag{16.1}$$

where Z_a and $\boldsymbol{R}_a$ are the atomic number and coordinate, respectively, and atomic units are used throughout. The ground-state charge $n(\boldsymbol{r})$ can be obtained by minimizing the total energy functional

$$E[n] = \int \mathrm{d}\boldsymbol{r}\; v_{\text{ext}}(\boldsymbol{r})n(\boldsymbol{r}) + F[n]\,, \tag{16.2}$$

with respect to variations of $n(\boldsymbol{r})$ over the possible ground-state charge densities. The functional $F[n]$ is the Hohenberg–Kohn functional which is independent of the system.

However, the explicit form of $F[n]$ is not known. For this reason Kohn and Sham resorted to constructing a viable set of single-particle equations by affirming that for any electron problem one can make fictitious single particle equations, subject to an external potential $v_{\text{eff}}(\boldsymbol{r})$, such that the interacting system ground-state density equals that of the noninteracting

one $n_{\text{eff}}(\boldsymbol{r})$ [16.3]

$$n(\boldsymbol{r}) = n_{\text{eff}}(\boldsymbol{r}) \,. \tag{16.3}$$

The auxiliary problem equations, the so-called Kohn–Sham (KS) equations, read as

$$\left[-\frac{\nabla_r^2}{2} + v_{\text{eff}}(\boldsymbol{r})\right]\varphi_i(\boldsymbol{r}) = \varepsilon_i\varphi_i(\boldsymbol{r}) \,, \tag{16.4}$$

and

$$n(\boldsymbol{r}) = \sum_{i=1}^{N} |\varphi_i(\boldsymbol{r})|^2 \,. \tag{16.5}$$

The KS equations can be worked out from the Hohenberg–Kohn variational principle which ensures that the functional $E[n]$ is stationary for small variations of the charge density from the one which guarantees the minimum energy, i.e., $n_{\text{eff}}(\boldsymbol{r})$ [16.3, 4]. One can find that

$$v_{\text{eff}}(\boldsymbol{r}) = v_{\text{ext}}(\boldsymbol{r}) + v_{\text{H}}([n], \boldsymbol{r}) + v_{\text{xc}}([n], \boldsymbol{r}) \,, \tag{16.6}$$

where $v_{\text{H}}(\boldsymbol{r})$ and $v_{\text{xc}}(\boldsymbol{r})$ are the Hartree and the exchange-correlation potential, respectively.

The KS approach is exact: its limitations are in regard to the approximated choice of the exchange-correlation potential defined as the functional derivative of the exchange-correlation functional,

$$\frac{\delta E_{\text{xc}}[n(\boldsymbol{r})]}{\delta n(\boldsymbol{r})} = v_{\text{xc}}(\boldsymbol{r}) \,. \tag{16.7}$$

Here $E_{\text{xc}}[n]$ includes the electron–electron functional minus the Coulomb classical one plus the kinetic energy functional difference between the (unknown) correct one and the single particle expression [16.4]. Approximations to $E_{\text{xc}}[n]$ will be discussed in the following section.

Finally, we wish to remark on some important points of the KS equations: (i) They can be solved self-consistently; (ii) they allow for a magnetic solution; (iii) differently from the Hartree–Fock (HF) approach their eigenvalues cannot be associated to ionization energies, since the Koopmans' theorem does not hold. Only the highest occupied KS eigenvalue is exactly the chemical potential of the system [16.5]. The KS eigenstates cannot be interpreted as one-electron orbitals since the sum of the squared magnitudes of the occupied orbitals, i.e., the charge density, is the fundamental quantity in DFT. However, both eigenfunctions and eigenvalues may often be considered as one-electron orbitals and energies with a good accuracy.

The Local Density Approximation

The local density approximation (LDA) functional can be defined by that of the exchange-correlation one for the homogeneous electron gas. Though a very simplified expression the LDA provides a useful guess for $E_{\text{xc}}[n(\boldsymbol{r})]$ of several condensed matter systems [16.3]. In a spin-polarized form the LDA exchange-correlation functional can be generalized to the local spin density approximation (LSDA) to be written as

$$E_{\text{xc}}[n]^{\text{LSDA}}[n_\uparrow, n_\downarrow] = \int n(\boldsymbol{r})\varepsilon_{\text{xc}}(n_\uparrow(\boldsymbol{r}), n_\downarrow(\boldsymbol{r}))\mathrm{d}\boldsymbol{r} \,, \tag{16.8}$$

where $n(\boldsymbol{r}) = n_\uparrow(\boldsymbol{r}) + n_\downarrow(\boldsymbol{r})$, and ε_{xc} is the exchange-correlation energy per particle for a homogeneous electron gas depending on its spin. Despite its simple expression the L(S)DA has produced many relevant results [16.6]. For example, the bulk constants, cohesive energies, and bulk moduli have been computed for C, Si, Ge with very small differences with respect to the experimental data, namely $\simeq 1\%$ for the bulk constants, $\simeq 4\%$ for the cohesive energies, and $\simeq 5\%$ for the bulk moduli. A detailed LDA-DFT study has demonstrated that the diamond structure is the most stable one for Si among several plausible ones [16.7]. The success of L(S)DA for systems with rapid changes in $n(\boldsymbol{r})$ can be explained by recalling a fundamental property of the exchange-correlation hole $n_{\text{xc}}(\boldsymbol{r}, \boldsymbol{r}')$, defined as [16.8]

$$n_{\text{xc}}(\boldsymbol{r}, \boldsymbol{r}') = \frac{n_2(\boldsymbol{r}, \boldsymbol{r}')}{n(\boldsymbol{r})} - n(\boldsymbol{r}) \,, \tag{16.9}$$

where $n_2(\boldsymbol{r}, \boldsymbol{r}')$ is the diagonal second-order density matrix, which represents the conditional probability of finding an electron in $\boldsymbol{r}'$ if there is one in $\boldsymbol{r}$. In an exact theory

$$\int n_{\text{xc}}(\boldsymbol{r}, \boldsymbol{r}')\mathrm{d}\boldsymbol{r}' = -1 \,. \tag{16.10}$$

The theorem in (16.10) is satisfied by the exchange-correlation hole in L(S)DA. We also observe that while the function $n_{\text{xc}}(\boldsymbol{r}, \boldsymbol{r}')$ is poorly estimated by L(S)DA, the corresponding exchange-correlation functional $E_{\text{xc}}^{\text{LSDA}}$

$$\begin{aligned} E_{\text{xc}}^{\text{LSDA}} &= \frac{1}{2}\int \mathrm{d}\boldsymbol{r}\, n(\boldsymbol{r}) \int \mathrm{d}\boldsymbol{r}' \frac{1}{|\boldsymbol{r}-\boldsymbol{r}'|} n_{\text{xc}}(\boldsymbol{r}, \boldsymbol{r}') \,, \\ &= \frac{1}{2}\int \mathrm{d}\boldsymbol{r} \int_0^\infty R^2 \mathrm{d}R \frac{1}{R} \int \mathrm{d}\Omega\, n_{\text{xc}}(\boldsymbol{r}, \boldsymbol{R}) \end{aligned} \tag{16.11}$$

only depends on the spherical average of $n_{\text{xc}}(\boldsymbol{r}, \boldsymbol{R})$ so that $E_{\text{xc}}^{\text{LSDA}}$ is often a reliable approximation to the

exchange correlation energy, since such a functional displays only a weak dependence on the exact shape of the exchange correlation hole [16.9].

The Generalized Gradient Approximation

Though being a very useful approximation, the L(S)DA is often unable to supply quantitatively correct predictions of physical quantities, e.g., it overestimates dissociation energies by $\approx 1\,\mathrm{eV}$ and determines inaccurate molecular atomization energies which turn out to be about 1 eV smaller than the real ones [16.10]. All these errors are much above the chemical accuracy of 43.36 meV. To amend such discrepancies it seemed rather obvious to introduce a semilocal exchange-correlation functional also dependent on the charge density. This expression is named the generalized gradient approximation (GGA) in which the exchange correlation functional $E_{\mathrm{xc}}^{\mathrm{GGA}}$ is given by

$$E_{\mathrm{xc}}^{\mathrm{GGA}} = \int f\big(n_{\uparrow}(\boldsymbol{r}), n_{\downarrow}(\boldsymbol{r}), \nabla n_{\uparrow}(\boldsymbol{r}), \nabla n_{\downarrow}(\boldsymbol{r})\big)\mathrm{d}\boldsymbol{r}\,. \tag{16.12}$$

Note that (16.12) is called the generalized gradient approximation because $E_{\mathrm{xc}}^{\mathrm{GGA}}$ does not simply include a gradient expansion of the exchange-correlation functional as occurs in the gradient expansion approximation. Such an approach does not fulfill some fundamental properties of the exchange-correlation hole leading to results worse than those by L(S)DA. The merit of the GGA is to describe the exchange correlation hole more realistically than a sheer expansion in the density. To this aim real-space cutoffs are introduced, and in analogy to L(S)DA the exchange hole is never positive, while the exchange and correlation holes integrate to minus one and zero, respectively [16.9, 11–13].

In [16.14] the GGA is extensively applied to several systems with consistent improvements in the calculated properties. First ionization energies of 30 atoms and atomization ones of simple hydrocarbons agree with the experimental ones within a 10% error. For three metals (Al, Na, Cs) studied with the stabilized jellium model very good estimates of the work function and the surface energy have been worked out [16.15]. The GGA functional unlike the L(S)DA is not unique and may contain empirical parameters. Among the most successful ones we recall the functional by Perdew and Wang (PW91) [16.11–14] by which the above-mentioned results were computed; and the subsequent Perdew, Burke, and Ernzerhof (PBE) [16.9, 16] and the revised PBE (revPBE) ones [16.17, 18]. The PBE functional is based on the PW91 one, but it exhibits a simpler and more transparent form, only satisfies physically important conditions, provides a precise account of the linear response of the homogeneous electron gas, and it scales correctly in the low- and high-density limit. For all these reasons, the PBE functional is routinely preferred to the PW91. As a detail the revPBE functionals substitute the value of the empirical parameter κ in the exchange functional with one which best matches the exchange function of the first-row atoms, which allows obtaining better chemisorption energies [16.17, 18].

Failures of the DFT-GGA Method

Despite the very good results outlined in the previous section, the GGA functional exhibits three important drawbacks:

(i) The presence of a spurious self-interaction [16.19];
(ii) The lack of discontinuities in the derivatives of the total energy at N integer number of particles [16.8, 20];
(iii) The erroneous exponential long-range decay interaction of an electron with a metal surface, for which an example is given in Fig. 16.1, and the inability to treat realistically the vdW interaction between two molecules or a molecule and a surface [16.21].

This last topic will be addressed later in this section. (i) We recall that in the Hartree–Fock method the self-interaction is correctly zero since for the same electron the Hartree and the exchange term cancel out. For an extended system of N electrons the right number of pair interactions is given by $N(N-1)/2$ and largely overcomes that of the self-interaction proportional to N. But for an atom or a small molecule the self-interaction correction (SIC) is a relevant one. For this reason, a modified functional to subtract spurious terms has been suggested which corrected very well the ionization energies of atoms [16.19]

$$E^{\mathrm{SIC}} = E^{\mathrm{approx}}[n^{\uparrow}, n^{\downarrow}] - \sum_{\alpha,\sigma}\left(J[n_{\alpha,\sigma}] + E^{\mathrm{approx}}[n_{\alpha,\sigma}, 0]\right)\,. \tag{16.13}$$

The expression E^{approx} is a conveniently approximated classical plus exchange-correlation functional, while J is the classical Coulomb one and hence the sum represents the SIC summed over all orbitals (α, σ). In (16.13) the self-interaction is subtracted for each orbital and creates an effective potential which is orbital dependent in the KS equations. We shall come back to this problem later.

(ii) It is well known that the variational formulation of DFT with the constraint of a fixed number of particles and external potential v_{ext} is expressed via the

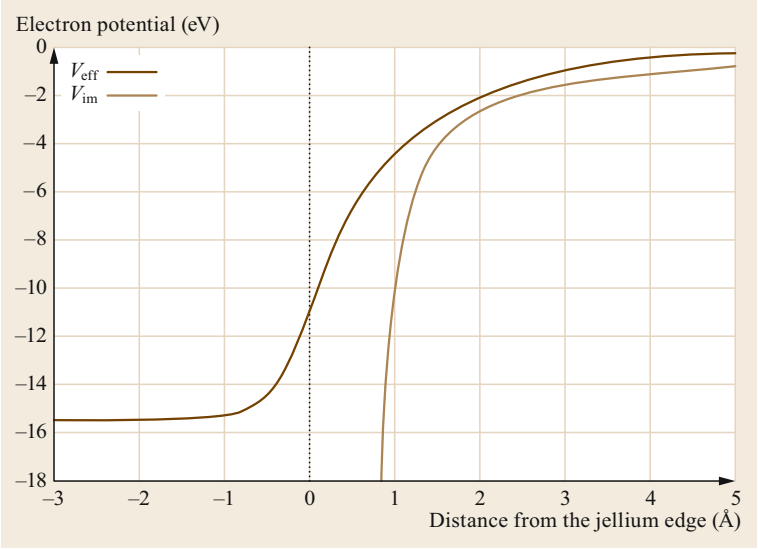

Fig. 16.1 Effective KS LDA potential at the surface of a jellium model having the aluminum density (*dark brown*). This curve shows an erroneous exponential decay towards vacuum following the one (correct) of the charge density. Hence, it misses the interaction of an electron with its image charge (whose potential is depicted by the *light brown line*)

Lagrange multiplier μ by

$$\delta\left(E[n]-\mu\int n(\boldsymbol{r})\mathrm{d}\boldsymbol{r}\right)=0\,, \tag{16.14}$$

which implies

$$\frac{\delta E[n]}{\delta n(\boldsymbol{r})}=\mu\,. \tag{16.15}$$

Following [16.22] (16.15) can be extended to a noninteger number of particles N by considering a mixture of pure states with fractional occupancy as an average. By assuming that $n_N(\boldsymbol{r})$ is the solution of (16.14) with particle number N the corresponding energy is $E_N = E[n_N]$ and

$$\frac{\partial E}{\partial N}=\mu(N)\,. \tag{16.16}$$

So the Lagrange multiplier μ is the exact chemical potential [16.4, 23].

By using fractional occupancy one can get the ground-state energy of the system on varying the particle number N. Such an energy is formed by piecewise segments joining with discontinuous derivatives at integer N and allows one to get the first ionization I and affinity energies A. For an atom with nuclear charge Z [16.4]

$$I=E(Z-1)-E(Z)\,, \tag{16.17}$$

$$A=E(Z)-E(Z+1)\,. \tag{16.18}$$

This behavior is described correctly by the exact DFT. Instead LDA and GGA calculate such fractional energies $E(Z)$ with an unphysical curvature and wrong minima at fractional occupancies. Such incorrect results are associated to the spurious self-interaction of fractional electrons introduced in the system and may be amended by adding a Hubbard-like term U to the LDA energy functional [16.20]: this approach is the so-called LDA+U method. We finally point out that occupancies entering the LDA+U functional are expressed as projections of the KS orbitals on a suitable localized basis set. For this reason and like SIC this functional is orbital dependent and nonlocal.

Orbital-Dependent Functionals

As pointed out in the previous section, orbital-dependent functionals could be a useful implementation to DFT. But we stress that in the KS equation the potential $v_{\text{eff}}(\boldsymbol{r})$ must be local and the same one for all orbitals to satisfy the Hohenberg–Kohn theorem [16.2]. So the orbitals to evaluate the exchange term must be KS orbitals which are generally different from the Hartree–Fock (HF) ones and generate an exchange energy other than the HF one and consequently two different correlation energies (i.e., the total energy, equal in all exact theories, minus the HF one) are determined in the two methods. Note that the KS orbitals depend on the charge density and are obtained solving the Schrödinger equation by a local multiplicative potential, while those computed by orbital-specific potentials are not. This is an important problem [16.10, 24] and much work has been devoted to it outside the scope of this review. We only remind the reader that in the optimized effective potential formalism it has been demonstrated that at first order in the density the energy functionals coincide when the variation between the KS potential and an orbital-dependent one is taken into account [16.10, 24]. Moreover, *Gilbert*'s theorem [16.25] established

that a nonlocal external potential determines uniquely the first-order density matrix, but from a known ground-state wavefunction the external potential v_{ext} is not given in a sole way [16.25].

A very popular class of orbital-dependent functionals are the hybrid ones which incorporate part of the exact exchange term from HF. First *Becke* realized that the adiabatic connection formula [16.26, 27] could be the correct tool to obtain rigorously the exchange correlation energy E_{xc} in the KS formalism and suggested the following expression [16.26]

$$E_{\text{xc}} \simeq \frac{1}{2}E_{\text{x}} + \frac{1}{2}E_{\text{xc}}^{\text{LSDA}} , \tag{16.19}$$

where E_{x} is the exchange energy of the KS orbitals. Such half exchange plus half LSDA contributions was improved into a three-parameter formula

$$E_{\text{xc}}^{\text{hyb}} = E_{\text{xc}}^{\text{LSDA}} + a_0\left(E_{\text{x}} - E_{\text{x}}^{\text{LSDA}}\right) + a_{\text{x}}\Delta E_{\text{x}}^{\text{GGA}} + a_{\text{c}}\Delta E_{\text{c}}^{\text{GGA}} , \tag{16.20}$$

where $\Delta E_{\text{x}}^{\text{GGA}}$ and $\Delta E_{\text{c}}^{\text{GGA}}$ are exchange and correlation gradient corrections to their respective L(S)DA expressions [16.10, 27]. A popular expression for the exchange correlation functional is that by *Becke*, Lee, Yang, and Parr (B3LYP) constituted by several terms with constants referred to thermochemical data. Such terms are: the LDA and HF exchange [16.28]; the gradient exchange correction by *Becke*; the Lee, Yang, Parr correlation [16.29]; the coefficients of local and gradient correlation functionals by Vosko, Wilk, and Nusair [16.30]. With this functional one obtains excellent atomization energies for the G2 set of molecules [16.31], and standard enthalpies of formation, ionization, affinity energies of the G3/99 set [16.32]. For these reasons such a semiempirical functional is widely used especially in the chemical scientific community [16.10]. Several other hybrid functionals have been proposed and we refer the reader to specialized papers [16.33, 34].

The van der Waals Interaction

The vdW or London dispersion interaction is a quantum effect due to the instantaneous zero-point fluctuations of electrons determining multipole moments on a quantum system which may induce other ones in other moieties, which interact with each other. Such a coupling is usually weaker than the electrostatic one but is pervasive in materials science becoming more important for larger molecules, noble gases, and organic molecule–surface systems. The polarizability of atoms, also depending on their environment, is fundamental to estimate the magnitude of the vdW forces [16.35–37]. The vdW coupling is attractive and behaves asymptotically as R^{-6} for two atoms/molecules at distance R, R^{-3} for a molecule–surface system, R^{-2} among two metal surfaces [16.37]. Such an interaction is a many-body phenomenon included in the exact DFT, but is not accounted for correctly by the GGA and hybrid functionals since they neglect instantaneous charge density fluctuations and correlations and solely consider semilocal correlations. The rigorous treatment of the vdW interactions should grasp their nonadditive and nonlocal character but models with pairwise potentials and fitted parameters can achieve good qualitative results in systems stemming from hybrid interfaces to biomolecular compounds [16.35].

In this section, we would like to outline three methods capable of treating the vdW interaction within DFT and which are suited to molecule–surface systems. First, the Rutgers–Chalmers collaborative efforts, say vdW DF and vdW DF2, succeeded in writing a seamless exchange-correlation functional as

$$E_{\text{xc}}^{\text{DF}} = E_{\text{x}}^{\text{GGA}} + E_{\text{c}}^{\text{LDA}} + E_{\text{c}}^{\text{nl}} , \tag{16.21}$$

where $E_{\text{x}}^{\text{GGA}}$ is the exchange energy in the revPBE approach, $E_{\text{c}}^{\text{LDA}}$ the LDA correlation energy, and E_{c}^{nl} the nonlocal correlation [16.38–40]. In this method, one treats the nonlocal functional starting from the adiabatic connection formula for the exact correlation energy, [16.38, 40], and then makes an expansion in the integrand to second order in $\hat{\varepsilon}$, $\hat{\varepsilon}$ being the dielectric constant treated in the plasmon pole approximation. By this approach, results in good agreement with experiments were calculated for the interaction energies of molecular dimers (duplexes) of the S22 complex set. A comparison with quantum chemistry results of vdW DF and vdW DF2 is shown in Fig. 16.2 [16.41]. The vdW DF treatment has also been proven to be accurate enough to study adsorption of organic molecules on solids, see *n*-alkane adsorption on C(0001) deposited on Pt(111) and *n*-butane on Cu(100), Cu(111), Au(111), and Pt(111) [16.40], and to investigate adsorption of organic molecules on solids, e.g., benzene and naphthalene on graphite [16.42].

A semiempirical method was devised by Grimme in which the vdW dispersion interaction between a couple of atoms is assumed to have the well-known asymptotic pairwise form, E_{disp}

$$E_{\text{disp}} = s_6 \sum_{i=1}^{N_{\text{at}}-1} \sum_{j=1}^{N_{\text{at}}} \frac{C_6^{ij}}{R_{ij}^6} f_{\text{damp}}(R_{ij}) , \tag{16.22}$$

and we denote the total functional as

$$E_{\text{DFT-D}} = E_{\text{KS-DFT}} + E_{\text{disp}} . \tag{16.23}$$

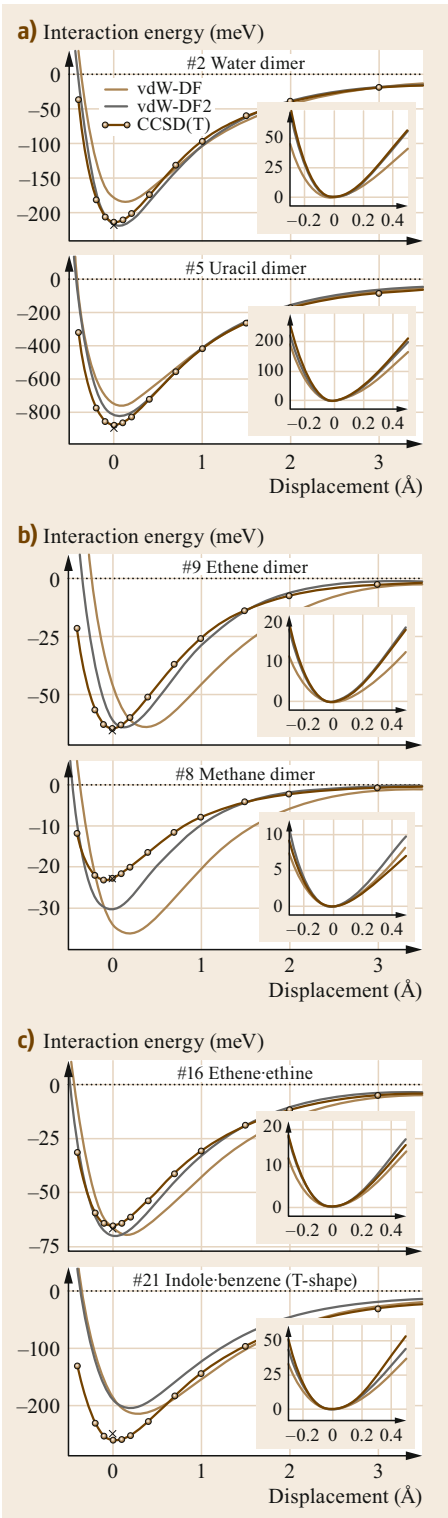

Fig. 16.2a–c Comparison between vdW DF and quantum chemistry (coupled cluster single-double and triple, CCSDT) potential energy curves, for the best and the worst case (among the S22 duplexes) of **(a)** hydrogen-bonded, **(b)** dispersion-dominated, and **(c)** mixed duplexes. *Insets* compare the shapes near the minima upon aligning to a common minimum point (Reprinted figure with permission from [16.41]. Coypright 2010 by the American Physical Society) ►

In (16.22) N_{at} is the number of atoms in the system, C_6^{ij} are the dispersion coefficients, R_{ij} the interatomic distances, s_6 is a scaling factor depending on the used approximate functional in the KS scheme. The damping function $f_{\text{damp}}(R_{ij})$ is equal to 1 for large R and becomes very small for R going to zero. In the D2 scheme the dispersion coefficients are given by a geometric mean of the atomic ones

$$C_6^{ij} = \sqrt{C_6^i C_6^j}\,. \tag{16.24}$$

As the coefficient C_6 is proportional to the ionization potential and the static dipole polarizability, it acts as a predetermined quantity which does not take into account modifications of the physical and chemical environment [16.43]. To consider such effects in the C_6 coefficients *Grimme*'s group later introduced the D3 scheme which takes into account the number of neighbors of each atom [16.44]. The larger the coordination the smaller the coefficient C_6^i of atom i, since the atom is somewhat compressed. In the numerical procedure one starts from a reference set of C_6 coefficients for each pair of atoms depending on their properties (location, hybridization). Interpolating among them by varying the number of neighbors one can obtain continuously changing C_6 values. The accuracy of this approach is confirmed by several results discussed in [16.44] and makes it a very useful tool in adsorption calculations also for organic molecules [16.45].

A different idea to take into account the environmental effects in the calculation of C_6^{ij} is to introduce the effective volume of an atom which is different from the free one. By using a Hirshfeld atomic partitioning weight $w_{\text{A}}(\boldsymbol{r})$ for atom A, the coefficient C_6^{AA} for an atom inside a molecule or a solid is scaled by the squared ratio of its volume in the molecule/solid and in the free atom within a self-consistent procedure. Then an equation for the coefficient between two atoms C_6^{AB} is provided in terms of C_6^{AA}, C_6^{BB} and the static atomic polarizability. Finally, the dispersion interaction is written as a pairwise summation like (16.22) [16.46]. This is often named the Tkachenko–Scheffler PBEvdW

method. Another approach within an atomic pair summation is the so called vdW-surf approach, which is more recent [16.47]. In this treatment many-body effects are taken into account by employing the Lifshitz–Zaremba–Kohn theory [16.48] to write the dispersion coefficient which includes the polarizability of the atoms and the dielectric constant of the solid. For a realistic calculation of adsorption energies one has also to take into account rapid variation of C_6^{AB} near the surface which may be described by a varying effective dimensionless volume, V^i_{eff}, to be determined via the Hirshfeld method. The effective $C^{ii}_{6,\text{eff}}$ coefficient attains the final form $C^{ii}_{6,\text{eff}} = [V^i_{\text{eff}}]^2 C^{ii}_{6,\text{bulk}}$ [16.47]. Accurate estimates of geometries and adsorption energies of perylene-3,4,9,10-tetracarboxylic dianhydride (PTCDA) on noble metals and Xe and benzene on transition metal surfaces have been worked out [16.47, 49]. For an up to date review on vdW interaction for adsorption of organic molecules at metals see [16.50].

Finally we wish to recall that both for a more accurate description of the ground state, and for excited ones, time dependent (TD) DFT and many-body perturbation theory are started being used with more stringent limitations of size [16.51].

16.2.2 Model Geometries

Cluster

The cluster model was introduced for the study of catalysis describing the system, i.e., a nanoparticle or a surface with an adsorbate, by a cluster of atoms plus the admolecule. Among the advantages of such an approach the treatment of localized effects, the convenient usage of computational chemistry methods. Difficulties may arise for the convergence of results with the cluster size and unwanted surface effects since the cluster displays several surfaces not just the one on which the adsorbate is located. This determines a large number of uncoordinated atoms and possibly surface charges to be compensated. The cluster model has proven successful, e.g., in evaluating the optical absorption spectra of adsorbed dyes [16.52] and, with suitable embedding techniques, in relation to the free energy of proton abstraction from water at $TiO_2(110)$ [16.53], but its relevance has historically decreased in favor of the slab approach. For recent reviews on the cluster model see [16.54, 55].

Slab

The slab approach describes the surface plus the adsorbate as a film of a few 2-D periodic layers accounting for the solid plus an adsorbate overlayer usually deposited on one of the two surfaces. On the 2-D periodic surface, for which the surface parallel momentum $\boldsymbol{K}$ is a good quantum number, by using Bloch waves as a linear combination of a set of localized orbitals l at lattice site i, say $\{\varphi_{\alpha i}\}$, the electronic energies can be obtained by the following secular equation for the wavefunction coefficient $c_{\beta j}$ [16.8]

$$\sum_{\beta j} \left(H_{\alpha i,\beta j} - E_{\boldsymbol{K}} S_{\alpha i,\beta j}\right) c_{\beta j} = 0 \,, \tag{16.25}$$

where $H_{\alpha i,\beta j}$ are the matrix elements of the KS Hamiltonian, while $S_{\alpha i,\beta j}$ represent the overlap ones. A way to recover three-dimensional (3-D) periodicity in the direction $\hat{z}$ normal to the surface is to repeat the slab adding a vacuum portion between replicas which has to be wide enough to avoid the spurious interaction [16.8, 56, 57]. A particularly useful basis set for this 3-D supercell geometry is represented by plane waves [16.8, 57]. If solved on a plane wave basis set, the supercell method requires a larger basis than the localized one of the 2-D slab approach but matrix elements of plane waves are easier to compute and converge. Indeed, for plane wave basis sets, the only parameter is the kinetic energy cutoff that can be increased without any bias. Practically, two kinetic energy cutoffs are chosen in representing the wavefunctions ($E_{c,\psi}$) and the charge density ($E_{c,\rho}$, with $E_{c,\rho} \neq E_{c,\psi}$ to properly describe ultrasoft pseudopotentials and ones with nonlocal core corrections). As a matter of fact the surface study within the supercell approach translates into a bulk problem but for a 2-D integration of the Brillouin zone, so the reader can be referred to textbooks on electronic structure calculation for practicalities [16.58].

The Extended Substrate

The models so far discussed provide computationally viable methods to calculate surface properties by systems that are finite in the direction orthogonal to the surface. However, one should not ignore that the thickness of the substrate in a typical experiment is several orders of magnitude larger and hence better represented by a semi-infinite one. For this reason, approaches based on Green's function accounting for the continuous spectrum of the solid were contrived. Such methods more recently formulated within DFT-KS include the Dyson equation [16.59–61], the embedded cluster [16.62–64], and Green's function matching techniques [16.65–68]. Owing to the extraordinary increase in computer performance in the last two decades, capable now of handling routine DFT simulations with several hundred atoms, the above methods have become less popular than the computationally simpler supercell approach to calculate adsorption geometries and energies. Such a technique also allows one to attain a very good description of bond structures, density of states (DOS), and spectroscopies of adsorbates. Only if the

detailed features of narrow peaks in the adsorbate projected density of states (PDOS) are required, e.g., to obtain information on the elastic linewidths of surface states, does the continuum of substrate states in the calculation appear to be beneficial [16.69]. Finally, we report that recently a Green's function approach adapted from quantum transport theory [16.70] has been successfully employed in the calculation of the lifetimes of the lowest unoccupied molecular orbital (LUMO) of organic molecules on rutile $TiO_2(110)$ [16.71] and of the LUMO of core-excited pyridine on Au(111) [16.72], via the inverse of the linewidth of this state. The former result may help in understanding charge transfer in dye-sensitized solar cells, the latter being bidirectional electron transport in femtosecond phenomena. To show the computational suitability of this approach for calculating the PDOS of molecules on solids compared to the finite size models we observe that the resolution of the LUMO PDOS of perylene compounds on a $(TiO_2)_{60}$ cluster is very approximate [16.73]. If one adopts a slab geometry, a 2-D unit cell of rutile $TiO_2(110)$ (3×1), and a required resolution of 2 meV in the PDOS for the fixed surface wavevector, one is forced to use more than 50 trilayers of semiconductor which would make the calculation very cumbersome. Instead using the above-mentioned Green's function method we can determine the PDOS on a molecular orbital of an adsorbate, Φ of energy E_Φ, by the imaginary part of the Green's function. Thus, we can fit the result with a Lorentzian function with full width at half maximum (fwhm) Γ [16.71]

$$P_\Phi \propto \frac{1}{\pi}\frac{\Gamma}{(E-E_\Phi)^2+\Gamma^2}\,. \tag{16.26}$$

16.3 Electronic States at Surfaces

Surface intrinsic electronic states, which decay exponentially both towards vacuum and bulk, may occur when 3-D bulk periodicity is broken by a surface. Traditionally, they are distinguished as *Shockley* [16.74] and *Tamm* [16.75] states. The derivation of such states is extensively described in several books [16.76, 77], which we refer the reader to for a thorough treatment. Here it suffices to outline the main properties.

16.3.1 Bulk Bands from the Surface Viewpoint

Given that bulk electronic states persist in the presence of the surface, their identification in terms of the surface symmetry is a necessary prerequisite for the description of genuine surface electronic states. This calls for obtaining the so-called *surface-projected band structure*. A 3-D wavevector $\boldsymbol{k}$ is decomposed in the components parallel and perpendicular to the surface, $\boldsymbol{k}=\boldsymbol{K}+\boldsymbol{k}_\perp$, so that bulk Block states $\epsilon_n(\boldsymbol{k})$, with n the band index, can be labeled by a joint index $(n,\boldsymbol{k}_\perp)$ and studied as a function of $\boldsymbol{K}$: $\epsilon_{n,\boldsymbol{k}_\perp}(\boldsymbol{K})$. Notice that, at variance of n, $\boldsymbol{k}_\perp$ can span a continuum of values so that energy ranges, rather than discrete values, are allowed for $\epsilon_{n,\boldsymbol{k}_\perp}(\boldsymbol{K})$.

As an example we consider a simple cubic solid within the tight-binding model, having a single band with analytic form $\epsilon(\boldsymbol{k})=-V[\cos(k_x a)+\cos(k_y a)+\cos(k_z a)]$, and derive the (001) surface band structure. Namely, we are interested in the energy ranges accessible at fixed $\boldsymbol{K}=(k_x,k_y)$ as a function of k_z in the interval $[-\pi/a,\pi/a]$. These ranges, evaluated at the high-symmetry points of the surface Brillouin zone, are $[-3V,-V]$ for $\boldsymbol{K}=\bar{\Gamma}$, $[-V,V]$ for $\boldsymbol{K}=\bar{\mathrm{X}}$, and $[V,3V]$ for $\boldsymbol{K}=\bar{\mathrm{M}}$. Overall, the band structure depicted in Fig. 16.3 is obtained.

As a more realistic example we consider the case of a face-centered-cubic metal, Cu(111). In practical ab initio calculation a bulk conventional unit cell with three atoms following the *ABC* stacking of atomic planes along the (111) direction can be constructed, and the bands plotted for different values of $\boldsymbol{k}_\perp$. One obtains a *spaghetti plot* becoming denser with a finer sampling of $\boldsymbol{k}_\perp$, that is reported in Fig. 16.4 as a gray area. Especially interesting is the presence of bulk-forbidden energy regions (surface-projected band gaps) where surface electronic states can exist. Such plots can be compared to the electronic structure in the presence of the surface. To that purpose, in Fig. 16.4 the states of a 30-atom-thick Cu(111) slab are reported, corresponding to 30 possible values of $\boldsymbol{k}_\perp$. There, additional features emerge, in the surface-projected band gaps or overlapping with bulk bands, that originate from the surface modification of the electronic potential and are discussed in the next paragraphs.

16.3.2 Shockley and Tamm States

In a simple picture of Shockley states we consider a periodic solid described by the nearly free electron model. Even if the lattice potential is treated as a small perturbation, its effect is to open up gaps in the band structure in which localized states may exist near the surface. Within the gap no solution is found for real wavevector $\boldsymbol{k}$. Formally, we look for wavefunctions with complex $\boldsymbol{k}$ and imaginary part $k_\mathrm{I}>0$. Assume that the lattice periodic potential is interrupted

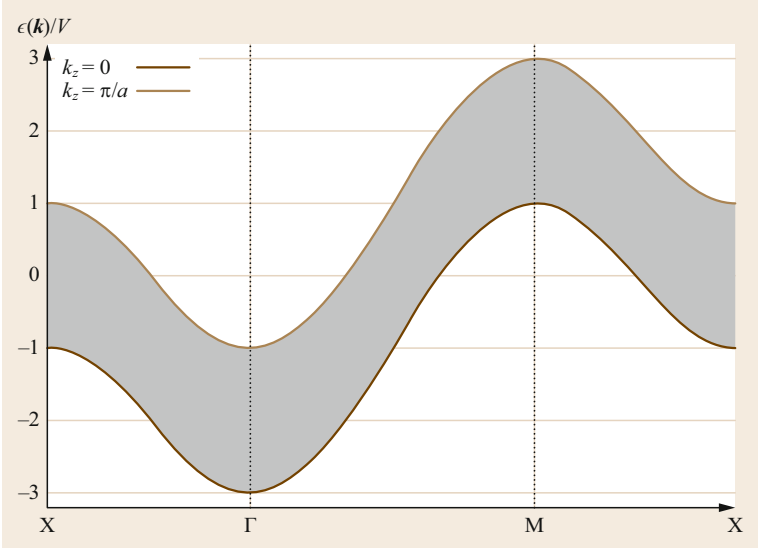

Fig. 16.3 Surface band structure of a tight-binding model of a simple cubic crystal with an s-like band

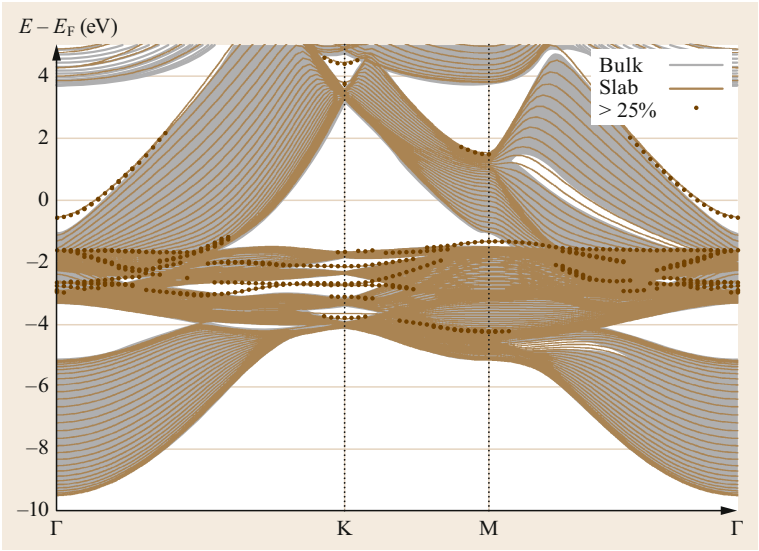

Fig. 16.4 Band structure of a slab consisting of 30 Cu(111) layers, calculated at the KS PBE level of theory in the absence of surface relaxations. *Brown circles* mark states whose weight on the first/last Cu layers is > 25%. The *gray shaded area* is the surface-projected band structure

at $z = z_0$ (z being the direction normal to the surface so that $\boldsymbol{r} \equiv (\boldsymbol{R}, z)$) by a step function of height W_0, a surface is created at $z = z_0$ and vacuum extends in the semi space $-\infty < z < z_0$. The complex wavefunction involves a factor $\exp(-k_I z)$ decreasing exponentially for positive and diverging for negative z_0, respectively. The latter solutions are incorrect for infinite bulk but are acceptable for a semi-infinite solid if they can be matched to decaying waves in vacuum of the form $\psi_{\text{out}} \propto \exp(\kappa z)\exp(\mathrm{i}\boldsymbol{K}\cdot\boldsymbol{R})$, where κ is real and positive and equal to

$$\kappa = \left[2\left(W_0 - E + \frac{K^2}{2}\right)\right]^{1/2} . \tag{16.27}$$

By equating the logarithmic derivatives of the wavefunctions, ψ_{in}, decaying into bulk, with ψ_{out} we obtain κ. Such a state localized at the surface is named the Shockley state.

An alternative way to describe surface states is to make use of the tight-binding method which is useful when the extension of the atomic orbitals in the solid is less than the interatomic spacing and so applicable to the study of narrow bands of transition metals and actinides. In this framework consider the slab model with infinite periodic atomic planes, identical atoms, and one atom per unit cell. In (16.25) one can write

$$c_{\alpha i(p)}(\boldsymbol{K}) = \exp(\mathrm{i}\boldsymbol{K}\cdot\boldsymbol{R}_i)c_{\alpha p}(\boldsymbol{K}) , \tag{16.28}$$

where $\boldsymbol{R}_i$ is a 2-D lattice vector while p labels the atomic plane of atom i. If P is the number of planes one solves a secular equation like (16.25) of dimension $lP \times lP$.

An elegant approach to compute the system bands is to avail oneself of a continued fraction technique within the single-particle Green's function. If we consider a linear chain in the Hückel approximation, i.e., there is a single non-zero resonance integral only for non nearest neighbors, with value β (with $\beta > 0$), while overlap is zero for orbitals in different sites, and modify the atomic orbital, say α_s for the first atom in the chain, two localized orbitals occur, that are named Tamm states. One with energy above that of the band for $\alpha_s > \beta$ and one below it for $\alpha_s < -\beta$. To take into account a simple solid with a chemisorbed atom Grimley also changed the resonance integral between the adatom and its nearest neighbor. According to the parameters one or two localized states may exist, which lying outside the band describe the formation of a localized bond [16.78]. A well-known example of Shockley and Tamm states is provided by the noble metal surfaces. For Cu(111) angle-resolved photoemission spectroscopy (ARPES) and DFT calculations [16.79–81] determined a fairly parabolic (sp) Shockley state, crossing the Fermi level, ε_F, along the $\bar{\Gamma}\bar{M}$ and $\bar{\Gamma}\bar{K}$ paths, with a minimum about 0.5 eV below ε_F. A d-like fairly dispersionless Tamm state was measured and computed just above the projected bulk d band around $\bar{M}$ and at about -2.0 eV below ε_F. See also Fig. 16.4. Along the direction $\bar{\Gamma}\bar{M}$ this state merges into the d band and becomes a surface resonant state, defined as a state which preserves an enhanced amplitude at the surface but propagates into bulk like a Bloch wave [16.82].

16.3.3 Quantum Well States

If we deposit ultrathin layers of atoms or molecules on the surface constituted of a different material one-dimensional (1-D) potential wells could be formed in the $\hat{z}$-direction. Such systems may display localized quantized states typical of a particle in a box and hence are named quantum well (QW) states. Several examples of such states are found in semiconductor heterostructures and metal atoms on metal surfaces. For a review on the latter systems see [16.83].

16.3.4 Image States

Together with Shockley and Tamm surface states a free surface exhibits surface states generated by the image potential (IP). In classical physics if an electron is at distance z from a metal, the electron–surface interaction can be calculated by replacing it with the interaction of an electron of charge e with a positive charge $-e$ (image charge) at position z inside the metal. One obtains

$$V_{\text{image}}^{\text{class}}(z) = -\frac{e^2}{4z} \,. \tag{16.29}$$

In a microscopic quantum treatment in which the metal is described by a semi-infinite jellium the distance z is substituted by that with reference to a plane with coordinate z_{image} which is the center of gravity of the metal polarization charge [16.85]. At large enough distances from the surface one can write

$$V_{\text{image}}(z) = -\frac{e^2}{4(z - z_{\text{image}})} \,. \tag{16.30}$$

The combination of the potential formed by the surface repulsive barrier (that occurs if a gap is present in the surface-projected bulk band structure) and of $V_{\text{image}}(z)$ generates weakly bound states with wavefunctions mainly located outside the surface [16.86]. They constitute a Rydberg-like series with energies E_n

$$E_n = \frac{-0.85}{(n+a)^2} \text{ eV} \,. \tag{16.31}$$

The constant a depends on the surface, the width of the energy gap, and its position with respect to vacuum. Inverse (IPES) and two-photon (2PP) photoemission spectroscopy are the experimental techniques of choice to investigate IP states (IPS). Finally, we remark on a new effect for IPS due to the spin–orbit Rashba effect [16.87]. Measurements performed with 2PP and circular dichroism coupled to DFT calculations with the phenomenological addition of the IP and based on the Green function embedding approach of *Ishida* [16.67] have shown that the spin–orbit interaction splits up the IPS with $n = 1$ on Au(001). Namely the energy splitting is zero at $\boldsymbol{K} = 0$ and increases along the $\bar{\Gamma}\bar{X}$ direction being larger than 20 meV for $\boldsymbol{K} = 0.25$ Å^{-1} [16.88].

16.3.5 Lifetimes of Surface States

The study of lifetimes of excited electron (or holes below the Fermi level) states is very important in physics. Their knowledge allows one to ascertain the duration and the extent of the influence of an excitation and they are strictly related to the dynamics of charge and energy transfer and of screening including the effect of surface vibrations. For a free metal surface, even when the elastic lifetime is infinite, other effects are present, namely the electron–electron interaction (inelastic lifetime) and the phonon one (vibrational lifetime). The former phenomenon leads to lower energy surface or bulk electrons together with the creation of an electron–hole pair. A nice schematic picture of such processes

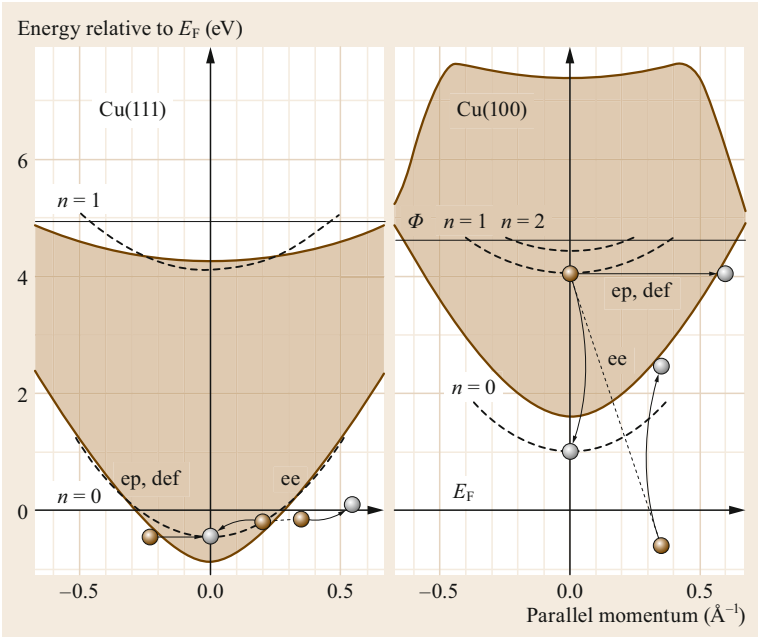

Fig. 16.5 Schematic projected bulk band structure (*shaded areas*) for the Cu(111) and Cu(100) surfaces with intrinsic surface-state bands ($n = 0$) and image-potential bands ($n \geq 1$). *Arrows* indicate possible electron–electron (ee), electron–phonon (ep), and defect (def) scattering processes (Reprinted with permission from [16.84] with permission from Elsevier)

for the Shockley state on Cu(111) and Cu(100) and IP bands is provided by [16.84, Fig. 1] which is repeated here (Fig. 16.5). While ARPES is limited to measuring lifetimes of hole states, scanning tunneling spectroscopy (STS) can explore those of states above and below the Fermi level. The interaction of an electron with the metal bands is described by the GW method using the random-phase approximation (RPA) or by time-dependent density functional theory (TDDFT) [16.89]. Results for the lifetimes, τ, of the (111) face of noble metals worked out by theory including the phonon contribution and STS experiments were found in excellent agreement. For Cu(111) at the band edge of the Shockley state both theory and experiments predict $\tau \approx 21$ meV [16.90].

16.3.6 Recent Results for Organic Adsorbates

Over the last 40 years several investigations have dealt with the modification of surface states by adsorption [16.91–93]. In this review we concentrate on very recent results regarding the effects of adsorption of organic molecules on surface states. To obtain a thorough understanding of the properties of the interface between an organic semiconductor and a metal, research has addressed by 2PP experiments the electronic states of hexa-cata-hexabenzocoronene (HBC), a promising photovoltaic material, on Cu(111) [16.94]. It is shown by increasing the coverage Θ from 0 to 2 ML (monolayers) that the Shockley state is quenched and the work function Φ of the HBC/Cu system decreases due to a combination of push back and electron transfer. New states appear at larger HBC coverage and are interpreted as IPS modified by the molecular layer on the metal. An interesting behavior of the Shockley state is found for NTCDA (1,4,5,8-naphthalene tetracarboxylic dianhydride) on Au(111) [16.95]. It is known that by deposition of a low amount of alkali atoms (Na) on noble metals an increase of the binding energy of the Shockley band occurs. The Shockley state is also sensitive to the presence of an organic film which displaces it upwards. In [16.95] the two effects are combined. First one covers Au(111) with a small amount of Na shifting down the Shockley state and then one deposits a monolayer of NTCDA: the Shockley state modifies its energy which appears very similar to that on clean Au(111) and suggests a very weak interaction between NTCDA and the metal. So this work outlines the importance of the behavior of Shockley states and the effect of alkali adatoms in controlling organic molecule adsorption and charge transfer. Among a variety of applications, scanning tunneling microscopy (STM) has been demonstrated to be able to induce nonlocal manipulations leading to molecular desorption [16.96]. The experiment considered chlorobenzene molecules on Si(111)-(7 × 7) and showed that charge injection from an STM tip with positive voltage V can cause molecular desorption once V reaches the desorption threshold. The effect decreases exponentially ($\simeq 100$ Å) from the location of the injected charge. From the electronic

point of view charge is transferred from the STM tip to a new surface state predominantly located at faulted rest and unfaulted rest atoms which is the threshold surface state for nonlocal desorption and hints at new ways of long-range surface manipulation via surface states [16.97].

16.4 Adsorption of Simple Atoms and Molecules

Adsorption is a phenomenon by which the surface of a solid links molecules from a gas or a liquid. It is generally a spontaneous one which is accompanied by a decrease of the free energy of the system and of entropy. The process is exothermic and the released heat is called heat of adsorption. Chemical adsorption or chemisorption requires a higher production of heat and often needs to overcome a barrier of activation energy. Physical adsorption or physisorption always occurs and asks for a lower energy of adsorption. Chemisorption does not always occur, but couples to physisorption when the molecules are closer to the surface and chemical bonds are formed.

The variety of adsorption phenomena, the possibility of covering only a small fraction of the solid surface (in percentage), a full layer or overlayer, from few to several layers, the enormous amount of different adsorbates from the simplest, hydrogen, to molecules with hundreds of atoms opens up an incredible number of new effects. This somewhat limits our treatment to prototypes of the main classes of adsorption.

16.4.1 Chemisorption of Simple Atoms and Molecules

The modern age of chemisorption started with *Grimley* [16.98] and later *Grimley* [16.99] and *Newns* [16.100] who independently adapted the Anderson model for magnetic impurities to chemisorption. They pointed out that the energy of an orbital of a chemisorbed atom is equal to $\varepsilon_{A\pm\sigma} = E_A + J_A n_{A\mp\sigma}$, where J_A is the Coulomb repulsion. So the effective energy of an orbital depends on its occupancy by an electron of opposite spin. Contrarily the occupancy of an orbital $n_{A\pm\sigma}$ depends on the distance of an orbital of opposite spin $\varepsilon_{A\mp\sigma}$ from the Fermi level. This indeed shows that chemisorption cannot be treated in a one-electron picture. We have seen how DFT progressed to supply a realistic tool to calculate the energetic and often with the help of experimental data the exact position of adsorbed molecules also with several atoms. Following Grimley and Newns, *Hammer* and *Norskov* [16.101] provided simple models to interpret the results by DFT which well account for the main trends of chemisorption and in which a fundamental role is played by the local density of states (LDOS). Take oxygen chemisorption on metals; we can imagine that this process occurs in two steps. First, the adsorbate 2p state interacts with the wide sp metal band and causes a single resonance. Its interaction with the narrower d band (strong coupling in the Grimely–Newns' model) splits it into two states: one bonding and the other one antibonding, below and above the d band, respectively. The adsorption energy can be written as $E_{ads} = E_0 + E_{hybr}$. Although the larger energy is the sp contribution, this is practically constant for all metals while the second term allows one to distinguish between different values of adsorption energy. In the case of Cu, Ag, and Au the antibonding band is completely filled and repulsive, while if we move on the left of the periodic table the antibonding state becomes depopulated as the d band shifts upwards and chemisorption becomes increasingly stronger: $\simeq -0.6$ eV (Ag); $\simeq -0.9$ eV (Pd); $\simeq -2.8$ eV (Ru); $\simeq -3.5$ eV (Tc); $\simeq -4.00$ eV (Mo); -4.2 eV (Nb), with the d band center roughly increasing from -4.0 to 2.0 eV, correspondingly.

To examine the molecular adsorption consider as a benchmark system the adsorption of CO. Experimental and theoretical studies suggest that electron donation from the CO 5σ filled orbital to the sp and d bands and backdonation from these bands to the 5π empty orbital is mainly the origin of this chemisorption phenomenon. The interaction with the sp band of the metals determines a downshift and broadening of 5σ and $2\pi^*$ orbitals, and with the d band, two bonding and two antibonding states below and above the pristine states. In conclusion, the d band contribution to the adsorption energy E_{d-ads} can be expressed in the form of a hybridization gain for the 5σ orbital and an orthogonalization cost for the 2π one. Analogously to oxygen if we move from noble metals to the right of the periodic table we span from dissociated CO (from Ag to Rh) to about -3.0 eV CO chemisorption for Nd.

Another fundamental question in chemisorption regards bond-making and breaking. For H dissociation bonding and antibonding states similar to atomic adsorption display a bond which is a little stretched. In this case, bonding and antibonding states similarly to atomic adsorption occur, while for stretched bonds the electronic structure of the molecule is alike that of the final state.

Very recently a sophisticated calculation was provided by *Schimka* et al., who abandoned the most recent functionals for alternative methods based on the many-

electron approach with the RPA [16.51]. In fact even for a small molecules like CO on Pt(111) the usual semilocal functionals tend to overestimate chemisorption energy and not provide the correct monoxide site. When exact Hartree–Fock exchange is combined with RPA we observe that the adsorption energy decreases which is due to interaction of the two frontier orbitals of CO, the 5σ and the $2\pi^*$ with the metal states. The 5σ orbitals are partially filled above ε_F determining a strong interaction in the atop site. The RPA also restores the correct order in energy for the most critical cases lowering the binding energy by 350−550 meV: −0.42 eV (adsorbed on Cu(111) in the top site) < −0.32 eV (Cu, face-centered cubic site, fcc); −1.31 eV (Pt top) < −1.23 eV (Pt fcc); and −1.43 eV (Rh top) < −1.28 eV (Rh, hexagonal close packed, hcp). Another example is benzene on ferromagnetic Ni(111). In the RPA the experimentally observed hollow site is favored while the total adsorption energy is instead lowered by RPA (−0.95 meV) compared to PBE (−0.65 meV) owing to a strong vdW bond.

Alkali Atoms on Metals

Among atomic adsorbates, alkali metal adsorbed on metal surfaces have been the subject of intense investigations in order to clarify fundamental issues in adsorption phenomena, as well as for their technological relevance as workfunction modifiers and surface dopants. Early description of this prototypical system dates to about 80 years ago with the Langmuir–Gurney model [16.102, 103]. The knowledge of this apparently simple system has remarkably improved during the last three decades showing the occurrence of various nontrivial phenomena overcoming the Langmuir–Gurney model, as reviewed by several authors in the past [16.104, 105] and more recently [16.106].

One example of peculiar phenomena lies in the correlated *vertical diffusion* motion observed for Na atoms on copper. Measurements of surface diffusion based on helium atom scattering for Na/Cu(001) have proven to be unable to explain an observed coverage dependence of the 2-D motion [16.107]. By high-resolution ^{3}He spin-echo, *Alexandrowicz* et al., [16.108] could demonstrate that experimental findings are accurately reproduced upon introducing an explicit dependence of the Na coordinate on the local adsorbate concentration, that is a time-dependent quantity at finite temperature, hence leading to a confined motion also along the surface normal, occurring on the same timescale as the diffusive motion. However, a coverage dependence of the Na–surface bond length is not expected [16.105]. DFT simulations [16.109] could eventually clarify this puzzle demonstrating that, while the Na−Cu bond is minimally affected by adsorbate concentration, the extent of the electronic density towards vacuum is modified considerably because of the dipole electric field induced by the other adsorbates. As the adsorbate distribution is inhomogeneous and time-dependent, this translates into a time evolution of the turning point for the scattered probe atoms. Related (yet static) electronic effects occur in emphasizing the corrugation of quasi-1-D structures observed by helium atom scattering (HAS) for Li and Na on Cu(001) as coverage approaches saturation, where changes in the atomic height are irrelevant. We will return to this case when discussing adsorption dipoles (Sect. 16.5.2).

Alkali atoms are also prototypical effects for the study of surface diffusion phenomena. Considering again Na on copper, the effects of step on surface diffusion have been studied by adopting a vicinal Cu(115) surface [16.110]. Motion is anisotropic and occurs prevalently parallel to the step edges, following intuition. Additionally, Na−Na collective effects described above are also anisotropic, pointing to a screened interaction for adsorbates on different terraces.

16.4.2 Physisorption of Noble Gases on Metals

Adsorption of noble gases is for several reasons an important topic in surface science. Already about 50 years ago *Scoles* et al. [16.111] and *Boato* et al. [16.112] performed the first experiments of diffraction of light noble atoms on solid surfaces. This technique has been extensively applied by *Toennies* et al. [16.113] and other scientists to obtain a detailed dispersion relationship of phonons on several surfaces. More recently, *Allison* et al. have employed beams of the fermion isotope ^{3}He to check the diffusion of alkali adatoms (Chap. 15) [16.114]. Ar, Kr, and Xe have been used for microscopic tribological models for perspective technological applications.

Being atoms with closed-shell systems, noble gases interact with a surface mainly with vdW or London dispersion forces by instantaneous dipoles. For this reason their bond to the surface is a physisorption one where we have already observed that DFT with semilocal corrections is not sufficient. The weakness of the interaction between the atom and the surface introduces the main complication since the adsorption energy is strongly dependent on correlation so that a local (semilocal) qualitative estimate, sufficient at shorter distances for a chemical bond, is insufficient to yield vdW energies, in which the polarizability of the probe and the long-wavelength dielectric constant are missing. Still LDA/GGA DFT treatments have supplied important information. A general property, validated by GGA-DFT, independent of the functional, is that the

equilibrium distance from the surface increases from Xe to Ar and it correlates with the adsorption energy that varies from a few meV for He to −320/−360 meV for the heaviest one, Xe. The results of *Da Silva* and *Stampfl* [16.115], confirmed by low-energy electron diffraction (LEED) measurements, found that Xe adatoms preferentially bind to low-coordination top sites instead of the highly coordinated hollow sites on metals because when charges of the atom and of the metal begin to overlap, Pauli repulsion is present and electrons are transferred more easily from atoms adsorbed on top sites than on hollow sites getting the atom closer on top. Nonlocal vdW DF functionals showed later that the hollow sites for Xe are maxima and the atop site a true minimum [16.51]. This phenomenon holds for close-packed surfaces, i.e., Pt(111), Pd(111), Cu(111) for Xe. However, a potential curve of a noble gas atom is erroneous when calculated by GGA-DFT. It is clear that a many-body seamless solution, as a function of distance from the surface, would be desirable for correct results.

A more subtle effect of He interacting with transition metal surfaces and the Cu(111) one, is the so-called anticorrugating effect. In fact elastic scattering measurements of He performed by *Rieder* et al. [16.116] on Rh(110) and Ni(110) showed intensities in the measured diffraction scans that can be reproduced by models in full disagreement with intuition: In order to explain their data, these authors had to assume that the corrugation profile seen by He is off phase with respect to the surface lattice atom positions, and that the classical turning point of the interaction potential is farther away at the short bridge position than at the top one, for a fixed kinetic energy of the impinging atom. GGA-DFT calculations by *Scheffler*'s group [16.117], which produce reasonable results at this atom–surface distance since the He surface potential is in its repulsive part, show that the property of s for He and p for Ne wavefunction facing the d metal ones at top and bridge position determine the anticorrugating effect. In a later paper on Cu(111), which explains very satisfactorily the anomalies of phonon spectra, anticorrugation was accounted for in terms of the relative kinetic energy ΔK of the electrons between top and bridge sites for the same impinging He kinetic energy. In other words, $\Delta K(\text{bridge}) > \Delta K(\text{top})$ and overcomes the electrostatic difference $\Delta U(\text{top}) > \Delta U(\text{bridge})$, with the exchange correlation term being negligible. Conversely, for a simple metal He/Al(111) the standard corrugation is observed and $\Delta K(\text{bridge}) < \Delta K(\text{top})$ [16.118].

Surface Properties Studied by Adsorption Phenomena

While the emphasis of adsorption studies may be more frequently on adsorbates, absorption and diffusion phenomena are also a tool to investigate surface properties. One obvious example is given by atom-scattering experiments. We would also like to mention a less direct example, where the observed atomic diffusion at a surface can be linked to the substrate approaching a structural transition [16.119]. Bulk cobalt is characterized by a hexagonal close-packed structure at ambient temperature and pressure, but thin Co films can be stabilized epitaxially on top of Fe(001) which acts as a template with square symmetry. Hence, a metastable body-centered-tetragonal structure is obtained up to about ten Co layers (after which the film transforms into hcp crystallites). Despite the fact that the atomistic structure of the surface remains unaltered, the diffusivity of Co adatoms has been shown to depend dramatically on film thickness: the process gradually evolves from an activated one, with a barrier of about half an eV on clean Fe(001), to being practically barrierless already at a thickness of 5 ML. Experimentally, this was determined by a statistical analysis of Co island size distributions, from which the diffusion coefficient was extracted, as a function of thickness and temperature. Density functional theory simulations then identified the transition state in the diffusion mechanism as a Co adatom occupying the bridge site, and that such site is stabilized by deformations in the substrate that increase in magnitude with film thickness. These deformations locally recover a structure in closer resemblance to the hexagonal one, so their energy cost drops to zero as the film approaches the structural transition.

16.5 Adsorption of Organic Molecules

The flexibility offered by natural and synthetic organic chemistry leads to a great deal of possible options in the choice of organic adsorbates. Example of classes of molecules having attracted significant interest in the literature for fundamental aspects and applications are self-assembled monolayers (SAMs), porphyrins, and polycyclic aromatic hydrocarbons (PAHs). Some examples are depicted in Fig. 16.6. Although the definition strictly applies to a wide class of molecules, with the SAM acronym one customarily denotes a specific class of self-assembled adsorbates where molecules are composed of a chemisorbed head group, a tail, and a functional termination. A prototypical case consists of *n*-alkanethiols where the anchoring group is a sulfur

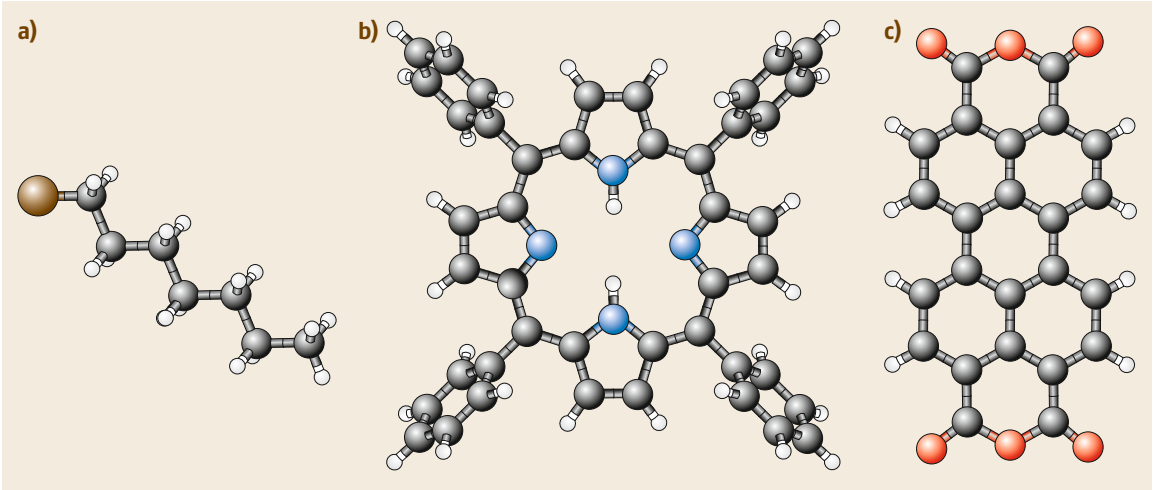

Fig. 16.6a–c Ball-stick model of example molecules for **(a)** SAM, showing an alkanethiol, **(b)** a porphyrin, here tetraphenylporphyrin, **(c)** a PAH, here PTCDA. *Gray*, *red*, *blue*, *smaller white*, and *larger brown balls* represent C, O, N, H, and S atoms, respectively

atom and the tail a $(-CH_2-)_n$ chain, see Fig. 16.6a, but many more configurations are possible [16.120]. These molecules find various applications in surface coatings. Porphyrins are molecules with enormous significance in biology and interesting catalytic properties. The case of tetraphenylporphyrin is shown in Fig. 16.6b. They can incorporate different metal centers which can be adjusted for tailored applications, and their properties and functionalities are characteristically influenced by interfacial interactions [16.121, 122].

Polycyclic aromatic hydrocarbons have attracted significant interest for organic electronic devices [16.123]. In the following, we will focus on this latter subset to select a few test cases for additional discussion. A popular molecule in surface science studies is PTCDA, which is shown in Fig. 16.6c.

16.5.1 Aromatic Molecules on Semiconductors and Metals: Configurations, Electronic and Spectroscopic Properties, π and σ Bands

Pentacene on TiO_2

The performance of an electronic device depends on a diversity of factors, including the structural, electronic, and spectroscopic properties of the very first layer of molecules at the hybrid interfaces within the device. The arrangement of the first molecules may steer the crystalline ordered growth of an organic active layer, [16.124] which is especially important since high quality of the organic crystal is required [16.125]. Also, the mobility within organic materials, also when high molecular ordering can be achieved, is optimal only for the directions maximizing intermolecular couplings [16.126]. Additionally, the ultimate transfer at a contact depends on the overlap of the molecular wavefunctions with the substrate ones.

An especially interesting and prototypical case that we take here as an example is constituted by pentacene ($C_{22}H_{14}$). This aromatic hydrocarbon is characterized by very high hole and electron mobility [16.127, 128] that exceeds that of amorphous silicon. The adsorption of pentacene on different substrates has therefore been widely studied both experimentally and theoretically. We select a few examples here to describe how different levels of interaction influence the growth.

The anisotropy of a weakly interacting substrate has proven effective to gently influence the molecular adsorbates, without affecting too strongly their electronic and spectroscopic properties. One such example is the case of pentacene on the rutile $TiO_2(110)$ surface. This surface is characterized by the formation of rows of protruding O atoms along the [001] crystal azimuth; rows are spaced ≈ 6.5 Å along $[1\bar{1}0]$ and atoms protrude by ≈ 1 Å with respect to surface Ti [16.129, 130], forming an ideal template to accommodate planar molecules as found for pentacene (other examples are perylene and its derivatives [16.131]). Submonolayer phases of pentacene on $TiO_2(110)$ have been studied by STM, HAS, and near-edge x-ray absorption fine structure (NEXAFS). These experiments have demonstrated the formation of a very ordered phase [16.132] with molecules adsorbed in a nearly planar geometry (tilt angle $\approx 25°$) and aligning along

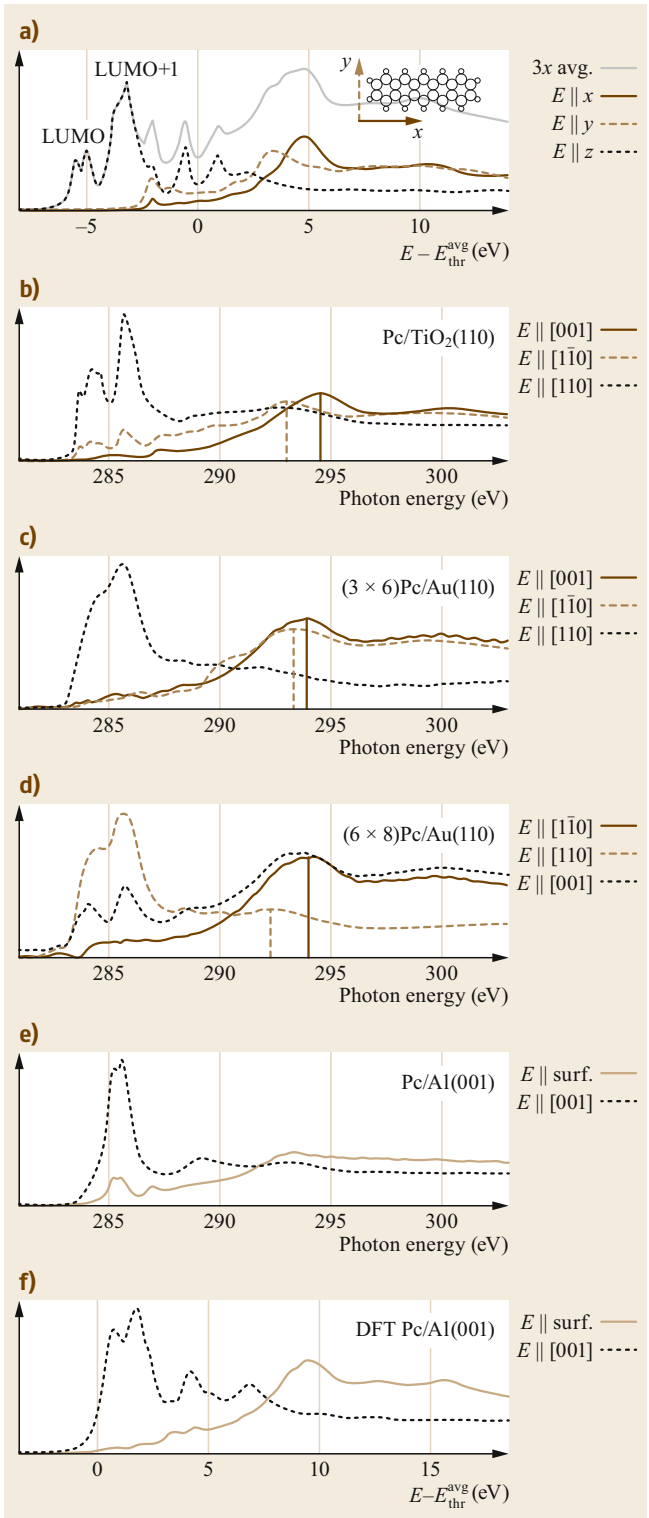

Fig. 16.7a–f NEXAFS spectrum of pentacene: **(a)** theoretical result for the gas phase [16.134]; **(b)** measured on TiO_2 [16.132]; **(c,d)** measured on Au(110) [16.135]; **(e)** measured and **(f)** computed for pentacene on Al(001) [16.136] ►

the $[1\bar{1}0]$ crystal azimuth with intermolecular distance dictated by coverage, and approaching that of the organic crystal at monolayer completion. In the other surface azimuth ([001]) intermolecular π–π attraction stabilizes stripes of pentacene. The NEXAFS spectrum of these molecules is reported in Fig. 16.7a for the gas phase (calculations shown as a reference) and in Fig. 16.7b for pentacene/TiO_2. It exhibits several characteristics testifying that the interaction with the substrate, although sufficiently strong as to drive the ordered phase, has only a minor influence on the molecular orbitals: molecular features are clearly resolved, not showing a hybridization-induced broadening present in other cases (see the other panels, discussed below); the spectra at monolayer coverage already resemble those of a thin overlayer and, once spherically averaged, gas-phase ones [16.133]. The ordered phase allows unprecedented analysis of the symmetry of the molecular orbitals that is only possible for stabilized molecules, and that is fully rationalized by theoretical simulations of the spectra based on the transition-potential approach [16.134] (Fig. 16.7a). One can identify the first unoccupied resonances as due to transitions to final bound states (LUMO, LUMO+1 and higher states) having π symmetry. For final unbound states $\approx 5\,\mathrm{eV}$ higher energy than that threshold, transitions to σ states emerge. Given the asymmetry of pentacene and the uneven length of its C–C bonds, the energy of σ states differ according to the dominant contribution of in-plane orbitals along the long or short molecular axis. Such an effect identifies an azimuthal dichroism in the spectra that can be used to resolve in-plane molecular orientation by NEXAFS, as was done to validate a model of perylene ($C_{20}H_{12}$) adsorption on the same surface, with the molecular axis along $[1\bar{1}0]$ where a rounded appearance of the molecules in the STM images could not be conclusive [16.131].

Pentacene on Silicon

The case of pentacene on silicon surfaces exhibits a completely different behavior. On this semiconductor, the molecule is found to strongly chemisorb. Several studies have highlighted possible configurations on Si(001)-(2 × 1). A work by the *Yates* group [16.137], combining STM with slab simulations at the PW91 level, revisited previous assignments and pointed out

the formation of six to eight Si−C covalent chemical bonds, and an adsorption energy of up to 128 kcal/mol. This is realized for a nearly flat molecule bridging between adjacent rows of Si dimers. Other configurations include strongly distorted pentacene with sp^3 hybridized C atoms. Consequently, a NEXAFS spectrum of pentacene on Si(001)-(2×1) reveals lost conjugation and missing contributions by peripheral C atoms at the otherwise expected $1s \rightarrow$ LUMO transition energy [16.138]. Chemisorption also occurs on Si(111)-(7×7). This strong interaction of pentacene with a silicon surface can be reduced by passivating the substrate with H [16.139] or by organic adsorbate functionalization [16.140].

Pentacene on Noble Metals

Adsorption of pentacene on metal surfaces also raised significant interest because of the occurrence of organic/inorganic interfaces at potential contacts. Among the noble metal surfaces, Au(111) is supposedly the one exhibiting the smallest interaction with the adsorbate. There, pentacene adsorbs in a mostly planar configuration. However, the interaction is still appreciable in inducing a weak bending of the molecule [16.141]. On Au(110) [16.135] different structures are observed: a (3×6) one, Fig. 16.7c, with planar molecules having their long axis along [001], exhibiting a significant broadening of the LUMO peaks and significantly smaller azimuthal dichroism than the one of free molecules. At higher coverage, a (6×8) structure forms where planar molecules coexist with ones having the long axis along the surface normal. The spectra of the two intermixed phases can be distinguished thanks to a different dependence on the experimental geometry in Fig. 16.7d. For example, π transitions are excited with $E \parallel [110]$ for flat-lying molecules and $E \parallel [001]$ for standing ones. Their comparison at about 285 eV in Fig. 16.7d testifies the dependence on adsorption angle of the electronic coupling of the π system with the substrate orbitals, with standing molecules leading to better resolved features and larger azimuthal dichroism. By increasing the interaction strength, silver and copper surfaces also present mostly planar molecules, with upwards bending of the molecule along its short axis. The mixing of the molecular and substrate electronic states becomes more relevant, featuring the filling of the lowest unoccupied molecular orbital on Ag(111) [16.142], Ag(110) [16.143], Cu(111) [16.144], Cu(001) [16.145], and Cu(110) [16.146]. Consequences of the LUMO filling are the possibility to detect such orbitals in photoemission experiments normally accessing the molecular states up to the highest occupied molecular orbital (HOMO) [16.143], and their reduced intensity or disappearance in NEXAFS.

Pentacene on Aluminum

As another metal of interest for device research, aluminum presents a stronger interaction that leads to a peculiar scenario. The adsorption of pentacene on Al(001) was studied by a combination of experimental and theoretical techniques [16.136]. It was found by reflection high-energy electron diffraction (RHEED) and STM that adsorption induces a reconstruction on the substrate, which appears as a rippling of Al rows along [100] having a corrugation of 30 pm in the STM images taken in exposed surface areas. The periodicity of these rows across $[1\bar{1}0]$ is 1.6 nm, the same as molecular stripes also identified in STM that extend along [100] with molecules having the long axis along [110]. From the theoretical point of view, the adsorption is somewhat intermediate between chemisorption and physisorption. If a DFT description with a semilocal functional is used, molecules are barely bound with GGA, whereas an adsorption energy of ≈ 2 eV is obtained with LDA showing an upward curvature (similarly to adsorption on Cu) [16.147]. The inclusion of vdW correction, there at the Grimme level, has a major impact on the GGA results. Of the possible adsorption sites compatible with the experimental orientation, all of them but one still present a mostly flat molecule with adsorption energy up to 1.50 eV. The other one, which is centered on a bridge site with the central C atoms on top of two Al atoms, is the most stable with an energy of 2.20 eV and features a V-shaped molecule. This configuration is depicted in Fig. 16.8 and is characterized by a V-angle at the center of 155° and a difference in C heights of 1.35 Å, with a deformation that costs, in the gas phase, an energy of 1.35 eV. This structure is stabilized by the optimal matching of the central C atoms with two Al ones, with a C−Al distance as small as 2.20 Å. This is only made possible, however, by the inclusion of dispersion forces: these allow a shorter distance between the aromatic rings and the surface, eventually allowing for the direct C−Al anchoring. Spectroscopic and microscopic properties simulated for molecules adsorbed in the V-shape are in very good agreement with the observations and corroborate this result. In particular, NEXAFS spectra reported in Fig. 16.7e (experiments) show that the molecules lie mostly face-on, with an effective tilt angle of the aromatic planes of $(28\pm5)°$ with respect to the surface, which takes into account molecular deformation and defect sites. Given the hybridization with metal states, a broadening of the molecular features could be expected similarly to the case of pentacene on Au(110). Differently from the gas phase, the signature of transitions to π^* orbitals is much narrower both in measured and computed (Fig. 16.7f) spectra, suggesting also in this case that filling of the LUMO takes place hence

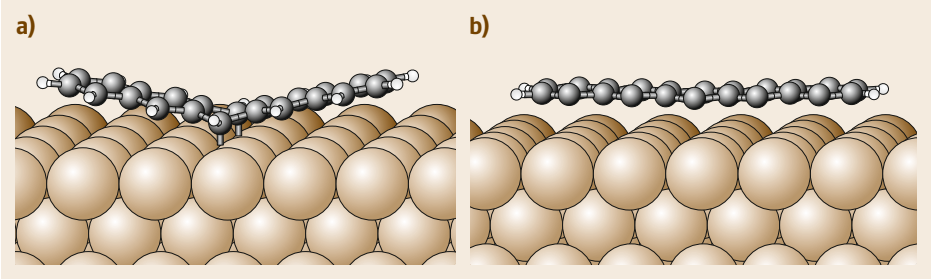

Fig. 16.8a,b Adsorption configuration of pentacene on Al(001) [16.136]. **(a)** Most-stable V-shaped configuration in the bridge site. **(b)** Flat-lying on a top site. *Balls* of *increasing size* denote H, C, and Al atoms

removing it from the unoccupied manifold of possible final states.

Band Symmetry and Spectroscopy

An effective tool for a rational analysis of spectra of adsorbed molecules is the identification of the molecular energy levels in the DOS and surface band structure of the system; Fig. 16.4 shows an example of a clean substrate. In this respect, many ab initio codes implement the possibility to project the surface bands onto the molecular eigenstates, typically computed by a separate calculation for the free molecule. As a result, one can visualize *fat bands*, where the color or size of the symbols in the *spaghetti plot* is proportional to the molecular contribution. Alternatively, a ***K***-resolved DOS (projected onto molecular orbitals) can be used and possibly superimposed as a color map on the usual surface band plot. The two approaches are conceptually equivalent and while the former may be more convenient to represent regions where only few bands appear, the latter is advantageous for high density of states and is the natural framework to describe the continuous spectrum of an extended substrate. The ***K***-resolved DOS is reported in Fig. 16.9 for thymine molecules forming rows of π-stacked molecules deposited on Si(001) [16.148]. In this case, the dispersion of HOMO- and LUMO-derived states (see insets) can be identified, allowing the distinction of molecular features and molecule-induced substrate ones in optical reflectance spectra.

16.5.2 Adsorption-Induced Charge Rearrangements/Induced Dipoles/Induced Spin Distributions

Induced Charge Rearrangements

Out of the various adsorption-induced phenomena, such as substrate relaxations, reconstructions, surfactant effects, etc., one of the most relevant and possibly easily visualized is the displacement of the electron density

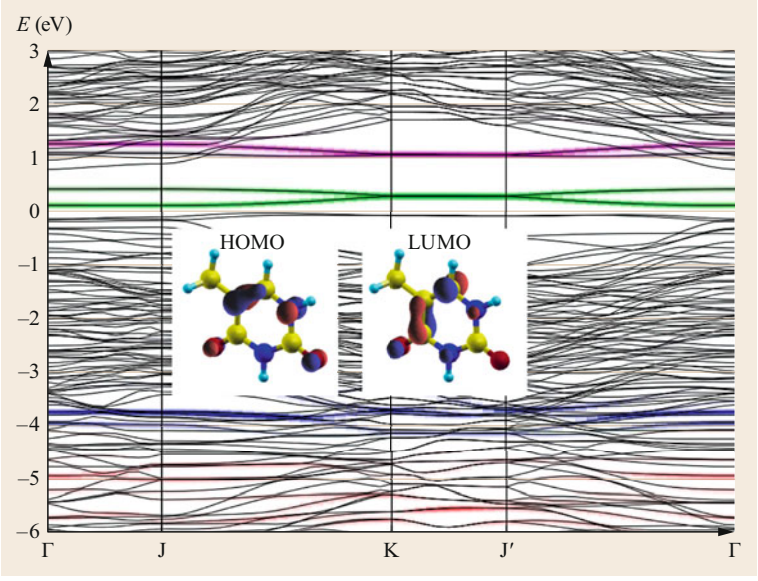

Fig. 16.9 Surface band structure of thymine molecules on Si(001) in the *dimer-bridge* configuration at half coverage [16.148] with molecular contributions shown as a color map of the ***K***-resolved DOS. HOMO and LUMO of gas-phase thymine are shown in the *insets*

of the combined system when that of the summed fragments is taken as a reference. That quantity, $\Delta\rho_{ads} = \rho_{mol/surf} - \rho^{gas}_{mol} - \rho^{clean}_{surf}$, is in principle exactly accessible by DFT where $\rho_{mol/surf}$, ρ^{gas}_{mol}, and ρ^{clean}_{surf} are the ground-state charge densities of the full system, of the free molecule, and of the clean substrate, respectively (the latter two commonly taken at the same coordinates they attain upon adsorption).

Let us take again as an example the case of adsorbed pentacene. A strong electronic charge reorganization at the interface occurs for various metals, see, e.g., [16.146] (also recall the filling of the LUMO of pentacene on a variety of substrates as presented in Sect. 16.5.1). The case of pentacene on Al(001) may serve as a tool to identify the relation between adsorption configurations and different charge displacements. To that purpose, in Fig. 16.10 the quantity $\Delta\rho_{ads}$ is reported for the two configurations, B chemisorbing with a V-shape (Fig. 16.10a,b) and T physisorbing nearly planar (Fig. 16.10c). The red color indicates regions of higher electron density and blue ones of lower density. By plotting in Fig. 16.10a the isosurfaces corresponding to an isovalue of $\pm 0.04\, e/\text{Å}^3$, accumulation of electron density in the C−Al bond formed at the center of the molecule can be seen. A corresponding charge depletion is instead observed in the vicinity of that bond at a smaller isovalue ($\pm 0.01\, e/\text{Å}^3$) in Fig. 16.10b. The net electron transfer from Al to the molecular region was estimated to amount to $0.56e$ [16.149]. To visualize any effect of electron density rearrangement in the physisorbed case, one has to take a lower isovalue $0.005\, e/\text{Å}^3$ in Fig. 16.10c.

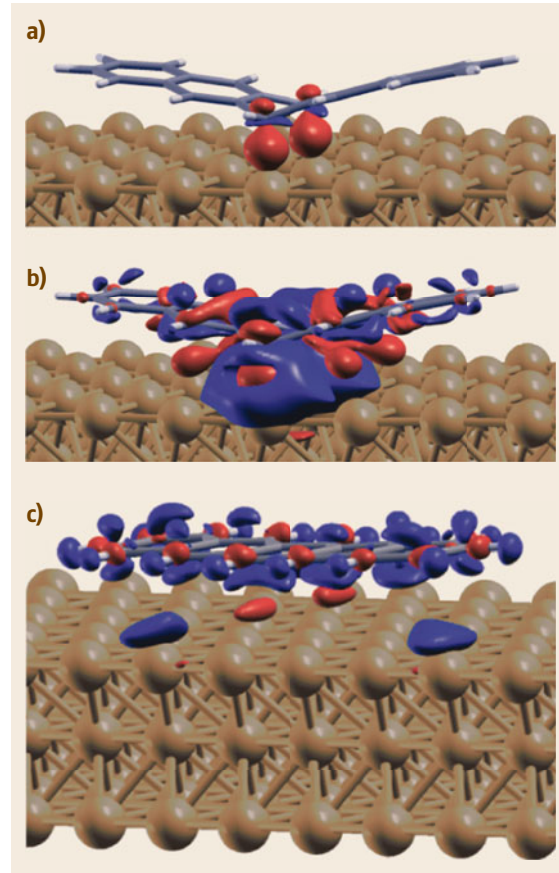

Fig. 16.10a–c Adsorption charge of pentacene on Al(001). **(a)** and **(b)** pentacene on the bridge site, showing surfaces at adsorption charge isovalues of **(a)** $\pm 0.04\, e/\text{Å}^3$ and **(b)** $\pm 0.01\, e/\text{Å}^3$. **(c)** Pentacene on the top site, with isovalues of $\pm 0.005\, e/\text{Å}^3$

Induced Dipoles

In relating the adsorption density rearrangements to workfunction changes one is tempted to express the dipole moment per adsorbed species at a given coverage as the product of the displaced charge (as estimated by Bader or related approaches) times an adsorption distance. However, as pointed out by *Bagus* and coworkers [16.150], several and often canceling terms contribute to the interface dipole so that the above expression is only formally valid. So one may have negatively charged adsorbates, like I/Cu(111), that decrease the surface workfunction contrary to expectations.

Also in the most simple and prototypical case of alkali atoms on a metal, several interesting phenomena may emerge.

For example, the charge displacement induced by adsorption of Cs on Cu(001) is depicted in Fig. 16.11a where we subtract from the electron density of the full system that of neutral Cs and of clean Cu(001). The first and more obvious feature is the transfer of electrons from the Cs region (diffuse red region centered at Cs) to the metal (see the blue region mostly located just above the surface layer). However, one can also appreciate: a localized polarization around the nearest Cu atoms that goes beyond earlier treatments by the jellium model [16.69]; a charge displacement in the region closer to the Cs nucleus, with negative/positive charge at larger/smaller distances, hence producing a dipole moment opposite to the total one. The latter effect corresponds to the polarization of the inner shell and reduces the total dipole moment especially for the heavier alkalis (by 11% for Cs, reducing dipole–dipole repulsions by 20%). The total dipole moment, as computed by DFT-PBE [16.151], produces a variation of the workfunction that at 0.06 ML coverage amounts to 1.97 eV, in excellent agreement with the measured value of 2.0 eV [16.152]. Lighter alkalis show qualitatively similar results, although reduced in magnitude [16.151].

It is noted that the surface dipole is a determined self-consistently. In particular, the experimental saturation of the workfunction change at a given coverage demonstrates the coverage dependence of the adsorption dipole as the overlayer is increasingly denser. Inhomogeneous changes in the local adsorbate density, while keeping the total coverage constant, also lead to interesting phenomena. For example, the dipole–dipole repulsion of adsorbed Na atom pairs on Cu(001) is modified from a pure R^{-3} law (R being the Na−Na distance) because of the reduction of the dipole moment as they come closer: neglecting this effect overestimates the repulsion energy by 20 meV when Na atoms are two Cu unit cells apart [16.153]. Reduction in the adsorption dipole induced by local density increases contributes to the stability of quasi-1-D structures observed and computed for Li/Cu(001) [16.154, 155] and Na/Cu(001) [16.156, 157] as saturation coverage is approached. Atom-scattering experiments demonstrate a 1-D corrugation of the probe–surface interaction that, linked to the surface electron density through the effective medium theory, is actually due to larger extension of the density towards vacuum, as the workfunction is locally reduced because of the increased density of dipoles. As an example, the electron density displacement for a high-coverage structure of Li/Cu(001) [16.155] is reported in Fig. 16.11b, where we show the difference between the adsorption charge density $\Delta\rho_{ads}$ for the full structure and a reference adsorption charge calculated by summing independent contributions by individual Li atoms at lower coverage. The accumulation of electron density in the red *pipe*-shaped region, probed by the experiments, indicates depolarization of the alkali–surface bond (see the blue region underneath) in favor of a metallic-like bond within Li atoms.

Induced Spin Distributions

Adsorption phenomena also have an interplay with spin-dependent phenomena. Cases of magnetic substrates where molecules can attain magnetic properties as a consequence of hybridization are reported (see, e.g., C_{60}/Fe_3O_4 [16.158] or pentacene on Co islands on copper [16.159]) or, conversely, ones of adsorbed magnetic molecules (e.g., porphyrins incorporating magnetic centers). The combination of a magnetic molecule with magnetic substrates [16.160] also raises significant interest for molecular spintronic devices.

However, it is intriguing to observe that adsorption can induce spin-polarization also for nonmagnetic molecules on nonmagnetic substrates. A case that has attracted particular interest is the one of covalent adsorption on graphene. Perfect clean graphene is spin-compensated and several techniques have been proposed to induce magnetic moment. *Casolo* and coworkers [16.161] already demonstrated that the adsorption of an H atom induces a net magnetic moment of $1\mu_B$ by effectively removing one p_z orbital from the π band of graphene: that, by Lieb's theorem for bipartite lattices, translates into the observed magnetism. The unpaired electron occupies a spin-polarized state (called *mid-gap state*) occurring right at the Dirac cone which is localized in space around the adsorbate given the vanishing substrate density of states, although periodic calculations show the appearance of bands in a small, size-dependent, energy gap. This effect is intimately related to modifications in the graphene lattice, rather than on the properties of the adsorbate, and was therefore extended to more general cases of covalently bonded organic molecules on graphene [16.162, 163] and carbon nanotubes [16.164]. The interested reader is referred to the review by *Martinazzo* for more details [16.165].

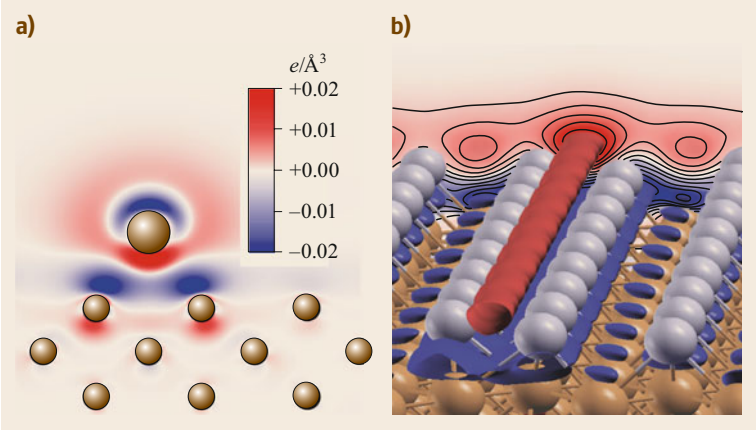

Fig. 16.11 (**a**) Side view of the adsorption charge for Cs/Cu(001). *Large* and *small circles* mark the position of Cs and Cu atoms, respectively. (**b**) Charge redistribution in forming 0.6 ML structures of Li/Cu(001), as compared to the individually adsorbed Li atoms. *Red regions* mark increased electron density. Isosurfaces are depicted at ± 0.01 Å^{-3}

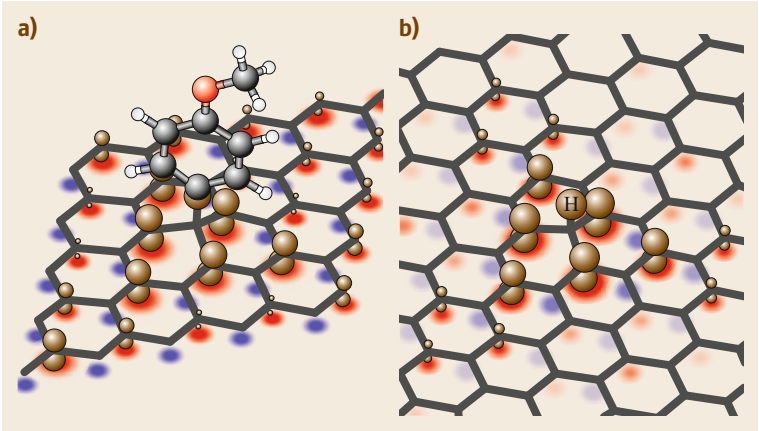

Fig. 16.12a,b Electron spin density $n_\uparrow - n_\downarrow$ for **(a)** methoxybenzene and **(b)** hydrogen adsorbed on graphene. The *red* isosurface corresponds to the value of $0.05\,e/\text{Å}^3$. *Red* and *blue shades* underneath are a false-color plot for values cut through a plane passing 0.65 Å below graphene and saturate at $\pm 0.02\,e/\text{Å}^3$

We recall few experimental facts. Observations of individual atoms and molecules on graphene are possible by the transmission electron microscope [16.166]. Hydrogen adsorption can be used to open a highly demanded band gap, as shown for H/graphene/Ir(111) [16.167]. Also, at low coverage hydrogen can induce a three-order-of-magnitude enhancement of the spin–orbit interaction in graphene [16.168]. Eventually, magnetic properties for organically functionalized graphene samples were measured showing the occurrence of antiferromagnetic domains [16.169].

The spin polarization of graphene with a covalent adsorbate is represented in Fig. 16.12 where we report the spin density $n_\uparrow - n_\downarrow$ for an adsorbed molecule (methoxybenzene, $CH_3OC_6H_5$) and atomic hydrogen, the latter computed for a larger (10×10 unit cell). We start by describing the case of anisole [16.163] in Fig. 16.12a. Upon covalent adsorption on a C atom belonging to one sublattice (A), that atom is lifted out of the carbon plane by 0.42 Å undergoing $sp^2 \rightarrow sp^3$ rehybridization. (This structural deformation costs 0.96 eV, which is subtracted from the adsorption energy leading to a final energy gain of only 0.32 eV despite the additional C–C bond.) The occupied mid-gap state is only minimally contributed directly by the adsorbate. Rather, it is mostly located at the nearest C atoms of the other sublattice (B), as evidenced by the spin density. A smaller and opposite spin polarization at the A sublattice can also be identified. As anticipated, very similar findings occur for adsorbed H, which is presented as a comparison in Fig. 16.12b.

Ultrafast Phenomena

We conclude this section by mentioning that adsorption-induced charge rearrangements and spin distributions can exhibit ultrafast time dependence (on the femtosecond timescale) in response to excitations. As an example, the adsorption charge of a core-excited adsorbed molecule is altered so as to accommodate an additional electron. This results in specific decay channels in de-excitation spectra [16.170] that are explained in terms of a modified $\Delta\rho_{\text{ads}}$ taking into account a filled LUMO orbital [16.72] injected from the substrate within a few fs to screen the perturbation. Returning to covalently functionalized graphene, a core-level excitation in the adsorbate is shown to disrupt the adsorption-induced magnetism on the fs time scale [16.171].

16.6 Conclusions

In this Chapter we have reviewed the progress made in adsorption and band structures in recent years. Adsorption energies have benefited from increased computer power and from new functionals and vdW implementation. Accuracies of maximum 200–300 meV in bonding have been accomplished. For surface bands a new area has opened up with the topic of adsorbed organic molecules. Especially with the help of synchrotron radiation methods and DFT approaches, the bands of organic adsorbates have been determined with great precision, including their orientation, tilting angle, and the formation of metal–semiconductor overlayers of particular interest for organic electronic devices and photovoltaics. In this respect, scanning tunneling microscopy and spectroscopy have also been of great help. New effects such as distance-surface manipulation of surface states have been foreseen.

References

16.1 K. Burke: Perspective on density functional theory, J. Chem. Phys. **136**, 150901 (2012)

16.2 P. Hohenberg, W. Kohn: Inhomogeneous electron gas, Phys. Rev. **136**, B864 (1964)

16.3 W. Kohn, L.J. Sham: Self-consistent equations including exchange and correlation effects, Phys. Rev. **140**, A1133 (1965)

16.4 R.M. Dreizler, E.K.U. Gross: *Density Functional Theory*, 3rd edn. (Springer, Berlin, Heidelberg 1990)

16.5 J.P. Perdew, M. Levy: Comment on "Significance of the highest occupied Kohn–Sham eigenvalue", Phys. Rev. B **56**, 16021 (1997)

16.6 M.T. Yin, M.L. Cohen: Ground-state properties of diamond, Phys. Rev. B **24**, 6121 (1981)

16.7 M.T. Yin, M.L. Cohen: Microscopic theory of the phase transformation and lattice dynamics of Si, Phys. Rev. Lett. **45**, 1044 (1980)

16.8 G.P. Brivio, M.I. Trioni: The adiabatic molecule-metal surface interaction: Theoretical approaches, Rev. Mod. Phys. **71**, 231 (1999)

16.9 J.P. Perdew, K. Burke, Y. Wang: Generalized gradient approximation for the exchange-correlation hole of a many-electron system, Phys. Rev. B **54**, 16533 (1996)

16.10 S. Kümmel, L. Kronik: Orbital-dependent density functionals: Theory and applications, Rev. Mod. Phys. **80**, 3 (2008)

16.11 Y. Wang, J.P. Perdew: Spin scaling of the electron-gas correlation energy in the high-density limit, Phys. Rev. B **43**, 8911 (1991)

16.12 W. Yang, J.P. Perdew: Correlation hole of the spin-polarized electron gas, with exact small-wave-vector and high-density scaling, Phys. Rev. B **43**, 13298 (1991)

16.13 J.P. Perdew, Y. Wang: Accurate and simple analytic representation of the electron-gas correlation energy, Phys. Rev. B **45**, 13244 (1992)

16.14 J.P. Perdew, J.A. Chevary, S.H. Vosko, K.A. Jackson, M.R. Pederson, D.J. Singh, C. Fiolhais: Atoms, molecules, solids, and surfaces: Applications of the generalized gradient approximation for exchange and correlation, Phys. Rev. B **46**, 6671 (1992)

16.15 J.P. Perdew, H.Q. Tran, K. Burke, E.D. Smith: Stabilized jellium: Structureless pseudopotential model for the cohesive and surface properties of metals, Phys. Rev. B **42**, 11627 (1990)

16.16 J.P. Perdew, K. Burke, M. Ernzerhof: Generalized gradient approximation made simple, Phys. Rev. Lett. **77**, 3865 (1996)

16.17 Y. Zhang, W. Yang: Comment on "Generalized gradient approximation made simple", Phys. Rev. Lett. **80**, 890 (1998)

16.18 B. Hammer, L.B. Hansen, J.K. Nørskov: Improved adsorption energetics within density-functional theory using revised Perdew–Burke–Ernzerhof functionals, Phys. Rev. B **59**, 7413 (1999)

16.19 J.P. Perdew, A. Zunger: Self-interaction correction to density-functional approximations for many-electron systems, Phys. Rev. B **23**, 3048 (1981)

16.20 M. Cococcioni, S. De Gironcoli: Linear response approach to the calculation of the effective interaction parameters in the LDA+U method, Phys. Rev. B **71**, 035105 (2005)

16.21 P. García-González, R.W. Godby: Many-body *GW* calculations of ground-state properties: Quasi-2D electron systems and van der Waals forces, Phys. Rev. Lett. **88**, 056406 (2002)

16.22 J.P. Perdew, M. Levy, J.L. Balduz Jr.: Density-functional theory for fractional particle number: Derivative discontinuities of the energy, Phys. Rev. Lett. **49**, 1691 (1982)

16.23 R. Parr, R.A. Donnell, M. Levy, W.E. Palke: Electronegativity: The density functional viewpoint, J. Chem. Phys. **68**, 3801 (1978)

16.24 S. Kümmel, J.P. Perdew: Optimized effective potential made simple: Orbital functionals, orbital shifts, and the exact Kohn–Sham exchange potential, Phys. Rev. B **68**, 035103 (2003)

16.25 T.L. Gilbert: Hohenberg–Kohn theorem for nonlocal external potentials, Phys. Rev. B **12**, 2111 (1975)

16.26 A.D. Becke: A new mixing of Hartree–Fock and local density-functional theories, J. Chem. Phys. **98**, 1372 (1993)

16.27 A.D. Becke: Density-functional thermochemistry. III. The role of exact exchange, J. Chem. Phys. **98**, 5648 (1993)

16.28 A.D. Becke: Density-functional exchange-energy approximation with correct asymptotic behavior, Phys. Rev. A **38**, 3098 (1988)

16.29 C. Lee, W. Yang, R.G. Parr: Development of the Colle-Salvetti correlation-energy formula into a functional of the electron density, Phys. Rev. B **37**, 785 (1988)

16.30 P.J. Stephens, F.J. Devlin, C.F. Chabalowski, M.J. Fritsch: Ab initio calculation of vibrational absorption and circular dichroism spectra using density functional force fields, J. Phys. Chem. Lett. **98**, 11623 (1994)

16.31 R.H. Hertwig, W. Koch: On the parameterization of the local correlation functional. What is Becke-3-LYP?, Chem. Phys. Lett. **268**, 345 (1997)

16.32 V.N. Staroverov, G.E. Scuseria, J. Tao, J.P. Perdew: Comparative assessment of a new nonempirical density functional: Molecules and hydrogen-bonded complexes, J. Chem. Phys. **19**, 12129 (2003)

16.33 R. Peverati, D.G. Truhlar: Quest for a universal density functional: The accuracy of density functionals across a broad spectrum of databases in chemistry and physics, Philos. Trans. R. Soc. A **372**, 20120476 (2016)

16.34 A. Stroppa, G. Kresse: The shortcomings of semi-local and hybrid functionals: What we can learn from surface science studies, New J. Phys. **10**, 063020 (2008)

16.35 A.M. Reilly, A. Tkachenko: Van der Waals dispersion interactions in molecular materials: Beyond pairwise additivity, Chem. Sci. **6**, 3289 (2015)
16.36 J. Klimes, A. Michaelides: Perspective: Advances and challenges in treating van der Waals dispersion forces in density functional theory, J. Chem. Phys. **137**, 128901 (2012)
16.37 C. Berland, V.R. Cooper, K. Lee, E. Schröder, T. Thonhauser, P. Hyldgaard, B.I. Lundqvist: Van der Waals forces in density functional theory: A review of the vdW-DF method, Rep. Prog. Phys. **78**, 066501 (2015)
16.38 Y. Andersson, D.C. Langreth, B.I. Lundqvist: Van der Waals interactions in density-functional theory, Phys. Rev. Lett. **76**, 102 (1996)
16.39 D.C. Langreth, M. Dion, H. Ryberg, E. Schröder, P. Hyldgaard, B.I. Lundqvist: Van der Waals density functional theory with applications, Int. J. Quantum Chem. **101**, 599 (2005)
16.40 M. Dion, H. Ryberg, E. Schröder, D.C. Langreth, B.I. Lundqvist: Van der Waals density functional for general geometries, Phys. Rev. Lett. **92**, 246401 (2005)
16.41 K. Lee, E.D. Murray, L. Kong, B.I. Lundqvist, D.C. Langreth: Higher-accuracy van der Waals density functional, Phys. Rev. B **82**, 081101(R) (2010)
16.42 S.D. Chakarova-Käck, E. Schröder, B.I. Lundqvist, D.C. Langreth: Application of van der Waals density functional to an extended system: Adsorption of benzene and naphthalene on graphite, Phys. Rev. Lett. **96**, 146107 (2006)
16.43 S. Grimme: Semiempirical GGA-type density functional constructed with a long-range dispersion correction, J. Comput. Chem. **27**, 1787 (2006)
16.44 S. Grimme, J. Antony, S. Ehrlich, H. Krie: A consistent and accurate ab initio dispersion correction DFT-D for the 94 elements H-Pu, J. Chem. Phys. **132**, 154104 (2010)
16.45 B. Shanigaram, R.K. Chitumalla, K. Bhanuprakash: Adsorption of TCNQ and F4-TCNQ molecules on hydrogen-terminated Si(111) surface: Van der Waals interactions included DFT study of the molecular orientations, Comput. Theor. Chem. **1084**, 174 (2016)
16.46 A. Tkatchenko, M. Scheffler: Accurate molecular van der Waals interactions from ground-state electron density and free-atom reference data, Phys. Rev. Lett. **102**, 073005 (2009)
16.47 V.G. Ruiz, W. Liu, E. Zojer, M. Scheffler, A. Tkatchenko: Density-functional theory with screened van der Waals interactions for the modeling of hybrid inorganic-organic systems, Phys. Rev. Lett. **108**, 146103 (2012)
16.48 E. Zaremba, W. Kohn: Van der Waals interaction between an atom and a solid surface, Phys. Rev. B **13**, 2270 (1976)
16.49 W. Liu, V.G. Ruiz, G. Zhang, B. Santra, X. Ren, M. Scheffler, A. Tkatchenko: Structure and energetics of benzene adsorbed on transition-metal surfaces: Density-functional theory with van der Waals interactions including collective substrate response, New J. Phys. **15**, 053046 (2013)
16.50 W. Liu, A. Tkatchenko, M. Scheffler: Modeling adsorption and reactions of organic molecules at metal surfaces, Acc. Chem. Res. **108**, 47 (2014)
16.51 L. Schimka, J. Harl, A. Stroppa, A. Gruneis, M. Marsman, F. Mitterdorfer, G. Kresse: Accurate surface and adsorption enegies from many-body pertubation theory, Nat. Mater. **9**, 741 (2010)
16.52 F. De Angelis, A. Tilocca, A. Selloni: Time-dependent DFT study of $[Fe(CN)_6]^{4-}$ sensitization of TiO_2 nanoparticles, J. Am. Chem. Soc. **126**, 15024 (2004)
16.53 T. Stecher, K. Reuter, H. Oberhofer: First-principles free-energy barriers for photoelectrochemical surface reactions: Proton abstraction at TiO_2(110), Phys. Rev. Lett. **117**, 276001 (2016)
16.54 A.A. Herzing, C.J. Kiely, A.F. Carley, P. Landon, G.J. Hutchings, H.-J. Freund: Identification of active gold nanoclusters on iron oxide supports for CO oxidation, Science **321**, 1331 (2008)
16.55 H.-J. Freund: Models for heterogeneous catalysts: Studies at the atomic level, Rend. Fis. Acc. Lincei **28**, 5 (2017)
16.56 M. Schlüter, J.R. Chelikowsky, S.G. Louie, M.L. Cohen: Self-consistent pseudopotential calculations for Si (111) surfaces: Unreconstructed (1×1) and reconstructed (2×1) model structures, Phys. Rev. B **12**, 4200 (1975)
16.57 M. Payne, M.P. Teter, D.C. Allan, T.A. Arias, J.D. Joannopoulos: Iterative minimization techniques for ab initio total-energy calculations: Molecular dynamics and conjugate gradients, Rev. Mod. Phys. **64**, 1045 (1992)
16.58 R.M. Martin: *Electronic Structure: Basic Theory and Practical Methods* (Cambridge Univ. Press, Cambridge 2004)
16.59 T.B. Grimley, C. Pisani: Chemisorption theory in the Hartree–Fock approximation, J. Phys. C **7**, 2831 (1974)
16.60 A.R. Williams, P.J. Feibelman, N.D. Lang: Green's-function methods for electronic-structure calculations, Phys. Rev. B **26**, 5433 (1982)
16.61 J. Bormet, J. Neugebauer, M. Scheffler: Chemical trends and bonding mechanisms for isolated adsorbates on Al(111), Phys. Rev. B **49**, 17242 (1994)
16.62 C. Pisani, F. Corá, R. Nada, R. Orlando: Hartree–Fock perturbed-cluster treatment of local defects in crystals I. The EMBED program: General features, Comput. Phys. Commun. **82**, 139 (1994)
16.63 S. Krüger, N. Rosch: The moderately-large-embedded-cluster method for metal surfaces; a density-functional study of atomic adsorption, J. Phys. Condens. Matter **6**, 8149 (1994)
16.64 N. Govind, Y.A. Wang, E.A. Carter: Electronic-structure calculations by first-principles density-based embedding of explicitly correlated systems, J. Chem. Phys. **110**, 7677 (1999)
16.65 J.E. Inglesfield: A method of embedding, J. Phys. C **14**, 3795 (1981)
16.66 M.I. Trioni, G.P. Brivio, S. Crampin, J.E. Inglesfield: Embedding approach to the isolated adsorbate, Phys. Rev. B **53**, 8052 (1996)

16.67 H. Ishida: Surface-embedded Green-function method: A formulation using a linearized-augmented-plane-wave basis set, Phys. Rev. B **63**, 165409 (2001)

16.68 J.E. Inglesfield: *The Embedding Method for Electronic Structure*, 1st edn. (IOP, Bristol 2016)

16.69 G.P. Brivio, G. Butti, S. Caravati, G. Fratesi, M.I. Trioni: Theoretical approaches in adsorption: Alkali adatom investigations, J. Phys. Condens. Matter **19**, 305005 (2007)

16.70 M. Brandbyge, J.-L. Mozos, P. Ordejón, J. Taylor, K. Stokbro: Density-functional method for nonequilibrium electron transport, Phys. Rev. B **65**, 165401 (2002)

16.71 G. Fratesi, C. Motta, M.I. Trioni, G.P. Brivio, D. Sánchez-Portal: Resonant lifetime of core-excited organic adsorbates from first principles, J. Phys. Chem. C **118**, 8775 (2014)

16.72 D. Cvetko, G. Fratesi, G. Kladnik, A. Cossaro, G.P. Brivio, L. Venkataraman, A. Morgante: Ultrafast electron injection into photo-excited organic molecules, Phys. Chem. Chem. Phys. **18**, 8264 (2016)

16.73 P. Persson, M.J. Lundqvist, R. Ernstorfer, W.A. Goddard III, F. Willig: Quantum chemical calculations of the influence of anchor-cum-spacer groups on femtosecond electron transfer times in dye-sensitized semiconductor nanocrystals, J. Chem. Theory Comput. **2**, 441 (2006)

16.74 W. Shockley: On the surface states associated with a periodic potential, Phys. Rev. **56**, 317 (1939)

16.75 I. Tamm: On the possible bound states of electrons on a crystal surface, Phys. Z. Sowjetunion **1**, 733 (1932)

16.76 M.C. Desjonqueres, D. Spanjaard: *Concepts in Surface Physics*, 2nd edn. (Springer, Berlin, Heidelberg 2013)

16.77 H. Lüth: *Solid Surfaces, Interfaces and Thin Films*, 5th edn. (Springer, Berlin, Heidelberg 2010)

16.78 T.B. Grimley: The molecular orbital theory of the interaction between an atom and a crystal surface, Proc. Phys. Soc. **72**, 103 (1958)

16.79 P.O. Gartland, B.J. Slagsvold: Transitions conserving parallel momentum in photoemission from the (111) face of copper, Phys. Rev. B **12**, 4047 (1975)

16.80 S.D. Kevan: Evidence for a new broadening mechanism in angle-resolved photoemission from Cu(111), Phys. Rev. Lett. **50**, 526 (1983)

16.81 S. Caravati, G. Butti, G.P. Brivio, M.I. Trioni, S. Pagliara, G. Ferrini, G. Galimberti, E. Pedersoli, C. Giannetti, F. Parmigiani: Cu(111) and Cu(001) surface electronic states. Comparison between theory and experiment, Surf. Sci. **600**, 3901 (2006)

16.82 A. Zangwill: *Physics at Surfaces* (Cambridge Univ. Press, Cambridge 1988)

16.83 M. Milun, P. Pervan, D.P. Woodruff: Quantum well structures in thin metal films: Simple model physics in reality?, Rep. Prog. Phys. **65**, 99 (2002)

16.84 P.M. Echenique, R. Berndt, E.V. Chulkov, T. Fauster, A. Goldmann, U. Höfer: Decay of electronic excitations at metal surfaces, Surf. Sci. Rep. **52**, 213 (2004)

16.85 N.D. Lang, W. Kohn: Theory of metal surfaces: Induced surface charge and image potential, Phys. Rev. B **7**, 3541 (1972)

16.86 E.V. Chulkov, V.M. Silkin, P.M. Echenique: Image potential states on metal surfaces: Binding energies and wave functions, Surf. Sci. **437**, 330 (1999)

16.87 A. Manchon, H.C. Koo, J. Nitta, S.M. Frolov, R.A. Duine: New perspectives for Rashba spin–orbit coupling, Nat. Mater. **14**, 871 (2015)

16.88 T. Nakazawa, N. Takagi, M. Kawai, H. Ishida, R. Arafune: Rashba splitting in an image potential state investigated by circular dichroism two-photon photoemission spectroscopy, Phys. Rev. B **94**, 115412 (2016)

16.89 G. Onida, L. Reining, A. Rubio: Electronic excitations: Density-functional versus many-body Green's-function approaches, Rev. Mod. Phys. **74**, 601 (2002)

16.90 J. Kliewer, R. Berndt, E.V. Chulkov, V.M. Silkin, P.M. Echenique, S. Crampin: Decay of electronic excitations at metal surfaces, Science **288**, 1399 (2000)

16.91 S.Å. Lindgren, L. Walldén: Cu surface state and Cs valence electrons in photoelectron spectra from the Cu(111)/Cs adsorption system, Solid State Commun. **28**, 283 (1978)

16.92 F.J. Himpsel, J.A. Knapp, D.A. Eastman: Angle resolved photoemission study of the electronic structure of chemisorbed hydrogen on Ni(111), Phys. Rev. B **19**, 2872 (1979)

16.93 S.Å. Lindgren, J. Paul, L. Walldén: Surface state energy shifts by molecular adsorption: Co on clean and Na covered Cu(111), Surf. Sci. **117**, 426 (1982)

16.94 S.-Y. Hong, P.-O. Yeh, I. Lee, J. Yu, J.I. Dadap, C. Nuckolls, R.M. Osgood: Coverage-dependent modification of the surface electronic structure of an organic-semiconductor-adsorbate layer, J. Phys. Chem. C **118**, 6214 (2014)

16.95 A. Bendounan, S. Ait-Ouazzou: Role of the Shockley state in doping of organic molecule monolayer, J. Phys. Chem. C **120**, 11456 (2016)

16.96 P.A. Sloan, S. Sakulsermsuk, R.E. Palmer: Nonlocal desorption of chlorobenzene molecules from the Si(111)(7×7) surface by charge injection from the tip of a scanning tunneling microscope: Remote control of atomic manipulation, Phys. Rev. Lett. **105**, 048301 (2010)

16.97 A. Manchon, H.C. Koo, J. Nitta, S.M. Frolov, R.A. Duine: New perspectives for Rashba spin–orbit coupling, Nat. Mater. **14**, 871 (2015)

16.98 T.B. Grimley: The molecular orbital theory of interaction between an atom and a crystal surface, Proc. Phys. Soc. A **72**, 103 (1958)

16.99 T.B. Grimley: The indirect interaction between atoms or molecules adsorbed on metals, Proc. Phys. Soc. A **90**, 751 (1967)

16.100 D.M. Newns: Self-consistent model of hydrogen chemisorption, Phys. Rev. **178**, 1123 (1969)

16.101 B. Hammer, J.K. Nørskov: Theoretical surface science and catalysis – Calculations and concepts, Adv. Catal. **45**, 71 (2000)
16.102 I. Langmuir: Vapor pressures, evaporation, condensation and adsorption, J. Am. Chem. Soc. **54**, 2798 (1932)
16.103 R.W. Gurney: Theory of electrical double layers in adsorbed films, Phys. Rev. **47**, 479 (1935)
16.104 J. Bormet, J. Neugebauer, M. Scheffler: Chemical trends and bonding mechanisms for isloated adsorbates on Al(111), Phys. Rev. B **49**, 17242 (1994)
16.105 R.D. Diehl, R. McGrath: Current progress in understanding alkali metal adsorption on metal surfaces, J. Phys. Condens. Matter **9**, 951 (1997)
16.106 M.I. Trioni, S. Achilli, E.V. Chulkov: Key ingredients of the alkali atom–metal surface interaction: Chemical bonding versus spectral properties, Prog. Surf. Sci. **88**, 160 (2013)
16.107 A. Cucchetti, S.C. Ying: Diffusion of Na atoms on a Cu(001) surface, Phys. Rev. B **60**, 11110 (1999)
16.108 G. Alexandrowicz, A. Jardine, H. Hedgeland, W. Allison, J. Ellis: Onset of 3D collective surface diffusion in the presence of lateral interactions: Na/Cu(001), Phys. Rev. Lett. **97**, 145103 (2006)
16.109 G. Fratesi, G. Alexandrowicz, M. Trioni, G.P. Brivio, W. Allison: Crucial electronic contributions to measures of surface diffusion by He atom scattering, Phys. Rev. B **77**, 235444 (2008)
16.110 O. Godsi, G. Corem, T. Kravchuk, C. Bertram, K. Morgenstern, H. Hedgeland, A.P. Jardine, W. Allison, J. Ellis, G. Alexandrowicz: How atomic steps modify diffusion and inter-adsorbate forces: Empirical evidence from hopping dynamics in Na/Cu(115), J. Phys. Chem. Lett. **6**, 4165 (2015)
16.111 M. Cavallini, G. Gallinari, L. Menegretti, G. Scoles, U. Valbusa: Rainbow scattering and the intermolecular potential of argon, Chem. Phys. Lett. **7**, 302 (1970)
16.112 G. Boato, P. Cantini, U. Garibaldi, A.C. Levi, R. Spedacini, G.E. Tommei: Diffraction and rainbow in atom surface scattering, J. Phys. C **6**, L394 (1973)
16.113 G. Brusdeylins, R.B. Doak, J.P. Toennies: Measurement of the dispersion relation for Rayleigh surface phonons of Li(100) by inelastic scattering of surface atoms, Phys. Rev. Lett. **46**, 437 (1981)
16.114 G. Fratesi, G. Alexandrowicz, M.I. Trioni, G.P. Brivio, W. Allison: Crucial electronic contributions to measures of surface diffusion by He atom scattering measurement, Phys. Rev. B **77**, 235444 (2008)
16.115 J.L.F. Da Silva, C. Stampfl: Trends in adsorption of noble gases He, Ne, Ar, Kr, and Xe on Pd(111)($\sqrt{3}\times\sqrt{3}$) *R*30°: All-electron density functional calculations, Phys. Rev. B **77**, 045401 (2008)
16.116 K.H. Rieder, G. Parschau, B. Burg: Experimental evidence for anticorrugating effects in He-metal interactions at surfaces, Phys. Rev. Lett. **71**, 1059 (1993)
16.117 M. Petersen, S. Wilke, P. Ruggerone, B. Kohler, M. Scheffler: Scattering of rare-gas atoms at a metal surface: Evidence of anticorrugation of the helium-atom potential energy surface and the surface electron density, Phys. Rev. Lett. **76**, 995 (1994)
16.118 N. Jean, M.I. Trioni, G.P. Brivio, V. Bortolani: Corrugating and anticorrugating static interactions in helium–atom scattering from metals, Phys. Rev. Lett. **92**, 013201 (2004)
16.119 A. Picone, M. Riva, G. Fratesi, A. Brambilla, G. Bussetti, M. Finazzi, L. Duò, F. Ciccacci: Enhanced atom mobility on the surface of a metastable film, Phys. Rev. Lett. **113**, 046102 (2014)
16.120 J.C. Love, L.A. Estroff, J.K. Kriebel, R.G. Nuzzo, G.M. Whitesides: Self-assembled monolayers of thiolates on metals as a form of nanotechnology, Chem. Rev. **105**, 1103 (2005)
16.121 W. Auwärter, D. Écija, F. Klappenberger, J.V. Barth: Porphyrins at interfaces, Nat. Chem. **7**, 105 (2015)
16.122 J.M. Gottfried: Surface chemistry of porphyrins and phthalocyanines, Surf. Sci. Rep. **70**, 259 (2015)
16.123 G. Witte, C. Wöll: Growth of aromatic molecules on solid substrates for applications in organic electronics, J. Mater. Res. **19**, 1889 (2004)
16.124 G.R. Dholakia, M. Meyyappan, A. Facchetti, T.J. Marks: Monolayer to multilayer nanostructural growth transition in n-type oligothiophenes on Au(111) and implications for organic field-effect transistor performance, Nano Lett. **6**, 2447 (2006)
16.125 C.-H. Chao, C.-H. Chan, F.-C. Wu, J.-J. Huang, S.Y. Lien, K.-W. Weng, H.-L. Cheng: Efficient hybrid organic/inorganic photovoltaic cells utilizing n-type pentacene and intrinsic/p-type hydrogenated amorphous silicon, Sol. Energy Mater. Sol. Cells **95**, 2407 (2011)
16.126 V.C. Sundar: Elastomeric transistor stamps: Reversible probing of charge transport in organic crystals, Science **303**, 1644 (2004)
16.127 Y.-Y. Lin, D.I. Gundlach, S.F. Nelson, T.N. Jackson: Pentacene-based organic thin-film transistors, IEEE Trans. Electron Devices **44**, 1325 (1997)
16.128 Y.-Y. Lin, D.I. Gundlach, S.F. Nelson, T.N. Jackson: Stacked pentacene layer organic thin-film transistors with improved characteristics, IEEE Electron Device Lett. **18**, 606 (1997)
16.129 U. Diebold: The surface science of titanium dioxide, Surf. Sci. Rep. **48**, 53 (2003)
16.130 C.L. Pang, R. Lindsay, G. Thornton: Structure of clean and adsorbate-covered single-crystal rutile TiO_2 surfaces, Chem. Rev. **113**, 3887 (2013)
16.131 G. Fratesi, V. Lanzilotto, S. Stranges, M. Alagia, G.P. Brivio, L. Floreano: High resolution NEXAFS of perylene and PTCDI: A surface science approach to molecular orbital analysis, Phys. Chem. Chem. Phys. **16**, 14834 (2014)
16.132 V. Lanzilotto, C. Sanchez-Sanchez, G. Bavdek, D. Cvetko, M.F. Lopez, J.A. Martin-Gago, L. Floreano: Planar growth of pentacene on the dielectric TiO_2(110) surface, J. Phys. Chem. C **115**, 4664 (2011)
16.133 M. Alagia, C. Baldacchini, M.G. Betti, F. Bussolotti, V. Carravetta, U. Ekström, C. Mariani, S. Stranges: Core-shell photoabsorption and photoelectron spectra of gas-phase pentacene: Experiment and theory, J. Chem. Phys. **122**, 124305 (2005)

16.134 G. Fratesi, V. Lanzilotto, L. Floreano, G.P. Brivio: Azimuthal dichroism in near-edge x-ray absorption fine structure spectra of planar molecules, J. Phys. Chem. C **117**, 6632 (2013)

16.135 G. Bavdek, A. Cossaro, D. Cvetko, C. Africh, C. Blasetti, F. Esch, A. Morgante, L. Floreano: Pentacene nanorails on Au(110), Langmuir **24**, 767 (2008)

16.136 A. Baby, G. Fratesi, S.R. Vaidya, L.L. Patera, C. Africh, L. Floreano, G.P. Brivio: Anchoring and bending of pentacene on aluminum (001), J. Phys. Chem. C **119**, 3624 (2015)

16.137 T. Suzuki, D.C. Sorescu, J.T. Yates: The chemisorption of pentacene on Si(001)-2×1, Surf. Sci. **600**, 5092 (2006)

16.138 H.-K. Lee, J.-H. Han, K.-J. Kim, T.-H. Kang, B. Kim: Configuration of pentacene ($C_{22}H_{14}$) films on Si(100)-2×1 studied by NEXAFS, Surf. Sci. **601**, 1456 (2007)

16.139 T. Shimada, H. Nogawa, T. Hasegawa, R. Okada, H. Ichikawa, K. Ueno, K. Saiki: Bulk-like pentacene epitaxial films on hydrogen-terminated Si(111), Appl. Phys. Lett. **87**, 061917 (2005)

16.140 K.P. Weidkamp, R.M. Tromp, R.J. Hamers: Epitaxial growth of large pentacene crystals on Si(001) surfaces functionalized with molecular monolayers, J. Phys. Chem. C **111**, 16489 (2007)

16.141 P.G. Schroeder, C.B. France, J.B. Park, B.A. Parkinson: Energy level alignment and two-dimensional structure of pentacene on Au(111) surfaces, J. Appl. Phys. **91**, 3010 (2002)

16.142 M. Pedio, B. Doyle, N. Mahne, A. Giglia, F. Borgatti, S. Nannarone, S.K.M. Henze, R. Temirov, F.S. Tautz, L. Casalis, R. Hudej, M.F. Danisman, B. Nickel: Growth of pentacene on Ag(111) surface: A NEXAFS study, Appl. Surf. Sci. **254**, 103 (2007)

16.143 D. Lüftner, T. Ules, E.M. Reinisch, G. Koller, S. Soubatch, F.S. Tautz, M.G. Ramsey, P. Puschnig: Imaging the wave functions of adsorbed molecules, Proc. Natl. Acad. Sci. U.S.A. **111**, 605 (2014)

16.144 K. Toyoda, I. Hamada, K. Lee, S. Yanagisawa, Y. Morikawa: Density functional theoretical study of pentacene/noble metal interfaces with van der Waals corrections: Vacuum level shifts and electronic structures, J. Chem. Phys. **132**, 134703 (2010)

16.145 A. Ferretti, C. Baldacchini, A. Calzolari, R. Di Felice, A. Ruini, E. Molinari, M. Betti: Mixing of electronic states in pentacene adsorption on copper, Phys. Rev. Lett. **99**, 046802 (2007)

16.146 K. Müller, A.P. Seitsonen, T. Brugger, J. Westover, T. Greber, T. Jung, A. Kara: Electronic structure of an organic/metal interface: Pentacene/Cu(110), J. Phys. Chem. C **116**, 23465 (2012)

16.147 M. Simeoni, S. Picozzi, B. Delley: An ab-initio study of pentacene on aluminum (100) surface, Surf. Sci. **562**, 43 (2004)

16.148 E. Molteni, G. Cappellini, G. Onida, G. Fratesi: Optical properties of organically functionalized silicon surfaces: Uracil-like nucleobases on Si(001), Phys. Rev. B **95**, 075437 (2017)

16.149 A. Baby, H. Lin, G.P. Brivio, L. Floreano, G. Fratesi: Core-level spectra and molecular deformation in adsorption: V-shaped pentacene on Al(001), Beilstein J. Nanotechnol. **6**, 2242 (2015)

16.150 P. Bagus, D. Käfer, G. Witte, C. Wöll: Work function changes induced by charged adsorbates: Origin of the polarity asymmetry, Phys. Rev. Lett. **100**, 126101 (2008)

16.151 G. Fratesi: Potential energy surface of alkali atoms adsorbed on Cu(001), Phys. Rev. B **80**, 045422 (2009)

16.152 C.A. Papageorgopoulos: Studies of separate adsorption and coadsorption of Cs and O_2 on Cu(100), Phys. Rev. B **25**, 3740 (1982)

16.153 G. Fratesi, A. Pace, G.P. Brivio: Short-range lateral interactions and depolarization of Na atoms on Cu surfaces, J. Phys. Condens. Matter **22**, 304005 (2010)

16.154 D.A. MacLaren, C. Huang, A.C. Levi, W. Allison: Coverage-dependent quantum versus classical scattering of thermal neon atoms from Li/Cu(100), J. Chem. Phys. **129**, 094706 (2008)

16.155 G. Fratesi: Depolarization and bonding in quasi-one-dimensional Na structures on Cu(001), Phys. Rev. B **84**, 155424 (2011)

16.156 A.P. Graham, J.P. Toennies: Helium-atom diffraction study of the submonolayer structures of sodium on Cu(001), Phys. Rev. B **56**, 15378 (1997)

16.157 C. Huang, G. Fratesi, D.A. MacLaren, W. Luo, G.P. Brivio, W. Allison: Charge redistribution in the formation of one-dimensional lithium wires on Cu(001), Phys. Rev. B **82**, 081413 (2010)

16.158 P.K.J. Wong, W. Zhang, G. van der Laan, M.P. de Jong: Hybridization-induced charge rebalancing at the weakly interactive $C_{60}/Fe_3O_4(001)$ spinterface, Org. Electron. **29**, 39 (2016)

16.159 Y.-H. Chu, C.-H. Hsu, C.-I. Lu, H.-H. Yang, T.-H. Yang, C.-H. Luo, K.-J. Yang, S.-H. Hsu, G. Hoffmann, C.-C. Kaun, M.-T. Lin: Spin-dependent molecule symmetry at a pentacene–Co spinterface, ACS Nano **9**, 7027 (2015)

16.160 H. Wende, M. Bernien, J. Luo, C. Sorg, N. Ponpandian, J. Kurde, J. Miguel, M. Piantek, X. Xu, P. Eckhold, W. Kuch, K. Baberschke, P.M. Panchmatia, B. Sanyal, P.M. Oppeneer, O. Eriksson: Substrate-induced magnetic ordering and switching of iron porphyrin molecules, Nat. Mater. **6**, 516 (2007)

16.161 S. Casolo, O.M. Løvvik, R. Martinazzo, G.F. Tantardini: Understanding adsorption of hydrogen atoms on graphene, J. Chem. Phys. **130**, 054704 (2009)

16.162 E.J.G. Santos, A. Ayuela, D. Sánchez-Portal: Universal magnetic properties of sp^3-type defects in covalently functionalized graphene, New J. Phys. **14**, 043022 (2012)

16.163 H. Lin, G. Fratesi, G.P. Brivio: Graphene magnetism induced by covalent adsorption of aromatic radicals, Phys. Chem. Chem. Phys. **17**, 2210 (2014)

16.164 E.J.G. Santos, D. Sánchez-Portal, A. Ayuela: Magnetism of covalently functionalized carbon nanotubes, Appl. Phys. Lett. **99**, 062503 (2011)

16.165 R. Martinazzo: Atomic-scale defects and impurities in graphene. In: *Graphene Science Handbook. Nanostructure and Atomic Arrangement*, ed. by M. Aliofkhazraei, N. Ali, W.I. Milne, C.S. Ozkan, S. Mitura, J.L. Gervasoni (CRC, Boca Raton 2016)
16.166 J.C. Meyer, C.O. Girit, M.F. Crommie, A. Zettl: Imaging and dynamics of light atoms and molecules on graphene, Nature **454**, 319 (2008)
16.167 R. Balog, B. Jørgensen, L. Nilsson, M. Andersen, E. Rienks, M. Bianchi, M. Fanetti, E. Lægsgaard, A. Baraldi, S. Lizzit, Z. Sljivancanin, F. Besenbacher, B. Hammer, T.G. Pedersen, P. Hofmann, L. Hornekær: Bandgap opening in graphene induced by patterned hydrogen adsorption, Nat. Mater. **9**, 315 (2010)
16.168 J. Balakrishnan, G. Kok Wai Koon, M. Jaiswal, A.H. Castro Neto, B. Özyilmaz: Colossal enhancement of spin-orbit coupling in weakly hydrogenated graphene, Nat. Phys. **9**, 284 (2013)
16.169 A.A. Komlev, T.L. Makarova, E. Lahderanta, P.V. Semenikhin, A.I. Veinger, T.V. Tisnek, G. Magnani, G. Bertoni, D. Pontiroli, M. Ricco: Magnetism of aniline modified graphene-based materials, J. Magn. Magn. Mater. **415**, 45 (2016)
16.170 J.B. Taylor, L.C. Mayor, J.C. Swarbrick, J.N. O'Shea, C. Isvoranu, J. Schnadt: Adsorption and charge transfer dynamics of bi-isonicotinic acid on Au(111), J. Chem. Phys. **127**, 134707 (2007)
16.171 A. Ravikumar, A. Baby, H. Lin, G.P. Brivio, G. Fratesi: Femtomagnetism in graphene induced by core level excitation of organic adsorbates, Sci. Rep. **6**, 24603 (2016)

Gian P. Brivio (deceased)

Gian Paolo Brivio was a Professor at the University of Milano-Bicocca(Italy) in Physics of Matter. His research focused on theoretical problems in surface and materials science. Specifically the investigation of magnetic effects in the interaction of molecules with graphene and adsorption of organic molecules on solids focusing on spectroscopic properties, excited states, and their lifetimes. He founded the European Doctoral Network in Physics and Chemistry of AdvancedMaterials (PCAM) in 2006. He had been Adjunct Professor at University Southern Denmark since 2015.

Guido Fratesi

Physics Department
University of Milano
Milano, Italy
guido.fratesi@unimi.it

Guido Fratesi is Associate Professor in Physics of Matter, the University of Milano. His research addresses surface systems and two-dimensional materials from first-principles theoretical approaches, especially for the properties of adsorbed organic molecules in relation to electron core-level techniques. He was co-organizer of the 17th Workshop on Dynamical Phenomena at Surfaces (2016) and of the 23rd and 24th Workshops of the European Theoretical Spectroscopy Facility (2018 and 2019).

Collective Part D

Part D Collective And Single Particle Excitations

Part D deals with collective and single-particle excitations at the surfaces of conductors. These excitations determine responses to photon and electron beams, energy transfer, and screening. As such, they impact on photoemission intensities and optical properties. Collective excitation at a surface is known as a surface plasmon (SP), which—in contrast to volume plasmons—corresponds to a transversally polarized mode. As such, the SP dispersion mixes with the light cone, giving rise to surface plasmon polaritons (SPPs) that are characterized by a lower group velocity (and hence a shorter wavelength) than light. SPPs may be excited by photons whenever the missing momentum is provided by a grating or surface disorder. They determine the Mie resonance at nanosized noble-metal particles, which produces the bright colors of the glass used in medieval cathedrals. SPPs are at the heart of plasmonic applications, including surface plasmon resonance spectroscopy and energy harvesting in solar cells.

Electronic excitations at metallic surfaces are important deexcitation channels for adsorbate vibrations and are responsible for nonadiabatic effects in adsorption processes, thus influencing chemical reactions. In contrast, SPs are too high in energy to contribute to energy dissipation under normal conditions. A notable exception is the recently discovered acoustic surface plasmon, which corresponds to the counterphase motion of the electrons of a Shockley surface state or a two-dimensional material such as graphene and an underlying three-dimensional electron gas. This mode is characterized by a much lower group velocity than polaritons, and therefore extends over a larger volume of phase space.

Chapter 17 is devoted to the theoretical underpinnings of the dielectric responses of quasi two-dimensional crystals to incident electron and photon beams, and covers a wide set of electronic and optical phenomena, such as the excitation of monopole, multipole, two-dimensional, and acoustic surface plasmons. First, the conventional formalism of the energy-loss functions is introduced, after which it is shown that a more general approach that takes into account the kinematics of the probing particle in the excitation process is required. Finally, the role of nonlocality in the response is addressed. This nonlocality leads to strong enhancement of the microscopic electric field at the surface, thus providing an explanation for photoyield data and multipole plasmon excitations.

Chapter 18 introduces the concepts of SP propagation and localized SP resonance. The surface plasmon frequency is determined by the bulk electron density, which typically leads to ultraviolet wavelengths. On the other hand, SP dispersion at wavelengths much smaller than those of light is dictated by surface properties, particularly the position of the induced charge with respect to the geometric surface plane. Since the latter sits outside the surface, the SP energy decreases with wavevector. The opposite happens for noble metal surfaces, as interband transitions displace the SP to lower frequencies, and this effect becomes less efficient with wavevector. Nanostructuring and adsorption-induced reconstructions are shown to affect the SP dispersion as well.

Chapter 19 covers plasmons in one- and two-dimensional (1-D and 2-D, respectively) systems. In contrast to ordinary surface plasmons of metallic bulk materials, the energy of a plasmon in a 1-D or 2-D system vanishes in the long wavelength limit, thus covering all energies from terahertz to the near-infrared, while the wavelength ranges from mesoscopic to nanometric. In the first part of the chapter, plasmons in 2-D systems are reviewed, including acoustic surface plasmons, which have a linear rather than a square-root-like dispersion. In the second part of the chapter, plasmon excitations in 1-D (linear chains) are presented, and it is shown that the slope of the dispersion is affected by the nature of the substrate and the separation between neighboring monoatomic chains.

Chapter 20 explores the theory of interband transitions, focusing on state-of-the-art ab initio methods with an emphasis on semiconductor surfaces. After providing a general theoretical framework for surface spectroscopies, the chapter reviews the main ab initio approaches based on density functional theory (DFT), Green's function (many-body theory or the GW method), the Bethe–Salpeter equation, and time-dependent DFT. Many examples of calculated spectra that are relevant to experimental electron spectroscopy of clean and modified surfaces of several semiconductors are included. Attention is also paid to the differences involved in extracting exciton binding energies using the GW, Bethe–Salpeter, and time-dependent DFT approaches. Despite theoretical and experimental difficulties, it is possible to match the surface interband transition spectrum to the surface morphology with high levels of accuracy and sensitivity to reconstructions.

17. Electron Energy-Loss and Photoelectron Spectroscopies of Surfaces and Two-Dimensional Crystals

Vladimir U. Nazarov, Eugene E. Krasovskii, Vyacheslav M. Silkin

Dielectric response of crystal surfaces and quasi two-dimensional (Q2-D) crystals to incident electrons and photons underlies a variety of electronic and optical phenomena, such as the excitation of monopole, multipole, two-dimensional (2-D), and acoustic plasmons, which have vast implications for optical and electron spectroscopies. This chapter covers model and electronic structure approaches to dynamic dielectric screening and discusses the development of the field from the pioneering works by R.H. Ritchie and P. Feibelman up to recent ab-initio developments. Starting with the quantum-mechanical expression for the microscopic dielectric response (Sect. 17.1), we explain the emergence of surface plasmon modes and discuss their structure based on simplified model systems. We further introduce an ab-initio approach to calculate the response function for realistic systems. We discuss how the excitations manifest themselves in the inelastic scattering of electrons reflected from a solid surface or a Q2-D crystal (Sect. 17.2), at first confining ourselves to the conventional formalism of energy-loss functions. We then demonstrate the necessity to go beyond this formalism and present the theory of the inelastic scattering of electrons, which takes into account the effect of the kinematics of the probing particle on the excitation process (Sect. 17.3). Finally, we show how the nonlocal response to the incident light leads to a strong enhancement of the microscopic electric field at the surface and how the total exciting field can be included into an ab-initio one-step photoemission theory to describe photoyield enhancement (Sects. 17.6 and 17.7).

M. Rocca, T.S. Rahman, L. Vattuone (Eds.), *Springer Handbook of Surface Science*, Springer Handbooks,
https://doi.org/10.1007/978-3-030-46906-1_17

17.1 Probing Solid Targets with Electrons and Light: What Kind of a Theory Do We Need?

Electron energy-loss spectroscopy (EELS) has by now developed into a very powerful experimental method for studying objects ranging from bulk solids (mimicked by sufficiently thick films), through thin films and surfaces of semi-bulk materials, to nano-objects of two and lower dimensionality. In the literature, the term EELS refers to two experimental techniques that are very different in their instrumental implementation. These are the more traditional high-resolution electron energy-loss spectroscopy (HREELS) [17.1, 2] and the newer version of the EELS in the transmission electron microscope (TEM) [17.3]. Fundamentally, both methods employ electron beams incident onto a target, which, after the inelastic scattering, are analyzed with respect to energy and momentum. In HREELS, electrons reflected from a solid surface are collected, with the incident energies usually ranging from several to several hundred eV. On the other hand, EELS in TEM employs incident energies in the range from tens to hundreds of keV, and it uses the transmission regime of electron scattering. Application of HREELS can be divided, in its turn, into two principal categories: those studying *electronic* excitations (with the energy losses roughly on the scale of 0.1−10 eV) and those concerned with *phononic* processes (with the losses roughly of the order of 10 meV). In the following, we will be exclusively dealing with electronic excitations, referring the reader interested in phonons to the corresponding literature (see [17.4–7], where the impact regime of the HREELS of surface phonons is considered).

The theory has almost always considered electronic excitations in HREELS and in the transmission EELS in TEM from very different perspectives. HREELS was traditionally treated within the concept of the *dipole* regime of scattering, while EELS in TEM was described within the *impact* regime. The former is characteristic of the inelastic scattering outside a target via long-range Coulomb interaction, while the latter concerns the short-range collisions with electrons of the target [17.8]. A notable exception from this picture has, however, been promoted in an approach founded in [17.9–11], which takes account of both the inelastic and elastic aspects of electron scattering at a solid target and, by this, does not require the artificial division of the scattering into the two different categories. Below, we adopt the latter approach and show that the two regimes can both be treated on the same footing, once a general expression for the double differential cross section of the electron scattering has been derived [17.9], from which those regimes follow as specific cases. Moreover, this approach reveals situations when the dipole and impact regimes intermix, thereby losing their distinct meaning, while the general formula holds and produces a consistent description of EELS [17.12, 13].

The methodology of this chapter is top down. In particular, results are not presented in chronological order. We first derive our main general expression for the inelastic double differential cross section of a charged projectile (electron, in particular) scattering on a solid (or atomic) target. We then demonstrate how this general result reduces to the known quantities (bulk and surface energy-loss functions, etc.) for particular targets and scattering geometries. We also emphasize cases when such a reduction is impossible and the scattering formalism must be used in its full extent. We will use atomic units ($\hbar = e = m = 1$) unless otherwise stated.

17.2 Inelastic Scattering of Electrons: General Formalism

The purpose of this section is to derive the differential cross section of an electron inelastic scattering on an arbitrary many (or few)-body system, representing it *in terms of the density-response function*. For simplicity, below we consider the zero temperature case. The interacting density-response function $\chi(\boldsymbol{r}, \boldsymbol{r}', \omega)$ determines the linear response of the particle density $n^{(1)}(\boldsymbol{r}, \omega)$ to the externally applied potential $v^{(1)}_{\rm ext}(\boldsymbol{r}, \omega)$, and it is defined by

$$n^{(1)}(\boldsymbol{r}, \omega) = \int \chi(\boldsymbol{r}, \boldsymbol{r}', \omega) v^{(1)}_{\rm ext}(\boldsymbol{r}', \omega) {\rm d}\boldsymbol{r}' \,. \qquad (17.1)$$

Below we will need an expression for χ in terms of the complete set of the eigenfunctions $|n\rangle$ and eigenvalues E_n of the many-body system under consideration, which, for self-containedness, we shortly derive as follows. We write down the Liouville equation [17.14]

$${\rm i}\frac{\partial \hat{\rho}}{\partial t} = \left[\hat{H}, \hat{\rho}\right], \qquad (17.2)$$

where

$$\hat{H} = \sum_{i=1}^{N}\left[-\frac{1}{2}\Delta_i + v_{\rm ext}(\boldsymbol{r}_i, t)\right] + \sum_{i<j}^{N}\frac{1}{|\boldsymbol{r}_i - \boldsymbol{r}_j|} \qquad (17.3)$$

is the time-dependent many-body Hamiltonian, and $\hat{\rho}$ is the many-body density matrix. Assuming the

time-dependent part of the external potential to be weak and assuming it to be monochromatic $v_{\rm ext}^{(1)}(\boldsymbol{r},t) = v_{\rm ext}^{(1)}(\boldsymbol{r},\omega)\mathrm{e}^{-\mathrm{i}\omega t}$, we linearize (17.2) to

$$\omega\hat{\rho}^{(1)} = \left[\hat{H}^{(0)},\hat{\rho}^{(1)}\right] + \left[\hat{H}^{(1)},\hat{\rho}^{(0)}\right], \tag{17.4}$$

where

$$\hat{H}^{(0)} = \sum_{i=1}^{N}\left[-\frac{1}{2}\Delta_i + v_{\rm ext}^{(0)}(\boldsymbol{r}_i)\right] + \sum_{i<j}^{N}\frac{1}{|\boldsymbol{r}_i-\boldsymbol{r}_j|}\,, \tag{17.5}$$

$$\hat{H}^{(1)} = \sum_{i=1}^{N} v_{\rm ext}^{(1)}(\boldsymbol{r}_i,\omega)\,. \tag{17.6}$$

Taking matrix elements of (17.4) between the many-body states $\langle n|$ and $|m\rangle$, we find for the perturbation of the density matrix

$$\langle n|\hat{\rho}^{(1)}|m\rangle = \frac{\delta_{m0}-\delta_{n0}}{E_m-E_n+\omega+\mathrm{i}\eta}\langle n|\hat{H}^{(1)}|m\rangle\,, \tag{17.7}$$

where an infinitesimal imaginary quantity $\mathrm{i}\eta$ has been added to the frequency to ensure the proper decay of the perturbation at $t=-\infty$.

The density perturbation is the trace (spur) of the density operator

$$\hat{n}(\boldsymbol{r}) = \sum_{i=1}^{N}\delta(\boldsymbol{r}_i-\boldsymbol{r}) \tag{17.8}$$

taken with the perturbation of the density matrix of (17.7). Therefore,

$$\begin{aligned} n^{(1)}(\boldsymbol{r},\omega) &= \mathrm{Sp}\left[\hat{\rho}^{(1)}\hat{n}\right] \\ &= \sum_{nm}\frac{\delta_{m0}-\delta_{n0}}{E_m-E_n+\omega+\mathrm{i}\eta}\langle m|\hat{n}(\boldsymbol{r})|n\rangle\langle n|\hat{H}^{(1)}|m\rangle \\ &= \int\sum_{nm}\frac{\delta_{m0}-\delta_{n0}}{E_m-E_n+\omega+\mathrm{i}\eta}\langle m|\hat{n}(\boldsymbol{r})|n\rangle\langle n|\hat{n}(\boldsymbol{r}')|m\rangle \\ &\quad\times v_{\rm ext}^{(1)}(\boldsymbol{r}',\omega)\mathrm{d}\boldsymbol{r}'\,. \end{aligned} \tag{17.9}$$

Comparing (17.9) and (17.1), we conclude that

$$\chi(\boldsymbol{r},\boldsymbol{r}',\omega) = \sum_{nm}\frac{\delta_{m0}-\delta_{n0}}{E_m-E_n+\omega+\mathrm{i}\eta} \times\langle m|\hat{n}(\boldsymbol{r})|n\rangle\langle n|\hat{n}(\boldsymbol{r}')|m\rangle\,, \tag{17.10}$$

which can be split into the reactive and the absorptive parts

$$\chi(\boldsymbol{r},\boldsymbol{r}',\omega) = \chi^{\rm R}(\boldsymbol{r},\boldsymbol{r}',\omega) + \mathrm{i}\chi^{\rm A}(\boldsymbol{r},\boldsymbol{r}',\omega)\,, \tag{17.11}$$

$$\chi^{\rm R}(\boldsymbol{r},\boldsymbol{r}',\omega) = \mathcal{P}\sum_{nm}\frac{\delta_{m0}-\delta_{n0}}{E_m-E_n+\omega} \times\langle m|\hat{n}(\boldsymbol{r})|n\rangle\langle n|\hat{n}(\boldsymbol{r}')|m\rangle\,, \tag{17.12}$$

$$\chi^{\rm A}(\boldsymbol{r},\boldsymbol{r}',\omega) = \pi\sum_{nm}(\delta_{n0}-\delta_{m0})\delta(E_m-E_n+\omega) \times\langle m|\hat{n}(\boldsymbol{r})|n\rangle\langle n|\hat{n}(\boldsymbol{r}')|m\rangle\,, \tag{17.13}$$

where $\mathcal{P}$ denotes the principal value. If, as we will always assume below, there is no magnetic field involved, $|n\rangle$ and $|n\rangle^*$ are eigenfunctions with the same eigenenergies E_n, from which it follows that

$$\chi^{\rm R}(\boldsymbol{r},\boldsymbol{r}',\omega) = \mathrm{Re}[\chi(\boldsymbol{r},\boldsymbol{r}',\omega)]\,, \tag{17.14}$$

$$\chi^{\rm A}(\boldsymbol{r},\boldsymbol{r}',\omega) = \mathrm{Im}[\chi(\boldsymbol{r},\boldsymbol{r}',\omega)]\,, \tag{17.15}$$

and

$$\chi(\boldsymbol{r}',\boldsymbol{r},\omega) = \chi(\boldsymbol{r},\boldsymbol{r}',\omega)\,. \tag{17.16}$$

17.2.1 Distorted-Waves Approach

The problem of the inelastic reflection of electrons at the surface cannot be solved within the Born approximation, since the reflection of electrons is the result of interaction with the lattice, which cannot be treated as weak.

Let us consider the scattering process schematically shown in Fig. 17.1. A projectile is elastically scattered by an atom or ion of the solid, and then it escapes into vacuum. While passing in the solid, it can suffer an inelastic scattering at the electron subsystem. We write down the many-body Hamiltonian of the target–projectile (the latter is assumed to be electron) system as

$$\hat{H} = \hat{H}_{\rm T} + \hat{H}_{\rm P} + \hat{H}_{\rm TP}\,, \tag{17.17}$$

$$\hat{H}_{\rm T} = \sum_{i=1}^{N}\left[-\frac{1}{2}\Delta_i + v_{\rm ext}(\boldsymbol{r}_i)\right] + \sum_{i<j}^{N}\frac{1}{|\boldsymbol{r}_i-\boldsymbol{r}_j|}\,, \tag{17.18}$$

$$\hat{H}_{\rm P} = -\frac{1}{2}\Delta + v_{\rm ext}(\boldsymbol{r})\,, \tag{17.19}$$

$$\hat{H}_{\rm TP} = \sum_{i=1}^{N}\frac{1}{|\boldsymbol{r}-\boldsymbol{r}_i|}\,. \tag{17.20}$$

In (17.18)–(17.20), $\boldsymbol{r}_i$ and $\boldsymbol{r}$ are positions of the electrons of the target and of the projectile, respectively.

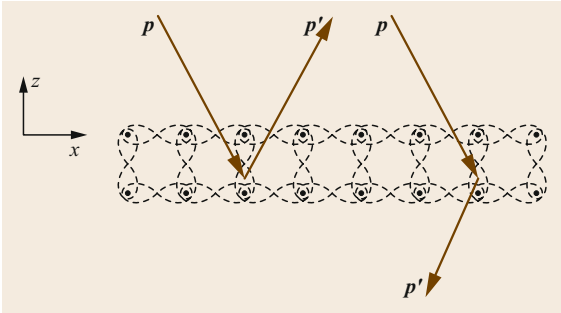

Fig. 17.1 Reflection and transmission geometries of the EELS experiment

Let us write down the differential cross section for an electron scattered from $|\boldsymbol{p}\rangle$ into $|\boldsymbol{p}'\rangle$ state with the transition of the solid from the ground state into an excited state of a complete orthonormal set of the eigenstates of the many-body system $|n\rangle$ [17.15]

$$\frac{\mathrm{d}\sigma}{\mathrm{d}\boldsymbol{p}'}(\boldsymbol{p}', n \leftarrow \boldsymbol{p}, 0) = \frac{(2\pi)^4}{p}\delta(E' - E)|\mathbf{t}(\boldsymbol{p}', n \leftarrow \boldsymbol{p}, 0)|^2 , \tag{17.21}$$

where E and E' are the total energies of the system before and after the collision, and $\mathbf{t}$ is the T-matrix on the energy surface [17.15] corresponding to the Hamiltonian (17.17). (The concept of $\mathbf{t}$-matrix is basic to the theory of both elastic and inelastic scattering [17.15]. Without going too much into theoretical details, for us it is important that (i) the differential cross section is quite generally expressed by the $\mathbf{t}$-matrix on the energy shell ($E = E'$) by (17.21), and (ii) $\mathbf{t}$-matrix itself can be conveniently expressed in the distorted-wave approximation by (17.25).) Let us assume that:

(i) The problem of the single-particle (elastic) scattering of the projectile can be solved exactly or to some good approximation with the Hamiltonian

$$\hat{H}_\mathrm{P}^0 = -\frac{1}{2}\Delta + V^0(\boldsymbol{r}) = -\frac{1}{2}\Delta + v_\mathrm{ext}(\boldsymbol{r}) + v^0(\boldsymbol{r}) . \tag{17.22}$$

At this point, we do not specify the potential $v^0(\boldsymbol{r})$, deferring this until later.

(ii) The potential

$$V^1 = \sum_{i=1}^{N} \frac{1}{|\boldsymbol{r} - \boldsymbol{r}_i|} - v^0(\boldsymbol{r}) \tag{17.23}$$

can be considered *weak*.

Then, according to (17.17),

$$\hat{H} = \hat{H}_\mathrm{T} + \hat{H}_\mathrm{P}^0 + V^1 . \tag{17.24}$$

We will consider V^1 as a perturbation and will solve the scattering problem in the first Born approximation with respect to V^1. Then, accounting for the perturbation of the first order, we obtain in the distorted-waves approximation [17.15]

$$\mathbf{t}(\boldsymbol{p}', n \leftarrow \boldsymbol{p}, 0) = \mathbf{t}^0(\boldsymbol{p}', n \leftarrow \boldsymbol{p}, 0) + \langle(\boldsymbol{p}', n)^{-0}|V^1|(\boldsymbol{p}, 0)^{+0}\rangle , \tag{17.25}$$

where $\mathbf{t}^0$ is $\mathbf{t}$ with the perturbation V^1 neglected,

$$|(\boldsymbol{p}, n)^{\pm 0}\rangle = \Omega_\pm|(\boldsymbol{p}, n)\rangle ,$$

where $\Omega_{\pm 0}$ are the Möller's operators of the scattering problem without perturbation [17.15], and $|\boldsymbol{p}\rangle$ are plane waves.

From here on, we will be interested in the scattering into the inelastic channel $|n\rangle \neq |0\rangle$ only. Then, since the solid is excited by the external perturbation, the first term in (17.25) is zero. Furthermore, if there is no perturbation, the scattering of the electron at the target does not depend on the electron subsystem, which leads to

$$|(\boldsymbol{p}, n)^{\pm 0}\rangle = |\boldsymbol{p}^\pm\rangle|n\rangle , \tag{17.26}$$

where $|\boldsymbol{p}^\pm\rangle$ are solutions of the Lippmann–Schwinger equation [17.15]

$$|\boldsymbol{p}^\pm\rangle = |\boldsymbol{p}\rangle + G^0\left(\frac{p^2}{2} \pm i0_+\right)V^0\,|\boldsymbol{p}^\pm\rangle . \tag{17.27}$$

Here, G^0 is the Green's function of a free particle. We can write by the use of (17.25) and (17.23)

$$\mathbf{t}(\boldsymbol{p}', n \leftarrow \boldsymbol{p}, 0) = \int \frac{\rho^*(\boldsymbol{r})\langle n|\hat{n}(\boldsymbol{r}')|0\rangle}{|\boldsymbol{r} - \boldsymbol{r}'|}\mathrm{d}\boldsymbol{r}\mathrm{d}\boldsymbol{r}' , \tag{17.28}$$

where

$$\rho(\boldsymbol{r}) = \langle \boldsymbol{r}|\boldsymbol{p}^+\rangle^* \langle \boldsymbol{r}|\boldsymbol{p}'^-\rangle . \tag{17.29}$$

Substituting (17.28) into (17.21), we have

$$\frac{\mathrm{d}\sigma}{\mathrm{d}\boldsymbol{p}'}(\boldsymbol{p}', n \leftarrow \boldsymbol{p}, 0) = \frac{(2\pi)^4}{p}\delta\left(\frac{p'^2}{2} + E_n - \frac{p^2}{2} - E_0\right) \times \int \frac{\rho^*(\boldsymbol{r})\langle n|\hat{n}(\boldsymbol{r}')|0\rangle}{|\boldsymbol{r} - \boldsymbol{r}'|}\frac{\rho(\boldsymbol{r}_1)\langle 0|\hat{n}(\boldsymbol{r}_1')|n\rangle}{|\boldsymbol{r}_1 - \boldsymbol{r}_1'|}\mathrm{d}\boldsymbol{r}\mathrm{d}\boldsymbol{r}'\mathrm{d}\boldsymbol{r}_1\mathrm{d}\boldsymbol{r}_1' , \tag{17.30}$$

where E_n are the energies of the electron subsystem in the corresponding states.

Regardless of the final state of the solid, the differential cross section is obtained from (17.30) by the summation over $|n\rangle$. This gives

$$\frac{\mathrm{d}\sigma}{\mathrm{d}\boldsymbol{p}'}(\boldsymbol{p}' \leftarrow \boldsymbol{p}) = \frac{(2\pi)^4}{p} \sum_n \delta\left(\frac{p'^2}{2} + E_n - \frac{p^2}{2} - E_0\right) \times \int \frac{\rho^*(\boldsymbol{r})\langle n|\hat{n}(\boldsymbol{r}')|0\rangle}{|\boldsymbol{r}-\boldsymbol{r}'|} \frac{\rho(\boldsymbol{r}_1)\langle 0|\hat{n}(\boldsymbol{r}_1')|n\rangle}{|\boldsymbol{r}_1-\boldsymbol{r}_1'|} \mathrm{d}\boldsymbol{r}\mathrm{d}\boldsymbol{r}'\mathrm{d}\boldsymbol{r}_1\mathrm{d}\boldsymbol{r}_1' \,. \tag{17.31}$$

On the other hand, with the use of (17.13), we can write

$$\chi^{\mathrm{A}}(\boldsymbol{r},\boldsymbol{r}',\omega) = \pi \sum_n \delta(E_n - E_0 + \omega)\langle n|\hat{n}(\boldsymbol{r})|0\rangle\langle 0|\hat{n}(\boldsymbol{r}')|n\rangle - \pi \sum_n \delta(E_0 - E_n + \omega)\langle 0|\hat{n}(\boldsymbol{r})|n\rangle\langle n|\hat{n}(\boldsymbol{r}')|0\rangle \,,$$

or, for $\omega > 0$ and taking into account that $E_n > E_0$,

$$\chi^{\mathrm{A}}(\boldsymbol{r},\boldsymbol{r}',\omega > 0) = -\pi \sum_n \delta(E_0 - E_n + \omega) \times \langle 0|\hat{n}(\boldsymbol{r})|n\rangle\langle n|\hat{n}(\boldsymbol{r}')|0\rangle \,. \tag{17.32}$$

Combining (17.31) and (17.32) with (17.15) and (17.16), we can write

$$\frac{\mathrm{d}\sigma}{\mathrm{d}\boldsymbol{p}'}(\boldsymbol{p}' \leftarrow \boldsymbol{p}) = -\frac{16\pi^3}{p} \times \mathrm{Im}\left(\int \frac{\rho^*(\boldsymbol{r})\chi(\boldsymbol{r}',\boldsymbol{r}_1',\omega)\rho(\boldsymbol{r}_1)}{|\boldsymbol{r}-\boldsymbol{r}'||\boldsymbol{r}_1-\boldsymbol{r}_1'|}\mathrm{d}\boldsymbol{r}\mathrm{d}\boldsymbol{r}'\mathrm{d}\boldsymbol{r}_1\mathrm{d}\boldsymbol{r}_1'\right), \tag{17.33}$$

where

$$\omega = \frac{p^2 - p'^2}{2} \,.$$

Equation (17.33) can be rewritten in the form of the double differential cross-section

$$\frac{\mathrm{d}^2\sigma}{\mathrm{d}\omega\mathrm{d}\Omega}(\boldsymbol{p}' \leftarrow \boldsymbol{p}) = -\frac{16\pi^3 p'}{p} \times \mathrm{Im}\left(\int \frac{\rho^*(\boldsymbol{r})\chi(\boldsymbol{r}',\boldsymbol{r}_1',\omega)\rho(\boldsymbol{r}_1)}{|\boldsymbol{r}-\boldsymbol{r}'||\boldsymbol{r}_1-\boldsymbol{r}_1'|}\mathrm{d}\boldsymbol{r}\mathrm{d}\boldsymbol{r}'\mathrm{d}\boldsymbol{r}_1\mathrm{d}\boldsymbol{r}_1'\right), \tag{17.34}$$

where $\mathrm{d}\Omega$ is the element of the solid angle. Equation (17.34) is the main result of this section. It is instructive to note that, since (17.34) relates the differential cross section of the inelastic scattering of the projectile to the absorption part of the density-response function, it is a variant of the fluctuation-dissipation theorem [17.16]. Another observation is that in (17.34), $\rho(\boldsymbol{r})$, given by (17.29) and (17.27), plays a role of a complex-valued charge density, which both excites our system and experiences the effect of its excitation.

At this point, we make a connection to the pretime-dependent density functional theory (TDDFT) literature on the inelastic diffraction [17.17–21] based on the concept of the mixed dynamic form factor (MDFF) [17.17]. We note that:

(i) Equation (17.34) can be also written in terms of MDFF rather than χ. Although the two forms are equivalent, expression via χ is of paramount importance for us, allowing us to invoke the linear-response TDDFT, for which χ is the key quantity [17.22].
(ii) For three-dimensional (3-D) crystals, (17.33) and (17.34) reduce to the results of [17.20], but their applicability is broader, permitting, in particular, their use in the Q2-D case, in the Laue (17.79), rather than Bloch function representation.

Up to this point we have not specified the potential $v^0(\boldsymbol{r})$ of (17.22), which has been added and subtracted from the total Hamiltonian. Since $v^0(\boldsymbol{r})$ is introduced to make the perturbation V^1 of (17.23) weak, one choice can be the Hartree potential. Another convenient choice of $v^0(\boldsymbol{r})$ is the sum of the Hartree and exchange-correlation potentials of the density functional theory (DFT). In the latter case, the single-particle Hamiltonian of (17.22) becomes the Kohn–Sham Hamiltonian [17.23], and the states $|\boldsymbol{p}^+\rangle$ and $|\boldsymbol{p}'^-\rangle$ of the projectile electron are obtained on the same footing as those of the electrons of the target.

17.3 Energy-Loss Functions

The traditional interpretation of the EELS of a bulk medium is known to be in terms of the bulk energy-loss function [17.24]

$$L_{\mathrm{b}}(\boldsymbol{q},\omega) = -\mathrm{Im}\left(\frac{1}{\epsilon(\boldsymbol{q},\omega)}\right), \tag{17.35}$$

where $\epsilon(\boldsymbol{q},\omega)$ is the wavevector and frequency-dependent dielectric function of the medium. In (17.35), $\boldsymbol{q}$ is the momentum, and ω is the energy transferred in the scattering event.

On the other hand, the reflection EELS at a surface of a semi-infinite medium is usually described with the

$g(\boldsymbol{q}_\parallel, \omega)$ function [17.25], where $\boldsymbol{q}_\parallel$ is the parallel-to-the-surface component of the transferred momentum. Deferring the definition of the g-function until below, here we write the surface energy-loss function in the long-wave limit as

$$L_s(\omega) = -\mathrm{Im}\left(\frac{1}{1+\epsilon(\omega)}\right) = -\frac{1}{2}\mathrm{Im}\left[g(\boldsymbol{q}_\parallel = \boldsymbol{0}, \omega)\right]. \tag{17.36}$$

In particular, (17.36) states that in *the long-wave limit*, the surface energy-loss function is determined by the bulk quantity $\epsilon(\omega)$. This, however, is not the case at $\boldsymbol{q}_\parallel \neq \boldsymbol{0}$, i.e., it would be meaningless to substitute the wavevector-dependent dielectric function into (17.36).

Since our equation (17.34) is general, the quantities of (17.35) and (17.36) must appear naturally from it at the corresponding conditions of the EELS setup. The purpose of this section is to demonstrate that it is, indeed, the case, which will give us insight into the general properties of our solution as well as set constraints on the applicability of the conventional approaches relying on the formulas of (17.35) and (17.36).

17.3.1 Bulk Scattering

Let us consider the transmission EELS through a film that is sufficiently thick, although penetrable, so that the surface scattering is of secondary importance, as schematized in Fig. 17.2. Let us neglect the projectile–ions interaction, considering only the scattering on the electron subsystem of the target. The reader can legitimately ask why this approximation can be made. If the target is a metal modeled with jellium and occupying the whole space, this is not an approximation, since, in this case, there is no crystal potential. Otherwise, it is difficult to justify this approximation a priori, and only a comparison with the results of the full theory of (17.34) can tell how important the effects of the elastic scattering on ions are. We, however, emphasize that the common use of (17.35) is based, most often implicitly, on the neglect of elastic scattering. Therefore, in (17.27), we now set $V^0(\boldsymbol{r}) = 0$, which leads to

$$\langle \boldsymbol{r}|\boldsymbol{p}^+\rangle = \langle \boldsymbol{r}|\boldsymbol{p}\rangle = \frac{\mathrm{e}^{\mathrm{i}\boldsymbol{p}\cdot\boldsymbol{r}}}{(2\pi)^{3/2}}\,,$$
$$\langle \boldsymbol{r}|\boldsymbol{p}'^-\rangle = \langle \boldsymbol{r}|\boldsymbol{p}'\rangle = \frac{\mathrm{e}^{\mathrm{i}\boldsymbol{p}'\cdot\boldsymbol{r}}}{(2\pi)^{3/2}}\,, \tag{17.37}$$

and, by (17.29),

$$\rho(\boldsymbol{r}) = \frac{\mathrm{e}^{\mathrm{i}(\boldsymbol{p}'-\boldsymbol{p})\cdot\boldsymbol{r}}}{(2\pi)^3}\,. \tag{17.38}$$

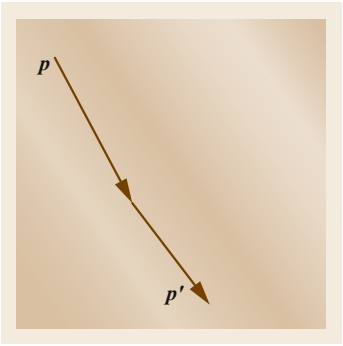

Fig. 17.2 Inelastic electron scattering in the bulk of a solid

Substituting (17.38) into (17.34), we have

$$\begin{aligned}\frac{\mathrm{d}^2\sigma}{\mathrm{d}\omega\mathrm{d}\Omega}(\boldsymbol{p}' \leftarrow \boldsymbol{p}) &= -\frac{p'}{4\pi^3 p}\mathrm{Im}\left(\int \frac{\chi(\boldsymbol{r}_1', \boldsymbol{r}', \omega)\mathrm{e}^{\mathrm{i}(\boldsymbol{p}'-\boldsymbol{p})\cdot(\boldsymbol{r}_1-\boldsymbol{r})}}{|\boldsymbol{r}-\boldsymbol{r}'||\boldsymbol{r}_1-\boldsymbol{r}_1'|}\mathrm{d}\boldsymbol{r}\mathrm{d}\boldsymbol{r}'\mathrm{d}\boldsymbol{r}_1\mathrm{d}\boldsymbol{r}_1'\right)\\ &= -\frac{4p'}{\pi p|\boldsymbol{p}-\boldsymbol{p}'|^4}\mathrm{Im}\left(\int \chi(\boldsymbol{r}_1, \boldsymbol{r}, \omega)\mathrm{e}^{\mathrm{i}(\boldsymbol{p}'-\boldsymbol{p})\cdot(\boldsymbol{r}_1-\boldsymbol{r})}\mathrm{d}\boldsymbol{r}\mathrm{d}\boldsymbol{r}_1\right)\\ &= -\frac{32\pi^2 p'}{p|\boldsymbol{p}-\boldsymbol{p}'|^4}\mathrm{Im}\left[\chi(\boldsymbol{p}-\boldsymbol{p}', \boldsymbol{p}-\boldsymbol{p}', \omega)\right],\end{aligned} \tag{17.39}$$

where the double Fourier transform of χ is

$$\chi(\boldsymbol{q}, \boldsymbol{q}', \omega) = \frac{1}{(2\pi)^3}\int \chi(\boldsymbol{r}, \boldsymbol{r}', \omega)\mathrm{e}^{\mathrm{i}(-\boldsymbol{q}\cdot\boldsymbol{r}+\boldsymbol{q}'\cdot\boldsymbol{r}')}\mathrm{d}\boldsymbol{r}\mathrm{d}\boldsymbol{r}'\,, \tag{17.40}$$

and in (17.39) χ is taken at $\boldsymbol{q} = \boldsymbol{q}' = \boldsymbol{p} - \boldsymbol{p}'$.

Equation (17.39) is the final result for a target of an arbitrary structure under the neglect of elastic scattering. We now consider a specific case of a uniform target occupying a box with a large size L with periodic boundary conditions. Then,

$$\chi(\boldsymbol{r}, \boldsymbol{r}', \omega) = \chi(\boldsymbol{r}-\boldsymbol{r}', \omega) \tag{17.41}$$

and

$$\chi(\boldsymbol{q}, \boldsymbol{q}', \omega) = \frac{\delta_{\boldsymbol{q}\boldsymbol{q}'}L^3}{(2\pi)^3}\chi(\boldsymbol{q}, \omega)\,, \tag{17.42}$$
$$\chi(\boldsymbol{q}, \omega) = \int \chi(\boldsymbol{r}, \omega)\mathrm{e}^{-\mathrm{i}\boldsymbol{q}\cdot\boldsymbol{r}}\mathrm{d}\boldsymbol{r}\,. \tag{17.43}$$

Substituting (17.42) into (17.39), we have

$$\frac{\mathrm{d}^2\sigma}{\mathrm{d}\omega\mathrm{d}\Omega}(\boldsymbol{p}' \leftarrow \boldsymbol{p}) = -\frac{4p'}{\pi|\boldsymbol{p}-\boldsymbol{p}'|^4 p}L^3\mathrm{Im}\left[\chi(\boldsymbol{p}-\boldsymbol{p}', \omega)\right]. \tag{17.44}$$

After dividing the differential cross section of (17.44) by the area $S = L^2$, we obtain the probability of the scattering per $\mathrm{d}\omega\mathrm{d}\Omega$ interval at the path length of L. Further division by L yields the probability to be scattered into the above interval per unit path length. In other words,

$$\frac{\mathrm{d}^3P}{\mathrm{d}\omega\mathrm{d}\Omega\mathrm{d}l}(\boldsymbol{p}' \leftarrow \boldsymbol{p}) = -\frac{4\mathrm{e}^2m^2p'}{\pi|\boldsymbol{p}-\boldsymbol{p}'|^4p}\mathrm{Im}\left[\chi(\boldsymbol{p}-\boldsymbol{p}',\omega)\right], \tag{17.45}$$

or taking account of the relation between the density-response function and the dielectric function

$$\frac{1}{\varepsilon(\boldsymbol{q},\omega)} = 1 + \frac{4\pi}{q^2}\chi(\boldsymbol{q},\omega), \tag{17.46}$$

we can write

$$\frac{\mathrm{d}^3P}{\mathrm{d}\omega\mathrm{d}\Omega\mathrm{d}l}(\boldsymbol{p}' \leftarrow \boldsymbol{p}) = -\frac{p'}{\pi^2|\boldsymbol{p}-\boldsymbol{p}'|^2p}\mathrm{Im}\left(\frac{1}{\varepsilon(\boldsymbol{p}-\boldsymbol{p}',\omega)}\right). \tag{17.47}$$

Equation (17.47) is the justification of the concept of the bulk energy-loss function, introduced in (17.35), the prefactor being a smooth function of p and p'.

17.3.2 Surface Scattering

In this section, we will introduce the concept of *dipole scattering* in the reflection EELS [17.25] (in the geometry of Fig. 17.3) and, following our methodology, we will show how it arises from the general formula of (17.34) as a specific case.

We define the dipole regime as a scattering during which the projectile (its wavefunction) does not enter the electron charge density of the target, so that the interaction is only via Coulomb forces at a distance (of course, the interaction is always via Coulomb forces, but we will see that *at a distance* makes a big difference).

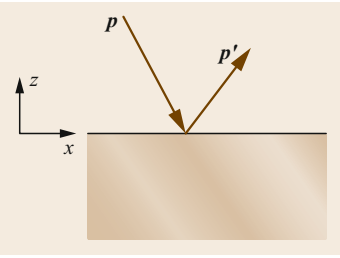

Fig. 17.3 Inelastic electron scattering from a semi-infinite solid in the reflection geometry

Let us assume that the target solid is uniform in the xy plane; we use the notation $\boldsymbol{r} \equiv (\boldsymbol{r}_\parallel, z)$. Then,

$$\langle \boldsymbol{r}|\boldsymbol{p}^+\rangle = \frac{\mathrm{e}^{\mathrm{i}\boldsymbol{p}_\parallel\cdot\boldsymbol{r}_\parallel}}{2\pi}\langle z|p_z^+\rangle,$$
$$\langle \boldsymbol{r}|\boldsymbol{p}'^-\rangle = \frac{\mathrm{e}^{\mathrm{i}\boldsymbol{p}'_\parallel\cdot\boldsymbol{r}_\parallel}}{2\pi}\langle z|p_z'^-\rangle, \tag{17.48}$$

and, by (17.29),

$$\rho(\boldsymbol{r}) = \frac{\mathrm{e}^{\mathrm{i}(\boldsymbol{p}'_\parallel-\boldsymbol{p}_\parallel)\cdot\boldsymbol{r}_\parallel}}{(2\pi)^2}\rho(z), \tag{17.49}$$

where

$$\rho(z) = \langle z|p_z^+\rangle^*\,\langle z|p_z'^-\rangle. \tag{17.50}$$

Substituting (17.49) into (17.34) and integrating over $\boldsymbol{r}_\parallel$ and $\boldsymbol{r}_{1\parallel}$, we have

$$\frac{\mathrm{d}^2\sigma}{\mathrm{d}\omega\mathrm{d}\Omega}(\boldsymbol{p}' \leftarrow \boldsymbol{p}) = -\frac{4\pi p'}{p}\mathrm{Im}\int \mathrm{e}^{-\mathrm{i}\boldsymbol{q}_\parallel\cdot\boldsymbol{r}'_\parallel}\mathrm{e}^{-q_\parallel|z-z'|}\rho^*(z)\chi(\boldsymbol{r}',\boldsymbol{r}'_1,\omega) \times \mathrm{e}^{\mathrm{i}\boldsymbol{q}_\parallel\cdot\boldsymbol{r}'_1}\mathrm{e}^{-q_\parallel|z_1-z'_1|}\rho(z_1)\mathrm{d}z\mathrm{d}\boldsymbol{r}'\mathrm{d}z_1\mathrm{d}\boldsymbol{r}'_1, \tag{17.51}$$

where $\boldsymbol{q}_\parallel = \boldsymbol{p}'_\parallel - \boldsymbol{p}_\parallel$, or

$$\frac{\mathrm{d}^2\sigma}{\mathrm{d}\omega\mathrm{d}\Omega}(\boldsymbol{p}' \leftarrow \boldsymbol{p}) = -\frac{4\pi p'}{p}\mathrm{Im}\int \mathrm{e}^{-q_\parallel|z-z'|}\rho^*(z)\chi(z',z'_1,q_\parallel,\omega) \times \mathrm{e}^{-q_\parallel|z_1-z'_1|}\rho(z_1)\mathrm{d}z\mathrm{d}z'\mathrm{d}z_1\mathrm{d}z'_1, \tag{17.52}$$

where, because of symmetry, $\chi(\boldsymbol{r},\boldsymbol{r}',\omega) = \chi(z,z',\boldsymbol{r}_\parallel - \boldsymbol{r}'_\parallel,\omega)$, and the 2-D Fourier transform was performed.

We now consider the case when the projectile never enters the charge density of the electrons of the target. We realize this by assuming that

$$\chi(z',z'_1,q_\parallel,\omega) = 0, \text{ if } z' > 0 \text{ or } z'_1 > 0, \tag{17.53}$$
$$\rho(z) = 0, \text{ if } z < 0. \tag{17.54}$$

Then, by (17.52),

$$\frac{\mathrm{d}^2\sigma}{\mathrm{d}\omega\mathrm{d}\Omega}(\boldsymbol{p}' \leftarrow \boldsymbol{p}) = -\frac{2q_\parallel p'}{p}\left|\int \mathrm{e}^{-q_\parallel z}\rho(z)\mathrm{d}z\right|^2\mathrm{Im}\left[g(q_\parallel,\omega)\right], \tag{17.55}$$

where the so-called g-function is defined by [17.25]

$$g(q_\parallel,\omega) = \frac{2\pi}{q_\parallel}\int \mathrm{e}^{q_\parallel z}\chi(z,z',q_\parallel,\omega)\mathrm{e}^{q_\parallel z'}\mathrm{d}z\mathrm{d}z'. \tag{17.56}$$

Furthermore, considering the definition of the density-response function χ, we can give the g-function of (17.56) the following interpretation. Let us apply to the system the external potential

$$v_{\text{ext}}(\boldsymbol{r},t) = \mathrm{e}^{\mathrm{i}\boldsymbol{q}_\parallel\cdot\boldsymbol{r}_\parallel + q_\parallel z - \mathrm{i}\omega t} \,. \tag{17.57}$$

Then, according to (17.56), the induced potential at large $z > 0$ outside the system is

$$g(q_\parallel,\omega)\mathrm{e}^{\mathrm{i}\boldsymbol{q}_\parallel\cdot\boldsymbol{r}_\parallel - q_\parallel z - \mathrm{i}\omega t} \,. \tag{17.58}$$

Having accurately introduced the concept of the dipole-scattering regime, it would be timely to address the question: What is, within our formalism, its opposite, known in the literature as the impact regime [17.25]? A simple answer reads: the impact regime takes place when there is no restriction on the incident electron to enter the electron density of the target. Then, formulas (17.34) and (17.29) must be used, examples of which we will see in Sects. 17.4.2 and 17.4.3.

Local-Response Model

Let us further see the simplifications arising within the approximation of the local response.

Let the $z > 0$ (region I) and $z < 0$ (region II) half-spaces be filled with vacuum and a medium of the dielectric function $\varepsilon(\omega)$, respectively, as schematized in Fig. 17.4. The boundary is assumed abrupt, and the dielectric function is wavevector independent. This model is referred to as local.

For this model, we can easily evaluate the g-function. Indeed, let the external potential be that of (17.57). The Poisson equation holds

$$\Delta v_{\text{ext}}(\boldsymbol{r},\omega) = -4\pi\rho_{\text{ext}}(\boldsymbol{r},\omega) \,, \tag{17.59}$$

where ρ_{ext} is the density of the external charges creating v_{ext}. Equations (17.59) and (17.57) lead to

$$\rho_{\text{ext}}(\boldsymbol{r},\omega) = 0 \,. \tag{17.60}$$

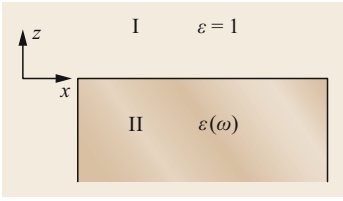

Fig. 17.4 Model of local response of a semi-infinite solid with the dielectric function $\varepsilon(\omega)$

On the other hand, it follows from the Gauss theorem

$$\nabla\cdot\boldsymbol{D}(\boldsymbol{r},\omega) = 4\pi\rho_{\text{ext}}(\boldsymbol{r},\omega) = 0 \tag{17.61}$$

and the material equation $\boldsymbol{D}(\boldsymbol{r},\omega) = \varepsilon(\omega)\boldsymbol{E}(\boldsymbol{r},\omega)$ that

$$\nabla\cdot\boldsymbol{E}(\boldsymbol{r},\omega) = 0 \,, \tag{17.62}$$

which holds in both regions I and II. Since $\boldsymbol{E}(\boldsymbol{r},\omega) = -\nabla v(\boldsymbol{r},\omega)$, in both regions we have

$$\Delta v(\boldsymbol{r},\omega) = 0 \,. \tag{17.63}$$

In our system, the $\boldsymbol{q}_\parallel$ component is conserved and, therefore, the solution of (17.63) can only be

$$v(\boldsymbol{r},\omega) = \mathrm{e}^{\mathrm{i}\boldsymbol{q}_\parallel\cdot\boldsymbol{r}_\parallel}\begin{cases}\mathrm{e}^{q_\parallel z} + A(\omega)\mathrm{e}^{-q_\parallel z}, & z > 0 \,,\\ B(\omega)\mathrm{e}^{q_\parallel z}, & z < 0 \,,\end{cases} \tag{17.64}$$

where $A(\omega)$ and $B(\omega)$ are constants in space, and the attenuation of the solution into the solid has been imposed. Then,

$$E_z(\boldsymbol{r},\omega) = -q_\parallel\mathrm{e}^{\mathrm{i}\boldsymbol{q}_\parallel\cdot\boldsymbol{r}_\parallel}\begin{cases}\mathrm{e}^{q_\parallel z} - A(\omega)\mathrm{e}^{-q_\parallel z}, & z > 0 \,,\\ B(\omega)\mathrm{e}^{q_\parallel z}, & z < 0 \,,\end{cases} \tag{17.65}$$

and

$$D_z(\boldsymbol{r},\omega) = -q_\parallel\mathrm{e}^{\mathrm{i}\boldsymbol{q}_\parallel\cdot\boldsymbol{r}_\parallel}\begin{cases}\mathrm{e}^{q_\parallel z} - A(\omega)\mathrm{e}^{-q_\parallel z}, & z > 0 \,,\\ \varepsilon(\omega)B(\omega)\mathrm{e}^{q_\parallel z}, & z < 0 \,.\end{cases} \tag{17.66}$$

Applying the boundary conditions of the continuity of $\boldsymbol{E}_\parallel$ (or, equivalently, of v) and of D_z at $z = 0$ [17.26], we find

$$A = \frac{1-\varepsilon(\omega)}{1+\varepsilon(\omega)} \,, \tag{17.67}$$

$$B = \frac{2}{1+\varepsilon(\omega)} \,. \tag{17.68}$$

Combining (17.67), (17.64), and (17.58), we arrive at

$$g(\omega) = \frac{1-\varepsilon(\omega)}{1+\varepsilon(\omega)} \,, \tag{17.69}$$

which is the final justification of formula (17.36).

17.4 Application to EELS of Metal Surfaces

Here, we will apply the formalisms introduced above to describe EELS from metal surfaces within models of increasing order of sophistication.

17.4.1 Dipole Scattering

Within the jellium model of a simple metal surface [17.28] and using the approximation of the dipole scattering (i.e., in terms of the g-function), *Tsuei* et al. [17.27] interpreted the multipole plasmon mode in alkali metals, which they detected experimentally. Their results for K and Na metals are reproduced in Fig. 17.5. As seen from the inset in Fig. 17.5a, the amplitude of the multipole plasmon is drastically underestimated compared to the experiment.

Another shortcoming of the purely dipole scattering theory is the oversimplification of the geometry of the experiment, including the incidence energy dependence of the EEL spectra. Indeed, according to (17.55), the $\boldsymbol{q}$ and ω dependence basically factorize in the expression for the differential cross section (apart from $p' = \sqrt{p^2 - 2\omega}$, which usually has an insignificant effect). This leads to dipole-mode spectra differing from each other at the same momenta and energy loss but at different geometries, by overall factors only, which does not matter, considering that the intensity scale is arbitrary.

We will see below that the unified theory of EELS, which does not separate the dipole and impact scatterings, lifts the above limitations.

17.4.2 Reflection of Electrons Under the Surface

The simplest possibility to go beyond the dipole regime is to allow for the incident electron penetration into the surface region, where the electron density of the target is nonzero or even into the bulk, doing this, however, simplistically by imposing an impenetrable potential barrier at a given depth under the surface. This pathway was implemented in [17.10] within the jellium model of a metal surface [17.28]. In this setup, the complex valued charge density is

$$\rho(z) = \left\{ \frac{\exp[\mathrm{i}q_\mathrm{f}(z-c)]}{\cos\theta_\mathrm{f}} + \frac{\exp[\mathrm{i}q_\mathrm{i}(z-c)]}{\cos\theta_\mathrm{i}} \right\} \frac{\Theta(z-c)}{4\pi} , \tag{17.70}$$

where $\Theta(z) = 0, 1$ if $z \lesseqgtr 0$, $q_{\mathrm{f,i}} = \pm(p' - p - q_\parallel \sin\theta_{\mathrm{f,i}})/\cos\theta_{\mathrm{f,i}}$ θ_i and θ_f are the angles of incidence and reflection, respectively, and $z = c$ is the position of the plane of reflection.

In [17.10], $\rho(z)$ of (17.70) was used in (17.52). The bulk, surface, and multipole plasmons, including their

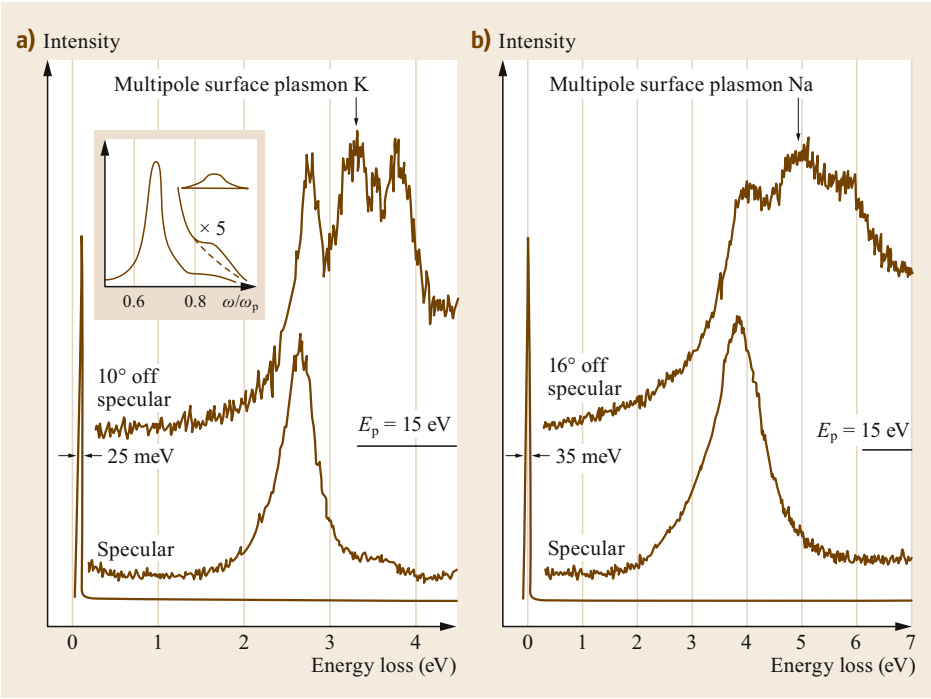

Fig. 17.5a,b EEL spectra for **(a)** K and **(b)** Na. The *bottom curves* in **(a)** and **(b)** are measurements in the specular direction, and the *top curves* are **(a)** 10° and **(b)** 16° off the specular direction, respectively. *Inset* in **(a)**: the calculated loss function $\mathrm{Im}[g(q,\omega)]$ at $q = 0.11\,\text{Å}^{-1}$. Reprinted with permission from [17.27]. Copyright (1990) by the American Physical Society

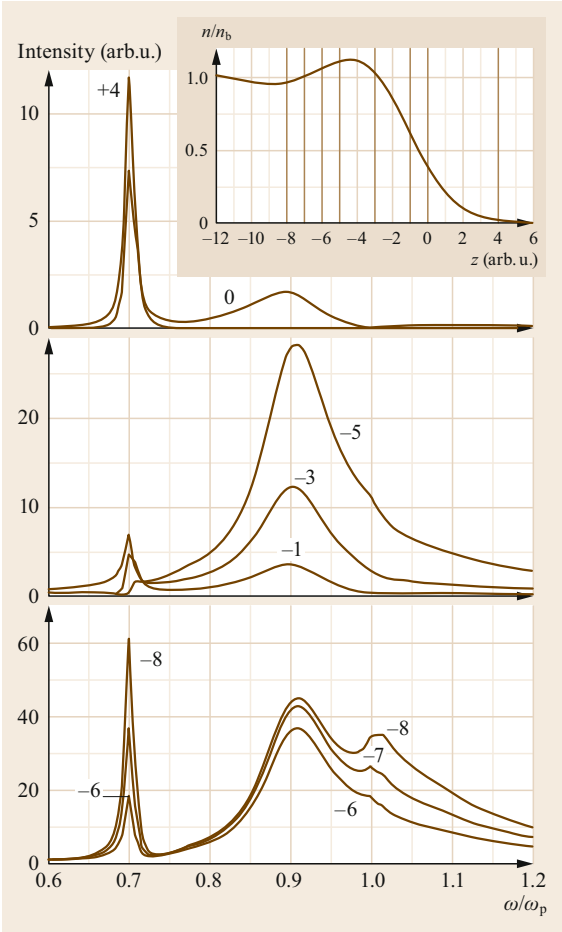

Fig. 17.6 Energy-loss function calculated for the K surface ($r_s = 5$) for reflection at different distances c from the jellium edge. The *inset* shows the positions of the penetration depths c inside the charge-density distribution profile at the surface; $E_p = 15\,\text{eV}$, $\theta_i = 50°$, and $\theta_f = 60°$. (Reproduced from [17.10])

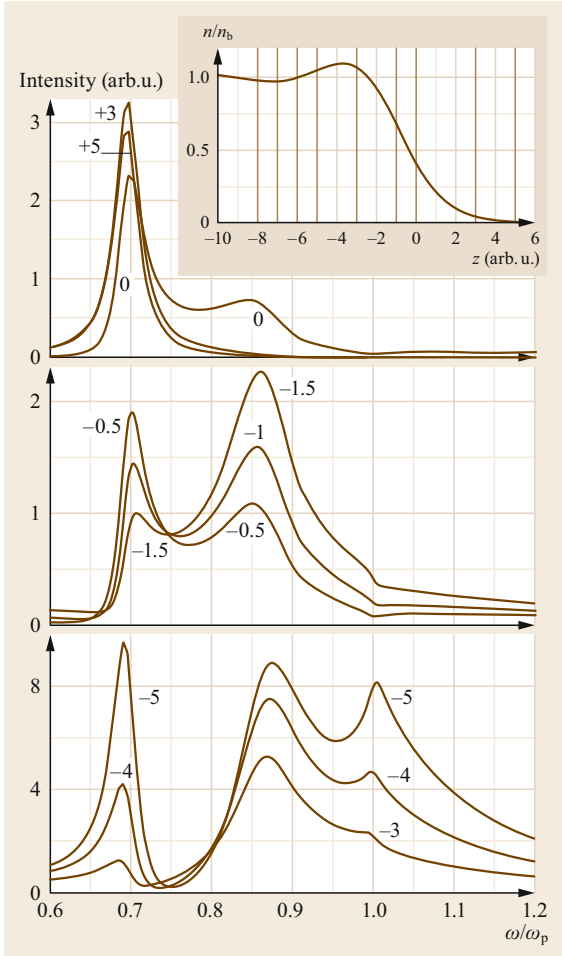

Fig. 17.7 Energy-loss function calculated for Na ($r_s = 4$) surface; $E_p = 15\,\text{eV}$, $\theta_i = 44°$, and $\theta_f = 60°$. (Reproduced from [17.10])

amplitudes, were found to be in good agreement with experiment, as can be seen from the comparison of Figs. 17.6 and 17.7 with Fig. 17.5.

This model was further improved by considering the elastic scattering of electrons within the kinematic theory of diffraction [17.11].

17.4.3 Target and Incident Electrons Treated on the Same Footing: EELS of the Ag Surface

It is obvious that the full implementation of the theory based on (17.34) and (17.29) in the case of the surface of a crystal would require a 3-D calculation of both the density-response function χ and the elastically scattered waves $|\boldsymbol{p}^+\rangle$ and $|\boldsymbol{p}'^-\rangle$, which, in this case, are the low-energy electron diffraction (LEED) wavefunctions. This ambitious program was fulfilled later in the case of the graphene target [17.13]. In this section, we will consider a step in that direction made in the calculation of EELS at the surface of silver [17.12].

Compared with the approach of [17.10], the improvement in [17.12] was to use the wavefunctions of the incident and reflected electron dictated by the crystal potential at the surface and in the bulk rather than those corresponding to the reflection from an infinite barrier at a fixed position. Therefore, the same Schrödinger, or rather Kohn–Sham, equations were solved both for the impinged electron and for the electrons of the target, the latter being necessary for calculation of the density-response function χ.

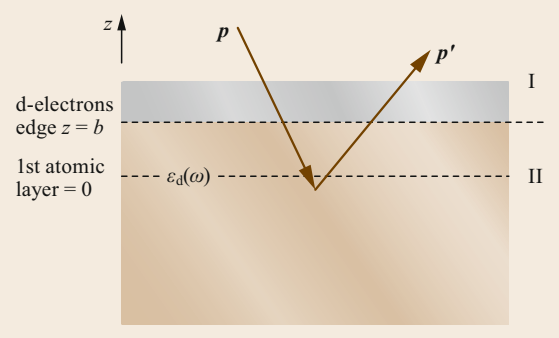

Fig. 17.8 Model used in the calculation of EELS from the Ag surface. (Reproduced from [17.12])

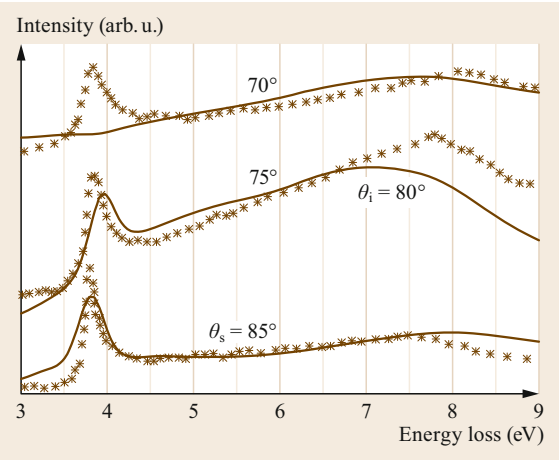

Fig. 17.9 High-resolution electron energy-loss spectra of the Ag(111) surface calculated within the framework of our theoretical approach in Sect. 17.4.3 (*solid lines*) compared to the experimental spectra of ten monolayers of Ag on the Ni(111) surface, the latter compiled from [17.29] (*symbols*). The energy of electrons in the incident beam is $E_p = 40\,\text{eV}$. (Reproduced from [17.12])

In order to facilitate calculations, a one-dimensional (1-D) model of the surface and the bulk crystal was used. An unfortunate artifact of this model is that it does not account for d-electrons of the Ag crystal, which significantly affects the dielectric response. To compensate for this deficiency, d-electrons were included

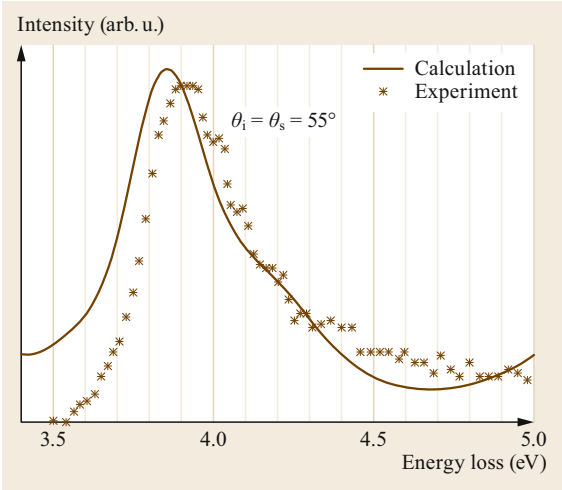

Fig. 17.10 High-resolution electron energy-loss spectrum of the Ag(111) surface calculated within the framework of our theoretical approach in Sect. 17.4.3 (*solid line*) for the specular reflection $\theta_i = \theta_s = 55°$. (Reproduced from [17.12])

phenomenologically through a background dielectric function $\varepsilon_d(\omega)$, as explained in detail in [17.30]. On the other hand, s-electrons were treated fully quantum-mechanically. The geometry of the model is shown in Fig. 17.8.

Within the aforementioned assumptions, the density-response function $\chi(z, z', q_\parallel, \omega)$ was obtained self-consistently, and then (17.52) was used to calculate the electron energy-loss spectrum.

The clear advantage of this approach is that it provides a means to study dependence of the EEL spectra on the experimental conditions, i.e., on the angles of incidence and reflection, and on the primary energy of the electrons. Representative calculated spectra are compared with the experiment in Figs. 17.9 and 17.10. While the comparison is, in general, satisfactory, the theory does not follow the experiment with larger wavevector transfer (Fig. 17.9, the spectrum with the angle of scattering of 70°). This is analyzed in detail in [17.12] and is attributed to the failure of the d-electrons' background dielectric function model at large wavevectors.

17.5 EELS of Q2-D Materials: Important Particulars

With the discovery of graphene [17.31], interest in Q2-D materials (materials macroscopic in two dimensions and microscopic in the third one) has grown, while EELS has become one of the important experimental techniques of their investigation [17.32]. It must be emphasized that our general formalism based on (17.33) and (17.34) remains fully applicable to Q2-D systems, and, moreover, it can be expected to be better suited in this case, considering that the first Born approximation for the inelastic scattering should hold

the more accurately the thinner a target is. While we defer the full theory until Sect. 17.5.4, for pedagogical reasons we start the considerations within the concept of energy-loss functions. In this section, we will limit ourselves to the description of the energy losses within the dipole regime, the latter having been introduced in Sect. 17.3.2. Below, we will focus on the distinctive features characteristic to Q2-D systems.

17.5.1 Supercell Method

To handle Q2-D crystals, calculations are generally performed with the use of the *supercell* method, which means that Q2-D layers are periodically replicated in space at a given distance d from each other, as shown in Fig. 17.11, and then standard 3-D solid-state methods are used for the resulting formally 3-D-periodic system. However, an important problem arises: in the calculation, the copies of the layers interact with each other and, therefore, the results obtained for the array of layers are not, generally speaking, the same as they would be for a single one. Moreover, it turns out that a simple increase of the interlayer distance d does not solve the problem, since, at sufficiently small $q_\parallel$ (long-wave response), the interaction between the copies remains strong. On the other hand, to give up the supercell approach and handle a single Q2-D system is usually computationally prohibitively expensive.

Fortunately, the elimination of the spurious interlayer interaction within the supercell method can be rigorously and efficiently performed in the following way. Let $\tilde{\chi}(\boldsymbol{q}_\parallel,\omega)=\tilde{\chi}_{\boldsymbol{G}\boldsymbol{G}'}(\boldsymbol{q}_\parallel,\omega)$ be the density-response function of the artificial supercell system, which includes the spurious interlayer interaction ($\boldsymbol{G}$ are the supercell reciprocal vectors). Then, the genuine density-response function of the single Q2-D system $\chi(\boldsymbol{q}_\parallel,\omega)$ free from the interlayer interaction can be restored as [17.33]

$$\chi(\boldsymbol{q}_\parallel,\omega)=\tilde{\chi}(\boldsymbol{q}_\parallel,\omega)\left[1+\mathbf{C}(\boldsymbol{q}_\parallel)\tilde{\chi}(\boldsymbol{q}_\parallel,\omega)\right]^{-1}\,, \tag{17.71}$$

where the matrix $\mathbf{C}_{\boldsymbol{G}\boldsymbol{G}'}$ is given by

$$\mathbf{C}_{\boldsymbol{G}\boldsymbol{G}'}(\boldsymbol{q}_\parallel)=F_{G_zG'_z}(|\boldsymbol{G}_\parallel+\boldsymbol{q}_\parallel|)\delta_{\boldsymbol{G}_\parallel\boldsymbol{G}'_\parallel}\,, \tag{17.72}$$

$$F_{G_zG'_z}(p)=\frac{4\pi(p^2-G_zG'_z)}{pd(p^2+G_z^2)(p^2+G_z'^2)} \times\cos\left(\frac{(G_z+G'_z)d}{2}\right)(1-\mathrm{e}^{-pd})\,, \tag{17.73}$$

and we have used the notation $\boldsymbol{G}\equiv(\boldsymbol{G}_\parallel,G_z)$.

17.5.2 The True Energy-Loss Function of a Q2-D Crystal

It must be emphasized that the correct energy-loss function to be used in the reflection EELS of Q2-D structures (as long as we are limited to the dipole regime), according to (17.55) and (17.56), is [17.33]

$$L_{\text{Q2-D}}(\boldsymbol{q}_\parallel,\omega)=-\frac{1}{2}\mathrm{Im}\left[g_{\text{Q2-D}}(\boldsymbol{q}_\parallel,\omega)\right], \tag{17.74}$$

where

$$g_{\text{Q2-D}}(\boldsymbol{q}_\parallel,\omega)=\frac{2\pi}{q_\parallel}\int \mathrm{e}^{q_\parallel z}\chi_{\mathbf{0}\mathbf{0}}(z,z',\boldsymbol{q}_\parallel,\omega)\mathrm{e}^{q_\parallel z'}\mathrm{d}z\mathrm{d}z'\,, \tag{17.75}$$

and not

$$-\mathrm{Im}\left(\frac{1}{\epsilon_{\text{Q2-D}}(\boldsymbol{q}_\parallel,\omega)}\right), \tag{17.76}$$

where

$$\frac{1}{\epsilon_{\text{Q2-D}}(\boldsymbol{q}_\parallel,\omega)}=1+\frac{2\pi}{q_\parallel}\int\chi_{\mathbf{0}\mathbf{0}}(z,z',\boldsymbol{q}_\parallel,\omega)\mathrm{d}z\mathrm{d}z'\,, \tag{17.77}$$

although the opposite is often assumed without justification. The latter energy-loss function is pertinent to the in-plane energy dissipation in the Q2-D system [17.33]. In the above equation, the subscripts at the response functions denote the zero in-plane reciprocal lattice vectors and select the long-wave response to the long-wave perturbation.

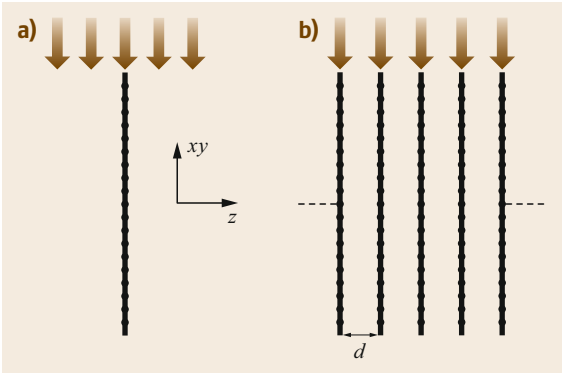

Fig. 17.11a,b 2-D material under an external field. **(a)** 2-D single-layer geometry and **(b)** 3-D super-cell geometry. (Reproduced from [17.33])

17.5.3 Results for Single-Layer and Multilayer Graphene

In [17.33], calculations using formulas (17.74)–(17.77) were performed. Results for monolayer pristine graphene are presented in Figs. 17.12 and 17.13.

A comparison of the theory with HEELS experiment for monolayer and bilayer graphene is shown in Fig. 17.14. We first note that the agreement between theory and experiment is much better in the case of the π-plasmon (upper panels) rather than for the $\pi+\sigma$ one. When making the comparison, we must take the following factors into account. As will be shown in Sect. 17.5.4, where we implement the theory that does not separate the dipole and impact mechanisms, the $\pi+\sigma$ plasmon is much more sensitive to the details of the elastic scattering than the π-plasmon is, the latter being well reproduced within the dipole mechanism. Since, on the one hand, the theory in this section is the dipole one, it is not surprising that for the $\pi+\sigma$ plasmon we have a worse agreement with experiment. On the other hand, the experiment in [17.34] was carried out with graphene on a substrate (of SiC (0001)) rather than with a standalone graphene. This would make the comparison of these experimental data to our full theory of Sect. 17.5.4 meaningless, the latter being sensitive to the details of the elastic scattering, which is very different for the standalone and the substrate-supported systems. The full theory with inclusion of the substrate is still to be built in the future.

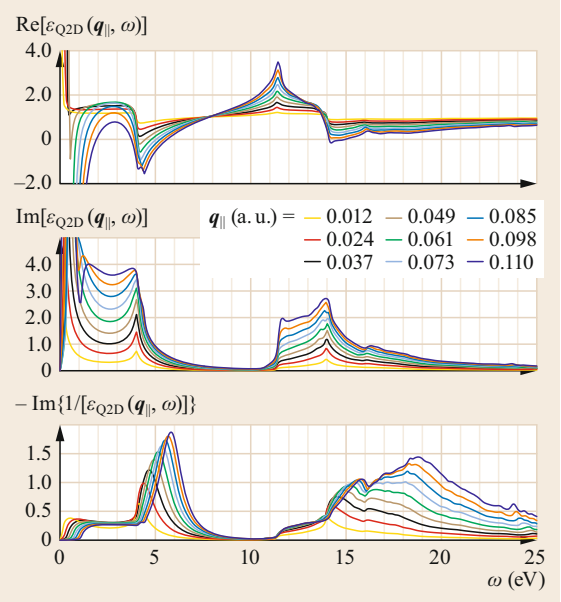

Fig. 17.12 Dielectric function of the pristine monolayer graphene obtained with (17.77) and the corresponding energy-loss function. Momentum $\boldsymbol{q}_\parallel$ is varied along the ΓM direction. (Reproduced from [17.33])

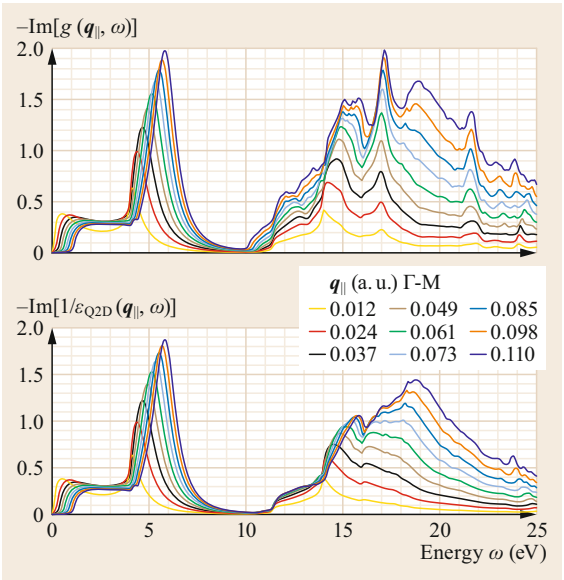

Fig. 17.13 The EELS-related energy-loss function $-1/2\mathrm{Im}\left[g_{Q2\text{-}D}(\boldsymbol{q}_\parallel,\omega)\right]$ (*upper panel*) compared to the energy-loss function $-\mathrm{Im}\left[1/\varepsilon_{Q2\text{-}D}(\boldsymbol{q}_\parallel,\omega)\right]$ (*lower panel*) for pristine monolayer graphene. (Reproduced from [17.33])

We note that all specific calculations considered above have required the knowledge of the interacting electrons density-response function $\chi(\boldsymbol{r},\boldsymbol{r}',\omega)$. The nontrivial methods of its numerical evaluation will be considered in Sects. 17.6.3 and 17.7.

17.5.4 Theory of EELS of Q2-D Crystals Beyond the Energy-Loss Functions Formalism

The one-step combined inelastic and elastic scattering theory, developed in Sect. 17.2.1 and resulting in expression (17.34) for the double differential cross section is best suited for applications to the HEELS of Q2-D crystals. This happens for two particular reasons. First, in the medium energy range of incident electrons ($\approx 10-100$ eV), the role of the elastic scattering grows very importantly, leading, in particular, to the appearance of the elastic *scattering resonances*, which were first predicted in [17.35] and then observed and studied experimentally [17.36–39]. Elastic scattering, therefore, can no longer be considered as constituting a smooth background to the sharp features due to inelastic processes, and both kinds of scattering must be included in the theory in their interrelations [17.13].

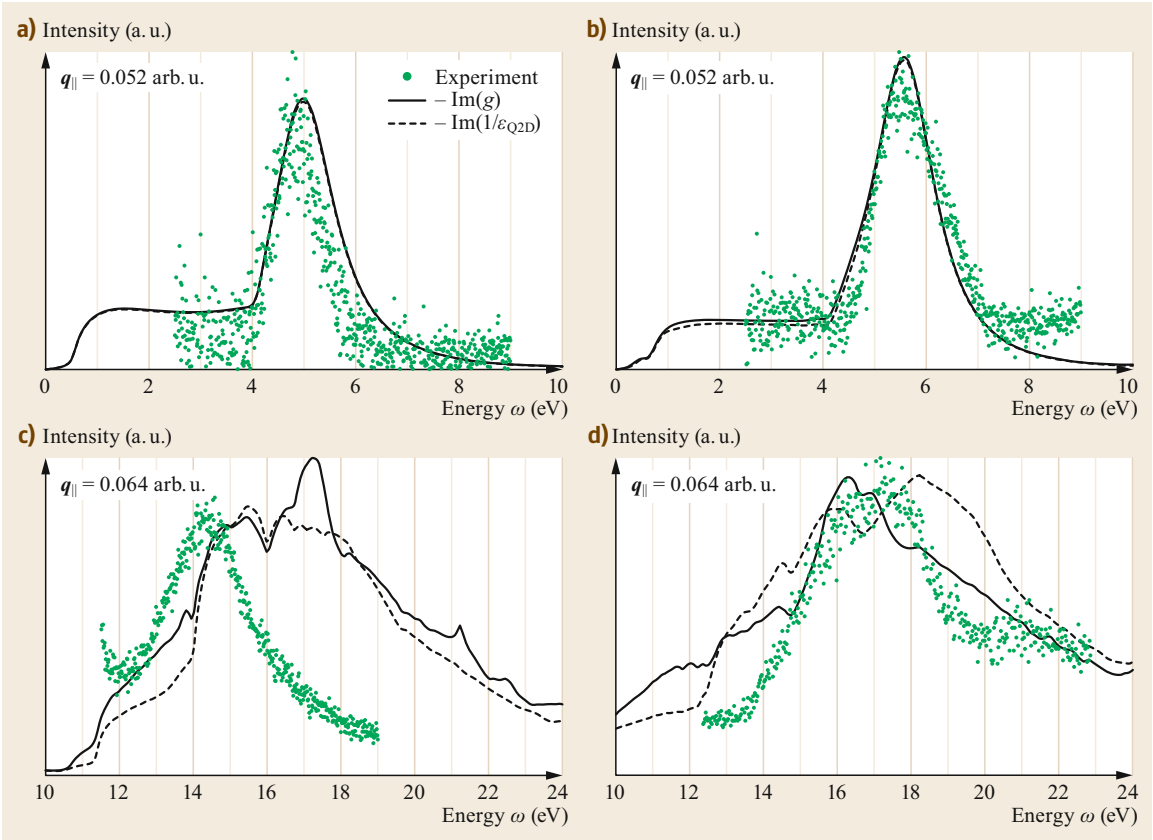

Fig. 17.14a–d The reflection EELS energy-loss function $-\mathrm{Im}\left[g_{\mathrm{Q2\text{-}D}}(\boldsymbol{q}_\parallel,\omega)\right]$ of (17.75) (*solid lines*) and the energy-loss function $-\mathrm{Im}\left[1/\varepsilon_{\mathrm{Q2\text{-}D}}(\boldsymbol{q}_\parallel,\omega)\right]$ of (17.77) (*dashed lines*) for monolayer **(a,c)** and bilayer **(b,d)** graphene in the energy range of π **(a,b)** and $\pi+\sigma$ **(c,d)** plasmons. *Green symbols* are the experimental HREELS data of [17.34]. The theoretical spectra have been roughly normalized to the experimental ones. (Reproduced from [17.33])

Secondly, in contrast to the surfaces of semi-infinite solids, Q2-D materials are the systems for which the method of Sect. 17.2.1 can be implemented without resorting to any sort of additional phenomenological ingredients. Indeed, the description of the energy losses in a semi-infinite solid necessarily requires the introduction of the *optical potential*. This is because we need a mechanism restricting electrons' exit to vacuum after penetrating arbitrarily deep into the target, without which mechanism the probability of the bulk losses diverges, leading to the break down of the first Born approximation for inelastic scattering [17.12]. In experiments, this restriction is ensured by the higher-order inelastic processes, which, however, cannot be included in the theory in the ab-initio fashion. The latter problem does not arise in the case of Q2-D materials, due to their microscopic thickness, making them ideal objects to be studied with the use of the theory of Sect. 17.2.1.

We proceed by noting that in a Q2-D crystal, the in-plane component of the wavevector is conserved to within a reciprocal lattice vector $\boldsymbol{G}_\parallel$. As a consequence, the density-response function becomes a matrix in the reciprocal lattice vectors $\chi_{GG'}(z,z',\boldsymbol{q}_\parallel,\omega)$, where $\boldsymbol{q}_\parallel$ belongs to the 2-D Brillouin zone (2-DBZ). Equation (17.34) can then be conveniently transformed to

$$\begin{aligned}
&\frac{1}{S}\frac{\mathrm{d}\sigma}{\mathrm{d}\omega\mathrm{d}\Omega}(\boldsymbol{p}'\leftarrow\boldsymbol{p})\\
&=-\frac{64\pi^5 p'}{p}\mathrm{Im}\left[\sum_{\substack{G\tilde{G}\\ G'\tilde{G}'}}\int \chi_{GG'}(z_1,z_1',\boldsymbol{q}_\parallel,\omega)\right.\\
&\times\frac{\mathrm{e}^{-|\boldsymbol{G}+\boldsymbol{q}_\parallel||z_1-z|}\mathrm{e}^{-|\boldsymbol{G}'+\boldsymbol{q}_\parallel||z_1'-z'|}}{|\boldsymbol{G}+\boldsymbol{q}_\parallel||\boldsymbol{G}'+\boldsymbol{q}_\parallel|}a^{+*}_{\boldsymbol{p},\boldsymbol{G}+\tilde{\boldsymbol{G}}}(z)a^{-}_{\boldsymbol{p}',\tilde{\boldsymbol{G}}+\boldsymbol{G}_0}(z)\\
&\left.\times a^{+}_{\boldsymbol{p},\boldsymbol{G}'+\tilde{\boldsymbol{G}}'}(z')a^{-*}_{\boldsymbol{p}',\tilde{\boldsymbol{G}}'+\boldsymbol{G}_0}(z')\,\mathrm{d}z\mathrm{d}z'\mathrm{d}z_1\mathrm{d}z_1'\right], \qquad (17.78)
\end{aligned}$$

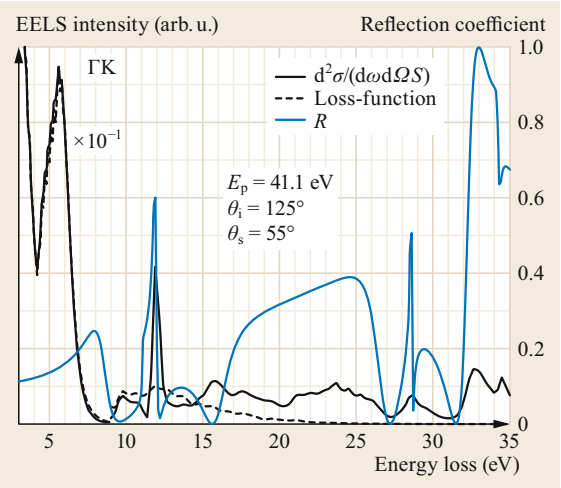

Fig. 17.15 Calculated EEL reflection spectrum of monolayer graphene (*thick black line*, full theory, (17.34)), the one calculated with the use of the surface loss function (*dashed line*, (17.55), (17.56)), and the coefficient of reflection (*thin blue line* plotted against the right *y*-axis). For better visualization, EEL spectra are split into two parts, the low-energy one is scaled by 0.1. See Fig. 17.16 for the definition of angles. (Reproduced from [17.13])

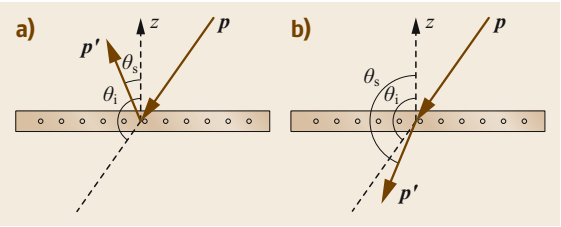

Fig. 17.16a,b Reflection **(a)** and transmission **(b)** geometries of the EELS experiment on a Q2-D crystal with the definition of angles. (Reproduced from [17.13])

where $a^{\pm}_{\boldsymbol{p},\boldsymbol{G}}(z)$ are the Fourier coefficients in the expansion (Laue representation [17.40])

$$\langle \boldsymbol{r}|\boldsymbol{p}^{\pm}\rangle = \sum_{\boldsymbol{G}} a^{\pm}_{\boldsymbol{p},\boldsymbol{G}}(z) \mathrm{e}^{\mathrm{i}(\boldsymbol{G}+\boldsymbol{p}_{\parallel})\cdot\boldsymbol{r}_{\parallel}} \,, \tag{17.79}$$

S is the normalization area, and $\boldsymbol{G}_0$ reduces the parallel component of the transferred momentum to the first Brillouin zone: $\boldsymbol{p}_{\parallel} - \boldsymbol{p}'_{\parallel} = \boldsymbol{q}_{\parallel} + \boldsymbol{G}_0$.

In [17.13], the approach based on (17.78) was implemented for Q2-D crystals and applied to monolayer and bilayer freestanding graphene. In Fig. 17.15, results corresponding to the experimental setup of HREELS are presented, where the reflection EEL spectrum of graphene calculated with the use of the present theory is plotted together with the reflection coefficient (the latter changing with $\boldsymbol{p}'$, while $\boldsymbol{p}$ is fixed). The energy of the incident electrons is $E_p = 41.1$ eV (the nonround primary energy in eV is due to the specific energy mesh in the wavefunction calculations), the angle of incidence is $\theta_i = 125°$, and the angle of scattering is $\theta_s = 55°$ (polar angles are relative to the positive z-axis, Fig. 17.16). It is instructive to note how the influence of the elastic scattering changes the spectrum in the energy range of the $\pi + \sigma$ plasmon, the latter extending broadly from about 10 to 25 eV within the energy-loss function approach [17.33]. A sharp peak in the reflection coefficient due to the diffraction resonance [17.35] at ≈ 11.9 eV leads to a peak in the EELS intensity at this energy. The same happens at ≈ 28.5 and 33 eV. Generally, the EEL spectrum becomes a product of the interplay of inelastic and elastic processes. At the same time, it would be an oversimplification to conclude that the EEL spectrum just follows the reflectance: In (17.34), the reflectance coefficient does not factorize and, therefore, the influence of the elastic scattering on the EELS is not straightforward. This can be observed in Fig. 17.15, considering a maximum in the EEL spectrum at ≈ 15.7 eV, where reflectance has a minimum.

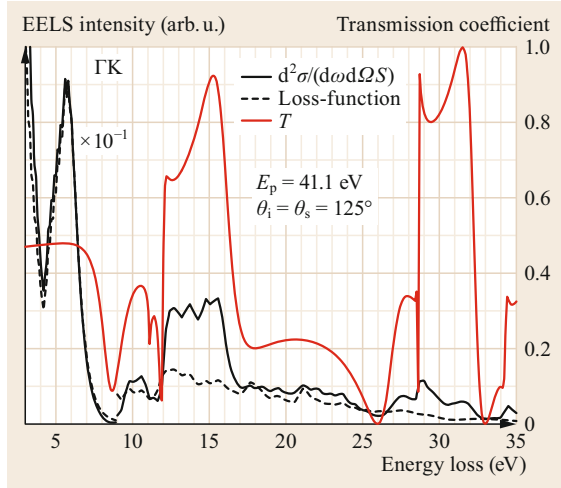

Fig. 17.17 Calculated EEL transmission spectrum of monolayer graphene (*thick line*, full theory, (17.34)), the one calculated with the use of the bulk loss function (*dashed line*, (17.47)), and the coefficient of transmission. See Fig. 17.16 for the definition of the angles. (Reproduced from [17.13])

Similar observations can be made from the EELS in the transmission geometry in comparison with the coefficient of transmission, as presented in Fig. 17.17. We conclude that the elastic scattering affects the EEL spectra dramatically, especially so in the region of the $\pi + \sigma$ plasmon and at higher energies. Different parts of

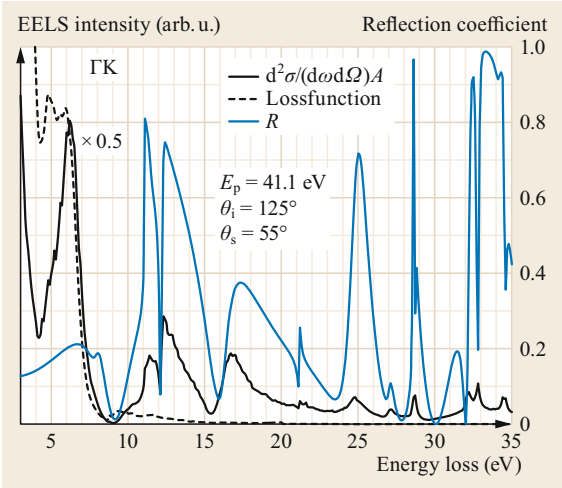

Fig. 17.18 Calculated EEL reflection spectrum of bilayer graphene (*thick black line*), the loss function (*dashed line*), and the coefficient of reflection (*blue*). In contrast to the monolayer case, the π-plasmon loss intensity is also influenced by the inclusion of the elastic scattering. (Reproduced from [17.13])

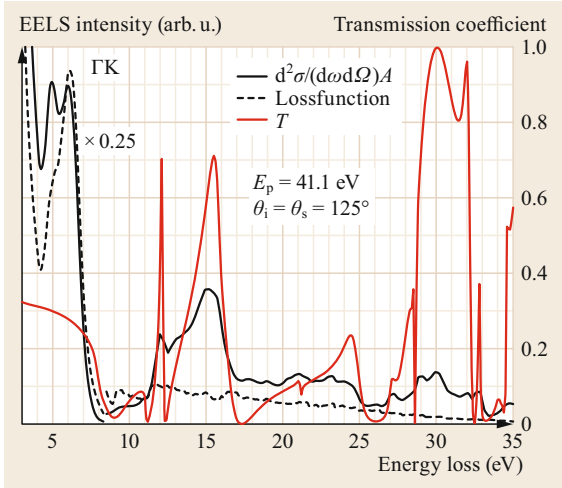

Fig. 17.19 Calculated EEL transmission spectrum of bilayer graphene (*thick black line*), the loss function (*dashed lines*), and the coefficient of transmission (*red*). In contrast to the monolayer case, the π-plasmon is also influenced by the inclusion of the elastic scattering. (Reproduced from [17.13])

the spectra are strongly enhanced and suppressed in the reflection and transmission regimes, which is mainly due to the presence of the diffraction resonances. These conclusions are supported by the spectra of the bilayer graphene in Figs. 17.18 and 17.19.

We argue that overcoming the limitations of the energy-loss functions formalism, the one-step simultaneous inelastic and elastic scattering approach can be expected to replace the former as a standard theoretical tool in the EELS of mesoscopic crystals.

17.6 Dielectric Screening in Photoemission

The alternating electric field of the light excites the electrons in the solid, and the electron promoted to a state with the energy higher than the surface potential barrier can leave the crystal, which is known as the photoelectric effect [17.41]. Apart from the probability to be excited, the probability of the photoelectron being detected with the same energy in vacuum depends on whether it would reach the surface without losing energy in inelastic collisions and on whether it would transmit through the surface or reflect back into the solid. The probability of inelastic scattering is expressed by the electron mean free path λ or electron lifetime τ, and the elastic scattering by the surface is reduced to time-reversed electron diffraction [17.42–45]. These aspects will be briefly discussed in Sect. 17.6.1. The excitation probability depends on the frequency and polarization of the incident light and also on the spatial structure of the electric field inside the solid, which may be strongly modified by the dielectric response of the electronic system, as we will discuss in Sects. 17.6.2 and 17.6.3.

Dielectric screening is most important at low photon energies, and this spectral region has recently become of special interest in angle-resolved photoemission spectroscopy [17.46–50], where a reduced inelastic scattering of the photoelectrons at low energies implies higher bulk sensitivity. A related issue is the design of laser-driven photocathodes of high quantum efficiency for free-electron lasers [17.51, 52]. Another rapidly growing field is laser-assisted time-resolved photoemission [17.53–58] based on the superimposed ultraviolet pulse and the laser pulse of $\omega = 1.7$ eV. In particular, in the streaking technique [17.53–57] the wave packet excited by the high-frequency pulse is accelerated by the laser field, and the energy shift of its spectrum is measured. In this relation, it is important to know how deeply the laser field penetrates into the solid and what its spatial structure is.

17.6.1 The Essence of the One-Step Photoemission Theory

If the interaction of the outgoing electron with the hole left behind can be neglected (the so-called sudden approximation [17.59]) and if the one-particle approach is adopted then the photocurrent is given by optical transitions from the initial states—eigenfunctions of the crystal Hamiltonian—to the time-reversed LEED states [17.42–44]. Indeed, it follows from the time-dependent perturbation theory that if an electron of initial energy E_i is excited by a harmonic perturbation $\hat{O}$ of frequency ω, the photoelectron wavefunction is

$$\Psi(\boldsymbol{r}) = \int \mathrm{d}\boldsymbol{r}'\, G^+(\boldsymbol{r},\boldsymbol{r}',E_\mathrm{f})\,\hat{O}\,\psi(\boldsymbol{r}')\,, \quad E_\mathrm{f} = E_\mathrm{i} + \omega\,. \tag{17.80}$$

This wave $|\Psi\rangle$ propagates in all directions, and it describes both external and internal photoemission. If we are interested in the probability of detecting the photoelectron outside the crystal at $\boldsymbol{r} \to +\infty$, then G^+ as a function of $\boldsymbol{r}'$ satisfies the Schrödinger equation everywhere in the half-space containing the crystal (but not the detector), and its asymptotic behavior at large $\boldsymbol{r}'$ can be inferred from the free-space Green's function G_0^+

$$G_0^+(\boldsymbol{r},\boldsymbol{r}',E) = -\frac{\exp\left(\mathrm{i}\sqrt{E}|\boldsymbol{r}-\boldsymbol{r}'|\right)}{2\pi|\boldsymbol{r}-\boldsymbol{r}'|} \tag{17.81}$$

and the resolvent identity [17.15, 42]

$$G^+(\boldsymbol{r},\boldsymbol{r}',E) = G_0^+(\boldsymbol{r},\boldsymbol{r}',E) + \int G_0^+(\boldsymbol{r},\boldsymbol{r}'',E)\,V(\boldsymbol{r}'')\,G^+(\boldsymbol{r}'',\boldsymbol{r}',E)\,\mathrm{d}\boldsymbol{r}''\,, \tag{17.82}$$

where $V(\boldsymbol{r})$ is the crystal potential. (We follow the arguments of *Adawi* [17.42] closely.) For $r \gg r'$, the dependences on $\boldsymbol{r}$ and $\boldsymbol{r}'$ of the free-space Green's function (17.81) factorize

$$G_0^+(\boldsymbol{r},\boldsymbol{r}',E) \to -\frac{\exp(\mathrm{i}kr)\exp(-\mathrm{i}\boldsymbol{k}\boldsymbol{r}')}{2\pi|\boldsymbol{r}|}, \quad \text{with } k = \sqrt{E} \quad \text{and } \boldsymbol{k} = k\frac{\boldsymbol{r}}{|\boldsymbol{r}|}\,. \tag{17.83}$$

From (17.82) and (17.83), the asymptotic formula for $G^+(\boldsymbol{r},\boldsymbol{r}',E)$ at $\boldsymbol{r} \to +\infty$ is

$$G^+(\boldsymbol{r},\boldsymbol{r}',E) = -\frac{1}{2\pi}\mathrm{e}^{\mathrm{i}kr} \times \left[\mathrm{e}^{-\mathrm{i}\boldsymbol{k}\boldsymbol{r}'} + \int G^+(\boldsymbol{r}',\boldsymbol{r}'',E)\,V(\boldsymbol{r}'')\,\mathrm{e}^{-\mathrm{i}\boldsymbol{k}\boldsymbol{r}''}\,\mathrm{d}\boldsymbol{r}''\right], \tag{17.84}$$

where we have used the identity $G^+(\boldsymbol{r}',\boldsymbol{r}'',E) = G^+(\boldsymbol{r}'',\boldsymbol{r}',E)$. For $\boldsymbol{r}'$ far from the crystal and $\boldsymbol{r}''$ inside the crystal, the function $G^+(\boldsymbol{r}',\boldsymbol{r}'',E)$ in the integrand contains only outgoing waves (in accord with its use in (17.80)). Thus, the expression in brackets contains a single *incoming* beam $\exp(-\mathrm{i}\boldsymbol{k}\boldsymbol{r}')$ coming from the detector and the outgoing beams due to the integral. The wavefunction that satisfies these conditions in vacuum is the LEED state $|\Phi\rangle$, cf., (17.37). Thus, the photocurrent J depends upon the probability of the transition from the initial state $|\mathrm{i}\,\boldsymbol{k}_\parallel\rangle$ to the *time reversed LEED state* $|\mathrm{f}\,\boldsymbol{k}_\parallel\rangle$

$$J(\omega,\boldsymbol{k}_\parallel) \approx \sqrt{E_\mathrm{f}-E_\mathrm{vac}}\left|\langle \mathrm{f}\,\boldsymbol{k}_\parallel|\,\hat{O}|\mathrm{i}\,\boldsymbol{k}_\parallel\rangle\right|^2\,, \tag{17.85}$$

where $\langle \boldsymbol{r}|\mathrm{f}\,\boldsymbol{k}_\parallel\rangle = \langle \boldsymbol{r}|\Phi\rangle^*$, and the notation $|\mathrm{i}\,\boldsymbol{k}_\parallel\rangle$ and $|\mathrm{f}\,\boldsymbol{k}_\parallel\rangle$ emphasizes that both initial and final states have a well-defined crystal momentum parallel to the surface $\boldsymbol{k}_\parallel$, but there is no translational invariance perpendicular to the surface. The initial states that belong to the $\boldsymbol{k}_\parallel$-projected bulk continuum are standing waves, which in the depth of the crystal, $z \to -\infty$, where the crystal potential is periodic, are a superposition of the incident wave and the Bloch waves reflected from the surface. (However, close to the surface the initial state wavefunction may have a more complicated structure). In the $\boldsymbol{k}_\parallel$-projected band gaps there may exist surface states, whose asymptotics at $z \to -\infty$ is a sum of evanescent Bloch waves, i.e., the waves with complex crystal momenta projections $k_\perp$. The initial state also has a band index, because there may be several degenerate states with the same $\boldsymbol{k}_\parallel$ and E_i, but here we drop it for brevity.

Photoemission is known to be a surface-sensitive phenomenon, which, in particular, manifests itself in the fact that the photocurrent from the surface state has the same order of magnitude as from the bulk bands (where the number of electrons is proportional to the thickness of the sample). The reason is the inelastic scattering of the outgoing electrons. In the one-step photoemission theory [17.42–45], the surface sensitivity is allowed for by the evanescent behavior of the LEED state, which is achieved by adding an absorbing potential $-\mathrm{i}V_\mathrm{i}$ to the Hamiltonian in the crystal half-space. Because the energy E is kept real, the imaginary optical potential forces the function $|\mathrm{f}\,\boldsymbol{k}_\parallel\rangle$ to decay in space, so that the wavevectors $k_\perp$ of all Bloch constituents of the LEED state become complex.

Computational methods for electron scattering by surfaces are based either on the layer KKR (Korringa–Kohn–Rostoker) multiple scattering technique [17.60–62] or on the Bloch-waves approach [17.63, 64]. In the latter case, one first determines the complex band structure of the semi-infinite substrate, i.e., finds for given E

and $\boldsymbol{k}_\parallel$ a number of relevant Bloch solutions with different $k_\perp$ and then connects a superposition of these partial waves to a plane-wave expansion in vacuum across the surface [17.65]. If the electron absorption is neglected, i.e., $V_\mathrm{i} = 0$, a finite number of the wavevectors $k_\perp$ are purely real, and they constitute the real $\boldsymbol{k}_\parallel$-projected band structure (propagating waves). Apart from that, for each E and $\boldsymbol{k}_\parallel$, there exists an infinite number of complex $k_\perp$, which constitute the complex band structure (evanescent waves) [17.66, 67]. For $V_\mathrm{i} \neq 0$, all $k_\perp$ become complex, and, similarly to the notion of the transmitted current, each partial wave can be ascribed *partial absorbed current* [17.68] according to the formula

$$j^\lambda = 2V_\mathrm{i} \int \left|\psi(k_\perp^\lambda, \boldsymbol{r})\right|^2 \mathrm{d}\boldsymbol{r}\,, \tag{17.86}$$

where the integration extends over the entire volume of the crystal. In the limit $V_\mathrm{i} \to 0$, (17.86) transforms into the usual expression for the transmitted current for the propagating waves ($\mathrm{Im}(k_\perp) \to 0$) and vanishes for the genuinely evanescent states (e.g., in a projected band gap, with $\mathrm{Im}(k_\perp)$ being the elastic decay rate). From the point of view of (17.85), the complex $k_\perp$ imply a broadening of the direct (crystal momentum conserving) transitions, and when the inelastic decay rate becomes comparable with the elastic one, the direct transitions picture becomes inapplicable [17.69].

17.6.2 The Optical Perturbation

The perturbation operator due to the optical electric field is expressed in terms of the vector potential $\boldsymbol{A}$ as

$$\hat{O} = \frac{1}{2c}\left[\boldsymbol{A}(\boldsymbol{r},\omega)\cdot\hat{\boldsymbol{p}} + \hat{\boldsymbol{p}}\cdot\boldsymbol{A}(\boldsymbol{r},\omega)\right], \tag{17.87}$$

where $\hat{\boldsymbol{p}} = -\mathrm{i}\nabla$ is the momentum operator. For photon energies up to far ultraviolet, the light wavelength is much larger than the dimensions of the crystal unit cell, so if the perturbing field in the solid has the same structure as in vacuum, then its spatial variations can be neglected, $\hat{\boldsymbol{p}}\cdot\boldsymbol{A} \approx 0$, and the perturbation operator would reduce to $\hat{O} = (1/c)\boldsymbol{A}\cdot\hat{\boldsymbol{p}}$. This is referred to as the dipole approximation. It may be sufficient at high enough photon energies, at which the electronic system virtually does not respond to the perturbation, $\epsilon \approx 1$. At lower energies, the effects of light refraction must be taken into account, and, in some cases, it is sufficient to include it via the macroscopic Fresnel equations based on the position-independent bulk dielectric constant of the solid [17.70–72].

Fresnel equations combined with the dipole approximation imply a certain form of the dependence of the photoemission intensity on the angle of incidence θ of the electromagnetic wave, which follows from the simple $\boldsymbol{A}(\theta)\cdot\boldsymbol{P}$ structure of the perturbing operator, where $\boldsymbol{P} = \langle \mathrm{f}\,\boldsymbol{k}_\parallel | -\mathrm{i}\nabla | \mathrm{i}\,\boldsymbol{k}_\parallel \rangle$ depends only on the initial and the final states, and $\boldsymbol{A}(\theta)$ depends on the macroscopic dielectric response. In many cases, pronounced deviations of $J(\theta)$ from this simple behavior were observed [17.73, 74], which pointed to the presence of another term in the perturbation operator. One term not included in the dipole approximation arises from the spatial inhomogeneity of the vector potential $\boldsymbol{A}(\boldsymbol{r},\omega)$ at the surface due to the simple fact that the field must change from its vacuum value to the asymptotics in the depth of the crystal given by macroscopic electrodynamics. This gives rise to the term $(1/2c)\hat{\boldsymbol{p}}\cdot\boldsymbol{A} = (-\mathrm{i}/2c)\,\mathrm{div}\,\boldsymbol{A}$, which may cause an asymmetric shape of the spectral peaks due to direct transitions [17.75, 76], or may lead to unexpectedly high intensity at the grazing incidence angle of p-polarized light [17.74], or may contribute to the circular dichroism [17.77, 78].

In the model considerations of [17.73–76], the vector potential was simply assumed to monotonically vary from its vacuum to its bulk value over a few angstroms wide surface region. A more refined treatment of the spatial inhomogeneity of $\boldsymbol{A}(\boldsymbol{r},\omega)$ requires a knowledge of the dielectric response in the surface region. The pronouncedly broken translational symmetry makes microscopic calculations very difficult, so the theoretical effort has been limited to simplest model systems. Nevertheless, the gross manifestations of the surface dielectric response in photoemission are well understood, as we show in the next section.

17.6.3 Nonlocal Dielectric Response

It has been known since the seminal works by *Feibelman* [17.79–81] that in metals, below the plasmon energy ω_p the microscopic fields generated at the surface by p-polarized light greatly enhance the emission intensity. Later, a vast experimental evidence of the enhancement of total photoyield ω_p was accumulated for simple metals [17.82–85]. Low-energy angle-resolved spectra in the constant initial state (CIS) mode were first reported for Al(100) [17.86, 87] and then for Be(0001) [17.88] and Al(111) [17.89].

Qualitatively, the emission enhancement is due to the excitation of a multipole surface plasmon [17.25, 91, 92], which was first predicted in 1970 by *Bennett* [17.93]. The multipole mode is a result of the nonlocal dielectric response at the surface. It was first calculated by *Feibelman* [17.79, 80] in the random phase approximation (RPA) for the response function in a jellium model. The local-field enhancement and the power absorption at the surface are analyzed in

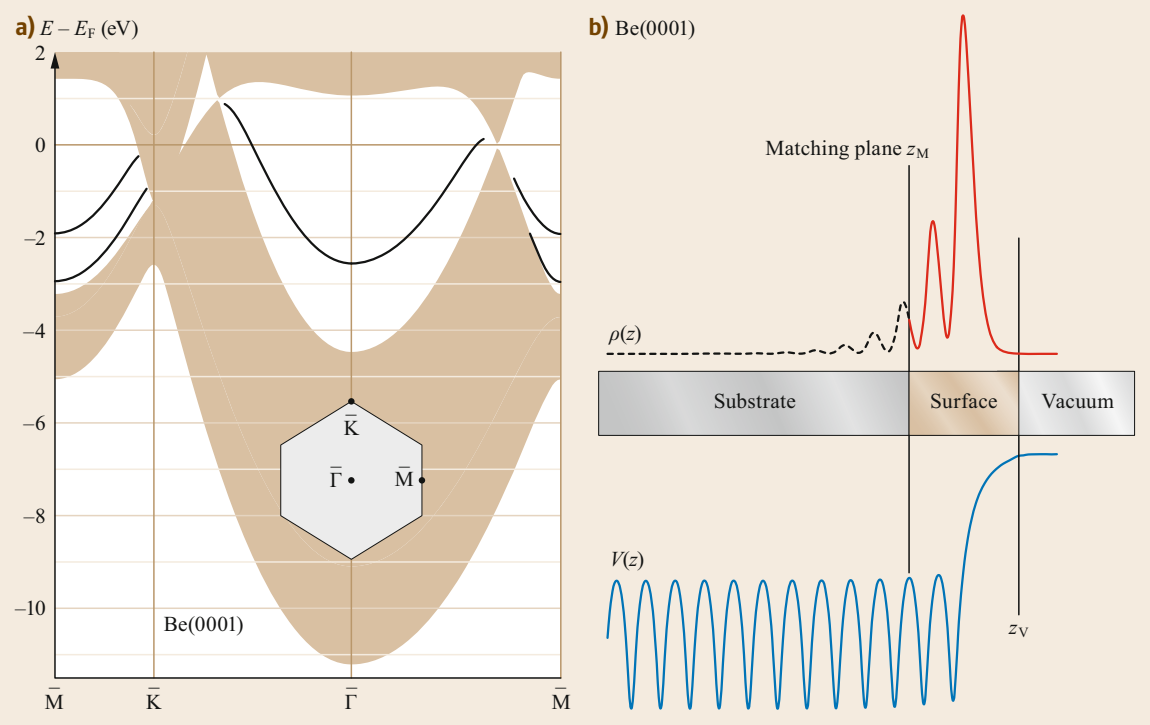

Fig. 17.20a,b Surface electronic structure of Be(0001). **(a)** The *shaded area* shows the $k_{\parallel}$ projected bulk band structure, and *lines* show calculated surface states. **(b)** Density profile $\rho(z)$ of the surface state at $\bar{\Gamma}$ and schematically shown crystal potential profile $V(z)$. The bulk band structure is calculated with a full-potential linear augmented plane wave method [17.90], and surface states are calculated with the embedding method of [17.65]; a fragment of a finite-thickness slab (from z_M to z_V) is embedded between a semi-infinite substrate and vacuum

detail in [17.81]. In metals with high electronic density, such as Al and Be, the multipole plasmon is only weakly manifested in electron energy-loss spectra [17.10] because it is blurred by a strong surface monopole plasmon, but it has a dramatic effect on photoemission intensities.

We will now introduce a quasi 1-D model to treat the nonlocal response within RPA and for Be(0001) demonstrate that the resulting total electric field combined with the (fully 3-D) one-step theory of photoemission fairly accurately describes the experimentally observed photoemission intensities. Beyond the jellium model, the present description includes (i) the nonfree-electron character of the photoemission initial and final states, (ii) the effect of optical absorption due to interband transitions on the *classical* Fresnel field, and (iii) the effect of crystallinity on the nonlocal dielectric response. The latter aspect allows for the damping due to electron-hole excitations (albeit underestimated) and eliminates the uncertainty of the jellium model [17.25] in locating the edge of the positive background relative to the crystal surface. The discussion below follows our work [17.94].

To calculate the self-consistent RPA response function χ, the Be(0001) surface is represented by a finite-thickness slab (60 atomic layers) inhomogeneous only along the direction z normal to the surface [17.95]. The model crystal potential $V(z)$ was constructed in [17.96, 97] so as to give the correct parameters of the gap at $\bar{\Gamma}$ and the location of the surface state (Fig. 17.20). (The scheme can be straightforwardly generalized to a true 3-D crystal potential, but this would require an enormous computational effort.)

In the quasi 1-D approach the z component of the electric field is the solution of the 1-D integral equation

$$\int \epsilon^{zz}(z,z',\omega)\mathcal{E}_z(z',\omega)\,\mathrm{d}z' = \mathcal{D}_z = \mathcal{E}_z^{\mathrm{vac}} \,. \quad (17.88)$$

The classical field in vacuum $\mathcal{E}_z^{\mathrm{vac}}$ is derived from the Fresnel equations using the experimental dielectric function ϵ_{mac} from [17.98], and the spatially varying total field inside the solid is obtained from the approximate microscopic theory. We thereby take into account the properties of the actual material in the bulk response but neglect the effect of the surface response on

reflection. Following the approach by *Samuelsen* and *Schattke* [17.99], we reduce the calculation of the response to the transverse field to the response to a scalar field, with the external scalar field taken as an evanescent wave

$$\phi^{\mathrm{ext}}(\boldsymbol{r}) = -\frac{2\pi}{q_\parallel}\exp(\mathrm{i}\boldsymbol{q}_\parallel \boldsymbol{r}_\parallel + q_\parallel z)\,. \tag{17.89}$$

The limit $q_\parallel \to 0$ is ensured by the numerical convergence of the results for $2\pi/q_\parallel$ much larger than the lattice constant.

The response of the electronic system to the external scalar field ϕ^{ext} is determined by the equation

$$\int \mathrm{d}z'\,\chi^0(z,z',q_\parallel,\omega)\phi^{\mathrm{tot}}(z',q_\parallel,\omega) = \int \mathrm{d}z'\,\chi(z,z',q_\parallel,\omega)\phi^{\mathrm{ext}}(z',q_\parallel,\omega)\,, \tag{17.90}$$

where ϕ^{tot} is the total self-consistent field, and the functions χ^0 and χ are the 2-D Fourier transforms of the noninteracting and interacting density-response functions, respectively. The noninteracting response function is derived from the single-particle eigenfunctions ψ_n, which, in the geometry of thick repeated slabs, are standing waves in the direction perpendicular to the surface, and they are independent of the Bloch vector $\boldsymbol{k}_\parallel$ parallel to the surface

$$\chi^0(z,z',q_\parallel,\omega) = 2\sum_{nm}\psi_n(z)\psi_m^*(z)\psi_n^*(z')\psi_m(z') \times \sum_{\boldsymbol{k}_\parallel}\frac{f_{\boldsymbol{k}_\parallel n} - f_{\boldsymbol{k}_\parallel+\boldsymbol{q}_\parallel m}}{E_{\boldsymbol{k}_\parallel n} - E_{\boldsymbol{k}_\parallel+\boldsymbol{q}_\parallel m} + \omega + \mathrm{i}\eta}\,. \tag{17.91}$$

Here, the sum over n and m comprises both occupied and unoccupied states, and $f_{\boldsymbol{k}_\parallel n} = \Theta(E_{\mathrm{F}} - E_{\boldsymbol{k}_\parallel n})$ are the Fermi occupation factors.

Within RPA, the interacting response function χ is the solution of the integral equation

$$\chi(z,z',q_\parallel,\omega) = \chi^0(z,z',q_\parallel,\omega) + \int \mathrm{d}z_1 \int \mathrm{d}z_2\,\chi^0(z,z_1,q_\parallel,\omega)v(z_1,z_2,q_\parallel)\chi(z_2,z',q_\parallel,\omega)\,, \tag{17.92}$$

where $v(z_1,z_2,q_\parallel)$ is the 2-D Fourier transform of the bare Coulomb interaction. In the present approach, the integral equation reduces to a linear algebra matrix equation (more details of the calculations are given in [17.95]). Finally, the solution of (17.88) $\mathcal{E}_z(z',\omega)$ is obtained from the solution ϕ^{tot} of (17.90) as its gradient $-\mathrm{d}\phi^{\mathrm{tot}}/\mathrm{d}z$ scaled so as to equal the z projection of the electric field of the electromagnetic wave in vacuum $\mathcal{E}_z^{\mathrm{vac}}$.

In jellium, light is absorbed only at the surface, and the absorbed power is proportional to the imaginary part of the centroid of the induced density $d_\perp(\omega)$ [17.81]. In a crystal, owing to the bulk local fields, the induced microscopic dipole moment extends to macroscopic distances, and surface and bulk absorption cannot be unambiguously separated. The surface absorption is, however, clearly seen in the energy-depth distribution $P(z,\omega)$ of the absorbed power; the results for 1-D crystal and jellium models of Be(0001) for p-polarized light incident at 45° are shown in Fig. 17.21 along with field intensity $I(z,\omega)$, which is the relevant quantity for photoemission. Above ω_{p}, bulk plasmons are excited, the momentum being provided by the surface; the plasmon wavevector increasing with energy is clearly seen for the jellium model, but for the crystalline Be, it is blurred by the stronger crystal fields. Below ω_{p}, the surface absorption peaks at the multipole plasmon energy $\omega_{\mathrm{m}} \approx 0.8\omega_{\mathrm{p}}$ in perfect agreement with the earlier jellium theory [17.81].

17.6.4 Photoemission from a Surface State

To see how the inclusion of the total exciting field into the perturbation operator $\hat{O}$ of (17.85) affects photoemission intensity, let us consider the emission from the surface state at $\bar{\Gamma}$ on Be(0001), see Fig. 17.20. Because it is located in a wide energy gap, its signal does not overlap with the bulk emission. The surface state is almost entirely localized within two outermost atomic layers (Fig. 17.20), so its spectrum cannot be understood in terms of direct transitions, and the evanescent part of the complex band structure is expected to play an important role. In addition, in spite of the small atomic number of Be, its unoccupied band structure is not free-electron-like, see Fig. 17.22a, as evident from the high-energy structures B–E in the $J(E)$ curve in Fig. 17.22b. Figure 17.22a relates these maxima to the complex band structure of the LEED states in the AΓA interval of the bulk Brillouin zone; the intensity is distributed over several conducting branches (i.e., partial waves that affect the escape of the photoelectron, see Sect. 17.6.1), and the observed spectrum results from a superposition of transition amplitudes to different Bloch waves. (For technical details of the calculation, see [17.94]).

Because we are interested in photoemission intensities we should pay attention to the effect of the absorbing potential $-\mathrm{i}V_{\mathrm{i}}(E)$, which controls the surface sensitivity in the calculations. In principle,

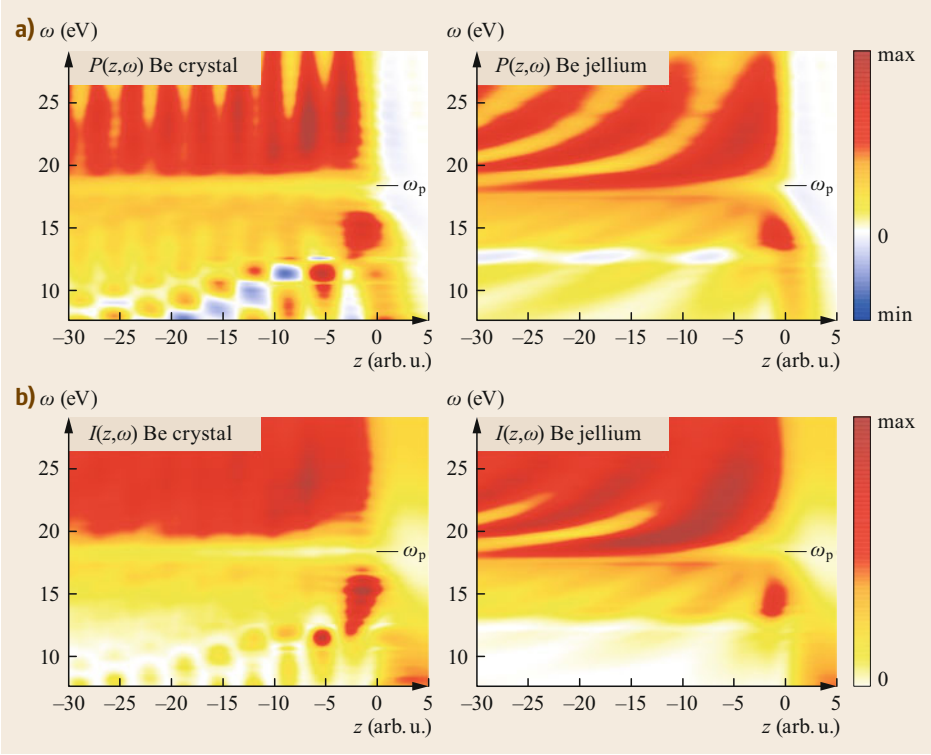

Fig. 17.21a,b Frequency-dependent spatial distribution of the electric field at the surface Be(0001). **(a)** Power absorption density $P(z,\omega) = [\omega/(4\pi)]\,\mathrm{Im}[\mathcal{D}_z E_z^*(z,\omega)]$ and **(b)** intensity $I(z,\omega) = |\mathcal{E}_z(z,\omega)|^2$. Calculations are for $q = 0.02$ (arb. u.)$^{-1}$. (Reproduced from [17.94])

this parameter can be obtained as the expectation value of the imaginary part of the self-energy operator [17.100], which can be calculated within the *GW* approximation [17.101, 102] from the ab-initio band structure [17.103]. However, for such a complicated electronic structure as that of Be, a reliable ab-initio calculation is still very difficult. In the present theory, V_i is the only unknown parameter, which, however, is known to be not strongly material dependent [17.104, 105] and to have a common behavior: V_i is close to zero at the Fermi energy, it increases sharply at the bulk plasma frequency ($\omega_p = 18.4$ eV for Be) and then steadily grows with energy. Assuming this shape, we deduced the function $V_i(E)$ (see the inset in Fig 17.22b) from the results for Al(100) [17.105] with an expected uncertainty of ± 0.5 eV (shown by shading). The variations of the emission intensity due to the uncertainty in V_i are shown by the shading of the $J(E)$ curve in Fig. 17.22b, and they are seen to be quite small compared to the intensity variations over the spectrum. Such weak sensitivity to the optical potential is a consequence of the strong spatial localization of the initial state.

The strongest peak A is at $\omega = 15$ eV, and it is entirely due to the enhancement of the exciting field caused by the multipole plasmon. Above ω_p, the higher intensity of the emission caused by the total field rather than by the incident field (dashed curve) is due to the classical response (described by the Fresnel formulas). In particular, when the reflected field is in phase with the incident field, a classical resonance occurs, which, for the incidence angle of 45°, is at $\omega_p\sqrt{2} = 26$ eV. However, in Be the classical resonance is very broad, and maximum B is, actually, a final state effect. For the comparison with the experiments [17.88], we scaled the $J(\omega)$ spectrum so as to match the measured curve over the interval 25–45 eV, the solid line in Fig. 17.22a. The theory rather accurately describes the intensity variation by two orders of magnitude in the interval 10–50 eV, which proves that the calculated exciting field is quite realistic, as well as are the final states. (The slow decrease of intensity above 50 eV may be due to experimental conditions.) We may conclude that the present model for the dielectric response, which is based on RPA and on 1-D crystallinity, is adequate for real surfaces.

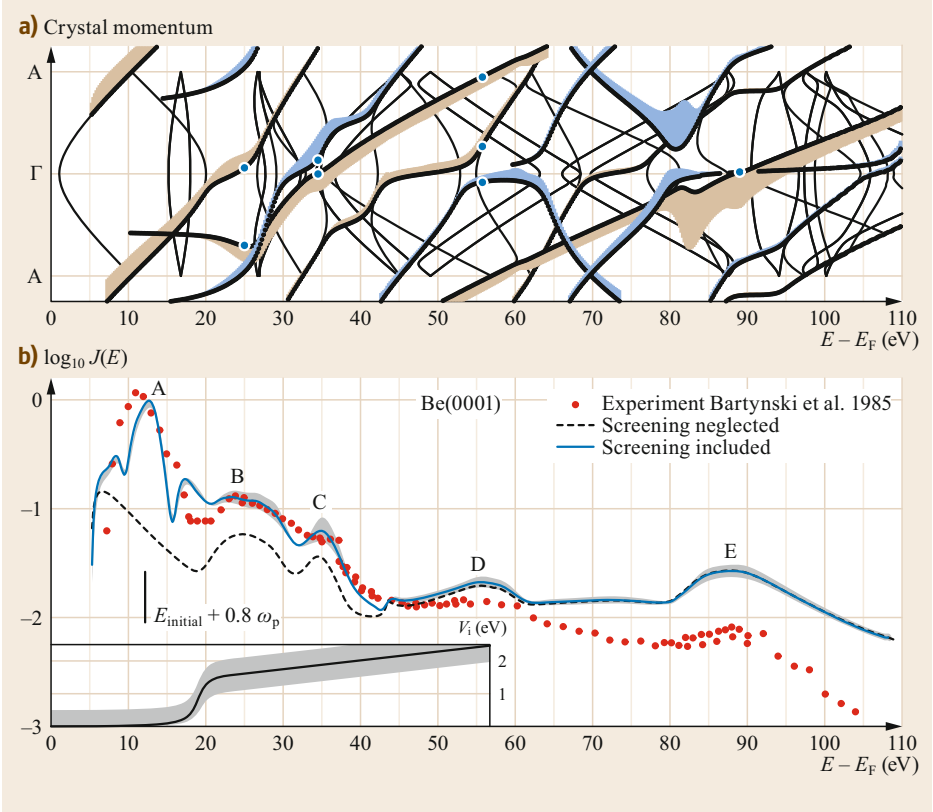

Fig. 17.22a,b Band structure analysis of the photoemission from the surface state at $\bar{\Gamma}$ on Be(0001). **(a)** Complex band structure of Be(0001) along the AΓA interval: *thin lines* are the (real) bulk band structure, $\mathrm{Im}(k_\perp = 0)$. *Thick lines* show Bloch waves that contribute to LEED states. Note that of the real band structure only the waves that move towards the surface contribute to the outgoing wave (which makes the thick lines asymmetric with respect to Γ). The vertical extent of the *shading* is proportional to the modulus (not squared) of the contribution to the matrix element from the individual partial wave. *Circles* indicate $k_\perp$ vectors of the Bloch waves at the maxima B–E. **(b)** Experimental [17.88] semilogarithmic intensity profile $\log_{10} J(\omega)$ (*circles*) of the $\bar{\Gamma}$ surface-state emission compared to the theory with (*solid line*) and without screening (*dashed line*). The *vertical bar* at $E - E_\mathrm{F} = 12\,\mathrm{eV}$ indicates the excitation energy of $0.8\omega_\mathrm{p}$. *Inset*: optical potential $V_\mathrm{i}(E)$. *Shading* shows the estimated uncertainty of V_i and in graph **(b)** the related intensity uncertainty. (Reproduced from [17.94])

17.7 Calculation of Response Functions

Here, we introduce an ab-initio method of the calculation of the response function for realistic systems with full inclusion of the electronic band structure. Also, we give some details of a simplified approach based on a 1-D model potential that simulates key features of the surface electronic structure.

17.7.1 Ab-initio Model

According to the time-dependent density-functional theory [17.106], the response function of interacting electrons χ is related to that of noninteracting electrons χ^0 through the integral equation

$$\chi(\boldsymbol{r},\boldsymbol{r}',\omega) = \chi^0(\boldsymbol{r},\boldsymbol{r}',\omega) + \int \mathrm{d}\boldsymbol{r}_1 \int \mathrm{d}\boldsymbol{r}_2\, \chi^0(\boldsymbol{r},\boldsymbol{r}_1,\omega)[v(\boldsymbol{r}_1,\boldsymbol{r}_2) + K^\mathrm{xc}(\boldsymbol{r}_1,\boldsymbol{r}_2,\omega)]\chi(\boldsymbol{r}_2,\boldsymbol{r}',\omega)\,, \quad (17.93)$$

where $v(\boldsymbol{r}_1,\boldsymbol{r}_2)$ is the Coulomb interaction potential, and $K^\mathrm{xc}(\boldsymbol{r}_1,\boldsymbol{r}_2,\omega)$ takes into account dynamical exchange-correlation effects. Many approximate forms for K^xc have been proposed. The simplest and most common approximation is RPA, in which K^xc is simply set to zero.

At the surface, the translational symmetry in the direction perpendicular to the surface is broken, and a direct application of (17.93) with full inclusion of the band structure would be a formidable task. One way to solve this problem is to resort to so-called repeated-slab geometry, where one constructs an artificial 3-D lattice with a unit cell containing a slab of a finite number of atomic layers representing the crystal surface of interest sandwiched between two vacuum spaces (cf., supercell geometry of Sect. 17.5.1). This cell is periodically repeated in the direction normal to the surface. For such geometry, one can perform 3-D Fourier transformation of all quantities and employ the computational codes developed for 3-D lattices. The only difference here is that the 2-DBZ is used, since the cell size in the direction perpendicular to the surface is substantially larger than its in-plane size.

For a 3-D periodic system, the integral equation (17.93) for χ transforms into a matrix equation, which for a given in-plane momentum transfer $\boldsymbol{q}_\parallel$ reads

$$\begin{aligned}&\chi_{GG'}(\boldsymbol{q}_\parallel,\omega)\\&=\chi^0_{GG'}(\boldsymbol{q}_\parallel,\omega)+\sum_{G_1}\sum_{G_2}\chi^0_{GG_1}(\boldsymbol{q}_\parallel,\omega)\left[\upsilon_{G_1}(\boldsymbol{q}_\parallel)\delta_{G_1G_2}\right.\\&\quad\left.+K^{\mathrm{xc}}_{G_1G_2}(\boldsymbol{q}_\parallel,\omega)\right]\chi_{G_2G'}(\boldsymbol{q}_\parallel,\omega)\,.\end{aligned}\tag{17.94}$$

The matrix elements of the response function of noninteracting electrons χ^0 are given by

$$\begin{aligned}&\chi^0_{GG'}(\boldsymbol{q}_\parallel,\omega)\\&=\frac{2}{S}\sum_{\boldsymbol{k}_\parallel}^{\text{2-DBZ}}\sum_{nn'}\frac{f_{\boldsymbol{k}_\parallel n}-f_{\boldsymbol{k}_\parallel+\boldsymbol{q}_\parallel n'}}{E_{\boldsymbol{k}_\parallel n}-E_{\boldsymbol{k}_\parallel+\boldsymbol{q}_\parallel n'}+(\omega+\mathrm{i}\eta)}\\&\quad\times\left\langle\psi_{\boldsymbol{k}_\parallel n}\right|\mathrm{e}^{-\mathrm{i}(\boldsymbol{q}_\parallel+\boldsymbol{G})\cdot\boldsymbol{r}}\left|\psi_{\boldsymbol{k}_\parallel+\boldsymbol{q}_\parallel n'}\right\rangle\\&\quad\times\left\langle\psi_{\boldsymbol{k}_\parallel+\boldsymbol{q}_\parallel n'}\right|\mathrm{e}^{\mathrm{i}(\boldsymbol{q}_\parallel+\boldsymbol{G}')\cdot\boldsymbol{r}}\left|\psi_{\boldsymbol{k}_\parallel n}\right\rangle,\end{aligned}\tag{17.95}$$

where the factor 2 accounts for spin, S is the normalization area, and the second sum runs over the band structure for each wavevector $\boldsymbol{k}_\parallel$ in the 2-DBZ, $f_{\boldsymbol{k}_\parallel n}=\{\exp[(E_{\boldsymbol{k}_\parallel n}-\mu)/T]+1\}^{-1}$ is the Fermi factor, with μ and T being the chemical potential and temperature of the electron gas, respectively; $E_{\boldsymbol{k}_\parallel n}$ and $\psi_{\boldsymbol{k}_\parallel n}$ are the one-particle eigenvalues and eigenfunctions, and η is a positive infinitesimal. For the evaluation of $E_{\boldsymbol{k}_\parallel n}$ and $\psi_{\boldsymbol{k}_\parallel n}$, one can employ a variety of methods developed within the framework of DFT. However, the computational cost of the evaluation of the matrix elements in (17.95) may be very different for different methods. The most efficient and simple computational realization is achieved in the plane-wave representation for the wavefunctions $\psi_{\boldsymbol{k}_\parallel n}$, but this limits the consideration to relatively simple elementary solids.

The evaluation of the χ^0 matrix is the most time-consuming part of the 3-D response calculations. In order to save computational time, one can first calculate [17.107, 108] the absorptive part of the χ^0 function according to (17.13), which, at $T=0$, takes the form

$$\begin{aligned}&\chi^{0A}_{GG'}(\boldsymbol{q}_\parallel,\omega)\\&=-\frac{2\pi}{S}\sum_{\boldsymbol{k}_\parallel}^{\text{2-DBZ}}\sum_{n}^{\text{occ}}\sum_{n'}^{\text{unocc}}\delta(E_{\boldsymbol{k}_\parallel n}-E_{\boldsymbol{k}_\parallel+\boldsymbol{q}_\parallel n'}+\omega)\\&\quad\times\left\langle\psi_{\boldsymbol{k}_\parallel n}\right|\mathrm{e}^{-\mathrm{i}(\boldsymbol{q}_\parallel+\boldsymbol{G})\cdot\boldsymbol{r}}\left|\psi_{\boldsymbol{k}_\parallel+\boldsymbol{q}_\parallel n'}\right\rangle\\&\quad\times\left\langle\psi_{\boldsymbol{k}_\parallel+\boldsymbol{q}_\parallel n'}\right|\mathrm{e}^{\mathrm{i}(\boldsymbol{q}_\parallel+\boldsymbol{G}')\cdot\boldsymbol{r}}\left|\psi_{\boldsymbol{k}_\parallel n}\right\rangle,\end{aligned}\tag{17.96}$$

where the sum over n (n') is limited to occupied (unoccupied) states. Another important problem is related to the long-range Coulomb interaction between oscillating charges in different slabs, which may introduce spurious effects in the response function χ. For instance, the plasmon dispersion is distorted in the long-wavelength limit. This issue is especially crucial, if one is interested in the dispersion of a 2-D plasmon [17.109]. Several recipes were proposed to solve this problem. One of the approaches [17.33] is described in Sect. 17.5.1. Implementation of this recipe in the first-principles calculations of the plasmonic structure of thin Pb(111) films demonstrated [17.110] its efficiency in the elimination of the spurious long-range Coulomb interaction between different slabs.

The ab-initio method to evaluate the response functions with full inclusion of the electronic band structure still has to be incorporated into the theories of the inelastic scattering of electrons and photoemission presented in previous sections. The recent progress in the numerical evaluation of response functions from first principles by different groups promises that this can be done in the nearest future. One of the main advantages of the ab-initio approach over the simple models based on a free-electron approximation is its ability to correctly describe both the energy and the lifetime of collective electronic excitations at the surfaces. The surface plasmon properties obtained with the surface response function evaluated with a full inclusion of the surface electronic structure demonstrated its efficiency: such calculations are able to reproduce the dispersion of the plasmon energy and lifetime for clean surfaces of the simple metals Mg(0001) [17.111–113], Al(111) [17.112], Be(0001) [17.114–116], and Pb(111) [17.110] very closely to the energy-loss experiments [17.117–119]. Moreover, since in this approach, the valence d electronic states are taken into account, the surface plasmon properties of the noble metals Cu(111) [17.120], Ag(111) [17.120, 121], and Au(111) [17.120, 122]

are well described as well, in agreement with the experiment [17.2]. Similar calculations were performed for Si(001) [17.123] and for surfaces with adsorbed layers, such as p(2×2)K/Be(0001) [17.124, 125], p(2×2)K/graphite [17.126], graphene/SiC(0001) and graphene/Al(111) [17.127], and H/Ag(111) [17.121] and monolayer and bilayer graphene [17.113, 127–133].

17.7.2 One-Dimensional Model

The results presented in this chapter are based on the response function χ^0 obtained with a simplified model, in which the band structure effects are included via the model potential of [17.97]. In contrast to the potential of the frequently used jellium model, the potential of [17.97] reproduces the key features of the surface band structure, namely the energy gap in the $\boldsymbol{k}_\parallel = 0$-projected bulk band structure and the energy of the surface state and the first image state. For simplicity, this model assumes the translational invariance and a free-electron-like dispersion for the electronic states in the plane of the surface. As a result, the wavefunctions are

$$\psi_{\boldsymbol{k}_\parallel n}(\boldsymbol{r}) = \frac{1}{\sqrt{S}} \mathrm{e}^{\mathrm{i}\boldsymbol{k}_\parallel \cdot \boldsymbol{r}_\parallel} \psi_n(z) \,, \tag{17.97}$$

and the corresponding single-particle energies are

$$E_{\boldsymbol{k}_\parallel n} = E_n + \frac{k_\parallel^2}{2m_n} \,, \tag{17.98}$$

where the energy E_n is obtained by solving the 1-D Schrödinger equation with the model potential, and m_n is the effective mass of the n-th energy band, which, in principle, may be different from unity (using the effective masses partially compensates for the averaging of the potential in the xy plane).

In this representation, the calculation of $\chi^0(\boldsymbol{r}, \boldsymbol{r}', \omega)$ reduces to the calculation of $\chi^0(z, z', q_\parallel, \omega)$ [17.134, 135], and the expression (17.95) for the response function of noninteracting electrons χ^0 becomes (17.91). In order to proceed one can expand the wavefunctions $\psi_n(z)$ in a Fourier series, again using a slab geometry for the surface description [17.134]. In this case, the Fourier representation of the noninteracting density-response function χ^0 takes the following form

$$\begin{aligned}
&\chi^0(z, z', q_\parallel, \omega) \\
&= \sum_{m=0}^{\infty} \sum_{n=0}^{\infty} \chi^{0+}_{mn}(q_\parallel, \omega) \cos\left(\frac{2\pi m}{d} z\right) \cos\left(\frac{2\pi n}{d} z'\right) \\
&\quad + \sum_{m=1}^{\infty} \sum_{n=1}^{\infty} \chi^{0-}_{mn}(q_\parallel, \omega) \sin\left(\frac{2\pi m}{d} z\right) \sin\left(\frac{2\pi n}{d} z'\right) ,
\end{aligned} \tag{17.99}$$

where d is the width of the unit cell composed of the atomic layers and the empty space.

Within the framework of RPA, the 2-D Fourier transform $\chi(z, z', q_\parallel, \omega)$ of the density-response function of an interacting electron system is obtained by solving the integral equation (17.92). All quantities entering (17.92) can be represented in the form of (17.99), which yields the following matrix equation for the coefficients $\chi^{\pm}_{m,n}(q_\parallel, \omega)$

$$\begin{aligned}
\chi^{\pm}_{mn}(q_\parallel, \omega) = \chi^{0\pm}_{mn}(q_\parallel, \omega) + \sum_{m', n'} \big[&\chi^{0\pm}_{mm'}(q_\parallel, \omega) v_{m'n'}(q_\parallel) \\
&\times \chi^{\pm}_{n'n}(q_\parallel, \omega) \big],
\end{aligned} \tag{17.100}$$

with $v_{mn}(q_\parallel)$ being the coefficients of the bare Coulomb interaction $v(z, z', q_\parallel)$. Further computational details of this approach can be found in [17.95].

17.8 Conclusions and Perspectives

We have reviewed the main challenges arising in the development of the theoretical approaches to the electron and photoemission spectroscopies of bulk, surface, and quasi 2-D solid systems. Over the years, the general trend of the transfer from model to ab-initio approaches have been clearly identified.

We have discussed the current state-of-the-art of the theory of EELS up to its very recent developments. A fundamental limitation of the traditional picture of the inelastic scattering of electrons at solid targets has been revealed. That is the neglect of the simultaneous *potential scattering* at the crystal lattice, which turns out to be critically important, especially for quasi 2-D materials in the energy range of incident electrons of $\approx 10-100$ eV, corresponding to the values used in high-resolution EELS. We have shown how this shortcoming can be overcome by the construction of the theory of one-step combined inelastic and elastic electron scattering. These results open a path to the *theoretically interpretable* application of HREELS for studying Q2-D materials with meV resolution, an unachievable limit with the presently available EELS in the TEM technique.

We have analyzed the results obtained with the new theory, which show a strong coupling between inelastic and elastic channels in monolayer and bilayer graphene in the HREELS regime. In particular, the excitation of

the $\pi + \sigma$ plasmon is dramatically affected by the scattering in the elastic channel. These theoretical findings constitute a strong motivation for performing HREELS experiments on free-standing Q2-D crystals, especially so in view of the recent advances in the HREELS techniques.

In our example calculations, we used the local-density approximation (LDA) to DFT for the ground-state calculations and RPA for the dynamic response calculations, respectively. This was done consciously for the sake of simplicity and considering that our goal was highlighting the coupling between inelastic and elastic processes, rather than studying the many-body effects in Q2-D materials, the latter problem having been addressed in a large body of literature ([17.136] and references therein). The basis of our approach, (17.78), however, remains valid at any level of (TD)DFT, allowing future inclusion of the many-body effects within the framework of this theory. At the same time, it must be noted that the supercell method might encounter difficulties in the presence of the long-range xc [17.137], in which case the *native* approaches [17.138] (considering a single Q2-D crystal from the very beginning) will be necessary. The well-known shortcomings of LDA and RPA [17.16] are the likely source of the remaining discrepancies between our calculations and experiment in the energy range of the $\pi + \sigma$ plasmon.

Finally, we argued that overcoming the limitations of the presently generally adopted energy-loss functions formalism, the theory of the simultaneous inelastic and elastic electron scattering can be expected to replace the previous approaches as a standard theoretical tool in the EELS of mesoscopic materials.

References

17.1 H. Ibach, D.L. Mills: *Electron Energy Loss Spectroscopy and Surface Vibrations* (Academic Press, New York 1982)

17.2 M. Rocca: Low-energy EELS investigation of surface electronic excitations on metals, Surf. Sci. Rep. **22**, 1–71 (1995)

17.3 R.F. Egerton: Electron energy-loss spectroscopy in the TEM, Rep. Prog. Phys. **72**, 016502 (2009)

17.4 M.-L. Xu, B.M. Hall, S.Y. Tong, M. Rocca, H. Ibach, S. Lehwald, J.E. Black: Energy dependence of inelastic electron scattering cross section by surface vibrations: Experimental measurement and theoretical interpretation, Phys. Rev. Lett. **54**, 1171–1174 (1985)

17.5 Z.Q. Wu, Y. Chen, M.L. Xu, S.Y. Tong, S. Lehwald, M. Rocca, H. Ibach: Adsorption distance of S on Ni(001): An electron-energy-loss-spectroscopy cross-section analysis of the Ni(001)-c(2x2) S system, Phys. Rev. B **39**, 3116–3124 (1989)

17.6 Y. Chen, S.Y. Tong, M. Rocca, P. Moretto, U. Valbusa, K.H. Bohnen, K.M. Ho: High-resolution electron energy-loss spectroscopy analysis of Ag(001): Discovery of a new surface longitudinal mode using first-principles phonon calculations, Surf. Sci. **250**, L389–L394 (1991)

17.7 M. Rocca, H. Ibach, S. Lehwald, T.S. Rahman: Surface phonon dispersion of surface and adsorbate layers. In: *Structure and Dynamics of Surfaces*, Topics in Current Physics, Vol. 41, ed. by P. von Blanckenhagen, W. Schommers (Springer, Berlin, Heidelberg 1986) p. 245

17.8 A. Liebsch, W.L. Schaich: Influence of a polarizable medium on the nonlocal optical response of a metal surface, Phys. Rev. B **52**, 14219–14234 (1995)

17.9 V.U. Nazarov: Analytical properties of dielectric response of semi-infinite systems and the surface electron energy loss function, Surf. Sci. **331–333**, 1157–1162 (1995)

17.10 V.U. Nazarov: Multipole surface-plasmon-excitation enhancement in metals, Phys. Rev. B **59**, 9866–9869 (1999)

17.11 V.U. Nazarov, S. Nishigaki: Inelastic low energy electron diffraction at metal surfaces, Surf. Sci. **482–485**, 640–647 (2001)

17.12 V.U. Nazarov, V.M. Silkin, E.E. Krasovskii: Role of the kinematics of probing electrons in electron energy-loss spectroscopy of solid surfaces, Phys. Rev. B **93**, 035403 (2016)

17.13 V.U. Nazarov, V.M. Silkin, E.E. Krasovskii: Probing mesoscopic crystals with electrons: One-step simultaneous inelastic and elastic scattering theory, Phys. Rev. B **96**, 235414 (2017)

17.14 L.D. Landau, E.M. Lifshitz: *Quantum Mechanics: The Non-Relativistic Theory* (Butterworth-Heinemann, London 1981)

17.15 J.R. Taylor: *Scattering Theory* (Wiley, New York 1972)

17.16 G.F. Giuliani, G. Vignale: *Quantum Theory of the Electron Liquid* (Cambridge Univ. Press, Cambridge 2005)

17.17 H. Kohl, H. Rose: Theory of image formation by inelastically scattered electrons in the electron microscope. In: *Advances in Electronics and Electron Physics*, Vol. 65, ed. by P.W. Hawkes (Academic Press, New York 1985) pp. 173–227

17.18 S.L. Dudarev, L.-M. Peng, M.J. Whelan: Correlations in space and time and dynamical diffraction of high-energy electrons by crystals, Phys. Rev. B **48**, 13408–13429 (1993)

17.19 L.J. Allen, T.W. Josefsson: Inelastic scattering of fast electrons by crystals, Phys. Rev. B **52**, 3184–3198 (1995)

17.20 P. Schattschneider, B. Jouffrey, M. Nelhiebel: Dynamical diffraction in electron-energy-loss spectrometry: The independent Bloch-wave model, Phys. Rev. B **54**, 3861–3868 (1996)

17.21 P. Schattschneider, M. Nelhiebel, H. Souchay, B. Jouffrey: The physical significance of the mixed dynamic form factor, Micron **31**, 333–345 (2000)

17.22 E.K.U. Gross, W. Kohn: Local density-functional theory of frequency-dependent linear response, Phys. Rev. Lett. **55**, 2850–2852 (1985)

17.23 W. Kohn, L.J. Sham: Self-consistent equations including exchange and correlation effects, Phys. Rev. **140**, A1133–A1138 (1965)

17.24 D. Pines: *Elementary excitations in solids* (Benjamin, New York 1963)

17.25 A. Liebsch: *Electronic excitations at metal surfaces* (Plenum, New York 1997)

17.26 L.D. Landau, E.M. Lifshitz: *Electrodynamics of continuous media* (Pergamon, New York 1960)

17.27 K.-D. Tsuei, E.W. Plummer, A. Liebsch, K. Kempa, P. Bakshi: Multipole plasmon modes at a metal surface, Phys. Rev. Lett. **64**, 44–47 (1990)

17.28 N.D. Lang, W. Kohn: Theory of metal surfaces: Charge density and surface energy, Phys. Rev. B **1**, 4555–4568 (1970)

17.29 A. Politano, V. Formoso, G. Chiarello: Collective electronic excitations in thin Ag films on Ni(111), Plasmonics **8**, 1683–1690 (2013)

17.30 V.M. Silkin, P. Lazić, N. Došlić, H. Petek, B. Gumhalter: Ultrafast electronic response of Ag(111) and Cu(111) surfaces: From early excitonic transients to saturated image potential, Phys. Rev. B **92**, 155405 (2015)

17.31 A.H. Castro Neto, F. Guinea, N.M.R. Peres, K.S. Novoselov, A.K. Geim: The electronic properties of graphene, Rev. Mod. Phys. **81**, 109–162 (2009)

17.32 T. Eberlein, U. Bangert, R.R. Nair, R. Jones, M. Gass, A.L. Bleloch, K.S. Novoselov, A. Geim, P.R. Briddon: Plasmon spectroscopy of free-standing graphene films, Phys. Rev. B **77**, 233406 (2008)

17.33 V.U. Nazarov: Electronic excitations in quasi-2D crystals: What theoretical quantities are relevant to experiment?, New J. Phys. **17**, 073018 (2015)

17.34 J. Lu, K.P. Loh, H. Huang, W. Chen, A.T.S. Wee: Plasmon dispersion on epitaxial graphene studied using high-resolution electron energy-loss spectroscopy, Phys. Rev. B **80**, 113410 (2009)

17.35 V.U. Nazarov, E.E. Krasovskii, V.M. Silkin: Scattering resonances in two-dimensional crystals with application to graphene, Phys. Rev. B **87**, 041405(R) (2013)

17.36 M. Pisarra, P. Riccardi, A. Sindona, A. Cupolillo, N. Ligato, C. Giallombardo, L. Caputi: Probing graphene interfaces with secondary electrons, Carbon **77**, 796–802 (2014)

17.37 J. Jobst, J. Kautz, D. Geelen, R.M. Tromp, S.J. van der Molen: Nanoscale measurements of unoccupied band dispersion in few-layer graphene, Nat. Commun. **6**, 8926 (2015)

17.38 F. Wicki, J.-N. Longchamp, T. Latychevskaia, C. Escher, H.-W. Fink: Mapping unoccupied electronic states of freestanding graphene by angle-resolved low-energy electron transmission, Phys. Rev. B **94**, 075424 (2016)

17.39 M. Krivenkov, D. Marchenko, J. Sánchez-Barriga, O. Rader, A. Varykhalov: Suppression of electron scattering resonances in graphene by quantum dots, Appl. Phys. Lett. **111**(16), 161605 (2017)

17.40 M. v. Laue: The diffraction of an electron-wave at a single layer of atoms, Phys. Rev. **37**, 53–59 (1931)

17.41 A. Einstein: Über einen die Erzeugung und Verwandlung des Lichtes betreffenden heuristischen Gesichtspunkt, Ann. Phys. **17**, 132 (1905)

17.42 I. Adawi: Theory of the surface photoelectric effect for one and two photons, Phys. Rev. **134**, A788–A798 (1964)

17.43 G.D. Mahan: Theory of photoemission in simple metals, Phys. Rev. B **2**, 4334–4350 (1970)

17.44 P.J. Feibelman, D.E. Eastman: Photoemission spectroscopy – correspondence between quantum theory and experimental phenomenology, Phys. Rev. B **10**, 4932–4947 (1974)

17.45 R.O. Kuzian, E.E. Krasovskii: One-step approach to ARPES from strongly correlated solids: A Mott-Hubbard system, Phys. Rev. B **94**, 115119 (2016)

17.46 T. Kiss, F. Kanetaka, T. Yokoya, T. Shimojima, K. Kanai, S. Shin, Y. Onuki, T. Togashi, C. Zhang, C.T. Chen, S. Watanabe: Photoemission spectroscopic evidence of gap anisotropy in an *f*-electron superconductor, Phys. Rev. Lett. **94**, 057001 (2005)

17.47 J.D. Koralek, J.F. Douglas, N.C. Plumb, Z. Sun, A.V. Fedorov, M.M. Murnane, H.C. Kapteyn, S.T. Cundiff, Y. Aiura, K. Oka, H. Eisaki, D.S. Dessau: Laser based angle-resolved photoemission, the sudden approximation, and quasiparticle-like spectral peaks in $Bi_2Sr_2CaCu_2O_{8+\delta}$, Phys. Rev. Lett. **96**, 017005 (2006)

17.48 T. Yamasaki, K. Yamazaki, A. Ino, M. Arita, H. Namatame, M. Taniguchi, A. Fujimori, Z.-X. Shen, M. Ishikado, S. Uchida: Unmasking the nodal quasiparticle dynamics in cuprate superconductors using low-energy photoemission, Phys. Rev. B **75**, 140513 (2007)

17.49 Y. Zhou, G.-L. Wang, C.-M. Li, Q.-J. Peng, D.-F. Cui, Z.-Y. Xu, X.-Y. Wang, Y. Zhu, C.-T. Chen, G.-D. Liu, X.-L. Dong, X.-J. Zhou: Sixth harmonic of a Nd:YVO 4 laser generation in KBBF for ARPES, Chin. Phys. Lett. **25**, 963 (2008)

17.50 T. Shimojima, K. Okazaki, S. Shin: Low-temperature and high-energy-resolution laser photoemission spectroscopy, J. Phys. Soc. Jpn. **84**, 072001 (2015)

17.51 E. Pedersoli, C.M.R. Greaves, W. Wan, C. Coleman-Smith, H.A. Padmore, S. Pagliara, A. Cartella, F. Lamarca, G. Ferrini, G. Galimberti, M. Montagnese, S. dal Conte, F. Parmigiani: Surface and bulk contribution to Cu(111) quantum efficiency, Appl. Phys. Lett. **93**, 183505 (2008)

17.52 D.H. Dowell, I. Bazarov, B. Dunham, K. Harkay, C. Hernandez-Garcia, R. Legg, H. Padmore, T. Rao, J. Smedley, W. Wan: Cathode R&D for future light sources, Nucl. Instrum. Methods Phys. Res. A **622**, 685–697 (2010)

17.53 A.L. Cavalieri, N. Muller, T. Uphues, V.S. Yakovlev, A. Baltuska, B. Horvath, B. Schmidt, L. Blumel, R. Holzwarth, S. Hendel, M. Drescher,

U. Kleineberg, P.M. Echenique, R. Kienberger, F. Krausz, U. Heinzmann: Attosecond spectroscopy in condensed matter, Nature **449**, 1029 (2007)

17.54 S. Neppl, R. Ernstorfer, A.L. Cavalieri, C. Lemell, G. Wachter, E. Magerl, E.M. Bothschafter, M. Jobst, M. Hofstetter, U. Kleineberg, J.V. Barth, D. Menzel, J. Burgdorfer, P. Feulner, F. Krausz, R. Kienberger: Direct observation of electron propagation and dielectric screening on the atomic length scale, Nature **517**, 342 (2015)

17.55 E.E. Krasovskii: Attosecond spectroscopy of solids: Streaking phase shift due to lattice scattering, Phys. Rev. B **84**, 195106 (2011)

17.56 A.G. Borisov, D. Sánchez-Portal, A.K. Kazansky, P.M. Echenique: Resonant and nonresonant processes in attosecond streaking from metals, Phys. Rev. B **87**, 121110 (2013)

17.57 E.E. Krasovskii, C. Friedrich, W. Schattke, P.M. Echenique: Rapid propagation of a Bloch wave packet excited by a femtosecond ultraviolet pulse, Phys. Rev. B **94**, 195434 (2016)

17.58 Z. Tao, C. Chen, T. Szilvási, M. Keller, M. Mavrikakis, H. Kapteyn, M. Murnane: Direct time-domain observation of attosecond final-state lifetimes in photoemission from solids, Science **353**, 62 (2016)

17.59 G. Borstel: Theoretical aspects of photoemission, Appl. Phys. A **38**, 193–204 (1985)

17.60 J.B. Pendry: *Low Energy Electron Diffraction: The Theory and Its Application to Determination of Surface Structure* (Academic Press, New York 1974)

17.61 J.B. Pendry: Theory of photoemission, Surf. Sci. **57**, 679–705 (1976)

17.62 J. Braun: The theory of angle-resolved ultraviolet photoemission and its applications to ordered materials, Rep. Prog. Phys. **59**, 1267 (1996)

17.63 D.S. Boudreaux, V. Heine: Band structure treatment of low energy electron diffraction intensities, Surf. Sci. **8**, 426–444 (1967)

17.64 J.B. Pendry: The application of pseudopotentials to low-energy electron diffraction II: Calculation of the reflected intensities, J. Phys. C **2**, 2273 (1969)

17.65 E.E. Krasovskii: Augmented-plane-wave approach to scattering of Bloch electrons by an interface, Phys. Rev. B **70**, 245322 (2004)

17.66 V. Heine: On the general theory of surface states and scattering of electrons in solids, Proc. Phys. Soc. **81**, 300 (1963)

17.67 V. Heine: Some theory about surface states, Surf. Sci. **2**, 1–7 (1964)

17.68 V.N. Strocov, E.E. Krasovskii, W. Schattke, N. Barrett, H. Berger, D. Schrupp, R. Claessen: Three-dimensional band structure of layered $TiTe_2$: Photoemission final-state effects, Phys. Rev. B **74**, 195125 (2006)

17.69 E.E. Krasovskii, K. Rossnagel, A. Fedorov, W. Schattke, L. Kipp: Determination of the hole lifetime from photoemission: Ti 3d states in $TiTe_2$, Phys. Rev. Lett. **98**, 217604 (2007)

17.70 A. Gerlach, R. Matzdorf, A. Goldmann: Experimental analysis of valence-band photoemission intensities for Cu(111) and Cu(100), Phys. Rev. B **58**, 10969–10974 (1998)

17.71 A. Chassé, L. Niebergall: Induced circular dichroism and spin polarization in the angular distribution of photoelectrons by optical properties of adsorbate systems, Surf. Sci. **546**, 57–63 (2003)

17.72 J. Hager, T. Michalke, R. Matzdorf: Correct application of Fresnel equations for intensity analysis of angle-resolved photoemission data, Surf. Sci. **600**, 1129–1133 (2006)

17.73 T. Michalke, A. Gerlach, K. Berge, R. Matzdorf, A. Goldmann: Interference of direct transitions and surface emission in ARPES studied by changing the light incidence angle, Phys. Rev. B **62**, 10544–10547 (2000)

17.74 F. Pforte, T. Michalke, A. Gerlach, A. Goldmann, R. Matzdorf: Strong contributions from surface electromagnetic fields to angle-resolved photoemission intensities of copper, Phys. Rev. B **63**, 115405 (2001)

17.75 T. Miller, W.E. McMahon, T.-C. Chiang: Interference between bulk and surface photoemission transitions in Ag(111), Phys. Rev. Lett. **77**, 1167–1170 (1996)

17.76 E.D. Hansen, T. Miller, T.-C. Chiang: Surface photoemission in Ag(100), Phys. Rev. B **55**, 1871–1875 (1997)

17.77 V.B. Zabolotnyy, S.V. Borisenko, A.A. Kordyuk, D.S. Inosov, A. Koitzsch, J. Geck, J. Fink, M. Knupfer, B. Büchner, S.-L. Drechsler, V. Hinkov, B. Keimer, L. Patthey: Disentangling surface and bulk photoemission using circularly polarized light, Phys. Rev. B **76**, 024502 (2007)

17.78 V.B. Zabolotnyy, E. Carleschi, T.K. Kim, A.A. Kordyuk, J. Trinckauf, J. Geck, D. Evtushinsky, B.P. Doyle, R. Fittipaldi, M. Cuoco, A. Vecchione, B. Büchner, S.V. Borisenko: Surface and bulk electronic structure of the unconventional superconductor Sr_2RuO_4: Unusual splitting of the β band, New J. Phys. **14**, 063039 (2012)

17.79 P.J. Feibelman: Self-consistent calculation of the surface photoelectric effect, Phys. Rev. Lett. **34**, 1092–1095 (1975)

17.80 P.J. Feibelman: Microscopic calculation of electromagnetic fields in refraction at a jellium-vacuum interface, Phys. Rev. B **12**, 1319–1336 (1975)

17.81 P.J. Feibelman: Surface electromagnetic fields, Prog. Surf. Sci. **12**, 287–407 (1982)

17.82 J. Monin, G.A. Boutry: Optical and photoelectric properties of alkali metals, Phys. Rev. B **9**, 1309–1327 (1974)

17.83 S.A. Flodstrom, J.G. Endriz: Investigation of the vectorial photoelectric effect in magnesium, Phys. Rev. B **12**, 1252–1256 (1975)

17.84 H. Petersen, S.B.M. Hagström: Optical excitation of the surface photoelectric effect of metals using synchrotron radiation, Phys. Rev. Lett. **41**, 1314–1317 (1978)

17.85 G. Jezequel: Surface-photoelectric-yield spectrum of indium below the plasmon energy, Phys. Rev. Lett. **45**, 1963–1966 (1980)

17.86 H.J. Levinson, E.W. Plummer, P.J. Feibelman: Effects on photoemission of the spatially varying

photon field at a metal surface, Phys. Rev. Lett. **43**, 952–955 (1979)
17.87 H.J. Levinson, E.W. Plummer: The surface photoeffect, Phys. Rev. B **24**, 628–638 (1981)
17.88 R.A. Bartynski, E. Jensen, T. Gustafsson, E.W. Plummer: Angle-resolved photoemission investigation of the electronic structure of Be: Surface states, Phys. Rev. B **32**, 1921–1926 (1985)
17.89 S.R. Barman, P. Häberle, K. Horn: Collective and single-particle excitations in the photoyield spectrum of Al, Phys. Rev. B **58**, R4285–R4288 (1998)
17.90 E.E. Krasovskii, F. Starrost, W. Schattke: Augmented Fourier components method for constructing the crystal potential in self-consistent band-structure calculations, Phys. Rev. B **59**, 10504–10511 (1999)
17.91 C. Schwartz, W.L. Schaich: Multipole surface plasmons and photoemission yield spectra, Phys. Rev. B **30**, 1059–1061 (1984)
17.92 K.-D. Tsuei, E.W. Plummer, A. Liebsch, K. Kempa, P. Bakshi: Multipole plasmon modes at a metal surface, Phys. Rev. Lett. **64**, 44–47 (1990)
17.93 A.J. Bennett: Influence of the electron charge distribution on surface-plasmon dispersion, Phys. Rev. B **1**, 203–207 (1970)
17.94 E.E. Krasovskii, V.M. Silkin, V.U. Nazarov, P.M. Echenique, E.V. Chulkov: Dielectric screening and band-structure effects in low-energy photoemission, Phys. Rev. B **82**, 125102 (2010)
17.95 V.M. Silkin, J.M. Pitarke, E.V. Chulkov, P.M. Echenique: Acoustic surface plasmons in the noble metals Cu, Ag, and Au, Phys. Rev. B **72**, 115435 (2005)
17.96 E.V. Chulkov, V.M. Silkin, P.M. Echenique: Image potential states on lithium, copper and silver surfaces, Surf. Sci. **391**, L1217–L1223 (1997)
17.97 E.V. Chulkov, V.M. Silkin, P.M. Echenique: Image potential states on metal surfaces: Binding energies and wave functions, Surf. Sci. **437**, 330–352 (1999)
17.98 E.D. Palik (Ed.): *Handbook of Optical Constants of Solids* (Academic Press, New York 1985)
17.99 D. Samuelsen, W. Schattke: Electromagnetic surface response for a solid with one-dimensional crystallinity, Phys. Rev. B **51**, 2537–2549 (1995)
17.100 D.W. Jepsen, F.J. Himpsel, D.E. Eastman: Single-step-model analysis of angle-resolved photoemission from Ni(110) and Cu(100), Phys. Rev. B **26**, 4039–4051 (1982)
17.101 L. Hedin: New method for calculating the one-particle green's function with application to the electron-gas problem, Phys. Rev. **139**, A796–A823 (1965)
17.102 L. Hedin, S. Lundqvist: Effects of electron–electron and electron–phonon interactions on the one-electron states of solids, Solid State Phys. **23**, 1–181 (1970)
17.103 C. Friedrich, S. Blügel, A. Schindlmayr: Efficient implementation of the *GW* approximation within the all-electron FLAPW method, Phys. Rev. B **81**, 125102 (2010)
17.104 E.E. Krasovskii, V.N. Strocov: Very-low-energy electron diffraction from TiS_2: Experiment and ab initio theory, J. Phys. Condens. Matter **21**, 314009 (2009)
17.105 E.E. Krasovskii, W. Schattke, P. Jiřiček, M. Vondráček, O.V. Krasovska, V.N. Antonov, A.P. Shpak, I. Bartoš: Photoemission from Al(100) and (111): Experiment and ab initio theory, Phys. Rev. B **78**, 165406 (2008)
17.106 M. Petersilka, U.J. Gossmann, E.K.U. Gross: Exictation energies from time-dependent density-functional theory, Phys. Rev. Lett. **76**, 1212 (1996)
17.107 F. Aryasetiawan, K. Karlsson: Energy loss spectra and plasmon dispersions in alkali metals: Negative plasmon dispersion in Cs, Phys. Rev. Lett. **73**, 1679–1682 (1994)
17.108 V.P. Zhukov, F. Aryasetiawan, E.V. Chulkov, I.G. de Gurtubay, P.M. Echenique: Corrected local-density approximation band structures, linear-response dielectric functions, and quasiparticle lifetimes in noble metals, Phys. Rev. B **64**, 195122 (2001)
17.109 A. Bergara, V.M. Silkin, E.V. Chulkov, P.M. Echenique: *Ab initio* dynamical response of metal monolayers, Phys. Rev. B **67**, 245402 (2003)
17.110 X. Zubizarreta, E.V. Chulkov, I.P. Chernov, A.S. Vasenko, I. Aldazabal, V.M. Silkin: Quantum-size effects in the loss function of Pb(111) thin films: An *ab initio* study, Phys. Rev. B **95**, 235405 (2017)
17.111 V.M. Silkin, E.V. Chulkov, P.M. Echenique: Band structure versus dynamical exchange-correlation effects in surface plasmon energy and damping: A first-principles calculation, Phys. Rev. Lett. **93**, 176801 (2004)
17.112 V.M. Silkin, E.V. Chulkov: Energy and lifetime of surface plasmon from first-principles calculations, Vacuum **81**, 186–191 (2006)
17.113 J. Yan, J.J. Mortensen, K.W. Jacobsen, K.S. Thygesen: Linear density response function in the projector augmented wave method: Applications to solids, surfaces, and interfaces, Phys. Rev. B **83**, 245122 (2011)
17.114 B. Diaconescu, K. Pohl, L. Vattuone, L. Savio, P. Hofmann, V.M. Silkin, J.M. Pitarke, E.V. Chulkov, P.M. Echenique, D. Farias, M. Rocca: Low-energy acoustic plasmons at metal surfaces, Nature **448**, 57 (2007)
17.115 V.M. Silkin, E.V. Chulkov, P.M. Echenique: Band structure effects in the surface plasmon at the Be(0001) surface, Radiat. Eff. Defects Solids **162**, 483–489 (2007)
17.116 V.M. Silkin, J.M. Pitarke, E.V. Chulkov, B. Diaconescu, K. Pohl, L. Vattuone, L. Savio, P. Hofmann, D. Fariñas, M. Rocca, P.M. Echenique: Band structure effects on the Be(0001) acoustic surface plasmon energy dispersion, Phys. Status Solidi (a) **205**, 1307–1311 (2008)

17.117 K.-D. Tsuei, E.W. Plummer, A. Liebsch, K. Kempa, P. Bakshi: Multipole plasmon modes at a metal surface, Phys. Rev. Lett. **64**, 44–47 (1990)

17.118 K.-D. Tsuei, E.W. Plummer, A. Liebsch, E. Pehlke, K. Kempa, P. Bakshi: The normal modes at the surface of simple metals, Surf. Sci. **247**, 302–326 (1991)

17.119 E.W. Plummer, K.-D. Tsuei, B.-O. Kim: The impact of the concept of a surface plasmon, Nucl. Instrum. Methods Phys. Res. B **96**, 448–459 (1995)

17.120 J. Yan, K.W. Jacobsen, K.S. Thygesen: Conventional and acoustic surface plasmons on noble metal surfaces: A time-dependent density functional theory study, Phys. Rev. B **86**, 241404 (2012)

17.121 J. Yan, K.W. Jacobsen, K.S. Thygesen: First-principles study of surface plasmons on Ag(111) and H/Ag(111), Phys. Rev. B **84**, 235430 (2011)

17.122 L. Vattuone, M. Smerieri, T. Langer, C. Tegenkamp, H. Pfnür, V.M. Silkin, E.V. Chulkov, P.M. Echenique, M. Rocca: Correlated motion of electrons on the Au(111) surface: Anomalous acoustic surface-plasmon dispersion and single-particle excitations, Phys. Rev. Lett. **110**, 127405 (2013)

17.123 N. Tancogne-Dejean, C. Giorgetti, V. Véniard: Optical properties of surfaces with supercell ab initio calculations: Local-field effects, Phys. Rev. B **92**, 245308 (2015)

17.124 V.M. Silkin, B. Hellsing, L. Walldén, P.M. Echenique, E.V. Chulkov: Photoelectron driven acoustic surface plasmons in $p(2\times2)$K/Be(0001): *Ab initio* calculations, Phys. Rev. B **81**, 113406 (2010)

17.125 V.M. Silkin, E.V. Chulkov, J.P. Echeverry, P.M. Echenique: Modification of response properties of the Be(0001) surface upon adsorption of a potassium monolayer: An ab initio calculation, Phys. Status Solidi (b) **247**, 1849–1857 (2010)

17.126 V. Chis, V.M. Silkin, B. Hellsing: Plasmaron excitations in $p(2\times2)$-K/graphite, Phys. Rev. B **89**, 205429 (2014)

17.127 J. Yan, K.S. Thygesen, K.W. Jacobsen: Nonlocal screening of plasmons in graphene by semiconducting and metallic substrates: First-principles calculations, Phys. Rev. Lett. **106**, 146803 (2011)

17.128 Y. Gao, Z. Yuan: Anisotropic low-energy plasmon excitations in doped graphene: An ab initio study, Solid State Commun. **151**, 1009–1013 (2011)

17.129 P. Wachsmuth, R. Hambach, M.K. Kinyanjui, M. Guzzo, G. Benner, U. Kaiser: High-energy collective electronic excitations in free-standing single-layer graphene, Phys. Rev. B **88**, 075433 (2013)

17.130 M. Pisarra, A. Sindona, P. Riccardi, V.M. Silkin, J.M. Pitarke: Acoustic plasmons in extrinsic free-standing graphene, New J. Phys. **16**, 083003 (2014)

17.131 D. Novko, V. Despoja, M. Šunjić: Changing character of electronic transitions in graphene: From single-particle excitations to plasmons, Phys. Rev. B **91**, 195407 (2015)

17.132 D. Novko, M. Šunjić, V. Despoja: Optical absorption and conductivity in quasi-two-dimensional crystals from first principles: Application to graphene, Phys. Rev. B **93**, 125413 (2016)

17.133 M. Pisarra, A. Sindona, M. Gravina, V.M. Silkin, J.M. Pitarke: Dielectric screening and plasmon resonances in bilayer graphene, Phys. Rev. B **93**, 035440 (2016)

17.134 A.G. Eguiluz: Dynamical density response function of a metal film in the random-phase approximation, Phys. Rev. Lett. **51**, 1907–1910 (1983)

17.135 A.G. Eguiluz: Self-consistent static-density-response function of a metal surface in density-functional theory, Phys. Rev. B **31**, 3303–3314 (1985)

17.136 D.A. Siegel, C.-H. Park, C. Hwang, J. Deslippe, A.V. Fedorov, S.G. Louie, A. Lanzara: Many-body interactions in quasi-freestanding graphene, Proc. Natl. Acad. Sci. U. S. A. **108**(28), 11365–11369 (2011)

17.137 J.F. Dobson, T. Gould, S. Lebègue: Layer response theory: Energetics of layered materials from semi-analytic high-level theory, Phys. Rev. B **93**, 165436 (2016)

17.138 P.E. Trevisanutto, G. Vignale: Ab initio electronic structure of quasi-two-dimensional materials: A "native" Gaussian-plane wave approach, J. Chem. Phys. **144**(20), 204122 (2016)

Vladimir U. Nazarov

National Research University (MIPT NRU)
Moscow Institute of Physics and Technology
Dolgoprudny, Russian Federation
nazarov@gate.sinica.edu.tw

Vladimir U. Nazarov received his PhD in 1990 from the Far-Eastern Branch of the Russian Academy of Sciences. He is now at Moscow Institute of Physics and Technology (National Research University), Russia, and he has worked, in the inverse chronological order, at Academia Sinica, Taiwan, Chonnam National University, South Korea, Kyushu Institute of Technology, Japan, and Institute for Automation and Control Processes, Russia. His scientific interests lie in the field of the fundamentals and applications of time-dependent density functional theory and low-dimensional materials.

Eugene E. Krasovskii

Dept. of Materials Physics
University of the Basque Country,
Donostia International Physics Center,
and IKERBASQUE, Basque Foundation for Science
Donostia-San Sebastián, Spain
eugene.krasovskii@ehu.eus

Eugene Krasovskii received his PhD from the Institute of Metal Physics in Kiev, Ukraine, in 1987. He worked at the Institute of Metal Physics, at the University of Kiel, Germany, and at the University of the Basque Country. Presently he is working on computational methods of solid-state theory, focused on the theory of electron diffraction, photoemission, and optical spectroscopy.

Vyacheslav M. Silkin

Dept. of Materials Physics
University of the Basque Country,
Donostia International Physics Center,
and IKERBASQUE, Basque Foundation for Science
Donostia-San Sebastián, Spain
waxslavas@ehu.es

Vyacheslav Silkin received his PhD from the Institute of Strength Physics and Material Science of the Russian Academy of Science at Tomsk, Russia (1990). He worked in the Institute of Strength Physics and Material Science in Russia, at the University of the Basque Country (Spain), and at Donostia International Physics Center (Spain). He is currently working on the dynamics of one-particle and collective electronic excitations in metals and their surfaces.

18. Surface Plasmons and Plasmonics

Mario Rocca

Surface plasmons (SPs) correspond to self-sustaining excitations of the electron gas of metals or semiconductors, i.e., to modulations of the density of such gas occurring at the surface of the body generating electric fields propagating along the surface and decaying exponentially perpendicular to it. Since the electric field at a metal surface is directed perpendicular to it, the SP corresponds to a transversely polarized wave. As such it may interact with light giving rise, in the long wavelength limit, to SP polaritons (SPPs) which are promising for plasmonics applications, i.e., SP-based electronics, since at any given frequency their wavelength is shorter than the one of light and may thus allow for a miniaturization of photonic devices. Excitation of SPPs by light requires matching of energy and wavevector and is thus possible only for rough surfaces or in the presence of gratings. As for bulk plasmons, the SP frequency is dictated by the electron density and falls typically between a couple and some tens of eV. Surface plasmons, therefore, cannot be excited thermally nor interact significantly with lattice vibrations but play a role whenever electronic degrees of freedom are involved as in electron and ion-surface scattering. Surface plasmon dispersion is dictated by surface properties and may depend on crystallographic surface and propagation direction. For small particles, resonant light absorption occurs whenever a closed path along the surface coincides with multiples of the SP wavelength (Mie resonance). If it falls in the visible range it determines the bright colors of metallic nanoparticles and can be exploited in energy harvesting in solar cells. SP resonances are, moreover, responsible for the amplification of the local electric field in nanoantennas and in surface-enhanced Raman spectroscopy, allowing Raman signals even for single isolated molecules to be recorded. Furthermore, the SP resonance influences the optical reflectivity and can therefore be easily monitored. Since the latter depends on the refractive index of the medium, surface modifications resulting from adsorption can be monitored in vacuum and electrochemical environments.

M. Rocca, T.S. Rahman, L. Vattuone (Eds.), *Springer Handbook of Surface Science*, Springer Handbooks,
https://doi.org/10.1007/978-3-030-46906-1_18

Surface plasmons are coherent excitations of the free-electron gas occurring at the interface of two materials. They are polarization waves propagating along the interface and evanescent normal to it, whereby the electromagnetic fields associated with the additional charge fall exponentially away from the interface.

Surface plasmons were first predicted by *Ritchie* in 1957 [18.1] and extensively studied in the following decades by *Raether* [18.2], *Kretschmann* [18.3], and *Otto* [18.4].

At variance with bulk plasmons, which correspond to longitudinal oscillations of the electron gas, SPs have transverse character and may therefore interact with light, a property which makes them attractive for applications. For this same reason at small wavevectors, where the SP dispersion crosses the light line, hybridization with electromagnetic radiation occurs giving rise to a mixed excitation: the surface plasmon polariton (SPP) (see [18.5] for a recent review of this topic). Direct excitation of an SP by light is, however, possible only when energy and wavevector match, a condition that is satisfied only for rough surfaces or in the presence of a grating which provides the missing momentum.

Evanescent light waves can be produced with a prism (a technique known as attenuated total reflection, Fig. 18.1). Above a certain angle of incidence, on the inside wall of the prism light undergoes total reflection, but the associated electromagnetic field spills over and reaches the metallic foil placed above it. Whenever energy and momentum match a SP, light is absorbed and the reflectivity decreases abruptly.

The metallic foil usually consists of the noble metals Au or Ag, since they have the sharpest resonances [18.7–9]. Shifts in the angle at which the resonance occurs may be induced by changes in the optical density close to the noble metal film. This effect forms the basis of surface plasmon resonance spectroscopy, a technique applied to monitor adsorption and desorption of molecules especially for the investigation of biointerfaces [18.6] and appreciated for its real-time and noninvasive nature.

SPs may otherwise be excited by charged particle beams, such as the swift electrons of a transmission electron microscope. Momentum transfer causes thereby a deflection in the trajectory and an energy loss as shown schematically in Fig. 18.2b for a 50-keV beam shot through Ag foils of different thickness. The electron energy-loss (EEL) spectra are shown in Fig. 18.2a. The lowest EEL peak at ≈ 3.63 eV corresponds to the excitation of the surface plasmon. The loss intensity is independent of film thickness since this mode can be excited only as long as the electron is *outside* of the foil. Conversely, the EEL at 3.78 eV is associated with the excitation of the bulk plasmon. Its intensity indeed scales with film thickness since it can be excited only while the electrons move *inside* the material. Energy and wavevector conservation allow the dispersion curve of both modes to be traced.

More recently, surface plasmon dispersion has been investigated with low kinetic energy electrons (kinetic energy of tens to hundreds of eV) for which the penetration into a metal surface is limited to just a few monolayers (MLs) [18.11–18] and the retrieved information is therefore highly surface sensitive. Such high-resolution electron energy-loss spectroscopy (HREELS) investigations allowed for a careful determination of the SP dispersion with wavevector, validating the theoretical forecast of a negative slope for simple metals [18.11, 19, 20] and stimulating new theory for noble metals where the dispersion was determined to be positive [18.21, 22]. The dispersion of the SP explains the size dependence of the Mie resonance in clusters [18.23–25], and impacts on the understand-

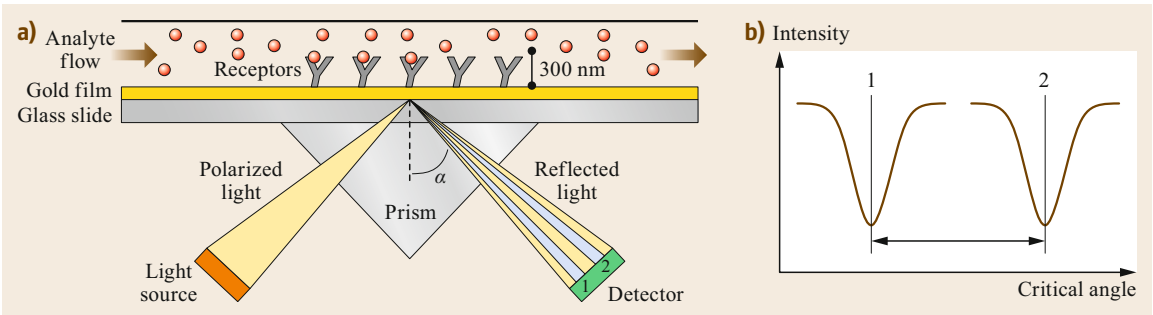

Fig. 18.1 **(a)** Kretschmann configuration used for biochemical sensing. A thin gold film is evaporated on a prism and put into contact with receptors and an analyte. The latter changes the refraction index in the thickness range of about 300 nm above the gold surface thereby causing a shift in the angular position at which absorption of light, caused by the excitation of SPPs, takes place. **(b)** Intensity of the reflected radiation versus angle with 1 and without 2 analyte. (Reprinted from [18.6], with permission from Elsevier)

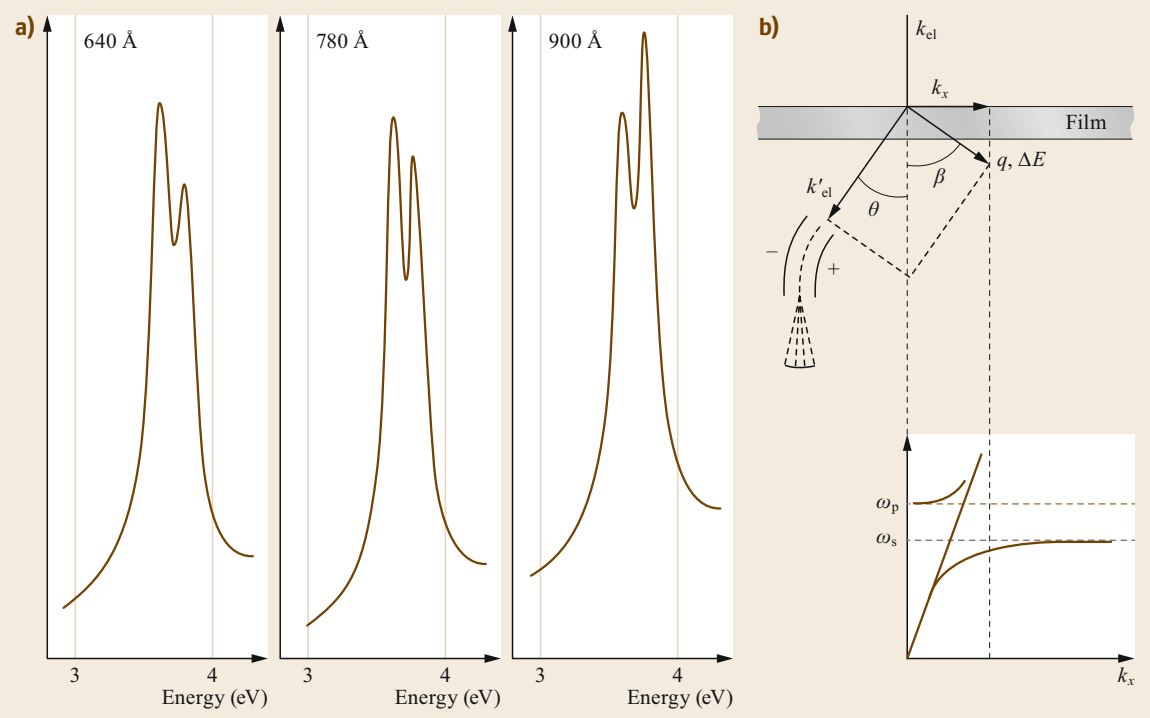

Fig. 18.2 **(a)** Electron energy-loss spectra recorded by swift electrons (kinetic energy 50 keV) moving through a thin Ag foil. The losses correspond to surface (3.63 eV) and bulk (3.78 eV) plasmon excitations. **(b)** Geometry of the experiment. The beam hits the foil along the surface normal and the electrons are recorded in transmission. The loss intensity of the bulk plasmon scales with the foil thickness. The *lower right panel* reports the dispersion of transverse modes with transferred momentum parallel to the surface k_x on a wavevector scale comparable to the one of photons in the visible range, i.e., 10^{-3} Å^{-1}. The hybridization of SPs and light gives rise to the SPP. (Reprinted by permission from **(a)** [18.10] and **(b)** [18.2], © Springer 1967, 1980)

ing of surface photoyield (PY), deexcitation mechanisms of adsorbates, and the origin of van der Waals forces [18.19, 21, 22].

A typical HREEL spectrum for an Ag surface showing the SP loss is reported in Fig. 18.3. It does not correspond to optimal investigation conditions since the impact energy of the electrons used in this experiment is relatively high implying an important integration of the inelastic signal over reciprocal space but it has been recorded over a wide energy-loss range. As one can see, the spectrum is dominated by a single peak. The bulk plasmon does not contribute appreciably to the inelastic signal and an important tail is present on the large energy-loss side due to the excitation of interband transitions. Changing the scattering geometry by moving out-of-specular within the dipolar cone allows for an accurate recording of the dispersion of the surface plasmon for wavevectors that are large compared to those of the light cone (Fig. 18.2b), a region which can only be accessed by optical methods.

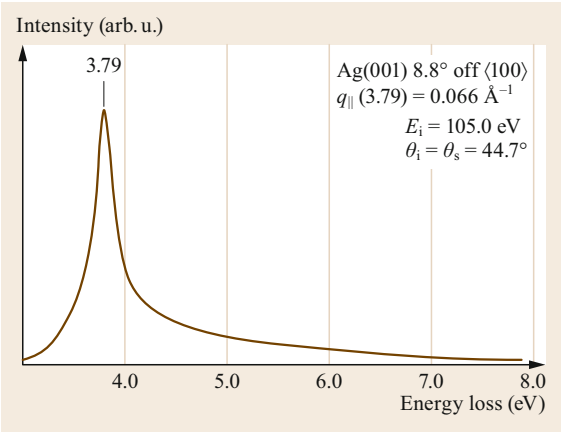

Fig. 18.3 Electron energy-loss spectrum recorded at a relatively large impact energy evidencing the loss due to the surface plasmon and the tail associated with interband transitions. (Reprinted from [18.22], with permission from Elsevier)

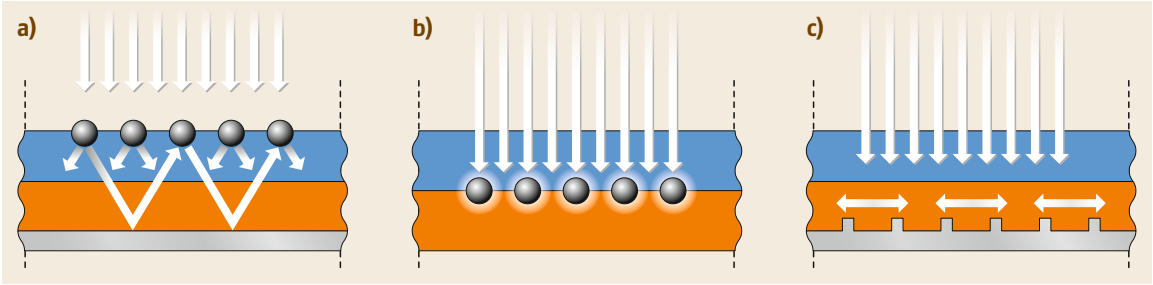

Fig. 18.4a–c Energy harvesting in plasmonic solar cells. Plasmonic nanoparticles are added to the junction in order to reduce the thickness of the cell to a few μm and save precious material while reducing the recombination of the charge carriers prior to their collection by the p-n junction. **(a)** Plasmonic particles at the surface reflect the light trapping it into the cell; **(b)** plasmonic particles at the interface trap the light by excitation of localized SPs; **(c)** SPPs are excited at the metal semiconductor interface. (Reprinted by permission from [18.26], © Springer 2000)

Fig. 18.5 The Lycurgus Cup (Reprinted by permission from [18.27], © Springer 2007)

The importance of SPs in applications grew over the years eventually giving rise to a new field of research called plasmonics. A search under the keyword *surface plasmon* yields some 64 000 papers over the past 20 years, while inserting the keyword *plasmonics* results in over 1000 papers appearing every year.

The interest in SPs and SPPs is motivated by their interaction with electromagnetic radiation which allows light to be squeezed in regions much smaller than the wavelength of the corresponding photon [18.28–30] and by energy harvesting in solar cells [18.26, 31]. Localization of light allows it to pass through subwavelength holes [18.32] and is promising for the construction of SP-based optoelectronic devices with nanosized dimensions [18.33, 34]. Finally, SP-based antennas are currently under investigation and look very promising for the generation of very high local electric fields. Results were reported for SP coupling to optical emitters [18.35–37], SP focusing [18.38, 39], building optical antennas at the nanoscale [18.40], SP-based integrated circuits [18.41, 42], SP-enhanced light-emitting diodes [18.43], as well as on negative refractive index materials [18.44–46].

In Fig. 18.4, schemes are reported for SP-based energy harvesting by light scattering of nanoparticles placed at the surface of a solar cell, at the p-n junction, and for SPP coupling by the corrugation introduced by a grating drawn in a metal back surface of the cell.

Two-dimensional (2-D) materials, such as graphene, can also sustain plasmons. This topic will not be treated here since it is reviewed in Chap. 19.

Surface plasmon-based nanotechnology is in reality an old technology, though it is now developed with knowledge-based insight. For example, the bright colors of the windows of Medieval cathedrals are due to Au and Ag nanoparticles of different diameter, embedded in the glass. The technique originates from late Roman times as witnessed by the magnificent Lycurgus Cup (now at the British Museum), which changes color when illuminated from the back (red) and front

(green) because of light absorption by localized SPs at the surface of the Au and Ag nanoparticles (Fig. 18.5).

The topic of SP dispersion has been summarized in 1995 [18.22]. Plasmonics applications in photovoltaic devices were reviewed more recently by *Atwater* and by *Polman* [18.26, 31]. An introduction to the surface plasmon topic may also be found in the some textbooks, see, e.g., [18.47].

18.1 Dynamical Screening at Surfaces

The dynamical screening of electric fields by a material is described by its dielectric response function ε which links the electric displacement field $\boldsymbol{D}$, generated by external charges only, with the electric field $\boldsymbol{E}$ to which all charges, i.e., including polarization charges, contribute. The response is thereby determined by the dependence on time t and space $\boldsymbol{r}$ of the external field $\boldsymbol{D}(t, \boldsymbol{r})$; $\boldsymbol{\varepsilon}$ is, in general, a tensor if the solid shows some anisotropy. Instead of performing complicated integrations over time delay and space distribution of the charges it is more convenient to look at the problem in reciprocal space performing a Fourier transform and reasoning in terms of frequency ω and wavevector $\boldsymbol{q}$ of the fields. The relationship between $\boldsymbol{D}$ and $\boldsymbol{E}$ simplifies then to the tensor product

$$\boldsymbol{D}(\omega, \boldsymbol{q}) = \boldsymbol{\varepsilon}(\omega, \boldsymbol{q})\, \boldsymbol{E}(\omega, \boldsymbol{q}) \,. \tag{18.1}$$

By definition, the component D_z normal to the interface is continuous across it while the one of the electric field E_z is discontinuous. If the only charges present at the interface are due to polarization, $\boldsymbol{E}$ will revert its direction across the interface, as schematically drawn in Fig. 18.6. A solution will then be possible at the particular frequency at which $\boldsymbol{\varepsilon}(\omega, \boldsymbol{q})$ also reverts its sign when crossing the interface.

If the interface is between a metal and a vacuum, an electric field generated by polarization charges may be sustained at the surface of the metal when the dielectric function of the metal $\varepsilon(\omega, q) = -1$. Such a condition is associated with the resonant excitation of an SP, a mode which propagates parallel to the interface in wavelike fashion and is characterized by a wavevector $q_\parallel$ (or by a wavelength $\lambda = 2\pi/q_\parallel$), an angular frequency, $\omega_{\mathrm{sp}}(q_\parallel)$, and a propagation velocity $v = \mathrm{d}\omega/\mathrm{d}q_\parallel$ parallel to the surface.

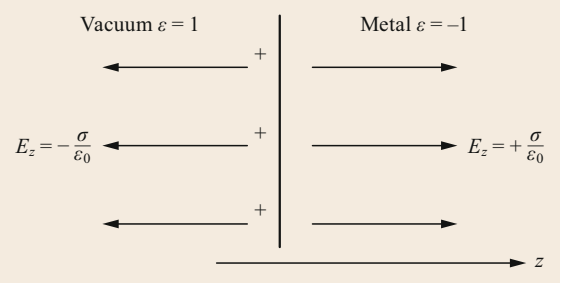

Fig. 18.6 Electric field across an interface with positive polarization charges. E is discontinuous while the field $D = \varepsilon E$ is continuous. Matching is possible only if ε changes sign across the interface

The electric fields associated with the polarization charges decrease exponentially away from the interface as $\mathrm{e}^{-|q_\parallel|z}$. Their penetration into the material is thus large at large wavelengths and very limited at large wavevectors. Excitation of surface plasmons makes up a very efficient screening mechanism for high-frequency external electric fields and determines thus to a large extent the high-frequency optical properties of surfaces.

For a free-electron gas one can easily demonstrate that the dielectric function is given by

$$\varepsilon(\omega) = 1 - \left(\frac{\omega_\mathrm{p}}{\omega}\right)^2 \,, \tag{18.2}$$

with ω_p plasma frequency. At ω_p, $\varepsilon(\omega) = 0$ so that according to (18.1) electric fields may exist in the bulk of the material even in the absence of external sources. This resonance condition corresponds to the excitation of volume or bulk plasmons, i.e., longitudinal waves with frequency ω_p, given by

$$\omega_\mathrm{p} = \sqrt{\frac{ne^2}{m^* \varepsilon_0}} \,, \tag{18.3}$$

in the international system units; n is thereby the density of the electron gas, e the elementary electric charge, m^* the effective mass of the involved electrons, ε_0 the dielectric constant of vacuum (for cgs units multiply the expression under the squareroot by $4\pi\varepsilon_0$).

Since for nonferromagnetic materials the magnetic permeability is very close to unity, the refraction index is given by $\sqrt{\varepsilon}$ and the body will be transparent to light above ω_p and opaque with a metallic shine below it since the refraction index is then purely imaginary. No absorption of electromagnetic radiation will take place if the imaginary part of the dielectric function is zero as in the case of the free-electron gas described by (18.2), but the waves will not be able to propagate inside it and be reflected back. In the case of alkali metals, ω_p falls in the near ultraviolet explaining the ultraviolet transparency of these materials.

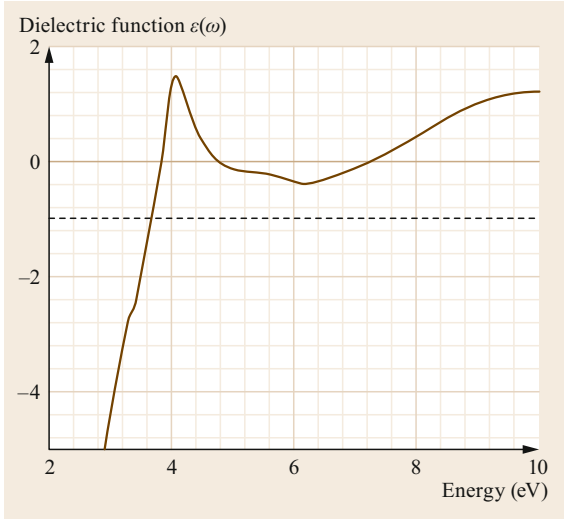

Fig. 18.7 Dielectric function for Ag. The interband transitions from the d bands to the Fermi level give an important contribution $> 3.8\,\text{eV}$ thus causing the shift of ω_p and ω_{sp} to lower energies. (Reprinted from [18.48], with permission from Elsevier) ►

As mentioned above the plasma resonance corresponds to a longitudinal excitation of the electron gas. Bulk plasmons, therefore, cannot be excited by photons since there is no matching in the polarization of the two waves. They are, conversely, excited by the swift electrons used in transmission electron microscopes (TEMs; Fig. 18.2a) and in ion-scattering experiments as long as electrons and ions are inside the material. Since ω_p depends quadratically on the three-dimensional wavevector $\boldsymbol{q}$, the transparency threshold scales with the inverse of the particle diameter since the wavelength of the excitations is limited by the size of the particles hosting it.

The $\varepsilon(\omega)$ is a bulk quantity and so is also its crossing of the -1 level, determining the value of the SP frequency, which is thus determined by bulk properties. For simple metals, (18.2) implies that $\omega_{sp} = \omega_p/\sqrt{2}$. In the presence of bound electrons contributing with ε_b to the dielectric function, the resonance is shifted to $\omega_{sp} = \omega_p/\sqrt{(2+\varepsilon_b)}$. The ratio ω_{sp}/ω_p will then be determined by the steepness of the $\varepsilon(\omega)$ curve in the region where this function changes from 0 to -1. The Ag case is shown in Fig. 18.7. For this metal the d-electron contribution shifts the surface plasma frequency from its free-electron value of 6.35 to 3.70 eV.

18.2 Surface Plasmon Dispersion

At variance with the frequency, the wavevector dependence of ω_{sp} is dictated by surface properties. Indeed, it depends on the position of the centroid of the polarization charge with respect to the geometric surface plane corresponding to halfway between the center of the atoms in the outermost layer and the center of the atoms of the first atomic layer which has been removed to form the surface.

Following *Feibelman* [18.20], the charge associated with the SP must be located above the geometric surface plane since there the electronic charge density is small and it costs less energy to add additional charge to the thinner, and therefore softer, electron gas. The model is schematized in Fig. 18.8a. The d parameters correspond to the centroid of the induced charge, located at $d_\perp$, and to the geometric surface coinciding with the jellium edge at $d_\parallel$.

Energy-dissipation mechanisms can be introduced by allowing for an imaginary part $d_\perp$. The dependence on frequency of real (distance) and imaginary (dissipation) parts of $d_\perp$ are reported in Fig. 18.8b as calculated by *Liebsch* [18.21] for simple metals with different density (expressed as usual by r_s, the radius of the sphere with a volume equivalent to the one available for each free electron in the unit cell (expressed in multiple of the Bohr radius a_0, $1\,a_0 \approx 0.5$ Å). In accord with Feibelman, $d_\perp$ is still outside of the jellium edge at the SP frequency and drops abruptly only at $\omega_m \approx 0.8\omega_p$ where the dissipation is largest especially for low-density materials ($r_s = 5$).

The additional charge associated with the SP generates a potential, which at any given location depends on its spatial distribution at the surface, i.e., on the wavelength of the SP. As mentioned above, at large wavelengths (small wavevectors) the surface plasmon potential penetrates deeply into the bulk, while at short wavelengths (large wavevectors) it will be confined to the near-surface region. Since the electronic charge density decreases exponentially with the distance from the surface, the SP will *see* a wavevector-dependent effective charge density n_{eff} largest at small wavevectors and smallest at short wavelengths. The surface plasma frequency will therefore decrease with SP wavevector. Given the $\sqrt{n}$ dependence of ω_p, for small wavevectors such dependence will be linear and correspond to a negative slope. This result has been confirmed experimentally for simple metals by HREELS [18.11, 18].

In Fig. 18.9, HREEL spectra are shown for a thick amorphous K film [18.11]. They were recorded by varying the angle of incidence of the incoming beam while keeping the scattering angle fixed and sweeping over

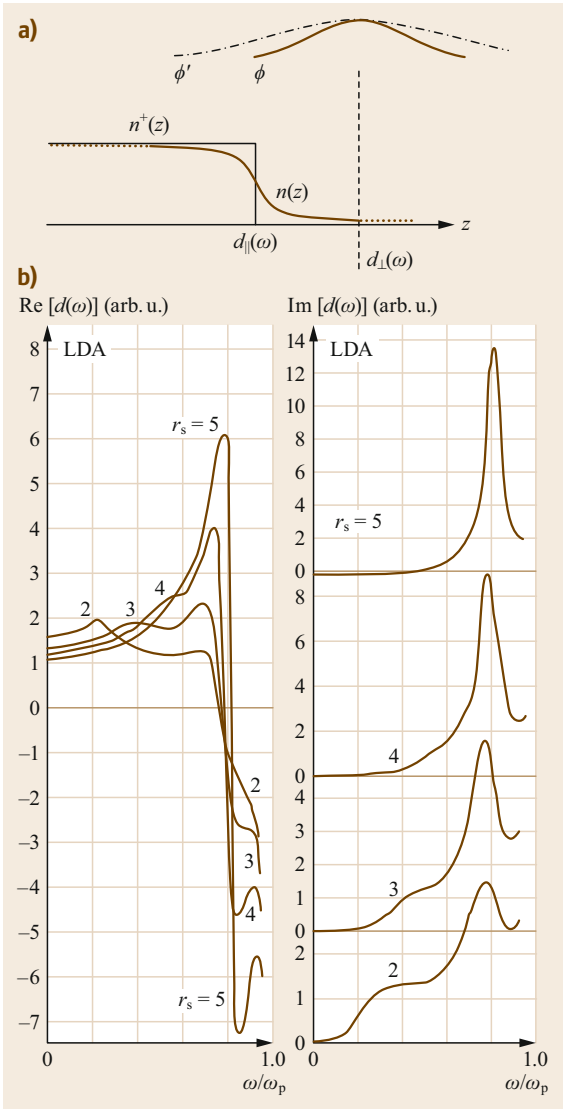

Fig. 18.8 **(a)** Position of the centroid of the oscillating charge associated with the SP, $d_\perp$, with respect to the geometric surface plane. The latter, coincides with the jellium edge and is indicated by $d_\parallel$ since it corresponds to the position where charge would be induced by an electric field oriented parallel to the surface. The electric potential associated with the additional charge is reported for two values of $q_\parallel$; ϕ' corresponds to a smaller $q_\parallel$ value than ϕ and is therefore restricted to a narrower region at the surface where the charge density is smaller, resulting in a wavevector dependence of n_{eff}. **(b)** Real (*left*) and imaginary (*right*) part of $d_\perp$ versus frequency parametric in the density of the material modelled by the parameter r_s (radius of the sphere at disposition of each electron, expressed in multiple of the Bohr radius). (Reprinted by permission from [18.21], © Springer 1997)

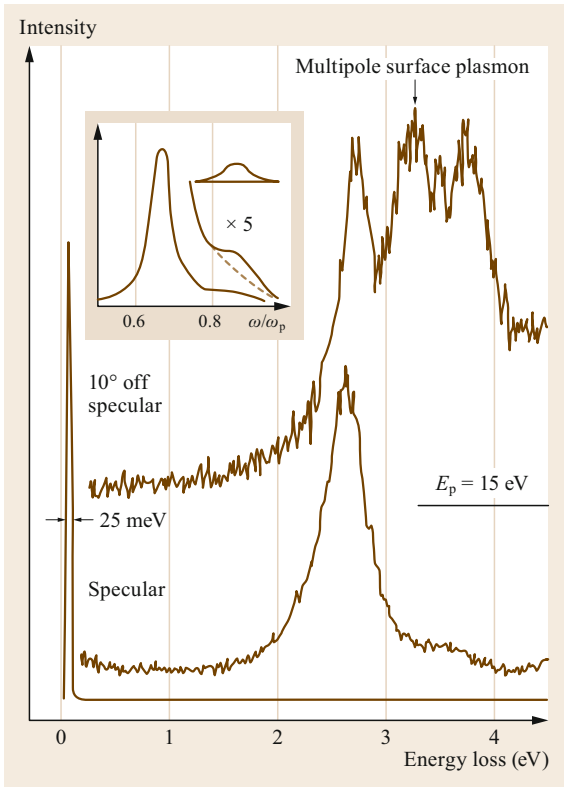

Fig. 18.9 HREEL spectra recorded for thick K films versus impinging angle of the electron beam, θ_i, for fixed scattering angle θ_s. The lowest frequency loss corresponds to the surface plasmon. Above $\theta_i = 50°$ also the multipole and the bulk plasmon losses are observed. (Reprinted with permission from [18.13]. Copyright (1990) by the American Physical Society)

the energy loss. Since the energy loss is comparable with the energy of the impinging electrons, scanning over energy implies sweeping also over exchanged parallel momentum.

As demonstrated by the Ewald construction reported in Fig. 18.10, the vanishing parallel momentum transfer condition at the SP energy of 2.6 eV occurs off specular. The SP loss peak moves then to a higher energy-loss value than for in-specular scattering. Plotting the position of the maximum of the energy loss versus exchanged momentum, calculated from the energy and parallel momentum conservation equations

$$\frac{\hbar^2 k_f^2}{2m} = \frac{\hbar^2 k_i^2}{2m} - \hbar\omega_{sp} \,, \tag{18.4}$$

$$k_{\parallel f} = k_{\parallel i} - q_\parallel \,, \tag{18.5}$$

with $\boldsymbol{k}_i$ and $\boldsymbol{k}_f$ wavevectors of the incident and scattered electrons, yields the data points reported in Fig. 18.11

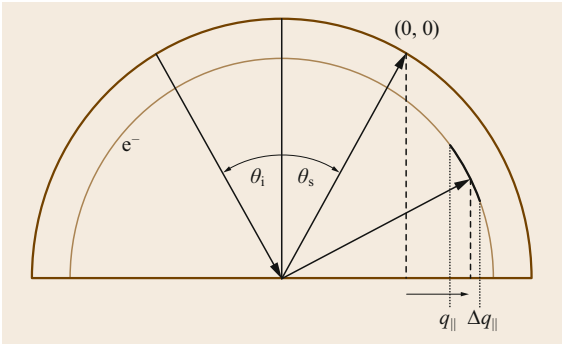

Fig. 18.10 Ewald construction showing the scattering geometry of the HREELS experiment; θ_i and θ_s correspond to incident and scattering angles, the *circle* to *on the energy shell*, i.e., to elastic scattering events for which $|k_f| = |k_i|$. Vanishing parallel momentum transfer is indicated by the *dashed vertical line* and corresponds to off-specular scattering for any nonzero energy-loss value (crossing point between *dashed line* and *light brown sphere* corresponding to a smaller final energy). The arc indicates the angular integration due to the acceptance of the spectrometer which translates into an integration over reciprocal space $\Delta q_\parallel$. The latter determines the quality of the HREEL spectra since achieving a good enough energy resolution is not problematic for the investigation of electronic excitations

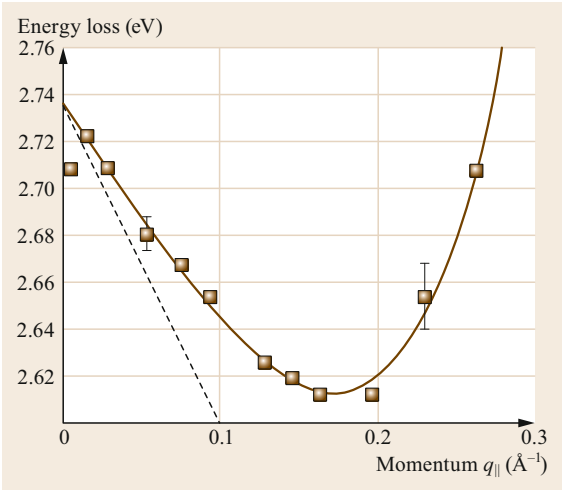

Fig. 18.11 Surface plasmon energy versus exchanged momentum for a thick K film. The dispersion is initially linear and negative. A quadratic term becomes important above 0.2 Å^{-1}. (Reprinted with permission from [18.11]. Copyright (1989) by the American Physical Society)

which nicely witness the negative dispersion up to some 0.1 Å^{-1} beyond which quadratic terms of bulk origin become important.

Back to Fig. 18.9, off-specular additional losses are apparent. They correspond to the multipole plasmon and to the bulk plasmon, respectively. The multipole corresponds to an excitation with an additional node in the normal direction. Excitation of multipole and bulk modes is more efficient for scattering conditions closer to normal incidence since the electrons penetrate then deeper inside the K film. Contrary to the excitation of the surface plasmon which is dipolar in nature, the one of the multipole mode is due to a different mechanism. Its cross section could be reproduced only recently by theory [18.49–52] and is treated thoroughly in Chap. 17.

The experimentally determined ratio of surface-to-volume plasmon energy for simple metals is reported in Table 18.1. As one can see the $1/\sqrt{2}$ ratio appropriate for a free-electron gas is respected quite accurately in experiment. The only important deviation is for Li for which band structure effects cannot be neglected.

The SP dispersion is well described by a polynomial fit. The values of the coefficients up to the fourth degree (A to D) are reported in Table 18.2 for the different simple metals. The quadratic term can be ascribed to the polarizability of the electron gas, an effect determining the dispersion also for the bulk plasmon, while no evident interpretations are possible for cubic and quartic terms. The order of magnitude of the quadratic term is in reasonable agreement with the quadratic coefficient of $\approx 2.2\,\text{eV}\text{Å}^2$ reported, e.g., for the bulk plasmon of Al [18.53]. The error bar on such terms is, however, quite large since the plasmon loss is heavily damped at large wavevector transfers. Indeed, the cubic term for K is associated to a very small quadratic term and the outcome could be flawed by a compensation effect in the curve fitting procedure.

According to Feibelman's theory the linear term of the dispersion is related to the position of the centroid of the induced charge $d_\perp(\omega)$ by

$$\omega_{sp}(q_\parallel) = \omega_{sp}(0)\left\{1 - \frac{1}{2}\left[d_\perp(\omega_{sp}) - d_\parallel(\omega_{sp})\right] q_\parallel + O\left(q_\parallel^2\right)\right\}. \quad (18.6)$$

The values extracted for the different simple metals are compared with theory in Table 18.3 and nicely confirm the calculated values quantitatively. The centroid of the induced charge lies accordingly on the average at some 0.7 Å above the geometric surface.

If a similar procedure is applied to the multiplasmon loss a linear positive dispersion with $q_\parallel$ is obtained. The multiplasmon frequency ω_{mp} is compared in Table 18.4 for the different simple metals. The ratio of

Table 18.1 Surface and bulk plasmon energies and line widths for simple metals. The $1/\sqrt{2} = 0.707$ condition on the frequency ratio of surface versus volume plasmon, expected for a free-electron gas is very well respected for all alkali and for Al except for Li

Metal surface	$\hbar\omega_{sp}$	$\Delta\hbar\omega_{sp}$	$\hbar\omega_p$	$\Delta\hbar\omega_p$	$\hbar\omega_{sp}/\hbar\omega_p$
Al(111)	10.9 [18.18]	3	15.34 [18.53]	0.5	0.71
Mg(0001)	7.38 [18.54]	1.2	10.4 [18.55]	0.7	0.71
Li(110)	4.28 [18.54]	0.5	7.12 [18.53]	2.2	*0.60*
Na film	3.98 [18.11]	0.6	5.72 [18.56]	0.4	0.79
K film	2.73 [18.11]	0.2	3.72 [18.56]	0.3	0.73
Rb film	2.46 [18.56]		3.41 [18.56]	0.6	0.72
Cs film	1.99 [18.11]	0.45	2.90 [18.56]	1.2	0.69

Table 18.2 Values of the coefficients resulting from a polynomial fit of the data. (Reprinted by permission from [18.12], Elsevier 1991)

Metal surface	$\hbar\omega_{sp}$	A (eV)	B (eV Å)	C (eV Å^2)	D (eV Å^3)
Al(111)	10.9	−3			
Mg(0001)	7.38	−3.02	9.78		
Li(110)	4.28	−0.87	2.11		
Na film	3.98	−1.56	2.47	−0.44	47.9
K film	2.73	−0.96	0.09	0.48	48.4
Rb film	2.46				
Cs film	1.99	−0.44	2.8	17.2	

Table 18.3 Values $d_\perp$ extracted from the linear coefficient of the measured dispersion curves compared to the result of random phase approximation (RPA) and local density approximation(LDA). RPA describes the experimental values more accurately since LDA fails in reproducing the tail of the electron density outside of the surface

Metal surface	$\hbar\omega_{sp}$ (eV)	$d_\perp(\omega_{sp})$ (Å)	d_{RPA} (Å)	d_{LDA} (Å)
Al(111)	10.3		0.4	0.6
Mg(0001)	7.38	0.82	0.6	1.0
Li(110)	4.28	0.48	0.8	1.4
Na film	3.98	0.73	0.9	1.9
K film	2.73	0.73	0.7	2.2
Rb film	2.46		0.6	2.2
Cs film	1.99	0.88	0.5	2.2

Table 18.4 Analysis of the multipole mode for the different simple metal surfaces as determined either by HREELS or by PY measurements. For Na, K, and Cs the dispersion with momentum could be determined and has a positive value. (Reprinted by permission from [18.12], © Elsevier 1991)

Metal surface	$\hbar\omega_{mp}$ (eV)	$\hbar\omega_{mp}/\hbar\omega_p$	$\Delta\hbar\omega_{mp}$ (eV)	Linear dispersion coefficient
Al	12.5 PY	0.83	3.3	
Mg	8.7 HREELS	0.84	2.3	
Li				
Na	4.7 HREELS	0.81	1.2	3.37
K	3.2 HREELS	0.84	0.7	2.47
Rb	2.8 PY	0.84	0.4	
Cs	2.4 HREELS	0.83	0.6	1.0

ω_{mp} to ω_p is always close to 0.84, the value expected for a free-electron gas. At ω_{mp} the PY is enhanced since the multiplasmon implies strong electric fields across the geometric surface plane. The dispersion of the multipole mode with transferred momentum is always positive.

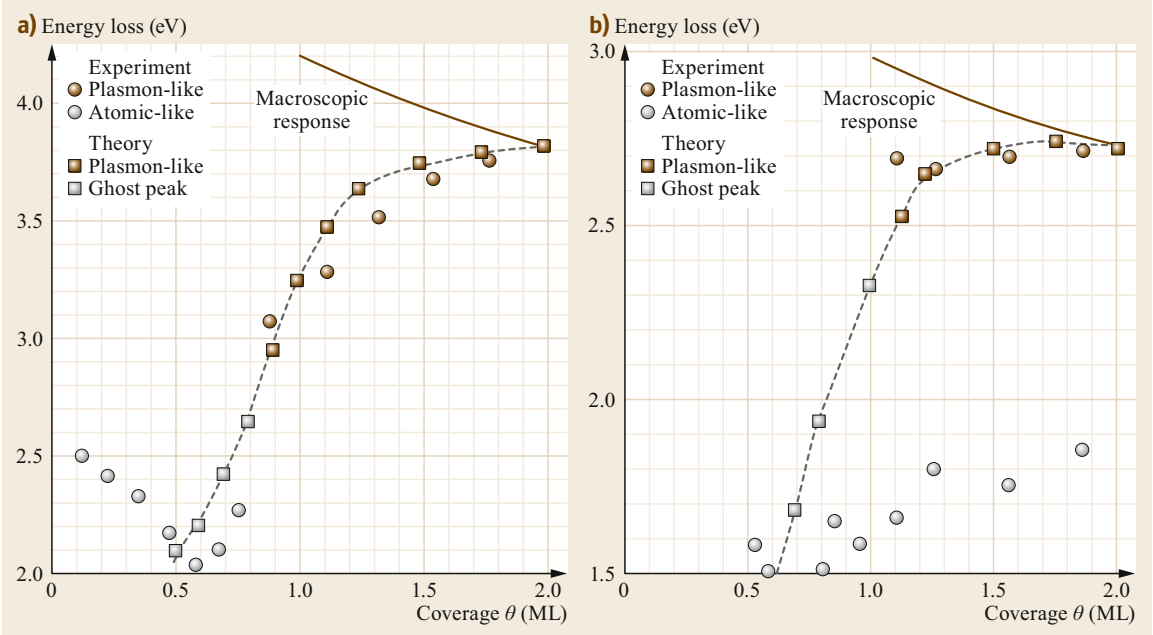

Fig. 18.12a,b Position of the losses in the surface plasmon region versus alkali film thickness: **(a)** Na/Al, **(b)** K/Al. The surface plasmon loss appears only after the completion of the first monolayer. At lower coverage the excitation is confined inside nanosized islands and is better described as a Mie resonance (see later the discussion for Ag clusters on Si(111)) or corresponds to an atomic-like excitation. The ghost peak corresponds to spectra in which because of inhomogeneity, both SP- and atomic-like modes are excited. (Reprinted with permission from [18.14]. Copyright (1991) by the American Physical Society)

The surface-loss spectra have been investigated also as a function of the thickness of the alkali film [18.14]. As shown in Fig. 18.12, the SP is excited only above one monolayer film thickness. At lower coverage the observed loss corresponds to a localized atomic-like excitation.

18.3 Lattice Effects on the Surface Plasmon Dispersion

Lattice effects on the surface plasmon frequency and dispersion, already evident for Li, become even more important for solid Hg. The experimental data are shown in Fig. 18.13 [18.57]. The data show a quite large scattering of the maximum of the energy-loss peaks due to the intrinsic broadness of the loss (1 eV). The initial slope of the dispersion is, however, clearly negative and can be reproduced by the stabilized jellium model which provides a better electronic density profile at the surface than normal jellium.

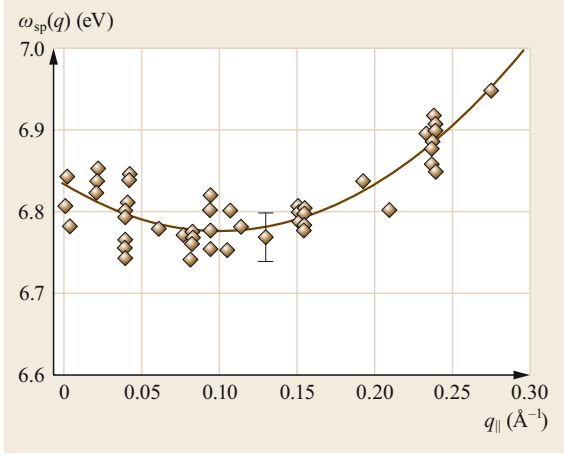

Fig. 18.13 SP dispersion for solid mercury. (Reprinted with permission from [18.57]. Copyright (1995) by the American Physical Society) ►

18.4 Effect of the Band Structure on Surface Plasmon Energy and Dispersion: The Case of Noble Metals

The situation is radically different for noble metals. In this case at the SP frequency important additional contributions to the surface response function come in due to the strongly bonded d-electrons localized around the ion cores. Their effect is to shift the plasma frequency (from the free-electron density value 9.6 eV to 3.78 eV

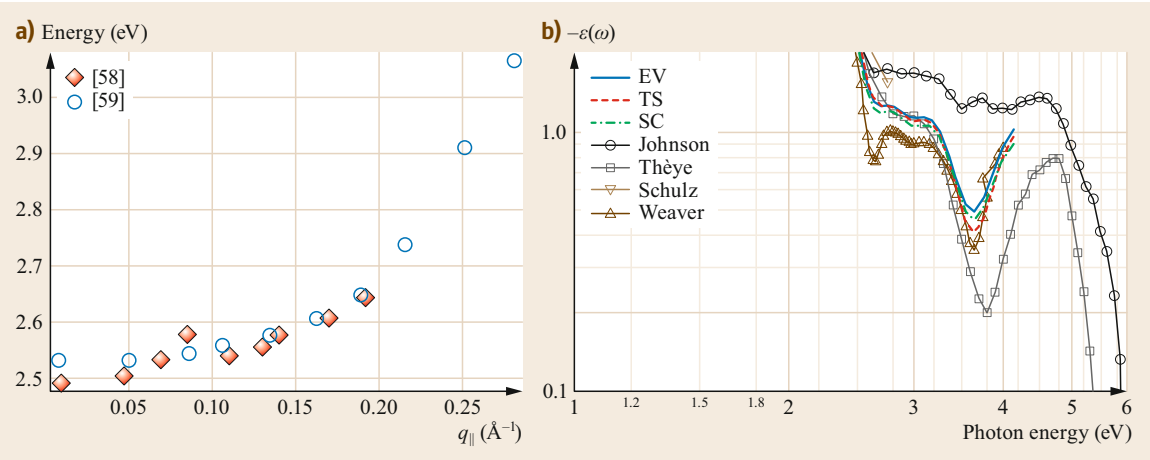

Fig. 18.14 **(a)** SP dispersion for Au(111) as published by *Park* and *Palmer* [18.58] and *Politano* et al. [18.59]. The data show a positive initial dispersion and a strong quadratic term. **(b)** Negative of the real part of the dielectric function in the relevant region according to different reports [18.60]. The *green curve* labeled SC corresponds to an Au(111) single crystal and crosses the $\varepsilon = -1$ value at around 3.2 eV, rather than at 2.5 eV shedding doubts on the assignment of the HREELS loss which corresponds rather to ε values close to -1.2. (Reprinted with permission from [18.60]. Copyright (1995) by the American Physical Society)

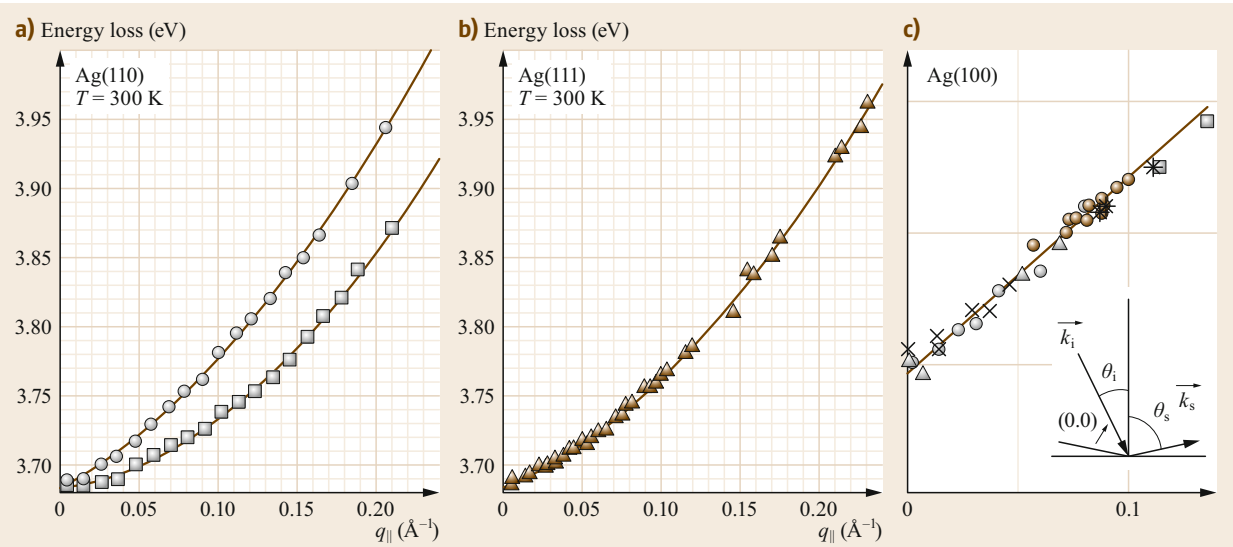

Fig. 18.15a–c Surface plasmon dispersion for **(a)** Ag(110), along the two high-symmetry directions of the strongly anisotropic surface (squares [110], circles [001]), **(b)** Ag(111), and **(c)** Ag(100). The data were recorded by HREELS for Ag(100) and by ELS-LEED for the other two surfaces. Notice the initial positive slope which is different for the different surfaces and anisotropic for Ag(110). The quadratic term is important for the (110) and (111) cases only. The different symbols for the dispersion of Ag(100) refer to data recorded for different impact energies ranging from 10 to 116 eV. (Reprinted with permission from [18.15] and [18.61]. Copyright (1990) and (1997) by the American Physical Society)

Table 18.5 Dispersion coefficients for Au(111) and for the different Ag surfaces as obtained by analyzing the HREELS data [18.15–17, 58, 59, 61]

Ag	Azimuth temperature	ω_{sp} (eV) $T = 100$ K	A (eV Å) $T = 100$ K	B (eV Å^2) $T = 100$ K	ω_{sp} (eV) $T = 300$ K	A (eV Å) $T = 300$ K	B (eV Å^2) $T = 300$ K
Ag(001)	⟨100⟩	3.71	1.4		3.69	1.4	0.06
Ag(001)	8.8° off ⟨100⟩				3.68	1.6	
Ag(001)	⟨110⟩				3.67	1.5	
Ag(110)	⟨001⟩	3.699	1.13	1.1			
Ag(110)	⟨1$\bar{1}$0⟩	3.705	0.42	2.06			
Ag(111)		3.708	0.60	2.2	3.692	0.64	2.0
Au(111)					2.49	0.40	1.70
Au(111)					2.46	0.12	10.75

in the case of Ag and from a similar value to 2.4 eV for Au). The dispersion with exchanged momentum is therefore determined not only by the effective charge density seen by the potential associated with the SP charge but also by the wavevector-dependent efficiency of the screening of d-electrons. *Seeing* the d-electrons less, implies a shift of the surface plasmon energy back to the unscreened value, i.e., towards higher energies. Globally, the effect on the surface plasmon dispersion becomes thus opposite to the one observed for simple metals and the dispersion slope is then positive. The centroid of the induced charge lies, however, still outside of the geometrical surface plane [18.21]. These effects were investigated experimentally for Au [18.58, 59] and Ag [18.15, 16, 61] surfaces.

The HREELS investigation of Au(111) is shown in Fig. 18.14a. The data show a fairly narrow peak at 2.5 eV which shows a positive dispersion and, at hand of the data for the dielectric function available at that time, was assigned to the SP excitation. According to more recent and more accurate optical investigations [18.60], however, such frequency does not correspond to $\varepsilon = -1$. The real part of ε remains indeed quite small from 2.5 to 6 eV (Fig. 18.14b) while the imaginary part of ε is large (around 6, not shown). The $\varepsilon = -1$ line is crossed thereby only at 3.2 eV. Further investigation is therefore needed to clarify the nature of the observed energy loss. Theoretical work in that direction is currently being performed [18.62].

The data for the SP dispersion of Ag are easier to interpret since in that case a very well-defined EEL peak is present at the frequency for which $\varepsilon(\omega) = -1$. The sharpness of the loss (full-width-at-half-maximum of only 50 meV for the Ag(111) surface, corresponding to a $\Delta E_{loss}/E_{loss}$ ratio close to 2%) allowed fine effects such as the face and the crystallographic direction dependence of the SP dispersion to be investigated.

The different Ag surfaces were investigated both by HREELS and by electron energy-loss-low-energy electron diffraction (ELS-LEED) [18.63], the latter being a technique performed with a spectrometer in which incident and scattering angles are set electronically rather than mechanically thus guaranteeing a higher reproducibility. The ELS-LEED spectrometer has also a better angular resolution which however translates into a momentum resolution comparable to the one of conventional HREELS since the incident and scattering beam directions are restricted to near-normal values. The results are reported in Fig. 18.15 while the coefficients resulting from the polynomial fit are collected in Table 18.5.

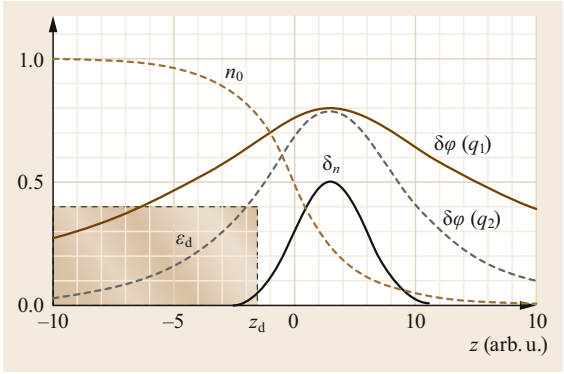

Fig. 18.16 Effective medium model for the plasmon dispersion on noble metal surfaces. The electric potential associated with the SP penetrates approximately one wavelength inside the surface. The effective charge density at large wavevectors is therefore less influenced by the effective medium describing the d-electrons than at small wavevectors. Since the effect of the effective medium is to shift the plasmon resonance to lower frequencies, ω_{sp} will increase with $q_\parallel$ giving a positive slope to the SP dispersion. (Reprinted by permission from [18.21], © Springer 1997)

Liebsch [18.21] modeled the effect of the localized d-electrons introducing an effective polarizable medium

mimicking their density and noticing that such medium is spatially localized closer to the nuclei than the sp-electrons (Fig. 18.16). He was then able to obtain a positive dispersion slope by placing the effective polarizable medium inside the jellium edge by some 0.8 Å. The different slope of the dispersion for the different crystal faces would then result from different positions of the polarizable medium with respect to the geometric surface. While this model gives a rational for the positive dispersion, it cannot reproduce the experimentally observed dependence of plasmon dispersion on crystal face even qualitatively since the position of the polarizable medium should be shallower for Ag(111) than for Ag(001) while the lattice spacing in the direction normal to the surface plane scales in the opposite way.

A merit of this model is, however, to explain the strong negative dispersion reported for Pd(110) [18.64] which is in accord with the fact that the SP frequency for this metal is at 7.8 eV with a marginal displacement with respect to the value expected for a free-electron gas with the density of Pd.

A more refined theoretical model was proposed by *Yan* et al. [18.65] who obtained the surface plasmon dispersion for Ag(111) as well as H/Ag(111) from first principles by calculating the q-dependent dielectric function.

18.5 Surface Plasmon Damping

The SP linewidth is determined by the damping mechanisms active at the surface, i.e., mainly by the possibility to decay into electron–hole pairs. A linear increase with $q_{\parallel}$ is therefore expected due to the increased phase space for transitions. This mechanism will, however, be largely ineffective as long as it is limited to intraband transitions. As soon as $\hbar\omega_{sp}(q_{\parallel})$ allows for the decay also via interband transitions, a sharp increase of the damping is therefore expected. This effect is shown in Fig. 18.17 for the Ag(001) surface [18.17]. The onset of interband transitions is clearly evident from the kink in the width versus wavevector curve at 0.1 $Å^{-1}$ or 3.82 eV. Interestingly, a smaller (and even negative) initial slope is observed for Ag(111) [18.61]. This indicates that the decay channels determining the plasmon line width at vanishing momentum become less effective with $q_{\parallel}$. The effect has not been investigated further.

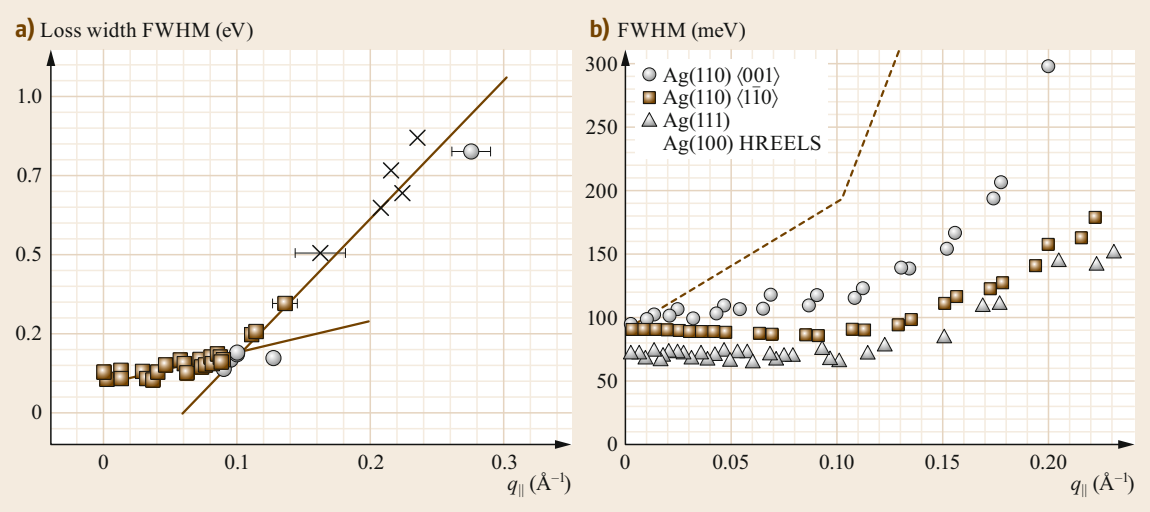

Fig. 18.17a,b Surface plasmon linewidth versus exchanged momentum for Ag(001) ((**a**) HREELS) and Ag(110) and Ag(111) ((**b**) ELS-LEED). The change in the slope is due to the onset of interband transitions involving the d-bands of Ag. ((**a**) Reprinted with permission from [18.17]. Copyright 1990 by the American Physical Society. (**b**) Reprinted from [18.61], with permission from Elsevier)

18.6 Multipole Plasmon Mode at Noble Metal Surfaces

Similar to the case of simple metals a multiplasmon mode is expected to be present also for the noble metals. By definition it corresponds to the frequency at which the real part of $d_\perp(\omega)$ crosses zero and one would therefore expect it to be in-between ω_s and ω_{sp} but no clear cut indications are drawn from theory. Resolving the multipole as a well-separated energy-loss peak is not possible for Ag due to the natural broadness of the SP. However, from the investigation of alkali metals it is evident that the multipole loss is excited most efficiently off specular (so its intensity is not expected to scale proportionally to the elastic reflectivity) and the intensity is largest at small $q_\parallel$ values.

As shown in Fig. 18.18, *Moresco* et al. [18.66] noticed small energy shifts at small $q_\parallel$ for experiments performed at different impact energy. The effect could not be ascribed to a more or less efficient excitation of the bulk plasmon since the latter is excited only when the electrons are below the surface and the penetration depth of the electron beam is a smooth function of energy. The shift must therefore be associated with the presence of contributions caused by different excitation mechanisms as is the case for the SP (excited by dipolar scattering) and the multipole (excited by a different mechanism).

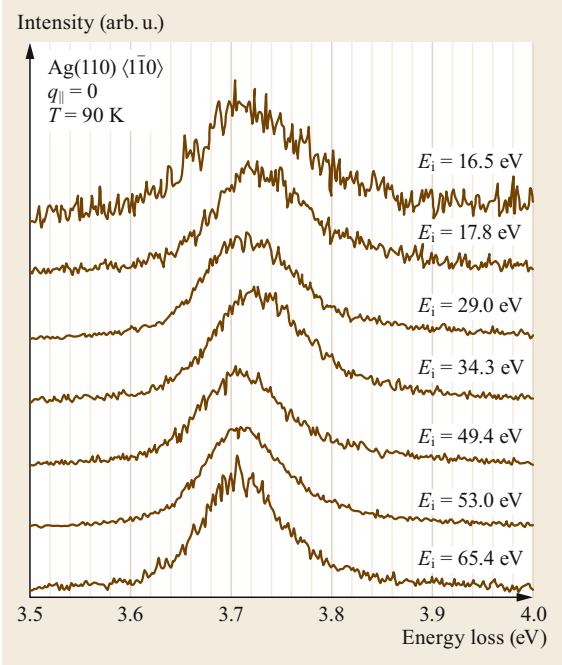

Fig. 18.18 HREEL spectra recorded with ELS-LEED for different impact energies. The position of the maximum was found to depend on the impact energy indicating a complex nature of the loss which must consist of two contributions excited by different excitation mechanisms. (Reprinted with permission from [18.66]. Copyright (1996) by the American Physical Society)

The evidence for an additional contribution is even stronger when looking at the apparent dispersion curves recorded at different impact energy. In some experimental conditions the curve flattens out at small wavevector (Fig. 18.19a for Ag(110) and Fig. 18.19b for Ag(111)). The loss is then definitively higher in frequency and broader than for conditions in which the maximum appears at the lowest energy. Similar observations had been made with HREELS (crosses in Fig. 18.19b).

Deconvoluting the energy-loss spectra with respect to SP and multipole contributions is not trivial since:

1. The width of the SP is not known (at $q_\parallel = 0$ it should be zero according to theory).
2. The width of the multipole is not known.
3. A background of electron–hole pairs is present whose exact shape is also not known.
4. The achievable signal-to-noise ratio does not allow accurate deconvolutions as for XPS data recorded with synchrotron radiation to be performed.

The authors proceeded therefore in a different way: They assumed that the sharpest peaks correspond to excitation of the SP only and determined the additional loss intensity by subtracting losses recorded at other impact energies. The result is shown in Fig. 18.20. It clearly shows a peak centered for $q_\parallel = 0$ at 3.74 eV at all impact energies and for both investigated Ag faces, (110) and (111). Such energy is too low to be due to the excitation of the volume plasmon as well as to the onset of interband transitions. A safe conclusion could therefore be drawn about the existence of a multipole mode for Ag.

This result was confirmed later by PY and angle-resolved photoemission measurements with low-energy photons performed by *Barman* et al. [18.67], who reported a multipole mode for Ag(111) at 3.7 eV for Ag(111) and Ag(100).

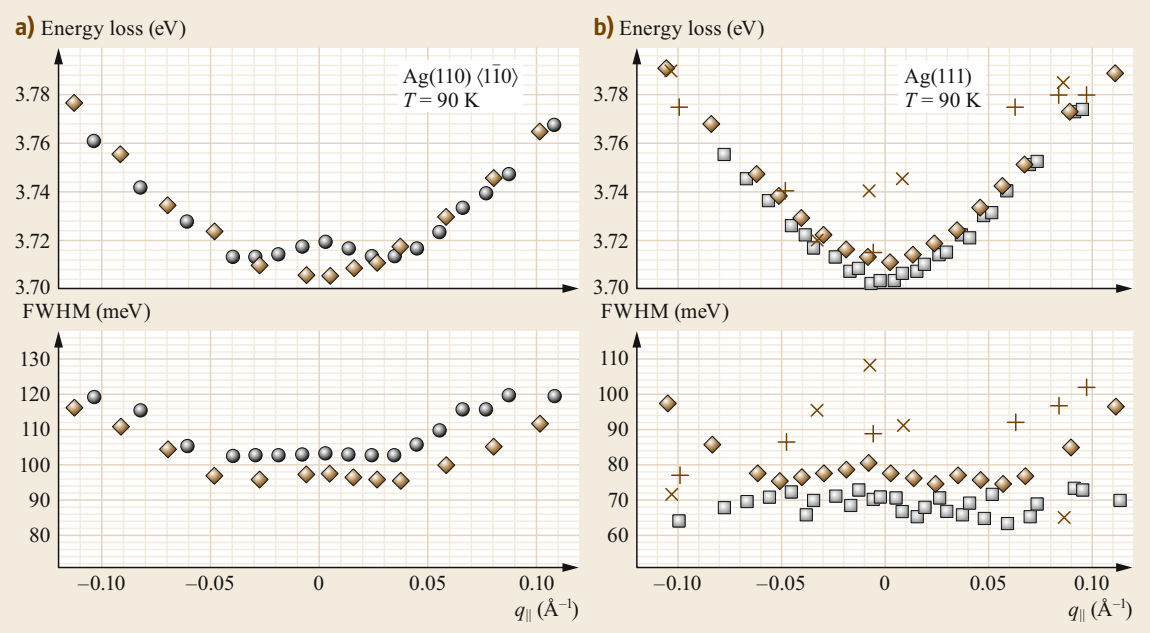

Fig. 18.19 **(a)** Collection of the energy losses and of the full-width-at-half maximum of the losses recorded with ELS-LEED for Ag(110) at 64.5 eV incident energy (*diamonds*) and 16.5 eV (*circles*). *Top*: SP energy; *bottom*: SP loss width versus $q_\parallel$. **(b)** Same as **(a)** but for Ag(111). The experiments have been performed both with ELS-LEED (*squares* $E_i = 20.1$ eV, *diamonds* $E_i = 51.5$ eV) as well as HREELS ($+$ $E_i = 10.7$ eV, $\times$ $E_i = 15.0$ eV). (Reprinted with permission from [18.66]. Copyright (1996) by the American Physical Society)

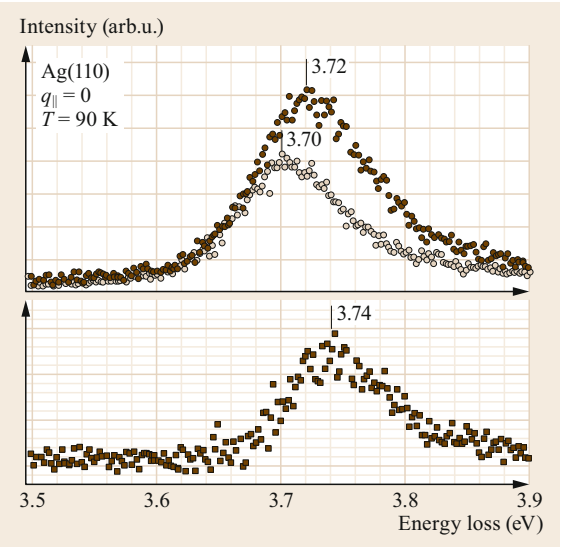

Fig. 18.20 Result of the subtraction of loss spectra recorded at different impact energies. The difference (*bottom panel*) is peaked at 3.74 eV, a value which coincides neither with $\omega_p = 3.78$ eV nor with the threshold of interband transitions, whose energy threshold is at 3.82 eV as determined from the dependence of the SP width versus $q_\parallel$. (Reprinted with permission from [18.66]. Copyright (1996) by the American Physical Society)

18.7 Temperature Dependence of the SP

Little work exists on the crystal temperature dependence of SPs, since only small effects are expected for electronic excitations. However, the SP loss on Ag is so sharp that it allows for very precise measurements of its energy. A small but non-negligible decrease with crystal temperature was indeed reported for both Ag(110) and Ag(111) (Fig. 18.21). Such an effect is compatible with the decrease of the electron gas density following thermal expansion.

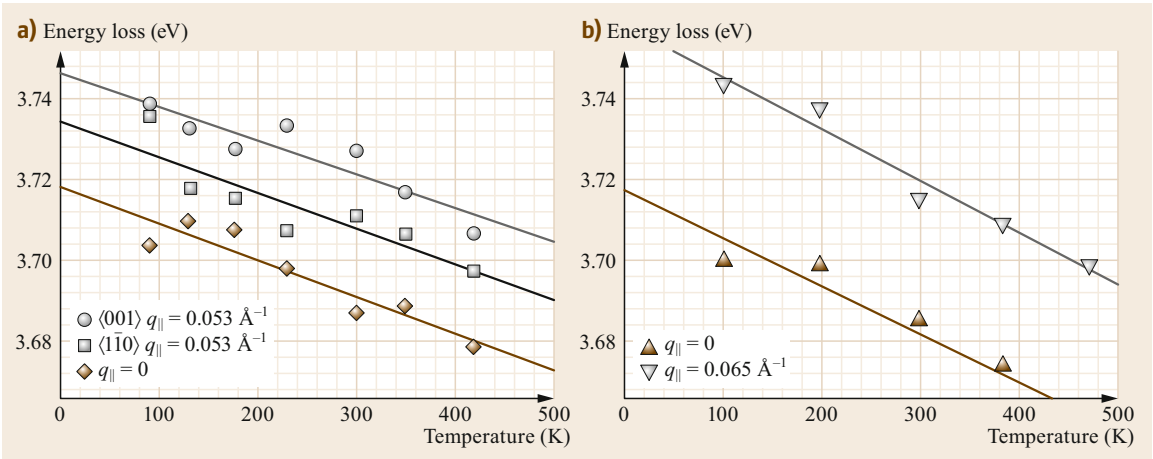

Fig. 18.21a,b SP energy versus crystal temperature at different values of $q_\parallel$ for **(a)** Ag(110) and **(b)** Ag(111). (Reprinted from [18.68], with permission from Elsevier)

18.8 Effect of Adsorption and of Surface Nanostructuring on Surface Plasmon Energy and Dispersion

Alkali metals induce an extended surface reconstruction on Ag(110) already at low coverage. 3% of K is sufficient to induce an extended (1×3) missing row reconstruction whereby one Ag row out of three is removed. With increasing K dose a (1×2) structure forms corresponding to 50% missing Ag atoms and finally the low-energy diffraction pattern evolves into a (1×3) structure at 30% K coverage corresponding to the removal of two out of three Ag rows. Models of these reconstructions are reported in Fig. 18.22c,d [18.69–71].

18.8.1 Alkali Metal Adsorption on Ag Surfaces

As shown in Fig. 18.22a,b the SP dispersion is differently affected for different K coverage and the effect is anisotropic with respect to crystal azimuth. The result of a polynomial fit of the dispersion curves is shown in Table 18.6.

At the lowest coverage, a change is visible only along ⟨001⟩, the direction along which the substrate atomic density decrease is dramatic since every third Ag row is removed. The linear term is thereby unaffected, while the quadratic term drops from 3.4 to 2 eV Å^2. The anisotropy of the surface becomes therefore larger.

The linear dispersion term is eventually affected with increasing K coverage. Indeed it doubles along the ⟨1$\bar{1}$0⟩ direction. The effect becomes dramatic as soon as the high coverage (1×3)-phase forms.

A slight drop occurs also for the frequency at $q_\parallel = 0$, the effect being systematic but within experimental error. Conversely, for larger K coverage ω_{sp} shifts remarkably from the bare surface value of 3.70 eV to 3.82 eV for 1.5 ML of K. The SP loss associated with K becomes apparent above half a monolayer coverage [18.69].

The effect on the ⟨1$\bar{1}$0⟩ direction becomes evident only for the largest K coverage. K adsorption, therefore, initially increases the azimuthal anisotropy. The most corrugated surface, however, is remarkably the least anisotropic at least with respect to the SP dispersion.

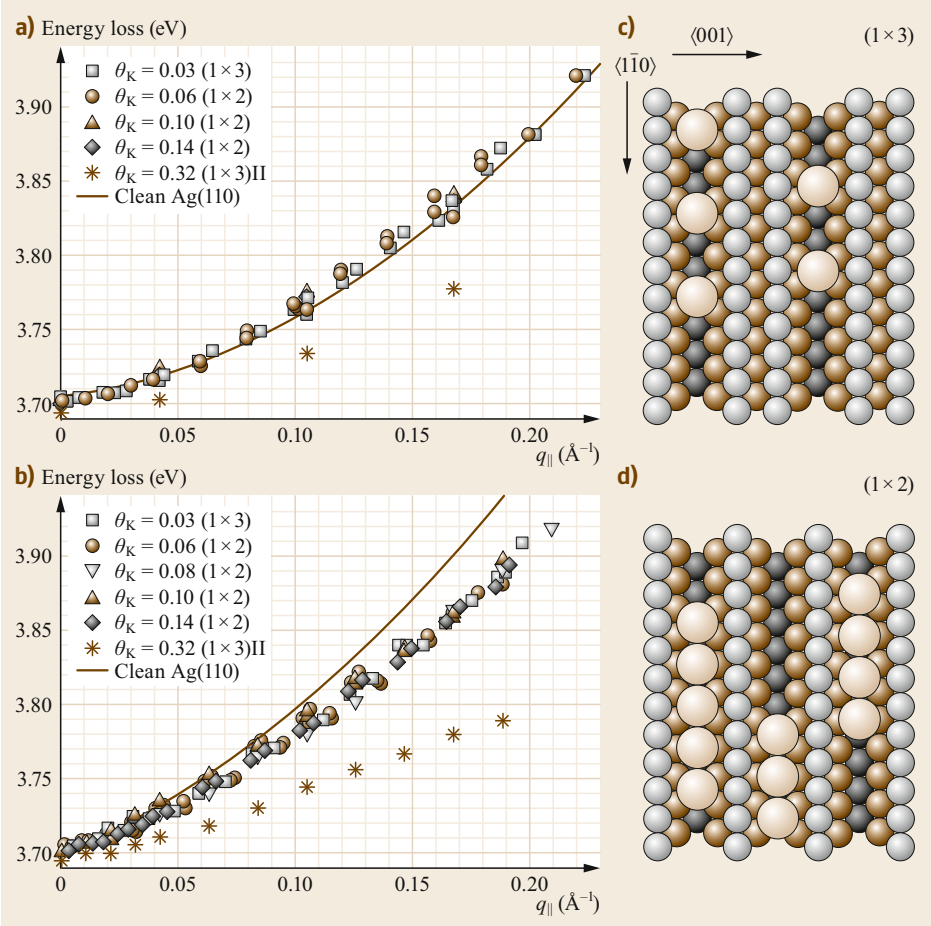

Fig. 18.22a–d Ag(110) SP dispersion for different K-induced reconstructions measured with ELS-LEED at 65.4-eV kinetic energy along the two high-symmetry directions: **(a)** ⟨1$\bar{1}$0⟩, **(b)** ⟨001⟩. With increasing K coverage the SP dispersion becomes markedly flatter especially along ⟨001⟩. Corresponding models are shown for the (1 × 3) **(c)** and (1 × 2) reconstruction **(d)**. (Reprinted from [18.70], with permission from Elsevier)

The effect of K adsorption on SP damping is shown in Fig. 18.23 for Ag(110) along both high-symmetry directions. Again at low coverage the effect is marginal along ⟨1$\bar{1}$0⟩ and larger along ⟨001⟩. At the highest coverage the surface becomes isotropic with respect to SP damping. Notably also the effect of the onset of interband transitions on SP damping is smoothed out.

Table 18.6 SP frequency and linear and quadratic dispersion coefficients along ⟨001⟩ and ⟨1$\bar{1}$0⟩. (Reprinted by permission from [18.69], © Elsevier 1999)

Coverage (ML)	Reconstruction	$\hbar\omega(0)$ (eV) ⟨001⟩	A (eV Å) ⟨001⟩	B (eV Å^2) ⟨001⟩	$\hbar\omega(0)$ (eV) ⟨1$\bar{1}$0⟩	A (eV Å) ⟨1$\bar{1}$0⟩	B (eV Å^2) ⟨1$\bar{1}$0⟩
0	(1 × 1)	3.700 ± 0.002	0.62 ± 0.04	3.4 ± 0.3	3.702 ± 0.003	0.26 ± 0.05	3.2 ± 0.2
0.03	(1 × 3)	3.700 ± 0.002	0.61 ± 0.05	2.1 ± 0.2	3.702 ± 0.002	0.27 ± 0.02	3.1 ± 0.1
0.06	(1 × 2)	3.699 ± 0.002	0.63 ± 0.02	1.9 ± 0.1	3.700 ± 0.002	0.36 ± 0.06	2.9 ± 0.3
0.08	(1 × 2)	3.698 ± 0.002	0.66 ± 0.08	2.0 ± 0.3			
0.10	(1 × 2)	3.698 ± 0.002	0.72 ± 0.03	1.6 ± 0.2	3.703 ± 0.005	0.46 ± 0.1	2.1 ± 0.8
0.14	(1 × 2)	3.698 ± 0.002	0.74 ± 0.06	1.4 ± 0.3	3.701 ± 0.005	0.39 ± 0.1	2.4 ± 0.8
0.32	(1 × 3)	3.693 ± 0.002	0.31 ± 0.07	0.95 ± 0.4	3.692 ± 0.005	0.21 ± 0.12	1.8 ± 0.7

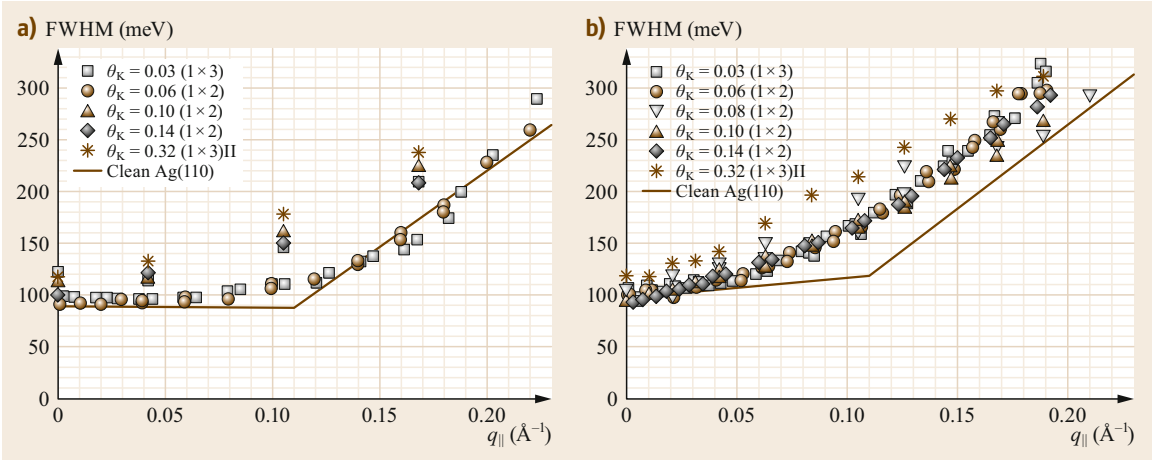

Fig. 18.23a,b Effect of K adsorption on the SP linewidth for **(a)** Ag(110) $\langle 1\bar{1}0\rangle$ and **(b)** Ag(110) $\langle 001\rangle$. (Reprinted from [18.70], with permission from Elsevier)

18.8.2 Effect of Surface Defectivity on Surface Plasmon Dispersion

SP dispersion has been investigated also with respect to the defectivity induced by sputtering at different crystal temperatures. The result for Ag(001) is shown in Fig. 18.24. The bare surface result corresponds to a purely linear dispersion which is at odds with the result of the other two low Miller index faces for which the linear coefficient of the dispersion is smaller and the quadratic one more important. Sputtering makes the curve more quadratic, as expected from the fact that atomic arrangements different from (001) are formed by the damaging action of the sputtering beam. The effect is, however, more marked at room than at low temperature since partial healing of the defects occurs. The difference could be only apparent since surface disorder implies also a worse resolution in reciprocal space which could shift up the SP at small $q_{\parallel}$ values.

In a different experiment the Ag(001) surface has been modified by oxygen adsorption. As shown in Fig. 18.25a, only a drop in the dispersion slope takes place when:

1. The surface is dosed at low temperature so that oxygen adsorption occurs molecularly on a non reconstructed substrate or
2. When adsorption occurs at room temperature where O adsorbs dissociatively and the O adatoms end up at fourfold hollow sites of a nonreconstructed substrate.

However, when the surface is dosed with oxygen at an intermediate temperature at which O_2 dissociates and

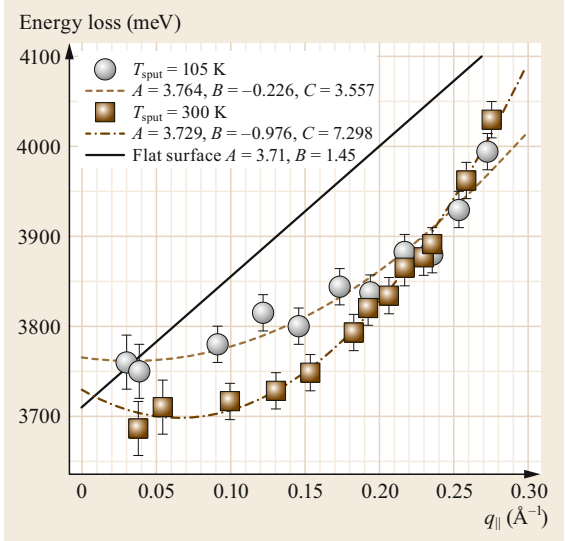

Fig. 18.24 SP dispersion for sputtered Ag(001) performed at 105 and 300 K. We note the drop in the linear dispersion term and the corresponding increase in the quadratic one. (Reprinted with permission from [18.72]. Copyright (2003) by the American Physical Society)

the surface reconstructs forming missing rows [18.74], then the dispersion becomes parabolic, see Fig. 18.25b.

Sputtering and oxygen adsorption indicate therefore that a qualitative change in the dispersion occurs upon surface reconstruction only. One possibility is that the reconstruction as well as sputtering kill a surface state at the X bar point of the 2-D Brillouin zone.

The outcome of the polynomial fits are reported in Table 18.7.

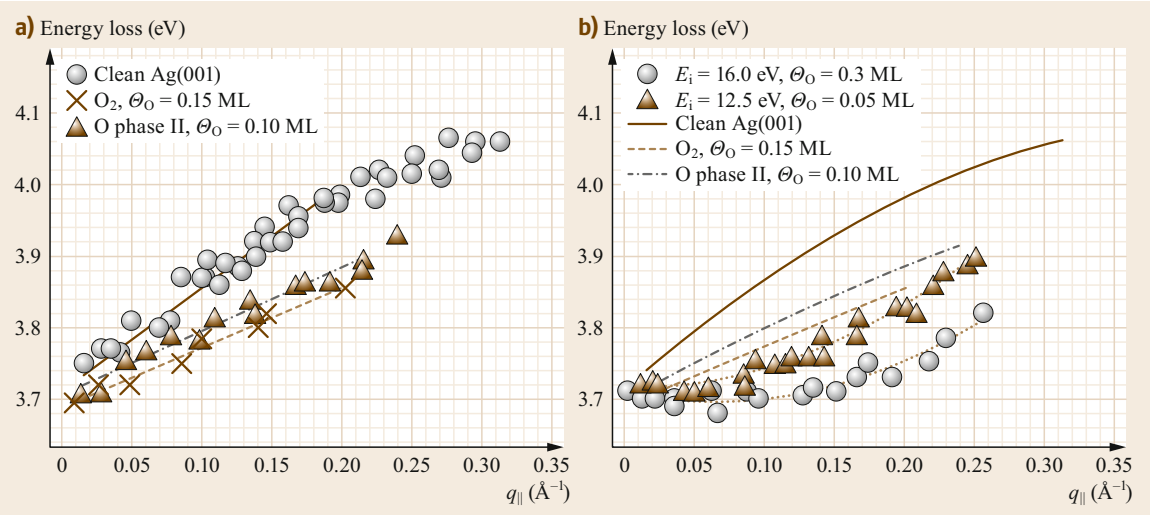

Fig. 18.25a,b SP dispersion of Ag(100) for different oxygen coverage. **(a)** O_2 and O in phase II correspond to a non reconstructed substrate. **(b)** O in phase I induces a missing row reconstruction of the surface. (Reprinted with permission from [18.73]. Copyright (2000) by the American Physical Society)

Table 18.7 SP dispersion coefficients for Ag(001) bare and following the adsorption of oxygen in different phases. Phase I corresponds to a reconstructed surface, while in phase II the O adatoms are adsorbed on a nonreconstructed substrate

Phase	Coverage (ML)	$\hbar\omega(0)$ (eV)	A (eV Å)	B (eV Å^2)
Bare Ag(001)		3.71	1.73 ± 0.13	-1.9 ± 0.4
O_2	0.15	3.69	0.86 ± 0.20	-0.1 ± 1.0
O phase II	0.10	3.70	1.1 ± 0.2	-0.9 ± 0.5
O phase I	0.05	3.71	0.0 ± 0.1	3.1 ± 0.5
O phase I	0.3	3.71	-0.4 ± 0.1	3.1 ± 0.5

The conclusion of these experiments is that, at least for Ag, both the linear and the quadratic terms of the dispersion are determined by surface properties (the only ones which may be affected by adsorbates or by surface disorder).

18.8.3 Other Reports on Adsorption-Induced Modifications of the Surface Plasmon Dispersion

An important modification of the SP dispersion was reported for Ag(111) by the group of *Kesmodel* [18.75] following dosing with Cl_2. The initial dispersion of the SP changes thereby from positive to negative. The data are reported in Fig. 18.26. Notably also the frequency at $q_{\parallel} = 0$ decreases, an effect which is not expected for an ultrathin film. The change of sign of the linear dispersion coefficient is ascribed to charge transfer between the Ag substrate and the molecular layer, although contributions due to plasmon screening via the Cl overlayer and surface chloride formation are mentioned as important factors as well.

Feng et al. [18.76] reported a similar effect upon adsorption of 2,3,5,6-tetrafluoro-7,7,8,8-tetracyanoquinodimethane (F4-TCNQ) on the same surface. In this case no change occurs for the SP frequency at $q_{\parallel} = 0$, but the SP frequency was then abnormally high already for the bare surface, an effect not explained by the authors which sheds doubt on the reliability of the experiment.

A change in dispersion and in SP frequency has been reported also for Au(111) following 4-ethylbenzenethiol and dodecanethiol adsorption [18.58]. This data should be considered with due care since, as discussed before, in this case the energy-loss maximum does not satisfy the $\varepsilon = -1$ condition.

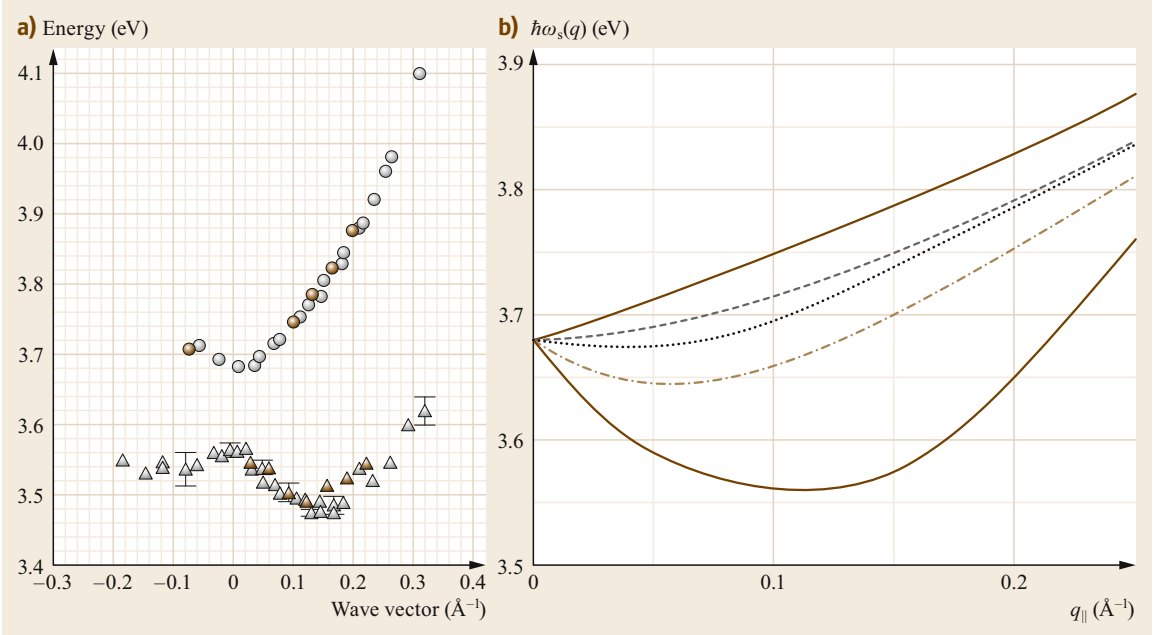

Fig. 18.26a,b Effect of Cl adsorption on Ag(111). **(a)** Experimental data for the bare surface (*circles*) and after adsorption of Cl. **(b)** Time-dependent density functional calculation of the dispersion curve. *Upper curve*: neutral Ag; *dashed curve*: charged Ag; *dotted curve*: neutral Ag with dielectric overlayer $\varepsilon = 2$; *dot dashed curve*: charged Ag with dielectric overlayer; *bottom solid curve*: neutral Ag with a surface layer consisting of AgCl $\varepsilon = 4$. (Reprinted with permission from [18.73]. Copyright (2000) by the American Physical Society)

18.9 Mie Resonance Shift and Surface Plasmon Dispersion

The Mie resonance [18.78] corresponds to a maximum of the optical cross section for metallic nanoparticles resulting from the excitation of the SP at their surface. The resonance condition is determined by the largest possible wavelength over a closed path on the surface of the cluster. In the limit of spherical particles only one

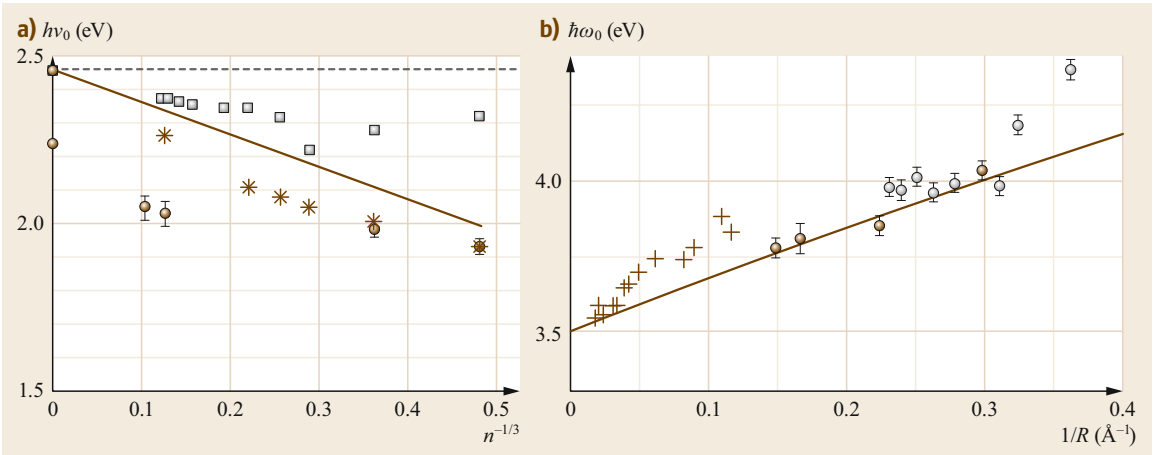

Fig. 18.27a,b Mie resonance dependence on cluster size for **(a)** K [18.23], and **(b)** Ag [18.25] nanoparticles. (Reprinted with permission from [18.23, 25]. Copyright (1992, 1993) by the American Physical Society)

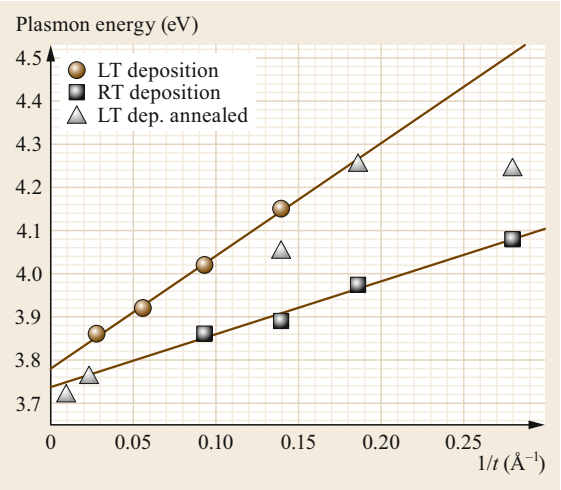

Fig. 18.28 Surface plasmon energy at vanishing momentum transfer for a thin Ag film deposited on Si(111) 7×7 plotted versus inverse of the film thickness t. (Reprinted with permission from [18.77]. Copyright (1999) by the American Physical Society)

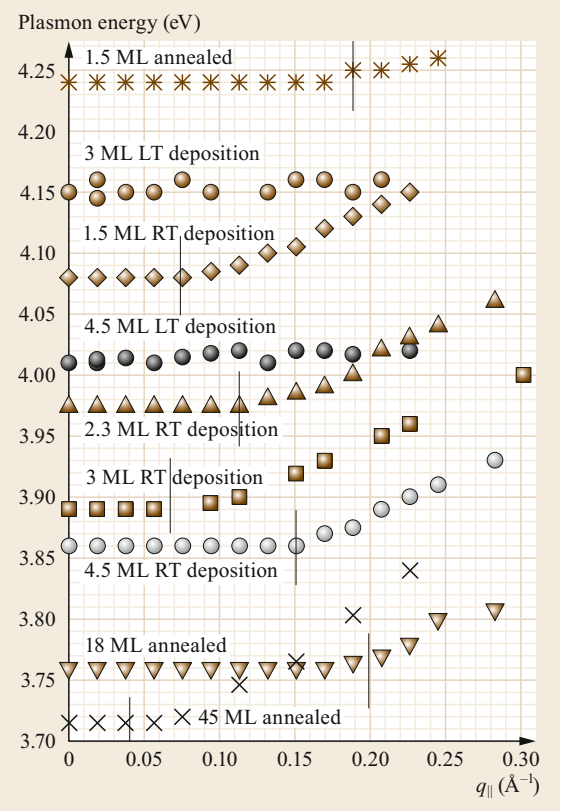

Fig. 18.29 SP dispersion for various preparation conditions for Ag films grown on Si(111) 7×7. (Reprinted with permission from [18.77]. Copyright (1999) by the American Physical Society)

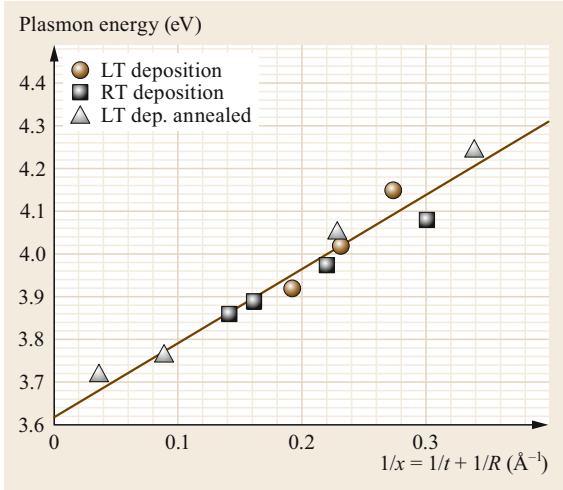

Fig. 18.30 Collection of the data of the SP energy recorded for Ag films grown on Si(111) 7×7 versus film thickness t and island size. Such a plot is equivalent to mapping the dependence of the SP energy versus surface-to-volume ratio of the islands. (Reprinted with permission from [18.77]. Copyright (1999) by the American Physical Society)

mode exists and the resonance corresponds to $2\pi R =$ wavelength $= 2\pi/q_{\parallel}$ with R radius of the nanoparticle. The $1/R$ dependence for the Mie resonance is thus equivalent to the $q_{\parallel}$ dependence of the SP frequency. As shown in Fig. 18.27, the effect has indeed opposite sign for bare K [18.23] and Ag [18.25] nanoparticles in perfect accord with the reasoning about simple and noble metals. Note that the asymptotic value of the frequency differs from the surface plasmon frequency since the limit is not a flat surface but the surface of a sphere.

The concept of the size dependence of Mie resonances was demonstrated to be useful also for the interpretation of SP excitations on ultrathin films deposited at surfaces if they consist of an ensemble of clusters. This is the case for silver deposited on Si(111) 7×7, which grows in flat cylinders of the size of half the 7×7-unit cell of the substrate and are terminated by a flat Ag(111) face. The data were apparently inconclusive since, as shown in Fig. 18.30, at vanishing $q_{\parallel}$ the SP energy took all possible values from 4.4 eV down to 3.7 eV. Plotting the data versus inverse film thickness, as suggested by [18.79], helped only partially. The reasoning is thereby that the film cannot support propagation of SP exceeding its thickness. The SP frequency is therefore determined by the largest supported wavelength. Depending on the sign of the SP dispersion the $1/t$ dependence arises naturally.

This analysis is reported in Fig. 18.28. As is evident the data points obtained after low-temperature

deposition followed by annealing are at odds with any reasonable dependence on film thickness.

More information could be gained from the inspection of data recorded versus wavevector transfer, see Fig. 18.29. They show an evident threshold beyond which dispersion is present while below it the SP behaves like an Einstein oscillator. For small $q_{\parallel}$ values the electron gas in the single clusters oscillates therefore in an uncorrelated way. The threshold value of $q_{\parallel}$ therefore permits the average lateral size of the clusters to be determined as $d = 2\pi/q_{\parallel}$.

When the data are plotted versus inverse thickness and inverse radius of the islands they finally fall on a straight line. Little reasoning will convince the reader that the $1/x$ in the abscissae is equivalent to the area versus volume ratio of the clusters. The dependence of the SP frequency is thus the same as the Mie resonance shift in anisotropic clusters.

18.10 Surface Plasmons and Surface Plasmon Polaritons

Since SP are transverse waves they may mix with light which gives rise to surface plasmon polaritons (SPP) in the long wavelength limit [18.5]. Such excitations are very interesting since they have larger wavevectors with respect to light at the corresponding frequency and allow therefore for its confinement especially at energies close to the one of the SP.

18.10.1 Dispersion of the Surface Plasmon Polariton

A typical dispersion curve of the SPP is reported in Fig. 18.31a for the Au/air interface. The slope of the dispersion depends on the dielectric with which gold is in contact. The SPP can thus have speeds up to 5 times lower than light and a correspondingly shorter wavelength. Confinement is, however, even stronger for frequencies closer to the SP frequency since the SPP dispersion curve bends then to the right. The phase and group velocities for the Ag and Au interfaces with air are shown in Fig. 18.31b. As one can see a further reduction by 30% occurs for Au at 2.25 eV [18.80].

18.10.2 Anisotropy of the Surface Plasmon Polariton Dispersion

As mentioned above the SP dispersion is anisotropic with respect to surface azimuth for Ag(110). Such anisotropy is present also for the SPP but with a reversed sign [18.7, 8]. The effect is pictorially summarized in Fig. 18.32. The apparent contradiction is due to the different origins of the anisotropy in the two ranges of exchanged momentum. At large wavevectors what matters is the microscopic position of the centroid of the induced charge and of the d-electrons with respect to the geometric surface plane. At short wavelengths the SPP anisotropy has a macroscopic origin being linked to the one of the interband transitions between surface states. A similar, but less clear cut result has been reported also for Au(110) [18.82].

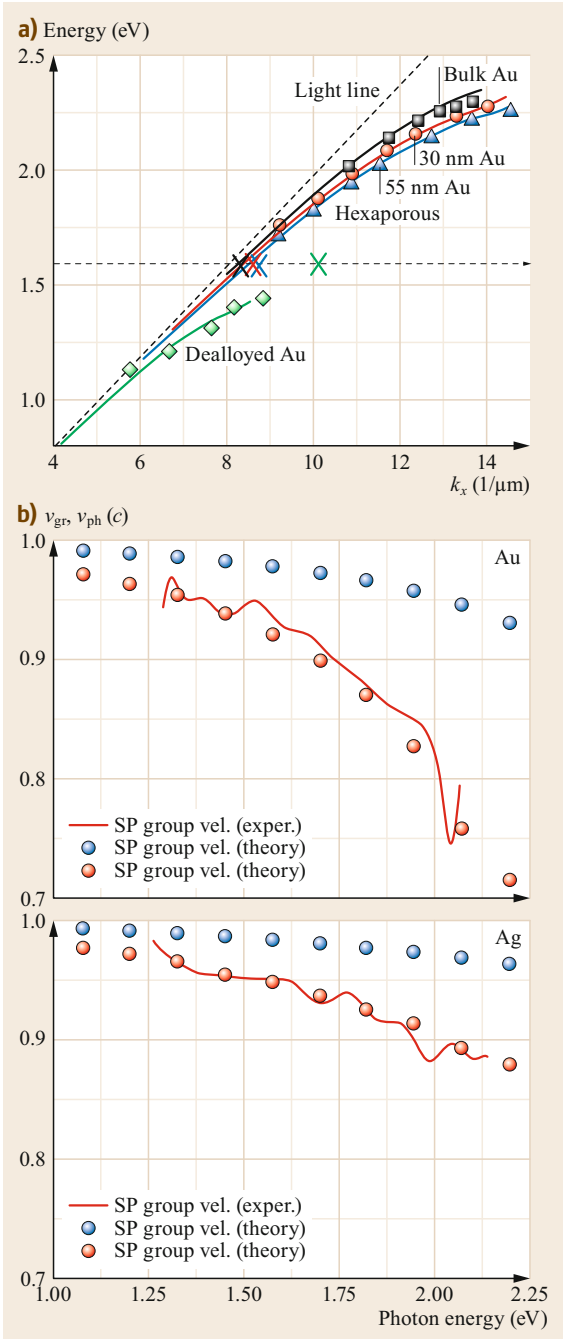

Fig. 18.31a,b SPP dispersion for Au and group **(a)** and phase velocities (expressed in terms of the velocity of light, c) for Au and Ag **(b)**. (Adapted with permission from [18.80] © IOP Publishing. Reproduced with permission. All rights reserved. And adapted with permission [18.81], The Optical Society (OSA))

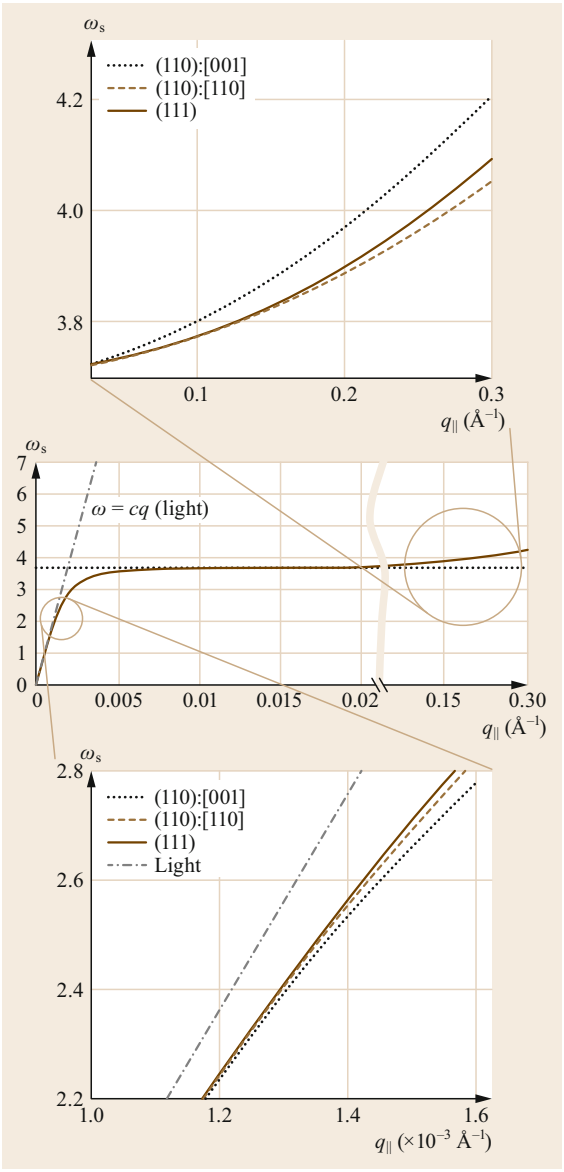

Fig. 18.32 The anisotropy of the Ag(110) surface is reflected both in the SP and in the SPP momentum range. The sign of the anisotropy is, however reversed, the frequency in $\langle 1\bar{1}0 \rangle$ direction being larger than along $\langle 100 \rangle$ for the SPP and smaller for the SP. (Reprinted from [18.19], with permission from Elsevier)

18.11 Conclusions and Perspectives

The surface science of conventional surface plasmons is by now a mature and well-understood topic. More recent papers by *Politano* et al. [18.83–86] analyzed the SP dispersion for Ag layers grown on Cu(111) and Ni(111). The perspectives of future work and discoveries are however in the applications of surface plasmons and surface plasmon polaritons mentioned in the introduction and in the new field of acoustic surface plasmons firstly reported for Be [18.87] and then for the noble metal surfaces [18.88–91] as well as for the 2-D monolayers [18.92] and naturally layered materials [18.93, 94] which are reviewed in Chap. 19.

References

18.1 R.H. Ritchie: Plasma losses by fast electrons in thin films, Phys. Rev. **106**, 874–881 (1957)

18.2 H. Raether: *Excitation of Plasmons and Interband Transitions by Electrons*, Springer Tracts in Modern Physics, Vol. 88, 1st edn. (Springer, Berlin 1980)

18.3 E. Kretschmann: Die Bestimmung optischer Konstanten von Metallen durch Anregung von Oberflächenplasmaschwingungen, Z. Phys. **241**, 313–324 (1971)

18.4 A. Otto: Excitation of nonradiative surface plasma waves in silver by the method of frustrated total reflection, Z. Phys. **216**, 398–410 (1968)

18.5 S.A. Maier: *Plasmonics: Fundamentals and Applications* (Springer, New York 2007)

18.6 S.G. Patching: Surface plasmon resonance spectroscopy for characterisation of membrane protein–ligand interactions and its potential for drug discovery, Biochim. Biophys. Acta **1838**, 43–55 (2014)

18.7 Y. Borensztein, W.L. Mochan, J. Tarriba, R.G. Barrera, A. Tadjeddine: Large anisotropy in the optical reflectance of Ag(110) single crystals: Experiment and theory, Phys. Rev. Lett. **71**(14), 2334 (1993)

18.8 J. Tarriba, W.L. Mochan: Collective surface modes of Ag single crystals, Phys. Rev. B **46**, 12902 (1992)

18.9 N. Sardana, T. Birr, S. Schenkler, C. Reinhardt, J. Schilling: Surface plasmons on ordered and bicontinuous spongy nanoporous gold, New J. Phys. **16**, 063053 (2014)

18.10 J. Daniels: Energieverlustmessungen an Silber mit hoher Energieauflösung, Z. Phys. **203**, 235 (1967)

18.11 K.D. Tsuei, E.W. Plummer, P.J. Feibelman: Surface plasmon dispersion in simple metals, Phys. Rev. Lett. **63**, 2256 (1989)

18.12 K.D. Tsuei, E.W. Plummer, A. Liebsch, E. Pehlke, K. Kempa, P. Bakshi: The normal modes at the surface of simple metals, Surf. Sci. **247**, 302 (1991)

18.13 K.D. Tsuei, E.W. Plummer, A. Liebsch, K. Kempa, P. Bakshi: Multipole plasmon modes at a metal surface, Phys. Rev. Lett. **64**, 44 (1990)

18.14 J.A. Gaspar, A.G. Eguiluz, K.D. Tsuei, E.W. Plummer: Elementary excitaions in alkali-metal overlayers probed by electron energy loss spectroscopy – Quantum mechanical effects, Phys. Rev. Lett. **67**, 2854 (1991)

18.15 M. Rocca, U. Valbusa: Angular dependence of dipole scatting cross section: Surface-plasmon losses on Ag(100), Phys. Rev. Lett. **64**, 2398 (1990)

18.16 M. Rocca, M. Lazzarino, U. Valbusa: Surface plasmon on Ag(110): Observation of linear and positive dispersion and strong azimuthal anisotropy, Phys. Rev. Lett. **69**, 2122 (1992)

18.17 M. Rocca, F. Biggio, U. Valbusa: Surface plasmon spectrum of Ag(001) measured by high resolution angle resolved EELS, Phys. Rev. B **42**, 2835 (1990)

18.18 G. Chiarello, V. Formoso, A. Santaniello, E. Colavita, L. Papagno: Surface plasmon dispersion and multiple surface plasmons in Al(111), Phys. Rev. B **62**, 12676 (2000)

18.19 W. Plummer, K.-D. Tsuei, B.-O. Kim: The impact of the concept of a surface plasmon, Nucl. Instrum. Methods Phys. Res. B **96**, 448 (1995)

18.20 P.J. Feibelman: Surface electromagnetic fields, Prog. Surf. Sci. **12**, 287 (1982)

18.21 A. Liebsch: *Electronic Excitations at Metal Surfaces* (Springer, New York 1997)

18.22 M. Rocca: Low energy EELS investigation of surface electronic excitations on metals, Surf. Sci. Rep. **22**, 1 (1995)

18.23 C. Brechignac, P. Caluzac, K. Kebaile, H. Leibgnier, A. Sarfati: Collective resonance in large free potassium cluster ions, Phys. Rev. Lett. **26**, 3916 (1992)

18.24 T. Reiner, M. Schmidt, C. Ellert, H. Haberland: Size dependence of the optical response of spherical sodium clusters, Phys. Rev. Lett. **74**, 1558 (1995)

18.25 J. Tiggesbaeumker, L. Koeller, K.-H. Meiwes-Broer, A. Liebsch: Blue shift of the Mie plasma frequency in Ag clusters and particles, Phys. Rev. A **48**, R1749 (1993)

18.26 H.A. Atwater, A. Polman: Plasmonics for improved photovoltaic devices, Nat. Mater. **9**, 205 (2000)

18.27 I. Freestone, N. Meeks, M. Sax, C. Higgitt: The Lycurgus Cup – A Roman nanotechnology, Gold Bull. **40**, 270 (2007)

18.28 G.I. Stegeman, R.F. Wallis, A.A. Maradudin: Excitation of surface polaritos by end-fire coupling, Opt. Lett. **8**, 386 (1983)

18.29 H.T. Miyazaki, Y. Kurokawa: Squeezing visible light-waves into a 3-nm-thick and 55-nm-long plasmon cavity, Phys. Rev. Lett. **96**, 097401 (2006)

18.30 A.G. Curto, J. Gómez Rivas: Confining light at the atomic scale, Nat. Nanophotonics **13**, 437 (2018)

18.31 A. Polman: Plasmonics applied, Science **322**, 868 (2008)

18.32 W.L. Barnes, A. Dereux, T.W. Ebbesen: Surface plasmon subwavelength optics, Nature **424**, 6950 (2003)

18.33 D.A. Iranzo, S. Nano, E.J.C. Dias, I. Epstein, C. Peng, D.K. Efetov, M.B. Lundeberg, R. Parret, J. Osmond, J.-Y. Hong, J. Kong, D.R. Englund, N.M.R. Peres, F.H.L. Koppens: Probing the ultimate plasmon confinement limits with a van der Waals heterostructure, Science **360**, 291–295 (2018)

18.34 A.M. Dubrovkin, B. Qiang, H.N.S. Krishnamoorthy, N.I. Zheludev, Q.J. Wang, J. Qi: Ultra-confined surface phonon polaritons in molecular layers of van der Waals dielectrics, Nat. Commun. **9**, 1762 (2018)

18.35 P. Andrew, W.L. Barnes: Energy transfer across a metal film mediated by surface plasmon polaritons, Science **306**, 1002–1005 (2004)

18.36 H. Mertens, H. Biteen, J.S. Atwater, H.A. Polman: Polarization-selective plasmon-enhanced Si quantum dot luminescence, Nano Lett. **6**, 2622–2625 (2006)

18.37 S. Kühn, U. Hakanson, L. Rogobete, V. Sandoghdar: Enhancement of single molecule fluorescence using a gold nanoparticle as an optical nano-antenna, Phys. Rev. Lett. **97**, 017402 (2006)

18.38 M.I. Stockman: Nanofocusing of optical energy in tapered plasmonic waveguides, Phys. Rev. Lett. **93**, 137404 (2004)

18.39 E. Verhagen, M. Spasenović, A. Polman, I. Kuipers: Nanowire plasmon excitation by adiabatic mode transformation, Phys. Rev. Lett. **102**, 203904 (2008)

18.40 P. Mühlschlegel, H.J. Eisler, O.J.F. Martin, B. Hecht, D.W. Pohl: Resonant optical antennas, Science **308**, 1607–1609 (2005)

18.41 H. Ditlbacher, J.R. Krenn, G. Schider, A. Leitner, F.R. Aussenegg: Two-dimensional optics with surface plasmon polaritons, Appl. Phys. Lett. **81**, 1762–1764 (2002)

18.42 S.I. Bozhevolnyi, V.S. Volkov, E. Devaux, J.Y. Laluet, T.W. Ebbesen: Channel plasmon subwavelength waveguide components including interferometers and ring resonators, Nature **440**, 508–511 (2006)

18.43 K. Okamoto, I. Niki, A. Shvartser, Y. Narukawa, T. Mukai, A. Scherer: Surface-plasmon-enhanced light emitters based on InGaN quantum wells, Nat. Mater. **3**, 601–605 (2004)

18.44 R.A. Shelby, D.R. Smith, S. Schultz: Experimental verification of a negative index of refraction, Science **292**, 77–79 (2001)

18.45 S. Linden, C. Enkrich, M. Wegener, J.F. Zhou, T. Koschny, C.M. Soukoulis: Magnetic response of metamaterials at 100 terahertz, Science **306**, 1351–1353 (2004)

18.46 N. Fang, H. Lee, C. Sun, X. Zhang: Sub-diffraction-limited optical imaging with a silver superlens, Science **308**, 534–537 (2005)

18.47 D. Sarid, W.A. Challener: *Modern Introduction to Surface Plasmons* (Cambridge Univ. Press, New York 2010)

18.48 E.D. Palik: *Handbook of Optical Constants of Solids* (Academic Press, London 1998)

18.49 V.U. Nazarov: Multipole surface-plasmon-excitation enhancement in metals, Phys. Rev. B **59**, 9866–9869 (1999)

18.50 V.U. Nazarov, S. Nishigaki: Inelastic low energy electron diffraction at metal surfaces, Surf. Sci. **482–485**, 640–647 (2001)

18.51 V.U. Nazarov, V.M. Silkin, E.E. Krasovskii: Role of the kinematics of probing electrons in electron energy-loss spectroscopy of solid surfaces, Phys. Rev. B **93**, 035403 (2016)

18.52 V.U. Nazarov, V.M. Silkin, E.E. Krasovskii: Probing mesoscopic crystals with electrons: On-step simultaneous inelastic and elastic scattering theory, Phys. Rev. B **96**, 235414 (2017)

18.53 E. Sprosser-Prou, A. Vom Felde, J. Fink: Aluminum bulk-plasmon dispersion and anisotropy, Phys. Rev. B **40**, 5799 (1989)

18.54 P.T. Sprunger, G.M. Watson, E.W. Plummer: The normal modes at the surface of Li and Mg, Surf. Sci. **269/270**, 551 (1992)

18.55 T. Kloos: Plasmaschwingungen in Al, Mg, Na und K angeregt durch schnelle Elektronen, Z. Phys. **265**, 225 (1973)

18.56 C. Kunz: Surface plasmon of Rb foils, Z. Phys. **196**, 311 (1966)

18.57 B. Kim, G. Lee, E.W. Plummer, P.A. Dowben, A. Liebsch: Mercury surface-plasmon dispersion: Experiment and theory, Phys. Rev. B **52**, 6057 (1995)

18.58 S.J. Park, R.E. Palmer: Plasmon dispersion of the Au(111) surface with and without self-assembled monolayers, Phys. Rev. Lett. **102**, 216805 (2009)

18.59 A. Politano, V. Formoso, G. Chiarello: Dispersion and damping of gold surfaces, Plasmonics **3**, 165 (2008)

18.60 R.L. Olmon, B. Slovick, T.W. Johnson, S.H. Oh, G.D. Boreman, M.B. Raschke: Optical dielectric function of gold, Phys. Rev. **86**, 235147 (2012)

18.61 F. Moresco, M. Rocca, V. Zielasek, T. Hildebrandt, M. Henzler: ELS-LEED study of electronic excitations on Ag(110) and Ag(111), Surf. Sci. **388**, 24 (1997)

18.62 O. Motornyi: *Ab initio Study of Electronic Surfaces States and Plasmons of Gold: Role of the Spin-Orbit Coupling and Surface Geometry*, PhD thesis (Ecole Polytechnique Paris, Paris 2018)

18.63 H. Claus, A. Büssenschütt, M. Henzler: Low energy electron diffraction with energy resolution, Rev. Sci. Instrum. **63**, 2195 (1992)

18.64 M. Rocca, S. Lizzit, B. Brena, G. Cautero, G. Comelli, G. Paolucci: The influence of d electrons on surface plasmon dispersion: Pd(110), J. Phys. Condens. Matter **7**, L611 (1995)

18.65 J. Yan, K.W. Jacobsen, K.S. Thygesen: First-principles study of surface plasmons on Ag(111) and H/Ag(111), Phys. Rev. B **84**, 235430 (2011)

18.66 F. Moresco, M. Rocca, V. Zielasek, T. Hildebrandt, M. Henzler: Evidence for the presence of the multipole plasmon mode on Ag surfaces, Phys. Rev. B **54**, 14333 (1996)

18.67 S.R. Barman, C. Biswas, K. Horn: Electronic excitations on silver surfaces, Phys. Rev. B **69**, 045413 (2004)

18.68 M. Rocca, F. Moresco, U. Valbusa: Temperature dependence of surface plasmons on Ag(001), Phys. Rev. B **45**, 1399 (1992)

18.69 F. Moresco, M. Rocca, T. Hildebrandt, M. Henzler: Collective excitations of thin films of disordered potassium adsorbed on Ag(110), Surf. Sci. **424**, 55 (1999)

18.70 F. Moresco, M. Rocca, T. Hildebrandt, V. Zielasek, M. Henzler: K adsorption on Ag(110): Effect on surface structure and electronic excitations, Surf. Sci. **424**, 62 (1999)

18.71 F. Moresco, M. Rocca, V. Zielasek, T. Hildebrandt, M. Henzler: Influence of surface interband transitions on surface plasmon dispersion, Europhys. Lett. **43**, 433–438 (1998)

18.72 L. Savio, L. Vattuone, M. Rocca: Surface plasmon dispersion on sputtered and nanostructured Ag(001), Phys. Rev. B **67**, 045406 (2003)

18.73 L. Savio, L. Vattuone, M. Rocca: Effect of surface interband transitions on surface plasmon dispersion O/Ag(001), Phys. Rev. B **61**, 7324 (2000)

18.74 M. Rocca, L. Savio, L. Vattuone, U. Burghaus, V. Palomba, N. Novelli, F. Buatier de Mongeot, U. Valbusa, R. Gunnella, G. Comelli, A. Baraldi, S. Lizzit, G. Paolucci: Phase transition of dissociatively adsorbed oxygen on Ag(001), Phys. Rev. B **61**, 213 (2000)

18.75 J.S. Kim, L.M. Chen, L.L. Kesmodel, P. Garcia Gonzales, A. Liebsch: Surface plasmon dispersion of Cl/Ag(111), Phys. Rev. B **56**, R4402 (1997)

18.76 B.J. Feng, H.J. Qin, J.H. He, X.Y. He, P. Cheng, L. Chen, K.H. Wu: Tuning the surface plasmon on Ag(111) by organic molecules, J. Appl. Phys. **112**, 023302 (2012)

18.77 F. Moresco, M. Rocca, T. Hildebrandt, M. Henzler: Observation of plasmon confinement for ultrathin nanostructured Ag films, Phys. Rev. Lett. **83**, 2238 (1999)

18.78 G. Mie: Beiträge zur Optik trüber Medien, speziell kolloidaler Metallösungen, Ann. Phys. **25**, 377 (1908)

18.79 Y. Borensztein, M. Roy, R. Alameh: Threshold and linear dispersion of the plasma resonance on thin Ag films, Europhys. Lett. **31**, 311 (1995)

18.80 V.V. Temnov, U. Woggon, J. Dintinger, E. Deveaux, T.E. Ebbesen: Surface plasmon interferometry: Measuring group velocity of surface plasmons, Opt. Lett. **32**, 1235 (2007)

18.81 W.L. Mochan, R.G. Barrera, Y. Borensztein, A. Tadjeddine: Optical reflectance anisotropy of Ag and Au single crystals, Physica A **207**, 334–339 (1994)

18.82 A. Politano, V. Formoso, E. Colavita, G. Chiarello: Probing collective electronic excitations in as deposited and modified Ag thin films grown on Cu(111), Phys. Rev. B **79**, 045426 (2009)

18.83 A. Politano, V. Formoso, G. Chiarello: Collective electronic excitations in thin Ag films on Ni(111), Plasmonics **8**, 1683–1690 (2013)

18.84 A. Politano, G. Chiarello: The influence of electron confinement, quantum size effects, and film morphology on the dispersion and the damping of plasmonic modes in Ag and Au thin films, Prog. Surf. Sci. **90**, 144 (2015)

18.85 A. Politano, G. Chiarello: Sputtering induced modification of the electronic properties of Ag/Cu(111), J. Phys. D **43**, 085302 (2010)

18.86 B. Diaconescu, K. Pohl, L. Vattuone, L. Savio, P. Hofmann, V.M. Silkin, J.M. Pitarke, E.V. Chulkov, P.M. Echenique, D. Farias, M. Rocca: Low-energy acoustic plasmons at metal surfaces, Nature **448**, 57 (2007)

18.87 K. Pohl, B. Diaconescu, L. Vattuone, G. Vercelli, V.M. Silkin, E.V. Chulkov, P.M. Echenique, M. Rocca: Acoustic surface plasmon on Cu(111), Europhys. Lett. **90**, 57006 (2010)

18.88 L. Vattuone, G. Vercelli, M. Smerieri, L. Savio, M. Rocca: Acoustic surface plasmon dispersion on nanostructured Cu(111), Plasmonics **7**, 323–329 (2012)

18.89 M. Smerieri, L. Vattuone, L. Savio, T. Langer, C. Tegenkamp, H. Pfnuer, V.M. Silkin, M. Rocca: Anisotropic dispersion and partial localization of acoustic surface plasmons on a stepped surface, Phys. Rev. Lett. **113**, 186804 (2014)

18.90 L. Vattuone, M. Smerieri, T. Langer, C. Tegenkamp, H. Pfnuer, M. Silkin, E.V. Chulkov, P.M. Echenique, M. Rocca: Correlated motion of electrons at Au(111) surface: Anomalous acoustic surface plasmon dispersion and single particle excitations, Phys. Rev. Lett. **110**, 127405 (2013)

18.91 J. Pischel, E. Welsch, O. Skibbe, A. Pucci: Acoustic surface plasmon on Cu(111) as an excitation in the mid-infrared range, J. Phys. Chem. C **117**(51), 26964–26968 (2013)

18.92 T. Nagao, T. Hildebrandt, M. Henzler, S. Hasegawa: Dispersion and damping of a two-dimensional plasmon in a metallic surface state band, Phys. Rev. Lett. **86**, 5747 (2001)

18.93 J. Lu, K.P. Loh, H. Huang, W. Chen, A.T.S. Wee: Plasmon dispersion on epitaxial graphene studied using high-resolution electron energy loss spectroscopy, Phys. Rev. B **80**, 113410 (2009)

18.94 T. Eberlein, U. Bangert, R.R. Nair, R. Jones, M. Gass, A.L. Bleloch, K.S. Novoselov, A. Geim, P.R. Briddon: Plasmon spectroscopy of free-standing graphene films, Phys. Rev. B **77**, 233406 (2008)

Mario Rocca

Dipt. di Fisica
Università di Genova
Genova, Italy
rocca@fisica.unige.it

Mario Rocca received his PhD in Physics at the University of Aachen (Germany) and is currently full professor of condensed matter physics at the University of Genova (Italy), where he leads a joint research group on Surface Science with CNR-IMEM. His major scientific achievements are on gas-surface interaction, ultrathin film growth, surface phonons and acoustic surface plasmons.

19. Plasmons in One and Two Dimensions

Herbert Pfnür, Christoph Tegenkamp, Luca Vattuone

This chapter will provide an overview of the properties of low-dimensional plasmons, discussing particularly characteristic examples. We will start with two-dimensional sheet plasmons (Sect. 19.1), concentrating on the plasmonic properties of the system most widely investigated in the recent past, graphene. Further emphasis will be given to low-dimensional plasmons coupled to other electron gases, which leads to linearization in the form of acoustic surface plasmons, but also to crossover of dimensionality, depending on plasmonic wavelengths. Finally we turn to quasi-one-dimensional systems and their corresponding plasmons, and try at the end to solve the puzzle of broad loss peaks but still fairly large plasmonic lifetimes.

Plasmons in low-dimensional systems represent an important tool for coupling energy into nanostructures and the localization of energy on the scale of only a few nanometers. Contrary to ordinary surface plasmons of metallic bulk materials, the dispersion of low-dimensional plasmons goes to zero in the long wavelength limit, thus covering a broad range of energies from terahertz to near-infrared, and from mesoscopic wavelengths down to those of just a few nanometers. Using specific, characteristic examples, we first review the properties of plasmons in two-dimensional (2-D) metallic layers from an experimental point of view. As demonstrated, tuning of their dispersion is possible by changes in charge carrier concentration in the partially filled 2-D conduction bands, but for a relativistic electron gas such as in graphene, only in the long wavelength limit. For short wavelengths, on the other hand, the dispersion turns out to be independent of the position of the Fermi level with respect to the Dirac point. A linear dispersion, seen under the latter conditions in graphene, can also be obtained in nonrelativistic electron gases by coupling between 2-D and 3-D (three-dimensional) electronic systems. As a well-investigated example, we discuss the acoustic surface plasmons in Shockley surface states, coupled with the bulk electronic system. Also, the introduction of anisotropy, e.g., by regular arrays of steps, seems to result in linearization (and to partial localization of the plasmons normal to the steps, depending on wavelengths). In quasi-one-dimensional (1-D) systems, such as arrays of gold chains on regularly stepped Si surfaces, only the dispersion is 1-D, whereas the shape and slope of the dispersion curves are dependent on the 2-D distribution of charge within each terrace and on coupling between wires on different terraces. In other words, the form of the confining quasi-1-D potential enters directly into the 1-D plasmon dispersion and offers new opportunities for tuning.

The long-range Coulomb interaction between valence electrons in metals results in collective plasma oscillations, as noted by *Pines* and *Bohm* [19.1, 2] as early as 1952. Plasmons exist in all dimensions [19.3]. The surface as the typical truncation of a bulk material imposes a new boundary condition on these collective plasma oscillations, resulting in localized states at the surface, called surface plasmons [19.4, 5]. In other words, the surface plasmon is the edge plasmon of a three-dimensional metal. Surface plasmons have a finite frequency in the long wavelength limit, which for a nearly free electron gas is located at $\omega_p/\sqrt{2}$, with

M. Rocca, T.S. Rahman, L. Vattuone (Eds.), *Springer Handbook of Surface Science*, Springer Handbooks,
https://doi.org/10.1007/978-3-030-46906-1_19

ω_p the bulk plasmon frequency, and a small dispersion with either positive or negative slope depending on the screening properties of the participating electronic orbitals [19.6, 7]. These properties of the surface plasmon also allow direct crossing of the surface plasmon dispersion with the light line and thus the direct interaction with light. The combined excitation of a surface plasmon in the presence of electromagnetic radiation is called a surface plasmon polariton (SPP), which represents the basis for the rapidly growing field of nanoplasmonics, opening the route for surface plasmon subwavelength optics [19.8], surface plasmon enhanced spectroscopy [19.9], near-field optics [19.10] and chemical applications [19.11, 12].

In this chapter, however, we will deal primarily with a different kind of collective low-energy excitations, generated in low-dimensional electron gases in one (1-D) and two dimensions (2-D). The most prominent examples are the 2-D sheet plasmons of a metallic monolayer that have been observed, e.g., in Ag or Dy monolayers on Si(111) [19.13, 14] and in monolayers of graphene on SiC or metal surfaces [19.15], but also the 2-D plasmons of partially filled surface states found on the clean surfaces of Be(0001) [19.16, 17], Cu(111) [19.18, 19] and Au(111) [19.20, 21], which result in so-called acoustic surface plasmons (ASP). Their relevance has two aspects: It is worthwhile to study the specifics of plasmonic excitations in low-dimensional systems in greater detail, since both partial localization and correlations are important [19.7]. Therefore, a quantitative theory for plasmonic excitations going beyond the nearly free electron gas model (NFEG) [19.22] is highly desirable. Secondly, much higher in-plane confinements of excitations can be achieved with plasmons associated with a 2-D electron gas, since their dispersion is much flatter than that of SPP, which allows for extraordinary confinement of energy from subterahertz to mid-infrared frequencies through the use of appropriate nanostructures providing the necessary momentum transfer. The $\sqrt{q}$-dependence of dispersion, however, makes a distortionless propagation of nonmonochromatic signals inherently impossible, since the different frequency components propagate at different velocities. This drawback can be overcome by the use of systems that have a linear rather than a square root dispersion. As we will illustrate later, a linear dependence of dispersion is always expected for low-D plasmons that are coupled and shielded by other 2-D or 3-D electron gases [19.23, 24]. This is particularly the case for metal surfaces supporting an electronic Shockley surface state (SS) with band dispersion crossing the Fermi level [19.25], which leads to the formation of the ASP.

The physics of experimentally accessible systems that exhibit quasi-1-D properties is still largely unexplored. The most obvious reason is their inherent instability, which allows their existence as isolated systems only at $T = 0\,\mathrm{K}$. 1-D properties can, however, be stabilized if embedded into a 2-D or 3-D environment. The interaction with these environments not only stabilizes these systems, but their feedback on 1-D properties opens a wide range of variability and enables them to be manipulated. Thus a variety of exotic phenomena such as charge and spin density waves becomes accessible and make them quite interesting objects to be studied [19.26, 27]. In this context, the arrays of atomic wires generated by self-assembly on semiconducting surfaces [19.28–32] are particularly attractive: they are geometrically strongly anisotropic [19.29, 33, 34], and they also exhibit quasi-1-D Fermi surfaces and/or even 1-D electronic transport properties under certain conditions. Depending on their chemical interaction with the substrate, but also on the details of the coupling of these wires mediated by the substrate, these ensembles reveal in part fundamentally different characteristics. As an example, bundles of In wires on Si(111) forming a (4×1) reconstruction are metallic at room temperature, but undergo a metal–insulator transition to form charge density waves below 130 K. In contrast, chains of Au on Ge(100), under special conditions, seem to reveal the spectroscopic signatures of a Luttinger liquid without any instabilities at low temperature [19.32, 35], although this behavior is still under discussion. Not only are quasi-1-D metal-insulator transitions observed [19.31, 36], but surface instabilities result in electronic stabilization of new facets. This stabilization is intimately coupled with changes in the electronic band structure leading, in some cases, to coupled spin and charge order [19.37, 38].

The 1-D properties are both visible by a combined view at geometry and occupied electronic states, and also manifest themselves in electronic excitations, which in the limit of pure 1-D behavior with its strong electronic correlations cannot be discriminated from collective plasmonic excitations [19.39]. As we will show later, although the identification of purely 1-D dispersion is easily possible [19.3, 40–43], the quantitative properties are explicitly dependent on the coupling to the environment. If the wires in arrays are essentially decoupled from each other, the strong confinement perpendicular to the chains leads to the generation of electronic subbands. As a consequence, the simultaneous excitation of subband plasmons and intersubband plasmon are observed [19.3, 41, 44]. In fact, various forms of interwire coupling [19.42, 45] lead partly to two-dimensional crossover in the quantitative dispersion properties that are also reflected in modifications of the band structure.

19.1 Sheet Plasmons

Historically, sheet plasmons were first observed as standing waves for a dilute 2-D electron system (2-DES) on a liquid He surface [19.46] at extremely low electron densities (few $10^6/\mathrm{cm}^2$). The square root dependence of the 2-D plasmon frequency was already seen in inversion layers of Si-MOS field effect transistors and in GaAlAs quantum well structures [19.47, 48]. These artificially tailored systems allowed only large electron spacing or long Fermi wavelengths ($\geq 1000\,\text{Å}$). Their energy dispersions were studied in a tiny wave-number region $q_\parallel \leq 0.01\,\text{Å}^{-1}$ where they can be described by classical local response theory and are also free from the lifetime broadening caused by Landau damping. Plasmons of Shockley surface states are other examples apart from 2-D metallic layers or stacks. Common to all these systems is that they are not freestanding, but are either on top of or embedded in a carrier material. Depending on its conductive properties, this material is responsible for shielding and modification of the electric field caused by the plasmons. Therefore, before we discuss specific examples, let us briefly summarize the theoretical ideas explained in more detail in Chap. 17.

19.1.1 Plasmon Dispersion for the 2-D Electron Gas

For a purely 2-D nearly free electron gas (NFEG), i.e., when no bulk electrons are present, theory predicts the existence of a surface plasmon exhibiting in the limit $q_\parallel \to 0$ a square root dependence of dispersion on $q_\parallel$; $q_\parallel$ is the component of the wave vector of the excitation parallel to the surface that is created in a scattering event. At least the next order, however, will be important in some cases (see later). Following *Stern* [19.22], the energy of the corresponding plasmon is given by

$$\omega_{2\text{-D}}^2 = e^2 \frac{E_\mathrm{F}}{2\epsilon' \pi \hbar^2} q_\parallel + \frac{3}{4} v_\mathrm{F}^2 q_\parallel^2 + \ldots \qquad (19.1)$$

with the Fermi energy E_F. For a freestanding 2-D system, ϵ' is just equal to the vacuum dielectric constant ϵ_0, whereas it becomes $\epsilon' = \epsilon_0 \epsilon$ when the 2-D electron gas is embedded in an insulating environment with dielectric function ϵ.

The first term in (19.1) is identical to the result for a thin metallic film obtained by the classical response theory [19.4], whereas the second term (and higher-order terms) results from the correlations in a 2-D Fermi gas and corresponding changes in the excitation spectrum. For the free electron gas, the 2-D electron density of occupied electronic states is related to E_F and to the effective mass $m^\star$ by

$$n_{2\text{-D}} = \frac{E_\mathrm{F} m^\star}{\pi \hbar^2} \,. \qquad (19.2)$$

On the contrary, for a relativistic electron gas with linear dispersion ($E = \hbar v_\mathrm{F} q_\parallel$), $n_{2\text{-D}}$ depends quadratically on E_F

$$n_{2\text{-D}} = \frac{E_\mathrm{F}^2}{\pi \hbar^2 v_\mathrm{F}^2} \qquad (19.3)$$

so that the leading term in (19.1) of the plasmon frequency at small $q_\parallel$ depends on electron density as $n_{2\text{-D}}^{1/4}$. Interestingly, the second term of (19.1) does not depend on the electron density in this case, since v_F is constant. As we shall show later, experiments confirm this prediction.

Screening by the environment due to embedding in or adsorption of a 2-D layer on a carrier material, or due to the presence of a bulk in the case of a surface state, will lead to modifications of (19.1). In the simplest case of adsorption of the 2-D layer on an insulating material, the resonances are far from the plasmon frequencies, and screening effects can be described by a dielectric constant, which is taken as the average of the dielectric constants of this material and of vacuum, so that ϵ' now reads $\epsilon' = \epsilon_0(\epsilon + 1)/2$.

In the case of a metallic surface state screened by the presence of 3-D electrons, theory predicts in the long wavelength limit the existence of two plasmons [19.7]: One corresponds to the high-frequency oscillation ω_h, in which 2-D and 3-D electrons oscillate in phase with each other. The other corresponds to a low-frequency oscillation in which both 2-D and 3-D electrons oscillate out of phase, characterized by a linear dispersion

$$\omega_\mathrm{l} = \alpha v_\mathrm{F}^{2\text{-D}} q_\parallel \,, \qquad (19.4)$$

where α is a constant with a value close to 1, and v_F is the 2-D Fermi velocity. Because of its linear dispersion, it is called acoustic surface plasmon (ASP).

As we shall later show, in the most common case, i.e., for Be(0001) [19.16], the 2-D Fermi velocity will be lower than that of the 3-D system, so that α is slightly larger than 1. However, there are cases, e.g., Au(111) [19.20] and Cu(111) [19.49], for which the 2-D Fermi velocity is higher than in 3-D, so that α is slightly lower than 1.

In order to understand the basic mechanism behind the ASP, let us compare the behavior of a conventional 2-D electron gas having a parabolic dispersion

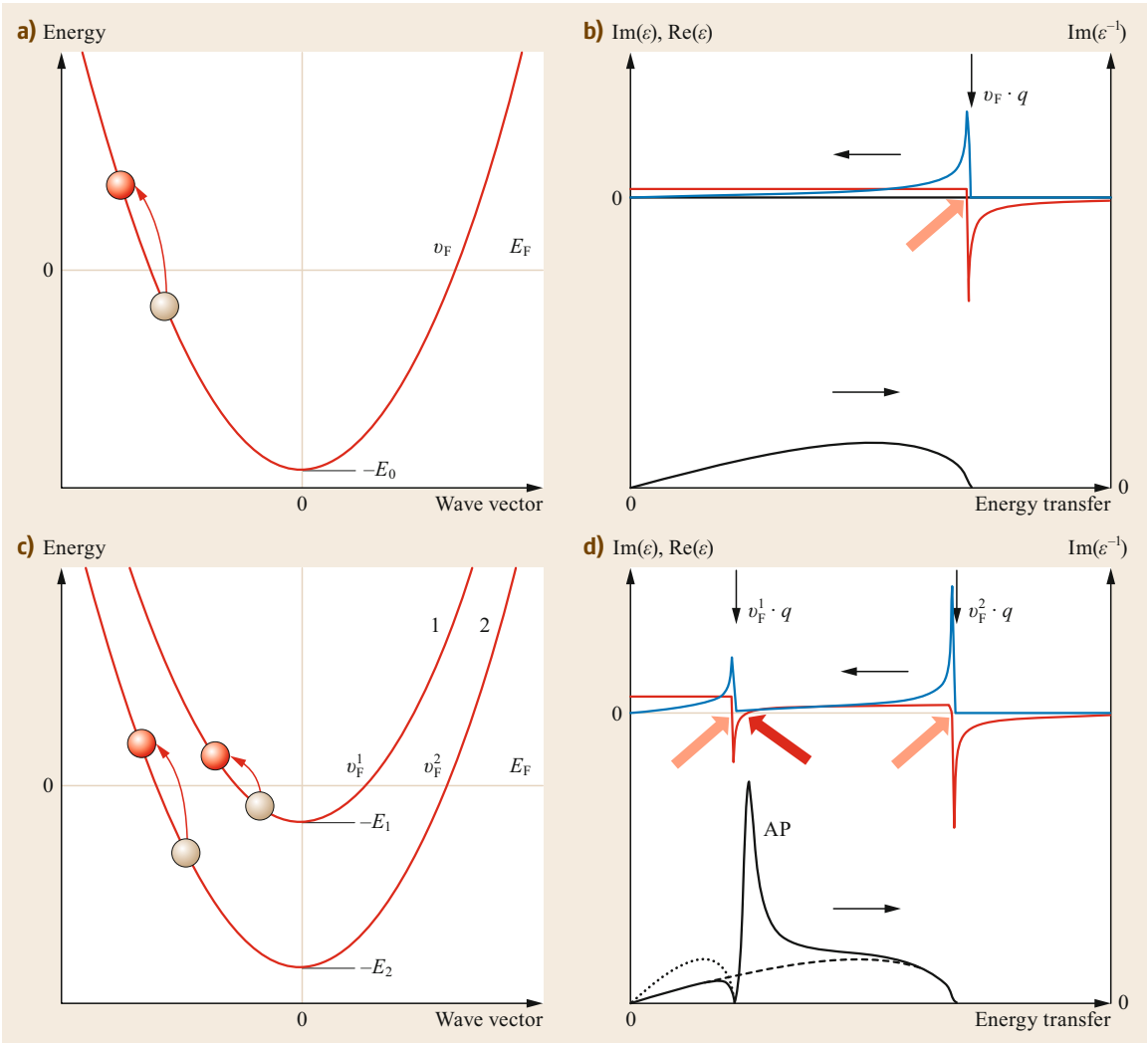

Fig. 19.1a–d Schematic of electronic excitations and decay in single- **(a,b)** and double-component **(c,d)** 2-D electron gases: Energy dispersion as a function of wave vector **(a,c)** with single-electron intraband transitions (*red arrows*). In **(b)** and **(d)**, the dielectric function ϵ with real (*red lines*) and imaginary parts (*blue lines*), and the loss function $\mathrm{Im}(1/\epsilon)$ (*black lines*) are plotted for an arbitrary but given small momentum transfer. Unobservable low-energy resonances are indicated by *light red arrows*. The observable feature, characterized by $\mathrm{Re}(\epsilon) = 0$ and a maximum in the loss function (and hence a small value in $\mathrm{Im}(\epsilon)$), is indicated by a *dark red arrow*. (Adapted with permission from [19.20]. © 2013 by the American Physical Society)

(Fig. 19.1a) with an electron gas consisting of two components with different Fermi velocities (Fig.19.1c). The corresponding dielectric function $\epsilon(\omega, \boldsymbol{k})$ for a given wave vector $\boldsymbol{k}$ (in the long wavelength limit) and the loss function $\mathrm{Im}(1/\epsilon)$ are shown Fig 19.1b,d. For the 2-D electron gas with only one component, the low-energy zero-crossing of $\mathrm{Re}[\epsilon(\omega, \boldsymbol{k})]$ is not associated with a peak in the loss function, and thus corresponds to the excitation of incoherent intraband electron–hole pairs. For a two-component electron gas, there exist three zero-crossings of $\mathrm{Re}[\epsilon(\omega, \boldsymbol{k})]$ at low energy. One is associated with a peak marked in the loss function $\mathrm{Im}(1/\epsilon)$. Since it lies just above the edge of single-particle transitions within the band with the lower Fermi velocity, it corresponds to a collective mode screened by the electrons located in the other band. In the long wavelength limit, i.e., for $q_\parallel \to 0$, the energies of both peaks in $\mathrm{Im}(\epsilon)$ disperse linearly with $q_\parallel$. The peak in the loss function, being limited by such linearly dispersing peaks, also exhibits a linear dispersion and thus satis-

fies (19.4). In the case of a Shockley surface state at a metal surface, the model still captures the essential physics, provided that one of the two components of the electron gas is associated to the 3-D electron system and that the coexistence of 3-D and 2-D electron gases in the same volume is properly considered.

It is worth mentioning here that this scenario of interacting electron gases is not limited to the specific case just discussed. For example, stacking of identical layers, separated by insulating spacers, considered theoretically in [19.23] also leads to coupling between electron gases and to linearization of plasmon dispersion. Even the anisotropy within the same 2-D band, e.g., in freestanding graphene at the K- and K′-points of the Brillouin zone, is predicted to lead to the formation of an ASP in addition to the standard sheet plasmon [19.50].

The plasmon dispersion can be measured experimentally by using (highly resolved) electron energy loss spectroscopy (HREELS). An instrument with simultaneous high energy and high momentum resolution is called ELS-LEED [19.51]. Electrons with energy E_i impinge at an angle θ_i with respect to the surface normal. Electrons can scatter elastically or inelastically. The energy spectrum of the electrons scattered at an angle θ_s from the surface normal may contain peaks at energy E_s. The energy lost (or gained) corresponds to the creation (or annihilation) of a collective excitation of energy E such that

$$E_\mathrm{i} = E + E_\mathrm{s} \,. \tag{19.5}$$

Note that E is positive when the excitation is created and negative if it is destroyed in the scattering event. The conservation of momentum in the direction parallel to the surface reads

$$k_{\mathrm{i},\parallel} = k_{\mathrm{s},\parallel} + q_\parallel + g_\parallel \,, \tag{19.6}$$

where $g_\parallel$ is any reciprocal lattice vector of the surface unit cell. Since before and after scattering the electron is a free particle (the same relationship holding also for any free particle with nonvanishing mass in the nonrelativistic limit), the modulus $k_{\mathrm{i},\parallel}$ of the parallel component $\boldsymbol{q}_\parallel$ of the wave vector is given by

$$k_{\mathrm{i},\parallel} = \frac{\sqrt{2mE_\mathrm{i}}}{\hbar} \cos\theta_\mathrm{i} \,. \tag{19.7}$$

The modulus $k_{\mathrm{s},\parallel}$ is given by a similar relationship. It is thus possible to obtain $q_\parallel$ and E, i.e., the dispersion relation of the collective excitation (or the energy and the momentum of the particle) created in the scattering event. Experiments performed for Ag on Si [19.13] and for $DySi_2$ [19.14] confirmed the prediction. At very long wavelengths, 2-D plasmons have low energy. However, they are unable to affect electron–phonon interaction and phonon dynamics close to the Fermi energy because of the square root dispersion.

19.1.2 Sheet Plasmons in 2-D

Metallic Layers

Here we discuss the prototype system Ag/Si(111) [19.13]. Similar results have been obtained for Dy/Si(111) [19.14]. The flat Ag/Si(111) system has been a prototype for the investigation of surface conductance on a low-doped Si substrate [19.52], in which metallic conductance has been shown to be associated with the formation of a $\sqrt{3}\times\sqrt{3}$R30° structure. Conductance can be changed by adding additional Ag atoms. In fact, such $\sqrt{3}$-structure was found to be a semi-metal [19.30], and metallicity is attained only by adding surplus Ag atoms to this structure [19.52]. The most natural explanation for this self-doping phenomenon seems to be the formation of a lattice gas in the second layer, as also suggested by a HREELS study as a function of Ag concentration [19.53]. The investigations on stepped Si(557) yield, however, are a somewhat different picture (see later).

In any case, 2-D metallicity can be generated in this system. Direct proof is found in the existence of a plasmonic excitation whose energy goes to zero at long wavelengths, i.e., no further excitation is necessary to create this plasmon. The first test for such a purely 2-D system has indeed been carried out in Ag/Si(111) at monolayer concentration [19.13]. The main results are shown in Fig. 19.2.

As shown in Fig. 19.2b, the dispersion can be well described by a 2-D nonrelativistic NFEG using the two terms given explicitly in (19.1). Within errors there was no angular dependence of the dispersion, but the slope of the dispersion changed when further Ag was added to the (already self-doped) $\sqrt{3}\times\sqrt{3}$R30°-Ag structure. From their fits, the authors determined electron concentrations of between 1.9 and $8\times10^{13}\,\mathrm{cm}^{-2}$ and an effective electron mass of around $0.3m_\mathrm{e}$. This result is in good agreement with data from angle-resolved photoemission (ARPES) for the same system [19.30]. From these numbers, an effective electron transfer of about one-third of an electron per surplus Ag atom was deduced. For the present case, the screening by the substrate can thus be accurately described by an effective dielectric constant of the interface.

Plasmons in the 2-D Relativistic Electron Gas

Since its ultimate discovery in 2004 [19.54], graphene has become one of the most studied materials in

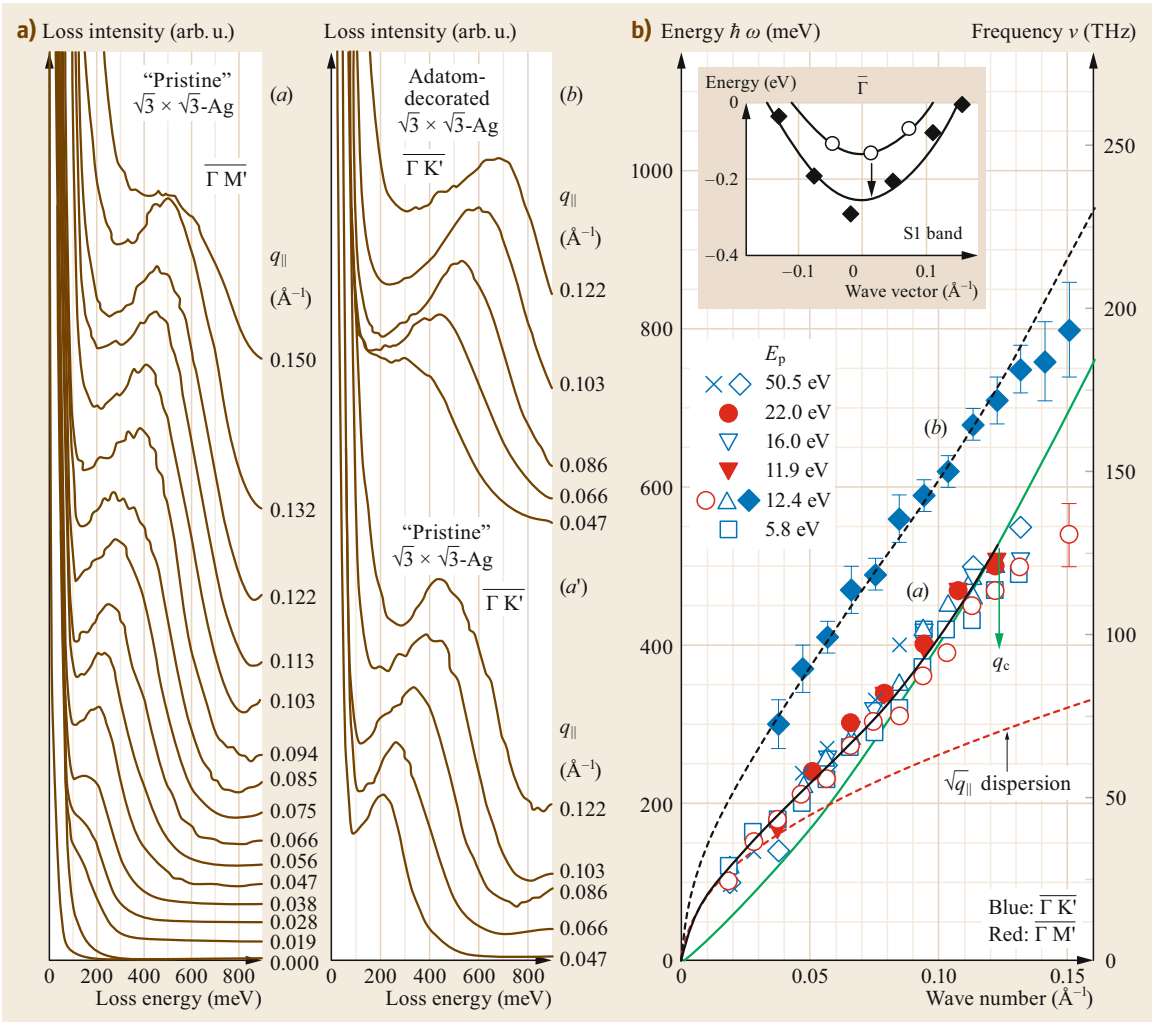

Fig. 19.2 **(a)** EELS spectra taken at an incident electron energy of $E_p = 12.4$ eV. For better visibility, the curves were shifted; the momentum transfer is given as parameter. (a) Scans along the $\overline{\Gamma M}$ direction (a′) and (b): Blueshift of losses due to the additional adatom decoration. **(b)** Plasmon dispersions of (a) a $\sqrt{3} \times \sqrt{3}$R30° ordered surface at a coverage slightly above 1 ML (monolayer) and (b) after further decoration with 0.15 ML of additional Ag. The *bold solid* and *dashed curves* are the fits within the nearly free electron gas model in RPA approximation. *Green curve*: upper edge of the single-particle excitation continuum. *Inset*: Schematic of the S1 surface band that is shifted below E_F by Ag coverages exceeding 1 ML. (Adapted with permission from [19.13]. © 2001 by the American Physical Society)

nanoscience. The coupling of light into flat and nanostructured graphene in the terahertz and far-infrared frequency regime using the plasmonic properties of graphene in order to form surface plasmon polaritons (SPP) has been a widely covered subject [19.55–57], and many potential applications have been suggested [19.58–61]. We refer the reader to these excellent reviews and will not elaborate on these topics here, since although in this range of frequencies subwavelength phenomena (compared with optical and infrared wavelengths) can be observed, the typical wavelengths of several micrometers do not allow entry into the nanoscale of 10 nm and below.

However, there is a unique property of 2-D plasmons that has become obvious by studying 2-D plasmons in graphene. Here we concentrate again on the low-energy plasmons. Other plasmons in graphene, in particular the standard π plasmon excitations, have been reviewed previously [19.15], and we refer the reader to this literature. At low $q_\parallel$ (typically in the range of μm^{-1}), i.e., at plasmon frequencies in the terahertz range, a series of studies have exploited the fact that

the plasmon frequencies of plasmon polaritons, i.e., the combined excitation of a plasmon in an external electromagnetic field, can be tuned by changing the carrier concentration in the graphene layer. This can be done most conveniently by using a gate voltage [19.62, 63]. Thus plasmon polaritons at a wavelength of a few hundred nanometers can be excited with light in the far- to mid-infrared range. This result is attractive because of its relatively low damping: decay lengths reaching 1 μm indeed allow us to foresee many potential applications including tunable infrared lasers [19.64], plasmonic quasicrystals [19.58], ultrasensitive detection down to the single-molecule level [19.65], improved photovoltaics [19.66] or nonlinear optics [19.67]. This tunability, however, is subject to physical limitations that we will further describe later.

Surprisingly, this tunability seems to completely disappear when $q_\parallel$ is in the range of $1\,\mathrm{nm}^{-1}$. An example is shown for graphene on Si-terminated 6H-SiC(0001) in Fig. 19.3. Figure 19.3a shows the plasmon dispersion, recorded with electron energy loss spectroscopy with simultaneous high momentum and high energy resolution [19.68]. These results agree well with those of [19.69]. The first layer of graphene on SiC grows on a carbon buffer layer. It turns out to be n-doped with a doping concentration of $1\times10^{13}\,\mathrm{cm}^{-2}$, and the Fermi level under these conditions to be about 400 meV above the Dirac point [19.68].

At very low $q_\parallel$, the dispersion is compatible with a $\sqrt{q_\parallel}$ dispersion, as predicted by the first term of (19.1). Deviation from this function is already evident at $q_\parallel < 0.03\,\text{Å}^{-1}$, similar to the Ag/Si(111) case discussed above. For $q_\parallel > 0.1\,\text{Å}^{-1}$, on the other hand, there is a linear slope of $1.35\pm0.1\times10^6\,\mathrm{m/s}$, very close to the Fermi velocity in graphene on SiC [19.70]. Between these two regimes there is a characteristic cusp that was ascribed to resonant damping, since the plasmon dispersion enters the continuum of single-particle interband transitions.

Qualitatively, the experimental dispersion curve follows the theoretical forecast for a 2-D Fermi gas of relativistic electrons within the random phase approximation (RPA) [19.71]. The resonant damping has not been considered in theory. Nevertheless, a cusp can be seen in theory (Fig. 19.4), which is therefore a characteristic property of the relativistic electron gas. It is much less pronounced than in experiment because damping is neglected in the theoretical calculation. Therefore, quantitative agreement between theory and experiment cannot be expected.

The main qualitative difference between the non-relativistic and the relativistic 2-D electron gas comes

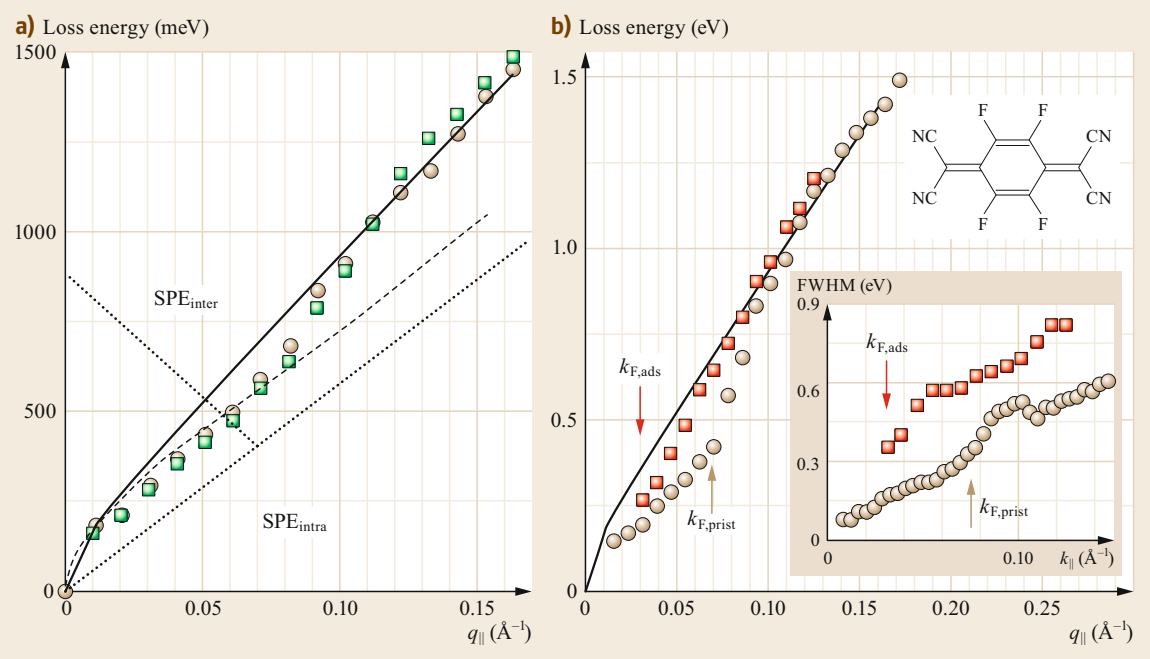

Fig. 19.3 **(a)** Plasmon dispersion for 1 ML graphene layer grown on H-etched SiC samples, measured at 300 K (*squares*) and at 80 K (*circles*). **(b)** Graphene plasmon dispersion before (*circles*) and after (*squares*) F4-TCNQ doping. *Lower inset*: changes in *k*-dependent half widths (same symbols as in main figure). *Upper inset*: stereographic model of F4-TCNQ. (Reprinted by permission from [19.68])

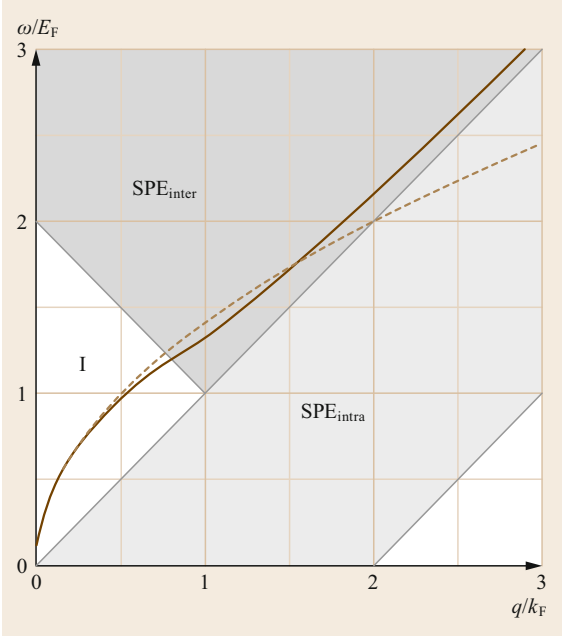

Fig. 19.4 Calculated plasmon dispersion for monolayer graphene within RPA on a substrate characterized by $\epsilon = 2.5$. The *dashed line* corresponds to the plasmon dispersion of a 2-D free electron gas with an electron density of $1 \times 10^{12}\,\mathrm{cm}^{-2}$. *Shaded areas* correspond to the continuum of intra- and interband single-particle excitations. (Adapted with permission from [19.71]. © 2007 by the American Physical Society)

from the second term in the expansion of plasmon dispersion, which becomes dominant for large $q_\parallel$. This term disperses linearly with a slope $\propto v_\mathrm{F}$, as already outlined above (19.1). For the relativistic electron gas of graphene, this limit is reached for $q_\parallel/k_\mathrm{F} > 1$ [19.71]. If this second term dominates, its slope, according to (19.1), does not depend on the embedding environment. Even more importantly, for the relativistic electron gas with a constant Fermi velocity, this term is independent of the doping level. Thus the slope of the dispersion in this limit should be usable as a calibration standard. This prediction can easily be tested.

One test is shown in Fig. 19.3b. Here, the plasmon dispersion curves are compared before and after covering the graphene layer with about one percent of a monolayer of 4F-TCNQ molecules at 300 K. F4-TCNQ is known to reduce the carrier density of graphene and hence to shift E_F downward [19.72]. As expected, the dip shifts to lower $q_\parallel$ values (to $\approx 0.03\,\mathrm{Å}^{-1}$). This shift is also seen in the resonance of the FWHM. Since the molecules added act as scattering centers, the loss structure is further broadened. This reduction of the doping concentration to $\approx 3 \times 10^{12}\,\mathrm{cm}^{-2}$ also reduces both E_F and k_F correspondingly. Therefore, the transition to the linear part of the dispersion happens at smaller $q_\parallel$, as expected from the considerations mentioned above, and the linear range is extended. The average slope of the linear part, however, remains unchanged, in accordance with a constant Fermi velocity and (19.1). Very similar behavior has been found for a quasi-freestanding graphene layer on SiC(0001), generated with a graphene buffer layer by intercalation with hydrogen, by gradual desorption of the hydrogen [19.73], which mainly shifts the Fermi level and thus the doping concentration.

A second example of this finding is shown by comparing these results with those obtained for graphene on Ir(111) [19.74, 75]. The growth of graphene on Ir is self-limited to a single layer by decomposition of hydrocarbons (ethylene) at temperatures around 1320 K, at a pressure of 2×10^{-7} Pa. It is characterized by a Fermi level very close to the Dirac point [19.76, 77], i.e., a doping concentration of less than $1 \times 10^{11}\,\mathrm{cm}^{-2}$. Therefore, and in accordance with the results just presented, only a linear slope can be observed within the $q_\parallel$ range resolvable with ELS-LEED. This result is shown in Fig. 19.5 together with the results obtained after doping the layer by intercalation with half a monolayer of Na and in comparison with those from SiC. Here we concentrate first on the lower dispersion branch. When the slope of the quasi-linear dispersion for graphene on Ir(111) is compared with that on SiC(0001) (Fig. 19.5b), they are virtually identical. While the more effective shielding of the metallic surface compared with SiC should lower the slope of dispersion [19.70], this shielding is not static and leads to a more complicated interaction between the 2-D electron gas of graphene and the 3-D electron gas in the conduction bands of Ir, which may compensate the expected redshift. However, this effect has not been studied quantitatively in this system. Completely linear dispersion has also been found for graphene on Pt(111) [19.15, 78]. The slope, however, is about 15% smaller than in the examples just shown, possibly due to different interaction and shielding compared with the Ir(111) substrate.

Intercalation of graphene on Ir(111) by half a monolayer of Na has the effect of strong n-doping of graphene due to a shift of the Fermi level of graphene by nearly 1 eV. As a consequence, the linearity of plasmon dispersion is seen over a reduced $q_\parallel$ range up to $0.1\,\mathrm{Å}^{-1}$, whereas for higher $q_\parallel$ values there is a tendency for leveling off. The slope measured in the linear $q_\parallel$ range is about 10% larger than with graphene on clean Ir(111). This is a remarkably small effect considering the change in doping level by about four orders of magnitude. On the other hand, both findings indicate

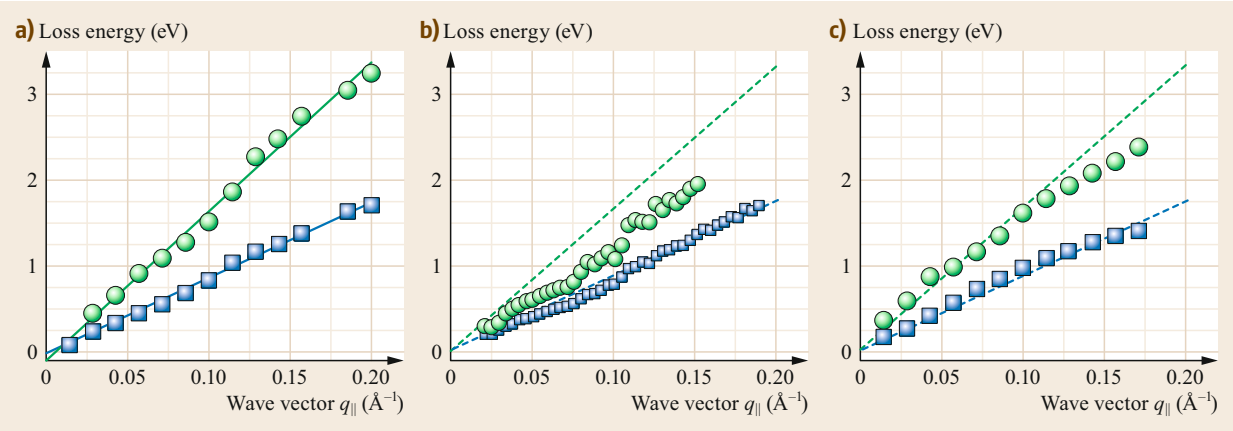

Fig. 19.5 **(a)** Plasmon dispersion of the two plasmonic branches of graphene on Ir(111). **(b)** Same type of data evaluation for graphene on SiC(0001) (n-doped layer $n \approx 10^{13}$ cm^{-2}). **(c)** Results for Na-intercalated graphene on Ir(111). The average linear slopes of **(a)** are drawn as *dashed lines* in the other graphs. While the *lower branches* correspond to the *standard* (or monopole) sheet plasmon, the others marked by *green symbols* have been assigned to multipole plasmons. (Reprinted by permission from [19.74])

that Na intercalation not only results in a rigid shift of the graphene bands, but also causes Na to interact more strongly with both graphene and Ir, resulting in the deviations measured. The increase in measured half widths of plasmon losses also points in this direction [19.74].

In view of (19.1), these results are not expected, since the doping level increases the first term of this equation considerably, so that it should dominate over a larger range of $q_{\|}$. A clear dependence of the plasmon dispersion has indeed been seen on SiC(0001) by varying the amounts of intercalated potassium [19.79]. In fact, due to the high doping level studied there, this first term of (19.1) dominates most of those results, and there is semi-quantitative agreement with the predictions of (19.1) with this assumption. At this point, we want to stress, however, that the findings of [19.79] are not in contradiction to the results found on Ir and the others discussed above. On the contrary, they fully agree with the predictions of (19.1). Since on a metal the screening is much more effective, the dielectric function is up to two orders of magnitude larger than for SiC, so that the first term of (19.1) is smaller by the same factor on metals like Ir or Pt as on SiC: the linear term in $q_{\|}$ thus already dominates at small $q_{\|}$. Moreover, the interaction with the shielding metal electrons leads to further linearization of the dispersion curves [19.23, 24], a mechanism not present on a semiconductor like SiC.

From these results we conclude that the tunability of the plasmon frequencies in the relativistic 2-D electron gas is possible only if the term $\propto \sqrt{q_{\|}}$ dominates the dispersion. The strong sensitivity of this term to the environment via its dielectric function ϵ influences both the accessible frequencies and the range of tunability. This range can easily be exceeded particularly on metals, where the term linear in $q_{\|}$ is responsible for the insensitivity of plasmon dispersion to the doping level and to the environment. This robustness has not yet been exploited, but is quite important for many potential applications.

Two-dimensional plasmons were also shown to couple to other excitations, in particular to phonons and single-electron excitations. The enhanced coupling of plasmons to single-particle excitations is quite well known: similar to the situation described above [19.68], due to opening of new decay channels, it causes resonantly enhanced damping. Similar phenomena have been observed in photoemission, but here the linear dispersion of (ideally) noninteracting single quasi-electrons and quasi-holes is modified close to the Dirac point by the interaction with the plasmon due to excitations of so-called plasmarons [19.80, 81]. For coupling between sheet plasmons and phonons, a prominent example is the coupling in graphene to the surface optical phonon of the underlying SiC on the Si-terminated surface [19.82, 83]. The coupling of this phonon was found to be remarkably robust. It cannot be quenched by intercalation or modifications of the intercalation. Instead, new coupled modes appear that are due to the coupling between the sheet plasmon with phonons of the intercalated material. Coupling of the plasmon with the internal LO phonon was found to be detectable only for bilayer graphene. This coupling may give a further handle to tailoring plasmonic properties.

Finally, we turn to the observation of multipole modes, which were identified for graphene on Ir(111)

and on SiC(0001) [19.74]. As evident from Fig. 19.5, these modes closely follow the dispersion of the basic mode, but with a different slope depending on the substrate material. On the metal, the ratio between slopes is roughly 2, while on SiC it is reduced to 1.4. The half widths of the multipole losses were found to be essentially the same as for the basic mode. Both modes appear at the same $q_{\parallel}$, so it seems that both modes are excited by the same mechanism. It is indeed only a matter of scattering cross section which one dominates. The different ratios of slope found on the metal and on the semiconductor, on the other hand, may be due again to different screening efficiency. These multipole modes in low-dimensional systems have not yet been explicitly considered theoretically, even if this improvement is highly desirable in order to gain deeper insight.

The Acoustic Surface Plasmon (ASP) for Be(0001), Cu(111) and Au(111)

As mentioned at the beginning of the chapter, a new mechanism governing linearization of plasmon dispersion comes into play when excitations of different electron gases are coupled. An important example is the 2-D electron gas of a Shockley surface state, which exists, e.g., on the close-packed surfaces of the noble metals (Ag(111), Au(111) and Cu(111)), but also on Be(0001). The 2-D sheet plasmon will inevitably be screened by the underlying 3-D electron gas of the metal. The ASP was first observed experimentally on Be(0001) with HREELS. Experimental data are shown in Fig. 19.6 along the $\overline{\Gamma M}$ direction for two different kinetic energies (7.26 and 10.74 eV, respectively) while keeping the scattering angle θ_s fixed (63.3° and 59.2°,

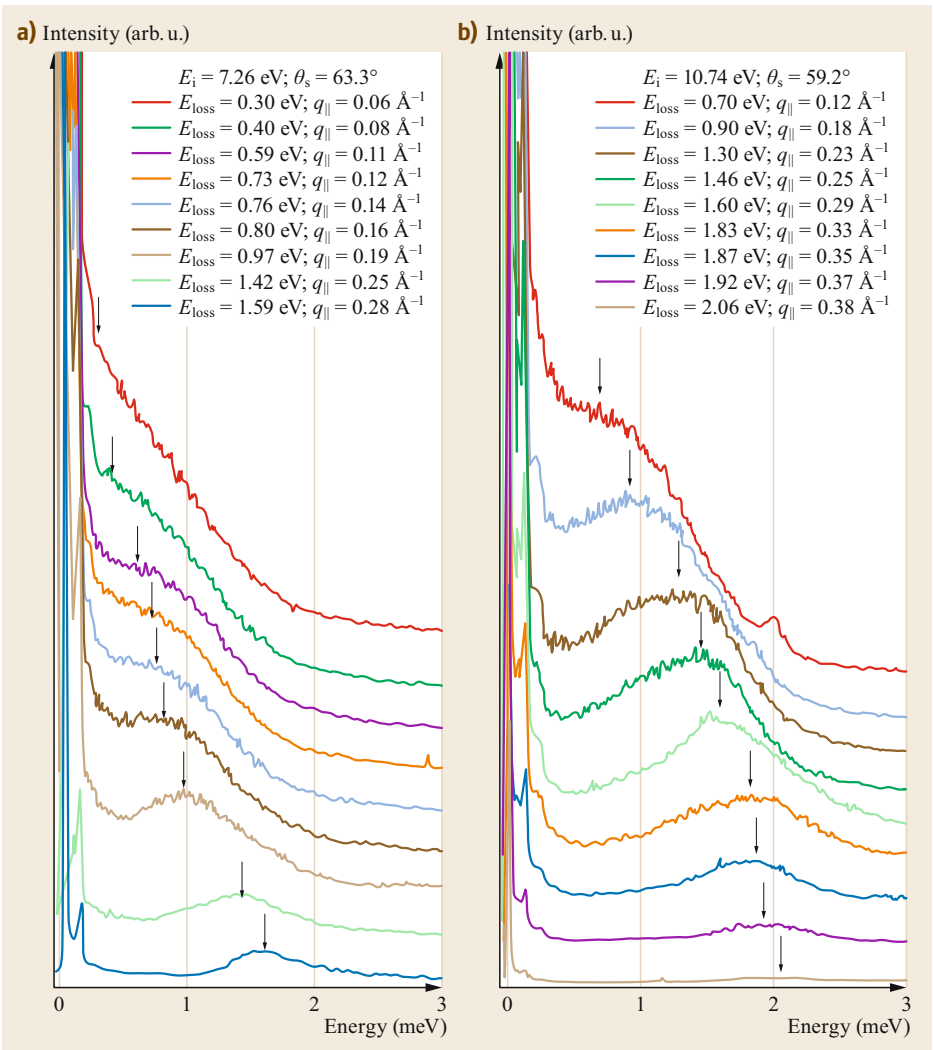

Fig. 19.6a,b HREEL spectra recorded for different scattering conditions starting from the specular direction (*uppermost spectra*) and moving out of specular for Be(0001). The *arrow* indicates the position of the energy loss feature. (After [19.16])

respectively) and changing the angle of incidence $\theta_i y$. The parallel momentum is obtained using (19.6).

It is apparent that a relatively broad energy loss feature is present and that it shifts to higher energy with increasing parallel wave vector. The position of the loss feature for several scattering conditions is shown in Fig. 19.7. The slope of the dispersion curve was found to be 5.5 eV Å (for comparison: 1 eV Å $\cong 1.52 \times 10^5$ m/s), slightly lower than predicted by a simplified 1-D model and in very good agreement with the prediction of a more accurate ab initio model. Measurements along ΓK were performed by another group [19.17]. The slope (group velocity) was found to be slightly higher (6.4 eV Å) than for the $\overline{\Gamma M}$ direction. Moreover, along the $\overline{\Gamma K}$ high-symmetry direction, the ASP has a greater width than along $\overline{\Gamma M}$, because the ASP dispersion is closer to the electron–hole pair continuum along $\overline{\Gamma K}$ [19.84].

The discovery of the ASP on Be(0001) triggered further measurements on other surfaces such as Cu(111) [19.18] and Au(111) [19.21], for which theory had already predicted its existence. For Au(111), actually two linearly dispersing losses were found [19.20], with group velocities of 3.95 and 8.1 eV Å, respectively. Only the latter loss was excited in [19.21]. A selection of spectra for different scattering conditions and the dispersion curves are shown in Fig. 19.8. According to time-dependent density functional theory (DFT) calculations [19.20], however, only the first with the lower slope corresponds to the ASP, whereas the second, higher-energy branch was assigned to an interband transition between a band edge of the bulk and the Shockley surface state. A further contribution to this loss from a multipole ASP cannot be excluded.

Interestingly, as seen from Fig. 19.8, the slope of the low-energy branch corresponds to a value of $\alpha < 1$ in (19.4), i.e., to a loss running slightly below the edge of the electron–hole pair continuum. As demonstrated theoretically [19.20], this is a particular screening effect of the surface state excitation by the bulk electrons. For Au(111), the electrons in the Shockley surface state close to the Fermi level have velocities higher than the corresponding majority of bulk electrons, thus leading to a value of α slightly lower than 1. The complication with two losses also appeared for the Cu(111) case, as a recent investigation with very high-energy resolution showed, i.e., the loss feature assigned to the ASP by *Pohl* et al. [19.18] actually consists of two losses. The component with the lowest slope among them was then assigned to the ASP for Cu(111), suggesting a scenario similar to Au(111) [19.49]. Thanks to the higher energy resolution, the width of the ASP is now lower than estimated before: using the time-energy principle of indeterminacy, it is thus possible to estimate the lifetime and the propagation length of the ASP, a parameter relevant for assessing the feasibility of ASP-based de-

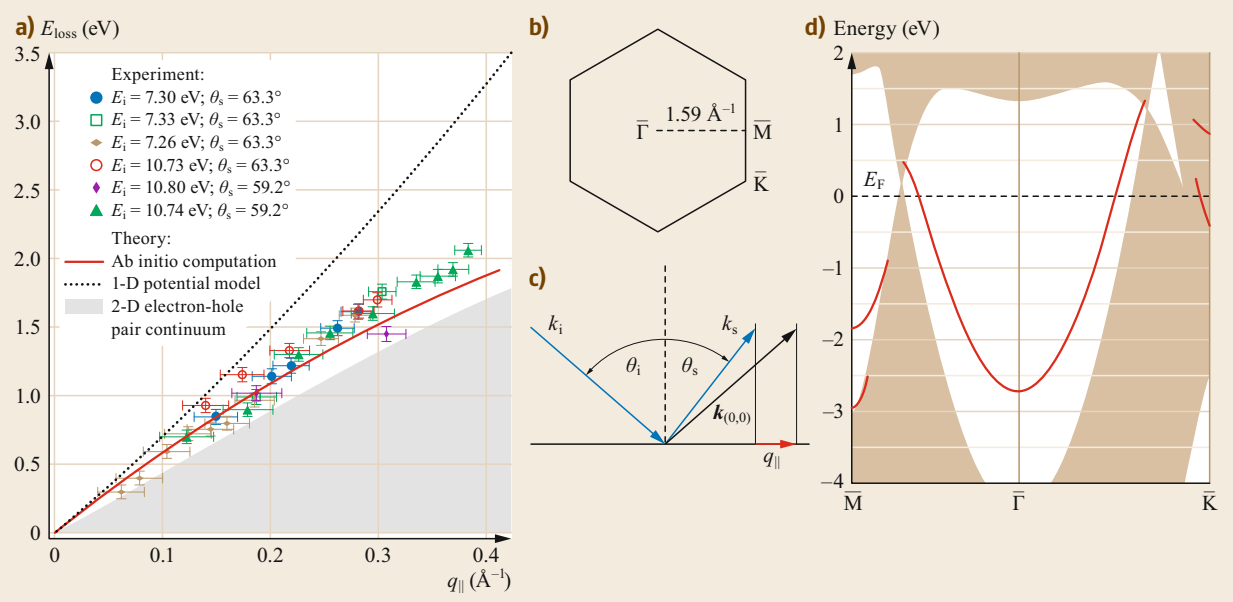

Fig. 19.7a–d Experimentally measured dispersion curve showing the energy of the ASP versus parallel wave vector. The theoretical predictions are also shown: *dotted black line* indicates the simpler 1-D model, while the *continuous red line* indicates the result of a more accurate ab initio calculation. The *shaded area* indicates the continuum of electron–hole excitations; **(b)** 2-D Brillouin zone; **(c)** schematic of the geometry of the experiment; **(d)** electronic structure of Be(0001) with the surface Shockley state in the gap. (After [19.16])

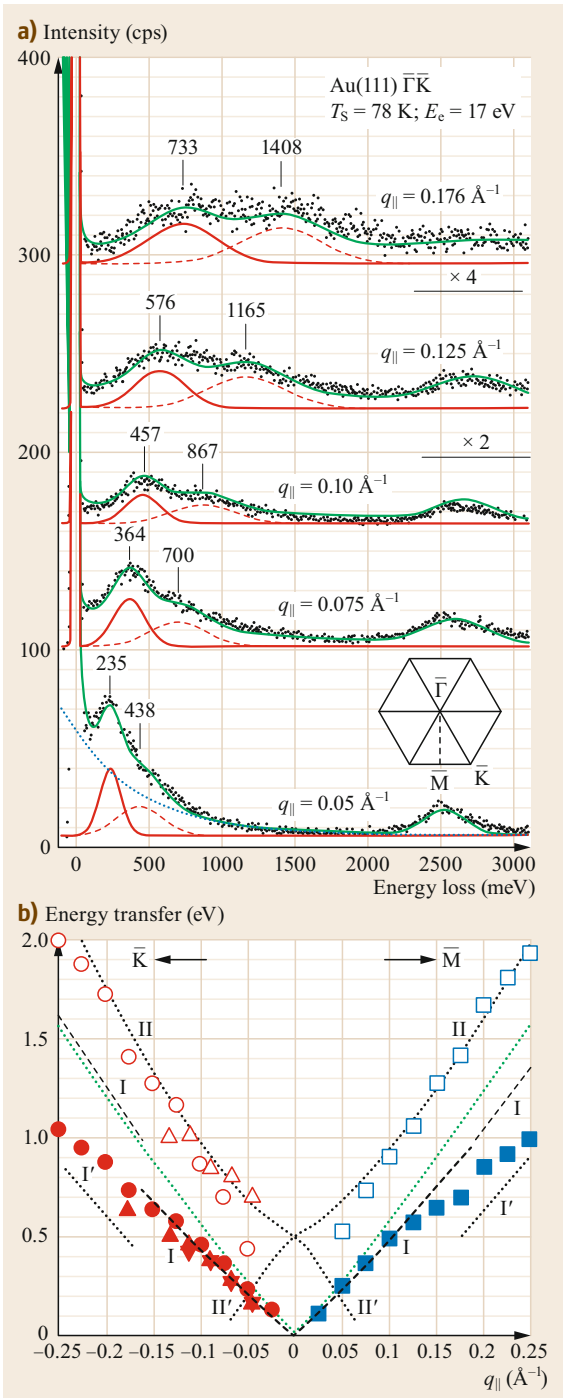

Fig. 19.8 **(a)** HREEL spectra recorded for different scattering conditions for Au(111). **(b)** Dispersion curves for the lower- and higher-energy branches as measured along the two high-symmetry directions are compared with the theoretical prediction (*dashed and dotted lines*). Different symbols correspond to different primary energies and surface temperatures; *squares and circles*: 17 eV and 78 K; *triangles pointing up*: 20 eV and RT; *triangles pointing down*: 13 eV and RT. (Adapted with permission from [19.20]. © 2013 by the American Physical Society) ►

vices. For a wavelength of 0.05 Å^{-1}, an FWHM (full width at half maximum) of the order of 20 meV has been estimated on Cu(111), corresponding to a propagation length of the order of 4 nm, a relatively low value. We shall discuss this important point again in the last section of the chapter.

ASP for Nanostructured and Regularly Stepped Surfaces

After having shown that the ASP exists for most of the surfaces for which it had been predicted, a quite natural question arises: How robust is this excitation? Is it affected by surface nanostructuring? In order to address such issues, experiments for both ion-bombarded Cu(111) and stepped Au surfaces were performed. In the former case, domes and pits of different sizes form upon ion bombardment, the morphology of which is determined by the interplay between thermal diffusion and removal of atoms by collision with the incoming ions. In the latter case, an ordered array of terraces separated by monatomic steps is present. The ASP turns out to be a relatively robust excitation: it is not destroyed by surface nanostructuring at either room temperature or 393 K, at least for moderate ion doses [19.19]. The linear best fit to the dispersion data yields a slope of (3.7 ± 0.5) eV Å. This value has to be compared with that found for the pristine surface ((4.33 ± 0.33) eV Å, [19.18]). As demonstrated by *Theilmann* et al. [19.85], the Shockley surface state (SSS) shifts from −0.4 to about −0.3 eV when the roughness of the Cu(111) surface is increased. This causes a decrease in the Fermi velocity and thus a decrease in the slope of the plasmon dispersion, in qualitative agreement with experiment. For large enough ion doses and when sputtering at 393 K, a non-dispersing loss was observed and tentatively assigned to a nonvertical inter-band transition from the bottom of the SSS to the Fermi level, the required momentum being provided by surface disorder [19.19].

With decreasing wavelength, plasmons also become more and more susceptible to scattering at atomic defects. This effect has clearly been seen for plasmons scattered at substrate steps in graphene on SiC(0001) [19.86]. On a metallic surface, scattering at steps is expected to be smaller due to the less directed bonds, but as was demonstrated for the regularly stepped Au(788) surface, it leads to subband formation and partial localization of plasmons. The (788) surface

consists of (111) terraces that are ≈ 40 Å wide, separated by monatomic steps. The choice of this particular terrace size is motivated by the fact that the distance between steps exceeds the critical value (around 20 Å for Au) beyond which the short-range interaction between steps becomes negligible, so that opening of an energy gap in the surface band structure can occur [19.87]. The choice of Au surfaces is motivated by their chemical inertness: the existence of the ASP is indeed closely related to the existence of a partly unoccupied Shockley surface state, which can in turn be destroyed by surface oxidation. The dispersion of the ASP for Au(788) was measured using an ELS-LEED setup [19.88].

The data are summarized in Fig. 19.9. Two losses with sound-like dispersion are present, denoted by I and II. The branch with the steeper slope originates from the ASP associated to the SSS of the (111) terraces, and has indeed a very similar slope as the ASP on flat Au(111). The branch with lower slope has no analogue on Au(111). Although full ab initio calculations are not feasible because the unit cell is too large, it was possible with the help of theoretical calculations to assign all the features observed experimentally [19.88].

In particular, we underline that:

1. Along the steps, two ASP modes exist. They have different group velocities determined by the Fermi velocities of two partly occupied SSS subbands.
2. The anisotropy introduced by the steps on Au(788) does not automatically lead to plasmon localization normal to the terraces.
3. The QW1 and QW2 subbands are still able to generate propagating plasmonic modes across the steps at wavelengths longer than the terrace width. The slightly different slopes of the modes parallel and normal to the steps reflect the anisotropy of the system.
4. Across the steps, plasmon localization becomes visible when $q_{\parallel}$ exceeds the reciprocal lattice vector of the periodic step array.

The interest in the effect of the presence of a regular array of steps on ASP existence and dispersion is not purely academic: It has been suggested indeed that vicinal surfaces might naturally provide a diffraction grating of nanometer size needed to couple the ASP with light [19.7]. Due to the large difference between the speed of light and the Fermi velocity in the Shockley surface state (almost three orders of magnitude!), an (infrared) photon with an energy of ≈ 0.5 eV could excite on Au(111) an ASP with a wavelength of ≈50 Å, provided that a diffraction grating is able to bridge the momentum gap. A hypothetical device effectively converting photons into ASP should therefore have a characteristic spacing of that order, i.e., about two/three orders of magnitude smaller than a traditional optoelectronic system operating at the same frequency.

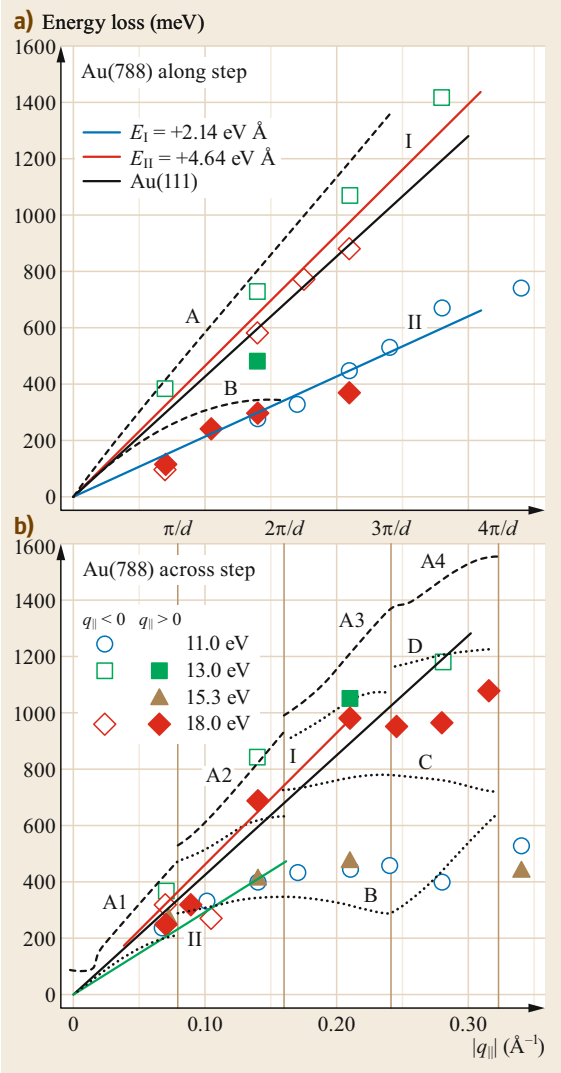

Fig. 19.9a,b Dispersion curves along **(a)** and across steps **(b)**. The *symbols* indicate the experimental data points, the *dotted lines* the results of the theoretical calculations. The best fits to the experimental data are shown by *colored lines*. (Adapted with permission from [19.88]. © 2014 by the American Physical Society)

Although some theoretical estimates for nanoparticles predict a low efficiency for the conversion of photons into ASPs [19.90], no experiments have yet been reported. In Table 19.1, experimental and theoretical values obtained for the slope of the ASP dispersion are summarized.

Table 19.1 Fermi velocity, experimentally determined slope of the dispersion, and experimental and theoretical α for different systems. The last row shows the theoretically predicted slope of the dispersion as estimated by the authors from Fig. 2c of [19.89]

System	Fermi velocity ($e^2/\hbar$)	Experimental slope (eV Å)	α_{exp}	α_{teo} (non ab initio: [19.24])
Be(0001)	0.41	5.5 [19.16]	1.08	–
Cu(111)	0.28	4.33 [19.18]	1.13	1.053
Cu(111)	0.28	3.11 [19.49]	0.81	–
Au(111)	0.35	3.95	0.83	1.032
Ag(111)	0.11	–	–	–
Ag(111)	–	–	–	≈ 7 [19.89]

Summarizing the ASP observations, it is apparent that the interaction between two electron gases provides a mechanism of mutual screening that leads to linearization of the dispersion, particularly also for small $q_\parallel$. Therefore, it is not described by (19.1), which at small $q_\parallel$ predicts a $\sqrt{q_\parallel}$ dependence.

The fact that α can be < 1, as observed for Au(111), so that the ASP runs below the electron–hole pair continuum, does not directly lead to overdamping of the ASP, as erroneously assumed before experimental evidence. Possible reasons are small overlap between SSS and bulk states, but also phase mismatch of wave functions, expressed by the different Fermi velocities of bulk and surface states.

The reliable calculation of these phenomena is still a challenge for simulations, as seen by two conflicting predictions for the Ag(111) surface: according to [19.89] this system should exhibit a slope even higher than for Au(111), while the non ab initio theory predicts a slope even lower than on Cu(111), in agreement with a third, independent calculation [19.91]. No experiments have measured the ASP dispersion for Ag(111), so this controversy remains open. On the other hand, the experiments carried out so far for ASP by HREELS measurements demonstrate that ambiguities due to the appearance of several losses can only be resolved by reliable quantitative theoretical descriptions.

19.2 Quasi-One-Dimensional Plasmons

As already demonstrated above for the case of Au(788), the introduction of extended defects such as steps on highly symmetric surfaces reduces the symmetry of surface states so significantly that subbands are formed, which are also visible by two separate subband plasmons for the two occupied subbands in the ground state. These plasmons, however, propagate across the steps for long wavelengths and are localized to single terraces only for wavelengths of the order of the terrace width. Therefore, they cannot be considered as quasi-one-dimensional.

On the other hand, the experimental observation of a purely 1-D dispersion of a plasmonic signal is clearly a necessary condition for quasi-1-D behavior, but is it sufficient? In the ideal case, a Tomonaga–Luttinger liquid may appear, in which, due to spin and charge separation of the lowest excitations, the plasmon should appear as a holon with a linear dispersion [19.92–94]. While there is no final answer to this question yet, in the following we will discuss systems in which the requirement of 1-D dispersion is clearly fulfilled: the formation of metallic chains of single atomic height on regularly stepped Si surfaces. Regular arrays of these chains are formed by self-organization, and the widths of the wires vary from single atomic chains to metallic strips that fill a whole (111) terrace, depending on the metal, but also on the step orientation. The main question is, of course, how strongly the potential 1-D properties of these wires are modified by their environment and the coupling to neighboring wires. As it turns out, there is again a wide variation in the strength of interaction, which still has to be understood.

A possible approach to 1-D plasmonic properties starts from a 2-D quasi-free electron gas that is confined to a wire of finite width by an appropriate potential. Within this model, following [19.95], the plasmon dispersion for a single isolated wire can be expressed as a function of the upper and lower boundaries of the electron–hole continuum of excitation, $\omega_\pm = q_\parallel^2/2 \pm q_\parallel k_F/m^\star$, as

$$\omega_p(q_\parallel) = \sqrt{\frac{\omega_-^2 - \omega_+^2 e^{A(q_\parallel)}}{1 - e^{A(q_\parallel)}}}\,, \tag{19.8}$$

with $A(q) = 2\pi q/\{m^\star g_s V(q)[1 - G(q)]\}$. $V(q)$ is the Fourier transform of the confining potential, $G(q)$ the local field correction factor due to electronic correlations, and g_s the spin degeneracy (1 or 2). Already this model yields to lowest order a dispersion linear in $q_\parallel$, contrary

to a 2-D electron gas. As one sees from (19.8), the dispersion depends not only on electron density (via k_F) and effective masses, but also explicitly on the form of the confining potential, and electronic correlations. For the coupling between wires, no such analytic expression can be given, but an approximate description of coupling, valid in the limit of small $q_\parallel$ [19.96–98], exists and will be discussed later for Au wires on Si surfaces.

19.2.1 Arrays of Quasi-1-D Wires with Small Coupling

From the few investigations of low-dimensional plasmons carried out on quasi-1-D systems so far, Ag/Si(557) [19.43, 99, 100] and $DySi_2$/Si(100)vic. [19.41] are those systems in which the properties of individual wires seem to be dominant, i.e., the coupling between wires is weak. Since the plasmonic properties of $DySi_2$/Si(100)vic. resemble those in the Ag/Si(557) system in many aspects, we concentrate here on the latter system.

As mentioned above, the Ag/Si(111) system is a prototype system for the investigation of 2-D plasmons, since carrier concentration in the Ag-modified Si surface state can be tuned by Ag surplus concentration. Similar properties have been found in the Ag/Si(557) system by investigation of the concentration-dependent plasmonic properties. Although the doping mechanism on the flat and stepped surfaces need not be exactly the same, these studies allow us to gain some surprising insights, not only into the doping mechanism, but also into general plasmonic properties in 1-D [19.43, 99, 100]. A possible reason for the decoupling of wires on different (111)-oriented mini-terraces in this system may be the separation of these terraces by (112)-oriented mini-facets, which contain three atomic double steps.

The atomic Ag wires formed in this system at coverages below 0.3 ML were found to be semiconducting. Therefore, low-energy plasmons do not exist below 0.3 ML. The formation of metallic wires is coupled to the appearance of $(\sqrt{3}\times\sqrt{3})$R30°-order on the (111)-

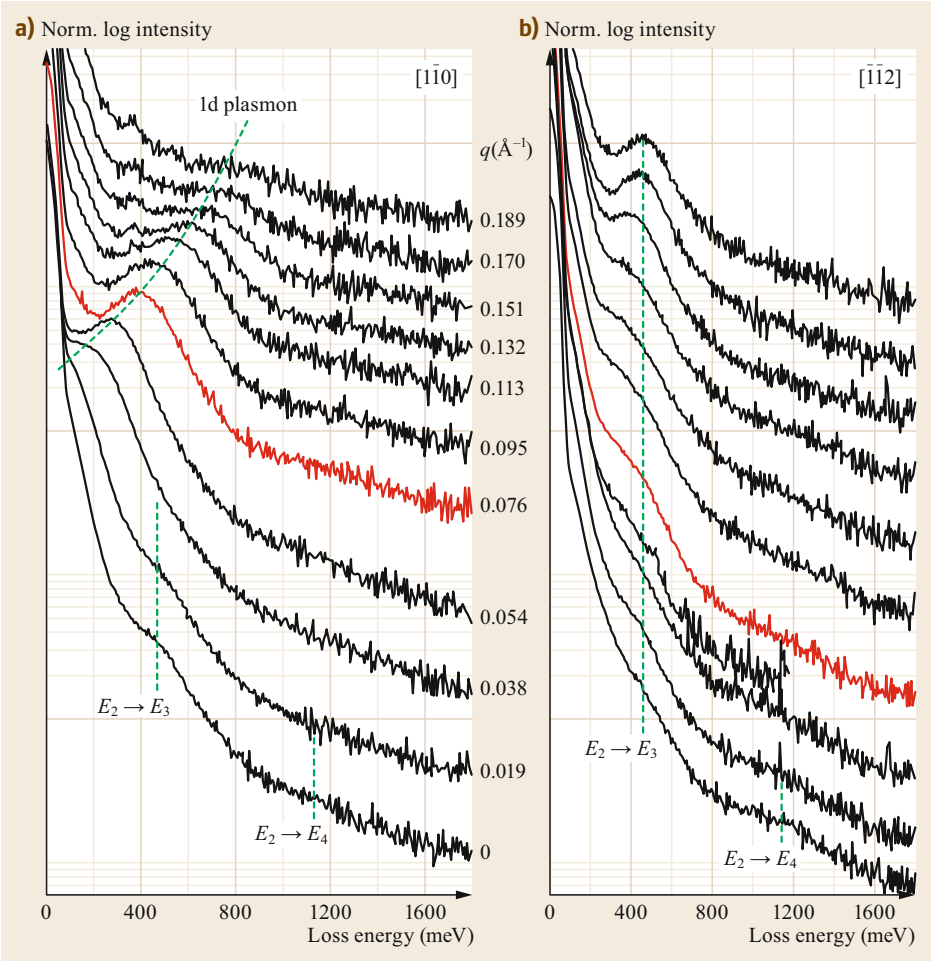

Fig. 19.10a,b EEL-spectra of 1 ML Ag/Si(557) along the [1$\bar{1}$0] **(a)** and [$\bar{1}\bar{1}$2] **(b)** directions taken at 300 K. Apart from the dispersing 1-D plasmon loss in **(a)**, two non-dispersing quantum well transitions $E_2 \rightarrow E_3$ and $E_2 \rightarrow E_4$ at 470 and 1160 meV are seen. Spectra are shifted for better visibility. (Reproduced by permission from [19.43], © IOP publishing 2013)

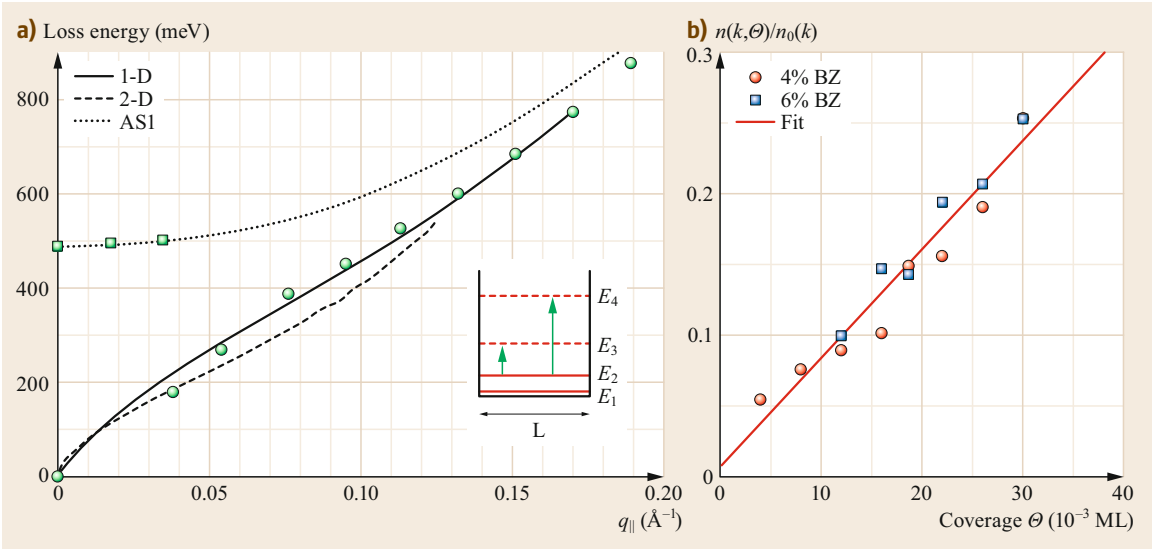

Fig. 19.11 **(a)** Dispersion along the [1$\bar{1}$0] direction. For comparison, the 2-D plasmon dispersion in Ag/Si(111) [19.13] is shown. The *dotted line* is a guide to the eye for AS1-mode. The AS2-branch is not shown. (Reproduced by permission from [19.43], © IOP publishing 2013) **(b)** Electron concentration, normalized to saturation, deduced from the position of the plasmonic losses as a function of Ag surplus concentration exceeding 1 ML. (Reproduced by permission from [19.99])

oriented mini-terraces, which have a local coverage of 1 ML.

As shown in Fig. 19.10, a clear 1-D dispersion was measured by EELS-LEED, which means that the triple steps between the (111) terraces act as insulating separators between the conducting strips. Indeed, the measured dispersion for the lowest plasmon mode, shown in Fig. 19.11b, agrees quantitatively with calculations [19.41] which assume a single strip of a 2-D electron gas that is confined by parabolic barriers to a width of 3.6 nm. Not only is the 1-D dispersion reproduced, but also the appearance of intersubband plasmons along the wires, which are expected to behave as coupled (and simultaneous) excitations of quantum well states and plasmons in these wires of finite width [19.44]. In the limit of long wavelengths they merge into the non-dispersing losses measured in the direction perpendicular to the wires (see Fig. 19.10b). They correspond to quantum well states normal to the wires. Their positions can be quantitatively fitted assuming a simple particle-in-a-box model with the measured wire width of 3.6 nm.

The metallic properties of the wires are not intrinsic, and instead are induced by extrinsic self-doping caused by Ag atoms adsorbed at the adjacent step edges, i.e., the bare Ag-wires with $\sqrt{3}\times\sqrt{3}$-order are semi-metallic. The doping atoms can be desorbed thermally without destroying the majority of Ag wires on the (111) terraces, but can be made metallic again by the tiniest amounts of post-adsorbed Ag atoms. Thus this system enables us to precisely determine the dependence of plasmon excitation energy on doping concentration in the range between 0.003 and 0.03 ML. Assuming that all parameters except the electron density remain constant, and that each surplus Ag atom contributes the same amount of charge to the system at low concentrations, we found that $E_{\mathrm{plasmon}} \propto \sqrt{n_{\mathrm{e}}}$, in agreement with theory (Fig. 19.11b). Remarkably, this dependence turns out to be universal, independent of dimension, and to be valid even for a Luttinger liquid. To the best of our knowledge, this is the first direct experimental verification of the $\sqrt{n_{\mathrm{e}}}$ dependence for plasmons in a quasi-1-D system.

This lateral doping mechanism on the atomic scale is most likely caused by the different binding strength of Ag atoms on terraces and at step edges. It leads to preferential trapping of Ag surplus atoms at the step edges and results in lateral band bending, as sketched in Fig. 19.12. As a consequence, the effective wire width is reduced with increasing doping concentration, since the doping chains of atoms are partially charged. Depending on the chemical differences between terrace and step, this charging also limits the maximum doping concentration. Impurity atoms of different sorts can change this situation drastically, but this has not yet been tested in any detail. These experiments also clearly ruled out the long-debated doping process by a lattice gas in the second Ag layer, which was found to be inactive with respect to the formation of a low-energy plasmon.

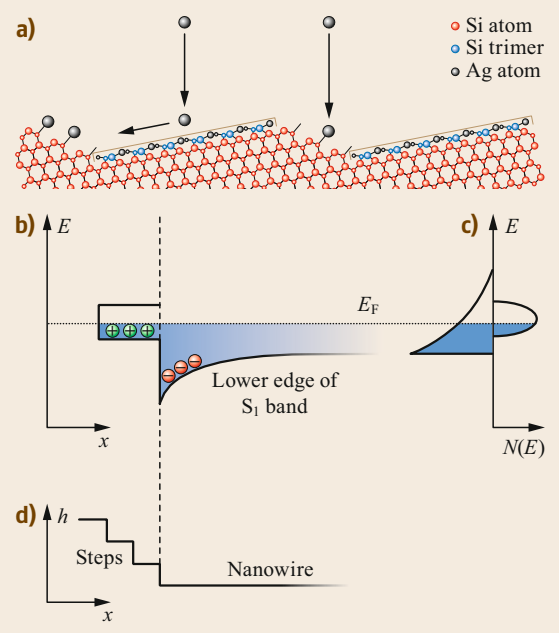

Fig. 19.12 **(a)** Sketch of doping mechanism by adsorption of surplus Ag atoms (*gray balls*) on both the uncovered steps and the Ag monolayer on flat terraces, where they diffuse and are trapped at step edges. **(b)** Lateral band bending resulting from different adsorption energies (and corresponding level filling **(c)** at terraces) and step edges, schematically shown in **(d)**. (Reproduced by permission from [19.100])

The final proof for this model came from the fact that, similar to the Pb/Si(557) system (Sect. 19.2.2), Ag/Si(557) also modifies surface and step energies, so that at high temperature (here 600 °C), the surface becomes unstable in the presence of a monolayer of Ag and tends to form larger (111) terraces and step bunches. Extended heating of the Ag-covered surface to 600 °C roughly doubled the average terrace size. This provided unique proof of the extrinsic doping mechanism, since the line doping concentration remains essentially constant at saturation, but the overall concentration is reduced with increasing terrace size, as the amount of electrons donated by the dopant atoms is distributed over the larger (111) terraces [19.100].

19.2.2 Between 1-D and 2-D: Pb/Si(557)

The situation is much less clear in the Pb/Si(557) system, although at first glance it looks quite similar to Ag/Si(557). For a critical coverage of 1.31 ML and at low temperature (below 78 K) the system clearly has 1-D properties in electrical conductance due to Fermi nesting and 1-D band filling induced by facet formation. Faceting locally transforms the surface into a (local)

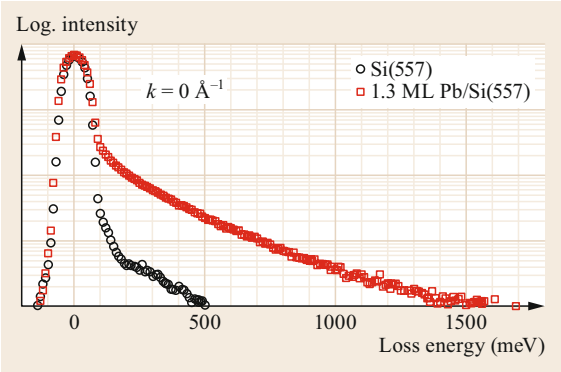

Fig. 19.13 Comparison of the electron loss spectra on clean Si(557) (*circles*) and that with 1.31 ML of Pb adsorbed at $q_{\parallel} = 0$. Due to the metallic property of the Pb layer, an exponentially decaying continuum of losses is seen (Drude tail). Primary energy $E_0 = 20$ eV. (Reproduced by permission from [19.42], © APS 2011)

(223) orientation [19.31, 36] that causes the opening of a small 1-D gap of 25 meV around the critical coverage. On the other hand, this high Pb concentration exhibits relatively strong electronic coupling between the terraces, so that the general appearance of the band structure is 2-D-like, but with 1-D properties close to the Fermi energy. This leads to the following intriguing question: are such 1-D properties still visible in collective electronic excitations with energies far higher than the bandgap of 25 meV? There may even be a transition between 1-D and 2-D behavior depending on the available decay processes into single-particle excitations.

The metallicity of the layer at 1.31 ML Pb coverage can be easily identified even qualitatively by comparing the electron energy loss spectra for the clean and Pb-covered Si(557) surface. Whereas for Si(557), only phonons can be created at small excitation energies, the continuum of low-energy electronic excitations in a metallic system results in a broad structureless background with exponentially decaying intensity as a function of loss energy. This is a clear signature of metallicity for the monolayer Pb/Si(557) system.

For the critical Pb concentration of 1.31 ML the HREELS spectra as a function of q both parallel and perpendicular to the terraces were measured at room temperature and with liquid-He cooling (Fig. 19.13). No clear temperature dependence was found. While a clearly dispersing loss peak was observed in the direction along the wires, no such loss was detected in the perpendicular direction. In other words, plasmonic excitations have a clear a 1-D dispersion at this Pb coverage. As seen from Fig. 19.14, the measured data points can be naturally extrapolated to zero momentum and zero energy. The dispersion can be quantitatively described by a model of a confined 2-D electron gas

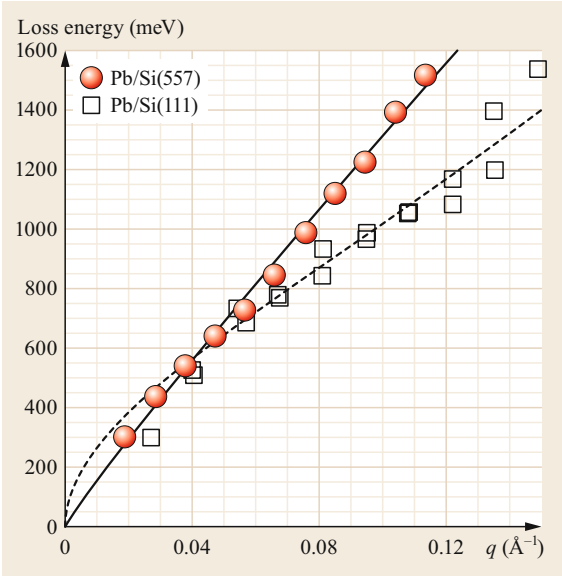

Fig. 19.14 Dispersion for 1.31 ML Pb on Si(557) parallel to the steps (*red balls*), compared with that obtained for the same coverage of Pb on Si(111). The *solid curve* is a quasi-1-D fit with $m^* = 0.4m_e$ and $N_{1\text{-D}} = 3.6 \times 10^7$ cm^{-1} (see text), whereas the *dashed curve* is a 2-D fit with the nearly free electron gas (NFEG) model with an effective mass of $0.4m_e$ and an electron density of $N_{2\text{-D}} = 2.4 \times 10^{14}$ cm^{-2}. (Reproduced by permission from [19.42], © APS 2011)

with local field corrections and correlations [19.44, 101] using a *single* four-atoms-wide metallic strip that is confined in a parabolic potential with the effective mass, m^*, and the 1-D electron density, N_D, given in the caption of Fig.19.14. Further details can be found in [19.42]. As also seen by the comparison with an analogous measurement for the isotropic Pb/Si(111) layer (see Fig. 19.14), there is a clear qualitative difference between a 1-D and a 2-D system (note that both dispersions must go through zero). Unlike the Ag/Si(557) system [19.43], however, no indications for quantum well confinement were detected.

The missing temperature dependence of the 1-D plasmonic dispersion can be taken as an indication that the physical mechanism for decoupling the plasmonic excitation on the various terraces cannot be related solely to Fermi nesting and opening of the 1-D bandgap. The absence of quantum well states means that the simple picture of a confining potential must be questioned. The key to this seemingly contradictory behavior may be hidden in the spin structure and the preferentially antiferromagnetic spin orientation on adjacent terraces, which leads to orthogonal electronic states. While there are no measurements, part of this spin correlation may still exist even at room temperature and consequently reduce the coupling. In the direction normal to the steps, the high resistance of steps [19.102], which at this Pb concentration turned out not to be covered by Pb [19.103], is already sufficient to prevent the formation of plasmon waves in this direction. This situation, however, is modified by the gradual filling of step edges with Pb at higher Pb concentrations.

Interestingly, the quasi-linear dispersion remains when the steps are decorated by Pb, as shown now by increasing Pb coverage to 1.4 ML. At this Pb concentration, about half of the Si step edges are decorated [19.104]. While these added chains increase the coupling between different terraces, the effective bandgap is also reduced [19.105]. Both changes in coupling parameters between terraces now lead to the behavior documented in Fig. 19.15. While there was no detectable signal for long wavelengths, losses and their dispersion were found both parallel and perpendicular to the steps for wavelengths shorter than 15 nm, and with quite small anisotropy of about 10%. This means that when switching on the coupling between terraces, dispersing plasmonic excitations appear with wavelengths that are more than ten times the terrace width.

It should be noted that a quasi-linear dispersion is still detected in both directions, similar to the Au(788) system discussed above. Anisotropy seems to be sufficient for the linearization of the plasmon dispersion. This finding may be obvious from (19.8) for the direction parallel to the wires, but not along the perpendicular direction. Unlike the Au(788) surface, we find here that propagating and dispersing plasmons normal to the wire direction are found only at wavelengths considerably shorter than the undistorted periodicity of (223) facets. This lack of periodicity for distances larger than 20 nm, of course, also makes it impossible to form long-wavelength plasmons here.

Thus there is a clear crossover behavior from 1-D to 2-D induced by a very small change in the surface concentration of Pb. At this moment there is neither a clear understanding of the underlying physical mechanism for the crossover nor a quantitative theory for the plasmonic excitations in these anisotropic low-D systems.

Interestingly, the metal-insulator transition of In/Si(111), historically the first well-investigated quasi-1-D system [19.28], was not only seen in DC conductance, but could also be detected by the disappearance of the plasmonic loss [19.3, 40], in contrast to the Pb/Si(557) system.

At first glance, these findings seem to be contradictory: the phase transitions in both systems are obviously of first order, though with opposite sign of temperature, the main difference lying in the structural changes in-

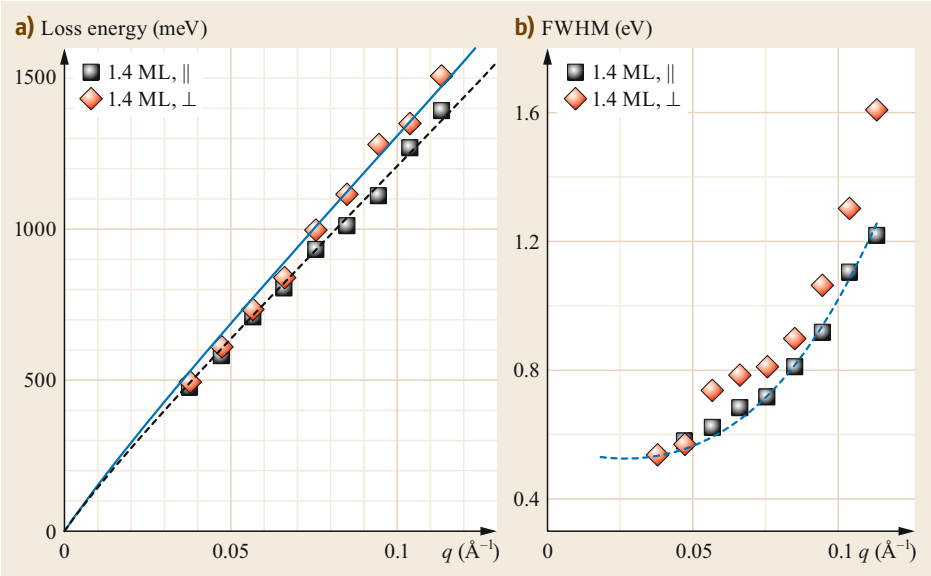

Fig. 19.15 **(a)** Dispersion parallel and perpendicular to the Si(557) steps. **(b)** Corresponding half widths (FWHM) of the measured losses. The *dashed curves* correspond to the results of 1.31 ML. (Reproduced by permission from [19.42])

volved. In Pb/Si(557) the Pb structure on each terrace essentially remains the same when going through the phase transition [19.106]. Only the average step distance is changed, by just 3.5% [19.103], which turns out to be sufficient to destroy the nesting condition at the critical coverage of 1.31 ML, and to form a sequence of charge density waves with varying periodicity and decreasing bandgap normal to the steps as a function of increasing Pb concentration [19.104]. The electronic changes in the band structure of this system associated with the metal–insulator transition also seem to be small. The plasmon excitation seems to be quite insensitive to these small electronic changes. This scenario contrasts very much with the strong structural and electronic changes in the In/Si(111) system when going from the (4×1) to the low-temperature (8×2) phase [19.33, 107], which involves melting and disappearance of the whole CDW system.

19.2.3 Coupling in Atomic Wires: Si(*hhk*)–Au

Au chains on regularly stepped Si(111) surfaces, tilted at various angles toward the $[\bar{1}\bar{1}2]$ direction, provide the narrowest possible arrays of chains consisting of either one or two atoms, depending on the type of step. Here, only double steps of Si separate the (111)-oriented terraces. Although purely 1-D dispersion along the chain direction is found, the lateral extension of the charge distribution, determined by both the structural motif and the terrace width, is found to explicitly influence the slope of the measured plasmon dispersion curves. In other words, the crossover into the second dimension is crucial for the quantitative interpretation of this quasi-1-D phenomenon, but is not completely described by existing theories.

Depending on coverage and step density, the widths of the Au-chains and their interwire spacing can be tuned, while their electronic band structures are still very similar. For example, 0.2 ML of Au on Si(557) results in growth of single-atom Au-chains and a row of Si-adatoms on each mini-terrace, with an interwire spacing of 19.2 Å [19.3, 108]. In contrast, Si(553) and Si(775)-Au host double Au chains in the center of the terrace [19.34, 109]. The interwire spacing is 14.8 for Si(553) and 21.3 Å for Si(775) [19.108, 110, 111]. For double Au chains, a nominal coverage of 0.48 ML on Si(553) and 0.32 ML on Si(775) results. Common to all these structures is a graphitic Si-honeycomb chain located at the step edges [19.108, 110, 111]. Each of these systems is characterized by metallic bands that are well known from angle-resolved photoemission (ARPES) measurements [19.108]. They only disperse along the chain direction $q_{\|}$, and have their minima at the zone boundary. Thus, the (equilibrium) electron density available for plasmonic excitations is also well known.

Here we compare the collective excitations in Si(553)-Au and Si(775)-Au, which have the same structural motif of the double gold chain. Furthermore, the Si(553)-Au system allows the coupling between wires to be varied, because it forms two phases. In the high-coverage (HCW) phase at Au coverage of 0.48 ML, all terraces are covered with a double strand of Au, whereas in the low-coverage (LCW) phase, at 0.21 ML, only every second terrace hosts the double gold chain [19.45, 112]. We will also make reference to the Si(557)-Au system with only a single gold chain.

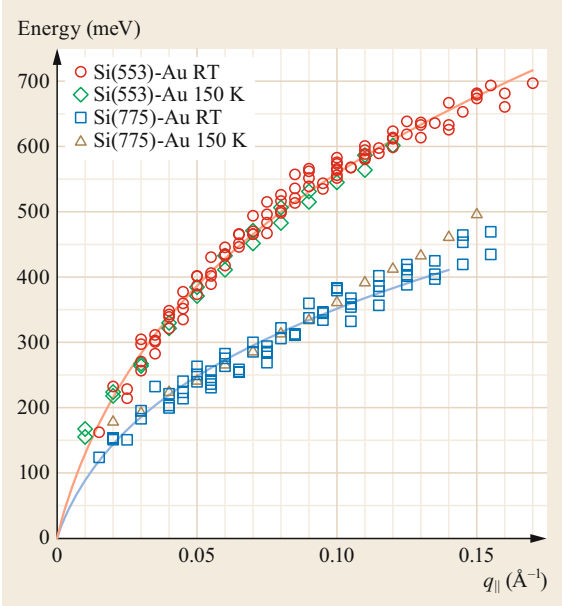

Fig. 19.16 Plasmon dispersion for Au quantum wires grown on Si(553) (HCW phase) and on Si(775). *Lines* are fits according to (19.9). For further details, see text. (Adapted with permission from [19.114]. © 2002 by the American Physical Society)

Interestingly, the step structure seems to have a significant influence on the coupling between wires on different terraces. While the Au wires on Si(553) and Si(775) seem to be strongly coupled, as shown later, this coupling was found to be weak for Au/Si(557) [19.95]. The plasmonic coupling between the wires in the ordered arrays, which is another aspect of dimensional crossover, is quantitatively modeled by existing mesoscopic theories [19.97, 98].

Contrary to the EELS spectra for Ag/Si(557) shown above, the spectra for all Au systems close to $q_\parallel = 0$ are structureless, apart from a small non-dispersing feature that dies out quickly with increasing $q_\parallel$. Metallicity is demonstrated by the exponentially decaying background intensity as a function of loss energy, known as the Drude tail [19.100], in agreement with findings from ARPES for the Si(553)-Au [19.108], scanning tunneling microscopy (STM) [19.113], and theory [19.111]. However, this result is at variance with the ARPES data for the Si(775)-Au [19.108] for reasons still to be explored. In the direction along the wires, clear loss features are observed, which shift to higher loss energies with increasing scattering angles, i.e., with increasing $q_\parallel$. In the $k_\perp$ direction, however, and similar to Ag/Si(557), no dispersing mode is seen.

The dispersion curves along the wires, derived from the loss maxima, are shown for Si(775)-Au and for the HCW phase of Si(553)-Au in Fig. 19.16. From the ARPES data cited above, the ratio of electron densities and effective masses is found to be virtually identical in the two systems for all surface bands. Therefore (19.9), and in spite of two existing bands, only one plasmon loss is expected, in agreement with our findings. Thus, for a true 1-D system, no dependence on terrace width, d, is expected to first order. This is obviously not the case, since a $1/d$ dependence is found. Using existing theories for a nearly free electron gas confined in quasi-1-D wires [19.40, 96, 97, 115], it was found that a quantitative fit was possible with a modified model of coupled wires sitting in a periodic array of square potentials at distance d [19.97, 98]. At small $q_\parallel$, the dispersion is given by

$$E = \hbar \sqrt{\frac{4ne^2}{(1+\epsilon)\epsilon_0 m^* a^2} q_\parallel a_0} \times \sqrt{K_0\left(\frac{q_\parallel a}{2\sqrt{2}}\right) + 2\sum_{l=1}^{L} K_0(q_\parallel l d)\cos(k_\perp l d)}\,, \tag{19.9}$$

where the first term of the product contains the electronic and structural properties of a single wire, the second the intrawire (first term under square root) and the interwire interaction; n is the electron density per unit length, e the elementary charge, m^* the effective mass. ϵ is the dielectric function of Si as partially embedding medium. K_0 are modified Bessel functions of zeroth order and second kind, $k_\perp$ is the momentum normal to the wires. If a (the effective wire width) is set equal to a_0 (a constant for normalization), (19.9) corresponds to the original formula given in [19.97, 98], which, however, turns out not to describe our findings. The ratio a_0/a accounts for both differences in structural motifs and effective wire widths of a single wire, and is the only free parameter in (19.9). In the array of square potentials, the first term under the second square root accounts for the self-interaction of a single wire, whereas the second term describes the interaction between different wires at multiple distances of d.

A further test of the sensitivity of the dispersion to the structural motif was carried out by fitting the published data of [19.3] for Si(557)-Au to (19.9). The Si(775) and Si(557) surfaces have almost the same terrace widths (21.2 versus 19.8 Å, respectively). However, for the best fit, the first term of (19.9) has to be a factor of 1.6 *larger* for Si(557)-Au than for Si(775)-Au. Taking the differences in n and the d-dependence from above for the two systems, the effective width a, as suggested in (19.9), is reduced by roughly a factor of 2 for Si(557)-Au compared with Si(775)-Au. These

results demonstrate that the dispersion is directly influenced not only by the periodicity, given by the wire distances d, but also by the *internal 2-D distribution* of the (excited) electron density within each wire. This result for Au/Si(557) is very much in agreement with the findings of [19.95]. Subband excitations, as in the Si(557)-Ag system, can be ruled out here as a possible source of the observed differences, since for these narrow structures and the given k_F, only the lowest subband of a quantum well is occupied. These results show that even in the case of purely 1-D plasmonic dispersion, there is a crossover to 2-D, and both the width of a wire on the atomic scale and the internal electronic distribution within the wire itself enter directly into the slope of plasmonic dispersion. Additional details, e.g., the choice of a_0, can be found in [19.45].

As it turns out, the LCW phase of Si(553)-Au can be described by the same formalism as (19.9) [19.114]. In fact, according to the analysis of *Song* et al. [19.112], the Au-covered terraces should have the same terrace width as in the HCW phase, whereas the empty terrace acts as separator between the Au wires.

This same effective wire width, however, does not reproduce the measured dispersion for the LCW phase, if we only assume a reduced coupling between wires due to their increased interwire distance from 14.8 to 32.7 Å. By actually fitting the data with a as a free parameter, we obtain an effective wire width of 8.8 Å, compared with 7.5 Å for the HCW phase. This effective spreading of the plasmon excitation on the terrace is in fact quite plausible. In the LCW phase, terraces not covered by gold are under tension [19.112], with the consequence of atomically rough edges. This gives the plasmon mode the ability to spill out more into the uncovered neighboring terrace by approximately $0.5a_\perp = 1.66$ Å. Assuming the same proportionality factor between terrace width and effective wire width as for the HCW phase [19.45], a corrected value of 8.5 Å is obtained that is very close to the value obtained here. Therefore, this result fits the general picture for the stepped Au-covered Si surfaces that the electron density spills out as far as possible, limited by the structure of the step edges, and expresses the crossover of two-dimensional properties on the one-dimensional plasmon dispersion. The effect of spill-out of electrons in the LCW phase compared with HCW may also be taken as indication of softening of the confining potential. A softer potential than the square would in fact have a qualitatively similar effect at constant effective wire width.

Summing up this section, we demonstrated that the Si(hhk)-Au systems offer the unique possibility to study both the spreading of the chain-induced electron density on the mini-terraces and the influence of wire coupling in plasmonic excitations of quasi-one-dimensional arrays of gold chains. As it turns out, there is an intriguing interplay between geometric terrace width and structural motif that influences the effective wire width, as is obvious from a comparison of, e.g., Si(775)-Au and Si(557)-Au. Coupling between wires, on the other hand, varies both with terrace size and with the step structure. These phenomena of course have a direct influence on the band structure in these systems. The relationship between plasmon dispersion and band structure is the subject of future investigations. Coming back to the Ag/Si(557) system, it is mainly the large average separation between terraces in the Si(557)-Ag system that makes them appear as essentially isolated wires. Weak coupling across Si(557) steps, which was found to be much weaker for Si(557)-Au than for Si(775)-Au, acts in the same direction.

19.3 Measured Peak Width of Plasmon Losses

So far, we have used only the information about peak positions, and have not discussed the line widths of the plasmon losses. These loss peaks were found to be fairly broad and not limited by the instrumental energetic resolution of the measurements. We discuss this problem using the recent example of Au/Si(553).

From a quick look at the measured width of the loss peaks, as shown in Fig. 19.17 for both Au phases on Si(553), particularly in the limit of $q_\parallel \to 0$, it is already obvious that these widths cannot be attributed to a lifetime, since in this limit the plasmonic excitation energies also go to zero. Consequently, the lifetimes have to go to infinity. Taking the measured width as lifetime would mean that the plasmonic excitation is highly overdamped, and plasmonic excitations would not exist. This is in sharp contrast to plasmons (at 125 meV) in comparable systems, where mean free paths exceeding 200 nm were observed [19.116]. Therefore, the FWHM at $k = 0$ must be the convolution of instrumental resolution in reciprocal space and in energy of the spectrometer, possibly also with a contribution caused by the short interaction time of the electron scattering process. The energy resolution of the instrument, however, cannot be the main source of the measured half widths—it accounts for only up to 10% of the measured FWHM. Geometric imperfections, as seen by the finite width in k for the elastic peak, is another source, since it will cause corresponding averaging over the disper-

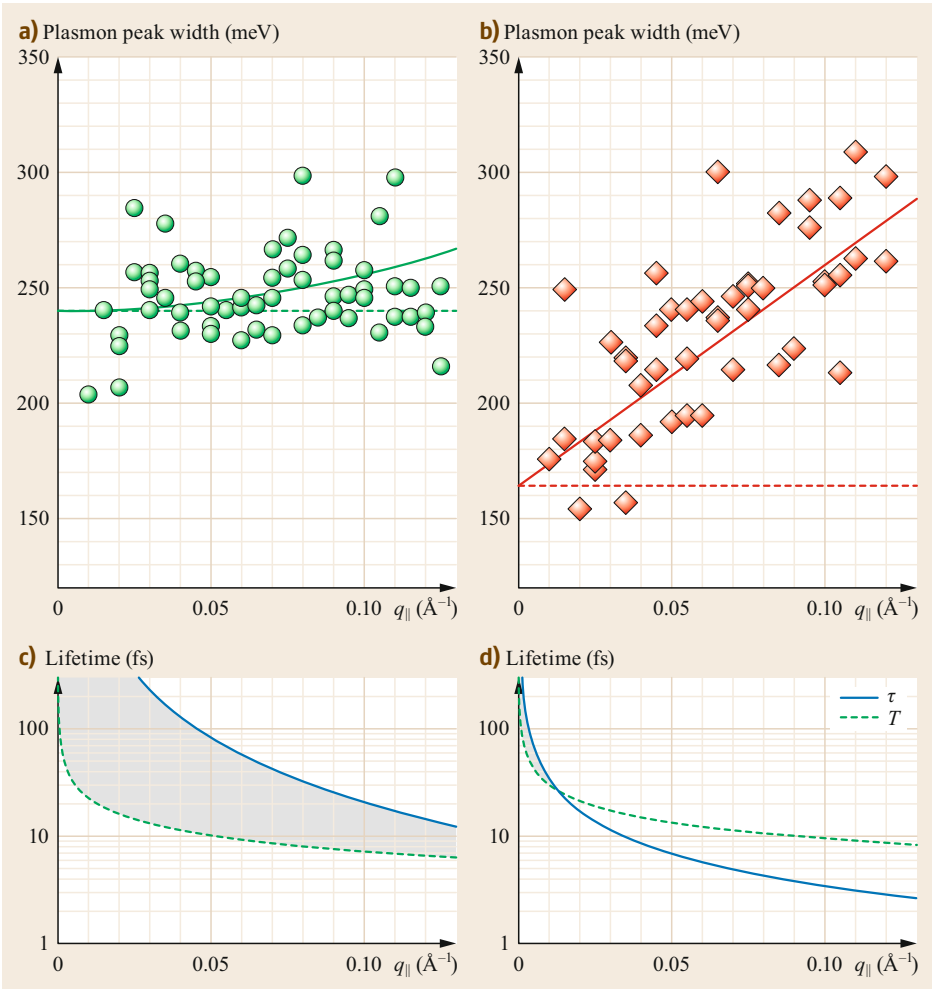

Fig. 19.17 **(a,b)** Plasmon peak widths for varying $q_\parallel$ as a measure of the change in plasmon lifetime for the HCW **(a)** and LCW phase **(b)**. **(c,d)** Estimated lifetimes τ from the data above after the subtraction of the *dashed* offset in comparison with the oscillation period T derived from the dispersion relations (see text). (Adapted by permission from [19.114], © IOP publishing 2016)

sion and thus energetic broadening. From systematic studies of LEED profile analysis, it can also be safely ruled out here as a main source of broadening. The finite k-space resolution of ± 0.01 Å^{-1}, however, can be the main source of broadening, as seen by a comparison with the slope of dispersion of the HCW phase from Fig. 19.16. Since this slope is generally lower by about 30% for the LCW phase than the HCW phase, the broadening in the limit of $q_\parallel \to 0$ is correspondingly reduced, as indeed seen in Fig. 19.17. Therefore, the short interaction time of the inelastically scattering electrons as the possible reason for broadening seems to play a minor role. It may, however, not be negligible in the present case, since only near-field multipole scattering can be effective here—dipole scattering cannot transfer the momentum necessary for excitation—the scattering process being closer to impact scattering [19.117].

Starting from the FWHM at $q = 0$ as an *instrumental* baseline, there is a tendency for a slight increase in FWHM by about 30 meV at $q_\parallel = 0.13$ Å for the HCW phase. This increase is much higher for the LCW phase and amounts to about 120 meV for the same range of $q_\parallel$. Two interpretations seem possible: broadening due to reduced lifetime with increasing energy of excitation, or inhomogeneous broadening caused by the existence of two plasmons.

For the HCW phase, lifetime broadening alone seems to be a possible explanation for the observed increase in FWHM as a function of $q_\parallel$, depicted in Fig. 19.17c. Using the procedures as just described, we approximated the increase in the peak widths by polynomial functions of second order (solid curves), subtracted the offset (dashed lines), and estimated the lifetime with Heisenberg's uncertainty principle of $\Delta E \Delta t \geq \hbar/2$, which yields the blue curve in Fig. 19.17c. This curve still represents a lower limit, since no broadening due to slight energetic differences in the two plasmon modes, especially at higher $q_\parallel$, was

assumed to exist. In any case, it is compatible with other data [19.116].

For the LCW phase, on the other hand, lifetime broadening as the main source of the increase in FWHM can be ruled out right away. Assuming that we can simply subtract the half widths of the baseline from the measured ones, the determined *lifetime* τ as a function of $q_\parallel$ quickly falls below the time T necessary for a single plasmon oscillation, as shown in Fig. 19.17d. Of course, this overdamped situation is unphysical. Therefore, it seems more realistic that a large part of the broadening seen is due to the existence of two plasmons.

From the large line widths of the plasmonic losses observed for both phases and their weak dependence on $q_\parallel$, we conclude that the main contribution is not due to short lifetimes, but even with the high momentum resolution of the present instrument is still mainly caused by the finite instrumental q-resolution, i.e., there is still a need for further experimental improvement. While the two plasmons originating from the two Au-induced electronic surface bands cannot be resolved in either HCW or LCW phases, their larger difference in excitation energy in the LCW phase leads to an additional contribution to the measured half widths.

19.4 Conclusions

Considerable knowledge has been gathered over the past 20 years on the dispersion of 2-D sheet plasmons. Plasmon dispersion in these systems—a few characteristic examples have been shown above—can be described surprisingly well by a nearly free electron gas, even with the modifications of massless fermions in a relativistic electron gas. The inclusion of correlation effects beyond RPA seems to have mainly a quantitative effect on the general slope of dispersion. At long wavelengths, the dependence on electron density of plasmons in a nonrelativistic electron gas, on the other hand, seems to follow the $\sqrt{n_e}$ dependence in all dimensions. Only in the relativistic case is it reduced to $\propto n^{1/4}$.

Furthermore, two main possibilities for linearization of plasmon dispersion have been identified that are quite important for potential signal transmission via plasmonic coupling. The first is due to the general form of plasmon dispersion (see 19.1), if the second term of this equation dominates. This condition depends on k_F, and it can be easily achieved at low electron concentrations and large $q_\parallel$. In the special case of a relativistic electron gas such as in graphene, it leads to the observed insensitivity of plasmon dispersion with respect to the doping level at large $q_\parallel$. In other words, the tunability of plasmons in graphene by changes of the doping level only exists at long wavelengths (terahertz to far-infrared range). The short wavelengths can still be used, but the strategy must be the selection of certain wavelengths, which are then quite robust against distortion. On metal surfaces in particular, this range is even more limited due to the large value of the real part of the dielectric function of metals at terahertz frequencies.

Linearization of plasmon dispersion already in the long wavelength limit can be achieved by coupling a 2-D electron gas to other 2-D or 3-D electron gases, leading to the acoustic surface plasmon (ASP). This property has been demonstrated for the Shockley surface states on Be(0001) and on the (111) surfaces of noble metals, but the concept is fairly general. For example, it might also be applicable for stacks of 2-D metallic sheets separated by insulating material, or for stacks of graphene sheets, thereby combining linear dispersion with tunability.

In the anisotropic 2-D case, which as a limit includes the quasi-1-D wires, the situation is less clear. While it is obvious that restriction of an electron gas to 1-D leads to linearization of the plasmon dispersion already to lowest order in $q_\parallel$, there is an explicit dependence of dispersion on the form of the confining potential. Furthermore, the crossover into the second dimension by explicit consideration of the wire width and the role of coupling of plasmonic excitations with the environment is a general problem whose description is still incomplete. Also, the role of correlations exceeding NFEG properties is still an open question. This sensitivity to the embedding environment, on the other hand, opens many still largely unexplored possibilities for tuning and manipulation on both the experimental and the theoretical side.

The present experimental setups, mainly electron loss spectroscopy (HREELS, EELS-LEED), still enable only limited studies of the dynamics of 2-D and 1-D plasmons. The main limit is k-space resolution. It is obvious that there is sensitivity to atomic-size defects such as steps, which increases as a function of $q_\parallel$ [19.86], i.e., there is high sensitivity to the quality of long-range order and its imperfection on the atomic scale.

The questions related to electronic effects in plasmon dynamics, on the other hand, are an urgent problem that has been touched upon qualitatively at best, as our examples show. Since the low-D plasmons are more strongly damped than, e.g., surface plasmons due to the conductive properties of the metallic sheets and wires, but also of their environment, it is clear that solving these questions will be a key issue for any application of these plasmons.

Acknowledgments. It is a pleasure to acknowledge the experimental contributions of the groups in Hannover and in Genova to several parts of this work, in particular by T. Block, U. Krieg, T. Lichtenstein, L. Savio, M. Smerieri and M. Rocca. We also strongly benefited from collaborations and discussions with the theory group at DIPC, San Sebastian, Spain, in particular by the collaboration with V.M. Silkin. Financial support for this work by the Deutsche Forschungsgemeinschaft, mainly through FOR1700 and project Pf238/28, is gratefully acknowledged.

References

19.1 D. Pines, D. Bohm: A collective description of electron interactions: II. Collective vs individual particle aspects of the interactions, Phys. Rev. **85**, 338 (1952)

19.2 D. Pines: Collective energy losses in solids, Rev. Mod. Phys. **28**, 184 (1956)

19.3 T. Nagao, S. Yaginuma, T. Inaoka, T. Sakurai: One-dimensional plasmon in an atomic-scale metal wire, Phys. Rev. Lett. **97**(11), 116802 (2006)

19.4 R.H. Ritchie: Plasma losses by fast electrons in thin films, Phys. Rev. **106**, 874 (1957)

19.5 H. Raether: *Surface Plasmons on Smooth and Rough Surfaces and on Gratings*, Springer Tracts in Modern Physics, Vol. 111 (Springer, Berlin, Heidelberg 1988)

19.6 A. Liebsch: *Electronic excitations at metal surfaces* (Plenum, New York 1997)

19.7 J.M. Pitarke, V.M. Silkin, E.V. Chulkov, P.M. Echenique: Theory of surface plasmons and surface-plasmon polaritons, Rep. Prog. Phys. **70**, 1 (2007)

19.8 W. Barnes, A. Dereux, T.W. Ebbesen: Surface plasmon subwavelength optics, Nature **424**, 824 (2003)

19.9 M. Jahn, S. Patze, I.J. Hidi, R. Knipper, A.I. Radu, A. Muhlig, S. Yuksel, V. Peksa, K. Weber, T. Mayerhofer, D. Cialla-May, J. Popp: Plasmonic nanostructures for surface enhanced spectroscopic methods, Analyst **141**, 756–793 (2016)

19.10 S. Kawata (Ed.): *Near Field Optics and Surface Plasmon Polaritons*, Topcis in Applied Physics, Vol. 81 (Springer, Berlin, Heidelberg 2001)

19.11 J. Grzelczak, M. Pérez-Juste, P. Mulvaney, L.M. Liz-Marzán: Shape control in gold nanoparticle synthesis, Chem. Soc. Rev. **37**, 1783 (2008)

19.12 N.J. Halas, S. Lal, W. Chang, S. Link, P. Nordlander: Plasmons in strongly coupled metallic nanostructures, Chem. Rev. **111**, 3913–3961 (2011)

19.13 T. Nagao, T. Hildebrandt, M. Henzler, S. Hasegawa: Dispersion and damping of a two-dimensional plasmon in a metallic surface-state band, Phys. Rev. Lett. **86**, 5747 (2001)

19.14 E.P. Rugeramigabo, T. Nagao, H. Pfnür: Experimental investigation of two-dimensional plasmons in a $DySi_2$ monolayer on Si(111), Phys. Rev. B **78**, 155402 (2008)

19.15 A. Politano, G. Chiarello: Plasmon modes in graphene: Status and prospect, Nanoscale **6**, 10927–10940 (2014)

19.16 B. Diaconescu, K. Pohl, L. Vattuone, L. Savio, P. Hofmann, V.M. Silkin, J.M. Pitarke, E.V. Chulkov, P.M. Echenique, D. Farias, M. Rocca: Low energy acoustic plasmons at metal surfaces, Nature **448**, 57 (2007)

19.17 M. Jahn, M. Muller, M. Endlich, N. Neel, J. Kröger, V. Chis, B. Hellsing: Oxygen vibrations and acoustic surface plasmon on Be(0001), Phys. Rev. B **86**, 085453 (2012)

19.18 K. Pohl, B. Diaconescu, G. Vercelli, L. Vattuone, V.M. Silkin, E.V. Chulkov, P.M. Echenique, M. Rocca: Acoustic surface plasmon on Cu(111), Europhys. Lett. **90**, 57006 (2010)

19.19 L. Vattuone, G. Vercelli, M. Smerieri, L. Savio, M. Rocca: Acoustic surface plasmon dispersion on nanostructured Cu(111), Plasmonics **7**(2), 323–329 (2012)

19.20 L. Vattuone, M. Smerieri, T. Langer, C. Tegenkamp, H. Pfnür, V. Silkin, E.V. Chulkov, P.M. Echenique, M. Rocca: Correlated motion of electrons at Au(111) surface: Anomalous acoustic surface plasmon dispersion and single particle excitations, Phys. Rev. Lett. **110**, 127405 (2013)

19.21 S. Park, R. Palmer: Acoustic plasmon on the Au(111) surface, Phys. Rev. Lett. **105**, 016801 (2010)

19.22 F. Stern: Polarizability of a two-dimensional electron gas, Phys. Rev. Lett. **18**, 546 (1967)

19.23 A. Bill, H. Morawitz, V.Z. Kresin: Electronic collective modes and superconductivity in layered conductors, Phys. Rev. B **68**, 144 (2003)

19.24 V.M. Silkin, J.M. Pitarke, E.V. Chulkov, P.M. Echenique: Acoustic surface plasmons in the noble metals Cu, Ag, and Au, Phys. Rev. B **72**, 115435 (2005)

19.25 V.M. Silkin, A. Garcia-Lekue, J.M. Pitarke, E.V. Chulkov, E. Zaremba, P.M. Echenique: Novel low-energy collective excitation at metal surfaces, Europhys. Lett. **66**, 260 (2004)

19.26 G. Güner: *Density Waves in Solids* (Addison Wesley, Boston 1994)

19.27 P. Snijders, H.H. Weitering: Electronic instabilities in self-assembled atom wires, Rev. Mod. Phys. **82**, 307 (2010)

19.28 H.W. Yeom, S. Takeda, E. Rotenberg, I. Matsuda, K. Horikoshi, J. Schaefer, C.M. Lee, S.D. Kevan, T. Ohta, T. Nagao, S. Hasegawa: Instability and charge density wave of metallic quantum chains on a silicon surface, Phys. Rev. Lett. **82**, 4898–4901 (1999)

19.29 J.N. Crain, A. Kirakosian, K.N. Altmann, C. Bromberger, S.C. Erwin, J.L. McChesney, J.-L. Lin, F.J. Himpsel: Fractional band filling in an atomic chain structure, Phys. Rev. Lett. **90**, 176805 (2003)

19.30 J.N. Crain, M.C. Gallagher, J.L. McChesney, M. Bissen, F.J. Himpsel: Doping of a surface band on Si(111)$\sqrt{3}\times\sqrt{3}-$Ag, Phys. Rev. B **72**, 045312 (2005)

19.31 C. Tegenkamp, Z. Kallassy, H. Pfnür, H.-L. Günter, V. Zielasek, M. Henzler: Switching between one and two dimensions: Conductivity of Pb-induced chain structures on Si(557), Phys. Rev. Lett. **95**, 176804 (2005)

19.32 C. Blumenstein, J. Schäfer, S. Mietke, S. Meyer, A. Dollinger, M. Lochner, X. Cui, L. Patthey, R. Matzdorf, R. Claessen: Atomically controlled quantum chains hosting a Tomonaga-Luttinger liquid, Nat. Phys. **7**, 776–780 (2011)

19.33 S. Wippermann, W.G. Schmidt: Entropy explains metal-insulator transition of the Si(111)-In nanowire array, Phys. Rev. Lett. **105**, 126102 (2010)

19.34 M. Krawiec: Structural model of the Au-induced Si(553) surface: Double Au rows, Phys. Rev. B **81**(11), 115636 (2010)

19.35 T. Tanikawa, I. Matsuda, T. Kanagawa, S. Hasegawa: Surface-state electrical conductivity at a metal-insulator transition on silicon, Phys. Rev. Lett. **93**, 016801 (2004)

19.36 C. Tegenkamp, T. Ohta, J.L. McChesney, H. Dil, E. Rotenberg, H. Pfnür, K. Horn: Coupled Pb chains on Si(557): Origin of one-dimensional conductance, Phys. Rev. Lett. **100**, 076802 (2008)

19.37 C. Tegenkamp, D. Lükermann, H. Pfnür, B. Slomski, G. Landolt, J.H. Dil: Fermi nesting between atomic wires with strong spin-orbit coupling, Phys. Rev. Lett. **109**, 266401 (2012)

19.38 C. Brand, H. Pfnür, G. Landolt, S. Muff, J.H. Dil, T. Das, C. Tegenkamp: Observation of correlated spin-orbit order in a strongly anisotropic quantum wire system, Nat. Commun. **6**, 8118 (2015)

19.39 T. Giamarchi: *Quantum Physics in One Dimension* (Clarendon, Oxford 2003)

19.40 T. Nagao, S. Yaginuma, T. Inaoka, T. Sakurai, D. Jeon: Sound-wave-like collective electronic excitations in Au atom chains, J. Phys. Soc. Jpn. **76**(11), 114714 (2007)

19.41 E.P. Rugeramigabo, C. Tegenkamp, H. Pfnür, T. Inaoka, T. Nagao: One-dimensional plasmons in ultrathin metallic silicide wires of finite width, Phys. Rev. B **81**, 165407 (2010)

19.42 T. Block, C. Tegenkamp, J. Baringhaus, H. Pfnür, T. Inaoka: Plasmons in Pb nanowire arrays on Si(557): Between one and two dimensions, Phys. Rev. B **84**(20), 205 (2011)

19.43 U. Krieg, C. Brand, C. Tegenkamp, H. Pfnür: One-dimensional collective excitations in Ag atomic wires grown on Si(557), J. Phys. Condens. Matter **25**(1), 014013 (2013)

19.44 T. Inaoka: Predicted energy-loss spectrum of two-dimensional plasmons in a metallic strip monolayer on a semiconductor surface, Phys. Rev. B **71**, 115305 (2005)

19.45 T. Lichtenstein, J. Aulbach, J. Schäfer, R. Claessen, C. Tegenkamp, H. Pfnür: Two-dimensional crossover and strong coupling of plasmon excitations in arrays of one-dimensional atomic wires, Phys. Rev. B **93**(16), 161408 (2016)

19.46 C.C. Grimes, G. Adams: Observation of two-dimensional plasmons and electron-Ripplon scattering in a sheet of electrons on liquid helium, Phys. Rev. Lett. **36**, 145–148 (1976)

19.47 S.J. Allen, D.C. Tsui, R.A. Logan: Observation of the two-dimensional plasmon in silicon inversion layers, Phys. Rev. Lett. **38**, 980–983 (1977)

19.48 B. Jusserand, D. Richards, G. Fasol, G. Weimann, W. Schlapp: Single particle excitations and plasmons in a single asymmetric modulation-doped GaAs quantum well, Surf. Sci. **229**, 394 (1990)

19.49 J. Pischel, E. Welsch, O. Skibbe, A. Pucci: Acoustic surface plasmon on Cu(111) as an excitation in the mid-infrared range, J. Phys. Chem. C **117**, 26964–26968 (2013)

19.50 M. Pisarra, A. Sindona, P. Riccardi, V. Silkin, J. Pitarke: Acoustic plasmons in extrinsic free-standing graphene, New J. Phys. **16**, 083003 (2014)

19.51 H. Claus, A. Büssenschütt, M. Henzler: Low-energy electron diffraction with energy resolution, Rev. Sci. Instrum. **63**, 2195 (1992)

19.52 S. Hasegawa, N. Sato, I. Shiraki, C.L. Petersen, P. Bøggild, T.M. Hansen, T. Nagao, F. Grey: Surface-state bands on silicon -Si(111)-$\sqrt{3}\times\sqrt{3}$-Ag surface superstructure, Jpn. J. Appl. Phys. **39**, 3815 (2000)

19.53 Y. Liu, R.F. Willis: The evolution of sheet-plasmon behavior in silver monolayers on Si(111)-($\sqrt{3}\times\sqrt{3}$)Ag surface, Surf. Sci. **603**(13), 2115–2119 (2009)

19.54 A. Castro Neto, F. Guinea, N. Peres, K. Novoselov, A. Geim: The electronic properties of graphene, Rev. Mod. Phys. **81**, 109–162 (2009)

19.55 Y. Wang, E.W. Plummer, K. Kempa: Foundations of plasmonics, Adv. Phys. **60**(5), 799–898 (2011)

19.56 F.J. Garcia de Abajo: Graphene plasmonics: Challenges and opportunities, ACS Photonics **1**(3), 135–152 (2014)

19.57 N.K. Emani, A.V. Kildishev, V.M. Shalaev, A. Boltasseva: Graphene: A dynamic platform for electrical control of plasmonic resonance, Nanophotonics **4**(2, SI), 214–223 (2015)

19.58 V.G. Achanta: Plasmonic quasicrystals, Prog. Quantum Electron. **39**, 1–23 (2015)

19.59 C.-H. Chou, F.-C. Chen: Plasmonic nanostructures for light trapping in organic photovoltaic devices, Nanoscale **6**(15), 8444–8458 (2014)

19.60 P.C. Eng, S. Song, B. Ping: State-of-the-art photodetectors for optoelectronic integration at telecommunication wavelength, Nanophotonics **4**(3), 277–302 (2015)

19.61 X. Gao, T.J. Cui: Spoof surface plasmon polaritons supported by ultrathin corrugated metal strip and their applications, Nanotechnol. Rev. **4**, 239–258 (2015)

19.62 Z. Fei, A.S. Rodin, G.O. Andreev, W. Bao, A.S. McLeod, M. Wagner, L.M. Zhang, Z. Zhao, M. Thiemens, G. Dominguez, M.M. Fogler, A.H.C. Neto, C.N. Lau, F. Keilmann, D.N. Basov: Gate-tuning of graphene plasmons revealed by infrared nano-imaging, Nature **487**, 82–85 (2012)

19.63 A. Woessner, M.B. Lundeberg, Y. Gao, A. Principi, P. Alonso-González, M. Carrega, K. Watanabe,

T. Taniguchi, G. Vignale, M. Polini, J. Hone, R. Hillenbrand, F.H.L. Koppens: Highly confined low-loss plasmons in graphene–boron nitride heterostructures, Nat. Mater. **14**, 421–425 (2015)

19.64 M. Pollini: Tuning terahertz lasers via graphene plasmons, Science **351**, 229–231 (2016)

19.65 K. Kneipp, Y. Wang, H. Kneipp, L.T. Perelman, I. Itzkan, R.R. Dasari, M.S. Feld: Single molecule detection using surface-enhanced Raman scattering (SERS), Phys. Rev. Lett. **78**, 1667–1670 (1997)

19.66 H.A. Atwater, A. Polman: Plasmonics for improved photovoltaic devices, Nat. Mater. **9**, 205213 (2010)

19.67 H. Harutyunyan, S. Palomba, J. Renger, R. Quidant, L. Novotny: Nonlinear dark-field microscopy, Nano Lett. **10**(12), 5076–5079 (2010)

19.68 C. Tegenkamp, H. Pfnür, T. Langer, J. Baringhaus, H.W. Schumacher: Plasmon electron-hole resonance in epitaxial graphene, J. Phys. Condens. Matter **23**(1), 012001 (2011)

19.69 Y. Liu, R.F. Willis, K.V. Emtsev, T. Seyller: Plasmon dispersion and damping in electrically isolated two-dimensional charge sheets, Phys. Rev. B **78**, 201403 (2008)

19.70 C. Hwang, D.A. Siegel, S.-K. Mo, W. Regan, A. Ismach, Y. Zhang, A. Zettl, A. Lanzara: Fermi velocity engineering in graphene by substrate modification, Sci. Rep. **2**, 590 (2012)

19.71 E.H. Hwang, S. Das Sarma: Dielectric function, screening, and plasmons in two-dimensional graphene, Phys. Rev. B **75**(20), 205418 (2007)

19.72 W. Chen, S. Chen, D.C. Qi, X.Y. Gao, A.T.S. Wee: Surface transfer p-type doping of epitaxial graphene, J. Am. Chem. Soc. **129**, 10418–10422 (2007)

19.73 T. Langer, H. Pfnür, C. Tegenkamp, S. Forti, K. Emtsev, U. Starke: Manipulation of plasmon electron-hole coupling in quasi-free-standing epitaxial graphene layers, New J. Phys. **14**(10), 103045 (2012)

19.74 H. Pfnür, T. Langer, J. Baringhaus, C. Tegenkamp: Multiple plasmon excitations in adsorbed two-dimensional systems, J. Phys. Condens. Matter **23**(11), 112204 (2011)

19.75 T. Langer, D. Förster, C. Busse, T. Michely, H. Pfnür, C. Tegenkamp: Sheet plasmons in buckled and undoped graphene, New J. Phys. **13**, 053006 (2011)

19.76 I. Pletikosić, M. Kralj, P. Pervan, R. Brako, J. Coraux, A.T. N'Diaye, C. Busse, T. Michely: Dirac cones and minigaps for graphene on Ir(111), Phys. Rev. Lett. **102**, 056808 (2009)

19.77 S. Rusponi, M. Papagno, P. Moras, S. Vlaic, M. Etzkorn, P.M. Sheverdyaeva, D. Pacilé, H. Brune, C. Carbone: Highly anisotropic Dirac cones in epitaxial graphene modulated by an island superlattice, Phys. Rev. Lett. **105**, 246803 (2010)

19.78 A. Politano, A.R. Marino, V. Formoso, D. Farías, R. Miranda, G. Chiarello: Evidence for acoustic-like plasmons on epitaxial graphene on Pt(111), Phys. Rev. B **84**, 033401 (2011)

19.79 S.Y. Shin, N.D. Kim, J.G. Kim, K.S. Kim, D.Y. Noh, K.S. Kim, J.W. Chung: Control of the π-plasmon in a single layer graphene by charge doping, Appl. Phys. Lett. **99**(8), 082110 (2011)

19.80 A. Bostwick, F. Speck, T. Seyller, K. Horn, M. Polini, R. Asgari, A.H. MacDonald, E. Rotenberg: Observation of plasmarons in quasi-freestanding doped graphene, Science **328**(5981), 999–1002 (2010)

19.81 A.L. Walter, A. Bostwick, K.-J. Jeon, F. Speck, M. Ostler, T. Seyller, L. Moreschini, Y.J. Chang, M. Polini, R. Asgari, A.H. MacDonald, K. Horn, E. Rotenberg: Effective screening and the plasmaron bands in graphene, Phys. Rev. B **84**, 085410 (2011)

19.82 R.J. Koch, T. Seyller, J.A. Schaefer: Strong phonon-plasmon coupled modes in the graphene/silicon carbide heterosystem, Phys. Rev. B **82**, 201413 (2010)

19.83 R.J. Koch, S. Fryska, M. Ostler, M. Endlich, F. Speck, T. Hänsel, J.A. Schaefer, T. Seyller: Robust phonon-plasmon coupling in quasifreestanding graphene on silicon carbide, Phys. Rev. Lett. **116**, 106802 (2016)

19.84 V. Silkin, J.M. Pitarke, E. Chulkov, B. Diaconescu, K. Pohl, L. Vattuone, L. Savio, P. Hofmann, D. Farıas, M. Rocca, P.M. Echenique: Band structure effects on the Be(0001) acoustic surface plasmon energy dispersion, Phys. Status Solidi (a) **205**, 1307–1311 (2008)

19.85 F. Theilmann, R. Matzdorf, A. Goldmann: High-resolution photoemission studies at rough Cu(111) surfaces: The influence of defect scattering and disorder-dependent dephasing processes, Surf. Sci. **420**, 33–42 (1999)

19.86 T. Langer, J. Baringhaus, H. Pfnür, H. Schumacher, C. Tegenkamp: Plasmon damping below the Landau regime: The role of defects in epitaxial graphene, New J. Phys. **12**, 033017 (2010)

19.87 J. Ortega, A. Mugarza, V. Pérez-Dieste, V. Repain, S. Rousset, A. Mascaraque: Probing wave functions at step superlattices: Confined versus propagating electrons, Mater. Sci. Eng. B **96**, 154–158 (2002)

19.88 M. Smerieri, L. Vattuone, L. Savio, T. Langer, C. Tegenkamp, H. Pfnür, V.M. Silkin, M. Rocca: Anisotropic dispersion and partial localization of acoustic surface plasmons on an atomically stepped surface: Au(788), Phys. Rev. Lett. **113**(18), 186804 (2014)

19.89 J. Yan, K. Jacobsen, K.S. Thygesen: Conventional and acoustic surface plasmons on noble metal surfaces: A time-dependent density functional theory study, Phys. Rev. B **86**, 241404 (2012)

19.90 M. Hrton, M.A. Poyli, V.M. Silkin, J. Aizpurua: Optical excitation of acoustic surface plasmons in metallic nanoparticles, Ann. Phys. **524**, 751–756 (2012)

19.91 J.-K. Ahn, Y.-I. Kim, K.-H. Kim, C.-J. Kang, M.C. Ri, S.-H. Kim: Simplified theory of the acoustic surface plasmons at the two-dimentional electron gas, Physica B **481**, 257–261 (2016)

19.92 S. Tomonaga: Remarks on Bloch's method of sound waves applied to many-fermion problems, Prog. Theor. Phys. **5**, 544–569 (1950)

19.93 J. Luttinger: An exactly soluble model of a many-fermion system, J. Math. Phys. (N.Y.) **4**, 1154 (1963)

19.94 J. Voit: One-dimensional Fermi liquids, Rep. Prog. Phys. **58**(9), 977 (1995)

19.95 R.K. Moudgil, V. Garg, K.N. Pathak: Confinement and correlation effects on plasmons in an atom-scale metallic wire, J. Phys. Condens. Matter **22**(13), 135003 (2010)

19.96 S. Das Sarma, W. Lai: Screening and elementary excitations in narrow-channel semiconductor microstructures, Phys. Rev. B **32**(2), 1401–1404 (1985)

19.97 Q. Li, S.D. Sarma: Plasmon excitations in one-dimensional lateral-quantum-wire superlattices, Phys. Rev. B **41**, 10268 (1990)

19.98 S. Das Sarma, E. Hwang: Dynamical response of a one-dimensional quantum-wire electron system, Phys. Rev. B **54**(3), 1936–1946 (1996)

19.99 U. Krieg, Y. Zhang, C. Tegenkamp, H. Pfnür: Tuning of one-dimensional plasmons by Ag-Doping in Ag-$\sqrt{3}$-ordered atomic wires, New J. Phys. **16**, 043007 (2014)

19.100 U. Krieg, T. Lichtenstein, C. Brand, C. Tegenkamp, H. Pfnür: Origin of metallicity in atomic Ag wires on Si(557), New J. Phys. **17**(4), 043062 (2015)

19.101 T. Inaoka: Low-dimensional plasmons in a metallic strip monolayer on a semiconductor surface, J. Phys. Soc. Jpn. **73**, 2201 (2004)

19.102 J. Rönspies, S. Wießell, H. Pfnür: The resistance of single atomic steps in ultrathin Pb nanowires on Si(557), Appl. Phys. A **100**(4), 1007–1012 (2010)

19.103 M. Czubanowski, A. Schuster, H. Pfnür, C. Tegenkamp: Temperature-driven refacetting phase transition in Pb chains on Si(557), Phys. Rev. B **77**, 174108 (2008)

19.104 M. Czubanowski, H. Pfnür, C. Tegenkamp: Atomic chain ordering with ultra-long periods: Pb/Si(557), Surf. Sci. **603**, L121–L124 (2009)

19.105 C. Tegenkamp, D. Lükermann, S. Akbari, M. Czubanowski, A. Schuster, H. Pfnür: Pb nanowires on vicinal Si(111) surfaces: Effects of refacetting on transport, Phys. Rev. B **82**, 205413 (2010)

19.106 H. Pfnür, C. Brand, M. Jaeger, J.P. Roenspies, C. Tegenkamp: Between one and two dimensions: Pb/Si(557) close to monolayer coverage, Surf. Sci. **643**, 79 (2016)

19.107 S. Wall, B. Krenzer, S. Wippermann, S. Sanna, F. Klasing, A. Hanisch-Blicharski, M. Kammler, W.G. Schmidt, M. Horn-von Hoegen: Atomistic picture of charge density wave formation at surfaces, Phys. Rev. Lett. **109**, 186101 (2012)

19.108 J.N. Crain, J.L. McChesney, F. Zheng, M.C. Gallagher, P.C. Snijders, M. Bissen, C. Gundelach, S.C. Erwin, F.J. Himpsel: Chains of gold atoms with tailored electronic states, Phys. Rev. B **69**, 125401 (2004)

19.109 J. Aulbach, S.C. Erwin, R. Claessen, J. Schäfer: Spin chains and electron transfer at stepped silicon surfaces, Nano Lett. **16**(4), 2698–2704 (2016)

19.110 I. Barke, F. Zheng, S. Bockenhauer, K. Sell, V.V. Oeynhausen, K.H. Meiwes-Broer, S.C. Erwin, F.J. Himpsel: Coverage-dependent faceting of Au chains on Si(557), Phys. Rev. B **79**(15), 155301 (2009)

19.111 S.C. Erwin, F.J. Himpsel: Intrinsic magnetism at silicon surfaces, Nat. Commun. **1**(5), 58 (2010)

19.112 I. Song, D.-H. Oh, H.-C. Shin, S.-J. Ahn, Y. Moon, S.-H. Woo, H.J. Choi, C.-Y. Park, J.R. Ahn: Direct momentum-resolved observation of one-dimensional confinement of externally doped electrons within a single subnanometer-scale wire, Nano Lett. **15**(1), 281–288 (2015)

19.113 J. Aulbach, J. Schäfer, S.C. Erwin, S. Meyer, C. Loho, J. Settelein, R. Claessen: Evidence for long-range spin order instead of a Peierls transition in Si(553)-Au chains, Phys. Rev. Lett. **111**, 137203 (2013)

19.114 T. Lichtenstein, C. Tegenkamp, H. Pfnür: Lateral electronic screening in quasi-one-dimensional plasmons, J. Phys. Condens. Matter **28**, 354001 (2016)

19.115 T. Inaoka, T. Nagao: Exchange-correlation effects on low-dimensional plasmons in an array of metallic quantum wires, Mater. Trans. **48**(4), 718–721 (2007)

19.116 F. Hötzel, K. Seino, C. Huck, O. Skibbe, F. Bechstedt, A. Pucci: Metallic properties of the Si(111)-5×2-Au surface from infrared plasmon polaritons and ab initio theory, Nano Lett. **15**(6), 4155–4160 (2015)

19.117 H. Ibach, D.L. Mills: *Energy electron loss spectroscopy and surface vibrations* (Academic Press, San Francisco 1982)

Herbert Pfnür

Festkörperphysik (Solid State Physics),
ATMOS
Leibniz Universität Hannover
Hannover, Germany
pfnuer@fkp.uni-hannover.de

Herbert Pfnür has been Professor of Experimental Physics at the Leibniz University of Hannover, Germany, since 1990. He started as a surface scientist, and his main research topics are all based on low-dimensional physics in ultrathin and ultrasmall systems down to the atomic scale, correlating structure and growth with electronic properties and excitations (such as plasmons), quantum correlations, instabilities, and electronic transport.

Christoph Tegenkamp

Institut für Physik
Technische Universität Chemnitz
Chemnitz, Germany
christoph.tegenkamp@physik.tu-chemnitz.de

Christoph Tegenkamp is Full Professor at TU Chemnitz. After his postdoc at the University of Maryland he returned to Hannover, where he worked on the functionalization of surfaces by molecules and quantum wires. Until 2017 he held a professorship for nano-electromechanical quantum systems. Among others, his current research is about spin-orbit effects in 1-D and 2-D electron gas systems and molecular electronics. He is on the Editorial Board of JPCM.

Luca Vattuone

Dipt. di Fisica
Università di Genova and IMEM-CNR Unità di Genova
Genova, Italy
vattuone@fisica.unige.it

Luca Vattuone received his PhD from the University of Genoa in 1994, worked as postdoc at Cambridge University (1995) and at Genoa University (1996–1999). In 1999 he became Staff Researcher and in 2012 Associate Professor of Condensed Matter Physics at Genoa University. His research activity focuses on the experimental investigation of gas–surface interactions and surface plasmons.

20. Ab Initio Theory of Interband Transitions

Conor Hogan, Maurizia Palummo, Olivia Pulci, Carlo Maria Bertoni

This chapter reviews the principles behind the theory and computation of interband transitions at surfaces. Particular emphasis is given to state-of-the-art ab-initio methodologies, and their application is illustrated through numerous practical examples in realistic surface systems. Following a simple introduction, we outline a general theoretical framework of surface spectroscopy, obtaining an expression for the surface response function that is appropriate for computation with ab-initio methods and for simulating various experimental spectroscopic techniques. We then revise the key ab-initio approaches, namely, density functional theory, Green's function-based many-body theory, and time-dependent density functional theory. The rest of the chapter presents examples of calculations at different levels of theory for various clean and modified surfaces of current interest, illustrating in each case the interplay between the surface geometry, electronic band structure, and interband excitations. Advanced concepts such as local field and excitonic effects at surfaces are highlighted. The chapter concludes with an outlook on challenges in the field and perspectives for future development.

While direct access to surface electronic bands and their dispersions in semiconductor and insulator surfaces is provided by standard experimental techniques such as electron photoemission, inverse photoemission, and scanning tunneling spectroscopies, optical spectroscopies were the first experimental tools—since surface studies really took off about 50 years ago—to yield insight into surface states by means of interband transitions. Nowadays, surface optical spectroscopies, especially when carried out in combination with first-principles simulations, constitute a truly powerful method for characterizing the geometrical and electronic properties of surfaces and interfaces [20.1].

M. Rocca, T.S. Rahman, L. Vattuone (Eds.), *Springer Handbook of Surface Science*, Springer Handbooks,
https://doi.org/10.1007/978-3-030-46906-1_20

20.1 General Theoretical Framework

According to standard band theory, interband transitions occur when an external perturbation—typically an incoming electromagnetic wave—excites an electron from an occupied electronic state into an unoccupied state by absorption of a photon. At a surface, the states taking part in these transitions can be of different character, such as: *true* surface states, i.e., those that lie within the bulk electronic gap and are usually localized within the topmost surface layers; surface *resonances*, which have energies overlapping with the (projected) bulk band structure and are more delocalized than true surface states; and *bulk* states that terminate at the surface and are modified by the change in potential. (See Chap. 16 for a thorough discussion of electronic states at surfaces.)

Figure 20.1 illustrates the connection between the surface band structure and the optical absorption spectrum for a few such possible interband transitions. The transitions indicated in a plot where the electronic bands are a function of the $\boldsymbol{k}$ wavevector in the surface Brillouin zone are almost vertical when the frequency of the light is in the optical range (from IR to UV) and there is no coupling with vibrational excitations. In this simplest picture of direct transitions of noninteracting particles, the absorption probability is

$$\text{Absorption} \propto \sum_{i,j} |\langle i|\boldsymbol{D}|j\rangle|^2 \delta(E_j - E_i - \hbar\omega) \,. \quad (20.1)$$

The sum spans occupied and unoccupied states i and j, $\boldsymbol{D}$ is the dipole operator related to the perturbation, and the delta ensures that a peak will occur when the incoming photon energy $\hbar\omega$ resonates with the energy difference $E_j - E_i$. If the matrix elements $\langle i|\boldsymbol{D}|j\rangle$ are assumed to be constant, it is clear that the optical spectrum is proportional to the joint density of states. Equation (20.1) is, of course, general to all systems. In the case of surfaces, however, the optical absorption can show peaks or shoulders arising from transitions between (Fig. 20.1) (a) true surface states, (b) bulk states, (c) surface resonances, or, indeed, combinations of these, with the peak intensity being determined by the appropriate matrix element. As surface states can lie inside the bulk gap, it is clear that the onset of optical transitions can occur at a lower energy than for the bulk material.

One major problem with using optical probes to study surfaces, however, is sensitivity. Indeed, the penetration depth of light is quite large—about 10 nm for photon energies between 2 and 4 eV in GaAs. Hence, whereas electron spectroscopies are naturally surface sensitive, optical methods are much more sensitive to the bulk. In order to circumvent this issue, techniques have been developed that allow information about the surface optical response to be extracted. Two such techniques are reflectance anisotropy spectroscopy (RAS), developed independently by *Aspnes* [20.2] and *Berkovits* et al. [20.3] in 1985, and surface differential reflectance spectroscopy (SDRS), used by *Chiarotti* et al. [20.4] for the first time in 1968 to study the Ge(111) surface—the first evidence of optical transitions involving surface states.

In RAS experiments, the difference in reflectivity for light polarized along two perpendicular directions

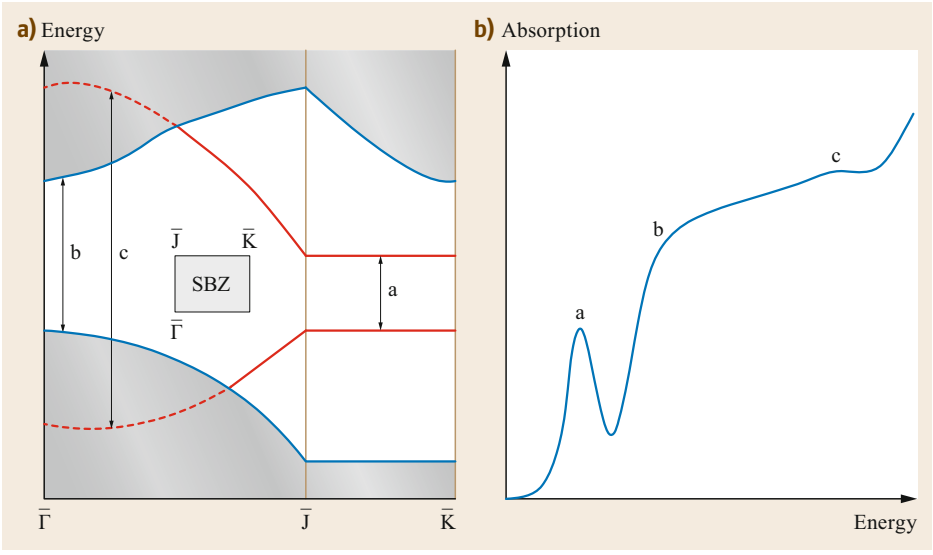

Fig. 20.1a,b Relationship between **(a)** the surface electronic band structure and **(b)** optical absorption due to typical interband transitions. Illustrated are transitions between true surface states a, projected bulk states b, and surface resonances c, respectively. SBZ denotes the surface Brillouin zone

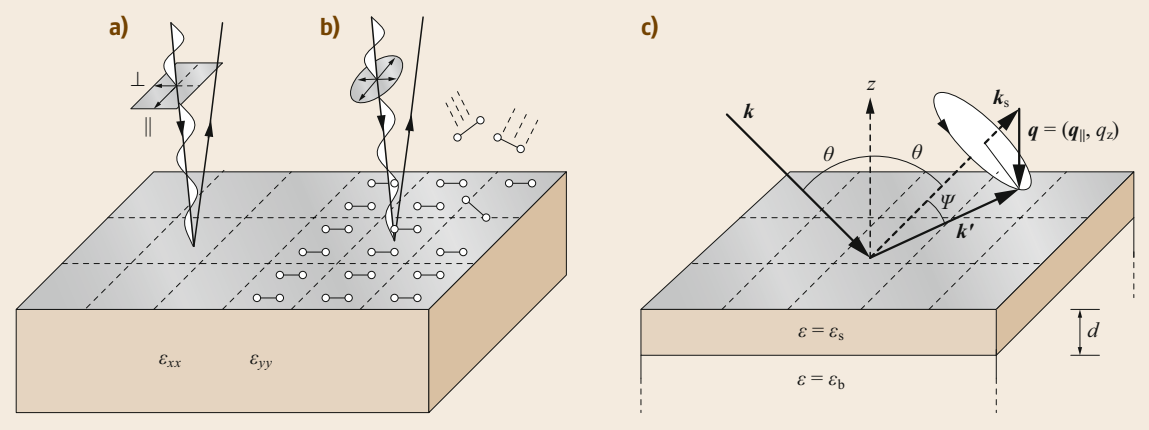

Fig. 20.2a–c Surface-sensitive optical and electronic spectroscopies. **(a)** Reflectance anisotropy spectroscopy (RAS). **(b)** Surface differential reflectance spectroscopy (SDRS). **(c)** Reflection/high-resolution electron energy-loss spectroscopy (REELS/HREELS). The surface response is represented by an anisotropic dielectric function **(a,b)** or an isotropic, three-layer model **(c)**

in the surface plane (x and y, usually parallel and perpendicular to the principal surface axes (Fig. 20.2a)) is measured. If the volume (bulk) is optically isotropic (e.g., in cubic materials), any observed signal must be due to the surface. As we will show later, such anisotropic signals are due to interband transitions involving states localized at, or modified by, the surface geometry. In the standard setup, RAS probes interband transitions in the 1.5−5.0 eV range, although this can be extended to the mid-IR and UV, and is thus sensitive to the full range of surface-derived transitions in semiconductors and insulators. For a recent review see [20.5, 6].

SDRS instead is based on measuring the change in reflectance due to chemical modification or deliberate contamination of the surface layer, typically via chemisorption of oxygen or hydrogen (Fig. 20.2b). Adsorption passivates (removes) the surface electronic states, thus modifying the optical response from the surface. Instead, the bulk response is unchanged and can thus be eliminated by measuring the reflectance change. SDRS is sensitive to *all* surface interband transitions, not only the anisotropic ones. It can easily measure transitions at low energies (≈ 0.5 eV). See [20.7] for a classic review and [20.8] for a modern application.

First-principles computation of interband transitions probed by these two spectroscopies are the main focus of this chapter. On the theoretical side (for some reviews, see [20.9–12]), simulation of RAS and SDRS has progressed beyond early dipole models and tight binding calculations and is nowadays capable of truly predictive analysis of experimental spectra based on first-principles atomistic simulations. Although other optical techniques exist that also probe interband transitions such as spectroscopic ellipsometry (SE) and nonlinear techniques such as surface second harmonic generation (SSHG) [20.1], we do not discuss them here, as they have been less studied at the ab-initio level (although progress is being made [20.13]). Interband transitions can also be probed by electron spectroscopies; the electric field associated with an electron beam impinging on a surface can induce interband excitations in a region well localized at the surface, with the resulting energy-loss function linked to the same response functions involved in the optical processes. In particular, reflection/high-resolution electron energy-loss spectroscopy (REELS/HREELS, Fig. 20.2c) can yield information that is complementary to that obtained with RAS or SDRS, and will also be considered here.

The chapter is organized as follows. Section 20.2 will introduce the theoretical framework for describing the response of a surface to photonic and electronic probes, respectively. The semi-infinite crystal surface itself will be modeled using a slab approximation, which allows the structure of the outer surface planes to differ from the geometry of the bulk planes. The microscopic slab polarizability α_s, together with the dielectric function of the underlying bulk material ε_b, will then be connected to the macroscopic (observable) RAS and SDRS signals in Sect. 20.2.1, and to the HREELS signal in Sect. 20.2.5.

Section 20.3 will discuss state-of-the-art ab-initio theoretical methods that allow the main microscopic ingredients, α_s and ε_b, to be calculated using quantum mechanical simulations. The basic framework for all atomistic simulations will be density functional theory (DFT), which is frequently used to compute the interband optical response in an independent particle (IP)

approximation. The effects of electron–electron interaction in the study of pair and collective excitations are addressed through many-body Green's function techniques and adequately approximated descriptions beyond the one-particle scheme. This is summarized in terms of single-particle excitations in Sect. 20.3.2 and two-particle excitations in Sect. 20.3.3. These methods constitute the state-of-the-art approach to calculate in an ab-initio framework the electronic and optical properties of materials beyond the mean-field DFT but including the so-called many-body effects (such as self-energy, local-field, and excitonic effects), allowing to improve the comparison with the experimental data and the predictive value of the simulations [20.11]. Section 20.3.4 shines a brief spotlight on an alternative way to include these effects by extending the capabilities of the DFT average-field approach to the description of excited states in the presence of a time-dependent perturbation: the time-dependent density functional theory (TDDFT).

Sections 20.4 and 20.5 will present examples of RAS, SDRS, and HREELS calculations performed mostly at the independent-particle level and applied to a range of clean and modified surfaces, respectively. In each case, we will show how atomistic simulations allow the surface spectra measured to be interpreted in terms of specific interband transitions linked to the surface geometry and the related electronic states. We will consider only semiconductor surfaces. Here, large rearrangements of the bonding geometry in the outermost layers occur, which allow the surfaces to stabilize energetically. In particular, the formation of dimers and their involvement in the interband transitions will be considered in Sects. 20.4.1 and 20.4.2. The influence of steps and defects, i.e., typical features of real surfaces, are briefly discussed in Sects. 20.4.3 and 20.4.4. Changes in the optical properties due to adsorption of atoms and molecules, and adlayer formation, will be discussed in Sect. 20.5. Although metal surfaces also show distinct interband peaks in their optical spectra, the major features are due to bulk dispersive effects, plasmons, and intraband transitions, which lie outside the scope of this chapter (see, instead, Chaps. 17 and 18). Nonetheless, theoretical studies of RAS/SDRS can be found for systems based on metal surfaces and ordered adsorbates such as Ag(111):Si [20.14], Ag(110) [20.15, 16], Cu(110) [20.16, 17], and Cu(110):CO [20.18].

Section 20.6 will discuss cases where it is strictly necessary to include correlation, excitonic, and local field effects well beyond a simple description in terms of a joint local density of states picture. Calculations of RAS and SDRS based on many-body Green's functions (Sect. 20.6.1) and TDDFT (Sect. 20.6.2) will show how the simple picture of electronic interband transitions begins to break down, especially where strongly bound excitons are present as on the C(100) surface (Sect. 20.6.3).

Finally, in Sect. 20.7 we will provide a glimpse of present and future challenges in the field and present some cases that are still open.

20.2 Theory of Surface Spectroscopy

In this section we establish the general phenomenological description of RAS, SDRS, and HREELS in terms of the surface and bulk dielectric functions. The recipe for the actual microscopic computation procedure that provides the link with surface interband transitions will be given in Sect. 20.3. We will not attempt to give an exhaustive account of the theory: for this, we refer the reader to the classic overview by *Del Sole* [20.19].

20.2.1 Surface Response Function

The reflected light from a surface carries information both on the surface and on the bulk, as the light wavelength in the infrared (IR), visible and near-UV regions is much larger than the surface reconstruction characteristic length usually involving only few atomic layers. Thus, the atomic reconstruction and electronic properties of surfaces by light reflectance can be investigated, depending on the ability to identify and to separate surface and bulk contributions. To this aim the surface sensitivity is achieved by measuring differences between signals, to enhance the surface contribution with respect to the bulk.

Classical electrodynamics provides the description of reflection and refraction laws at the abrupt interface between vacuum and a continuous dispersive medium of dielectric function $\epsilon(\omega)$, through the matching of the parallel component of the electric field $\boldsymbol{E}$ and of the perpendicular component of the electric displacement field $\boldsymbol{D}$. Neglecting spatial dispersion, $\boldsymbol{D}(\omega) = \epsilon(\omega)\boldsymbol{E}(\omega)$. The Fresnel equations give the reflectivities when the electric field vector is parallel to the plane of incidence (p-polarization),

$$R_{\mathrm{p}} = \frac{\epsilon(\omega)q_z - q'_z}{\epsilon(\omega)q_z + q'_z} \qquad (20.2)$$

and perpendicular (s-polarization)

$$R_s = \frac{q_z - q_z'}{q_z + q_z'} , \tag{20.3}$$

where q_z and q_z' are the components perpendicular to the surface of the light wavevector in vacuum and in the bulk, respectively.

A fully microscopic model must take into account the local dependence of $\boldsymbol{D}(\boldsymbol{r}, \omega)$, and $\boldsymbol{E}(\boldsymbol{r}, \omega)$,

$$\boldsymbol{D}_\alpha(\boldsymbol{r}, \omega) = \sum_\beta \int \mathrm{d}^3\boldsymbol{r}' \epsilon_{\alpha\beta}(\boldsymbol{r}, \boldsymbol{r}'; \omega) \boldsymbol{E}_\beta(\boldsymbol{r}', \omega) . \tag{20.4}$$

where α and β label the cartesian coordinates and $\epsilon_{\alpha\beta}(\boldsymbol{r}, \boldsymbol{r}'; \omega)$ is the microscopic dielectric matrix of the whole vacuum–surface system and interface. In the case of homogeneous systems, $\epsilon_{\alpha\beta}(\boldsymbol{r}, \boldsymbol{r}'; \omega) \approx \epsilon_{\alpha\beta}(|\boldsymbol{r} - \boldsymbol{r}'|; \omega)$ and (20.4) simplifies if the wavelength of the electric field $\boldsymbol{E}_\beta(\boldsymbol{r}', \omega)$ is large in the region where the microscopic dielectric function is nonvanishing, because $|\boldsymbol{r}' - \boldsymbol{r}|$ is of the order of some Å. Then the relation becomes local

$$\boldsymbol{D}_\alpha(\boldsymbol{r}, \omega) = \sum_\beta \epsilon_{\alpha\beta}(\omega) \boldsymbol{E}_\beta(\boldsymbol{r}, \omega) \tag{20.5}$$

and the dielectric tensor components

$$\epsilon_{\alpha\beta}(\omega) = \int \mathrm{d}^3\boldsymbol{r}' \epsilon_{\alpha\beta}(|\boldsymbol{r} - \boldsymbol{r}'|; \omega) \tag{20.6}$$

do not depend on position $\boldsymbol{r}$ because of the overall translational invariance of the crystal at long wavelengths. However, in real crystals, the atomic structure introduces a spatial inhomogeneity in the electron density at a microscopic level. This means that an external spatially constant perturbing field can induce fluctuations on the scale of the interatomic distances in the material, giving rise to additional internal microscopic fields. These are known as *local field effects*, that we can neglect only at a first approximation. It has been shown that local-field effects are important in some cases [20.20, 21]. In crystals with cubic symmetry, the dielectric tensor is diagonal and can be written as $\epsilon_{\alpha\beta}(\omega) = \epsilon(\omega)\delta_{\alpha\beta}$, where the *isotropic dielectric function* $\epsilon(\omega)$ appears.

Even neglecting the local-field effects, the dielectric function at the crystal–vacuum interface is intrinsically nonlocal and inhomogeneous. The dependence of the dielectric response on the coordinate perpendicular to the surface plane (z) should be considered. In the case of a system composed by vacuum for $z < 0$ and a semi-infinite solid for $z \geq 0$, (20.4) can be written for fields with a plane-wave dependence on coordinates and a phase of the form $\exp[\mathrm{i}(q_x x + q_z z - \omega t)]$ (the wavevector lies in the incidence plane xz). The resulting expression is given by

$$D_\alpha(q_x, z; \omega) = \sum_\beta \int \mathrm{d}z' \epsilon_{\alpha\beta}(q_x, z, z'; \omega) \times E_\beta(q_x, z'; \omega) , \tag{20.7}$$

which is valid in the long-wavelength limit $q_x \to 0$. In this case, the q_x-dependence can be omitted, and $\epsilon_{\alpha\beta}(z, z'; \omega)$ in this limit is a *macroscopic* nonlocal dielectric tensor (with the dimension of the inverse of a length) that describes the dielectric response of a medium nonuniform in the z-direction and, in principle, includes all nonlocal corrections in the normal plane in the long-wavelength limit.

The first attempt to solve Maxwell's equations for a realistic macroscopic model of a surface was done by *McIntyre* and *Aspnes* [20.22], where a surface layer of thickness d of a few Å, with a dielectric constant ϵ_s, was put in between the vacuum and a bulk region, with $\epsilon_v = 1$ and $\epsilon_b(\omega)$, respectively, and neglecting the surface anisotropy and nonlocality. The inhomogeneity was approximated by an abrupt step in both boundaries. The corrections to the Fresnel expressions at first order in $(\omega/c)d$, for $\Delta R_s(\omega)/R_s(\omega)$ and $\Delta R_p(\omega)/R_p(\omega)$ were found. They reduce to a simple expression that is the same for both cases when the incident angle is $\theta = 0°$ (normal incidence)

$$\frac{\Delta R_{s,p}(\omega)}{R_{s,p}(\omega)} = \frac{4\omega d}{c} \operatorname{Im}\left\{\frac{\epsilon_s(\omega) - \epsilon_b(\omega)}{\epsilon_b(\omega) - 1}\right\} . \tag{20.8}$$

The general formulae at $\theta \neq 0$ are not reported here, but this *three-layer model* was widely used at that time to interpret spectra and appeared to fail for high θ values, especially at grazing incidence.

In 1979, *Bagchi* et al. [20.23] developed a perturbation procedure to consider the variations in the vicinity of the surface. In their model, the bulk was assumed to be local, while the surface response was anisotropic with respect to the zz-component of the dielectric tensor. Employing a jellium model for the half-space $z > 0$, the field components are not continuous at the interface except for E_x, E_y and D_z, which are continuous functions and can be perturbatively calculated. The Fresnel formulae for the reflectivity for both s- and p-polarized light were given for the thickness of the surface $d \ll \lambda$.

Later on, *Del Sole* [20.24] found two general expressions of the corrections to Fresnel formulae for large anisotropies allowing in-plane anisotropy. They

can describe real crystals. In the case of s-polarized light, Del Sole obtained

$$\frac{\Delta R_{\mathrm{s}}(\omega)}{R_{\mathrm{s}}(\omega)} = \frac{4\omega}{c}\cos\theta\ \mathrm{Im}\left\{\frac{\Lambda_{yy}(\omega)}{\epsilon_{\mathrm{b}}(\omega)-1}\right\}, \tag{20.9}$$

while for p-polarization

$$\frac{\Delta R_{\mathrm{p}}(\omega)}{R_{\mathrm{p}}(\omega)} = \frac{4\omega}{c}\cos\theta \times \mathrm{Im}\left\{\frac{\left[\epsilon_{\mathrm{b}}(\omega)-\sin^2\theta\right]}{\left[\epsilon_{\mathrm{b}}(\omega)-1\right]}\frac{\Lambda_{xx}(\omega)+\epsilon_{\mathrm{b}}^2(\omega)\sin^2\theta\Lambda_{zz}(\omega)}{\left[\epsilon_{\mathrm{b}}(\omega)\cos^2\theta-\sin^2\theta\right]}\right\}; \tag{20.10}$$

$\Lambda_{ij}(\omega)$ (where i and j can be the Cartesian indices x, y), and $\Lambda_{zz}(\omega)$ are averaged response functions that account for nonlocal surface contributions and are given by [20.24]

$$\Lambda_{ij}(\omega) = \int \mathrm{d}z \int \mathrm{d}z' \left[\epsilon_{ij}(z,z';\omega) - \delta_{ij}\delta(z-z')\epsilon_0(z;\omega)\right] - \int \mathrm{d}z \int \mathrm{d}z' \int \mathrm{d}z'' \int \mathrm{d}z''' \epsilon_{iz}(z,z';\omega) \times \epsilon_{zz}^{-1}(z',z'';\omega)\epsilon_{zi}(z'',z''';\omega) \tag{20.11}$$

and

$$\Lambda_{zz}(\omega) = \int \mathrm{d}z \int \mathrm{d}z' \left[\epsilon_{zz}^{-1}(z,z';\omega) - \delta(z-z')\epsilon_0^{-1}(z;\omega)\right], \tag{20.12}$$

where

$$\epsilon_0(z;\omega) = \theta(z)\epsilon_{\mathrm{b}}(\omega) + \theta(-z) \tag{20.13}$$

is the *abrupt* interface dielectric function of the bulk plus the vacuum. The inverse kernel $\epsilon_{zz}^{-1}(z,z';\omega)$ is defined by

$$\int \mathrm{d}z''\epsilon_{zz}(z,z'';\omega)\epsilon_{zz}^{-1}(z'',z';\omega) = \delta(z-z')\,. \tag{20.14}$$

All these surface response functions $\Lambda_{\alpha\beta}(\omega)$ have the dimensions of length as they are multiple integrals of the dielectric tensor $\epsilon_{\alpha\beta}(z,z'';\omega)$. We remark that only longitudinal (diagonal) components appear in (20.9) and (20.10), as the quantities Λ_{xy} and Λ_{yx} will be present only in the second-order mixing terms of s and p light.

In principle, (20.11) and (20.12) can include all many-body and local-field effects [20.25].

20.2.2 Connection with Experiment

As mentioned in the introduction, the surface response functions can be probed experimentally by a variety of experimental techniques. Surface differential reflectance spectroscopy (SDRS), also abbreviated to SDR and DRS, is based on measuring the change in reflectance after a chemical modification of the surface (typically the deposition of a layer of oxygen or hydrogen) quenches the specific features coming from surface bands and the clean surface reconstructions: $\mathrm{SDRS} = (R_{\mathrm{oxidized}} - R_{\mathrm{clean}})/R_{\mathrm{clean}}$. In terms of the modified Fresnel reflectivities, this is written as

$$\frac{\Delta R_{\mu}(\omega)}{R_{\mu}(\omega)} = \left(\frac{\Delta R_{\mu}(\omega)}{R_{\mu}(\omega)}\right)_{\mathrm{clean}} - \left(\frac{\Delta R_{\mu}(\omega)}{R_{\mu}(\omega)}\right)_{\mathrm{modified}}. \tag{20.15}$$

Here, μ denotes s or p light polarization. By taking the reflectance difference, the unmodified bulk contribution cancels out, and any observed signal should be related to the surface modification. The percentage difference of the spectra is related to the surface structure of the clean surface and to the surface electronic state sensitivity upon adsorption.

Reflectance anisotropy spectroscopy (RAS), also known as reflectance difference spectroscopy (RDS), measures the difference in reflectance by a change of the linear polarization of light between two principal axes (x and y) along the surface. For cubic crystals, the bulk optical response is isotropic, and any observed reflectance anisotropy should be related to the break of symmetry of the surface region or from nonlinear effects. The latter are usually small, although measurable, and can be neglected in a typical RAS measurement. For crystals with uniaxial symmetry, like wurtzite, RAS can be applied when the surface normal is parallel to the c-axis. The RAS technique has some advantages over SDRS, since it does not need a reference system where the structural surface features are assumed to be canceled in a uniform and isotropical way. It has been used to follow in situ the epitaxial growth to verify the layer by layer deposition [20.26–28]. Interpretation of the RAS signal is also simpler, since only the knowledge of the atomic structure of the clean surface is necessary. RAS experimental setups measure the polarization state of the reflected light,

$$\frac{\Delta\tilde{r}}{\tilde{r}} = \frac{\tilde{r}_x - \tilde{r}_y}{(\tilde{r}_x + \tilde{r}_y)/2}\,, \tag{20.16}$$

where $\tilde{r}_\alpha = [\Delta R_\alpha(\omega)/R_\alpha(\omega)]_{\mathrm{clean}}$, for light polarized along the α axis. The RAS signal is commonly given in terms of the reflectance $\Delta R/R$ or of the complex

Fresnel reflectivities $\Delta\tilde{r}/\tilde{r}$. The latter is usually used for setups where both real and imaginary parts can be measured. The two quantities are related, and for small amplitudes the relation is $\Delta R/R = 2\,\mathrm{Re}\,\Delta\tilde{r}/\tilde{r}$.

The previous description is based on a general dielectric model that accounts for all possible effects of nonlocal field corrections and anisotropy through the explicit dependence of the function $\Lambda_{\alpha\beta}(\omega)$ on $\epsilon_{\alpha\beta}(z,z',\omega)$ and its inverse. From an explicit form of these ingredients we could calculate directly, for instance, the difference between (20.9) and (20.10). Conversely, we could fit the functions $\Lambda_{\alpha\beta}(\omega)$ from the experimental RAS and SDRS signals themselves [20.29, 30]. For instance, in the case of normal incidence, we can write the RAS signal as

$$\frac{\Delta R}{R} = \frac{4\omega}{c}\,\mathrm{Im}\left\{\frac{\Lambda_{yy}(\omega)-\Lambda_{xx}(\omega)}{\epsilon_\mathrm{b}(\omega)-1}\right\}. \tag{20.17}$$

Since $\Lambda_{yy}(\omega)-\Lambda_{xx}(\omega)$ can be written as a length d multiplied by the difference of two effective complex dielectric susceptibilities at surfaces, $\Delta\epsilon_{\mathrm{s,eff}}(\omega) = \Delta\epsilon'_{\mathrm{s,eff}}(\omega) + \mathrm{i}\Delta\epsilon''_{\mathrm{s,eff}}(\omega)$, and $\epsilon_\mathrm{b}(\omega)$ is also complex, we can write

$$\frac{\Delta R}{R} = \frac{4\omega d}{c}\left[A(\omega)\Delta\epsilon''_{\mathrm{s,eff}}(\omega) - B(\omega)\Delta\epsilon'_{\mathrm{s,eff}}(\omega)\right], \tag{20.18}$$

where

$$A(\omega) = \frac{\epsilon'_\mathrm{b}-1}{(1-\epsilon'_\mathrm{b})^2+(\epsilon''_\mathrm{b})^2},$$
$$B(\omega) = \frac{\epsilon''_\mathrm{b}}{(1-\epsilon'_\mathrm{b})^2+(\epsilon''_\mathrm{b})^2} \tag{20.19}$$

are functions that depend only on the bulk substrate. Thus, the surface and the bulk contribution can be identified in particular conditions [20.29].

20.2.3 Slab Approximation

If we possess a microscopic quantum description of the electronic structure of the semi-infinite crystal, we can obtain, in principle, its response functions and make a comparison with the experimental results. However, identification of the proper ingredients at the level of the phenomenological description developed above (at an appropriate level of approximation) is a heavy task to perform. The electronic properties of a semi-infinite crystal, occupying a half-space $z>0$, are difficult to treat in practice [20.31], and it is simpler to describe the surface and bulk with a stack of a finite but sufficient number of atomic planes embedded in a vacuum region. The slab of atomic planes has a surface periodicity that is determined by the surface reconstruction, if present. A vacuum region with a thickness comparable to that of the atomic slab is added. This structure can be periodically repeated to obtain a 3-D (three-dimensional) periodic structure thereby accessible to the software tools designed for 3-D crystal band structures (even if large unit cells are necessary). The unit cell (supercell) has the 2-D (two-dimensional) surface cell of the surface with area A as its basis and a height L equal to the slab thickness plus the width of the vacuum region. Many phenomena in surfaces are relatively short range in nature, so that the surface region d_s where the system differs with respect to the bulk is restricted to a few atomic planes and is, indeed, much less than L. The number of atomic layers that are used in a slab calculation can vary from 10 to 30, depending on the surface, its reconstruction, and the phenomena to be described. Nonetheless, any calculation has to be tested for convergence with respect to the number of atomic planes and the total thickness of the unit cell.

The quantities Λ_{yy} and Λ_{xx} that appear in (20.9) and (20.10) are the only ingredients required at $\theta = 0$, and they can be interpreted in terms of the polarizability that can be obtained from a slab calculation. To do this, we consider the first term in (20.11), as in most cases, the second term with four integrations does not give relevant contributions. For an interface between semi-infinite vacuum and bulk, we have

$$\Lambda_{ij}(\omega) = \int_{-\infty}^{\infty}\mathrm{d}z\int_{-\infty}^{\infty}\mathrm{d}z'[\epsilon_{ij}(z,z';\omega) - \delta_{ij}\delta(z-z')\epsilon_0(z;\omega)]\,. \tag{20.20}$$

We can put $i=j=(x,y)$ and observe that the upper limit in the first integration can be limited to a value d, with $d>0$ and also $d>d_\mathrm{s}$

$$\Lambda_{ii}(\omega) = \int_{-\infty}^{d}\mathrm{d}z\int_{-\infty}^{\infty}\mathrm{d}z'[\epsilon_{ii}(z,z';\omega)-\delta(z-z')] - [\epsilon_\mathrm{b}(\omega)-1]d\,. \tag{20.21}$$

Figure 20.3 describes the matching of the semi-infinite model with the microscopic slab calculation. If d is sufficiently larger than the thickness of the surface region d_s, where some difference between the electronic structures of the semi-infinite crystal and the bulk are present, the difference does not depend on the value of d, and it converges rapidly to a fixed value. We notice, however, that the second term has some uncertainty in

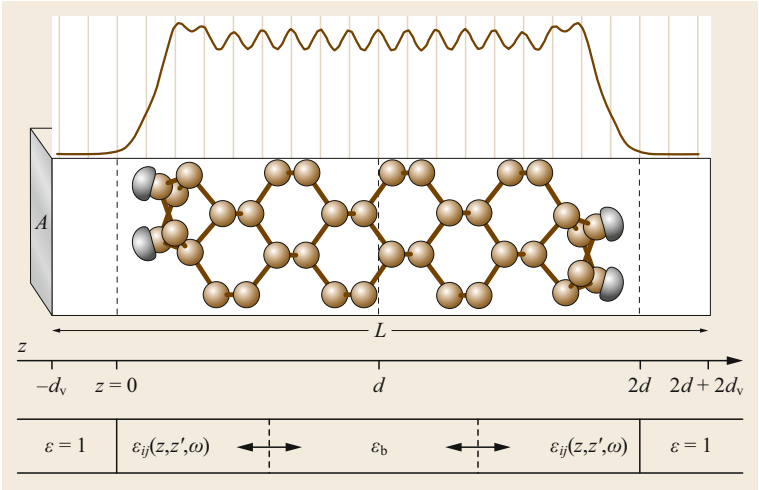

Fig. 20.3 Schematic of the bulk–surface–vacuum interfaces and the corresponding atomic slab. In the *upper part* of the figure, a slab of 16 atomic planes presenting surface reconstruction at the two sides is shown with atomic positions and sketches of the surface states of dangling bond type. The slab is confined by vacuum regions, and the whole is inside a repeated cell of thickness L, to recover 3-D periodicity. The electron charge density obtained from the valence states, laterally integrated, as a function of z, is also shown, and we can see the partial spilling of charge into the vacuum at the two surfaces. In the *lower part* of the figure, the ingredients of the phenomenological model are shown. The boundaries between the regions where the surface response functions match the bulk ones are mobile, as indicated by the *arrows*

the phenomenological model because the semi-infinite bulk has a cut plane located at some arbitrary $z=0$, not well defined with respect to the last atomic positions at the surface (Fig. 20.3).

Using a repeated slab calculation, we can identify the lower integration limit $(-\infty)$ with $z=-d_v$, the *midpoint* of the vacuum region; $z=0$ is the coordinate of the ideal surface plane in the abrupt interface plane (rather arbitrary); and $z=d$ is the middle of the slab. Thus, the supercell has $L=2d+2d_v$, and we can evaluate (20.21) as

$$\Lambda_{ii}^{hs}(\omega)=4\pi\alpha_{ii}^{hs}(\omega)-(\epsilon_b-1)d\,, \qquad (20.22)$$

where $i=x,y$ and α_{ii}^{hs} is the half-slab polarizability

$$4\pi\alpha_{ii}^{hs}(\omega)=\int_{-d_v}^{d}dz\int_{-d_v}^{2d+d_v}dz'[\epsilon_{ii}(z,z';\omega)-\delta(z-z')]\,. \qquad (20.23)$$

The half-slab polarizability can be directly calculated in an independent-particle scheme or including the electron–electron interaction from a many-body perturbative approach. For nonsymmetric slabs (where front and back surfaces are not equivalent), the half-slab polarizability for one surface can be extracted using a real-space cut function [20.32].

20.2.4 Independent Particle Response

In order to express $\alpha_{ii}^{hs}(\omega)$ in terms of independent particle or quasiparticle energies and wavefunctions, we have to use the RPA (random-phase approximation) without the local-field effects (Sect. 20.3.1) form of the imaginary part of the slab polarizability that is related by time-dependent perturbation theory to the transition probability induced by the radiation between the slab eigenstates [20.33]

$$\mathrm{Im}\left\{4\pi\alpha_{ii}^{hs}(\omega)\right\}=\frac{4\pi^2e^2}{m^2\omega^2A}\sum_{\boldsymbol{k}}\sum_{v,c}|p_{vc,k}^{i}|^2 \times\delta(E_c(\boldsymbol{k})-E_v(\boldsymbol{k})-\hbar\omega)\,. \qquad (20.24)$$

Here, $p_{vc,k}^{i}$ is the matrix element of the i-th Cartesian component of the momentum between valence and conduction states at a given $\boldsymbol{k}$; the sum over $\boldsymbol{k}$ is over the 2-D surface Brillouin zone; and $E_c(\boldsymbol{k})$ and $E_v(\boldsymbol{k})$ are the energies of the single/quasiparticle states involved in the transition between valence and conduction bands. A factor of 2 due to the spin degeneracy of the bands is compensated by the division by 2 of the half-slab evaluation of these diagonal (xx) and (yy) terms. The imaginary part can be used to obtain $\mathrm{Re}[4\pi\alpha_{ii}^{hs}(\omega)]$ through the Kramers–Kronig relations. To be consistent, the quantity $\epsilon_b(\omega)$ that appears in (20.22) and in (20.9) and (20.10) should be calculated at the same lev-

els of approximation from the long-wavelength limit of the RPA bulk dielectric function, computing the imaginary part and then deriving the real part. These are thus truly *microscopic* versions of the response functions, without including local-field effects.

In summary, therefore, the functions $4\pi\alpha_{ii}^{\mathrm{hs}}(\omega)$ for the half-slab are thus evaluated at a first-level approximation in the RPA-independent particle (IP) scheme, using a Kohn–Sham picture (as particles seeing the same effective field), or in an independent quasiparticle (IQP) picture (as quasiparticles moving in a nonlocal and state-dependent potential). Having obtained $4\pi\alpha_{ii}^{\mathrm{hs}}(\omega)$, one can then use (20.22) and finally use the appropriate explicit expressions of relative reflectances.

Note that the use in (20.24) of self-consistent energy eigenvalues and eigenvalues coming from the Kohn–Sham equations of DFT or from a self-energy equation, coupled with the RPA approximation for the polarizability, is a particular choice. In practical studies, surface dielectric properties are often computed in this way. The framework can be extended to include local-field corrections and other many-body corrections with respect to the self-energy, as we will show in Sect. 20.3; however, this comes with a high computational cost. Nevertheless, the IP approach can very often offer a reasonably good interpretation of the experimental data in terms of surface interband transitions, as Sects. 20.4 and 20.5 will show.

20.2.5 Electron Energy-Loss Spectroscopy

Electron energy-loss spectroscopy (EELS) is a powerful and versatile technique for characterizing materials across a wide range of excitations. When used in a reflection geometry, with incident electrons in the 1−10 eV range, the technique is known as reflection or high-resolution electron energy-loss spectroscopy (REELS/HREELS) and is sensitive to surface excitations, including interband transitions [20.34]. In fact, HREELS can be used to probe the surface anisotropic response in the visible–UV range in a manner complementary to RAS but with a much higher sensitivity (by two orders of magnitude) [20.35, 36].

According to standard dipole scattering theory, the electron scattering probability is given by the product of a kinematic term and the surface loss term [20.37],

$$P(\boldsymbol{q}_\parallel,\omega) = 2\left(\frac{me}{\hbar^2\pi}\right)^2 \frac{1}{\cos\varphi_\mathrm{i}}\frac{k'}{k}\frac{q_\parallel}{|q_\parallel^2+q_\perp^2|^2} \times \mathrm{Im}\, g(\boldsymbol{q}_\parallel,\omega)\,, \tag{20.25}$$

where $\boldsymbol{k}$ and $\boldsymbol{k}'$ are the wavevectors of the incident and scattered electrons, such that $\boldsymbol{q}_\parallel = \boldsymbol{k}_\parallel - \boldsymbol{k}'_\parallel$ and $q_\perp = k_\perp - k'_\perp$ are the transferred momenta parallel and perpendicular to the surface. The energy transfer is $\hbar\omega = \hbar^2[k^2 - k'^2]/2m$. The surface loss function itself can be expressed in terms of an *effective* dielectric function $\epsilon_{\mathrm{eff}}(q_\parallel,\omega)$, which takes into account all surface and bulk excitations

$$\mathrm{Im}\{g(\omega)\} = \mathrm{Im}\left\{\frac{-2}{1+\epsilon_{\mathrm{eff}}(q_\parallel,\omega)}\right\}. \tag{20.26}$$

Within a simple picture of a semi-infinite bulk crystal, this expression, inverted, reduces to a simple average of the bulk ($\epsilon_{\mathrm{eff}} = \epsilon_\mathrm{b}$) and vacuum ($\epsilon_\mathrm{v} = 1$) response function.

Assuming the more realistic picture of an anisotropic surface layer of the dielectric tensor $\epsilon_\mathrm{s} = \mathrm{diag}(\epsilon_{\mathrm{sx}}, \epsilon_{\mathrm{sy}}, \epsilon_{\mathrm{sz}})$, lying atop an anisotropic (cubic) bulk (three-layer model), the effective dielectric function can be written as [20.38, 39]

$$\epsilon_{\mathrm{eff}}(q_\parallel,\omega) = \epsilon_\mathrm{s}\frac{\epsilon_\mathrm{s}+\epsilon_\mathrm{b}+(\epsilon_\mathrm{b}-\epsilon_\mathrm{s})\mathrm{e}^{-2q_\parallel d\sqrt{\epsilon_{\mathrm{sx}}/\epsilon_{\mathrm{sz}}}}}{\epsilon_\mathrm{s}+\epsilon_\mathrm{b}-(\epsilon_\mathrm{b}-\epsilon_\mathrm{s})\mathrm{e}^{-2q_\parallel d\sqrt{\epsilon_{\mathrm{sx}}/\epsilon_{\mathrm{sz}}}}}\,, \tag{20.27}$$

where $\epsilon_\mathrm{s} = \sqrt{\epsilon_{\mathrm{sx}}\epsilon_{\mathrm{sz}}}$ is the geometric mean and ϵ_b the dielectric function of the bulk. The appropriate expressions for an anisotropic bulk response (e.g., for II-VI wurtzite surfaces) have been derived by *Esquivel-Sirvent and Noguez* [20.40].

The connection to the surface interband transitions can be more clearly seen by considering the well-known limit of (20.27) when $q_\parallel d \ll 1$[20.37, 38]

$$\epsilon_{\mathrm{eff}}(q_\parallel,\omega) \simeq \epsilon_\mathrm{b} + q_\parallel d\left(\epsilon_{\mathrm{sx}} - \frac{\epsilon_\mathrm{b}^2}{\epsilon_{\mathrm{sz}}}\right). \tag{20.28}$$

Clearly for $q_\parallel \to 0$ or $d \to 0$, $\epsilon_{\mathrm{eff}}(q_\parallel,\omega)$ tends to ϵ_b; for very large $q_\parallel$, $\epsilon_{\mathrm{eff}}(q_\parallel,\omega)$ can be shown to tend to ϵ_s. Thus, the HREELS signal contains terms ultimately proportional to $\mathrm{Im}\{\epsilon_{\mathrm{sx}}\}$ and/or $\mathrm{Im}\{\epsilon_\mathrm{b}\}$, which can be resolved experimentally under the appropriate kinematic conditions or computed using a three-layer model.

In practical calculations, the optical dielectric functions ($q \to 0$) are often used where the experimental momentum transfer is small [20.39]. A theoretical scheme for computing HREELS spectra beyond the three-layer model, including nonlocality and full q-dependence, is given in [20.41].

20.3 Ab-initio Approach

The theoretical framework developed in the previous section is quite general and can be applied to phenomenological or (semi-)empirical descriptions of the surface dielectric response. In this section, we focus on state-of-the-art ab-initio approaches that allow parameter-free and quantitatively correct calculations of surface interband excitations. Although the simple band picture of interband transitions depicted in Fig. 20.1 offers a clear and intuitive explanation of the connection between surface electronic states and optical or energy-loss spectra, the reality is more complicated. Electrons and holes are, after all, *interacting* particles and feel the effects of long and short-range screening by themselves and by other particles in the system.

In the following, we will outline the three-step procedure that will allow us to compute, in an ab-initio framework, the electronic and optical properties of materials beyond mean-field density functional theory and including so-called many-body effects (such as self-energy and excitonic effects). This will allow us to improve the comparison with the experimental data and add truly predictive value to the simulations [20.11]. The steps are:

1. Density functional theory calculation of surface geometry and electronic structure
2. Many-body perturbation theory (Green's function method) to obtain quasiparticle energy bands via the GW approximation
3. Solution of the Bethe–Salpeter equation to describe particle–hole interactions.

This theoretical scheme is quite general and nowadays is applied to systems of different chemical character and dimensionality, from bulk to surfaces, nanostructures, molecules, and organic or hybrid compounds. Figure 20.4 summarizes the various levels of approximation for computing interband excitations that will be considered.

In Sect. 20.6, we will show how the application of the full three-step procedure to several simple semiconducting and insulating surfaces has been of fundamental importance for understanding the exact nature of the optical interband features measured in the experiments. In discussing the calculation of the dielectric properties of a material we will remain quite general, speaking in terms of the macroscopic dielectric function $\epsilon_{\mathrm{M}}(\omega)$. For the case of surfaces, which are the main topic here, the half-slab polarizability $4\pi\alpha_{ii}^{\mathrm{hs}}$ introduced in Sect. 20.2.1 can be obtained by multiplying the macroscopic dielectric function by half the cell thickness. This section will end with an alternative method to the three-step procedure that has become popular in recent years: the time-dependent density functional theory (TDDFT) [20.42].

20.3.1 Density Functional Theory

Density functional theory (DFT) [20.43] in the Kohn–Sham (KS) formalism [20.44] is a very powerful computational approach to predict a wide range of chemical and physical properties of materials of different dimensionality, including surfaces. In their 1964 work [20.43], *Hohenberg* and *Kohn* demonstrated that the ground-state energy of a system of N interacting electrons in an external potential $V_{\mathrm{ext}}(\boldsymbol{r})$ is a functional of the electronic density which is minimized at the true ground state density of the system. In a following paper in 1965 [20.44], *Kohn* and *Sham* reformulated the variational problem of the functional energy minimization in terms of the solution of a set of one-particle self-consistent equations (Kohn–Sham equations)

$$\left[-\frac{1}{2}\nabla^2 + V_{\mathrm{eff}}^{\mathrm{KS}}(\boldsymbol{r})\right]\phi_i(\boldsymbol{r}) = \epsilon_i\phi_i(\boldsymbol{r})\,, \qquad (20.29)$$

where the electron density of the interacting system is reproduced by the sum of the densities of N independent particles described by the Kohn–Sham wavefunctions $n(\boldsymbol{r}) = \sum_i^N |\phi_i(\boldsymbol{r})|^2$, and the effective potential is the sum of the external potential, the Hartree potential,

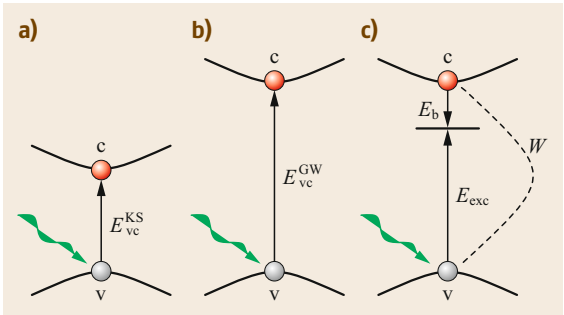

Fig. 20.4a–c Ab-initio approaches for computing interband excitations, in order of increasing difficulty. **(a)** Independent particle approximation (IP) using DFT (Kohn–Sham) energies and wavefunctions. **(b)** Independent quasiparticle approximation (IQP) using GW energies and wavefunctions, which typically opens the DFT band gap and yields higher excitation energies. **(c)** Interacting quasiparticle approximation within the Bethe–Salpeter equation (BSE) approach, allowing formation of bound excitons below the GW gap. Equivalent physical results can also be obtained with TDDFT

and the exchange-correlation (xc) potential: $V_{\rm eff}^{\rm KS}(\boldsymbol{r}) = V_{\rm ext}(\boldsymbol{r}) + V_{\rm H}(\boldsymbol{r}) + V_{\rm xc}(\boldsymbol{r})$. Here, $V_{\rm xc}$ is explicitly defined as the functional derivative with respect to the density of the exchange-correlation energy $E_{\rm xc}[n]$ that is a universal functional of the density and contains, in principle, all the many-body effects, but it is actually the unknown part since the theory does not provide an explicit analytical form of it. Hence, the approximations made to calculate this contribution are of crucial importance for the success of the approach. Most DFT calculations of periodic materials adopt local [20.44] or semilocal [20.45] forms for the exchange-correlation energy.

From the solution of the KS equations it is possible to obtain the ground-state electronic total energy as

$$E_{\rm tot} = \sum_i^N \epsilon_i - \frac{1}{2}\int {\rm d}\boldsymbol{r}'{\rm d}\boldsymbol{r}\frac{n(\boldsymbol{r})n(\boldsymbol{r}')}{|\boldsymbol{r}-\boldsymbol{r}'|} + E_{\rm xc}[n] - \int {\rm d}\boldsymbol{r} V_{\rm xc}(\boldsymbol{r})n(\boldsymbol{r})\,. \tag{20.30}$$

In the Born–Oppenheimer approximation, the ionic contribution can be added to the electronic total energy and, by means of the use of the Hellman–Feynman theorem, the electronic forces on the ions can be calculated. Within such a scheme (and thanks to efficient algorithms) DFT simulations are nowadays used to search for the equilibrium geometry of complex systems such as relaxed or reconstructed surfaces, clean and covered with adsorbates. The outcome of these calculations gives both the equilibrium geometry of the surface, as well as the band structure of the Kohn–Sham equations that can be considered as a first effective picture of the electron bands.

Within this approach, the Kohn–Sham eigenvalues are introduced as Lagrange multipliers, hence, their interpretation as excitation energies of the real system has no theoretical foundation. In fact, their interpretation as electron addition or removal energies leads to the well-known band gap problem of DFT: the electronic band gaps predicted by the theory are typically 30–50% (sometimes even more) smaller than the experimental ones. Nonetheless, KS eigenvalues and wavefunctions are often used as a first approximation in optical properties calculations and used directly in the simple interband picture depicted in Fig. 20.4a and represented by (20.24). As a result, computed spectra are generally redshifted with respect to the experiment. For systems with a gap, this can be corrected using a so-called *scissors* shift Δ that opens the gap, as long as an appropriate renormalization recipe is used [20.46]. The value of the shift can be estimated from GW calculations or used ad hoc. Due to fortuitous cancelations when differences are computed, this approximation (DFT-IP plus scissors) often works well for calculations of RAS and SDRS.

20.3.2 Green's Function Theory—GW

An appropriate theoretical framework for treating electronic excitations is the many-body perturbation theory based on a Green's function formalism. This allows us to improve the description of the electronic charged and neutral excited states and to give reliable predictive results, overcoming the DFT-KS single-particle scheme. In the second quantization formalism, the propagation of an electron added or extracted in an interacting N-electron system is described by the time-ordered single-particle Green's function [20.47]

$$G(1,2) = -{\rm i}\,\langle \Phi_N |\, T(\hat{\psi}_{\rm H}(1)\hat{\psi}_{\rm H}^{\dagger}(2))\,|\Phi_N\rangle\,. \tag{20.31}$$

Here $1 = (x_1, t_1)$ (where t_1 is a time coordinate, while $x_1 = (\sigma_1, \boldsymbol{r}_1)$ indicate the spin and spatial coordinate and a similar definition stands for 2, ...); $|\Phi_N\rangle$ is the ground state of the interacting N-particle system, $\hat{\psi}_{\rm H}, \hat{\psi}_{\rm H}^{\dagger}$ are the field operators in the Heisenberg representation, and T is Wick's time-ordering operator. We here assume that the system is in equilibrium and at zero temperature. For a more extended formulation, we refer to several textbooks [20.47, 48].

In principle, from the knowledge of Green's function, one can calculate the ground-state total energy and the expectation value of any single-particle operator. Moreover, using the so-called Lehman representation of G, it can be shown that its poles in the complex-frequency space correspond to the charged excitation energies of the many-body system [20.48]. Nevertheless, $|\Phi_N\rangle$ being an unknown quantity in an arbitrary interacting N-particle system, (20.31) does not provide a practical way to calculate G and all the related physical quantities. Starting from the equation of motion for G and using its spectral representation, it can be shown that the electronic excitations of the many-body interacting system correspond to the eigenvalues of the so-called quasiparticle (QP) equation, [20.48, 49]

$$\left(-\frac{1}{2}\nabla^2 + V_{\rm ext} + V_{\rm H}\right)\Phi_i^{\rm QP}(x) + \int \Sigma(x,x',\epsilon_i^{\rm QP})\Phi_i^{\rm QP}(x'){\rm d}x' = \epsilon_i^{\rm QP}\Phi_i^{\rm QP}(x)\,, \tag{20.32}$$

where a nonlocal, time-dependent, non-Hermitian operator, the *self-energy* Σ, appears. The self-energy can be thought of as the effective potential that the electron

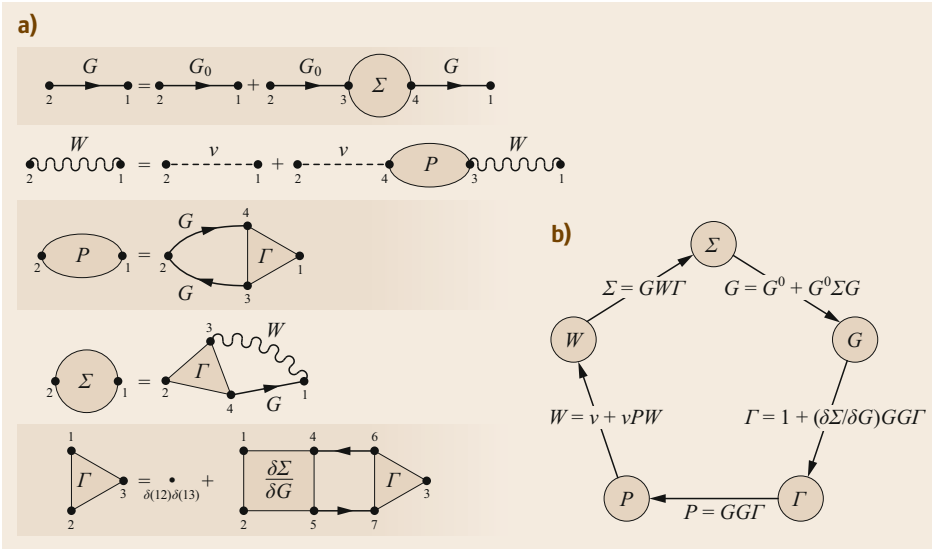

Fig. 20.5 **(a)** The five Hedin equations are written in terms of Feynman diagrams. **(b)** The same equations are represented in the so-called *Hedin's Pentagon*, which illustrates the idea of solving the set of five Hedin equations through an iterative procedure

or the hole added to the system feels due to the change in the charge distribution induced by its own presence. With respect to KS electrons which are completely independent particles, the quasiparticles can be seen as weakly interacting dressed electrons characterized by finite lifetimes which are related to the imaginary part of the complex eigenvalues ϵ_i^{QP} [20.49–51].

Suitable approximation for the self-energy can be found using the so-called *Hedin equations* [20.52], a closed set of equations (Fig. 20.5) that connects the self-energy Σ and the Green's function G to other fundamental functions characterizing the system such as the vertex function Γ, the polarization P, and the screened Coulomb interaction W

$$\Sigma(1,2) = \mathrm{i}\int G(1,3)\Gamma(3,2,4)W(4,1)\mathrm{d}(34)\,, \tag{20.33}$$

$$W(1,2) = v(12) + \int v(13)P(3,4)W(4,2)\mathrm{d}(34)\,, \tag{20.34}$$

$$P(1,2) = -\mathrm{i}\int G(1,3)G(4,1)\Gamma(3,4,2)\mathrm{d}(34)\,, \tag{20.35}$$

$$\Gamma(1,2,3) = \delta(12)\delta(13) + \int \frac{\delta\Sigma(1,2)}{\delta G(4,5)} G(4,6)G(7,5)\Gamma(6,7,3)\mathrm{d}(4567)\,, \tag{20.36}$$

where v is the bare Coulomb interaction. Here, the presence of commas indicates the separate dependence on the different variable sets, while the absence of commas indicates the dependence on the difference of spatial coordinates and times. The symbols d(34) and d(4567) indicate that multiple integrations must be performed on the space coordinates and time and a sum of spin variables must be done for every numerical label.

These equations cannot be solved exactly but are a good starting point for various approximations of Σ. Hedin proposed an iterative solution of these equations starting with $\Sigma = 0$ (this corresponds to the Hartree approximation). This way, at the first iteration step, the vertex function, the polarization, and the self-energy are

$$G = G_0; \quad \Gamma(1,2,3) = \delta(12)\delta(13)\,; \tag{20.37}$$

$$P(1,2) = -iG(1,2)G(2,1);$$
$$\Sigma(1,2) = iG(1,2)W(2,1)\,. \tag{20.38}$$

The Green's function G is computed using the noninteracting particle Green function G_0, and the screening is constructed within the random phase approximation (RPA). In practical calculations, the quasiparticle energies are generally computed in a first-order perturbative scheme, starting from the DFT Kohn–Sham eigenvalues and eigenfunctions. This is the so-called G_0W_0 perturbative approximation of the self-energy. The computation of quasiparticle energies within this approach nowadays represents a sufficiently refined method for band structure calculations of materials [20.53]. A few successful applications of this approach for the QP band structure of insulating and semiconducting surfaces will be discussed in Sect. 20.6, but other examples can be found in the literature. Optical excitations can also be considered at this level by replacing the KS eigenvalues with the GW ones in an appropriate manner [20.54]; such a scheme is depicted in Fig. 20.4b, and examples will appear later in the chapter. Several self-consistent GW schemes have been proposed in the

last years [20.55, 56] but have rarely been applied to surfaces [20.57]. Computationally less expensive, self-consistent GW_0, updating only energies in G, is instead a method often used to estimate the quasiparticle energies also for surfaces [20.58].

20.3.3 The Bethe–Salpeter Equation

The macroscopic dielectric function $\epsilon_{\mathrm{M}}(\omega)$ is the crucial physical quantity that is needed to describe the optical properties of surfaces (and materials in general). It can be obtained at different levels of accuracy in the theoretical ab-initio framework we are describing here, starting from the simplest independent particle (Sects. 20.2.1 and 20.3.1) or quasiparticle approximation (Sect. 20.3.2) up to the inclusion of local-field and excitonic effects by solving the Bethe–Salpeter equation (BSE). First of all, it is worth remembering that $\epsilon_{\mathrm{M}}(\omega)$ is not the simple average of the microscopic quantity but, following the *Adler* and *Wiser* formulation, it is [20.20, 21]

$$\epsilon_{\mathrm{M}}(\omega) = \lim_{\boldsymbol{q}\to\boldsymbol{0}} \frac{1}{\epsilon^{-1}_{\boldsymbol{G}=\boldsymbol{0},\boldsymbol{G}'=\boldsymbol{0}}(\boldsymbol{q},\omega)} \,, \tag{20.39}$$

where $\boldsymbol{G}$ are the reciprocal lattice vectors. This formula relies on the fact that, in an inhomogeneous material, while the macroscopic field varies with frequency ω and has the Fourier component of vanishing wavevector, the microscopic field varies with the same frequency but with a mix of wavevectors $\boldsymbol{q}+\boldsymbol{G}$. These microscopic fluctuations induced by the external perturbation are at the origin of the local-field effects and reflect the spatial inhomogeneity of the material.

At the microscopic level ϵ is related to the irreducible polarization function P by the following equation: $\epsilon(1,2) = \delta(12) - \int v(1,3)P(3,2)\mathrm{d}3$. As we discussed in the previous section, the simplest approximation is to consider the electron and hole propagators as independent and use $P = -\mathrm{i}GG$. We will refer to this approach as the random phase approximation without local fields (RPA-noLF)). It can be shown that it is exactly equivalent to using the so-called Fermi golden rule

$$\mathrm{Im}\{\epsilon(\omega)\} \propto \sum_{i,f} |\langle\phi_i| D \left|\phi_f\right\rangle|^2 \delta(\varepsilon_i - \varepsilon_f - \hbar\omega) \,, \tag{20.40}$$

where D is the dipole operator and the DFT-KS or the QP eigenfunctions and eigenvalues can be used.

For the case of surfaces in a repeated slab geometry, this equation multiplied by the half-thickness of the cell and the appropriate prefactor, gives the half-slab polarizability, which is then used to calculate RAS and SDRS at the independent (quasi) particle level of approximation (i.e., it reduces to (20.24)). While the local-field effects can be taken into account using (20.39), the solution of the Bethe–Salpeter equation, for coupled electron and hole propagators, allows us to describe local fields and the electron-hole interaction on the same footing.

More than two decades of applications of the BSE approach have shown that the optical spectra of materials calculated for different dimensionalities can result in much better agreement with experiments. Unfortunately, such calculations are very demanding from a computational point of view, especially for complex materials. In the case of surfaces, its application has, up to now, mainly remained limited to simple reconstructions of elemental semiconducting surfaces.

Starting from the GW approximation for the self-energy and multiplying the vertex function by $-\mathrm{i}GG$, it can be shown that a four-point integral equation for a generalized reducible polarization ${}^4\bar{P}(1,2;3,4)$ can be obtained at the second iterative step of the Hedin equations (see [20.49] for a full derivation) as

$$\begin{aligned} {}^4\bar{P}(1,1';2,2') = {}& {}^4P_{\mathrm{IQP}}(1,1';2,2') \\ & + \int \mathrm{d}(33'44')\, {}^4P_{\mathrm{IQP}}(1,1';3,3') \\ & \times K(3,3';4,4')\, {}^4\bar{P}(4,4';2,2') \end{aligned} \tag{20.41}$$

where the kernel K contains two contributions [20.59]

$$\begin{aligned} K(1,1',2,2') = {}& \delta(1,1')\delta(2,2')\bar{v}(1,2) \\ & - \delta(12)\delta(1'2')W(1,1') \,. \end{aligned} \tag{20.42}$$

The term $\bar{v}$ is the unscreened Coulomb potential where the long-range ($\boldsymbol{G}=0, \boldsymbol{q}\to 0$) Fourier transform component is set as zero. When spin is not explicitly treated, this term acquires a factor of 2 for singlet excitons. The second term, $-W$, is the screened Coulomb attraction between the electron and the hole. While this last term is obtained from the functional derivative of the self-energy, the first term (here using $\bar{v}$ to obtain the macroscopic dielectric function instead of the microscopic one) formally comes from the functional derivative of the Hartree potential [20.60], which enters in the equation for the reducible polarization function.

Rewriting this equation in transition space, using the basis of the KS wavefunctions ϕ_{n_k}, the Bethe–Salpeter equation becomes

$$\begin{aligned} \bar{P} &= [1 + P_{\mathrm{IQP}}K]^{-1}\bar{P}_{\mathrm{IQP}} \\ &= [H^{\mathrm{exc}} - I\omega]^{-1}_{(n_1,n_2),(n_3,n_4)}(f_{n_4} - f_{n_3}) \,, \end{aligned} \tag{20.43}$$

where an effective excitonic Hamiltonian is introduced, defined as

$$H^{\mathrm{exc}}_{(n_1,n_2),(n_3,n_4)} = (E_{n_2} - E_{n_1})\delta_{n_1,n_3}\delta_{n_2,n_4} + (f_{n_2} - f_{n_1}) \times \int \mathrm{d}\boldsymbol{r}_1\,\mathrm{d}\boldsymbol{r}'_1\,\mathrm{d}\boldsymbol{r}_2\,\mathrm{d}\boldsymbol{r}'_2\;\phi_{n_1}(\boldsymbol{r}_1)\,\phi^*_{n_2}(\boldsymbol{r}'_1) \times K(\boldsymbol{r}_1,\boldsymbol{r}'_1,\boldsymbol{r}_2,\boldsymbol{r}'_2)\,\phi^*_{n_3}(\boldsymbol{r}_2)\,\phi_{n_4}(\boldsymbol{r}'_2)\,. \tag{20.44}$$

Then, using the spectral representation [20.49] for the inverse of a matrix, the interacting polarization can be obtained by solving an effective eigenvalue problem

$$\sum_{(n_3,n_4)} H^{\mathrm{exc}}_{(n_1,n_2),(n_3,n_4)} A^{(n_3,n_4)}_{\lambda} = E_{\lambda} A^{(n_1,n_2)}_{\lambda}\,. \tag{20.45}$$

In particular, it can be shown that for the calculation of the optical properties of extended systems such as surfaces (at least in one of the three spatial directions): (i) one needs to include only transitions with positive frequency [20.49] (i.e., (n_1, n_2) and (n_3, n_4) are pairs made of one valence and one conduction band, respectively); (ii) only transitions with the same $\boldsymbol{k}$ for the initial and final states can be included. Then, the macroscopic dielectric function reads as

$$\epsilon_{\mathrm{M}}(\omega) = 1 + \lim_{\boldsymbol{q}\to 0} v(\boldsymbol{q}) \sum_{\lambda} \frac{\left|\sum_{v,c;\boldsymbol{k}} \langle v,\boldsymbol{k}-\boldsymbol{q}|\mathrm{e}^{-\mathrm{i}\boldsymbol{q}\boldsymbol{r}}|c,\boldsymbol{k}\rangle A^{(\mathrm{v,c};\boldsymbol{k})}_{\lambda}\right|^2}{E_{\lambda}-\omega}\,. \tag{20.46}$$

The meaning of this equation is clear; instead of a simple sum of independent-particle optical matrix elements (interband transitions), the latter are weighted by the excitonic eigenstates A_λ. This occurs because the electron–hole Hamiltonian (20.45) is not diagonal due to the presence of the nondiagonal excitonic kernel.

This formulation allows us to interpret optical spectra (like absorption, reflectivity, transmission, EELS, etc.) in terms of mixing of single-particle interband transitions. Moreover, the excitation energies in the denominator of (20.46) are related to the excitonic eigenvalues E_λ which, in the case of reduced-dimensionality systems or low-dielectric screening, can be smaller with respect to the difference between the quasiparticle energy of occupied and unoccupied states. This difference quantifies the exciton binding energy. With reference to the schematic shown in Fig. 20.4c, E_λ is the excitonic eigenvalue E_{exc}, and E_{b} the exciton binding energy.

In summary, a three step procedure (DFT, GW, and BSE) of increasing computational cost is required if excitonic effects have to be included. It is clear that this approach cannot be applied to very complex systems, and indeed, full GW and Bethe–Salpeter calculations are generally done only for systems composed of few tens of atoms.

20.3.4 TDDFT

An alternative approach to calculate the optical properties of materials is the time-dependent density functional theory (TDDFT) [20.61], which is formally a powerful tool for the description of *neutral* excited states. In fact, TDDFT is, in principle, exact for neutral excited-state properties, and its simplicity relies on the fact that a two-point response function, instead of the four-point response function of the Bethe–Salpeter approach, is needed. The rigorous generalization of DFT to time-dependent external fields was proposed in [20.61, 62], where a theory similar to the Hohenberg–Kohn–Sham one was developed, albeit for time-dependent potentials.

Several reviews of the foundation of TDDFT and its applications can be found elsewhere [20.42, 63, 64]. In contrast to DFT, no energy minimum principle is available, and the evolution of the system is described by the quantum-mechanical action. The true time-dependent density is that which makes the action stationary. Minimizing the action, it is possible to obtain a set of time-dependent Kohn–Sham equations. Since all observables are unique functionals of the density, in principle, any property can be exactly obtained by the Kohn–Sham time-dependent formalism. TDDFT casts all many-body effects into the dynamical exchange-correlation kernel $f_{\mathrm{xc}}(r,t;r',t') = \delta v_{\mathrm{xc}}(r,t)/\delta n(r't')$, where $v_{\mathrm{xc}}(r,t)$ is the time-dependent exchange-correlation potential. A reliable calculation of absorption spectra relies on a good approximation to $f_{\mathrm{xc}}(r,t;r',t')$. The simplest approximation, the adiabatic extension of the static LDA (ALDA), fails to yield good absorption spectra in extended systems, although it is surprisingly good in some molecules and small clusters [20.65].

This failure is due to the lack, in the ALDA, of the long-range tail of the kernel, which is essential for the calculation of absorption spectra in extended systems, while the same term has little effect in small systems. Two derivations of approximate xc kernels with a long-range tail, based on the comparison with BSE results, have appeared. In the former approach, due to *Reining* and others [20.66], the basic assumption is the equivalence of the four-point polarizability of the BSE with the two-point polarizability of TDDFT (this equivalence is, in fact, rigorous only for the two-point contraction of the BSE polarizability), while the latter approach [20.67, 68] expands the xc correlation kernel to first order in the screened e–h interaction W. Quite

surprisingly, in spite of the different assumptions, both derivations yield the same formula for $f_{xc}(r,t;r',t')$, and spectra calculated for some bulk semiconductors and insulators [20.66, 67] result in very good agreement with experiment. Even the occurrence of strongly bound excitons [20.68] is equally well described within BSE and the TDDFT approach.

According to [20.67], the xc kernel is expanded to first order in the screened Coulomb potential, W, yielding

$$f_{xc} = P_0^{-1} P^{(1)} P_0^{-1} \,, \tag{20.47}$$

where $P^{(1)}$ is the first-order (in W) contribution to the irreducible polarizability P of many-body theory. Then, the irreducible polarizability is calculated according to the TDDFT formulation

$$P = P_0 + P_0 f_{xc} P \,. \tag{20.48}$$

Since P, f_{xc} etc. are all two-point quantities, TDDFT is, in principle, computationally less demanding than the BSE, and it could be employed in the case of more complex systems, like surfaces, nanostructures, biological molecules, and so on, where the BSE is hardly usable. Surfaces are especially difficult to study, since a large number of k-points and transitions have to be included in the excitonic Hamiltonian, rendering its diagonalization a bottleneck. Hence, it is of crucial importance to check the reliability of TDDFT optical spectra also in these cases. A practical illustration of the method will be given in Sect. 20.6.2 for Si(111)-(2×1).

20.4 Clean Semiconductor Surfaces

In the following three sections, we demonstrate how ab-initio simulations of the surface interband excitations yield a direct understanding of the surface geometry and electronic structure, and in many cases, help to interpret the experimental data. In this section, a few typical clean surfaces will be discussed. In particular, we will focus on different aspects of the (001) and (111) surfaces in elemental group IV and III-V compounds. For the most part, calculations will be discussed at the level of the independent particle approximation. In fact, it will become clear that surface spectra calculations at this level (based simply upon interband excitations between Kohn–Sham eigenstates, i.e., (20.24)) often yield a qualitatively correct description of the surface response due to fortuitous cancelation of terms in the RAS (20.16) and SDRS (20.15). This gives the advantage of allowing a straightforward interpretation of surface optical spectra in terms of interband transitions between well-defined electronic surface states.

For systems with a gap within DFT, the application of a simple *scissors* operator to open the KS gap (either chosen ad hoc or based on knowledge of GW/GW-BSE calculations) can even lead to quantitatively good agreement with experiments. This feature has allowed RAS and SDRS calculations to be applied to large and complicated systems that otherwise would not be tractable with a full MBPT or TDDFT approach. Section 20.6 will illustrate where higher order-effects, such as those from strongly bound excitons, are required.

20.4.1 Dimer Geometry

The main structural motif associated with (001) surfaces is the *dimer*. The spectral signature of dimer-induced states on the surface optical properties has been studied across many group-V and III-V(001) surfaces, including InP(001) [20.69, 70], GaP(001) [20.71, 72] and GaAs(001) [20.73–75]. However, the Si(100) surface is perhaps the most deeply studied of them all and is thus a good candidate to examine in detail. It has a simple structure based on rows of buckled dimers with well-defined surface states and a small reconstruction area; this has allowed it to be studied at various levels of theory, from tight binding, through DFT-IP, to GW-BSE. It is also an important template for simulating atomic and molecular adsorption, as will become clear in Sect. 20.5.

The first DFT-IP calculations on Si(100) established the connection between the surface dimers and the optical signal [20.76] and demonstrated that the correct geometry contains rows of alternating buckled Si dimers, most likely in a $c(4\times2)$ reconstruction [20.77]. A layer-by-layer spatial decomposition of the RAS signal [20.32] yielded a more complete picture of the various spectral features. A key fingerprint of the Si dimer is a sharp negative peak S_1 around 1.6 eV in the RAS, as shown in Fig. 20.6a. Analysis of the surface dielectric function (Fig. 20.6b) reveals that the S_1 peak arises from transitions between π and π^* orbitals running *parallel* to the dimer rows that are localized within the first few surface layers (Fig. 20.6c). Intra-dimer contributions are also present, but are much weaker. Both SDRS [20.77] and HREELS [20.39] (Fig. 20.6b) resolve a further surface-related feature S_0 below 1 eV, which appears to be due to transitions near the Γ points between bulk states and the π^* surface states, as shown.

Interpretation of experimental spectra at higher energy is more complicated, since much of the response

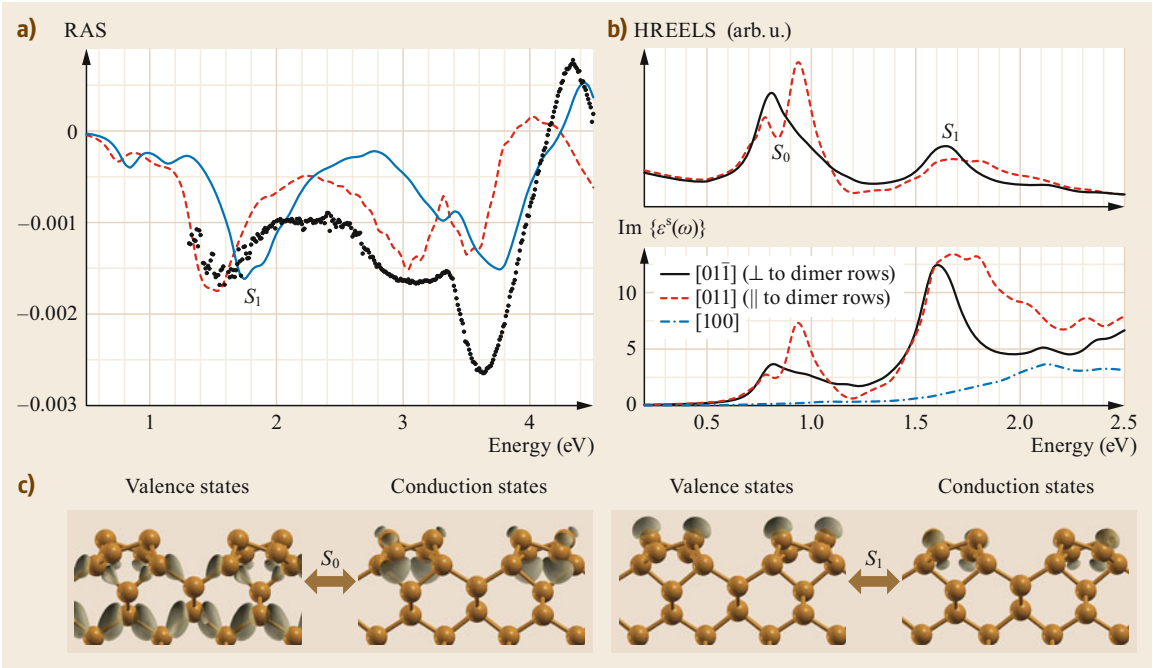

Fig. 20.6a–c Optical properties of the Si(100) surface. **(a)** RAS computed within DFT-IP plus scissors (*solid blue line*) and GW-BSE (*dashed red line*), compared with experimental data (adapted by permission from [20.78]). **(b)** HREELS and imaginary part of surface dielectric function. **(c)** Isosurfaces of wavefunctions contributing to the main optical peaks (Reprinted with permission from [20.39]. Copyright (2009) by the American Physical Society)

comes from bulk layers deep below the surface; indeed, the oscillation around 4 eV is characteristic of interband transitions between surface perturbed bulk states near E_2. The broad structure around 3 eV is of particular interest. Experimental evidence, coupled with the lack of a clear peak in the DFT-IP spectra, indicated that it arises from *steps* (this is discussed in more detail in Sect. 20.4.3). However, more advanced calculations of the ideal clean surface performed at the GW-BSE level [20.78] (see the red dashed curve in Fig. 20.6a) also produce a peak at this energy, suggesting that it can actually be a feature of the clean surface—due, in this case, to the presence of weakly bound excitons. Nonetheless, it is clear that the simpler DFT-IP scheme in this case succeeds in explaining most of the experimental data; surfaces exhibiting stronger excitonic effects are discussed in Sect. 20.6.

20.4.2 Dimer Composition

The GaAs(001)-c(4 × 4) surface offers a nice example of the sensitivity of interband transitions to small changes in the surface structure and chemistry. For many years, the c(4 × 4) surface was thought to be composed of a symmetric (or possibly asymmetric) triplet of As–As dimers (homodimers), as illustrated in Fig. 20.7. However, *Ohtake* et al. [20.79, 80] proposed that a new mixed dimer (heterodimer) structure, consisting of three Ga–As dimers, would form instead of the more As-rich surface if the preparation conditions were modified (specifically, if As_4 fluxes are used instead of As_2 during molecular beam epitaxial growth). The formation of two distinct structural phases α and β is clear from the RAS spectra measured.

Ab-initio calculations [20.81] of the RAS performed at the DFT-IP+scissors level provide strong confirmation of the proposals of *Ohtake* et al. [20.80]: the symmetric dimer calculations yield a relatively weak, single-peaked feature at 1.6 eV in agreement with the β-phase measurements, while the mixed dimer model yields a broader, stronger peak around 2.0 eV, as in the observed α phase data. The origin of the former feature was shown [20.36] to be derived from interband transitions between filled dangling bonds on the threefold coordinated As atoms backbonded to the dimers and empty π^* orbitals of the As–As dimers. Additional empty states at the Ga atoms are available on the mixed dimer surface, explaining the two-peaked RAS signal. A thorough decomposition of the various peaks in the GaAs(001)-c(4 × 4) RAS, by means of (20.19) is given in [20.29].

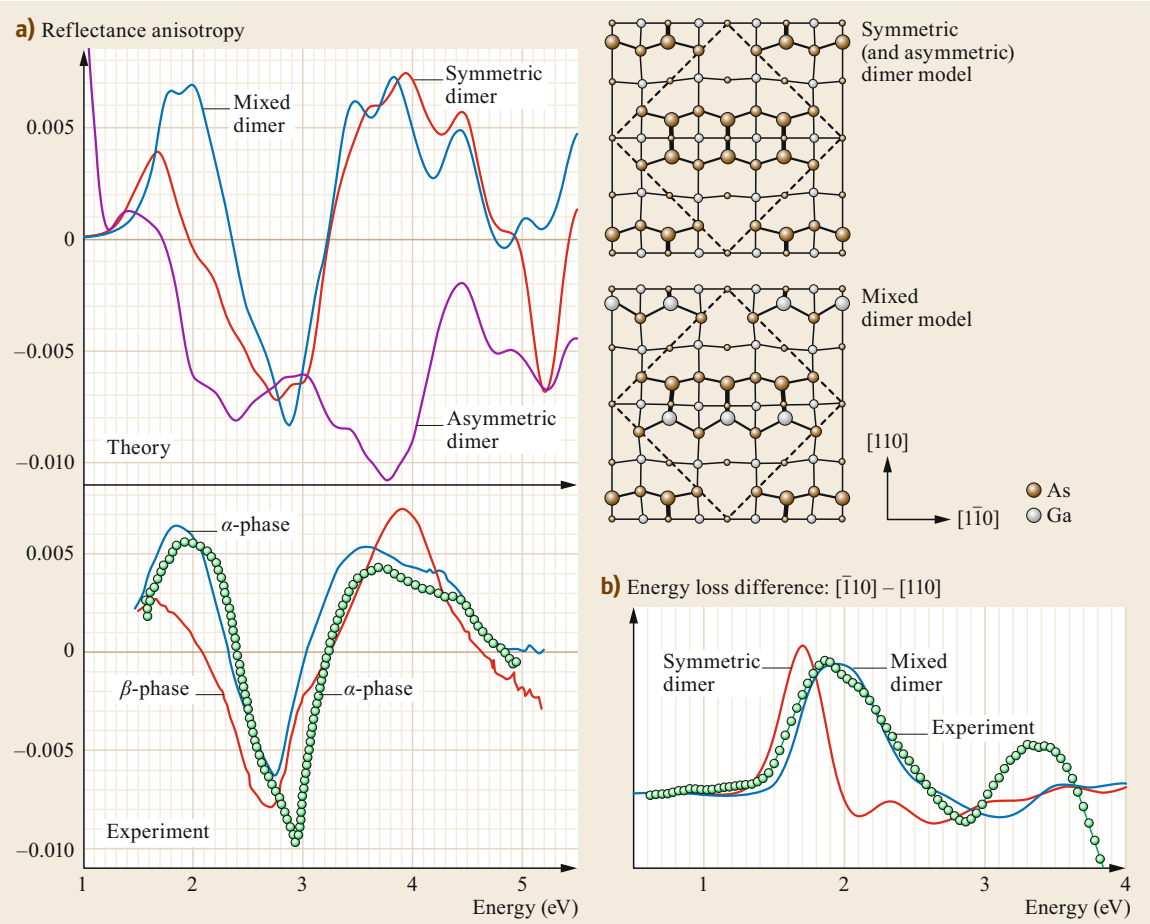

Fig. 20.7a,b Interband transitions at the GaAs(001)-c(4 × 4) surface probed by **(a)** optical (RAS) and **(b)** electronic (HREELS) spectroscopies. **(a)** Calculations from [20.81], measurements from [20.80] (*lines*) and [20.36] (*dots*). **(b)** Calculations from [20.41] and measurements from [20.36]. See text for details

These calculations highlight the remarkable sensitivity of surface optical spectra to the chemical composition of single surface bonds. The difference between the two surface models becomes even more apparent in HREELS spectra, which also probe interband transitions in ϵ_2, as explained in Sect. 20.2.5, but offer a higher surface sensitivity. Figure 20.7 reports calculations [20.41] using a simple three-layer model for the same surface models and experimental data from [20.36] for the β-phase. In this case, the difference is even more striking than before and stresses the one-to-one correspondence between RAS and HREELS where surface interband transitions are involved. Better agreement with experiments above 3 eV can be obtained by properly accounting for the nonlocality of $\epsilon(z, z', \omega)$, as discussed in [20.41].

20.4.3 Stepped Surfaces

The supercell framework allows perfectly aligned surface terraces to be constructed and studied. Real surfaces, however, exhibit a wealth of features that are difficult to account for in first-principles studies, such as defects, steps, adatoms, contaminants, strain, multiple domains, and so on. Although experimentalists strive to prepare model surfaces, these additional features are generally unavoidable, and in some cases even desired. In many cases, these deviations from the ideal surface lead to important features in the surface dielectric response and need to be accounted for or mitigated in calculations. Their influence on the surface interband spectra will be discussed in the following.

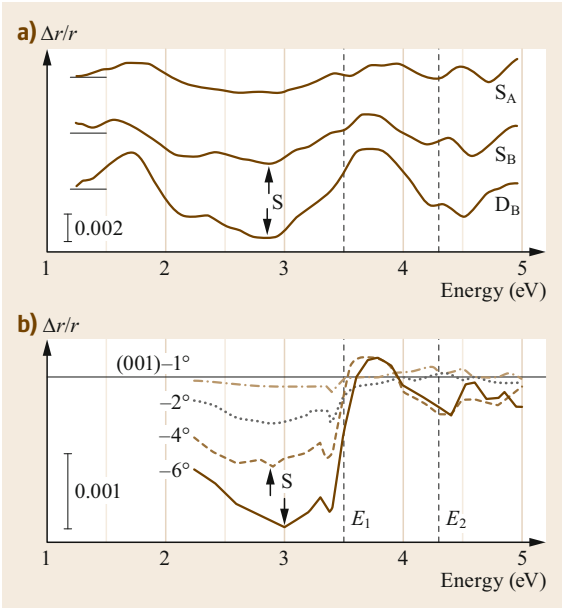

Fig. 20.8a,b Optical anisotropy signal arising from steps on Si(100). **(a)** DFT-IP calculations for single (S_A, S_B) and double (D_B) type steps. **(b)** Experimental data for different miscut angles (Reprinted with permission from [20.82]. Copyright (2001) by the American Physical Society)

Steps on Si(001)

The first ab-initio study of the influence of steps on the surface optical anisotropy was carried out by *Schmidt* et al. [20.82] and focused on the Si(001) surface. Nominally prepared Si(100) typically phase separates into a balanced mixture of (1×2) and (2×1)-oriented domains separated by single height steps. As RAS measures a macroscopic average, the generated signal is close to zero. In order to generate a nonzero RAS signal, a 4° offcut is often used, which forces the surface to form double-height steps and thus favor a single phase. The ab-initio calculations, shown in Fig. 20.8, demonstrated that single and double-height steps both generate broad negative signals above the gap in the 2.0–3.5 eV range, in agreement with experimental observations [20.83]. The signals are largely caused by perturbations of bulk wavefunctions by the anisotropic surface potential generated by the steps [20.82].

Steps on C(100):H

Hydrogenation of diamond surfaces brings three main effects. First, it enhances the semiconducting character of the surface. Secondly, new empty states, hydrogen-related, appear in the forbidden gap, near the Γ point, with nearly free electron character. Third, the electron affinity becomes negative, making hydrogenated diamond an appealing candidate as a cold cathode emitter.

The electronic properties of the ideal C(100)2×1:H surface have been studied by *Marsili* and *Pulci* [20.84] at the DFT and GW level. Its optical properties, for the nominally flat and for vicinal C(001):H surfaces, have been investigated experimentally and computed theoretically at the DFT level, in [20.85]. The experimental RAS shows an almost zero response for the 0° nominally flat surface, a negative broad signal for the 2° surface, and a broad positive signal, becoming negative above 3.5 eV, for the 4° surface.

Calculations performed simulating the presence of single and double steps of the *Chadi* [20.86] and of the *Tsai* and *Yeh* type [20.87] give indications that the single steps appearing in the C(001):H vicinal surface are more compatible with the Chadi geometrical model S_B (that is, with C dimers parallel to the single-step edges). In the case of double steps, instead, the comparison of the experimental and calculated RAS [20.85] gives hints towards the D_A Chadi geometrical model, that is with C dimers of the upper terrace perpendicular to the double-step edges.

Si(110)-(16 × 2)

Si(110) surfaces can be obtained with different high-temperature treatment in various reconstructions with different unit cell sizes. The most stable one is a long-range reconstruction that consists of alternately raised and lowered terraces in a huge (16×2) cell. From the results of STM topography a realistic model of the system was proposed by *Stekolnikov* et al. [20.88], which contains chains of pentamers on both terraces and single-layer height rebonded steps. The SDRS signal has been computed [20.30] ab initio, including TDDFT methods, and compared with experiments. A main SDRS peak at 1.8 eV was assigned to interband transitions involving states localized on the pentamers. However, the overall agreement is weak, suggesting that the structural model is not complete.

Vicinal Surfaces

Vicinal surfaces are currently a hot topic in surface and material science (Chap. 12), as the formation of regular step and terrace arrays offers a natural template for surface functionalization by atoms, molecules, or nanostructures, as well as a gateway to studying and harnessing novel physical phenomena. Changing the vicinal angle changes the step structure and terrace width, and thus also the density of nanostructures and the coupling between them. Although clean vicinal surfaces have been studied experimentally, theoretical work has focused on adsorbate-stabilized reconstructions, as they offer more regular step/terrace combinations and smaller unit cells. In particular, the Si(*hhl*)-Au surfaces have been studied intensively with

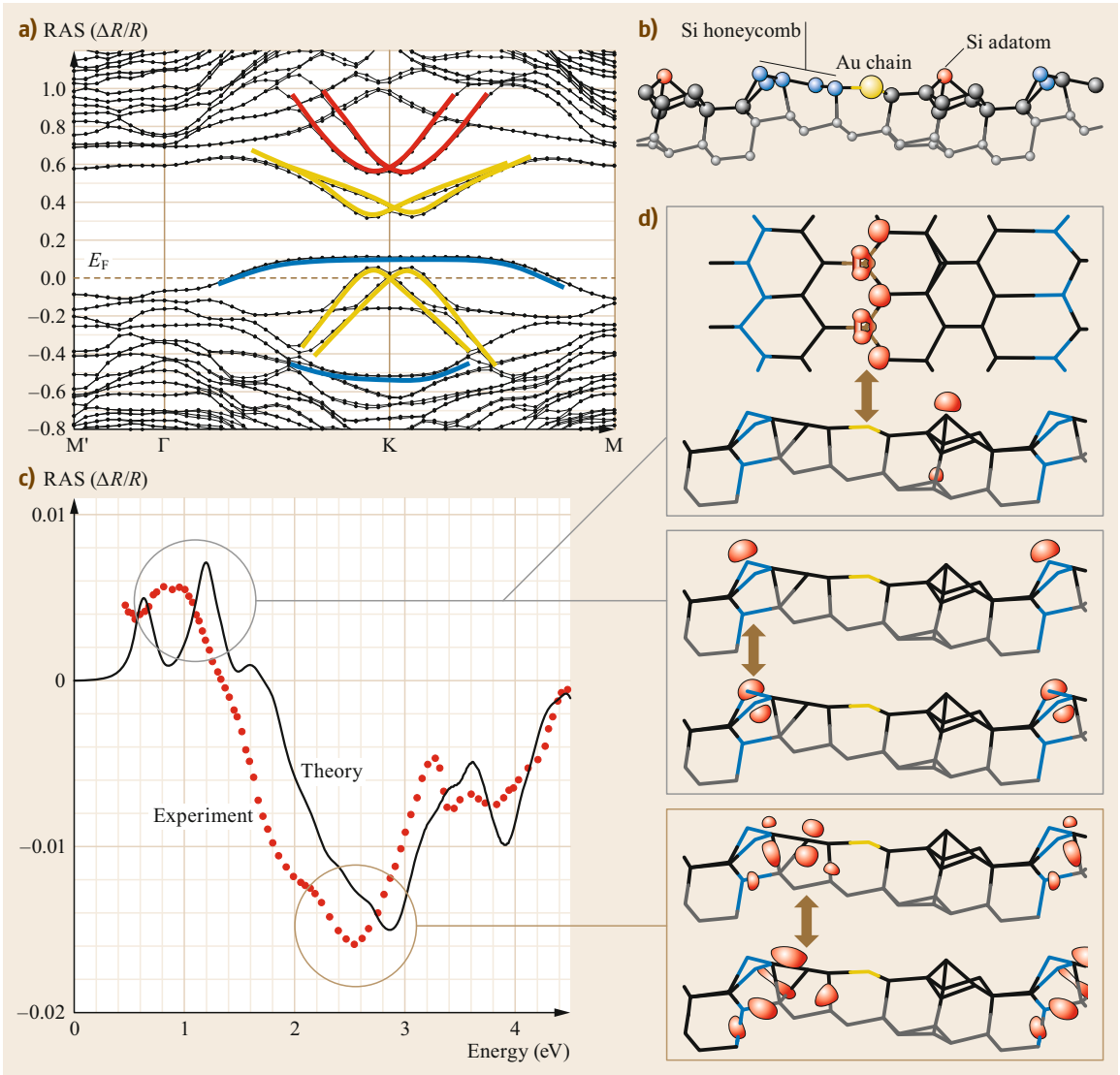

Fig. 20.9a–d Optical and electronic properties of the vicinal Si(557)-Au surface. **(a)** DFT-LDA band structure, with surface states at step-edge dangling bonds (*blue lines*), at the Au−Si chain (*gold*), and at Si adatoms (*red lines*), relative to the Fermi level. **(b)** Atomic structure (side view, topmost layers). **(c)** Computed RAS spectrum (DFT-IP plus scissors) compared with experimental data from [20.89]. **(d)** Filled (*bottom*) and empty (*top*) electronic states involved in the main interband transitions contributing to the peaks indicated in **(c)**

optical probes. There are several reasons for this. First, the Au-stabilized surfaces form regular single-height steps along [110] that border narrow terraces containing atomic chains of Au that can stretch for hundreds of Å. The array of quasi-1-D (quasi-one-dimensional) nanostructures are strongly anisotropic and, therefore, perfect for studying by using RAS, as it should be easy to decouple optical excitations along and perpendicular to the step edges and Au chains. Secondly, the unreconstructed Si(111) surface is naturally isotropic within the surface plane, and thus any observed anisotropy is strongly related to the formation of reconstructions that lower the symmetry. Thirdly, the RAS signal is rich with features in the 1–5 eV range and has similar, but not identical, spectra across the range of different vicinal angles and Au coverages. RAS spectra have been reported on Si(557)-Au, Si(553)-Au, and Si(775)-Au [20.90, 91].

As an example, we consider the Si(557)-Au surface (carefully analyzed by *Hogan* et al. [20.92]) and focus on the role of the step geometry on the surface interband transitions. Figure 20.9b shows a side view of the surface geometry. Besides the Au-chain embedded in the terrace and the presence of adatoms, the step edge is made of a characteristic Si honeycomb structure with dangling bonds lying right at the edge itself. (This honeycomb motif actually appears to be a feature common to all Si(*hhl*)-Au surfaces.) The Au chains, adatoms and Si dangling bonds all give rise to distinct surface states in the computed band structure (Fig. 20.9a); the latter states are partially filled. Calculations of the surface optical anisotropy (Fig. 20.9c) at the DFT-IP+scissors level appear in excellent agreement with the experimental data, thus allowing the experimental peaks to be interpreted in terms of the surface geometry. Most of the signal, i.e., 0.5–4.0 eV, in fact derives from transitions involving either the step edge Si orbitals lying close to the Fermi level or deeper-lying π/π^*-like orbitals of the honeycombs themselves (Si=Si bonds). Contributions from the Au chains are restricted to low energy and have a smaller overall contribution. The fact that most of the RAS signal derives from the step atoms explains the almost universally similar nature of the RAS signals observed across the Si(*hhl*)-Au family of vicinal surfaces [20.89].

20.4.4 Defects

Defects are the bugbear of surface preparation, and their presence can make interpretation of experimental data difficult. In some cases, however, some may actually drive formation of the lowest energy reconstruction, an example being subsurface Ga antisite defects on Sb-rich GaSb(001) [20.93]. On this surface, second-layer As atoms are substituted by Ga atoms in order to reduce or eliminate the metallicity of long dimer-chain reconstructions (effectively by doping the system with holes). The optical anisotropy of GaSb(001) shows features typical of (001) surfaces, with peaks and troughs deriving from interband transitions from occupied dangling bonds to dimer antibonding orbitals. Subsurface Ga substitution only weakly perturbs the geometry, which can nonetheless be detected in low energy (1 eV) peaks involving extended dimer chain orbitals. More importantly, however, the change in level occupation associated with the loss of metallicity is reflected in stronger changes in the spectrum at 2.5 eV, bringing the computed spectra more in line with the measured data [20.94].

20.5 Adsorbate-induced Effects

Adsorbates and adlayers have a marked effect on the surface optical properties. They can modify the interband transitions of the clean surface in various ways: by quenching such transitions (e.g., by destroying one or all of the optically active electronic states); by perturbing existing states (e.g., by changing the potential felt by states terminating at the surface); by introducing new optically active states; by stabilizing new surface reconstructions (as discussed for Au on vicinal Si(111) in Sect. 20.4.3); and so on.

It is important for the surface scientist to understand the extent of these changes. Undetected contaminants can lead to incorrect conclusions regarding the surface electronic structure. An interesting case is that of the InP(001)-(2×1) surface, which was understood (via STM) to consist of rows of buckled phosphorus dimers. However, such a structure should yield a metal in apparent violation of electron counting rules and in contradiction with the measured surface band gap of over 1.0 eV. The mystery was resolved with the help of DFT calculations of the RAS [20.95], which proved that the surface, which was prepared using metalorganic vapor phase epitaxy, was actually hydrogen stabilized. On the other hand, the induced change in the surface optical spectra due to passivants can be used to interpret the signal of the *clean* surface, at least in terms of surface or bulk-related transitions (the former being more sensitive to surface contaminants). This idea, in fact, encapsulates the technique of surface differential reflectance spectroscopy (SDRS), described in Sect. 20.2.1 and encapsulated by (20.15).

In the following, we outline how these effects can manifest in surface interband spectra through atomic, molecular, and layer adsorption.

20.5.1 Atomic Adsorption

Hydrogen

Being the most accessible passivant and contaminant, hydrogen and oxygen have been by far the most commonly used adsorbates in semiconductor surface optical and HREELS studies. Hydrogen adsorption is relatively easy to model within ab-initio calculations, as it tends to adsorb dissociatively at well-defined sites such as dangling bonds. Generally speaking, the main effect of H adsorption is to passivate the surface dangling bonds and, thereby, quench surface optical transitions occurring below the onset of bulk-like transitions near the E_1 peak energy. In the case of Si(100), this yields a quenched signal in RAS [20.78] and HREELS [20.97]

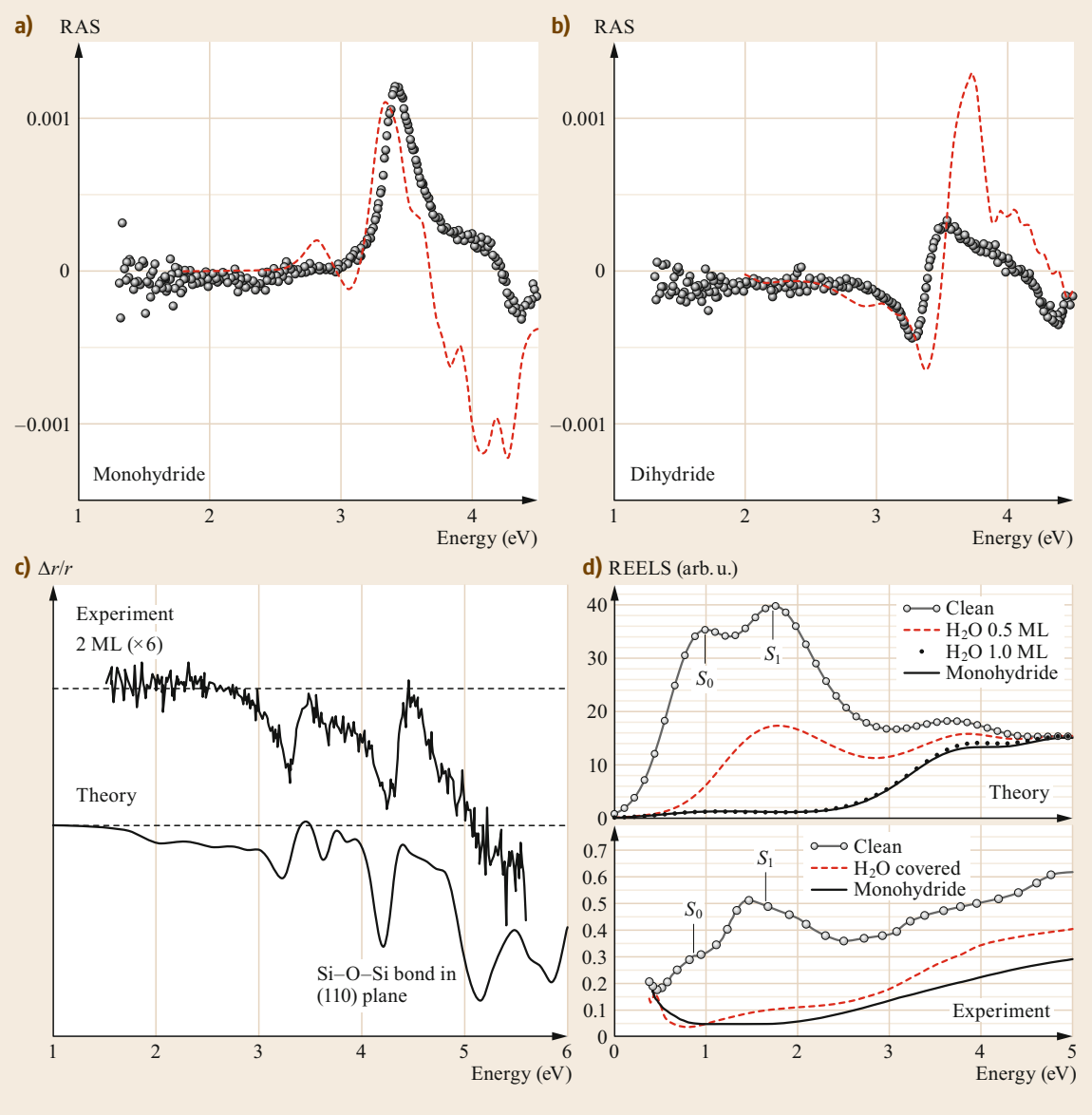

Fig. 20.10a–d Optical and energy-loss spectra of Si(100) with adsorbates. **(a)** RAS of monohydride and **(b)** dihydride passivated Si(100), computed using BSE and compared with experiments. **(c)** RAS of oxidized Si(100) using DFT-IP. **(d)** REELS of monohydride and water-contaminated surface ((**a**,**b**) reprinted with permission from [20.78]. Copyright 2009 by the American Physical Society. **(c)** reprinted with permission from [20.96] Copyright 2005 by the American Physical Society. **(d)** Reprinted with permission from [20.97])

below 3 eV, and pronounced peaks in SDRS [20.78] at 1.5 (at least in the calculations) and 3 eV. However, H adsorption can also change the surface structure, as shown in Fig. 20.10. Monohydride formation (Fig. 20.10a) on Si(100) leaves dimers intact, while (Fig. 20.10b) dihydride formation induces dimer breaking. The latter manifests as a characteristic SDRS peak at 3.8 eV, while the reduced strain also leads to a quite different surface-induced bulk anisotropy, as seen in RAS.

Similar quenching of π–π^* transitions has been noted on C(100):H terraces, leaving a zero RAS signal below 4.5 eV [20.84, 85, 98]. On GaAs(110):H, a similar mechanism results in a zero RAS below 3 eV, while the SDRS shows contributions across the

2.0–4.0 eV range from surface and perturbed bulk contributions [20.99]. The mechanism is slightly different on P-rich GaP(001)-$(2\times1)/(2\times2)$ [20.100] and InP(001)-(2×1) [20.95] surfaces. Here, H has a fundamental role in stabilizing the systems by passivating half of the dangling bond states on (buckled) P dimers. Strong optical anisotropies persist around 2.6 eV due to interband transitions between filled states on the remaining P dangling bonds and empty dimer antibonding orbitals.

Oxygen

The influence of oxygen adsorption on semiconductor surface interband transitions is complicated by the fact that the adsorption mechanisms are not thoroughly understood, and the preferred sites not uniquely defined [20.101, 102]. On Si(100), which is by far the mostly widely investigated using ab-initio schemes, theoretical simulations of the optical response reveal that the initial states of oxidation at room temperature are marked by oxygen insertion into dimers and (primarily) their backbonds [20.101, 103–105], i.e., forming Si–O–Si bonds. This causes strong perturbations on the dimer–dimer interactions, changing the dispersion of the surface localized bands and eventually pushing them outside the gap. In the RAS, this is reflected by a general quenching of the clean surface signals and a uniformly broad signal in SDRS [20.105]. During thermal oxidation, on the other hand, layer-by-layer growth of the oxide layer occurs and is reflected by oscillations in the optical anisotropy [20.106]. This was explained by *Fuchs* et al. [20.96] as deriving from strain perturbations on the Si bulk wavefunctions by oxygen being incorporated into Si–Si bonds below the interface (Fig. 20.10c); the disordered oxide layers above the interface only have a minor impact on the optical anisotropy. Complicated mechanisms also accompany oxygen adsorption on GaAs(001) surfaces [20.107], although the breaking of, and substitution into, As dimers (leaving Ga–O–Ga bonds) has been suggested using HREELS simulations (Fig. 20.10d) [20.108].

Alkali Metals

While oxygen and hydrogen are representative of the electronegative end of the periodic table of elements ($\chi = 3.5$ and 2.0, respectively), it is interesting to consider the effect that adsorption of more *electropositive* species such as alkali atoms can have on the surface interband spectra. Low coverages of Cs ($\chi = 0.8$) in particular have been investigated on As-rich GaAs(001) surfaces using RAS [20.109]. The observed effect on the surface optical response is the addition of a strong broad negative signal across the 3.0–5.0 eV range; similar studies using K ($\chi = 0.9$) and Na ($\chi = 1.0$) adsorption, or on Ga-rich surfaces, exhibit very similar changes in the experimental signal [20.110], hinting that the underlying mechanism is universal.

DFT calculations [20.109, 111] on GaAs(001) revealed that Cs adsorption only weakly perturbs the clean surface geometry. Instead, strong surface dipoles are created due to electronic charge transfer from the alkali to the surface, and furthermore, new surface resonance states are induced. The calculations attribute the induced optical signal both to perturbations of surface-terminating bulk states (through the change in the surface potential) and to bulk-like transitions involving Cs-induced resonance states. Although small site-dependent signals at low energy (2.0 eV) can directly arise from interband transitions involving Cs-substrate bonds, the primary influence of electropositive elements on the RAS remains, therefore, somewhat *indirect*, in strong contrast to more electronegative elements.

20.5.2 Adsorbate-stabilized Reconstructions

Besides atomic adsorbates that mainly perturb or passivate the surface structure, there is a huge number of adsorbate-stabilized surface reconstructions, many of which have been investigated using RAS or SDRS simulations. These include Si(001)-(1×1):Sb [20.112], GaAs(110):Sb/As [20.113], and the aforementioned H-stabilized P-rich (001) surfaces of GaP [20.100] and InP [20.95]. However, there are also many cases in which adsorbates generate highly anisotropic surface nanostructures that are ideal for studying using RAS. In particular, Si(111) offers a natural template for growth of quasi-1-D nanowires. Within the typical experimental convention, positive RAS signals correspond to excitations parallel to the wires. Indium adsorption induces metallic (4×1) and semiconducting (8×2) phases containing fairly broad In *ribbons*, which can be distinguished and interpreted using RAS [20.114–116]. Although the RAS signals of the two phases (Fig. 20.11a) are dominated by broad negative signals across 1.2–3.0 eV, sharp positive peaks are present in the mid-infrared. Both phases feature a peak at 0.50 eV due to transitions between bonding and nonbonding In chain states, as expected. However, only the hexagon model features a peak at 0.72 eV (0.53 eV in the calculation), related to the additional In–In bonds between the two zigzag rows, which allows the two models to be distinguished [20.115].

Li and Ag induce the so-called (3×1) honeycomb chain-channel reconstruction, wherein the metal atoms form single-atom wires between Si honeycomb chains (the same honeycomb motifs noted in Sect. 20.4.3). Also in this case, the optical spectrum (Fig. 20.11b)

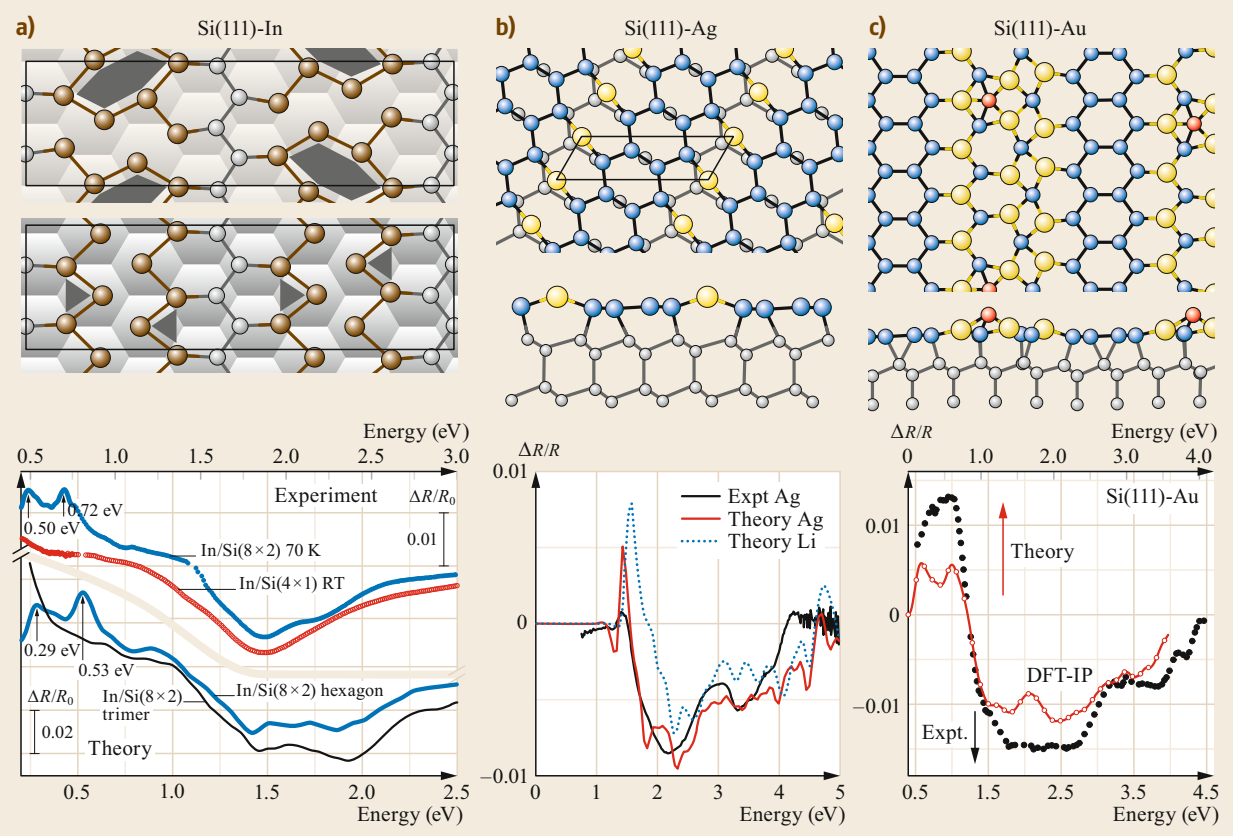

Fig. 20.11a–c Structural models and RAS of adsorbate stabilized Si(111) reconstructions (theory and experiment). **(a)** Hexagon and trimer models of the Si(111)-In nanowire array. **(b)** Ag and Li honeycomb chain-channel reconstructions, computed using a hybrid-DFT approach [20.117]. **(c)** Triple atomic Au nanowires on Si(111). ((**a**) Reprinted with permission from [20.115]. Copyright 2009 by the American Physical Society. **(b)** Adapted with permission from [20.117]. Copyright 2013 by the American Physical Society. **(c)** Reprinted with permission from [20.118] Copyright 2013 by the American Physical Society)

is negative across the 1.8–4.5 eV range, being dominated by interband transitions involving π^*-like surface states localized on the Si honeycomb atoms [20.117], although a small positive structure appears at 1.5 eV due to transitions involving occupied states at the honeycomb edge. The same Si honeycombs also dominate in the case of the Si(111)-(5×2):Au surface [20.118, 119]. Although the precise Au coverage is still a matter of discussion, computed RAS spectra using a 0.6 monolayer (ML) coverage model of triple Au chains, and Si adatoms are in good agreement [20.118] with experimental data (Fig. 20.11c). Again, in this case, the spectra are dominated by Si honeycomb and localized Si-Au states. However, a fairly sharp positive feature, corresponding to *intrachain* optical transitions, is found around 1 eV.

Thus, in contrast to expectations, the optical spectra of adsorbates forming quasi-1-D atomic chains are not dominated by electronic transitions along the chain direction; instead, their presence is reflected indirectly in the optical signals of the adsorbate-stabilized substrate geometry. Weaker positive signals related to extended states along the atomic chains appear below 1.5 eV; experiments report that they are sensitive to surface quality.

20.5.3 Molecular Adsorption

As in the atomic case, the influence of molecular adsorption on surface interband excitations largely occurs through modification or quenching of signals from the clean surface (i.e., the molecule–substrate bonding), at least within the typical experimental range of $\approx$ 1.5–5.0 eV. Simulations have, up to now, focused primarily on the Si(100) surface.

H_2O adsorption on Si(001) has been explored theoretically using RAS [20.120] and HREELS [20.97] (Fig. 20.10d). In both cases, partial coverage of the

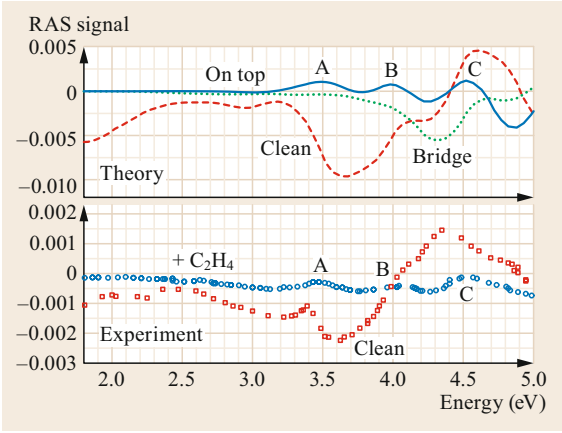

Fig. 20.12 RAS of ethylene adsorption on Si(001). Theory (*top*), for clean, on-top and bridge sites, respectively; and experiment (*bottom*), for clean and 1 ML coverage of C_2H_4. The contribution of steps has been subtracted from the measured clean surface signal

surface results simply in attenuation of the RAS or HREELS spectra. At full coverage, dissociation of the H_2O molecule across the Si dimers passivates all surface dangling bonds and removes the dimer-related (π, π^*) surface states (Sect. 20.4.1), thus killing the prominent peak(s) arising from interband transitions below 1.8 eV. At higher energy, both RAS and HREELS show bulk-related features (around E_1 and E_2) that persist after adsorption.

Organic molecules offer more interesting possibilities. DFT-IP level studies have been performed for adsorption of a number of such molecules on Si(001). Neither acetylene [20.121] nor ethylene [20.122, 123] cause dimer cleavage. However, the induced optical signal remains sensitive to the adsorption geometry, i.e., parallel (on-top) or perpendicular (bridge site) to the dimer. Whereas on-top adsorption kills the inter-dimer (chain) peak at 1.7 eV by removing dimer empty states, the bridge site suppresses positive intradimer contributions and enhances the negative inter-dimer peak [20.122]. A comparison with experiments (Fig. 20.12) demonstrates that the on-top configuration is, in fact, favored. Both cyclopentene [20.124, 125] and uracil [20.126] may cause further perturbations on the surface response, e.g., through dimer breaking or oxygen insertion, and various adsorption geometries are possible, along with a general attenuation of the clean surface signals around E_1 and E_2.

A notable example of where the molecular adsorbate was thought to have a more direct influence on the surface optical anisotropy is the case of 9,10-phenanthrenequinone on Si(100) [20.125, 127], which introduces a characteristic new peak at 5.2 eV in the experimental data. Intra-molecular π–π^* excitations were proposed to explain this peak based on gas-phase spectra [20.128]. However, the ab-initio calculations [20.127] showed that, while π–π^* transitions do contribute to the optical anisotropy of the molecular layer, the adsorption-modified Si bulk states are dominant across the full spectral range.

Last, we note that differential reflectance spectroscopy can be used to probe the molecular adsorbate layer itself if nonreactive surfaces are used. This idea was widely applied in [20.8, 129] to the study of organic epitaxial films using molecules whose chromophores generate the dominant optical signal. However, the need to use GW-BSE to study the optical response of such organic layers has limited their appearance in theoretical studies [20.130].

20.5.4 Adlayers

Since visible light can penetrate several hundred nm into a crystal, it is a useful probe of buried interfaces [20.131], capping layers [20.90], and adlayers [20.132]. An interesting example of the latter that has been investigated using RAS and DFT-IP calculations is the Si(105)-Ge surface. Its geometry has long been established as the *rebonded step* (RS) model [20.133], which consists of a smooth, highly reconstructed Ge layer (about 5 Å thick) atop a Si(105) substrate. The main reconstruction motif is a curious 6-atom *horseshoe* structure composed of three dimers and stabilized by the in-plane strain due to the Si-Ge lattice parameter mismatch.

Fazi et al. [20.134] measured the RAS of this surface and compared it with ab-initio calculations assuming the RS model and obtained excellent agreement

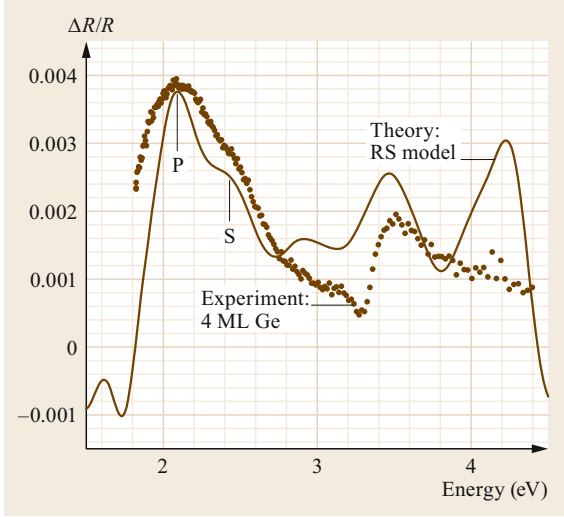

Fig. 20.13 Measured and computed RAS of the Si(105)-Ge rebonded step (RS) surface reconstruction

between them (Fig. 20.13). The main features P and S in the spectrum derive from interband transitions from occupied bulk-like states lying ≈ 1 eV below the valence band maximum to empty surface states lying inside the bulk gap. In the case of the main peak P, these surface states are, in fact, physically localized well *below* the horseshoe structure on the surface—a curious fact considering the density of surface dimers—near the location of the Si-Ge interface itself. Fazi and colleagues used this unique character to cast light on the microscopic structure of the Si-Ge interface. By monitoring the RAS signal during growth and comparing it with calculations for different Ge coverages and interface models (sharp/gradient/disordered), they confirmed that a sharp interface is present and demonstrated the connection between the surface optical spectra and the interface chemistry. This highlights the sensitivity of interband transitions to the bond stoichiometry of subsurface layers, in a similar fashion to the dimer composition on GaAs(001) discussed in Sect. 20.4.2.

20.6 Excitonic and Local-Field Effects

The importance of excitonic effects on the dielectric response of materials has been known for quite a long time [20.135]. The presence of the interaction between the electron and the hole pairs in the optical excitation process in spectroscopical measurements like light absorption or reflectivity, or electron energy loss, has an effect on the spectral line shapes above the gap and the formation of bound exciton states below it. Due to the low screening, the latter phenomenon is particularly evident in insulators or in low-dimensional systems, where binding energies of the order of 1 eV are observed. The relevance of these effects at several surface terminations of simple elemental semiconductors is now well established. This knowledge has been reached thanks to a systematic comparison of experimental RAS/SDRS and photoemission data with theoretical results obtained by DFT and MBPT calculations. In particular, strongly bound surface-state excitons have been found at the (111)-(2×1) surface of Si [20.136, 137], in Ge, [20.138] and C(111) [20.57], and at the (100)-(2×1) termination of diamond [20.139, 140].

As we will show in this section, the exciton dynamics has a one-dimensional character due to the peculiar atomic reconstruction of these surfaces (along the dimer rows in C(100) and along the Pandey chains [20.141] in Si and Ge(111)). For this reason, it is more difficult for electrons and holes not to feel their mutual interaction, which leads to bound excitons with binding energies (BE) ranging from a few tens of eV in Si and Ge, to 1 eV or slightly less in diamond. The large exciton binding energy observed at the C(100) surface—about four times larger with respect to that found in Si and Ge (111)—has been explained in terms of its reduced static screening with respect to Si (111), and will be the focus of Sect. 20.6.3.

20.6.1 BSE Approach to Group IV (111) Surfaces

The (111) termination is the natural cleavage surface of the most important group-IV semiconductors like silicon, germanium, and diamond, and for this reason, it is the most widely and deeply studied. It shows different geometric structures depending on preparation and actual temperature of the sample, but upon cleavage in ultra-high vacuum (UHV) and at low temperature the low energy electron diffraction (LEED) pattern is compatible with a (2×1) reconstruction. Angle-resolved photoemission measurements performed on the (111)-(2×1) termination of Si and Ge reveal the presence

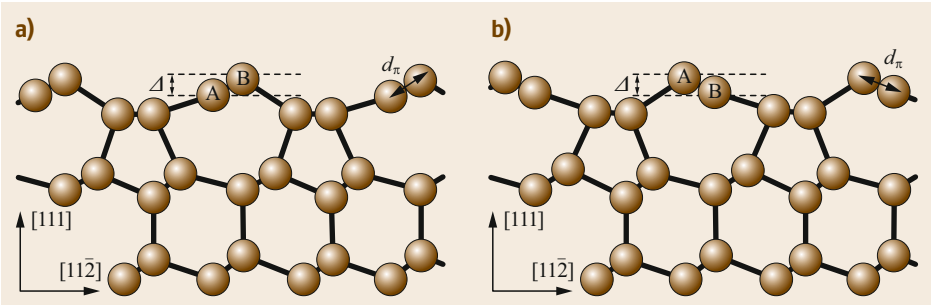

Fig. 20.14a,b Atomic structure of the negative (**a**) and positive (**b**) buckling chain model. The distance d_π between atom A and atom B is the bond length along the Pandey chain, while the difference in height Δ between atom A and atom B is the buckling amplitude

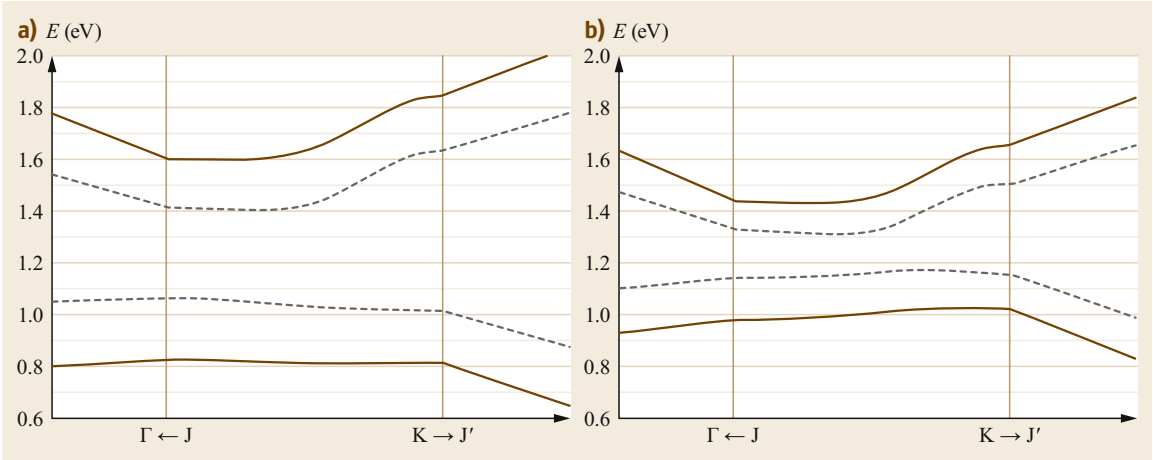

Fig. 20.15a,b DFT (*dashed line*) and GW (*solid line*) band structure around the Fermi energy of the Si(111)-(2 × 1) positive **(a)** and negative **(b)** buckling chain model

of an occupied and unoccupied surface band. SDRS data are, instead, characterized by a strong optical anisotropy with a peak for light polarized along the Pandey chains at 0.45 eV for Si, and at 0.49 eV for Ge. The Pandey model featuring five and seven-member rings of atoms in the surface bilayer can explain most of the experimental spectroscopic data of the (111)-(2 × 1) reconstruction of silicon and germanium.

Theoretical simulations have revealed the presence of two geometries, generally identified as positive and negative buckling (or right and left isomers, respectively), as shown in Fig. 20.14, which are almost degenerate in energy. For both Si and Ge, the energy difference between the two isomers is very small; in fact, one can assume that the two geometries are energetically degenerate within the accuracy of the DFT method. It should thus be expected that both isomers could coexist in nature. However, recent low-temperature angle-resolved ultraviolet photoemission spectroscopy and scanning tunneling microscopy and spectroscopy (STM and STS) measurements, together with state-of-the-art first-principles excited-state calculations demonstrated that for highly n-doped Si(111), both isomers coexist at the surface [20.145]. For undoped samples, the standard Pandey chain model [20.141] (right chain or positive buckling) yields a good comparison with SDRS data for Si(111)-(2 × 1), while for Ge(111)-(2 × 1) a better agreement between experiment and theory is obtained considering the negative buckling reconstruction (Fig. 20.14).

The reason of the dominance of one isomer over the other is not completely clear. A possibility is that the dominant structure is cleavage induced. For both isomers of Si and Ge surfaces, the band structure exhibits two surface bands, i.e., one is mainly composed of an occupied dangling-bond state (D_{up}) on the externally shifted atom and the other is an empty dangling-bond state (D_{down}). Figure 20.15 reports the theoretical GW band structures obtained for both isomers by *Violante* et al. [20.137]. The band structure of the right isomer is consistent with previously published data calculated within the same theoretical approach [20.136]. The quasi-particle band structures of positive and negative buckling show a small band dispersion along the JK direction while a larger dispersion is observed along the perpendicular direction corresponding in real space to the Pandey chain direction. This is due to the fact that the coupling between the orbitals is very strong along the chain, while the interaction among the chains is weak. In Fig. 20.16 the corresponding GW band structures [20.138] of the two isomers for Ge(111)-(2 × 1) are reported, showing qualitatively similar behavior to that described for Si. More specifically, the surface state bands along the JK direction have a larger dispersion in Ge with respect to the Si case, suggesting a larger interaction among the Pandey chains in Ge. In both cases the surface gap calculated for the negative isomer results smaller with respect to the positive isomer indicating the differences due to the underlying bulk geometry. In Si(111)-(2 × 1) with negative buckling the occupied and empty surface bands result flatter and more parallel with respect to those of the positive Pandey chain model. A minimum gap of 0.44 eV near JK/2 occurs for negative buckling, while for the positive buckling a minimum gap of 0.77 eV is observed near J. For Ge(111)-(2 × 1) the dispersion of the empty D_{down} band between J and K is different from the positively buckled chain. For the positive isomer the minimum direct gap results to be 0.88 eV and is located along the JK direction. For the negatively buckled isomer the minimum direct surface gap is significantly smaller, amounting to 0.66 eV.

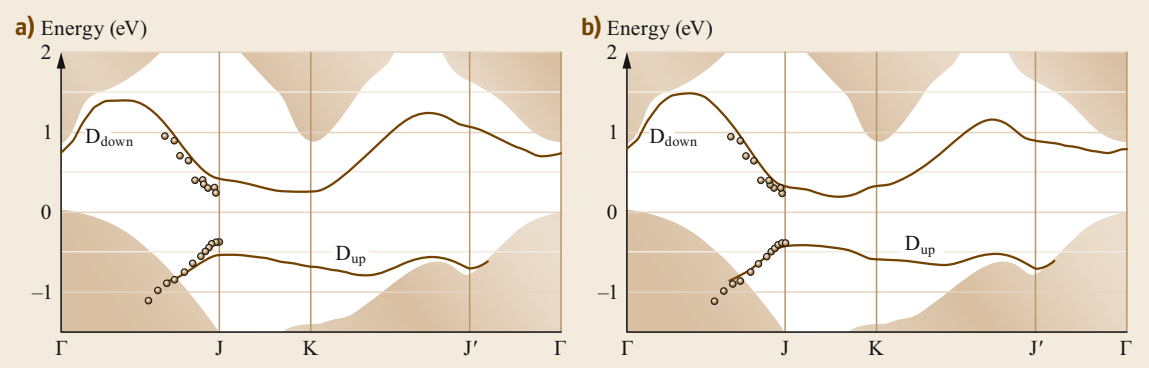

Fig. 20.16a,b GW band structure of the Ge(111)-(2 × 1) surface. **(a)** Positive buckling chain model. **(b)** Negative buckling chain model. The *brown area* represents the bulk state region. Experimental data (*dots*) from [20.142–144]

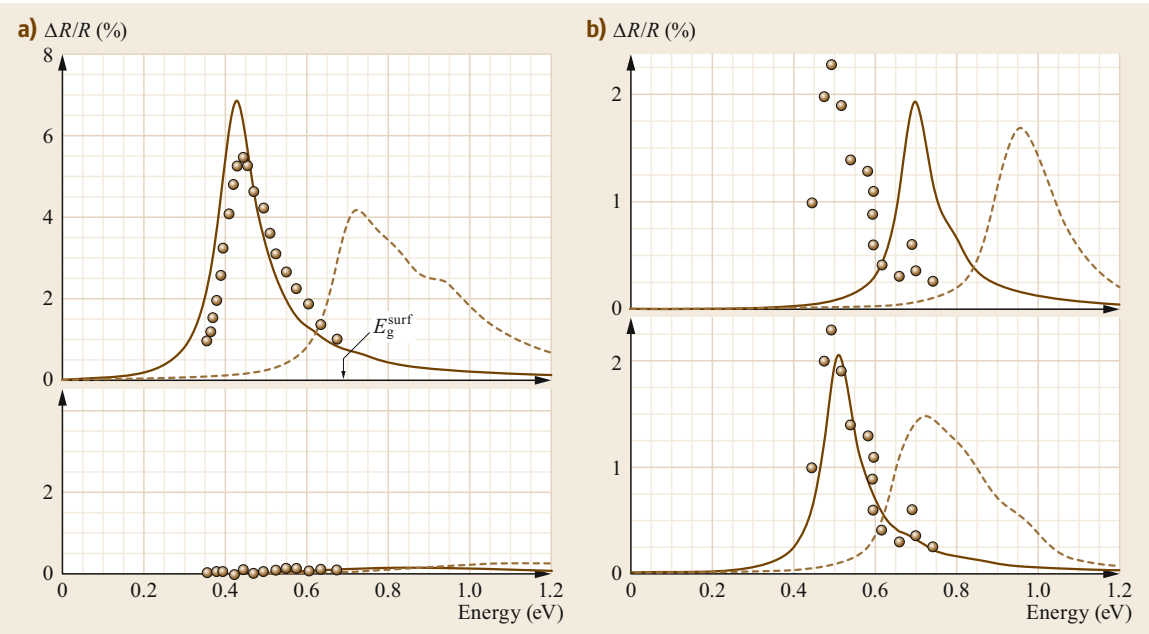

Fig. 20.17 **(a)** SDRS spectra at normal incidence of the positively buckled Si(111)-(2 × 1) surface, compared with experiments [20.146] (*dots*). The *solid* (*dashed*) *curves* include (neglect) electron–hole interaction. The electric field is parallel (*top*) and perpendicular (*bottom*) to the Pandey chains. **(b)** SDRS of the Ge(111)-(2 × 1) surface for positive (*top*) and negative (*bottom*) buckling chain models, compared with experimental data from [20.147] (*dots*)

The presence of the Pandey chains gives rise to a large anisotropy in the optical properties, as demonstrated by various experimental SDRS and RAS spectra measured at these surfaces since 1980 [20.146, 148, 149]. A large optical peak for light polarized along the Pandey chain direction is visible in the experimental spectra at 0.45 eV for Si and 0.49 eV for Ge. The comparison of the SDRS data with the corresponding BSE theoretically computed spectra clearly reveals the excitonic nature of this optical feature and the dominance of the negative isomer at the Ge surface and of the positive buckling in Si. In both surfaces, the excitonic effects are quite strong, drastically modifying the optical spectra calculated at the independent quasiparticle (IQP) level. *Rohlfing* and *Louie* [20.136] performed the first ab-initio BSE calculation of the SDRS of Si(111)-(2 × 1). Using the positive buckling Pandey chain model, they obtained a very good agreement with the experimental optical SDRS spectrum, proving the presence of a bound surface exciton and of the dominance of the right isomer in normally doped samples (Fig. 20.17a). RAS spectra recently computed

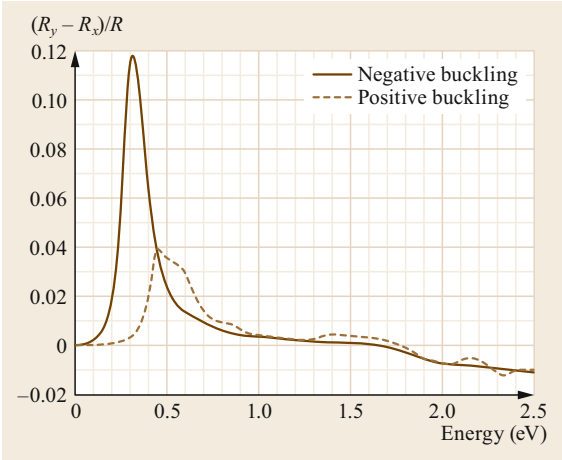

Fig. 20.18 RAS spectra of Si(111)-2 × 1 for positive and negative buckling structures, calculated within BSE; y is the [110] direction, parallel to the Pandey chains, and x is the [112] direction, perpendicular to the chains. An artificial broadening of 0.05 eV has been included

by *Violante* et al. [20.137] confirm this result. In this work, the authors extended the analysis to the negative bucking model, and Fig. 20.18 reports their RAS spectra calculated at the BSE level for both isomers.

Figure 20.17b shows the comparison of the SDRS experimental spectra with theoretical curves obtained at the IQP and BSE level of approximation, both for the negative and positive isomer of Ge(111)-(2 × 1) [20.138]. From Fig. 20.17 it is clear that the good agreement with experiment is, in this case, obtained by considering the negative chain model as the dominant reconstruction.

From the electronic and the optical experimental and theoretical data, the excitonic binding energy results to be 0.32 eV (0.13 eV) for the positive (negative) isomer in Si [20.137], while the corresponding values for Ge are 0.18 eV for the positive and 0.15 eV for the negative isomer [20.138]. The smaller binding energy for negative buckling isomers is consistent with the narrower electronic gaps and is a consequence of a more effective screening. The exciton is localized at the surface, along the chain for both isomers, and it is almost one-dimensional along the [110] direction, as a direct consequence of the weak interaction between the chains. The amplitude of probability of the electron is very large on the same chain where the hole is located, and it is already much weaker on the neighboring chains. The spatial distribution of the lowest excitonic wavefunction along this direction is different for the two isomers, as demonstrated for Si, where the probability to find the excited electron, keeping the hole position fixed along a Pandey chain, ranges over a larger

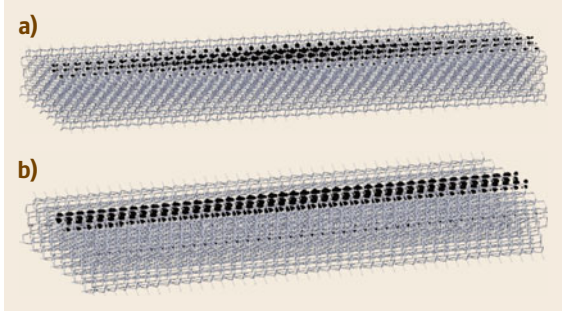

Fig. 20.19a,b Spatial distribution of the surface exciton at the Si(111)-(2 × 1) positive and negative buckling chain models. **(a)** Positive buckling, **(b)** negative buckling

distance along the [110] direction and decays to nearly zero in 80 Å for the positive buckling model, but still remains large for the negative buckling, with an estimated excitonic *length* larger than 80 Å (Fig. 20.19). As a consequence, the excitonic peak calculated is sharper in the case of negative buckling.

To conclude we can state that the accurate comparison of the results of ab-initio DFT plus MBPT simulations including the electron–hole interaction in the BSE approach, with the available experimental data have revealed that: i) in both Si and Ge(111)-(2 × 1) surfaces, the optical spectrum is dominated by the presence of bound surface excitons, with binding energy of the order of 0.25 eV; ii) the excitonic spatial distribution is highly anisotropic at the surface with the amplitude of the electron very large in the same Pandey chain where the hole is created. This analysis is obviously not accessible within the simpler one-particle picture of independent optical interband transitions.

20.6.2 Si(111)-(2 × 1) from TDDFT

As mentioned before, TDDFT is, in principle, exact for describing neutral excitations, and its advantage lies in the fact that the two-point response function $\chi(r, r', \omega)$ is needed instead of the four-point function of the Bethe–Salpeter approach. However, the exact form of the key ingredient of this approach, which is the exchange-correlation xc kernel f_{xc}, is unknown and needs to be approximated. The simplest and most used scheme for molecular systems, the adiabatic local density approximation (ALDA), is known to fail in extended systems such as surfaces. Other refined kernels have been derived in the last years but never tested on surfaces [20.67, 68, 150], while a nonlocal, static kernel with the correct long-range behavior, known as the RORO kernel [20.150] has been successfully applied only to three-dimensional systems. Moreover, several authors have derived another more elaborate nonlo-

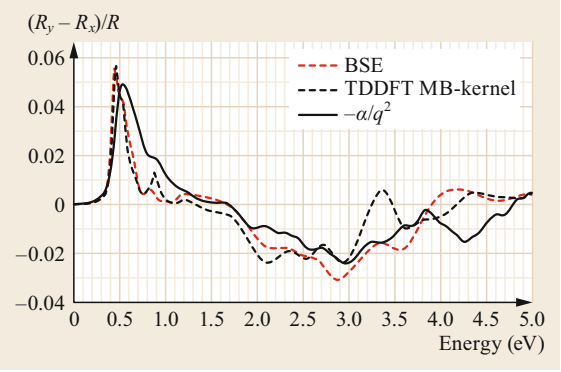

Fig. 20.20 Calculated RAS for Si(111)-(2 × 1) (positive buckling model) using different approaches: the Bethe–Salpeter equation; the TDDFT many-body kernel; and the TDDFT RORO [20.150] kernel with $\alpha = +0.2$

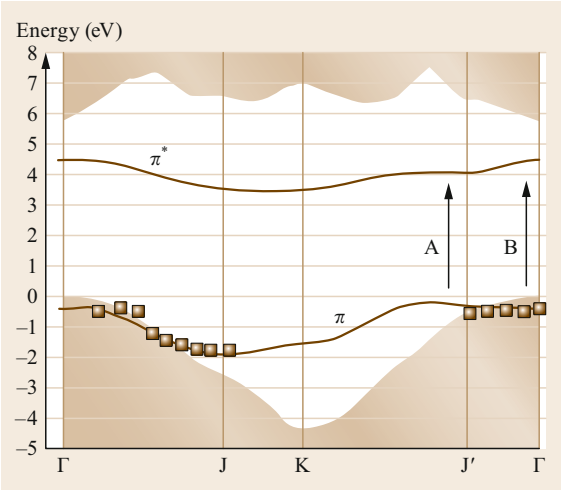

Fig. 20.21 Quasiparticle band structure of C(100)-(2 × 1) along high-symmetry lines of the surface Brillouin zone. *Brown regions* indicate the projected bulk band structure; *solid lines* are the dimer surface states. The *vertical arrows* indicate the two one-particle vertical transitions associated to the main optical peaks called A and B. Experimental data from [20.152]

cal and energy-dependent exchange-correlation kernel starting from the parallelism of the response function in TDDFT and many-body schemes. Also in this case, bulk and one-dimensional materials were studied, yielding a very good agreement with the BSE and experimental spectra.

Pulci et al. [20.151] selected Si(111)-(2 × 1) as a prototype surface for testing the performance of these different exchange-correlation kernels in TDDFT calculations to describe the surface optical properties. They showed how ALDA clearly fails to reproduce the excitonic optical peak of this surface, while the many-body derived TDDFT kernel reproduced a spectrum in very good agreement with the BSE one, both for transitions across surface states, where strong excitonic effects occur, and for bulk-like transitions (Fig. 20.20). Interestingly, using the static α/q^2 RORO kernel [20.150] the agreement with BSE results worsens slightly, but it is still very satisfactory.

20.6.3 Strongly-Bound Excitons on C(100)

At variance with Si(100), the lowest energy configuration of C(100) is the (2 × 1) unbuckled dimer reconstruction. While the tilting of dimer atoms at Si(100) breaks the surface symmetry and opens the gap between surface bands, the C(100)-(2 × 1) surface with symmetric dimers is already semiconducting, and a Jahn–Teller-like transition does not occur. Moreover, the localized nature of the C-2p orbital leads to a strong tendency to form a π bond within each dimer, giving a smaller interaction with neighboring dimers with respect to the case of silicon. The electronic band structure, obtained including the GW corrections, is shown in Fig. 20.21 together with direct photoemission data [20.152]. The agreement between theory and experiment is very good. The QP corrections do not affect the dispersion much but increase the LDA gaps between occupied and empty surface states by 1.8−2.1 eV. The minimum surface gap is indirect (along J′–K), and the surface bands are almost parallel near J′. This feature, together with the low dielectric screening of diamond, is the main reason for the formation of a strongly-bound exciton. The different behavior at the Si and diamond (100) surfaces is related to the different surface band structure of the two surfaces; while in the case of C(100) both surface LDA bands are within the gap (as in the case of the Si(111)-(2 × 1) and Ge(111)-(2 × 1) surfaces), with the empty one just in the middle of the gap; in the case of Si(100), both surface bands are energetically close to bulk bands.

Regarding the optical properties of this surface, several theoretical works, performed at different stages of approximation (DFT, GW, BSE), reported a strong anisotropy of the surface dielectric function for light polarized along and perpendicular to the dimer rows [20.76, 98]. Figure 20.22 reports results obtained from DFT-IP, GW-IQP, and BSE simulations (see [20.140] for more details). In the top panel (DFT-IP level), we see that two peaks (A and B), at 2.4 and 3 eV, which are due to surface-state to surface-state transitions, are present only for light polarized along the dimers (full lines) while for light polarized perpendicular to the dimers (dashed lines) the absorption onset occurs at 3.8 eV. On the central panel (self-energy

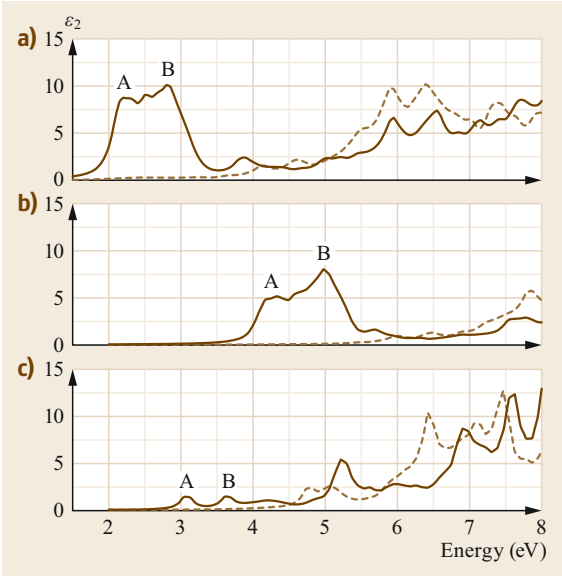

Fig. 20.22a–c Imaginary part of the surface dielectric functions of C(100)-(2 × 1) computed for light polarized along the dimers (*solid lines*) and in the perpendicular direction (*dashed lines*), computed at different levels of theory: **(a)** DFT-IP, **(b)** GW, and **(c)** GW (self-energy) + LFE (local-field effects) + BSE (excitonic effects). An artificial broadening of 0.1 eV has been used

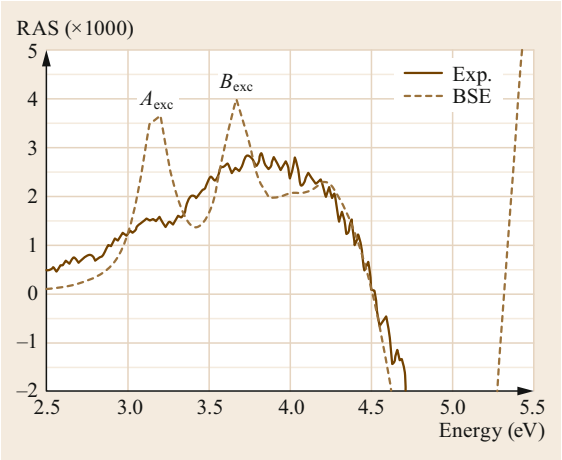

Fig. 20.23 RAS signal of the C(100) surface, calculated including excitonic, self-energy, and local-field effects (*dashed line*), compared with the experimental spectrum (*solid line*). A_{exc}, B_{exc} indicate the two bound excitons corresponding to the two one-particle transitions indicated with labels A and B in Fig. 20.21 (Reprinted with permission from [20.139]. Copyright (2005) by the American Physical Society)

effects included) we observe that the GW dielectric functions are essentially blue shifted by about 1.9 eV with respect to the DFT curves. Finally, on the third panel, when the e–h attractive interaction (W) and the local field effects ($\bar{v}$) are included through the solution of the Bethe–Salpeter equation, the surface dielectric function is redshifted by about 1 eV, and a significant shape and intensity modification is observed.

In Fig. 20.23, the RAS theoretical and experimental spectra are reported, the former at the BSE level of approximation, showing how the inclusion of local-field and excitonic effects provides a good agreement with experimental data. The inclusion of the electron–hole interaction in the calculation has dramatic effects: two strongly bound excitons (A_{exc} and B_{exc} in Fig. 20.23) develop from the corresponding one-particle transitions ([20.139, Fig. 3]). Good agreement with the experimental RAS curve behavior is also obtained in the region of interband transitions, with a deep negative contribution above 4.5 eV. This can be explained by the formation of bound excitons (with a binding energy of 0.9 eV), which induces a transfer of oscillator strength to lower energies for light polarized parallel to the dimers with a consequent depletion at higher frequencies.

The importance of excitonic and local-field effects in this surface is also clearly visible in the EELS spectrum [20.140]. Figure 20.24 reports the theoretical EEL spectra, obtained including many-body effects (Fig. 20.24b), are compared with the experimental data [20.153] (Fig. 20.24a). The experimental loss function is characterized by three main peaks located at 3.5, 4.7, and 5.9 eV. One can see that the agreement of the theoretical results with the experiment is reasonably good (Fig. 20.24b). The lowest energy double-peak (centered around 3.5 eV) is due to the excitation of the surface-state excitons, appearing at 3.1 and 3.8 eV in the surface dielectric functions; the calculated double peak corresponds well to the asymmetric experimental structure around 3.4 eV. The calculated structure at about 5 eV is due to surface state to surface state transitions, and the higher structures are mixed surface state to bulk state transitions.

In the interpretation of semiconductor surface optical data there has been a persistent discussion about the role of local-field effects. In fact, it is generally supposed that they are more important at the surface than in the bulk due to an increased inhomogeneity of the charge density, but due to the complexity of the problem, frequently these effects were studied by modeling the surface by a lattice of polarizable point atoms. In fact, the C(100) surface is an example where the optical anisotropy observed can be mainly attributed to the importance of local-field effects. Keeping in mind the atomic geometry of the surface reconstruction, it is clear that along the [011] direction, parallel

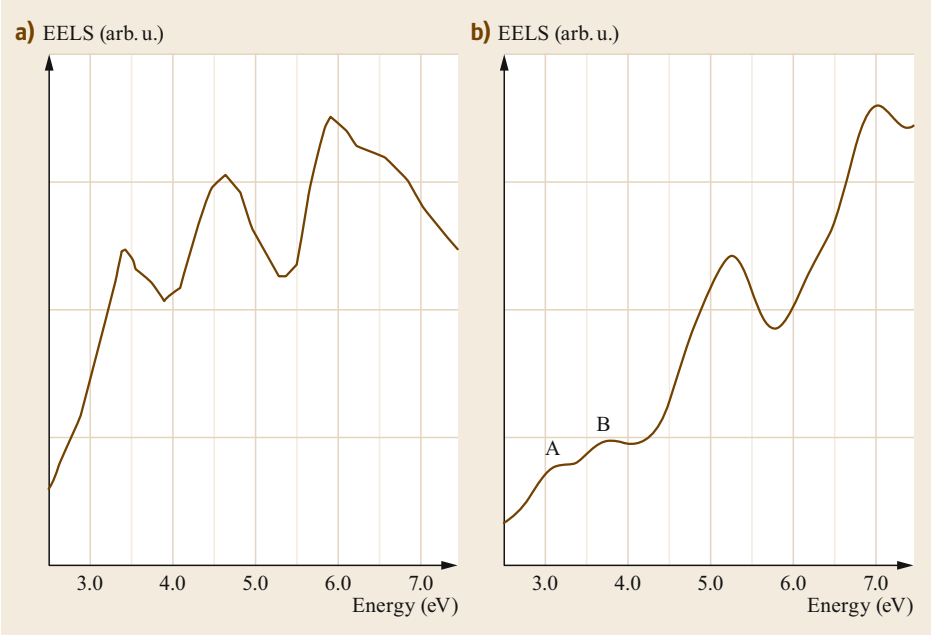

Fig. 20.24a,b Electron energy-loss spectrum of C(100)-(2 × 1). **(a)** Experimental data [20.153]. **(b)** Theoretical spectrum including excitonic effects

to the dimers (and perpendicular to the dimer rows), wide vacuum regions between the surface atoms are present, while in the $[0\bar{1}1]$ direction (which is the direction of the dimer rows) the atomic distances are similar to the bulk ones. In other words, the electric field for light polarized along [011] undergoes a surface distortion, such as to keep, according to Maxwell's boundary conditions, its electric displacement constant within the dimer rows and in between them. This can induce a strong reduction of the electric field within the dimer rows, and hence of the dielectric response for light polarized along the dimers ([011] direction). A similar anisotropic behavior of local-field effects (the so-called *depolarization effect*) has been observed in other strongly anisotropic systems like nanowires and nanotubes [20.154].

20.7 Concluding Remarks

We conclude this chapter with some comments on the practical challenges that face researchers in the field of surface interband excitations and mention some open questions.

First of all, we note that most of the systems discussed in this chapter correspond to relatively simple surfaces with small unit cells. Real surfaces can be much more complex, however. Even low-index surfaces can have huge unit cell reconstructions (e.g., Si(110)-(16 × 2) and Si(111)-(7 × 7)), vicinal surfaces like Si(557), adsorbate-stabilized nanostructured surfaces such as Ge(100):Au, and large systems containing d or f orbitals present an even tougher challenge. Other aspects of complexity derive from phenomena such as mixed domains, strain, surface charging, defects, and dislocations. Computation of optical properties in such systems can generally only be described using the simplest ab-initio approach, i.e., at the DFT-IP level, since self-energy calculations and the inclusion of excitonic and local-field effects become prohibitively heavy for slabs with hundreds of atoms inside large supercells. Other effects (strain, for instance, can penetrate hundreds of atomic layers) simply lie beyond any current ab-initio approach. However, we have seen that even in some of the simplest structures, the anisotropy of localized states make the DFT-IP approach unreliable. In these cases, the combined effects of quasiparticle, excitonic, and local-field corrections must be included in the description of the optical spectra. We expect that these phenomena may become even more important in highly nanostructured surfaces. Promising attempts have been made to avoid using GW and BSE using hybrid DFT functionals [20.117, 119], and fast and accurate TDDFT kernels (*bootstrap* kernels) may offer an alternative solution. The accuracy of these methods in surface systems, with respect to more

accurate GW-BSE approaches, needs to be carefully tested.

Another difficult task is the separation of the bulk and surface effects in the optical properties, due to the presence of *bulk-like* interband signals that are shifted or modified in shape by the presence of the surface. These effects can arise from interband transitions involving deep surface resonances or bulk states terminated at the surface, and often this identification remains a challenge. Although attempts have been made to understand the *derivative-like signals*, as in the spectra around E_1 and E_2 [20.155], respectively, at 2.6–3.0 and 4.5–4.7 eV in GaAs(110) [20.156], a microscopic understanding in terms of surface geometry is lacking. Another point is the effect of the use of finite slabs to model the surface-bulk systems. Although computation of optical spectra has a more critical dependence on the slab size thickness than, say, electron spectroscopy, there is no need to move beyond the slab model toward semi-infinite models in the computation of interband transitions if adequately thick slabs are used.

With regard to specific systems, a case that still seems unsolved is the (111) surface of diamond. After cleavage, the surface is not reconstructed, as the surface dangling bonds are mostly saturated by hydrogen atoms. After annealing at 700 K, hydrogen desorbs and the surface forms a (2×1) reconstruction. Total energy calculations indicate a Pandey chain geometry with no buckling and no dimerization as the most stable structure for the clean surface. In DFT-LDA calculations, this flat geometry gives origin to two surface bands nearly degenerate along the $\bar{J}$–$\bar{K}$ direction of the C(111)-(2×1) surface Brillouin zone. However, experimental RAS measurements show a peak extending from 1.1 to 2.8 eV with a maximum at 1.47 eV [20.157]. The experimental studies have been continued more recently [20.158], considering also the modifications of the RAS spectra induced by oxygen adsorption, comparing the shapes of surface spectra at the three (111)-(2×1) surfaces of C, Si and Ge, and their behavior upon adsorption, confirming for C the previous results and a shift similar to Si and reduction of the peak strength with oxygen uptake.

Calculation of GW corrections at the lowest level of approximation does not significantly open the gap along $\bar{J}$–$\bar{K}$ even if the effect is stronger elsewhere in the Brillouin zone. Inclusion of BSE corrections goes in the opposite direction and reduces the excitation energy. A detailed analysis [20.122] showed that the shape and location of the experimental peak can be obtained, if excitonic effects are included, only with an artificial opening of the gap by 1.8 eV. Further theoretical work [20.159] addressed this point, confirming the discrepancy between theory and experiments (always assuming this *ideal* flat surface reconstruction and the absence of defects in the theoretical computation). It has been suggested that the presence of low hydrogen contamination, defects, steps, and terraces could be responsible for the opening of the gap. A more accurate analysis is required, in both experiment and theory, to understand to what extent the interband excitations are due to the geometry of the clean surface, or to the presence of bonded hydrogen atoms and other surface steps or defects.

Thus, it is clear that even the simplest systems need further study. It is not surprising that another such surface presents aspects still to be clarified: the highly-studied Si(111)-(2×1) surface (now 40 years under investigation!). From a theoretical point of view, despite the very small difference in the total energy values of the two geometries, the energetically most stable reconstruction should be the *negative buckling* Pandey model, as obtained in the case of Ge. Experimentally, instead, the *positive buckling* isomer is seen, with the former occurring just in hyperdoped silicon samples. Again, the presence of defects, steps, and terraces could stabilize the positive buckling and be responsible for the observed preference. We have seen that the RAS spectra corresponding to the two geometries are significantly different, and this, in conjunction with other experimental local probes, can offer further tools of investigation.

To conclude, we note that 50 years of experimental study of surface optical properties, together with the development in the last four decades of theoretical methods well beyond the DFT-IP picture, have provided reliable tools for understanding surface interband excitations. Despite the technical difficulties present both in experiment and theory, it is now possible to describe the connection between surface interband transitions and the surface geometry to a high degree of sensitivity (including, as we have illustrated, details of the surface structure, stoichiometry, and composition). *Real* surfaces, featuring more complex geometries and morphology, will soon be accessible in the near future through combined experimental and theoretical studies, while simpler problematic cases still invite further investigation.

Acknowledgments. In this perspective, this chapter is dedicated to Wolfgang Richter and to Rodolfo Del Sole, as a tribute to their great contribution, through experiment and theory, to the understanding of surfaces.

References

20.1 J.F. McGilp: Probing surface and interface structure using optics, J. Phys. Condens. Matter **22**(8), 084018 (2010)

20.2 D.E. Aspnes: Above-bandgap optical anisotropies in cubic semiconductors: A visible–near ultraviolet probe of surfaces, J. Vac. Sci. Technol. B **3**(5), 1498 (1985)

20.3 V.L. Berkovits, I.V. Makarenko, T.A. Minashvili, V.I. Safarov: Optical transitions on GaAs [110] surface, Solid State Commun. **56**(5), 449–450 (1985)

20.4 G. Chiarotti, G. Del Signore, S. Nannarone: Optical detection of surface states on cleaved (111) surfaces of Ge, Phys. Rev. Lett. **21**(16), 1170–1172 (1968)

20.5 P. Weightman, D.S. Martin, R.J. Cole, T. Farrell: Reflection anisotropy spectroscopy, Rep. Prog. Phys. **68**(6), 1251–1341 (2005)

20.6 C. Noguez, O. Pulci: Quantum mechanical calculations of electronic and optical properties of surfaces. In: *Quantum Chemical Calculations of Surfaces and Interfaces of Materials*, ed. by V.A. Basiuk, P. Ugliengo (American Scientific Publishers, Los Angeles 2009) pp. 217–248

20.7 P. Chiaradia, G. Chiarotti: Surface differential reflectance–experiment. In: *Photonic Probes of Surfaces*, ed. by P. Halevi (Elsevier, Amsterdam 1995) p. 97

20.8 R. Forker, T. Fritz: Optical differential reflectance spectroscopy of ultrathin epitaxial organic films, Phys. Chem. Chem. Phys. **11**(13), 2142–2155 (2009)

20.9 G. Onida, W.G. Schmidt, O. Pulci, M. Palummo, A. Marini, C. Hogan, R. Del Sole: Theory for modeling the optical properties of surfaces, Phys. Status Solidi (a) **188**(4), 1233–1242 (2001)

20.10 M. Palummo, O. Pulci, R. Del Sole, A. Marini, P. Hahn, W.G. Schmidt, F. Bechstedt: The Bethe–Salpeter equation: A first-principles approach for calculating surface optical spectra, J. Phys. Condens. Matter **16**(39), S4313 (2004)

20.11 O. Pulci, M. Marsili, E. Luppi, C. Hogan, V. Garbuio, F. Sottile, R. Magri, R. Del Sole: Electronic excitations in solids: Density functional and Green's function theory, Phys. Status Solidi (b) **242**, 2737–2750 (2005)

20.12 W.G. Schmidt, K. Seino, P.H. Hahn, F. Bechstedt, W. Lu, S. Wang, J. Bernholc: Calculation of surface optical properties: From qualitative understanding to quantitative predictions, Thin Solid Films **455/456**, 764–771 (2002)

20.13 S.M. Anderson, N. Tancogne-Dejean, B.S. Mendoza, V. Véniard: Theory of surface second-harmonic generation for semiconductors including effects of nonlocal operators, Phys. Rev. B **91**(7), 075302 (2015)

20.14 C. Hogan, O. Pulci, P. Gori, F. Bechstedt, D.S. Martin, E.E. Barritt, A. Curcella, G. Prevot, Y. Borensztein: Optical properties of silicene, Si/Ag(111), and Si/Ag(110), Phys. Rev. B **97**(19), 195407 (2018)

20.15 S. Bouarab, M. Mebarki, A. Ziane, M. Khan: Ab initio origin of optical anisotropy in Ag(110), Phys. Rev. B **63**(19), 195409 (2001)

20.16 P. Monachesi, M. Palummo, S.R. Del, R. Ahuja, O. Eriksson, R. Del Sole: Reflectance anisotropy spectra of Cu and Ag (110) surfaces from ab initio theory, Phys. Rev. B **64**(11), 5421 (2001)

20.17 P. Monachesi, M. Palummo, R. Del Sole, A. Grechnev, O. Eriksson: Ab initio calculation of depth-resolved optical anisotropy of the Cu(110) surface, Phys. Rev. B **68**(3), 035426 (2003)

20.18 P. Monachesi, L. Chiodo: Optical response of the copper surface to carbon monoxide deposition, Phys. Rev. Lett. **93**(11), 116102 (2004)

20.19 R. Del Sole: Reflectance spectroscopy–Theory. In: *Photonic Probes of Surfaces*, ed. by P. Halevi (Elsevier, Amsterdam 1995) p. 131

20.20 S.L. Adler: Quantum theory of the dielectric constant in real solids, Phys. Rev. **126**(2), 413–420 (1962)

20.21 N. Wiser: Dielectric constant with local field effects included, Phys. Rev. **129**(1), 62–69 (1963)

20.22 J.D.E. McIntyre, D.E. Aspnes: Differential reflection spectroscopy of very thin surface films, Surf. Sci. **24**(2), 417–434 (1971)

20.23 A. Bagchi, R.G. Barrera, A.K. Rajagopal: Perturbative approach to the calculation of the electric field near a metal surface, Phys. Rev. B **20**(12), 4824–4838 (1979)

20.24 R. Del Sole: Microscopic theory of optical properties of crystal surfaces, Solid State Commun. **37**(7), 537–540 (1981)

20.25 R. Del Sole, E. Fiorino: Macroscopic dielectric tensor at crystal surfaces, Phys. Rev. B **29**(8), 4631–4645 (1984)

20.26 D.E. Aspnes, J.P. Harbison, A.A. Studna, L.T. Florez: Application of reflectance difference spectroscopy to molecular-beam epitaxy growth of GaAs and AlAs, J. Vac. Sci. Technol. A **6**(3), 1327 (1988)

20.27 G. Bauer, W. Richter (Eds.): *Optical Characterization of Epitaxial Semiconductor Layers* (Springer, Berlin, Heidelberg 1996)

20.28 M.A. Herman, W. Richter, H. Sitter: *Epitaxy*, Springer Series in Materials Science, Vol. 62 (Springer, Berlin, Heidelberg 2004)

20.29 C. Hogan, R. Del Sole: Optical properties of the GaAs(001)-c(4x4) surface: Direct analysis of the surface dielectric function, Phys. Status Solidi (b) **242**(15), 3040–3046 (2005)

20.30 E. Ferraro, C. Hogan, M. Palummo, R. Del Sole: Optical properties of the long-range Si(110)-(16x2) reconstruction from first principles, Phys. Status Solidi (b) **249**(6), 1148–1154 (2012)

20.31 S. Brodersen, W. Schattke: Calculation of the dielectric function for a semi-infinite crystal, Phys. Rev. B **66**(15), 153303 (2002)

20.32 C. Hogan, R. Del Sole, G. Onida: Optical properties of real surfaces from microscopic calculations of the dielectric function of finite atomic slabs, Phys. Rev. B **68**(3), 035405 (2003)

20.33 F. Manghi, R. Del Sole, A. Selloni, E. Molinari: Anisotropy of surface optical properties from first-

principles calculations, Phys. Rev. B **41**, 9935 (1990)
20.34 L. Vattuone, L. Savio, M. Rocca: High-resolution electron energy loss spectroscopy (HREELS): A sensitive and versatile surface tool. In: *Surface Science Techniques*, ed. by G. Bracco, B. Holst (Springer, Berlin, Heidelberg 2013) pp. 499–529
20.35 A. Balzarotti, M. Fanfoni, F. Patella, F. Arciprete, E. Placidi, G. Onida, R. Del Sole: The GaAs(001)-c(4x4) surface: A new perspective from energy loss spectra, Surf. Sci. **524**(1–3), L71–L76 (2003)
20.36 F. Arciprete, C. Goletti, E. Placidi, P. Chiaradia, M. Fanfoni, F. Patella, C. Hogan, A. Balzarotti: Surface versus bulk contributions from reflectance anisotropy and electron energy loss spectra of the GaAs(001)-c(4x4) surface, Phys. Rev. B **68**(12), 125328 (2003)
20.37 H. Ibach, D.L. Mills: *Electron energy loss spectroscopy and surface vibrations* (Academic Press, New York 1982)
20.38 A. Selloni, R. Del Sole: Optical and electron energy-loss spectra of Si(111)2x1, Surf. Sci. **168**(1–3), 35–45 (1986)
20.39 L. Caramella, C. Hogan, G. Onida, R. Del Sole: High-resolution electron energy loss spectra of reconstructed Si(100) surfaces: First-principles study, Phys. Rev. B **79**(15), 155447 (2009)
20.40 R. Esquivel-Sirvent, C. Noguez: Electron energy loss for anisotropic systems: Application to GaN ($10\bar{1}0$), Phys. Rev. B **58**(11), 7367–7372 (1998)
20.41 C. Hogan, M. Palummo, R. Del Sole: Theory of dielectric screening and electron energy loss spectroscopy at surfaces, C. R. Phys. **10**(6), 560–574 (2009)
20.42 E.K.U. Gross, J.F. Dobson, M. Petersilka: Density functional theory of time-dependent phenomena. In: *Density Functional Theory II*, ed. by R.F. Nalewajski (Springer, Berlin, Heidelberg 1996) pp. 81–172
20.43 P. Hohenberg, W. Kohn: Inhomogeneous electron gas, Phys. Rev. **136**(3B), B864–B871 (1964)
20.44 W. Kohn, L.J. Sham: Self-consistent equations including exchange and correlation effects, Phys. Rev. **140**(4A), A1133–A1138 (1965)
20.45 J.P. Perdew, Y. Wang: Pair-distribution function and its coupling-constant average for the spin-polarized electron gas, Phys. Rev. B **46**(20), 12947–12954 (1992)
20.46 R. Del Sole, R. Girlanda: Optical properties of semiconductors within the independent-quasiparticle approximation, Phys. Rev. B **48**(16), 11789–11795 (1993)
20.47 A.L. Fetter, J.D. Walecka: *Quantum Theory of Many-particle Systems* (Dover, London 2003) p. 565
20.48 G. Stefanucci, R. Van Leeuwen: *Nonequilibrium Many-body Theory of Quantum Systems* (Cambridge Univ. Press, Cambridge 2013)
20.49 G. Onida, L. Reining, A. Rubio: Electronic excitations: Density-functional versus many-body Green's-function approaches, Rev. Mod. Phys. **74**(2), 601–659 (2002)
20.50 P.M. Echenique, J.M. Pitarke, E.V. Chulkov, A. Rubio: Theory of inelastic lifetimes of low-energy electrons in metals, Chem. Phys. **251**(1–3), 1–35 (2000)
20.51 A. Marini, R. Del Sole, A. Rubio, G. Onida: Quasiparticle band-structure effects on the d hole lifetimes of copper within the GW approximation, Phys. Rev. B **66**(16), 161104 (2002)
20.52 L. Hedin: New method for calculating the one-particle Green's function with application to the electron-gas problem, Phys. Rev. **139**(3A), A796–A823 (1965)
20.53 W.G. Aulbur, L. Jönsson, J.W. Wilkins: Quasiparticle calculations in solids, Solid State Phys. **54**, 1–218 (1999)
20.54 O. Pulci, G. Onida, R. Del Sole, L. Reining: Ab initio calculation of self-energy effects on optical properties of GaAs(110), Phys. Rev. Lett. **81**(24), 5374–5377 (1998)
20.55 M. van Schilfgaarde, T. Kotani, S. Faleev: Quasiparticle self-consistent GW theory, Phys. Rev. Lett. **96**(22), 226402 (2006)
20.56 F. Caruso, P. Rinke, X. Ren, A. Rubio, M. Scheffler: Self-consistent GW: All-electron implementation with localized basis functions, Phys. Rev. B **88**(7), 075105 (2013)
20.57 M. Marsili, O. Pulci, F. Bechstedt, R. Del Sole: Electronic structure of the C(111) surface: Solution by self-consistent many-body calculations, Phys. Rev. B **72**(11), 115415 (2005)
20.58 J. Deslippe, G. Samsonidze, D.A. Strubbe, M. Jain, M.L. Cohen, S.G. Louie: BerkeleyGW: A massively parallel computer package for the calculation of the quasiparticle and optical properties of materials and nanostructures, Comput. Phys. Commun. **183**(6), 1269–1289 (2012)
20.59 W. Hanke: Dielectric theory of elementary excitations in crystals, Adv. Phys. **27**(2), 287–341 (1978)
20.60 G. Strinati: Application of the Green's functions method to the study of the optical properties of semiconductors, Riv. Nuovo Cimento **11**(12), 1–86 (1988)
20.61 E. Runge, E.K.U. Gross: Density-functional theory for time-dependent systems, Phys. Rev. Lett. **52**(12), 997–1000 (1984)
20.62 E.K.U. Gross, W. Kohn: Local density-functional theory of frequency-dependent linear response, Phys. Rev. Lett. **55**(26), 2850–2852 (1985)
20.63 M. Casida: Time-dependent density functional response theory of molecular systems: Theory, computational methods, and functionals. In: *Recent Developments and Applications of Modern Density Functional Theory*, ed. by J.M. Seminario (Elsevier, Amsterdam 1996) p. 391
20.64 J.F. Dobson, G. Vignale, M.P. Das (Eds.): *Electronic Density Functional Theory: Recent Progress and New Directions* (Springer, New York 1998)
20.65 V. Olevano, M. Palummo, G. Onida, R. Del Sole: Exchange and correlation effects beyond the LDA on the dielectric function of silicon, Phys. Rev. B **60**(20), 14224–14233 (1999)

20.66 F. Sottile, V. Olevano, L. Reining: Parameter-free calculation of response functions in time-dependent density-functional theory, Phys. Rev. Lett. **91**(5), 056402 (2003)

20.67 G. Adragna, R. Del Sole, A. Marini: Ab initio calculation of the exchange-correlation kernel in extended systems, Phys. Rev. B **68**(16), 165108 (2003)

20.68 A. Marini, R. Del Sole, A. Rubio: Bound excitons in time-dependent density-functional theory: Optical and energy-loss spectra, Phys. Rev. Lett. **91**(25), 256402 (2003)

20.69 W.G. Schmidt, N. Esser, A.M. Frisch, P. Vogt, J. Bernholc, F. Bechstedt, M. Zorn, T. Hannappel, S. Visbeck, F. Willig, W. Richter: Understanding reflectance anisotropy: Surface-state signatures and bulk-related features in the optical spectrum of InP(001)(2x4), Phys. Rev. B **61**(24), R16335–R16338 (2000)

20.70 O. Pulci, K. Lüdge, P. Vogt, N. Esser, W.G. Schmidt, W. Richter, F. Bechstedt: First-principles study of InP and GaP(001) surfaces, Comp. Mater. Sci. **22**(1/2), 32–37 (2001)

20.71 N. Esser, T. Hannappel, S. Visbeck: GaP (001) and InP(001): Reflectance anisotropy and surface geometry, J. Vac. Sci. Technol. B **17**(4), 1691–1696 (1999)

20.72 W.G. Schmidt, J.L. Fattebert, J. Bernholc, F. Bechstedt: Self-energy effects in the optical anisotropy of GaP(001), Surf. Rev. Lett. **06**(06), 1159–1165 (1999)

20.73 A.I. Shkrebtii, N. Esser, W. Richter, W.G. Schmidt, F. Bechstedt, B.O. Fimland, A. Kley, R. Del Sole: Reflectance anisotropy of GaAs(100): Theory and experiment, Phys. Rev. Lett. **81**(3), 721–724 (1998)

20.74 W.G. Schmidt, F. Bechstedt, K. Fleischer, C. Cobet, N. Esser, W. Richter, J. Bernholc, G. Onida: GaAs(001): Surface structure and optical properties, Phys. Status Solidi (a) **188**(4), 1401–1409 (2001)

20.75 F. Arciprete, C. Goletti, E. Placidi, C. Hogan, P. Chiaradia, M. Fanfoni, F. Patella, A. Balzarotti: Surface states at the GaAs(001)2x4 surface, Phys. Rev. B **69**(8), 081308 (2004)

20.76 C. Kress, A. Shkrebtii, R. Del Sole: Surface reflectance anisotropy of C(100) and Si(100) ab initio calculations within the pseudopotential plane wave approach, Surf. Sci. **377–379**, 398–403 (1997)

20.77 M. Palummo, G. Onida, R. Del Sole, B.S. Mendoza: Ab initio optical properties of Si (100), Phys. Rev. B **60**(4), 2522 (1999)

20.78 M. Palummo, N. Witkowski, O. Pluchery, R. Del Sole, Y. Borensztein: Reflectance-anisotropy spectroscopy and surface differential reflectance spectra at the Si(100) surface: Combined experimental and theoretical study, Phys. Rev. B **79**(3), 035327 (2009)

20.79 A. Ohtake, J. Nakamura, S. Tsukamoto, N. Koguchi, A. Natori: New structure model for the GaAs(001)-c(4x4) surface, Phys. Rev. Lett. **89**(20), 206102 (2002)

20.80 A. Ohtake, P. Kocán, J. Nakamura, A. Natori, N. Koguchi: Kinetics in surface reconstructions on GaAs(001), Phys. Rev. Lett. **92**(23), 236105 (2004)

20.81 C. Hogan, E. Placidi, R. Del Sole: Geometric structure and optical properties of the GaAs(001)-c(4×4) surface, Phys. Rev. B **71**(4), 041308 (2005)

20.82 W.G. Schmidt, F. Bechstedt, J. Bernholc: Terrace and step contributions to the optical anisotropy of Si(001) surfaces, Phys. Rev. B **63**(4), 045322 (2001)

20.83 S. Jaloviar, J.-L. Lin, F. Liu, V. Zielasek, L. McCaughan, M. Lagally: Step-induced optical anisotropy of vicinal Si(001), Phys. Rev. Lett. **82**(4), 791–794 (1999)

20.84 M. Marsili, O. Pulci: The fascinating physics of carbon surfaces: First-principles study of hydrogen on C(0 0 1), C(1 1 1) and graphene, J. Phys. D **43**(37), 374016 (2010)

20.85 M. Schwitters, D. Martin, P. Unsworth, T. Farrell, J. Butler, M. Marsili, O. Pulci, P. Weightman: Contribution of steps to optical properties of vicinal diamond (100):H surfaces, Phys. Rev. B **83**(8), 085402 (2011)

20.86 D.J. Chadi: Stabilities of single-layer and bilayer steps on Si(001) surfaces, Phys. Rev. Lett. **59**(15), 1691–1694 (1987)

20.87 M.-H. Tsai, Y.-Y. Yeh: Molecular-dynamics calculations of energetics and geometries of steps on diamond C(001), Phys. Rev. B **58**(4), 2157–2160 (1998)

20.88 A.A. Stekolnikov, J. Furthmüller, F. Bechstedt: Long-range surface reconstruction: Si(110)-(16x2), Phys. Rev. Lett. **93**(13), 136104 (2004)

20.89 N. McAlinden, J.F. McGilp: New evidence for the influence of step morphology on the formation of Au atomic chains on vicinal Si(111) surfaces, Europhys. Lett. **92**(6), 67008 (2010)

20.90 N. McAlinden, J.F. McGilp: Using surface and interface optics to probe the capping, with amorphous Si, of Au atom chains grown on vicinal Si(111), J. Phys. Condens. Matter **21**(47), 474208 (2009)

20.91 C. Braun, C. Hogan, S. Chandola, N. Esser, S. Sanna, W.G. Schmidt: Si(775)-Au atomic chains: Geometry, optical properties, and spin order, Phys. Rev. Mater. **1**(5), 055002 (2017)

20.92 C. Hogan, N. McAlinden, J.F. McGilp: Optical characterization of gold chains and steps on the vicinal Si(557) surface: Theory and experiment, Phys. Status Solidi (b) **249**(6), 1095–1104 (2012)

20.93 C. Hogan, R. Magri, R. Del Sole: Role of surface structural motifs on the stability and reflectance anisotropy spectra of Sb-rich GaSb(001) reconstructions, Phys. Rev. B **83**(15), 155421 (2011)

20.94 C. Hogan, R. Magri, R. Del Sole: Spontaneous Formation of surface antisite defects in the stabilization of the Sb-rich GaSb(001) surface, Phys. Rev. Lett. **104**(15), 157402 (2010)

20.95 W.G. Schmidt, P. Hahn, F. Bechstedt, N. Esser, P. Vogt, A. Wange, W. Richter: InP(001)-(2x1) surface: A hydrogen stabilized structure, Phys. Rev. Lett. **90**(12), 126101 (2003)

20.96 F. Fuchs, W. Schmidt, F. Bechstedt: Understanding the optical anisotropy of oxidized Si(001) surfaces, Phys. Rev. B **72**(7), 075353 (2005)

20.97 C. Hogan, L. Caramella, G. Onida: Simulation of the oxidation pathway on Si(100) using high-resolution EELS, Phys. Status Solidi (b) **249**(6), 1132–1139 (2012)

20.98 V.I. Gavrilenko, F. Bechstedt: Theory of reflectance anisotropy of clean and hydrogenated (001) diamond surfaces, Phys. Rev. B **56**(7), 3903–3906 (1997)

20.99 O. Pulci, M. Palummo, A.J. Shkrebtii, G. Onida, R.D. Sole, R. Sel Sole: Theoretical study of the surface optical properties of clean and hydrogenated GaAs (110), Phys. Status Solidi (a) **175**(1), 71–76 (1999)

20.100 P.H. Hahn, W.G. Schmidt, F. Bechstedt, O. Pulci, R. Del Sole: P-rich GaP(001)(2x1)/(2x2) surface: A hydrogen adsorbate structure determined from first principles calculations, Phys. Rev. B **68**(3), 033311 (2003)

20.101 A. Incze, R. Del Sole, G. Onida: Ab initio study of reflectance anisotropy spectra of a submonolayer oxidized Si(100) surface, Phys. Rev. B **71**(3), 035350 (2005)

20.102 C. Goletti, L. Fazi, C. Hogan, L. Persichetti, A. Sgarlata, M. Palummo, A. Balzarotti: Early oxidation stages of the strained Ge/Si(105) surface: A reflectance anisotropy spectroscopy study, Phys. Status Solidi (b) **252**(1), 87–94 (2015)

20.103 F. Fuchs, W.G. Schmidt, F. Bechstedt: Initial stage of Si(001) surface oxidation from first-principles calculations, J. Phys. Chem. B **109**(37), 17649–17653 (2005)

20.104 N. Witkowski, K. Gaál-Nagy, F. Fuchs, O. Pluchery, A. Incze, F. Bechstedt, Y. Borensztein, G. Onida, R. Del Sole: All-optical determination of initial oxidation of Si(100) and its kinetics, Eur. Phys. J. B **66**(4), 427–431 (2008)

20.105 K. Gaál-Nagy, A. Incze, G. Onida, Y. Borensztein, N. Witkowski, O. Pluchery, F. Fuchs, F. Bechstedt, R. Del Sole: Optical spectra and microscopic structure of the oxidized Si(100) surface: Combined in situ optical experiments and first principles calculations, Phys. Rev. B **79**(4), 045312 (2009)

20.106 T. Yasuda, S. Yamasaki, M. Nishizawa, N. Miyata, A. Shklyaev, M. Ichikawa, T. Matsudo, T. Ohta: Optical anisotropy of oxidized Si(001) surfaces and its oscillation in the layer-by-layer oxidation process, Phys. Rev. Lett. **87**(3), 037403 (2001)

20.107 D. Paget, C. Hogan, V. Berkovits, O. Tereshchenko: Surface and bulk origin of the optical anisotropy of As-rich GaAs(001) and Ga1-xInxAs(001), Phys. Rev. B **67**(24), 245313 (2003)

20.108 E. Placidi, C. Hogan, F. Arciprete, M. Fanfoni, F. Patella, R. Del Sole, A. Balzarotti: Adsorption of molecular oxygen on GaAs(001) studied using high-resolution electron energy-loss spectroscopy, Phys. Rev. B **73**(20), 205345 (2006)

20.109 C. Hogan, D. Paget, O. Tereshchenko, L. Reining, G. Onida: Optical anisotropy induced by cesium adsorption on the As-rich c(2x8) reconstruction of GaAs(001), Phys. Rev. B **69**(12), 125332 (2004)

20.110 C. Hogan, D. Paget, O.E. Tereshchenko, R. Del Sole: Effect of adsorption of electronegative and electropositive elements on the surface optical anisotropy of GaAs(001), Phys. Status Solidi (c) **2981**(8), 2976–2981 (2003)

20.111 C. Hogan, D. Paget, Y. Garreau, M. Sauvage, G. Onida, L. Reining, P. Chiaradia, V. Corradini: Early stages of cesium adsorption on the As-rich c(2x8) reconstruction of GaAs(001): Adsorption sites and Cs-induced chemical bonds, Phys. Rev. B **68**(20), 205313 (2003)

20.112 J. Power, O. Pulci, A. Shkrebtii, S. Galata, A. Astropekakis, K. Hinrichs, N. Esser, R. Sole, W. Richter: Sb-induced (1x1) reconstruction on Si(001), Phys. Rev. B **67**(11), 115315 (2003)

20.113 O. Pulci, K. Fleischer, M. Pristovsek, S. Tsukamoto, R. Del Sole, W. Richter: Structural analysis by reflectance anisotropy spectroscopy: As and Sb on GaAs(110), J. Phys. Condens. Matter **16**(39), S4367–S4374 (2004)

20.114 S. Wang, W. Lu, W.G. Schmidt, J. Bernholc: Nanowire-induced optical anisotropy of the Si(111)-In surface, Phys. Rev. B **68**(3), 035329 (2003)

20.115 S. Chandola, K. Hinrichs, M. Gensch, N. Esser, S. Wippermann, W.G. Schmidt, F. Bechstedt, K. Fleischer, J.F. McGilp: Structure of Si(111)-In nanowires determined from the midinfrared optical response, Phys. Rev. Lett. **102**(22), 226805 (2009)

20.116 E. Speiser, S. Chandola, K. Hinrichs, M. Gensch, C. Cobet, S. Wippermann, W.G. Schmidt, F. Bechstedt, W. Richter, K. Fleischer, J.F. McGilp, N. Esser: Metal-insulator transition in Si(111)-(4x1)/(8x2)-In studied by optical spectroscopy, Phys. Status Solidi (b) **247**(8), 2033–2039 (2010)

20.117 S. Jorgji, J.F. McGilp, C.H. Patterson: Reflectance anisotropy spectroscopy of Si(111)-(3x1)Li and Ag surfaces, Phys. Rev. B **87**(19), 195304 (2013)

20.118 C. Hogan, E. Ferraro, N. McAlinden, J.F. McGilp: Optical fingerprints of Si honeycomb chains and atomic gold wires on the Si(111)-(5x2)-Au surface, Phys. Rev. Lett. **111**(8), 087401 (2013)

20.119 C.H. Patterson, S. Banerjee, J.F. McGilp: Reflectance anisotropy spectroscopy of the Si(111)–(5x2)Au surface, Phys. Rev. B **94**(16), 165417 (2016)

20.120 K. Seino, W.G. Schmidt: H_2O on Si(001): Surface optical anisotropy from first-principles calculations, Surf. Sci. **571**(1–3), 157–160 (2004)

20.121 P.L. Silvestrelli, O. Pulci, M. Palummo, R. Del Sole, F. Ancilotto: First-principles study of acetylene adsorption on Si(100): The end-bridge structure, Phys. Rev. B **68**(23), 235306 (2003)

20.122 M. Marsili, N. Witkowski, O. Pulci, O. Pluchery, P.L. Silvestrelli, R. Del Sole, Y. Borensztein: Adsorption of small hydrocarbon molecules on Si surfaces: Ethylene on Si(001), Phys. Rev. B **77**(12), 125337 (2008)

20.123 M. Marsili, O. Pulci, M. Palummo, P.L. Silvestrelli, R. Del Sole: Electronic and optical properties of

acetylene and ethylene on Si(001), Superlattices Microstruct. **46**(1/2), 240–245 (2009)
20.124 W. Lu, W.G. Schmidt, J. Bernholc: Cycloaddition reaction versus dimer cleavage at the Si(001): C_5H_8 interface, Phys. Rev. B **68**(11), 115327 (2003)
20.125 W.G. Schmidt, F. Fuchs, A. Hermann, K. Seino, F. Bechstedt, R. Passmann, M. Wahl, M. Gensch, K. Hinrichs, N. Esser, S. Wang, W. Lu, J. Bernholc: Oxidation- and organic-molecule-induced changes of the Si surface optical anisotropy: Ab initio predictions, J. Phys. Condens. Matter **16**(39), S4323–S4334 (2004)
20.126 K. Seino, W.G. Schmidt: Reflectance anisotropy of uracil covered Si(0 0 1) surfaces: Ab initio predictions, Surf. Sci. **548**(1–3), 183–186 (2004)
20.127 A. Hermann, W.G. Schmidt, F. Bechstedt: Phenanthrenequinone adsorbed on Si(001): Geometries, electronic properties, and optical response, J. Phys. Chem. B **109**(16), 7928–7933 (2005)
20.128 C.A. Hacker, R.J. Hamers: Optical and electronic anisotropy of a π-conjugated molecular monolayer on the silicon(001) surface, J. Phys. Chem. B **107**(31), 7689–7695 (2003)
20.129 R. Forker, M. Gruenewald, T. Fritz: Optical differential reflectance spectroscopy on thin molecular films, Annu. Rep. Prog. Chem. Sect. C **108**, 34 (2012)
20.130 G. Bussetti, M. Campione, L. Ferraro, L. Raimondo, B. Bonanni, C. Goletti, M. Palummo, C. Hogan, L. Duò, M. Finazzi, A. Sassella: Probing two-dimensional vs three-dimensional molecular aggregation in metal-free tetraphenylporphyrin thin films by optical anisotropy, J. Phys. Chem. C **118**(29), 15649–15655 (2014)
20.131 O. Supplie, S. Brückner, O. Romanyuk, H. Döscher, C. Höhn, M.M. May, P. Kleinschmidt, F. Grosse, T. Hannappel: Atomic scale analysis of the GaP/Si(100) heterointerface by in situ reflection anisotropy spectroscopy and ab initio density functional theory, Phys. Rev. B **90**(23), 235301 (2014)
20.132 W. Lu, W.G. Schmidt, E.L. Briggs, J. Bernholc: Optical anisotropy of the SiC(001)-(3x2) surface: Evidence for the two-adlayer asymmetric-dimer model, Phys. Rev. Lett. **85**(20), 4381–4384 (2000)
20.133 P. Raiteri, D. Migas, L. Miglio, A. Rastelli, H. von Känel: Critical role of the surface reconstruction in the thermodynamic stability of {105} Ge pyramids on Si(001), Phys. Rev. Lett. **88**(25), 103–106 (2002)
20.134 L. Fazi, C. Hogan, L. Persichetti, C. Goletti, M. Palummo, A. Sgarlata, A. Balzarotti: Intermixing and buried interfacial structure in strained Ge/Si(105) facets, Phys. Rev. B **88**(19), 195312 (2013)
20.135 F. Bassani, G. Pastori Parravicini: *Electronic States and Optical Transitions in Solids* (Pergamon, New York 1975)
20.136 M. Rohlfing, S.G. Louie: Excitons and optical spectrum of the Si(111)-(2x1) surface, Phys. Rev. Lett. **83**(4), 856–859 (1999)
20.137 C. Violante, A. Mosca Conte, F. Bechstedt, O. Pulci: Geometric, electronic, and optical properties of the Si(111)2x1 surface: Positive and negative buckling, Phys. Rev. B **86**(24), 245313 (2012)
20.138 M. Rohlfing, M. Palummo, G. Onida, R. Del Sole: Structural and optical properties of the Ge(111)-(2x1) surface, Phys. Rev. Lett. **85**(25), 5440–5443 (2000)
20.139 M. Palummo, O. Pulci, R. Del Sole, A. Marini, M. Schwitters, S.R. Haines, K.H. Williams, D.S. Martin, P. Weightman, J.E. Butler: Reflectance anisotropy spectra of the diamond (100)-(2x1) surface: Evidence of strongly bound surface state excitons, Phys. Rev. Lett. **94**(8), 087404 (2005)
20.140 M. Palummo, O. Pulci, A. Marini, L. Reining, R. Del Sole: Ab initio calculation of many-body effects on the EEL spectrum of the C(100) surface, Phys. Rev. B **74**, 235431 (2006)
20.141 K.C. Pandey: New π-bonded chain model for Si(111)-(2×1) surface, Phys. Rev. Lett. **47**(26), 1913–1917 (1981)
20.142 J.M. Nicholls, B. Reihl: Antibonding surface state band of the Ge(111)2x1 surface, Surf. Sci. **218**(1), 237–245 (1989)
20.143 J.M. Nicholls, G.V. Hansson, U.O. Karlsson, R.I.G. Uhrberg, R. Engelhardt, K. Seki, S.A. Flodström, E.E. Koch: Confirmation of a highly dispersive dangling-bond band on Ge(111)-2x1, Phys. Rev. Lett. **52**(17), 1555–1558 (1984)
20.144 J.M. Nicholls, G.V. Hansson, R.I.G. Uhrberg, S.A. Flodström: Experimental dangling-bond band on the Ge(111)-(2x1) surface, Phys. Rev. B **27**(4), 2594–2597 (1983)
20.145 G. Bussetti, B. Bonanni, S. Cirilli, A. Violante, M. Russo, C. Goletti, P. Chiaradia, O. Pulci, M. Palummo, R. Del Sole, P. Gargiani, M.G. Betti, C. Mariani, R.M. Feenstra, G. Meyer, K.H. Rieder: Coexistence of negatively and positively buckled isomers on n^+-doped Si(111)-2x1, Phys. Rev. Lett. **106**(6), 067601 (2011)
20.146 P. Chiaradia, A. Cricenti, S. Selci, G. Chiarotti: Differential reflectivity of Si(111)2x1 surface with polarized light: A test for surface structure, Phys. Rev. Lett. **52**(13), 1145–1147 (1984)
20.147 S. Nannarone, P. Chiaradia, F. Ciccacci, R. Memeo, P. Sassaroli, S. Selci, G. Chiarotti: Surface states in Si(111)2x1 and Ge(111)2x1 by optical reflectivity, Solid State Commun. **33**(6), 593–595 (1980)
20.148 G. Chiarotti, S. Nannarone, R. Pastore, P. Chiaradia: Optical absorption of surface states in ultra-high vacuum cleaved (111) surfaces of Ge and Si, Phys. Rev. B **4**(10), 3398–3402 (1971)
20.149 C. Goletti, G. Bussetti, F. Arciprete, P. Chiaradia, G. Chiarotti: Infrared surface absorption in Si(111)-2x1 observed with reflectance anisotropy spectroscopy, Phys. Rev. B **66**(15), 153307 (2002)
20.150 L. Reining, V. Olevano, A. Rubio, G. Onida: Excitonic effects in solids described by time-dependent density-functional theory, Phys. Rev. Lett. **88**(6), 066404 (2002)
20.151 O. Pulci, A. Marini, M. Palummo, R. Del Sole: Test of long-range exchange-correlation kernels of time-dependent density functional theory at surfaces: Application to Si(111)2×1, Phys. Rev. B **82**(20), 205319 (2010)

20.152 R. Graupner, F. Maier, J. Ristein, L. Ley, C. Jung: High-resolution surface-sensitive C 1 s core-level spectra of clean and hydrogen-terminated diamond (100) and (111) surfaces, Phys. Rev. B **57**(19), 12397–12409 (1998)
20.153 T.W. Mercer, P.E. Pehrsson: Surface state transitions on the reconstructed diamond C(100) surface, Surf. Sci. **399**(1), L327–L331 (1998)
20.154 A.G. Marinopoulos, L. Reining, A. Rubio, N. Vast: Optical and loss spectra of carbon nanotubes: Depolarization effects and intertube interactions, Phys. Rev. Lett. **91**(4), 046402 (2003)
20.155 R. Del Sole, G. Onida: Surface versus crystal-termination effects in the optical properties of surfaces, Phys. Rev. B **60**(8), 5523–5528 (1999)
20.156 O. Pulci, G. Onida, R. Del Sole, A. Shkrebtii: Ab initio calculation of the reflectance anisotropy of GaAs(110), Phys. Rev. B **58**(4), 1922–1927 (1998)
20.157 G. Bussetti, C. Goletti, P. Chiaradia, T. Derry: Optical gap between dangling-bond states of a single-domain diamond C(111)-2x1 by reflectance anisotropy spectroscopy, Europhys. Lett. **79**(5), 57002 (2007)
20.158 B. Bonanni, G. Bussetti, A. Violante, P. Chiaradia, C. Goletti: Confinement effects in π-bonded chains at group IV semiconductor (111) surfaces, J. Phys. Condens. Matter **25**(48), 485008 (2013)
20.159 A.I. Shkrebtii, M. Marsili, E. Heritage, O. Pulci, R. Del Sole, F. Bechstedt: Defect induced modification of the surface gap and optical properties of C(111)2x1 surface, Phys. Status Solidi (a) **209**(4), 669–674 (2012)

Conor Hogan

Institute of Structure of Matter (ISM-CNR)
National Research Council of Italy
Rome, Italy
conor.hogan@ism.cnr.it

Dr Conor Hogan received his PhD in Physics from Trinity College Dublin (2001). He joined the Italian National Research Council (CNR) in 2005 and became a permanent Researcher in 2009 at the Institute of Structure of Matter (ISM) in Rome. His research interests include simulation of surface and interface spectroscopies from first principles, excitations in organic molecules and nanostructures, structural and electronic properties of 2D materials, and development of the Yambo code.

Maurizia Palummo

Dept. of Physics and INFN
University of Rome "Tor Vergata"
Rome, Italy
maurizia.palummo@roma2.infn.it

Professor Maurizia Palummo obtained her PhD in Physics in 1994. Following several postdoctorate and research positions, she has been Associate Professor at the Department of Physics of the University of Rome "Tor Vergata" since 2017. The main focus of her present research is on the ab-initio calculation of electronic and optical properties of surfaces, organic molecules, and derivatives and nanostructures, mainly nanowires and novel 2D materials.

Olivia Pulci

Dept. of Physics, and INFN
University of Rome "Tor Vergata"
Rome, Italy
olivia.pulci@roma2.infn.it

Professor Olivia Pulci obtained her PhD in Physics from the University of Rome "Tor Vergata" (1996). She was Researcher at Rome Tor Vergata until 2010, when she took up her present post as Associate Professor in Physics. Her research interests include ab-initio calculations of the electronic and optical properties of low-dimensional semiconductor structures (including surfaces, novel 2D systems, nanocrystals), but also of ice, water, and of cellulose for cultural heritage preservation.

Carlo M. Bertoni

Dept. of Physics, Informatics and Mathematics
University of Modena and Reggio Emilia
Modena, Italy
carlo.m.bertoni@gmail.com

Carlo Maria Bertoni graduated in physics (1970). He became Full Professor of Quantum Theory of Solids (University of Rome "Tor Vergata", 1987) and in Theoretical Physics (University of Modena, 1994). He served as Dean of the Faculty of Science (University of Modena, 2005-2012). His research fields include electronic, structural and vibrational properties of solids, low-dimensional systems, nanoscience, surfaces and interfaces, and theory of electron and X-ray spectroscopies using synchrotron radiation.

Part E Surface Magnetism

Part E Surface Magnetism

Part E is devoted to surface magnetism. Because translational invariance in the direction normal to the surface is broken at the surface itself, and due to the low dimensionality, broken bonds, and reduced coordination associated with surfaces, the magnetic properties of a surface or thin film may differ substantially from those of the same material in bulk form. On the other hand, a surface is also a template that can be used to grow magnetic nanostructures for magnetic memories. For the latter application, one has to keep in mind that the magnetic properties of the clusters depend on the magnetic coupling with the support. Decoupling from a metal substrate can be realized with ultrathin oxide films. A wide set of applications can be foreseen, covering information technology (data storage, processing, sensing), energy harvesting, power conversion (thermoelectric and spin-motive devices), and medicine (nanoparticles for drug targeting and hyperthermia).

Chapter 21 provides a pedagogic and broad introduction to surface magnetism starting from the fundamental concepts of the band structure model, which can be used to explain spin and orbital magnetic moments, exchange interactions, and magnetic anisotropy in low-dimensional structures. Solid surfaces, thin films, and noncollinear spin configurations including one-dimensional atomic chains and single-atom magnets are addressed. The latter represent magnetic structures at the ultimate size limit.

Chapter 22 focuses on the magnetic properties of transition metal oxide surfaces and thin films. After establishing a framework that distinguishes magnetic metal oxides from metallic magnetic materials, the chapter describes experimental methods that are used for sample preparation as well as to characterize the surface geometries and magnetic properties of these materials. Oxide/metal interface engineering through the use of buffer layers is covered as well. In the final section of the chapter, the interplay between magnetic and chemical properties is discussed.

21. Magnetic Surfaces, Thin Films and Nanostructures

Pietro Gambardella, Stefan Blügel

This chapter presents a pedagogical overview on fundamental aspects of surface and interface magnetism that have implications for the understanding of a broad variety of nanoscale magnetic and spintronic phenomena. We introduce general concepts derived from electronic band structure models to explain the evolution of the spin and orbital magnetic moments, exchange interaction, and magnetic anisotropy in low-dimensional structures. Trends due to the reduced symmetry and atomic coordination are emphasized, including the effects of spin–orbit coupling and the Dzyaloshinskii–Moriya interaction. We present spin Hamiltonian models that capture the collective behavior of a magnetic lattice and enable the description of the low-energy spin excitations as well as of the onset of magnetic order as a function of temperature in systems of arbitrary size and dimension. Finally, we illustrate the magnetic behavior of exemplary surface systems, such as the surfaces of bulk crystals, ultrathin films, non-collinear spin structures, and atomically engineered spin networks, including one-dimensional atomic chains and single-atom magnets.

Surface magnetism is a vast subject that has ramifications in several areas of condensed matter physics, materials science, and nanotechnology. Because the surface is what we can see and touch of a magnet, one could argue that the study of surface magnetism is as old as magnetism itself. However, the recognition that the surface properties of magnets are distinct from those of the bulk came relatively late, thanks to the work of Louis Néel, Francis Bitter, and others in the second half of the twentieth century. Starting in the 1970s, the development of increasingly sophisticated and reliable surface preparation methods, as well as of sensitive analysis techniques, revolutionized the field and brought surface magnetism to the forefront of fundamental and applied research. Today, the study of surfaces and interfaces overlaps with the fields of nanomagnetism and spintronics, forming one of the most lively areas of magnetism.

M. Rocca, T.S. Rahman, L. Vattuone (Eds.), *Springer Handbook of Surface Science*, Springer Handbooks,
https://doi.org/10.1007/978-3-030-46906-1_21

Surfaces have a dual nature. On the one hand, a surface represents the abrupt termination of a bulk crystal. As such, one may expect that the properties of a magnet will change in the proximity of the uppermost surface layers due to the reduced atomic coordination. On the other hand, a surface is a platform that can be used to fabricate and manipulate magnetic nanostructures. By using physical vapor deposition methods, such as molecular beam epitaxy or sputtering, and either top-down or bottom-up patterning techniques, structures of almost arbitrary shape and composition can be assembled. These structures present magnetic and electronic properties that do not exist in the bulk. Such a diversity of nano- and heterostructures underpins a wide spectrum of applications, ranging from information technology (data storage, processing, sensing) to energy harvesting, power conversion (thermoelectric and spin-motive devices), and medicine (nanoparticles for immunoassays, drug targeting, and hyperthermia).

The theoretical approaches used to predict and describe the magnetic properties of surfaces are based on either itinerant electronic band structure models extended from the bulk to low-dimensional systems or ligand field models extended from few atoms to structures of increasing size. As is typical in the description of correlated electron systems, the choice of one approach or another largely depends on the degree of electron localization as well as on the phenomena under investigation. In magnetic metals, for example, the unpaired electrons in the outer shells of the magnetic atoms are neither fully itinerant nor fully localized, which results in a rich variety of electronic and magnetic effects.

Despite this diversity, most of the peculiar features of surface magnetism can be attributed to a few basic facts, namely the change of the atomic coordination number and symmetry breaking. The purpose of this chapter is to present a pedagogical overview of these effects, focusing on ground-state properties such as the saturation magnetization, magnetic anisotropy, and critical temperature, as well as on the behavior of magnetic atoms in different coordination environments. The emphasis is on metal systems, but many of the concepts introduced here are general and can be extrapolated to insulators, semiconductors, and two-dimensional materials. Nonequilibrium effects, such as magnetization dynamics, magnetotransport properties, and voltage- or current-induced magnetization switching, are not treated explicitly. For a detailed description of these topics, we refer to more extensive reviews on ultrathin metal films [21.1–9], multiferroic heterostructures and oxide interfaces [21.10–12], magnetic clusters and nanoparticles [21.13–16], and single atoms [21.17–21]. Comprehensive reviews also exist on nonequilibrium effects such as spin dynamics in confined geometries [21.22–25], ultrafast magnetism [21.26], magnetotransport phenomena [21.27–32], as well as current-induced spin torques and magnetization switching [21.33–35].

21.1 Fundamentals

This section provides an overview of the theoretical concepts used to predict and analyze the magnetic ground state of surfaces and low-dimensional structures. The magnetic ground-state properties are determined by (i) the formation of local moments of different sizes, (ii) the interactions responsible for magnetic order as well as for the magnetic coupling at interfaces or across spacer layers, and (iii) the magnetic anisotropy energy, which couples the direction of the magnetization to the lattice and determines the easy and hard axes of magnetization. Table 21.1 compares the magnetic energies involved in (i)–(iii) with the structural and compositional ground-state energies of typical transition metals. From the relative importance of the different energies, it is evident that the formation of local magnetic moments has a considerable influence on the stability and structural arrangement of surfaces and interfaces. Since the local moments may change quite substantially in different coordination environments, materials with new and unknown phases [21.36], crystal structures, and magnetic structures [21.37] are to be expected. The anisotropy energy is a rather small quantity, being energetically nearly decoupled from the rest, but it has a strong influence on the stability and finite-temperature properties of thin films and nanoparticles. An important point related to (i) and (ii) is that the broken inversion symmetry of

Table 21.1 Typical ground-state energies for 3d metal films

Property	Energy (eV/atom)
Cohesive energy	5.5
Local moment formation	1.0
Alloy formation	0.5
Magnetic order	0.2
Structural relaxation	0.05
Magnetic anisotropy	10^{-4}–10^{-2}

surfaces and interfaces, which is common to all nanostructures, gives rise not only to the well-known symmetric Heisenberg exchange interaction but also to antisymmetric exchange, viz. the so-called Dzyaloshinskii–Moriya interaction (DMI), which favors non-collinear spin alignment (Sect. 21.1.6). Depending on the strength of the DMI, chiral or vortex-like spin structures such as spirals and skyrmions can emerge in thin magnetic films deposited on nonmagnetic substrates. Predicting the magnetic ground state of a low-dimensional magnetic system is therefore a highly nontrivial problem.

Historically, itinerant models of magnetism based on ab initio band structure calculations have been used to predict the magnetic ground state of metallic ferromagnets and antiferromagnets at zero temperature. On the other hand, the magnetism of complex spin structures, stemming from either itinerant or localized spins, has been almost exclusively discussed within the framework of spin lattice Hamiltonians, such as the Heisenberg and Ising models. Due to necessity of taking spin fluctuations into account, the temperature dependence of the magnetization has also been treated using spin lattice models. More recent approaches map the results of ab initio calculations onto Heisenberg-type Hamiltonians to study the thermodynamical properties of bulk and low-dimensional magnets [21.38]. In the following, we give a basic introduction to both itinerant and localized models of magnetism with an emphasis on dimensionality effects relevant to understanding the behavior of surfaces and nanostructures.

21.1.1 Stoner Model

This subsection focuses on the dimensional aspect of itinerant magnetism, in particular of those systems including d electrons, as relevant for the magnetic ground-state properties of metallic surfaces, heterostructures, and nanoparticles. Considering the vast number of possible systems, which grows quickly with the types of constituent atoms, the surface and interface orientation, the chemical and structural roughness at interfaces, and the electronic nature of the substrate (metal, semiconductor, or insulator), an exhaustive review of such effects is impractical. Instead, we discuss chemical trends for transition metals to develop an intuition of the dimensional aspects that influence the magnetic behavior of metallic surfaces, interfaces, multilayers, ultrathin films, and magnetic clusters deposited on surfaces. The simplest low-dimensional systems are isolated atoms, whose spin moments as a function of the number of d electrons are well described by Hund's first rule: the spins of all electrons in an atom are aligned parallel to each other as long as no quantum state is occupied more than once. Thus, nearly all of the 30 transition-metal atoms have magnetic spin moments. The largest possible d moments occur at the center of each series, i.e., 5 μ_B for Cr and Mn in the 3d series. On the other hand, it is well known that only 5 of the 30 transition metals remain magnetic in their bulk crystalline phase: Co and Ni are ferromagnetic, Cr is antiferromagnetic, and Mn and Fe are ferromagnetic or antiferromagnetic depending on their crystal structure (Fig. 21.1). Low-dimensional transition metals should fall in between these two extremes. Also, systems that are nonmagnetic as bulk metals may be magnetic at the surface or as nanostructures.

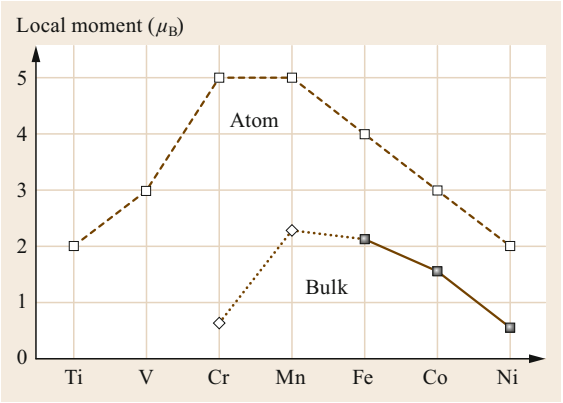

Fig. 21.1 Local magnetic moments of isolated 3d atoms (*empty squares* connected by *dashed line*), ferromagnetic (*solid squares* connected by *solid line*) and antiferromagnetic (*diamonds connected* by *dotted line*) 3d bulk metals. The magnetism of the atom includes only the moment due to the d electrons. For the bulk metals, the experimental spin moments are shown

Spontaneous magnetic moments in itinerant electron systems form due to the repulsive electron–electron interactions and Pauli exclusion principle, which favor either parallel or antiparallel alignment of the spin moments on neighboring lattice sites. Elements in the first half of the 3d series, if magnetic such as Cr and Mn, tend to develop antiferromagnetic exchange interactions. This is because the d-states at the bottom of the band have bonding character and singlet-like wavefunctions, with large amplitudes between atomic sites. As the electrons are more likely to be found close to each other, Pauli's exclusion principle forces their spins to be antiparallel. Elements in the second half of the 3d series, such as Fe, Co, and Ni, on the other hand, tend to develop ferromagnetic exchange interactions. This is because the wavefunctions in the upper half of the d-band have predominantly antibonding character, with a node between atomic sites. As a result, the d electrons are more localized, with a tendency to align their

spins parallel to each other. Exchange is usually introduced into band structure calculations by means of an exchange–correlation potential, which shifts the energy eigenvalues by a constant amount $\mp(1/2)Im_S$, where m_S is the local spin magnetic moment given by the integral of the magnetization density over the atomic unit cell and I is the exchange integral (the Stoner parameter). In the rigid band approximation, the energy eigenvalues for spin up ($\uparrow$) and spin down ($\downarrow$) electrons are thus given by

$$\varepsilon_\nu^{\uparrow,\downarrow}(\boldsymbol{k}) = \varepsilon_\nu^0(\boldsymbol{k}) \mp \frac{1}{2} I m_S \,, \tag{21.1}$$

where $\varepsilon_\nu^0(\boldsymbol{k})$ is the energy dispersion of the electron states in the absence of exchange, $\boldsymbol{k}$ is the electron's wavevector, and ν is a band index. The densities of states (DOS) $n^{\uparrow,\downarrow}(E)$ are also shifted compared with the DOS $n^0(E)$ of the nonmagnetic metal

$$n^{\uparrow,\downarrow}(E) = \sum_\nu \int_{\mathrm{BZ}} \delta\left(E - \varepsilon_\nu^{\uparrow,\downarrow}\right) \mathrm{d}\boldsymbol{k} = n^0\left(E \pm \frac{1}{2} I m_S\right) , \tag{21.2}$$

where the integral is over the Brillouin zone. From (21.2), one obtains the number N of electrons and m_S as the sum and difference, respectively, of the occupied spin-up and spin-down states integrated up to the Fermi energy E_F,

$$N = \int^{E_F} \left[n^0\left(E + \frac{1}{2} I m_S\right) + n^0\left(E - \frac{1}{2} I m_S\right) \right] \mathrm{d}E \,, \tag{21.3}$$

$$m_S = \int^{E_F} \left[n^0\left(E + \frac{1}{2} I m_S\right) - n^0\left(E - \frac{1}{2} I m_S\right) \right] \mathrm{d}E \,. \tag{21.4}$$

Equations (21.3) and (21.4) can be solved self-consistently with the condition of charge neutrality that determines N, thus E_F gives nonmagnetic solutions $m_S \neq 0$ only if the so-called Stoner criterion is satisfied, namely

$$I n^0(E_F) > 1 \,. \tag{21.5}$$

The Stoner criterion is thus an instability condition that expresses the competition between the exchange interaction that drives the system into ferromagnetism for large I and the kinetic energy of the electrons. The kinetic energy increases if the system becomes magnetic, as exchange splitting raises the energy of the spin-down (minority) states above E_F. However, if $n^0(E_F)$ is large, a large gain in exchange energy can be realized for relatively little cost in kinetic energy. The rigid band shift exemplified in (21.1) is a simplified model that works well for small values of the exchange splitting energy Im_S, as is the case for bulk ferromagnets. Although deviations can be found for thin films, as the magnetic moments and thus the exchange splitting are large, this model provides a good basis for discussing trends in magnetic moment formation across the Periodic Table as well as dimensionality effects. Moreover, the Stoner criterion can be generalized to antiferromagnetic as well as non-collinear spin structures by introducing a staggered susceptibility $\chi_{\boldsymbol{q}}$ that describes the tendency to form a frozen spin wave of wavevector $\boldsymbol{q}$ and is proportional to the local DOS, which favors the formation of stable moments for $I\chi_{\boldsymbol{q}}(E_F) > 1$ [21.6].

21.1.2 Role of the Coordination Number

The exchange integral I is an intra-atomic, element-specific quantity that, in the simplest approximation, is independent of the local environment, the structure, and the site of a given atom, e.g., in the surface or bulk. According to *Gunnarsson* [21.39] and *Janak* [21.40], the global trend

$$I_{3d} > I_{4d} > I_{5d} \tag{21.6}$$

is found for the exchange integrals of the 3d, 4d, and 5d transition-metal series. Focusing on the d electrons as those relevant for itinerant magnetism, the DOS depends on both the coordination number N_{nn} and the hopping matrix elements h_d between the d-states. This can be understood as follows: The integral of the d-DOS (corresponding to states with angular momentum quantum number $l = 2$) is $\int_W n_l(E)\mathrm{d}E = 2l + 1$, where W is the bandwidth of the d-states. Thus, in the simplest approximation possible (i.e., a rectangular-shaped DOS), one can assume that the local DOS scales inversely proportionally to the bandwidth W,

$$n(E_F) \propto \frac{1}{W} \,. \tag{21.7}$$

In the atomic limit, the bandwidth converges to zero, the Stoner criterion is always fulfilled, and moments in accordance with Hund's first rule will be found. In general, the DOS consists of contributions from electrons in s, p, d, and f states. For transition metals, by far the largest contribution comes from the d electrons, and the d–d hybridization determines the shape of the DOS. Therefore, in the following discussion, we restrict our-

selves to d electrons and write

$$n(E_F) \approx n_d(E_F) \approx \frac{1}{W_d} . \tag{21.8}$$

The average local bandwidth $\overline{W}_d(\boldsymbol{R}_i)$ for atom i at position $\boldsymbol{R}_i$ can be estimated in a nearest-neighbor tight-binding model, applicable for the itinerant but tightly bound d electrons of transition-metal atoms, as

$$W_d \approx \overline{W}_d(\boldsymbol{R}_i) = 2\sqrt{N_{nn}(\boldsymbol{R}_i)}\, h_d(R_{nn}) . \tag{21.9}$$

According to (21.9), the bandwidth depends on two quantities: (a) the hopping matrix element h_d of the d electrons and (b) the number of nearest-neighbor atoms N_{nn} (the coordination number). The influence of these parameters is discussed below.

(a) h_d depends on the overlap of the d wavefunctions, decreasing with increasing distance R_{nn} to the nearest-neighbor atoms. For a given lattice constant, h_d increases with the extension of the wavefunction or, equivalently, the number of nodes. Figure 21.2 shows a schematic of the bandwidths of 3d, 4d, and 5d bulk transition metals, together with the bandwidths of rare earths and actinides. In line with the arguments of increasing number of nodes from 3d to 5d wavefunctions, a clear *macrotrend* emerges in the transition-metal series, which can be summarized as follows

$$\begin{aligned} h_{3d} < h_{4d} < h_{5d} &\Longrightarrow W_{3d} < W_{4d} < W_{5d} \\ &\Longrightarrow n_{3d} > n_{4d} > n_{5d} . \end{aligned} \tag{21.10}$$

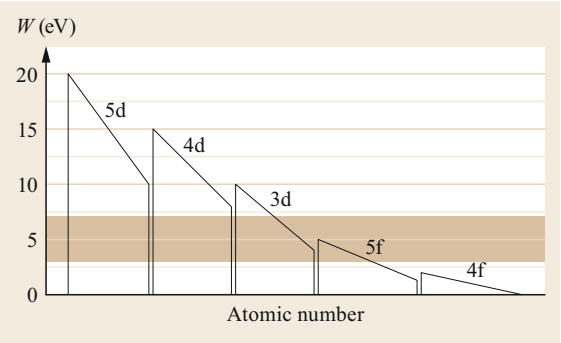

Fig. 21.2 Schematic illustration of bandwidth W of transition metals together with rare earths (4f) and actinides (5f) in the bulk phase. The 5f electrons of the early actinides and the 3d electrons of transition metals from the middle to the end of the 3d series (Cr to Ni) show itinerant magnetism, whereas the late actinides and the rare earths are best described by a localized electron picture with magnetic properties determined, to a good approximation, by Hund's rules. The *shaded rectangle* indicates the region favorable for band magnetism. Above the rectangle magnetism is suppressed, while below the rectangle localized (atomic) magnetism is preferred

Within each transition-metal series, there exists in addition a microtrend: due to the incomplete screening of the Coulomb potential of the nucleus by the d electrons, the d wavefunctions are more extended at the beginning than at the end of the series, thus the hopping matrix element is larger at the beginning than at the end of the series, which has consequences for the bandwidth W and DOS $n(E_F)$.

(b) The smaller the value of N_{nn}, the smaller the d–d hybridization and the width of the d-bands. Consider, for example, an atom in the environment of a face-centered cubic (fcc) crystal ($N_{fcc} = 12$), in the (001) surface ($N_{(001)} = 8$), in a two-dimensional (001) monolayer (ML) film ($N_{ML} = 4$), and in a monatomic chain ($N_{chain} = 2$), keeping the nearest-neighbor distance fixed ($R_{nn} = \text{const}$) and the bond strength fixed ($h_d = \text{const}$). Under these circumstances, one obtains for the ratio of the bandwidths

$$W_d^{chain} : W_d^{ML} : W_d^{(001)} : W_d^{fcc} = 0.41 : 0.58 : 0.82 : 1 , \tag{21.11}$$

or the local DOS

$$n_d^{chain} : n_d^{ML} : n_d^{(001)} : n_d^{fcc} = 2.45 : 1.73 : 1.22 : 1 . \tag{21.12}$$

The important message of (21.11) and (21.12) is that the reduction of the coordination number leads to less d–d hybridization and thus band narrowing, and the tendency towards magnetism is considerably increased. The reduction of the coordination number is hence responsible for the fact that the magnetism is enhanced at surfaces as compared with bulk, and the magnetism of ultrathin films should be larger than at surfaces. A nice manifestation of these arguments is shown in Fig. 21.3a, where the spin-resolved DOS of single-monolayer Fe and of a single Fe atom adsorbed on the Au(111) surface are calculated from first principles [21.41]. Clearly, the width of the 3d-band of the single Fe atom is smaller than that of the Fe monolayer and much smaller compared with the Au 5d-band, whereas $n(E_F)$ is largest for the single Fe atom. Accordingly, the spin and magnetic moments of the single Fe atoms are larger than those of the Fe monolayer, and both are enhanced relative to the bulk Fe moments. The arguments put forward here for the increased ferromagnetism in reduced dimension can be carried over directly to antiferromagnetism. Additionally, one can expect that transition metals, which are nonmagnetic as bulk metals, will become magnetic at surfaces or as ultrathin films.

The magnetic properties are expected to depend also on the surface or film orientation, because along with

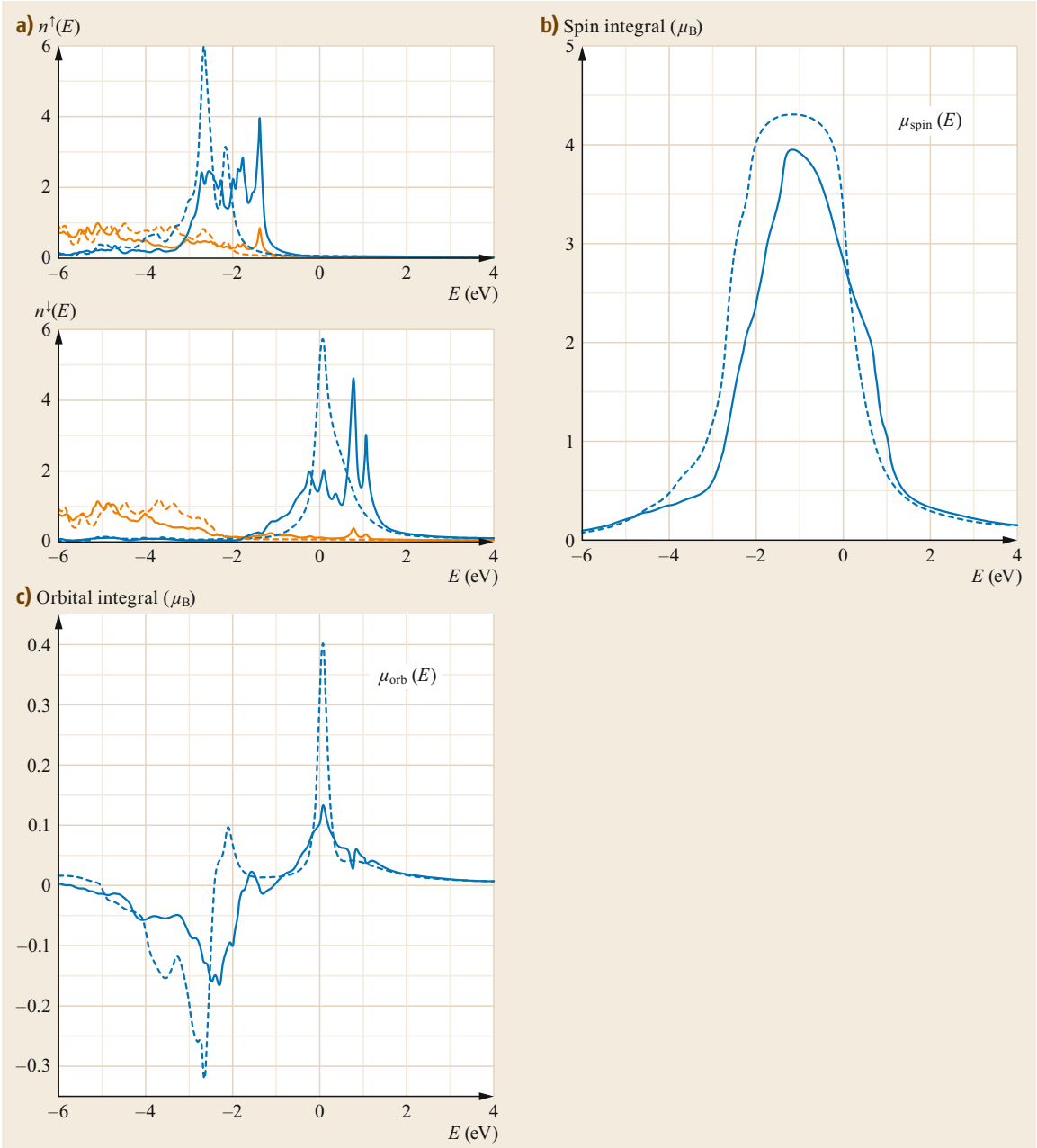

Fig. 21.3 **(a)** Spin-resolved DOS of 1 ML of Fe/Au(111) (*solid lines*) and a single Fe atom on Au(111) (*dashed lines*) calculated ab initio using density functional theory. *Blue* and *yellow lines* represent the DOS projected on Fe and Au orbitals, respectively. Supported atoms are treated as a perturbation on the clean surface using a relativistic impurity Green function formalism [21.42]. **(b,c)** Spin and orbital magnetic moment per Fe atom as a function of energy relative to the Fermi level. Note that the spin moment is maximum and the orbital moment is minimum at $E \approx -1$ eV, corresponding to a half-filled d-band, in agreement with the first and second Hund rules. Figure courtesy of *Šipr* and *Minár*, based on calculations reported in [21.41, 43]

Table 21.2 Coordination number N_{nn}, interlayer distance t, point symmetry S, and packing density ρ (fraction of area of surface unit cell covered by atoms represented by touching spheres) for an fcc lattice. Only the three low-index surfaces, (001), (011), and (111), are considered. a is the lattice parameter of the simple cubic unit cell

Surface	N_{nn}	S	t/a	ρ
(111)	9	C_{3v}	0.5774	0.9068
(001)	8	C_{4v}	0.5000	0.7854
(011)	7	C_{2v}	0.3536	0.5554

a change of the surface orientation goes a change of the coordination number N_{nn} (Table 21.2) as well as a change of the nearest-neighbor distance $R_{\parallel}$ between the surface atoms and the distance $R_{\perp}$ between the surface atoms and the atoms in the next layer. For an fcc lattice, the (111) surface is the most densely packed one, leading to the smallest enhancement of the magnetic moments. Among the three low-index surfaces with orientation (001), (011), and (111), the (011) surface is the most open. For the latter, we expect the largest magnetic moments. At surfaces or ultrathin films with body-centered cubic (bcc) lattice structure, the trend should be exactly the opposite. The most densely packed surface is the (011) surface, for which we expect the smallest enhancement of the magnetic moments. The (111) surface is the most open. This surface is already close to a stepped one.

The coordination number discussed so far is an important aspect in interface magnetism but not the whole story. Further important aspects have to be taken into account to provide a qualitatively correct description of magnetism at surfaces and interfaces, as described below.

Point Symmetry

The disruption of the translational symmetry perpendicular to a surface or interface reduces the point symmetry. Degeneracies typical for cubic bulk metals may be lifted. One example is the threefold-degenerate t_{2g} orbital, which is split into a twofold-degenerate state and a nondegenerate state at a (001) surface. This symmetry breaking induces a splitting or broadening of the DOS and makes magnetism unfavorable. A famous victim of this scenario is Pd. Bulk Pd has a large DOS at the Fermi level, which contributes to a large exchange-enhanced susceptibility. Thus, bulk Pd is nearly ferromagnetic. The band narrowing experienced at the surface due to the reduction of the coordination number should drive the surface of Pd into a ferromagnetic state, but this is not the case. Instead, the change of the surface symmetry splits the states at the Fermi energy, broadens the DOS, and counteracts the band narrowing. The surface of Pd(001) thus remains nonmagnetic.

Shift of the d-Band Relative to the sp-Band

Compared with an isolated atom, the d electrons in a solid are in a state of compression. Therefore, their energy levels are positioned at a much higher energy than in an atom. At the surface, the charge density of the d electrons can relax and their energy levels move downwards, closer to the bottom of the sp-band, leading to an increase of the number of d electrons. This downward shift is often facilitated by a significant hybridization of the d electrons with sp electrons or holes in the case of a transition-metal film deposited on a nonmagnetic metal substrate. As depicted in Fig. 21.4a, this effects leads to a Lorentzian tail of the DOS. If this tail is positioned close to the Fermi energy, magnetism can be drastically reduced due to the decrease of the Fermi-level DOS. An example of this effect is a single Ni monolayer on Cu(100), for which the local Ni moment amounts to 0.33 μ_B, which is smaller than the magnetic moment of Ni atoms at the Ni(100) surface (0.72 μ_B). For the same reason, a monolayer of Pd on Ag(100) is nonmagnetic, whereas small Pd clusters support the formation of 4d magnetic moments [21.44, 45]. In both cases, we would expect an increase of the moment due to the reduction of the coordination number by a factor two when compared with the respective (100) surfaces. On the other hand, elements at the beginning of the transition-metal series such as V profit from this effect, and magnetism can appear more likely.

sp–d Dehybridization

The main carriers of itinerant magnetism are the d electrons. In free atoms, the number of d electrons is an integer. In metallic systems, the number of d electrons is noninteger and depends on, besides the dominating d–d hybridization, the hybridization with the s and p electrons. Due to sp–d hybridization, the d-states below the Fermi energy are mixed into unoccupied sp hybrids, which reduces the number of d electrons in bulk systems compared with free atoms. If the coordination number decreases or the nearest-neighbor distance increases, the d-states become more localized, leading to sp–d dehybridization and a consequent increase in the occupation of the d-states, as illustrated in Fig. 21.4b. Surfaces and monolayers, with their smaller coordination numbers, therefore have a higher number of d electrons favorable for magnetism.

Charge Neutrality

Local charge neutrality has to be fulfilled to avoid the appearance of strong Coulomb forces. Band narrowing (at interfaces) automatically means that the number

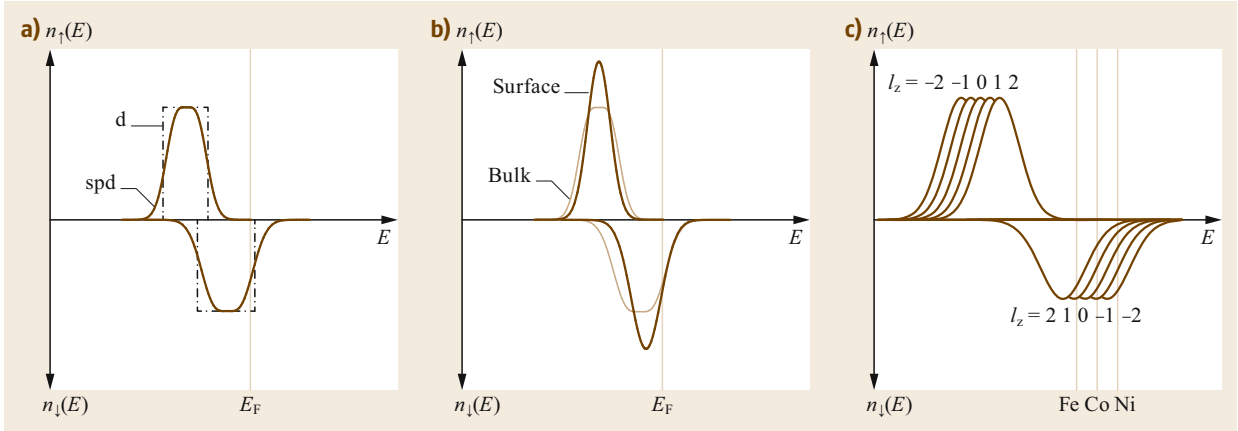

Fig. 21.4 **(a)** Schematic illustration of hybridization of d electrons of a magnetic layer with sp electrons, e.g., of the substrate. The *dot-dashed* (*solid*) line shows the d-projected DOS in the absence (presence) of sp–d hybridization. **(b)** Schematic illustration of the role of sp–d dehybridization on the DOS of the d electrons. The integrated density of d-states for the surface is larger than for the bulk. Note also that the exchange splitting between majority and minority states is larger for the surface because of the upward shift of the minority DOS. **(c)** Schematic DOS of a 3d bulk metal, showing the hybridization of states with different orbital angular momentum quantum number l_z. The spin–orbit coupling partially removes the degeneracy between the $+l_z$ and $-l_z$ states, inducing a net orbital moment. The *dashed line* indicates the approximate position of the Fermi level for Fe, Co, and Ni. (Adapted by permission from [21.46] © APS 1990)

of electrons must change. To avoid charged interfaces, a realignment of the center of gravity of the bands occurs (Fig. 21.4b). The d band, which moved to lower energy in order to relax the compression, now moves upwards again. Due to this upward shift in energy, the minority and majority electrons depopulate by different amounts. Together with the change of the number of majority electrons due to the sp–d dehybridization, this effect leads to an increase of the magnetic moment. All together, we find a complex alignment of each band, which depends on the symmetry of the Bloch wavefunctions.

Strong and Weak Ferromagnets

Strong ferromagnets (magnets with filled majority band) are less sensitive to changes of the coordination number and the lattice parameter relative to weak ferromagnets (magnets with partly occupied majority bands). Neglecting these interwoven effects has been a source of confusion in the past. They are readily included by performing self-consistent first-principles calculations.

21.1.3 Spin and Orbital Moments

The magnetic moment discussed in the previous section, given by (21.4), is clearly a consequence of the imbalance of spin-up and spin-down electrons caused by intraatomic exchange–correlation effects and is, therefore, a pure spin magnetic moment. The narrowing of the d-projected DOS as well as the shifts of the center of gravity of the majority and minority d bands with reduced coordination number generally result in an increase of m_S at surfaces and low-dimensional structures, as seen in Fig. 21.3 for the case of Fe monolayers and adatoms on Au(111). From atomic physics, moreover, we know that the total magnetic moment is the sum of the spin and orbital contributions, $\boldsymbol{m} = \boldsymbol{m}_S + \boldsymbol{m}_L$. In a classical picture, the orbital moment results from the orbital motion of the electron revolving around the nucleus. To obtain a finite orbital moment, the symmetry in the number of electrons revolving clock- or counterclockwise must be broken, which we refer to as broken orbital degeneracy. Generally, three mechanisms can enable such symmetry breaking: (i) Coulomb correlation effects, as known for single atoms, which lead to Hund's second rule, (ii) the spin–orbit interaction, and (iii) the scalar spin chirality $\kappa = \boldsymbol{S}_i \cdot (\boldsymbol{S}_j \times \boldsymbol{S}_k)$, involving at least three atoms with a non-coplanar spin texture. The first two mechanisms are ubiquitous and well characterized [21.47–50]. Mechanism (iii), on the other hand, is rather new and restrained to non-collinear spin systems [21.51]. The scalar spin chirality κ originates from the non-coplanarity between three neighboring spins, and replaces the spin–orbit interaction in giving rise to an emergent effective magnetic field, which is the source of *topological orbital magnetization*. Such an effect is present, e.g., in skyrmions, where the topological orbital magnetization is proportional to the topological charge of the skyrmion [21.52] and can

Table 21.3 Local spin (m_S) and orbital (m_L) magnetic moments in units of μ_B calculated using the generalized gradient approximation to density functional theory for Fe, Co, and Ni atoms in bulk crystals (D = 3), unsupported (111) monolayers (D = 2), atomic chains (D = 1), and free atoms (D = 0). For the bulk crystals the variation of the orbital moment with the direction is small, but for films and chains the orbital moments parallel (∥) and perpendicular (⊥) to the film plane or chain axis are given. The lattice spacing is chosen as if the film or chain had been grown epitaxially on a Pt(111) substrate

D	Fe			Co			Ni		
	m_S	m_L		m_S	m_L		m_S	m_L	
		∥	⊥		∥	⊥		∥	⊥
3	2.05	0.05		1.59	0.08		0.62	0.05	
2	3.07	0.07	0.10	2.09	0.20	0.19	0.94	0.18	0.14
1	3.22	0.72	0.27	2.32	0.98	0.77	1.18	0.84	0.44
0	4	2		3	3		2	3	

be comparable in magnitude to the orbital moments due to the spin–orbit interaction [21.53, 54].

Table 21.3 reports representative values of m_S and m_L calculated by density functional theory for structures of various dimensions (D). In line with the arguments presented in Sect. 21.1.2, we observe that the spin moment increases in going from 3-D to 0-D structures as a result of the decrease in coordination number of the magnetic atoms. The calculations yield very small bulk orbital moments: $m_L = 0.05\,\mu_B$, $0.08\,\mu_B$ and $0.05\,\mu_B$ for bcc Fe, hexagonal close-packed (hcp) Co, and fcc Ni. It is well known that the orbital moments are quenched in the bulk due to crystal-fields effects. In metals, moreover, the broadening of the 3d levels due to sp–d hybridization contributes to the simultaneous occupation of electronic states with orbital quantum numbers $l_z = \pm 1$ and $l_z = \pm 2$ [21.46, 55], as shown in Fig. 21.4c. Larger orbital moments are obtained for crystal structures with noncubic crystal-field symmetry, such as hcp Co, and, more prominently, in 2-D and 1-D structures due to the reduced hybridization (Fig. 21.3). However, it is important to realize that these enhanced orbital moments are still significantly smaller than the corresponding free atom values, as given by Hund's second rule (last row in Table 21.3). Note that first-principles calculations based on local spin density approximation or the generalized gradient approximation typically underestimate orbital moments. In literature, several methods have been discussed to overcome this problem [21.56–58]; for example, the orbital moments of bulk magnets increase by about a factor of 2 if Brooks' orbital polarization is applied [21.59, 60] and even more in low dimensions [21.61]. A systematic comparison of density functional theory (DFT) results for free-standing and Pt-supported Fe and Co magnets in various dimensions using the local spin density approximation can be found in the works of *Komelj* et al. [21.62] and *Ederer* et al. [21.63].

Despite being smaller than the spin moment, the orbital moment plays a major role in determining the preferred orientation of the magnetization in crystalline as well as low-dimensional structures. At the atomic level, the coupling between m_L and m_S is established by the spin–orbit interaction

$$\mathcal{H}_{so} = \frac{1}{r}\frac{dV(r)}{dr}(\boldsymbol{s}\cdot\boldsymbol{l}) = \xi(r)\boldsymbol{s}\cdot\boldsymbol{l}\,, \tag{21.13}$$

where $V(r)$ is the radially symmetric Coulomb potential, and $\boldsymbol{s}$ and $\boldsymbol{l}$ are the one-electron spin and orbital angular momentum operators, respectively. Since the radial derivative of the potential in a crystal is largest in the vicinity of a nucleus, we can expect that the major contribution to the spin–orbit interaction will come from this region. Furthermore, since for small r the potential will be Coulomb like ($V = -(Z/r)$), the radial expectation value of $\xi(r)$ leads to a material-dependent spin–orbit coupling constant ξ that is roughly proportional to the square of the atomic number, $\xi \propto Z^2$ [21.64]. The spin–orbit interaction additionally provides a mechanism to promote the formation of finite orbital moments in systems in which crystal-field and hybridization effects would otherwise completely quench m_L [21.46, 48, 49, 55]. In a solid where the symmetry of the electronic states ψ_i is such that the zeroth-order orbital moment $m_L = -\mu_B \sum_i \langle\psi_i|\boldsymbol{l}|\psi_i\rangle = 0$, the spin–orbit interaction admixes states that carry no orbital momentum, e.g., the d_{xy} and $d_{x^2-y^2}$ orbitals, such that their combination forms an orbital moment in the z direction. In perturbation theory using the first-order correction for the wavefunctions, the expectation value of the orbital moment can be written as

$$\begin{aligned} m_L &= -\mu_B\langle\boldsymbol{l}\rangle \\ &= -\mu_B \sum_{i,j} \frac{\langle\psi_i|\boldsymbol{l}|\psi_j\rangle\langle\psi_j|\mathcal{H}_{so}|\psi_i\rangle}{\varepsilon_i - \varepsilon_j} \\ &\qquad \times f(\varepsilon_i)[1 - f(\varepsilon_j)]\,, \end{aligned} \tag{21.14}$$

where f is the Fermi function ensuring that the state ψ_i is occupied and ψ_j is unoccupied. In a metal where sev-

eral bands cross the Fermi level E_F, it is basically the sum of all contributions from the bands near E_F that determines the orbital moment.

Anisotropy of the Orbital Moment

The dependence of m_L on atomic coordination in systems of reduced dimensionality and interfaces is best understood in terms of a schematic model that includes the effects of crystal field, hybridization, and spin–orbit interaction for the exemplary case of a free-standing and supported d-metal monolayer [21.49, 50, 65, 66]. Figure 21.5 shows the schematic DOS and crystal-field splitting of a free-standing Co monolayer and of a supported Co monolayer on a strongly interacting substrate such as Pd, Pt, or Au. Following *Stöhr* [21.66], we assume that the d-band is substantially exchange split and more than half-filled, so that the majority band does not contribute to m_L and we only have to consider the partially filled minority band. The d orbitals at each lattice site experience a crystal field V that leads to a splitting of these levels. If the surface normal is assumed to be in the z-direction, the d_{xy} and $d_{x^2-y^2}$ orbitals will experience a crystal-field splitting $2V_\parallel$ that is different from the splitting $2V_\perp$ of the out-of-plane d_{zx}, d_{yz}, and d_{z^2} orbitals. In a band picture, these splittings can be translated into bandwidths $W_\parallel \propto V_\parallel$ and $W_\perp \propto V_\perp$. Assuming that the minority band is half-filled, which is approximately correct for Co, the energy splittings appearing in the denominator of (21.14) are $\varepsilon_{d_{xy}} - \varepsilon_{d_{x^2-y^2}} = 2V_\parallel$ and $\varepsilon_{d_{yz,xz}} - \varepsilon_{d_{z^2}} = 2V_\perp$. Calculating the matrix elements of the orbital moment operator between the different d orbitals and using the ratio $R = V_\perp/V_\parallel$, (21.14) allows us to calculate the in-plane and out-of-plane orbital moments [21.65, 66]

$$m_L^\parallel = \frac{\xi\mu_B}{2V_\parallel}\left(\frac{3}{R} + \frac{2}{R+1}\right) \quad \text{and} \quad m_L^\perp = 4\frac{\xi\mu_B}{2V_\parallel} \,. \tag{21.15}$$

Equation (21.15) shows that $m_L^\parallel$ and $m_L^\perp$ are inversely proportional to the bandwidths of the out-of-plane and in-plane oriented states, respectively. This result is intuitively clear, since, e.g., $m_L^\perp$ originates from the in-plane motion of the electrons that is favored by the hopping between the d_{xy} and $d_{x^2-y^2}$ states, separated by $V_\parallel$. The more these two levels are split in energy, the more difficult it will be for the electron to *circle* around the atom and, therefore, to form an orbital moment.

In the case of a free-standing monolayer (Fig. 21.5a), the strongest electronic interactions are in-plane, which leads to $R < 1$ and $m_L^\parallel > m_L^\perp$. This is also the case of Co monolayers on weakly interacting substrates such as Cu. On the other hand, substrates made of heavy elements with rather delocalized 4d and 5d states favor strong hybridization with the 3d out-of-plane orbitals of Co, leading to $R > 1$ and $m_L^\perp > m_L^\parallel$ (Fig. 21.5b). Taking typical values for 3d-metal monolayers, viz. a spin–orbit coupling strength of $\xi \approx 75\,\text{meV}$ and bandwidths of $W^\parallel \approx 3\,\text{eV}$ and $W^\perp \approx 2\,\text{eV}$, one estimates orbital moments of $m_L^\parallel = 0.28\,\mu_B$ and $m_L^\perp = 0.20\,\mu_B$ for a free standing system, in agreement with the ab initio results

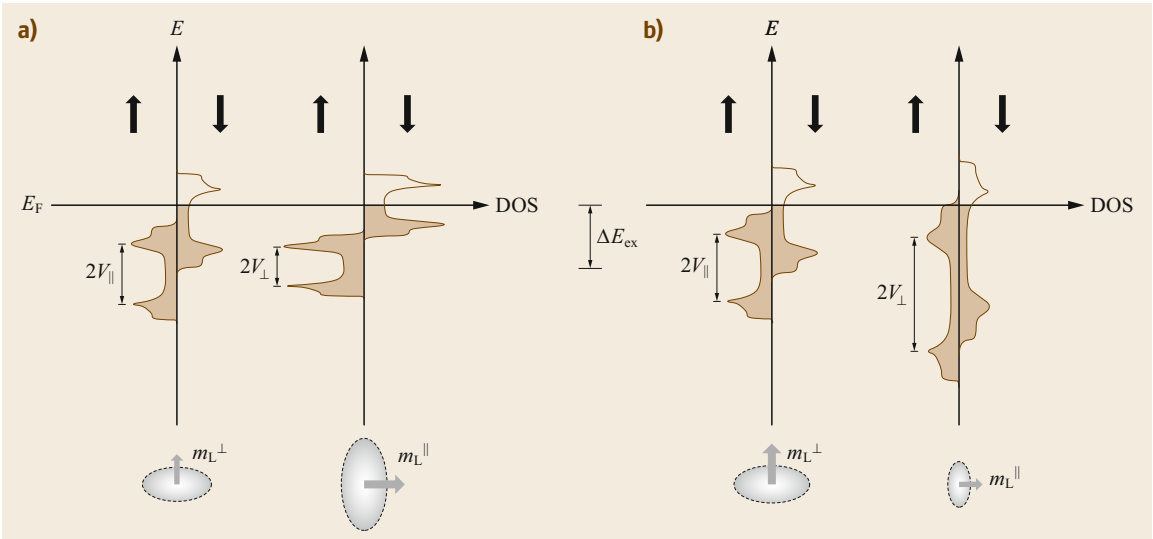

Fig. 21.5a,b Schematic spin-resolved DOS and crystal-field splitting of **(a)** a free-standing Co monolayer and **(b)** a Co monolayer supported on Pt or Au. The different crystal-field splitting for in-plane and out-of-plane orbitals leads to different in-plane and out-of-plane bandwidths. The splittings shown here are representative of electronic states with $\boldsymbol{k}$ wavevector close to the center of the Brillouin zone. (Adapted from [21.66], © Elsevier 1999)

reported in Table 21.3. This simple model thus captures the main mechanisms leading to the enhancement and anisotropy of the orbital moment, which, as we shall see later, plays a fundamental role in determining the magnitude of the magnetocrystalline anisotropy.

21.1.4 Magnetic Anisotropy

The behavior of a magnetic material in an applied field is typically anisotropic. This means that, besides the isotropic exchange interaction, there are additional interactions that make the total energy depend on the orientation of the magnetization with respect to a reference frame tied to the crystal or the geometrical axes of the sample. This orientation-dependent energy contribution is called the magnetic anisotropy energy, E_{MAE}. Without magnetic anisotropy, magnetism would have been hard to discover and exploit. In some way or another, most applications of magnetic materials hinge on the fact that it is easier to magnetize a magnet in one direction than another. Among other things, the magnetic anisotropy is responsible for the occurrence of easy and hard axes, stabilizes magnetic order against thermal fluctuations in low-dimensional systems where the exchange interaction alone would not suffice, and limits the width of a magnetic domain wall. Magnetic anisotropy, for example, is responsible for the bistability of magnetic domains with uniaxial symmetry, which allows the two possible magnetization directions in space to be interpreted in terms of bits 0 or 1 and makes magnetic materials valuable as storage media.

Phenomenological expressions for the magnetic anisotropy energy can be obtained by expanding the free magnetic energy in powers of the direction cosines of the magnetization along the three coordinate axes and retaining only those terms compatible with the symmetry of the crystal. The magnetic anisotropy energy of cubic and hexagonal surfaces is usually given as a function of the azimuthal and polar angles ϕ and θ of the magnetization direction relative to the crystal axes x, y, and z:

1. *Tetragonal symmetry:* (001) surface of cubic crystals

$$E_{\mathrm{MAE}} = K_1 \sin^2\theta + K_2 \sin^4\theta + K_3 \sin^4\theta \cos 4\phi + \ldots \qquad (21.16)$$

2. *Orthorhombic symmetry:* (011) surface of cubic crystals

$$E_{\mathrm{MAE}} = K_1 \sin^2\theta + K_1' \sin^2\theta \cos 2\phi + K_2 \sin^4\theta + K_2' \sin^4\theta (10\sin^2\phi - 3\sin^4\phi) + \ldots \qquad (21.17)$$

3. *Hexagonal symmetry:* (111) surface of cubic crystals or (0001) surface of hexagonal crystals

$$E_{\mathrm{MAE}} = K_1 \sin^2\theta + K_2 \sin^4\theta + K_3 \sin^6\theta + K_3' \sin^6\theta \cos 6\phi + \ldots \qquad (21.18)$$

General expressions for E_{MAE} for different crystal symmetries are given, e.g., in [21.67, 68]. The anisotropy constants $K_{1,2,3,\ldots}$ depend sensitively on the chemical composition and dimensionality of the system, which ultimately determine the electronic band structure. The microscopic origins of the magnetic anisotropy are the spin–orbit interaction (21.13) and the magnetic dipolar interaction, which give rise to the magnetocrystalline anisotropy and shape anisotropy, respectively. Both interactions contribute to the total anisotropy energy

$$E_{\mathrm{MAE}} = E_{\mathrm{MCA}} + E_{\mathrm{shape}} \,. \qquad (21.19)$$

Magnetocrystalline Anisotropy

The magnetocrystalline anisotropy (MCA) can be explained by the interplay of crystal-field effects and spin–orbit coupling. The latter couples the (isotropic) spin moment to the (anisotropic) orbital moment, which is determined by the symmetry and type of the partially filled orbital states at the magnetic ion's site (21.15). The relationship between the MCA energy and m_{L} can thus be exemplified by means of the perturbation model presented in Sect. 21.1.3 [21.49, 50, 65, 66]. In the absence of spin-flip terms (i.e., when the majority and minority band are well separated by the exchange interaction), the spin–orbit coupling changes the total energy in second-order perturbation theory as [21.50]

$$\langle \mathcal{H}_{\mathrm{so}} \rangle = \sum_{i,j} \frac{|\langle \psi_j | \mathcal{H}_{\mathrm{so}} | \psi_i \rangle|^2}{\varepsilon_i - \varepsilon_j} \mathrm{f}(\varepsilon_i)[1 - \mathrm{f}(\varepsilon_j)] \propto -\frac{\xi}{4\,\mu_{\mathrm{B}}} \widehat{\boldsymbol{s}} \cdot \left(\boldsymbol{m}_{\mathrm{L}}^{\downarrow} - \boldsymbol{m}_{\mathrm{L}}^{\uparrow} \right) \,, \qquad (21.20)$$

where $\widehat{\boldsymbol{s}}$ is the direction of the spin moment, and $\boldsymbol{m}_{\mathrm{L}}^{\downarrow}$ and $\boldsymbol{m}_{\mathrm{L}}^{\uparrow}$ are the orbital moment vectors of the spin-down and spin-up bands, respectively. If the spin-up band is completely filled, the energy $\langle \mathcal{H}_{\mathrm{so}} \rangle$ is proportional to the size of the orbital moment. E_{MCA} is the difference of $\langle \mathcal{H}_{\mathrm{so}} \rangle$ for two different magnetization directions and is therefore proportional to the anisotropy of the orbital moment,

$$E_{\mathrm{MCA}} = \langle \mathcal{H}_{\mathrm{so}}(\widehat{\boldsymbol{s}}^{\parallel}) \rangle - \langle \mathcal{H}_{\mathrm{so}}(\widehat{\boldsymbol{s}}^{\perp}) \rangle \propto -\frac{\xi}{4\,\mu_{\mathrm{B}}} \left(m_{\mathrm{L}}^{\parallel} - m_{\mathrm{L}}^{\perp} \right) \,. \qquad (21.21)$$

This relationship between orbital moment anisotropy and MCA was first derived by *Bruno* [21.49] and has

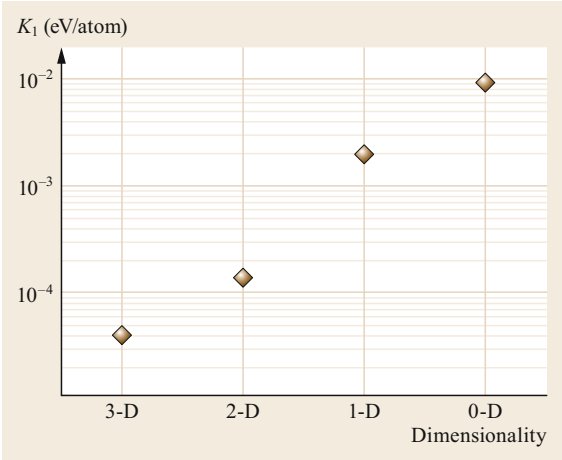

Fig. 21.6 Values of magnetocrystalline anisotropy energy per Co atom in a 3-D hcp crystal, 2-D monolayer film on Pt(111), and 1-D monatomic chain on Pt(997), and as 0-D single atoms on Pt(111). (Adapted by permission from [21.72, 73], © SpringerNature 2003)

been experimentally verified in 2-D thin films [21.69–71] as well as in 1-D and 0-D systems [21.72–74]. According to (21.21), the easy axis of magnetization is the direction with the largest m_L. The magnetic anisotropy energy is thus the energy cost required to rotate the magnetization away from the easy axis, which can be visualized as the torque exerted by the orbital moment on the spin moment during the rotation of the magnetization [21.75].

In 3-D cubic crystals, m_L is very small and nearly isotropic since all the d orbitals have balanced $\pm l_z$ contributions. The MCA energy is consequently small: on the order of 0.005 meV/atom in bulk fcc metals such as Fe and Ni, and about 0.05 meV/atom in crystals with uniaxial symmetry such as hcp Co. Low-dimensional systems, however, present strongly enhanced orbital moments due to the broken symmetry and reduced atomic coordination [21.69, 72–74, 76–78]. The MCA thus increases quite spectacularly in these systems, with typical values of 0.1−1 meV/atom in 2-D layers, and 1−10 meV/atom in 1-D and 0-D nanostructures (Fig. 21.6). The anisotropy of the orbital moment also explains the emergence of perpendicular magnetic anisotropy in thin films, as obtained from (21.15) and (21.21) in the limit of strong substrate hybridization ($R > 1$, see Fig. 21.5b).

Shape Anisotropy

In contrast to the MCA, the shape anisotropy is a non-relativistic effect that originates from magnetostatic dipolar interactions. This anisotropy is closely related to the demagnetizing field $\boldsymbol{B}_{\rm dem}$ produced by the spatial distribution of the magnetization in materials of finite shape. In uniformly magnetized samples of ellipsoidal shape, the demagnetizing field can be written as

$$\boldsymbol{B}_{\rm dem} = -\mathfrak{N}\mu_0\boldsymbol{M}\,, \quad \text{with} \quad B_{{\rm dem},i} = -\mathfrak{N}_{ij}\mu_0 M_j\,, \tag{21.22}$$

where $\boldsymbol{M}$ is the magnetization, μ_0 is the magnetic permeability of vacuum, $\mathfrak{N}$ is the demagnetization tensor, and $i, j = x, y, z$. As is well known from classical electromagnetism, $\boldsymbol{B}_{\rm dem}$ opposes the magnetization inside a magnet due to the tendency of the dipolar field to oppose the field produced by neighboring dipoles. If x, y, z are the principal axes of a sample with ellipsoidal shape, $\mathfrak{N}$ is a diagonal 3×3 matrix with unit trace. The demagnetizing factors $\mathfrak{N}_{xx}$, $\mathfrak{N}_{yy}$, and $\mathfrak{N}_{zz}$ have very simple expressions in a 2-D thin film ($\mathfrak{N}_{xx} = \mathfrak{N}_{yy} = 0$, and $\mathfrak{N}_{zz} = 1$ if the surface normal is along z) and a 1-D wire ($\mathfrak{N}_{xx} = 0$, $\mathfrak{N}_{yy} = \mathfrak{N}_{zz} = 1/2$ if the wire axis is along x). The magnetostatic self-energy associated with the demagnetizing field is

$$E_{\rm dem} = -\frac{1}{2}\int_V \boldsymbol{M}\cdot\boldsymbol{B}_{\rm dem}{\rm d}V = +\frac{1}{2}\mu_0\int_V \boldsymbol{M}\cdot\mathcal{R}\cdot\boldsymbol{M}{\rm d}V\,, \tag{21.23}$$

where the integration is performed over the magnet's volume V. The magnetization tends to adopt a configuration that minimizes this energy, and the shape anisotropy is essentially the difference of $E_{\rm dem}$ for a magnetic body magnetized along two different directions, e.g., x and z

$$\begin{aligned} E_{\rm shape} &= E_{\rm dem}(\boldsymbol{M} \parallel \boldsymbol{x}) - E_{\rm dem}(\boldsymbol{M} \parallel \boldsymbol{z}) \\ &= \frac{1}{2}\mu_0(\mathfrak{N}_{zz} - \mathfrak{N}_{xx})M^2 V\,. \end{aligned} \tag{21.24}$$

It is easy to see that the minimization of $E_{\rm shape}$ in a 2-D magnetic thin film requires $\boldsymbol{M}$ to lie in the film's plane, and that the larger the volume (i.e., the thickness) of the film, the more this tendency will be accentuated. For bcc Fe, for instance, with a bulk magnetic moment of 2.215 μ_B/atom ($M = 1.71 \times 10^6$ A/m) and a lattice constant of 5.42 arb.u., the effective shape anisotropy constant $K_{\rm shape} = (1/2)\mu_0 M^2$ is equal to -0.140 meV/atom (1.8 MJ/m^3). In bulk samples, thick films, or polycrystalline layers without a preferred grain orientation, and patterned nanostructures, the shape anisotropy is frequently the dominant form of anisotropy. The minimization of the demagnetizing energy (21.23) is also the driving force for the spontaneous formation of magnetic domains. The structure of the domains and domain walls, however, is ultimately

determined by the competition between diverse factors, including exchange, MCA, and DMI, for which we refer the reader to specialized monographs [21.79–81].

Equations (21.22)–(21.24) assume that the magnetization arises from a continuous magnetic medium; therefore, K_{shape} is the same for all atoms irrespective of their position. For thin films and wires of a few atomic layers, however, this assumption is no longer valid. In such a case, the magnetic dipole–dipole energy has to be evaluated explicitly instead of E_{dem}. In transition metals, the magnetization distribution around the atom is almost spherical and can thus be treated to a good approximation as a collection of discrete magnetic dipoles arranged regularly on a crystalline lattice. The dipolar energy E_{dip} per atom experienced by a dipole at site i due to the presence of ferromagnetically aligned dipoles on all other sites j can then be expressed as

$$E_{\text{dip}}^{(i)}(\theta) = K_{\text{dip}}^{(i)} \cos^2\theta = \frac{1}{2}\frac{\mu_0}{4\pi}\sum_{j(j\neq i)}\frac{m_i m_j}{R_{i,j}^3}\left(1-3\cos^2\theta_{ij}\right) , \quad (21.25)$$

where θ_{ij} is the angle between the direction of the magnetic moment m of the dipoles at sites i or j given in units of the Bohr magneton μ_{B} and the vector $\boldsymbol{R}_{i,j}$ connects atoms i and j. The θ dependence expresses explicitly the fact that the dipole–dipole interaction contributes to the magnetic anisotropy. Obviously, in thin films and wires, the anisotropy energy depends on the position of the atom i relative to the surface or wire axis, respectively (in contrast to E_{shape}). For crystalline thin wires and films, the sum in (21.25) can be evaluated straightforwardly using fast-converging summation techniques [21.82, 83]. *Draaisma* and *de Jonge* [21.84] have worked out in detail the layer-dependent dipolar anisotropy $K_{\text{dip}}^{(i)}$. In general, the outer atoms experience values of K_{dip} that are appreciably smaller than those of the inner layers, which finally approach K_{shape}. The inner atoms reach 95% of K_{shape} at ≈ 15 Å below the surface. The exact details depend on the crystal structure and surface orientation; e.g., a reduction between 25 and 45% of K_{shape} was reported for a (100)-oriented fcc or bcc monolayer, respectively. The dipolar interaction is also sensitive to the interface or surface roughness, which is always present on real films. According to *Bruno* [21.85], the roughness gives rise to an effective perpendicular contribution to the shape anisotropy whose order of magnitude depends on the parameters characterizing the roughness.

Effective Anisotropy Field

The different sources of magnetic anisotropy add up and compete to determine the preferential orientation of the magnetization in a given sample. Consider, for example, the case of a thin film with uniaxial MCA given by $K_1 \sin^2\theta$, where θ is the angle between the surface normal and the magnetization. If $K_1 > 0$, the MCA will favor the perpendicular direction. This term, however, will compete with the shape anisotropy $E_{\text{shape}} = -(1/2)\mu_0 M^2 \sin^2\theta$ that favors the in-plane direction. The total anisotropy energy per unit volume is therefore

$$E_{\text{MAE}} = \left(K_1 - \frac{1}{2}\mu_0 M^2\right)\sin^2\theta = K_{\text{eff}}\sin^2\theta , \quad (21.26)$$

where K_{eff} is the effective anisotropy constant of the film that determines the in-plane ($K_{\text{eff}} < 0$) or out-of-plane ($K_{\text{eff}} > 0$) orientation of the magnetization. Note that, for practical purposes, it is often customary to define a fictitious *magnetic anisotropy field* $\boldsymbol{B}_{\text{K}}$ to represent the strength of the magnetic anisotropy on an equal footing with an applied magnetic field. Such a field is defined by setting $E_{\text{MAE}} = -(1/2)V\boldsymbol{M}\cdot\boldsymbol{B}_{\text{K}}$, which, for a thin film with uniaxial anisotropy along z, gives $\boldsymbol{B}_{\text{K}} = -\Re\mu_0\boldsymbol{M} + (2K_1/M)(\boldsymbol{M}\cdot z/M)z$.

Temperature Dependence of the Magnetic Anisotropy

In general, both types of magnetic anisotropy are temperature-dependent quantities. Whereas the shape anisotropy simply scales as $M(T)^2$, the MCA has a more complex temperature dependence (see also Sect. 21.3.2). Intuitively, a reduction of the MCA is expected with increasing temperature not only because the saturation magnetization decreases, but also because thermal vibrations smear out the effects of the crystal field. Thus, one expects that the MCA will vanish much faster than the magnetization as a function of temperature. Theoretical models of single-ion anisotropies yield a power law [21.86, 87]

$$\frac{K_l(T)}{K_l(0)} = \left[\frac{M(T)}{M(0)}\right]^{l(l+1)/2} , \quad (21.27)$$

where l is the order of each term in a spherical harmonic expansion of the MCA energy. In cubic systems, K contains terms of order $l = 4$ and the exponent is 10; in uniaxial systems, K is formed by terms with $l = 2$, leading to an exponent of 3. It must be noted, however, that the MCA of itinerant magnetic systems often deviates from this power law; in hcp Co, for example, K_1

($l = 2$) changes sign at ≈ 500 K, leading to a transition from uniaxial to easy-plane anisotropy. Furthermore, (21.27) implies that MCA vanishes at the Curie temperature, which is hard to understand given that the local magnetic moments survive the ferromagnetic–paramagnetic transition and the spin–orbit coupling is independent of temperature. Alternative approaches to calculate the temperature dependence of the MCA from first principles are described, e.g., in [21.88–90]. In thin films, the temperature-dependent effective anisotropy scales with the film thickness and surface magnetization [21.90].

21.1.5 Spin Hamiltonians

Effective spin models have been developed to capture the microscopic exchange mechanisms among magnetic atoms and reduce the problem of modeling arbitrary magnetic configurations to the spin degree of freedom, whereby the details of the electronic structure are included into effective exchange parameters. In general, the Hamiltonian of such a system may contain contributions from the isotropic and anisotropic exchange interactions, DMI, magnetocrystalline anisotropy, dipolar interactions, as well as the coupling of the spin and orbital moments to an external magnetic field (Zeeman interaction). The spins localized on lattice sites i, j are considered as either classical vectors or quantum operators $\boldsymbol{S}$, with equal magnitude $|\boldsymbol{S}|^2 = S^2$ or $|\boldsymbol{S}|^2 = S(S+1)$ on all sites, respectively. Working with a spin Hamiltonian offers various advantages, as it permits (i) an efficient search for the magnetic ground state, (ii) the calculation of dynamical properties such as the magnon dispersion or magnetic excitations, and (iii) the calculation of thermal properties such as the critical temperature. One of the most familiar spin lattice models is the Heisenberg Hamiltonian

$$\mathcal{H} = -\sum_{i,j} J_{ij} \boldsymbol{S}_i \cdot \boldsymbol{S}_j \,, \tag{21.28}$$

where the exchange interaction between the spins is isotropic and described by the pair interaction J_{ij}. In model spin systems, J_{ij} can be safely approximated by the ferromagnetic ($J_1 > 0$) or antiferromagnetic ($J_1 < 0$) nearest-neighbor (nn) interaction, i.e., $J_{ij} = 0$ for all i, j, except for $J_{\mathrm{nn}} = J_1$. Although in magnetic insulators J_1 often dominates over the rest of the more distant pairs, an attempt to reproduce the magnetic complexity or T_c solely from J_1 produces results of limited validity. In itinerant transition-metal magnets, depending on the Fermi surface, J_{ij} between distant pairs are required to model the properties reliably even though J_1 is usually the largest interaction.

The Heisenberg model allows one to construct a zero-temperature phase diagram of relevant spin states as a function of the exchange parameters J_{ij}, including non-collinear spin states. For example, a spin spiral state with a propagation vector $\boldsymbol{q}$ in the first Brillouin zone is a fundamental solution of the Heisenberg model of classical spins for a Bravais lattice. For such structures, it is convenient to write the spin on lattice sites in terms of their discrete Fourier-transformed equivalents

$$\boldsymbol{S}(\boldsymbol{q}) = \frac{1}{N} \sum_n \boldsymbol{S}_n \mathrm{e}^{-\mathrm{i}\boldsymbol{q}\boldsymbol{R}_n} \quad \text{and} \quad J(\boldsymbol{q}) = \sum_n J_{0n} \mathrm{e}^{-\mathrm{i}\boldsymbol{q}\boldsymbol{R}_n} \,. \tag{21.29}$$

Exploiting the translational invariance of the lattice, we can then rewrite (21.28) as

$$\mathcal{H} = -N \sum_{\boldsymbol{q}} J(\boldsymbol{q}) \boldsymbol{S}(\boldsymbol{q}) \cdot \boldsymbol{S}(-\boldsymbol{q}) \,, \tag{21.30}$$

where we have to ensure that the length of all spins $\boldsymbol{S}_n^2 = S^2$ is conserved on all sites n. This condition is fulfilled by solutions of the type [21.91]

$$\boldsymbol{S}_n = S[\hat{\boldsymbol{e}}_x \cos(\boldsymbol{q} \cdot \boldsymbol{R}_n) + \hat{\boldsymbol{e}}_y \sin(\boldsymbol{q} \cdot \boldsymbol{R}_n)] \,, \tag{21.31}$$

where the unit vectors $\hat{\boldsymbol{e}}_x$ and $\hat{\boldsymbol{e}}_y$ are orthogonal to each other and have otherwise arbitrary directions. Equation (21.31) describes a spiral spin density wave as shown in the lower half of Fig. 21.7. A more general form of spiral spin density waves can be obtained for a magnetization precessing around a cone with an opening angle ϑ, which can be understood as a superposition of a flat spin spiral and a ferromagnetic state

$$\begin{aligned} \boldsymbol{S}_n = S[&\hat{\boldsymbol{e}}_x \cos(\boldsymbol{q} \cdot \boldsymbol{R}_n) \sin\vartheta \\ &+ \hat{\boldsymbol{e}}_y \sin(\boldsymbol{q} \cdot \boldsymbol{R}_n) \sin\vartheta + \hat{\boldsymbol{e}}_z \cos\vartheta] \,, \end{aligned} \tag{21.32}$$

as shown in the upper half of Fig. 21.7. From (21.30), one can conclude that the spiral spin density wave with

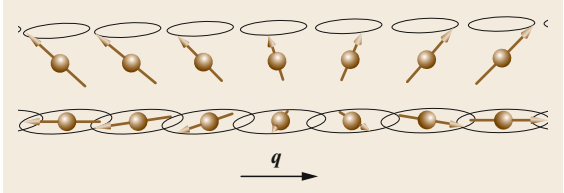

Fig. 21.7 Spiral spin density wave or spin spiral propagating along the wavevector $\boldsymbol{q}$. The upper spiral represents a coned spiral with a cone angle of 45°; the bottom spiral represents a flat spiral, with a cone angle of 90°. Both spirals exhibit a counterclockwise rotational sense expressed by a chirality vector parallel to the z-axis

the lowest total energy will be the one with the propagation vector $\boldsymbol{Q}$ that maximizes $J(\boldsymbol{q})$. These will be preferably the high-symmetry points in the Brillouin zone of $\boldsymbol{q}$-vectors, and then high-symmetry lines. For example, if $\boldsymbol{Q}=0$ maximizes $J(\boldsymbol{q})$, the solution corresponds to the ferromagnetic state; if $\boldsymbol{Q}=\hat{\boldsymbol{e}}_z(\pi/a_z)$ and a_z is the lattice constant in the z-direction, then the structure is layered antiferromagnetic in the z-direction.

Exchange interactions beyond the classical Heisenberg model, such as biquadratic, four-spin three-site and four-spin four-site interactions, can be derived from a perturbation expansion of the Hubbard model [21.92, 93]. Note also that, in recent years, there has been an effort to develop multiscale approaches to calculate the material-specific exchange parameters and magnetic properties from first principles and map them onto spin lattice Hamiltonians, thus enabling the modeling of realistic systems over mesoscopic dimensions [21.6].

21.1.6 Dzyaloshinskii–Moriya Interaction

In 1957, *Dzyaloshinskii* [21.94] predicted on the basis of symmetry arguments the presence of a chiral magnetic interaction of the form

$$\mathcal{H}_{\mathrm{DM}}=\sum_{i,j}\boldsymbol{D}_{ij}\cdot(\boldsymbol{S}_i\times\boldsymbol{S}_j)\,, \tag{21.33}$$

where the Dzyaloshinskii vector $\boldsymbol{D}$ depends on the symmetry of the system and on the direction of the vector connecting the two sites i and j in real space. This interaction is now referred to as the DMI or antisymmetric exchange interaction [21.95]. Necessary conditions for the occurrence of the DMI are a structural assymmetry and a spin–orbit interaction. The strength of $\boldsymbol{D}$ depends also on details of the electronic structure. The DMI can be understood as the spin–orbit contribution to the total energy due to a rotating or winding magnetic structure. The existence of the DMI has far-reaching consequences. Depending on the sign, the symmetry properties, and the value of $\boldsymbol{D}_{ij}$, collinear ferro- or antiferromagnetic structures become unstable and are replaced by a non-collinear magnetic structure with one specific chirality, $\boldsymbol{c}=\boldsymbol{S}_i\times\boldsymbol{S}_{i+1}$, either right-handed ($c>0$) or left-handed ($c<0$). The DMI is fundamentally different from the direct, kinetic, or metallic exchange interactions, which are caused exclusively by the Coulomb interaction. These interactions are symmetric; i.e., two magnetic configurations with right-handed ($\uparrow\rightarrow$) or left-handed ($\uparrow\leftarrow$) alignment of the magnetic moments have the same energy. The nature of the DMI favors non-collinear magnetic structures and is responsible for weak ferromagnetism, i.e., the occurrence of small net magnetic moments in otherwise antiferromagnetic materials. In the context of bulk magnetic materials, one may think of hematite (Fe_2O_3), a mineral with an antiferromagnet exchange ($J<0$), as an example. The canting angle between neighboring spins can be estimated from a simple two-site model

$$\mathcal{H}_{\mathrm{DMI}}=-J\boldsymbol{S}_1\cdot\boldsymbol{S}_2+\boldsymbol{D}\cdot(\boldsymbol{S}_1\times\boldsymbol{S}_2)\,. \tag{21.34}$$

Assuming that the spins $\boldsymbol{S}_1$ and $\boldsymbol{S}_2$ are located in the same plane, then the energy depends only on the angle θ between the antiferromagnetically aligned spins,

$$E=-JS^2\cos(\pi-\theta)+DS^2\sin(\pi-\theta)\,. \tag{21.35}$$

Minimization of this expression yields the equilibrium canting angle $\tan(\pi-\theta)=-D/J$. For atoms in a periodic lattice, if D is large, spin–orbit energy is gained by a strong winding (large θ) of the magnetic texture. For small D the period of the winding magnetic texture becomes large (small θ), and may be much larger than the period of the crystal lattice. In this case one works with the micromagnetic formulation of the DMI, which can be found in [21.56].

Since the Dzyaloshinskii vector $\boldsymbol{D}$ is an axial vector, $\mathcal{H}_{\mathrm{DMI}}$ has the most general form of an antisymmetric tensor of second rank that is second order in spin $\boldsymbol{S}$. Typically, the combination of hopping of spin-polarized electrons and the presence of the spin–orbit interaction can produce such a term. The microscopic details depend on the specific material system and are described using different microscopic models. In 1960, *Moriya* identified the spin–orbit interaction as the microscopic origin of the DMI in magnetic insulators by treating the spin–orbit interaction on top of the superexchange mechanism [21.96]. Moriya also derived a set of symmetry rules that determine under which circumstances the DMI will occur. These rules are general and apply also to metallic systems. Considering two magnetic ions located at sites A and B, respectively, and the point C bisecting the straight line AB, the following five Moriya rules are obtained:

(i) When a center of inversion is located at C: $\boldsymbol{D}=0$
(ii) When a mirror plane perpendicular to AB passes through C: $\begin{cases}\boldsymbol{D}\parallel\text{mirror plane}\\ \text{or}\quad \boldsymbol{D}\perp\text{AB.}\end{cases}$
(iii) When there is a mirror plane including A and B: $\boldsymbol{D}\perp$ mirror plane.
(iv) When a twofold rotation axis perpendicular to AB passes through C: $\boldsymbol{D}\perp$ twofold axis.
(v) When there is an n-fold ($n\geq 2$) axis along AB: $\boldsymbol{D}\parallel$ AB.

The strength of the DMI can be estimated as $D\propto|(\xi/\Delta E)|J$, where ΔE is roughly the energy difference

between the ground states and the first excited states of the two magnetic ions. The DMI is thus first order in the spin–orbit interaction, here expressed in terms of the spin–orbit coupling constant ξ (Sect. 21.1.3), in contrast to the magnetocrystalline anisotropy (Sect. 21.1.4) that is at least second order. It is thus clear that $D = 0$ in the case of a mirror symmetry or point of inversion between the two ions. In other words, the DMI exists only between two *different* atoms. However, *different* need not mean different ion species; it can just mean different chemical environments, such as in a bipartite lattice, where the symmetry of the electronic orbitals changes between the two types of lattice site.

Today we understand that the DMI (21.33) is the lowest order chiral interaction in a sequence of higher-order interactions that are systematically derivable [21.97, 98]. An example are the chiral four-spin interactions of the type $(\boldsymbol{S}_i \cdot \boldsymbol{S}_j)(\boldsymbol{S}_k \times \boldsymbol{S}_l)$ [21.99], which are necessary to describe the chiral magnetism of Fe chains on Re(0001). Novel types of interactions are the topological chiral interactions [21.97], which do not depend on the vector spin chirality $\boldsymbol{c}_{ij} = \boldsymbol{S}_i \times \boldsymbol{S}_j$ but on the scalar spin chirality $\kappa_{ijk} = \boldsymbol{S}_i \cdot (\boldsymbol{S}_j \times \boldsymbol{S}_k)$, that breaks the time inversion symmetry and causes a topological orbital moment (Sect. 21.1.3). The interaction of the topological orbital moments brings about terms of the type κ_{ijk}^2 and the triple index suggests energy gain not through the formation of a rotating magnetic structure but a curved one.

The DMI in metals has been discussed in relationship to different hopping mechanisms using different microscopic models that go back to *Smith* [21.100], *Fert* and *Levy* [21.28, 101], and *Kanamori* and coworkers [21.102]. *Fert* and *Levy* [21.101] derived an expression for the antisymmetric exchange interaction mediated by the Ruderman–Kittel–Kasuya–Yosida (RKKY) coupling for two magnetic atoms in spin glasses doped with heavy impurity atoms, i.e., impurity atoms with a large atomic number and thus a large spin–orbit interaction. This model is also applicable to magnetic adatoms on surfaces, for which the DMI can be interpreted as an equilibrium manifestation of the Byshkov–Rashba interaction [21.103–105]. Consider, for example, a thin magnetic film on a substrate with the vacuum potential on one side and the potential of the substrate on the other side. This inversion asymmetry leads to a gradient of the potential that can be interpreted to a first approximation as an electric field normal to the film surface. In the rest frame of moving electrons, the electric field $\boldsymbol{E}$ appears via the Lorentz transformation as an intrinsic $\boldsymbol{k}$ dependent magnetic field $\boldsymbol{B} \propto \boldsymbol{k} \times \boldsymbol{E}$ oriented parallel to the film plane, which then interacts with the spin $\boldsymbol{s}$ of the conduction electron, giving rise to an additional term in the Hamiltonian, similar to (21.13) in the context of spin–orbit coupling. Here, instead of an orbital motion, a linear motion of an electron with momentum $\boldsymbol{k}$ in an electric field oriented along $\boldsymbol{e}_z$ is considered. This so-called Rashba effect [21.106] is described by an Hamiltonian $\mathcal{H}_\mathrm{R} = \alpha_\mathrm{R} \boldsymbol{s} \cdot (\boldsymbol{k} \times \boldsymbol{e}_z)$, where the strength of the Rashba parameter, α_R, is determined, e.g., by the asymmetry of the wavefunction due to the asymmetry of the potential or the electric field, respectively, and the spin–orbit coupling strength ξ of the electrons involved. The magnetic interaction between the localized spins $\boldsymbol{S}_i$ at lattice site i and $\boldsymbol{S}_j$ at lattice site j is caused by conduction electrons which hop from site i to site j and back. Electrons in a magnetic film propagate in an exchange field $\pm 1/2 I m_\mathrm{S}$ (21.1), the bands are exchange split, and the time-inversion symmetry is lost. Due to the spin–orbit interaction caused by the Bychkov–Rashba term, electrons experience a kinetic energy with an additional weak spin-dependent potential which depends on the propagation direction $\boldsymbol{k}$ of the electrons. Thus, the motion from site i to j and the back motion from j to i is slightly different. The same is true for the time-reversed process, i.e., the electron hopping first from site j to i and then back. At first sight, both processes look identical, and indeed both contribute equally to the isotropic Heisenberg exchange in (21.28). However, the presence of the spin–orbit interaction in conjunction with the broken inversion symmetry introduces a complex phase factor into the conventional hopping between the sites i and j [21.107, 108]. This factor provides an antisymmetric component to the hopping, such that the two processes do not cancel out identically [21.109]. Instead, it gives rise to a DMI term equivalent to (21.33), which is proportional to α_R and falls off almost linearly with the distance between magnetic and nonmagnetic atoms. Extending the concept of an electric field originating from broken inversion symmetry beyond the simple Bychkov–Rashba model, it has been found that the DMI in multilayer systems can be related to the differences in the workfunctions [21.110] or electronegativities [21.111] of the interface layers. In an atomic picture, the minimal model that exemplifies such an antisymmetric exchange interaction is shown in Fig. 21.8 and consists of three atoms, at least two of which are magnetic, representing the magnetic film, while one has a strong spin–orbit interaction, representing the substrate. Typical values of D for 3d/5d metal interfaces are in the range of $0.5{-}2\,\mathrm{mJ/m^2}$ for magnetic layers that are about $t = 2$–6 atoms thick, which corresponds to $\approx (0.25 - 1)t\,\mathrm{meV}$ per interface atom. The sign of D changes between 5d elements in the first and second half of the transition-metal layer, reflecting the sign of the spin–orbit coupling. Interfaces between 3d metals and oxides, such as Co/MgO and Co/AlO_x,

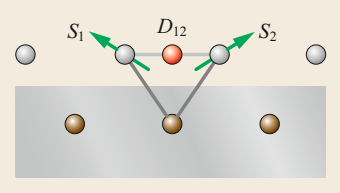

Fig. 21.8 Schematic diagram of DMI interaction at the interface between a magnetic layer (*top*) and a heavy metal (*bottom*), inducing a canting of spins S_1 and S_2 on adjacent lattice sites

also present significant DMI [21.112, 113]. Methods used to measure the strength of the DMI include field- and current-driven domain wall displacement measurements [21.114, 115] as well as Brillouin light scattering, which measures the nonreciprocal propagation of spin waves [21.116, 117].

Surprisingly, the effects of the DMI on the magnetism of surface systems were discovered only recently [21.118]. One reason for this late discovery is probably that the DMI has traditionally been neglected in the study of metal systems, since most metals crystallize in structures with centrosymmetric symmetry. However, recent studies have shown that the DMI plays an important role in defining the spin configuration of low-dimensional magnets, such as spin spirals in 2-D [21.118–120] or 1-D systems [21.121–123], as well as non-collinear magnetism in 0-D structures [21.124–126]. This type of interaction is decisive also in defining the chirality of magnetic domain walls [21.127–129], in the formation of magnetic skyrmions (Sect. 21.4) [21.130–137], as well as in the coupling of nanomagnets at surfaces [21.138].

21.1.7 Critical Phenomena

It is well known that magnetic excitations in itinerant ferromagnets are basically of two different types, namely Stoner excitations associated with longitudinal fluctuations of the magnetization, and spin-waves or magnons, which correspond to collective transverse fluctuations of the magnetization direction. Near the bottom of the excitation spectrum, the density of states of magnons is considerably greater than that of Stoner excitations, so that the thermodynamics in the low-temperature regime is completely dominated by magnons, while Stoner excitations can be safely ignored. Thus, it seems reasonable to extend this approximation up to the critical temperature, to neglect the Stoner excitation systematically, and to describe the transversal fluctuations using the Heisenberg model expressed in (21.28). More advanced theoretical models adopt this approach by mapping first-principles exchange parameters onto Heisenberg-type Hamiltonians to study the thermodynamical properties of bulk and low-dimensional magnets [21.139]. Below the critical temperature, the so-called Curie temperature T_C for ferromagnets or the Néel temperature, T_N, for magnets with more complex magnetic phases, including antiferromagnets, the spontaneous magnetization remains finite, while it is zero above T_C. The phase transition is second order; i.e., the spontaneous magnetization M_s, which is the order parameter characterizing the phase transition, vanishes continuously at T_C. A second-order phase transition is governed by the principle of universality, according to which the behavior of the system close to a phase transition does not depend on the details of the system itself, such as its material parameters or geometry, but rather on the symmetry group of the order parameter and the dimensionality of both the lattice and spin vector [21.140, 141].

Critical Temperature

Within the assumptions of the Heisenberg model, the magnetic moment at each lattice site is given by $\boldsymbol{m}_i = -g\mu_B \boldsymbol{S}_i$, where g is the Landé g-factor and μ_B is the Bohr magneton, and the magnetization is

$$\boldsymbol{M} = -\frac{g\mu_B}{NL^D}\sum_{i=1}^{N}\boldsymbol{S}_i\,, \tag{21.36}$$

where N is the total number of sites in the lattice and L^D ($D = 3, 2, 1, 0$) is the *volume* of the lattice. By solving (21.36) self-consistently in the mean-field approximation (MFA), one obtains the well-known result

$$k_B T_C^{MFA} = \frac{2}{3} N_{nn} J_1 S^2\,, \tag{21.37}$$

where k_B is the Boltzmann constant, N_{nn} is the coordination number of nearest-neighbor atoms, and J_1 is the interaction strength introduced in Sect. 21.1.5. For more complex structures, such as a 3-D system exhibiting a helical spin spiral ground state with wavevector $\boldsymbol{Q}$, the critical temperature is given by

$$k_B T_N^{MFA} = \frac{2}{3} S^2 J(\boldsymbol{Q}) \tag{21.38a}$$

and

$$k_B T_C^{MFA}(\mathrm{nn}) = \frac{2}{3} S^2 N_{nn} J_1\,. \tag{21.38b}$$

The MFA gives the right proportionality of T_C with respect to the number of neighbors, but it has also a few deficiencies. Besides overestimating T_C for 3-D systems by about 20%, T_C^{MFA} does not depend on the lattice structure or the dimensionality of the system.

These shortcomings can be remedied by treating the Heisenberg model in the random-phase approximation (RPA) [21.38, 142], which gives

$$\frac{1}{k_B T_N^{RPA}} = \frac{3}{4}\frac{1}{NS^2}\sum_{\boldsymbol{q}}\left(\frac{1}{J(\boldsymbol{Q})-J(\boldsymbol{q})} + \frac{1}{J(\boldsymbol{Q})-\frac{1}{2}J(\boldsymbol{q}+\boldsymbol{Q})-\frac{1}{2}J(\boldsymbol{q}-\boldsymbol{Q})}\right) \quad (21.39a)$$

and

$$k_B T_C^{RPA}(\mathrm{nn}) = \frac{2}{3}S^2 N_{\mathrm{nn}} J_1 \begin{cases} 0.660 & \mathrm{sc} \\ 0.718 & \mathrm{bcc} \\ 0.744 & \mathrm{fcc} \end{cases} . \quad (21.39b)$$

The RPA gives weight to the low-energy magnon excitations $E(q) \propto J(\boldsymbol{Q}) - J(\boldsymbol{q})$ in the summation over all modes. This provides estimates of T_C that are in close vicinity to those obtained by numerical analysis using classical Monte Carlo simulations [21.143, 144].

Both approximations show that T_C and T_N depend on the number of nearest neighbors; one therefore expects these critical temperatures to decrease if the dimensionality of the system is reduced. However, both approximations show a qualitatively different behavior for low-dimensional magnets. The mean-field approximation overestimates the tendency for long-range order and always predicts a phase transition to ferromagnetic order in the Heisenberg model, no matter whether we have a 1-D, 2-D, or 3-D system, whereas $T_C^{RPA} = 0$ already for 2-D systems. This is consistent with the theorem of *Mermin* and *Wagner* [21.145], which states that, in two dimensions, there is no spontaneous long-range ferromagnetic order for isotropic Heisenberg models with a short-range interaction

$$\sum_j J_{ij} r_{ij}^2 < \infty$$

at finite temperature. In thin films, however, long-range order at finite temperature is stabilized by the magnetic anisotropy, which is practically always present, either due to MCA or dipolar interactions [21.146]. The magnetic anisotropy opens a gap Δ in the excitation spectrum of the spin waves, $E(q) \propto \Delta + J(\boldsymbol{Q}) - J(\boldsymbol{q})$, and suppresses low-energy long-wavelength fluctuations which occur at low temperatures. According to the renormalization group analysis of *Erickson* and *Mills* [21.147, 148], the critical temperature in two dimensions, $T_C^{(2\text{-D})}$, scales as

$$T_C^{(2\text{-D})} = T_C^{(3\text{-D})} \frac{2}{\ln\left(\frac{3\pi}{4}\frac{k_B T_C^{(3\text{-D})}}{K}\right)} , \quad (21.40)$$

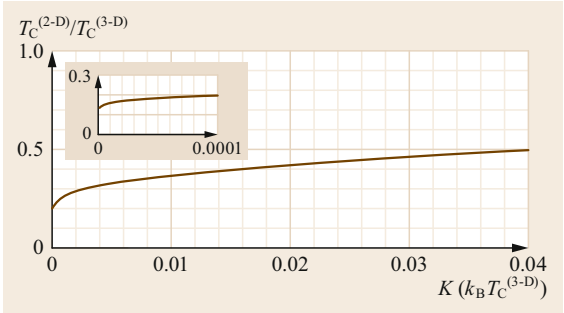

Fig. 21.9 Critical temperature of a two-dimensional magnet as function of the uniaxial anisotropy following (21.40). The function starts at zero for $K = 0$. Note its rapid growth in the vicinity of the origin, as shown in the inset at magnified scale

where the critical temperature of the three-dimensional Heisenberg model is renormalized by a logarithmic factor which depends on the strength of the uniaxial magnetic anisotropy K (Sect. 21.1.4). This result is displayed in Fig. 21.9. T_C vanishes in the isotropic limit ($K \to 0$) in accordance with the Mermin–Wagner theorem. Interestingly, for finite K, there is a rapid increase of T_C, reaching reasonable values, of, e.g., 20% of the critical temperature in 3-D systems, for anisotropy values of less than a percent of the ferromagnetic coupling constant. Consider, for example, Fe, with a shape anisotropy of 0.140 meV, which corresponds to 1.63 K on the temperature scale. This is only 0.14% of the Curie temperature of Fe, $T_C^{(3\text{-D})}(\mathrm{Fe}) = 1183\,\mathrm{K}$, but already causes a Curie temperature for a Fe film of $T_C^{(2\text{-D})}(\mathrm{Fe}) = 0.27 T_C^{(3\text{-D})}(\mathrm{Fe}) = 320\,\mathrm{K}$. A detailed treatment of T_C for 2-D monolayers with either out-of-plane or in-plane anisotropy is presented in [21.146, 149].

Thus, for any finite anisotropy, there is a critical temperature at which the spin degree of freedom is frozen, i.e., the dimensionality of the spin is reduced from three for the Heisenberg model to one, viz. spin up and spin down. In terms of universality, the Heisenberg model with any finite anisotropy value belongs to the universality class of the Ising model, and the Ising model shows a phase transition in 2-D.

In 1-D, even the Ising model does not show long-range order at finite temperature. However, in quasi-1-D magnetic chains (i.e., chains of finite size), there is a so-called blocking temperature below which a finite chain has a spontaneous and remanent magnetization, with long-range metastable order in the chain (Sect. 21.5). In reality, this magnetic order is accompanied by a slow relaxation [21.151]. The relaxation time depends on the magnetic anisotropy and can be long relative to the observation time, such that a quasi-1-D chain appears as a ferromagnet, as verified experimentally [21.72].

Table 21.4 Critical exponents for the 3-D mean-field approximation, 3-D Heisenberg model ($n = 3$), 3-D planar (or xy) model ($n = 2$), and 3-D and 2-D Ising models ($n = 1$), where n is the dimensionality of the spin vector. The values are taken from Rushbrooke et al. [21.150]

	MFA	3-D Heisenberg	3-D planar	3-D Ising	2-D Ising
β	1/2	0.35–0.385	1/3	5/16	1/8
γ	1	7/5	4/3	5/4	7/4
δ	3	5	5	5	15
ν	1/2	0.735	0.67	0.64	1

Scaling Laws

Beyond the MFA, the temperature-dependent behavior of systems described by spin lattice Hamiltonians is usually derived by means of high-temperature ($T \propto T_C$) and low-temperature ($T \ll T_C$) power series expansions of the relevant thermodynamic properties [21.152].

High-Temperature Limit. In the vicinity of the critical point T_C, the functions $f(T)$ of interest are assumed to have power-law singularities of the form

$$f(T) \approx A \left(1 - \frac{T}{T_C}\right)^{-\lambda} , \qquad (21.41)$$

where λ is the critical exponent and A is called the amplitude of the singularity. For the saturation magnetization, one thus expects

$$M_s(T) \propto \left(1 - \frac{T}{T_C}\right)^{\beta} , \quad \text{for} \quad T \to T_C^- , \qquad (21.42)$$

and $M_s(T) = 0$ for $T > T_C$. Moreover, as T approaches T_C, the response of the system to an external field is very large, so that the isothermal magnetic susceptibility diverges at T_C

$$\chi(T) \propto \left(\frac{T}{T_C} - 1\right)^{-\gamma} , \quad \text{for} \quad T \to T_C^+ . \qquad (21.43)$$

Related to the diverging susceptibility is the correlation length ξ, one of the most fundamental features of a critical point, which also diverges at T_C. ξ defines the range r over which the magnetic correlations decay, typically following an exponential function at large r and $T > T_C$: $\langle M(r)M(r=0)\rangle \propto \exp(-r/\xi)$. It is found that ξ varies as

$$\xi \propto \left(\frac{T}{T_C} - 1\right)^{-\nu} , \quad \text{for} \quad T \to T_C^+ . \qquad (21.44)$$

Finally, the application of a magnetic field H induces a finite magnetization at $T = T_C$ and above. The relation between H and M_s, called a magnetic isotherm, shows the following critical behavior

$$M_s(H, T_C) \propto H^{1/\delta} , \quad \text{for} \quad H \to 0^+ . \qquad (21.45)$$

Although there is no proof that such expressions are generally correct, (21.42)–(21.45) agree with exact solutions, when available, as well as experimental data [21.153]. Values of the critical exponents β, γ, ν, and δ are reported in Table 21.4 for different lattice models. In contrast to the MFA, the critical exponents are independent of the number N_{nn} of nearest neighbors because they describe the magnet's behavior at macroscopic length scales, which is dominated by long-range fluctuations and does not depend on the atomic environment. Another notable result of universal critical behavior is that fluctuations become increasingly important as the dimensionality of a system is reduced, as illustrated by the critical exponents of the 3-D and 2-D Ising model, and by the absence of spontaneous magnetic order for the isotropic 2-D Heisenberg model and 1-D Ising model.

Low-Temperature Limit. At low temperature, the free energy of a magnetic system can be expanded in ascending powers of the temperature. The expansion parameter is the dimensionless ratio $k_B T/J_1$ or, equivalently (21.39), T/T_C. Once the free energy is known, most of the other thermodynamic quantities of interest can be easily calculated. For a 3-D cubic lattice of identical spins with isotropic exchange coupling between nearest neighbors described by the Hamiltonian in (21.28), *Dyson* showed that the saturation magnetization in zero external field is approximated by

$$M_s(T) = M_s(0) + a_1 \left(\frac{T}{T_C}\right)^{3/2} + a_2 \left(\frac{T}{T_C}\right)^{5/2} + a_3 \left(\frac{T}{T_C}\right)^{7/2} + a_4 \left(\frac{T}{T_C}\right)^{4} + \mathcal{O}\left(\frac{T}{T_C}\right)^{9/2} , \qquad (21.46)$$

where the coefficients a_i depend on the type of cubic lattice as well as on the spin value S [21.154]. Such a power-series development is limited to low temperature ($T \lesssim (1/4)T_C$). The behavior of the ferromagnet in the critical region cannot be determined even if all terms in the expansion are supposed to be accu-

rately known, because effects of order $\exp[-J_1/(k_BT)]$, which play a decisive role at temperatures around the order–disorder transition where $k_BT \propto J_1$, are neglected. Equation (21.46) is derived by a detailed analysis of the spin wave excitations in a ferromagnet, considering deviations of the energy spectrum from the quadratic dispersion law as well as the mutual interactions between spin waves.

The concept of a spin wave (or magnon, the associated quantized excitation analog to a phonon) is fundamental to understand the low-temperature behavior of any magnetic system. In such collective excitations of the spin lattice, spins on adjacent sites have nearly parallel magnetic moments and the energy cost of a spin flip $\propto J_1$ is spread over one wavelength $2\pi/q$, where $\boldsymbol{q}$ is the wavevector of the spin wave. In the limit of infinite wavelength, a spin wave corresponds to a constant rotation of all spins that does not change their orientation relative to each other. As a result, such an excitation costs no energy. For this reason, spin wave energies can be very small, on the order of μeV per atom, which makes them accessible by thermal fluctuations on an energy scale of k_BT down to the lowest temperature.

Spin waves are eigenstates of the Heisenberg Hamiltonian in (21.28)–(21.30) with eigenvalues

$$\hbar\omega(\boldsymbol{q}) = S\hbar^2[J(0) - J(\boldsymbol{q})] \approx \mathcal{A}q^2 + \dots , \qquad (21.47)$$

where $\mathcal{A}$ is the so-called exchange stiffness parameter, which is a scalar for materials with cubic crystal structure but may be a tensor otherwise. The above approximation is valid at small wavevectors and is responsible for the leading term of order $T^{3/2}$ in the low-temperature expansion in (21.46). This term was first derived by Bloch by assuming that the density of reversed spins is so small that the interaction between two or more spin waves can be neglected. Corrections to the quadratic dispersion relationship in (21.47) are responsible for higher-order terms in the expansion, whereas spin-wave interactions in the spontaneous magnetization start manifesting themselves only at order T^4 [21.154]. This result can be explained by considering that spin waves excited at low temperature have long wavelengths and are basically coherent small-amplitude movements of a great number of atomic spins, such that mutual disturbances due to the overlapping of spin waves at the same atomic site are very small.

At finite temperature, all thermodynamic quantities, including the magnetization, must be calculated from a statistical average of the ground state and excited states. As each spin wave corresponds to the inversion of a single spin, i.e., carries $\hbar/2$ angular momentum, the saturation magnetization at finite temperature is equal to the saturation magnetization at zero temperature minus the average number of excited spin waves, namely

$$M_s(T) = M_s(0) - \frac{g\mu_B}{NL^D}\sum_{\boldsymbol{q}} \frac{1}{e^{\hbar\omega(\boldsymbol{q})/(k_BT)} - 1} , \qquad (21.48)$$

where the term in the sum is the expectation value of the magnon number operator at thermodynamic equilibrium, which obeys Bose–Einstein statistics. By changing the wavevector summation into an integral over the first Brillouin zone, assuming $\hbar\omega(q) = \mathcal{A}q^2$, and keeping track of the dimensionality D of the system, we obtain

$$M_s(T) = M_s(0) - g\mu_B \frac{\Omega_D}{(2\pi)^D} \times \int_0^\infty \frac{1}{e^{\mathcal{A}q^2/(k_BT)} - 1} q^{D-1} dq , \qquad (21.49)$$

where $\Omega_{3\text{-D}} = 4\pi$, $\Omega_{2\text{-D}} = 2\pi$, and $\Omega_{1\text{-D}} = 1$. Since the integrand is proportional to q^{D-3} at small wavevectors, the integral diverges in 1-D and 2-D. This results, which coincides with the Mermin–Wagner theorem [21.145], is a consequence of the diverging number of low-energy magnons at any finite temperature in isotropic 1-D and 2-D systems. However, as stated in Sect. 21.1.7 on the *critical temperature*, any interaction that breaks spherical symmetry, such as a magnetic field H or anisotropy energy K, is sufficient to stabilize magnetic order in 2-D. In such a case, the magnon dispersion relation writes $\hbar\omega(q) = \mathcal{A}q^2 + g\mu_BH + K$ and, assuming $k_BT \gg g\mu_BH + K$, (21.49) becomes

$$M_s(T) = M_s(0) - g\mu_B \frac{k_BT}{4\pi\mathcal{A}t} \ln \frac{k_BT}{g\mu_BH + K} , \qquad (21.50)$$

where t is the thickness of the 2-D layer [21.155, 156]. Thus, since the magnon number is approximately independent of t, and the logarithmic factor is almost constant except near $T = 0\,\mathrm{K}$, the magnetization decreases approximately proportional to T/t rather than $T^{3/2}$ as in Bloch's theory. On the high-energy side, the range of validity of (21.50) is determined by the energy interval over which the spin wave modes with wavevector q_z in the direction perpendicular to the film plane can be safely ignored. For a film of thickness t, $q_z = n_z(\pi/t)$, where $n_z = 0, \pm1, \dots$ Therefore, no mode with $q_z \neq 0$ can be excited if $k_BT < \mathcal{A}(\pi^2/t^2)$. On the low-energy side, (21.50) assumes that the thermal energy is large enough to overcome the gap in the magnon spectrum induced by either the field or anisotropy energy, such that $k_BT > g\mu_BH + K$. The overall tendency expected in thin films is a faster decrease of $M_s(T)$ compared with bulk 3-D magnets at low temperature.

21.1.8 Superparamagnetism

In the absence of magnetic anisotropy, the magnetization of any ferromagnetic system (as well as the Néel vector of an antiferromagnet) would oscillate randomly in time due to thermal fluctuations. In most bulk magnets and antiferromagnets, however, the presence of magnetic anisotropy of either crystalline or dipolar origin stabilizes the magnetization along one of the easy axes of the system, either globally or at the level of individual domains. As the total magnetic anisotropy energy scales with the volume, structures with a reduced number of atoms such as nanoparticles, nanowires, and small surface clusters present a transition from a paramagnetic-like behavior at high temperature to a ferromagnetic-like state below the so-called blocking temperature T_b. This transition occurs as the total anisotropy energy NK, given by the product of the number of atoms N and the anisotropy energy per atom K, becomes larger than the thermal energy $k_B T$. Unlike the Curie temperature, however, T_b does not correspond to a thermodynamic phase transition but to the kinetics of the relaxation process over the NK energy barrier. Therefore, the value of T_b depends on the timescale of the experimental observations and not only on the material properties of the system. Because the atomic spins are still strongly coupled by exchange in small structures, systems that present this type of behavior are called *superparamagnetic* in order to distinguish them from ordinary paramagnetic systems.

Here, following [21.157, 158], we present an analytical model describing the transition from blocking to superparamagnetism of an ensemble of monodisperse noninteracting particles. We assume that the magnetic particles have uniaxial out-of-plane anisotropy NK and are thus characterized by two local minima of the magnetic energy as a function of the angle θ between the surface normal and the magnetization $\boldsymbol{M}$ (see inset of Fig. 21.10). The anisotropy energy at zero field is the energy associated with the barrier that has to be overcome as a transition state during magnetization reversal. The rate of barrier crossing for an ensemble of monodisperse particles, all having identical values of K and M, or the time average of this rate for a single particle, is described for small fields by an Arrhenius expression

$$\nu = \nu_0 \mathrm{e}^{-(K+\boldsymbol{M}\cdot\boldsymbol{B})/(k_B T)} , \qquad (21.51)$$

where typically $\nu_0 = 10^9 - 10^{10}\,\mathrm{s}^{-1}$ [21.159]. At zero field, the relaxation time τ is given by $\tau = 1/2\nu = \tau_0 \exp[NK/(k_B T)]$, with $\tau_0 = 1/2\nu_0$. The barrier is readily overcome if $T > T_b = NK/\{k_B \ln[1/(\omega\tau_0)]\}$, where ω is related to the observation time $t = 2\pi/\omega$, given, e.g., by the sweep frequency of the external magnetic field used to measure χ. T_b is the temperature at which the ensemble reaches half of its thermodynamic equilibrium susceptibility χ_{eq}. For $T > T_b$ the particles are superparamagnetic, and $\chi(T) = \chi_{eq}(T)$. For $T < T_b$ the particles are blocked in a fixed magnetization state (up or down), hence $\chi(T) = 0$. In the vicinity of T_b, the state of the system is determined by the kinetics of barrier crossing. The zero-field susceptibility of the ensemble of monodisperse particles can be calculated numerically by solving the master equations for the occupation of the two energy minima and allowing for thermal fluctuations around these minima (see red dots in Fig. 21.10) [21.157]. Alternatively, in the limit of small fields, the real part of the complex zero-field susceptibility can be derived analytically by linearization

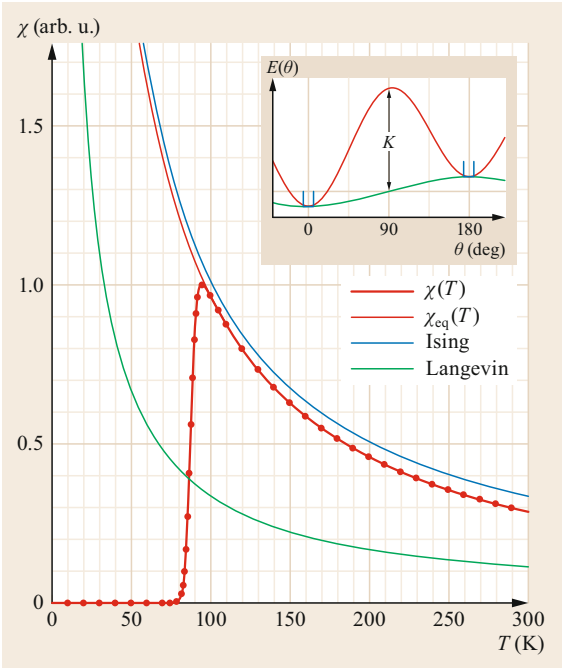

Fig. 21.10 Zero-field magnetic susceptibility $\chi(T)$ for an ensemble of monodisperse, uniaxial particles ($NK = 200\,\mathrm{meV}$, $M = 1500\,\mathrm{atoms} \times 2.1\,\mu_B = 182\,\mathrm{meV/T}$, field sweep with $\omega/(2\pi) = 0.3\,\mathrm{Hz}$). The analytical model (*thick red curve*) describes well the blocking-to-superparamagnetic transition, as evidenced by comparison with the numerical calculation (*red dots*). The equilibrium zero-field susceptibility, χ_{eq}, is shown as *thin red curve*. $\chi(T)$ derived from the Ising model (two states: up and down) and Langevin model (continuum of states, no anisotropy, only the Zeeman energy $-\boldsymbol{M}\cdot\boldsymbol{B}$ is present) are shown for comparison. *Inset*: Energy of a uniaxial monodomain particle as a function of the orientation of $\boldsymbol{M}$ with respect to an out-of-plane external field $\boldsymbol{B}$ in the Ising model, Langevin model, and the full model incorporating the anisotropy energy NK. (Reprinted by permission from [21.157], © SpringerNature 2003)

of the master equations, which gives [21.157, 160, 161]

$$\chi(T) = \frac{1}{1+\omega^2\tau^2}\chi_{\mathrm{eq}}(T)\,, \quad \text{where}$$

$$\chi_{\mathrm{eq}}(T) = M^2\left\{\frac{\mathrm{e}^{NK/(k_\mathrm{B}T)}}{\sqrt{\pi NKk_\mathrm{B}T\,\mathrm{erf}\left[\sqrt{NK/(k_\mathrm{B}T)}\right]}} - \frac{1}{(NK)^2}\right\}. \tag{21.52}$$

Figure 21.10 shows that the analytical solution for $\chi(T)$ (full red line) perfectly reproduces the numerical one, even though the former includes only the maximum energy NK via the relaxation time, whereas the latter takes into account the full energy curve. Note that, despite the fact that the particles are monodisperse, the transition from blocked to superparamagnetic behavior occurs over a finite temperature range $\Delta T = 2k_\mathrm{B}T_\mathrm{b}^2/(NK)$. The maximum of χ is located just above T_b and approximately given by $M^2/(k_\mathrm{B}T_\mathrm{b}) \propto M^2/K$. The figure also shows the infinite anisotropy limit (Ising model, blue curve) and the vanishing anisotropy limit (Langevin model, green curve). Ensembles of polydisperse magnetic particles can be modeled by calculating a weighted average of (21.52) while taking into account the finite size distribution of the particles and the dispersion of the parameters N, M, and K.

21.2 Surfaces of Bulk Crystals

Owing to the relation between the magnetic moment and coordination number, the surface magnetization of bulk ferromagnets is typically enhanced relative to the interior of the material. Theoretical studies of the magnetism of transition-metal surfaces can be summarized as follows: Magnetic moments have been found for all investigated surfaces of Cr, Fe, fcc and hcp Co, and Ni [21.162]. The surface of Mn has not been investigated in depth, due to the many possible bulk ground states of Mn. The enhancement of the calculated moments at the Co and Ni surfaces is relatively small. Co and Ni are strong ferromagnets, so that the enhancement is basically due to the sp–d dehybridization. On the other hand, Cr is a weak antiferromagnet and Fe is a weak ferromagnet (or antiferromagnet, depending on the lattice spacing), so that additional majority d-states can be occupied at the expense of minority d-states at the surface, leading to a greater enhancement of the magnetic moment. Because of the reduced coordination of open surfaces, the magnetic moment of a Ni atom at the Ni(110) surface is larger than that of a Ni atom at the Ni(100) surface. The smallest moment is found for the close-packed Ni(111) surface. For bcc Fe, the situation is slightly different: Here also the smallest moment is found for the close-packed (110) surface, but the largest moment is not found for the most open Fe(111) surface but for the (100) surface. Both the (100) and (111) surfaces have four atoms with nearest-neighbor bulk distance, but they differ in the number of next-nearest neighbor atoms and their distribution in the surface and subsurface layers. In general, the screening of the surface due to the d electrons is rather efficient. The surface-induced perturbation of the magnetic moments does not penetrate deep into the bulk. The moments at the fcc Co(100) and hcp Co(0001) surface already reach the bulk value in the first or at most second layer below the surface. For bcc (100) surfaces such as those of Fe or Cr, the perturbation penetrates slightly deeper into the bulk because the change of the surface moments is greater. Additionally, for bcc metals with half d-band filling, the bcc pseudogap in the density of states provides worse screening of the surface perturbation and the surface states can penetrate deeper into the bulk. Figure 21.11 shows a comparison of the layer-resolved magnetic moments calculated for Fe(100) and Fe(110).

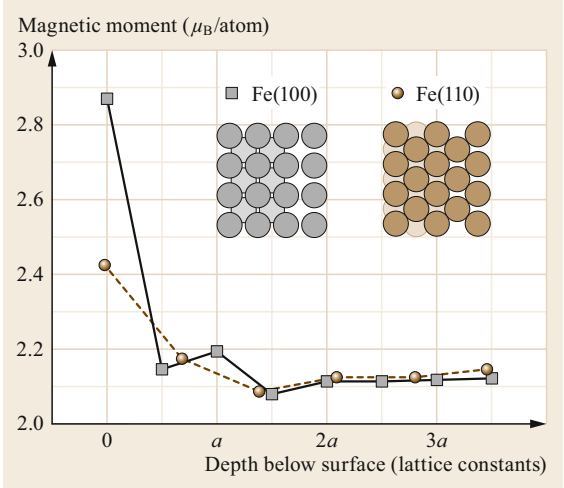

Fig. 21.11 Layer-resolved local magnetic Fe moment from the surface to bulk for Fe(100) and Fe(110). (Adapted by permission from [21.163], © Handschuh 1997)

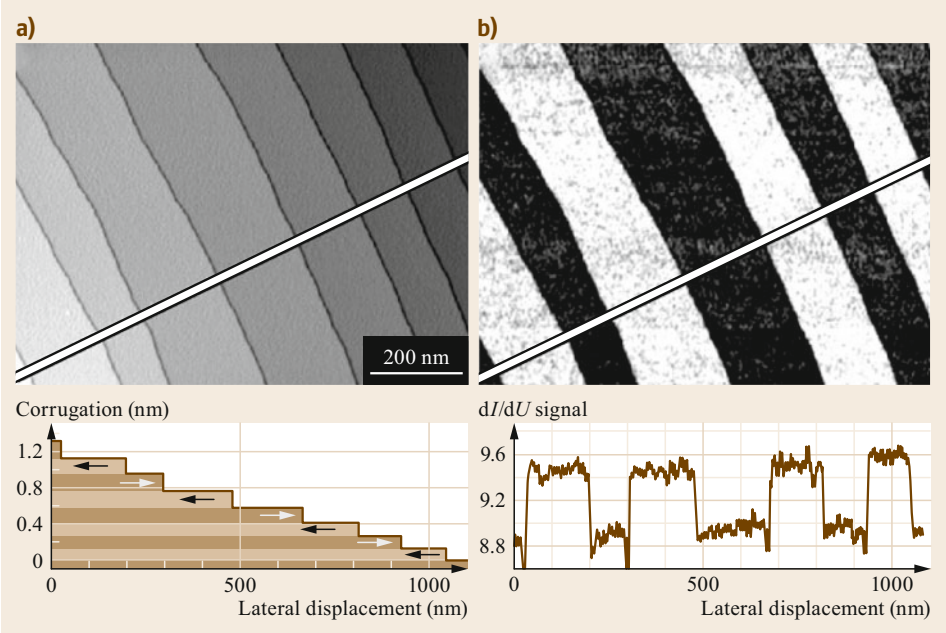

Fig. 21.12 **(a)** STM image of Cr(001) surface. Nine terraces separated by monatomic steps are visible. **(b)** Simultaneously acquired spin-resolved dI/dU map at $U = -290\,\mathrm{mV}$ sample bias. The signal changes at every step between low and high due to antiparallel magnetization of adjacent terraces. (Reprinted by permission from [21.164], © Am. Phys. Soc. 2002)

Due to symmetry breaking, materials that have antiferromagnetic or non-collinear spin structures in the bulk may present different types of magnetic order at the surface. A famous example is bcc Cr, which has a layered antiferromagnetic structure along the (001) direction modulated by an incommensurate spin density wave with wavevector $\boldsymbol{Q} = (2\pi/a)(0, 0, Q)$, where a is the lattice parameter of Cr and $Q = 0.952 \approx 19/20$. The spin density wave in bulk Cr can be ascribed to the so-called nesting between parallel sheets of the paramagnetic Fermi surface, which gives rise to a peak in the $\boldsymbol{q}$-dependent spin susceptibility $\chi_{\boldsymbol{q}}$ at the nesting wavevector $\boldsymbol{q} = \boldsymbol{Q}$. At the surface, one may envisage that the Fermi surface topology alters and that no spin density wave appears. This problem has been investigated both theoretically and experimentally [21.165–167]. Spin-polarized scanning tunneling microscopy (STM) and neutron scattering studies have confirmed that the Cr(001) surface consists of ferromagnetically ordered planes with an in-plane magnetization that inverts between adjacent terraces separated by monatomic step edges (Fig. 21.12). As the magnetization direction alternates over a large number of terraces without any change in the spin-polarized contrast, the surface magnetic structure cannot be described appropriately by a simple continuation of the bulk spin density wave. Rather, the surface pins the maximum of the spin density wave as well as the direction of the spins such that the Cr magnetic moments align along the easy (100) direction, likely due to strong in-plane surface anisotropy [21.167].

Another interesting consequence of the reduced surface coordination is that elements that are nonmagnetic in the bulk may present magnetic surfaces, such as V(100), Rh(100), and Pd(001). For both V(100) and Rh(100), the situation is controversial, as there are experimental and theoretical investigations suggesting surface magnetism, while others argue for the opposite [21.168–171]. Probably, Rh(100) is at the edge of becoming magnetic. For the (100) surface of Pd, which exhibits a strong Stoner-enhanced susceptibility in the bulk, no surface magnetism was found. However, although both the bulk and (001) surface of V, Ru, Rh, and Pd metals are nonmagnetic, theoretical calculations predict that the M_xV_{1-x} alloys with M = Ru, Rh, Pd are magnetic due to the shift of the d_{z^2} surface state, common to all bcc (100) surfaces, towards the Fermi energy, which increases $n(E_F)$ [21.172].

From the investigation of the layer dependence of the local moments from the surface to the bulk, we draw the important conclusion that the changes of the local moment due to the reduced coordination environment are limited approximately to the first and second topmost layers. In the context of thin metal films, this observation means that the effect of surfaces and interfaces will extend over a very limited thickness range.

21.3 Ultrathin Films

Much of the progress in the field of magnetism and spintronics over the last 50 years has been due to the development of refined techniques to grow high-quality thin films and complex multilayers with controlled thickness, stoichiometry, and crystal structure. The methods of choice for the growth of magnetic thin films are based on physical vapor deposition and include thermal and electron-beam evaporation as well as direct-current (DC) and radiofrequency (RF) sputtering. Whereas sputtering is used extensively at high throughput for producing polycrystalline films and coatings for the magnetic recording industry, molecular beam epitaxy (MBE) is used to deposit single-crystal layers with controlled lattice structure and orientation, mostly for fundamental investigations. The extreme sensitivity of the magnetic properties to the film structure and interfaces makes it impractical to present a detailed overview of the relevant growth processes here, which are necessarily specific to each system. For more details on the growth of magnetic metal films by MBE on metal and semiconducting substrates we refer to [21.1, 173, 174], respectively; the growth of magnetic oxide films has been reviewed in [21.175, 176]. Another factor that contributed enormously to the understanding of magnetic thin films is the emergence of surface science techniques capable of probing the magnetization with atomic-scale detail, sub-nanosecond temporal resolution, and element sensitivity. A synopsis of some of the main techniques employed in the study of surface magnetism is presented in Table 21.5. Finally, the development of ab initio and micromagnetic computational approaches has provided unprecedented insight into the electronic structure and magnetic configuration of finite-size systems, including equilibrium as well as nonequilibrium properties. In the following, we describe some of the most peculiar properties of magnetic thin films.

21.3.1 Magnetic Moments

The magnetic moments of thin films vary as a function of thickness. There are two factors that are responsible for this behavior. First, because of the reduced coordination of the magnetic atoms in a few-layer-thick film, the width of the d-band is typically smaller than in bulk systems. As a consequence (Sect. 21.1.2), the exchange splitting as well as the Fermi-energy DOS increase relative to the bulk (Fig. 21.4), driving up the magnetic moments and favoring the formation of stable magnetic states (21.5) for a much wider variety of transition-metal elements than just the bulk 3d ferromagnets and antiferromagnets. Second, the electronic hybridization between film and substrate also affects the d-bandwidth; For instance, substrates that are wide-bandgap insulators, such as MgO(100), allow for the formation of two-dimensional electron bands within the bandgap of the substrate material. In this case, the impact on the magnetization of the film due to the substrate is expected to be small. The same is true for noble-metal substrates, which have d-bands well below the Fermi energy. Even in the monolayer limit, the width of the d-band is not significantly broadened by the d–d interaction with the substrate, and magnetism is restricted to the monolayer. Increasing the d–d hybridization by choosing appropriate nonmagnetic transition-metal substrates, such as Pd, Pt, or W, however, leads to a considerable broadening of the monolayer bands and also introduces a significant spin polarization of the substrate. Broadening of the d-band can also be caused by d–sp hybridization, particularly in the case of metallic substrates with a large free-electron density such as Al, which generally leads to a reduction of the d magnetic moments [21.183, 195].

As transition-metal monolayers on noble-metal substrates are the classical systems exhibiting 2-D magnetism, we present in Fig. 21.13a systematic theoretical

Table 21.5 Synopsis of experimental techniques that are widely used in the investigation of magnetic thin films and nanostructures. Typical sensitivity values are given for measurement times ranging from a few seconds to a few hours. Units of μ_B/cm^2 can be converted into surface coverage by recalling, e.g., that 1 ML $\approx 1.5\times10^{15}$ atoms/cm^2 for the (111) surface of Pt or (100) surface of Cu. Additional microscopy techniques are described in [21.187]

Technique	Measured quantity	Sensitivity	Probing depth	Lateral resolution	References
SQUID	Magnetic flux	$5\times10^{13}\ \mu_B$	–	–	[21.177]
MOKE	Kerr rotation	10^{10}–$10^{14}\ \mu_B/cm^2$	10–20 nm	$\geq 0.5\,\mu m$	[21.178–180]
FMR	Resonant magnetic field	10^{10}–$10^{14}\ \mu_B/cm^2$	$\approx 1\,\mu m$	–	[21.68, 181]
XMCD	Element-specific m_S and m_L	10^{12}–$10^{14}\ \mu_B/cm^2$	≤ 5 nm	–	[21.182, 183]
XPEEM	Element-specific m_S and m_L	$10^{14}\ \mu_B/cm^2$	≤ 5 nm	20–50 nm	[21.182, 184]
MFM	Magnetic field gradient	10 μT	Near surface	10–50 nm	[21.185–188]
NVM	Magnetic field	1 μT	Near surface	20–50 nm	[21.189–191]
SP-STM	Tunneling resistance	$\leq 1\ \mu_B$	≤ 1 nm	≤ 1 Å	[21.192–194]

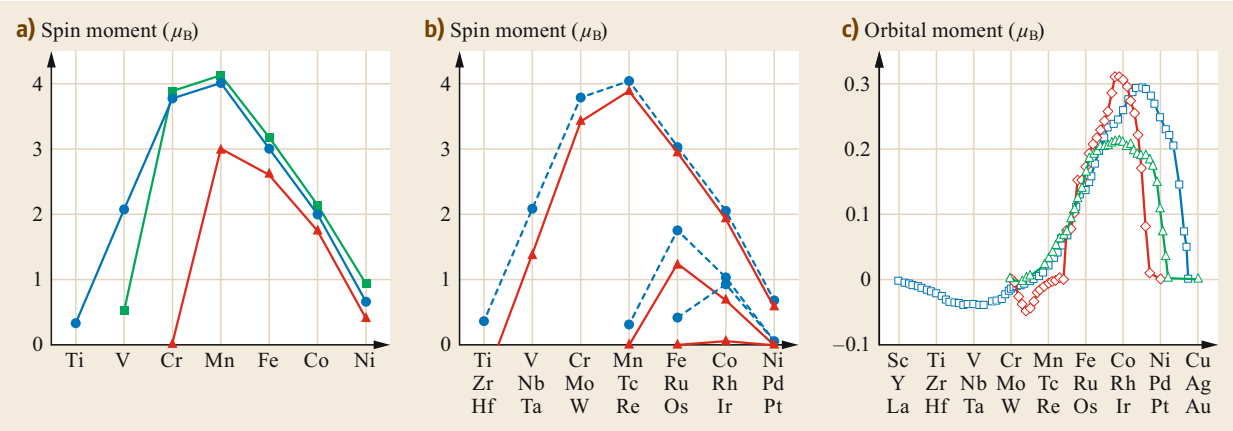

Fig. 21.13 **(a)** Local spin magnetic moments as calculated for ferromagnetic 3d metal monolayers on Ag(100) [21.196] (*dots*), Pd(100) [21.197] (*squares*), and Cu(001) [21.36] (*triangles*), and **(b)** 3d, 4d [21.198], and 5d monolayers on Ag(001) [21.199] (*dots*) and Ag(111) [21.200] (*triangles*). **(c)** Local orbital magnetic moments calculated for free-standing ferromagnetic 3d (*squares*), 4d (*triangles*), and 5d (*diamonds*) monolayers. The lateral lattice constant corresponds to that of Ag(100), although, in contrast to **(a,b)**, the layers are unsupported. The calculations are carried out for films with noninteger atomic number Z. The data are averages of the in-plane and out-of-plane moments

calculations of the magnetic moments of all possible 3d, 4d, and 5d transition-metal monolayers on Ag(001). In the ideal case of a pseudomorphic (001) monolayer, all the 3d metals (Ti, V, Cr, Mn, Fe, Co, and Ni) have a ferromagnetic ground state, whereas Tc, Ru, and Rh are ferromagnetic among the 4d metals, and Os and Ir are ferromagnetic among the 5d metals. The local magnetic moments are very large, not only for the 3d monolayers, but surprisingly also for the 4d and 5d ones. In the 3d series, the overall trend of the local moments follows Hund's first rule. The largest local moment of about $4\,\mu_B$ is found for Mn, whereas from Mn to Ni the magnetic moment decreases in steps of $1\,\mu_B$. The latter is a consequence of the strong ferromagnetism in these monolayers. The magnetic moments of Ti, V, and Cr monolayers show a pronounced dependence on the substrate: Ti is magnetic on Ag(100) but nonmagnetic on Pd(100), the magnetic moment of V is reduced by more than $1.5\,\mu_B$ when changing the substrate from Ag to Pd, whereas for Cr the magnetic moment changes from $3.8\,\mu_B$ on Ag(100) or Pd(100) to zero on Cu(100). Although not as dramatic, such a reduction is also visible for Mn. The drastic reduction of the monolayer moments is caused by the decrease of the lattice constants in the sequence Ag to Pd to Cu as well as by the increase of d–sp hybridization on Cu. When comparing the results of the local moments between 3d, 4d, and 5d monolayers on Ag(001), an interesting trend is observed: The element with the largest magnetic moment among each transition-metal series shifts from Mn to Ru (isoelectronic to Fe) and finally to Ir (isoelectronic to Co), respectively. Experimental investigations of Rh and Ru layers on Ag(100), however, have failed to provide evidence for finite 4d magnetic moments, even at low temperature [21.201]. Calculations have further shown that including the spin–orbit interactions significantly reduces the magnetic spin moment of the 5d metal monolayers, and depending on the interlayer relaxation, the spin moment might be suppressed [21.202].

On the (111) surface of an fcc crystal or the (0001) surface of an hcp crystal, the coordination number changes from 4 to 6 relative to the (100) surface, and the symmetry changes from fourfold to threefold or sixfold, respectively. Figure 21.13b exemplifies the general trend that the magnetic moments of the sixfold-coordinated monolayers on Ag(111) are smaller in magnitude than those of the fourfold-coordinated ones on Ag(001). The greater reduction of the magnetic moments is found at the beginning of the 3d series, where the wavefunctions are more extended than at the end of the series. Changing the coordination number from 4 to 6 does not change the local moments of Mn, Fe, Co, and Ni significantly. One consequence of this result is that no dramatic difference in the formation of large local moments is expected for monolayers that do not grow pseudomorphically on any substrate, but keep an average distance between atoms similar to the pseudomorphic films. The heavier metals are more affected by the change in coordination, however, because of the increasing degree of delocalization of the d wavefunction when going from the 3d to the 4d and 5d series.

Experimental investigations of the magnetic moments of ultrathin films, and of low-dimensional magnets in general, are complicated by the fact that the

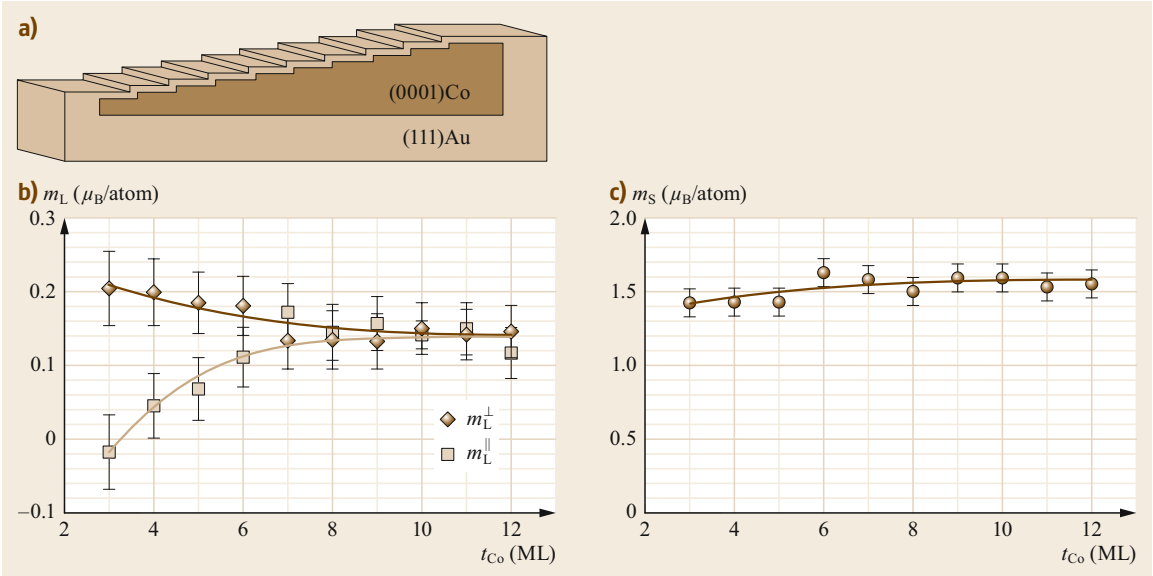

Fig. 21.14 **(a)** Schematic of Au/Co(3–12 ML)/Au wedge sample grown by molecular epitaxy on a float-glass substrate. The film has (111) texture after annealing and has a perpendicular easy axis at small Co thickness but in-plane easy axis for Co layers ≥ 11 ML. **(b)** In-plane ($m_L^\parallel$) and out-of-plane ($m_L^\perp$) orbital moments determined by XMCD as a function of Co thickness. **(c)** Angle-averaged spin moment. The measurements were performed at room temperature; the spin moment decreases with decreasing Co thickness, due to a drop in T_C. (Adapted by permission from [21.182], © SpringerNature 2007)

saturation magnetization is strongly temperature dependent (Sects. 21.1.7 and 21.3.3), which makes it hard to compare m_S and m_L between different systems, unless low temperatures and/or high magnetic fields are applied. Nonetheless, one generally finds that the magnetic moments of 3d films that form sharp interfaces with weakly interacting substrates tend to increase with reduced thickness [21.1, 203]. The presence of surface steps, which introduce lower-coordination sites relative to a smooth 2-D film, also has measurable effects on the magnetization [21.204]. Importantly, the different coordination environment inside the films relative to the bottom and top interfaces leads to a thickness-dependent distribution of the local magnetization [21.205, 206]. However, the magnetic moment measured by most experimental techniques is an average quantity over the film thickness. By artificially separating the bulk and surface magnetic moments, m^b and m^s, respectively, one may expect such an average moment to vary as $m = m^b + (m^s - m^b)t_s/t$, where t is the total thickness of the film and t_s is the effective thickness of the surface or interface region over which the effects of the reduced coordination are significant (typically 1 or 2 ML). This formula also accounts for the formation of magnetic dead layers ($m^s = 0$), which occur due to strong electronic hybridization with the substrate or, more often, intermixing between magnetic and nonmagnetic species at diffuse interfaces. One should be careful, however, because structural effects, e.g., due to strain relaxation, may also lead to substantial changes of the magnetic moment [21.207, 208] or even of the magnetic phase as a function of thickness [21.3]. Fcc Fe films grown on Cu(100) constitute a famous example of a system for which the magnetic order depends sensitively on the lattice parameter and growth mode [21.1, 209, 210].

The orbital magnetic moment can be deduced from x-ray magnetic circular dichroism (XMCD) measurements, in which dipolar selection rules allow for the separation of m_S and m_L [21.213–215] as well as from the g-factor shifts detected in angular-dependent ferromagnetic resonance spectra of thin films [21.68, 216]. Figure 21.14 shows m_S and m_L measured at room temperature on a thin Co wedge sandwiched between two Au layers. Whereas m_S does not change significantly, as the expected increase of the spin moment is masked by the decrease of T_C, m_L changes strongly with decreasing Co thickness. Moreover, the anisotropy of the orbital moment $m_L^\perp - m_L^\parallel$ increases from nearly zero to $\approx 0.24\,\mu_B$ in the 3-ML-thick film. In the model outlined in Sect. 21.1.3, this trend shows that the contribution to the Co orbital moment from the in-plane orbitals (d_{xy} and $d_{x^2-y^2}$) becomes larger than that from the out-of-plane orbitals (d_{xz}, d_{yz}, and d_{z^2}), indicating that the d–d hybridization at the Co/Au interface is

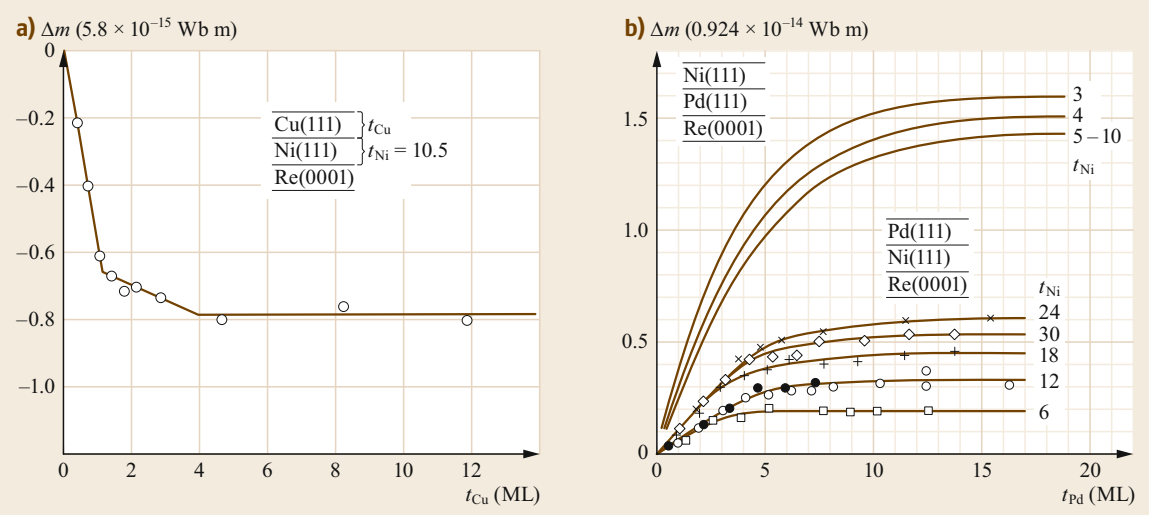

Fig. 21.15 **(a)** Decrease of magnetic moment in a 10.5-ML-thick Ni(111) film induced by Cu coating. The decrease Δm is given in units of the bulk monolayer moment of 5.8×10^{-15} Wb m, versus the number of coating Cu layers, t_{Cu}. (Reprinted by permission from [21.211], © Elsevier 1985). **(b)** Increase of magnetic moment Δm caused by a Pd(111) film of t_{Pd} atomic layers deposited below (*solid lines*) or on top (*data points*) of a Ni(111) film of t_{Ni} layers. (Reprinted by permission from [21.212], © Am. Phys. Soc. 1984)

stronger than the in-plane hybridization (Fig. 21.5b). The stronger out-of-plane orbital moment also explains the perpendicular magnetic anisotropy observed in this system for Co films ≤ 11 ML [21.69]. In general, an increase of m_L of up to 50% is detected in thin films and monolayer structures [21.76, 216–218]. A similar increase is reported for the ratio m_L/m_S, which signifies that m_L is more sensitive than m_S to changes of the atomic coordination environment and band filling (Fig. 21.13c), in line with the hierarchy of the Hund's rules.

Induced Magnetic Moments at Interfaces

If the substrate and the capping layer affect the interfacial moments of a magnetic film, the reciprocal effect also occurs. Magnetic films (and adsorbates in general) can induce sizable moments in otherwise nonmagnetic materials via the so-called *magnetic proximity effect*, which is due to the exchange splitting of hybridized wavefunctions at interfaces. These effects were recognized very early on by *Gradmann* and collaborators, who studied the magnetization of Fe, Co, and Ni layers capped by Cu, Ag, and Pd [21.1, 212, 219]. Figure 21.15a shows the decrease of the moment of Cu/Ni/Re(0001) layers as a function of the Cu coverage due to the hybridization of the Ni d bands with the Cu sp bands, and the increase of the total moment of Ni/Pd/Re(0001) and Pd/Ni/Re(0001) layers due to the formation of induced moments in Pd. Proximity effects are prominent in nonmagnetic metals that are close to a magnetic Stoner instability such as Pd and Pt (Sect. 21.1.1).

Recent investigations have exploited the element sensitivity of XMCD to separately measure the magnetic moments of the ferromagnetic films and the induced magnetic moments in the nonmagnetic layers [21.218, 220, 221]. Figure 21.16a shows the XMCD spectra of polycrystalline W, Ir, and Pt in Fe/W, Fe/W, and Co/Pt multilayers. The finite XMCD signal shows that all the 5d elements have acquired sizable induced moments, with m_S and m_L extracted from the XMCD sum rules indicated next to the spectra [21.221]. The different sign of the XMCD spectra shows that W is coupled antiparallel with respect to the ferromagnetic layer, in contrast to Ir and Pt, which are coupled parallel to it. This behavior originates from a general trend in the transition-metal series with d band filling, whereby elements with less than a half-filled d shell have a negative interatomic exchange integral J, whereas elements with more than a half-filled d shell have a positive J. Figure 21.16b shows the layer-dependent magnetic moment profile reconstructed for a Ni_6/Pt_5 multilayer using data from layers with different Ni and Pt thicknesses [21.218]. The data evidence how the changes in magnetic moment (reduction of the Ni moment and induction of the Pt moment) are layer specific and confined to the atoms next to the interface.

Importantly, proximity effects at the interface between nonmagnetic metals, e.g., Pt, and magnetic oxides such as garnets [21.222] or ferrites [21.223, 224],

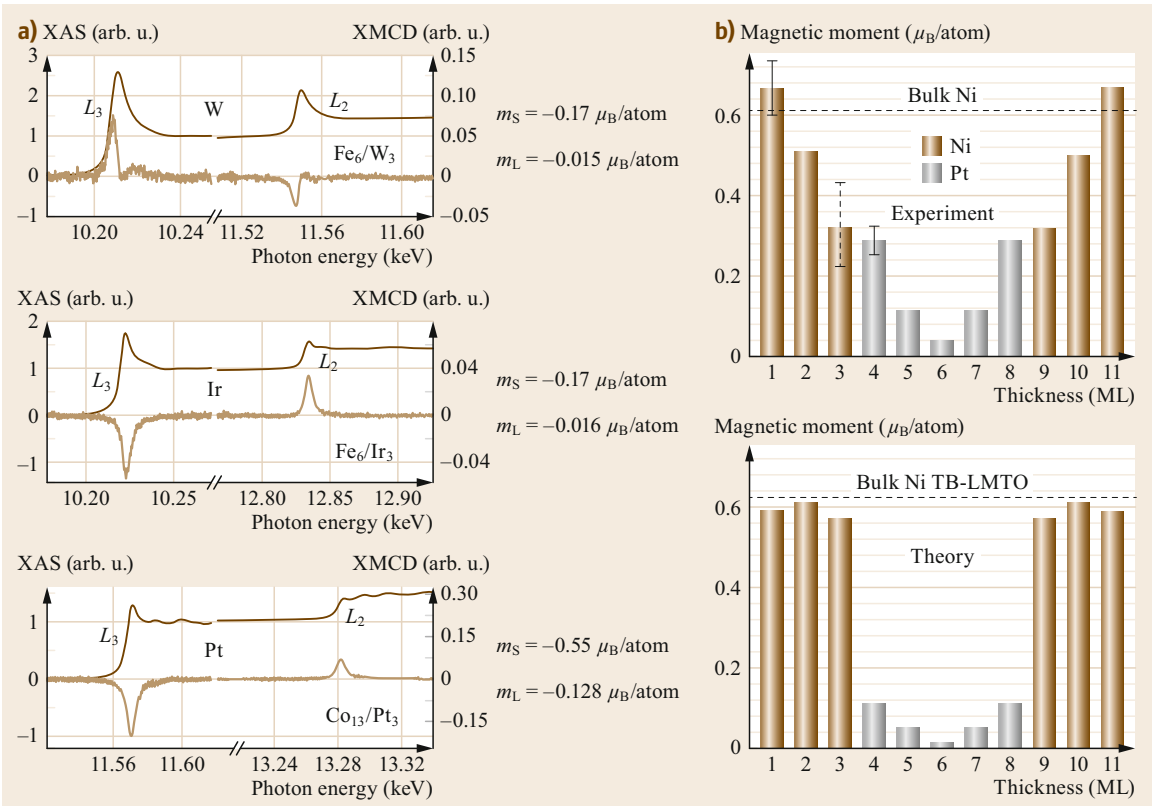

Fig. 21.16 **(a)** x-Ray absorption (*top*) and XMCD (*bottom*) spectra measured at the $L_{3,2}$ edges of W, Ir, and Pt in Fe/W, Fe/Ir, and Co/Pt multilayers measured at 10 K in a magnetic field of 5 T applied normal to the film plane. The *indexes* indicate the thickness in units of ML. (Reprinted by permission from [21.221], © Wiley 2003) **(b)** Magnetic moment profile of a Ni_6/Pt_5 multilayer measured by XMCD (*top*) and calculated by the tight-binding linearized muffin-tin orbital method (*bottom*). (Reprinted by permission from [21.218], © Am. Phys. Soc. 2000)

are typically much smaller than for 3d metal films due to the localization of the 3d wavefunctions in the oxide compounds. Such effects, which depend strongly on the quality of the oxide interface [21.222, 225], are currently under intense investigation to understand the magnetotransport properties of nonmagnetic metal films deposited on ferrimagnetic insulators [21.226].

21.3.2 Magnetic Anisotropy

There are three important sources of magnetic anisotropy in thin films, which are related to the reduced symmetry as well as to the crystalline structure of 2-D layers: (i) the shape anisotropy discussed in Sect. 21.1.4, (ii) the reduced or modified coordination of atoms at surfaces, interfaces, or step edges [21.1, 227–231], and (iii) the distortion of the lattice due to strain between the magnetic layers and the substrate, resulting in a magnetoelastic energy contribution [21.1, 232–234]. (ii) and (iii) are related to the anisotropy of the orbital moment in a noncubic environment, which produces a strong enhancement of the MCA.

First-principles calculations reveal that the MCA energy of free-standing (100) transition-metal monolayers is a strong function of band filling [21.229–231]. Calculations by Blügel et al. show that the uniaxial anisotropy constant K_{MCA} is negative between Fe and Cu, peaks at -4.75 meV between Co and Ni, is positive for Fe, and oscillates between positive and negative values from Fe to Ti with amplitude $|K_{MCA}| < 0.2$ meV. Thus, among the 3d metal elements, only the Fe(100) monolayer has an out-of-plane magnetization direction. The strong dependence of K_{MCA} on the occupation of the d-band explains why the MCA is extremely sensitive to electrical gating and oxidation, which has important consequences for the realization of voltage-controlled memory devices [21.9, 235–237]. The calculations also show that K_{MCA} reaches values of 12.32 meV for Os and -13.50 meV for Ir, reflecting the strong increase of the MCA in 5d monolayers due

to their large spin–orbit coupling. Although the magnetism of 5d monolayers is purely theoretical, such an increase shows that the MCA of the induced 5d moments at interfaces can be very strong and even surpass that of the magnetic 3d layers.

Any discussion of the magnetic anisotropy of thin films, however, should include the influence of the substrate and capping layers on (i) and (ii) described above. In the spirit of the model introduced in Sect. 21.1.4, the electronic interaction with the substrate tends to decrease the in-plane orbital moment. This effect alone may not be sufficient to force a change of sign of K_{MCA}, e.g., from negative (favoring in-plane magnetization) to positive (favoring out-of-plane magnetization). For example, K_{MCA} calculated for a Co monolayer on a weakly interacting substrate such as Ag(100) is $-1.33\,\mathrm{meV}$, which adds to the negative in-plane shape anisotropy. However, heavy-metal substrates with strong spin–orbit interactions, which have in addition a large Stoner-enhanced susceptibility, such as W or Pt, can modify the MCA of the interface atoms and also develop strongly anisotropic induced moments, thus determining the overall magnetic anisotropy of the film. This situation is typical for Co films on Pt(111), Pd(111), and Au(111), and multilayers containing the same combination of Co and nonmagnetic elements [21.228, 238, 239]. Interfacial bonding to electronegative atoms, such as oxygen, provides another means to strongly influence the MCA of metal films, even in the absence of heavy metals [21.9, 240]. The axial bonds that develop between O and 3d atoms when, e.g., or MgO or AlO_x are deposited on Fe or Co, or vice versa, induce a crystal-field splitting that favors a very strong out-of-plane orbital moment and the consequent out-of-plane anisotropy [21.74, 241, 242]. This effect is exploited to stabilize the perpendicular magnetization of magnetic tunnel junction devices that utilize CoFeB and MgO as the magnetic electrode and insulating barrier, respectively [21.243].

Extensive reviews have been published on experimental measurements concerning the magnetic anisotropy of transition-metal films on metal substrates [21.1, 68, 232, 244], multilayers [21.245], semiconductors [21.174, 246, 247], and oxide interfaces [21.9]. Rather than presenting an exhaustive overview of different systems, we focus here on general trends, highlighting two cases that are representative of thin-film behavior. To facilitate the discussion, it is common practice to separate the volume-like contributions to the effective anisotropy constants, K^{V} (energy per unit volume), from the interface term K^{I} (energy unit per area). This separation is justified qualitatively by observing that, if more than one or two layers of magnetic material are deposited as a thin film, the layers that are not forming an interface (with the vacuum or the substrate) are expected to exhibit more bulk-like properties. The effective magnetic anisotropy constant K^{eff} of a magnetic layer of thickness t is thus

$$K^{\mathrm{eff}} = K^{\mathrm{V}} + \frac{K^{\mathrm{I}}}{t} \,. \tag{21.53}$$

The two anisotropy constants in (21.53) contain contributions of the dipolar and the spin–orbit-derived anisotropy. Thus, we can write for the volume term $K^{\mathrm{V}} = K^{\mathrm{V}}_{\mathrm{shape}} + K^{\mathrm{V}}_{\mathrm{MCA}}$, and for the interface term $K^{\mathrm{I}} = K^{\mathrm{I}}_{\mathrm{shape}} + K^{\mathrm{I}}_{\mathrm{MCA}}$. In such a model, $K^{\mathrm{V}}_{\mathrm{MCA}}$ includes the thickness-independent crystalline and magnetoelastic contributions, whereas K^{I} includes all the thickness-dependent effects. $K^{\mathrm{V}}_{\mathrm{shape}}$ is the shape anisotropy due to the average dipolar energy as obtained by the continuum theory (21.24), while $K^{\mathrm{I}}_{\mathrm{shape}}$ is the contribution due to the reduction of the dipole anisotropy field experienced by the atoms in the surface or interface region calculated using (21.25). Because the negative shape anisotropy has a constant value per atom and thus increases with thickness, the magnetization of thick films is usually in-plane, with a few exceptions due, e.g., to tetragonally distorted crystal structures. For thicknesses smaller than 1–2 nm, however, $K^{\mathrm{I}}_{\mathrm{MCA}}$ can dominate K^{V} and determine the easy axis. If these terms have different signs, a reorientation transition of the easy axis can occur.

Co layers deposited on Pt(111), by either molecular beam epitaxy or sputtering, represent a prototype system in which such a spin reorientation transition occurs due to a positive K^{I} and negative $K^{\mathrm{V}}_{\mathrm{shape}}$. Figure 21.17 shows that the product $K^{\mathrm{eff}} t_{\mathrm{Co}}$ of a (111)-textured $AlO_x/\mathrm{Co}(t_{\mathrm{Co}})/\mathrm{Pt}$ layer changes from positive to negative as a function of thickness, leading to an out-of-plane to in-plane spin transition for $t_{\mathrm{Co}} > 1\,\mathrm{nm}$ [21.249], as expected based on (21.53). The measurements additionally show that the threshold thickness shifts from 1.35 nm in the as-deposited layers to more than 3 nm after annealing at 598 K for 30 min. This effect is attributed to the migration of oxygen through the Al capping layer to the Co interface, leading to the homogeneous formation of Co–O–Al bonds over the interface and a consequent increase of the perpendicular anisotropy of the top Co surface. The increase of the perpendicular anisotropy due to oxidation is also confirmed by exposing as-grown Al/Co/Pt trilayers to an rf oxygen plasma, as shown in Fig. 21.18a. Whereas the pristine Al/Co/Pt structure has in-plane anisotropy, progressive oxidation leads to an out-of-plane easy axis and square magnetization loops (Fig. 21.18b). The perpendicular anisotropy, reflected by the coercivity in Fig. 21.18c, has a maximum coinciding with full oxidation of the top Co interface

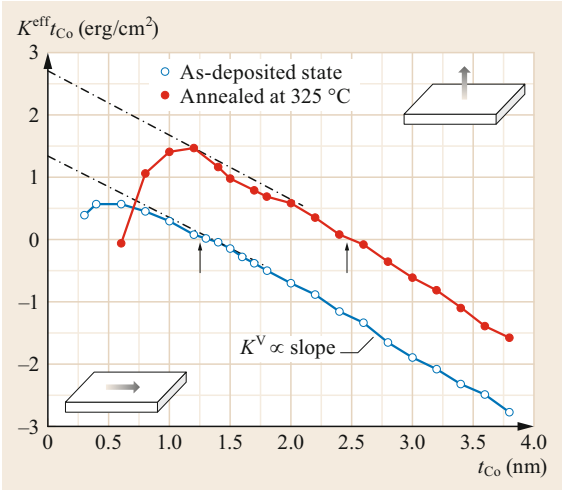

Fig. 21.17 Variation of product of effective anisotropy energy K^{eff} and Co thickness t_{Co} as a function of Co thickness for as-deposited and annealed polycrystalline films of Pt(2)/Cu(2)/AlO_x(0.5)/Co(t_{Co})/Pt(20)/Ta(2) grown by sputtering on a SiO_2 wafer. The thickness of each layer is given in nanometers in the parentheses. The oxide layer is obtained by natural oxidation of Al in an oxygen pressure. The sum of the interface terms, K^{I}, is given by the intersection with the ordinate axis, whereas the volume-like contribution, K^{V}, is deduced from the slope of the curve. The *thin arrows* indicate the thickness at which the spin reorientation transition occurs. (Reprinted by permission from [21.9], © Am. Phys. Soc. 2017)

and declines afterwards due to overoxidation of the Co layer [21.248]. From the slope of $K^{\text{eff}}t_{\text{Co}}$ in Fig. 21.17, one deduces that the effective bulk anisotropy is essentially the demagnetizing energy of the Co layer ($-\mu_0 M^2/2$) and does not change with oxidation. The sum of the interfacial anisotropy at the Co/Pt and AlO_x/Co interfaces, given by the y-axis intercept of $K^{\text{eff}}t_{\text{Co}}$, however, increases sharply after annealing, giving $K^{\text{I}} = 2.8\,\text{mJ/m}^2$ ($1\,\text{mJ/m}^2 = 1\,\text{erg/cm}^2$). Note that $1\,\text{mJ/m}^2 \approx 0.5\,\text{meV/atom}$ for a *single* Co layer, assuming the same atomic density as for a Pt(111) monolayer. Since the anisotropy of the Co/Pt interface is in the range of $0.6-1.4\,\text{mJ/m}^2$ [21.250, 251], this result implies that K^{I} at the AlO_x/Co interface is in the range of $1.4-2.2\,\text{mJ/m}^2$, i.e., comparable to that of the Co/Pt interface. Similar enhancements of the perpendicular anisotropy are obtained at the MgO/CoFe interface [21.252], which is quite remarkable considering the weak spin–orbit coupling of Co, AlO_x, and MgO [21.9].

A different case is that of epitaxial Ni layers grown on Cu(100) [21.232, 233, 253]. Here the interface anisotropy is negative, which leads to an in-plane easy axis of the thinner Ni films. However, Ni grows pseudomorphically on Cu(001) with an in-plane lattice constant that is 1.6% larger compared with fcc Ni. To compensate this strain, the vertical spacing between the Ni layers contracts, leading to a crystalline structure with face-centered tetragonal (fct) symmetry. According to the arguments presented in Sect. 21.1.4, we would now expect that $V_\perp > V_\parallel$, therefore $R > 1$ and a crystalline volume term $K^{\text{V}}_{\text{MCA}}$ that favors perpendicular magnetization. Indeed, a plot of K^{eff} as a function of $1/t_{\text{Ni}}$ (Fig. 21.19a) shows that K^{I} is negative, $\approx -85\,\mu\text{eV/atom}$ at room temperature, whereas $K^{\text{V}}_{\text{MCA}}$ is positive, $\approx 30\,\mu\text{eV/atom}$, which is more than an order of magnitude larger compared with fcc Ni. By estimating the compensation point at which $K^{\text{eff}} = 0$, we would expect an in-plane to out-of-plane spin reorientation transition at around $t_{\text{Ni}} = 5-6\,\text{ML}$. However, as the shape anisotropy contributes another $-10\,\mu\text{eV/atom}$ to K^{V}, the transition actually sets in at $\approx 7\,\text{ML}$. In very thick films, the structure of Ni relaxes back to fcc and K^{V} decreases until the influence of the shape anisotropy brings the easy axis back in-plane.

The two examples presented above show how the nature of the interfaces as well as of the *bulk* crystalline structure of the film concur in determining the orientation of the magnetization, together with the shape anisotropy. Surfaces with reduced in-plane symmetry, due to either the presence of steps [21.204, 254–256] or inequivalent bonding geometries [21.246, 257], further show preferential in-plane directions, captured by higher-order anisotropy constants in (21.17); for example, symmetry breaking at atomic steps of ultrathin Fe films grown on stepped Ag(001) induces a uniaxial magnetic anisotropy with the easy axis parallel to the step edges, which scales quadratically with the step density [21.255]. In such a case, the origin of the step-induced magnetic anisotropy is almost independent of the Fe film thickness, which has been attributed to a long-range distortion of the cubic symmetry of Fe [21.258]. In other cases, however, local effects due to the reduced coordination of the step atoms dominate the anisotropy behavior, as shown, e.g., by the abrupt 90° switching of the in-plane easy axis for 20-ML-thick Co films grown on stepped Cu(001) upon step decoration by only 0.03 ML of Cu [21.259]. Such local step-edge effects are also responsible for oscillations of the MCA during layer-by-layer growth of Co on Cu(001), as the film morphology alternates between filled and incompletely filled atomic layers [21.260]. Other morphology-related effects are due to electron confinement, which, in crystalline films, has been

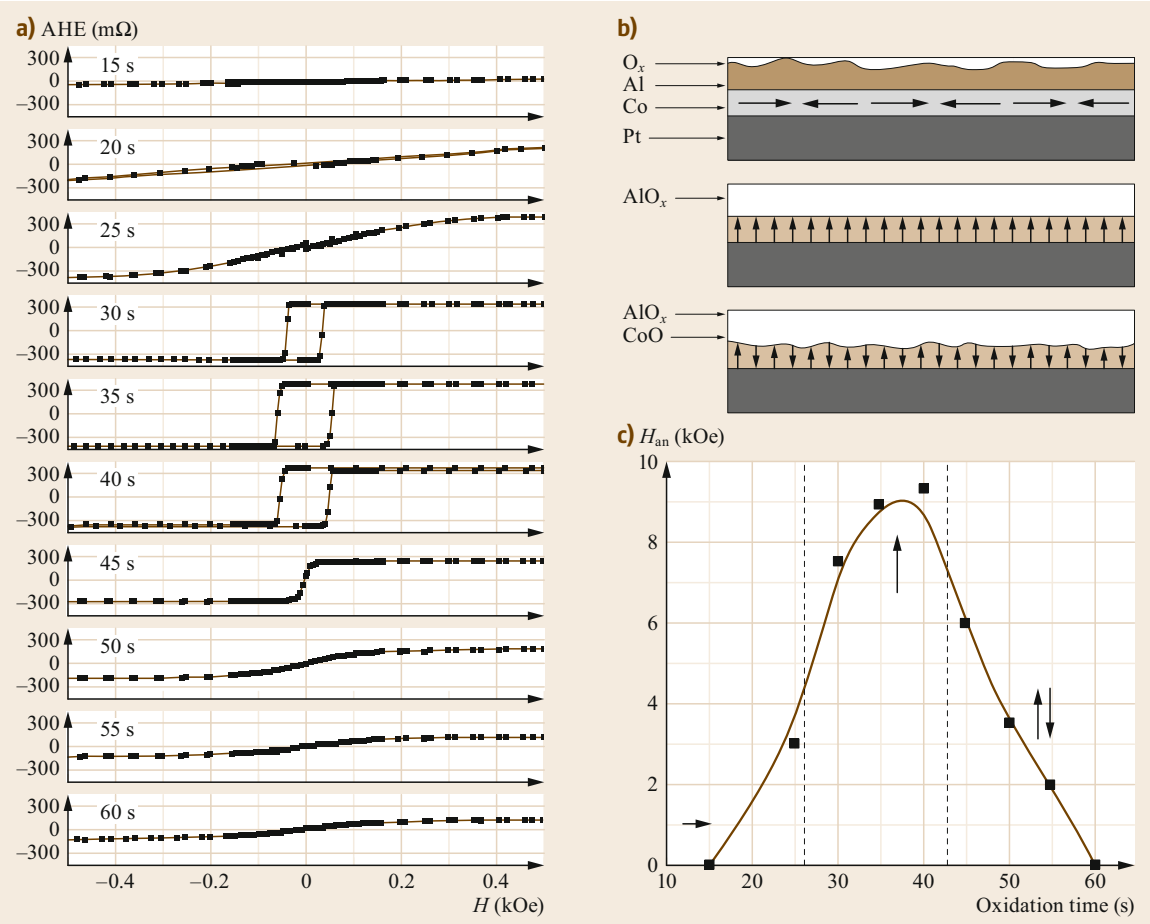

Fig. 21.18 **(a)** Magnetization loops of $AlO_x(1.6)/Co(0.6)/Pt(3)$ trilayers measured by the anomalous Hall effect (AHE) as a function of out-of-plane magnetic field for various plasma oxidation times. **(b)** Schematics of the interface oxidation process showing underoxidized (*top*), optimally oxidized (*middle*), and overoxidized (*bottom*) Co layers. **(c)** Effective anisotropy field versus oxidation time. (Reprinted by permission from [21.248], © Am. Inst. Phys. 2008)

shown to lead to oscillations of the MCA due to the formation of quantum well states in either a nonmagnetic metal cap layer [21.261] or the ferromagnetic layer itself [21.262].

Finally, magnetic anisotropies are temperature-dependent quantities, as mentioned in Sect. 21.1.4 and illustrated in Fig. 21.19b for the second- and fourth-order anisotropy constants of Ni/Cu(001) [21.253]. The different temperature dependence of the surface, volume, and shape anisotropies may give rise to spin reorientation transitions as a function of temperature [21.244]. Such transitions have been observed, e.g., in Fe films on Cu(001) and Ag(001) [21.263–265], which evolve from out-of-plane at low temperature to in-plane at high temperature, as well as in Ni/Cu(001), which shows the opposite behavior [21.253].

21.3.3 Temperature Dependence of Magnetic Order

The temperature dependence of magnetic order is different in thin films relative to bulk materials (Sect. 21.1.7). Magnetic films grown pseudomorphically on nonmagnetic substrates with appropriate lattice spacing allow for the investigation of the order–disorder phase transition in a layerwise fashion, provided that the films are thermodynamically stable, i.e., that their microstructure does not change with temperature.

Curie Temperature

The first extensive studies of magnetic order in ferromagnetic films were carried out by Gradmann and coworkers for epitaxial NiFe and Co layers grown on

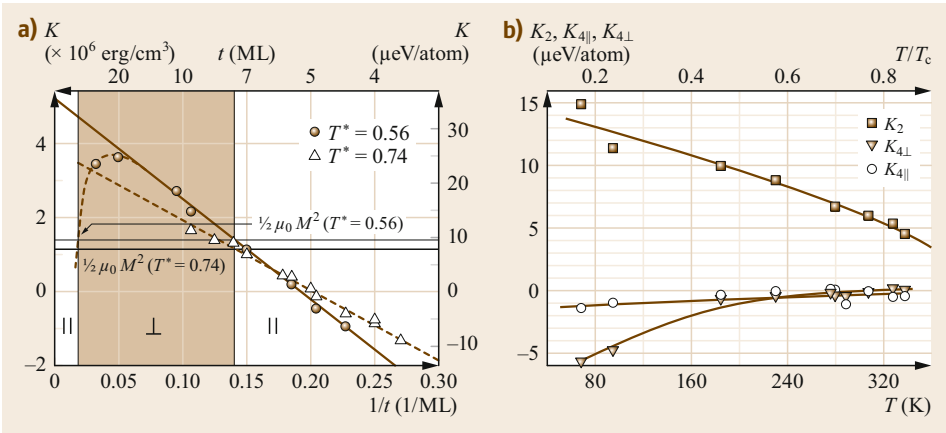

Fig. 21.19 **(a)** Effective anisotropy energy K of epitaxial Ni layers grown on Cu(100) as a function of Ni thickness for two reduced temperatures $T^* = T/T_C$. The *shaded area* is the perpendicularly magnetized phase where the crystalline anisotropy exceeds the shape anisotropy, indicated by the *solid* and *dashed horizontal lines* for the two temperatures. (Reprinted by permission from [21.232], © Springer 1996). **(b)** Temperature dependence of the anisotropy constants K_2 and K_4 determined for a 7–8 ML thick Ni/Cu(001) film. Note that $K_{4\parallel} \neq K_{4\perp}$ as a result of the tetragonally distorted structure of the Ni film, and that the convention used to number the K_i indexes here is different from that used in (21.17) (Reprinted by permission from [21.253], © Am. Phys. Soc. 1997)

Cu(111) as well as for Ni on Re(0001) and Fe on W(110) [21.1, 266, 267]. The results evidenced a drastic decrease of the Curie temperature T_C when the film thickness approached the monolayer limit, as shown in Fig. 21.20. The decrease of T_C is related to the reduced coordination of the magnetic atoms, as discussed in Sect. 21.1.7 for the Heisenberg model. Qualitatively, the decrease of the average coordination number $\overline{N}$, schematized in Fig. 21.20b, leads to a $1/t$ decrease of T_C. The data in Fig. 21.20c agree with the reduction of

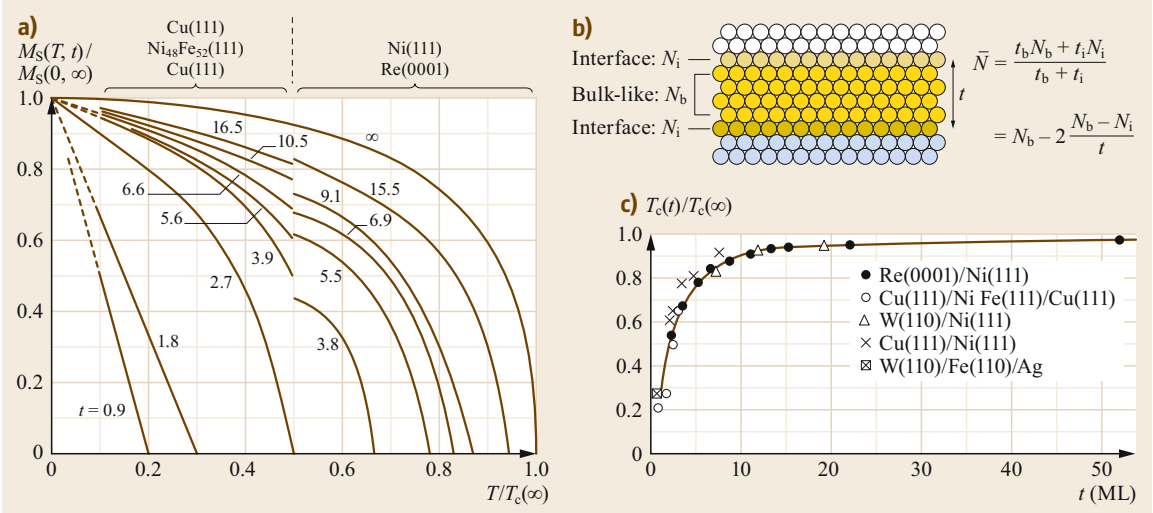

Fig. 21.20a–c Dependence of spontaneous magnetization $M_s(T, t)$ on temperature T (normalized to the Curie temperature $T_C(\infty)$ of the bulk material) and the number t of atomic layers, given as parameters for $Ni_{48}Fe_{52}(111)$ films on Cu(111) ($T < 0.5T_C(\infty)$) and Ni(111) films on Re(0001) ($T > 0.5T_C(\infty)$). Data for bulk Ni are shown for comparison. **(b)** Schematic diagram of the change of the average coordination number $\overline{N}$ for a thin film. **(c)** Normalized Curie temperature versus number of atomic layers t for different densely packed cubic transition-metal films. (Adapted by permission from [21.1], © Elsevier 1993)

T_C relative to the bulk Curie temperature $T_C(\infty)$ predicted by finite-size scaling models [21.268–270],

$$\frac{T_C(\infty) - T_C(t)}{T_C(\infty)} = \left(\frac{t_0}{t}\right)^{1/\nu} , \qquad (21.54)$$

where t_0 is a constant and ν is the critical exponent of the spin–spin correlation length introduced in Sect. 21.1.7. The values of $1/\nu$ vary from 1 in the mean-field case to 2 depending on the boundary conditions assumed for the magnetic film and the geometry of the lattice. The curves in Fig. 21.20c are well reproduced by $1/\nu = 1.27 \pm 0.2$, although (21.54) is strictly valid only for a 3-D layered system ($t > 4$ ML) with thickness-independent magnetic anisotropy. For thinner films, higher ordering temperatures than predicted by (21.54) are actually observed, consistent with the fact that T_C increases with surface anisotropy (21.40). Studies of Ni layers grown on Cu(110), Cu(100), and Cu(111) also reveal that T_C depends on the symmetry of the lattice and interlayer spacing [21.271].

The morphology and, thereby, the magnetic properties of ultrathin films depend strongly on the preparation conditions. Although it is possible to grow smooth 2-D monolayers with sharp interfaces, care must be taken to adjust the deposition conditions in order to achieve wetting and layer-by-layer growth while minimizing interdiffusion [21.272, 273]. A well-known example is that of bcc Fe films grown on W(110), which have been characterized by low-energy electron diffraction (LEED), Auger, and STM, and studied by conversion electron Mössbauer spectroscopy [21.1, 272, 274], torsion oscillation magnetometry [21.203, 275], spin-polarized LEED [21.276, 277], the magnetooptic Kerr effect [21.278, 279], as well as spin-polarized STM [21.192, 280–283]. The relative contributions of the first, second, and bulk-like Fe layers can be distinguished by their different magnetic hyperfine fields as measured by Mössbauer spectroscopy [21.274, 284]. For thickness $t < 0.2$ ML, the films are pseudomorphic, as observed by LEED and STM, and the monolayer component alone is present in the Mössbauer spectra, independent of the preparation temperature ($T_{prep} =$ 300 or 475 K) and despite the large misfit of 9.4% between the lattice constants of W and Fe. Wetting in this case is favored by the large difference between the surface energy of the substrate and overlayer. For $t > 0.8$ ML, the growth mode depends sensitively on T_{prep}. For films deposited at $T_{prep} = 300$ K, second-layer Fe islands form on top of a closed and thermodynamically stable pseudomorphic monolayer, whereas for films grown at $T_{prep} \geq 475$ K, step-flow growth leads to the formation of continuous double-layer stripes on top of the first layer, accompanied by the appearance of nonperiodic dislocation lines along the [001] direction to relax the accumulated tensile strain in the Fe lattice [21.192, 272, 285], as shown in Fig. 21.21.

The surfaces of thicker films are atomically smooth. The changes of the Curie temperature as a function of T_{prep} reported in Fig. 21.22 for Fe/W(110) capped by Ag reflect the fact that the morphology of films prepared at 475 K is stable for 0.35 ML $< t <$ 1.2 ML, and $T_C = (282 \pm 3)$ K is an intrinsic property of the Ag-covered monolayer (uncapped Fe films have $T_C \propto$ 210 K [21.274]). As T_C does not depend on the Fe coverage in the sub-monolayer regime, one concludes also that the lateral size of the monolayer patches is sufficiently large that finite-size effects of the 2-D lattice can be ignored. In contrast, the strong increase of T_C with t for films grown at $T_{prep} = 300$ K indicates that the morphology of the Fe films is not stable and that Fe islands of increasing size form or coalesce with increasing T_{prep} [21.272]. Note also that the first and second Fe layer have in-plane and out-of-plane anisotropy, respectively, and that on vicinal substrates with a terrace width of less than 10 nm, Fe stripes grown on adjacent terraces couple antiparallel, both effects having an influence on T_C [21.275–280].

Low-Temperature Behavior

The low-temperature behavior of the saturation magnetization is determined, as in bulk systems, by the excitation of spin waves (Sect. 21.1.7, *Scaling Laws*). According to (21.46) and (21.50), the reduced magnetization $M_s(T)/M_s(0)$ should scale as $1 - T \ln T \approx 1 - T$ for $T < T_C/2$. In experiments, however, deviations from this trend have been reported depending on the temperature range and anisotropy barriers specific to each system as well as extrinsic factors (e.g., overlapping magnetic signals resulting from magnetic layers with different interfaces or a superparamagnetic phase). The low-temperature magnetization can nonetheless be approximated by a dependence of the type

$$\frac{M_s(T)}{M_s(0)} = 1 - bT^{\alpha} , \qquad (21.55)$$

where b is an effective spin wave parameter and α varies from 1 in the case of an ideal 2-D layer with finite magnetic anisotropy to 3/2 for sufficiently thick ferromagnetic layers, as expected according to Bloch's law. A detailed description of low-temperature magnetization measurements of thin films is reported in [21.1, 2].

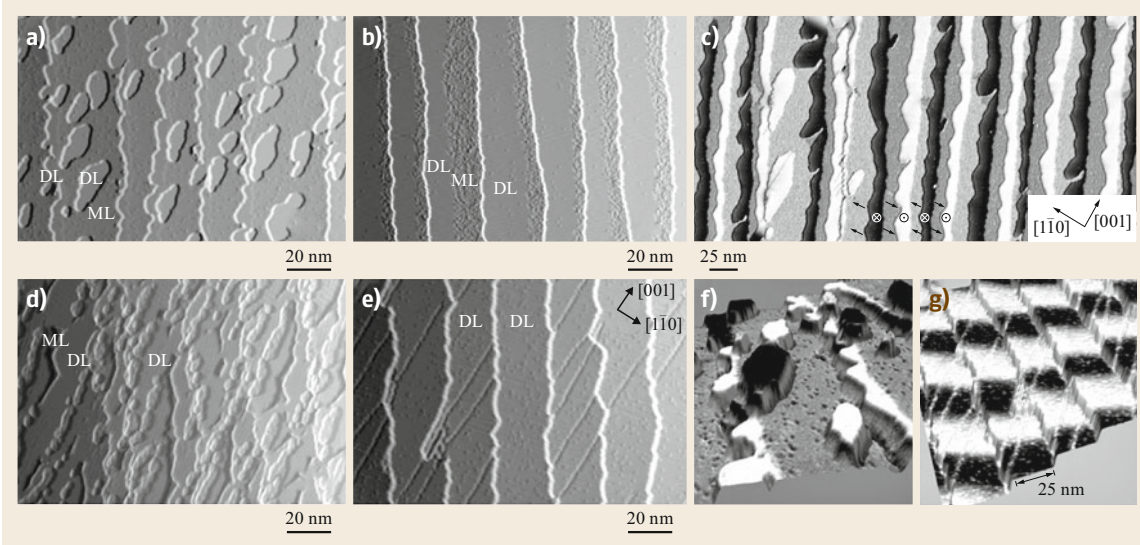

Fig. 21.21a–g Growth and magnetic structure of Fe on W(110). **(a)** For coverage $t = 1.3$ ML deposited at $T_{prep} = 300$ K, second-layer Fe islands grow irregularly on top of the first pseudomorphic Fe layer. **(b)** $t = 1.6$ ML and $T_{prep} = 550$ K. Fe grows in a step-flow mode, forming a sequence of monolayer stripes alternating with double-layer stripes where the second layer overlaps the first. **(c)** $t = 2.1$ ML and $T_{prep} = 300$ K. The second layer is connected but not closed. Third-layer islands form on top of dislocation lines. **(d)** $t = 2.0$ ML and $T_{prep} = 550$ K. Continuous film with dislocation lines along [001]. **(e)** Spin-polarized STM image of a smooth 1.4 ML Fe/W(110) film taken with a Gd-coated tip with canted magnetization. Both out-of-plane and in-plane contrast are visible on double- and monolayer Fe, respectively. Note the antiparallel alignment of adjacent out-of-plane Fe domains induced by dipolar coupling. **(f)** Rendering of the topographic and out-of-plane magnetic contrast of Fe double-layer islands prepared by evaporation of 1.3 ML Fe at $T_{prep} = 300$ K. **(g)** Same for a continuous double layer prepared at $T_{prep} = 550$ K. With increasing coverage, the magnetic structure of the double-layer stripes evolves into a spin spiral constituted by alternate up and down domains with periodicity of ≈ 50 nm separated by in-plane chiral domain walls [21.283]. (Reprinted by permission from [21.282], © Am. Phys. Soc. 2002)

21.4 Non-collinear Spin Configurations

For a long time, one of two possible magnetic orders, either ferromagnetic or antiferromagnetic, with collinear spin orientation in single domain regions was considered as the ground state of surfaces and ultrathin films. Progress in theoretical and experimental methods led to the realization that non-collinear spin structures can have a lower energy compared with collinear ones, thanks to either antiferromagnetic interactions frustrated by geometric contraints imposed by the crystal, Heisenberg-type interactions competing between different pairs of atoms or Heisenberg exchange competing with the antisymmetric exchange. In the following, we discuss how such effects can give rise to periodic frustrated spin lattices, 1-D periodic chiral textures (spin spirals), 1-D localized chiral textures (chiral domain walls), and 2-D localized or periodic chiral textures (skyrmions and skyrmion lattices, respectively).

21.4.1 Frustrated Systems

In general, magnetic frustration is a phenomenon where the geometry of the crystal lattice or the competition of different interactions imposes constraints on the energy minimization of the global spin texture, thus preventing pairs of neighboring spins from adopting a configuration with minimal bond energy.

The first case is exemplified by materials with antiferromagnetic nearest-neighbor interactions deposited on a triangular lattice, such as the (111) and (0001) surfaces of an fcc and hcp crystal, respectively, on which the antiferromagnetic alignment of neighboring spins is frustrated by geometry. The epitaxial growth of such ultrathin films has been studied intensively using various experimental techniques. In particular, pseudohexagonal c(8 × 2)Mn films on Cu(100) [21.286], Mn films on the (111) surfaces of fcc Pd [21.287],

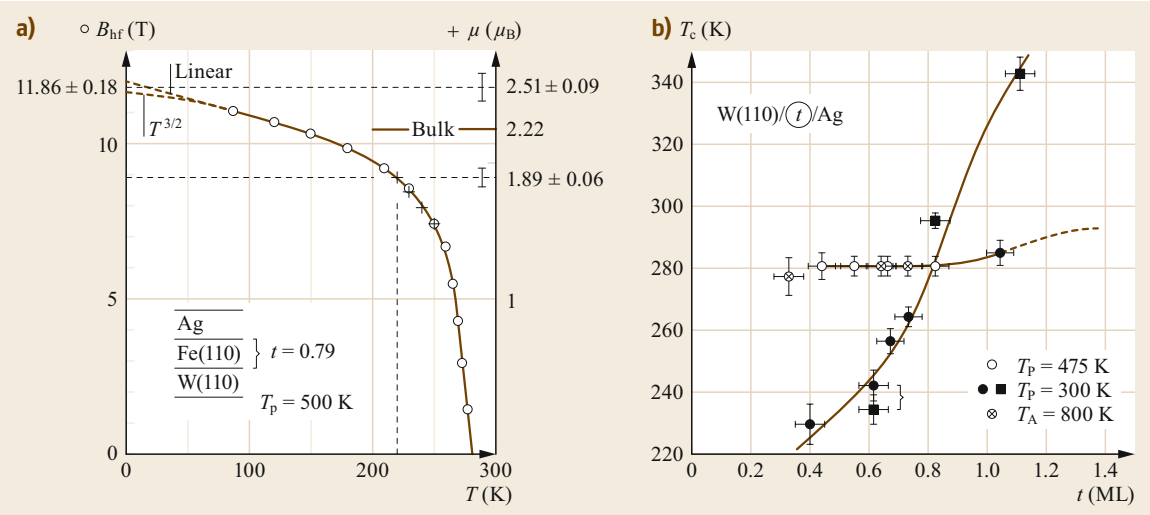

Fig. 21.22 **(a)** Magnetization of a pseudomorphic monolayer of Fe on W(110) grown at 500 K and capped by Ag measured by torsion oscillator magnetometry (*crosses*) and Mössbauer spectroscopy (*circles*). The Curie temperature is 282 K. The *right-hand scale* shows that the saturation magnetic moment per Fe atom exceeds that of bulk Fe. The *solid line* represents a $(1-bT^{3/2})$ fit. (Reprinted by permission from [21.203], © Am. Phys. Soc. 1989) **(b)** Curie temperature of Fe films on W(110), coated with Ag, measured by conversion electron Mössbauer spectroscopy. The samples were prepared at 300 and 475 K or prepared at 300 and annealed at 800 K before coating. (Reprinted by permission from [21.272], © Springer 1989)

Ir [21.288], Cu [21.289–291], and MgO [21.292], and on the (0001) surface of Ru [21.293] and Co [21.294] have been prepared and analyzed. However, other ultrathin hexagonal films, e.g., Cr and V on Pt(111) and Ru(0001) [21.295–297], have also been investigated. Detailed investigations of the magnetic structure have been carried out in selected cases by means of spin-polarized STM [21.298]. From a theoretical point of view, even when neglecting the effects of spin–orbit coupling, a large variety of spin ground states are possible, depending on the relative magnitude and sign of the nearest- and next-nearest-neighbor exchange coupling constants, J_1 and J_2, respectively. If J_2 is zero or positive (ferromagnetic), then there are only two possible magnetic ground states, determined by the sign of J_1, the ferromagnetic and the antiferromagnetic 120° Néel state. But small negative values of J_2 are already sufficient to allow for an infinite number of magnetic states, namely commensurate or incommensurate spin spiral states with wavevector $\boldsymbol{Q}$ along any high-symmetry line of the surface (Sect. 21.1.5). Examples are shown in Fig. 21.23 for three particular cases of spin spirals: the rowwise antiferromagnetic state ($\boldsymbol{Q} = \overline{\mathrm{M}}$), the 120° Néel state ($\boldsymbol{Q} = \overline{\mathrm{K}}$), and the so-called 3Q-state, a 3-D non-collinear spin structure on a 2-D lattice with four chemically identical atoms per surface unit cell, where the relative angle between all nearest-neighbor spins is given by the tetrahedron angle of 109.47°. The 3Q-state is formed as a linear combination of the three rowwise antiferromagnetic structures orthogonal in spin space, each having one of the three $\boldsymbol{Q}$-vectors corresponding to a different $\overline{\mathrm{M}}$-point of the surface Brillouin zone. From the viewpoint of the Heisenberg model (21.28), the single- and triple-Q state have the same energy, but both are discriminated by higher-order spin-interaction such as the biquadratic or four-spin interactions. Ab initio calculations of 3d monolayers with or without a Cu(111) substrate show that the energy differences between different magnetic states change due to the presence of the substrate, but the magnetic ground state remains unaltered: Cr/Cu(111) exhibits the 120° Néel state and Mn/Cu(111) the 3Q-structure, which is 17 meV lower in energy than the 1Q-state, while Fe/Cu(111) is ferromagnetic ($\boldsymbol{Q} = \overline{\Gamma}$). Experimental investigations have identified the 120° Néel state for monolayer Mn/Ag(111) [21.299] and Fe/Re(0001) [21.300] and the 3Q-state for monolayer Mn/Re(0001) [21.301].

The second case of frustration refers to competing exchange interactions. Suppose a chain of 3 identical atoms of spin $S = 1$ at equidistant lattice sites subject to a nearest neighbor exchange interaction J_1 between atom 1 and 2 as well as atom 2 and 3 and a next-nearest neighbor interaction J_2 between atom 1 and 3. Referring to the Heisenberg model (21.28) and assuming between neighboring atoms the same canting angle θ of the lo-

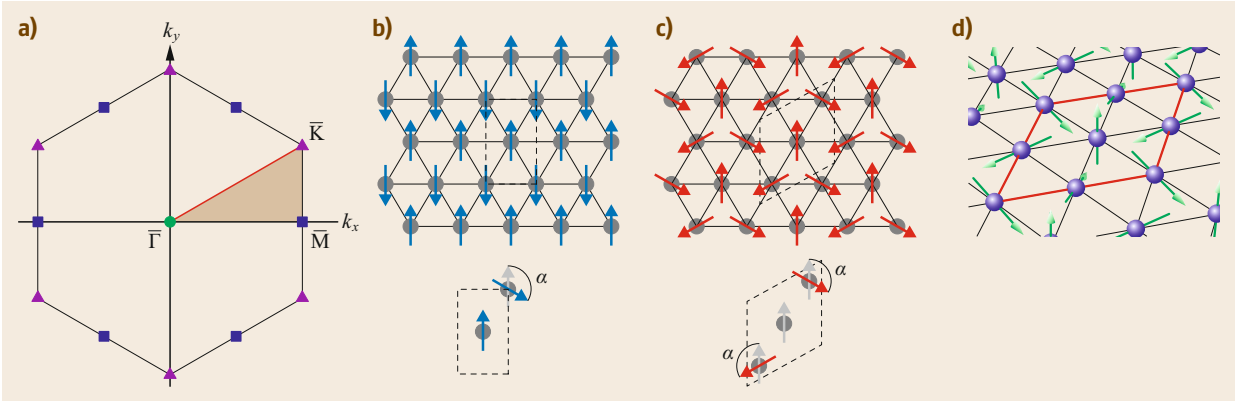

Fig. 21.23 **(a)** The *hexagon* shows the first Brillouin zone of the 2-D hexagonal Bravais lattice. The *brown-shaded area* indicates the irreducible part. **(b)** The rowwise antiferromagnetic structure. **(c)** The coplanar non-collinear 120° Néel structure. Indicated are the corresponding two- and three-atom unit cells and the continuous paths, which connect the corresponding magnetic structure to the FM state. **(d)** The 3Q-structure, with spins pointing in all three directions of the spin space. Note that, due to the neglect of the spin–orbit interaction, only the relative orientation of the moments is specified

cal moments, the magnetic energy of the system is given by $E(\theta) = -2J_1\cos(\theta) - J_2\cos(2\theta)$. The energy minimization leads to the solutions $\sin(\theta) = 0$, which refers to the ferromagnetic state ($\theta = 0°$) with the energy $E_{\mathrm{FM}} = -2J_1 - J_2$ if all atoms couple ferromagnetically ($J_1, J_2 > 0$), or to the antiferromagnetic state $\theta = 180°$) with equal energy $E_{\mathrm{AFM}} = -2|J_1| - J_2$, if the nearest neighbor interaction is antiferromagnetic and the next-nearest neighbor ferromagnetic ($J_1 < 0, J_2 > 0$). However, if the nearest neighbor interaction is ferromagnetic and the next-nearest interaction is antiferromagnetic ($J_1 > 0, J_2 < 0$) or all interactions are antiferromagnetic ($J_1 < 0, J_2 < 0$), then neither the ferro- nor the antiferromagnetic chain satisfies the interactions between all pairs of atoms. Subsequently, the energy of the collinear state will be higher than $-2|J_1| - |J_2|$ and rises depending on J_1 and J_2 until a non-collinear solution with a non-trivial canting angle of $\cos(\theta_{\mathrm{NC}}) = -J_1/(2J_2)$ becomes lower in energy. This happens if $-3/4|J_1| < J_2 < 0$ and the energy amounts to $E(\theta_{\mathrm{NC}}) = 3/2J_1^2/J_2 - J_2$. The canting angle follows from a ratio of exchange interactions. It is interesting to compare this canting angle with the one discussed in (21.35), which followed from a competion between Heisenberg exchange and DMI. Since the DMI is a spin–orbit phenomenon, its energy scale is typically one order of magnitude smaller than the exchange interaction. Translating this simple model to periodic structures such as films and chains shows that exchange frustration leads to magnetic structures with short pitches, often on the atomic scale, whereas the DMI-stabilized noncollinear structures can be of a different scale. A nice example is Mn/W(110) [21.118] in comparison to Mn/W(100) [21.119]. Both have the same chemical composition, in both Mn is grown on lattices that give no cause for geometric frustration, both exhibit spin-spiral ground states, but the periods of the magnetic spirals are 12 nm versus 2.2 nm, clearly indicating that the latter is due to exchange competition and the former to the DMI. We conclude that exchange frustration offers a path of producing small localized magnetic textures.

21.4.2 Chiral Spin Spirals

Magnetic films or clusters on surfaces, including multilayer structures, present broken inversion symmetry along the surface normal, which, together with spin–orbit coupling, gives rise to antisymmetric exchange or DMI (Sect. 21.1.6). The DMI competes with the symmetric exchange and the anisotropy energy: whereas the latter terms favor collinear spin alignment, the DMI favors a spatially spiraling magnetic structure with a specific rotational direction. In this context, a completely new class of chiral magnets has been recently established, being made of monolayers and ultrathin films or heterostructures of 3d metals, where the DMI interaction and magnetic chirality are introduced due to the presence of heavy-metal surfaces and interfaces. In some instances, the DMI introduces chiral ground states, e.g., in Mn/W(110) [21.118], Mn/W(100) [21.119], Fe/Ir(111) [21.134, 302, 303], Pd/Fe/Ir(111) [21.135], and biatomic Fe chains on the (5×1)-Ir(001) reconstruction [21.123]. If the magnetic structure changes on a mesoscopic length scale, the non-collinear magnetization can be described by a continuous vector field $\boldsymbol{m}(\boldsymbol{r})$ with $|\boldsymbol{m}| = 1$. In the simplest case, $\boldsymbol{m}$ varies only along one spatial coordinate x and the energy of a magnetic configuration can be described

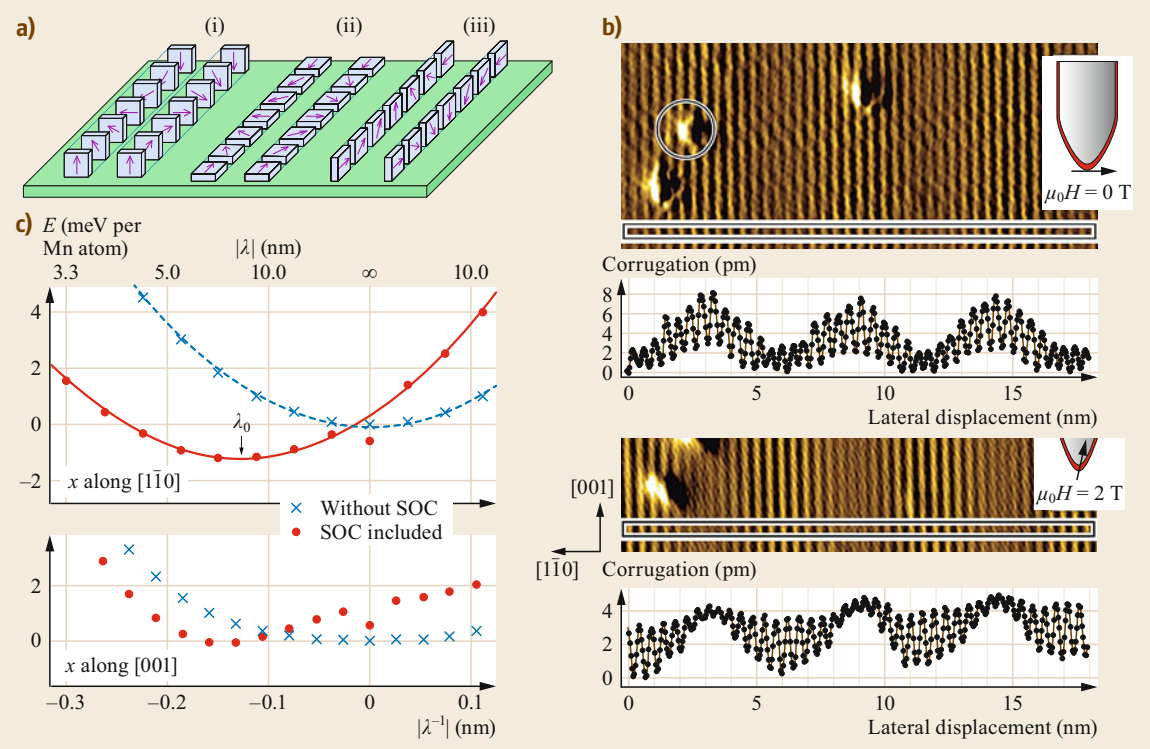

Fig. 21.24 **(a)** Schematics of right- and left-handed spin spirals with different rotation axes on a symmetric surface. For (i) and (ii), the right- and left-handed spirals are mirror images of each other. In (iii), the surface breaks the mirror symmetry. Therefore, the two spirals in (iii) are not equivalent to each other and may differ in energy. The left-rotating cycloidal spiral shown in (iii) corresponds to the one found for 1 ML Mn on W(110), a system with local antiferromagnetic order. **(b)** Spin-polarized STM images of the Mn monolayer on W(110) and corresponding line sections taken with a ferromagnetic Fe-coated tip at external fields of 0 T (*top*) and 2 T (*bottom*). As sketched in the *insets*, the external field rotates the tip magnetization from in-plane to out-of-plane, shifting the position of maximum spin contrast. The stripes on the nanometer scale represent the local antiferromagnetic structure. On a larger length scale, however, the image shows a spiral structure that is driven by the DMI, as seen in the line profiles at the bottom of each image. **(c)** Electronic energy of a homogeneous spin spiral depending on the period length $|\lambda|$. The sign of λ depends on the rotational direction. The *data points* show the results obtained from electronic structure calculations, and the *lines* indicate the fits with the terms of (21.57). (**(b,c)** reprinted with permission from [21.118], © SpringerNature 2007)

by a simple micromagnetic energy functional of the form

$$E(\boldsymbol{m}) = \int \mathrm{d}x \left[\frac{A}{4\pi^2} \left(\frac{\mathrm{d}\boldsymbol{m}(x)}{\mathrm{d}x} \right)^2 + \boldsymbol{m}(x)^{\mathsf{T}} \cdot \overleftrightarrow{\mathcal{K}} \cdot \boldsymbol{m}(x) + \frac{\boldsymbol{D}}{2\pi} \cdot \left(\boldsymbol{m}(x) \times \frac{\mathrm{d}\boldsymbol{m}(x)}{\mathrm{d}x} \right) \right], \tag{21.56}$$

where the spin stiffness A represents the exchange interactions that favor collinear spin alignment, the symmetric anisotropy tensor $\overleftrightarrow{\mathcal{K}}$ accounts for the preferred orientation of the magnetization with respect to the crystal lattice, and the micromagnetic Dzyaloshinskii vector $\boldsymbol{D}$, also called spiralization vector, is nonzero only if the underlying crystal structure does not possess inversion symmetry. The DMI breaks the degeneracy of right- and left-handed spin rotations, thus favoring either a right- or left-handed spiral magnetic structures (Fig. 21.24a; note that only cycloidal spin spirals of type (iii) have nondegenerate right- and left-handed states).

Monolayer Mn/W(110) is an exemplary system where DMI-induced cycloidal spin spirals are observed, characterized by a fixed rotation axis and $(\mathrm{d}\boldsymbol{m}/\mathrm{d}x)^2 = \text{const}$ [21.118]. Figure 21.24b shows a constant-current spin-polarized STM image measured on an atomically flat Mn layer on W(110) using a Fe-coated probe tip sensitive to the in-plane magnetization. The spin-polarized STM data reveal periodic stripes running

along the [001] direction, with an interstripe distance of 0.47 nm matching the surface lattice constant along the $[1\bar{1}0]$ direction. This contrast stems from the local c(2 × 2)-antiferromagnetic structure [21.304]. The line profile further reveals that the magnetic amplitude is not constant but modulated with a period of about 6 nm along this direction. Imaging the surface using an Fe-coated tip with out-of-plane magnetization shows that the maximum contrast of the long-wave modulation is achieved where the in-plane spin signal exhibits a minimum (Fig. 21.24c), consistent with the contrast expected of a spin spiral propagating along the $[1\bar{1}0]$ direction with magnetic moments rotating from in-plane to out-of-plane. For such a homogeneous spiral, (21.56) simplifies to

$$E = A\lambda_0^{-2} + D\lambda_0^{-1} + \overline{K}\,, \tag{21.57}$$

where the integration is performed over one period length $|\lambda_0|$, the sign of λ_0 distinguishes between right- and left-handed spirals, and $\overline{K}$ is the anisotropy energy averaged over the spiral. The energy given by (21.57) is lower for the spiral than for the antiferromagnetic state if the DMI overcomes the average energy penalty per atom for spins spiraling in a plane rather than pointing along a preferred easy axis of magnetization, that is, if $D^2 > 4A\overline{K}$. The period of the optimal homogeneous spiral is thus given by $\lambda_0 = -2A/D$. Density functional theory calculations, reported in Fig. 21.24c, show how the energy of the Mn/W(110) monolayer depends on the direction and period of the spin spiral. The calculated parameters are $A = 94\,\mathrm{meV\,nm^2}$, $D = 24\,\mathrm{meV\,nm}$, and $\overline{K} = 0.6\,\mathrm{meV}$ per Mn atom [21.118]. Notably, considering only isotropic exchange (no spin–orbit interaction), the total energy minimum occurs for the antiferromagnetic state. Introducing spin–orbit coupling has two effects: first, it shifts the energy of the antiferromagnetic state by $\overline{K}$; second, it breaks the inversion symmetry between right- and left-handed spin rotation, leading to a DMI that contributes a term linear in λ^{-1} to the total energy. As a result, the minimum energy now appears for a left-handed (cycloidal) spin spiral along the $[1\bar{1}0]$ direction (a spin spiral along the [001] direction is energetically unfavorable because of the greater anisotropy energy cost for spins pointing along [001]).

In general, the energy minimization of (21.56) leads to an inhomogeneous spin spiral [21.305], whereby the degree of inhomogeneity is controlled by a positive dimensionless parameter $\kappa = (4/\pi)^2 A\overline{K}/D^2$, into which all three micromagnetic parameters A, D and $\overline{K}$ in (21.56) enter. For the parameter set $\kappa \in [0, 1[$ a periodic spin spiral takes the lowest energy. The spiral is homogeneous for infinitesimally small positive κ and becomes maximally inhomogeneous if κ approaches 1. For example, for Mn/W(110), $\kappa = 0.3$ [21.306]. For a double-layer of Fe/W(110) (see also discussion in Sect. 21.3.3), κ is close to 1 or larger than 1 depending on the strain induced into the system in response of cutting angle or step width, respectively, of the W(110) crystal. At $\kappa = 1$ a phase transition occurs from a spin-spiral state ground state to a ferromagnetic state with chiral domain walls.

21.4.3 Chiral Domain Walls

When the exchange interaction is much stronger than the DMI, the preferred ground state is the collinear one, but the DMI can still force the formation of chiral domain walls, as, e.g., in Fe/W(110) [21.128, 282], Co/Pt(111) [21.307], $[\mathrm{Co/Ni}]_n$/Pt(111) and Ir(111) [21.80], and Ni/Fe/Cu(001) [21.308, 309], as shown in Fig. 21.25, as well as canting of the magnetization at the edge of laterally confined magnetic structures [21.310]. The effects of the DMI on domain walls are readily observed in ultrathin films with perpendicular anisotropy, where the DMI induces a transition from achiral Bloch (helical-like) walls, favored by dipolar interactions, to homochiral Néel (cycloidal-like) walls for sufficiently large values of D [21.128, 129, 309]. Figure 21.25a–c shows schematic diagrams of the different domain wall types typically observed in ultrathin films with perpendicular anisotropy. As seen for $[\mathrm{Co/Ni}]_n$ multilayers grown on Pt(111) and Ir(111), shown in Fig. 21.25d–f, the domain wall chirality depends on the substrate as well as on the thickness of the magnetic film [21.80]. The opposite chirality observed at the Ni/Pt(111) and Ni/Ir(111) interfaces is due to the opposite sign of the DMI in these systems. Achiral walls can be obtained either by depositing a thin Ir layer on Pt in order to compensate the DMI or by increasing the magnetic film thickness in order to favor Bloch walls. Experimental and simulated phase diagrams of the domain wall chirality and its dependence on the DMI and magnetic anisotropy parameters are shown in Fig. 21.25g–j. The chirality of the domain walls plays a fundamental role in determining the domain wall motion [21.81, 129, 311–313] and the polarity of current-induced switching by spin–orbit torques in thin films and nanostructures [21.35, 314]. Similar to Fig. 21.25a, the chirality reported for 3d layers grown on Pt, such as the AlO_x/Co/Pt films typically used for investigating switching and domain wall motion, is left handed [21.307, 314–316]. In simple one-dimensional domain wall models, the effects of the DMI in such systems can be included by considering an effective in-plane chiral field $B_{\mathrm{DMI}} = D/M\delta$, where $\delta = \pi\sqrt{A/\overline{K}}$ is the domain wall width. The DMI

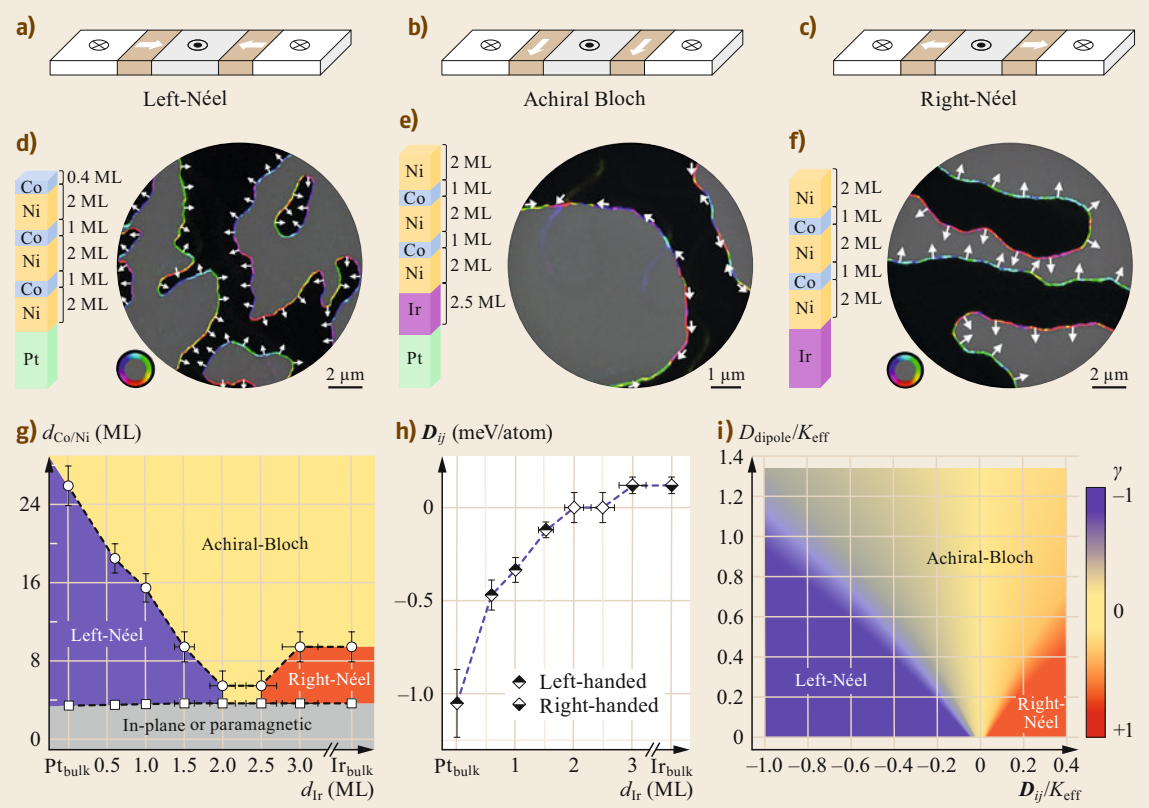

Fig. 21.25a–i Schematic domain wall configurations for **(a)** left-handed Néel, **(b)** achiral Bloch, and **(c)** right-handed Néel domain walls. **(d–f)** Real-space observation of domain walls in $[Co/Ni]_n$ multilayers grown on **(d)** Pt(111), **(e)** Ir(2.5 ML)/Pt(111), and **(f)** Ir(111). Images obtained by compound spin-polarized low-energy electron microscopy. The *color wheel* represents the direction of the in-plane magnetization in each image pixel. *White arrows* show the in-plane spin orientations in the domain walls. **(g)** Experimental domain wall type and chirality phase diagram for the multilayers shown in **(e,f)**. The *square dots* indicate the transition from in-plane anisotropy to out-of-plane anisotropy, and *circular dots* indicate the transition from chiral Néel walls to achiral Bloch walls. **(h)** Estimated DMI deduced from the data (*circles*) plotted in **(g)**. **(i)** Monte Carlo-simulated phase diagram of the domain wall chirality, where D_{dipole} corresponds to the strength of dipole interaction and K_{eff} corresponds to the effective magnetic anisotropy. The asymmetry γ quantifies the chirality as 1 (right-handed), 0 (achiral), or −1 (left-handed). (Adapted by permission from [21.80], © SpringerNature 2013)

further alters the dynamical properties of collinear ferromagnetic films, as found for the magnon dispersion in Fe/W(110) [21.317] as well as in Co, Co/Ni, and $Ni_{80}Fe_{20}$ films sputtered on Pt [21.116, 117, 318].

21.4.4 Skyrmions

Besides inducing 1-D spiral spin states and chiral domain wall configurations, the DMI also stabilizes 2-D spin textures known as chiral magnetic *skyrmions*. Skyrmions are vortex-like axially symmetric structures in which the magnetic moments rotate coherently across the center, as shown in Fig. 21.26. However, in contrast to a magnetic vortex, the magnetic moments in a skyrmion point into a unique three-dimensional direction and consequently have a topology that cannot be *unwound* in a continuous way to form, e.g., a collinear magnetic state. In mathematical terms, a skyrmion is a smooth, localized, and topologically stable field configuration which maps from real space to an order parameter space with a nontrivial topology and has particle-like properties [21.319] and has particle-like properties. The topological index of the field is called the 2-D winding number or the topological charge of the skyrmion, which, for a 2-D magnetic texture, is given by

$$\mathcal{W} = \frac{1}{4\pi} \int \boldsymbol{m} \cdot \left(\frac{\partial \boldsymbol{m}}{\partial x} \times \frac{\partial \boldsymbol{m}}{\partial y} \right) \mathrm{d}x\mathrm{d}y \,. \qquad (21.58)$$

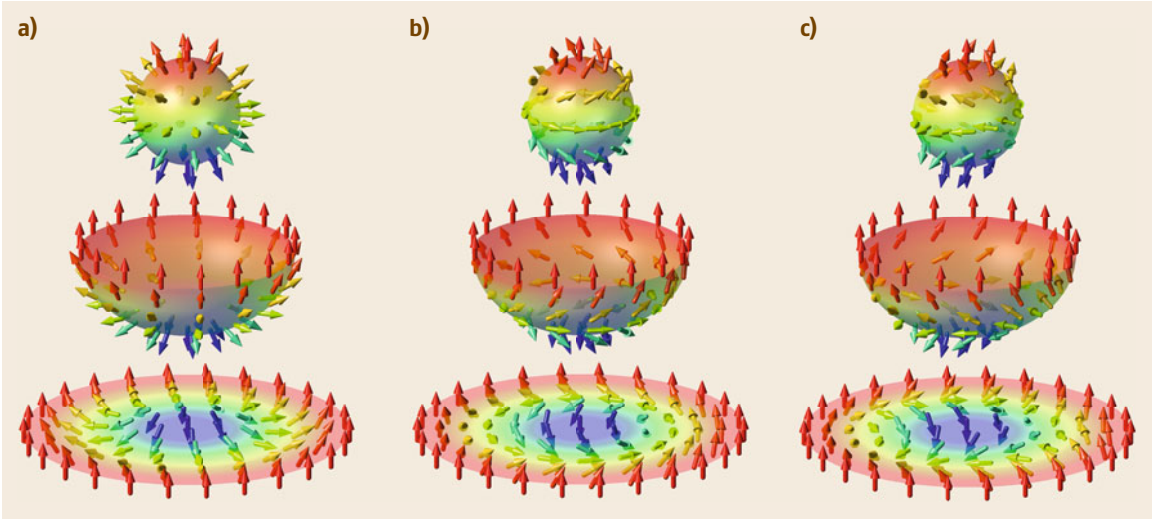

Fig. 21.26 **(a)** Schematic picture of a Néel skyrmion and its mapping onto a sphere (hedgehog configuration), **(b)** of a Bloch skyrmion (*combed* hedgehog configuration) and **(c)** antiskyrmion or multichiral skyrmion, for which the winding sense of the magnetic moments changes between clock- and counterclockwise in orthogonal spatial directions. The color code describes the value of the z-component of the magnetisation with *red* (*blue*) representing $m_z = +1$ (-1). (Figures courtesy of K. Everschor-Sitte, from [21.319])

The sign of $\mathcal{W}$ is defined by the orientation of the magnetization in the ferromagnetic background, which is taken along the positive z-direction of an external magnetic field. Each topological class characterized by an integer $\mathcal{W}$ corresponds to a spatial distribution of magnetic moments wound $\mathcal{W}$ times around a sphere, as shown in Fig. 21.26, where the boundary of the skyrmion (*infinity*) is mapped onto the north pole. For example, a magnetic film with uniform magnetization has $\mathcal{W} = 0$, a vortex has $\mathcal{W} = \pm 1/2$, whereas both Néel- and Bloch-type skyrmions have $\mathcal{W} = -1$ and antiskyrmions $\mathcal{W} = +1$. From the skyrmion core to the ferromagnetic rim, skyrmions have a unique winding sense of the magnetization, clockwise or counterclockwise depending on the sign of the DMI. Antiskyrmions or multichiral skyrmions have both winding senses, but along orthogonal directions. Following the magnetization density 360° around the antiskyrmion core, Bloch and Néel-type magnetization textures with different windings alternate. The type of skyrmion or the choice of an antiskyrmion depends on the lattice symmetry. For example, Bloch-type skyrmions are a consequence of a cubic lattice, Néel-type skyrmions are a consequence of interface geometry in particular with (100) and (111) surface orientation. An exception are interfaces with C_{2v} symmetry or lower symmetry, like the bcc or fcc (110) surfaces. On these surfaces, skyrmions and antiskyrmions can become stable simultaneously [21.320]. Néel and Bloch skyrmions differ in that the former are mapped to spins pointing outwards or inwards of the unit sphere, as in a hedgehog structure, whereas the latter are mapped to spins that rotate clockwise or counterclockwise around the sphere (Fig. 21.26). Although the real-space spin configurations appear different for Néel and Bloch skyrmions, both have the same topological charge, thus live in the same topological subsector, and the two structures are topologically equivalent. Consequently, a Bloch skyrmion can be continuously deformed into a Néel skyrmion by 90° rotation of the spins, and vice versa. Note that skyrmions differ quite substantially in the dynamical and excitation properties from bubble-like spin textures that have been extensively studied in the past in perpendicularly magnetized systems such as hexagonal ferrites [21.321], uniaxial garnets [21.322, 323], and single-crystalline Co(0001) films [21.324]. Magnetic bubbles in these materials are stabilized by dipole interactions rather than by the DMI, which gives rise to a rich variety of spin textures with nonuniform chirality and topologies, and therefore arbitrary topological winding numbers [21.323].

Whether a system supports the formation of skyrmions and skyrmion lattices, as opposed to uniform magnetic domains or spiral spin states, depends on the interplay of the parameters appearing in (21.34) and (21.56) with the addition of the Zeeman interaction due to an external magnetic field. A skyrmion lattice can either be the ground state of the system, if high-order exchange interactions [21.134] or dipolar interactions [21.137] are present, or emerge out of a spin spiral phase by the application of an ex-

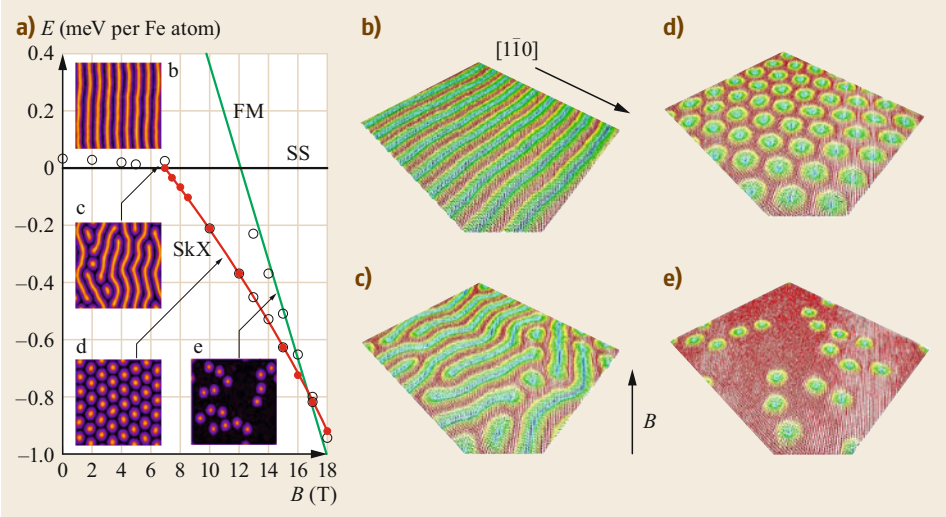

Fig. 21.27 **(a)** Low-temperature phase diagram calculated for fcc-Pd/1 ML Fe/Ir(111) as a function of a magnetic field applied perpendicular to the film. The energy per Fe atom of the spin spiral (SS), skyrmion lattice (SkX), and saturated ferromagnetic (FM) states are shown by *black*, *red*, and *green lines*, respectively. *Open circles* indicate the energy of mixed states. *Insets* show the simulated spin-polarized scanning tunneling microscopic images for an out-of-plane magnetized tip of the spin structures that are displayed in **(b–e)**. **(b–e)** A *red color* denotes magnetic moments pointing up, that is, in the direction of the magnetic field, while *blue spins* point in the opposite direction. (Reprinted by permission from [21.325], © SpringerNature 2014)

ternal magnetic field as metastable state [21.131, 132, 135]. Magnetic skyrmions of the Bloch type were first experimentally observed in non-centrosymmetric bulk MnSi single crystals [21.131] and in other compounds that have the same cubic B20 crystal structure, such as $Fe_{1-x}Co_xSi$ [21.132] and FeGe [21.133]. Symmetry breaking due to interfaces and strong spin–orbit coupling facilitate the formation of Néel-type skyrmions in ultrathin magnetic layers deposited on heavy metals such as Pt, Ir, and W. Low-temperature spin-polarized STM studies evidenced the formation of a skyrmion-like lattice with periodicity of about 1 nm for a pseudomorphic Fe monolayer on Ir(111) [21.134]. For this system, the competition between the magnetic exchange interaction and DMI determines the periodicity, and the DMI imposes a unique rotational sense, whereas the two-dimensional lattice is stabilized by a four-spin interaction. Adding a single nonmagnetic layer of Pd on Fe/Ir(111) changes the magnetic properties such that the ground state is a spin spiral with a period about seven times longer than the skyrmion lattice of the uncovered Fe/Ir(111) surface, and a skyrmion lattice appears only in an applied magnetic field of the order of 1 T. In contrast to the spin spiral state, which is magnetically compensated, the hexagonal skyrmion lattice exhibits a net magnetization and is, therefore, favored by the Zeeman energy. For the same reason, at even larger fields, the system evolves into a saturated ferromagnetic state [21.135]. This behavior, schematized in Fig. 21.27, is typical for field-induced skyrmion lattices. For this particular system, ab initio electronic structure calculations [21.325] show that the change of ground state from Fe/Ir(111) to Pd/Fe/Ir(111) is not due to a decrease of the DMI, which is mainly determined by the Ir interface and does not depend significantly on the 4d transition-metal overlayer. Rather, the addition of Pd increases the exchange interaction among the Fe atoms relative to Fe/Ir(111), as the nearest-neighbor exchange interaction in a hexagonal Fe monolayer depends on the d-band filling of the substrate and can be tuned from ferro- to antiferromagnetic [21.326]. Thus, in Pd/Fe/Ir(111), the energy barrier separating the skyrmion phase from the uniform ferromagnetic phase is lower relative to Fe/Ir(111), and comparable to k_BT at measurement temperatures of ≈ 10 K. In these conditions, thermally activated switching between topologically distinct states occurs. Moreover, skyrmions can be imprinted or annihilated one by one into the ferromagnetic phase, e.g., by voltage sweeps with the STM tip, as the switching rate and direction can be controlled by the spin-polarized current as well as by the presence of atomic defects that act as preferred nucleation and pinning sites for the skyrmions [21.135].

Skyrmions are also found in ultrathin ferromagnetic/heavy-metal layers deposited by sputtering, such as

$[Ir/Co/Pt]_n$ and $[Ta/Co/Pt]_n$ multilayers [21.136, 327], $TaO_x/CoFeB/Ta$, $AlO_x/Co/Pt$, and $MgO/CoFeB/W$ trilayers [21.137, 328, 329]. In these materials, the magnetic anisotropy, DMI, and exchange parameters that control the skyrmion stability and size can be easily tuned by adjusting the nature and thickness of the films that comprise the multilayers. Such systems are also of interest to create and manipulate skyrmions in racetrack-type devices [21.330], which has raised hopes of fabricating skyrmion-based magnetic memories and logic devices based on the same technology as that developed for magnetoresistance devices. It shall be noted, however, that despite their topological protection, skyrmions are neither indestructible nor insensitive to the pinning potential of the medium in which they form, and do not move faster than domain walls at comparable current densities. Their potential for spintronic applications therefore remains to be established. On the other hand, skyrmions represent an interesting system for studying the interaction of nontrivial topological magnetic textures with externally applied magnetic and electric fields. For further information on this topic, we refer to recent monographs [21.331–334].

21.4.5 Synthetic Spin Structures

The non-collinear spin structures described in Sects. 21.4.2–21.4.4 form spontaneously whenever the DMI is strong enough to offset the interactions that favor collinear spin states, namely the exchange interaction and magnetic anisotropy, in (21.56). It is possible, however, to tune the balance of such interactions in order to induce the formation of artificial spin structures that have a predetermined size, shape, and topology. Spatial modulation of the magnetic anisotropy can be achieved using ion irradiation [21.335–339], oxidation [21.9, 138, 340], and electric gating [21.235, 236, 341]. Likewise, it is possible to tune the DMI [21.112], e.g., by electric gating [21.342]. Local reduction of the perpendicular magnetic anisotropy induced by ion irradiation was used to introduce low-field domain nucleation sites in Pt/Co multilayer strips [21.335, 339], which allows one to modulate the formation and flow of chiral domain walls [21.339, 343]. Alternatively, selective oxidation can be used to pattern regions with in-plane and out-of-plane magnetic anisotropy next to each other [21.138]. In the presence of the DMI, the magnetization in two adjacent regions with orthogonal magnetization experiences a chiral coupling (21.33), favoring spin configurations with a specific handedness. For example, in $Pt/Co/AlO_x$ trilayers with adjacent out-of-plane regions pointing either *up* (↑) or *down* (↓) and in-plane regions pointing either *left* (←) or *right* (→), the DMI favors the left-handed →↑ and ↓→ configurations over the right-handed ones ←↑ and ↓←. It can be shown that, below a critical size, the magnetic behavior of the coupled regions is predominantly determined by the lateral chiral coupling induced by the DMI [21.138]. Indeed, if the energy associated with the chiral coupling is larger than the energy barrier to switch one or both magnetic regions, the direction of the magnetization in one region effectively controls the magnetization in the adjacent region, leading to a lateral exchange bias. Therefore, this coupling, mediated by chiral domain walls between out-of-plane and in-plane magnetic regions, provides a powerful means to engineer the lateral interactions between nanomagnets, which is an alternative to long-range dipolar fields. As the dipolar interaction is nonlocal and scales inversely with the volume of the magnets, the chiral coupling induced by the DMI is significantly stronger than the dipolar coupling in nanometer-sized structures and thin films. Coupled out-of-plane/in-plane building blocks can be used to fabricate synthetic antiferromagnets with linear or curved geometry, artificial spin lattices with checkerboard or frustrated antiferromagnetic interactions, and even synthetic skyrmions with an arbitrary number of windings [21.138]. Examples of such structures are shown in Fig. 21.28. The DMI thus provides a tool to design arrays of non-collinear nanomagnets with tunable couplings, which can be used, e.g., to realize nanomagnet logic gates [21.344], reconfigurable magnonic crystals, as well as current-induced switching between multistate magnetic configurations [21.138].

21.5 One-Dimensional Atomic Chains

Owing to the reduced number of neighbors contributing to the exchange interaction, thermal fluctuations become more disruptive with decreasing dimensionality. As a result, magnetism in 1-D structures is more sensitive to temperature effects compared with 2-D systems. In fact, whereas in 2-D the introduction of dipolar coupling or an arbitrarily small anisotropy of spin–orbit origin is sufficient to establish long-range magnetic order [21.345], in 1-D low-energy spin wave excitations, i.e., fluctuations in the relative alignment of adjacent spins, are more effective in breaking long-range order for obvious topological reasons [21.346, 347]. Even in the 1-D Ising model, i.e., the extreme anisotropic limit of the Heisenberg model in (21.28), magnetic order is forbidden in the absence of an external field for any $T > 0$. A simple thermodynamic argument, due to Lan-

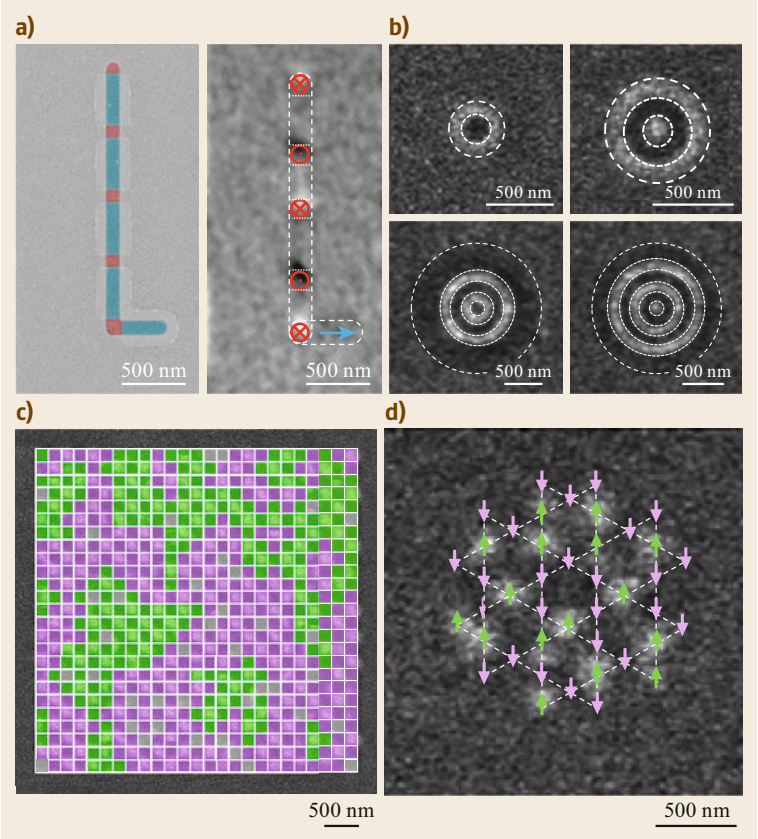

Fig. 21.28a–d Examples of artificial magnetic structures that can be realized by exploiting the DMI at surfaces. All structures consist of Pt/Co/AlO_x trilayers with alternate out-of-plane and in-plane magnetized regions patterned by selective oxidation. **(a)** Synthetic antiferromagnetic chain consisting of ferromagnetic Co dots with alternate up/down orientation (*red*) mediated by in-plane magnetized Co regions (*blue*). **(b)** Synthetic skyrmions with arbitrary number of windings. **(c)** Artificial spin lattice consisting of out-of-plane elements acting as Ising-like moments (*squares*) that are antiferromagnetically coupled via in-plane spacers (*thin white lines*). Two different antiferromagnetic domains are *shaded in green* and *purple*. **(d)** Artificial kagome spin lattice. The *green* and *purple arrows* indicate the orientation of the magnetization of the out-of-plane vertices. *Bright* and *dark contrast* in the images correspond to magnetization pointing up and down, respectively. (Reprinted by permission from [21.138], © Am. Assoc. Adv. Sci. 2019)

dau, exemplifies this point very clearly as a function of the system size [21.348]. Consider a chain consisting of N magnetic moments described by the Ising Hamiltonian $H = -J\sum_{i=1}^{N-1} S_{zi}S_{zi+1}$, with nearest-neighbor exchange coupling energy $J > 0$ (ferromagnetic interaction). The ground-state energy of the system is $E_0 = -J(N-1)$ and corresponds to the situation where all the moments are aligned, as shown in Fig. 21.29a. The lowest-lying excitations are those in which a single break occurs at any one of the N sites. There are $N-1$ equivalent such excited states, all with the same energy $E = E_0 + 2J$, shown in Fig. 21.29b. At a given temperature T, the change in free energy due to these excitations is $\Delta G = 2J - k_\mathrm{B}T\ln(N-1)$. For $N \to \infty$, the entropy term prevails and we have $\Delta G < 0$ at any finite temperature. The ferromagnetic state becomes unstable to thermal fluctuations. For chains of finite length, however, if $(N-1) < \mathrm{e}^{2J/(k_\mathrm{B}T)}$, ferromagnetic order is energetically stable. Assuming $2J = 10\,(20)$ meV, we get an upper limit of $N \approx 10\,(100)$ atoms at $T = 50$ K. Such conclusions apply to an ideal 1-D lattice of spin point vectors in both the ferromagnetic and antiferromagnetic case. An antiferromagnetic system, however, presents additional complications. If the spins in the Heisenberg Hamiltonian are considered as classical vectors, then the ground state of a 1-D chain is easily found to be the alternate up–down configuration shown in Fig. 21.29c, viz. the so-called Néel state. Note that, depending on whether N is odd or even, the chain may or may not have a net magnetization. When the quantum nature of the spins is considered, the situation is radically different. The eigenstates of the quantum antiferromagnetic Heisenberg Hamiltonian are then given by a superposition of states, each representing a classical spin configuration (Fig. 21.29d). As a consequence, contrary to the ferromagnetic case, we cannot assign a well-defined orientation to individual atomic spins in the ground state of an antiferromagnetic quantum system; the spins are entangled, inseparable from each other. Such an effect, which is well known for the wavefunctions describing the triplet singlet pair $1/\sqrt{2}(|\uparrow\downarrow\rangle \pm |\downarrow\uparrow\rangle)$ of a two-electron molecular bond, is generally present in antiferromagnetic 2-D and 1-D low-dimensional magnetic systems and is discussed more at length in [21.349, 350].

Historically, experimental investigations on 1-D magnetic systems have concentrated on bulk insulating crystals consisting of arrays of linear chains

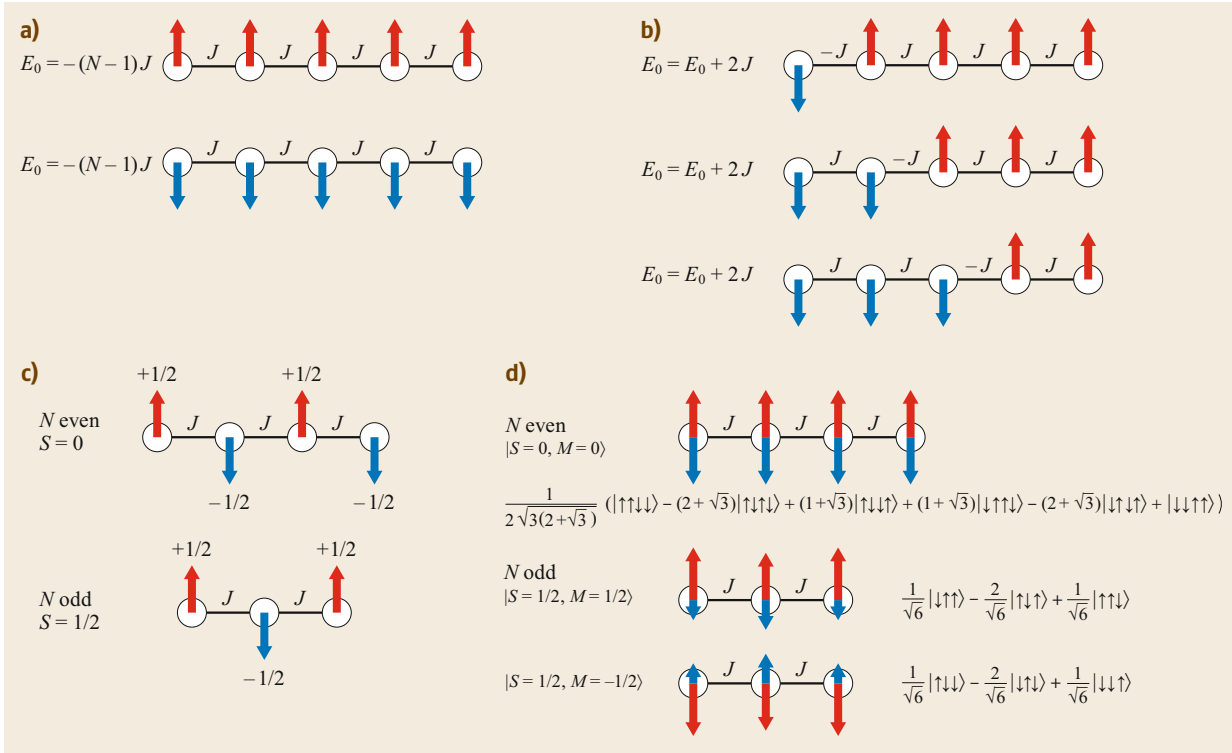

Fig. 21.29 **(a)** Equivalent ground-state configurations of a ferromagnetic Ising spin chain in zero applied magnetic field. **(b)** Lowest-energy excited states. **(c)** Néel ground state of antiferromagnetic Ising classical spin chains with $N = 3$, 4 atoms. **(d)** Ground state of antiferromagnetic quantum chains with spin 1/2. The length of the *arrows* represents the relative probability for each spin to point up or down. The corresponding wavefunctions are also given

of exchange-coupled transition-metal ions separated by nonmagnetic atom spacers and characterized by weak interchain interactions [21.349, 353, 354]. One example is tetramethylammonium manganese chloride, which typically exhibits antiferromagnetic coupling and 1-D paramagnetic behavior down to $T \approx 1$ K [21.355]. Molecular ferri- and ferromagnetic chain-like compounds containing magnetically anisotropic ions also allow the realization of 1-D Ising model systems, so called *single-chain magnets*, which display slow relaxation of the magnetization on a macroscopic time scale [21.356], as predicted by *Glauber* in the 1960s [21.151]. Surface science studies of 1-D magnetism are based on two approaches, namely the deposition of magnetic atoms on templated nonmagnetic surfaces [21.72, 357] and the atom-by-atom fabrication of single-atomic chains using scanning probe manipulation [21.358, 359]. In the first approach, the atomic steps of a nonmagnetic vicinal surface are used as a deposition template for the magnetic atoms, thus producing a large number of nanowires in a parallel process. The average thickness and spatial separation of the wires can be controlled independently using the coverage and surface miscut angle, respectively. The high wire density and overall uniformity of these systems allow for their investigation using powerful spatially integrating spectroscopic techniques, such as angle-resolved photoemission and XMCD. In the second approach, chains with a well-defined number of atoms and lattice spacing can be assembled one atom at a time and investigated locally using spin-polarized STM and inelastic tunneling spectroscopy. In both cases, the transition from 1-D to 2-D magnetic behavior can be studied in the same material system by simply varying the coverage of the magnetic atoms, which makes surface studies of magnetism very appealing.

21.5.1 Self-Assembly of 1-D Chains on Template Surfaces

Arrays of continuous, quasi-1-D monolayer-thick stripes of a magnetic metal on top of a nonmagnetic substrate are obtained by exploiting self-assembly on vicinal surfaces [21.360], for which the control of the stripe width can be pushed down to the monatomic limit [21.351, 352, 361–364]. Depending on the sur-

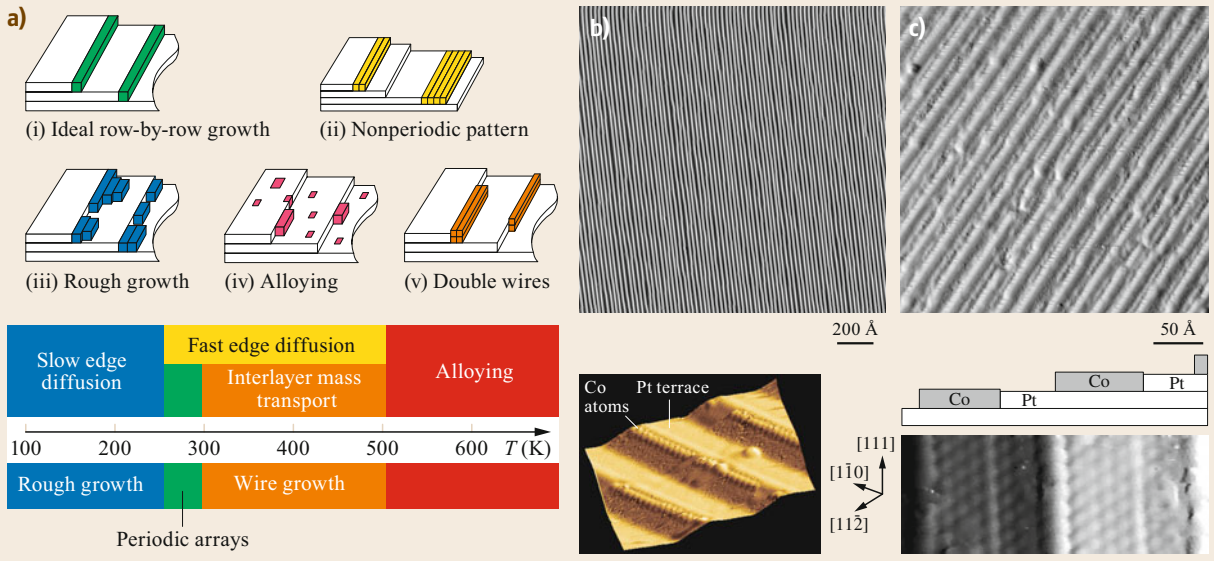

Fig. 21.30 **(a)** Schematic representation of the growth modes of Co on a stepped Pt(997) surface as a function of the substrate temperature. **(b)** STM topograph of the periodic step structure of Pt(997) (*top*) and of monatomic Co chains adjacent to the Pt steps (*bottom*). **(c)** STM image of 0.6 ML Co deposited at $T = 250$ K on Pt(997); the step-down direction is from *right* to *left*. Row-by-row growth conserves the original step pattern, forming regular stripes that run parallel to the Pt steps. The *bottom image* shows a detail of two adjacent steps with atomically resolved Co chains and Pt terraces. (Adapted by permission from [21.73, 351, 352], © Am. Phys. Soc. 2000, Elsevier 2003)

face temperature, adatoms on vicinal surfaces tend to self-assemble into chain-like structures at the lower side of the step edges, where the binding energy is largest [21.362, 365]. Growth proceeds either as a smooth step-wetting process [21.351, 352, 366, 367] or as nucleation of two-dimensional (2-D) islands at the step edges [21.368], provided that the adatom displacement prior to nucleation is larger than the terrace width of the substrate. Figure 21.30a shows different scenarios of heteroepitaxy on a stepped substrate, as derived from the growth of Co on the vicinal Pt(997) surface. We distinguish:

(i) The ideal case of row-by-row growth
(ii) Chains of different widths due to interlayer crossing of the adatoms
(iii) Formation of irregular 2-D islands at the step edges
(iv) Alloying
(v) Formation of double-layer-thick stripes.

In preparing arrays of 1-D chains for spectroscopic investigation with spatially integrating probes, one must focus on the conditions that favor the ideal case (i). As a general trend, 1-D chain formation is limited at low temperature by slow edge-diffusion processes and at high temperature by interlayer diffusion and, eventually, by alloying between the metal adspecies and the substrate.

Figure 21.30b shows an STM image of the Pt(997) surface, which has an average terrace width of 20.2 ± 2.9 Å [21.369], corresponding to a step density of $5 \times 10^6\,\mathrm{cm}^1$. Periodic arrays of Co chains grow only between 250 and 290 K [21.351]. A monatomic chain array is obtained as the coverage equals the inverse of the number of atomic rows in the substrate terraces, i.e., 0.125 ML ($1\,\mathrm{ML} = 1.5 \times 10^{15}\,\mathrm{atoms/cm}^2$) for Pt(997). The average length of a continuous Co chain is estimated to be ≈ 80 atoms from the average kink density per Pt step obtained by STM. As the coverage increases to more than a monatomic chain per terrace, Co grows in a row-by-row mode (Fig. 21.30c). This approach was first explored by *Elmers* et al. [21.276] in a study of wide Fe stripes (> 10 nm) on vicinal W(110), which show in-plane anisotropy and a relaxation-free ferromagnetic phase transition due to dipolar-induced coupling across adjacent stripes [21.278, 280, 281]. Deposition on stepped substrates has also been used to investigate the magnetic behavior of quasi-1-D Fe stripes on stepped Cu(111) [21.370, 371] and Au(778) [21.372], as well as of Fe and Co stripes on Pd(110) [21.373–375]. Recent investigations have shown that step decoration can be used also to produce bimetallic 1-D alloys [21.361, 376, 377] as well as transition-metal

oxide chains [21.378, 379], which may have either ferromagnetic or antiferromagnetic couplings [21.380].

21.5.2 Magnetic Properties and Magnetic Order in 1-D Chains

In the limit of atomically thin metal chains, tight-binding [21.381–383] as well as ab initio electronic calculations predict large exchange splittings and strongly increased m_S and m_L relative to those of the bulk and 2-D monolayers [21.62, 63, 384–388] as well as MCA energies exceeding 1 meV per atom [21.384, 385, 389–392], which are attributed to the reduced d-bandwidth in 1-D structures as well as interactions with the substrate. Angle-resolved photoemission measurements of Co monatomic chains grown along the step edges of Pt(997) corroborate the prediction of large exchange splitting of the Co 3d-states (2.1 eV) [21.393] compared with thin films (1.4−1.9 eV) or bulk Co (1.4 eV) [21.394, 395], suggesting that m_S is on the order of $2\,\mu_B$/atom [21.360], i.e., $\approx 0.4\,\mu_B$/atom larger compared to bulk Co. Extensive XMCD investigations performed on the Co/Pt(997) system have allowed the measurement of the Co magnetic moment as a function of chain width [21.72, 73, 396]. Most strikingly, the m_L of the monatomic Co chains reaches up to $0.68\,\mu_B$/atom, representing an almost fivefold enhancement relative to bulk hcp Co and being more than twice the value found for a Co monolayer on Pt(997). The lateral thickness of the chains has a strong influence on m_L, which drops already to $0.37\,\mu_B$/atom in biatomic chains [21.396].

Figure 21.31 shows the magnetization of Co chains with different atomic thicknesses deposited on Pt(997), measured along the easy (filled symbols) and hard (open symbols) axes at 45 and 10 K. The significant dependence of the magnetization on the direction of the applied field indicates a very strong magnetic anisotropy, which increases from $K = 0.17$ meV/atom in the 2-D monolayer limit up to $K = 2.0$ meV/atom in the monatomic chains. Further, both K and the easy axis direction oscillate as a function of the chain thickness (top diagrams in Fig. 21.31 and [21.396]). This behavior is specific of 1-D metal systems and was predicted by tight-binding calculations for both free-standing [21.381] and supported [21.383] 1-D Co chains. The canting of the easy axis in the plane perpendicular to the chains is due to symmetry breaking at the Pt step edges [21.385, 391, 392]. The DMI at the step edge does not change the magnetic order in the Co chain but selects homochiral Néel-walls over Bloch-walls [21.121].

The magnetic response of the Co chains as a function of field at $T = 45$ K shows reversible behavior with zero remanent magnetization, thus indicating the absence of long-range ferromagnetic order. However, the shape of the magnetization curve reveals the presence of short-range order, i.e., of significant interatomic exchange coupling in the chains. For noninteracting paramagnetic moments, in fact, the magnetization would be significantly smaller and nearly linear up to 6 T. By lowering the sample temperature to 10 K, the magnetization of the monatomic chains becomes hysteretic, indicating a transition to a long-range ferromagnetic ordered state with finite remanence extended over the whole sample. The observation of long-range ferromagnetic order might appear in contrast to the predicted absence of magnetism in 1-D systems. However, similar to the single-chain molecular magnets, the ferromagnetic state in the chains is a metastable state stabilized by the large MCA barriers, which allow ferromagnetic order to persist over timescales equal to or longer than the measurement time. The observed behavior is therefore that of a 1-D superparamagnetic system, i.e., a system composed by segments, or spin blocks, each containing N_c exchange-coupled Co atoms, whose resultant magnetization orientation is not stable due to thermal fluctuations. Fits of the magnetization of the monatomic chains above the blocking temperature performed using a classical spin block model [21.351] yield $N_c = 15$ atoms and $K = 2{-}0$ meV/atom, as well as a total magnetic moment per Co atom of $\approx 3.8\,\mu_B$/atom, including the spin and orbital Co moments as well as the induced moment on Pt. The same curves can be fit using a finite-size transfer matrix algorithm using the Heisenberg Hamiltonian [21.346]

$$\mathcal{H} = -\sum_{i=1}^{N_c-1} J\boldsymbol{S}_i \cdot \boldsymbol{S}_{i+1} - \sum_{i=1}^{N_c} [K(S_i^z)^2 + g_{\text{Co–Pt}}\mu_B \boldsymbol{B} \cdot \boldsymbol{S}_i] \,, \qquad (21.59)$$

where $J = 20$ meV, $K = 3.3$ meV, $|\boldsymbol{S}_i|^2 = 1$, $g_{\text{Co–Pt}} = 3.8$, and $N_c = 80$. The two approaches yield consistent results, apart from the *magnetic length* of the chains. This is not so surprising given that the spin block model does not include the possibility of spin excitations inside each block. Although the structural analysis of the Pt(997) surface yields atomically straight step edges with a length of ≈ 80 lattice sites, the actual magnetic length of the chains can be also influenced by dislocations, substitutional impurities, and contaminants that can never be completely eliminated in experiments. Inhomogeneities of the chain length and thickness are likely also responsible for the reduced remanence relative to the saturation magnetization observed at 10 K.

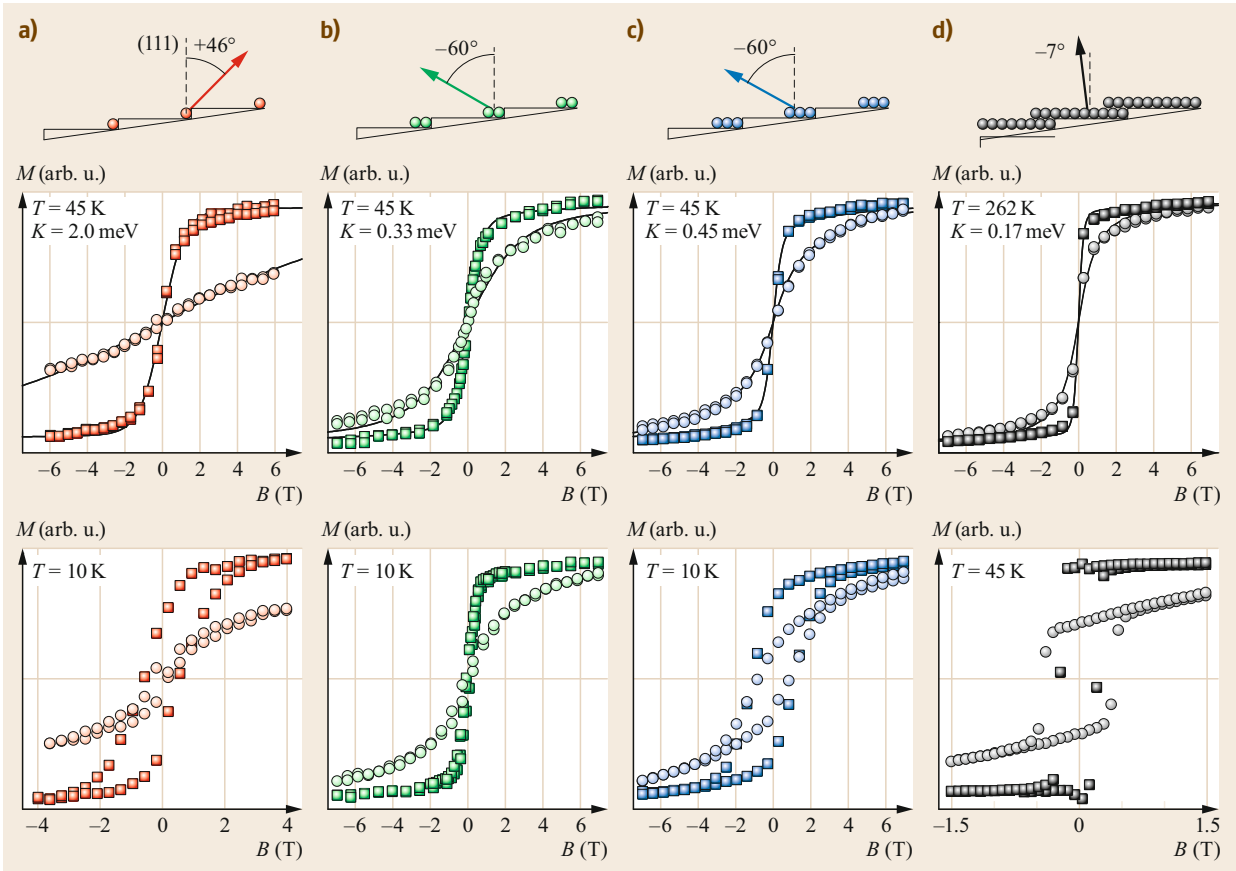

Fig. 21.31a–d Magnetization of **(a)** monatomic, **(b)** biatomic, and **(c)** triatomic chains and **(d)** 1.3 ML Co on Pt(997) along the easy and hard directions (*filled* and *open symbols*, respectively), measured above and below the blocking temperature. The easy axis is indicated by the *arrows* in the top diagrams. The data points represent the XMCD at the L_3 Co edge (779 eV) normalized by the L_3 absorption edge jump. *Solid lines* are fits to the data according to a classical spin block model. (Reprinted by permission from [21.72, 396], © SpringerNature 2002, Am. Phys. Soc. 2004)

As the system evolves towards a 2-D film and the number of exchange-coupled Co atoms in the chains increases (Fig. 21.31b–d), a stronger tendency towards magnetic order is expected. Contrary to expectations, however, the two-atom chains do not exhibit long-range magnetic order, even at low temperature (Fig. 21.31b, bottom panel). In this case, the tendency towards order is counteracted by the drastic reduction of K, consistent with the reduction of m_L. Paradoxically, therefore, the 1-D character of the monatomic chains favors magnetic bistability rather than disrupting it, owing to the enhanced magnetic anisotropy energy of the low-coordinated Co atoms. Eventually, a fully coalesced magnetic layer forms (Fig. 21.31b–d), showing properties typical of a 2-D film (Sect. 21.3).

Equation (21.59) further allows modeling of size- and site-dependent spin correlation effects along the monatomic chains. Because the spins at the two ends of a chain lack one magnetic neighbor, the first and last spins along the chains can fluctuate more freely than those in the middle, leading to the confinement of entropy close to the end spins. Figure 21.32 shows the site dependence of the average easy-axis spin projection $\langle S_i^z \rangle$ in the presence of an applied field $B_z = 2\,\mathrm{T}$ at $T = 45\,\mathrm{K}$. The profiles obtained for segments of different lengths N are compared with the expectation value for the infinite chain [21.397]. Translational invariance is broken for any segment but for the infinite chain, and $\langle S_i^z \rangle$ decreases symmetrically with respect to the middle of the segment while moving towards the end spins. Note that the asymptotic value for the infinite chain is never reached for segments smaller than $N = 50$. From the above discussion, it is evident that, depending on temperature, finite-size effects play a central role in determining the magnetization of 1-D systems.

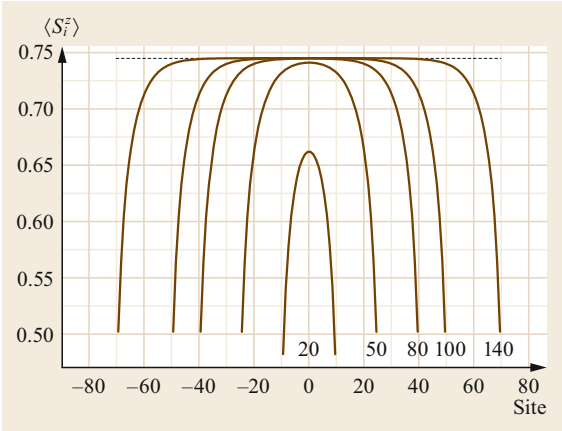

Fig. 21.32 Site dependence of $\langle S_i^z \rangle$ of monatomic Co chains shown for different lengths of the segments at $T = 45\,\mathrm{K}$ in zero applied field. The site index is enumerated starting from the middle of each segment. The *dashed line* corresponds to the infinite chain expectation value. (Reprinted by permission from [21.346], © Springer 2006)

21.5.3 Local Couplings and Excitations in 1-D Chains

Atom manipulation by low-temperature STM has opened up the possibility of assembling and probing magnetic chains of well-defined length and couplings on flat substrates. STM also provides a means to locally probe the ground state and spin excitation spectrum of the assembled structures using spin-polarized tunneling [21.192, 193] and inelastic tunneling spectroscopy [21.398, 399]. Adatom chains assembled on insulating substrates such as Cu_2N typically display localized electron behavior characterized by antiferromagnetically or ferromagnetically coupled integer or half-integer spins, providing a nice example of finite-size 1-D spin lattices [21.358, 359, 400]. Adatom chains assembled on metal surfaces, on the other hand, allow the study of the formation of delocalized quantum states and Kondo correlation effects in 1-D structures that incorporate *defects*, i.e., magnetic and nonmagnetic species, such as $CoCu_nCo$ chains on Cu(111) [21.401, 402]. Recently, ferromagnetic chains assembled on s-wave superconducting substrates with strong spin–orbit coupling have been proposed as a simple realization of a topological superconductor [21.403, 404]. Such 1-D chains with nearest-neighbor hopping, large exchange splitting of the d bands, and proximity-induced pairing carry zero-energy excitations at the chain ends, which are regarded as a solid-state equivalent to Majorana fermions in particle physics. Examples of these systems are Fe and Co chains on Pb(110), as described in [21.405, 406]. In the following, we describe two examples of ferromagnetic [21.358] and antiferromagnetic [21.359] chains assembled on insulating substrates in order to illustrate the rich physics accessible by STM spectroscopy.

Figure 21.33a shows a schematic diagram and STM image of a single-atomic layer of Cu_2N formed by N implantation on Cu(001). This layer has insulating properties, which prevents direct hybridization between the d electrons of magnetic adatoms with the Cu(001) sp-bands. Transition-metal adatoms deposited at cryogenic temperature on Cu_2N/Cu(001) adsorb on top of the Cu sites and can be manipulated by the STM tip using pick-up and release voltage pulses of opposite polarity. Figure 21.33b shows the atom-by-atom construction of a chain of nine Mn atoms positioned on neighboring Cu sites along the [100] direction, at a distance of 0.36 nm from each other. Inelastic electron tunneling spectroscopy performed by positioning the tip of the STM on top of the Mn atoms was used to determine the ground state and spin excitation spectrum of chains of different length, as shown in Fig. 21.33c. This technique is based on the increase of the conductance of a tunnel junction when the energy of the tunneling electrons matches that of a vibrational or magnetic excitation of the sample, thus opening an inelastic conduction channel that adds to the elastic conductance [21.398, 407]. In the case of magnetic atoms, $\mathrm{d}I/\mathrm{d}V$ conductance steps correspond to spin-flip excitations that change the spin projection S_z but leave the total spin S unchanged. The energy of these excitations, given by $-eV$, where V is the STM bias voltage, generally depends on the applied magnetic field, magnetic anisotropy, and exchange coupling to neighbor atoms. The $\mathrm{d}I/\mathrm{d}V$ spectra of Mn chains consisting of one to ten atoms at zero field display a striking dependence on the parity of the chain. At $V < 1\,\mathrm{mV}$, the spectra of odd-length chains, including a single Mn atom, exhibit a narrow dip in conductance centered at 0 V, typical of spin-flip excitations of a ground state with $S > 0$. None of the even-length chains, however, exhibit a spin-flip excitation: the spectra are flat near $V = 0$, at both zero and high magnetic field. The absence of spin-flip excitations in even-length chains is attributed to a ground state with $S = 0$. The alternation of the ground-state spin between zero and nonzero values is consistent with the compensation and uncompensation of the total Mn spin for even- and odd-length chains, respectively, indicating that the Mn spins are antiferromagnetically coupled. At larger bias voltages, both odd and even chains, with the exception of a single Mn atom, present large $\mathrm{d}I/\mathrm{d}V$ steps in conductance at voltages that are symmetric with respect to $V = 0$. These features can be analyzed by calculating the spin excitation spectrum starting from the Heisenberg Hamiltonian (21.28).

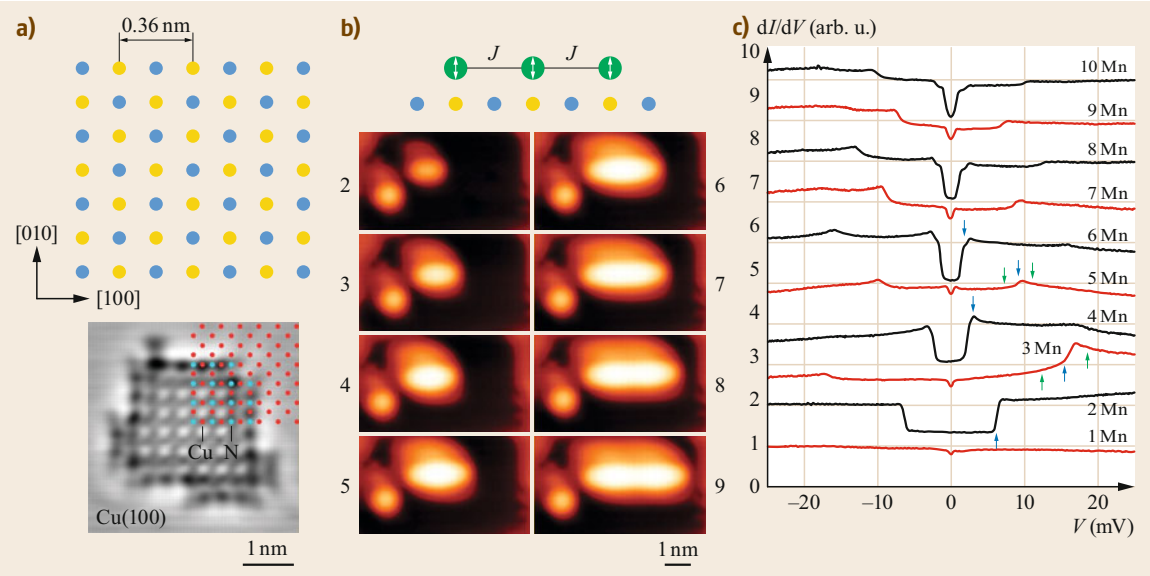

Fig. 21.33 **(a)** *Top*: Lattice model of a Cu_2N island on Cu(001). Cu atoms are shown as *yellow dots*, N atoms as *blue dots*. *Bottom*: constant-current STM topograph of a Cu_2N island on Cu(001). **(b)** STM images of the building of a Mn chain two to nine atoms long on Cu_2N. The top diagram shows the coupling between adjacent Mn spins, likely mediated by superexchange through the intervening N atom. **(c)** Conductance spectra of Mn chains on Cu_2N. Spectra were taken with the tip positioned above the center of chains of Mn atoms of length one to ten at $T = 0.6$ K and $B = 0$ T. Spectra on chains containing an odd (even) number of atoms are shown in *red* (*black*) to emphasize the parity dependence. *Blue arrows* indicate the lowest energy spin-changing excitation obtained from the isotropic Heisenberg model with $J = 6.2$ meV and $S = 5/2$. For comparison, *green arrows* indicate the same excitation with $S = 2$ (lower voltage) and $S = 3$ (higher voltage) on the trimer and pentamer; the same excitation with $S = 2$ and $S = 3$ is not distinguishable from $S = 5/2$ on the dimer, tetramer, and hexamer chains. (Adapted by permission from [21.358], © Am. Assoc. Adv. Sci. 2006)

Overall, the excitation energies of the chains can be well reproduced by assuming an antiferromagnetic exchange coupling constant $J = -6.2 \pm 0.3$ meV and a local spin $S_{Mn} = 5/2$ [21.358]. The magnetic anisotropy (i.e., the zero-field splitting parameter) is small in such a case, consistent with the orbital singlet state of Mn atoms with spin 5/2. An important point of this study is that the energy of the conductance steps turned out to be the same irrespective of the position of the STM tip along the chains, which suggests that the excited states are collective entangled states rather than single-atom spin flips, consistently with the picture drawn in Fig. 21.29d. Such states have also been reported for odd-length Mn chains assembled on Ni(110) [21.408].

In the Mn chains, the formation of entangled quantum spin states is favored by the large value of J relative to the on-site magnetic anisotropy energy K. By decreasing the ratio J/K, however, the classical Néel states with alternate spin orientation on each atom (Fig. 21.29c) can be stabilized. This situation is realized for Fe atoms aligned along the [010] rows of Cu_2N/Cu(001) with interatomic distance equal to 0.72 nm [21.359]. In these chains, the Fe spins couple antiferromagnetically with strength $J = 1.2$ meV and have an out-of-plane magnetic anisotropy of $K \approx 1.5$ meV [21.409]. Spin-polarized STM images of a linear eight-atom chain clearly distinguish the two Néel ground states, as shown in Fig. 21.34a,b. By applying a voltage > 7 meV between the chains and a magnetic tip, the spin configuration can be switched between the two Néel states with a probability that depends on the magnetic orientation of the tip, as expected for spin transfer torque, as well as on the position of the tip, due to the larger susceptibility of the spins at the two ends of a magnetic chain (Fig. 21.32 and [21.346]). The switching rate increased rapidly when either the bias voltage or tunneling current increased. Below the threshold for current-induced switching, the switching between opposite Néel states is either thermally activated or induced by quantum tunneling. The thermal switching rates of linear chains of Fe atoms with varying length $(1 \times n)$ and arrays of two coupled chains $(2 \times n)$ are shown in Fig. 21.34c. All structures containing eight or more atoms are stable at 0.5 K, whereas spontaneous fluctuations between the two Néel states set in with increasing temperature. Structures with more

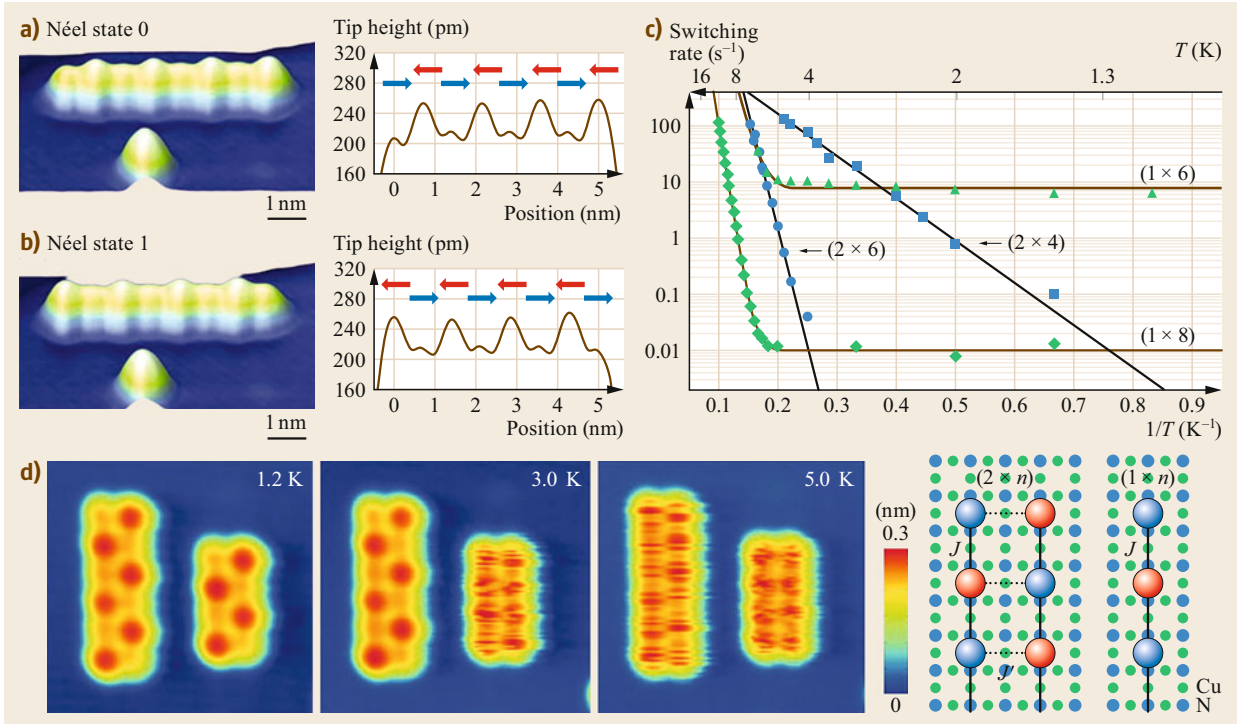

Fig. 21.34 **(a)** Spin-polarized STM image of a linear chain of eight Fe atoms assembled on a Cu_2N overlayer on Cu(001). The *line* profile on the *right-hand side* shows the alternate alignment of the Fe spins in the Néel state '0'. **(a)** Same as **(b)** for the Néel state '1'. **(c)** Arrhenius plot of the switching rates for different Fe arrays as determined by two-state noise of the tunneling current ($< 10^3\ s^{-1}$) and a pump–probe voltage scheme ($> 10^3\ s^{-1}$). **(d)** Thermal stability of antiferromagnetic arrays. *From left to right*: STM images of (2×6) and (2×4) arrays of Fe atoms at 1.2, 3.0, and 5.0 K. Both arrays have stable Néel states at 1.2 K, but the smaller array switched rapidly during the imaging at 3.0 K. At 5.0 K, both arrays switched rapidly. Image size 7.7×7.7 nm. A schematic of the atomic positions of Fe and Cu_2N substrate atoms is also shown (Cu atoms, *yellow*; N atoms, *light blue*). *Ball colors* depict the spin alignment of one Néel state, with *red* being parallel and *blue* antiparallel to the tip's spin. (Adapted by permission from [21.359], © Am. Assoc. Adv. Sci. 2012)

atoms remain stable to higher temperatures owing to the increase of the total anisotropy energy (Fig. 21.34d). Above 5 K, the switching rates of the (1×6), (1×8), and (2×6) arrays follow an Arrhenius law like (21.51) with exponential prefactors on the order of $10^8\ s^{-1}$ and reversal barriers of 7–12 meV, which are comparable to the threshold for voltage-induced switching and the energy $2S^2J = 9.6$ meV (assuming $S = 2$ for Fe) required to create a single Ising domain wall within one of the chains (Sect. 21.5). Below 5 K, the switching rates of the (1×6) and (1×8) chains become independent of temperature due to quantum tunneling of the magnetization between the two degenerate ground states, similar to molecular magnets [21.410] and magnetic nanoparticles [21.159]. Quantum tunneling rates can be decreased by increasing the chain length as well as by coupling two chains, e.g., from (1×6) to (2×6). Even a weak interchain coupling $J' = 0.03$ meV markedly suppresses quantum tunneling, as shown in Fig. 21.34c. These measurements also evidence the anisotropy of the exchange coupling ($J \gg J'$) due to the anisotropy of the superexchange interaction mediated by the Cu_2N substrate. Note that the sign of J depends on the alignment of the Fe atoms relative to the crystal axes, which allows for studying ferromagnetically coupled chains on the same surface [21.400, 411].

Overall, the examples presented in this section evidence the rich magnetic behavior and diverse properties of ferromagnetic and antiferromagnetic spin chains on different surfaces. Besides the possibility of preparing such systems by self-assembly or atom manipulation techniques, surfaces allow for in-depth investigations of the chain properties using photon and electron spectroscopy techniques, which provide unprecedented insight into the magnetism of 1-D systems.

21.6 Single-Atom Magnets

Magnetic atoms on surfaces represent the ultimate limit of monodisperse magnets. Although individual atoms generally present paramagnetic behavior, their investigation provides clues to fundamental and practical issues in magnetism, such as the dependence of the magnetization on system size, atomic coordination, and composition [21.17–21]. The spin and orbital magnetic moments, exchange coupling, and magnetic ordering of such systems can be tuned by tiny changes of dimensions and coupling to the environment [21.73, 124, 158, 183, 194, 412]. The magnetic anisotropy energy per atom can be increased by up to three orders of magnitude with respect to bulk materials, leading to metastable (blocked) magnetic states at low temperature [21.72, 359, 413, 414]. Depending on the system size and interaction with the host medium, the magnetization can behave as a classical vector or be quantized, leading to effects such as magnetic hysteresis, the typical macroscale property of a magnet, as well as quantum tunneling and phase interference effects, which are characteristic of microscopic systems [21.415–417]. Moreover, magnets made of one or a few atoms organized into regular patterns allow for the investigation of the ultimate limits of magnetic storage and quantum computation in novel materials [21.418–420].

Progress in the manipulation and probing of single atoms has allowed the study of the influence of the binding sites on the magnetic moments, anisotropy, and relaxation time with unprecedented spatial and temporal resolution. Inelastic electron tunneling spectroscopy gives direct access to the atomic spin excitations of both individual magnetic atoms and nanostructures (Sect. 21.5.3), providing information on the quantum properties of engineered spin structures at surfaces, albeit mostly on thin insulating layers [21.359, 398, 400, 409, 421, 422]. The development of pump–probe techniques based on spin-polarized STM [21.74, 359, 423] has made it possible to measure the spin relaxation time of individual atoms [21.44, 59], while the recent introduction of electron spin resonance (ESR) STM [21.242, 424, 425] allows for the exploration of the coherent dynamics of individual magnetic atoms of surfaces [21.419, 420] as well as sensitive measurements of the relatively weak, long-range dipolar interactions among adatoms [21.418, 426].

From a different perspective, controlling the bonding, diffusion, and nucleation processes of adatoms at surfaces offers many opportunities to tune the adatom–substrate interaction as well as to construct multiatom magnetic clusters with tailored shape and dimensions [21.427]. Adatoms and clusters may further be considered as the precursors of thin films, as the growth of magnetic mono- and multilayers is typically initiated by the deposition of transition-metal atoms from the vapor phase onto a nonmagnetic substrate. Investigating substrate–impurity hybridization and coordination effects thus provides basic understanding and useful guidelines to tailor the magnetization and magnetic anisotropy of nanomagnets and optimize sensitive interface properties that govern the performance of magnetic storage media and spintronic devices.

Although most transition-metal and rare-earth atoms possess a magnetic moment in the gas phase, the survival of this moment when an atom is placed on a nonmagnetic metal surface is not granted. For transition metals, the competition between the intraatomic Coulomb interactions and the kinetic energy associated with electron delocalization caused by hybridization of the adatom and the electronic states of the substrate may result in either magnetic or nonmagnetic ground states [21.195]. For moderate hybridization between the adatom and host electron states, the Anderson model [21.428] describes well the formation of a magnetic moment. Many-body spin-flip processes may also lead to the Kondo effect, the screening of the local moment by conduction electron spins [21.429], which can be directly visualized by scanning tunneling spectroscopy [21.19, 430, 431]. In the following, we describe the conditions that favor the emergence of strong local moments and magnetic anisotropy in single atoms at surfaces. Depending on the coupling of the magnetic degrees of freedom of the adatoms with the electronic and phononic baths of the substrate, single atoms may display fast spin relaxation, bistable magnetic states, or coherent quantum behavior.

21.6.1 Transition-Metal Atoms

In most cases, a transition-metal atom deposited on a metallic substrate presents reduced m_S and m_L compared with the gas phase (Fig. 21.1). The adatoms still follow Hund's first rule, with maximal moments at the center of each series; however, their magnetic moment assumes smaller, noninteger values relative to the free atoms. For example, a gas-phase Co atom with seven electrons in the d-shell has $m_S = 3$ and $m_L = 3\,\mu_B$, which reduce to about $m_S = 2$ and $m_L = 1\,\mu_B$ on Pt(111) owing to charge transfer from the substrate and hybridization of the Co 3d states [21.73]. The larger relative decrease of m_L compared with m_S is related to the hierarchy of Hund's rules, as electron delocalization reduces the Coulomb repulsion effects within the d-states. Note that the local moments tend to decrease further with increased coordination, as shown by experiments

and calculations performed for clusters and monolayer films. On the other hand, owing to the reduced atomic coordination, elements that are nonmagnetic in the bulk may display sizable magnetic moments as adatoms, including 4d and 5d elements (Sect. 21.1.2). This allows for a much broader choice of elements in the construction of atomic-scale magnets.

XMCD [21.17, 183] and photoemission [21.195] studies show that the electronic valence of single Co atoms typically changes from d^7 in the gas phase to d^8 upon deposition on a metal surface. Experiments on alkali-metal films, for which the electron density increases from Cs to Li, indicate that the delocalization of the 3d-states increases with the electron density of the substrate, being maximum on Li [21.183]. The delocalization of the 3d-states causes a progressive decrease of m_S and m_L, which eventually leads to a nonmagnetic ground state due to Kondo screening of the local moments by the substrate conduction electrons [21.195]. On transition-metal substrates, on the other hand, the admixture of adatom and substrate d-states leads to unequal filling of orbitals with different symmetry and hence to strong anisotropy of m_L (Sect. 21.1.3, *Anisotropy of the Orbital Moment*). As the spin–orbit interaction couples m_L and m_S, a strong magnetic anisotropy is also expected, as schematized in Fig. 21.35 for $Co_1/Pt(111)$.

XMCD experiments and ab initio calculations also show that m_L and the MCA energy K of small Co_N clusters are correlated and dramatically sensitive to unitary changes of the atomic coordination [21.73, 432], as shown in Fig. 21.36. This tendency, governed by lateral adatom–adatom interactions as well as substrate–adatom interactions, continues from adatoms to clusters and thin films until, eventually, values of m_L and m_S close to bulk are reached (Fig. 21.36). The decreasing trend of K with atomic coordination must be taken into account if more atoms are assembled together with the aim of obtaining clusters with total magnetic anisotropy strong enough to stabilize ferromagnetic behavior against thermal fluctuations. Structures where the shape and composition are tuned so as to control the coordination of the magnetic atoms and maximize m_L and K, such as core–shell 2-D particles [21.157], 1-D atomic wires (Sect. 21.5), 2-D metalorganic networks, and single molecules [21.433–436], offer several opportunities to prevent a drastic decrease of K.

The high magnetic anisotropy of 3d adatoms on heavy-metal surfaces such as Pt, Pd, Ir, and W suggests that the magnetic moment of a single atom may become stable below a certain temperature, as the spin relaxation time τ increases exponentially with the ratio $K/(k_BT)$ (Sect. 21.1.8). Whereas this would certainly occur for a classical spin, spin-flip scattering with the conduction electrons of the substrate [21.422] and spin–phonon coupling [21.48] severely limit the stability of the magnetic moment in realistic situations. In addition, zero-point quantum spin fluctuations, which are a direct consequence of Heisenberg's uncertainty principle, can alter the magnetic ground state by effectively reducing the magnetic anisotropy energy barrier, which in turn reduces the magnetic stability [21.437, 438]. Indeed, no indication of magnetic remanence was observed for $Co_1/Pt(111)$ [21.73], even down to 0.3 K [21.439], while the longest τ reported for $Fe_1/Pt(111)$ is 3 ns at 0.3 K [21.440].

Electron scattering from a conductive surface can be effectively suppressed by introducing a thin insulating layer between the substrate and the magnetic adatoms. Such a layer additionally allows for tuning the phonon density of states of the surface as well as the symmetry and strength of the ligand field experienced by the adatoms, with the aim of reducing the spin–phonon relaxation and quantum tunneling rates, respectively. A first experiment performed on $Co_1/MgO/Ag(001)$ showed that the insertion of a few-monolayer-thick MgO spacer led to a drastic increase of τ, up to $232 \pm 17\,\mu s$ at 0.6 K in a magnetic field of 1 T. In this case, spin-flip transitions involving ground and excited states prevent even larger τ values from being reached [21.74].

The preferred binding site of Co on MgO(001) is on top of oxygen with four Mg atoms as neighbors, resulting in C_{4v} symmetry (Fig. 21.37). The dominant bond is between the out-of-plane d-orbitals of Co and p-orbitals of O, resulting in a nearly uniaxial ligand field (Fig. 21.37). This axial coordination plays a major role in determining the magnetic ground state of the adatoms as well as the energy separation of the lowest excited states, in particular the *zero-field splitting* between the two lowest spin doublets. The effects of the axial ligand field are shown in Fig. 21.37 by adopting a simplified one-electron picture of the Co d-orbitals (Fig. 21.37c) and a many-electron multiplet scheme including electronic interactions and spin–orbit coupling (Fig. 21.37e) derived from analysis of x-ray absorption spectra [21.74]. As seen in Fig. 21.37c, the axial field splits the 3d orbitals into three groups with different magnetic quantum numbers (0, 1, and 2) without breaking the degeneracy between the $d_{x^2-y^2}$, d_{xy} and d_{xz}, d_{yz} orbitals. This splitting preserves the orbital moment of the free atom along the vertical axis, leading to a ground state with $m_L \approx 3\,\mu_B$. A more detailed analysis carried out using multiplet ligand field theory [21.441, 442] reveals that the Co ground state is a mixed d^7 and $d^8\underline{1}$ configuration, where $\underline{1}$ describes a ligand hole on the O site, which arises due to charge transfer between the Co d-states and O 2p-states via the

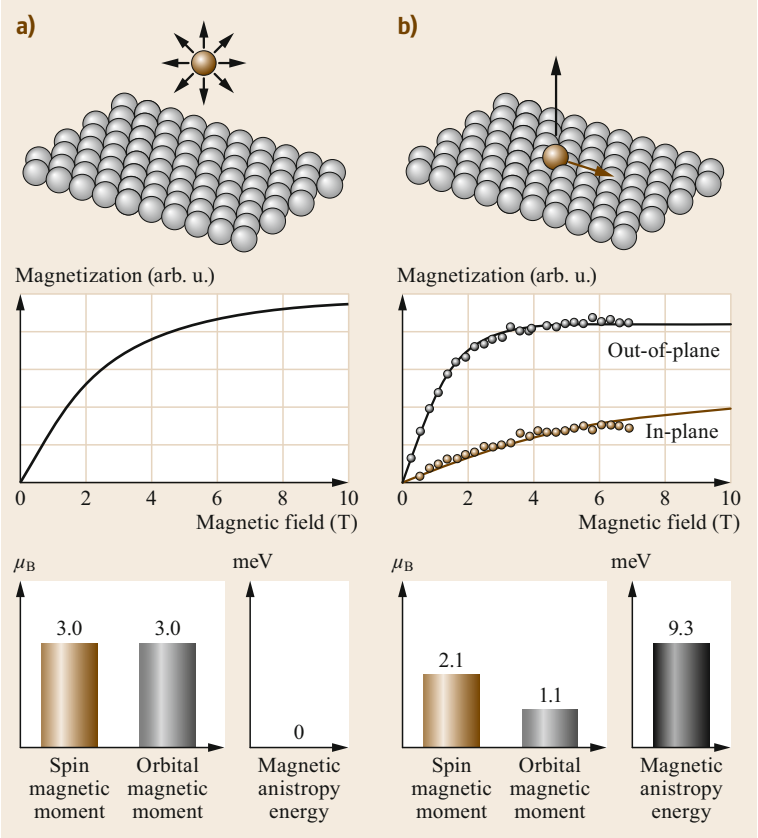

Fig. 21.35a,b Schematic representation of the symmetric and asymmetric environment of a magnetic atom in the gas phase **(a)** and on a close-packed metal surface **(b)**, respectively. The spin and orbital magnetic moment of a gas-phase Co atom are given by Hund's rules for a d^7 electronic configuration and compared with that of an individual Co atom deposited on the Pt(111) surface. The field-dependent magnetization is represented in **(a)** by a Brillouin function in the absence of magnetic anisotropy. In **(b)**, symmetry breaking and Co–Pt hybridization induce strong anisotropy of the magnetization measured out-of-plane (*black*) and close to in-plane (*brown*). (Reprinted by permission from [21.17], © Elsevier 2009)

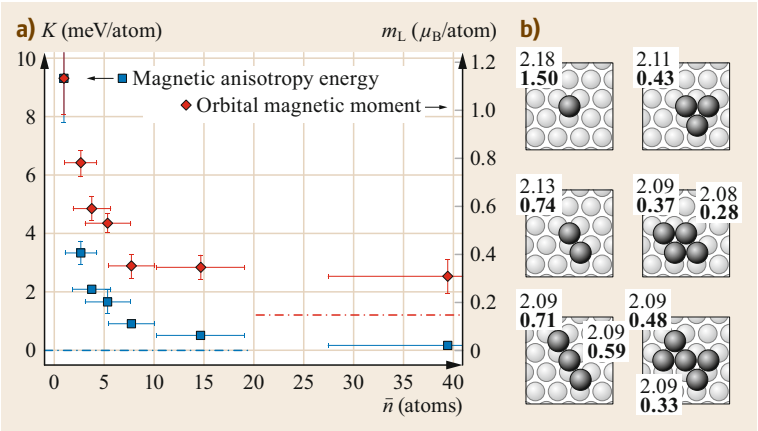

Fig. 21.36 **(a)** Orbital moment m_L and uniaxial anisotropy energy K as functions of average cluster size $\bar{n}$ for Co_n/Pt(111). For comparison, the *red* and *blue dashed-dotted lines* show m_L and K of bulk hcp-Co, respectively. The *error bars* on the horizontal scale represent the standard deviation of the size distribution determined by STM. **(b)** m_S (*bold print*) and m_L (*normal print*) calculated using density functional theory for different atoms in the Co_n/Pt(111) clusters. (Reprinted by permission from [21.73], © Am. Assoc. Adv. Sci. 2003)

d_{z^2} orbital. The evolution of the calculated Co states as a function of ligand field splitting and spin–orbit interaction (Fig. 21.37e) shows that the lowest energy level is a doublet with $L_z = \pm 2.91 \otimes S_z = \pm 1.27$, where L_z and S_z are the projections of the total orbital and spin moments on the axial direction. The spin moment is slightly less than the free atom value of $S = 3/2$ because of mixing of the ground-state terms ^{4}F and ^{2}F of the d^7 and d^8 configurations, respectively. Since both terms have $L = 3$, however, configuration mixing does not reduce the total orbital moment. The first excited level, with $L_z = \pm 2.54 \otimes S_z = \pm 0.39$, lies 58 meV above the ground state. This zero-field splitting, which can also be measured by inelastic tunneling spectroscopy [21.74], is the largest ever found for a 3d transition-metal element and represents an upper limit

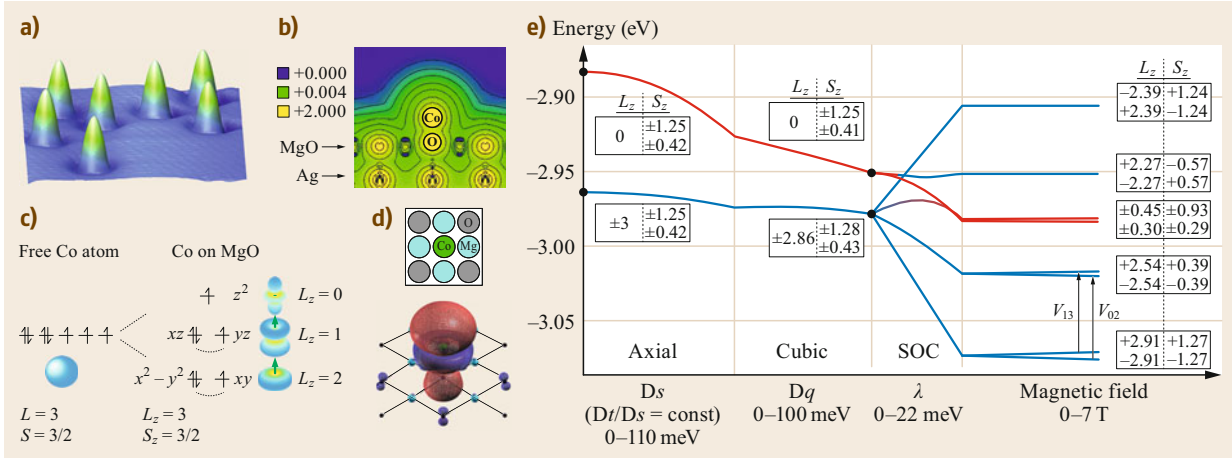

Fig. 21.37 **(a)** Constant-current STM image of seven Co atoms on 1 ML of MgO on Ag(100) at $T = 1.2$ K. **(b)** DFT-calculated structure and valence electron charge density of one Co atom atop an oxygen atom in 1 ML MgO on Ag(100). The charge density color scale is in atomic units. **(c)** Schematic model of the orbital occupancy of Co in the ^4F term ($L = 3$, $S = 3/2$) of a free atom (*left*), and Co on the MgO surface (*right*), with remaining large orbital degeneracy ($L_Z = 3$, $S_Z = 3/2$). The orbital moment is preserved along the axial direction by the symmetry of the ligand field. **(d)** Top view of the atomic structure (*top*) and oblique view of the positive (*red*) and negative (*blue*) spin density of the valence electrons of Co calculated by DFT (*bottom*). **(e)** Lowest energy levels obtained by multiplet simulations of the x-ray absorption spectra as a function of ligand field, spin–orbit coupling, and applied magnetic field. The *color code* of the energy levels highlights the different orbital symmetry of the states: *blue* for E and *red* for B_2. The two transitions seen in inelastic tunneling spectroscopy are indicated by *arrows*. (Reprinted by permission from [21.74], © Am. Assoc. Adv. Sci. 2014)

of K for single atoms. The key to such a large splitting is the nearly unquenched orbital moment of the lowest energy levels, which allows the $S_z = \pm 3/2$ states to be maximally split from the $S_z = \pm 1/2$ states by the spin–orbit interaction. In such a case, the zero-field splitting is equal to $\lambda L_z \Delta S_z = \lambda L_z \approx 60$ meV, where $\lambda \approx -20$ meV is the atomic spin–orbit coupling constant of Co. This value reaches the full magnitude of the spin–orbit coupling energy available to a Co atom, in contrast to most molecular and solid-state systems, where the orbital moment is quenched by the ligand field and the zero-field splitting has a second-order dependence on λ^2 [21.49, 443].

Achieving a large magnetic anisotropy requires breaking the spatial symmetry of the atomic wavefunctions without quenching the orbital magnetization. The most promising strategy to preserve the large orbital moment of a free atom and induce uniaxial anisotropy is to use low-coordination geometries, as shown for atoms bound to oxygen sites on MgO(001) or on the threefold-coordinated sites of a (111) surface [21.73, 444], as well as for molecular complexes with axially coordinated metal species [21.445–449]. This strategy can also be adapted to extended thin films, where perpendicular magnetic anisotropy is induced by depositing thin oxide layers, such as MgO and AlO_x, on 3d ferromagnetic layers, such as Co, Fe, or CoFe (Sect. 21.3.2).

21.6.2 Rare-Earth Atoms

The gas-phase electronic configuration of the rare-earth atoms is $[Xe]6s^25d^04f^n$. Because the partially filled 4f shell is shielded from the environment by the outer filled $5s^2$ and $5p^6$ shells, the spin and orbital magnetic moments of the 4f electrons retain large, atomic-like values even in a bulk environment. In free atoms, the total angular momentum J, which is the vector sum of the momenta S and L of the 4f shell, and its projection J_z are good quantum numbers. The electronic levels of a given configuration split according to J, with energy determined by the intraatomic Coulomb interaction and spin–orbit coupling. Each level is a $(2J + 1)$-degenerate multiplet. When the ions are incorporated into a crystal or deposited onto a surface, the ligand field partially lifts the degeneracy of the J-manifolds, splitting states with different $|J_z|$ over several tens of meV according to the strength and symmetry of the crystal potential. This splitting determines the magnitude of the total magnetic moment as well as the magnetic anisotropy of the rare-earth ions. Magnetic and electric hyperfine interactions provide additional structure to the energy levels, which is relevant for understanding spin coherence and relaxation processes.

Isolated rare-earth impurities in bulk dielectric crystals are currently being investigated for quantum mem-

ory and optical signal processing applications [21.450]. These systems combine long optical and spin state coherence times with the possibility of controlling light–matter interactions using external electric and magnetic fields. In the context of surface magnetism, rare-earth ions provide an alternative to transition metals to explore magnetic bistability and quantum coherence in single atoms, taking advantage of the quantized nature of J and J_z as well as of the multiplicity of the electronic levels. The angular symmetry of the ligand field provided by the surface determines the symmetry of the quantum states and thereby their coupling via tunneling matrix elements. Therefore, depending on the symmetry of the ligand field, the magnetic moment may be protected from direct quantum tunneling between the two $\pm J_z$ ground states as well as from reversal induced by single-electron spin flips [21.444, 451].

In principle, rare-earth atoms can have either a divalent $(6s6p5d)^2 4f^n$ or trivalent $(6s6p5d)^3 4f^{n-1}$ electronic configuration, where divalent and trivalent refer to the occupancy of the (6s6p5d)-derived valence band. Most rare earths are divalent as free ions and trivalent in the bulk [21.452–454], although mixed valencies have been reported for several of the early lanthanides [21.455–458] and Tm [21.459]. Bulk lattice–ion interactions are well understood in the framework of spin Hamiltonians including ligand field effects [21.460–462]. For rare-earth atoms in low-coordination environments, such as for surfaces [21.463–466], thin films [21.467], small clusters [21.468, 469], and adatoms, the 4f occupancy may be different with respect to the bulk. Tm atoms on W(110) are trivalent [21.470]. Dy, Ho, Er, and Tm atoms adsorbed on Pt(111), Cu(111), Ag(100), and Ag(111) assume a trivalent (divalent) configuration when the sum of the $4f \rightarrow 5d$ promotion energy and intershell coupling energy is low (high) and the substrate density of states at the Fermi level is large (low) [21.454]. On oxide surfaces such as MgO, the prevalent configuration is trivalent, whereas Dy atoms on graphene/Ir(111) are divalent [21.471]. The MCA of trivalent rare-earth atoms is on the order of a few meV/atom and typically larger than that of divalent atoms.

Similar to the transition metals, rare-earth atoms adsorbed on metallic surfaces behave as paramagnets [21.454, 472, 473]. Ho atoms deposited on MgO(100) thin films grown on Ag(100), on the other hand, display long-lived remanent magnetization, with a relaxation time that depends on the MgO thickness [21.414]. Not only do the Ho atoms show magnetic bistability, they also have an exceptionally large coercive field and present magnetic hysteresis up to 40 K, a temperature substantially higher than the blocking temperature of most single-molecule magnets on comparable time scales. The adsorption site, XMCD spectra, and magnetic hysteresis of an ensemble of Ho atoms on 7 ML of MgO/Ag(001) measured at 6.5 K are shown in Fig. 21.38a–c. The spin relaxation time of this system measured at 10 K by XMCD is $\tau \approx 1600 \pm 100$ s at low field (0.01 T) and $\approx 1200 \pm 100$ s at high field (6.8 T). Thus, the Ho atoms on MgO retain a long relaxation time even at very high field, in contrast with single-molecule magnets, which typically exhibit faster relaxation at high field because of phonon scattering and level crossing [21.446, 474–477]. Comparable magnetic lifetimes are reported down to 2.5 K, implying that, < 10 K, relaxation is essentially driven by non-thermal processes. Moreover, measurements taken at different photon fluxes show that τ is mostly limited by the secondary-electron cascade generated by the absorbed x-rays. The scattering with these hot electrons reduces the magnetic lifetime [21.478]. The relaxation times measured by XMCD hence represent a lower bound on the intrinsic τ. Indeed, spin-polarized STM measurements demonstrate that τ exceeds several hours at temperatures < 4 K [21.418].

These exceptional properties originate from a combination of factors. XMCD [21.414] and inelastic tunneling spectroscopy measurements [21.479] show that the Ho atoms on top of oxygen sites have a $4f^{10}$ electronic configuration with $J = 8$. The C_{4v} symmetry of the oxygen adsorption site determines a ligand field with strong (weak) axial (fourfold) components, resulting in a ground-state doublet with either $J_z = \pm 7$ or $J_z = \pm 8$ character, depending on the interpretation of the available experimental data. The $J_z = \pm 7$ ground state is protected from quantum tunneling and first-order electron spin excitations ($\Delta m = 0, \pm 1$) at any external magnetic field [21.451], which prevents magnetization reversal by electron scattering. However, theoretical calculations indicate that spin–phonon coupling is the most relevant mechanism allowing for spin relaxation of Ho/MgO, for both $J_z = \pm 7$ and $J_z = \pm 8$ ground states. The very low density of vibrational modes in the MgO layer at low energy strongly suppresses first-order scattering with phonons ($\Delta m = \pm 1, \pm 2$). The absence of Ho–MgO vibrational modes in the region of hyperfine level crossing can further slow down relaxation at low fields, as observed for $TbPc_2$ molecules grafted onto suspended nanotubes [21.480].

The reversal processes that are triggered by the scattering with conduction electrons and with the soft phonon modes of the metal substrate are expected to depend strongly on the thickness of the MgO layer. Indeed, the hysteresis loops of Ho atoms become narrower when the thickness of the MgO film is reduced below 4 ML, and they almost close for a thickness of 2 ML [21.414]. Hence, symmetry protection against first-order reversal is not a sufficient condition to pre-

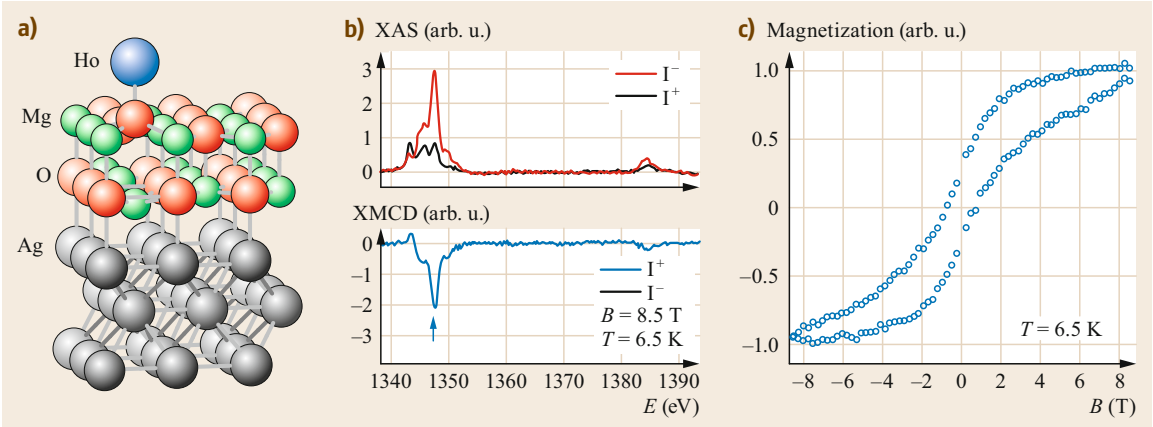

Fig. 21.38 **(a)** Adsorption geometry of a Ho atom on top of oxygen on 2 ML of MgO on Ag(100) calculated by DFT. **(b)** x-Ray absorption and XMCD spectra taken at the Ho $M_{4,5}$ edges (3d → 4f transitions) for an ensemble of individual Ho adatoms deposited on seven monolayers of MgO on Ag(100) at 6.5 K in a field of 8.5 T applied perpendicular to the sample's surface. The Ho coverage corresponds to 0.01 ML referred to the Ag(100) lattice. **(c)** Magnetization as a function of applied field recorded at the maximum of the XMCD signal (see *arrow* in **(b)**). (Adapted by permission from [21.414], © Am. Assoc. Adv. Sci. 2016)

vent magnetization reversal. To obtain long magnetic lifetimes in single atoms, efficient decoupling from the electron and phonon bath of the substrate is required. Notably, the magnetic lifetime of the Ho atoms on MgO is much longer than for Ho ions in $HoPc_2$ [21.481] and Ho-doped dielectric crystals [21.482], likely because of the larger level splitting and the smaller number of vibration modes allowed for atoms adsorbed on surfaces.

Reading and Writing the Magnetic States of Single Atoms

Recent experiments have demonstrated that it is possible to read and write the magnetic state of individual Ho atoms on MgO using spin-polarized STM [21.418, 479]. The Ho states can be sensed by measuring either the tunnel magnetoresistance [21.193] or the shift of the electron spin resonance (ESR) spectrum measured on a nearby Fe atom [21.242] and written by spin-polarized current pulses, as shown in Fig. 21.39. At bias voltages $V < 73$ mV, i.e., below the first spin excitation threshold accessible by STM, the tunneling magnetoresistance is stable for hours at low temperature. At larger bias, discrete changes in conductance are observed, separated by plateaus of long residence times in the high- and low-conductance states (Fig. 21.39b). The switching rate increases linearly with the tunnel current, indicating that it is limited by a single-electron process with a switching probability on the order of 10^{-9} per tunneling electron (Fig. 21.39c). The rate depends in a nonlinear way on the bias voltage (Fig. 21.39d), reflecting transition energies between different magnetic states of Ho on MgO. To write the Ho state, repeated current pulses at $V > 150$ mV are applied to an Ho atom, until a change in magnetoresistance measured at $V = 50$ mV indicates that the magnetic moment has switched. The magnetic origin of the long-lived states is confirmed by single-atom ESR on a nearby Fe atom, which shows that the resonance peak of Fe shifts by almost 1 GHz as the dipolar field produced by the Ho magnetic moment changes sign upon switching (Fig. 21.39e).

ESR-STM measurements also allow for estimating the magnetic moment of Ho by measuring the resonance shift as a function of the Fe–Ho distance [21.418]. The out-of-plane magnetic moment estimated by ESR-STM is $10.1 \pm 0.1\ \mu_B$, which is compatible with the 4f magnetic moment expected of a pure $J_z = 8$ state, but about $1\ \mu_B$ larger than that of a pure $J_z = 7$ state, as well as significantly larger than the magnetic moment estimated by XMCD [21.414]. Whereas the latter discrepancy may be due to the incomplete magnetic saturation of Ho atom ensembles measured by XMCD at high field, owing to their extremely long relaxation times, it remains to be established whether part of the total magnetic moment measured by ESR-STM arises from the polarization of the d and 6s-electrons or of the nearest-neighbor oxygen 2p-states [21.479].

STM measurements further show that the magnetic bistability of Ho extends to relatively high temperature. The first spontaneous magnetization reversal events are measured at 45 K with a relaxation time of ≈ 66 s. The high temperature required to activate thermally induced switching confirms the weak interaction between the magnetic quantum states and lattice vibrations. Strikingly, this temperature is close to the onset of Ho

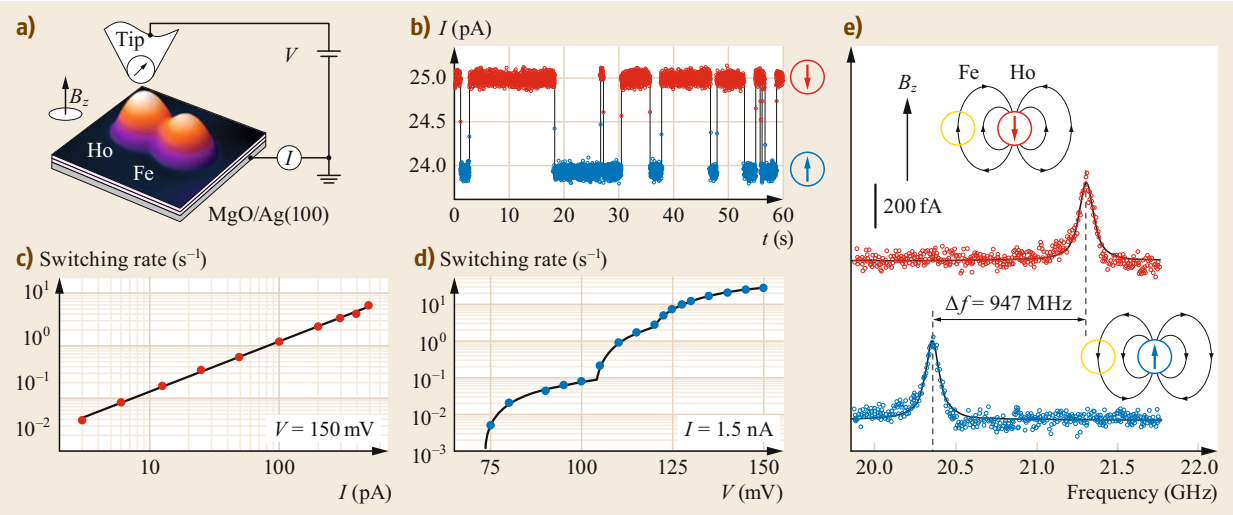

Fig. 21.39 **(a)** Schematic of a spin-polarized STM tip and topographic image of a Ho and an Fe atom on 2 ML of MgO. **(b)** The tunnel current recorded on a Ho atom shows switching between two magnetic states (*red*, down; *blue*, up) with long residence time ($V = 150$ mV, current set point $I = 25$ pA). At these tunneling conditions, switching is induced by tunneling electrons. **(c)** Switching rate measured as a function of current at constant $V = 150$ mV. **(d)** Bias dependence of the switching rate at constant current ($I = 1.5$ nA) showing three rate-increasing thresholds at 73, 104, and 119 mV. **(e)** ESR spectra of an Fe atom located at a distance of 1.4 nm from a Ho atom in the high-conductance (*top*, *red*) and low-conductance (*bottom*, *blue*) state. The ESR measurements were performed by adding a radiofrequency voltage of ≈ 15 mV at 10–30 GHz to the dc bias voltage in the presence of an external magnetic field providing 100 mT out-of-plane, which induces a Zeeman splitting of ≈ 20.8 GHz for Fe [21.242]. The *inset schematics* show the dipolar field of the Ho atom in the up and down states. All data were recorded at a temperature of 1.2 K. (Adapted by permission from [21.418], © SpringerNature 2017)

diffusion from the oxygen to the bridge site of the MgO lattice [21.479], providing further confirmation of the extremely weak spin–phonon coupling in this system. Stiff insulating spacer layers such as MgO therefore effectively decouple the electronic and phononic degrees of freedom of the adatoms from the substrate bath, opening novel possibilities to probe and manipulate atomic spins and their environment in a controlled way.

21.7 Outlook and Perspectives

The experiments on single atoms presented in the last section exemplify the extraordinary series of theoretical and experimental breakthroughs in surface and interface magnetism that have occurred over the past three decades. The ability to build and probe magnetic structures with tunable interactions one atom at a time, in controlled environments, and on timescales that extend from thousands of seconds to the sub-ns regime, provides direct experimental access to emergent phenomena at surfaces as well as a stringent test of equilibrium and nonequilibrium models of magnetic systems relevant for condensed-matter and statistical physics. This level of control has been instrumental in enabling large scale commercial applications of surface and interface magnetic systems, such as magnetic sensors, data storage media for hard drives, and magnetic random access memories. Beyond these achievements lie several possibilities for future research and technological developments.

21.7.1 Merging Functionalities

Worldwide demand for data storage, processing, and communication rates is expanding at a rapid pace. At the same time, the exponential increase in capability, and corresponding decrease in size and cost, of electronic devices captured by Moore's Law is coming to an end as the smallest device features approach the atomic scale. One way out of this conundrum is to develop a new generation of materials and devices that integrate more functions in a seamless manner, such as memory and logic or signal transduction and data transfer. Magnetic systems that couple the electronic charge with the orbital and spin de-

grees of freedom can serve this purpose, e.g., by allowing for on-chip low-power information transfer at GHz to THz frequency, beyond-complementary metal–oxide–semiconductor (CMOS) logic-in-memory architectures, as well as novel biosensing and quantum sensing techniques. Many of these applications rely on the fine engineering of the magnetic and electrical response of thin films and nanostructures. The great variety of magnetic parameters (magnetization, anisotropy, damping, domain structure), couplings (exchange bias, RKKY, DMI, dipolar) and transport properties (several types of magnetoresistance and Hall effects, spin torques) that can be tuned in these systems provides a tell-tale demonstration of the versatile functions of magnetic surfaces and interfaces.

21.7.2 Novel 2-D Materials

Originally restricted to metallic thin films, investigations of surface and interface magnetism now encompass all classes of materials: metals, semimetals, topological insulators, semiconductors, and insulators. A recent subject of research are atomically thin crystals produced by either exfoliation or chemical vapor deposition of van der Waals materials, so-called 2-D materials. Examples include ferromagnetic insulators, such as single-layer chromium trihalides, itinerant ferromagnets such as iron germanium tellurides, as well as antiferromagnets. Whereas most of the theoretical concepts and experimental techniques used for the investigation of 2-D magnetic materials are common to those developed for magnetic thin films, these materials open novel perspectives due to the broad range of couplings and electron correlation phenomena that can be obtained in van der Waals heterostructures. Besides their fundamental interest, future studies shall address the potential for technological impact of such materials, which hinges on achieving robust magnetic order above room temperature and on finding efficient ways for large-scale fabrication of 2-D heterostructures.

21.7.3 Neuromorphic Computing

Taking into consideration the Hopfield relation between early neural networks, spin-glass transitions, and spin models, localized topological spin textures open new opportunities to include neuromorphic computing functionalities in magnetic films. In this context, skyrmions and antiskyrmions have been proposed to realize reservoir computing networks, which exploit the complex dynamics of nonlinear systems for sequential data processing [21.483]. This suggestion is based on the fact that pinned skyrmions deform under the action of a current, which modifies their transport properties and leads to nonlinear current–voltage characteristics. The degree of nonlinearity has been suggested to depend strongly on the character of the chiral states constituting the magnetic texture [21.484]. Correspondingly, the interaction of skyrmions with currents and magnons can result in a manifold of internal degrees of freedom that can be utilized for achieving neural networks functionalities.

21.7.4 Quantum Computing

Quantum computing promises unprecedented capabilities for certain computational tasks such as prime factorization, decryption, and quantum many-body problems. The basic building block of a quantum computer is the quantum mechanical bit (qubit), which can represent arbitrary quantum superpositions of two basis states. Magnetic atoms at surfaces with a magnetic doublet ground state well-separated from other states can serve as model systems for spin qubits. By changing the substrate, adsorption site, and proximity to other magnetic species, the coupling and decoherence of quantum spins can be studied with atomic-scale precision in different environments. The development of scanning probe techniques that can probe and manipulate quantum coherence in single atoms is very promising in this respect (Sect. 21.6). Furthermore, helical spin chains and ferromagnetic chains of transition-metal atoms on superconducting substrates offer the possibility to realize topological qubits based on the formation of so-called Majorana bound states [21.21]. These states are nonlocal zero-energy quasiparticle excitations that emerge in superconductors in the presence of spin–orbit coupling and broken time reversal symmetry. Majorana qubits are topologically protected against perturbations and obey non-Abelian exchange statistics, two properties that make them very appealing for fault-tolerant topological quantum computation [21.485].

References

21.1 U. Gradmann: Magnetism in ultrathin transition metal films. In: *Handbook of Magnetic Materials*, Vol. 7, ed. by K.H.J. Buschow (Elsevier, Amsterdam 1993) pp. 1–96

21.2 H.J. Elmers: Ferromagnetic monolayers, J. Mod. Phys. B **09**(24), 3115–3180 (1995)

21.3 M. Wuttig, X. Liu (Eds.): *Ultrathin Metal Films: Magnetic and Structural Properties*, Springer Tracts in Modern Physics, Vol. 206 (Springer, Berlin, Heidelberg 2004)

21.4 B. Heinrich, J. Anthony, C. Bland (Eds.): *Ultrathin Magnetic Structures I–IV*, Vol. 1 (Springer, Berlin, Heidelberg 2005)

21.5 P. Poulopoulos, K. Baberschke: Magnetism in thin films, J. Phys. Condens. Matter **11**(48), 9495 (1999)

21.6 S. Blügel: Reduced dimensions I: Magnetic moment and magnetic structure. In: *Magnetism Goes Nano: 36th IFF Spring School*, ed. by S. Blügel, T. Brückel, C.M. Schneider (Forschungszentrum Jülich, Jülich 2005)

21.7 M. Przybylski, J. Kirschner: Surface Magnetism. In: *Surface and Interface Science* (Wiley-Blackwell, New-York 2014) pp. 679–742, Chap. 7

21.8 F. Hellman, A. Hoffmann, Y. Tserkovnyak, G.S.D. Beach, E.E. Fullerton, C. Leighton, A.H. MacDonald, D.C. Ralph, D.A. Arena, H.A. Dürr, P. Fischer, J. Grollier, J.P. Heremans, T. Jungwirth, A.V. Kimel, B. Koopmans, I.N. Krivorotov, S.J. May, A.K. Petford-Long, J.M. Rondinelli, N. Samarth, I.K. Schuller, A.N. Slavin, M.D. Stiles, O. Tchernyshyov, A. Thiaville, B.L. Zink: Interface-induced phenomena in magnetism, Rev. Mod. Phys. **89**, 025006 (2017)

21.9 B. Dieny, M. Chshiev: Perpendicular magnetic anisotropy at transition metal/oxide interfaces and applications, Rev. Mod. Phys. **89**(2), 025008 (2017)

21.10 R. Ramesh, N.A. Spaldin: Multiferroics: Progress and prospects in thin films, Nat. Mater. **6**(1), 21–29 (2007)

21.11 P. Zubko, S. Gariglio, M. Gabay, P. Ghosez, J.-M. Triscone: Interface physics in complex oxide heterostructures, Annu. Rev. Condens. Matter Phys. **2**(1), 141–165 (2011)

21.12 M. Trassin: Low energy consumption spintronics using multiferroic heterostructures, J. Phys. Condens. Matter **28**(3), 033001 (2015)

21.13 I.M.L. Billas, A. Châtelain, W.A. de Heer: Magnetism of Fe, Co and Ni clusters in molecular beams, J. Magn. Magn. Mater. **168**(1), 64–84 (1997)

21.14 J. Bansmann, S.H. Baker, C. Binns, J.A. Blackman, J.-P. Bucher, J. Dorantes-Dávila, V. Dupuis, L. Favre, D. Kechrakos, A. Kleibert, K.-H. Meiwes-Broer, G.M. Pastor, A. Perez, O. Toulemonde, K.N. Trohidou, J. Tuaillon, Y. Xie: Magnetic and structural properties of isolated and assembled clusters, Surf. Sci. Rep. **56**(6), 189–275 (2005)

21.15 D. Fiorani: *Surface Effects in Magnetic Nanoparticles*, Vol. 48 (Springer, New York 2005) pp. 1305–1308

21.16 D.J. Sellmyer, R. Skomski: *Advanced Magnetic Nanostructures* (Springer, New York 2006)

21.17 H. Brune, P. Gambardella: Magnetism of individual atoms adsorbed on surfaces, Surf. Sci. **603**(10-12), 1812–1830 (2009)

21.18 H. Brune, P. Gambardella: Atomic and molecular magnets on surfaces. In: *Fundamentals of Picoscience*, ed. by K.D. Sattler (CRC, Boca Raton 2013) pp. 447–470

21.19 M. Ternes: Probing magnetic excitations and correlations in single and coupled spin systems with scanning tunneling spectroscopy, Prog. Surf. Sci. **92**(1), 83–115 (2017)

21.20 F. Delgado, J. Fernández-Rossier: Spin decoherence of magnetic atoms on surfaces, Prog. Surf. Sci. **92**(1), 40–82 (2017)

21.21 B.W. Heinrich, J.I. Pascual, K.J. Franke: Single magnetic adsorbates on s-wave superconductors, Prog. Surf. Sci. **93**(1), 1–19 (2018)

21.22 B. Hillebrands, K. Ounadjela (Eds.): *Spin Dynamics in Confined Magnetic Structures I–III*, Topics in Applied Physics, Vol. 83 (Springer, Berlin, Heidelberg 2003)

21.23 K. Zakeri: Elementary spin excitations in ultrathin itinerant magnets, Phys. Rep. **545**(2), 47–93 (2014)

21.24 V.V. Kruglyak, S.O. Demokritov, D. Grundler: Magnonics, J. Phys. D Appl. Phys. **43**(26), 264001 (2010)

21.25 A.V. Chumak, V.I. Vasyuchka, A.A. Serga, B. Hillebrands: Magnon spintronics, Nat. Phys. **11**, 453 (2015)

21.26 A. Kirilyuk, A.V. Kimel, T. Rasing: Ultrafast optical manipulation of magnetic order, Rev. Mod. Phys. **82**, 2731–2784 (2010)

21.27 T.R. McGuire, R.I. Potter: Anisotropic magnetoresistance in ferromagnetic 3D alloys, IEEE Trans. Magn. **11**(4), 1018–1038 (1975)

21.28 A. Fert: Magnetic and transport properties of metallic multilayers, Mater. Sci. Forum **439**, 59–60 (1990)

21.29 I. Zutic, J. Fabian, S. Das Sarma: Spintronics: Fundamentals and applications, Rev. Mod. Phys. **76**(2), 323–410 (2004)

21.30 E.Y. Tsymbal, I. Zutic: *Handbook of Spin Transport and Magnetism* (CRC, Boca Raton 2011)

21.31 J. Sinova, S.O. Valenzuela, J. Wunderlich, C.H. Back, T. Jungwirth: Spin Hall effect, Rev. Mod. Phys. **87**, 1213 (2015)

21.32 V. Baltz, A. Manchon, M. Tsoi, T. Moriyama, T. Ono, Y. Tserkovnyak: Antiferromagnetic spintronics, Rev. Mod. Phys. **90**, 015005 (2018)

21.33 M.D. Stiles, J. Miltat: Spin-transfer torque and dynamics. In: *Spin Dynamics in Confined Magnetic Structures III*, ed. by B. Hillebrands, A. Thiaville (Springer, Berlin, Heidelberg 2006) pp. 225–308

21.34 P. Gambardella, I.M. Miron: Current-induced spin–orbit torques, Philos. Trans. R. Soc. A **369**, 3175–3197 (2011)

21.35 A. Manchon, I.M. Miron, T. Jungwirth, J. Sinova, J. Železný, A. Thiaville, K. Garello, P. Gambardella: Current-induced spin–orbit torques in ferromagnetic and antiferromagnetic systems, Rev. Mod. Phys. **91**, 035004 (2019)

21.36 S. Blügel: Magnetically stabilized surface alloys, Appl. Phys. A **63**, 595 (1996)

21.37 P. Kurz, G. Bihlmayer, K. Hirai, S. Blügel: Three-dimensional spin structure on a two-dimensional lattice: Mn/Cu(111), Phys. Rev. Lett. **86**, 1106 (2001)

21.38 I. Turek, J. Kudrnovský, M. Diviš, M. Franek, G. Bihlmayer, S. Blügel: First-principles study of the electronic structure and exchange interactions in bcc europium, Phys. Rev. B **68**, 224431 (2003)

21.39 O. Gunnarsson: Band model for magnetism of transition metals in the spin-density-functional formalism, J. Phys. F **6**, 587 (1976)

21.40 J.F. Janak: Uniform susceptibilities of metallic elements, Phys. Rev. B **16**, 255 (1977)

21.41 S. Bornemann, O. Šipr, S. Mankovsky, S. Polesya, J.B. Staunton, W. Wurth, H. Ebert, J. Minár: Trends in the magnetic properties of Fe, Co, and Ni clusters and monolayers on Ir(111), Pt(111), and Au(111), Phys. Rev. B **86**, 104436 (2012)

21.42 H. Ebert, D. Ködderitzsch, J. Minár: Calculating condensed matter properties using the KKR-Green's function method–recent developments and applications, Rep. Prog. Phys. **74**(9), 096501 (2011)

21.43 O. Šipr, J. Minár, H. Ebert: On the importance of the magnetic dipole term Tz in analyzing X-ray magnetic circular dichroism spectra of clusters, Europhys. Lett. **87**, 67007 (2009)

21.44 S. Blügel: Magnetism of 4d and 5d transition metal adlayers on Ag(001): Dependence on the adlayer thickness, Phys. Rev. B **51**, 2025 (1995)

21.45 M. Moseler, H. Häkkinen, R.N. Barnett, U. Landman: Structure and magnetism of neutral and anionic palladium clusters, Phys. Rev. Lett. **86**, 2545–2548 (2001)

21.46 O. Eriksson, B. Johansson, R.C. Albers, A.M. Boring, M.S.S. Brooks: Orbital magnetism in Fe, Co, and Ni, Phys. Rev. B **42**, 2707–2710 (1990)

21.47 R.D. Cowan: *The Theory of Atomic Structure and Spectra* (Univ. California Press, Oakland 1981)

21.48 A. Abragam, B. Bleaney: *Electron Paramagnetic Resonance of Transition Ions* (Oxford Univ. Press, Oxford 2012)

21.49 P. Bruno: Tight-binding approach to the orbital magnetic moment and magnetocrystalline anisotropy of transition-metal monolayers, Phys. Rev. B **39**, 865 (1989)

21.50 G. van der Laan: Microscopic origin of magnetocrystalline anisotropy in transition metal thin films, Phys. Condens. Matter **10**, 3239 (1998)

21.51 R. Shindou, N. Nagaosa: Orbital ferromagnetism and anomalous Hall effect in antiferromagnets on the distorted fcc lattice, Phys. Rev. Lett. **87**, 116801 (2001)

21.52 M. dos Santos Dias, J. Bouaziz, M. Bouhassoune, S. Blügel, S. Lounis: Chirality-driven orbital magnetic moments as a new probe for topological magnetic structures, Nat. Commun. **7**, 13613 (2016)

21.53 J.-P. Hanke, F. Freimuth, A.K. Nandy, H. Zhang, S. Blügel, Y. Mokrousov: Role of Berry phase theory for describing orbital magnetism: From magnetic heterostructures to topological orbital ferromagnets, Phys. Rev. B **94**, 121114 (2016)

21.54 J.-P. Hanke, F. Freimuth, S. Blügel, Y. Mokrousov: Prototypical topological orbital ferromagnet γ-FeMn, Sci. Rep. **7**, 41078 (2017)

21.55 S. Frota-Pessôa: Magnetic behavior of 3 d impurities in Cu, Ag, and Au: First-principles calculations of orbital moments, Phys. Rev. B **69**(10), 104401 (2004)

21.56 M.S.S. Brooks: Calculated ground state properties of light actinide metals and their compounds, Physica B **130**, 6 (1985)

21.57 I.V. Solovyev, A.I. Liechtenstein, K. Terakura: Is Hund's second rule responsible for the orbital magnetism in solids?, Phys. Rev. Lett. **80**, 5758–5761 (1998)

21.58 I.V. Solovyev: Orbital polarization in itinerant magnets, Phys. Rev. Lett. **95**, 267205 (2005)

21.59 O. Eriksson, M.S.S. Brooks, B. Johansson: Orbital polarization in narrow-band systems: Application to volume collapses in light lanthanides, Phys. Rev. B **41**, 7311 (1991)

21.60 O. Hjortstam, J. Trygg, J.M. Wills, B. Johansson, O. Eriksson: Calculated spin and orbital moments in the surfaces of the 3d metals Fe, Co, and Ni and their overlayers on Cu(001), Phys. Rev. B **53**, 9204 (1996)

21.61 B. Nonas, I. Cabria, R. Zeller, P.H. Dederichs, T. Huhne, H. Ebert: Strongly enhanced orbital moments and anisotropies of adatoms on the Ag(001) surface, Phys. Rev. Lett. **86**, 2146–2149 (2001)

21.62 M. Komelj, C. Ederer, J.W. Davenport, M. Fähnle: From the bulk to monatomic wires: An ab initio study of magnetism in Co systems with various dimensionality, Phys. Rev. B **140407**(R), 66 (2002)

21.63 C. Ederer, M. Komelj, M. Fähnle: Magnetism in systems with various dimensionalities: A comparison between Fe and Co, Phys. Rev. B **68**, 052402 (2003)

21.64 A.R. Mackintosh, O.K. Andersen: The electronic structure of transition metals. In: *Electrons at the Fermi surface*, ed. by M. Springford (Cambridge Univ. Press, London 1980) p. 149

21.65 D.-S. Wang, R. Wu, A.J. Freeman: First-principles theory of surface magnetocrystalline anisotropy and the diatomic-pair model, Phys. Rev. B **47**(22), 14932 (1993)

21.66 J. Stöhr: Exploring the microscopic origin of magnetic anisotropies with X-ray magnetic circular dichroism (XMCD) spectroscopy, J. Magn. Magn. Mater. **200**, 470 (1999)

21.67 R.R. Birss: *Symmetry and Magnetism*, Vol. 863 (North-Holland, Amsterdam 1964)

21.68 M. Farle: Ferromagnetic resonance of ultrathin metallic layers, Rep. Prog. Phys. **61**(7), 755 (1998)

21.69 D. Weller, J. Stöhr, R. Nakajima, A. Carl, M.G. Samant, C. Chappert, R. Mégy, P. Beauvillain, P. Veillet, G.A. Held: Microscopic origin of magnetic anisotropy in Au/Co/Au probed with x-ray magnetic circular dichroism, Phys. Rev. Lett. **75**, 3752–3755 (1995)

21.70 H.A. Dürr, G. van der Laan, D. Spanke, F.U. Hillebrecht, N.B. Brookes: Electron-correlation-induced magnetic order of ultrathin Mn films, Phys. Rev. B **56**, 8156–8162 (1997)

21.71 N. Nakajima, T. Koide, T. Shidara, H. Miyauchi, H. Fukutani, A. Fujimori, K. Iio, T. Katayama, M. Nývlt, Y. Suzuk: Perpendicular magnetic anisotropy caused by interfacial hybridization via enhanced orbital moment in Co/Pt multilayers: Magnetic circular x-ray dichroism study, Phys. Rev. Lett. **81**, 5229 (1998)

21.72 P. Gambardella, A. Dallmeyer, K. Maiti, M.C. Malagoli, W. Eberhardt, K. Kern, C. Carbone: Ferromagnetism in one-dimensional monatomic metal chains, Nature **416**(6878), 301–304 (2002)

21.73 P. Gambardella, S. Rusponi, M. Veronese, S.S. Dhesi, C. Grazioli, A. Dallmeyer, I. Cabria,

R. Zeller, P.H. Dederichs, K. Kern, C. Carbone, H. Brune: Giant magnetic anisotropy of single cobalt atoms and nanoparticles, Science **300**(5622), 1130–1133 (2003)

21.74 I.G. Rau, S. Baumann, S. Rusponi, F. Donati, S. Stepanow, L. Gragnaniello, J. Dreiser, C. Piamonteze, F. Nolting, S. Gangopadhyay, O.R. Albertini, R.M. Macfarlane, C.P. Lutz, B.A. Jones, P. Gambardella, A.J. Heinrich, H. Brune: Reaching the magnetic anisotropy limit of a 3d metal atom, Science **344**(6187), 988–992 (2014)

21.75 C. Nistor, T. Balashov, J.J. Kavich, A.L. Rizzini, B. Ballesteros, G. Gaudin, S. Auffret, B. Rodmacq, S.S. Dhesi, P. Gambardella: Orbital moment anisotropy of Pt/Co/AlO_x heterostructures with strong Rashba interaction, Phys. Rev. B **84**(5), 054464 (2011)

21.76 M. Tischer, O. Hjortstam, D. Arvanitis, J.H. Dunn, F. May, K. Baberschke, J. Trygg, J.M. Wills, B. Johansson, O. Eriksson: Enhancement of orbital magnetism at surfaces: Co on Cu(100), Phys. Rev. Lett. **75**, 1602–1605 (1995)

21.77 H.A. Dürr, E. Dudzik, S.S. Dhesi, J.B. Goedkoop, G. van der Laan, M. Belakhovsky, C. Mocuta, A. Marty, Y. Samson: Chiral magnetic domain structures in ultrathin FePd films, Science **284**, 2166 (1999)

21.78 S.S. Dhesi, H.A. Dürr, G. van der Laan, E. Dudzik, N.B. Brookes: Electronic and magnetic structure of thin Ni films on Co/Cu(001), Phys. Rev. B **60**, 12852 (1999)

21.79 A. Hubert, R. Schäfer: *Magnetic Domains: The Analysis of Magnetic Microstructures* (Springer, Berlin, Heidelberg 2008)

21.80 G. Chen, T. Ma, H. Kwon, C. Won, Y. Wu, A.K. Schmid: Tailoring the chirality of magnetic domain walls by interface engineering, Nat. Commun. **4**, 2671 (2013)

21.81 E. Martinez, S. Emori, N. Perez, L. Torres, G.S.D. Beach: Current-driven dynamics of Dzyaloshinskii domain walls in the presence of in-plane fields: Full micromagnetic and one-dimensional analysis, J. Appl. Phys. **115**, 213909 (2014)

21.82 J. Topping: On the mutual potential energy of a plane network of doublets, Proc. R. Soc. A **114**, 67–72 (1927)

21.83 L. Szunyogh, B. Újfalussy, P. Weinberger: Magnetic anisotropy of iron multilayers in Au(001): First-principles calculations in terms of the fully relativistic spin-polarized screened KKR method, Phys. Rev. B **51**, 9552–9559 (1995)

21.84 H.J.G. Draaisma, W.J.M. de Jonge: Surface and volume anisotropy from dipole–dipole interactions in ultrathin ferromagnetic films, J. Appl. Phys. **64**, 3610 (1988)

21.85 P. Bruno: Dipolar magnetic surface anisotropy in ferromagnetic thin films with interfacial roughness, J. Appl. Phys. **64**(6), 3153–3156 (1988)

21.86 H.B. Callen, E. Callen: The present status of the temperature dependence of magnetocrystalline anisotropy, and the l(l+1)2 power law, J. Phys. Chem. Solids **27**(8), 1271–1285 (1966)

21.87 S. Chikazumi, C.D. Graham: *Physics of Ferromagnetism* (Oxford Univ. Press, Oxford 2009)

21.88 J.B. Staunton, L. Szunyogh, A. Buruzs, B.L. Gyorffy, S. Ostanin, L. Udvardi: Temperature dependence of magnetic anisotropy: An ab initio approach, Phys. Rev. B **74**, 144411 (2006)

21.89 Á. Buruzs, P. Weinberger, L. Szunyogh, L. Udvardi, P.I. Chleboun, A.M. Fischer, J.B. Staunton: Ab initio theory of temperature dependence of magnetic anisotropy in layered systems: Applications to thin Co films on Cu(100), Phys. Rev. B **76**, 064417 (2007)

21.90 P. Asselin, R.F.L. Evans, J. Barker, R.W. Chantrell, R. Yanes, O. Chubykalo-Fesenko, D. Hinzke, U. Nowak: Constrained Monte Carlo method and calculation of the temperature dependence of magnetic anisotropy, Phys. Rev. B **82**, 054415 (2010)

21.91 K. Yosida: *Theory of Magnetism*, Springer Series in Solid-State Sciences, Vol. 122 (Springer, Berlin, Heidelberg 1996)

21.92 M. Takahashi: Half-filled Hubbard model at low temperature, J. Phys. C **10**(8), 1289–7301 (1977)

21.93 M. Hoffmann, S. Blügel: Systematic derivation of realistic spin models for beyond-Heisenberg solids, Phys. Rev. B **101**(2), 024418 (2020)

21.94 I.E. Dzialoshinskii: Thermodynamic theory of "weak" ferromagnetism in antiferromagnetic substances, Sov. Phys. JETP **5**(6), 1259–1272 (1957)

21.95 D. Treves, S. Alexander: Observation of antisymmetric exchange interaction in yttrium orthoferrite, J. Appl. Phys. **33**(3), 1133–1134 (1962)

21.96 T. Moriya: Anisotropic superexchange interaction and weak ferromagnetism, Phys. Rev. **120**(1), 91 (1960)

21.97 S. Grytsiuk, J.-P. Hanke, M. Hoffmann, J. Bouaziz, O. Gomonay, G. Bihlmayer, S. Lounis, Y. Mokrousov, S. Blügel: Topological–chiral magnetic interactions driven by emergent orbital magnetism, Nat. Commun. **11**, 511 (2020)

21.98 S. Mankovsky, S. Polesya, H. Ebert: Extension of the standard Heisenberg Hamiltonian to multi-spin exchange interactions, Phys. Rev. B **101**(17), 174401 (2020)

21.99 A. Lászlóffy, L. Rózsa, K. Palotás, L. Udvardi, L. Szunyogh: Magnetic structure of monatomic Fe chains on Re(0001): Emergence of chiral multispin interactions, Phys. Rev. B **99**(18), 184430 (2019)

21.100 D.A. Smith: New mechanisms for magnetic anisotropy in localised S-state moment materials, J. Magn. Magn. Mater. **1**(3), 214–225 (1976)

21.101 A. Fert, P.M. Levy: Role of anisotropic exchange interactions in determining the properties of spin-glasses, Phys. Rev. Lett. **44**, 1538–1541 (1980)

21.102 M. Kataoka, O. Nakanishi, A. Yanase, J. Kanamori: Antisymmetric spin interaction in metals, J. Phys. Soc. Jpn. **53**(10), 3624–3633 (1984)

21.103 K.-W. Kim, H.-W. Lee, K.-J. Lee, M.D. Stiles: Chirality from interfacial spin-orbit coupling effects in magnetic bilayers, Phys. Rev. Lett. **111**, 216601 (2013)

21.104 A. Kundu, S. Zhang: Dzyaloshinskii–Moriya interaction mediated by spin-polarized band with

Rashba spin–orbit coupling, Phys. Rev. B **92**(9), 094434 (2015)
21.105 J. Bouaziz, M. dos Santos Dias, A. Ziane, M. Benakki, S. Blügel, S. Lounis: Chiral magnetism of magnetic adatoms generated by Rashba electrons, New J. Phys. **19**(2), 023010 (2017)
21.106 Y.A. Bychkov, E.I. Rashba: Oscillatory effects and the magnetic-susceptibility of carriers in inversion layers, J. Phys. C **17**(33), 6039–6045 (1984)
21.107 N. Hatano, R. Shirasaki, H. Nakamura: Non-Abelian gauge field theory of the spin-orbit interaction and a perfect spin filter, Phys. Rev. A **75**(3), 032107 (2007)
21.108 S.-H. Chen, C.-R. Chang: Non-Abelian spin-orbit gauge: Persistent spin helix and quantum square ring, Phys. Rev. B **77**(4), 045324 (2008)
21.109 A. Rückriegel, P. Kopietz: Spin currents, spin torques, and the concept of spin superfluidity, Phys. Rev. B **95**(10), 104436 (2017)
21.110 Y.-K. Park, D.-Y. Kim, J.-S. Kim, Y.-S. Nam, M.-H. Park, H.-C. Choi, B.-C. Min, S.-B. Choe: Experimental observation of the correlation between the interfacial Dzyaloshinskii–Moriya interaction and work function in metallic magnetic trilayers, NPG Asia Mater. **10**(10), 995–1001 (2018)
21.111 H. Jia, B. Zimmermann, G. Michalicek, G. Bihlmayer, S. Blügel: Electric dipole moment as descriptor for interfacial Dzyaloshinskii-Moriya interaction, Phys. Rev. Mater. **4**(2), 024405 (2020)
21.112 F. Freimuth, S. Blügel, Y. Mokrousov: Berry phase theory of Dzyaloshinskii–Moriya interaction and spin–orbit torques, J. Phys. Condens. Matter **26**(10), 104202 (2014)
21.113 H. Yang, O. Boulle, V. Cros, A. Fert, M. Chshiev: Controlling Dzyaloshinskii–Moriya interaction via chirality dependent layer stacking, insulator capping and electric field, Sci. Rep. **8**, 12356 (2018)
21.114 A. Hrabec, N.A. Porter, A. Wells, M.J. Benitez, G. Burnell, S. McVitie, D. McGrouther, T.A. Moore, C.H. Marrows: Measuring and tailoring the Dzyaloshinskii-Moriya interaction in perpendicularly magnetized thin films, Phys. Rev. B **90**(2), 020402(R) (2014)
21.115 S. Emori, E. Martinez, K.-J. Lee, H.-W. Lee, U. Bauer, S.-M. Ahn, P. Agrawal, D.C. Bono, G.S.D. Beach: Spin Hall torque magnetometry of Dzyaloshinskii domain walls, Phys. Rev. B **90**(18), 184427 (2014)
21.116 M. Belmeguenai, J.-P. Adam, Y. Roussigné, S. Eimer, T. Devolder, J.-V. Kim, S. Mourad Cherif, A. Stashkevich, A. Thiaville: Interfacial Dzyaloshinskii–Moriya interaction in perpendicularly magnetized Pt/Co/AlO_x ultrathin films measured by Brillouin light spectroscopy, Phys. Rev. B **91**, 180405(R) (2015)
21.117 H.T. Nembach, J.M. Shaw, M. Weiler, E. Jué, T.J. Silva: Linear relation between Heisenberg exchange and interfacial Dzyaloshinskii–Moriya interaction in metal films, Nat. Phys. **11**(10), 825 (2015)
21.118 M. Bode, M. Heide, K. von Bergmann, P. Ferriani, S. Heinze, G. Bihlmayer, A. Kubetzka, O. Pietzsch, S. Blugel, R. Wiesendanger: Chiral magnetic order at surfaces driven by inversion asymmetry, Nature **447**, 190–193 (2007)
21.119 P. Ferriani, K. von Bergmann, E.Y. Vedmedenko, S. Heinze, M. Bode, M. Heide, G. Bihlmayer, S. Blügel, R. Wiesendanger: Atomic-scale spin spiral with a unique rotational sense: Mn monolayer on W(001), Phys. Rev. Lett. **101**, 027201 (2008)
21.120 B. Santos, J.M. Puerta, J.I. Cerda, R. Stumpf, K. von Bergmann, R. Wiesendanger, M. Bode, K.F. McCarty, J. de la Figuera: Structure and magnetism of ultra-thin chromium layers on W(110), New J. Phys. **10**(1), 013005 (2008)
21.121 B. Schweflinghaus, B. Zimmermann, M. Heide, G. Bihlmayer, S. Blügel: Role of Dzyaloshinskii–Moriya interaction for magnetism in transition-metal chains at Pt step edges, Phys. Rev. B **94**, 024403 (2016)
21.122 J. Honolka, T.Y. Lee, K. Kuhnke, D. Repetto, V. Sessi, P. Wahl, A. Buchsbaum, P. Varga, S. Gardonio, C. Carbone, S.R. Krishnakumar, P. Gambardella, M. Komelj, R. Singer, M. Fähnle, K. Fauth, G. Schütz, A. Enders, K. Kern: Complex magnetic phase in submonolayer Fe stripes on Pt(997), Phys. Rev. B **79**, 104430 (2009)
21.123 M. Menzel, Y. Mokrousov, R. Wieser, J.E. Bickel, E. Vedmedenko, S. Blügel, S. Heinze, K. von Bergmann, A. Kubetzka, R. Wiesendanger: Information transfer by vector spin chirality in finite magnetic chains, Phys. Rev. Lett. **108**, 197204 (2012)
21.124 A.A. Khajetoorians, M. Steinbrecher, M. Ternes, M. Bouhassoune, M. dos Santos Dias, S. Lounis, J. Wiebe, R. Wiesendanger: Tailoring the chiral magnetic interaction between two individual atoms, Nat. Commun. **7**, 10620 (2016)
21.125 S. Mankovsky, S. Bornemann, J. Minár, S. Polesya, H. Ebert, J.B. Staunton, A.I. Lichtenstein: Effects of spin–orbit coupling on the spin structure of deposited transition-metal clusters, Phys. Rev. B **80**, 014422 (2009)
21.126 A. Antal, B. Lazarovits, L. Udvardi, L. Szunyogh, B. Újfalussy, P. Weinberger: First-principles calculations of spin interactions and the magnetic ground states of Cr trimers on Au(111), Phys. Rev. B **77**, 174429 (2008)
21.127 A. Kubetzka, O. Pietzsch, M. Bode, R. Wiesendanger: Spin-polarized scanning tunneling microscopy study of 360° walls in an external magnetic field, Phys. Rev. B **67**, 020401 (2003)
21.128 M. Heide, G. Bihlmayer, S. Blügel: Dzyaloshinskii–Moriya interaction accounting for the orientation of magnetic domains in ultrathin films: Fe/W(110), Phys. Rev. B **78**(14), 140403 (2008)
21.129 A. Thiaville, S. Rohart, E. Jué, V. Cros, A. Fert: Dynamics of Dzyaloshinskii domain walls in ultrathin magnetic films, Europhys. Lett. **100**(5), 57002 (2012)
21.130 U.K. Rößler, A.N. Bogdanov, C. Pfleiderer: Spontaneous skyrmion ground states in magnetic metals, Nature **442**(7104), 797 (2006)
21.131 S. Mühlbauer, B. Binz, F. Jonietz, C. Pfleiderer, A. Rosch, A. Neubauer, R. Georgii, P. Böni:

Skyrmion lattice in a chiral magnet, Science **323**(5916), 915–919 (2009)
21.132 X.Z. Yu, Y. Onose, N. Kanazawa, J.H. Park, J.H. Han, Y. Matsui, N. Nagaosa, Y. Tokura: Real-space observation of a two-dimensional skyrmion crystal, Nature **465**(7300), 901 (2010)
21.133 X.Z. Yu, N. Kanazawa, Y. Onose, K. Kimoto, W.Z. Zhang, S. Ishiwata, Y. Matsui, Y. Tokura: Near room-temperature formation of a skyrmion crystal in thin-films of the helimagnet FeGe, Nat. Mater. **10**(2), 106 (2011)
21.134 S. Heinze, K. Von Bergmann, M. Menzel, J. Brede, A. Kubetzka, R. Wiesendanger, G. Bihlmayer, S. Blügel: Spontaneous atomic-scale magnetic skyrmion lattice in two dimensions, Nat. Phys. **7**(9), 713 (2011)
21.135 N. Romming, C. Hanneken, M. Menzel, J.E. Bickel, B. Wolter, K. von Bergmann, A. Kubetzka, R. Wiesendanger: Writing and deleting single magnetic skyrmions, Science **341**(6146), 636–639 (2013)
21.136 C. Moreau-Luchaire, C. Moutafis, N. Reyren, J. Sampaio, C.A.F. Vaz, N. Van Horne, K. Bouzehouane, K. Garcia, C. Deranlot, P. Warnicke, P. Wohlhuter, J.M. George, M. Weigand, J. Raabe, V. Cros, A. Fert: Additive interfacial chiral interaction in multilayers for stabilization of small individual skyrmions at room temperature, Nat. Nanotechnol. **11**(8), 444 (2016)
21.137 O. Boulle, J. Vogel, H.X. Yang, S. Pizzini, D.D. Chaves, A. Locatelli, T.O. Mentes, A. Sala, L.D. Buda-Prejbeanu, O. Klein, M. Belmeguenai, Y. Roussigne, A. Stashkevich, S.M. Cherif, L. Aballe, M. Foerster, M. Chshiev, S. Auffret, I.M. Miron, G. Gaudin: Room-temperature chiral magnetic skyrmions in ultrathin magnetic nanostructures, Nat. Nanotechnol. **11**(5), 449–454 (2016)
21.138 Z. Luo, T. Phuong Dao, A. Hrabec, J. Vijayakumar, A. Kleibert, M. Baumgartner, E. Kirk, J. Cui, T. Savchenko, G. Krishnaswamy, L.J. Heyderman, P. Gambardella: Chirally coupled nanomagnets, Science **363**(6434), 1435–1439 (2019)
21.139 I. Turek, J. Kudrnovský, V. Drchal, P. Bruno: Exchange interactions, spin waves, and transition temperatures in itinerant magnets, Philos. Mag. **86**, 1713–1752 (2006)
21.140 C. Domb, D.L. Hunter: On the critical behaviour of ferromagnets, Proc. Phys. Soc. **86**(5), 1147 (1965)
21.141 R.B. Griffiths: Thermodynamic functions for fluids and ferromagnets near the critical point, Phys. Rev. **158**, 176–187 (1967)
21.142 S.V. Tyablikov: *Methods of Quantum Theory of Magnetism* (Plenum, San Diego 1967)
21.143 N. Metropolis, A.W. Rosenbluth, M.N. Rosenbluth, A.H. Teller, E. Teller: Equation of state calculations by fast computing machines, J. Chem. Phys. **21**, 1087–1092 (1953)
21.144 D.P. Landau, K. Binder: *A Guide to Monte Carlo Simulations in Statistical Physics* (Cambridge Univ. Press, Cambridge 2000)
21.145 N.D. Mermin, H. Wagner: Absence of ferromagnetism or antiferromagnetism in one- or two-dimensional isotropic Heisenberg models, Phys. Rev. Lett. **17**, 1133 (1966)
21.146 P. Bruno: Magnetization and Curie temperature of ferromagnetic ultrathin films: The influence of magnetic anisotropy and dipolar interactions, Mater. Res. Soc. Symp. Proc. **231**, 299 (1991)
21.147 R.P. Erickson, D.L. Mills: Anisotropy–driven long–range order in ultrathin ferromagnetic films, Phys. Rev. B **43**, 11527 (1991)
21.148 D.L. Mills: Thermodynamic properties of ultrathin ferromagnetic films. In: *Ultrathin Magnetic Structures*, Vol. I, ed. by J.A.C. Bland, B. Heinrich (Springer, Berlin, Heidelberg 1994) pp. 91–121
21.149 W. Dürr, D. Kerkmann, D. Pescia: Experimental advances in two-dimensional magnetism, Int. J. Mod. Phys. B **4**(03), 401–435 (1990)
21.150 G.S. Rushbrooke, G.A. Baker Jr., P.J. Wood: Heisenberg model. In: *Phase Transitions and Critical Phenomena*, Vol. 3, ed. by C. Domb, M.S. Green (Academic Press, New York 1974) p. 245
21.151 R.J. Glauber: Time-dependent statistics of the Ising model, J. Math. Phys. **4**, 294 (1963)
21.152 C. Domb, M.S. Green: *Phase Transitions and Critical Phenomena*, Vol. 3 (Academic Press, New York 1974)
21.153 P. Heller: Experimental investigations of critical phenomena, Rep. Prog. Phys. **30**(2), 731 (1967)
21.154 F.J. Dyson: Thermodynamic behavior of an ideal ferromagnet, Phys. Rev. **102**, 1230–1244 (1956)
21.155 U. Gradmann: Ferromagnetism near surfaces and in thin films, Appl. Phys. **3**(3), 161–178 (1974)
21.156 R. Jelitto: Zur spontanen Magnetisierung dünner ferromagnetischer Schichten, Z. Naturforsch. A **19**(13), 1581–1591 (1964)
21.157 S. Rusponi, T. Cren, N. Weiss, M. Epple, P. Buluschek, L. Claude, H. Brune: The remarkable difference between surface and step atoms in the magnetic anisotropy of two-dimensional nanostructures, Nat. Mater. **2**, 546–551 (2003)
21.158 P. Gambardella, H. Brune, S.S. Dhesi, P. Bencok, S.R. Krishnakumar, S. Gardonio, M. Veronese, C. Grazioli, C. Carbone: Paramagnetic Mn impurities on Ge and GaAs surfaces, Phys. Rev. B **72**(4), 045337 (2005)
21.159 W. Wernsdorfer: Classical and quantum magnetization reversal studied in nanometer-sized particles and clusters, Adv. Chem. Phys. **118**, 99–190 (2007)
21.160 R.W. Chantrell, N.Y. Ayoub, J. Popplewell: The low field susceptibility of a textured superparamagnetic system, J. Magn. Magn. Mater. **53**(1/2), 199–207 (1985)
21.161 O. Fruchart, P.-O. Jubert, C. Meyer, M. Klaua, J. Barthel, J. Kirschner: Vertical self-organization of epitaxial magnetic nanostructures, J. Magn. Magn. Mater. **239**(1-3), 224–227 (2002)
21.162 A.J. Freeman, R.Q. Wu: Electronic structure theory of surface, interface and thin-film magnetism, J. Magn. Magn. Mater. **100**(1), 497–514 (1991)
21.163 S. Handschuh: *Zusammenhang zwischen magnetischem Moment und Hyperfeinfeld an Grenzflächen von Eisenschichten: Experiment und Theorie*, PhD Thesis (Univ. Cologne, Cologne 1994)

21.164 M. Kleiber, M. Bode, R. Ravlić, N. Tezuka, R. Wiesendanger: Magnetic properties of the Cr(001) surface studied by spin-polarized scanning tunneling spectroscopy, J. Magn. Magn. Mater. **240**(1), 64–69 (2002)

21.165 S. Blügel, D. Pescia, P.H. Dederichs: Ferromagnetism versus antiferromagnetism of the Cr(001) surface, Phys. Rev. B **39**, 1392–1394 (1989)

21.166 G. Bihlmayer, T. Asada, S. Blügel: Electronic and magnetic structure of the (001)-surfaces of V, Cr, and V/Cr, Phys. Rev. B **62**, R11937 (2000)

21.167 T. Hänke, S. Krause, L. Berbil-Bautista, M. Bode, R. Wiesendanger, V. Wagner, D. Lott, A. Schreyer: Absence of spin-flip transition at the Cr(001) surface: A combined spin-polarized scanning tunneling microscopy and neutron scattering study, Phys. Rev. B **71**, 184407 (2005)

21.168 S. Ohnishi, C.L. Fu, A.J. Freeman: Local spin density total energy study of surface magnetism: V(100), J. Magn. Magn. Mater. **50**(2), 161–168 (1985)

21.169 I. Morrison, D.M. Bylander, L. Kleinman: Ferromagnetism of the Rh(001) surface, Phys. Rev. Lett. **71**, 1083–1086 (1993)

21.170 J.-H. Cho, M. Scheffler: Surface relaxation and ferromagnetism of Rh(001), Phys. Rev. Lett. **78**, 1299–1302 (1997)

21.171 A. Goldoni, A. Baraldi, G. Comelli, S. Lizzit, G. Paolucci: Experimental evidence of magnetic ordering at the Rh(100) surface, Phys. Rev. Lett. **82**, 3156–3159 (1999)

21.172 I. Turek, S. Blügel, J. Kudrnovský: Magnetic nature of (100) surfaces of bcc RuV, RhV, and PdV binary alloys, Phys. Rev. B **57**, R11065 (1998)

21.173 R. Bertacco, M. Cantoni, M. Riva, A. Tagliaferri, F. Ciccacci: Epitaxial growth and characterization of layered magnetic nanostructures, Appl. Surf. Sci. **252**(5), 1754–1764 (2005)

21.174 G.A. Prinz: Magnetic metal films on semiconductor substrates. In: *Ultrathin Magnetic Structures II*, ed. by B. Heinrich, J.A.C. Bland (Springer, Berlin, Heidelberg 1994)

21.175 S.A. Chambers: Epitaxial growth and properties of thin film oxides, Surf. Sci. Rep. **39**(5), 105–180 (2000)

21.176 L.W. Martin, Y.-H. Chu, R. Ramesh: Advances in the growth and characterization of magnetic, ferroelectric, and multiferroic oxide thin films, Mater. Sci. Eng. Rep. **68**(4), 89–133 (2010)

21.177 M. Sawicki, W. Stefanowicz, A. Ney: Sensitive SQUID magnetometry for studying nanomagnetism, Semicond. Sci. Technol. **26**(6), 064006 (2011)

21.178 Z.Q. Qiu, S.D. Bader: Surface magneto-optic Kerr effect, Rev. Sci. Instrum. **71**(3), 1243–1255 (2000)

21.179 R.M. Osgood III, S.D. Bader, B.M. Clemens, R.L. White, H. Matsuyama: Second-order magneto-optic effects in anisotropic thin films, J. Magn. Magn. Mater. **182**(3), 297–323 (1998)

21.180 C. Stamm, C. Murer, M. Berritta, J. Feng, M. Gabureac, P.M. Oppeneer, P. Gambardella: Magneto-optical detection of the spin Hall effect in Pt and W thin films, Phys. Rev. Lett. **119**(8), 087203 (2017)

21.181 B. Heinrich, J.F. Cochran: Ultrathin metallic magnetic films: Magnetic anisotropies and exchange interactions, Adv. Phys. **42**, 523 (1993)

21.182 J. Stöhr, H.-C. Siegmann: *Magnetism: From Fundamentals to Nanoscale Dynamics*, Springer Series in Solid-State Sciences, Vol. 152 (Springer, Berlin, Heidelberg 2007)

21.183 P. Gambardella, S.S. Dhesi, S. Gardonio, C. Grazioli, P. Ohresser, C. Carbone: Localized magnetic states of Fe, Co, and Ni impurities on alkali metal films, Phys. Rev. Lett. **88**, 047202 (2002)

21.184 A. Locatelli, E. Bauer: Recent advances in chemical and magnetic imaging of surfaces and interfaces by XPEEM, J. Phys. Condens. Matter **20**(9), 093002 (2008)

21.185 D. Rugar, H.J. Mamin, P. Guethner, S.E. Lambert, J.E. Stern, I. McFadyen, T. Yogi: Magnetic force microscopy: General principles and application to longitudinal recording media, J. Appl. Phys. **68**(3), 1169–1183 (1990)

21.186 H.J. Hug, B. Stiefel, P.J.A. van Schendel, A. Moser, R. Hofer, S. Martin, H.-J. Güntherodt, S. Porthun, L. Abelmann, J.C. Lodder, G. Bochi, R.C. O'Handley: Quantitative magnetic force microscopy on perpendicularly magnetized samples, J. Appl. Phys. **83**(11), 5609–5620 (1998)

21.187 H. Hopster, H.P. Oepen: *Magnetic Microscopy of Nanostructures* (Springer, Berlin, Heidelberg 2006)

21.188 O. Kazakova, R. Puttock, C. Barton, H. Corte-León, M. Jaafar, V. Neu, A. Asenjo: Frontiers of magnetic force microscopy, J. Appl. Phys. **125**(6), 060901 (2019)

21.189 L. Rondin, J.-P. Tetienne, T. Hingant, J.-F. Roch, P. Maletinsky, V. Jacques: Magnetometry with nitrogen-vacancy defects in diamond, Rep. Prog. Phys. **77**(5), 056503 (2014)

21.190 R. Schirhagl, K. Chang, M. Loretz, C.L. Degen: Nitrogen-vacancy centers in diamond: Nanoscale sensors for physics and biology, Annu. Rev. Phys. Chem. **65**(1), 83–105 (2014)

21.191 C.L. Degen, F. Reinhard, P. Cappellaro: Quantum sensing, Rev. Mod. Phys. **89**, 035002 (2017)

21.192 M. Bode: Spin-polarized scanning tunnelling microscopy, Rep. Prog. Phys. **66**(4), 523 (2003)

21.193 R. Wiesendanger: Spin mapping at the nanoscale and atomic scale, Rev. Mod. Phys. **81**, 1495–1550 (2009)

21.194 S. Loth, K. von Bergmann, C.P. Lutz, A.J. Heinrich: Spin-polarized spin excitation spectroscopy, New J. Phys. **12**, 125021 (2010)

21.195 C. Carbone, M. Veronese, P. Moras, S. Gardonio, C. Grazioli, P.H. Zhou, O. Rader, A. Varykhalov, C. Krull, T. Balashov, A. Mugarza, P. Gambardella, S. Lebègue, O. Eriksson, M.I. Katsnelson, A.I. Lichtenstein: Correlated electrons step by step: Itinerant-to-localized transition of fe impurities in free-electron metal hosts, Phys. Rev. Lett. **104**, 117601 (2010)

21.196 S. Blügel, P.H. Dederichs: Ferromagnetism and antiferromagnetism of 3d metal overlayers on noble-metal substrates, Europhys. Lett. **9**, 597 (1989)

21.197 S. Blügel: Strong ferromagnetism of 3d-metal overlayers on Pd(001), Europhys. Lett. **7**, 743 (1988)

21.198 S. Blügel: Ferromagnetism of 4d-metal monolayers on Ag and Au and Pd(001) surfaces, Europhys. Lett. **18**, 257 (1992)

21.199 S. Blügel: Two-dimensional ferromagnetism of 3d, 4d, and 5d transition metal monolayers on noble metal (001) substrates, Phys. Rev. Lett. **68**, 851–854 (1992)

21.200 J. Redinger, S. Blügel, R. Podloucky: Ferromagnetism of 4d and 5d transition-metal monolayers on Ag(111), Phys. Rev. B **51**, 13852 (1995)

21.201 J. Honolka, K. Kuhnke, L. Vitali, A. Enders, K. Kern, S. Gardonio, C. Carbone, S.R. Krishnakumar, P. Bencok, S. Stepanow, P. Gambardella: Absence of local magnetic moments in Ru and Rh impurities and clusters on Ag(100) and Pt(997), Phys. Rev. B **76**(14), 144412 (2007)

21.202 B. Újfalussy, L. Szunyogh, P. Weinberger: Magnetism of 4d and 5d adlayers on Ag(001) and Au(001): Comparison between a nonrelativistic and a fully relativistic approach, Phys. Rev. B **51**, 12836–12839 (1995)

21.203 H.J. Elmers, G. Liu, U. Gradmann: Magnetometry of the ferromagnetic monolayer Fe(110) on W(110) coated with Ag, Phys. Rev. Lett. **63**, 566–569 (1989)

21.204 M. Albrecht, U. Gradmann, T. Furubayashi, W.A. Harrison: Magnetic moments in rough Fe surfaces, Europhys. Lett. **20**(1), 65 (1992)

21.205 J. Korecki, M. Przybylski, U. Gradmann: Thermal variation and spatial distribution of local magnetization in ultrathin Fe(110) films, J. Magn. Magn. Mater. **89**(3), 325–334 (1990)

21.206 J.M. Tonnerre, E. Jal, E. Bontempi, N. Jaouen, M. Elzo, S. Grenier, H.L. Meyerheim, M. Przybylski: Depth-resolved magnetization distribution in ultra thin films by soft X-ray resonant magnetic reflectivity, Eur. Phys. J. Spec. Top. **208**(1), 177–187 (2012)

21.207 S. Hope, J. Lee, P. Rosenbusch, G. Lauhoff, J.A.C. Bland, A. Ercole, D. Bucknall, J. Penfold, H.J. Lauter, V. Lauter, R. Cubitt: Thickness dependence of the total magnetic moment per atom in the Cu/Ni/Cu/Si(001) system, Phys. Rev. B **55**, 11422–11431 (1997)

21.208 P. Ohresser, G. Ghiringhelli, O. Tjernberg, N.B. Brookes, M. Finazzi: Magnetism of nanostructures studied by x-ray magnetic circular dichroism: Fe on Cu(111), Phys. Rev. B **62**(9), 5803 (2000)

21.209 D. Li, M. Freitag, J. Pearson, Z.Q. Qiu, S.D. Bader: Magnetic phases of ultrathin Fe grown on Cu(100) as epitaxial wedges, Phys. Rev. Lett. **72**(19), 3112 (1994)

21.210 H.L. Meyerheim, J.-M. Tonnerre, L. Sandratskii, H.C.N. Tolentino, M. Przybylski, Y. Gabi, F. Yildiz, X.L. Fu, E. Bontempi, S. Grenier, J. Kirschner: New model for magnetism in ultrathin fcc Fe on Cu(001), Phys. Rev. Lett. **103**, 267202 (2009)

21.211 E. Bergter, U. Gradmann, R. Bergholz: Magnetometry of the Ni(111)/Cu(111) interface, Solid State Commun. **53**(7), 565–567 (1985)

21.212 U. Gradmann, R. Bergholz: Magnetization of Pd(111) films by contact with ferromagnetic Ni(111) films, Phys. Rev. Lett. **52**(9), 771 (1984)

21.213 B.T. Thole, P. Carra, F. Sette, G. van der Laan: X-ray circular dichroism as a probe of orbital magnetization, Phys. Rev. Lett. **68**, 1943–1946 (1992)

21.214 P. Carra, B.T. Thole, M. Altarelli, X. Wang: X-ray circular dichroism and local magnetic fields, Phys. Rev. Lett. **70**(5), 694–697 (1993)

21.215 C.T. Chen, Y.U. Idzerda, H.-J. Lin, N.V. Smith, G. Meigs, E. Chaban, G.H. Ho, E. Pellegrin, F. Sette: Experimental confirmation of the x-ray magnetic circular dichroism sum rules for iron and cobalt, Phys. Rev. Lett. **75**, 152–155 (1995)

21.216 A.N. Anisimov, M. Farle, P. Poulopoulos, W. Platow, K. Baberschke, P. Isberg, R. Wäppling, A.M.N. Niklasson, O. Eriksson: Orbital magnetism and magnetic anisotropy probed with ferromagnetic resonance, Phys. Rev. Lett. **82**(11), 2390 (1999)

21.217 Y. Wu, J. Stöhr, B.D. Hermsmeier, M.G. Samant, D. Weller: Enhanced orbital magnetic moment on Co atoms in Co/Pd multilayers: A magnetic circular x-ray dichroism study, Phys. Rev. Lett. **69**, 2307–2310 (1992)

21.218 F. Wilhelm, P. Poulopoulos, G. Ceballos, H. Wende, K. Baberschke, P. Srivastava, D. Benea, H. Ebert, M. Angelakeris, N.K. Flevaris, D. Niarchos, A. Rogalev, N.B. Brookes: Layer-resolved magnetic moments in Ni/Pt multilayers, Phys. Rev. Lett. **85**, 413–416 (2000)

21.219 J. Kohlhepp, H. Fritzsche, H.-J. Elmers, U. Gradmann: Magnetic polarization of epitaxial Cr and Pd by a Co(0001) substrate, J. Magn. Magn. Mater. **148**(1/2), 95–96 (1995)

21.220 M.G. Samant, J. Stöhr, S.S.P. Parkin, G.A. Held, B.D. Hermsmeier, F. Herman, M. Van Schilfgaarde, L.-C. Duda, D.C. Mancini, N. Wassdahl, R. Nakajima: Induced spin polarization in Cu spacer layers in Co/Cu multilayers, Phys. Rev. Lett. **72**, 1112–1115 (1994)

21.221 F. Wilhelm, P. Poulopoulos, A. Scherz, H. Wende, K. Baberschke, M. Angelakeris, N.K. Flevaris, J. Goulon, A. Rogalev: Interface magnetism in 3d/5d multilayers probed by X-ray magnetic circular dichroism, Phys. Status Solidi (a) **196**(1), 33–36 (2003)

21.222 S. Geprägs, S. Meyer, S. Altmannshofer, M. Opel, F. Wilhelm, A. Rogalev, R. Gross, S.T.B. Goennenwein: Investigation of induced Pt magnetic polarization in $Pt/Y_3Fe_5O_{12}$ bilayers, Appl. Phys. Lett. **101**(26), 262407 (2012)

21.223 T. Kuschel, C. Klewe, J.-M. Schmalhorst, F. Bertram, O. Kuschel, T. Schemme, J. Wollschläger, S. Francoual, J. Strempfer, A. Gupta, M. Meinert, G. Götz, D. Meier, G. Reiss: Static magnetic proximity effect in $Pt/NiFe_2O_4$ and Pt/Fe bilayers investigated by x-ray resonant magnetic reflectivity, Phys. Rev. Lett. **115**, 097401 (2015)

21.224 M. Collet, R. Mattana, J.-B. Moussy, K. Ollefs, S. Collin, C. Deranlot, A. Anane, V. Cros, F. Petroff, F. Wilhelm, A. Rogalev: Investigating magnetic

proximity effects at ferrite/Pt interfaces, Appl. Phys. Lett. **111**(20), 202401 (2017)
21.225 T. Kikkawa, M. Suzuki, J. Okabayashi, K. Uchida, D. Kikuchi, Z. Qiu: E.iji Saitoh: Detection of induced paramagnetic moments in Pt on $Y_3Fe_5O_{12}$ via x-ray magnetic circular dichroism, Phys. Rev. B **95**, 214416 (2017)
21.226 S.Y. Huang, X. Fan, D. Qu, Y.P. Chen, W.G. Wang, J. Wu, T.Y. Chen, J.Q. Xiao, C.L. Chien: Transport magnetic proximity effects in platinum, Phys. Rev. Lett. **109**, 107204 (2012)
21.227 L. Néel: Anisotropie magnétique superficielle et surstructures d'orientation, J. Phys. Radium **15**(4), 225–239 (1954)
21.228 P. Bruno, J.-P. Renard: Magnetic surface anisotropy of transition metal ultrathin films, Appl. Phys. A **49**(5), 499–506 (1989)
21.229 J.G. Gay, R. Richter: Spin anisotropy of ferromagnetic films, Phys. Rev. Lett. **56**, 2728–2731 (1986)
21.230 C. Li, A.J. Freeman, H.J.F. Jansen, C.L. Fu: Magnetic anisotropy in low-dimensional ferromagnetic systems: Fe monolayers on Ag(001), Au(001), and Pd(001) substrates, Phys. Rev. B **42**, 5433–5442 (1990)
21.231 G.H.O. Daalderop, P.J. Kelly, M.F.H. Schuurmans: Magnetic anisotropy of a free-standing Co monolayer and of multilayers which contain Co monolayers, Phys. Rev. B **50**, 9989 (1994)
21.232 K. Baberschke: The magnetism of nickel monolayers, Appl. Phys. A **62**(5), 417–427 (1996)
21.233 O. Hjortstam, K. Baberschke, J.M. Wills, B. Johansson, O. Eriksson: Magnetic anisotropy and magnetostriction in tetragonal and cubic Ni, Phys. Rev. B **55**(22), 15026 (1997)
21.234 D. Sander: The correlation between mechanical stress and magnetic anisotropy in ultrathin films, Rep. Prog. Phys. **62**(5), 809 (1999)
21.235 M. Weisheit, S. Fahler, A. Marty, Y. Souche, C. Poinsignon, D. Givord: Electric field-induced modification of magnetism in thin-film ferromagnets, Science **315**(5810), 349–351 (2007)
21.236 T. Maruyama, Y. Shiota, T. Nozaki, K. Ohta, N. Toda, M. Mizuguchi, A.A. Tulapurkar, T. Shinjo, M. Shiraishi, S. Mizukami, Y. Ando, Y. Suzuki: Large voltage-induced magnetic anisotropy change in a few atomic layers of iron, Nat. Nanotechnol. **4**(3), 158–161 (2009)
21.237 W.-G. Wang, M. Li, S. Hageman, C.L. Chien: Electric-field-assisted switching in magnetic tunnel junctions, Nat. Mater. **11**(1), 64 (2012)
21.238 P.F. Carcia, A.D. Meinhaldt, A. Suna: Perpendicular magnetic anisotropy in Pd/Co thin film layered structures, Appl. Phys. Lett. **47**(2), 178–180 (1985)
21.239 W.B. Zeper, F.J.A.M. Greidanus, P.F. Carcia, C.R. Fincher: Perpendicular magnetic anisotropy and magneto-optical Kerr effect of vapor-deposited Co/Pt-layered structures, J. Appl. Phys. **65**(12), 4971–4975 (1989)
21.240 S. Monso, B. Rodmacq, S. Auffret, G. Casali, F. Fettar, B. Gilles, B. Dieny, P. Boyer: Crossover from in-plane to perpendicular anisotropy in Pt/CoFe/AlO_x sandwiches as a function of Al oxidation: A very accurate control of the oxidation of tunnel barriers, Appl. Phys. Lett. **80**(22), 4157–4159 (2002)
21.241 H.X. Yang, M. Chshiev, B. Dieny, J.H. Lee, A. Manchon, K.H. Shin: First-principles investigation of the very large perpendicular magnetic anisotropy at Fe/MgO and Co/MgO interfaces, Phys. Rev. B **84**, 054401 (2011)
21.242 S. Baumann, F. Donati, S. Stepanow, S. Rusponi, W. Paul, S. Gangopadhyay, I.G. Rau, G.E. Pacchioni, L. Gragnaniello, M. Pivetta, J. Dreiser, C. Piamonteze, C.P. Lutz, R.M. Macfarlane, B.A. Jones, P. Gambardella, A.J. Heinrich, H. Brune: Origin of perpendicular magnetic anisotropy and large orbital moment in Fe atoms on MgO, Phys. Rev. Lett. **115**(23), 237202 (2015)
21.243 S. Ikeda, K. Miura, H. Yamamoto, K. Mizunuma, H.D. Gan, M. Endo, S. Kanai, J. Hayakawa, F. Matsukura, H. Ohno: A perpendicular-anisotropy CoFeB-MgO magnetic tunnel junction, Nat. Mater. **9**(9), 721–724 (2010)
21.244 P.J. Jensen, K.H. Bennemann: Magnetic structure of films: Dependence on anisotropy and atomic morphology, Surf. Sci. Rep. **61**(3), 129–199 (2006)
21.245 M.T. Johnson, P.J.H. Bloemen, F.J.A. Den Broeder, J.J. De Vries: Magnetic anisotropy in metallic multilayers, Rep. Prog. Phys. **59**(11), 1409 (1996)
21.246 G. Wastlbauer, J.A.C. Bland: Structural and magnetic properties of ultrathin epitaxial Fe films on GaAs(001) and related semiconductor substrates, Adv. Phys. **54**(2), 137–219 (2005)
21.247 A.T. Hindmarch: Interface magnetism in ferromagnetic metal–compound semiconductor hybrid structures, Spin **01**(01), 45–69 (2011)
21.248 A. Manchon, S. Pizzini, J. Vogel, V. Uhlír, L. Lombard, C. Ducruet, S. Auffret, B. Rodmacq, B. Dieny, M. Hochstrasser, G. Panaccione: X-ray analysis of the magnetic influence of oxygen in Pt/Co/AlO_x trilayers, J. Appl. Phys. **103**(7), 07–A912 (2008)
21.249 Y. Dahmane, S. Auffret, U. Ebels, B. Rodmacq, B. Dieny: Perpendicular magnetic anisotropy at Co/AlO_x interface, IEEE Trans. Magn. **44**(11), 2865–2867 (2008)
21.250 V.W. Guo, B. Lu, X. Wu, G. Ju, B. Valcu, D. Weller: A survey of anisotropy measurement techniques and study of thickness effect on interfacial and volume anisotropies in Co/Pt multilayer media, J. Appl. Phys. **99**(8), 08–E918 (2006)
21.251 K. Yakushiji, T. Saruya, H. Kubota, A. Fukushima, T. Nagahama, S. Yuasa, K. Ando: Ultrathin Co/Pt and Co/Pd superlattice films for MgO-based perpendicular magnetic tunnel junctions, Appl. Phys. Lett. **97**(23), 232508 (2010)
21.252 L.E. Nistor, B. Rodmacq, S. Auffret, A. Schuhl, M. Chshiev, B. Dieny: Oscillatory interlayer exchange coupling in MgO tunnel junctions with perpendicular magnetic anisotropy, Phys. Rev. B **81**, 220407 (2010)
21.253 M. Farle, B. Mirwald-Schulz, A.N. Anisimov, W. Platow, K. Baberschke: Higher-order magnetic anisotropies and the nature of the spin-reorientation transition in face-centered-tetragonal Ni(001)/Cu(001), Phys. Rev. B **55**(6), 3708 (1997)

21.254 A. Berger, U. Linke, H.P. Oepen: Symmetry-induced uniaxial anisotropy in ultrathin epitaxial cobalt films grown on Cu(1 1 13), Phys. Rev. Lett. **68**, 839–842 (1992)

21.255 R.K. Kawakami, E.J. Escorcia-Aparicio, Z.Q. Qiu: Symmetry-induced magnetic anisotropy in Fe films grown on stepped Ag(001), Phys. Rev. Lett. **77**(12), 2570 (1996)

21.256 D. Repetto, T.Y. Lee, S. Rusponi, J. Honolka, K. Kuhnke, V. Sessi, U. Starke, H. Brune, P. Gambardella, C. Carbone, A. Enders, K. Kern: Structure and magnetism of atomically thin Fe layers on flat and vicinal Pt surfaces, Phys. Rev. B **74**(5), 054408 (2006)

21.257 J.J. Krebs, B.T. Jonker, G.A. Prinz: Properties of Fe single-crystal films grown on (100) GaAs by molecular-beam epitaxy, J. Appl. Phys. **61**(7), 2596–2599 (1987)

21.258 Y.Z. Wu, C. Won, Z.Q. Qiu: Magnetic uniaxial anisotropy of Fe films grown on vicinal Ag(001), Phys. Rev. B **65**, 184419 (2002)

21.259 W. Weber, C.H. Back, A. Bischof, D. Pescia, R. Allenspach: Magnetic switching in cobalt films by adsorption of copper, Nature **374**(6525), 788–790 (1995)

21.260 W. Weber, C.H. Back, A. Bischof, C. Würsch, R. Allenspach: Morphology-induced oscillations of the magnetic anisotropy in ultrathin Co films, Phys. Rev. Lett. **76**, 1940–1943 (1996)

21.261 W. Weber, A. Bischof, R. Allenspach, C. Würsch, C.H. Back, D. Pescia: Oscillatory magnetic anisotropy and quantum well states in Cu/Co/Cu(100) films, Phys. Rev. Lett. **76**, 3424–3427 (1996)

21.262 J. Li, M. Przybylski, F. Yildiz, X.D. Ma, Y.Z. Wu: Oscillatory magnetic anisotropy originating from quantum well states in Fe films, Phys. Rev. Lett. **102**, 207206 (2009)

21.263 D.P. Pappas, K.-P. Kämper, H. Hopster: Reversible transition between perpendicular and in-plane magnetization in ultrathin films, Phys. Rev. Lett. **64**, 3179–3182 (1990)

21.264 R. Allenspach, A. Bischof: Magnetization direction switching in Fe/Cu(100) epitaxial films: Temperature and thickness dependence, Phys. Rev. Lett. **69**, 3385–3388 (1992)

21.265 A. Berger, H. Hopster: Nonequilibrium magnetization near the reorientation phase transition of Fe/Ag(100) films, Phys. Rev. Lett. **76**(3), 519 (1996)

21.266 U. Gradmann, J. Müller: Flat ferromagnetic, epitaxial 48Ni/52Fe(111) films of few atomic layers, Phys. Status Solidi (b) **27**(1), 313–324 (1968)

21.267 R. Bergholz, U. Gradmann: Structure and magnetism of oligatomic Ni(111)-films on Re(0001), J. Magn. Magn. Mater. **45**(2/3), 389–398 (1984)

21.268 G.A.T. Allan: Critical temperatures of Ising lattice films, Phys. Rev. B **1**, 352–356 (1970)

21.269 M.E. Fisher, M.N. Barber: Scaling theory for finite-size effects in the critical region, Phys. Rev. Lett. **28**, 1516–1519 (1972)

21.270 C. Domb: Critical temperature of finite systems in d dimensions, J. Phys. A **6**(9), 1296 (1973)

21.271 R. Zhang, R.F. Willis: Thickness-dependent Curie temperatures of ultrathin magnetic films: Effect of the range of spin-spin interactions, Phys. Rev. Lett. **86**(12), 2665 (2001)

21.272 U. Gradmann, M. Przybylski, H.J. Elmers, G. Liu: Ferromagnetism in the thermodynamically stable monolayer Fe(110) on W(110), coated by Ag, Appl. Phys. A **49**(6), 563–571 (1989)

21.273 G. Moulas, A. Lehnert, S. Rusponi, J. Zabloudil, C. Etz, S. Ouazi, M. Etzkorn, P. Bencok, P. Gambardella, P. Weinberger, H. Brune: High magnetic moments and anisotropies for Fe_xCo_{1-x} monolayers on Pt(111), Phys. Rev. B **78**(21), 214424 (2008)

21.274 M. Przybylski, U. Gradmann, J. Korecki: Magnetic hyperfine fields near the W(110)/Fe(110)-interface, J. Magn. Magn. Mater. **69**(2), 199–205 (1987)

21.275 N. Weber, K. Wagner, H.J. Elmers, J. Hauschild, U. Gradmann: Nanoscale spatial switching of magnetic anisotropy in pseudomorphic Fe(110) on W(110), Phys. Rev. B **55**, 14121–14124 (1997)

21.276 H.J. Elmers, J. Hauschild, H. Höche, U. Gradmann, H. Bethge, D. Heuer, U. Köhler: Submonolayer magnetism of Fe(110) on W(110): Finite width scaling of stripes and percolation between islands, Phys. Rev. Lett. **73**, 898–901 (1994)

21.277 H.J. Elmers, J. Hauschild, H. Fritzsche, G. Liu, U. Gradmann, U. Köhler: Magnetic frustration in ultrathin Fe films, Phys. Rev. Lett. **75**, 2031–2034 (1995)

21.278 J. Hauschild, H.J. Elmers, U. Gradmann: Dipolar superferromagnetism in monolayer nanostripes of Fe(110) on vicinal W(110) surfaces, Phys. Rev. B **57**, R677–R680 (1998)

21.279 H.J. Elmers, J. Hauschild, U. Gradmann: Reorientation of magnetization states in Fe-nanostripe arrays on stepped W(110) caused by adsorption of CO, H_2 and O_2, J. Magn. Magn. Mater. **198–199**, 222–224 (1999)

21.280 O. Pietzsch, A. Kubetzka, M. Bode, R. Wiesendanger: Real-space observation of dipolar antiferromagnetism in magnetic nanowires by spin-polarized scanning tunneling spectroscopy, Phys. Rev. Lett. **84**, 5212–5215 (2000)

21.281 M. Pratzer, H.J. Elmers, M. Bode, O. Pietzsch, A. Kubetzka, R. Wiesendanger: Atomic-scale magnetic domain walls in quasi-one-dimensional Fe nanostripes, Phys. Rev. Lett. **87**, 127201 (2001)

21.282 A. Kubetzka, M. Bode, O. Pietzsch, R. Wiesendanger: Spin-polarized scanning tunneling microscopy with antiferromagnetic probe tips, Phys. Rev. Lett. **88**, 057201 (2002)

21.283 S. Meckler, N. Mikuszeit, A. Preßler, E.Y. Vedmedenko, O. Pietzsch, R. Wiesendanger: Real-space observation of a right-rotating inhomogeneous cycloidal spin spiral by spin-polarized scanning tunneling microscopy in a triple axes vector magnet, Phys. Rev. Lett. **103**, 157201 (2009)

21.284 M. Przybylski, I. Kaufmann, U. Gradmann: Mössbauer analysis of ultrathin ferromagnetic Fe(110) films on W(110) coated by Ag, Phys. Rev. B **40**, 8631–8640 (1989)

21.285 M. Bode, R. Pascal, R. Wiesendanger: Scanning tunneling spectroscopy of Fe/W(110) using iron covered probe tips, J. Vac. Sci. Technol. A **15**(3), 1285–1290 (1997)

21.286 T. Flores, M. Hansen, M. Wuttig: Structure and growth of Mn on Cu(100), Surf. Sci. **279**, 251 (1992)

21.287 D. Tian, H. Li, S.C. Wu, F. Jona, P.M. Marcus: Atomic and electronic structure of thin films of Mn on Pd111, Phys. Rev. B **45**, 3749–3754 (1992)

21.288 S. Andrieu, H.M. Fischer, M. Piecuch, A. Traverse, J. Mimault: Structure of Mn films grown on (111) and (001) fcc Ir determined by EXAFS and the multiple-scattering approach, Phys. Rev. B **54**, 2822–2829 (1996)

21.289 D. Tian, A.M. Begley, F. Jona: New metastable phase of Mn by epitaxy on Cu111, Surf. Sci. **273**(1), L393–L398 (1992)

21.290 I.L. Grigorov, J.C. Walker: Structural and magnetic properties of Mn epitaxially grown on Cu(111) (abstract), J. Appl. Phys. **81**(8), 3907–3907 (1997)

21.291 I.L. Grigorov, J.C. Walker, M.E. Hawley, G.W. Brown, M. Lütt, M.R. Fitzsimmons: Structural and magnetic properties of "expanded" Mn, J. Appl. Phys. **83**(11), 7010–7012 (1998)

21.292 I.L. Grigorov, M.R. Fitzsimmons, I.-L. Siu, J.C. Walker: Observation and analysis of multidomain epitaxy of α-Mn on MgO(111), Phys. Rev. Lett. **82**, 5309–5312 (1999)

21.293 A.S. Arrott, B. Heinrich, S.T. Purcell, J.F. Cochran, K.B. Urquhart: Engineering magnetic materials on the atomic scale (invited), J. Appl. Phys. **61**(8), 3721–3728 (1987)

21.294 K. Ounadjela, P. Vennegues, Y. Henry, A. Michel, V. Pierron-Bohnes, J. Arabski: Structural changes in metastable epitaxial Co/Mn superlattices, Phys. Rev. B **49**, 8561–8573 (1994)

21.295 K. Zhang, M. Kuhn, U. Diebold: Growth and structure of ultrathin Cr films on Pt(111), Surf. Sci. **371**(2), 223–234 (1997)

21.296 M. Albrecht, J. Pohl, H. Wider, E.U. Malang, J. Köhler, K. Friemelt, E. Bucher: V and Cr on Ru surfaces, Surf. Sci. **397**(1), 354–360 (1998)

21.297 M. Sambi, G. Granozzi: Ultrathin V films on Pt(111): A structural study by means of X-ray photoelectron spectroscopy and diffraction, Surf. Sci. **426**(2), 235–250 (1999)

21.298 K. von Bergmann, A. Kubetzka, O. Pietzsch, R. Wiesendanger: Interface-induced chiral domain walls, spin spirals and skyrmions revealed by spin-polarized scanning tunneling microscopy, J. Phys. Condens. Matter **26**(39), 394002 (2014)

21.299 C.L. Gao, W. Wulfhekel, J. Kirschner: Revealing the 120° antiferromagnetic Néel structure in real space: One monolayer Mn on Ag(111), Phys. Rev. Lett. **101**, 267205 (2008)

21.300 S. Ouazi, A. Kubetzka, K. von Bergmann, R. Wiesendanger: Enhanced atomic-scale spin contrast due to spin friction, Phys. Rev. Lett. **112**, 076102 (2014)

21.301 J. Spethmann, S. Meyer, K. von Bergmann, R. Wiesendanger, S. Heinze, A. Kubetzka: Discovery of magnetic single- and triple-q states in Mn/Re(0001), Phys. Rev. Lett. **124**(22), 227203 (2020)

21.302 K. v. Bergmann, S. Heinze, M. Bode, E.Y. Vedmedenko, G. Bihlmayer, S. Blügel, R. Wiesendanger: Observation of a complex nanoscale magnetic structure in a hexagonal Fe monolayer, Phys. Rev. Lett. **96**, 167203 (2006)

21.303 K. von Bergmann, S. Heinze, M. Bode, G. Bihlmayer, S. Blügel, R. Wiesendanger: Complex magnetism of the Fe monolayer on Ir(111), New J. Phys. **9**(10), 396–396 (2007)

21.304 S. Heinze, M. Bode, A. Kubetzka, O. Pietzsch, X. Nie, S. Blügel, R. Wiesendanger: Real-space imaging of two-dimensional antiferromagnetism on the atomic scale, Science **288**, 1805 (2000)

21.305 Y.A. Izyumov: Modulated, or long-periodic, magnetic structures of crystals, Sov. Phys. Usp. **27**(11), 845–867 (1984)

21.306 B. Zimmermann, M. Heide, G. Bihlmayer, S. Blügel: First-principles analysis of a homochiral cycloidal magnetic structure in a monolayer Cr on W(110), Phys. Rev. B **90**(11), 115427 (2014)

21.307 J.P. Tetienne, T. Hingant, L.J. Martinez, S. Rohart, A. Thiaville, L.H. Diez, K. Garcia, J.P. Adam, J.V. Kim, J.F. Roch, I.M. Miron, G. Gaudin, L. Vila, B. Ocker, D. Ravelosona, V. Jacques: The nature of domain walls in ultrathin ferromagnets revealed by scanning nanomagnetometry, Nat. Commun. **6**, 6733 (2015)

21.308 G. Chen, J. Zhu, A. Quesada, J. Li, A.T. N'Diaye, Y. Huo, T.P. Ma, Y. Chen, H.Y. Kwon, C. Won, Z.Q. Qiu, A.K. Schmid, Y.Z. Wu: Novel chiral magnetic domain wall structure in Fe/Ni/Cu(001) films, Phys. Rev. Lett. **110**, 177204 (2013)

21.309 T.N.G. Meier, M. Kronseder, C.H. Back: Domain-width model for perpendicularly magnetized systems with Dzyaloshinskii–Moriya interaction, Phys. Rev. B **96**, 144408 (2017)

21.310 N. Mikuszeit, O. Boulle, I.M. Miron, K. Garello, P. Gambardella, G. Gaudin, L.D. Buda-Prejbeanu: Spin-orbit torque driven chiral magnetization reversal in ultrathin nanostructures, Phys. Rev. B **92**(14), 144424 (2015)

21.311 S. Emori, U. Bauer, S.-M. Ahn, E. Martinez, G.S.D. Beach: Current-driven dynamics of chiral ferromagnetic domain walls, Nat. Mater. **12**(7), 611–616 (2013)

21.312 K.-S. Ryu, L. Thomas, S.-H. Yang, S. Parkin: Chiral spin torque at magnetic domain walls, Nat. Nanotechnol. **8**(7), 527–533 (2013)

21.313 M. Baumgartner, P. Gambardella: Asymmetric velocity and tilt angle of domain walls induced by spin–orbit torques, Appl. Phys. Lett. **113**(24), 242402 (2018)

21.314 M. Baumgartner, K. Garello, J. Mendil, C.O. Avci, E. Grimaldi, C. Murer, J.X. Feng, M. Gabureac, C. Stamm, Y. Acremann, S. Finizio, S. Wintz, J. Raabe, P. Gambardella: Spatially and time-resolved magnetization dynamics driven by spin–orbit torques, Nat. Nanotechnol. **12**(10), 980–986 (2017)

21.315 S. Pizzini, J. Vogel, S. Rohart, L.D. Buda-Prejbeanu, E. Jué, O. Boulle, I.M. Miron, C.K. Safeer,

S. Auffret, G. Gaudin, A. Thiaville: Chirality-induced asymmetric magnetic nucleation in Pt/Co/AlO_x ultrathin microstructures, Phys. Rev. Lett. **113**(4), 047203 (2014)

21.316 C.K. Safeer, E. Jué, A. Lopez, L. Buda-Prejbeanu, S. Auffret, S. Pizzini, O. Boulle, I. Mihai Miron, G. Gaudin: Spin-orbit torque magnetization switching controlled by geometry, Nat. Nanotechnol. **11**(2), 143–146 (2016)

21.317 K. Zakeri, Y. Zhang, T.-H. Chuang, J. Kirschner: Magnon lifetimes on the Fe(110) surface: The role of spin–orbit coupling, Phys. Rev. Lett. **108**, 197205 (2012)

21.318 K. Di, B. Li Zhang, H. Siah Lim, S. Choon Ng, M. Hau Kuok, J. Yu, J. Yoon, X. Qiu, H. Yang: Direct observation of the Dzyaloshinskii–Moriya interaction in a Pt/Co/Ni film, Phys. Rev. Lett. **114**, 047201 (2015)

21.319 K. Everschor-Sitte, M. Sitte: Real-space Berry phases: Skyrmion soccer (invited), J. Appl. Phys. **115**(17), 172602 (2014)

21.320 M. Hoffmann, B. Zimmermann, G.P. Müller, D. Schürhoff, N.S. Kiselev, C. Melcher, S. Blügel: Antiskyrmions stabilized at interfaces by anisotropic Dzyaloshinskii–Moriya interactions, Nat. Commun. **8**(1), 308 (2017)

21.321 R.C. Sherwood, J.P. Remeika, H.J. Williams: Domain behavior in some transparent magnetic oxides, J. Appl. Phys. **30**(2), 217–225 (1959)

21.322 A.H. Bobeck, E.G. Spencer, L.G. Van Uitert, S.C. Abrahams, R.L. Barns, W.H. Grodkiewicz, R.C. Sherwood, P.H. Schmidt, D.H. Smith, E.M. Walters: Uniaxial magnetic garnets for domain wall "bubble" devices, Appl. Phys. Lett. **17**(3), 131–134 (1970)

21.323 A.P. Malozemoff, J.C. Slonczewski: *Magnetic Domain Walls in Bubble Materials: Advances in Materials and Device Research*, Vol. 1 (Academic Press, New York 2016)

21.324 P.J. Grundy, R.S. Tebble, D.C. Hothersall: Cylindrical domains observed in thin cobalt crystals, J. Phys. D **4**(1), 174 (1971)

21.325 B. Dupé, M. Hoffmann, C. Paillard, S. Heinze: Tailoring magnetic skyrmions in ultra-thin transition metal films, Nat. Commun. **5**, 4030 (2014)

21.326 B. Hardrat, A. Al-Zubi, P. Ferriani, S. Blügel, G. Bihlmayer, S. Heinze: Complex magnetism of iron monolayers on hexagonal transition metal surfaces from first principles, Phys. Rev. B **79**, 094411 (2009)

21.327 S. Woo, K. Litzius, B. Kruger, M.Y. Im, L. Caretta, K. Richter, M. Mann, A. Krone, R.M. Reeve, M. Weigand, P. Agrawal, I. Lemesh, M.A. Mawass, P. Fischer, M. Klaui, G.R.S.D. Beach: Observation of room-temperature magnetic skyrmions and their current-driven dynamics in ultrathin metallic ferromagnets, Nat. Mater. **15**(5), 501 (2016)

21.328 W.J. Jiang, P. Upadhyaya, W. Zhang, G.Q. Yu, M.B. Jungfleisch, F.Y. Fradin, J.E. Pearson, Y. Tserkovnyak, K.L. Wang, O. Heinonen, S.G.E. te Velthuis, A. Hoffmann: Blowing magnetic skyrmion bubbles, Science **349**(6245), 283–286 (2015)

21.329 S. Jaiswal, K. Litzius, I. Lemesh, F. Buttner, S. Finizio, J. Raabe, M. Weigand, K. Lee, J. Langer, B. Ocker, G. Jakob, G.S.D. Beach, M. Klaui: Investigation of the Dzyaloshinskii–Moriya interaction and room temperature skyrmions in W/CoFeB/MgO thin films and microwires, Appl. Phys. Lett. **111**(2), 022409 (2017)

21.330 J. Sampaio, V. Cros, S. Rohart, A. Thiaville, A. Fert: Nucleation, stability and current-induced motion of isolated magnetic skyrmions in nanostructures, Nat. Nanotechnol. **8**(11), 839 (2013)

21.331 N. Nagaosa, Y. Tokura: Topological properties and dynamics of magnetic skyrmions, Nat. Nanotechnol. **8**(12), 899 (2013)

21.332 R. Wiesendanger: Nanoscale magnetic skyrmions in metallic films and multilayers: A new twist for spintronics, Nat. Rev. Mater. **1**(7), 16044 (2016)

21.333 J. Ping Liu, Z. Zhang, G. Zhao: *Skyrmions: Topological Structures, Properties, and Applications* (CRC, Boca Raton 2016)

21.334 W. Jiang, G. Chen, K. Liu, J. Zang, S.G.E. te Velthuis, A. Hoffmann: Skyrmions in magnetic multilayers, Phys. Rep. **704**, 1–49 (2017)

21.335 T. Devolder, C. Chappert, V. Mathet, H. Bernas, Y. Chen, J.P. Jamet, J. Ferré: Magnetization reversal in irradiation-fabricated nanostructures, J. Appl. Phys. **87**(12), 8671–8681 (2000)

21.336 R. Hyndman, P. Warin, J. Gierak, J. Ferré, J.N. Chapman, J.P. Jamet, V. Mathet, C. Chappert: Modification of Co/Pt multilayers by gallium irradiation—Part 1: The effect on structural and magnetic properties, J. Appl. Phys. **90**(8), 3843–3849 (2001)

21.337 T. Devolder, J. Ferré, C. Chappert, H. Bernas, J.-P. Jamet, V. Mathet: Magnetic properties of He^+-irradiated Pt/Co/Pt ultrathin films, Phys. Rev. B **64**, 064415 (2001)

21.338 R. Lavrijsen, J.H. Franken, J.T. Kohlhepp, H.J.M. Swagten, B. Koopmans: Controlled domain-wall injection in perpendicularly magnetized strips, Appl. Phys. Lett. **96**(22), 222502 (2010)

21.339 J.H. Franken, M. Herps, H.J.M. Swagten, B. Koopmans: Tunable chiral spin texture in magnetic domain-walls, Sci. Rep. **4**, 5248 (2014)

21.340 C. Bi, Y. Liu, T. Newhouse-Illige, M. Xu, M. Rosales, J.W. Freeland, O. Mryasov, S. Zhang, S.G.E. te Velthuis, W.G. Wang: Reversible control of Co magnetism by voltage-induced oxidation, Phys. Rev. Lett. **113**, 267202 (2014)

21.341 M. Schott, A. Bernand-Mantel, L. Ranno, S. Pizzini, J. Vogel, H. Béa, C. Baraduc, S. Auffret, G. Gaudin, D. Givord: The skyrmion switch: Turning magnetic skyrmion bubbles on and off with an electric field, Nano Lett. **17**(5), 3006–3012 (2017)

21.342 T. Srivastava, M. Schott, R. Juge, V. Křižáková, M. Belmeguenai, Y. Roussigné, A. Bernand-Mantel, L. Ranno, S. Pizzini, S.-M. Chérif, A. Stashkevich, S. Auffret, O. Boulle, G. Gaudin, M. Chshiev, C. Baraduc, H. Béa: Large-voltage tuning of Dzyaloshinskii–Moriya interactions: A route to-

ward dynamic control of skyrmion chirality, Nano Lett. **18**(8), 4871–4877 (2018)
21.343 J.H. Franken, H.J.M. Swagten, B. Koopmans: Shift registers based on magnetic domain wall ratchets with perpendicular anisotropy, Nat. Nanotechnol. **7**, 499 (2012)
21.344 Z. Luo, A. Hrabec, T.P. Dao, G. Sala, S. Finizio, J. Feng, S. Mayr, J. Raabe, P. Gambardella, L.J. Heyderman: Current-driven magnetic domain-wall logic, Nature **579**(7798), 214–218 (2020)
21.345 M. Bander, D.L. Mills: Critical temperature in 2D, Phys. Rev. B **38**, 12015 (1988)
21.346 A. Vindigni, A. Rettori, M.G. Pini, C. Carbone, P. Gambardella: Finite-sized Heisenberg chains and magnetism of one-dimensional metal systems, Appl. Phys. A **82**(3), 385–394 (2006)
21.347 D.S.G. Bauer, P. Mavropoulos, S. Lounis, S. Blügel: Thermally activated magnetization reversal in monatomic magnetic chains on surfaces studied by classical atomistic spin-dynamics simulations, J. Phys. Condens. Matter **23**(39), 394204 (2011)
21.348 L.D. Landau, E.M. Lifshitz: *Statistical Physics*, Vol. 5 (Pergamon, New York 1959)
21.349 L.J. de Jongh, A.R. Miedema: Experiments on simple magnetic model systems, Adv. Phys. **23**, 1–260 (1974)
21.350 D. Welz: Zero-point fluctuation in quasi one-dimensional antiferromagnets: Theory and experiment, J. Phys. Condens. Matter **5**(22), 3643–3652 (1993)
21.351 P. Gambardella, M. Blanc, L. Burgi, K. Kuhnke, K. Kern: Co growth on Pt(997): From monatomic chains to monolayer completion, Surf. Sci. **449**(1–3), 93–103 (2000)
21.352 P. Gambardella, M. Blanc, H. Brune, K. Kuhnke, K. Kern: One-dimensional metal chains on Pt vicinal surfaces, Phys. Rev. B **61**(3), 2254–2262 (2000)
21.353 D.W. Hone, P.M. Richards: One- and two-dimensional magnetic systems, Ann. Rev. Mater. Sci. **4**, 337 (1974)
21.354 A. Caneschi, D. Gatteschi, N. Lalioti, C. Sangregorio, R. Sessoli, G. Venturi, A. Vindigni, A. Rettori, M.G. Pini, M.A. Novak: Cobalt(II)-nitronyl nitroxide chains as molecular magnetic nanowires, Angew. Chem. Int. Ed. **40**, 1760 (2001)
21.355 R. Dingle, M.E. Lines, S.L. Holt: Linear-chain antiferromagnetism in $[(CH_3)_4N][MnCl_3]$, Phys. Rev. **187**, 643 (1969)
21.356 K.S. Pedersen, A. Vindigni, R. Sessoli, C. Coulon, R. Clérac: Single-chain magnets. In: *Molecular Magnetic Materials: Concepts and Applications*, ed. by B. Sieklucka, D. Pinkowicz (Wiley, Weinheim 2016) pp. 131–159
21.357 P. Gambardella: Magnetism in monatomic metal wires, J. Phys. Condens. Matter **15**(34), S2533–S2546 (2003)
21.358 C.F. Hirjibehedin, C.P. Lutz, A.J. Heinrich: Spin-coupling in engineered atomic structures, Science **312**, 1021 (2006)
21.359 S. Loth, S. Baumann, C.P. Lutz, D.M. Eigler, A.J. Heinrich: Bistability in atomic-scale antiferromagnets, Science **335**(6065), 196–199 (2012)
21.360 F.J. Himpsel, J.E. Ortega, G.J. Mankey, R.F. Willis: Magnetic nanostructures, Adv. Phys. **47**, 511 (1998)
21.361 P. Gambardella, K. Kern: Ni growth on vicinal Pt(111): Low temperature exchange and formation of ordered surface alloys, Surf. Sci. **475**(1–3), L229–L234 (2001)
21.362 P. Gambardella, H. Brune, K. Kern, V.I. Marchenko: Equilibrium island-size distribution in one dimension, Phys. Rev. B **73**(24), 245425 (2006)
21.363 S. Shiraki, H. Fujisawa, M. Nantoh, M. Kawai: The growth of Fe, Ni and Co on vicinal Au(111) surfaces, Appl. Surf. Sci. **237**, 284 (2004)
21.364 T.F. Mocking, P. Bampoulis, N. Oncel, B. Poelsema, H.J.W. Zandvliet: Electronically stabilized nanowire growth, Nat. Commun. **4**, 2387 (2013)
21.365 F. Picaud, C. Ramseyer, C. Girardet, P. Jensen: Confinement effects on the growth of adsorbates: Interpretation of the formation of monoatomic Ag wires on Pt(997), Phys. Rev. B **61**, 16154 (2000)
21.366 F.J. Himpsel, K.N. Altmann, R. Bennewitz, J.N. Crain, A. Kirakosian, J.-L. Lin, J.L. McChesney: One-dimensional electronic states at surfaces, J. Phys. Condens. Matter **13**, 11097 (2001)
21.367 F.J. Himpsel, J.E. Ortega: Edge state and terrace state for Cu on W(331) and W(110), Phys. Rev. B **50**, 4992 (1994)
21.368 J. de la Figuera, M.A. Huerta-Garnica, J.E. Prieto, C. Ocal, R. Miranda: Fabrication of magnetic quantum wires by step–flow growth of cobalt on copper surfaces, Appl. Phys. Lett. **66**, 1006 (1995)
21.369 E. Hahn, H. Schief, V. Marsico, A. Fricke, K. Kern: Orientational instability of vicinal Pt surfaces close to (111), Phys. Rev. Lett. **72**, 3378 (1994)
21.370 J. Shen, R. Skomski, M. Klaua, H. Jenniches, S. Sundar Manoharan, J. Kirschner: Magnetism in one dimension: Fe on Cu(111), Phys. Rev. B **56**, 2340 (1997)
21.371 J. Shen, M. Klaua, P. Ohresser, H. Jenniches, J. Barthel, C.V. Mohan, J. Kirschner: Structural and magnetic phase transitions of Fe on stepped Cu(111), Phys. Rev. B **56**, 11134 (1997)
21.372 H. Fujisawa, S. Shiraki, M. Furukawa, M. Nantoh, M. Kawai, T. Nakamura, T. Muro: Electronic and magnetic structures of Fe on a vicinal Au(111) surface, J. Electron Spectrosc. Relat. Phenom. **144**, 519 (2005)
21.373 D. Li, B. Roldan Cuenya, J. Pearson, S.D. Bader, W. Keune: Magnetism of step-decorated Fe on Pd(110), Phys. Rev. B **64**, 144410 (2001)
21.374 C. Yu, D. Li, J. Pearson, S.D. Bader: Alignment of self-assembled magnetic nanostructures: Co dot chains and stripes on grooved Ru(0001), Appl. Phys. Lett. **79**, 3848 (2001)
21.375 L. Yan, M. Przybylski, Y. Lu, W.H. Wang, J. Barthel, J. Kirschner: Fabrication and uniaxial magnetic anisotropy of Co nanowires on a Pd(110) surface, Appl. Phys. Lett. **86**, 102503 (2005)
21.376 P. Gambardella, M. Blanc, K. Kuhnke, K. Kern, F. Picaud, C. Ramseyer, C. Girardet, C. Barreteau, D. Spanjaard, M.C. Desjonqueres: Growth of composition-modulated Ag/Co wires on Pt(997), Phys. Rev. B **64**(4), 45404 (2001)

21.377 W. Essolaani, F. Picaud, C. Ramseyer, P. Gambardella, M. Said, D. Spanjaard, M.C. Desjonqueres: Formation of one-dimensional ordered alloy at step edges: An atomistic study of the (2×1) Ni-Pt alloy on the Pt(997) surface, Surf. Sci. **605**(9/10), 917–922 (2011)

21.378 F. Li, F. Allegretti, S. Surnev, F.P. Netzer: Oxide–metal nanowires by oxidation of a one-dimensional Mn-Pd alloy: Stability and reactivity, Langmuir **26**(21), 16474–16480 (2010)

21.379 L.-Y. Ma, A. Picone, M. Wagner, S. Surnev, G. Barcaro, A. Fortunelli, F.P. Netzer: Structure and electronic properties of CoO nanostructures on a vicinal Pd(100) surface, J. Phys. Chem. C **117**(36), 18464–18474 (2013)

21.380 P. Ferstl, L. Hammer, C. Sobel, M. Gubo, K. Heinz, M.A. Schneider, F. Mittendorfer, J. Redinger: Self-organized growth, structure, and magnetism of monatomic transition-metal oxide chains, Phys. Rev. Lett. **117**, 046101 (2016)

21.381 J. Dorantes-Dávila, G.M. Pastor: Magnetic anisotropy of one-dimensional nanostructures of transition metals, Phys. Rev. Lett. **81**, 208 (1998)

21.382 L. Zhou, D. Wang, Y. Kawazoe: Orbital correlation and magnetocrystalline anisotropy in one-dimensional transition-metal systems, Phys. Rev. B **60**, 9545 (1999)

21.383 R. Félix-Medina, J. Dorantes-Dávila, G.M. Pastor: Spin moments, orbital moments and magnetic anisotropy of finite-length Co wires deposited on Pd(110), New J. Phys. **4**, 100 (2002)

21.384 B. Lazarovits, L. Szunyogh, P. Weinberger: Magnetic properties of finite Co chains on Pt(111), Phys. Rev. B **67**, 024415 (2003)

21.385 A.B. Shick, F. Máca, P.M. Oppeneer: Anomalous ferromagnetism of a monatomic Co wire at the Pt(111) surface step edge, Phys. Rev. B **69**, 212410 (2004)

21.386 M. Weinert, A.J. Freeman: Magnetism of linear chains, J. Magn. Magn. Mater. **38**, 23 (1983)

21.387 D. Spišák, J. Hafner: Reconstruction and magnetic structure of ultrathin γ-Fe films on Cu(111) Phys, Rev. B **67**, 134434 (2003)

21.388 Y. Mokrousov, G. Bihlmayer, S. Blügel, S. Heinze: Magnetic order and exchange interactions in monoatomic 3*d* transition-metal chains, Phys. Rev. B **75**, 104413 (2007)

21.389 J. Hong, R.Q. Wu: First principles calculations of magnetic anisotropy energy of Co monatomic wires, Phys. Rev. B **67**, 020406(R) (2003)

21.390 J. Hong, R.Q. Wu: Magnetic properties of Co nanochains, Phys. Rev. B **70**, 060406 (2004)

21.391 B. Újfalussy, B. Lazarovits, L. Szunyogh, G.M. Stocks, P. Weinberger: Ab initio spin dynamics applied to nanoparticles: Canted magnetism of a finite Co chain along a Pt(111) surface step edge, Phys. Rev. B **70**, 100404 (2004)

21.392 S. Baud, C. Ramseyer, G. Bihlmayer, S. Blügel: Relaxation effects on the magnetism of decorated step edges: Co/Pt(664), Phys. Rev. B **73**, 104427 (2006)

21.393 A. Dallmeyer, C. Carbone, W. Eberhardt, C. Pampuch, O. Rader, W. Gudat, P. Gambardella, K. Kern: Electronic states and magnetism of monatomic Co and Cu wires, Phys. Rev. B **61**, R5133 (2000)

21.394 C.M. Schneider, J. Kirschner: Magnetism at surfaces and in Ultrathin films. In: *Electronic Structure*, Handbook of Surface Science, Vol. 2, ed. by K. Horn, M. Scheffler (Elsevier, Amsterdam 2000) pp. 511–668

21.395 W. Clemens, T. Kachel, O. Rader, E. Vescovo, S. Blügel, C. Carbone, W. Eberhardt: Quantum size effects and the enhancement of the exchange splitting in ultrathin Co overlayers on Cu(100), Solid State Commun. **81**(9), 739–744 (1992)

21.396 P. Gambardella, A. Dallmeyer, K. Maiti, M.C. Malagoli, S. Rusponi, P. Ohresser, W. Eberhardt, C. Carbone, K. Kern: Oscillatory magnetic anisotropy in one-dimensional atomic wires, Phys. Rev. Lett. **93**(7), 077203 (2004)

21.397 M. Blume, P. Heller, N.A. Lurie: Classical one-dimensional Heisenberg magnet in an applied field, Phys. Rev. B **11**, 4483 (1975)

21.398 A.J. Heinrich, J.A. Gupta, C.P. Lutz, D.M. Eigler: Single-atom spin-flip spectroscopy, Science **306**, 466 (2004)

21.399 S. Loth, K. von Bergmann, M. Ternes, A.F. Otte, C.P. Lutz, A.J. Heinrich: Controlling the state of quantum spins with electric currents, Nat. Phys. **6**, 340 (2010)

21.400 A. Spinelli, B. Bryant, F. Delgado, J. Fernandez-Rossier, A.F. Otte: Imaging of spin waves in atomically designed nanomagnets, Nat. Mater. **13**(8), 782 (2014)

21.401 J. Lagoute, C. Nacci, S. Fölsch: Doping of monatomic Cu chains with single Co atoms, Phys. Rev. Lett. **98**, 146804 (2007)

21.402 N. Néel, R. Berndt, J. Kröger, T.O. Wehling, A.I. Lichtenstein, M.I. Katsnelson: Two-site Kondo effect in atomic chains, Phys. Rev. Lett. **107**, 106804 (2011)

21.403 A.Y. Kitaev: Unpaired Majorana fermions in quantum wires, Phys. Usp. **44**(10S), 131 (2001)

21.404 J. Li, H. Chen, I.K. Drozdov, A. Yazdani, B.A. Bernevig, A.H. MacDonald: Topological superconductivity induced by ferromagnetic metal chains, Phys. Rev. B **90**(23), 235433 (2014)

21.405 S. Nadj-Perge, I.K. Drozdov, J. Li, H. Chen, S. Jeon, J. Seo, A.H. MacDonald, B.A. Bernevig, A. Yazdani: Observation of Majorana fermions in ferromagnetic atomic chains on a superconductor, Science **346**(6209), 602–607 (2014)

21.406 M. Ruby, B.W. Heinrich, Y. Peng, F. von Oppen, K.J. Franke: Exploring a proximity-coupled Co chain on Pb(110) as a possible Majorana platform, Nano Lett. **17**(7), 4473–4477 (2017)

21.407 B.C. Stipe, M.A. Rezaei, W. Ho: Single-molecule vibrational spectroscopy and microscopy, Science **280**(5370), 1732–1735 (1998)

21.408 S. Holzberger, T. Schuh, S. Blügel, S. Lounis, W. Wulfhekel: Parity effect in the ground state localization of antiferromagnetic chains coupled to a ferromagnet, Phys. Rev. Lett. **110**, 157206 (2013)

21.409 C.F. Hirjibehedin, C.Y. Lin, A.F. Otte, M. Ternes, C.P. Lutz, B.A. Jones, A.J. Heinrich: Large magnetic anisotropy of a single atomic spin embedded in a surface molecular network, Science **317**, 1199 (2007)

21.410 J.R. Friedman, M.P. Sarachik, J. Tejada, R. Ziolo: Macroscopic measurement of resonant magnetization tunneling in high-spin molecules, Phys. Rev. Lett. **76**(20), 3830 (1996)

21.411 B. Bryant, A. Spinelli, J.J.T. Wagenaar, M. Gerrits, A.F. Otte: Local control of single atom magnetocrystalline anisotropy, Phys. Rev. Lett. **111**(12), 127203 (2013)

21.412 L. Zhou, J. Wiebe, S. Lounis, E. Vedmedenko, F. Meier, S. Blügel, P.H. Dederichs, R. Wiesendanger: Strength and directionality of surface RKKY-interaction mapped on the atomic scale, Nat. Phys. **6**, 187 (2010)

21.413 A. Ako Khajetoorians, J. Wiebe, B. Chilian, R. Wiesendanger: Realizing all-spin based logic operations atom by atom, Science **332**(6033), 1062–1064 (2011)

21.414 F. Donati, S. Rusponi, S. Stepanow, C. Wackerlin, A. Singha, L. Persichetti, R. Baltic, K. Diller, F. Patthey, E. Fernandes, J. Dreiser, Z. Sljivancanin, K. Kummer, C. Nistor, P. Gambardella, H. Brune: Magnetic remanence in single atoms, Science **352**(6283), 318–321 (2016)

21.415 W. Wernsdorfer: Classical and quantum magnetization reversal studied in nanometer-sized particles and clusters, Adv. Chem. Phys. **118**, 99 (2001)

21.416 W. Wernsdorfer: Quantum dynamics in molecular nanomagnets, C. R. Chim. **11**(10), 1086–1109 (2008)

21.417 J.S. Miller, D. Gatteschi: Molecule-based magnets, Chem. Soc. Rev. **40**, 3065–3066 (2011)

21.418 F.D. Natterer, K. Yang, W. Paul, P. Willke, T. Choi, T. Greber, A.J. Heinrich, C.P. Lutz: Reading and writing single-atom magnets, Nature **543**, 226 (2017)

21.419 K. Yang, Y. Bae, W. Paul, F.D. Natterer, P. Willke, J.L. Lado, A. Ferrón, T. Choi, J. Fernández-Rossier, A.J. Heinrich, C.P. Lutz: Engineering the eigenstates of coupled spin-1/2 atoms on a surface, Phys. Rev. Lett. **119**, 227206 (2017)

21.420 P. Willke, W. Paul, F.D. Natterer, K. Yang, Y. Bae, T. Choi, J. Fernández-Rossier, A.J. Heinrich, C.P. Lutz: Probing quantum coherence in single-atom electron spin resonance, Sci. Adv. **4**(2), eaaq1543 (2018)

21.421 A. Mugarza, C. Krull, R. Robles, S. Stepanow, G. Ceballos, P. Gambardella: Spin coupling and relaxation inside molecule-metal contacts, Nat. Commun. **2**, 490 (2011)

21.422 J.-P. Gauyacq, N. Lorente, F.D. Novaes: Excitation of local magnetic moments by tunneling electrons, Prog. Surf. Sci. **87**(5–8), 63–107 (2012)

21.423 S. Loth, M. Etzkorn, C.P. Lutz, D.M. Eigler, A.J. Heinrich: Measurement of fast electron spin relaxation times with atomic resolution, Science **329**, 1628 (2010)

21.424 Y. Manassen, R.J. Hamers, J.E. Demuth, A.J. Castellano Jr.: Direct observation of the precession of individual paramagnetic spins on oxidized silicon surfaces, Phys. Rev. Lett. **62**, 2531–2534 (1989)

21.425 T.S. Seifert, S. Kovarik, C. Nistor, L. Persichetti, S. Stepanow, P. Gambardella: Single-atom electron paramagnetic resonance in a scanning tunneling microscope driven by a radio-frequency antenna at 4 K, Phys. Rev. Res. **2**(1), 013032 (2020)

21.426 T. Choi, W. Paul, S. Rolf-Pissarczyk, A.J. Macdonald, F.D. Natterer, K. Yang, P. Willke, C.P. Lutz, A.J. Heinrich: Atomic-scale sensing of the magnetic dipolar field from single atoms, Nat. Nanotechnol. **12**, 420 (2017)

21.427 H. Brune, M. Giovannini, K. Bromann, K. Kern: Self-organized growth of nanostructure arrays on strain relief patterns, Nature **394**, 451 (1998)

21.428 P.W. Anderson: Localized magnetic states in metals, Phys. Rev. **124**, 41 (1961)

21.429 P. Nozieres, A. Blandin: Kondo effect in real metals, J. Phys. **41**(3), 193–211 (1980)

21.430 J. Li, W.D. Schneider, R. Berndt, B. Delley: Kondo scattering observed at a single magnetic impurity, Phys. Rev. Lett. **80**, 2893 (1998)

21.431 V. Madhavan, W. Chen, T. Jamneala, M.F. Crommie, N.S. Wingreen: Tunneling into a single magnetic atom: Spectroscopic evidence of the Kondo resonance, Science **280**(5363), 567–569 (1998)

21.432 P. Gambardella, S. Rusponi, T. Cren, N. Weiss, H. Brune: Magnetic anisotropy from single atoms to large monodomain islands of Co/Pt(111), C. R. Phys. **6**(1), 75–87 (2005)

21.433 P. Gambardella, S. Stepanow, A. Dmitriev, J. Honolka, F.M.F. de Groot, M. Lingenfelder, S. Sen Gupta, D.D. Sarma, P. Bencok, S. Stanescu, S. Clair, S. Pons, N. Lin, A.P. Seitsonen, H. Brune, J.V. Barth, K. Kern: Supramolecular control of the magnetic anisotropy in two-dimensional high-spin Fe arrays at a metal interface, Nat. Mater. **8**(3), 189–193 (2009)

21.434 J. Bartolomé, F. Bartolomé, L.M. Garcia, G. Filoti, T. Gredig, C.N. Colesniuc, I.K. Schuller, J.C. Cezar: Highly unquenched orbital moment in textured Fe-phthalocyanine thin films, Phys. Rev. B **81**(19), 195405 (2010)

21.435 S. Stepanow, P.S. Miedema, A. Mugarza, G. Ceballos, P. Moras, J.C. Cezar, C. Carbone, F.M.F. de Groot, P. Gambardella: Mixed-valence behavior and strong correlation effects of metal phthalocyanines adsorbed on metals, Phys. Rev. B **83**, 220401 (2011)

21.436 S. Stepanow, A.L. Rizzini, C. Krull, J. Kavich, J.C. Cezar, F. Yakhou-Harris, P.M. Sheverdyaeva, P. Moras, C. Carbone, G. Ceballos, A. Mugarza, P. Gambardella: Spin tuning of electron-doped metal-phthalocyanine layers, J. Am. Chem. Soc. **136**(14), 5451–5459 (2014)

21.437 J. Ibañez-Azpiroz, M. dos Santos Dias, S. Blügel, S. Lounis: Zero-point spin-fluctuations of single adatoms, Nano Lett. **16**(7), 4305–4311 (2016)

21.438 J. Ibañez-Azpiroz, M. dos Santos Dias, S. Blügel, S. Lounis: Spin-fluctuation and spin-relaxation effects of single adatoms from first principles, J. Phys. Condens. Matter **30**(34), 343002 (2018)

21.439 F. Meier, L. Zhou, J. Wiebe, R. Wiesendanger: Revealing magnetic interactions from single-atom magnetization curves, Science **320**(5872), 82–86 (2008)

21.440 J. Hermenau, M. Ternes, M. Steinbrecher, R. Wiesendanger, J. Wiebe: Long spin-relaxation times in a transition-metal atom in direct contact to a metal substrate, Nano Lett. **18**(3), 1978–1983 (2018)

21.441 G. van der Laan, B.T. Thole: Strong magnetic x-ray dichroism in 2*p* absorption spectra of 3*d* transition-metal ions, Phys. Rev. B **43**, 13401–13411 (1991)

21.442 F. de Groot, A. Kotani: *Core Level Spectroscopy of Solids* (CRC, Boca Raton 2008)

21.443 B.R. McGarvey: Electron spin resonance of transition-metal complexes. In: *Transition Metal Chemistry*, Vol. 3, ed. by R.L. Carlin (Marcel Dekker, New York 1966)

21.444 T. Miyamachi, T. Schuh, T. Märkl, C. Bresch, T. Balashov, A. Stöhr, C. Karlewski, S. André, M. Marthaler, M. Hoffmann, M. Geilhufe, S. Ostanin, W. Hergert, I. Mertig, G. Schön, A. Ernst, W. Wulfhekel: Stabilizing the magnetic moment of single holmium atoms by symmetry, Nature **503**, 242–246 (2013)

21.445 A.M. Bryan, W.A. Merrill, W.M. Reiff, J.C. Fettinger, P.P. Power: Synthesis, structural, and magnetic characterization of linear and bent geometry cobalt(II) and nickel(II) amido complexes: Evidence of very large spin-orbit coupling effects in rigorously linear coordinated Co^{2+}, Inorg. Chem. **51**(6), 3366–3373 (2012)

21.446 J.M. Zadrozny, D.J. Xiao, M. Atanasov, G.J. Long, F. Grandjean, F. Neese, J.R. Long: Magnetic blocking in a linear iron(I) complex, Nat. Chem. **5**(7), 577–581 (2013)

21.447 J.D. Rinehart, M. Fang, W.J. Evans, J.R. Long: A N23–radical-bridged terbium complex exhibiting magnetic hysteresis at 14 K, J. Am. Chem. Soc. **133**(36), 14236–14239 (2011)

21.448 J. Klatyk, W. Schnelle, F.R. Wagner, R. Niewa, P. Novák, R. Kniep, M. Waldeck, V. Ksenofontov, P. Gütlich: Large orbital moments and internal magnetic fields in lithium nitridoferrate(I), Phys. Rev. Lett. **88**, 207202 (2002)

21.449 A. Jesche, R.W. McCallum, S. Thimmaiah, J.L. Jacobs, V. Taufour, A. Kreyssig, R.S. Houk, S.L. Bud'ko, P.C. Canfield: Giant magnetic anisotropy and tunnelling of the magnetization in $Li_2(Li_{1-x}Fe_x)N$, Nat. Commun. **5**, 3333 (2014)

21.450 C.W. Thiel, T. Böttger, R.L. Cone: Rare-earth-doped materials for applications in quantum information storage and signal processing, J. Lumin. **131**(3), 353–361 (2011)

21.451 C. Hübner, B. Baxevanis, A.A. Khajetoorians, D. Pfannkuche: Symmetry effects on the spin switching of adatoms, Phys. Rev. B **90**, 155134 (2014)

21.452 B.T. Thole, G. van der Laan, J.C. Fuggle, G.A. Sawatzky, R.C. Karnatak, J.-M. Esteva: 3*d* x-ray-absorption lines and the $3d^94f^{n+1}$ multiplets of the lanthanides, Phys. Rev. B **32**(8), 5107–5118 (1985)

21.453 J.B. Goedkoop, B.T. Thole, G. van der Laan, G.A. Sawatzky, F.M.F. de Groot, J.C. Fuggle: Calculations of magnetic x-ray dichroism in the 3d absorption spectra of rare-earth compounds, Phys. Rev. B **37**(4), 2086–2093 (1988)

21.454 A. Singha, R. Baltic, F. Donati, C. Wackerlin, J. Dreiser, L. Persichetti, S. Stepanow, P. Gambardella, S. Rusponi, H. Brune: 4*f* occupancy and magnetism of rare-earth atoms adsorbed on metal substrates, Phys. Rev. B **96**(22), 224418 (2017)

21.455 A. Kotani, Y. Toyozawa: Optical spectra of core electrons in metals with an incomplete shell. I. Analytic features, J. Phys. Soc. Jpn. **35**(4), 1073–1081 (1973)

21.456 O. Gunnarsson, K. Schönhammer: Electron spectroscopies for Ce compounds in the impurity model, Phys. Rev. B **28**, 4315–4341 (1983)

21.457 J.C. Parlebas, A. Kotani: Photoemission theory of mixed valent semiconductors, J. Appl. Phys. **57**(8), 3191–3193 (1985)

21.458 Y. Hammoud, J.C. Parlebas, F. Gautier: Mixed-valent impurity model in rare-earth semiconducting compounds, J. Phys. C **18**(36), 6603–6614 (1985)

21.459 N. Mårtensson, B. Reihl, R.A. Pollak, F. Holtzberg, G. Kaindl, D.E. Eastman: Single-site mixed valence of thulium: A comparative photoemission study of $Tm_xY_{1-x}Se$ and $Tm_xY_{1-x}S$, Phys. Rev. B **26**, 648–653 (1982)

21.460 K.W.H. Stevens: Matrix elements and operator equivalents connected with the magnetic properties of rare earth ions, Proc. Phys. Soc. A **65**(3), 209–215 (1952)

21.461 B. Johansson: Energy position of 4*f* levels in rare-earth metals, Phys. Rev. B **20**, 1315–1327 (1979)

21.462 C. Rudowicz, S.K. Misra: Spin-Hamiltonian formalisms in electron magnetic resonance (EMR) and related spectroscopies, Appl. Spectrosc. Rev. **36**(1), 11–63 (2001)

21.463 G.K. Wertheim, G. Crecelius: Divalent surface state on metallic samarium, Phys. Rev. Lett. **40**, 813–816 (1978)

21.464 B. Johansson: Valence state at the surface of rare-earth metals, Phys. Rev. B **19**, 6615–6619 (1979)

21.465 A. Stenborg, O. Björneholm, A. Nilsson, N. Mårtensson, J.N. Andersen, C. Wigren: Valence changes and core-level shifts of Sm adsorbed on Mo(110), Phys. Rev. B **40**, 5916–5923 (1989)

21.466 E. Lundgren, J.N. Andersen, R. Nyholm, X. Torrelles, J. Rius, A. Delin, A. Grechnev, O. Eriksson, C. Konvicka, M. Schmid, P. Varga: Geometry of the valence transition induced surface reconstruction of Sm(0001), Phys. Rev. Lett. **88**, 136102 (2002)

21.467 M. Domke, C. Laubschat, M. Prietsch, T. Mandel, G. Kaindl, W.D. Schneider: Experimental proof for coordination-dependent valence of Tm metal, Phys. Rev. Lett. **56**, 1287–1290 (1986)

21.468 L. Peters, I. Di Marco, M.S. Litsarev, A. Delin, M.I. Katsnelson, A. Kirilyuk, B. Johansson, B. Sanyal, O. Eriksson: Valence and spectral properties of rare-earth clusters, Phys. Rev. B **92**, 035143 (2015)

21.469 L. Peters, S. Ghosh, B. Sanyal, C. van Dijk, J. Bowlan, W. de Heer, A. Delin, I. Di Marco, O. Eriksson, M.I. Katsnelson, B. Johansson, A. Kirilyuk: Magnetism and exchange interaction of small rare-earth clusters; Tb as a representative, Sci. Rep. **6**, 19676 (2016)

21.470 C. Nistor, A. Mugarza, S. Stepanow, P. Gambardella, K. Kummer, J.L. Diez-Ferrer, D. Coffey, C. de la Fuente, M. Ciria, J.I. Arnaudas: Structure and magnetism of Tm atoms and monolayers on W(110), Phys. Rev. B **90**(6), 064423 (2014)

21.471 R. Baltic, M. Pivetta, F. Donati, C. Wäckerlin, A. Singha, J. Dreiser, S. Rusponi, H. Brune: Superlattice of single atom magnets on graphene, Nano Lett. **16**(12), 7610–7615 (2016)

21.472 F. Donati, A. Singha, S. Stepanow, C. Wackerlin, J. Dreiser, P. Gambardella, S. Rusponi, H. Brune: Magnetism of Ho and Er atoms on close-packed metal surfaces, Phys. Rev. Lett. **113**(23), 237201 (2014)

21.473 M. Steinbrecher, A. Sonntag, M. dos Santos Dias, M. Bouhassoune, S. Lounis, J. Wiebe, R. Wiesendanger, A.A. Khajetoorians: Absence of a spin-signature from a single Ho adatom as probed by spin-sensitive tunneling, Nat. Commun. **7**, 10454 (2016)

21.474 R. Sessoli, D. Gatteschi, A. Caneschi, M.A. Novak: Magnetic bistability in a metal-ion cluster, Nature **365**(6442), 141–143 (1993)

21.475 N. Ishikawa, M. Sugita, T. Ishikawa, S. Koshihara, Y. Kaizu: Lanthanide double-decker complexes functioning as magnets at the single-molecular level, J. Am. Chem. Soc. **125**(29), 8694–8695 (2003)

21.476 M. Mannini, F. Pineider, C. Danieli, F. Totti, L. Sorace, P. Sainctavit, M.-A. Arrio, E. Otero, L. Joly, J.C. Cezar, A. Cornia, R. Sessoli: Quantum tunnelling of the magnetization in a monolayer of oriented single-molecule magnets, Nature **468**(7322), 417–421 (2010)

21.477 L. Ungur, J.J. Le Roy, I. Korobkov, M. Murugesu, L.F. Chibotaru: Fine-tuning the local symmetry to attain record blocking temperature and magnetic remanence in a single-ion magnet, Angew. Chem. Int. Ed. **126**(17), 4502–4506 (2014)

21.478 J. Dreiser, R. Westerström, C. Piamonteze, F. Nolting, S. Rusponi, H. Brune, S. Yang, A. Popov, L. Dunsch, T. Greber: X-ray induced demagnetization of single-molecule magnets, Appl. Phys. Lett. **105**(3), 032411 (2014)

21.479 F.D. Natterer, F. Donati, F. Patthey, H. Brune: Thermal and magnetic-field stability of holmium single-atom magnets, Phys. Rev. Lett. **121**, 027201 (2018)

21.480 M. Ganzhorn, S. Klyatskaya, M. Ruben, W. Wernsdorfer: Strong spin-phonon coupling between a single-molecule magnet and a carbon nanotube nanoelectromechanical system, Nat. Nanotechnol. **8**, 165 (2013)

21.481 N. Ishikawa, M. Sugita, W. Wernsdorfer: Nuclear spin driven quantum tunneling of magnetization in a new lanthanide single-molecule magnet: Bis(phthalocyaninato)holmium anion, J. Am. Chem. Soc. **127**(11), 3650–3651 (2005)

21.482 R. Giraud, W. Wernsdorfer, A.M. Tkachuk, D. Mailly, B. Barbara: Nuclear spin driven quantum relaxation in $LiY_{0.998}Ho_{0.002}F_4$, Phys. Rev. Lett. **87**, 057203 (2001)

21.483 G. Bourianoff, D. Pinna, M. Sitte, K. Everschor-Sitte: Potential implementation of reservoir computing models based on magnetic skyrmions, AIP Advances **8**(5), 055602 (2018)

21.484 M. Redies, F.R. Lux, J.-P. Hanke, P.M. Buhl, G.P. Müller, N.S. Kiselev, S. Blügel, Y. Mokrousov: Distinct magnetotransport and orbital fingerprints of chiral bobbers, Phys. Rev. B **99**(14), 140407(R) (2019)

21.485 S.D. Sarma, M. Freedman, C. Nayak: Majorana zero modes and topological quantum computation, npj Quantum Inf. **1**(1), 15001 (2015)

Pietro Gambardella

Laboratory for Magnetism and Interface Physics, Department of Materials
ETH Zurich
Zurich, Switzerland
pietro.gambardella@mat.ethz.ch

Pietro Gambardella graduated in physics from the University of Genova and obtained his PhD from EPFL, Switzerland. He was a postdoc at Max Planck Institut for Solid State Physics and research assistant at EPFL. In 2006, he was appointed ICREA Research Professor at the Catalan Institute of Nanotechnology before joining ETH Zurich as Full Professor in 2013. His research interests include magnetism, spintronics, surfaces, and interfaces, as well as x-ray and scanning probe techniques.

Stefan Blügel

Peter Grünberg Institute and Institute for Advanced Simulation
Forschungszentrum Jülich
Jülich, Germany
s.bluegel@fz-juelich.de

Stefan Blügel received his PhD in physics from RWTH-Aachen University. Since 2002, he has been the director of the Quantum Theory of Materials Institute at Peter Grünberg Institute, and in 2003 he joined RWTH-Aachen as Full Professor. He is one of the founding directors of the Institute of Advanced Simulation. His research interests include materials-specific theory and supercomputing of electronic properties, focusing on quantum materials and topology, spintronics, magnetism, and materials for nanoelectronics.

22. Magnetic Properties of Oxide Surfaces and Films

Alberto Brambilla, Andrea Picone, Marco Finazzi, Lamberto Duò, Franco Ciccacci

This chapter discusses the interesting magnetic properties of low-dimensional oxides, especially transition metal (TM) oxides (Sect. 22.1), which have long been the focus of scientific investigations. In recent years, researchers have taken a particular interest in low-dimensional TM oxide systems, especially ultrathin films (in the nanometer thickness range) that typically develop at surfaces and interfaces. In this respect, interfaces are at the heart of the magnetic phenomena associated with low-dimensional systems containing magnetic oxides. Understanding and mastering the physics of interfaces is therefore crucial if we are to manipulate the magnetic properties of such small-scale systems. Thus, several experimental techniques that allow the chemical compositions and magnetic properties of surfaces and interfaces to be probed have been developed over the last century, some of which are described in Sect. 22.2.

We also discuss various physical aspects of interfaces between magnetic transition metal oxides (TMO) and other magnetic layers (usually magnetic TMs). Since the ferromagnetic (FM) elemental metals (Fe, Co, and Ni) react strongly with oxygen, chemical interactions at those O/M interfaces can influence their magnetic properties. In Sect. 22.3, we consider the use of buffer layers—ultrathin layers of a different oxide or metal incorporated at the O/M interface—as a strategy for controlling such reactions. Finally, Sect. 22.4 provides an overview of the influence of interface chemistry on the magnetic coupling at O/M interfaces.

22.1 Overview

Oxides are compounds that are naturally abundant and have long been widely exploited for technological applications ranging from electronics to catalysis. In their natural forms, oxides possess important magnetic properties. For example, the first permanent magnets to be discovered were lodestones—rocks containing spontaneously magnetized iron oxide Fe_3O_4 (magnetite, which is ferrimagnetic (FI)).

Magnetic oxides have been widely studied and are extensively employed in their bulk forms and in low-dimensional systems (down to the nanometer scale). There are already a large number of books and reviews that discuss the general properties of oxides, so in this chapter we only briefly mention their general solid-state properties (i.e., their structural, electronic, and chemical features).

M. Rocca, T.S. Rahman, L. Vattuone (Eds.), *Springer Handbook of Surface Science*, Springer Handbooks,
https://doi.org/10.1007/978-3-030-46906-1_22

22.1.1 Crystalline and Electronic Properties

Oxides are typically ionic compounds containing metal cations and oxygen anions. The bonds in oxides can range from strongly ionic to notably covalent, depending largely on the electronegativity of the cations. This range of bonding leads to a great variety of crystal structures and electronic properties. Many oxides are good insulators, while a number of them (such as cuprates [22.1]) exhibit conducting or even superconducting behavior.

Crystal Structure

The crystal structure of an oxide is determined by its stoichiometry and the coordination number(s) of the cationic species in the oxide. In metal oxides, the crystal structure is typically based on an oxygen sublattice with either face-centered cubic (fcc) or hexagonal close packed (hcp) symmetry, with the metal cations occupying octahedral and tetrahedral interstitial sites. Variations in stoichiometry and the sites that are occupied by cations lead to a myriad of possible crystal structures of oxides, some of which are listed in Table 22.1.

This range of possible crystal structures is even greater for ultrathin oxides grown epitaxially on metallic substrates, as the interaction of the oxide with the substrate can induce the development of new phases that are not found in the corresponding bulk materials. As an example, ultrathin (monolayer (ML)) TiO_2 and reduced (TiO_x) films with various peculiar structures have been obtained through pseudo-epitaxial growth on different substrates: rutile TiO_2(110) crystals, hexagonal reconstructions, and ordered arrays of titanium oxide nanodots have been prepared on Ni(110) [22.2]; rectangular and hexagonal phases are also seen when ultrathin TiO_x films are stabilized on Pt(111) [22.3]; and exotic structures such as those with a pinwheel shape appear when TiO_2 is grown on herringbone-reconstructed Au(111) surfaces [22.4].

Low-dimensional oxides with exotic mesoscopic morphologies can also be obtained by exploiting structural features of the substrates, such as those associated with growth on vicinal surfaces. In addition, such an approach permits the stabilization of one-dimensional (1-D) and two-dimensional (2-D) nanostructures, i.e., nanowires and nanostripes. One example is CoO on Pd(1 1 23), which is vicinal to Pd(100). In this case, quasi-1-D CoO nanostripes grow in a pseudomorphically strained hexagonal phase. The driving mechanism for this process is step decoration [22.5]. The same mechanism is responsible for the stabilization of 2-D Mn oxide nanostripes grown on the stepped Pd(1 1 21) surface, which is also vicinal to Pd(100) [22.6]. Note that the mismatch between the MnO and the Pd lattices, about 14%, is relatively large. Interactions with the edges of the steps offer the oxide a path to strain relaxation, thus permitting the formation of well-ordered structures, as displayed in Fig. 22.1.

Besides its interaction with the substrate, another aspect that strongly influences the structure of an ultrathin oxide is the employed growth procedure. A significant example of this is the growth of ultrathin MgO films on Fe(001); it was shown that the optimal growth conditions depend on a delicate balance between the oxygen partial pressure during the reactive deposition of Mg and the growth rate maintained by the Mg evaporator [22.7]. For instance, an excessively high oxygen pressure leads to unwanted substrate oxidation; on the other hand, low growth rates give oxygen-deficient MgO films. There is typically a narrow window of growth parameters that are suitable for generating ultrathin oxide films with the desired quality, as exemplified by Fig. 22.2.

Electronic Structure

Oxides are commonly considered to be insulating materials. However, their electronic properties vary significantly depending on the cations in and the stoichiometry of the oxide. A wide range of bandgaps are seen for oxides, meaning that many oxides are very good insulators (e.g., MgO), some have semiconductor-like properties (e.g., TiO_2), while others are conductors (e.g., V_2O_3) or even superconductors (e.g., cuprates, such as $YBa_2Cu_3O_7$). Indeed, metal–insulator transitions occur for some oxides (e.g., V_2O_3, Ti_2O_3) at particular temperatures.

Table 22.1 List of common oxide crystal structures with examples

Structure	Magnetic examples	Nonmagnetic examples
Halite (rock salt)	NiO, CoO, FeO	MgO
Wurtzite	–	ZnO
Spinel	Fe_3O_4	Al_2MgO_4
Perovskite	$La_{0.67}Sr_{0.33}MnO_3$ (LSMO)	$SrTiO_3$
Corundum (sapphire)	Fe_2O_3, Cr_2O_3	Al_2O_3
Rutile	CrO_2	TiO_2
Pyrochlore	$Gd_2Ti_2O_7$	$Y_2Ti_2O_7$
Garnet	$Y_3Fe_5O_{12}$ (YIG)	$Y_3Al_5O_{12}$ (YAG)

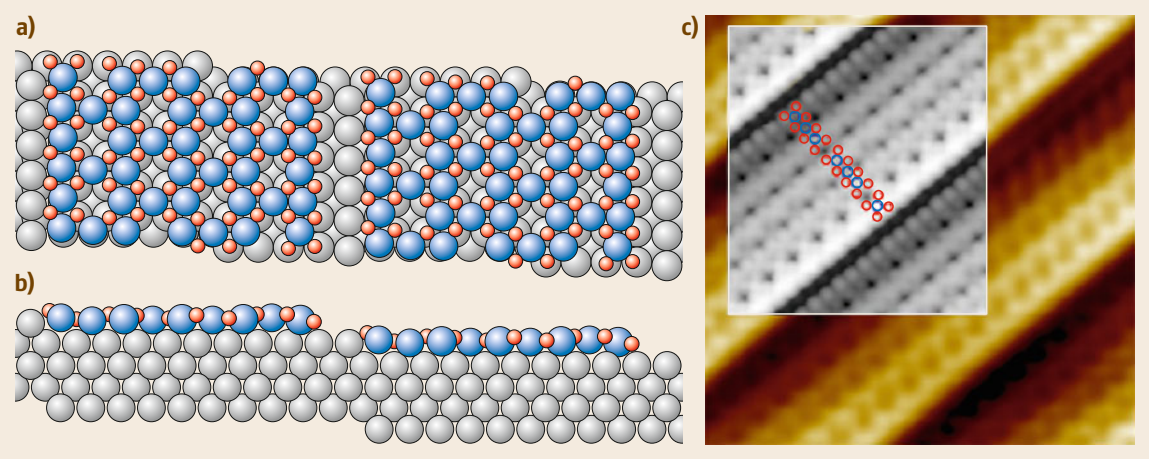

Fig. 22.1a–c Panels **(a)** and **(b)** display top and side views of the c(4×2)-$Mn_{14}O_{20}$/Pd(1 1 21) structural model. *Large* (*blue*) and *small* (*red*) adatoms indicate manganese and oxygen atoms, respectively, adsorbed on a Pd(1 1 21) substrate represented by *light gray spheres*. Panel **(c)** compares the experimental (0.4 V; 100 pA) and calculated (*inset*) STM images (Reprinted with permission from [22.6]. © 2012 by the American Physical Society)

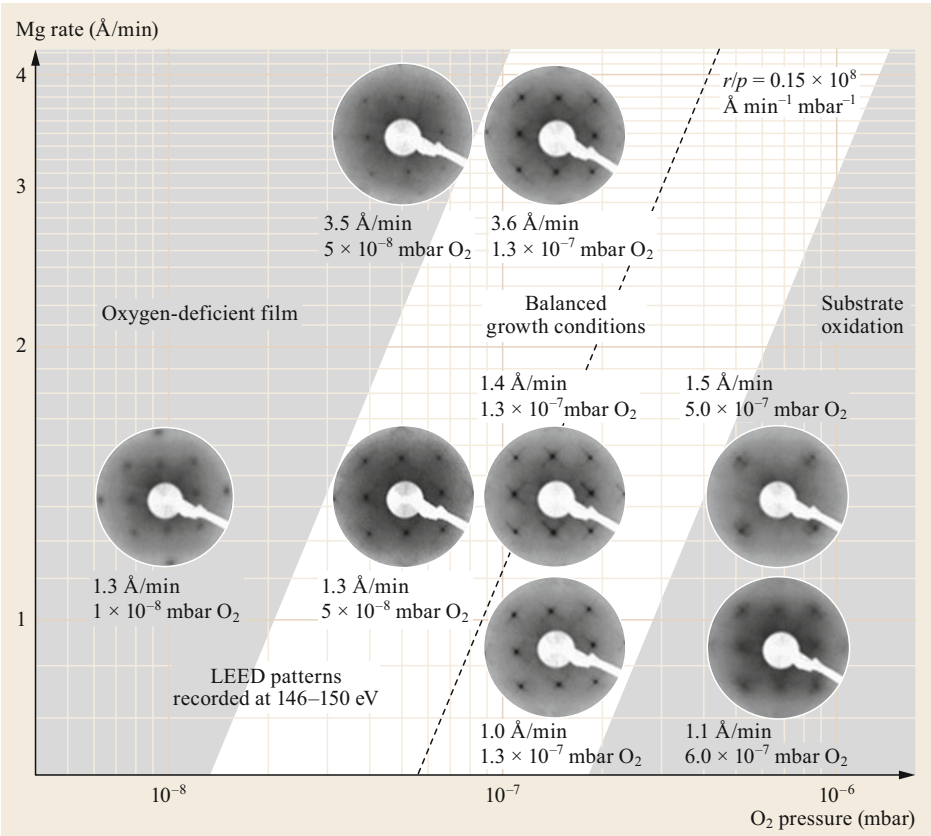

Fig. 22.2 Low-energy electron diffraction (LEED) patterns of 8 ML MgO films grown on Fe(001) at room temperature under different O_2 partial pressures and at various Mg deposition rates (Reprinted from [22.7], with permission from Elsevier)

Given the different characteristics exhibited by different oxides, they are often categorized into non-TM oxides and TM oxides. Magnetic oxides typically belong to the latter category, as also indicated by Table 22.1.

A common feature of non-TM oxides is that the valence and conduction states of the M atoms exhibit either s or p symmetry. This situation leads to far fewer possibilities than for TM oxides: either a wide-bandgap insulating oxide containing an element from the first two groups of the periodic table, such as MgO ($E_g = 7.8\,\text{eV}$), or a smaller bandgap insulating oxide that is based on elements in groups that occur after the TMs in the periodic table, such as ZnO ($E_g = 3.3\,\text{eV}$). Note that the bandgap of ZnO is substantially altered in the presence of defects or doping, which can yield semiconducting oxides (ZnO is an example, as is SnO_2).

TM oxides are instead characterized by the role played by d atomic orbitals, leading to a huge variety of possible cation oxidation states and to issues linked to the symmetry of the crystal field. The first aspect stems from the fact that the energy associated with a d^n configuration barely changes when n changes by ± 1, resulting in several stable oxides with different stoichiometries. The different electronic configurations of the different oxidation states of the cation also correspond to different crystallographic structures, as shown for several TMs in Table 22.2. A crucial feature of TM oxides is that the band resulting from d orbital overlap is typically narrower than that resulting from the overlap of s and p orbitals. For this reason, band formation competes with other effects such as electron–electron and electron–phonon interactions, giving rise to effects such as the well-known Mott transition [22.8]. The relative strength of the interaction between cations in TM oxides also provides the potential for long-range magnetic ordering, such as that seen in NiO and other magnetic insulators.

22.1.2 Origin of Magnetism in Transition Metal Oxides

The long-range magnetism exhibited by ferromagnets is generated by the exchange interaction. This quantum-mechanical effect occurs when wavefunctions of ions that are nearest neighbors in the lattice overlap. However, magnetic ions are not usually adjacent to each other in oxides. The occurrence of long-range magnetic order in oxides may be interpreted as arising through the indirect coupling of magnetic ions; in other words, the wavefunctions of two magnetic ions overlap with that of a nonmagnetic ion adjacent to both of the magnetic ones. The most important indirect exchange mechanisms are called superexchange and double exchange.

Superexchange typically occurs in ionic solids such as TM oxides, and involves the states that participate in the bonding between the metal and the oxygen atoms, namely 3d TM atoms and 2p valence states of oxygen. In particular, superexchange generates long-range antiferromagnetic (AF) order in several TM monoxides such as NiO, CoO, FeO, and MnO. This mechanism is often described schematically, as shown in Fig. 22.3 [22.9]. In this figure, the hypothetical ground-state (GS) distribution of electrons in the magnetically active (i.e., not completely filled) subshells is depicted

Table 22.2 Electronic configuration of the 3d shell and corresponding crystal structures for some 3d transition metal oxides

	Bixbyite	Rutile	Corundum	Rock salt	Spinel	Other
$3d^0$	Sc_2O_3	TiO_2	–	–	–	TiO_2 (anatase and brookite) V_2O_5 (orthorhombic) CrO_3 (orthorhombic)
$3d^1$	–	VO_2 ($T > 340\,\text{K}$)	Ti_2O_3	–	–	–
$3d^2$	–	CrO_2	V_2O_3	TiO_x ($0.6 < x < 1.28$)	–	–
$3d^3$	–	β-MnO_2	Cr_2O_3	VO_x ($0.8 < x < 1.3$)	–	–
$3d^4$	Mn_2O_3	–	–	–		–
					Mn_3O_4	
$3d^5$	–	–	α-Fe_2O_3	MnO		–
					Fe_3O_4	
$3d^6$	–	–	–	FeO		–
					Co_3O_4	
$3d^7$	–	–	–	CoO		–
$3d^8$	–	–	–	NiO	–	–
$3d^9$	–	–	–	–	–	CuO (monoclinic)
$3d^{10}$	–	–	–	–	–	Cu_2O (cubic) ZnO (wurtzite)

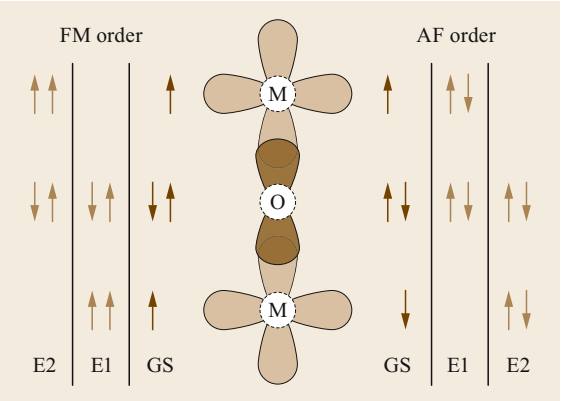

Fig. 22.3 Schematic of the superexchange mechanism. GS indicates the ground-state configuration; E1 and E2 are two possible excited configurations (see text)

with black arrows in the case of FM or AF order, where the direction of the arrow indicates the electron spin direction in the metal ion. Possible excited states are shown as gray arrows. It is found that the indicated excited states are allowed by the exclusion principle for the AF case but are forbidden for the FM case. This implies that, in the former case, electrons can be delocalized over the whole ionic structure, thus lowering the total energy of the system, leading to an AF ground state.

Double exchange refers in particular to cases with a mixed-valence magnetic cation; e.g., Fe_3O_4 (Fig. 22.4) contains both Fe^{2+} and Fe^{3+} ions. This mechanism, which was originally proposed to explain the magnetoconductivity of some oxides (e.g., doped perovskites), involves electrons hopping from one magnetic cation to another through a common O^{2-} ion. The 2p shell of the latter is full, so the process occurs in two steps (hence the term *double exchange*): an electron is transferred from the occupied oxygen state to one of the cations (e.g., Fe^{3+}), leaving an unoccupied level that receives a second electron from the other cation (in this case Fe^{2+}). Both processes occur without spin flipping, which is unfavorable according to Hund's rules,

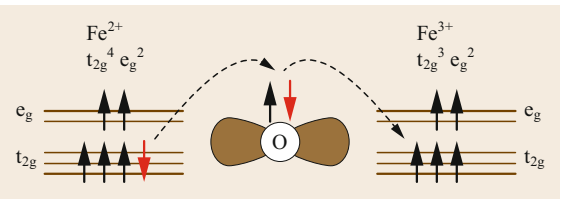

Fig. 22.4 Schematic of the double exchange mechanism for Fe_3O_4. *Arrows* indicate the direction of electron spin. The schematic assumes that hopping is permitted due to FM alignment between the ions (see text)

so hopping is only allowed when the two cations have the same magnetic structure, i.e., when their spins are parallel. The double exchange process, just like the superexchange process, results in the delocalization of the electron over the entire M-O-M system (which is then said to be of mixed valence), thus lowering its total energy. Another important example of a compound in which the double exchange mechanism is active is lanthanum strontium manganite $La_{1-x}Sr_xMnO_3$ (LSMO), which is known to possess a rich electronic phase diagram that depends on the doping level x and includes a FM phase.

22.1.3 Surfaces and Interfaces

Magnetic oxide thin films and surfaces are commonly prepared on FM surfaces, as discussed in the following sections. Elemental ferromagnetic TMs (Fe, Co, and Ni) react strongly with oxygen. Therefore, when they form interfaces with oxides, relevant oxidation/reduction (redox) processes would be expected to occur. This often results in the formation of defective oxides and/or oxidized metallic surfaces.

The various magnetic TMOs that can form when TMs are oxidized or at the interface between the TMO and TM can be inferred by calculating the standard enthalpy (heat) of formation $\Delta_f H^0$ of each oxide considered. This is the enthalpy change during the reaction in which the oxide is formed from its constituent elements in their standard states (the redox process in particular), which is normally calculated assuming the initial presence of 1 mol of oxygen. The lower the value of $\Delta_f H^0$, the more thermodynamically favorable the oxide formation. Table 22.3 provides a list of $\Delta_f H^0$ values in kJ/mol for the formation of a number of magnetically relevant oxides at 298.15 K. These enthalpies are taken from [22.10, 11], and the compounds are listed in order of increasing magnitude of $\Delta_f H^0$. The table also reports the magnetic order exhibited by each oxide, and its magnetic ordering temperature (the Curie temperature for FM oxides and the Néel temperature for AF oxides). $\Delta_f H^0$ values for the nonmagnetic (NM; i.e., materials with no long-range magnetic order) oxides MgO and Al_2O_3, which are frequently used as substrates for the growth of metallic thin films, are also shown for reference.

Redox reactions at oxide interfaces directly influence the magnetic properties of the sample. If we consider, for instance, the interfaces between AF TMOs such as NiO and CoO and FM TMs such as Fe, Co, and Ni, a comprehensive study by *Regan* et al. [22.12] utilizing x-ray absorption spectroscopy (XAS) showed how reactions at the interface between oxygen and metal layers always resulted in the reduction of the

Table 22.3 Standard enthalpy (heat) of formation values $\Delta_f H^0$ (at 298.15 K), types of magnetic order, and magnetic ordering temperatures for some magnetic oxides

Molecular formula	Name	$\Delta_f H^0$ (kJ/mol)	Magnetic order	Ordering temperature (K)
CoO	Cobalt(II) oxide	−237.9	AF	292
NiO	Nickel(II) oxide	−240.6	AF	523
FeO	Iron(II) oxide	−272.0	AF	198
MnO	Manganese(II) oxide	−385.2	AF	116
CrO_2	Chromium(IV) oxide	−598.0	FM	390
MgO	Magnesium oxide	−601.6	NM	–
Fe_2O_3	Iron(III) oxide	−824.2	AF	950
Co_3O_4	Cobalt(II,III) oxide	−891.0	AF	40
Fe_3O_4	Iron(II,III) oxide	−1118.4	FI	858
Cr_2O_3	Chromium(III) oxide	−1139.7	AF	307
$FeWO_4$	Iron(II) tungstate	−1155.0	AF	76
Mn_3O_4	Manganese(II,III) oxide	−1387.8	FI	43
Al_2O_3	Aluminum oxide (corundum)	−1675.7	NM	–
$CoFe_2O_4$	Cobalt ferrite	−20 000.0	FI	793
$NiFe_2O_4$	Nickel ferrite	−20 000.0	FI	858

former and/or the oxidation of all of the latter for all combinations of the above materials. Both the redox reaction products and the thickness of the reduced/oxidized region (typically a few atomic layers at room temperature (RT)) can typically be predicted based on the $\Delta_f H^0$ values of the oxides involved. For instance, a NiO or CoO layer is reduced more strongly when it is next to a metallic Fe layer than when it is next to a cobalt or nickel metal layer, since Fe oxides have lower enthalpies of formation than Co or Ni oxides. The magnetic properties of the Fe oxides formed at the interface depend on their magnetic environment; e.g., when NiO thin films are grown on Fe(001) by reactive deposition, the FI oxide Fe_3O_4 has been reported to form at the interface, as demonstrated by the x-ray absorption spectrum presented in the left panel of Fig. 22.5. The magnetization vector of the Fe_3O_4 layer was observed to be parallel to that of the Fe(001) substrate, which was parallel to the surface and aligned along one of the [100] in-plane directions [22.13]. On the other hand, when a thin layer of Fe_3O_4 was realized by oxidizing an Fe(110) substrate, antiparallel magnetic coupling of the overlayer with the substrate was observed [22.14], as displayed in Fig. 22.6.

In other cases, particularly when a thin metallic Fe overlayer is grown on a NiO(100) substrate (i.e., in reverse order with respect to the example provided above), the growth conditions lead to the formation of a different Fe oxide at the interface: FeO [22.15]. As reported in Table 22.3, the latter is characterized by AF order, leading to a completely different magnetic environment for an otherwise analogous interface. More examples of the interplay between interface chemistry and magnetic properties are provided in Sect. 22.4.

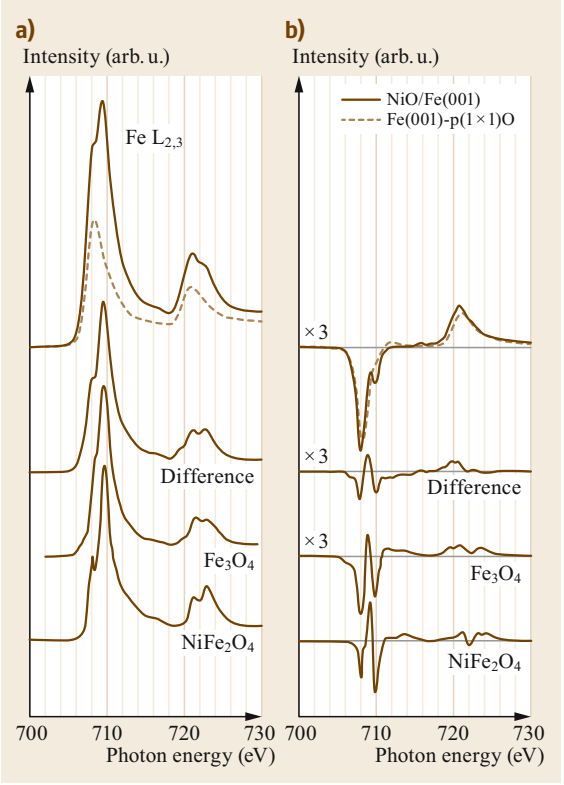

Fig. 22.5a,b Comparison of the Fe $L_{2,3}$ XAS **(a)** and x-ray magnetic circular dichroism (XMCD) spectra **(b)** of 20 ML NiO/Fe(001) and Fe(001)-p(1×1)O. After normalization, the spectra obtained for Fe(001)-p(1×1)O were multiplied by a factor of 0.5. The difference spectra are compared to the XAS and XMCD spectra of Fe_3O_4 and $NiFe_2O_4$ (Reprinted from [22.13], with permission from Elsevier)

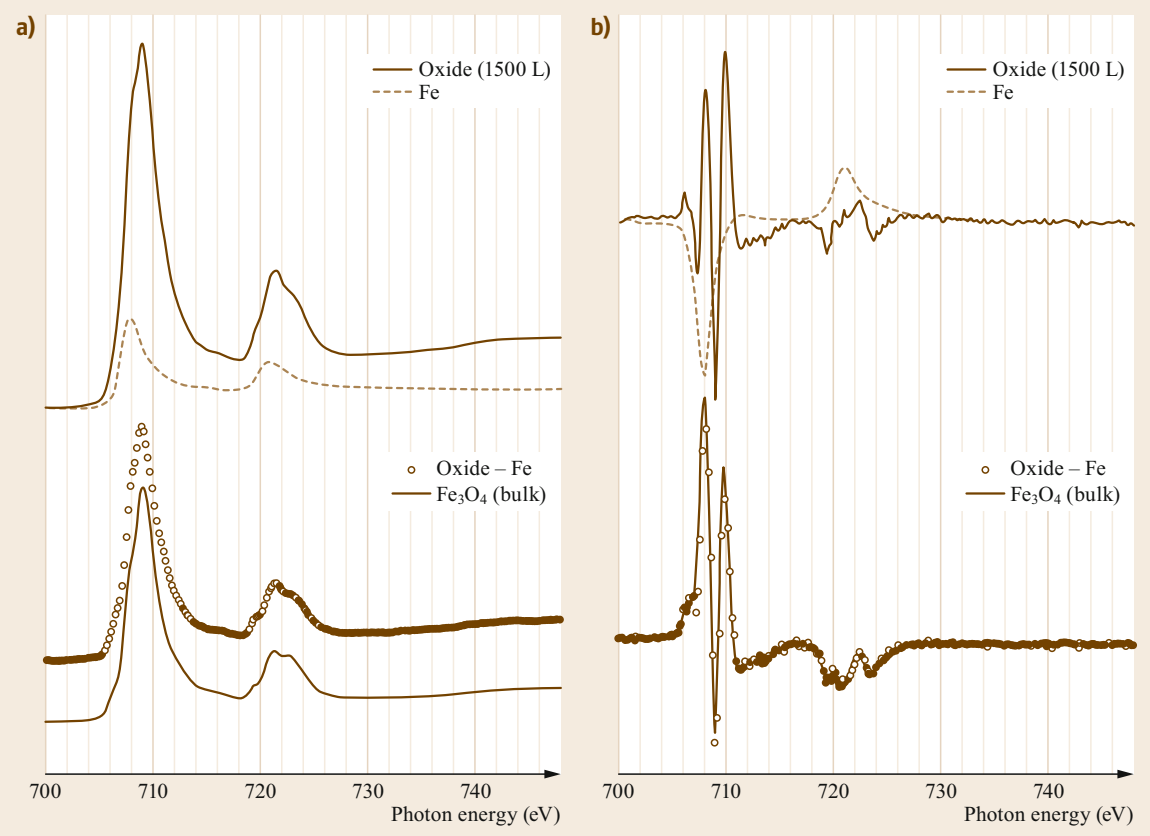

Fig. 22.6 **(a)** Fe $L_{2,3}$ XAS spectra acquired for an Fe film exposed to 1500 L oxygen (*top, solid line*) and for metallic Fe (*top, dotted line*). The Fe-subtracted spectrum (*bottom, open circles*) is compared to the bulk Fe_3O_4 spectrum (*bottom, solid line*). **(b)** Same as **(a)**, but for magnetic circular dichroism (MCD) curves. To aid comparison, the sign of the MCD for the bulk Fe_3O_4 has been reversed (Reprinted from [22.14], with permission from Elsevier)

22.2 Experimental Methods

Since oxides are used in many scientific and technological fields, a large number of experimental methods are employed for their preparation and characterization. The methods applied often depend on the approach used. Here, we limit ourselves to a survey of the most important experimental methods associated with thin and ultrathin films of magnetic oxides.

The formation of thin and ultrathin MOs usually involves chemical reactions that may modify the chemical and physical properties (including the magnetic properties) of the substrate, resulting in various possible interfaces. This is a particularly important consideration for TM substrates, as discussed in Sect. 22.1, and one that necessitates tight control over the growth procedure, particularly during the early stages of MO oxide growth. This in turn implies that a controlled environment is required, along with (typically) ultrahigh vacuum (UHV) conditions (base pressures on the order of 10^{-10} mbar) and the ability to monitor sample properties even when the thickness of the growing MO is in the sub-ML range. The sample preparation approaches and experimental characterization methods that are best suited to such goals are those typical of surface science studies. The most relevant methods for studying MO are briefly described in the following section.

22.2.1 Sample Preparation and Growth

The growth of thin and ultrathin films under controlled conditions is usually achieved via physical vapor methods. The most widely used of these is molecular beam epitaxy (MBE), which is well known as a technique for

growing semiconductors and involves the use of molecular beams of the deposited elements. These beams are produced by heating solid state sources and travel a short distance to the crystalline substrate in UHV or a controlled atmosphere. The latter case is particularly common in oxide thin film growth, where the molecular beam of the cationic element is evaporated in an oxygen atmosphere (this oxygen atmosphere can either be molecular, achieved by simply connecting a pure O_2 bottle to a leak valve, or atomic, which requires more complicated tools such as plasma sources). Such an approach is often called reactive deposition.

The word *epitaxy* refers to the development of a thin film on a crystalline substrate where the crystal structure of the thin film is dictated by that of the substrate. This influence of the substrate on the structure of the thin film can be exploited to produce crystalline thin films of very high quality as well as metastable structures that have no stable equivalents in the bulk, as discussed earlier.

MBE sources can be either very simple evaporation cells or more sophisticated effusion cells (such as Knudsen cells). The simplest cell consists of a hot filament that either directly heats a solid piece of the source material or a crucible containing the material if the latter is in powder form or has a low melting temperature (for example). In some cases, electron bombardment is employed to heat up the source (particularly when higher temperatures are needed), which can be achieved by simply establishing an appropriate voltage difference between the filament and source. More sophisticated cells often include shutters that are employed to isolate the sample from the molecular beam during preheating and calibration phases, as well as temperature monitoring systems such as thermocouples.

MBE is particularly well suited for growing ultrathin films (down to the sub-ML range) as it permits very small evaporation rates (on the order of 1 ML/min) and is performed in UHV. For the same reasons, MBE is not practical for realizing relatively thick films (on the order of hundreds of nm or more) or for industrial applications.

Other physical deposition techniques can provide higher rates and require less demanding environments. Sputtering is a very common method of growing thin films that involves accelerating a beam of (typically Ar^+) ions towards a target containing the source material, causing the ejection of target atoms (or small clusters) which are then directed onto a substrate surface. This technique is very versatile and robust in terms of the quality, uniformity, and purity of the grown film. Both simple and ternary oxides, as well as other compounds and alloys, can be produced by sputtering deposition starting from a target of the material to be grown or by (for instance) mixing oxygen with the argon in the ion source. The high speed of this process makes it particularly applicable for the preparation of samples comprising several different thin film layers (such as multilayer stacks used in spin valves).

Another versatile physical method employed in research laboratories is pulsed laser deposition (PLD). In this technique, high-power laser pulses are directed onto a target in a dedicated vacuum chamber, causing the ablation of the target material. This ablated material ionizes and forms a plasma plume that is directed toward a substrate, where the material is deposited. The stoichiometric composition of the target is generally preserved on the substrate. This method is used to grow complex magnetic oxides such as manganites for instance.

A further method of preparing ultrathin oxide films is through the oxidation of a metallic substrate by direct exposure to oxygen. This approach is clearly limited to the formation of native MO films. The thermodynamics (in particular the enthalpies of formation reported in Table 22.3) and kinetics of the oxidation process determine the compound that forms during the process. Another relevant aspect of direct oxidation is the fact that the crystal structure of the MO often does not correspond to that of the parent metallic crystal. For instance, bulk Co has a hexagonal close-packed (hcp) structure, while bulk CoO possesses a face-centered cubic (fcc) structure. Ultrathin MO films of high crystalline quality are therefore only rarely prepared by direct oxidation; one such example is alumina Al_2O_3 ultrathin film (a few ML in thickness) prepared on the alloy NiAl(110), where the film is stabilized by oxidation and subsequent annealing [22.16].

22.2.2 Chemical and Structural Characterization

In the following sections, the main spectroscopic and microscopic experimental techniques used in structural and chemical analyses of oxide surfaces are described.

Spectroscopic Techniques

The spectroscopic methods that are used to characterize surfaces and ultrathin films are those typically employed in experimental surface science. Such methods feature high surface sensitivity, meaning that they allow the experimenter to explore properties associated with the topmost layers of a sample, with probing depths on the order of a nanometer or less. Electrons are suitable probes for achieving such sensitivity, since the inelastic mean free path (IMFP) of an electron with an energy of a few tens of eV is typically less than 1 nm, even in oxides. The energy dependence of the IMFP of

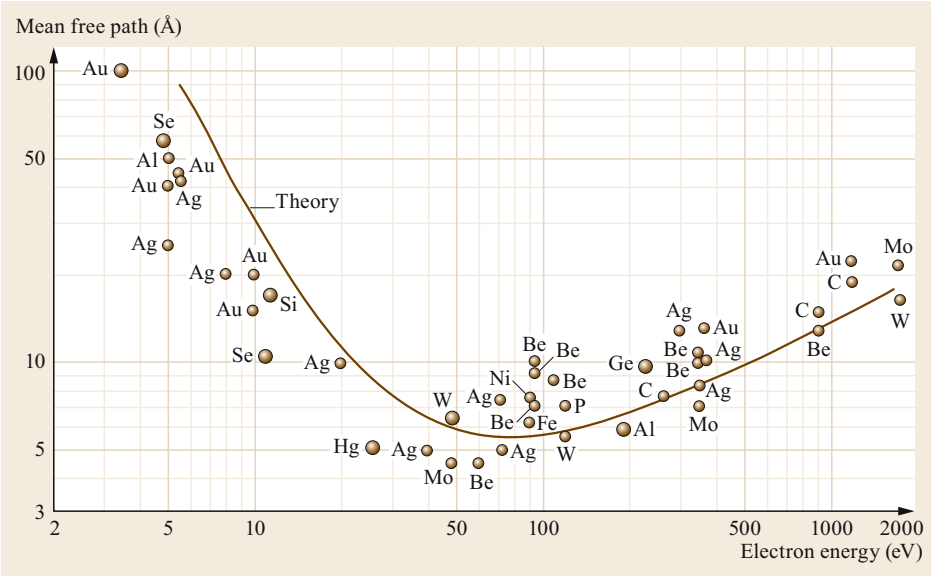

Fig. 22.7 Quasi-universal curve of the inelastic mean free path of an electron in a solid. *Points* are experimental data and the *continuous line* is the theoretical curve. Experimental data from [22.17, 18]; theoretical data from [22.19] (Reprinted by permission from [22.20], © Cambridge Univ. Press 1988)

an electron in a solid exhibits a quasi-universal curve, an example of which is reported in Fig. 22.7. The reference work of *Seah* and *Dench* [22.21] proposes the following heuristic equation for evaluating the IMFP λ_{IMFP} in an inorganic compound (such as an oxide): $\lambda_{\mathrm{IMFP}} = 143/E^2 + 0.054\sqrt{E}$, where the electron kinetic energy E is in eV and the resulting IMFP is in nanometers. The IMFP is related to the length d that electrons travel into the solid by the attenuation of the electron beam intensity with respect to the initial intensity I_0 as follows: $I(d) = I_0 \mathrm{e}^{-d/\lambda_{\mathrm{IMFP}}}$.

Photoemission spectroscopy (PES) is one of the tools most commonly used to investigate the electronic and chemical properties of surfaces. This technique allows the binding energy of an electron photoemitted from the sample following the absorption of a photon of energy $h\nu$ to be calculated via the energy balance $E_{\mathrm{K}} = h\nu - E_{\mathrm{B}} - \phi_{\mathrm{a}}$, where E_{K} is the electron kinetic energy as measured by an energy analyzer, E_{B} is the electron binding energy, and ϕ_{a} is the analyzer work function. Photon energies in the ultraviolet (UV; up to a few tens of eV) or the soft x-ray region (on the order of 1 keV) allow the binding energies of electrons from the valence band and from core levels to be probed, respectively. The same technique is therefore usually denoted UPS (ultraviolet photoemission spectroscopy) or XPS (x-ray photoemission spectroscopy), depending on the energy range of the photons employed. XPS is also known as ESCA (electron spectroscopy for chemical analysis), as the electron binding energy is specific to each element. Thus, identifying the energies of the most intense peaks in an XPS/ESCA spectrum allows the elements present to be discerned.

When analyzing compounds, one of the most useful features of XPS is the chemical shift effect, which is the shift in energy of core-level peaks that occurs when the chemical environment of the element is changed. Although the core levels are not directly involved in chemical bonding, such bonding changes the electrostatic potential generated by the valence electrons, which in turn influences the binding energies of the core electrons. In oxides, the chemical shift depends on the oxidation state, the lattice sites, and the ionic environment. In general, larger binding energies are measured for the core levels in oxides than for the core levels in the cationic element in the metallic state. The example shown in Fig. 22.8 relates to TiO_2, the 2p core-level peaks of which show a relatively large chemical shift (almost 5 eV) when compared to those of metallic Ti. Other less evident features, such as different symmetries of the XPS line shapes of the metallic and oxide materials, are not discussed here.

Other effects are responsible for variations in the core-level line shapes in XPS, among which we will briefly mention the final-states effect known as *shake up*. This effect arises because the creation of a positively charged core hole during the photoemission process induces a decrease in the electron density near to that core hole, which in turn reduces the kinetic energy of the outgoing electron such that a peak appears at higher binding energy. This effect is observed in particular in magnetic TM monooxides such as CoO and NiO, as demonstrated by the spectra reported in Fig. 22.9. In the latter, shake-up peaks relating to the Ni $2p_{3/2}$ and Ni $2p_{1/2}$ core levels of a NiO sample are indicated. Multiplet splitting is also apparent; this occurs

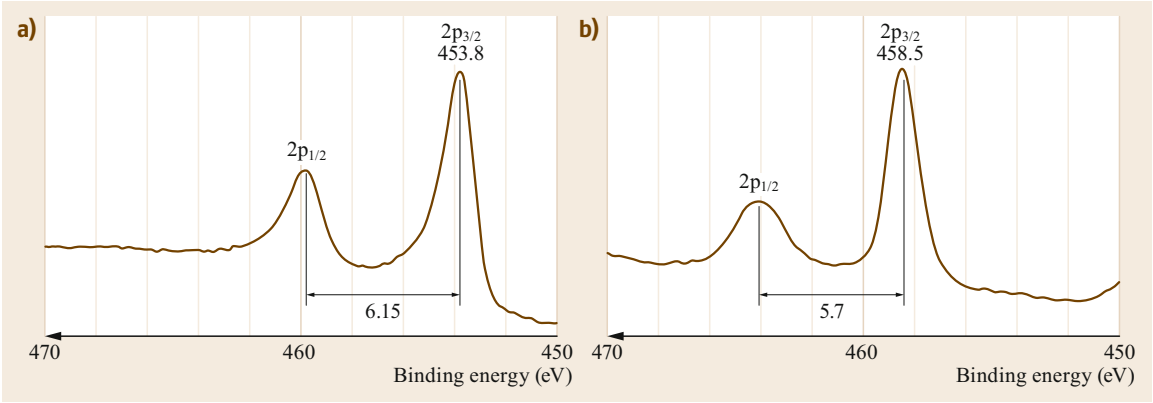

Fig. 22.8a,b XPS spectra of the 2p core levels of **(a)** Ti and **(b)** TiO_2 (Reprinted by permission from [22.22], © PerkinElmer 1979)

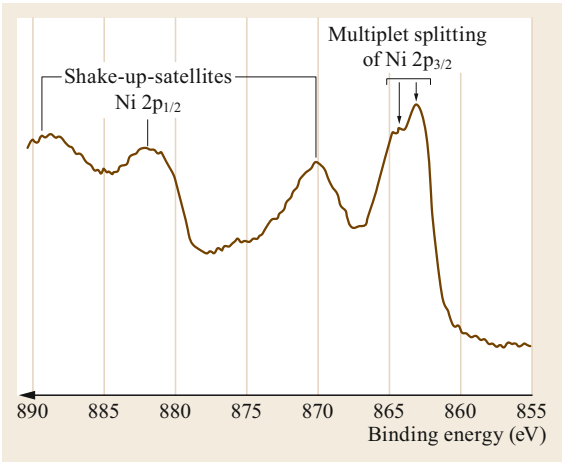

Fig. 22.9 Ni 2p shake-up and multiplet splitting features in the 2p core-level region of the XPS spectrum of a NiO sample (Reprinted from [22.23], with permission from Elsevier)

due to the presence of unpaired electrons in the valence band [22.23].

We should also mention charging effects, which are common in insulating samples such as sufficiently thick nondefective oxides. Electron emission generates a positive charge at the sample surface that cannot be neutralized by a negative charge from the ground reservoir. The outgoing electron is attracted by this positive charge, which decreases the measured kinetic energy (or artificially increases the binding energy). It is sometimes possible for the correct energy values to be retrieved by utilizing a well-known core level peak as a reference, thus permitting the energy scale to be calibrated. Another way of avoiding charging effects is to employ a charge neutralizer, i.e., an electron gun that directs negative charge to the sample surface. However, this approach must also be thoroughly calibrated, since there is a risk of negatively charging the surface if the neutralizing electron beam is too intense.

Another widely used electron-based spectroscopic technique is Auger electron spectroscopy (AES), which makes use of the well-known Auger effect, a nonradiative route for an ion with a core hole (created by exciting the sample with either electrons or photons) to relax to a lower-energy state. This relaxation results in the emission of a so-called Auger electron, and the kinetic energy of this electron depends on the set of core levels of the involved atom, which gives AES the element specificity that makes it a valuable method of identifying the chemical species at the surface of a sample, similar to XPS. Another similarity to the latter technique is its surface sensitivity, as typical kinetic energies of Auger electrons as measured with laboratory instruments are on the order of tens to hundreds of eV. As a matter of fact, Auger electrons can also be observed in XPS spectra, thus allowing the chemical composition of the sample to be cross-checked. Peak positions in AES spectra are also influenced by the chemical environment and exhibit chemical shifts comparable to those of XPS peaks. However, this behavior is often overlooked in AES because AES peaks are usually larger and have more complicated line shapes.

At this point, it is worth mentioning the use of synchrotron radiation as a source for spectroscopy experiments on low-dimensional materials. The high intensities, energies, and spatial resolutions of such sources as well as their tunability over a wide energy range make them ideal for spectroscopic and microscopic investigations of nanostructures.

X-ray absorption spectroscopy (XAS) in the soft x-ray range (about 100–1000 eV) is often used as a reference spectroscopic technique. This is a core-level

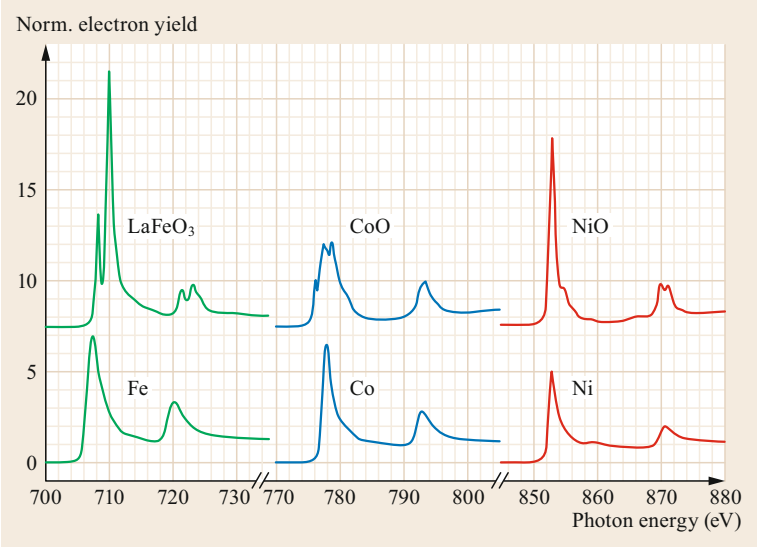

Fig. 22.10 XAS spectra obtained at the $L_{2,3}$ edges of elemental Fe, Co, and Ni (*lower row*) and cationic Fe, Co, and Ni in oxide compounds (*upper row*) (Adapted from [22.24])

spectroscopic method, implying that it is sensitive to the chemical environment and thus also useful for studying compounds. The associated physical mechanism is the absorption of a photon by a core-level electron (at specific absorption edges) that is promoted to an unoccupied state just above the Fermi level. The core hole then relaxes through both radiative and nonradiative processes, and the resulting secondary electrons are collected and measured as the signal. Here, we focus on a region on the order of 10 eV above the absorption edge (sometimes called x-ray absorption near-edge structure, XANES), whereas larger energy windows may include other information too (e.g., structural order), and the XAS in such cases is generally termed extended x-ray absorption fine structure (EXAFS) [22.25].

XAS spectra of TMs are typically taken at the so-called L-edge, which corresponds to $2p \rightarrow 3d$ electronic transitions that occur following the absorption of photons in the soft x-ray range, i.e., between about 700 and 900 eV for Fe, Co and Ni, as shown in Fig. 22.10 [22.24]. More precisely, these spectra contain two broad peaks that relate to L_2 (originating from $2p_{1/2}$ states) and L_3 (originating from $2p_{3/2}$ states) absorption edges, which are split by the spin–orbit interaction. Such transitions are regulated by dipole selection rules and are therefore linked to the 3d valence states, which are responsible for the magnetic properties of TMs. When TMs are included as cations in oxides, their XAS spectra develop a complicated fine structure called multiplet structure, which is influenced by crystal field and multiplet effects. The latter reflect various interactions between valence holes and electrons that are not discussed here.

Microscopy Techniques

Spatially resolved investigations of a sample surface can be realized at several length scales by exploiting various probes. Here, we limit our discussion to just a few examples involving probes that are suited for investigating matter (in particular oxides) at the nanometer scale. These probes are again electrons with low kinetic energies, photons in the soft x-ray range, and small tips in scanning probe approaches. Furthermore, we focus on techniques that are also implemented as magnetic imaging tools.

Photoemission electron microscopy (PEEM) is a microscopy counterpart to PES, where an UV/x-ray photon beam is directed onto a sample, leading to the emission of photoelectrons, which are then scattered by the surrounding atoms. The resulting secondary electrons that leave the sample are transferred by means of an electron optical column to a dedicated imaging system. Just as in PES, the sample depth probed by PEEM is very thin (in the nm range), making it a surface-sensitive technique. Electron collection is achieved using several electron optical elements, as described in [22.26]. A high lateral resolution of less than 20 nm can be obtained using state-of-the-art instruments by limiting the energy range and angular dispersion of the electron beam (at the expense of intensity).

Of particular interest to us in the context of this chapter is the version of PEEM that uses x-ray beams to excite photoelectrons, which is known as x-ray photoelectron emission microscopy (X-PEEM). Synchrotron radiation sources are frequently exploited to excite photoemitted electrons in X-PEEM, particularly for

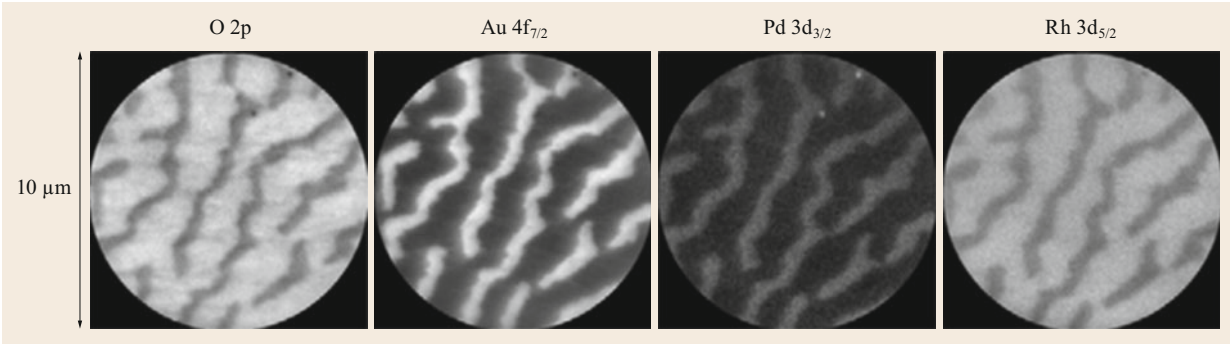

Fig. 22.11 X-PEEM images illustrating the formation of stationary patterns of Au and Pd on Rh(110) along with phase separation of Au and Pd from O (Reprinted from [22.27]. © IOP Publishing. Reproduced with permission. All rights reserved)

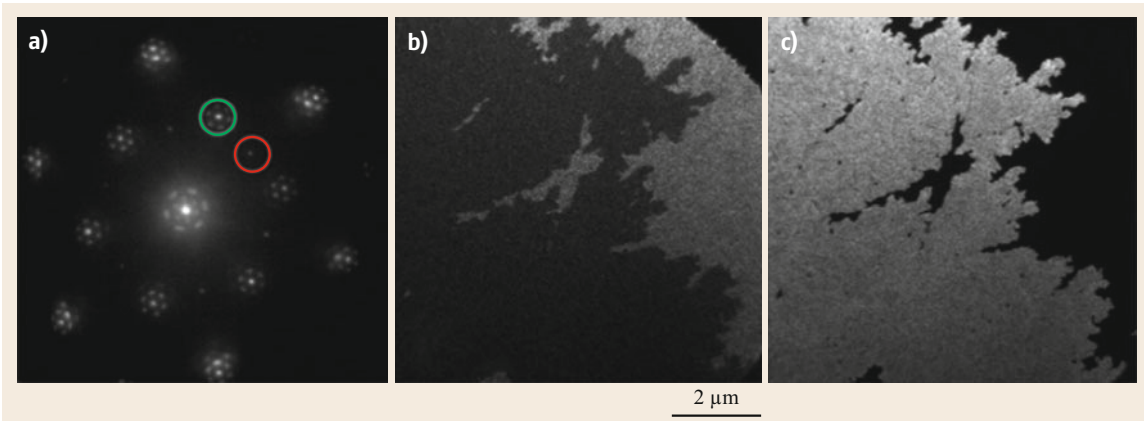

Fig. 22.12a–c Steps involved in phase identification for iron oxide films using **(a)** LEED and **(b,c)** LEEM structures. Images **(b)** and **(c)** focus on the *green*- and *red-labeled* LEED spots in **(a)**, which correspond to bright areas with corundum and spinel structures, respectively. The electron energy in all measurements was 38 eV (Reprinted from [22.28], with permission from Elsevier)

low-dimensional systems. For such systems, X-PEEM also facilitates chemical contrast, which is obtained by tuning the incident photon energy at the absorption edges of the various elements. Furthermore, the abovementioned problem with low counting rates when attempting to achieve high-resolution performance is mitigated by the high flux of synchrotron sources.

As an example of the ability of X-PEEM to resolve chemical species, Fig. 22.11 shows four images of the same sample surface obtained with photoemission energies corresponding to the indicated core levels. The sample is Rh(110) modified with Au and Pd of sub-ML coverage, and this material has been used as a catalyst for water formation. This leads to reorganization and phase separation within Au and Pd adlayers, which are spectator species (they do not actively participate in the reaction but they do block some active sites on the surface). The phase separation is clearly visible in the energy-resolved X-PEEM images [22.27].

Among the various electron microscopy techniques available, one particular method exploits low-energy (on the order of 1–100 eV) electrons and is therefore known as low-energy electron microscopy (LEEM) [22.29]. In this method, the probe is an electron beam that impinges on the sample and is backscattered towards a screen through an electron optical column. The typical spatial resolution of this approach is high (about 10 nm laterally). An important feature of the technique is the ability to image surface structures in situ and in real time, even at relatively high temperatures, which makes LEEM a very powerful tool for studying surface phase transformations, mainly by aiding the identification of the different phases. The example presented in Fig. 22.12 is phase identification for an iron oxide film containing mixed phases. LEEM also allows for the acquisition of low-energy electron diffraction (LEED) patterns. Figure 22.12a shows that these patterns are related to the presence of differ-

ent crystal structures, namely corundum (green circle) and spinel (red circle). By selecting the momentum of the emitted electrons, different LEEM images can be acquired, as shown in Fig. 22.12b,c. Further chemically sensitive measurements (not shown) revealed the presence of both Fe_3O_4 and Fe_2O_3 (the latter also in different phases) [22.28].

Finally, scanning probe techniques are widely exploited in the study of low-dimensional systems. The most well known are atomic force microscopy (AFM) [22.30] and scanning tunneling microscopy (STM) [22.31], both of which utilize sharp tips that are placed in close proximity (subnanometer range) to a sample surface and scanned laterally by piezoelectric actuators, allowing the surface morphology to be measured.

AFM is based on the detection of attractive and repulsive interactions between the apex atoms in the probe tip and atoms on the surface of the sample. The tip is typically mounted on a cantilever that bends to a degree that depends on its hardness and the strength of the interactions, which have different effective ranges; for instance, chemical interactions are short-range interactions whereas van der Waals and electrostatic interactions are longer-range interactions. The strengths of the different types of interactions depend on the system that is probed. Measurements can either be static (the bending of the cantilever is measured directly) or dynamic (the cantilever is oscillated close to resonance and the interaction forces influence the frequency, amplitude, or phase of the oscillations).

In STM, a metallic tip is brought in close proximity to (a few angstroms from) the surface of a conducting sample, leading to an overlap of the wavefunction of the apex atom in the probe tip with surface electronic states. If an electrostatic potential is applied between the probe tip and the surface, the quantum tunneling of electrons is facilitated. A tunneling current can therefore be measured that depends strongly on the tip–sample distance, which is the reason for the extremely high spatial resolution (atomic level) of STM.

AFM is a straightforward choice when examining insulating materials because, unlike STM, the sample and tip do not need to be conductors. This is particularly useful for thick oxides that, in principle, cannot be investigated using STM (although they can be made sufficiently conductive for STM using specific strategies, e.g., by producing defects [22.32]).

Figure 22.13 shows, as an example, an AFM topographic image of the surface of a thin (8 ML) MgO film on Fe(001). MgO is a wide-gap insulator and is therefore difficult to study with STM unless it is present as ultrathin layers on conducting substrates (see later in this chapter). Figure 22.13 reveals, in particular, the development of directional step edges that form due to the presence of misfit dislocations [22.7].

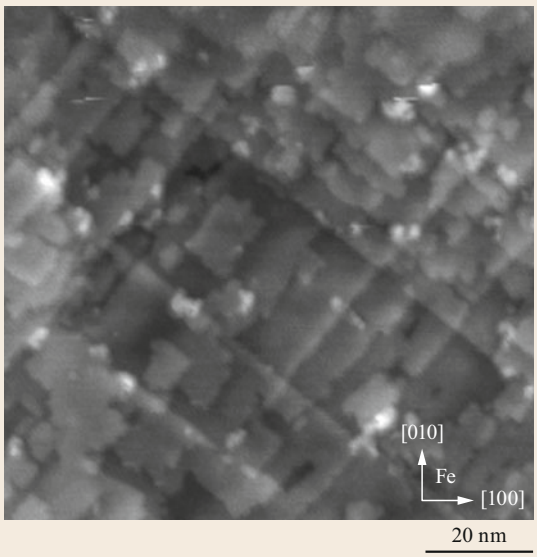

Fig. 22.13 AFM image of an 8 ML thick MgO film on Fe(001) (Reprinted from [22.7], with permission from Elsevier)

On the other hand, STM is widely used for ultrathin oxide films because it is often performed in UHV conditions, and these are the conditions that are usually applied when samples of this nature are investigated. An example of the use of STM in this context was shown earlier in the chapter: see Fig. 22.1. Very high quality STM images of ultrathin oxides with atomic resolution have also been obtained in many other cases. Figure 22.14 shows two examples relating to a 2 ML thick MgO film deposited on Ag(001) and a FeO monolayer grown on Pt(111). In their bulk forms, both oxides have a rock salt crystal structure (Table 22.1) that develops along different crystallographic planes in the images due to the epitaxial relationships of the oxides with their respective substrates (see also Sect. 22.2.1).

22.2.3 Magnetic Measurements

For thin and ultrathin magnetic oxide films, it is also necessary to experimentally characterize the magnetic properties of the samples. All of the methods discussed in earlier sections can be implemented as a magnetic variant, as described below.

Magnetic Spectroscopic Techniques

In magnetized FM samples, the internal magnetic field acts as a quantization direction for electron spin, mean-

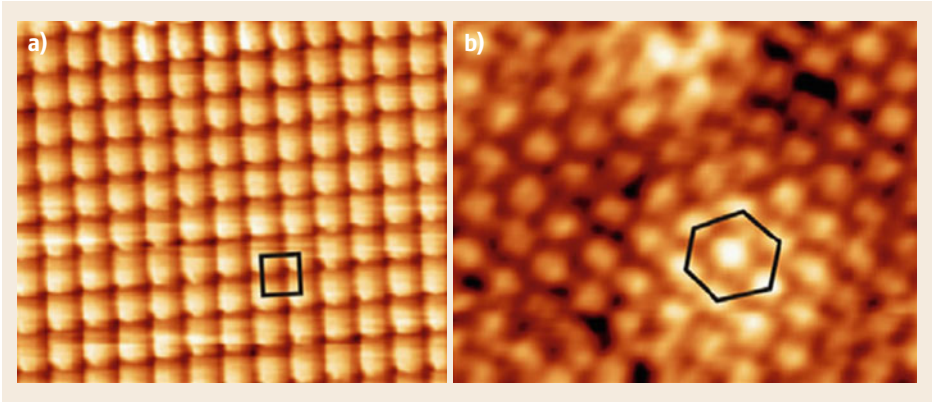

Fig. 22.14a,b STM images of **(a)** 2 ML MgO/Ag(001) and **(b)** 1 ML FeO/Pt(111) (both images show regions $3.5 \times 2.9\,\mathrm{nm}^2$ in size). Both oxides have a rock salt structure, but they expose different crystallographic planes due to differences in substrate symmetry (Reprinted from [22.33], with permission from Elsevier)

ing that the electrons emitted in photoemission experiments have a spin quantum number. This allows the spin polarization P of the photoelectrons to be defined as follows:

$$P = \frac{N_\uparrow - N_\downarrow}{N_\uparrow + N_\downarrow} , \qquad (22.1)$$

where the up and down arrows refer to the spin direction with respect to the quantization axis. The measurement of P in PES experiments is achieved by adding spin detectors (polarimeters) to the standard equipment, leading to a method known as spin-polarized PES (SPPES) or spin-resolved PES (SRPES). Polarimeters are commonly used to measure spin scattering asymmetries, although they have the drawback of dramatically reducing the signal intensity. State-of-the-art instruments and synchrotron radiation measurements can largely bypass this limitation, making SPPES an important method for deriving information on the spin-resolved electronic structures of magnetic materials.

As an example, Fig. 22.15 presents PES and SPPES spectra for a $CrO_2(100)$ epitaxial film on TiO_2. As also mentioned in Table 22.3, CrO_2 is a FM oxide with an ordering temperature that is above RT in its bulk form. *Fujiwara* et al. [22.34] report SPPES measurements obtained at both RT and 40 K that are consistent with this characterization. The difference in the spin-polarized density of states is also related to the half-metallicity of CrO_2.

A different approach can be employed to measure spin-polarized electronic states in XAS experiments. In such experiments, dipole transitions do not allow spin flips, so, in principle, it is possible to measure the number of d holes with up and down spin provided that either spin-up or spin-down electrons can be selectively excited by the x-ray beam. This is achieved by using circularly polarized photons, which are available in dedicated beamlines of synchrotron radiation facilities. In x-ray magnetic circular dichroism (XMCD), XAS spectra with oppositely (either right or left) circularly polarized x-ray photons are acquired and then subtracted from each other. The XMCD signal is therefore proportional to the difference in spin-up and spin-down holes in the d shell, and its sign provides information on the direction of the sample magnetization. The strongest signal is obtained when the magnetization is parallel to the propagation direction of the photon beam. As it is based on XAS, XMCD also provides elemental and shell specificity, thus permitting the identification of magnetized species in multicomponent (e.g., multilayer) samples. Furthermore, it has been demonstrated that simple sum rules can be used to quantitatively determine spin and orbital angular momenta from XMCD spectra.

As an example, Fig. 22.16 reports one of the first XMCD measurements, which was performed on a Ni(111) crystal [22.35]. The opposite signs of the XMCD peaks at the two absorption edges are typical of XMCD spectra of all FM TMs.

Just as for XMCD, it is possible to acquire XAS spectra with linearly polarized x-ray photons where the polarization direction is either in or out of the synchrotron plane. Subtracting such spectra from each other leads to an x-ray magnetic linear dichroism (XMLD) spectrum. The XMLD signal is not related to the magnetization vector $\boldsymbol{M}$ (unlike in XMCD), which is zero in an AF material, but to the direction of the local magnetic moments. This implies that XMLD is a very special method: a magnetic spectroscopy that is sensitive to the AF order of a sample. On the other hand, an XMLD signal can be also produced by nonmagnetic properties, such as asymmetry of the crystal field of the

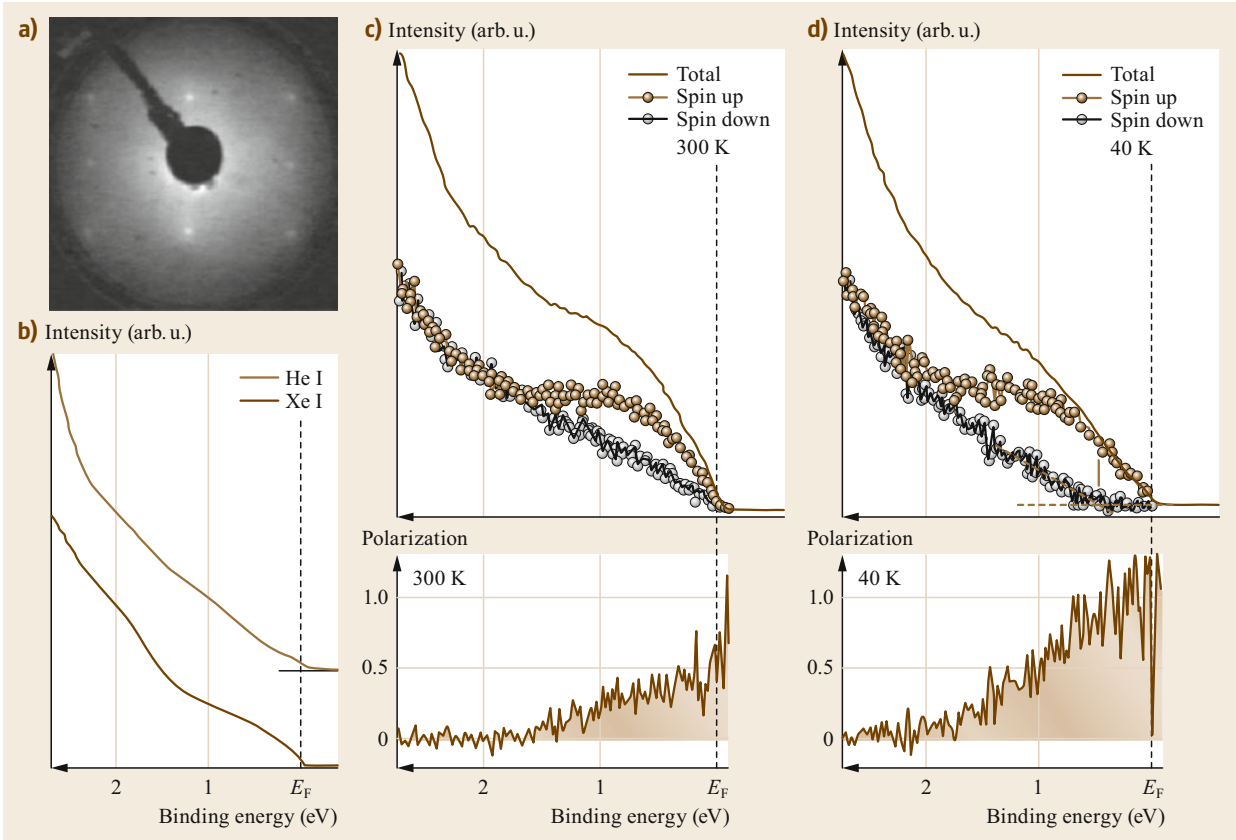

Fig. 22.15 **(a)** LEED pattern of $CrO_2(100)/TiO_2$ ($E = 45\,eV$). **(b)** Valence-band spin-integrated PES spectra measured at $h\nu = 21.2\,eV$ (He I) and $h\nu = 8.44\,eV$ (Xe I) at 300 K. **(c,d)** Spin-resolved photoemission spectra measured via the Xe I line and the corresponding energy dependence of the spin polarization at 300 and 40 K, respectively (Reprinted from [22.34], with the permission of AIP Publishing)

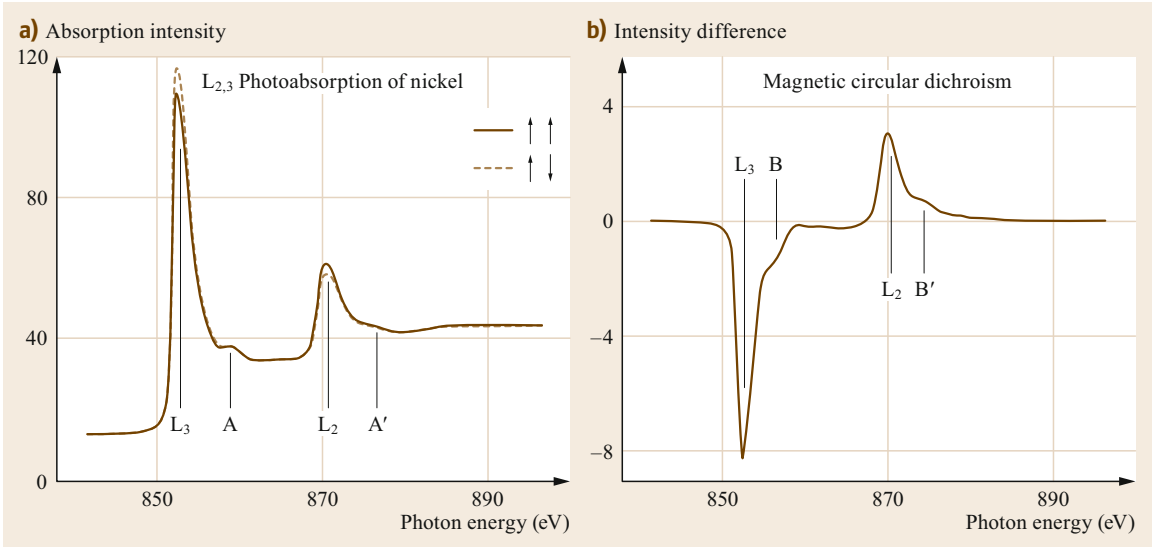

Fig. 22.16 XAS **(a)** and XMCD spectra **(b)** obtained for a Ni(111) crystal (Reprinted with permission from [22.35]. © 1990 by the American Physical Society)

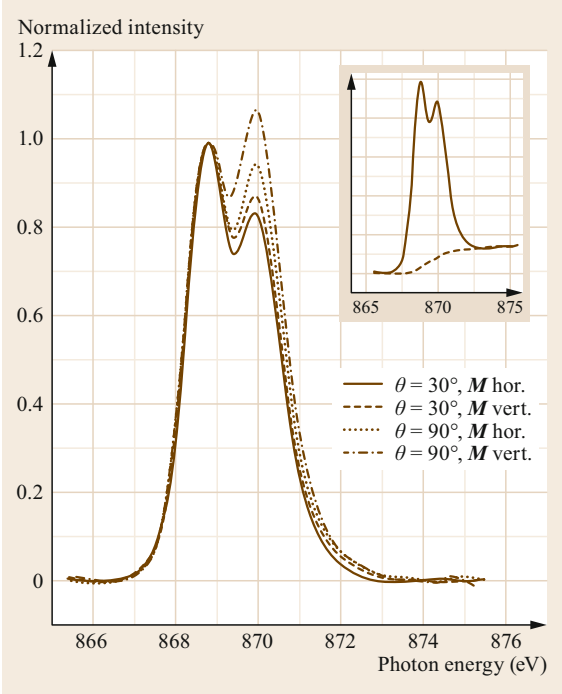

Fig. 22.17 Normalized Ni L_2 absorption spectra obtained at 180 K for a 7 ML NiO/Fe(001) sample. θ is the angle between the x-ray polarization direction and the surface normal; $\boldsymbol{M}$ refers to the substrate magnetization. *Inset*: raw spectrum with background (Reprinted with permission from [22.36]. © 2004 by the American Physical Society)

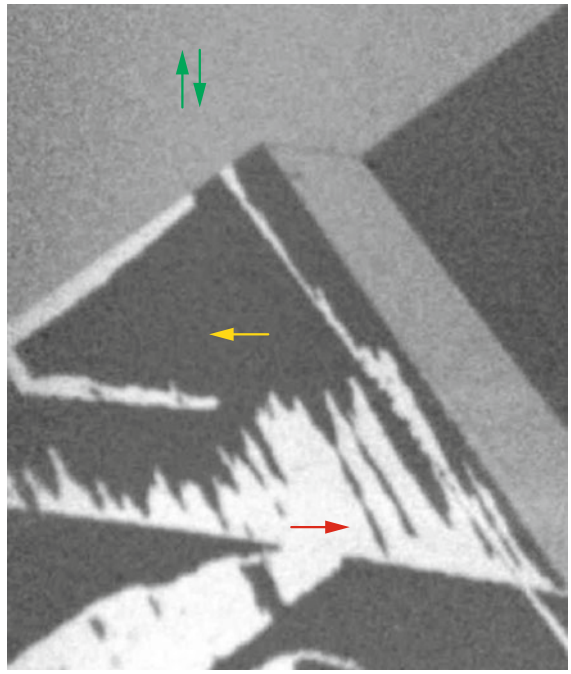

Fig. 22.18 XMCD-PEEM images of Fe(001) domains in an Fe/NiO/Fe trilayer (NiO thickness: 1.4 nm). The x-rays' propagation direction is parallel to the horizontal axis in the image. The *arrows* indicate the directions of the FM domains. The field of view is about 75 μm. The image was acquired at the PEEM-2 beamline of the ALS synchrotron (Berkeley, USA) (Reprinted by permission from [22.37], © Brambilla 2005)

sample. Thus, care must be taken when analyzing the experimental data.

In the example shown in Fig. 22.17, XMLD spectra were acquired for an ultrathin (7 ML) NiO film on Fe(001). The spectra were obtained at the Ni L_2 edge for different measurement geometries, i.e., either normal ($\theta = 90°$) or grazing ($\theta = 30°$) incidence and with the substrate magnetization $\boldsymbol{M}$ in either the horizontal or the vertical plane (i.e., parallel or perpendicular to the x-ray linear polarization direction, respectively). Since the crystal field shows fourfold symmetry about the NiO(001) surface normal, it provides a constant contribution as a function of the azimuth, so the difference between the spectra acquired at normal incidence with crossed polarizations is due to the presence of long-range AF order in the measured film [22.36].

Magnetic Microscopic Techniques

The different responses of magnetic samples upon the absorption of differently polarized x-rays can also be exploited to obtain a magnetic contrast in images acquired with an X-PEEM microscope. This involves implementing the XMCD and XMLD techniques to realize XMCD-PEEM and XMLD-PEEM measurements. Such measurements are performed by acquiring images at photon energies corresponding to peaks in the XMCD and XMLD spectra of a magnetic element present in the sample with different circular or linear polarizations. The acquired images are then subtracted from each other and normalized in order to obtain the magnetic contrast image. Since the resolution of state-of-the-art X-PEEM microscopes can be as low as 10 nm, the images can reveal details of the magnetic domain and domain wall microstructure in both FM and in AF materials using XMCD and XMLD, respectively.

As an example, Fig. 22.18 shows XMCD-PEEM images of Fe domains in an Fe/NiO/Fe trilayer [22.37, 38]. Here, the incident direction of the x-ray beam was parallel to the horizontal axis of the image. The magnetization in the black domains differs from that in the white domains by 180°, as indicated by the red and yellow arrows, while domains differing in magnetization by 90° with respect to the white domains are not resolved (gray areas).

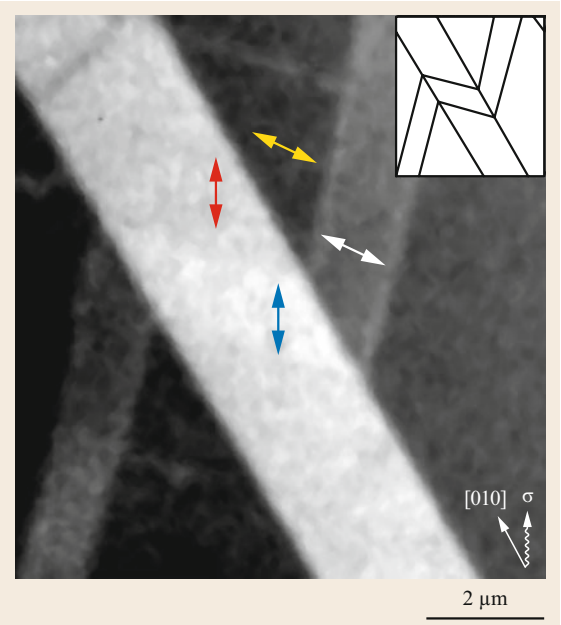

Fig. 22.19 XMLD-PEEM image of the surface of a NiO(001) crystal. The different gray tones correspond to different AF domain orientations (Reprinted with permission from [22.39]. © 2001 by the American Physical Society) ◄

An example of XMLD-PEEM is shown in Fig. 22.19, which presents the AF domain configuration of a cleaved NiO(001) crystal. Here, the linear polarization was in the synchrotron plane and the beam direction was 30° from the [010] sample direction, as indicated in the inset. Four different gray tones are discernible, which relate to four different AF domains. Note that the direction of the local magnetic moments has both in-plane and out-of-plane components; see [22.39] for a full description.

There is also a spin-polarized version of LEEM (SPLEEM), in which spin-polarized electrons are directed onto the sample. The polarization $\boldsymbol{P}$ of the impinging electron beam can potentially be oriented in any direction; low-energy electrons are either backscattered or absorbed depending on their spin and on the sample magnetization $\boldsymbol{M}$, so the reflected electron beam permits the imaging of magnetic domains and domain walls in FM samples [22.41].

Figure 22.20 demonstrates the ability of SPLEEM to resolve FM domains with a lateral resolution of few tens of nm in different spatial directions. The figure compares the magnetic domain configuration in a thin (11 ML) Co film on Ir(111) with that in a thin Co film intercalated beneath graphene that had previously been grown on the same Ir(111) substrate. In the former case, the Co magnetization is in the plane of the film,

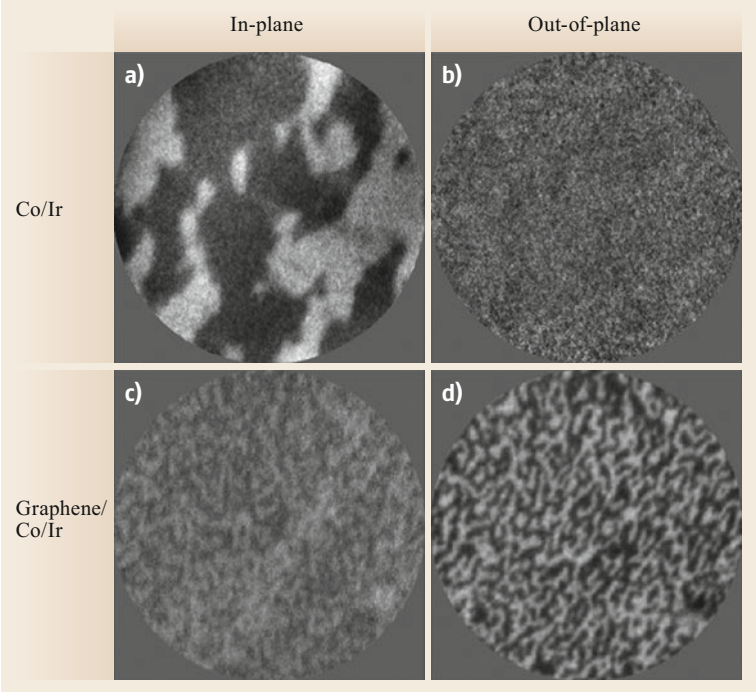

Fig. 22.20a–d SPLEEM images (field of view: 10 μm) of 11 ML of Co deposited on Ir(111) **(a,b)** and intercalated at the graphene/Ir(111) interface **(c,d)** (Reprinted from [22.40], with the permission of AIP Publishing)

whereas it is in the out-of-plane direction in the latter case [22.40].

There are also magnetic versions of both AFM and STM: magnetic force microscopy (MFM) [22.42] and spin-polarized scanning tunneling microscopy (SP-STM) [22.43], respectively.

In MFM, the FM sample produces a magnetic stray field that is detected by measuring the force it exerts on another small magnetic element, the tip. This approach is very similar to standard AFM, although the measured forces are usually considerably smaller. It is worth noting that a strong force would correspond to a strong magnetic interaction between the tip and the sample, which could potentially modify the magnetic configuration of the latter (clearly an unwanted effect). In a typical situation, the tip is tens of nm away from the surface, and bending of the order of a nm is measured [22.44]. MFM measurements are therefore usually performed in the dynamic mode (see above). So far, MFM has generally been employed in magnetic recording research, largely because it does not require specific sample preparation procedures, magnetic recording media have smooth surfaces and very high stray fields, and such media are not strongly influenced by external magnetic fields.

Figure 22.21 shows a typical FM domain configuration in a commercial hard disk; this configuration represents the recorded tracks [22.42].

In magnetic materials, the exchange interaction introduces a term that removes the spin degeneracy of the electronic bands. Provided that magnetized tips are employed, this implies that the tunneling probability in STM is dependent on the relative orientation of the magnetization vectors of the tip and sample, a scheme very similar to that used in magnetic tunneling junctions [22.45]. Since different tunneling probabilities reflect different apparent heights in the sample topography, this SPSTM approach permits the visualization of magnetic domains with the high spatial resolution typical of STM. In particular, it is possible to show that a magnetic contrast is obtained by mapping the differential conductance $\mathrm{d}I/\mathrm{d}V$, where I is the tunneling current and V is the applied bias [22.46].

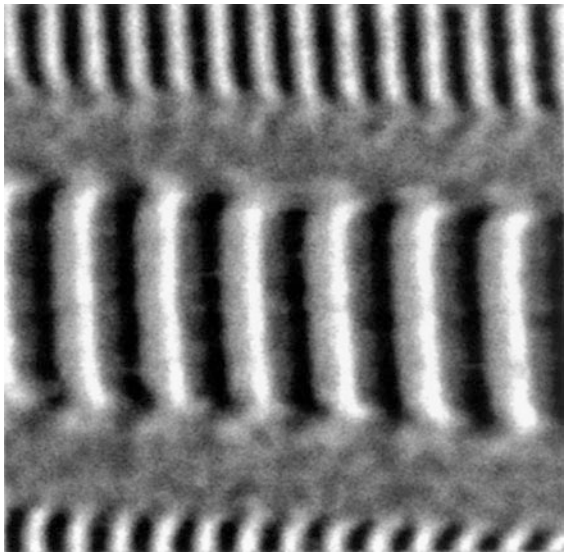

Fig. 22.21 Standard MFM image of recorded tracks on a hard disk. The image size is $12 \times 12\,\mu\mathrm{m}$ (Reprinted by permission from [22.42], © Ann. Revs. 1999)

One important aspect of SPSTM measurements is the preparation of suitable magnetized tips, which should be able to guarantee both high spatial resolution, high spin polarization, and very low stray fields to ensure that the magnetic configuration of the sample is not perturbed. One of the most successful methods of achieving this is to coat a standard W tip with an ultrathin layer of magnetic material such as Fe or Cr. In-plane or out-of-plane (with respect to the sample surface) magnetization of the tip can be realized by selecting an appropriate material and thickness for the coating [22.43].

An interesting example of the magnetic imaging capabilities of SPSTM is given by the measurement of Cr(001) crystal surfaces. Cr is termed a topological AF, as each (001) layer is FM and the magnetizations of the adjacent layers are opposite to each other, resulting in an AF structure overall. Therefore, when observing the Cr(001) surface, each terrace step separating an odd number of layers also separates oppositely magnetized FM domains. This is clearly apparent in Fig. 22.22, which compares the topography of a Cr(001) surface characterized by several single-layer steps (Fig. 22.22a) to a differential conductance map, which reveals oppositely magnetized FM domains (Fig. 22.22b) characterized by different gray tones [22.46].

Optical Methods: The Magneto–Optic Kerr Effect

The magneto-optic Kerr effect (MOKE) is the phenomenon where the properties of a linearly polarized laser beam change as it is reflected from the surface of a FM sample. The changes of interest are typically either a rotation of the direction of polarization or a shift in the ellipticity of the light, both of which are proportional to the magnetization of the sample. The depth sensitivity of MOKE is on the order of tens of nm, and it can be performed in different geometries by illuminating the sample at different angles of incidence. The application of a variable external magnetic field $\boldsymbol{H}$ per-

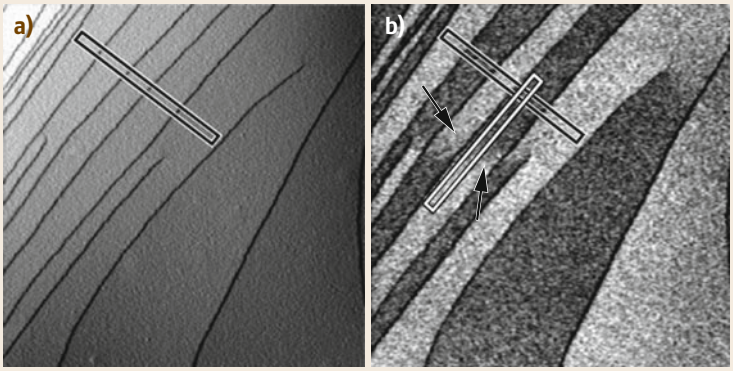

Fig. 22.22 **(a)** STM topographic image (1 μm × 1 μm) of the Cr(001) surface, where all terraces are separated by monoatomic steps. The data were obtained with an Fe-coated tip. **(b)** Spin-polarized differential conductance map of the same surface region. The *arrows* indicate the presence of a more complicated micromagnetic structure corresponding to screw dislocations (Reprinted with permission from [22.46]. © 2000 by the American Physical Society)

mits the acquisition of magnetic hysteresis loops. In the polar configuration (i), the beam hits the surface at normal incidence and the measured effect is related to the out-of-plane component of $\boldsymbol{M}$. In the longitudinal configuration (ii), the angle of incidence of the light is not zero and $\boldsymbol{H}$ is applied within the plane of incidence and parallel to the sample surface. Note that the polarization of the light can either be transverse magnetic or transverse electric and there is no longitudinal Kerr effect at normal incidence. In the transverse configuration (iii), $\boldsymbol{H}$ is perpendicular to the plane of incidence (which is, again, not normal to the surface). In this configuration, only a transverse magnetic polarized beam generates the Kerr effect.

This set of different measurement geometries permits vector magnetometry—the full spatial determination of the magnetization vector $\boldsymbol{M}$ during the hysteresis loop, as exemplified by Fig. 22.23, which relates to a 180 nm thick CoNiO film [22.47]. It is important to note that MOKE is a relative magnetometry technique, i.e., it is not able to measure the absolute value of $\boldsymbol{M}$.

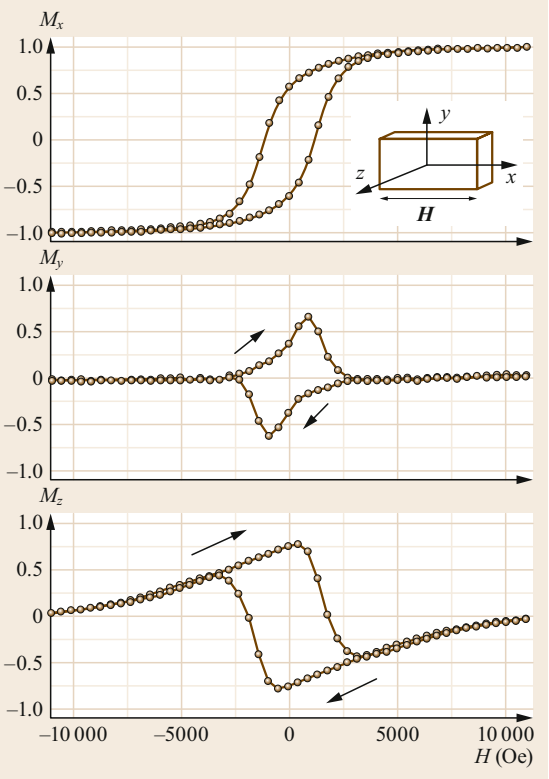

Fig. 22.23 Reduced components of the magnetization vector as a function of the applied magnetic field $\boldsymbol{H}$ of a 180 nm thick CoNiO film. The components are normalized to the saturation value of $\boldsymbol{M}$ (Reprinted from [22.47], with the permission of AIP Publishing)

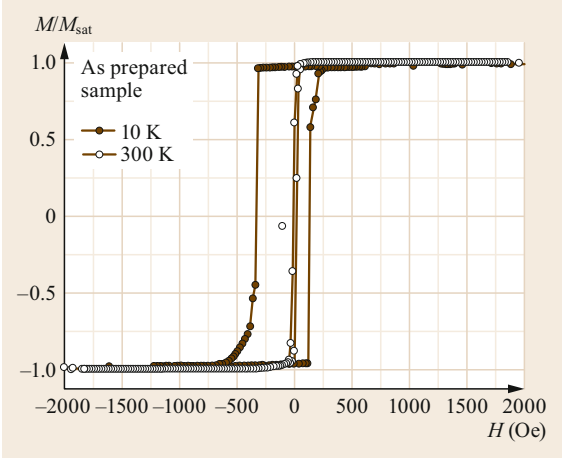

Fig. 22.24 Hysteresis loops of an Fe layer (21 nm thick) deposited on a CoO film (33 nm thick). *Open dots*: RT measurements obtained above the Néel temperature. *Filled dots*: magnetization reversal observed after field cooling to 10 K (Reprinted with permission from [22.48]. © 2007 by the American Physical Society)

The MOKE technique has been widely applied to the characterization of AF magnetic oxides included in layered FM/AF structures that exhibit the exchange bias (EB) effect [22.49]. This effect is seen when a system featuring a FM/AF interface undergoes a field cooling procedure starting from a temperature intermediate between the ordering (Curie) temperature of the FM material and the ordering (Néel) temperature of the AF material and finishing below the latter under the influence of an externally applied magnetic field. Due to the interaction between the magnetic moments at the interface, a unidirectional magnetic anisotropy is established in the sample. This can be observed as a rigid shift (EB field, H_E) of the hysteresis loop of the FM/AF system, which is usually accompanied by an increase in the coercive field H_C. AF oxides, especially NiO and CoO, have been widely studied as AF layers in EB systems [22.50].

Figure 22.24 shows the occurrence of both effects in an Fe/CoO bilayer. The MOKE loop at 300 K was obtained for an unbiased sample (open dots), whereas that at 10 K (filled dots) was attained subsequently to field cooling and clearly shows a large increase in H_C and a shift of the hysteresis loop of about 100 Oe [22.48].

22.3 Engineering Oxide–Metal Interfaces with Buffer Layers

The physical properties of layered metal–oxide heterostructures depend strongly on the atomistic details of the oxide–metal interface, so fine control of the boundary region is required to obtain specific functionalities [22.10, 50–53]. The structure and chemical composition of metal–oxide interfaces can be tailored by exploiting an appropriate buffer layer, i.e., a nanometer-thick film inserted between the substrate and the overlayer. The presence of oxide or metal buffer layers can assist the growth of oxide films on metallic substrates as well as the deposition of metallic films on oxide surfaces.

22.3.1 Buffer Layers

According to the recent literature, the presence of a buffer layer can affect the oxide–metal heterostructure in the following ways:

1. *It influences the chemical composition of the oxide–metal interface.* During the formation of an oxide–metal layered system, the metallic layer is often oxidized [22.12, 54, 55]. This oxidation occurs for two main reasons: (i) whenever an oxide film is grown via reactive deposition on highly oxidizable metallic substrates such as those composed of FM elements, the oxygen-rich atmosphere induces the development of a thin native oxide layer on the substrate [22.7, 56]; (ii) if the metallic layer can form an oxide compound that is more thermodynamically stable than the oxide it is interfaced with, migration of oxygen atoms triggers the reduction of the oxide and the oxidation of the metal [22.57, 58]. In case (i), the presence of the buffer layer can hinder substrate oxidation by preventing direct contact between its surface and gaseous oxygen, while in case (ii) it may inhibit interfacial redox reactions.
2. *It promotes the stabilization of high-quality interfaces between metals and their native oxides.* The crystal structure of a metal is often very different from that of its native oxide. For instance, Mg and Co crystallize with a hexagonal close-packed lattice, while the corresponding monoxides MgO and CoO adopt a cubic rock salt structure. Because of this symmetry mismatch, the oxidation of bulk metals results in poor-quality interfaces or even in the development of amorphous oxide layers. This drawback can be circumvented by growing metastable films, i.e., films that mimic the crystal structure of the substrate. By growing a suitable metastable phase, good epitaxy with the native oxide can be obtained [22.59–61].
3. *It can be used to tailor the morphology of metallic films grown on oxide substrates.* In epitaxial growth, the overlayer wets the substrate if the condition $\gamma_f + \gamma_{f/s} \leq \gamma_s$ is satisfied, where γ_f and γ_s are the surface free energies of the film and the substrate, respectively, while $\gamma_{f/s}$ quantifies the interaction between the substrate and the overlayer [22.62, 63].

Due to the low surface free energies of oxides, weakly interacting metals deposited on oxide surfaces generally nucleate 3-D islands. On the other hand, covering the oxide surface with a buffer layer of another oxide or metal prior to the deposition of a metal can provide a template for the growth of two-dimensional metallic films. Effective buffer layers are metals or oxides that interact strongly with their oxide or metal counterparts.

The following sections discuss some examples of the use of metallic or oxide buffer layers to tune the chemical compositions and/or the morphological structures of metal oxide heterostructures.

22.3.2 Metallic Buffer Layers

Ni and Co films on an Fe(001) surface are prototypical examples of magnetic metallic buffer layers used for the growth of epitaxial oxides on a FM metallic substrate. When NiO or CoO are grown directly on Fe(001) by reactive deposition, extensive oxidation of the substrate is observed [22.13, 64, 65]. This oxidation can be suppressed to some degree (but not prevented) by passivating the clean Fe(001) surface with 1 ML of oxygen, yielding an Fe(001)-p(1×1)O surface [22.66–70]. Figure 22.25a displays XAS spectra acquired after the deposition of NiO on an Fe(001)-p(1×1)O surface.

The XAS spectrum obtained at the Fe $L_{2,3}$ edges from Fe(001)-p(1×1)O is characterized by two peaks at about 708 and 722 eV. After the deposition of 20 ML of NiO, multiplet fine structure develops, as shown in Fig. 22.25a, indicating the chemical modification of the substrate. A comparison of the spectra of Fe oxides is provided in the top panel of Fig. 22.25a. It is apparent that a considerable amount of Fe oxide develops during NiO growth, and that the amount of Fe oxide increases as the system is annealed up to 350 °C. Finally, annealing at higher temperatures induces the dissolution of both NiO and Fe oxide, restoring the pristine metallic shape of the Fe peaks. Oxidation of the substrate also occurs with the deposition of CoO on the Fe(001)-p(1×1)O surface, as revealed by the XPS spectra shown in Fig. 22.25b. The Fe 2p peaks acquired on 1 ML CoO/Fe(001)-p(1×1)O can be obtained through the convolution of the Fe 2p transitions characteristic of Fe(001)-p(1×1)O (solid line), Fe_3O_4 (dotted line), and FeO (dashed line). Figure 22.25b also reveals that the thickness of the Fe oxide increases as the amount of CoO deposited increases.

The substrate oxidation observed at the interfaces NiO/Fe(001)-p(1×1)O and CoO/Fe(001)-p(1×1)O is mainly due to the gaseous oxygen used during the reactive deposition. As a matter of fact, assuming a typical deposition rate of 1 ML/min for Ni or Co and a background oxygen pressure of 10^{-6} mbar, the ratio of oxygen molecules that reach the surface to metal atoms

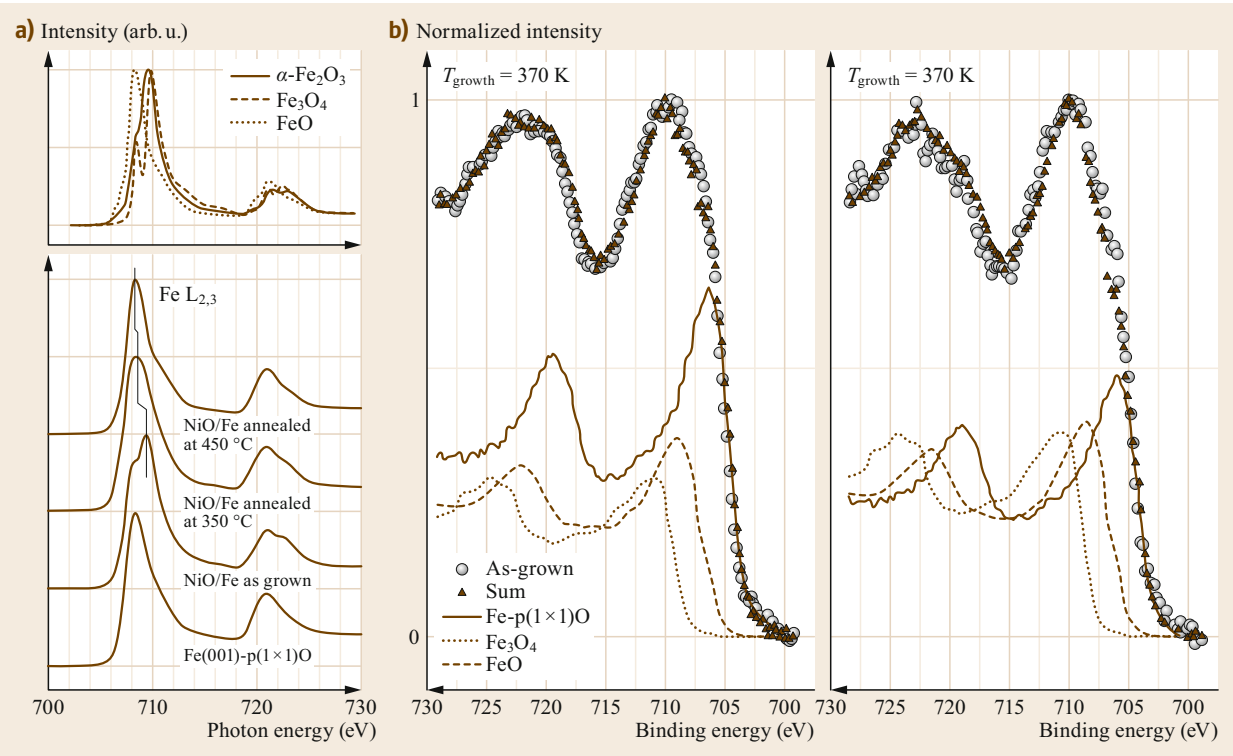

Fig. 22.25 **(a)** XAS spectra obtained at the Fe $L_{2,3}$ edges in the total electron yield mode from as-grown Fe(001)-p(1×1)O and 20 ML NiO/Fe(001) after annealing at 350 and 450 °C. Reference curves measured at the Fe $L_{2,3}$ edges from α-Fe_2O_3, Fe_3O_4, and FeO are shown at the *top* (Reprinted with permission from [22.13]. © 2004 by the American Physical Society). **(b)** *Open dots* Fe 2p XPS spectra from 1 ML CoO/Fe-p(1×1)O (*left*) and 5 ML CoO/Fe-p(1×1)O (*right*) bilayers. *Triangles* represent the sum of the Fe-p(1×1)O substrate spectrum (*solid*), the Fe_3O_4 spectrum (*dotted*), and the FeO (*dashed*) reference spectrum (Reprinted from [22.64], with permission from Elsevier)

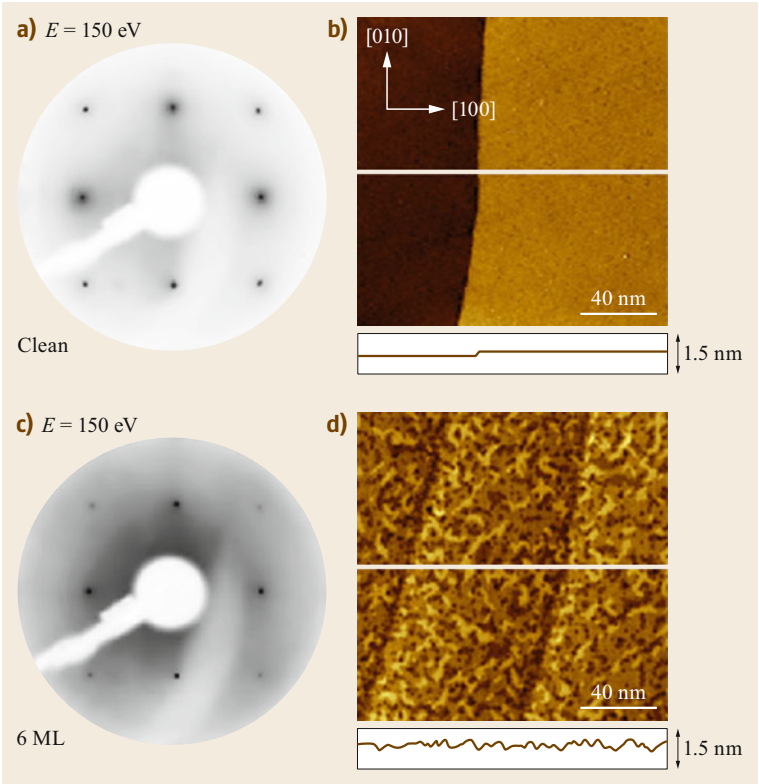

Fig. 22.26a–d LEED patterns and STM constant-current images acquired on the Fe(001) substrate **(a,b)** and after the deposition of a 6 ML thick Ni film **(c,d)** (Reprinted from [22.71]. © IOP Publishing. Reproduced with permission. All rights reserved)

that reach the surface is about 45, implying that the substrate is already covered with a native oxide layer when NiO or CoO starts to nucleate on Fe(001).

In order to avoid direct contact between the oxygen molecules and the Fe(001) surface, a Ni (Co) film can be deposited on the substrate before NiO (CoO) growth. In the following, we will see that it is important to choose an appropriate buffer layer to protect the substrate from oxidation. Bulk Ni crystallizes in a face-centered cubic (fcc) structure with a lattice constant of 352 pm, considerably smaller than that of fcc NiO (417 pm). However, ultrathin Ni films deposited on the Fe(001) surface adopt a body-centered cubic structure (bcc) with the same lattice constant as that of the Fe substrate [22.71, 73]. Figure 22.26a,c display LEED patterns measured on an Fe(001) substrate and a 5 ML thick Ni film, respectively. The diffraction patterns show the same unit cell, revealing that the Ni film grows pseudomorphically on the Fe(001) substrate. Figure 22.26b,d present STM images acquired on the surfaces of Fe(001) and 6 ML Ni/Fe(001), respectively. The bare surface displays atomically flat terraces separated by monoatomic steps, while the surface roughness increases slightly after Ni deposition.

In order to explore the possibility of using it as a protective coating against Fe oxidation, an ultrathin Ni film grown on Fe(001) was exposed to molecular oxygen [22.72, 75]. Figure 22.27a shows the evolution of AES curves acquired at normal (solid lines) and grazing (dotted lines) emission angles. The shape of the low kinetic energy peaks of AES is particularly sensitive to the chemical states of the surface elements, so it can be used to check their oxidation states [22.76]. The spectrum of the as-deposited sample (black curve) is characterized by two peaks at about 46 and 61 eV, corresponding to metallic Fe and Ni, respectively. Exposure to oxygen results in the appearance of a shoulder at lower kinetic energy than the metallic Fe peak. This feature indicates the presence of Fe oxide, as testified by the top spectrum (green curve), which was acquired for Fe(001) oxidized with 50 L of O_2. The Fe oxide peak becomes larger with increasing oxygen exposure (blue curve) and subsequent annealing in a vacuum (brown curve). Therefore, oxidation of the Ni/Fe(001) sample triggers the segregation of Fe from the bulk to the surface, where it is oxidized. Comparison of the STM images acquired before (Fig. 22.27d) and after (Fig. 22.27c) oxidation reveals that oxygen exposure causes surface roughening. Annealing in vacuum

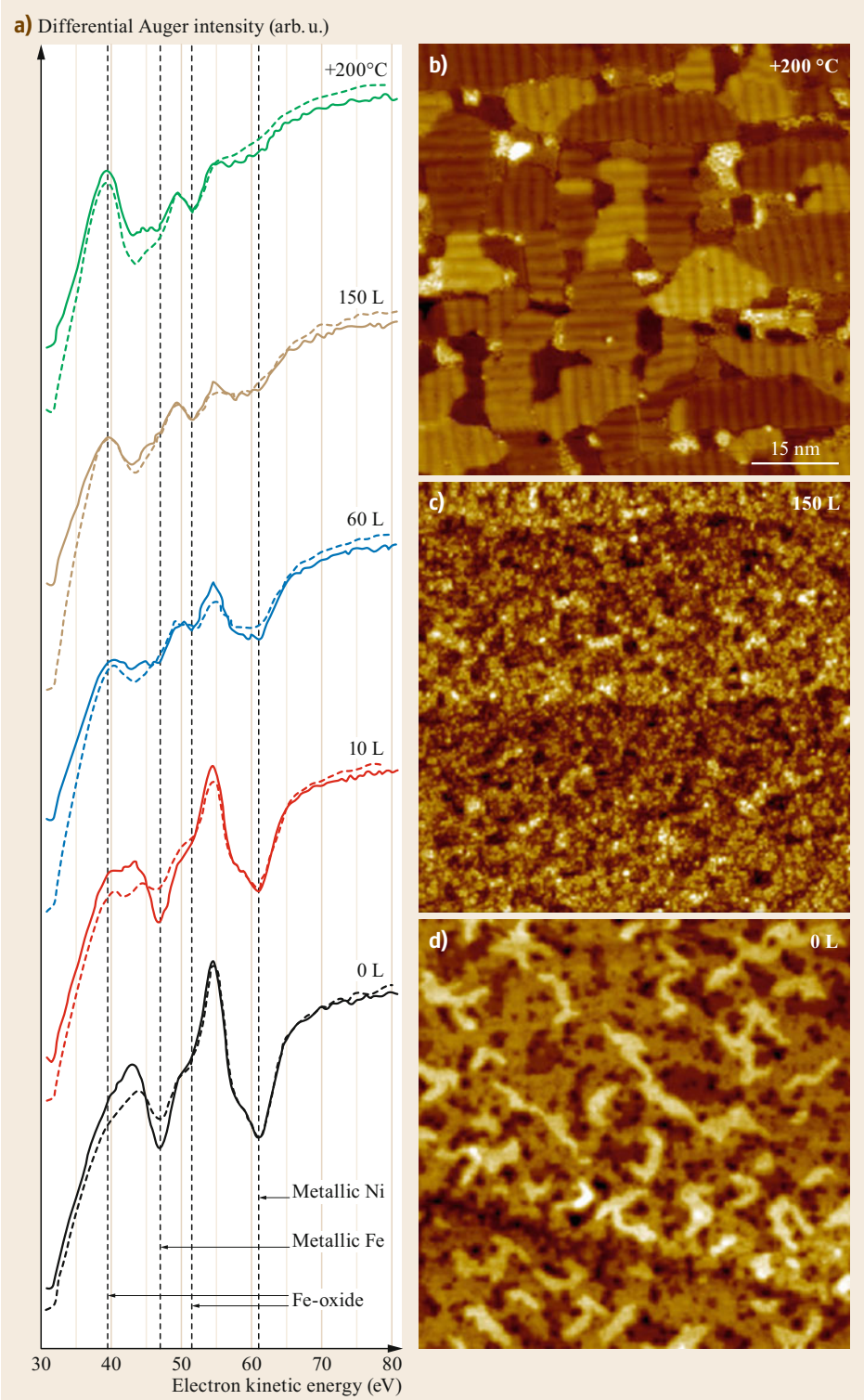

Fig. 22.27
(a) Auger spectra acquired after the exposure of a 5 ML thick Ni/Fe(001) layer to between 0 L (*black*) and 150 L (*brown*) of oxygen. The *top spectrum* was obtained for the oxidized sample after it was annealed in UHV. *Solid* and *dashed curves* correspond to spectra acquired at normal and grazing emission angles, respectively. **(d)** STM image obtained for the pristine Ni/Fe(001) sample. **(b,c)** Ni and Fe samples oxidized with 150 L of O_2 and subsequently annealed at 200 °C in UHV, respectively (Reprinted from [22.72], with permission from Elsevier)

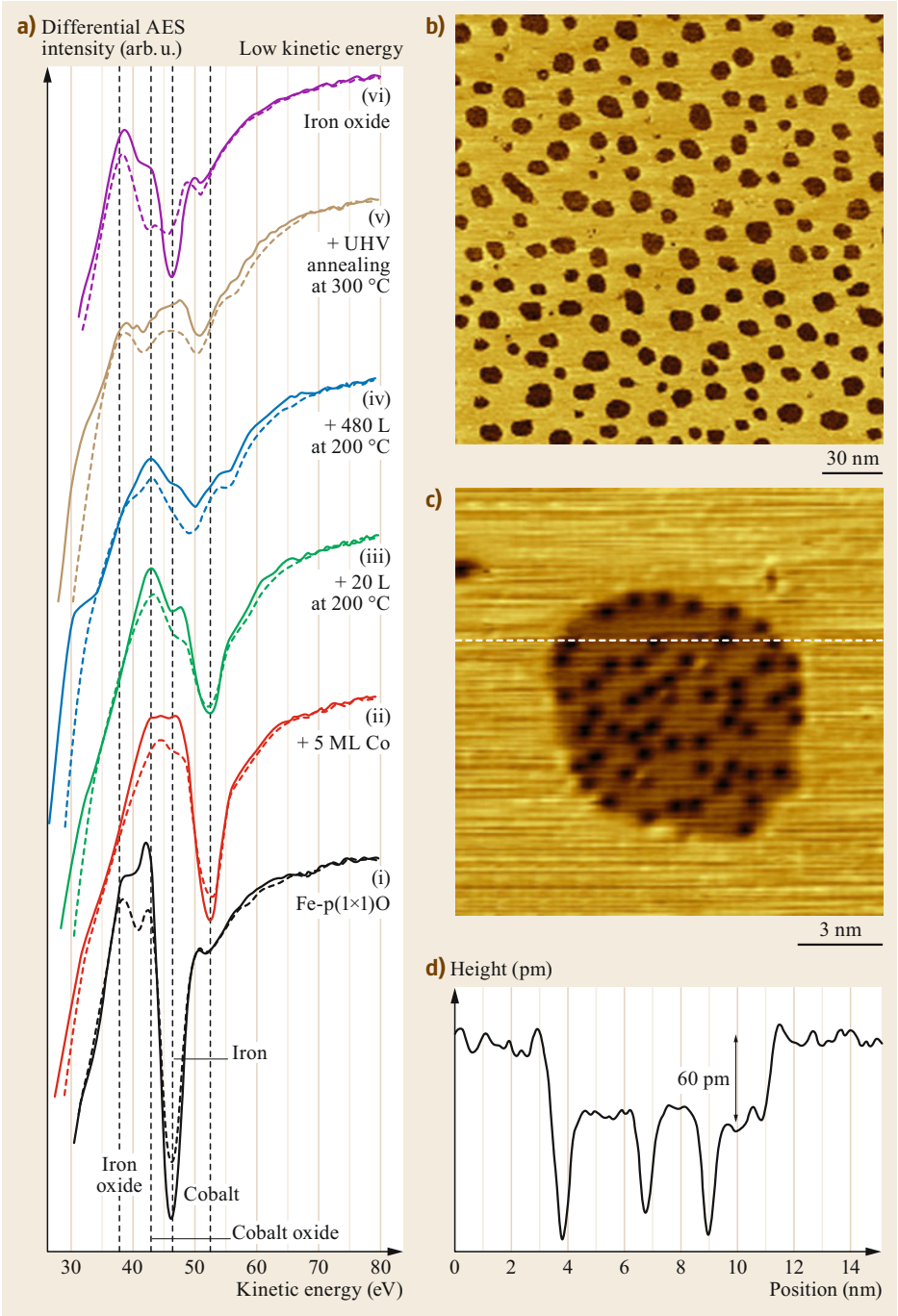

Fig. 22.28 ⟨a⟩ AES spectra acquired after the growth and oxidation of 5 ML of Co on an Fe-p(1×1)O substrate. The *top curve* is the reference spectrum of oxidized Fe. ⟨b,c⟩ Constant-current STM images of the Co film after exposure to 2 L of O_2. The profile corresponds to the *dashed line* in ⟨c⟩ (Reprinted (adapted) with permission from [22.74]. © 2016 American Chemical Society)

(Fig. 22.27b) restores the atomically flat surface. This surface is characterized by a nanometric Moiré pattern arising from interference of the topmost hexagonal FeO(111) layer (not shown; see [22.72]) with the square Ni/Fe(001) substrate. In conclusion, the Ni buffer layer cannot prevent the oxidation of the Fe(001) substrate, indicating that the NiO/Fe(001) interface is highly unstable.

A completely different oxidation path is observed when a Co buffer layer is used to protect the Fe(001) substrate. As in the case of Ni, Co grows on Fe(001) as a tetragonally distorted body-centered cubic (bcc)

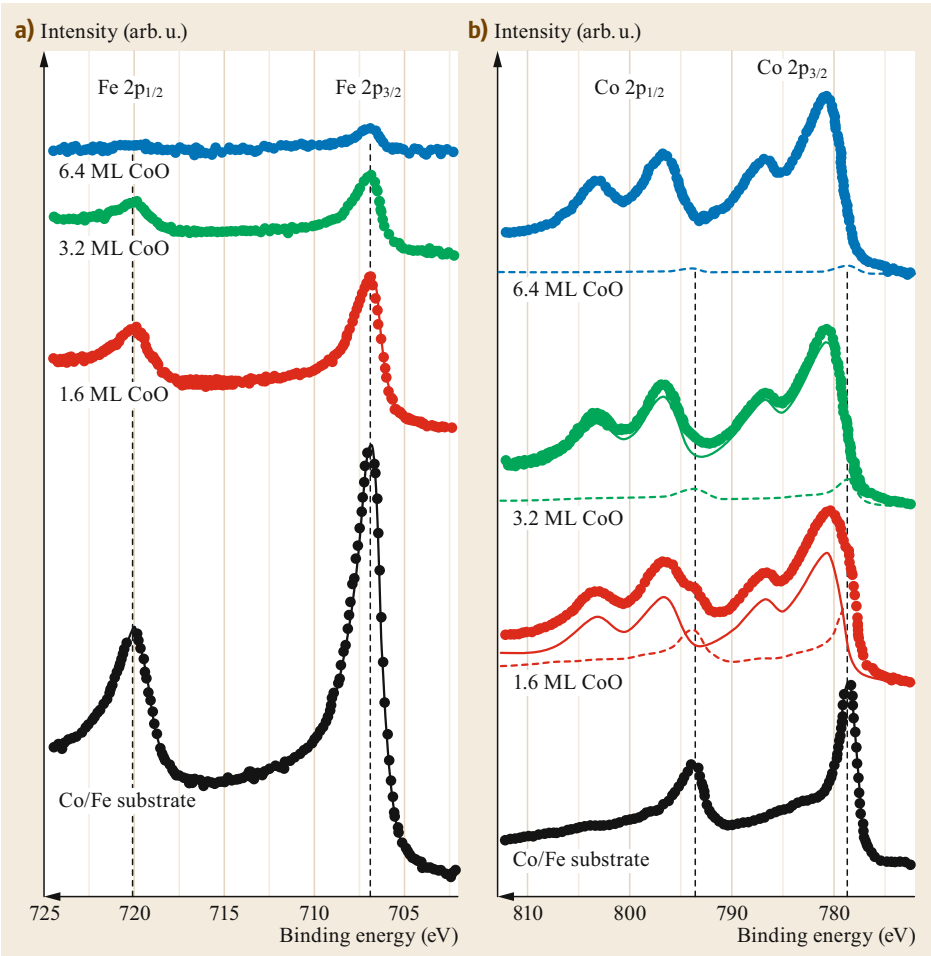

Fig. 22.29a,b XPS spectra obtained for various levels of CoO coverage. *Co/Fe substrate* refers to the surface of a 5 ML thick Co film grown on Fe-p(1×1)O. **(a)** Fe 2p peaks (*circles* are the raw data, *continuous lines* are fits to the data). **(b)** Co 2p energy region (*circles* are the raw data, *continuous lines* are fits to data for the oxidized components; *dashed lines* are fits to data for the metallic components) (Reprinted from [22.77], with permission from Elsevier)

metastable phase [22.78, 79]. The data presented in the following relate to a Co film grown on an Fe(001)-p(1×1)O surface [22.74], but similar results were observed when a Co buffer layer was stabilized on oxygen-free Fe(001). Figure 22.28a displays AES spectra measured for the Fe(001)-p(1×1)O (black curve), the 5 ML Co film (red curve), and after dosing with 20 L (green curve) and 480 L (blue curve) of oxygen. In contrast to the case in which Ni/Fe(001) is oxidized, no Fe oxide signature is observed in the spectra. However, if the sample is annealed to 300 °C in UHV, a small amount of Fe oxide can be discerned (brown curve). Figure 22.28b and c present STM images of the oxidized sample showing the nucleation of defective CoO_x islands. Due to the tunneling conditions used for the imaging, the islands appear as depressions with respect to the substrate, as indicated by the line profile drawn in Fig. 22.28d. Moreover, atomic-scale defects are visible inside the islands; these defects were assigned to oxygen vacancies [22.74].

Due its chemical stability, the Co/Fe(001) bilayer is a promising template for growing sharp CoO/Fe interfaces [22.77]. Figure 22.29 displays the XPS spectra acquired in the Fe 2p and Co 2p energy regions after the reactive deposition of increasing amounts of CoO. The Fe 2p peak position is that of metallic Fe at every step of CoO deposition, while the shape of the Co 2p doublet approaches that of oxidized Co, indicating the development of a stoichiometric oxide.

The absence of Fe oxidation also influences the morphology of the growing film. While CoO deposited directly on Fe(001)-p(1×1)O is characterized by a featureless mesoscopic morphology [22.65], the film grown on the Co buffer layer consists of a periodic array of islands (Fig. 22.30). The ordered nucleation of CoO is due to the presence of a network of misfit dislocations at the CoO/Fe(001) interface.

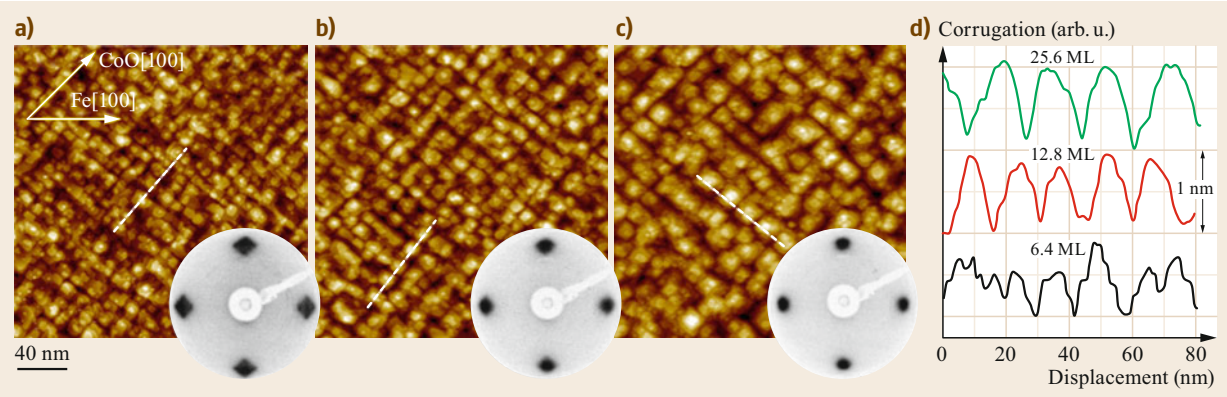

Fig. 22.30a–d STM images of 6.4 ML CoO **(a)**, 12.8 ML CoO **(b)**, and 25.6 ML CoO films **(c)**. The *insets* show the corresponding LEED patterns acquired with an electron beam energy of 50 eV. **(d)** displays the topographic profiles measured along the *white dashed lines* in the STM images (Reprinted from [22.77], with permission from Elsevier)

22.3.3 Oxide Buffer Layers

This section explores how oxide buffer layers have been successfully used to control both the interfacial chemical reactions and the morphologies of oxide–metal heterostructures.

Allegretti et al. used a CoO buffer layer inserted between NiO and Co to obtain a chemically sharp interface between an AF oxide and a FM metal [22.80]. Figure 22.31a shows the XPS Co and Ni $2p_{3/2}$ peaks acquired after the deposition of metallic Co on a NiO(001) surface. According to the upper curve, if the Co film is deposited at 100 K, its spectrum is characterized by the Co^0 component only. On the other hand, heating the Co/NiO sample at 550 K triggers the oxidation of Co, as revealed by the presence of a Co^{2+} component in the lower spectrum. The chemical instability of the Co/NiO(001) interface is also indicated by the evolution of the Ni $2p_{3/2}$ peak, as displayed in Fig. 22.31c. There are no discernible signatures of metallic N in the spectra acquired for the NiO surface (top) and the Co-covered sample at 100 K (middle), while a significant fraction of Ni^0 is present after heating.

The redox reaction can be prevented by depositing a 1–2 ML thick CoO buffer layer on the NiO before the growth of Co. Figure 22.31b displays the Co $2p_{3/2}$ peaks measured for the as-deposited CoO film (lower spectrum), those measured after the growth of metallic Co at 100 K (middle spectrum), and those measured after annealing the sample at 550 K (upper spectrum). These spectra imply that Co retains metallic character. Accordingly, after checking the Ni $2p_{3/2}$ spectra displayed in Fig. 22.32d, it is clear that there are no discernible signatures of Ni^0 at any step in the experiment.

Nozaki et al. recently used an ultrathin Fe_2O_3 layer to improve the crystalline quality of ultrathin Co films deposited on a MgO(001) surface [22.81]. Figure 22.32a displays reflection high-energy electron diffraction (RHEED) images acquired after the growth of 1 nm thick Co film on MgO. The faint diffraction spots indicate the development of 3-D Co islands that preferentially expose their hcp Co(1120) surfaces. On the other hand, if the MgO(001) surface is covered with a 0.2 nm thick Fe_2O_3 layer (Fig. 22.32b), the diffraction pattern becomes sharper, suggesting that a continuous and flat Co film develops. Interestingly, if the thickness of the Fe_2O_3 buffer layer is increased to 0.4 nm (Fig. 22.32c), a new diffraction pattern corresponding to a Co film with bcc structure develops.

22.4 Chemical and Magnetic Properties in Low-Dimensional Transition Metal Oxides

One of the main influences on the magnetic properties of a layered heterostructure is the chemical composition of its interfaces [22.82–88]. The magnetic order of a crystal depends on the chemical environment of the atoms that constitute the the crystal. For instance, Ni and Co are FM metals, but their native monoxides (NiO, CoO) are antiferromagnetically ordered. The situation is even more complex for elements that form several stable oxides, each characterized by a different stoichiometry and magnetic configuration. For example,

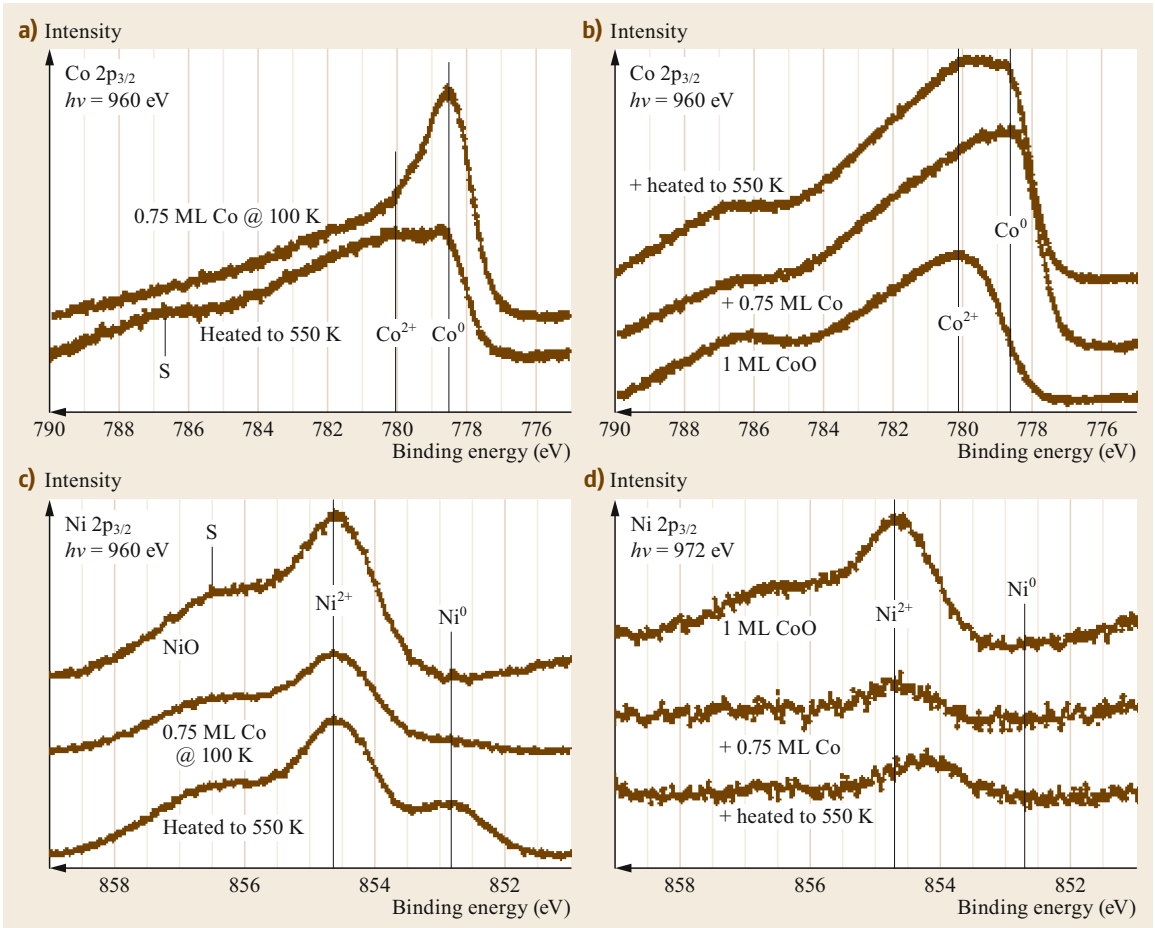

Fig. 22.31a–d Co $2p_{3/2}$ **(a)** and Ni $2p_{3/2}$ XPS spectra **(c)** acquired on the pristine 20 ML NiO(100) surface after the growth of 0.75 ML Co metal at 100 K and after annealing at 550 K, as well as Co $2p_{3/2}$ **(b)** and Ni $2p_{3/2}$ XPS spectra **(d)** of pristine 1 ML CoO(100) on NiO(100) after the deposition of 0.75 ML Co metal on the CoO(100) surface at 100 K and after increasing the temperature of this surface to 550 K (Reprinted from [22.80], with permission from Elsevier)

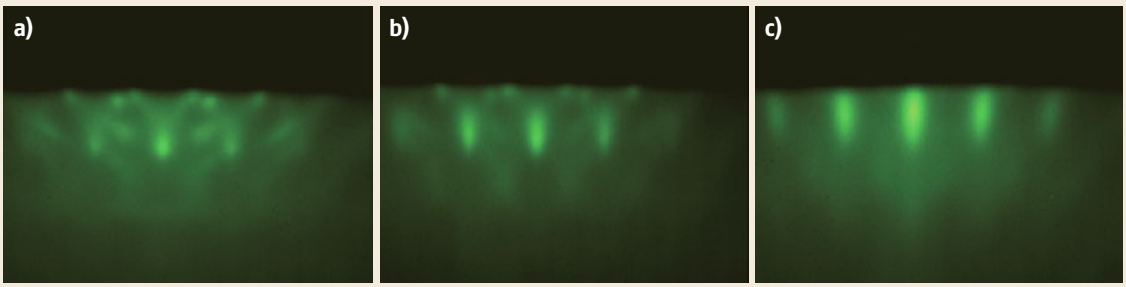

Fig. 22.32 **(a)** RHEED image of a 1 nm thick Co film deposited on pristine MgO. **(b,c)** RHEED images acquired after the deposition of 1 nm of Co on 0.2 and 0.4 nm thick Fe_2O_3 buffer layers, respectively (Reprinted from [22.81], with the permission of AIP Publishing)

FM Fe can form AF hematite (α-Fe_2O_3) and wüstite (FeO) as well as FI magnetite (Fe_3O_4) and maghemite (γ-Fe_2O_3). Heterostructures containing multivalent elements are often characterized by the presence of mixed phases, so a detailed knowledge of the interface composition is required to obtain the desired magnetic properties.

22.4.1 Influence of Interface Chemistry on Exchange Coupling

The influence of the chemical state at the interface on the magnetic properties of CoO/Fe(001) bilayers was recently investigated by *Młynczak* et al. [22.89]. Figure 22.33a presents hysteresis loops acquired in the Fe[110] direction for CoO/Fe samples containing different amounts of Fe oxide at the interface. The reference sample was obtained by growing CoO on Fe(001), the overoxidized sample by exposing the Fe(001) surface to 30 L of O_2 before CoO deposition, and the underoxidized sample by covering the Fe(001) surface with a thin Co buffer layer prior to reactive deposition. The hysteresis loops measured at 30 K for the three samples (displayed in Fig. 22.33a) demonstrate that the interface chemistry strongly influences the magnetization of the sample. Figure 22.33b displays both H_C and the exchange bias field (H_E) as functions of the temperature. These curves show that increasing the amount of iron oxide at the interface raises the temperature at which H_C starts to increase. Since the increase in H_C can be related to the establishment of AF order in the pinning layer, these data suggest that the presence of Fe_3O_4 increases the Néel temperature of CoO.

As discussed in Sect. 22.3.2, the oxidation of Fe in CoO/Fe(001) bilayers can be completely suppressed by inserting a sufficiently thick Co buffer layer into the interface. The magnetic properties of the CoO/Co/Fe(001) system have recently been investigated using MOKE [22.90]. The bare Fe(001) surface possesses two axes along which magnetization is easiest (known as *easy axes*): the [100] and [010] crystallographic directions. Due to the fourfold symmetry of the Fe(001) surface, the hysteresis loops measured in the [100] and [010] directions are identical (not shown). Figure 22.34 displays hysteresis loops acquired for a 25 ML CoO/5 ML Co/Fe(001) system. Due to the considerable thickness of the Fe substrate (more than 300 ML), EB is not observed in this system. However, the Co oxide layer strongly influences the magnetic properties of the Fe(001) substrate. The hysteresis curve acquired in the [100] direction is a square loop, i.e., the magnetization inverts in a single jump.

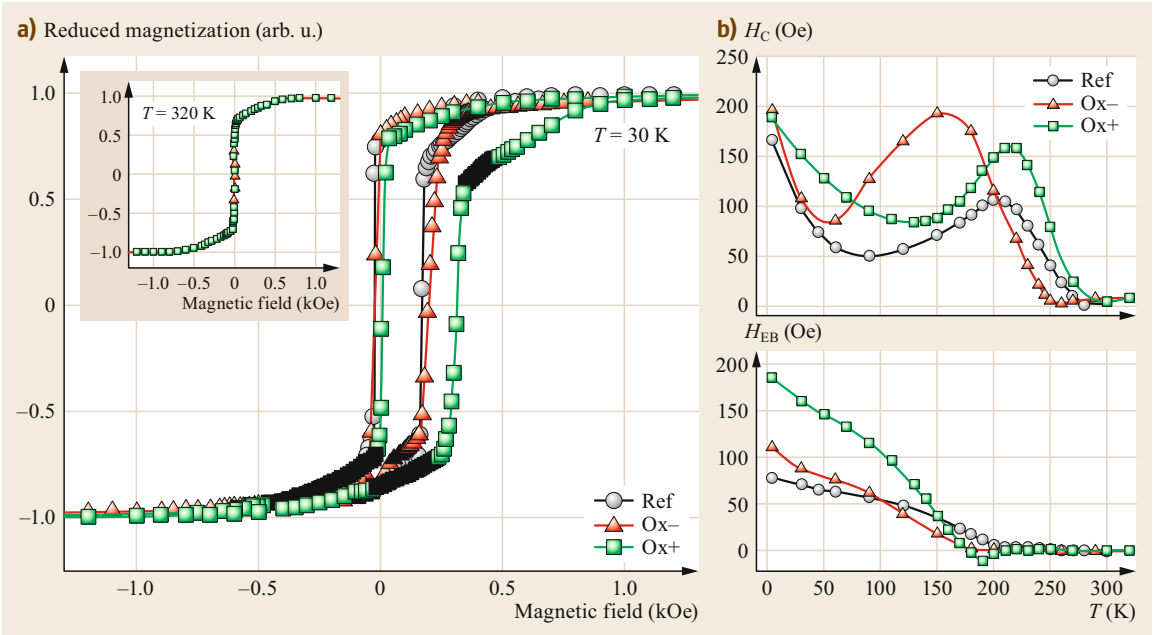

Fig. 22.33 **(a)** Magnetic hysteresis loops acquired at 30 K for the reference sample of CoO on Fe(001) (*empty circles*), an underoxidized sample (Ox−; *red triangles*), and an overoxidized sample (Ox+; *green squares*) with the magnetic field applied in the Fe[110] direction after field cooling (FC) at −20 kOe. The *inset* shows the loops measured at 320 K. **(b)** Temperature dependence of the coercive field (H_C) and that of the exchange bias field (H_{EB}). The *solid lines* are guides for the eye (Reprinted from [22.89], with permission from Elsevier)

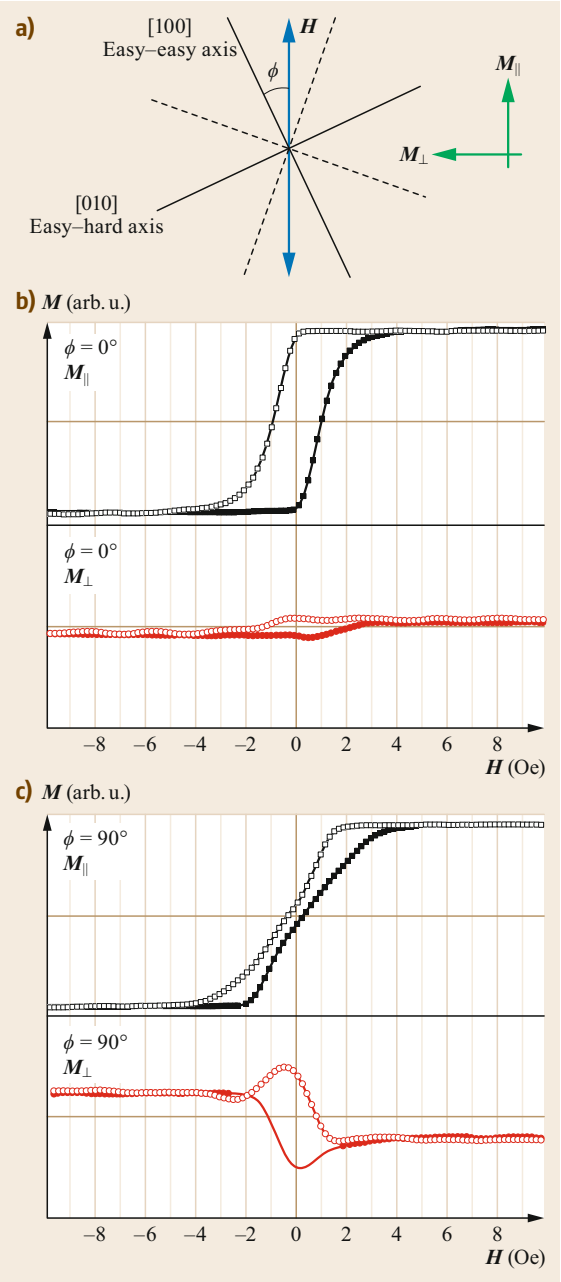

Fig. 22.34a–c MOKE hysteresis loops of the in-plane magnetization of a 25 ML CoO/5 ML Co/Fe(001) sample. The components parallel ($\boldsymbol{M}_{\parallel}$) and perpendicular ($\boldsymbol{M}_{\perp}$) to the applied field $\boldsymbol{H}$ are shown for different azimuthal angles. *Open* and *full symbols* correspond to decreasing and increasing loop branches, respectively. The experimental geometry is sketched in **(a)**, where the *continuous lines* represent the easy axes and the *dashed lines* show the axes along which magnetization is most difficult. **(b,c)** Hysteresis loops acquired in the [100] and [010] crystallographic directions, respectively (Reprinted from [22.90], with the permission of AIP Publishing) ◄

On the other hand, magnetization inversion in the [010] direction involves two jumps with two different H_C values, which are more visible in the magnetic vector component perpendicular to the applied field ($\boldsymbol{M}_{\perp}$). Such measurements suggest that during the hysteresis loop along the [010] axis, magnetic domains form with $\boldsymbol{M}$ parallel to the Fe [100] axis. The different magnetic inversions along the two nominally equivalent directions of Fe(001) can be explained by assuming that the CoO overlayer induces in-plane uniaxial magnetic anisotropy in the system, making magnetization along the [100] axis easier than that along the [010] axis [22.91, 92].

Chemical reactions at the metal–oxide interface can also induce EB in systems where the FM layer is coupled with a NM oxide. Using MOKE and magnetic second harmonic generation (MSHG), *Fan* et al. showed that the formation of a thin layer of AF FeO at the MgO/Fe(001) interface can pin the magnetization of the Fe atoms located at the interface with MgO [22.93]. Figure 22.35 shows hysteresis loops of Fe in the bulk (Fig. 22.35b–d) and at the interface (Fig. 22.35e–g) for different interfacial oxygen contents. While the bulk curves are all centered on $\boldsymbol{H} = 0$, the magnetization at the interface exhibits EB at sufficiently high interfacial oxygen concentrations.

22.4.2 Spin Transport

Magnetic tunnel junctions (MTJs) are devices consisting of two FM metals separated by a thin insulator. If the thickness of the insulator is small enough, electrons can tunnel across the junction when a voltage is applied. The electrical resistance (R) of the junction depends on the relative orientation of the magnetizations of the two electrodes, so different logic states can be obtained by writing the magnetic state of the MTJ. The parameter that quantifies the resistance asymmetry when the magnetizations of the electrodes are antiparallel (AP) or parallel (P) is the tunnel magnetoresistance (TMR), defined as $(R_{AP}–R_P)/R_P$. Large TMR values can be obtained using fully epitaxial Fe/MgO/Fe layers [22.95, 96]. These large values have been ascribed to Δ_1 majority spin electronic states of Fe(001), which decay slowly inside the MgO barrier [22.97]. For the P configuration, electrons tunnel efficiently across the barrier because the Δ_1 states that penetrate inside the MgO barrier match those present in the other Fe layer. On the other hand, for the AP configuration, the Δ_1 states are only present in one Fe electrode, so the electrons

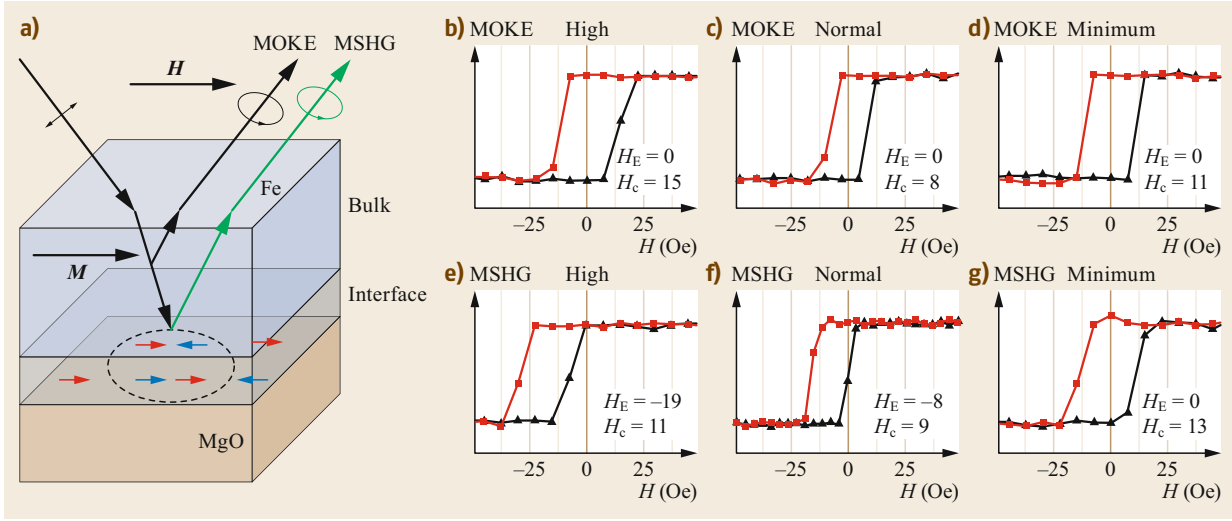

Fig. 22.35a–g Hysteresis loops acquired for MgO/Fe(001) in the bulk and at the interface with MOKE and magnetic second harmonic generation, respectively. **(a)** Experimental setup: the magnetic field H is applied in the plane along the easy axis [010] of Fe(001). The *top* and *bottom panels* show magnetization in the bulk and at the interface, respectively, for samples with high, normal, and low interfacial oxygen contents (From [22.93])

are reflected at the MgO/Fe interface. This scenario suggests that spin transport across a MTJ is strongly dependent on the interfaces between the FM metals and the oxide, so the chemical composition of the latter is expected to play a fundamental role. In the following, we discuss two examples in which chemical modifications influence MTJ performance: (i) the presence of an Fe oxide layer at the bottom MgO/Fe interface and (ii) the presence of oxygen vacancies in the MgO barrier.

In the former case, *Zhang* et al. studied the influence of an FeO layer on the electronic properties of the MgO/Fe interface via first-principles calculations [22.94]. Figure 22.36 compares the spatial dis-

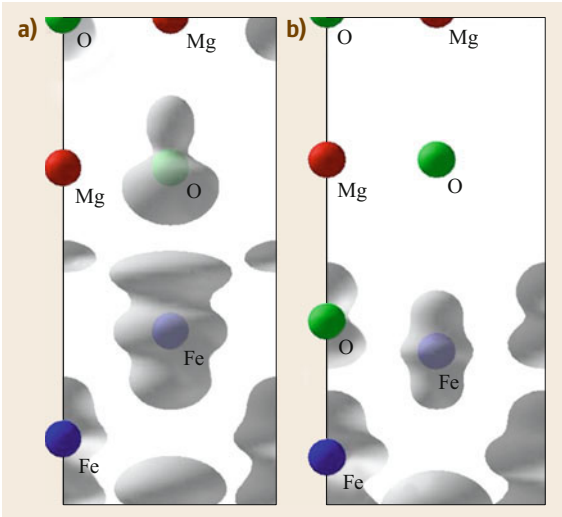

Fig. 22.36a,b The partial density of states at the Fermi energy due to the Δ_1 state in the majority spin channel near the interface region. **(a)** Without the FeO layer. **(b)** With the FeO layer (Reprinted with permission from [22.94]. © 2003 by the American Physical Society)

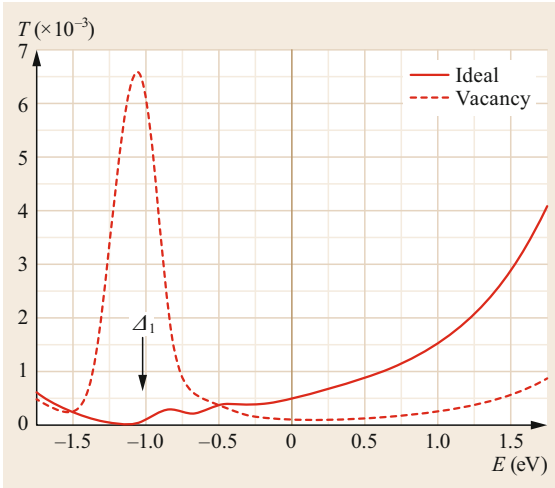

Fig. 22.37 Majority-spin transmission probability T as function of the energy E per cell in Fe/5 ML of MgO/Fe(001) for ideal MgO and for MgO with oxygen vacancies. The *arrow* indicates the bottom of the majority Δ_1 band (Reprinted from [22.98], with the permission of AIP Publishing)

tribution of the Δ_1 state for a MgO/Fe interface (Fig. 22.36a) to that for a MgO/FeO/Fe interface (Fig. 22.36b) and shows that the presence of the FeO layer strongly hinders the penetration of the electron wavefunction into the MgO barrier. The weaker coupling of the Δ_1 state to the MgO layer reduces the tunneling current of the majority spin channel and consequently the TMR. The postulated increase in R_p due to the oxidation of the Fe(001) bottom electrode was experimentally confirmed by *Bonell* et al. [22.99] and *Zermatten* et al. [22.100].

Modifying the MgO barrier can also influence the performance of the MTJ. *Velev* et al. studied the influence of O vacancies (F centers) on spin-dependent tunneling in Fe/MgO/Fe(001) magnetic tunnel junctions [22.98]. Figure 22.37 presents the transmission probability T as a function of the energy for perfect MgO (continuous line) and MgO with oxygen vacancies (dashed line). The transmission of the MTJ with vacancies drops markedly around E_F compared to that of a perfect MTJ. This reduction in majority-spin transmission can be explained by noting that tunneling electrons are scattered by the oxygen vacancies from slowly decaying states with $K = 0$ to electronic states with larger parallel K that are characterized by faster decay inside the MgO barrier.

22.5 Conclusions and Perspectives

In this chapter, we have focused on the magnetic properties of ultrathin oxide films grown epitaxially on metallic substrates. This topic was discussed from a surface science perspective, i.e., by considering model systems in UHV conditions. In the first part of the chapter, we analyzed the subtle interplay between the magnetic order of the oxide and its structural and electronic properties. The complexity of this problem requires a multifarious experimental approach involving both spin-resolved spectroscopic and microscopic techniques, as described in the second section of the chapter. The magnetic properties of metal–oxide multilayers are strongly related to the physicochemical coupling between the epitaxial film and the substrate. In this context, the third section of the chapter described how the structure and the chemical composition of the oxide–metal interface can be tailored by inserting an appropriate buffer layer. Finally, through the use of selected examples, we showed in the fourth section of the chapter how even a minor modification to the chemical composition of the interface can strongly influence the magnetic coupling between the ferromagnetic substrate and the oxide overlayer as well as the spin transport properties of a magnetic tunnel junction.

Turning our attention to future perspectives in this area of research, we can identify several lines of development. First, most of the literature in this area is focused on binary transition metal oxides; there have been relatively few studies of more complex systems such as ternary oxides. Multicomponent oxides with multiferroic order (such as rare earth manganites) are particularly interesting due to their application in magnetoelectronic devices. Another still largely unexplored field is heterostructures composed of an ultrathin oxide and two-dimensional materials (graphene, MoS_2, h-BN, etc.). It is expected that new layered van der Waals crystals of this nature will be synthesized through the epitaxial growth of monolayer oxides, expanding the library of two-dimensional materials that are available.

References

22.1 M.R. Norman: The challenge of unconventional superconductivity, Science **332**, 196 (2011)

22.2 T.V. Ashworth, C.A. Muryn, G. Thornton: Nanodots and other low-dimensional structures of titanium oxides, Nanotechnology **16**, 3041 (2005)

22.3 G. Barcaro, E. Cavaliere, L. Artiglia, L. Sementa, L. Gavioli, G. Granozzi, A. Fortunelli: Building principles and structural motifs in TiO_x ultrathin films on a (111) substrate, J. Phys. Chem. C **116**, 13302 (2012)

22.4 C. Wu, M.S.J. Marshall, M.R. Castell: Surface structures of ultrathin TiO_x films on Au(111), J. Phys. Chem. C **115**, 8643 (2011)

22.5 L.-Y. Ma, A. Picone, M. Wagner, S. Surnev, G. Barcaro, A. Fortunelli, F.P. Netzer: Structure and electronic properties of CoO nanostructures on a vicinal Pd(100) surface, J. Phys. Chem. C **117**, 18464 (2013)

22.6 C. Franchini, F. Li, S. Surnev, R. Podloucky, F. Allegretti, F.P. Netzer: Tailor-made ultrathin manganese oxide nanostripes: 'Magic widths' on Pd(1 1 N) terraces, J. Phys. Condens. Matter **24**, 042001 (2012)

22.7 A. Tekiel, S. Fostner, J. Topple, Y. Miyahara, P. Grütter: Reactive growth of MgO overlayers on Fe(001) surfaces studied by low-energy electron

diffraction and atomic force microscopy, Appl. Surf. Sci. **273**, 247 (2013)
22.8 V.E. Henrich, P.A. Cox: *The Surface Science of Metal Oxides* (Cambridge Univ. Press, Cambridge 1996)
22.9 S. Blundell: *Magnetism in Condensed Matter* (Oxford Univ. Press, Oxford 2001)
22.10 A. Picone, M. Riva, A. Brambilla, A. Calloni, G. Bussetti, M. Finazzi, F. Ciccacci, L. Duò: Reactive metal–oxide interfaces: A microscopic view, Surf. Sci. Rep. **71**, 32 (2016)
22.11 D.R. Lide (Ed.): *CRC Handbook of Chemistry and Physics* (CRC, Boca Raton 2010)
22.12 T.J. Regan, H. Ohldag, C. Stamm, F. Nolting, J. Lüning, J. Stöhr, R.L. White: Chemical effects at metal/oxide interfaces studied by x-ray absorption spectroscopy, Phys. Rev. B **64**, 214422 (2001)
22.13 M. Finazzi, A. Brambilla, L. Duò, G. Ghiringhelli, M. Portalupi, F. Ciccacci, M. Zacchigna, M. Zangrando: Chemical effects at the buried NiO/Fe(001) interface, Phys. Rev. B **70**, 235420 (2004)
22.14 H.-J. Kim, J.-H. Park, E. Vescovo: Oxidation of the Fe(110) surface: An Fe_3O_4(111)/Fe(110) bilayer, Phys. Rev. B **61**, 15284 (2000)
22.15 P. Luches, L. Pasquini, S. Benedetti, V. Bellini, S. Valeri, F. Manghi, R. Rüffer, F. Boscherini: Interfacial magnetic structure in Fe/NiO(001), Phys. Rev. B **83**, 094413 (2011)
22.16 M.S. Chen, D.W. Goodman: Ultrathin, ordered oxide films on metal surfaces, J. Phys. Condens. Matter **20**, 264013 (2008)
22.17 T.N. Rhodin, J.W. Gadzuk: *The Nature of the Surface Chemical Bond* (North-Holland, Amsterdam 1979)
22.18 G.A. Somorjai: *Chemistry in Two Dimensions* (Cornell Univ. Press, Ithaka 1981)
22.19 D.R. Penn: Electron mean free paths for free-electron-like materials, Phys. Rev. B **13**, 5248 (1976)
22.20 A. Zangwill: *Physics at Surfaces* (Cambridge Univ. Press, Cambridge 1988)
22.21 M.P. Seah, W.A. Dench: Quantitative electron spectroscopy of surfaces: A standard data base for electron inelastic mean free paths in solids, Surf. Interf. Anal. **1**, 2–11 (1979)
22.22 C.D. Wagner, W.M. Riggs, L.E. Davis, J.F. Moulder: *Handbook of X-ray Photoelectron Spectroscopy*, 1st edn. (Perkin-Elmer Corp., Eden Prairie 1979)
22.23 S. Tougaard: Surface analysis, x-ray photoelectron spectroscopy. In: *Elsevier Reference Module in Chemistry, Molecular Sciences and Chemical Engineering*, ed. by J. Reedijk (Elsevier, Waltham 2013)
22.24 J. Stöhr: Magnetic dichroism spectroscopy and microscopy, https://www-ssrl.slac.stanford.edu/stohr/xmcd.htm
22.25 H. Wende: Recent advances in x-ray absorption spectroscopy, Rep. Prog. Phys. **67**, 2105 (2004)
22.26 W. Kuch: Imaging magnetic microspectroscopy. In: *Magnetic Microscopy of Nanostructures*, ed. by H. Hopster, H.P. Oepen (Springer, Berlin, Heidelberg 2005) pp. 1–28
22.27 A. Locatelli, E. Bauer: Recent advances in chemical and magnetic imaging of surfaces and interfaces by XPEEM, J. Phys. Condens. Matter **20**, 093002 (2008)
22.28 F. Genuzio, A. Sala, T. Schmidt, D. Menzel, H.-J. Freund: Phase transformations in thin iron oxide films: Spectromicroscopic study of velocity and shape of the reaction fronts, Surf. Sci. **648**, 177 (2016)
22.29 E. Bauer: Low energy electron microscopy, Rep. Prog. Phys. **57**, 895 (1994)
22.30 Y. Seo, W. Jhe: Atomic force microscopy and spectroscopy, Rep. Prog. Phys. **71**, 016101 (2008)
22.31 G. Binnig, H. Rohrer: Scanning tunneling microscopy from birth to adolescence, Rev. Mod. Phys. **59**, 615 (1987)
22.32 D.A. Bonnell, J. Garra: Scanning probe microscopy of oxide surfaces: Atomic structure and properties, Rep. Prog. Phys. **71**, 044501 (2008)
22.33 N. Nilius: Properties of oxide thin films and their adsorption behavior studied by scanning tunneling microscopy and conductance spectroscopy, Surf. Sci. Rep. **64**, 595 (2009)
22.34 H. Fujiwara, M. Sunagawa, K. Terashima, T. Kittaka, T. Wakita, Y. Muraoka, T. Yokoya: Intrinsic spin polarized electronic structure of CrO_2 epitaxial film revealed by bulk-sensitive spin-resolved photoemission spectroscopy, Appl. Phys. Lett. **106**, 202404 (2015)
22.35 C.T. Chen, F. Sette, Y. Ma, S. Modesti: Soft-x-ray magnetic circular dichroism at the L2,3 edges of nickel, Phys. Rev. B **42**, 7262(R) (1990)
22.36 M. Finazzi, M. Portalupi, A. Brambilla, L. Duò, G. Ghiringhelli, F. Parmigiani, M. Zacchigna, M. Zangrando, F. Ciccacci: Magnetic anisotropy of NiO epitaxial thin films on Fe(001), Phys. Rev. B **69**, 014410 (2004)
22.37 A. Brambilla: Properties of NiO and Fe Magnetic Thin Films in Layered Structures, Dissertation, Politecnico di Milano (2005)
22.38 A. Brambilla, P. Biagioni, N. Rougemaille, A.K. Schmid, A. Lanzara, L. Duò, F. Ciccacci, M. Finazzi: Nano-sized magnetic instabilities in Fe/NiO/Fe(001) epitaxial thin films, Thin Solid Films **515**, 712 (2006)
22.39 H. Ohldag, A. Scholl, F. Nolting, S. Anders, F.U. Hillebrecht, J. Stöhr: Spin reorientation at the antiferromagnetic NiO(001) surface in response to an adjacent ferromagnet, Phys. Rev. Lett. **86**, 2878 (2001)
22.40 N. Rougemaille, A.T. N'Diaye, J. Coraux, C. Vo-Van, O. Fruchart, A.K. Schmid: Perpendicular magnetic anisotropy of cobalt films intercalated under graphene, Appl. Phys. Lett. **101**, 142403 (2012)
22.41 K. Grzelakowski, E. Bauer: A flange-on type low energy electron microscope, Rev. Sci. Instrum. **67**, 742 (1995)
22.42 U. Hartmann: Magnetic force microscopy, Annu. Rev. Mater. Sci. **29**, 53 (1999)
22.43 R. Wiesendanger: Spin mapping at the nanoscale and atomic scale, Rev. Mod. Phys. **81**, 149 (2009)
22.44 L. Abelmann, A. van den Bos, C. Lodder: Magnetic force microscopy – towards higher resolution. In: *Magnetic Microscopy of Nanostructures*, ed. by

H. Hopster, H.P. Oepen (Springer, Berlin, Heidelberg 2005), Chap. 12
22.45 J.S. Moodera, G.-X. Miao, T.S. Santos: Frontiers in spin-polarized tunneling, Phys. Today **63**, 46 (2010)
22.46 M. Kleiber, M. Bode, R. Ravlić, R. Wiesendanger: Topology-induced spin frustrations at the Cr(001) surface studied by spin-polarized scanning tunneling spectroscopy, Phys. Rev. Lett. **85**, 4606 (2000)
22.47 P. Vavassori: Polarization modulation technique for magneto-optical quantitative vector magnetometry, Appl. Phys. Lett. **77**, 1605 (2000)
22.48 G. Nowak, A. Remhof, F. Radu, A. Nefedov, H.-W. Becker, H. Zabel: Structural and magnetic properties of stoichiometric epitaxial CoO/Fe exchange-bias bilayers, Phys. Rev. B **75**, 174405 (2007)
22.49 A.E. Berkowitz, K. Takano: Exchange anisotropy – A review, J. Magn. Magn. Mater. **200**, 552 (1999)
22.50 M. Finazzi, L. Duò, F. Ciccacci: Magnetic properties of interfaces and multilayers based on thin antiferromagnetic oxide films, Surf. Sci. Rep. **64**, 139 (2009)
22.51 S. Surnev, A. Fortunelli, F.P. Netzer: Structure–property relationship and chemical aspects of oxide–metal hybrid nanostructures, Chem. Rev. **113**(6), 4314–4372 (2013)
22.52 Q. Fu, T. Wagner: Interaction of nanostructured metal overlayers with oxide surfaces, Surf. Sci. Rep. **62**(11), 431–498 (2007)
22.53 H.-J. Freund, S. Shaikhutdinov, N. Nilius: Model studies on heterogeneous catalysts at the atomic scale, Top. Catal. **57**(10–13), 822–832 (2014)
22.54 A.R. Chourasia: Investigation of chemical reactivity at the M/CuO interfaces (where M = Fe, Co, or Ni), J. Appl. Phys. **112**, 024323 (2012)
22.55 L. Duò, M. Portalupi, M. Marcon, R. Bertacco, F. Ciccacci: Epitaxial thin NiO films grown on Fe(0 0 1) and the effect of temperature, Surf. Sci. **518**, 234 (2002)
22.56 A. Brambilla, A. Calloni, G. Berti, G. Bussetti, L. Duò, F. Ciccacci: Growth and interface reactivity of titanium oxide thin films on Fe(001), J. Phys. Chem. C **117**(18), 9229–9236 (2013)
22.57 S. Benedetti, P. Luches, M. Liberati, S. Valeri: Chemical reactions and interdiffusion at the Fe/NiO(001) interface, Surf. Sci. **572**(23), L348–L354 (2004)
22.58 R. Abrudan, J. Miguel, M. Bernien, C. Tieg, M. Piantek, J. Kirschner, W. Kuch: Structural and magnetic properties of epitaxial Fe/CoO bilayers on Ag(001), Phys. Rev. B **77**, 014411 (2008)
22.59 S. Valeri, A. Borghi, G. Gazzadi, A. di Bona: Growth and structure of cobalt oxide on (001) bct cobalt film, Surf. Sci. **423**(23), 346–356 (1999)
22.60 G. Gazzadi, A. Borghi, A. di Bona, S. Valeri: Epitaxial growth of CoO on the (001) surface of bct cobalt, Surf. Sci. **402/404**, 632–635 (1998)
22.61 O. Dugerjav, H. Kim, J.M. Seo: Growth of a crystalline and ultrathin MgO film on Fe(001), AIP Advances **1**(3), 032156 (2011)
22.62 E. Bauer: Phänomenologische Theorie der Kristallabscheidung an Oberflächen. I, Z. Kristallogr. **110**, 372–394 (1958)
22.63 J.A. Venables, G.D.T. Spiller, M. Hanbucken: Nucleation and growth of thin films, Rep. Prog. Phys. **47**, 399 (1984)
22.64 A. Brambilla, P. Sessi, M. Cantoni, L. Duò, M. Finazzi, F. Ciccacci: Epitaxial growth and characterization of CoO/Fe(001) thin film layered structures, Thin Solid Films **516**(21), 7519–7524 (2008)
22.65 A. Brambilla, A. Picone, M. Finazzi, L. Duo, F. Ciccacci: Scanning tunneling microscopy investigation of CoO/Fe(001) and Fe/CoO/Fe(001) layered structures, Surf. Sci. **605**, 95 (2011)
22.66 F. Donati, P. Sessi, S. Achilli, A.L. Bassi, M. Passoni, C.S. Casari, C.E. Bottani, A. Brambilla, A. Picone, M. Finazzi, L. Duò, M.I. Trioni, F. Ciccacci: Scanning tunneling spectroscopy of the Fe(001)-p(1×1)O surface, Phys. Rev. B **79**, 195430 (2009)
22.67 A. Picone, G. Fratesi, A. Brambilla, P. Sessi, F. Donati, S. Achilli, L. Maini, M.I. Trioni, C.S. Casari, M. Passoni, A. Li Bassi, M. Finazzi, L. Duò, F. Ciccacci: Atomic corrugation in scanning tunneling microscopy images of the Fe(001)-p(1×1)O surface, Phys. Rev. B **81**, 115450 (2010)
22.68 S.S. Parihar, H.L. Meyerheim, K. Mohseni, S. Ostanin, A. Ernst, N. Jedrecy, R. Felici, J. Kirschner: Structure of O/Fe(001)-p(1×1) studied by surface x-ray diffraction, Phys. Rev. B **81**, 075428 (2010)
22.69 W. Feng, H.L. Meyerheim, K. Mohseni, O. Brovko, V.S. Stepanyuk, N. Jedrecy, R. Felici, J. Kirschner: Misfit-induced modification of structure and magnetism in O/Fe(001)-p(1×1), Phys. Rev. Lett. **110**, 235503 (2013)
22.70 A. Picone, A. Brambilla, A. Calloni, L. Duò, M. Finazzi, F. Ciccacci: Oxygen-induced effects on the morphology of the Fe(001) surface in out-of-equilibrium conditions, Phys. Rev. B **83**, 235402 (2011)
22.71 G. Bussetti, M. Riva, A. Picone, A. Brambilla, L. Duò, M. Finazzi, F. Ciccacci: Martensitic transition during Ni growth on Fe(001): Evidence of a precursor phase, New J. Phys. **14**(5), 053048 (2012)
22.72 M. Riva, A. Picone, G. Bussetti, A. Brambilla, A. Calloni, G. Berti, L. Duò, F. Ciccacci, M. Finazzi: Oxidation effects on ultrathin Ni and Cr films grown on Fe(001): A combined scanning tunneling microscopy and Auger electron spectroscopy study, Surf. Sci. **621**, 55–63 (2014)
22.73 A.V. Mijiritskii, P.J.M. Smulders, V.Y. Chumanov, O.C. Rogojanu, M.A. James, D.O. Boerma: Structure of Ni overlayers on bcc Fe(100), Phys. Rev. B **58**, 8960–8966 (1998)
22.74 A. Picone, M. Riva, A. Brambilla, D. Giannotti, O. Ivashko, G. Bussetti, M. Finazzi, F. Ciccacci, L. Duò: Atomic scale insights into the early stages of metal oxidation: A scanning tunneling microscopy and spectroscopy study of cobalt oxidation, J. Phys. Chem. C **120**, 5233–5241 (2016)
22.75 A. Calloni, G. Berti, A. Brambilla, M. Riva, A. Picone, G. Bussetti, M. Finazzi, F. Ciccacci, L. Duò:

Electron spectroscopy investigation of the oxidation of ultra-thin films of Ni and Cr on Fe(0 0 1), J. Phys. Condens. Matter **26**(44), 445001 (2014)

22.76 A.G. Sault: Quantitative analysis of Auger lineshapes of oxidized iron, Appl. Surf. Sci. **74**(3), 249–262 (1994)

22.77 A. Brambilla, A. Picone, D. Giannotti, M. Riva, G. Bussetti, G. Berti, A. Calloni, M. Finazzi, F. Ciccacci, L. Duo: Self-organized nano-structuring of CoO islands on Fe(001), Appl. Surf. Sci. **362**, 374–379 (2016)

22.78 A. Picone, M. Riva, G. Fratesi, A. Brambilla, G. Bussetti, M. Finazzi, L. Duò, F. Ciccacci: Enhanced atom mobility on the surface of a metastable film, Phys. Rev. Lett. **113**, 046102 (2014)

22.79 M. Riva, A. Picone, D. Giannotti, A. Brambilla, G. Fratesi, G. Bussetti, L. Duò, F. Ciccacci, M. Finazzi: Mesoscopic organization of cobalt thin films on clean and oxygen-saturated Fe(001) surfaces, Phys. Rev. B **92**, 115434 (2015)

22.80 F. Allegretti, G. Parteder, M. Ramsey, S. Surnev, F. Netzer: The formation of sharp NiO(1 0 0)–cobalt interfaces, Surf. Sci. **601**(14), L73–L76 (2007)

22.81 T. Nozaki, H. Kubota, A. Fukushima, S. Yuasa: Interface engineering using an Fe oxide insertion layer for growing a metastable bcc-Co on MgO(001), Appl. Phys. Lett. **106**(2), 022405 (2015)

22.82 H. Ohldag, T.J. Regan, J. Stöhr, A. Scholl, F. Nolting, J. Lüning, C. Stamm, S. Anders, R.L. White: Spectroscopic identification and direct imaging of interfacial magnetic spins, Phys. Rev. Lett. **87**, 247201 (2001)

22.83 R. Bali, M.M. Soares, A.Y. Ramos, H.C.N. Tolentino, F. Yildiz, C. Boudot, O. Proux, M. De Santis, M. Przybylski, J. Kirschner: Magnetic and structural properties of the Fe layers in CoO/Fe/Ag(001) heterostructure, Appl. Phys. Lett. **100**(13), 132403 (2012)

22.84 E. Młyńczak, P. Luches, S. Valeri, J. Korecki: NiO/Fe(001): Magnetic anisotropy, exchange bias, and interface structure, J. Appl. Phys. **113**(23), 234315 (2013)

22.85 P.K. Manna, E. Skoropata, Y.-W. Ting, K.-W. Lin, J.W. Freeland, J. van Lierop: Interface mixing and its impact on exchange coupling in exchange biased systems, J. Phys. Condens. Matter **28**, 486004 (2016)

22.86 Q.Y. Xu, G. Ni, H. Sang, Y.W. Du: The exchange coupling of a NiO/FeNi bilayer with interdiffused interface, J. Phys. Condens. Matter **13**, 5047 (2001)

22.87 E. Młyńczak, B. Matlak, A. Kozioł-Rachwał, J. Gurgul, N. Spiridis, J. Korecki: Fe/CoO(001) and Fe/CoO(111) bilayers: Effect of crystal orientation on the exchange bias, Phys. Rev. B **88**, 085442 (2013)

22.88 C.A.F. Vaz, E.I. Altman, V.E. Henrich: Exchange bias and interface electronic structure in Ni/Co_3O_4(011), Phys. Rev. B **81**, 104428 (2010)

22.89 E. Młyńczak, J. Gurgul, J. Przewoźnik, D. Wilgocka-Ślzak, K. Freindl, N. Spiridis, J. Korecki: Effect of interfacial iron oxidation on the exchange bias in CoO/Fe bilayers, Appl. Surf. Sci. **304**, 86–90 (2014)

22.90 D. Giannotti, H. Hedayat, G. Vinai, A. Picone, A. Calloni, G. Berti, M. Riva, G. Bussetti, F. Boschini, P. Torelli, G. Panaccione, E. Carpene, C. Dallera, M. Finazzi, A. Brambilla: Magnetic anisotropy at the buried CoO/Fe interface, Appl. Phys. Lett. **109**, 232401 (2016)

22.91 R.P. Cowburn, S.J. Gray, J.A.C. Bland: Multijump magnetic switching in in-plane magnetized ultrathin epitaxial Ag/Fe/Ag(001) films, Phys. Rev. Lett. **79**, 4018 (1997)

22.92 R.P. Cowburn, S.J. Gray, J. Ferre, J.A.C. Bland, J. Miltat: Magnetic switching and in-plane uniaxial anisotropy in ultrathin Ag/Fe/Ag(100) epitaxial films, J. Appl. Phys. **78**, 7210 (1995)

22.93 Y. Fan, K.J. Smith, G. Luepke, A.T. Hanbicki, R. Goswami, C.H. Li, H.B. Zhao, B.T. Jonker: Exchange bias of the interface spin system at the Fe/MgO interface, Nat. Nanotechnol. **8**(6), 438–444 (2013)

22.94 X.-G. Zhang, W.H. Butler, A. Bandyopadhyay: Effects of the iron-oxide layer in Fe–FeO–MgO–Fe tunneling junctions, Phys. Rev. B **68**, 092402 (2003)

22.95 J. Mathon, A. Umerski: Theory of tunneling magnetoresistance of an epitaxial Fe/MgO/Fe(001) junction, Phys. Rev. B **63**, 220403 (2001)

22.96 S. Yuasa, T. Nagahama, A. Fukushima, Y. Suzuki, K. Ando: Giant room-temperature magnetoresistance in single-crystal Fe/MgO/Fe magnetic tunnel junctions, Nat. Mater. **3**, 868–871 (2004)

22.97 W.H. Butler, X.G. Zhang, T.C. Schulthess, J.M. MacLaren: Spin-dependent tunneling conductance of Fe/MgO/Fe sandwiches, Phys. Rev. B **63**, 54416 (2001)

22.98 J.P. Velev, K.D. Belashchenko, S.S. Jaswal, E.Y. Tsymbal: Effect of oxygen vacancies on spin-dependent tunneling in Fe/MgO/Fe magnetic tunnel junctions, Appl. Phys. Lett. **90**, 072502 (2007)

22.99 F. Bonell, S. Andrieu, A.M. Bataille, C. Tiusan, G. Lengaigne: Consequences of interfacial Fe–O bonding and disorder in epitaxial Fe/MgO/Fe(001) magnetic tunnel junctions, Phys. Rev. B **79**, 224405 (2009)

22.100 P.J. Zermatten, F. Bonell, S. Andrieu, M. Chshiev, C. Tiusan, A. Schuhl, G. Gaudin: Influence of oxygen monolayer at Fe/MgO interface on transport properties in Fe/MgO/Fe(001) magnetic tunnel junctions, Appl. Phys. Exp. **5**, 023001 (2012)

Alberto Brambilla

Dipartimento di Fisica
Politecnico di Milano
Milano, Italy

Alberto received his PhD in Physics at Politecnico di Milano (Italy) in 2005, with an experimental activity focused on the investigation of thin films and interfaces of magnetic materials, oxides, and semiconductors through ultrahigh vacuum spectroscopy and microscopy techniques. He was a researcher at CNISM and became Assistant Professor (2008) and then Associate Professor (2014) in the Physics Department of Politecnico di Milano.

Andrea Picone

Dipartimento di Fisica
Politecnico di Milano
Milano, Italy
andrea.picone@polimi.it

Andrea Picone received his PhD in Physics (2012) from the Politecnico di Milano. During his PhD he focused on the characterization of the structural and electronic properties of transition metal oxides. Currently, his scientific interest lies in the study of layered systems formed by ultrathin oxides and ferromagnetic metals, with emphasis on the interplay between interface chemistry and magnetic coupling. He is author of 27 scientific papers in international peer-reviewed journals.

Marco Finazzi

Dipartimento di Fisica
Politecnico di Milano
Milano, Italy

Marco Finazzi received his PhD in Physics in 1994 from the Politecnico di Milano. Since 2001 he has carried out his scientific activity in the Physics Department of Politecnico di Milano, where he became Full Professor in 2016. He teaches experimental physics and physics of low-dimensional systems. His main fields of interest span from the physics of the transport of spin in solid-state systems to nano-optics and plasmonics.

Lamberto Duò

Dipartimento di Fisica
Politecnico di Milano
Milano, Italy

Lamberto Duò received his PhD from Politecnico di Milano in 1987. He was then appointed as Staff Scientist in the Physics Department of Politecnico di Milano, where he subsequently became Full Professor. Professor Duò has worked on electron spectroscopies of highly correlated electron systems, spin-resolved electron spectroscopies of magnetic systems with low dimensionality and scanning near-field optical microscopy of magnetic nanostructures. He is author of over 150 publications.

Franco Ciccacci

Dipartimento di Fisica
Politecnico di Milano
Milano, Italy

Franco Ciccacci received his Doctor's degree in Physics at Università di Roma La Sapienza. He is currently Full Professor of Experimental Physics at Politecnico di Milano. His research activities include surface physics, production, and detection of spin-polarized electron beams, electron spectroscopy from solids, also with synchrotron radiation and spin resolution, thin film magnetism, deposition of nanostructured materials for spintronics. He is author of over 200 scientific papers in international journals.

Part F

Lattice Dy

Part F Lattice Dynamics

Part F is devoted to lattice dynamics. Atoms in solids vibrate around their equilibrium positions in a potential determined by interactions with their neighbors and by their electronic configuration, including the pronounced effect of their conduction electrons, if present. In the harmonic approximation, all terms in the Taylor expansion of the interaction potential beyond the quadratic are neglected, which is reasonable for small oscillations around the equilibrium positions. The solutions of the equation of motion are then noninteracting normal modes and their quanta are called phonons. When the solid is truncated, the translational invariance normal to the surface is lost and the phonon spectrum changes. The wavevector is two-dimensional at the surface, and the spectrum consists of the projection of the bulk states and of additional modes characterized by an amplitude that decreases away from the surface (surface phonons and resonances). Such modes arise due to the lack of inversion symmetry at the surface and play an essential role in determining phenomena such as energy dissipation in gas–surface interactions and surface diffusion. The surface phonon spectrum has been determined by two main methods: thermal energy He atom scattering and angle-resolved high-resolution electron energy loss spectroscopy (HREELS) performed with low-energy electrons. In addition, phonons at vanishing momenta can be excited by infrared light. Recent advances in HREELS allow the acquisition of the full phonon spectrum after just a few hours of work instead of weeks, opening the door to the study of more reactive systems.

Phonons are eigenstates of the harmonic Hamiltonian and thus have infinite lifetimes. However, the interaction potential is not exactly harmonic, causing phonon lines to have a finite energy width. Phonons are often computed within the Born–Oppenheimer approximation, which may break down under specific conditions. Such is the case for Kohn anomalies, which may be particularly strong at surfaces due to the reduced dimensionality, or for superconductivity, which can have a higher critical temperature at the surface.

Chapter 23 provides a detailed introduction to surface phonon spectra and the theoretical methods used to calculate them, including force constant models and ab initio methods. The results from theoretical predictions are compared to experimental results for several different kinds of solid surfaces. The final part of this chapter addresses problems that are still unresolved despite the advances made in this field over the past decades.

Chapter 24 is devoted to the theoretical description of the electron–phonon interaction, which determines many physical phenomena such as superconductivity, Kohn anomalies, photoemission, and the dynamics of excited electrons and holes. Current computational and experimental techniques are covered. A summary of the results obtained for elemental and adsorbate-covered metal surfaces, thin films, and metallic states on the surfaces of topological insulators is also provided.

Chapter 25 explores experimental results on surface vibrations obtained by STM-IETS (scanning tunneling microscopy–inelastic tunneling spectroscopy). This technique combines the atomic-scale spatial resolution of STM with the chemical sensitivity of vibrational spectroscopy. The chapter addresses the selection rules of STM-IETS, which are quite different from those pertinent to HREELS and infrared reflection spectroscopy. Vibrations at alkenethiol self-assembled monolayers are presented as an example.

Chapter 26 takes an unconventional approach to the topics of this session, showing how a detailed description of the chemical composition of a surface can be obtained through the combined use of multiple experimental techniques: infrared (IR) spectroscopy, low-energy ion scattering (LEIS), and x-ray photoemission spectroscopy (XPS). This information is required to understand several surface chemical and physical processes, such as thin-film growth, surface functionalization, catalysis, and near-surface diffusion.

23. Surface Phonons: Theoretical Methods and Results

Giorgio Benedek, Marco Bernasconi, Davide Campi, J. Peter Toennies, Matthieu J. Verstraete

The theoretical methods currently in use for the calculation of surface phonon dispersion curves and how they have evolved from the phenomenological force-constant models to the present day first principles theories are discussed. A selection of paradigmatic examples for the different classes of crystal surfaces is presented with comparisons to the experimental data obtained from helium atom scattering or electron energy-loss spectroscopy.

In Sect. 23.1, this chapter presents a general introduction to the concepts and methods in the theory of surface lattice dynamics. This is followed by a survey of theoretical developments, from the early theories, extending the original Born–von Kármán approach to the dynamics of crystal surfaces, to recent first-principles treatments based on the density functional theory. Since all theoretical methods, whether phenomenological or ab-initio, have their own domain of applicability, they will be illustrated in Sect. 23.2 according to the role that the electronic structure plays in lattice dynamics with a few paradigmatic examples of surface phonon calculations at the different levels of approximation. The final part on the density functional perturbation theory (DFPT) will only present examples that are particularly challenging today, requiring functionals including spin–orbit coupling and van der Waals contributions. These examples concern the surfaces of heavy 6sp elements and some topological insulator compounds. Some open problems concerning DFPT and expected future developments are briefly mentioned in the concluding Sect. 23.3.

Surfaces play a fundamental role in all branches of nanotechnology. In particular, a detailed knowledge of surface dynamics is essential for the structural and functional characterization of nanostructures. The study of quantized surface vibrations—surface phonons—enables us to learn about the forces at a solid surface, or between the surface and adsorbed molecules. This understanding makes it possible to elucidate and exploit a wide variety of transport and optical properties and functions involving phonons, either directly or via electron–phonon interaction.

Learning about the nature of things by studying their motion is an old concept: "Igitur impossibile est de aliqua re cognoscere, quòd fit natura, non cognoscendo motum" (It is therefore impossible to learn what nature makes about anything without knowing its motion) [23.1]. Most of what we know about the inner constitution of our planet comes from seismology, and it was in the realm of seismology that the study of solid surface dynamics started in the last two decades of the nineteenth century with the fundamental work of *Lord Rayleigh* [23.2, 3]. This work demonstrated for a semi-infinite elastic, homogeneous, and isotropic solid, the existence of acoustic waves propagating along the surface with a frequency proportional to the wavevector and decaying exponentially inside the solid. The decay length was shown to be proportional to the surface wavelength, as expected from a simple scale law: *a homogeneous semi-infinite continuum looks the same at any length scale*. Thus, surface waves, which originally explained the slow but most destructive long-wave component of earthquakes (Rayleigh waves (RWs)), exist at

M. Rocca, T.S. Rahman, L. Vattuone (Eds.), *Springer Handbook of Surface Science*, Springer Handbooks,
https://doi.org/10.1007/978-3-030-46906-1_23

any scale, from the surface of planets to that of large nuclei, and, therefore, at the surface of crystal lattices. The intrinsic inhomogeneity of the solid at the atomic scale causes a deviation from the frequency-wavevector proportionality when wavelengths become comparable to the interatomic distances: the RW phase velocity is no longer constant but exhibits a dispersion. The detailed study of the dispersion relation $\omega(\boldsymbol{Q})$ of the frequency ω versus the wavevector $\boldsymbol{Q}$ is a rich source of information about the structure, the forces, and the interactions occurring at the surface of any solid material, much in the same way seismic RWs provide information about the constitution and inhomogeneities of the Earth's crust. Surface waves like RWs, which obey the fundamental scaling law illustrated above, are said to be *macroscopic*, otherwise they are called *microscopic*.

Rayleigh waves, however, do not come alone. Elastic-wave displacements are vectors with three possible components, so that two other acoustic surface waves may exist, possibly only at finite wavevectors, with polarization vectors orthogonal to those of Rayleigh waves. On the atomic scale, the solid is a periodic lattice with a unit cell that contains one or more atoms. In the latter case, the unit cell, besides its three degrees of freedom associated with the translations of its center of mass, has internal degrees of freedom. The vibrational modes of the lattice associated with these degrees of freedom have frequencies that do not vanish for $\boldsymbol{Q} \to 0$ and are known as optical vibrations, since they determine the infrared optical properties in ionic crystals. The creation of a free surface in a polyatomic crystal and the consequent break of translational symmetry in the direction normal to surface bring forth surface vibrations of optical nature. In general, they have as many dispersion curves as the crystal unit cell has internal degrees of freedom. Unlike Rayleigh waves, the frequencies of optical surface modes do not vanish at $\boldsymbol{Q} = 0$, and their penetration lengths remain very short, in general on the scale of the lattice distances. Thus, optical surface modes carry specific information on the surface geometry and local interactions, which makes their study of primary interest in the physics of nanostructures. The spectrum of surface vibrations is further enriched by the presence at the surface of adsorbed chemical species or by the deposition of ultrathin films, and much can be learnt about their properties from surface phonon spectroscopy.

For a more detailed discussion of the concepts and methods summarized in the following Sects. 23.1 and 23.2, the reader is referred to [23.4, Chaps. 3–5], which has recently appeared. Chapter 11 of this Springer Handbook also contains a comprehensive discussion and analysis of the important measurements of the surface phonon dispersion curves of insulators, semiconductors, and metals. Extended lists of measured surface phonon dispersion curves that have been analyzed with the different methods presented in this chapter can be found in the Landolt–Börnstein chapter [23.5] and in the appendices of the very recent monograph [23.4].

Although several early theoretical studies on surface phonons anticipated the advent of their spectroscopy, the great progress in the theoretical modeling and ab-initio methods for the surface dynamics of real surfaces would not have been possible without the parallel development of powerful experimental techniques, notably high-resolution electron energy loss (HREELS) spectroscopy, with the first evidence of a microscopic surface mode obtained by *Harald Ibach* in 1971 [23.6], and helium atom scattering (HAS), also in 1971, with the first observation of RWs from angular distributions by *Brian Williams* [23.7, 8]. HAS surface phonon spectroscopy moved from the detection of phonon signatures in angular distributions, with an essential contribution from the Genoa group [23.9–14], to time-of-flight (TOF) spectroscopy, by which the RW speed in LiF(001) was measured [23.15]. The real breakthrough was, however, the realization of nozzle-beam sources with a high speed ratio [23.16], which enabled high-resolution TOF spectroscopy and the measurement of surface phonon dispersion curves in ionic crystals [23.17–19] and metals [23.20, 21]. Good results for Cu(001) were also obtained as early as 1981 by measuring the energy loss with a LiF analyzer crystal [23.22], a method which was not adopted further. In the same year, intriguing results were reported for Ni(111) with Ne atom scattering [23.23], which are worth mentioning, not only for being the first observation of RWs in a metal surface with atom scattering but also for the possible assignment of an unexplained branch to acoustic surface plasmons [23.4]. A rich collection of review articles and books from the early 1990s on kept the pace of the progress in surface phonon HAS spectroscopy and related theory [23.24–51], including the realization of ^{3}He spin-echo spectroscopy, anticipated by *DeKieviet* et al. [23.52] and fully realized by the Cavendish group with an unprecedented resolution in the neV range [23.53, 54]. A full account of HAS spectroscopy from the origin to present can be found in the recent monograph and book mentioned above [23.4, 5].

In parallel with these developments, HREELS in the impact regime also acquired the necessary resolution for an accurate determination of the surface phonon dispersion curves, mostly on conducting materials [23.55–57]. Transition metal and noble metal surfaces have served as a benchmark for HREELS studies [23.58–70] and for early first-principles calculations of surface dynamics [23.66–68]. The important role of these surfaces in catalytical processes stimulated further extensive investigations on the vibrational spectra

of adsorbed phases and overlayers [23.65]. HAS and HREELS basically provide the same information of surface phonon dispersion curves, generally in excellent agreement. It was soon realized that on semiconductor and metals they rely on rather different mechanisms with respect to the energy and momentum transfer to surface phonons. While electrons in the impact regime are directly scattered by the ion cores, He atoms at thermal energy are scattered by the electron density at the surface and can only transfer energy and momentum to ion cores through electron–phonon coupling (Sect. 23.2). In other words, HAS and HREELS provide valuable complementary information on surface dynamics [23.32, 46]. This understanding was fostered by the continued feedback between experiment and theory.

23.1 Concepts and Methods of Surface Lattice Dynamics

In order to describe the vibrational dynamics of a crystalline solid [23.71–75], its potential energy U is Taylor-expanded in the time-dependent displacements $\boldsymbol{u}(l\kappa, t) \equiv \boldsymbol{u}(l\kappa)$ of the atoms with respect to their equilibrium positions $\boldsymbol{r}_{l\kappa}$, defined by the conditions $\partial U/\partial \boldsymbol{r}_{l\kappa} = 0$

$$U = U_0 + \frac{1}{2}\sum_{ll'\kappa\kappa'} \frac{\partial^2 U}{\partial \boldsymbol{r}_{l\kappa}\partial \boldsymbol{r}_{l'\kappa'}} \boldsymbol{u}(l\kappa)\boldsymbol{u}(l'\kappa') + \frac{1}{6}\sum_{ll'l''\kappa\kappa'\kappa''} \frac{\partial^3 U}{\partial \boldsymbol{r}_{l\kappa}\partial \boldsymbol{r}_{l'\kappa'}\partial \boldsymbol{r}_{l''\kappa''}} \boldsymbol{u}(l\kappa)\boldsymbol{u}(l'\kappa')\boldsymbol{u}(l''\kappa'') + \ldots \quad (23.1)$$

where U_0 is the static potential energy. Here, $\boldsymbol{r}_{l\kappa}$ stands for $\boldsymbol{r}_{l\kappa} \equiv l_1\boldsymbol{a}_1 + l_2\boldsymbol{a}_2 + l_3\boldsymbol{a}_3 + \boldsymbol{d}(\kappa)$, where $\boldsymbol{a}_m$ $(m = 1, 2, 3)$ are the basis vectors of the lattice, the integer indices l_m run from 0 to $N_m - 1$, with $N_1N_2N_3$ the number of unit cells of the crystal, and $\boldsymbol{d}(\kappa)$ $(\kappa = 1, 2, \ldots, s)$ define the relative positions of the s atoms inside each unit cell. The derivatives,

$$\frac{\partial^2 U}{\partial r_{l\kappa\alpha}\partial r_{l'\kappa'\beta}} \equiv R_{\alpha\beta}\left(l\kappa, l'\kappa'\right), \quad (23.2)$$

where α and β label the vector components, which define the harmonic atom–atom (two-body) *force constant matrix*. The cubic and further higher-order terms in the expansion of U determine a variety of important anharmonic effects in lattice dynamics, such as thermal expansion, thermal resistance, and phonon–phonon interaction. They are usually neglected (*harmonic approximation*) in the theory of surface dynamics and are treated perturbatively to obtain the above temperature-dependent properties. According to Born–von Kármán theory, the equations of motion in the harmonic approximation for the atomic vibrations of a crystal lattice are given by

$$-M_\kappa \ddot{u}_\alpha(l\kappa, t) = \Sigma_{l'\kappa'\beta} R_{\alpha\beta}(lk, l'\kappa') u_\beta(l'\kappa', t)\,, \quad (23.3)$$

where M_κ is the mass of the κ-th atom in the unit cell.

The theory of surface lattice dynamics in its classical Born–von Kármán formulation [23.76–81] considers two steps. In the first step, the bulk phonons, which are solutions of the dynamical equation for the crystal lattice with 3-D boundary conditions, are *projected* onto new coordinates appropriate to 2-D boundary conditions. In the second step, the effects of the surface perturbation arising from the removal of the periodic boundary condition in the direction normal to the surface are considered. The bulk phonons which are most affected by the surface perturbation transform into surface localized phonons, e.g., the Rayleigh waves (RWs), or in-band surface resonances, e.g., the anomalous longitudinal (AL) acoustic resonance in metal surfaces.

23.1.1 Surface-Projected Bulk Phonon Bands

In the first step, the 3-D lattice is viewed as generated by two-dimensional (2-D) translations in the $(\boldsymbol{a}_1, \boldsymbol{a}_2)$ plane of a large unit cell containing sN_3 atoms. Such a 2-D representation of a crystal is called the *slab representation* of a crystal. In this representation, the solutions of the atomic equations of motion are Bloch waves with 2-D wavevectors $\boldsymbol{Q}$ in the $(\boldsymbol{a}_1, \boldsymbol{a}_2)$ plane and angular frequencies $\omega_{\boldsymbol{Q}\nu}$

$$u_\alpha(l\kappa, t) \propto u_\alpha(l_3\kappa, \boldsymbol{Q}\nu) \times \exp[\mathrm{i}\boldsymbol{Q}\cdot(l_1\boldsymbol{a}_1 + l_2\boldsymbol{a}_2) - \mathrm{i}\omega_{\boldsymbol{Q}\nu}t]\,. \quad (23.4)$$

Here, the sets (l_1, l_2) and (l_3, κ) are used to label the slab cells in two dimensions and the atoms inside each slab cell, respectively, whereas the branch index ν labels the $3sN_3$ phonon solutions of (23.3) for each wavevector $\boldsymbol{Q}$. The latter are obtained by inserting (23.4) into (23.3) as a solution of the eigenvalue equation

$$M_\kappa\omega^2_{\boldsymbol{Q}\nu}u_\alpha\left(l_3\kappa, \boldsymbol{Q}\nu\right) = \sum_{\beta l'_3\kappa'} R_{\alpha\beta}\left(l_3\kappa, l'_3\kappa', \boldsymbol{Q}\right) u_\beta\left(l'_3\kappa', \boldsymbol{Q}\nu\right), \quad (23.5)$$

where

$$R_{\alpha\beta}\left(l_3\kappa, l_3'\kappa', \boldsymbol{Q}\right) = \sum_{l_1 l_2} R_{\alpha\beta}\left(l\kappa, l'\kappa'\right) \exp\left[\mathrm{i}\boldsymbol{Q}\cdot(l_1\mathrm{a}_1 + l_2\mathrm{a}_2)\right] \quad (23.6)$$

are the 2-D Fourier transform of the force constants given by (23.2). Equation (23.6) defines the set of $\boldsymbol{Q}$-*dependent interplanar force constants*. As in the 3-D case, the set of modes of given ν for all values of $\boldsymbol{Q}$ forms the ν-th phonon branch, and the function $\omega_{\boldsymbol{Q}\nu}$ is its dispersion relation (Fig. 23.1b). From the solution of (23.5), the eigenfrequencies $\omega_{\boldsymbol{Q}\nu}$ and the displacement vectors $u_\alpha(l_3\kappa, \boldsymbol{Q}\nu)$, known as the $\boldsymbol{Q}$-*dependent planar displacements*, are obtained. The quantized physical displacement of the (l,κ)-th atom, with $l = (l_1 l_2 l_3)$, for the $(\boldsymbol{Q},\nu)$-th phonon mode is then given by

$$u_\alpha(l\kappa, \boldsymbol{Q}\nu, t) = \left(\frac{\hbar}{2N_1 N_2 M_\kappa \omega_{\boldsymbol{Q}\nu}}\right)^{1/2} e_\alpha(l_3\kappa, \boldsymbol{Q}\nu) \times \exp\left[\mathrm{i}\boldsymbol{Q}\cdot(l_1\boldsymbol{a}_1 + l_2\boldsymbol{a}_2) - \mathrm{i}\omega_{\boldsymbol{Q}\nu}t\right], \quad (23.7)$$

where the *eigenvectors* $e_\alpha(l_3\kappa, \boldsymbol{Q}\nu)$ form an orthogonal complete set in their $3sN_3$ space and are normalized to unity. The eigenvectors determine the polarization of the displacement field amplitude and are, therefore, termed *polarization vectors*. The factor $(N_1N_2)^{-1/2}$ ensures the normalization to unity of the exponential plane waves, so that the eigenwaves $(N_1N_2)^{-1/2}\, e_\alpha(l_3\kappa, \boldsymbol{Q}\nu)\exp[\mathrm{i}\boldsymbol{Q}\cdot(l_1\boldsymbol{a}_1 + l_2\boldsymbol{a}_2)]$ form an orthonormal, complete set in the full crystal space (*normal modes*).

Since the periodic boundary condition is still maintained also for the third translation $N_3\boldsymbol{a}_3$, the above solutions are just those of the 3-D lattice, which have been relabeled to correspond to a 2-D representation. The eigenfrequencies $\omega_{\boldsymbol{Q}\nu}$, for each $\boldsymbol{Q}$ and for ν varying from 1 to $3sN_3$, now form $3s$ bands, each one containing N_3 modes. For an infinitely thick slab ($N_3 \to \infty$), the individual modes can no longer be resolved, and the bands become continuous. They are referred to as *bulk phonon bands* projected onto the $(\boldsymbol{a}_1, \boldsymbol{a}_2)$ plane.

The correspondence between the two and three-dimensional representations of the phonon branches inside a solid with 3-D periodic boundary conditions is illustrated in Fig. 23.1. The 3-D dispersion surface in Fig. 23.1a is generated by the phonon energies as a function of the 3-D wavevector $\boldsymbol{q}$. The 2-D representation is then obtained by splitting $\boldsymbol{q}$ into a 2-D component $\boldsymbol{Q}$, which is parallel to the atomic planes of the slab, and a normal component q_z, namely $\boldsymbol{q} = (\boldsymbol{Q}, q_z)$. Each curve in the 2-D representation (Fig. 23.1b) represents

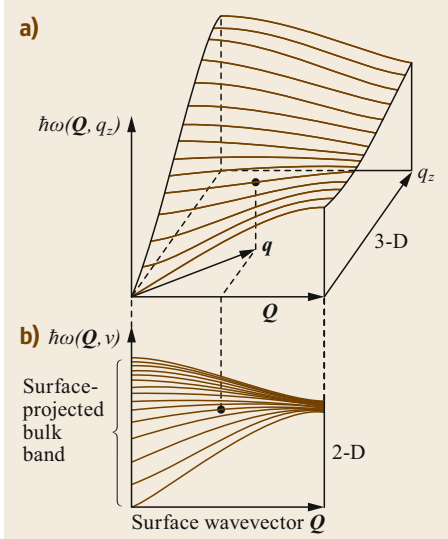

Fig. 23.1 **(a)** The energy surface $\hbar\omega(\boldsymbol{Q}, q_z)$ generated by the dispersion curves of an acoustic bulk phonon within a periodic slab with N_3 layers is plotted as a function of parallel $(\boldsymbol{Q})$ and normal (q_z) wavevector components. **(b)** This set of dispersion curves is converted into a 2-D band $\hbar\omega_{\boldsymbol{Q}\nu}$. The normal component q_z is replaced by an index ν labeling all the N_3 modes of the band with the same parallel wavevector $\boldsymbol{Q}$. In this example, there are 15 dispersion curves corresponding to the $N_3 = 15$ atomic layers of the slab. If the unit cell of the original periodic crystal contains s atoms, there will be $3s$ such bands, and index ν will label altogether $3sN_3$ modes for each value of the parallel wavevector $\boldsymbol{Q}$

the phonon energy as a function of $\boldsymbol{Q}$ for a given value of q_z. Thus, each bulk phonon branch generates just as many curves as the number of possible values of q_z, that is, N_3. The resulting set of curves is referred to as the *surface-projected* bulk band.

If the unit cell contains s atoms, then it has $3s$ degrees of freedom, and the total phonon spectrum is made up of $3s$ different, partially superimposed surface-projected bands. Thus, for each value of $\boldsymbol{Q}$ in the 2-D representation, there are altogether $3sN_3$ modes, which are conveniently labeled by a single index ν. The corresponding frequency distribution within all the bands is given by the *total* $\boldsymbol{Q}$-*selected phonon density of states* (DOS)

$$D_0(\boldsymbol{Q}, \omega) = \frac{1}{N_3}\sum_\nu \delta(\omega - \omega_{\boldsymbol{Q},\nu})\,. \quad (23.8)$$

Similarly, the $\boldsymbol{Q}$-*selected DOS projected* onto a specific plane l_3, sublattice κ, and polarization α is defined

as

$$D_{0\alpha}(\kappa l_3 \boldsymbol{Q}, \omega) = \frac{1}{N_3} \sum_{\nu} |e_\alpha(l_3\kappa, \boldsymbol{Q}\nu)|^2 \delta\left(\omega - \omega_{\boldsymbol{Q},\nu}\right), \quad (23.9)$$

respectively. Clearly $\sum_{l_3\kappa\alpha} D_{0\alpha}(l_3\kappa\boldsymbol{Q}, \omega) = D_0(\boldsymbol{Q}, \omega)$ due to eigenvector normalization.

23.1.2 Effects of the Surface Perturbation

So far, only a macroscopic-sized crystal slab with three-dimensional periodic boundary conditions has been dealt with, where the layer for $l_3 = N_3 - 1$ is connected to the first layer ($l_3 = 0$) by the same bulk interatomic forces that act between any other pair of adjacent layers (Fig. 23.2a). By the requirements of periodic boundary conditions along the $\boldsymbol{a}_3(z)$ direction, the reduction in the coordination of the atoms at a physical surface and the changes in the force constants at the surface were not accounted for in the above discussion.

A surface is created at a 2-D boundary Σ, if all the interatomic forces connecting atoms across Σ are broken apart. This way, the periodic boundary conditions along the z-axis are lifted, and two free surfaces are created at $l_3 = 0$ and $N_3 - 1$ (Fig. 23.2b). The original periodic lattice has now been transformed into a finite slab with two free surfaces. Only the atoms in the two surface regions A and B are affected by the cut of forces across Σ. This operation leads to a perturbation of the force constant matrix and a consequent change of eigenfrequencies and eigenvectors. The perturbation matrix has nonzero elements only within a subspace σ that encompasses the regions A and B. When the two surfaces are identical, the problem can be reduced to that of a single surface of a semi-infinite lattice by using a new set of symmetrized coordinates and letting $N_3 \to \infty$ (Fig. 23.2c) [23.82–84]. The size of the new perturbation subspace σ' is one half of that for a finite slab.

The 2-D Fourier transform of the perturbation matrix $\boldsymbol{\Lambda}_{\alpha\beta}(l_3\kappa, l_3'\kappa', \boldsymbol{Q})$ due to the creation of the two free surfaces needs to be added to the unperturbed lattice dynamical matrix $R_{0,\alpha\beta}(l_3\kappa, l_3'\kappa', \boldsymbol{Q})$ to give, in matrix notation, a new eigenvalue equation

$$[\mathbf{R}_0(\boldsymbol{Q}) + \boldsymbol{\Lambda}(\boldsymbol{Q})\boldsymbol{u} - \mathbf{M}\omega^2]\boldsymbol{u} = 0\,. \quad (23.10)$$

Once the perturbation matrix is known, there are two classical ways to solve it. One is the direct diagonalization of the $3sN_3 \times 3sN_3$ dynamical matrix for a sufficiently thin slab (*slab method*). If the goal is to know the surface dynamics of a macroscopic crystal, N_3 has to be much larger than the size of $\boldsymbol{\Lambda}$, although within the limits of the available computational power. This is not a serious limitation for phenomenological force-constant models, but may still be a problem for first-principles calculations.

The second way to solve (23.10) is based on the *Green's function method*. It has the advantage that the diagonalization problem is reduced from the large space of dynamical matrix to the much smaller space of the perturbation, with a modest computational effort for the calculation of complex-valued Green's functions of the unperturbed crystal. With the advent of fast computers, the direct diagonalization has become the method of choice, although the present extension of surface dynamics studies to complex surfaces and adsorbates, and the calculation of their vibrational response functions may revive the interest in the Green's function method

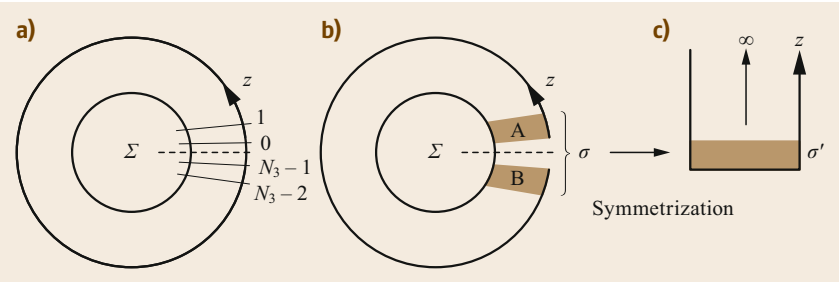

Fig. 23.2 **(a)** Representation of a lattice with periodic boundary conditions in the z direction. The *broken line* indicates the boundary plane Σ located between the 0-th and the $N_3 - 1$-st lattice planes. **(b)** When all the interactions connecting atoms across the boundary plane Σ are set to zero the periodic boundary conditions in the z direction normal to the boundary plane are lifted and the original periodic lattice is transformed into a slab with two parallel free surfaces. The periodicity is preserved in two independent directions parallel to the surfaces. The atoms affected by the perturbation are located in the surface regions A and B. **(c)** For identical surfaces, a symmetry transformation allows for the reduction of the perturbation subspace σ to one half of it (σ'), and for $N_3 \to \infty$, the slab problem transforms into that for a semi-infinite lattice with one single surface

and its implementation with density functional perturbation theory.

The Slab Method: Polarization and Classification of Surface Modes

In order to obtain useful information about the surface dynamics of the semi-infinite crystal from the direct numerical diagonalization of (23.10), the number of layers N_3 has to be chosen large enough so that the spectral features of the surface layers are clearly distinguished from those of the bulk. This is nicely illustrated in Fig. 23.3, which shows the phonon dispersion curves of a (111)-oriented slab of a monoatomic face-centered cubic (fcc) lattice for an increasing number of layers from 1 to 15. The calculation is based on the mass and nearest-neighbor force constants of copper. A single free-standing layer ($N_3 = 1$) shows only the three acoustic branches of shear vertical (SV), shear horizontal (SH), and longitudinal (L) polarization. The addition of a second layer ($N_3 = 2$) leads to three optical phonon branches, also of SV, SH, and L polarization, which have clear, avoided crossings with the acoustic branches of similar polarization. With additional layers, the number of modes increases at the rate of three new branches per layer, eventually leading to thicker and thicker phonon bands. Most of these branches are essentially those of bulk phonons projected onto the surface, as illustrated in Fig. 23.1, but already at ten layers, the effects of the surfaces become apparent with some branches that are well separated from relatively dense bands. The *spectral* localization of these isolated phonon branches corresponds to a *spatial* localization of their eigenvectors in the surface region where the perturbation is effective. These isolated branches are, therefore, attributed to *surface localized modes*.

When the penetration length of the surface wave is much less than the slab thickness, the frequencies of the pair of modes arising at the two surfaces of the slab are practically degenerate. In a slab of infinite thickness the two surfaces are independent of each other and the frequencies of the *microscopic* surface mode frequencies are equal, which is equivalent to replacing the thick slab with a semi-infinite crystal with a single surface.

The polarization and degree of localization of surface phonons can be assessed from the $\boldsymbol{Q}$-selected DOS projected on different planes and atomic coordinates, (23.9). Since the surface itself is not a mirror-symmetry plane the SV and L components of the displacements are coupled and out-of-phase with respect to each other, leading to an *elliptical* polarization. The plane containing the L and SV components is called the *sagittal plane*. When there is a sagittal plane that is also a mirror symmetry plane of the lattice, the polarization ellipse lies on the sagittal plane, and the polarization is more precisely called *sagittal*. Depending on the dominant component in the sagittal plane, the modes with sagittal polarization are designated as either quasi-transverse ($\approx$ SV) or quasi-longitudinal ($\approx$ L). On the other hand, in the case that the sagittal plane is not a mirror plane, as occurs, e.g., in the $\overline{\Gamma K}$ and $\overline{MK}$ directions of fcc(111) surfaces (Fig. 23.3), the polarization ellipse is rotated with respect to the sagittal plane, and the sagittal and SH components are mixed. Thus, the polarizations of $\approx$ SV and $\approx$ L modes may only be quasi-sagittal, and that of SH modes only quasi-SH.

Some slab eigenmodes may have a strong amplitude enhancement at the surface, and, therefore, a large projected DOS, even though their frequency lies within a bulk phonon band. This happens when their eigenvectors are either orthogonal or quasi-orthogonal to the eigenvectors of the bulk band. The first case is that of an *embedded surface mode*, giving a δ-function inside the perturbed projected DOS; the second case that of a *surface phonon resonance*, whose origin and nature are better described within the Green's function formalism introduced in the next section. Note that the eigenvector orthogonality characterizing an embedded surface mode may only occur along sagittal mirror symmetry directions; away from these directions these modes become resonances. For certain anisotropic surfaces along particular directions, the RW are actually embedded in the SH bulk band and are also known as pseudosurface modes (PSM).

Surface phonon branches are conventionally labeled by S_j ($j = 1, 2, 3, \ldots$), depending on their acoustic or optical character and polarization. In the example of Fig. 23.3, for $N_3 = 15$, the acoustic surface mode S_1 corresponds, in the long-wave limit ($Q \to 0$) to the Rayleigh wave (RW), then becomes elliptically polarized $\approx$ SV and pure (SV) at the zone boundary. The gap surface modes S_2 and S_3 are associated with the L bulk phonon band. In principle, each surface-projected bulk phonon band has its own surface branch. For example, the SH and L bulk bands generate, respectively, an SH acoustic surface branch (S_7), and an $\approx$ L acoustic surface branch, (S_6), (not shown in Fig. 23.3), which eventually end up as S_2 or S_3 at the zone boundaries. The $\approx$ L acoustic surface branch, which is detached from the lower edge of the L band, is normally superimposed on the SV transverse band and is, therefore, a resonance, sharing with the SV bulk modes its weak SV component. The velocities of both acoustic surface modes S_6 and S_7 for $\boldsymbol{Q} \to 0$, tend to the respective bulk velocities; thus, both surface modes have no surface wave counterpart in the elastic semi-infinite continuum and are, therefore, microscopic. In most metal surfaces, the $\approx$ L acoustic surface branch becomes anomalously soft with increasing $\boldsymbol{Q}$. For this reason, it is called the

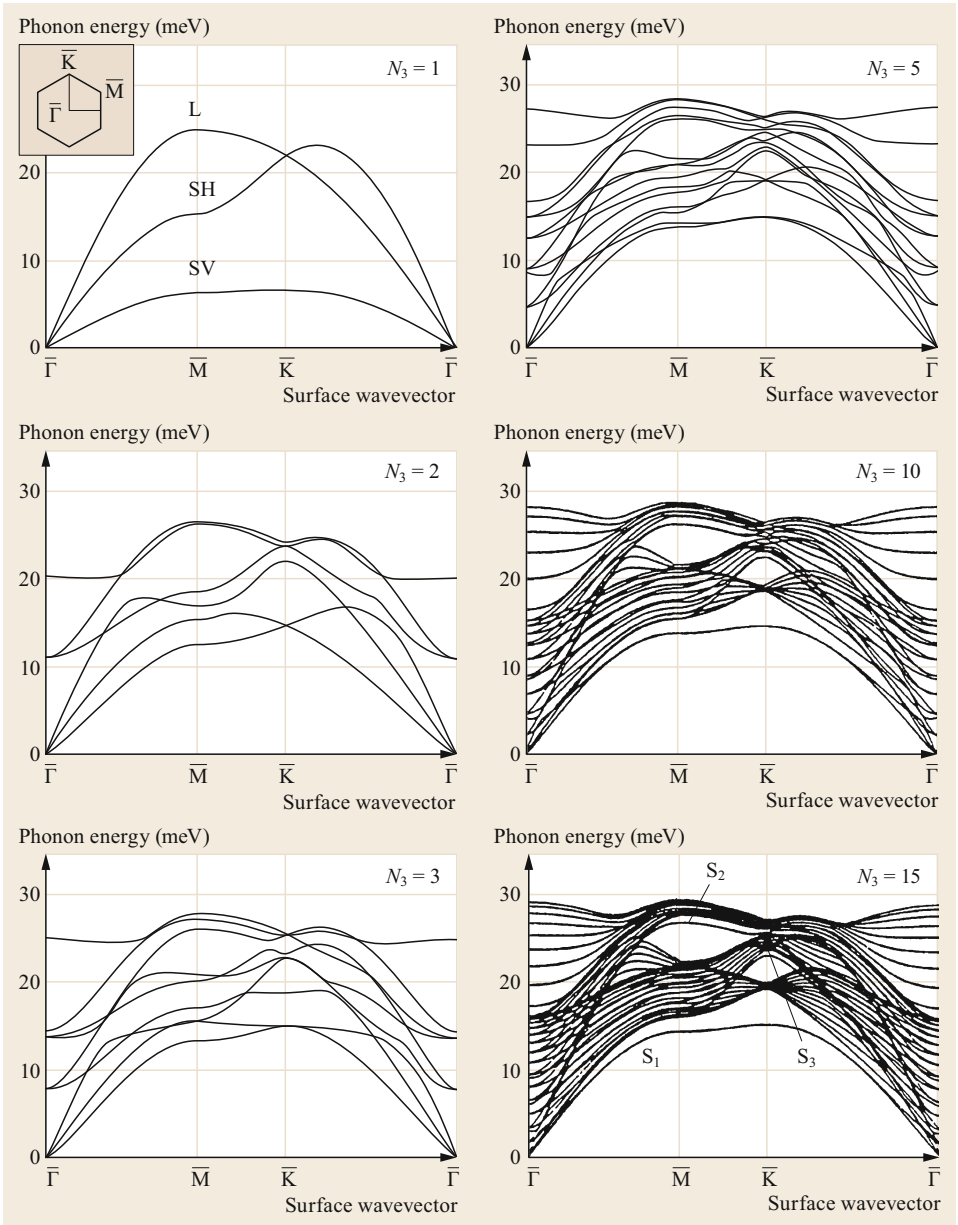

Fig. 23.3 The evolution to the surface phonon dispersion curves of an fcc(111) along the symmetry directions for an increasing number of layers, calculated with one single nearest-neighbor force constant, which gives the best fit of copper bulk phonons [23.4]. For a single layer ($N_3 = 1$) only the three acoustic modes of shear vertical (SV), shear horizontal (SH), and longitudinal (L) polarization occur (the *inset* shows the surface Brillouin zone with the symmetry directions), while for $N_3 > 1$ there are an increasing number of optical phonon branches. For $N_3 = 15$ the number of layers is sufficiently large to show a clear separation of the surface phonon branches (the Rayleigh wave branch S_1 and two gap modes S_2 and S_3) from the closely spaced surface-projected bulk bands

anomalous longitudinal surface phonon resonance and is usually labeled S_3.

In diatomic crystals, the three additional optical phonon branches lead to a corresponding number of additional surface phonon branches. In ionic crystals, e.g., NaCl, at $\boldsymbol{Q} = 0$ there is a degenerate pair of optical surface modes of L and SH polarizations, which are known as *Lucas modes* and are, respectively, labeled

S_4 and S_5. In addition, there is also a detached optical surface mode of SV polarization labeled S_2 (*Wallis mode*), which eventually ends in the gap S_2 mode at the zone boundary. Note that also monoatomic metals often behave as diatomic lattices at the surface due to surface relaxation, which confers a bilayer structure to the surface region. In this case, pairs of surface Lucas modes and an upper Wallis mode can be recognized, although, in general, they have the character of a resonance, except where they become localized gap modes. Another interesting case is that of diatomic crystals made of equal or nearly equal atom masses, which can be viewed as an approximate monoatomic lattice with a surface unit cell twice as large as the real one. In this case, additional surface optical branches originate from the folding at the zone boundaries of the acoustic modes. Folded RWs (denoted by S_8) are known to occur, e.g., in NaF(001), KCl(001), and also in Si(111)2×1.

In layered crystals, surface modes may have their largest amplitude at the n-th layer (with $n = 1$ the surface layer) and are usually labeled by SVn, SHn, and Ln, while Greek letters are often preferred for the quantum-well modes of thin films.

The Green's Function Method

For values of ω corresponding to localized surface modes that fall outside the spectrum $\{\omega_\nu\}$ of $\mathbf{R}_0(\boldsymbol{r})$, the matrix $\mathbf{R}_0(\boldsymbol{Q}) - \mathbf{M}\omega^2$ can be inverted and (23.10) can be rewritten as

$$\left\{\mathbf{I} - [\mathbf{M}\omega^2 - \mathbf{R}_0(\boldsymbol{Q})]^{-1}\boldsymbol{\Lambda}(\boldsymbol{Q})\right\}\boldsymbol{u} = 0\,, \quad \omega \notin \{\omega_n\}\,. \tag{23.11}$$

Nonvanishing eigenvectors of (23.11) are obtained for each $\boldsymbol{Q}$ at the values of ω fulfilling the equation

$$\det\left\{\mathbf{I} - [\mathbf{M}\omega^2 - \mathbf{R}_0(\boldsymbol{Q})]^{-1}\boldsymbol{\Lambda}(\boldsymbol{Q})\right\} = 0\,, \quad \omega \notin \{\omega_n\}\,. \tag{23.12}$$

The determinant of this linear equation is taken in the small subspace of the perturbation matrix $\boldsymbol{\Lambda}(\boldsymbol{Q})$ and not in the large space of the matrix $\mathbf{R}_0(\boldsymbol{Q})$. The reduction of the problem from the large space of the slab to the small space of the perturbation is the central idea of the Green's function (GF) method [23.72, 82, 84–90].

The Green's function method also provides a suitable framework to describe another important effect of the surface perturbation, the emergence of resonances in the spectrum of bulk mode frequencies. For $N_3 \to \infty$, the set of eigenfrequencies $\{\omega_\nu\}$ constituting the spectrum of the unperturbed matrix $\mathbf{R}_0(\boldsymbol{Q})$ tends to a continuum, and at any frequency ω of this spectrum, there is an eigenvector $\boldsymbol{u}_0$, which solves the unperturbed dynamical problem. The problem to be solved is, therefore, the calculation of the distortion of the unperturbed waves produced by a localized perturbation, and it can be treated within scattering theory. For a frequency ω falling inside $\{\omega_\nu\}$, (23.10) can be transformed into

$$\boldsymbol{u} = \boldsymbol{u}_0 + \mathbf{G}_0(\boldsymbol{Q}, \omega^2)\boldsymbol{\Lambda}(\boldsymbol{Q})\boldsymbol{u}\,, \quad \omega \in \{\omega_\nu\}\,, \tag{23.13}$$

where $\boldsymbol{u}_0$ is an eigenvector of $\mathbf{R}_0(\boldsymbol{Q})$ for the eigenfrequency ω and

$$\mathbf{G}_0(\boldsymbol{Q}, \omega^2) = [\mathbf{M}(\omega^2 + \mathrm{i}0^+) - \mathbf{R}_0(\boldsymbol{Q})]^{-1}\,, \quad \omega \in \{\omega_\nu\} \tag{23.14}$$

is the unperturbed GF matrix, defined as the analytical continuation of $[\mathbf{M}\omega^2 - \mathbf{R}_0(\boldsymbol{Q})]^{-1}$ into the complex plane. The shift of the frequency ω away from the real axis by the infinitesimal quantity $\mathrm{i}0^+$ into the upper complex half-plane allows for the inversion in (23.14) for ω^2 inside the spectrum of $\mathbf{R}_0(\boldsymbol{Q})$. In scattering theory, (23.13) is known as the Lippmann–Schwinger equation [23.91]. Its formal solution is given by

$$\begin{aligned}\boldsymbol{u} &= \left[\mathbf{I} - \mathbf{G}_0\left(\boldsymbol{Q}, \omega^2\right)\boldsymbol{\Lambda}(\boldsymbol{Q})\right]^{-1}\boldsymbol{u} \\ &= \boldsymbol{u}_0 + \mathbf{G}_0\left(\boldsymbol{Q}, \omega^2\right)\mathbf{T}\left(\boldsymbol{Q}, \omega^2\right)\boldsymbol{u}_0\,,\end{aligned} \tag{23.15}$$

where

$$\mathbf{T}\left(\boldsymbol{Q}, \omega^2\right) \equiv \boldsymbol{\Lambda}(\boldsymbol{Q})\left[\mathbf{I} - \mathbf{G}_0\left(\boldsymbol{Q}, \omega^2\right)\boldsymbol{\Lambda}(\boldsymbol{Q})\right]^{-1}\,, \tag{23.16}$$

is the transition matrix (or simply the **T**-matrix) and has nonzero elements only in the subspace of the perturbation $\boldsymbol{\Lambda}$. Equation (23.15) is viewed as the solution of a scattering problem with the eigenvector $\boldsymbol{u}$ given by the sum of the incident wave $\boldsymbol{u}_0$ and the scattered wave $\mathbf{G}_0\mathbf{T}\boldsymbol{u}_0$ produced by the perturbation $\boldsymbol{\Lambda}$, which here acts as a scattering potential. In general, the perturbed wave $\boldsymbol{u}$ in (23.15) is not normalized in the same way as $\boldsymbol{u}_0$ and may need to be multiplied by a normalization constant.

Owing to the factor $[\mathbf{I} - \mathbf{G}_0\boldsymbol{\Lambda}]^{-1}$, called the *resonant denominator*, the elements of the **T**-matrix are all proportional to

$$\begin{aligned}&\frac{1}{\det(\mathbf{I} - \mathbf{G}_0\boldsymbol{\Lambda})} \\ &= \frac{\mathrm{e}^{\mathrm{i}\theta}}{|\mathrm{Re}[\det(\mathbf{I} - \mathbf{G}_0\boldsymbol{\Lambda})] + i\mathrm{Im}[\det(\mathbf{I} - \mathbf{G}_0\boldsymbol{\Lambda})]|}\,,\end{aligned} \tag{23.17}$$

where the argument

$$\theta = -\arctan \frac{\mathrm{Im}[\det(\mathbf{I}-\mathbf{G}_0\mathbf{\Lambda})]}{\mathrm{Re}[\det(\mathbf{I}-\mathbf{G}_0\mathbf{\Lambda})]} \tag{23.18}$$

gives the phase shift between the incident and the scattered wave [23.86, 87]. According to (23.16) and (23.17) a resonance enhancement of the **T**-matrix and, therefore, of the amplitude of the perturbed wave with respect to the incident wave, occurs at frequencies ω where

$$\mathrm{Re}\{\det[\mathbf{I}-\mathbf{G}_0(\boldsymbol{Q},\omega^2)\mathbf{\Lambda}(\boldsymbol{Q})]\} = 0\,. \tag{23.19}$$

This equation is a generalization of (23.12). It gives the frequencies of both surface resonances, for ω inside $\{\omega_\nu\}$, and localized modes, for ω outside $\{\omega_\nu\}$. In the latter case, the determinant of (23.19) is a real function. According to (23.18) a resonance occurs when the phase shift θ between the incident and the scattered wave is equal to $\pi/2$. This corresponds exactly to the case of a forced mechanical oscillator, with the incident wave playing the role of external oscillating force and the scattered wave that of the oscillator response. The scattered part of the wave becomes very large with respect to the incident wave.

In general, the size of the matrix $\mathbf{\Lambda}$ subspace σ' is determined by the range of the interatomic force constants. However, it was shown [23.84] that even in the presence of long-range Coulomb forces, as in ionic crystals, the symmetry operation reducing σ to σ' leads to a perturbation matrix whose elements decay exponentially for increasing l_3, l_3'. This justifies using a cut-off and working with a small perturbation matrix. Moreover, for intrinsic surface perturbations resulting in a relaxed unreconstructed surface, the translational and rotational invariance conditions, which must be fulfilled by the perturbed force constant matrix, define a set of effective surface force constants in terms of $\boldsymbol{Q}=0$ elements of the inverse unperturbed projected Green's functions [23.84]. Such internal self-consistency tests of the intrinsic surface perturbation of the alkali halide (001) surfaces [23.82, 92] can probably be extended to more complex intrinsic surfaces of current interest.

Surface localized modes and resonances yield important features in the perturbed density of phonon states, as shown in the following definitions. By means of the identities

$$\frac{1}{\omega^2-\omega_\nu^2+\mathrm{i}0^+} = \frac{1}{\omega^2-\omega_\nu^2} - \mathrm{i}\pi\delta\left(\omega^2-\omega_\nu^2\right)\,, \tag{23.20}$$

$$\delta(\omega^2-\omega_\nu^2) = \frac{1}{2\omega}\left[\delta\left(\omega-\omega_\nu\right)+\delta\left(\omega+\omega_\nu\right)\right], \tag{23.21}$$

the *total unperturbed* $\boldsymbol{Q}$-selected DOS can be written as

$$D_0(\boldsymbol{Q},\omega) = -\frac{2\omega}{\pi}\mathrm{Tr}\{\mathrm{Im}[\mathbf{M}\mathbf{G}_0(\boldsymbol{Q},\omega^2)]\}\,. \tag{23.22}$$

The *total perturbed* $\boldsymbol{Q}$-selected DOS, $D(\boldsymbol{Q},\omega)$, is defined in a similar way

$$D(\boldsymbol{Q},\omega) = -\frac{2\omega}{\pi}\mathrm{Tr}\{\mathrm{Im}[\mathbf{M}\mathbf{G}(\boldsymbol{Q},\omega^2)]\}\,, \tag{23.23}$$

where

$$\begin{aligned} G\left(\boldsymbol{Q},\omega^2\right) &= \left[\mathbf{M}\left(\omega^2+\mathrm{i}0^+\right)-\mathbf{R}_0(\boldsymbol{Q})-\mathbf{\Lambda}(\boldsymbol{Q})\right]^{-1} \\ &= \left[\mathbf{I}-\mathbf{G}_0\left(\boldsymbol{Q},\omega^2\right)\mathbf{\Lambda}(\boldsymbol{Q})\right]^{-1}\mathbf{G}_0\left(\boldsymbol{Q},\omega^2\right), \end{aligned} \tag{23.24}$$

is the *perturbed GF-matrix*. The change in the DOS can be expressed, after some algebra, as

$$\begin{aligned} &\Delta D\left(\boldsymbol{Q},\omega^2\right) \equiv D\left(\boldsymbol{Q},\omega^2\right) - D_0\left(\boldsymbol{Q},\omega^2\right) \\ &= -\frac{1}{\pi}\frac{\partial}{\partial\omega}\mathrm{Im}\left\{\ln\det\left[\mathbf{I}-\mathbf{G}_0\left(\boldsymbol{Q},\omega^2\right)\mathbf{\Lambda}(\boldsymbol{Q})\right]\right\} \\ &= \frac{1}{\pi}\frac{\partial\theta}{\partial\omega}\,. \end{aligned} \tag{23.25}$$

The diagonal elements

$$D_{0,l_3\kappa\alpha}(\boldsymbol{Q},\omega) = -\frac{2\omega}{\pi}\mathrm{Im}[\mathbf{M}\mathbf{G}_0(\boldsymbol{Q},\omega^2)]_{l_3\kappa\alpha,l_3\kappa\alpha}\,, \tag{23.26}$$

$$D_{l_3\kappa\alpha}\left(\boldsymbol{Q},\omega\right) = -\frac{2\omega}{\pi}\mathrm{Im}\left[\mathbf{M}\mathbf{G}\left(\boldsymbol{Q},\omega^2\right)\right]_{l_3\kappa\alpha,l_3\kappa\alpha} \tag{23.27}$$

are the unperturbed $\boldsymbol{Q}$-selected DOS *projected* onto the l_3-th plane, the κ-th sublattice and polarization α, and the corresponding *perturbed projected* $\boldsymbol{Q}$-selected DOS, respectively.

In the limit $N_3 \to \infty$, the densities of phonon states become continuous functions for ω inside $\{\omega_\nu\}$. Moreover, the perturbed phonon densities display δ-functions at certain frequencies ω_S outside $\{\omega_\nu\}$, which correspond to the localized surface modes. When they lie in the continuum $\{\omega_\nu\}$ of bulk modes, they exhibit sharp peaks at the resonance frequencies ω_R. By expanding the resonant denominator around ω_R, where its real part vanishes, a Lorentzian peak is obtained in the phonon density change [23.82, 91, 92]

$$\Delta D\left(\boldsymbol{Q},\omega\right) \cong \frac{1}{\pi}\frac{\Gamma/2}{\left(\omega-\omega_R\right)^2+(\Gamma/2)^2}\,, \tag{23.28}$$

$$\omega \approx \omega_R\,,$$

with a full width at half maximum (FWHM) given by

$$\Gamma = \frac{2\mathrm{Im}\{\det\left[\mathbf{I} - \mathbf{G}_0\left(\boldsymbol{Q}, \omega_\mathrm{R}^2\right)\boldsymbol{\Lambda}(\boldsymbol{Q})\right]\}}{\frac{\partial}{\partial\omega}\,\mathrm{Re}\{\det\left[\mathbf{I} - \mathbf{G}_0\left(\boldsymbol{Q}, \omega^2\right)\boldsymbol{\Lambda}(\boldsymbol{Q})\right]\}|_{\omega=\omega_\mathrm{R}}} \,. \tag{23.29}$$

From (23.28) and (23.29), it follows that the perturbed GF has a pole in the complex plane at $z = \omega_\mathrm{R} - \mathrm{i}\Gamma/2$ corresponding to a resonance. In order to fulfill causality [23.86, 87], by which the response, i.e., the scattered wave, follows the stimulus, i.e., the incident wave, Γ has to be positive. The same also holds for localized modes, for which, however, $\Gamma \to 0^+$ and the corresponding peaks in $D(\boldsymbol{Q}, \omega)$, (23.28), become δ-functions. Note that a solution ω_R of (23.19), which yields a negative Γ, does not contribute a real resonance but leads to an *antiresonance*, i.e., a depletion region in $D(\boldsymbol{Q}, \omega)$ with respect to $D_0(\boldsymbol{Q}, \omega)$. Such depletion regions compensate for the density of states transferred to localized and real resonant modes.

From the computational point of view, the GF method has the great advantage that all the diagonalizations are performed in the perturbation subspace rather than in the whole slab space. This advantage, however, is lost to some extent due to the comparatively difficult task of calculating the matrix elements of the complex-valued Green's functions, which require integrations over the bulk Brillouin zone with special care for frequencies around van Hove singularities [23.75, 92, 93]. For this reason, the GF method is nowadays less popular than the direct diagonalization of the whole slab dynamical matrix discussed above, the latter method now being more expedient due to the availability of fast computers.

On the other hand, the GF method provides a convenient framework for the calculation of the various vibrational response functions of the surface, for example, the inelastic atom-scattering cross section [23.4, Chap. 7]. Such response functions can, in general, be expressed in terms of the time-dependent displacement-displacement correlation function $\langle \widehat{u}_\alpha(l\kappa, t)\widehat{u}_\beta(l'\kappa', 0)\rangle_T$, where

$$\widehat{u}_\alpha\left(l\kappa, t\right) = \sum_{\boldsymbol{Q}\nu} u_\alpha\left(l_3\kappa, \boldsymbol{Q}\nu\right) \mathrm{e}^{\mathrm{i}\boldsymbol{Q}\cdot\boldsymbol{r}_l} \left(b^+_{\boldsymbol{Q}\nu}\mathrm{e}^{\mathrm{i}\omega_{\boldsymbol{Q}\nu}t} + b^-_{\boldsymbol{Q}\nu}\mathrm{e}^{-\mathrm{i}\omega_{\boldsymbol{Q}\nu}t}\right) \tag{23.30}$$

is the displacement field operator, $b^+_{\boldsymbol{Q}\nu}$ and $b_{\boldsymbol{Q}\nu}$ are phonon creation and annihilation operators, respectively, and $\langle\ldots\rangle_T$ means the thermal average at temperature T. With some little algebra, it is found that

$$\int_{-\infty}^{\infty} \mathrm{d}t\mathrm{e}^{\mathrm{i}\omega t}\left\langle \widehat{u}_\alpha(l\kappa, t)\widehat{u}_\beta(l'\kappa', 0)\right\rangle_T = -\frac{2\hbar}{1 - \mathrm{e}^{-\hbar\omega/(k_\mathrm{B}T)}}\mathrm{Im}[G_{\alpha\beta}(l\kappa, l'\kappa', \omega^2)] \,, \tag{23.31}$$

where $G_{\alpha\beta}(l\kappa, l'\kappa', \omega^2)$ are the GF-matrix elements in the direct lattice space and the 2-D Fourier transforms of the elements of $G(\boldsymbol{Q}, \omega^2)$ [23.72, 75].

23.2 The Role of Electrons in Surface Dynamics

As anticipated in the introduction to this chapter, the experimental and theoretical study of surface phonons aims at understanding the basic atomic scale interactions operating at the surface of different classes of solid materials. The methods illustrated in Sect. 23.1 rely on the force constant matrix introduced by (23.2). After recognizing the essential role of valence electrons in determining bulk force constants in the 1960s, theoretical surface dynamics gradually moved away from force-constant models, which in various ways indirectly included the electronic degrees of freedom, to first-principles methods based on density functional theory. At the same time, powerful new experimental methods were developed, like high-resolution electron energy loss (HREELS), helium atom scattering (HAS), and, more recently, inelastic x-ray (IXS) spectroscopies. In particular, besides providing high-resolution data on surface phonon dispersion curves, HAS qualifies as a unique tool to detect deep subsurface modes in conducting materials through the so-called *quantum sonar effect* [23.94, 95]. This enables the direct measurement of the mode-selected electron–phonon coupling strength (*mode-λ spectroscopy*) in these systems [23.94, 96, 97]. A thorough report on HAS theory and data for the surface phonon dispersion curves of more than 200 surfaces of single crystals, ultrathin films, and adsorbed layers can be found in the Landolt–Börnstein collection and the chapter and monograph mentioned above [23.4, 5].

23.2.1 From Rigid Ions to Shell Models

The early lattice force-constant models considered atoms as hard massive spheres (rigid ion (RI) model)

disregarding the actual shape of the valence electron distribution and its deformation during the atomic motion. Historically, the rigid ion model was first used for the bulk [23.101] and surface dynamics of ionic crystals [23.102]. Due to its simplicity, it is still in use as a first-order approach to the surface dynamics especially in complex systems [23.103]. Moreover, it provides a fair approximation for the surface dynamics of close-shell monoatomic crystals like rare-gas solids.

The surface dispersion curves for Xe(111) measured with HAS (Fig. 23.4; [23.100]) are very well reproduced by the RI model with a single nearest-neighbor central force constant but with a 15% softening of the force constant at the surface layer [23.98]. This model, originally introduced by *Hall* et al. for Cu(111) [23.99], permits us to assign the observed modes above the RW (S_1) to the longitudinal acoustic (S_3) and to the optical surface resonances S_2 and S_4. The fact that these resonances are observed by HAS despite their prevalent localization in the second atomic layer is attributed to an unexpected electron–phonon interaction due to the comparatively large polarizability of surface Xe atoms, which also provides a mechanism for the 15% surface force constant softening at the surface. This effect of the electron–phonon interaction is confirmed by the first-principles DFPT calculation reproduced in Fig. 23.4b [23.98]. Despite the fact that the calculated S_2 resonance is about 15% above the HAS experimental data, the DFPT calculation predicts the S1 mode at the same frequency as the RI calculation with a 15% softening.

The electronic susceptibility plays a crucial role in determining the phonon dispersion relations in all three classes of solids, insulators, semiconductors, and metals. Since in lattice dynamics atoms are treated as discrete entities, the indirect forces between ion cores that are mediated by the interposed electrons can be approximately modeled by additional degrees of freedom associated either with the deformation (polarization) of the electronic shells in closed-shell insulators, or the motion of the bond charges in covalent of partially covalent semiconductors, or the charge density oscillations in free-electron conductors. There is a wide class of models where many-body effects are accounted for by a set of electronic coordinates harmonically coupled to the ion core coordinates in the adiabatic approximation [23.104–107]. In particular, the shell model (SM), formulated independently by *Dick* and *Overhauser* [23.108] and *Cochran* [23.109, 110] for the analysis of the phonon dispersion curves in insulators, gives excellent results also for the surface dynamics of ionic crystals within the slab method [23.111–117].

In the SM, the valence electron shells can be rigidly displaced with respect to ion cores, which corresponds to dipolar polarization. More sophisticated versions of the SM, including shell deformabilities of

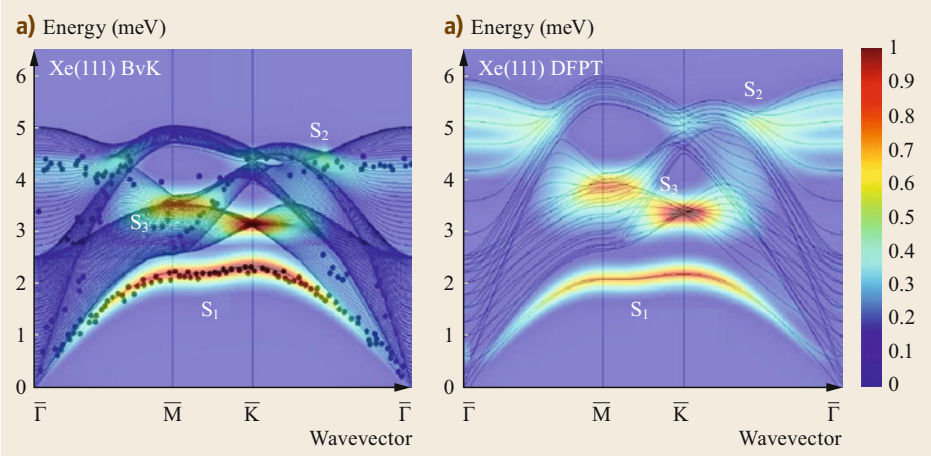

Fig. 23.4 **(a)** An RI model calculation for the Xe(111) surface [23.98], similar to the RI calculation of *Hall* et al. for Cu(111) [23.99], with one single bulk nearest-neighbor central force constant. By reducing the force constant in the first layer by 15% it was possible to reproduce the frequencies of the RW (or S_1) modes, and the S_3 and S_2 resonances observed with HAS (*black dots*) [23.98, 100]. The color code indicates the surface-projected phonon density. The prevalent second-layer displacements of the S_2 resonance and of S_3 at the $\overline{\mathbf{M}}$-point are attributed to an important electron–phonon (e–ph) interaction resulting from the large Xe atom polarizability. This also explains the 15% surface force constant softening. **(b)** This effect of the e–ph interaction is confirmed by a first-principles DFPT calculation [23.98], which is in general agreement with the HAS data, except that the S_3 and S_2 resonances are too high in frequency by about 12 and 20%, respectively

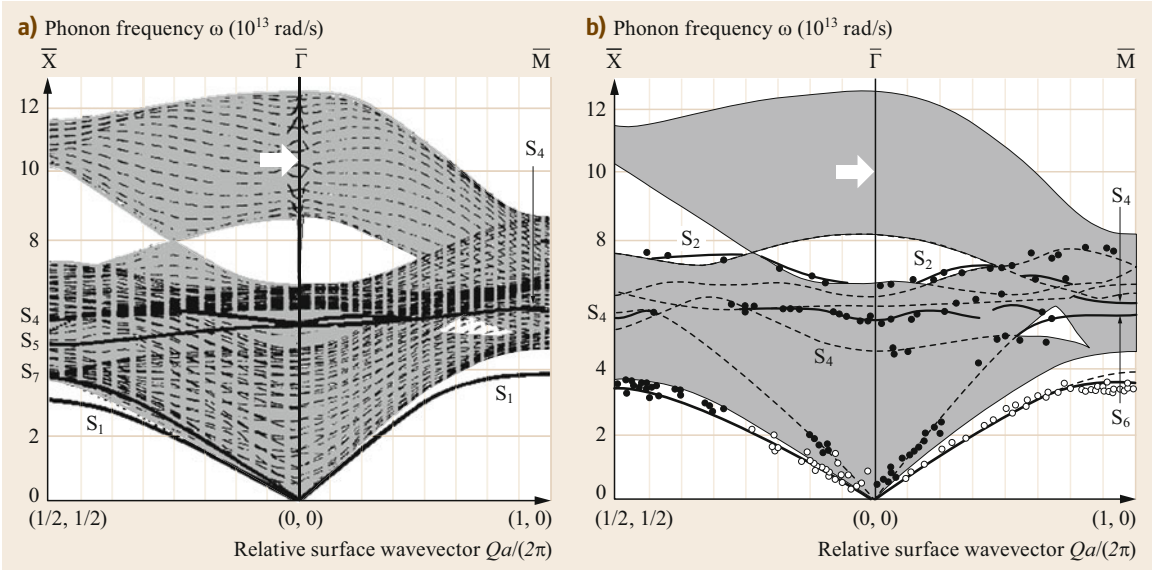

Fig. 23.5a,b Surface phonon dispersion curves of LiF(001) along the symmetry directions calculated with **(a)** the shell model (SM) and the slab method (all polarizations) [23.117] and **(b)** with the breathing-shell model (BSM) and the Green's function (GF) method (only sagittal polarization ⊥) [23.83, 118]. The better resolution of the GF method in **(b)** permits us to resolve additional surface modes, like the optical branches S_2 and S_4 and the sagittal acoustic branch S_6; S_1 is the Rayleigh wave, and S_4 the longitudinal Lucas mode [23.119]. The S_5 and S_7 branches in the SM calculation, shown in **(a)**, are the SH Lucas mode and the SH Alldredge mode, respectively [23.112]. The slab calculation also shows the signature of the macroscopic Fuchs and Kliever (FK surface phonon polariton) (*white arrow*) [23.120, 121]. The GF method predicts the existence of the FK mode, provided the surface depolarization field is added to the surface polarization [23.82]. HAS data points are from (○) [23.17–19] and (●) [23.122]. Some data points follow the band edges, where there are maxima of the surface-projected DOS

monopolar (breathing shell model, BSM [23.123, 124]) and/or quadrupolar types (quadrupolar shell model, QSM [23.125, 126]), have been used for a more precise description of the dynamical polarization phenomena in different classes of ionic compounds. In combination with the GF method, the BSM proved to give excellent results in the calculation of alkali halide surface phonons [23.82–84, 92], as seen in Fig. 23.5a for LiF(001) in comparison with a slab SM calculation (Fig. 23.5a) and the HAS data. In particular, the BSM, unlike SM, predicts the correct S_2 optical branch and the $\overline{M}$-point softening of the RW (S_1), in agreement with HAS data. Zone-boundary RW softening has been explained as being due to the surface increase of the F^- ion polarizability. As shown in the previous section, the GF method directly provides the vibrational response functions for a semi-infinite crystal, thus being particularly suited to the calculation of inelastic HAS spectra [23.118, 127, 128].

In transition metal compounds, characterized by open shells, more degrees of freedom are needed to represent the response of the valence electrons. This led to the formulation of the double-shell model (DSM), where more than one shell per atom is included [23.129], and the cluster model (CM), where hybridized shells of the transition metal atom with those of the surrounding ligand ions are considered [23.130]. The CM, combined with the GF method, proved efficient for the study of surface phonon superconducting anomalies in TiN(001) [23.131, 132], accounting for the surface DOS excess measured by neutron inelastic scattering (NIS) in nanometric powders [23.133, 134].

As seen in Fig. 23.6a, the calculated surface phonon dispersion curves present important Kohn anomalies in the quasi-L ($\underline{S_6}$) mode at about 2/3 of the Brillouin zone (BZ) in the $\overline{\Gamma M}$, the same position as for the longitudinal acoustic (LA) bulk mode, and in the RW (S_1), shifted to 1/2 of the BZ. Such features are called *superconducting anomalies*, since they are attributed to the electron–phonon interaction responsible for the superconductivity in this class of materials. The comparison between the calculated surface-excess phonon DOS (Fig. 23.6b) with that observed with NIS (above) shows a softening of the surface gap S_2 and of the RW modes indicated by vertical arrows in Fig. 23.6a and horizontal arrows in Fig. 23.6b. In order to obtain a quantitative agreement, an enhancement of the electron–phonon interaction in the surface layer is required. As discussed

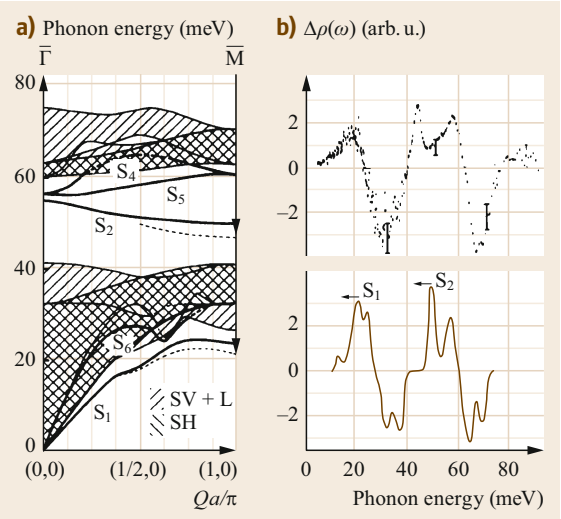

Fig. 23.6 **(a)** A cluster shell model (CM) Green's function calculation of the surface phonon dispersion curves of TiN(001) [23.131]. **(b)** The DOS from neutron inelastic scattering (NIS) from nanometric powders [23.134] (*top*) is compared with the corresponding surface-excess phonon density from the CM-GF calculation (*bottom*). The *vertical arrows* in **(a)**, which correspond to the *horizontal arrows* in **(b)**, show the softening of the surface phonon. An increase of the electron–phonon interaction at the surface yields good agreement between theory and experiment

in [23.131], this would imply a slight increase of the superconducting T_c for nanocrystals smaller in size than the coherence length.

In covalent or partially covalent crystals, the many-body effects due to the bonding electrons, e.g., the three-body angle-bending force constants, have been well described by the valence force field (VFF) theory [23.135, 136] and the Keating model (KM) [23.137, 138], with useful results in the dynamical theory of covalent semiconductors [23.139]. These methods provided the basis for the bond charge model (BCM) [23.140–146], which includes new adiabatic degrees of freedom associated with the valence electrons of the covalent bonds. Following *Fleszar* and *Resta*'s demonstration that BCM stands on a solid first-principles quantum mechanical basis [23.147], the BCM extension to treat π-bonding electrons [23.148] provided a reliable and efficient tool for surface dynamics of covalent semiconductors [23.148], III–V compounds [23.149], and graphite [23.150, 151]. Two basic examples of BCM calculations for the native Si(111) 2×1 and C(0001) surfaces are shown in Figs. 23.7 and 23.8. The 2×1 reconstructed Si(111) surface is characterized by the presence of π-bonded chains (atoms 1, 2 in the left upper inset of Fig. 23.7), which host a flat surface phonon branch at about 10 meV. The large number of surface phonon branches, substantially confirmed by subsequent DFPT calculations [23.152], is due to the extended surface perturbation associated with the sequence of five and sevenfold atomic rings (Fig. 23.7, left inset). The surface displacements of the surface phonons at $\overline{\Gamma}$ are shown in the left inset in Fig. 23.7. Of special interest are the two modes above the bulk phonon maximum with in-plane polarization normal to the chains and the $I_z(00{+}{+})$ mode at 55 meV, which is localized on the fivefold ring. It is the first microscopic surface phonon observed with HREELS by *Ibach* in 1971 [23.6].

The success of BCM in dealing with semiconductor surfaces with π-bonded chains naturally led to graphite, where BCM, although less popular, proved to be superior to the Born–von Kármán treatments with many parameters [23.165–169]. A six-parameter BCM calculation for C(0001) [23.150, 151], shown in Fig. 23.8a, compares quite well with the HREELS data [23.155–158] and to a minor extent with DFT-LDA and DFT-GGA calculations [23.154], shown in Fig. 23.8b. Some of the critical points of discrepancy are indicated in Fig. 23.8 by arrows. For example, the TA-ZO and LA-LO quasi-degeneracies at the $\overline{M}$ point predicted by a DFT-GGA calculation are not found in the HREELS data. On the other hand, DFT-GGA calculations reproduce quite well more recent inelastic x-ray spectroscopy (IXS) data [23.159], which, however, show relevant differences to the HREELS data, presumably because of the different penetration lengths of the two probes.

23.2.2 The Multipole Expansion Method

A feature common to all versions of shell and bond-charge models is the description of the electronic response to the atomic motion through suitable dynamical coordinates harmonically coupled to the ion coordinates. A unifying framework is provided by the multipole expansion (ME) method, originally formulated for lattice dynamics by *Allen* [23.170] as a special representation of the general microscopic theory constructed within a set of local basis functions [23.171–183]. This method, allowing for a general and efficient phenomenological treatment of the electronic degrees of freedom, proved quite successful in reproducing the anomalous dispersion curves of transition metals such as niobium [23.170], and later for the analysis of surface phonon anomalies in noble metals [23.184]. The microscopic basis of the ME method makes it suitable for either a first-principles calculation or a phenomenological parametrization known, in metal surface dynamics, as the pseudocharge (PC) model [23.185, 186]. Besides providing a convenient framework for the calculation of phonon dispersion curves, the ME method

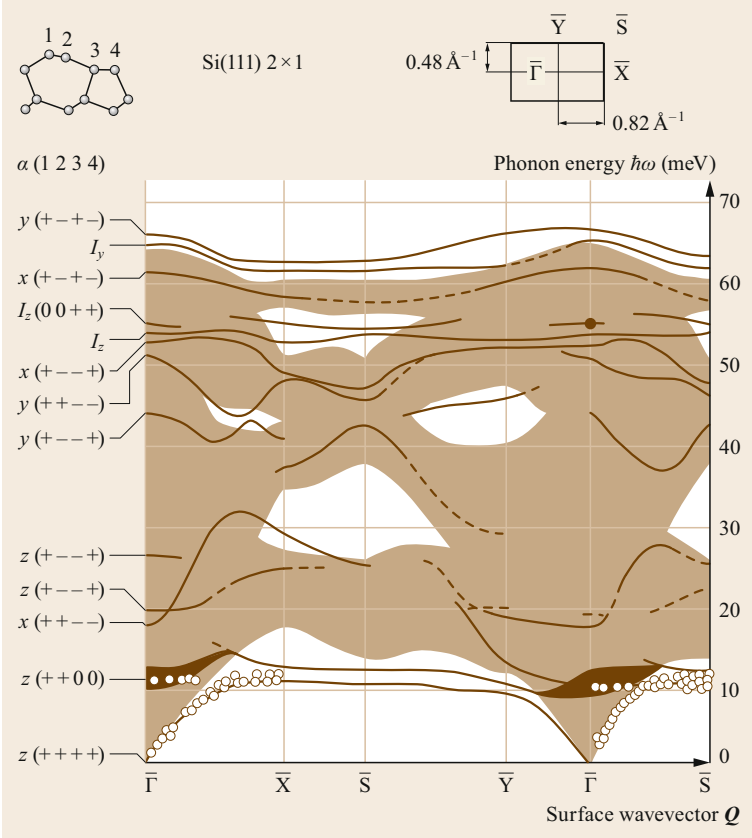

Fig. 23.7 BCM surface phonon dispersion curves of the native Si(111) 2×1 surface along the symmetry directions (*right-hand inset*) [23.148]. The zone center displacements of the four surface atoms (*left-hand inset*) are schematically indicated (I_y and I_z are modes with prevalent amplitudes at the interface between the reconstructed surface region and the undisturbed bulk below). The *hatched areas* represent the surface projected bulk phonon bands, the *dark areas* show the width of the 10 meV flat surface mode resulting from the folding of the RW and associated with the oscillations of the π-bonded chain (atoms 1–2 in *left-hand inset*). The experimental HAS data points (○) [23.153] are also shown. The large number of resonances (including the 55 meV mode (●) observed by *Ibach* with HREELS [23.6]), and optical surface modes localized in the gaps and above the bulk maximum reflect the complex surface reconstruction with a periodic sequence of five and sevenfold rings

has the special merit of providing the phonon-induced surface charge density oscillations, which are directly related to the inelastic HAS intensities and the corresponding mode-selected electron–phonon coupling. Although the ME method for the surface dynamics of ordinary metal surfaces has presently been superseded by efficient ab-initio methods such as the DFPT, it was revived recently for the interpretation of inelastic HAS spectra from more complex surfaces, such as those of topological insulators [23.187–189]. Actually, the ME method, besides providing a local-basis representation of DFPT, has the advantage of being easily extendable to treat nonadiabatic dynamics.

The essence of the ME method is the following. As in DFT, the total energy of the lattice system is written as the sum of the energy E_{ion} due to the direct interaction of the ion cores and the energy of the electrons given by a functional of the electron charge density $n(\boldsymbol{r})$ [23.190]

$$E = E_{\mathrm{ion}} + F[n(\boldsymbol{r})] + \int v_{\mathrm{ion}}(\boldsymbol{r}) n(\boldsymbol{r}) \mathrm{d}^3 r \,. \qquad (23.32)$$

The functional $F[n(\boldsymbol{r})]$ includes the electron–electron potential energy, as well as the kinetic energy; $v_{\mathrm{ion}}(\boldsymbol{r})$ is the external potential acting on the electron system. The electron density is expanded over an orthonormal set of localized basis functions $Y_\Gamma\,(\boldsymbol{r}-\boldsymbol{r}_{l\lambda})$, centered at convenient special points $\boldsymbol{r}_{l\lambda} = \boldsymbol{r}_l + \boldsymbol{r}_\lambda$, with $\boldsymbol{r}_l$ a unit cell position and $\boldsymbol{r}_\lambda$ a special point position within the unit cell

$$n(\boldsymbol{r}) = \sum_{\Gamma l\lambda} C_\Gamma(l\lambda) Y_\Gamma\,(\boldsymbol{r}-\boldsymbol{r}_{l\lambda}) \,. \qquad (23.33)$$

The basis functions $Y_\Gamma(\boldsymbol{x})$ are conveniently chosen as products of a radial function and an angular harmonic function transforming as the Γ-th irreducible representation of the point group at $\boldsymbol{r}_{l\lambda}$. Thus, Γ labels the harmonic order and its components and (23.32) is actually an ME of the charge density.

In a rigid-atom (ion) insulator, the electronic shells coincide with the atoms (ions), and no additional degree of freedom is needed. In a dipolar shell model (SM), the shells can move rigidly with respect to ion cores; in this case, Γ takes three values corresponding to the three components of an oscillating dipole, and the coefficients $C_\Gamma(l\lambda)$ are displacement vectors dynamically coupled to the atom (ion) core displacements $\boldsymbol{u}(l\kappa)$. In the breathing shell model (BSM),

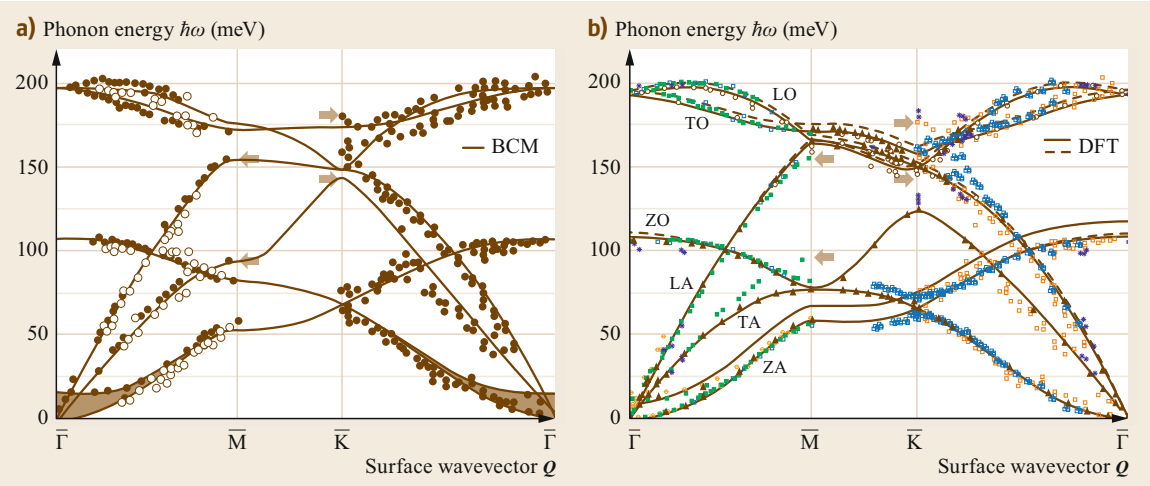

Fig. 23.8a,b Theoretical dispersion curves for the (0001) surface of graphite. **(a)** Calculated with BCM by *Benedek* and *Onida* [23.150], and **(b)** with ab-initio DFT-local density approximation (LDA, *dashed line*) and DFT-generalized gradient approximation (GGA, (*solid line*) by *Wirtz* and *Rubio* [23.154]. The data points in **(a)** are from HREELS (*open circles*: *Wilkes* et al. [23.155], *full circles*: *Oshima* et al. [23.156, 157], *Siebentritt* et al. [23.158]); data points in **(b)** from IXS (*black full triangles* [23.159], *black open circles* [23.160]), HREELS (*green full square* and *red open squares* [23.156–158], *blue open squares* [23.161]), double-resonance Raman scattering (DRRS), *blue crosses* [23.162]), infrared absorption (*open red triangles* [23.163]), and neutron scattering data (*orange open diamonds* [23.164]). The *arrows* mark the end points of the transverse acoustic (TA) and LA branches at $\overline{\mathrm{M}}$, and of the transverse optical (TO) branch at $\overline{\mathrm{K}}$ as obtained from HREELS, which are well reproduced by BCM but show significant differences from the IXS data, in turn well reproduced by the ab-initio calculations

the atomic shell can also have a breathing (spherical) deformation, and the $C_\Gamma(l\lambda)$ are scalar coefficients. For quadrupolar shell deformations, considered in the QSM, the coefficients $C_\Gamma(l\lambda)$ are (combinations of) components of a symmetric tensor. In metals, free-electron delocalization can be accounted for by electronic *shells*, denoted pseudocharges (PCs), which are centered at symmetry points of the unit cell away from ion positions, whereas valence electron shells are located at the ion positions. In general, the larger effects come from delocalized shells representing free electrons, and the dipolar components may be sufficient to account for the dynamical oscillations of the charge density.

The coefficients $C_\Gamma(l\lambda)$ are now split into their static and dynamic parts,

$$C_\Gamma(l\lambda, t) = C^0_\Gamma(l\lambda) + c_\Gamma(l\lambda, t)\,, \tag{23.34}$$

and the dynamic PC multipolar components $c_\Gamma(l\lambda)$ (omitting hereafter the argument t) are treated on the same footing as the displacement vectors. Similar to (23.1), the potential energy, is now expanded around its equilibrium value U_0 with respect to both the atomic displacements $\boldsymbol{u}(l\kappa)$ and PC components $c_\Gamma(l\lambda)$

$$\begin{aligned} U = U_0 &+ \frac{1}{2}\sum_{l\kappa\alpha,l'\kappa'\beta} R_{\alpha\beta}\left(l\kappa, l'\kappa'\right) u_\alpha(l\kappa) u_\beta(l'\kappa') \\ &+ \frac{1}{2}\sum_{l\kappa\alpha,l'\lambda'\Gamma'} \left[T_{\alpha\Gamma'}\left(l\kappa, l'\lambda'\right)\right. \\ &\left. + T^+_{\Gamma'\alpha}\left(l'\lambda', l\kappa\right)\right] u_\alpha(l\kappa) c_{\Gamma'}(l'\lambda') \\ &+ \frac{1}{2}\sum_{l\lambda\Gamma,l'\lambda'\Gamma'} H_{\Gamma\Gamma'}\left(l\lambda, l'\lambda'\right) c_\Gamma(l\lambda) c_{\Gamma'}(l'\lambda')\,, \end{aligned} \tag{23.35}$$

where the first-order derivatives are set to zero at equilibrium, and only quadratic terms in the dynamic variables are retained (*harmonic approximation*). The force-constant matrices for the atom–atom, atom–PC, and PC–PC interactions are, respectively, given by

$$\begin{aligned} R_{\alpha\beta}(l\kappa, l'\kappa') &= \frac{\partial^2 U}{\partial u_{l\kappa,\alpha}\partial u_{l'\kappa'\beta}} \\ &= \frac{\partial^2 E_{\mathrm{ion}}}{\partial u_{l\kappa,\alpha}\partial u_{l'\kappa'\beta}} + \int \mathrm{d}\boldsymbol{r} n(\boldsymbol{r}) \frac{\partial^2 v_{\mathrm{ion}}(\boldsymbol{r})}{\partial r_{l\kappa,\alpha}\partial r_{l'\kappa',\beta}} \\ &\equiv R^{\mathrm{ion}}_{\alpha\beta}(l\kappa, l'\kappa') + R^{\mathrm{el}}_{0,\alpha\beta}(l\kappa, l'\kappa')\,, \end{aligned} \tag{23.36}$$

$$T_{\alpha\Gamma}\left(l\kappa,l'\lambda'\right)=\frac{\partial^2 U}{\partial u_\alpha(l\kappa)\partial c_\Gamma(l'\lambda')}$$
$$=\frac{1}{V}\int \mathrm{d}^3 r\left[\frac{\partial\delta E_{\mathrm{tot}}}{\delta n(\boldsymbol{r})\partial u_\alpha(l\kappa)}\right]Y\left(\boldsymbol{r}-\boldsymbol{r}_{l'\lambda'}\right)$$
$$=\int \mathrm{d}^3 r\left[\frac{\partial v_{\mathrm{ion}}(\boldsymbol{r})}{\partial u_\alpha(l\kappa)}\right]Y_\Gamma\left(\boldsymbol{r}-\boldsymbol{r}_{l'\lambda'}\right), \qquad (23.37)$$

and

$$H_{\Gamma\Gamma'}\left(l\lambda,l'\lambda'\right)=\frac{\partial^2 U}{\partial c_\Gamma(l\lambda)\partial c_{\Gamma'}\left(l'\lambda'\right)}$$
$$=\frac{1}{V^2}\iint \mathrm{d}^3 r\mathrm{d}^3 r'\left[\frac{\delta^2 E_{\mathrm{tot}}}{\delta n(\boldsymbol{r})\delta n\left(\boldsymbol{r}'\right)}\right]$$
$$\times Y_\Gamma\left(\boldsymbol{r}-\boldsymbol{r}_{l\lambda}\right)Y_{\Gamma'}\left(\boldsymbol{r}-\boldsymbol{r}_{l'\lambda'}\right). \qquad (23.38)$$

As will be shown in Sect. 23.2.4, (23.48), only the pure electronic part $F(\boldsymbol{n})$ of the total energy functional will appear in (23.38). The atom–atom force-constant matrix, (23.36), is the sum of two terms, one related to the change of the atom–atom potential energy produced by a quadratic atom displacement, the other to the change of the electronic energy produced by the same quadratic atom displacement. The atom–PC force-constant matrix and its transposed PC–atom matrix express the electron–phonon interaction, while the PC–PC force constant matrix is related to the static electron susceptibility $\chi(\boldsymbol{r},\boldsymbol{r}')$ in the local basis representation, i.e.,

$$H^{-1}_{\Gamma\Gamma'}\left(l\lambda,l'\lambda'\right)=-\iint \mathrm{d}^3 r\mathrm{d}^3 r' Y_\Gamma\left(\boldsymbol{r}-\boldsymbol{r}_{l\lambda}\right)\chi\left(\boldsymbol{r},\boldsymbol{r}'\right)$$
$$\times Y^{+}_{\Gamma'}\left(\boldsymbol{r}-\boldsymbol{r}_{l'\lambda'}\right). \qquad (23.39)$$

The eigenvalue equations for the atomic and PC coordinates read

$$M_\kappa\omega^2 u_\alpha(l\kappa)=\sum_{l'\kappa'\beta}R_{\alpha\beta}\left(l\kappa,l'\kappa'\right)u_\beta(l'\kappa')$$
$$+\sum_{\Gamma l'\lambda'}T_{\alpha\Gamma}\left(l\kappa,l'\lambda'\right)c_\Gamma(l'\lambda'), \qquad (23.40)$$

$$\mu_\Gamma\omega^2 c_\Gamma(l\lambda)=\sum_{l'\kappa'\alpha}T^{+}_{\alpha\Gamma}(l\lambda,l'\kappa')u_\alpha(l'\kappa')$$
$$+\sum_{l'\lambda'\Gamma'}H_{\Gamma\Gamma'}(l\lambda,l'\lambda')c_{\Gamma'}(l'\lambda'), \qquad (23.41)$$

where ω is the angular frequency, and μ_Γ is the PC effective mass.

Equations (23.40) and (23.41) can be formally transformed into a dynamical equation for the atomic displacements and one providing the corresponding charge-density oscillations, now written in vector-matrix notation

$$\mathbf{M}\omega^2\boldsymbol{u}=[\mathbf{R}^{\mathrm{ion}}+\mathbf{R}^{\mathrm{el}}-\mathbf{T}(\mathbf{H}-\mu\omega^2)^{-1}\mathbf{T}^{+}]\boldsymbol{u}, \qquad (23.42)$$

$$\boldsymbol{c}=-(\mathbf{H}-\mu\omega^2)^{-1}\mathbf{T}^{+}\boldsymbol{u}. \qquad (23.43)$$

The *phonon dynamics* in the adiabatic approximation is obtained from (23.42) after setting $\mu=0$. The formalism coincides with the DFPT treatment (see later) [23.191] via the transcription, in the adiabatic approximation,

$$\sum_{\nu\boldsymbol{k}}^{\mathrm{occ}}\left\langle\psi_{\nu\boldsymbol{k}}\left|\frac{\partial^2 v_{\mathrm{ion}}(\boldsymbol{r})}{\partial u_\alpha(l\kappa)\,\partial u_\beta\left(l'\kappa'\right)}\right|\psi_{\nu\boldsymbol{k}}\right\rangle$$
$$=\int \mathrm{d}^3 r n(\boldsymbol{r})\frac{\partial^2 v_{\mathrm{ion}}(\boldsymbol{r})}{\partial u_\alpha\left(l\kappa\right)\partial u_\beta\left(l'\kappa'\right)}\quad\Rightarrow\quad\mathbf{R}^{\mathrm{el}}_0, \qquad (23.44)$$

$$\sum_{\nu\boldsymbol{k}}^{\mathrm{occ}}\left\langle\frac{\partial\psi_{\nu\boldsymbol{k}}}{\partial u_\alpha(l\kappa)}\left|\frac{\partial v_{\mathrm{ion}}(\boldsymbol{r})}{\partial u_\beta(l'\kappa')}\right|\psi_{\nu\boldsymbol{k}}\right\rangle+\mathrm{c.c.}$$
$$=\int \mathrm{d}^3 r\frac{\partial n(\boldsymbol{r})}{\partial u_\alpha(l\kappa)}\frac{\partial v_{\mathrm{ion}}(\boldsymbol{r})}{\partial u_\beta(l'\kappa')}$$
$$=\iint \mathrm{d}^3 r\mathrm{d}^3 r'\frac{\partial v_{\mathrm{ion}}(\boldsymbol{r})}{\partial u_\alpha(l\kappa)}\chi(\boldsymbol{r},\boldsymbol{r}')\frac{\partial v_{\mathrm{ion}}(\boldsymbol{r}')}{\partial u_\beta(l'\kappa')}$$
$$\Rightarrow\quad-\mathbf{T}\mathbf{H}^{-1}\mathbf{T}^{+}, \qquad (23.45)$$

where the sums are performed over the occupied electronic states of wavefunctions $|\psi_{\nu\boldsymbol{k}}\rangle$, band index ν, and wavevector $\boldsymbol{k}$.

The ME method offers a conceptually simple, although computationally demanding, scheme for the treatment of nonadiabatic effects, e.g., the nonadiabatic Kohn anomalies as produced by avoided crossings between a surface phonon dispersion curve and that of an electron–hole excitation [23.192, 193]. Moreover, when no adiabatic approximation is imposed, also the electronic collective excitations as represented by the dynamics of the PC coordinates, and their coupling to the phonon dynamics can be obtained from the joint solution of (23.42) and (23.43), as long as the electronic effective masses μ_Γ can be assigned in some way so as to appropriately model the frequency-dependent inverse electron susceptibility matrix $\mathbf{H}_{\Gamma\Gamma'}(l\lambda,l'\lambda';\omega)$. The dynamical equation for the PC coordinates and the equation providing the motion of atoms eventually following the electron density oscillations can be more

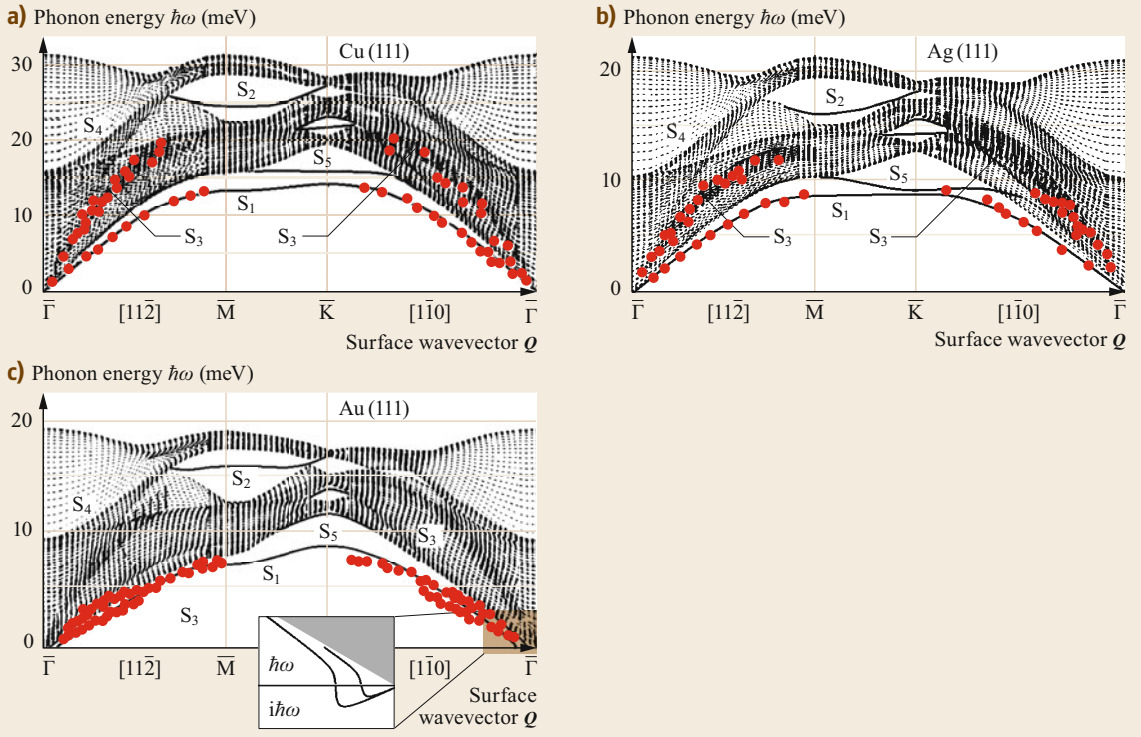

Fig. 23.9a–c PC model calculation of the surface phonon dispersion curves for **(a)** Cu(111), **(b)** Ag(111) and **(c)** Au(111) [23.184]. For Cu(111) and Ag(111), the PC model reproduces the RW (S_1) and the longitudinal acoustic resonance (S_3) dispersion curves in good agreement with HAS data (*full circles*) [23.21]. The PC calculation for Au(111), although including PC components up to octupoles, yields unstable surface acoustic branches at very small wavevectors (*inset*), consistent with the known $23 \times \sqrt{3}$ reconstruction of this surface [23.21]. The apparent doubling of the S_1 branch observed by HAS in both symmetry directions can be associated with two different domain orientations

conveniently written as

$$\mu\omega^2 \boldsymbol{c} = [\mathbf{H} - \mathbf{T}^+(\mathbf{R} - \mathbf{M}\omega^2)^{-1}\mathbf{T}^+]\boldsymbol{c}\,, \qquad (23.46)$$

$$\boldsymbol{u} = -(\mathbf{R} - \mathbf{M}\omega^2)^{-1}\mathbf{T}\boldsymbol{c}\,. \qquad (23.47)$$

In this case, the adiabatic approximation may consist in letting the atomic mass matrix $\mathbf{M}$ go to infinity so that only charge-density oscillations in a rigid lattice are obtained from the dynamical equation $\mu\omega^2\boldsymbol{c} = \mathbf{H}\boldsymbol{c}$ and $\boldsymbol{u} = 0$. When the dispersion curves of low-energy surface electronic collective excitations, such as occur in acoustic surface plasmons (ASPs), intersect the surface phonon spectrum, the coupling of the PC to the atom degrees of freedom is expected to lead to an avoided crossing between the ASP and surface-phonon branches and, even more importantly, to a renormalizing of the effective mass of the electron.

The ME method has been used in its phenomenological adiabatic PC model version with good results in the analysis of the dispersion curves and HAS spectra of 3d noble metals [23.184, 194] (Fig. 23.9). For Cu(111) and Ag(111), the PC model correctly predicts, besides the RW (S_1) dispersion curves, the longitudinal resonance S_3 observed with HAS. The S_3 resonance, later recognized as a peculiar feature of practically all metal surfaces, originates from the lower edge of the LA bulk band, showing a large anomalous softening towards the zone edge with an increasing localization on the second surface layer. Its anomalous softening, as well as its comparatively large HAS intensity were both explained by the PC model as clear manifestations of electron–phonon interaction [23.185, 186]. As originally shown by *Bortolani* et al. [23.195, 196], the S_1 and S_3 dispersion curves as well as their HAS intensities can, in principle, be reproduced with a simple BvK force constant model, at the cost, however, of a large unphysical softening of the surface constants. The PC model had the merit of elucidating the nature of the anomalous L resonance, similarly to what was obtained with another powerful approach, the embedded-atom (EA) method [23.197–203], also providing an effective semiempirical way to account for

the effects of the electron–phonon interaction in surface dynamics [23.194] (see the following section).

The PC model for the bulk dynamics of gold requires PC components to octupole order to account for the large anisotropy at the surface. When applied to the dynamics of the ideal (unreconstructed) Au(111) surface (Fig. 23.9), the PC model, while reproducing the HAS data for the RW (S_1) branch quite well, yields unstable surface acoustic branches at very small wavevectors (inset), consistently with the instability and the $23 \times \sqrt{3}$ reconstruction of this surface [23.204]. The apparent doubling of the S_1 branch observed by HAS in both symmetry directions has been attributed to an ultrasoft S_3 branch, on the basis of a molecular dynamics analysis [23.205]. An alternative explanation is a doubling of the RW due to two different domain orientations of the reconstructed surface. On the other hand, no HAS data corresponds to the anomalous resonance S_3 predicted by the PC model, suggesting that the surface PCs do not respond to the motion of the second layer atoms as a consequence of their stabilization into a charge-density wave (CDW) of the reconstructed phase. More recent high-resolution ^{3}He-spin-echo scattering measurements by *McIntosh* et al. [23.206] have given clear evidence of phason excitations of the quasi-incommensurate $23 \times \sqrt{3}$-Au(111) surface, in agreement with earlier molecular dynamics (MD) predictions [23.207]. This system offers an example where the ME method would permit a description of both phonon and phason dynamics and their possible coupling. The large size of the unit cell, and the possible need for a nonadiabatic treatment, still make this kind of dynamical problems difficult to access for present ab-initio methods.

Another interesting case is that of Xe(111) surface dynamics (Fig. 23.4). As can be seen in Fig. 23.10, the experimental HAS dispersion curves of the noble gas crystal Xe(111) [23.98, 100] exactly match also those calculated with the PC model for Cu(111) after a rescaling by about a factor of 6 for the larger mass and softer force constants. As discussed above, this agreement is also obtained with the simplest RI model, but the observation with HAS of the optical SV2 and L2 branches localized on the second layer would not be explained, unless there are corresponding surface charge density oscillations. This is actually the mechanism that is accounted for by the PC model, and is confirmed by DFPT, as is discussed in the next section.

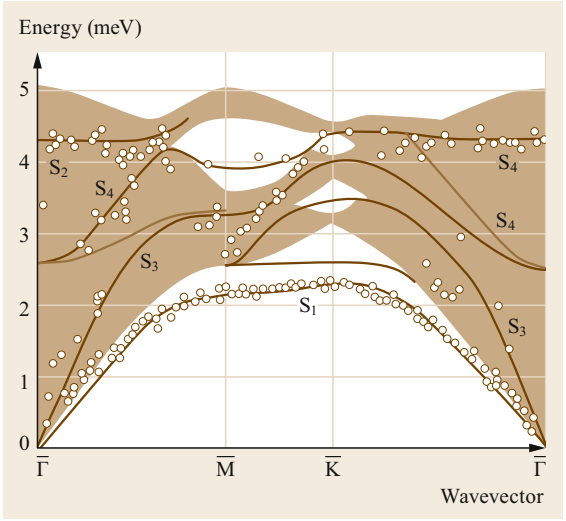

Fig. 23.10 The HAS dispersion curves of Xe(111) (*red dots*, Fig. 23.4 [23.98, 100]) are very well fitted by the PC calculation for Cu(111), Fig. 23.9, after a rescaling by a factor 6.2 to account for the larger mass and softer force constants. The observation by HAS of the optical subsurface resonances S_2 and S_3 localized on the second atomic layer is actually explained by the PC model as being due to the associated oscillations of the surface PCs. Although a closed-shell atom, Xe, has a large polarizability by which the second layer atom displacements yield large oscillations (polarizations) of the atomic shells in the surface layer

23.2.3 From Semiempirical to Full Ab-initio Methods

The great progress made in the theory and calculations of the electronic band structure in all kinds of solids during the last three decades has made it possible to evaluate the electronic contributions to the total energy of solids as a function of the atomic positions. This development has opened up a new phase in the theory of surface dynamics. In insulators and semiconductors, short-range repulsive force constants can be derived directly from the overlap of atomic orbitals. In more general terms, the interatomic force constants can be obtained from a tight-binding (TB) scheme for the electronic structure, provided that the dependence on the interatomic distances of the Coulomb and hopping integrals between neighboring atoms are known [23.213]. Such integrals are, in turn, determined either from fitting procedures (empirical TB) or from first-principles calculations of the electronic structure. The TB methods give reliable results for the surface phonon frequencies of covalent and III–V semiconductors [23.214] with a reasonable computational effort. In the semiempirical total energy method (SETE) developed by *Pollmann* and coworkers [23.215, 216] an empirical TB scheme is used to calculate the band structure contribution to the total energy, whereas the short-range repulsive contribution is expressed by phenomenological pair potentials.

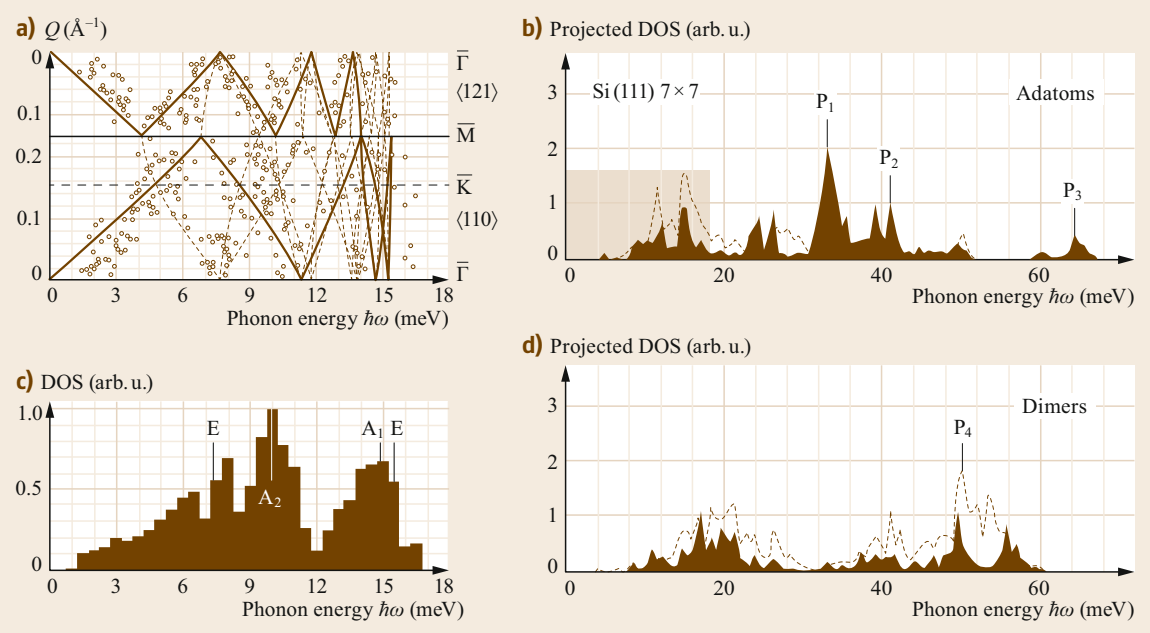

Fig. 23.11 **(a)** The RW and low-energy (acoustic) phonon dispersion curves of prevalent SV polarization along the symmetry directions of the Si(111)-7×7 reconstructed surface as measured by HAS (●) [23.208]. The data are fitted by a sine curve for the ideal 1×1 surface folded 49 times within the 7×7 surface Brillouin zone (*full lines*: ×1; *dasheed lines*: ×2). **(c)** Acoustic SV phonon DOS generated from the density of the HAS data multiplied by 2ω. The *arrows* indicate the lowest $Q = 0$ frequencies obtained by *Štich* et al. [23.209–211] with a first-principles MD and the multiple-signal classification algorithm. Symmetry labels refer to the irreducible representations of the C_{3V} group. This acoustic DOS from HAS agrees fairly well with the calculated DOS projected onto the adatoms **(b)** (*shaded rectangle*) from the Car–Parrinello molecular-dynamics simulation of *Kim* et al. [23.212] (*brown area*: SV component; *dashed lines*: horizontal component). This is consistent with the fact that adatoms are the most prominent features of the 7×7 surface [23.212]. **(d)** Poor agreement is found instead with the DOS projected onto the atom dimers or the free-surface and backbone atoms (not shown) of the 7×7 unit cell

First-principles tight-binding (FPTB) methods derived from the Varma–Weber TB theory of transition metal dynamics [23.217, 218] have been used to approach difficult problems, such as the dynamics and instabilities of tungsten and molybdenum(001) surfaces [23.219, 220]. Complex surface dynamics problems, such as those involving extensively reconstructed surfaces, have also been investigated with quantum molecular dynamics based on the tight-binding Hamiltonian. A sample of calculations by *Kim* et al. [23.212] for the Si(111)-7×7 reconstructed surface is shown in Fig. 23.11 and compared with the DOS derived from HAS measurements for the folded RW [23.208] and the zone-center phonon energies calculated by *Štich* et al. [23.209–211] with first-principles MD. Indeed, the TB scheme in combination with molecular dynamics has become an efficient tool due to the invention of linear-scaling simulation codes where the computational time increases linearly with the number N of atoms [O(N) codes] [23.221–225].

For free-electron metals, such as alkali and alkaline earth metals and aluminum, significant progress in lattice dynamics was achieved with the use of pseudopotentials [23.228–230], with which the effects of electronic screening on the electron–ion interactions can be accounted for in a perturbation calculation. Within the pseudopotential perturbation (PPP) theory, the electron-mediated interaction is shown to be proportional to the Fourier-transformed product of the squared pseudopotential times the density (dielectric) response function of the interacting electrons [23.231, 232]. Along those lines, a microscopic theory of lattice dynamics based on the density response (DR) can be formulated in general terms and implemented at various levels of approximation [23.171–183]. The DR-PPP theory was applied to the surface dynamics of alkali metals by *Calandra* et al. [23.233–235], who derived the screening from an infinite-barrier model, and by *Eguiluz* et al. [23.236–238] in a state-of-the-art, self-consistent calculation

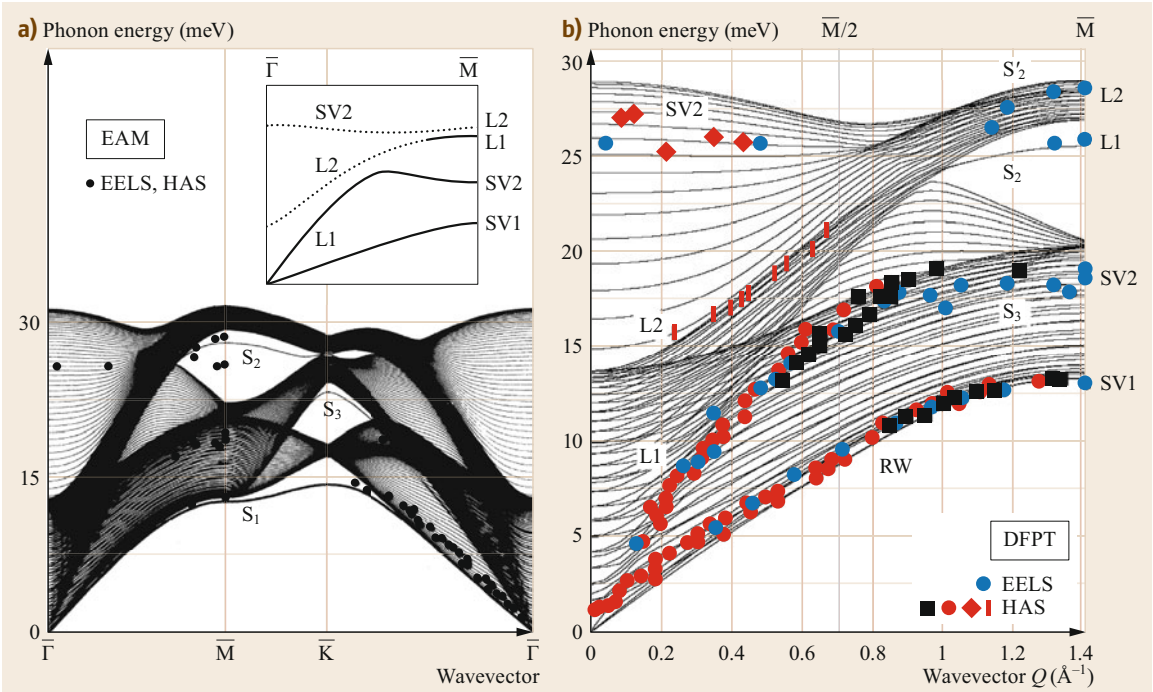

Fig. 23.12 (a) The surface phonon dispersion curves of Cu(111) calculated with the embedded-atom model (EAM) [23.226] and a selection of HAS [23.5, 185] and HREELS data [23.99, 227]. The *inset* shows the complex avoided crossings of the L1 acoustic branch in the $\overline{\Gamma M}$ direction with the optical branches of L2 and SV2 polarization [23.5, 194], where 1 and 2 indicate a prominent localization in the first and second surface layers, respectively. The EAM dispersion curves compare very well with the DFPT calculations shown in **(b)** along the $\overline{\Gamma M}$ direction together with a complete set of HAS and HREELS measurements [23.5, 185, 227]. The *black dots* in **(a)** are identical to the HREELS data plotted in **(b)**

for sp-bonded surfaces such as Al(001), (110), and (111) [23.239]. The PPP theory is less successful with noble and transition metals, where the localized d electrons contribute a strong pseudopotential that cannot be treated within a perturbation theory [23.240, 241].

The total energy of an atom in a host electronic system and the many-body interactions with the surrounding atoms mostly depend upon the immersion energy of that atom into the electron density contributed by the neighboring atoms. From the knowledge of this immersion energy and its dependence on the positions of neighboring atoms, the dynamical matrix can be obtained for the calculation of both bulk and surface phonons. The first-principles basis of this approach can be traced back to the Kohn–Sham (KS) theory of impurities in jellium [23.242], to the subsequent calculations for hydrogen [23.243–245] and He [23.246, 247] impurities, and to the theory of chemisorption [23.248, 249], as well as the quasi-atom concept introduced by *Stott* and *Zaremba* [23.250, 251] within the uniform-density approximation (UDA). Various semiempirical methods based on this concept are available [23.252]. These include the embedded atom method (EAM) [23.197–203], the effective medium (EM) theory [23.253–255], and methods relying on special forms of the many-body interaction, such as the Finnis–Sinclair (FS) [23.256] or tight-binding second moment (TBSM) potentials [23.257–259], the glue model (GM) [23.260–262], and the equivalent crystal (EC) model [23.263].

Figure 23.12 compares an EAM calculation of Cu(111) dispersion curves [23.226] with a more recent DFPT calculation and a complete set of HREELS [23.227] and HAS data [23.5, 185] in the $\overline{\Gamma M}$ direction. The agreement of both EAM and DFPT calculations with experimental data is very good. Many valuable results have been produced with the EAM approach for sp as well as for transition and noble metals, also for complex (vicinal, adsorbate) surfaces with large surface unit cells. For example, the EAM calculations by *Sklyadneva* et al. [23.264] for the (211) and (511) surfaces of copper reproduce the HAS measurements performed by *Witte* et al. [23.265] very well.

Conceptually, EAM as well as the other semiempirical methods provide a microscopic basis for the cluster shell model and, on the other hand, a surrogate for challenging ab-initio calculations based on density functional theory [23.190, 266, 267]. Moreover, these quantum semiempirical approaches are easily implemented in efficient molecular dynamics schemes and have produced a considerable number of interesting results for a wide spectrum of surface dynamical phenomena, mostly for metals.

The density functional theory of electrons in solids is founded on the Hohenberg–Kohn theorem [23.266], which states that the total energy E of a system is related in a unique way to its electron density function $n(\boldsymbol{r})$ via a (generally unknown) functional $E[n(\boldsymbol{r})]$. A trial functional is constructed through the Kohn–Sham eigenfunctions of an effective one-electron Hamiltonian [23.242], where the Coulomb interactions are derived from the density $n(\boldsymbol{x})$ itself. The exchange and correlation term, which represents the unknown part of the functional E, can be approximated with suitable local or semilocal functionals of the density [23.267, 268], commonly within the local-density approximation (LDA) [23.269] or the generalized-gradient approximation (GGA) [23.270–272]. Through a self-consistency loop the functional E is minimized and the electronic density $n(\boldsymbol{r})$ determined. This makes DFT the most powerful method for first-principles calculation of the ground-state total energy, albeit a computationally demanding one.

There are different ways to calculate the phonon frequencies from DFT. A first route to a first-principles (FP) DFT lattice dynamics is based on the determination, through molecular dynamics simulations at sufficiently low temperature, of the velocity–velocity correlation function, from which the phonon spectrum is derived by a Fourier transform. A major breakthrough in this direction was the Car–Parrinello method (CPM) [23.273], where the coefficients of Kohn-Sham wavefunctions expanded on a plane-waves basis set are treated as classical time-dependent variables, together with the nuclear coordinates. The evolution of this set of coordinates in time, within the adiabatic approximation, fully describes the quantum dynamics of the entire system. The CPM is highly demanding in terms of computer time and memory. However, nowadays it is possible to perform Car–Parrinello molecular dynamics (CP-MD) for 1000 atoms to extract velocity–velocity correlation functions. Thus, the CPM provides an important reference frame for many surface dynamical problems, including the calculation of surface phonons in semiconductors [23.274–276]. It remains a popular and efficient application of density functional theory to time-dependent problems.

In 1989, *Sankey* and *Niklewski* developed a less computationally demanding approach to ab-initio molecular dynamics based on a first-principles tight-binding (FPTB) scheme [23.277]. The tight-binding matrix elements are constructed within a density functional local density approximation (DF-LDA) theory, where the total energy is represented by a Harris functional [23.278], and the Kohn–Sham wavefunctions are approximated by a set of local pseudoatomic orbitals [23.277]. This theory was successfully applied to the calculation of the surface phonon densities for low-index surfaces of diamond by *Alfonso* et al. [23.279, 280].

A second approach to FP lattice dynamics is the frozen-phonon method (FPM) [23.281–285] where the effective interatomic force constants are obtained from a calculation of the total energy $E[n(\boldsymbol{r})]$ for the atoms slightly shifted from their equilibrium positions. There are two main variants of this method. In the first one, phonon energies are determined by a quadratic fit of the total energy changes produced by displacing the atoms according to a pattern that corresponds to a normal mode. This procedure can be applied only in those cases in which phonon eigenvectors are completely determined by symmetry and are, thus, known a priori; moreover, only phonons at $\boldsymbol{q} = 0$ can be studied using a single unit cell. To deal with phonons at finite $\boldsymbol{q}$, a supercell commensurate with $\boldsymbol{q}$ is needed. In surface dynamics, this technique encounters the difficulty that the displacement pattern of any surface phonon, even at symmetry points, is not precisely known in principle. Thus, its application is limited to particular cases, e.g., for adsorbates that are largely decoupled from the substrate.

The second variant exploits the possibility of calculating the forces with little computational effort by means of the Hellmann–Feynman (HF) theorem. Once the ground-state properties have been determined, a small displacement of atom l will produce forces acting on each atom l', and, thus, an entire row of the dynamical matrix can be computed. The complete dynamical matrix can be constructed by performing all the symmetry-independent displacements. This method has the advantage that it does not need a priori knowledge of the phonon eigenvectors and allows us to construct the whole real-space force-constant matrix. Hence, its Fourier transform provides the dynamical matrix for any arbitrary wavevector $\boldsymbol{q}$. In many cases, the effective interatomic force constants have long-range terms, due to conduction electrons in metals, which develop Friedel oscillations around a local disturbance [23.288, 289], or to electrical dipole–dipole interactions in ionic compounds. In these cases, computationally demanding large supercells must be used to

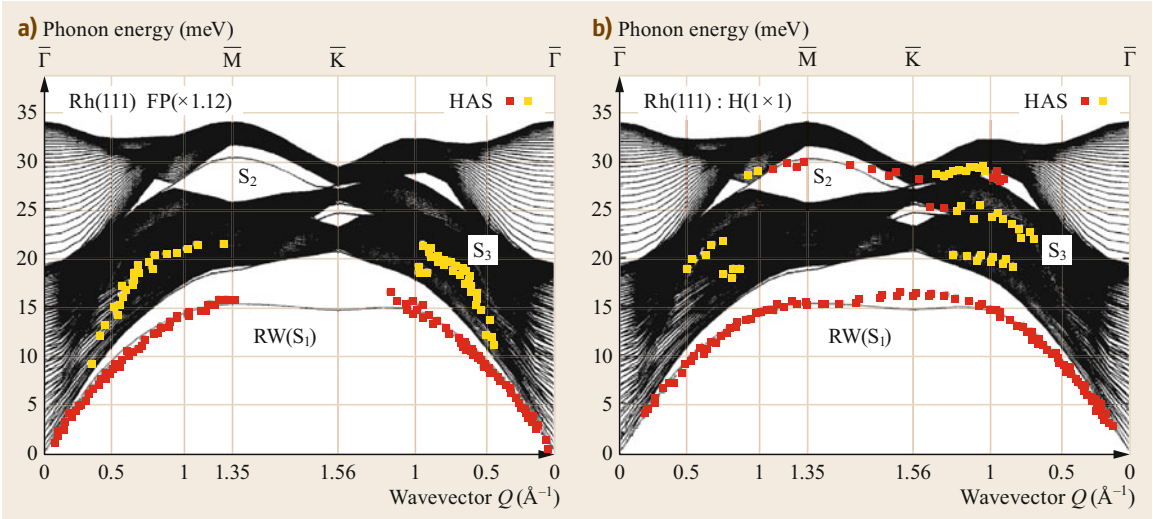

Fig. 23.13a,b First-principles calculations of the surface phonon dispersion curves for Rh(111) [23.286], rescaled by a factor 1.12 (12% stiffening) reproduce quite well the surface acoustic branches S_1 and S_3 measured with HAS [23.287] for both clean **(a)** and hydrogen-covered **(b)** surfaces, and the optical branch S_2, only observed for Rh(111):H(1×1). An additional HAS feature at 20 meV, close to the acoustic SH branch and more visible for the H-covered surface, may be related to the lack of mirror symmetry in the $\overline{\Gamma K}$ direction

ensure good convergence. Recent developments extend these force-fitting methods to anharmonic couplings, either at $T = 0$ [23.290, 291] or renormalized at finite T [23.292–294].

Bohnen, Ho, and coworkers successfully employed these methods using DFT with a pseudopotential and Kohn–Sham orbitals expanded on a plane wave basis for the surfaces of simple metals [23.295–300]. For noble metals, they obtained good results using a mixed basis of plane waves and localized orbitals [23.301–303]. Figure 23.13a shows a calculation for Rh(111) in which total energy density functional (DF) calculations of the force constants up to the 12th neighbors were performed by derivation of HF forces; both norm-conserving (P1) and ultrasoft nonnorm-conserving (P2) pseudopotentials were used [23.286]. The calculation based on P1 (displayed in Fig. 23.13 [23.286]), yields a good fit of the surface phonon dispersion curves measured with HAS for both the clean Fig. 23.13a and the hydrogen-covered Fig. 23.13b Rh(111) surfaces [23.287], after rescaling the theoretical dispersion curves by a factor 1.12 (12% stiffening). The near identity of the S1 and S3 branches for clean and H-covered surfaces and the good agreement of the HAS S_2 gap mode for the H-covered surface with the (rescaled) clean surface calculation indicate, as argued by *Witte* et al. [23.287], that H surface passivation of Rh(111), unlike that of Ni(100), Pt(111), and W(001), does not alter the surface force constants.

The third route to ab-initio surface lattice dynamics originates from the density response (DR) method, in which the dynamical matrix is obtained by calculating the second-order derivatives of the total energy directly with respect to the atomic positions. By virtue of the Hellman–Feynman theorem the derivatives of $E[n(\boldsymbol{x})]$ become integral expressions of the potential and density derivatives. Within linear response theory, the latter can be expressed in terms of a DR function. This way, a first-principles formulation of the DR theory is obtained for lattice dynamics, where the DR function is expressed as the second-order functional derivative of E with respect to $n(\boldsymbol{r})$ [23.183]. The DR function has to be obtained self-consistently by summing over matrix elements of the perturbing potential between occupied and unoccupied Kohn–Sham states [23.304–308]. With such a pseudopotential approach *Eguiluz* and *Quong* obtained very good results for the dynamics of the three low index surfaces of aluminum [23.239, 304, 305]. Since the DR is a ground-state property, the sum over unoccupied Kohn–Sham states can be avoided via the use of Green's functions, as was done in various implementations of the DR method. The Eguiluz–Quong FP-DR approach is in many respects a theory of the dielectric function and may be regarded as a different formulation of the density functional perturbation theory (DFPT) developed by *Baroni* and coworkers [23.191, 309, 310].

The good performance of DFPT in reproducing the experimental HAS and HREELS dispersion curves for most solid surfaces rests on the preliminary accurate determination of the equilibrium surface relaxation and its temperature dependence [23.311]. *Dal Corso* et al. successfully calculated the bulk phonon dispersion curves of Cu, Ag, and Au using a DFPT based on Vanderbilt's ultrasoft pseudopotentials [23.312]. The DFPT method was further applied by *dal Corso* to the surface dynamics of the Cu(001) surface [23.313] in combination with either the *Perdew*, *Burke*, and *Ernzerhof* generalized-gradient approximation (GGA) [23.272] or LDA [23.269]. The GGA yields a substantially better agreement with HAS and HREELS experimental data. A thorough analysis of the above developments in ab-initio phonon dynamics of metal surfaces up to DFPT can be found in *Heid* and *Bohnen*'s review [23.299].

A summary of the DFPT formalism is presented in the next section, as it provides not only the surface phonon dispersion curves but also the mode-selected electron–phonon coupling strengths, which are necessary ingredients in the calculation of inelastic HAS intensities for conducting surfaces.

23.2.4 Density Functional Perturbation Theory

DFT allows us to efficiently investigate the ground-state properties of a system of N interacting electrons in a generic external potential $V(\boldsymbol{x})$ by considering the electronic density $n(\boldsymbol{x})$ instead of the many-body wavefunctions as the fundamental quantity to describe the system. The theoretical basis of DFT rests on the Hohenberg and Kohn theorems [23.266], which, together with the Rayleigh–Ritz variational principle, state that the electronic part of the total energy

$$E_{\mathrm{el}}[n(\boldsymbol{x})] = F[n(\boldsymbol{x})] + \int n(\boldsymbol{x}) v_{\mathrm{ion}}(\boldsymbol{x}) \mathrm{d}\boldsymbol{x} \,, \qquad (23.48)$$

is a unique functional of the electron density $n(\boldsymbol{x})$, which is minimized by the ground-state electronic density corresponding to the external (ion) potential $v_{\mathrm{ion}}(\boldsymbol{x})$, and its minimum corresponds to the ground-state energy. The functional $F[n(\boldsymbol{x})]$ is a sum of the kinetic energy functional $T[n(\boldsymbol{x})]$ for the interacting system, of the classical Hartree term $J[n(\boldsymbol{x})]$ for the electron–electron interaction and the nonclassical contribution $E_{\mathrm{ncl}}[n(\boldsymbol{x})]$ to the electron–electron interaction. Of these functionals, only $J[n(\boldsymbol{x})]$ is known. The Kohn–Sham theorem [23.242] suggests a reasonable approximation to the $F[n(\boldsymbol{x})]$ functional. Their *ansatz* is to calculate the exact kinetic energy of a noninteracting system $T_{\mathrm{s}}[n(\boldsymbol{x})]$ in an external effective potential which provides the same ground-state density as the interacting one and rewrite the functional as $F[n(\boldsymbol{x})] = T_{\mathrm{s}}[n(\boldsymbol{x})] + J[n(\boldsymbol{x})] + E_{\mathrm{xc}}[n(\boldsymbol{x})]$, where $E_{\mathrm{xc}}[n(\boldsymbol{x})]$ incorporates the unknown terms arising from the exchange and correlation energy. Reliable approximations are available for the exchange-correlation functional, such as the local-density approximation (LDA) [23.269] and the generalized-gradient approximation (GGA) [23.272]. These have turned out to be particularly good in most cases, with the exception of highly correlated systems, especially with d and f electrons.

The variation of the energy functional, (23.48), with respect to $n(\boldsymbol{x})$ and with the constraint that the number of electrons is fixed, provides the external effective potential of the auxiliary non-interacting system, which finally leads to the Kohn–Sham equations

$$\left(-\frac{\hbar^2}{2m}\frac{\partial^2}{\partial \boldsymbol{x}^2} + V_{\mathrm{SCF}}(\boldsymbol{x})\right)\psi_n(\boldsymbol{x}) = \varepsilon_n \psi_n(\boldsymbol{x}) \,, \qquad (23.49)$$

where the effective (self-consistent) potential V_{SCF} is given by

$$V_{\mathrm{SCF}}(\boldsymbol{x}) = v_{\mathrm{ion}}(\boldsymbol{x}) + e^2 \int \frac{n(\boldsymbol{x}')}{|\boldsymbol{x}-\boldsymbol{x}'|}\mathrm{d}\boldsymbol{x}' + \frac{\delta E_{\mathrm{xc}}}{\delta n(\boldsymbol{x})} \qquad (23.50)$$

and

$$n(\boldsymbol{x}) = 2\sum_{n=1}^{N/2} |\psi_n(\boldsymbol{x})|^2 \,. \qquad (23.51)$$

The self-consistent solution of (23.50) and (23.51), normally by iteration from an initial guess of $n(\boldsymbol{x})$, yields the ground-state charge density and energy. It is straightforward to show that the Hellmann–Feynman theorem holds in the framework of DFT. Thus, the forces and force constants and the first and second derivatives of the total energy with respect to the ionic positions can be written as functionals of the ground-state charge density as

$$\boldsymbol{F}_l = -\frac{\partial E}{\partial \boldsymbol{r}_l} = -\frac{\partial E_{\mathrm{ion}}}{\partial \boldsymbol{r}_l} - \int n(\boldsymbol{x}) \frac{\partial v_{\mathrm{ion}}(\boldsymbol{x})}{\partial \boldsymbol{r}_l}\mathrm{d}\boldsymbol{x} \,, \qquad (23.52)$$

$$\begin{aligned}
\Phi\left(ll'\right) &= \frac{\partial^2 E(\boldsymbol{r})}{\partial \boldsymbol{r}_l \partial \boldsymbol{r}_{l'}} \\
&= \frac{\partial^2 E_{\mathrm{ion}}(\boldsymbol{r})}{\partial \boldsymbol{r}_l \partial \boldsymbol{r}_{l'}} + \int n(\boldsymbol{x}) \frac{\partial^2 v_{\mathrm{ion}}(\boldsymbol{x})}{\partial \boldsymbol{r}_l \partial \boldsymbol{r}_{l'}}\mathrm{d}\boldsymbol{x} \\
&\quad + \int \frac{\partial n(\boldsymbol{x})}{\partial \boldsymbol{r}_l}\frac{\partial v_{\mathrm{ion}}(\boldsymbol{x})}{\partial \boldsymbol{r}_{l'}}\mathrm{d}\boldsymbol{x} \\
&= \frac{\partial^2 E_{\mathrm{ion}}(\boldsymbol{r})}{\partial \boldsymbol{r}_l \partial \boldsymbol{r}_{l'}} + \int n(\boldsymbol{x}) \frac{\partial^2 v_{\mathrm{ion}}(\boldsymbol{x})}{\partial \boldsymbol{r}_l \partial \boldsymbol{r}_{l'}}\mathrm{d}\boldsymbol{x} \\
&\quad - \iint \frac{\partial v_{\mathrm{ion}}(\boldsymbol{x})}{\partial \boldsymbol{r}_l}\chi\left(\boldsymbol{x},\boldsymbol{x}'\right)\frac{\partial v_{\mathrm{ion}}(\boldsymbol{x}')}{\partial \boldsymbol{r}_{l'}}\mathrm{d}\boldsymbol{x}\mathrm{d}\boldsymbol{x}' \,.
\end{aligned} \qquad (23.53)$$

In the last term of (23.53), the density derivative has been explicitly written in terms of the electron susceptibility $\chi(\boldsymbol{x},\boldsymbol{x}')$ (independent to the lowest order of ion positions) in order to show the one-to-one correspondence of (23.53) with the ME force constant matrix, (23.44)–(23.45).

In the calculation of the DFPT force constant matrix it is not necessary to evaluate first the electron susceptibility. To first-order the derivatives $\partial V_{\mathrm{SCF}}/\partial \boldsymbol{r}_l$, $\partial\psi/\partial \boldsymbol{r}_l$, $\partial n(\boldsymbol{x})/\partial \boldsymbol{r}_l$ (the latter needed in (23.53)) can be obtained by solving self-consistently the variation of the Kohn–Sham equation (23.49)

$$(H_{\mathrm{SCF}}-\varepsilon_n)\,\frac{\partial\psi_n(\boldsymbol{x})}{\partial \boldsymbol{r}_l} = -\left(\frac{\partial V_{\mathrm{SCF}}(\boldsymbol{x})}{\partial \boldsymbol{r}_l}-\frac{\partial\varepsilon_n}{\partial \boldsymbol{r}_l}\right)\psi_n(\boldsymbol{x})\,, \tag{23.54}$$

where

$$\frac{\partial V_{\mathrm{SCF}}(\boldsymbol{x})}{\partial \boldsymbol{r}_l} = \frac{\partial v_{\mathrm{ion}}(\boldsymbol{x})}{\partial \boldsymbol{r}_l} + e^2\int\frac{1}{|\boldsymbol{x}-\boldsymbol{x}'|}\frac{\partial n(\boldsymbol{x}')}{\partial \boldsymbol{r}_l}\mathrm{d}\boldsymbol{x}' + \int\frac{\delta^2 E_{\mathrm{xc}}}{\delta n(\boldsymbol{x})\delta n(\boldsymbol{x}')}\frac{\partial n(\boldsymbol{x}')}{\partial \boldsymbol{r}_l}\mathrm{d}\boldsymbol{x}'\,, \tag{23.55}$$

$$\frac{\partial\varepsilon_n}{\partial \boldsymbol{r}_l} = \langle\psi_n|\,\frac{\partial V_{\mathrm{SCF}}}{\partial \boldsymbol{r}_l}\,|\psi_n\rangle\,. \tag{23.56}$$

This approach is particularly effective, since only occupied states are needed to evaluate the right-hand side of (23.54) [23.314], whereas the standard perturbation theory approach, based on the expansion in eigenfunctions of the unperturbed Hamiltonian, would require sums over the full spectrum of the zero order Hamiltonian. An alternative formulation of DFPT, worked out by *Gonze* [23.315, 316], can be obtained on the basis of a variational principle. It can be shown [23.191] that the two formulations are substantially equivalent, although with relevant differences in their implementation; while the latter proceeds from the perturbative expansion of the Kohn–Sham energy functional and a minimization, the former requires the self-consistent solution of linear equations by means of the Green's function method.

As discussed by *Baroni* et al. in their review article [23.191], DFPT has a strong advantage over other ab-initio methods that require supercells. To treat a $\boldsymbol{q}\neq 0$ perturbation, the $\boldsymbol{q}$-space Fourier components of the perturbation in DFPT are independent, up to a reciprocal lattice vector $\boldsymbol{G}$. To first order, a $\boldsymbol{q}$-component of the perturbation can only admix an electronic eigenfunction of wavevector $\boldsymbol{k}$ with eigenfunctions of wavevector $\boldsymbol{k}+\boldsymbol{q}$. This allows us to readily obtain the Fourier components of the force constant matrix and the phonon frequencies at any arbitrary $\boldsymbol{q}$-point. In polar materials, where the contribution from the macroscopic electric field is naturally present in the ion–ion part of the force constant matrix, the effect of the electronic density response can be accounted for by simply replacing the bare ion charges in the non-analytic part of the dynamical matrix with effective Born charges [23.191], similarly to what is done with shell models [23.73, 75].

In the case of conducting materials, there may be the problem that the number of $\boldsymbol{k}$-points needed to correctly describe the effects related to the presence of a Fermi surface could be prohibitively large. An efficient implementation of DFPT for metallic systems, based on the energy level broadening by a smearing function was proposed by *de Gironcoli* [23.317]. Another effective approach, based on a different treatment of the perturbation, is that of *Eguiluz* and *Quong* mentioned above [23.304]. Even with the use of the latter technique, however, the phonon dispersion curves for metals within DFPT can critically depend on the sampling of $\boldsymbol{k}$- and $\boldsymbol{q}$-points and may meet some difficulty in dealing with Kohn anomalies.

In practical calculations, the bare electron-nucleus interaction $v_{\mathrm{ion}}(\boldsymbol{x})$ is often replaced by a pseudopotential that takes into account the effects of core electrons, and only valence electrons are treated explicitly. DFPT was first implemented within the framework of a plane-wave basis set expansion for Kohn–Sham states [23.318, 319] and using norm-conserving pseudopotentials [23.320, 321]. This paradigm was used extensively and with great success to study bulk and surface phonons of semiconductors and simple metals. The need to deal with transition metals within a pseudopotential and a plane-wave approach (without needing a huge basis set), led to the development of ultrasoft pseudopotentials [23.322]. Their use within DFPT was implemented by *dal Corso* et al. [23.312] and *dal Corso* [23.313]. The further development of fully relativistic pseudopotentials and their inclusion in the linear-response code paved the way to the inclusion of spin–orbit coupling and the study of its effect on phonon modes and electron–phonon interactions [23.323–328]. An alternative approach to materials is the use of a local or mixed basis set instead of plane waves. Significant progress in this field was made by *Savrasov* and *Andersen* [23.329], who implemented a new full potential linear muffin-tin orbital (LMTO) method, and DFPT has been implemented in several full-potential linearized augmented plane wave (FLAPW) codes [23.330–332].

The subsequent introduction of nonlocal exchange-correlation corrections provided an effective, although not yet completely satisfactory, way to treat van der Waals interactions within the framework of DFT [23.333–338]. In particular, their inclusion in DFPT codes, together with spin–orbit coupling, can

substantially improve the performance of DFPT, especially for layered crystals with heavy atoms and weak interlayer bonding.

DFPT is nowadays one of the most popular methods for the calculations of phonons and has been implemented in some of the most widely used simulation codes, like Quantum ESPRESSO [23.339], ABINIT [23.323, 340], Vienna Ab Initio Simulation Package (VASP) [23.341], and Cambridge Serial Total-Energy Package (CASTEP) [23.342]. To date, the surface phonon dispersion curves for about 50 different solid surfaces have been calculated with DFPT and have generally been found to be in good agreement with HAS and HREELS experimental data, so as to endow DFPT with highly predictive power. A fairly complete list of references of surface phonon calculations can be found in two Springer monographs [23.4, 5].

23.2.5 DFPT Surface Phonons for Heavy Elemental Solids and Compounds

A challenging testing ground for DFPT including spin–orbit coupling (SOC) and van der Waals (VdW) interaction is the calculation of the surface phonon dispersion curves and the electron–phonon interaction in 6sp metals and topological insulator compounds, for which detailed experimental HAS data are now available. This is discussed in the following sections.

Cs(110), Ba(0001)

Recent DFPT calculations of the surface phonon dispersion curves for the Cs(110) surface of a free-standing 11 monolayer (ML) slab are shown in Fig. 23.14 and compared with HAS data measured on a 25 ML Cs(110) film on Pt(111) at two different temperatures [23.343, 344]. The equilibrium configuration and the phonon dispersion curves for bulk cesium and for the Cs(110) surface were obtained with density functional theory and DFPT as implemented in the Quantum ESPRESSO code [23.339] with the Perdew–Burke–Ernzerhof (PBE) approximation for the exchange-correlation functional [23.272], norm-conserving pseudopotentials with nonlinear core corrections, and a 30 Ry cutoff on the plane wave expansion of Kohn–Sham orbitals. The experimental equilibrium lattice parameter (6.141 Å) was well reproduced by DFPT (6.171 Å) without SOC and VdW corrections, supporting the conjecture that their effects have opposite sign and cancel out to a good extent.

Besides the fact that little was known before about the phonon dispersion curves of cesium even in the bulk, another interesting aspect of the HAS study of very soft Cs films during growth beyond single monolayers was the assessment of their surface structure and

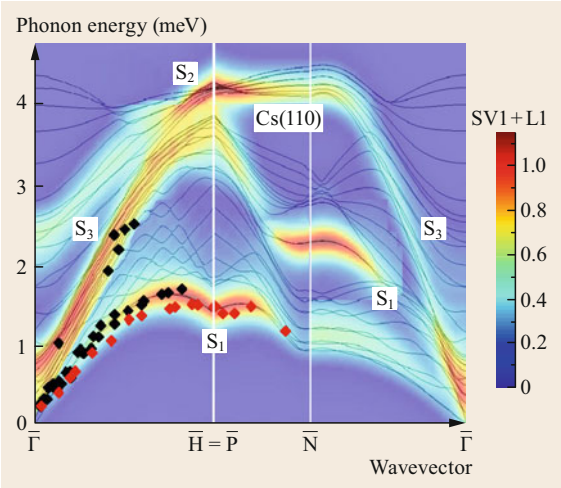

Fig. 23.14 Comparison of the surface phonon dispersion curves calculated with DFPT for 25 ML Cs(110)/Pt(111), represented with their surface-projected DOS (*color code aside*), with HAS data measured at a temperature of 40 K (*black lozenges*) and 100 K (*red lozenges*) for phonon creation processes. The colors indicate the surface-projected DOS for the sagitally polarized first-layer phonons. The comparatively weak electron–phonon interaction only permitted distinct observation of the RW (S_1) and a part of the longitudinal surface resonance S_3 [23.343, 344]

orientation [23.344, 345]. Little is known about alkali surfaces from low-energy electron diffraction (LEED) studies, besides a pioneering study on Na(110) and its oxide [23.346]. Soft materials like cesium are also characterized by a comparatively large anharmonicity, especially at the surface. The HAS data in Fig. 23.14 indicate in the Rayleigh wave dispersion curve in the $\overline{\Gamma H}$ direction a 17% softening for an increase of temperature from 40 to 100 K, corresponding to an anharmonicity coefficient $x_{e,s} = 0.037$ [23.4, 347]. This value is appreciably larger than the values found for the surfaces of other free electron metals (e.g., $x_{e,s} = 0.024$ for aluminum surfaces), consistently with a surface Debye temperature as low as 48 K [23.4, 344]. Also the electron–phonon interaction, expressed by the mass-enhancement factor λ and derived for the Cs(110) surface from the temperature dependence of the Debye–Waller (DW) exponent turns out to be slightly larger ($\lambda = 0.186$) [23.97, 343] than the bulk value $\lambda = 0.14$ known from the literature [23.348].

HAS studies of the barium surface are only available for Ba 1-3 monolayers on Cu(001) [23.349]. Of special interest is the Ba bilayer, which exhibits a twisted dodecagonal 4-D structure, Ba(0001), with $\lambda = 0.29$ [23.350], also slightly larger than the Ba bulk value ($\lambda = 0.27$) [23.348].

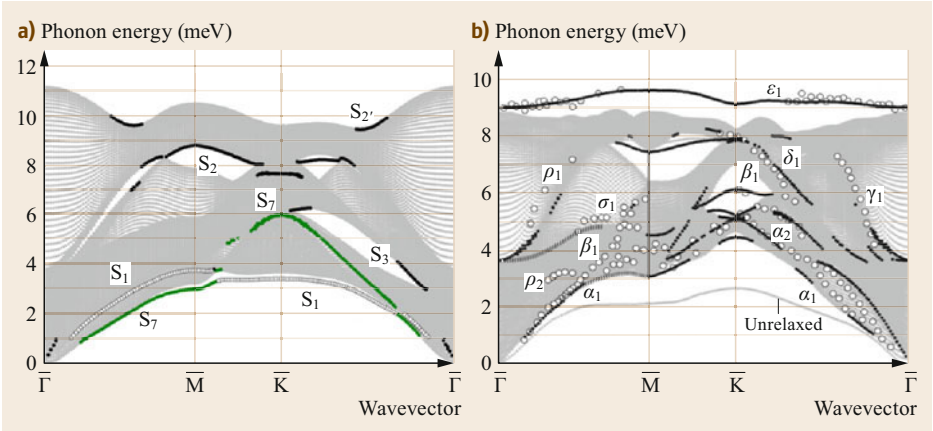

Fig. 23.15a,b The surface dynamics (*dark gray* and *small symbols*) of Tl(0001) **(a)** and Pb(111) **(b)** calculated with DFPT including SOC [23.351, 352]. For Pb(111), the soft RW branch (*light gray full line*) for the ideal unrelaxed surface is also shown. The strong surface bilayer contraction predicted at equilibrium lifts the RW branch up to the bulk acoustic edge (α_1) and the optical branch ε_1 well above the maximum of the bulk phonon band, in very good agreement with the HAS data (*open circles*) [23.353]. *Greek letter labels* are those of [23.353], while for Tl(0001), the labels S_j have the usual meaning. No important relaxation effect is predicted in Tl(0001) **(a)** due to the small surface bilayer contraction

Tl(0001), Pb(111)

The spin–orbit coupling has been found to have significant effects in the DFPT surface dynamics of 6sp metals. Figure 23.15 compares two DFPT calculations of the surface phonon dispersion curves of Tl(0001) [23.351] and Pb(111) [23.352], including SOC. Both surfaces are characterized by a contraction of the first surface bilayer, which is quite large in lead (-4.5% with SOC, -4.7% without SOC) but rather small in thallium (-0.2% with and without SOC). Such contractions, and their difference in the two surfaces, are reflected in the appearance of a localized surface phonon branch above the maximum of the bulk phonon continuum. While in Pb(111) this optical branch, denoted by ε_1 in Fig. 23.15b, lies well above the bulk density all along the surface Brillouin zone, in Tl(0001) the optical mode S_2' (Fig. 23.15b) is localized above the bulk maximum only around one half of the zone in both symmetry directions. The large surface bilayer contraction in Pb(111) also yields a strong stiffening of the RW branch towards the zone boundary. As can be seen in Fig. 23.15b, the surface relaxation shifts the RW branch for the ideal unrelaxed surface (light gray full line) upwards to very near the lower bulk band edge. In Tl(0001), the RW (S_1 in Fig. 23.15a) runs above the SH (S_7) branch in the $\overline{\Gamma}\overline{M}$ direction, and is, therefore, a pseudo-surface wave (PSW) branch, but this is due to the peculiar elastic constants and not to surface relaxation.

This unusual behavior of Pb(111) surface dispersion curves is confirmed by the available HAS data [23.353], which agree very well with the calculated upper branch ε_1 and the RW branch (α_1) running along the lower edge of the acoustic bulk band. Also, the other branches, here labeled with Greek letters as in [23.353], are well reproduced by theory, confirming the good performance of DFPT with the inclusion of SOC. It is interesting to note that VdW terms do not seem to have relevant effects, the surface equilibrium structure with relaxation and the local change of force constants having mostly a chemical origin. This may not be so for Tl(0001), where surface relaxation is much smaller, but no published HAS data are available to date for a similar comparison.

The specific contribution of SOC on the phonon spectrum can be singled out by comparing the surface-projected phonon DOS of Tl(0001) calculated with and without the spin–orbit interaction. As shown in Fig. 23.16 [23.351], the acoustic modes, notably the RWs (S_1) at the zone boundary contributing the main DOS peak at 3.1 meV, are shifted by SOC to higher energy by +7.0%, while the highest optical modes (mainly S_2') are shifted downward by about the same absolute amount, corresponding to a fractional shift of -2.3% (arrows).

The effects of SOC are more evident in Pb(111). DFPT calculations on ultrathin Pb(111) films on a (rigid) Cu(111) substrate not including SOC have been reported for different film thicknesses ranging from 3 to 7 ML [23.353–355]. The highest surface optical mode, identified as a stretching of the surface bilayer is generally above the experimental data, with the largest discrepancy of about 9% for 6 ML, but a reasonable agreement for 7 ML, which indicates an oscillatory character for the misfit, with a period similar to that of the surface bilayer contraction [23.355]. A comparison

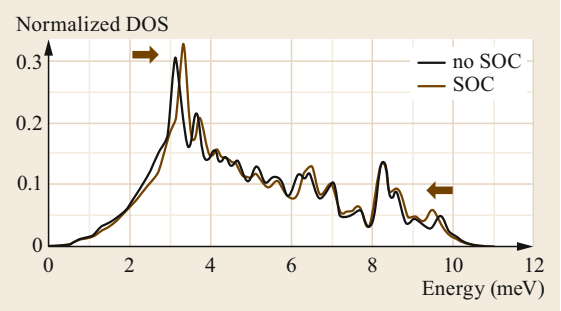

Fig. 23.16 The surface-projected phonon DOS of Tl(0001) calculated with DFPT including (*brown line*) or excluding (*black line*) SOC [23.351]. The *arrows* underscore the sections of the spectrum most affected by SOC. The first low-energy peak associated with zone-boundary RWs shifts to higher energy by +7.0% with the inclusion of SOC, whereas the highest-energy peak at 9.7 meV, corresponding to the S_2' optical mode, is softened by about −2.3%

of the HAS data for a 3 ML-Pb(111) film on a Cu(111) substrate with the DFPT dispersion curves without and with SOC is shown in Fig. 23.17. The periodicity of the Pb film is locked into that of Cu(111) with the respective lattice distances in the ratio 4 : 3 and a superstructure unit cell containing 9 Pb atoms and 16 Cu atoms (Fig. 23.17b). For this reason, the dispersion curves are conveniently represented in the Brillouin zone of the surface superstructure (Fig. 23.17c).

As shown in Fig. 23.17a, the addition of SOC generally yields an improved agreement with experiment, with the expected softening of the upper optical branch ε_1 and of the folded acoustic branch α_1. On the contrary, mode ε_2 localized at the film substrate is stiffened by SOC, also leading to a good agreement with experiment. It is, however, noted that the SOC softening of the σ_1 branch at $\overline{\Gamma}$ spoils the good agreement obtained without SOC. In general, these results are qualitatively valid for thicker films, as well as for the Pb(111) surface of the semi-infinite solid.

Bi(111)

Bismuth surfaces have been extensively investigated for a broad spectrum of interesting properties, as discussed in the excellent review by *Hofmann* [23.359]. The rhombohedral layered structure of bismuth is constituted by a pile of atomic bilayers with strong intrabilayer bonds and weaker interactions between bilayers. This leads to a peculiar set of phonon dispersion curves for Bi(111), characterized by a large gap between the acoustic bands, where bilayers move as quasi-rigid

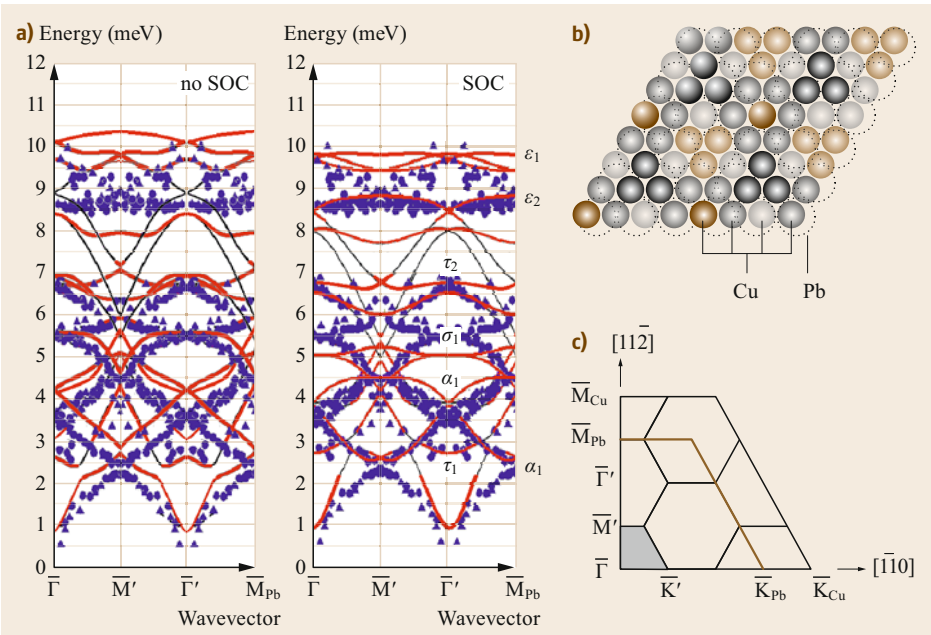

Fig. 23.17 **(a)** DFPT calculation of the phonon dispersion curves of a 3 ML-Pb(111) film on a Cu(111) substrate assumed to be rigid without (*left*) and with SOC (*right*), compared with HAS data (*blue symbols*) in the [11$\bar{2}$] symmetry direction [23.353, 354]. **(b)** The unit cell of the Pb(111)/Cu(111) superstructure with 9 Pb atoms (*broken circles*) and 16 Cu atoms (*smaller circles with different colors* indicating inequivalent atoms). **(c)** A quadrant of the Cu(111) surface BZ including the BZ of Pb(111) (*brown line boundaries*) and that of the superstructure (*gray area*) [23.354]

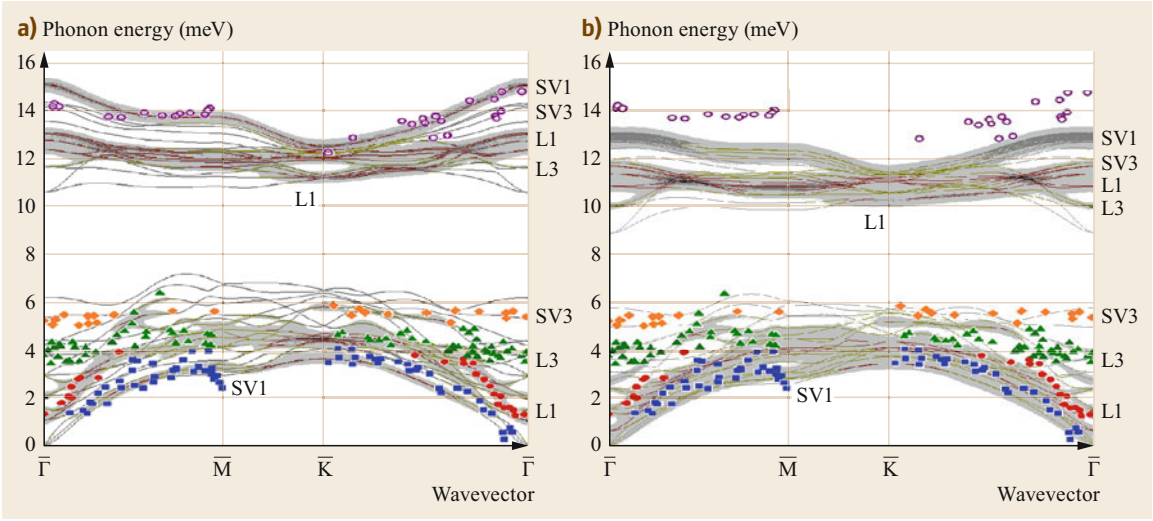

Fig. 23.18a,b DFPT surface dynamics of Bi(111) **(a)** without SOC [23.356] and **(b)** with SOC [23.95, 357] compared with HAS data [23.356, 358]

entities, and the optical bands hosting intralayer vibrations [23.356–358, 360, 361]. The trend in the surface bilayer contraction, small in Tl(0001) and large in Pb(111), in Bi(111) is manifested by a bilayer reorganization of the entire lattice. From DFPT, the softening induced by SOC of the intralayer phonon modes is found to be quite large (Fig. 23.18), whether localized mostly in the first (SV1 and L1 branches) or in the second bilayer (SV3 and L3 branches), its average amount being as large as about −15% [23.357]. Actually, *Chis* et al. showed that the spin–orbit part of the electron–phonon interaction, more than the SOC effect on the band structure, is responsible for such a large softening [23.357]. The SOC softening remains appreciable for the upper modes of the acoustic band and decreases in the lower part of the spectrum.

Surprisingly, for Bi(111) the experimental HAS data are, however, in good agreement with the DFPT calculations without SOC, whereas the DFPT-SOC calculation gives substantially softer surface optical branches. A careful HAS study of the Bi(111) optical modes exploiting resonance enhancement (Fig. 23.19; [23.358]) confirms the good agreement with a DFPT calculation without SOC for both the SV and L modes localized in the first bilayer (SV1,2 and L1), as well as for the SV mode in the second bilayer (SV3). It is likely that van der Waals interaction plays an important role in Bi(111) surface dynamics so as to compensate the misfit found with the inclusion of SOC. To our knowledge, no investigation has been made in this direction so far.

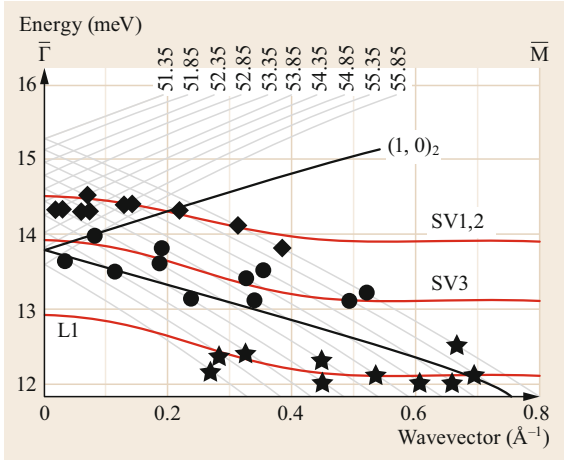

Fig. 23.19 A HAS study based on resonance enhancement of the optical surface branches of Bi(111) in the $\overline{\Gamma}\overline{\mathrm{M}}$ direction gives dispersion curves (*lozenges*, *full circles* and *stars*) in good agreement with DFPT calculations without SOC (*red curves*) [23.358]. *Light gray lines* represent the HAS scan curves for a narrow interval of incident He beam angles, whose intersections with the resonance curve $(1,0)_2$ (*black line*) for the second He bound state and the exchange of a G = (1, 0) surface reciprocal vector give the energy and wavevector of the surface phonon involved

Po(001) and the Heavier 6sp Elements

Polonium is the only elemental solid with a stable low-temperature, simple-cubic (sc) phase with one atom per unit cell (α-Po), eventually turning into a rhombohedral phase (β-Po) at around room temperature. A theoreti-

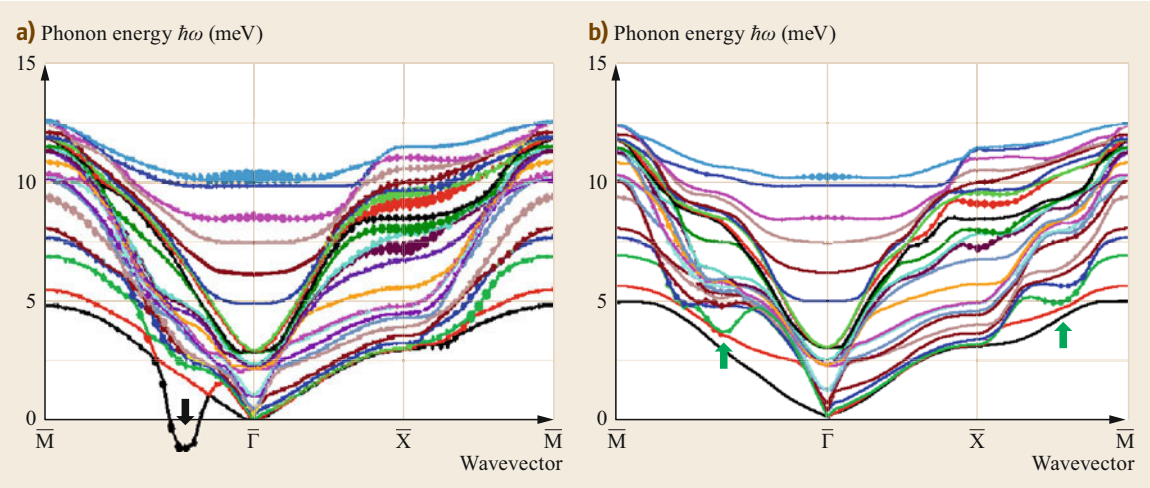

Fig. 23.20a,b DFPT calculations of the phonon dispersion curves for the (001) surface of a 8 ML free-standing slab of simple-cubic α-polonium without **(a)** and with SOC **(b)** [23.362]. In this case, SOC removes an unstable phonon ((**a**), *downward arrow*) lifting the Kohn anomaly within the bulk phonon band and inducing another one at the zone's middle ((**b**), *upward arrows*)

cal study of α-Po bulk and surface dynamics based on a force constant model [23.363] is confirmed by a state-of-the-art DFPT calculation [23.364], which demonstrated that the unusual stability of the sc lattice is due to an important change of the Fermi surface produced by the large SOC, dramatically reducing the nesting areas and the related Kohn anomalies. The DFPT Kohn anomalies lead to a hardening of the phonon energies, which is just opposite to what is found for lead and bismuth, and, in general, for simple metals. A natural question was whether the surface (001) of polonium is stable as well and what the role of SOC is. A DFPT calculation for a free-standing 8-ML slab without and with SOC [23.362], illustrated in Fig. 23.20a,b, shows that in the absence of SOC, a surface mode is, indeed, unstable in the $\overline{\Gamma}\overline{\mathrm{M}} \equiv [100]$ direction at about one third of the BZ. As can be seen in Fig. 23.20b, the addition of SOC stabilizes the surface by lifting the anomaly within the bulk phonon band and shifting its wavevector to about one half of the BZ, while leaving most of the other modes almost unchanged. Another anomaly appears, however, in the middle of the BZ boundary $\overline{\mathrm{XM}}$ with no consequence for the surface stability. No experimental study of the surface dispersion curves has been possible so far for α-Po(001) due to its radioactivity; the lifetime of the most stable natural isotope ^{210}Po is only 138.4 days, whereas the most stable synthetic isotope, ^{209}Po with a lifetime of 103 years is very expensive.

Even more difficult would be the experimental study of surface phonons for the crystalline forms of the remaining two 6sp elements, astatine and radon. From the theoretical point of view, information on the band structure of these elemental solids is found in [23.365]. The most stable (synthetic) isotope of astatine, ^{211}At, has a lifetime of only 7.21 h. A DFT calculation including SOC and dispersion forces by *Hermann* et al. [23.366] predicts that under normal conditions, it is an atomic metallic solid with a tetragonal lattice (space group $I4/mmm$), and that above 13 GPa, it has an fcc structure. Interestingly, without SOC astatine is predicted to be a molecular solid like other halogens. The only vibrational information of the atomic metallic phase of solid astatine is the calculated Debye frequency, which corresponds to an energy of 16.8 meV [23.366], which is considerably higher than the maximum bulk phonon energy of α-Po(001).

Radon, the last 6sp element, has been carefully investigated [23.367] not only for the general interest in rare gas overlayers but particularly for environmental reasons, radon being one of the main radioactive atmospheric contaminants. Far from being an inert noble gas, it has a chemistry similar to that of Xe, and in its expected fcc crystalline form it would have interesting surface properties similar to those of Xe(111) [23.98]. Unfortunately, the short lifetime of the most stable isotope ^{222}Rn (3.82 days) prevents the growth of films of even a few layers for investigation. For fcc-Rn there is, however, a calculation of the Debye temperature based on the phenomenological Mie–Lennard-Jones (MLJ) potential [23.368]. Although at the interatomic distances of the solid, the Tang–Toennies potential [23.369] would be more appropriate, the MLJ value of 53 K, corresponding to a Debye frequency in energy units of 4.56 meV, is only

slightly less than the DFPT maximum phonon energy in Xe(111), equal to 4.8 meV [23.98]. The predictive power of DFT and DFPT is severely challenged when applied to condensed forms of heavy and superheavy atoms. The future possibility to deposit a few-layer films of these highly radioactive elements for the investigation of their dynamical properties will provide an important testing ground.

Topological Insulator Surfaces

Topological insulator surfaces provide another important testing ground for DFPT surface dynamics. Figure 23.21 reproduces two recent DFPT calculations for three quintuple layers (QLs) of $Bi_2Se_3(111)$ [23.370, 371] and $Sb_2Te_3(111)$ [23.370, 372], together with recent HAS investigations of the surface phonons of the $Bi_2Se_3(111)$ surface [23.189, 371]. The first measurements by *Zhu* et al. [23.189], supported by a theoretical analysis based on the ME model, gave some evidence of a strong Kohn anomaly in the lowest optical mode at about 5 meV for a wavevector $Q = 2k_F \cong 0.23$ Å^{-1} corresponding to the Fermi level transition across the Dirac cone. More recent HAS measurements with higher resolution [23.371], reported in Fig. 23.21a, reproduce the calculated DFPT dispersion curves quite well, but do not show any anomaly. Since an electronic transition across the Dirac cone of a topological material implies a spin reversal, it can couple to a phonon only via the spin–orbit part of the electron–phonon interaction. Moreover, as discussed below for $Bi_2Te_3(111)$, the presence of a Kohn anomaly depends very much on the actual position of the Fermi level, which can be moved up and down by surface defects and doping, and eventually cut the associated quantum-well states within the surface band bending. These apparently conflicting results may actually hide a complex scenario, which it would be worth investigating further.

The spin–orbit interaction provides the fundamental mechanism for the nontrivial electronic structure of topological insulators. It is, therefore, expected to also affect the surface phonon dispersion curves, the major effect being a substantial softening of the optical modes, as observed above for Bi(111). On the other hand, the DFPT calculation with no SOC and no van der Waals (VdW) correction for $Bi_2Se_3(111)$ yields good agreement with HAS over the entire dispersion curve. The more precise micro-Raman measurements by *Shahil* et al. [23.373] on exfoliated samples of few quintuple layers (QL) of $Bi_2Se_3(111)$ and $Sb_2Te_3(111)$ predict energies of 21.5 and 20.5 meV for the highest A_{1g} Raman-active mode, respectively, slightly softer than the corresponding SV1 modes at $\overline{\Gamma}$. The discrepancy in $Bi_2Se_3(111)$ may indicate that the SOC softening exceeds the VdW hardening, while the better agreement in $Sb_2Te_3(111)$ speaks for a substantial cancellation of the two corrections.

A similar misfit occurs for $Bi_2Te_3(111)$ between the highest $\overline{\Gamma}$-point mode calculated with DFPT with no SOC or VdW (Fig. 23.22a; [23.374, 375]) and the corresponding *Shahil* et al. micro-Raman A_{1g} energy [23.373] (Fig. 23.22b), also suggesting a SOC softening larger than the VdW stiffening. The DFPT calculation of the lower part of the spectrum is in excellent agreement with the high-resolution ^{3}He-spin-echo (HeSE) scattering data shown in Fig. 23.23a. Also in this case, the deep Kohn anomaly reported at $Q =$

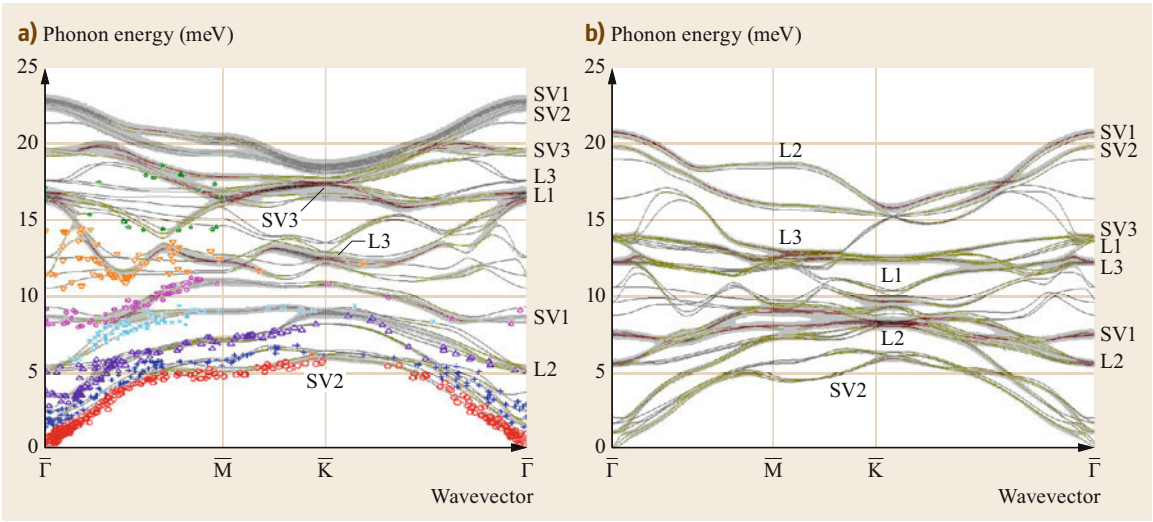

Fig. 23.21 (a) DFPT dispersion curves for three quintuple layers of $Bi_2Se_3(111)$ [23.370, 371] and **(b)** of $Sb_2Te_3(111)$ [23.370, 372]. The calculations do not include SOC or van der Waals corrections. HAS data [23.371] for $Bi_2Se_3(111)$ are also reported with symbols of different colors according to the assignment to different phonon branches

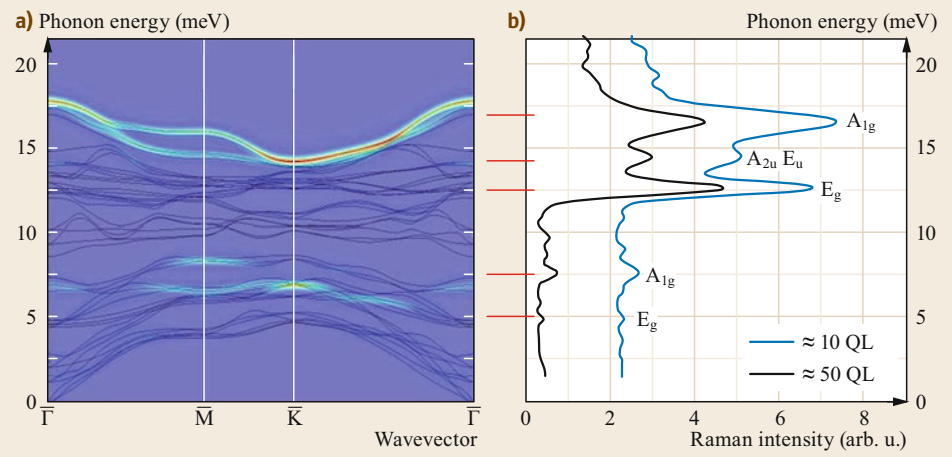

Fig. 23.22 **(a)** DFPT dispersion curves for three quintuple layers (QLs) of $Bi_2Te_3(111)$ (same color code for surface-projected DOS as in Fig. 23.14) calculated with no SOC or VdW corrections [23.374, 375]. **(b)** The micro-Raman spectra measured by *Shahil* et al. [23.373] for exfoliated few-QL samples agree well with the corresponding calculated modes at $\overline{\Gamma}$, except for the highest calculated A_{1g}, which is above the experimental value

$2k_F \cong 0.18\,\text{Å}^{-1}$ in a previous HAS study by *Howard* et al. [23.376, 377] is not found in the HeSE measurements, nor in the DFPT calculation. However, the inspection of the DOS associated with the RW and the L acoustic branches as measured with HeSE scattering (Fig. 23.23b) reveals an incipient sharp Kohn anomaly in the L branch at about one half of the zone [23.374, 375], which could correspond to an electron–phonon coupling involving Fermi-level quantum-well states within the surface band bending [23.378].

The implication of quantum-well electronic states at a band-bending accumulation layer in surface phonon anomalies is also transparent in a recent Brillouin scattering study of the RW and L dispersion curves in the GHz spectral region of a 50 nm $Bi_2Te_3(111)$ film on a GaAs substrate (Fig. 23.23c; [23.379]). The fact that the anomalies occur at a wavevector corresponding to a penetration depth of the surface waves approximately equal to the film thickness means that the electron–phonon coupling is with the excitations of the two-dimensional electron gas (2DEG) at the Bi_2Te_3/GaAs interface. The surface waves at smaller wavevectors become the Sezawa waves of the supported film.

Heid et al. [23.380] recently demonstrated (including SOC) that the weak electron–phonon interaction due to Dirac electrons in this class of topological insulators is strongly enhanced when the Fermi level is shifted above the minimum of the conduction band, so as to cut the surface 2DEG minibands. This work demonstrates that the major contribution to electron–phonon coupling comes from the higher optical phonons above 10 meV, i.e., those which most perturb the electronic states within the QLs.

A final remark concerns surface phonons in this class of topological insulators. Although the QLs are commonly considered to be held together by weak van der Waals interactions, there is no gap in the surface phonon DOS between the acoustic (interlayer) and the optical (intralayer) phonon bands, unlike what occurs in Bi(111) and Sb(111). Optical bands, as is visible in Figs. 23.21 and 23.22, exhibit unusually strong dispersions with large avoided crossings and character exchanges. This peculiar behavior appears to be a signature of the important electron–phonon effects affecting the optical branches and is represented in DFPT by the last term of (23.53).

23.3 Some Open Problems

Despite the great progress and success of DFPT in the calculation of surface phonons of all kinds of crystal lattices, there is an intrinsic limitation in the size of systems that can be approached within a reasonable central processing unit (CPU) time. The size limitation mainly concerns the number of atomic layers that can be chosen in the slab and the spatial extension of the surface unit cell. Complex structures with extended surface unit cells can be approached only at the expense of the number of layers, yielding coarse surface-projected phonon densities. As long as the surface modes are well localized, their dispersion curves can be obtained with

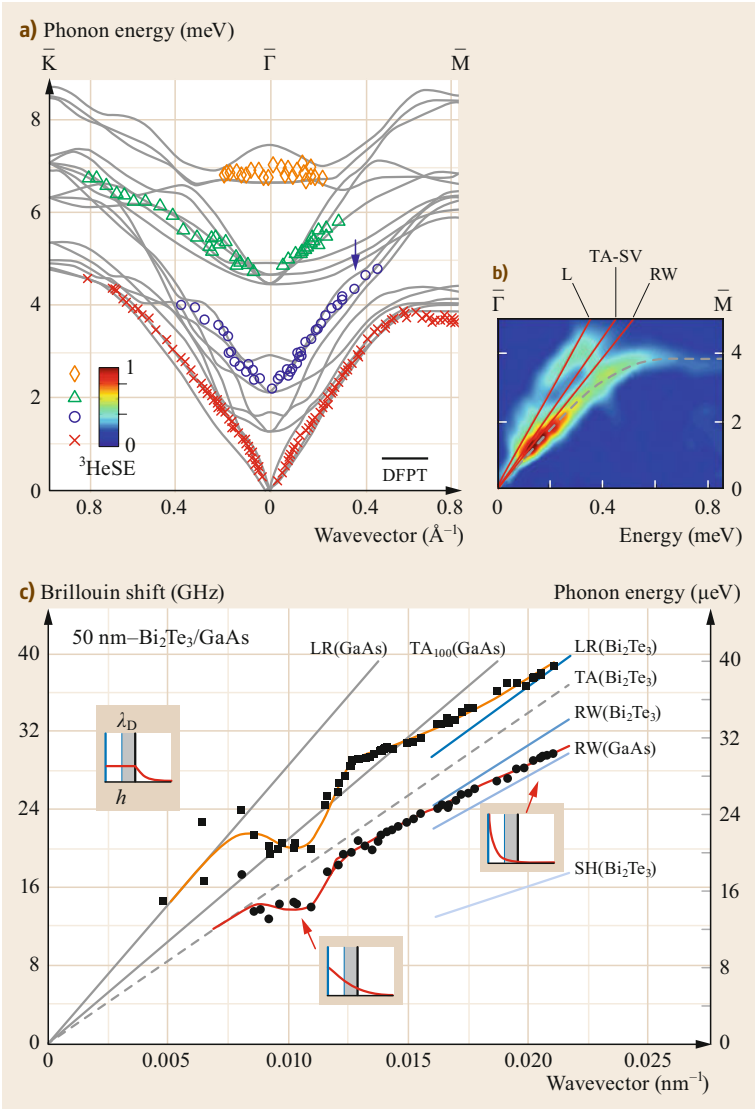

Fig. 23.23 **(a)** DFPT calculation of the dispersion curves for three QLs of Bi_2Te_3(111) in the low-energy part of the spectrum compared with HeSE scattering data (*symbols in color*) [23.375]. **(b)** The DOS associated with the RW and the L acoustic branches as measured with HeSE reveals an incipient sharp Kohn anomaly in the L branch at about one half of the zone (*arrow* in **(a)**), which could correspond to a coupling with a Fermi level transition involving surface quantum-well states [23.374, 375]. **(c)** Kohn anomalies in the RW and L branches of a 50 nm film of Bi_2Te_3(111) on a GaAs substrate are also found in the GHz spectral region with Brillouin scattering (*full circles* and *squares*) [23.379]. The fact that the anomalies occur at a wavevector corresponding to a penetration depth approximately equal to the film thickness (*insets* in **(c)**) implies that the electron–phonon coupling is with the interface 2DEG excitations

sufficient precision, even with a slab model of a few layers. The condition is that the surface phonon penetration length should be much shorter than the slab thickness. However, surface resonances are as important as localized surface modes in the calculation of various surface response functions, and their dispersion curves can hardly be recognized in slabs with a too few layers, especially in the case of large surface unit cells. In general, a simple scaling argument suggests that a semi-infinite crystal can be reliably modeled by a slab as long as the thickness is much larger than the linear size of the cell (or the number of layers is much larger than the number of atoms composing the unit cell).

This problem needs to be carefully considered for the prediction and interpretation of the HAS spectra. After being recognized to carry information on both localized surface modes and resonances and also on subsurface modes having their largest amplitude several layers beneath the surface, it became clear that ab-initio simulations with only a few atomic layers would be insufficient. Efficient expedients have to be introduced, like that of sandwiching a thick slab with ab-initio bulk force constants between the two halves of a thin slab with its ad-hoc ab-initio force constants. This way, sufficiently reliable dense surface projected DOS can be obtained and resonant features identified. From earlier discussions, it appears that the Green's function formalism is most appropriate for dealing with energy-dependent vibrational response functions and resonances. Provided that the eigenfrequencies

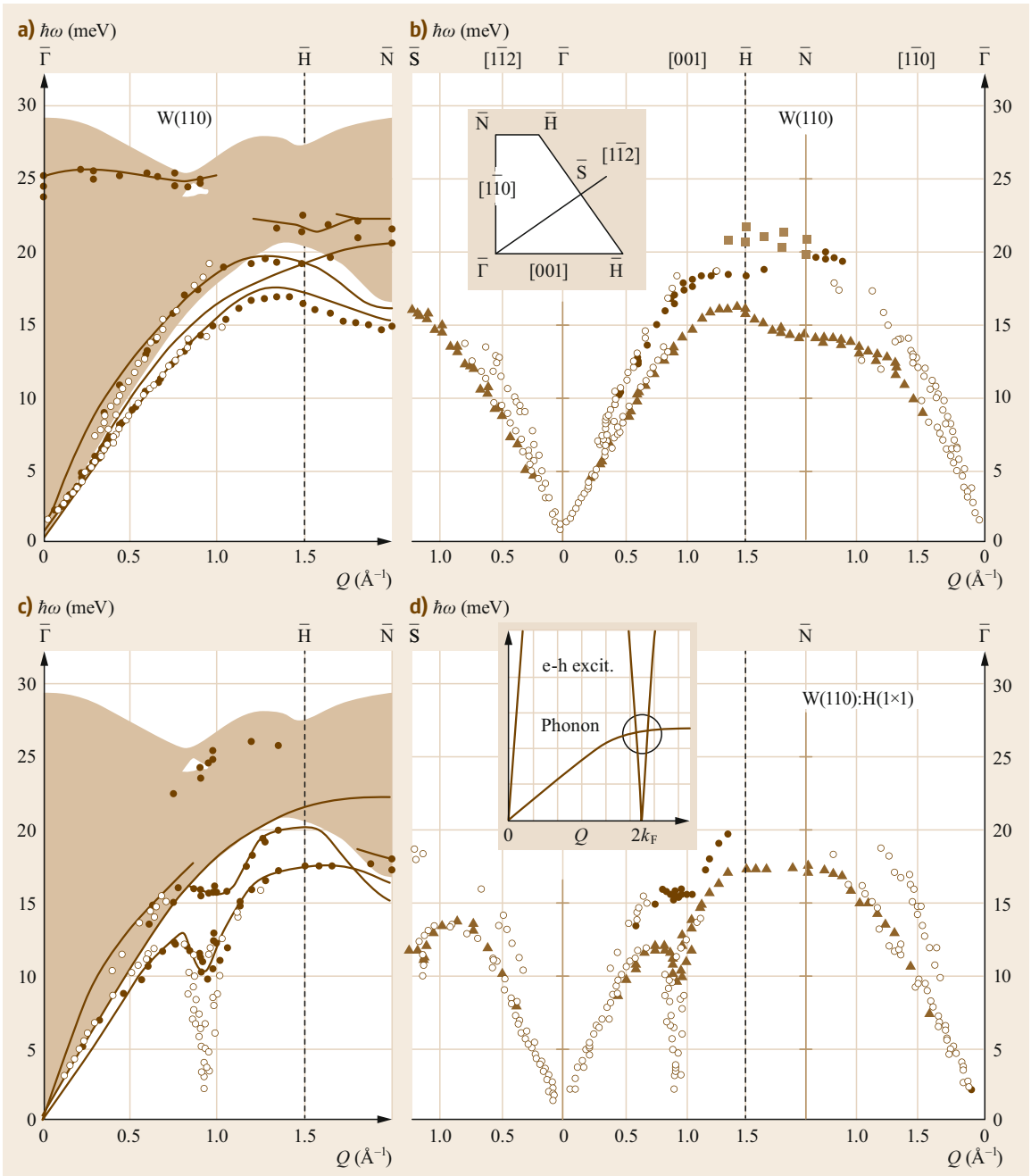

Fig. 23.24a–d Surface phonon dispersion curves of clean **(a,b)** and H-covered **(c,d)** W(110), calculated with DFPT **(a,c)** [23.381] and measured with HAS (*open symbols*) [23.382–385] and HREELS (*full symbols*) [23.386, 387]. The *inset* in **(b)** shows the irreducible part of the surface Brillouin zone with the symmetry directions. The H monolayer induces a deep nonadiabatic anomaly in the $\overline{\Gamma}\overline{\mathrm{H}}$ direction due to an avoided crossing between the surface phonons and the electron–hole (e–h) excitations in the quasi-1-D electronic band of the hydrogen rows, as is illustrated in the *inset* in **(d)**

and eigenvectors of the bulk phonons are known, the Green's function formalism can also be applied to extended surface unit cells, since the coordinate space to deal with is reduced from that of the entire slab to that of the perturbation. Thus, one of the possible and highly desired developments in the field would be the implementation of the Green's function method for DFPT surface dynamics.

Another challenge for DFPT is represented by the nonadiabatic manifestations of electron–phonon interaction, like, e.g., the sharp Kohn anomalies occurring in quasi-one-dimensional free-electron systems at the surface of metals. A well-known example is that of W(110) covered with an atomic hydrogen monolayer. Figure 23.24 collects the surface phonon dispersion curves of the clean W(110) surface (Fig. 23.24a,b) and of W(110):H(1×1) (Fig. 23.24c,d), calculated with DFPT (Fig. 23.24a,c) [23.381] and measured with HREELS (full symbols) [23.386, 387] and HAS (open symbols) [23.382–385]. The inset in Fig. 23.24b shows the irreducible part of the surface Brillouin zone with the symmetry directions on the bcc(110) surface. The H monolayer induces a deep Kohn anomaly in the $\overline{\Gamma\mathrm{H}}$ direction, whose nonadiabatic character is due to an avoided crossing between the surface phonon branches and the electron–hole excitations in the quasi-1-D electronic band of the hydrogen rows, as is illustrated in the inset of Fig. 23.24d [23.388].

While the DFPT calculation [23.381] for the clean surface accounts very well for the experimental dispersion curves, that for the H-covered surface fails to reproduce the deep anomaly. The anomalies obtained by DFPT originate, as expected, from the corresponding $2k_{\mathrm{F}}$ nesting at the Fermi level [23.389, 390], but due to the adiabatic approximation required by DFPT, the predicted anomaly in the RW is much shallower than the sharp anomaly seen in the HAS experiment. At the two avoided crossings, the surface phonon is converted into an electron–hole excitation, with atoms moving less and less and electrons oscillating more and more, and vice versa. Since HREELS in the impact regime mostly interacts with core electrons, it only detects phonon-like excitations and can follow the anomalous dispersion curve only as long as the atomic displacements are sufficiently large. If the adiabatic approximation could be avoided in DFPT calculations, then it would be possible to deal with this and other similar nonadiabatic phenomena like, e.g., phonon-induced chemical reactions at surfaces, etc. As discussed in Sect. 23.2.2, the ME method provides a phenomenological approach to nonadiabatic phonon dynamics (see, e.g., the PC model fit of W(110):H(1×1) and Mo(110):H(1×1) anomalies in [23.388]), but the specific role of the electronic band structure and electron–hole excitations at the Fermi level can only be accounted for by a full development of a nonadiabatic DFPT, hopefully in the near future.

Acknowledgments. We are grateful to Evgueni V. Chulkov, Pedro M. Echenique, and Irina Yu. Sklyadneva (DIPC, San Sebastian, Spain), Wolfgang Ernst and Toni Tamtögl (TU Graz, Austria), Daniel Farìas (Universidad Autonoma, Madrid, Spain), Salvador Miret-Artès (CSIC, Madrid, Spain), and Dick Manson (Clemson University, SC, USA) for several useful discussions and a fruitful collaboration on some of the recent and most challenging aspects of surface dynamics summarized in the last sections of the present chapter. Two of us (JPT and GB) also acknowledge several useful discussions in the early days of HAS theory and surface dynamics with the late Gian Paolo Brivio, to whose memory this review is dedicated.

References

23.1 Ioannes Duns Scotus (1265–1308): *Physicorum Aristotelis Quaestiones*, Tom. II, Lib. III–4 (L. Durand, Lyon 1639)

23.2 J.W. Strutt (Baron Rayleigh): On waves propagated along the plane surface of an elastic solid, Proc. Lond. Math. Soc. **17**, 4 (1885)

23.3 J.W. Strutt (Baron Rayleigh): *The Theory of Sound* (MacMillan, London 1896), Reprinted by Dover, New York 1945

23.4 G. Benedek, J.P. Toennies: *Atomic-Scale Dynamics at Surfaces – Theory and Experimental Studies with Helium Atom Scattering* (Springer, Berlin, Heidelberg 2018), Chap. 3

23.5 G. Benedek, D. Campi, J.P. Toennies: Interaction of atoms with surfaces and surface phonons. In: *Physics of Solid Surfaces, Subvol. A*, Landolt-Börnstein, New Ser., Subvol. 45A, ed. by P. Chiaradia, G.F. Chiarotti (Springer, Berlin, Heidelberg 2015) pp. 572–646, Chap. 10

23.6 H. Ibach: Surface vibrations of silicon detected by low-energy electron spectroscopy, Phys. Rev. Lett. **27**, 253 (1971)

23.7 B.R. Williams: Scattering of helium atoms by phonons in the (001) surface of LiF at 150 °K, J. Chem. Phys. **55**, 3220 (1971)

23.8 B.F. Mason, B.R. Williams: The inelastic scattering of He and Ne from a (001) surface of sodium fluoride, J. Chem. Phys. **61**, 2765 (1974)

23.9 G. Boato, P. Cantini: Experiments on scattering of light atomic beams from crystal surfaces. In: *Dynamics Aspects of Surface Physics*, ed. by F.O. Goodman (Compositori, Bologna 1974) p. 707

23.10 P. Cantini, G.P. Felcher, R. Tatarek: Inelastic resonant transitions of atoms on a LiF surface, Phys. Rev. Lett. **37**, 606 (1976)

23.11 P. Cantini, P. Tatarek, G.P. Felcher: Selective adsorption in elastic and inelastic scattering of He and Ne from LiF(001) surface, Surf. Sci. **68**, 104–112 (1977)

23.12 G. Benedek, G. Boato: Scattering of thermal atoms from crystal surfaces, Europhys. News **8**(4), 5–8 (1977)

23.13 G. Boato, P. Cantini, R. Tatarek, S. Terreni: Atomic vibrations at the (0001) graphite surface studied by He atom scattering, Surf. Sci. **114**, 485–497 (1982)

23.14 G. Boato, P. Cantini: Diffraction of neutral atoms and molecules from crystalline surfaces, Adv. Electron. Electron Phys. **60**, 95–160 (1983)

23.15 J.M. Horne, D.R. Miller: Single-Rayleigh-phonon interaction in the scattering of He from LiF(001), Phys. Rev. Lett. **41**, 511–514 (1978)

23.16 G. Brusdeylins, J.P. Toennies, H.-D. Meyer, K. Winkelmann: Production of helium nozzle beams with very high speed ratios. In: *Rarefied gas dynamics; 10th Int. Symp., Aspen* (American Institute of Aeronautics and Astronautics, New York 1977) pp. 1047–1059

23.17 G. Brusdeylins, R.B. Doak, J.P. Toennies: Observation of surface phonons in inelastic scattering of He atoms from LiF(001) crystal surfaces, Phys. Rev. Lett. **44**, 1417 (1980)

23.18 G. Brusdeylins, R.B. Doak, J.P. Toennies: Measurement of the dispersion relation for Rayleigh surface phonons of LiF(001) by inelastic scattering of He atoms, Phys. Rev. Lett. **46**, 437 (1981)

23.19 G. Brusdeylins, R.B. Doak, J.P. Toennies: High-resolution helium time-of-flight studies of Rayleigh surface-phonon dispersion curves of LiF, NaF, and KCl, Phys. Rev. B **27**, 3662 (1983)

23.20 R.B. Doak, U. Harten, J.P. Toennies: Anomalous surface phonon dispersion relations for Ag(111) measured by inelastic scattering of He atoms, Phys. Rev. Lett. **51**, 578 (1983)

23.21 U. Harten, J.P. Toennies, C. Woll: Helium time-of-flight spectroscopy of surface-phonon dispersion curves of the noble metals, Faraday Discuss. Chem. Soc. **80**, 137 (1985)

23.22 B.F. Mason, B.R. Williams: Inelastic atom scattering from a Cu(001) surface and an ordered adsorbed layer of Xe atoms at 16 K, Phys. Rev. Lett. **46**, 1138–1142 (1981)

23.23 B. Feuerbacher, R.F. Willis: Momentum transfer cutoff in the scattering of neon atoms from a nickel (111) surface, Phys. Rev. Lett. **526**, 47–50 (1981)

23.24 J.P. Toennies: The study of the forces between atoms of single crystal surfaces from experimental phonon dispersion curves. In: *Solvay Conf. Surf. Sci.*, Springer Ser. Surf. Sci., Vol. 14, ed. by F.W. de Wette (Springer, Berlin 1989) pp. 248–290

23.25 V. Bortolani, N.H. March, M.P. Tosi (Eds.): *Interaction of Atoms and Molecules with Solid Surfaces* (Plenum, New York 1990)

23.26 T.B. Grimley: Gas–surface interactions. In: *Interaction of Atoms and Molecules with Solid Surfaces*, ed. by V. Bortolani, N.H. March, M.P. Tosi (Plenum, New York 1990) pp. 25–52

23.27 W. Kohn: Theory of atom–surface collisions. In: *Interaction of Atoms and Molecules with Solid Surfaces*, ed. by V. Bortolani, N.H. March, M.P. Tosi (Plenum, New York 1990) pp. 53–70

23.28 H. Ibach: Surface vibration spectroscopy. In: *Interaction of Atoms and Molecules with Solid Surfaces*, ed. by V. Bortolani, N.H. March, M.P. Tosi (Plenum, New York 1990) pp. 325–356

23.29 F. García-Moliner: Basic vibrational properties of surfaces. In: *Interaction of Atoms and Molecules with Solid Surfaces*, ed. by V. Bortolani, N.H. March, M.P. Tosi (Plenum, New York 1990) pp. 71–116

23.30 C. Wöll: Phonons on surfaces: the importance of structure and adsorbates, Appl. Phys. A **53**, 377–387 (1991)

23.31 F.W. de Wette, W. Kress (Eds.): *Surface Phonons*, Springer Ser. Surf. Sci., Vol. 21 (Springer, Berlin, Heidelberg 1991)

23.32 J.P. Toennies: Experimental determination of surface phonons by helium atom and electron energy loss spectroscopy. In: *Surface Phonons*, ed. by F.W. de Wette, W. Kress (Springer, Berlin 1991) pp. 111–166

23.33 V. Celli: Theory of helium scattering from surface phonons. In: *Surface Phonons*, ed. by F.W. de Wette, W. Kress (Springer, Berlin 1991) pp. 167–192

23.34 R.B. Doak, D.J. Auerbach: Single phonon inelastic helium scattering. In: *Atomic and Molecular Beam Methods*, Vol. 2, ed. by G. Scoles, D.C. Laine, U. Valbusa (Oxford Univ. Press, New York 1992) p. 384

23.35 E. Hulpke (Ed.): *Helium Atom Scattering from Surfaces* (Springer, Berlin, Heidelberg 1992)

23.36 G. Benedek, J.P. Toennies: Helium atom scattering spectroscopy of surface phonons: genesis and achievements. In: *Surface Science: The First Thirty Years*, ed. by C.B. Duke (Elsevier, Amsterdam 1994)

23.37 G. Benedek, J.P. Toennies: Helium atom scattering spectroscopy of surface phonons: genesis and achievements, Surf. Sci. **299/300**, 587–611 (1994)

23.38 G. Comsa: Surface scattering of thermal energy He beams: from the proof of the wave nature of atoms to a versatile and efficient surface probe, Surf. Sci. **299/300**, 77 (1994)

23.39 V. Celli: Interaction of atoms with surfaces. In: *Physics of Solid Surfaces*, Landolt-Börnstein, New Series III, Vol. 24, ed. by G. Chiarotti (Springer, Berlin, Heidelberg 1995) p. 278, Part C

23.40 R.F. Wallis, S.Y. Tong: Surface phonons. In: *Physics of Solid Surfaces*, Landolt-Börnstein, New Series III, Vol. 24, ed. by G. Chiarotti (Springer, Berlin, Heidelberg 1995) p. 434, Part B

23.41 F. Hofmann, J.P. Toennies: High-resolution helium atom time-of-flight spectroscopy of low-frequency vibrations of adsorbates, Chem. Rev. **96**, 1307 (1996)

23.42 M.C. Desjonquères, D. Spanjaard: Vibrations at surfaces. In: *Concepts in Surface Physics* (Springer, Berlin, Heidelberg 1996), Chap. 3

23.43 S.A. Safron: High-resolution helium atom scattering as a probe of surface vibrations. In: *Advances in Chemical Physics*, Vol. XCV, ed. by I. Prigogine, S.A. Rice (Wiley, New York 1996)

23.44 B. Gumhalter: Single-and multiphonon atom–surface scattering in the quantum regime, Phys. Rep. **351**, 1 (2000)

23.45 G.D. Billing: *Dynamics of Molecule Surface Interactions* (Wiley, New York 2000)

23.46 M. Rocca: Surface phonon dispersion. In: *Physics of Covered Surfaces, I. Adsorbate Layers on Surfaces*, ed. by H.P. Bonzel (Springer, Heidelberg, Berlin 2002) pp. 1–68

23.47 J.R. Manson: Energy transfer to phonons in atom and molecule collisions with surfaces. In: *Surface Dynamics*, Vol. 3, ed. by W.N. Unertl (North Holland, Amsterdam 2006)

23.48 W. Widdra: Vibrations at surfaces. In: *Surface and Interface Science*, ed. by K. Wandelt (Wiley-VCH, Weinheim 2012) pp. 773–814

23.49 L. Vattuone, G. Bracco, M. Smerieri, L. Savio, M. Rocca: Supersonic molecular beams studies of surfaces. In: *Dynamics of Gas–Surface Interactions*, Springer Ser. Surf. Sci., Vol. 50, ed. by R. Díez Muiño, H. Busnengo (Springer, Berlin, Heidelberg 2013) pp. 1–23

23.50 R. Díez Muiño, H. Busnengo (Eds.): *Dynamics of Gas–Surface Interactions* (Springer, Berlin, Heidelberg 2013)

23.51 G.G. Rusina, E.V. Chulkov: Phonons on the clean metal surfaces and in adsorption structures, Russ. Chem. Rev. **82**(6), 483–510 (2013)

23.52 M. DeKieviet, D. Dubbers, C. Schmidt, D. Scholz, U. Spinola: $_3$He spin echo: new atomic beam technique for probing phenomena in the neV range, Phys. Rev. Lett. **75**, 1919 (1995)

23.53 A.P. Jardine, S. Dworski, P. Fouquet, G. Alexandrowicz, D.J. Riley, G.Y.H. Lee, J. Ellis, W. Allison: Ultrahigh-resolution spin-echo measurement of surface potential energy landscapes, Science **304**, 1790 (2004)

23.54 A.P. Jardine, H. Hedgeland, G. Alexandrowicz, W. Allison, J. Ellis: Helium-3 spin-echo: principles and application to dynamics at surfaces, Prog. Surf. Sci. **84**, 323–379 (2009)

23.55 H. Ibach, D.L. Mills: *Electron Energy Loss Spectroscopy and Surface Vibrations* (Academic Press, New York 1982)

23.56 S. Lehwald, J.M. Szeftel, H. Ibach, T.S. Rahman, D.L. Mills: Surface phonon dispersion of Ni(100) measured by inelastic electron scattering, Phys. Rev. Lett. **50**, 518 (1983)

23.57 X. Mu-Liang, B.M. Hall, S.Y. Tong, M. Rocca, H. Ibach, S. Lehwald, J.E. Black: Energy dependence of inelastic electron scattering cross section by surface vibrations: experimental measurement and theoretical interpretation, Phys. Rev. Lett. **54**, 1171 (1985)

23.58 H. Ibach: *Electron Energy Loss Spectrometers: The Technology of High Performance*, Springer Ser. Opt. Sci., Vol. 63 (Springer, Berlin, Heidelberg 1991)

23.59 H. Ibach: Electron energy loss spectroscopy: the vibration spectroscopy of surfaces, Surf. Sci. **299/300**, 116 (1994)

23.60 H. Ibach, M. Balden, S. Lehwald: Recent advances in electron energy loss spectroscopy of surface vibrations, J. Chem. Soc. Faraday Trans. **92**, 4771–4774 (1996)

23.61 H. Ibach: *Physics of Surfaces and Interfaces* (Springer, Berlin, Heidelberg 2007), Chap. 7

23.62 M. Rocca, H. Ibach, S. Lehwald, M.L. Xu, B.M. Hall, Y.S. Tong: Electron–phonon scattering and structure analysis. In: *The Structure of Surfaces*, ed. by M.A. van Hove, S.Y. Tong (Springer, Berlin, Heidelberg 1985) pp. 156–162

23.63 S. Lehwald, J.M. Szeftel, H. Ibach, T.S. Rahman, G.L. Mills: EELS study of the dynamics of clean Ni(100): surface phonons and surface resonances, Surf. Sci. **171**, 632–642 (1986)

23.64 S. Lehwald, M. Rocca, H. Ibach, T.S. Rahman: Surface phonon dispersion of ordered overlayers, J. Electron Spectrosc. Relat. Phenom. **38**, 29–44 (1986)

23.65 M. Rocca, H. Ibach, S. Lehwald, T.S. Rahman: Surface phonon dispersion of surface and adsorbate layers. In: *Structure and Dynamics of Surfaces I*, ed. by W. Schommers, P. von Blanckenhagen (Springer, Berlin, Heidelberg 1987) pp. 245–276

23.66 J.L. Erskine, E.-J. Jeong, J. Yater, Y. Chen, S.Y. Tong: Detection of odd symmetry shear modes at metal surfaces by inelastic electron scattering: experiment and theory, J. Vac. Sci. Technol. A **8**, 2649 (1990)

23.67 Y. Chen, S.Y. Tong, M. Rocca, P. Moretto, U. Valbusa, K.H. Bohnen, K.M. Ho: High-resolution electron energy loss spectroscopy analysis of Ag(001): discovery of a new surface longitudinal mode using first-principles phonon calculations, Surf. Sci. **250**, L389 (1991)

23.68 Y. Chen, S.Y. Tong, J.S. Kim, L.L. Kesmodel, T. Rodach, K.P. Bohnen, K.M. Ho: Characterization of surface phonons on Cu(001) and Ag(001): first-principles phonon calculations with experimental and theoretical studies of high-resolution electron-energy-loss spectra, Phys. Rev. B **44**, 11394 (1991)

23.69 M. Rocca, U. Valbusa: EELS cross-section of surface phonons on Ag(001), Nuovo Cim. **15D**, 493–499 (1993)

23.70 L. Vattuone, M. Rocca, L. Savio: High resolution electron energy loss spectroscopy (HREELS): a sensitive and versatile surface tool. In: *Surface Science Techniques*, Springer Ser. Surf. Sci., Vol. 51, ed. by G. Bracco, B. Holst (Springer, Berlin, Heidelberg 2013) pp. 499–529, Chap. 17

23.71 M. Born, K. Huang: *Dynamical Theory of Crystal Lattices* (Clarendon, Oxford 1998)

23.72 A.A. Maradudin, E.W. Montroll, G.H. Weiss, I.P. Ipatova: *Theory of Lattice Dynamics in the*

Harmonic Approximation, Solid State Physics, Suppl. 3 (Academic Press, New York 1971)
23.73 W. Cochran: *The Dynamics of Atoms in Crystals* (Arnold, London 1973)
23.74 P. Brüesch: *Phonons: Theory and Experiments. Lattice Dynamics and Models of Interatomic Forces* (Springer, Berlin, Heidelberg, New York 1982)
23.75 H. Böttger: *Principle of the Theory of Lattice Dynamics* (Akademie-Verlag, Berlin 1983), Sect. 1.4
23.76 M. Born, T. von Kármán: Über Schwingungen in Raumgittern, Phys. Z. **13**, 297 (1912)
23.77 R.F. Wallis: Effects of surfaces in lattice dynamics. In: *Dynamical Properties of Solids*, Vol. 2, ed. by G.K. Horton, A.A. Maradudin (North-Holland, Amsterdam 1975) p. 443
23.78 J.E. Black: Surface phonons: metals. In: *Dynamical Properties of Solids*, Vol. 6, ed. by G.K. Horton, A.A. Maradudin (Elsevier, Amsterdam 1990) p. 179
23.79 R.E. Allen, G.P. Alldredge, F.W. de Wette: Surface modes of vibration in monatomic crystals, Phys. Rev. Lett. **23**, 1285 (1969)
23.80 R.E. Allen, G.P. Alldredge, F.W. de Wette: Studies of vibrational surface modes, Phys. Rev. B **4**, 1648–1661 (1971)
23.81 A.A. Maradudin, P. Mazur, E.W. Montroll, G.H. Weiss: Remarks on the vibrations of diatomic lattices, Rev. Mod. Phys. **30**, 173 (1958), App. A
23.82 L. Miglio, G. Benedek: Study of surface phonons by means of the Green's function method. In: *Structure and Dynamics of Surfaces II*, ed. by W. Schommers, P. von Blanckenhagen (Springer, Berlin, Heidelberg 1987) p. 35
23.83 G. Benedek, L. Miglio: The Green's function method in the surface lattice dynamics of ionic crystals. In: *Surface Phonons*, Springer Ser. Surf. Sci., Vol. 21, ed. by F.W. deWette, W. Kress (Springer, Berlin, Heidelberg 1991) pp. 37–66
23.84 G. Benedek: Surface lattice dynamics of ionic crystals by the Green function method, Phys. Status Solidi (b) **58**, 661 (1973)
23.85 G. Benedek, G.P. Brivio, L. Miglio, V.R. Velasco: Dispersion relations of surface phonons in LiF(001) and NaF(001), Phys. Rev. B **26**, 497 (1982)
23.86 S. Doniach, E.H. Sondheimer: *Green's Function for Solid State Physics* (Benjamin, London 1974), Reprinted by Imperial College Press, London 1998
23.87 E.N. Economou: *Green's Function in Quantum Physics* (Springer, Berlin, Heidelberg 1978)
23.88 I.M. Lifshitz, L.M. Rozenzweig: Dynamics of lattice filling half-space, Zh. Eksp. Teor. Fiz. **18**, 1012 (1948), in Russian
23.89 I.M. Lifshitz, A.M. Kosevich: The dynamics of a crystal lattice with defects, Rep. Prog. Phys. **29**(I), 217 (1966)
23.90 G. Benedek: Dynamics of solid surfaces, Phys. Mag. **7**(suppl.), 1 (1985)
23.91 B.A. Lippmann, J. Schwinger: Variational principles for scattering processes, Phys. Rev. **79**, 469 (1950)
23.92 G. Benedek: The Green function approach to the surface lattice dynamics of ionic crystals, Surf. Sci. **61**, 603 (1976)
23.93 L. van Hove: Correlations in space and time and born approximation scattering in systems of interacting particles, Phys. Rev. **95**, 249 (1954)
23.94 I.Y. Sklyadneva, G. Benedek, E.V. Chulkov, P.M. Echenique, R. Heid, K.-P. Bohnen, J.P. Toennies: Mode-selected electron–phonon coupling in superconducting Pb nanofilms determined from He atom scattering, Phys. Rev. Lett. **107**, 095502 (2011)
23.95 G. Benedek, M. Bernasconi, K.-P. Bohnen, D. Campi, E.V. Chulkov, P.M. Echenique, R. Heid, I.Y. Sklyadneva, J.P. Toennies: Unveiling mode-selected electron–phonon interactions in metal films by helium atom scattering, Phys. Chem. Chem. Phys. **16**, 7159–7172 (2014)
23.96 J.R. Manson, G. Benedek, S. Miret-Artès: Electron–phonon coupling strength at metal surfaces directly determined from the helium atom scattering Debye–Waller factor, J. Phys. Chem. Lett. **7**, 1016–1021 (2016)
23.97 G. Benedek, S. Miret-Artès, J.P. Toennies, J.R. Manson: Electron–phonon coupling constant of metallic overlayers from specular He atom scattering, J. Phys. Chem. Lett. **9**, 76–83 (2018)
23.98 D. Campi, M. Bernasconi, G. Benedek, J.P. Toennies: Surface dynamics of Xe(111): an ambiguous nobility, J. Phys. Chem. C **119**, 14579–14584 (2015)
23.99 B.M. Hall, D.L. Mills, M.H. Mohamed, L.L. Kesmodel: Surface lattice dynamics of Cu(111), Phys. Rev. B **38**, 5856 (1988)
23.100 A. Šiber, B. Gumhalter, A.P. Graham, J.P. Toennies: He atom scattering and theoretical study of the surface phonons of a simple benchmark system: Xe(111), Phys. Rev. B **63**, 115411 (2001)
23.101 E.W. Kellermann: Theory of the vibrations of the sodium chloride lattice, Philos. Trans. R. Soc. A **238**, 513 (1940)
23.102 S.Y. Tong, A.A. Maradudin: Normal modes of a semi-infinite ionic crystal, Phys. Rev. **181**, 1318 (1969)
23.103 L. Philippe, P. Lambin, P. Senet, A.A. Lucas: Phonon structure of thin films of the YBaCuO compound, Appl. Supercond. **2**, 135 (1994)
23.104 W. Cochran, R.A. Cowley: Phonons in perfect crystals. In: *Encyclopedia of Physics 25/2a* (Springer, Berlin, Heidelberg 1967) p. 83
23.105 J.R. Hardy: Phenomenological models in lattice dynamics. In: *Dynamical Properties of Solids*, Vol. 1, ed. by G.K. Horton, A.A. Maradudin (North-Holland, Amsterdam 1974) p. 157, Chap. 3
23.106 H. Bilz, B. Gliss, W. Hanke: Title: Theory of phonons in ionic crystals. In: *Dynamical Properties of Solids*, Vol. 1, ed. by G.K. Horton, A.A. Maradudin (North-Holland, Amsterdam 1974) p. 343, Chap. 6
23.107 H. Bilz, W. Kress: *Phonon Dispersion Relations in Insulators* (Springer, Berlin, Heidelberg 1976)
23.108 B.C. Dick, A.W. Overhauser: Theory of the dielectric constants of alkali halide crystals, Phys. Rev. **112**, 90 (1958)
23.109 W. Cochran: Theory of the lattice vibrations of germanium, Phys. Rev. Lett. **2**, 495 (1959)

23.110 W. Cochran: Crystal stability and the theory of ferroelectricity, Adv. Phys. **9**, 387 (1960)

23.111 T.S. Chen, G.P. Alldredge, F.W. de Wette, R.E. Allen: Surface and pseudosurface modes in ionic crystal, Phys. Rev. Lett. **26**, 1543 (1971)

23.112 G.P. Alldredge: Shear-horizontal surface waves on the (001) face of cubic crystals, Phys. Lett. **41A**, 291 (1972)

23.113 T.S. Chen, G.P. Alldredge, F.W. de Wette, R.E. Allen: Surface modes of vibration in the rigid-Ion model of NaCl, Phys. Rev. B **6**, 627 (1972)

23.114 T.S. Chen, G.P. Alldredge, F.W. de Wette: Distribution of surface phonon branches in RbF and RbCl, Solid State Commun. **10**, 941 (1972)

23.115 T.S. Chen, G.P. Alldredge, F.W. de Wette: Surface phonons for the (001) face of lithium fluoride, Phys. Lett. **40 A**, 401 (1972)

23.116 V.L. Zoth, G.P. Alldredge, F.W. de Wette: On the existence of long-wavelength shear-horizontal surface waves on the bcc (001) surface, Phys. Lett. **47A**, 247 (1974)

23.117 T.S. Chen, F.W. de Wette, G.P. Alldredge: Studies of vibrational surface modes in ionic crystals. I. Detailed shell-model studies for the unrelaxed (001) face of seven crystals having the rocksalt structure, Phys. Rev. B **15**, 1167 (1977)

23.118 G. Benedek, R.B. Doak, J.P. Toennies: Surface-phonon spectroscopy of LiF(001) by inelastic scattering of He atoms: theory and interpretation of time-of-flight spectra, Phys. Rev. B **28**, 7277 (1983)

23.119 A.A. Lucas: Phonon modes of an ionic crystal slab, J. Chem. Phys. **48**, 3156 (1968)

23.120 R. Fuchs, K.L. Kliever: Optical modes of vibration in an ionic crystal slab, Phys. Rev. **140**, A2076 (1965)

23.121 A.D. Boardman (Ed.): *Electromagnetic Surface Modes* (Wiley, New York 1982)

23.122 G. Bracco, M. D'Avanzo, C. Salvo, R. Tatarek, F. Tommasini: Observation of acoustic and optical surface phonons in LiF(001) by inelastic He scattering, Surf. Sci. **189/190**, 684 (1987)

23.123 U. Schröder: A new model for lattice dynamics ("breathing shell model"), Solid State Commun. **4**, 347 (1966)

23.124 U. Schröder, V. Nüsslein: Calculations of dispersion curves and specific heat for LiF and NaCl using the breathing shell model, Phys. Status Solidi (b) **21**, 309 (1967)

23.125 K. Fischer, H. Bilz, R. Haberkorn, W. Weber: Covalency and deformability of Ag^+-ions in the lattice dynamics of silver halide, Phys. Status Solidi (b) **54**, 285 (1972)

23.126 W. Kress, P. Roedhammer, H. Bilz, W.D. Teuchert, A.N. Christensen: Phonon anomalies in transition-metal nitrides: TiN, Phys. Rev. B **17**, 111 (1978)

23.127 G. Benedek: Surface lattice dynamics. In: *Dynamic Aspects of Surface Physics*, ed. by F.O. Goodman (Compositori, Bologna 1974) p. 605

23.128 D. Eichenauer, J.P. Toennies: Theory of one-phonon assisted adsorption and desorption of He atoms from a LiF(001) single crystal surface. In: *Dynamics on Surfaces*, ed. by B. Pullman, J. Jortner, A. Nitzan, B. Gerber (Reidel, Dordrecht 1984) p. 1

23.129 W. Weber: Lattice dynamics of transition-metal carbides, Phys. Rev. B **8**, 5082 (1973)

23.130 A.N. Christensen, W. Kress, M. Miura, N. Lehner: Phonon anomalies in transition-metal nitrides: HfN, Phys. Rev. B **28**, 977 (1983), and references therein

23.131 G. Benedek, M. Miura, W. Kress, H. Bilz: Anomalies in the surface–phonon dispersion of TiN(001), Phys. Rev. Lett. **52**, 1907 (1984)

23.132 G. Benedek, M. Miura, W. Kress, H. Bilz: Surface phonon anomalies in superconducting transition metal compounds, Surf. Sci. **148**, 107 (1984)

23.133 S.W. Musser, K.H. Rieder: Influence of surface force-constant changes on surface-mode frequencies, Phys. Rev. B **2**, 3034 (1970)

23.134 K.H. Rieder, W. Drexel: Observation of vibrational surface modes in the acousto-optical bulk gap of TiN, Phys. Rev. Lett. **34**, 148 (1975)

23.135 E.B jr . Wilson, J.C. Decius, P.C. Cross: *Molecular Vibrations* (McGraw-Hill, New York 1955)

23.136 R. Tubino, L. Piseri, G. Zerbi: Lattice dynamics and spectroscopic properties by a valence force potential of diamondlike crystals: C, Si, Ge, and Sn, J. Chem. Phys. **6**, 1022 (1972)

23.137 P.N. Keating: First- and second-order dipole moments of homopolar crystals, Phys. Rev. **140A**, 369 (1965)

23.138 P.N. Keating: Effect of invariance requirements on the elastic strain energy of crystals with application to the diamond structure, Phys. Rev. **145**, 637 (1966)

23.139 S.K. Sinha: Phonons in semiconductors, Crit. Rev. Solid State Sci. **3**, 273 (1973)

23.140 J.C. Phillips: Covalent bond in crystals. I. Elements of a structural theory, Phys. Rev. **166**, 832 (1968)

23.141 R.M. Martin: A simple bond charge model for vibrations in covalent crystals, Chem. Phys. Lett. **2**, 268 (1968)

23.142 R.M. Martin: Dielectric screening model for lattice vibrations of diamond-structure crystals, Phys. Rev. **186**, 871 (1969)

23.143 F.A. Johnson: A bond charge model of lattice dynamic, Proc. R. Soc. A **339**, 73 (1974)

23.144 W. Weber: New bond-charge model for the lattice dynamics of diamond-type semiconductors, Phys. Rev. Lett. **33**, 371 (1974)

23.145 K.C. Rustagi, W. Weber: Adiabatic bond charge model for the phonons in A3B5 semiconductor, Solid State Commun. **18**, 637 (1976)

23.146 W. Weber: Adiabatic bond charge model for the phonons in diamond, Si, Ge, and α–Sn, Phys. Rev. B **15**, 4789 (1977)

23.147 A. Fleszar, R. Resta: Real-space force constants for lattice dynamics in silicon and germanium in the adiabatic bond-charge model, Phys. Rev. B **34**, 7140 (1986)

23.148 L. Miglio, P. Santini, P. Ruggerone, G. Benedek: Dynamics of extensively reconstructed surfaces: Si(111) 2×1, Phys. Rev. Lett. **62**, 3070 (1989)

23.149 P. Santini, L. Miglio, G. Benedek, U. Harten, P. Ruggerone, J.P. Toennies: Dynamics and structural assessment of open semiconductor surfaces: GaAs(110), Phys. Rev. B **42**, 11942 (1990)

23.150 G. Benedek, G. Onida: Bulk and surface dynamics of graphite with the bond charge model, Phys. Rev. B **47**, 16471 (1993)

23.151 G. Benedek, F. Hoffmann, G. Onida, P. Ruggerone, L. Miglio: Surface phonons in layered crystals: theoretical aspects, Surf. Sci. Rep. **20**, 3 (1994)

23.152 M. Zitzlsperger, R. Honke, P. Pavone, U. Schröder: Ab initio calculation of the structure, the electronic states and the phonon dispersion of the Si(111)-(2×1) surface, Surf. Sci. **377**, 108 (1997)

23.153 U. Harten, J.P. Toennies, C. Wöll: Observation of a 10-meV Einstein oscillator mode on the Si(111)(2×1) surface, Phys. Rev. Lett. **57**, 2947 (1986)

23.154 L. Wirtz, A. Rubio: The phonon dispersion of graphite revisited, Solid State Commun. **131**, 141–152 (2004)

23.155 J.L. Wilkes, R.E. Palmer, R.F. Willis: Phonons in graphite studied by EELS, J. Electron Spectrosc. Relat. Phenom. **44**, 355 (1987)

23.156 C. Oshima, T. Aizawa, R. Souda, Y. Ishizawa, Y. Sumiyoshi: Surface phonon dispersion curves of graphite (0001) over the entire energy region, Solid State Commun. **65**, 1601 (1988)

23.157 C. Oshima, A. Nagashima: Ultra-thin epitaxial films of graphite and hexagonal boron nitride on solid surfaces, J. Phys. Condens. Matter **9**, 1 (1997)

23.158 S. Siebentritt, R. Pues, K.-H. Rieder, A.M. Shikin: Surface phonon dispersion in graphite and in a lanthanum graphite intercalation compound, Phys. Rev. B **55**, 7927 (1997)

23.159 M. Mohr, J. Maultzsch, E. Dobardžić, S. Reich, I. Milošević, M. Damnjanović, A. Bosak, M. Krisch, C. Thomsen: Phonon dispersion of graphite by inelastic x-ray scattering, Phys. Rev. B **76**, 035439 (2007)

23.160 J. Maultzsch, S. Reich, C. Thomsen, H. Requardth, P. Ordejòn: Phonon dispersion in graphite, Phys. Rev. Lett. **92**, 075501 (2004)

23.161 H. Yanagisawa, T. Tanaka, Y. Ishida, M. Matsue, E. Rokuta, S. Otani, C. Oshima: Analysis of phonons in graphene sheets by means of HREELS measurement and ab initiocalculation, Surf. Interface Anal. **37**, 133 (2005)

23.162 A. Grüneis, R. Saito, T. Kimura, L.C. Cancado, M.A. Pimienta, A. Jorio, A.G. Souza Filho, G. Dresselhaus, M.S. Dresselhaus: Determination of two-dimensional phonon dispersion relation of graphite by Raman spectroscopy, Phys. Rev. B **65**, 155405 (2002)

23.163 R.J. Nemanich, G. Lucovsky, S.A. Solin: Optical probes of the lattice dynamics of graphite, Mater. Sci. Eng. **31**, 157 (1977)

23.164 R. Nicklow, N. Wakabayashi, H.G. Smith: Lattice dynamics of pyrolytic graphite, Phys. Rev. B **5**, 4951 (1972)

23.165 E. de Rouffignac, G.P. Alldredge, F.W. De Wette: Lattice dynamics of graphite slabs, Phys. Rev. B **23**, 4208 (1981)

23.166 G.P. Alldredge, E. de Rouffignac, B. Firey, F.W. de Wette: Inadvertent symmetries in a lattice-dynamical model of graphite, Phys. Rev. B **29**, 3712 (1984)

23.167 M. Maeda, Y. Kuramoto, C. Horie: Phonon dispersion relations of graphite, J. Phys. Soc. Jpn. Lett. **47**, 337 (1979)

23.168 R. Al-Jishi, G. Dresselhaus: Lattice-dynamical model for graphite, Phys. Rev. B **26**, 4514 (1982)

23.169 T. Aizawa, R. Souda, S. Otani, Y. Ishizawa, C. Oshima: Anomalous bond of monolayer graphite on transition-metal carbide surfaces, Phys. Rev. Lett. **64**, 768 (1990)

23.170 P.B. Allen: Charge-density distortions and lattice dynamics: a general theory and application to Nb, Phys. Rev. B **16**, 5139 (1977)

23.171 L.J. Sham: Electronic contribution to lattice dynamics in insulating crystal, Phys. Rev. **188**, 1431 (1969)

23.172 R.M. Pick, M.H. Cohen, R.M. Martin: Microscopic theory of force constants in the adiabatic approximation, Phys. Rev. B **1**, 910 (1970)

23.173 R.M. Pick, M.H. Cohen, R.M. Martin: Microscopic theory of force constants in the adiabatic approximation, Phys. Rev. B **1**, 910 (1970)

23.174 W. Hanke: Microscopic theory of dielectric screening and lattice dynamics in the Wannier representation, Phys. Rev. B **8**, 4585–4591 (1973)

23.175 L.J. Sham: Electronic influence on lattice dynamics. In: *Elementary Excitations in Solids, Molecules, and Atoms*, NATO Advanced Study Institute Series (Series B: Physics), Vol. 2, ed. by J.T. Devreese, A.B. Kunz, T.C. Collins (Springer, Boston, MA 1974) pp. 1–23

23.176 W. Hanke, L.J. Sham: Local-field and excitonic effects in the optical spectrum of a covalent crystal, Phys. Rev. B **12**, 4501 (1975)

23.177 W. Hanke, L.J. Sham: Many-particle effects in the optical spectrum of a semiconductor, Phys. Rev. B **21**, 4656 (1980)

23.178 P.E. van Camp, V.E. van Doren, J.T. Devreese: Microscopic screening and phonon dispersion of silicon: moment expansion for the polarizability, Phys. Rev. Lett. **42**, 1224 (1979)

23.179 R. Resta, A. Baldereschi: Local-field effects and zone-center phonons in Si, Ge, GaAs, and ZnSe, Phys. Rev. B **24**, 4839 (1981)

23.180 P.E. van Camp, V.E. van Doren, J.T. Devreese: Consistent microscopic calculation of phonons in Si, Phys. Rev. B **25**, 4270 (1982)

23.181 R. Resta: Local-field effects and phonon screening in polar semiconductors, Phys. Rev. B **27**, 3620 (1983)

23.182 P.E. van Camp, V.E. van Doren, J.T. Devreese: Ab initio phonon dispersion curves of Si, Phys. Rev. B **31**, 4089 (1985)

23.183 C. Falter: A unifying approach to lattice dynamical and electronic properties of solids, Phys. Rep. **164**, 1 (1988)

23.184 C.S. Jayanthi, H. Bilz, W. Kress, G. Benedek: Nature of surface-phonon anomalies in noble metals, Phys. Rev. Lett. **59**, 795 (1987)

23.185 C. Kaden, P. Ruggerone, J.P. Toennies, G. Zhang, G. Benedek: Electronic pseudocharge model for the Cu(111) longitudinal-surface-phonon anomaly observed by helium-atom scattering, Phys. Rev. B **46**, 13509 (1992)

23.186 C. Kaden, P. Ruggerone, J.P. Toennies, G. Zhang, G. Benedek: Surface lattice dynamics and inelastic He scattering in Cu(111), Nuovo Cim. D **14**, 627 (1992)

23.187 X. Zhu, Y. Yao, H.C. Hsu, F.C. Chou, M. El-Batanouny: Temperature-dependent anomalies in the structure of the (001) surface of $LiCu_2O_2$, Surf. Sci. **605**, 376 (2011)

23.188 X. Zhu, L. Santos, R. Sankar, S. Chikara, C. Howard, F.C. Chou, C. Charmon, M. El-Batanouny: Interaction of phonons and Dirac fermions on the surface of Bi_2Se_3: a strong Kohn anomaly, Phys. Rev. Lett. **107**, 186102 (2011)

23.189 X.T. Zhu, L. Santos, C. Howard, R. Sankar, F.C. Chou, C. Chamon, M. El-Batanouny: Electron–phonon coupling on the surface of the topological insulator Bi_2Se_3 determined from surface–phonon dispersion measurements, Phys. Rev. Lett. **108**, 185501 (2012)

23.190 R.G. Parr, W. Yang: *Density Functional Theory of Atoms and Molecules* (Oxford Univ. Press, New York 1989)

23.191 S. Baroni, S. de Gironcoli, A. Dal Corso, P. Giannozzi: Phonons and related crystal properties from density-functional perturbation theory, Rev. Mod. Phys. **73**, 515 (2001)

23.192 E. Hulpke, J. Lüdecke: Hydrogen-induced phonon anomaly on the W(110) surface, Phys. Rev. Lett. **68**, 2846 (1992)

23.193 E. Hulpke, J. Lüdecke: The giant surface phonon anomaly on hydrogen saturated W(110) and Mo(110), Surf. Sci. **287/288**, 837 (1993)

23.194 G. Benedek, M. Bernasconi, V. Chis, E. Chulkov, P.M. Echenique, B. Hellsing, J.P. Toennies: Theory of surface phonons at metal surfaces: recent advances, J. Phys. Condens. Matter **22**, 084020 (2010)

23.195 V. Bortolani, A. Franchini, F. Nizzoli, G. Santoro: Explanation of the anomalous peak observed in He-atom scattering from Ag(111), Phys. Rev. Lett. **52**, 429 (1984)

23.196 V. Bortolani, A. Franchini, G. Santoro: Santoro surface phonon calculations in metals and comparison with experimental techniques. In: *Electronic Structure, Dynamics, and Quantum Structural Properties of Condensed Matter*, ed. by J.T. Devreese, P. van Camp (Springer, Boston 1985) pp. 401–449

23.197 M.S. Daw, M.I. Baskes: Semiempirical, quantum mechanical calculation of hydrogen embrittlement in metals, Phys. Rev. Lett. **50**, 1285 (1983)

23.198 M.S. Daw, M.I. Baskes: Embedded-atom method: derivation and application to impurities, surfaces, and other defects in metals, Phys. Rev. B **29**, 6443 (1984)

23.199 J.S. Nelson, E.C. Sowa, M.S. Daw: Calculation of phonons on the Cu(100) surface by the embedded-atom method, Phys. Rev. Lett. **61**, 1977 (1988)

23.200 P.R. Underhill: An investigation of the anomalous surface phonon softening on noble metal (111) surfaces using the embedded atom method, Surf. Sci. **200**, L441 (1988)

23.201 N. Luo, W. Xu, S. Shen: Application of the embedded atom method to surface-phonon dispersions on Cu(100), Solid State Commun. **67**, 837 (1988)

23.202 M.S. Daw, S.M. Foiles, M.I. Baskes: The embedded-atom method: a review of theory and applications, Mater. Sci. Rep. **9**, 251–310 (1993)

23.203 J.S. Nelson, M.S. Daw, E.C.S. Sowa: Embedded atom calculations of the Cu (001), (111), and (110) surface phonon spectra, Superlattices Microstruct. **7**, 259 (1990)

23.204 U. Harten, A.M. Lahee, J.P. Toennies, C. Wöll: Observation of a soliton reconstruction of Au(111) by high-resolution helium-atom diffraction, Phys. Rev. Lett. **54**, 2619 (1985)

23.205 X.Q. Wang: Anomalous surface phonons of the reconstructed Au(111): a molecular-dynamics simulation, Phys. Rev. Lett. **67**, 1294 (1991)

23.206 E.M. McIntosh, P.R. Kole, M. El-Batanouny, D.M. Chisnall, J. Ellis, W. Allison: Measurement of the phason dispersion of misfit dislocations on the Au(111) surface, Phys. Rev. Lett. **110**, 086103 (2013)

23.207 R. Ravelo, M. El-Batanouny: Molecular-dynamics study of the reconstructed Au(111) surface: low temperature, Phys. Rev. B **40**, 9574 (1989)

23.208 G. Benedek, G. Lange, P. Ruggerone, J.P. Toennies: Lattice dynamics of the (7×7) reconstructed Si(111) surface from high-resolution helium atom scattering, Europhys. Lett. **41**, 647 (1998)

23.209 I. Štich, K. Terakura, B.E. Larson: First-principles finite-temperature characterization of dynamics of the Si(111)-7×7, Phys. Rev. Lett. **74**, 4491 (1995)

23.210 I. Štich, J. Kohanoff, K. Terakura: Low-temperature atomic dynamics of the Si(111)-7×7, Phys. Rev. B **54**, 2642 (1996)

23.211 I. Štich: First-principles finite-temperature simulation of surface dynamics: Si(111)-(7×7), Surf. Sci. **368**, 152 (1996)

23.212 J. Kim, F.S. Khan, M. Yeh, J.W. Wilkins: Surface phonons of the Si(111)-7×7 reconstructed surface, Phys. Rev. B **52**, 14709 (1995)

23.213 W. Harrison: *Electronic Structure and the Properties of Solids* (Dover, New York 1988)

23.214 Y.R. Wang, C.B. Duke: Rotational surface phonons on (110) cleavage surfaces of zincblende-structure compound semiconductors, Surf. Sci. **205**, L755 (1988)

23.215 B. Sandfort, A. Mazur, J. Pollmann: Surface phonons of hydrogen-terminated semiconductor surfaces. I. The H:Si(111)-(1×1) surface, Phys. Rev. B **51**, 7139 (1995)

23.216 A. Mazur, B. Sandfort, V. Gräschus, J. Pollmann: Phonons at hydrogen-terminated Si and diamond surfaces. In: *Festkörperprobleme*, Advances in Solid State Physics, Vol. 36, ed. by R. Helbig (Springer, Berlin, Heidelberg 1997) pp. 181–201

23.217 C.M. Varma, W. Weber: Phonon dispersion in transition metals, Phys. Rev. B **21**, 6142 (1979)

23.218 W. Weber: First principles lattice dynamics of transition metals. In: *The Electronic Structure of Complex Systems*, NATO ASI Series (Series B: Physics), Vol. 113, ed. by P. Phariseau, W.M. Temmermann (Springer, Boston, MA 1984) pp. 345–462

23.219 X.W. Wang, W. Weber: Surface-phonon instabilities of W(001), Phys. Rev. Lett. **58**, 1452 (1987)

23.220 X.W. Wang, C.T. Chan, K.-H. Ho, W. Weber: Role of surface-state nesting in the incommensurate reconstruction of Mo(001), Phys. Rev. Lett. **60**, 2066 (1988)

23.221 F. Mauri, G. Galli, R. Car: Orbital formulation for electronic-structure calculations with linear system-size scaling, Phys. Rev. B **47**, 9973 (1993)

23.222 P. Ordejòn, D. Drabold, M. Grunbach, R. Martin: Unconstrained minimization approach for electronic computations that scales linearly with system size, Phys. Rev. B **48**, 14646 (1993)

23.223 S. Goedecker, L. Colombo: Efficient linear scaling algorithm for tight-binding molecular dynamics, Phys. Rev. Lett. **74**, 122 (1994)

23.224 S. Goedecker: Linear scaling electronic structure methods, Rev. Mod. Phys. **71**, 1085 (1999)

23.225 L. Colombo, M. Rosati: Parallel tight-binding molecular dynamics simulations on symmetric multi-processing platforms, Comput. Phys. Commun. **128**, 108 (2000)

23.226 S. Nelson, M.S. Daw, E.C. Sowa: Cu(111) and Ag(111) surface-phonon spectrum: the importance of avoided crossings, Phys. Rev. B **40**, 1465 (1989)

23.227 M.H. Mohamed, L.L. Kesmodel, B.M. Hall, D.L. Mills: Surface phonon dispersion on Cu(111), Phys. Rev. B **37**, 2763 (1988)

23.228 L.J. Sham: A calculation of the phonon frequencies in sodium, Proc. R. Soc. A **283**, 33 (1965)

23.229 W. Harrison: *Pseudopotentials in the Theory of Metals* (Benjamin, New York 1966)

23.230 A.O.E. Animalu, F. Bonsignori, V. Bortolani: The phonon spectra of alkali metals and aluminium, Nuovo Cim. B **44**, 159 (1966)

23.231 E.G. Brovman, Y.M. Kagan: Dlinnovolnovye fonony v metallakh, Zh. Eksp. Teor. Fiz. **57**, 1329 (1970), Engl. Transl.: Long-wave phonons in metals, Sov. Phys. JETP 30:721 (1970)

23.232 E.G. Brovman, Y.M. Kagan: Phonons in nontransition metals, Soviet Physics Uspekhi **17**, 125–152 (1974), Translated from Usp. Fiz. Nauk 112, 369–426 (1974)

23.233 C. Beatrice, C. Calandra: Surface screening effects in the vibrational spectra of simple metal surfaces, Phys. Rev. B **10**, 6130 (1983)

23.234 C. Calandra, A. Catellani, C. Beatrice: Surface vibrations of Na(001) and K(001) surfaces, Surf. Sci. **148**, 90 (1984)

23.235 C. Calandra, A. Catellani, C. Beatrice: Pseudopotential theory of the vibrational properties of simple metal surfaces, Surf. Sci. **152/153**, 814 (1985)

23.236 A.G. Eguiluz: Dynamical density response function of a metal-film in the random-phase approximation, Phys. Rev. Lett. **51**, 1097 (1983)

23.237 A.G. Eguiluz: Self-consistent static-density-response function of a metal surface in density-functional theory, Phys. Rev. B **31**, 3303 (1985)

23.238 A.G. Eguiluz: Electronic screening at the surface of an sp-bonded metal, Phys. Scr. **36**, 651 (1987)

23.239 J.A. Gaspar, A.G. Eguiluz, M. Gester, A. Lock, J.P. Toennies: Resonances in the surface-phonon spectrum of an sp-bonded metal, Phys. Rev. Lett. **66**, 337 (1991)

23.240 W.A. Harrison: Transition-metal pseudopotentials, Phys. Rev. **181**, 1036 (1969)

23.241 J.A. Moriarty: Density-functional formulation of the generalized pseudopotential theory. II, Phys. Rev. B **26**, 1754 (1982)

23.242 W. Kohn, L.J. Sham: Self-consistent equations including exchange and correlation effect, Phys. Rev. A **140**, 1133 (1965)

23.243 Z.D. Popovic, M.J. Stott: Nonlinear, self-consistent theory of proton screening in metals applied to hydrogen in Al and Mg, Phys. Rev. Lett. **33**, 1164 (1974)

23.244 E. Zaremba, W. Kohn: Theory of helium adsorption on simple and noble-metal surfaces, Phys. Rev. B **15**, 12769 (1977)

23.245 E. Zaremba, L.M. Sander, H.B. Shore, J.H. Rose: Self-consistent screening of a proton in jellium, J. Phys. F **7**, 1763 (1977)

23.246 M.D. Whitmore: Helium heat of solution in Al and Mg using non-linear self-consistent screening of the nucleus, J. Phys. F **6**, 1259 (1976)

23.247 J.K. Nørskov: Electronic structure of H and He in metal vacancies, Solid State Commun. **24**, 691 (1977)

23.248 D.S. Larsen, J.K. Nørskov: Calculated energies and geometries for hydrogen impurities in Al and Mg, J. Phys. F **9**, 1975 (1980)

23.249 J.K. Nørskov, N.D. Lang: Effective-medium theory of chemical binding: application to chemisorption, Phys. Rev. B **21**, 2131 (1980)

23.250 M.J. Stott, E. Zaremba: A model for light impurities in metals, Solid State Commun. **32**, 1297 (1979)

23.251 M.J. Stott, E. Zaremba: Quasiatoms: an approach to atoms in nonuniform electronic system, Phys. Rev. B **22**, 1564 (1980)

23.252 A.E. Carlsson: Beyond pair potentials in elemental transition metals and semiconductors. In: *Solid State Physics*, Vol. 43, ed. by H. Ehrenreich, D. Turnbull (Academic Press, Boston 1990) pp. 1–91

23.253 W.K. Jacobsen, J.K. Nørskov, M.J. Puska: Interatomic interactions in the effective-medium theory, Phys. Rev. B **35**, 7423 (1987)

23.254 P.D. Ditlevsen, J.K. Nørskov: The surface phonons of Cu(111), J. Electron Spectrosc. Relat. Phenom. **54/55**, 237 (1990)

23.255 P.D. Ditlevsen, J.K. Nørskov: Vibrational properties of aluminum, nickel and copper surfaces, Surf. Sci. **254**, 261 (1991)

23.256 M.W. Finnis, J.E. Sinclair: A simple empirical N-body potential for transition metals, Philos. Mag. A **50**, 45 (1984)

23.257 V. Rosato, M. Guillope, B. Legrand: Thermodynamical and structural properties of f.c.c. transi-

tion metals using a simple tight-binding model, Philos. Mag. A **59**(2), 321 (1989)
23.258 J. Guevara, A.M. Llois, M. Weismann: Model potential based on tight-binding total-energy calculations for transition-metal systems, Phys. Rev. B **52**, 11509 (1995)
23.259 F. Raouafi, C. Barreteau, M.C. Desjonquères, D. Spanjaard: The phonon spectra of low and high index surfaces of copper, Surf. Sci. **507**, 748 (2002)
23.260 F. Ercolessi, E. Tosatti, M. Parrinello: Au(100) reconstruction in the glue model, Surf. Sci. **177**, 314 (1986)
23.261 F. Ercolessi, M. Parrinello, E. Tosatti: Simulation of gold in the glue model, Philos. Mag. A **58**, 513 (1988)
23.262 X.Q. Wang, G.L. Chiarotti, F. Ercolessi, E. Tosatti: Anomalous high-frequency modes of "missing-row" reconstructed (110) surfaces, Phys. Rev. B **38**, 8131 (1988)
23.263 J.R. Smith, A. Banerjea: New approach to calculation of total energies of solids with defects: surface-energy anisotropies, Phys. Rev. Lett. **59**, 2451 (1987)
23.264 I.Y. Sklyadneva, G.G. Rusina, E.V. Chulkov: Vibrational states on vicinal surfaces of Al, Ag, Cu and Pd, Surf. Sci. **416**, 17 (1998)
23.265 G. Witte, J. Braun, A. Lock, J.P. Toennies: Helium-atom-scattering study of the dispersion curves of step-localized phonons on Cu(211) and Cu(511), Phys. Rev. B **52**, 2165 (1995)
23.266 P. Hohenberg, W. Kohn: Inhomogeneous electron gas, Phys. Rev. **136**, 864 (1964)
23.267 E.K.U. Gross, R.M. Dreizler (Eds.): *Density Functional Theory* (Plenum, New York 1994)
23.268 R.M. Martin: *Electronic Structure: Basic Theory and Pratical Methods* (Cambridge Univ. Press, Cambridge 2004)
23.269 J.P. Perdew, A. Zunger: Self-interaction correction to density-functional approximations for many-electron systems, Phys. Rev. B **23**, 5048 (1981)
23.270 A.D. Becke: Density-functional exchange-energy approximation with correct asymptotic behavior, Phys. Rev. A **38**, 3098 (1988)
23.271 J.P. Perdew: Unified theory of exchange and correlation beyond the local density approximation. In: *Electronic Structure of Solids*, ed. by P. Ziesche, H. Eschrig (Akademie, Berlin 1991) pp. 11–20
23.272 J.P. Perdew, K. Burke, M. Ernzerhof: Generalized gradient approximation made simple, Phys. Rev. Lett. **77**, 3865 (1996)
23.273 R. Car, M. Parrinello: Unified approach for molecular dynamics and density-functional theory, Phys. Rev. Lett. **55**, 2471 (1985)
23.274 A. Ancilotto, W. Andreoni, A. Selloni, R. Car, M. Parinello: Surface phonons from ab-initio molecular dynamics: Si(111) 2×1. In: *Phonons 89*, ed. by S. Hunklinger, W. Ludwig, G. Weiss (World Scientific, Singapore 1990) p. 931
23.275 F. Ancillotto, W. Andreoni, A. Selloni, R. Car, M. Parrinello: Structural, electronic, and vibrational properties of Si(111)-2×1 from ab initio molecular dynamics, Phys. Rev. Lett. **65**, 3148 (1990)
23.276 R. di Felice, A.I. Shkrebtii, F. Finocchi, C.M. Bertoni, G. Onida: Surface vibrations at clean and hydrogenated GaAs(110) from ab-initio molecular dynamics, J. Electron Spectrosc. Relat. Phenom. **64/65**, 697 (1993)
23.277 O.F. Sankey, D.J. Niklewski: Ab initio multicenter tight-binding model for molecular-dynamics simulations and other applications in covalent systems, Phys. Rev. B **40**, 3979 (1989)
23.278 J. Harris: Simplified method for calculating the energy of weakly interacting fragments, Phys. Rev. B **31**, 1770 (1985)
23.279 D.R. Alfonso, D.A. Drabold, S.E. Ulloa: Phonon modes of diamond (100) surfaces from ab initio calculations, Phys. Rev. B **51**, 1989 (1995)
23.280 D.R. Alfonso, D.A. Drabold, S.E. Ulloa: Structural, electronic, and vibrational properties of diamond (100), (111), and (110) surfaces from ab initio calculation, Phys. Rev. B **51**, 14669 (1995)
23.281 V. Heine, D. Weaire: Pseudopotential theory of cohesion and structure. In: *Solid State Physics*, Vol. 24, ed. by H. Ehrenreich, F. Seitz, T. Turnbull (Academic Press, New York 1970) pp. 249–463
23.282 H. Wendel, R.M. Martin: Theory of structural properties of covalent semiconductors, Phys. Rev. B **19**, 5251 (1979)
23.283 K. Kunc, R.M. Martin: Density-functional calculation of static and dynamic properties of GaAs, Phys. Rev. B **24**, 2311 (1981)
23.284 M.T. Yin, M.L. Cohen: Theory of lattice-dynamical properties of solids: application to Si and Ge, Phys. Rev. B **26**, 3259 (1982)
23.285 K.M. Ho, C.L. Fu, B.N. Harmon, W. Weber, D.R. Hamann: Vibrational frequencies and structural properties of transition metals via total-energy calculations, Phys. Rev. Lett. **49**, 673 (1982)
23.286 K.-P. Bohnen, A. Eichler, J. Hafner: First principles calculations of surface phonons on Rh(111), Surf. Sci. **368**, 222 (1996)
23.287 G. Witte, J.P. Toennies, C. Woll: Comparison of surface phonon dispersion curves for clean and hydrogen covered Rh(111) surfaces, Surf. Sci. **323**, 228 (1995)
23.288 J. Friedel: Metallic alloys, Nuovo Cim. **7**, 287 (1958)
23.289 W.A. Harrison: *Solid State Theory* (Dover, New York 1979), Chap. II
23.290 W. Li, J. Carete, N.A. Katcho, N. Mingo: ShengBTE: a solver of the Boltzmann transport equation for phonons, Comput. Phys. Commun. **185**, 1747 (2014)
23.291 A. Togo, I. Tanaka: First principles phonon calculations in materials science, Scr. Mater. **108**, 1 (2015)
23.292 P. Souvatzis, D. Legut, O. Eriksson, K.I. Katsnelson: Ab initio study of interacting lattice vibrations and stabilization of the β-phase in Ni-Ti shape-memory alloy, Phys. Rev. B **81**, 092201 (2010)
23.293 O. Hellman, I.A. Abrikosov, S.I. Simak: Lattice dynamics of anharmonic solids from first principles, Phys. Rev. B **84**, 180301(R) (2011)
23.294 I. Errea, M. Calandra, F. Mauri: First-principles theory of anharmonicity and the inverse isotope effect in superconducting palladium-hy-

dride compounds, Phys. Rev. Lett. **111**, 177002 (2013)
23.295 K.M. Ho, K.P. Bohnen: First-principles calculation of surface phonons on the Al(110) surface, Phys. Rev. Lett. **56**, 934 (1986)
23.296 K.M. Ho, K.P. Bohnen: Surface-phonon calculations for the Al(110) surface, Phys. Rev. B **38**, 12897 (1988)
23.297 K.P. Bohnen, K.M. Ho: First principles calculation of lattice relaxation and surface phonons on Al(100), Surf. Sci. **207**, 105 (1988)
23.298 K.P. Bohnen, K.M. Ho: Structure and dynamics at metal surfaces, Surf. Sci. Rep. **19**, 99 (1993)
23.299 R. Heid, K.-P. Bohnen: Ab initio lattice dynamics of metal surfaces, Phys. Rep. **387**, 151 (2003)
23.300 T. Rodach, K.P. Bohnen, K.M. Ho: First-principles study of the Na(110) surface, Surf. Sci. **209**, 481 (1989)
23.301 A.M. Lahee, J.P. Toennies, C. Wöll, K.P. Bohnen, K.M. Ho: Comparison of helium atom scattering surface phonon dispersion curves of the (1×2) reconstructed Au(110) surface with first-principle calculations, Europhys. Lett. **10**, 261 (1989)
23.302 T. Rodach, K.P. Bohnen, K.M. Ho: First principles calculations of lattice relaxation at low index surfaces of Cu, Surf. Sci. **286**, 66 (1993)
23.303 T. Rodach, K.P. Bohnen, K.M. Ho: First principles calculations of surface phonons for Cu(110), Surf. Sci. **296**, 123 (1993)
23.304 A.E. Eguiluz, A.A. Quong: Electronic screening in metals: from phonons to plasmons. In: *Dynamical Properties of Solids*, Vol. 7, ed. by G.K. Horton, A.A. Maradudin (North-Holland, Amsterdam 1995) pp. 425–507, Chap. 6
23.305 A.A. Quong, B.M. Klein: Self-consistent-screening calculation of interatomic force constants and phonon dispersion curves from first principles, Phys. Rev. B **46**, 10734 (1992)
23.306 A.A. Quong, A.G. Eguiluz: First-principles evaluation of dynamical response and plasmon dispersion in metals, Phys. Rev. Lett. **70**, 3955 (1993)
23.307 R.F. Wallis, A.A. Maradudin, V. Bortolani, A.G. Eguiluz, A.A. Quong, A. Franchini, G. Santoro: Comparison between phenomenological and pseudopotential force constants for the lattice dynamics of Al, Phys. Rev. B **48**, 6043 (1993)
23.308 A.A. Quong: First-principles determination of the interatomic-force-constant tensor of Au, Phys. Rev. B **49**, 3226 (1994)
23.309 M. Buongiorno Nardelli, S. Baroni, P. Giannozzi: Phonon softening and high-pressure low-symmetry phases of cesium iodide, Phys. Rev. Lett. **69**, 1069 (1992)
23.310 P. Giannozzi, S. de Gironcoli, P. Pavone, S. Baroni: Ab initio calculation of phonon dispersions in semiconductors, Phys. Rev. B **43**, 7231 (1993)
23.311 J. Xie, S. de Gironcoli, S. Baroni, M. Scheffler: Temperature-dependent surface relaxations of Ag(111), Phys. Rev. B **59**, 970 (1999)
23.312 A. dal Corso, A. Pasquarello, A. Baldereschi: Density-functional perturbation theory for lattice dynamics with ultrasoft pseudopotentials, Phys. Rev. B **56**, R11369 (1997)
23.313 A. dal Corso: Density-functional perturbation theory with ultrasoft pseudopotentials, Phys. Rev. B **64**, 235118 (2001)
23.314 S. Baroni, P. Giannozzi, A. Testa: Green's-function approach to linear response in solids, Phys. Rev. Lett. **58**, 1861 (1987)
23.315 X. Gonze: Perturbation expansion of variational principles at arbitrary order, Phys. Rev. A **52**, 1086 (1995)
23.316 X. Gonze: Adiabatic density-functional perturbation theory, Phys. Rev. A **52**, 1096 (1995)
23.317 S. de Gironcoli: Lattice dynamics of metals from density-functional perturbation theory, Phys. Rev. B **51**, 6773 (1995)
23.318 W.E. Pickett: Pseudopotential methods in condensed matter applications, Comput. Phys. Rep. **9**, 115 (1989)
23.319 M.C. Payne, M.P. Teter, D.C. Allen, T.A. Arias, J.D. Joannopoulos: Iterative minimization techniques for ab initio total-energy calculations: molecular dynamics and conjugate gradients, Rev. Mod. Phys. **64**, 1045 (1992)
23.320 D.R. Hamann, M. Schluter, C. Chiang: Norm-conserving pseudopotentials, Phys. Rev. Lett. **43**, 1494 (1979)
23.321 L. Kleinman, D.M. Bylander: Efficacious form for model pseudopotentials, Phys. Rev. Lett. **48**, 1425 (1982)
23.322 D. Vanderbilt: Soft self-consistent pseudopotentials in a generalized eigenvalue formalism, Phys. Rev. B **41**, 7892 (1990)
23.323 X. Gonze, J.-M. Beuken, R. Caracas, F. Detraux, M. Fuchs, G.-M. Rignanese, L. Sindic, M. Verstraete, G. Zerah, F. Jollet, M. Torrent, A. Roy, M. Mikami, P. Ghosez, J.-Y. Raty, D.C. Allan: First-principles computation of material properties: the ABINIT software project, Comput. Mater. Sci. **25**, 478 (2002)
23.324 X. Gonze, G.-M. Rignanese, M. Verstraete, J.-M. Beuken, Y. Pouillon, R. Caracas, F. Jollet, M. Torrent, G. Zerah, M. Mikami, P. Ghosez, M. Veithen, J.-Y. Raty, V. Olevano, F. Bruneval, L. Reining, R.W. Godby, G. Onida, D.R. Hamann, D.C. Allan: A brief introduction to the ABINIT software package, Z. Kristallogr. **220**, 558 (2005)
23.325 A. Dal Corso, A. Mosca Conte: Spin-orbit coupling with ultrasoft pseudopotentials: application to Au and Pt, Phys. Rev. B **71**, 115106 (2005)
23.326 A. Dal Corso: Density functional perturbation theory for lattice dynamics with fully relativistic ultrasoft pseudopotentials: application to fcc-Pt and fcc-Au, Phys. Rev. B **76**, 054308 (2007)
23.327 M.J. Verstraete, M. Torrent, F. Jollet, G. Zérah, X. Gonze: Density functional perturbation theory with spin-orbit coupling: phonon band structure of lead, Phys. Rev. B **78**, 045119 (2008)
23.328 A. Dal Corso: Ab initio phonon dispersions of face centered cubic Pb: effects of spin–orbit coupling, J. Phys. Condens. Matter **20**, 445202 (2008)

23.329 S.Y. Savrasov, O.K. Andersen: Linear-response calculation of the electron–phonon coupling in doped $CaCuO_2$, Phys. Rev. Lett. **77**, 4430 (1996)

23.330 R. Yu, H. Krakauer: Linear-response calculations within the linearized augmented plane-wave method, Phys. Rev. B **49**, 4467 (1994)

23.331 R. Kouba, A. Taga, C. Ambrosch-Draxl, L. Nordström, B. Johansson: Phonons and electron–phonon interaction by linear-response theory within the LAPW method, Phys. Rev. B **64**, 184306 (2001)

23.332 J. K. Dewhurst, S. Sharma, L. Nordström, F. Cricchio, O. Grånäs, E. K. U. Gross: The Elk Code Manual. Version 5.3.25, http://elk.sourceforge.net

23.333 M. Dion, H. Rydberg, E. Schroeder, D.C. Langreth, B.I. Lundquist: Van der Waals density functional for general geometries, Phys. Rev. Lett. **92**, 246401 (2004)

23.334 K. Lee, E.D. Murray, L. Kong, B.I. Lundquist, D.C. Langreth: Higher-accuracy van der Waals density functional, Phys. Rev. B **82**, 081101 (2010)

23.335 V. Cooper: Van der Waals density functional: an appropriate exchange functional, Phys. Rev. B **81**, 161104 (2010)

23.336 S. Grimme, J. Antony, S. Ehrlich, S. Krieg: A consistent and accurate ab initio parametrization of density functional dispersion correction (DFT-D) for the 94 elements H-Pu, J. Chem. Phys. **132**, 154104 (2010)

23.337 T. Thonhauser, S. Zuluaga, C.A. Arter, K. Berland, E. Schröder, P. Hyldgaard: Spin signature of nonlocal correlation binding in metal–organic frameworks, Phys. Rev. Lett. **115**, 136402 (2015)

23.338 S. Azadi, R.E. Cohen: Low-pressure phase diagram of crystalline benzene from quantum Monte Carlo, J. Chem. Phys. **145**, 064501 (2016)

23.339 P. Giannozzi, S. Baroni, N. Bonini, M. Calandra, R. Car, C. Cavazzoni, D. Ceresoli, G.L. Chiarotti, M. Cococcioni, I. Dabo, A. Dal Corso, S. de Gironcoli, S. Fabris, G. Fratesi, R. Gebauer, U. Gerstmann, C. Gougoussis, A. Kokalj, M. Lazzeri, L. Martin-Samos, N. Marzari, F. Mauri, R. Mazzarello, S. Paolini, A. Pasquarello, L. Paulatto, C. Sbraccia, S. Scandolo, G. Sclauzero, A.P. Seitsonen, A. Smogunov, P. Umari, R.M. Wentzcovitch: QUANTUM ESPRESSO: a modular and open-source software project for quantum simulations of materials, J. Phys. Condens. Matter **21**, 395502 (2009)

23.340 X. Gonze, B. Amadon, P.-M. Anglade, J.-M. Beuken, F. Bottin, P. Boulanger, F. Bruneval, D. Caliste, R. Caracas, M. Côté, T. Deutsch, L. Genovese, P. Ghosez, M. Giantomassi, S. Goedecker, D.R. Hamann, P. Hermet, F. Jollet, G. Jomard, S. Leroux, M. Mancini, S. Mazevet, M.J.T. Oliveira, G. Onida, Y. Pouillon, T. Rangel, G.-M. Rignanese, D. Sangalli, R. Shaltaf, M. Torrent, M.J. Verstraete, G. Zerah, J.W. Zwanziger: ABINIT: first-principles approach to material and nanosystem properties, Comput. Phys. Commun. **180**, 2852 (2009)

23.341 G. Kresse, J. Furtmüller: Efficient iterative schemes for ab initio total-energy calculations using a plane-wave basis set, Phys. Rev. B **54**, 11169 (1996)

23.342 S.J. Clark, M.D. Segall, C.J. Pickard, P.J. Probert, K. Refson, M.C. Payne: First principles methods using CASTEP, Z. Kristallogr. **220**(5/6), 567 (2005)

23.343 D. Campi, M. Bernasconi, G. Benedek, A.P. Graham, J.P. Toennies: Surface lattice dynamics and electron–phonon interaction in cesium ultrathin films, Phys. Chem. Chem. Phys. **19**, 16358 (2017)

23.344 E. Hulpke, J. Lower, A. Reichmuth: Strain and confined resonances in ultrathin alkali-metal films, Phys. Rev. B **53**, 13901 (1996)

23.345 A. Politano, G. Chiarello, G. Benedek, E.V. Chulkov, P.M. Echenique: Vibrational spectroscopy and theory of alkali metal adsorption and co-adsorption on single-crystal surfaces, Surf. Sci. Rep. **68**, 305–389 (2013)

23.346 S. Andersson, J.P. Pendry, P.M. Echenique: Low energy electron diffraction from Na(110) and Na_2O(111) surface, Surf. Sci. **65**, 539 (1977)

23.347 G. Benedek, J.P. Toennies: Systematic trends in the normal enhancement of the phonon anharmonicity at the surface of metals, Phys. Rev. B **46**, 13643 (1992)

23.348 P.B. Allen: Empirical electron-phonon λ values from resistivity of cubic metallic elements, Phys. Rev. B **36**, 2920 (1987)

23.349 A. Bartholmei, P. Fouquet, G. Witte: Growth and dynamics of ultrathin barium films on Cu(100), Surf. Sci. **473**, 227 (2001)

23.350 G. Benedek, J.R. Manson, S. Miret-Artès: The electron–phonon interaction of low-dimensional and multi-dimensional materials from he atom scattering, Advanced Materials **32**, 2002072 (2020)

23.351 I.Y. Sklyadneva, R. Heid, K.-P. Bohnen, P.M. Echenique, G. Benedek, E.V. Chulkov: The effect of spin–orbit coupling on the surface dynamical properties and electron–phonon interaction of Tl(0001), J. Phys. Chem. A **115**, 7352 (2011)

23.352 I.Y. Sklyadneva, R. Heid, K.-P. Bohnen, P.M. Echenique, E.V. Chulkov: Surface phonons on Pb(111), J. Phys. Condens. Matter **24**, 104004 (2012)

23.353 J. Braun, P. Ruggerone, G. Zhang, J.P. Toennies, G. Benedek: Surface phonon dispersion curves of thin Pb films on Cu(111), Phys. Rev. B **79**, 205423 (2009)

23.354 G.G. Rusina, S.D. Borisova, S.V. Eremeev, I.Y. Sklyadneva, E.V. Chulkov, G. Benedek, J.P. Toennies: Surface dynamics of the wetting layers and ultrathin films on a dynamic substrate: (0.5–4) ML Pb/Cu(111), J. Phys. Chem. C **120**, 22304 (2016)

23.355 F. Calleja, A.L. Vázquez de Parga, E. Anglada, J.J. Hinarejos, R. Miranda, F. Yndurain: Crystallographic and electronic contribution to the apparent step height in nanometer-thin Pb(111) films grown on Cu(111), New J. Phys. **11**, 123003 (2009)

23.356 A. Tamtögl, P. Kraus, M. Mayrhofer-Reinhartshuber, W.E. Ernst, D. Campi, M. Bernasconi,

G. Benedek: Surface and subsurface phonons of Bi(111) measured with helium atom scattering, Phys. Rev. B **87**, 035410 (2013)

23.357 V. Chis, G. Benedek, P.M. Echenique, E.V. Chulkov: Phonons in ultrathin Bi(111) films: role of spin-orbit coupling in electron–phonon interaction, Phys. Rev. **87**, 075412 (2013)

23.358 P. Kraus, A. Tamtögl, M. Mayrhofer-Reinhartshuber, G. Benedek, W.E. Ernst: Resonance-enhanced inelastic He-atom scattering from subsurface optical phonons of Bi(111), Phys. Rev. B **87**, 245433 (2013)

23.359 P. Hofmann: The surfaces of bismuth: Structural and electronic properties, Prog. Surf. Sci. **81**, 191 (2006)

23.360 G.Q. Huang, J. Yang: Surface lattice dynamics and electron–phonon interaction in ultrathin Bi(111) film, J. Phys. Condens. Matter **25**, 175004 (2013)

23.361 M. Alcántara Ortigoza, I.Y. Sklyadneva, R. Heid, E.V. Chulkov, T.S. Rahman, K.-P. Bohnen, P.M. Echenique: Ab initio lattice dynamics and electron–phonon coupling of Bi(111), Phys. Rev. B **90**, 195438 (2014)

23.362 M. Verstraete, G. Benedek: Lattice dynamics of polonium: symmetry breaking phase transitions and surface phonons. In: *Mater. Res. Soc. Symp. Proc. Ser*, Vol. 1404E (2011), Paper W1.11

23.363 A. Khater, R. Tigrine, B. Bourahla: Polonium bulk and surface vibrational dynamics, Phys. Status Solidi (b) **246**, 1614 (2009)

23.364 M.J. Verstraete: Phases of polonium via density functional theory, Phys. Rev. Lett. **104**, 035501 (2010)

23.365 D.A. Papaconstantopoulos: *Handbook of the Band Structure of Elemental Solids: From Z = 1 to Z = 112*, 2nd edn. (Springer, Berlin, Heidelberg 2015) pp. 400–427

23.366 A. Hermann, R. Hofmann, N. Ashcroft: Condensed astatine: monatomic and metallic, Phys. Rev. Lett. **111**, 116404 (2013)

23.367 R. Eichler, M. Schädel: Adsorption of radon on metal surfaces: a model study for chemical investigations of elements 112 and 114, J. Phys. Chem. B **106**, 5413 (2002)

23.368 M. Magomedov: The calculation of the parameters of the Mie–Lennard-Jones potential, High Temp. **44**, 513 (2006)

23.369 K.T. Tang, J.P. Toennies: The van der Waals potentials between all the rare gas atoms from He to Rn, J. Chem. Phys. **118**, 4976 (2003)

23.370 D. Campi: *Atomistic simulation of thermal transport and vibrational properties in phase change materials*, Dissertation (University Milano-Bicocca, Milan 2015)

23.371 A. Ruckhofer, D. Campi, M. Bremholm, Ph Hofmann, G. Benedek, M. Bernasconi, W.E. Ernst, A. Tamtögl: THz surface excitations and electron-phonon coupling in Bi_2Se_3(111) from helium atom scattering, Phys. Rev. Res. **2**, 023186 (2020)

23.372 D. Campi, M. Bernasconi, G. Benedek: Ab-initio calculation of surface phonons at the Sb_2Te_3(111) surface, Surf. Sci. **678**, 46–51 (2018)

23.373 K.M.F. Shahil, M.Z. Hossain, V. Goyal, A.A. Balandin: Micro-Raman spectroscopy of mechanically exfoliated few-quintuple layers of Bi_2Te_3, Bi_2Se_3, and Sb_2Te_3 materials, J. Appl. Phys. **111**, 054305 (2012)

23.374 A. Tamtögl, D. Campi, M. Bremholm, E.M.J. Hedegaard, B.B. Iversen, M. Bianchi, P. Hofmann, N. Marzari, G. Benedek, J. Ellis, W. Allison: Surface phonon dispersion of Bi_2Te_3(111): evidence for a prominent surface acoustic wave and the role of van der Waals Interactions, arXiv:1803.11184v1 [cond-mat.mtrl-sci] (2018)

23.375 A. Tamtögl, D. Campi, M. Bremholm, E.M.J. Hedegaard, B.B. Iversen, M. Bianchi, P. Hofmann, N. Marzari, G. Benedek, J. Ellis, W. Allison: Nanoscale surface dynamics of Bi_2Te_3(111): observation of a prominent surface acoustic wave and the role of van der Waals interactions, Nanoscale **10**(30), 14627–14636 (2018)

23.376 C. Howard, M. El-Batanouny: Connecting electron and phonon spectroscopy data to consistently determine quasiparticle-phonon coupling on the surface of topological insulators, Phys. Rev. B **89**, 075425 (2014)

23.377 C. Howard, M. El-Batanouny, R. Sankar, F.C. Chou: Anomalous behavior in the phonon dispersion of the (001) surface of Bi_2Te_3 determined from helium atom-surface scattering measurements, Phys. Rev. B **88**, 035402 (2013)

23.378 S.V. Eremeev, M.G. Vergniory, T.V. Menshchikova, A.A. Shaposhnikov, E.V. Chulkov: The effect of van der Waal's gap expansions on the surface electronic structure of layered topological insulators, New J. Phys. **14**, 113030 (2012)

23.379 M. Wiesner, A. Trzaskowska, B. Mroz, S. Charpentier, S. Wang, Y. Song, F. Lombardi, P. Lucignano, D. Campi, M. Bernasconi, G. Benedek, F. Guinea, A. Tagliacozzo: The electron–phonon interaction at deep Bi_2Te_3-semiconductor interfaces from Brillouin light scattering, Sci. Rep. **7**, 16449 (2017)

23.380 R. Heid, I.Y. Sklyadneva, E.V. Chulkov: Electron-phonon coupling in topological surface states: The role of polar optical modes, Sci. Rep. **7**, 1095 (2017)

23.381 C. Bungaro, S. de Gironcoli, S. Baroni: Theory of the anomalous Rayleigh dispersion at H/W(110) surfaces, Phys. Rev. Lett. **77**, 2491 (1996)

23.382 J. Lüdecke: *Vergleichende Untersuchung der sauberen und adsorbatbedeckten W(110) und Mo(110)-Oberfläche mit hoch auflösender Helium-Atomstrahlstreuung*, Bericht 15 (Max-Planck-Institut für Strömungsforschung, Göttingen 1984)

23.383 E. Hulpke, J. Lüdecke: Vibrational properties of the clean W(110) surface and of different hydrogen adsorbate phases studied by helium atom scattering, Surf. Sci. **272**, 289 (1992)

23.384 E. Hulpke, J. Lüdecke: The giant surface phonon anomaly on hydrogen saturated W(110) and Mo(110), Surf. Sci. **287/288**, 837 (1993)

23.385 E. Hulpke, J. Lüdecke: Surface phonon anomaly induced by adsorption, J. Electron Spectrosc. Relat. Phenom. **64/65**, 641 (1993)

23.386 M. Balden, S. Lehwald, E. Preuss, H. Ibach: Surface phonons of the clean and H-covered W(110) surface measured with EELS, Surf. Sci. **309**, 1141 (1994)

23.387 M. Balden, S. Lehwald, H. Ibach, D.L. Mills: Hydrogen covered W(110) surface: a hydrogen liquid with a propensity for one-dimensional order, Phys. Rev. Lett. **73**, 854 (1994)

23.388 G. Benedek, M. Pardo, J.P. Toennies: Theory of inelastic atom scattering from surface electron–hole and plasmon excitations. In: *Highlights on Spectroscopies of Semiconductors and Nanostructures*, Conf. Proc., Vol. 94, ed. by G. Guizzetti, A.C. Andreani, F. Marabelli, M. Patrini (SIF, Bologna 2007) pp. 151–167

23.389 B. Kohler, P. Ruggerone, M. Scheffler, E. Tosatti: Enhanced electron–phonon coupling at the Mo and W(110) surfaces induced by adsorbed hydrogen, Z. Phys. Chem. **197**, 193 (1996)

23.390 B. Kohler, P. Ruggerone, M. Scheffler: Anomalies in He atom scattering spectra of the H-covered Mo(110) and W(110) surfaces, Surf. Sci. **368**, 213 (1996)

Giorgio Benedek

Department of Materials Science – U5
University of Milano-Bicocca
Milano, Italy

Donostia International Physics Center (DIPC)
Donostia/San Sebastián, Spain
giorgio.benedek@unimib.it

Giorgio Benedek is Emeritus Professor of Structure of Matter in the Department of Materials Science of the University of Milano-Bicocca, Milan, Italy and Visiting Professor at the Donostia International Physics Center (DIPC) in Donostia/San Sebastian, Basque Country, Spain. His main interests lie in the theory of surface dynamics, inelastic helium atom scattering from crystal surfaces, and surface electron–phonon interaction.

Marco Bernasconi

Department of Materials Science
University of Milano-Bicocca
Milano, Italy
marco.bernasconi@unimib.it

Marco Bernasconi received his PhD from SISSA-Trieste. He is Full Professor of Theoretical Condensed Matter Physics and Dean of the PhD School in Materials Science and Nanotechnology at the University of Milano-Bicocca, Italy. His main interests are in electronic structure calculations and molecular dynamics simulations of materials for applications in microelectronics, photonics, and energy.

Davide Campi

Theory and Simulation of Materials and National Centre for Computational Design and Discovery of Novel Materials
Ecole Polytechnique Fédérale de Lausanne
Lausanne, Switzerland
davide.campi@epfl.ch

Davide Campi is currently EPFL/Marie-Curie Postdoctoral Fellow at the École Polytechnique Fédérale de Lausanne (Switzerland). He received his PhD in Nanostructures and Nanotechonology from the University of Milano-Bicocca (Italy) in 2016. His research mainly focuses on the theory of phonons and electron–phonon interaction in low-dimensional materials. He has several collaborations with experimental groups in helium-atom scattering spectroscopy.

J. Peter Toennies

Max-Planck-Institut fuer Dynamik und Selbstorganisation
Goettingen, Germany

Jan Peter Toennies is Emeritus Scientific Member and former Director of the Department of Molecular Interactions of the Max Planck Institute for Dynamics and Self-Organization (MPI-DS) in Göttingen, Germany. Professor Toennies continues his research at MPI-SD, presently focused on intermolecular potentials, quantum fluid helium and hydrogen clusters, helium atom scattering from crystal surfaces, and quantum flow dynamics of solid helium.

Matthieu J. Verstraete

Nanomat/Q-Mat/CESAM, ETSF – Institut de Physique, Bat. B5a 3/7
Université de Liège
Liège, Belgium
matthieu.verstraete@uliege.be

Matthieu J. Verstraete is Professor of Physics at the University of Liège, Belgium, and chairs the ETSF Steering Committee. He specializes in first-principles theory of electrons, phonons, their ultrafast dynamics and coupling, with implementation in open-source codes and spearheading community-wide efforts for integration and interoperability. Applications include thermoelectric and spin-caloritronic devices, 2-D materials and their heterostructures, and metallic alloys.

24. Electron–Phonon Interaction on Metallic Surfaces, Overlayers and Thin Films

Rolf Heid, Irina Y. Sklyadneva, Evgueni V. Chulkov

The electron–phonon interaction (EPI) lies at the heart of many physical phenomena like electrical and heat conductivity, phonon-mediated superconductivity, dynamics of excited electrons and holes, and various temperature-dependent phenomena. Knowledge of EPI is therefore of profound interest in condensed matter physics.

This chapter provides an introduction to the EPI on metallic surfaces, overlayers, and thin films. Section 24.1 describes the basic concepts of the renormalization of electronic quasiparticles, which manifests itself in finite lifetimes of excited electrons or holes and kinks in electronic band dispersions. A central quantity is the electron self-energy, which incorporates dissipative processes induced by scattering of virtual phonons. Sections 24.2 and 24.3 present current computational and experimental techniques, respectively, which allow the energy- and momentum-dependence of these phenomena to be analyzed in great detail. A compilation of results for elemental and adsorbate-covered metal surfaces, thin films, and metallic states on the surface of topological insulators is given in Sect. 24.4. Finally, EPI-related phenomena are discussed from the perspective of the surface phonons in Sect. 24.5.

Electron–phonon interaction (EPI) is one of the fundamental many-body interactions always present in a solid material. In the last two decades this research field has gained new impetus in the context of surface science, because surfaces provide a unique platform for these studies as they allow a more direct and controlled access to the relevant electronic and phononic quasiparticles than the bulk counterpart. In addition, EPI is important for a detailed understanding of a variety of surface-related phenomena, like surface relaxation or surface phase transitions. As it changes the properties of both electronic and vibrational quasiparticles, it also has an impact on various dynamical processes at surfaces.

Fundamental aspects of EPI in crystalline solids have been reviewed in the classic book of *Grimvall* [24.1]. The steady improvement of experimental and theoretical techniques led to a rise in studies of EPI properties on surfaces. This research field is characterized by a fruitful interrelation of theory and experiment. On the one hand, theoretical models provide microscopic interpretations of experimental data, while on the other hand high-precision experiments serve as tests for the accu-

M. Rocca, T.S. Rahman, L. Vattuone (Eds.), *Springer Handbook of Surface Science*, Springer Handbooks,
https://doi.org/10.1007/978-3-030-46906-1_24

racy of theoretical approaches. For further reading, we refer the reader to several review articles that deal with EPI on surfaces from different perspectives [24.2–10].

In this chapter, we will address studies of EPI for metallic surfaces, overlayers, and thin films. Not discussed are layered materials, like cuprate or iron-pnictide/chalcogenide superconductors, or charge-density wave compounds, like transition-metal dichalcogenides, where EPI has been studied with similar techniques, but where the emphasis was placed on bulk properties. We also do not include EPI studies of 2-D materials like graphene, which are topics of separate chapters in this handbook. While we briefly introduce several spectroscopic and theoretical techniques, this is done only in the context of their applications to gain information about the EPI. The reader is referred to other chapters of this handbook for more detailed presentations of these techniques.

24.1 Basic Concepts

In this section, an introduction to the fundamental aspects of electron–phonon interaction, its influence on electronic quasiparticles, and its quantification is presented. In the following, we adopt atomic units with $\hbar = 1$, where $\hbar$ is Planck's constant.

24.1.1 Renormalization of Electronic Quasiparticles

The central quantity describing the renormalization of electronic quasiparticles is the electron self-energy Σ. It is a momentum- and energy-dependent quantity that describes the effect of interactions of a quasiparticle with its environment. The relationship between the self-energy and the renormalized Green's function G is given by the Dyson equation

$$G(\boldsymbol{k}\nu,\epsilon) = [\epsilon - \epsilon_{\boldsymbol{k}\nu} - \Sigma(\boldsymbol{k}\nu,\epsilon)]^{-1} \,. \tag{24.1}$$

Here the electronic state is denoted by a momentum $\boldsymbol{k}$ and band index ν. The unrenormalized or bare energy is $\epsilon_{\boldsymbol{k}\nu}$, which is taken relative to the Fermi level ϵ_F. For not too large self-energies, the spectral function of the quasiparticle,

$$A(\boldsymbol{k}\nu,\epsilon) = -2\mathrm{Im}\{G(\boldsymbol{k}\nu,\epsilon+\mathrm{i}\delta)\} \,, \tag{24.2}$$

possesses a well-defined peak which is shifted from the original quasiparticle energy and acquires a finite linewidth. Here, δ denotes a positive infinitesimal number. The shifted energy is connected to the real part of Σ by

$$\overline{\epsilon}_{\boldsymbol{k}\nu} = \epsilon_{\boldsymbol{k}\nu} - \mathrm{Re}\{\Sigma(\boldsymbol{k}\nu,\overline{\epsilon}_{\boldsymbol{k}\nu})\} \,, \tag{24.3}$$

while the imaginary part determines the linewidth (full-width-at-half-maximum)

$$\Gamma_{\boldsymbol{k}\nu} = -2\mathrm{Im}\{\Sigma(\boldsymbol{k}\nu,\overline{\epsilon}_{\boldsymbol{k}\nu})\} \,. \tag{24.4}$$

The inverse linewidth gives the lifetime of the quasiparticle,

$$\tau_{\boldsymbol{k}\nu} = \frac{1}{\Gamma_{\boldsymbol{k}\nu}} \,. \tag{24.5}$$

The self-energy can be represented by an infinite series of Feynman diagrams. In the case of the electron–phonon interaction, the dominant contribution comes from the lowest-order diagram schematically shown in Fig. 24.1, which describes a virtual exchange of a phonon mode, and leads to [24.1]

$$\begin{aligned}\Sigma(\boldsymbol{k}\nu,\epsilon) = \frac{1}{N_q}\sum_{\boldsymbol{q}j}\sum_{\nu'} |g^{\boldsymbol{q}j}_{\boldsymbol{k}+\boldsymbol{q}\nu',\boldsymbol{k}\nu}|^2 \\ \times\left[\frac{b(\omega_{\boldsymbol{q}j})+f(\epsilon_{\boldsymbol{k}+\boldsymbol{q}\nu'})}{\epsilon+\omega_{\boldsymbol{q}j}-\epsilon_{\boldsymbol{k}+\boldsymbol{q}\nu'}+\mathrm{i}\delta}\right. \\ \left.+\frac{b(\omega_{\boldsymbol{q}j})+1-f(\epsilon_{\boldsymbol{k}+\boldsymbol{q}\nu'})}{\epsilon-\omega_{\boldsymbol{q}j}-\epsilon_{\boldsymbol{k}+\boldsymbol{q}\nu'}+\mathrm{i}\delta}\right] .\end{aligned} \tag{24.6}$$

The q-summation runs over N_q points in the first Brillouin zone. Temperature dependence enters via the Fermi and Bose distribution functions $f(\epsilon) = 1/(\mathrm{e}^{\epsilon/(k_\mathrm{B}T)}+1)$ and $b(\epsilon) = 1/(\mathrm{e}^{\epsilon/(k_\mathrm{B}T)}-1)$, respectively, where k_B is Boltzmann's constant; $\omega_{\boldsymbol{q}j}$ denotes the energy of the phonon mode with momentum $\boldsymbol{q}$, while j

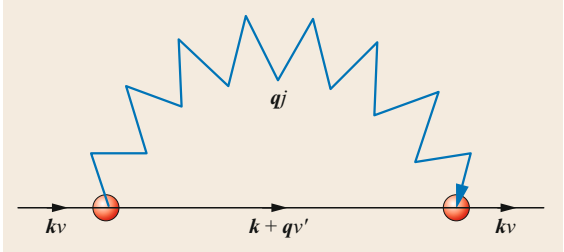

Fig. 24.1 Schematic drawing of the lowest-order contribution to the electron self-energy coming from the electron–phonon interaction. Straight and zigzag lines represent electron and phonon Green's functions, respectively

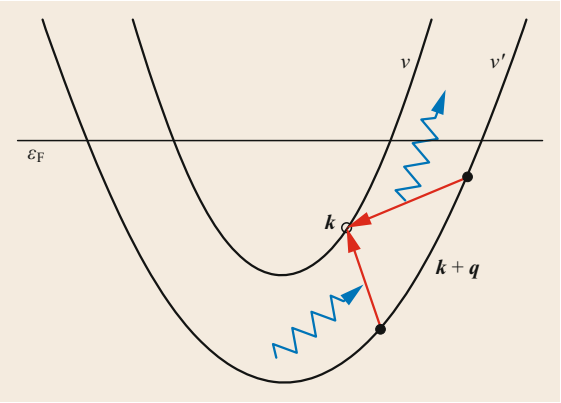

Fig. 24.2 Schematic drawing of the scattering processes that contribute to the self-energy of a hole quasiparticle ($\boldsymbol{k}\nu$), indicating electronic transitions (*red arrows*) and emitted or absorbed phonons (*blue zigzag lines*)

indexes the phonon branch. The electron–phonon vertex $g^{\boldsymbol{qj}}_{\boldsymbol{k}+\boldsymbol{q}\nu',\boldsymbol{k}\nu}$ represents the probability amplitude to scatter an electron/hole from a state ($\boldsymbol{k}\nu$) to ($\boldsymbol{k}+\boldsymbol{q}\nu'$) via the phonon mode ($\boldsymbol{qj}$). Higher order diagrams are supposed to be small in virtue of the Migdal theorem and are usually neglected [24.11].

An illustration of the physical processes described by (24.6) is given in Fig. 24.2. When a hole quasiparticle is created below the Fermi energy, electrons can scatter virtually from states with higher or lower energies, which is accompanied by a simultaneous emission or absorption of a phonon, respectively. Similarly, an electronic quasiparticle created at energies above the Fermi level can scatter virtually into other unoccupied states, again emitting or absorbing a phonon. These two types of processes are represented by the first and second term in (24.6), respectively.

The imaginary part of Σ can be written in the form [24.6]

$$\begin{aligned}&\mathrm{Im}\{\Sigma(\boldsymbol{k}\nu,\epsilon)\}\\&=-\pi\int_0^\infty \mathrm{d}\omega\,\left\{\alpha^2F^+_{\boldsymbol{k}\nu}(\epsilon,\omega)[b(\omega)+f(\omega+\epsilon)]\right.\\&\left.\quad+\alpha^2F^-_{\boldsymbol{k}\nu}(\epsilon,\omega)[b(\omega)+f(\omega-\epsilon)]\right\},\end{aligned}\tag{24.7}$$

where the two spectral functions defined by

$$\begin{aligned}\alpha^2F^\pm_{\boldsymbol{k}\nu}(\epsilon,\omega)&=\frac{1}{N_q}\sum_{\boldsymbol{qj}}\delta(\omega-\omega_{\boldsymbol{qj}})\\&\quad\times\sum_{\nu'}|g^{\boldsymbol{qj}}_{\boldsymbol{k}+\boldsymbol{q}\nu',\boldsymbol{k}\nu}|^2\delta(\epsilon-\epsilon_{\boldsymbol{k}+\boldsymbol{q}\nu'}\pm\omega)\end{aligned}\tag{24.8}$$

correspond to the emission (+) and absorption (−) processes. Combining (24.7) with (24.4) gives an expression for the quasiparticle linewidth due to electron–phonon interaction

$$\begin{aligned}\Gamma_{\boldsymbol{k}\nu}&=2\pi\int_0^\infty \mathrm{d}\omega\,\left\{\alpha^2F^+_{\boldsymbol{k}\nu}(\overline{\epsilon}_{\boldsymbol{k}\nu},\omega)[b(\omega)+f(\omega+\overline{\epsilon}_{\boldsymbol{k}\nu})]\right.\\&\left.\quad+\alpha^2F^-_{\boldsymbol{k}\nu}(\overline{\epsilon}_{\boldsymbol{k}\nu},\omega)[b(\omega)+f(\omega-\overline{\epsilon}_{\boldsymbol{k}\nu})]\right\}.\end{aligned}\tag{24.9}$$

A formula for the real part of the self-energy can be derived directly from (24.7), but in practice it is more convenient to make use of the Kramers–Kronig relation

$$\mathrm{Re}\{\Sigma(\boldsymbol{k}\nu,\epsilon)\}=\frac{1}{\pi}\int \mathrm{d}\epsilon'\frac{\mathrm{Im}\{\Sigma(\boldsymbol{k}\nu,\epsilon')\}}{\epsilon-\epsilon'}\,.\tag{24.10}$$

The second δ-function in (24.8) expresses the energy conservation and differs for emission and absorption by the sign of the phonon frequency. Because energies related to lattice vibrations are often much smaller than the relevant electronic energies, emission or absorption of a phonon mainly changes the momentum of the electron, while the associated energy change is negligible. Therefore, the difference between the two spectral functions is often very small, and one can resort to the so-called quasielastic approximation

$$\begin{aligned}\alpha^2F^\pm_{\boldsymbol{k}\nu}(\overline{\epsilon}_{\boldsymbol{k}\nu},\omega)&\approx\alpha^2F_{\boldsymbol{k}\nu}(\omega)\\&=\frac{1}{N_q}\sum_{\boldsymbol{qj}}\delta(\omega-\omega_{\boldsymbol{qj}})\sum_{\nu'}|g^{\boldsymbol{qj}}_{\boldsymbol{k}+\boldsymbol{q}\nu',\boldsymbol{k}\nu}|^2\\&\quad\times\delta(\overline{\epsilon}_{\boldsymbol{k}\nu}-\epsilon_{\boldsymbol{k}+\boldsymbol{q}\nu'})\,,\end{aligned}\tag{24.11}$$

which gives a simplified expression for the linewidth

$$\begin{aligned}\Gamma_{\boldsymbol{k}\nu}&\approx2\pi\int_0^\infty \mathrm{d}\omega\alpha^2F_{\boldsymbol{k}\nu}(\omega)\\&\quad\times[2b(\omega)+f(\omega+\overline{\epsilon}_{\boldsymbol{k}\nu})+f(\omega-\overline{\epsilon}_{\boldsymbol{k}\nu})]\,.\end{aligned}\tag{24.12}$$

The spectral function $\alpha^2F_{\boldsymbol{k}\nu}(\omega)$ bears some similarities with the well-known Eliashberg function used in the strong-coupling theory of phonon-mediated superconductivity. The important difference is that it is associated to an individual electron state ($\boldsymbol{k}\nu$) and describes the effect of coupling to all other electronic states which can be reached by exchange of a single phonon.

In the derivation presented above, the Dyson equation (24.1) is evaluated directly on the real axis. This approximation breaks down when the self-energy becomes too large. More generally, the quasiparticle properties are determined from the poles of the renormalized

Green's function in the complex plane, i.e., for complex energies ϵ. Such a scheme has been developed by *Eiguren* et al. [24.12, 13]. Application to the surface band renormalization of H/W(110) led, for large coupling strength, to a complex behavior of the renormalized spectral function like multipeak structures, which can no longer be interpreted within a simple quasiparticle picture.

24.1.2 Electron–Phonon Coupling Strength

The strength of the renormalization depends on three factors: (i) available final electronic states $(\boldsymbol{k}+\boldsymbol{q}\nu')$, (ii) available phonon modes connecting the initial to the final states, and (iii) the probability for this scattering given by $|g^{\boldsymbol{q}j}_{\boldsymbol{k}+\boldsymbol{q}\nu',\boldsymbol{k}\nu}|^2$. A convenient dimensionless measure of the average coupling strength is the electron–phonon coupling constant

$$\lambda_{\boldsymbol{k}\nu} = 2\int \mathrm{d}\omega \frac{\alpha^2 F_{\boldsymbol{k}\nu}(\omega)}{\omega} \,. \tag{24.13}$$

It is a property of the individual quasiparticle $(\boldsymbol{k}\nu)$ and depends both on momentum and band index. It can be directly connected to measurable quantities in two ways. The first one is the high-temperature behavior of electronic linewidth. Under the condition $T \gg \omega_{\max}$, where $\omega_{\max}$ is the maximum phonon frequency, the linewidth becomes linear in T and (24.12) simplifies to

$$\Gamma_{\boldsymbol{k}\nu} \approx 2\pi\lambda_{\boldsymbol{k}\nu} k_\mathrm{B} T \,. \tag{24.14}$$

Thus, $\lambda_{\boldsymbol{k}\nu}$ is given by the slope of the linear increase of the linewidth at sufficiently high temperatures. The second route is via the self-energy and is based on the exact relationship

$$\lambda_{\boldsymbol{k}\nu} = \left.\frac{\partial \mathrm{Re}\{\Sigma(\boldsymbol{k}\nu,\epsilon)\}}{\partial\epsilon}\right|_{\epsilon=\epsilon_\mathrm{F},T=0} \,. \tag{24.15}$$

Thus, $\lambda_{\boldsymbol{k}\nu}$ also determines the slope of the real part of the self-energy at the Fermi energy ϵ_F in the limit $T \to 0\,\mathrm{K}$. The real part of self-energy can be extracted from measurements of the renormalized quasiparticle dispersion at low temperatures.

Both routes, via the temperature-dependent linewidth or the low-energy behavior of the self-energy, have been widely utilized to determine the coupling constant from experimental data. We will discuss the applied techniques in more detail in Sect. 24.3.

24.2 Computational Approaches

Renormalization of electronic quasiparticles is typically a process involving many phonon modes, which also differ in the way they couple to the relevant electronic states. Interpretation of experiments is therefore quite involved and must be combined with theoretical guidance. Simple models have been widely used in analyzing experimental data, but they provide only limited information about the most relevant phonons involved. Significant advances in microscopic approaches in the last decade have made very detailed calculations of all relevant quantities possible today.

24.2.1 Simple Models

We will discuss here two types of simple models, the Einstein and the Debye model. The Einstein model provides an instructive look into the renormalization process. It assumes the coupling of a single dispersionless phonon branch of frequency Ω. The spectral function then consists of a single δ-type peak represented by

$$\alpha^2 F_{\boldsymbol{k}\nu}(\omega) = \lambda_\mathrm{E}\frac{\Omega}{2}\delta(\omega-\Omega) \,. \tag{24.16}$$

The corresponding electron self-energy for $T \to 0$ is depicted in Fig. 24.3a. In this limit, only phonon emission processes contribute and the imaginary part exhibits a characteristic step at Ω. Physically this means that if a quasiparticle is created within an energy range smaller than Ω around the Fermi level, this state cannot decay via emission of a single phonon. For energies larger than Ω this decay channel is opened. The real part of the self-energy possesses a maximum at the phonon frequency. As a result, the renormalized dispersion shown in Fig. 24.3b exhibits a kink-like structure right at the phonon energy.

The Einstein model is only appropriate if the electron–phonon interaction is dominated by a single dispersionless optical mode. A more common situation is that the surface states are coupled to many vibrations with a continuous frequency spectrum. Then, the Debye model is more appropriate. This ansatz assumes that all phonon modes contribute equally to the total coupling, such that the spectral function is proportional to the phonon density of states. The latter is approximated by a Debye spectrum [24.4, 14]

$$\alpha^2 F_{\boldsymbol{k}\nu}(\omega) = \lambda_\mathrm{D}\frac{\omega^2}{\omega_\mathrm{D}^2} \,,\ \omega \le \omega_\mathrm{D} \,. \tag{24.17}$$

The Debye frequency ω_D characterizes the maximum phonon frequency, while λ_D denotes the coupling con-

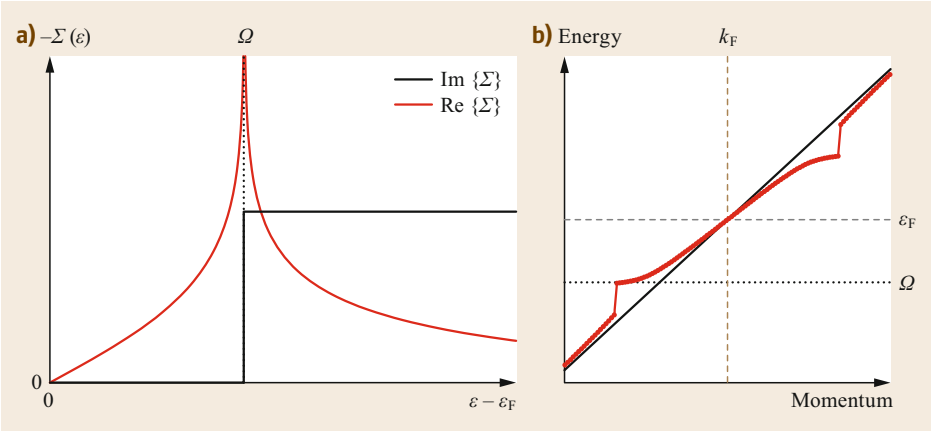

Fig. 24.3a,b Illustration of the renormalization of an electronic band for a model of coupling to an Einstein-type phonon branch with energy Ω. **(a)** Real and imaginary part of the electron self-energy. **(b)** Renormalized quasiparticle dispersion, displaying a kink at the phonon energy

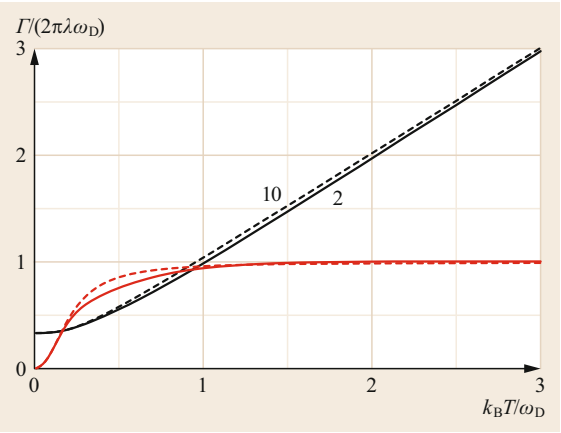

Fig. 24.4 Linewidth as a function of temperature (*black lines*) as well as the temperature derivative (*red lines*) for the Debye model for two values of the ratio $\epsilon_{k\nu}/\omega_D$

stant. The temperature dependence of the linewidth obtained with this model using (24.12) is shown in Fig. 24.4. Its functional form depends on the ratio of the quasiparticle energy $\epsilon_{k\nu}$ and ω_D. The linear-in-T regime is typically reached at temperatures slightly above ω_D/k_B.

The complete functional form of $\Gamma(T)$ provides a convenient basis for fitting data should the linear-in-T regime not be reachable. The fit result depends on the chosen ω_D and often the bulk ω_D is chosen. However, for surfaces that possess a larger surface relaxation or an electronic structure distinct from the bulk, ω_D is adjusted to account for a surface phonon spectrum that deviates from the bulk, or even two-dimensional variants of the Debye spectrum are used [24.2].

24.2.2 Microscopic Models

A calculation of EPI-related quantities requires the knowledge of three ingredients:

(i) electronic surface band structure including electronic wavefunctions
(ii) phonon spectrum comprising vibrations of the bulk material, and localized phonon modes present at the surface and
(iii) first-order variation of the screened potential induced by atom displacements, which determine the electron–phonon matrix elements.

Steps towards an atomistic calculation of EPI on surfaces were first made by the development of microscopic models, which for each of the three ingredients independently introduce simplifying approximations. Such a model approach was proposed in [24.15, 16] based on the following assumptions:

(i) The one-electron states were derived from a one-dimensional potential representing the crystal potential at the surface. The form of the potential was constructed in such a way as to reproduce various properties of the surface electronic structure, like surface-projected bulk gaps or energies of surface and image states [24.17].
(ii) Lattice dynamical properties were obtained from a force-constant model with a single parameter, and the surface vibrations were calculated by applying this model to a slab geometry [24.18].
(iii) The first-order variation of the screened potential was represented by *Ashcroft* pseudopoten-

tials [24.19], which were screened either with the Thomas–Fermi approximation or the random-phase approximation. In metals, screening is crucial to obtain realistic values for the electron–phonon matrix elements.

This model approach is restricted to surface states derived from s-p orbitals only, and works for metals with simple and compact lattice structures, where the simplified description of the lattice dynamics is justified. It was therefore applied predominantly to compact surfaces of fcc noble and transition metals, and to surfaces of Al. This approach was later extended by introducing two-dimensional potentials to describe the one-electron states, which improved the description of the electronic surface structure in the case of more anisotropic surfaces like the (110) surfaces of fcc noble metals [24.20]. To handle overlayers, phonons were calculated from the more sophisticated embedded atom model [24.21, 22].

24.2.3 Ab Initio Calculations

Density-functional theory is nowadays a well established approach to calculate electronic structure properties in a wide range of material classes. It starts from the quantum-mechanical description and provides material-specific information about the one-electron wavefunctions and energies. Besides, also the lattice dynamics and electron–phonon interaction can be calculated within the same framework. The most efficient scheme is based on a linear-response technique and is called density-functional perturbation theory [24.23–26]. It allows calculation of the first-order response of the electronic system with respect to an atomic displacement in a self-consistent procedure, from which the phonon properties can be derived. Importantly, this approach automatically incorporates screening effects. In addition, it provides the first-order variation of the potential needed for the electron–phonon matrix elements.

There are presently a growing number of studies applying this technique to the EPI on surfaces. Surfaces are represented by finite-size slabs, which must be chosen thick enough to converge to the surface properties of a semi-infinite system [24.27]. The bottleneck of such ab initio studies is usually the calculation of the phonons, which quickly becomes very expensive with increasing slab thickness. Furthermore, the evaluation of EPI quantities requires fine meshes in momentum space for both phonons and electron–phonon matrix elements, which is typically handled by elaborate interpolation schemes [24.28, 29].

24.3 Experimental Determination of Electron–Phonon Coupling Strength

In this chapter we briefly recapitulate the different experimental approaches used to extract the electron–phonon coupling in surface states.

24.3.1 Angle-Resolved Photoemission Spectroscopy

The most widely used experimental technique to obtain information about the strength of the electron–phonon interaction at surfaces is angle-resolved photoemission spectroscopy (ARPES), which allows the properties of individual electronic quasiparticles to be accessed. In the photoemission process, an incoming photon is absorbed and excites an electron from an occupied state into a vacuum state. In the so-called sudden approximation, one assumes that after photon absorption the photoelectron does not interact further with the system left behind. Without energy and momentum resolution effects, the photoemission intensity can be written as [24.30]

$$I(\boldsymbol{k},\epsilon,T) = I_0(\boldsymbol{k}) f(\epsilon,T) A(\boldsymbol{k},\epsilon,T)\,. \tag{24.18}$$

For simplicity, the discussion is restricted to a single electronic band, $\boldsymbol{k}$ denotes the momentum of the photoelectron and ϵ its energy relative to the Fermi level, I_0 is proportional to the square of the matrix element describing the excitation process and depends on the momentum of the photoelectron as well as on the energy and polarization of the incoming photon, and f is the Fermi distribution function. In (24.18) the temperature dependence of the quantities is shown explicitly. The one-particle spectral function A contains all information about the initial electronic state, and is connected to the one-particle Green's function via

$$A(\boldsymbol{k},\epsilon,T) = -2\mathrm{Im}\{G(\boldsymbol{k},\epsilon,T)\}\,. \tag{24.19}$$

This can be expressed in terms of the electronic self-energy with the help of (24.1) as

$$A(\boldsymbol{k},\epsilon,T) = -\frac{2\mathrm{Im}\{\Sigma(\boldsymbol{k},\epsilon,T)\}}{[\epsilon-\epsilon_{\boldsymbol{k}}-\mathrm{Re}\{\Sigma(\boldsymbol{k},\epsilon,T)\}]^2+[\mathrm{Im}\{\Sigma(\boldsymbol{k},\epsilon,T)\}]^2}\,. \tag{24.20}$$

On the basis of this general relationship, two major routes have been pursued to extract information about the self-energy from ARPES experiments, which are described in the following.

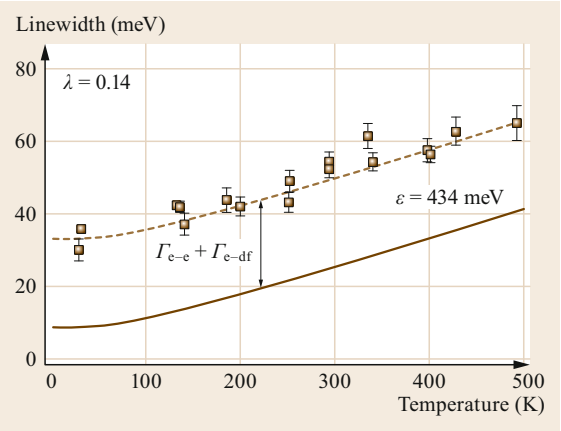

Fig. 24.5 Example of a temperature-dependent linewidth. Data points (*filled squares*) for the Cu(111) surface state at $\overline{\Gamma}$ taken from [24.31] (Data points taken from [24.6], © IOP Publishing & Deutsche Physikalische Gesellschaft. CC-BY-NC-SA)

Measurement of Temperature-Dependent Linewidth

A straightforward procedure to determine the linewidth Γ of an electronic state is by scanning the photoemission intensity as a function of energy for a fixed momentum $\boldsymbol{k}$. For electronic states with binding energies larger than typical phonon energies, the energy dependence in the self-energy can be neglected to a good approximation. Such a scan takes a Lorentzian shape with a full-width-at-half-maximum $\Gamma(T) = 2|\mathrm{Im}\{\Sigma(T)\}|$. In general, it is the sum of three contributions, $\Gamma = \Gamma_{e-ph} + \Gamma_{e-e} + \Gamma_{df}$. Apart from the linewidth from the electron–phonon interaction (Γ_{e-ph}), it contains contributions from inelastic electron–electron scattering processes (Γ_{e-e}), and elastic scattering of electrons from defects at the surface (Γ_{df}). As the latter two contributions are often very weakly dependent on temperature, $\Gamma(T)$ equals $\Gamma_{e-ph}(T)$ up to a constant shift. Figure 24.5 shows an example for a measurement of the Cu(111) surface state, which lies at the surface Brillouin zone center ($\overline{\Gamma}$) at a binding energy of 434 meV [24.31]. The measured T-dependence of the linewidth can be described by a constant plus $\Gamma_{e-ph}(T)$ calculated from (24.12) with the Debye model (24.17). Even without modeling, the coupling constant λ could be directly extracted from the data from the slope at higher temperature via (24.14). This simple analysis breaks down, however, when the concentration of surface defects varies strongly within the same temperature range, which is the case for defects with a low excitation barrier, and causes a significant T-dependence of Γ_{df}. Then the T-dependence of Γ_{e-ph} cannot be extracted directly from the data. Such a complication has been discussed for Al(100) and Au(111) surfaces [24.32, 33].

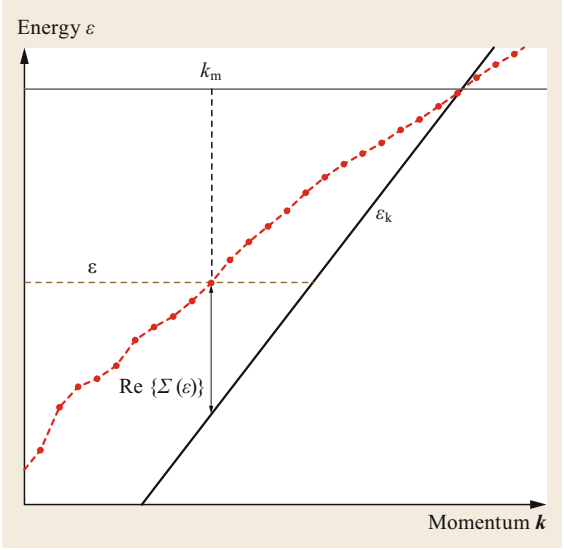

Fig. 24.6 Sketch of extraction of self-energy from ARPES measurements

Extraction of Electron Self-Energy

The most direct way to extract information about the self-energy from ARPES experiments is to record momentum distribution curves (MDCs). An MDC represents photoemission intensity as a function of $\boldsymbol{k}$ at constant kinetic energy of the photoelectron, i.e., at constant ϵ, and at constant photon energy. For an analysis of an MDC, one typically assumes that the $\boldsymbol{k}$ dependence of both the self-energy and the prefactor I_0 in (24.18) can be neglected. This approximation is reasonable, if one takes data restricted to a sufficiently small momentum range. The $\boldsymbol{k}$ dependence in (24.18) then stems solely from the bare dispersion $\epsilon_{\boldsymbol{k}}$, and an MDC along a one-dimensional direction in momentum space takes the form

$$I(k) \propto \frac{1}{[\epsilon - \epsilon_k - \mathrm{Re}\{\Sigma(\epsilon, T)\}]^2 + [\mathrm{Im}\{\Sigma(\epsilon, T)\}]^2} \,. \tag{24.21}$$

For constant ϵ and T, this MDC exhibits a maximum at k_m given by

$$\epsilon - \epsilon_{k_m} - \mathrm{Re}\{\Sigma(\epsilon, T)\} = 0 \,. \tag{24.22}$$

This relationship is sketched in Fig. 24.6. At the same time, an MDC provides also information about $\mathrm{Im}\{\Sigma\}$. This is seen most easily for the case where the bare band is described by a linear dispersion, $\epsilon_k = v(k - k_F)$, with v the slope. The MDC then takes the form of a Lorentzian, and the real and imaginary part of the self-energy can be extracted directly from the position of its

maximum k_m and from its linewidth W (full-width-at-half-maximum) as

$$\mathrm{Re}\{\Sigma(\epsilon,T)\} = \epsilon - v(k_m - k_F)\,,$$
$$\mathrm{Im}\{\Sigma(\epsilon,T)\} = -v\frac{W}{2}\,. \qquad (24.23)$$

The main difficulty of this approach lies in the fact that the determination of both real and imaginary parts of the self-energy involves the bare dispersion which is not known. Two strategies have been applied to deal with this problem. The first is to determine the bare dispersion from measurements of the band dispersion at higher binding energies, where the renormalization by phonons becomes negligible, or to take it from band structure calculations, which do not include many-body corrections.

The second approach rests on the Kramers–Kronig relation (24.10) connecting the real and imaginary part of the self-energy. Combined with the experimental information, it is used to set up a self-consistent procedure to simultaneously determine the self-energy and the bare dispersion. This approach is appealing because it does not require any a priori knowledge about the bare dispersion. Its accuracy, however, depends crucially on the proper modeling of the high-energy parts of the self-energy. These high-energy tails needed for the Kramers–Kronig relation are not directly accessible experimentally [24.34].

After having obtained the self-energy functions, the remaining task is to extract the underlying electron–phonon coupling quantities. Using (24.15), the coupling constant $\lambda_{\boldsymbol{k}\nu}$ can be determined from the slope of $\mathrm{Re}\{\Sigma(\epsilon)\}$ at ϵ_F in the limit $T \to 0\,\mathrm{K}$. Complications arise due to finite energy and momentum resolution present in actual experiments, and the presence of the Fermi distribution function in the expression (24.18) for the photoemission intensity [24.35, 36], which hampers the self-energy analysis in close vicinity to ϵ_F and limits the accuracy of the coupling constant $\lambda_{\boldsymbol{k}\nu}$ obtained via (24.15). Extraction of complete self-energies is restricted to cases where the renormalization effects are large enough to be resolved experimentally. Therefore, most commonly this technique is applied to occupied states close to the Fermi level. For further reading we refer to [24.6, 30, 37].

A more ambitious task is to extract the complete EPI spectral function $\alpha^2F_{\boldsymbol{k}\nu}$ (24.11) from the self-energy. A practical procedure, proposed in [24.38], is based on the approximate relationship between the spectral function and the real part of the self-energy [24.1]

$$\mathrm{Re}\{\Sigma(\boldsymbol{k}\nu,\epsilon)\} = \int \mathrm{d}\omega\alpha^2F_{\boldsymbol{k}\nu}(\omega)\int \mathrm{d}x\frac{2f(x+\epsilon)}{x^2-\omega^2}\,. \qquad (24.24)$$

This expression can be derived from (24.6) and (24.8) in the quasielastic approximation and by replacing the spectral function by its value at the Fermi level

$$\alpha^2F_{\boldsymbol{k}\nu}(\omega) \approx \alpha^2F_{\boldsymbol{k}\nu}(\overline{\epsilon}_{\boldsymbol{k}\nu} \to \epsilon_F,\omega)\,. \qquad (24.25)$$

These simplifications are reasonable if the electronic structure behaves smoothly around ϵ_F on the scale of phonon energies. From measurements of $\mathrm{Re}\{\Sigma(\epsilon)\}$, the spectral function is obtained by inverting the integral equation (24.24). Because a direct inversion tends to be numerically unstable, a fitting procedure employing the maximum entropy method (MEM) has been developed [24.4, 38], which allows additional physical constraints for the spectral function to be built in without severe restrictions on its shape. This scheme is more robust against data noise than the direct inversion, but still relies on high-precision data. Besides application to the EPI on the Be(0001) surface [24.4, 38–40] this MEM fitting procedure has been used in several studies of the electronic renormalization of layered cuprate superconductors [24.41–45].

24.3.2 Time-Resolved Angle-Resolved Photoemission Spectroscopy

The presence of a surface typically creates a variety of loosely bound states, whose wave functions are located close to the surface and whose energies lie between the Fermi energy ϵ_F and the vacuum energy E_{vac}. These unoccupied surface states are not accessible with the ARPES technique described so far. The state must be first populated before its dynamics can be studied. This is achieved by two-photon photoemission spectroscopy (2PPE), which is a well established technique nowadays [24.46, 47].

The principles of the 2PPE excitation process are illustrated in Fig. 24.7. A first light pulse, called the pump pulse, excites an electron from a state below ϵ_F into an

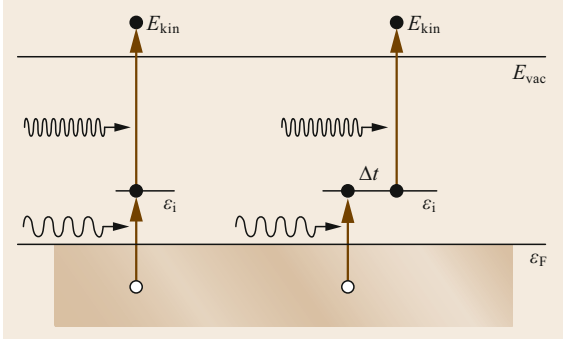

Fig. 24.7 Illustration of the two-photon photoemission process

unoccupied intermediate state with energy ϵ_i above ϵ_F. A second light pulse, also called the probe pulse, then lifts the electron above the vacuum level E_{vac}. It finally escapes the surface with a kinetic energy E_{kin} which is recorded by an energy analyzer. Further information about the dynamics of the intermediate state is gained when the probe pulse is delayed with respect to the pump pulse by a delay time Δt. For this time-dependent 2PPE, one distinguishes two modes of data acquisition:

(i) Energy-resolved 2PPE spectra: the emission rate is measured as a function of E_{kin} at a fixed delay time. Such spectra provide information about the energy and the linewidth Γ of the intermediate state.

(ii) Time-resolved 2PPE spectra: the emission rate is recorded as a function of the delay time for a particular kinetic energy. When the kinetic energy is chosen to record the intermediate state, the measured intensity is proportional to the population of this state. Time-resolved spectra then reflect the decay of the population in the time domain, which often exhibits a simple exponential behavior

$$I \propto I_0 e^{\Delta t/\tau_i} , \qquad (24.26)$$

from which the intrinsic lifetime τ_i of the intermediate state can be deduced directly.

Because the 2PPE process is a second-order excitation, analysis of the recorded intensities is quite involved. In particular, the linewidth Γ obtained by the energy-resolved 2PPE is not only determined by the intrinsic lifetime $(1/\tau_i)$, but contains further contributions from quasielastic scattering processes. The latter do not change the population of the intermediate state, but cause a relaxation of the quantum phase relation between the states involved in the excitation. This phenomenon is called dephasing. An elaborate analysis of the 2PPE linewidth is, e.g., presented in [24.47]. Therefore, the true intrinsic lifetime is determined only by mode (ii). Complications may arise if several intermediate states are present. In this case, the population dynamics must be described by a coupled set of rate equations, whose solution provides the individual lifetimes [24.48]. Determination of the electron–phonon coupling λ then proceeds in the same way as for the occupied states described in Sect. 24.3.1, namely from linear T-dependence of the intrinsic linewidths $\Gamma_i(T) = 1/\tau_i(T)$ using (24.14).

24.3.3 Scanning–Tunneling Spectroscopy

Another approach to analyze the intrinsic lifetime of surface states utilizes the scanning-tunneling microscopy (STM) technique, which is described in more detail in Chaps. 8 and 25. The metallic tip is first positioned on top of the surface. For a fixed distance between tip and surface, the tunneling current I is recorded as function of the bias voltage V between the tip and surface. This measurement mode is also called scanning-tunneling spectroscopy (STS). When the electronic structure of the tip is featureless, the differential conductance dI/dV is directly proportional to the density of states of the surface.

In the presence of a surface state, an additional tunneling channel is opened, when V is raised to the bottom of the surface band (Fig. 24.8). This is reflected as a step in dI/dV as a function of V. A finite lifetime of the surface state gives rise to a broadening of the step. *Li* et al. have utilized a numerical evaluation of the tunneling conductance within a many-body perturbation framework to establish a quantitative connection between the measured width of the step and the intrinsic lifetime [24.49]. In this way, the total linewidth of the surface state at the bottom of the surface band is probed. An advantage of this technique is that prior to the spectroscopic measurements, the STM can be used to characterize in situ the surface properties and to identify appropriate defect-free areas, which eliminates defect scattering as a contribution to the lifetime. Also this technique is applicable to both occupied and unoccupied surface states. Limitations arise from

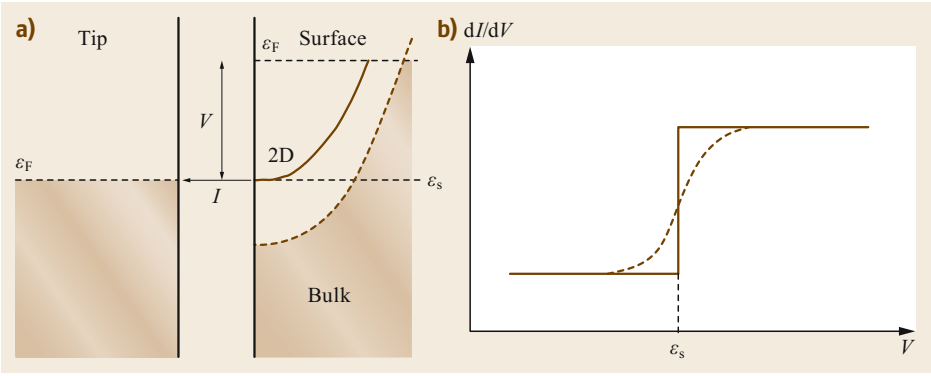

Fig. 24.8a,b Illustration of scanning–tunneling spectroscopy of a surface state: Energy level scheme **(a)** and differential conductance **(b)**

the low temperatures typically required for operating the STM, which prevents temperature-dependent studies to discriminate between the electron–electron and electron–phonon contributions to the lifetime. This has been circumvented by taking estimates for the electron–electron contribution from calculations [24.50]. Furthermore, this technique does not resolve the momenta of the tunneling electrons, and is only applicable to states at the bottom (or top) of the surface band, where the tunneling conductance shows well-resolved steps.

24.4 Electron–Phonon Coupling of Electronic Surface States

In this section, we give a compilation of the various studies devoted to the electron–phonon interaction of electronic surface states. This research is characterized by close links between experimental and theoretical investigations, which mutually stimulated each other and whose techniques were steadily improved. The field covers a wide range of metallic surfaces, ranging from elemental surfaces to adsorbate covered surfaces and recently to metallic surface states of topological insulators.

24.4.1 Elemental Metal Surfaces

A collection of results for elemental metal surfaces is given in Table 24.1. Al(100) and Mg(0001) are examples of nearly free electron metals. Both Al(100) and Mg(0001) surfaces show surface states around $\overline{\Gamma}$ with a parabolic dispersion. For Al(100) the surface band falls into a small bulk-projected band gap, while for Mg(0001) the surface state lies in the energy range of bulk-projected states and penetrates more deeply into the bulk. Experiments and ab initio calculations agree in that the electron–phonon coupling of these surface states is comparable to the average coupling in the bulk materials (0.43 [24.51] and 0.29–0.35 [24.52] for Al and Mg, respectively). A slight increase at $\overline{\Gamma}$ for Al(100) was attributed to an additional decay channel via the Rayleigh surface mode [24.51]. The similarity of the coupling between surface and bulk states indicates that the surface modes dominantly couple to bulk states, which lie close in energy because of the smallness of the bulk-projected band gap. Significantly larger couplings are predicted for the occupied and unoccupied surface states at the $\overline{\mathrm{X}}$ point. The simple electronic structure has also stimulated the application of model approaches for Al(100), but the obtained couplings deviate significantly from both experimental and ab initio results.

Extensive studies of EPI were devoted to the (0001) and $(10\overline{1}0)$ surfaces of Be [24.3]. Be bulk is characterized by strongly covalent bonding and has a very low electronic density of states (DOS) at the Fermi energy. Consequently, its EPI is rather small with $\lambda = 0.21 - 0.24$ [24.1, 96]. Be surfaces display a qualitatively different electronic structure [24.97]. At Be(0001), a surface state is located in a wide band gap, which enhances the DOS and renders the surface more metallic. For the surface state around $\overline{\Gamma}$ experiments obtained a large range of coupling values of 0.6–1.2 at ϵ_F. Part of this spread has been attributed to the difficulty of finding appropriate models to fit the T dependence of the measured linewidths. The bulk phonon spectrum extends to rather high frequencies ($\approx 80\,\mathrm{meV}$), which would require temperatures $T > 1000\,\mathrm{K}$ to reach the linear regime. Also it was suggested that the relevant surface-phonon spectrum is significantly softer than the bulk spectrum. More recent experiments based on the extraction of self-energies revealed a pronounced anisotropy of the coupling at ϵ_F. A similar anisotropy has been found in theoretical studies, although on average smaller couplings are obtained. A similar situation is encountered for Be$(10\overline{1}0)$. A free-electron like surface state exists in the wide gap around the $\overline{\mathrm{A}}$ point, which again enhances the DOS at the Fermi energy with respect to the bulk. For this surface state, discrepancies between experimental values of 0.65–0.7 and theoretical results of ≈ 0.2 remained unresolved. In contrast, for the second surface state at $\overline{\mathrm{A}}$ at higher binding energy, experiment and theory agree on an intermediate coupling of 0.45–0.5, which is still twice as large as the bulk value.

Surfaces of the noble metals Cu, Ag, and Au have played an important role in EPI research. The (111) surface of these metals possesses a Shockley-type surface state around $\overline{\Gamma}$ in the L-gap of the bulk. Another Shockley-type surface state exists at the $\overline{\mathrm{Y}}$ point of the (110) surface. These states are well localized within a few surface layers. Theoretical modeling with different degrees of sophistication has been applied to this class of surfaces. The surface states can be described by approximating the surface potential by one- or two-dimensional model potentials. Furthermore, the lattice dynamics can be approximated by a single-force-constant model, which facilitates a realistic modeling of the surface phonon spectrum. Experiment and theory coincide in that the coupling strength is rather similar for all noble metal surfaces with λ in the range of 0.1–0.2. It reflects the small coupling encountered in the bulk materials (for example, calculations gave 0.14 and 0.17 for Cu and Au, respectively [24.98, 99]). An even smaller value was obtained for another surface state at $\overline{\mathrm{M}}$ of the Cu(100) surface. An exception seemed to be the EPI in the surface state of Au(111), where ini-

Table 24.1 EPI parameters for electronic states of elemental metal surfaces. Experimental results are from ARPES measurements, if not stated otherwise

Surface	k point	E (eV)	λ	Γ_{e-ph} (0 K) (meV)	Method	References
Al(100)	$\overline{\Gamma}$	−2.75	cw 0.51		Γ fit	[24.32]
			0.23		Model	[24.16]
			0.23	18	Model	[24.16]
			0.51	35	ai	[24.51, 53, 54]
				26	Model	[24.27]
	$\overline{X}$	−4.55	0.78(4)	50	ai	[24.51, 55]
		1.23	0.65	42	ai	[24.51]
	$k_F^{\overline{\Gamma}\to\overline{M}}$	0	0.67(5)		Re$\{\Sigma\}$ slope	[24.56]
	k_F	0	0.55		Model	[24.16]
			0.45		ai	[24.51]
Mg(0001)	$\overline{\Gamma}$	−1.63	0.27(2)	21	Γ fit	[24.57]
			0.28	19	ai	[24.52, 58]
	$\overline{M}$	−0.95	0.38	20	ai	[24.52, 58, 59]
Be(0001)	$\overline{\Gamma}$	−2.78	0.87		Γ fit	[24.60, 61]
			0.38		ai	[24.62]
			0.21		ai	[24.63]
	$k_F^{\overline{\Gamma}\to\overline{M}}$	0	1.18(7)		Re$\{\Sigma\}$ slope	[24.64, 65]
			1.17		ai	[24.63]
			0.70(8)		MEM	[24.4]
			1.1		MEM	[24.39]
			0.94		MEM	[24.40]
	$k_F^{\overline{\Gamma}\to\overline{M}/\overline{K}}$	0	0.7(1)		Re$\{\Sigma\}$ slope	[24.61]
	$k_F^{\overline{\Gamma}\to\overline{K}}$	0	0.9		MEM	[24.39]
			0.88		ai	[24.62]
			0.48		ai	[24.63]
Be(10$\overline{1}$0)	$\overline{A}$	−0.42	0.65(3)	84	Γ fit	[24.66, 67]
			0.16		ai	[24.68]
	$\overline{A}$	−2.73	0.49(4)		Γ fit	[24.66, 67]
			0.44		ai	[24.68]
	$k_F^{\overline{A}\to\overline{\Gamma}}$	0	0.68(8)		MEM	[24.38]
			0.22		ai	[24.68]
	$k_F^{\overline{A}\to\overline{L}}$	0	0.18		ai	[24.68]
Cu(111)	$\overline{\Gamma}$	−0.390	0.14(2)	30	Γ slope	[24.31]
			0.137(15)		Γ slope	[24.69]
			cw 0.137	8	Γ + Re$\{\Sigma\}$ slope	[24.70]
				24	STS	[24.50]
			0.16	7.3	Model	[24.15, 16]
				5.7	Model	[24.27]
	$\overline{M}$	−1.932	0.085(15)		Γ slope	[24.69]
Cu(110)	$k_F^{\overline{\Gamma}\to\overline{Y}}$	0	0.17(2)	7	Re$\{\Sigma\}$ slope	[24.71]
			0.160		ai	[24.71]
	$\overline{Y}$	−0.510	0.23(2)		Γ slope	[24.72]
			0.155	7.7	ai	[24.71]
			0.24	9.6	Model	[24.20, 73]
		1.7	0.08	4.2	Model	[24.20, 73, 74]
Cu(100)	$\overline{M}$	−1.8	0.09(2)		Γ slope	[24.69, 75]

cw: consistent with; ai: ab initio; Γ slope: coupling from linear slope of $\Gamma(T)$; Γ fit: coupling from model fit of $\Gamma(T)$; Re$\{\Sigma\}$ slope: coupling from linear slope of Re$\{\Sigma(\epsilon)\}$ at ϵ_F; Σ fit: model fit to $\Sigma(\epsilon)$; MEM: maximum entropy method; 2PPE: two-photon photoemission spectroscopy; STS: scanning tunneling spectroscopy

Table 24.1 (continued)

Surface	k point	E (eV)	λ	Γ_{e-ph} (0 K) (meV)	Method	References
Ag(111)	$\overline{\Gamma}$	−0.063		6	STS	[24.50, 76]
			0.12	3.7	Model	[24.15, 16]
Ag(110)	$\overline{Y}$	−0.106	0.28		Model	[24.20, 73, 77]
		1.6	0.08		Model	[24.20, 73, 78]
Au(111)	$\overline{\Gamma}$	−0.487	0.34(1)		Γ slope	[24.76, 79]
				18	STS	[24.50]
			cw 0.11		Γ fit	[24.32]
			0.11	3.6	Model	[24.16]
			0.15	4.5	Model	[24.33]
Mo(110)	$k_F^{\overline{\Gamma}\to\overline{N}}$	0	0.52		Γ slope	[24.80]
Mo(112)	$k_F^{\overline{\Gamma}\to\overline{X}}$	0	0.42		Σ fit	[24.81]
			0.46		ai+Model	[24.82]
V(100)	k_F	0	1.45		Re{Σ} slope	[24.83]
Pd(111)	$\overline{\Gamma}$	1.26	cw 0.08		2PPE Γ slope	[24.29]
			0.08	19	ai	[24.29]
Pd(110)	$\overline{Y}$	1.38	0.17		Model	[24.20, 73]
	$\overline{Y}$	3.4	0.03		Model	[24.20, 73]
α-Ga(010)	$\overline{C}$	−1.1	1.4(1)		Γ fit	[24.84]
			1.17(4)		Γ fit	[24.85]
Sb(111)	$k_F^{\overline{\Gamma}\to\overline{K}}$	0	0.22(3)		Γ slope	[24.86]
	k_F^{av}		0.27		ai	[24.87]
Bi(111)	$k_F^{\overline{\Gamma}\to\overline{M}}$	0	0.60(5)		Σ fit	[24.88]
	$k_{inner}^{\overline{\Gamma}\to\overline{M}}$	−0.025	0.40(5)		Γ slope	[24.36]
		−0.37	0.97		ai	[24.89]
	$k_{outer}^{\overline{\Gamma}\to\overline{M}}$	−0.30	0.46		ai	[24.89]
	k_F^{av}		0.39		ai	[24.90]
Bi(110)	$k_F^{\overline{\Gamma}\to\overline{X_2}}$	0	0.27(2)		Γ fit	[24.35]
	$k_F^{\overline{M}\to\overline{X_2}}$	0	0.19(3)		Γ fit	[24.35]
Bi(100)	$\overline{\Gamma}\to\overline{K_2}$	0.07–0.33	0.20(2)–0.72(5)		Γ slope	[24.91]
Tl(0001)	k_F^{av}		1.01		ai	[24.92]
Gd(0001)	$\overline{\Gamma}$	≈ -0.2	≈ 1.0		Γ slope	[24.93]
	$\approx\overline{\Gamma}$	−0.182	1.3	11.7	STS Γ fit	[24.94, 95]
		0.491	1.5		STS Γ fit	[24.94, 95]
Lu(0001)	$\approx\overline{\Gamma}$	0.0023		0.05	STS	[24.94]
Ho(0001)	$\approx\overline{\Gamma}$	−0.090		10.3	STS	[24.94]

cw: consistent with; ai: ab initio; Γ slope: coupling from linear slope of $\Gamma(T)$; Γ fit: coupling from model fit of $\Gamma(T)$; Re{Σ} slope: coupling from linear slope of Re{$\Sigma(\epsilon)$} at ϵ_F; Σ fit: model fit to $\Sigma(\epsilon)$; MEM: maximum entropy method; 2PPE: two-photon photoemission spectroscopy; STS: scanning tunneling spectroscopy

tially a λ of 0.34 was deduced from the T-dependent linewidth [24.79], but a reanalysis of the data taking into account thermally excited defects showed that they are consistent with the smaller value of 0.11 obtained from calculations [24.32, 33].

The $\overline{\Gamma}$ surface state in Au(111) is well known to show a Rashba-type splitting due to spin–orbit coupling. Such a splitting could be resolved also for Cu(111) in a recent ARPES experiment, which was a prerequisite for extracting the correct self-energy at the Fermi energy. The derived λ compared favorably with ab initio calculations [24.71].

Transition metals are characterized by an active involvement of d states in the electronic structure at the Fermi energy. They often possess a sizable electron–phonon coupling in the bulk and one therefore expects them to exhibit larger surface EPI effects. Indeed the first extraction of an electron self-energy was achieved

for a surface band at the Mo(110) surface with a $\lambda = 0.52$, which was even enhanced compared to the bulk value of 0.42 [24.80]. A coupling comparable to the bulk was found for a band observed at the Mo(112) surface [24.81], although a recent analysis of the surface band structure suggested that the observed band has a dominant bulk-like character. A large surface enhancement of the coupling was found for the V(100) surface state with a measured $\lambda = 1.45$ vastly exceeding the bulk value of 0.8–1.2 [24.98].

The Shockley-type states at $\overline{\Gamma}$ of the (111) and (110) surfaces of Pd have also been investigated. In contrast to the (111) and (110) surfaces of noble elements, these Pd surface states lie above ϵ_F and are unoccupied. A very small coupling of $\lambda = 0.08$ for the (111) surface state observed in a two-photon-photoemission experiment was explained theoretically by a strong reduction of the bulk states available for the decay above ϵ_F. A more extensive theoretical calculation predicted that the coupling strength of other surface-localized states below ϵ_F varies strongly with the energy and momentum and could reach values up to 1.4 [24.100, 101], significantly exceeding the Pd bulk value (0.35–0.69 [24.98]).

α-Ga is another elemental metal with a large EPI in the bulk ($\lambda = 0.98$ [24.1]). The (010) surface supports a surface state which builds an electron pocket around the $\overline{C}$ point at the corner of the surface Brillouin zone. T-dependent linewidth measurements for the state at $\overline{C}$ suggested a very large coupling of 1.4. This value was reduced to 1.17 in a later study, which identified the presence of a surface phase transition. Still the EPI is enhanced with respect to the bulk.

The semimetals Bi and Sb are characterized by a pseudogap with small Fermi surfaces and a very low DOS. Consequently the EPI in the bulk is very small, with $\lambda = 0.13$ [24.90] and 0.17 [24.87] for Bi and Sb, respectively. In contrast, their surfaces are much more metallic due to the presence of surface states positioned in large projected band gaps. For Bi all low-indexed surfaces (100), (110), and (111) have been studied experimentally. Spin–orbit coupling (SOC) has a large effect on their surface electronic structure [24.102]. In Bi bulk, electronic states always come in pairs because of the Kramers degeneracy. The loss of inversion symmetry at the surface induces large spin splittings of the surface bands, with large impact on the band dispersion and Fermi-level crossings. The largest couplings were found for Bi(111). This hexagonal surface hosts two types of Fermi surfaces, a circular one around $\overline{\Gamma}$ and six lobes stretched along the $\overline{\Gamma M}$ direction. While the Fermi surface around $\overline{\Gamma}$ is difficult to access because it lies in a region of surface-projected bulk states, the EPI of states at the inner part of the lobe-like Fermi surface has been studied in several ARPES

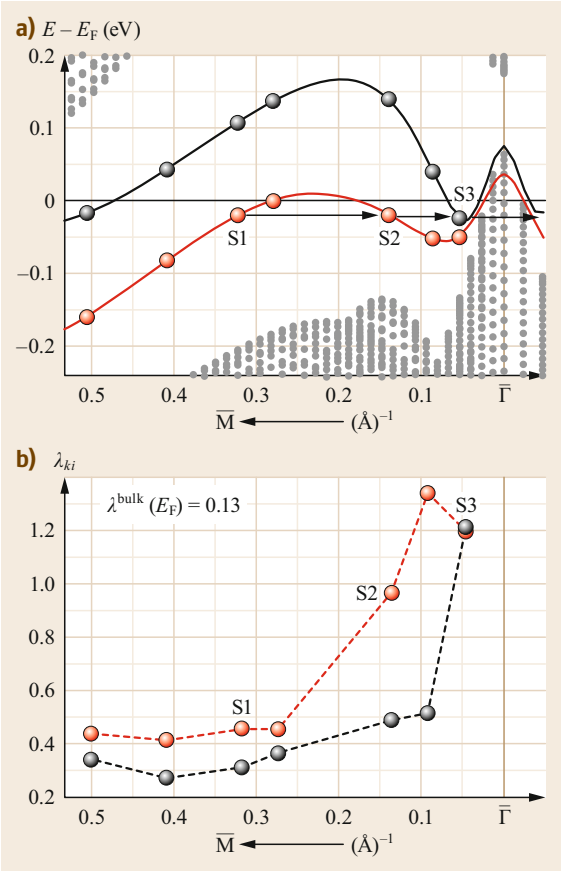

Fig. 24.9 (a) Surface band structure of Bi(111) and **(b)** variation of the coupling constant calculated with an ab initio approach. (Reprinted with permission from [24.89]. Copyright (2014) by the American Physical Society)

experiments. It has been argued that the seemingly different results obtained could be reconciled if the finite energy resolution of the spectrometer is taken into account [24.35]. A reanalysis of the data suggested a coupling of the order of 0.4, consistent with an ab initio calculation of the momentum-averaged coupling for a five-bilayer slab [24.103]. A more detailed ab initio study of the momentum-resolved EPI for these surface states has been performed recently [24.89]. As shown in Fig. 24.9, it revealed couplings of 0.4–0.5 over a wide range of momentum and energy for states of the surface band which crosses the Fermi energy. The enhancement with respect to the bulk was in part attributed to coupling within the same surface band. However, for states close to $\overline{\Gamma}$ a strong increase of λ was found, which could be traced back to a coupling to bulk-like states at $\overline{\Gamma}$ mediated by long-wavelength phonons of low frequency [24.89].

At Bi(110) the surface states build two Fermi surfaces consisting of hole pockets at $\overline{\Gamma}$ and $\overline{M}$. Moderate

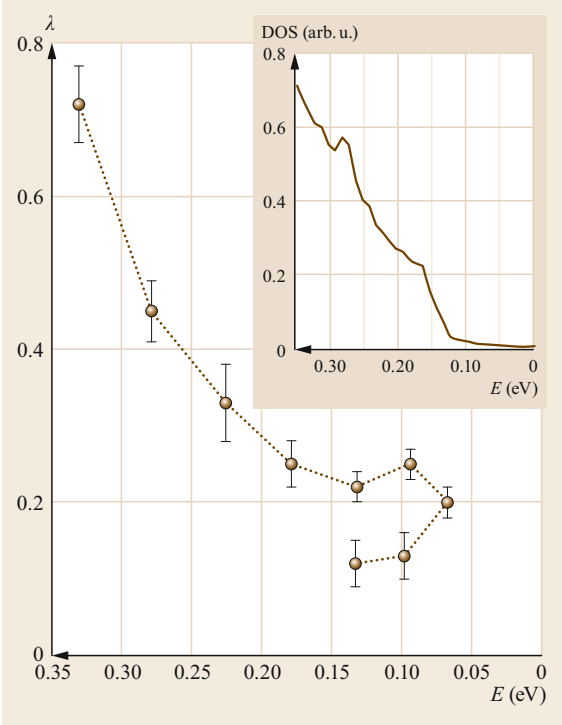

Fig. 24.10 Electron–phonon coupling λ of the surface state of Bi(100) along the $\overline{\Gamma M}$ direction as a function of the binding energy. The *inset* shows the density of states of bulk Bi in the same energy range. (Reprinted with permission from [24.91]. Copyright (2003) by the American Physical Society)

couplings were found in both cases for surface states at ϵ_F. For Bi(100), a distinct dependence of the coupling on the binding energy was observed for a surface band along the $\overline{\Gamma M}$ line. For increasing momentum, this band disperses upwards from an energy of 330 meV below ϵ_F and reaches a maximum of 70 meV below ϵ_F. With decreasing binding energy a large drop of λ from 0.72 to 0.20 was found (Fig. 24.10). Because the bulk DOS shows a similar energy dependence, namely a drop from a high DOS at large binding energies to a low DOS region near ϵ_F, the energy dependence of the EPI was interpreted as reflecting the change in the number of bulk states available for decay via phonons. This implies that the decay of these surface states predominantly happens into bulk-like states.

Albeit SOC is smaller for Sb, dispersion of the surface bands and Fermi surface shapes at the Sb(111) surface closely resemble those of Bi(111). In this case, only weak coupling seems to exist. While one ARPES experiment suggested a coupling slightly enhanced over the bulk value [24.86], a more recent experiment could not detect any sizable renormalization of the surface band at ϵ_F [24.104]. A small EPI is also supported by an ab initio calculation of a Fermi surface average obtained for a slab geometry [24.87].

Another element with strong SOC and large bulk EPI is Pb with $\lambda = 1.55$ [24.98]. Its surfaces, however, do not support well-localized surface states. An ARPES study of the (110) surface revealed a strong band renormalization near the Fermi-level crossing of a bulk state [24.70]. A similar situation is encountered for the (0001) surface of Tl, where an ab initio investigation merely found surface resonances. Yet, the momentum-averaged coupling strength of 1.01 was enhanced with respect to the bulk value of 0.87 [24.92].

The EPI has also been investigated for the (0001) surfaces of the lanthanide metals Gd, Ho, and Lu. The (0001) surface hosts a $5d_{z^2}$-like surface state (Tamm state) in the projected band gap near $\overline{\Gamma}$. The exchange interaction with the 4f magnetic moments splits the surface state into an occupied majority-spin state and an unoccupied minority-spin state [24.105]. Both ARPES and STS experiments on Gd(0001) indicated a large EPI in the range 1.0−1.3 for the occupied majority-spin state, and an even larger coupling of 1.5 was obtained by STS for the unoccupied minority-spin state. Ho(0001) and Lu(0001) were investigated only by STS, and no estimate for λ was given.

24.4.2 Adsorbate Covered Surfaces and Thin Films

Materials with confined geometries on the nanoscale exhibit pronounced quantum-size effects, which manifest themselves in their peculiar electronic and vibrational properties. Adsorbate-covered surfaces provide a natural platform to study such quantum-size effects and to investigate their consequences for the electron–phonon interaction. When metals are deposited as monolayers (MLs) or ultrathin films on a substrate, they exhibit an electronic structure different from the bulk material. The confinement of the electronic motion in the direction vertical to the film gives rise to quantum-well states (QWS), which may interact more effectively with the adsorbate vibrations resulting in an enhanced EPI. Variation of the film thickness can be used to tailor these properties. Key results are summarized in Table 24.2.

Mono- and Submonolayer Coverage

Well-studied examples of strong electron–phonon interaction for an overlayer system are hydrogen monolayers on Mo or W metals. The EPI in the surface electronic structure of H/W(110) has been investigated by ARPES. This system hosts several hydrogen-related surface states forming different Fermi surface pockets. For the band S_1 building an elliptic hole pocket around

Table 24.2 EPI parameters for electronic states at overlayers and quantum-well states of thin films. Experimental results are from ARPES measurements, if not stated otherwise

Surface	Coverage (ML)	k point	E (eV)	λ	Γ_{e-ph} (0 K) (meV)	Method	References
H/W(110)	1	$k_F^{\overline{\Gamma}\to\overline{S}}$ (S_1)	0	1.4(1)		Re{Σ} slope	[24.106]
		k_F (S_1)	0	0–0.8(2)		Re{Σ} slope	[24.107]
			0	0.8–1.1		ai	[24.12]
		k_F (S_2)	0	0.7–0.9		ai	[24.12]
D/W(110)	1	$k_F^{\overline{\Gamma}\to\overline{S}}$ (S_1)	0	0.8		Re{Σ} slope	[24.106]
Au/Mo(112)	1	$k_F^{\overline{\Gamma}\to\overline{X}}$	0	0.70		Σ fit	[24.108]
		k_F^{av}	0	0.68		ai	[24.108]
Na/Cu(111)	1	$\overline{M}$	−0.1	0.24		Γ slope	[24.109]
				0.14	5.4	Model	[24.21]
	0.25	$\overline{M}$			9(3)	STS	[24.110]
Cs/Cu(111)	0.25	$\overline{M}$	−0.025	0.18	3.3	Model	[24.111, 112]
			0.408		7.5(30)	STS	[24.110]
Bi/Cu(100)	0.5	$\overline{M}$	−2.1 (E_1)	0.23(1)		Γ slope	[24.113]
		$\overline{X}$	−1.2 (E_4)	0.9(1)		Γ slope	[24.113]
			−1.0 (E_5)	1.1(1)		Γ slope	[24.113]
Bi/Ag(111)	1/3	$\approx\overline{\Gamma}$	–(0.7–0.2)	0.55(4)		Γ slope	[24.114]
Ag/V(100)	1–8	$\overline{\Gamma}$	QWS	0.2–1.0		Γ slope	[24.83]
Ag/Fe(100)	1–15	$\overline{\Gamma}$	QWS	0.3–1.0		Γ slope	[24.115]
Ag/Cu(111)		$\overline{\Gamma}$	QWS	0.11–0.16		Γ slope	[24.116]
Pb/Si(111)	15–28	$\overline{\Gamma}$	QWS	0.71–1.07		Γ slope	[24.117]
	4–10	$\overline{\Gamma}$	uQWS		15–60	STS	[24.118]
			uQWS	1.45–1.6		ai	[24.118]
	5, 7, 12	$\overline{\Gamma}$	oQWS	0.7–1.0		Γ slope	[24.119]
			oQWS	1.0–1.6		ai	[24.119]
	1	k_F^{av}	0	0.72		ai	[24.120]
	2–6	k_F^{av}	0	1.05–1.38		ai	[24.121]
	4–10	k_F^{av}	0	1.5–2.1		ai	[24.122]

QWS: quantum-well state; uQWS: unoccupied QWS; oQWS: occupied QWS; ai: ab initio; Γ slope: coupling from linear slope of $\Gamma(T)$; Γ fit: coupling from model fit of $\Gamma(T)$; Re{Σ} slope: coupling from linear slope of Re{$\Sigma(\epsilon)$} at ϵ_F; Σ fit: coupling from model fit of $\Sigma(\epsilon)$; STS: Scanning tunneling spectroscopy

the $\overline{S}$ point, a split in the dispersion close to ϵ_F was observed, at a binding energy corresponding to an H adsorbate mode frequency (Fig. 24.11). By replacing hydrogen with deuterium, the split size was reduced and its energy position moved closer to ϵ_F. This isotope effect demonstrated that the renormalization is indeed invoked by the adsorbate [24.106]. A later study succeeded in extracting the real part of the self-energy for various directions around the hole pocket. Derived coupling strengths varied between 0 and 0.8 partly exceeding $\lambda = 0.2$ of W bulk [24.107]. H/W(110) was also examined by an ab initio approach, where the Dyson equation (24.1) was solved self-consistently in the complex energy plane. It was found that the interaction with the adsorbate vibrations leads to a breakdown of the simple quasiparticle picture and results in complex shapes of the spectral functions, whose maxima mimic the measured band splittings [24.12, 13]. This strong electron–phonon interaction also has a dramatic effect on the vibrational properties of the adlayer. Large phonon anomalies of the adsorbate modes have been observed for hydrogenated (100) and (110) surfaces of W and Mo, which will be discussed in more detail in Sect. 24.5.

Several experimental and theoretical studies were devoted to Na/Cu(111). Deposition of Na on the Cu(111) surface leads to a QWS inside the surface-projected bulk gap of Cu around $\overline{\Gamma}$. For a full monolayer (ML) coverage, this state resides about 0.1 eV below ϵ_F at $\overline{\Gamma}$ [24.123]. The experimental coupling of 0.24 obtained from the slope of the temperature-dependent linewidth surpassed theoretical estimates of λ for both Na (0.16) and Cu (0.15) bulk [24.109]. Several microscopic model calculations of the EPI with varying degrees of sophistication have been applied to this system [24.2, 21, 124, 125]. Results depended sensitively

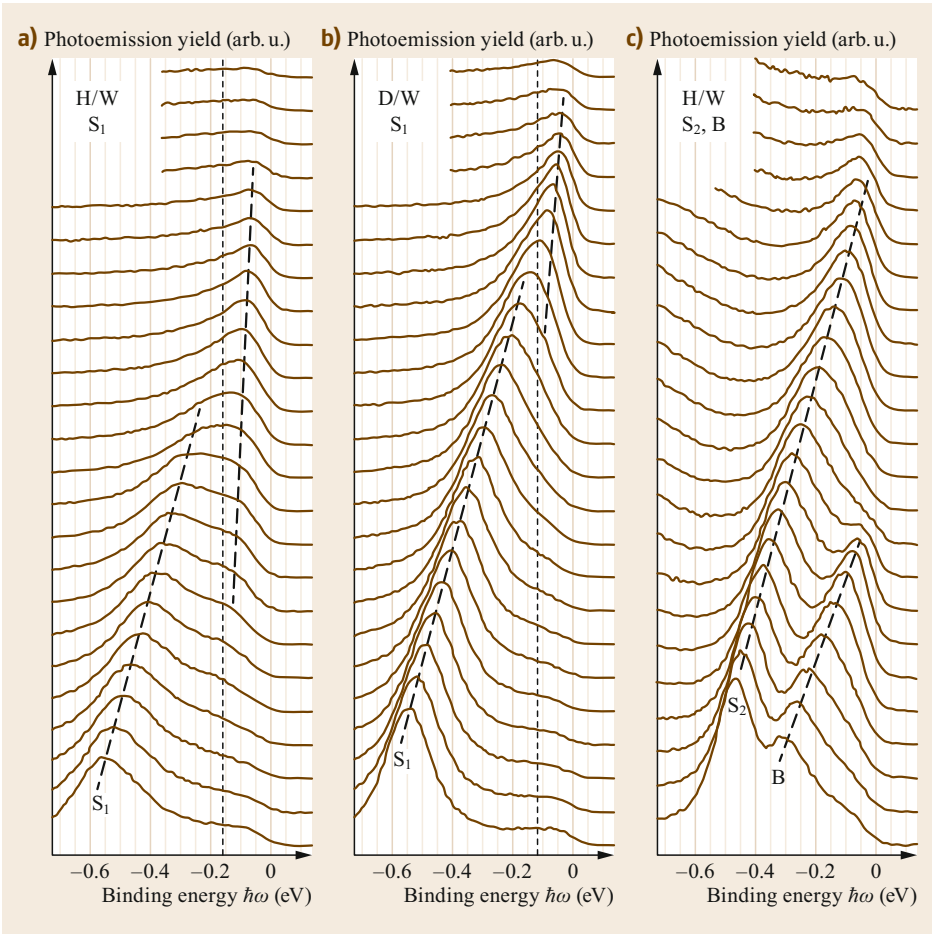

Fig. 24.11a–c Dispersion of the surface bands of H and D monolayers on W(110) as measured by ARPES along $\overline{\Gamma S}$. S_1 and S_2 denote two different surface bands, B is a bulk band in the same energy region. (Reprinted with permission from [24.106]. Copyright (2000) by the American Physical Society)

on the choice of the vibrational spectrum relevant for the coupling, suggesting that an accurate description of the surface vibrational spectrum including the overlayer is required for a reliable quantitative calculation of the EPI. Coupling strengths of similar magnitude have also been found in a model study of 0.25-ML coverage of Cu(111) by Cs, which builds an ordered (2×2) overlayer [24.112].

Au/Mo(112) is another example of a monolayer adsorbate system with a coupling that is significantly enhanced over the bulk value. In an ARPES experiment, bulk and (112)-derived surface states of Mo were found to strongly hybridize with a state originating from the Au overlayer. At ϵ_F a large coupling of 0.70 was derived from the self-energy. An ab initio calculation gave almost the same value for the momentum-averaged coupling at ϵ_F.

Submonolayer coverages of Bi on noble metal surfaces possess dispersive electronic states which are hybridized with the substrate electronic states and are spin-split due to the strong spin–orbit interaction related to Bi. The EPI has been studied for two cases, a 1/3 monolayer on Ag(111) and a half-monolayer coverage on Cu(100). In both cases, the surfaces reconstruct. For the $(\sqrt{3} \times \sqrt{3})$R30° Bi/Ag(111) surface, a large Rashba-type splitting of a surface band was observed near $\overline{\Gamma}$. It exhibited a strong coupling of about 0.55 with a rather weak dependence on the binding energy. For c(2×2)Bi/Cu(100), even larger values for λ were extracted for states at the surface Brillouin zone boundary $\overline{X}$ point. In both cases, the surface states are likely hybrid states involving states derived from both adsorbate and substrate atoms. These cases again exemplify that the coupling in adsorbate systems can by far exceed the bulk coupling strengths of the individual metals.

Quantum-Well States in Thin Films

The variation of the EPI in QWS with the thickness of the film has been systematically investigated for ultrathin Ag films on different metal substrates, Fe(100), V(100), and Cu(111). In each case, QWS develop in the projected band gap around $\overline{\Gamma}$. Their binding ener-

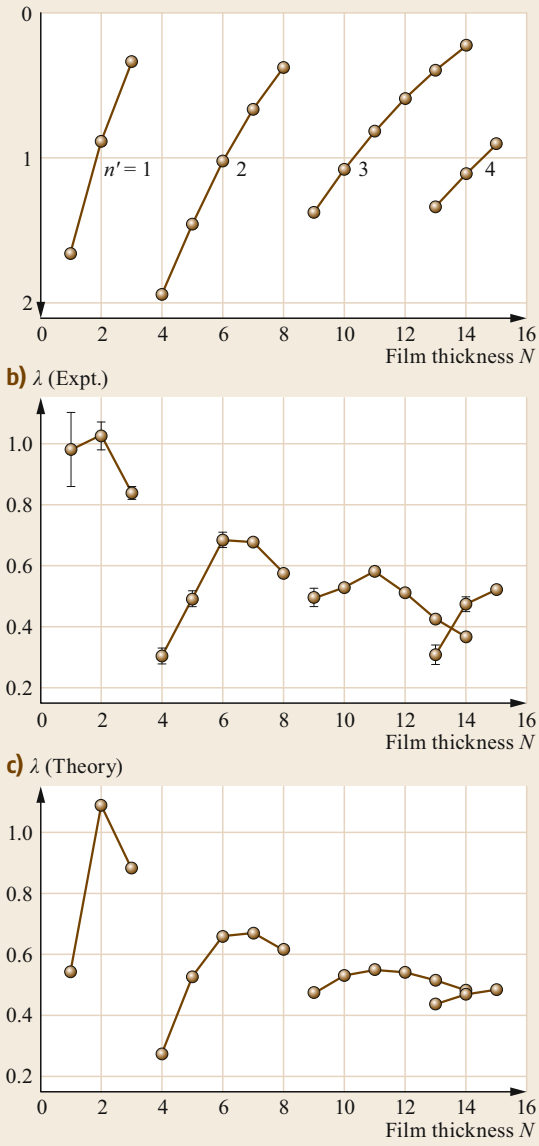

Fig. 24.12 **(a)** Experimental binding energies and **(b)** electron–phonon coupling constant in the $\overline{\Gamma}$ quantum-well state of Ag films on Fe(100) as a function of the thickness given in number of monolayers (N). **(c)** shows results of a model calculation. (Reprinted with permission from [24.115]. Copyright (2002) by the American Physical Society)

gies vary significantly with the thickness of the film and also depend on the type of substrate. In an early study, the QWS of Ag films on Cu(111) showed little variations of λ with the film thickness, and was similar to the coupling in Ag bulk [24.116]. In contrast, both studies on the (100) metal surfaces found a strong and nonmonotonous variation of λ with the thickness. The largest values of order 1 were obtained for the very thin films. Figure 24.12 exemplifies this behavior for Ag films on Fe(100) [24.115]. Most values by far exceed the value of λ for bulk Ag. It has been proposed that the large coupling is an interface effect and has its origin in a large potential step at the interface seen by the QWS, which enhances the electron–phonon coupling matrix elements. A simple modeling based on this idea could reproduce the main trends including the observed oscillatory behavior in λ as a function of thickness, but a detailed microscopic calculation to substantiate this explanation has not been performed until now.

Ultrathin films of Pb are another intensively studied overlayer system. The coupling of individual QWS were investigated in several ARPES experiments, where λ values were extracted from the T-slope of the linewidth. For films of 15–28 ML thickness, an oscillatory behavior of the EPI with the number of layers was observed [24.117]. For thinner films ($\leq$ 12 ML) the deduced λ for the QWS of the order of 0.7–1.0 was significantly lower than the bulk value. Ab initio calculations suggested that this reduction is linked to the presence of a substrate, whose impact on the EPI grows the thinner the films become [24.119].

Unoccupied QWS of Pb films with 4–10 ML thickness were studied by a combined scanning tunneling spectroscopy and ab initio approach [24.118]. From T-dependent STS measurements the electron–electron contribution Γ_{e-e} could be separated from the electron–phonon contribution Γ_{e-ph}. The linewidth showed a quadratic dependence on the QWS energy, which was attributed to Γ_{e-e}. Comparison with ab initio calculations suggested that the extracted $\Gamma_{e-ph}(T = 0)$ values are compatible to values of λ in the range 1.45–1.6 for most of the QWS, which are close to the Pb bulk value of 1.55.

Pb thin films also exhibit peculiar superconducting properties. Pb bulk is a strong-coupling superconductor with a large average coupling constant of $\lambda = 1.55$ and a bulk transition temperature of $T_c = 7.2$ K. Atomically flat islands of Pb(111) with large lateral extension can be prepared on various substrates (Si(111) or Cu(111)) with high control on the number of monolayers. Scanning tunneling spectroscopy can be used to identify the superconducting transition temperature as the temperature, where a gap in the electronic density of states opens at ϵ_F. These studies show that T_c is reduced when the film thickness decreases, but superconductivity survives for films as thin as 5 ML [24.126]. For thicknesses smaller than 30 ML, T_c showed an oscillatory dependence [24.117]. Even for a 1-ML coverage of Pb on Si(111), a superconducting transition was

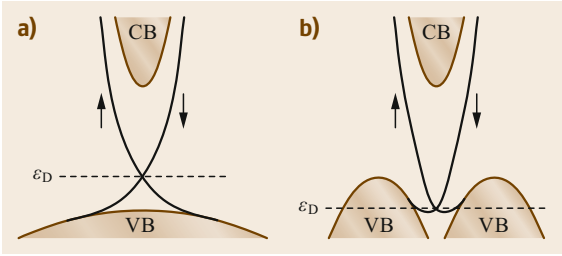

Fig. 24.13a,b Schematic drawing of the band structure at the (0001) surface of the topological insulators Bi_2Se_3 **(a)** and Bi_2Te_3 **(b)**. CB: bulk conduction band; VB: bulk valence band; ϵ_D: energy position of the Dirac point

found ($T_c = 1.83\,K$) [24.127]. In this case, however, the structure of the Pb overlayer differs from a (111) surface layer. Because of this interest in superconducting properties, several theoretical studies focused on the calculation of Fermi-surface-averaged EPI for Pb films. It has been noted that spin–orbit coupling has a significant influence on the coupling strength and cannot be neglected [24.122].

24.4.3 Topological Insulators

Topological insulators are materials whose electronic structure is topologically distinct from a normal insulator. In the bulk, they possess an electronic band gap like an ordinary insulator, but the topological property forces the presence of gapless edge states. A variety of topological insulators have been theoretically predicted and experimentally identified, and exist in both two and three dimensions (2-D and 3-D). A survey of recent work on EPI for topological insulators has been given in [24.136], and for further reading we refer to the reviews [24.137–140].

In the context of EPI at surfaces, research focused on the surface states of 3-D topological insulators. Here, the edge states manifest themselves as metallic (gapless) surface states with peculiar properties. In Fig. 24.13, the surface electronic structure of two prominent examples of 3-D topological insulators, Bi_2Se_3 and Bi_2Te_3, is sketched schematically. The metallic surface bands are located at the center of the surface Brillouin zone and span the energy-gap region between the bulk valence and conduction bands. At a single crossing point, called the Dirac point (with energy ϵ_D), they possess a linear dispersion. This 2-D dispersion represents a so-called Dirac cone, well known from the electronic structure of graphene. But here the situation differs in that each band is single degenerate, and the spin direction of each state is locked perpendicular to its momentum. This peculiar spin structure is promising for applications related to spin-polarized transport.

The topological origin of the surface state has the consequence that it is robust against perturbations at the surface, which do not break time-reversal symmetry, like nonmagnetic impurities. This argument strictly holds only in the single-particle picture, but could be violated by many-body interactions. This motivated several investigations to quantify the strength of the electron–phonon interaction in topological surface states. Studies concentrated on the (0001) surface of the 3-D topological insulators Bi_2Se_3 and Bi_2Te_3. Results are collected in Table 24.3. Both compounds are layered materials built from neutral five-layer blocks (quintuple layers), which are only weakly bound by van der Waals-type interactions. This allows an easy cleavage of samples to prepare the (0001) surface, which is oriented parallel to the layers. The existence of the topological surface state has been verified experimentally [24.141].

Table 24.3 EPI parameters for electronic surface states of topological insulators. Experimental results are from ARPES measurements, if not stated otherwise

Surface	k point	$\epsilon_F - \epsilon_D$ (eV)	$E - \epsilon_F$ (eV)	λ	Method	Reference
Bi_2Se_3(0001)		0.25–0.3	–(0.2–0.25)	0.25(5)	Γ slope	[24.128]
		0.23–0.27	–(0–0.02)	0.08	Γ slope	[24.129]
	$k_F^{\bar{\Gamma}\to\bar{K}}$	0.3	0	≈ 3	Re{Σ} slope	[24.130]
		0.35	0	0.17	Re{Σ} slope	[24.131]
	k_F^{av}	0.2	0	0.42	Model	[24.132]
		0.5	0	0.25	Model	[24.133]
Bi_2Te_3(0001)	$k_F^{\bar{\Gamma}\to\bar{K}}$	0.08	0	< 0.01	Re{Σ} slope	[24.131]
		0.3	0	0.19	Re{Σ} slope	[24.131]
	k_F^{av}		0	0.05	ai	[24.103]
		0.05	0	0.13	Model	[24.134]
		0.1	0	0.01	Model	[24.135]

ai: ab initio; Γ slope: coupling from linear slope of $\Gamma(T)$; Re{Σ} slope: coupling from linear slope of Re{$\Sigma(\epsilon)$} at ϵ_F; Model: continuum model for coupling to acoustic modes

For Bi_2Se_3, the Dirac point falls within the bulk band gap, and for uncharged samples its energy coincides with the Fermi energy. Sample preparation typically leads to slightly electron-doped bulk materials, which results in an upward shift of the Fermi level, and may also lead to a partial filling of the bulk conduction bands. The degree of doping can be characterized by the energy distance $\epsilon_F - \epsilon_D$. ARPES measurements have given quite diverse results for the EPI. An early experiment [24.142] could not detect an electron–phonon self-energy, suggestive of a very small coupling. Later studies gave values for λ ranging from 0.08 to 0.25 [24.128, 129, 131]. Even $\lambda \approx 3$ has been deduced from the measured renormalization of the quasiparticle dispersion [24.130]. The authors suggested, however, that this large value does not originate only from the EPI, but also includes coupling to low-energy spin plasmons.

In the case of Bi_2Te_3, the Dirac point overlaps with the energy region of the bulk valence states, which naturally leads to a partial occupation of the upper part of the Dirac cone even for undoped bulk samples. ARPES experiments by *Chen* et al. [24.131] found a pronounced dependence of the EPI coupling strength on the doping. A very small λ for hole-doped samples contrasted an enhanced coupling for electron-doped ones. Anisotropy of the EPI related to the hexagonal symmetry of the (0001) surface has recently been studied in an ARPES experiment [24.143]. Close to the Dirac point, the electronic dispersion is rather isotropic. At about 200 meV above the Dirac point, the dispersion along the $\overline{\Gamma}$–$\overline{M}$ direction flattens markedly as compared to the $\overline{\Gamma}$–$\overline{K}$ direction. Constant energy contours change from a circular to a hexagonally warped shape. Simultaneously, the lifetime broadenings become anisotropic, with larger broadenings found along $\overline{\Gamma}$–$\overline{K}$. It was proposed that modifications of the spin texture in the warped Dirac cone could be responsible for an anisotropy of the spin-dependent scattering.

Beside these direct probes of the quasiparticle properties, additional experiments providing more indirect information about the coupling strength are briefly mentioned here. Time-resolved ARPES or pump-probe experiments analyzed the ultrafast carrier dynamics related to the surface state [24.144–146]. Further information was gained from transport measurements [24.147, 148] and optical spectroscopy [24.149, 150]. Finally, investigations of the surface phonon spectrum with helium-atom scattering spectroscopy indicated unusual phonon anomalies, which were attributed to a strong coupling to the topological surface states [24.151–153]. The approach to quantify the EPI from the phonon perspective will be addressed further in Sect. 24.5.

On the theoretical side, the coupling of topological surface states with acoustic modes has been studied based on a continuum model [24.132–135]. This approach considers the interaction of the surface electrons with long-wavelength acoustic phonons, which also includes contributions from surface-localized vibrations like the Rayleigh mode, but neglects contributions from optical phonons. Despite a similar framework, no consensus was reached on the strength of the EPI (Table 24.3). Contribution from optical phonon modes were taken into account in an ab initio calculation for a thin film of Bi_2Te_3 [24.103]. Results for the average λ suggested a very small coupling.

24.5 Electron–Phonon Interaction and Phonons

The interaction between electrons and atomic vibrations does not only affect the electronic quasiparticles, but also renormalizes the vibrational quasiparticles, i.e., the phonons. In analogy to the electronic quasiparticles, the EPI gives rise to changes in the phonon frequencies and evokes finite lifetimes. Because of the reduced dimensionality at the surface, these renormalization effects can be more pronounced for surface vibrations than for phonons in the bulk.

The topic of surface phonons is covered in Chap. 23 of this Springer Handbook. We briefly mention here the three spectroscopic techniques used to measure surface phonon dispersion and related properties:

(i) Helium atom scattering (HAS): it utilizes inelastic scattering of He atoms at a surface which creates or annihilates a phonon. The He atom does not penetrate the surface, but is reflected a few Å above the surface atoms. This makes this technique very surface sensitive.

(ii) High-resolution electron energy-loss spectroscopy (HREELS): this technique uses inelastic electron scattering processes to gain information about the lattice vibrations. It is less surface sensitive than HAS because electrons penetrate the surface.

(iii) Inelastic x-ray scattering (IXS) at grazing incidence: IXS is nowadays a common technique to probe bulk phonons, because x-rays penetrate deeply into the bulk. However, if the angle of the incoming x-ray is chosen to be smaller than the angle for total reflection, the so-called grazing incidence condition, the inelastic scattering acquires a much higher surface sensitivity.

In this section, we first introduce the basic quantities describing the phonon renormalization, and define related measures of the EPI. Then we give a survey of the most dramatic effects of the EPI on surface phonons. Finally, we discuss methods to extract information about the EPI from measurements of surface phonon properties.

24.5.1 Renormalization of Phonons

The starting point is the expression for the renormalized phonon Green's function in terms of the phonon self-energy Π [24.1],

$$D(\boldsymbol{q}j,\omega) = \frac{2\omega_{\boldsymbol{q}j}}{\omega^2 - \omega_{\boldsymbol{q}j}^2 - 2\omega_{\boldsymbol{q}j}\Pi(\boldsymbol{q}j,\omega)} , \qquad (24.27)$$

where the phonon is characterized by the momentum $\boldsymbol{q}$ and branch index j. It is linked to the bare Green's function $D_0(\boldsymbol{q}j,\omega) = 1/(\omega-\omega_{\boldsymbol{q}j}) - 1/(\omega+\omega_{\boldsymbol{q}j})$ by the Dyson equation $D^{-1} = D_0^{-1} - \Pi$, with $\omega_{\boldsymbol{q}j}$ denoting the bare frequency, i.e., the frequency a vibration would have without the interaction with the electrons. The spectral function of the phonon is given by $-2\mathrm{Im}\{D(\boldsymbol{q}j,\omega)\}$. For small self-energies, it will still show a quasiparticle peak, which is, however, broadened and its center is shifted away from the bare frequency $\omega_{\boldsymbol{q}j}$. The finite linewidth is proportional to the inverse lifetime and connected with $\mathrm{Im}\{\Pi\}$, while the frequency shift is related to $\mathrm{Re}\{\Pi\}$.

The phonon self-energy can be expressed as an infinite series of Feynman diagrams. Figure 24.14 shows schematically the graph for the lowest-order contribution from the EPI to the imaginary part of the self-energy, which describes a virtual electron-hole excitation. This leads to the expression

$$\mathrm{Im}\{\Pi(\boldsymbol{q}j,\omega)\} = \pi\frac{1}{N_k}\sum_{\boldsymbol{k}\nu\nu'} |g^{\boldsymbol{q}j}_{\boldsymbol{k}+\boldsymbol{q}\nu',\boldsymbol{k}\nu}|^2 \times [f(\epsilon_{\boldsymbol{k}\nu}) - f(\epsilon_{\boldsymbol{k}+\boldsymbol{q}\nu'})] \times \delta[\omega + \epsilon_{\boldsymbol{k}\nu} - \epsilon_{\boldsymbol{k}+\boldsymbol{q}\nu'}] . \qquad (24.28)$$

N_k is the number of points used in the k summation. Equation (24.28) depends on temperature via the Fermi distribution function f. The phonon linewidth induced by the EPI is given as

$$\gamma_{\boldsymbol{q}j}(T) = -2\mathrm{Im}\{\Pi(\boldsymbol{q}j,\omega_{\boldsymbol{q}j})\} . \qquad (24.29)$$

Because phonon energies are often much smaller than typical electronic energies, $\gamma_{\boldsymbol{q}j}$ has a weak T-dependence and it is justified to take its $T \to 0$ limit [24.154]

$$\gamma_{\boldsymbol{q}j}(T=0) \approx 2\pi\omega_{\boldsymbol{q}j}\frac{1}{N_k}\sum_{\boldsymbol{k}\nu\nu'} |g^{\boldsymbol{q}j}_{\boldsymbol{k}+\boldsymbol{q}\nu',\boldsymbol{k}\nu}|^2 \times \delta(\epsilon_{\boldsymbol{k}\nu})\delta(\epsilon_{\boldsymbol{k}+\boldsymbol{q}\nu'}) . \qquad (24.30)$$

To arrive at this form, the phonon frequency appearing in the δ-function in (24.28) was neglected. This approximation works usually very well, except in the limit $\boldsymbol{q} \to 0$ for metals, because there the energy difference $\epsilon_{\boldsymbol{k}\nu} - \epsilon_{\boldsymbol{k}+\boldsymbol{q},\nu}$ becomes arbitrarily small.

Equation (24.30) becomes relevant in the context of phonon-mediated superconductivity. The interaction between electrons and phonons gives rise to an effective attractive electron–electron interaction which leads to the formation of Cooper pairs as the basis of a superconducting state. The microscopic theory of superconductivity based on this phonon-mediated paring has been developed by *Bardeen* et al. [24.155] and extended by *Eliashberg* [24.156] to the strong coupling regime. The central quantity in describing the pairing interaction is the so-called Eliashberg function

$$\alpha^2F(\omega) = \frac{1}{N(\epsilon_\mathrm{F})}\frac{1}{N_q}\frac{1}{N_k}\sum_{\boldsymbol{q}j,\boldsymbol{k}\nu\nu'} |g^{\boldsymbol{q}j}_{\boldsymbol{k}+\boldsymbol{q}\nu',\boldsymbol{k}\nu}|^2 \times \delta(\omega-\omega_{\boldsymbol{q}j})\delta(\epsilon_{\boldsymbol{k}\nu})\delta(\epsilon_{\boldsymbol{k}+\boldsymbol{q}\nu'}) . \qquad (24.31)$$

Here $N(\epsilon_\mathrm{F}) = 1/N_k\sum_{\boldsymbol{k}\nu}\delta(\epsilon_{\boldsymbol{k}\nu})$ is the electronic density of states at the Fermi energy per spin. $\alpha^2F(\omega)$ represents a measure of the pairing strength mediated by phonons of energy ω. The sum in (24.31) extends over all phonon modes and averages over possible interaction paths involving electronic states at the Fermi energy, weighted by the corresponding scattering probability as given by the EPI matrix elements.

On the basis of the Eliashberg function one defines the coupling constant

$$\lambda_\mathrm{sc} = 2\int \mathrm{d}\omega \frac{\alpha^2F(\omega)}{\omega} . \qquad (24.32)$$

This quantity is a dimensionless measure of the average coupling strength of a material related to pairing, and plays a central role in characterizing superconducting properties like the transition temperature. Using (24.31)

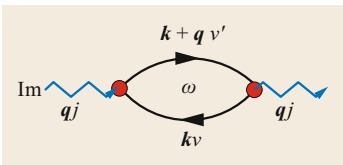

Fig. 24.14 Schematic drawing of the lowest-order contribution to the imaginary part of the phonon self-energy from interaction with electrons

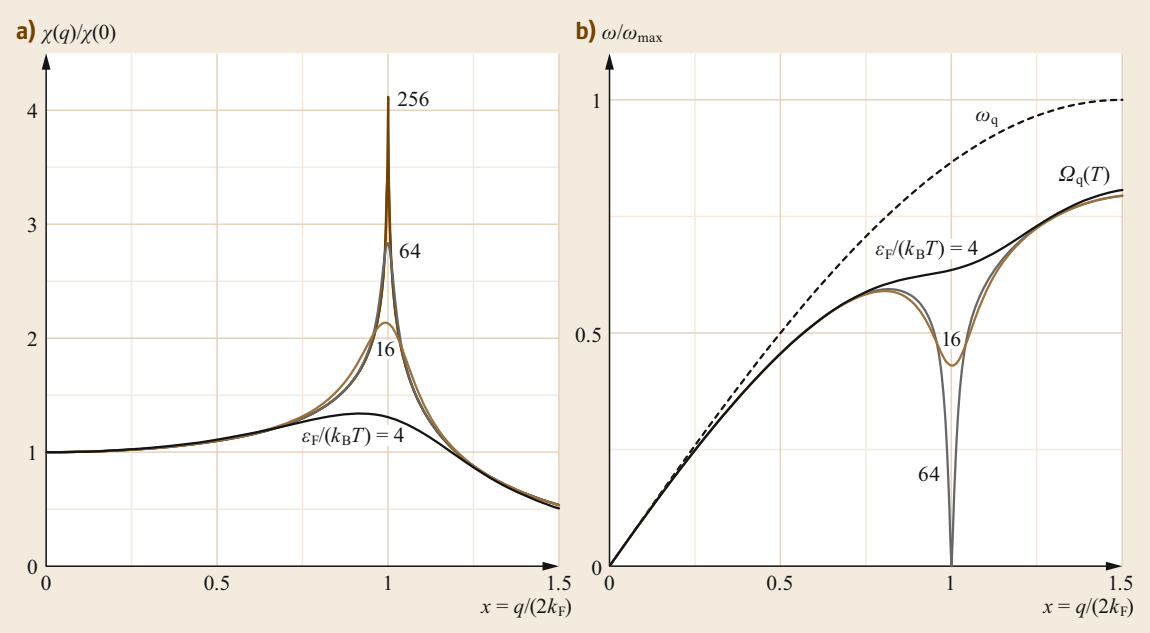

Fig. 24.15a,b Schematic drawing of a Kohn anomaly. The charge susceptibility **(a)** and phonon renormalization **(b)** as a function of temperature for a one-dimensional Fermi gas

and (24.30) the coupling constant can be expressed as a sum of contributions from individual phonon modes,

$$\lambda_{sc} = \frac{1}{\pi N(\epsilon_F)} \frac{1}{N_q} \sum_{qj} \frac{\gamma_{qj}}{\omega_{qj}^2} . \qquad (24.33)$$

This motivates the definition of a mode-selected coupling constant as

$$\lambda_{qj} = \frac{1}{\pi N(\epsilon_F)} \frac{\gamma_{qj}}{\omega_{qj}^2} , \qquad (24.34)$$

which is the property of an individual phonon. Then the total coupling is just given by the momentum average over all mode-selected coupling constants and summed over all phonon branches

$$\lambda_{sc} = \frac{1}{N_q} \sum_{qj} \lambda_{qj} . \qquad (24.35)$$

λ_{sc} can be also linked to the coupling strength defined for individual electronic states. Combining (24.11) and (24.13) one finds

$$\lambda_{sc} = \frac{1}{N(\epsilon_F)} \frac{1}{N_k} \sum_{k\nu} \lambda_{k\nu} \delta(\epsilon_{k\nu}) . \qquad (24.36)$$

Thus, λ_{sc} represents the average coupling strength of all electronic states at the Fermi level.

24.5.2 Kohn Anomalies of Surface Phonons

A Kohn anomaly is a pronounced softening of phonons which is induced by a specific coupling to electronic states in the vicinity of the Fermi level. The softening occurs in a small momentum range and becomes enhanced when lowering the temperature. If strong enough, it can result in an instability of the phonon and evokes a structural phase transition. The physics of the Kohn anomaly is most easily demonstrated for the model of a one-dimensional noninteracting electron gas. The renormalized phonon frequency can be expressed by the charge susceptibility $\chi_q(T)$ as [24.157]

$$\Omega_q^2(T) = \omega_q^2 + 2\omega_q g^2 \chi_q(T) , \qquad (24.37)$$

where ω_q denotes the bare frequency, and g is an effective coupling constant and is assumed to be independent of momentum q. Figure 24.15 sketches the renormalization of an acoustic branch coupled to a one-dimensional electron gas; χ_q is peaked at $2k_F$, where k_F is the Fermi wavevector, and diverges in the limit $T \to 0$. This induces a sharp dip in the phonon dispersion at $q = 2k_F$, which grows when lowering T, and eventually leads to a lattice instability at a finite temperature. As a consequence, the structure changes and the electronic charge density develops a spatial modulation called a charge-density wave (CDW).

In dimensions larger than one, the divergency of χ is usually washed out. Exceptions are situations where a so-called Fermi surface nesting occurs. Two larger sections of the Fermi surface exist which are parallel to each other and differ by a constant vector $\boldsymbol{q}_c$. In this case $\chi_{q_c}(T)$ exhibits a pronounced T dependence. The nesting condition can be easier fulfilled in 2-D than in 3-D. Promising candidates are layered materials with weak binding orthogonal to the layers, which exhibit quasi-2-D electronic structures. They possess Kohn-type anomalies already in the bulk. In a few cases, however, Kohn anomalies were observed in surface phonon branches, whose properties differed markedly from that of the bulk. An example is $2H$-$TaSe_2$, where the Rayleigh mode measured by HAS displayed a T-dependent anomaly. It was located at one-half of the reduced Brillouin zone, in contrast to the bulk anomaly in the longitudinal acoustic branch, which occurred at two-thirds of the zone [24.158]. In a comparative study of bulk and surface phonons of $2H$-$NbSe_2$ using IXS under grazing incidence conditions, the Kohn anomaly was found to be significantly deeper in energy at the surface than in the bulk [24.159]. It was suggested that the strengthening of the anomaly originates from a structural relaxation in the topmost layers [24.160].

Hydrogen-covered surfaces of Mo(110) and W(110) are classical examples where Kohn anomalies in the surface phonon dispersion were detected, which have no counterpart in the bulk. Figure 24.16 shows measurements from both HAS and HREELS, which indicate very sharp phonon anomalies in acoustic branches after adsorption of H on the W(110) surface [24.161]. Subsequent ab initio calculations found that the H adsorption evokes surface electronic states, whose Fermi surface contour shows the required nesting property. Thus, the observed dip was interpreted as a Kohn anomaly related to the adsorbate-induced surface state [24.162]. The anomalous acoustic branches involve to a larger extend vibrations of the substrate atoms. A complementary HREELS measurement of the adsorbate vibrations at energies of ≈ 100 meV detected similar anomalous dips, which occur at the same wave vector as for the acoustic branches [24.163]. The observation of an electronic surface state by ARPES and its very peculiar dispersion, discussed in the previous section, further corroborated this explanation [24.106].

The pronounced temperature dependence of the phonon frequency at the critical wavevector of the Kohn anomaly has been used by *Kröger* et al. [24.8, 165] to obtain a quantitative estimate of the electron–phonon coupling strength. They applied an analytic expression for the frequency renormalization which was derived for a one-dimensional free-electron gas [24.157]

$$\Omega_{q_c}^2(T) = \omega_{q_c}^2 \left[1 - \lambda_c \ln\left(\frac{1.14\epsilon_F}{k_B T}\right)\right] . \qquad (24.38)$$

Here, an effective coupling constant related to the critical phonon mode is introduced, which is connected to the coupling constant g introduced in (24.37) by $\lambda_c = 2g^2 N(\epsilon_F)/\omega_{q_c}$. From measurements of $\Omega_{q_c}(T)$ at two temperatures (100 and 293 K) and identifying ϵ_F with the bottom edge of the electron band, which takes part in the quasi one-dimensional Fermi surface nesting, they derived values of $\lambda_c \approx 0.11$ and 0.13 for H/Mo(110) and H/W(110), respectively. These values are significantly smaller than coupling constants $\lambda = 0.7-1.4$ obtained from a renormalization analysis of electronic states (Table 24.2).

Recent measurements of the (0001) surface phonon dispersion of the topological insulators Bi_2Se_3 and Bi_2Te_3 suggested the existence of an optical surface phonon branch with an unusual dispersion and a V-shaped minimum [24.151, 153]. The minimum occurs at small momenta of approximately the size of the Dirac cone of the topological surface state. This observation has been interpreted as a strong Kohn anomaly originating from the interaction of this phonon branch with the topological surface state. The dispersion was analyzed within an empirical lattice-dynamical model, which in addition to the direct ion–ion Coulomb forces also accounts for the electronic degrees of freedom by dynamically deformable pseudo charges. The presence of the surface state is modeled by dipolar pseudo charges at the surface, which are more deformable than those in the bulk. This model was able to reproduce the dispersion and the V-shaped minimum of the surface phonon branch. The dispersion of the anomalous branch was analyzed within the empirical model to obtain an estimate for the real part of the phonon self-energy [24.152, 153]. A Kramers–Kronig transformation was then utilized to calculate the related imaginary part of the self-energy. With the help of (24.29) and (24.34) this was linked to the phonon linewidth and mode-selected coupling constant λ_{qj}. Averaging over all modes of the anomalous branch gave values of 0.43 and 1.44 for Bi_2Se_3 and Bi_2Te_3, respectively. These values represent lower limits for the total coupling λ_{sc}, which would require summation over all branches. Such a strong coupling to the surface state should also result in an unusual renormalization of the electronic surface states [24.166], which has not been reported so far (Table 24.3).

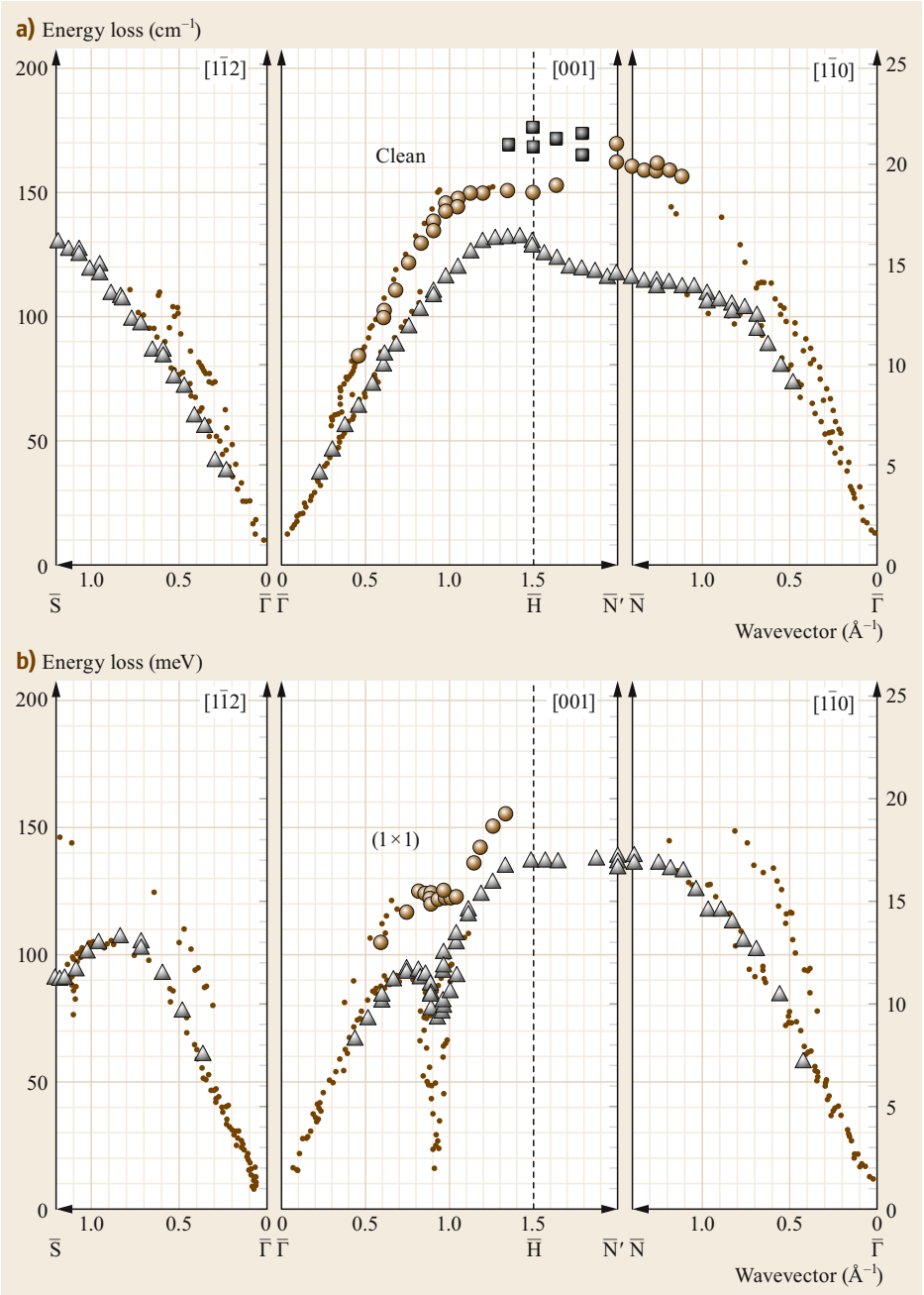

Fig. 24.16a,b Dispersion of surface phonons of the clean W(110) surface **(a)** and the H/W(110) surface **(b)**. Shown are data from HREELS for the Rayleigh wave (*triangles*) and the longitudinally polarized surface phonons of the first (*circles*) and second (*squares*) layer. The *dots* denote HAS results from [24.164]. (Reprinted from [24.161], with permission from Elsevier)

24.5.3 Mode-Selected Coupling from Phonon Measurements

Details of the EPI on surfaces are encoded in the mode-selected coupling constants λ_{qj} defined in (24.34). Inelastic Helium atom scattering (HAS) experiments on thin films have shown that this technique may provide direct access to this quantity.

The inelastic scattering of an He atom off a surface happens near the classical turning point, which typically lies a few Å above the topmost surface layer. The scattering probability for creation or annihilation of a single phonon is determined by the size of the modulation of the electronic density at this turning point induced by the phonon vibration. It has been common wisdom that only surface phonons with large vibrational am-

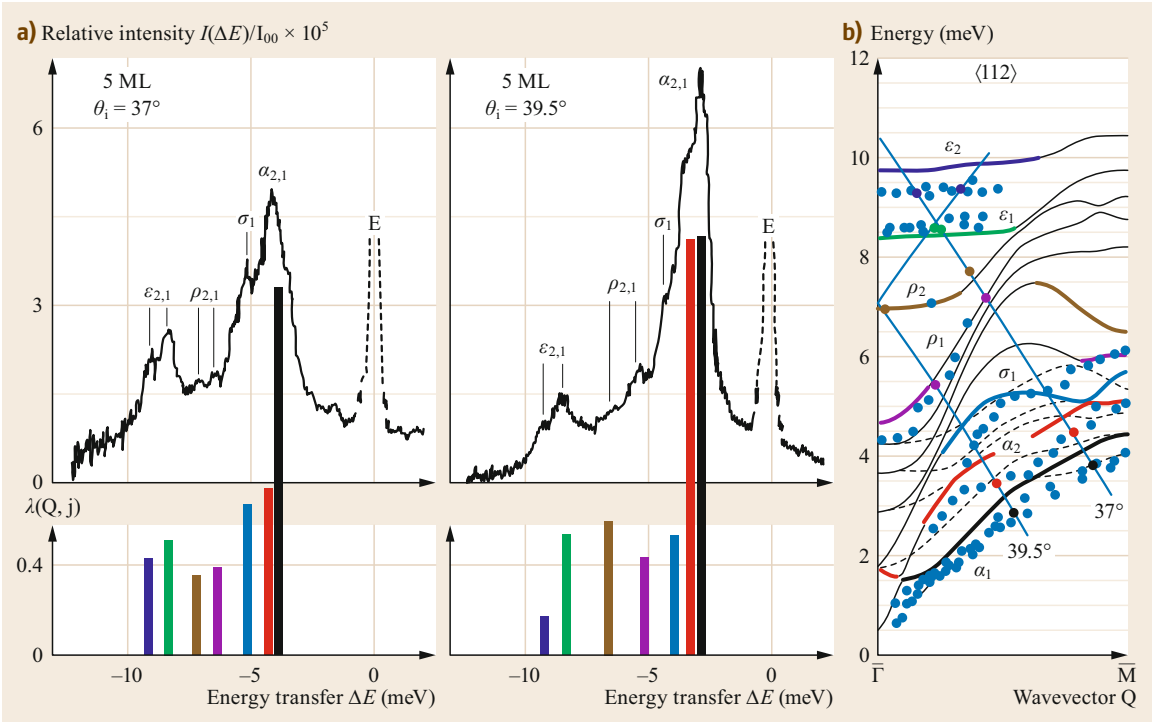

Fig. 24.17 **(a)** Example of HAS energy-gain spectra for a five-monolayer Pb film on a Cu(111) substrate in the ⟨112⟩ direction (*upper panel*), calculations of the mode-selected coupling constants (*lower panel*), and **(b)** the corresponding scan curves across the phonon dispersion. (Reproduced adapted from [24.167] with permission of PCCP Owner Societies)

plitudes in the topmost surface layer create sufficiently large density modulations to be detected by HAS. This view has been challenged by HAS measurements of the phonon modes of thin Pb(111) films on Cu(111), which resulted in surprisingly rich spectra [24.168]. Comparison with ab initio calculations suggested that modes localized deeper below the surface or even at the interface to the substrates were detected. A theoretical analysis of the scattering process showed that under conditions appropriate for the confined geometry of the film, the HAS scattering probability is [24.167, 169]

$$P(\boldsymbol{k}_i, \boldsymbol{k}_f) \propto f(\Delta E) \sum_{qj} \lambda_{qj} \delta(\Delta E - \omega_{qj}) \,. \qquad (24.39)$$

Here $\boldsymbol{k}_i$, $\boldsymbol{k}_f$ denote the initial and final momenta of the He atom, and ΔE the energy transfer in the scattering process. $f(\Delta E)$ represents a kinematic prefactor which is a slowly varying function of the energy transfer ΔE. (24.39) demonstrates that the scattering probability or the HAS amplitude is approximately proportional to the mode-selected coupling constants λ_{qj}. This relationship is supported by comparison of HAS spectra with ab initio calculations of λ_{qj}. Figure 24.17 shows an example for a 5-ML Pb(111) film on Cu(111) for two different scan curves. Both peak positions and amplitudes of the spectra agree well with calculated phonon energies and mode-selected coupling constants. These findings show that HAS is a promising spectroscopy tool to measure the branch and momentum dependence of the mode-selected coupling constants. It offers an experimental path to identify those phonon modes which are most relevant for the superconducting pairing in thin films, and to study the variation of the pairing interaction with the film thickness.

24.6 Conclusions

Surfaces provide an ideal platform to study the interaction of electronic and vibrational degrees of freedom in much detail. Steady advances in experimental techniques and computational methods led in recent years to an intensified investigation of EPI-related phenomena. The close link between experiment and theory has

been proven to be mutually fruitful. While increasing experimental resolution provides improved quantitative estimates serving as benchmarks for calculational approaches, theory gives additional insight into the interpretation of the data.

In this chapter, we presented an overview of investigations of electron–phonon interaction at metallic surfaces, overlayers, and thin films. The main focus was placed on the renormalization of electronic quasiparticles, which can be most directly probed by surface spectroscopy techniques. We have also discussed the effects of EPI on surface vibrational properties, which, when strong enough, can trigger surface phase-transitions inducing structural reconstructions. Various cases have been identified, where the interaction strength at the surface is significantly enhanced over the bulk value. A better understanding of the EPI of confined electronic states, e.g., quantum-well states of thin films, and its relation to thin film superconductivity may help to control or even allow the design of desired properties by choosing proper thicknesses or geometries. More recently, the relevance of EPI for the stability of topological surface states has been recognized. In view of the increasing number of compounds with topologically nontrivial electronic structures, like topological insulators, Dirac or Weyl metals, whose interesting physics rests on the stability of surface or edge states, precise knowledge about the intrinsic EPI of these states will become increasingly important for future applications.

References

24.1 G. Grimvall: *The Electron–phonon Interaction in Metals*, Selected Topics in Solid State Physics (Elsevier North-Holland, Amsterdam, New York, Oxford 1981)

24.2 B. Hellsing, A. Eiguren, E.V. Chulkov: Electron–phonon coupling at metal surfaces, J. Phys. Condens. Matter **14**(24), 5959 (2002)

24.3 E.W. Plummer, J. Shi, S.-J. Tang, E. Rotenberg, S.D. Kevan: Enhanced electron–phonon coupling at metal surfaces, Prog. Surf. Sci. **74**(1–8), 251–268 (2003)

24.4 S.-J. Tang, J. Shi, B. Wu, P.T. Sprunger, W.L. Yang, V. Brouet, X.J. Zhou, Z. Hussain, Z.-X. Shen, Z. Zhang, E.W. Plummer: A spectroscopic view of electron–phonon coupling at metal surfaces, Phys. Status Solidi (b) **241**(10), 2345–2352 (2004)

24.5 B. Hellsing, A. Eiguren, E.V. Chulkov, P.M. Echenique: Electron–phonon coupling and lifetimes of excited surface states, Surf. Sci. **593**(1–3), 12–18 (2005)

24.6 P. Hofmann, I.Y. Sklyadneva, E.D.L. Rienks, E.V. Chulkov: Electron–phonon coupling at surfaces and interfaces, New J. Phys. **11**(12), 125005 (2009)

24.7 E.V. Chulkov, A. Zugarramurdi, S.S. Tsirkin, X. Zubizarreta, I.A. Nechaev, I.Y. Sklyadneva, S.V. Eremeev: Electronic structure and excitations on clean and nanostructured metal surfaces, Eur. Phys. J. B **75**, 37–47 (2010)

24.8 J. Kröger: Electron–phonon coupling at metal surfaces, Rep. Prog. Phys. **69**(4), 899 (2006)

24.9 J. Kröger: Nonadiabatic effects on surfaces: Kohn anomaly, electronic damping of adsorbate vibrations, and local heating of single molecules, J. Phys. Condens. Matter **20**(22), 224015 (2008)

24.10 P.M. Echenique, R. Berndt, E.V. Chulkov, T. Fauster, A. Goldmann, U. Höfer: Decay of electronic excitations at metal surfaces, Surf. Sci. Rep. **52**(7/8), 219–317 (2004)

24.11 A.B. Migdal: Interaction between electrons and lattice vibrations in a normal metal, Sov. Phys. JETP **7**, 996–1001 (1958)

24.12 A. Eiguren, C. Ambrosch-Draxl: Complex quasiparticle band structure induced by electron–phonon interaction: Band splitting in the $1\times$ 1H/W(110) surface, Phys. Rev. Lett. **101**, 036402 (2008)

24.13 A. Eiguren, C. Ambrosch-Draxl, P.M. Echenique: Self-consistently renormalized quasiparticles under the electron–phonon interaction, Phys. Rev. B **79**, 245103 (2009)

24.14 N.S. Luo, P. Ruggerone, J.P. Toennies, G. Benedek: Electron–phonon coupling at metal surfaces probed by helium atom scattering, Phys. Scr. **T49**, 584 (1993)

24.15 A. Eiguren, B. Hellsing, F. Reinert, G. Nicolay, E.V. Chulkov, V.M. Silkin, S. Hüfner, P.M. Echenique: Role of bulk and surface phonons in the decay of metal surface states, Phys. Rev. Lett. **88**, 066805 (2002)

24.16 A. Eiguren, B. Hellsing, E.V. Chulkov, P.M. Echenique: Phonon-mediated decay of metal surface states, Phys. Rev. B **67**, 235423 (2003)

24.17 E.V. Chulkov, I. Sarria, V.M. Silkin, J.M. Pitarke, P.M. Echenique: Lifetimes of image-potential states on copper surfaces, Phys. Rev. Lett. **80**, 4947–4950 (1998)

24.18 J.E. Black, F.C. Shanes, R.F. Wallis: Surface vibrations on face centered cubic metal surfaces: The (111) surfaces, Surf. Sci. **133**(1), 199–215 (1983)

24.19 N.W. Ashcroft: Electron–ion pseudopotentials in metals, Phys. Lett. **23**(1), 48–50 (1966)

24.20 S.S. Tsirkin, S.V. Eremeev, E.V. Chulkov: Model pseudopotential for the (110) surface of fcc noble metals, Surf. Sci. **604**(9/10), 804–810 (2010)

24.21 S.V. Eremeev, I.Y. Sklyadneva, P.M. Echenique, S.D. Borisova, G. Benedek, G.G. Rusina, E.V. Chulkov: Electron–phonon coupling in a

sodium monolayer on Cu(111), Surf. Sci. **601**(18), 4553–4556 (2007)
24.22 S.D. Borisova, G.G. Rusina, S.V. Eremeev, G. Benedek, P.M. Echenique, I.Y. Sklyadneva, E.V. Chulkov: Vibrations in submonolayer structures of Na on Cu(111), Phys. Rev. B **74**, 165412 (2006)
24.23 N.E. Zein: Density functional calculations of elastic moduli and phonon spectra of crystals, Sov. Phys. Solid State **26**, 1825 (1984)
24.24 S. Baroni, P. Giannozzi, A. Testa: Green's-function approach to linear response in solids, Phys. Rev. Lett. **58**, 1861–1864 (1987)
24.25 S. Baroni, S. de Gironcoli, A. Dal Corso, P. Giannozzi: Phonons and related crystal properties from density-functional perturbation theory, Rev. Mod. Phys. **73**, 515–562 (2001)
24.26 R. Heid, K.-P. Bohnen: Ab initio lattice dynamics of metal surfaces, Phys. Rep. **387**(5/6), 151–213 (2003)
24.27 A. Nojima, K. Yamashita, B. Hellsing: Model Eliashberg functions for surface states, Appl. Surf. Sci. **254**(23), 7938–7941 (2008)
24.28 A. Eiguren, C. Ambrosch-Draxl: Wannier interpolation scheme for phonon-induced potentials: Application to bulk MgB_2, W, and the (1×1) H-covered W(110) surface, Phys. Rev. B **78**, 045124 (2008)
24.29 I.Y. Sklyadneva, R. Heid, V.M. Silkin, A. Melzer, K.-P. Bohnen, P.M. Echenique, T. Fauster, E.V. Chulkov: Unusually weak electron–phonon coupling in the Shockley surface state on Pd(111), Phys. Rev. B **80**, 045429 (2009)
24.30 A. Damascelli, Z. Hussain, Z.-X. Shen: Angle-resolved photoemission studies of the cuprate superconductors, Rev. Mod. Phys. **75**, 473–541 (2003)
24.31 B.A. McDougall, T. Balasubramanian, E. Jensen: Phonon contribution to quasiparticle lifetimes in Cu measured by angle-resolved photoemission, Phys. Rev. B **51**, 13891–13894 (1995)
24.32 M.F. Jensen, T.K. Kim, S. Bengió, I.Y. Sklyadneva, A. Leonardo, S.V. Eremeev, E.V. Chulkov, P. Hofmann: Thermally induced defects and the lifetime of electronic surface states, Phys. Rev. B **75**, 153404 (2007)
24.33 S.V. Eremeev, E.V. Chulkov: Effect of point defects on the temperature dependence of the linewidth of a surface electronic state on the Au(111) surface, Phys. Solid State **51**(4), 854–859 (2009)
24.34 A.A. Kordyuk, S.V. Borisenko, A. Koitzsch, J. Fink, M. Knupfer, H. Berger: Bare electron dispersion from experiment: Self-consistent self-energy analysis of photoemission data, Phys. Rev. B **71**, 214513 (2005)
24.35 C. Kirkegaard, T.K. Kim, P. Hofmann: Self-energy determination and electron–phonon coupling on Bi(110), New J. Phys. **7**(1), 99 (2005)
24.36 J.E. Gayone, C. Kirkegaard, J.W. Wells, S.V. Hoffmann, Z. Li, P. Hofmann: Determining the electron–phonon mass enhancement parameter λ on metal surfaces, Appl. Phys. A **80**(5), 943–949 (2005)
24.37 T. Cuk, D.H. Lu, X.J. Zhou, Z.-X. Shen, T.P. Devereaux, N. Nagaosa: A review of electron–phonon coupling seen in the high-T_c superconductors by angle-resolved photoemission studies (ARPES), Phys. Status Solidi (b) **242**(1), 11–29 (2005)
24.38 J. Shi, S.-J. Tang, B. Wu, P.T. Sprunger, W.L. Yang, V. Brouet, X.J. Zhou, Z. Hussain, Z.-X. Shen, Z. Zhang, E.W. Plummer: Direct extraction of the Eliashberg function for electron–phonon coupling: A case study of Be$(10\bar{1}0)$, Phys. Rev. Lett. **92**, 186401 (2004)
24.39 T. Chien, E.D.L. Rienks, M.F. Jensen, P. Hofmann, E.W. Plummer: Anisotropic electron–phonon coupling on a two-dimensional circular Fermi contour, Phys. Rev. B **80**, 241416 (2009)
24.40 T. Chien, X. He, S.-K. Mo, M. Hashimoto, Z. Hussain, Z.-X. Shen, E.W. Plummer: Electron–phonon coupling in a system with broken symmetry: Surface of Be(0001), Phys. Rev. B **92**, 075133 (2015)
24.41 X.J. Zhou, J. Shi, T. Yoshida, T. Cuk, W.L. Yang, V. Brouet, J. Nakamura, N. Mannella, S. Komiya, Y. Ando, F. Zhou, W.X. Ti, J.W. Xiong, Z.X. Zhao, T. Sasagawa, T. Kakeshita, H. Eisaki, S. Uchida, A. Fujimori, Z. Zhang, E.W. Plummer, R.B. Laughlin, Z. Hussain, Z.-X. Shen: Multiple bosonic mode coupling in the electron self-energy of $(La_{2-x}Sr_x)CuO_4$, Phys. Rev. Lett. **95**, 117001 (2005)
24.42 E. Schachinger, J.P. Carbotte: Finite band inversion of angular-resolved photoemission in $Bi_2Sr_2CaCu_2O_{8+\delta}$ and comparison with optics, Phys. Rev. B **77**, 094524 (2008)
24.43 J.M. Bok, J.H. Yun, H.-Y. Choi, W. Zhang, X.J. Zhou, C.M. Varma: Momentum dependence of the single-particle self-energy and fluctuation spectrum of slightly underdoped $Bi_2Sr_2CaCu_2O_{8+\delta}$ from high-resolution laser angle-resolved photoemission, Phys. Rev. B **81**, 174516 (2010)
24.44 L. Zhao, J. Wang, J. Shi, W. Zhang, H. Liu, J. Meng, G. Liu, X. Dong, J. Zhang, W. Lu, G. Wang, Y. Zhu, X. Wang, Q. Peng, Z. Wang, S. Zhang, F. Yang, C. Chen, Z. Xu, X.J. Zhou: Quantitative determination of Eliashberg function and evidence of strong electron coupling with multiple phonon modes in heavily overdoped $(Bi,Pb)_2Sr_2CuO_{6+\delta}$, Phys. Rev. B **83**, 184515 (2011)
24.45 J.H. Yun, J.M. Bok, H.-Y. Choi, W. Zhang, X.J. Zhou, C.M. Varma: Analysis of laser angle-resolved photoemission spectra of $Ba_2Sr_2CaCu_2O_{8+\delta}$ in the superconducting state: Angle-resolved self-energy and the fluctuation spectrum, Phys. Rev. B **84**, 104521 (2011)
24.46 H. Petek, S. Ogawa: Femtosecond time-resolved two-photon photoemission studies of electron dynamics in metals, Prog. Surf. Sci. **56**(4), 239–310 (1997)
24.47 M. Weinelt: Time-resolved two-photon photoemission from metal surfaces, J. Phys. Condens. Matter **14**(43), R1099 (2002)
24.48 P.S. Kirchmann, U. Bovensiepen: Ultrafast electron dynamics in Pb/Si(111) investigated by two-photon photoemission, Phys. Rev. B **78**, 035437 (2008)

24.49 J. Li, W.-D. Schneider, R. Berndt, O.R. Bryant, S. Crampin: Surface-state lifetime measured by scanning tunneling spectroscopy, Phys. Rev. Lett. **81**, 4464–4467 (1998)

24.50 J. Kliewer, R. Berndt, E.V. Chulkov, V.M. Silkin, P.M. Echenique, S. Crampin: Dimensionality effects in the lifetime of surface states, Science **288**(5470), 1399–1402 (2000)

24.51 I.Y. Sklyadneva, E.V. Chulkov, P.M. Echenique: Electron–phonon interaction on an Al(001) surface, J. Phys. Condens. Matter **20**(16), 165203 (2008)

24.52 A. Leonardo, I.Y. Sklyadneva, V.M. Silkin, P.M. Echenique, E.V. Chulkov: Ab initio calculation of the phonon-induced contribution to the electron-state linewidth on the Mg(0001) surface versus bulk Mg, Phys. Rev. B **76**, 035404 (2007)

24.53 I.Y. Sklyadneva, A. Leonardo, P.M. Echenique, E.V. Chulkov: Electron–phonon contribution to hole linewidth of the surface state on Al(001), Surf. Sci. **601**(18), 4022–4024 (2007)

24.54 E.V. Chulkov, A. Leonardo, I.Y. Sklyadneva, V.M. Silkin: Dynamics of electrons and holes at surfaces, Appl. Surf. Sci. **254**(1), 383–386 (2007)

24.55 H.J. Levinson, F. Greuter, E.W. Plummer: Experimental band structure of aluminum, Phys. Rev. B **27**, 727–747 (1983)

24.56 J. Jiang, K. Shimada, H. Hayashi, H. Iwasawa, Y. Aiura, H. Namatame, M. Taniguchi: Coupling parameters of many-body interactions for the Al(100) surface state: A high-resolution angle-resolved photoemission spectroscopy study, Phys. Rev. B **84**, 155124 (2011)

24.57 T.K. Kim, T.S. Sørensen, E. Wolfring, H. Li, E.V. Chulkov, P. Hofmann: Electron–phonon coupling on the Mg(0001) surface, Phys. Rev. B **72**, 075422 (2005)

24.58 A. Leonardo, I.Y. Sklyadneva, P.M. Echenique, E.V. Chulkov: Electron–phonon interaction in magnesium: From the monolayer to the Mg(0001) surface, Surf. Sci. **601**(18), 4018–4021 (2007)

24.59 F. Schiller, M. Heber, V.D.P. Servedio, C. Laubschat: Electronic structure of Mg: From monolayers to bulk, Phys. Rev. B **70**, 125106 (2004)

24.60 T. Balasubramanian, E. Jensen, X.L. Wu, S.L. Hulbert: Large value of the electron–phonon coupling parameter ($\lambda = 1.15$) and the possibility of surface superconductivity at the Be(0001) surface, Phys. Rev. B **57**, R6866–R6869 (1998)

24.61 S. LaShell, E. Jensen, T. Balasubramanian: Nonquasiparticle structure in the photoemission spectra from the Be(0001) surface and determination of the electron self energy, Phys. Rev. B **61**, 2371–2374 (2000)

24.62 A. Eiguren, S. de Gironcoli, E.V. Chulkov, P.M. Echenique, E. Tosatti: Electron–phonon interaction at the Be(0001) surface, Phys. Rev. Lett. **91**, 166803 (2003)

24.63 I.Y. Sklyadneva, E.V. Chulkov, P.M. Echenique, A. Eiguren: Electron–phonon interaction and hole (electron) lifetimes on Be(0001), Surf. Sci. **600**(18), 3792–3794 (2006)

24.64 M. Hengsberger, D. Purdie, P. Segovia, M. Garnier, Y. Baer: Photoemission study of a strongly coupled electron–phonon system, Phys. Rev. Lett. **83**, 592–595 (1999)

24.65 M. Hengsberger, R. Frésard, D. Purdie, P. Segovia, Y. Baer: Electron–phonon coupling in photoemission spectra, Phys. Rev. B **60**, 10796–10802 (1999)

24.66 T. Balasubramanian, L.I. Johansson, P.A. Glans, C. Virojanadara, V.M. Silkin, E.V. Chulkov, P.M. Echenique: Surface electronic band structure and $\bar{A}$ surface state lifetimes at the Be($10\bar{1}0$) surface: Experiment and theory, Phys. Rev. B **64**, 205401 (2001)

24.67 S.-J. Tang, Ismail, P. T. Sprunger, E. W. Plummer: Electron–phonon coupling and temperature-dependent shift of surface states on Be($10\bar{1}0$), Phys. Rev. B **65**, 235428 (2002)

24.68 I.Y. Sklyadneva, R. Heid, P.M. Echenique, K.-P. Bohnen, E.V. Chulkov: Electron–phonon coupling in surface electronic states on Be($10\bar{1}0$), Phys. Rev. B **83**, 195437 (2011)

24.69 R. Matzdorf, G. Meister, A. Goldmann: Phonon contributions to photohole linewidths observed for surface states on copper, Phys. Rev. B **54**, 14807–14811 (1996)

24.70 F. Reinert, B. Eltner, G. Nicolay, F. Forster, S. Schmidt, S. Hüfner: The electron–phonon self-energy of metallic systems determined by angular resolved high-resolution photoemission, Physica B **351**(3/4), 229–234 (2004)

24.71 J. Jiang, S.S. Tsirkin, K. Shimada, H. Iwasawa, M. Arita, H. Anzai, H. Namatame, M. Taniguchi, I.Y. Sklyadneva, R. Heid, K.-P. Bohnen, P.M. Echenique, E.V. Chulkov: Many-body interactions and Rashba splitting of the surface state on Cu(110), Phys. Rev. B **89**, 085404 (2014)

24.72 P. Straube, F. Pforte, T. Michalke, K. Berge, A. Gerlach, A. Goldmann: Photoemission study of the surface state at $\bar{Y}$ on Cu(110): Band structure, electron dynamics, and surface optical properties, Phys. Rev. B **61**, 14072–14077 (2000)

24.73 S.V. Eremeev, S.S. Tsirkin, E.V. Chulkov: Phonon-induced scattering of excited electrons and holes on (110) noble metal surfaces, Phys. Rev. B **82**, 035424 (2010)

24.74 O. Zeybek, A.M. Davarpanah, S.D. Barrett: Electronic surface states of Cu(110) surface, Surf. Sci. **600**(24), 5176–5181 (2006)

24.75 R. Matzdorf, G. Meister, A. Goldmann: Temperature-dependent photoemission spectra from Cu(100) and Cu(111) surfaces, Surf. Sci. **286**(1), 56–65 (1993)

24.76 F. Reinert, G. Nicolay, S. Schmidt, D. Ehm, S. Hüfner: Direct measurements of the *L*-gap surface states on the (111) face of noble metals by photoelectron spectroscopy, Phys. Rev. B **63**, 115415 (2001)

24.77 A. Gerlach, G. Meister, R. Matzdorf, A. Goldmann: High-resolution photoemission study of the $\bar{Y}$

surface state on Ag(110), Surf. Sci. **443**(3), 221–226 (1999)
24.78 A. Goldmann, V. Dose, G. Borstel: Empty electronic states at the (100), (110), and (111) surfaces of nickel, copper, and silver, Phys. Rev. B **32**, 1971–1980 (1985)
24.79 S. LaShell, B.A. McDougall, E. Jensen: Electron–phonon mass enhancement parameter of the $\overline{\Gamma}$ surface state on Au(111) measured by photoemission spectroscopy, Phys. Rev. B **74**, 033410 (2006)
24.80 T. Valla, A.V. Fedorov, P.D. Johnson, S.L. Hulbert: Many-body effects in angle-resolved photoemission: Quasiparticle energy and lifetime of a Mo(110) surface state, Phys. Rev. Lett. **83**, 2085–2088 (1999)
24.81 N. Wu, Y.B. Losovyj, K. Fukutani, P.A. Dowben: The electron–phonon coupling at the Mo(112) surface, J. Phys. Condens. Matter **22**(24), 245501 (2010)
24.82 I.N. Yakovkin, P.A. Dowben: A density functional theory study of the electron–phonon coupling at the Mo(112) surface, J. Phys. Condens. Matter **23**(22), 225503 (2011)
24.83 M. Kralj, A. Šiber, P. Pervan, M. Milun, T. Valla, P.D. Johnson, D.P. Woodruff: Temperature dependence of photoemission from quantum-well states in Ag/V(100): Moving surface–vacuum barrier effects, Phys. Rev. B **64**, 085411 (2001)
24.84 P. Hofmann, Y.Q. Cai, C. Grütter, J.H. Bilgram: Electron–lattice interaction on α-Ga(010), Phys. Rev. Lett. **81**, 1670–1673 (1998)
24.85 C. Søndergaard, C. Schultz, S. Agergaard, S.V. Hoffmann, Z. Li, P. Hofmann, H. Li, C. Grütter, J.H. Bilgram: Interplay between electronic structure and surface phase transition on α-Ga(010), Phys. Rev. B **67**, 165422 (2003)
24.86 K. Sugawara, T. Sato, S. Souma, T. Takahashi, M. Arai, T. Sasaki: Fermi surface and anisotropic spin–orbit coupling of Sb(111) studied by angle-resolved photoemission spectroscopy, Phys. Rev. Lett. **96**, 046411 (2006)
24.87 D. Campi, M. Bernasconi, G. Benedek: Phonons and electron–phonon interaction at the Sb(111) surface, Phys. Rev. B **86**, 075446 (2012)
24.88 C.R. Ast, H. Höchst: Two-dimensional band structure and self-energy of Bi(111) near the $\overline{\Gamma}$ point, Phys. Rev. B **66**, 125103 (2002)
24.89 M. Alcántara Ortigoza, I.Y. Sklyadneva, R. Heid, E.V. Chulkov, T.S. Rahman, K.-P. Bohnen, P.M. Echenique: *Ab initio* lattice dynamics and electron–phonon coupling of Bi(111), Phys. Rev. B **90**, 195438 (2014)
24.90 G.Q. Huang, J. Yang: Surface lattice dynamics and electron–phonon interaction in ultrathin Bi(111) film, J. Phys. Condens. Matter **25**(17), 175004 (2013)
24.91 J.E. Gayone, S.V. Hoffmann, Z. Li, P. Hofmann: Strong energy dependence of the electron–phonon coupling strength on Bi(100), Phys. Rev. Lett. **91**, 127601 (2003)
24.92 I.Y. Sklyadneva, R. Heid, K.-P. Bohnen, P.M. Echenique, G. Benedek, E.V. Chulkov: The effect of spin–orbit coupling on the surface dynamical properties and electron–phonon interaction of Tl(0001), J. Phys. Chem. A **115**(25), 7352–7355 (2011)
24.93 A.V. Fedorov, T. Valla, F. Liu, P.D. Johnson, M. Weinert, P.B. Allen: Spin-resolved photoemission study of photohole lifetimes in ferromagnetic gadolinium, Phys. Rev. B **65**, 212409 (2002)
24.94 A. Bauer, A. Mühlig, D. Wegner, G. Kaindl: Lifetime of surface states on (0001) surfaces of lanthanide metals, Phys. Rev. B **65**, 075421 (2002)
24.95 A. Rehbein, D. Wegner, G. Kaindl, A. Bauer: Temperature dependence of lifetimes of Gd(0001) surface states, Phys. Rev. B **67**, 033403 (2003)
24.96 I.Y. Sklyadneva, E.V. Chulkov, W.-D. Schöne, V.M. Silkin, R. Keyling, P.M. Echenique: Role of electron–phonon interactions versus electron–electron interactions in the broadening mechanism of the electron and hole linewidths in bulk Be, Phys. Rev. B **71**, 174302 (2005)
24.97 E.W. Plummer, J.B. Hannon: The surfaces of beryllium, Prog. Surf. Sci. **46**(2), 149–158 (1994)
24.98 S.Y. Savrasov, D.Y. Savrasov: Electron–phonon interactions and related physical properties of metals from linear-response theory, Phys. Rev. B **54**, 16487–16501 (1996)
24.99 R. Bauer, A. Schmid, P. Pavone, D. Strauch: Electron–phonon coupling in the metallic elements Al, Au, Na, and Nb: A first-principles study, Phys. Rev. B **57**, 11276–11282 (1998)
24.100 I.Y. Sklyadneva, R. Heid, K.-P. Bohnen, E.V. Chulkov: Electron–phonon coupling in the surface electronic states on Pd(111), New J. Phys. **11**(10), 103038 (2009)
24.101 I.Y. Sklyadneva, S.S. Tsirkin, S.V. Eremeev, R. Heid, K.-P. Bohnen, E.V. Chulkov: Contribution of phonons to the line width of surface electronic states on Pd(111), Phys. Solid State **53**(12), 2508–2514 (2011)
24.102 P. Hofmann: The surfaces of bismuth: Structural and electronic properties, Prog. Surf. Sci. **81**(5), 191–245 (2006)
24.103 G.Q. Huang: Surface lattice vibration and electron–phonon interaction in topological insulator Bi_2Te_3(111) films from first principles, Europhys. Lett. **100**(1), 17001 (2012)
24.104 Z. Xie, S. He, C. Chen, Y. Feng, H. Yi, A. Liang, L. Zhao, D. Mou, J. He, Y. Peng, X. Liu, Y. Liu, G. Liu, X. Dong, L. Yu, J. Zhang, S. Zhang, Z. Wang, F. Zhang, F. Yang, Q. Peng, X. Wang, C. Chen, Z. Xu, X. Zhou: Weak electron–phonon coupling and unusual electron scattering of topological surface states in Sb(111) by laser-based angle-resolved photoemission spectroscopy, Chin. Phys. Lett. **31**(6), 067305 (2014)
24.105 R. Wu, C. Li, A.J. Freeman, C.L. Fu: Structural, electronic, and magnetic properties of rare-earth metal surfaces: hcp Gd(0001), Phys. Rev. B **44**, 9400–9409 (1991)
24.106 E. Rotenberg, J. Schaefer, S.D. Kevan: Coupling between adsorbate vibrations and an electronic surface state, Phys. Rev. Lett. **84**, 2925–2928 (2000)

24.107 E. Rotenberg, S.D. Kevan: Electron–phonon coupling in W(110)-(1×1)H, J. Electron Spectrosc. Relat. Phenom. **126**(1–3), 125–132 (2002)

24.108 K. Fukutani, H. Hayashi, I.N. Yakovkin, T. Habuchi, D. Hirayama, J. Jiang, H. Iwasawa, K. Shimada, Y.B. Losovyj, P.A. Dowben: Enhanced electron–phonon coupling at the Au/Mo(112) surface, Phys. Rev. B **86**, 205432 (2012)

24.109 A. Carlsson, B. Hellsing, S.-Å. Lindgren, L. Walldén: High-resolution photoemission from a tunable quantum well: Cu(111)/Na, Phys. Rev. B **56**, 1593–1600 (1997)

24.110 C. Corriol, V.M. Silkin, D. Sánchez-Portal, A. Arnau, E.V. Chulkov, P.M. Echenique, T. von Hofe, J. Kliewer, J. Kröger, R. Berndt: Role of elastic scattering in electron dynamics at ordered alkali overlayers on Cu(111), Phys. Rev. Lett. **95**, 176802 (2005)

24.111 M. Breitholtz, V. Chis, B. Hellsing, S.-Å. Lindgren, L. Walldén: Overlayer resonance and quantum well state of Cs/Cu(111) studied with angle-resolved photoemission, LEED, and first-principles calculations, Phys. Rev. B **75**, 155403 (2007)

24.112 A. Nojima, K. Yamashita, B. Hellsing: Model calculation of the electron–phonon coupling in Cs/Cu(111), Phys. Rev. B **78**, 035417 (2008)

24.113 P. Gargiani, S. Lisi, M.G. Betti, A.T. Ibrahimi, F. Bertran, P. Le Fèvre, L. Chiodo: Orbital dependent Rashba splitting and electron–phonon coupling of 2D Bi phase on Cu(100) surface, J. Chem. Phys. **139**(18), 184707 (2013)

24.114 D. Guan, M. Bianchi, S. Bao, E. Perkins, F. Meier, J.H. Dil, J. Osterwalder, P. Hofmann: Strongly enhanced electron–phonon coupling in the Rashba-split state of the Bi/Ag(111) surface alloy, Phys. Rev. B **83**, 155451 (2011)

24.115 D.-A. Luh, T. Miller, J.J. Paggel, T.-C. Chiang: Large electron–phonon coupling at an interface, Phys. Rev. Lett. **88**, 256802 (2002)

24.116 K. Takahashi, A. Tanaka, M. Hatano, H. Sasaki, S. Suzuki, S. Sato: Electron–phonon interaction of quantum-well states on Ag nanofilms studied by temperature-dependent photoemission spectroscopy, Surf. Sci. **433–435**, 873–877 (1999)

24.117 Y. Guo, Y.-F. Zhang, X.-Y. Bao, T.-Z. Han, Z. Tang, L.-X. Zhang, W.-G. Zhu, E.G. Wang, Q. Niu, Z.Q. Qiu, J.-F. Jia, Z.-X. Zhao, Q.-K. Xue: Superconductivity modulated by quantum size effects, Science **306**(5703), 1915–1917 (2004)

24.118 I.-P. Hong, C. Brun, F. Patthey, I.Y. Sklyadneva, X. Zubizarreta, R. Heid, V.M. Silkin, P.M. Echenique, K.-P. Bohnen, E.V. Chulkov, W.-D. Schneider: Decay mechanisms of excited electrons in quantum-well states of ultrathin Pb islands grown on Si(111): Scanning tunneling spectroscopy and theory, Phys. Rev. B **80**, 081409 (2009)

24.119 M. Ligges, M. Sandhofer, I.Y. Sklyadneva, R. Heid, K.-P. Bohnen, S. Freutel, L. Rettig, P. Zhou, P.M. Echenique, E.V. Chulkov, U. Bovensiepen: Electron–phonon coupling in quantum-well states of the Pb/Si(111) system, J. Phys. Condens. Matter **26**(35), 352001 (2014)

24.120 J. Noffsinger, M.L. Cohen: Superconductivity in monolayer Pb on Si(111) from first principles, Solid State Commun. **151**(6), 421–424 (2011)

24.121 J. Noffsinger, M.L. Cohen: First-principles calculation of the electron–phonon coupling in ultrathin Pb superconductors: Suppression of the transition temperature by surface phonons, Phys. Rev. B **81**, 214519 (2010)

24.122 I.Y. Sklyadneva, R. Heid, K.-P. Bohnen, P.M. Echenique, E.V. Chulkov: Mass enhancement parameter in free-standing ultrathin Pb(111) films: The effect of spin-orbit coupling, Phys. Rev. B **87**, 085440 (2013)

24.123 N. Fischer, S. Schuppler, R. Fischer, T. Fauster, W. Steinmann: Electronic structure of a single layer of Na on Cu(111), Phys. Rev. B **43**, 14722–14725 (1991)

24.124 B. Hellsing, J. Carlsson, L. Walldén, S.-Å. Lindgren: Phonon-induced decay of a quantum-well hole: One monolayer Na on Cu(111), Phys. Rev. B **61**, 2343–2348 (2000)

24.125 E.V. Chulkov, J. Kliewer, R. Berndt, V.M. Silkin, B. Hellsing, S. Crampin, P.M. Echenique: Hole dynamics in a quantum-well state at Na/Cu(111), Phys. Rev. B **68**, 195422 (2003)

24.126 C. Brun, I.-P. Hong, F. Patthey, I.Y. Sklyadneva, R. Heid, P.M. Echenique, K.-P. Bohnen, E.V. Chulkov, W.-D. Schneider: Reduction of the superconducting gap of ultrathin Pb islands grown on Si(111), Phys. Rev. Lett. **102**, 207002 (2009)

24.127 T. Zhang, P. Cheng, W.-J. Li, Y.-J. Sun, G. Wang, X.-G. Zhu, K. He, L. Wang, X. Ma, X. Chen, Y. Wang, Y. Liu, H.-Q. Lin, J.-F. Jia, Q.-K. Xe: Superconductivity in one-atomic-layer metal films grown on Si(111), Nat. Phys. **6**, 104–108 (2010)

24.128 R.C. Hatch, M. Bianchi, D. Guan, S. Bao, J. Mi, B.B. Iversen, L. Nilsson, L. Hornekær, P. Hofmann: Stability of the Bi_2Se_3(111) topological state: electron–phonon and electron–defect scattering, Phys. Rev. B **83**, 241303 (2011)

24.129 Z.-H. Pan, A.V. Fedorov, D. Gardner, Y.S. Lee, S. Chu, T. Valla: Measurement of an exceptionally weak electron–phonon coupling on the surface of the topological insulator Bi_2Se_3 using angle-resolved photoemission spectroscopy, Phys. Rev. Lett. **108**, 187001 (2012)

24.130 T. Kondo, Y. Nakashima, Y. Ota, Y. Ishida, W. Malaeb, K. Okazaki, S. Shin, M. Kriener, S. Sasaki, K. Segawa, Y. Ando: Anomalous dressing of Dirac fermions in the topological surface state of Bi_2Se_3, Bi_2Te_3, and Cu-doped Bi_2Se_3, Phys. Rev. Lett. **110**, 217601 (2013)

24.131 C. Chen, Z. Xie, Y. Feng, H. Yi, A. Liang, S. He, D. Mou, J. He, Y. Peng, X. Liu, Y. Liu, L. Zhao, G. Liu, X. Dong, J. Zhang, L. Yu, X. Wang, Q. Peng, Z. Wang, S. Zhang, F. Yang, C. Chen, Z. Xu, X.J. Zhou: Tunable Dirac fermion dynamics in topological insulators, Sci. Rep. **3**, 2411 (2013)

24.132 S. Giraud, A. Kundu, R. Egger: Electron–phonon scattering in topological insulator thin films, Phys. Rev. B **85**, 035441 (2012)

24.133 S. Das Sarma, Q. Li: Many-body effects and possible superconductivity in the two-dimensional metallic surface states of three-dimensional topological insulators, Phys. Rev. B **88**, 081404 (2013)

24.134 S. Giraud, R. Egger: Electron–phonon scattering in topological insulators, Phys. Rev. B **83**, 245322 (2011)

24.135 V. Parente, A. Tagliacozzo, F. von Oppen, F. Guinea: Electron–phonon interaction on the surface of a three-dimensional topological insulator, Phys. Rev. B **88**, 075432 (2013)

24.136 X. Zhu, C. Howard, J. Guo, M. El-Batanouny: Electron–phonon coupling on the surface of topological insulators. In: *Recent Research Developments in Surface Science*, Vol. 2, ed. by S.G. Pandalai (Research Signpost, Jagathy 2013) pp. 93–120

24.137 M.Z. Hasan, C.L. Kane: *Colloquium*: topological insulators, Rev. Mod. Phys. **82**, 3045–3067 (2010)

24.138 X.-L. Qi, S.-C. Zhang: Topological insulators and superconductors, Rev. Mod. Phys. **83**, 1057–1110 (2011)

24.139 M.Z. Hasan, J.E. Moore: Three-dimensional topological insulators, Annu. Rev. Condens. Matter Phys. **2**(1), 55–78 (2011)

24.140 H. Weng, R. Yu, X. Hu, X. Dai, Z. Fang: Quantum anomalous Hall effect and related topological electronic states, Adv. Phys. **64**, 227–282 (2015)

24.141 D. Lu, I.M. Vishik, M. Yi, Y. Chen, R.G. Moore, Z.-X. Shen: Angle-resolved photoemission studies of quantum materials, Annu. Rev. Condens. Matter Phys. **3**(1), 129–167 (2012)

24.142 S.R. Park, W.S. Jung, C. Kim, D.J. Song, C. Kim, S. Kimura, K.D. Lee, N. Hur: Quasiparticle scattering and the protected nature of the topological states in a parent topological insulator Bi_2Se_3, Phys. Rev. B **81**, 041405 (2010)

24.143 J. Sánchez-Barriga, M.R. Scholz, E. Golias, E. Rienks, D. Marchenko, A. Varykhalov, L.V. Yashina, O. Rader: Anisotropic effect of warping on the lifetime broadening of topological surface states in angle-resolved photoemission from Bi_2Te_3, Phys. Rev. B **90**, 195413 (2014)

24.144 Y.-P. Lai, H.-J. Chen, K.-H. Wu, J.-M. Liu: Temperature-dependent carrier-phonon coupling in topological insulator Bi_2Se_3, Appl. Phys. Lett. **105**(23), 232110 (2014)

24.145 J.A. Sobota, S.-L. Yang, D. Leuenberger, A.F. Kemper, J.G. Analytis, I.R. Fisher, P.S. Kirchmann, T.P. Devereaux, Z.-X. Shen: Distinguishing bulk and surface electron–phonon coupling in the topological insulator Bi_2Se_3 using time-resolved photoemission spectroscopy, Phys. Rev. Lett. **113**, 157401 (2014)

24.146 M. Weis, K. Balin, R. Rapacz, A. Nowak, M. Lejman, J. Szade, P. Ruello: Ultrafast light-induced coherent optical and acoustic phonons in few quintuple layers of the topological insulator Bi_2Te_3, Phys. Rev. B **92**, 014301 (2015)

24.147 D. Kim, Q. Li, P. Syers, N.P. Butch, J. Paglione, S.D. Sarma, M.S. Fuhrer: Intrinsic electron–phonon resistivity of Bi_2Se_3 in the topological regime, Phys. Rev. Lett. **109**, 166801 (2012)

24.148 M.V. Costache, I. Neumann, J.F. Sierra, V. Marinova, M.M. Gospodinov, S. Roche, S.O. Valenzuela: Fingerprints of inelastic transport at the surface of the topological insulator Bi_2Se_3: Role of electron–phonon coupling, Phys. Rev. Lett. **112**, 086601 (2014)

24.149 Y.D. Glinka, S. Babakiray, T.A. Johnson, D. Lederman: Thickness tunable quantum interference between surface phonon and Dirac plasmon states in thin films of the topological insulator Bi_2Se_3, J. Phys. Condens. Matter **27**(5), 052203 (2015)

24.150 Y.D. Glinka, S. Babakiray, D. Lederman: Plasmon-enhanced electron–phonon coupling in Dirac surface states of the thin-film topological insulator Bi_2Se_3, J. Appl. Phys. **118**(13), 135713 (2015)

24.151 X. Zhu, L. Santos, R. Sankar, S. Chikara, C. Howard, F.C. Chou, C. Chamon, M. El-Batanouny: Interaction of phonons and Dirac fermions on the surface of Bi_2Se_3: A strong Kohn anomaly, Phys. Rev. Lett. **107**, 186102 (2011)

24.152 X. Zhu, L. Santos, C. Howard, R. Sankar, F.C. Chou, C. Chamon, M. El-Batanouny: Electron–phonon coupling on the surface of the topological insulator Bi_2Se_3 determined from surface-phonon dispersion measurements, Phys. Rev. Lett. **108**, 185501 (2012)

24.153 C. Howard, M. El-Batanouny, R. Sankar, F.C. Chou: Anomalous behavior in the phonon dispersion of the (001) surface of Bi_2Te_3 determined from helium atom-surface scattering measurements, Phys. Rev. B **88**, 035402 (2013)

24.154 P.B. Allen: Neutron spectroscopy of superconductors, Phys. Rev. B **6**, 2577–2579 (1972)

24.155 J. Bardeen, L.N. Cooper, J.R. Schrieffer: Theory of superconductivity, Phys. Rev. **108**, 1175–1204 (1957)

24.156 G.M. Eliashberg: Interactions between electrons and lattice vibrations in a superconductor, Sov. Phys. JETP **11**, 696 (1960)

24.157 G. Grüner: *Density Waves in Solids*, Frontiers in Physics (Perseus, Cambridge 1994)

24.158 G. Benedek, G. Brusdeylins, C. Heimlich, L. Miglio, J.G. Skofronick, J.P. Toennies, R. Vollmer: Shifted surface-phonon anomaly in 2*H*-$TaSe_2$, Phys. Rev. Lett. **60**, 1037–1040 (1988)

24.159 B.M. Murphy, H. Requardt, J. Stettner, J. Serrano, M. Krisch, M. Müller, W. Press: Phonon modes at the 2*H*-$NbSe_2$ surface observed by grazing incidence inelastic x-ray scattering, Phys. Rev. Lett. **95**, 256104 (2005)

24.160 B.M. Murphy, M. Müller, J. Stettner, H. Requardt, J. Serrano, M. Krisch, W. Press: Investigating surface dynamics with inelastic x-ray scattering, J. Phys. Condens. Matter **20**(22), 224001 (2008)

24.161 B. Kohler, P. Ruggerone, M. Scheffler: Anomalies in He atom scattering spectra of the H-covered

Mo(110) and W(110) surfaces, Surf. Sci. **368**(1), 213–221 (1996)
24.162 B. Kohler, P. Ruggerone, M. Scheffler: Ab initio study of the anomalies in the He-atom-scattering spectra of H/Mo(110) and H/W(110), Phys. Rev. B **56**, 13503–13518 (1997)
24.163 J. Kröger, S. Lehwald, M. Balden, H. Ibach: Anomalous dispersion of adsorbate phonons of Mo(110)-H, Phys. Rev. B **66**, 073414 (2002)
24.164 E. Hulpke, J. Lüdecke: Surface phonon anomaly induced by adsorption, J. Electron Spectrosc. Relat. Phenom. **64**, 641–649 (1993)
24.165 J. Kröger, S. Lehwald, H. Ibach: Estimation of the electron–phonon coupling parameter of Mo(110)-H and W(110)-H, Phys. Rev. B **69**, 201404 (2004)
24.166 C. Howard, M. El-Batanouny: Connecting electron and phonon spectroscopy data to consistently determine quasiparticle-phonon coupling on the surface of topological insulators, Phys. Rev. B **89**, 075425 (2014)
24.167 G. Benedek, M. Bernasconi, K.-P. Bohnen, D. Campi, E.V. Chulkov, P.M. Echenique, R. Heid, I.Y. Sklyadneva, J.P. Toennies: Unveiling mode-selected electron–phonon interactions in metal films by helium atom scattering, Phys. Chem. Chem. Phys. **16**, 7159–7172 (2014)
24.168 J. Braun, P. Ruggerone, G. Zhang, J.P. Toennies, G. Benedek: Surface phonon dispersion curves of thin Pb films on Cu(111), Phys. Rev. B **79**, 205423 (2009)
24.169 I.Y. Sklyadneva, G. Benedek, E.V. Chulkov, P.M. Echenique, R. Heid, K.-P. Bohnen, J.P. Toennies: Mode-selected electron–phonon coupling in superconducting Pb nanofilms determined from He atom scattering, Phys. Rev. Lett. **107**, 095502 (2011)

Rolf Heid

Institute for Quantum Materials and Technologies
Karlsruhe Institute of Technology
Karlsruhe, Germany
rolf.heid@kit.edu

Rolf Heid received his PhD in Physics (1991) from the University of Karlsruhe and his Habilitation (2002) from the University of Regensburg, where he served as a lecturer for 10 years. His research focuses on electronic and vibrational properties of solids and as their interaction, and the development of computational tools based on density functional theory. Applications comprise various metallic compounds, superconductors, and their surfaces and interfaces, as well as nanomaterials and topological systems.

Irina Y. Sklyadneva

Donostia International Physics Center (DIPC)
Donostia/San Sebastián, Spain
swxskski@ehu.eus

Irina Sklyadneva received her PhD in Physics from Tomsk State University in 1990, focusing on electronic properties of bulk metals and metal surfaces. She has been working at the Donostia International Physics Center (DIPC) (Basque Country, Spain) since 2003. Her research interests focus on lattice dynamics and electron–phonon coupling in metals, topological insulators, Dirac and Weyl semimetals, as well as in thin films and layered materials.

Evgueni V. Chulkov

Faculty of Chemical Sciences, Materials Physics Department
University of the Basque Country, UPV/EHU
Donostia-San Sebastián, Spain
evgenivladimirovich.tchoulkov@ehu.eus

Evgueni Chulkov received his PhD in Physics from Tomsk State University (1980), focusing on electronic and thermo-dynamic properties of metals and alloys. He is Professor in the Material Physics Department at the University of the Basque Country. His research interest lies in electronic structure and single-particle and collective excitations in metallic materials and on their surfaces, topological insulators, Dirac and Weyl semimetals, thin films, and electron–electron, electron–phonon, and electron–magnon interactions.

25. Spatially Resolved Surface Vibrational Spectroscopies

Tadahiro Komeda, Norio Okabayashi

Herein, we discuss the STM-IETS (scanning tunneling microscopy-inelastic electron tunneling spectroscopy) technique in the following order. After briefly mentioning conventional IETS (inelastic electron tunneling spectroscopy), STM-IETS experimental results are introduced focusing on similarities and differences to conventional IETS. The working principle behind STM-IETS for the detection of vibrational modes is considered by reviewing recent progress in STM-IETS theoretical calculations. In addition, experimental setups to improve the quality of the IET (inelastic electron tunneling) spectrum, including low-temperature measurements, electronics (especially the use of the lock-in amplifier), and IET signal mapping are reviewed. With this information, we discuss in detail STM-IETS measurements performed on an alkanethiol self-assembled monolayer (SAM) formed on an Au(111) surface. This molecule is often employed as a standard sample for the examination of IETS observations with atom-scale electrodes, which are used in single-molecule electronics investigations. STM-IETS reveals not only C–H stretching mode, which often appears as a prominent feature in IET spectra, but also other vibrational features in the so-called fingerprint region including vibrational modes which are beneficial for distinguishing functional groups. A comparison with recent calculations shows excellent agreement. In addition, partial deuteration of the molecule can provide more information about the site of the molecule where the excitation of the vibrational mode occurs. A selection rule or propensity for IETS detection is then discussed on the basis of a combination of these experimental investigations and theoretical simulations.

This chapter reviews recent IETS studies. IETS is an all-electron spectroscopy method used to detect the energy of an excitation process at surfaces/interfaces. The ability of IETS to reveal the vibrational modes of molecules was first demonstrated by Jaklev using a metal–insulator–metal (M–I–M) tunneling device, in which the molecule is buried in the insulating layer. The successful measurement of IET spectra with a scanning tunneling microscope (STM) combines atom-scale spatial resolution with chemical

M. Rocca, T.S. Rahman, L. Vattuone (Eds.), *Springer Handbook of Surface Science*, Springer Handbooks,
https://doi.org/10.1007/978-3-030-46906-1_25

sensitivity, and is thus considered a powerful tool for surface characterization. However, the working principle behind STM-IETS is different to other vibrational detection techniques like infrared spectroscopy for which a dipole excitation is the main excitation mechanism.

25.1 Surface Spectroscopy

IETS is a technique to observe elemental excitations of species present in the tunneling junction. IET spectra are obtained by analyzing the tunneling current variation as a function of the voltage between the tunneling gap. Thus, it is an all-electron spectroscopy technique. The capability of IETS to obtain information about chemical properties of the interface was reported soon after the invention of tunneling devices such as the Esaki diode [25.1]. IETS can extract the excitation energies of vibrational modes of a molecule, phonons of metals and insulators, magnons and spin-flip processes of the magnetic bulk or atom/molecule in the tunneling gap (Fig. 25.1a).

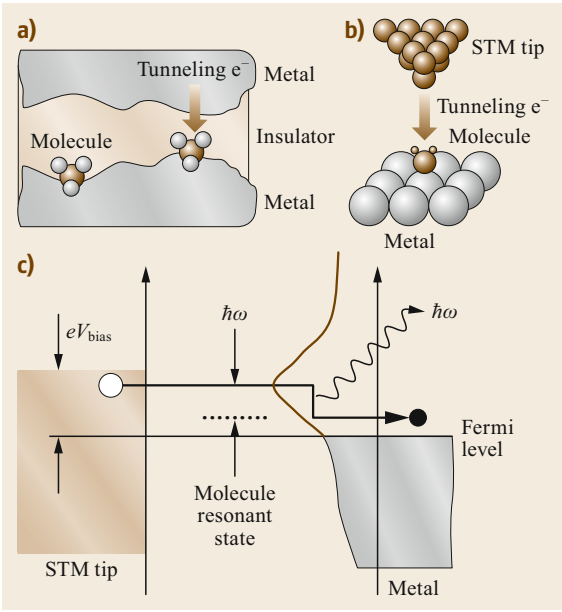

Fig. 25.1a–c Schematic drawing of an inelastic tunneling spectroscopy measurement on molecules showing **(a)** conventional IETS with a metal–insulator–metal tunneling junction (molecules buried in its interface) and **(b)** an STM setup and **(c)** a tunneling electron emitted from an STM tip is trapped in a molecule-induced resonant state. The electron moves after a short time into the metal substrate. During the process the electron could excite a phonon or molecule's vibration with an energy $\hbar\omega$. (Reprinted from [25.2], with permission from Elsevier)

25.1.1 Inelastic Tunneling Spectroscopy

The pioneering works by *Jaklevic* and *Lambe* detected clear vibrational features of molecules buried in the interface [25.3]. This result was achieved by measuring current and voltage across a metal–insulator–metal (M–I–M) device whose interface contains a target molecule. The work was followed by more research into the fields of basic science of molecular spectroscopy and applications like catalysis. The IETS technique was able to provide much higher resolution than infrared adsorption spectroscopy (IRAS) could offer at that time. These reports have already been reviewed in detail [25.4, 5].

The characteristic features of the IETS technique have been summarized by *Mazur* and *Hipps* as follows [25.6]. Firstly, IETS has much higher sensitivity than that provided by IRAS and Raman spectroscopy. With less than 10^{13} molecules, IETS can provide a complete spectrum. Secondly, overtone and combination bands usually have a low intensity, thus allowing easier identification of the fundamental modes. Thirdly, optically forbidden transitions may be observed as strong bands, and one can obtain spectra in the *IR-opaque* regions.

However, in the 1990s, IETS surface and interface research activity declined. This occurred mainly because of the availability of few methods to characterize the properties of the molecules in the interface. Moreover, to judge structural and electronic properties of adsorbates on surfaces the results of many surface science techniques must be combined, which cannot be realized for the IETS sample. In addition, the lack of a strict selection rule in IETS compared to that in IRAS measurements makes this technique less attractive to determine the molecular configuration on the surface. However, the appearance of STM has changed this situation. With STM for IETS measurements, the drawbacks of IETS can be compensated, allowing IETS to be a useful technique in the investigation of vibrations at surfaces (Fig. 25.1b).

25.1.2 Scanning Tunneling Microscope Technique

An energy diagram for the tunneling process is expressed in a simplified 1-D barrier in Fig. 25.2a. Elec-

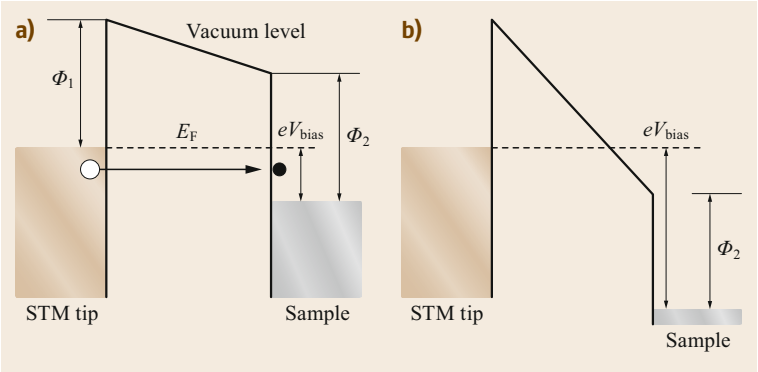

Fig. 25.2a,b Schematic drawing of an energy diagram for tunneling in a simplified 1-D barrier: **(a)** normal tunneling and **(b)** Fowler–Nordheim tunneling. (Reprinted from [25.2], with permission from Elsevier)

trons can tunnel from the tip to the unoccupied states of the substrate in the energy range between the Fermi level (E_F) and $E_F - V_{bias}$. If a slow variation of local density of state (LDOS) both for the substrate and for the tip can be assumed, tunneling current versus V_{bias} should show the Ohmic behavior.

To see characteristic features of the tunneling current compared to the conventional electron source, it is worth noting the difference in energy range of the two techniques with reference to the sample's Fermi level. The energy of electrons available from conventional electron sources should be *above* the vacuum level of the sample, while tunneling electrons can be injected to the states *below* the vacuum level.

At the same time there are several constricting conditions for the tunneling electrons. First, an available energy range of tunneling electrons is limited to that close to the work function ($\approx 4-5$ eV for normal metals). If V_{bias} exceeds the work function as shown in Fig. 25.2b, the tunneling current shows a drastic increase because the width of the tunneling barrier becomes thinner thus moving into the Fowler–Nordheim (FN) tunneling region [25.7, 8]. In the FN tunneling region, the lateral spatial resolution is limited to ≈ 30 Å [25.9, 10] so that no atomic resolution is feasible.

The next issue is the maximum value of the tunneling current. The smaller the tunneling gap, the higher the obtained tunneling current. It can be estimated that the tip is separated from the substrate by ≈ 1 Å for the tunneling gap of 1 MΩ. If the distance is further reduced then a chemical bonding appears between the two and irreversible changes to the properties of the surface are made. The expected current for 1 MΩ gap resistance is $\approx 5\,\mu$A at the maximum available voltage for the STM mode [25.11–13].

Despite these limits, the tunneling current from an STM tip can provide a variety of unique features, which have been used for electron-induced phenomena [25.14].

25.1.3 Chemical Analysis with Electron Probe

There are various surface analytical techniques with the electron-in and electron-out configuration, which include Auger spectroscopy and high-resolution electron energy-loss spectroscopy (HR-EELS). Although Auger spectroscopy has the capability to identify the element of targets, the lateral resolution of the Auger signal still does not reach the atomic-scale region.

The HR-EELS technique is a sensitive analysis method to detect vibrational modes of molecules and phonon of substrates. The energy range of the incident electrons is similar to that used in the STM measurement and practically all vibrational modes of molecules can be detected. The selection rule of HR-EELS contributes to the determination of the molecule's bonding configuration on the surface. These features mean that the HR-EELS technique is widely used.

In order to understand whether the detection mechanism of the vibration mode of HR-EELS and IETS are similar or not, we briefly review the HR-EELS technique.

25.1.4 Excitation of Vibrational Modes with Electrons

The experimental setup of HR-EELS can be described as follows. Incident electrons, which are monochromatized in energy with the use of a monochromator, are injected onto the sample surface with energy of a few eV. The electrons scattered from the sample are analyzed in terms of energy and the energy distribution of these electrons are plotted. The peaks in the spectrum correspond to the yield of the electrons that lost certain energy from that of the incident electrons due to the vibrational excitation. The energy, strength, and width of these peaks can be analyzed to identify the chemical species, adsorption sites, and electronic and structural configuration of the adsorbates [25.15].

The vibration excitation mechanism of HR-EELS has been investigated in detail both for theoretical and experimental aspects. The mechanism can be classified into three groups: (1) dipole excitation, (2) impact scattering, and (3) negative ionic resonant scattering [25.2].

Dipole Excitation

The injected electron produces an electric field that varies with time. The oscillating field causes the excitation of the vibration of the adsorbed molecules [25.16]. The interaction occurs through long-range fields, and the excitation is expected to occur far away from the molecule (typically 100 Å). Generally, the momentum transfer is small. The selection rule of dipole scattering can be derived from the analysis of the matrix elements in the Golden rule $|\langle F|\gamma E|I\rangle|^2$, where I/F are the initial/final vibrational states. The coupling Hamiltonian is expressed as γE, where γ is the dipole moment operator formed by the intra-adsorbate nuclear motion of the vibrational mode, and E is the electric field at the adsorbate site. The vibrational modes that have a nonzero matrix element are the dipole active modes. In addition, we should pay attention to the image potential for an understanding of the selection rule. The dipoles perpendicular to the surface are reinforced by their image dipoles which emphasize the excitation. Conversely, the image potential for the dipole moment parallel to the surface creates a dipole in a direction reversed from the original one, thus canceling out the total dipole moment. As the momentum transfer is small, the inelastic component due to dipolar losses is distributed along the specular direction of the reflected electrons [25.15].

Impact Scattering

A second excitation mechanism is called impact scattering, which is characteristic of EELS only [25.17]. In the impact scattering channel, the dipole selection rule is no longer valid and a contribution from dipole-inactive modes to the inelastic cross-section can be detected [25.18]. Experimentally, this component is observed in the nonspecular direction where the intensity of the dipole component is drastically reduced. These losses are excited in the proximity of the surface. The injected electron interacts with the ion core in the range of a few Å from the center. The interaction is short range compared with the dipole scattering. The interaction mechanism is more complicated than dipole scattering and multiple scattering should be considered.

Theoretically, the formation of a deformed potential due to the excitation of a vibrational mode is considered, which scatters the incoming electron to different momentum and energy. Thus, if a particular vibrational quantum (energy $\hbar\omega_s$; wavevector Q_s) is excited and the initial vector of the electron changes from k^I to k^s in momentum, the following matrix element M results [25.15];

$$M(k^I, k^s; +s) = \langle n_s + 1|f(k^s, k^I; R)|n_s\rangle = \sqrt{(n_s+1)}\sqrt{\frac{\hbar}{2M\omega_s}}\frac{\partial f}{\partial Q_s}\,, \tag{25.1}$$

$$\frac{\partial f}{\partial Q_s} = \sum_{i\alpha}\left(\frac{\partial f}{\partial R_{i\alpha}}\right)_0 \frac{\xi_{i\alpha}}{\sqrt{M_i}}\,, \tag{25.2}$$

where n_s is the occupation number of the vibration quantum, f is the scattering amplitude, R is the position of the nuclei, M is the reduced mass, and $\xi_{i\alpha}$ denotes the amplitude of the displacement of nucleus i in the Cartesian direction α due to a given vibrational motion.

Negative Ion Resonance Scattering

This excitation is well known for gas-phase molecules. In the excitation process, the incident electron is temporally trapped in an unoccupied electronic state of a molecule. The charging of the molecule can cause a structural rearrangement, including the elongation/-contraction of the distance between nuclei. Such kinetic movement of nuclei is called a shape resonance.

It is well established that the excitation of vibrational modes of molecules is greatly enhanced in this resonance scattering process for gas-phase molecules [25.19]. For example, the differential vibrational cross-section shows the resonant enhancement at ≈ 9.5 eV for gas-phase O_2, which corresponds to the resonance energy for the formation of a negative ion of O_2 [25.20].

However, there are a very limited number of reports of successful observations of negative ion resonance for molecules on surfaces using HR-EELS. One of the reasons is the shorter lifetime of the negative ionic state for adsorbed molecules compared to gas-phase molecules due to the presence of a decay path associated with the formation of a chemical bond between molecule and substrate. Experimentally, the lifetime of a negative ionic state can be evaluated from the spectra of inverse photoemission spectroscopy, where the intrinsic broadening (Γ) reflects the lifetime (τ) of the ionic state. It has been reported that $\Gamma \approx 0.4$ eV for free CO molecules, and $\Gamma \approx 1.5$–2.5 eV when chemisorbed on Ni [25.21] and Cu [25.22]. For this reason, negative ion resonance has been reported on physisorbed molecules (N_2) on evaporated silver films [25.23]. In this case, the lifetime of the resonance is indeed relatively long due to the weak coupling between the molecule and the surface, which enhances the excitation of vibrational modes. More recently, the mechanisms of inelastic electron scattering were studied for adsorbed O_2 on Ag(110) and on Ag(111) using HR-EELS [25.24].

25.2 STM-IETS Experiments and Theory

The excitation of a vibrational mode of a molecule in the STM junction is schematically illustrated in Fig. 25.1c. The model is based on resonant tunneling in which an electron tunnels from the tip to the substrate leaving a molecule in a resonant state, the energy of which is dissipated into the substrate.

25.2.1 Detection of Vibrational Mode with IETS

For electron tunneling through a molecule, in addition to the elastic electron path, processes appear in which it loses energy by exciting a vibrational mode. Since the maximum energy which can be lost in the inelastic process is eV_{bias}, the process occurs only when the energy relation of $eV_{\mathrm{bias}} > \hbar\omega$ is satisfied. The appearance of the new channel that causes the inelastic process contributes to the increase of the conductance ($\mathrm{d}I/\mathrm{d}V$). The relation of I–V, $\mathrm{d}I/\mathrm{d}V$, and $\mathrm{d}^2I/\mathrm{d}V^2$ curves are schematically shown in Fig. 25.3. In the $\mathrm{d}^2I/\mathrm{d}V^2$ curve, two peaks are expected at symmetric energy positions but with reverse polarity [25.4, 6].

Let us consider whether the vibrational excitation mechanisms shown in the HR-EELS section can account for the STM-IETS mechanism. It should be noted that there exist distinct differences in the properties of the incident electrons between the two methods. First, the interaction at long distance of ≈ 100 Å, which causes the major part of dipole scattering of HR-EELS, cannot be realized in the IET process where the electron source is located within 10 Å. Second, the electrons tunnel into and interact with the states located between E_{F} and the vacuum level (in the case where electrons are injected into a sample). Because of the lowering of the lowest unoccupied molecular orbital (LUMO) level with respect to the gas phase for adsorbed molecules, gas-induced resonance states are often observed in this energy range.

The vibrational excitation in STM-IETS is likely caused by a combination of the impact and resonant scattering processes.

25.2.2 Examples of STM-IETS

Measurements of IETS spectra within the STM setup (STM-IETS) started with the pioneering work of Ho's group. However, the phenomenon had been already predicted theoretically shortly after the invention of STM [25.26]. The first IETS measurement was per-

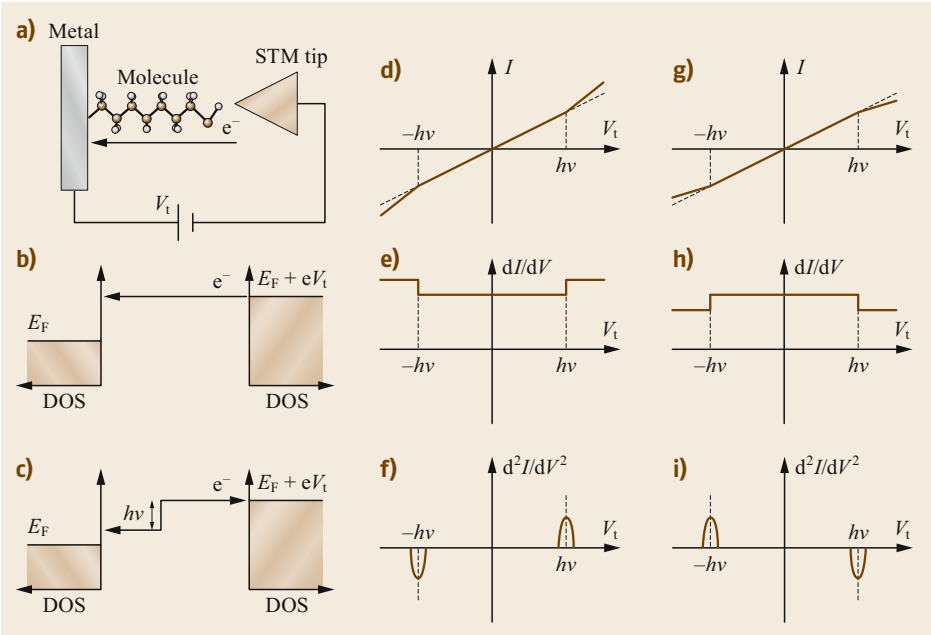

Fig. 25.3a–i Schematic view of **(a)** the tunneling process through a molecule on the surface, **(b)** elastic and **(c)** inelastic tunneling processes. **(d–f)** Effect of the inelastic process on I versus V, $\mathrm{d}I/\mathrm{d}V$ versus V, and $\mathrm{d}^2I/\mathrm{d}V^2$ versus V, respectively, where the inelastic current is increased while increasing the bias V_{t} (positive peak). **(g–i)** Similar to **(d–f)**, however, here the inelastic current is decreased while increasing the bias (negative peak). This case can be seen for O_2/Ag(110), where the density of states of the adsorbate-induced state near the Fermi level is higher, and for Au wire bridging small gap electrodes. (Reprinted from [25.25], with permission from Elsevier)

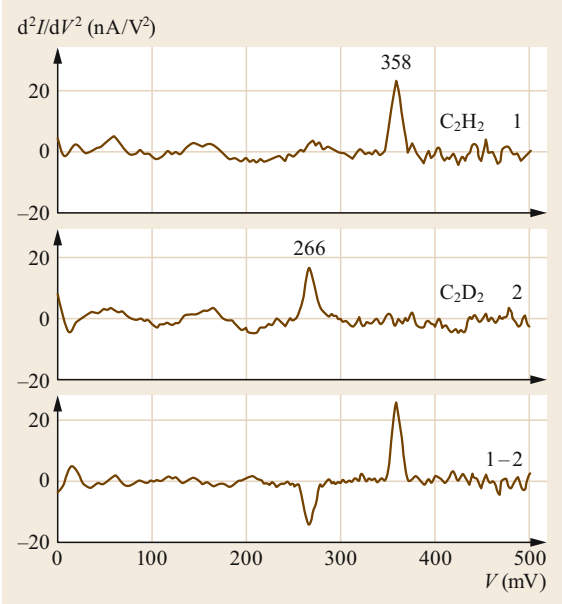

Fig. 25.4 Background difference d^2I/dV^2 spectra for C_2H_2 (1) and C_2D_2 (2), taken with the same STM tip, showing peaks at 358 and 266 mV, respectively. The spectrum *at the bottom* corresponds to (1) subtracted by (2), which contributes more background subtraction. (Reprinted with permission from [25.29]. Copyright (1998) by the American Physical Society)

formed for an acetylene (C_2H_2) molecule adsorbed on a Cu(100) surface [25.27]. The results showed an increase in the tunneling conductance at 358 mV due to the excitation of the C−H stretching mode (ν(C−H)). An isotopic shift to 266 mV was observed for deuterated acetylene (C_2D_2) (Fig. 25.4). The conductance change due to the excitation of the ν(C−H) mode was estimated to be $\approx 4.2\%$. It is interesting to compare STM-IETS results with the ones obtained with conventional IETS, which utilize the metal–insulator–molecule–metal tunnel device, for hydrocarbons. The ν(C−H) mode was measured as the strongest feature also in the conventional IETS spectra; the conductance change of 1.8% was observed for a complex silane molecule containing aminopropyltrimethoxy [25.6, 28].

Thereafter, measurement of STM-IETS spectra of CO molecules were performed; vibrations of four isotopes of CO on Cu(001) and Cu(110) at 8 K were measured by STM-IETS [25.30]. The low-energy mode observed at 36 mV was assigned to the hindered rotation mode (R-mode) which causes a conductance change of 15%, i.e., larger than that for ν(C−H). The C−O stretch is detected at 256 mV, which is close to the energy obtained using the HR-EELS technique. However, the conductance change is small ($\approx 1.5\%$) and it was claimed that the peak intensity is close to the detection limit of STM-IETS at the time of the report. It is intriguing to note that the detected intensity for the ν(C−O) mode is weak, while this mode typically gives rise to intense features in HR-EELS. We can thus argue that the excitation mechanisms involved in IETS and HR-EELS are different.

Notably, the hindered translational mode (T-mode) and M−CO stretching mode are not observed [25.30]. It is interesting to see whether the appearance and disappearance of specific vibrational modes in STM-IETS can be related to the properties of these modes. Let us examine their relaxation time (τ), which indicates how long the vibrational mode lasts once it is excited [25.31]. Experimental results for τ are 2 ps for the CO stretch mode [25.32], and a similar value is reported for the R-mode [25.33]. Conversely, τ is ≈ 40 ps for the T-mode [25.34], and $\tau > 10$ ps for the CO−Pt(111) stretch mode [25.35]. With use of an insulating layer between the molecule and the substrate, the lifetime of the vibrational modes can be increased and the IETS yield is larger (Sect. 25.3). However, the life-time and the IETS yield of the T-mode and R-mode of the CO molecule shows a reverse tendency. This point will be discussed later with a theoretical model.

Another example of the protruded feature in the positive sample bias of IETS spectra was reported for a pyridine molecule adsorbed on a Cu(001) surface by *Lauhon* and *Ho* [25.36]. They compared IETS results for pyridine and benzene molecules, where a clear feature of the ν(C−H) mode is only observed for the pyridine molecule case.

The appearance/disappearance of the ν(C−H) feature in IETS spectra with a chemical change of the molecule was reported for a benzene molecule adsorbed on a Cu(110) surface [25.37]. A benzene molecule is adsorbed on Cu(110) with a flat-lying configuration. When electrons are injected into the benzene molecule, it causes the dehydrogenation of the molecule and changes the bonding to the upright configuration (Fig. 25.5).

IETS spectra obtained, respectively, on the Cu(110) substrate (I), on the benzene molecule (II), and on the benzene molecule after tunneling electron dosing (III) are shown in Fig. 25.6a. We see IETS features only for spectrum (III), which are marked with arrows in the figure at the energies of 372 and −380 mV. The isotope effect was also examined and the IETS spectra obtained after dosing tunneling electrons to a deuterated benzene molecule are shown in Fig. 25.6b, where we see the ν(C−H) feature shift to 275 mV for the heavy isotope. These results can be rationalized if the ν(C−H) vibrational mode appears only after the change of the bonding configuration of the benzene molecule into the upright position.

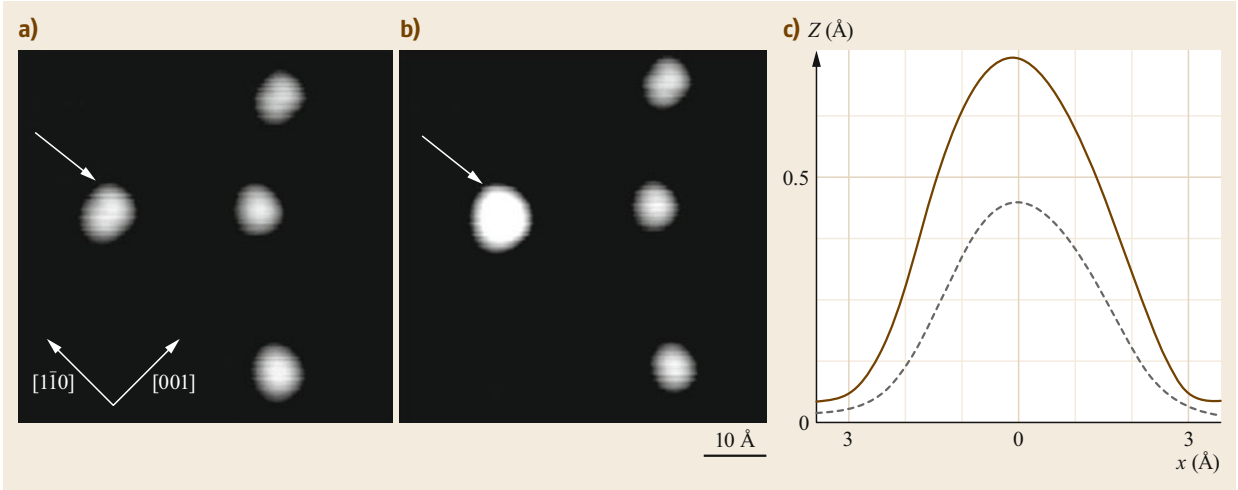

Fig. 25.5a–c Topographic image of the molecules of benzene and its reacted product. The observation conditions are the tunneling current 0.6 nA, the sample bias voltage of −500 mV, and the area 43×43 Å^2. The target molecule of benzene is shown by the *arrow* in **(a)**. It becomes brighter in **(b)** after the dosing of tunneling electrons with the energy of 4 eV (sample bias positive) for 0.2 s. **(c)** Apparent height of the benzene molecule (*dashed line*) and its reacted product (*solid line*). The height of the reacted product is 44% greater than that of the original benzene molecule. (Reprinted from [25.38], with the permission of AIP Publishing)

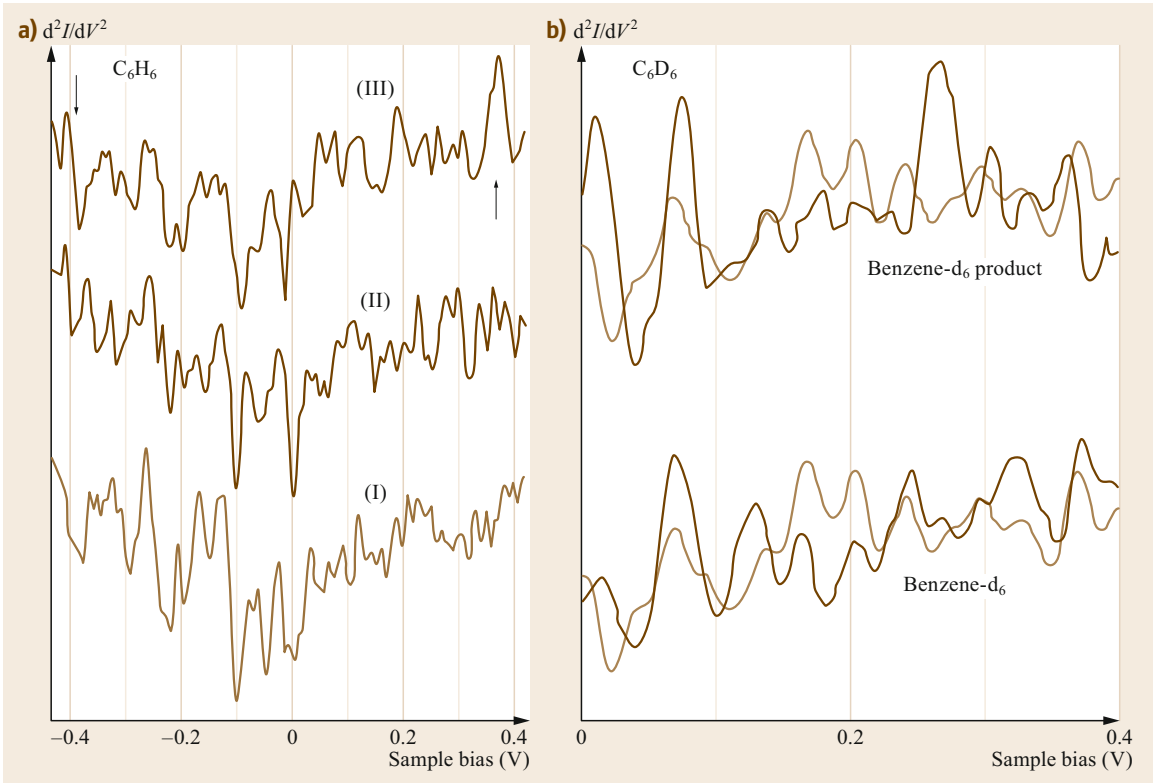

Fig. 25.6 **(a)** Vibrational spectra (dI^2/dV^2 versus V plot) obtained on the clean Cu(110) surface (I), the benzene molecule (II), and its reacted product (III) by STM-IETS taken at a gap resistance of 1 GΩ and $V_{rms} = 5$ mV modulation at 398 Hz. The spectra are the averages of 20 scans for the bias range between −0.4 and 0.4 V. **(b)** STM-IETS spectra on the deuterated benzene molecule (C_6D_6) and its reacted product. On both spectra, the spectrum of the Cu substrate is superimposed by a thin line [25.38]

There are no established selection rules for IETS, but it has been inferred empirically in the conventional IETS studies that stronger intensities are obtained for optically active modes than for the optically forbidden modes [25.4]. Since the ν(C−H) mode has a dipole moment along the surface normal for the upright configuration realized both for pyridine and dehydrogenated benzene molecules, the observed IETS spectra go along with this rule, even though the dipole excitation is less likely for STM-IETS. It can also be rationalized from a different viewpoint, i.e., the vibrational modes are effectively excited if the nuclei motions are along the tunneling current direction, which will be examined later.

25.2.3 Spectra Shape of IETS

There are several reports where the STM-IETS features in the positive energy region appear as dips instead of peaks (Fig. 25.3g,h). This shows a large difference from the results of IETS with metal oxide tunneling devices, in which almost all features appear as peaks for positive energy values.

Hahn et al. revealed two vibrational modes showing a *decrease* in conductance at ±82.0 and ±38.3 mV sample bias for a single oxygen molecule chemisorbed on the fourfold hollow sites of an Ag(110) surface at 13 K [25.37]. *Pascual* et al. detected low energy adsorbate–substrate (external or hindered) vibrational modes of benzene molecules adsorbed on an Ag(110) surface [25.39]. These IETS features are found to be strongly sensitive to the adsorption properties, and more interestingly the vibrational spectra of molecules close to kink sites exhibit a characteristic Fano-like line shape.

Agrait et al. reported similar dips in the IETS for free-standing gold atomic chains of up to seven atoms in length [25.40]. The dip features are derived from the phonon modes whose frequencies are determined by the length of the chain.

Persson and Baratoff have claimed that there appears a case where the dI/dV ($V > 0$) decreases at the threshold voltage instead of the *increase* observed for the normal case illustrated in Fig. 25.3 [25.41]. This happens when the elastic channel suffers an effect of backscattering of elastic electrons by exciting and reabsorbing a vibrational mode at the threshold energy. The backscattering might reduce the intensity of an elastic component. Experimentally, we can only measure the sum of the elastic and the inelastic component. Thus, the shape of the IETS spectra is not always protruded; it can be a dip or remain flat even if the inelastic component gives a positive contribution for the conductance change.

Such an increase of the backscattering appears when the LDOS of resonance states is high. Resonance states are defined as molecular orbitals of adsorbates broadened after interacting with metal substrate levels. When the LDOS of the resonance states is high (low) at the Fermi level, it is called on-resonance (off-resonance). Most conventional IETS experiments have been performed on molecules adsorbed on inert Al_2O_3 oxide and the off-resonant condition is expected in these cases. It is suggested that this is the main reason why protruded peaks are observed in the IET spectrum ($V > 0$) in most observations [25.41]. One of a few examples in which such a dip is observed corresponds to the case in which methyl isocyanide molecules are adsorbed on alumina-supported rhodium particles, which can be an evidence of the importance of the resonant coupling process [25.42]. *Persson* claimed that such a behavior is characteristic for negative ion resonance and neither dipole nor impact scattering induce such behavior [25.41].

Recently, *Paulsson* et al. reported a theoretical model to explain the switch between the peak and dip in IETS [25.43]. They chose four different IETS results and performed theoretical simulations. The four cases included IETS investigations of oligo phenylene ethynylene (OPE) [25.44] (Fig. 25.7a) and a gold chain connected to two Au electrodes [25.40] (Fig. 25.7b), and STM-IETS investigations of CO chemisorbed on Cu(111) [25.45] (Fig. 25.7c) and O_2 on Ag(110) [25.37] (Fig. 25.7d). In the case of OPE on gold (Fig. 25.7a) and CO on Cu(111) (Fig. 25.7c) peaks are observed at positive bias values of the d^2I/dV^2 versus V. Conversely, for the gold chain (Fig. 25.7b) and for O_2 on Ag(110) (Fig. 25.7d) peaks are present for negative bias and dips are present at positive bias.

The proposed model illustrates an electron transport between two electrodes assuming a single electronic state for each, where the electron transfer is considered in terms of the ratio of molecular coupling to two electrodes (α) and transmission (τ) [25.43]. According to this model, the maximum transmission is described by $\tau_{max} = 4\alpha/(1+\alpha)^2$ (thick line in Fig. 25.8) and a crossover point, where the shape of the d^2I/dV^2 spectrum changes from the peak to the dip, is described by $\tau_{crossover} = \tau_{max}/2$ (red dashed line in Fig. 25.8). The diagram in Fig. 25.8 indicates that for a given coupling ratio, if the transmission is higher than half-maximum, the inelastic back scattering prevails over the inelastic forward scattering, leading to the decreased tunneling probability.

The four samples treated here are located in the phase diagram as follows: (a) The OPE molecule is connected similarly to the two electrodes via strong chemical bonds ($\alpha \approx 1$) and the electronic state responsible for the transport is far from the Fermi level

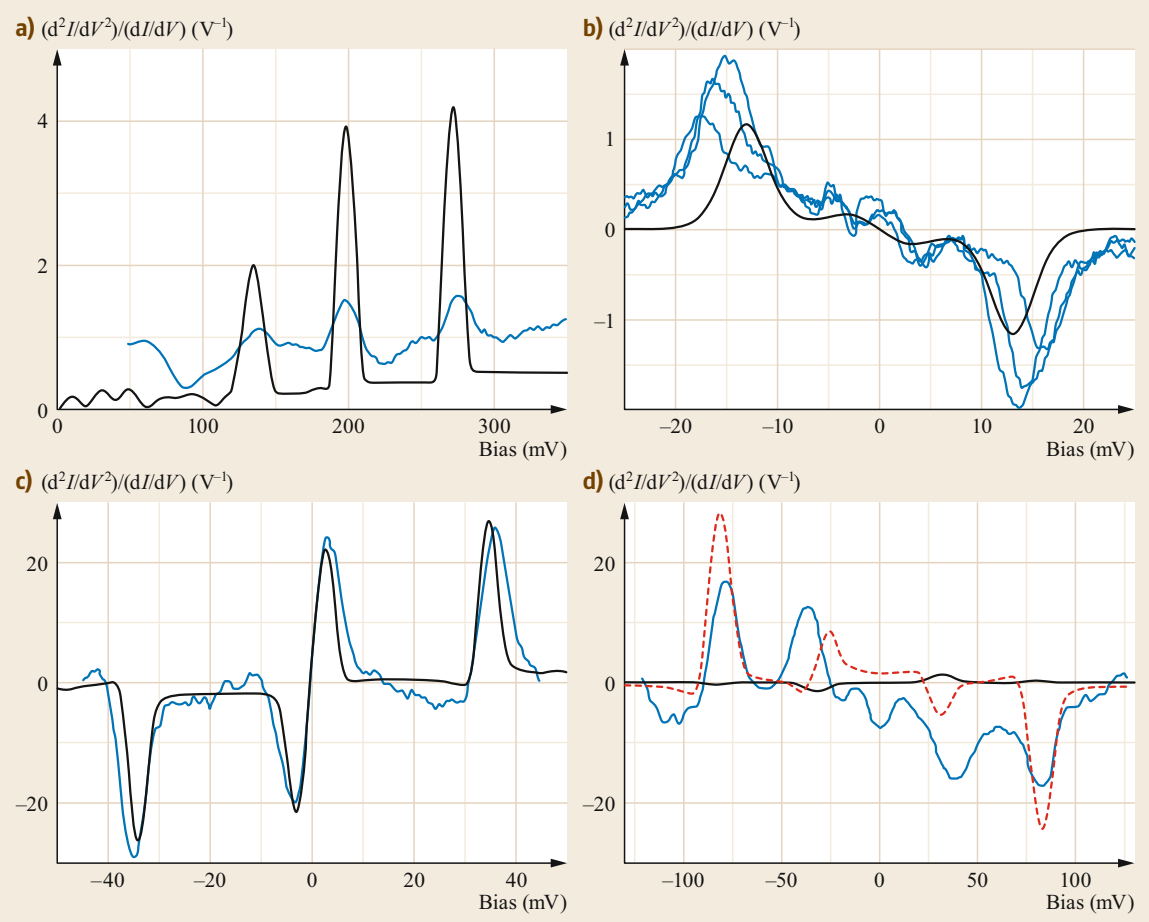

Fig. 25.7a–d Experimental (*blue lines*) and calculated (*black lines*) IETS for **(a)** OPE molecule on Au(111) electrodes [25.44], **(b)** Au chain connected to Au(100) electrodes [25.40], **(c)** CO molecule on Cu(111) [25.45], and **(d)** O_2 molecule on Ag(110) [25.37]. In case **(d)**, the Fermi energy in the calculation has been shifted manually $\Delta\varepsilon_F = -0.6\,\text{eV}$ to match the experiment (*red dashed line*). The calculation data originate from [25.46]. For the STM configurations **(c)** and **(d)**, the calculated IETS is compared with a rescaled d^2I/dV^2. (Reprinted with permission from [25.46]. Copyright (2008) by the American Physical Society)

($\tau \approx 0$). Thus, the OPE is located in the upper left part of the phase diagram, which provides the peaks in the d^2I/dV^2 versus V plot at positive bias. (b) The gold chain is also connected strongly and symmetrically to the two electrodes ($\alpha \approx 1$), however, the transmission is higher than the half-maximum, and the system ends up in the upper right corner of the phase diagram providing the dips. Systems (c) CO/Cu(111) and (d) O_2/Ag(110) have both been investigated by STM, therefore the coupling is antisymmetric ($\alpha \approx 0$). Conversely, the transmissions are considerably different between the CO and the O_2 molecule. This is caused by the different electronic structure of CO and O_2 after being adsorbed on Cu(111) and Ag(110) substrates, respectively. If the resonant states of O_2/Ag(110) and CO/Cu(111) are compared, the former, originated from $1\pi_g$ level, has a much higher density near the Fermi level than the latter. Thus, the tunneling conditions in the bias range near the Fermi level are off-resonant and on-resonant for the CO/Cu(111) and O_2/Ag(110) cases, respectively. Because of this contrast, the CO case is located to the left of the crossover line (providing the peaks) and the O_2 case is located to the right of the crossover line (providing the dips) [25.43]. Besides this qualitative consistency between experiment and theory, numerical calculations based on DFT (density functional theory) and NEGF (nonequilibrium Green's function) (Sect. 25.2) formalism reproduce the experimental observations well in quantitative terms (black lines in Fig. 25.7) [25.43].

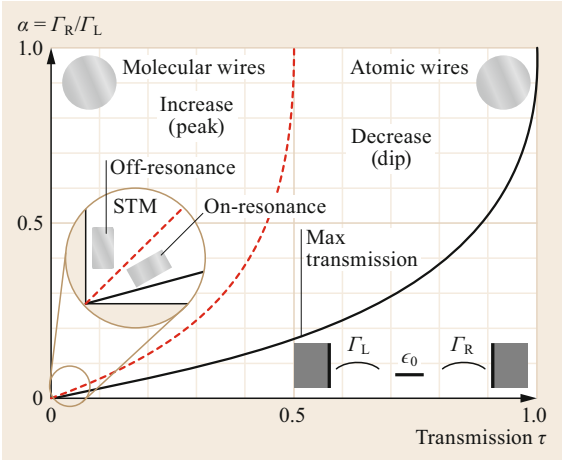

Fig. 25.8 Phase diagram for a one-level model. A state specified by ε_0 is coupled with left and right electrodes with strength Γ_L and Γ_R, respectively. For an STM measurement, electrode L and electrode R represent the substrate and the tip, respectively. The *inset* illustrates the sign of the conductance change at the onset of inelastic tunneling. At a given coupling ratio, the elastic transmission has an upper bound max (*black line*), and the inelastic conductance change undergoes a sign change at crossover $t_{\text{crossover}} = t_{\max}/2$ (*red dashed line*). (Reprinted with permission from [25.46]. Copyright (2008) by the American Physical Society)

25.2.4 Theory of IETS

The IETS ν(C−H) mode features observed for the acetylene molecule, which has a much stronger intensity compared to other modes, has attracted attention and theoretical calculations have been performed. The mechanism behind the appearance of strong intensity was discussed by *Lorente* et al. [25.47] and *Mingo* and *Makoshi* [25.48]. Both of them calculated the matrix elements in which the initial electronic state i makes a transition to the final state f caused by the presence of a deformation potential [25.49]. The deformation potential is the change of one-electron potential by the nucleus movement accompanying the vibrational mode of the molecule.

More precisely, *Lorente* et al. presented the following formula for it [25.47]

$$|\langle\phi_\lambda|\delta v|\phi_\mu\rangle|^2 \,, \tag{25.3}$$

where $\langle\phi_\lambda|$ and $|\phi_\mu\rangle$ are the final and initial electronic states in the resonant states calculated by the DFT. The deformation potential δv is thereby expressed in the form of $\partial v = \sqrt{\hbar/2M\omega}\,\partial v/\partial Q$, where M is the reduced mass, Q the coordinate of the atoms involved in the vibration, and v is a one-electron potential energy.

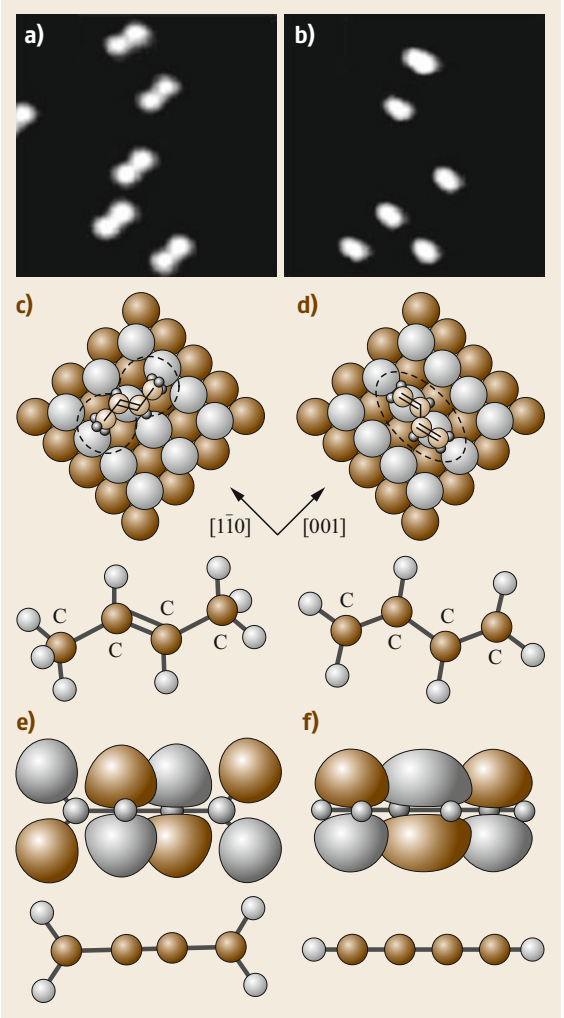

Fig. 25.9a–f The STM images, bonding configuration and structure of the molecules for **(a,c)** *trans*-2-butene and **(b,d)** 1,3-butadiene. Contour of the molecule orbital of the LUMO state is shown for **(e)** *trans*-2-butene and **(f)** for 1,3-butadiene. Note a portion of the LUMO orbital is located in the CH_3 group of *trans*-2-butene in **(e)**

Note that $\sqrt{\hbar/2M\omega}$ corresponds to the amplitude of the vibrational mode.

If we compare (25.1) for the impact scattering mechanism of HR-EELS with (25.3), we find similarities between these two theoretical treatments. The theory shown by Lorente does not include the formation of a temporary negative ion explicitly proposed by *Persson* and *Baratoff* [25.49]. Mingo et al. showed that the weak intensities of all vibrational modes detected for the acetylene molecule other than the ν(C−H) mode is due to the destructive interference between different atomic orbitals. *Mii* et al. used the Green func-

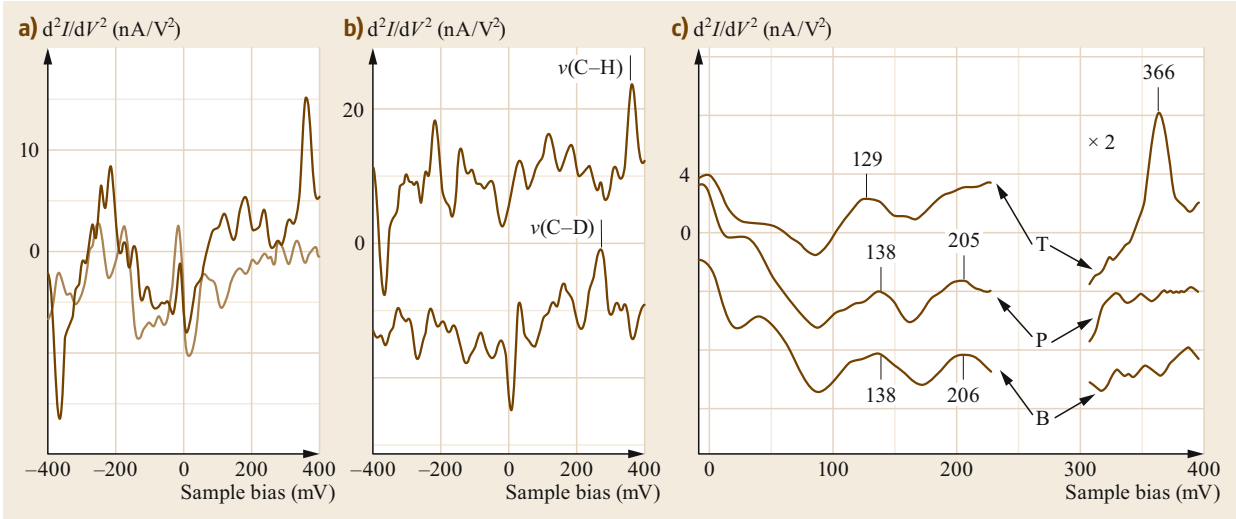

Fig. 25.10 **(a)** Vibrational spectra obtained for the clean Pd(110) surface (*light brown line*) and *trans*-2-butene (*dark brown line*) by STM-IETS reported at a gap resistance of 1 GΩ with a 14.1 mV (rms) ac modulation at 397 Hz. The spectra correspond to averages of four scans from −400 to +400 mV. **(b)** Vibrational spectra for *trans*-2-buten (*upper line*) and *trans*-2-buten-d_8 (*lower line*) after background subtraction. The change in conductance for the peaks at ±366 mV (268 mV) is 6% (5%) at positive sample bias, and 7% (3%) at negative sample bias, for the C−H (C–D) stretching mode of *trans*-2-butene (*trans*-2-butene-d_8). **(c)** Vibrational spectra for *trans*-2-butene (*curve* T), the reaction product (*curve* P), and 1,3-butadiene (*curve* B) shown in Fig. 25.9f. The spectra were taken at a gap resistance of 200 MΩ within the range of 0−230 mV, in the region where dehydrogenation does not occur, and 1.5 GΩ within the range of 300–400 mV. (Reprinted with permission from [25.50]. Copyright (2002) by the American Physical Society)

tional method on the basis of the Anderson Hamiltonian to calculate such differences in different vibrational modes [25.51, 52].

Here we examine how these theoretical treatments reproduce actual IETS spectra observed for molecules other than acetylene. *Kim* et al. reported IETS spectra measured for trans-2-butene (C_4H_8) and 1,3-butadiene (C_4H_6) molecules adsorbed on a Pd(110) surface [25.50]. The topographic image and the model of the bonding configuration are illustrated in Fig. 25.9a,c, respectively for the *trans*-2-butene molecule, and in Fig. 25.9b,d for the 1,3-butadiene molecule. The former has a C=C bond at the center of the molecule, and two CH_3 groups are attached to both ends of the C=C bond. The butadiene molecule has two C=C bonds inside the molecule.

For the IETS spectra, a clear peak was observed at 365 mV corresponding to the ν(C−H) mode for the *trans*-2-butene molecule (Fig. 25.10), whose peak intensity is almost as strong as that observed for an acetylene molecule on Cu(100) [25.27, 53]. However, this feature cannot be observed for the 1,3-butadiene molecule in spite of their similar structure and the existence of C−H species.

The origin of the different intensities of the ν(C−H) mode observed for the two molecules can be explained as follows. We see these two molecules have a significant difference in the electronic state at the energy close to the Fermi level. The molecular orbital (MO) of the LUMO level for *trans*-2-butene and 1,3-butadiene molecules are shown in Fig. 25.9e,f, respectively. The LUMO level shifts downwards from the gas phase after adsorption on the surface, and forms a resonant state near the Fermi level. The MO of the LUMO level can be seen at the C−H bond in the CH_3 group for the *trans*-2-butene molecule, but it is absent for the butadiene molecule. The model proposed by Lorente suggests that the coupling between the initial and the final state expressed in (25.3) determines the IETS signal intensity.

We can assume that the deformation potential δv should be distributed at the bond related to the vibrational mode (the C−H bond for the case of the C−H stretching mode). The IETS signal should be strong only when the densities of the electronic states of ϕ_λ and ϕ_μ have large components at the bond for the vibration mode. Thus, the absence of the MO of the LUMO level at the C−H bond for the butadiene molecule might be responsible for the weak intensity of the ν(C−H) mode.

In addition, the bonding strength between the molecule and the substrate should be considered as a factor

that determines the IETS signal strength. This is especially so in the case where the negative ion resonance participates in the vibration excitation, because the excitation probability of vibration modes should increase in the case where the lifetime of the negative ion state is longer. It is speculated that a weaker interaction between the CH_3 group and the substrate for the *trans*-2-butene molecule than that of the CH_2 group for the butadiene molecule might enhance the excitation probability of the ν(C−H) mode.

25.2.5 Calculation Methods for IETS

Recently, a calculation method combining DFT and NEGF calculations successfully reproduced the experimental results [25.49, 54, 55].

The NEGF method correctly describes the corrections to the elastic current and can describe experiments in which the current increases and/or decreases due to inelastic scattering. The calculation covers IETS phenomena not only for the STM setup but also for an atom chain which bridges two electrodes. The current variation gives rise to peaks and/or dips in the second derivative. The main disadvantage of the NEGF method is that it consumes a large computational resource. The recently developed lowest-order expansion (LOE) approximation of the NEGF method makes it feasible to calculate the IETS from large-scale DFT calculations [25.46, 54, 56]. In addition, the emission rate calculation in the LOE approximation is identical to Fermi's golden rule expression. The LOE can therefore provide physical insights into the scattering processes and allow derivation of selection rules for IETS from first-principle calculations.

NEGF clearly shows how the current is coupled with the vibrations through the junction. To simplify these expressions, two approximations are used. The first assumption is that only the lowest order e–ph coupling matters. The second is that the density of states varies slowly near the Fermi level, which allows the integration over energy to be carried out analytically.

In the low-temperature limit, the power dissipation from the electrons into the vibrational system is then given by

$$P = \sum_{\lambda} \frac{(\hbar\omega)^2}{\pi\hbar}[n_{\mathrm{B}}(\hbar\omega) - n_{\lambda}]\mathrm{Tr}(M_{\lambda}AM_{\lambda}A) + \frac{\hbar\omega}{e}\gamma_{\lambda} \begin{cases} 0; & |eV| < \hbar\omega\,, \\ |eV| - \hbar\omega; & |eV| > \hbar\omega\,, \end{cases} \tag{25.4}$$

where $\hbar\omega$ is the energy of the target vibrational mode, $n_{\mathrm{B}}(\hbar\omega)$ the Bose–Einstein distribution, n_{λ} the occupation of the vibrational mode, M_{λ} the e–ph interaction, A the spectral function, and γ_{λ} the emission rate which will be discussed later [25.54, 56]. The first term drives the vibrational system towards equilibrium with the electrons. The second term describes vibrational heating where the emission rate is given by

$$\gamma_{\lambda} = \frac{e}{\pi\hbar}(M_{\lambda}A_{\mathrm{L}}M_{\lambda}A_{\mathrm{R}}) = \frac{4\pi e}{\hbar}\sum_{l,r}|\langle\Psi_r|M_{\lambda}|\Psi_l\rangle|^2\,, \tag{25.5}$$

where A_{L}, A_{R} are the spectral functions of the two lead electrodes connecting the scattering region. The scattering rate can further be rewritten in terms of the scattering states of the two lead electrodes ($|\Psi_{\mathrm{r}}\rangle$ or $|\Psi_{\mathrm{l}}\rangle$). Equation (25.5) thereby resembles Fermi's golden rule and if the scattering states are known, selection rules based on the symmetry of the scattering states and e–ph coupling can be derived.

The forward (back) scattering forms a peak (dip) in IETS. The variation of the current can be estimated by

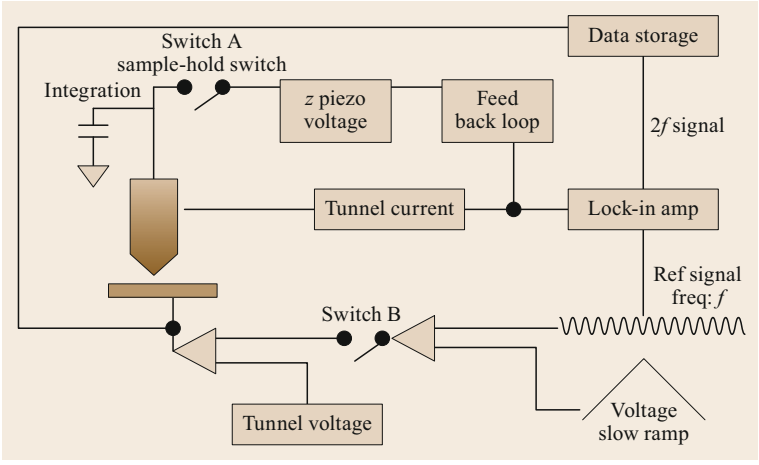

Fig. 25.11 A schematic drawing of an STM-IETS setup. IETS spectroscopy is measured by turning off the feedback circuit (switch A) and applying slow-ramping voltage in which a sine-shape modulation voltage is superimposed (frequency ≈ 797 Hz) to the sample bias by closing switch B. The differentiation of the tunneling current is executed by the use of a lock-in amplifier. (Reprinted from [25.2], with permission from Elsevier)

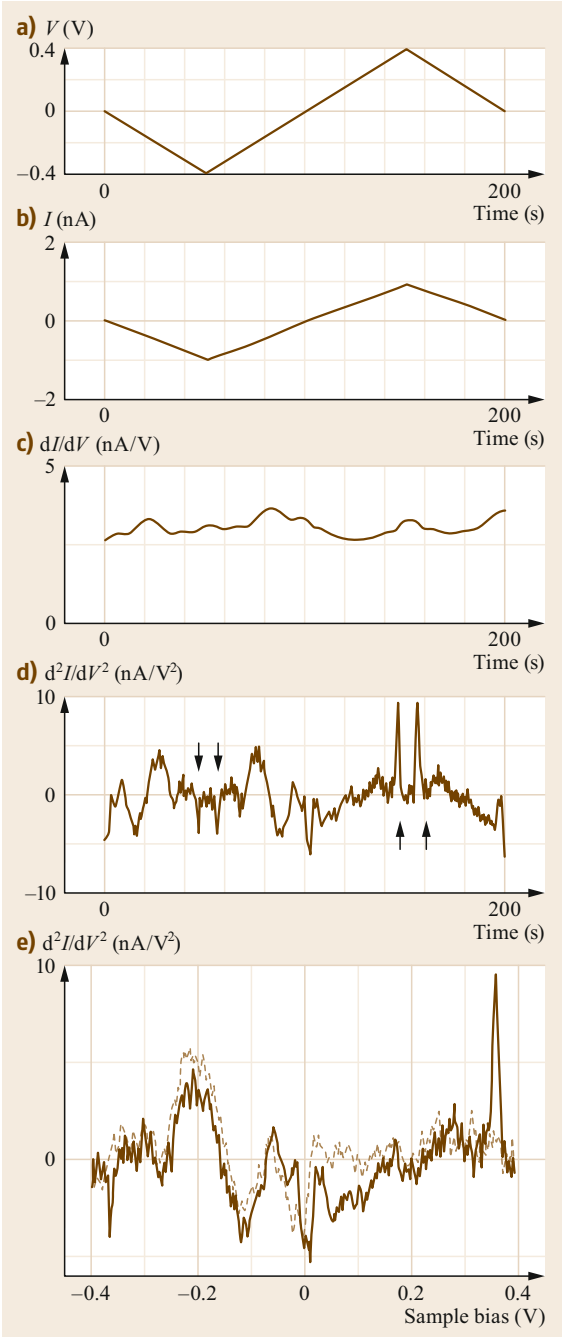

Fig. 25.12a–e Variation of sample bias **(a)**, and tunneling current **(b)**, the output of the lock-in amplifier of the harmonic **(c)**, and the second harmonic component **(d)** as a function of the measurement time of the STM-IETS of a *trans*-2-butene molecule on Pd(110). All graphs are the average of 16 cycles of the measurements (see text). The *arrows* indicate sharp features corresponding to the ν(C−H) vibrational mode. **(e)** The d^2I/dV^2 versus V spectra obtained on a *trans*-2-butene molecule (*solid curve*) and on the bare Pd(110) surface (*dashed curve*). (Reprinted from [25.59], with the permission of AIP Publishing) ►

the scattering rate which can be evaluated using (25.5), which will be introduced later on in this chapter. The crossover from peak to dip in simplified models occurs at a transmission of 1/2 [25.46].

25.2.6 Experimental Setup of STM-IETS

An example of the experimental setup used in STM-IETS is shown in Fig. 25.11. Conventional STS measurement can be executed by recording the I–V curve followed by numerical differentiation. This procedure is possible because the natural width of electronic states is of the order of ≈ 1 eV and there is no special technical difficulty in taking the numerical derivative of the I–V curve. Conversely, the vibrational features have quite a narrow peak width of the order of 1 mV, which makes it quite difficult to obtain d^2I/dV^2 by numerical differentiation. Instead, lock-in amplifier detection using a voltage modulation method is required. The measurement of the lock-in amplifier signal requires a relatively long acquisition time of the order of ≈ 100 s to get a single spectrum. The change of relative location between the tip and the molecule may then be critical; stability is therefore required both for lateral and horizontal directions. Attention should be paid to both the mechanical stability of the STM head and to the reproducibility of the control electronics [25.57, 58].

An example of an IETS measurement is shown in Fig. 25.12a–d, where the variation of bias voltage, tunneling current, dI/dV, and d^2I/dV^2 are displayed as a function of time. The data were obtained for a *trans*-2-butene molecule adsorbed on Pd(110). The curves of d^2I/dV^2 versus V are shown in Fig. 25.12e by comparing the spectra obtained on the bare metal substrate (dashed line) and on the adsorbate (solid line). Sharp features can be identified at the sample bias of −363 and 360 mV only in the spectrum obtained on the molecule. The former appears as a dip and the latter is a peak which satisfies the conditions for the assignment to a vibration-induced feature. The intensity of the positive peak is $\approx 9.5\,\mathrm{nA/V^2}$ and the full-width-at-half-maximum (FWHM) is ≈ 12 mV. Though there are several other vibrational modes, they are not as obvious as the mode identified as the ν(C−H) mode [25.59].

Low-Temperature STM System

As mentioned above, IETS is an all-electron spectroscopy method whose resolution has a linear relation with the system temperature except for the modulation

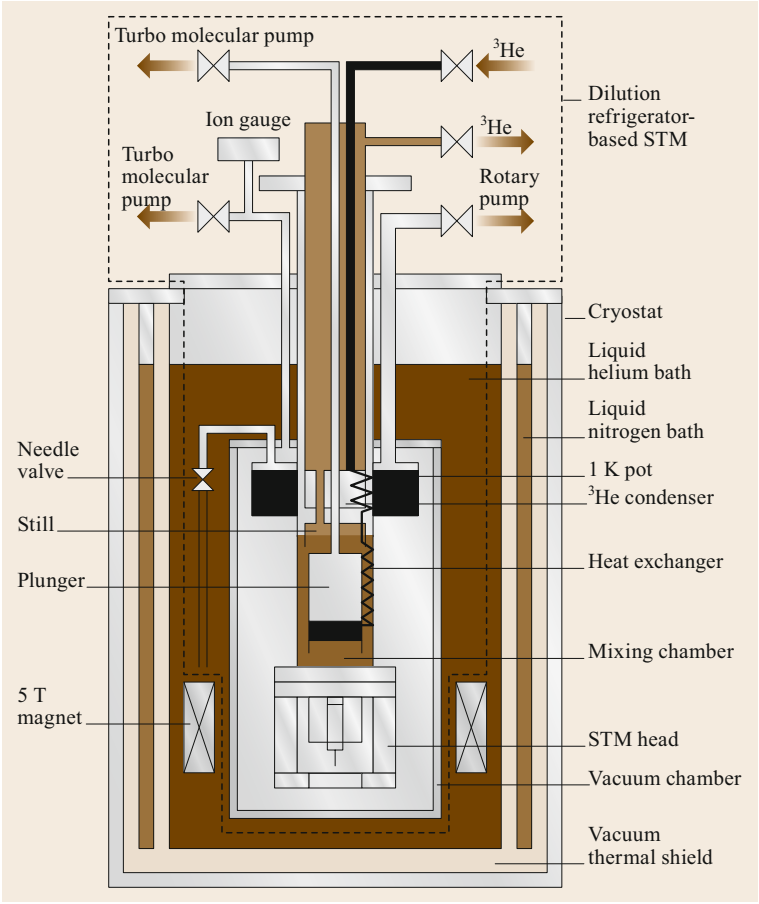

Fig. 25.13 Schematic of a compact ultralow-temperature STM system. The cryostat is mounted on a vibration-isolation table (not shown). (From [25.60]. © IOP Publishing. Reproduced with permission. All rights reserved)

voltage and the intrinsic peak width. Thus, lowering the temperature of the STM system is beneficial both for mechanical stabilization (elimination of the thermal drift) and for improvement of the resolution of the IETS spectroscopy. An example of an STM system based on a dilution refrigerator-type STM is shown in Fig. 25.13 [25.60]. The cryostat and dilution refrigerator (TC330-SCM and TS-3H100, Taiyo Nissan, Japan), and the STM unit (USSS-9990, Unisoku, Japan) are both commercially available. The cryostat consists of a 57 L liquid helium bath, a 26 L liquid nitrogen bath, a vacuum thermal shield, and a 5-T superconducting electromagnet. The cryostat is mounted on a vibration-isolation table (AWF-1510DTU, Meiritsu Seiki Co., Japan) (not shown). By using this setup and operating the dilution refrigerator, we can acquire IET spectra at a temperature of 260 mK [25.60]. However, for the vibrational spectroscopy of alkanethiol molecules the resolution of the spectra at 260 mK showed no improvement over those obtained at 4.4 K because of other experimental factors. Details of the operating principles of the dilution refrigerator are given elsewhere [25.60].

This system is operated by cooling with liquid He and once filled to full volume, the STM can work at a stable temperature of 4.4 K for 48–72 h without requiring a further supply of liquid He.

The dilution-refrigerator-based STM system is illustrated in Fig. 25.14a while the STM head is shown in Fig. 25.14b. A sample can be transferred from the bottom of the STM unit. The STM system can be operated in the following two configurations:

1. The system works in a stand-alone manner. The sample is loaded in an inert gas atmosphere, followed by pumping with a turbo molecular pump (TMP) for 24 h. After that, the system is immersed into the liquid He bath. The operation of the TMP is discontinued once the bath is filled with liquid He. The wall of the chamber works as a cryogenic pump.
2. The bottom of the STM system of Fig. 25.14a is connected to a Ultrahigh Vacuum (UHV) system via a connection which goes through the liquid He bath. With the use of a long vertical magnetic loading

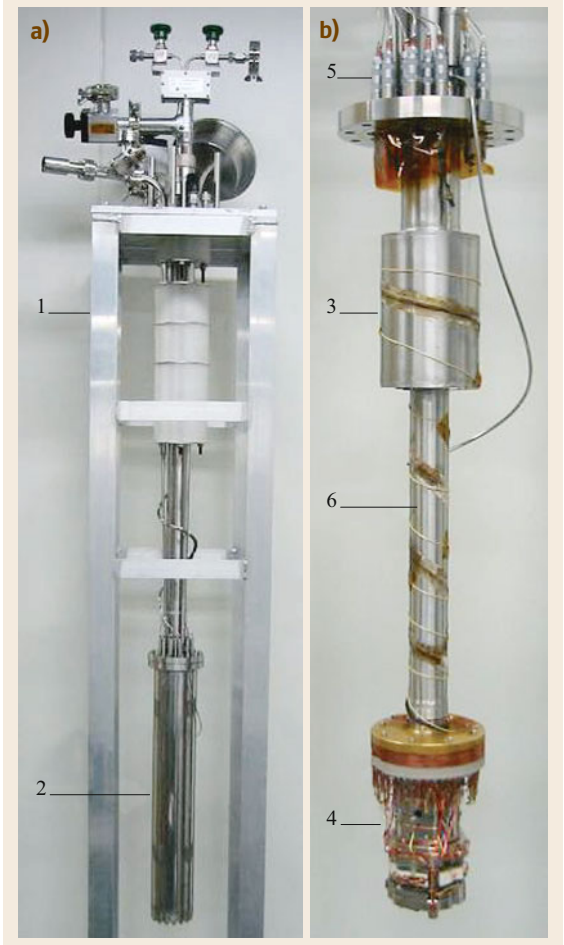

Fig. 25.14 (a) The dilution refrigerator-based STM, (1) support table, (2) vacuum chamber; **(b)** the inner structure of the vacuum chamber, (3) 1 K pot, (4) STM head, (5) wires for the scanner piezo, shear piezo, sample bias and thermometer, (6) circular cylinder. (From [25.60].)

system, the sample can be prepared in a separated preparation chamber and transferred into the STM head under UHV conditions. The second method is more straightforward in terms of the sample surface quality compared to the first one. However, the He cryostat dewar must be disassembled for the maintenance of the STM head. The particular study shown below for the alkanethiol molecule was performed using the first method.

The coarse motion of the STM is operated using a slip and stick motion, which allows for a maximum movement of the X–Y stage of ± 0.5 mm. The maximum scan area of the STM piezo tube for X–Y is $3.4 \times 3.4\,\mu m^2$ at 300 K and $1.0 \times 1.0\,\mu m^2$ below 4.4 K. The coarse motion and scanning of the STM is controlled by commercially available units (PMC100 and SPM100, RHK, Troy) and operated using their accompanied software (XPM, RHK, Troy).

Measurement of I–V Derivative by Using Lock-in Amp

The normal inelastic signal originating from a vibrational mode with energy $h\nu$ appears as a step-like feature at the sample bias of $h\nu/e$ in the dI/dV curve and a peak or a dip at the sample bias of $h\nu/e$ in the d^2I/dV^2 curve. Use of a lock-in amplifier is effective for obtaining high-precision dI/dV and d^2I/dV^2 curves. A schematic of the IETS measurement system is shown in Fig. 25.15a. The modulation voltage ($\Delta V \sin(2\pi ft)$) is applied to the sample bias (V). In this case, the tunneling current (I) can be approximated as

$$I[V + \Delta V \sin(2\pi ft)] \approx I(V) + \frac{dI}{dV}\Delta V \sin(2\pi ft) + \frac{d^2I}{dV^2}\frac{(\Delta V)^2}{4}\sin\left(4\pi ft - \frac{\pi}{2}\right) + \frac{d^2I}{dV^2}\frac{(\Delta V)^2}{4}\,. \quad (25.6)$$

Hence, dI/dV can be obtained by detecting the AC current modulated at f, and d^2I/dV^2 can be obtained by detecting the AC component modulated at $2f$ where the phase of the modulation current is delayed by $-90°$ compared to that of the modulation voltage. The modulation frequency was set in the range between 500 and 1000 Hz, and the cutoff frequency of the preamplifier was set to 1.5 kHz. The tunneling current was converted to a voltage signal by a preamplifier (IVP-PGA and IVP-200, RHK, Troy), which was then divided into two paths: one is to an input of an STM controller (SPM100, RHK, Troy), for gap control, and the other to a lock-in amplifier (NF5640, NF Corp., Yokohama), for the conductance and the IET signal measurement. The output of the lock-in amplifier was recorded using an STM controller (Fig. 25.15a).

The phase shift between the modulation voltage and output modulation current resulting from the wiring and tunnel-junction configuration should be calibrated beforehand with the method described as follows. First, the STM tip is retracted by a few tens of nm from the surface to a point where the tunneling current cannot be detected. Next, a modulation bias with frequency f is applied to the sample, producing an AC current (displacement current) with frequency f. This AC current is produced solely due to the capacitance between tip and

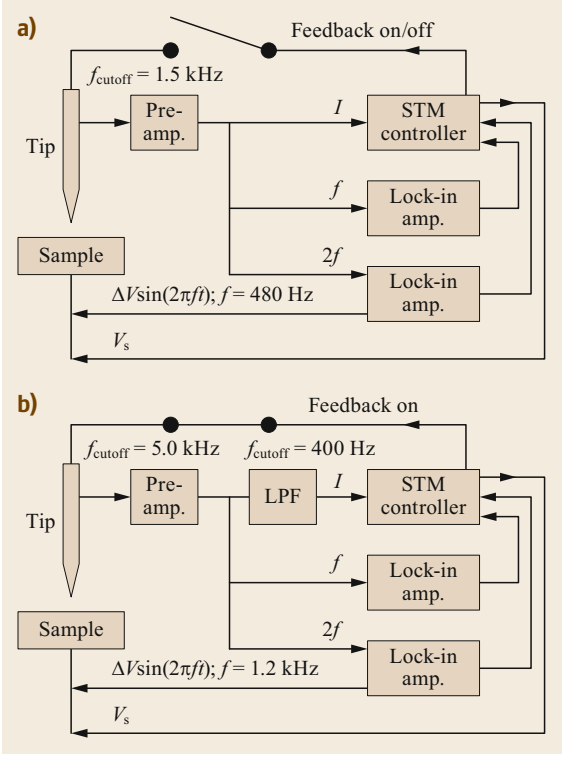

Fig. 25.15a,b Schematic drawing of **(a)** a conventional IETS measurement system and **(b)** an improved mapping system for the IET signal (From [25.61]. © IOP Publishing. Reproduced with permission. All rights reserved)

sample. By maximizing the magnitude of the AC current using the lock-in amplifier, the phase shift between the input modulation voltage and output modulation current can be determined. The phase shift for the frequency $2f$ can also be estimated by repeating the same procedure. This phase shift is stable and it is not necessary to repeat the phase determination process once it has been determined.

25.2.7 Spatial Mapping of IETS

Mapping of IET signals is an effective method for visualizing the distribution of a characteristic feature of a molecule on a surface [25.45, 62]. *Sainoo* et al. reported a mapping method of IET signals using a conventional measurement system (Fig. 25.15a), where the feedback loop is activated during the mapping process [25.59]. In order to minimize the effect of the modulation voltage on the feedback loop, they employed a high-frequency modulation voltage and a low time constant on the feedback loop. However, the restriction of the time constant on the feedback loop and remnant effects of the modulation voltage on the feedback system prevent a good topographic image and IETS mapping from being obtained for a high tunneling resistance sample like alkanethiol SAMs. Actually, in a mapping experiment using the same setup, it was not possible to obtain satisfactory IET mapping for a hexanethiol SAM.

In order to solve this problem, the AC component of the tunneling current signal, which is used for gap-distance control, is minimized [25.61]. This is achieved by inserting a low-pass filter (3314, NF Corp., Yokohama) between the preamplifier and the STM controller (Fig. 25.15b), which results in a reduction of the feedback response by the modulation voltage. The modulation frequency is set at 1.2 kHz, the cutoff frequency of the preamplifier at 5 kHz and the cutoff frequency of the low-pass filter at 400 Hz. The attenuation slope of the low-pass filter was 48 dB/oct, making the transmission rate of the modulation current less than 0.1% at 1.2 kHz. Under this condition, we could see no change in the modulation current for frequency f at the input of the lock-in amplifier, with or without the feedback loop engaged.

25.3 Survey of STM–IETS Reports for Various Systems

Here we examine examples of STM-IETS measured for various systems.

Organic molecules have often been targeted by IETS measurements. Investigation of a pyridine molecule on Ag(110) was reported by *Hahn* and *Ho* [25.63]. It revealed a C−H stretching mode at 378 meV and the isotope shift to 282 meV when deuterated.

Sainoo et al. reported a measurement for the cis-butene molecule on Pd(110) [25.64]. The IETS features were detected at 37 and 358 meV, which are assigned to the metal-molecule stretching mode and the C−H stretching mode, respectively.

In addition, they measured the yield of the rotation of the molecule as a function of the energy of the injected electrons, which they called *action spectroscopy* and is supposed to yield supplemental information for the vibration modes detected by STM-IETS. The result shows an enhancement of the rotation at 110 and at 115 meV, which are assigned to the excitations of C−C stretch and C−H bending modes, respectively, according to the energies reported for those modes. They claim that some modes are more apparent in action spectroscopy than in STM-IETS.

Since the bonding strength between the molecule and the substrate, and consequently the life-time of the vibrational mode has a substantial effect on the yield of the STM-IETS signal, much effort has been put into the search for a good substrate. The substrate NiAl(110) after oxidation was used to decrease the interaction between the molecule and the substrate, since the oxide can still show an atomic-scale flatness. *Nilius* et al. demonstrated that an attachment of CO molecules to a Pd atom, both of which are adsorbed on oxidized NiAl(110), is possible by using the atom manipulation technique [25.65]. The CO's hindered rotational mode is then measured at 40 meV and the C−O stretching mode at 258 meV, whose energies are appropriate for the formation of metal-CO clusters. Liu et al. measured the STM-IETS for the molecule of 4,7,12,15-tetrakis[2,2]paracyclophane (DMAS-PCP) on the same surface. A feature at 25 meV is assigned to out-of-lane C−C−N and CC−C bending, and that at 179 meV is assigned to in-plane CC−H bending, in addition the feature at 365 meV corresponds to the C−H stretch in the CH_2 group [25.66].

Organic molecules consisting of a large number of atoms have also been investigated with STM-IETS techniques. One example is a tetramantane diamondoid molecule adsorbed on Au(111), in which a feature was detected at 356 meV corresponding to the C−H stretching mode [25.62]. A tetracyanoethylene (TCNE) molecule on Cu(111) was reported to show features at 5.1, 13.3, 21.9, 35.7 meV originating from $=C-(CN)_2$ rocking modes [25.67]. Phthalocyanine molecules, a popular molecule in surface science investigations, have also been investigated with the IETS technique. A double-layer island of cobalt phthalocyanine (CoPc) on Cu(111) showed a feature at 20 meV, which was attributed to a vibration mode of the benzene ring against the substrate [25.68]. Mugarza reported the vibration modes of CuPc and NiPc adsorbed on an Ag(100) surface. Various modes in the energy range between −100 and 100 meV were detected. The authors claimed that the observed modes imply distortion of Cu−N bonds. The vibrational features are observed when the tip is placed in the center of the molecule, while the Kondo resonance feature due to the presence of an unpaired π orbital is observed at the perimeter of the molecule [25.69].

In addition, fullerene groups have been studied by STM-IETS from the early stages of this research. *Pascual* et al. measured STM-IETS for C_{60} on Ag(110), in which a feature at 52 meV was detected and was assigned to the $H_g(\omega_2)$ mode [25.70]. They found an intensity variation which is correlated with the adsorption configuration. The results were explained considering that symmetry of the resonant states associated with the vibrational mode determines the intensity of the IETS feature. The IETS spectrum of metallofullerene of Gd@C82 adsorbed on Ag(001) shows a feature at 43 meV which appears in a spatially restricted region. This feature is assigned to the cage mode and the spatial localization is attributed to the distribution of the electronic state with which the vibrational mode is coupled [25.71].

Phonons of metal substrates were investigated by *Gawronski* et al. using STM-IETS. They detected phonons at surfaces at 9 and 21 meV for Au(111) and Cu(111) surfaces, respectively. It should be noted that the spatial variation of the phonon excitation for Au(111) measured by mapping IETS signals displays an atomic resolution, which is explained in terms of site-specific phonon excitation probabilities [25.72].

25.4 In-Depth Analysis of IETS of an Alkanethiol Molecule

As stated already, the combination of STM and IETS can be beneficial. STM can give atomic-scale resolution and be combined with other surface-science analysis techniques. Meanwhile, in recent studies of molecular electronics or single-molecule devices there has been rising interest in IETS measurements. Such studies became feasible thanks to the development of electrodes with an atomic-scale gap, between which a molecular bridge is formed. It is necessary to execute chemical analysis for a molecule in the gap, and IETS is a promising technique. However, even for an identical molecule, the IETS spectra fluctuate among various types of devices [25.25]. Thus, an effort has been made to compare IETS data systematically for alkanethiol SAM films. The molecules form a well-defined SAM on a Au(111) surface, which has been characterized with a variety of surface analysis techniques [25.73].

25.4.1 Nonisotope Alkanethiol SAM

Several devices with such atomic-scale electrodes and alkanethiol SAM are illustrated in Fig. 25.16. Figure 25.16a shows a mechanical break junction (MBJ) system [25.74]. By bending a thin foil of metal mechanically, it is possible to make a crack in the foil and use it as a nm-scale gap. The gap size can then be controlled by the pushing force.

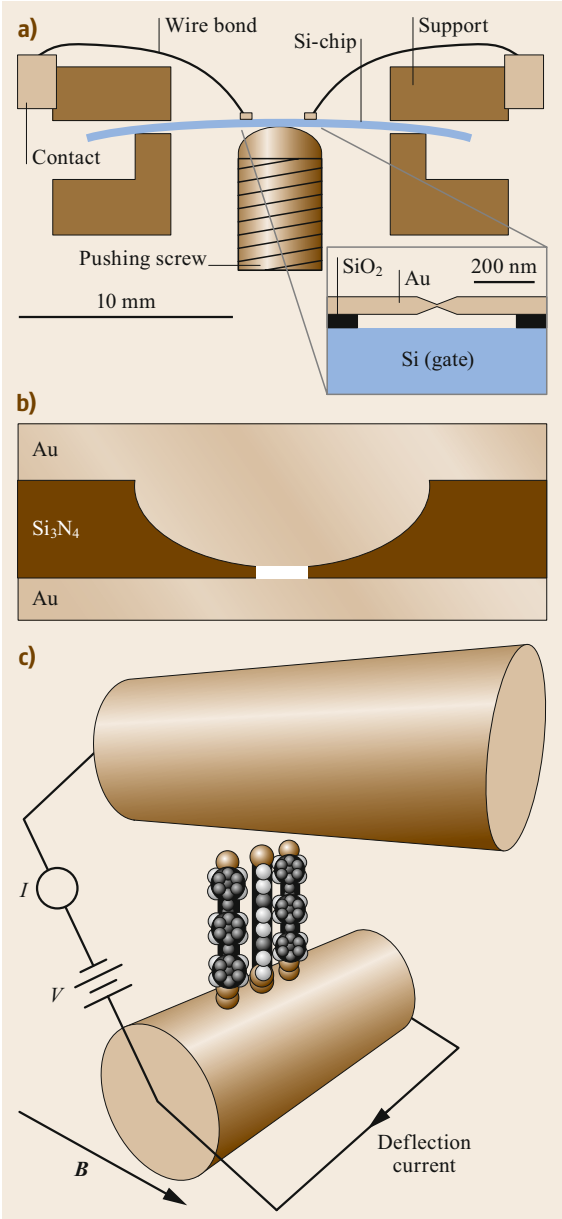

Fig. 25.16a–c Devices employed for single-molecule measurement: **(a)** mechanical break junction. (Adapted with permission from [25.74], Copyright 2008 American Chemical Society) **(b)** Nanopore device. (From [25.75]. Reprinted with permission from AAAS) **(c)** Cross-wire devices. (Reprinted with permission from [25.76]. Copyright 2002 by the American Physical Society)

A device fabricated with a more sophisticated Si process is shown in Fig. 25.16b and called the *nanopore* device [25.77]. In the particular device shown here, an Si_3N_4 film is formed above an Au substrate, which is scratched by an etching technique. The etching makes the Si_3N_4 thinner with a shape described in the figure. Eventually a hole appears in the center and the etching is stopped. By using this procedure, it is possible to make a nm-scale hole on an Au substrate. On the Au surface through the hole, the alkanethiol SAM is formed, which is covered by a top Au electrode. The final device consists of a monolayer of alkanethiol molecules of limited lateral size.

A *cross wire* device is shown in Fig. 25.16c [25.76]. First, an Au wire whose surface is covered with the alkanethiol SAM is prepared. Then a second Au wire with a bare surface is placed near the first wire. The two wires are attached using the electromagnetic force between them.

Macroscopic vibrational spectroscopies using IRAS and HR-EELS have been reported for alkanethiol SAMs. For example, the investigation of vibrational modes with energies between a few tens and 200 meV provides information inherent to the molecules in question. These modes can be used to identify the molecules investigated, thus they are called fingerprint modes. As already discussed, the vibrational modes corresponding to changes in the dipole moment perpendicular to the surface normal appear as strong peaks [25.78].

Before going into the discussion of IETS, we examine the results of HR-EELS measurements for vibrational features of an alkanethiol SAM. *Kato* et al. prepared alkanethiol SAMs on Au(111) surfaces with various lengths $(CH_3(CH_2)_{n-1}S/Au(111)$, $2 \leq n \leq 18)$ [25.79]. With their sample preparation, they could fabricate a SAM with large, well-ordered domains. By virtue of this sample property, they were able to obtain good EELS signals in dipole scattering. Vibrational modes like the CH_2 rocking mode at 89 meV, the CH_3 s-deformation mode at 171 meV, and the CH_3 d-deformation or CH_2 scissor modes at 180 meV are clearly visible (Fig. 25.17). Besides these large signals, weak features are identified, including Au–S stretching modes at 28 and 32 meV, a CH_3 rocking mode at 113 meV, a C–C stretching mode at 130 meV, and a CH_2 twist mode at 157 meV.

Among these detected signals, the CH_3 s-deformation mode with the energy of 171 meV shows a strong even–odd effect on the number of carbon atoms that constitute the alkyl chain. When it is even (odd), the signal becomes strong (weak). This result is consistent with the geometrical structure of the alkanethiol SAM shown in the inset of Fig. 25.17. In the case of the even number, the terminal methyl group points in a direction perpendicular to the surface. Thus, the change in dipole moment perpendicular to the surface is large, providing strong dipole scattering. Conversely, in the case of an odd carbon number, the terminal methyl group points in

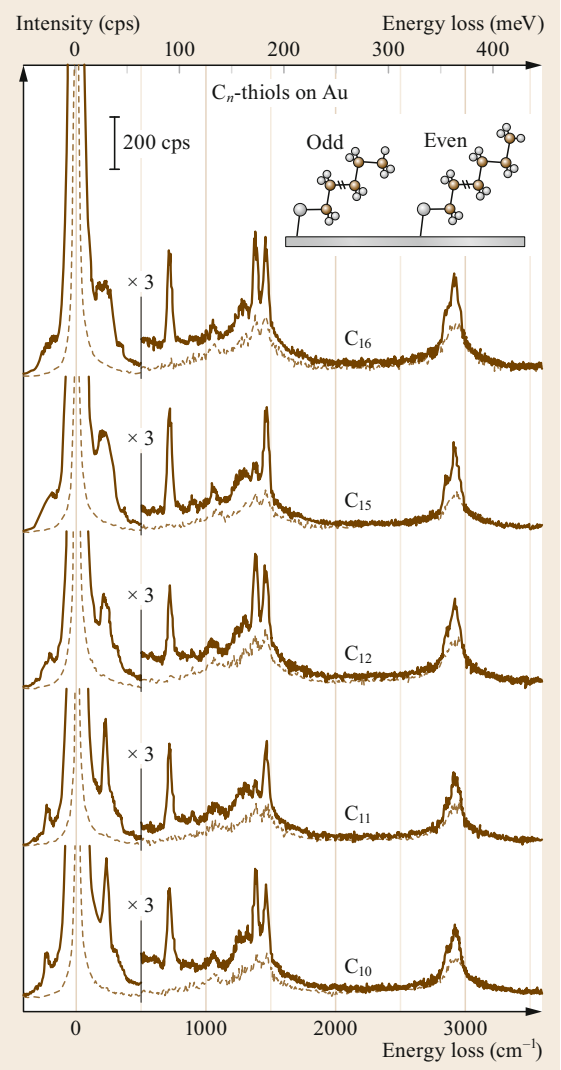

Fig. 25.17 HR-EEL spectra for various alkanethiol (C_n-thiol) SAMs on Au. The *solid* and *dashed lines* correspond to specular spectra detected at 60° and off-specular spectra detected at 42°, respectively. The *inset* shows schematic models of an alkanethiol SAM structure for an odd and even number of carbons. (Reprinted adapted with permission from [25.79]. Copyright (2002) American Chemical Society)

a direction parallel to the surface, resulting in a smaller change in the dipole moment in the perpendicular direction and little dipole scattering.

Kato et al. also investigated impact scattering for alkanethiol SAMs with EELS, where the vibrational signals, prominent in dipole scattering, such as the CH_2 rocking mode at 89 meV, the CH_3 s-deformation mode at 171 meV, and the CH_3 d-deformation or CH_2 scissor mode at 180 meV, are decreased and become comparable to the peak intensity of the C−C stretching signal at 130 meV (see the dashed lines in Fig. 25.17). In other words, the selection rules for impact scattering are more relaxed than those for dipole scattering.

The even–odd effect of an alkanethiol SAM is also observed in IRAS for the C−H stretching mode of the terminal methyl group [25.80]. The terminal methyl group points in a perpendicular direction when the carbon number is even. In this case, the change in dipole moment originating from the symmetric stretch of the methyl group is larger than that in the case of an odd carbon number. Thus, the strong C−H symmetric stretching signal is detected in the case of an even carbon number, but not when there is an odd number of carbons.

Formation of Alkanethiol SAM and STM

A SAM film of alkanethiol can be formed following established methods [25.73]. First, Au/mica sample (Keysight Technologies, Santa Rosa) is annealed in air using a hydrogen torch. Immediately upon annealing, the sample is immersed in an ethanol solution of octanethiol (1 mM) for 24 h or hexane solution of octanethiol (1 mM) for 6 min, and rinsed with ethanol before being inserted into the vacuum chamber for the STM inspection.

The use of partially/fully deuterated alkanethiol SAMs contributes to the peak assignment of the IETS peaks. Partially deuterated alkanethiols can be synthesized from commercially available $CD_3(CH_2)_7Br$ and $CH_3(CH_2)_6CD_2Br$ (C/D/N Isotopes, Point-Claire) following the established scheme [25.81]. Gas chromatography–mass spectrometry showed that the purity of the final product was 94.4% ($CD_3(CH_2)_7SH$) and 98.7% ($CH_3(CH_2)_6CD_2SH$), respectively.

Figure 25.18 shows a topographic image of the prepared octanethiol SAM on an Au(111) surface measured at 4.4 K, where the sample bias (V_s) and current (I_t) of the set point are $V_s = -2.5$ V and $I_t = 83$ pA, respectively [25.82]. An ordered structure of the octanethiol SAM with $(\sqrt{3} \times \sqrt{3})$R30° structure in register with the substrate of Au(111) is visible, which is consistent with previous reports [25.73] and the theoretical simulations (Fig. 25.19). Note that this well-ordered structure is usually observed before and after IETS measurements, i.e., showing the stability of the surface condition.

The gap between the tip and molecule should be measured before performing the IETS measurement. This can be examined by monitoring the tunneling current while the gap distance is varied, which is often called I–z spectroscopy. The I versus z curve shown in Fig. 25.20 was measured by approaching the tip at a rate of ≈ 0.35 Å/s from the initial position ($z = 0$)

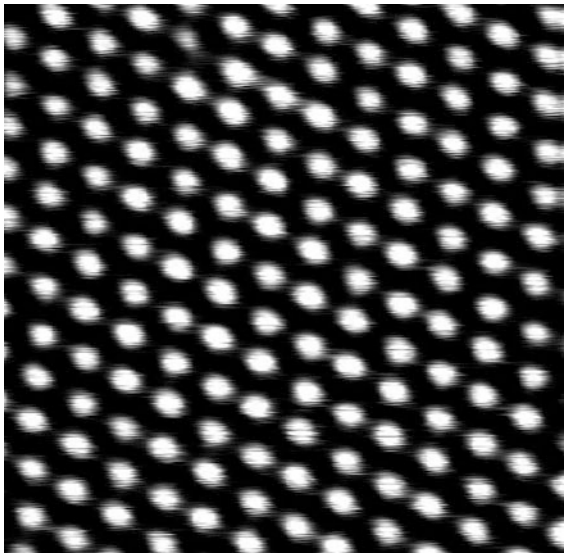

Fig. 25.18 Topographic STM image of an octanethiol SAM on Au(111) ($5.4 \times 5.4\,\mathrm{nm}^2$, $I_t = 83\,\mathrm{pA}$, and $V_s = -2.5\,\mathrm{V}$). (Reprinted with permission from [25.82]. Copyright (2008) by the American Physical Society)

defined by the conditions of $I_t = 10\,\mathrm{pA}$ and $V_s = 500\,\mathrm{mV}$, where the vertical axis is expressed on a log scale [25.82]. The measured I versus z curve can be fitted with a straight line at the initial stage of approach ($z < -1.5\,\text{Å}$). This fitting curve can be expressed as $I \propto \exp(-\alpha z)$ with $\alpha = 2.0\,\text{Å}^{-1}$, where the decay constant α is comparable with those previously reported for the vacuum tunneling barrier of $\alpha = 2.4\,\text{Å}^{-1}$ [25.83]. After reaching $z = -1.5\,\text{Å}$, which gives $I_t \approx 0.2\,\mathrm{nA}$ at $V_s = 500\,\mathrm{mV}$, the curve shows a bend and is deviated from a straight line. The slope after the bend can be estimated as $I \propto \exp(-\beta z)$, with $\beta = 1.1\,\text{Å}^{-1}$ at its initial stage. However, β becomes smaller when the tip gets closer to the surface. The decay rate of the tunneling current through a monolayer of alkanethiol SAM was previously analyzed by *Bumm* et al. for SAMs with various chain lengths ($CH_3(CH_2)_{n-1}S$) [25.84]. They employed a two-layer model in which the vacuum layer and the SAM layer were assumed to have independent decay constants for the electron tunneling. With this model, the tunneling current variation with the SAM layer thickness was estimated to be $I \propto \exp(-\beta z)$ with $\beta = 1.2\,\text{Å}^{-1}$ [25.84]. The tip and the SAM are in contact at $z = -1.5\,\text{Å}$ and the electron decay length in the SAM layer is close to the value that has been determined by Bumm et al. shortly after the contact. The decay length becomes smaller with further approach of the tip to the substrate, which is speculated to be due to a conformational change in the molecule layer caused by the tip.

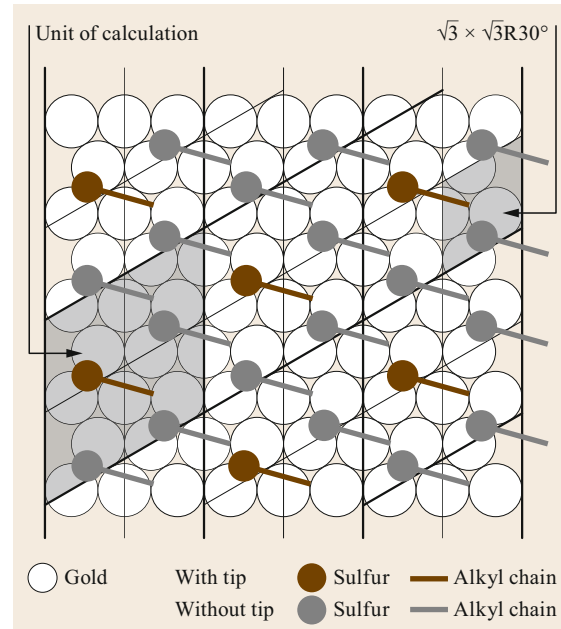

Fig. 25.19 Schematic showing an octanethiol SAM on Au(111). The unit cell used in the IETS calculation is shown by *thick black lines*. The STM tip modeled by one protruding Au atom was placed approximately over the end group of the octanethiol whose alkyl chain and sulfur atom are depicted in *brown* (*gray* for without the tip). (Reprinted from [25.25], with permission from Elsevier)

IETS of Alkanethiol SAM

In this section, we examine the detail of an IET spectrum for an octanethiol SAM on Au(111) at 4.4 K. Before recording the IETS measurement a good topographic image like that shown in Fig. 25.18 is collected with a junction resistance of usually a few tens of GΩ. For the IETS measurement, the tip was placed on a protrusion of the STM image and was brought close to the surface and the junction resistance is reduced to 0.5 GΩ ($V_s = 500\,\mathrm{mV}$, $I_t = 1\,\mathrm{nA}$). This set point was chosen because higher current is required for the IETS than for topographic imaging to improve the signal-to-noise ratio. Judging from the I–z curve in Fig. 25.20, the tip is about 1.5 Å inside the molecule layer from the contact point. Further lateral tracking of the tip position was not executed. However, the drift of the tip along the lateral direction was limited and was less than one unit of the alkanethiol lattice (5 Å) for 1 day. The data of I versus V, $\mathrm{d}I/\mathrm{d}V$ versus V, and $\mathrm{d}^2I/\mathrm{d}V^2$ versus V were simultaneously recorded both for the increasing and decreasing voltage ramp between 500 and −500 mV, where the feedback loop was open for 14 min. For this interval, the current change due to the

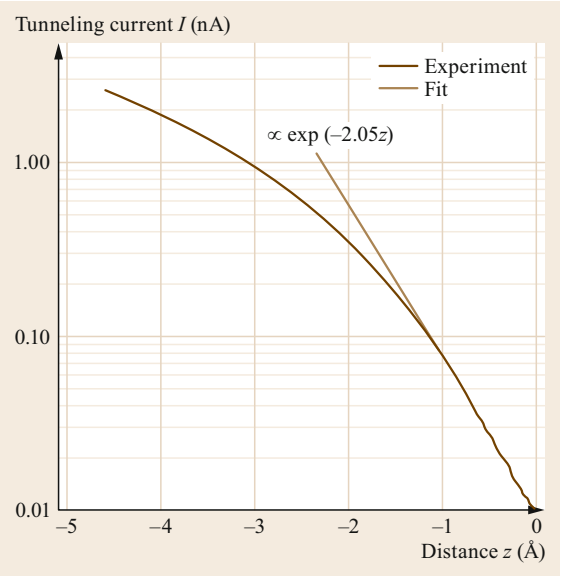

Fig. 25.20 Variation in the tunneling current when the tip approaches the surface (I–z curve). The tip approached at a rate of ≈ 0.35 Å/s from the initial position of $I_t = 0.01$ nA and $V_s = 500$ mV. The *linear line* is the result of a least square fit with a function of $I \propto \exp(-\alpha z)$. (Reprinted with permission from [25.82]. Copyright (2008) by the American Physical Society)

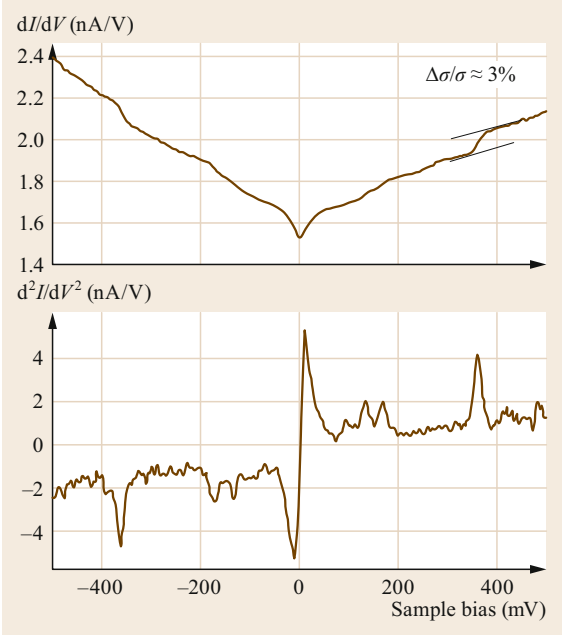

Fig. 25.21 Plot of d^2I/dV^2 versus V for an octanethiol SAM on Au(111) at 4.4 K. The tip was positioned at $I_t = 1$ nA and $V_s = 500$ mV. A modulation voltage of $V_{rms} = 7.2$ mV has been added. The plot is an average of 32 cycles of measurements, taking ≈ 7 min for each cycle. (Reprinted with permission from [25.82]. Copyright (2008) by the American Physical Society)

thermal drift along the vertical direction was less than 3% in average. The spectra in Fig. 25.21 are an average over 32 scans, each of which took 7 min, with a total acquisition time of about 4 h. A modulation voltage of 7.2 mV (rms) and a modulation frequency of 480 Hz were used. It was confirmed that the tunneling current at 480 and 960 Hz contained no periodic noise by executing its fast Fourier transform. The time constants of the two lock-in amplifiers were both set at 100 ms.

The acquired d^2I/dV^2 versus V and dI/dV versus V plots are shown in Fig. 25.22 [25.82]. The vertical axis was calibrated by comparing the numerical derivation of the I versus V and dI/dV versus V curves with the outputs of the lock-in amplifiers. The d^2I/dV^2 versus V curve shows features that appear at symmetric energy positions with respect to the Fermi level with a reversed polarity (Fig. 25.22). These features satisfy all the conditions required to assign them as vibrational features [25.4]. Among several peaks originating from vibrational modes, we can see that a prominent feature appears at the energy of ± 361 mV which can be attributed to the C−H stretching mode (ν(C−H)). In the papers so far reported, the ν(C−H) feature dominates the IET spectra. The other vibrational features are less obvious, except for the metal–molecule vibration modes [25.27, 50, 58, 64]. Conversely, the spectrum of Fig. 25.21 shows clear peaks between 50 and 200 meV. They also satisfy the criteria for assigning them to the vibrational modes, which include C−H bending modes and a C−C stretching mode. The conductance change ($\Delta\sigma/\sigma$), estimated from dI/dV, is $\approx 3.0\%$ for the C−H stretching mode (361 mV) and $\approx 1.2\%$ for the CH bending mode (171 mV). The measured $\Delta\sigma/\sigma$ for the C−H stretching mode exceeds 10% in the case of the C_2H_2 molecule [25.27]. However, other modes like C−H bending and C−C stretching were not detected. Thus, the detection of C−H bending and C−C stretching modes in the current study indicates a high yield of these modes for the alkanethiol SAM. Precise assignment of these modes and reasons for the high yields are discussed in later sections.

Tuning of Experimental Conditions for Better IETS

Here the calibration of the IETS spectra is discussed. As an example, the spectra obtained for the alkanethiol SAM is shown in Fig. 25.22. The brown lines in Fig. 25.22a–c, correspond to I, dI/dV (output of the lock-in amplifier), and d^2I/dV^2 (output of the other

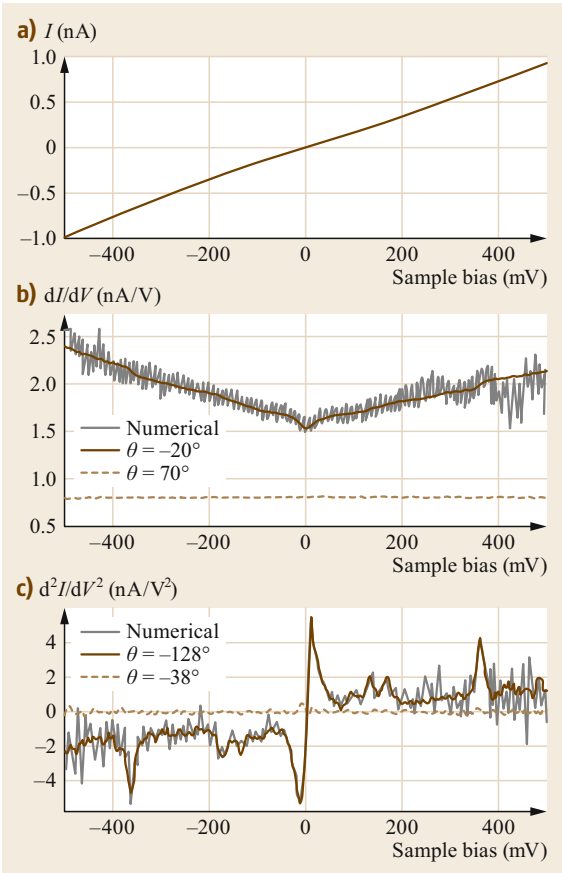

Fig. 25.22 **(a)** I versus V for the octanethiol SAM at 4.4 K ($V_s = 500$ mV, $I_t = 1$ nA). **(b)** The *brown line* corresponds to the dI/dV versus V acquired by the lock-in amplifier with the adjusted phase condition. The *gray line* is the numerical derivation of the I versus V. The *dashed line* is the output of the lock-in amplifier measuring the f component where the phase was 90° different from that in the case of the *brown line*. **(c)** The *brown line* is the d^2I/dV^2 versus V acquired by the other lock-in amplifier with the adjusted phase condition. The *gray line* is the numerical derivation of the dI/dV (*brown line* in **(b)**). The *dashed line* is the output of the other lock-in amplifier measuring the $2f$ component where the phase is 90° different from that in the case of the *brown line*. (From [25.60]. © IOP Publishing. Reproduced with permission. All rights reserved)

lock-in amplifier), respectively [25.60]. The gray line in Fig. 25.22b is the numerical derivation of I versus V, by which the absolute value of dI/dV versus V, obtained with the lock-in amplifier, is determined. The one for the d^2I/dV^2 (brown line in Fig. 25.22c) is also determined by repeating the same process. Note that the fluctuation in the noise level of the dI/dV versus V and d^2I/dV^2 versus V curves by the lock-in amplifiers are smaller than those obtained by the numerical derivations.

The dashed line in Fig. 25.22b is the output of the lock-in amplifier for the f component, where the phase is rotated by 90° from that of the brown line in Fig. 25.22b. The dashed line is almost constant for the entire bias voltage range, indicating that the phase of the lock-in amplifier for the measurement of the dI/dV versus V is correct. The capacitance between the tip and the sample, calculated from the magnitude of the dashed line, is 250 fF. The dashed line in Fig. 25.22c is the current component at the frequency of $2f$ detected by the other lock-in amplifier where the phase is rotated by 90° from that of the brown line in Fig. 25.22c. It also shows that the magnitude of the dashed line is zero for the bias range, which indicates that the phase for the d^2I/dV^2 versus V measurement is also correct.

The FWHM of the IET signal is described by the following relation

$$W^2 = (1.7V_{\mathrm{mod}})^2 + \left(\frac{5.4kT}{e}\right)^2 + W_1^2 , \qquad (25.7)$$

where k is the Boltzmann constant, T is the temperature, V_{mod} is the modulation voltage (rms), and W_1 is the intrinsic width of the peak [25.85]. Figure 25.23a shows a normalized d^2I/dV^2 versus V spectra in the energy range near the C–H stretching mode ($T = 4.4$ K, $V_s = 500$ mV, $I_t = 1$ nA), where the modulation voltage was systematically changed from 25.2 to 5.2 mV (rms) [25.60]. We can see a decrease of the peak width with a decrease in the modulation voltage. By further decreasing the modulation voltage to 2.7 mV, the peak seems to split into two components with energies located at 359 and 365 mV (Fig. 25.23b), both of which appear in the symmetric position around the Fermi level with the inversed polarity. To reach this accuracy, the spectra were averaged over 680 and 1600 scans, which took about 11 and 27 h, for the positive sample bias and the negative sample bias, respectively. In Fig. 25.23c, an IRA spectrum examined for the prepared octanethiol SAM on the Au surface is shown as a reference. Similar results had been reported previously [25.86–88] with the following peak assignment: peak A at 354 meV CH_2 symmetric stretch, peak B at 357 meV the CH_3 symmetric stretch by Fermi resonance, peak C at 362 meV the CH_2 antisymmetric stretch, peak D at 364 meV the CH_3 symmetric stretch by Fermi resonance, and peak E at 368 meV the CH_3 antisymmetric stretch.

In the IETS spectra obtained with $V_{\mathrm{mod}} = 2.7$ mV, a saddle is visible in the peak of Fig. 25.23b. In order to further discuss the origin of these two peaks, a smaller modulation voltage must be employed to obtain a higher resolution. However, the signal-to-noise

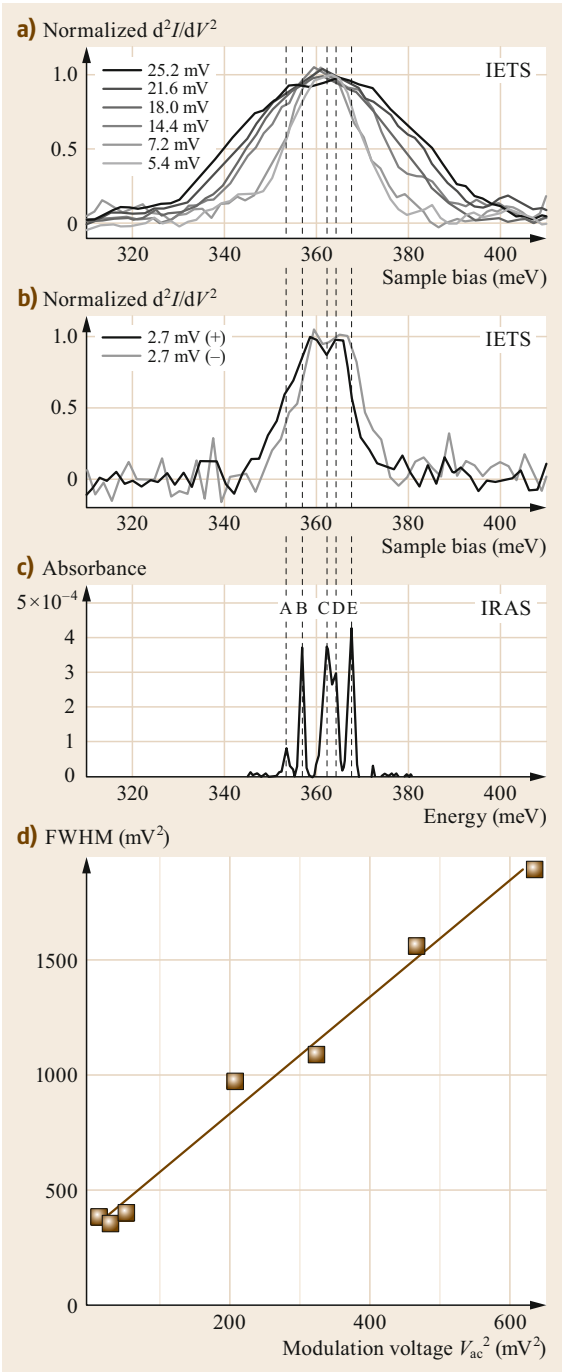

Fig. 25.23 **(a)** Normalized d^2I/dV^2 spectra around the energy of a C−H stretching mode for the octanethiol SAM at 4.4 K, where the modulation voltage is systematically varied ($V_s = 500$ mV, $I_t = 1$ nA). **(b)** The same as **(a)**, but in this case, the modulation voltage is 2.7 mV and the d^2I/dV^2 spectrum for negative bias is also shown. **(c)** Infrared reflection absorption spectrum for the octanethiol SAM on an Au surface at room temperature. **(d)** The square of FWHM of the CH stretching peak is plotted as a function of the square of the modulation voltage. (From [25.60]. © IOP Publishing. Reproduced with permission. All rights reserved) ►

ratio hampers the use of a smaller modulation bias voltage. Instead, a partial deuteration method is employed where all hydrogen atoms of the methyl group are replaced by deuterium atoms.

In Fig. 25.23d, the squares of FWHM of the C−H stretching peaks are plotted as a function of the square of the modulation voltage [25.60]. The solid line is the result of a least square fitting of the experimental results expressed by $W^2 = (1.6V_{mod})^2 + 352$. This experimental observation is reproduced by (25.7), though because of experimental error there is a slight discrepancy in the prefactor of V_{mod}. This relationship between the FWHM and modulation voltage is consistent with the previous report for C_2H_2 molecules on Cu(100) [25.57]. Considering that $5.4kT/e = 2.0$ mV at $T = 4.4$ K, W_1 is estimated to be 19 mV. This value is similar to the energy difference between peak A and E in Fig. 25.23c (14 meV).

In the previous section, we see that a higher resolution of the C−H stretching mode in IETS spectra can be obtained by reducing the modulation voltage. The same thing can be seen for the vibrational modes in the fingerprint region, as shown in Fig. 25.24 [25.82]. The modulation voltage V_{mod} is decreased to 3.6 meV, i.e., half of that used in Fig. 25.22 ($V_s = 500$ mV, $I_t = 1$ nA, $T_{sample} = 4.4$ K). The data is an average over 464 scans, which took about 24 h to be collected. Reference EELS data is shown in Fig. 25.24a. The energy positions of the detected vibrational features are compared with the result of the HR-EELS, and the assigned modes are listed in Table 25.1 with reference to HR-EELS, IRAS, and Raman spectroscopy [25.79, 86–89]. By comparison to these spectroscopic data, the IETS peaks can be assigned as follows: peak A is Au−S stretching, D is C−S stretching or CH_2 rocking, E is CH_3 rocking, F is C−C stretching, K is CH_3 s-deformation or CH_2 wagging, and L is CH_2 scissoring or CH_3 d-deformation. For some peaks, such as peaks E, K, and L, there are two candidates that can be discriminated using the technique of partial deuteration, as discussed later. Through such a comparison with the HR-EELS and IRAS data, we can conclude that STM-IETS is a useful tool for vibrational analysis of adsorbates.

Theory Versus Experiment

The overall property of the IET spectrum for an octanethiol SAM is compared to that obtained theoreti-

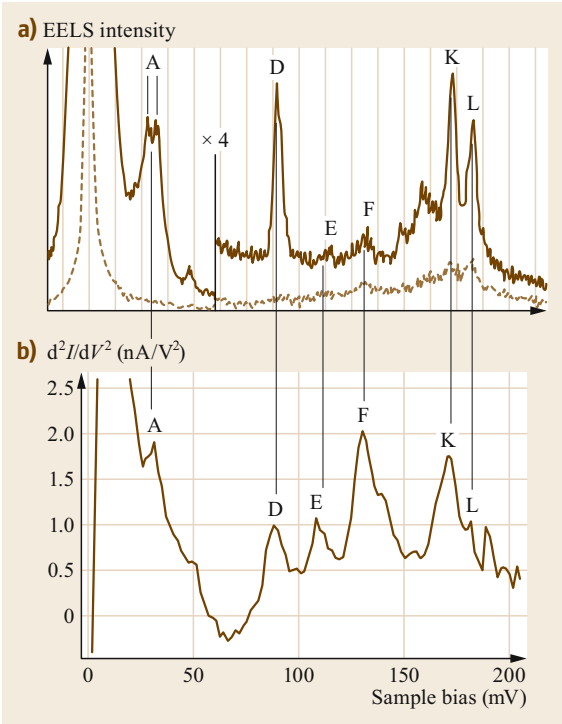

Fig. 25.24 **(a)** HR-EEL spectrum for an octanethiol SAM [25.79] and **(b)** high-resolution IET spectrum for the energy region of the C−C stretching mode and C−H bending mode of the octanethiol SAM ($V_s = 500$ mV, $I_t = 1$ nA, $V_{mod} = 3.6$ mV (rms), and $T = 4.4$ K) [25.82]. The peaks can be assigned as (A) Au−S stretching, (D) C−S stretching or CH_2 rocking, (E) CH_3 rocking, (F) C−C stretching, (K) CH_3 s-deformation or CH_2 wag, and (L) CH_2 scissor or CH_3 d-deformation. (Reprinted from [25.25], with permission from Elsevier)

Table 25.1 The vibrational features of the current data are compared with the EELS data [25.79] and the expected modes are listed with reference to the HR-EELS, IRAS, and Raman data [25.79, 86–89]

Peak	STM-IETS (meV)	EELS (meV)	Expected mode
A	31	28/32	Au−S stretch
D	88	81/89	ν(S−C)/CH_2 rock
E	108	113	CH_3 rock
F	130	130	ν(C−C)
K	171	172	CH_3 s-deform./CH_2 wag
L	182	180	CH_3 d-deform./CH_2 scissor

cally in Fig. 25.25 [25.90]. The IETS peaks deduced both by experiment and theory are approximately symmetric with the applied bias and the features of the IET spectrum can be divided into (i) the low bias anomaly caused by the large number of low-energy vi-

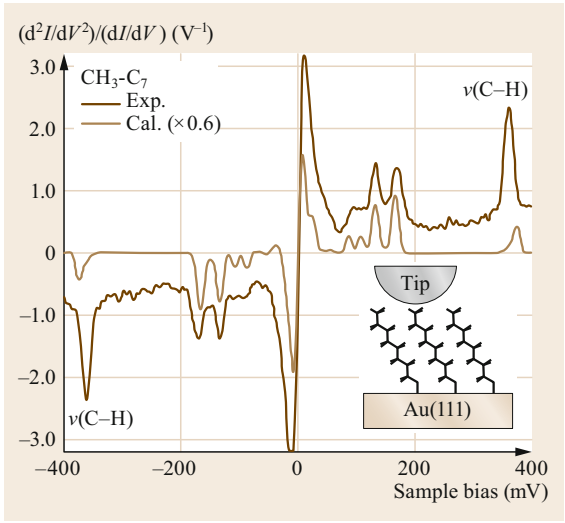

Fig. 25.25 Comparison between experimental (*dark brown*) and calculated (*light brown*) IET spectra for an octanethiol SAM. The broadening in both experiment and theory is determined by the temperature (4.4 K) and the lock-in modulation voltage ($V_{mod} = 7.2$ mV). (From [25.91]. © IOP Publishing. Reproduced with permission. All rights reserved)

brations, including gold phonons, (ii) the fingerprint region (≈ 50–200 meV, that can be used for a chemical identification of the molecule) that includes ν(C−S), ν(C−C), and CH bending modes, and (iii) C−H stretch modes (ν(C−H) ≈ 360 meV). Overall, the calculated IET spectrum reproduces that obtained by experiment. However, there are the following discrepancies: (i) magnitude of the zero bias anomaly [25.44], where we note that the low-frequency vibrations originating from the Au(111) substrate are not included in the calculations, (ii) intensity of the ν(C−H) mode is severely underestimated by theory. To investigate the latter problem, a partially deuterated alkanethiol is employed in a later section.

Comparison to Other Tunneling Junctions

In this section, we compare the STM-IETS results with those of the crossed-wire electrodes [25.44] and nanopore electrodes [25.77] (Fig. 25.26). The IET spectra measured using crossed-wire electrodes show extraordinarily good agreement with the current data, both in the energy positions and the relative intensities of the peaks. Even the anomaly at low bias shows a good agreement. Conversely, the comparison with the results obtained by using nanopore electrodes shows a poor agreement with those of STM-IETS. The results obtained by the nanopore experiment show a low intensity for the C−H stretching mode with a derivative-like line

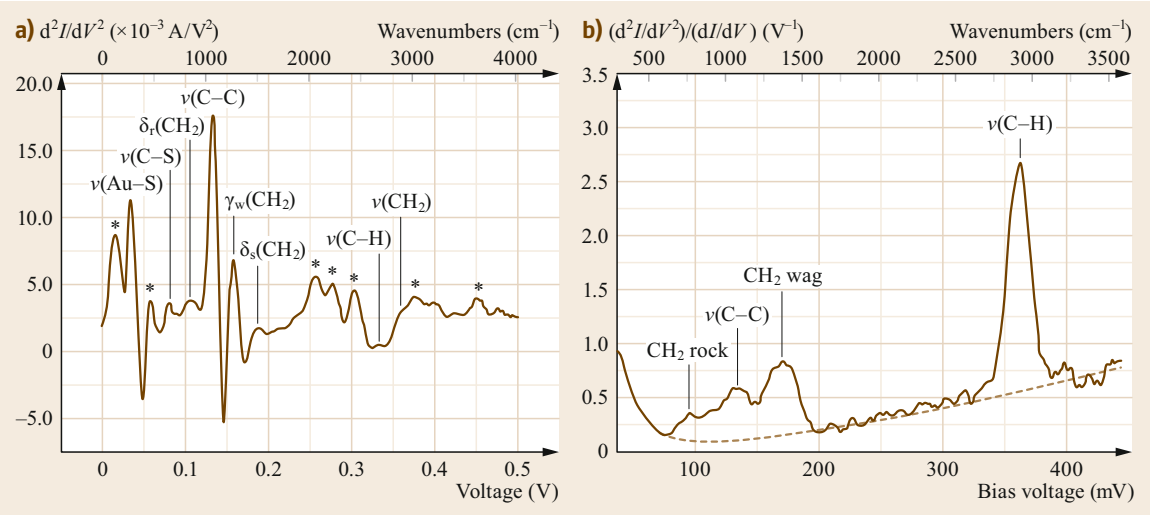

Fig. 25.26a,b IET spectra of **(a)** an octanedithiol ($HS(CH_2)_8SH$) SAM using a nanopore junction. (Reprinted adapted with permission from [25.77]. Copyright (2004) American Chemical Society) **(b)** An undecanethiol ($CH_3(CH_2)_{10}SH$) SAM using a crossed-wire junction. (Reprinted adapted with permission from [25.44]. Copyright (2004) American Chemical Society)

shape, and unidentified peaks at ≈ 250–500 meV. Recently, *Yu* et al. fabricated a molecular junction using a crossed-wire whereby metal impurities were intentionally incorporated among the molecules [25.92]. The junction with metal impurities shows peaks similar to those observed by *Wang* et al. [25.77], suggesting the possibility of the incorporation of metal impurities during the formation process of the top electrodes in the nanopore device. We should consider that the crossed-wire junction lead electrodes to less damage of the alkanethiol molecules in the junctions.

25.4.2 IETS Using Isotope Labeling of an Alkanethiol SAM

The use of deuterated molecules of an octanethiol SAM enables a more precise assignment of the IETS peaks. Both partially deuterated alkanethiols and fully deuterated alkanethiols can form a SAM on Au(111) surfaces, where $(\sqrt{3}\times\sqrt{3})R30°$ periodicity in relation to the Au(111) substrate is observed, as is also the case for the normal alkanethiol.

Isotope Labeling for IETS

The results of IETS for partially and fully deuterated octanethiols, including normal octanethiols, are summarized in Fig. 25.27 ($V_s = 500$ mV, $I_t = 1$ nA, and $T = 4.4$ K) [25.90]. We show the calculated energy positions of several expected vibrational modes for those molecules in Fig. 25.27b, where the vibrational modes (labeled D–L) are specified at the top. For the non-deuterated molecule, a conclusive peak comparison with the experiment is hampered by the overlapping of peaks at similar energies. However, further analysis using the isotope shift of the deuterated molecules enables a much more precise assignment, wherein calculated isotope shifts (Fig. 25.27b) were compared to the corresponding IET spectra (Fig. 25.27c).

Among the expected vibrational peaks, some were not detected in the experimental IET spectra. We mark the detected peaks by solid lines and undetected peaks by dashed lines in Fig. 25.27b, so that we can identify the dominant vibrational mode in the overlapping peaks. For example, peak E is composed of two overlapping peaks, the CH_3 rock and CH_2 twist modes, in the nondeuterated molecule. These two modes are separated in energy by the deuteration of the methyl group $CD_3(CH_2)_7$, but the CH_2 twist mode is not observed at the expected position. This result indicates a small yield for the CH_2 twist mode, and it is concluded that peak E is dominated by the CH_3 rocking mode for the normal molecule. Through similar arguments, the peaks K and L can be assigned to CH_2 wag and CH_2 scissor modes, respectively.

The fully deuterated molecule shows more complicated isotope shifts due to the coupling between the C–C stretching and CD bending modes. In this case, the calculated IET spectra can be employed to identify peaks g and h. The calculation shows that peak g is a vibrational mode with the combined character of C–C stretching and CH_2 wagging, and peak h is a vibrational mode that accompanies the C–C stretch and

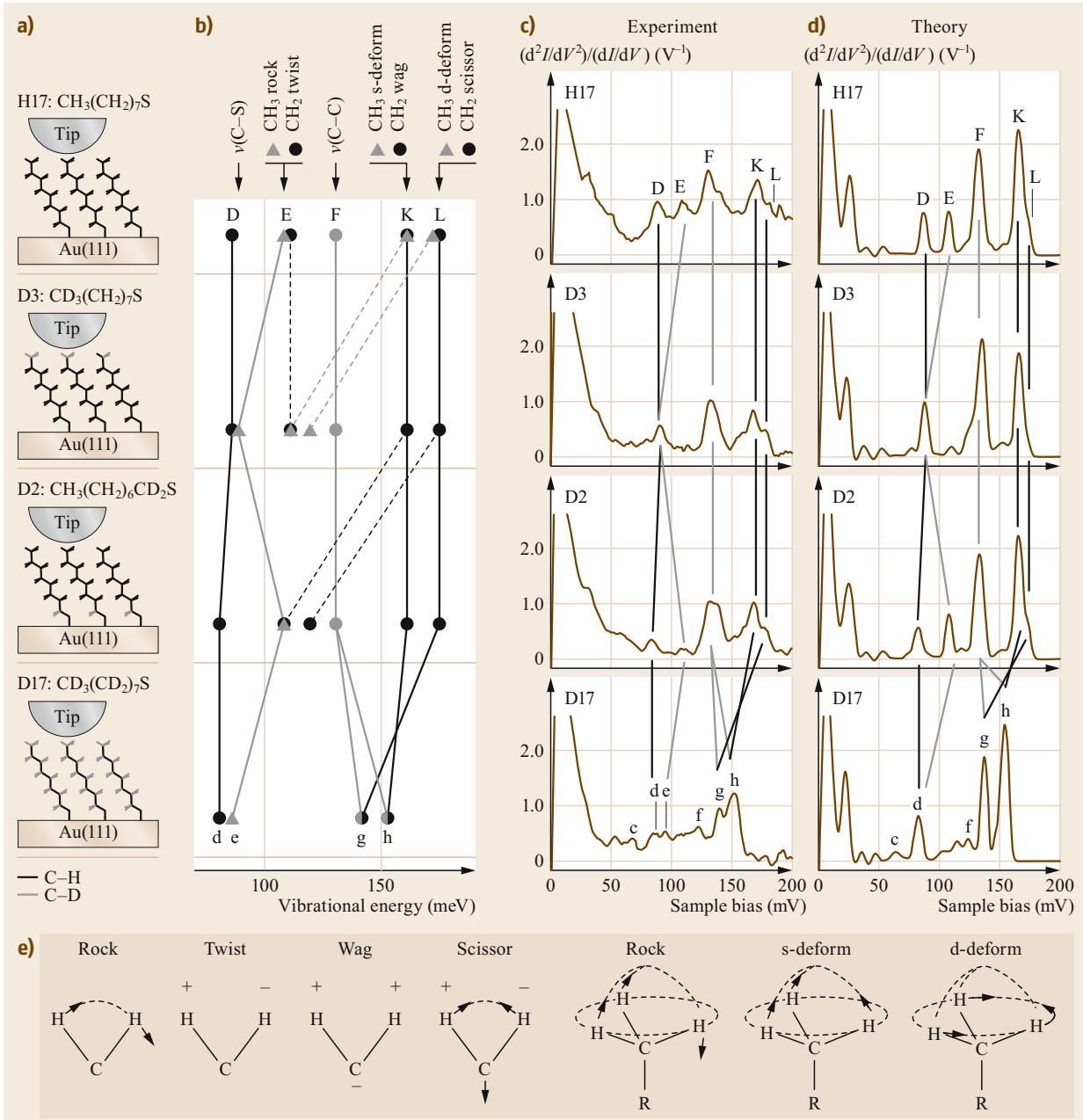

Fig. 25.27a–e IET spectra of deuterated alkanethiol SAMs. **(a)** Sketch showing the partial deuteration of C–H bonds, in which isotopes of $CH_3(CH_2)_7S$ [H17], $CD_3(CH_2)_7S$ [D3], $CH_3(CH_2)_6CD_2S$ [D2], and $CD_3(CD_2)_7S$ [D17] are shown. **(b)** Calculated isotope shifts used to identify which vibrational modes contribute to the IET spectrum, **(c)** experimental IET spectra with the isotope shifts of individual IETS peaks highlighted, **(d)** calculated IET spectra using the NEGF-DFT method, **(e)** illustration of the various bending modes. In **(b)**, the *solid* (*dashed*) lines correspond to observed (not observed) IETS modes (see text). The peaks D, E, F, K, and L originate from ν(S–C), CH_3 rocking, ν(C–C), CH_2 wagging, and CH_2 scissoring, respectively, and peaks g and h are ν(C–C) coupled with CD bending modes. (Reprinted adapted with permission from [25.90]. Copyright (2010) American Chemical Society)

Table 25.2 Summary of IETS peaks

Molecule	Mark	Experiment (meV)	Calculation (meV)	Main mode
$CH_3(CH_2)_7S$	D	88	87	ν(S−C)[a]
	E	108	107	CH_3 rock
	F	130	132	ν(C−C)
	K	171	165	CH_2 wag[b]
	L	182	173	CH_2 scissor[c]
	M	361	368	ν(C−H)
$CD_3(CH_2)_7S$	D/E	90	88	ν(S−C)/CD_3[d] rock
	F	132	135	ν(C−C)
	K	167	166	CH_2 wag
	L	178	172	CH_2 scissor
	i	255	256	$\nu_s(CD_3)$
		273	278	$\nu_{as}(CD_3)$
	M	360	364	$\nu(CH_2)$
$CH_3(CH_2)_6CD_2S$	D	83[e]	82[e]	ν(S−C)[a]
	E	108	108	CH_3 rock
	F	132	133	ν(C−C)
	K	169	165	CH_2 wag[b]
	L	180	173	CH_2 scissor[c]
	i	265	282	ν(C−D)
	M	360	374	ν(C−H)
$CD_3(CD_2)_7S$	c	68	63	CD_2 rock[f]
	d	84[e]	82[e,g]	ν(S−C)
	e	95	–	CD_3 rock[h]
	f	123	124	CCC deform
	g	140	137	ν(C−C)[i]
	h	152	154	ν(C−C)[i]
	i	271	277	ν(C−D)

[a,b,c] Overlap with small contributions from [a] CH_2 rocking, [b] CH_3 s-deformation, and [c] CH_3 d-deformation.
[d] By deuteration of the methyl group, CH_3 rocking overlaps with peak D.
[e] Deuteration of the bottom methylene red-shifts the ν(S−C) mode by ≈ 5 meV.
[f] Deuteration of the methylene groups shifts the CH_2 rocking mode, previously overlapping with peak D, to peak c.
[g] From theory, peak d originates from the prominent ν(C−S) at 82 mV and a weak CD_3 rocking mode at 85 mV.
[h] Tentative assignment.
[i] Coupled with CD bending modes. The isotope shifts in the full-deuteration case are not straightforward; sometimes the isotope shift couples modes, e.g., peaks g and h [25.90]

CH_2 scissor. We can see that the character of the vibrational mode for fully deuterated alkanethiols is similar to that for the normal molecules.

We note that the calculated vibrational energies agree with those obtained by experiment within an accuracy of a few percent (Table 25.2). In addition, both the relative peak heights and the absolute magnitude of the IETS peaks are well reproduced, the latter showing an agreement within a factor of three (although additional broadening mechanisms are not considered).

Selection Rule or Propensity

As shown in previous sections, we precisely assigned IETS active modes for alkanethiol molecules. Here, using Fermi's golden rule we discuss why such modes are active in IETS. The first eigenchannel with the largest transmission for the alkanethiol SAM has σ-type symmetry originating from the C−C bonds (Fig. 25.28). This eigenchannel exponentially decreases as the electrons tunnel through the molecule. The σ-character implies a strong coupling of tunneling electrons to vibrational modes modifying the C−C bond lengths of the alkyl chain, since these modes also show σ-type symmetry. In fact, many of the IETS active modes, i.e., C−C stretch (peak F), CH_2 wag (K), and scissor (L), accompany a substantial displacement in the C−C bond length. In contrast, the inactive modes, CH_2 rock and twist, do not accompany a C−C displacement. By using this simple rule, we can also understand the strengths of the IETS sig-

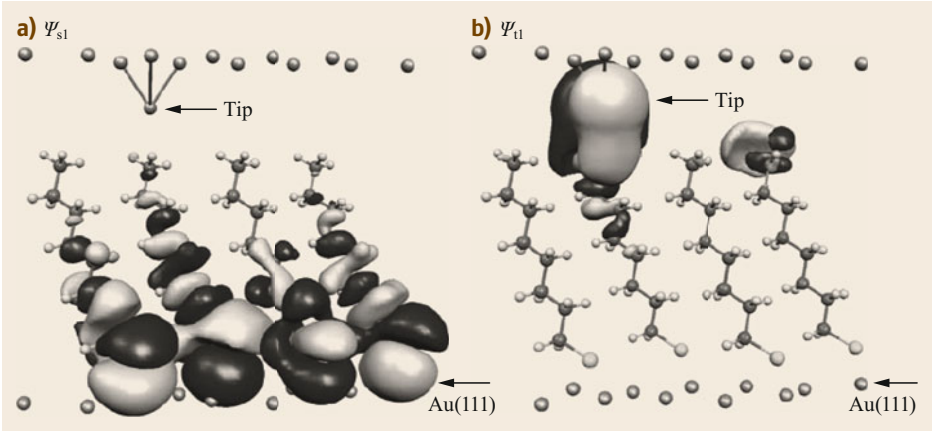

Fig. 25.28a,b Scattering states at the Fermi level. Maximally transmitting scattering states (eigenchannels) incident from (**a**) substrate side and (**b**) tip side. The color (*black/white*) of the isosurface plots indicate the sign of the scattering state. (Reprinted adapted with permission from [25.90]. Copyright (2010) American Chemical Society)

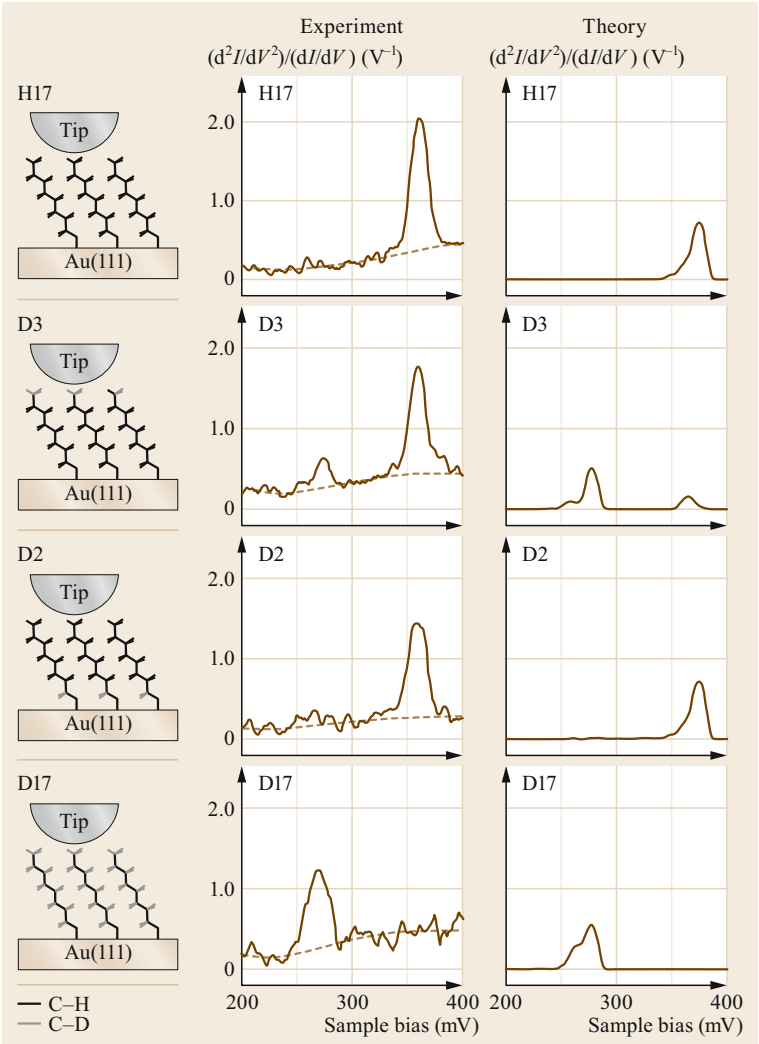

Fig. 25.29 ν(C−D) and ν(C−H) regions of IET spectra. Experimental and theoretical IET spectra for $CH_3(CH_2)_7S$ (H17), $CD_3(CH_2)_7S$ (D3), $CH_3(CH_2)_6CD_2S$ (D2), and $CD_3(CD_2)_7S$ (D17) ($V_{rms} = 7.2$ mV). The *dashed lines* show the estimated background signal. (Reprinted adapted with permission from [25.90]. Copyright (2010) American Chemical Society)

nals, e.g., the scissor mode has less C−C character than the wagging mode, which is reflected in the IETS intensity.

Site Selectivity of IETS

Upon identification of the vibrational signals we can qualitatively understand how each part of a molecule contributes to the IET spectra. As shown in Fig. 25.27c, the IETS intensity of peaks F (ν(C−C)), K (CH_2 wag), and L (CH_2 scissor) do not appreciably change with deuteration of the CH_2 closest to the sulfur atom ($CH_3(CH_2)_6CD_2S$). The IETS weight is therefore not predominantly determined from this part of the molecule in contrast to the report by *Beebe* et al. [25.93].

A more quantitative discussion is possible by examining the C−H stretch modes. For the four alkanethiol molecules with different deuterated groups, the ν(C−D) and ν(C−H) regions of the IET spectra are shown in Fig. 25.29. In contrast to the fingerprint area, the comparison between the experiment and theory for the C−H stretching region is not straightforward. When we compare the nondeuterated and fully deuterated cases shown in Fig. 25.29, the C−H vibrational energy shows an isotope shift from 361 to 271 meV, which agrees well with what is expected from the effective mass variation. The IETS intensity in the fully deuterated case also decreases by a factor of $\approx 1\sqrt{2}$. The decrease in IETS intensity might be due to the weakened e–ph coupling which originates from the lowered vibration amplitude of the normal mode with the mass increase [25.54–56]. In order to estimate the IET signal amplitude and the position dependence, the experimental IET signals are integrated after subtracting the interpolated background as indicated in Fig. 25.29a. The estimated intensities after this process are shown in Table 25.3. The integrated peak areas of the C−H stretching mode for the normal molecule and the C−D stretching modes for the fully deuterated molecule are denoted by ν(C−H, all) and ν(C−D, all), respectively.

As can be seen from Table 25.3, the measured signal intensity of ν(C−H) and ν(C−D) can be well explained with a model in which all hydrogen atoms in the molecule contribute equally to the IETS signal, i.e., the signal is proportional to the number of H and D atoms. When the terminal methyl group is deuterated (Fig. 25.29b), the area of the ν(C−D, CD_3) peak is $\approx 28\%$ of ν(C−D, all), while the ν(C−H) peak is decreased from ν(C−H, all) by $\approx 16\%$. Although there is a certain discrepancy between the two numbers, the increase/decrease is roughly consistent with a substitution ratio of 18% (3 out of 17 hydrogen atoms). We also find a similar tendency for the methylene group, where the peak area of ν(C−D) is $\approx 14\%$ of ν(C−D, all) and the ν(C−H) is reduced by $\approx 23\%$ from ν(C−H, all), which is comparable to $2/17$ ($\approx 12\%$). This behavior is also consistent with the discussion earlier for CH_2 wagging and CH_2 scissoring modes, where we showed that the contributions from the methylene group closest to the Au electrode are small. These discussions do not agree with the previous report [25.93] that the contribution of the methylene group closest to the electrode is notably enhanced due to its location close to the metal substrate. From a theoretical viewpoint, the exponential decay in the scattering states originating from the Au electrode and STM tip (Fig. 25.28) will cancel in Fermi's golden rule. On the basis of this picture, it is difficult to imagine that the IETS weights are significantly different for different parts of the molecule.

Table 25.3 Relative peak area of ν(C−D) and ν(C−H) signals in the experiment. The standard (100%) of the ν(C−D) (ν(C−H)) signal is the peak area for $CD_3(CD_2)_7S$ ($CH_3(CH_2)_7S$) [25.90]

Molecule	ν(C−D)	ν(C−H)
$CH_3(CH_2)_7S$	–	100%
$CD_3(CH_2)_7S$	28%	84%
$CH_3(CH_2)_6CD_2S$	14%	77%
$CD_3(CD_2)_7S$	100%	–

The intensity of the ν(C−H) mode deduced by theory is severely underestimated compared to that found by experiment. Comparing the IET spectra of normal alkanethiol (hereafter denoted by CH_3-C_7) to the one of the methyl group deuterated alkanethiol (hereafter denoted by CD_3-C_7) allows us to investigate this problem in more detail [25.90]. The isotope-shifted ν(C−D) signal was observed for CD_3-C_7 (Fig. 25.30b). A small peak at 255 meV and a large peak at 273 meV are then compared to IRAS data [25.94], the higher energy peak with the larger intensity can be assigned to the asymmetric C−D stretching mode of CD_3 (275 meV by IR-$\nu_{as}(CD_3)$ [25.94] and 278 meV by theory) and the lower energy peak with smaller intensity to the symmetric C−D stretching mode of the CD_3 (258 meV by IR-$\nu_s(CD_3)$ [25.94] and 256 meV by theory). The measured peak area ratio of $\nu_{as}(CD_3)$ to $\nu_s(CD_3)$ was 80 : 20, as estimated using Gaussian fitting. This value is comparable to the theoretical values of 84 and 16%, underlining the quantitative agreement for the CH_3 modes.

As mentioned for the tip position on the octanethiol SAM film, there is no gap between the tip and the molecule if the IETS is measured with the set-point mentioned above. One might wonder whether the touching of the tip and the molecule might have some effect on the spectra. This can be checked by using shorter alkanethiols (methyl-group deuterated hexanethiols: $CD_3-(CH_2)_5-S$) where IETS measurement

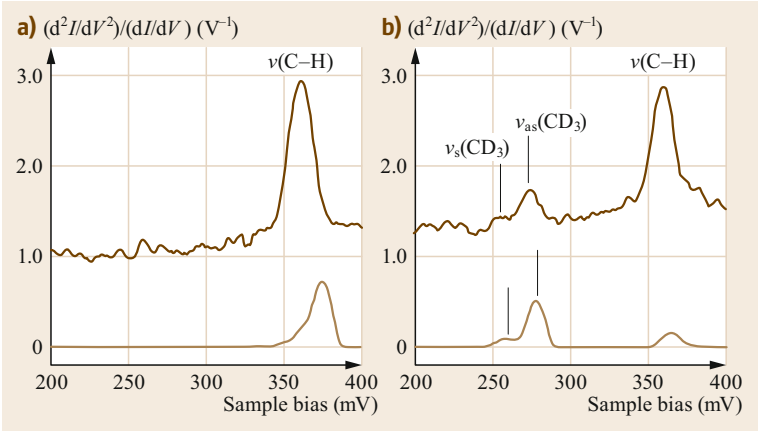

Fig. 25.30a,b IET spectra for the C−D and C−H stretch regions (ν(C−D) and ν(C−H)) for CH_3-C_7 **(a)** and CD_3-C_7 **(b)** SAMs on Au(111). The *dark brown* and *light brown* are the experimental and theoretical spectra, respectively ($V_{mod} = 7.2$ mV). (Reprinted adapted with permission from [25.90]. Copyright (2010) American Chemical Society)

with a tunneling gap between tip and molecule is possible. The result shows that the asymmetric mode in $\nu(CD_3)$ is still dominant in the IET signal even when a vacuum gap exists between the sample and the tip.

The analysis of $\nu_s(CH_3)$ and $\nu_{as}(CH_3)$ modes enables the examination of the empirical selection rule discussed for the conventional IETS that is mentioned in the previous section, e.g., stronger intensities are obtained for optically active modes than for the optically forbidden modes [25.4]. This implies a mechanism that tunneling electrons interact with the dynamic dipole moments of a molecule via the long-range Coulomb force [25.95]. The strength of these dipole moments will be enhanced by image charges when they point along the surface normal and reduced when they lie parallel to the surface. Thus, one can argue that the main IET signal comes from the vibrational modes whose dynamic dipole moments point along the surface normal. However, the results for the $\nu_s(CH_3)$ and $\nu_{as}(CH_3)$ modes obtained by the STM-IETS measurements are inconsistent with this rule. This is because the strong IET signal comes from the asymmetric CH_3 stretch mode which has a much smaller dynamic dipole moment along the surface normal than the symmetric stretch [25.87]. The discrepancy implies that it is inadequate to consider the long-range Coulomb interaction as the mechanism for the vibration excitation, which was discussed in the conventional IETS experiments.

The changes in the ν(C−H) region of the IET spectra upon deuteration of the methyl group can help the

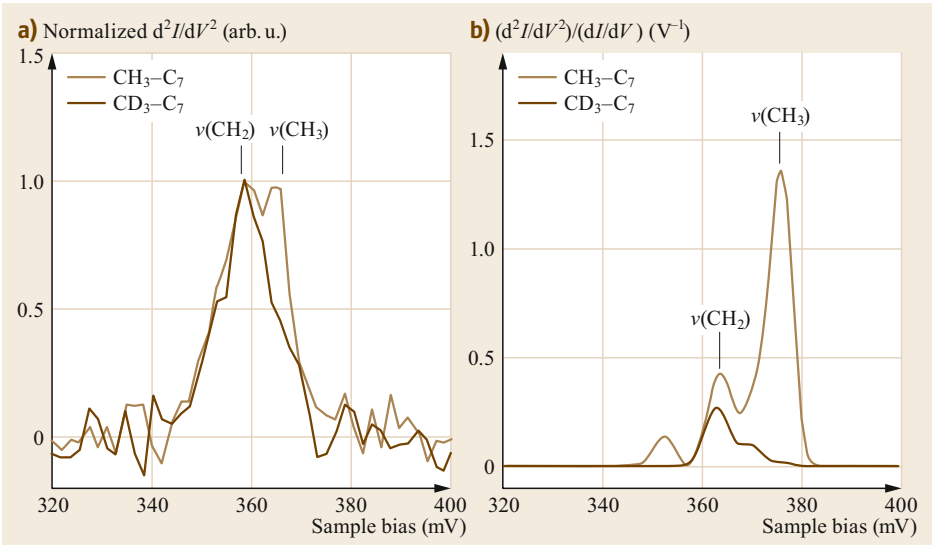

Fig. 25.31 **(a)** Experimental and **(b)** theoretical high-resolution IETS around the ν(C−H) modes for CH_3-C_7 (*dark brown*) and CD_3-C_7 (*light brown*) SAMs on Au(111) ($V_{mod} = 2.7$ mV). The experimental IETS intensity is normalized such that the peak height is 1 for both cases. (Reprinted with permission from [25.82]. Copyright (2008) by the American Physical Society)

assignment of the modes in the ν(C−H) region. The dark brown and light brown lines in Fig. 25.31a show the high-resolution IET spectra for CH_3-C_7 and CD_3-C_7, respectively. IETS spectra with a higher resolution are obtained with a smaller modulation voltage (V_{mod} = 2.7 mV). For the CH_3-C_7 (light brown line), two peaks can be seen at energies of 359 and 365 meV, while for CD_3-C_7 (dark brown line) we only observe a single peak whose energy is identical to that of the lower energy component of the light brown curve. The peak-area ratio of the low energy component to the high energy one was estimated using Gaussian functions to be 5 : 1. Since the ν(C−H) signal for the CD_3-C_7 molecule is expected to originate only from the CH_2 group, we can assign the components of 359 and 365 meV to the CH_2 and CH_3 groups, respectively. Taking into account the fact that using IRAS the CH_2 symmetric and asymmetric modes are observed at 354 and 362 meV, respectively [25.87, 88], the presence of a lower energy CH_2 IET peak centered at 359 meV indicates that the IET intensity is composed of the asymmetric and symmetric CH_2 stretch modes with an approximately equal contribution. Note that the symmetric C−H stretching mode of the CH_2 and the asymmetric C−H stretching mode of CH_2 are not distinguished in IETS (Fig. 25.31a) owing to the small energy splitting (8 meV), however, that is not the case for the C−D stretching mode of the CD_3 (Fig. 25.30b) owing to the large energy splitting (17 meV). IRAS data further provides the symmetric and asymmetric stretch modes of the CH_3 group ($\nu_s(CH_3)$ and $\nu_{as}(CH_3)$) at 360 and 367 meV. The latter value is close to the high-energy peaks of the IET spectra and is consistent with the conclusion that the asymmetric mode is dominant for the methyl group. The experimental data therefore indicate that the majority of the C−H stretch IET signal originates from the CH_2 groups with approximately equal weights for $\nu_s(CH_2)$ and $\nu_{as}(CH_2)$. It is observed that a smaller ratio (1 : 5) of the ν(C−H) signal originates from the CH_3 group, for which the asymmetric CH_3 stretch dominates over the symmetric stretch mode.

Intermolecular and Intramolecular Tunneling

In the previous section, we summarized the experimentally observed features of the C−H stretching signal. In the C−H stretching energy region ($\approx$ 350−380 meV), the comparison between experimental and theoretical calculations is less satisfactory than that for the fingerprint region. For example, the calculated vibrational energies are consistently 5−10 meV larger than the experimental data ($\nu_s(CH_3)$ = 353 and 365 meV, $\nu_{as}(CH_3)$ = 375 meV, $\nu_s(CH_2)$ = 363 meV, and $\nu_{as}(CH_2)$ = 369 meV). In addition, the IETS amplitude for the $\nu(CH_2)$ mode is severely underestimated by theory (Fig. 25.30) [25.91]. Since the quantitative agreement between the experiment and the calculation is good for the $\nu(CD_3)$ modes, the poor performance for the $\nu(CH_2)$ modes is puzzling. However, one may propose the hypothesis that the discrepancy is due to inelastic intermolecular scattering. The process is either that the $\nu(CH_2)$ modes scatter the intermolecular tunneling electrons, and/or that the existence of the excited $\nu(CH_2)$ modes change the transport through the molecule under the tip (Fig. 25.32a). This idea could explain the poor agreement between theory and experiment since DFT is not well suited for describing intermolecular interactions. In addition, the magnitude of the e–ph coupling for the $\nu(CH_2)$ modes should be large between the molecules and could thus enable intermolecular hopping.

The calculations indicate that intermolecular scattering is indeed important. As shown in Fig. 25.32b, the majority of the current is carried by the elastic process whose energy-resolved current density [25.91] is shown in Fig. 25.32c for a positive tip bias case. Here, approximately 75% of the current passes through the molecule closest to the tip (second molecule from the left in the figures), i.e., intramolecular tunneling (Fig. 25.32a) is dominant in the elastic process. The change in current densities due to the inelastic scattering is also calculated focusing on the $\nu(CH_2)$ excitation process. In this case, electrons start at E_{high} and end at E_{low} by exciting the vibration of $h\nu$ (Fig. 25.32b). The current densities at E_{high} (before excitation) and E_{low} (after excitation) are shown in Fig. 25.32d,e, respectively, where the former gradually decreases throughout the SAM as the electrons are scattered to E_{low}. In the inelastic tunneling case, 62% of the current enters through the molecule closest to the tip (second molecule from the left in the figures). This value is lower than that found in the case of the elastic process and indicates that the electrons take a more intermolecular path than in the elastic process. In addition, Fig. 25.32d,e show a smaller part of the current entering the molecule under the tip (second molecule from the left in Fig. 25.32d) than exiting (Fig. 25.32e). The enhancement of the $\nu(CH_2)$ component with the increase of the intermolecular current can be understood with a simplified model with using a propensity rule of IET spectroscopy that the C−H stretching mode is efficiently excited with electron flow along the C−H bond direction [25.4, 5]. Since the bond of C−H of CH_2 in the alkanethiol molecule is rather normal than parallel to the molecular axis, the increase of the intermolecular component of the current flow enhances the IET component from the C−H stretching mode of the CH_2 species.

The intermolecular tunneling was examined for an elastic process, where the conductivity of a SAM

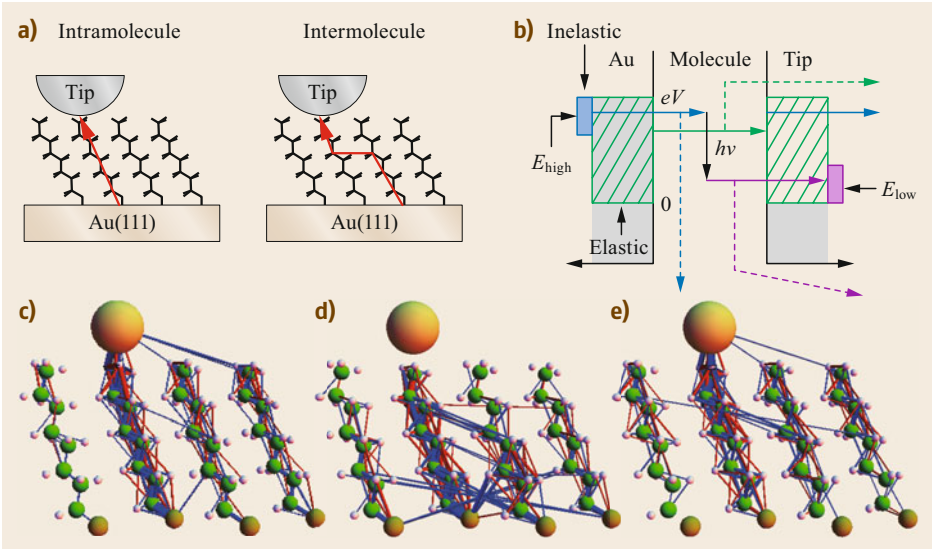

Fig. 25.32 **(a)** Intra- and intermolecular current paths, **(b)** schematics of the energy-resolved elastic and inelastic processes. Current density plots of the elastic component **(c)** and inelastic components **(d)** before and **(e)** after the $\nu(CH_2)$ excitation, where the *cylindrical area* is proportional to the current density (normalized) and *blue* (*red*) indicates electrons flowing upwards (downwards). (Reprinted adapted with permission from [25.90]. Copyright (2010) American Chemical Society)

sample was measured by a conductive atomic force microscopy (AFM) [25.96–98]. The result shows that the conductivity of alkanethiol SAMs increases with the tilt angle of the molecules [25.96–98]. In order to understand this observation, *Frederiksen* et al. performed first-principle calculations for SAMs by changing the density of alkanethiol molecules on a substrate while keeping the SAM structure [25.98]. They found a slight increase of conductance with increasing molecular density, which supports the contribution of intermolecular tunneling.

Despite the support from such a DFT calculation, there is still no definitive proof that the underestimated intensity of the $\nu(CH_2)$ component originates from the lack of the intermolecular scattering in the current DFT calculation. Alternative models such as supramolecular structures in the SAM should therefore be studied further.

25.5 Mapping of IETS Signals

In this section, we examine how the spatial mapping of the IETS can contribute to the recognition of a single molecule. The first example is a simultaneous observation of the topographic image and the vibrational mapping where *trans*-2-butene and butadiene molecules are coadsorbed. In the experiments, the bias voltage is set at $V_s = 360\,\text{mV}$, which gives the maximum intensity for $\nu(\text{C}-\text{H})$ of the *trans*-2-butene molecule, and the tunneling current is set at 1 nA. The modulation voltage ($V_{pp} = 18\,\text{mV}$, 797 Hz) is superimposed on the sample bias. A scanning from left to right takes 10 s. The time constant of the lock-in amplifier is set at 30 ms.

25.5.1 Spatial Mapping of IETS Features

The topographic image is shown in Fig. 25.33a. The area contains two *trans*-2-butene molecules and one butadiene molecule, which are labeled T and B, respectively. The *trans*-2-butene molecule appears as a dumbbell-shaped protrusion [25.50]. The separation of the two protrusions observed within the molecule is less prominent than the one obtained with smaller bias voltages ($V_s = 100\,\text{mV}$) [25.50]. The butadiene molecule is observed as an oval-shaped protrusion. The frequency of the modulation is high enough for the feedback loop setup, and the effect of the superimposed modulation voltage cannot be identified in the topographic image.

The mapping of the vibrational feature shows a clear increase in $\text{d}^2I/\text{d}V^2$ at the positions of the *trans*-2-butene molecules. As is indicated by the color index, the maximum $\text{d}^2I/\text{d}V^2$ intensity is $\approx 10\,\text{nA/V}^2$ which is close to the value obtained by the single-point IETS. The positions of the feature obtained in the forward scan and in the backward scan show little change, which

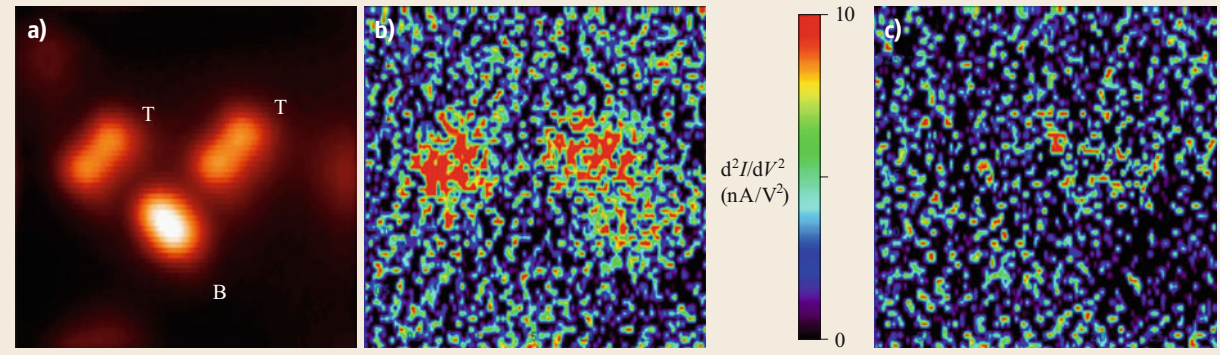

Fig. 25.33a–c Simultaneous observation of the topographic image **(a)**, and the mapping of d^2I/dV^2 intensity **(b)**, on the surface which contains both *trans*-2-butene (label T) and butadiene (label B) molecules. The tip scans the area with the feedback loop on (tunneling conditions of $V_{sample} = 360\,mV$ and $I_{tunnel} = 1\,nA$, area $43 \times 43\,Å^2$). The color bar index for d^2I/dV^2 intensity corresponds to the range from 0 to $10\,nA/V^2$. No image processing including the Fourier transfer process is performed. **(c)** A reference image of d^2I/dV^2 mapping obtained at $V_{sample} = 300\,mV$, which shows no obvious structures at the positions of the molecules. (Reprinted from [25.59], with the permission of AIP Publishing)

indicates that the combination of the scan speed and the time constant of the lock-in amplifier is adequate. However, we cannot see any characteristic feature at the position corresponding to the butadiene molecule. This is consistent with the previous report [25.50]. In spite of the existence of a C−H bond in the butadiene molecule, the ν(C−H) feature is hardly observed.

As a reference, the mapping of d^2I/dV^2 obtained at $V_s = 300\,mV$ is shown in Fig. 25.33c. In this image no features are observed either for the *trans*-2-butene molecules nor the butadiene molecules. These results have clearly indicated that chemically sensitive molecular recognition is possible using this simple d^2I/dV^2 mapping technique.

25.5.2 Hydrogenated Alkanethiol in a Matrix of Deuterated Alkanethiol SAMs

Mapping of IET signals for an alkanethiol SAM composed of hydrogenated alkanethiol (H-alkanethiol) and deuterated alkanethiol (D-alkanethiol) can provide information on the tunneling passage of electrons in the SAM. In order to execute this investigation, an identification of the isotope molecule inserted into the matrix of alkanethiol is required. A SAM sample composed of H- and D-alkanethiol can be prepared by dipping the Au substrate into an ethanol solution containing a minority of H-alkanethiol and a majority of D-alkanethiol. If the length of the molecule is different, e.g., using $CH_3(CH_2)_7S$ as the H-alkanethiol and $CD_3(CD_2)_5S$ as the D-alkanethiol, the mixture of the molecules can be confirmed from a topographic image of the SAM (Fig. 25.34). Here, bright and dim spots correspond to the H-octanethiols and D-hexanethiols, respectively. The ratio of the number of bright to dim spots is 1 : 19, which is identical within errors to the ratio of the constituents (1 : 25) in the ethanol solution from which the SAM was prepared. This observation indicates that when the length of the molecule is similar, the mi-

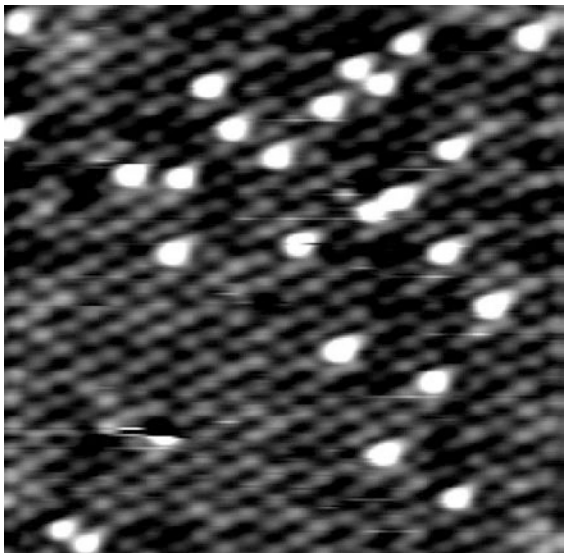

Fig. 25.34 STM image of $CH_3(CH_2)_7S$ and $CD_3(CD_2)_5S$ coadsorbed SAM on Au(111). Sample bias of 1.5 V, current of 9 pA, scan area of 10 nm × 10 nm, temperature of 4.4 K. *Bright* and *dim spots* correspond to the hydrogenated octanethiols and deuterated hexanethiols, respectively. The ratio of the number of bright to dim spots is 1 : 19, which is almost identical to the ratio of the constituents (1 : 25) in the ethanol solution from which the SAM was prepared. (Reprinted from [25.61], with the permission of AIP Publishing)

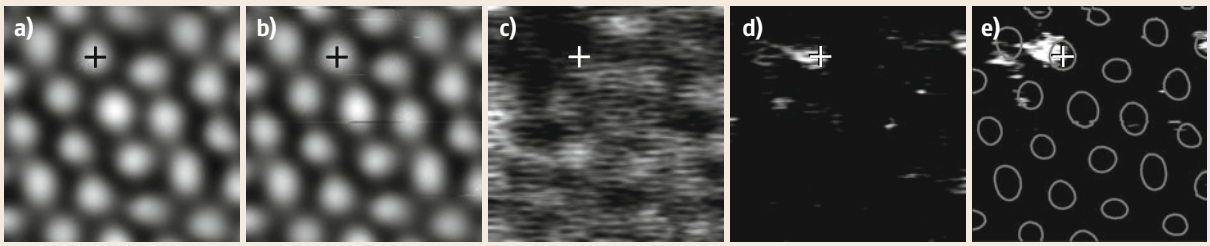

Fig. 25.35a–e STM images of $CH_3(CH_2)_5S$ and $CD_3(CD_2)_5S$ coadsorbed SAMs on Au(111) with a ratio of H : D = 1 : 9 for **(a)** $V_s = 264\,mV$ and $I_t = 264\,pA$, and **(b)** $V_s = 362\,mV$ and $I_t = 362\,pA$. The scan range is $2.2\,nm \times 2.2\,nm$. Maps of the IET signal with **(c)** $V_s = 264\,mV$ and **(d)** $V_s = 362\,mV$, which were simultaneously measured with **(a)** and **(b)**, respectively. **(e)** Difference between **(c)** and **(d)**. *Circles* of *gray lines* represent the contour of the *bright spot* in the topographic image. (Reprinted from [25.61], with the permission of AIP Publishing)

nor molecule is inserted into the matrix of the major molecule in an isolated manner, i.e., phase separation does not occur, in contrast to the case of the SAM formed by two molecules with significantly different molecular lengths [25.99, 100].

25.5.3 Mapping the IET Signal for an Alkanethiol SAM

Next, we look at the case where D-alkanethiol and H-alkanethiol molecules with the same length are mixed [25.90]. The ratio of the H-alkanethiol to D-alkanethiol in the solution was 1 : 9. Figure 25.35a,b shows topographic images of the thus-prepared SAM surface with a sample bias of 264 mV (corresponding to the C−D stretching mode) and 362 mV (C−H stretching mode), respectively. No obvious differences in either topographic image can be seen, which is in contrast to the case of Fig. 25.34. Note that the lateral drift of the STM image was less than 0.2 Å in a single mapping process (1.4 h), therefore the scan areas of Fig. 25.35a,b are almost identical. Figure 25.35c,d shows the IET maps simultaneously acquired with topographic images of Fig. 25.35a,b, respectively. In contrast to the identical topographic images, we can see a decrease in the signal from the C−D stretching mode around the cross mark, see Fig. 25.35c, and an increase in the C−H stretching signal around the same mark, see Fig. 25.35d.

This can be more clearly visualized by differentiating Fig. 25.35c,d. By this method we can identify an H-hexanethiol molecule at the cross mark (Fig. 25.35e). There is an additional molecule in the upper right image that can be attributed to an H-hexanethiol molecule, and thus two H-hexanethiol molecules are identified out of a total of 25 molecules. This is a reasonable value considering that the mixture ratio of the H- to D-molecules was 1 : 9.

The tunneling resistance used in these IET maps was 1 GΩ (264 mV/264 pA or 362 mV/362 pA). When the resistance is lowered, the signal-to-noise ratio of the IET signals improves. However, this induces the problem of the interaction between the tip and sample. The tunneling resistance of several tens of GΩ is used for topographic imaging, which yielded routinely good data. We speculate that a slight shift of the bright areas in the IET map and the topographic image is due to such tip-substrate interaction problems.

This problem may be solved by improving the signal-to-noise ratio in the tunneling current, which would allow us to use a smaller tunneling current and hence a wider tunneling gap. If this can be realized, the modulation voltage can be decreased from the current setting of 28.8 mV to a smaller value, which should contribute to visualizing the small energy differences between vibrational modes. This improved signal-to-noise ratio also clarifies the importance of the intermolecular tunneling process. The degree of the intermolecular process is shown by comparing the IET spectra for the case where the STM tip is above an H-alkanethiol molecule surrounded by D-alkanethiols with the case where the STM tip is placed above an H-alkanethiol molecule surrounded by the same H-alkanethiol molecules. Investigation of the intermolecular process using the IETS mapping technique is ongoing.

25.6 Summary

Recent progress of STM-IETS is reviewed. After the pioneering work of Ho's group on the detection of vibrational modes of a C_2H_2 molecule on a Cu surface, STM-IETS measurements have been performed for a variety of systems. In addition, we see a greater variety of molecules and electrodes have been in-

vestigated, which include STM-IETS measurement of atomic chains of metals and the use of other types of nanoscale devices with an atomic-scale gap distance. In most cases, vibration/phonon features appear as an increase of the conductance at the threshold energy of a vibrational mode (corresponding to a peak in a d^2I/dV^2 spectrum for $V > 0$). This is consistent with the results of the conventional M–I–M tunneling devices, in which only a few examples showed a decrease of the conductance out of the vast number of investigated molecules. For this type of IETS feature, a theoretical model using an approach similar to the one used to describe impact scattering in HR-EELS can account for the observed STM-IETS behavior. Conversely, the decrease of the conductance for $V > 0$ is observed for cases of adsorbates with a strong bonding with the substrate and a metal chain connected to two electrodes. The dip of d^2I/dV^2 for $V > 0$ is explained using a resonant model which is realized with a strong coupling of the gap species to the electrodes. The absence of this type of signal in the IETS data of M–I–M tunneling devices might be due to the fact that no strong bonding is formed between the molecule and the electrode. We introduced an advanced theoretical simulation that can account both for the increase and decrease of the conductance.

We discussed the IETS measurement of alkanethiol SAMs in detail, which may be used as a standard molecule for comparisons of IET spectra obtained with various configurations of electrodes. The IET spectrum obtained for the octanethiol SAM shows clear features in the fingerprint region, which can be directly compared with HR-EELS data and proves the ability of STM-IETS. Using isotope labeling, precise peak assignment is enabled, which suggests that IETS active modes are accompanied by a substantial C−C displacement. A comparison between the experimental IETS data and theoretical simulations shows a good overall agreement. In addition, fine features, such as the ratio of the symmetric CH_3 stretching signal to antisymmetric CH_3 stretching signal, are reproduced well by the simulation. The only exception is found in the large underestimation of the CH_2 stretching signal by the calculation. In order to interpret this discrepancy, a hypothesis that the intermolecular tunneling process enhances the CH_2 stretching signal has been proposed. The process of intermolecular hopping of the electron is underestimated by DFT.

In the final section, we demonstrated the effectiveness of IET mapping for a butene molecule and alkanethiol SAM. Increasing the sensitivity of the IETS mapping methods is pivotal to clarifying the importance of the intermolecular process.

The demand for chemical identification with atomic-scale resolution is increasing. As we can see, vibrational spectroscopy can play a crucial role in chemical identification, and we therefore expect an expansion of research utilizing the IETS technique.

References

25.1 L. Esaki: New phenomenon in narrow germanium p-n junctions, Phys. Rev. **109**, 603 (1958)

25.2 T. Komeda: Chemical identification and manipulation of molecules by vibrational excitation via inelastic tunneling process with scanning tunneling microscopy, Prog. Surf. Sci. **78**, 41–85 (2005)

25.3 R.C. Jaklevic, J. Lambe: Molecular vibration spectra by electron tunneling, Phys. Rev. Lett. **17**, 1139–1140 (1966)

25.4 P.K. Hansma: *Tunneling Spectroscopy* (Plenum, New York 1982)

25.5 D.G. Walmsley, J.L. Tomlin: Compilation of inelastic electron tunnelling spectra of molecules chemisorbed on metal oxides, Prog. Surf. Sci. **18**, 247–447 (1985)

25.6 U. Mazur, K.W. Hipps: Inelastic electron tunneling spectroscopy. In: *Handbook of Vibrational Spectroscopy*, Vol. 1, ed. by J. Chalmers, P. Griffiths (Wiley, New York 2002) pp. 812–829

25.7 J.G. Simmons: Generalized formula for the electric tunnel effect between similar electrodes separated by a thin insulating film, J. Appl. Phys. **24**, 1793 (1963)

25.8 R.H. Fowler, L. Nordheim: Electron emission in intense electric fields, Proc. R. Soc. A **119**, 173 (1928)

25.9 R.S. Becker, J.A. Golovchenko, B.S. Swartzentruber: Electron interferometry at crystal-surfaces, Phys. Rev. Lett. **55**, 987–990 (1985)

25.10 A.J. Caamaño, Y. Pogorelov, O. Custance, J. Méndez, A.M. Baró, J.Y. Veuillen, J.M. Gómez-Rodríguez, J.J. Sáenz: Field emission interferometry with the scanning tunneling microscope, Surf. Sci. **426**, L420–L425 (1999)

25.11 U. Dürig, J.K. Gimzewski, D.W. Pohl: Experimental observation of forces acting during scanning tunneling microscopy, Phys. Rev. Lett. **57**, 2403–2406 (1986)

25.12 U. Dürig, O. Züger, D.W. Pohl: Force sensing in scanning tunnelling microscopy: Observation of adhesion forces on clean metal surfaces, J. Microsc. **152**, 259–267 (1988)

25.13 U. Dürig, O. Züger, D.W. Pohl: Observation of metallic adhesion using the scanning tunneling microscope, Phys. Rev. Lett. **65**, 349–352 (1990)

25.14 G. Binnig, N. Garcia, H. Rohrer: Conductivity sensitivity of inelastic scanning tunneling microscopy, Phys. Rev. B **32**, 1336–1338 (1985)

25.15 H. Ibach, D.L. Mills: *Electron Energy Loss Spectroscopy and Surface Vibrations* (Academic Press, New York 1982)

25.16 D. Šokčević, Z. Lenac, R. Brako, M. Šunjić: Excitation of adsorbed molecule vibrations in low

energy electron scattering, Z. Phys. B **28**, 273–281 (1977)
25.17 C.H. Li, S.Y. Tong, D.L. Mills: Large-angle inelastic electron-scattering from adsorbate vibrations – Basic theory, Phys. Rev. B **21**, 3057–3073 (1980)
25.18 M. Rocca, H. Ibach, S. Lehwald, T.S. Rahman: Surface phonon dispersion of surface and adsorbate layers. In: *Structure and Dynamics of Surfaces I*, ed. by W. Schommers, P. von Blanckenhagen (Springer, Berlin, Heidelberg 1986) pp. 245–276
25.19 G.J. Schulz: Resonances in electron impact on diatomic molecules, Rev. Mod. Phys. **45**, 423–486 (1973)
25.20 S.F. Wong, M.J.W. Boness, G.J. Schulz: Vibrational excitation of O_2 by electron impact above 4 eV, Phys. Rev. Lett. **31**, 969–972 (1973)
25.21 F.J. Himpsel, T. Fauster: Empty orbitals of adsorbates determined by inverse ultraviolet photoemission, Phys. Rev. Lett. **49**, 1583–1586 (1982)
25.22 J. Rogozik, H. Scheidt, V. Dose, K.C. Prince, A.M. Bradshaw: The 2π-derived level in the adsorption system CO/Cu(110), Surf. Sci. **145**, L481–L487 (1984)
25.23 J.E. Demuth, D. Schmeisser, P. Avouris: Resonance scattering of electrons from N_2, CO, O_2, and H_2 adsorbed on a silver surface, Phys. Rev. Lett. **47**, 1166–1169 (1981)
25.24 R. Franchy, F. Bartolucci, F. Buatier De Mongeot, F. Cemic, M. Rocca, U. Valbusa, L. Vattuone, S. Lacombe, K. Jacobi, K.B.K. Tang, R.E. Palmer, J. Villette, D. Teillet-Billy, J.P. Gauyacq: Negative ion resonances of O_2 adsorbed on Ag surfaces, J. Phys. Condens. Matter **12**, R53–R82 (2000)
25.25 N. Okabayashi, M. Paulsson, T. Komeda: Inelastic electron tunneling process for alkanethiol self-assembled monolayers, Prog. Surf. Sci. **88**, 1–38 (2013)
25.26 A. Baratoff, B.N.J. Persson: Theory of the local tunneling spectrum of a vibrating adsorbate, J. Vac. Sci. Technol. A **6**, 331–335 (1988)
25.27 B.C. Stipe, M.A. Rezaei, W. Ho: Inducing and viewing the rotational motion of a single molecule, Science **279**, 1907–1909 (1998)
25.28 K.W. Hipps, U. Mazur: An inelastic electron tunneling spectroscopy study of the complexation reaction of $CoBr_2$ and $CoCl_2$ with silane modified alumina, Surf. Sci. **207**, 385–400 (1989)
25.29 B.C. Stipe, M.A. Rezaei, W. Ho: Single-molecule vibrational spectroscopy and microscopy, Science **280**, 1732–1735 (1998)
25.30 L.J. Lauhon, W. Ho: Single-molecule vibrational spectroscopy and microscopy: CO on Cu(001) and Cu(110), Phys. Rev. B **60**, R8525–R8528 (1999)
25.31 M. Headgordon, J.C. Tully: Molecular-orbital calculations of the lifetimes of the vibrational-modes of CO on Cu(100), Phys. Rev. B **46**, 1853–1856 (1992)
25.32 M. Morin, N.J. Levinos, A.L. Harris: Vibrational energy transfer of CO/Cu(100): Nonadiabatic vibration/electron coupling, J. Chem. Phys. **96**, 3950–3956 (1992)
25.33 C.J. Hirschmugl, G.P. Williams, F.M. Hoffmann, Y.J. Chabal: Adsorbate-substrate resonant interactions observed for CO on Cu(100) in the far infrared, Phys. Rev. Lett. **65**, 480–483 (1990)
25.34 B.N.J. Persson: Surface resistivity and vibrational damping in adsorbed layers, Phys. Rev. B **44**, 3277–3296 (1991)
25.35 R. Ryberg: The metal-molecule stretch vibrational mode studied by infrared spectroscopy; CO on Pt(111), J. Electron Spectrosc. Relat. Phenom. **54–55**, 65–80 (1990)
25.36 L.J. Lauhon, W. Ho: Single-molecule chemistry and vibrational spectroscopy: Pyridine and benzene on Cu(001), J. Phys. Chem. A **104**, 2463–2467 (2000)
25.37 J.R. Hahn, H.J. Lee, W. Ho: Electronic resonance and symmetry in single-molecule inelastic electron tunneling, Phys. Rev. Lett. **85**, 1914–1917 (2000)
25.38 T. Komeda, Y. Kim, Y. Fujita, Y. Sainoo, M. Kawai: Local chemical reaction of benzene on Cu(110) via STM-induced excitation, J. Chem. Phys. **120**, 5347–5352 (2004)
25.39 J.I. Pascual, J.J. Jackiw, Z. Song, P.S. Weiss, H. Conrad, H.P. Rust: Adsorbate-substrate vibrational modes of benzene on Ag(110) resolved with scanning tunneling spectroscopy, Phys. Rev. Lett. **86**, 1050–1053 (2001)
25.40 N. Agraït, C. Untiedt, G. Rubio-Bollinger, S. Vieira: Onset of energy dissipation in ballistic atomic wires, Phys. Rev. Lett. **88**, 216803 (2002)
25.41 B.N.J. Persson: Inelastic vacuum tunneling, Phys. Scr. **38**, 282–290 (1988)
25.42 A. Bayman, P.K. Hansma, W.C. Kaska: Shifts and dips in inelastic-electron-tunneling spectra due to the tunnel-junction environment, Phys. Rev. B **24**, 2449–2455 (1981)
25.43 M. Paulsson, T. Frederiksen, H. Ueba, N. Lorente, M. Brandbyge: Unified description of inelastic propensity rules for electron transport through nanoscale junctions, Phys. Rev. Lett. **100**, 226604 (2008)
25.44 J.G. Kushmerick, J. Lazorcik, C.H. Patterson, R. Shashidhar, D.S. Seferos, G.C. Bazan: Vibronic contributions to charge transport across molecular junctions, Nano Lett. **4**, 639–642 (2004)
25.45 A.J. Heinrich, C.P. Lutz, J.A. Gupta, D.M. Eigler: Molecule cascades, Science **298**, 1381–1387 (2002)
25.46 M. Paulsson, T. Frederiksen, H. Ueba, N. Lorente, M. Brandbyge: Unified description of inelastic propensity rules for electron transport through nanoscale junctions, Phys. Rev. Lett. **100**, 226604 (2008)
25.47 N. Lorente, M. Persson, L.J. Lauhon, W. Ho: Symmetry selection rules for vibrationally inelastic tunneling, Phys. Rev. Lett. **86**, 2593–2596 (2001)
25.48 N. Mingo, K. Makoshi: Calculation of the inelastic scanning tunneling image of acetylene on Cu(100), Phys. Rev. Lett. **84**, 3694–3697 (2000)
25.49 B.N.J. Persson, A. Baratoff: Inelastic electron tunneling from a metal tip: The contribution from resonant processes, Phys. Rev. Lett. **59**, 339 (1987)
25.50 Y. Kim, T. Komeda, M. Kawai: Single-molecule reaction and characterization by vibrational excitation, Phys. Rev. Lett. **89**, 126104 (2002)

25.51 T. Mii, S. Tikhodeev, H. Ueba: Theory of vibrational tunneling spectroscopy of adsorbates on metal surfaces, Surf. Sci. **502**, 26–33 (2002)

25.52 T. Mii, S.G. Tikhodeev, H. Ueba: Spectral features of inelastic electron transport via a localized state, Phys. Rev. B **68**, 205406 (2003)

25.53 B.C. Stipe, M.A. Rezaei, W. Ho: Coupling of vibrational excitation to the rotational motion of a single adsorbed molecule, Phys. Rev. Lett. **81**, 1263–1266 (1998)

25.54 T. Frederiksen, M. Paulsson, M. Brandbyge, A.-P. Jauho: Inelastic transport theory from first principles: Methodology and application to nanoscale devices, Phys. Rev. B **75**, 205413 (2007)

25.55 N. Lorente, M. Persson: Theory of single molecule vibrational spectroscopy and microscopy, Phys. Rev. Lett. **85**, 2997–3000 (2000)

25.56 T. Frederiksen, N. Lorente, M. Paulsson, M. Brandbyge: From tunneling to contact: Inelastic signals in an atomic gold junction from first principles, Phys. Rev. B **75**, 235441–235448 (2007)

25.57 L.J. Lauhon, W. Ho: Effects of temperature and other experimental variables on single molecule vibrational spectroscopy with the scanning tunneling microscope, Rev. Sci. Instrum. **72**, 216–223 (2001)

25.58 B.C. Stipe, M.A. Rezaei, W. Ho: Localization of inelastic tunneling and the determination of atomic-scale structure with chemical specificity, Phys. Rev. Lett. **82**, 1724–1727 (1999)

25.59 Y. Sainoo, Y. Kim, T. Komeda, M. Kawai: Inelastic tunneling spectroscopy using scanning tunneling microscopy on *trans*-2-butene molecule: Spectroscopy and mapping of vibrational feature, J. Chem. Phys. **120**, 7249–7251 (2004)

25.60 N. Okabayashi, T. Komeda: Inelastic electron tunneling spectroscopy with a dilution refrigerator based scanning tunneling microscope, Meas. Sci. Technol. **20**, 095602 (2009)

25.61 N. Okabayashi, T. Komeda: Identification of a deuterated alkanethiol inserted in a hydrogenated alkanethiol self-assembled monolayer by mapping of an inelastic tunneling signal, Rev. Sci. Instrum. **81**, 084101–084104 (2010)

25.62 Y. Wang, E. Kioupakis, X. Lu, D. Wegner, R. Yamachika, J.E. Dahl, R.M.K. Carlson, S.G. Louie, M.F. Crommie: Spatially resolved electronic and vibronic properties of single diamondoid molecules, Nat. Mater. **7**, 38–42 (2008)

25.63 J.R. Hahn, W. Ho: Imaging and vibrational spectroscopy of single pyridine molecules on Ag(110) using a low-temperature scanning tunneling microscope, J. Chem. Phys. **124**, 204708 (2006)

25.64 Y. Sainoo, Y. Kim, T. Okawa, T. Komeda, H. Shigekawa, M. Kawai: Excitation of molecular vibrational modes with inelastic scanning tunneling microscopy processes: Examination through action spectra of *cis*-2-butene on Pd(110), Phys. Rev. Lett. **95**, 246102 (2005)

25.65 N. Nilius, T.M. Wallis, W. Ho: Vibrational spectroscopy and imaging of single molecules: Bonding of CO to single palladium atoms on NiAl(110), J. Chem. Phys. **117**, 10947–10952 (2002)

25.66 N. Liu, C. Silien, W. Ho, J.B. Maddox, S. Mukamel, B. Liu, G.C. Bazan: Chemical imaging of single 4,7,12,15-tetrakis[2.2]paracyclophane by spatially resolved vibrational spectroscopy, J. Chem. Phys. **127**, 244711 (2007)

25.67 T. Choi, S. Bedwani, A. Rochefort, C.-Y. Chen, A.J. Epstein, J.A. Gupta: A single molecule Kondo switch: Multistability of tetracyanoethylene on Cu(111), Nano Lett. **10**, 4175–4180 (2010)

25.68 A.F. Takacs, F. Witt, S. Schmaus, T. Balashov, M. Bowen, E. Beaurepaire, W. Wulfhekel: Electron transport through single phthalocyanine molecules studied using scanning tunneling microscopy, Phys. Rev. B **78**, 233404 (2008)

25.69 A. Mugarza, C. Krull, R. Robles, S. Stepanow, G. Ceballos, P. Gambardella: Spin coupling and relaxation inside molecule-metal contacts, Nat. Commun. **2**, 490 (2011)

25.70 J.I. Pascual, J. Gómez-Herrero, D. Sánchez-Portal, H.-P. Rust: Vibrational spectroscopy on single C-60 molecules: The role of molecular orientation, J. Chem. Phys. **117**, 9531–9534 (2002)

25.71 M. Grobis, K.H. Khoo, R. Yamachika, X.H. Lu, K. Nagaoka, S.G. Louie, M.F. Crommie, H. Kato, H. Shinohara: Spatially dependent inelastic tunneling in a single metallofullerene, Phys. Rev. Lett. **94**, 136802 (2005)

25.72 H. Gawronski, M. Mehlhorn, K. Morgenstern: Imaging phonon excitation with atomic resolution, Science **319**, 930–933 (2008)

25.73 J.C. Love, L.A. Estroff, J.K. Kriebel, R.G. Nuzzo, G.M. Whitesides: Self-assembled monolayers of thiolates on metals as a form of nanotechnology, Chem. Rev. **105**, 1103–1169 (2005)

25.74 A.R. Champagne, A.N. Pasupathy, D.C. Ralph: Mechanically adjustable and electrically gated single-molecule transistors, Nano Lett. **5**, 305–308 (2005)

25.75 M.A. Reed, C. Zhou, C.J. Muller, T.P. Burgin, J.M. Tour: Conductance of a molecular junction, Science **278**, 252–254 (1997)

25.76 J.G. Kushmerick, D.B. Holt, J.C. Yang, J. Naciri, M.H. Moore, R. Shashidhar: Metal-molecule contacts and charge transport across monomolecular layers: Measurement and theory, Phys. Rev. Lett. **89**, 086802 (2002)

25.77 W.Y. Wang, T. Lee, I. Kretzschmar, M.A. Reed: Inelastic electron tunneling spectroscopy of an alkanedithiol self-assembled monolayer, Nano Lett. **4**, 643–646 (2004)

25.78 A. Kudelski: Characterization of thiolate-based mono- and bilayers by vibrational spectroscopy: A review, Vib. Spectrosc. **39**, 200–213 (2005)

25.79 H.S. Kato, J. Noh, M. Hara, M. Kawai: An HREELS study of alkanethiol self-assembled monolayers on Au(111), J. Phys. Chem. B **106**, 9655–9658 (2002)

25.80 S.C. Chang, I. Chao, Y.T. Tao: Structures of self-assembled monolayers of aromatic-derivatized thiols on evaporated gold and silver surfaces – Implication on packing mechanism, J. Am. Chem. Soc. **116**, 6792–6805 (1994)

25.81 Z. Li, Z. Wu, F. Luo: Synthesis and antifungal activities of alkyl *N*-(1,2,3-thiadiazole-4-carbonyl) carbamates and *S*-alkyl *N*-(1,2,3-thiadiazole-4-

carbonyl) carbamothioates, J. Agric. Food Chem. **53**, 3872–3876 (2005)
25.82 N. Okabayashi, Y. Konda, T. Komeda: Inelastic electron tunneling spectroscopy of an alkanethiol self-assembled monolayer using scanning tunneling microscopy, Phys. Rev. Lett. **100**, 217801 (2008)
25.83 L. Olesen, M. Brandbyge, M.R. Sørensen, K.W. Jacobsen, E. Lægsgaard, I. Stensgaard, F. Besenbacher: Apparent barrier height in scanning tunneling microscopy revisited, Phys. Rev. Lett. **76**, 1485–1488 (1996)
25.84 L.A. Bumm, J.J. Arnold, T.D. Dunbar, D.L. Allara, P.S. Weiss: Electron transfer through organic molecules, J. Phys. Chem. B **103**, 8122–8127 (1999)
25.85 J. Klein, A. Léger, M. Belin, D. Défourneau, M.J.L. Sangster: Inelastic-electron-tunneling spectroscopy of metal-insulator-metal junctions, Phys. Rev. B **7**, 2336 (1973)
25.86 M.D. Porter, T.B. Bright, D.L. Allara, C.E.D. Chidsey: Spontaneously organized molecular assemblies. 4. Structural characterization of *n*-alkyl thiol monolayers on gold by optical ellipsometry, infrared spectroscopy, and electrochemistry, J. Am. Chem. Soc. **109**, 3559–3568 (1987)
25.87 S.-C. Chang, I. Chao, Y.-T. Tao: Structure of self-assembled monolayers of aromatic-derivatized thiols on evaporated gold and silver surfaces: Implication on packing mechanism, J. Am. Chem. Soc. **116**, 6792–6805 (1994)
25.88 R.G. Nuzzo, L.H. Dubois, D.L. Allara: Fundamental studies of microscopic wetting on organic surfaces. 1. Formation and structural characterization of a self-consistent series of polyfunctional organic monolayers, J. Am. Chem. Soc. **112**, 558–569 (1990)
25.89 M.A. Bryant, J.E. Pemberton: Surface Raman scattering of self-assembled monolayers formed from 1-alkanethiols: Behavior of films at Au and comparison to films at Ag, J. Am. Chem. Soc. **113**, 8284–8293 (1991)
25.90 N. Okabayashi, M. Paulsson, H. Ueba, Y. Konda, T. Komeda: Site selective inelastic electron tunneling spectroscopy probed by isotope labeling, Nano Lett. **10**, 2950–2955 (2010)
25.91 N. Okabayashi, M. Paulsson, H. Ueba, Y. Konda, T. Komeda: Inelastic tunneling spectroscopy of alkanethiol molecules: High-resolution spectroscopy and theoretical simulations, Phys. Rev. Lett. **104**, 077801 (2010)
25.92 L.H. Yu, C.D. Zangmeister, J.G. Kushmerick: Origin of discrepancies in inelastic electron tunneling spectra of molecular junctions, Phys. Rev. Lett. **98**, 206803 (2007)
25.93 J.M. Beebe, H.J. Moore, T.R. Lee, J.G. Kushmerick: Vibronic coupling in semifluorinated alkanethiol junctions: Implications for selection rules in inelastic electron tunneling spectroscopy, Nano Lett. **7**, 1364–1368 (2007)
25.94 É. Garand, J.F. Picard, P. Rowntree: Inter- and intramolecular temperature-dependent vibrational perturbations of alkanethiol self-assembled monolayers, J. Phys. Chem. B **108**, 8182–8189 (2004)
25.95 D.J. Scalapino, S.M. Marcus: Theory of inelastic electron-molecule interactions in tunnel junctions, Phys. Rev. Lett. **18**, 459 (1967)
25.96 Y. Qi, I. Ratera, J.Y. Park, P.D. Ashby, S.Y. Quek, J.B. Neaton, M. Salmeron: Mechanical and charge transport properties of alkanethiol self-assembled monolayers on a Au(111) surface: The role of molecular tilt, Langmuir **24**, 2219–2223 (2008)
25.97 H. Song, H. Lee, T. Lee: Intermolecular chain-to-chain tunneling in metal-alkanethiol-metal junctions, J. Am. Chem. Soc. **129**, 3806–3807 (2007)
25.98 T. Frederiksen, C. Munuera, C. Ocal, M. Brandbyge, M. Paulsson, D. Sanchez-Portal, A. Arnau: Exploring the tilt-angle dependence of electron tunneling across molecular junctions of self-assembled alkanethiols, ACS Nano **3**, 2073–2080 (2009)
25.99 S. Chen, L. Li, C.L. Boozer, S. Jiang: Controlled chemical and structural properties of mixed self-assembled monolayers of alkanethiols on Au(111), Langmuir **16**, 9287–9293 (2000)
25.100 A.V. Shevade, J. Zhou, M.T. Zin, S. Jiang: Phase behavior of mixed self-assembled monolayers of alkanethiols on Au(111): A configurational-bias Monte Carlo simulation study, Langmuir **17**, 7566–7572 (2001)

Tadahiro Komeda

Institute of Multidisciplinary Research for Advanced Materials (IMRAM)
Tohoku University
Sendai, Japan
tadahiro.komeda.a1@tohoku.ac.jp

Tadahiro Komeda is currently Professor at the Institute of Multidisciplinary Research for Advanced Materials (IMRAM, Tagen) at Tohoku University, Japan. He received his PhD from Kyoto University, Japan. He joined Tohoku University as Full Professor in 2003. His research group works on developing chemical-analysis techniques for molecular electronic and spintronic device materials using scanning probe microscopes.

Norio Okabayashi

School of Mathematics and Physics
Kanazawa University
Kanazawa, Japan
okabayashi@staff.kanazawa-u.ac.jp

Norio Okabayashi is an Assistant Professor at the School of Mathematics and Physics at Kanazawa University. He obtained his PhD at the University of Tokyo in 2004. After completing 3 postdoctoral fellowships, at Tohoku University and elsewhere, he started working at his current position in 2012. His present research concerns inelastic electron tunneling spectroscopy combined with atomic force microscopy.

26. Adsorption Sites, Bonding Configurations, Reactions and Mass Transport Surface

Eric C. Mattson, Yves J. Chabal

Section 26.2 discusses the essential concepts of infrared (IR) spectroscopy as it pertains to studies of surfaces and interfaces, focusing on different potential measurement geometries and the type of information that can be extracted from an IR absorption measurement. Section 26.3 provides a brief overview of low-energy ion scattering (LEIS)-based quantification of surface composition and thin film structure. The fundamentals of x-ray photoemission spectroscopy (XPS) have already been covered in a previous chapter and are therefore not addressed here. Section 26.4 presents examples from a variety of different fields to illustrate how the combination of these three techniques has yielded quantitative information on adsorption sites, bonding configurations, surface reactions, and mass transport. These examples include ultrashallow monolayer doping of semiconductors, growth of ultrathin metal oxide layers, characterization of catalyst model surface structure, reactivity of transition-metal surfaces with nitrogen and hydrogen plasmas, dielectric surface etching and functionalization, and gas storage in nanoporous materials.

Infrared (IR) spectroscopy, low-energy ion scattering (LEIS), and x-ray photoemission spectroscopy (XPS) are widely used techniques for a broad range of studies of surface chemistry and composition. IR absorption measurements directly probe the chemical bonds at surfaces and in thin films through excitation of vibrational transitions, providing a fingerprint of the bonds present in the absorbing material. LEIS measurements probe the elemental composition of an ultrashallow (< 1 nm) surface region and can yield static depth profiles of the first 5–10 nm of a surface region. XPS measurements detect the photoelectron yield and binding energy of the core level of each particular element, thereby providing in-depth information on the nature of the chemical bonds and oxidation states of the elements present. When used in combination, these three techniques can provide a detailed description of the amount and types of chemical species present at surfaces, which yields quantitative insight into many surface chemical and physical processes such as thin film growth, surface functionalization, catalysis, and near-surface diffusion. In this chapter, we review some basic principles of IR

M. Rocca, T.S. Rahman, L. Vattuone (Eds.), *Springer Handbook of Surface Science*, Springer Handbooks,
https://doi.org/10.1007/978-3-030-46906-1_26

spectroscopy and LEIS spectroscopy, noting that XPS has been covered in detail in another chapter of this handbook. We discuss how these three complementary techniques can be applied to understand surface reactions and mass transport for a variety of different applications, and we discuss specific problems that highlight the type of information that can be extracted from the combined techniques.

26.1 Surface Techniques Survey

Adsorbate bonding and structure, surface reaction products and mechanisms, and mass transport are complex elements underlying many important technological problems ranging from microelectronics to energy conversion and storage. Fundamental studies of these phenomena often require a multi-technical approach in order to quantitatively evaluate a given process or reaction. While there exist many experimental probes that can determine adsorption sites and bonding configurations, or characterize surface reactions and mass transport, the combination of vibrational spectroscopy, core-level photoemission, and low-energy ion scattering (LEIS) spectroscopies is uniquely suited to study all of these phenomena in situ on quantitative footing when performed together. The most convenient choice for vibrational spectroscopy is infrared (IR) absorption, which provides the highest energy resolution, good sensitivity, and structural information obtained from polarized radiation (thanks to versatility in experimental geometries). Additionally, IR measurements can be carried out under conditions that do not require ultrahigh vacuum. IR absorption measurements not only offer a direct probe of the chemical bonds present in an adsorbed layer by excitation of optically active vibrational modes, but can also provide rich information on the electronic structure of condensed-phase systems, although the latter is less frequently done. LEIS measurements can directly determine the identity and concentration of atoms present in the outermost layer of a surface, and can also offer static depth profiles of subsurface species within a depth of 5−10 nm. Finally, XPS measurements give the identity and chemical state of the elements present in the outermost ≈ 5 nm of the surface region. The collective strengths of these techniques enable a quantitative analysis of surface chemical structure, composition, and reactivity, and resolve ambiguities that could arise from the measurements of the individual techniques taken on their own.

26.2 IR Measurements of Surfaces and Thin Films

Vibrational spectroscopic methods, and IR spectroscopy in particular, have played an important role in the development of surface science. The strength of vibrational spectroscopy lies in its ability to identify the chemical nature of adsorbates and reaction products and their local symmetry and bonding configuration through measurements of the vibrational frequencies and intensities of adsorbates. Under the most favorable conditions, the number frequencies of modes observed in a vibrational spectroscopy experiment can be used to deduce the site symmetry of an adsorbate on the basis of factor group analysis of the possible bonding configurations. In the investigation of thin films, vibrational measurements probe, depending on the measurement conditions, the transverse-optical (TO) and/or longitudinal-optical (LO) phonon modes of the adlayer, which can yield information on structure, crystallinity or local order, thickness, and dielectric properties.

Many aspects of IR spectroscopy offer unique advantages over other surface-sensitive vibrational spectroscopic techniques such as high-resolution electron energy loss spectroscopy (HREELS) or sum-frequency generation (SFG) spectroscopy. Some of these advantages include excellent energy resolution (10^{-4} eV), high sensitivity ($< 1\%$ of a monolayer, depending on dynamic dipole moment and measurement geometry), versatility of potential measurement geometries, and the ability to simultaneously probe optically active electronic transitions such as free carrier absorption. While these characteristics render IR spectroscopy a very powerful technique, the nature and degree of quantitation that can be extracted from experiments can be further improved when performed in conjunction with other quantitative techniques that provide additional information on coverage and chemical state of the substrate. For example, IR measurements provide rich information on the chemical and structural nature of an adsorbate, but are not always sensitive to the chemical state of the substrate atoms. Additionally, quantification of the amount of a given species on a surface (i.e., the coverage) from an IR measurement alone is challenging without some form of calibration. In contrast,

techniques such as XPS and LEIS are inherently quantitative and sample both the adsorbate and substrate. They can supplement the information gaps and provide information that, when used in conjunction with IR measurements, provides a comprehensive and quantitative picture of structure and chemical bonding at surfaces. These techniques will be addressed in subsequent sections. In this section, we focus on important aspects of IR spectroscopic measurements specific to the study of surfaces and interfaces, many of which have been the subject of numerous books and reviews [26.1–8]; here we summarize some of the most important topics with emphasis on the type of information that can be extracted from different experimental approaches. We further note that, though IR spectroscopy is the focus of the current section, the strength of other vibrational techniques (such as HREELS) with their own respective advantages should not be underestimated. Similarly, in the context of this chapter, numerous multi-technique approaches combining HREELS, photoemission, ion scattering methods, or combinations thereof [26.9–12] have also been conducted to address many complex scientific problems.

26.2.1 IR Absorption and Normal Vibrations

The fundamental principles of IR spectroscopic measurements ranging from molecular to extended systems have been discussed at length in numerous books and review articles; here we discuss the most important aspects of the theory as it pertains to an understanding of surface phenomena, and a more detailed theoretical framework can be found in the references given. IR radiation interacts with matter primarily through coupling of the electric field of the IR photons with the motion of charges in a molecule or material. In the case of vibrational excitation, a photon excites a vibrational mode such that a time-dependent dipole moment (i.e., *dynamical dipole moment*) is formed as a result of the atomic displacements that occur during the vibration. Analogously, a photon can couple to the motion of electrons in a solid to promote an electron to a higher energy state through dynamical dipoles formed as a result of electronic motion or the difference in charge distribution between the two states. In both cases, photon absorption is mediated by the formation of time-dependent dipole moments that form as a result of the excitation, which comprises a general selection rule for IR absorption: for a given transition to have IR activity, the excited state must produce a dynamical dipole moment. This selection rule, applicable to both molecular and condensed-phase systems, is derived from the golden rule for the transition probability per unit time, where the radiation field is treated as a time-dependent perturbation. In the case of a vibrational excitation, it is found that the integral over space τ

$$\int \psi_f^* \boldsymbol{\mu}_\xi \psi_i \mathrm{d}\tau \,, \tag{26.1}$$

must be nonzero in order for a transition to occur [26.13]. Here, $\boldsymbol{\mu}_\xi$ is the component of the dipole moment along the direction of the electric field polarization, and ψ_i and ψ_f the initial and final vibrational states. The intensity of an IR mode in the gas phase is ultimately dependent upon the value of the integral (26.1), which can be evaluated to give the intensity of a vibrational mode

$$\int \psi_f^* \boldsymbol{\mu}_\xi \psi_i \mathrm{d}\tau = \left(\frac{h}{8\pi^2 c\upsilon}\right)^{1/2} \frac{\partial \boldsymbol{\mu}_\xi}{\partial Q} \,. \tag{26.2}$$

Here, h is Planck's constant, c the speed of light, ν the vibrational frequency, and Q the normal coordinate, which describes the atomic displacements that occur during vibration. Thus, IR intensities are governed by the *change* in the dipole moment of the molecule that occurs as a result of the vibration.

The normal modes of vibration of molecules, or phonons in the case of extended systems, are determined with the methods of discrete group theory, which use symmetry to evaluate both the atomic displacements that occur during a vibration and the selection rules that determine which types of modes are IR (or Raman) active [26.13, 14]. Using standard methods that take into account the symmetry of the vibrating moiety, the number and character of normal modes of vibration of a given molecule or solid can be determined, allowing for the modes observed in an IR experiment to be linked to a specific chemical structure. It can be shown that the dipole moment transforms under symmetry operations in the same way as translation (e.g., x, y, and z), and therefore any vibration belonging to the same irreducible representation as x, y, or z will be IR active. When an atom or molecule adsorbs on a surface, the symmetry is lowered by the presence of the substrate, and the vibrations of the adsorbed complex may be different from those of the gas-phase molecule. While in simple cases the normal modes of the adlayer can be intuitively inferred, in general a full group-theoretical treatment is used to understand the normal modes of a given adsorbate structure [26.3], particularly for large or complex molecules. The vibrations of an adlayer are connected to those of a gas-phase analog by correlation tables that relate the irreducible representations of the point group of the molecule to those of the surface unit cell group. Often, the reduced symmetry in the adsorbed state can lead to splitting of otherwise degenerate modes, or activity of otherwise IR-inactive modes.

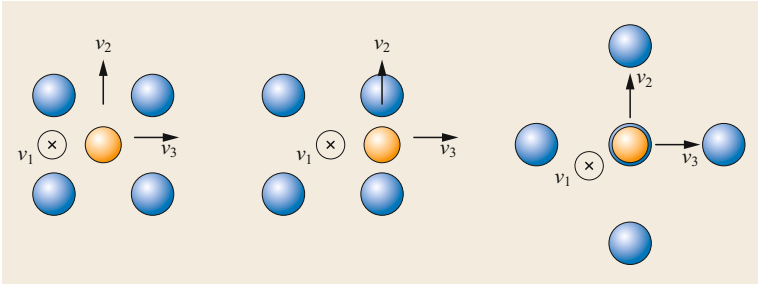

Fig. 26.1 Frustrated translational modes of an adatom adsorbed at surface sites of different symmetry

In addition, translational and rotational degrees of freedom of the free molecule become vibrational degrees of freedom of an adsorbed molecule. Therefore, consideration of the symmetry of an adsorbate complex is often critical in properly identifying its chemical state and adsorption configuration.

As an example, we first consider adsorption of a single atom on a surface. In its free state, a single atom has only translational degrees of freedom, which in turn become frustrated translational modes in the adsorbed state. Thus, three modes are in principle detectable in a vibrational measurement. The number of modes observed in an IR (or HREELS) experiment can be used to infer the site symmetry of the atom. Consider first adsorption of the atom at a fourfold hollow site as in Fig. 26.1a; here, one mode is associated with the frustrated translation perpendicular to the surface (ν_1), and the remaining two modes (ν_2, ν_3) are frustrated translations parallel to the surface. Because of the symmetry of the site group, however, the two remaining translational modes are equivalent, and therefore their frequencies degenerate. Consider next adsorption at a bridge site, as in Fig. 26.1b; in this case we have, as before, a frustrated translation normal to the surface (ν_1) and two frustrated translations parallel to the surface (ν_2, ν_3). In this case, however, the degeneracy between the ν_2 and ν_3 modes is lifted, and the two modes would be expected to have distinct frequencies. In the case of adsorption on an atop site as in Fig. 26.1c, the ν_2 and ν_3 are again degenerate, and it would therefore be difficult to distinguish the adsorption configurations in Fig. 26.1a,c; however, the frequency of the ν_1 mode would be expected to be significantly different between the atop and hollow configurations due to the different levels of coordination to the surface. Similar mode-counting arguments can be made to understand the bonding configuration for small molecules, although the situation becomes more complicated because both internal modes and frustrated rotations must also be considered. In some cases, the internal modes can also be used to infer the symmetry of the adsorption site; for instance, the C−O stretching frequency of CO adsorbed on metal surfaces is known to decrease with increasing coordination to the surface [26.15], and can therefore be used to deduce its adsorption configuration. While mode-counting arguments can potentially be very useful in vibrational spectroscopy, the challenge, particularly with IR spectroscopy, is that often not all modes are observed. This can result from selection rules associated with the substrate (discussed below) or, more often, a limited accessible spectral range. Frustrated rotations and parallel translations often lie in the far-IR region, which is a particularly difficult region due to the need for special sources, detectors, and window materials; therefore, low-frequency vibrations are more readily detectable with HREELS. Nevertheless, for light adsorbates, mode-counting arguments in conjunction with measured frequencies and intensities can shed a great deal of light on bonding configuration, particularly when used in conjunction with first-principles modeling.

26.2.2 Measurement Geometries

External Reflection

For the case of strongly absorbing substrates, in particular metals, the external reflection geometry is most frequently used (Fig. 26.2a). Because of selection rules discussed below, an IR beam is incident upon a reflective surface at a large angle of incidence, and the spectrum of the adlayer is determined by the difference in reflectivity of the clean versus adsorbate-covered substrate. Early calculations by *Greenler* [26.16] showed that the coupling of the normal (p-polarized) component of the electric field at a metal surface to an adsorbate mode with a dynamical dipole moment component oriented perpendicular to the surface was significantly enhanced at grazing-incidence angles (Fig. 26.3), with the optimal incidence angle determined by the dielectric function of the metal substrate. In contrast, the parallel (s-polarized) component of the electric field immediately above the surface cancels out almost entirely due to the phase change that occurs upon reflection. Thus, measurements employing the reflection geometry are most frequently performed at grazing (83−88°) angles of incidence to maximize the signal due to

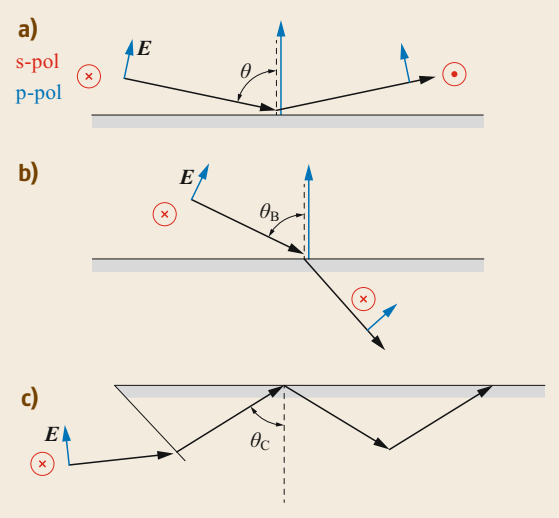

Fig. 26.2a–c Schematic diagram of measurement geometries used for IR spectroscopic measurements. **(a)** In the external reflection geometry, the beam is incident at a large angle with respect to the surface normal. A standing wave is generated between the incident and reflected beams. The normal components of the two beams add constructively, while the tangential components cancel one another due to the phase change occurring upon reflection. **(b)** Depiction of the transmission geometry with the angle of incidence equal to the Brewster angle, as discussed in the text. Here, reflection of the p-polarized component of the light is suppressed, leading to a partially polarized transmitted beam. **(c)** In the multiple internal reflection geometry, the beam is incident upon the sample from a beveled edge, and the beam transmitted into the sample is incident at an angle of incidence greater than the critical angle. The beam undergoes multiple internal reflections from both faces of the sample before finally exiting from the opposite beveled edge

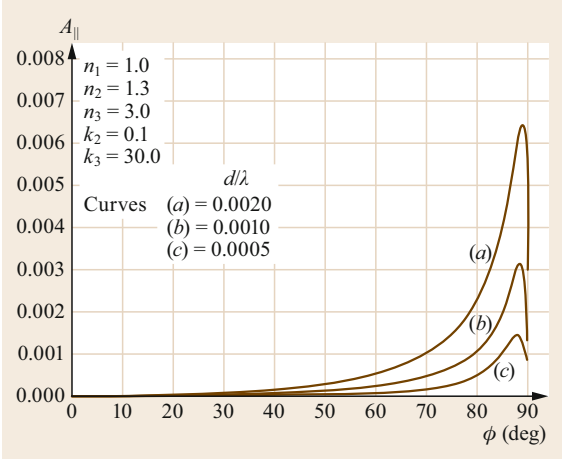

Fig. 26.3 Absorption factor for the three-layer model for reflection measurements from metal surfaces as a function of angle of incidence for p-polarized radiation (Reprinted from [26.16], with the permission of AIP Publishing)

the adlayer. Experiments performed in this fashion are frequently referred to as infrared reflection-absorption spectroscopy (IRRAS) or reflection-absorption infrared spectroscopy (RAIRS). Such measurements have traditionally been used to study adsorption and reactivity at metal surfaces, but the technique has recently been shown to be useful for the study of adsorbed layers on transparent oxide substrates as well [26.17, 18].

The detection of vibrational modes of an adlayer on a metallic substrate is subject to the so-called metal surface selection rule. The selection rule dictates that only vibrational modes that produce a dynamical dipole moment with a component perpendicular to the surface can be detected in an IRRAS experiment. The physical origin for this rule is as follows: The formation of a dipole moment immediately above the surface results in image charges that screen the field of the dipole in the metal. In the case of a dipole moment oriented parallel to the surface, the image charges produce a dipole moment oriented opposite that of the vibration, leading to a cancellation of the net dipole moment associated with the vibration. In contrast, the dipole moment associated with the image charge induced by a perpendicular adsorbate vibration is oriented parallel to that of the adsorbate; consequently, the adsorbate and image dipoles add constructively so that the net dipole moment is nonzero and the vibration is IR active. While the metal surface selection rule provides an intuitive picture for IR activity at metal surfaces, care must be taken when correlating atomic displacements of a particular vibration with dynamical dipole moments to infer whether the vibration is IR active or not. Some cases are straightforward; for instance, the adsorption of CO on most metal surfaces results in the molecular axis nearly parallel to the surface normal. Consequently, the C–O stretch produces a strong dynamical dipole moment perpendicular to the surface, and the vibration is readily detected. An example is illustrated in Fig. 26.4a, which shows RAIRS spectra from CO adsorbed on Pd(100) at 300 K [26.19]. Bands at 1983 and 2096 cm^{-1} are readily detected and assigned to CO bonded at bridge and atop sites. In other cases, however, the situation is more complex. The O–O stretching mode of O_2 adsorbed on Pt(111) provides such an example. Here, it is well established through near-edge x-ray absorption fine structure (NEXAFS) measurements [26.21] that the molecule adsorbs at a Pt-top site with its molecular axis parallel to the surface. Therefore, a stretching vibration that yields atomic displacements parallel to the

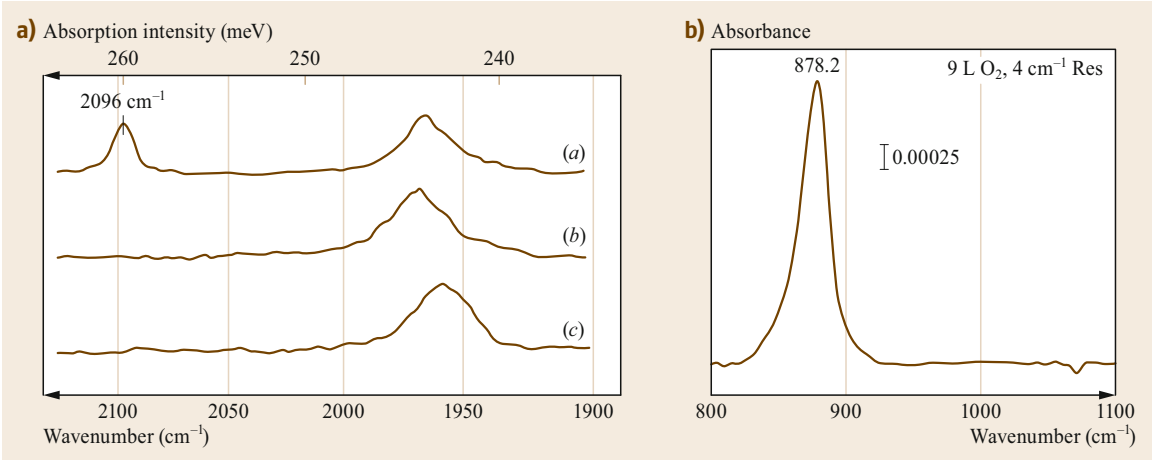

Fig. 26.4a,b IRRAS spectra of CO adsorbed on Pd(100) **(a)** and O_2 adsorbed on Pt(111) **(b)**. **(a)** Reprinted from [26.19], with permission from Elsevier. **(b)** Reprinted adapted with permission from [26.20]. Copyright 1994 American Chemical Society

surface would not be expected to have IR activity, and yet experiments show [26.20] that the mode is clearly observed, as in Fig. 26.4b, *Fan* and *Trenary* [26.20] framed the metal surface selection rule into a simple group theoretical argument: a vibrational mode is considered to be symmetry-allowed if it belongs to the same irreducible representation as the surface normal. In the case of the O_2/Pt(111) system, the molecule adsorbs with C_{2v} site group symmetry, and therefore the surface normal, which transforms like z, belongs to the A_1 irreducible representation. Therefore, the group theoretical arguments presented by Fan and Trenary would suggest that any vibration of the Pt−O_2 complex with A_1 symmetry should be IR active according to the selection rule. Indeed, both the O−O stretch and the Pt−O_2 stretch belong to the A_1 irreducible representation and are therefore IR active. Several notes were made regarding the physical origin for the IR activity of the O−O stretch. First, in conjunction with expansion/contraction of the O−O bond, a net perpendicular displacement of the entire molecule takes place during the O−O stretching vibration, accounting for $\approx 10\%$ of the total atomic displacements during the vibration. Second, a perpendicular charge transfer between the metal substrate and adsorbate takes place in registry with parallel O−O stretching displacements, giving rise to a dipole moment perpendicular to the surface and responsible for the considerable intensity of the mode. A similar reasoning was invoked for the case of the IR activity of the (totally symmetric) C−C stretching mode on ethylene/Pt(111), another case where the C−C bond was known to be parallel to the surface. For this system, the IR activity was proposed to originate from mixing of the C−C bond stretching with the wagging motion of the methylene groups, which is perpendicular to the surface. The possibility of adsorbate–substrate charge transfer during the C−C bond stretching/compression was also acknowledged as possibly contributing to the appreciable intensity of the mode.

Transmission

The IR transmission geometry (Fig. 26.2b), arguably the most versatile geometry for IR absorption measurements, can be applied to surface studies of a range of different types of substrates, from transparent or weakly absorbing materials, to powders and supported catalysts, and even sufficiently thin metal thin films on transparent substrates. Developments in spectrometers, sources, and detectors over the past 20 years have improved the throughput of the beam for typical benchtop sources such that the signal-to-noise ratio (SNR) obtainable for a single pass (through both surfaces of a double-side polished crystal) is sufficient to observe submonolayer coverage of adsorbed species, as will be shown below. Unlike the multiple internal reflection (MIR) geometry (1.1.3), the beam enters the sample from the surface of interest, and there is no need for edge beveling. This enables a much simpler configuration for temperature control of the sample through direct resistive heating of the sample itself, in the case of semiconductor surfaces. Furthermore, the measurements can be performed at arbitrary angles of incidence and, coupled with the use of polarization, provide detailed information on the structure of adsorbed complexes. The IR intensity transmitted through a sample of thickness d follows a Beer's law dependence, $I = I_0 e^{-\alpha d}$, and the absorbance is defined as $A = -\log(I/I_0)$. Here, I_0 is the intensity of the incident

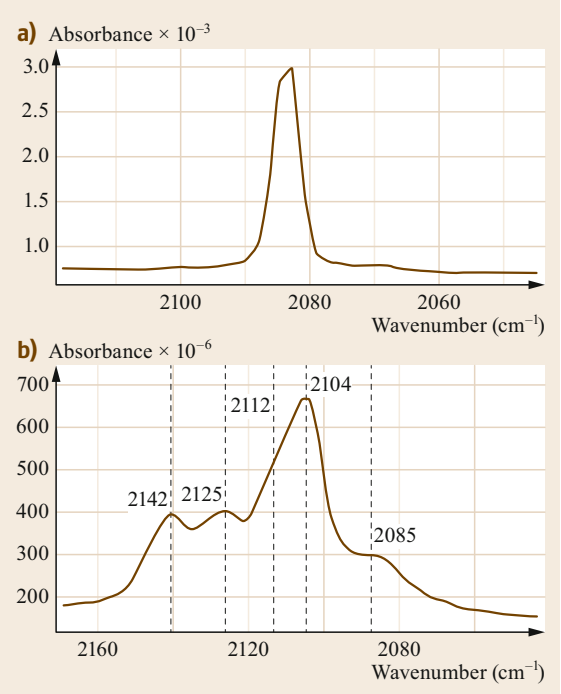

Fig. 26.5a,b IR absorption spectra of H-terminated Si(111) prepared by HF and NH_4F etching **(a)** and H-terminated Si(100) prepared NH_4F etching **(b)** measured using the Brewster's angle transmission geometry

IR beam, I that of the transmitted beam, and α the absorptivity of the material. In the case of semiconductor substrates, which are usually partially absorbing in the IR, the background attenuation due to bulk absorption can be substantial. With transmission measurements, an interesting option is to use p-polarized radiation at the Brewster angle of the substrate (Fig. 26.2b), thus suppressing reflection losses (i.e., interferences) and enhancing the transmitted signal. Another advantage of this geometry is that, since the incident beam contains electric field components both parallel and perpendicular to the surface, vibrational modes of all orientations are probed. When measurements are used in conjunction with a polarizer, this allows for the determination of the orientation of adsorbate bonds. In studies of supported thin films, both LO and TO modes are detected. In contrast, at normal incidence the beam is naturally polarized perpendicular to the plane of incidence (s-polarized), and therefore only the parallel components of adsorbate or TO phonon modes are detected. In supported particle or pressed powder samples, normal incidence is ordinarily used for simplicity, since the constituents are randomly oriented. Alternatively, for highly scattering powders or pellets, the diffuse reflectance geometry can be used. In this case, the beam is incident along the surface normal, and mirrors collect the diffusely scattered light and refocus into the detector. A procedure known as the Kubelka–Munk transformation is applied to the spectra to account for mixing of the real and imaginary parts of the refractive index that result from resonant Mie scattering.

As an example, Fig. 26.5a,b shows IR absorption spectra of NH_4F-etched Si(111) and Si(100) surfaces, respectively, collected from Brewster's angle transmission measurements. Here, the reference measurements are those of the same crystals prior to etching. In the case of Si(111) surfaces, a single intense peak is observed, associated with the atop monohydride species that fully passivate the surface [26.22]. In the case of Si(100) surfaces, a much more complicated absorption profile is observed. Previous scanning tunneling microscopy (STM) investigations showed the surface morphology to be quasi-atomically flat, and polarized multiple internal reflection (MIR) measurements (discussed later) identified bands associated with strained monohydride, strained dihydride, and unstrained dihydride [26.23]. In the spectrum shown in Fig. 26.5b recorded in transmission mode, the bands observed at 2104 and 2112 cm^{-1} are associated with unstrained dihydrides, those at 2085 and 2142 cm^{-1} with strained dihydrides, and the band at 2125 cm^{-1} with strained monohydride. Several important points can be taken from these spectra. First, the SNR obtained from a single-pass transmission measurement is sufficient to clearly observe bands associated with surface species, at least for reasonably high coverage and/or strong or sharp modes. Second, the higher spectral resolution obtainable with IR measurements than with corresponding HREELS permits examination of distinct chemical species located within close spectral proximity.

Multiple Internal Reflection

In the MIR geometry (Fig. 26.2c), the beam is internally incident upon the surface–vacuum interface at an angle exceeding the critical angle, such that the beam is totally internally reflected multiple times by the front and back surfaces of the sample. This is typically accomplished by beveling the edges so that an external beam can enter the crystal at normal incidence with a bevel angle that achieves the angle of incidence required for total internal reflection. The clear advantage of this experimental geometry is the amplification of the signal from the surface due to the fact that the IR beam interacts with the surface multiple times, and is therefore the geometry of choice for examining very low-coverage and/or low-intensity modes. Another advantage of MIR spectroscopy is that, for typical angles of incidence, the measurements are equally sensitive to normal and parallel components of surface vibrations [26.1]. As

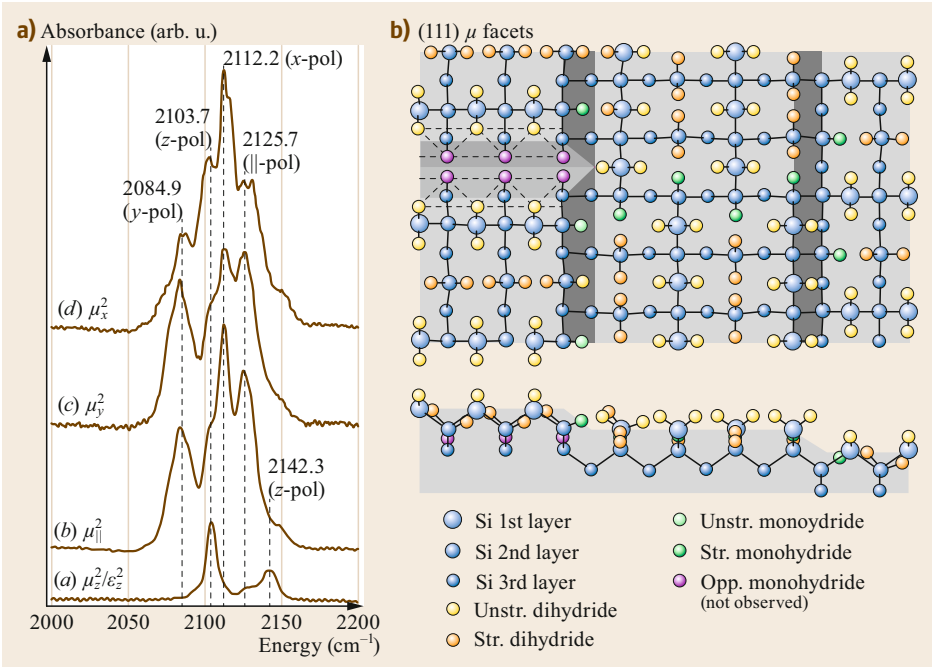

Fig. 26.6a,b Polarization-resolved MIR measurements enabled extraction of the Cartesian components of the dynamical dipole moment in the NH_4F-etched Si(100) **(a)**, and enabled the structural characterization of a complex hydride termination of the surface **(b)** (Reprinted adapted with permission from [26.23]. Copyright (2010) American Chemical Society)

for the case of the transmission geometry, polarization can be employed to extract information on the structure of adsorbed layers. One drawback of MIR measurements is the need to bevel the short edges of the samples and to keep them clear for IR beam access. The latter requirement prevents a uniform resistive heating because the short edges cannot support metal clamps over their whole length. In addition, the much longer optical path length of the radiation results in complete attenuation even in regions of weak substrate absorption. For example, the weak multiphonon absorption of Si renders the entire spectral region below 1400 cm^{-1} completely inaccessible. Nevertheless, MIR spectroscopy has offered significant insight into a number of complex systems [26.23–29]. *Hines* and coworkers performed polarization-resolved MIR spectroscopic studies of NH_4F-etched Si(100) surfaces in conjunction with scanning tunneling microscopy measurements [26.23]. STM images of the etched surfaces showed a structure composed of long rows, 0.9 Å in height and separated by 7.7 Å (exactly twice the distance between adjacent Si atoms). Polarized MIR spectra offered chemical insight into the identity of terminal H atoms. The spectra were computationally decomposed to deconvolute the Cartesian components of the dipole moments associated with each of the vibrations in the Si–H stretching region (Fig. 26.6a). A total of five distinct modes were observed, two of which had IR activity originating from dynamical dipole moments perpendicular to the surface, while three had activity originating from mostly parallel dipole moments. From existing literature and their relative splitting, two bands (2103.7 and 2112.2 cm^{-1}) were readily assigned to the asymmetric and symmetric vibrations, respectively, of unstrained dihydride species. Based on high-resolution STM imaging, these groups were found to exist in one-atom-thick rows, with the molecular plane perpendicular to the row direction. The adjacent missing rows showed characteristics consistent with dihydride termination in the STM images, and the polarization and splitting of the bands at 2084.9 and 2142.3 cm^{-1} were assigned to the asymmetric and symmetric vibrations of strained dihydrides rotated 90° about the surface normal with respect to the orientation of the unstrained dihydrides. The remaining band at 2125.7 cm^{-1} was attributed to strained monohydrides present at surface defects. The integration of high-resolution STM imaging and polarization-resolved MIR spectroscopy therefore led to the structural model depicted in Fig. 26.6b. Structural determination in the case of such a complex chemical termination highlights the advantages of the MIR technique: high sensitivity, spectral resolution, and polarization specificity.

Microscopy

While surface science has evolved primarily through the investigation of well-defined model systems, many current directions involve complex and inhomogeneous systems that may have variability at microscopic length scales. Potential applications include catalyst particles,

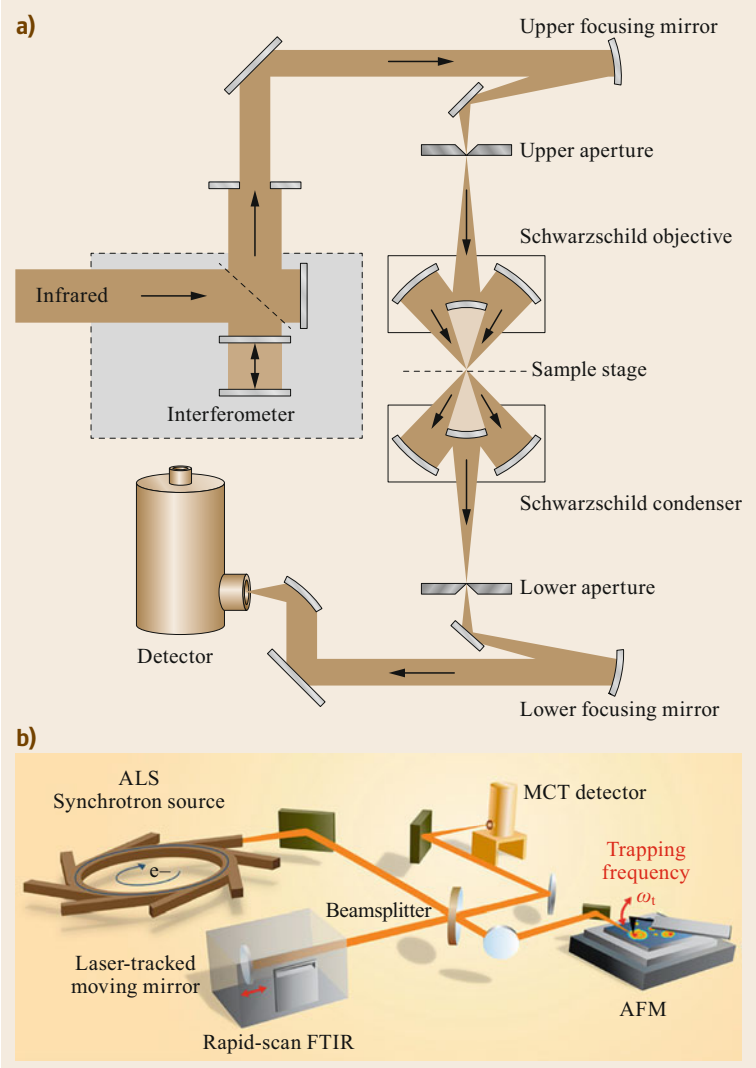

Fig. 26.7 **(a)** Optical arrangement used in typical far-field-based IR microspectroscopy, employing Schwarzschild optics and transmission geometry. **(b)** Experimental arrangement for broadband s-SNOM coupled to a synchrotron source (Reprinted from [26.30, 31], with the permission of AIP Publishing)

exfoliated films and 2-D (two-dimensional) materials, and microelectronic devices. In addition to conventional ultrahigh vacuum UHV-based surface science techniques that sample macroscopic sample areas, microscopic techniques (e.g., IR microscopy) have recently emerged and can be employed to study surface phenomena under high or atmospheric pressure. IR-based microscopy is particularly challenging, for a number of reasons. First, the comparatively long wavelength of IR radiation limits the obtainable resolution due to diffraction [26.30, 32, 33]. Second, the amount of light that can be focused on the sample is limited by the source size; typical lab-based Globar sources have a relatively low emittance, and therefore measurements performed at magnifications such that the resolution is diffraction-limited are usually subject to very poor SNR, hindering the study of weak signals originating from surfaces. The use of synchrotron radiation overcomes this problem, however, as the effective source size is small but has very high brightness. Most surface science-based studies using microscopy configurations have employed a synchrotron-based source.

Conventional far-field IR microscopy employs a Schwarzschild optical design (Fig. 26.7a). In the normal-incidence transmission geometry, an IR beam is focused onto the sample by a condenser lens, transmitted through the sample, and refocused onto a detector by an objective lens. In the normal-incidence reflection geometry, the incident and reflected beams are focused using the same Schwarzschild lens. Apertures are used before and after the condenser and objective lenses, respectively, to control the area illuminated and

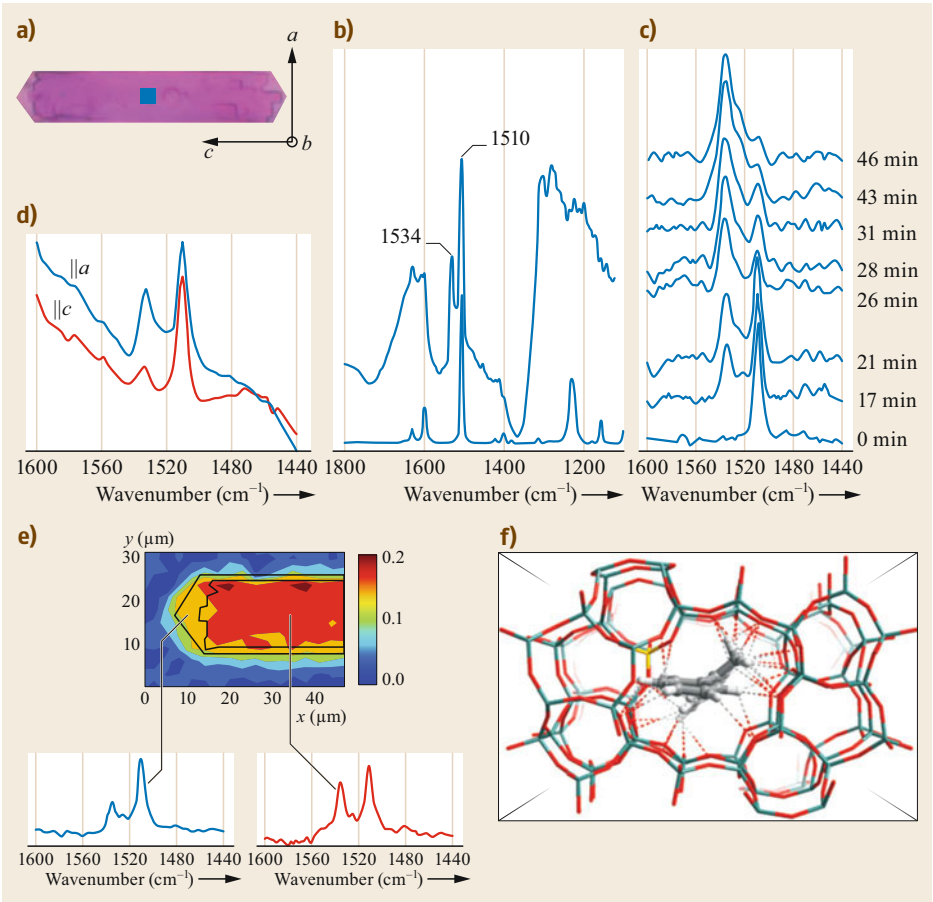

Fig. 26.8 **(a)** Optical image of the H-ZSM-5 crystal; **(b)** IR spectrum of an H-ZSM-5 crystal contacted with 4-fluorostyrene (*top*) compared with that of liquid 4-fluorostyrene (*bottom*); **(c)** 1440–1600 cm^{-1} region of the IR spectra taken in situ during the 4-fluorostyrene oligomerization reaction; **(d)** in situ IR spectra taken with light polarizations parallel and perpendicular to the crystal axis; **(e)** intensity of the IR band at 1534 cm^{-1} mapped over the crystal after reaction and the IR spectra taken from the edge and the body of the crystal; **(f)** optimized geometry of linear conjugated carbocation formed during styrene oligomerization in the straight channel of H-ZSM-5 (Reproduced from [26.34] with permission of The Royal Society of Chemistry)

measured. In this confocal geometry, imaging is accomplished by raster-scanning the sample through the illuminated area to generate spatially resolved spectral maps. Alternatively, recent developments in focal-plane array (FPA) detectors have also enabled wide-field imaging [26.35] that circumvents the need for raster scanning. Specialized optics also exist for grazing-incidence reflection microscopy.

While the constraints imposed by conventional microscope optics and stage control make vacuum conditions challenging, a number of groups have developed cells to enable simultaneous microscopy and in situ modification of surfaces or films. *Stavitski* and *Weckhuysen* [26.34] used in situ synchrotron-based IR spectromicroscopy to study the catalytic conversion of thiophene derivatives over a single microcrystal of the zeolite catalyst H-ZSM-5. Synchrotron-based transmission measurements, in conjunction with coherent anti-Stokes Raman scattering (CARS) measurements, were able to identify the chemical nature of the reactants and products, as seen from the IR spectra taken as a function of reaction time (Fig. 26.8b,c). In addition, polarization analysis has enabled the evaluation of the relative orientation of the product molecules with respect to the channel structure of the crystal (Fig. 26.8f). Imaging studies as a function of time have verified that both the reactants and products are concentrated within the interior of the crystal rather than the edges, demonstrating the potential of imaging studies in determining reactive sites of catalyst particles.

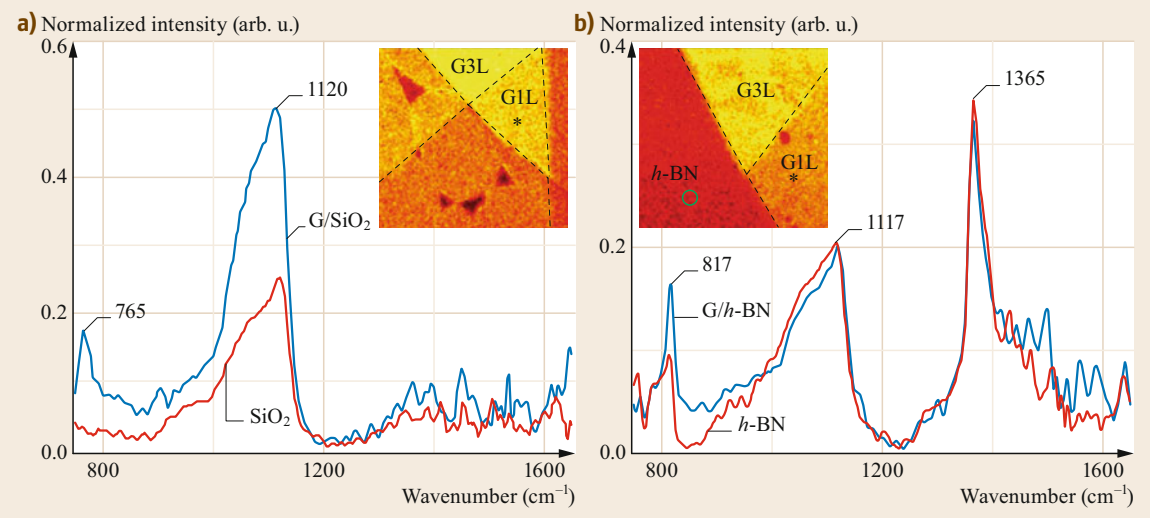

Fig. 26.9 **(a)** Synchrotron infrared nanoscopy (SINS) spectra of clean and graphene-covered SiO_2. **(b)** SINS spectra of BN and graphene-covered BN, showing enhancement of the LO BN phonon mode at 817 cm^{-1} (Reproduced from [26.36] with permission of The Royal Society of Chemistry)

In addition to conventional far-field spectromicroscopy, near-field IR spectromicroscopy coupled with atomic force microscopy AFM has recently been demonstrated [26.37, 38], as shown in Fig. 26.7b. Here, an IR beam is focused onto the apex of an AFM tip; the tip effectively serves as an antenna, and the scattering amplitude is measured. Ultrabroadband spectrally resolved images are obtainable when a synchrotron beam is used as the light source [26.31], and the technique is referred to as scattering-scanning near-field optical microscopy (s-SNOM) or synchrotron infrared nanospectroscopy (SINS). In this geometry, AFM images are collected in parallel with IR spectra; the obtainable spatial resolution is not limited by diffraction but rather by the size of the AFM tip, yielding spatial resolution much higher than that achieved with conventional optics. In one recent demonstration, *Barcelos* et al. [26.36] used SINS to examine graphene/BN heterostructures on SiO_2. Figure 26.9 shows SINS spectra from heterostructures composed of graphene/SiO_2 (Fig. 26.9a) and graphene/h-BN (Fig. 26.9b). The insets show the corresponding s-SNOM images, generated from the total spectral intensity integrated over the entire bandwidth, enabling visualization of the locations of single- and few-layer graphene flakes. The positions from which the spectra are extracted are indicated in the s-SNOM maps in the insets. The spectra in Fig. 26.9a compare the intensity of the SiO_2 surface phonon for a bare SiO_2 surface and a graphene/SiO_2 interface. The increase in the SiO_2 mode originates from coupling of the charge carriers in the graphene sheet to the SiO_2 surface phonon. SINS spectra acquired from graphene/hBN/SiO_2 are compared with those acquired from hBN/SiO_2 in Fig. 26.9b. As before, the SiO_2 surface phonon mode is identified at 1120 cm^{-1}, and modes due to hBN phonons can be observed at 1365 cm^{-1} (TO out-of-plane mode) and 817 cm^{-1} (LO in-plane mode). Interestingly, the spectra from the graphene/hBN heterostructure showed a significant enhancement (70%) of the LO hBN mode at 817 cm^{-1}, and this enhancement was ascribed to a coupling between the plasmons in the graphene sheet and the surface phonons of the hBN to form a hybrid surface plasmon–phonon polariton (SPPP). Additional measurements were performed on a region in which a bubble formed between the graphene sheet and the hBN substrate such that a void of ≈ 40 nm was formed. Interestingly, the SiO_2 and TO hBN modes were no longer detectable, as they were outside the ≈ 25–30 nm interaction volume of the AFM tip; however, the (enhanced) LO hBN mode at 817 cm^{-1} was detected, confirming the long-range nature of the interaction between the LO hBN phonons and the graphene plasmons. Such measurements highlight the unique information that can be obtained when IR spectroscopy can be performed with < 50 nm spatial resolution.

26.2.3 Low-Energy Electronic Excitations at Surfaces

In addition to exciting vibrational modes of adsorbates, IR light can couple to electronic excitations near the Fermi level, providing information on the electronic structure of a surface or film, similarly to how optically

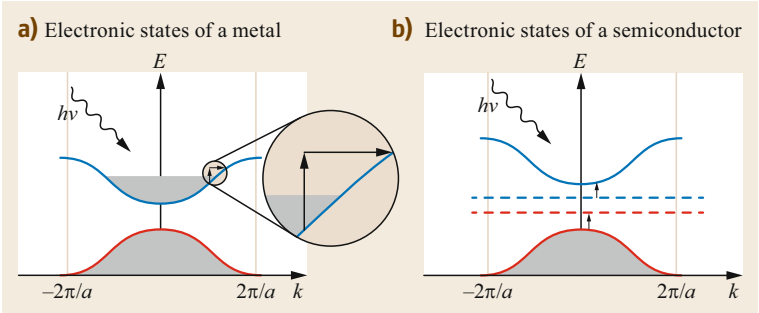

Fig. 26.10a,b IR active electronic excitations in solids. In the intraband absorption process **(a)**, an electron is promoted to a higher energy state within the same band, and momentum is conserved via phonons or other scattering processes. In the interband absorption process **(b)**, a photon promotes an electron to a higher energy state within a different band. Transitions of this type can occur, for example, between the valence and conduction bands of semiconductors, impurity states, and bulk valence and conduction bands, or between surface-state bands and bulk valence and conduction bands (Reprinted from [26.2], with permission from Elsevier)

active transitions are probed in the bulk. Figure 26.10 shows a schematic describing the different types of absorption processes that can take place in metals and semiconductors. In a metal or doped semiconductor, the conduction band is partially filled, and intraband excitations, in which an electron is promoted to a higher energy state within the same band, can be excited. Interband transitions, also commonly referred to as free carrier absorption, give a characteristic Lorentzian line shape centered at zero frequency that decays throughout the mid-IR or visible region at a rate depending on the carrier density, effective mass and relaxation time. An electronic absorption of this type is often well described within the Drude model, in which the frequency-dependent conductivity σ is related to the relaxation time, carrier density, and effective mass as

$$\sigma(\omega) = \frac{Ne^2}{m^*} \frac{1}{\frac{1}{\tau} - \mathrm{i}\omega} , \qquad (26.3)$$

where N is the carrier density, τ the relaxation time, e the electronic charge, m^* the effective mass, and ω the frequency. Within the context of this model, fitting a broadband IR absorption spectrum to a Drude-type functional dependence (26.3) can be used to quantify the conductivity of a surface or thin film; the primary challenge is discriminating between signals arising from the surface and bulk, particularly in the case of metals. One approach is to collect the spectrum of the clean surface of interest, and then quench the associated surface states (e.g., by dosing the surface with oxygen or another species) to prepare a reference surface in which intraband transitions are not present. Alternatively, one can study a differential spectrum to examine the *change* in the conductivity of the surface resulting from a certain process (adsorption, surface reconstruction, etc.). Quantification of the differential spectrum can then proceed through the differential analog of (26.3).

A field of current interest in which optical probes of the conductivity of the surface provide unique insight is the investigation of topological insulators. Stoichiometric crystals of these materials are expected to possess an insulating bulk phase, while the surfaces are characterized by symmetry-protected metallic states. A challenge in optical studies of metallic surface states in topological insulators is that crystal impurities incorporated during growth can give rise to a free carrier response that may be difficult to distinguish from that of the metallic surface states. One such study was conducted by *Post* et al. [26.39], where IR spectroscopic studies were performed on the alloyed topological insulator (TI) $(Bi,Sb)_2Te_3$. In that work, a combination of Fourier transform and time-domain spectroscopic measurements were used to extract the optical conductivity of the sample (Fig. 26.11). Contributions due to phonon modes (6 and 8 meV) were deconvoluted from the Drude peak due to the free carrier response (broadband modulation that increases with decreasing frequency). The oscillator strength of the Drude peak in the experimental conductivity spectra was compared with that obtained from calculations of the free carrier response from a linearly dispersing metallic surface state. The authors found that at sufficiently low temperature (< 100 K), the magnitude of the Drude oscillator strength reached the upper limit predicted by the theoretical model, indicating that the free carrier response was not dominated by bulk carriers. This finding was significant for the field, as it provided a road map for discriminating bulk and surface free carrier absorption to enable future studies of the physics of TIs.

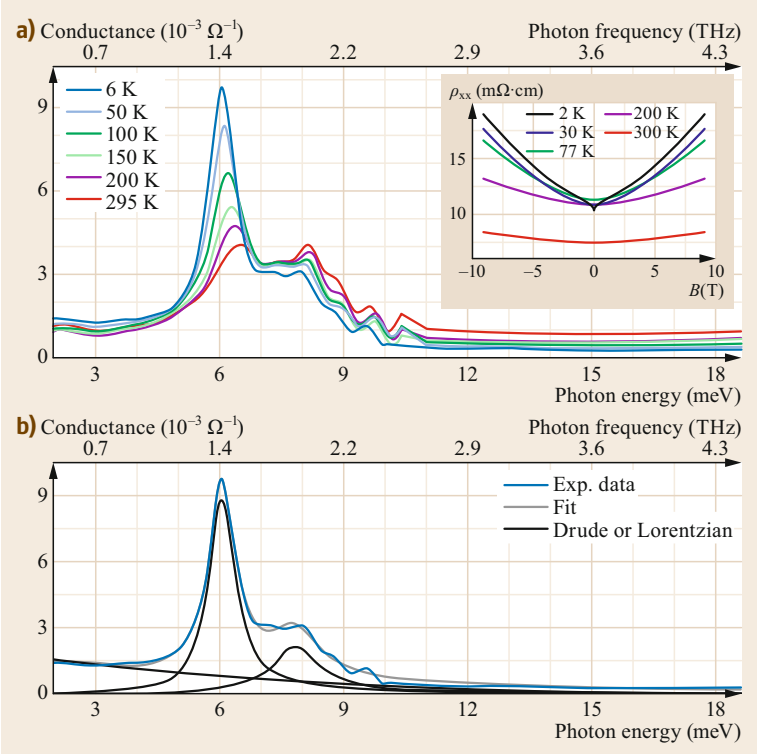

Fig. 26.11 **(a)** Temperature-dependent spectrum of the conductance spectra of $(Bi, Sb)_2Te_3$ as a function of temperature. The bands at 6 and 8 meV are due to phonon resonances, and the broad baseline change is due to the free carrier response. **(b)** Drude–Lorentz model fit of the 6 K experimental conductance (Reprinted with permission from [26.39]. Copyright (2015) by the American Physical Society)

Absorption of IR light can also excite interband excitations from metals and semiconductors, as depicted in Fig. 26.10b. Here, an electron is promoted from a state in a band below the Fermi level to a different band above the Fermi level. These transitions can take place for states in the bulk valence and conduction bands, between surface states and bulk bands, or between donor or acceptor impurity states and bulk or surface bands. The distribution of optically active interband transitions in a material as a function of energy is referred to as the joint density of states (JDOS), the general expression of which follows the form

$$\rho_{cv}(\hbar\omega) = \frac{2}{8\pi^3}\iint \frac{dS}{|\nabla_k (E_c - E_v)|_{E_c - E_v = \hbar\omega}} , \quad (26.4)$$

where the integral is carried out over the Fermi surface, and E_c and E_v are the bottom and top of the conduction and valence bands, respectively. The points at which the denominator vanishes, known as critical points, provide distinct optical markers in the JDOS that provide information on the curvature of the bands giving rise to the transition. The shape of the singularities in the JDOS can follow one of several different functional forms (four possibilities exist for a 3-D (three-dimensional) system versus three for a 2-D system) depending on the dispersion of the bands of interest, and therefore be used to infer details on the electronic band structure of the system through a process known as critical point analysis. As for the case of intraband transitions, the challenge is discriminating the surface versus bulk signals; similar approaches can be used for those described above, i.e., quenching the surface state or examining the overall change in absorption.

IR spectroscopic measurements of interband transitions in graphene and its multilayer analogs have yielded much insight into its electronic structure. In one such example, IR spectroscopy was used to measure the band gap of bilayer graphene as a function of electrical gating. In work by *Zhang* et al. [26.40], field-effect transistor devices employing graphene as the semiconducting element were fabricated and examined as a function of gate voltage using synchrotron-based transmission measurements (Fig. 26.12). In comparing the measured absorption spectra with predictions based on the tight-binding model, they were able to demonstrate tunability of the band gap of bilayer graphene by varying the voltage of the top and bottom gate electrodes.

An important consideration arises when studying the surface electronic structure of metals using the reflection-absorption geometry. Calculations of the electric field of a grazing-incidence IR beam reflected from a metal surface have shown that, immediately

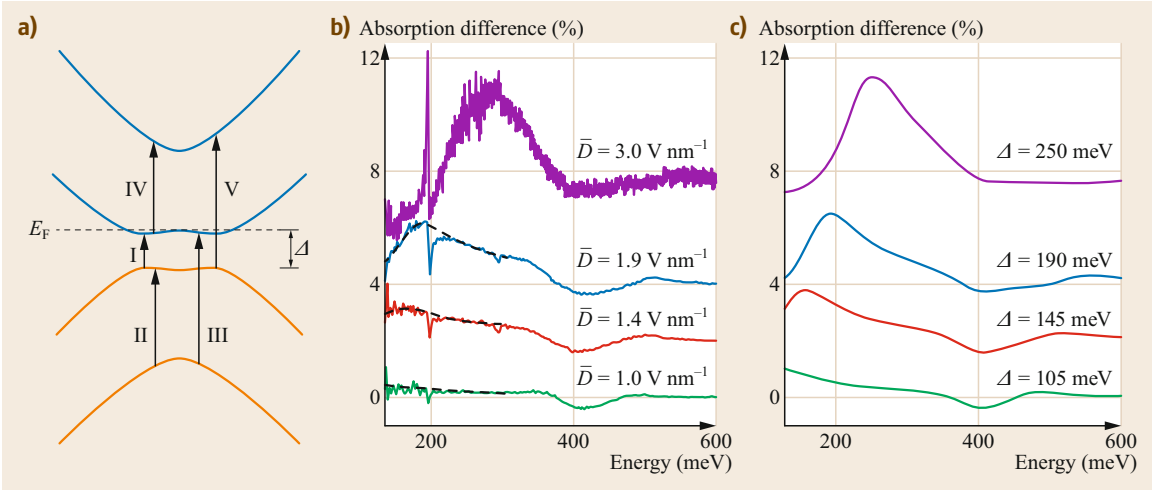

Fig. 26.12 **(a)** Schematic of possible interband transitions in electrically gated bilayer graphene. **(b)** Experimental IR spectra of a top- and bottom-gated bilayer graphene flake as a function of the electric displacement field. **(c)** Tight-binding predictions of the absorption spectra of bilayer graphene under the displacement fields corresponding to the experimental data in **(b)** (Reprinted by permission from [26.40], © Nature 2009)

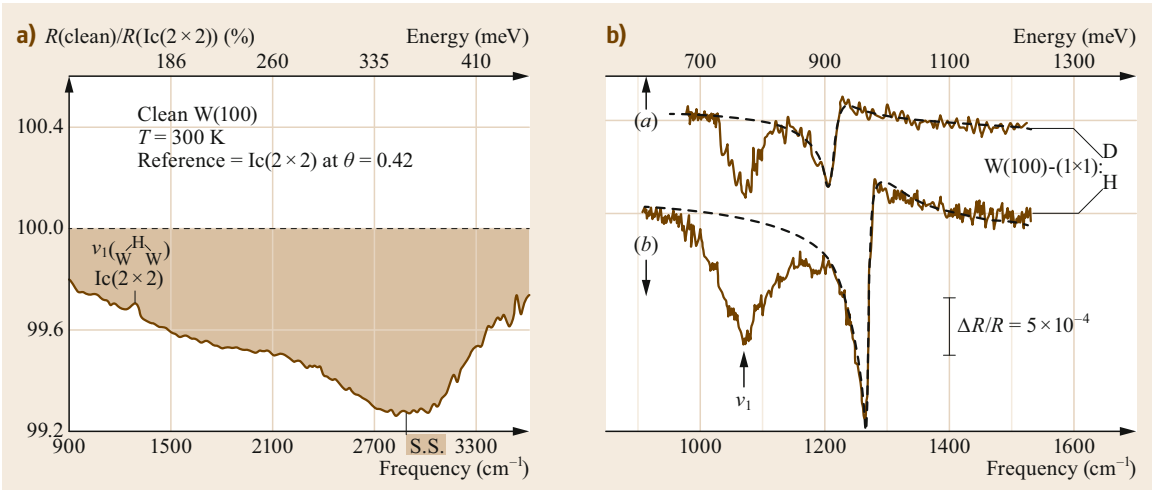

Fig. 26.13 **(a)** Surface-state absorption from clean W(100) using IRRAS. Here, the reference measurement is the H-terminated Ic(2 × 2) reconstruction of the surface, in which the surface states of interest are quenched by the H-passivation. **(b)** IRRAS spectra of H/W(100) showing a Fano line shape due to parallel adsorbate frustrated modes (Reprinted with permission from [26.41, 42], Copyright (1988, 1985) by the American Physical Society)

above the surface, the tangential (s-polarized) component of the field is suppressed due to the phase change upon reflection (or alternatively the boundary condition requiring the s-component to be continuous), while the normal component of the p-polarized radiation is enhanced by addition of the incident and reflected components. In contrast, *below* the surface, the radiation is strongly refracted, resulting in a much stronger tangential component than normal component [26.1]. An example of such a measurement is shown in Fig. 26.13, where the electronic absorption of clean, unreconstructed W(100) is shown to give rise to a strong broadband feature throughout the mid-IR [26.41]. In light of the geometric considerations discussed above, the origin of this feature was associated with d-band surface states with x^2-y^2 symmetry.

In certain cases, the dominance of the excitation of transitions parallel to the surface (below the surface) leads to nonadiabatic coupling of these electronic levels to adsorbate vibrations parallel to the surface (above the

surface) [26.43–45], detected as a Fano-shaped modulation of the electronic absorption. Persson has argued the generality of the phenomena, demonstrating that parallel frustrated adsorbate translations or vibrations with zero dynamical dipole moment parallel to the surface should always manifest strong anti-absorption resonances or Fano line shapes [26.43]; however, later work established selection rules determined by the parity of the vibrational and electronic states involved, as well as the magnitude of the density of states at the Fermi level, that determine whether such vibrations are detectable [26.45, 46]. Experimentally, the first observation of detection of a formally dipole-forbidden mode was reported by *Chabal* [26.41] for IRRAS measurements of H on W(100) (Fig. 26.13b). Here, the symmetric stretch is observed as a normal absorption band (1070 cm^{-1}), while an additional mode is detected at 1270 cm^{-1} with a highly asymmetric line shape. This mode was originally assigned to the overtone of the W−H wag mode, but later suggested to be associated with the W−H asymmetric stretch on the basis of the symmetry of the surface electronic states measured by photoemission and believed to be involved in the coupling; these states have an even symmetry with respect to the (001) mirror plane, suggesting that the vibrational mode should also have even parity such as the asymmetric stretch. Similar anti-absorption resonances originating from parallel adsorbate modes have since been observed for H/Mo(100) [26.41], CO/Cu(100), and H/Cu(111) [26.47].

26.3 Low-Energy Ion Scattering

Low-energy ion scattering (LEIS), also known as ion scattering spectroscopy (ISS), is a highly surface-sensitive experimental method that enables the determination of the elemental composition of the outermost atomic layer of a solid, and can provide varying degrees of insight into surface atomic structure [26.48–51]. In this technique, a beam of noble gas atoms is ionized and accelerated to an energy within the range 0.1−10 keV before being directed onto a sample surface. A fraction of the incident ions undergo collisions with the surface atoms and are scattered without being neutralized (possibly through reionization processes). The scattered ions are detected after passing through an energy analyzer and, based on their final kinetic energy, the masses of the atoms by which they scatter are determined. In this fashion, the different elements present at the surface of a material are quantified. The surface selectivity of LEIS signals originates from the low energy of the incident ions and the very high probability that an incident ion will become neutralized upon interaction with a solid surface. The concepts of shadowing and blocking can be used to further understand the preferential selectivity of surface signals in LEIS versus ion scattering measurements performed at higher energies (e.g., MEIS, RBS). Shadowing arises from the scattering of an incident projectile, which modifies its trajectory such that atoms situated within a certain volume behind the target atom cannot act as scattering centers and are therefore invisible to the incident beam. The volume shadowed by the target atom is referred to as the shadow cone. Similarly, an ion scattered by a target atom and subsequently scattered again by another target atom establishes an additional shadowed region behind the second target atom, known as the blocking cone. As illustrated in Fig. 26.14, the relative sizes of the shadow cones (relative to a typical inorganic crystal structure) depend on the ion incident energy. At high energies (MeV), as is the case of RBS, the shadow cones are narrow. In contrast, at energies typical of LEIS, the shadow cones are of the order of interatomic spacings, since the low energy of the projectile will cause its trajectory to deviate strongly around a relatively weak interaction potential. The larger shadow cone in the case of LEIS means that the probability for an incident projectile to

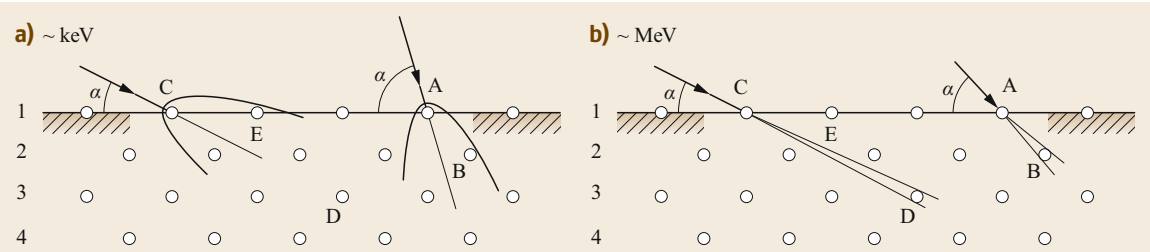

Fig. 26.14a,b Schematic diagrams of the shadow cone relative to interatomic dimensions in the case of LEIS **(a)** and RBS **(b)** (Reprinted from [26.52], with permission from Elsevier)

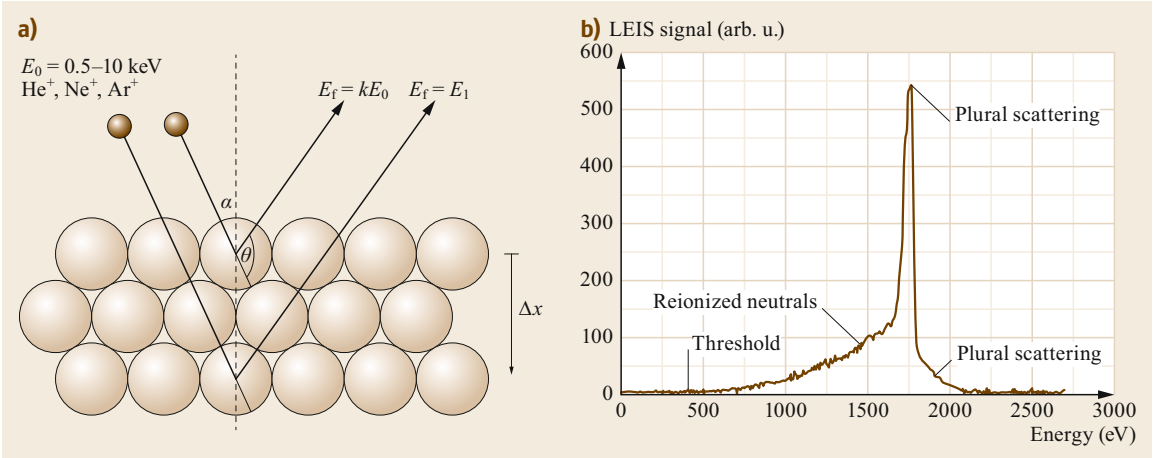

Fig. 26.15 **(a)** Experimental scheme for LEIS measurements; noble gas ions incident upon a surface at an angle α from the surface normal are scattered into an angle θ with energy kE_0. **(b)** Features in a typical LEIS spectrum illustrated for 3 keV He^+ scattered from polycrystalline Al (Reprinted from [26.50], with permission from Elsevier)

penetrate and exit the surface without scattering and/or becoming neutralized is negligibly small, and therefore the binary scattering peaks in LEIS spectra are generally representative of elements present at the outermost layer of the surface.

Quantification of the relative amounts of the respective elements at the surface may be carried out by evaluating the total ion yield associated with each element and scaled by a calibration factor determined by measurement of samples with known surface concentrations. This poses the most challenging problem, for a number of reasons. First, calibration can be challenging because of the need to obtain well-defined standards with known surface concentrations. This is often done using a pure crystal or thin film for the reference measurement; however, for many elements (such as N, O, Cl, F, and many others) there exists no pure elemental material that can be used for this purpose. Second, there exist certain cases in which the ion yield is dependent upon the coverage or density of the species in question, and such cases are referred to as suffering from *matrix effects*.

In addition to providing information on the composition of the outermost atomic layer, analysis of experimental LEIS spectra also provide a static, nondestructive depth profile of the first 5−10 nm within the surface of a sample [26.50, 53]. Quantification of depths and concentrations of relevant species is accomplished through the use of simulations that statistically treat the interaction between an atom beam of interest with a target sample [26.54]. Lastly, information from LEIS has the potential to give valuable insight into surface structure and bonding configurations, and measurements performed under certain conditions enable surface crystallography with elemental specificity [26.55]. In the following sections, we review the fundamental principles of LEIS measurements, with emphasis on recent developments of the technique and illuminating examples that highlight the type of information that can be extracted.

26.3.1 Identification of Surface Elements and Concentrations from Binary Collisions

In a typical LEIS measurement, a monochromated beam of ions (typically noble gases; He, Ne, and/or Ar) is ionized, accelerated and incident upon a sample surface at an angle α, as shown in Fig. 26.15. Some fraction of the incident ions undergo a single elastic scattering process without being neutralized, and subsequently scatter at an angle θ with respect to the angle of incidence. The ions scattered within some angular range are then collected into an energy analyzer and subsequently detected to produce a spectrum showing the number of ions detected as a function of energy. Within the binary collision approximation (BCA), conservation of energy and momentum gives for the final energy E_f of an ion of mass m_1 scattered from an atom of mass m_2 through an angle θ with respect to the surface normal [26.48–50]

$$E_f = \left(\frac{\cos\theta \pm \sqrt{(m_2/m_1)^2 - \sin^2\theta}}{1 + \frac{m_2}{m_1}} \right)^2 E_0 \,. \quad (26.5)$$

The final energy of the ions in an LEIS measurement is a direct function of the mass of the scattering atom, and can therefore be used to deduce the elemental composition of the surface atoms. There are, however,

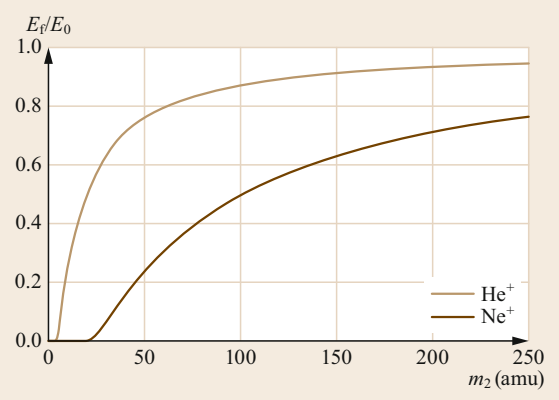

Fig. 26.16 Energy lost during binary collisions for He^+ and Ne^+ projectiles as a function of the mass of the scattering atoms based on (26.5). Here, a scattering angle of 145° is assumed

combinations of masses and angles for which backscattering does not occur. For instance, elements lighter than that of the probing ions cannot be detected (e.g., H using He^+); similarly, first-row elements cannot be detected by backscattering when Ne^+ is used as the projectile. In practice, the choice of probe ion is made on the basis of the elements being targeted. While Ne^+ cannot detect first-row elements, He^+ may not be sufficient to resolve heavy elements that are close in mass. Figure 26.16 shows the dependence of the final projectile energy as a function of the mass of scattering atoms for He^+ and Ne^+ projectiles based on the solutions of (26.5), assuming a scattering angle of 145°. Clearly, the values of E_f/E_o for heavy masses (e.g., > 50 amu) are very similar when He^+ is used as the projectile and therefore may not be sufficient to resolve elements of similar mass. In contrast, the values of E_f vary much more rapidly in the 50−100 amu region when Ne^+ is used as the projectile. For resolving even heavier elements, Ar^+ or Kr^+ can be used.

The ions scattered from binary collisions generally give the most prominent features in an LEIS spectrum and are used for evaluation of surface concentrations, but ions that undergo more complicated scattering processes are also detected. In addition to ions that undergo single scattering, many of the incident ions will penetrate below the surface and suffer multiple inelastic events. Of these neutralized ions, some will undergo trajectories that bring them back to the surface, and a fraction will become reionized at the surface such that they can be detected in a measured spectrum. As these species undergo multiple collisions as well as potential inelastic scattering events, they will ultimately be detected with final energies lower than that of the binary collision peak. The reionized neutrals can give rise to various structures in an LEIS spectrum ranging from tails to distinct peaks depending on the distribution of the scattering elements. Additionally, an incident ion can also scatter elastically from two or more surface atoms without becoming neutralized. Such multiple scattering events can be described by applying (26.5) twice, with the initial energy of the second collision treated as the final energy of the first collision. In such events, the final energy of the scattered ions is actually greater than that of an ion scattered through the same angle with a single binary collision; consequently, features due to plural scattering are observed at energies greater than that of the binary collision peak. Figure 26.15b shows an LEIS spectrum for 3 keV He^+ ions scattered from a polycrystalline Al target, where these representative scenarios are illustrated. A clear sharp peak from the He^+–Al binary collision is observed with a low-energy tail due to ions that become neutralized and are ultimately reionized after undergoing multiple scattering events below the surface. On the high-energy side of the binary collision peak, a shoulder due to elastic plural scattering is observed.

While the features due to plural scattering and reionized neutrals can yield valuable information, as will be discussed below, the binary collision peak (also referred to as the *surface peak*) is generally the most useful and widely used feature in the spectrum for quantification of surface species. The yield of ions scattered from a particular element is directly related to the surface concentration of the element in question

$$S_i = \frac{I_p}{e} t \xi R \eta_i N_i \tag{26.6}$$

Here, S_i is the number of ions detected, I_p the primary beam current, e the electronic charge, t the measurement time, R a correction factor determined by surface roughness (equal to 1 for flat surfaces), η_i and N_i the sensitivity factor and surface concentration, respectively, for the element in question, and ξ an instrumental factor into which the characteristics of the analyzer and detector are absorbed. The elemental sensitivity factor is determined by the differential scattering cross section $d\sigma_i/d\Omega$ and the fraction incident ions that do not become neutralized upon interaction with the surface, known as the ion fraction P_i^+

$$\eta_i = P_i^+ \frac{d\sigma_i}{d\Omega} \tag{26.7}$$

In general, the elemental sensitivity factors are not necessarily known, and ξ and η_i are determined through calibration measurements of appropriate standards. If the η_i is independent of the number and type of surrounding atoms, i.e., absent matrix effects, the calibration can be performed on any sample in which

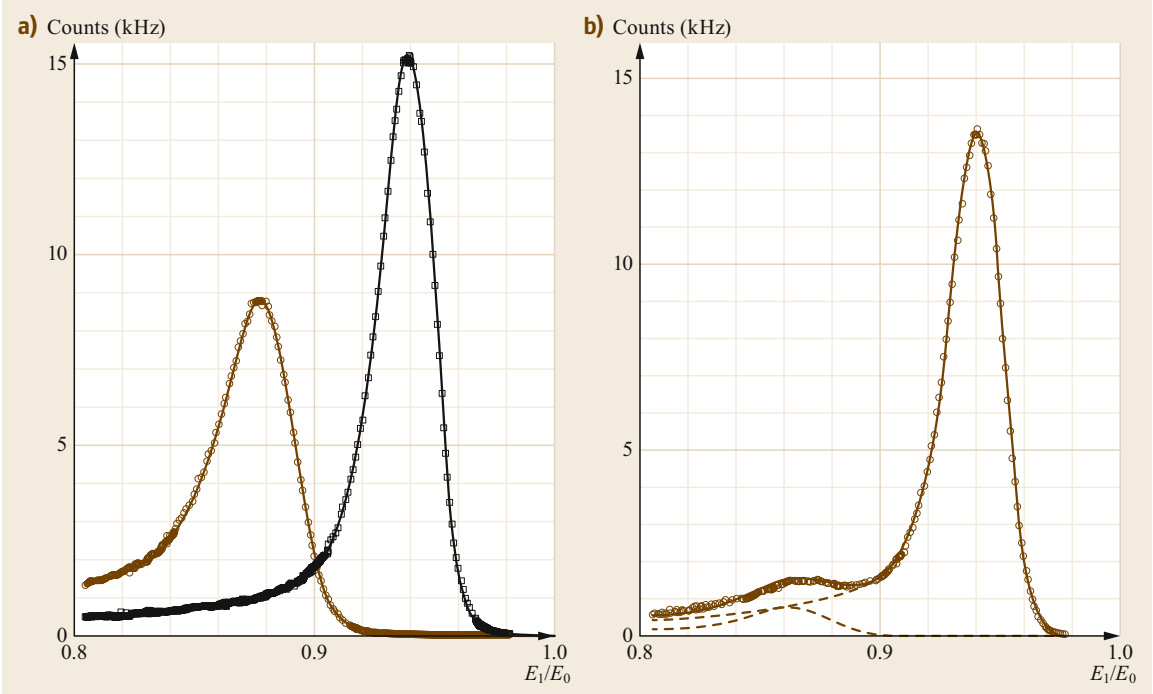

Fig. 26.17a,b 2 keV He^+ LEIS spectra of pure Pt and Ru standards **(a)** and an annealed PtRu alloy **(b)** (Reprinted from [26.56], with permission from Elsevier)

the atomic surface concentration is known. One such application in which this approach is readily used is quantification of the elemental composition of alloyed metals used in catalysts, as this knowledge provides insight into the active sites in various catalytic processes [26.57–61]. For example, *Gasteiger* et al. [26.56] used LEIS to determine the surface composition of a series of PtRu alloys following sputtering or annealing. In their work, pure Pt and Ru reference samples were prepared and measured to evaluate the ion yield of the respective elements (Fig. 26.17a). With this calibration, it was possible to determine the surface composition of the alloy materials from measurements such as that in Fig. 26.17b. In doing so, they were able to determine that the surface concentration was predominantly bulk-terminated in the case of surfaces cleaned only by Ar^+ sputtering, whereas a differential enrichment of surface Pt was observed for surfaces annealed to 800 °C.

In the case of the a surface partially covered by an adsorbate layer, the signal due to the substrate atoms is reduced due to blocking by the adlayer [26.48, 49]. Consequently, the form for the signal of the substrate atoms (26.6) is modified to incorporate blocking by the adsorbates as

$$S_s = \frac{I_p}{e} t\xi R\eta_i \left(N_S - \alpha N_{ads}\right), \tag{26.8}$$

where N_s is the density of surface substrate atoms and N_{ads} that of adsorbate atoms; α is a factor introduced to describe how many substrate atoms are blocked by a single adsorbate, and is determined by the adsorbate geometry and scattering cross-section, which determine the shape of the adsorbate's shadow cone. At high coverage, the shadow cones from neighboring adsorbates merge and the shadowing coefficient decreases. The latter generally has a unitary order of magnitude, and if known can be used to determine the coverage of an adsorbate-covered surface. Similarly, this information can be used to determine various aspects of the adsorbate geometry, discussed in more detail below.

26.3.2 Charge Transfer Processes

As discussed above, the fate of an ion in the 0.1–10 keV energy range incident upon a surface can follow one of several paths. While ions that undergo binary collisions without being neutralized provide the most straightforward evaluation of the surface composition, understanding neutralization and reionization can give insight into the sensitivity of the measurement toward different materials and structures. The processes underlying charge exchange between a surface and a fast projectile are complex, and a comprehensive discussion is available elsewhere [26.48, 50] and is beyond the scope

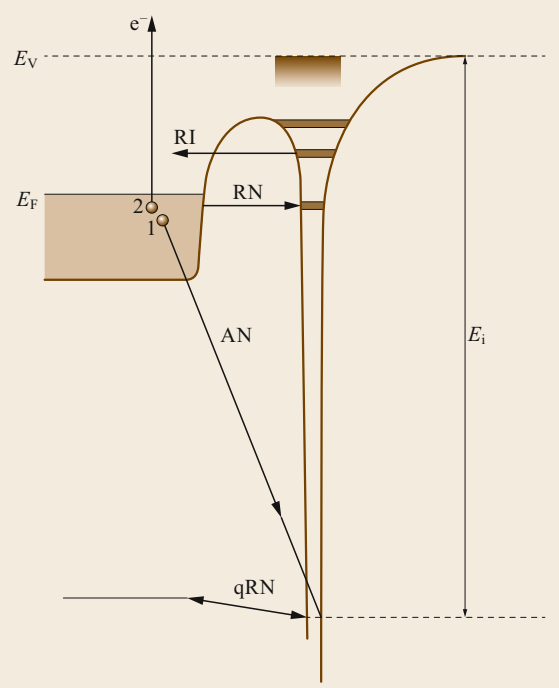

Fig. 26.18 Schematic energy diagram representing the processes of RN, RI, AN, and qRN in terms of the projectile and target levels (Reprinted from [26.48], with permission from Elsevier)

of this chapter. Here we present a qualitative review of the basic principles of neutralization and reionization that are of significance for LEIS measurements. Figure 26.18 shows a scheme depicting the principle charge exchange processes that give rise to neutralization and reionization of ions in the LEIS regime. When a fast, typically positively charged projectile approaches a surface, image charges induced in the solid lead to a broadening and can decrease the binding energy of the electronic states of the projectile due to repulsion between the electrons of the projectile and surface, leading to an increase in the energy of the highest electronic levels of the projectile relative to vacuum [26.62]. As the distance between the surface and projectile becomes increasingly small, the states of the projectile can begin to interact with those of the surface. In the process of resonant neutralization (RN), electrons in the conduction band of the crystal are resonant with unoccupied states of the projectile and proceed to tunnel into the unoccupied states, as depicted in Fig. 26.18. In the reverse process (*resonance ionization*, RI), electrons from the highest occupied orbital of a neutral projectile atom tunnel into the conduction band of the crystal, and the projectile becomes reionized. In *quasi*-resonant neutralization (qRN), electrons in a core-level of the surface may be nearly resonant with the ground state of the projectile, and tunneling between the levels can lead to neutralization. Such processes are heavily dependent on the energy of the projectile atom, since the probability for tunneling oscillates as a function of the time integral of the potential energy difference between the incoming (ionized) and outgoing (neutralized) states. This effect leads to strong oscillations in the ion fraction as a function of the incident projectile energy that are also dependent on the matrix, and such oscillations have been observed in systems such as He^+ scattering from Pb [26.63] and Ne^+ scattering from Au [26.64]. In Auger neutralization (AN), an electron from the substrate neutralizes the projectile, either by directly decaying to the ground state or through an intermediate metastable excited state, in conjunction with excitation of another substrate electron or plasmon. Alternatively, a substrate electron can fill a core-hole of the projectile, leading to emission of an Auger electron originating from an excited state of the projectile in a process known as indirect Auger de-excitation. Lastly, neutralization of an incident ion or reionization of a neutralized projectile can occur via collision-induced processes [26.65]. Here, a neutralized projectile atom becomes reionized when it approaches sufficiently close to a target atom as to promote a core-level state (e.g., the He 1s) to an energy that, at a certain critical distance from the target atom, is equal in energy to an excited (ionized) state. Consequently, an electron can be transferred to the target, and the projectile scatters in an ionized final state. Similarly, the reverse process can occur to yield collision-induced neutralization. Importantly, reionization provides a pathway of detection for which ions that become neutralized penetrate the surface and, through multiple scattering events, return to the surface.

The cycle of neutralization and reionization comes with an energy cost. It has been reported that for He projectiles in general, the complete neutralization and reionization process costs a total of $20+\varepsilon$ eV to transfer an electron to a He level at an energy ε above the Fermi level of the substrate. Thus, ions detected from reionization processes are always detected at energies below that of the binary collision peak. Take for example the hydrogen-terminated Si(111) surface. Figure 26.19 shows 3 keV He^+ spectra taken from Si(111)−H surfaces prepared by HF and NH_4F etching as-prepared and after sputtering with Ar^+ to remove the adsorbed H and yield a clean Si(111) surface. While in the case of the clean surface a clear, intense Si binary collision peak is observed, the H-terminated surface shows only a weak peak due to blocking of the Si atoms by atop H. In addition, the Si peak in this case appears shifted by ≈ 20 eV to lower energy. The physical interpreta-

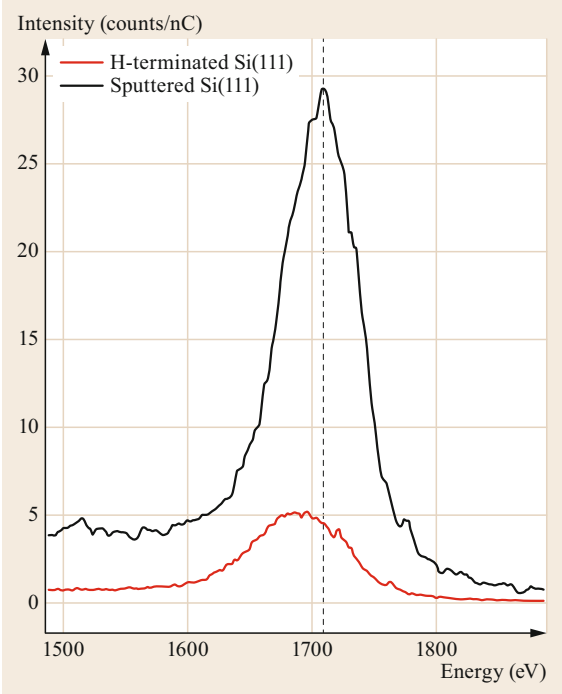

Fig. 26.19 3 keV He^+ LEIS spectra of hydrogen-terminated Si(111) before (*red*) and after (*black*) Ar^+ sputtering, demonstrating a ≈ 20 eV shift of the Si peak

tion for this effect is that the incident He^+ ions have undergone multiple scattering processes, initially with adsorbed H, that allowed them to penetrate the surface and scatter from Si atoms before being reionized. This neutralization and reionization cycle occurs at an energy cost close to 20 eV, leading to a lower apparent energy at which the Si atoms are detected.

26.3.3 Analysis of Subsurface Signals

Projectile ions that penetrate the surface and undergo multiple scattering trajectories within the bulk suffer additional energy losses as a result of various elastic and inelastic processes. Of the fraction of these particles that scatter back to the surface and are reionized, the total energy lost will be greater than the minimum required for the neutralization and charging cycles. With the appropriate a priori knowledge of the system, these signals can provide important information on the identity, location, and density of subsurface atoms. For example, Fig. 26.20a shows an 8 keV He^+ LEIS spectra of a multilayer system comprising a 1.2 nm HfO_2 film with a 2 nm Al_2O_3 cap. Here, the surface peaks for Al and O are at their expected positions for a binary collision based on (26.5), but the Hf peak is shifted to lower energy than that expected for surface Hf. In general, for the subsurface signals, the redshift in the peak position correlates with the depth of the scattering elements, while the width of the peak is related to their depth distribution or thickness. *Brüner* et al. [26.54] developed a method for quantification of these subsurface signals using a variation of the transport of ions in matter (TRIM) code [26.66] developed for Rutherford backscattering (RBS) data, known as TRBS. The approach involves calculating the scattering trajectory of a neutral projectile of a given energy for a particular model structure. The charge state of the projectiles is taken into account by assuming that the measured spectra are the product of the energy distribution of backscattered neutral particles with the ion fraction of the surface. In general, the material-dependent parameters needed for the calculations are not necessarily known, in particular the electronic stopping correction factor, which determines the projectile energy lost through nuclear and electronic processes within the material, and the reionization function, which determines the probability that an ion of a particular energy will be reionized at the surface. Fortunately, these parameters can be evaluated through the measurement of the appropriate standards in conjunction with TRBS modeling. The electronic stopping factor for a given material can be determined by comparing measurements of thin film structures of thickness known from other methods with TRBS simulations to determine the value that accurately reproduces the characteristics of the experiment. The probability for reionization at the surface or ion fraction is a function that is acutely dependent on the composition of the surface, and therefore must be determined specifically for the surface of interest. In practice, measurements of standards are performed over a reasonably large energy range such that the functional dependence of the ion fraction can be accurately determined and is unobscured by low-energy features due to secondary sputtered ions. Once measured, the surface peaks are subtracted off, and the measured spectrum is assumed to be the product of the ion fraction with the spectrum of backscattered neutrals; therefore, the ion fraction is determined by dividing the experimental spectrum by the simulated spectrum. Once these parameters have been determined, simulated LEIS spectra can be calculated for arbitrary structures for comparison with experiment. Brüner and coworkers found that for the case of the Al_2O_3/HfO_2 system used for the initial study, the approach described above was largely successful for determining the thicknesses of the respective components of the heterostructures (Table 26.1) despite some minor discrepancies in one sample.

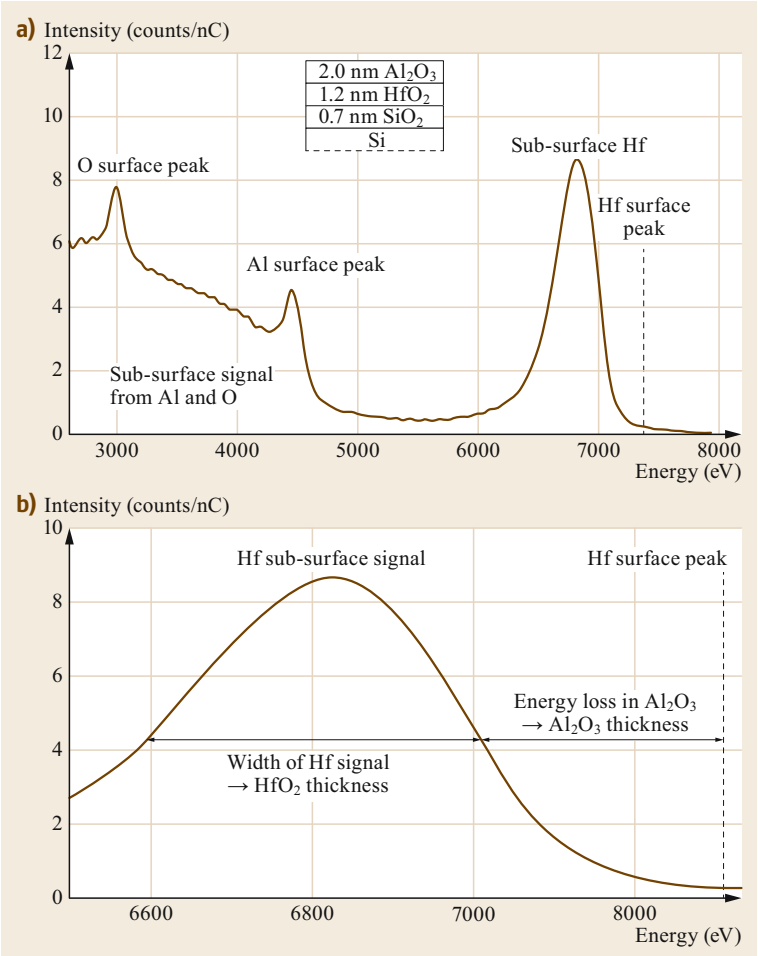

Fig. 26.20a,b 8 keV He^+ LEIS spectra of a 1.2 HfO_2 film with a 2 nm Al_2O_3 cap supported on Si with a native oxide. **(a)** Shows that Al and O are observed at the positions expected for surface peaks, but the Hf signal is shifted to lower energy than that expected for a surface peak. **(b)** Shows how the subsurface Hf signal relates to information about the multilayer structure of the sample (Reprinted from [26.54], with the permission of AIP Publishing)

Table 26.1 Nominal sample structure determined through x-ray reflectivity (XRR) and LEIS+TRBS simulations in work by *Brüner* et al. (Reprinted by permission from [26.54], © Am. Inst. Phys. Publ. 2014)

Sample	XRR measurements (nm)		LEIS and TRBS simulation (nm)	
	Al_2O_3 cap	HfO_2 layer	Al_2O_3 cap	HfO_2 layer
1	2.0	1.2	2.0	1.2
2	1.0	1.8	1.8	1.8
3	2.8	0.7	2.8	0.5

26.3.4 Structural Analysis

LEIS measurements, in addition to providing the complete elemental composition of a surface, can yield valuable information on surface atomic structure. Depending on the measurement configuration, projectile characteristics, and numerical analysis, different types of information and degrees of detail on the structure of surfaces can be obtained. Such structural information can range from qualitative orientation of adsorbates and surface terminations to local symmetry and identity of nearest neighbor atoms, and even crystallographic studies yielding the complete structure of the surface unit cell.

The first and most straightforward approach to characterization of the surface atomic structure employs the principle of shadowing to make qualitative inferences regarding the bonding position of different elements on the surface. With some a priori knowledge of the surface structure, the idea that atoms that lie within the shadow cone of another atom will be invisible in single-scattering peaks can be used to qualitatively deduce the locations of the atoms of interest. Some of the earliest demonstrations of the strength of LEIS were in evaluating the surface terminations of non-centrosymmetric crystals such as CdS and ZnS [26.67]. Early studies on the opposite ⟨111⟩ polar faces of ZnS and the ⟨0001⟩ faces of CdS detailed the termination of these crys-

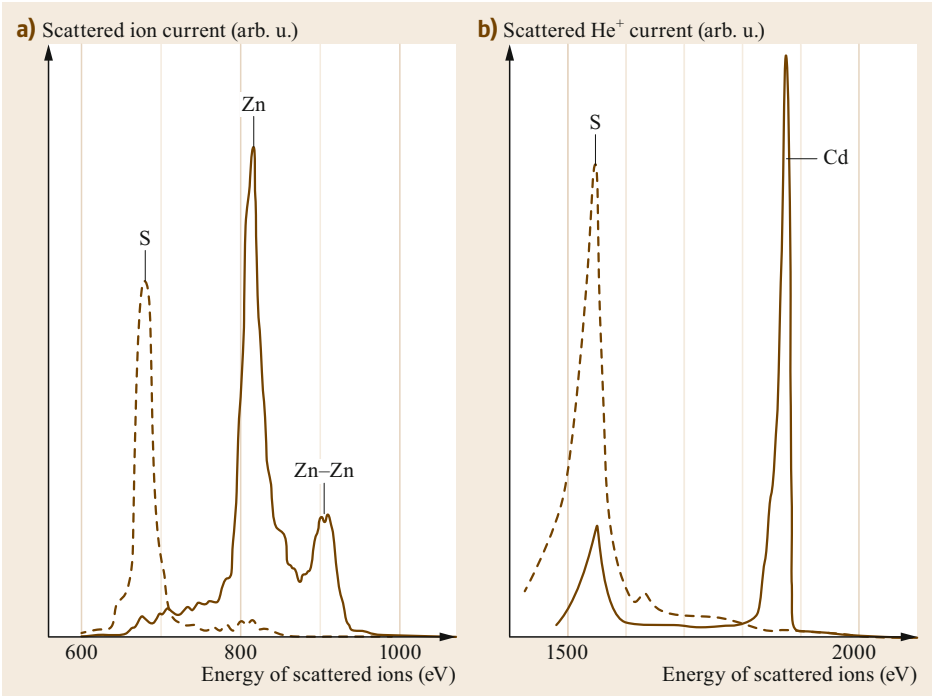

Fig. 26.21a,b He^+ LEIS spectra from opposite polar faces of ZnS **(a)** and CdS **(b)** (Reprinted from [26.67], with permission from Elsevier)

tals. In the case of ZnS, 1 keV Ne^+ spectra (Fig. 26.21) showed terminations in which only Zn and S, respectively, were detected for the opposite faces, suggesting a bulk termination as a reasonable approximation of the surface structure. Similar results were obtained for the opposite faces of CdS.

The approach in which the shadowing of atoms is employed to deduce their relative location can be further used to characterize adsorbate structures, as was done for an early study of CO adsorption on polycrystalline Ni [26.68]. Here, 1.8 keV He^+ LEIS spectra were taken from Ni foils dosed with CO, and an O peak of area approximately five times that of C was observed. The author noted that, with the similar masses and therefore scattering cross sections of O and C, a ratio of approximately 1 : 1 would be expected if the C and O atoms were randomly distributed on the surface. The observation of such a larger magnitude of the O peak was taken to mean that the CO molecules bonded perpendicular to the surface via the C atom, leading to increased visibility of O relative to C. This conclusion was in agreement with structural models derived from previous IR [26.69] and LEED [26.70] studies on similar systems. While the interpretation here is straightforward and could have been derived by complementary techniques alone, other cases in which the symmetry of the surface is evaluated by LEED are often less straightforward, as a given LEED pattern could originate from a number of potential structures. One of many such instances in which LEIS data have aided in structure determination is in the O/Ag(110). *Heiland* et al. [26.71] used LEIS in conjunction with LEED to determine the structure of the (2×1) reconstruction of the Ag(110) surface formed after dosing with 7000 L oxygen. In their work, they measured the ion yield for 500 eV He^+ ions scattered along the [100] and [110] directions (parallel and perpendicular to the atomic rows of the (110) surface) and observed a very strong variation in the O signal along these different directions (Fig. 26.22a). On the basis of this variation, they were able to discriminate between three possible structural models that could give rise to a (2×1) LEED pattern (Fig. 26.22b–d). From inspection, the structure depicted in Fig. 26.22b would not be expected to give strong azimuthal shadowing dependence, since the O is situated in the outermost plane and its nearest neighbors along the [100] direction are spaced comparatively far apart. Similarly, it was argued that only a moderate shadowing effect could be expected for the structure in Fig. 26.22c. In contrast, the structure depicted in Fig. 26.22d would be expected to give a strong shadowing effect for scattering perpendicular to the atomic rows due to the close proximity of the bridge site to the Ag nearest neighbors, which are situated at an elevated position relative to the O atoms. Arguments of this nature can be used to differentiate between different structural models, and the approach is most favorable in the case of well-ordered crystalline substrates.

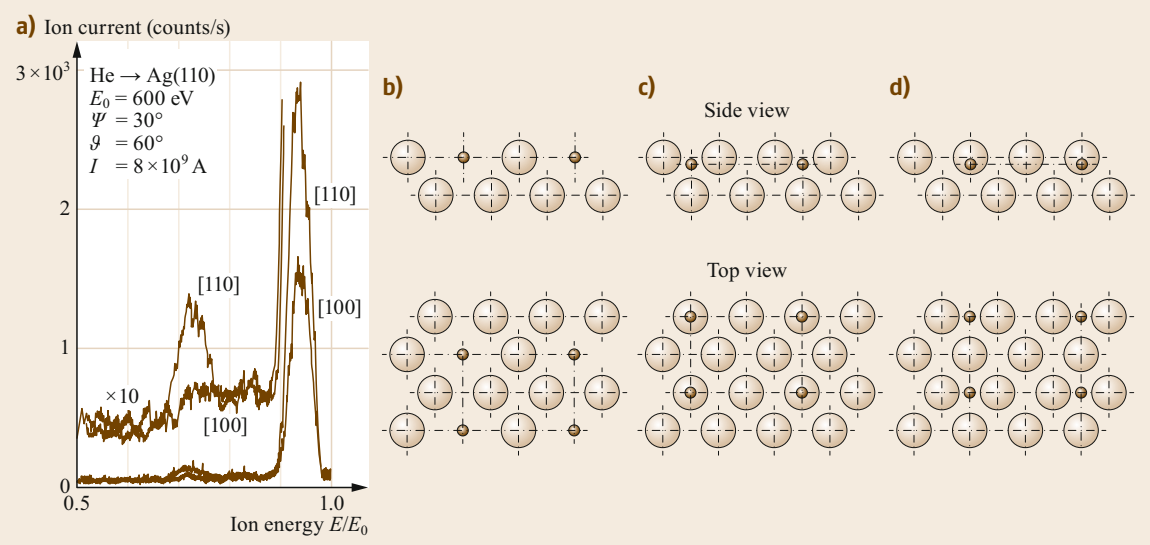

Fig. 26.22 **(a)** Experimental He^+ LEIS spectra of O-covered Ag(110) taken along different crystallographic orientations. **(b–d)** Potential structural models for O on Ag(110) that could give rise to a (2×1) LEED pattern (Reprinted from [26.71], with permission from Elsevier)

A second approach to atomic structure characterization using LEIS employs the principles of multiple scattering to infer information about the relative positions and identities of nearest neighbor atoms. In addition to undergoing binary collisions, an incident ion can undergo multiple collisions involving smaller scattering angles that add up to the total scattering angle. The final projectile energy in such a process is greater than that which would be measured for a single binary collision with the same total scattering angle, which can be seen by applying (26.5) twice. While this effect can be undesirable in the identification or quantification of surface elements, it can yield valuable insight into local structural environments. The final energy of the projectile after two or more collisions is dependent on the masses of all target atoms involved, and multiple scattering peaks can be used to infer the identity and potentially the location of nearest neighbor atoms. Some early theoretical work was performed to correlate multiple scattering features with underlying structures by employing simple models of the surface, such as simple atom chains [26.72], and this approach was largely successful for qualitatively reproducing many of the physical aspects of the experiments. Quantitative structural analysis, however, requires the use of indirect methods for structure determination through simulation of ion scattering experiments for different structural models [26.72–75]. Even so, in the case of close-packed and well-ordered surfaces, multiple scattering features in experimental data can often yield the identity of nearest neighbor atoms by inspection. Multiple scattering effects tend to be most pronounced in the case of low energies, heavy projectiles, and small angles of incidence and scattering angles. Therefore, while the use of high energies is typically used to circumvent multiple scattering features in experimental spectra, the use of heavy, (e.g., Ne^+, Ar^+) projectiles at low energy ($\approx 500\,eV$) can be used to amplify the measurability of multiple scattering features. In addition, the use of alkali projectiles has been shown to increase the ion fraction significantly [26.76, 77], and therefore the prospects for observing features due to multiple scattering are much more favorable.

Brongersma and *Mul* [26.78] performed measurements on the (111) and $(\bar{1}\bar{1}\bar{1})$ surfaces of GaP, as shown in Fig. 26.23. Here, the measurements are performed in a specular geometry along the $\langle 11\bar{2}\rangle$ direction with 350 eV Ne^+ and a scattering angle of 45°. The surfaces measured at room temperature are dominated by a broad feature due to recoiled Ga and P atoms; this effect is circumvented when the measurements are performed at 450 °C. In the case of the (111) surface, a binary collision peak due to Ga was observed in conjunction with new peaks due to Ga–P and Ga–Ga scattering, whereas only a Ga single-scattering peak was observed from measurement of the $(\bar{1}\bar{1}\bar{1})$ surface. The observation of the latter peak was indicative of surface reconstruction, since in the case of the unreconstructed surface, calculations indicated that blocking by P would make double scattering by nearest-neighbor Ga atoms impossible. This assessment was in agreement with a previous LEED study showing a (2×2) LEED

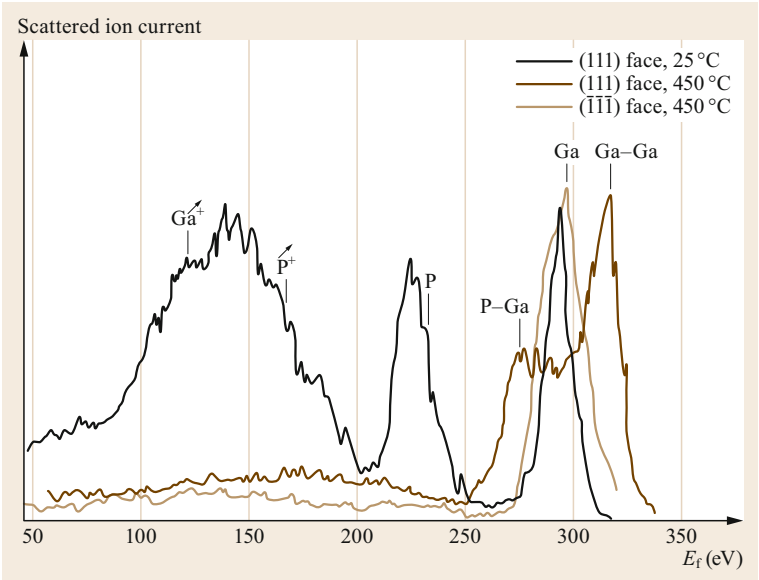

Fig. 26.23 350 eV Ne^+ LEIS spectra from GaP(111) and $(\bar{1}\bar{1}\bar{1})$ surfaces at room temperature and 450 °C (Reprinted from [26.78], with permission from Elsevier)

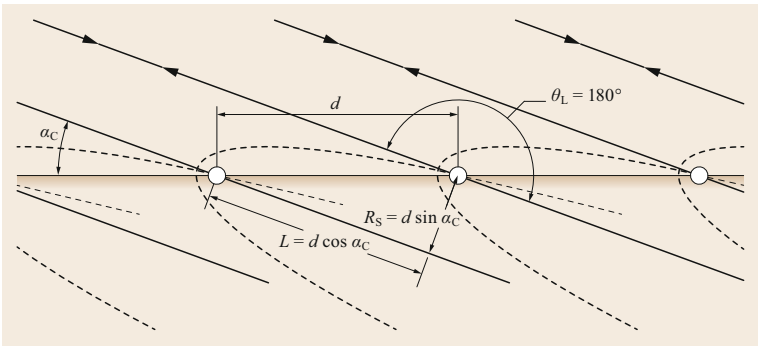

Fig. 26.24 Experimental geometry from ICISS. Backscattered ions are measured as a function of incidence angle. For angles less than some critical angle α_c, shadowing effects prevent backscattering, so that angle-dependent measurements can yield the dimensions of the shadow cone (Reprinted from [26.52], with permission from Elsevier)

pattern on the same surface upon annealing to 500 °C. In addition, the observation of a Ga–P peak indicated a position of the surface P atoms different from that of the bulk, and the authors suggested that additional measurements as a function of scattering angle and azimuth could further clarify the details of the reconstruction.

The most quantitative approach for determination of the atomic structure of surfaces originates from methods that measure the shape of the shadow cone. In impact-collision ion scattering spectroscopy (ICISS) [26.52, 55], the energy distribution of a beam of scattered ions is measured as a function of incidence angle at grazing angles along specific crystallographic directions. Rather than measuring the specularly reflected beam, the ions which are backscattered through a scattering angle of approximately 180° are measured. The principle of the measurement of the shadow cone can be understood by considering a chain of atoms as in Fig. 26.24a. For incidence angles greater than some critical angle α_c, the shadow cones of neighboring atoms completely block one another, and no backscattering occurs. As the angle of incidence approaches the critical angle, backscattering begins to increase. By considering the geometry of the system, it can be seen that the angle at which backscattering becomes possible is directly related to the interatomic spacing and the radius of the shadow cone. Since the shadow cone is specific to the element under consideration, the dimensions of the shadow cone for a particular element can be determined by measurement of systems in which the lattice constants are known and then applied to the unknown system. Importantly, for this geometry, only shadowing effects affect the measured data, and the combined effects of shadowing and blocking that are intractable in specular scattering are decoupled.

Aono et al. [26.79] used ICISS to study the (2×1) reconstruction of Si(100), performing measurements as a function of both the polar (incident) angle and azimuthal angle of the surface with respect to ⟨110⟩, as in Fig. 26.25a. In particular, the spectra measured at graz-

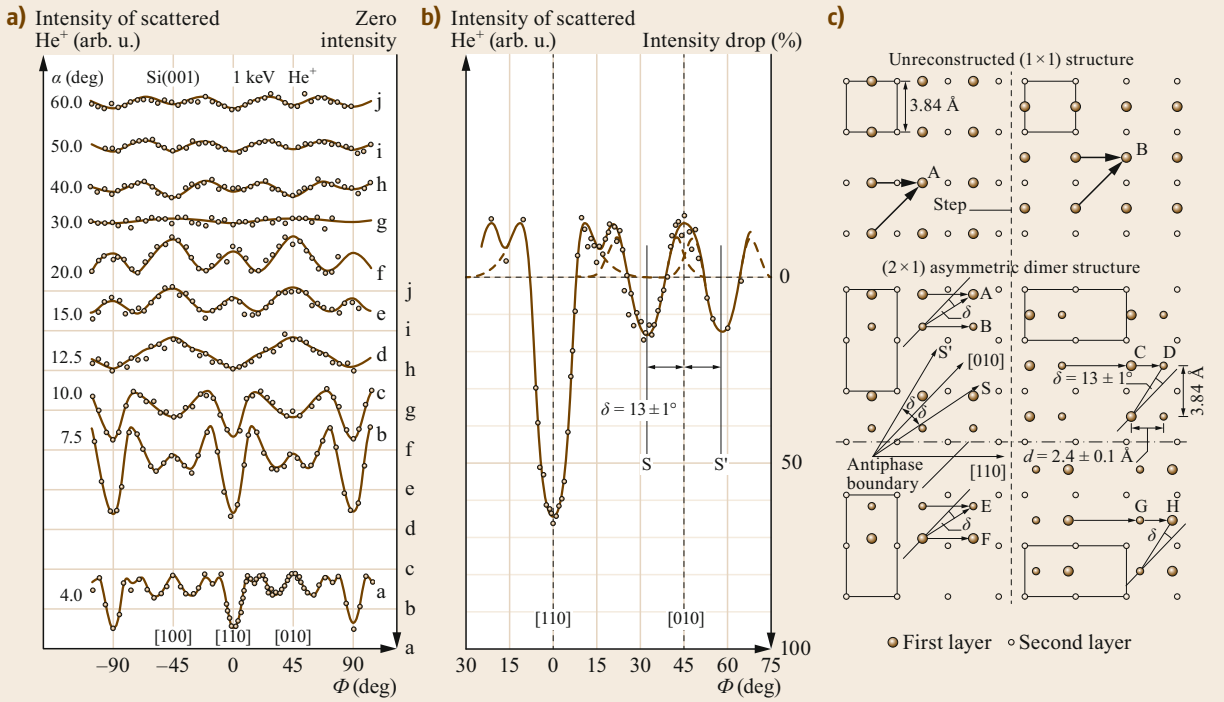

Fig. 26.25 **(a)** 1 keV He^+ ICISS spectra taken as a function of incident angle and azimuth, with a magnified version of the 4° spectrum shown in **(b)**. **(c)** Shows structural models of the Si(100) surface, comparing the directions for shadowing in the unreconstructed (top) and (2 × 1) (bottom) surfaces (Reprinted with permission from [26.79]. Copyright (1982) by the American Physical Society)

ing incidence (magnified in Fig. 26.25b) show several distinct minima due to shadowing effects, accompanied by maxima at their periphery due to channeling. These minima, along the [110] direction and along directions rotated by 13° with respect to [100], indicate shadowing effects in orientations different from those expected for the bulk-terminated surface (along both [110] and [100], Fig. 26.25c), as was expected. Rather, these observations are consistent with the asymmetric dimer structure, as shown in Fig. 26.25d. Here, shadowing effects are expected for the [110] azimuth and for azimuths at some angles denoted δ from [100], in good agreement with the measured data. From the measured value of δ, the authors where able to determine the Si−Si dimer bond length of 2.4 Å. Such approaches have been used to investigate the structure of a number of systems ranging from metals to adsorbate systems and defect analysis [26.80–86].

26.3.5 Matrix Effects

In all cases discussed above, matrix effects, in which the ion yield is determined by its surrounding environment, can have a significant impact on the quantitation of LEIS data. Previous reviews have discussed in detail the origin of matrix effects arising from different charge transfer processes, and *Brongersma* et al. [26.50] discussed several methods for identifying whether matrix effects are present in a given system in conjunction with approaches to remedy matrix effects of different physical origins. The most straightforward of these approaches, in an approach developed by *Jacobs* et al. [26.87], involves comparison of the energy dependence of the ion yield of the elements in the sample of interest. Because the ion fraction is acutely dependent on the incident ion energy, any potential differences in the neutralization probability between the unknown and standard samples will be highlighted. In the absence of matrix effects, the ratio between the LEIS intensity of a given element in the unknown and reference samples should remain constant as a function of energy. Similarly, another approach for evaluating whether matrix effects are present involves plotting the logarithm of the ion fraction against the perpendicular component of the projectile velocity. A linear relation is expected, and its slope is given by a characteristic velocity that should be the same for a given element in different matrices, assuming that neutralization via Auger processes

is dominant. Additional experimental checks on matrix effects are described in detail in [26.50]. These include examination of the energy dependence of the ion yield ratios in the case of compounds, which should be independent of incident energy on the basis of the above arguments, measurement of the angular dependence of the ion yield, and use of the total signal in the case of binary compounds in which samples of varying composition are available.

Once it has been established whether matrix effects play a significant role in the system of interest, quantification can proceed in one of several ways. In the absence of matrix effects, evaluation of the concentrations of surface atoms can be done in a straightforward manner using the appropriate calibration samples and appropriately applying (26.6). If it is determined that matrix effects are present, the manner in which the quantification proceeds is dependent on the type of neutralization mechanism. For the case in which the matrix effects arise from b-RN, oscillations in the ion yield as a function of energy are observed and represent the dependence of the probability for tunneling between core-level states of the target and discrete states of the projectile given the projectile velocity. It was pointed out, given a survey of systems with known matrix effects, that effects of this origin can almost always be circumvented by using Ne^+ as the projectile rather than He^+ [26.50]. In addition, working at higher energies (> 3 keV) can suppress the matrix effects, since the amplitude of the oscillations of the ion yield is damped at high energies. In general, the use of higher energies is effective in suppressing matrix effects of different origins, as the perpendicular component of the projectile velocity is increased and the time of interaction between the projectile and target is reduced.

The other primary class of matrix effects is found with low-work-function systems; here, the situation is more complicated because the effects of the matrix on the ion yield cannot be attributed to one specific neutralization mechanism, since energy-dependent RN processes play a large role in addition to other mechanisms, particularly collision induced (CI) neutralization. While the use of higher energies can potentially alleviate matrix effects in low-work-function systems, a more rigorous approach to quantification for low-work-function materials was presented by *Cortenraad* et al. [26.88]. Here, it is assumed that when the work function of the surface reaches a sufficiently low value, RN becomes pronounced- and the ion fraction is determined by the population of the projectile atomic level at a distance from the target atoms known as the freezing distance. The ion fraction associated with RN processes can then be described as

$$P^+_{\mathrm{RN}} = \exp\left(-C\frac{|\varepsilon_\mathrm{a} - \varepsilon_\mathrm{F}|}{v}\right), \tag{26.9}$$

where ε_a is the energy of the first excited state of the projectile at the freezing distance, ε_F is the Fermi energy, v is the perpendicular component of the projectile velocity, and C is a constant. In the correction process, the ion fraction is first determined as a function of the work function range of interest, enabling determination of the constant C in (26.9). With this information, the contribution to the ion fraction from RN can be determined. If the contribution to the ion fraction from other mechanisms is known from, e.g., low coverage measurements, then the contribution from RN can be discriminated. From such a process one can generate a curve of the ion fraction due to RN as a function of work function, enabling subsequent quantification for surfaces of arbitrary elemental composition.

26.3.6 Conclusions

LEIS has been shown to be a highly sensitive tool for the determination of the elemental composition of the outermost layer of a surface. Quantification in the majority of cases is straightforward, with the use of appropriate standards with known surface concentrations. The presence of matrix effects, in which the ion fraction of a given element is determined by its surroundings, can be readily identified using standard methods. While quantification can be more challenging in these few cases, a number of methods exist to circumvent these challenges and perform quantitative analysis. Beyond the determination of the surface composition, LEIS measurements afford the possibility of performing static depth profiles in the outer 5–10 nm of the surface region, enabling examination of multilayer structures and diffusion processes. Lastly, the high surface sensitivity of LEIS can be exploited to extract structural details of surfaces and, under certain measurement conditions, perform surface crystallography.

26.4 Combining IR, XPS, and LEIS Measurements

The previous two sections have described the principles of IR absorption and LEIS spectroscopy in investigating a variety of surface phenomena. Here, we illustrate how the combination of all three techniques (IR, LEIS, XPS) is a necessary and powerful means for deriving quantitative information regarding surface composition,

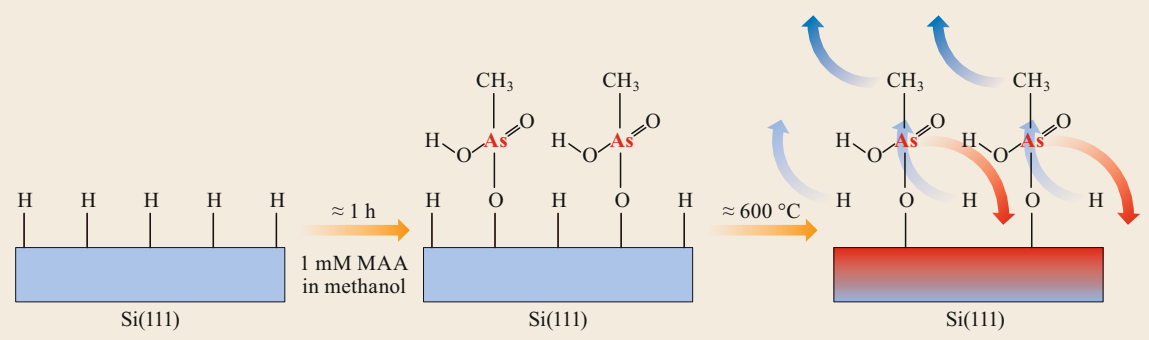

Fig. 26.26 Schematic of MAsA functionalization of Si(111)−H and subsequent MLD process. As-grafted surfaces contain MAsA coordinated via monodentate Si−O−As bonds to the substrate. Annealing to 600 °C results in loss of the organic tail and subsequent diffusion of As into the bulk

structure, and reactivity that would not have been accessible in experiments with one or even two of these techniques taken on their own. We have selected relatively recent examples of systems that are important for microelectronics, catalysis, and energy (e.g., gas storage).

26.4.1 Ultrashallow Doping with Methylarsenic Acid/Si(111)–H

Progressive device downscaling and new device structures have given rise to challenges in semiconductor device manufacturing, as many of the approaches for materials engineering used in existing device technology have reached fundamental limits in the length scales for which they are practical. For example, the design of 3-D ultrashallow junctions requires precise and shallow doping, which is not possible with conventional doping processes such as ion implantation. Consequently, monolayer doping (MLD) has recently been developed [26.89, 90] for doping semiconductor nanostructures that circumvents this issue. In the MLD process, a semiconductor surface is first functionalized with an organic molecule containing the desired dopant (e.g., P, B, As). The essential attributes of this molecule are the ability to chemically bond with the surface (Si−H or SiO_2−OH) and to self-assemble on the surface thanks to an organic tail. The procedure then involves annealing to sufficiently high temperature to decompose the ligands of the adsorbed functional group and subsequently drive the dopants into the bulk via diffusion processes. Initially, it was not clear whether the dopant atom might evaporate during this annealing step, and an oxide capping layer was deposited on the organic layer. However, the example below shows that such a capping layer is not necessary. While this approach has shown great promise for doping ultrashallow surface regions [26.89–95], quantitative mechanistic studies of these processes are needed to obtain sufficient information to properly engineer the combined process.

For instance, *Longo* et al. [26.96] examined MLD of H-terminated Si(111) and Si(100) surfaces using methylarsenic acid (MAsA) to achieve n-type doping via As diffusion into the bulk. Here, a combination of in situ transmission IR absorption (Brewster's angle incidence), XPS, and LEIS measurements were used as experimental probes to guide the ab initio modeling of the entire MLD process. Si(111)−H surfaces were prepared using conventional HF and NH_4F treatments [26.22] and functionalized with MAsA by immersion into a 10^{-3} mol methanol solution at 65 °C in a glove box for 12 h [26.96]. Specifically, the MAsA is chemically attached to Si−H in a monodentate structure by reaction of one of its As−OH bonds to form a Si−O−As bond as in Fig. 26.26, similar to grafting of methylphosphonic acid to H-terminated Si(111) [26.92, 97]. Figure 26.27a shows the absorption spectrum of the as-grafted surface referenced to the surface following HF etching. The data show modes associated with C−H stretching of methyl groups (2800–3000 cm^{-1}), As=O stretching (1180 cm^{-1}), As−O stretching (1080 cm^{-1}), and As−O-H bending (925 cm^{-1}). Analysis of the Si−H stretching mode from ex situ IR spectra of the functionalized surfaces indicated that, due to steric interactions, the MAsA coverage was approximately two-thirds monolayer, with the rest of the surface remaining H-terminated. For this study, all subsequent annealing was performed in a UHV cluster system combining separate chambers for LEIS, IR, and XPS measurements, with in situ UHV sample transfer. As illustrated in Fig. 26.27b, the IR absorption spectra recorded as a function of annealing temperature provided insight into the thermally driven evolution of the adlayer; upon annealing to 600 K, loss of the hydrocarbon stretching band and a blueshift of the Si−H stretching band were observed, indicating the decomposition of the molecule

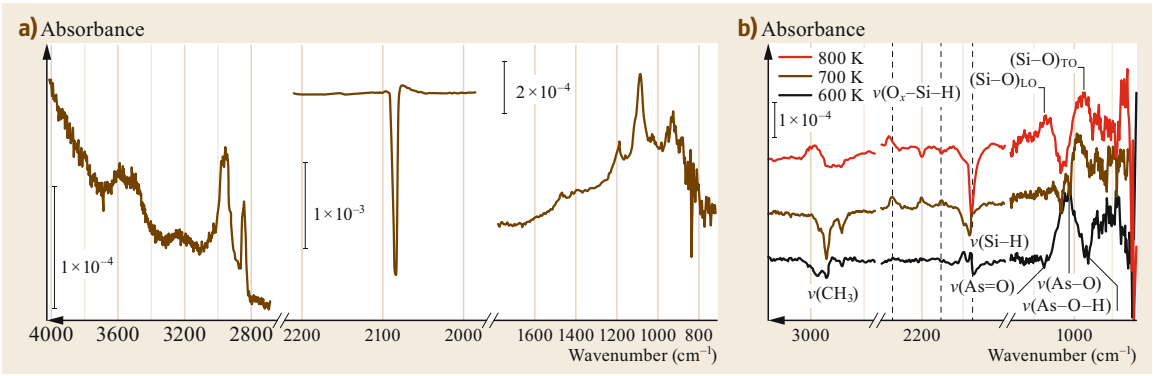

Fig. 26.27 **(a)** IR absorption spectrum of MAsA/Si(111)−H referenced to the clean Si(111)−H surface, and **(b)** differential IR spectra of MAsA/Si(111)−H taken as a function of temperature during UHV annealing (Reprinted adapted with permission from [26.96]. Copyright (2016) American Chemical Society)

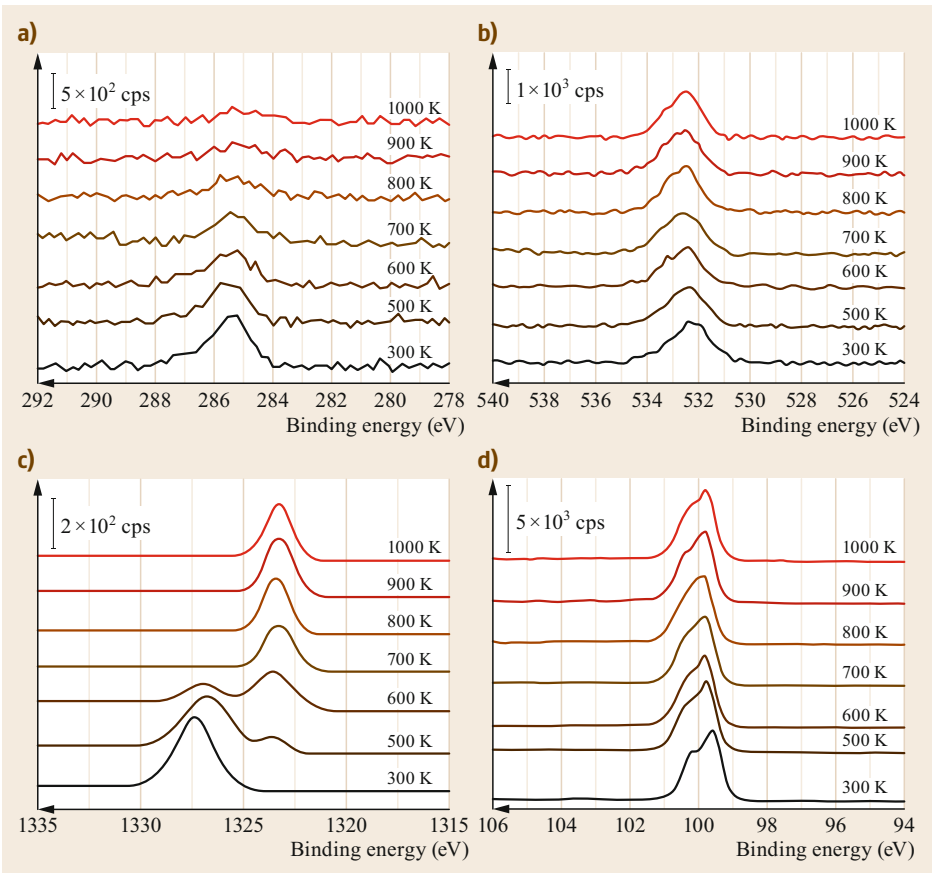

Fig. 26.28 **(a)** C 1s, **(b)** O 1s, **(c)** As $2p_{3/2}$ and **(d)** Si 2p spectra of MAsA/Si(111)−H surfaces as a function of UHV annealing (Reprinted adapted with permission from [26.96]. Copyright (2016) American Chemical Society)

with the insertion of one oxygen atom in the Si−Si back-bonds. In addition, an increase in the intensity of the As−O stretching mode at 1100 cm^{-1} was observed, likely due to changes in the dynamical dipole moments associated with the vibration following the loss of the organic tail, accompanied by relaxation of the geometric structure. Upon annealing to 700 K, the hydrocarbon band intensity continued to weaken, and the appearance of further blueshifted Si−H stretch bands indicated that additional oxygen atoms from the AsO_x groups were incorporated into the Si back-bonds into higher oxidation states for Si (O_2−Si−H at 2200 cm^{-1}

and O_3−Si−H at 2270 cm^{-1}). The incorporation and local agglomeration of oxygen was clearly identified by the appearance of SiO_x TO and LO Si−O phonon bands at 960 and 1178 cm^{-1}, respectively, involving Si−O−Si stretching vibrations [26.98–100]. Finally, upon annealing to 800 K, a loss of intensity of the As−O band at 1100 cm^{-1} was observed with a consolidation of the Si−H stretch band at 2270 cm^{-1}, associated with the O_3−Si−H groups, indicating complete decomposition of the arsonate groups and further incorporation and agglomeration of O atoms into the substrate. In summary, the IR absorption data provide good markers for chemical modification (e.g., loss of organic tail, oxygen incorporation in Si) but cannot determine exactly the behavior of As. In particular, it cannot be established whether As desorbs.

XPS measurements provided complementary information by determining the oxidation state of As and the evolution of C and O atoms during the annealing process, as illustrated in Fig. 26.28. For instance, the carbon concentration originating from the organic tail of the molecules starts to decrease at 500 K, at which stage the oxidation state of the As begins to change, as seen by the emergence of a shoulder of lower binding energy in the As $2p_{3/2}$ spectrum. Further reduction of the As atom continues at higher temperatures, until the C 1s core level is below the limit of detection by 1000 K, an important finding given that prior MLD studies found that incorporated capping layers suffered from residual C contamination [26.89].

While the chemical evolution of all species (As, O, C, H) could be determined from IR and XPS measurements, providing a guide as to the chemistry taking place as a function of temperature, these techniques provided no information on the spatial diffusion of As, and even the fact that As would not desorb from the surface. To answer this question, LEIS is by far the best technique, as it can track and quantify the As concentration in the near-surface region. Using 3 keV He^+ ions that are best suited to detecting both light (C, O) and heavier (As) atoms, spectra were recorded as a function of temperature. Figure 26.29a shows the energy range corresponding to the As binary collision region (Fig. 26.29a), providing evidence that little change takes place between 300 and 973 K apart from intensity variations due to blocking effects. Upon annealing to 1023 K, however, a low-energy tail emerged; by 1073 K, the binary collision peak had split into a doublet with a redshifted component at 2300 eV, and the intensity of the surface peak at 2375 eV had decreased dramatically. Annealing to 1125 K resulted in a reduction of the surface peak to below the detection limit, and only the 2300 eV peak remained; further annealing led to an additional low-energy peak at 2225 eV, with a broadened distribution of the intensity in that region. The origin of these peak shifts can only be attributed to diffusion of As into the subsurface region. In Sect. 26.3, it was shown that LEIS can detect sub-

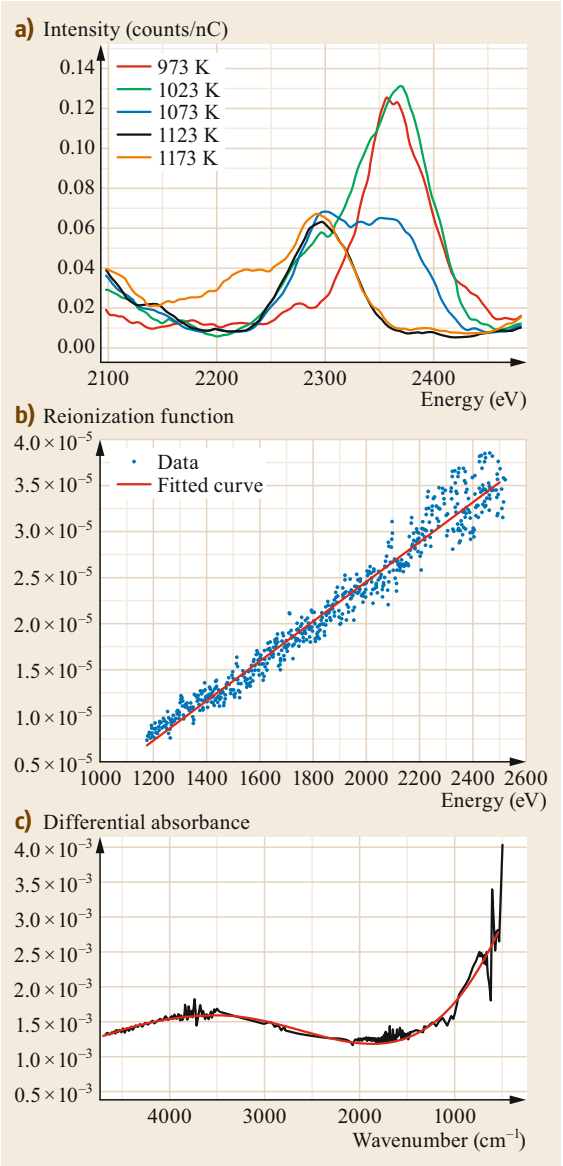

Fig. 26.29 **(a)** 3 keV He^+ LEIS spectra in the As binary collision region for MAsA/Si(111)−H surface as a function of UHV annealing. **(b)** Determination of the reionization function for the Si(111) surface annealed to 1123 K. **(c)** Broadband IR spectra showing the low-frequency Drude behavior and broad absorption band between 3000 and 5000 cm^{-1} due to an interband transition (Reprinted adapted with permission from [26.96]. Copyright (2016) American Chemical Society)

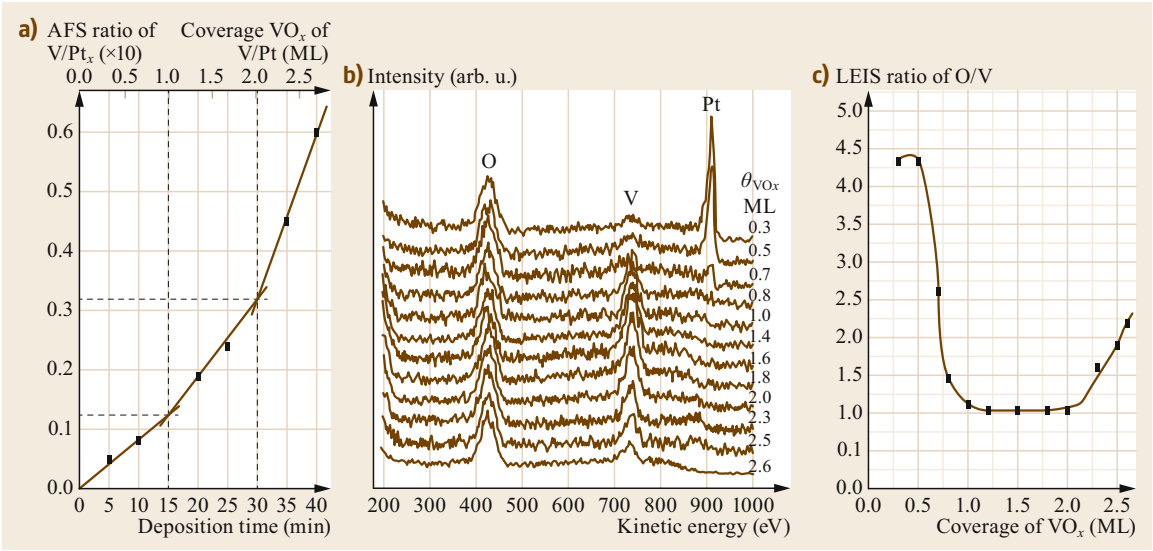

Fig. 26.30 **(a)** Coverage of VO_x determined by AES measurements as a function of deposition time; **(b)** LEIS measurements of VO_x overlayers as a function of coverage; **(c)** V:O intensity ratio of LEIS spectra as a function of coverage (Reproduced from [26.101] with permission of The Royal Society of Chemistry)

surface elements via neutrals that penetrate into the bulk and subsequently become reionized at the surface following backscattering by subsurface atoms, as demonstrated for $Al_2O_3/HfO_2/SiO_x$ multilayers. Here, the progressive shifts to lower energy and the intensity decreases of the As peak are attributed to the migration of As below the surface, and the depth of the As was inferred by TRBS simulations in a manner similar to that demonstrated by *Brüner* et al. [26.54] for the $Al_2O_3/HfO_2/SiO_x$ multilayer system. The initial shift seen at 1073 K corresponds to a depth of 0.7 nm, and the systematic shift to lower energy demonstrates unambiguously the diffusion of As into the bulk. Furthermore, quantification of the signal allows for the extraction of the dopant concentration. The reionization function of the surface can be determined, as discussed in Sect. 26.3, by dividing the measured LEIS spectrum by the spectrum simulated by TRBS for backscattered neutrals with the same projectile/target combination and experimental geometry. The resulting function has a linear dependence on energy, as was observed for the case of HfO_2 (Fig. 26.29b). With this knowledge, the concentration of As could be extracted, and was found to be 3×10^{21} As/cm^3. These values are consistent with all the As penetrating into the Si substrate, even though there was no oxide capping layer to confine the dopant (thought to be necessary in previous studies) [26.89, 90, 102, 103]. The doping effect was further demonstrated by broadband IR spectra (i.e., focusing on the electrical response of the Si substrate) recorded over a large temperature window (Fig. 26.29c). Spectra obtained by referencing 973 K data to 573 K, for instance, show a characteristic Drude response and a broad high-frequency absorption band between the conduction band and unoccupied higher-lying bands (Fig. 26.29c), an unequivocal demonstration of n-type doping. Thus, the combination of these three techniques, supplemented with first-principles modeling, was essential to derive a rigorous quantification of the complete MLD process for As doping of oxide-free Si(111) surfaces. This work provides a methodology that is applicable to other systems with arbitrary substrate/dopant concentrations.

26.4.2 Metal Oxide Growth: VO_x/Pt(111)

Vanadium oxides have interesting physical and chemical properties, particularly valuable for heterogeneous catalysis, as they support a number of reactions [26.104, 105]. In light of the appealing properties of supported VO_x catalysts (and similar systems), fundamental studies on the relationships between film structure and oxidation states with functional properties such as catalytic activity and selectivity are of importance for their development and optimization. In one such study, *Tang* et al. [26.101] combined LEIS, XPS, HREELS, and IRRAS to study the growth and oxidation of ultrathin vanadium films on Pt(111) substrates. Here, ultrathin films (0–3 ML) were deposited under ultrahigh vacuum (UHV) by evaporation of V onto a clean Pt(111) crystal, followed by oxidation under different conditions. Initial oxidation was done by exposing the VO_x-evaporated

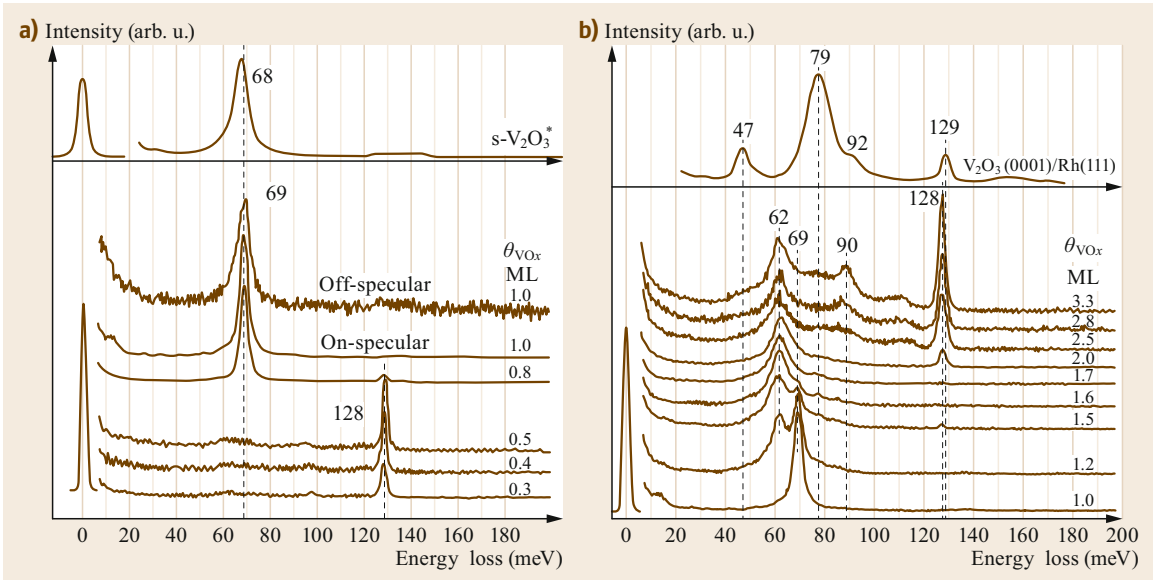

Fig. 26.31a,b HREELS spectra of VO_x overlayers as a function of coverage for **(a)** $0\,\text{ML} < \theta \leq 1\,\text{ML}$ and **(b)** $1\,\text{ML} \leq \theta \leq 3\,\text{ML}$ (Reproduced from [26.101] with permission of The Royal Society of Chemistry)

layer to 10^{-7} Torr O_2 for 10 min at 623 K. Different durations of evaporation and subsequent oxidation were used to control the coverage and number of monolayers deposited. LEIS and Auger electron spectroscopy (AES) were used to monitor the surface coverage and termination of the VO_x films. HREELS and IRRAS measurements were used to characterize the bonding between V and O, while XPS correlated the oxidation states of the films with the oxidation treatments.

Figure 26.30 shows the variation in the LEIS and AES signals observed as a function of V deposition time and subsequent VO_x coverage θ after 10^{-7} Torr O_2 oxidation. For low coverage, $0\,\text{ML} < \theta < 1\,\text{ML}$, the signal due to the Pt substrate gradually decreases until becoming undetectable as a complete monolayer is formed. Taken with the Auger data, these results provide a measure of the coverage of the substrate. In addition, the O/V intensity ratio extracted from the LEIS spectra show a marked decrease for coverage greater than 0.5 ML. The O/V ratio remains nearly constant between 1 and 2 ML, before undergoing a sharp increase for > 2 ML.

Figure 26.31a shows HREELS spectra taken from the corresponding coverage in Fig. 26.30. For coverage ≤ 0.5 ML, the spectra are dominated by a single peak at 128 meV ($1032\,\text{cm}^{-1}$), attributed to vanadyl V=O stretching, originating from structures such as those depicted in Fig. 26.32a. At coverage greater than 0.5 ML, the 128 meV peak disappears, and a new mode at 69 meV is observed, similar to that observed in s-V_2O_3. Thus the data indicate that as the coverage increased, isolated VO_x groups coalesced to form a continuous layer in which the V=O double bonds are broken to link neighboring VO_x groups. On the basis of mode-counting arguments, the authors were able to distinguish between potential ML structures, citing a structure of the type shown in Fig. 26.32b*(a)* as most consistent with the data. The decrease in the O/V LEIS intensity ratio for coverage less than 0.5 ML is consistent with this model, given the more open structure in Fig. 26.32b*(a)* than that in which the O atom is directly on top of the V, as in Fig. 26.32a*(a)–(c)*. This mechanism, in which the isolated VO_x units coalesce at high coverage to form bridging O at the expense of vanadyl groups, was further verified by performing co-adsorption studies in which CO was dosed for coverage < 0.5 mL; here again the authors observed only the 69 meV band and concluded that the isolated VO_x units are *compressed* into continuous V_2O_3 units due to competition for adsorption sites.

For overlayers between 1 and 2 ML, the structure formed is more complex and is observed in conjunction with a $(3\sqrt{3} \times 6)$ LEED pattern. The phonon modes observed in the HREELS spectra in this regime (Fig. 26.31b) show new features below 100 meV, but no modes indicative of vanadyl groups. A band is observed at 62 meV, and its intensity increases at the expense of the 69 meV band intensity; furthermore, the frequency of this feature can be used to infer a bonding configuration as shown in Fig. 26.32c*(a)* based on the frequencies expected for VO_x in different oxidation states. For films between 2 and 3 ML, new modes at 80 and 90 meV are

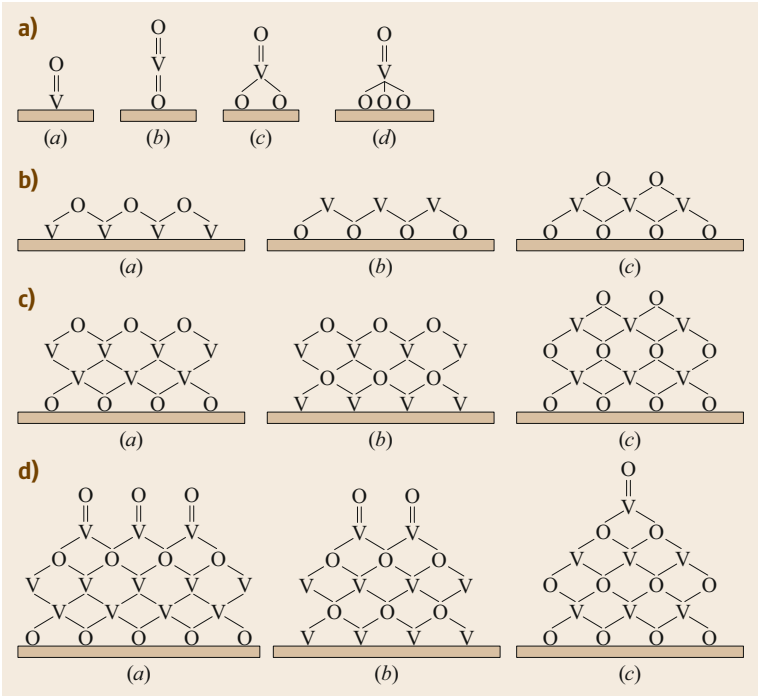

Fig. 26.32a–d Potential structures of VO_x overlayers for coverage of **(a)** < 0.5 ML, **(b)** 1 ML, **(c)** 2 ML, **(d)** 3 ML (Reproduced from [26.101] with permission of The Royal Society of Chemistry)

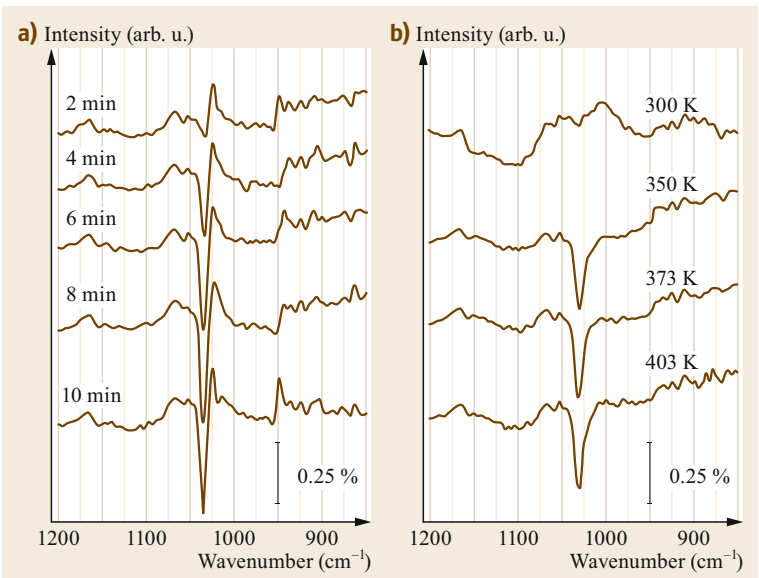

Fig. 26.33a,b IRRAS spectra of **(a)** 0.9 ML VO_x exposed to 1 Torr O_2 at room temperature and **(b)** 3 ML VO_x exposed to 1 Torr O_2 at indicated temperatures (Reproduced from [26.101] with permission of The Royal Society of Chemistry)

observed in conjunction with the reappearance of the mode at 128 meV, while the mode at 62 meV remains, suggesting that the formation of the third monolayer did not perturb the structure of the underlying 2 ML. In addition, above 2 ML, the intensity ratio O/V extracted from the LEIS of O and V increases quickly, and together with the reappearance of the 129 meV band, these observations point to a vanadyl termination. Thus, structural models such as those shown in Fig. 26.32d*(a)–(c)* describe the complete 3 ML structure.

In an attempt to further increase the V oxidation state, samples with 1 and 3 ML VO_x layers were brought to a high-pressure chamber connected to the UHV chamber and oxidized with 1 Torr O_2 at different times and temperatures while in situ IRRAS measurements were performed (Fig. 26.33a). In both the 0.9 and 3 ML sam-

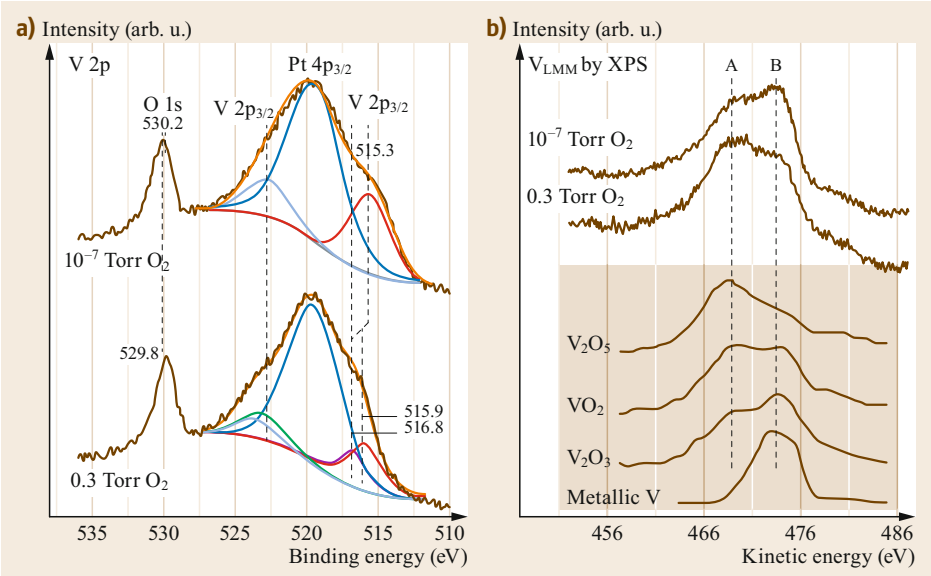

Fig. 26.34 **(a)** V 2p and O 1s spectra of 3 ML VO_x exposed to 10^{-7} Torr O_2 (*top*) and 0.3 Torr O_2 (*bottom*), with corresponding LMM Auger spectra shown in **(b)** with comparison to V/VO_x standards (Reproduced from [26.101] with permission of The Royal Society of Chemistry)

ples, additional oxidation could be achieved by formation of additional vanadyl units, as evidenced by a strong mode at the V=O stretching feature at 1038 cm^{-1} in the IRRAS spectra. The fact that the exposure to higher partial pressures of O_2 led to oxidation states greater than that observed for V_2O_3 was further verified by XPS measurements, as shown in Fig. 26.34a,b. Here, 3 ML VO_x films oxidized with 10^{-7} Torr O_2 and 0.3 Torr O_2 were examined; analysis of small core-level shifts toward higher binding energy by careful deconvolution of the spectrum of the sample oxidized with 0.3 Torr O_2 revealed the presence of higher oxidation states as inferred from IRRAS measurements. While these data are complicated by the overlapping Pt $4p_{3/2}$ line of the substrate, the V_{LMM} Auger lines from the XPS data also show the same trend when compared with standards of V, V_2O_3, VO_2, and V_2O_5. Together with the V 2p spectra, the data indicate that the 3 ML films oxidized using 10^{-7} Torr O_2 are in the oxidation state of V_2O_3, while films oxidized with 0.3 Torr O_2 are in mixed valence states that appear similar to a mixture of VO_2 and V_2O_5. Thus, the combination of vibrational spectroscopy (in this case both IR and HREELS measurements) with LEIS and XPS was again essential to derive quantitative information on the atomic structure and bonding configurations of thin films. This work demonstrates a powerful approach for studying growth reactions.

26.4.3 Catalyst Surface Structure: Au–Pd Alloys on Mo(110)

Bimetallic alloys have long been recognized for their unique, often enhanced or selective catalytic activity, which is generally very different from that of the constituent components [26.106]. As catalytic processes are dominated by the interaction between the target molecules and the outermost atoms present at the catalyst surface, a thorough understanding of the surface composition and structure is essential for a mechanistic understanding and optimization of catalytic reactions. In these systems, it is generally thought that both ligand effects (due to heteronuclear charge transfer) and ensemble effects (due to a particular number of atoms in some geometric orientation) potentially play a role in catalytic activity. XPS, LEIS, and IR measurements are frequently used for the characterization of catalyst materials and associated reactions, as in situ techniques can yield information including the complete surface composition, chemical state of the elements at the surface, and details regarding the identity and structure of adsorbates *under* reaction conditions. When performed in parallel, the combination of these approaches can provide a comprehensive picture of surface chemistry that can then be linked to catalytic activity.

Goodman and coworkers [26.107, 108] performed such mechanistic studies to establish the correlation of surface structure with catalytic activity for Pd-Au alloy surfaces. Such Pd-Au catalysts are effective for CO oxidation, vinyl acetate synthesis, hydrodechlorination of $CClF_2$, hydrogenation reactions, and other surface reactions [26.109–112]. For these studies, they synthesized the alloys by physical vapor deposition of Pd and Au onto Mo(110) substrates followed by annealing to various temperatures to tune the surface composition. To investigate a potential role of the order in which the respective metals were deposited, experiments were

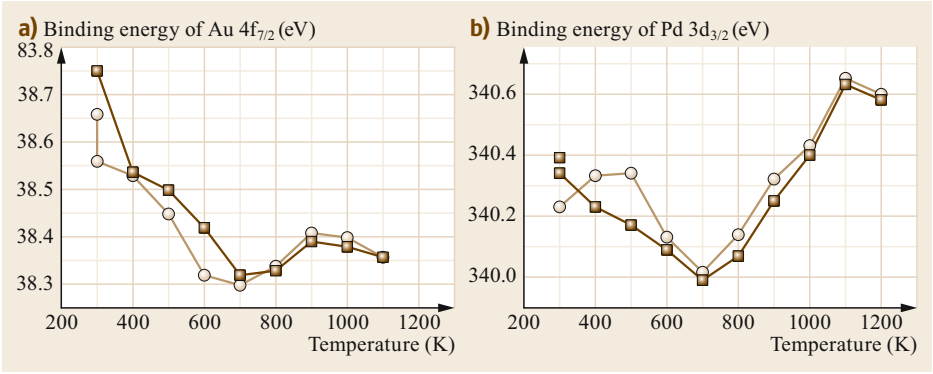

Fig. 26.35a,b Binding energy of the Au $4f_{7/2}$ **(a)** and Pd $3d_{3/2}$ **(b)** levels from Au-Pd alloys as a function of temperature determined from XPS measurements (Reprinted adapted with permission from [26.107]. Copyright (2005) American Chemical Society)

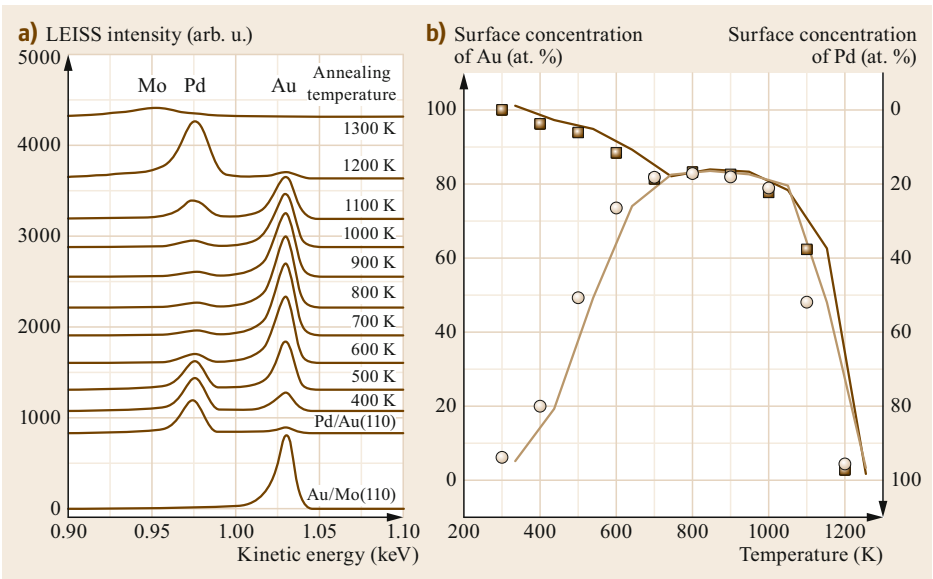

Fig. 26.36 **(a)** LEIS spectra of Pd/Au/Mo(110) as a function of annealing temperature, and **(b)** extracted surface concentrations for Au-Pd alloys annealed to different temperatures for films in which Pd was deposited first (*circles*) and Au was deposited first (*squares*) (Reprinted adapted with permission from [26.107]. Copyright (2005) American Chemical Society)

carried out for both 5 ML Au/5 ML Pd/Mo(110) (i.e., Pd deposited first) and 5 ML Pd/5 ML Au/Mo(110) (Au deposited first). Figure 26.35 shows the binding energies, measured by XPS, of the Au $4f_{7/2}$ and Pd $3d_{3/2}$ peaks following deposition and subsequent annealing. Clearly, similar results were observed for both Pd deposited first and Au deposited first. Upon annealing to 700 K, both the Au 4f and Pd 3d levels continuously shift to lower binding energies by 0.45 and 0.15 eV, respectively, as compared with pure Au and Pd. Upon annealing to higher temperatures (1000 K), the Pd 3d level progressively shifts toward higher binding energy, while Au begins to desorb (disappearance of Au $4f_{7/2}$ level). Some important results were derived from these data. First, the core-level shifts provided direct evidence of alloying following annealing. Second, the core-level shifts observed were attributed to a charge-compensation model, where Au gains sp electrons and loses d electrons, whereas the opposite is the case for Pd. Charge compensation such as that described above falls under the classification of ligand effects, one potential factor determining the catalytic properties of bimetallic alloys.

LEIS was then used to determine the surface composition at each stage of annealing. Figure 26.36a shows 1.1 keV He^+ LEIS spectra of the Pd/Au/Mo(110) films

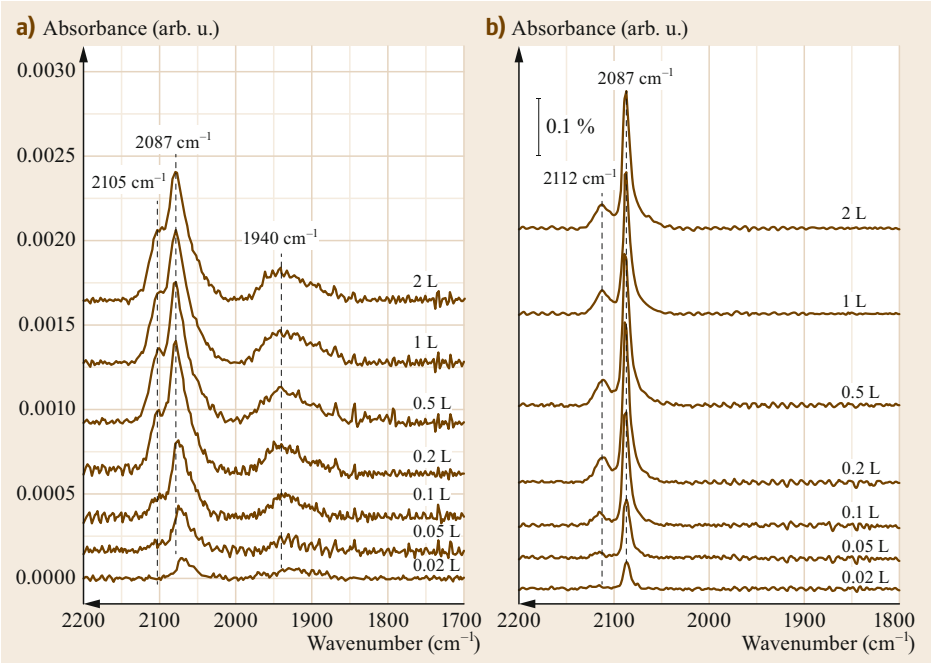

Fig. 26.37a,b IRRAS spectra from Pd-Au alloys taken as a function of CO exposure in films annealed to 600 K **(a)** and 800 K **(b)** (Reprinted adapted with permission from [26.107]. Copyright (2005) American Chemical Society)

as a function of deposition and processing. Deposition of 5 ML Au onto Mo(110) leads to a total disappearance of the Mo peak, indicating complete wetting of the surface. Following deposition of 5 ML Pd onto the 5 ML Au/Mo(110) surface, a peak emerges at the position expected for Pd, while a small feature due to Au is still observable, indicating that some degree of intermixing takes place at room temperature. Above 700 K, the intensity of the Au peak increases continuously, and the relative Pd and Au intensities remain nearly constant between 700 and 1000 K. Upon annealing to temperatures > 1000 K, the intensity of the Au peak begins to decrease because of Au desorption, leading to a Pd-enriched surface. From the measured data and use of the appropriate standards, the authors are able to compute the surface concentration of Au and Pd at each annealing temperature, as shown in Fig. 26.36b. Beginning from room temperature, the surface Au concentration increases continuously until a stable $Au_{0.8}Pd_{0.2}$ alloy is formed at 700 K, which remains until 1000 K.

Further experiments studying the IR response of adsorbed CO on surfaces prepared under different conditions provided additional insight into the surface structure. Here, the surfaces were dosed with CO at 80 K and measured using the IRRAS geometry (discussed in Sect. 26.2). Figure 26.37a shows IRRAS spectra obtained from of a 5 ML Pd/5 ML Au/Mo(110) film annealed to 600 K following exposure to different doses of CO. Such annealing leads to a surface Pd concentration of 27%. At low doses (0.1 L), two modes are observed at 2087 and 1940 cm^{-1}. The mode at 1940 cm^{-1} is characteristic of CO bonded at a bridge site, while that at 2087 cm^{-1} is in the frequency region expected for CO adsorbed at an atop site. Above 0.2 L, an additional band is observed at 2105 cm^{-1} and saturates for doses > 5 L. On the basis of existing literature, the 2105 cm^{-1} band is assigned to CO adsorbed at an Au atop site, the band at 2087 cm^{-1} to a Pd atop site, and the band at 1940 cm^{-1} to a Pd bridge site. Similar experiments were performed on an analogous sample annealed to 800 K, leading to a lower (18%) surface Pd concentration. Below 0.1 L, a single feature was observed at 2087 cm^{-1}, while a feature was observed at 2112 cm^{-1} with additional exposure (> 0.1 L). In this case, no features due to multi-coordinated CO are observed, supporting the assignment of the 1940 cm^{-1} band as originating from a Pd bridge site. Rather, only adsorption at Pd and Au atop sites takes place at low Pd concentrations. These observations point to the absence of Pd ensembles (dimers, trimers, patches, etc.) on the 800 K-annealed surface, but clearly indicate their presence on the 600 K-annealed surface (containing 27% surface Pd). With the combination of in situ IR, XPS, and LEIS techniques, both ligand effects and ensemble effects can be investigated in detail, and ultimately correlated to catalytic reaction mechanisms and performance.

26.4.4 Magnetic Surfaces: Metal Plasma Cleaning and Nitridation

Ferromagnetic thin films form the basis for spintronics devices, commonly used for memory and logic applications [26.113]. For instance, multilayer structures have been constructed to separate ferromagnetic, typically first-row transition metal, layers and insulating spin-filter layers. Central to the performance of these devices is the chemical state of the interface between the ferromagnetic electrode and the spin-filter layer, as antiferromagnetic oxide impurities can lead to scattering and spin decoherence. Nitridation is one potential route toward modification of such surfaces, and transition-metal nitrides that interface easily with the magnetic electrode layers could therefore be used as barrier and/or spin valve layers. Additionally, transition metals and their nitrides are becoming increasingly utilized in a wide variety of catalytic processes [26.114–118]. Consequently, understanding the surface composition, structure, and reactivity of these materials is of high importance.

In one study, hydrogen and nitrogen plasmas were used to etch the native oxide from Co thin films and subsequently form an ultrathin surface nitride layer [26.119]. In situ IRRAS, LEIS, and XPS were employed to thoroughly investigate the surface composition and structure during each step of the treatment. In this study, Co thin films on Si were first cleaned in UHV using an H_2/Ar inductively coupled plasma (ICP) with the sample maintained at 200 °C, and the surface chemical composition was monitored by in situ IRRAS measurements performed as a function of plasma exposure time. The IR spectra were collected in reflection during plasma exposure and referenced to the reflectivity of the surface immediately before plasma exposure (Fig. 26.38). The dependence on the plasma exposure measured by IRRAS revealed that surface carbonates (1400–1600 cm^{-1}) were etched first, and that the metal oxide ($\approx 600\,cm^{-1}$) was etched only after the carbonates were removed, presumably due to initial protection of a cobalt carbonate overlayer. The O 1s and Co 2p XP spectra associated with plasma-cleaned surfaces (Fig. 26.39) showed Co primarily in its metallic form, with a submonolayer coverage of O primarily in the form of adsorbed hydroxyl groups with relatively little metal oxide (Fig. 26.39c). The respective coverage of hydroxyl and metal oxide was estimated from measurements to be 21 and 4% of a monolayer, respectively. It was postulated that the relatively high partial pressure of water present when backfilling the UHV chamber with an H_2 plasma ($> 10^{-8}$ Torr, measured from a mass spectrometer after turning off the plasma source) was mainly responsible for both hydroxyl and metal oxidation during H_2 plasma treatment.

Nitridation of the cleaned surface was then achieved at room temperature via nitrogen ICP under UHV conditions, *after* removal of the native metal oxide. As in the case of the hydrogen plasma treatment, IRRAS measurements were performed in situ to monitor the evolution of the surface species as a function of N_2 plasma exposure time, as shown in Fig. 26.40. Several important features were noted. First, a band at 1795 cm^{-1} in the spectrum collected within the first

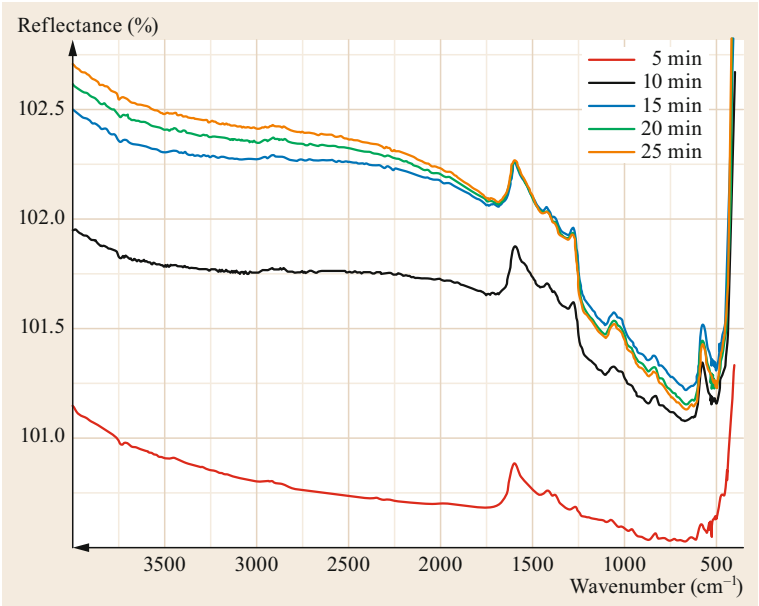

Fig. 26.38 In situ IRRAS spectra taken from Co surfaces at 473 K as a function of exposure to hydrogen plasma

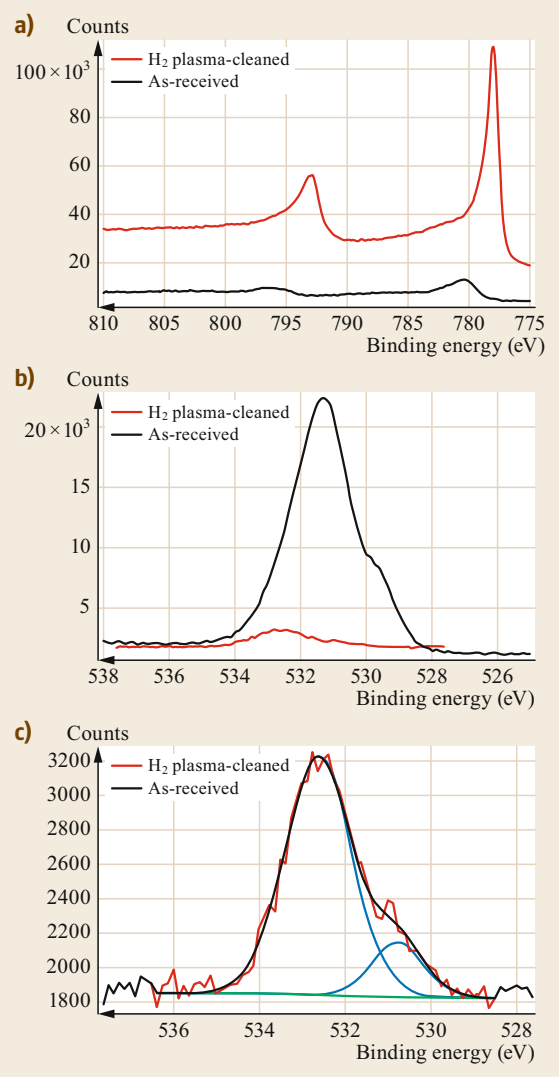

Fig. 26.39a–c XPS spectra of as-received and plasma-cleaned Co films. **(a)** Co 2p and **(b)** O 1s levels, **(c)** deconvolution of the O 1s spectrum into peaks due to hydroxyl (533 eV) and metal oxide (530.5 eV)

2.5 min of plasma exposure was attributed to adsorbed NO. With progressive exposure to the plasma, the intensity of this band diminished concomitantly with the emergence and growth of a band at 2187 cm^{-1}, associated with NO^+. The presence of NO likely originated from interactions between the N_2 plasma and the oxygen in the silica tube of the plasma source, initially leading to the incorporation of oxygen into the film in the form of NO. In addition to these sharp vibrational features, a change in the broadband absorption was noted (centered around 1700 cm^{-1}), assigned to internal transitions between degenerate d levels split by spin–orbit coupling, which was observed in many compounds containing Co in the 2+ state, including CoO [26.120]. Finally, a weak positive contribution at 600 cm^{-1} was attributed to Co–N stretching vibrations. The observation of an upward-pointing band associated with bond formation was unusual for the case of an absorbing layer on a metal substrate, as ordinarily the presence of an absorbing moiety on a metal surface will result in a downward-pointing band in the reflectivity spectrum (signifying light absorption). The observation of an upward-pointing band due to Co–N bond formation was ultimately determined to result from a complex optical effect arising from the intense broadband electronic absorption due to spin–orbit split d–d excitations. An investigation employing optical modeling of the substrate and overlayer dielectric functions revealed that the CoN electronic resonance induces a strong dispersion of the dielectric function in the low-frequency region in which the Co–N peak was observed, leading to a positive contribution of the Co–N band relative to the baseline. The weak features between 1000 and 1300 cm^{-1} were attributed to incomplete cancellation of the SiO_2 phonons of the underlying SiO_2 layer, arising from differences in the degree of attenuation following nitridation.

An analysis of the Co 2p core-level position (0.4 eV shift from the metallic Co position) and the relative intensities of the Co 2p and N 1s core levels in the XPS measurements (Fig. 26.41a,b) indicated that the ultrathin surface layer is CoN, with a Co/N stoichiometry of 1 : 1. Based on the attenuation of the substrate signal (Fe 2p core level), the intensity of thickness of this layer was derived to be 1.5 nm.

To determine the chemical composition of the surface layer, LEIS measurements were performed after surface nitridation. Interestingly, the LEIS spectra of the nitrided surface displayed only a very weak Co peak (Fig. 26.41c,d), shifted with respect to its position on the clean surface by 10–20 eV, indicating that the Co atoms are subsurface. This finding is consistent with the first layer being fully passivated by N and O. In addition, measurements performed as a function of Ar^+ sputtering showed that the O signal was localized at the outer surface, and not present throughout the entire 1.5 nm of the film. Through the application of these three combined techniques, the chemistry of the near-surface region could be tracked at each stage of treatment to show that (i) an ultrathin CoN layer is formed when clean Co surfaces are exposed to nitrogen plasma, (ii) oxygen is incorporated into the films from the plasma source in the form of NO^+, and (iii) the oxygen impurities are predominantly localized at the outermost surface and not throughout the entire nitrided region.

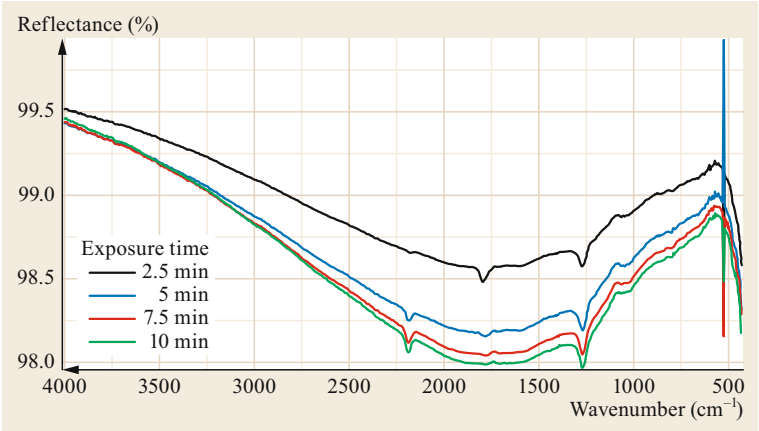

Fig. 26.40 IRRAS spectra obtained during nitrogen plasma treatment of Co surfaces. Here, the reference measurement is that of the clean surface before exposure to nitrogen plasma

A similar approach was employed to study the more complex but industrially relevant alloy surface CoFeB [26.121]. In that case, the films were crystallized by annealing to 673 K, followed by Ar^+ sputtering to remove the remaining oxide. In situ IRRAS spectra taken during nitrogen plasma treatment showed trends similar to those observed for Co nitridation, with the formation of NO^+ and a variation in the broadband absorbance throughout the mid-IR. In this case, two vibrational bands were observed in the Co–N/Fe–N

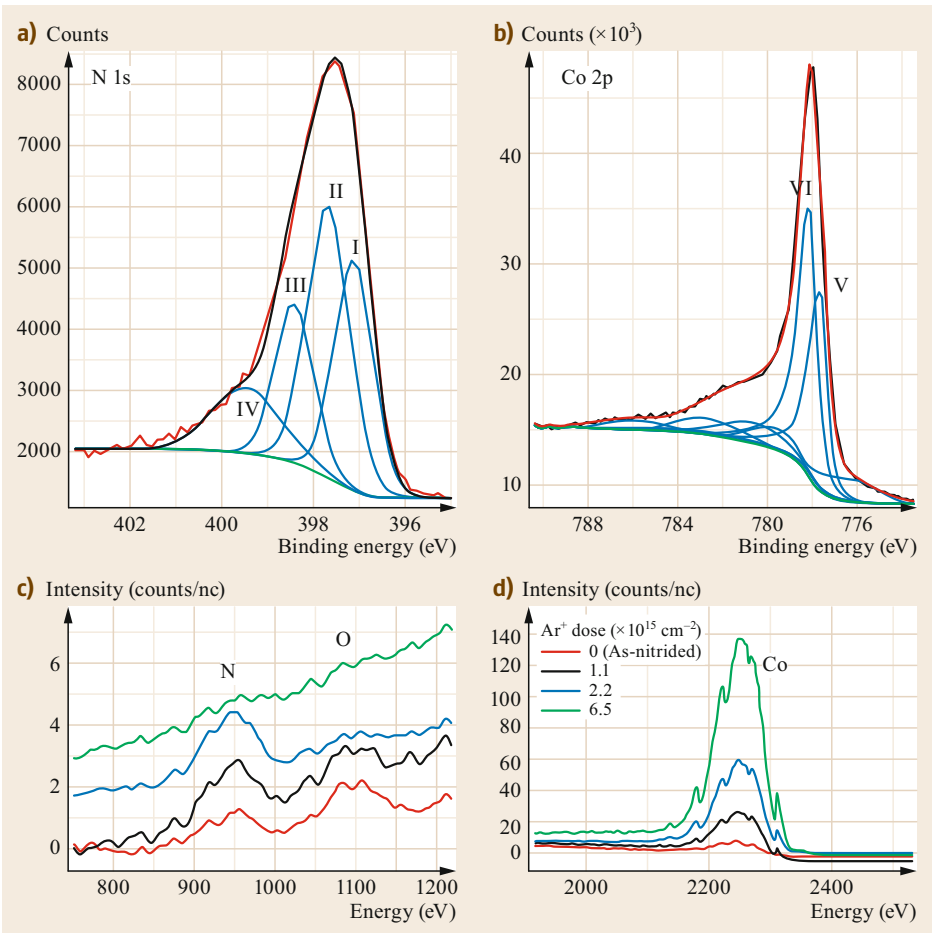

Fig. 26.41 **(a)** N 1s and **(b)** Co 2p spectra from nitrided Co films. Peaks labeled I, II, III, and IV in **(c)** are due to surface-shifted CoN, fully coordinated CoN, Co oxynitride, and NO^+, respectively. Peaks V and VI in **(d)** are due to the underlying Co substrate and the CoN overlayer, respectively. **(c,d)** 3 keV He^+ LEIS spectra from the same films taken as a function of Ar^+ sputtering (Reprinted from [26.119], with the permission of AIP Publishing)

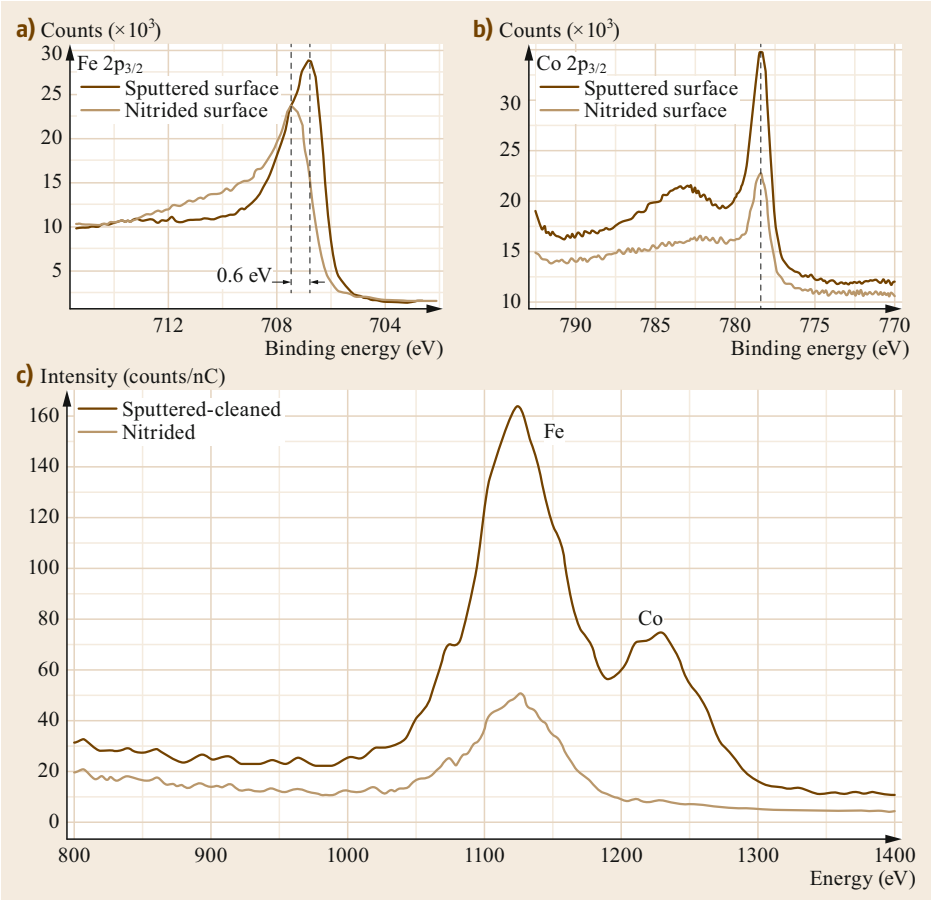

Fig. 26.42
(a) Fe $2p_{3/2}$ and **(b)** Co $2p_{3/2}$ spectra of sputter-cleaned and nitrided CoFeB films. **(c)** 5 keV Ne^+ LEIS spectra of sputter-cleaned and nitrided CoFeB films (Reprinted from [26.121], with the permission of AIP Publishing)

stretching region, consistent with the formation of a nitrogen-rich film, such as Fe_2N_3.

XPS and LEIS measurements were collected for the clean surface and following nitridation. The XPS spectra revealed a substantial shift of the Fe 2p core level but not the Co 2p core level, the intensity of the latter being much more heavily attenuated (Fig. 26.42a,b). These results suggest a preferential reactivity of the Fe atoms with nitrogen in the alloy and little reactivity of Co, which was further supported by LEIS measurements using 5 keV Ne^+ to resolve the similar masses of Co and Fe. The LEIS measurements showed that both Fe and Co were initially present on the clean surface, but only Fe was detectable following nitridation (Fig. 26.42c), consistent with Co absorption into the film after Fe reaction with N to form iron nitride. These results suggest that the formation of iron nitride is energetically more favorable than cobalt nitride. Quantification of the Fe 2p and N 1s spectra suggest that the stoichiometry of the iron nitride film is Fe_2N_3, significantly higher than the FeN obtained through plasma nitridation of an Fe(100) single crystal. This finding is further supported by the number, frequencies, and relative intensities of the bands observed in the Fe−N stretching region. Additional measurements of the surfaces following annealing showed that the process was partially reversible, and that the Fe_2N_3 layer decomposed following annealing to 673 K, leaving some residual N likely occupying interstitial sites in the form of Fe_4N [26.122]. The Fe/Co surface concentration did not reach the original level observed for the clean surface, but rather had a Co surface concentration less than half that of the clean surface, pointing to a potential method to tune the Fe/Co ratio of the surface of CoFeB alloys relative to the bulk. This example illustrates again how the three techniques are used in a complementary fashion, each providing critical information that would not have been unambiguous from the individual techniques taken on their own. Furthermore, the in situ capabilities of the system used in this work enabled all three techniques to be performed on the exact same sample without contamination during transfers, providing an extra degree of confidence in the results.

26.4.5 Dielectric Surfaces: Termination of HF-etched Si_3N_4

Silicon nitride (Si_3N_4) is employed for a number of applications in microelectronic devices, such as dielectric spacers and diffusion barriers. The surfaces of Si_3N_4 films readily oxidize when exposed to ambient conditions to form a Si-rich N-depleted region, which can interfere with applications dependent on the surface composition (functionalization or integration with other materials). It is therefore important to remove the native oxide or oxynitride and to control and understand the resulting termination after oxide removal typically achieved by HF etching. HF etching of Si_3N_4 had been studied by several groups [26.124–127], with conflicting reports on the resulting surface species present after etching, ranging from complete NH_x termination to surficial Si–H and Si–F. To clarify the relationship between the chemical termination of the etched surfaces and conditions used for HF treatment and subsequent rinsing, *Liu* et al. [26.123, 128] performed a combination of IR absorption, XPS, and LEIS measurements as a function of chemical treatment. Figure 26.43 shows the IR absorption spectra of the Si_3N_4 samples following HF etching and either direct nitrogen drying or rinsing with toluene, methanol water, acetonitrile (ACN), or dimethyl sulfoxide. The intense negative peaks at 838 and 1122 cm^{-1} are associated with the weakening of Si_3N_4 phonon modes associated with etching of the bulk nitride. When HF-etched surfaces were not immediately rinsed in deionized (DI) water, intense modes were observed at 3330 and 1440 cm^{-1} associated with N–H stretching and bending vibrations, respectively. However, a more careful examination of these spectra revealed that they could not be due to NH_x termination of the Si_3N_4 surfaces. Instead, the frequency of the 1440 cm^{-1} mode is known to be characteristic of the bending mode of NH_4^+

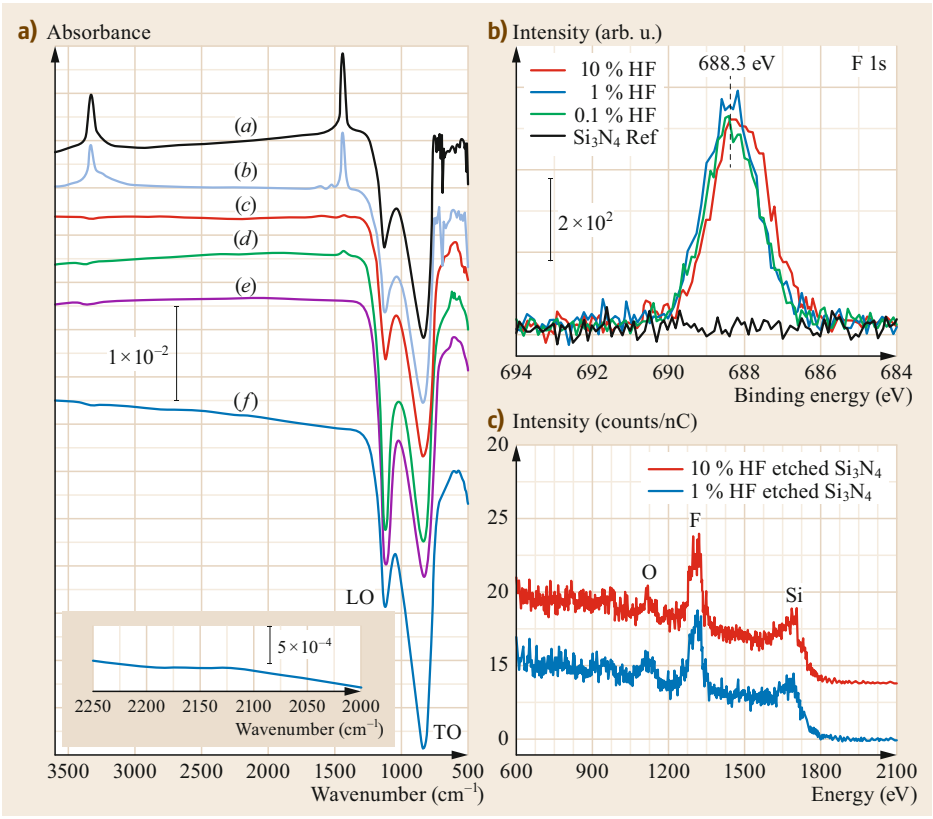

Fig. 26.43 **(a)** Transmission IR absorption spectra of HF-etched Si_3N_4 films and *(a)* directly dried with N_2 with no water rinsing, *(b)* dried with nitrogen and soaked in toluene overnight, *(c)* dried with nitrogen and soaked in methanol overnight, *(d)* directly rinsed with dimethyl sulfoxide and dried with nitrogen, *(e)* directly rinsed with acetonitrile and dried with nitrogen, and *(f)* directly rinsed with deionized water and dried with nitrogen. **(b)** F 1s XP spectra of Si_3N_4 films etched with different concentrations of HF and directly rinsed with water. **(c)** 3 keV He^+ LEIS spectra of Si_3N_4 etched with 1% and 10% HF and directly rinsed with water (Reprinted from [26.123], with the permission of AIP Publishing)

ions, pointing to the adsorption of ammonium salts on the surface.

Indeed, subsequent atomic force microscopy (AFM) measurements of surfaces prepared without immediate rinsing or rinsing with a nonpolar solvent clearly showed the presence of deposits at the surface with typical dimensions > 100 nm. On the basis of the reactants involved and position of the observed IR modes, these particles were determined to be $(NH_4)_2SiF_6$ salts. The finding that improper rinsing could yield IR features that were previously interpreted as originating from NH_x surface chemical functionalities explained these previous observations of HF-etched surfaces, since immediate rinsing was not reported, particularly because IR measurements of surfaces that were immediately rinsed with appropriate solvents showed only a very weak band at 1550 cm^{-1} (instead of 1440 cm^{-1}) that could originate from no more than ≈ 10% of a NH_x monolayer, and its quantification is discussed below. Furthermore, no features that could be attributed to surficial Si−H bonds were detected. Thus, despite reports claiming complete hydrogen termination of the HF-etched surfaces, the data pointed to the need for a more refined model for the composition of the etched surface.

XPS (Fig. 26.43b) and LEIS (Fig. 26.43c) measurements were employed to identify the elements present at the surface and their chemical state. Both He^+ LEIS and XPS measurements showed the presence of Si, F, and O at the surface, in relative amounts that were independent of the HF concentration used for etching (from 0.1 to 10%). The F 1s core level (Fig. 26.43b) is characterized by a single symmetric peak at 688.3 eV binding energy, consistent with the formation of a Si−F bond and not N−F bonding, indicating a single-chemical environment for surface F atoms. Residual physisorbed atmospheric contaminants were ruled out as the origin of this signal, as the F signal did not initially disappear as gentle gas-cluster ion beam (GCIB) sputtering (Fig. 26.44) was used to remove weakly adsorbed species in a gradual layer-by-layer fashion. Interestingly, prolonged GCIB bombardment of the surface led to complete elimination of F, but not of O; rather, there was an additional component in the O 1s spectrum shifted by ≈ 0.6 eV toward lower binding energy (after accounting for charging effects). The redshifted position, and the fact that this peak persists even after all surface F is removed, point to the fact that some O atoms are located in the subsurface region. All the observations taken together suggest that there are two chemically distinct oxygen moieties as a result of HF etching: a surficial hydroxyl group and O atoms inserted into the Si back-bonds to form Si−O−Si.

Quantification of the relative amounts of the surface species present (atop F, hydroxyl, and amine groups) posed a challenging problem that required a multifaceted approach to yield physically meaningful results. Often, XPS coverage is evaluated based on the attenuation of the substrate due to an adlayer, and the degree of attenuation is determined from measurements of the substrate under identical conditions with and without the adlayer. Unfortunately, since the substrate comprises largely light elements, even the comparatively gentle GCIB method used to remove the F and O lead to preferential sputtering of the N in the substrate, rendering this approach inaccurate. An alternative method was used to circumvent this problem: a system with a well-defined one-third monolayer coverage [26.129] of atop Si−F species was produced and measured as a calibra-

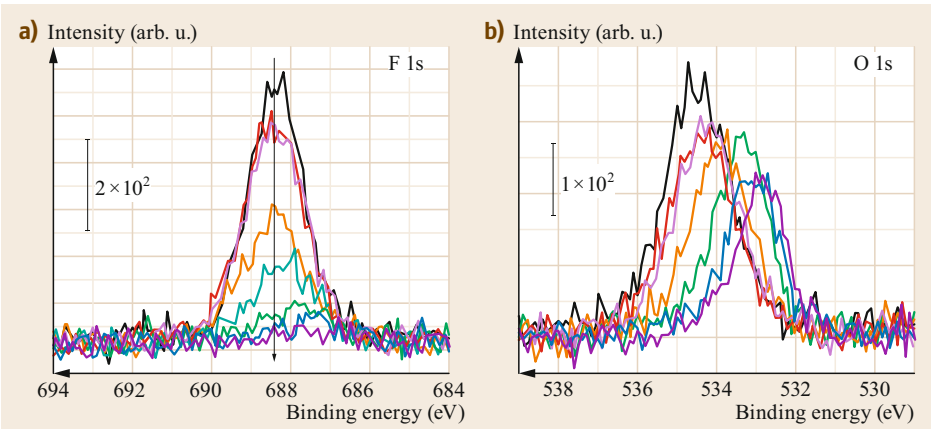

Fig. 26.44 F 1s **(a)** and O 1s **(b)** XP spectra of HF-etched Si_3N_4 films prepared with proper water rinsing as a function of GCIB sputtering. The spectra correspond to the following GCIB-sputtering sequence: no sputtering, 5 kV 30 s and 1 min net sputtering, followed by 10 kV for net sputtering times of 15 s, 45 s, 2 min, 6 min, 11 min, and 16 min (Reprinted from [26.128], with the permission of AIP Publishing)

tion for XPS intensities. With this information, it was possible to then quantify the amount of F present at the surface of the HF-etched Si_3N_4 surfaces: ≈ 70% F monolayer.

Quantification of the coverage of $-NH_2$ groups at the surface cannot be accomplished through the XPS measurements with calibrations standards, as the N 1s is dominated by the signal from the substrate; an alternative method for evaluating the coverage involved performing a chemical titration of existing NH_x surface groups via surface reactions and quantification of the resulting reaction products. In particular, the IR intensity of the C−H stretching modes in organic aldehydes, known to be preferentially reactive toward amine groups, were used to quantify the amount of $-NH_2$ initially present. In this manner, the total number of molecules reacted with the HF-etched surface was estimated at $17 \pm 5\%$ of a monolayer, when an organic functionalized SiO_2 surface was used to calibrate the C−H stretching intensity of a complete monolayer.

Similarly, quantification of surface Si−OH was achieved using a target molecule that reacts preferentially with hydroxyl groups, in this case chlorodimethyloctadecylsilane (CDMODS). Following reaction, the measured loss at the O−H stretch intensity was $\approx 37 \pm 16\%$ of the loss following identical reaction conditions with a fully OH-terminated SiO_2 surface. Assuming complete reaction with all surface hydroxyl groups, the OH coverage is therefore estimated at $37 \pm 16\%$ monolayer. Interestingly, despite having lost considerably less OH than for the corresponding reaction on SiO_2, the etched Si_3N_4 surface showed hydrocarbon content nearly equal to that observed for SiO_2, suggesting additional potential reaction sites. LEIS measurements of CDMODS-functionalized Si_3N_4 (Fig. 26.45) after annealing to remove the organic groups showed an F/Si ratio of $76 \pm 11\%$ of that observed for the etched Si_3N_4 surface with similar thermal treatment but no CDMODS functionalization, indicating that surficial F atoms are removed during the reaction to expose additional reactive sites as one additional route toward incorporation of CDMODS onto the surface.

In this complex and inhomogeneous system, identification and quantification of the final surface termination was particularly challenging, as several chemical moieties were present depending on the treatment, and no technique taken on its own was sensitive to all species present at the surface. Only the combination of IR, XPS, and LEIS made it possible to identify and control the HF-etched Si_3N_4 surface and arrive at a method for selective functionalization, by first performing a Schiff base reaction with aldehydes and the NH_2 groups, and then reaction with silanes and the OH groups, using molecules with different head groups.

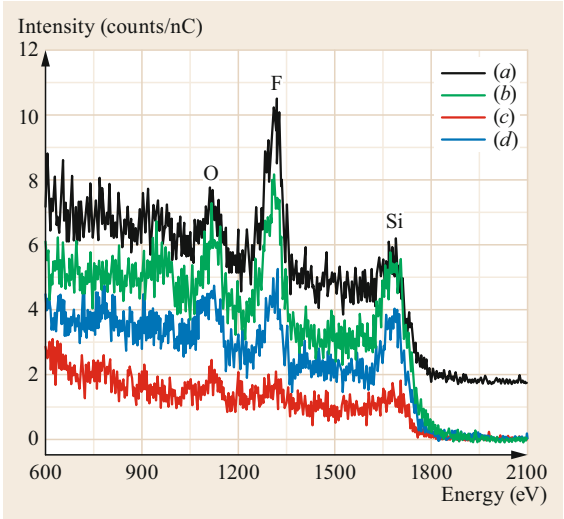

Fig. 26.45 3 keV He^+ LEIS spectra of HF-etched Si_3N_4 films *(a)* immediately after water rinsing, *(b)* after annealing the film in *(a)* to 873 K, *(c)* etched and CDMODS-reacted Si_3N_4 measured at 303 K, and *(d)* the film in *(c)* measured after annealing to 873 K (Reprinted from [26.128], with the permission of AIP Publishing)

26.4.6 Mass Transport in Complex and Irregular Surfaces and Nanostructures

Metal–organic frameworks (MOFs), crystalline nanoporous materials comprising metal ions or clusters linked by organic ligands, are emerging as key materials for applications such as energy storage, gas capture and separation, sensors, and even biomedicine. A major challenge in optimizing their performance for these applications is the relatively weak adsorption energy and therefore inefficient retention of many target molecules. While modification or functionalization of the ligands is one route toward selective retention of specific molecules, *Tan* et al. [26.130] examined a new and more universal approach to enable retention of molecules in MOFs by adding a capping layer to the surface of the MOF channels to prevent out-diffusion following gas loading. Focusing on a particular MOF with a channel structure (MOF-74, Fig. 26.46a), they demonstrated that by introducing a *sticky* molecule (4 Torr) such as ethylenediamine (EDA) after CO gas loading (40 Torr), a monolayer-thick molecular cap was formed, preventing the escape of loaded CO molecules. The rationale for this approach was to block the channel structure with a relatively bulky molecule that interacts sufficiently with the MOF surface to remain adsorbed and prevent out-diffusion of the trapped molecules, as shown by the schematic in Fig. 26.45b.

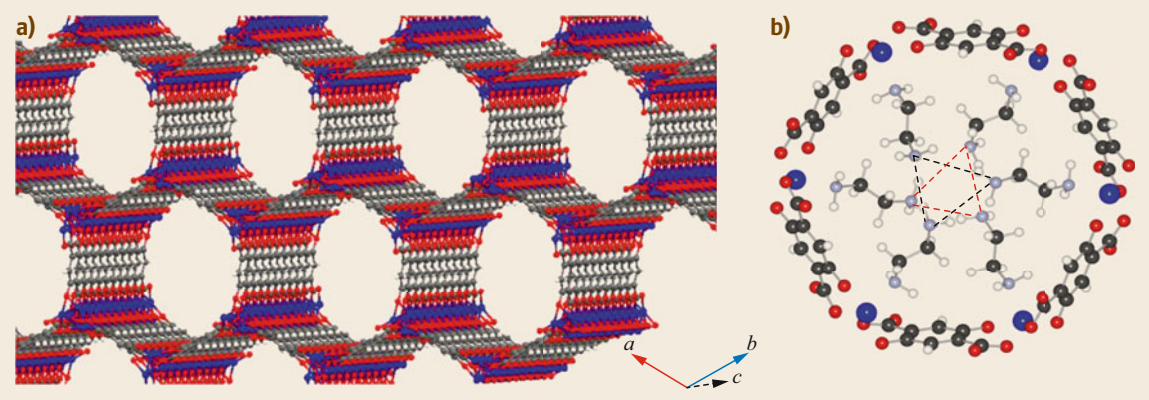

Fig. 26.46 **(a)** Schematic of the MOF-74 structure. **(b)** Optimized geometry of EDA adsorbed at the channel openings (Reprinted by permission from [26.130], © Nature 2016)

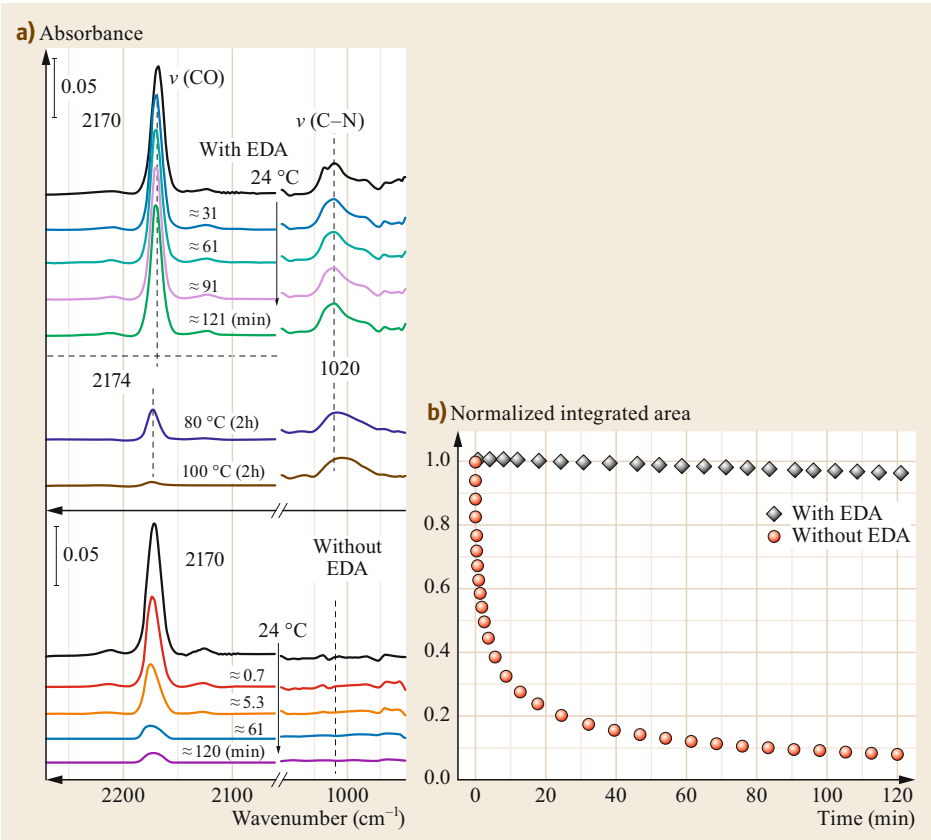

Fig. 26.47 **(a)** *Top panel*: IR absorption spectra following CO loading and capping as a function of evacuation time. *Middle panel*: thermal stability of the loaded/capped system. *Bottom panel*: IR absorption spectra as a function of evacuation time following CO loading in the absence of an EDA cap. **(b)** Integrated area of the CO stretching features in Fig. 26.39a as a function of evacuation time (Reprinted by permission from [26.130], © Nature 2016)

The gas loading, capping, and pump-down process was monitored in situ and as a function of time using IR spectroscopy. The measurements were performed in a high-pressure cell enabling normal incident transmission measurements on pressed powders of the MOF material. Figure 26.47a shows differential IR spectra taken as a function of time following CO loading, EDA capping, and pump-down. The data show modes assigned to the C≡O stretch of the trapped molecules and C−N stretching of the adsorbed EDA, both of which remain nearly constant over the course of the two hours during which the experiment was performed. In contrast, the bottom panel shows analogous measurements taken on samples loaded

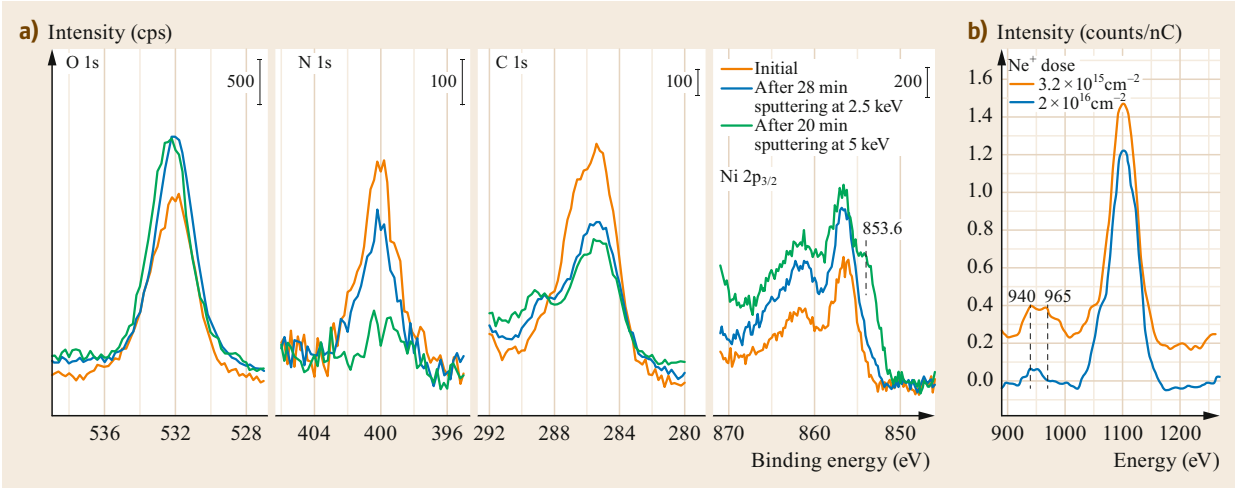

Fig. 26.48 **(a)** O 1s, N 1s, C 1s, and Ni 2p core-level spectra of loaded and capped Ni-MOF74 as a function of GCIB sputter time. **(b)** 3 keV He^+ LEIS spectra of loaded and capped Ni-MOF74 as a function of sputtering using 5 keV Ne^+ (Reprinted by permission from [26.130], © Nature 2016)

identically with CO but not capped with EDA; the data show that, following evacuation for 2 h, the CO signature is reduced to less than 10% of its initial value. To quantify the temporal stability of trapped gases, the integrated intensity of the C≡O stretch recorded as a function of time after pump-down is shown in Fig. 26.47b for the experiments with and without the EDA capping layer. Clearly, the presence of the EDA has the effect of preventing the trapped CO molecules from exiting the MOF through the pore channels, and therefore serves to confine the gases within the MOFs.

To test the theory that the EDA was adsorbed on the exterior surface of the channels, XPS and LEIS measurements were performed. Figure 26.48a shows O 1s, N 1s, C 1s, and Ni 2p XP spectra of the loaded, capped MOF system as-prepared and as a function GCIB sputtering. Again, the GCIB can be regarded as a *gentle* sputtering technique that is ideal for removing light elements at the surface one layer at a time. The data show that, as a function of GCIB sputtering time, the surface N signal decreases to the detection limit of the instrument, but the C, O, and Ni peaks, representative of the bulk of the MOF, are maintained. These data point to the fact that any N-containing moieties are located close to the surface. LEIS measurements were performed on loaded, capped MOF samples to further verify the localization of the EDA layers. Data collected with 3 keV He^+ (Fig. 26.48b) clearly show a peak due to N at the surface of the MOF samples. The peak appeared as a doublet with components centered at ≈ 940 and 960 eV, showing unambiguously that N is present at the outermost region of the surface, and supporting the model of the EDA molecules residing in a position as depicted in Fig. 26.46b to *cap* the channels. Prolonged sputtering with 5 keV showed an elimination of the 960 eV component, and only the 940 eV component remained. These data can again be interpreted as N atoms lying directly below the surface, as the 20 eV shift observed relative to the position of the surface peak is well matched for the energy cost for a complete neutralization and reionization cycle, as discussed in Sect. 26.3. The persistence of this subsurface peak following further sputtering was ascribed to the irregular geometry of the (powder) samples, rendering many sites, such as those residing at grain boundaries or regions blocked by neighboring particles, invisible to the sputtering beam but accessible through the process of multiple scattering and reionization. This work thus demonstrates an approach for characterizing surface reactions and mass transport in complex and irregular surfaces and nanostructures, even hybrid organic-inorganic materials.

26.5 Conclusions and Outlook

This chapter has illustrated how combined vibrational (in particular IR), XPS, and LEIS measurements enable quantitative, comprehensive analysis of studies of adsorbate structures and bonding configurations, sur-

face reactions, and mass transport for a wide variety of systems. The examples presented above demonstrate how the information derived from experiments combining these techniques can unravel specific properties (e.g., catalytic reactivity, thin film growth, semiconductor doping) of the system of interest. From these examples, several overarching conclusions are reached:

1. More often than not, a single experimental probe is insufficient to fully understand a given surface structure, reaction, etc. The combined assets of the techniques discussed here can strengthen the conclusions of each individual technique, enabling quantitation and insight that would not be possible for a single technique used alone.
2. The different interaction volumes of IR photons, XPS photoelectrons, and LEIS ions can be used in a complementary way to deduce the relative location of a given species with respect to the surface. IR absorption measurements probe the greatest depth (throughout the complete sample for the case of transmission and MIR measurements and one-half the skin depth for the case of IRRAS with metal surfaces, typically ≈ 30 nm), but signals originating only from the surface can be discriminated through the use of a proper reference measurement. XPS effectively performs an average over the outermost $\approx$ 5 nm weighted by the depth of the atom from which the photoelectrons originate. The surface peaks in LEIS originate from only the outermost 1–2 atomic layers, although subsurface signals (characterized by a shift in the energy of the backscattered ions) can provide static depth profiles up to $\approx 5-10$ nm. These effects can yield information on different aspects of a given system; for example, details on chemical bonding of an adsorbate overlayer from IR absorption, chemical state of the substrate from XPS, and diffusion processes from LEIS.
3. While the examples presented here have shown a synergistic marriage between IR, LEIS, and XPS measurements, other combinations of surface-sensitive techniques are also clearly valuable for studies of bonding configurations, surface reactions, and mass transport. For example, many of the studies discussed in this chapter combine LEIS or IR measurements with LEED in the study of ordered structures, which can provide further structural insight into many systems. Similarly, combining the spectroscopic techniques discussed above with scanning probe microscopy such as STM can provide further information on coverage, surface morphology, bonding configurations, and surface electronic structure [26.9]. As is often the case, the most useful combinations (e.g., STM and IR) are also the most difficult to realize in practice, but the efforts are worth it!

As experimental developments have continued to improve, and initial results on these combined techniques have demonstrated the value of this multi-technique approach, the motivation for developing other synergistic combinations increases. Hopefully, this chapter will add to this motivation.

References

26.1 Y.J. Chabal: Surface infrared spectroscopy, Surf. Sci. Rep. **8**, 211–357 (1988)

26.2 C.J. Hirschmugl: Frontiers in infrared spectroscopy at surfaces and interfaces, Surf. Sci. **500**, 577–604 (2002)

26.3 N. Sheppard, J. Erkelens: Vibrational spectra of species adsorbed on surfaces: forms of vibrations and selection rules for regular arrays of adsorbed species, Appl. Spectrosc. **38**, 471–485 (1984)

26.4 H.G. Tompkins: Infrared reflection-absorption spectroscopy. In: *Methods of Surface Analysis*, Methods and Phenomena, Vol. 1, ed. by A.W. Czanderna (Elsevier, Amsterdam 1975), Chap. 10

26.5 W. Suetaka: *Surface Infrared and Raman Spectroscopy* (Springer, New York 1995)

26.6 V.P. Tolstoy, I.V. Chernyshova, V.A. Skryshevsky: *Handbook of Infrared Spectroscopy of Ultrathin Films* (Wiley, Hoboken 2003)

26.7 J.T. Yates, T.E. Madey: *Vibrational Spectroscopy of Molecules on Surfaces* (Springer, New York 1987)

26.8 F.M. Hoffmann: Infrared reflection-absorption spectroscopy of adsorbed molecules, Surf. Sci. Rep. **3**, 107–192 (1983)

26.9 J. Pal, M. Smerieri, E. Celasco, L. Savio, L. Vattuone, M. Rocca: Morphology of monolayer MgO films on Ag(100): switching from corrugated islands to extended flat terraces, Phys. Rev. Lett. **112**(12), 126102 (2014)

26.10 A. Pfau, K.D. Schierbaum: The electronic structure of stoichiometric and reduced CeO_2 surfaces—an XPS, UPA and HREELS study, Surf. Sci. **321**, 71–80 (1994)

26.11 S.C. Street, C. Xu, D.W. Goodman: The physical and chemical properties of ultrathin oxide films, Ann. Rev. Phys. Chem. **48**, 43–68 (1997)

26.12 D.R. Mullins, D.R. Huntley, S.H. Overbury: The nature of the sulfur induced surface reconstruction on Ni(111), Surf. Sci. **323**, L287–L292 (1995)

26.13 P.M.A. Sherwood: *Vibrational Spectroscopy of Solids* (Cambridge Univ. Press, Cambridge 1972)

26.14 E.B. Wilson, J.C. Decius, P.C. Croscc: *Molecular Vibrations* (Dover, Mineola 1955)

26.15 P. Hollins: The influence of surface-defects on the infrared spectra of adsorbed species, Surf. Sci. Rep. **16**, 51–94 (1992)

26.16 R.G. Greenler: Infrared study of adsorbed molecules on metal surfaces by reflection techniques, J. Chem. Phys. **44**, 310–315 (1966)

26.17 G.A. Kimmel, M. Baer, N.G. Petrik, J. VandeVondele, R. Rousseau, C.J. Mundy: Polarization- and azimuth-resolved infrared spectroscopy of water on TiO_2(110): anisotropy and the hydrogen-bonding network, J. Phys. Chem. Lett. **3**, 778–784 (2012)

26.18 N.G. Petrik, G.A. Kimmel: Adsorption geometry of CO versus coverage on TiO_2 from s- and p-polarized infrared spectroscopy, J. Phys. Chem. Lett. **3**, 3425–3430 (2012)

26.19 A.M. Bradshaw, F.M. Hoffmann: Chemisorption of carbon-monoxide on palladium single crystal surfaces-IR spectroscopic evidence for localized site adsorption, Surf. Sci. **72**, 513–535 (1978)

26.20 J. Fan, M. Trenary: Symmetry and the surface infrared selection rule for the determination of the structure of molecules on metal surfaces, Langmuir **10**, 3649–3657 (1994)

26.21 D.A. Outka, J. Stöhr, W. Jark, P. Stevens, J. Solomon, R.J. Madix: Orientation and bond length of molecular oxygen on Ag(110) and Pt(111): a near-edge x-ray-absorption fine-structure study, Phys. Rev. B **35**, 4119–4122 (1987)

26.22 G.S. Higashi, Y.J. Chabal, G.W. Trucks, K. Raghavachari: Ideal hydrogen termination of the Si-(111) surface, Appl. Phys. Lett. **56**, 656–658 (1990)

26.23 I.T. Clark, B.S. Aldinger, A. Gupta, M.A. Hines: Aqueous etching produces Si(100) surfaces of near-atomic flatness: strain minimization does not predict surface morphology, J. Phys. Chem. C **114**, 423–428 (2010)

26.24 C. Mui, J.H. Han, G.T. Wang, C.B. Musgrave, S.F. Bent: Proton transfer reactions on semiconductor surfaces, J. Am. Chem. Soc. **124**, 4027–4038 (2002)

26.25 C. Mui, G.T. Wang, S.F. Bent, C.B. Musgrave: Reactions of methylamines at the Si(100)-2×1 surface, J. Chem. Phys. **114**, 10170–10180 (2001)

26.26 X. Zhang, E. Garfunkel, Y.J. Chabal, S.B. Christman, E.E. Chaban: Stability of HF-etched Si(100) surfaces in oxygen ambient, Appl. Phys. Lett. **79**, 4051–4053 (2001)

26.27 M.R. Vilar, J. El Beghdadi, F. Debontridder, R. Artzi, R. Naaman, A.M. Ferraria, A.M.B. do Rego: Characterization of wet-etched GaAs(100) surfaces, Surf. Interface Anal. **37**, 673–682 (2005)

26.28 M. Shinohara, T. Kuwano, Y. Akama, Y. Kimura, M. Niwano, H. Ishida, R. Hatakeyama: Interaction of hydrogen-terminated Si(100), (110), and (111) surfaces with hydrogen plasma investigated by in situ real-time infrared absorption spectroscopy, J. Vac. Sci. Technol. A **21**, 25–31 (2003)

26.29 K.J. Uram, U. Jansson: The adsorption of disilane on Si(111)-7×7 as studied by multiple internal-reflection spectroscopy, Surf. Sci. **249**, 105–116 (1991)

26.30 G.L. Carr: Resolution limits for infrared microspectroscopy explored with synchrotron radiation, Rev. Sci. Instrum. **72**, 1613–1619 (2001)

26.31 H.A. Bechtel, E.A. Muller, R.L. Olmon, M.C. Martin, M.B. Raschke: Ultrabroadband infrared nanospectroscopic imaging, Proc. Natl. Acad. Sci. U.S.A. **111**, 7191–7196 (2014)

26.32 E.C. Mattson, M.J. Nasse, M. Rak, K.M. Gough, C.J. Hirschmugl: Restoration and spectral recovery of mid-infrared chemical images, Anal. Chem. **84**, 6173–6180 (2012)

26.33 E. Levenson, P. Lerch, M.C. Martin: Spatial resolution limits for synchrotron-based infrared spectromicroscopy, Infrared Phys. Technol. **51**, 413–416 (2008)

26.34 E. Stavitski, B.M. Weckhuysen: Infrared and Raman imaging of heterogeneous catalysts, Chem. Soc. Rev. **39**, 4615–4625 (2010)

26.35 M.J. Nasse, M.J. Walsh, E.C. Mattson, R. Reininger, A. Kajdacsy-Balla, V. Macias, R. Bhargava, C.J. Hirschmugl: High-resolution Fourier-transform infrared chemical imaging with multiple synchrotron beams, Nat. Methods **8**, 413–U58 (2011)

26.36 I.D. Barcelos, A.R. Cadore, L.C. Campos, A. Malachias, K. Watanabe, T. Taniguchi, F.C.B. Maia, R. Freitas, C. Deneke: Graphene/h-BN plasmon–phonon coupling and plasmon delocalization observed by infrared nanospectroscopy, Nanoscale **7**, 11620–11625 (2015)

26.37 B. Knoll, F. Keilmann: Near-field probing of vibrational absorption for chemical microscopy, Nature **399**, 134–137 (1999)

26.38 R. Hillenbrand, T. Taubner, F. Keilmann: Phonon-enhanced light-matter interaction at the nanometre scale, Nature **418**, 159–162 (2002)

26.39 K.W. Post, B.C. Chapler, M.K. Liu, J.S. Wu, H.T. Stinson, M.D. Goldflam, A.R. Richardella, J.S. Lee, A.A. Reijnders, K.S. Burch, M.M. Fogler, N. Samarth, D.N. Basov: Sum-rule constraints on the surface state conductance of topological insulators, Phys. Rev. Lett. **115**, 116804 (2015)

26.40 Y.B. Zhang, T.T. Tang, C. Girit, Z. Hao, M.C. Martin, A. Zettl, M.F. Crommie, Y.R. Shen, F. Wang: Direct observation of a widely tunable bandgap in bilayer graphene, Nature **459**, 820–823 (2009)

26.41 J.E. Reutt, Y.J. Chabal, S.B. Christman: Coupling of H vibration to substrate electronic states in Mo(100)-P(1×1)H and W(100)-P(1×1)H – example of strong breakdown of adiabaticity, Phys. Rev. B **38**, 3112–3132 (1988)

26.42 Y.J. Chabal: Electronic damping of hydrogen vibration on the W(100) surface, Phys. Rev. Lett. **55**, 845–848 (1985)

26.43 B.N.J. Persson, A.I. Volokitin: On the origin of anti-absorption resonances in adsorbate vibrational spectroscopy, Chem. Phys. Lett. **185**, 292–297 (1991)

26.44 B.N.J. Persson: Surface resistivity and vibrational damping in adsorbed layers, Phys. Rev. B **44**, 3277–3296 (1991)

26.45 Z.Y. Zhang, D.C. Langreth: Electronic damping of adsorbate fundamental and overtone vibrations at metal-surfaces, Phys. Rev. B **39**, 10028–10046 (1989)

26.46 K.E. Smith, S.D. Kevan: Nonadiabatic adsorbate vibrational damping and surface electronic-structure – H on W(001), Phys. Rev. Lett. **64**, 567–570 (1990)

26.47 C.L.A. Lamont, B.N.J. Persson, G.P. Williams: Dynamics of atomic adsorbates – hydrogen on Cu(111), Chem. Phys. Lett. **243**, 429–434 (1995)

26.48 H. Niehus, W. Heiland, E. Taglauer: Low-energy ion scattering at surfaces, Surf. Sci. Rep. **17**, 213–303 (1993)

26.49 E. Taglauer, W. Heiland: Surface analysis with low-energy ion scattering, Appl. Phys. **9**, 261–275 (1976)

26.50 H.H. Brongersma, M. Draxler, M. de Ridder, P. Bauer: Surface composition analysis by low-energy ion scattering, Surf. Sci. Rep. **62**, 63–109 (2007)

26.51 T.M. Buck: Low-energy ion scattering spectrometry. In: *Methods of Surface Analysis*, Methods and Phenomena, Vol. 1, ed. by A.W. Czanderna (Elsevier, Amsterdam 1975), Chap. 3

26.52 M. Aono: Quantitative surface structure analysis by low-energy ion scattering, Nucl. Instrum. Methods Phys. Res. B **2**, 374–383 (1984)

26.53 A. Rafati, R. ter Veen, D.G. Castner: Low-energy ion scattering: determining overlayer thickness for functionalized gold nanoparticles, Surf. Interface Anal. **45**, 1737–1741 (2013)

26.54 P. Brüner, T. Grehl, H. Brongersma, B. Detlefs, E. Nolot, H. Grampeix, E. Steinbauer, P. Bauer: Thin film analysis by low-energy ion scattering by use of TRBS simulations, J. Vac. Sci. Technol. A **33**, 01A122 (2015)

26.55 M. Aono, C. Oshima, S. Zaima, S. Otani, Y. Ishizawa: Quantitative surface atomic geometry and two-dimensional surface electron-distribution analysis by a new technique in low-energy ion scattering, Jpn. J. Appl. Phys. **20**, L829–L832 (1981)

26.56 H.A. Gasteiger, P.N. Ross, E.J. Cairns: LEIS and AES on sputtered and annealed polycrystalline Pt-Ru bulk alloys, Surf. Sci. **293**, 67–80 (1993)

26.57 V.R. Stamenkovic, B.S. Mun, K.J.J. Mayrhofer, P.N. Ross, N.M. Markovic: Effect of surface composition on electronic structure, stability, and electrocatalytic properties of Pt-transition metal alloys: Pt-skin versus Pt-skeleton surfaces, J. Am. Chem. Soc. **128**, 8813–8819 (2006)

26.58 V. Stamenkovic, T.J. Schmidt, P.N. Ross, N.M. Markovic: Surface segregation effects in electrocatalysis: kinetics of oxygen reduction reaction on polycrystalline Pt_3Ni alloy surfaces, J. Electroanal. Chem. **554**, 191–199 (2003)

26.59 J.P. Jacobs, A. Maltha, J.G.H. Reintjes, J. Drimal, V. Ponec, H.H. Brongersma: The surface of catalytically active spinels, J. Catal. **147**, 294–300 (1994)

26.60 W.P. Zhou, X.F. Yang, M.B. Vukmirovic, B.E. Koel, J. Jiao, G.W. Peng, M. Mavrikakis, R.R. Adzic: Improving electrocatalysts for O_2 reduction by fine-tuning the Pt-support interaction: Pt monolayer on the surfaces of a $Pd_3Fe(111)$ single-crystal alloy, J. Am. Chem. Soc. **131**, 12755–12762 (2009)

26.61 K. Luo, T. Wei, C.W. Yi, S. Axnanda, A.W. Goodman: Preparation and characterization of silica supported Au-Pd model catalysts, J. Phys. Chem. B **109**, 23517–23522 (2005)

26.62 H. Winter: Image charge effects in ion surface scattering, J. Phys. Condens. Matter **8**, 10149–10183 (1996)

26.63 R.L. Erickson, D.P. Smith: Oscillatory cross-sections in low-energy Ion scattering from surfaces, Phys. Rev. Lett. **34**, 297–299 (1975)

26.64 H.H. Brongersma, T.M. Buck: Selected topics in low-energy Ion scattering-surface segregation in Cu-Ni alloys and ion neutralization, Surf. Sci. **53**, 649–658 (1975)

26.65 M. Draxler, R. Gruber, H.H. Brongersma, P. Bauer: Velocity scaling of ion neutralization in low energy ion scattering, Phys. Rev. Lett. **89**, 263201 (2002)

26.66 J.F. Ziegler: *The Stopping and Ranges of Ions in Matter* (Pergamon, New York 1977)

26.67 H.H. Brongersma, P.M. Mul: Absolute configuration assignment of molecules and crystals in discussion, Chem. Phys. Lett. **19**, 217–220 (1973)

26.68 D.P. Smith: Scattering of low-energy noble gas ions from metal surfaces, J. Appl. Phys. **38**, 340–347 (1967)

26.69 H.L. Pickering, H.C. Eckstrom: Heterogeneous reaction studies by infrared absorption, J. Phys. Chem. **63**, 512–517 (1959)

26.70 R.L. Park, H.E. Farnsworth: CO adsorption + interaction with oxygen on (110) nickel, J. Chem. Phys. **40**, 2354 (1964)

26.71 W. Heiland, F. Iberl, E. Taglauer, D. Menzel: Oxygen adsorption on (110) silver, Surf. Sci. **53**, 383–392 (1975)

26.72 D.G. Armour, G. Carter, A.G. Smith: A theoretical treatment of low energy ion back-scattering from a row of gold atoms, Radiat. Eff. **3**, 175–181 (1970)

26.73 M.T. Robinson, I.M. Torrens: Computer simulation of atomic-displacement cascades in solids in binary-collision approximation, Phys. Rev. B **9**, 5008–5024 (1974)

26.74 A.L. Boers: Multiple ion scattering, Surf. Sci. **63**, 475–500 (1977)

26.75 E. Taglauer, W. Heiland: Investigation of chain effect in scattering of low-energy noble-gas ions from a Ni(110) surface, Surf. Sci. **33**, 27 (1972)

26.76 H. Niehus, G. Comsa: Ion-scattering spectroscopy in the impact collision mode (ICISS) – surface-structure information from noble-gas and alkali-ion scattering, Nucl. Instrum. Methods Phys. Res. B **15**, 122–125 (1986)

26.77 H. Niehus: Low-energy Ion-scattering for the determination of the locations of surface atoms, Nucl. Instrum. Methods Phys. Res. **218**, 230–234 (1983)

26.78 H.H. Brongersma, P.M. Mul: Analysis of outermost atomic layer of a surface by low-energy ion scattering, Surf. Sci. **35**, 393–412 (1973)

26.79 M. Aono, Y. Hou, C. Oshima, Y. Ishizawa: Low-energy ion-scattering from the Si(001) surface, Phys. Rev. Lett. **49**, 567–570 (1982)

26.80 M. Izumi, Y. Konishi, T. Nishihara, S. Hayashi, M. Shinohara, M. Kawasaki, Y. Tokura: Atomically defined epitaxy and physical properties of strained $La_{0.6}Sr_{0.4}MnO_3$ films, Appl. Phys. Lett. **73**, 2497–2499 (1998)

26.81 J.A. Yarmoff, D.M. Cyr, J.H. Huang, S. Kim, R.S. Williams: Impact-collision ion-scattering spectroscopy of Cu(110) and Cu(110)-(2×1)-O using 5-KeV $^6Li^+$, Phys. Rev. B **33**, 3856–3868 (1986)

26.82 T. Ohnishi, K. Takahashi, M. Nakamura, M. Kawasaki, M. Yoshimoto, H. Koinuma: A-site layer terminated perovskite substrate: $NdGaO_3$, Appl. Phys. Lett. **74**, 2531–2533 (1999)

26.83 M. Yoshimoto, T. Maeda, K. Shimozono, H. Koinuma, M. Shinohara, O. Ishiyama, F. Ohtani: Topmost surface-analysis of $SrTiO_3$(001) by coaxial impact-collision ion-scattering spectroscopy, Appl. Phys. Lett. **65**, 3197–3199 (1994)

26.84 T. Fujino, M. Katayama, K. Inudzuka, T. Okuno, K. Oura, T. Hirao: Surface hydroxyl formation on vacuum-annealed TiO_2, Appl. Phys. Lett. **79**, 2716–2718 (2001)

26.85 M. Aono, Y. Hou, R. Souda, C. Oshima, S. Otani, Y. Ishizawa: Direct analysis of the structure, concentration, and chemical activity of surface atomic vacancies by specialized low energy ion scattering spectroscopy – TiC(001), Phys. Rev. Lett. **50**, 1293–1296 (1983)

26.86 C.R. Parkinson, M. Walker, C.F. McConville: Reaction of atomic oxygen with a Pt(111) surface: chemical and structural determination using XPS, CAICISS and LEED, Surf. Sci. **545**, 19–33 (2003)

26.87 J.P. Jacobs, S. Reijne, R.J.M. Elfrink, S.N. Mikhailov, H.H. Brongersma, M. Wuttig: Quantification of the composition of alloy and oxide surfaces using low-energy ion-scattering, J. Vac. Sci. Technol. A **12**, 2308–2313 (1994)

26.88 R. Cortenraad, A.W.D. van der Gon, H.H. Brongersma, S.N. Ermolov, V.G. Glebovsky: Quantification of the surface composition of low-work function surfaces using low-energy ion scattering, Surf. Interface Anal. **31**, 200–205 (2001)

26.89 J.C. Ho, R. Yerushalmi, Z.A. Jacobson, Z. Fan, R.L. Alley, A. Javey: Controlled nanoscale doping of semiconductors via molecular monolayers, Nat. Mater. **7**, 62–67 (2008)

26.90 J.C. Ho, R. Yerushalmi, G. Smith, P. Majhi, J. Bennett, J. Halim, V.N. Faifer, A. Javey: Wafer-scale, sub-5 nm junction formation by monolayer doping and conventional spike annealing, Nano Lett. **9**, 725–730 (2009)

26.91 J.C. Ho, A.C. Ford, Y.L. Chueh, P.W. Leu, O. Ergen, K. Takei, G. Smith, P. Majhi, J. Bennett, A. Javey: Nanoscale doping of InAs via sulfur monolayers, Appl. Phys. Lett. **95**, 072108 (2009)

26.92 R.C. Longo, K. Cho, W.G. Schmidt, Y.J. Chabal, P. Thissen: Monolayer doping via phosphonic acid grafting on silicon: microscopic insight from infrared spectroscopy and density functional theory calculations, Adv. Funct. Mater. **23**, 3471–3477 (2013)

26.93 T. Alphazan, L. Mathey, M. Schwarzwälder, T.-H. Lin, A.J. Rossini, R. Wischert, V. Enyedi, H. Fontaine, M. Veillerot, A. Lesage, L. Emsley, L. Veyre, F. Martin, C. Thieuleux, C. Copéret: Monolayer doping of silicon through grafting a tailored molecular phosphorus precursor onto oxide-passivated silicon surfaces, Chem. Mater. **28**, 3634–3640 (2016)

26.94 Z.Y. Sun, O. Hazut, B.C. Huang, Y.P. Chiu, C.S. Chang, R. Yerushalmi, L.J. Lauhon, D.N. Seidman: Dopant diffusion and activation in silicon nanowires fabricated by ex situ doping: a correlative study via atom-probe tomography and scanning tunneling spectroscopy, Nano Lett. **16**, 4490–4500 (2016)

26.95 O. Hazut, B.C. Huang, A. Pantzer, I. Amit, Y. Rosenwaks, A. Kohn, C.S. Chang, Y.P. Chiu, R. Yerushalmis: Parallel p-n junctions across nanowires by one-step ex situ doping, ACS Nano **8**, 8357–8362 (2014)

26.96 R.C. Longo, E.C. Mattson, A. Vega, W. Cabrera, K. Cho, Y.J. Chabal, P. Thissen: Mechanism of arsenic monolayer doping of oxide-free Si(111), Chem. Mater. **28**, 1975–1979 (2016)

26.97 P. Thissen, O. Seitz, Y.J. Chabal: Wet chemical surface functionalization of oxide-free silicon, Prog. Surf. Sci. **87**, 272–290 (2012)

26.98 K.T. Queeney, M.K. Weldon, J.P. Chang, Y.J. Chabal, A.B. Gurevich, J. Sapjeta, R.L. Opila: Infrared spectroscopic analysis of the Si/SiO_2 interface structure of thermally oxidized silicon, J. Appl. Phys. **87**, 1322–1330 (2000)

26.99 M.K. Weldon, B.B. Stefanov, K. Raghavachari, Y.J. Chabal: Initial H_2O-induced oxidation of Si(100)-(2×1), Phys. Rev. Lett. **79**, 2851–2854 (1997)

26.100 B.B. Stefanov, A.B. Gurevich, M.K. Weldon, K. Raghavachari, Y.J. Chabal: Silicon epoxide: unexpected intermediate during silicon oxide formation, Phys. Rev. Lett. **81**, 3908–3911 (1998)

26.101 Z.Y. Tang, S.L. Wang, L.H. Zhang, D. Ding, M.S. Chen, H.L. Wan: Effects of O_2 pressure on the oxidation of VO_x/Pt(111), Phys. Chem. Chem. Phys. **15**, 12124–12131 (2013)

26.102 W.P. Voorthuijzen, M.D. Yilmaz, W.J.M. Naber, J. Huskens, W.G. van der Wiel: Local doping of silicon using nanoimprint lithography and molecular monolayers, Adv. Mater. **23**, 1346–1350 (2011)

26.103 J. O'Connell, G.A. Verni, A. Gangnaik, M. Shayesteh, B. Long, Y.M. Georgiev, N. Petkov, G.P. McGlacken, M.A. Morris, R. Duffy, J.D. Holmes: Organo-arsenic molecular layers on silicon for high-density doping, ACS Appl. Mater. Interfaces **7**, 15514–15521 (2015)

26.104 S. Surnev, M.G. Ramsey, F.P. Netzer: Vanadium oxide surface studies, Prog. Surf. Sci. **73**, 117–165 (2003)

26.105 M. Abu Haija, S. Guimond, Y. Romanyshyn, A. Uhl, H. Kuhlenbeck, T.K. Todorova, M.V. Ganduglia-Pirovano, J. Dobler, J. Sauer, H.J. Freund: Low temperature adsorption of oxygen on reduced V_2O_3(0001) surfaces, Surf. Sci. **600**, 1497–1503 (2006)

26.106 M.A.C. Nascimento: *Theoretical Aspects of Heterogeneous Catalysis* (Kluwer, Dordrecht 2001)

26.107 C.W. Yi, K. Luo, T. Wei, D.W. Goodman: The composition and structure of Pd-Au surfaces, J. Phys. Chem. B **109**, 18535–18540 (2005)

26.108 M.S. Chen, D. Kumar, C.W. Yi, D.W. Goodman: The promotional effect of gold in catalysis by palladium-gold, Science **310**, 291–293 (2005)

26.109 C.J. Baddeley, R.M. Ormerod, A.W. Stephenson, R.M. Lambert: Surface-structure and reactivity in the cyclization of acetylene to benzene with Pd overlayers and Pd/Au surface alloys on Au(111), J. Phys. Chem. **99**, 5146–5151 (1995)

26.110 Y.F. Han, D. Kumar, D.W. Goodman: Particle size effects in vinyl acetate synthesis over Pd/SiO_2, J. Catal. **230**, 353–358 (2005)

26.111 M. Legawiec-Jarzyna, A. Srebowata, Z. Karpinski: Hydrodechlorination of dichlorodifluoromethane (CFC-12) over Pd/Al_2O_3 and $Pd-Au/Al_2O_3$ catalysts, React. Kinet. Catal. Lett. **79**, 157–163 (2003)

26.112 A.M. Venezia, V. La Parola, B. Pawelec, J.L.G. Fierro: Hydrogenation of aromatics over $Au-Pd/SiO_2-Al_2O_3$ catalysts; support acidity effect, Appl. Catal. A **264**, 43–51 (2004)

26.113 I. Žutić, J. Fabian, S. Das Sarma: Spintronics: fundamentals and applications, Rev. Mod. Phys. **76**, 323–410 (2004)

26.114 R. Razzaq, C. Li, M. Usman, K. Suzuki, S. Zhang: A highly active and stable $Co_4N/\gamma-Al_2O_3$ catalyst for CO and CO_2 methanation to produce synthetic natural gas (SNG), Chem. Eng. J. **262**, 1090–1098 (2015)

26.115 Z. Yao, X. Zhang, F. Peng, H. Yu, H. Wang, J. Yang: Novel highly efficient alumina-supported cobalt nitride catalyst for preferential CO oxidation at high temperatures, Int. J. Hydrog. Energ. **36**, 1955–1959 (2011)

26.116 Z. Yao, A. Zhu, J. Chen, X. Wang, C.T. Au, C. Shi: Synthesis, characterization and activity of alumina-supported cobalt nitride for NO decomposition, J. Solid State Chem. **180**, 2635–2640 (2007)

26.117 M.Y. Zheng, X.W. Chen, R.H. Cheng, N. Li, J. Sun, X.D. Wang, T. Zhang: Catalytic decomposition of hydrazine on iron nitride catalysts, Catal. Commun. **7**, 187–191 (2006)

26.118 R.B. Anderson: Iron nitrides as Fischer–Tropsch catalysts, Adv. Catal. **5**, 355–384 (1953)

26.119 E.C. Mattson, D.J. Michalak, W. Cabrera, J.F. Veyan, Y.J. Chabal: Initial nitride formation during plasma-nitridation of cobalt surfaces, Appl. Phys. Lett. **109**, 091602 (2016)

26.120 R. Newman, R.M. Chrenko: Infrared absorption from $L \cdot S$ splittings in Co^{2+} salts, Phys. Rev. **115**, 1147–1152 (1959)

26.121 E.C. Mattson, D.J. Michalak, J.F. Veyan, Y.J. Chabal: Cobalt and iron segregation and nitride formation from nitrogen plasma treatment of CoFeB surfaces, J. Chem. Phys. **146**, 052805 (2017)

26.122 C. Navío, M.J. Capitán, J. Álvarez, R. Miranda, F. Yndurain: Formation of a non-magnetic metallic iron nitride layer on bcc Fe(100), New J. Phys. **12**, 073004 (2010)

26.123 L.H. Liu, W.J.I. Debenedetti, T. Peixoto, S. Gokalp, N. Shafiq, J.F. Veyan, D.J. Michalak, R. Hourani, Y.J. Chabal: Morphology and chemical termination of HF-etched Si_3N_4 surfaces, Appl. Phys. Lett. **105**, 261603 (2014)

26.124 V.M. Bermudez: Wet-chemical treatment of Si_3N_4 surfaces studied using infrared attenuated total reflection spectroscopy, J. Electrochem. Soc. **152**, F31–F36 (2005)

26.125 L.M. Loewenstein, C.M. Tipton: Chemical etching of thermally oxidized silicon-nitride-comparison of wet and dry etching methods, J. Electrochem. Soc. **138**, 1389–1394 (1991)

26.126 D. Watanabe, H. Aoki, M. Itano, T. Kezuka, C. Kimura, T. Sugino: High selectivity (SiN/SiO_2) etching using an organic solution containing anhydrous HF, Microelectron. Eng. **86**, 2161–2164 (2009)

26.127 J. Mertens, E. Finot, O. Heintz, M.H. Nadal, V. Eyraud, A. Cathelat, G. Legay, E. Bourillot, A. Dereux: Changes in surface stress, morphology and chemical composition of silica and silicon nitride surfaces during the etching by gaseous HF acid, Appl. Surf. Sci. **253**, 5101–5108 (2007)

26.128 L.H. Liu, D.J. Michalak, T.P. Chopra, S.P. Pujari, W. Cabrera, D. Dick, J.F. Veyan, R. Hourani, M.D. Halls, H. Zuilhof, Y.J. Chabal: Surface etching, chemical modification and characterization of silicon nitride and silicon oxide-selective functionalization of Si_3N_4 and SiO_2, J. Phys. Condens. Matter **28**(9), 094014 (2016)

26.129 D.J. Michalak, S.R. Amy, D. Aureau, M. Dai, A. Esteve, Y.J. Chabal: Nanopatterning Si(111) surfaces as a selective surface-chemistry route, Nat. Mater. **9**, 266–271 (2010)

26.130 K. Tan, S. Zuluaga, E. Fuentes, E.C. Mattson, J.F. Veyan, H. Wang, J. Li, T. Thonhauser, Y.J. Chabal: Trapping gases in metal organic frameworks with a selective surface molecular barrier layer, Nat. Commun. **7**, 13871 (2016)

Eric C. Mattson

Dept. of Materials Science and Engineering
University of Texas at Dallas
Dallas, TX, USA

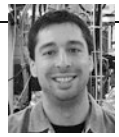

Eric Mattson obtained his BS and PhD degrees in Physics from the University of Wisconsin-Milwaukee. He joined the Chabal research group in the Materials Science Department at UT-Dallas as a Postdoctoral Researcher in 2014. His research has focused on understanding surface modification and reactivity of industrially- relevant systems using ultrahigh vacuum-based in-situ spectroscopic methods.

Yves J. Chabal

Dept. of Materials Science and Engineering
University of Texas at Dallas
Dallas, TX, USA
chabal@utdallas.edu

Yves Chabal holds a Texas Instrument Distinguished Chair in Nanoelectronics at the University of Texas at Dallas, where he directed the Laboratory for Surface Modification, an interdisciplinary research center. His research has included development of sensitive spectroscopic methods to characterize surfaces and interfaces, atomic layer deposition, biosensors, materials and surface modifications for energy, photovoltaics and hydrogen storage applications, twodimensional materials, and nanoenergetic materials and interfaces.

Gas Surfa

Part G

Part G Gas Surface Interaction

Part G deals with the gas–surface interaction, a process that is pivotal to our understanding of catalysts and sensors and their optimization. Interactions between gas species and surfaces depend on the nature and strength of the bond between the atom or molecule and the surface, the site occupied by the admolecules (for nondissociative adsorption) or the fragments or adatoms (if bond breaking occurs), the formation of ordered overlayers, and the interactions between the adsorbates. This information is required to obtain a fundamental understanding of adsorption and desorption processes. Adsorption may be governed by physical forces alone (van der Waals interactions between the atom/molecule and the substrate responsible for physisorption) or by the formation of chemical bonds with the substrate (chemisorption). In the former case, the molecule is barely affected, and its vibrational modes are almost unchanged. In the latter case, the internal bonds may be significantly modified and the frequencies of the vibrational modes exhibit important shifts. The chemisorption interaction can then lead to partial or complete dissociation of the reactants, and the resulting radicals can act as promoters or poisons in catalytic reactions. Interactions between adsorbates and their ability to diffuse on the surface can lead to the formation of ordered adlayers stabilized by either direct interactions between the admolecules or substrate-mediated interactions. Such ordered structures can be used as templates or active coatings in applications.

Chapter 27 provides an introduction to the topic of this section, and describes recent first-principles methods employed to calculate the adsorption energy. These methods are explored in great length by examining the subtleties of CO adsorption on a number of metal and nonmetal surfaces. Surface reactions are then addressed using transition state theory and activation energy calculations performed via first-principles methods. The chapter also discusses the solution to the so-called CO puzzle—the long-standing disagreement between experimental results and theoretical predictions regarding the adsorption site of CO on Pt(111).

Chapter 28 covers nonadiabatic effects in most common gas–surface reactions in the local density friction approximation (LDFA). In particular, the chapter describes the roles of friction and energy dissipation in the scattering of atoms and molecules, in their dissociation, and in the subsequent relaxation of hot atoms. It also addresses Eley–Rideal and hot-atom abstraction processes as well as desorption induced by intense femtosecond laser pulses, thus exemplifying the power of the LDFA approach.

Chapter 29 provides an overview of self-assembling monolayers (SAMs) formed by organic molecules at surfaces. This topic is particularly relevant to molecular electronics, sensor design, pharmacology, biocompatibility, hygiene, and biofouling. The formation of covalent structures and the self-assembly of thiols and amino acids are given as examples. The apparently huge number of possible arrangements is rationalized by considering the relative magnitudes of the interactions of the molecules with the substrate and each other, as well as the constraints imposed by the structure of the substrate on which the overlayer is grown.

Chapter 30 deals with the energetics of adsorption. The chapter reviews data obtained with a single-crystal calorimeter for the adsorption of simple molecules at single-crystal surfaces, as well as more recent results regarding the adsorption of molecules at clusters and the adhesion of metal atoms at oxide surfaces. Microcalorimetry can provide information on atom/molecule–surface interaction strengths that is not attainable with other experimental methods, and can act as a benchmark to test state-of-the-art theoretical calculations.

Chapter 31 describes a rigorous kinetic approach to adsorption, diffusion, desorption, and surface reactions in terms of macroscopic variables such as rate equations for local coverage or partial coverage. When local equilibrium is not applicable, an approach based on nonequilibrium statistical mechanics involving time-dependent distribution functions is required. The chapter covers the theory for adsorbates that remain in quasi-equilibrium throughout the desorption process and the theory for a lattice gas model with multiple interactions. Examples are provided for the adsorption and desorption of hydrogen on Rh(311) and the coupled desorption and site conversion of coadsorbates for $(NO + O)/Ru(001)$. In the final part, recent advances in the theory of kinetic lattice gas models regarding nondissociative adsorption and precursor-mediated adsorption and desorption are discussed.

Chapter 32 reviews results on the dependence of the sticking probability on the vibrational and rotational states of the reactants in the gas phase. Initially, information about the role of the internal degrees of freedom in adsorption was obtained by examining the internal states of scattered molecules and making use of a detailed balance. Later, methods of preparing gas-phase molecules in well-defined rotational and vibrational states were developed. This permitted the direct measurement of the sticking probability in at least partially defined quantum states. Selected results obtained by preparing molecules in supersonic beams through laser, hexapole, and collisional alignment are presented. These demonstrate the pivotal role of stereodynamics in the reaction at hand and the role of vibrational and rotational energy in overcoming activation energy barriers.

27. Gas Surface Interaction and Surface Reactions

Ziyun Wang, Peijun Hu, Qingfeng Ge

The gas–surface interaction and surface reactions are important aspects of surface science. In this chapter, fundamental concepts along with some of the latest findings in these two subject areas are reviewed, with a focus on the results of first-principles calculations. The chapter is divided into two parts, with the first exploring the gas–surface interaction (Sect. 27.1) and the second discussing surface reactions (Sect. 27.2).

In the first part, we summarize recent developments in the use of first-principles methods to calculate the adsorption energy of a gas on a surface, and we illustrate these developments using the adsorption of CO as an example. Furthermore, the relationship between surface electronic structure and adsorption energy is explored for the adsorption of a gas on surfaces of both metallic and sp^2-carbon materials. Two models for predicting adsorption are then considered, and an example of catalyst screening using the chemical potential is given.

In the second part of the chapter, we first explain transition state theory and show how to calculate the activation energy using first-principles methods. The Brønsted–Evans–Polanyi (BEP) relationship and representative surface reaction mechanisms are then reviewed. After that, the characteristics of active sites on the surfaces of metals and metal oxides are illustrated with examples. Finally, a short perspective on the future of research into gas–surface interactions and surface reactions using first-principles methods is provided.

The gas–surface interaction and surface reactions are of great importance in surface science and heterogeneous catalysis, so they have been extensively studied using many experimental techniques. However, the microscopic details of gas–surface interactions and (especially) surface reactions are still unclear due to the limited time and size resolutions of such techniques. First-principles calculations offer an alternative method of studying gas–surface interactions and surface reactions at atomic scales. In the last few decades, a large number of investigations of gas–surface interactions and surface reactions have been carried out using first-principles calculations. Indeed, due to increased computing power and the development of computational algorithms, first-principles calculations have become one of the most important tools used in surface science and heterogeneous catalysis research. In this chapter, the results of first-principles calculations are used to review some theories regarding gas–surface interactions and surface reactions. Some examples of these kinds of interactions and reactions are included for illustrative purposes. We also discuss some related computational methods and their development. This chapter is divided into two sections corresponding to gas–surface interactions and surface reactions, respectively.

M. Rocca, T.S. Rahman, L. Vattuone (Eds.), *Springer Handbook of Surface Science*, Springer Handbooks,
https://doi.org/10.1007/978-3-030-46906-1_27

27.1 The Gas–Surface Interaction

Gas–surface interactions have many important applications in physics and chemistry. In particular, such interactions are crucial to heterogeneous catalysis. Almost all gas–solid reactions in heterogeneous catalysis start with the adsorption of the reactant molecules on a surface. The adsorption of the product species that form on a surface following a catalyzed reaction is dependent on their interaction with that surface. The gas–surface interaction influences the level of catalytic activity and selectivity during heterogeneous catalysis and is central to the behavior of many getter materials, such as zeolites and activated carbon.

The adsorption energy is one of the main properties associated with any gas–surface interaction. This energy can be determined using first-principles calculations: the energy of a gas molecule adsorbed on a surface and the corresponding energies of the gas molecule and the surface alone can be calculated directly by solving the Schrödinger equation, and the energy difference between these states yields the adsorption energy. However, approximations are used in first-principles methods, especially in density functional theory (DFT), which is the most widely used first-principles method, and this utilization of approximations can lead to low accuracy when using first-principles methods to calculate the adsorption energies for some systems. For instance, DFT fails to correctly predict the adsorption energy and site for CO on some metal surfaces; this issue is known as the *CO puzzle* [27.1]. In an attempt to solve the CO puzzle, many computational methods have been applied to improve the accuracy of the adsorption energies generated by first-principles calculations. In this section, we provide a general overview of the use of first-principles calculations to derive adsorption energies, and we discuss the development of new methods that could be used to solve the CO puzzle by providing a more precise description of the gas–surface interaction.

A detailed knowledge of the electronic structure of the surface involved is essential when probing gas–surface interactions. This is because a deep understanding of the relationship between the surface electronic structure and the gas–surface interaction is needed to elucidate the changes in the surface electronic structure that occur upon the adsorption of a gas molecule at a surface and the differences in gas adsorption strength between different surfaces. Therefore, some studies of the relationship between electronic structure and adsorption energy are discussed in Sect. 27.1.2.

As mentioned above, the gas–surface interaction is crucial to the activities of many catalytic and getter materials. The adsorption strength is a very important influence on the activities of these materials. Indeed, better catalysts have been developed by tailoring the adsorption energy through appropriate engineering of the surface structure [27.2, 3]. Furthermore, the rational design of catalytic materials can be achieved by searching for surface structures with desirable adsorption energies [27.4]. Therefore, understanding the relationship between adsorption energy and surface structure is key to speeding up the discovery of novel materials with particular gas–surface interactions. In Sect. 27.1.3, some recent results on the relationship between adsorption energy and surface structure are discussed.

In Sect. 27.1.4, we present an example of determining the gas–surface interaction using first-principles calculations. This example illustrates catalyst design based on the calculation of adsorption energy using density functional theory. The application of the concept of chemical potential to heterogeneous catalysis, which represents the most recent approach to understanding catalytic activity based on the adsorption energy, is also discussed. Finally, an example involving the design of an active counter electrode (CE) material for application to the triiodide reduction reaction in dye-sensitized solar cells is provided.

27.1.1 Calculating the Adsorption Energy

Before describing first-principles calculations of the adsorption energy in gas–surface interactions, it is important to introduce the model used to describe the surface in the calculations. Two basic models are used in adsorption energy calculations: the cluster model and the slab model. The former normally treats the adsorbate, the adsorption site atoms, and the nearby surface atoms as a supermolecule (cluster), whereas the latter considers the surface to be a periodic slab. One of the advantages of the cluster model is that, because it involves fewer atoms, less computation is needed than for the slab method. However, the accuracy of the cluster model is usually insufficient. Thus, although the slab model normally requires more computational effort, it gives a more accurate description of surface structure and properties in general. Advances in computational power have therefore led to the increasing use of the slab model to study gas–surface interactions. Herein, we focus on adsorption calculations performed using the slab model.

Figure 27.1 shows a typical example of a slab model of a CO molecule interacting with Pd(111), where Pd(111) is modeled using a (2×2) periodic unit cell containing four surface Pd atoms. In normal first-principles calculations of adsorption energy, the

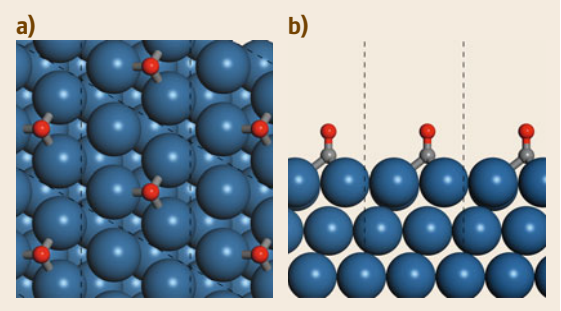

Fig. 27.1a,b Illustration of the slab model of the interaction of a CO molecule with Pd(111). Pd, C, and O atoms are shown in *blue*, *gray*, and *red*, respectively

adsorption energies of the adsorbate at different adsorption sites are determined in turn, and the most stable site is treated as the adsorption site. As shown in Fig. 27.1, the most favorable adsorption site of CO on Pd(111) is the threefold hollow site. The adsorbate is replicated through the application of periodic boundary conditions (Fig. 27.1). Therefore, the size of the unit cell needs to be large enough to avoid interactions with the adsorbate in neighboring unit cells. Alternatively, a small unit cell can be employed to measure the adsorbate–adsorbate interaction when the surface coverage is high. Using the slab model, the adsorption energy of the gas molecule on the surface (E_{ads}) can be obtained as the difference between the energy of the gas bonded with the surface ($E_{\text{gas+surf}}$) and the sum of the energies of the gas molecule (E_{gas}) and surface (E_{surface}) when they are not interacting, i.e.,

$$E_{\text{ads}} = E_{\text{gas+surf}} - E_{\text{gas}} - E_{\text{surf}} \,. \tag{27.1}$$

According to this definition, the more negative the adsorption energy, the stronger the gas surface interaction. Using this method and model, the adsorption energies associated with both physical adsorption and chemisorption of the gas molecule on the surface can be calculated. The accuracy of the calculated adsorption energy value depends on the first-principles method applied. In most cases, especially for metal surfaces, DFT gives values that are reasonably close to the corresponding experimental values; however, rather inaccurate adsorption energies and even incorrect adsorption site predictions are generated for some systems using normal DFT methods. This section begins with a discussion of one of the most famous failures of DFT: its inability to accurately calculate the adsorption energy of CO on Pt(111). The reasons for this *CO puzzle* are discussed in terms of the electronic structures of the CO molecule and the surface, and some corrections based on an understanding of these electronic structures are also explored. The last section focuses on the utilization of different calculation methods (DFT+U and the random phase approximation) to solve this puzzle. The process of solving the CO puzzle illustrates how first-principles methods are used and developed to better understand the electronic structures of gas–surface interactions and to more accurately predict adsorption energies and sites.

The CO Puzzle

The CO puzzle refers to the strong disagreement between the adsorption sites of CO on (mainly) Pt(111) predicted by first-principles calculations and those observed experimentally. This discrepancy was first discussed by *Feibelman* et al. [27.1]. Experimentally, CO is found to prefer atop or bridge sites on Pt(111). For example, *Blackman* et al. [27.5] examined a disordered one-third monolayer of CO on Pt(111) at 160 K using diffuse low-energy electron diffraction analysis. Their results suggested that (88±5)% of the CO molecules are located at atop sites while (12±5)% are at bridge sites. Furthermore, *Schweizer* et al. [27.6] developed an empirical potential energy surface for CO/Pt(111) by fitting infrared measurements of the CO stretch frequency and peak width at different temperatures and for various CO coverages. They found that the difference between the atop and bridge sites was around 60 meV upon extrapolating to zero coverage, and that the atop site was more favorable. Similar results have also been obtained using many different techniques, such as diffraction, vibrational spectroscopy, and scanning probe microscopy, which are reviewed in the original paper on the CO puzzle [27.1]. Experimental results indicate that each CO molecule binds to a single Pt atom and agree with the theoretical determined energy difference between adsorptions at atop sites and bridge sites. Threefold hollow adsorption was only very rarely observed in the experimental studies.

Interestingly, most DFT methods fail to predict the preferred adsorption site. *Feibelman* et al. [27.1] calculated CO adsorption on Pt(111) using different calculation methods and codes, as shown in Table 27.1, including the Vienna ab initio simulation package (VASP) with ultrasoft pseudopotentials (USP), Blöchl's projector augmented wave (PAW) approach, the Dacapo code with USP, and full-potential, linearized, augmented plane wave (FP-LAPW). The exchange-correlation functionals in both the local density approximation (LDA) and the generalized gradient approximation (GGA) were considered too. A series of coverage values were taken into account, ranging from 1/12 to 1/3. The results shown in Table 27.1 suggest that the binding energies at the fcc hollow site are stronger than those at the atop site—a conclusion at odds with the

Table 27.1 Binding energies at a fcc hollow site relative to those at an atop site on CO/Pt(111) for different supercells, coverages (θ), methods, and exchange-correlation (XC) functionals. The binding energy is defined as shown in (27.1), so a more negative value indicates stronger binding. All data are adapted from the paper by *Feibelman* et al. [27.1]

Supercell	θ (ML)	Method	XC funct.	ΔBE (eV)
$3\times2\sqrt{3}$	$\frac{1}{12}$	VASP, USP	PW91	−0.25
2×2	$\frac{1}{4}$	Dacapo, USP	PW91	−0.23
2×2	$\frac{1}{4}$	Dacapo, USP	PBE	−0.24
2×2	$\frac{1}{4}$	Dacapo, USP	RPBE	−0.16
2×2	$\frac{1}{4}$	Dacapo, USP	LDA	−0.45
$c(4\times2)$	$\frac{1}{4}$	VASP, USP	LDA	−0.41
$c(4\times2)$	$\frac{1}{4}$	Dacapo, USP	PW91	−0.23
$c(4\times2)$	$\frac{1}{4}$	VASP, USP	PW91	−0.18
$c(4\times2)$	$\frac{1}{4}$	VASP, PAW	PW91	−0.13
$\sqrt{3}\times\sqrt{3}-R30°$	$\frac{1}{3}$	Dacapo, USP	PW91	−0.23
$\sqrt{3}\times\sqrt{3}-R30°$	$\frac{1}{3}$	FP-LAPW	PW91	−0.10

experimental results. This disagreement is known as the CO/Pt(111) puzzle. In addition to Pt(111), calculations on Cu(111) also predict the wrong preferred adsorption site: angle-resolved photoemission extended fine structure (ARPEFS) and spectroscopic analysis indicated that CO prefers atop sites at a coverage of 1/3 ML, while DFT-GGA calculations predicted that the hcp hollow site would be the most stable. On the other hand, DFT-GGA calculations correctly predicted that CO/Pd(111) and CO/Ni(111) were the threefold sites.

Feibelman et al. [27.1] also explored some possible reasons for the disagreement between the experimentally observed and theoretically deduced preferred sites for CO adsorption. First, they proposed that the experimentally observed phenomenon may be due to the adsorption of CO at a Pt adatom on Pt(111). They calculated the CO adsorption energy at a Pt adatom on Pt(111) and found it to be 40 meV greater than that at a fcc hollow site. However, the energy gain is not sufficient to stabilize Pt adatoms on Pt(111), as the adatom formation energy is unfavorable by 1.07 eV. Secondly, the possible influence of hydrogen atoms on the experimentally observed adsorption energy and sites was examined using a model that included subsurface hydrogen. However, the inclusion of subsurface hydrogen did not make the atop-bridge configuration more favorable than the hollow sites. Thirdly, the relativistic correction and spin polarization were accounted for, but neither led to a preference for atop-site bonding. Lastly, the effects of correcting for the zero-point energy and the vibrational entropy were examined. The zero-point energies of CO adsorbed at the atop and fcc sites were found to be 218 and 196 meV, respectively, meaning that the zero-point energy destabilizes the atop site more than the fcc site. The vibrational entropy contribution, calculated via the harmonic approximation, is 0.083 meV/K higher for an atop site than for a fcc site at ≈ 300 K. Consequently, even though the entropic contribution stabilizes adsorption at the atop site by 25 meV at 300 K, this contribution is not enough to make the atop site more stable than the fcc site at 300 K. Furthermore, most surface science experiments are performed at low temperatures, which reduces the entropic contribution. Therefore, DFT calculations underestimate the preference of CO for adsorption at low-coordination sites.

The HOMO–LUMO Gap and the Singlet–Triplet CO Excitation Energy

As mentioned above, normal DFT methods fail to correctly predict the preferred site for the adsorption of CO on Pt(111). In order to solve this CO puzzle, a better understanding of the adsorption of CO on Pt(111) is required. The Blyholder model [27.7] is one of the most widely accepted models of CO adsorption on a transition metal surface. With some modifications [27.8, 9], this model can be used to probe the difference between adsorption at atop sites and adsorption at hollow sites. According to the model, there are two main contributions to CO adsorption on Pt(111): 5σ donation and 2π backdonation. The former refers the mixing of the highest occupied molecular orbital (HOMO) of CO, 5σ, with the d_{z^2} states of the surface, while the latter corresponds to the interaction between the lowest unoccupied molecular orbital (LUMO) of CO, 2π, and the d_{yz} and d_{xz} states of the surface. Donation from 5σ and backdonation to 2π occur during CO adsorption at both atop and hollow sites, although donation from 5σ tends to make CO adsorb at the atop site whereas 2π backdonation favors the hollow sites.

Kresse et al. [27.10] investigated CO adsorption on Pt(111) using four different PAW potentials generated with different core radii. The adsorption energies at atop and hollow sites obtained with the four potentials are quite different, as shown in Table 27.2. As the pseudopotential core radius increases, the adsorption energy

Table 27.2 Difference in binding energy ΔE between CO adsorption at an atop site and CO adsorption at a fcc sites on Pt(111), the adsorption energy for a fcc site E_{fcc}, and the one-electron DFT HOMO–LUMO ($5\sigma - 2\pi$) gap E_{gap} for various PAW potentials. The pseudopotential core radius of the p wavefunction r_c and the optimized CO bond length d are also listed for each PAW potential. The binding energy is defined as shown in (27.1) (i.e., a more negative value indicates stronger binding). All the data are adapted from the paper by *Kresse* et al. [27.10]

	r_c (arb. u.)	d (Å)	E_{gap} (eV)	ΔE (meV)	E_{fcc} (eV)
Hard PAW	1.1	1.134	7.01	−105	−1.67
Standard PAW	1.5	1.142	6.91	−126	−1.72
PAW	1.7	1.162	6.71	−180	−1.83
Soft PAW	1.85	1.18	6.48	−243	−1.91

of CO at fcc Pt(111) strengthens. At the same time, the HOMO–LUMO gap decreases. The downwards shift of the LUMO enhances the interaction between the 2π orbital and d states. As discussed above, 2π backdonation contributes more to adsorption at the hollow sites than adsorption at the atop sites. Thus, the decrease in the HOMO–LUMO gap leads to a preference for the hollow site, as shown in Table 27.2. Based on the aforementioned facts, increasing the HOMO–LUMO gap may be a promising way to make atop sites more favorable than hollow ones. However, there is an upper limit on the HOMO–LUMO gap within the PAW approximation, which gives an energy difference of −105 meV, as shown in Table 27.2. A DFT+U-inspired method of shifting the LUMO of CO further upwards was proposed by *Kresse* et al. [27.10]. DFT+U is a revised electronic method based on the framework of traditional DFT. The basic idea of DFT+U is to treat the strong on-site Coulomb interaction of localized electrons with an additional term that is not correctly described by LDA or GGA. The correction proposed by Kresse et al. is

$$E_{DFT+U} = E_{DFT} + \frac{U}{2}\sum_{\sigma=1}^{2}\sum_{i=1}^{2}\left(\rho_i^{\sigma} - \rho_i^{\sigma}\rho_i^{\sigma}\right) , \quad (27.2)$$

where E_{DFT+U} and E_{DFT} are the modified and conventional density functionals; σ is an index for the spin, and ρ_i^{σ} are the occupancies of the two LUMO orbitals for the up and down spins. *Kresse* et al. [27.10] found that when U equals 0.5 eV, the adsorption energies given by this DFT+U functional for both atop and hollow sites are the same. When $U = 0.75$ eV, the atop site is 60 meV more favorable than the hollow site and the adsorption energies decrease from 1.72 to 1.39 eV, which is in better agreement with experiments. These results suggest that the position of the LUMO plays an important role in the site preference prediction.

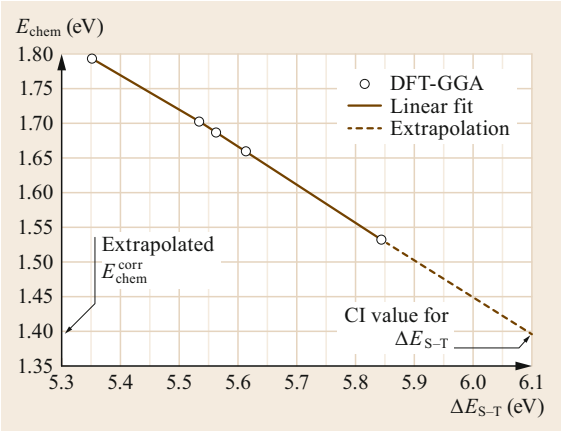

Fig. 27.2 Relationship between the adsorption energy of CO on Pt(111) E_{chem} and the singlet–triplet excitation energy ΔE_{S-T} for five pseudopotential sets (*circles*). (Reprinted with permission from [27.11], Copyright (2004) by the American Physical Society)

The DFT+U-type functional mentioned above provides one possible solution to the CO puzzle. However, the value of U is not known and can only be determined by fitting the experimental data, which is a difficult task. *Mason* et al. [27.11] proposed a first-principles extrapolation method to evaluate CO adsorption energies on a series of metal surfaces, including Pt, Rh, Pd, and Cu. They found that, like the HOMO–LUMO gap, there was a linear relation between the CO adsorption energy E_{chem} and the singlet–triplet excitation energy ΔE_{S-T}, as shown in Fig. 27.2. Similar linear relationships were also observed for the other investigated surfaces, including Pt(111), Rh(111), Pd(111), Cu(111), Pt(100), Rh(100), Pd(100), and Cu(100).

The value of ΔE_{S-T} obtained from coupled-cluster and configuration-interaction (CI) quantum-chemical calculations is very accurate and agrees well with the experimental value of ΔE_{S-T} (6.095 eV). However, *Mason* et al. [27.11] showed that the DFT-GGA always underestimates the value of ΔE_{S-T} no matter which pseudopotential set is used, which is one of the main reasons that the adsorption energies of CO on transition metal surfaces are overestimated by DFT-GGA. This led to the proposal of a first-principles extrapolation method based on the aforementioned linear relation and the ΔE_{S-T} value from the coupled-cluster and CI methods,

$$E_{chem}^{corr} = E_{chem}^{GGA} + \left(\Delta E_{S-T}^{CI} - \Delta E_{S-T}^{GGA}\right)\frac{\delta E_{chem}^{GGA}}{\delta E_{S-T}^{GGA}} , \quad (27.3)$$

where E_{chem}^{corr} and E_{chem}^{GGA} are the corrected adsorption energy determined by this extrapolation method and the

original energy from DFT-GGA, respectively. ΔE_{S-T}^{CI} and ΔE_{S-T}^{GGA} are the CO singlet–triplet excitation energies from the CI and DFT-GGA methods, respectively. $\delta E_{chem}^{GGA}/\delta E_{S-T}^{GGA}$ is the slope of the linear relation shown in Fig. 27.2b. Using this extrapolation method, the adsorption site for CO on Pt(111) was correctly predicted, as the adsorption energy at the atop site 0.163 eV was found to be more favorable than that at the hcp hollow site. Furthermore, the adsorption energy of CO on Cu(111) was calculated as 0.621 eV at the atop site and 0.610 eV at the bridge site, respectively, which reproduce the experimental results mentioned in the last section. In general, the average error of this extrapolation method was found to be 0.16 eV (13%)—much lower than the average error of 0.38 eV (30%) of PBE, which is a simple yet reasonably accurate method for correcting the results of normal DFT.

Hybrid DFT and the Random Phase Approximation

In the previous section, the CO puzzle was mainly attributed to the incorrect estimation of the HOMO–LUMO gap from DFT calculations. Two different methods based on parameter fitting with respect to the experimental values and high-level quantum chemistry calculations were introduced. However, these methods can only be used for the adsorption of CO on transition metals and similar systems with known experimental results. General methods that more accurately reflect the electronic structures of both the gas molecule and the surface, thus providing a better quantitative description of the gas–surface interaction, are necessary to solve the CO puzzle for all systems. In this section, two successful state-of-the-art methods of predicting the adsorption site for CO/Pt(111) are reviewed: hybrid DFT and the random phase approximation (RPA).

The exact exchange-correlation (XC) functional should be a truly nonlocal quantity that depends on the electronic density at two different points. However, the most popular DFT methods use either LDA or GGA XC functionals, which are local and semilocal, respectively. Furthermore, the use of independent exchange and correlation causes a general self-interaction error in DFT. One way to reduce the errors caused by these issues is to use a hybrid DFT method with a Hartree–Fock exchange component. *Reimers* and coworkers [27.12] showed that the hybrid PBE0 XC functional can predict the correct adsorption site for CO on Pt(111). The Hartree–Fock exchange component is included in the PBE GGA functional by introducing an extra parameter, i.e.,

$$E^{PBE0} = \alpha E^{exx} + (1-\alpha)E_{PBE}^{X} + E_{PBE}^{c}\,, \qquad (27.4)$$

where E^{exx} is the Hartree–Fock exchange and E_{PBE}^{X} and E_{PBE}^{c} are the exchange and correlation energies for the PBE GGA functional, respectively. The parameter α is optimized to 0.25 for PBE0. Using the hybrid DFT method, the HOMO–LUMO gap energy is calculated to be 9.42 eV, which is more than 2 eV higher than the HOMO–LUMO gap energies given by all of the local and semilocal functionals. The PBE0 HOMO and LUMO energies are -10.01 and -0.60 eV, respectively, while PBE gives -8.40 eV for the HOMO energy and -1.37 eV for the LUMO energy. Therefore, the HOMO–LUMO gap for gas-phase CO calculated using PBE0 is much higher than that calculated by PBE, which indicates that PBE0 and PBE should give significantly different adsorption energies based on the discussion in the last section. The PBE0-calculated adsorption energy of CO at the atop site is -1.80 eV according to *Reimers* and coworkers [27.12], which is 0.27 eV higher than that provided by PBE. Interestingly, the PBE0-derived adsorption energy of CO at the fcc site is -1.67 eV, indicating that PBE0 correctly predicts the preferred adsorption site. Therefore, hybrid DFT offers one way to solve the CO puzzle without using fitted parameters from experiments (except for the exchange contribution α in (27.4)). However, as suggested in the original paper [27.12], a band gap is artificially introduced by the hybrid functional for calculations of the Pt(111) surface, even though Pt is a conductor with a continuous band structure. In summary, even though the hybrid DFT method correctly identifies the preferred adsorption site, some minor defects in the approach it uses to calculate the band structures of conductors may limit its use in metal systems.

Besides their inability to correctly identify the preferred adsorption site, *Schimka* et al. [27.13] suggested that semilocal density functionals also tend to underestimate the surface energy. As shown in Fig. 27.3, there is a linear relation between the adsorption energies and the adsorption energies of CO at Pt atop and Rh atop sites for various semilocal and hybrid functionals. However, the experimental values for Pt and Rh (the orange points in Fig. 27.3) are far from the lines, suggesting that none of these functionals can accurately reproduce the experimental values for both the adsorption energy and the surface energy at the same time. Therefore, it is necessary to trade off accuracy in the adsorption energy for inaccuracy in the surface energy or vice versa. For instance, the Becke–Lee–Yang–Parr (BLYP) functional, a strong gradient correction, gives an accurate value for the adsorption energy of CO on Rh(111) but fails to precisely predict the surface energy. One the other hand, PBEsol, which corresponds to

an extremely weak semilocal gradient, reproduces the surface energy reasonably well but overestimates the adsorption energy. In order to solve this issue, *Schimka* et al. [27.13] implemented a state-of-art RPA method, GW-RPA [27.14], with exact Hartree–Fock exchange and RPA correlation energy. As shown in Fig. 27.3, the CO adsorption energies and surface energies of both Pt and Rh calculated using GW-RPA are not correlated with any of the other functionals. The points relating to GW-RPA data for both Pt and Rh (the green points in Fig. 27.3) are close to the corresponding points for the experimental data (orange points). Furthermore, the GW-RPA-predicted adsorption sites on various surfaces (e.g., Cu, Rh, Ru, Pd, and Pt) agree with those observed experimentally. The electronic structures of CO and the surfaces were also obtained using different methods and then compared. The PBE functional was found to give a good fit to the electronic structure of Pt(111) but to underestimate the HOMO–LUMO gap of the CO molecule, as mentioned above. Hybrid functionals are electronic methods that admix a certain amount of Fock exchange with a local or semilocal density functional. One hybrid method, HSE, reproduces the experimental HOMO and LUMO positions and the HOMO–LUMO gap rather accurately, but its description of the band structure of Pt(111) is rather inaccurate. GW-RPA, on the other hand, offers reasonable fits to the electronic structures of both Pt(111) and gas-phase CO. In summary, RPA is an excellent parameter-free tool for calculating the adsorption energy in gas–surface interactions. With the development of new first-principles methods, descriptions of gas–surface interactions will become more accurate and will be obtained more rapidly.

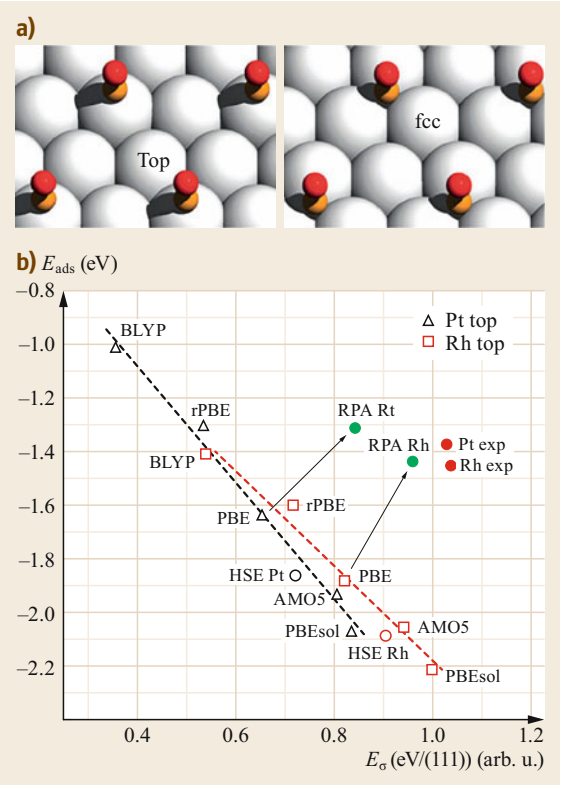

Fig. 27.3 **(a)** CO adsorption geometries considered for a (2×2) surface cell. **(b)** Plot of the adsorption energy at the atop site versus the surface energy (specified per unit area, u. a.) for Pt(111) and Rh(111). The data obtained using various semilocal functionals are plotted. (From [27.13])

27.1.2 Electronic Structure and Adsorption Energy

The relationship between the electronic structure of the surface and the adsorption energy is very important for gas–surface interactions. This relationship gives us considerable insight not only into the electron transfer that occurs in a gas–surface interaction but also into the general trend in adsorption energy for metal surfaces across the periodic table. One of the most popular models of electronic structure and adsorption energy is the d-band center, which was first proposed by *Hammer* and *Nørskov* to explain the inertness of gold [27.15]. In this section, we first review the d-band center model to unravel the relationship between electronic structure and adsorption energy. An example of the use of the d-band center theory is given. Finally, a model that allows us to understand the relationship between the electronic structure and the activity of an sp^2 material is provided.

The d-Band Center

Gold is the noblest of all metals. It has the lowest bond strength of most gas and liquid molecules. In order to understand the nobility of gold, *Hammer* and *Nørskov* [27.15] calculated the adsorption and desorption of a hydrogen molecule on four different surfaces (Au, Cu, Ni, and Pt) using a self-consistent DFT method. They found that the activities of these metal surfaces increased in the order Au < Cu < Pt < Ni. On Ni(111) and Pt(111), the dissociation of hydrogen is barrierless and hydrogen atoms on these surfaces are more stable than gas-phase hydrogen. On Cu(111), there is a small barrier to hydrogen dissociation and the enthalpy change involved is slightly negative. Au(111) is the most inert surface. It is unfavorable for hydrogen dissociation both thermodynamically and kinetically.

In order to elucidate why a gold surface is so noble, Hammer and Nørskov studied electronic transfer during the adsorption and dissociation of hydrogen on

various surfaces. As shown in Fig. 27.4, two different components contribute to the interaction between hydrogen and a transition metal surface. The first is the interaction of the 1s state of hydrogen with metal s bands (Fig. 27.4a), which causes the adsorption state to broaden. Interactions with metal s bands should therefore be attractive, and they should be similar for all four surfaces (Au, Cu, Ni, and Pt) because the s–s coupling matrix element is similar for all metal surfaces. The second component is the interaction between the 1s state of hydrogen and metal d states, which gives rise to both bonding and antibonding orbitals, as shown in Fig. 27.4b. If only bonding orbitals are occupied, this interaction should be attractive, while there is no hybridization energy if both bonding and antibonding orbitals are filled. Therefore, the gas–surface interaction depends strongly on whether an antibonding state is filled. Because the antibonding states lie above the d states, the energy of the center of the d states relative to the Fermi level is a good indicator of the gas–surface interaction. As shown in Fig. 27.5, there is only one resonance on a metal surface with a low d-band center position (DOS on the left in Fig. 27.5), indicating weak chemisorption. Upon increasing the d-band center position, the antibonding states become more significant and the gas–surface interactions become stronger. Therefore, the inertness of gold is due to its low d-band center. It is worth mentioning that the inertness of gold (as compared to other group 11 metals) is also due to the relativistic effect. The relativistic effect scales as approximately Z^2 and therefore becomes very important for heavy elements. The stability of the $6s^2$ configuration of gold due to relativistic contraction makes it much harder for gold than for Ag and Cu to adsorb hydrogen.

The d-Band Center and Adsorption Energy

The d-band center model is one of the most successful models, and the d-band center position has been found to be correlated with the adsorption energy in many different systems. In this section, the relationship between the d-band center position and the adsorption energy on near-surface alloys (NSAs) is reviewed.

NSAs are alloys where a solute metal is present near the surface of a host metal. Such alloys are used in heterogeneous catalysis to tune the adsorption properties. For example, the CO adsorption energy on thin platinum layers over Ru(0001) is lower than that on Pt(111) [27.17]. *Greeley* and *Mavrikakis* [27.18] screened the hydrogen adsorption and dissociation processes on a group of NSAs using DFT calculations. Two different NSA models were considered, namely overlayers and subsurface alloys. Overlayer alloys have one layer of solute metal on the host metal surface, whereas

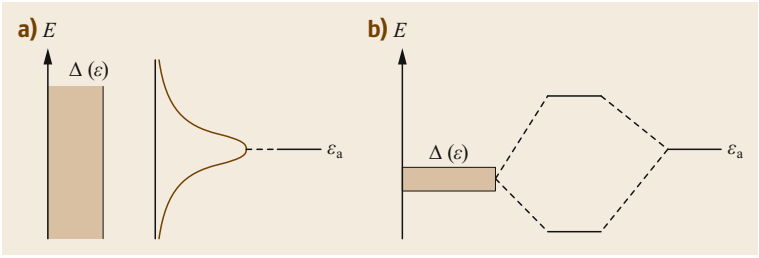

Fig. 27.4a,b The local density of states (DOS) at an adsorbate for interactions with **(a)** a metal s band and **(b)** a transition metal d band. (Reprinted from [27.16], with permission from Elsevier)

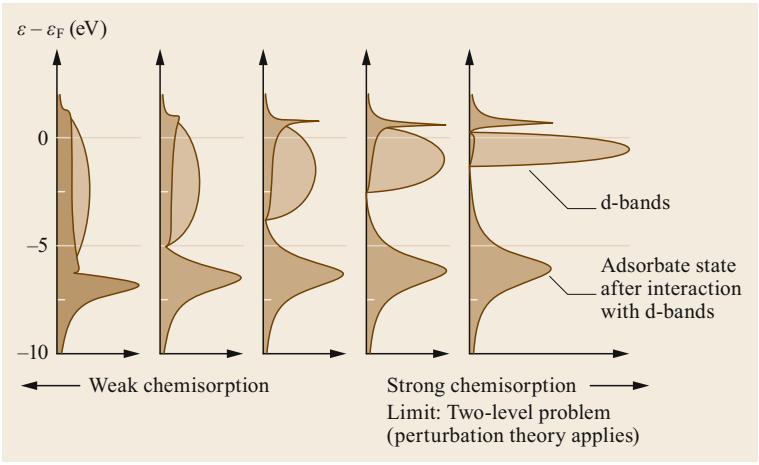

Fig. 27.5 The local DOS projected onto an adsorbate state interacting with the d bands at a surface. (Reprinted from [27.16], with permission from Elsevier)

the surface and bulk atoms in subsurface alloys are host metal atoms and there is one layer of solute metal in the subsurface.

Greeley and Mavrikakis first evaluated the stabilities of the NSAs using two different criteria: the segregation energy and the difference in hydrogen binding energy between the solute and the host metal (more details can be found in [27.18]). The hydrogen atom adsorption energies and hydrogen molecule dissociation barriers on stable NSAs were calculated. The hydrogen atom adsorption energies were found to be lower than those on pure metals. The adsorption energies on the NSAs were generally weaker than those on most pure metal surfaces, and the adsorption strengths on the NSAs were mostly found to be weaker than those on Pt and comparable to those on Cu and Au. As discussed in the last section, Cu and Au do not permit hydrogen adsorption and dissociation at their surfaces; thus, given their similar adsorption strengths to Cu and Au, these NSAs should not permit hydrogen dissociation. Interestingly, the dissociation barriers on all the NSAs were found to be below 0.6 eV, and most were as low as 0.2 eV, making them much lower than the barriers on Cu and Au. In order to understand the trends in adsorption energy on these NSAs, the position of the d-band center was calculated for each NSA. As shown in Fig. 27.6, a linear relation was observed between the binding energy of a hydrogen atom and the position of the d-band center for the alloy. As the d-band center increases in energy, the bond energy of the hydrogen atom increases, suggesting that the d-band center model is sufficient to accurately model the gas–surface interactions on NSAs. Note that three different linear relations

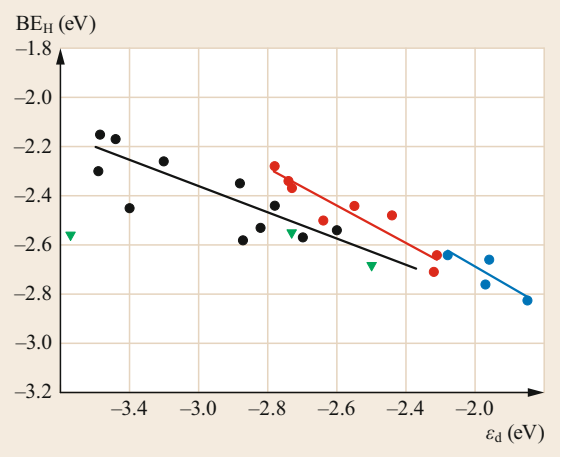

Fig. 27.6 Correlation of the binding energy of atomic hydrogen, BE_H, with the d-band center of the corresponding surface. (From [27.18])

are evident in Fig. 27.6; this can be explained by the different coupling matrix elements of the host metals.

Electronic Structures of Nonmetal Surfaces

In addition to metals, nonmetallic materials—especially sp^2-carbon materials—have attracted a great deal of attention in the field of heterogeneous catalysis. For example, *Su* and coworkers [27.19] found that carbon nanotubes with modified surfaces can efficiently catalyze the dehydrogenation of *n*-butane to butenes with good recyclability. The relationship between electronic structure and adsorption strength is key to understanding the adsorption process in these sp^2-carbon materials and developing new catalysts based on nonmetallic materials.

Hu and coworkers [27.20] investigated the adsorption energies of oxygen molecules and oxygen atoms on graphene and graphene oxide with different oxygen-containing groups at different sites. They considered armchair edge, zigzag edge, and basal plane sites along with five different groups: carboxyl, hydroxyl, ketone, aldehyde, and epoxy groups. The dissociation barrier for an oxygen molecule was also calculated. All of the results are shown in Table 27.3. Based on these results, the adsorption energy of an oxygen atom at particular sites on graphene without any oxygen-containing groups decreases in the order armchair > zigzag > basal plane. However, the introduction of oxygen-containing groups affects the adsorption energy dramatically. In order to understand the variations in adsorption energy that occur upon changing the adsorption site and the oxygen-containing group present, the electron transfer process must be investigated. During the adsorption and dissociation of the oxygen molecule, electrons are transferred from the graphene surface to the antibonding orbital of the oxygen molecule, weakening the O–O bond. The easier it is for electrons to be transferred, the more favorable the adsorption and dissociation of oxygen molecules. On the other hand, the electrons are in a delocalized orbital on the graphene surface. As the electron transfers from the surface to the oxygen molecule, the hybridization of the carbon changes from sp^2 to sp^3, meaning that a new atomic p orbital can bond with the adsorbed oxygen atom. Therefore, the ease with which carbon atoms can switch from sp^2 to sp^3 hybridization is another important indicator of the adsorption energy.

Based on the discussion above, the trend in the adsorption energy of oxygen at different sites on graphene without oxygen-containing groups can be explained as follows. The adsorption of oxygen molecules on the basal plane requires that two carbon atoms change from sp^2 to sp^3 hybridization. These two carbon atoms are involved in four six-atom rings, so the reaction will affect

Table 27.3 Results of DFT calculations of the initial state (IS) and the transition state (TS) and final state (FS) for the dissociation of oxygen on graphene and graphene oxide. The chemisorption energy of O (O_{atom}) is also listed in the table for comparison. All of the energies are given in eV with respect to the gas-phase molecule. All results are adapted from [27.20]

Site	Group	IS	TS	FS	O_{atom}
Armchair	Graphene	0.62	1.19	0.33	−0.15
	Ketone	0.61	0.99	−0.68	−0.26
	Carboxyl	0.48	1.08	0.12	−0.32
	Hydroxyl	0.28	0.88	−0.14	−0.29
	Aldehyde	0.26	0.89	−0.41	−0.46
	Epoxy	0.32	0.72	−0.02	−0.41
Zigzag	Graphene	1.05	1.42	0.03	0.18
	Ketone	0.69	1.29	−0.34	−0.16
	Carboxyl	0.93	1.51	−0.07	0.18
	Hydroxyl	0.83	0.96	−0.68	0.13
	Aldehyde	0.83	1.31	−0.14	0.02
	Epoxy	0.23	0.70	−0.69	−0.48
Basal plane	Graphene	2.05	2.69	1.47	0.90
	Hydroxyl	1.14	1.56	0.73	0.26
	Epoxy	1.37	2.03	0.87	0.42

the delocalization of the electrons in those four rings. Therefore, shifts in hybridization are difficult for carbon atoms in the basal plane. The weakest adsorption energy of an oxygen atom in the basal plane is therefore 0.90 eV. For adsorption at zigzag edges, the oxygen molecule is adsorbed on two carbon atoms, but only two rings are affected in this case due to the structure of the zigzag edge. Thus, the adsorption energy of an oxygen atom at a zigzag edge is much more favorable than it is on the basal plane. The adsorption of an oxygen atom at an armchair edge is also favorable, with an adsorption energy of −0.15 eV. When the oxygen molecule is adsorbed on the armchair edge, only one ring structure is affected (the geometries of these surfaces are explained in [27.20]). In summary, the adsorption at each site is related to the number of six-atom rings that are affected by the adsorption, indicating the presence of a structural effect. This variation in adsorption energy with site is, however, an electronic effect, namely differences in the ease of deconstructing the delocalized orbitals on graphene.

The effect of changing the oxygen-containing group present does not seem to be as clear as the above-described trend in adsorption energy upon changing the adsorption site. Unlike the metal surface, the electrons involved in the adsorption of the oxygen molecule on sp^2-carbon material are the delocalized electrons (the p_z electrons). The projected density of states (PDOS) of the p_z band of graphene with different oxygen-containing groups was obtained using DFT. In Fig. 27.7, PDOSs are shown for zigzag edges without any oxygen-containing group (Fig. 27.7a), with an epoxy group (Fig. 27.7b), and with a carboxyl group (Fig. 27.7c). Due to the existence of different oxygen-containing groups, the electronic structures of these surfaces are quite different. To quantitatively evaluate the difference between the electronic structures of these surfaces, we introduced the concept of the p_z-band center, which is defined in a similar manner to the d-band center. The position of the p_z-band center for each of the three graphene structures is indicated by a dashed line in Fig. 27.7. This corresponds to −3.53 eV for the pure zigzag edge, −3.02 eV for the zigzag edge with an epoxy group, and −3.71 eV for the zigzag with a carboxyl group. Interestingly, the oxygen dissociation barrier on a zigzag edge is highest for the zigzag edge with a carboxyl group (1.51 eV). The p_z-band center has the lowest value for the carboxyl group at all three sites. The p_z-band center of the epoxy group is the highest for all three sites. The presence of this group also leads to the highest oxygen dissociation activity at zigzag edges, as shown in Table 27.3. A linear relation between the p_z-band center energy and the oxygen dissociation barrier is shown in Fig. 27.7, suggesting that the p_z-band center is a good indicator of the activity of an sp^2-carbon material. A similar relation between the adsorption energy of the oxygen molecule on zigzag edges with oxygen-containing groups and the HOMO energy of a benzene molecule with the corresponding groups was found by *Hu* and coworkers [27.20]. Both energies depend on the level of electron delocalization, illustrating the effects of oxygen-containing groups on the delocalized electrons.

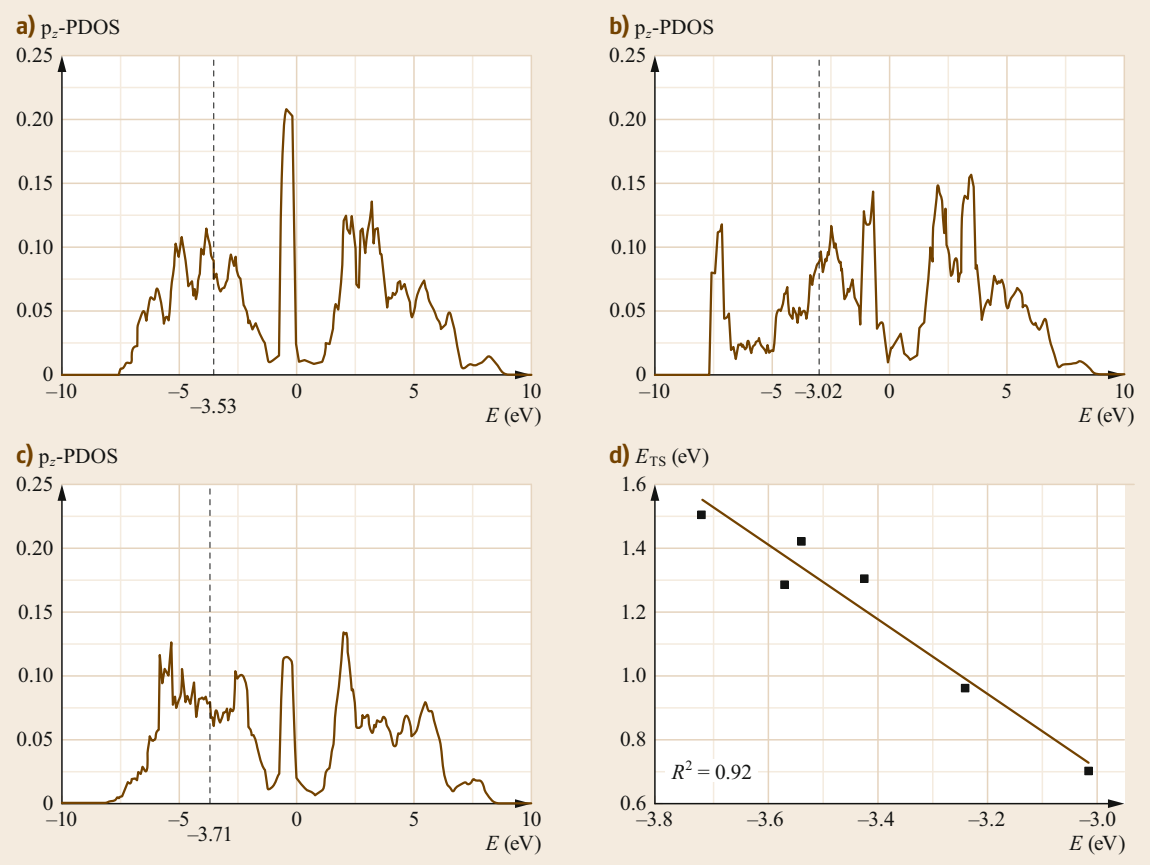

Fig. 27.7a–d The p_z partial density of states (p_z-PDOS) and the p_z-band center for **(a)** zigzag edges, **(b)** zigzag edges with epoxy groups, and **(c)** zigzag edges with carboxyl groups; **(d)** the correlation between the energy of the p_z-band center and the energy of the TS. The *dashed lines* indicate the positions of p_z-band centers

27.1.3 Predicting the Adsorption Energy

The ability to accurately predict the adsorption energy is crucial when attempting to rationally design materials with specific adsorption properties. In other words, a quantitative description of the relationship between surface structure and adsorption energy can enhance our understanding of adsorption energy trends among various materials and speed up the design of new materials. The relationship between electronic structure and adsorption energy mentioned in the last section permits a deep understanding of the electron transfer involved in gas–surface interactions. It can also be used to predict adsorption energies. However, calculating the projected DOS for surface atoms is a very time-consuming task compared to calculating the adsorption energy, which limits its applicability to the high-throughput screening of materials. Moreover, even though the electronic structure of a material is one of its fundamental structural properties, it is hard to engineer the electronic structure based on our current knowledge of surface science. More direct properties need to be introduced if we are to predict adsorption energies. In this section, two examples of methods that allow adsorption energy prediction are discussed for two different systems, namely nanoparticles and alloys.

Generalized Coordination Numbers

Almost all surfaces have different types of sites (e.g., terrace, edge, and corner sites). Some of these sites are associated with high catalytic activities; for instance, B5 sites are important in ammonia [27.21] and Fischer–Tropsch synthesis [27.22]. Furthermore, the activities of some catalytic systems are correlated with particle size. Thus, the relationships between the adsorption energy and the properties of different sites on metal particles are very important.

Calle-Vallejo et al. [27.23] carried out a systematic investigation of the prediction of adsorption energies of various species on nanoparticles based on DFT cal-

culation results. Palladium nanoparticles were chosen due to their important applications in heterogeneous catalysis and electrochemistry. They calculated the adsorption energies of *O, *O_2, *OH, *OOH, *H_2O, and *H_2O_2 (* denotes the adsorption site) on three different nanoparticles: Pt_{201}, Pt_{79}, and Pt_{38} (more details on the modeling performed can be found in the original work [27.23]). One of the most important differences between types of adsorption sites is the chemical environment, namely the number of neighboring atoms—the coordination number. This parameter is arguably the easiest surface property which can be calculated directly. For example, a Pt atom on the Pt(111) surface is surrounded by six surface atoms and three subsurface atoms, giving a coordination number of nine. *Calle-Vallejo* et al. [27.23] compared the adsorption energies of *OH at different sites on nanoparticles. They are plotted as the coordination numbers of the corresponding adsorption sites in Fig. 27.8. In general, there is a linear relation between the coordination number and the adsorption energy: as the coordination number decreases, the adsorption energy increases because the level of unsaturation at the adsorption site rises. However, the mean absolute error (MAE) in this relation is 0.09 eV and the maximum error is 0.33 eV, which could be improved.

To improve the prediction accuracy for the adsorption energy, *Calle-Vallejo* et al. [27.23] introduced the concept of the *generalized coordination number* ($\overline{\mathrm{CN}}$) of an atom i with n_i nearest neighbors, which they defined as

$$\overline{\mathrm{CN}}(i) = \sum_{j=1}^{n_i} \mathrm{cn}(j) \frac{n_j}{\mathrm{cn}_{\max}} , \qquad (27.5)$$

where cn(j) is the coordination number of the j-th neighboring atom and $n_j/\mathrm{cn}_{\max}$ is the weight of the given atom. This definition incorporates the environments of neighboring atoms (note that examples of the calculation of the generalized coordination number can be found in [27.23]). Using the generalized coordination number instead of the usual coordination number roughly halves the MAE (to 0.056 eV) and the maximum error (to 0.161 eV), as shown in Fig. 27.8. The adsorption energies of all the other species mentioned above were also found to correlate well with the generalized coordination number, which therefore represents an efficient approach to adsorption prediction. Recently, *Calle-Vallejo* et al. [27.24] proposed the use of coordination–activity plots to predict catalytic activity based on the generalized coordination number. This approach led to the discovery of highly active sites of Pt(111), which were subsequently confirmed experimentally.

Bonding Contribution Equation

The generalized coordination number offers an efficient approach to predicting adsorption energies at different sites on nanoparticles. However, at present, only the generalized coordination numbers of pure metal surfaces and nanoparticles are considered. This is a problem because surfaces containing more than one metallic element, such as alloys, play a very important role in heterogeneous catalysis. For example, the $Pt_3Ni(111)$ alloy surface was found to be tenfold more active in the oxygen reduction reaction than the pure Pt(111) surface [27.2]. Given that there are a large number of possible combinations of metals, and that the ratio of the metals can also be varied, there are an enormous number of possible alloys with a wide range of adsorption properties—an ideal situation for catalyst design. Elucidating the relationship between alloy structure and adsorption energy is therefore the key to accelerating

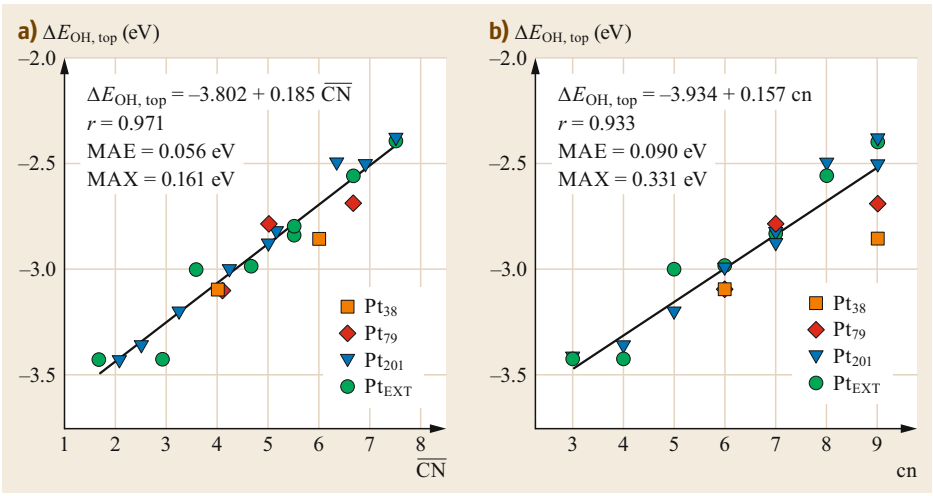

Fig. 27.8a,b Plots of the adsorption energy of *OH atop versus the generalized **(a)** and usual **(b)** coordination numbers of the site to which the adsorbate is bound. (Reprinted by permission from [27.23], © 2014 Wiley)

the design of alloy surfaces with defined adsorption properties.

We proposed an explicit equation with three chemically meaningful terms, which we denoted the *bonding contribution equation* [27.25], to quantitatively account for the surface structures and the adsorption energies of alloy systems. To begin with, we considered the adsorption of oxygen atoms on alloys with one solute metal. If the oxygen is adsorbed at a fcc hollow site, there are four possible types of adsorption site atoms: an atom connected to oxygen (type I), a surface atom near a type I atom (type II), and two types of subsurface atoms (types III and IV; the types of adsorption site atoms are discussed in more detail in [27.25]). We found that the adsorption energy of an oxygen atom on the surface of an alloy with one solute metal can be evaluated using the equation

$$E_{\text{predicted}} = gca \,, \tag{27.6}$$

where g is the generalized parameter, c is the contribution factor, and a is the intrinsic bonding ability of the solute metal. The intrinsic bonding ability is the adsorption energy of oxygen on the close-packed surface of solute metal atoms. The contribution factor is used to distinguish between the different substitution positions. A bond-counting contribution factor (BCCF) was introduced, with values of $7/27$, $-2/9$, $-2/27$, and $-3/27$, respectively, for types I, II, III, and IV in a Pt(111)-p(2×2) unit cell (more details are given in [27.25]). We compared the adsorption energies predicted using this equation with those calculated from DFT and found that the MAE was only 0.07 eV, as shown in Fig. 27.9.

In real alloy systems, the surface may contain multiple solute metals or more substitutions. We therefore extended the bonding contribution equation to consider alloys with n substitutions and obtained

$$E_{\text{ad}} = \sum_{i=1}^{n} gc_i a_i \,. \tag{27.7}$$

This equation can be used to calculate the adsorption energies of multiple solute metals in an alloy. We randomly generated 100 alloy surfaces based on Pt(111)-p(2×2) with two or three substitutions, and a comparison of the energies predicted using this equation with those calculated using DFT is shown in Fig. 27.9b. In general, the MAE for the comparison of predicted and calculated adsorption energies was 0.10 eV. Considering that alloys are relatively complicated systems, this MAE is reasonable and implies that the equation could be used as a prescreening method during catalyst design. To further test the generality of our bonding contribution equation, we also considered alloy surfaces with a different unit cell size, namely Pt(111)-p(3×3) (Fig. 27.9c), and a different adsorbate, namely CO (Fig. 27.9d). The corresponding MEAs were found to be below 0.12 eV, suggesting that the bonding contribution equation accurately predicts the adsorption energy.

27.1.4 Catalyst Design Based on the Adsorption Energy

The adsorption energy plays an important role in catalytic activity, and effective catalysts should facilitate adsorption energies that are in the optimal range for reactants, intermediates, and products. Determining this optimal range is a pivotal step when designing or screening catalytic materials. In this section, we discuss how this interval can be evaluated based on the chemical potential. Design work that uses this interval is then briefly reviewed.

To obtain the optimal adsorption energy interval, *Cheng* and *Hu* [27.26] introduced chemical potentials into the theory of heterogeneous catalysis [27.26]. In their work, using the Langmuir adsorption paradigm, they expressed the chemical potential of surface species i as

$$\begin{aligned}\mu(T,\theta_i) &= \mu_i^0(T) + RT\ln\left(\frac{\theta_i}{\theta_*}\right)\\ &= E^{\text{total}} + \Delta\mu_i(T) + RT\ln\left(\frac{\theta_i}{\theta_*}\right),\end{aligned} \tag{27.8}$$

where θ_i and θ_* are the coverage of species i and the free-site coverage, respectively, while $\mu_i^0(T)$ is the standard chemical potential of i at temperature T, which can be calculated by applying a thermal correction $\Delta\mu_i(T)$ to the total energy E^{total}. The process of a normal reaction involving heterogeneous catalysis starts from the reactant in the gas phase. After a series of adsorption and surface reactions, the key intermediate forms. Then, after surface reactions of the intermediate, the products desorb from the surface. During this catalyzed process, the chemical potentials should decrease step by step from reactants to intermediates to products, i.e.,

$$\mu_{\text{R}} > \mu_{\text{I}} > \mu_{\text{P}} \,. \tag{27.9}$$

Based on (27.9), the chemical potential of the intermediate state is

$$\mu_{\text{I}} = \mu_{\text{I}}^0 + RT\ln\left(\frac{\theta_{\text{I}}}{\theta_*}\right). \tag{27.10}$$

Furthermore, as proposed in [27.26], the coverage of free site θ_* is often on the order of 10^{-2}–10^{-1} ML in

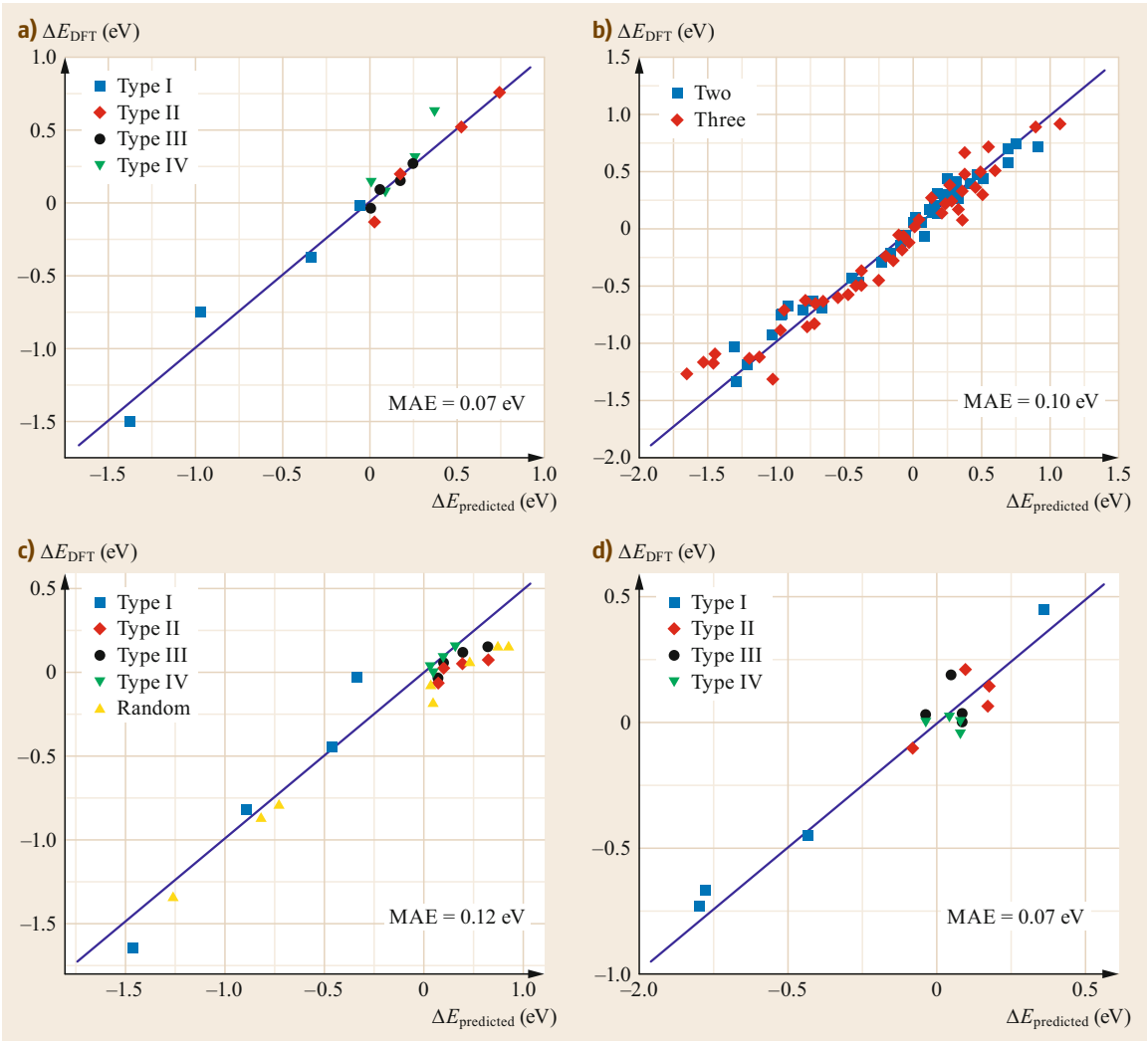

Fig. 27.9a–d Comparison of the adsorption energies predicted using the bonding contribution equation with those calculated using DFT for **(a)** oxygen on alloys of Pt(111) p(2 × 2) with one substituted atom, **(b)** oxygen on randomly generated alloys of Pt(111) p(2 × 2) with two or three substituted atoms, **(c)** oxygen on alloys of Pt(111) p(3 × 3) with one substituted atom, and **(d)** CO on alloys of Pt(111) p(2 × 2) with one substituted atom. (This figure is from our unpublished work [27.25])

the steady state, which leads to a coverage-dependent term $RT\ln(\theta_I/\theta_*)$, denoted ε, which takes values in the small interval 0.1–0.2 eV at 500 K. In other words, the chemical potential of intermediate I for a good catalyst should be

$$\mu_I^0 + \varepsilon > \mu_I > \mu_I^0 - \varepsilon \text{ or } \mu_I \approx \mu_I^0 \,. \qquad (27.11)$$

Combining (27.10) and (27.11) yields a general principle for identifying a good catalyst,

$$\mu_R + \varepsilon > \mu_I^0 > \mu_P - \varepsilon \,, \qquad (27.12a)$$

or approximately

$$\mu_R > \mu_I^0 > \mu_P \,. \qquad (27.12b)$$

Based on this principle, a good catalyst can be identified using the following approach. A chemical potential region (the blue zone in Fig. 27.10) is formed which has the chemical potential of the reactants μ_R and the chemical potential of the products μ_P as upper and lower bounds, respectively. A catalyst with a chemical potential in this zone is most likely to be reactive according to (27.12) (e.g., catalyst C with $\mu_{I,C}^0$ in Fig. 27.10). Due

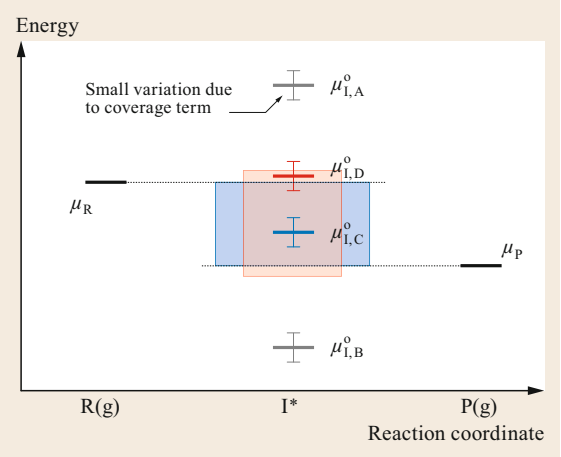

Fig. 27.10 Searching for good catalysts based on their chemical potentials. (Reprinted by permission from [27.26], © 2011 Wiley)

to the coverage-dependent term ε, the region can be extended (red zone in Fig. 27.10). The chemical potential of a good catalyst (such as catalyst D in Fig. 27.10) should occur within this region, whereas catalysts with chemical potentials outside the red zone (e.g., catalysts A and B in Fig. 27.10) are unlikely to be good catalysts.

Based on the design strategy mentioned above, a novel counter electrode (CE) material for use as an catalyst in the triiodide reduction reaction (IRR) employed in dye-sensitized solar cells was discovered. In the IRR, the chemisorption energy of the key intermediate—an iodine atom—on the catalyst should be in the approximate interval 0.33−1.20 eV, as derived from (27.12). The adsorption energies of an iodine atom on many promising CE materials were calculated and checked to see if they were within the adsorption energy window mentioned above. Several known good catalysts for IRR were found to give adsorption energies within the desired range, including Pt, WO_3, WC, NiS, CoS, MoC, and MoN. Furthermore, two surfaces that had not previously been considered in this context were also found to give adsorption energies within the required range, namely the $Fe_2O_3(012)$ and $Fe_2O_3(104)$ surfaces of α-Fe_2O_3. To verify these theoretical predictions, pure-phase Fe_2O_3 was synthesized via a simple modified hydrothermal method [27.27]. Based on its photovoltaic data, the overall energy-conversion efficiency of this α-Fe_2O_3 was found to be 6.96%, which is remarkably similar to that of Pt (7.32%). These results suggest that α-Fe_2O_3 is a suitable catalyst for the reduction of triiodide to iodide.

27.2 Surface Reactions

Surface reactions are another important area of surface science. In heterogeneous catalysis, the adsorbed reactants undergo a series of surface reactions that lead to the final products. Understanding these surface reactions is crucial if we are to optimize the activity and selectivity of heterogeneous catalysts, determine the limitations of current catalysts, and develop better catalytic materials.

The reaction rate of a surface reaction is arguably the most important kinetic property. In the first part of this section, we introduce the use of transition state theory to quantitatively evaluate the reaction rate in terms of the activation energy. We then describe the calculation of the activation energy using first-principles methods and consider the details of the reaction process at the atomic level. The BEP relation, one of the most important relations in heterogeneous catalysis, is also discussed.

The steps involved in a surface reaction (i.e., the reaction mechanism) are a fundamental aspect of heterogeneous catalysis. Three different reaction mechanisms are reviewed, using the most recent results from DFT calculations as examples. We also briefly introduce the concept of active sites and give examples of such sites on a metal and a metal oxide.

Besides these topics, there are many other active areas of research in surface reactions using DFT calculations, such as microkinetic modeling, the effects of surface reconstruction, the volcano curve, and new catalytic materials. In this section, we choose three fundamental areas that have strong connections to surface science and the gas–surface interactions discussed earlier in the chapter.

27.2.1 Reaction Rate and Activation Energy

The reaction rate is one of the most important kinetic properties of a surface reaction. For an elementary reaction in which the reactants and products are located on a surface, the reaction rate is related to the rate constant of the reaction and the surface coverages of the reactant and product species. In his well-known equation, Arrhenius proposed that the rate constant (k) depends on the temperature as

$$k = Ae^{-\frac{E_a}{RT}} , \qquad (27.13)$$

where A is the pre-exponential factor, T and R are the temperature and the universal gas constant, respectively, and E_a is the activation energy. When this equation was proposed, the physical meanings of the pre-exponential factor and the activation energy were unclear. However, transition state theory (TST)—introduced by Eyring, Polanyi, and Evans—provides a solid theoretical foundation for the Arrhenius equation. TST assumes an equilibrium energy distribution among all possible quantum states at all points along the reaction coordinate. The probability of finding a molecule in a particular quantum state is proportional to the Boltzmann distribution $\exp[\Delta E/(k_B T)]$. It is also assumed that a chemical reaction proceeds from one local minimum (corresponding to the reactants) to another (corresponding to the products) via a saddle point (known as the transition state, TS) on the potential energy surface of nuclear coordinate space. If the transition-state molecule is in equilibrium with the reactant, the reaction rate constant is given by

$$k = \frac{k_B T}{h} e^{-\frac{\Delta^{\neq} G^{\circ}}{RT}} , \tag{27.14}$$

where $\Delta^{\neq} G^{\circ}$ is the standard Gibbs free energy difference between the IS and the TS, k_B is Boltzmann's constant, and h is Plank's constant, respectively. Using the equation

$$\Delta^{\neq} G^{\circ} = \Delta^{\neq} H^{\circ} - T\Delta^{\neq} S^{\circ}, \tag{27.15}$$

the rate constant can be written as

$$k = \frac{k_B T}{h} e^{-\frac{\Delta^{\neq} S^{\circ}}{R}} e^{-\frac{\Delta^{\neq} H^{\circ}}{RT}} , \tag{27.16}$$

where $\Delta^{\neq} H^{\circ}$ and $\Delta^{\neq} S^{\circ}$ are the enthalpy and entropy differences between the IS and the TS, respectively. In TST, the reaction rate is directly linked to the activation energy. The activation energy can be calculated as the energy difference between the TS and the IS. We now show how the transition state is located and the activation energy is calculated for CO oxidation on Pt(111) using DFT, and we discuss the relation between the change in enthalpy and the activation energy, which is known as the *BEP relation*.

Transition State for CO Oxidation

CO oxidation is a typical surface reaction that is effectively catalyzed by certain transition metals such as platinum, which has been used to remove CO and other pollutants from exhaust emissions. Understanding the process of CO oxidation and the reaction barrier on platinum is therefore important both scientifically and industrially. *Alavi* et al. [27.28] carried out a pioneering study on the transition state for and activation energy of CO oxidation on Pt(111).

Alavi et al. [27.28] used both the LDA and GGA functionals to investigate the oxidation of CO on Pt(111)-p(2×2). The reaction was assumed to start with the coadsorption of the oxygen atom and CO, with the oxygen atom at the hollow site and CO at the atop site. A new method of searching for the transition state, namely the *constrained minimization scheme*, was introduced to locate the transition state for CO oxidation. The distance between the carbon atom in CO and the adsorbed oxygen atom (O–CO) is fixed in this method, and the structure is optimized by relaxing all remaining orthogonal degrees of freedom. The state with vanishing forces along the reaction coordinate (O–CO) is considered to be the transition state. The pathway for CO oxidation from the IS to the FS via the TS was identified using this method, as shown in Fig. 27.11. In the geometry of the IS (Fig. 27.11a), oxygen is adsorbed at a hollow site and CO is adsorbed at an atop site nearby. As the reaction proceeds, the CO moves from the atop site to another neighboring atop site near the oxygen atom (Fig. 27.11b–e), while the oxygen atom also moves from the hollow site to a lower bridge site (Fig. 27.11e). The forces on both CO and O vanish at the geometry shown in Fig. 27.11e, suggesting that CO and O are at atop and bridge sites, respectively, in the transition state for the oxidation of CO on Pt(111). After the transition state, the CO moves towards O, as shown in Fig. 27.11f–h. Figure 27.11f shows the final state of the CO oxidation process—a chemisorbed CO_2 molecule. This CO_2 molecule is highly bent and asymmetric, and the length of the newly formed CO bond is significantly longer than that of the gas-phase molecule. Regarding the changes in energy, the reaction barrier is 1.01 eV when calculated using LDA and 1.05 eV according to GGA. This work reported the first transition state and low-energy pathway for CO oxidation on Pt(111), and the constrained minimization scheme for locating the transition state is still widely used today [27.29, 30]. This work suggests that DFT calculations are a powerful tool for understanding surface reaction processes and calculating the activation energies of these reactions.

The oxidation of CO on other transition metals such as Ru(001) and Rh(111) was also studied by *Hu* and coworkers [27.31, 32] using the constrained minimization scheme. They found that CO oxidation only proceeds on these metal surfaces when (i) the surface oxygen becomes activated upon shifting from the hollow site to the bridge site (as discussed above) and (ii) the CO approaches the activated surface oxygen atom from the correct direction. They also found that the energy change of the CO movement in the CO oxidation is negligible, while the activation of the oxygen atom upon moving from the hollow site to the bridge site

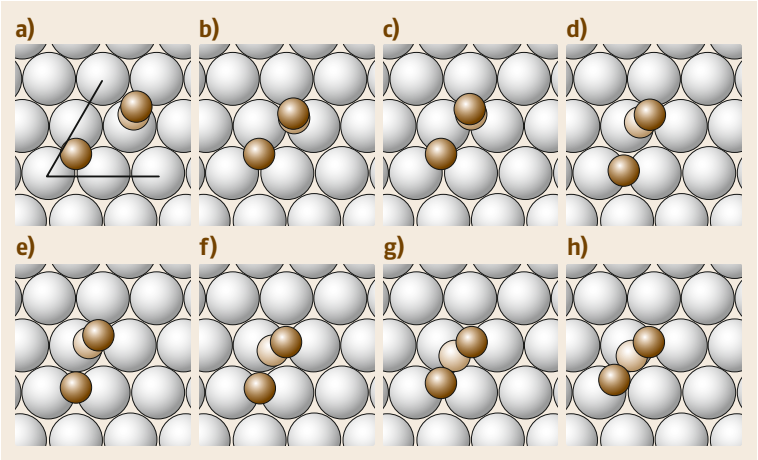

Fig. 27.11a–h Geometries along the reaction pathway for the oxidation of CO on Pt(111), ranging from the initial state **(a)** to the final state **(h)**. The Pt atoms are represented by the *largest spheres*, the O atoms are denoted by the *darkest spheres*, and the C atoms are shown as *light brown spheres*. (Reprinted with permission from [27.28], Copyright (1998) by the American Physical Society)

requires a considerable amount of energy. Thus, the reaction barrier is mainly determined by the scission of the O–metal bond. One may ask why the oxygen atom must move from a hollow site to a bridge site to become activated for catalytic CO oxidation. In order to answer this question, *Zhang* and *Hu* [27.31] investigated CO oxidation on Rh(111) using DFT. They discovered that the 2p orbitals of oxygen are almost completely filled due to strong bonding with three metal atoms at the hollow site. As shown in Fig. 27.12a, when the oxygen atom is activated upon shifting from the hollow to the bridge site, there is no significant change in the LDOS along the p_x axis but the LDOS decreases considerably along the p_y axis, which suggests that the p_y orbital is activated and available to form a new bond. At the same time, CO needs to diffuse to the atop site in the p_y direction, as shown in Fig. 27.12. Therefore, the oxygen atom is inactive at the hollow site because its 2p orbitals are almost fully occupied, so it must be activated by moving to the bridge site before it can react with CO.

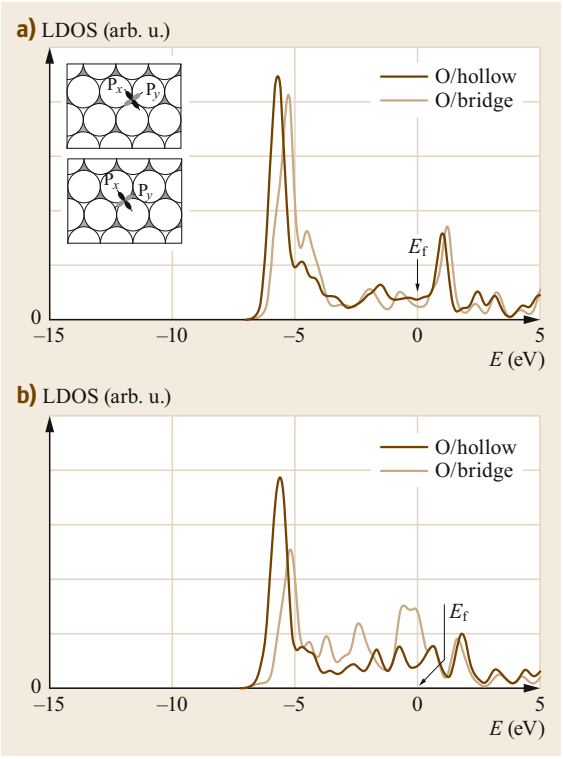

Fig. 27.12a,b Local density of states (LDOS) projected onto a point 0.4 Å away from the center of the oxygen atom along the p_x axis **(a)** or the p_y axis **(b)** for the oxygen at the hollow and bridge sites. The *inset* depicts the bonding of the $2p_x$ and $2p_y$ orbitals of the oxygen atom with metal atoms. (Reprinted with permission from [27.31], Copyright (2000) American Chemical Society)

The BEP Relation

In previous sections, we discussed the calculation of the adsorption energy and the activation energy—two of the most important energetic results for gas–surface interactions and surface reactions—using DFT. Are these two properties, one of which is from thermodynamics and the other is from kinetics, correlated? According to DFT calculations, they are indeed related. The BEP relation is a widely utilized relation between the adsorption energy and the activation energy that is used to analyze elementary surface reactions. The typical form of the BEP relation for an elementary surface reaction is

$$E_a = \alpha \Delta H + \beta \,, \qquad (27.17)$$

where E_a and ΔH are the activation energy and the enthalpy change for this reaction, respectively. α and β are the two BEP parameters, which vary with the type of surface reaction considered. The BEP relation therefore suggests that the activation energy is linearly correlated with the enthalpy change for surface reactions of the

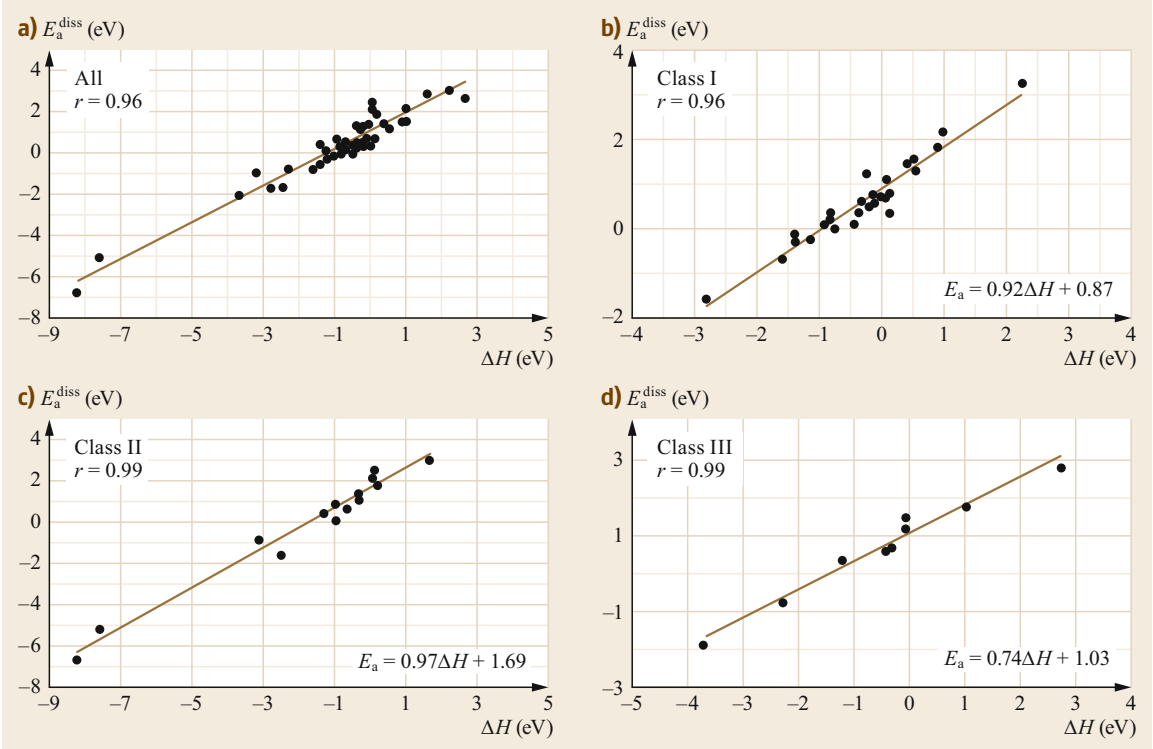

Fig. 27.13a–d Plots of activation energy (E_a^{diss}) against enthalpy change (ΔH) for **(a)** more than 50 elementary reaction steps, **(b)** discrete adsorbate dehydrogenation reactions (class I); **(c)** diatomic dissociation and hydrocarbon cracking reactions (class II), and **(d)** triatomic dissociation reactions (class III). (Reprinted with permission from [27.33], Copyright (2003) American Chemical Society)

same type. In other words, the more thermodynamically favorable the reaction, the lower the activation energy is likely to be. The BEP relation for surface reactions was proposed by several groups around the year 2000 based on DFT calculations. *Pallassana* and *Neurock* [27.34] demonstrated that both the hydrogenation and dehydrogenation of ethylene follow the BEP relation on bimetallic Pd alloy surfaces. *Logadottir* et al. [27.35] found that the adsorption energy of N_2 and the activation energy for N_2 dissociation are linearly correlated in ammonia synthesis. Two different lines with different α and β values are found for different reaction structures, namely terrace and step sites. *Liu* and *Hu* [27.36] also developed a model that links the activation energy, chemisorption energies, and the bonding energy. Following these pioneering reports, many other examples of BEP relations for different reactions that explain the activities of many surface reactions were reported; these have been reviewed by van *Santen* et al. [27.37].

The parameters α and β in the BEP relation are very important and are the key to predicting activation energies from enthalpy changes. They vary for different types of reactions and reaction sites. In order to explore how these parameters vary for different reactions, *Michaelides* et al. [27.33] investigated the activation energies and enthalpy changes for more than 50 dissociation reactions. As shown in Fig. 27.13a, they found a linear relation between the activation energies and enthalpy changes of all these reactions. Interestingly, the reactions were classified into three different classes, each of which had its own BEP relation. The first class corresponded to dehydrogenation reactions, including O–H and C–H bond cleavage. The values of the slope and the intercept for the BEP relation in this case were found to be 0.92 and 0.87, respectively (Fig. 27.13b). The α and β values for class II reactions, corresponding to diatomic dissociation and hydrocarbon cracking, were very different from those for class I, as shown in Fig. 27.13c. The third class of reaction corresponded to triatomic activation (Fig. 27.13d), for instance the dissociation of molecules such as CO_2, NO_2, and N_2O. Michaelides et al. suggested that the differences in the BEP parameters of the three classes are related to the activation energies of the reverse association reactions.

27.2.2 Reaction Mechanisms

In the previous section, we described the use of DFT to calculate the activation energy and locate the transition state. These results can then be used to determine the detailed steps involved in the surface reaction, i.e., the reaction mechanism. In this section, we discuss the investigation of reaction mechanisms using DFT. Two main reaction mechanisms, namely the Langmuir–Hinshelwood (LH) and Eley–Rideal (ER) mechanisms, are reviewed using the oxidation of CO as an example. The Mars–van Krevelen (MvK) mechanism, which is widely used for metal oxide and some other surfaces, is also introduced.

The Langmuir–Hinshelwood and Eley–Rideal Mechanisms

There are two main widely accepted reaction mechanisms for surface reactions: the LH and ER mechanisms. The processes involved in these two mechanisms are illustrated in Fig. 27.14. In the LH mechanism (Fig. 27.14a), the reaction begins with the adsorption of both reactants. The adsorbed reactant species then diffuse across the surface, eventually coming into contact, reacting, and generating the product species. Finally, the products desorb to the gas phase. On the other hand, only one reactant is initially adsorbed at the surface in the ER mechanism, as shown in Fig. 27.14b. The other reactant (the white ball in Fig. 27.14b) couples with the adsorbed reactant (the brown ball in Fig. 27.14b) from the gas phase. The last step is the desorption of the resulting products. Both mechanisms are found to occur in various surface reactions; interestingly, most catalytic surface reactions prefer the LH mechanism [27.38].

To understand why the LH mechanism is generally preferred in catalytic surface reactions, *Baxter* and *Hu* [27.38] investigated the LH and ER pathways for CO oxidation on Pt(111). Both of these mechanisms start with CO in the gas phase and oxygen atoms (generated by the dissociation of adsorbed oxygen molecules) on the surface. In the LH mechanism, the CO is first adsorbed on the surface. The CO then couples with surface oxygen, forming CO_2. In the ER mechanism, CO from the gas phase couples directly with the surface oxygen. Using the constrained minimization scheme, *Baxter* and *Hu* located the transition states of both reactions [27.38]. Surprisingly, the activation energies of the ER and LH mechanisms were calculated to be 0.72 and 1.05 eV, respectively. The same phenomenon was also observed on the Ru(001) surface; in this case, the activation energy for CO oxidation via the ER mechanism was found to be 0.41 eV lower than that for the LH mechanism [27.39]. Furthermore, a linear relation between the total bond strength of the initial reaction state and the reaction barrier was found [27.38]. This linear relation helped to explain why the ER mechanism had a lower activation energy than the LH mechanism: to allow oxygen atoms to couple with gas-phase CO in the ER mechanism, the bonding between the oxygen atoms and surface metal atoms needs to be relatively weak. In the LH mechanism, the surface CO and oxygen must be activated before they can react, which requires more energy than the ER mechanism. Therefore, the barrier to the ER mechanism is generally lower than that to the LH mechanism.

These findings obviously contrast with the statement that most surface reactions follow the LH mechanism. To answer this paradox, the energy profiles for both mechanisms of CO oxidation on Pt(111) were compared, as shown in Fig. 27.15. The ER mechanism has two conditions: first, the gas-phase CO should be located above the surface oxygen in the correct orientation; second, the CO must possess enough energy to

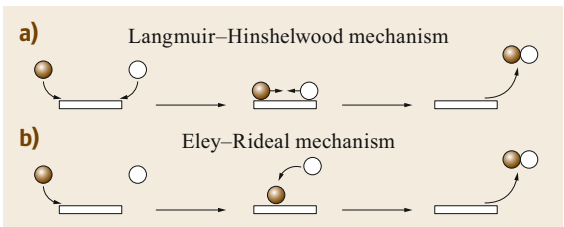

Fig. 27.14a,b Schematics of the (a) Langmuir–Hinshelwood and (b) Eley–Rideal mechanisms. The *brown* and *white balls* represent the two reactants

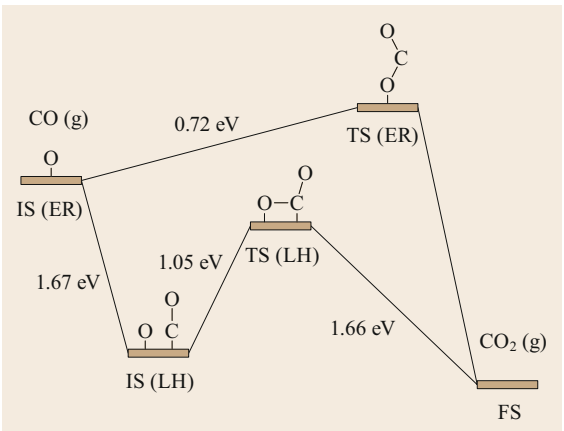

Fig. 27.15 Total energy profiles for CO oxidation on Pt(111) via the LH and ER mechanisms. (Reprinted with permission from [27.33], Copyright (2003) American Chemical Society)

overcome the reaction barrier to the ER mechanism. On the other hand, the adsorption energy of CO on Pt(111) is 1.67 eV, so the adsorption of CO is favorable thermodynamically, and the surface coverage of CO should be high. Thus, surface oxygen is more likely to couple with surface CO than with gas-phase CO. Furthermore, the entropy of gas-phase CO at the reaction temperature can also change the overall picture. When entropy is taken into account, the barrier to the ER mechanism increases due to the increase in the entropy of the gas-phase CO. On the other hand, changing the entropy of the gas-phase CO only affects the adsorption energy of CO. Therefore, taking the effect of temperature into consideration, the barrier to the ER mechanism will increase whereas the barrier to the LH mechanism will be almost unaffected. Thus, even though the total energy barrier to the LH mechanism is higher than that to the ER mechanism, CO prefers to react with oxygen via the LH mechanism.

MvK Mechanism

Another common mechanism besides the LH and ER mechanisms is the MvK mechanism. In MvK, the lattice components of the surface are involved in the reaction. For example, the lattice oxygen on a metal oxide surface may react with an adsorbate, forming an oxygen vacancy. The lattice oxygen is then regenerated via the dissociation of a gas-phase oxygen molecule. In this section, we explore the mechanisms for methane oxidation on nickel-doped cobalt oxide, which are typical examples of the MvK mechanism.

Nickel-doped cobalt oxide ($NiCo_2O_4$) was found to be an excellent catalyst for complete methane oxidation by *Tao* et al. [27.30]. This catalyst facilitates the complete oxidation of methane at temperatures from 350 to 550 °C. To investigate the reaction mechanism for enhanced methane oxidation on $NiCo_2O_4$, DFT calculations were implemented [27.30]. To begin with, the stabilities of all the facets with low Miller indices were evaluated based on the surface energies. $NiCo_2O_4$(100), $NiCo_2O_4$(110)-A, and $NiCo_2O_4$(110)-B were found to be stable, given their low surface energies. The barriers to the dissociative adsorption of methane on these three surfaces were then calculated to evaluate their activities. The Ni on the $NiCo_2O_4$(110)-B surface was observed to be the most active site for methane activation, with a dissociation barrier of 0.52 eV. Based on all of the above knowledge, the mechanism for methane oxidation on $NiCo_2O_4$(110)-B was investigated. Two favorable reaction pathways were discovered, as shown in Fig. 27.16; both are typical examples of the MvK mechanism as they involve the lattice oxygen.

On the $NiCo_2O_4$(110)-B surface, both the nickel and cobalt atoms are bonded to two lattice oxygen atoms, as shown in Fig. 27.16. The reaction starts with the dissociative adsorption of CH_4, in which CH_3 is adsorbed at a nickel site while the dissociated hydrogen atom is accepted by a nearby lattice oxygen, forming

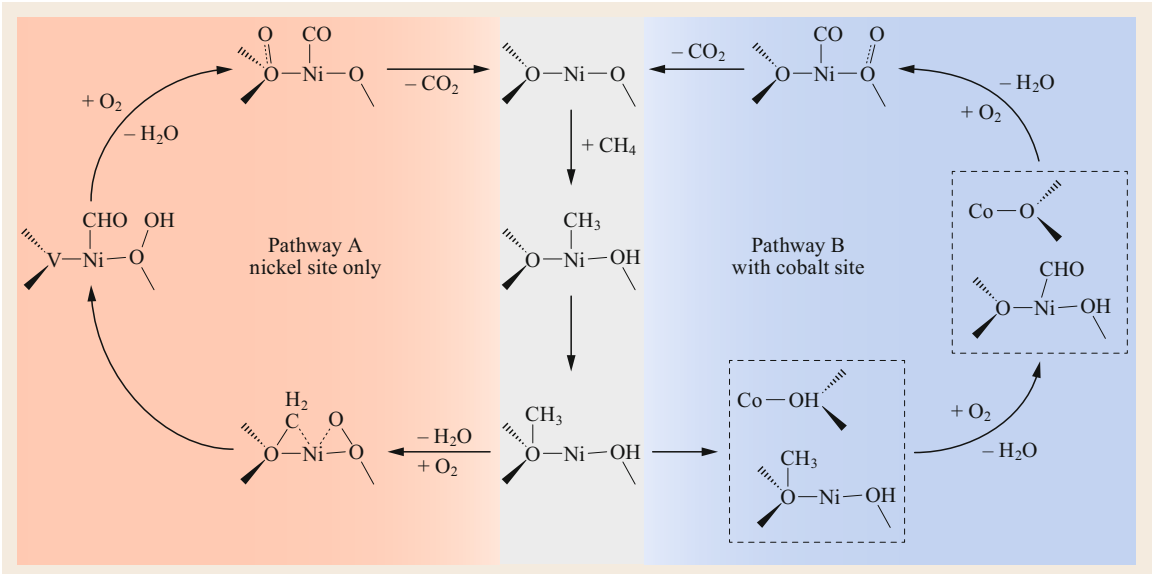

Fig. 27.16 Two reaction pathways for the complete oxidation of methane on a type I $NiCo_2O_4$(110)-B crystal. Pathway A (*red*) involves dehydrogenation at a nickel site only, whereas pathway B (*blue*) also involves Ni but includes dehydrogenation at a nearby Co site. V donates the oxygen vacancy

a OH group. It is then favorable for the CH_3 to couple with another lattice oxygen, yielding CH_3O. Next, there are two possible pathways: pathway A, which only involves the nickel site, or pathway B, which involves both nickel and cobalt sites. These pathways are depicted in red and black, respectively, in Fig. 27.16.

In pathway A, CH_3O is dehydrogenated by the surface OH group. The resulting H_2O desorbs, leaving an oxygen vacancy, and an oxygen molecule is adsorbed at this vacancy (lower left in Fig. 27.16). The formation of an oxygen vacancy and the regeneration of lattice oxygen are central processes in the MvK mechanism. As shown in Fig. 27.16, the C–H bond in CH_2O then dissociates with the help of the adsorbed oxygen molecule, which leads to CHO and OOH species (middle left in Fig. 27.16). Further dehydrogenation of CHO is favorable, and the H_2O that is generated desorbs before another oxygen molecule is adsorbed, just as in the step described above. At the end of the reaction cycle, the CO is oxidized by the oxygen molecule and the resulting CO_2 desorbs to the gas phase.

Pathway B is similar to pathway A except that the dehydrogenations of CH_3O and CH_2O are assisted by the lattice oxygen of a nearby cobalt site. According to DFT calculations, pathway B is more favorable than pathway A, suggesting that the synergistic effect of the nickel and cobalt sites is the reason for the enhanced catalytic activity of $NiCo_2O_4$(110)-B. The lattice oxygen plays very important roles in both pathways, which are two typical examples of the MvK mechanism. The assistance provided by lattice oxygen atoms in the dehydrogenation and oxidation steps and the regeneration of the lattice oxygen are the main reasons for the unique catalytic properties of metal oxide materials.

27.2.3 Active Sites

There are many reaction sites on most catalyst surfaces. These sites possess different chemical environments, oxidation states, and local geometries, and therefore different catalytic behaviors. Normally only a few sites exhibit high catalytic activities for a specific reaction. These sites are known as the *active sites*. Some reactions are catalyzed by only one specific site on a surface (the other sites are completely inert). In heterogeneous catalysis, a good understanding of the active sites is required to appropriately engineer the structure of the catalyst at the atomic level. In this section, we provide examples of active sites with different oxidation states.

Under realistic reaction conditions (especially those required for oxidation), there may be sites with different oxidation states, which tend to have different catalytic activities and associated reaction mechanisms. One well-known example is the so-called pressure gap in catalytic CO oxidation at a ruthenium surface [27.40, 41]. Under ultrahigh vacuum conditions, the ruthenium surface exhibits a low activity for CO oxidation, whereas the surface can efficiently catalyze CO oxidation under oxygen-rich conditions. The high activity of ruthenium under these reaction conditions was discovered to be due to the formation of a ruthenium oxide film that is active in CO oxidation [27.41]. The reason for the difference in activity between the metal and the metal oxide is very complex. Below, we review a recent DFT study of the dehydrogenation of cyclohexanol on copper and copper oxide surfaces that highlights the difference between a metal and a metal oxide in this context.

The catalytic dehydrogenation of cyclohexanol to cyclohexanone is of great importance in the manufacture of nylon, and copper-based catalysts are among the most promising. However, experimental studies were unable to clarify the active site for cyclohexanol dehydrogenation on copper-based catalysts. Therefore, to identify the active site and the mechanism for cyclohexanol dehydrogenation on copper-based catalysts, *Wang* et al. [27.42] carried out a DFT+U study of the dehydrogenation of cyclohexanol on copper and copper oxide. Two sites with different oxidation states—monovalent copper oxide and metallic copper—were considered. Six facets were taken into account: Cu(100), Cu(110), Cu(111), Cu_2O(100), Cu_2O(110), and Cu_2O(111). Based on their calculated surface energies, the Cu(111) and Cu_2O(111) were found to be the most stable metallic and oxide facets, respectively. As shown in Fig. 27.17, the surface structures of Cu(111) and Cu_2O(111) are quite different: there are four reaction sites on close-packed Cu(111), namely the top, bridge, and two hollow sites (fcc and hcp); whereas Cu_2O(111) is hexagonally structured, with two different copper sites—coordinatively saturated (Cu_{CSA}) and unsaturated (Cu_{CUS}) copper. These completely different surface structures are likely to result in different catalytic activities.

Using DFT calculations, the adsorption free energy of the reactant cyclohexanol at the reaction temperature, 260 °C, was found to be 0.74 and −0.45 eV on Cu(111) and Cu_2O(111), respectively. Therefore, reactant adsorption on the metallic copper surface is unfavorable under reaction conditions; adsorption on Cu_2O(111) is preferred. The adsorption sites on Cu(111) and Cu_2O(111) are the top and Cu_{CUS} sites, respectively. Thus, the high adsorption energy on Cu_2O(111) may be due to the activity of the low-coordination copper site. The dehydrogenation of cyclohexanol was then investigated, and the effective barriers on Cu(111) and Cu_2O(111) were calculated to be 1.77 and 1.53 eV, respectively, which suggests that Cu_2O(111) is likely

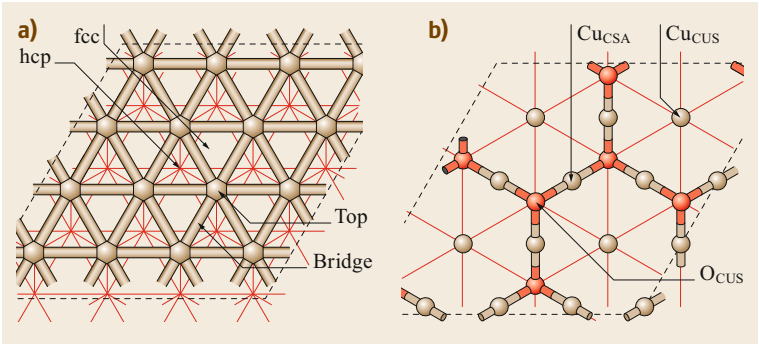

Fig. 27.17a,b The surface structures of and the possible reaction sites on **(a)** Cu(111) and **(b)** Cu_2O(111). The ball and stick notation is used for surface atoms whereas all of the subsurface atoms are depicted using a point and line notation. (Reprinted from [27.42], with permission from Elsevier)

to be the active site in cyclohexanol dehydrogenation. Based on this work, it is apparent that the significant structural differences between sites with different oxidation states are a major reason for the difference in catalytic activity between these sites.

Active site determination is one of the most complicated aspects of modeling surface reactions. Aside from oxide sites, carbide, hydride, sulfide, and/or nitride sites may be active sites in some reactions. Furthermore, there are many facets of metallic surfaces with different structures, such as terrace, step, and kink structures. The active sites for some novel catalysts such as metal-organic frameworks, metal-free catalysts, and single-atom catalysts are largely unknown. First-principles methods may offer efficient approaches for probing the active sites of these materials.

27.3 Perspectives

In this chapter, we have seen that first-principles calculations are powerful tools that allow us to obtain a deeper understanding of the gas–surface interaction and surface reactions. Results for energy parameters such as the adsorption energy and the activation energy can easily be obtained from first-principles calculations, as can structural details such as the geometries of the adsorbed molecules, transition states, and intermediate states in surface reactions. These results lead to a clearer understanding of gas–surface interactions and surface reactions. Aided by first-principles calculations, some new theoretical frameworks have been proposed, including the d-band center theory, the generalized coordination number, the bonding contribution equation, and the BEP relation, all of which were reviewed in this chapter. First-principles calculations were also found to be helpful for understanding the reaction mechanisms and the active sites of surface reactions, as mentioned above. Even though first-principles calculations have become an important tool in surface science, the following challenges must still be addressed:

- The affordable first-principles methods that are currently used to investigate gas–surface interactions and surface reactions are not yet accurate enough to achieve high chemical accuracy, while high-level first-principles methods are generally too expensive. Accurate first-principles methods for reasonably large systems are still to be developed.
- Most of the energy values obtained using first-principles methods are total energies. In real systems, free energies must be accounted for when determining gas–surface interactions and surface reactions. While it is straightforward to compute free energy gas-phase molecules or species on surfaces, it is quite time-consuming for systems containing liquids. Fast methods to calculate the free energies of solid/liquid interfaces are desirable.
- Under realistic reaction conditions, there are many factors that may change the behavior of ideal models in first-principles calculations, such as the effects of water and the adsorbate–adsorbate interaction. These effects must be considered, as doing so should lead to a better understanding of gas–surface interactions and surface reactions in real systems.

References

27.1 P.J. Feibelman, B. Hammer, J.K. Norskov, F. Wagner, M. Scheffler, R. Stumpf, R. Watwe, J. Dumesic: The CO/Pt(111) puzzle, J. Phys. Chem. B **105**, 4018–4025 (2001)

27.2 V.R. Stamenkovic, B. Fowler, B.S. Mun, G. Wang, P.N. Ross, C.A. Lucas, N.M. Marković: Improved oxygen reduction activity on $Pt_3Ni(111)$ via increased surface site availability, Science **315**, 493–497 (2007)

27.3 V. Stamenkovic, B.S. Mun, K.J.J. Mayrhofer, P.N. Ross, N.M. Markovic, J. Rossmeisl, J. Greeley, J.K. Nørskov: Changing the activity of electrocatalysts for oxygen reduction by tuning the surface electronic structure, Angew. Chem. Int. Ed. **45**, 2897–2901 (2006)

27.4 Z. Wang, P. Hu: Towards rational catalyst design: A general optimization framework, Philos. Trans. R. Soc. A **374**, 20150078 (2016)

27.5 G.S. Blackman, M.L. Xu, D.F. Ogletree, M.A. Van Hove, G.A. Somorjai: Mix of molecular adsorption sites detected for disordered CO on Pt(111) by diffuse low-energy electron diffraction, Phys. Rev. Lett. **61**, 2352–2355 (1988)

27.6 E. Schweizer, B.N.J. Persson, M. Tüshaus, D. Hoge, A.M. Bradshaw: The potential energy surface, vibrational phase relaxation and the order-disorder transition in the adsorption system Pt{111}-CO, Surf. Sci. **213**, 49–89 (1989)

27.7 G. Blyholder: Molecular orbital view of chemisorbed carbon monoxide, J. Phys. Chem. **68**, 2772–2777 (1964)

27.8 A. Föhlisch, M. Nyberg, J. Hasselström, O. Karis, L.G.M. Pettersson, A. Nilsson: How carbon monoxide adsorbs in different sites, Phys. Rev. Lett. **85**, 3309–3312 (2000)

27.9 H. Aizawa, S. Tsuneyuki: First-principles study of CO bonding to Pt(111): validity of the Blyholder model, Surf. Sci. **399**, L364–L370 (1998)

27.10 G. Kresse, A. Gil, P. Sautet: Significance of single-electron energies for the description of CO on Pt(111), Phys. Rev. B **68**, 073401 (2003)

27.11 S.E. Mason, I. Grinberg, A.M. Rappe: First-principles extrapolation method for accurate CO adsorption energies on metal surfaces, Phys. Rev. B **69**, 161401 (2004)

27.12 Y. Wang, S. de Gironcoli, N.S. Hush, J.R. Reimers: Successful a priori modeling of CO adsorption on Pt(111) using periodic hybrid density functional theory, J. Am. Chem. Soc. **129**, 10402–10407 (2007)

27.13 L. Schimka, J. Harl, A. Stroppa, A. Grüneis, M. Marsman, F. Mittendorfer, G. Kresse: Accurate surface and adsorption energies from many-body perturbation theory, Nat. Mater. **9**, 741–744 (2010)

27.14 L. Hedin: New method for calculating the one-particle green's function with application to the electron-gas problem, Phys. Rev. **139**, A796–A823 (1965)

27.15 B. Hammer, J.K. Norskov: Why gold is the noblest of all the metals, Nature **376**, 238–240 (1995)

27.16 B. Hammer, J.K. Norskov: Theoretical surface science and catalysis – calculations and concepts, Adv. Catal. **45**, 71–129 (2000)

27.17 A. Schlapka, M. Lischka, A. Groß, U. Käsberger, P. Jakob: Surface strain versus substrate interaction in Heteroepitaxial metal layers: Pt on Ru(0001), Phys. Rev. Lett. **91**, 016101 (2003)

27.18 J. Greeley, M. Mavrikakis: Alloy catalysts designed from first principles, Nat. Mater. **3**, 810–815 (2004)

27.19 J. Zhang, X. Liu, R. Blume, A. Zhang, R. Schlögl, D.S. Su: Surface-modified carbon nanotubes catalyze oxidative dehydrogenation of *n*-butane, Science **322**, 73–77 (2008)

27.20 Z. Wang, B. Yang, Y. Wang, Y. Zhao, X.M. Cao, P. Hu: Identifying the trend of reactivity for sp^2 materials: an electron delocalization model from first principles calculations, Phys. Chem. Chem. Phys. **15**, 9498–9502 (2013)

27.21 A. Logadottir, J.K. Norskov: Ammonia synthesis over a Ru(0001) surface studied by density functional calculations, J. Catal. **220**, 273–279 (2003)

27.22 J. Cheng, P. Hu, P. Ellis, S. French, G. Kelly, C.M. Lok: Some understanding of Fischer–Tropsch synthesis from density functional theory calculations, Top. Catal. **53**, 326–337 (2010)

27.23 F. Calle-Vallejo, J.I. Martínez, J.M. García-Lastra, P. Sautet, D. Loffreda: Fast prediction of adsorption properties for platinum nanocatalysts with generalized coordination numbers, Angew. Chem. Int. Ed. **53**, 8316–8319 (2014)

27.24 F. Calle-Vallejo, J. Tymoczko, V. Colic, Q.H. Vu, M.D. Pohl, K. Morgenstern, D. Loffreda, P. Sautet, W. Schuhmann, A.S. Bandarenka: Finding optimal surface sites on heterogeneous catalysts by counting nearest neighbors, Science **350**, 185–189 (2015)

27.25 Z. Wang, P. Hu: Formulating the activity contribution equation in heterogeneous catalysis: A quantitative description of the relationship between surface structure and adsorption energy (unpublished)

27.26 J. Cheng, P. Hu: Theory of the kinetics of chemical potentials in heterogeneous catalysis, Angew. Chem. Int. Ed. **50**, 7650–7654 (2011)

27.27 Y. Hou, D. Wang, X.H. Yang, W.Q. Fang, B. Zhang, H.F. Wang, G.Z. Lu, P. Hu, H.J. Zhao, H.G. Yang: Rational screening low-cost counter electrodes for dye-sensitized solar cells, Nat. Commun. **4**, 1583 (2013)

27.28 A. Alavi, P.J. Hu, T. Deutsch, P.L. Silvestrelli, J. Hutter: CO oxidation on Pt(111): an ab initio density functional theory study, Phys. Rev. Lett. **80**, 3650–3653 (1998)

27.29 Y. Mao, Z. Wang, H.-F. Wang, P. Hu: Understanding catalytic reactions over zeolites: A density functional theory study of selective catalytic reduction of NO_x by NH_3 over Cu-SAPO-34, ACS Catalysis **6**(11), 7882–7891 (2016)

27.30 F.F. Tao, J.J. Shan, L. Nguyen, Z. Wang, S. Zhang, L. Zhang, Z. Wu, W. Huang, S. Zeng, P. Hu: Understanding complete oxidation of methane on spinel

oxides at a molecular level, Nat. Commun. **6**, 7798 (2015)
27.31 C.J. Zhang, P. Hu: Why must oxygen atoms be activated from hollow sites to bridge sites in catalytic CO oxidation?, J. Am. Chem. Soc. **122**, 2134–2135 (2000)
27.32 C. Zhang, P. Hu, A. Alavi: A general mechanism for CO oxidation on close-packed transition metal surfaces, J. Am. Chem. Soc. **121**, 7931–7932 (1999)
27.33 A. Michaelides, Z.P. Liu, C.J. Zhang, A. Alavi, D.A. King, P. Hu: Identification of general linear relationships between activation energies and enthalpy changes for dissociation reactions at surfaces, J. Am. Chem. Soc. **125**, 3704–3705 (2003)
27.34 V. Pallassana, M. Neurock: Electronic factors governing ethylene hydrogenation and dehydrogenation activity of pseudomorphic Pd_{ML}/Re(0001), Pd_{ML}/Ru(0001), Pd(111), and Pd_{ML}/Au(111) surfaces, J. Catal. **191**, 301–317 (2000)
27.35 A. Logadottir, T.H. Rod, J.K. Nørskov, B. Hammer, S. Dahl, C.J.H. Jacobsen: The Brønsted–Evans–Polanyi relation and the volcano plot for ammonia synthesis over transition metal catalysts, J. Catal. **197**, 229–231 (2001)
27.36 Z.P. Liu, P. Hu: General trends in CO dissociation on transition metal surfaces, J. Chem. Phys. **114**, 8244–8247 (2001)
27.37 R.A. van Santen, M. Neurock, S.G. Shetty: Reactivity theory of transition-metal surfaces: A Brønsted–Evans–Polanyi linear activation energy-free-energy analysis, Chem. Rev. **110**, 2005–2048 (2010)
27.38 R.J. Baxter, P. Hu: Insight into why the Langmuir–Hinshelwood mechanism is generally preferred, J. Chem. Phys. **116**, 4379–4381 (2002)
27.39 C.J. Zhang, P. Hu, A. Alavi: A density functional theory study of CO oxidation on Ru(0001) at low coverage, J. Chem. Phys. **112**, 10564–10570 (2000)
27.40 H. Over, M. Muhler: Catalytic CO oxidation over ruthenium—bridging the pressure gap, Prog. Surf. Sci. **72**, 3–17 (2003)
27.41 H. Over, Y.D. Kim, A.P. Seitsonen, S. Wendt, E. Lundgren, M. Schmid, P. Varga, A. Morgante, G. Ertl: Atomic-scale structure and catalytic reactivity of the RuO_2(110) surface, Science **287**, 1474 (2000)
27.42 Z. Wang, X. Liu, D.W. Rooney, P. Hu: Elucidating the mechanism and active site of the cyclohexanol dehydrogenation on copper-based catalysts: A density functional theory study, Surf. Sci. **640**, 181–189 (2015)

Ziyun Wang

University of Toronto
Toronto, Canada
ziyunwang.wang@utoronto.ca

Dr. Ziyun Wang studied for his PhD (2012–2015) and research fellowship (2015–2017) at Queen's University Belfast with Prof. Peijun Hu and Prof. Chris Hardacre (University of Manchester). From 2017 to 2018, he was a postdoc with Prof. Jens Nørskov and Dr. Thomas Bligaard at Stanford University. He is currently a postdoc with Prof. Ted Sargent at the University of Toronto.

Peijun Hu

p.hu@qub.ac.uk

Peijun Hu received a lectureship at Queen's University Belfast in 1995, where he was promoted to a reader in 2001 and to a professor in 2004. In 2009, he was elected a member of Royal Irish Academy. Since joining Queen's University, he has developed a strong research group with a special interest in theoretical chemistry, particularly heterogeneous catalysis, and has developed some new theories for heterogeneous catalysis.

Qingfeng Ge

qge@chem.siu.edu

Dr. Qingfeng Ge is a professor and Distinguished Scholar at the Department of Chemistry and Biochemistry of Southern Illinois University in Carbondale, as well as Associate Editor of the *Journal of CO_2 Utilization*. Dr. Ge was educated in Tianjin University, worked as a research associate at Copenhagen University and Cambridge University, and was a research scientist at the University of Virginia before joining SIUC in 2003.

28. Nonadiabatic Effects in Gas–Surface Dynamics

Maite Alducin, Ricardo Díez Muiño, J. Iñaki Juaristi

In this chapter, we will provide the theoretical foundations on which the local-density friction approximation (LDFA) is based and examples of its application to gas–surface interaction problems. With this aim, first in Sect. 28.2 we will review the derivation of the stopping power (energy lost per unit path length) for an atom or molecule traveling through a uniform electron gas in the strong coupling limit, i.e., when its velocity is lower than the Fermi velocity of the system. Real systems present electronic density nonlinearities. For this reason in Sect. 28.3, we show how this method for calculating the stopping power has been successful to reproduce and explain experimental energy-loss measurements for ions/atoms traveling through real solids and interacting with metal surfaces. The last part of Sect. 28.3 is devoted to the description of the LDFA method that accounts for the effect of energy losses in the dynamics of thermal and hyperthermal gas particles interacting with metal surfaces. Its implementation both in molecular dynamics performed in precalculated potential energy surfaces (PESs) and in ab-initio molecular dynamics is also discussed. Finally, an overview of the knowledge acquired during last years by the application of the LDFA will be presented in Sect. 28.4. In particular, we will analyze the importance of electron–hole (e–h) pair excitations in different gas–surface elementary processes that involve atoms and molecules of practical interest, such as H, N, H_2, N_2, and H_2O. The analysis will mostly review the results obtained for the dissociative and nondissociative adsorption, for the Eley–Rideal and hot-atom recombinations and for the scattering of these gas species on different metal surfaces. As a general conclusion, it will be shown that e–h pair excitations are typically relevant for long-lasting processes. The last part of this section will review recent applications of the LDFA to model the desorption dynamics of atoms or molecules induced by femtosecond laser pulses. A summary of this chapter is provided in Sect. 28.5.

In regard to metal surfaces, there is ample consensus in accepting that low-energy electrons can already be excited by thermal and hyperthermal atoms and molecules. Still, the remaining open question is how the different gas–surface elementary processes are affected by such low-energy electronic excitations. Here, we review recent progress in the theoretical understanding of nonadiabatic effects in most common gas–surface elementary reactions. The LDFA, which is the focus of this chapter, provides the ideal theoretical framework to

M. Rocca, T.S. Rahman, L. Vattuone (Eds.), *Springer Handbook of Surface Science*, Springer Handbooks,
https://doi.org/10.1007/978-3-030-46906-1_28

efficiently account for the low-energy electronic excitations in present state-of-the-art gas–surface simulations and, as such, the LDFA has been decisive in achieving this understanding. The LDFA has been applied to study nonadiabatic effects in the scattering of atoms and molecules, in the dissociation of molecules and subsequent relaxation of the nascent hot atoms, and also recently in Eley–Rideal and hot-atom recombinative abstraction processes. All these studies provide us with some hints to establish under what circumstances these excitations become efficient and may, hence, affect a specific process. A general observation is that the nature of these excitations usually requires long-lasting interactions at the surface in order to observe deviations from the adiabatic behavior. As a final and interesting remark, we will also show that the LDFA has been successfully applied to simulate desorption processes induced by intense femtosecond laser pulses, provided that desorption is actually mediated by the laser–created hot-metal electrons.

28.1 Modeling Gas–Surface Interaction

Modeling the interaction dynamics of thermal and hyperthermal molecules and atoms with metal surfaces is relevant to understanding the mechanisms and properties that rule the reactivity of a given gas–surface system. In the end, this understanding will pave the way to the control of surface processes at the atomic and molecular scale. Traditionally, theoretical studies of the elementary processes arising in gas–solid interfaces relied on the Born–Oppenheimer approximation (BOA), which assumes that electrons adapt instantaneously to the nuclear motion. As a consequence, the interaction between the gas particle and the metal can be described using a single adiabatic potential energy surface to perform either classical or quantum molecular dynamics calculations.

Obviously, the adiabatic approximation facilitates the theoretical treatment of these processes. Nevertheless, since the incidence energy of the gas particles is quite low, in the range of tens of meVs up to a few eV, an accurate theoretical description of the dynamical gas–surface interaction usually requires first principles at the level of density functional theory (DFT), as well as inclusion of at least all the degrees of freedom of the gas species involved in the event. Once these conditions are fulfilled, there are various examples in the literature proving the reasonable success of the adiabatic approximation in describing the fundamental properties in most elementary gas–surface processes: dissociation [28.1–7], recombination between incoming gas-atoms and adsorbates [28.8–10], angular distribution and rovibrational states of the scattered gas species [28.11–14], and diffraction peaks [28.1, 15–17], to cite few.

However, since in a metal there is no energy threshold for electronic excitations, even a slow atom/molecule moving close to the surface excites e–h pairs. The chemicurrents measured upon adsorption of thermal atoms and molecules on metal surfaces provide experimental evidence supporting this idea [28.18]. The aim is then to understand how these low-energy excitations revert on the different processes occurring at the gas–solid interface. In this respect, the challenge in present gas–surface dynamics simulations is to provide a reliable description of these electronic excitations while keeping the level of accuracy reached with the full-dimensional adiabatic calculations. Different models have been developed to account for this energy-dissipation channel in the scattering and adsorption of gas species on metals [28.19–25]. Among them, one method that allows us to include this effect in both of the advanced approaches used in multidimensional dynamics simulations—molecular dynamics performed in precalculated potential energy surfaces of DFT quality and ab-initio molecular dynamics—is the local-density friction approximation (LDFA) [28.23]. Briefly, in this method a friction force is introduced in the classical equations of motion. The corresponding friction coefficient is a function of the value of the surface electronic density, calculated with DFT, at the position of the moving atom. The value of the friction coefficient itself is also calculated with DFT for the same atom moving through a uniform electron gas of that density.

28.2 Theory of Electronic Friction in a Free Electron Gas

The uniform electron gas model has been widely used in condensed matter physics to describe metallic systems. Its origins go back to the early work of Drude, Bohr, and Sommerfeld. According to the electron gas model, the valence electrons of a solid move freely through the volume. This approximation can be further

supported with the use of the jellium model, in which the solid ion cores are smoothed into a constant background of positive charge that compensates in average the Coulomb interaction of a constant electronic density n_0.

For decades, the theoretical study of the interaction between moving atomic particles and metallic media was based on the electron gas picture. An ion traveling through an electron gas creates a perturbation in the electronic density. A rearrangement of the medium electronic density is generated due to the Coulomb potential of the projectile. The metal electrons are piled up in a spatial region near the charge in order to screen the long-range Coulomb interaction. In this framework, the stopping power, i.e., the energy lost per unit path length by the particle, is the retarding force that this screening charge exerts on the atom.

Starting in the 1950s, a large body of literature on stopping power based on linear theory emerged. In the linear approximation, the moving projectile is considered a small perturbation to the electronic medium. The response of the latter can, thus, be represented by a linear response function, quite often in the random-phase approximation. Linear response is, however, quantitatively inaccurate in the regime in which the Sommerfeld parameter Z/v is not much lower than 1 ($Z/v \ll 1$; atomic units, a.u., are used throughout unless otherwise stated). In the definition of the Sommerfeld parameter, Z is the charge of the moving projectile, and v is the relative velocity of the collision between the projectile and the medium electrons. The relative velocity in the collision v is roughly the projectile velocity, when this is large enough. For very slow projectiles, however, v can be estimated from the Fermi velocity of the medium electrons. In practice, then, linear theory works well for low charges, fast projectiles, or high-electron density media. Under other circumstances, alternative nonperturbative models must be used.

In the strong perturbation regime, a customary way to introduce the theoretical calculation of the energy loss in an electron gas is scattering theory. The energy lost by a projectile in motion inside a free-electron gas is, thus, obtained from the change in linear momentum arising in the collisions between the moving projectile and the medium electrons. Taking advantage of the difference in masses between the incoming atomic projectile and the electrons, the rest frame of the projectile can be considered as the system of reference in the calculation. The change in projectile velocity and, therefore, the projectile energy loss is in this picture a consequence of the momentum transfer in the electron scattering off the projectile potential.

The practical difficulties in this scheme are, in principle, twofold. The first one is the calculation of the scattering potential and the scattering properties in an accurate way. In the limit of vanishing velocities of the projectile, the scattering potential can be self-consistently calculated using density functional theory (DFT). For increasing velocities, however, the calculation of the self-consistent potential can be more involved. The second difficulty is a correct evaluation of the flux of electrons colliding with the projectile. In the case of vanishing velocities, again, the problem is simplified, and only electrons at the Fermi level contribute. For larger velocities, the level occupancy can be described using the shifted Fermi sphere (SFS) description introduced by *Schönhammer* [28.26].

In 1999, *Salin* et al. showed [28.27] that this scattering approach is equivalent to an adiabatic evolution of the electron gas from its initial homogeneous distribution to a final state in which the projectile is dynamically screened. They proved this equivalence by using the ensemble Kohn–Sham (KS) method within the local-density approximation. The equivalence requires, of course, that the KS potential and the KS wave functions are used to obtain the scattering properties. In [28.27], it was demonstrated that the stopping power must be linearly dependent with its velocity for low values and shows that, in practice, it is roughly linear up to velocities similar to the Fermi velocity of the medium electrons. It nicely also shows the connection between the scattering theory of energy loss and DFT-like approaches based on the calculation of the asymmetric change in the electronic density induced by the projectile.

It is only in recent years that more sophisticated calculations based on time-dependent density functional theory (TDDFT) have become available. TDDFT provides a self-consistent, nonperturbative, time-domain treatment of electron dynamics in many body systems. Therefore, TDDFT calculations of the energy loss are, in principle, valid over the full range of velocities, from the quasistatic limit to the high-velocity regime, keeping the accuracy of nonperturbative methods. *Quijada* et al. used big jellium clusters to mimic the stopping power in metallic solids [28.28]. Beyond the electron-gas picture, TDDFT has been also used to obtain the stopping power of atoms in solids [28.29–33] and to study general electronically nonadiabatic effects of slow atoms and molecules on metal surfaces [28.22, 34].

28.2.1 Scattering Theory

In the following, we will restrict ourselves to the case of an atom or molecule moving inside an infinite homogeneous electron gas with a velocity $\boldsymbol{v}$ much lower than the Fermi velocity of the electrons in the medium v_F

($v \ll v_F$). The mass of the projectile M is much larger than that of the electrons in the medium ($M \gg 1$). We will use the scattering-theory formulation to obtain simplified expressions for the stopping power in terms of some scattering magnitudes. We mentioned before that this approach, even if based on classical binary collisions between the moving projectile and the medium electrons, is actually equivalent to a fully quantum-mechanical DFT description of the energy-loss process. We proceed with the scattering approach, nevertheless, because it provides an intelligible picture of the mechanisms that give rise to the energy exchange.

The density of the electron gas before the entrance of the incident particle is constant n_0. The electron gas parameter r_s can be obtained from the density through $1/n_0 = 4\pi r_s^3/3$ and is related to the Fermi momentum k_F through $k_F^3 = 9\pi/(4r_s^3)$. For zero temperature, all occupied electron states have a momentum q lower than k_F, obeying a Fermi distribution $g_0(\boldsymbol{q})$

$$g_0(\boldsymbol{q}) = \frac{1}{4\pi^3}\Theta(k_F - q)\,, \tag{28.1}$$

where $\Theta(x)$ is the Heaviside step function. The electronic density of the electron gas is recovered by integration

$$n_0 = \int \mathrm{d}^3\boldsymbol{q}\, g_0(\boldsymbol{q})\,. \tag{28.2}$$

The energy lost by the moving projectile arises from the exchange of momentum with the medium electrons due to sequential individual collisions along the trajectory. The net momentum transferred to the projectile by the flux of electrons is, thus, the origin of the retarding force.

It is easier to calculate the momentum transfer in the inertial system of reference of the moving projectile. Under the infinite-mass approximation ($M \gg 1$), the projectile system of reference actually coincides with the center of mass of the system. Let us, respectively, call $\boldsymbol{P} = M\boldsymbol{v}$ and $\boldsymbol{P}' = M\boldsymbol{v}'$ the linear momenta of the projectile before and after the collision. The change in momentum of the projectile will be then $\Delta\boldsymbol{P} = \boldsymbol{P}' - \boldsymbol{P}$. In the same way, we define $\boldsymbol{k}$ and $\boldsymbol{k}'$ as the momenta of a single electron before and after the collision in the center-of-mass reference frame; $\Delta\boldsymbol{k} = \boldsymbol{k}' - \boldsymbol{k}$ is thus the change in momentum. Conservation of momentum and energy requires that

$$\Delta\boldsymbol{P} = -\Delta\boldsymbol{k}\,, \tag{28.3}$$

$$\Delta E = -\Delta\epsilon\,, \tag{28.4}$$

where ΔE is the kinetic energy transferred to the projectile

$$\Delta E = \frac{(P')^2}{2M} - \frac{(P)^2}{2M} \tag{28.5}$$

and $\Delta\epsilon$ is the change in kinetic energy of the electron after the collision

$$\Delta\epsilon = \frac{(k')^2}{2} - \frac{(k)^2}{2}\,. \tag{28.6}$$

Using these equations and substituting $\boldsymbol{P}' = \boldsymbol{P} - \Delta\boldsymbol{k}$ in (28.4), we find that

$$\begin{aligned}\Delta E &= \frac{1}{2M}\left[(\Delta k)^2 - 2\boldsymbol{P}\Delta\boldsymbol{k}\right] \\ &= \frac{\boldsymbol{P}}{M}(\boldsymbol{k} - \boldsymbol{k}') = \boldsymbol{v}(\boldsymbol{k} - \boldsymbol{k}')\,,\end{aligned} \tag{28.7}$$

where terms of order $\approx (1/M)$ have been neglected. This infinite mass approximation implicitly implies that changes in the projectile velocity v during the collision are negligible. Otherwise said, there is no recoil.

So far, we have obtained the energy transferred to the moving projectile due to a well-defined collision with a single electron. The next step is to obtain the total energy transferred to the projectile due to the total flux of electrons encountered by the projectile per unit time. In the system of reference of the projectile (i.e., the center of mass), the homogeneous electron gas moves with a velocity $-\boldsymbol{v}$. The velocities of the incident electrons are correspondingly shifted by a vector $-\boldsymbol{v}$ following a simple Galilean transformation. Therefore, again in the case of zero temperature, the occupancy of the electronic states can be obtained from a shifted Fermi sphere distribution $g(\boldsymbol{k})$

$$g(\boldsymbol{k}) = \frac{1}{4\pi^3}\Theta(k_F - |\boldsymbol{k} + \boldsymbol{v}|)\,. \tag{28.8}$$

The flux of electrons $N(\boldsymbol{k})$ with momentum $\boldsymbol{k}$ per unit area and per unit time is, thus,

$$N(\boldsymbol{k}) = k\, g(\boldsymbol{k})\, \mathrm{d}^3\boldsymbol{k}\,. \tag{28.9}$$

In order to know how many of them emerge with a final momentum $\boldsymbol{k}'$ after the collision, we need to introduce a new function, namely, the differential scattering cross section $\sigma(\boldsymbol{k}, \boldsymbol{k}')$ [28.35]. In scattering theory and for a fixed center of scattering, i.e., a static potential $V(\boldsymbol{r})$, $\sigma(\boldsymbol{k}, \boldsymbol{k}')$ measures the proportionality factor between the number of particles scattered with a final momentum $\boldsymbol{k}'$ and the initial number of incident particles per unit area and per unit time with a momentum $\boldsymbol{k}$. It can be expressed in terms of the complex scattering amplitude $f(\boldsymbol{k}, \boldsymbol{k}')$ through

$$\sigma(\boldsymbol{k}, \boldsymbol{k}') = |f(\boldsymbol{k}, \boldsymbol{k}')|^2\,. \tag{28.10}$$

For a spherically symmetric potential $V(r)$, the angular dependence is much simplified, and the scattering cross

section $\sigma(\boldsymbol{k},\boldsymbol{k}')$ only depends on the relative angle between $\boldsymbol{k}$ and $\boldsymbol{k}'$. Here, we will, in principle, keep the more general nonspherical case and go to the spherical limit later. If there is no energy transferred to additional channels in the global collision, the scattering in the center of mass is elastic, and the moduli are equal $k = k'$. With these ingredients, and knowing the energy transferred in a single collision given by (28.7), it is easy to calculate the total energy transferred per unit time to the projectile by the electron gas $\mathrm{d}E/\mathrm{d}t$ as

$$\frac{\mathrm{d}E}{\mathrm{d}t} = \frac{\boldsymbol{P}}{M}\int \mathrm{d}^3\boldsymbol{k}\,\mathrm{d}\Omega_{k'}\,k\,g(\boldsymbol{k})\,(\boldsymbol{k}-\boldsymbol{k}')\,\sigma(\boldsymbol{k},\boldsymbol{k}')\,. \tag{28.11}$$

Using that $\boldsymbol{P} = M\boldsymbol{v}$, we can obtain the stopping power S, defined as the energy lost by the projectile per unit path length as

$$\begin{aligned} S &= -\frac{1}{v}\frac{\mathrm{d}E}{\mathrm{d}t} \\ &= -\boldsymbol{u}_v\int \mathrm{d}^3\boldsymbol{k}\,\mathrm{d}\Omega_{k'}k^2\,g(\boldsymbol{k})\,(\boldsymbol{u}_{\boldsymbol{k}}-\boldsymbol{u}_{\boldsymbol{k}'})\,\sigma(\boldsymbol{k},\boldsymbol{k}')\,, \end{aligned} \tag{28.12}$$

where we have denoted $\boldsymbol{u}_{\boldsymbol{a}}$ as a unitary vector along the direction defined by vector $\boldsymbol{a}$ and we use a global negative sign to follow the traditional sign convention. The stopping power has dimensions of force and can be viewed as the retarding force acting on the projectile.

In scattering by a spherically symmetric potential, it is customary and useful to define an additional magnitude, the momentum-transport cross section, or transport cross section, for a given initial electron momentum $\boldsymbol{k}$. For the general case of a nonspherical potential, the correspondent magnitude $\boldsymbol{\sigma}^{\mathrm{T}}(\boldsymbol{k})$ keeps a vectorial character and can be defined as

$$\boldsymbol{\sigma}^{\mathrm{T}}(\boldsymbol{k}) = \int \mathrm{d}\Omega_{k'}\,(\boldsymbol{u}_{\boldsymbol{k}}-\boldsymbol{u}_{\boldsymbol{k}'})\,\sigma(\boldsymbol{k},\boldsymbol{k}')\,. \tag{28.13}$$

The combination of (28.12) and (28.13) conveys a simplified expression for the stopping power

$$S = -\boldsymbol{u}_v\int \mathrm{d}^3\boldsymbol{k}\,k^2\,g(\boldsymbol{k})\,\boldsymbol{\sigma}^{\mathrm{T}}(\boldsymbol{k})\,. \tag{28.14}$$

If we call $\sigma_v^{\mathrm{T}}(\boldsymbol{k}) = \boldsymbol{u}_v\boldsymbol{\sigma}^{\mathrm{T}}(\boldsymbol{k})$, the component of the transport cross section $\boldsymbol{\sigma}^{\mathrm{T}}(\boldsymbol{k})$ along the direction defined by the velocity $\boldsymbol{v}$ and we explicitly express that the integration over $\boldsymbol{k}$ is constrained by the shifted Fermi sphere (SFS) distribution $g(\boldsymbol{k})$ defined by (28.8), we can further simplify the equation for the stopping force

$$S = \frac{-1}{4\pi^3}\int_{\mathrm{SFS}} \mathrm{d}^3\boldsymbol{k}\,k^2\,\sigma_v^{\mathrm{T}}(\boldsymbol{k})\,. \tag{28.15}$$

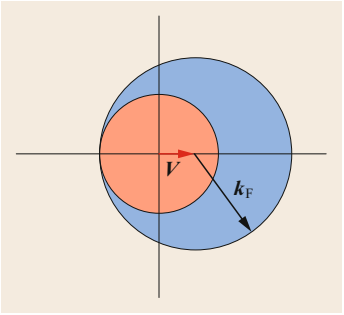

Fig. 28.1 Simplified sketch of the shifted Fermi sphere distribution of electron momenta. The *blue sphere* represents the $\boldsymbol{k}$-distribution of occupied electron states, shifted by a vector $\boldsymbol{v}$ from the origin. The *red sphere* shows the electron states that can be neglected in practice

Figure 28.1 shows a graphical representation of the SFS in $\boldsymbol{k}$-space. Since the scattering is elastic in the system of reference of the center of mass, the Pauli principle forbids all scattering events within the orange sphere. Effective scattering events are only available from occupied states in the blue area into unoccupied electron states, outside the Fermi sphere. In practice, we notice that the imposed SFS restriction (i.e., the Heaviside function $\Theta(k_{\mathrm{F}} - |\boldsymbol{k}+\boldsymbol{v}|)$) only accounts for all electronic states that are initially occupied. Due to the Pauli principle, an additional constraint should be imposed, namely that the final states with momentum $\boldsymbol{k}'$ must be unoccupied before the collision. However, there is no need to enforce this condition in the calculation because of the symmetry properties of the scattering cross section. Time-reversal symmetry implies that

$$\sigma(\boldsymbol{k},\boldsymbol{k}') = \sigma(-\boldsymbol{k}',-\boldsymbol{k})\,. \tag{28.16}$$

In addition, for potentials with parity symmetry [$V(\boldsymbol{r}) = V(-\boldsymbol{r})$], the following condition is fulfilled

$$\sigma(\boldsymbol{k},\boldsymbol{k}') = \sigma(-\boldsymbol{k},-\boldsymbol{k}')\,. \tag{28.17}$$

Therefore, the scattering from $\boldsymbol{k}$ to an occupied final state $\boldsymbol{k}'$, which is quantum mechanically forbidden, will be in the calculation canceled by the contribution from the process $\boldsymbol{k}' \to \boldsymbol{k}$.

Under these symmetry properties, the overall angular integration, when the full solid angles Ω_k and Ω_k' are

scanned, vanishes

$$\int \mathrm{d}\Omega_k \, \mathrm{d}\Omega_{k'} \, (\boldsymbol{u}_{\boldsymbol{k}} - \boldsymbol{u}_{\boldsymbol{k}'}) \, \sigma(\boldsymbol{k}, \boldsymbol{k}') = 0 \, . \tag{28.18}$$

The initial $\boldsymbol{k}$ states that contribute to the integration must, therefore, fulfill the following conditions

$$\begin{aligned} |\boldsymbol{k}| &\geq k_\mathrm{F} - v \\ |\boldsymbol{k} + \boldsymbol{v}| &\leq k_\mathrm{F} \, . \end{aligned} \tag{28.19}$$

In practice, the SFS constraint means that there are some restrictions in the angular integration over the angle Ω_k. If it were not the case, the total integration over Ω_k and Ω'_k in (28.11) would be zero (see (28.18)) and so would be the energy loss $\mathrm{d}E/\mathrm{d}t$. If we call γ_{kv} the angle between the vectors $\boldsymbol{k}$ and $\boldsymbol{v}$, then

$$|\boldsymbol{k} + \boldsymbol{v}| = (k^2 + v^2 + 2kv \cos\gamma_{kv})^{1/2} \, . \tag{28.20}$$

In the limit $v \to 0$,

$$|\boldsymbol{k} + \boldsymbol{v}| =_{v\to 0} k + v \cos\gamma_{kv} \, , \tag{28.21}$$

the allowed values of k are

$$k_\mathrm{F} - v \leq k \leq k_\mathrm{F} - v \cos\gamma_{kv} \, , \tag{28.22}$$

and the stopping force of (28.15) can be approximated as

$$S = \lim_{v\to 0} \left[\frac{-1}{4\pi^3} \int \mathrm{d}\Omega_k \int_{k_\mathrm{F}-v}^{k_\mathrm{F}-v\cos\gamma_{kv}} \mathrm{d}k \, k^4 \sigma_{\boldsymbol{v}}^\mathrm{T}(\boldsymbol{k}) \right] . \tag{28.23}$$

This limit can be easily obtained. If we call

$$F[\boldsymbol{k}] = \int \mathrm{d}k \, k^4 \, \sigma_{\boldsymbol{v}}^\mathrm{T}(\boldsymbol{k}) \, , \tag{28.24}$$

then the stopping force of (28.23) can be obtained through a Taylor expansion

$$\begin{aligned} S &= \frac{-1}{4\pi^3} \int \mathrm{d}\Omega_k \lim_{v\to 0} \left[\int_{k_\mathrm{F}-v}^{k_\mathrm{F}-v\cos\gamma_{kv}} \mathrm{d}k \, k^4 \sigma_{\boldsymbol{v}}^\mathrm{T}(\boldsymbol{k}) \right] \\ &= \frac{-1}{4\pi^3} \int \mathrm{d}\Omega_k \lim_{v\to 0} \left\{ F[\boldsymbol{k}]|_{k=k_\mathrm{F}-v\cos\gamma_{kv}} - F[\boldsymbol{k}]|_{k=k_\mathrm{F}-v} \right\} \\ &= \frac{-1}{4\pi^3} \int \mathrm{d}\Omega_k \left\{ F[\boldsymbol{k}_\mathrm{F}] - v\cos\gamma_{kv} \frac{\partial F[\boldsymbol{k}]}{\partial k}|_{k=k_\mathrm{F}} \right. \\ &\qquad \left. - \left[F[\boldsymbol{k}_\mathrm{F}] - v \frac{\partial F[\boldsymbol{k}]}{\partial k}|_{k=k_\mathrm{F}} \right] \right\} \\ &= \frac{-1}{4\pi^3} \int \mathrm{d}\Omega_k \, (1 - \cos\gamma_{kv}) \, v \, k_\mathrm{F}^4 \, \sigma_{\boldsymbol{v}}^\mathrm{T}(\boldsymbol{k}_\mathrm{F}) \, . \end{aligned} \tag{28.25}$$

Because of (28.18), the first term of the integral in (28.25) vanishes, and we can keep a simplified expression for the stopping force

$$S = \frac{1}{4\pi^3} \, v \int \mathrm{d}\Omega_k \, \cos\gamma_{kv} \, k_\mathrm{F}^4 \, \sigma_{\boldsymbol{v}}^\mathrm{T}(\boldsymbol{k}_\mathrm{F}) \, . \tag{28.26}$$

Notice that this stopping force depends linearly on velocity and, therefore, is a friction force. Quite often, the friction force is written in terms of a friction coefficient η that is simply the proportionality factor between S and v

$$\eta = \frac{S}{v} = \frac{1}{4\pi^3} \int \mathrm{d}\Omega_k \, \cos\gamma_{kv} \, k_\mathrm{F}^4 \, \sigma_{\boldsymbol{v}}^\mathrm{T}(\boldsymbol{k}_\mathrm{F}) \, . \tag{28.27}$$

28.2.2 Spherical Symmetry

Now let us go to the simplest case, in which the scattering potential is spherically symmetric. When $V(\boldsymbol{r}) = V(r)$, the modulus of the transport cross section (28.13) does not depend at all on the incident direction of the electron momentum $\boldsymbol{k}$. The only angular variable that plays a role is the scattering angle $\beta_{kk'}$ between the incident momentum $\boldsymbol{k}$ and the exit momentum $\boldsymbol{k}'$. The angular integral in (28.13) can then be easily performed by considering the $\boldsymbol{k}$ vector as the OZ-axis (Fig. 28.2). In this way, $\beta_{kk'}$ becomes the polar angle $\theta_{k'}$, and the integral over the azimuthal angle $\varphi_{k'}$ keeps as contributions to the final output only the projections of $\boldsymbol{u}_{\boldsymbol{k}'}$ over $\boldsymbol{u}_{\boldsymbol{k}}$. Therefore, the transport cross section in the spherical case can be obtained from (28.13) as

$$\begin{aligned} \boldsymbol{\sigma}_\mathrm{sph}^\mathrm{T}(\boldsymbol{k}) = 2\pi \int \mathrm{d}\,(\cos\beta_{kk'}) \, [(1 - \cos\beta_{kk'}) \\ \times \sigma(k, \cos\beta_{kk'}) \, \boldsymbol{u}_{\boldsymbol{k}}] \, . \end{aligned} \tag{28.28}$$

Formally speaking, this is still a vectorial quantity along the $\boldsymbol{u}_{\boldsymbol{k}}$-direction, which has been considered as the OZ-axis. In practice, however, let us keep just the scalar

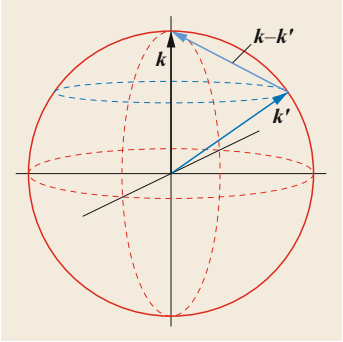

Fig. 28.2 The geometry used in momentum space to perform the integration. The OZ-axis is considered to be along the direction of the vector $\boldsymbol{k}$

value as

$$\sigma^{\mathrm{T}}_{\mathrm{sph}}(k) = 2\pi \int \mathrm{d}\,(\cos\beta_{kk'})\,(1-\cos\beta_{kk'}) \times \sigma(k,\cos\beta_{kk'})\,, \tag{28.29}$$

which is the standard definition of the transport cross section in scattering theory when applied to spherical potentials [28.36].

The calculation of the stopping power in the spherical case is now obtained directly from (28.26). The component of the transport cross section on the $\boldsymbol{v}$-direction is

$$\sigma^{\mathrm{T}}_{\boldsymbol{v}}(k_{\mathrm{F}}) = \sigma^{\mathrm{T}}_{\mathrm{sph}}(k_{\mathrm{F}})\,\cos\gamma_{kv}\,, \tag{28.30}$$

and the stopping force can be obtained as

$$\begin{aligned} S &= \frac{1}{4\pi^3}\,v \int \mathrm{d}\varphi_k \mathrm{d}(\cos\gamma_{kv})\cos^2\gamma_{kv}\,k_{\mathrm{F}}^4\,\sigma^{\mathrm{T}}_{\mathrm{sph}}(k_{\mathrm{F}}) \\ &= \frac{1}{2\pi^2}\,v\,k_{\mathrm{F}}^4\,\sigma^{\mathrm{T}}_{\mathrm{sph}}(k_{\mathrm{F}}) \int_{-1}^{1} \mathrm{d}(\cos\gamma_{kv})\,\cos^2\gamma_{kv} \\ &= \frac{1}{3\pi^2}\,v\,k_{\mathrm{F}}^4\,\sigma^{\mathrm{T}}_{\mathrm{sph}}(k_{\mathrm{F}}) \\ &= n_0\,v\,k_{\mathrm{F}}\,\sigma^{\mathrm{T}}_{\mathrm{sph}}(k_{\mathrm{F}})\,. \end{aligned} \tag{28.31}$$

Equation (28.31) again shows explicitly that, in the limit of zero velocity (quasistatic limit), the stopping power depends linearly on the velocity v. This linear dependence is actually a consequence of the shift in the Fermi sphere of occupied electronic levels. One can show, however, that the linearity in v is kept for increasing values of the velocity, provided that the scattering potential includes terms beyond the monopolar term [28.27].

One of the advantages of (28.31) is that it can be used to simplify the actual calculation of the electronic stopping. For spherical potentials whose range is shorter than the Coulomb potential, the transport cross section $\sigma^{\mathrm{T}}_{\mathrm{sph}}(k)$ can be easily expressed in terms of the phase shifts $\delta_l(k)$ of the continuum wave functions. For each partial wave l, the phase shift measures the difference in phase between the asymptotic forms of the radial wave function with or without the scattering potential [28.35]. The phase shifts $\delta_l(k)$ determine completely all properties of the scattering process at infinity. The transport cross section can be obtained from the phase shifts as [28.36]

$$\sigma^{\mathrm{T}}_{\mathrm{sph}}(k) = \frac{4\pi}{k^2}\sum_{l=0}^{\infty}(l+1)\sin^2\left[\delta_l(k)-\delta_{l+1}(k)\right]\,, \tag{28.32}$$

and the electronic stopping, or friction force, can consequently be written from (28.31) as

$$S = \frac{4\pi}{k_{\mathrm{F}}}\,n_0\,v\sum_{l=0}^{\infty}(l+1)\sin^2\left[\delta_l(k_{\mathrm{F}})-\delta_{l+1}(k_{\mathrm{F}})\right]\,. \tag{28.33}$$

Let us here explicitly write the form of the friction coefficient η that, according to (28.27), is just the proportionality factor between S and v

$$\eta = \frac{4\pi}{k_{\mathrm{F}}}\,n_0\sum_{l=0}^{\infty}(l+1)\sin^2\left[\delta_l(k_{\mathrm{F}})-\delta_{l+1}(k_{\mathrm{F}})\right]\,. \tag{28.34}$$

In practice, the number of phase shifts that is required in the sum over l-components is usually very limited. The calculation of the electronic stopping power in the limit of zero velocities is, therefore, reduced to the obtention of a few partial-wave phase shifts in a spherical scattering potential, which is a relatively simple numerical problem. The accuracy of the final result for S will certainly depend on the accuracy of the scattering potential employed.

In the case of a charged atomic projectile moving inside a free-electron gas, accurate calculations date back to the early 1980s and based the calculation of the scattering potential on density functional theory (DFT) [28.37]. DFT provides, in principle, an exact description of the scattering problem in the static limit, although approximations are required to account for the exchange-correlation term. The electronic density around the projectile is calculated in a self-consistent way, and so it is the effective potential.

Early DFT-based calculations of the electronic stopping power already showed the necessity of using a nonperturbative description of the projectile screening and remarked the quantitative difference with previous calculations based on linear theory [28.37, 38] in the quasistatic limit. Figure 28.3 explicitly shows this difference for the case of hydrogen and helium projectiles in an electron gas. A great success of DFT-based calculations was the prediction of oscillations in the stopping power dependence on the projectile charge, the so-called Z_1-oscillations [28.38]. The oscillating structure is a signature of the formation of closed shells and of the appearance of resonances in the continuum. We will discuss these in further detail in Sects. 28.3.1 and 28.3.2.

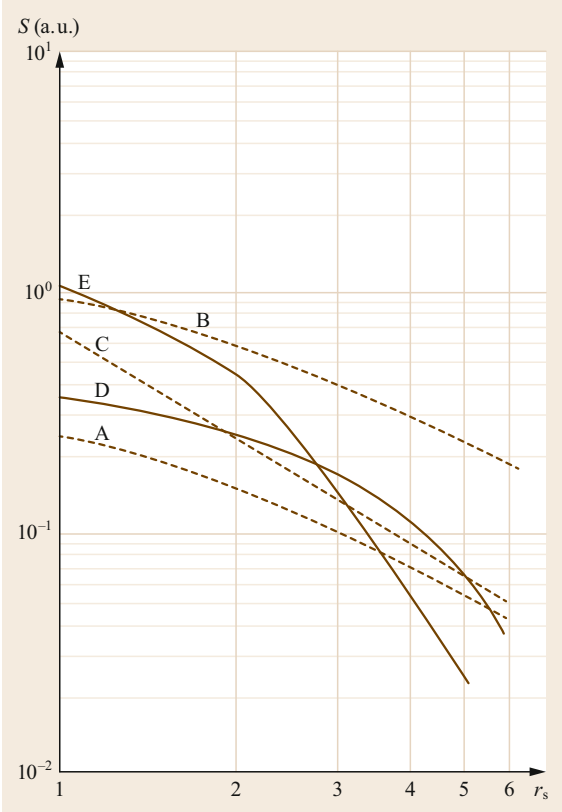

Fig. 28.3 Stopping power (here $S = (\mathrm{d}W/\mathrm{d}R)/v$) of different atomic particles as a function of the electron density parameter r_s. *Curves* A and B show the results of linear response theory for hydrogen and helium, respectively. *Curve* C is a different linear response calculation for singly-ionized helium. *Curves* D and E, respectively, are the DFT results for hydrogen and helium (Reprinted with permission from [28.38]. Copyright (2016) by the American Physical Society)

28.2.3 Axial Symmetry

Although there is no additional complication from the conceptual point of view, the algebra and numerics of the computation of the electronic stopping power when the scattering potential presents axial symmetry is more cumbersome. This is the case, for instance, in the calculation of the stopping power for diatomic molecules or in the study of the vicinage effect, which is defined as the difference between the energy loss of the molecule and that of the isolated atoms forming the molecule.

A convenient geometry in this case is to consider that the velocity vector $\boldsymbol{v}$ lies on the XZ-plane and that the symmetry axis of the potential is the OZ-axis. Let us denote by α the angle between $\boldsymbol{v}$ and the OZ-axis and again by γ_{kv} the angle between $\boldsymbol{k}$ and $\boldsymbol{v}$.

The vectorial transport cross section $\boldsymbol{\sigma}^{\mathrm{T}}(\boldsymbol{k})$ of (28.13) can then be projected into two components, namely $\sigma_{\parallel}^{\mathrm{T}}(\boldsymbol{k})$ and $\sigma_{\perp}^{\mathrm{T}}(\boldsymbol{k})$. They represent the components parallel and perpendicular to the symmetry axis, respectively. In the case of a moving dimer, for instance, they would correspond to the components parallel and perpendicular to the dimer axis. The stopping power or friction force S is now a function of the angle α, i.e., of the angle between the velocity $\boldsymbol{v}$ and the symmetry axis, and can be written as [28.39]

$$S(\alpha) = \eta_{\parallel}\, v\, \cos^2\alpha + \eta_{\perp}\, v\, \sin^2\alpha\,, \tag{28.35}$$

with

$$\eta_{\parallel} = \frac{k_{\mathrm{F}}^4}{4\pi^3}\int \mathrm{d}\Omega_k\, \sigma_{\parallel}^{\mathrm{T}}(\boldsymbol{k}_{\mathrm{F}})\, \cos\theta_k\,, \tag{28.36}$$

and

$$\eta_{\perp} = \frac{k_{\mathrm{F}}^4}{4\pi^3}\int \mathrm{d}\Omega_k\, \sigma_{\perp}^{\mathrm{T}}(\boldsymbol{k}_{\mathrm{F}})\, \sin\theta_k\, \cos\varphi_k\,; \tag{28.37}$$

$\eta_{\parallel}$ and $\eta_{\perp}$, respectively, are the friction coefficients for an axially symmetric system moving in a direction parallel or perpendicular to its symmetry axis. Due to the axial symmetry of the problem, the parallel component $\eta_{\parallel}$ accounts for the friction coefficient in both the OX and OY-directions. For any other orientation of the symmetry axis, the friction force is a combination of $\eta_{\parallel}$ and $\eta_{\perp}$ through (28.35).

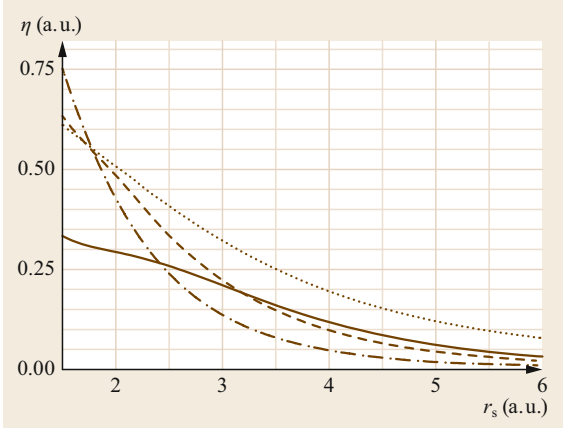

Fig. 28.4 Friction coefficients for H_2 as a function of the electronic density parameter r_s. *Solid line*: H_2 moving parallel to its axis ($\eta_{\parallel}(H_2)$). *Dashed line*: H_2 moving perpendicular to its axis ($\eta_{\perp}(H_2)$). *Dotted line*: twice the friction coefficient of atomic H ($2\eta(H)$). *Dash-dotted line*: friction coefficient of He ($\eta(He)$). (Reprinted with permission from [28.39]. Copyright (2016) by the American Physical Society)

The solution of the scattering problem in the axially symmetric case permits to go beyond the independent atom approximation in the calculation of the friction force. The energy lost by a dimer in a metallic medium, for instance, is not equivalent to the energy lost by its two atomic components independently. This effect was quantitatively evaluated in [28.39] for the case of a hydrogen molecule moving in a free-electron gas. Figure 28.4 shows that the friction force of the molecule, either with the axis aligned in a direction perpendicular or parallel to the velocity vector, is of the same order of magnitude as the friction force that the two hydrogen atoms would suffer independently considered. Some differences arise in the final value, however, due to interference effects between the two centers.

28.3 Fundamentals of the Local-Density Friction Approximation

As shown in the previous section, the energy loss in the excitation of electrons by low-velocity atomic particles traveling through systems in which the electronic density is constant is well established. However, in all real systems, the electronic density is not uniform, and it is a function of the position. In particular, this is the case in the surface of a solid, where there exist large density gradients, but also in the bulk of metals in which the electronic density is correlated with the atomic positions and for which the uniform jellium model represents just an approximation.

This section aims to show how the friction coefficients obtained within the jellium model have been used to successfully describe the energy loss of atomic particles in real systems. We will first focus on the energy loss of keV ions traveling with velocities lower than the Fermi velocity of the electrons, both inside the bulk and at the surface of metals. Next, we will describe how this methodology has been extended in order for it to be applied for thermal and hyperthermal gas–surface dynamics simulations within the so-called local-density friction approximation (LDFA) [28.23]. The section will end by presenting the latter developments, which allow incorporating the LDFA into ab-initio molecular dynamics simulations (AIMD), in what is known as ab-initio molecular dynamics with electronic friction (AIMDEF) [28.40–43].

28.3.1 Energy Loss of keV Ions in Metals

The first comparison of the theoretical model of Sect. 28.2 with experiments was performed for H projectiles in [28.44] shortly after introduction of the model in [28.37]. Specifically, the stopping power (i.e., friction force) calculated via (28.33) was compared to the experimental data measured in 20 different metals and semiconductors. The energy of the H projectiles was of the order of the keV, which implies velocities lower than the Fermi velocity of the target. The level of agreement between theory and experiments was considered satisfactory in all cases. At this point, some clarifications on the comparison done in [28.44] are in order. First, although the ions traveling through the solid do necessarily probe regions of different electronic density, these variations were disregarded in this work. In fact, the results for each solid depended on just a single parameter, namely, the average valence band electronic density. Second, (28.33) is, in principle, only strictly valid in the quasistatic limit ($v \to 0$) in virtue of the approximations done in its derivation, as explained above. However, the agreement with the experiment was observed up to velocities of the projectile close to the Fermi velocity of the target, i.e., the proportionality of the stopping power with the projectile velocity was kept up to these velocities. Lastly, no band-gap effect was observed for semiconductors, which showed the same behavior as metals. This last fact is, indeed, related to the relatively high energy of the projectiles used in these experiments. Note that in the quasistatic limit, (28.33), which assumes no threshold for electronic excitations, does not apply to semiconductors.

The calculations were extended to projectiles with atomic number $Z_1 > 2$ in [28.38]. Remarkably, the experimentally observed Z_1 oscillations in the stopping power were naturally obtained within this level of theory. These oscillations reflect the shell structure of the atomic projectile. Briefly, the appearance of scattering resonances close to the Fermi level for some values of Z_1 lead to relatively large values of the stopping power. For increasing values of Z_1, former resonances become bound states, but at the same time, new scattering resonances may appear at certain Z_1. As a result, a nonmonotonic dependence of the stopping power on Z_1 is found. Furthermore, note that the values of Z_1, for which the maxima and minima of the stopping power take place, also depend on the screening, or in other words, on the electronic density of the target. In [28.38], the authors compared available experimental data for $1 \leq Z_1 \leq 20$ ions traveling within bulk carbon and aluminum with velocities in the range $v = 0.25–0.83$ a.u. [28.45–48] with the theoretical predic-

tions for the stopping power. As done in [28.44], each material was modeled in the calculations by the average valence electronic density. As an overall trend, the experimental Z_1 oscillations were qualitatively reproduced by the theory. However, quantitative agreement was only obtained for $Z_1 < 7$, while the stopping power was underestimated by the theory for larger values of Z_1. Likely reasons for the quantitative differences could be the neglect of electronic density variations inside the solid, as well as deviation from straight trajectories not considered in the theoretical calculations. This conclusion can be reached by a comparison with the experimental data obtained for well-channeled ions, which was also performed in [28.44]. In a given crystal channel, the electronic density variations are lower than for random conditions, therefore the neglect of electronic density variations and deviation in the trajectories should be less important in this case. Experimental data obtained for projectiles traveling through the ⟨110⟩ and ⟨111⟩ channels of Si [28.49] were compared with the theoretical stopping power calculated using the average electronic density of each channel. In accordance with the previous argument, it was observed that the quantitative agreement between experiments and theory in this case was much better than for random conditions. Subsequent works in which the experimental stopping power for ions traveling through the ⟨110⟩ channel of gold [28.50] was compared with the nonlinear theory of [28.38], showed a similar good agreement for the Z_1 oscillations [28.51, 52].

28.3.2 Energy Loss of keV Ions Scattered off Metal Surfaces

A clear situation in which the electronic density probed by the projectile along its trajectory is nonuniform is that of an ion/atom scattered off a metal surface. Typically, in these experiments, grazing incidence conditions are used in order to keep the normal energy of the projectiles low. The latter condition is important to guarantee that the projectiles are reflected above the surface without penetration even for incidence energies in the keV range [28.53, 54].

For projectiles velocities larger than the Fermi velocity of the metal electrons, an accurate description of the energy loss at metal surfaces can be obtained within linear response theory [28.55–60] (see also the discussion of the Sommerfeld parameter in Sect. 28.2). Briefly, one calculates the energy loss per unit path length of an ion traveling parallel to the surface at different distances from it in terms of the surface response function. In this way, one obtains the so-called distance-dependent stopping power that combined with a calculation of the projectile trajectory allows one to obtain the energy loss experienced by the reflected particle.

However, at velocities lower than the Fermi velocity of the metal electrons, the projectile represents a strong perturbation, and linear response theory is no longer a valid description. A successful way to treat this problem has been to calculate the friction coefficient using the formalism presented in the previous section. The justification for using a bulk model to calculate the electronic energy loss at the surface of a metal is that most of the energy loss of the scattered particle takes place in the part of its trajectory close to the turning point [28.61]. In this region, the projectile is close to the surface atomic layer, i.e., well embedded in the surface electronic density, and, therefore, a bulk calculation of the friction force must necessarily be a good approximation.

Several works have used this idea in order to understand experimental measurements of the energy loss of keV atomic projectiles grazingly scattered off metal surfaces. The simplest model that has been used is based on the calculation of an interaction length L between the projectile and the surface. This interaction length is defined as the length of the trajectory of the projectile that lies within a given distance from the surface topmost atomic layer. Typically, this distance is of the order of the jellium edge. In order to obtain the energy loss in a given trajectory, the interaction length L is subsequently multiplied by the bulk stopping power S, i.e., $\Delta E = LS$. This approach has been used successfully to explain, for instance, the channeling effects in the energy loss of ions scattered off metal surfaces [28.62, 63]. Another application has been the study of the dependence on the charge state of nitrogen ions scattered off aluminum surfaces [28.64, 65].

A step forward from the previous scheme consists in evaluating distance-dependent stopping powers in terms of the average electronic density at a given distance from the surface. Let us discuss in more detail the combined experimental and theoretical work of [28.66], in which this approach was used. In experiments performed by *Winter* [28.66], the energy loss of ions with atomic numbers $1 \leq Z_1 \leq 20$ scattered off an Al(111) surface was measured as a function of the incidence angle ϕ_{in}. All ions had the same velocity $v = 0.5$ a.u. By performing trajectory calculations using Moliere-type interatomic potentials, these data allowed us to extract the experimental distance-dependent stopping powers $S_{\text{exp}}(z)$. The corresponding theoretical results were obtained as follows. For each distance from the surface z, the lateral average ab-initio electronic density of the aluminum surface $n_0(z)$ was calculated.

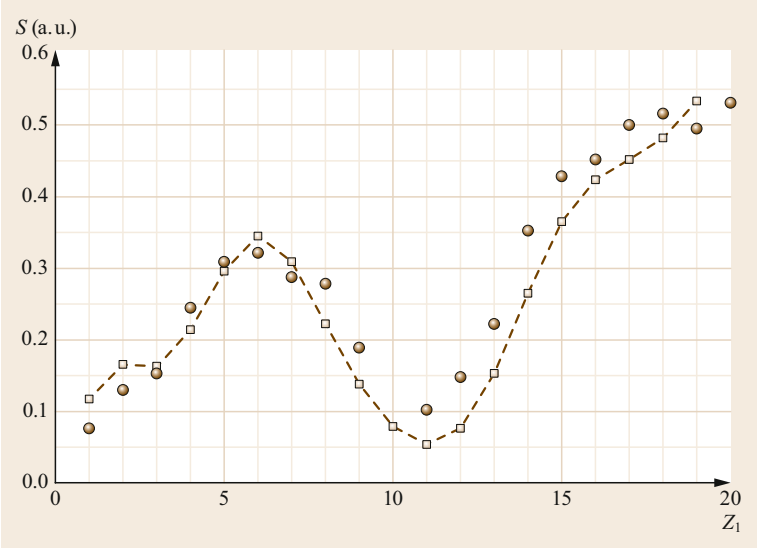

Fig. 28.5 Stopping power of ions with velocity $v = 0.5$ a.u. as a function of their atomic number Z_1 moving parallel to the Al(111) surface at a distance of 0.6 Å from the topmost layer. The data from grazing scattering experiments $S_{exp}(z)$ (*solid circles*) is compared to the theoretical $S_{theo}(z)$ obtained using (28.33) for the lateral average electronic density at 0.6 Å from the surface (*open squares*). *Dashed lines* are used to guide the eye. Data taken from [28.66]

Subsequently, the theoretical distance-dependent stopping powers $S_{theo}(z)$ were obtained for the 20 ions by introducing $n_0(z)$ in (28.33). Figure 28.5 shows the comparison between $S_{exp}(z)$ and $S_{theo}(z)$ for a distance to the topmost layer of 0.6 Å. The agreement is excellent and shows the adequacy of the local density picture. In fact, it is the most stringent test of the theory so far and represents strong support for the use of the local density friction model that we will present in the next section. It should be mentioned that for larger distances from the surface, the agreement was not that excellent, mostly for ions with $Z_1 > 14$. The discrepancies were attributed to the nonuniformity of the density and the increasing importance of the density gradients at large distances from the surface. However, it must be stressed that for ions with $Z_1 < 14$, the order of magnitude of the experimental and theoretical stopping powers were the same. In fact, except for $Z_1 = 2$ and $Z_1 = 3$ at the largest analyzed distances, the ratios between the two quantities were well below a factor of 2.

28.3.3 The Local-Density Friction Approximation (LDFA)

When going from keVs to thermal and hyperthermal energies, the chemical aspects of the interaction of atoms and molecules with metal surfaces in a way becomes richer. Thus, in addition to scattering events, a variety of elementary reactive processes can be identified: adsorption of atoms and molecules, dissociation, recombination between gas-phase species and adsorbates, desorption, etc. Considering that the incidence energy of the gas particles is quite low, in the range of tens of meV up to a few eV, accurate and precise theoretical calculations based on DFT that accounts for the full dimensionality of the problem are required in order to understand the properties that rule all these processes.

As stated in the introduction to this chapter, state-of-the-art simulations of the dynamics of gas–surface elementary process are based on the BOA and consist in solving either classically or quantum mechanically the equations of motion that are ruled by the adiabatic forces acting on those atoms involved in the process. Typically, one defines the initial conditions of the simulations by fixing the initial energy and angle of incidence of the incoming atom/molecule, which are usually the variables that are controlled in molecular beams experiments, and performing a Monte Carlo sampling over the rest of the degrees of freedom. For a given experimental situation, reliable statistics require the calculation of a large number of trajectories that differ in the initial value of the dynamical variables that are not controlled by the experimental setup.

The so-called ab-initio molecular dynamics (AIMD) is a powerful and flexible method to deal with gas–surface dynamics [28.67, 68]. In AIMD, the adiabatic forces between the atoms in the system are calculated at each integration step of the classical dynamics equations using DFT and the Hellmann–Feynman theorem. A clear advantage of AIMD is that it enables the description of the surface-atom movement in a natural way. Therefore, AIMD calculations are instrumental in studying events where the gas–surface interaction times are comparable to those of the surface motion (phonons). As a disadvantage, we note that

AIMD numerical calculations can be computationally expensive. However, their use has become affordable in the last years, even for multidimensional problems requiring refined statistics. Thus, in Sect. 28.3.4, we will describe how the effect of electronic excitations has been incorporated into AIMD.

Nonetheless, in recent years, most state-of-the-art calculations of gas–surface processes performed have relied on the construction of the multidimensional adiabatic PES that can be later used for classical or quantum calculations of the dynamics. Adiabatic PESs are usually built from thousands of DFT-calculated energies that are subsequently interpolated following one of the accurate numerical schemes developed for this purpose [28.69–72]. Compared to AIMD, the great advantage of this alternative approach is that once the PES has been constructed, the additional computational cost of the classical dynamics calculations is negligible. The latter enables us to run a large number of trajectories to achieve a reliable statistical sampling of the process under consideration. The main disadvantage of this approach is the difficulty to obtain high accuracy in the interpolation procedure, which may affect the evaluation of the energy exchange with the surface lattice and temperature effects.

The (energy-conserving) adiabatic approximation applied to either AIMD or molecular dynamics simulations performed on multidimensional frozen-surface PESs have been very successful in describing many gas–surface interaction phenomena. Nevertheless, since in a metal there is no energy threshold to create electronic excitations, any atom/molecule interacting with a metal surface will generate these excitations and, in principle, their effect should be included in the dynamics.

Nonadiabatic effects due to low-energy e–h pair excitations can be effectively introduced in the classical equations of motion through a dissipative force acting on the gas-phase species, as (28.33) suggests, and as also derived within a different theoretical framework in [28.19]. Determining a realistic value of the friction coefficient specific for each system has been the focus of several theoretical studies [28.19, 20, 25, 73, 74]. Among these, the local-density friction approximation (LDFA) [28.23] provides an efficient framework to calculate the position-dependent friction coefficient, while capturing the relevant physical aspects of the low-energy electronic excitations. The physics behind the LDFA is grounded in the practical application of (28.33) to the stopping power of atoms on metal surfaces described in Sect. 28.3.2. Within the LDFA, the position-dependent friction coefficient $\eta(\boldsymbol{r}_i)$ of a gas-phase atom i is simply a function of the (bare) surface-electron density at the position of the atom, $n_{\mathrm{sur}}(\boldsymbol{r}_i)$. In the original LDFA [28.23], $n_{\mathrm{sur}}(\boldsymbol{r}_i)$ was calculated with DFT using the same conditions used to calculate the adiabatic PES—but without including the gas-species. The friction coefficient at each point of the trajectory is, subsequently, approximated by that corresponding to an electron gas with electronic density $n_0 = n_{\mathrm{sur}}(\boldsymbol{r}_i)$. As a further approximation when applied to molecules, correlation effects in η between the atoms conforming the molecule, i.e., the vicinage effect described in Sect. 28.2.3, are neglected. Therefore, in the case of a diatomic molecule and assuming the frozen-surface approximation, the equation of motion for each of the atoms of the molecule takes the following form

$$m_i \frac{\mathrm{d}^2 \boldsymbol{r}_i}{\mathrm{d}t^2} = -\nabla_i V(\boldsymbol{r}_i, \boldsymbol{r}_j) - \eta(\boldsymbol{r}_i) \frac{\mathrm{d}\boldsymbol{r}_i}{\mathrm{d}t} \,, \tag{28.38}$$

where $\boldsymbol{r}_i, \boldsymbol{r}_j$ are the position vectors of atoms i, j of the molecule, and m_i is the mass of atom i. The first term on the right-hand side of (28.38) is the adiabatic force obtained from the six-dimensional (6-D) PES $V(\boldsymbol{r}_i, \boldsymbol{r}_j)$, and the second term on the right-hand side is the dissipative force experienced by atom i. Note that, for simplicity, (28.38) assumes that the electronic system is at 0 K. This is a good approximation for the usual surface temperatures employed in most gas–surface experiments, since the e–h-pair distribution hardly deviates from its ground state at 0 K. In cases of extremely high electronic temperatures ($T_e > 1000$ K), the effect of the excited electrons on the gas atom/molecule can be incorporated by adding a random force, as described below. In Sect. 28.4, we review different studies that use the LDFA formalism to analyze the effect of e–h excitations in the reaction and scattering of hyperthermal atoms and molecules at metal surfaces.

Although without using a DFT-based PES to calculate the adiabatic force, molecular dynamics with electronic friction, in which the friction coefficient is calculated in terms of the local density and using (28.33), have been performed by various groups. It is worth mentioning the work of *Li* and *Wahnström* [28.75], in which the dynamics of hydrogen diffusion in Pd was analyzed using a potential based on the embedded-atom method. Also *Valdés* and coworkers performed molecular dynamics with local electronic friction to study the energy loss of keV ions in different projectile–surface interaction systems using parametrized interatomic potentials and image potential corrections [28.76–80].

Another interesting aspect is that the LDFA method can be readily combined with the generalized Langevin oscillator model (GLO) [28.81, 82]. This way, energy

exchange with both lattice vibrations and electronic excitations can be incorporated into the dynamics, while keeping the accuracy of a multidimensional ab-initio PES for the gas–metal interaction. The joined LDFA+GLO dynamics formulation [28.83] has allowed us to disentangle the relative importance of electronic and phononic excitations in the scattering and adsorption of gas particles at surfaces, as well as in recombinative processes between gas particles and adsorbates, as will be reviewed in Sect. 28.4.

Nonadiabaticity is undoubtedly the driving force behind the ultrafast photochemistry on metals triggered in femtosecond laser experiments [28.84]. The theoretical challenge is to disentangle the mechanisms that rule this complex phenomena and, in this respect, the LDFA can also be a powerful tool in certain cases, which we describe next.

As was shown by *Tully* et al. [28.85, 86], molecular dynamics with electronic friction based on precalculated multidimensional ground-state PESs can also be used to simulate desorption of adsorbates from metal surfaces induced by femtosecond laser pulses working in the so-called DIMET (desorption induced by multiple electronic transitions) regime. In DIMET, the desorption process is surface mediated [28.84]. The laser pulse generates the excitation of the metal electrons, and the energy is subsequently transferred from the electronic system to the adsorbates that can eventually desorb. As a consequence, the simulation of DIMET can be efficiently performed with a two step approach. First, the excitation of the electronic system by the laser pulse is accounted for in terms of a time-dependent electronic temperature T_e that is obtained within the two-temperature model (2TM) [28.87]. In this model, one solves the following coupled equations for the electron T_e and phonon T_{ph} temperatures

$$C_e \frac{\partial T_e}{\partial t} = \frac{\partial}{\partial z}\kappa \frac{\partial T_e}{\partial z} - g\,(T_e - T_{ph}) + S(z,t)\,,$$
$$C_{ph} \frac{\partial T_{ph}}{\partial t} = g(T_e - T_{ph})\,. \qquad (28.39)$$

In these equations, C_e is the electron heat capacity, C_{ph} is the phonon heat capacity, κ is the electron thermal conductivity, g is the electron–phonon coupling constant, and $S(z,t)$ is the absorbed laser power per unit volume. Subsequently, the dynamics of each desorbing adsorbate i is modeled using a Langevin equation that is obtained by extending (28.38) to finite electronic temperatures. The latter consists in including a random fluctuating force $\boldsymbol{R}_i$ that results from the scattering of heated electrons with the adsorbate. The resulting Langevin equation reads

$$m_i \frac{\mathrm{d}^2 \boldsymbol{r}_i}{\mathrm{d}t^2} = -\nabla_i V(\boldsymbol{r}_i, \boldsymbol{r}_j) - \eta(\boldsymbol{r}_i)\frac{\mathrm{d}\boldsymbol{r}_i}{\mathrm{d}t} + \boldsymbol{R}_i[T_e(t), \eta(\boldsymbol{r}_i)]\,. \qquad (28.40)$$

The electronic fluctuating force $\boldsymbol{R}_i$ is connected through the second fluctuation-dissipation theorem to the electronic friction force via the electronic temperature T_e and is modeled by a Gaussian white noise with the following variance

$$\mathrm{Var}[\boldsymbol{R}_i(T_e, \eta)] = \frac{2k_B T_e(t)\eta(\boldsymbol{r}_i)}{\Delta t}\,, \qquad (28.41)$$

where k_B is the Boltzmann constant, and Δt is the integration time step of the simulation. Combining (28.40) with the GLO model, the effect of the laser-heated phonons on the desorption process can also be modeled. In such a case, the phonon temperature $T_{ph}(t)$, obtained from the 2TM, is taken as the temperature of the corresponding thermal bath. The two-step approach described, combined or not with GLO, has been successful in simulating femtosecond laser-induced desorption experiments in the DIMET regime [28.88–91].

28.3.4 Ab-initio Molecular Dynamics with Electronic Friction (AIMDEF)

Standard AIMD simulations can naturally include the energy transfer between the gas-phase species and the surface lattice by just allowing the surface atoms to move according to the DFT-calculated forces. The temperature of the metal during the simulation can also be controlled using any of the thermostats available in the present ab-initio codes. Still, standard AIMD does not incorporate electronic excitation effects. In this respect, the first realization of an accurate and joint description of the two main energy exchange channels (e–h pairs and phonons) in gas–surface dynamics simulations is the AIMDEF method developed in [28.40] and later improved in [28.41, 42]. Within AIMDEF, the effect of low-energy electronic excitation on the dynamics of the gas species is obtained via an electronic friction force that is also calculated on-the-fly. This is done by incorporating the LDFA scheme in the ab-initio program.

This methodology has been implemented in the VASP package [28.92, 93], and it was first applied to study the relaxation of the nascent hot atoms created upon dissociation of H_2 on Pd(100) [28.40]. In this first AIMDEF implementation, the bare surface-electron density, which determines the LDFA friction coefficients, was approximated by the electron density

of the bare frozen-surface calculated self-consistently with DFT, $n_{\mathrm{sur}}^{\mathrm{FS}}$. In other words, the surface-electron density changes caused by the surface-atom displacements were neglected. This is a reasonable approximation only in those cases where the surface atoms barely move, as was the case in [28.40, 94] due to the large mass mismatch between the hydrogen atoms and the target palladium/platinum atoms. Unfortunately, in most situations, the surface-atom displacements are expected to cause appreciable changes in the surface-electron density n_{sur}. This means that this density needs to be known at any instant t. The latter complicates the use of the LDFA in usual AIMDEF simulations because only the electron density of the whole system, i.e., gas species and surface atoms, is calculated self-consistently at each integration step. This limitation was solved in [28.41–43], where two valid methods were proposed that enable calculating an approximated surface-electron density of the moving surface atoms at almost no additional computational cost.

In the first one, the surface-electron density is calculated at each time step t as the superposition of the ground-state electron densities of the isolated individual surface atoms n_j^{atom}, i.e.,

$$n_{\mathrm{sur}}^{\mathrm{AS}}(\boldsymbol{r}_i, t) = \sum_{j=1}^{N_{\mathrm{sur}}} n_j^{\mathrm{atom}}(\boldsymbol{r}_i, t) \,, \tag{28.42}$$

where the summation index j runs over all surface atoms N_{sur}. This method successfully accounts for the movement of the surface atoms at each time step, but it obviously misses the charge redistribution upon formation of bonds between the surface atoms.

The second method corrects this misbehavior by making use of the Hirshfeld partitioning scheme [28.95] in order to subtract the contribution of the gas-phase atoms from the self-consistent density of the whole system $n^{\mathrm{SCF}}(\boldsymbol{r}_i, t)$. More precisely, the bare surface-electron density is approximated at each t by

$$n_{\mathrm{sur}}^{\mathrm{H}}(\boldsymbol{r}_i, t) = n^{\mathrm{SCF}}(\boldsymbol{r}_i, t)\left[1 - \sum_{n=1}^{N_{\mathrm{A}}} w_n(\boldsymbol{r}_i, t)\right],$$
$$w_n(\boldsymbol{r}_i, t) = \frac{n_n^{\mathrm{atom}}(\boldsymbol{r}_i, t)}{\sum_{m=1}^{N} n_m^{\mathrm{atom}}(\boldsymbol{r}_i, t)}, \tag{28.43}$$

where the indexes m and n run, respectively, over the total number of atoms in the system N and in the gas-phase species/adsorbate N_{A}. In this equation, the Hirshfeld weighting factor $w_n(\boldsymbol{r}_i, t)$ represents the contribution of the n-th atom to the electron density of the whole system at $\boldsymbol{r}_{\mathrm{i}}$. Thus, the factor

$$\left[1 - \sum_{n=1}^{N_{\mathrm{A}}} w_n(\boldsymbol{r}_i, t)\right],$$

defines the weight corresponding to the system without the contribution of the adsorbate. These new methods to calculate the bare surface electronic density when performing AIMDEF simulations [28.41–43] have also already been implemented in VASP. A detailed discussion on the performance of each of them can be found in [28.42]. Note in passing that the Hirshfeld partitioning scheme was used by *Rittmeyer* et al. to calculate the vibrational lifetimes of molecules on metal surfaces [28.96]. The authors propose using it as an attempt to include correlation effects between the atoms forming the molecules in the original LDFA scheme, but noting that its use is only justified for adsorbates on metals and not for the general gas–surface scattering dynamics. The difference with respect to (28.43) is that only the weighting factor of the atom for which the friction coefficient is calculated, i.e., $w_i(\boldsymbol{r}_i, t)$, is subtracted from n^{SCF}.

28.4 The Local-Density Friction Approximation Applied to Elementary Gas–Surface Processes

Even if e–h pair excitations were soon recognized as an efficient energy drain in the interaction of fast atoms with solids and surfaces [28.31, 53, 56, 66, 97–99], their relevance in gas–surface interactions that involve energies up to a few eV can depend strongly on the specific elementary process and the specific system under study. The aim of this section is to provide an overview of the knowledge acquired in recent years in this matter and for which the different *flavors* of the LDFA applied to molecular dynamics simulations have proven to be very useful. We present this analysis for each of the elementary gas–surface processes that are usually treated in the literature.

28.4.1 Scattering of Atoms and Molecules off Metal Surfaces

The advantages of scattering experiments conducted with supersonic molecular beams in characterizing the dynamics of gas–surface interactions are conveniently discussed in the literature [28.102–105]. Combined with other techniques, one can extract valuable infor-

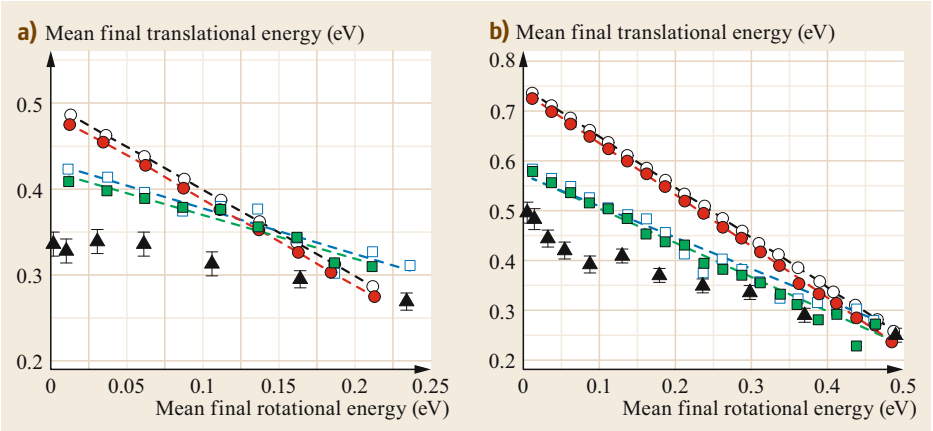

Fig. 28.6a,b Mean final translational energy versus mean final rotational energy of the N_2 molecules reflected from W(110) for normal incidence and detection angles and two incidence energies: **(a)** $E_i = 0.5\,\text{eV}$, **(b)** $E_i = 0.75\,\text{eV}$. The results of the simulations performed in [28.100] with the adiabatic approximation (*open circles*), the LDFA (*red, filled circles*), the GLO (*blue, open squares*), and the LDFA+GLO (*green, filled squares*) calculations are compared to the experimental data of [28.101] (*black, filled triangles*) for $T_s = 1200\,\text{K}$

mation by directly measuring different properties of the scattered beam, as these references show.

A magnitude directly accessible in scattering experiments is the energy-loss distribution of the reflected molecules/atoms. In the case of molecules, inelastic scattering can occur not only as a consequence of the energy loss into the surface by either phonon or electronic excitations, but also because of possible rovibrational (de)excitations facilitated by the interaction with the surface. The rovibrational inelastic contribution can be experimentally identified using sophisticated quantum-state detection techniques [28.106–110]. Still, the contribution of phonons and e–h pairs seems inaccessible at present, and it is at this point that theoretical simulations become a useful counterpart. Next, we provide selected examples where the LDFA contributed to us gaining further insight into the role of e–h pairs and phonon excitations.

The LDFA was used in combination with the GLO model to understand the factors contributing to the rotationally inelastic scattering of a rotationally cold N_2 beam from W(110). Experimentally, the molecules were found to lose around 30% of their incidence energy for low-exit rotational states, while the energy loss was lower for those molecules scattered at high-exit rotational states [28.101]. Classical molecular dynamics simulations performed in [28.100] with different approximations:

(i) using the frozen-surface adiabatic approximation (sometimes denoted BOSS from Born–Oppenheimer with static surface)
(ii) including only e–h pair excitations (LDFA)
(iii) including only energy exchange with the lattice (GLO), and
(iv) including both energy-dissipation channels by combining the LDFA and the GLO model in the equations of motion (LDFA+GLO)

showed that the contribution of e–h-pair excitations is very minor, most of the energy being dissipated into the surface lattice (phonons). This is shown in Fig. 28.6, where the results of the four types of simulations are compared with the experimental data. Figure 28.6 represents the average exit-translational energy as a function of the exit-rotational energy E_{rot} for the scattered molecules for two incidence energies. The steep decrease obtained in the adiabatic calculations (constant total energy), which simply reflects that rotational excitation occurs at expense of translational energy, are at variance with the experimental observations. Inclusion of e–h-pair excitations does not alter these results significantly. Only those simulations that account for phonon excitations (GLO and LDFA+GLO) capture the experimental observation that more energy is lost at low-exit rotational states. The authors argued that those molecules that are rotationally excited at the expense of the translational energy while approaching the surface—as dictated by the PES corrugation—, are more inefficient at transferring energy to the lattice. This idea was already illustrated in [28.112] by using a simplified kinematic model. Focusing on the comparison between the GLO(+LDFA) results and experiments in more detail, the still slightly larger loses observed in experiments at low E_{rot} might be due to recombination of the dissociated molecules that desorb at the exper-

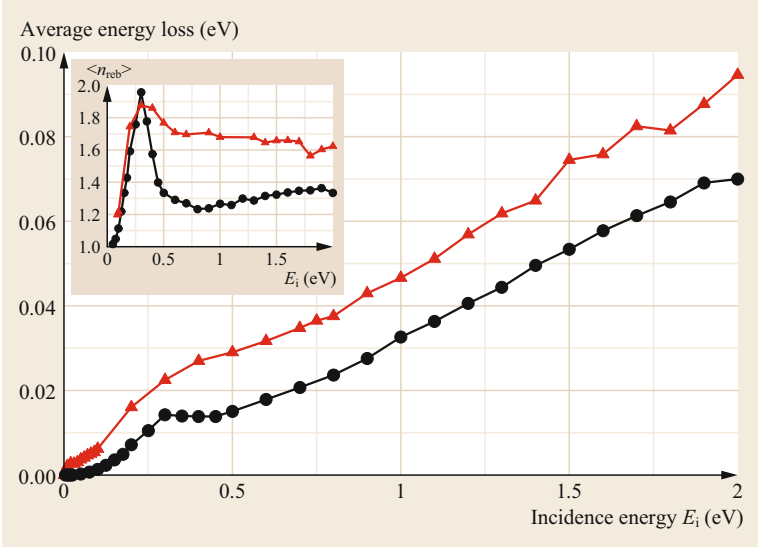

Fig. 28.7 Mean energy loss of the N_2 molecules reflected from W(110) (*black circles*) and W(100) (*red triangles*) as a function of the incidence energy E_i and for normal incidence. *Inset*: corresponding average number of rebounds. Results taken from the LDFA simulations of [28.111]

imental $T_s = 1200\,K$, but preferentially at the lowest internal energies.

Theoretically, more direct evidence for the minor energy losses caused by e–h pair-excitations in this system is provided in Fig. 28.7, which displays the mean energy loss into e–h pair-excitations as a function of the incidence energy of the scattered N_2. The results were obtained from LDFA simulations [28.111]. In all cases, the energy loss is less than 10% of the N_2 incidence energy. Slightly larger energy losses are obtained for N_2 scattered off the W(100) surface. This difference between the two crystal faces was rationalized in terms of the different N_2 dynamics. The molecules stay close to the surface on W(100) longer than on W(110), which contributes to exciting more electrons. The number of rebounds plotted in the inset is an example of the more prominent trapping-like dynamics followed on W(100). The energy-loss distributions taken from [28.111] and plotted in Fig. 28.8 provide a better understanding of the factors ruling the differences between the two surfaces. In both cases, there is a two-peak structure that correlates with the classical turning point Z_{min} of the reflected N_2. In general, the high-energy loss peak is mainly due to those molecules that probe the closest distances to the surface, where the electronic density is high. In contrast, the low-energy peaks correspond to molecules that are reflected at larger distances, i.e., in low electron density regions. This is what we observe in the insets of Fig. 28.8, where the Z_{min} distributions are plotted separately for the trajectories that give rise to the low-energy (shadow bars) and high-energy (open bars) loss peaks. As mentioned above, the number of rebounds is another factor that can affect the energy losses. A close inspection of the trajectories contributing to the low-energy loss peak shows that only around 0.1% of these trajectories show more than one rebound before being reflected. However, in the case of the high-energy loss peak, 62% (24%) of the trajectories with $E_i = 0.75\,eV$ ($E_i = 1.5\,eV$) experience two to four rebounds before being reflected from the W(100) surface. Similarly, percentages of about 30% (6%) are found for the high-energy loss peak in the W(110) case. Comparing both surfaces, the larger percentages found on the W(100) surface contribute to also explaining that the high-energy loss peak is shifted to higher energies as compared with the one appearing in the W(110) energy-loss spectra.

Also minor seems to be the role of e–h pairs in the scattering of O_2 off Ag(111). This system was extensively studied by *Raukema* et al. using a supersonic molecular beam apparatus that permitted incidence energies ranging from 0.4 to 1.8 eV [28.113]. Among other magnitudes, the authors measured the energy loss distribution of the scattered molecules using different incidence conditions (Θ_i, E_i). The distributions exhibit a distinctive behavior that was not observed with N_2 or Ar beams on the same surface. These individual features were particularly apparent at final scattering angles close to the surface normal. The O_2 scattered above the specular angle are characterized by high-energy losses that under large normal incidence energy conditions can exceed those predicted from the *hard-sphere scattering* or Baule model. The latter is a simplified model that describes a two-body collision assuming energy and momentum conservation while neglecting the internal degrees of freedom [28.114]. Molecular dynamics calculations performed with the GLO model and a DFT-based 6-D PES were already able to nicely

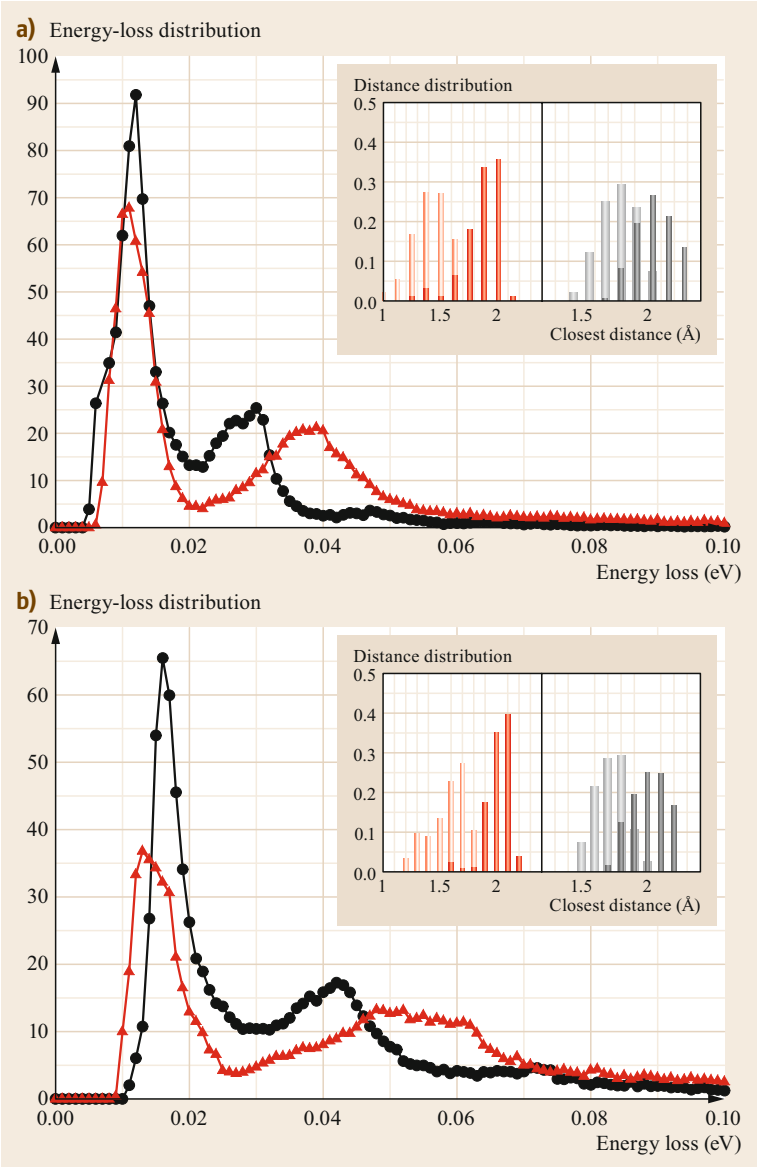

Fig. 28.8a,b Energy-loss distribution of the N_2 molecules reflected from the W(110) (*black circles*) and W(100) (*red triangles*) surfaces when impinging normal to the surface with an initial incidence energy $E_i = 0.75\,\text{eV}$ **(a)** and $E_i = 1.5\,\text{eV}$ **(b)**. The *insets* show for each incidence condition and surface the classical turning point distribution of the molecules contributing to the low-energy (*shadowed bars*) and high-energy (*open bars*) peaks. Results taken from the LDFA simulations of [28.111]

reproduce all these experimental features [28.14]. The experimental energy-loss distributions are compared with the GLO simulations in Fig. 28.9. Specifically, this figure shows the angularly resolved final-to-initial translational energy ratio distributions of O_2 scattered from Ag(111) at different incidence conditions. Values of $\langle E_f\rangle/\langle E_i\rangle < 1$ show that the molecule has lost translational energy after reflection, and the larger energy losses correspond to the smaller energy ratios. In general, the experimental data (Fig. 28.9a) show that the energy loss increases with the incidence energy, the former being higher at $\Theta_i = 40°$. The results of the GLO calculations, which only include energy exchange and dissipation with the surface lattice, are plotted in Fig. 28.9b. The qualitative agreement with the experimental data is remarkable. In spite of its simplicity, the GLO model reproduces the shape and trends of the $\langle E_f\rangle/\langle E_i\rangle$ distributions, as well as the dependence on E_i and Θ_i. A detailed analysis on how the parallel and perpendicular translational energy are effectively exchanged due to PES corrugation explains the peculiar shape of the distributions. Energy exchange with the surface is favored under backscattering conditions, i.e., the higher the perpendicular energy during the collision, the larger the energy loss. Hence, the energy transfer from parallel to perpendicular motion experienced by

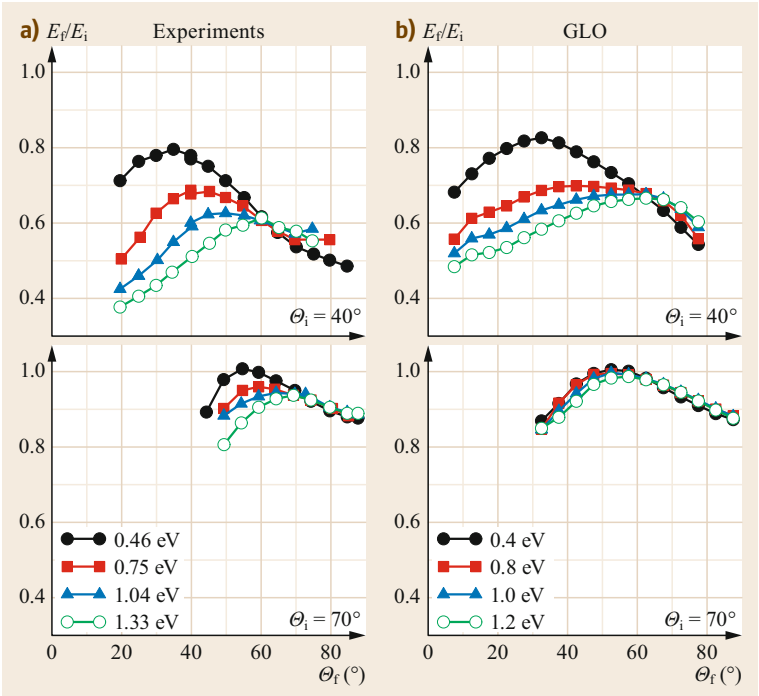

Fig. 28.9a,b Angularly resolved final-to-initial energy distributions of O_2 scattered off Ag(111) under different incidence conditions (Θ_i, E_i). The experimental data by *Raukema* et al. [28.113] **(a)** are compared with the GLO simulations performed in [28.14] **(b)** (Reprinted with permission from [28.14]. Copyright (2014) by the American Physical Society)

the O_2 molecules scattered above the specular angle ($\Theta_f < \Theta_i$) is the reason why they have a larger energy loss than those scattered quite below the specular angle whose energy has been predominantly transferred into the parallel motion. Furthermore, as E_i increases, the molecules get closer to the surface, and the result is a larger energy transfer, as observed in Fig. 28.9.

Meyer and *Reuter* also found that the energy loss of O_2 scattered off Pd(100) is dominated by energy exchange to the lattice rather than to e–h pairs [28.115, 116]. The authors performed calculations of a few trajectories following the method of [28.25] to calculate the energy dissipated into electronic excitations, while phonons excitations were modeled with their own QM/Me method [28.116].

Considering the molecule-to-surface atom mass ratios, the minor effects that e–h pair excitations seem to have on the scattering properties of the aforementioned systems can, to some extent, be masked by the more efficient phonon excitation mechanism. In this respect, the scattering of H_2 on metals can be considered a better alternative to gain further insight into the ingredients that determine the relevance of e–h pairs. Actually, this interaction has been widely investigated for decades as the prototype to test the validity of the Born–Oppenheimer approximation in the thermal/hyperthermal regime [28.1, 4, 5, 117–119]. Among the magnitudes that can be particularly sensitive to the fine details of the molecule–surface interaction—i.e., to its multidimensional nature and to the existence of nonadiabatic contributions—are the state-to-state elastic and inelastic scattering probabilities.

In [28.120], the LDFA was used to analyze possible nonadiabatic effects in the state-to-state scattering of H_2 and D_2 off the Cu(111) surface. The results for the vibrational survival probabilities of $H_2(v_i = 1, J_i = 1)$ and $D_2(v_i = 1, J_i = 2)$ obtained from quasi-classical (QC) calculations, which include the initial zero-point energy of the molecules, are reproduced in Fig. 28.10a,b, respectively. In general, the LDFA survival probabilities are slightly larger than the adiabatic ones. The calculations were performed for two 6-D PESs that differ from each other in the exchange-correlation functional (PW91 and SRP). The effect of e–h pairs is slightly larger for the more reactive PW91-PES because the molecules can approach closer to the surface, where the electron density and, hence, the effective coupling to the valence-band electrons is larger. A common feature observed in all the 6-D calculations is the decrease of the vibrational survival probability as increasing the incidence energy, the decrease being more pronounced for H_2 than for D_2. This kind of behavior has been experimentally observed in the scattering of H_2 off Cu(111) [28.121], as well as in the scattering of H_2 [28.122] and D_2 [28.123] from Cu(100), for which a similar isotope effect to that ob-

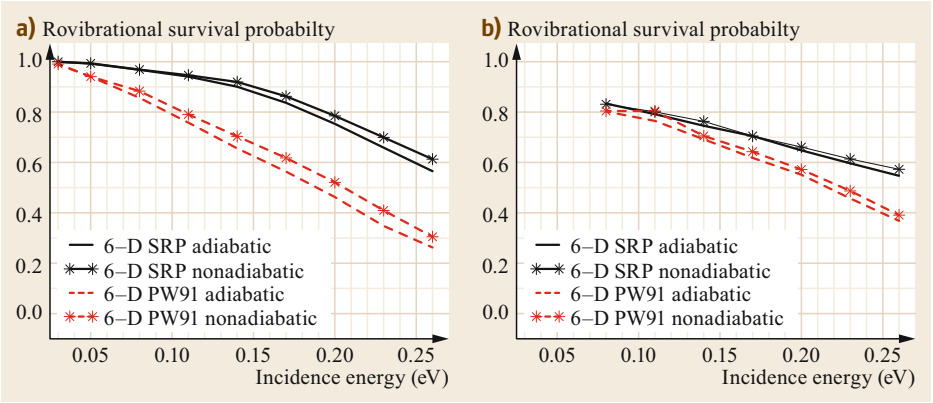

Fig. 28.10a,b Adiabatic (*lines*) and nonadiabatic (*lines with stars*) QC simulations of the rovibrational survival probability as a function of the incidence energy for **(a)** $H_2(\nu_i = 1, J_i = 1)$ and **(b)** $D_2(\nu_i = 1, J_i = 1)$ impinging on Cu(111) at normal incidence. Results obtained in [28.120] from 6-D molecular dynamics calculations performed with the SRP-PES developed by *Diaz* et al. [28.4] (*black lines* and *stars*) and a 6-D PW91-PES (*red lines* and *stars*)

tained theoretically by Muzas et al. with the PW91-PES is also observed. The same authors showed that the rotational excitation/de-excitation probabilities do not change significantly either when accounting for e–h pair excitations (Fig. 28.11). Interestingly enough, the effect is to decrease the excitation probabilities while increasing the survival and de-excitation probabilities. In principle, one would be tempted to assume that at each E_i, the changes caused by e–h pair-excitations in the D_2 isotopologue should be smaller because of its slower velocity. While this is the case for the survival probabilities of Fig. 28.10, in the case of the rotational excitation probabilities of Fig. 28.11, this is not that clear and seems to depend on the exchange correlation functional, which shows the complexity of the 6-D dynamics in a corrugated PES.

The scattering of thermal/hyperthermal atoms off metal surfaces has also motivated various experimental and subsequent theoretical studies in an attempt to gain further insight into the energy transfer mechanisms and, in particular, into the role played by e–h-pair excitations.

Using effusive beams of N atoms scattered from Ag(111) at $T_s = 500\,\mathrm{K}$ and an incidence angle (with respect to the surface normal) $\Theta_i = 60°$, *Ueta* et al. in-

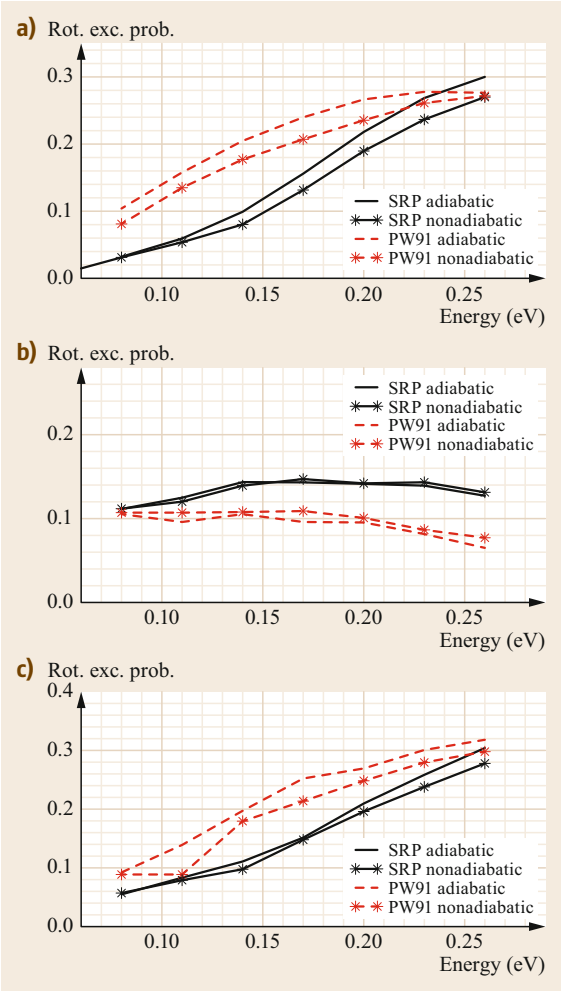

Fig. 28.11a–c Adiabatic and nonadiabatic QC simulations of the rovibrational excitation/de-excitation probability as a function of the incidence energy for **(a)** $H_2(\nu_i = 1, J_i = 1 \to J_f = 3)$, **(b)** $D_2(\nu_i = 1, J_i = 2 \to J_f = 0)$, and **(c)** $D_2(\nu_i = 1, J_i = 2 \to J_f = 4)$. Molecules impinge on Cu(111) at normal incidence. Colors and symbols as in Fig. 28.10 (Reprinted from [28.120], with the permission of AIP Publishing) ►

vestigated the energy loss as a function of the in-plane (polar) scattering angle [28.124]. The final-to-initial energy ratio measured increases with the outgoing (polar) angle Θ_f of the scattered N atoms (Θ_f is also referred to the surface normal). Specifically, it yields values between 0.6 and 0.9 for angles $\Theta_f < \Theta_i$, and it steeply increases above 1 for the grazing outgoing angles ($\Theta_f > 50°$), suggesting an unexpectedly large energy transfer from the surface to the atoms. The effusive beam with a nominal average kinetic energy $\langle E_i \rangle = 4.3\,\text{eV}$, however, carries a mixture of N atoms with diverse kinetic energies, as the large full-width-at-half-maximum (FWHM) of $\approx 5.0\,\text{eV}$ manifests. Classical dynamics simulations performed for monoenergetic N beams with a well-defined incidence energy showed that N always loses energy ($\langle E_f \rangle / \langle E_i \rangle < 1$ for all Θ_f), although in agreement with experiments, the energy losses are larger, the larger the outgoing angle Θ_f [28.125]. The experimental measurements were only reproduced when performing simulations that mimic the experimental effusive beam. A careful analysis of the trajectories showed that the apparent energy gain occurs because only the most energetic atoms in the beam ($E_i > 4.3\,\text{eV}$) are scattered at grazing angles. As a result, the average final energy at these angles exceeds the initial $\langle E_i \rangle = 4.3\,\text{eV}$. Furthermore, by comparing the results obtained from simulations that include or do not include e–h-pair excitations and/or phonons, the authors demonstrate that only a small percentage of the energy is lost into e–h pairs [28.125].

Interestingly enough, a completely different conclusion is obtained in the case of H atoms scattered from Au(111) and Cu(111) [28.126–128]. AIMD simulations of the scattering of 5 eV H-atoms predicted experimentally realizable conditions where only about 2% of the incident energy should be lost into metal phonon excitations [28.126, 127]. Higher experimental losses should, hence, be attributed to e–h pairs. As a rough estimation, the authors used the position and velocities from the AIMD trajectories to compute within the LDFA the energy lost into e–h pairs and already predicted that the electronic and not the phononic would be the dominant energy-loss channel in these systems. Similar conclusions were obtained for H/Au(111) from nonadiabatic molecular dynamics simulations based on the LDFA and the effective-medium theory [28.128], which were finally confirmed experimentally in [28.129]. Using incidence and detection angles $\Theta_i = \Theta_f = 45°$ along the $[10\bar{1}]$-direction and incidence energies ranging from 0.99to 3.33 eV, both theory and experiments found a considerable fractional energy loss $(E_i - \langle E_f \rangle)/E_i = 0.33 \pm 0.01$, which the theoretical simulations permit us to identify as being dominated by the electronic excitations.

28.4.2 Adsorption of Atoms and Molecules on Metals

The validity of the BOA in describing the interaction of (thermal/hyperthermal) molecules with metal surfaces has been extensively investigated in the context of dissociative adsorption. There are various examples showing that the experimental adsorption probabilities are rather well described within the adiabatic approximation, provided that an accurate potential-energy surface and the relevant degrees of freedom are included in the dynamics simulations. Unfortunately, the inherent limitations of present DFT to accurately describe on the same footing the large and small gradient density regions important in gas–surface interactions complicates this task in many cases. As a result, the calculated dissociation probabilities can vary strongly with the exchange-correlation functional used in the description [28.4, 130–132], a methodological restriction that cannot be overlooked when the comparison to experiments is used to extract the possible effects of e–h pairs in the dissociation mechanism.

Electronic nonadiabatic effects in the dissociative adsorption have been studied using the LDFA for a few systems that are, however, representative of most relevant situations. Dissociation of H_2 on Cu(110) is an activated process that requires the molecule to have a minimum energy to overcome the potential energy barrier leading to dissociation. The lowest barriers are located close to the surface (below 1 Å), where the electron density is usually large, and for the molecule quite elongated (i.e., for an internuclear distance $r \geq 1.17$ Å). In this type of late-barrier systems, the effect of e–h pairs is to decrease the dissociation probability because the molecule loses part of its total energy before arriving at the barrier. Classical trajectory simulations performed for H_2/Cu(110) showed that this reduction is, however, very minor [28.23]. Similar conclusions have been obtained for the dissociative adsorption of H_2O [28.133], as well as CH_4 and their partially deuterated isotopologues on Ni(111) [28.134]. These systems are particularly interesting because state-resolved gas–surface experiments have revealed a strong mode dependence in promoting dissociation [28.135–137]. Quasiclassical simulations performed on these systems that accounted for e–h-pair excitations show through the LDFA that none of these mode-specificity properties are significantly altered by e–h pairs [28.133, 134].

There are different factors that contribute to the generally minor effects that e–h-pair excitations have in the final dissociative probabilities of those systems characterized by a direct and fast dissociation process. The energy loss into low-energy electronic excitations is proportional to the friction coefficient, the projectile

velocity, and the length traveled. In the region where the density is high, the molecule–surface potential is, in many cases, highly repulsive and causes a substantial reduction of the kinetic energy of the molecules. In addition, a common property of the aforementioned dissociation processes is that all of them involve short time scales. Therefore, even if friction coefficient values were large because of the high-density regions the molecule might be probing, the short time spent by the molecules in those regions together with the reduction in the velocity cause a marginal energy loss that hardly affects the dissociation process itself.

The role of e–h pairs in the dissociation of N_2 on W(100) and W(110) was studied within the LDFA in [28.23, 111]. The process is in both cases quite complex, as it strongly depends on the incidence conditions. At normal incidence and energies $> 0.5\,\mathrm{eV}$ dissociation is dominated by a rather direct process. However, the difference is that the energy barriers to N_2 dissociation are located in the so-called *entrance channel*, i.e., at larger distances from the surface where the molecule still preserves its gas-phase equilibrium bond length because of a still weak interaction with the surface. Under such conditions it is not surprising that the contribution to the dissociation probability of the direct dissociation events is basically unchanged by e–h pairs. The dissociation dynamics change drastically at lower E_i, namely, $< 0.2\,\mathrm{eV}$ for $N_2/W(100)$ and $< 0.5\,\mathrm{eV}$ for $N_2/W(110)$. Under such circumstances, dissociation proceeds in both W surfaces through an indirect mechanism, in which the molecules are first dynamically trapped around the molecular chemisorption wells during a few picoseconds (1−2 ps on W(110) and 5−10 ps on W(100)) before finding the path leading to dissociation. The analysis in [28.111] shows that the effect of e–h pairs is to increase the dissociation probabilities mediated by this indirect mechanism. Interestingly, such an effect is opposite to that observed on the aforementioned examples of direct and late-barrier dissociation events, but can be easily understood once we recognize the different energy landscapes ruling the process in each case. A common feature in $N_2/W(110)$ and $N_2/W(100)$ is that from the bottom of the adsorption well, the energy barriers to desorption are, on average, higher than those to dissociation. Hence, once the molecule is trapped on the surface and starts to dissipate energy, dissociation becomes energetically favored. Yet, the effect is quite minor with corrections to the dissociation probabilities on both surfaces of about 10−15% at most. Even if the time the molecules spend on the surface probing the high-density regions before dissociation is considerably long, the dissociation event itself, being ruled by early barriers, is actually decided once the molecules become trapped by the chemisorption well, or, in general, by the attractive parts of the PES. Thus, the excitation of the low-energy electrons that become important at ulterior times cannot alter the outcome of the dissociating trajectories much.

Taking into consideration all the above examples, we can speculate that the ideal dissociation conditions for which nonadiabatic effects may still be determinant should combine late-barrier together with trapping-mediated dynamics. Unless these conditions are met, one should expect that the adiabatic approximation suffices to provide a reasonable description of the dissociation process, at 1250 least in its initial stages, as we discuss next.

At first sight, the theoretically predicted insignificance of e–h pairs in the gas–surface processes described so far contrasts with existing experiments, proving that they are efficiently excited even under thermal gas–surface conditions. Detection of low-energy solid-state e–h-pair excitations is technically feasible by means of Schottky diode devices, which consist of ultrathin metal films grown on semiconductor substrates. Hot charge carriers (electrons/holes) excited during the exothermic adsorption of atoms and molecules on metals are detected as *chemicurrents* on the diode [28.18, 138, 139]. Using this technique, a variety of exothermic chemical reactions that constitute a representative sample of relevant gas–surface interactions, such as physisorption, chemisorption, dissociation, and recombinative desorption, have been investigated to conclude that a large fraction of the energy is dissipated into e–h pairs in view of the correlation found between chemicurrent intensities and adsorption energies. The question, then, is how to reconcile theory and experiments in this matter.

Studies focused on the subsequent relaxation of the adsorbing gas species rather than on the initial adsorption process itself have been decisive in understanding the role of the low-energy excited electrons [28.40–43, 140]. In [28.141], the relaxation of the nascent H atoms formed upon dissociation of H_2 on Pd(100) was first studied using AIMD, which only includes dissipation into phonons, and more recently in [28.40, 41, 43] using the newly developed AIMDEF method explained in Sect. 28.3.4. The authors show that, although e–h-pair effects are usually irrelevant on the molecule bond-breaking timescale—which explains the success of the adiabatic approach and the minor corrections to the dissociation probabilities discussed above—, it is an efficient dissipative channel in the subsequent relaxation of the resulting hot products that propagate until they reach thermal equilibrium with the surface. The results for H relaxation are particularly striking, as it was found that energy dissipation into e–h pairs occurs at a rate

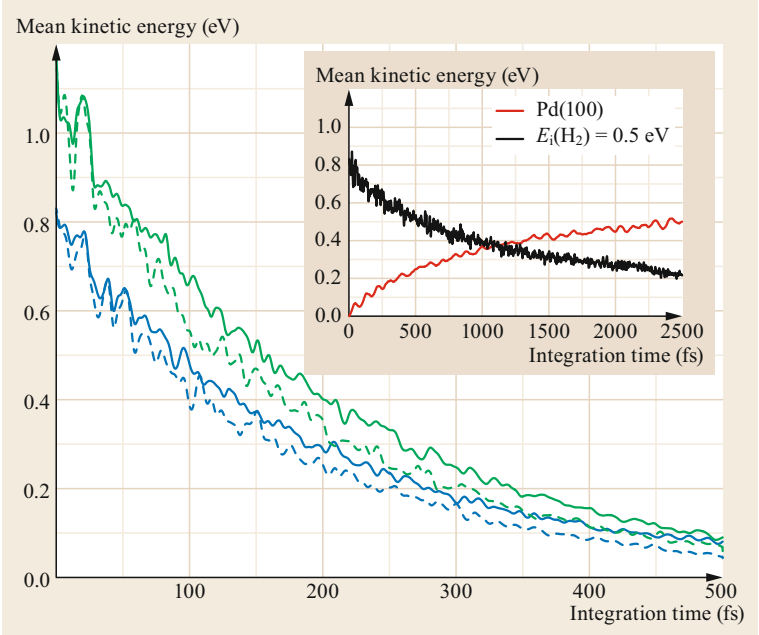

Fig. 28.12 Time evolution of the mean kinetic energy of H_2 upon dissociation on Pd(100) as calculated from the LDFA-based AIMDEF simulations in [28.40]. *Blue* (*green*) *lines* correspond to H_2 impinging with $E_i = 0.5(1.0)$ eV. *Solid* (*dashed*) *lines* represent the AIMDEF results obtained in frozen-surface (nonfrozen-surface) simulations. *Inset*: mean H_2 (*black line*) and Pd (*red line*) kinetic energy obtained from nonfrozen-surface AIMD simulations without electronic friction (Reprinted with permission from [28.40]. Copyright (2014) by the American Physical Society)

five times faster than dissipation into phonons. This can be observed in Fig. 28.12, where the H_2 kinetic energy averaged over all the dissociated trajectories is plotted as a function of time for H_2 beams with 0.5 and 1.0 eV of incidence energy. The evolution is represented from the instant at which the molecule is considered dissociated (i.e., when the internuclear distance is > 1.5 Å). Note that the kinetic energy starts at a value larger than the initial E_i because of the energy gained by the molecule in the dissociation process. In order to quantify the contribution of phonons and e–h pairs to the relaxation process, the authors performed three types of simulations: frozen-surface (FS) AIMDEF calculations in which the surface atoms are not allowed to move (FS+AIMDEF; nonfrozen-surface (NFS) AIMDEF calculations that allow for the movement of the atoms in the two topmost surface layers (NFS+AIMDEF); and nonfrozen surface AIMD simulations that do not include electronic friction (NFS+AIMD).

In the 0.5 eV H_2 beam case, ≈ 1 ps is needed to reduce the kinetic energy down to 0.4 eV when only the phononic channel is included (NFS+AIMD, see inset in Fig. 28.12), while ≈ 0.14 ps are enough to observe the same decrease, when only e–h pairs excitations are considered (blue solid line in Fig. 28.12). Comparing the NFS+AIMDEF and FS+AIMDEF results, the relaxation rate is slightly larger in the former case, i.e., when both energy dissipation mechanisms are included, than in the latter. However, the small differences found between both types of simulations (dashed versus solid lines in Fig. 28.12) is a clear indication of the relaxation process being strongly dominated by e–h pairs.

The minor role of phonons in the relaxation of H on metals is directly related to its small mass compared with that of the usual metal atoms of interest. The competition between e–h pairs and phonons during the adsorption and relaxation processes of heavier atoms and molecules was also studied in [28.41–43, 140]. Together, all these studies cover different mass ratios between the gas species and the metal atoms that provide a wider perspective on the role played by each energy-dissipation channel. The adsorption of N atoms on Ag(111) was investigated by *Martin-Gondre* et al. [28.140], who performed molecular dynamics simulations on a three-dimensional (3-D) PES and included the role of phonons and e–h-pairs by combining the GLO and the LDFA. The same system was later analyzed by means of AIMDEF simulations, which permits, in principle, a more accurate and realistic description of the surface-atom movement and, importantly, of the interplay between the two energy dissipation mechanisms. The overall conclusions extracted in both studies are similar though, and we will only review those of [28.140] that take advantage of the low computational cost to monitor the adsorption process until the atom is fully accommodated and relaxed in the well.

Figure 28.13 shows the total energy of the adsorbing N atoms against time as calculated when accounting for energy dissipation into both phonons and e–h pairs (LDFA+GLO), and when only one of the mechanisms is considered (the LDFA for e–h pairs and the GLO

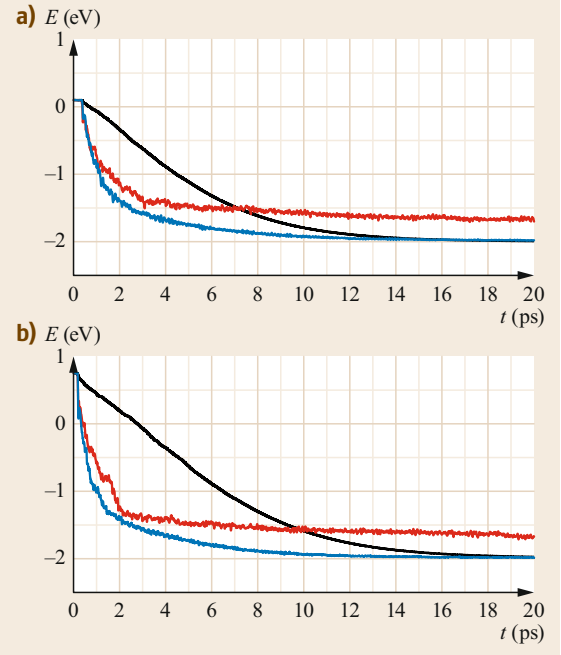

Fig. 28.13a,b Time evolution of the total (potential plus kinetic) energy of N atoms adsorbing on Ag(111). Results obtained in [28.140] from three-dimensional (3-D) molecular dynamics based on the LDFA (*black curves*), GLO (*red curves*), and LDFA+GLO (*blue curves*) simulations for an incidence angle of 40° and two different energies: **(a)** $E_i = 0.10\,\text{eV}$, **(b)** $E_i = 0.75\,\text{eV}$. Surface temperature is $T_s = 500\,\text{K}$ (Reprinted from [28.140], with permission from Elsevier)

for phonons). Figure 28.13 corresponds to N atoms impinging from vacuum at 40° with respect to the surface normal and with an initial kinetic energy of 0.1 eV (Fig. 28.13a) and 0.75 eV (Fig. 28.13b). Compared with the somehow similar initial decay of the LDFA+GLO and GLO curves at times below 1(2) ps for $E_i = 0.1(0.75)\,\text{eV}$, the slower decay of the LDFA one at each E_i shows that, in contrast to the relaxation of H atoms, the initial steps of the adsorption of N on Ag(111) are primarily controlled by the energy exchange to the surface lattice. It is at longer times when the contribution of e–h pairs becomes crucial. We can infer this statement from the comparison between the LDFA+GLO and GLO curves at times 1(2)–10 ps. While the GLO results reach an almost steady plateau, the additional incorporation of e–h pairs (LDFA+GLO curves) results in a slow but continuous decay that causes an additional energy loss of around 0.5 eV at 10 ps.

It is meaningful to follow the evolution of the adsorbing N over the surface unit cell that is plotted in Fig. 28.14 at times $t = 10$ (red dots) and $t = 20$ ps (blue

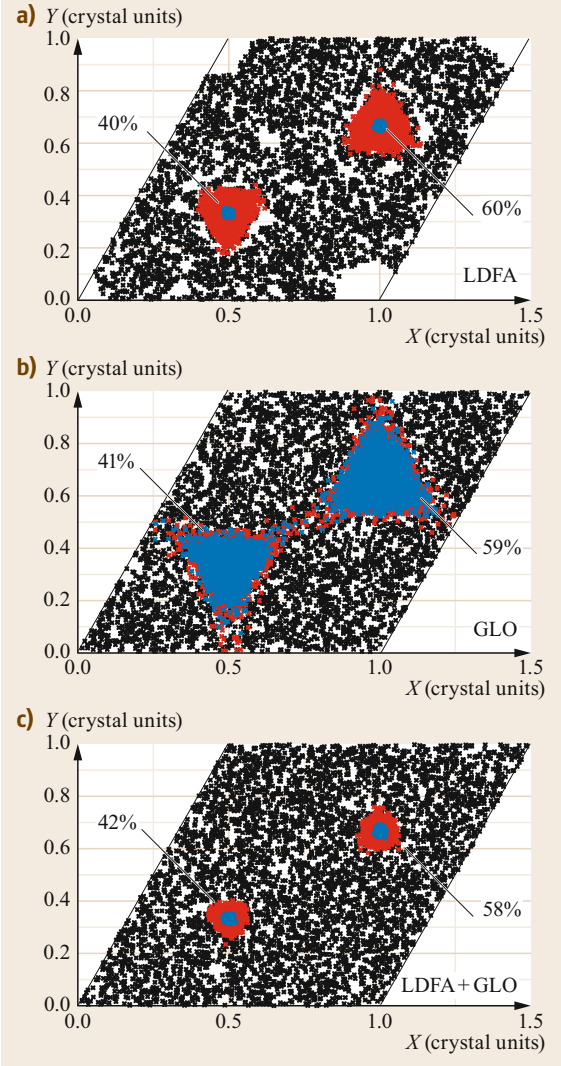

Fig. 28.14a–c Initial (*black dots*) and final (*colored dots*) (X, Y) positions of the adsorbing N over the Ag(111) surface unit cell as obtained in [28.140] for the LDFA **(a)**, GLO **(b)**, and LDFA+GLO **(c)**. Incidence conditions: $E_i = 0.1\,\text{eV}$ and $\Theta_i = 40°$. *Red* (*blue*) *dots* correspond to the final atomic positions after an integration time of 10(20) ps. The percentage of atoms adsorbed at the fcc and hcp sites is also indicated. For clarity, all points have been merged into one elementary cell with the Ag atoms located at the corners of the cell and the fcc(hcp) hollow located in the upper (lower) part of the cell. The GLO and LDFA+GLO simulations performed at $T_s = 500\,\text{K}$ (Reprinted from [28.140], with permission from Elsevier)

dots), as obtained from the three types of simulations. In all cases, the atoms are already located over the fcc and hcp hollow sites that correspond to the position of the stable and metastable adsorption wells,

respectively. Apart from this common feature, there are notable differences in the (X, Y)-distributions obtained by each model. At $t = 10$ ps, the LDFA+GLO distribution is the narrowest, showing that the adsorbing atoms are quite well localized already at the adsorption wells. Interestingly, the GLO model gives a quite broad distribution, also when compared to the LDFA one. The different degrees of localization observed in the three cases is well correlated with the amount of energy lost by the N atoms in each type of simulation. The increasing efficiency of the electronic dissipation channel in the long-time term is more apparent after noting the still broad distribution obtained with the GLO model at 20 ps, which contrasts highly to the well-defined LDFA and LDFA+GLO positions. All in all, the in-depth analysis of [28.140] shows that the relevant energy dissipation channels at the beginning and at the end of the dynamics are different. Indeed, the fast energy loss due to phonons during the 2 or 3 first picoseconds of the dynamics will promote the trapping of N atoms, preventing any reflection process. Nevertheless, since e–h pairs are continuously excited as long as the adsorbing species moves, the final position of the adsorbed atoms is ruled by the latter dissipation channel.

Molecular adsorption of N_2 on Fe(110) is an additional and more extreme example of adsorption dominated by energy dissipation into phonons. Using the different types of AIMD and AIMDEF simulations aimed to isolate the contribution of each energy-dissipation channel that were described above, *Novko* et al. [28.41, 43] showed that no adsorption event occurs when only e–h-pair excitations are included in the simulations (FS+AIMDEF). Furthermore, the relaxation rates obtained when accounting for phonons with (NFS+AIMDEF) and without (AIMD) e–h-pair excitations are rather similar. Figure 28.15 shows the time evolution of the N_2 mean kinetic energy, which is obtained as an average over all adsorbing NFS+AIMDEF trajectories. This system is characterized by three molecular adsorption wells that have quite different properties regarding their adsorption energies and their position and configuration on the surface. For this reason, Figure 28.15 shows the mean kinetic energy separated for each of the wells. The *top-vertical* well with $E_a = -0.31$ eV occurs for the molecule atop an Fe atom and oriented vertical to the surface, while the *bridge-parallel* ($E_a = -0.22$ eV) and *hollow-parallel* ($E_a = -0.49$ eV) wells correspond to the molecule lying parallel to the surface with their center of mass over bridge and hollow sites, respectively. At the end of the simulation, the kinetic energy of those molecules that end up on the less bounded bridge site is only of few tens of meV, as an indication of the molecules having reached the bottom of the well (note that the zero-point energy was neglected in all the simulations). At

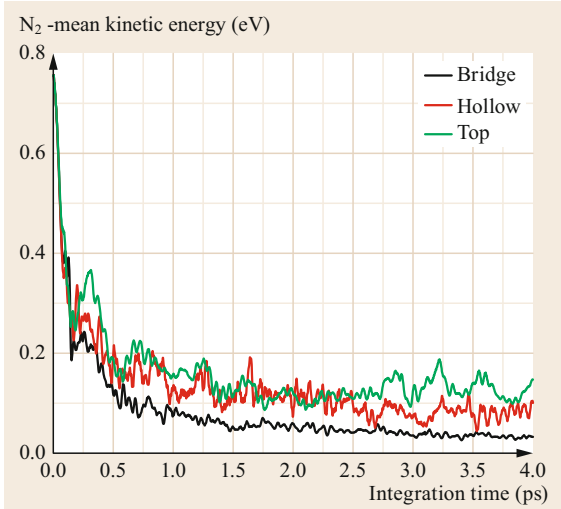

Fig. 28.15 Time evolution of the mean kinetic energy of N_2 adsorbing on Fe(110) at each of the three different molecular wells. Results obtained from the LDFA-based AIMDEF simulations in [28.41, 42] using the Hirshfeld density partitioning scheme to account for the surface density changes caused by the Fe displacements in nonfrozen-surface calculations. Incidence conditions $E_i = 0.75$ eV and normal incidence

first thought, the results showing that the kinetic energy of the molecules adsorbing at the *top-vertical* well remains larger than that of the molecules adsorbing on the *hollow-parallel* one seems contradictory to the corresponding E_a values and show the slower thermalization of the molecules on the top well. As shown in [28.43], this happens because both energy-loss channels depend strongly on the adsorption configuration. At the top site, the molecule lies further from the surface, where the electron density is lower, and thus, the e–h-pair excitations are less efficient. The comparison of the additional AIMD simulations performed in [28.43] showed that the phonon excitation channel is also less efficient at the top site.

The competition between the two energy dissipation channels can easily be quantified by calculating the amount of energy transferred from the adsorbates to e–h pairs and to the lattice. For a single atomic trajectory, the former contribution as a function of time can be evaluated from the path integration of the friction force on each gas atom along its trajectory, i.e.,

$$E_{eh}(t) = \sum_{i=1}^{N_{step}} \eta(\boldsymbol{r}_i)|\boldsymbol{v}_i|^2 \Delta t \,, \qquad (28.44)$$

where $\eta(\boldsymbol{r}_i)$ and $\boldsymbol{v}_i$ are, respectively, the friction coefficient and velocity of the atom at the integration step i,

and Δt is the constant time step used in the integration. The mean energy lost into e–h pairs is calculated as an average over the available number of trajectories $\langle E_{eh}(t)\rangle$. In the case of molecules, the contributions of all the atoms are added. The energy transferred to the lattice atoms is the sum of the instantaneous kinetic energy of the surface atoms $\langle E_{kin}(t)\rangle$ and the instantaneous variation of the potential energy due to lattice distortions $\langle E_{pot}(t)\rangle$. The former can be easily calculated at each time step t during the AIMDEF simulation, while the latter requires additional and separated calculations of the potential energy associated to the distorted surface lattice but without including the adsorbing gas species (see [28.41, 43] for a detailed description).

Figure 28.16 reproduces the mean energy dissipated into each mechanism for the relaxation of the nascent H atoms formed upon dissociation of H_2 on Pd(100) and the adsorption of N_2 on Fe(110), as calculated in [28.41]. In the e–h-pair-dominated H/Pd(110) system, the energy transferred to e–h pairs is around more than two times larger than the total energy transferred to the lattice after just 0.5 ps. A completely opposite behavior is obviously observed for the phonon-dominated N_2/Fe(110) system in which we observe that the energy lost into phonons at the end of the simulation time (4 ps) is almost four times the energy released into the e–h pairs. In the first stages of the dynamics, at $t < 0.5$ ps, a rapid energy transfer takes place from the molecule to the surface lattice. In fact, this fast energy transfer fully accounts for the adsorption process in the N_2/Fe(110) system. After this short period of time, while $\langle E_{ph}\rangle$ reaches a plateau, $\langle E_{eh}\rangle$ increases monotonically. Interestingly, we observe that despite the phononic channel dominating the N_2 relaxation, the energy lost to e–h pairs is by no means negligible. Actually, no matter how dissimilar the adsorption and relaxation processes are, in close similarity to the observations made for the adsorption of N on Ag(111), we also observe for H/Pd(100) and N_2/Fe(110) that the energy loss into the lattice occurs at the initial stages of the adsorption process. Specifically, the sum of the $\langle E_{kin}(t)\rangle$ and $\langle E_{pot}(t)\rangle$ curves remains basically constant in H/Pd(100) and N_2/Fe(110) after the first ≈ 0.1 and 0.8 ps, respectively. In contrast, since neither the H atoms nor the N_2 molecules are fully relaxed and accommodated in their respective wells, the e–h pairs are still an active energy drain, as is apparent from the increasing behavior of the corresponding curve during the whole integration time. The H atoms that are close to the bottom of the well exhibit an almost saturated $\langle E_{eh}\rangle$ curve.

28.4.3 Atom–Atom Recombinative Abstraction on Covered Surfaces

The catalytic properties of surfaces depend on the competition among the different elementary processes that characterize the gas–surface interaction [28.142]. While molecular and dissociative adsorption are usually the initial steps responsible for populating the surface with at least part of the desired reactants, most surface reactions involve at the latest stage the recombination of two or more species to conform the final molecular compound that desorbs. The surface catalycity and the replenishment of the surface active sites will depend on the efficiency of these recombi-

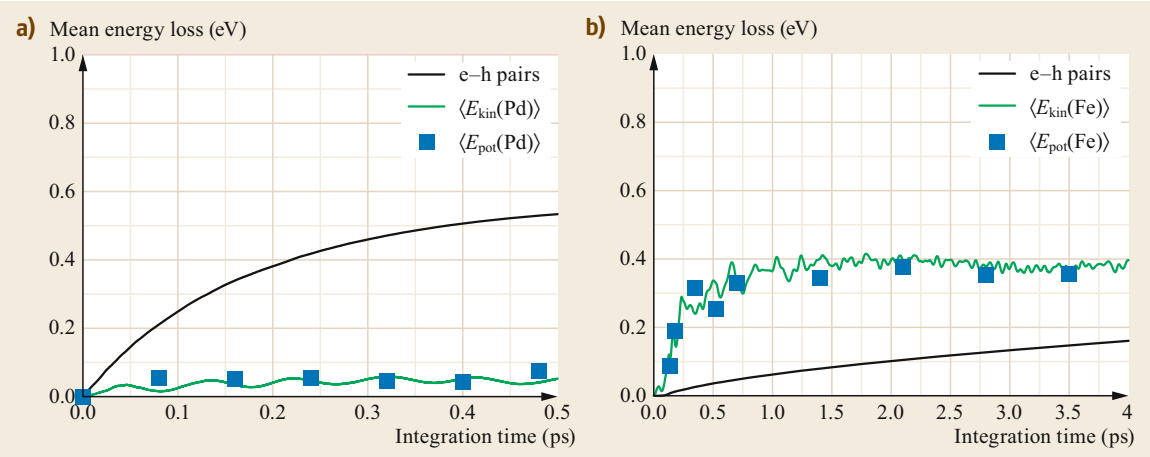

Fig. 28.16a,b Energy transferred to the surface upon adsorption of H on Pd(100) **(a)** and N_2 on Fe(110) **(b)** resolved into the different energy dissipation channels: e–h-pair excitations (*black curves*), kinetic energy of surface atoms $\langle E_{kin}(t)\rangle$ (*green curves*), and potential energy of the surface $\langle E_{pot}(t)\rangle$ (*blue squares*). Results obtained in [28.41] from AIMDEF simulations based on the LDFA with the Hirshfeld density partitioning scheme proposed in [28.42]

nation processes. Then, it comes as no surprise that many pioneering investigations were focused precisely on identifying all possible processes involving recombination [28.143–146]. Originally postulated as an atom exchange, the single-collision Eley–Rideal (ER) process is now assigned to the direct recombination of an incoming gas-phase species with a surface adsorbate to conform a molecular compound that desorbs during the collision. Closely related to it, the hot-atom (HA) abstraction process differs in that the gas-phase species experiences few collisions with the surface prior recombination. The extreme alternative to the ER mechanism is the Langmuir–Hinshelwood recombination, in which the species involved in the reaction are fully thermalized with the surface. In this section, we will focus on the recombination processes triggered by incident gas atoms, namely, ER and HA abstraction events.

Due to the usual fast nature of the single-collision ER abstraction, most of the theoretical studies performed on different systems were conducted under the adiabatic approximation or by only taking into account energy dissipation into the lattice phonons [28.8, 148–155]. The effect of e–h pairs in ER processes has been analyzed by *Galparsoro* et al. [28.147]. The authors investigated the ER recombination of H–H and N–N on two different W surfaces and performed 6-D quasiclassical dynamics simulations in which both energy dissipation mechanisms, namely, e–h pairs and phonons, were included within the LDFA and GLO models. Among other observations—all focused on the ER recombination in the ideal limit of a single adsorbate—, it was found that phonon excitations reduce the N–N ER cross section by about 10–50%, depending on the incidence energy and the crystal face. However, phonon excitations hardly affect the H–H abstraction due to the large mismatch between the masses of H and W atoms. Regarding e–h-pair excitations, the behavior observed when comparing N–N ER and H–H ER is just the opposite. Specifically, e–h pairs have a very minor effect on the N–N ER recombination cross section, but they can modify the adiabatic H–H ER cross section by as much as 36%.

The authors also evaluated the energy exchanged between the molecule and the metal separating the contributions of each of the energy-dissipation channels. The results for the H–H and N–N recombinations are reproduced in Figs. 28.17 and 28.18, respectively. By comparing both figures, we observe that the energy loss due to phonon excitations is about one order of magnitude higher for the N–N recombination than for the H–H recombination, in agreement with the mass mismatch between N and W being smaller than that between H and W. In contrast, energy dissipation due to e–h pair excitations is about three times larger for the H–H recombination than for the N–N recombination, despite the fact that the friction coefficients at equal electron density are significantly higher for N than for H [28.23, 37]. The authors attribute this somewhat counterintuitive result to the combination of two main factors. First, the comparative analysis of the trajectories showed that H atoms get closer to the surface and, therefore, probe regions of higher electronic density than N atoms do. Second, for similar collision energies the friction force and, hence, the electronic energy loss is larger for H than for N, due to the corresponding higher velocity of the former (28.44). As a final remark on the comparison between the two energy dissipation channels, note that even if phonons are the main energy-loss channel for N_2 formation, the electronic excitations are by no means negligible in this case. However, the H–H recombination on W surfaces can be safely described without including phonon excitations, as their

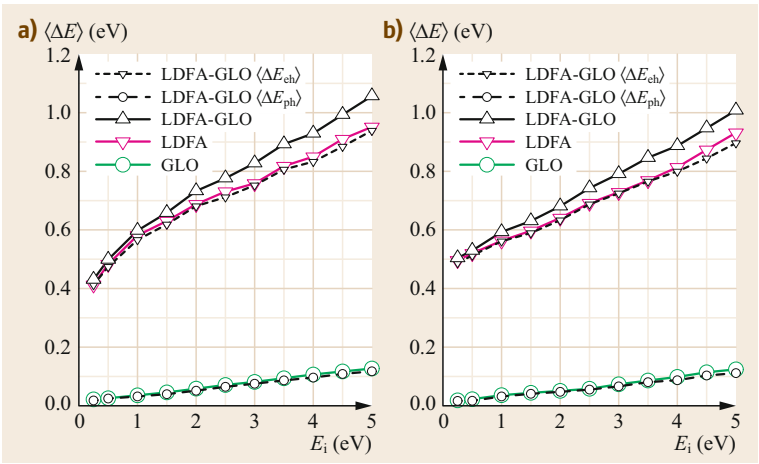

Fig. 28.17a,b Dependence of the average energy loss $\langle \Delta E \rangle$ on the incidence energy E_i for **(a)** H–H/W(100) and **(b)** H–H/W(110). Results obtained in [28.147] for the LDFA (*magenta down-triangles*), GLO (*green circles*) and LDFA-GLO (*black up-triangles*) simulations. For the LDFA-GLO calculations, the average energy loss into phonons $\langle \Delta E_{ph} \rangle$ (*black circles* and *dashed lines*) and into e–h-pair excitations $\langle \Delta E_{e-h} \rangle$ (*black down-triangles* and *dashed lines*) are also shown (Reprinted with permission from [28.147]. Copyright (2015) American Chemical Society)

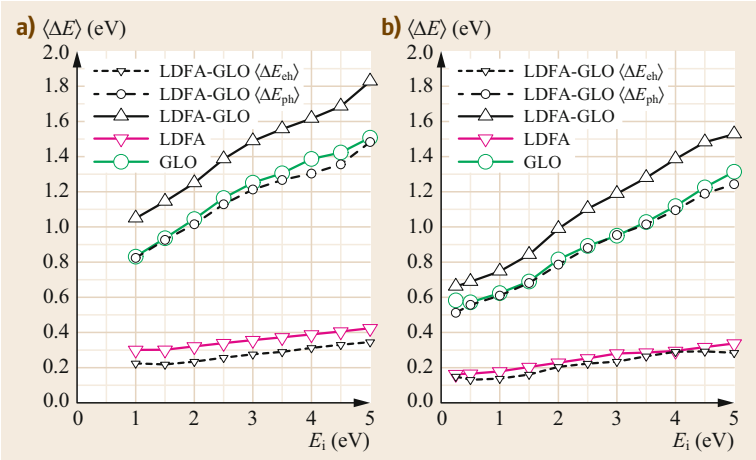

Fig. 28.18a,b Dependence of the average energy loss $\langle \Delta E \rangle$ on the incidence energy E_i for **(a)** N–N/W(100) and **(b)** N–N/W(110). Results obtained in [28.147] for the LDFA (*magenta down-triangles*), GLO (*green circles*) and LDFA-GLO (*black up-triangles*) simulations. For the LDFA-GLO calculations, the average energy loss into phonons $\langle \Delta E_{ph} \rangle$ (*black circles* and *dashed lines*) and into e–h-pair excitations $\langle \Delta E_{e-h} \rangle$ (*black down-triangles* and *dashed lines*) are also shown (Reprinted with permission from [28.147]. Copyright (2015) American Chemical Society)

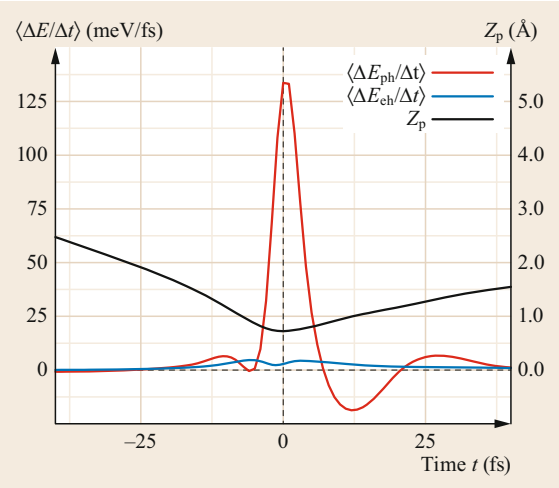

Fig. 28.19 Energy-loss rate of the incident N ($t < 0$) and nascent N_2 ($t > 0$) going into phonons (ΔE_{ph}, in *red*) and into e–h pairs (ΔE_{e-h}, in *blue*). *The right y-axis* indicates the values of the average z position of the projectile z_p (in *black*). Data from the LDFA+GLO simulations of N + N/W(100) at $E_i = 1.5$ eV (Reprinted with permission from [28.147]. Copyright (2015) American Chemical Society)

effect on the cross sections and energy loss is negligible [28.147].

The analysis provided in [28.147] on the time evolution of each energy-loss process along the ER trajectories is very instructive. Figure 28.19 displays the average energy-loss rate to phonons $\langle \Delta E_{ph}/\Delta t \rangle$ and to metal electrons $\langle \Delta E_{eh}/\Delta t \rangle$ as a function of time for N + N/W(100) at $E_i = 1.5$ eV. For each ER trajectory, the energy-loss rates are calculated by evaluating at each integration step Δt the contribution of each energy-loss channel (see [28.147] for details). The average over trajectories is calculated after setting in each case the origin of time ($t = 0$) at the instant the projectile reaches the classical turning point. As is shown in Fig. 28.19, most of the energy dissipated into the surface lattice occurs at the classical turning point (see the large symmetric peak centered at $t \approx 0$ fs, which amounts to ≈ 0.76 eV). Afterwards, the forming molecule gains and loses energy, but the energy exchange in these cases is considerably smaller. At first sight, the electronic energy-loss rate, which vanishes at the classical turning point with the z-component of the projectile velocity, is rather symmetric around this point, although slightly smaller along the outgoing ($t > 0$) part of the trajectory as compared to the losses experienced for $t < 0$. Even if the surface-electron density is rather similar along the incoming ($t < 0$) and outgoing ($t > 0$) parts of the trajectory, the projectile loses an important part of its kinetic energy into phonons upon the first collision with the surface. As a result, the electronic friction force and, correspondingly, the energy loss decrease for the remaining (outgoing) part of the trajectory. A similar analysis of the time evolution of each energy-loss mechanism is plotted in Fig. 28.20 for H + H/W(100) at $E_i = 1.5$ eV. Qualitatively, the behavior of the electronic and phononic channels is similar to that described for the N–N recombination case. Thus, the largest energy transfer to the surface lattice occurs close to the classical turning point as expected, while the energy-dissipation rate into e–h pairs, despite being rather symmetric along the incoming and outgoing parts of the trajectories, is slightly smaller in the latter part. It is very illustrative, however, that there are large quantitative differences that exist between the two systems, which provide evidence as to what mechanism rules the total energy loss in each case.

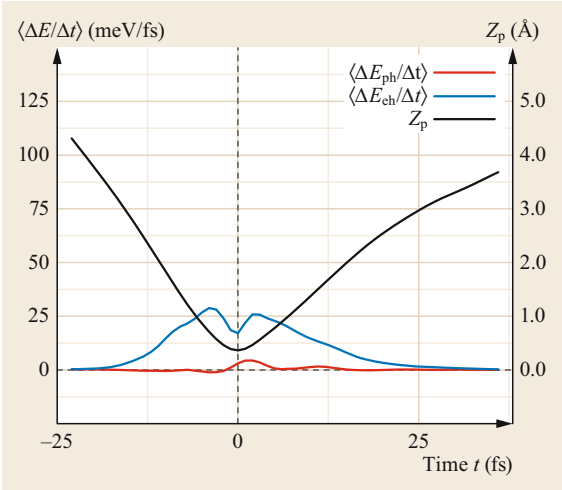

Fig. 28.20 Same as Fig. 28.19 for H + H/W(100) and $E_i = 1.5$ eV. Data extracted from the LDFA+GLO simulations performed in [28.147]

The usually long-lasting HA recombination, which involves hyperthermal diffusion of the impinging atom on the surface, in principle, meets all the necessary conditions for being significantly affected by the dissipation of energy into e–h-pair excitations. This problem has been studied for the scattering of H atoms from the H-covered W(110) surface [28.156]. Strikingly, the commonly accepted idea of HA recombination being dominant over the single-collision ER mechanism—and actually confirmed with adiabatic simulations performed for the same system [28.9]—is drastically affected when e–h-pair excitations come into play. This is what the LDFA simulations performed by *Galparsoro* et al. show in [28.156]. According to these authors, the HA recombination process is notably diminished in favor of H adsorption on the surface, particularly at low coverages and E_i. The comparison between the adiabatic and the LDFA cross sections *per* adsorbate is reproduced in Fig. 28.21 for all possible recombination processes and for two distinct coverages, namely, $\Theta = 0.25$ and 1 ML. In these simulations, a H–H recombination event is counted as ER when the molecule is formed after the first rebound of the projectile and moves definitively toward the vacuum and as *primary* HA when the projectile suffers more than one collision before recombining. Finally, when recombination involves two target atoms, the event is classified as *secondary* HA recombination. Figure 28.21 shows that nonadiabatic effects mainly affect the two HA recombination mechanisms, while the ER recombination hardly changes in agreement with what was also found in the single-adsorbate limit discussed above. The reduction experienced by the primary and secondary HA cross sections is more severe at the low-coverage and low-incident energies. Additional analysis of the energy lost by the projectile along the trajectory reveals that the incoming H atom rapidly dissipates into the efficient e–h pair production all the necessary energy the molecule requires to escape from the attractive surface regions. At low coverages, the longer time required for a projectile to collide with an adsorbate increases the efficiency of the electronic energy loss and, in turn, decreases the probability of recombination and desorption.

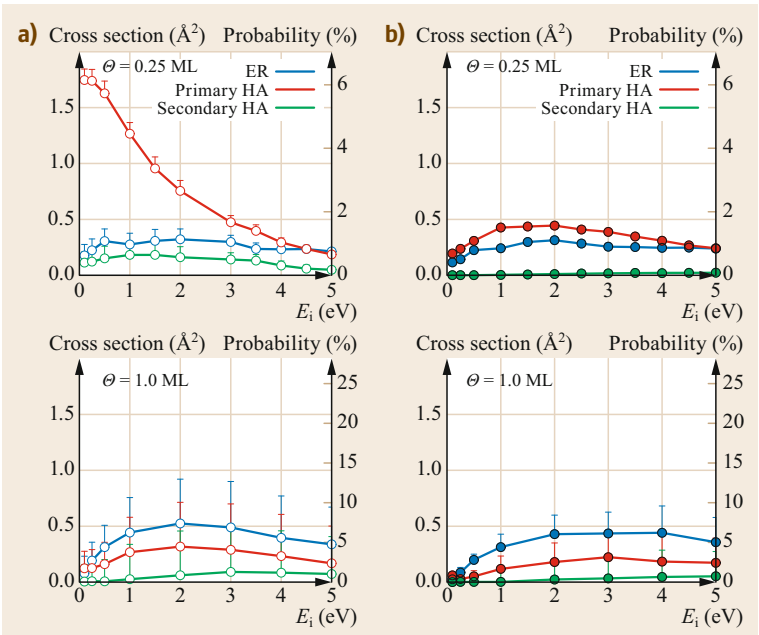

Fig. 28.21a,b ER and HA cross sections for H–H/W(110) calculated with **(a)** adiabatic BOSS [28.9] and **(b)** LDFA molecular dynamics simulations in [28.156] for H-coverages of 0.25 and 1.0 ML. *Error bars* indicate the uncertainties coming from the multiadsorbate CRP–interpolated PES

28.4.4 Femtosecond Laser-Induced Desorption

As described in Sect. 28.3.3, *Tully* and coworkers showed that the physics ruling the femtosecond laser-induced desorption of adsorbates from metal surfaces can be reasonably modeled by a Langevin-type equation in the case of UV/Vis lasers operating at large fluences, i.e., when desorption occurs via multiple electronic excitations (DIMET regime) [28.85, 86]. These early works simulated the laser-induced desorption of CO from Cu(100) using empirical potentials to describe the molecule–surface interaction. The recombinative desorption of H_2/D_2 from a saturated Ru(0001):H/D(1×1) surface was experimentally investigated in [28.157, 158] using 120−130 fs laser pulses at a wavelength centered ≈ 800 nm. Among their findings, the large isotope effect observed between the H_2 and D_2 desorption yields ($Y(H_2)/Y(D_2)$) that decreases from about a factor 22 to 5 as the laser fluence is roughly varied from 50 to 120 J/m^2 was particularly remarkable. As reported on other DIMET experiments, a nonlinear increase of yields with laser fluence was also observed. Other key observations were a clearly nonequal partitioning of the energy of desorbing particles into translation, vibration, and rotation, the linear increase of energies with fluence, a Maxwell–Boltzmann velocity distribution of desorbing particles with an unusually *hot* temperature, and a preference of helicopter versus cartwheel rotation. All these issues were studied by *Saalfrank* and coworkers using different level theories in [28.88, 159, 160]. Of interest for the present chapter devoted to the LDFA, it is remarkable the success of the 6-D molecular dynamics simulations performed in the context of the Langevin equation and the LDFA to account for the friction and random forces at each integration step [28.88]. The authors conclude that most of the experimental observations are actually consequence of the corrugated adiabatic PES. This conclusion notes first the importance of accounting for at least the degrees of freedom of the adsorbates (6-D), and second, that the recombination is a *low* nonadiabatic process in the sense that it is governed by low-energy electron excitations. These are the ideal working conditions under which the LDFA is particularly efficient, and it thus explains its adequacy in describing most of the experimental observations quantitatively.

Even if electrons are the driven agents in most of the fs-laser desorption systems studied, and, therefore, theoretical models have primarily focused on them, the recent theoretical study of [28.89] predicts that also the laser-excited phonons can contribute and rule the desorption process. Following the aforementioned works, *Lončarić* et al. treat the laser-induced surface excitation trough the 2TM [28.87] (Sect. 28.3.3), while the multidimensional dynamics of the adsorbates is described by a classical Langevin equation, in which the friction and random forces account for the action of the heated electrons, the latter being calculated with the LDFA as in [28.88]. The novelty of [28.89] is the additional use of the GLO model to also include the effect of the energy exchange between the molecule and the heated surface lattice in the desorption dynamics. The effect of the laser-induced excited phonons in photodesorption is compared with that of electronic excitations, taking the desorption of O_2 from Ag(110) as a case study. The system is theoretically appealing for this purpose, because DFT-PBE predicts the existence of the four distinct O_2 adsorption wells depicted in Fig. 28.22 that correspond to the molecule lying parallel to the surface at different heights Z from the surface, the latter being relevant because of the different surface-electron densities that the O atoms probe. In the 6-D (frozen surface) PES, the adsorption energies E_a, surface-electron density at the position of the O atom (given in terms of the electron mean radius r_s), and the geometries are as follows:

(i) The short-bridge site (SB) well with $E_a = -0.33$ eV and $r_s = 3.57$ a.u. has the molecular center of mass (CM) at $Z = 2.20$ Å over the short-bridge site with the molecular axis oriented along the $[1\bar{1}0]$-direction
(ii) The long-bridge site (LB) well with $E_a = -0.24$ eV, $r_s = 3.82$ a.u., and CM at $Z = 1.98$ Å over the long-bridge site is oriented along the [001]-direction
(iii) The H001 well with $E_a = -0.24$ eV, $r_s = 2.62$ a.u., and its CM at $Z = 1.29$ Å over the hollow site is oriented along the [001]-direction, and
(iv) The H110 well with $E_a = -0.21$ eV, $r_s = 2.57$ a.u., and CM at $Z = 1.09$ Å is also over the hollow site, but oriented along the $[1\bar{1}0]$-direction.

Figure 28.22 reproduces the theoretical desorption yields Y as a function of the laser fluence F for each adsorption well. In all cases, we observe the characteristic superlinear desorption yields ($Y = aF^n$ with $n > 1$) expected for multielectron excitations. For all the laser fluences considered, the highest desorption yields are obtained for H110, followed by H001, LB, and SB. The exponent n of the power law is also different for each well, its value decreasing from $n = 5.8$ for desorption from the SB well down to $n = 2.6$ for desorption from the H110 well. Both results can be mostly related to the differences in the adsorption energies of the dif-

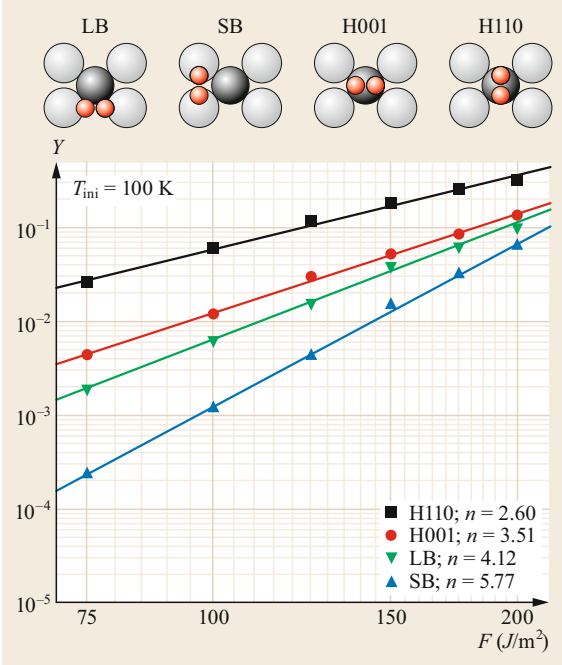

Fig. 28.22 Desorption yields Y as a function of the laser fluence F calculated in [28.89] for each of the O_2 adsorption wells that exists on Ag(110) (see *inset*). *Lines* are obtained by fitting each set of data to the equation $Y = aF^n$ (Reprinted with permission from [28.89]. Copyright (2016) by the American Physical Society)

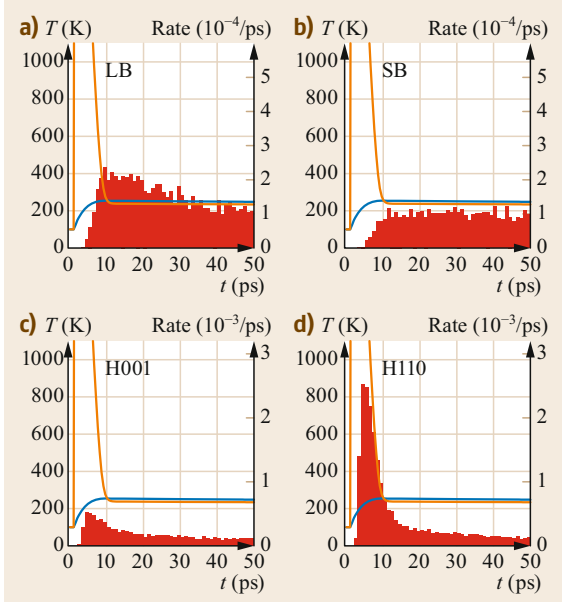

Fig. 28.23a–d Desorption rates (*right ordinate*) calculated for $F = 200\,\mathrm{J/m^2}$ and each adsorption well in [28.89] using a time interval of 1 ps. Electron (*orange line*) and phonon (*blue line*) temperatures calculated from the 2TM are also shown (*left ordinate*). Bridge wells: **(a)** LB, **(b)** SB; hollow wells: **(c)** H001, **(d)** H110 (Reprinted with permission from [28.89]. Copyright (2016) by the American Physical Society)

ferent wells. The highest desorption yield and lowest exponent correspond to the well with the lowest E_a and vice versa. However, the adsorption energy itself is not the only property ruling the desorption process. The LB and H001 wells have the same adsorption energy (−0.24 eV), but the yields are consistently larger for desorption from the H001 well than from the LB one. The authors showed by comparing the time dependence of T_e and T_{ph} as obtained from the 2TM to the desorption rates from each of the wells that this effect is related to the desorption process being, respectively, ruled by the laser-excited phonons and the laser-excited e–h pairs in the bridge and hollow wells. These results are shown in Fig. 28.23 for $F = 200\,\mathrm{J/m^2}$. There are remarkable differences between the bridge wells (LB and SB) and the hollow wells (H001 and H110) observed not only in the magnitude of the desorption rates, but also in their time evolution. While the desorption rates for the hollow wells seem to follow the time evolution of T_e—with a delay of around 3.5 ps though—, the desorption rates from the bridge sites are not much affected by the high increase of T_e at short times, and it is at longer times, once T_e and T_{ph} are equilibrated, when the desorption rates from LB and SB reach their highest values. It is worth to mentioning that the desorption rate from SB seems to follow the time evolution of T_{ph}, but also with a certain delay. All these observations suggest that while desorption from the hollow sites is mainly an electron-mediated effect, where the energy transfer from the electrons excited by the laser pulse to the adsorbed molecule plays a dominant role, its effect on desorption from the bridge sites is less relevant. In these cases, desorption seems to occur as a consequence of the laser-mediated phonon excitations. The authors further confirmed these ideas by performing additional calculations in which only the effect of either the heated electrons (LDFA with $T_e(t)$) or heated phonons (GLO with $T_{ph}(t)$) was included in the desorption dynamics. In the case of desorption from the hollow sites, the LDFA yields and rates were significantly larger than GLO ones, while the opposite behavior was observed for desorption from the bridge wells. The minor effect of the heated electrons on the bridge wells can be understood by realizing that the molecule on these wells is located at intermediate distances from the surface where the electron density is small (compare the aforementioned different r_s values probed by the O atoms at the different adsorption wells). The general predic-

tion that can be extracted from the theoretical analysis of [28.89] is that multiple electron excitations are, indeed, expected to be the main mechanism ruling fs-laser desorption in the case of chemisorbed species, while the laser-heated phonons will dominate in the case of physisorbed adsorbates.

28.5 Conclusion

In this chapter, we have reviewed recent developments based on the LDFA to study the effect of low-energy electronic excitations in elementary gas–surface processes. We have shown that the LDFA constitutes a valuable tool to incorporate such effects in multidimensional molecular dynamics calculations and that its flexibility has already allowed its implementation in AIMD simulations.

Several conclusions have been already made by the application of the LDFA to different gas–surface interaction problems. In the case of the scattering of hyperthermal molecules, such as N_2 or O_2 and atoms as N from metal surfaces, the contribution of the electronic excitations to the energy loss has been found to be very minor. In these cases, the energy loss is dominated by phonon excitations that take place as a result of the collision of the projectile with the surface. On the contrary, for the lighter H projectiles, phonon contribution to the energy loss is much reduced. Indeed, in this case, electronic excitations have been found to be the dominant mechanism, and the LDFA has successfully reproduced the energy loss measured.

Regarding dissociative adsorption of molecules at surfaces, two different scenarios can be distinguished. In the case of activated direct dissociation, electronic excitations reduce the adsorption probabilities, because the molecule loses part of its energy before arriving at the energy barrier that governs the process. However, since the time scale for this process is usually very short, the amount of energy loss is very reduced, and the adsorption probabilities remain nearly unchanged. A different picture arises in the case of indirect dissociation preceded by trapping of the molecule in the adsorption well. In this case, once the molecule is trapped it starts to lose energy efficiently by exciting e–h pairs. If from the bottom of the chemisorption well the barriers to desorption are on average larger than those of dissociation, energy loss favors the latter over the former, giving rise to an increase in the dissociative adsorption probabilities. Nevertheless, even in this case, the effect is usually very minor, because most of the dissociation is decided before the trapping of the molecule takes place.

Although the effect of electronic excitations in the adsorption probabilities is very minor, their role on the relaxation and thermalization of hot adsorbates at surfaces is very important. Depending on the mass ratio between the adsorbate and the surface atoms, phonon excitations or electronic excitations dominate the relaxation process. For instance, the relaxation of hot H adsorbates is fully dominated by the electronic excitations, while for N atoms and N_2 molecules, phonon excitations have been shown to be the dominant energy-dissipation channel. Nevertheless, it has been demonstrated that even in these phonon-dominated cases, the energy transferred to the electronic system during the relaxation process is substantial, since e–h pairs are responsible of the final accommodation in the adsorption wells.

Similar conclusions are extracted for Eley–Rideal and hot-atom recombinative abstraction processes occurring between gas-phase and adsorbed atoms at metal surfaces. Phonon excitations can substantially affect N–N recombination probabilities but can be safely neglected in the case of H–H recombination. On the contrary, electronic excitations have a large impact in H–H recombination probabilities but hardly affect N–N recombination. A remarkable result found recently is the dramatic reduction of the hot-atom mechanism for H–H recombination when electronic excitations are included at low coverages and low projectile-incidence energies.

Finally, we have shown how the LDFA can also be used to describe energy transfer from heated electrons to adsorbates at metal surfaces in terms of a classical Langevin equation. This has a direct application to the simulation of femtosecond laser-induced desorption of adsorbates at metal surfaces in the DIMET regime. Combination of the LDFA with the GLO method allows us to treat the coupling of the adsorbates to the laser-excited electrons and phonons. In this way, for instance, it has been shown that the desorption of O_2 from the Ag(110) surface can be governed by phonon or by electron excitations simultaneously, depending on the characteristics of the adsorption well in which the molecule is initially located. A natural future development in this field would be the implementation of the Langevin dynamics with heated electrons within the AIMDEF scheme. This would allow us to model laser induced desorption dynamics within AIMD for the first time, allowing for independent atom-surface movement. Such a methodology will represent an important step forward in the modelization and understanding of the photodesorption dynamics.

References

28.1 P. Nieto, E. Pijper, D. Barredo, G. Laurent, R.A. Olsen, E.-J. Baerends, G.-J. Kroes, D. Farías: Reactive and nonreactive scattering of H_2 from a metal surface is electronically adiabatic, Science **312**(5770), 86–89 (2006)

28.2 M. Alducin, R. Díez Muiño, H.F. Busnengo, A. Salin: Why N_2 molecules with thermal energy abundantly dissociate on W(100) and not on W(110), Phys. Rev. Lett. **97**, 056102 (2006)

28.3 C. Díaz, J.K. Vincent, G.P. Krishnamohan, R.A. Olsen, G.J. Kroes, K. Honkala, J.K. Nørskov: Multidimensional effects on dissociation of N_2 on Ru(0001), Phys. Rev. Lett. **96**(9), 096102 (2006)

28.4 C. Díaz, E. Pijper, R.A. Olsen, H.F. Busnengo, D.J. Auerbach, G.J. Kroes: Chemically accurate simulation of a prototypical surface reaction: H_2 dissociation on Cu(111), Science **326**(5954), 832–834 (2009)

28.5 A. Groß: Ab initio molecular dynamics simulations of the adsorption of H_2 on palladium surfaces, Chem. Phys. Chem. **11**(7), 1374–1381 (2010)

28.6 I. Goikoetxea, J. Beltrán, J. Meyer, J.I. Juaristi, M. Alducin, K. Reuter: Non-adiabatic effects during the dissociative adsorption of O_2 at Ag(111): A first-principles divide and conquer study, New J. Phys. **14**(1), 013050 (2012)

28.7 I. Goikoetxea, J.I. Juaristi, R. Díez Muiño, M. Alducin: Surface strain improves molecular adsorption but hampers dissociation for N_2 on the $\{Fe/W\}(110)$ surface, Phys. Rev. Lett. **113**, 066103 (2014)

28.8 M. Blanco-Rey, E. Díaz, G.A. Bocan, R. Díez Muiño, M. Alducin, J.I. Juaristi: Efficient N_2 formation on Ag(111) by Eley–Rideal recombination of hyperthermal atoms, J. Phys. Chem. Lett. **4**, 3704–3709 (2013)

28.9 R. Pétuya, P. Larregaray, C. Crespos, P. Aurel, H.F. Busnengo, A.E. Martínez: Scattering of atomic hydrogen off a H-covered W(110) surface: hot-atom versus Eley–Rideal abstraction dynamics, J. Phys. Chem. C **119**(6), 3171–3179 (2015)

28.10 R. Pétuya, M.A. Nosir, C. Crespos, R. Díez Muiño, P. Larregaray: Isotope effects in Eley–Rideal and hot-atom abstraction dynamics of hydrogen from tungsten (100) and (110) surfaces, J. Phys. Chem. C **119**(27), 15325–15332 (2015)

28.11 H.F. Busnengo, E. Pijper, G.J. Kroes, A. Salin: Rotational effects in dissociation of H_2 on Pd(111): quantum and classical study, J. Chem. Phys. **119**(23), 12553–12562 (2003)

28.12 K.R. Geethalakshmi, J.I. Juaristi, R. Díez Muiño, M. Alducin: Non-reactive scattering of N_2 from the W(110) surface studied with different exchange-correlation functionals, Phys. Chem. Chem. Phys. **13**, 4357–4364 (2011)

28.13 F. Nattino, C. Díaz, B. Jackson, G.-J. Kroes: Effect of surface motion on the rotational quadrupole alignment parameter of D_2 reacting on Cu(111), Phys. Rev. Lett. **108**, 236104 (2012)

28.14 I. Goikoetxea, J. Meyer, J.I. Juaristi, M. Alducin, K. Reuter: Role of physisorption states in molecular scattering: a semilocal density-functional theory study on O_2/Ag(111), Phys. Rev. Lett. **112**, 156101 (2014)

28.15 D. Farías, C. Díaz, P. Rivière, H.F. Busnengo, P. Nieto, M.F. Somers, G.J. Kroes, A. Salin, F. Martín: In-plane and out-of-plane diffraction of H_2 from metal surfaces, Phys. Rev. Lett. **93**, 246104 (2004)

28.16 D. Barredo, G. Laurent, C. Díaz, P. Nieto, H.F. Busnengo, A. Salin, D. Farías, F. Martín: Experimental evidence of dynamic trapping in the scattering of H_2 from Pd(110), J. Chem. Phys. **125**(5), 051101 (2006)

28.17 M. del Cueto, A.S. Muzas, G. Füchsel, F. Gatti, F. Martín, C. Díaz: Role of van der Waals forces in the diffraction of noble gases from metal surfaces, Phys. Rev. B **93**, 060301 (2016)

28.18 H. Nienhaus: Electronic excitations by chemical reactions on metal surfaces, Surf. Sci. Rep. **45**, 1 (2002)

28.19 M. Head-Gordon, J.C. Tully: Molecular dynamics with electronic frictions, J. Chem. Phys. **103**(23), 10137–10145 (1995)

28.20 J.R. Trail, D.M. Bird, M. Persson, S. Holloway: Electron–hole pair creation by atoms incident on a metal surface, J. Chem. Phys. **119**(8), 4539–4549 (2003)

28.21 A.C. Luntz, M. Persson: How adiabatic is activated adsorption/associative desorption?, J. Chem. Phys. **123**(7), 074704 (2005)

28.22 M. Lindenblatt, E. Pehlke: Ab Initio simulation of the spin transition during chemisorption: H/Al(111), Phys. Rev. Lett. **97**, 216101 (2006)

28.23 J.I. Juaristi, M. Alducin, R. Díez Muiño, H.F. Busnengo, A. Salin: Role of electron–hole pair excitations in the dissociative adsorption of diatomic molecules on metal surfaces, Phys. Rev. Lett. **100**(11), 116102 (2008)

28.24 N. Shenvi, S. Roy, J.C. Tully: Dynamical steering and electronic excitation in NO scattering from a gold surface, Science **326**, 829 (2009)

28.25 M. Timmer, P. Kratzer: Electron–hole spectra created by adsorption on metals from density functional theory, Phys. Rev. B **79**, 165407 (2009)

28.26 K. Schönhammer: Nonlinear friction in a homogenous electron gas: exact results, Phys. Rev. B **37**, 7735–7737 (1988)

28.27 A. Salin, A. Arnau, P.M. Echenique, E. Zaremba: Dynamic nonlinear screening of slow ions in an electron gas, Phys. Rev. B **59**, 2537–2548 (1999)

28.28 M. Quijada, A.G. Borisov, I. Nagy, R. Díez Muiño, P.M. Echenique: Time-dependent density-functional calculation of the stopping power for protons and antiprotons in metals, Phys. Rev. A **75**, 042902 (2007)

28.29 A.V. Krasheninnikov, Y. Miyamoto, D. Tománek: Role of electronic excitations in ion collisions with carbon nanostructures, Phys. Rev. Lett. **99**, 016104 (2007)

28.30 J.M. Pruneda, D. Sánchez-Portal, A. Arnau, J.I. Juaristi, E. Artacho: Electronic stopping power in LiF from first principles, Phys. Rev. Lett. **99**, 235501 (2007)

28.31 M. Ahsan Zeb, J. Kohanoff, D. Sánchez-Portal, A. Arnau, J.I. Juaristi, E. Artacho: Electronic stopping power in gold: the role of *d* electrons and the H/He anomaly, Phys. Rev. Lett. **108**, 225504 (2012)

28.32 A. Castro, M. Isla, J. Martíz, J.A. Alonso: Scattering of a proton with the Li_4 cluster: Nonadiabatic molecular dynamics description based on time-dependent density-functional theory, Chem. Phys. **399**, 130–134 (2012)

28.33 A. Lim, W.M.C. Foulkes, A.P. Horsfield, D.R. Mason, A. Schleife, E.W. Draeger, A.A. Correa: Electron elevator: excitations across the band gap via a dynamical gap state, Phys. Rev. Lett. **116**, 043201 (2016)

28.34 M. Grotemeyer, E. Pehlke: Electronic energy dissipation during scattering of vibrationally excited molecules at metal surfaces: *ab initio* simulations for HCl/Al(111), Phys. Rev. Lett. **112**, 043201 (2014)

28.35 C. Cohen-Tannoudji, B. Diu, F. Laloë: *Quantum Mechanics* (Wiley, New York 1977)

28.36 B.H. Bransden, C.J. Joachain: *Physics of Atoms and Molecules*, 2nd edn. (Pearson Education Limited, Harlow 2003)

28.37 P.M. Echenique, R.M. Nieminen, R.H. Ritchie: Density functional calculation of stopping power of an electron gas for slow ions, Solid State Commun. **37**(10), 779–781 (1981)

28.38 P.M. Echenique, R.M. Nieminen, J.C. Ashley, R.H. Ritchie: Nonlinear stopping power of an electron gas for slow ions, Phys. Rev. A **33**, 897–904 (1986)

28.39 R. Díez Muiño, A. Salin: Energy and angular momentum transfer in the excitation of electron–hole pairs by slow dimers, Phys. Rev. B **62**, 5207–5215 (2000)

28.40 M. Blanco-Rey, J.I. Juaristi, R. Díez Muiño, H.F. Busnengo, G.J. Kroes, M. Alducin: Electronic friction dominates hydrogen hot-atom relaxation on Pd(100), Phys. Rev. Lett. **112**, 103203 (2014)

28.41 D. Novko, M. Blanco-Rey, J.I. Juaristi, M. Alducin: Ab initio molecular dynamics with simultaneous electron and phonon excitations: application to the relaxation of hot atoms and molecules on metal surfaces, Phys. Rev. B **92**, 201411 (2015)

28.42 D. Novko, M. Blanco-Rey, M. Alducin, J.I. Juaristi: Surface electron density models for accurate ab initio molecular dynamics with electronic friction, Phys. Rev. B **93**, 245435 (2016)

28.43 D. Novko, M. Blanco-Rey, J.I. Juaristi, M. Alducin: Energy loss in gas-surface dynamics: electron–hole pair and phonon excitation upon adsorbate relaxation, Nucl. Instrum. Methods B **382**, 26–31 (2016)

28.44 A. Mann, W. Brandt: Material dependence of low-velocity stopping powers, Phys. Rev. B **24**, 4999–5003 (1981)

28.45 J.H. Ormrod, H.E. Duckworth: Stopping cross sections in carbon for low-energy atoms with Z less than 12, Can. J. Phys. **41**(9), 1424–1442 (1963)

28.46 J.H. Ormrod, J.R. Macdonald, H.E. Duckworth: Some low-energy atomic stopping cross sections, Can. J. Phys. **43**(2), 275–284 (1965)

28.47 D. Ward, H.R. Andrews, I.V. Mitchell, W.N. Lennard, R.B. Walker, N. Rud: Systematics for the Z1-oscillation in stopping powers of various solid materials, Can. J. Phys. **57**(5), 645–656 (1979)

28.48 G. Höberg: Electronic and nuclear stopping cross sections in carbon for light mass ions of 4.5 to 46 keV energy, Phys. Status Solidi (b) **48**(2), 829–841 (1971)

28.49 F.H. Eisen: Channeling of medium-mass ions through silicon, Can. J. Phys. **46**(6), 561–572 (1968)

28.50 J. Böttiger, F. Bason: Energy loss of heavy ions along low-index directions in gold single crystals, Radiat. Eff. **2**(2), 105–110 (1969)

28.51 I. Nagy, A. Arnau, P.M. Echenique: Nonlinear stopping power and energy-loss straggling of an interacting electron gas for slow ions, Phys. Rev. A **40**, 987–994 (1989)

28.52 P.M. Echenique, A. Arnau, M. Penalba, I. Nagy: Stopping power of low velocity ions in solids, Nucl. Instrum. Methods B **56**, 345–347 (1991)

28.53 H. Winter: Collisions of atoms and ions with surfaces under grazing incidence, Phys. Rep. **367**(5), 387–582 (2002)

28.54 K. Kimura, M. Hasegawa, M.-H. Mannami: Energy loss of MeV light ions specularly reflected from a SnTe(001) surface, Phys. Rev. B **36**, 7–12 (1987)

28.55 J.I. Juaristi, F.J. García de Abajo: Energy loss in grazing proton-surface collisions, Nucl. Instrum. Methods B **90**(1), 252–256 (1994)

28.56 J.I. Juaristi, F.J. García de Abajo, P.M. Echenique: Energy loss of MeV protons specularly reflected from metal surfaces, Phys. Rev. B **53**, 13839–13850 (1996)

28.57 M.A. Cazalilla, J.I. Juaristi: Energy loss of fast protons specularly reflected from metal surfaces, Nucl. Instrum. Methods B **157**(1–4), 104–109 (1999)

28.58 M. Alducin, V.M. Silkin, J.I. Juaristi, E.V. Chulkov: Effect of surface band structure in the energy loss of ions at surfaces, Nucl. Instrum. Methods B **193**(1–4), 585–589 (2002)

28.59 M. Alducin, V.M. Silkin, J.I. Juaristi, E.V. Chulkov: Energy loss of ions at metal surfaces: band-structure effects, Phys. Rev. A **67**, 032903 (2003)

28.60 M. Alducin, J.I. Juaristi: Energy loss in the interaction of atomic particles with solid surfaces. In: *Theory of the Interaction of Swift Ions with Matter. Part 1*, Advances in Quantum Chemistry, Vol. 45, ed. by J.R. Sabin, E. Brandas (Elsevier, San Diego 2004) pp. 223–245

28.61 J.I. Juaristi: Energy loss of ions interacting with metal surfaces, Nucl. Instrum. Methods B **230**(1–4), 148–157 (2005)

28.62 A. Robin, W. Heiland, J. Jensen, J.I. Juaristi, A. Arnau: Channeling effects observed in energy-loss

spectra of nitrogen ions scattered off a Pt(110) surface, Phys. Rev. A **64**, 052901 (2001)
28.63 A. Robin, M. Reiniger, A. Närmann, M. Schleberger, J.I. Juaristi, W. Heiland: Trajectory straggling and nonlinear effects in the energy loss of surface-channeled ions, Phys. Rev. B **67**, 165409 (2003)
28.64 J.I. Juaristi, A. Arnau, P.M. Echenique, C. Auth, H. Winter: Charge state dependence of the energy loss of slow ions in metals, Phys. Rev. Lett. **82**, 1048–1051 (1999)
28.65 J.I. Juaristi, A. Arnau, P.M. Echenique, C. Auth, H. Winter: Charge state dependence of the energy loss of slow nitrogen ions reflected from an aluminum surface under grazing incidence, Nucl. Instrum. Methods B **157**(1–4), 87–91 (1999)
28.66 H. Winter, J.I. Juaristi, I. Nagy, A. Arnau, P.M. Echenique: Energy loss of slow ions in a nonuniform electron gas, Phys. Rev. B **67**, 245401 (2003)
28.67 A. Groß, M. Bockstedte, M. Scheffler: *Ab initio* molecular dynamics study of the desorption of D_2 from Si(100), Phys. Rev. Lett. **79**, 701–704 (1997)
28.68 A. Groß: Reactions at surfaces studied by ab initio dynamics calculations, Surf. Sci. Rep. **32**(8), 291–340 (1998)
28.69 H.F. Busnengo, A. Salin, W. Dong: Representation of the 6D potential energy surface for diatomic molecule near a solid surface, J. Chem. Phys. **112**(17), 7641–7651 (2000)
28.70 J. Ischtwan, M.A. Collins: Molecular potential energy surfaces by interpolation, J. Chem. Phys. **100**(11), 8080–8088 (1994)
28.71 S. Lorenz, M. Scheffler, A. Groß: Descriptions of surface chemical reactions using a neural network representation of the potential-energy surface, Phys. Rev. B **73**(11), 115431 (2006)
28.72 J. Behler, S. Lorenz, K. Reuter: Representing molecule-surface interactions with symmetry-adapted neural networks, J. Chem. Phys. **127**(1), 014705 (2007)
28.73 B. Hellsing, M. Persson: Electronic damping of atomic and molecular vibrations at metal surfaces, Phys. Scr. **29**(4), 360 (1984)
28.74 J.R. Trail, M.C. Graham, D.M. Bird: Electronic damping of molecular motion at metal surfaces, Comput. Phys. Commun. **137**, 163 (2001)
28.75 Y. Li, G. Wahnström: Nonadiabatic effects in hydrogen diffusion in metals, Phys. Rev. Lett. **68**, 3444–3447 (1992)
28.76 J.E. Valdés, P. Vargas, L. Guillemot, V.A. Esaulov: Effect of oxygen adsorption on the energy losses in grazing scattering of hydrogen ions on Ag(110), Nucl. Instrum. Methods B **256**(1), 81–85 (2007)
28.77 J.E. Valdés, P. Vargas, C. Celedón, E. Sánchez, L. Guillemot, V.A. Esaulov: Electronic density corrugation and crystal azimuthal orientation effects on energy losses of hydrogen ions in grazing scattering on a Ag(110) surface, Phys. Rev. A **78**, 032902 (2008)
28.78 L. Chen, J.E. Valdés, P. Vargas, V.A. Esaulov: Surface channelling and energy losses of 4 keV hydrogen and fluorine ions in grazing scattering on Au(111) and missing row reconstructed Au(110) surfaces, J. Phys. Condens. Matter **22**(34), 345005 (2010)
28.79 L. Chen, J. Shen, J.E. Valdés, P. Vargas, V.A. Esaulov: Energy loss of keV fluorine ions scattered off a missing-row reconstructed Au(110) surface under grazing incidence, Phys. Rev. A **83**, 032901 (2011)
28.80 L. Chen, J.E. Valdés, P. Vargas, J. Shen, V.A. Esaulov: Energy losses of H and F ions in grazing scattering on a missing row reconstructed Au(110) surface, Phys. Scr. **2011**(T144), 014042 (2011)
28.81 S.A. Adelman, J.D. Doll: Generalized Langevin equation approach for atom/solid-surface scattering: general formulation for classical scattering off harmonic solids, J. Chem. Phys. **64**(6), 2375–2388 (1976)
28.82 J.C. Tully: Dynamics of gas–surface interactions: 3D generalized Langevin model applied to fcc and bcc surfaces, J. Chem. Phys. **73**(4), 1975–1985 (1980)
28.83 M. Alducin, R. Díez Muiño, J.I. Juaristi: Energy dissipation channels in reactive and non-reactive scattering at surfaces. In: *Dynamics of Gas-Surface Interactions: Atomic-level Understanding of Scattering Processes at Surfaces*, Springer Series in Surface Sciences, Vol. 50, ed. by R. Díez Muiño, H.F. Busnengo (Springer, Berlin, Heidelberg 2013) pp. 371–388
28.84 P. Saalfrank: Quantum dynamical approach to ultrafast molecular desorption from surfaces, Chem. Rev. **106**(10), 4116–4159 (2006)
28.85 C. Springer, M. Head-Gordon, J.C. Tully: Simulations of femtosecond laser-induced desorption of CO from Cu(100), Surf. Sci. **320**(1/2), L57–L62 (1994)
28.86 C. Springer, M. Head-Gordon: Simulations of the femtosecond laser-induced desorption of CO from Cu(100) at 0.5 ML coverage, Chem. Phys. **205**(1/2), 73–89 (1996)
28.87 S.I. Anisimov, B.L. Perel'man Kapeliovich: Electron emission from metal surfaces exposed to ultrashort laser pulses, Sov. Phys. JETP **39**, 375 (1974)
28.88 G. Füchsel, T. Klamroth, S. Monturet, P. Saalfrank: Dissipative dynamics within the electronic friction approach: the femtosecond laser desorption of H_2/D_2 from Ru(0001), Phys. Chem. Chem. Phys. **13**, 8659–8670 (2011)
28.89 I. Lončarić, M. Alducin, P. Saalfrank, J.I. Juaristi: Femtosecond-laser-driven molecular dynamics on surfaces: Photodesorption of molecular oxygen from Ag(110), Phys. Rev. B **93**, 014301 (2016)
28.90 I. Lončarić, M. Alducin, P. Saalfrank, J.I. Juaristi: Femtosecond laser pulse induced desorption: a molecular dynamics simulation, Nucl. Instrum. Methods B **382**, 114–118 (2016)
28.91 R. Scholz, G. Floß, P. Saalfrank, G. Füchsel, I. Lončarić, J.I. Juaristi: Femtosecond-laser induced dynamics of CO on Ru(0001): deep insights from a hot-electron friction model including surface motion, Phys. Rev. B **94**, 165447 (2016)

28.92 G. Kresse, J. Furthmüller: Efficiency of ab-initio total energy calculations for metals and semiconductors using a plane-wave basis set, Comput. Mater. Sci. **6**(1), 15–50 (1996)

28.93 G. Kresse, J. Furthmüller: Efficient iterative schemes for ab initio total-energy calculations using a plane-wave basis set, Phys. Rev. B **54**, 11169–11186 (1996)

28.94 P. Saalfrank, J.I. Juaristi, M. Alducin, M. Blanco-Rey, R. Díez Muiño: Vibrational lifetimes of hydrogen on lead films: an ab initio molecular dynamics with electronic friction (AIMDEF) study, J. Chem. Phys. **141**(23), 234702 (2014)

28.95 F.L. Hirshfeld: Bonded-atom fragments for describing molecular charge densities, Theoret. Chim. Acta **44**, 129 (1977)

28.96 S.P. Rittmeyer, J. Meyer, J.I. Juaristi, K. Reuter: Electronic friction-based vibrational lifetimes of molecular adsorbates: beyond the independent-atom approximation, Phys. Rev. Lett. **115**, 046102 (2015)

28.97 J.F. Ziegler, J.P. Biersack: *The Stopping and Range of Ions in Matter* (Springer, Boston 1985)

28.98 P. Bauer, F. Kastner, A. Arnau, A. Salin, P.D. Fainstein, V.H. Ponce, P.M. Echenique: Phase effect in the energy loss of H projectiles in Zn targets: experimental evidence and theoretical explanation, Phys. Rev. Lett. **69**, 1137–1139 (1992)

28.99 D. Goebl, K. Khalal-Kouache, D. Roth, E. Steinbauer, P. Bauer: Energy loss of low-energy ions in transmission and backscattering experiments, Phys. Rev. A **88**, 032901 (2013)

28.100 L. Martin-Gondre, M. Alducin, G.A. Bocan, R. Díez Muiño, J.I. Juaristi: Competition between electron and phonon excitations in the scattering of nitrogen atoms and molecules off tungsten and silver metal surfaces, Phys. Rev. Lett. **108**, 096101 (2012)

28.101 T.F. Hanisco, A.C. Kummel: Rotationally inelastic scattering of N_2 from W(110), J. Vac. Sci. Technol. A **11**(4), 1907–1913 (1993)

28.102 A.W. Kleyn: Molecular beams and chemical dynamics at surfaces, Chem. Soc. Rev. **32**, 87–95 (2003)

28.103 R.D. Beck, A.L. Utz: Quantum-state resolved gas/surface reaction dynamics experiments. In: *Dynamics of Gas-Surface Interactions: Atomic-level Understanding of Scattering Processes at Surfaces*, Springer Series in Surface Sciences, Vol. 50, ed. by R. Díez Muiño, H.F. Busnengo (Springer, Berlin, Heidelberg 2013) pp. 179–212

28.104 D. Farías, R. Miranda: Thermal energy atomic and molecular beam diffraction from solid surfaces. In: *Dynamics of Gas-Surface Interactions: Atomic-level Understanding of Scattering Processes at Surfaces*, Springer Series in Surface Sciences, Vol. 50, ed. by R. Díez Muiño, H.F. Busnengo (Springer, Berlin, Heidelberg 2013) pp. 51–73

28.105 L. Vattuone, G. Bracco, M. Smerieri, L. Savio, M. Rocca: Supersonic molecular beam studies of surfaces. In: *Dynamics of Gas–Surface Interactions: Atomic-level Understanding of Scattering Processes at Surfaces*, Springer Series in Surface Sciences, Vol. 50, ed. by R. Díez Muiño, H.F. Busnengo (Springer, Berlin, Heidelberg 2013) pp. 1–23

28.106 G.O. Sitz: Gas surface interactions studied with state-prepared molecules, Rep. Prog. Phys. **65**(8), 1165 (2002)

28.107 M.P. Schmid, P. Maroni, R.D. Beck, T.R. Rizzo: Molecular-beam/surface-science apparatus for state-resolved chemisorption studies using pulsed-laser preparation, Rev. Sci. Instrum. **74**(9), 4110–4120 (2003)

28.108 A.M. Wodtke, D. Matsiev, D.J. Auerbach: Energy transfer and chemical dynamics at solid surfaces: the special role of charge transfer, Prog. Surf. Sci. **83**(3), 167–214 (2008)

28.109 L.B.F. Juurlink, D.R. Killelea, A.L. Utz: State-resolved probes of methane dissociation dynamics, Prog. Surf. Sci. **84**(3/4), 69–134 (2009)

28.110 L. Vattuone, L. Savio, F. Pirani, D. Cappelletti, M. Okada, M. Rocca: Interaction of rotationally aligned and of oriented molecules in gas phase and at surfaces, Prog. Surf. Sci. **85**(1–4), 92–160 (2010)

28.111 I. Goikoetxea, J.I. Juaristi, M. Alducin, R. Díez Muiño: Dissipative effects in the dynamics of N_2 on tungsten surfaces, J. Phys. Condens. Matter **21**(26), 264007 (2009)

28.112 J. Kimman, C.T. Rettner, D.J. Auerbach, J.A. Barker, J.C. Tully: Correlation between kinetic-energy transfer to rotation and to phonons in gas-surface collisions of NO with Ag(111), Phys. Rev. Lett. **57**(16), 2053–2056 (1986)

28.113 A. Raukema, R.J. Dirksen, A.W. Kleyn: Probing the (dual) repulsive wall in the interaction of O_2, N_2, and Ar with the Ag(111) surface, J. Chem. Phys. **103**(14), 6217–6231 (1995)

28.114 B. Baule: Theoretische Behandlung der Erscheinungen in verdünnten Gasen, Ann. Phys. **44**, 145 (1914)

28.115 J. Meyer, K. Reuter: Electron–hole pairs during the adsorption dynamics of O_2 on Pd(100): exciting or not?, New J. Phys. **13**(8), 085010 (2011)

28.116 J. Meyer, K. Reuter: Modeling heat dissipation at the nanoscale: an embedding approach for chemical reaction dynamics on metal surfaces, Angew. Chem. Int. Ed. **53**(18), 4721–4724 (2014)

28.117 A. Groß: Dynamics of molecule–surface interactions from first principles. In: *Surface Dynamics*, The Chemical Physics of Solid Surfaces, Vol. 11, ed. by D.P. Woodruff (Elsevier, Amsterdam 2003) pp. 1–26

28.118 G.J. Kroes, C. Díaz, E. Pijper, R.A. Olsen, D.J. Auerbach: Apparent failure of the Born–Oppenheimer static surface model for vibrational excitation of molecular hydrogen on copper, Proc. Natl. Acad. Sci. U. S. A. **107**(49), 20881–20886 (2010)

28.119 G.-J. Kroes, C. Diaz: Quantum and classical dynamics of reactive scattering of H_2 from metal surfaces, Chem. Soc. Rev. **45**, 3658–3700 (2016)

28.120 A.S. Muzas, J.I. Juaristi, M. Alducin, R. Díez Muiño, G.J. Kroes, C. Díaz: Vibrational deexcitation and rotational excitation of H_2 and D_2 scattered from

Cu(111): adiabatic versus non-adiabatic dynamics, J. Chem. Phys. **137**(6), 064707 (2012)
28.121 A. Hodgson, P. Samson, A. Wight, C. Cottrell: Rotational excitation and vibrational relaxation of $H_2(\upsilon = 1, J = 0)$ scattered from Cu(111), Phys. Rev. Lett. **78**, 963–966 (1997)
28.122 E. Watts, G.O. Sitz: State-to-state scattering in a reactive system: H_2(v=1,J=1) from Cu(100), J. Chem. Phys. **114**, 4171 (2001)
28.123 L.C. Shackman, G.O. Sitz: State-to-state scattering of D2 from Cu(100) and Pd(111), J. Chem. Phys. **123**, 064712 (2005)
28.124 H. Ueta, M.A. Gleeson, A.W. Kleyn: Scattering of hyperthermal nitrogen atoms from the Ag(111) surface, J. Phys. Chem. A **113**(52), 15092–15099 (2009)
28.125 L. Martin-Gondre, G.A. Bocan, M. Blanco-Rey, M. Alducin, J.I. Juaristi, R. Díez Muiño: Scattering of nitrogen atoms off Ag(111) surfaces: a theoretical study, J. Phys. Chem. C **117**, 9779–9790 (2013)
28.126 M. Pavanello, D.J. Auerbach, A.M. Wodtke, M. Blanco-Rey, M. Alducin, G.J. Kroes: Adiabatic energy loss in hyperthermal H atom collisions with Cu and Au: a basis for testing the importance of nonadiabatic energy loss, J. Phys. Chem. Lett. **4**, 3735 (2013)
28.127 G.-J. Kroes, M. Pavanello, M. Blanco-Rey, M. Alducin, D.J. Auerbach: Ab initio molecular dynamics calculations on scattering of hyperthermal H atoms from Cu(111) and Au(111), J. Chem. Phys. **141**(5), 054705 (2014)
28.128 S.M. Janke, D.J. Auerbach, A.M. Wodtke, A. Kandratsenka: An accurate full-dimensional potential energy surface for H/Au(111): importance of nonadiabatic electronic excitation in energy transfer and adsorption, J. Chem. Phys. **143**(12), 124708 (2015)
28.129 O. Bünermann, H. Jiang, Y. Dorenkamp, A. Kandratsenka, S.M. Janke, D.J. Auerbach, A.M. Wodtke: Electron–hole pair excitation determines the mechanism of hydrogen atom adsorption, Science **350**(6266), 1346–1349 (2015)
28.130 G.A. Bocan, R. Díez Muiño, M. Alducin, H.F. Busnengo, A. Salin: The role of exchange-correlation functionals in the potential energy surface and dynamics of N_2 dissociation on W surfaces, J. Chem. Phys. **128**(15), 154704 (2008)
28.131 M. Wijzenbroek, D.M. Klein, B. Smits, M.F. Somers, G.-J. Kroes: Performance of a non-local van der Waals density functional on the dissociation of H_2 on metal surfaces, J. Phys. Chem. A **119**(50), 12146–12158 (2015)
28.132 L. Martin-Gondre, J.I. Juaristi, M. Blanco-Rey, R. Díez Muiño, M. Alducin: Influence of the van der Waals interaction in the dissociation dynamics of N_2 on W(110) from first principles, J. Chem. Phys. **142**(7), 074704 (2015)
28.133 B. Jiang, M. Alducin, H. Guo: Electron–hole pair effects in polyatomic dissociative chemisorption: water on Ni(111), J. Phys. Chem. Lett. **7**(2), 327–331 (2016)
28.134 X. Luo, B. Jiang, J.I. Juaristi, M. Alducin, H. Guo: Electron–hole pair effects in methane dissociative chemisorption on Ni(111), J. Chem. Phys. **145**(4), 044704 (2016)
28.135 R.D. Beck, P. Maroni, D.C. Papageorgopoulos, T.T. Dang, M.P. Schmid, T.R. Rizzo: Vibrational mode-specific reaction of methane on a nickel surface, Science **302**(5642), 98–100 (2003)
28.136 D.R. Killelea, V.L. Campbell, N.S. Shuman, A.L. Utz: Bond-selective control of a heterogeneously catalyzed reaction, Science **319**(5864), 790–793 (2008)
28.137 P.M. Hundt, B. Jiang, M.E. van Reijzen, H. Guo, R.D. Beck: Vibrationally promoted dissociation of water on Ni(111), Science **344**(6183), 504–507 (2014)
28.138 B. Gergen, H. Nienhaus, W.H. Weinberg, E.W. McFarland: Chemically induced electronic excitations at metal surfaces, Science **294**, 2521 (2001)
28.139 B. Schindler, D. Diesing, E. Hasselbrink: Electronic excitations induced by hydrogen surface chemical reactions on gold, J. Chem. Phys. **134**(3), 034705 (2011)
28.140 L. Martin-Gondre, G.A. Bocan, M. Alducin, J.I. Juaristi, R. Díez Muiño: Energy dissipation channels in the adsorption of N on Ag(111), Comput. Theor. Chem. **990**(0), 126–131 (2012)
28.141 A. Groß: Ab initio molecular dynamics study of hot atom dynamics after dissociative adsorption of H_2 on Pd(100), Phys. Rev. Lett. **103**, 246101 (2009)
28.142 G. Ertl: Reactions at surfaces: from atoms to complexity (Nobel lecture), Angew. Chem. Int. Ed. **47**(19), 3524–3535 (2008)
28.143 I. Langmuir: Part II. Heterogeneous reactions. Chemical reactions on surfaces, Trans. Faraday Soc. **17**, 607–620 (1922)
28.144 D.D. Eley, E.K. Rideal: Parahydrogen conversion on tungsten, Nature **146**, 401–402 (1940)
28.145 D.D. Eley, E.K. Rideal: The catalysis of the parahydrogen conversion by tungsten, Proc. R. Soc. A **178**, 429–451 (1941)
28.146 D.D. Eley: The interchange of hydrogen in the adsorbed film on tungsten, Proc. R. Soc. A **178**, 452–464 (1941)
28.147 O. Galparsoro, R. Pétuya, J.I. Juaristi, C. Crespos, M. Alducin, P. Larregaray: Energy dissipation to tungsten surfaces upon Eley-Rideal recombination of N_2 and H_2, J. Phys. Chem. C **119**(27), 15434 (2015)
28.148 B. Freiesleben Hansen, G.D. Billing: Hydrogen and deuterium recombination rates on a copper surface, Surf. Sci. **373**(1), L333–L338 (1997)
28.149 T. Kammler, J. Kuppers: Interaction of H atoms with Cu(111) surfaces: adsorption, absorption, and abstraction, J. Chem. Phys. **111**(17), 8115–8123 (1999)
28.150 S. Shimokawa, A. Namiki, M.N. Gamo, T. Ando: Temperature dependence of atomic hydrogen-induced surface processes on Ge(100): thermal desorption, abstraction, and collision-induced desorption, J. Chem. Phys. **113**(16), 6916–6925 (2000)
28.151 Z.B. Guvenc, X. Sha, B. Jackson: The effects of lattice motion on Eley–Rideal and hot atom reactions: quasiclassical studies of hydrogen re-

combination on Ni(100), J. Phys. Chem. B **106**(33), 8342–8348 (2002)
28.152 M. Cacciatore, E. Christoffersen, M. Rutigliano: Adsorption site and surface temperature effects in CO formation on Pt(111): a new semiclassical study, J. Phys. Chem. A **108**(41), 8810–8818 (2004)
28.153 M. Rutigliano, M. Cacciatore: Isotope and surface temperature effects for hydrogen recombination on a graphite surface, Chem. Phys. Chem. **9**(1), 171–181 (2008)
28.154 E. Quintas-Sanchez, C. Crespos, P. Larregaray, J.-C. Rayez, L. Martin-Gondre, J. Rubayo-Soneira: Surface temperature effects on the dynamics of N_2 Eley–Rideal recombination on W(100), J. Chem. Phys. **138**(2), 024706 (2013)
28.155 R. Pétuya, C. Crespos, E. Quintas-Sánchez, P. Larregaray: Comparative theoretical study of H_2 Eley–Rideal recombination dynamics on W(100) and W(110), J. Phys. Chem. C **118**(22), 11704–11710 (2014)
28.156 O. Galparsoro, R. Pétuya, J.I. Juaristi, C. Crespos, M. Alducin, P. Larregaray: Hydrogen abstraction from metals surface: when electron–hole pair excitations strongly affect hot-atom recombination, Phys. Chem. Chem. Phys. **18**, 31378–31383 (2016)
28.157 D.N. Denzler, C. Frischkorn, C. Hess, M. Wolf, G. Ertl: Electronic excitation and dynamic promotion of a surface reaction, Phys. Rev. Lett. **91**, 226102 (2003)
28.158 S. Wagner, C. Frischkorn, M. Wolf, M. Rutkowski, H. Zacharias, A.C. Luntz: Energy partitioning in the femtosecond-laser-induced associative D_2 desorption from Ru(0001), Phys. Rev. B **72**, 205404 (2005)
28.159 T. Vazhappilly, T. Klamroth, P. Saalfrank: Femtosecond-laser desorption of H_2 (D_2) from Ru(0001): quantum and classical approaches, J. Phys. Chem. C **113**, 7790–7801 (2009)
28.160 G. Füchsel, T. Klamroth, J.C. Tremblay, P. Saalfrank: Stochastic approach to laser-induced ultrafast dynamics: the desorption of H_2/D_2 from Ru(0001), Phys. Chem. Chem. Phys. **12**, 14082–14094 (2010)

Maite Alducin

Centro de Física de Materiales CFM/MPC (CSIC-UPV/EHU)
Donostia-San Sebastián, Spain
maite.alducin@ehu.eus

Maite Alducin obtained her PhD degree in Physics from Euskal Herriko Unibertsitatea (UPV/EHU). In 2007, she obtained a permanent position as CSIC researcher in Centro de Física de Materiales (CFM) in Donostia-San Sebastián. Her initial research focused on linear response theory and charge transfer processes of ions at metals. At present, her research is mainly focused on gas–surface reactive dynamics with a special interest in nonadiabatic effects at metal surfaces.

Ricardo Díez Muiño

Centro de Física de Materiales CFM/MPC (CSIC-UPV/EHU)
Donostia-San Sebastián, Spain
rdm@ehu.eus

Ricardo Díez Muiño received his PhD from Euskal Herriko Unibertsitatea (UPV/EHU) in Donostia-San Sebastián. In 2003, he obtained a permanent position as CSIC researcher in Centro de Física de Materiales (CFM). In addition to his position at CFM, he is Director of DIPC. His main fields of research are condensed matter theory and chemical physics, in particular the theory of electronic excitations in metallic systems, and atomic and molecular physics.

J. Iñaki Juaristi

Depto de Física de Materiales
Facultad de Químicas UPV/EHU
Donostia-San Sebastián, Spain
josebainaki.juaristi@ehu.eus

Joseba Iñaki Juaristi obtained his PhD degree in Physics (1996) from Euskal Herriko Unibertsitatea (UPV/EHU), where he became Tenured Professor in 2001. His initial research focused on the theoretical study of the electronic excitations generated in the interaction of atomic particles with metals and their surfaces. His research currently focuses on the modelization of gas–surface interactions, with special attention paid to the role played by electronic excitations in the dynamics.

29. Self-assembly of Organic Molecules at Metal Surfaces

Gianangelo Bracco, Marco Smerieri, Letizia Savio

Adsorption and self-assembly of organic molecules at surfaces is a key issue in nanoscience and nanotechnology for the many possible uses of hybrid organic–inorganic interfaces. Depending on the nature of the molecules, applications are foreseen in the fields of molecular electronics, sensoristics, pharmacology, biocompatibility, hygiene and biofouling. As a consequence, there has been a large effort in the last few years to determine the structure of the layers and to unravel the mechanisms at the basis of the self-assembly process.

In Sect. 29.1 we describe the different possibilities of self-assembly at metal surfaces. For sake of clarity, we group the different examples depending on the category of molecules which are employed. Section 29.2 will deal with covalent bonding and formation of organometallic compounds starting from hydrocarbon precursors. Section 29.3 will be dedicated to noncovalent bonding and divided into three subsections devoted, respectively, to π-conjugated systems, to the formation of self-assembled monolayers of thiols and to small biological molecules, mainly amino acids (Sect. 29.3.3), at surfaces.

29.1 Molecular Engineering of Surfaces

The characterization of the physical–chemical interactions at the hybrid organic–inorganic interface and the assembly mechanisms of the so-called hybrid nanocomposites is a major challenge in nanoscience. In fact, depending on the nature of the molecule, many possible applications are foreseen in several fields of science and engineering. Large aromatic compounds are particularly interesting for their use in nanoelectronics [29.1, 2], sensoristics and, if coupled with a suitable metal atom in an organometallic compound, for nanocatalysis and spintronics. On the other hand, clarifying the interaction of small biological molecules as amino acids and peptides with metal and oxide surfaces is mandatory to gain useful insight for the possible use of such systems in pharmacology applications [29.3], to solve biocompatibility issues and to prevent fouling and biocorrosion phenomena. Finally, we remark that the presence of an organic layer can modify the interfacial properties of the surface on which it is deposited, for instance by changing the reactivity of surface atoms or behaving as an electrically insulating film. Therefore, solid surfaces coated with an organic self-assembled monolayer (SAM) can present well-defined properties: SAMs provide a convenient, flexible, and simple way to tailor the interfacial properties of metals, metal oxides, and semiconductors.

Molecular engineering is an important field of research in nanoscience, since the accurate control of the position, electronic properties, intermolecular interactions and molecule–substrate interface of functional molecules is fundamental for molecular electronics [29.4]. Several techniques for the construction of well-defined molecular architectures have been developed so far, e.g., manipulation, nanofabrication and nanolithography [29.5–7]. Exploiting the spontaneous assembly of the molecular units on suitable surfaces or nanoparticles is of course a simple and advantageous method to realize low-dimensional quantum-confined

M. Rocca, T.S. Rahman, L. Vattuone (Eds.), *Springer Handbook of Surface Science*, Springer Handbooks,
https://doi.org/10.1007/978-3-030-46906-1_29

geometries [29.2, 8] and to achieve reproducible and scalable results. On the other hand, the availability of extended and regular patterns at the nanoscale is a key issue also for fields as sensoristics, nanocatalysis and spintronics. Indeed, suitable guest molecules/atoms can be selectively accommodated in the cavities of nanoporous networks for sensing purposes, molecular (chiral) recognition, or templating. E.g., fullerene and fullerene derivatives are prospective building blocks for functional nanostructures when deposited on metal surfaces but, at low coverage, they are too mobile and not stable enough for use in molecular devices. When deposited on a template formed by a self-assembled glycine layer on Cu(111), isolated fullerene molecules can be immobilized and form a regular pattern [29.9]. Similarly, the nanocavities can provide functional spaces for heterogeneous catalytic reactions if they host a reactive molecular species or a metal atom acting as catalyst. Depending on the magnetic properties of the metal, metal–organic networks may also be relevant for spintronic applications.

Molecular engineering involves quite often large organic molecules, typically aromatic compounds, which may also be specially designed or modified for specific purposes, e.g., by adding a metal atom or a desired functional group [29.10–13]. However, self-assembly is a process occurring very often with molecules present in nature and especially with molecules of biological interest. Indeed, the term was firstly used in biology to indicate the phenomenon in which complementary molecular units find each other and form a stable complex (sub)system. It is remarkable, in this respect that one of the first observations was that of spontaneous association of entire and infectious viruses from their separated nucleic acid and protein components [29.14]. The self-assembly of biomolecules at surfaces opens up wide perspectives [29.15–18]. Due to the complexity of the systems, so far only the simplest species have been investigated at the molecular level. The natural selectivity of nucleic acids suggests these molecules to be a good model system and, indeed, several 1-D and 2-D hydrogen-bonded structures were observed on Cu(111) [29.19, 20] and Cu(110) [29.21]. However, achieving unique routes toward low-dimensional nanostructures of nucleic acids is often nontrivial [29.20]. For this reason, the attention has concentrated on amino acids and oligopeptides [29.17, 18]. Amino acids are the basic constituents of proteins. Short peptides are the simplest organized structure formed by amino acids and still do not present the additional complication of folding, typical of proteins or of long peptides. Therefore, they have a structure simple enough to be assumed as a model for the chemisorption of biofunctional molecules but they are also suitably *complex* to offer precious information on the fundamental mechanisms governing the hybrid organic–inorganic interface. Last but not least, all the natural amino acids except glycine are chiral. Since the surface reactivity can be modified by exploiting the intrinsic chirality of amino acids and peptides, their action as a chiral modifier is a crucial issue for chiral separation or enantioselective heterogeneous catalysis.

Before proceeding with the description of the self-assembly concepts, it is worth mentioning that there is some confusion in literature about the proper terminology to be employed. In fact, spontaneous organization of separate units in an ordered system can occur at the nanoscale, but it can also be a mesoscale phenomenon, especially when dealing with biological systems. In this latter case, the term self-organization is probably more appropriate. A potential classification scheme is the one proposed by *Barth* [29.15], according to which:

- *Self-assembly* consists in the spontaneous formation of spatially textured architectures of well-defined geometry, stable under equilibrium conditions. Self-assembly proceeds in closed systems by synergic interaction of clearly identifiable functional units. The free energy minimization leads to identical and reproducible patterns.
- The term *self-organized growth* indicates regular arrangements of units controlled by mesoscale force fields or kinetic limitations arising in processes accompanying matter accumulation. These structures are uniform to a certain extent but, a priori, not identical at the atomic or molecular scale.
- *Self-organization* is associated with spatiotemporal order phenomena in open systems and away from thermodynamic equilibrium.

Only self-assembly phenomena at the nanoscale will be treated in this chapter. The examples reported here will deal mainly with noble metal surfaces since they (especially Cu) are the most common substrates used to investigate the hybrid organic–inorganic interface [29.17, 22–24].

Formation of spatially organized molecular architectures at surfaces can involve different kinds of intermolecular and molecule–substrate bonding, which can be roughly classified as covalent or noncovalent bondings.

Covalent bonding implies bond-breaking and subsequent saturation of the dangling bond towards the surface, towards a metal adatom with the formation of an organometallic compound or towards another molecule. Usually the molecule dissociates by loosing a H atom. This is indeed the case for all amino acids adsorbing in the anionic form [29.24], for thiols binding at the metal surface through their sulfur group [29.3, 25] and

for some aromatic compounds [29.11, 26]. However, if the molecule is modified by introducing an additional element or functional group (such as a halogen atom or a methyl group), this particular bonding is probably the weakest and the first one to be broken [29.11, 13, 27]. This process has been observed and exploited, e.g., for the formation of organometallic chains from halogenated hydrocarbon precursors.

Finally, formation of covalent bonds within adjacent molecules may lead to the synthesis of new molecular species, e.g., to peptides when starting from amino acids or to polymeric structures when the precursor is a hydrocarbon molecule, preferably already inserted in an organometallic assembly. Since this last process requires energy, it is usually activated by providing external energy in the form of heat, light, or even electron injection.

Noncovalent bonding, on the contrary, is driven mainly by electrostatic forces. Van der Waals interactions and hydrogen bond formation are the most common driving mechanisms, though other ionic interactions and substrate-mediated long-range forces may play a role [29.24, 28, 29]. In addition, supramolecular ordered patterns, i.e., a hierarchical organization of self-assembled structures, can take place under some conditions. Van der Waals interactions are evident, e.g., in lamellar structures of flat-lying chain-like hydrocarbon species realized at solid–liquid interfaces [29.23] or in self-assembled monolayers of alkanethiols [29.25], but they are present for whatever system. Their weakness often prevents a clear understanding of their relevance, though with recent progress in density functional theory (DFT) their contribution can now be taken into account with a good degree of approximation [29.30, 31]. Hydrogen bonding, which is mostly due to electrostatic interactions [29.32], is probably the most common type of noncovalent intermolecular interaction [29.22, 24]. More generally, charged or polar moieties can form H bridges or other electrostatic coupling schemes. An even stronger, albeit nonselective, bonding occurs in the ionic self-assembly, explored in solution-based systems [29.33]. In 3-D, the strength of ionic bonds typically exceeds that of H-bridges; however, appreciable screening may intervene on metals. A special electrostatic interaction is the zwitterionic bonding in amino acids [29.18]. In addition, indirect substrate-mediated effects may be operative and influence the molecular mobility and self-assembly process [29.29].

To understand the self-assembly mechanisms and to unravel the geometry of the molecular patterns, several factors have to be considered, among which adsorption, mobility, lateral interactions and molecule–substrate interactions. All of them depend on the atomic environment, chemical nature and symmetry

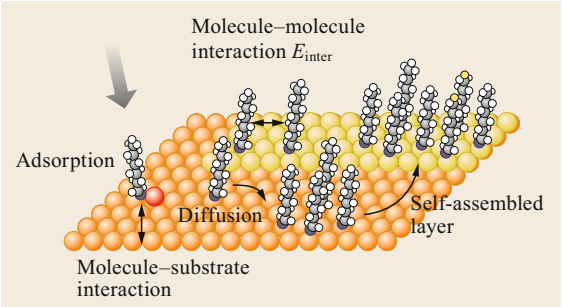

Fig. 29.1 Scheme of the mechanisms controlling molecular self-assembly on surfaces. *From left to right*: (i) Molecules from the gas phase hit the surface and are adsorbed on it. (ii) The molecules diffuse on the surface and get into contact with other molecules. (iii) Intermolecular bonds are established and an ordered layer forms. (Reprinted from [29.37], with permission from Elsevier)

of the substrate [29.12, 17, 34]. The accurate balancing of all these factors allows for the appearance of supramolecular order and determines the stable geometry of the self-assembled pattern. As an example, we anticipate here that alanine adsorb on Cu(110) in the anionic form [29.35], as many other amino acids. Since the molecule–substrate interaction is quite strong, this molecule organizes to form chiral clusters of six or eight units, interspersed with chiral channels exposing the bare metal atoms, in order to release the stress due to the lattice mismatch and to keep registry with the substrate. Glutamic acid on Ag(100), on the contrary, arranges in extended monolayer islands fully covering the Ag terraces, since the interaction with the silver substrate is weak and intermolecular forces prevail [29.36].

Noncovalent self-assembly between molecules can be schematized with the three-step process represented in Fig. 29.1 and including: adsorption, diffusion, molecular recognition and islands formation:

i) *Adsorption.* A flux of molecules is directed towards a well-prepared surface and the single units adsorb on it, usually in a definite configuration and at specific sites. For small organic species on metals, typical adsorption energies of $0.5\,\mathrm{eV} < E_{ad} < 10\,\mathrm{eV}$ per molecule and molecule–substrate bond energies in the range of 0.3–5 eV per functional group are reported [29.38], the precise value being strongly dependent on substrate reactivity, symmetry and electronic properties. Since the structures of interest must be stable at room temperature (RT), E_{ad} should exceed $\approx 1\,\mathrm{eV}$ according to the desorption rate equation for an isolated species

$$\Gamma_{des} = \nu_0 \mathrm{e}^{-\beta E^*} , \qquad (29.1)$$

where $\nu_0 = 10^{13}\,\mathrm{s}^{-1}$, $\beta = [k_\mathrm{B}T]^{-1}$ and E^* is the corresponding energy barrier.
The coupling of the molecule to the atomic lattice confines the adsorbate and influences its conformation. If the molecules are anchored to the substrate with a specific functional group, the adsorption configuration may depend on coverage and/or annealing of the layer [29.36, 37, 39, 40]. If the species is flexible enough, molecular deformation can occur [29.41, 42], while the symmetry reduction associated with the 2-D confinement may induce a rich variety of chirality phenomena [29.17, 21, 43]. All this information is indicative of the key role of the molecule–substrate interaction in the adsorption process and in the determination of the final self-assembled geometry. In addition, if molecule–substrate interactions are relevant, rearrangements of the substrate atomic lattice may occur. Step faceting and bouncing has indeed been observed on deposition of amino acids at Cu(001) [29.18, 44]. Conversely, naturally reconstructed or artificially patterned surfaces can provide anisotropic templates with preferential adsorption sites, thus steering peculiar self-assembled geometries [29.45, 46].

ii) *Diffusion.* The molecules diffuse on the surface. Surface migration and 2-D rotation are thermally activated processes associated with energy barriers $0.05\,\mathrm{eV} < E_\mathrm{m} < 3\,\mathrm{eV}$ and $E_\mathrm{rot} \approx E_\mathrm{m}$, respectively [29.15]. Considering the simplified case of a unique migration energy barrier for diffusion of isolated species and using a rate equation of the same form as (29.1), it is evident that self-assembly at RT can be achieved if $E_\mathrm{m} \leq 0.5\,\mathrm{eV}$. Migration barriers are adsorption configuration-dependent [29.47] and usually reflect the anisotropy of the surface. They can be tuned also by suitable modification of the molecular structure, e.g., by adding specific functional groups.
For site-specific bonding, the adsorbates have a specific orientation with respect to the substrate atomic lattice. Two-dimensional rotations are therefore possible and, as diffusion, require thermal activation and follow a similar rate law. Detailed studies characterizing rotational motion are rare and limited to small molecules [29.48] but the order expressed in 2-D self-assembly provides clear indirect evidence of this phenomenon [29.17, 22, 23].

iii) *Molecular recognition and formation of regular architectures*. The mobile molecules are adsorbed in configurations promoting molecular recognition and the formation of lateral noncovalent bonds between functional groups. Then, the self-assembly of low-dimensional nanosystems is mediated by the selectivity and directionality of hydrogen bonds or metal–ligand interactions, but also by bonding schemes based on nonspecific interactions. One or more types of noncovalent bond formation mechanisms can be involved, depending on the characteristics of both the surface and the molecular species; the typical energy gain for the formation of the self-assembled geometry is $0.02\,\mathrm{eV} < E_\mathrm{as} < 2.5\,\mathrm{eV}$ [29.15].

The study of the detailed adsorption configuration and of the self-assembly patterns of molecules at surfaces is often an experimental challenge, which requires a combination of powerful tools. The scanning tunneling microscope (STM) is certainly a fundamental instrument for this kind of investigation. It allows to determine the surface morphology at the atomic level, to manipulate individual molecules to create specific patterns or to induce specific chemical reactions [29.49–51], but also to gain spectroscopic information (scanning tunneling spectroscopy, STS) on individual molecules [29.52]. The limit of this technique is the lack of chemical information, since STS analysis is limited to the valence band region and it is extremely local and technically demanding. For this reason, microscopic investigation is usually complemented by spectroscopic experiments aimed at defining the chemical state of the molecule as a whole and of its different functional groups. Core level photoemission spectroscopy, either with laboratory and synchrotron x-ray sources, is largely employed in this respect. For the simplest molecules, as amino acids, also infrared (IR) spectroscopy is of common use. Though interpreting a vibrational spectrum can be a bit more complicated than reading an XPS one, IR spectroscopy is a photon-based technique and thus presents the great advantage of working also in ambient conditions, not necessarily in ultrahigh vacuum. This is important in the study of biological molecules, which are often deposited from solution and investigated in liquid environment. Moreover, in some cases, biointerfaces may be damaged by x-ray irradiation, while they are not perturbed by the less-energetic photons in the IR region.

Experimental investigation must be complemented by DFT and other model calculations, which help to shed light onto structure and properties of the molecule–surface system. For example, the following points can be addressed:

i) The nature of the intermolecular interactions at play in molecular layers at surfaces
ii) The structure of the layer
iii) For chiral adsorbates, the mechanisms by which the chirality at the molecular level is expressed in the 2-D system
iv) Chiral recognition.

The theoretical approach can bring spectacular breakthroughs in the description of adsorbed molecules and provide precious information to interpret experimental data and to better understand the structural and environmental factors affecting molecular adsorption and ordering on a surface. The first DFT studies of complex systems neglected Van der Waals interaction and were thus affected by a systematic error in their predictions; these forces are taken into account in the more modern functionals, thus increasing significantly also the quantitative agreement with the experimental data.

In this chapter we will provide a brief overview of this topic by presenting a few examples for significant categories of molecules and considering the nature of the interaction with the substrate and with the neighboring adsorbates. We will start describing the formation of covalent structures and the surface-assisted polymerization of organic compounds. Then, we will move to noncovalent, intermolecular bonding, analyzing first the case of self-assembled monolayers of thiol molecules and then focusing on small biological molecules, such as amino acids.

29.2 Organometallic Compounds and Covalent Bond Networks

Recent research interests in the field of surface-supported organic monolayers focus on two main topics: the growth of epitaxial grapheme [29.53, 54] and the production of surface covalent organic frameworks [29.13, 26, 55–57]. In fact, nowadays it is well established that bottom-up fabrication of surface nanostructures guarantees a final product of better quality in terms of uniformity, low defectivity and, hence, transport properties with respect to the top-down approach. In this frame, 1-D and 2-D organometallic compounds and coordination polymers have attracted large attention because they are often thermally more stable [29.10, 58] than structures based on the weaker electrostatic interactions or hydrogen bonds [29.59]. Organometallic structures may evolve into polymeric chains/networks through activated formation of new covalent bonds, while in other cases the covalent assembly forms without this intermediate step.

Most of this surface-confined chemistry has been directed by specific functionalization of the organic components—typically introducing halogen atoms or carboxylate, pyridyl, or carbonitrile functionalities—in order to create covalently bound macromolecular structures with controlled shape and size. The concept of surface-assisted covalent bonding is schematized in Fig. 29.2 for the tetra(4-bromophenyl)porphyrin (Br_4TPP) molecule [29.26]: a chemically stable, central molecular unit with a specific function (e.g., a peculiar electronic/magnetic/catalytic property) is equipped with several legs, some of which may be modified by the introduction of a functionalized termination. After thermal dissociation of the substituent atoms (either on the surface or in the evaporator), the monomer building blocks are connected with each other through the activated legs, directly on the surface, by thermal diffusion. The ability to design and synthesize molecules with a different number and relative arrangement of predefined connection points allows the construction of various topologies, such as dimers, linear chains and two-dimensional arrays. This is shown in the bottom part of Fig. 29.2 for tetraphenylporphyrin (TPP) modified with one, two or four Br terminations and deposited on Au(111). Upon sufficient heating, the molecules become activated and connect on the surface forming molecular arrays, the topology of which depends on the molecular design (Fig. 29.2b). If only one Br substituent is used (BrTPP), each building block provides only one reactive site and dimer formation occurs. If the porphyrin building blocks are modified with two Br atoms in a linear geometry (*trans*-Br_2TPP), long, linear chains are observed, while the use of four Br substituents (Br_4TPP) enables the construction of two-dimensional networks. Accordingly, no macromolecular structures can be formed starting from pure (i.e., nonhalogenated) TPP molecules. These results clearly show that the architecture of the nanostructures can be precisely controlled through the position of active endgroups in the chemical structure of the molecular building blocks. The covalent nature of the formed bonds is confirmed by DFT calculations and manipulation experiments.

If a similar process occurs with the participation of metal atoms, usually provided by the substrate, we assist with the formation of organometallic chains as those reported in the examples of Fig. 29.3 and in top panels of Fig. 29.4. *Fan* et al. [29.60] deposited 4,4″-dibromo-*meta*-terphenyl (DMTP; see Fig. 29.3c for the molecular structure) on Cu(111) at $T \geq 300$ K. DMTP dissociates by C–Br bond scission and the resulting *meta*-terphenyl fragments form stable organometallic structures based on C–Cu–C bonds. At RT (Fig. 29.3a), both cyclic oligomers of the type (*meta*-terphenyl-Cu)$_n$ (with $n = 6, 8, 14, 16, 18, 22$ marked by *arrows*) and zig-zag polymer chains form. The latter ones have a repeat unit length of 26.5 Å, are oriented $\pm 5.0°$ off the $\langle 0\bar{1}1 \rangle$ direction of the underlying Cu(111) substrate and can bend by angles of 60°, 120° or 180° (i.e., backfold). Islands formed by these chains are elongated

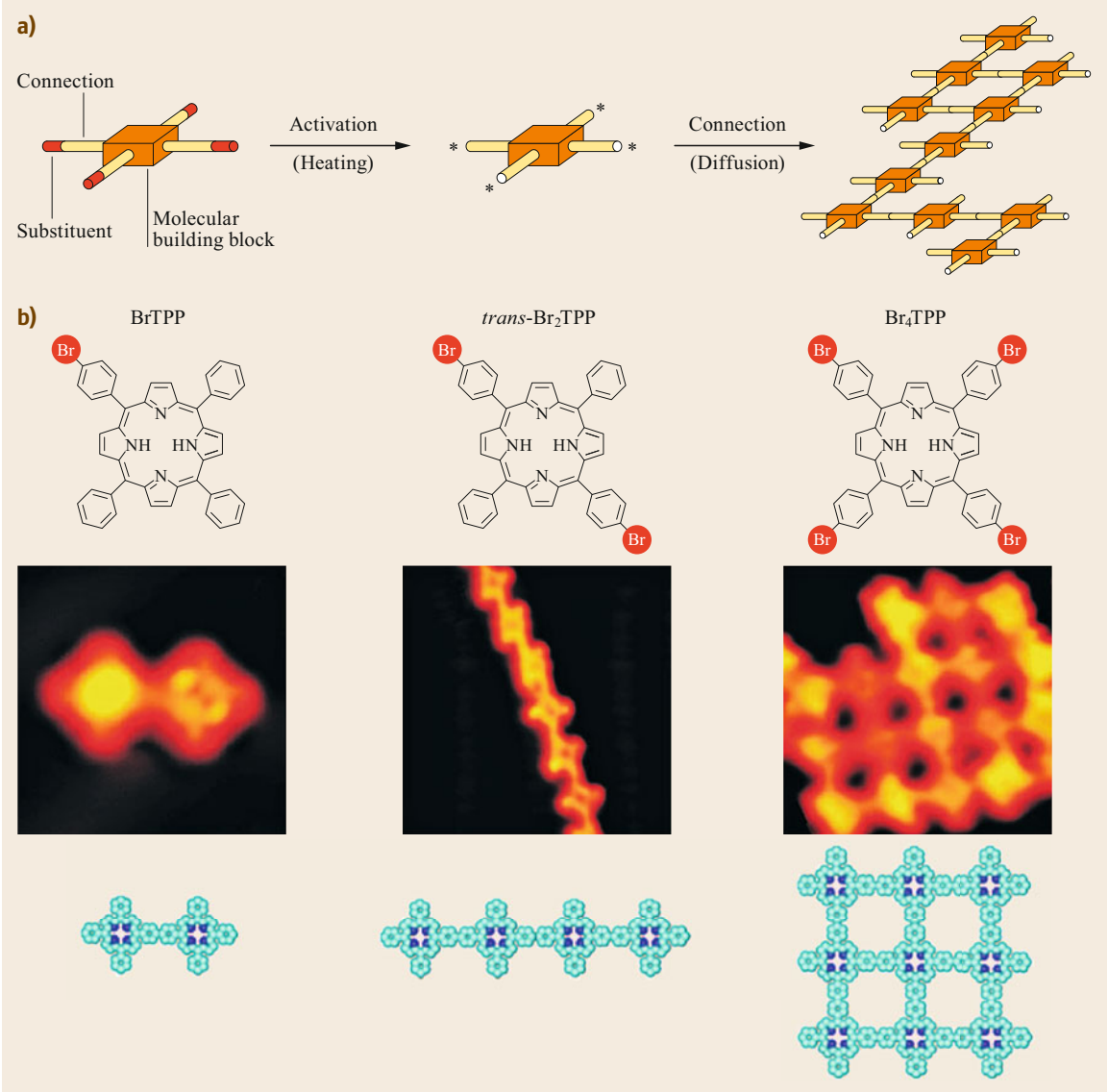

Fig. 29.2 **(a)** Schematic representation of the formation of covalently bound networks by connecting activated molecular building blocks. **(b)** Macromolecular architectures obtained from different TPP monomer building blocks modified with one, two and four Br substituents. The *top row* shows the chemical structure of the molecular precursors; the *middle row* reports detailed STM images of the nanostructures formed upon covalent bonding ($5 \times 5\,nm^2$, $10 \times 10\,nm^2$ and $8.5 \times 8.5\,nm^2$, respectively). The chemical structure of the final assemblies is schematized in the *bottom row*. (After [29.26])

along the chain direction. The Cu atoms involved in the metal–organic structure stem partly from the terraces, as witnessed by the formation of vacancy islands at high coverage. Macrocycles appear at room temperature and below, whereas only chains are formed at higher T (Fig. 29.3b). Such behavior indicates that chains are thermodynamically favored, probably because of the high packing density that is reached when they organize into islands and that allows a maximum of lateral van der Waals interactions. Finally, the evidence of C–Cu–C bond formation but not of direct C–C bond formation suggests that Cu adatoms participate in the C–Br bond scission, so that Br is directly replaced by Cu.

Halogenated (aromatic) hydrocarbons often form organometallic compounds with carbon–metal–carbon bonds. These nanostructures may then act as intermediates in the surface-assisted Ullmann reaction [29.62, 63] leading to the synthesis of covalent assemblies [29.57,

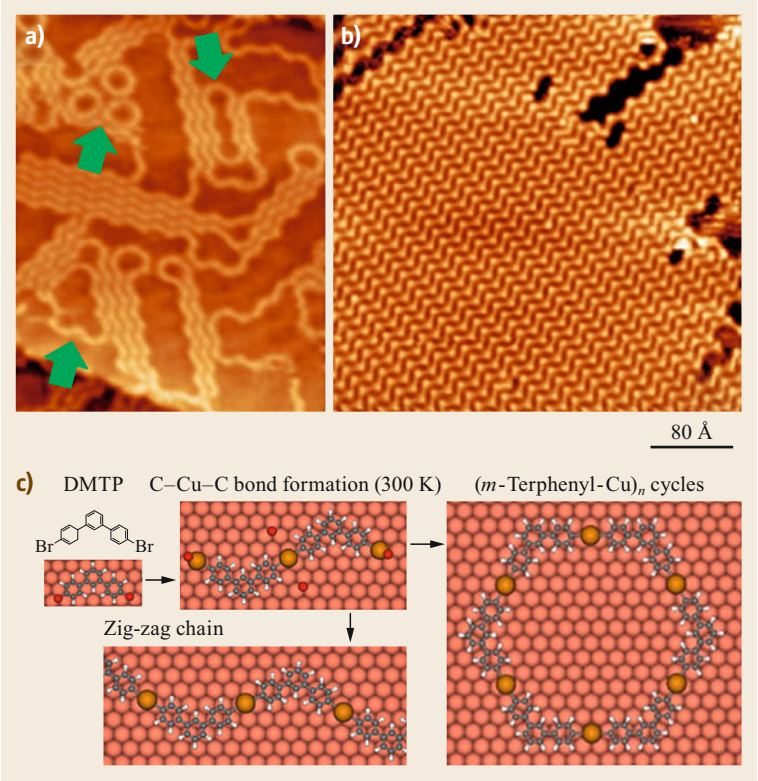

Fig. 29.3 **(a)** STM image of the Cu(111) surface after deposition of 0.55 ML of DMTP at RT ($V = -2.75$ V, $I = 0.08$ nA). Both the macrocycles $(MTP\text{-}Cu)_6$, $(MTP\text{-}Cu)_{14}$ and $(MTP\text{-}Cu)_{16}$ (marked by *green arrows*) and folded zig-zag chains are present. **(b)** STM image of the Cu(111) surface after deposition of 0.77 ML DMTP at $T = 440$ K ($V = -3.6$ V, $I = 0.02$ nA). **(c)** Reaction scheme leading to the formation of the observed structures. Color code: *white*, hydrogen; *grey*, carbon; *red*, bromine; underlying Cu(111) surface atoms are shown by *orange spheres*. (Reprinted with permission from [29.60]. Copyright (2015) American Chemical Society)

64–66]. This process consists of two steps since the dehalogenation of the precursor molecule and the formation of an organometallic intermediate with metal atoms extracted from the surface is followed by a surface-catalyzed C–C bond formation. Ullman coupling has been deeply investigated and exploited in several surface-mediated polymerization processes [29.51, 60, 67]. In fact, if additional energy is provided, dehydrogenation and C–C bond formation may occur and the formation of polymer chains or networks is observed [29.11, 68, 69]. Recently, this process has been exploited especially for the controlled growth of graphene nanoribbons (GNRs). These 1-D nanostructures are of extreme interest for the use of graphene-based materials in nanoelectronics because, contrary to extended graphene layers, they have a band gap. Since the latter depends on the width and on the edge geometry of the ribbons [29.13, 70], their fabrication presents strong requirements of uniformity and reproducibility, which are usually not satisfied by top-down fabrication methods [29.71, 72]. The bottom-up approach gives better results and, indeed, the synthesis of GNRs is a good example of surface-assisted covalent coupling. The large variety of studies performed evinces how the final product strongly depends on growth parameters as the nature and geometry of the substrate and the molecular structure. E.g., 10,10′-dibromo-9,9′-bianthryl (DBBA), a very common precursor used for the synthesis of $N = 7$ armchair GNRs, polymerizes into GNRs both on Au(111) and on Cu(111) but on the less-reactive substrate higher temperatures are necessary to activate the intermediate and final steps of the reaction [29.69]. On the other hand, the same thermal treatment that leads to GNR formation on Cu(111) produces quasizero dimension flat nanographene units on Cu(110) because, in this case, the Ullman coupling reaction is blocked by the strong anisotropy of the surface [29.73]. The nature of the molecule is another crucial ingredient to determine the geometry of the final self-assembled covalent structures and of the GNRs in particular. On Ag(111), straight $N = 7$ armchair GNRs can be fabricated starting from DBBA, while chevron-type GNRs with alternating widths of $N = 6$ and $N = 9$ are obtained using 6,11-dibromo-1,2,3,4-tetraphenyltriphenylene monomers [29.13]. Several aromatic molecules self-assemble in well-organized organometallic compounds [29.65, 74, 75] but only in a few cases complete dehydrogenation and C–C covalent bond formation are reported [29.11, 13, 57, 76]. Recently, a comparison between the thermal evolution of 5,11-dibromotetracene (DBT) [29.61] and of 1,6-dibromopyrene (DBP) [29.11] layers deposited on

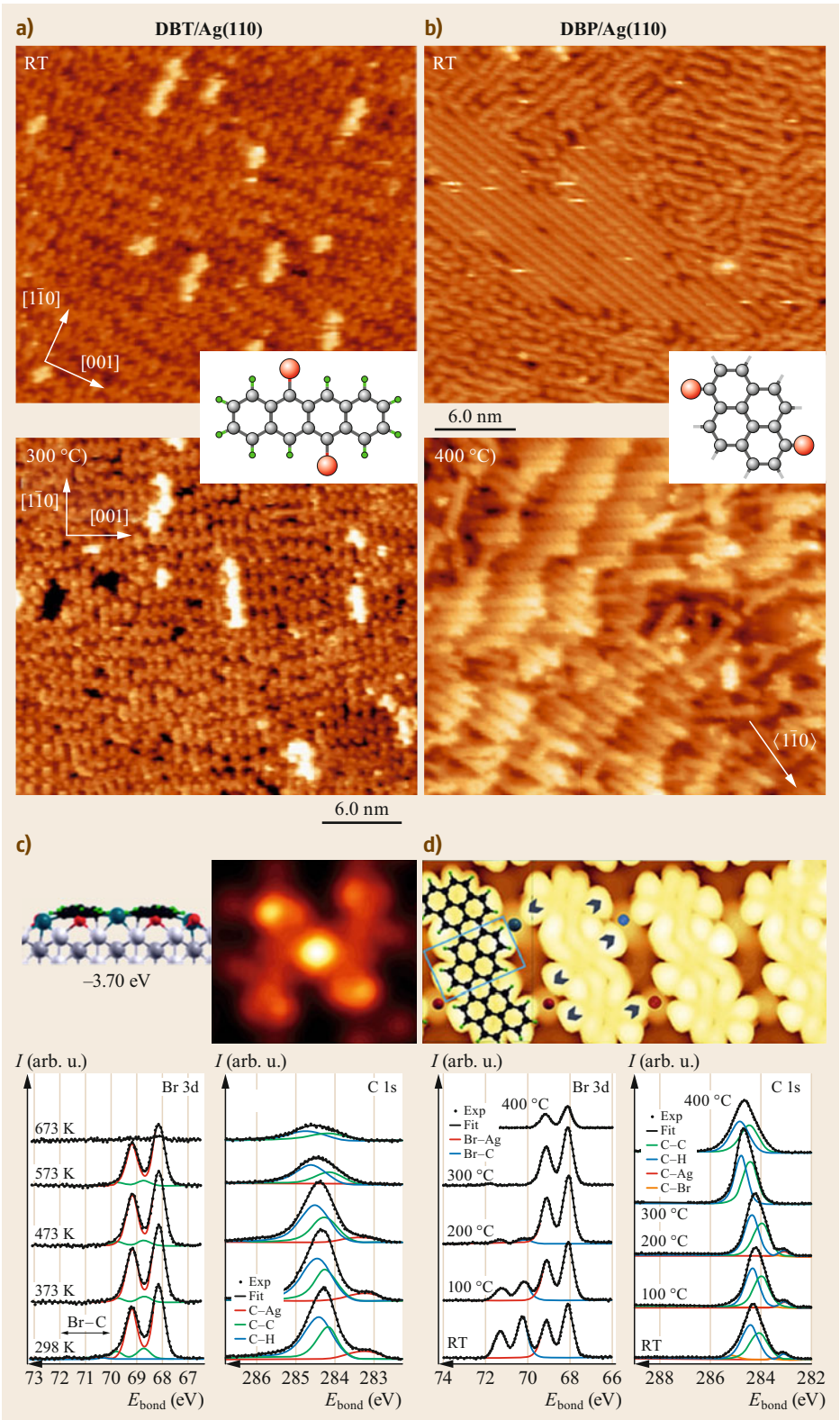
a)
DBT/Ag(110)
RT
[1$\bar{1}$0]
[001]
300 °C)
[1$\bar{1}$0]
[001]
b)
DBP/Ag(110)
RT
6.0 nm
400 °C)
⟨1$\bar{1}$0⟩
6.0 nm
c)
–3.70 eV
d)
I (arb. u.)
Br 3d
673 K
573 K
473 K
373 K
Br–C
298 K
73 72 71 70 69 68 67
E_{bond} (eV)
I (arb. u.)
C 1s
Exp
Fit
C–Ag
C–C
C–H
286 285 284 283
E_{bond} (eV)
I (arb. u.)
Br 3d
400 °C
Exp
Fit
Br–Ag
Br–C
300 °C
200 °C
100 °C
RT
74 72 70 68 66
E_{bond} (eV)
I (arb. u.)
C 1s
400 °C
Exp
Fit
C–C
C–H
C–Ag
C–Br
300 °C
200 °C
100 °C
RT
288 286 284 282
E_{bond} (eV)

Fig. 29.4 **(a,c)** Formation of –tetracene–Ag–organometallic chains on Ag(110). **(a)** *Top*: STM image of (0.9 ± 0.1) ML of DBT deposited on Ag(110) at RT ($V = 1$ V, $I = 1.4$ nA). *Bottom*: Same as top, after annealing to 300 °C for 10 min ($V = 0.84$ V, $I = 5.89$ nA). **(c)** *Top*: Optimized geometry and simulated STM image of the DBT–Ag–DBT dimer, which best reproduces the experimentally observed images. *Black*, *green*, *red*, and *grey balls* correspond to C, H, Br, and Ag atoms, respectively. Different shades of *grey* are used to identify the Ag layers, while the Ag adatoms are colored in *blue*. *Bottom*: XPS spectra of the Br 3d and C 1s regions showing the thermal evolution of 0.4 ML of DBT deposited on Ag(110) at RT. **(b,d)** GNRs formation from DBP/Ag(110). **(b)** *Top*: STM image of the Ag(110) surface covered with 0.7 ML of DBP deposited at RT ($V = 0.5$ V, $I = 28$ nA). *Bottom*: Arrays of ordered GNRs formed upon annealing a DBP multilayer to 150 °C for 15 min and then to 400 °C for 3 min. **(d)** *Top*: Simulated STM image of the DBP trimer, which best reproduces the experimentally observed structures. The optimized geometry is superimposed on the *left side*. *Bottom*: XPS spectra of the Br 3d and C 1s regions showing the thermal evolution of 1.2 ML of DBP deposited on Ag(110) at RT. For all STM images, size: 30×30 nm^2. (Reproduced from [29.11] with permission of The Royal Society of Chemistry. And reprinted with permission from [29.61]. Copyright (2016) American Chemical Society) ◄

Ag(110) has revealed a completely different behavior of these dihalogenated molecules, having very similar molecular weight but different conformation (Fig. 29.4). In both cases, debromination of molecules in contact with the metal substrate and formation of organometallic structures involving Ag adatoms occur already at RT. This is witnessed by the observation of elongated chains in the STM images (top row in Fig. 29.4a,b) and by the presence of Br–Ag and C–Ag components in the XPS spectra (bottom row in Fig. 29.4c,d). However, for DBT, organometallic dimers (as the one simulated in the top row in Fig. 29.4c) and trimers are the most common configurations at submonolayer coverage. Longer structures as those of the top row in Fig. 29.4a may be observed only at a nominal coverage close to 1 ML. Such features are stable up to $T = 300$ °C (bottom row in Fig. 29.4a), above which temperature the majority of the organic overlayer desorbs, as confirmed also by the significant reduction of the XPS intensity. On the contrary, at $\approx$ 300 °C the organometallic –DBP–Ag-chains disappear and the DBP monomers undergo further dehydrogenation and C–C coupling. Between 300 and 475 °C, GNRs are observed on the surface (bottom row in Fig. 29.4b), arranged in disordered patterns, in ordered arrays or in a polymer network depending on annealing temperature and preparation conditions. The graphenic nature of these ribbons is deduced from the up-shift towards 285 eV of the C 1s binding energy observed in the XPS spectra > 300 °C. Their internal structure could be determined by comparison of high-resolution STM images with the outcome of DFT simulations for a DBP trimer (top row in Fig. 29.4d).

The different results obtained in the experiments of Fig. 29.4 are explained considering that, for the DBT/Ag(110) system, significant substrate-precursor interaction leading to a flat-lying geometry and steric hindrance between the molecular units inhibit covalent coupling. Substrate directed adsorption between the $\langle 1\bar{1}0 \rangle$ atomic rows also suppresses dehydrogenative coupling at mild temperatures. This does not hold for DBP, which has a roundish shape. This result underlines the importance of geometrical and steric factors in the choice of the precursor molecule. In addition, as evident in the top row in Fig. 29.4d, the GNRs produced from the DBP precursor present a regular sequence of edge sites, with two zig-zag sites alternating to one armchair site. This opens the way to the perspective of tuning the shape and dimension of nanoribbons (and hence the correlated electronic properties) by choosing suitably tailored or purposefully designed molecular precursors.

As is evident from the previous examples, the use of halogenated precursors, as well as of molecules modified with other functionalized terminations, is very common. The presence of specific and often interlocking functional groups helps to achieve the assembly of a desired structure, e.g., by providing a privileged direction for new covalent bond formation. However, there are significant examples of organometallic structures and surface-assisted polymerization of nonfunctionalized molecules.

Schulz et al. [29.77] followed the synthesis of chiral GNRs on Cu(111) from three different bianthryl precursors (dibromo-, dichloro-, or halogen-free bianthryl) and found that, irrespective of the bianthryl precursor, the Ullmann route is inactive, and instead, identical chiral (3,1) GNRs are formed. This behavior, at variance with the one observed on the corresponding Ag and Au surfaces [29.13, 78], is due to the stronger molecule–surface interaction on Cu(111), which stabilizes the radical after halogen–carbon bond scission and reduces the energy barrier for C–H bond activation. Consequently, C–H bond activation occurs at a lower temperature than aryl–aryl coupling, resulting in similar intermolecular carbon–carbon bond formation for halogenated and nonhalogenated bianthryl species. The ring-closure reaction through cyclodehydrogenation yields, as a final product, the fully aromatic chiral GNR.

Haq et al. and *Hanke* et al. [29.10, 79] recently demonstrated that formation of organometallic

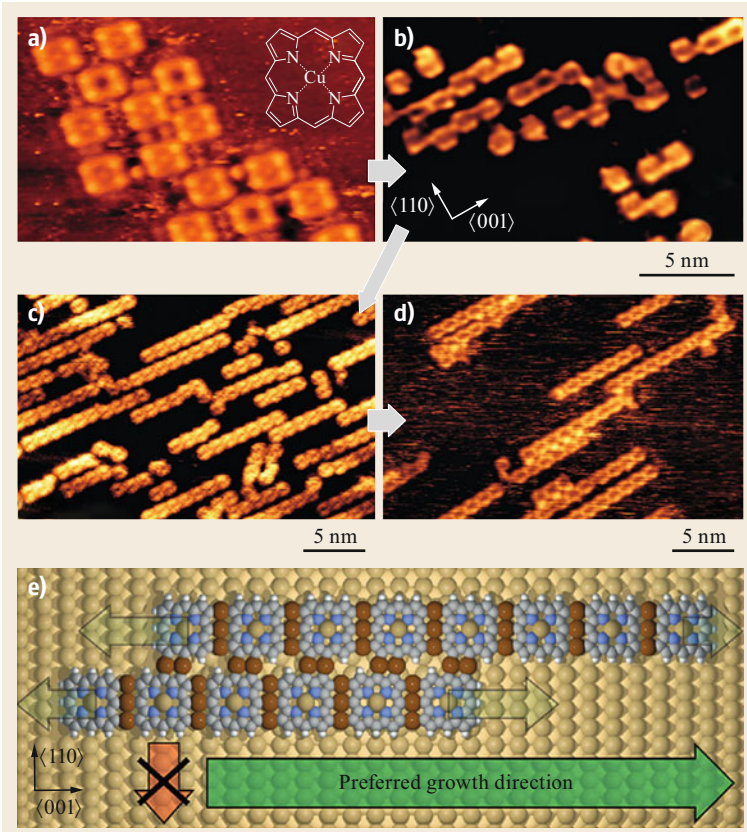

Fig. 29.5a–e Formation of covalently bound Cu-porphyrin chains on Cu(110) (see *inset* in **(a)** for the molecular structure). **(a)** Upon deposition at RT, the molecules form islands and capture Cu adatoms. **(b)** Annealing to 300–330 °C initiates C–Cu–C bond formation. Different intermediate states involving one or two connecting Cu atoms are observed. **(c)** Formation of porphyrin chains, one macrocycle wide, occurs upon annealing to ≈ 375 °C. **(d)** At 400 °C oriented porphyrin chains are observed. No more than two chains are connected in parallel. The porphyrin centers in the parallel chains are offset by a single lattice spacing in the ⟨001⟩ direction. **(e)** Model representation for the central chain in **(d)**, showing the orientation on the Cu(110) surface rows and the growth direction (*green arrow*). The *red arrow* denotes the direction in which no further growth is seen. (Reprinted with permission from [29.79]. Copyright (2011) American Chemical Society)

chains can be achieved with completely unfunctionalized porphyrins (H_2-porphyrin, Cu-porphyrin, Zn(II)-diphenylporphyrin and diphenylporphyrin) adsorbed on Cu(110) and subsequently heated to several hundred °C. Figure 29.5 shows the case of unsubstituted Cu-porphyrin. In a heat-to-connect assembly strategy, the surface was used as the only means to activate, connect, and direct the self-assembly into 1-D chains that are coupled by organometallic C–Cu–C bonds. In fact, the structures obtained after annealing to $T \geq 375\,°C$ are highly ordered and form one-dimensional chains on the surface only in the ⟨001⟩ direction (i.e., perpendicular to the Cu rows as shown in Fig. 29.5c). By combining STM analysis with DFT calculations and by considering several possible geometries, the authors explain this effect as related to the commensurability of the adsorbate with the surface. During the annealing process, several different porphyrin–porphyrin couplings occur with increasing numbers of connecting Cu adatoms. Extended 2-D assemblies were never observed but, at $T = 400\,°C$ (Fig. 29.5d), parallel chains could sometimes bind together forming fused double-rows, which are predicted to be the most stable adsorbate structure. Therefore, a chemical and energetic driving force toward a full two-dimensional self-assembly exists, though the process is self-limited to two to three parallel coupled chains. The impossibility of forming an extended 2-D pattern is explained in terms of the stress induced in the adsorbate by the self-assembly: only the ⟨001⟩ direction provides the proper lattice spacing that enables the molecule to fit without significant distortion. This result highlights the critical role of the Cu(110) surface structure in directing the assembly and opens perspectives in surface engineering.

29.3 Noncovalent Bonding

When noncovalent bonding occurs, self-assembly is driven by other kinds of interactions, which are usually weaker and mainly of electrostatic nature: ionic bonding, hydrogen bonding, Van der Waals interactions and, sometimes, long-range interactions mediated by the substrate. Except for the last one, all these forces

are also active in three dimensions and are responsible not only for the formation of molecular aggregates (e.g., the formation of molecular crystals) but also for the particular conformation of complex molecules (e.g., peptide or protein folding). The molecules within the noncovalent assembly can form a covalent bond with the substrate, as in the case of thiol SAMs [29.80–83] and of deprotonated amino acid species [29.18], or be physisorbed [29.84, 85]. The same molecular species can adsorb in either of the two chemical states depending on experimental conditions [29.36, 85].

The selectivity and directionality of hydrogen bonds [29.32] offer an excellent means for noncovalent synthesis [29.86] and for the formation of 2-D architectures on surfaces. Hydrogen-bonded nanostructures with distinct shape can be realized on surfaces starting from a wide variety of molecules, especially when exploiting suitable functional groups. The geometrical complementarity, promoting the formation of multiple weak linkages [29.86], is important and at the basis of molecular recognition phenomena. More generally, H-bridges can form between charged or polar moieties. Ionic bonds are expected to be stronger than H-bridges. This is, indeed, true in three dimensions, while for molecules supported on a metal surface they can be weakened by the presence of an appreciable screening effect.

Noncovalent self-assembly has been observed for many kinds of molecules. In the following we will briefly report a few examples of planar, extended π-systems, of thiol SAMs and of ordered patterns of small biological molecules, which we consider the most representative categories when discussing self-assembly phenomena at surfaces.

29.3.1 π-Conjugated Molecules

On appropriate substrates, π-systems adsorb in flat-lying geometries favoring lateral molecular recognition. If the molecules are modified with peripheral functional groups favoring H-bond formation, the supramolecular assembly process takes advantage of both the energetics and the directionality of H-bonding. Moieties for head-to-tail or lateral coupling have been tested and the results suggest that, in general, species with functional groups providing geometrical (steric) or electronic complementarity can be employed. A typical example is provided by carboxyphenyl-substituted porphyrins deposited on Au(111). These molecules interact with each other by forming a double H-bond bridge between the terminal carboxyl groups; depending on the number and position of carboxyl terminations in each porphyrin, two- or four-membered clusters are observed [29.87].

In the following we discuss the cases of trimesic acid [29.85] (TMA, 1,3,5-benzenetricarboxylic acid, $C_6H_3(COOH)_3$) and 4-[*trans*-2-(pyrid-4-ylvinyl)] benzoic acid [29.88] (PVBA), which represent prototype materials for supramolecular self-assemblies. Due to its trigonal structure, TMA is a model system for the understanding of supramolecular geometries in 2-D. PVBA, on the contrary, is a linear molecule and therefore tends to organize into 1-D structures. Presenting two chiral enantiomers when constrained in 2-D, it is of interest for the understanding of chiral recognition at surfaces.

In the temperature range $192\,\mathrm{K} < T < 280\,\mathrm{K}$, TMA on Cu(001) [29.85] forms islands of flat-lying molecules in which the honeycomb motif prevails, though some small areas of more densely packed molecules are always present (Fig. 29.6a–d). As represented in the scheme of Fig. 29.6d, the honeycomb superstructure is stabilized by hydrogen-bond-mediated dimerization of the self-complementary carboxyl groups. Due to the chemical activity of the Cu substrate, the low-temperature arrangement is substituted by stripe-shaped supramolecular structures if deposition is performed at $T = 300\,\mathrm{K}$ (Fig. 29.6e–g). This organizational change is associated with a deprotonation of the molecules, leading to carboxylate formation and an upright bonding geometry, as schematically shown in Fig. 29.6g.

The molecule 4-[*trans*-2-(pyrid-4-ylvinyl)] benzoic acid (PVBA; see Fig. 29.7a for the molecular structure of λ- and δ-enantiomers) was adsorbed at Au(111) and at Ag(111) surfaces [29.88] and it was demonstrated that chiral correlation can extend over mesoscopic length without intimate molecular contact.

When small amounts of PVBA are evaporated on the achiral surface, because of the stochastic nature of the deposition process, an equal and evenly distributed population of λ- and δ-species is expected. However, at RT PVBA molecules are quite mobile and they self-assemble in supramolecular twin chains stabilized by formation of hydrogen bonds (Fig. 29.7b). As evident from STM images, the constituent molecular rows can have two relative displacements, related by a mirror symmetry. Therefore, chiral recognition is active and the twin chains display supramolecular chirality. To understand the mechanism driving this chiral recognition process, molecular dynamics (MD) simulations based on a force field were performed. The most stable configuration, schematized in Fig. 29.7b, is the one in which the chains are stabilized by strong head-to-tail OH$\cdots$N hydrogen bonds between PVBA endgroups. In addition, antiparallel arrangement of adjacent rows and their relative shift allows the negatively charged double-bonded O atoms to point towards the pyridile moiety of the

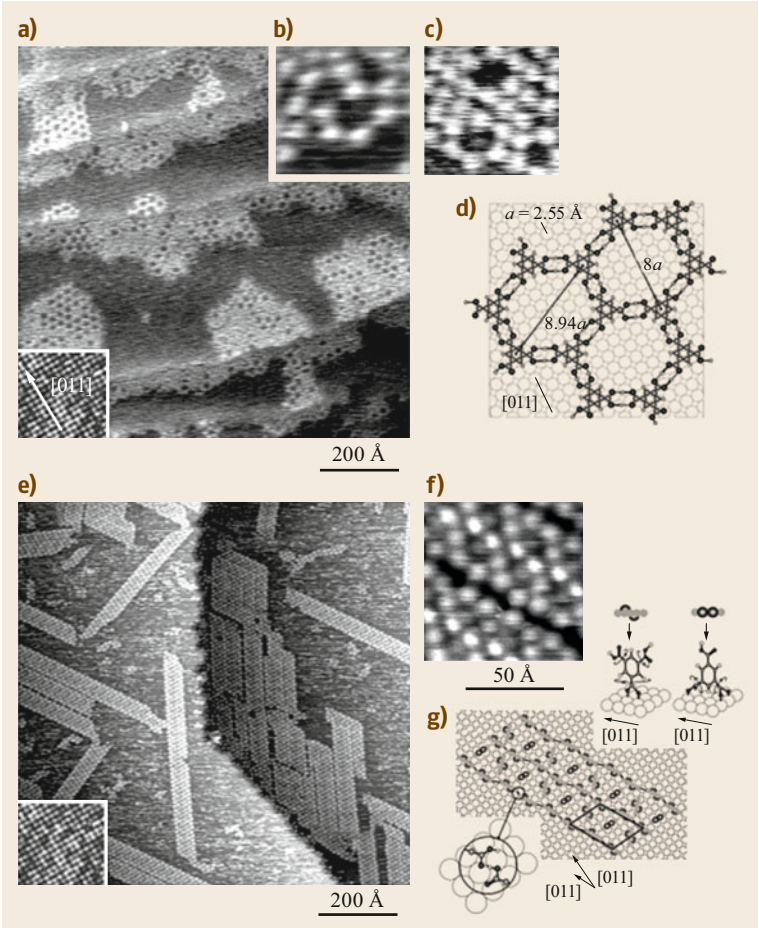

Fig. 29.6 (**a–d**) TMA on Cu(001). Low-temperature phase, produced by depositing the molecule on the Cu(001) surface at 240 K. The STM overview (**a**) shows compact TMA islands decorating atomic steps ($100 \times 100\,\mathrm{nm}^2$, $V = 0.39\,\mathrm{V}$, $I = 1.11\,\mathrm{nA}$). *Inset*: Atomically resolved Cu(001) surface. (**b,c**) Details of the honeycomb structure formed and of a 90° rotated honeycomb mesh coexisting with close-packed TMA molecules, respectively. (**d**) Structural model and characteristic dimensions of the honeycomb network with individual TMA centered at substrate hollow sites. Hydrogen bonds between adjacent units are marked. Color code: oxygen atoms are *black*, carbon atoms are *light grey circles*, hydrogen atoms are *white*. (**e–g**) Stripe phase, produced by deposition of TMA at RT. The STM overview (**e**) ($100 \times 100\,\mathrm{nm}^2$, $V = 0.75\,\mathrm{V}$, $I = 0.54\,\mathrm{nA}$) shows four distinct orientations of the islands. *Inset*: Atomically resolved pristine Cu(001) surface. (**f**) High-resolution image of a five-TMA-wide island ($V = 1.54\,\mathrm{V}$, $I = 0.2\,\mathrm{nA}$). (**g**) Proposed structural model for the striped supramolecular arrangement of (**f**). The stripe orientation and the Cu(001) azimuth are indicated. Two possible anchoring geometries of TMA-derived carboxylates are shown in the *top-right* corner while a possible H-bonding geometry along the stripe orientation is indicated in the *bottom-left* one. The unit cell of the structure is marked. Color code as in (**d**). (Reprinted with permission from [29.85]. Copyright (2002) American Chemical Society)

adjacent molecule, with consequent H-bond formation and stabilization of the twin chains (formation energy of $\approx 0.2\,\mathrm{eV/molecule}$). Chiral recognition within the twin chain structure can be rationalized: the crooked shape of the molecule promotes optimal sideward bonding of the carboxylic acid group only when it smoothly matches the bending of its antiparallel counterpart, which corresponds to the condition of identical chirality. It is more intriguing to observe that the twin chains form nanogratings extending over micrometer-size domains. On Ag(111) the periodicity of such nanogratings could be tuned by varying the PVBA coverage. All twin chains in each domain have the same chirality, so that the homochiral pattern extends over mesoscopic length. The authors exclude that the self-replication of supramolecular chirality is a phenomenon mediated

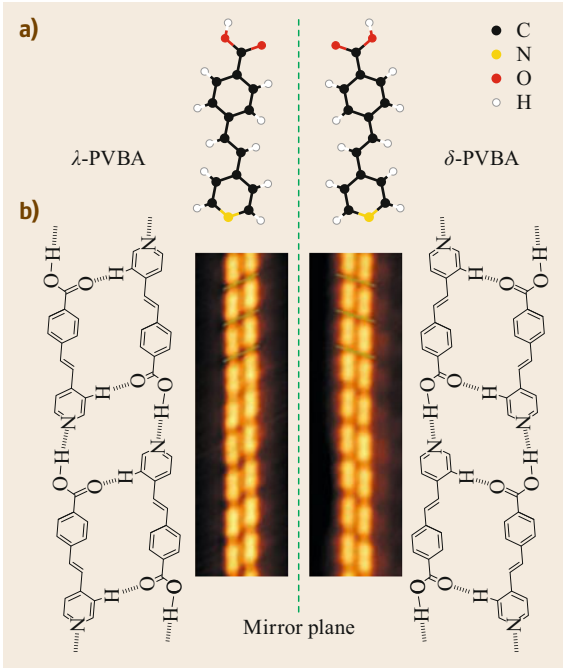

Fig. 29.7 **(a)** λ and δ enantiomer of PVBA upon confinement to two dimensions. The *dashed line* indicates the mirror symmetry plane. **(b)** STM topographs and corresponding models of the two possible *twin chain* supramolecular arrangements observed upon self-assembly of PVBA on Ag(111) at RT (image size 40×135 Å^2; measured at 77 K). In the models, hydrogen bonds are indicated by *dashes*. (Reprinted with permission from [29.88]. Copyright (2001) by the American Physical Society)

by the surface. They demonstrate indeed that the effect takes place in the course of the gratings' evolution and that it is driven by the formation of metastable molecular structures (observed at low temperature) interconnecting the molecular chains.

29.3.2 Self-Assembled Monolayers of Thiols

Another interesting class of molecules is the one represented by thiols, i.e., organosulfur compounds that contain a SH group. In fact, sulfur has a strong affinity to transition metal surfaces [29.25] and therefore, usually, the S–H bond breaks, the thiolate unit anchors onto the metal surface through the S atom and the dissociated H atom recombines with the one originating from another molecule and desorbs in the form of H_2. In fact, SAMs are assemblies formed onto the surface of a solid by the adsorption of organic molecular constituents having a chemical functionality, the headgroup, with a specific affinity for the substrate and organizing spontaneously into structures with crystalline (or semicrystalline) order through noncovalent, electrostatic or van der Waals interactions. Adsorption is also possible on the surface of liquids, as in the case of mercury [29.89, 90], but that case will be not treated here. In this section, we will limit our description to the main results obtained, in particular, for alkanethiols, while further information on SAMs and gold–sulfur interaction can be found in recent reviews [29.80–83, 91].

After the first observation that polar organic compounds diluted in nonpolar solvents adsorbed on solid surfaces forming well-oriented monolayers [29.92], pioneering work on the deposition of organic compounds exploiting the S–Au interaction was started by *Nuzzo* and *Allara* in 1983 [29.93, 94]. They investigated disulfides that spontaneously produced an ordered organic film by the simple immersion of the substrate in a solution of the compound: this technique is an alternative to the more complex procedure necessary for the growth of Langmuir–Blodgett films [29.95] and can be usefully employed for the growth of SAMs of alkanethiols [29.96].

The most studied among the different thiols-substrate systems are SAMs of alkanethiols (R–SH) on Au(111). Since gold is inert toward corrosion and oxidation, the growth can be performed also with the substrate kept in ambient conditions. Usually the thiolate moiety (R–S–) is thought to anchor on Au surfaces through a S–Au covalent bond of ≈ 2.1 eV [29.82], which is strong enough to displace adventitious organic species that always adsorb onto the surface in ambient conditions.

The molecular structure of some alkanethiols is shown in Fig. 29.8. The so-called normal alkanethiols (Fig. 29.8a, sometimes indicated as C_nSH or simply C_n, with n the number of carbon atoms in the alkyl chain) consist in an alkyl chain (R) terminated on one side, with a thiol (–SH) headgroup and on the other side, with a methyl group (the so-called endgroup or tailgroup). It is possible to synthesize compounds with different endgroups, such as those shown in Fig. 29.8b,d) and many others (e.g., $-CF_3$, $-NH_2$, $-CN$, $-SO_3H$, etc.), thus obtaining functionalized alkanethiols to be employed in SAM formation [29.97–102].

In Fig. 29.8e a dialkyl-disulfide is also shown. Symmetric disulfides with structure R–S–S–R produce SAMs identical to the ones obtained by alkanethiols having the same alkyl chain [29.104], but their solubility is generally lower than for thiols and the adsorption kinetic can be different.

Two main phases can be foreseen for SAMs of alkanethiols: the lying-down phase and the standing-up phase. In the limit of very low coverage, isolated molecules interact only with the substrate: the thiol molecule anchors its headgroup to the surface and the

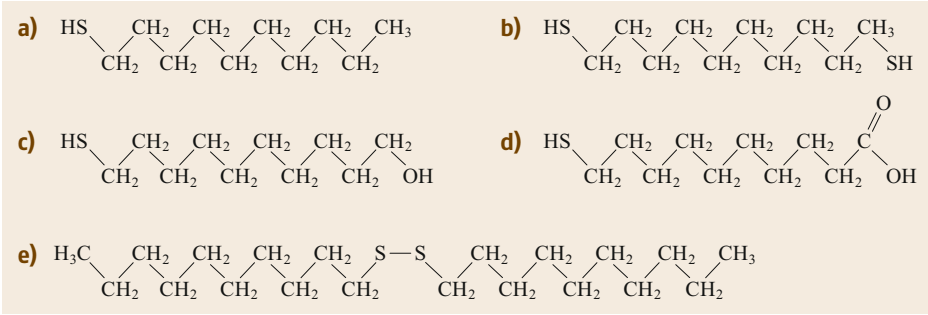

Fig. 29.8a–e A few examples of compounds used to form self-assembled monolayers. The compounds are plotted with a number of carbon atoms $n = 10$. **(a)** Normal alkanethiols (*n*-alkanethiols), endgroup is a methyl group: $HS-(CH_2)_{n-1}-CH_3$; **(b)** α,ω-alkanedithiols, endgroup is a thiol group: $HS-(CH_2)_n-SH$; **(c)** ω-mercaptoalkanol, endgroup is an alcohol group: $HS-(CH_2)_n-OH$; **(d)** ω-mercaptoalkane carboxylic acid, endgroup is a carboxylic acid group: $HS-(CH_2)_{n-1}-COOH$; **(e)** 1,1′-dialkyl-disulfide, two identical *n*-alkanethiolates are connected by a disulfide S–S bond: $CH_3-(CH_2)_{n-1}-S-S-(CH_2)_{n-1}-CH_3$. (Reprinted from [29.103], with permission from Elsevier)

interaction of the rest of the molecule with the surface determines adsorption in a flat-lying configuration. As shown by *Poirier* [29.105], the isolated molecules are highly mobile on the surface. On increasing the coverage the molecules start to interact with each other and the lying-down phase acquires a periodic order, the so-called striped phases (STM image in Fig. 29.9b). At intermediate coverage other lying-down phases are observed (Fig. 29.9c–e and following Fig. 29.16, where also a model for these assemblies is presented). Above a critical molecular density, the intermolecular interaction gets stronger and can compete with the interaction with the substrate. Therefore the standing-up phase grows and covers almost all the surface, except for a few vacancy islands, which are clearly visible as dark features (Fig. 29.9f). In this phase the molecules stand with their axis at about 30° from the normal and arrange in a $(\sqrt{3}\times\sqrt{3})$R30° superstructure with hexagonal lattice rotated by 30° with respect to the lattice of the Au(111) substrate. In fact, the nearest neighbor distance for Au atoms ($a = 2.88$ Å) is too short to accommodate the alkyl chains, while they can occupy next-nearest sites at a distance of $\sqrt{3}a = 4.99$ Å. Assuming as the standard model that S binds at threefold hollow site at this $\sqrt{3}a$ distance, the hexagonal lattice for the SAM is shown in Fig. 29.10a. Such configuration does not maximize the lateral van der Waals interactions between the alkyl chains within the SAMs. In order to minimize the free energy of the layer, the molecules adopt a tilted conformation reducing their distance, as shown in Fig. 29.10b.

Therefore, at high coverage, the substrate surface is covered with the alkanethiol SAM in the standing-up phase, i.e., the sulfur headgroup anchors the molecules to the gold substrate and the exposed surface presents the endgroups of the compound. As a consequence, as mentioned before, the organic film can change the physico-chemical properties of the gold substrate through its functionalization. This explains why this type of organic material is so attractive, not only for studying self-assembling but also in such diverse fields of applications such as sensing [29.108], molecular electronics [29.109], molecular switching [29.110], control of protein adsorption [29.111, 112], and surface patterning [29.113–115]. In fact, they are an example of the modular concept of organic chemistry: as shown schematically in Fig. 29.10b, they present the same sulfur–gold anchor, a spacer represented by the alkyl chain that decouples the metal surface from the endgroup and the environment and a functional endgroup with tunable properties.

An alkanethiol SAM can be grown on gold by following two different procedures [29.103], i.e., deposition from the gas phase or from the liquid phase:

a) In gas phase deposition, also known as physical vapor deposition (PVD), the gold sample is exposed to the vapor of the compound in vacuum. This is a very clean method for producing a self-assembled monolayer, since contamination from the environment can be minimized and the substrate can be prepared with the usual procedure of ion sputtering and annealing cycles and checked by typical surface science techniques. In gas phase deposition, the molecular flux depends on the vapor pressure of the evaporant. Therefore, this growth method is efficient for the production of low-coverage SAMs in the lying-down phase and is useful to study the early stages of the dynamics of the assembly at submonolayer coverage, e.g., the striped phases. On the contrary, the standing-up phase can form only if the vapor pressure of the compound is high enough and it can be more difficult to be achieved

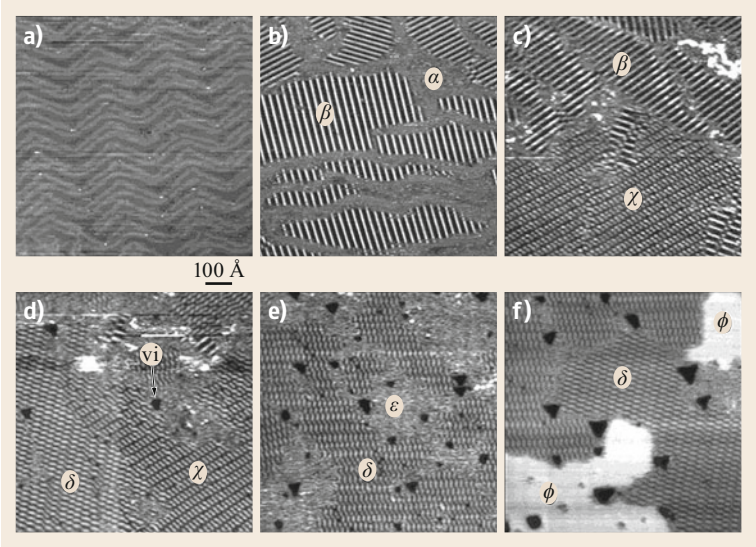

Fig. 29.9a–f STM images of the isothermal growth at 22 °C of decanethiol in ultrahigh vacuum. **(a)** Herringbone reconstruction of the clean Au(111). **(b)** Exposing the surface to a small dose of decanethiol, the formation of different domains of the striped β-phase in coexistence with a highly mobile α-phase, i.e., a two-dimensional gas, was observed. Au reconstruction was lifted in the regions covered with the β-phase. The growth proceeds with an increase of the β-regions. **(c)** When the surface is saturated by β, a new χ-phase was observed to nucleate in coexistence with β. **(d)** With a further increase in the surface coverage, another new δ-phase is formed that coexists with χ. Moreover, dark features are also observed: these pits are Au vacancy islands (vi). **(e)** At even higher surface coverage, a new disordered ε-phase was observed in coexistence with δ. **(f)** At higher surface coverage, ε-phase is replaced by the standing-up ϕ-phase, which coexists with δ. At saturation, the surface is covered with the ϕ-phase. (Reprinted with permission from [29.106]. Copyright (2001) American Chemical Society)

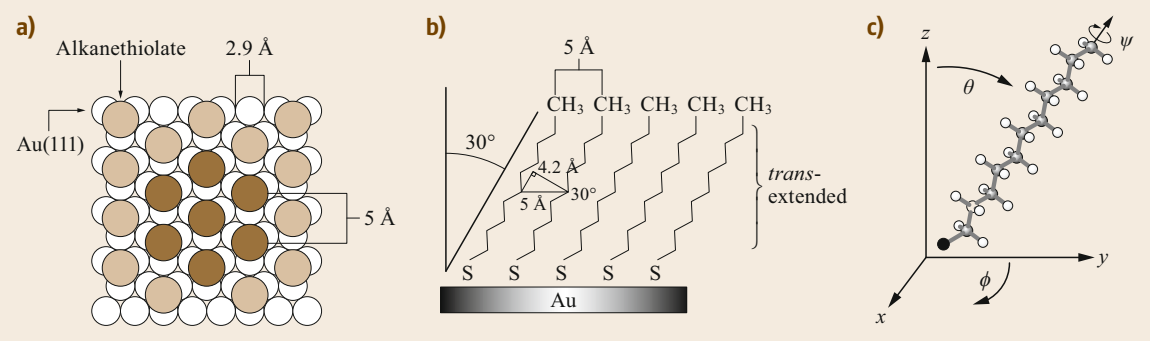

Fig. 29.10 **(a)** Top view of the structure of alkanethiol SAMs on Au(111): *open circles* are gold atoms in a hexagonal close-packed arrangement, *shaded circles* represent alkanethiolate adsorbates. *Darker circles* show the hexagonal $(\sqrt{3} \times \sqrt{3})$R30° structure of the film. **(b)** Side view of the same structure: alkanethiolates with their alkyl chains tilted 30° to pack more closely molecules in a *trans*-extended conformation, with minimum distance between adjacent chains of about 4.2 Å. **(c)** Scheme of the orientation of a decanethiol molecule with all-*trans* chain in a SAM on Au(111): tilt angle θ, tilt azimuthal direction ϕ, twist of the molecular plane ψ. (Reprinted from [29.103, 107], with permission from Elsevier)

especially with long chain molecules (for $n > 11$) and solid compounds (for $n > 17$). We also mention that for solid compounds, alternative deposition techniques such as the supersonic organic molecular beam deposition (SuOMBD) [29.116] can be employed. SuOMBD exploits the heating and sublimation of the compound in a flow of a carrier gas and the supersonic expansion of the seeded mixture

through a nozzle. The molecular flux is still very low, which allows to investigate molecular adsorption in the limit of zero-coverage [29.117]. On the other hand, since the compound is transported to the speed of the carrier gas, it can reach hyperthermal energies, available to the molecule to overcome adsorption or diffusion barriers if present.

b) In liquid deposition the gold sample is immersed in a solution of the compound to be deposited. The solution is a complex environment and the dynamic aspects of this form of deposition are difficult to characterize with the same type of details as for the case of gas-phase studies. However, the evolution of the structural phases formed during the self-assembly is similar to that for assembly from the gas phase [29.118–120]. Figure 29.11 schematizes the adsorption process in presence of solvent molecules. The kinetics of film growth can be influenced by the presence of the solvent, modifying the adsorption picture we have described previously [29.107]. In fact, physisorbed solvent molecules can be present on the gold surface after the immersion of the substrate and those molecules must be displaced to allow the thiol to adsorb. In particular, for long chains, adsorption of a lying-down thiol molecule requires to displace a number of solvent molecules greater than the one needed to adsorb in a standing-up conformation. Therefore, standing-up thiolate domains can form directly when depositing from solution and could also be favored over the formation of a striped phase. Moreover, solvent molecules can also favor the transition from the lying-down to the standing-up conformation due to additional interactions (alkyl chain-solvent and solvent–substrate interactions). In liquid deposition, it is also possible to control the chemisorption of the alkanethiol electrochemically [29.121] but this topic will be not treated here.

As explained above, a standing-up phase is easily obtained with liquid deposition. This is the most common protocol for preparing SAMs on gold since it does not require a complex vacuum system but only a suitable solvent for the compound. A freshly prepared (or flame annealed) supported gold film is immersed into a dilute (1−10 mM, rarely also micromolar) ethanolic solution of thiols for several hours at room temperature. The adsorption starts with a fast process: in fact, after a few seconds or few minutes, an adsorbate with a high coverage is obtained. On the other hand, the film contains defects and, in order to minimize them, incubation times of some hours (or sometimes some days) are necessary: the reorganization process to maximize the density of molecules is slow, in particular for long alkyl

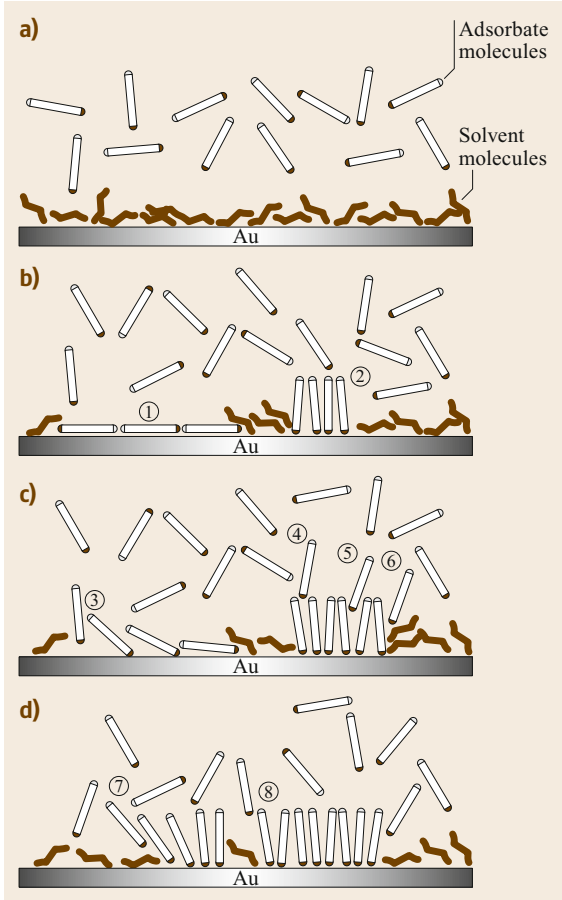

Fig. 29.11a–d Illustration of the adsorption processes in solution. The first steps correspond to a fast growth regime. **(a)** The adsorbate molecules in solution approach the gold substrate, which is coated with a layer of physisorbed solvent molecules (Note: the solvent molecules surrounding the adsorbate molecules have been omitted for clarity.) **(b)** The adsorbate molecules displace the solvent molecules to form either lying-down domains (1) or upright domains (2). **(c)** Additional adsorbate molecules incorporate into the lying-down domains and initiate a transition to an upright domain (3). Alternatively, adsorbate molecules can impinge on the surface (4), within the boundaries (5) or at the boundaries (6) of upright domains and incorporate into them. **(d)** The upright domains formed from either the lying-down phase (7) or direct adsorption (8) continue to grow until maximum coverage is attained. (Reprinted from [29.107], with permission from Elsevier)

chains. Besides the immersion time, the parameters that can affect the SAM structure and formation rate are the type of solvent, the temperature, the concentration and structure of the adsorbate (such as its chain length), the adsorbate purity and the cleanliness of the sub-

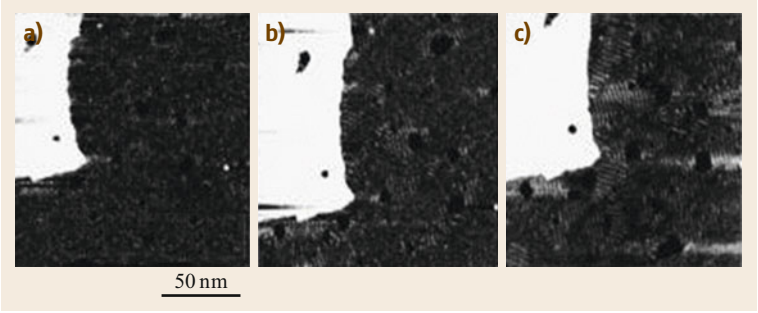

Fig. 29.12a–c Images acquired during the self-assembly process of $C_{15}SH$ in a 0.5 μM heptane solution. **(a)** Just upon addition of the modifying solution droplets, **(b)** 1 min and **(c)** 4 min later. The *black dots* are the pit-like defects. (Reprinted with permission from [29.119]. Copyright (1998) American Chemical Society)

strate. Alkanethiol SAMs obtained from liquid phase deposition using alternative solvents to ethanol (such as toluene, tetrahydrofuran, dimethylformamide, acetonitrile, cyclooctane) do not differ significantly from those formed from ethanolic solutions [29.96]. Ethanol has the advantage of being cheap, available with high purity, of low toxicity and to solvate a variety of alkanethiols with varying degrees of polar character and chain length.

Temperatures of the solution above RT improve the kinetics of the layer formation and reduce the number of defects in the SAM, producing larger domains [29.122]. Post-treatment of the deposited film up to 85 °C did not show any loss of molecules, while some changes were observed starting from 100 °C, that evolved into a severe deterioration of the monolayer topography at 115 °C [29.123].

Immersion time and concentration parameters are inversely related, longer times being required for lower concentrations. On the other hand, the minimum concentration to deposit a SAM must be $> 1\,\mu M$, as demonstrated by experiments on SAMs obtained by immersion for a week in solutions with concentrations $\approx 1\,\mu M$. It was indeed shown that the physical properties of the SAM are not the same as those formed starting from more concentrated solutions [29.96], probably because impurities are deposited along with thiols and this fact hinders the use of extremely dilute solutions except for the investigation of the initial stages of the adsorption in liquid [29.118–120].

As mentioned before, SAMs contain defects. Impurities can be introduced in the film during the deposition process, which is especially true when the compound is provided from immersion in solution. Considering the substrates, the evaporated gold films present many grains with boundaries that limit the crystallinity of the SAM. Also, when single crystals are employed, steps are always present. Even on large grains, the $(\sqrt{3} \times \sqrt{3})$ registry of the thiol molecules with the substrate can determine orientational and translational domain boundaries with the presence of missing rows. Including also the molecular tilt, the organic film is in general formed by domains with different alignments. On the other hand, the typical $(23 \times \sqrt{3})$ reconstruction of Au(111) (the so-called herringbone reconstruction [29.124–126], as shown in Fig. 29.9), is lifted after SAM formation, leaving in turn monatomic-height vacancies [29.127–129]. The origin of these pit-like defects, shown in Figs. 29.9 and 29.12 for deposition from the gas and from the liquid phase, respectively, can be understood by considering the different atomic density of the reconstructed and unreconstructed Au(111) surface. Indeed, the atom density in the $(23 \times \sqrt{3})$ reconstruction is 4.3% higher than in the unreconstructed gold surface; the change in the atom density induced by adsorption causes a relaxation of the surface, with the formation of single-atom vacancies that subsequently nucleate into large vacancy islands [29.128, 130]. The topography of the organic film faithfully replicates the underneath topography of these defects. Finally, intrinsic defects of the film are related to the chain of alkanethiolate. In fact, all the chains should be in the all-*trans* configuration but some molecules can present gauche defects, as shown in Fig. 29.13.

Let's consider in more detail the different phases obtained by vapor deposition. Figure 29.14 reports the low-energy atom diffraction (LEAD) patterns measured versus time (i.e., at different doses) during exposure of Au(111) at 278 K to decanethiol [29.131]. The evolution of the SAM structure is evident; from the ordered striped phase, the layer passes through an intermediate phase which does not show any diffraction pattern (a film without a long-range ordering) and finally it reaches the standing-up configuration, with a new diffraction pattern. The main peak is associated with the $(\sqrt{3} \times \sqrt{3})$R30° periodicity but, at the highest dose, a superlattice peak corresponding to the so-called c(4×2) structures appears.

Schreiber et al. [29.132] studied the uptake curve, ranging over four orders of magnitude, of decanethiol on Au(111) at RT (Fig. 29.15). Diffraction data are reported together with the evolution of the XPS signal, which provides an estimation of mass coverage. After the fast completion of the striped phase (measured by

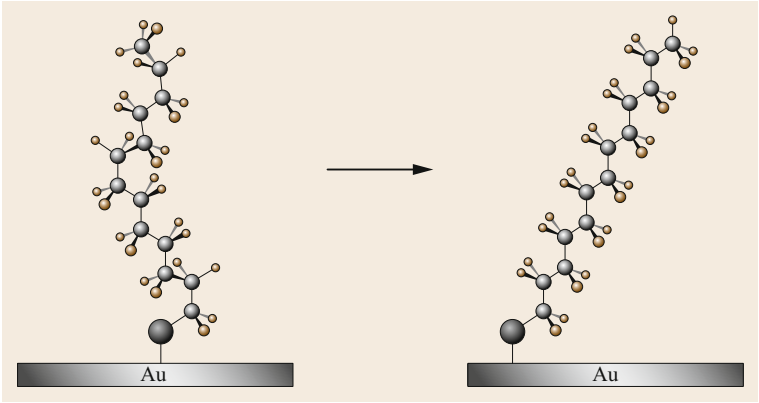

Fig. 29.13 Chain straightening from a molecule with gauche kinks to a *trans*-extended conformation. (Reprinted from [29.107], with permission from Elsevier)

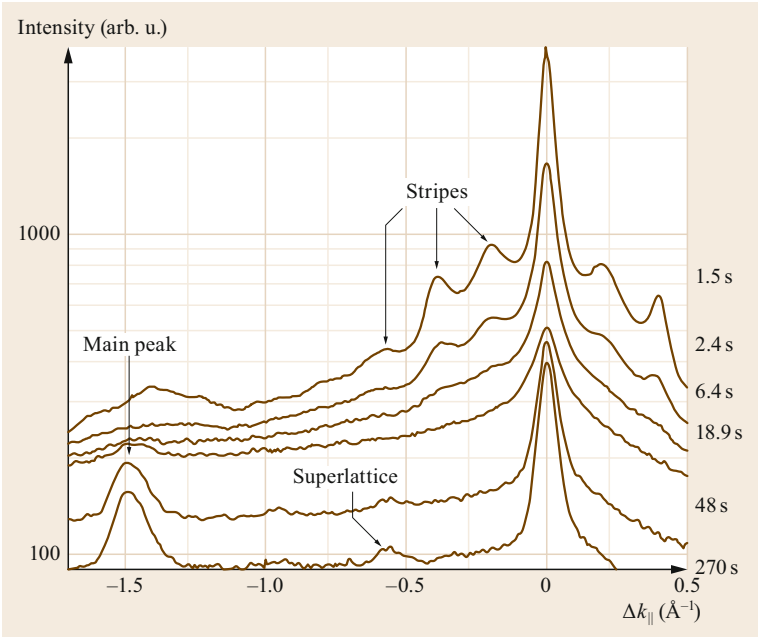

Fig. 29.14 Evolution of the LEAD pattern during the growth of decanethiol on Au(111) at 278 K. (Reprinted from [29.31], with permission from Elsevier)

LEAD after an exposure of a few tens of langmuir), the amount of sulfur remains almost constant up to an exposure of about 1000 L, above which the standing-up phase (and in particular the c(4 × 2) one) starts to form, as evinced by LEAD and grazing incident x-ray diffraction.

For the striped phase, LEED measurements by *Dubois* et al. [29.133] and LEAD studies by *Camillone* et al. [29.134, 135] showed that the lying-down molecules form a rectangular $(p \times \sqrt{3})$ unit cell, where p is the number of Au spacings of 2.88 Å. Of course, the value of p is chain length-dependent and close to twice the one found in the corresponding bulk phases of the molecule; for decanethiol, p was ≈ 11, corresponding to a spacing of ≈ 32 Å. On the other hand, different lying-down phases could be grown [29.136]. For instance, with a small displacement of every second row of stripes in the perpendicular direction, the primitive rectangular cell transforms to a centered one very similar in terms of area per molecule [29.137, 138].

STM investigations provided further information on lying-down phases also on small domains that are not resolved in diffraction [29.105, 139–141]. Figure 29.16a–d shows a sequence of STM images of a Au(111) surface at 293 K [29.139] with a low thiolate coverage. Different lying-down phases coexist on the surface [29.105], namely the ordered structures β, χ^* (it is a variant of the χ-phase of Fig. 29.9), and δ, and the disordered ε-phase. At very low coverage a phase of isolated molecules with high mobility, called α-phase [29.105], is present (not shown in Figs. 29.16, 29.9 and [29.105]). The four images are

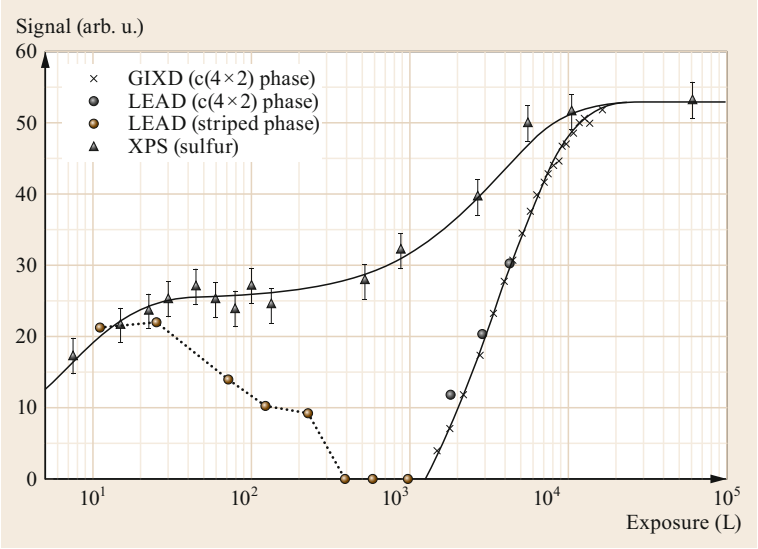

Fig. 29.15 Decanethiol deposition on Au(111) single crystal at 300 K by vapor-phase deposition in ultrahigh vacuum. Different measured signals versus thiols exposure are shown. XPS: signal from sulfur 1s. LEAD and grazing incident x-ray diffraction data correspond to the particular phase formed at the given coverage. (Reprinted from [29.103], with permission from Elsevier)

acquired with a time lapse of 420 s and it is evident that the boundaries between two phases are changing in time. The β-phase is a striped phase in which the decanethiolate molecules are lying flat on the Au(111) surface and are arranged in an alternating head-to-head and tail-to-tail registry (Fig. 29.16g) with a corrugation of 0.5 nm along the row direction and a periodicity of 3.3 nm across the stripes. The δ-phase is similar, but the tails of the molecules are lying partly on top of each other. Therefore the stripe width is only 7.5 times the nearest-neighbor gold distance (2.2 nm), with a periodicity $(5\sqrt{3}\times\sqrt{3})$R30°. The χ^*-phase is a mixture of small β- and δ-domains and shows a dynamical behavior with a switching between the stripe components. The disordered ε-phase does not show any structure but the height profiles are consistent with decanethiolate molecules lying flat on the Au(111) substrate. In the images of Fig. 29.16a–d, the δ-phase covers completely the lower terrace (top part of the image) and remains stable with time. The β and χ^*-domains occupy the upper terrace (bottom part) and partially convert into each other with time. Vacancy islands with a single layer depth also show some dynamics since they change size and, in most cases, a well-ordered β-phase is observed inside them.

At higher coverage, a standing-up phase is formed. For long chains ($n > 9$) the structure has a $(\sqrt{3}\times\sqrt{3})$R30° registry, as expected from the packing of molecules on Au(111). The alkyl chains are tilted by an angle θ and twisted by an angle ψ, according to the notation reported in Fig. 29.10c. Depending on the endgroup, these angles are in the range 28°–40° and 50°–55°, respectively, as determined by IR spectroscopy [29.142]. A study performed with x-ray diffraction on n-alkanethiols with $10 \le n \le 30$ [29.143] showed two different regimes: $32° < \theta < 34°$ for $10 \le n < 15$ and $30° < \theta < 31°$ for $15 < n \le 30$. The tilt direction from the next-nearest neighbor was $\approx 15°$ for the former regime and between 4° and 9° for the latter.

Finally, for a full coverage SAM, the formation of an overlayer was discovered by LEAD [29.144] and confirmed by x-ray diffraction [29.145, 146] and STM [29.147, 148] (Fig. 29.17). It is usually referred to as c(4 × 2) using an unconventional notation; in fact the unit cell size is referred to as the $(\sqrt{3}\times\sqrt{3})$R30° overlayer of molecules. With respect to the Au(111) lattice, the structure is more appropriately denoted as $(3\times 2\sqrt{3})$.

The evidence for two inequivalent molecules in the c(4 × 2) structure means a break of the hexagonal symmetry. A possible explanation is the difference in twist angle between the inequivalent molecules. However, x-ray data [29.149] suggested that the difference should be also related to the different adsorption site of the headgroup. In fact, a study performed with x-ray standing waves (XSW) [29.150] showed that there are two distinct lateral and vertical positions for sulfur. This was in contrast with the single site predicted by the standard model and based on the observation that elemental sulfur adsorbs on transition metal surfaces at highly coordinated sites, such as the threefold hollow site on fcc(111) surfaces (e.g., S/Ni(111) [29.151]). The XSW investigation [29.150] also showed that the results for striped phases are indistinguishable from standing-up ones.

STM studies could determine the sulfur position but, if the alkanethiolates in the SAMs are too long, the Au–S interface is buried underneath the hydrocar-

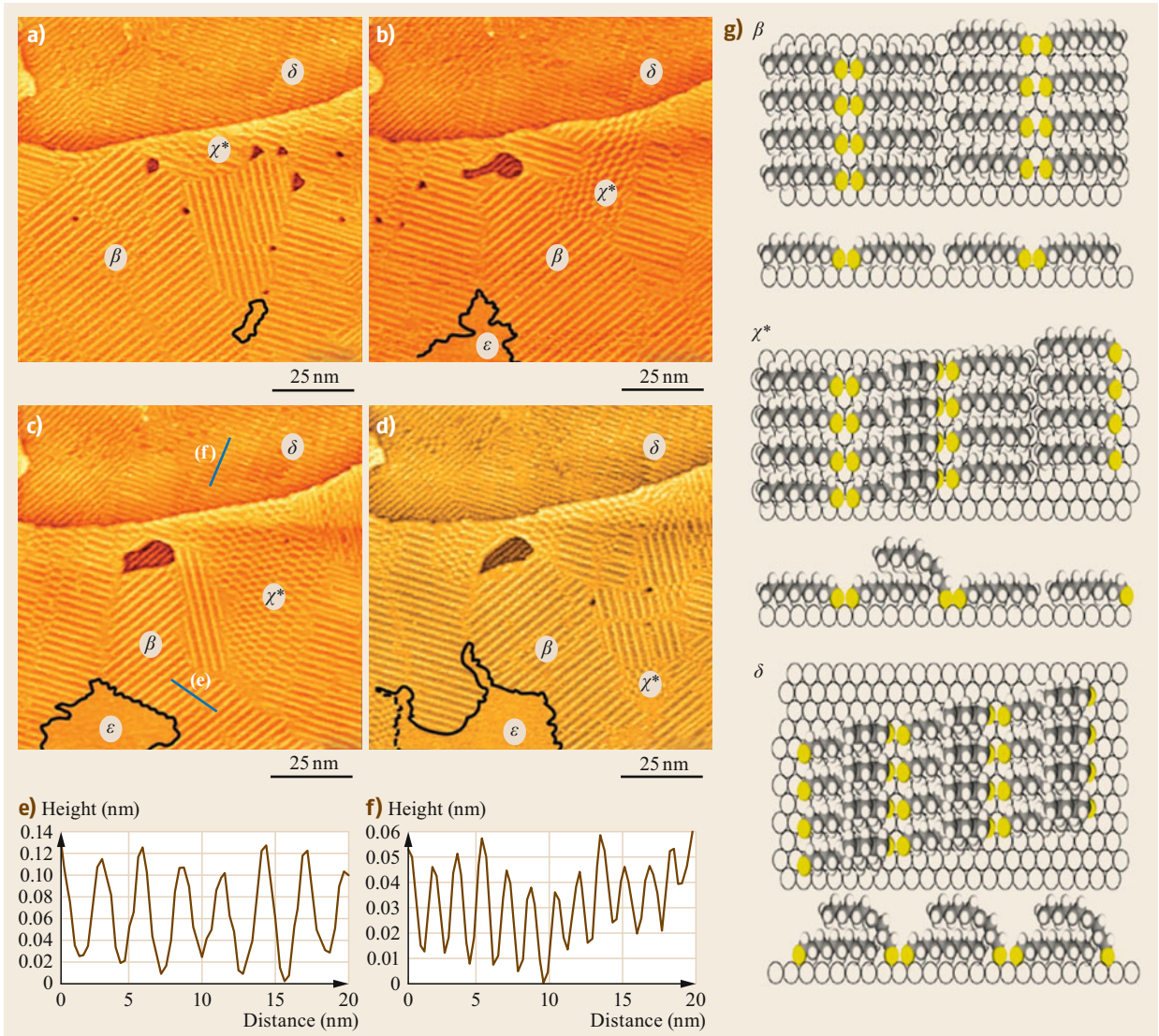

Fig. 29.16 (a–d) Sequence of STM images of a decanethiolate SAM on Au(111) at 293 K ($V = 1.2$ V, $I = 190$ pA). Regions β, δ, and χ^* are ordered phases while ε is a disordered phase. The *solid line* marks a domain boundary between the β-phase and the disordered ε-phase, while the *dashed line* marks a χ^*-ε-domain boundary. Consecutive images were measured with a time lapse of 420 s. Line profiles **(e,f)** were taken across the β and δ-phases in **(c)**, respectively. The stripe widths are **(e)** 3.3 nm and **(f)** 2.2 nm. **(g)** Schematic representation of top and side views of β-, χ^*-, and δ-phases. For the sake of simplicity metal–thiolate bond is represented here by a simple bond between a sulfur atom and a gold atom of the Au(111) substrate. (Reprinted with permission from [29.139]. Copyright (2013) American Chemical Society)

bon chains. Therefore, short chain alkanethiols SAMs attracted a lot of interest both for the possibility of a direct imaging of headgroups and because they can be simulated more easily.

For methylthiolate SAMs, the shortest and apparently simpler *n*-alkanethiol, *Dishner* et al. [29.152] reported a coexistence between $(2\sqrt{3} \times 3)$ and $(2\sqrt{3} \times \sqrt{3})$R30° structures. The latter was confirmed by *Danisman* et al. [29.153], while a new (3×4) structure was observed [29.154–156]. At low temperature, the (3×4) was coexistent with the previously mentioned hexagonal phases but He atom diffraction and LEED data did not support the $(2\sqrt{3} \times 3)$ [29.156]. Moreover, the (3×4) diffraction pattern disappeared

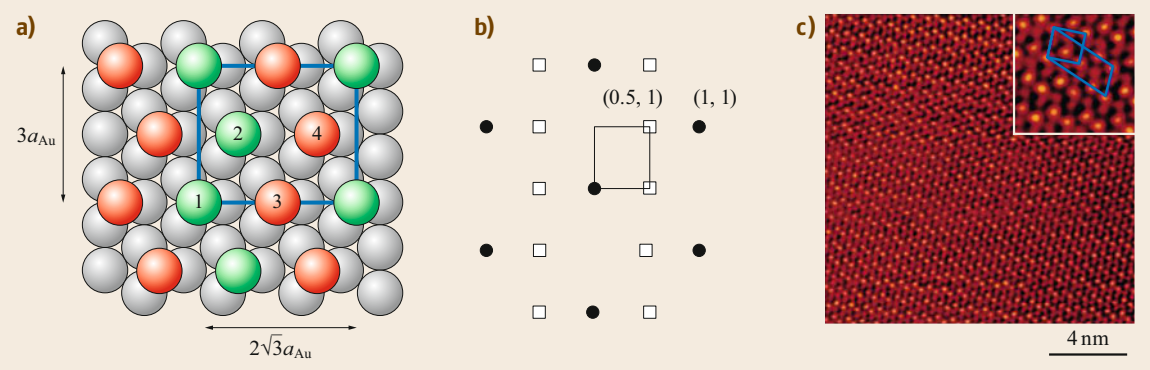

Fig. 29.17a–c A c(4×2) superlattice (or rectangular $(3\times 2\sqrt{3})$ overlayer, if expressed with respect to the lattice spacing of the Au substrate) of decanethiol on Au(111). Two-dimensional schematic view of the structure in real space **(a)** and in reciprocal space **(b)** and corresponding STM image **(c)**. Diffraction peaks: *full circles* correspond to the hexagonal $(\sqrt{3}\times\sqrt{3})$R30° periodicity, *open squares* are related to the superlattice. The systematic absence of superlattice peaks with integer indices, such as (1, 0), (1, 2), etc., indicates the presence of symmetry equivalent molecules in the unit cell of the overlayer. In particular, the pair of molecules labeled 1 and 2 and the distinct pair labeled 3 and 4. (Reprinted with permission from [29.148]. Copyright (2003) American Chemical Society)

at (315±10) K, leaving only the hexagonal overlayer and this transition was reversible. More recent studies have suggested that the $(\sqrt{3}\times\sqrt{3})$R30° periodicity might not be the real character for RS–Au bonding [29.157]. In fact, experimental observations supported by calculations [29.129, 158, 159] showed that the sulfur headgroup is not directly adsorbed to Au(111) and that the gold adatoms play a role in forming the SAM. The creation of gold adatoms is consistent with the observation of vacancy islands on thiol-covered surfaces; adatoms were observed to coexist with striped phases [29.127]; adatoms can also assist the dissociation [29.160] and stabilize the structure [29.161], and could explain the relatively high mobility in SAMs. Another indirect suggestion that adatoms are involved in the alkanethiols SAMs is the study of surface morphology after the removal of an octanethiolate SAM. Large triangular Au islands were observed to form where the SAM was present [29.162]. For example, after water dissociation under the STM tip, the resulting hydrogen determines the breaking of the Au–S bond of an octanethiol SAM and the release of gold adatoms [29.163]. Going back to the methylthiolate-gold system, the distance between the two methyl groups in the CH_3S–Au–SCH_3 complexes is too large, so that the complex does not directly fit into a $(\sqrt{3}\times\sqrt{3})$R30° lattice [29.164]. On the other hand, in the structural model by *Mazzarello* et al. [29.158] a dynamic equilibrium between adatom-methylthiolate complexes and bridge-bonded thiolate species adjacent to vacancy creates a disordered monolayer in which the average structure satisfies the $(\sqrt{3}\times\sqrt{3})$ symmetry. Alternatively, *Voznyy* et al. found a $(3\times 4\sqrt{3})$R30° structure for methylthiolate [29.159] and, using the previous idea of the disordered phase by assuming a $(3\times 4\sqrt{3})$ with reduced long-range order at 75% of saturation coverage, they were able to show that the corresponding diffraction pattern showed a $(\sqrt{3}\times\sqrt{3})$ periodicity although, locally, the unit cell is different. Voznyy et al. also discussed the possibility to transform *trans*-complexes into their *cis*-isomers of the $(3\times 4\sqrt{3})$ structure to describe the c(4×2) of long chain SAMs.

Figure 29.18 shows STM images, measured on a low-coverage methylthiolate film on Au(111) by *Voznyy* et al. [29.159]. The analysis of the images shows adatom complexes in which sulfur atoms bind covalently both to the Au adatom of the complex and to surface gold atoms, besides preserving the radical methyl tail. Those complexes are chiral due to the presence of different substituents around the sulfur atoms which, by using the stereochemical nomenclature, can be both *S*-type or *R*-type. The complex is a *trans*-isomer if both sulfur atoms are of the same type, *R* or *S* (Fig. 29.18f for the *R*-type case); otherwise it is a *cis*-isomer, as in Fig. 29.18g. For the two isomers, the authors calculated a difference in adsorption energy < 0.1 eV but with a barrier of 0.50 eV to transform an isomer into the other. Moreover, the authors observed the formation of stripes in which the complexes are in the same *trans*-configuration, but on increasing coverage, they did not observe a 2-D-ordering; this fact is probably related to a weak or even repulsive interstripe interaction. Instead, this 2-D ordering was observed for propylthiolate ($n = 3$), for which there is an increase of van der Waals interactions between tails. It is also interesting

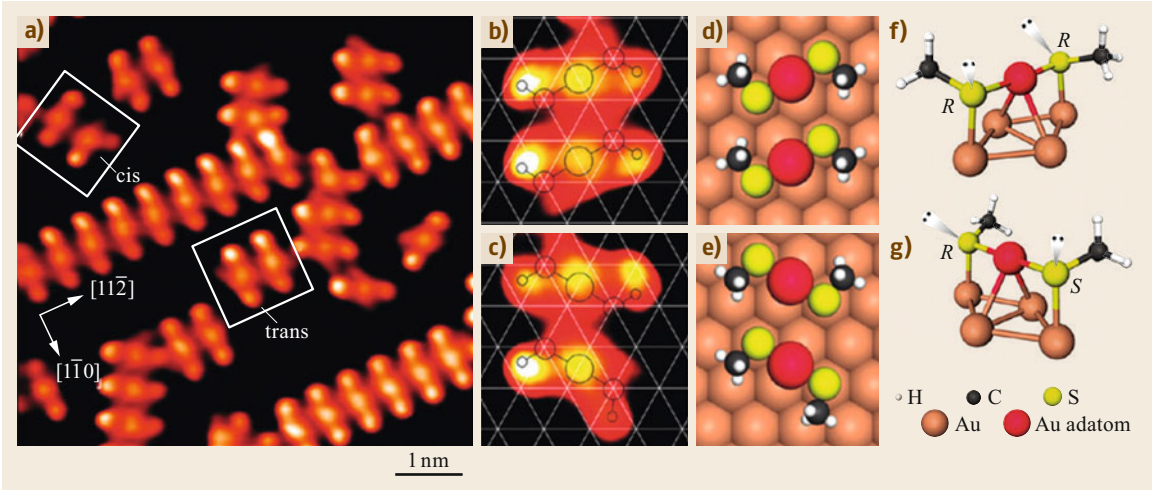

Fig. 29.18a–g Methylthiolate at low coverage on Au(111). **(a)** STM image. *White squares* indicate the different complexes reported in the enlarged images of panels **(b)** and **(c)**. Panel **(b)** refers to adjacent *trans*-$(CH_3)_2Au$ complexes; panel **(c)** shows adjacent *cis*- and *trans*-adatom complexes. The superimposed triangulation represents the Au lattice. The corresponding schematic models are shown in panels **(d)** and **(e)**, respectively. Panels **(f)** and **(g)** show the DFT optimized structures for *trans*- and *cis*-configurations. (Reprinted with permission from [29.159]. Copyright (2009) American Chemical Society)

that in this last case the authors found a chiral recognition between the 1-D stripes, since adjacent stripes present alternating *R*,*R* and *S*,*S* symmetries [29.159].

A (3×4) structure was also observed for ethanethiolate ($n = 2$) [29.165, 166] and propylthiolate ($n = 3$) SAMs [29.166], while not observed for butylthiolate ($n = 4$) [29.167]. Therefore, the experiments show that, at $n = 4$, steric hindrance and van der Waals interactions between chains start to compete with the headgroup–Au interaction to produce the hexagonal structure of long chain SAMs.

The gold adatoms seem to be a general feature for the adsorption of thiolates on Au(111). On the one hand, the structure of short chain thiolates seems based on dithiolate complexes; on the other hand, XSW experiments on hexylthiolate ($n = 6$) and octylthiolate ($n = 8$) SAMs demonstrated that such species also bind to gold adatoms but form *R*,*S*-Au_{ad} complexes with a single thiolate [29.168]. More generally, considering thiols with a structure different from a simple alkyl chain, STM studies on low-coverage benzenethiol on Au(111) revealed the role of gold adatoms; in fact phenylthiolate was observed to self-assemble into surface-bonded complexes with gold adatoms [29.169]. Instead, mercaptobenzoic acid, the thiolate which was observed to form gold adatom complexes on gold clusters [29.170], adsorbs on Au(111) without the formation of vacancy islands; the observed gold islands present a low coverage and are not consistent with Au-adatom models [29.171].

29.3.3 Amino Acids

Finally, a large category of molecules which naturally undergo self-assembly are small molecules of biological interest. Indeed, the first investigations on the H-bond-mediated assembly on surfaces were stimulated by the observation of selective base pairing of nucleic acids. DNA nucleotides were therefore among the first biological molecules to be studies on surfaces in a controlled way, i.e., with the approach typical of surface science and with the aim of understanding the phenomena at the molecular level [29.19, 20]. However, most surface science studies on the anchoring and self-assembly of biological molecules have been performed on amino acids and short peptides [29.17, 18]. The reasons are manifold. First, amino acids are the basic constituents of peptides and proteins, while oligopeptides represent the simplest organized structure formed by amino acids. Thus, the structure of these molecules is simple enough to use these systems as models for the chemisorption of biofunctional molecules. On the other hand, they are *complex* enough to provide useful information on the fundamental mechanisms governing the hybrid organic–inorganic interface. Finally, all the twenty natural amino acids, except glycine, are chiral. Since it is now established that the surface reactivity can be modified by exploiting the intrinsic chirality of amino acids and peptides [29.174, 175], their action as a chiral modifier is crucial for chiral separation or enantio-selective heterogeneous catalysis.

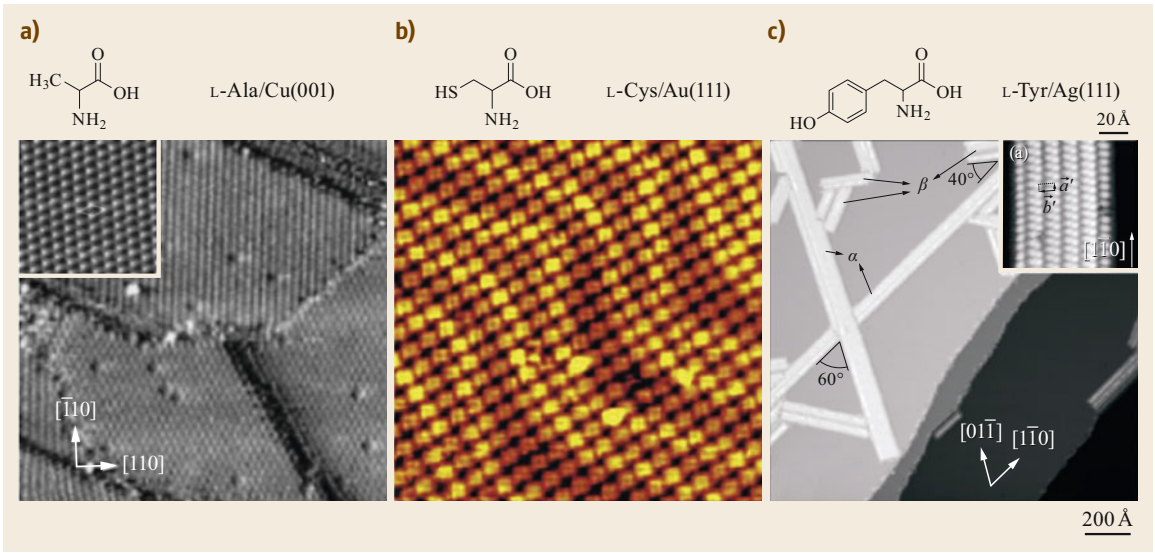

Fig. 29.19a–c STM images showing a self-assembled geometry detected for different amino acid species on Cu, Au and Ag surfaces, respectively. **(a)** L-alanine/Cu(001) (image size $22.5 \times 22.5\,\mathrm{nm}^2$, $V = -1.0\,\mathrm{V}$, $I = 1.0\,\mathrm{nA}$). The image shows large domains of the of the $c(2 \times 4)$ superstructure, which forms in two equivalent orientations. *Inset*: Molecule-resolved image of the $c(2 \times 4)$ superstructure in one orientation ($5.5 \times 5.5\,\mathrm{nm}^2$, $V = -1.0\,\mathrm{V}$, $I = 0.6\,\mathrm{nA}$). A $c(2 \times 4)$ unit cell is outlined. **(b)** One of the different molecular structures formed by L-cysteine on Au(111) depending on substrate temperature and surface coverage. The underlying herringbone reconstruction of Au(111) is preserved (image size $22 \times 23\,\mathrm{nm}^2$). **(c)** L-tyrosine deposited on Ag(111) at 170 K and then annealed to 320 K. Supramolecular self-assembled domains extend under the influence of the underlying substrate symmetry (image size $200 \times 200\,\mathrm{nm}^2$, $V = 0.5\,\mathrm{V}$, $I = 0.1\,\mathrm{nA}$). *Inset*: Enlargement of the 2-D L-tyrosine supramolecular nanoribbons on Ag(111) ($V = 0.5\,\mathrm{V}$, $I = 0.07\,\mathrm{nA}$). (Reprinted from [29.37, 172], with permission from Elsevier, reprinted with permission from [29.173]. Copyright (2010) American Chemical Society)

Most of the studies on self-assembly of amino acids at metal surfaces has been performed on Cu and other noble metals, though a few works on transition metals as Pt, Pd and Ni have been reported [29.176–180]. The results underline the role of the substrate, which is determined mainly by its reactivity, but also the existence of some common features. The general trend is that amino acids adsorb on Cu, Au and Ag surfaces at RT in the monolayer regime, self-assembling in ordered structure of various geometry, depending on experimental conditions (Fig. 29.19). Multilayers form rarely at 300 K [29.181], while they are observed at lower T.

Almost all the twenty natural amino acids have been deposited on Cu surfaces. The comparison among results on the different systems allows to draw a global picture in which both similarities and differences related to the surface geometry and/or to the molecular structure are evinced. This same comparison is much less straightforward on other metal surfaces, which have been investigated less systematically.

Amino acid adsorption can occur either in the neutral, in the anionic or in the zwitterionic form. The occurrence of zwitterionic adsorption is immediately evinced by XPS analysis of the layer since the presence of a charged $-NH_3^+$ functionality causes an upshift on the N 1s photoemission line (from a binding energy $E_b(\mathrm{N\,1s}) < 400\,\mathrm{eV}$ to $E_b(\mathrm{N\,1s}) \approx 401\,\mathrm{eV}$). On the other hand, adsorption in the anionic/zwitterionic form is evinced also by the presence of well-defined bands in the reflection adsorption infra red spectrum of each amino acid species. As an example, for Ala/Cu(110) direct evidence of an anionic species at low coverage is given by the presence of the symmetric stretch vibration of the carboxylate functionality, $\nu_s(\mathrm{COO}^-)$, at $1411\,\mathrm{cm}^{-1}$ (Fig. 29.20; [29.39]).

Molecules in direct contact with the Cu surface adsorb, in general, in the anionic form, while zwitterionic adsorption is characteristic of the multilayer. A common adsorption configuration can be identified for the different amino acids: the simplest species bind to the Cu surface in a μ_2 or μ_3 configuration, depending on coverage and annealing temperature. As shown in Fig. 29.20 for the case of alanine, they correspond, respectively, to the situation in which two or three bind-

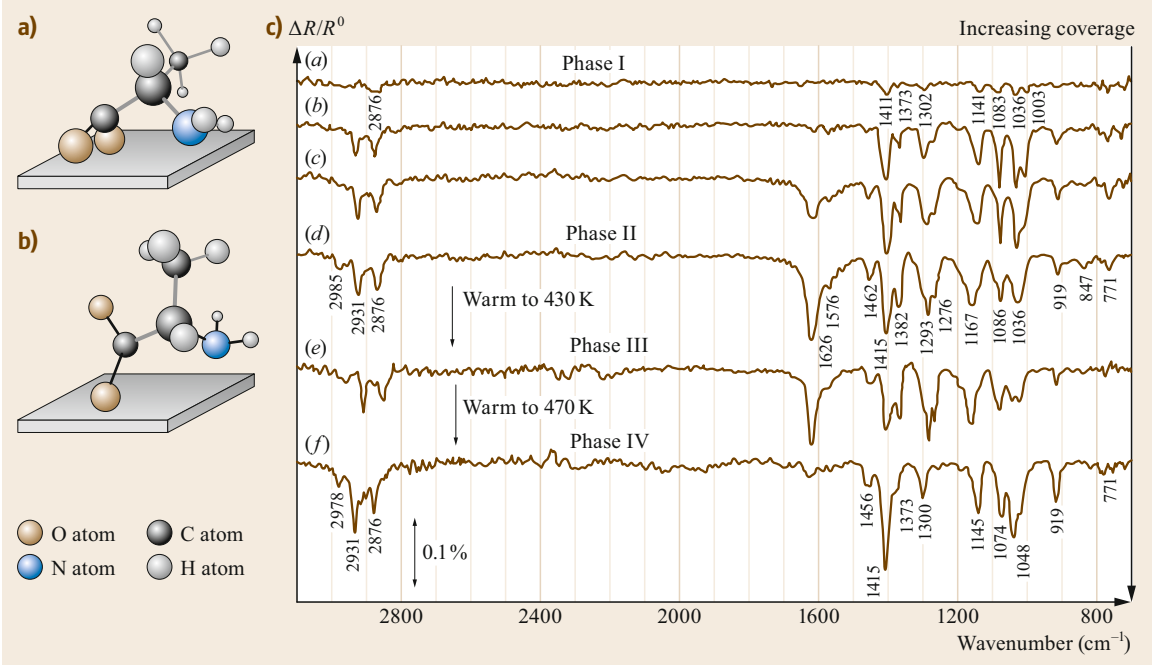

Fig. 29.20a–c Representation of the μ_3 and μ_2 bonding schemes discussed in the text, for the case of *S*-alaninate on Cu(110). **(a)** In the μ_3 configuration the two carboxylate oxygens are equidistant from the surface. This is evinced in RAIRS data (spectra (*a*) and (*b*) in **(c)**) by the intensity of the symmetric carboxylate stretch vibration, $\nu_s(\mathrm{COO}) = 1411\,\mathrm{cm}^{-1}$, and by the absence of the corresponding asymmetric stretch, $\nu_{as}(\mathrm{COO})$, expected around $1625\,\mathrm{cm}^{-1}$. Further analysis of the RAIR spectrum suggests that the OCO plane of the carboxylate group must be tilted towards the surface plane and that the plane of the NH_2 group lies almost parallel to the surface. **(b)** In the μ_2 configuration (spectra (*c*)–(*e*) in **(c)**), on the contrary, one O atom points away from the surface, as revealed by the strong intensity of the $\nu_{as}(\mathrm{COO})$ mode at $1626\,\mathrm{cm}^{-1}$, and the methyl group is held almost vertical along the surface normal. **(c)** The identification of phase I to IV is coherent with the STM analysis discussed in Fig. 29.21. (Reprinted from [29.39], with permission from Elsevier)

ing points are present. In μ_2 configuration, usually the molecule binds through the N atom and one O atom of the carboxylate/carboxylic group, with the second O atom protruding into the vacuum. In the more stable μ_3 configuration, the N atom and both carboxylate O atoms are bound to the surface. For the smallest amino acids, like glycine and alanine, the side chain protrudes towards the vacuum. On the contrary, if the side chain is more complex and contains additional, possibly reactive functional groups, it may bend towards the surface and anchor to it in a fourth point (μ_4 conformation). This behavior has been observed, e.g., for lysine on Cu(110) [29.182] and for serine on Cu(531) [29.183].

An immediate consequence of the very similar adsorption conformation of the different amino acid species is that these molecules self-assemble on the surface forming similar long-range adsorption patterns, as demonstrated by LEED and STM data. Three distinct phases may form on Cu surfaces with increasing molecular density:

i) The 2-D gas, at low coverage. This phase is driven by repulsive interaction among the molecules, which are very mobile on the surface so that they cannot be imaged by STM
ii) The intermediate phase, in which *standing* molecules align in short rows and are stabilized by intermolecular H-bonds
iii) The solid phase, consisting of extended, ordered superstructures.

The (3×2) superstructure is the most stable pattern observed on Cu(110) for simple molecules as *Gly* and *Ala* [29.39, 184, 185] (Fig. 29.21d), but also for more complex ones as *Lys* [29.186]. At saturation coverage, the other amino acids usually organize in less-dense superstructures, due to the need of accommodating larger molecules. In all cases, hydrogen bonding is essential for the stabilization of the layer.

The case of alanine on Cu(110) is paradigmatic of how the self-assembly behavior of amino acids can

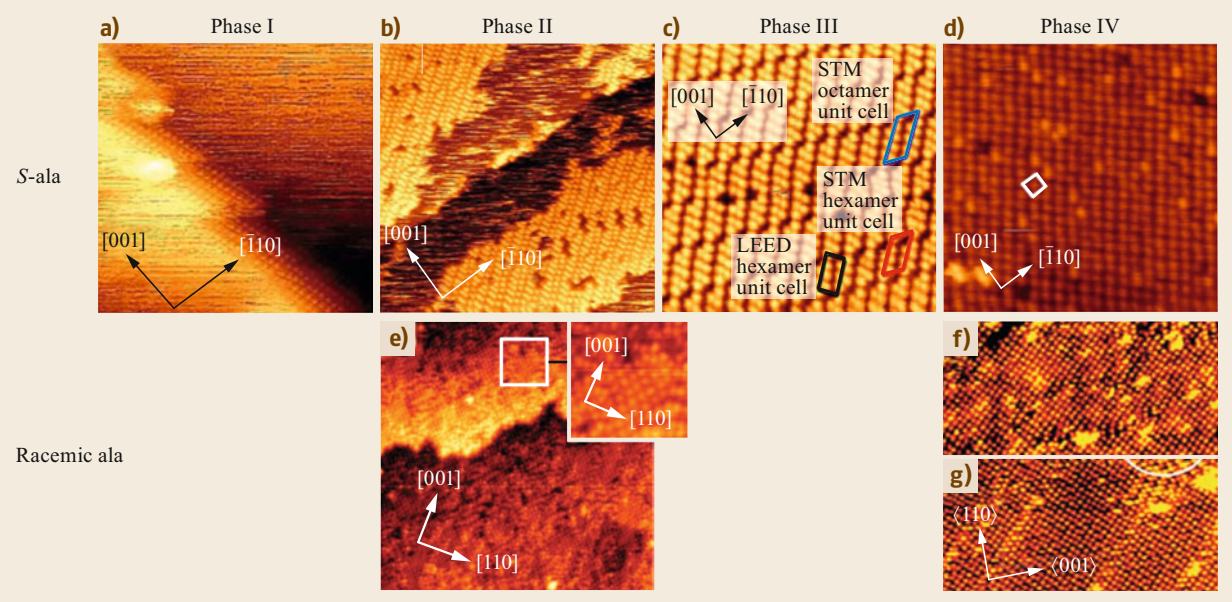

Fig. 29.21a–g STM images showing the various geometries of alaninate on Cu(110) obtained under different experimental conditions. *Top row*: *S*-alanine/Cu(110). **(a)** Phase I, showing alaninate molecules at step edges and streaky areas on terraces (image size $29.2 \times 24.6\,\mathrm{nm}^2$, $V = 1.02\,\mathrm{V}$, $I = 1.08\,\mathrm{nA}$). **(b)** Phase II, showing the details of chiral chains covering large terraces (image size $25.4 \times 24.6\,\mathrm{nm}^2$, $V = 2.08\,\mathrm{V}$, $I = 1.97\,\mathrm{nA}$). **(c)** Phase III. The image shows size-selected clusters of 6 or 8 molecules (image size $12.7 \times 12.3\,\mathrm{nm}^2$, $V = 2.08\,\mathrm{V}$, $I = 1.97\,\mathrm{nA}$). Hexamer clusters occupy a unit mesh of $17.5\,\text{Å} \times 9\,\text{Å}$ and octamer clusters a unit mesh of $21.5\,\text{Å} \times 9\,\text{Å}$. The corresponding unit cells as determined by STM and the hexamer unit cell determined by LEED are marked. The hexamer unit cell in matrix notation is (5,3,3,1) according to STM and (2,2,5,3) according to LEED. **(d)** Phase IV. The STM image shows the achiral (3×2) reconstruction (image size $12.7 \times 12.3\,\mathrm{nm}^2$, $V = 2.83\,\mathrm{V}$, $I = 1.14\,\mathrm{nA}$; annealing temperature 453 K). The unit cell (marked in the figure) contains two molecules and measures $7.2\,\text{Å} \times 7.6\,\text{Å}$. *Bottom row*: racemic alanine/Cu(110). **(e)** Phase II showing patches of achirally ordered molecules (image size $40 \times 40\,\mathrm{nm}^2$, $V = 0.36\,\mathrm{V}$, $I = 0.15\,\mathrm{nA}$). The *inset* is an enlargement of the area marked by the *square* and shows the details of the local order of racemic phase II. **(f)** Racemic phase IVa associated with the distorted (3×2) LEED pattern (image size $22.4 \times 11.2\,\mathrm{nm}^2$, $V = 1.05\,\mathrm{V}$, $I = 0.17\,\mathrm{nA}$). **(g)** Racemic phase IVb associated with the true (3×2) LEED pattern (image size $22.4 \times 11.2\,\mathrm{nm}^2$, $V = 1.49\,\mathrm{V}$, $I = 0.59\,\mathrm{nA}$). (Reprinted from [29.34], with permission from Elsevier)

depend on experimental conditions and how chirality plays a role in this process. For this reason, we are going to treat it in some details in the following. According to RAIRS data, in the multilayer regime, stable below room temperature, the molecules are predominantly in a zwitterionic state, as expected for solid alanine [29.187]. Conversely, adsorption in the 300–470 K temperature range always yields to the formation of an alaninate species, as witnessed by the sequence of RAIRS spectra of Fig. 29.20.

This picture, relatively simple from the spectroscopic point of view, gets much more complicated when the morphology of the alanine layers is taken into account. STM analysis reveals, indeed, a polymorphic behavior of the L-Ala/Cu(110) system [29.35, 39], with the identification of four different surface structural phases depending on alanine coverage and surface temperature (Fig. 29.21). At low coverage and RT, a disordered phase occurs, in which the alaninate molecules are found concentrated in small areas close to the steps (phase I in Fig. 29.21a). Due to the high mobility of individual alaninate units, no STM images could be recorded for the molecular species at terraces, even if RAIRS data show a significant growth of the molecules in the μ_3 configuration (spectra (*a*) and (*b*) in Fig. 29.20c). Increasing the coverage, molecules at terraces get to interact with each other and self-assemble into chains some tens of nanometers long and aligned in the $\langle\bar{1}12\rangle$ direction (phase II in Fig. 29.21b). The chain structure is not homogeneous, since single chains (formed by individual alaninate units) and double chains (consisting of paired molecules) turn into each other every few molecular units along the chain length. We note that $\langle\bar{1}12\rangle$ is not a symmetry direction of the Cu(110) surface; therefore, the system is starting to organize in a chiral fashion. Spectroscopic anal-

ysis indicates the coexistence of alaninate molecules both in μ_3 and in μ_2 conformation (spectrum (*d*) in Fig. 29.20c). The creation of the μ_2 species at higher coverage is attributed to kinetic factors since only the μ_3 species is formed at all Θ. Interestingly, the authors suggest that the μ_2 species triggers chain formation at the terraces, and thus that the presence of alaninate units in this configuration is essential for supramolecular chiral organization.

Upon annealing of phase II, the RAIRS spectra remain unaltered (trace (*e*) in Fig. 29.20c), indicating that molecules in both the μ_3 and μ_2 configuration are still present. Instead, the alaninate chains evolve into a highly ordered chiral overlayer (phase III in Fig. 29.21c) formed by clusters of 6 or 8 units lined up in pairs in the ⟨110⟩ direction and with an overall growth direction broadly parallel to the nonsymmetric $\langle\bar{1}12\rangle$. In phase III, 2-D chirality is expressed at the macroscopic length scale, since size-defined chiral clusters self-assemble into a defined chiral array with chiral channels and spaces of bare metal left between them. The identical experiment performed with *R*-alanine produces the mirror image domain [29.188]. To determine the long-range order of the overlayer, several models of individual hexamers are proposed [29.35, 39], involving a different proportion of molecules in μ_3 and in μ_2 conformation on an unreconstructed or a reconstructed Cu(110) surface.

The chiral chains of phase II are precursors to the size-selected clusters of phase III. Both the chains of variable width observed at RT and the the peculiar organization in small, size-selected clusters at the higher temperature are the result of a competition between intermolecular forces and molecule–substrate interaction. Above a critical cluster size, the stress induced by maintaining optimum adsorption sites for the alaninate molecules and by maximizing the intermolecular interactions leads to a fracture in the assembly of the chains, opening two possible scenarios. In the former case, molecules can be forced away from their optimal adsorption site by intermolecular interactions; alternatively, the strength of the chemisorption bond forces surface reconstruction in order to optimize adsorption geometry. The former mechanism may well dominate at room temperature (phase II), where the barrier to significant reconstruction cannot be overcome. On the other hand, the higher temperature required to create phase III suggests that metal reconstruction may accompany the formation of regular size-selected clusters. The competition between molecule–molecule and molecule–metal interactions is a phenomenon to be generally taken into account on self-assembly processes. The behavior observed in the case of Ala/Cu(110) indicates a predominance of molecule–metal interactions. On the contrary, on less-reactive substrates such as Ag, intermolecular forces prevail and the formation of extended amino acid layers is observed [29.36, 189].

Further heating of the Ala/Cu(110) system in phase III to 470 K causes substantial changes in the RAIR spectra (trace (*f*) in Fig. 29.20c), indicating full conversion of μ_2 alaninate units into the μ_3 geometry. According to LEED and STM data, a new achiral (identical for both *S*- and *R*-alaninate) organization of the molecules appears on the surface (phase IV in Fig. 29.21d), characterized by a (3×2) superstructure with two molecules per unit cell ($\Theta = 1/3$) and by a pseudoglide plane in the ⟨001⟩ direction. This overlayer is stable up to 520 K. DFT analysis [29.190] found that, in the lowest energy configuration, each unit cell of the (3×2) enantiopure overlayer contains two molecules with opposite footprint chirality. The result is coherent with photoelectron diffraction measurements [29.191], which indicate the existence of two molecules with slightly different local adsorption sites within the (3×2) unit cell.

The formation of chiral/achiral overlayers starting from L-ala and depending on experimental condition indicates that chirality is a factor to be strictly monitored and considered when dealing with the self-assembly of amino acid species. Therefore, it is interesting to understand what happens when a racemic mixture is deposited on the surface. Separation of enantiomers within racemic crystals has been known for some time, while chiral recognition at surfaces has been investigated more recently but is nowadays a well-established phenomenon [29.17]. Despite that, there is not a straightforward behavior for surface chiral segregation—the formation of enantio-pure domains of opposite chirality—and each amino acid/metal system needs to be tracked separately. In general, if heterochiral interactions prevail, a racemic layer forms. This is the case for adsorption of racemic alanine on Cu(110) [29.188], for which formation of achiral domains is observed and the suppression of some of the phases present for the enantio-pure species occurs. In particular, while the disordered phase I is observed also for racemic alanine, phase II is significantly different. STM images show achiral patches with poor long-range order (Fig. 29.21e) and the LEED pattern, consisting of split and faint spots, confirms this picture. Also the thermal evolution of the racemic system follows an alternative path with respect to the one observed for the enantio-pure layer. Racemic phase II converts directly into the achirally organized phase IV at $T = 358$ K. The (3×2) overlayer of the racemic alanine mixture differs from the one described for pure *S*-alaninate since: (a) a smaller energy barrier is required for the racemic mixture, because both the energetically preferred foot-

prints of *S*- and *R*-alaninate can be accommodated at the surface. (b) The (3×2) structure presents initially a glide plane (see phase IVa in Fig. 29.21f), as in the case of *S*-alaninate, but the coverage can be further increased to create a *true* (3×2) LEED pattern with no glide plane (see phase IVb in Fig. 29.21g).

On the contrary, if homochiral interactions dominate, chiral segregation of enantiomers is favored. An example in this respect is provided by racemic Cys deposited on Au(110) [29.192]. The molecules organize in domains of dimers identical to those observed in previous experiments performed using pure enantiomers, while no new structures associated to the pairing of molecules of opposite chirality are found. Therefore, dimers are either of the LL form (rotated clockwise) or of the DD form (rotated anticlockwise), suggesting that the dimerization of the cysteine molecules is highly enantioselective, with each molecule binding exclusively to partners of the same chirality.

Chiral recognition is the preliminary step to chiral separation of D- and L-enantiomers, which is a key issue for chemical and pharmaceutical industries. This process can be enhanced by the use of suitable chiral surfaces and, in this respect, the case of serine adsorption at high Miller index Cu surfaces is emblematic. Distinct enantio-resolution ability was observed on Cu(110), where the L- and D-enantiomers aggregate in well-ordered islands, and on the stepped Cu(643) and Cu(3 1 17) surfaces [29.193, 194]. However, since the two enantiomers have very similar adsorption energies, chiral separation is not straightforward. On Cu(531), on the contrary, the difference in adsorption energies between D- and L-serine is significant and this is the reason why many theoretical and experimental efforts focused on exploring the adsorption configurations and enantioselective ability of serine on this surface [29.183, 195, 196]. Very recently, *Wang* et al. calculated the adsorption geometries and energetics of D- and L-serine at the (531) face of Cu, Ag, Au, and Pd [29.197]. Cu(531) is the most efficient in chiral separation due to the conformational strain imposed both on the molecule and on the substrate upon adsorption of D-serine. In addition, enantio-selectivity is predicted to be enhanced up to 36% by decorating the (110) and the (311) microfacets of Cu(531) with Ni atoms.

Focusing the attention back to the self-assembly process and to the forces involved, we recall that, in the above-mentioned case of Ala/Cu(110), the molecule–substrate interaction is the driving force of the self-assembly mechanism. On the contrary, if a less-reactive metal is employed, intermolecular interactions may prevail and interesting phenomena can be observed. This is indeed the case of glutamic acid on Ag. Though adsorption of this amino acid has been investigated on all low Miller index surfaces [29.36, 84, 189, 198], the L-Glu/Ag(100) system has been unravelled in great detail [29.28, 36, 84].

As shown in Fig. 29.22, L-Glu self-assemble on Ag(100) forming single-layer islands, the geometry and extension of which changes by varying the surface temperature between 250 and 350 K. A row-like structure is observed at $T = 250$ K (Fig. 29.22a), a comb-like structure at $T = 300$ K (Fig. 29.22b), while a flower-like (Fig. 29.22c) and a square-like (Fig. 29.22d) structure coexist at $T = 350$ K. XPS analysis indicates that, in all cases, the Glu units are in the nonzwitterionic form. The co-presence of comb-like and flower-like domains at the transition temperature $T = 325$ K, combined with the thermal evolution measured by XPS, suggests the existence of several local minima in the energy diagram of the Glu/Ag(100) system.

The two assemblies observed at 350 K were reproduced by DFT-D calculations [29.28, 84] and simulated STM images in very good agreement with the experimental ones confirm the validity of the proposed models (Fig. 29.23). At variance with the majority of cases reported in literature, the *square* structure consists of neutral molecules physisorbed on the surface through weak vdW forces, while H-bonds between carboxyl groups and the formation of a OCOH–OCOH–OCOH–OCOH cycle at the vertex of the squares are the main driving force for the self-assembly (Fig. 29.23b).

The flower structure (Fig. 29.23a,c,e) is formed by 50% of deprotonated Glu units in upstanding conformation and arranged in the bright tetrameric units. The other molecules are in the neutral form and lie flat on the surface. This configuration is characterized by glutamate anions strongly bound to the surface and by the physisorbed surrounding Glu molecules, which conserve some degree of freedom in the layer. As evident from the table in Fig. 29.23, the *flower* and the *square* assemblies have similar dispersion energy and H-bond interaction energy but, as a consequence of the different chemical states of the Glu molecules, the binding energy to the substrate is significantly different. This is therefore a good example of how the balance among the different forces acting on the molecules may affect their final configuration. In addition, the thermodynamical isostability of the two assemblies at 350 K is explained by considering entropic factors which have a strong stabilizing impact on the poorly adsorbed *square* structure [29.199]. The transition from one structure to the other is expected to be kinetically possible thanks to the low reactivity of the Ag(100) surface.

Finally, it is worth considering self-assembly of amino acids at metal surfaces also in view of their perspective role as base catalysts for enantioselective

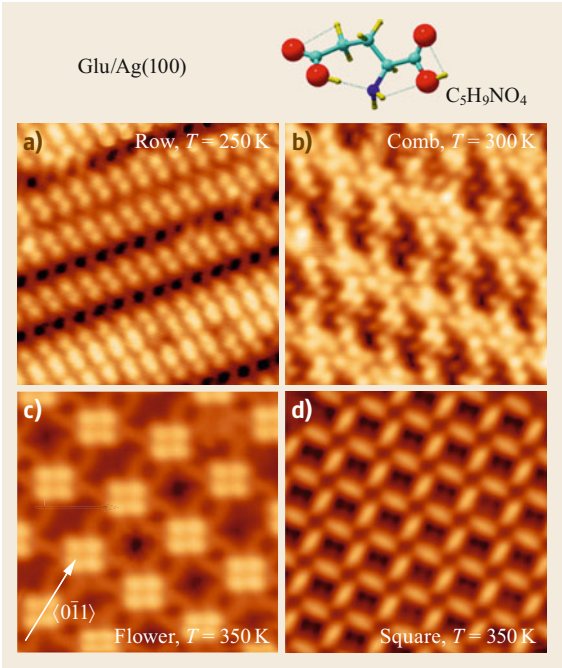

Fig. 29.22a–d Overview of the self-assembled structures observed upon L-Glu deposition on Ag(100) at different T (image size 80 Å × 80 Å). **(a)** *Row* structure: The amino acids lie flat on the surface and form long, one-molecule-wide rows oriented ≈ 40° off the $\langle 0\bar{1}1\rangle$ direction. In each row, adjacent molecules are separated by (6.5 ± 0.2) Å and their molecular axis is at an angle of ≈ 65° with respect to $\langle 0\bar{1}1\rangle$. The estimated local coverage is $\Theta_{Glu} \approx 0.09$ ML. **(b)** *Comb* structure: The surface is covered by large monolayer islands consisting of elongated features oriented along the $\langle 0\bar{1}1\rangle$ directions (periodicity ≈ 26 Å). Each feature is formed by a linear backbone (two lines of molecules separated by (5.6 ± 0.2) Å) and by additional Glu units inserted as *teeth* at ≈ 45° (periodicity (14.0 ± 0.2) Å, $\Theta_{Glu} \approx$ 0.09 ML). **(c)** *Flower* structure: Clusters of four molecules (the *flowers*) are linked by *sticks* showing a lower contrast. Adjacent maxima within each tetramer are separated by 5.8 and 5.4 Å, respectively. Tetramers form a square pattern with the main axes aligned within 5° with the $\langle 0\bar{1}1\rangle$ directions (periodicity ≈ 21 Å). The sticks are also oriented in the high symmetry direction of the substrate. The Glu local coverage is $\Theta_{Glu} = 0.14$ ML but, considering that only a fraction of the surface is covered by Glu islands, the overall coverage is likely to be significantly smaller. **(d)** *Square* structure: Glu molecules are physisorbed and lie flat on the surface, 4.6 Å above the surface plane. They arrange in a square geometry oriented ≈ 20° off $\langle 1\bar{1}0\rangle$. The axis of the Glu units is oriented ≈ 10° off the $\langle 1\bar{1}0\rangle$ direction, so that a chiral pattern forms in self-assembled islands. The average dimensions of the single squares are $a = (13.2 \pm 0.8)$ Å and $b = (12.2 \pm 0.7)$ Å for the sides and $c = (19.7 \pm 0.8)$ Å for the diagonal, from which a local coverage $\Theta_{Glu} \approx 0.10$ ML is deduced. (Reprinted with permission from [29.36]. Copyright (2011) American Chemical Society) ◄

reactions, the importance of which is growing and growing due to the demand of pharmaceutical and chemical industries for large quantities of optically pure chemicals. Though several studies on enantioselective systems have been performed on Cu, which is also the most investigated substrate in this respect [29.17], it is in this field that amino acid adsorption at transition metals becomes of interest. Enantioselectivity is transferred to the metal substrate by adsorption of a chiral species (modifiers) but, so far, only a few categories of enantioselective heterogeneous catalytic processes have been investigated at the fundamental level. Among them, we mention the enantioselective hydrogenation of α-keto esters over Pt-based systems and the asymmetric hydrogenation of β-keto esters over Ni-based catalysts [29.174, 175]. On Ni-based materials the most studied chiral modifiers are (*R*,*R*)-tartaric acid [29.200, 201] and (*S*)-glutamic acid [29.202]. The latter species shows a peculiar behavior as a modifier, since the chirality of the final product in the hydrogenation of β-keto esters depends on T_{ev} (Fig. 29.24). Glu adsorption below 350 K results in a preference for the *R*-enantiomer, while Glu adsorption above 350 K favors the *S* species [29.174]. (*S*)-Glu adsorption at Ni(111) and at Ni/Au bimetallic systems was thoroughly investigated by the group of *Baddeley* [29.202–204], who also studied the chemical activity of the chirally modified (*S*)-Glu/Ni catalyst with respect to the simplest β-keto ester, i.e., methylacetoacetate (MAA) [29.180, 205]. By combining STM images with RAIRS results, they could demonstrate that (*S*)-Glu initially adsorbs on Ni(111) at 300 K in the zwitterionic form and prevalently at steps. With increasing coverage (Fig. 29.25a) the terraces are populated by molecules in the form of anionic monoglutamate. Small areas in which the molecules present an ordered $(\sqrt{7} \times \sqrt{7})$R19.1° geometry (local coverage 0.14 ML) or a $(3\sqrt{3} \times 3\sqrt{3})$R30° geometry (local coverage 0.11 ML) appear. Such structures are stabilized by hydrogen bonding. The extent of ordering is limited, since the authors estimate the ordered domains to cover 10–20% of the surface and to have a typical diameter of ≈ 10 nm, but it increases by annealing the surface to 350 K (Fig. 29.25b). On the contrary, further heating to 400 K (Fig. 29.25c) changes the nature of the adlayer: it consists now of 1-D structures, probably stabilized by H-bonding interactions between neighboring molecules and extending along the close-packed Ni directions.

Energy	Flower assembly (eV/molecule)		Square assembly (eV/molecule)	
E_{total}	−2.83		−1.29	
E_{disp}	−0.82	29%	−0.38	29%
E_{H_bond}	−0.75	26%	−0.89	69%
E_{bind}	−1.26	45%	−0.02	2%

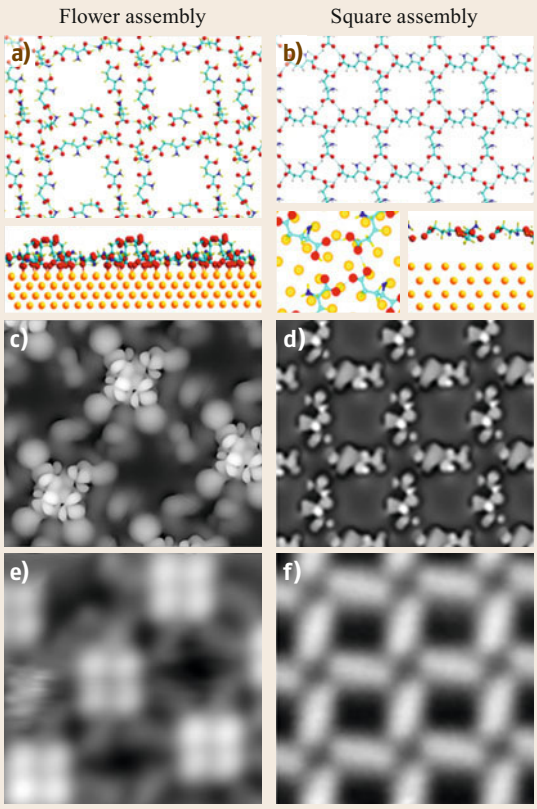

Fig. 29.23a–f The Table summarizes the adsorption, binding and cohesion energies of the *flower* and *square* assemblies formed by Glu/Ag(100) at $T = 350$ K (energies in eV per GLU molecule). **(a,b)** Optimized geometry of the assemblies. The molecular density of the calculated structure is 1.95×10^{18} Glu molecule/m^2 (mixture of neutral and radical species) for the *flower* assembly **(a)** and 1.39×10^{18} Glu molecule/m^2 for the *square* assembly **(b)**. **(c,d)** Simulated STM image deduced from the configuration in **(a,b)** for $V = 1.0$ V. The good agreement with the corresponding experimental image, reported in **(e,f)**, is evident. (Reprinted with permission from [29.28, 84, 199]. Copyright (2013, 2010, 2014) American Chemical Society)

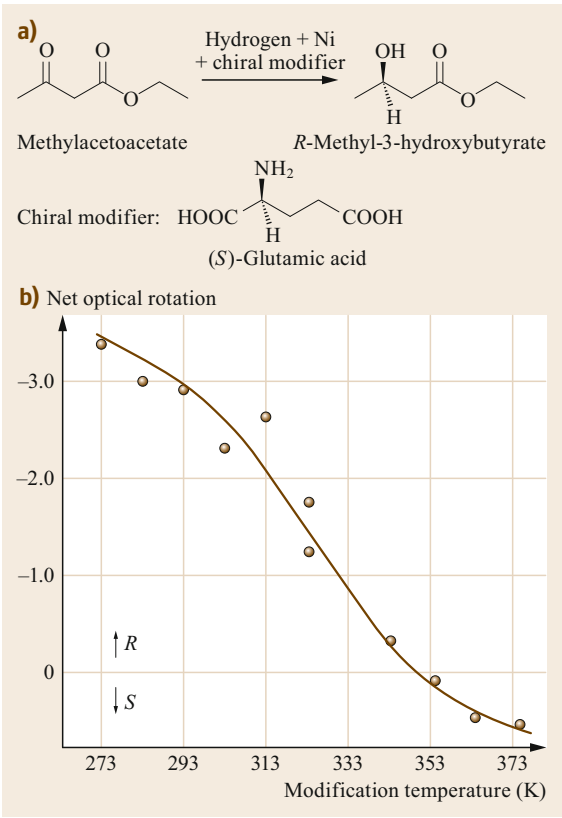

Fig. 29.24 (a) Reaction scheme for the enantioselective hydrogenation of β-keto esters over Ni catalysts in presence of (*S*)-glutamic acid. **(b)** Net optical rotation of the methyl-3-hydroxybutyrate product formed over (*S*)-Glu modified Ni catalysts as a function of modification temperature. (Reprinted from [29.202], with permission from Elsevier)

Deposition of the amino acid at $T = 350$ K produces a surface ordering similar to the one obtained upon annealing the 300 K layer but, in addition, it causes a restructuring of the step edges, which assume a *saw-tooth* appearance. Chiral faceting of the step edges upon adsorption of a chiral molecule is a phenomenon already documented for several systems, e.g., for Lys/Cu(001) [29.44] and Glu/Ag(110) [29.189], and it can be relevant in explaining the different enantioselective properties of the catalyst at 300 and at 350 K. In fact, MAA adsorption at 300 K occurs mainly in the diketo tautomeric form (with a direct interaction between the NH_3^+ group of zwitterionic Glu and the ketone group of the MAA molecules) if the (*S*)-Glu chiral modifier is pre-deposited at 300 K. Conversely, it occurs in the enol form if Glu deposition is performed at 350 K [29.205]. In liquid solution, the nature of the final product is also influenced by pH. The more protonated the Glu modifier is, more diketones tend to form. The optimum enantioselective catalytic performance occurs

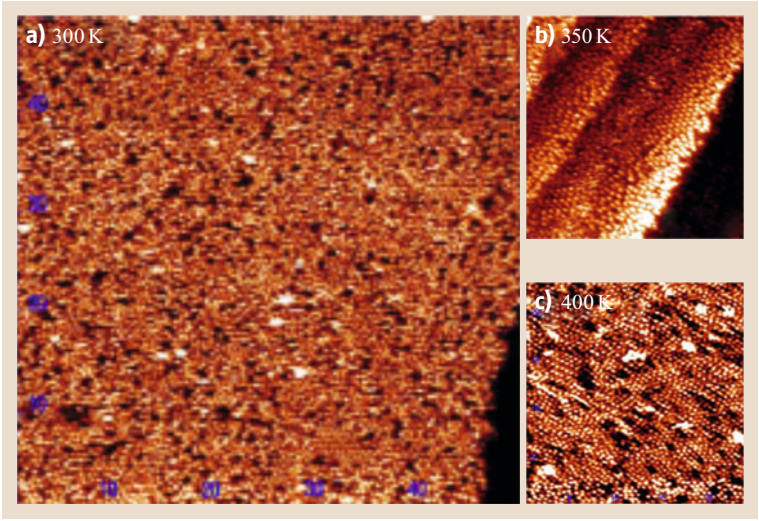

Fig. 29.25 **(a)** STM images of a high-coverage (*S*)-Glu/Ni(111) layer produced at 300 K (image size $49.7 \times 49.7\,\mathrm{nm}^2$; $I = 0.34\,\mathrm{nA}$; $V = 0.55\,\mathrm{V}$). **(b)** STM image obtained after annealing the sample in **(a)** to 350 K (image size $21.4 \times 21.4\,\mathrm{nm}^2$, $I = 0.32\,\mathrm{nA}$; $V = 0.36\,\mathrm{V}$). **(c)** Same as **(b)** after annealing the layer to 400 K (image size $23.5 \times 23.5\,\mathrm{nm}^2$; $I = 0.30\,\mathrm{nA}$; $V = 0.54\,\mathrm{V}$). (Reprinted from [29.202], with permission from Elsevier)

following modification at pH 5, at which the keto/enol ratio continues to drop with increasing modification temperature. Since (*S*)-Glu adsorbs in the zwitterionic form at 300 K and low coverage and in the anionic form with step restructuring at 350 K, the switch in the preferred enantiomeric product with modification temperature may be related to the ability of Glu to behave either as an amino acid or as a chiral diacid (as tartaric acid).

29.4 Conclusions

In this chapter we have presented a necessarily incomplete overview of the self-assembly process occurring at surfaces at the nanoscale. The few examples reported here should provide an overview of the different self-assembly mechanisms and of the different kinds of molecules involved in this process. We also believe that they should convey to the reader the idea of the wide range of possibilities opened by self-assembly to control the structure and properties of the organic–inorganic interface by choosing the most suitable molecular species.

References

29.1 A.E. Nel, L. Mädler, D. Velegol, T. Xia, E.M.V. Hoek, P. Somasundaran, F. Klaessig, V. Castranova, M. Thompson: Understanding biophysicochemical interactions at the nano–bio interface, Nat. Mater. **8**, 543–557 (2009)

29.2 Y. Pennec, W. Auwärter, A. Schiffrin, A. Weber-Bargioni, A. Riemann, J.V. Barth: Supramolecular gratings for tuneable confinement of electrons on metal surfaces, Nat. Nanotechnol. **2**, 99–103 (2007)

29.3 J.C. Love, L.A. Estroff, J.K. Kriebel, R.G. Nuzzo, G.M. Whitesides: Self-assembled monolayers of thiolates on metals as a form of nanotechnology, Chem. Rev. **105**, 1103–1170 (2005)

29.4 C. Joachim, J.K. Gimzewski, A. Aviram: Electronics using hybrid-molecular and mono-molecular devices, Nature **408**, 541–548 (2000)

29.5 Z. Xu, Y. Fu, W. Han, D. Wei, H. Jiao, H. Gao: Recent developments in focused ion beam and its application in nanotechnology, Curr. Nanosci. **12**, 696–711 (2016)

29.6 F.C. Simeone, C. Albonetti, M. Cavallini: Progress in micro- and nanopatterning via electrochemical lithography, J. Phys. Chem. C **113**, 18987–18994 (2009)

29.7 H.-D. Yu, M.D. Regulacio, E. Ye, M.-Y. Han: Chemical routes to top-down nanofabrication, Chem. Soc. Rev. **42**, 6006–6018 (2013)

29.8 K. Ariga, H. Ito, J.P. Hill, H. Tsukube: Molecular recognition: From solution science to nano/materials technology, Chem. Soc. Rev. **41**, 5800–5835 (2012)

29.9 K. Kanazawa, A. Taninaka, H. Huang, M. Nishimura, S. Yoshida, O. Takeuchi, H. Shigekawa: Scanning tunneling microscopy-/spectroscopy on self-assembly of a glycine/Cu(111) nanocavity array, Chem. Commun. **47**, 11312–11314 (2011)

29.10 S. Haq, F. Hanke, M.S. Dyer, M. Persson, P. Iavicoli, D.B. Amabilino, R. Raval: Clean coupling of unfunctionalized porphyrins at surfaces to give highly oriented organometallic oligomers, J. Am. Chem. Soc. **133**, 12031–12039 (2011)

29.11 M. Smerieri, I. Píš, L. Ferrighi, S. Nappini, A. Lusuan, C. Di Valentin, L. Vaghi, A. Papagni, M. Cattelan, S. Agnoli, E. Magnano, F. Bondino, L. Savio: Synthesis of graphene nanoribbons with a defined mixed edge-site sequence by surface assisted polymerization of (1,6)-dibromopyrene on Ag(110), Nanoscale **8**, 17843–17853 (2016)

29.12 F. Rosei, M. Schunack, Y. Naitoh, P. Jiang, A. Gourdon, E. Laegsgaard, I. Stensgaard, C. Joachim, F. Besenbacher: Properties of large organic molecules on metal surfaces, Prog. Surf. Sci. **71**, 95–146 (2003)

29.13 J. Cai, P. Ruffieux, R. Jaafar, M. Bieri, T. Braun, S. Blankenburg, M. Muoth, A.P. Seitsonen, M. Saleh, X. Feng, K. Müllen, R. Fasel: Atomically precise bottom-up fabrication of graphene nanoribbons, Nature **466**, 470–473 (2010)

29.14 A. Klug: From macromolecules to biological assemblies (Nobel Lecture), Angew. Chem. Int. Ed. **22**, 565–582 (1983)

29.15 J.V. Barth: Molecular architectonic on metal surfaces, Annu. Rev. Phys. Chem. **58**, 375–407 (2007)

29.16 H. Cölfen, S. Mann: Higher-order organization by mesoscale self-assembly and transformation of hybrid nanostructures, Angew. Chem. Int. Ed. **42**, 2350–2365 (2003)

29.17 S.M. Barlow, R. Raval: Complex organic molecules at metal surfaces: Bonding, organisation and chirality, Surf. Sci. Rep. **50**, 201–341 (2003)

29.18 D. Costa, C.M. Pradier, F. Tielens, L. Savio: Adsorption and self-assembly of bio-organic molecules at model surfaces: A route towards increased complexity, Surf. Sci. Rep. **70**, 449–453 (2015)

29.19 T. Kawai, H. Tanaka, T. Nakagawa: Low dimensional self-organization of DNA-base molecules on Cu(111) surfaces, Surf. Sci. **386**, 124–136 (1997)

29.20 M. Furukawa, H. Tanaka, T. Kawai: The role of dimer formation in the self-assemblies of DNA base molecules on Cu(111) surfaces: A scanning tunneling microscope study, J. Chem. Phys. **115**, 3419–3423 (2001)

29.21 Q. Chen, N.V. Richardson: Enantiomeric interactions between nucleic acid bases and amino acids on solid surfaces, Nat. Mater. **2**, 324–328 (2003)

29.22 J.V. Barth, J. Weckesser, N. Lin, A. Dmitriev, K. Kern: Supramolecular architectures and nanostructures at metal surfaces, Appl. Phys. A **76**, 645–652 (2003)

29.23 S. De Feyter, F.C. De Schryver: Two-dimensional supramolecular self-assembly probed by scanning tunneling microscopy, Chem. Soc. Rev. **32**, 139–150 (2003)

29.24 D. Costa, P.A. Garrain, M. Baaden: Understanding small biomolecule-biomaterial interactions: A review of fundamental theoretical and experimental approaches for biomolecule interactions with inorganic surfaces, J. Biomed. Mater. Res. A **101**, 1210–1222 (2013)

29.25 A. Ulman: Formation and structure of self-assembled monolayers, Chem. Rev. **96**, 1533–1554 (1996)

29.26 L. Grill, M. Dyer, L. Lafferentz, M. Persson, M.V. Peters, S. Hecht: Nano-architectures by covalent assembly of molecular building blocks, Nat. Nanotechnol. **2**, 687–691 (2007)

29.27 S. Nappini, I. Píš, G. Carraro, E. Celasco, M. Smerieri, L. Savio, E. Magnano, F. Bondino: On-surface synthesis of different boron–nitrogen–carbon heterostructures from dimethylamine borane, Carbon **120**, 185–193 (2017)

29.28 I. Tranca, M. Smerieri, L. Savio, L. Vattuone, D. Costa, F. Tielens: Unraveling the self-assembly of the (*S*)-glutamic acid "flower" structure on Ag(100), Langmuir **29**, 7876–7884 (2013)

29.29 S. Blankenburg, W.G. Schmidt: Glutamic acid adsorbed on Ag(110): Direct and indirect molecular interactions, J. Phys. Condens. Matter **21**, 185001 (2009)

29.30 J. Klimeš, D.R. Bowler, A. Michaelides: Van der Waals density functionals applied to solids, Phys. Rev. B **83**, 195131 (2011)

29.31 M. Dion, H. Rydberg, E. Schröder, D.C. Langreth, B.I. Lundqvist: Van der Waals density functional for general geometries, Phys. Rev. Lett. **92**, 246401 (2004)

29.32 T. Steiner: The hydrogen bond in the solid state, Angew. Chem. Int. Ed. **41**, 48–76 (2002)

29.33 C.F.J. Faul, M. Antonietti: Ionic self-assembly: Facile synthesis of supramolecular materials, Adv. Mater. **15**, 673–683 (2003)

29.34 L. Dong, W. Wang, T. Lin, K. Diller, J.V. Barth, J. Liu, B.Z. Tang, F. Klappenberger, N. Lin: Two-dimensional hierarchical supramolecular assembly of a silole derivative and surface-assisted chemical transformations, J. Phys. Chem. C **119**, 3857–3863 (2015)

29.35 S.M. Barlow, S. Louafi, D. Le Roux, J. Williams, C. Muryn, S. Haq, R. Raval: Supramolecular assembly of strongly chemisorbed size-and shape-defined chiral clusters: *S*- and *R*-alanine on Cu(110), Langmuir **20**, 7171–7176 (2004)

29.36 M. Smerieri, L. Vattuone, T. Kravchuk, D. Costa, L. Savio: (*S*)-Glutamic acid on Ag(100): Self-assembly in the nonzwitterionic form, Langmuir **27**, 2393–2404 (2011)

29.37 A. Kühnle: Self-assembly of organic molecules at metal surfaces, Curr. Opin. Colloid Interface Sci. **14**, 157–168 (2009)

29.38 A. Nilsson, L.G.M. Pettersson: Chemical bonding on surfaces probed by x-ray emission spectroscopy and density functional theory, Surf. Sci. Rep. **55**, 49–167 (2004)

29.39 S.M. Barlow, S. Louafi, D. Le Roux, J. Williams, C. Muryn, S. Haq, R. Raval: Polymorphism in supramolecular chiral structures of *R*- and *S*-alanine on Cu(1 1 0), Surf. Sci. **590**, 243–263 (2005)

29.40 X. Zhao, R.G. Zhao, W.S. Yang: Self-assembly of L-tryptophan on the Cu(001) surface, Langmuir **18**, 433–438 (2002)

29.41 A. Gerlach, F. Schreiber, S. Sellner, H. Dosch, I.A. Vartanyants, B.C.C. Cowie, T.-L. Lee, J. Zegenhagen: Adsorption-induced distortion of $F_{16}CuPc$ on Cu(111) and Ag(111): An x-ray standing wave study, Phys. Rev. B **71**, 205425 (2005)

29.42 T. Yokoyama, S. Yokoyama, T. Kamikado, S. Mashiko: Nonplanar adsorption and orientational ordering of porphyrin molecules on Au(111), J. Chem. Phys. **115**, 3814–3818 (2001)

29.43 R. Raval: Chiral expression from molecular assemblies at metal surfaces: Insights from surface science techniques, Chem. Soc. Rev. **38**, 707–721 (2009)

29.44 X. Zhao: Fabricating homochiral facets on Cu(001) with L-lysine, J. Am. Chem. Soc. **122**, 12584–12585 (2000)

29.45 S. Linden, D. Zhong, A. Timmer, N. Aghdassi, J.H. Franke, H. Zhang, X. Feng, K. Müllen, H. Fuchs, L. Chi, H. Zacharias: Electronic structure of spatially aligned graphene nanoribbons on Au(788), Phys. Rev. Lett. **108**, 216801 (2012)

29.46 R. Otero, Y. Naitoh, F. Rosei, P. Jiang, P. Thostrup, A. Gourdon, E. Lægsgaard, I. Stensgaard, C. Joachim, F. Besenbacher: One-dimensional assembly and selective orientation of Lander molecules on an O–Cu template, Angew. Chem. Int. Ed. **43**, 2092–2095 (2004)

29.47 J.A. Miwa, S. Weigelt, H. Gersen, F. Besenbacher, F. Rosei, T.R. Linderoth: Azobenzene on Cu(110): Adsorption site-dependent diffusion, J. Am. Chem. Soc. **128**, 3164–3165 (2006)

29.48 L.J. Lauhon, W. Ho: Single molecule thermal rotation and diffusion: Acetylene on Cu(001), J. Chem. Phys. **111**, 5633–5636 (1999)

29.49 D.M. Eigler, E.K. Schweizer: Positioning single atoms with a scanning tunnelling microscope, Nature **344**, 524–526 (1990)

29.50 J.R. Hahn, W. Ho: Oxidation of a single carbon monoxide molecule manipulated and induced with a scanning tunneling microscope, Phys. Rev. Lett. **87**, 166102 (2001)

29.51 S.-W. Hla, L. Bartels, G. Meyer, K.-H. Rieder: Inducing all steps of a chemical reaction with the scanning tunneling microscope tip: Towards single molecule engineering, Phys. Rev. Lett. **85**, 2777–2780 (2000)

29.52 W. Ho: Single-molecule chemistry, J. Chem. Phys. **117**, 11033–11061 (2002)

29.53 R. Mas-Ballesté, C. Gómez-Navarro, J. Gómez-Herrero, F. Zamora: 2D materials: To graphene and beyond, Nanoscale **3**, 20–30 (2011)

29.54 M. Batzill: The surface science of graphene: Metal interfaces, CVD synthesis, nanoribbons, chemical modifications, and defects, Surf. Sci. Rep. **67**, 83–115 (2012)

29.55 J.W. Colson, W.R. Dichtel: Rationally synthesized two-dimensional polymers, Nat. Chem. **5**, 453–465 (2013)

29.56 L. Lafferentz, V. Eberhardt, C. Dri, C. Africh, G. Comelli, F. Esch, S. Hecht, L. Grill: Controlling on-surface polymerization by hierarchical and substrate-directed growth, Nat. Chem. **4**, 215–220 (2012)

29.57 A. Basagni, F. Sedona, C.A. Pignedoli, M. Cattelan, L. Nicolas, M. Casarin, M. Sambi: Molecules–oligomers–nanowires–graphene nanoribbons: A bottom-up stepwise on-surface covalent synthesis preserving long-range order, J. Am. Chem. Soc. **137**, 1802–1808 (2015)

29.58 D. Heim, D. Écija, K. Seufert, W. Auwärter, C. Aurisicchio, C. Fabbro, D. Bonifazi, J.V. Barth: Self-assembly of flexible one-dimensional coordination polymers on metal surfaces, J. Am. Chem. Soc. **132**, 6783–6790 (2010)

29.59 J.V. Barth, J. Weckesser, G. Trimarchi, M. Vladimirova, A. De Vita, C. Cai, H. Brune, P. Günter, K. Kern: Stereochemical effects in supramolecular self-assembly at surfaces: 1-D versus 2-D enantiomorphic ordering for PVBA and PEBA on Ag(111), J. Am. Chem. Soc. **124**, 7991–8000 (2002)

29.60 Q. Fan, J.M. Gottfried, J. Zhu: Surface-catalyzed C–C covalent coupling strategies toward the synthesis of low-dimensional carbon-based nanostructures, Acc. Chem. Res. **48**, 2484–2494 (2015)

29.61 I. Píš, L. Ferrighi, T.H. Nguyen, S. Nappini, L. Vaghi, A. Basagni, E. Magnano, A. Papagni, F. Sedona, C. Di Valentin, S. Agnoli, F. Bondino: Surface-confined polymerization of halogenated polyacenes: The case of dibromotetracene on Ag(110), J. Phys. Chem. C **120**, 4909–4918 (2016)

29.62 F. Ullmann, J. Bielecki: Ueber Synthesen in der Biphenylreihe, Ber. Dtsch. Chem. Ges. **34**, 2174–2185 (1901)

29.63 M. Di Giovannantonio, M. El Garah, J. Lipton-Duffin, V. Meunier, L. Cardenas, Y.F. Revurat, A. Cossaro, A. Verdini, D.F. Perepichka, F. Rosei, G. Contini: Insight into organometallic intermediate and its evolution to covalent bonding in surface-confined Ullmann polymerization, ACS Nano **7**, 8190–8198 (2013)

29.64 W. Wang, X. Shi, S. Wang, M.A. Van Hove, N. Lin: Single-molecule resolution of an organometallic intermediate in a surface-supported Ullmann coupling reaction, J. Am. Chem. Soc. **133**, 13264–13267 (2011)

29.65 Q. Fan, C. Wang, Y. Han, J. Zhu, J. Kuttner, G. Hilt, J.M. Gottfried: Surface-assisted formation, assembly, and dynamics of planar organometallic macrocycles and zigzag shaped polymer chains with C–Cu–C bonds, ACS Nano **8**, 709–718 (2014)

29.66 M.O. Blunt, J.C. Russell, N.R. Champness, P.H. Beton: Templating molecular adsorption using a covalent organic framework, Chem. Commun. **46**, 7157–7159 (2010)

29.67 J. Eichhorn, T. Strunskus, A. Rastgoo-Lahrood, D. Samanta, M. Schmittel, M. Lackinger: On-surface Ullmann polymerization via intermediate organometallic networks on Ag(111), Chem. Commun. **50**, 7680–7682 (2014)

29.68 P. Ruffieux, J. Cai, N.C. Plumb, L. Patthey, D. Prezzi, A. Ferretti, E. Molinari, X. Feng, K. Müllen, C.A. Pignedoli, R. Fasel: Electronic structure of

atomically precise graphene nanoribbons, ACS Nano **6**, 6930–6935 (2012)
29.69 K.A. Simonov, N.A. Vinogradov, A.S. Vinogradov, A.V. Generalov, E.M. Zagrebina, N. Mårtensson, A.A. Cafolla, T. Carpy, J.P. Cunniffe, A.B. Preobrajenski: Effect of substrate chemistry on the bottom-up fabrication of graphene nanoribbons: Combined core-level spectroscopy and STM study, J. Phys. Chem. C **118**, 12532–12540 (2014)
29.70 P. Han, K. Akagi, F. Federici Canova, H. Mutoh, S. Shiraki, K. Iwaya, P.S. Weiss, N. Asao, T. Hitosugi: Bottom-up graphene-nanoribbon fabrication reveals chiral edges and enantioselectivity, ACS Nano **8**, 9181–9187 (2014)
29.71 X. Li, X. Wang, L. Zhang, S. Lee, H. Dai: Chemically derived, ultrasmooth graphene nanoribbon semiconductors, Science **319**, 1229–1232 (2008)
29.72 L. Jiao, L. Zhang, X. Wang, G. Diankov, H. Dai: Narrow graphene nanoribbons from carbon nanotubes, Nature **458**, 877–880 (2009)
29.73 K.A. Simonov, N.A. Vinogradov, A.S. Vinogradov, A.V. Generalov, E.M. Zagrebina, G.I. Svirskiy, A.A. Cafolla, T. Carpy, J.P. Cunniffe, T. Taketsugu, A. Lyalin, N. Mårtensson, A.B. Preobrajenski: From graphene nanoribbons on Cu(111) to nanographene on Cu(110): Critical role of substrate structure in the bottom-up fabrication strategy, ACS Nano **9**, 8997–9011 (2015)
29.74 C. Zhang, Q. Sun, H. Kong, L. Wang, Q. Tana, W. Xu: On-surface synthesis of organometallic complex *via* metal–alkene interactions, Chem. Commun. **50**, 15924–15927 (2014)
29.75 M. Chen, J. Xiao, H.-P. Steinrück, S. Wang, W. Wang, N. Lin, W. Hieringer, J.M. Gottfried: Combined photoemission and scanning tunneling microscopy study of the surface-assisted Ullmann coupling reaction, J. Phys. Chem. C **118**, 6820–6830 (2014)
29.76 A. Kimouche, M.M. Ervasti, R. Drost, S. Halonen, A. Harju, P.M. Joensuu, J. Sainio, P. Liljeroth: Ultra-narrow metallic armchair graphene nanoribbons, Nat. Commun. **6**, 10177 (2015)
29.77 F. Schulz, P.H. Jacobse, F. Federici Canova, J. van der Lit, D.Z. Gao, A. van den Hoogenband, P. Han, R.J.M. Klein Gebbink, M.-E. Moret, P.M. Joensuu, I. Swart, P. Liljeroth: Precursor geometry determines the growth mechanism in graphene nanoribbons, J. Phys. Chem. C **121**, 2896–2904 (2017)
29.78 H. Huang, D. Wei, J. Sun, S.L. Wong, Y.P. Feng, A.H. Castro Neto, A.T.S. Wee: Spatially resolved electronic structures of atomically precise armchair graphene nanoribbons, Sci. Rep. **2**, 983 (2012)
29.79 F. Hanke, S. Haq, R. Raval, M. Persson: Heat-to-connect: Surface commensurability directs organometallic one-dimensional self-assembly, ACS Nano **5**, 9093–9103 (2011)
29.80 P. Maksymovych, O. Voznyy, D.B. Dougherty, D.C. Sorescu, J.T. Yates: Gold adatom as a key structural component in self-assembled monolayers of organosulfur molecules on Au(111), Prog. Surf. Sci. **85**, 206–240 (2010)
29.81 D.P. Woodruff: The interface structure of n-alkylthiolate self-assembled monolayers on coinage metal surfaces, Phys. Chem. Chem. Phys. **10**, 7211–7221 (2008)
29.82 E. Pensa, E. Cortés, G. Corthey, P. Carro, C. Vericat, M.H. Fonticelli, G. Benítez, A.A. Rubert, R.C. Salvarezza: The chemistry of the sulfur–gold interface: In search of a unified model, Acc. Chem. Res. **45**, 1183–1192 (2012)
29.83 T. Bürgi: Properties of the gold–sulphur interface: From self-assembled monolayers to clusters, Nanoscale **7**, 15553–15567 (2015)
29.84 M. Smerieri, L. Vattuone, D. Costa, F. Tielens, L. Savio: Self-assembly of (*S*)-glutamic acid on Ag(100): A combined LT-STM and ab initio investigation, Langmuir **26**, 7208–7215 (2010)
29.85 A. Dmitriev, N. Lin, J. Weckesser, J.V. Barth, K. Kern: Supramolecular assemblies of trimesic acid on a Cu(100) surface, J. Phys. Chem. B **106**, 6907–6912 (2002)
29.86 L.J. Prins, D.N. Reinhoudt, P. Timmerman: Noncovalent synthesis using hydrogen bonding, Angew. Chem. Int. Ed. **40**, 2382–2426 (2001)
29.87 T. Yokoyama, T. Kamikado, S. Yokoyama, S. Mashiko: Conformation selective assembly of carboxyphenyl substituted porphyrins on Au (111), J. Chem. Phys. **121**, 11993–11997 (2004)
29.88 J. Weckesser, A. De Vita, J.V. Barth, C. Cai, K. Kern: Mesoscopic correlation of supramolecular chirality in one-dimensional hydrogen-bonded assemblies, Phys. Rev. Lett. **87**, 961011–961014 (2001)
29.89 N. Muskal, I. Turyan, D. Mandler: Self-assembled monolayers on mercury surfaces, J. Electroanal. Chem. **409**, 131–136 (1996)
29.90 A. Iakovlev, D. Bedrov, M. Müller: Molecular dynamics simulation of alkylthiol self-assembled monolayers on liquid mercury, Langmuir **33**, 744–754 (2017)
29.91 H. Häkkinen: The gold–sulfur interface at the nanoscale, Nat. Chem. **4**, 443–455 (2012)
29.92 W.C. Bigelow, D.L. Pickett, W.A. Zisman: Oleophobic monolayers, J. Colloid Sci. **1**, 513–538 (1946)
29.93 R.G. Nuzzo, D.L. Allara: Adsorption of bifunctional organic disulfides on gold surfaces, J. Am. Chem. Soc. **105**, 4481–4483 (1983)
29.94 R.G. Nuzzo, F.A. Fusco, D.L. Allara: Spontaneously organized molecular assemblies. 3. Preparation and properties of solution adsorbed monolayers of organic disulfides on gold surfaces, J. Am. Chem. Soc. **109**, 2358–2368 (1987)
29.95 A. Ulman: *An Introduction to Ultrathin Organic Films: From Langmuir–Blodgett to Self-Assembly* (Academic Press, San Diego 1991)
29.96 C.D. Bain, E.B. Troughton, Y.T. Tao, J. Evall, G.M. Whitesides, R.G. Nuzzo: Formation of monolayer films by the spontaneous assembly of organic thiols from solution onto gold, J. Am. Chem. Soc. **111**, 321–335 (1989)

29.97 H. Hamoudi, V.A. Esaulov: Selfassembly of α,ω-dithiols on surfaces and metal dithiol heterostructures, Ann. Phys. **528**, 242–263 (2016)

29.98 H.-J. Himmel, K. Weiss, B. Jäger, O. Dannenberger, M. Grunze, C. Wöll: Ultrahigh vacuum study on the reactivity of organic surfaces terminated by OH and COOH groups prepared by self-assembly of functionalized alkanethiols on Au substrates, Langmuir **13**, 4943–4947 (1997)

29.99 S.M. Mendoza, I. Arfaoui, S. Zanarini, F. Paolucci, P. Rudolf: Improvements in the characterization of the crystalline structure of acid-terminated alkanethiol self-assembled monolayers on Au(111), Langmuir **23**, 582–588 (2007)

29.100 J. Pflaum, G. Bracco, F. Schreiber, R. Colorado Jr., O.E. Shmakova, T.R. Lee, G. Scoles, A. Kahn: Structure and electronic properties of CH_3- and CF_3-terminated alkanethiol monolayers on Au(111): A scanning tunneling microscopy, surface x-ray and helium scattering study, Surf. Sci. **498**, 89–104 (2002)

29.101 W.A. Marmisollé, D.A. Capdevila, E. de la Llave, F.J. Williams, D.H. Murgida: Self-assembled monolayers of NH_2-terminated thiolates: Order, pK_a, and specific adsorption, Langmuir **29**, 5351–5359 (2013)

29.102 M.J. Esplandiú, H. Hagenström, D.M. Kolb: Functionalized self-assembled alkanethiol monolayers on Au(111) electrodes: 1. Surface structure and electrochemistry, Langmuir **17**, 828–838 (2001)

29.103 F. Schreiber: Structure and growth of self-assembling monolayers, Prog. Surf. Sci. **65**, 151–256 (2000)

29.104 H.A. Biebuyck, C.D. Bain, G.M. Whitesides: Comparison of organic monolayers on polycrystalline gold spontaneously assembled from solutions containing dialkyl disulfides or alkanethiols, Langmuir **10**, 1825–1831 (1994)

29.105 G.E. Poirier: Coverage-dependent phases and phase stability of decanethiol on Au(111), Langmuir **15**, 1167–1175 (1999)

29.106 G.E. Poirier, W.P. Fitts, J.M. White: Two-dimensional phase diagram of decanethiol on Au(111), Langmuir **17**, 1176–1183 (2001)

29.107 R. Colorado Jr., T.R. Lee: Thiol-based self-assembled monolayers: Formation and organization. In: *Encyclopedia of Materials: Science and Technology*, ed. by K.H.J. Buschow, R.W. Cahn, M.C. Flemings, B. Ilschner, E.J. Kramer, S. Mahajan, P. Veyssière (Elsevier, Oxford 2001) pp. 9332–9344

29.108 N.K. Chaki, K. Vijayamohanan: Self-assembled monolayers as a tunable platform for biosensor applications, Biosens. Bioelectron. **17**, 1–12 (2002)

29.109 G. Heimel, L. Romaner, E. Zojer, J.-L. Bredas: The interface energetics of self-assembled monolayers on metals, Acc. Chem. Res. **41**, 721–729 (2008)

29.110 J. Gao, L. Tang, S. Holmes, F. Li, R.E. Palmer, Q. Guo: Surface-induced symmetry reduction in molecular switching: Asymmetric *cis–trans* switching of CH_3S–Au–SCH_3 on Au(111), Nanoscale **8**, 19787–19793 (2016)

29.111 E. Ostuni, R.G. Chapman, R.E. Holmlin, S. Takayama, G.M. Whitesides: A survey of structure–property relationships of surfaces that resist the adsorption of protein, Langmuir **17**, 5605–5620 (2001)

29.112 I. Solano, P. Parisse, F. Gramazio, O. Cavalleri, G. Bracco, M. Castronovo, L. Casalis, M. Canepa: Spectroscopic ellipsometry meets AFM nanolithography: About hydration of bioinert oligo(ethylene glycol)-terminated self-assembled monolayers on gold, Phys. Chem. Chem. Phys. **17**, 28774–28781 (2015)

29.113 Y. Xia, G.M. Whitesides: Soft lithography, Annu. Rev. Mater. Sci. **28**, 153–184 (1998)

29.114 G.-Y. Liu, S. Xu: Nanometer scale fabrication of self-assembled monolayers: Nanoshaving and nanografting. In: *Inorganic Materials Synthesis*, ACS Symposium Series, Vol. 727 (American Chemical Society, Washington 1999) pp. 199–208

29.115 K. Salaita, Y. Wang, C.A. Mirkin: Applications of dip-pen nanolithography, Nat. Nanotechnol. **2**, 145–155 (2007)

29.116 S. Iannotta, T. Toccoli, F. Biasioli, A. Boschetti, M. Ferrari: Highly ordered films of quaterthiophene grown by seeded supersonic beams, Appl. Phys. Lett. **76**, 1845–1847 (2000)

29.117 E. Albayrak, S. Karabuga, G. Bracco, M.F. Danışman: Investigation of the deposition and thermal behavior of striped phases of unsymmetric disulfide self-assembled monolayers on Au(111): The case of 11-hydroxyundecyl decyl disulfide, J. Chem. Phys. **142**, 014703 (2015)

29.118 R. Yamada, K. Uosaki: In situ, real time monitoring of the self-assembly process of decanethiol on Au(111) in liquid phase. A scanning tunneling microscopy investigation, Langmuir **13**, 5218–5221 (1997)

29.119 R. Yamada, K. Uosaki: In situ scanning tunneling microscopy observation of the self-assembly process of alkanethiols on gold(111) in solution, Langmuir **14**, 855–861 (1998)

29.120 S. Xu, S.J.N. Cruchon-Dupeyrat, J.C. Garno, G.-Y. Liu, G.K. Jennings, T.-H. Yong, P.E. Laibinis: In situ studies of thiol self-assembly on gold from solution using atomic force microscopy, J. Chem. Phys. **108**, 5002–5012 (1998)

29.121 F. Ma, R.B. Lennox: Potential-assisted deposition of alkanethiols on Au: Controlled preparation of single- and mixed-component SAMs, Langmuir **16**, 6188–6190 (2000)

29.122 R. Yamada, H. Wano, K. Uosaki: Effect of temperature on structure of the self-assembled monolayer of decanethiol on Au(111) surface, Langmuir **16**, 5523–5525 (2000)

29.123 E. Delamarche, B. Michel, H. Kang, C. Gerber: Thermal stability of self-assembled monolayers, Langmuir **10**, 4103–4108 (1994)

29.124 U. Harten, A.M. Lahee, J.P. Toennies, C. Wöll: Observation of a soliton reconstruction of Au(111) by high-resolution helium-atom diffraction, Phys. Rev. Lett. **54**, 2619–2622 (1985)

29.125 A.R. Sandy, S.G.J. Mochrie, D.M. Zehner, K.G. Huang, D. Gibbs: Structure and phases of the Au(111) surface: X-ray-scattering measurements, Phys. Rev. B **43**, 4667–4687 (1991)

29.126 E. Torres, G.A. DiLabio: A density functional theory study of the reconstruction of gold(111) surfaces, J. Phys. Chem. C **118**, 15624–15629 (2014)

29.127 G.E. Poirier: Mechanism of formation of Au vacancy islands in alkanethiol monolayers on Au(111), Langmuir **13**, 2019–2026 (1997)

29.128 G. Yang, G. Liu: New insights for self-assembled monolayers of organothiols on Au(111) revealed by scanning tunneling microscopy, J. Phys. Chem. B **107**, 8746–8759 (2003)

29.129 P. Maksymovych, D.C. Sorescu, J.T. Yates: Gold-adatom-mediated bonding in self-assembled short-chain alkanethiolate species on the Au(111) surface, Phys. Rev. Lett. **97**, 146103 (2006)

29.130 G.E. Poirier: Characterization of organosulfur molecular monolayers on Au(111) using scanning tunneling microscopy, Chem. Rev. **97**, 1117–1128 (1997)

29.131 P. Schwartz, F. Schreiber, P. Eisenberger, G. Scoles: Growth kinetics of decanethiol monolayers self-assembled on Au(111) by molecular beam deposition: An atomic beam diffraction study, Surf. Sci. **423**, 208–224 (1999)

29.132 F. Schreiber, A. Eberhardt, T.Y.B. Leung, P. Schwartz, S.M. Wetterer, D.J. Lavrich, L. Berman, P. Fenter, P. Eisenberger, G. Scoles: Adsorption mechanisms, structures, and growth regimes of an archetypal self-assembling system: Decanethiol on Au(111), Phys. Rev. B **57**, 12476–12481 (1998)

29.133 L.H. Dubois, B.R. Zegarski, R.G. Nuzzo: Molecular ordering of organosulfur compounds on Au(111) and Au(100): Adsorption from solution and in ultrahigh vacuum, J. Chem. Phys. **98**, 678–688 (1993)

29.134 N. Camillone III, P. Eisenberger, T.Y.B. Leung, P. Schwartz, G. Scoles, G.E. Poirier, M.J. Tarlov: New monolayer phases of *n*-alkane thiols self-assembled on Au(111): Preparation, surface characterization, and imaging, J. Chem. Phys. **101**, 11031–11036 (1994)

29.135 N. Camillone, T.Y.B. Leung, P. Schwartz, P. Eisenberger, G. Scoles: Chain length dependence of the striped phases of alkanethiol monolayers self-assembled on Au(111): An atomic beam diffraction study, Langmuir **12**, 2737–2746 (1996)

29.136 F. Balzer, R. Gerlach, G. Polanski, H.-G. Rubahn: Chain length dependence of the structure of alkane thiol films on Au(111), Chem. Phys. Lett. **274**, 145–151 (1997)

29.137 R. Gerlach, G. Polanski, H.-G. Rubahn: Structural manipulation of ultrathin organic films on metal surfaces: The case of decane thiol/Au(111), Appl. Phys. A **65**, 375–377 (1997)

29.138 H. Kondoh, C. Kodama, H. Sumida, H. Nozoye: Molecular processes of adsorption and desorption of alkanethiol monolayers on Au(111), J. Chem. Phys. **111**, 1175–1184 (1999)

29.139 K. Sotthewes, H. Wu, A. Kumar, G.J. Vancso, P.M. Schön, H.J.W. Zandvliet: Molecular dynamics and energy landscape of decanethiolates in self-assembled monolayers on Au(111) studied by scanning tunneling microscopy, Langmuir **29**, 3662–3667 (2013)

29.140 G.E. Poirier, M.J. Tarlov, H.E. Rushmeier: Two-dimensional liquid phase and the $p \times \sqrt{3}$ phase of alkanethiol self-assembled monolayers on Au(111), Langmuir **10**, 3383–3386 (1994)

29.141 R. Staub, M. Toerker, T. Fritz, T. Schmitz-Hübsch, F. Sellam, K. Leo: Flat lying pin-stripe phase of decanethiol self-assembled monolayers on Au(111), Langmuir **14**, 6693–6698 (1998)

29.142 R.G. Nuzzo, L.H. Dubois, D.L. Allara: Fundamental studies of microscopic wetting on organic surfaces. 1. Formation and structural characterization of a self-consistent series of polyfunctional organic monolayers, J. Am. Chem. Soc. **112**, 558–569 (1990)

29.143 P. Fenter, A. Eberhardt, K.S. Liang, P. Eisenberger: Epitaxy and chainlength dependent strain in self-assembled monolayers, J. Chem. Phys. **106**, 1600–1608 (1997)

29.144 N. Camillone, C.E.D. Chidsey, G. Liu, G. Scoles: Superlattice structure at the surface of a monolayer of octadecanethiol self-assembled on Au(111), J. Chem. Phys. **98**, 3503–3511 (1993)

29.145 P. Fenter, P. Eisenberger, K.S. Liang: Chain-length dependence of the structures and phases of $CH_3(CH_2)_{n-1}SH$ self-assembled on Au(111), Phys. Rev. Lett. **70**, 2447–2450 (1993)

29.146 F. Schreiber: Self-assembled monolayers: From simple model systems to biofunctionalized interfaces, J. Phys. Condens. Matter **16**, R881–R900 (2004)

29.147 G.E. Poirier, M.J. Tarlov: The c(4 × 2) superlattice of *n*-alkanethiol monolayers self-assembled on Au(111), Langmuir **10**, 2853–2856 (1994)

29.148 G. Yang, G. Liu: New insights for self-assembled monolayers of organothiols on Au(111) revealed by scanning tunneling microscopy, J. Phys. Chem. B **107**, 8746–8759 (2003)

29.149 P. Fenter, A. Eberhardt, P. Eisenberger: Self-assembly of *n*-alkyl thiols as disulfides on Au(111), Science **266**, 1216–1218 (1994)

29.150 P. Fenter, F. Schreiber, L. Berman, G. Scoles, P. Eisenberger, M.J. Bedzyk: On the structure and evolution of the buried S/Au interface in self-assembled monolayers: X-ray standing wave results, Surf. Sci. **412/413**, 213–235 (1998)

29.151 Y. Kitajimaa, S. Yagi, T. Yokoyama, A. Imanishi, S. Takenaka, T. Ohta: Surface structures of SNi(111) in $(\sqrt{3} \times \sqrt{3})R30^\circ$ and $(5\sqrt{3} \times 2)$ phases studied by surface extended x-ray absorption fine structure spectroscopy, Surf. Sci. **320**, L89–L94 (1994)

29.152 M.H. Dishner, J.C. Hemminger, F.J. Feher: Direct observation of substrate influence on chemisorption of methanethiol adsorbed from the gas phase onto the reconstructed Au(111) surface, Langmuir **13**, 2318–2322 (1997)

29.153 M.F. Danışman, L. Casalis, G. Bracco, G. Scoles: Structural investigation of monolayers prepared by deposition of $(CH_3S)_2$ on the (111) face of single-crystal gold, J. Phys. Chem. B **106**, 11771–11777 (2002)

29.154 H. Kondoh, H. Nozoye: Low-temperature ordered phase of methylthiolate monolayers on Au(111), J. Phys. Chem. B **103**, 2585–2588 (1999)

29.155 V. De Renzi, R. Di Felice, D. Marchetto, R. Biagi, U. del Pennino, A. Selloni: Ordered (3×4) high-density phase of methylthiolate on Au(111), J. Phys. Chem. B **108**, 16–20 (2004)

29.156 D. Cavanna, G. Bracco, V. De Renzi, V. Corradini, R. Biagi, U. del Pennino: Ordered phases and temperature behaviour of CH_3S self-assembled monolayers on Au(111), J. Phys. Condens. Matter **19**, 305019 (2007)

29.157 L. Tang, F. Li, W. Zhou, Q. Guo: The structure of methylthiolate and ethylthiolate monolayers on Au(111): Absence of the $(\sqrt{3} \times \sqrt{3})R30^\circ$ phase, Surf. Sci. **606**, L31–L35 (2012)

29.158 R. Mazzarello, A. Cossaro, A. Verdini, R. Rousseau, L. Casalis, M.F. Danisman, L. Floreano, S. Scandolo, A. Morgante, G. Scoles: Structure of a CH_3S monolayer on Au(111) solved by the interplay between molecular dynamics calculations and diffraction measurements, Phys. Rev. Lett. **98**, 16102 (2007)

29.159 O. Voznyy, J.J. Dubowski, J.T. Yates, P. Maksymovych: The role of gold adatoms and stereochemistry in self-assembly of methylthiolate on Au(111), J. Am. Chem. Soc. **131**, 12989–12993 (2009)

29.160 X. Fan, X. Fang, R. Ran, W. Ming Lau: Density functional theory study of the adsorption of methanthiol on Au(111): Role of gold adatoms, Physica E Low Dimens. Syst. Nanostruct. **59**, 248–253 (2014)

29.161 J. Lee, J.S. Boschen, T.L. Windus, P.A. Thiel, D.-J. Liu: Stabilization of X–Au–X complexes on the Au(111) surface: A theoretical investigation and comparison of X = S, Cl, CH_3S, and SiH_3S, J. Phys. Chem. C **121**, 3870–3879 (2017)

29.162 N.A. Kautz, S.A. Kandel: Alkanethiol/Au(111) self-assembled monolayers contain gold adatoms: Scanning tunneling microscopy before and after reaction with atomic hydrogen, J. Am. Chem. Soc. **130**, 6908–6909 (2008)

29.163 F.-S. Li, W. Zhou, Q. Guo: Uncovering the hidden gold atoms in a self-assembled monolayer of alkanethiol molecules on Au(111), Phys. Rev. B **79**, 113412 (2009)

29.164 Q. Guo, F. Li: Self-assembled alkanethiol monolayers on gold surfaces: Resolving the complex structure at the interface by STM, Phys. Chem. Chem. Phys. **16**, 19074 (2014)

29.165 M. Kawasaki, H. Nagayama: Observation of highly ordered 3×4 phase of ethanethiol self-assembled monolayer on Au(111), Chem. Lett. **30**, 942–943 (2001)

29.166 J. Gao, F. Li, Q. Guo: Balance of forces in self-assembled monolayers, J. Phys. Chem. C **117**, 24985–24990 (2013)

29.167 A. Chaudhuri, D.C. Jackson, T.J. Lerotholi, R.G. Jones, T.-L. Lee, B. Detlefs, D.P. Woodruff: Structural investigation of Au(111)/butylthiolate adsorption phases, Phys. Chem. Chem. Phys. **12**, 3229–3238 (2010)

29.168 M. Yu, N. Bovet, C.J. Satterley, S. Bengió, K.R.J. Lovelock, P.K. Milligan, R.G. Jones, D.P. Woodruff, V. Dhanak: True nature of an archetypal self-assembly system: Mobile Au-thiolate species on Au(111), Phys. Rev. Lett. **97**, 166102 (2006)

29.169 P. Maksymovych, J.T. Yates: Au adatoms in self-assembly of benzenethiol on the Au(111) surface, J. Am. Chem. Soc. **130**, 7518–7519 (2008)

29.170 P.D. Jadzinsky, G. Calero, C.J. Ackerson, D.A. Bushnell, R.D. Kornberg: Structure of a thiol monolayer-protected gold nanoparticle at 1.1 Å resolution, Science **318**, 430–433 (2007)

29.171 E. Pensa, A.A. Rubert, G. Benitez, P. Carro, A. González Orive, A. Hernández Creus, R.C. Salvarezza, C. Vericat: Are 4-mercaptobenzoic acid self-assembled monolayers on Au(111) a suitable system to test adatom models?, J. Phys. Chem. C **116**, 25765–25771 (2012)

29.172 X. Zhao, R.G. Zhao, W.S. Yang: Adsorption of alanine on Cu(001) studied by scanning tunneling microscopy, Surf. Sci. **442**, L995–L1000 (1999)

29.173 J. Reichert, A. Schiffrin, W. Auwärter, A. Weber-Bargioni, M. Marschall, M. Dell'Angela, D. Cvetko, G. Bavdek, A. Cossaro, A. Morgante, J.V. Barth: L-tyrosine on Ag(111): Universality of the amino acid 2D zwitterionic bonding scheme?, ACS Nano **4**, 1218–1226 (2010)

29.174 Y. Izumi: Modified Raney nickel (MRNi) catalyst: Heterogeneous enantio-differentiating (asymmetric) catalyst. In: *Advances in Catalysis, Vol. 32*, ed. by D.D. Eley, H. Pines, P.B. Weisz (Academic Press, New York 1983) pp. 215–271

29.175 G. Webb, P.B. Wells: Asymmetric hydrogenation, Catal. Today **12**, 319–337 (1992)

29.176 M. Mahapatra, L. Burkholder, Y. Bai, M. Garvey, J.A. Boscoboinik, C. Hirschmugl, W.T. Tysoe: Formation of chiral self-assembled structures of amino acids on transition-metal surfaces: Alanine on Pd(111), J. Phys. Chem. C **118**, 6856–6865 (2014)

29.177 G. Feng, L. Zhenjun, W. Yilin, L. Burkholder, W.T. Tysoe: Chemistry of glycine on Pd(111): Temperature-programmed desorption and x-ray photoelectron spectroscopic study, J. Phys. Chem. C **111**, 9981–9991 (2007)

29.178 P. Löfgren, A. Krozer, J. Lausmaa, B. Kasemo: Glycine on Pt(111): A TDS and XPS study, Surf. Sci. **370**, 277–292 (1997)

29.179 K.E. Wilson, C.J. Baddeley: Chiral assemblies of nickel lysinate via the corrosive adsorption of (*S*)-lysine on Ni/Au{111}, Surf. Sci. **629**, 102–107 (2014)

29.180 T.E. Jones, A.E. Rekatas, C.J. Baddeley: Influence of modification pH and temperature on the interaction of methylacetoacetate with (*S*)-glutamic acid-modified Ni{111}, J. Phys. Chem. C **111**, 5500–5505 (2007)

29.181 E.M. Marti, C. Methivier, C.M. Pradier: (*S*)-Cysteine chemisorption on Cu(110), from the gas or liquid phase: An FT-RAIRS and XPS study, Langmuir **20**, 10223–10230 (2004)

29.182 T. Eralp, A. Shavorskiy, G. Held: The adsorption geometry and chemical state of lysine on Cu{110}, Surf. Sci. **605**, 468–472 (2011)

29.183 T. Eralp, A. Cornish, A. Shavorskiy, G. Held: The study of chiral adsorption systems using synchrotron-based structural and spectroscopic techniques: Stereospecific adsorption of serine on Au-modified chiral Cu{531} surfaces, Top. Catal. **54**, 1414–1428 (2011)

29.184 R.B. Rankin, D.S. Sholl: Assessment of heterochiral and homochiral glycine adlayers on Cu(110) using density functional theory, Surf. Sci. **548**, 301–308 (2004)

29.185 Z.V. Zheleva, T. Eralp, G. Held: Complete experimental structure determination of the p(3 × 2) phase of glycine on Cu{110}, J. Phys. Chem. C **116**, 618–625 (2012)

29.186 V. Humblot, C. Méthivier, R. Raval, C.M. Pradier: Amino acid and peptides on Cu(1 1 0) surfaces: Chemical and structural analyses of L-lysine, Surf. Sci. **601**, 4189–4194 (2007)

29.187 G. Jones, L.B. Jones, F. Thibault-Starzyk, E.A. Seddon, R. Raval, S.J. Jenkins, G. Held: The local adsorption geometry and electronic structure of alanine on Cu{1 1 0}, Surf. Sci. **600**, 1924–1935 (2006)

29.188 S. Haq, A. Massey, N. Moslemzadeh, A. Robin, S.M. Barlow, R. Raval: Racemic versus enantiopure alanine on Cu(110): An experimental study, Langmuir **23**, 10694–10700 (2007)

29.189 T.E. Jones, C.J. Baddeley, A. Gerbi, L. Savio, M. Rocca, L. Vattuone: Molecular ordering and adsorbate induced faceting in the Ag{110}-(*S*)-glutamic acid system, Langmuir **21**, 9468–9475 (2005)

29.190 R.B. Rankin, D.S. Sholl: Structure of enantiopure and racemic alanine adlayers on Cu(110), Surf. Sci. **574**, L1–L8 (2005)

29.191 D.I. Sayago, M. Polcik, G. Nisbet, C.L.A. Lamont, D.P. Woodruff: Local structure determination of a chiral adsorbate: Alanine on Cu(1 1 0), Surf. Sci. **590**, 76–87 (2005)

29.192 A. Kühnle, T.R. Linderoth, B. Hammer, F. Besenbacher: Chiral recognition in dimerization of adsorbed cysteine observed by scanning tunnelling microscopy, Nature **415**, 891–893 (2002)

29.193 T. Eralp, A. Shavorskiy, Z.V. Zheleva, G. Held, N. Kalashnyk, Y. Ning, T.R. Linderoth: Global and local expression of chirality in serine on the Cu{110} surface, Langmuir **26**, 18841–18851 (2010)

29.194 Y. Yun, A.J. Gellman: Enantiospecific adsorption of amino acids on naturally chiral Cu{3,1,17}$^{R\text{or}S}$ Surfaces, Langmuir **31**, 6055–6063 (2015)

29.195 H.S. Song, J.W. Han: Tuning the surface chemistry of chiral Cu(531)^{S} for enhanced enantiospecific adsorption of amino acids, J. Phys. Chem. C **119**, 15195–15203 (2015)

29.196 T. Eralp, A. Ievins, A. Shavorskiy, S.J. Jenkins, G. Held: The importance of attractive three-point interaction in enantioselective surface chemistry: Stereospecific adsorption of serine on the intrinsically chiral Cu{531} surface, J. Am. Chem. Soc. **134**, 9615–9621 (2012)

29.197 Y. Wang, S. Yang, M. Fuentes-Cabrera, S. Li, W. Liu: Enhancing enantiomeric separation with strain: The case of serine on Cu(531), J. Am. Chem. Soc. **139**, 8167–8173 (2017)

29.198 M. Smerieri, L. Vattuone, M. Rocca, L. Savio: Spectroscopic evidence for neutral and anionic adsorption of (*S*)-glutamic acid on Ag(111), Langmuir **29**, 6867–6875 (2013)

29.199 D. Costa, M. Smerieri, I. Tranca, L. Savio, L. Vattuone, F. Tielens: DFT atomistic thermodynamics applied to elucidate the driving force behind glutamic acid self-assemblies on silver (100) surface, J. Phys. Chem. C **118**, 29874–29879 (2014)

29.200 V. Humblot, S. Haq, C. Muryn, W.A. Hofer, R. Raval: From local adsorption stresses to chiral surfaces: (*R*,*R*)-Tartaric acid on Ni(110), J. Am. Chem. Soc. **124**, 503–510 (2002)

29.201 T.E. Jones, C.J. Baddeley: A RAIRS, STM and TPD study of the Ni/*R*,*R*-tartaric acid system: Modelling the chiral modification of Ni nanoparticles, Surf. Sci. **513**, 453–467 (2002)

29.202 T.E. Jones, M.E. Urquhart, C.J. Baddeley: An investigation of the influence of temperature on the adsorption of the chiral modifier, (*S*)-glutamic acid, on Ni{1 1 1}, Surf. Sci. **587**, 69–77 (2005)

29.203 A.G. Trant, T.E. Jones, T.C.Q. Noakes, P. Bailey, C.J. Baddeley: Adsorption of (*S*)-glutamic acid induces segregation of Ni at bimetallic Au/Ni surfaces, Surf. Sci. **604**, 300–307 (2010)

29.204 A.G. Trant, T.E. Jones, C.J. Baddeley: Thermal treatment of glutamic acid-modified nickel nanoclusters on Au{111} leads to the formation of one-dimensional metal-organic coordination networks, J. Phys. Chem. C **111**, 10534–10540 (2007)

29.205 T.E. Jones, C.J. Baddeley: Investigating the mechanism of chiral surface reactions: The interaction of methylacetoacetate with (*S*)-glutamic acid modified Ni{111}, Langmuir **22**, 148–152 (2006)

Gianangelo Bracco

Dipartimento di Fisica
Università di Genova
Genova, Italy
bracco@fisica.unige.it

Gianangelo Bracco received his PhD in Physics from the University of Genoa (1987). In 2015, he was appointed Associate Professor of Experimental Physics in the Department of Physics at the University of Genoa, where is currently continuing his activity on the study of surface properties and molecular beams. The results of his scientific activity have been published in more than 110 publications in journals and books.

Marco Smerieri

Istituto dei Materiali per l'Elettronica ed il Magnetismo
Consiglio Nazionale delle Ricerche
Genova, Italy

Marco Smerieri is a researcher of the National Research Council of Italy (CNR) at the Institute of Materials for Electronics and Magnetism (IMEM). He received his PhD in Physics at the University of Genoa in 2010. His research activity focuses on the field of experimental surface science with particular attention to the investigation of molecule–surface interactions at the nanoscopic level.

Letizia Savio

Istituto dei Materiali per l'Elettronica ed il Magnetismo
Consiglio Nazionale delle Ricerche
Genova, Italy
letizia.savio@imem.cnr.it

Letizia Savio is a researcher at the Istituto dei Materiali per l'Elettronica ed il Magnetismo of CNR, Italy. She received her PhD in Physics at the Universita degli Studi di Genova in 2002. Her research interests are centered on the investigation of molecule–surface interactions at the nanoscopic level, with particular focus on the hybrid organic–inorganic interfaces and on self-assembly phenomena at metal surfaces and 2-D layers.

30. Energetics of Adsorption: Single Crystal Calorimetry

Luca Vattuone, David A. King

Adsorption energy is a fundamental thermodynamic quantity in the description of gas–surface interactions. In general, it depends not only on the ad-species and on the chemical nature of the substrate but also on the surface coverage and the density and nature of the surface defects. It can also be significantly affected by the presence of coadsorbates and by temperature when the latter determines a different arrangement of species on the substrate or even the formation of different moieties at the surface. On the one hand, the measure of the heat of adsorption by the isosteric method can be used only in selected cases, where adsorption occurs reversibly and a reliable control of the coverage over a large enough range of temperatures is experimentally accessible. On the other hand, temperature-programmed desorption, which until now has been the most widely used technique, is not applicable when adsorption occurs irreversibly, and care is needed to properly analyze the experimental data, especially when the heat of adsorption is strongly coverage dependent. Single-crystal calorimetry (SCAC) provides a means of overcoming most such limitations. Since it is impossible to cover all the results obtained by this technique in a single review, a rich bibliography is provided and only selected results (in the opinion of the authors) are summarized here. The first section addresses the results obtained by the infrared calorimeter of the Cambridge group, which mostly deals with the coverage dependence of the heat of adsorption of different gases on single-crystal (both low and high Miller index) surfaces. The second section deals with the results obtained by the pyroelectric calorimeter by the Washington group, which cover both the adsorption of large organic molecules and of non-gaseous species. The impressive results obtained to date have drawn other research groups into the field, and new designs have appeared that enable, for example, the study of the adsorption of gas molecules at the surface of nanoparticles and at oxide surfaces. The last section of this chapter is devoted to such results.

M. Rocca, T.S. Rahman, L. Vattuone (Eds.), *Springer Handbook of Surface Science*, Springer Handbooks,
https://doi.org/10.1007/978-3-030-46906-1_30

The heat of adsorption of molecules at surfaces is a key thermodynamic parameter for the understanding of adsorption and reaction at surfaces and, consequently, also for heterogeneous catalysis. It is also a key parameter in providing a test for the first principles quantum theory calculations now widely used to study processes at surfaces.

30.1 Methods for Calorimetry

The isosteric method, which measures the pressure required to keep a constant coverage of the adsorbate at the surface as a function of temperature, can be effectively used only when it is possible to check the equilibrium coverage in a reliable way over a large enough range of temperatures. It cannot, thus, be employed when irreversible adsorption occurs, and it can be affected by the changes in the arrangements of adsorbates at the surface while the temperature and the pressure are being modified [30.1]. Thermal desorption spectroscopy (TDS or TPD) is more routinely used, since it is compatible with conventional UHV experimental setups; it cannot, however, be used when desorption does not occur. Moreover, the extraction of thermodynamic data from TPD curves is affected significantly by the method employed for the analysis. The basic idea of calorimetry is to measure the temperature change occurring at the surface when adsorption occurs. While measurements for non monocrystalline surfaces have been conducted over a long period of time [30.2], measurements for single-crystal surfaces became systematically available only in the 1990s. After a few previous attempts by *Kyser* and *Masel* [30.3], the first single-crystal calorimeter was developed by the group of *King* in Cambridge [30.4, 5], and a systematic investigation of adsorption of different gases at single-crystal surfaces was undertaken. These results have already been reviewed in detail [30.1]. Here, we shall present only some of them: the effect of promoters on the heat of adsorption, the measurement of the energy difference between surface phases, the heat of reaction, lateral interactions among adsorbates, and the role of defects in adsorption. The main limitation of the first Cambridge calorimeter, which essentially monitored the change in the infrared emission caused by the temperature increase upon adsorption, was the restriction to room temperature adsorption and to nonactivated systems. A different calorimeter, based on pyroelectric detection, was then developed by the same group; this calorimeter allowed the measurement of heats of adsorption at different temperatures [30.6]. This design was extensively improved by the group of *Campbell* [30.7, 8] at Washington University in Seattle, who extended the method to the measurement of the heat of adsorption of metals and of nanoparticles at surfaces. Some of their latest achievements will also be reviewed in this chapter. Recently, similar experimental setups have been developed also by other research groups [30.9, 10] improving the sensitivity and extending the set of systems for which the heat of adsorption can be measured.

30.2 Definition of the Heat of Adsorption

Adsorption at surfaces is an exothermic process, and the differential molar enthalpy change is, thus, negative. According to the usual convention we define the differential molar adsorption heat q as its opposite. The isosteric adsorption heat q_{st} is defined according to the Clausius–Clapeyron equation

$$q_{\mathrm{st}}(\theta) = -R\left[\frac{\partial \ln P}{\partial(1/T)}\right]_{\theta} , \qquad (30.1)$$

where P is the pressure, T the absolute temperature, R the gas constant, and θ the fractional surface coverage. In practice it is necessary to measure the change in the gas pressure needed to keep the fractional surface coverage constant while changing the temperature. This approach suffers from two drawbacks: firstly it can be applied only when adsorption takes place reversibly, and secondly, a reliable indicator of the actual surface coverage is needed; θ can be checked in different ways, i.e., monitoring the work function, the diffraction pattern, or some specific spectroscopic signal (vibrational or electronic) related to the adsorbate, but care is needed since these indicators may be affected in some cases also by change in the temperature, especially because a relatively wide range of temperatures is required for an accurate measurement. Moreover, when the temperature is increased, the pressure required to maintain a constant coverage may increase beyond the capabilities of traditional UHV techniques, thus further limiting the practical feasibility of this approach. An example is reported in Fig. 30.1, which shows the pioneering work of *Tracy* and *Palmberg* [30.11]. They first measured the

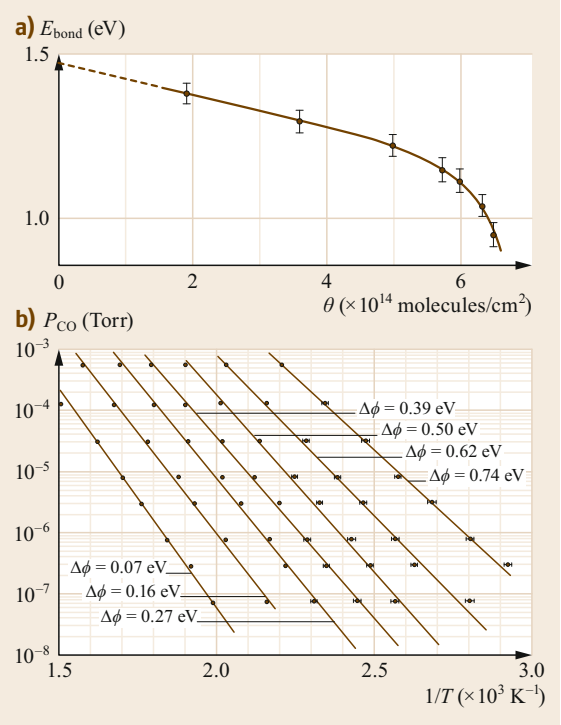

Fig. 30.1 **(a)** Heat of adsorption as a function of coverage for CO on Pd(100). **(b)** Pressure as a function of the inverse temperature required to keep a constant CO coverage on Pd(100). Coverage is monitored by the work function of the surface. *Curves* corresponding to different work functions and, thus, to different coverages are reported (Adapted from [30.11], with permission from Elsevier) ◄

change in the work function $\Delta\Phi$ of Pd(100) as a function of temperature for different CO pressures. From these curves of pressure versus inverse temperature were obtained (Fig. 30.1b). The coverage of CO on Pd(100) is monitored by monitoring the work function. The coverage for each $\Delta\Phi$ was obtained as follows. In a series of experiments CO was adsorbed at room temperature until the work function changed by $\Delta\Phi$.

The sample was then rapidly flashed to 500 °C; the integral of the pressure rise is proportional to the amount of CO that has desorbed. The absolute calibration of the coverage was possible using the c(4 × 2)-45° low-energy electron diffraction (LEED) pattern which corresponds to a coverage of 0.5 ML. Using the Clapeyron equation, the heat of adsorption as a function of θ is obtained.

30.3 Experimental Setups

As outlined above, the basic principle behind the development of a single-crystal calorimeter (SCAC in the following) is the measurement of the change in the temperature of a sample upon adsorption of a measured dose of adsorbate. In order to obtain a quantitative result for the heat of adsorption it is necessary to measure accurately and reliably the heat released to the sample upon adsorption and the amount of adsorbing gas. The result was attained by using sample of very low thermal capacity (i.e., single crystals with a radius of some mm, and a thickness of some micrometers) and by dosing the desired gas by use of a supersonic molecular beam (SMB). The flux of the SMB is measured prior to each experiment by a spinning rotor gauge. The surface of the sample is then exposed at normal incidence using a pulsed SMB and the sticking probability and the increase in the temperature are measured simultaneously. The coverage is obtained by integrating the amount of gas adsorbed at each pulse. The different SCAC setups can be classified on the basis of the method used to measure the heat released and the temperature change.

The calorimeter initially developed by the group of King (Fig. 30.2a) measures the change in the infrared intensity emitted by the back of the sample upon adsorption of gas. The intensity is measured by a suitable IR detector and is calibrated by comparing the signal measured upon adsorption with the one recorded when the clean surface is exposed to a laser of known power impinging at normal incidence and correcting for the reflectivity of the sample at the laser wavelength. The reflectivity is measured in a separate experiment by optical methods. The change in radiated power from the back of the crystal is proportional to the third power of the temperature times the change in T due to adsorption. The sensitivity, thus, drops as T^3 and for this reason the infrared detection technique is inadequate for low-temperature measurements.

In order to overcome this limitation another detector was developed that employs the pyrolectric effect; the increase in the temperature produced by adsorption is measured by monitoring the pyroelectric signal in place of the IR emission. In the first design [30.6], the detector element was a $LiTaO_3$ wafer 0.3 mm thick onto which AuCr electrodes had been deposited. The single crystal (which had a thickness of $\approx 2\,\mu$m) was bonded to the wafer by cold welding onto an intermediate layer of polycrystalline Ni, which, in turn, was

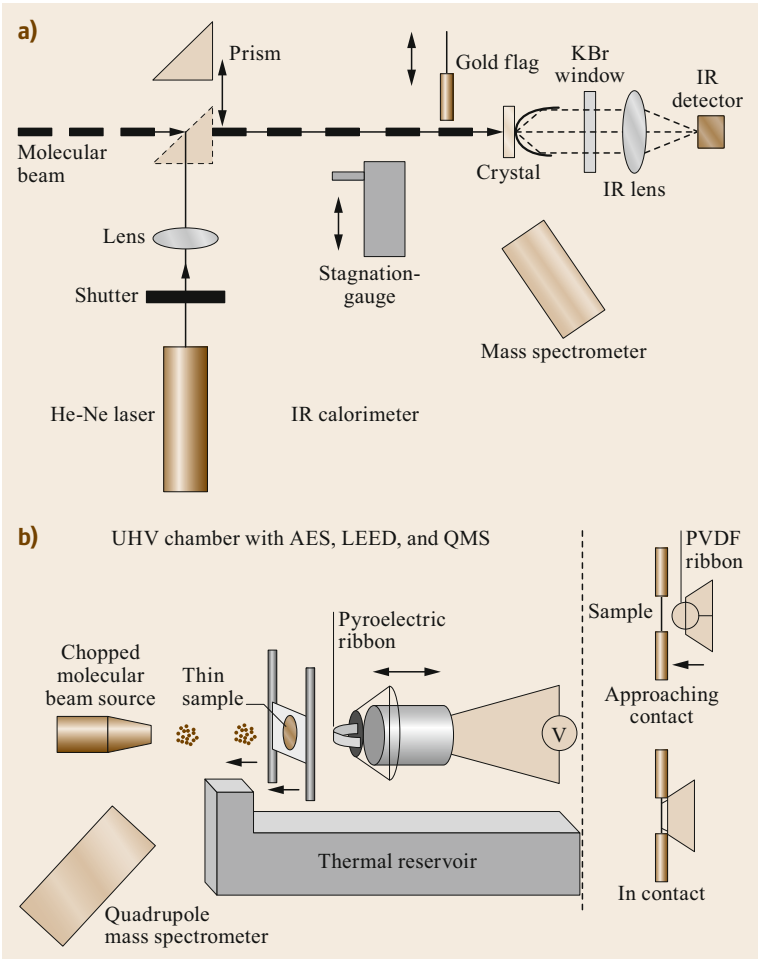

Fig. 30.2 **(a)** The Cambridge calorimeter (Adapted from [30.5], with permission from Elsevier). **(b)** The pyroelectric calorimeter in Washington (Adapted from [30.7], with the permission of AIP Publishing)

evaporated onto one AuCr electrode. The voltage signal generated between the two electrodes was passed through a specially designed high-impedance amplifier and then acquired digitally. In subsequent designs (Fig. 30.2b) [30.7, 8], a pyroelectric ribbon is moved carefully until it touches the backside of the sample and the pyroelectric signal is recorded. A similar method is used in the latest experimental setups [30.9, 10].

30.4 Overview of Experimental Results by the Cambridge Group

A very large amount of data has been obtained by the Cambridge group starting from the 1990s. We shall briefly overview the most significant results in the opinion of the authors. We shall consider the following topics here:

a) The dissociative adsorption of oxygen from the regime of chemisorption to the onset of oxidation on low Miller index Ni surfaces
b) The effect of surface temperature and potassium precoverage on Ni oxidation
c) The experimental determination of the energy difference between surface phases
d) The effect of lateral interactions between adsorbates on the heat of adsorption and their role in surface chemistry
e) The heat of adsorption in presence of defects
f) Heat of adsorption of hydrocarbons and determination of the metal–C bond energy
g) The heat of reaction for CO oxidation
h) The determination of prefactors for desorption.

30.4.1 Dissociative Adsorption

Dissociative oxygen adsorption and substrate oxidation are among the most common phenomena occurring when reactive surfaces are exposed to O_2. Figure 30.3a shows the sticking probability s measured at normal incidence and at room temperature (RT) by the King and Wells method using a pulsed supersonic molecular beam of O_2 impinging onto a clean Ni(100) surface. By integrating s over the exposure time and multiplying it by the beam flux it is possible to obtain the total amount of oxygen that has adsorbed (apparent oxygen adatom coverage). In Fig. 30.3a, s is plotted versus such apparent coverage. Three regimes are present:

i) Initially s is large (≈ 0.55) and decreases rapidly with increasing exposure to the beam.
ii) After reaching a minimum s increases again and remains relatively large (> 0.1) until an apparent coverage of ≈ 5 ML of oxygen adatoms is reached.
iii) Thereafter, s remains constant, indicating that a stable regime has been attained in which the amount of oxygen adsorbing during the length of the pulse is desorbed in the time between two subsequent pulses.

The contributions of these three regimes have been deconvoluted and are shown by the continuous lines in the figure. Figure 30.3b shows the net sticking probability (obtained by subtracting the reversible contribution to s) as a function of the net adatom coverage (obtained by subtracting the amount of oxygen that desorbs between subsequent pulses). The first regime corresponds to the rapid building up of an adsorbed oxygen layer, while the second one indicates the formation of an oxide layer at the surface. Ni oxidation is believed to start at nucleation points and to go on by island growth. Oxygen incorporation occurs only at the edges of the islands; after an initial increase s reaches a maximum and decreases as long as islands get larger until the oxide growth stops at ≈ 3.5 ML. Formation of a thicker oxide then becomes extremely slow or suppressed under the experimental conditions of this experiment.

Figure 30.3c shows the heat of adsorption as a function of coverage for Ni(100), as well as for the other low Miller index surfaces (Ni(110) and Ni(111)) at RT. The heat of adsorption is relatively large for all surfaces but exhibits different behaviors. On Ni(100) a rapid decrease with increasing coverage is present. This decrease is due to repulsive lateral interactions between second-nearest neighbors. The interaction between third-nearest neighbors must be, on the contrary, weakly attractive, since an ordered $p(2\times 2)$ structure forms. For Ni(110), the initial heat (475 kJ/mol) is lower than for Ni(100), and the drop with θ is less steep because of the formation of Ni–O chains, which shield the O atoms, thus decreasing the magnitude of repulsive interactions between them. Also, for Ni(111),

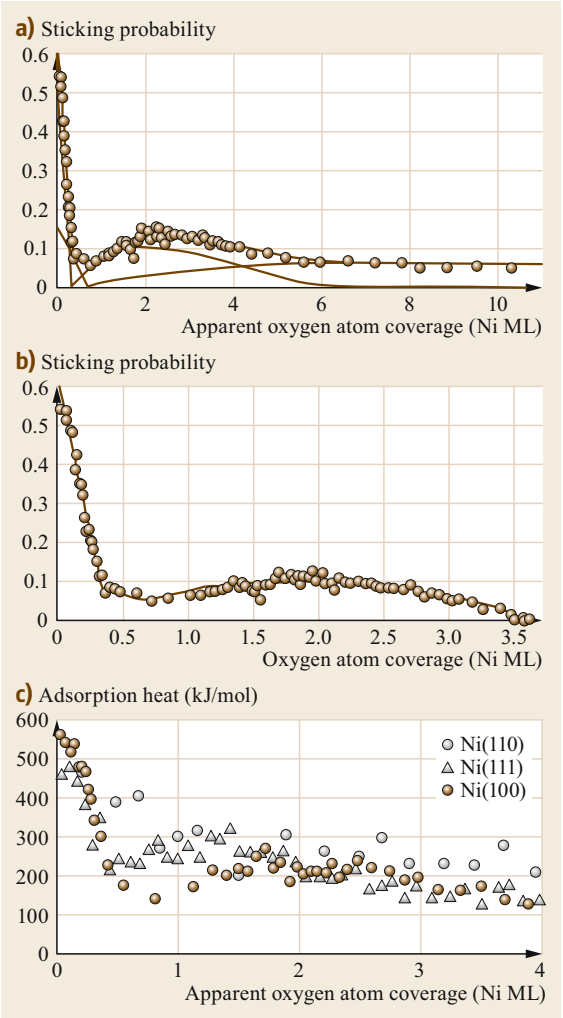

Fig. 30.3 **(a)** Sticking probability versus apparent O adatom coverage on Ni(100) at RT, showing the chemisorption, oxidation, and reversible regimes. The *smooth line* running through the experimental data is the sum of the other lines used to fit the data, including two *straight lines* as an empirical fit to the chemisorption sticking probability, a peaked curve corresponding to oxidation by island growth, and a curve corresponding to reversible molecular oxygen adsorption. **(b)** Net sticking probability (obtained from the one in **(a)** by subtracting the reversible contribution) as a function of absolute coverage. **(c)** Oxygen differential adsorption heat on different Ni single-crystal surfaces at 300 K (Reprinted from [30.12], with the permission of AIP Publishing)

q is initially (440 kJ/mol) lower than for Ni(100), since adsorption occurs at threefold hollow sites; q initially increases due to the rearrangements of the adatoms at the surface to minimize the repulsive interactions. Such a reordering is made possible by the presence of an effective precursor-mediated adsorption path (evident from $s(\theta)$, which is, however, not reported here). Repulsive interactions set in thereafter, causing a decrease of q. The three low Miller index surfaces studied here behave similarly in the oxidation regime with heat of adsorption of the order of 200 kJ/mol. Finally, when oxide growth stops, and reversible adsorption of oxygen starts to occur on the oxide film, the heat of adsorption decreases to ≈ 87 kJ/mol.

30.4.2 Surface Temperature and Potassium Precoverage on Ni Oxidation

The heat of adsorption of O_2 on Ni(100) was also measured as a function of the surface temperature using a pyroelectric detector [30.12]. The results are shown in Fig. 30.4. It is apparent that: i) for $\theta \leq 0.25$ ML, q is constant (and possibly slightly increasing with θ) at 410 K, while it is initially lower and decreases with increasing coverage for lower temperatures. ii) Above 0.25 ML, q decreases rapidly at 410 K than at lower T. A simple Monte Carlo simulation using a lattice-gas model provides a consistent explanation for all these observations [30.12]. The interaction between first neighbors is prohibitively high, since the saturation coverage does not exceed 0.5 ML in the chemisorption regime. The interaction between second-nearest neighbors must be strongly repulsive (by 30 kJ/mol) in order to account for the sudden drop observed at 410 K above 0.25 ML when the sites of the c(2 × 2) structure starts to be occupied. The third-nearest neighbors' interaction must be weakly attractive (by 1.5 kJ/mol) to explain the tendency to form the p(2 × 2) structure and in this way to account for the slight increase in q between 0 and 0.25 ML at 410 K. Since 0.25 ML is the coverage expected for an ordered p(2 × 2) overlayer, these findings indicate that at 410 K, the mobility of the O adatoms is high enough to allow the system to minimize the repulsive interactions by avoiding the occupation of second-nearest neighbor sites and possibly even to maximize the heat of adsorption, exploiting the fact that third-nearest neighbor interaction is weakly attractive. At RT, on the contrary, the mobility is not high enough to allow for the formation of a fully-ordered overlayer; repulsive interactions show up already < 0.25 ML, because of the occupation of second-nearest neighbor sites. This effect becomes even more evident at 90 K, where the limit of immobile adsorbate is reached and a nearly monotonic decrease in q is observed. The effect

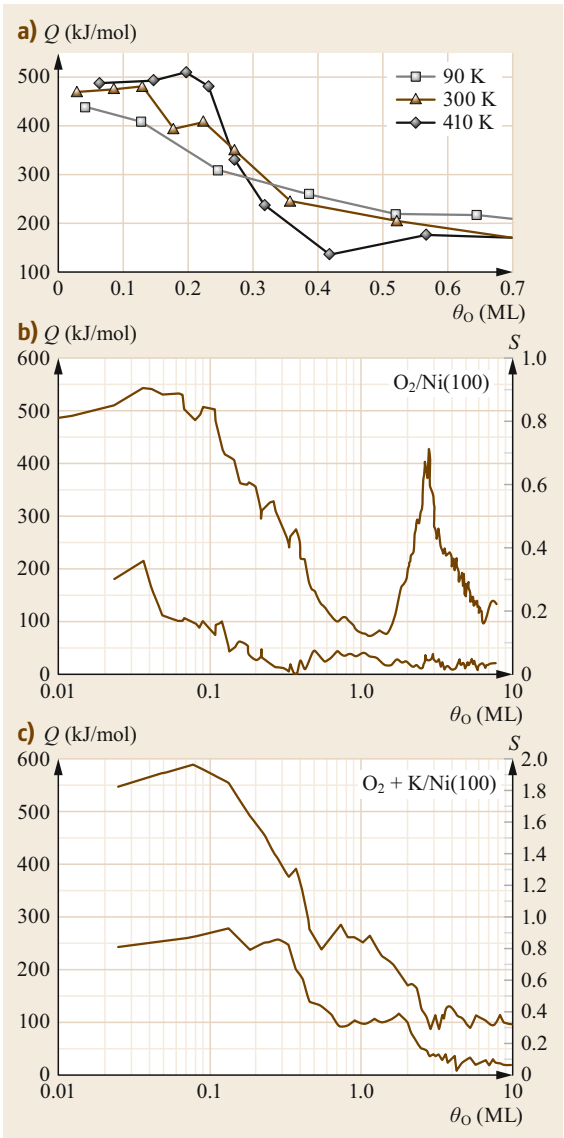

Fig. 30.4 **(a)** Differential heat of adsorption of O_2 on Ni(100) versus apparent O adatom coverage on Ni(100) at different temperatures in the low-coverage regime (Adapted from [30.12], with the permission of AIP Publishing). **(b)** Sticking probability (*lower graph*) and differential heat (*upper graph*) for O_2 on Ni(100) at RT without K. **(c)** Sticking probability (*lower graph*) and differential heat (*upper graph*) for O_2 on Ni(100) at RT for a K precoverage of 0.3 ML (Reprinted from [30.13], with permission from Elsevier)

of K preadsorption [30.15] on q and s for oxygen adsorption on Ni(100) is apparent from Fig. 30.4b,c. For $\theta_K = 0.3$ ML, the initial sticking coefficient is 0.85, i.e., more than two times larger than for the bare Ni(100)

surface, and remains constant up to $\theta_O = 0.33$. The heat of adsorption is initially higher (by 40 kJ/mol) than for the bare surface and decreases similarly with increasing coverage. In the range of coverage corresponding to the formation of the oxide, the presence of K completely modifies the behavior of the system; s remains nearly constant up to an oxygen coverage of 2 ML, while q is constant until 1.3 ML of oxygen and decreases towards the reversible adsorption regime afterwards. The presence of K thus affects the kinetics much more effectively than the thermodynamics of oxygen adsorption at Ni(100). The increased charge density in the surface region due to K adsorption increases the probability of dissociation of O_2 in the molecular precursor. For a K precoverage > 0.15 ML, the molecular state is stabilized and the rate of oxidation of the substrate is increased. The measurements of the effect of the K precoverage on the heat of adsorption of O_2 on Ni(111) and Ni(100) are discussed in larger detail in [30.1].

30.4.3 Energy Difference Between Surface Phases

We now show that it is possible to use microcalorimetry also to measure the energy difference between surface phases, information previously obtained only by theoretical methods [30.16]. It is known that the bare Pt(100) surface can exist at RT in two different phases: a metastable (1 × 1) and a hex phase. Upon annealing to 500 K the (1 × 1) phase turns into the hex one. It is, however, possible to adsorb molecules such as CO (or NO) at RT starting from both phases and ending with a (1 × 1) phase. The differential heat of adsorption of CO was then measured at RT starting from both

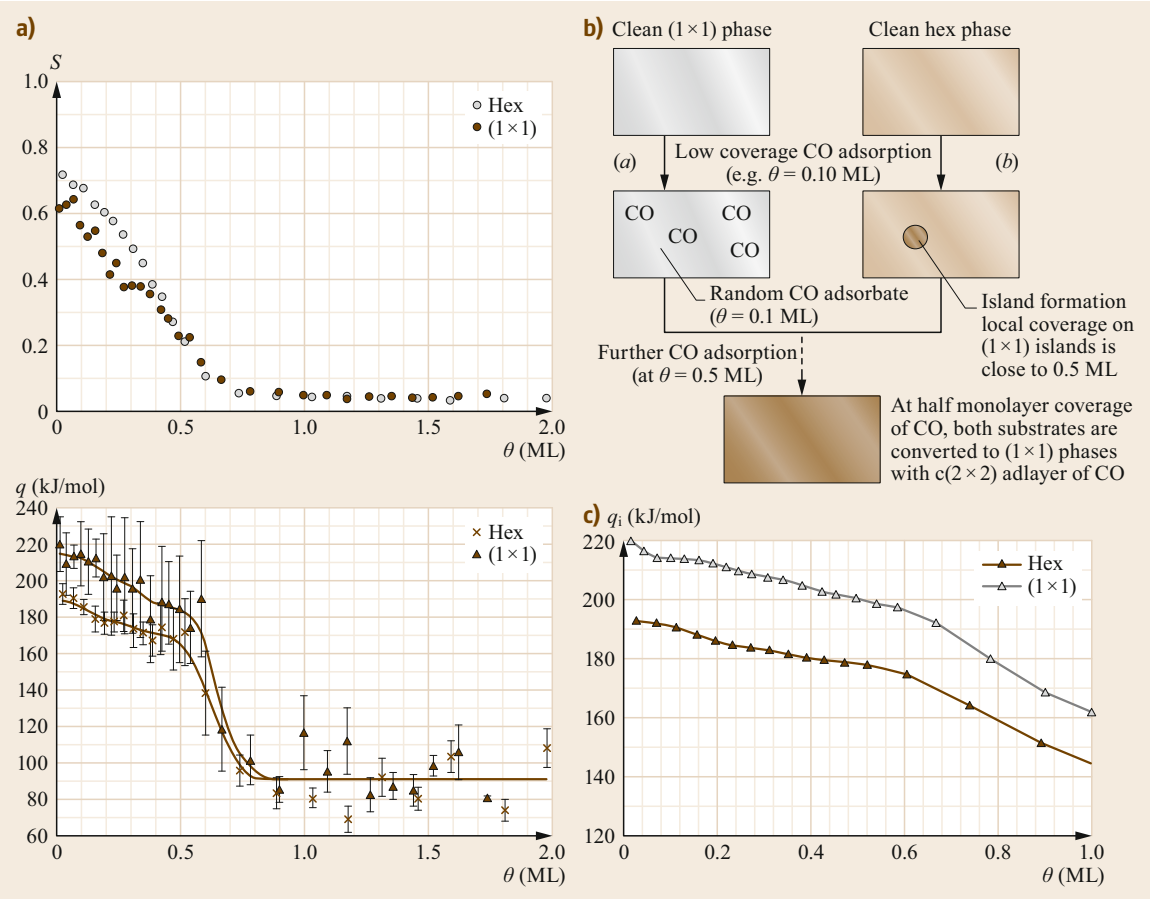

Fig. 30.5 **(a)** Sticking probability S (*top*) and differential heat of adsorption q (*bottom*) for CO adsorption on Pt(100)-hex and Pt(100)-(1 × 1) at RT. **(b)** The two initial states of clean Pt(100), the two different CO adsorption pathways (*a* and *b*), and the identical final state, Pt(100)-(1 × 1)–c(2 × 2)-CO. The difference in the integral adsorption heat q_i **(c)** along paths *a* and *b* is the energy difference between the initial states (12 kJ/mol). ([30.1], © ACS 1998; adapted from [30.14], with the permission of AIP Publishing)

phases. Since the final state is the same, i.e., a c(2 × 2) CO-covered (1 × 1) phase with a coverage of 0.5 ML, by comparing the integral heat of adsorption it was possible to obtain experimentally the energy difference between the hex and the (1 × 1) phase [30.16]. The integral heat of adsorption is defined as

$$q_{\mathrm{int}}(\theta) = \frac{\int q_{\mathrm{diff}} \mathrm{d}\theta}{\int \mathrm{d}\theta} \,. \tag{30.2}$$

The difference between the integral heats q_{int} at a coverage of 0.5 ML multiplied by the coverage is, thus, equal to the difference in energy between the bare hex and (1 × 1) phases, which comes out to be 12 kJ/mol.

30.4.4 The Role of Lateral Interactions in Surface Chemistry

The heat of adsorption of molecules is often strongly coverage dependent. Such dependence can arise for different reasons: direct and indirect interactions between adsorbed molecules, coexistence of molecular and dissociative adsorption, etc. Lateral interactions may arise from three contributions: dipole–dipole interaction, Pauli repulsion, and substrate-mediated interactions.

Dipole–dipole interactions are long-range forces but they are too small to explain the experimentally observed decrease in q. Pauli repulsion is definitely stronger, but since it arises from the overlap of electron wavefunctions it can play a role only between first neighbors. Thus, we can conclude that the major contribution to lateral interactions is provided by substrate-mediated interactions. They can be either repulsive or attractive, and their magnitude can be estimated by the change in the heat of adsorption with increasing coverage. One example is provided in Fig. 30.6 for CO adsorption on Pt(111). For $\theta =$ 0.33 ML, a $(\sqrt{3} \times \sqrt{3})$R30° overlayer of CO molecules forms (Fig. 30.6). In this structure, each CO admolecule is surrounded by six next-nearest neighbors. If we assume that adsorbate–adsorbate interactions can be described as sum of forces between couples of molecules (or atoms), i.e., if pairwise addictivity holds, then the repulsive interaction ω_2 can be easily estimated

$$\omega_2 = \frac{q(0) - q(0.33)}{6} = 3.8\,\mathrm{kJ/mol}\,. \tag{30.3}$$

Lateral interactions play a key role in surface chemistry. A paradigmatic example is provided in Fig. 30.7. The differential heat of adsorption of NO on the bare Ni(100) is initially quite high and decreases rapidly with increasing NO coverage, due to lateral interactions. The relatively high initial value indicates that dissociative adsorption takes place. The same figure shows also the differential heat for NO on the same surface precovered with different amounts of O adatoms; the initial heat decreases rapidly with increasing O precoverage. The data can be modeled by considering the sites occupied by the adatoms generated by the dissociation of

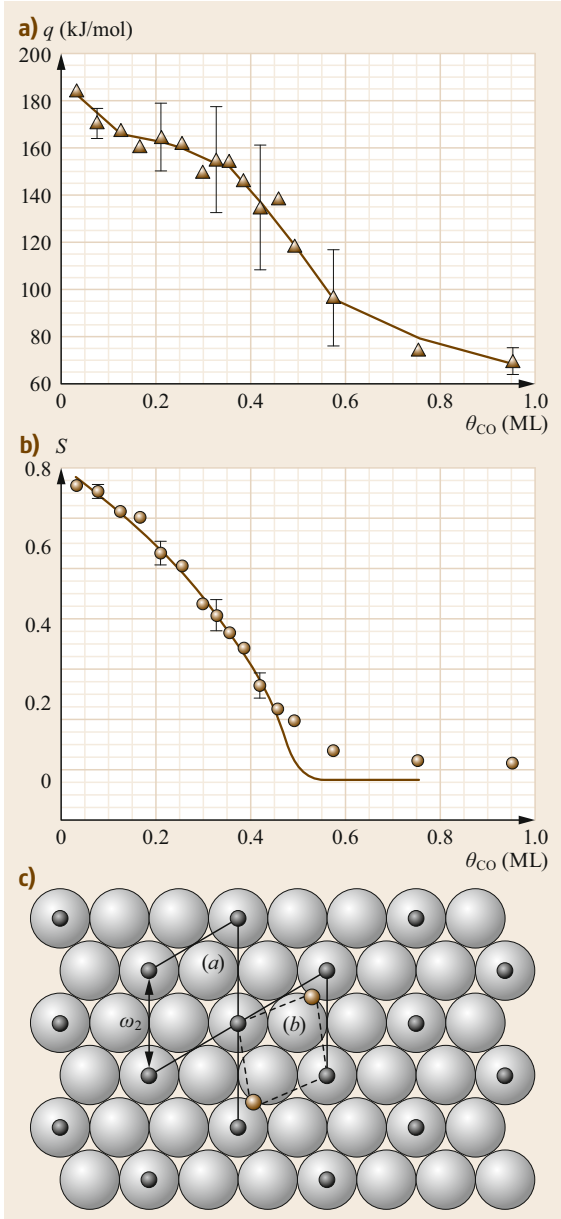

Fig. 30.6a–c Differential heat of adsorption for CO on Pt(111) **(a)** and sticking probability **(b)** versus coverage and **(c)** model of the $(\sqrt{3} \times \sqrt{3})$R30° (Adapted from [30.17], with the permission of AIP Publishing)

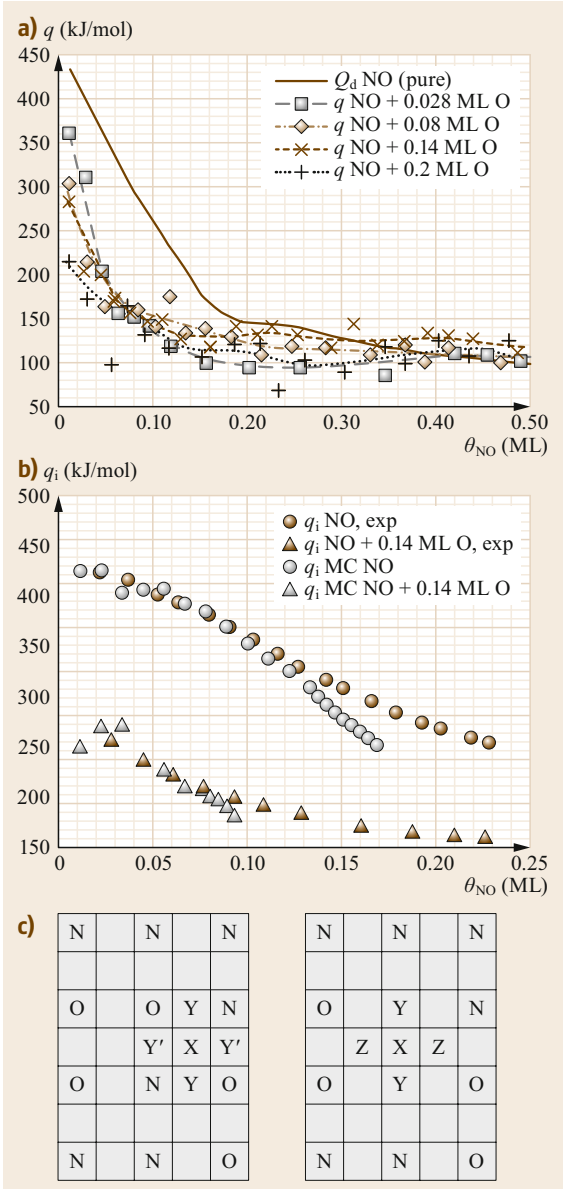

Fig. 30.7a–c Differential heat q **(a)** and integral heat q_i **(b)** of adsorption on NO on Ni(100) for different precoverages of O atoms (MC: Monte Carlo simulation). **(c)** Possible adsorption sites for the NO molecule (X) and for the N and O adatoms resulting from its dissociation (Y, Y′ and Z. See text.) (Adapted from [30.18], with the permission of AIP Publishing; [30.19], © Wiley 1996)

NO into N and O adatoms or by the oxygen adatoms generated by the dissociation of O_2 [30.18]. The integral heat is shown in Fig. 30.7b. The model (MC) assumes an initial heat of adsorption equal to the experimentally measured initial value and fits the decrease in the heat of adsorption by assuming the same repulsive interaction between N–O, N–N, and O–O adatoms in second-nearest neighboring sites. Occupation of first-neighbor sites does not occur, as indicated by the value of the saturation coverage in the chemisorption regime, which is < 0.5 ML. The model properly describes the data up to a certain coverage of adatoms (≈ 0.12 ML for the bare surface and ≈ 0.09 ML for a surface precovered with O adatoms) and thereafter drops more rapidly than experimentally observed. Above such coverage, the experimentally measured differential heat exhibits a plateau, which is assigned to nondissociative chemisorption. We can, thus, draw the following picture. As long as lateral interactions are not too strong, the heat of adsorption is higher for dissociative than for molecular adsorption, and O and N adatoms form. Dissociation eventually ends (and molecular chemisorption starts) at the coverage for which the heat of dissociative adsorption falls below the heat of molecular chemisorption.

The schematic in Fig. 30.7c clarifies what happens in the different geometrical arrangements of the O and N adatoms present on the surface. If a NO molecule lands at the X site, the adatoms resulting from its dissociation can try to occupy second and third-neighbor sites. If the preadsorbed adatoms occupy the sites shown in the left part of the scheme, dissociative adsorption cannot occur because occupation of first-neighbor sites is forbidden. If, on the contrary, the sites around the X site are free, dissociation can occur by occupying the Y sites. Occupation of the Z sites is not expected to occur, it being thermodynamically less favored. These results indicate that the array of empty sites that are required for dissociative adsorption to occur is quite demanding if the repulsive interactions are large, as in the present case. The model is able to describe consistently both the coverage dependence of q and of the sticking probability (not shown, [30.19]). We expect this scenario to occur for several different systems; a similar argument has, in fact, been invoked to explain the onset of molecular adsorption for NO on Ni(211) [30.20, 21].

30.4.5 Heat of Adsorption at Defects

It is well established that high Miller index surfaces can be model systems for the investigation of adsorption at well-defined defects; such surfaces indeed exhibit a high amount of majority defects arranged in a regular way [30.22]. Several stepped surfaces have been studied by microcalorimetry (i.e., adsorption of CO on Fe(211) [30.23], of NO on Ni(211) [30.20], O_2 and NO on stepped Pt surfaces [30.24], and O_2 on Ni(211) [30.21]). Here, we will summarize here the results obtained for two different cases: oxygen adsorp-

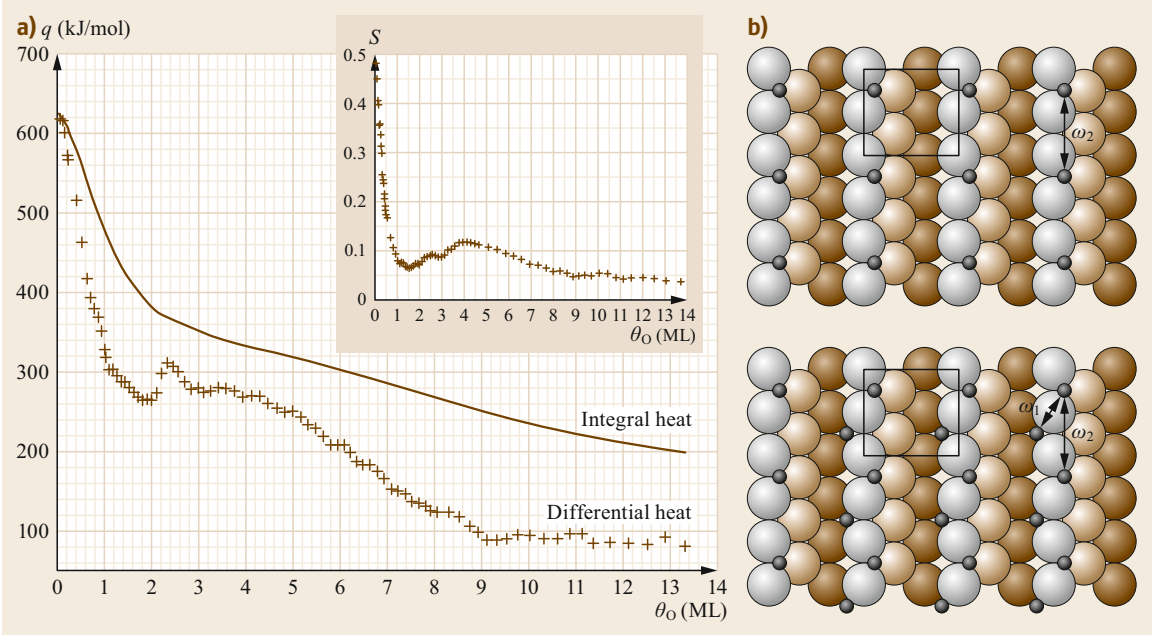

Fig. 30.8 **(a)** Differential and integral heat of adsorption for O_2 on Ni(211) as a function of the O adatom coverage. The *inset* shows the coverage dependence of the sticking probability. **(b)** Model of the (211) surface with the sites occupied at 0.5 ML (*top*) and at 1 ML (*bottom*) oxygen coverage. The contributions to pairwise lateral repulsive interactions between adatoms at different distances are shown schematically (see text) (Adapted from [30.21], © 2004 American Chemical Society)

tion on stepped Ni(211) [30.21] and NO dissociation on stepped Pt surfaces [30.24]. In Fig. 30.8, the differential heat of adsorption and the sticking probability of O_2 on Ni(211) are reported as a function of the apparent adatom coverage. The initial differential heat of adsorption q (620 kJ/mol) is significantly higher than for low Miller index surfaces (Fig. 30.3) because of the presence of low-coordinated adsorption sites at the steps; q then decreases rapidly with coverage due to strong lateral repulsions between adatoms until a coverage of 1.8 ML of oxygen adatoms is reached. The drop in q from 620 to 460 kJ/mol between 0 and 0.5 ML is due to repulsions between adatoms at a distance of about 4.98 Å (corresponding to $\omega_2 = 40$ kJ/mol in Fig. 30.8). At 1 ML, q has dropped to 300 kJ/mol due to an additional repulsive interaction between adatoms at a distance of 3.45 Å. The addition of further adatoms at the steps would cause further and stronger repulsive interactions between adatoms; at this coverage, the steps are, thus, saturated and adsorption at terrace sites must set in until a coverage of 1.8 ML is reached. At this coverage, q suddenly increases, reaching a maximum value of 310 kJ/mol at 2.3 ML and remains constant at about 270 kJ/mol up to 4 ML. The coverage dependence of the differential heat of adsorption is closely related to the sticking probability shown in the inset of Fig. 30.8. As for low Miller index surfaces, oxidation starts at nucleation points on the surface and proceeds via formation of islands of oxide. The number of sites at the boundaries of the islands increases until the islands starts to merge; at this point, the length of the island boundaries progressively diminishes, and the sticking probability approaches zero. Above this point, q decreases slowly to attain the steady-state value of 90 kJ/mol around 9 ML. In Fig. 30.9, the differential heat and the sticking probability for NO adsorption on Pt(111), Pt(211) and Pt(411) are compared. The fcc(211) surface consists of two-atom wide (111) terraces separated by a single-atom step of (100) orientation. The fcc(411) surface is more complex; it consists of two terraces of (100) character, one being two atoms wide and the other one atom wide, separated by a single-atom step of (111) orientation. The sticking probability behaves similarly on these surfaces; it decreases quite slowly with coverage, indicating that a precursor mechanism is active and is not affected significantly by the presence of an ordered array of steps or by the size of the terraces. The initial differential heat of adsorption is, on the contrary, significantly affected by the presence of the steps: q is higher on the (411) surface (217 kJ/mol), intermediate on Pt(211) (192 kJ/mol), and lower on Pt(111)

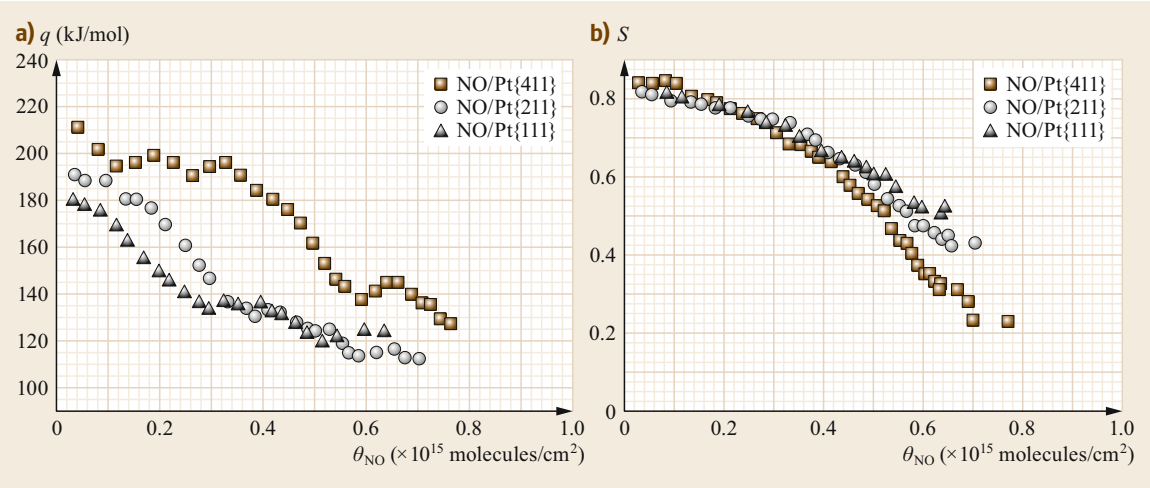

Fig. 30.9a,b Differential heat **(a)** and sticking probability **(b)** for NO adsorption on low and high Miller index Pt surfaces (Adapted from [30.24], with permission from Elsevier)

(182 kJ/mol). This result is consistent with the following trend: NO adsorbs molecularly on Pt(111), while it dissociates at steps on Pt(211) and Pt(411). The amount of dissociated NO is found to be greater for the latter surface because of the larger size of the (100) facets on Pt(411). For Pt(211), q indeed indicates dissociative adsorption up to 0.26 molecules/cm^2, while a similar argument suggests dissociative adsorption to occur up to 0.31 molecules/cm^2 for Pt(411). At higher coverage, when the steps are saturated, molecular adsorption sets in, thus explaining the similar heat of adsorption observed for Pt(111) and Pt(211). For Pt(411), q remains relatively high up to a larger coverage; probably incoming NO molecules will not be as close to the adsorbed N and O adatoms and lateral interactions are, thus, weaker, and a lower drop in q is observed [30.24].

30.4.6 Heat of Adsorption of Hydrocarbons

The measurement of the heat of adsorption of hydrocarbons is particularly relevant, since it also provides a way to determine the metal–C bond energy. This value cannot be obtained by thermal desorption experiments because adsorption of hydrocarbons at reactive metal surfaces in most cases occurs irreversibly, producing many different surface species, with different degrees of dehydrogenation and with different rehybridizations of the C–C bond inside the molecule. An essay of such complexity is provided in Fig. 30.10, which shows the heat of adsorption of a simple hydrocarbon like ethene (C_2H_4) on different Pt surfaces. The different initial value of q and its different coverage dependences can only be understood by considering that different radicals form. On Pt(100)-hex [30.25] quad-σ acetylene forms on the bare surface, followed by ethylidyne between 0.06 and 0.18 ML. At higher coverage di-σ ethylene forms. Finally, reversible adsorption of π-bonded ethylene occurs. These assignments explain the decrease in q and the plateau present at the different coverages. On Pt(100)-(1×1), the situation is similar, except for the fact that ethylidyne does not form because of the absence of threefold sites on this surface; quad-σ acetylene forms on the bare surface, followed by di-σ-bonded ethylene, and then by reversibly adsorbed π-bonded ethylene. For Pt(110), the situation is quite different; it has been suggested that ethylylidine (C–CH_2–) forms on the bare-surface bonding in the troughs of the (1×2) missing-row reconstruction. The next species is ethylidyne (C–CH_3), which probably adsorbs on the (111) microfacets of the Pt(110) surface; above 0.5 ML, di-σ ethylene and then reversibly adsorbed π-bonded ethylene are observed [30.26]. On Pt(111) [30.27] an unusual, nonmonotonic, dependence of q on coverage is obtained. In the present case, several reactions can occur

Ia) $C_2H_4(g) + 2^* \rightarrow CHCH_3(a)$
Ib) $CHCH_3(a) + 2^* \rightarrow CCH_3(a) + H(a)$
II) $C_2H_4(g) + 3^* + H(a) \rightarrow CCH_3(a) + H_2(g)$

At low coverage, no loss of hydrogen by recombination takes place, and reactions Ia) and Ib) occur. At 0.17 ML, reaction II) starts to occur, and a minimum in q is observed, since hydrogen desorption is endothermic. After consuming all the preadsorbed H, eventually formation of ethylidyne (reaction Ib) occurs. As the ethylidyne islands grow, fewer and fewer threefold sites are available and only bridge sites are vacant. They then favor the for-

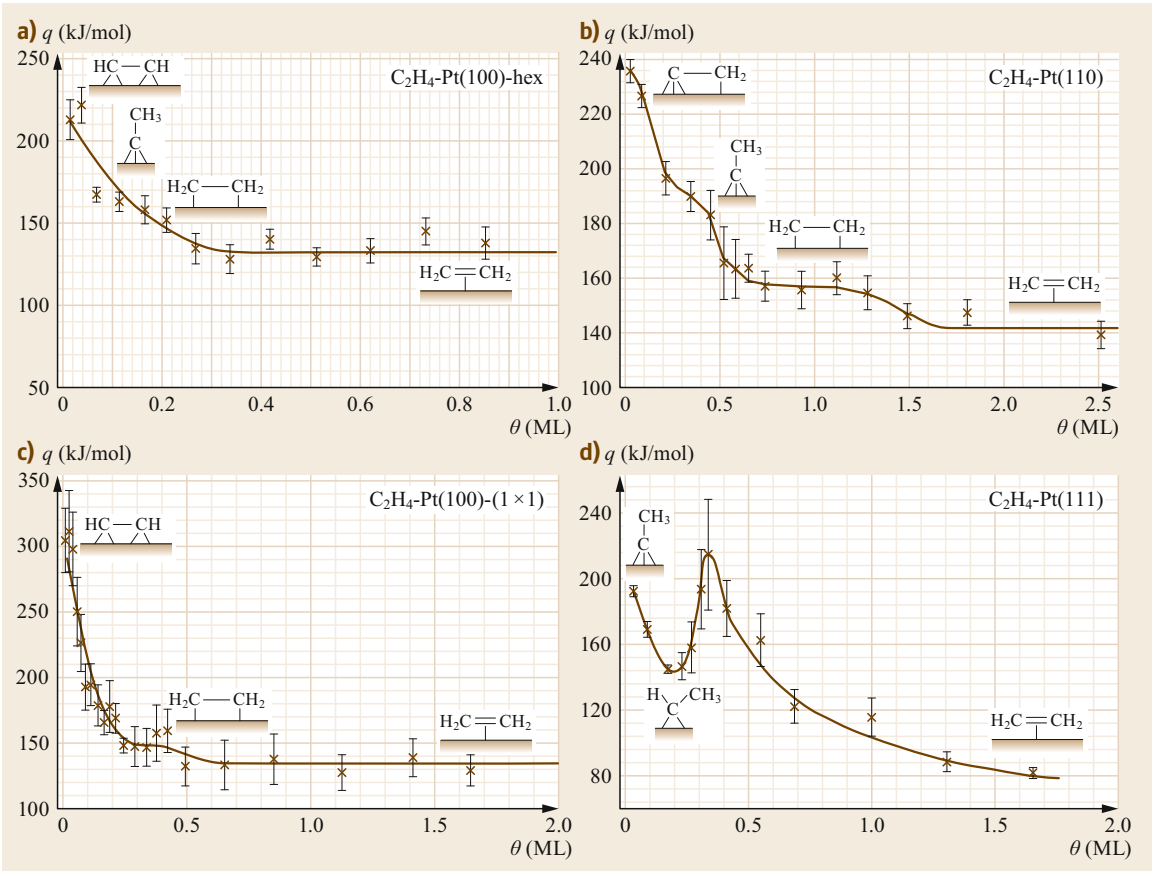

Fig. 30.10a–d Differential heat of adsorption for C_2H_4 adsorption on (**a**) Pt(100)-hex, (**b**) Pt(100), (**c**) Pt(110)-(1 × 1), and (**d**) Pt(111) at RT ((**a**,**c**) Adapted from [30.25], with permission from Elsevier; (**b**,**d**) adapted from [30.26], © 1995 by the American Physical Society)

mation of $CHCH_3$ and direct formation of ethylidyne stops. Since no H_2 is lost by desorption, the measured heat of adsorption increases, giving rise to a maximum at ≈ 0.35 ML. Thereafter, q decreases again, declining towards reversible π-bonded ethylene adsorption. Similar experiments were performed also for Pd(100) and Ni(100). On Pd(100), adsorption of ethylene occurs reversibly at RT, and the measurement of q is difficult. The data for Ni(100) are shown in Fig. 30.11. As for Pt surfaces, the interpretation of the results relies entirely on the identification of the species present on the surface. According to the literature (see the original papers and [30.1] for details), CH and CCH initially forms on this surface. The initial heat is associated with the formation of methylidyne (CH) followed by acetylide (CCH). The heat of adsorption was measured at RT also for acetylene on Ni(100) and Pd(100). The results are shown in Fig. 30.11. On Ni(100), the formation of CH and then of CCH can account for the observed results. The lower value observed for Pd(100) is explained by the fact that on the latter surface, dehydrogenation does not occur and that di-σ acetylene is present at low coverage after exposure at RT. The calorimetric data have, thus, been used to estimate the metal–carbon bond energy for Pt, Ni, and Pd. The results are summarized in Table 30.1. It is apparent that the metal–C bond energy is strongly dependent on the nature of the substrate, being 20% higher for Pt than

Table 30.1 Averaged metal–C bond energies as obtained from SCAC. (Data from [30.1])

Surface	Metal–C bond energy (kJ/mol)
Pt(110)	242
Pt(111)	244
Pt(100)	240
Pd(100)	171
Ni(100)	205

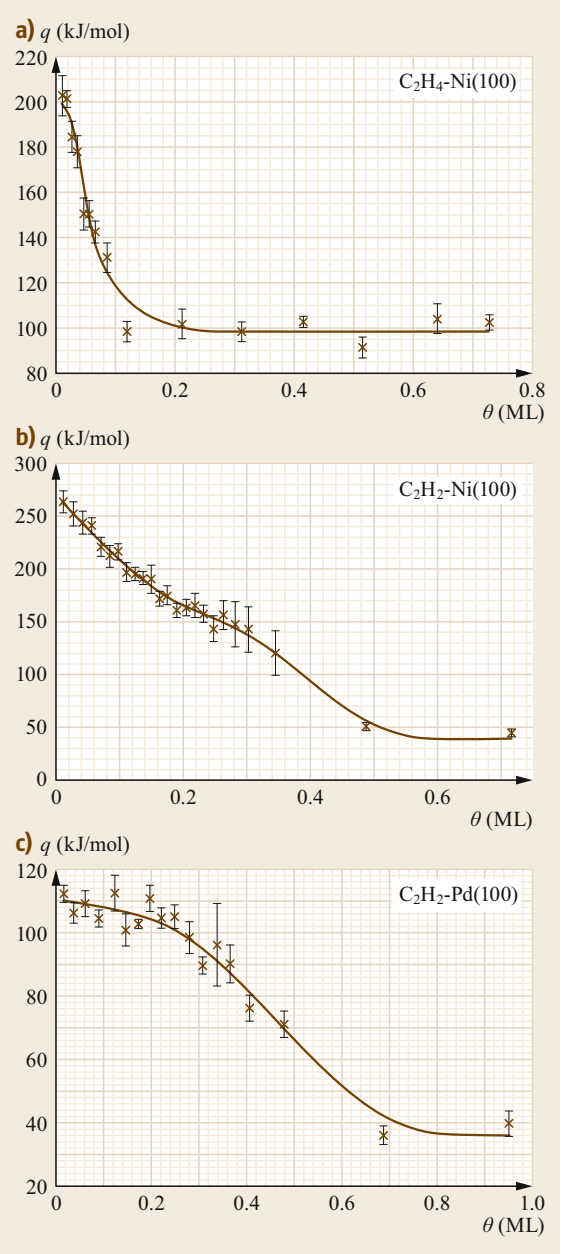

Fig. 30.11a–c Differential heat of adsorption for C_2H_4 adsorption on Ni(100) **(a)** and for C_2H_2 adsorption on Ni(100) **(b)** and Pd(100) **(c)** (Adapted from [30.28], with permission from Elsevier)

for Ni and 30% higher than for Pd. It is, however, nearly independent of the surface structure, at least for Pt surfaces. The database should be extended further in order to gain deeper insight into such general trends [30.29].

30.4.7 Heat of Reaction: CO Oxidation

The heat of adsorption of CO on an oxygen precovered surfaces have been measured calorimetrically for Pt(110) [30.30] and Pt(111) [30.17]. The results of the experiments are shown in Fig. 30.12. The initial heat measured when CO is adsorbed onto an O-precovered surface is 177 kJ/mol for Pt(110) and 157 kJ/mol for Pt(111). The heat of reaction ΔH_r can be easily estimated by considering the reaction

$$\mathrm{CO(g) + O(Pt) \rightarrow CO_2(g)} \qquad (30.4)$$

and it reads

$$\begin{aligned}\Delta H_r &= \Delta H_f(\mathrm{CO_2}) - \Delta H_f(\mathrm{CO(g)}) - \Delta H_f(\mathrm{O(Pt)}) \\ &= (-171 \pm 16)\,\mathrm{kJ/mol}\,.\end{aligned} \qquad (30.5)$$

If the CO_2 molecules would leave the surface without any excess energy, we would expect a differential heat of adsorption for CO on an oxygen-covered surface of 171 kJ/mol. The difference between the calculated heat of reaction and the measured differential heat is (-6 ± 17) kJ/mol and is, thus, compatible with a vanishing excess energy. On the contrary, when O_2 is dosed on a CO-precovered Pt(110) surface, the measured differential heat is 190 kJ/mol. Indeed, the following relations hold

$$\mathrm{O_2(g) + 2\,CO(Pt) \rightarrow 2\,CO_2(g)} \qquad (30.6)$$

and this reads

$$\begin{aligned}\Delta H_r &= 1\Delta H_f(\mathrm{CO_2}) - 2\Delta H_f(\mathrm{CO(Pt)}) - \Delta H_f(\mathrm{O_2})(\mathrm{g}) \\ &= (-287 \pm 24)\,\mathrm{kJ/mol}\,.\end{aligned} \qquad (30.7)$$

An adsorption heat of 287 kJ/mol would be measured if the reaction products would leave the surface without excess energy. The measured value of the differential heat is, however, significantly lower than expected! These results indicate that the desorbing CO_2 molecules have an average kinetic energy of (49 ± 21) kJ/mol [30.1]. Adsorption of CO on O-precovered Pt(111) leads to similar results [30.17].

30.4.8 Frequency Factor for Desorption

In all SCAC experiments, a steady state is reached characterized by a constant sticking probability and a constant differential heat of adsorption. In order to

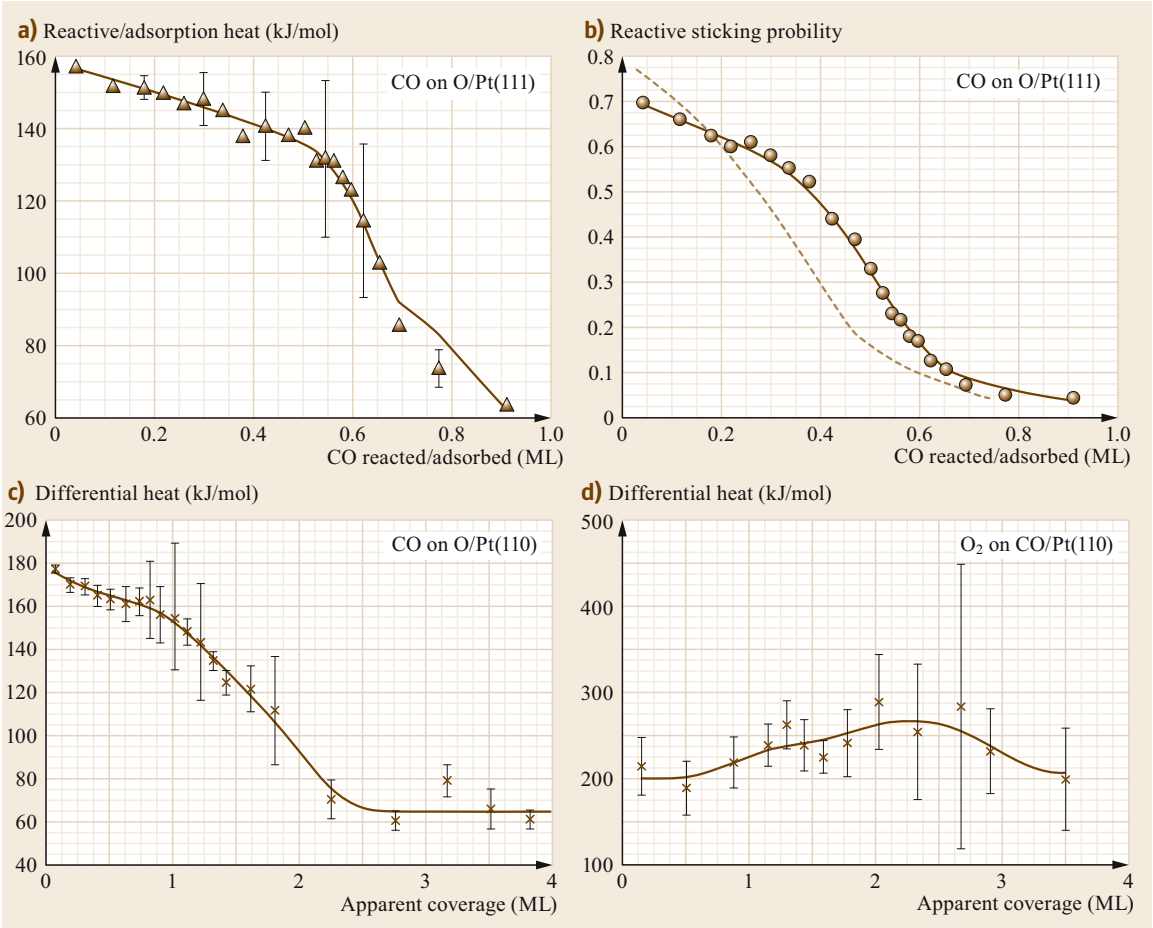

Fig. 30.12a–d Differential heat of adsorption (a) and sticking probability (b) for CO adsorption on Pt(111) precovered with a saturation coverage of oxygen. ([30.17], © AIP 1997). Differential heat of adsorption for: CO adsorption on O-saturated Pt(110) (c) and for O_2 adsorption on CO-saturated Pt(110) (d) (Adapted from [30.1], © 1998 American Chemical Society)

understand the meaning of this fact we must remember that in a SCAC experiment, a pulsed molecular beam is used. Typically, pulses last for 50 ms and are separated by 2.5 s. When a steady state is reached, the molecules adsorbed during each pulse desorb in the time between subsequent pulses. The number of molecules adsorbing during each pulse is, thus, just the number of molecules present in each pulse multiplied by the sticking probability. It is usual to express the rate of desorption using the following expression

$$\frac{\mathrm{d}\theta}{\mathrm{d}t} = \nu_{\mathrm{des}}(\theta)^n \mathrm{e}^{-q/(RT)} \,, \tag{30.8}$$

where n is the desorption order and ν_{des} the desorption frequency factor (also called prefactor for desorption). Since the number of molecules desorbing in the time between pulses is equal to the number of molecules adsorbing during the pulses in the steady-state region, it should be possible to determine ν_{des}. Since under steady-state conditions the Gibbs free energy change for adsorption vanishes, it is possible to determine also the entropy change due to adsorption directly from the calorimetric data

$$\Delta G = \Delta H - T\Delta S = 0 \,, \tag{30.9}$$

and then

$$\Delta S = \frac{\Delta H}{T} = -\frac{q}{T} \,. \tag{30.10}$$

The standard entropy for a gas can be calculated using the law of perfect gases as

$$S = S^0 - R \ln\left(\frac{p}{p^0}\right), \tag{30.11}$$

where S^0 is the standard entropy of the gas (i.e., 198 J/(K mol) for CO at 1 atm and 298 K), p the gas pressure, and p^0 the standard pressure. By using the experimentally obtained ΔH, it is possible to extract the differential entropy of the adsorbed phase S_a

$$S_a = S^0 - R \ln\left(\frac{p}{p^0}\right) - \frac{q}{T}. \tag{30.12}$$

The results of this analysis for CO adsorption at RT on different single-crystal Ni surfaces are summarized in Table 30.2. The extraction of prefactors from calorimetric data, however, requires some care. The same analysis for CO Pt(110) [30.31] leads to a prefactor for desorption of $2.5 \times 10^{(9\pm1.2)}$ Hz. This is a value that is remarkably lower than usually assumed ($\approx 10^{14}$ Hz)! The reason for this discrepancy is that the desorption rate is not exactly given by (30.8). This simple and widely-used expression is somewhat oversimplified, since it neglects several processes that may take place; for example, a mobile precursor may be involved also in desorption, thus providing a path back to the chemisorbed state. If these processes are considered, the desorption rate is reduced by a factor F, which can be written as [30.33]

Table 30.2 Differential heat q_{ss}, S_a and frequency factor for desorption as obtained from steady-state conditions for CO adsorption on different Ni surfaces (data taken from [30.32])

System	q_{ss} (kJ/mol)	S_a	ν_{des} (Hz)
CO/Ni(111)	95	71	3×10^{14}
CO/Ni(100)	99	58	1×10^{15}
CO/Ni(110)	101	50	3×10^{15}

$$F = f_d + f_m\left[1 - \left(1 + \frac{f_d}{f_a}\right)^{-1}\left(1 + K\frac{\theta}{1-\theta}\right)^{-1}\right], \tag{30.13}$$

where f_d, f_m, and f_a are the probabilities of desorption, migration to a neighbor site, and chemisorption for a molecule in the precursor state; K is the Kisliuk constant. The smaller K is, the more mobile the precursor, while $K = 1$ represents an immobile precursor. Since F cannot be directly obtained by the experimental data, care must be taken in extracting the frequency factor directly from steady-state values using (30.8).

30.5 Overview of Experimental Results by the Washington Group

The main limitations of the Cambridge IR calorimeter arise from the need to operate it at room temperature and to use pulsed supersonic molecular beams of gases. In particular, the IR setup did not allow the study of activated adsorption systems, adsorption of gases with low vapor pressure around room temperature, and adsorption of nongaseous species (such a metals). Most of these limitations were overcome by the use of pyroelectric detectors, which enabled an extension of the range of temperatures at which the measurements can be performed, and by the development of modified sources enabling also the use of effusive beams of low vapor pressure molecules [30.7, 8] and adatoms [30.34–37].

A large set of systems have been investigated in such ways obtaining calorimetric data regarding in particular:

a) Heat of adsorption of both simple [30.38–41] and more complex organic compounds [30.42–50] and subsequent determination of bond energies and heat of formation of chemically important radicals
b) Heat of adsorption of adatoms at both metal [30.51, 52], oxides [30.53–60], semiconductors [30.61], and insulating surfaces [30.62].

Dedicated reviews have appeared [30.37, 63–67] and just a few selected examples will be highlighted here.

30.5.1 Heat of Adsorption of "Large" Molecules at Surfaces

The supersonic molecular beam source successfully used for gases by the Cambridge group cannot be used to dose molecules having a vapor pressure < 100 Torr at room temperature. Under these conditions, an effusive beam with a source operating < 400 K can be used for molecules with a vapor pressure between 0.01 and 100 Torr at room temperature [30.7, 8]. The source is schematically shown in Fig. 30.13. Thanks to this improvement it was possible to measure the heat of adsorption and the sticking probability of species like benzene and other larger organic molecules with mo-

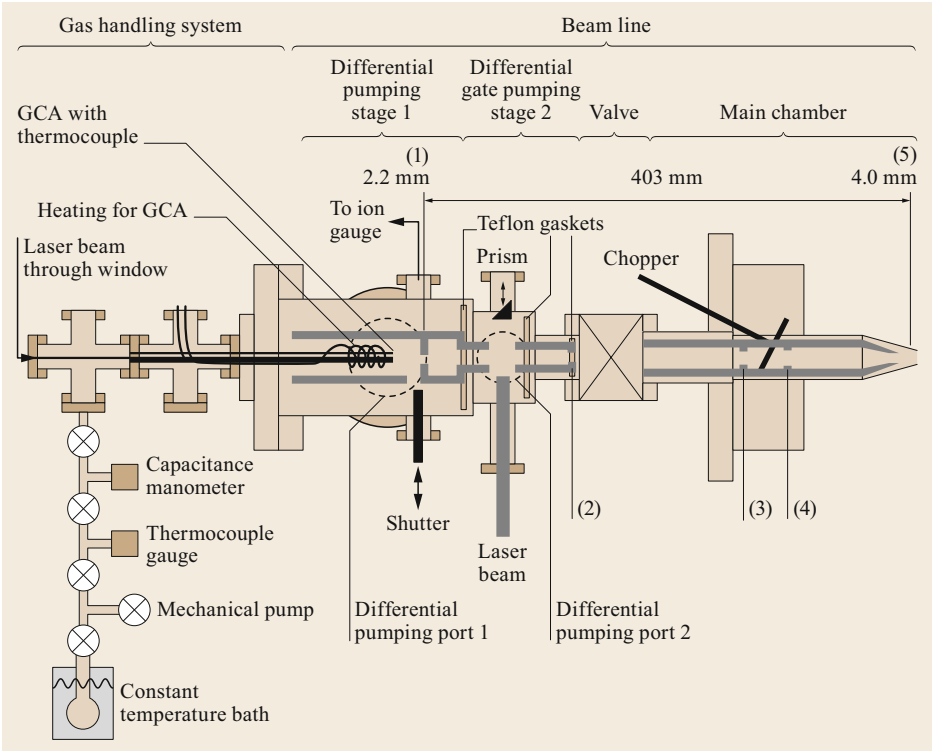

Fig. 30.13 Schematic of the effusive molecular beam and its separate elements: gas handling system and beam line, with five orifices indicated by numbers: (1)–(5). The beam line consists of two differential pumping stages separated from the main chamber by a gate valve. The purpose of the gas handling system is to deliver the low vapor pressure molecules in the constant temperature bath, kept at 280 K, to the glass capillary array (GCA). The temperature of the GCA is monitored by a thermocouple and is resistively heated to maintain a temperature of 300 K. The line between the constant temperature bath and the GCA is maintained at 290 K, using heating tape, to prevent condensation of the low vapor pressure molecules along the way. The beam line consists of five orifices, only two of which are beam defining: (1) and (5). The inner diameter (ID) of (1) and (5) are 2.2 and 4.0 mm, respectively, and the distance between them is 403 mm. Orifices (2), (3), and (4), which are not beam defining, but only slightly larger, have IDs of 2.8, 3.8, and 4.0 mm, respectively. Also indicated are ports for the laser and prism for calibration with the laser beam, the shutter, used to stop the molecular beam, and the chopper, used to chop both the laser and molecular beams (Adapted from [30.7], with the permission of AIP Publishing)

lar mass exceeding 70 g/mol. The measurement of the heat of adsorption of such "large" organic molecules sometimes presents some additional complexity, which is schematically shown in Fig. 30.14 for the case of cyclohexene adsorption on Pt(111).

The lower trace in Fig. 30.14a shows the QMS signal when the molecular beam hits the inert gold flag. The duration of the pulse is 50 ms. The above trace shows the QMS trace when the molecular beam hits the Pt(111) surface. It is apparent that the cyclohexene signal does not end when the molecular beam is interrupted but continues thereafter. This result indicates that, under the conditions of that experiment (263 K and coverage > 0.15 ML) transient desorption occurs off the surface.

The corresponding calorimetric signal exhibits a more complex behavior. Firstly, there is a delay between the instant at which adsorption and release of heat starts and the onset of the calorimetric signal, because of the limited thermal contact between the Pt(111) sample and the pyroelectric polymer. The heat deposited by the molecules is measured by the slope of the calorimetry pulse during the initial steep rise, typically 40–140 ms after the pulse hits the sample. Since the calorimetry signal after the initial steep rise is not used for calculating the amount of heat deposited, any desorption occurring after that point in time (140 ms) is neglected in the evaluation of q. However, desorption occurring during the first 140 ms will affect the measured heat. In order to account for this

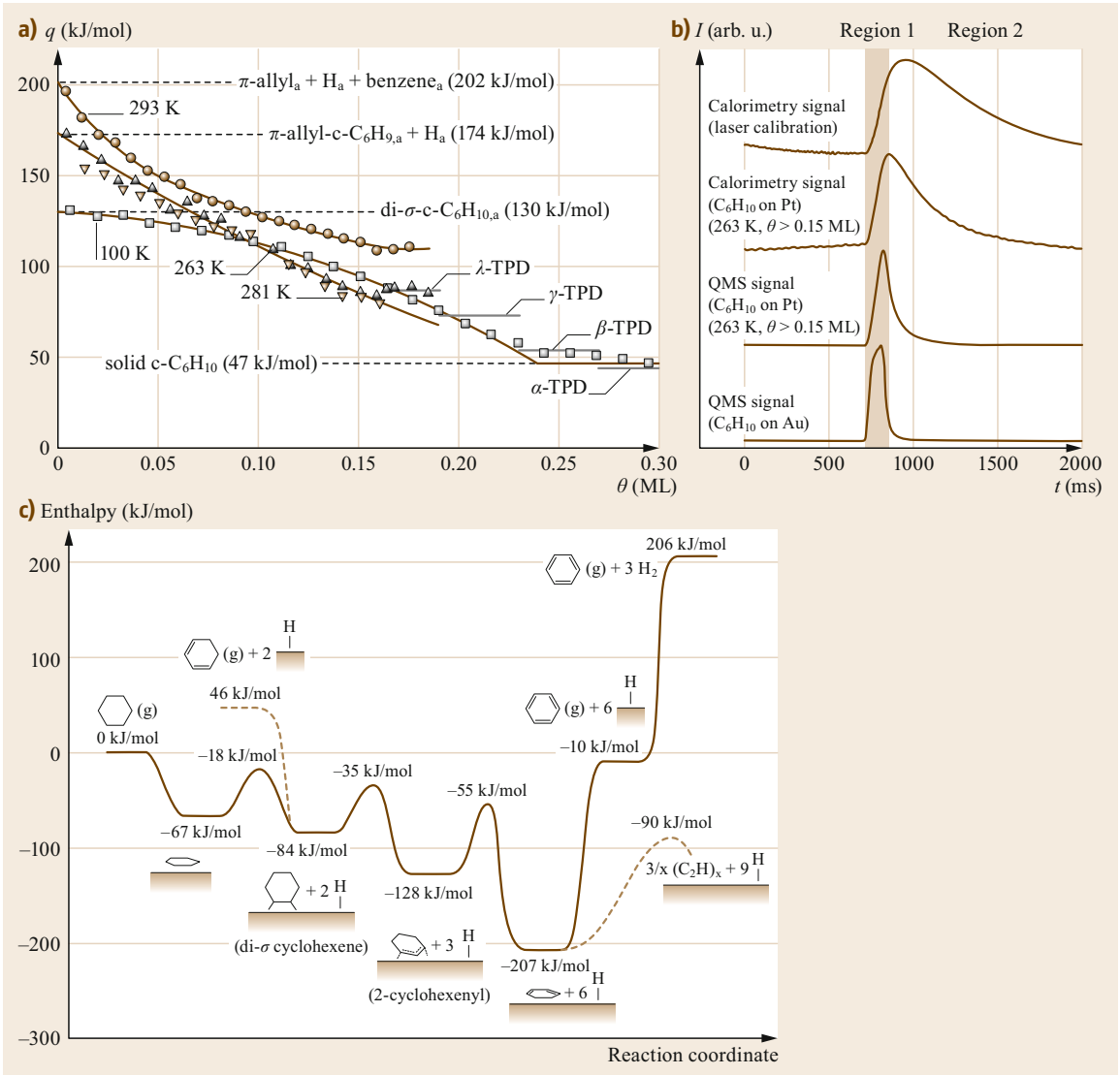

Fig. 30.14 **(a)** Differential heat of adsorption for cyclohexene adsorption on Pt(111). **(b)** Comparison of the pyroelectric and QMS signal versus time (see text). **(c)** Energetic of cyclohexane dehydrogenation on Pt(111), as obtained by calorimetric data. Only the heats of adsorption of H_2 and cyclohexane were obtained by analysis of TPD data (see the original papers for details) ([30.63], © Roy. Soc. Chem. 2008; adapted from [30.44], © 2008 American Chemical Society)

effect, a correction was introduced [30.44]. A short-time sticking probability was defined as the fraction of the impinging molecules, which is considered to determine the heat of adsorption. This fraction is higher than the fraction of molecules, which has not desorbed before the next cyclohexene pulse starts to hit the surface (the so-called "long-term sticking probability") and which is used to determine the surface coverage. This somewhat rough correction, which is essentially a linear interpolation scheme neglecting desorption after the pulse has reached its maximum intensity, is sufficient when transient desorption is limited. Its validity is questionable when transient desorption is relevant, e.g., for cyclohexene adsorption Pt(111) at 263 K and > 0.15 ML; q for cyclohexene on Pt(111) was measured as a function of coverage for temperatures in the range from 100 to 300 K. The results are shown in Fig. 30.14. At 100 K, cyclohexene adsorbs as di-σ-bonded cyclohexene with an initial adsorption heat of 130 kJ/mol. From this calorimetric result and using the standard enthalpy of formation of gas phase cyclohexene (−5 kJ/mol), the standard enthalpy of for-

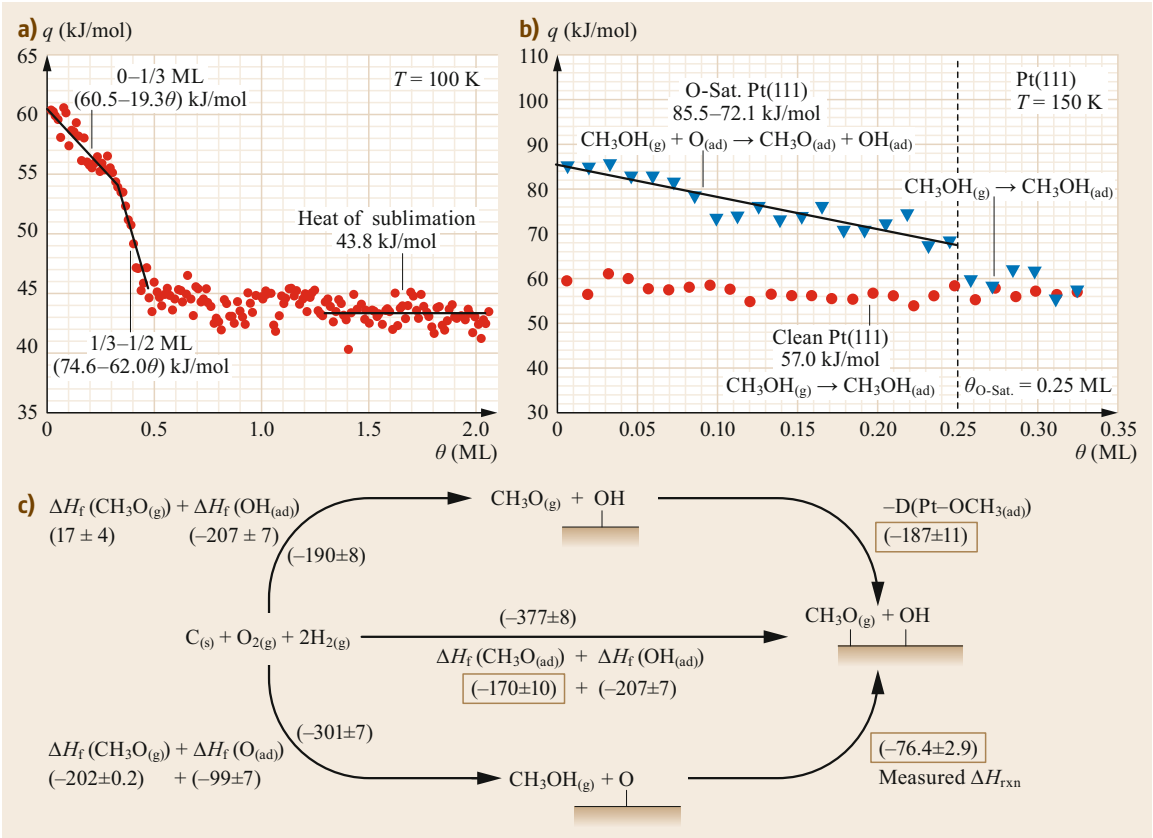

Fig. 30.15 **(a)** Differential heat of adsorption of methanol on clean Pt(111) at 100 K versus total methanol coverage. **(b)** Differential heat of adsorption of methanol versus total methanol coverage on (*circles*) clean and (*triangles*) oxygen-saturated Pt(111) at 150 K. **(c)** Thermodynamic cycle at 150 K used in calculating the bond enthalpy and standard heat of formation of adsorbed methoxy. The values are expressed in kJ/mol (Adapted from [30.45], © 2012 American Chemical Society)

mation of adsorbed di-σ-bonded cyclohexene was obtained (−135 kJ/mol). A similar argument was used to analyze the experimental data recorded at 281 K; at this temperature, cyclohexene dehydrogenates upon adsorption, forming adsorbed 2-cyclohexenyl (π-allyl-c-C_6H_9) plus a hydrogen adatom. The initial heat of adsorption is 174 kJ/mol, so adding the heat of formation of gas cyclohexene and one-half the heat of adsorption of H_2 on Pt(111) (72 kJ/mol), the heat of formation of adsorbed π-allyl-c-C_6H_9 was estimated (−143 kJ/mol). Finally, from the measured heat of adsorption of benzene on Pt(111) at 300 K (197 kJ/mol) and using the enthalpy of formation of gaseous benzene (83 kJ/mol), the standard enthalpy of formation of adsorbed benzene was found (−114 kJ/mol). By combining all these calorimetric data a partial energy landscape of the dehydrogenation of cyclohexane to benzene on Pt(111) was obtained. The reader is referred to the original papers for the details of this complex diagram, which nicely illustrates the extent of information attainable from calorimetry [30.42, 44, 63]. Inspection of the diagram provides deeper understanding of cyclohexane and cyclohexene dehydrogenation as well as of benzene hydrogenation in presence of a Pt catalyst. In particular, since the barrier for cyclohexene desorption is higher than the barrier for its further dehydrogenation it is difficult to stop the dehydrogenation of cyclohexane to cyclohexene. Similarly, the barrier for benzene desorption is too high at low coverage, thus explaining why no benzene is obtained from dehydrogenation of cyclohexane and cyclohexene. It is, however, possible to obtain benzene by increasing the coverage of co-adsorbed species; this way, the barrier to overcome for further dehydrogenation increases and desorption of benzene becomes competitive with its dissociation.

Under the high-pressure conditions at which real catalysts operate, the desorption of dehydrogenated products is, thus, kinetically competitive with complete

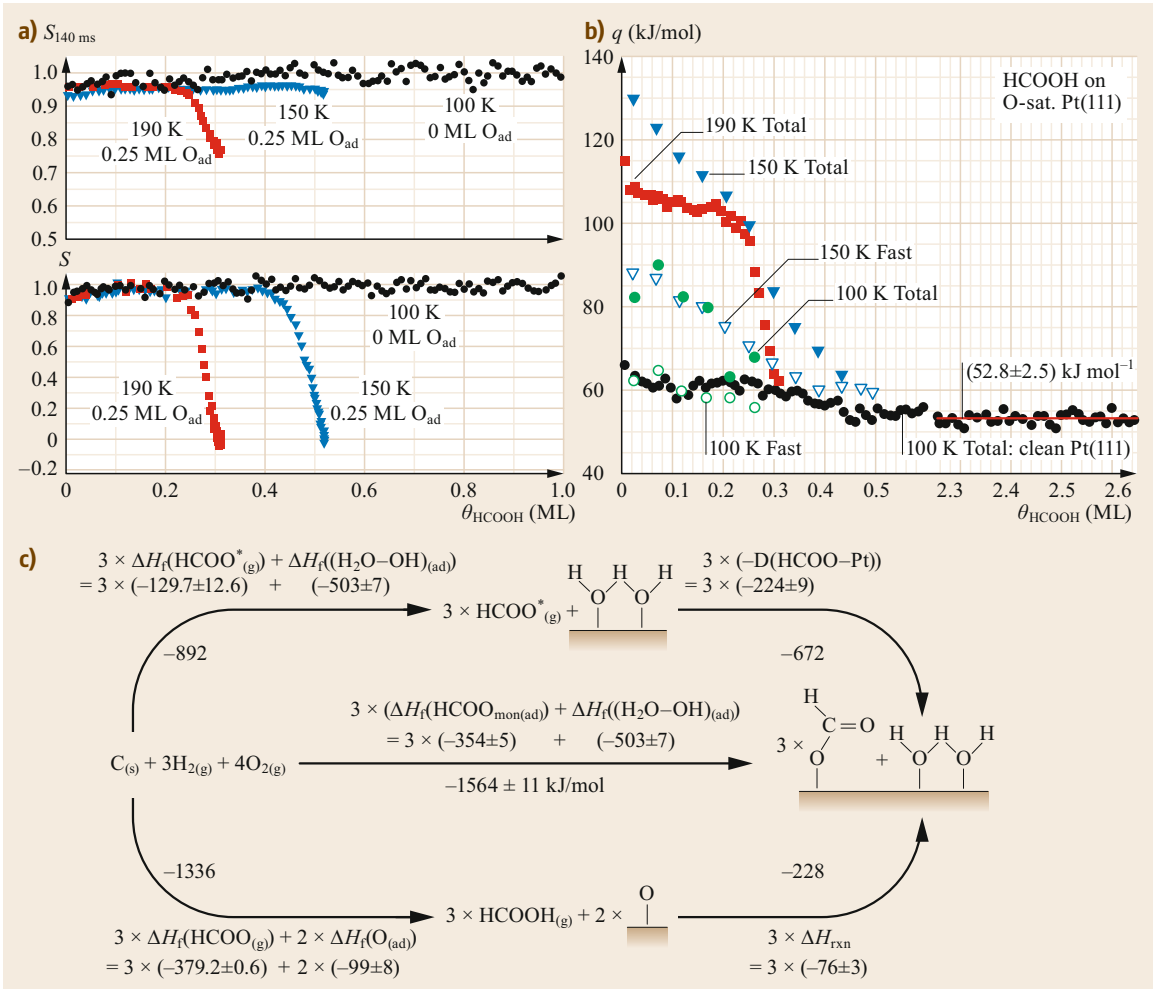

Fig. 30.16 **(a)** Short-term (*upper panel*) and long-term sticking probabilities (*lower panel*) of formic acid on clean Pt(111) at 100 K and O-saturated Pt(111) at 150 and 190 K as a function of the total formic acid coverage. **(b)** Heats of adsorption measured at various temperatures on clean Pt(111) at 100 K (*black circles*) and O-saturated Pt(111) at 100 K (*hollow* and *solid green circles*), 150 K (*hollow* and *solid blue triangles*), and 190 K (*red squares*) as a function of total coverage of adsorbed HCOOH, irrespective of its final structure. *Hollow symbols* represent fast heat deposition steps, while *solid symbols* represent total heats (i.e., the sum of fast and slow steps). The multilayer heat of adsorption is indicated by a *red line* through the 100 K data in the *lower right corner*. **(c)** Thermodynamic cycle used to determine the enthalpy of formation of adsorbed monodentate formate on Pt(111) and its HCOOPt(111) bond enthalpy from the integral fast S1 heat of adsorption at 150 K and 3/8 ML, shown as the *bottom right-hand step*. The values are expressed in kJ/mol (Adapted from [30.49], © 2014 American Chemical Society)

dehydrogenation. Note that the latter should also be avoided to completely coke the catalyst itself.

Campbell and co-workers undertook a systematic investigation of the heat of adsorption of several species on Pt(111) surfaces: methanol on an oxygen precovered surface to obtain methoxy [30.45] (Fig. 30.15), formic acid on oxygen-saturated Pt(111) to obtain formate [30.49] (Fig. 30.16) and water on oxygen precovered Pt(111) [30.38]. The results are summarized in Table 30.3, reporting the adiabatic PtOR bond dissociation enthalpies for three oxygen-bound molecular fragments to the Pt(111) surface: deuterated hydroxyl (OD) [30.38], monodentate formate (O(O)CH) [30.49], and methoxy (OCH_3) [30.45], where R is the part of the fragment bonded with oxygen. Quite interestingly, these ROPt(111) bond enthalpies vary linearly with the ROH bond enthalpies in the corresponding gas-phase molecules (water, methanol, and formic acid), and the

Table 30.3 Adiabatic RO–Pt(111) and gas phase R–OH bond strengths. The values are expressed in kJ/mol (data taken from [30.41])

Adsorbed species	ΔH_f^0	Gas phase R–OH bond strength	Measured bond enthalpy for RO–Pt(111)
–OD	-210 ± 7	500	248 ± 7
–O(O)CH	-353 ± 10	469 ± 13	224 ± 13
$-OCH_3$	-170 ± 12	437	187 ± 11

slope is compatible with 1.00. This result resembles the known trend for organometallic complexes and is explained by the local character of chemical bonding, even on extended metal surfaces. It is, thus, possible to predict bond enthalpies for many other molecular fragments at metal surfaces and derive the energetics of relevant catalytic reactions [30.41].

30.5.2 Heat of Adsorption of Metal Adatoms at Surfaces

The measurement of the heat of adsorption of metal adatoms at surfaces [30.68] became feasible thanks to substantial upgrades of the Cambridge calorimeter. Such modifications involved both the source and the detector of the released heat. The heat of adsorption q for Ag on Si(100)-(2 × 1) is shown in Fig. 30.17. Chopped pulses of a silver atom beam from a hot effusive source are directed at the surface of a thin Si(100) sample, releasing energy into the crystal upon adsorption. This causes a small transient temperature rise, detected by a thin pyroelectric polymer ribbon pressed into contact with the backside of the crystal during the measurement. The signal provided by the pyroelectric detector is calibrated by comparison with the signal produced by light pulses of known energy provided by a He-Ne laser. The sticking probability is obtained by measuring the amount of metal in a pulse that is reflected off the sample with a line-of-sight quadrupole mass spectrometer. The incident flux is measured with a quartz crystal microbalance. For adsorption on the bare surface, $q = 347$ kJ/mol. It decreases rapidly until at 0.55 ML it drops below the bulk heat of sublimation of Ag (285 k/mol). At 1 ML, q rises again reaching a value compatible with the bulk heat of sublimation at 2.5 ML. The sticking probability is surprisingly monotonic; indeed, it increases with coverage despite the complicated behavior of q.

The data can be rationalized as follows. The initial value of q is higher than the value expected for isolated

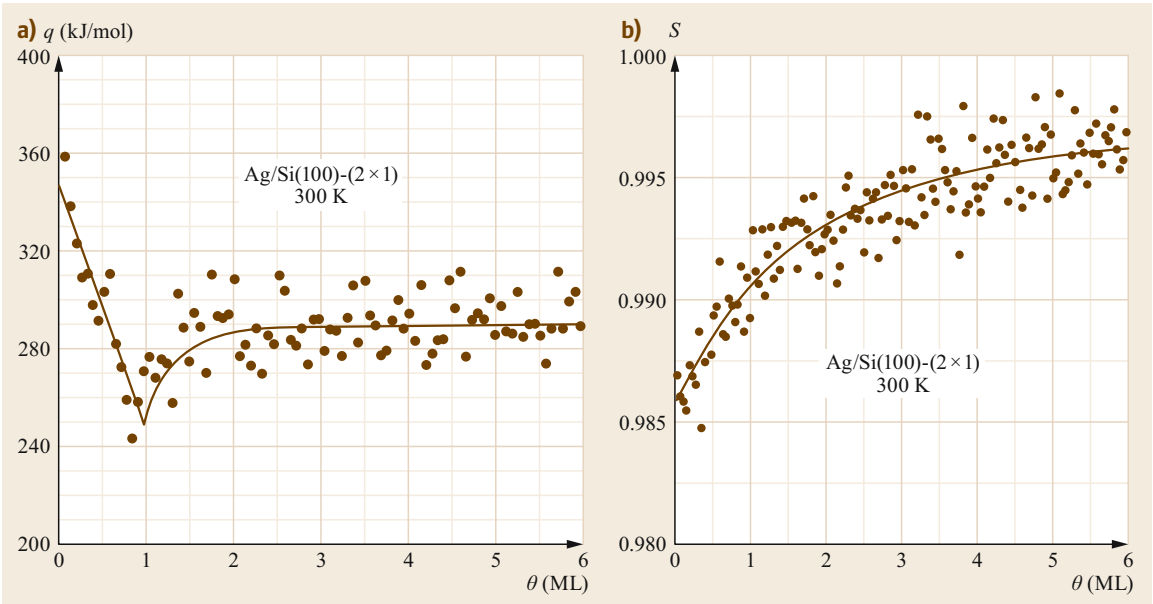

Fig. 30.17 **(a)** Heat of adsorption of Ag atoms on Si(100)-(1 × 2) versus adatom coverage. The *solid curve* is formed by a linear fit to the data over the first ML and a double exponential fit to the data at coverages > 1.0 ML. **(b)** Sticking probability of Ag atoms on the same substrate (Adapted from [30.61], © 2001 by the American Physical Society)

adatoms due to the formation of chains of adatoms. Such elongated Ag islands, seen by STM at 300 K up to a coverage of 1 ML, would normally imply attractive Ag–Ag interactions. The observation of a globally decreasing q with coverage implies that they are, on the contrary, repulsive. The formation of Ag–Si bonds induces significant strain in the neighboring surface sites, thus explaining the overall repulsive interaction between islands. If the growth were controlled by thermodynamics alone, 3-D growth should start ≈ 0.55 ML i.e., when q becomes lower than the heat of sublimation. Due to kinetic constraints, this happens, however, only ≈ 1 ML; indeed, at such a coverage, q rises quickly towards the bulk sublimation value. Once large 3-D particles have formed on top of the wetting layer, they provide more stable sites for Ag than in the wetting layer. This example shows that the information provided by calorimetry can be successfully used to explain the different regimes in the growth of metallic films on different substrates.

The same kind of measurements are able to also highlight size effects in the growth of nanoparticles. The calorimeter measures sticking probability and heat of adsorption versus coverage. In order to obtain information on the effect of particle size it is necessary to correlate the coverage with the size of the nanoparticles. Quantitative analysis of spectral intensities in Auger electron spectroscopy and ion scattering spectroscopy for the different elements as a function of Ag coverage was employed to characterize the growth morphology of the Ag films on magnesia and ceria surfaces. The data were well fitted by assuming that the Ag grows as three-dimensional (3-D) Ag particles with an hemispherical shape and a fixed, coverage independent, number N of Ag particles for unit of area. The data are not sensitive to the exact shape of the nanoparticles but are very sensitive to their aspect ratio. The analysis of Auger data showed that, > 0.03 ML, N is independent of coverage. Dividing the Ag coverage (atoms/cm^2) by N (particles/cm^2), the average number of Ag atoms per particle is obtained at any given Ag coverage. Measurement of q for Ag adsorption on different substrates was performed and compared as a function of particle size and of the number of atoms in the nanoparticle. The results are summarized in Fig. 30.18. It is apparent that the initial value of q, i.e., the value proper to very small particles, is strongly dependent on the nature of the substrate; for nanoparticles containing < 1000 atoms, Ag atoms are 30–70 kJ/mol more stable when they are deposited on ceria than on MgO surfaces.

This result nicely explains the pivotal role of the support in the sintering of nanoparticles. As long as a metal atom is less stable in a nanoparticle of a certain size than in the bulk, it will prefer to move and to form larger particles. The point is that this driving force for sintering drops below 10 kJ/mol for Ag nanoparticles of 400 atoms (3 nm) on ceria and for nanoparticles of 3000 atoms (6 nm) on MgO(100). For nanoparticles consisting of ≈ 5000 atoms, the energy of the added atoms reaches the value of the bulk metal also on MgO. Data for Pb exhibits a similar behavior [30.56].

Very recently, a similar study was performed also for Cu deposited on ceria. By comparing the heat of

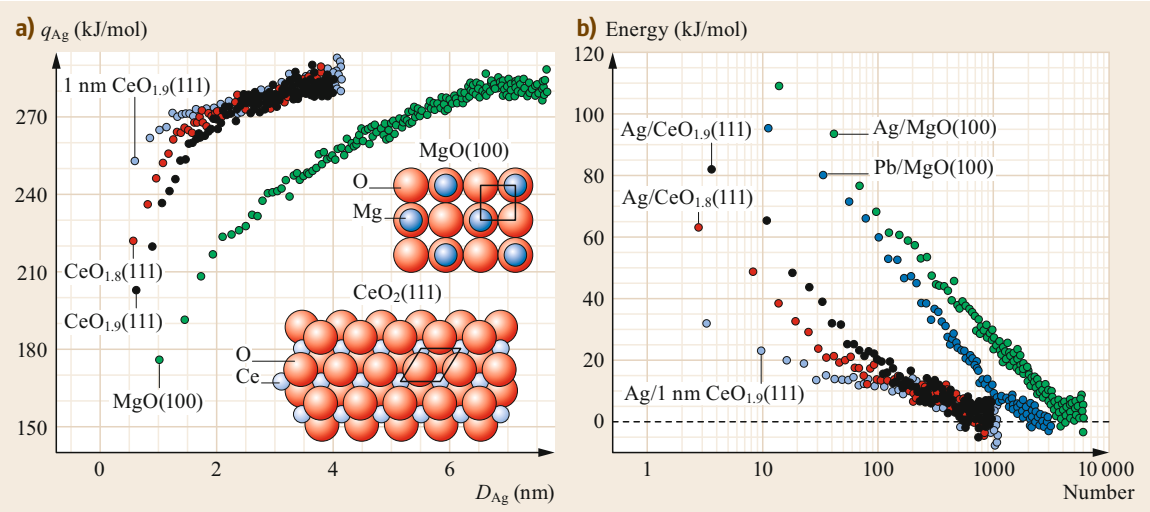

Fig. 30.18 **(a)** Measured heat of Ag atom adsorption q_{Ag} versus the Ag particle diameter D_{Ag} to which it adds, for Ag adsorption onto four different surfaces. **(b)** Measured energy of a Ag atom, relative to its energy in bulk Ag(solid), versus the number of metal atoms already in the particle, for Ag particles on different surfaces (From [30.58]. Reprinted with permission from AAAS)

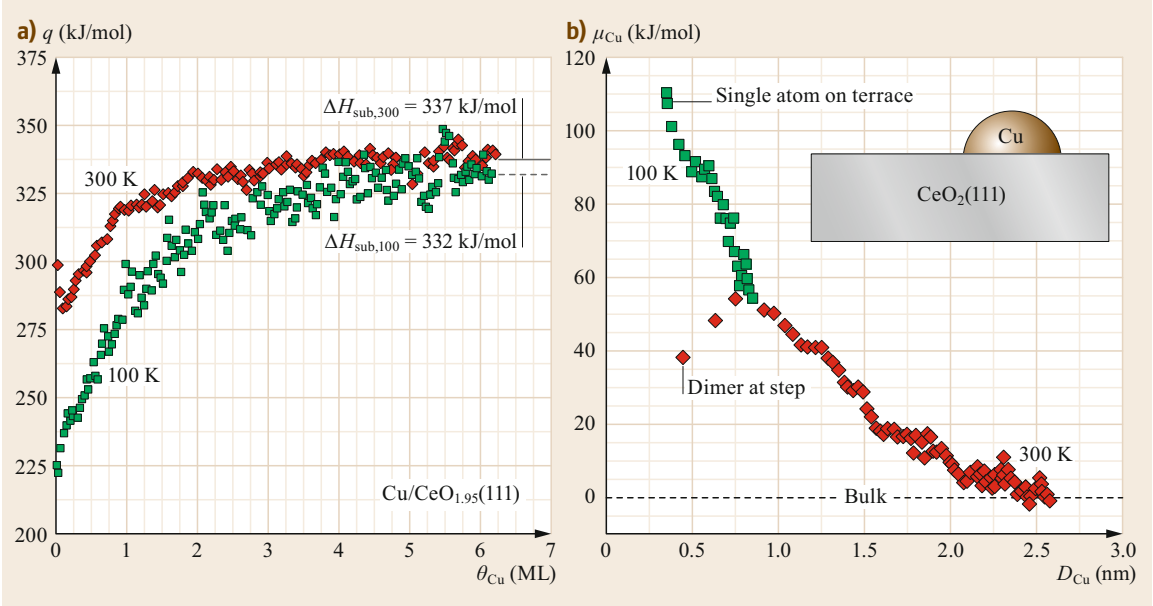

Fig. 30.19 **(a)** Cu atom heat of adsorption at 300 K (*diamonds*) and 100 K (*squares*) on $CeO_{1.95}(111)$ as a function of Cu coverage. **(b)** Chemical potential of Cu atoms in Cu nanoparticles on $CeO_{1.95}(111)$ relative to that in bulk Cu (solid) versus the effective diameter of the Cu particle down to the single atom limit (Adapted from [30.67], © 2015 American Chemical Society)

adsorption at 300 and at 100 K, it was possible to obtain the chemical potential as a function of particle size [30.67]. Ion scattering spectroscopy (ISS) was employed to determine the number of nanoparticles for unit of area; the normalized ISS signals directly provide the fraction of the ceria surface, which is masked by Cu particles, and the fraction of the total maximum Cu signal (due to complete coverage by Cu) that is observed at any given Cu coverage. The heat of adsorption for Cu nanoparticles with a diameter from 0.45 to 0.8 nm is lower at 100 K than at room temperature by some 30–50 kJ/mol on the same $CeO_{1.95}(111)$ surface; this difference was attributed to cluster nucleation on terrace sites at 100 K and at step-edge sites at 300 K. Hence, at 100 K, the number of nanoparticles for unit of area (5.3×10^{13} particles/cm^2) is about seven times higher than at 300 K (7.8×10^{12} particles/cm^2). Since the entropic contribution to the free energy changes very little with particle size compared with the enthalpic one, the chemical potential of a metal atom in a particle of diameter D, $\mu(D)$, is higher than that in the bulk metal, $\mu(\infty)$, by an amount equal to the heat of sublimation of bulk Cu minus the differential heat of Cu adsorption at diameter D. It is, thus, possible to obtain $\mu(D)$ from the calorimetrically measured q as a function of particle size. The results are shown in Fig. 30.19. The chemical potential decreases with increasing particle size. The Cu chemical potential is 110 kJ/mol higher for isolated Cu adatoms on stoichiometric terrace sites than for Cu in nanoparticles exceeding 2.5 nm diameter, where it reaches the bulk Cu(solid) limit. In Cu dimers, the Cu chemical potential is notably 57 kJ/mol lower at step edges than on stoichiometric terrace sites.

We finally mention the possibility to use metal adatoms to characterize the defectivity of oxide surfaces [30.57]. Figure 30.20 shows the heat of adsorption for Ca and Li on pristine and ion-bombarded MgO. While ion sputtering causes a strong increase in the initial adsorption energy for Li on MgO(100) at 300 K, the initial adsorption energy for Ca is independent of the extent of sputtering. In order to explain this intriguing result, density functional theory (DFT) calculations were also performed. DFT revealed that while Ca adatoms thermally diffuse to look for the remaining defect sites, Li adatoms remain blocked when they reach a terrace site nearby an occupied step or kink site. The measured dependence was simulated with a kinetic model taking the binding energies and the adatom migration barriers provided by DFT as inputs. The lines is the figure show the result of this model, which evidently captures the essential physics ruling the behavior of this system.

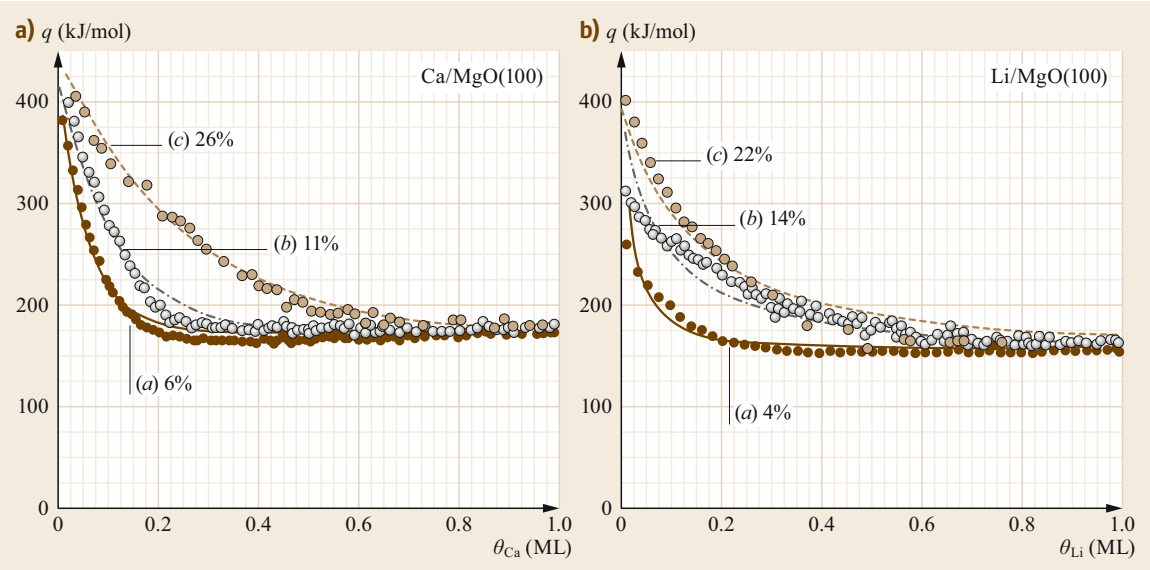

Fig. 30.20a,b Heat of adsorption of Ca (**a**) and Li (**b**) versus coverage at 300 K for adsorption on (*a*) pristine MgO(100) and (*b*) and (*c*) MgO(100) irradiated with increasing Ar^+ ion doses (from 10^{14} to 10^{16} ions/cm^2) to create more defects. Each curve is labeled with the percentage of total MgO sites that were defect sites (Adapted from [30.57], © 2009 American Chemical Society)

30.6 Results of Other Research Groups

The impressive achievements of single-crystal calorimetry obtained in Cambridge and in Washington stimulated further developments of the technique [30.9, 10]. In recent years, some papers have appeared focussing on the heat of adsorption of gases at nanoparticles of different size [30.69], on water adsorption at oxide surfaces [30.70], on the adsorption of chiral molecules [30.71], and on the effect of surface temperature on the coverage dependence of the heat of adsorption [30.72]. Such results are briefly reviewed in the final part of this chapter.

30.6.1 Heat of Adsorption of CO on Pd Nanoparticles

Although results obtained on single-crystal surfaces have provided valuable insight into the behavior of more complex systems, researchers are presently trying to investigate directly adsorption and reactions on nanoparticles supported on oxide substrates. Such efforts have also increased the range of operation of microcalorimetry. Figure 30.21 shows the dependence of the heat of adsorption of CO and of O_2 on Pd nanoparticles of different size deposited on a thin Fe_3O_4 film grown on Pt(111). By depositing different amounts of Pd on the film, nanoparticles of different sizes were obtained. The particle size was determined by STM the smallest nanoparticles correspond to ≈ 120 atoms/particle, while largest ones consist of ≈ 4900 atoms/particle. The data are compared with the results obtained for a Pd(111) single crystal. The dependence of the initial adsorption energy for oxygen on the particle size exhibits a clear trend. It strongly rises from about 205 to 250–275 kJ/mol when moving from Pd(111) to large Pd nanoclusters where it passes through a maximum and decreases thereafter, reaching a value of 205 kJ/mol on the smallest Pd nanoparticles. The initial rise is accounted for by the fact that on Pd(111) oxygen adatoms adsorb at threefold-hollow sites, while on large Pd nanoclusters, oxygen first occupies undercoordinated sites at the edges of the particle, which usually have a higher heat of adsorption. For smaller nanoparticles, the first sites to be occupied are still undercoordinated sites at the edges. The decrease of q is, thus, due to a pure size effect; in smaller nanoparticles, the lattice spacing is lower, the d bands are downshifted [30.74], and this causes a significant decrease in the heat of adsorption [30.75]. The decrease of the particle size causes, moreover, a lower van der Waals contribution to the heat of adsorption, thus resulting in an overall decreasing value. The data for the initial heat of adsorption of CO on the same nanopar-

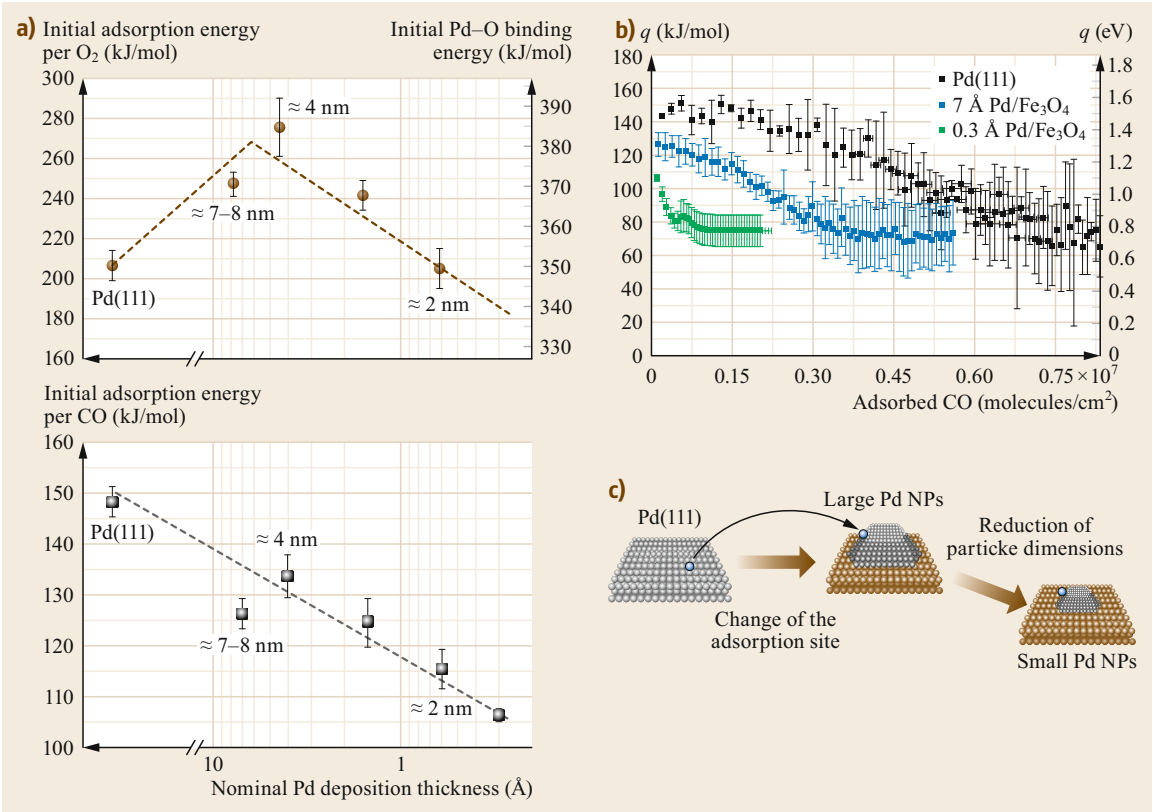

Fig. 30.21 **(a)** Initial adsorption energy for (*upper panel*) O_2 and (*lower panel*) CO molecules plotted as a function of the nominal Pd coverage on the $Fe_3O_4/Pt(111)$ samples with the nominal deposition thickness of 0.3 (only for CO), 0.6, 1.5, 4, and 7 Å and on the Pd(111) single-crystal surface. Next to the data points, the average diameters of the Pd particles are given. Error bars show the standard error of the mean. The *dashed lines* are given to guide the eye. **(b)** Adsorption heat of CO on Pd(111) and on a $Pd/Fe_3O_4/Pt(111)$ model catalyst plotted as a function of CO surface coverage. Each curve is an average of four to six experimental runs measured on freshly prepared samples. **(c)** A model describing two microscopic trends affecting the binding energy: the local configuration of the adsorption site, and the particle size. NPs = nanoparticles (Adapted from [30.73], © 2010 by the American Physical Society; [30.69], © Wiley VCH 2013)

ticles exhibits, on the contrary, a monotonic decrease with particle size. Since the heat of adsorption of CO on Pd(111) does not change so much from terrace to corner sites, the behavior of the heat of adsorption is dominated by size effects over the whole range considered in these studies.

30.6.2 Heat of Adsorption of Propylene Oxide

In Fig. 30.22, the heat of adsorption of the *R* and *S* enantiomers of propylene oxide on bare and NEA-covered Pt(111) surfaces are reported. 1-(1-Naphthyl)ethylamine (NEA) is a model chiral modifier; it has an aromatic group for binding to a metal surface and an amino group close to the chiral centre capable of hydrogen bonding. Adsorption of *S*- and *R*-propylene oxide (PO) on the bare Pt(111) surface shows an initial heat of adsorption of 50 decreasing to 42−43 kJ/mol at a coverage of $\approx 1.5\times10^{14}$ molecules/cm^2 corresponding to 1 PO molecule every 10 P atoms. Above this coverage, *q* either goes through a small local maximum (*S*-PO) or, rather, remains constant (*R*-PO) up to the coverage of 4.1×10^{14} molecules/cm^2. Saturation is then reached at a coverage of 5.5×10^{14} molecules/cm^2. When PO adsorbs on the pristine Pt(111) surface, its binding energy rapidly reaches a constant level; this plateau is most likely due to the formation of PO islands. After some PO nuclei consisting of a few PO molecules are formed on the surface, further PO molecules diffuse to the boundary of these nuclei and adsorb with a constant binding energy. It is only after the PO surface coverage increases to such an extent that neighboring PO islands start to coalesce that the binding

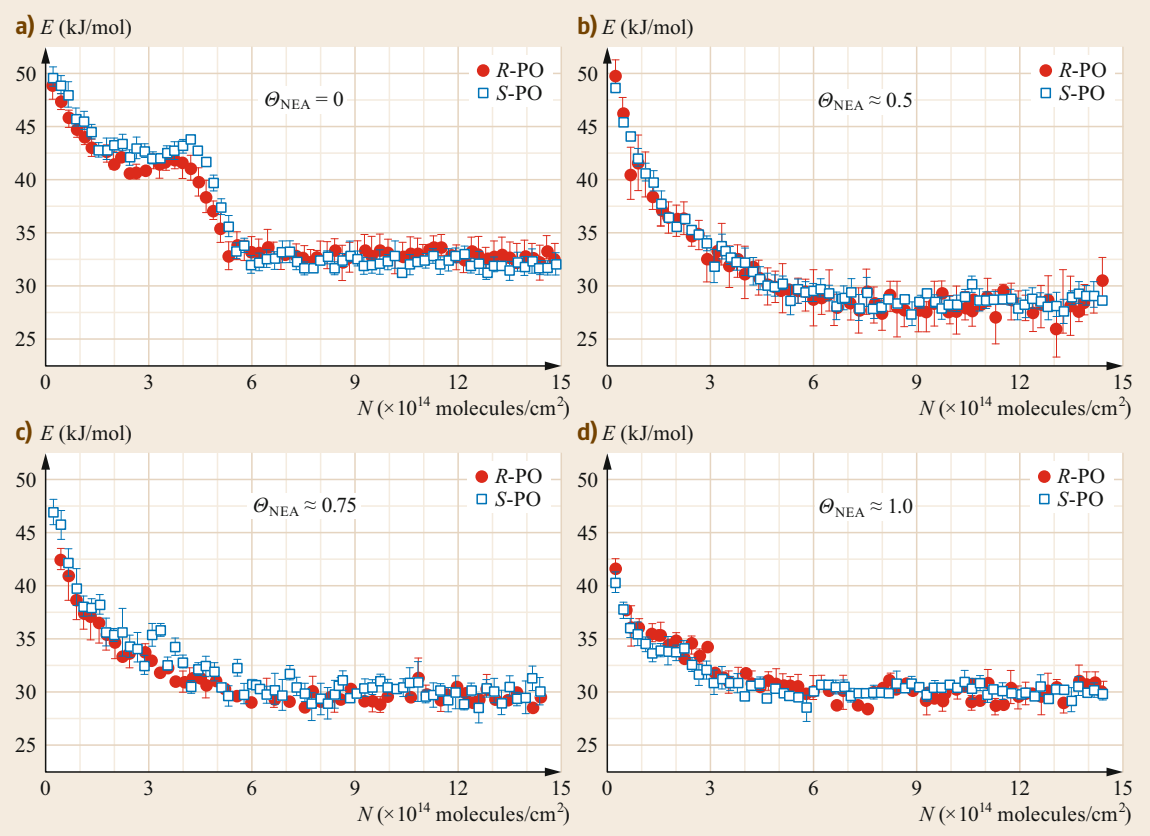

Fig. 30.22a–d Adsorption energy of *S*-PO and *R*-PO as a function of the number of adsorbed molecules on **(a)** bare Pt(111), as well as *R*-NEA-covered Pt(111) with the *R*-NEA relative coverage of **(b)** 0.5; **(c)** 0.75; **(d)** 1. The data points are averages of 35 independent measurements; the error bars show the error of the mean value. ([30.71], published by the PCCP Owner Societies licensed under a Creative Commons Attribution 3.0 Unported Licence 2015)

energy of the last incoming PO molecules decreases and approaches the value characteristic for PO adsorption in the second layer. The coverage dependence of q changes completely if NEA is present on the surface; as evident from Fig. 30.22b–d a monotonically decreasing heat of adsorption is measured in this case. When the surface is covered with 50% of NEA, i.e., when half of the surface still exposes Pt atoms, the plateau in q has completely disappeared. Most likely, there is a preferred adsorption of PO in the vicinity of NEA, preventing PO island formation on the still available metal sites. All these results suggest a preferential interaction between PO and the adsorbed modifier possibly resulting in the formation of a complex between these molecules.

30.6.3 Heat of Adsorption of Water at Metal and Oxide Surfaces

We conclude our review by presenting in Fig. 30.23 the microcalorimetric results for H_2O adsorption on Pt(111) and on two thin iron-oxide films. On Pt(111) and on FeO/Pt(111), the heat of adsorption is initially 47 kJ/mol and remains nearly constant until ice is formed. On Fe_3O_4(111)/Pt(111), q is initially much higher (87 kJ/mol) and decreases thereafter, monotonically leveling at a coverage of 1.2×10^{15} molecules/cm^2. The high value of q is indicative of water dissociation. Measurements performed at different temperatures are shown in Fig. 30.23b. The initial adsorption energy at higher temperatures reaches 101 kJ/mol and decreases, leveling off at a lower coverage without forming multilayer ice. An increase of the initial binding energy from 87 kJ/mol at 120 K to 101 kJ/mol at temperatures > 180 K is most likely related to a kinetic hindrance of water dissociation at 120 K. Since the initial adsorption energy remains constant for all temperatures > 180 K, this value can be considered as the true thermodynamic value that is not affected by the slow kinetics of water dissociation. The leveling of q corresponds, as is usual in calorimet-

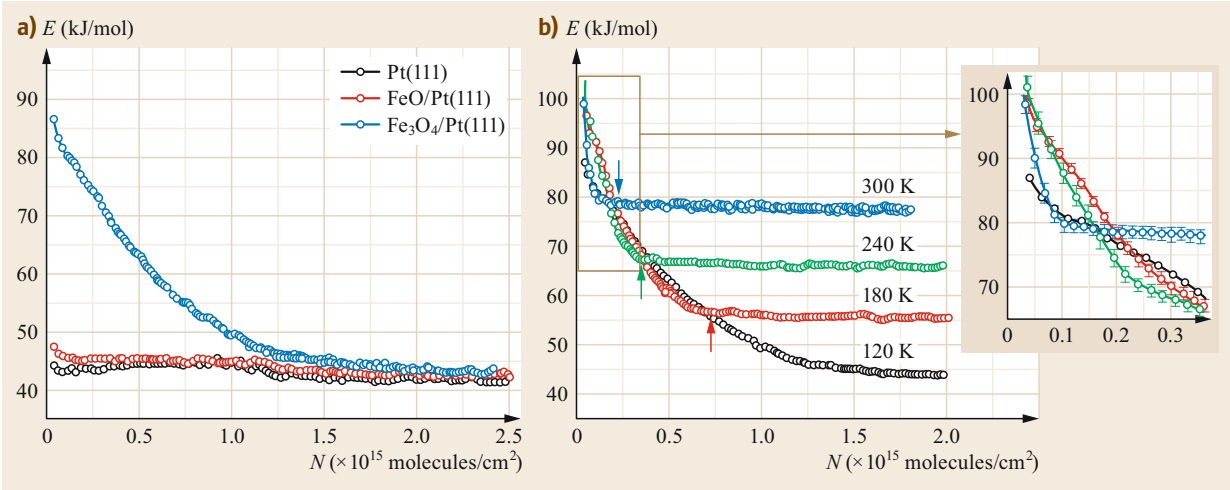

Fig. 30.23 **(a)** Differential adsorption energy measured at 120 K plotted as a function of the number of adsorbed H_2O molecules for Pt(111), FeO(111)/Pt(111), and Fe_3O_4 (111)/Pt(111). **(b)** Differential adsorption energy of H_2O on Fe_3O_4(111)/Pt(111) as a function of the number of adsorbed H_2O molecules measured at different temperatures. ([30.70], © Wiley VCH 2015)

ric experiments using pulsed beams, to a steady-state equilibrium between molecules adsorbing during the water pulse and molecules desorbing in the time between subsequent pulses. The initial heat of adsorption at high temperature is higher than that obtained by thermal desorption methods (65 kJ/mol) [30.76]. These calorimetric data shed light on a possible failure of the generally-accepted simple model of water dissociation leading to two individual OH groups. IRAS measurements using isotopically labeled water molecules and DFT calculations suggested, on the contrary, a more complex mechanism: a dimer form consisting of one H_2O molecule dissociated into two OH groups and another nondissociated H_2O molecule [30.70].

30.7 Conclusions

Although SCAC is only about 20 years old, it has already developed into a mature and powerful technique. The complexity of the experimental setups and the need for accurate calibrations are still probably limiting its further utilization despite the huge amount of information that could be provided.

In our opinion, we foresee and welcome two possible future directions of development:

a) A systematic use of the existing SCAC setups with an extension of the sets of investigated systems, thus enriching the amount of data and the development of a more extended database covering more and more systems of catalytic interest. In this effort, the calorimetric information provided by SCAC will, however, need more and more precise identification of the moieties forming upon adsorption, which can be provided mainly by spectroscopic techniques, as has already happened for the analysis of calorimetric data obtained for simple organic molecules.

b) Further developments of the technique will be necessary to allow the investigation of currently inaccessible adsorption systems, in particular of activated adsorption systems. This direction will most likely require the use of supersonic beams to overcome adsorption barriers and to attain high-enough adsorption probabilities and, thus, an acceptable signal-to-noise ratio in the calorimetric signal.

References

30.1 W.A. Brown, R. Kose, D.A. King: Femtomole adsorption calorimetry on single-crystal surfaces, Chem. Rev. **98**, 797–832 (1998)

30.2 S. Cerny: Adsorption microcalorimetry in surface science studies sixty years of its development into a modern powerful method, Surf. Sci. Rep. **26**, 1–59 (1996)

30.3 D.A. Kyser, R.J. Masel: Design of a calorimeter capable of measuring heats of adsorption on single crystal surfaces, Rev. Sci. Instrum. **58**, 2141–2144 (1987)

30.4 C.E. Borroni-Bird, D.A. King: An ultrahigh vacuum single crystal adsorption microcalorimeter, Rev. Sci. Instrum. **62**, 2177–2185 (1991)

30.5 A. Stuck, C.E. Wartnaby, Y.Y. Yeo, J.T. Stuckless, N. Al-Sarraf, D.A. King: An improved single crystal adsorption calorimeter, Surf. Sci. **349**, 229–240 (1996)

30.6 S.J. Dixon-Warren, M. Kovar, C.E. Wartnaby, D.A. King: Pyroelectric single crystal adsorption microcalorimetry at low temperatures: Oxygen on Ni{100}, Surf. Sci. **307–309**, 16–22 (1994)

30.7 H.M. Ajo, H. Ihm, D.E. Moilanen, C.T. Campbell: Calorimeter for adsorption energies of larger molecules on single crystal surfaces, Rev. Sci. Instrum. **75**, 4471–4480 (2004)

30.8 W. Lew, O. Lytken, J.A. Farmer, M.C. Crowe, C.T. Campbell: Improved pyroelectric detectors for single crystal adsorption calorimetry from 100 to 350 K, Rev. Sci. Instrum. **81**, 024102 (2010)

30.9 J.-H. Fischer-Wolfarth, J. Hartmann, J.A. Farmer, J.M. Flores-Camacho, C.T. Campbell, S. Schauermann, H.-J. Freund: An improved single crystal adsorption calorimeter for determining gas adsorption and reaction energies on complex model catalysts, Rev. Sci. Instrum. **82**, 024102 (2011)

30.10 P. Hörtz, R. Schäfer: A compact low-temperature single crystal adsorption calorimetry setup for measuring coverage dependent heats of adsorption at cryogenic temperatures, Rev. Sci. Instrum. **85**, 074101 (2014)

30.11 J.C. Tracy, P.W. Palmberg: Simple technique for binding energy determinations: CO on Pd(100), Surf. Sci. **14**, 274–277 (1969)

30.12 J.T. Stuckless, C.E. Wartnaby, N. Al-Sarraf, St J.B. Dixon-Warren, M. Kovar, D.A. King: Oxygen chemisorption and oxide film growth on Ni{100}, {110}, and {111}: Sticking probabilities and microcalorimetric adsorption heat, J. Chem. Phys. **106**, 2012–2030 (1997)

30.13 N. Al-Sarraf, J.T. Stuckless, C.E. Wartnaby, D.A. King: Adsorption microcalorimetry and sticking probabilities on metal single crystal surfaces, Surf. Sci. **283**, 427–437 (1993)

30.14 Y.Y. Yeo, L. Vattuone, D.A. King: Energetics and kinetics of CO and NO adsorption on Pt{100}: Restructuring and lateral interactions, J. Chem. Phys. **104**, 3810–3821 (1996)

30.15 N. Al-Sarraf, J.T. Stuckless, D.A. King: Direct measurement of potassium-promoted change in heat of adsorption of CO on Ni{100}, Nature **360**, 243–245 (1992)

30.16 Y.Y. Yeo, C.E. Wartnaby, D.A. King: Calorimetric measurement of the energy difference between two solid surface phase, Science **268**, 1731–1732 (1995)

30.17 Y.Y. Yeo, L. Vattuone, D.A. King: Calorimetric heats for CO and oxygen adsorption and for the catalytic CO oxidation reaction on Pt{111}, J. Chem. Phys. **106**, 392–401 (1997)

30.18 L. Vattuone, Y.Y. Yeo, D.A. King: Adatom bond energies and lateral interaction energies from calorimetry: NO, O_2, and N_2 adsorption on Ni{100}, J. Chem. Phys. **104**, 8096–8102 (1995)

30.19 L. Vattuone, Y.Y. Yeo, D.A. King: Lateral interactions as the determinant in the switch from molecular to dissociative chemisorption: NO on Ni{100}, Catal. Lett. **41**, 119–123 (1996)

30.20 A.D. Karmazyn, V. Fiorin, D.A. King: Calorimetric studies of NO on Ni{2 1 1}: Criteria for switching from dissociative to molecular adsorption, Surf. Sci. **547**, 184–192 (2003)

30.21 A.D. Karmazyn, V. Fiorin, D.A. King: Direct sticking and differential adsorption heats as probes of structural transitions: O_2 on the stepped Ni{211} surface, J. Am. Chem. Soc. **126**, 14273–14277 (2004)

30.22 L. Vattuone, L. Savio, M. Rocca: Bridging the structure gap: Chemistry of nanostructured surfaces at well-defined defects, Surf. Sci. Rep. **63**, 101–168 (2008)

30.23 D. Borthwick, V. Fiorin, S.J. Jenkins, D.A. King: Facile dissociation of CO on Fe{2 1 1}: Evidence from microcalorimetry and first-principles theory, Surf. Sci. **602**, 2325–2332 (2008)

30.24 V. Fiorin, D. Borthwick, D.A. King: Microcalorimetry of O_2 and NO on flat and stepped platinum surfaces, Surf. Sci. **603**, 1360–1364 (2009)

30.25 Y.Y. Yeo, A. Stuck, C.E. Wartnaby, R. Kose, D.A. King: Microcalorimetric study of ethylene adsorption at 300 K on Pt{100}-hex and Pt{100}-(1 × 1), J. Mol. Catal. **131**, 31–38 (1998)

30.26 A. Stuck, C.E. Wartnaby, Y.Y. Yeo, D.A. King: Microcalorimetric study of ethylene on Pt{110}-(1 × 2), Phys. Rev. Lett. **74**, 578–581 (1995)

30.27 Y.Y. Yeo, A. Stuck, C.E. Wartnaby, D.A. King: Microcalorimetric study of ethylene adsorption on the Pt{111} surface, Chem. Phys. Lett. **259**, 28–36 (1996)

30.28 L. Vattuone, Y.Y. Yeo, R. Kose, D.A. King: Energetics and kinetics of the interaction of acetylene and ethylene with Pd{100} and Ni{100}, Surf. Sci. **447**, 1–14 (2000)

30.29 H. Gross, C.T. Campbell, D.A. King: Metal–Carbon bond energies for adsorbed hydrocarbons from calorimetric data, Surf. Sci. **572**, 179–190 (2004)

30.30 C.E. Wartnaby, A. Stuck, Y.Y. Yeo, D.A. King: Calorimetric measurement of catalytic surface reaction heat: CO oxidation on Pt{110}, J. Chem. Phys. **102**, 1855–1858 (1995)

30.31 C.E. Wartnaby, A. Stuck, Y.Y. Yeo, D.A. King: Microcalorimetric heats of adsorption for CO, NO, and

oxygen on Pt{110}, J. Phys. Chem. **100**, 12483–12488 (1996)
30.32 J.T. Stuckless, N. Al-Sarraf, C. Wartnaby, D.A. King: Calorimetric heats of adsorption for CO on nickel single crystal surface, J. Chem. Phys. **99**, 2202–2212 (1993)
30.33 D.A. King: The influence of weakly bound intermediate states on thermal desorption kinetics, Surf. Sci. **64**, 43–51 (1977)
30.34 J.T. Stuckless, N.A. Frei, C.T. Campbell: A novel single-crystal adsorption calorimeter and additions for determining metal adsorption and adhesion energies, Rev. Sci. Instrum. **69**, 2427–2438 (1998)
30.35 C.T. Campbell, J.C. Sharp, Y.X. Yao, E.M. Karp, T.L. Silbaugh: Insights into catalysis by gold nanoparticles and their support effects through surface science studies of model catalysts, Faraday Discuss. **152**, 227–239 (2011)
30.36 J.R.V. Sellers, T.E. James, S.L. Hemmingson, J.A. Farmer, C.T. Campbell: Adsorption calorimetry during metal vapor deposition on single crystal surfaces: Increased flux, reduced optical radiation, and real-time flux and reflectivity measurements, Rev. Sci. Instrum. **84**, 123901 (2013)
30.37 S. Schauermann, T.L. Silbaugh, C.T. Campbell: Single-crystal adsorption calorimetry on well-defined surfaces: From single crystals to supported nanoparticles, Chem. Rec. **14**, 759–774 (2014)
30.38 W. Lew, M.C. Crowe, E.M. Karp, O. Lytken, J.A. Farmer, L. Árnadóttir, C. Schoenbaum, C.T. Campbell: The energy of adsorbed hydroxyl on Pt(111) by microcalorimetry, J. Phys. Chem. C **115**, 11586–11594 (2011)
30.39 W. Lew, M.C. Crowe, C.T. Campbell, J. Carrasco, A. Michaelides: The energy of hydroxyl coadsorbed with water on Pt(111), J. Phys. Chem. C **115**, 23008–23012 (2011)
30.40 E.M. Karp, C.T. Campbell, F. Studt, F. Abild-Pedersen, J.K. Nørskov: Energetics of oxygen adatoms, hydroxyl species and water dissociation on Pt(111), J. Phys. Chem. C **116**, 25772–25776 (2012)
30.41 E.M. Karp, T.L. Silbaugh, C.T. Campbell: Bond energies of molecular fragments to metal surfaces track their bond energies to H atoms, J. Am. Chem. Soc. **136**, 4137–4140 (2014)
30.42 H. Ihm, H.M. Ajo, J.M. Gottfried, P. Bera, C.T. Campbell: Calorimetric measurement of the heat of adsorption of benzene on Pt(111), J. Phys. Chem. B **108**, 14627–14633 (2004)
30.43 J.M. Gottfried, E.K. Vestergaard, P. Bera, C.T. Campbell: Heat of adsorption of naphthalene on Pt(111) measured by adsorption calorimetry, J. Phys. Chem. B **110**, 17539–17545 (2006)
30.44 O. Lytken, W. Lew, J.J.W. Harris, E.K. Vestergaard, J.M. Gottfried, C.T. Campbell: Energetics of cyclohexene adsorption and reaction on Pt(111) by low-temperature microcalorimetry, J. Am. Chem. Soc. **130**, 10247–10257 (2008)
30.45 E.M. Karp, T.L. Silbaugh, M.C. Crowe, C.T. Campbell: Energetics of adsorbed methanol and methoxy on Pt(111) by microcalorimetry, J. Am. Chem. Soc. **134**, 20388–20395 (2012)
30.46 T.L. Silbaugh, J.B. Giorgi, Y. Xu, A. Tillekaratne, F. Zaera, C.T. Campbell: Adsorption energy of *tert*-butyl on Pt(111) by dissociation of *tert*-butyl iodide: Calorimetry and DFT, J. Phys. Chem. C **118**, 427–438 (2013)
30.47 E.M. Karp, T.L. Silbaugh, C.T. Campbell: Energetics of adsorbed CH_3 and CH on Pt(111) by calorimetry: Dissociative adsorption of CH_3I, J. Phys. Chem. C **117**, 6325–6336 (2013)
30.48 E.M. Karp, T.L. Silbaugh, C.T. Campbell: Energetics of adsorbed CH_3 on Pt(111) by calorimetry, J. Am. Chem. Soc. **135**, 5208–5211 (2013)
30.49 T.L. Silbaugh, E.M. Karp, C.T. Campbell: Energetics of formic acid conversion to adsorbed formates on Pt(111) by transient calorimetry, J. Am. Chem. Soc. **136**, 3964–3971 (2014)
30.50 C.A. Wolcott, I.X. Green, T.L. Silbaugh, Y. Xu, C.T. Campbell: Energetics of adsorbed CH_2 and CH on Pt(111) by calorimetry: The dissociative adsorption of diiodomethane, J. Phys. Chem. C **118**, 29310–29321 (2014)
30.51 H. Larsen, D.E. Starr, C.T. Campbell: Enthalpies of adsorption of metal atoms on single-crystalline surfaces by microcalorimetry, J. Chem. Thermodyn. **33**, 333–345 (2001)
30.52 J.F. Zhu, S.F. Diaz, L.R. Heeb, C.T. Campbell: Adsorption of Pb on NiAl(1 1 0): Energetics and structure, Surf. Sci. **574**, 34–42 (2005)
30.53 D.E. Starr, D.J. Bald, J.E. Musgrove, J.T. Ranney, C.T. Campbell: Microcalorimetric measurements of the heat of absorption of Pb on well-defined oxides: MgO(100) and p(2×1)-oxide on Mo(100), J. Chem. Phys. **114**, 3752–3764 (2001)
30.54 D.E. Starr, S.F. Diaz, J.E. Musgrove, J.T. Ranney, D.J. Bald, L. Nelen, H. Ihm, C.T. Campbell: Heat of absorption of Cu and Pb on hydroxyl-covered MgO(100), Surf. Sci. **515**, 13–20 (2002)
30.55 D.E. Starr, C.T. Campbell: Low-temperature adsorption microcalorimetry: Pb on MgO(100), J. Phys. Chem. B **105**, 3776–3782 (2001)
30.56 C.T. Campbell, S.C. Parker, D.E. Starr: The effect of size-dependent nanoparticle energetics on catalyst sintering, Science **298**, 811–814 (2002)
30.57 J.A. Farmer, C.T. Campbell, L. Xu, G. Henkelman: Defect sites and their distributions on MgO(100) by Li and Ca adsorption calorimetry, J. Am. Chem. Soc. **131**, 3098–3103 (2009)
30.58 J.A. Farmer, C.T. Campbell: Ceria maintains smaller metal catalyst particles by strong metal-support bonding, Science **329**, 933–936 (2010)
30.59 J.C. Sharp, Y.X. Yao, C.T. Campbell: Silver nanoparticles on Fe_3O_4(111): Energetics by Ag adsorption calorimetry and structure by surface spectroscopies, J. Phys. Chem. C **117**, 24932–24936 (2013)
30.60 T.E. James, S.L. Hemmingson, T. Ito, C.T. Campbell: Energetics of Cu adsorption and adhesion onto reduced CeO_2(111) surfaces by calorimetry, J. Phys. Chem. C **119**, 17209–17217 (2015)
30.61 D.E. Starr, J.T. Ranney, J.H. Larsen, J.E. Musgrove, C.T. Campbell: Measurement of the energetics of metal film growth on a semiconductor: Ag/Si(100)-(2×1), Phys. Rev. Lett. **87**, 106102 (2001)

30.62 M. Smedh, S.F. Diaz, C.T. Campbell: Adsorption and adhesion energies of Pb on (1×1)-Mo_2C/Mo(100) by calorimetry, Phys. Rev. B **67**, 205401 (2003)
30.63 O. Lytken, W. Lew, C.T. Campbell: Catalytic reaction energetics by single crystal adsorption calorimetry: Hydrocarbons on Pt(111), Chem. Soc. Rev. **37**, 2172–2179 (2008)
30.64 M.C. Crowe, C.T. Campbell: Adsorption microcalorimetry: Recent advances in instrumentation and application, Annu. Rev. Anal. Chem. **4**, 41–58 (2011)
30.65 C.T. Campbell, L. Árnadóttir, J.R.V. Sellers: Kinetic prefactors of reactions on solid surfaces, Z. Phys. Chem. **227**, 1435–1454 (2013)
30.66 C.T. Campbell: The energetics of supported metal nanoparticles: Relationships to sintering rates and catalytic activity, Acc. Chem. Res. **46**, 1712–1719 (2013)
30.67 T.E. James, S.L. Hemmingson, C.T. Campbell: Energy of supported metal catalysts: From single atoms to large metal nanoparticles, ACS Catalysis **5**, 5673–5678 (2015)
30.68 J.T. Stuckless, D.E. Starr, D.J. Bald, C.T. Campbell: Metal adsorption calorimetry and adhesion energies on clean single-crystal surfaces, J. Chem. Phys. **107**, 5547–5553 (1997)
30.69 M. Peter, J.M. Flores-Camacho, S. Adamovski, L.K. Ono, K.-H. Dostert, C.P. O'Brien, B. Roldan Cuenya, S. Schauermann, H.-J. Freund: Trends in the binding strength of surface species on nanoparticles: How does the adsorption energy scale with the particle size?, Angew. Chem. Int. Ed. **52**, 5175–5179 (2013)
30.70 P. Dementyev, K.-H. Dostert, F. Ivars-Barceló, C.P. O'Brien, F. Mirabella, S. Schauermann, X. Li, J. Paier, J. Sauer, H.-J. Freund: Water interaction with iron oxides, Angew. Chem. Int. Ed. **54**, 13942–13946 (2015)
30.71 P. Dementyev, M. Peter, S. Adamovsky, S. Schauermann: Chirally-modified metal surfaces: Energetics of interaction with chiral molecules, Phys. Chem. Chem. Phys. **17**, 22726–22735 (2015)
30.72 P. Hörtz, P. Ruff, R. Schäfer: A temperature dependent investigation of the adsorption of CO on Pt(111) using low-temperature single crystal adsorption calorimetry, Surf. Sci. **639**, 66–69 (2015)
30.73 J.-H. Fischer-Wolfarth, J.A. Farmer, J.M. Flores-Camacho, A. Genest, I.V. Yudanov, N. Rösch, C.T. Campbell, S. Schauermann, H.-J. Freund: Particle-size dependent heats of adsorption of CO on supported Pd nanoparticles as measured with a single-crystal microcalorimeter, Phys. Rev. B **81**, 241416(R) (2010)
30.74 B. Hammer, Y. Morikawa, J.K. Nørskov: CO chemisorption at metal surfaces and overlayers, Phys. Rev. Lett. **76**, 2141–2144 (1996)
30.75 I.V. Yudanov, M. Metzner, A. Genest, N. Rösch: Size-dependence of adsorption properties of metal nanoparticles: A density functional study on palladium nanoclusters, J. Phys. Chem. C **112**, 20269–20275 (2008)
30.76 W. Weiss, W. Ranke: Surface chemistry and catalysis on well-defined epitaxial iron-oxide layers, Prog. Surf. Sci. **70**, 1–151 (2002)

Luca Vattuone

Dipt. di Fisica
Università di Genova and IMEM-CNR Unità di Genova
Genova, Italy
vattuone@fisica.unige.it

Luca Vattuone received his PhD from the University of Genoa in 1994, worked as postdoc at Cambridge University (1995) and at Genoa University (1996–1999). In 1999 he became Staff Researcher and in 2012 Associate Professor of Condensed Matter Physics at Genoa University. His research activity focuses on the experimental investigation of gas–surface interactions and surface plasmons.

David A. King

The Foreign and Commonwealth Office
London, UK
dk@camkas.co.uk

Sir David is Exec Chair, Centre for Climate Repair at Cambridge, and Partner at SYSTEMIQ. He was UK Climate Envoy, 2013–2017, UK Government Chief Scientific Adviser, 2000–2007, and Professor of Physical Chemistry at the universities of Liverpool (1974–1988) and Cambridge (1988–2000). He has published over 500 papers on surface science and catalysis. He has received many international awards and honors.

31. Kinetics of Adsorption, Desorption and Reactions at Surfaces

H. Jürgen Kreuzer

We review the kinetic theories of adsorption, desorption, surface diffusion, and surface reactions, emphasizing the physics and chemistry underlying these processes. In particular, the need for local equilibrium in setting up macroscopic rate equations is discussed in detail, in particular for lattice–gas models. Several examples, such as hydrogen adsorption on rhodium surfaces and desorption from a coadsorbate, are presented. To go beyond the macroscopic level, one needs further details of the kinetics, such as the time evolution of correlators (in addition to the coverages), which are furnished by kinetic lattice–gas models, which also cover surface diffusion. An important point demonstrated in this chapter is the need for a consistent explanation of all data on a particular adsorbate system, including not only desorption spectra but also coverage and temperature-dependence of sticking coefficients and, last but not least, all thermodynamic data, such as adsorption isobars and heats of adsorption.

In Sect. 31.2, we present the theory for adsorbates that remain in quasi-equilibrium throughout the desorption process, in which case a few macroscopic variables, namely the partial coverages θ_r and their rate equations, are needed. We introduce the lattice–gas model and discuss results ranging from noninteracting adsorbates to systems with multiple interactions treated essentially exactly with the transfer-matrix method in Sect. 31.2.1. In Sect. 31.3, we discuss two examples to show the utility of theoretical approaches: adsorption and desorption of hydrogen on Rh(311) and coupled desorption and site conversion of coadsorbates: (NO+O)/Ru(001). In Sect. 31.4, we then proceed to the mesoscopic level by outlining recent advances in the theory of the kinetic lattice–gas model, such as nondissociative adsorption, and precursor-mediated adsorption and desorption. Finally, we make some concluding remarks in Sect. 31.5.

Surface processes such as adsorption, desorption, surface diffusion, and surface reactions can be described at the macroscopic level by writing kinetic equations for macroscopic variables, in particular rate equations for the (local) coverage or for partial coverages. This can be done rigorously by using the framework of nonequilibrium thermodynamics, which itself is based on the concept of local equilibrium [31.1]. The latter is established over length scales that are large compared to a mean free path and slow on the scale of the collision time. If this cannot be guaranteed, then a set of macroscopic variables is not sufficient, and an approach based on nonequilibrium statistical mechanics involving time-dependent distribution functions must be invoked.

M. Rocca, T.S. Rahman, L. Vattuone (Eds.), *Springer Handbook of Surface Science*, Springer Handbooks,
https://doi.org/10.1007/978-3-030-46906-1_31

31.1 Surface Reaction

The kinetic lattice–gas model, based on a Markovian master equation, is an example of such a theory. The greater details that can be described in such a theory involve time-dependent correlation functions. Going beyond phenomenological approaches, one must start from a microscopic Hamiltonian of the coupled gas–solid system and derive a rigorous master equation for which transition probabilities are calculated from first principles. So far, this program has only been completed for phonon-mediated physisorption kinetics, as is reviewed in a monograph by *Kreuzer* and *Gortel* [31.2].

A theory of surface processes must provide a consistent description and explanation of the experimental data available on a particular adsorbate system. For adsorption, it is the coverage and temperature-dependence of the sticking coefficient. For desorption, it is the desorption rate of the various desorbing species, again as a function of coverage and temperature. This may be either the isothermal desorption rate or the rate of temperature-programmed desorption (TPD). In the latter experimental setup, the adsorbate is prepared for different initial coverages at low temperature, and the substrate is then heated to give a (preferably linear) rise in temperature, during which the desorption products are detected. With time-resolved EELS and IR spectroscopies, some species remaining at the surface can also be monitored with which the partial coverages of the theory must agree. In addition, LEED can be used to record, via the scattering intensities, the time evolution of local correlations in the adsorbate, which thus must also be provided by the theory. Lastly, because any kinetic theory yields the equilibrium properties of the adsorbate via its time-independent solution, these must be consistent with the measured equilibrium properties of the system, such as adsorption isotherms and isobars, the heat of adsorption and the differential entropy, and correlation functions, all as a function of coverage and temperature. Only when a large set of kinetic data and all equilibrium data are explained satisfactorily within the same theory, can one claim to have a realistic model of the system.

31.2 Desorption with Fast Surface Diffusion

If surface diffusion is fast on the time scale of desorption, the adsorbate is maintained in equilibrium throughout the desorption process, i.e., all correlation functions attain their equilibrium values at the remaining coverage $\theta(t)$ at temperature $T(t)$. Thus, the adsorbate can be uniquely characterized by its chemical potential, $\mu(\theta(t), T(t))$. Take as an example desorption of an adsorbate that shows coexistence of a dense and a dilute two-dimensional phase in a certain range of coverage and temperature, then during desorption the distribution between the two phases will be in equilibrium at the remaining coverage $\theta(t)$ and the attained temperature $T(t)$, i.e., a description of the desorption process is possible with only a few macroscopic variables.

To derive an explicit expression of the rate of desorption, we restrict ourselves for the moment to nondissociative adsorption. Other systems will be dealt with later. We look at a situation where the gas phase pressure of a molecular species, P, is different from its value, $\overline{P}$, the equilibrium pressure needed to have a coverage θ at temperature T. There is then an excess flux to re-establish equilibrium between gas phase and adsorbate, so that we can write [31.3–6]

$$\frac{\mathrm{d}\theta}{\mathrm{d}t} = S(\theta, T)(P - \overline{P})\frac{a_\mathrm{s}\lambda_\mathrm{th}}{h}\,, \tag{31.1}$$

where

$$\lambda_\mathrm{th} = \frac{h}{(2\pi m k_\mathrm{B} T)^{1/2}} \tag{31.2}$$

is the thermal wavelength, a_s is the area of one adsorption cell, and h is Planck's constant. Next, we express the equilibrium pressure in terms of the gas-phase chemical potential, μ_g,

$$\overline{P} = \frac{k_\mathrm{B}T}{\lambda_\mathrm{th}^3} Z_\mathrm{int} \mathrm{e}^{\mu_\mathrm{g}/(k_\mathrm{B}T)}\,. \tag{31.3}$$

Here, Z_int is the intramolecular partition function accounting for rotations and vibrations. However, in equilibrium, the chemical potential in the gas phase is equal to that in the adsorbate, μ_a, so that we can write the desorption rate in (31.1) as

$$R_\mathrm{d} = S(\theta, T)\frac{a_\mathrm{s}^2}{\lambda_\mathrm{th}}\frac{k_\mathrm{B}T}{h} Z_\mathrm{int} \mathrm{e}^{\mu_\mathrm{a}/(k_\mathrm{B}T)}\,. \tag{31.4}$$

This is the principal result for the rate of desorption from an adsorbate that remains in quasi-equilibrium throughout desorption. Noteworthy is the clear separation into a dynamic factor, the sticking coefficient $S(\theta, T)$ and a thermodynamic factor involving single-particle partition functions and the chemical potential

of the adsorbate. The sticking coefficient is a measure of the efficiency of energy transfer in adsorption. Since energy supply from the substrate is required for desorption, the sticking coefficient, albeit usually at a higher temperature, must appear in the desorption rate as well by the detailed balance argument. The sticking coefficient cannot be obtained from thermodynamic arguments but must be calculated from a microscopic or mesoscopic theory, or be postulated in a phenomenological approach, based on experimental evidence for a particular system.

For dissociative adsorption [31.7], i.e., for systems in which the gas phase is predominantly molecules that dissociate into fragments A and B on the surface (not necessarily atoms), the desorption rate is given by

$$R_{\mathrm{d}}(\mathrm{A}+\mathrm{B}\rightarrow\mathrm{AB}) = S_{\mathrm{dis}}(\theta_{\mathrm{A}},\theta_{\mathrm{B}},T)\frac{a_{\mathrm{s}}^2}{\lambda_{\mathrm{th}}} \times \frac{k_{\mathrm{B}}T}{h} Z_{\mathrm{int}}^{(\mathrm{A})} Z_{\mathrm{int}}^{(\mathrm{B})} \mathrm{e}^{(\mu_{\mathrm{A}}+\mu_{\mathrm{B}})/(k_{\mathrm{B}}T)} , \tag{31.5}$$

where $S_{\mathrm{dis}}(\theta_{\mathrm{A}},\theta_{\mathrm{B}},T)$ is the dissociative sticking coefficient at the indicated partial coverages and at the desorption temperature.

This approach is adaptable to more complicated systems, such as multilayer growth and reactive processes, provided that the individual species remain in local equilibrium, allowing, of course, for dissociation and reaction disequilibria.

31.2.1 Lattice-Gas Models

Most microscopic theories of adsorption and desorption are based on the lattice–gas model. One assumes that the surface of a solid can be divided into two-dimensional cells, labeled i, for which one introduces microscopic variables $n_i = 1$ or 0, depending on whether or not cell i is occupied by an adsorbed gas particle. (The connection with magnetic systems is made by a transformation to spin variables $\sigma_i = 2n_i - 1$.) In its simplest form, a lattice–gas model is restricted to the submonolayer (ML) regime and to gas–solid systems, in which the surface structure and the adsorption sites do not change as a function of coverage. To introduce the dynamics of the system, one writes a model Hamiltonian, which, for the simplest system of a one-component adsorbate with one adsorption site per unit cell, is

$$H = E_{\mathrm{s}}\sum_i n_i + V_{1n}\sum_{\langle ij\rangle} n_i n_j + V_{2n}\sum_{\langle ij'\rangle} n_i n_{j'} + \ldots \tag{31.6}$$

Here, E_{s} is a single-particle energy, and V_{1n} and V_{2n} are the two-particle interactions between nearest neighbors $\langle ij\rangle$ and next-nearest neighbors $\langle ij'\rangle$, respectively. Interactions between farther neighbors and many-particle interactions can be easily added. As long as the (average) number of particles in the adsorbate does not change, which is the case for systems in equilibrium, or for diffusion studies, the first term in (31.6) is constant and can be dropped from further consideration. However, if we want to study adsorption–desorption kinetics, the number of particles in the adsorbate changes as a function of time, and a proper identification of E_{s} is mandatory. Arguing that the lattice–gas Hamiltonian should give the same Helmholtz free energy as a microscopic Hamiltonian (for noninteracting particles), one can show that the proper identification is given by

$$E_{\mathrm{s}} = -V_0 - k_{\mathrm{B}}T\ln(q_3 q_{\mathrm{int}}) , \tag{31.7}$$

where V_0 is the (positive) binding energy of an isolated particle on the surface. Moreover,

$$q_3 = q_z q_{xy} \tag{31.8}$$

is the vibrational partition function of an adsorbed particle with (in the harmonic approximation)

$$q_z = \frac{\mathrm{e}^{h\nu_z/(2k_{\mathrm{B}}T)}}{\mathrm{e}^{h\nu_z/(k_{\mathrm{B}}T)}-1} \tag{31.9}$$

its component for the motion perpendicular to the surface. Likewise, q_{xy} is the partition function for the motion parallel to the surface. We have also made adjustment for the fact that the internal partition function for rotations and vibrations of an adsorbed molecule might be changed from its free gas-phase value Z_{int} to q_{int}, if some of the internal degrees of freedom become frozen out or frustrated.

31.2.2 Chemical Potential

Equations (31.1), (31.4), and (31.5) show that to determine the equilibrium properties of an adsorbate and also the adsorption–desorption and dissociation kinetics under quasi-equilibrium conditions, we need to calculate the chemical potential as a function of coverage and temperature. The simplest case is a single-component adsorbate. The case of dissociative equilibrium with both atoms and molecules present on the surface has been reported elsewhere [31.7].

For a noninteracting molecular adsorbate, the chemical potential is given by

$$\mu_{\mathrm{a}}(\theta,T) = -V_0 + k_{\mathrm{B}}T\left[\ln\left(\frac{\theta}{1-\theta}\right) - \ln(q_3 q_{\mathrm{int}})\right] . \tag{31.10}$$

Inserted into (31.3) this gives the Langmuir isotherm

$$\overline{P} = \frac{k_B T}{\lambda_{th}^3} Z_{int} e^{\mu_a/(k_B T)} = \frac{k_B T}{\lambda_{th}^3} \frac{Z_{int}}{q_3 q_{int}} e^{-V_0/(k_B T)} \frac{\theta}{1-\theta} , \tag{31.11}$$

from which we get the isosteric heat of adsorption

$$\begin{aligned} Q_{iso}(\theta, T) &= k_B T \left. \frac{\partial \ln \overline{P}}{\partial T} \right|_\theta \\ &= V_0 + \frac{5}{2} k_B T - k_B T^2 \frac{\partial}{\partial T} \ln \left(\frac{q_3 q_{int}}{Z_{int}} \right) \end{aligned} \tag{31.12}$$

and the differential entropy

$$\Delta s(\theta, T) = \overline{s} - s_G = -k_B \ln \left(\frac{\overline{P}}{P_0} \right) - Q_{iso}(\theta, T) , \tag{31.13}$$

where

$$\overline{s} = \left. \frac{\partial S}{\partial n} \right|_{T,P,A} \tag{31.14}$$

is the differential entropy of the adsorbate and s_G that of the gas phase; P_0 is the pressure of the reference state.

Similarly, we obtain the rate of desorption

$$R_d = S(\theta, T) \frac{\theta}{1-\theta} \frac{a_s}{\lambda_{th}^2} \frac{k_B T}{h} \frac{Z_{int}}{q_3 q_{int}} e^{-V_0/(k_B T)} . \tag{31.15}$$

Note that if sticking is controlled by site exclusion only, i.e., if $S(\theta, T) = S_0(T)(1-\theta)$, this rate is that of a first-order reaction at low coverage. This simple picture breaks down when either the sticking coefficient depends differently on the coverage, as it does, for instance, for precursor-mediated adsorption, or when lateral interactions become important. It then does not make much physical sense to talk about the order of the desorption process.

To gain some qualitative insight into the effect of lateral interactions, it is useful to employ simple analytical approximations in the calculation of the chemical potential of which the quasichemical approximation is the best suited. We split the chemical potential into a noninteracting part (31.10) and a term due to lateral interactions, $\mu_a = \mu_a^{(ni)} + \mu_a^{(lat)}$, and obtain for the latter, for c nearest-neighbor interactions only,

$$\mu_a^{(lat)}(\theta, T) = c V_{1n} + \frac{1}{2} c k_B T \ln \left(\frac{\alpha - 1 + 2\theta}{\alpha + 1 - 2\theta} \frac{1-\theta}{\theta} \right) , \tag{31.16}$$

where

$$\alpha^2 = 1 - 4\theta(1-\theta) \left[1 - e^{-V_{1n}/(k_B T)} \right] . \tag{31.17}$$

This adds to the isosteric heat, which now reads

$$Q_{iso}(\theta, T) = Q_{iso}(0, T) + \frac{1}{2} c V_{1n} \left(\frac{1 - \alpha - 2\theta}{\alpha} \right) . \tag{31.18}$$

For a large repulsive interaction, $V_{1n}/(k_B T) \gg 1$, Q_{iso} exhibits two distinct and essentially constant values for $\theta \lessgtr 1/2$, because for $\theta < 1/2$, adsorbed particles are essentially isolated from each other by the mutual repulsion on nearest-neighbor sites, whereas, for $\theta > 1/2$, those particles that have c neighbors have their binding energy reduced by cV_{1n}. The consequence of this energetics on desorption is that in temperature-programmed desorption, one observes one desorption peak for initial coverages $\theta_0 < 1/2$, essentially that of a noninteracting adsorbate, and, for initial coverages $\theta > 1/2$, an additional peak at lower temperature for desorption out of a local environment of c neighbors.

Such analytic approximations based on clusters of particles quickly become mathematically intractable with variation in cluster size, geometry, and range of interactions [31.8, 9].

31.2.3 Transfer-Matrix Method

With the availability of computers, the transfer-matrix method [31.10] emerged as an alternative and powerful technique for the study of the cooperative phenomena of adsorbates resulting from interactions [31.11, 12]. Quantities are calculated exactly on a semi-infinite lattice. Coupled with finite-size scaling towards the infinite lattice, the technique has proved popular for the determination of phase diagrams and critical-point properties of adsorbates ([31.13–19] and magnetic spin systems [31.20–22], and further references therein). Application to other aspects of adsorbates, e.g., the calculation of desorption rates and heats of adsorption, has been more recent [31.23–26]. Sufficient accuracy can usually be obtained for the latter without scaling and essentially exact results are possible. In the following, we summarize the elementary but important aspects of the method to emphasize the ease of application. Further details can be found in the above references.

To introduce the transfer-matrix method, we repeat some well-known facts for a 1-D (one-dimensional) lattice gas of N_s sites with nearest-neighbor interactions, V_{1n} [31.27]. Its grand canonical partition function is

given by

$$\Xi(T,N_\mathrm{s},\mu)=\sum_{\boldsymbol{n}}\mathrm{e}^{-[H(\boldsymbol{n})-\mu N(\boldsymbol{n})]/(k_\mathrm{B}T)}\,, \tag{31.19}$$

$$N(\boldsymbol{n})=\sum_{i=1}^{N_\mathrm{s}} n_i\,, \tag{31.20}$$

where $\boldsymbol{n}=(n_1,n_2,\ldots,n_{N_\mathrm{s}},n_{N_\mathrm{s}+1}=n_1)$ specifies one of the 2^{N_s} microstates of the (two-state) adsorbate, with cyclic boundary conditions imposed. Substituting the Hamiltonian (31.6), we can rewrite Ξ as a sum over products

$$\begin{aligned}\Xi&=\sum_{\boldsymbol{n}}\prod_{i=1}^{N_\mathrm{s}}T(n_i,n_{i+1})\,,\\&=\sum_{\boldsymbol{n}}T(n_1,n_2)T(n_2,n_3)\ldots T(n_{N_\mathrm{s}},n_1)\,,\end{aligned} \tag{31.21}$$

$$T(n_i,n_{i+1})=\exp\left[\frac{\varepsilon}{2}(n_i+n_{i+1})-\upsilon n_i n_{i+1}\right], \tag{31.22}$$

with

$$\varepsilon=\frac{\mu-E_\mathrm{s}}{k_\mathrm{B}T}\quad\text{and}\quad\upsilon=\frac{V_{1n}}{k_\mathrm{B}T}\,.$$

If the factors $T(n_i,n_{i+1})$ are regarded as the elements of a 2×2 matrix in the basis $\{|0\rangle,|1\rangle\}$ for each site i ($z=\exp(\varepsilon)$; $y=\exp(-\upsilon)$)

$$\mathbf{T}=\begin{pmatrix}T(0,0)&T(0,1)\\T(1,0)&T(1,1)\end{pmatrix}=\begin{pmatrix}1&z^{1/2}\\z^{1/2}&zy\end{pmatrix}\,, \tag{31.23}$$

then the summation over states in (31.21) is equivalent to matrix multiplication, e.g.,

$$\sum_{n_2=0,1}T(n_1,n_2)T(n_2,n_3)=T^2(n_1,n_3)\,, \tag{31.24}$$

where $T^2(n_1,n_3)$ is an element of the matrix $\mathbf{T}^2$. Summing over all intermediate states gives

$$\begin{aligned}\Xi&=\sum_{n_1=0,1}T^{N_\mathrm{s}}(n_1,n_1)=\mathrm{tr}[\mathbf{T}^{N_\mathrm{s}}]\\&=\lambda_1^{N_\mathrm{s}}+\lambda_2^{N_\mathrm{s}}\,,\end{aligned} \tag{31.25}$$

where $\lambda_{1,2}$ are the eigenvalues of the transfer-matrix $\mathbf{T}$. With $\lambda_2<\lambda_1$ the second term becomes insignificant for *large* N_s, so that all thermodynamic information about the system is contained in the largest eigenvalue of the transfer matrix.

One obtains the coverage as

$$\begin{aligned}\theta(T,\mu)&=\frac{\langle N\rangle}{N_\mathrm{s}}=\frac{1}{N_\mathrm{s}}\left.\frac{\partial\ln\Xi}{\partial(\beta\mu)}\right|_{T,N_\mathrm{s}}\\&=\left.\frac{\partial\ln(\lambda_1)}{\partial(\beta\mu)}\right|_{T,N_\mathrm{s}}\,,\end{aligned} \tag{31.26}$$

with

$$\beta=\frac{1}{k_\mathrm{B}T}\,.$$

To avoid numerical differentiation (which is inherently unstable) one uses the fact that an eigenvalue can be expressed as $\lambda_1=\boldsymbol{v}_1^\mathrm{L}\mathbf{T}\boldsymbol{v}_1^\mathrm{R}$, where $\boldsymbol{v}_1^{\mathrm{L,R}}$ are the corresponding normalized left and right eigenvectors. Differentiation of the eigenvalue with respect to any parameter is then equivalent to the differentiation of the transfer matrix, and one finds

$$\begin{aligned}\theta(T,\mu)&=\frac{z}{\lambda_1}\boldsymbol{v}^\mathrm{L}\left.\frac{\partial\mathbf{T}}{\partial z}\right|_{T,N_\mathrm{s}}\boldsymbol{v}^\mathrm{R}\\&=\sum_{k=1,2}p_k v_{1k}^2\,,\end{aligned} \tag{31.27}$$

where $\boldsymbol{v}_1^\mathrm{L}=(\boldsymbol{v}_1^\mathrm{R})^\mathrm{T}=\boldsymbol{v}_1=(v_{11},v_{12})$ in the basis in which the first and second components are the empty ($p_1=0$) and occupied ($p_2=1$) sites, respectively. Thus, the problem of finding the coverage as a function of temperature and chemical potential is reduced to the determination of the (largest) eigenvalue and corresponding eigenvector of a matrix of Boltzmann factors. Other information can be readily extracted in the same way, for instance, the (average) nearest-neighbor correlation function is given by

$$\begin{aligned}\langle n_i n_{i+1}\rangle&=\frac{1}{N_\mathrm{s}\Xi}\sum_{\boldsymbol{n}}\sum_{i=1}^{N_\mathrm{s}}n_i n_{i+1}\mathrm{e}^{-[H(\boldsymbol{n})-\mu N(\boldsymbol{n})]/(k_\mathrm{B}T)}\\&=-\frac{1}{N_\mathrm{s}}\left.\frac{\partial\ln\Xi}{\partial(\beta V_{1n})}\right|_{T,N_\mathrm{s}}=\frac{y}{\lambda_1}\boldsymbol{v}^\mathrm{L}\left.\frac{\partial\mathbf{T}}{\partial y}\right|_{T,N_\mathrm{s}}\boldsymbol{v}^\mathrm{R}\,.\end{aligned} \tag{31.28}$$

The transfer-matrix method extends rather straightforwardly to more than one dimension, systems with multiple interactions, more than one adsorption site per unit cell, and more than one species by enlarging the basis in which the transfer matrix is defined. Explicit details are given elsewhere [31.28]. The construction of the transfer matrices and associated numerical procedures is essentially the same for these systems, and such calculations are done routinely [31.29]. If

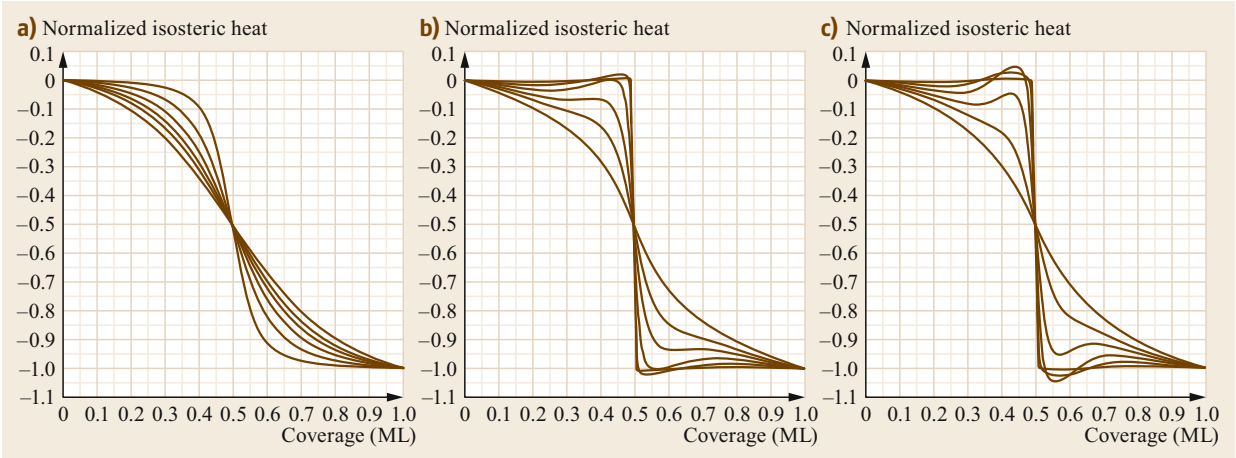

Fig. 31.1a–c Normalized isosteric heat, $(Q_{\mathrm{iso}}(\theta,T)-Q_{\mathrm{iso}}(0,T))/4V_{1n}$, as a function of coverage for first-neighbor repulsion on a square lattice, for temperatures (*top to bottom* at 0.2 ML) $k_{\mathrm{B}}T/V_{1n}=0.25$, 0.35, 0.45, 0.55, 0.65, and 0.85. **(a)** Quasichemical approximation, see (31.16); **(b)** transfer-matrix result for $M=4$; and **(c)** for $M=8$

there are two or more nonreacting (but interacting) species on the surface, then the partial coverages depend on the chemical potentials specified for each species.

As an example of the quality of the quasichemical approximation versus the transfer-matrix method, in Fig. 31.1 we show the isosteric heat for repulsive first-neighbor interactions on a square lattice [31.25].

31.3 Examples

Our first example of the utility of the theoretical approach to thermal desorption kinetics is a study of the thermodynamics and adsorption and desorption kinetics of hydrogen on Rh(311) obtained from an anisotropic lattice–gas model [31.30].

31.3.1 Adsorption and Desorption of Hydrogen on Rh(311)

Understanding this complex system will also allow us to make predictions (without any further information) for hydrogen adsorption on the Rh(110) and Rh(111) surfaces. For the Rh(311) surface, we need to consider three and fourfold coordinated adsorption sites, first-neighbor attraction along the closed-packed $[01\bar{1}]$-direction, and first and second-neighbor and trio repulsions in the $[1\bar{1}\bar{2}]$-direction to account for $(1\times n)$ structures at coverages $\theta=1/4$, $1/3$, $1/2$ and $2/3$, as shown in Fig. 31.2 [31.30].

In Fig. 31.3, we give the experimental and the best-fit theoretical TPD curves, which show very good agreement [31.30].

LEED intensities were also measured during desorption (Fig. 31.4) [31.30]. Because they are proportional to the square of density–density correlations, and the latter can be calculated from the transfer matrix, simultaneously with the chemical potential, one can further elucidate the structures and show their influence on TPD. The two-site correlators of interest are

$$C_k=\langle n_{rc}n_{r,c+k}\rangle\,, \tag{31.29}$$

which for $k=1,2,3$ give the probabilities of finding first, second and third-neighbor sites occupied in the $[1\bar{1}\bar{2}]$-direction. For a completely disordered adsorbate, these correlators have the value θ^2. At sufficiently low temperature, they attain the values $(C_1,C_2,C_3)=(0,0,1/3)$, $(0,1/2,0)$ and $(1/3,1/3,2/3)$ at $\theta=1/3$, $1/2$, and $2/3$ for the 1×3-H, 1×2-H and 1×3-2H structures of Fig. 31.2, respectively.

The LEED intensities are calculated from

$$I(\boldsymbol{k},T)=I_0\sum_{i,j=1}^{M}\langle n_in_j\rangle \mathrm{e}^{\mathrm{i}\boldsymbol{k}\cdot(\boldsymbol{r}_i-\boldsymbol{r}_j)} \tag{31.30}$$

in terms of two-particle correlators. Because of the attraction in the $[01\bar{1}]$-direction, the correlators do not crucially depend on the interparticle spacings in this direction. Ordering is, therefore, mainly reflected in the variation of the correlators in the $[1\bar{1}\bar{2}]$-direction and,

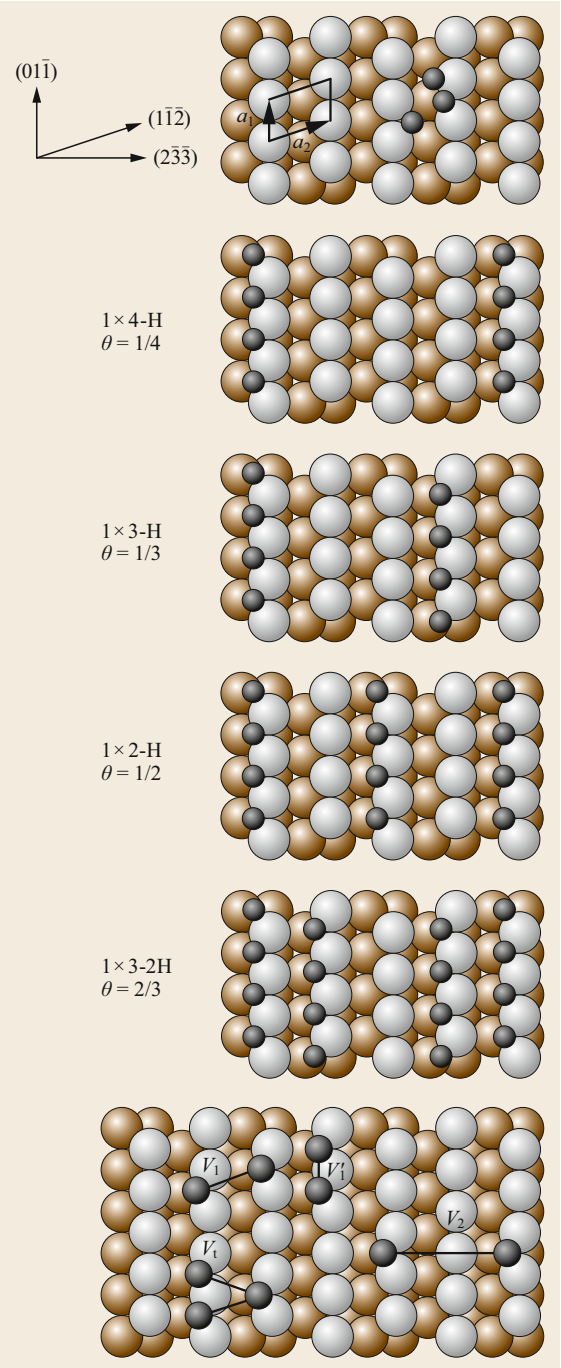

Fig. 31.2 Ordered structures of hydrogen on Rh(311) and model interactions

consequently, we can simplify the calculation and use the two-site correlators calculated in the finite direction of the transfer matrix. The experimental LEED intensities for third-order and half-order spots are reproduced by theory without any further adjustments in the lattice–gas Hamiltonian used to fit the TPD spectra (Fig. 31.4) [31.30].

Because the Rh(311) surface can be thought of as consisting of portions of (111) and (110) surfaces, the lattice–gas model for the (311) surface contains all the necessary parameters for these surfaces as well. Thus, without any further fitting, one can immediately calculate the TPD spectra for these surfaces as well. It turns out to be an excellent fit to the corresponding experimental data [31.30]. This again demonstrates the power of a theoretical approach that is geared to explain *all* available data, thermodynamic and kinetic, on a system; in this case, hydrogen adsorption on three different Rh surfaces.

31.3.2 Coupled Desorption and Site Conversion of Coadsorbates: (NO+O)/Ru(001)

The (NO+O)/Ru(001) system constitutes a good example of complex desorption-site conversion with the advantage that the geometrical structures, the coverages, as well as detailed spectroscopic information on all participating species are available experimentally. A combined set of desorption data and vibrational spectra with in situ determination of partial coverages in desorption that show site conversion for both increasing and decreasing temperatures. This system is understood in detail by modeling the (NO+O) coadsorbate layer on Ru(001) as a lattice gas that accounts for the adsorbate structure and site conversion, and explains the TPD spectra [31.31]. The unusual features of the TPD spectra result in part from the dramatic coverage dependence of the sticking coefficient induced by site exclusion.

It has been found that ≈ 0.5 ML of NO (relative to Ru surface atoms) can be postadsorbed within the (2×1)-O/Ru(001) layer at $\theta_O = 0.5$ ML. For this combined (NO+O) coverage of 1 ML both O and NO reside in hcp-hollow sites, arranged in alternating close-packed O and NO rows (Fig. 31.5) [31.31].

The detailed geometry has been determined by LEED-IV [31.32]. Heating of the layer (at $1\,\mathrm{K\,s^{-1}}$) leads to NO desorption at 250–350 K in a broad peak until 0.25 ML NO is left on the surface (Fig. 31.6); no oxygen leaves the surface in this range. LEED-IV analysis of the remaining layer shows that now the oxygen atoms sit in equal numbers of hcp and fcc sites in a honeycomb arrangement, and the NO molecules sit in on-top sites at the centers of the O hexagons (Fig. 31.5). It appears probable that the conversion of oxygen-site occupancy occurs simultaneously with desorption of half the initial NO coverage. Only upon further heating

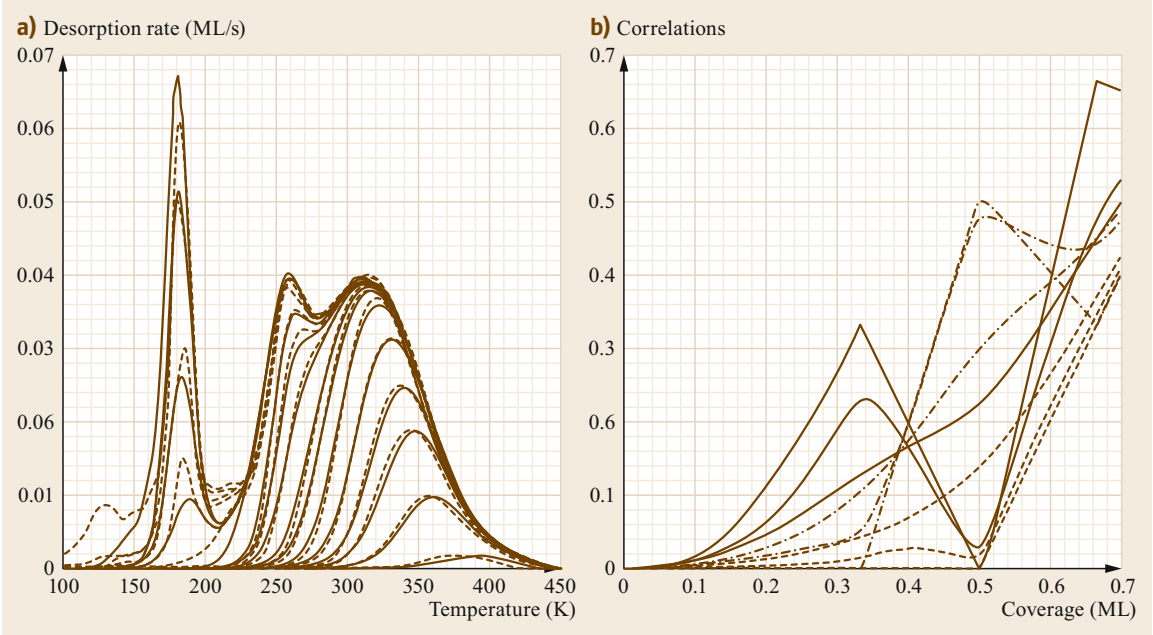

Fig. 31.3 **(a)** Model TPD spectra (*solid lines*) and experimental data (*dashed lines*) for H on Rh(311) for initial coverages in the range 0.01−0.68 ML. Heating rate 10 K/s. Surface-energy parameters: $V_0 = 2.647\,\text{eV}$, $V'_{1n} = -0.029\,\text{eV}$, $V_{1n} = 0.035\,\text{eV}$, $V_{2n} = 0.022\,\text{eV}$, $V_{\text{trio}} = 0.011\,\text{eV}$; vibrational frequencies $2\times10^{13}\,\text{s}^{-1}$, $1.3\times10^{13}\,\text{s}^{-1}$, $5\times10^{10}\,\text{s}^{-1}$; site area $a_s = 12A^2$; dissociation energy $D_0 = 4.478\,\text{eV}$; $T_{\text{vib}} = 6332\,\text{K}$, $T_{\text{rot}} = 87.6\,\text{K}$. **(b)** Isothermal correlators as a function of coverage for temperatures 350, 220, and 100 K (with sharpest features at lowest temperature): C_1 (*dotted line*), C_2 (*long-short dashed line*), and C_3 (*solid line*)

to 420 K is more NO released in a very narrow temperature interval. The oxygen atoms, none of which desorb, return to their original (2×1)-O arrangement at hcp sites. These coupled phenomena constitute a good example of complex desorption with site conversion, with the advantage that the geometrical structures, the coverages, as well as detailed spectroscopic information on all participating species are well known. In particular, vibrational spectra for in-situ determination of partial coverages have been measured not only in desorption and conversion for increasing temperatures, but also for the reverse process. We have studied this system in detail with a suitable theoretical model for desorption, the results of which are compared with the experimental data.

The (NO+O) coadsorbate layer on Ru(001) was modeled as a lattice gas that will account for the adsorbate structure and explain the TPD spectra. To reduce the complexity of the system to manageable proportions the quarter monolayer of O in a was fixed in a (2×2) structure at the hcp sites of a hexagonal lattice. The remaining quarter monolayer of O can sit either on hcp sites to form a (2×1)-O superlattice or on neighboring fcc sites with a weaker binding energy. The NO sits either on the empty rows of hcp sites between the rows of the (2×1)-O structure or on neighboring on-top sites. Lateral interactions of the coadsorbates are mainly those of mutual site exclusion, but long-range repulsive (dipole–dipole) interactions must also be accounted for.

As for the kinetics it was kept as simple as possible but sufficient to account for the main features of desorption and site conversion. Rather than resorting to a complex kinetic lattice–gas model (for which more experimental data would be needed to fix all the parameters) a simple model was used that ignores the details of lateral interactions but includes them summarily in a mean field theory accounting, most importantly, for long-range dipolar forces. An important fact to understand is the coverage dependence of the sticking coefficient, calculated in the framework of a kinetic lattice–gas model, drops dramatically by several orders of magnitude beyond a quarter monolayer of NO. This delays desorption (the desorption rate contains the sticking coefficient!) of the last quarter of NO until it finally blows off explosively in a very narrow temperature range (Fig. 31.6) [31.31].

More work in the NO plus O adsorbate can be found in a follow-up paper [31.33]. Additional applications of the transfer-matrix method to adsorption and desorption kinetics deal with other molecules on low index metal

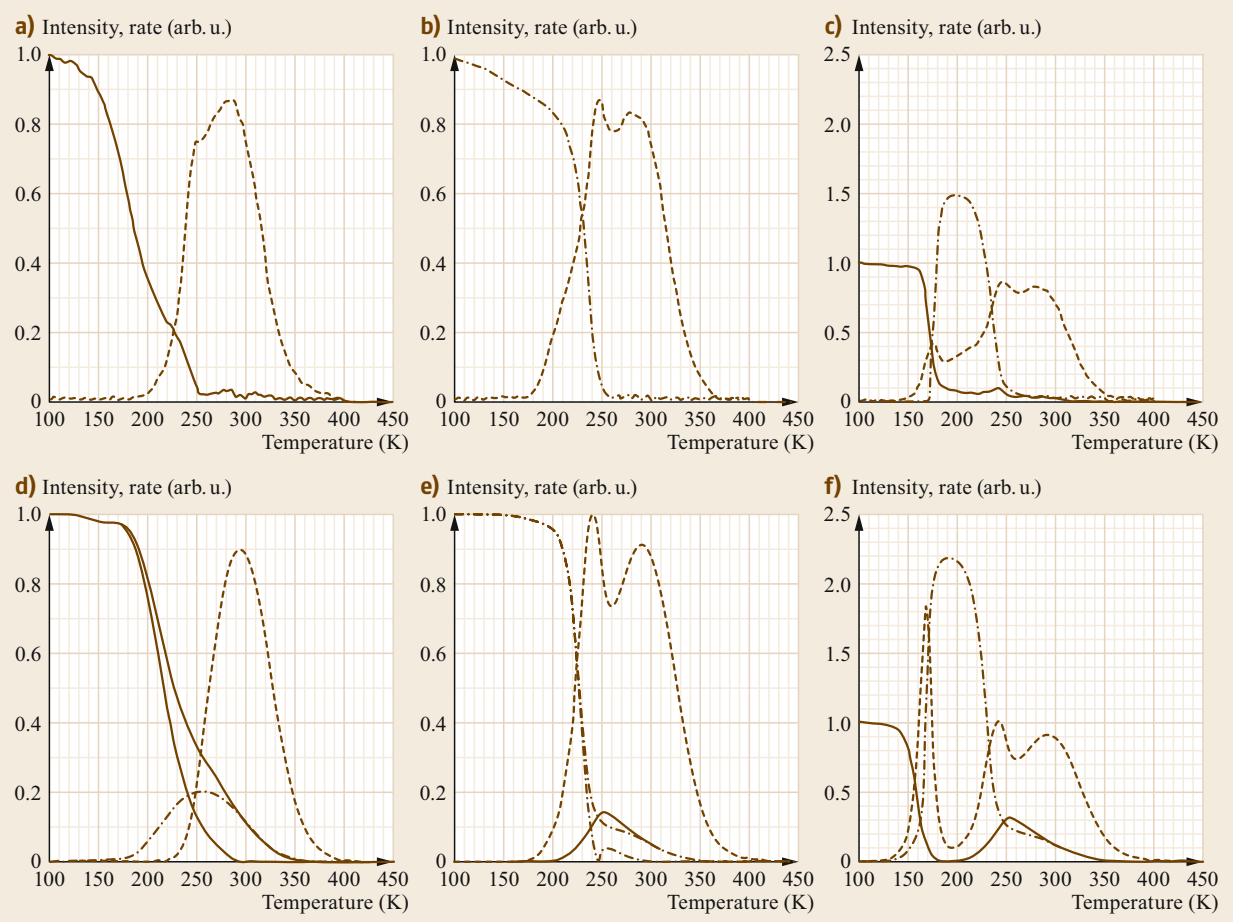

Fig. 31.4 **(a–c)** Experimental LEED intensitiesfor (1×3) (*solid line*) and (1×2) (*long-short dashed line*) structures and corresponding TPD rates (*dotted lines*) as a function of desorption temperature for approximate initial coverages 1/3, 1/2, and 2/3 ML. **(d–f)** Theoretical LEED intensities, calculated with (31.39), and theoretical TPD rates for these initial coverages. Heating rate 1 K/s

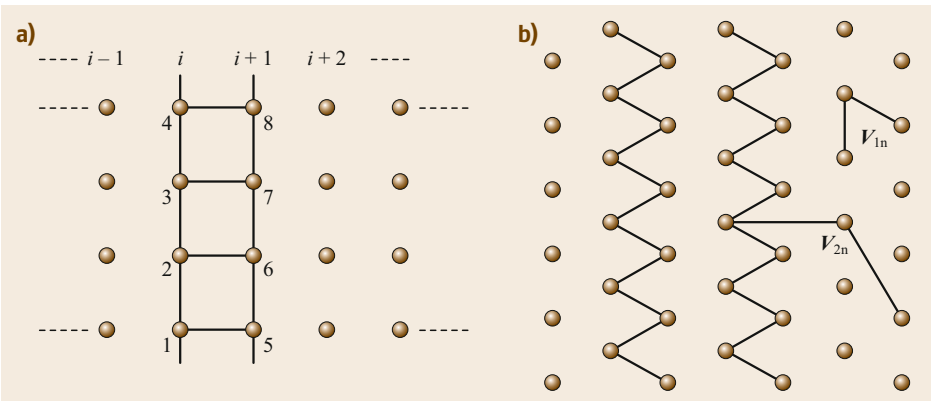

Fig. 31.5 **(a)** Schematic of a semi-infinite square lattice of width four sites, nearest-neighbor interactions indicated. **(b)** The 24 sites involved in the construction of the transfer matrix for nearest and next-nearest neighbor interactions on a hexagonal lattice for $M = 6$

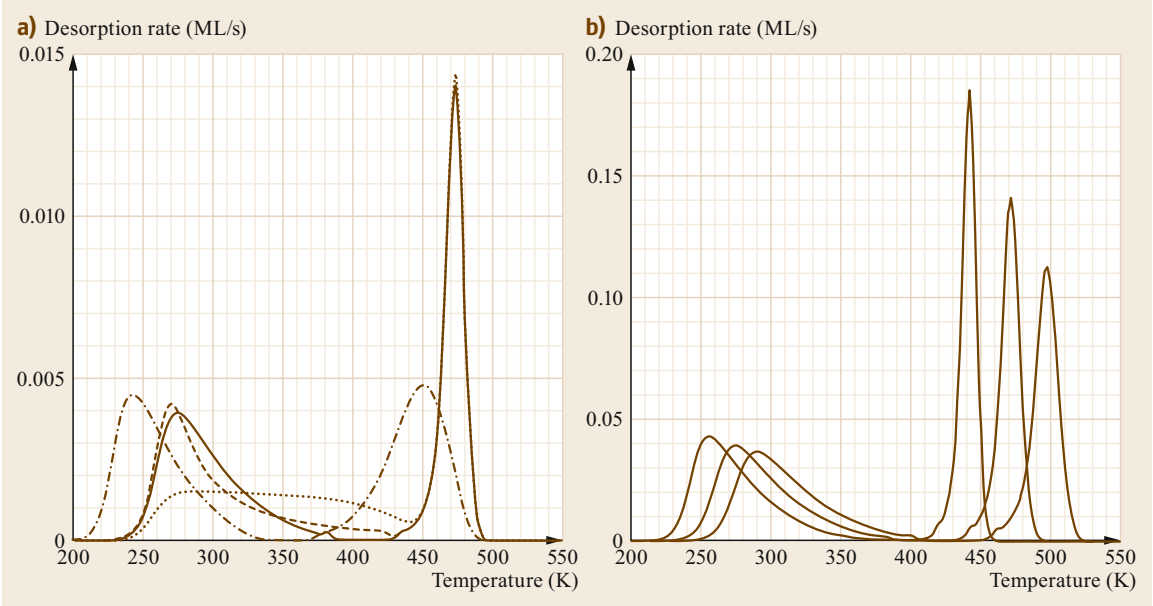

Fig. 31.6a,b TPD spectra for the models including long-range interactions for initial NO coverage $\theta_0 = 0.5$ ML and $1\,\mathrm{K\,s^{-1}}$. **(a)** Phenomenological model, (19) from [31.29], with $p = 1/4$, $\mu_{\mathrm{dip}}(\theta^{\max}) = 0.57\,\mathrm{eV}$ (*solid line* for site-exclusion sticking), classical dipole assembly model, (17) from [31.29], with $M^2(0)/a^3 = 0.19\,\mathrm{eV}$, $b = 2$ (*dashed line*), mean field, (19) from [31.29], with $p = 1$, maximum shift 0.57 eV (*dotted line*). **(b)** Best fit with $p = 1/4$ for heating rates of 0.05, 1, and $10\,\mathrm{K\,s^{-1}}$. Desorption rates scaled by ×200, ×10, ×1, respectively

surfaces [31.34–40], multilayers [31.41–43], multisite stepped surfaces [31.44], and co-adsorbates [31.31, 45–53].

A similar approach has been used to study dissociative adsorption and associative desorption [31.54, 55].

31.4 Kinetic Lattice-Gas Models

If it cannot be guaranteed that the adsorbate remains in local equilibrium during its time evolution, then a set of macroscopic variables is not sufficient, and an approach based on nonequilibrium statistical mechanics involving time-dependent distribution functions must be invoked. The kinetic lattice–gas model is an example of such a theory [31.56]. It is derived from a Markovian master equation, but is not totally microscopic in that it is based on a phenomenological Hamiltonian. We demonstrate this approach with two examples: (i) an adsorbate with nondissociative adsorption, and (ii) precursor-mediated adsorption and desorption. Our basic assumption is that the kinetic phenomena of adsorption, desorption, and surface diffusion can be described as Markov processes, with the occupation numbers in the Hamiltonian (31.6) as stochastic variables.

31.4.1 Nondissociative Adsorption

We introduce a function $P(\boldsymbol{n}, t)$, which gives the probability that the state $\boldsymbol{n} = (n_1, n_2, \ldots, n_{N_s})$ is realized at time t, where N_s is now the total number of adsorption sites on the surface. It satisfies a master equation

$$\frac{\mathrm{d}P(\boldsymbol{n}, t)}{\mathrm{d}t} = \sum_{\boldsymbol{n}'} [W(\boldsymbol{n}, \boldsymbol{n}')P(\boldsymbol{n}', t) - W(\boldsymbol{n}', \boldsymbol{n})P(\boldsymbol{n}, t)] \,, \tag{31.31}$$

where $W(\boldsymbol{n}', \boldsymbol{n})$ are the transition probabilities per unit time that the system changes from a state $\boldsymbol{n}$ to $\boldsymbol{n}'$. They are not completely arbitrary but must satisfy detailed balance

$$W(\boldsymbol{n}', \boldsymbol{n}) \mathrm{e}^{-\beta\left[H(\boldsymbol{n}) - \mu \sum_{i(\boldsymbol{n})} n_i\right]} = W(\boldsymbol{n}, \boldsymbol{n}') \mathrm{e}^{-\beta\left[H(\boldsymbol{n}') - \mu \sum_{i(\boldsymbol{n}')} n_i'\right]} \,. \tag{31.32}$$

To specify these transition probabilities we make the further assumption that the residence time of a particle in a given adsorption site is much longer than the time of an individual transition to or from that state, either in exchange with the gas phase in adsorption and desorption, or for hopping across the surface in diffusion. In such situations there will be only one individual transition at any instant of time, and the transition probabilities can be summed, one at a time, over all possible processes (adsorption, desorption, diffusion) and over all adsorption sites on the surface. To implement this, we first write

$$W(\boldsymbol{n}', \boldsymbol{n}) = W_{\text{ad-des}}(\boldsymbol{n}', \boldsymbol{n}) + W_{\text{diff}}(\boldsymbol{n}', \boldsymbol{n}) \tag{31.33}$$

as a sum of adsorption–desorption and diffusion terms. For the former, we then write the most general power series in the occupation numbers [31.57]

$$\begin{aligned} &W_{\text{ad-des}}(\boldsymbol{n}', \boldsymbol{n}) \\ &= w_0 \sum_l \left[(1-n_l) \left(1 + A_1 \sum_{l'} n_{l'} + A_2 \sum_{l'l''} n_{l'} n_{l''} + \ldots \right) \right. \\ &\quad \left. + D_0 n_l \left(1 + D_1 \sum_{l'} n_{l'} + D_2 \sum_{l'l''} n_{l'} n_{l''} + \ldots \right) \right] \\ &\quad \times \delta\left(n'_l, 1-n_l\right) \prod_{l' \neq l} \delta(n'_l, n_l) \, . \end{aligned} \tag{31.34}$$

Here the sums over l', l'' run over the neighbors of l. The highest term is a product of $(c+1)$ factors with c the coordination number of the lattice.

Detailed balance imposes a set of restrictions on the coefficients A_n, D_n; e.g., if there is only one adparticle present, say in site i, so that $n_i = 1$ and all other $n_j = 0, j \neq i$, then (31.43) gives

$$w_0 D_0 \mathrm{e}^{-E_\mathrm{s}/(k_\mathrm{B}T)} = w_0 \, , \tag{31.35}$$

so that

$$D_0 = \mathrm{e}^{\beta(E_\mathrm{s}-\mu)} \, . \tag{31.36}$$

Note that w_0 cannot be fixed by detailed balance, the reason being that it contains the information about the energy exchange with the solid, which is not contained in the static lattice–gas Hamiltonian. However, by comparison with the phenomenological rate equation (31.1), we can identify it as

$$w_0 = S_0 \frac{P \lambda_{\text{th}} a_\mathrm{s}}{h} \, . \tag{31.37}$$

To obtain the other coefficients we next specify that two particles are adsorbed on neighboring sites, $n_i = n_{i+a} = 1$, with all other sites empty and obtain

$$1 + A_1 = (1 + D_1)\mathrm{e}^{-\beta V_{1n}} \, . \tag{31.38}$$

From situations where three and four neighboring sites are occupied we obtain, respectively,

$$1 + 2A_1 + A_2 = (1 + 2D_1 + D_2)\mathrm{e}^{-2\beta V_{1n}} \, , \tag{31.39}$$

$$1 + 3A_1 + 3A_2 + A_3 = (1 + 3D_1 + 3D_2 + D_3)\mathrm{e}^{-3\beta V_{1n}} \, , \tag{31.40}$$

and so on, for a total of c constraints (and nearest-neighbor interactions only). If longer-ranged interactions are included, this introduces further coefficients and half as many further constraints.

The fact that detailed balance provides only half the number of constraints to fix the unknown coefficients in the transition probabilities is not really surprising considering that, if it would fix them all, then the static (lattice–gas) Hamiltonian would dictate the kind of kinetics possible in the system. Again, this cannot be because this Hamiltonian does not include the energy-exchange dynamics between adsorbate and substrate. As a result, any functional relation between the A and D coefficients in (31.34) must be postulated ad hoc (or calculated from a microscopic Hamiltonian that accounts for coupling of the adsorbate to the lattice or electronic degrees of freedom of the substrate). Several scenarios have been discussed in the literature [31.57].

The simplest choice is to set all $A_i = 0$ in (31.34). Physically, this means that an adsorbing particle will not experience any interactions with its prospective neighbors and sticking is solely controlled by the availability of sites. Thus, the sticking coefficient becomes (for $A_i = 0$)

$$S(\theta, T) = S_0(T)(1-\theta) \, . \tag{31.41}$$

The sticking coefficient at zero coverage, $S_0(T)$, contains the dynamic information about the energy transfer from the adsorbing particle to the solid, which gives rise to its temperature dependence, for instance, an exponential Boltzmann factor for activated adsorption.

The desorption kinetics are thus specified by

$$D_\mathrm{r} = \left(\mathrm{e}^{\beta V_{1n}} - 1\right)^r \tag{31.42}$$

for $r = 1$–c. Because $(\mathrm{e}^\alpha - 1)n = \mathrm{e}^{n\alpha} - 1$ for $n = 0, 1$, we can rewrite (31.34) as

$$\begin{aligned} &W_{\text{ad-des}}(\boldsymbol{n}', \boldsymbol{n}) \\ &= w_0 \sum_l \left[(1-n_l) + D_0 n_l \exp\left(\beta V_{1n} \sum_j n_l n_j \right) \right] \\ &\quad \times \delta\left(n'_l, 1-n_l\right) \prod_{l' \neq l} \delta\left(n'_l, n_l\right) , \end{aligned} \tag{31.43}$$

implying that the local environment enters the desorption rate via a Boltzmann factor. This kind of kinetics has been termed Langmuir kinetics; it contains simple desorption kinetics and trivial adsorption due to site exclusion only. This interconnection between adsorption and desorption is dictated by the principle of detailed balance: if an adsorption system with nondissociative adsorption does not show the linear decrease of sticking as a function of coverage, then its desorption kinetics is most likely also not controlled by (31.51); if direct sticking and desorption are still maintained, then Langmuir kinetics must be abandoned. (Precursors, i.e., nondirect adsorption and desorption, can also alter the kinetics, and this will be discussed below.)

Insisting on the Langmuir kinetics is overly restrictive because in most systems sticking is not controlled by site exclusion only. Because the energy transfer in the adsorption process takes place within angstroms of the surface, the adsorbing particle actually experiences the interaction with particles already adsorbed on neighboring sites in more or less the same way as desorbing particles do, i.e., a lateral repulsion (attraction) will aid (hinder) desorption (desorption). Thus, making the effect of lateral interactions symmetric for adsorption and desorption, one would set $A_\mathrm{r} = -D_\mathrm{r}$; we have called this the interaction kinetics. More generally, one can assume a linear relationship (although this is only dictated by arguments of simplicity) and find

$$A_\mathrm{r} = \gamma_\mathrm{C} D_\mathrm{r} \tag{31.44}$$

$$D_\mathrm{r} = \frac{\mathrm{e}^{r\beta V_{1n}} - 1}{1 - \gamma_\mathrm{C}\mathrm{e}^{r\beta V_{1n}}} - \binom{r}{1} D_1 - \binom{r}{2} D_2 - \ldots - \binom{r}{r-1} D_{r-1} \,. \tag{31.45}$$

This completes the adsorption–desorption kinetics.

Turning next to diffusion we consider hopping from a site l to its neighbors $l+a$ and write

$$\begin{aligned} W_\mathrm{diff}(\boldsymbol{n}', \boldsymbol{n}) &= w_\mathrm{diff} \sum_{l,a} \Bigg[n_l (1 - n_{l+a}) \Bigg(1 + B_1 \sum_{l'} n_{l'} + B_2 \sum_{l'l''} n_{l'} n_{l''} + \ldots \Bigg) \\ &\quad \times \Bigg(1 + \widetilde{B}_1 \sum_{l'} n_{l'} + \widetilde{B}_2 \sum_{l'l''} n_{l'} n_{l''} + \ldots \Bigg) \Bigg] \\ &\quad \times \delta\left(n'_l, 1 - n_l\right) \delta\left(n'_{l+a}, 1 - n_{l+a}\right) \prod_{l' \neq l, i+a} \delta\left(n'_l, n_l\right) . \end{aligned} \tag{31.46}$$

The individual hopping rate (per unit time) is given by w_diff, which most likely contains a Boltzmann factor to account for an activation barrier to diffusion. The sums over l' and l'' run over the neighbors of l (with the exception of $l+a$) and $l+a$ (with the exception of l), respectively. The terms with the coefficients B_i account for the fact that hopping will be enhanced (hindered) if the particle in its initial state experiences a repulsive (attractive) interaction with some neighbors. Likewise, via the terms with $\widetilde{B}_i$, hopping will be reduced (enhanced), if the particle tries to jump into a site that is surrounded by occupied sites, with which the particle will interact repulsively (attractively). Detailed balance, again, imposes conditions on these coefficients similar to those in (31.53) and (31.54) for adsorption and desorption.

To study the time evolution of the adsorbate we define the coverage

$$\theta(t) = \langle \bullet \rangle = N_\mathrm{s}^{-1} \sum_i \sum_{\boldsymbol{n}} n_i P(\boldsymbol{n}, t) \tag{31.47}$$

and obtain its equation of motion by multiplying the master equation (31.43) with n_i and summing over all sites and states. This will introduce on its right-hand side n-site correlation functions that will be site independent, if it can be assured that the adsorbate remains homogeneous throughout its time evolution. For a square lattice, as an example, we find

$$\begin{aligned} \frac{\mathrm{d}\theta}{\mathrm{d}t} = S(\theta, T) \frac{P\lambda_\mathrm{th} a_\mathrm{s}}{h} - r_\mathrm{des} \Bigg[& \langle \bullet \rangle + 4 D_1 \langle \bullet\bullet \rangle \\ & + D_2 \left(4 \left\langle \begin{matrix} \bullet & \\ \bullet & \bullet \end{matrix} \right\rangle + 2 \langle \bullet \quad \bullet \quad \bullet \rangle \right) \\ & + 4 D_3 \left\langle \begin{matrix} & \bullet & \\ \bullet & \bullet & \bullet \end{matrix} \right\rangle + D_4 \left\langle \begin{matrix} \bullet & & \\ \bullet & \bullet & \\ \bullet & & \bullet \end{matrix} \right\rangle \Bigg] , \end{aligned} \tag{31.48}$$

where we introduced a symbolic notation

$$\begin{aligned} \langle \circ \rangle &= 1 - \langle \bullet \rangle \,, \\ \langle \circ\bullet \rangle &= N_\mathrm{s}^{-1} \sum_{\boldsymbol{n}} (1 - n_i) n_{i+a} P(\boldsymbol{n}, t) \,, \\ \left\langle \begin{matrix} \bullet & \\ \bullet & \bullet \end{matrix} \right\rangle &= N_\mathrm{s}^{-1} \sum_{\boldsymbol{n}} (1 - n_i) n_{i+a} n_{i+a'} P(\boldsymbol{n}, t) \,. \end{aligned} \tag{31.49}$$

The sticking coefficient in (31.57) is given explicitly by

$$\begin{aligned} S(\theta, T) = S_0(T) \Bigg[& \langle \circ \rangle + 4 A_1 \langle \circ\bullet \rangle \\ & + A_2 \left(4 \left\langle \begin{matrix} \bullet & \\ \circ & \bullet \end{matrix} \right\rangle + 2 \langle \bullet \quad \circ \quad \bullet \rangle \right) \end{aligned}$$

$$+4A_3\left\langle \begin{smallmatrix} \bullet & \bullet \\ \circ & \bullet \end{smallmatrix} \right\rangle + A_4\left\langle \begin{smallmatrix} \bullet & \bullet \\ \circ & \bullet \end{smallmatrix} \right\rangle \Bigg] . \quad (31.50)$$

In addition to the temperature dependence of $S_0(T)$, we have the correlation functions, which also determine its coverage dependence.

The correlators (31.59) are subject to similar equations of motion involving yet higher correlators, the whole hierarchy being equivalent to the original master equation. For instance, for the two-particle correlator, we have

$$\begin{aligned}
\frac{\mathrm{d}\langle\bullet\bullet\rangle}{\mathrm{d}t} = 2S_0(T)\frac{P\lambda_{\mathrm{th}}a_{\mathrm{s}}}{h}\Bigg[& (1+A_1)\langle\circ\bullet\rangle \\
& +(A_1+A_2)\left(\langle\bullet\circ\bullet\rangle + 2\left\langle \begin{smallmatrix} \bullet & \bullet \\ \circ & \bullet \end{smallmatrix} \right\rangle\right) \\
& +3(A_2+A_3)\left\langle \begin{smallmatrix} \bullet & \bullet \\ \circ & \bullet \end{smallmatrix} \right\rangle \\
& +(A_3+A_4)\left\langle \begin{smallmatrix} \bullet & \bullet \\ \bullet & \circ \end{smallmatrix} \right\rangle\Bigg] \\
-2r_{\mathrm{des}}\Bigg[& (1+D_1)\langle\bullet\bullet\rangle \\
& +(D_1+D_2)\left(\langle\bullet\bullet\bullet\rangle + 2\left\langle \begin{smallmatrix} \bullet & \bullet \\ \bullet & \bullet \end{smallmatrix} \right\rangle\right) \\
& +3(D_2+D_3)\left\langle \begin{smallmatrix} \bullet & \bullet \\ \bullet & \bullet \end{smallmatrix} \right\rangle \\
& +(D_3+D_4)\left\langle \begin{smallmatrix} \bullet & \bullet \\ \bullet & \bullet \end{smallmatrix} \right\rangle\Bigg] .
\end{aligned} \quad (31.51)$$

To describe an arbitrary nonequilibrium evolution of the adsorbate we need the whole hierarchy or at least a suitably truncated subset. We can close the hierarchy at the level of two-site correlators by a factorization of higher correlators with one site overlap [31.58, 59]

$$\left\langle \begin{smallmatrix} \bullet & \bullet & \bullet \end{smallmatrix} \right\rangle = \left\langle \begin{smallmatrix} \bullet & \bullet \\ \bullet & \bullet \end{smallmatrix} \right\rangle = \frac{\langle\bullet\bullet\rangle^2}{\langle\bullet\rangle} , \quad (31.52)$$

$$\left\langle \begin{smallmatrix} \bullet & \bullet \\ \bullet & \bullet \end{smallmatrix} \right\rangle = \frac{\langle\bullet\bullet\rangle^3}{\langle\bullet\rangle^2} , \quad (31.53)$$

$$\left\langle \begin{smallmatrix} \bullet & \bullet \\ \bullet & \circ \end{smallmatrix} \right\rangle = \frac{\langle\bullet\circ\rangle^3}{\langle\circ\rangle^2} . \quad (31.54)$$

This is the simplest closure and corresponds, for the equilibrium solution, to the quasichemical approximation (31.16). If higher accuracy is required, one must keep larger correlators and factor with larger overlap. As an example with two-site overlap, one writes

$$\left\langle \begin{smallmatrix} \bullet & \bullet \\ \bullet & \bullet \end{smallmatrix} \right\rangle = \left\langle \begin{smallmatrix} \bullet & \bullet \end{smallmatrix} \right\rangle^2 \frac{1}{\langle\bullet\bullet\rangle} , \quad (31.55)$$

which results in three coupled nonlinear equations of motion for $\langle\bullet\rangle$, $\langle\bullet\bullet\rangle$, and $\left\langle \begin{smallmatrix} \bullet & \bullet \\ \bullet & \bullet \end{smallmatrix} \right\rangle$.

In one dimension the truncation of the equations of motion has been worked out in detail [31.59]. This has allowed an accurate examination of the role of diffusion in desorption and implications for the Arrhenius analysis in nonequilibrium situations. The largest deviations from the desorption kinetics of a mobile adsorbate obviously occur for an immobile adsorbate where surface diffusion is negligible throughout the temperature range of desorption.

Next, we explore the implications of assuming that surface diffusion is much faster than desorption, so that, during desorption, the structure of the adsorbate rearranges itself appropriately for equilibrium at the instantaneous coverage and temperature. As a result, all correlators also assume their equilibrium values and are, thus, only functions of (instantaneous) coverage and temperature. In such a system the adsorbate is thus in local or quasi-equilibrium on the surface, although during desorption there is no overall equilibrium with the three-dimensional gas phase above the adsorbate. Because for a system in quasi-equilibrium the correlators are known (equilibrium) functions of coverage and temperature, we need only one macroscopic equation to describe the time evolution. This equation has a remarkable structure. First, we note that the equilibrium solution, $\mathrm{d}\theta/\mathrm{d}t = 0$, in (31.57) gives for the chemical potential

$$\mathrm{e}^{\beta\mu} = \frac{\overline{P}}{k_{\mathrm{B}}TZ_{\mathrm{int}}}\lambda_{\mathrm{th}}^3 = \frac{\mathrm{e}^{-\beta V_0}}{q_3 q_{\mathrm{int}}}\frac{\langle\bullet\rangle + 4D_1\langle\bullet\bullet\rangle_0 + \ldots}{\langle\circ\rangle + 4A_1\langle\circ\bullet\rangle_0 + \ldots} , \quad (31.56)$$

where all correlators attain their equilibrium values, indicated by the subscript zero, and should be calculated from the (canonical or grand canonical) partition function, or equivalently from the right-hand sides of their (coupled) equations of motion.

With the help of (31.65) we can now rewrite the equation of motion for the coverage (31.57) for a system maintained in quasi-equilibrium by fast surface diffusion as

$$\frac{\mathrm{d}\theta}{\mathrm{d}t} = S(\theta,T)\frac{a_{\mathrm{s}}\lambda_{\mathrm{th}}}{h}P - S(\theta,T)\frac{a_{\mathrm{s}}}{\lambda_{\mathrm{th}}^2}\frac{k_{\mathrm{B}}TZ_{\mathrm{int}}}{h}\mathrm{e}^{\beta\mu(\theta,T)} , \quad (31.57)$$

where the sticking coefficient is given, as a function of coverage and temperature by (31.59). This is precisely the phenomenological rate equation presented in (31.1) with, however, the sticking coefficient specified explicitly, and is valid for any system. To reiterate: the desorption rate in (31.66) now consists of two factors: (i), the equilibrium fugacity of the adsorbate, $e^{\beta\mu}$, controlling the adsorbate energetics and structure, and (ii), the sticking coefficient controlling the gas-substrate energy transfer in adsorption and desorption. Such factorizations, or similar ones, must always be possible for processes that proceed through a sequence of local equilibrium states because they are completely described by equations of motion for the relevant thermodynamic variables, and the factorization ensures that the equilibrium state is independent of the kinetics. An application of this approach has been presented for oxygen adsorption and desorption from silver [31.40].

31.4.2 Adsorption and Desorption via Precursors

To further demonstrate the power of the kinetic lattice–gas approach we briefly review the work on precursor-mediated adsorption and desorption [31.60, 61]. We consider an adsorbate in which, in addition to the most strongly-bound chemisorbed (or physisorbed) adsorbed state, the adparticles can also be found in intrinsic or extrinsic precursor states. One introduces three sets of occupation numbers, $n_i = 0$ or 1, $m_i = 0$ or 1, and $l_i = 0$ or 1, depending on whether the final adsorbed (chemisorbed) state, the intrinsic precursor state (above an empty adsorbed state) or the extrinsic precursor state (above an occupied adsorbed state) are empty or occupied. The static properties of this lattice gas are controlled by a Hamiltonian

$$\begin{aligned} H = {} & E_{\mathrm{s}}^{(\mathrm{c})} \sum_i n_i + E_{\mathrm{s}}^{(\mathrm{i})} \sum_i m_i + E_{\mathrm{s}}^{(\mathrm{e})} \sum_i l_i \\ & + V_{1n}^{(\mathrm{c})} \sum_{i,a} n_i n_{i+a} + V_{1n}^{(\mathrm{i})} \sum_{i,a} m_i n_{i+a} \\ & + V_{1n}^{(\mathrm{e})} \sum_{i,a} n_i l_i n_{i+a} + \ldots \end{aligned} \tag{31.58}$$

The single-particle free energies are given by

$$E_{\mathrm{s}}^{(\mathrm{r})} = -V_R - k_{\mathrm{B}} T \ln\left(q_3^{(\mathrm{r})} q_{\mathrm{int}}^{(\mathrm{r})}\right), \tag{31.59}$$

(r = c, i, e) in terms of their respective binding energies and partition functions. Furthermore, $V_{1n}^{(\mathrm{c})}$ is the lateral interaction between two particles in the adsorbed state in nearest-neighbor sites, and $V_{1n}^{(\mathrm{i})}$ and $V_{1n}^{(\mathrm{e})}$ are the interactions between a particle in the intrinsic or extrinsic precursor state in cell i and a particle in the adsorbed state in a neighboring site. Longer-ranged interactions can easily be added as done elsewhere [31.61]. To describe the time evolution of the adsorbate we use a kinetic lattice–gas model recently developed to study the effect of lateral interactions on sticking. For the coverages of the three states, we obtain the kinetic equations

$$\begin{aligned} \frac{\mathrm{d}\langle n\rangle}{\mathrm{d}t} = {} & S_{\mathrm{C}}^0(T)(1-\langle n\rangle)\widetilde{S}_{\mathrm{C}} \frac{a_{\mathrm{s}}\lambda_{\mathrm{th}}}{h} P - r_{\mathrm{C}}\widetilde{f}_{\mathrm{C}}\langle n\rangle \\ & + w_{\mathrm{CI}}\left[\widetilde{f}_{\mathrm{CI}}\langle m\rangle - \left(\frac{a_{\mathrm{C}}}{a_{\mathrm{I}}}\right)\widetilde{f}_{\mathrm{IC}}\langle n\rangle\right] \\ & + z w_{\mathrm{CE}}\left[\widetilde{f}'_{\mathrm{CE}}(1-\langle n\rangle)\langle l\rangle - \left(\frac{a_{\mathrm{C}}}{a_{\mathrm{E}}}\right)\widetilde{f}'_{\mathrm{CE}}\langle n\rangle^2\right], \end{aligned} \tag{31.60}$$

$$\begin{aligned} \frac{\mathrm{d}\langle m\rangle}{\mathrm{d}t} = {} & S_{\mathrm{I}}^0(T)\widetilde{S}_{\mathrm{I}}(1-\langle n\rangle)\frac{a_{\mathrm{s}}\lambda_{\mathrm{th}}}{h} P - r_{\mathrm{I}}\widetilde{f}_{\mathrm{I}}\langle m\rangle \\ & - w_{\mathrm{CI}}\left[\widetilde{f}_{\mathrm{CI}}\langle m\rangle - \left(\frac{a_{\mathrm{C}}}{a_{\mathrm{I}}}\right)\widetilde{f}_{\mathrm{IC}}\langle n\rangle\right] + w_{\mathrm{II}} + w_{\mathrm{IE}}, \end{aligned} \tag{31.61}$$

$$\begin{aligned} \frac{\mathrm{d}\langle l\rangle}{\mathrm{d}t} = {} & S_{\mathrm{E}}^0(T)\theta\widetilde{S}_{\mathrm{E}}\frac{a_{\mathrm{s}}\lambda_{\mathrm{th}}}{h} P - r_{\mathrm{E}}\widetilde{f}_{\mathrm{E}}\langle l\rangle + w_{\mathrm{EE}} - w_{\mathrm{IE}} \\ & - z w_{\mathrm{CE}}\left[\widetilde{f}'_{\mathrm{CE}}(1-\langle n\rangle)\langle l\rangle - \left(\frac{a_{\mathrm{C}}}{a_{\mathrm{E}}}\right)\widetilde{f}'^2_{\mathrm{EC}}\langle n\rangle^2\right]. \end{aligned} \tag{31.62}$$

The constants r_{C} and w_{IC} etc. are specified in terms of microscopic parameters and the functions $\widetilde{f}_{\mathrm{C}}$, $\widetilde{f}_{\mathrm{I}}$, $\widetilde{f}_{\mathrm{IC}}$, etc., account for the various lateral interactions between the particles in the adsorbed and precursor states. We have factored out an explicit dependence on the coverages so that in the absence of any lateral interactions, these functions are all equal to 1.

To obtain the equilibrium conditions for the adsorbate we use (31.2) with $P = \overline{P}$ and obtain for the chemical potential of the adsorbate as a function of coverage and temperature

$$e^{\mu_{\mathrm{C}}/(k_{\mathrm{B}}T)} = \frac{h\lambda_{\mathrm{th}}^2}{k_{\mathrm{B}}TZ_{\mathrm{int}}a_{\mathrm{s}}} \frac{a_{\mathrm{C}}\widetilde{f}_{\mathrm{C}}}{\widetilde{S}_{\mathrm{C}}} \frac{\langle n\rangle}{1-\theta}, \tag{31.63}$$

$$e^{\mu_{\mathrm{I}}/(k_{\mathrm{B}}T)} = \frac{h\lambda_{\mathrm{th}}^2}{k_{\mathrm{B}}TZ_{\mathrm{int}}a_{\mathrm{s}}} \frac{r_{\mathrm{I}}\widetilde{f}_{\mathrm{I}}}{S_{\mathrm{I}}^0(T)(1-\theta)\widetilde{S}_{\mathrm{I}}}\langle m\rangle, \tag{31.64}$$

$$e^{\mu_{\mathrm{E}}/(k_{\mathrm{B}}T)} = \frac{h\lambda_{\mathrm{th}}^2}{k_{\mathrm{B}}TZ_{\mathrm{int}}a_{\mathrm{s}}} \frac{r_{\mathrm{E}}\widetilde{f}_{\mathrm{E}}}{S_{\mathrm{E}}^0(T)\theta\widetilde{S}_{\mathrm{E}}}\langle l\rangle, \tag{31.65}$$

$$\widetilde{f}_{\mathrm{CI}}\langle m\rangle = \left(\frac{a_{\mathrm{C}}}{a_{\mathrm{I}}}\right)\widetilde{f}_{\mathrm{IC}}\langle n\rangle, \tag{31.66}$$

$$\widetilde{f}_{\mathrm{CE}}\langle l\rangle = \left(\frac{a_{\mathrm{C}}}{a_{\mathrm{E}}}\right)\widetilde{f}_{\mathrm{EC}}\langle n\rangle \,, \tag{31.67}$$

where $\mu_{\mathrm{C}} = \mu_{\mathrm{I}} = \mu_{\mathrm{E}}$.

To obtain the equilibrium sticking coefficient we assume that at an ambient pressure P_0, the adsorbate is in equilibrium at a temperature T with partial coverages n_0, m_0, and l_0. We then increase the pressure slightly to $P = P_0 + \Delta P$ and linearize the rate equations in the increase in the precursor coverages $\Delta m = \langle m\rangle - m_0$ and $\Delta l = \langle l\rangle - l_0$. If adsorption into and desorption from the precursors is much faster than transitions from the precursors into the adsorbed state, we can ignore terms proportional to $\Delta n = \langle n\rangle - \theta$ on the right-hand side of (31.69)–(31.71) and also assume that the precursors will be in a steady state. It has been shown that the sticking coefficient is then given by [31.61]

$$\begin{aligned} &S(\theta,T) \\ &= S_{\mathrm{C}}(\theta,T) + S_{\mathrm{I}}(\theta,T)\frac{w_{\mathrm{CI}}\widetilde{f}_{\mathrm{CI}}X_1 + z w_{\mathrm{CE}}\widetilde{f'}_{\mathrm{CE}}Y_1(1-\theta)}{X_1X_2 - Y_1Y_2} \\ &\quad + S_{\mathrm{E}}(\theta,T)\frac{w_{\mathrm{CI}}\widetilde{f}_{\mathrm{CI}}Y_2 + z w_{\mathrm{CE}}\widetilde{f'}_{\mathrm{CE}}X_2(1-\theta)}{X_1X_2 - Y_1Y_2} \,. \end{aligned} \tag{31.68}$$

If we suppress the exchange of particles between the intrinsic and extrinsic precursors, $w_{\mathrm{IE}} = 0$, we obtain

$$\begin{aligned} S(\theta,T) &= S_{\mathrm{C}}(\theta,T) + S_{\mathrm{I}}(\theta,T)\frac{w_{\mathrm{CI}}\widetilde{f}_{\mathrm{CI}}}{r_{\mathrm{I}}\widetilde{f}_{\mathrm{I}} + w_{\mathrm{CI}}\widetilde{f}_{\mathrm{CI}}} \\ &\quad + S_{\mathrm{E}}(\theta,T)\frac{z w_{\mathrm{CE}}\widetilde{f'}_{\mathrm{CE}}(1-\theta)}{r_{\mathrm{E}}\widetilde{f}_{\mathrm{E}} + z w_{\mathrm{CE}}\widetilde{f'}_{\mathrm{CE}}(1-\theta)} \,, \end{aligned} \tag{31.69}$$

$$= S_{\mathrm{C}}(\theta,T) + S_{\mathrm{intr}}(\theta,T) + S_{\mathrm{extr}}(\theta,T) \,. \tag{31.70}$$

Only under this condition are the three adsorption channels independent of each other. This is the standard scenario always used in interpreting data. However, this is only one scenario because if, on the other hand, the exchange between the two precursors is the fastest process on the surface, we obtain

$$\begin{aligned} S(\theta,T) &= S_{\mathrm{C}}(\theta,T) + [S_{\mathrm{I}}(\theta,T) + S_{\mathrm{E}}(\theta,T)] \\ &\quad \times \frac{\left(w_{\mathrm{CI}}\widetilde{f}_{\mathrm{CI}}a_{\mathrm{E}} + z w_{\mathrm{CE}}\widetilde{f'}_{\mathrm{CE}}a_{\mathrm{I}}\theta\right)(1-\theta)}{\left\{\left(r_{\mathrm{I}}\widetilde{f}_{\mathrm{I}} + w_{\mathrm{CI}}\widetilde{f}_{\mathrm{CI}}\right)a_{\mathrm{I}}\theta + a_{\mathrm{E}}(1-\theta)\right\} \\ &\quad \times \left[r_{\mathrm{E}}\widetilde{f}_{\mathrm{E}} + z w_{\mathrm{CE}}\widetilde{f'}_{\mathrm{CE}}(1-\theta)\right]\Big\}} \,, \end{aligned} \tag{31.71}$$

and the two precursor channels of adsorption are maximally coupled, and straightforward interpretation is at a loss. One can study the desorption kinetics in the presence of precursors along similar lines.

31.5 Concluding Remarks

In this review article, we have tried to show that an analytical approach to the thermodynamics and the kinetics of adsorbates is not restricted to simple systems but can deal with rather complicated situations in a systematic approach such as multisite and multicomponent systems with or without precursor-mediated adsorption and surface reconstruction, including multilayers/subsurface species. This approach automatically ensures that such fundamental principles as detailed balance are implemented properly.

For the equilibrium properties and for the kinetics under quasi-equilibrium conditions for the adsorbate, the transfer-matrix technique is a convenient and accurate method to obtain not only the chemical potentials, as a function of coverage and temperature, but all other thermodynamic information, e.g., multiparticle correlators. We emphasize the economy of the computational effort required for the application of the technique. In particular, because it is based on an analytic method it does not suffer from the limitations of time and accuracy inherent in statistical methods such as Monte Carlo simulations. The task of variation of Hamiltonian parameters in the process of fitting a set of experimental data (thermodynamic and kinetic) is both fast and systematic. To date, the most accurate modeling of desorption and thermodynamic data has been obtained by this method.

For adsorbates out of local equilibrium, an analytic approach to the kinetic lattice–gas model is a powerful theoretical tool by which, in addition to numerical results, explicit formulae can be obtained to elucidate the underlying physics. This allows one to extract simplified pictures of and approximations to complicated processes, as shown above with precursor-mediated adsorption as an example. This task of theory is increasingly overlooked with the trend to use cheaper computer power for numerical simulations. Unfortunately, many of the simulations of adsorbate kinetics are based on unnecessarily oversimplified assumptions (for example, constant sticking coefficients, constant pref-

actors etc.), which rarely are spelled out because the physics has been introduced in terms of a set of computational instructions rather than formulating the theory rigorously, e.g., based on a master equation.

Ultimately, the coverage and temperature dependence of the kinetic and equilibrium properties of an adsorbate are the result of interactions of the adsorbed species with the substrate and with each other. In the ideal scenario, one would start the theoretical development with quantum-mechanical calculations of the potential energy surfaces for the coupled adsorbate-substrate system. If the system can be approximately described by a lattice–gas model, one then has all the necessary information to specify the interaction parameters in the corresponding lattice–gas Hamiltonian. All equilibrium and kinetic properties then follow from a good theory. This scenario has been initiated for oxygen on Ru(001) using density functional theory for the energy calculations [31.53]. This approach—density functional calculations, lattice–gas modeling, and kinetic theory—provides the necessary link between the fundamental interactions of the adsorbate and the macroscopic theories of equilibrium and kinetics. It is parameter free and, thus, should lead to a deeper understanding of surface physics and chemistry. The application of density-functional theory in a multidimensional approach to catalysis has been discussed in a recent review [31.62].

References

31.1 H.J. Kreuzer: *Nonequilibrium Thermodynamics and Its Statistical Foundations* (Oxford Univ. Press, Oxford 1981)

31.2 H.J. Kreuzer, Z.W. Gortel: *Physisorption Kinetics* (Springer, Berlin 1986)

31.3 H.J. Kreuzer, S.H. Payne: Equilibria and dynamics of gas adsorption on heterogeneous solid surfaces. In: *Studies in Surfaces Science and Catalysis*, ed. by W. Rudszinski, W.A. Steele, G. Zgrablich (Elsevier, Amsterdam 1997) p. 153

31.4 H.J. Kreuzer, S.H. Payne: Nonequilibrium thermodynamics of a two-phase adsorbate, Surf. Sci. **198**, 235–262 (1988)

31.5 H.J. Kreuzer, S.H. Payne: Desorption from a two-phase adsorbate: zero or fractional order, Surf. Sci. **200**, L433–L440 (1988)

31.6 S.H. Payne, H.J. Kreuzer: Nonequilibrium thermodynamics of a two-phase adsorbate: lattice gas and van der Waals models, Surf. Sci. **205**, 153–176 (1988)

31.7 H.J. Kreuzer, S.H. Payne, A. Drozdowski, D. Menzel: Theory of dissociative and nondissociate adsorption and desorption, J. Chem. Phys. **110**, 6982–6999 (1999)

31.8 J.M. Honig: Adsorption theory from the viewpoint of orderdisorder theory. In: *The Solid–Gas Interface*, ed. by E.A. Flood (Marcel Dekker, New York 1967) pp. 371–412

31.9 D.M. Burley: Closed form approximations for lattice systems. In: *Phase Transitions and Critical Phenomena*, Vol. 2, ed. by C. Domb, M.S. Green (Academic Press, New York 1972) pp. 329–374

31.10 C. Domb: On the theory of cooperative phenomena in crystals, Adv. Phys. **9**, 245–361 (1960)

31.11 L.K. Runnels, L.L. Combs: Exact finite method of lattice statistics. I. Square and triangular lattice gases of hard molecules, J. Chem. Phys. **45**, 2482–2492 (1966)

31.12 F.H. Ree, D.A. Chesnut: Phase transition of a hard-core lattice gas. The square lattice with nearest-neighbor exclusion, J. Chem. Phys. **45**, 3983–4003 (1966)

31.13 L.K. Runnels: Lattice gas theories of melting. In: *Phase Transitions and Critical Phenomena*, Vol. 2, ed. by C. Domb, M.S. Green (Academic Press, New York 1972) pp. 305–328

31.14 W. Kinzel, M. Schick: Extent of exponent variation in a hard-square lattice gas with second-neighbor repulsion, Phys. Rev. B **24**, 324–328 (1981)

31.15 W. Kinzel, W. Selke, K. Binder: Phase transitions on centred rectangular lattice gases: a model for the adsorption of H on Fe(110), Surf. Sci. **121**, 13–31 (1982)

31.16 P.A. Rikvold, W. Kinzel, J.D. Gunton, K. Kaski: Finite-size-scaling study of a two-dimensional lattice-gas model with a tricritical point, Phys. Rev. B **28**, 2686–2892 (1983)

31.17 P.A. Rikvold, K. Kaski, J.D. Gunton, M.C. Yalabik: Finite-size scaling study of a lattice-gas model for oxygen chemisorbed on tungsten, Phys. Rev. B **29**, 6285–6294 (1984)

31.18 N.C. Bartelt, T.L. Einstein: Triangular lattice gas with first-and second-neighbor exclusions: continuous transition in the four-state Potts universality class, Phys. Rev. B **30**, 5339–5341 (1984)

31.19 N.C. Bartelt, T.L. Einstein, L.D. Roelofs: Transfer-matrix approach to estimating coverage discontinuities and multicritical-point positions in two-dimensional lattice-gas phase diagrams, Phys. Rev. B **34**, 1616–1623 (1986)

31.20 W. Kinzel, M. Schick: Phenomenological scaling approach to the triangular Ising antiferromagnet, Phys. Rev. B **23**, 3435–3441 (1981)

31.21 N.H. Fuchs, S. Gartenhaus: Sparse-matrix analysis of spin-(1/2) Ising systems, Phys. Rev. B **31**, 7261–7273 (1985)

31.22 N.H. Fuchs: Transfer-matrix analysis for Ising models, Phys. Rev. B **41**, 2173–3183 (1990)

31.23 A.V. Myshlyavtsev, V.P. Zhdanov: The effect of nearest-neighbour and next-nearest-neighbour lateral interactions on thermal desorption spectra, Chem. Phys. Lett. **162**, 43–46 (1989)

31.24 A.V. Myshlyavtsev, J.L. Sales, G. Zgrablich, V.P. Zhdanov: The effect of three-body interactions on thermal desorption spectra, J. Stat. Phys. **58**, 1029–1039 (1990)

31.25 S.H. Payne, H.J. Kreuzer, L.D. Roloefs: Isosteric heat of adsorption for repulsive interactions, Surf. Sci. Lett. **259**, 781–786 (1991)

31.26 S.H. Payne, Z. Jun, H.J. Kreuzer: Lattice gas with multiple interactions: isosteric heat and thermal desorption, Surf. Sci. **264**, 185–196 (1992)

31.27 C.J. Thompson: *Mathematical Statistical Mechanics* (Princeton Univ. Press, Princeton 1979)

31.28 H.J. Kreuzer, S.H. Payne: Theoretical approaches to the kinetics of adsorption, desorption and reactions at surfaces. In: *Computational Methods in Surface and Colloid Science*, ed. by M. Borowko (Marcel Dekker, New York 2000) pp. 439–479

31.29 H.J. Kreuzer, S.H. Payne: ASTEK program package for the Analysis and Simulation of Thermal Equilibrium and Kinetics of gases adsorbed on solid surfaces

31.30 S.H. Payne, H.J. Kreuzer, W. Frie, L. Hammer, K. Heinz: Adsorption and desorption of hydrogen on Rh(311) and comparison with other Rh surfaces, Surf. Sci. **421**, 279–295 (1999)

31.31 H.J. Kreuzer, S.H. Payne, P. Jakob, D. Menzel: Coupled desorption and site conversion of co-adsorbates: a lattice gas analysis of thermal desorption and spectroscopic data of (NO+O)/Ru(001), Surf. Sci. **424**, 36–54 (1999)

31.32 C.T. Rettner, M.N.R. Ashfold (Eds.): *Dynamics of Gas-Surface Collisions* (Royal Society of Chemistry, Cambridge 1991)

31.33 S.H. Payne, J.S. McEwen, H.J. Kreuzer, D. Menzel: Lateral interactions and nonequilibrium in adsorption and desorption. 2. A lattice gas model for $(2\times2)-(30-NO)$/Ru(001), Surf. Sci. **600**, 4560–4569 (2006)

31.34 S.H. Payne, H.J. Kreuzer, K.A. Peterlinz, T.J. Curtiss, C. Uebing, S.J. Sibener: Coverage dependent desorption kinetics of CO from Rh(111): a theoretical analysis, Surf. Sci. **272**, 102–110 (1992)

31.35 H.J. Kreuzer, Z. Jun, S.H. Payne, W. Nichtl-Pecher, L. Hammer, K. Müller: Thermal desorption kinetics of hydrogen on rhodium(110), Surf. Sci. **303**, 1–15 (1994)

31.36 D.C. Skelton, D.H. Wei, S.D. Kevan: Non-monotonic lateral interactions in CO/Pt(111), Surf. Sci. **320**, 77–84 (1994)

31.37 D.H. Wei, D.C. Skelton, S.D. Kevan: Trends in lateral interactions between CO chemisorbed on low index copper surfaces, Surf. Sci. **326**, 167–176 (1995)

31.38 D.H. Wei, D.C. Skelton, S.D. Kevan: Desorption and molecular interactions on surfaces: C) Rh(110), CORh(100) and CORh(111), Surf. Sci. **381**, 49–64 (1997)

31.39 H.J. Kreuzer, S.H. Payne, M. Grunze, C. Wöll: Adsorption and desorption of N_2 on Ni(110): entropy versus energy, Z. Phys. Chem. **202**, 273–296 (1997)

31.40 F. Buatier de Mongeot, M. Rocca, A. Cupolillo, U. Valbusa, H.J. Kreuzer, S.H. Payne: Sticking and thermal desorption of O_2 on Ag(001), J. Chem. Phys. **106**, 711–718 (1997)

31.41 S.H. Payne, H.J. Kreuzer: Multilayer adsorption and desorption, Surf. Sci. **338**, 261–278 (1995)

31.42 S.H. Payne, H.J. Kreuzer, A. Pavlovska, E. Bauer: Multilayer adsorption and desorption: Au and Cu on Mo (110), Surf. Sci. **345**, L1–L10 (1996)

31.43 W. Widdra, P. Trischberger, W. Friess, D. Menzel, S.H. Payne, H.J. Kreuzer: Rare-gas thermal desorption from flat and stepped platinum surfaces: lateral interactions and the influence of dimensionality, Phys. Rev. B **57**, 4111–4126 (1998)

31.44 S.H. Payne, H.J. Kreuzer: Adsorption and thermal desorption on stepped surfaces, Surf. Sci. **399**, 135–159 (1998)

31.45 P.A. Rikvold, J.B. Collins, G.D. Hansen, J.D. Gunton: Three-state lattice gas on a triangular lattice as a model for multicomponent adsorption, Surf. Sci. **203**, 500–524 (1988)

31.46 J.B. Collins, P. Sacramento, P.A. Rikvold, J.D. Gunton: Lateral interactions in catalyst poisoning, Surf. Sci. **221**, 277–298 (1989)

31.47 P.A. Rikvold, M.R. Deakin: Lateral interactions and enhanced adsorption, Surf. Sci. **249**, 180–193 (1991)

31.48 D.C. Skelton, D.H. Wei, S.D. Kevan: Molecular interactions and cooperativity in coadsorption: CO + NoPt(111), Surf. Sci. Lett. **355**, 319–324 (1996)

31.49 S.H. Payne, J.S. McEwen, H.J. Kreuzer, D. Menzel: Adsorption and desorption of CO on Ru(0001): a comprehensive analysis, Surf. Sci. **594**, 240–262 (2005)

31.50 T. Niedermayer, H. Schlichting, D. Menzel, S.H. Payne, H.J. Kreuzer: Thermal and non-thermal kinetics of helium monolayers on Pt(111), Phys. Rev. B **71**, 045427 (2005)

31.51 J.S. McEwen, S.H. Payne, H.J. Kreuzer, M. Kinne, R. Denecke, H.-P. Steinrück: Adsorption and desorption of CO on Pt(111): a comprehensive analysis, Surf. Sci. **545**, 47–69 (2003)

31.52 S.H. Payne, G. Ledue, J.C. Michael, H.J. Kreuzer, R. Wagner, K. Christmann: Analysis and theory of multilayer desorption: Ag on Re, Surf. Sci. **512**, 151–164 (2002)

31.53 C. Stampfl, M. Scheffler, H. Pfnür, H.J. Kreuzer, S.H. Payne: First principles theory of surface thermodynamics and kinetics, Phys. Rev. Lett. **83**, 2993–2996 (1999)

31.54 H.J. Kreuzer, S.H. Payne, A. Drozdowski, D. Menzel: Theory of dissociative and nondissociate adsorption and desorption, J. Chem. Phys. **110**, 6982–6999 (1999)

31.55 T. Niedermayer, H. Schlichting, D. Menzel, S.H. Payne, H.J. Kreuzer: Photo- and thermodesorption of helium on Pt(111), Phys. Rev. Lett. **89**, 126101–126104 (2002)

31.56 K. Kawasaki: Kinetics of Ising models. In: *Phase Transitions and Critical Phenomena*, Vol. 2, ed. by C. Domb, M.S. Green (Academic Press, New York 1972) pp. 443–501

31.57 H.J. Kreuzer, Z. Jun: Kinetic lattice gas model: Langmuir, Ising and interaction kinetics, Appl. Phys. A **51**, 183–195 (1990)

31.58 A. Wierzbicki, H.J. Kreuzer: Kinetic lattice gas model: a systematic closure approximation, Surf. Sci. **257**, 417–426 (1991)
31.59 S.H. Payne, A. Wierzbicki, H.J. Kreuzer: Kinetic lattice gas model in one dimension: I. Canonical approach, Surf. Sci. **291**, 242–260 (1993)
31.60 H.J. Kreuzer: Kinetic lattice gas model with precursors, Surf. Sci. **238**, 305–316 (1990)
31.61 H.J. Kreuzer: Theory of sticking: the effect of lateral interactions, J. Chem. Phys. **104**, 9593–9612 (1996)
31.62 K. Reuter: Ab initio thermodynamics and first-principles microkinetics for surface catalysis, Catal. Lett. **146**, 541–563 (2016)

Hans Jürgen Kreuzer

Department of Physics and Atmospheric Science
Dalhousie University
Halifax, Canada
h.j.kreuzer@dal.ca

Hans Jürgen Kreuzer, born 1942 in Germany, Canadian Citizen. MSc 1966 (Bonn), Dr. rer. nat. 1967 (Bonn), Professor of Physics U. Of Alberta 1971-82, Killam Research Professor and A.C. Fales Professor of Theoretical Physics, Dalhousie University since 1982. Publications: 330 research articles, 8 books, 270 invited talks, 5 patents. Worked and published in elementary particle theory, condensed matter, nonequilibrium statistical mechanics, solid state physics, surface science, polymer science, biophysics, holography, physics and chemistry in high electric fields. Honors and Awards: Lady Davies Professor, Technion, Haifa, Israel (1977), Guest Fellow of the Royal Society, London (1987), Fellow of the Max-Planck Society, Germany (1988), Heinrich-Welcker Guest Professor, University of Erlangen-Nürnberg, Germany (1992), Fellow of the Royal Society of Canada (1993), Humboldt Research Prize (1995, 2008), Honorary Professor, Wuhan Institute of Technology (2010), Visiting Professor, Sun Yat-sen University. Founder and owner of 4-Deep Inwater Imaging, a company that manufactures digital holographic and fluorescence microscopes based on his patents, see www.4-deep.com.

32. State Resolved Sticking Probability in Gas–Surface Interaction

Luca Vattuone, Michio Okada

This chapter provides selected examples of experimental investigations addressing the role of rotational and vibrational energy in adsorption at surfaces. Such information can generally be obtained in different ways characterized by different degrees of state selectivity. The first part of the chapter deals with the effect of rotational energy, while the second considers the effect of vibrational energy. The former investigations compared the behavior of rotationally hot and cold molecular beams by measuring the sticking probability on well-defined surfaces under controlled, ultrahigh-vacuum conditions. When detection of the rotational state of gas-phase molecules became feasible, a large amount of information was obtained indirectly: researchers first determined experimentally the rotational state of desorbing (or scattered) molecules and then used microreversibility (otherwise called detailed balance) arguments to extract information on the effect of the rotational states on the sticking probability. In recent years, methods to prepare molecules in partially and, in some cases, even fully defined rotational quantum states were developed. The central part of the section highlights recent results obtained using electrostatic and finally magnetic hexapoles. The first section of the chapter ends by reviewing results obtained by exploiting the velocity dependence of the degree of alignment of molecules seeded with inert carriers in a supersonic molecular beam. A brief selection of results obtained with laser methods concludes this section. Laser methods are on the contrary indispensable for the preparation of vibrationally excited molecules, which is the topic of the second section of the chapter. The relative roles of kinetic and vibrational energy are discussed, and the concepts of entrance and late barrier in the potential energy surface are introduced. Pioneering experiments showing greater specificity in surface reactions are briefly reviewed.

The reactivity of a surface towards a gas species can be measured by the adsorption (or sticking) probability S, defined as

$$S = \frac{\mathrm{d}\Theta}{\mathrm{d}\chi} = \frac{\mathrm{d}\Theta}{\Phi \mathrm{d}t}\,, \tag{32.1}$$

where Θ is the coverage, χ is the exposure, and Φ is the flux; $\Theta(\chi)$ is defined as the ratio between the number of molecules adsorbed (impinging) on unit area n_s and the surface density of atoms on the substrate n_0. These are substrate-dependent dimensionless quantities usually expressed in monolayers (ML). Alternatively, the exposure can be expressed in another, substrate-independent quantity, the Langmuir (L). One Langmuir corresponds to an exposure of 10^{-6} Torr lasting for 1 s; For example, exposing a surface to a gas pressure of 10^{-7} Torr for 10 s corresponds to 1 L. The Langmuir is more often used in backfilling experiments, i.e., when the uptake of the gas is performed by exposing the surface to a predefined pressure p for a certain time. To convert from L to ML and back, it is necessary to use

M. Rocca, T.S. Rahman, L. Vattuone (Eds.), *Springer Handbook of Surface Science*, Springer Handbooks,
https://doi.org/10.1007/978-3-030-46906-1_32

elementary kinetic theory. For an ideal gas, the number of molecules crossing a unit area in unit time is given by

$$\frac{dN}{dAdt} = \frac{N}{4V}\langle v\rangle = p\sqrt{\frac{1}{2\pi kTm}}\,, \tag{32.2}$$

where m is the mass of the gas, k is Boltzmann's constant, and T is the temperature of the gas. The sticking probability S of a gas species at a surface is a function of several variables which describe the status of the molecule (kinetic energy (E) and vibrational (ν), rotational (J), and electronic quantum state), of the surface (temperature (T), coverage (Θ) of different adsorbates, density of defects, etc.), and of the direction of impingement of the molecule (polar (θ) and azimuthal (ϕ) angles of incidence).

$$S = S(E, \nu, J, \ldots; T, \Theta, \ldots; \theta, \phi)\,. \tag{32.3}$$

In general, S can be estimated by considering the change in the coverage produced by a certain exposure. If the exposure is performed by backfilling the experimental chamber, the so-estimated S is averaged over the angles of incidence θ and ϕ, over the Maxwellian energy distribution of molecules at the temperature T of the gas, and over all the internal degrees of freedom of the molecules.

The use of supersonic molecular beams has enabled the direct measurement of the dependence of S on the polar (θ) and azimuthal (ϕ) angles of incidence, on energy E, and at least partly, on internal variables [32.1]. The direction of impingement of molecules onto the surface (i.e., θ, ϕ) can indeed be controlled by rotating the sample with respect to the direction of the molecular beam. The kinetic energy E of the molecules of the gas of interest can be tuned within a relatively large range by seeding them into a carrier gas (usually He or another inert gas) or changing the temperature of the molecular beam source T_N; E is given by

$$E = \frac{m}{<m>} < \frac{\gamma}{\gamma - 1} > kT_N\,, \tag{32.4}$$

where m is the mass of a molecule of the gas and $<m>$ is the average mass of the molecules in the beam (which depends on the masses and concentration of the molecule and of the carrier gas), while γ is the ratio between the specific heats at constant pressure and constant volume.

Changing T_N affects not only the kinetic energy but also the internal state of the molecules in the source, before the occurrence of the supersonic expansion. Despite the fact that, even at room temperature (RT), a high fraction of rotationally excited molecules are present inside the molecular beam source, at the end of the supersonic expansion, the molecules are in general rotationally cold. This is due to the rotational relaxation that occurs during the supersonic expansion.

However, at the end of the supersonic expansion, the molecules retain at least partial memory of their initial state: a significant increase in T_N thus indeed determines also a change of the rotational temperature of the molecules in the beam; for example, the rotational temperature of a pure ethene beam is of the order of 10 K for $T_N = 300$ K but increases to ≈ 100 K for $T_N = 900$ K [32.2].

In contrast, the collisions between the molecules during the supersonic expansion do not allow for significant vibrational relaxation, so that the population of vibrationally excited states at the end of the expansion depends essentially on the temperature T_N of the source. However, even when operating the nozzle at high T_N, only a small fraction of vibrationally excited molecules can be obtained. The reason is quite simple: the typical energy of intramolecular vibrational quanta is on the order of at least 0.1 eV (i.e., for wagging modes) and can reach values close to or > 0.4 eV (for CH and OH stretching modes), so the probability of thermal excitation of vibrational modes is quite low. Moreover, all the vibrational modes can be excited, so the use of a supersonic molecular beam alone does not achieve state selectivity.

Nonthermal methods are thus mandatory to achieve a significant fraction of vibrationally hot molecules or for the preparation of molecules in controlled vibrational states. The molecules in the beam can be used to perform uptake experiments and obtain information about the dependence of the sticking probability on at least some of the dynamical variables. S is often determined using the so-called retarded reflector method (or method of *King* and *Wells* [32.3], KW in the following).

In this method, the partial pressure of the molecules of interest is monitored using a quadrupole mass spectrometer as a function of time. As sketched in Fig. 32.1, when the molecular beam is allowed into the chamber hosting the sample, an increase in the pressure is recorded. However, an inert flag (flag 2) close to the sample prevents the beam from striking the surface of the sample. At a later time, the inert flag is removed so that the beam can hit the sample. A decrease of the partial pressure proportional to the sticking probability is then obtained. When the coverage no longer increases, a steady state is reached and the partial pressure remains constant.

This method allows accurate measurements of S with a sensitivity on the order of 1%. Calibration of the coverage is also possible provided that the intensity of

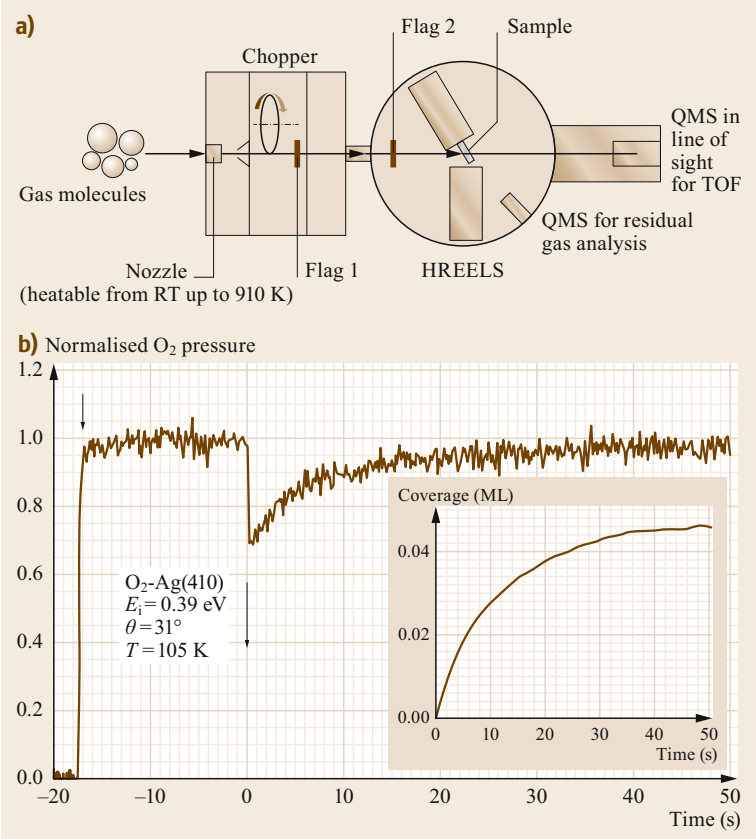

Fig. 32.1a,b Schematic of direct reflector method. **(a)** The setup used in Genoa to measure the sticking probability: it couples a supersonic molecular beam with an ultrahigh-vacuum chamber hosting the sample, a quadrupole mass spectrometer for residual gas analysis, and another one for time-of-flight measurements. The vibrational spectrometer (HREELS, high-resolution electron energy-loss spectroscopy) allows verification of the chemical state of adsorbed species. **(b)** A typical KW trace. When flag 1 is turned down, the molecular beam enters the UHV chamber and the partial pressure (of O_2 in this case) rises to a steady-state value determined by the incoming flux and the pumping speed of the chamber. As long as flag 2 remains up, the beam does not hit the surface. When flag 2 is also turned down, the beam strikes the sample, a fraction S of the molecules sticks to the surface, and the partial pressure drops. When saturation coverage is reached (or when the adsorption probability becomes lower than the experimental sensitivity), the partial pressure recovers its initial value. The inset shows the coverage as a function of time (Reprinted from [32.4], with permission from Elsevier. From [32.5] © IOP Publishing. Reproduced with permission. All rights reserved)

the beam can be determined independently. The coverage can thus be obtained by integrating S over time

$$\Theta(t) = \Phi \int_0^t S(\tau)\mathrm{d}\tau \,. \tag{32.5}$$

This method has been used extensively over the years to measure S for a wide set of systems. This chapter is organized into two different sections, covering the role of rotational and vibrational degrees of freedom, respectively.

32.1 Effect of Rotational Energy on S

The fundamental importance of the role of rotational energy has stimulated extensive theoretical and experimental investigations, and the field is still developing. We thus focus here on some of the most recent results, providing thus only a partial overview of this field; the more specialized reader is referred to dedicated review papers [32.6–23].

To avoid possible misunderstandings, we briefly recall the definition of molecular polarization for a distribution of rotating molecules.

The most straightforward way to do this is to consider the polarization of the angular momentum vector of the molecules, which defines their axis of rotation. While the total angular momentum of a closed-shell molecule arises purely from its rotational motion, in an open-shell molecule there may also be a contribution from electronic angular momentum. Defining the spatial polarization in terms of the total angular momentum vector also provides a way to treat polarization in atoms, in which the only contribution to the total angular momentum is electronic, in the form of spin and electronic orbital angular momentum [32.22].

In this respect, we must distinguish between alignment and orientation. For an aligned distribution, all vectors are aligned along a single axis (or sometimes in a plane) but without a preferred direction: equal numbers of arrows pointing in the up and down directions are then present. For an oriented distribution, on the other hand, the vectors have both a preferred axis and a preferred direction.

From a more formal point of view, let us consider the quantum-mechanical angular momentum vector $\boldsymbol{J}$ and its projection onto the axis defined by the velocity of the molecules M_J.

A beam of molecules which are aligned (but not oriented) have an isotropic distribution of M_J with equal population of positive and negative values of M_J, while a beam of oriented molecules have an anisotropic distribution of M_J.

Experimental investigations on the role of rotational degrees of freedom in molecule–surface interactions can employ both indirect and direct methods. In the former case, the rotational state of the molecules impinging on the surface is not controlled and information about the dependence of the sticking probability on the rotational state is obtained indirectly by analyzing the rotational state of scattered/desorbing molecules (mostly using laser methods) and applying detailed balance arguments. Such methods are addressed in the next subsection.

In direct methods, on the contrary, the rotational state of the incoming molecules is at least partially controlled and the sticking probability is measured directly using the King and Wells method. In pioneering *direct* studies, information was obtained by comparing the behavior of rotationally cold and hot beams obtained by increasing the temperature of the molecular beam source. Later, methods to prepare molecules in at least partially selected states appeared; electrostatic hexapole methods are presented first, followed by very recent results obtained using the magnetic hexapole technique. We then review the main results obtained by using collisional alignment and, finally, experiments performed by preparing the molecules in defined rotational states using laser methods.

32.1.1 Indirect Results Obtained by Use of Detailed Balance

The interaction of H_2 and D_2 with surfaces has been studied extensively both theoretically and experimentally. *Rettner* et al. [32.24] determined the state-resolved flux $I(E,\theta,T,\nu,J)$ for H_2 molecules desorbing off Cu(111) for different rotational states J and for molecules in the fundamental vibrational state $\nu = 1$. The flux of molecules leaving the surface was probed by laser ionization detection, and time-of-flight distributions were obtained by recording the flight times of the photoions to a multichannel plate detector. H_2 molecules were detected quantum-state specifically by laser ionization via a two-photon resonance to the H_2 E,F$^1\Sigma_g^+$ state. Detailed balance, when applied to adsorption/desorption processes, states that, for a system at equilibrium, the rate of adsorption is equal to the rate of desorption for any subset of molecules of the equilibrium flux striking the surface. It has been shown that the principle of detailed balance can be applied to relate adsorption/reflection measurements to desorption measurements made on systems at equilibrium and quasiequilibrium, e.g., under the conditions established in a molecular beam experiment [32.25].

$I(E,\theta,T,\nu,J)$ is related, in the limit of small coverage, to the state-resolved initial sticking probability, $S_0(E,\theta,T,\nu,J)$, via the relationship

$$\begin{aligned} &I(E,\theta,T.\nu,J)\sin\theta\mathrm{d}\theta\mathrm{d}\phi\mathrm{d}E \\ &\propto S_0(E;\theta,T,\nu,J)N(\nu,J,T)E\mathrm{e}^{-\frac{E}{kT}} \\ &\quad\times\cos\theta\sin\theta\mathrm{d}\theta\mathrm{d}\phi\mathrm{d}E\,, \end{aligned} \tag{32.6}$$

where T is the surface temperature, $N(\nu,J,T)$ is the Boltzmann population of state (ν,J), and $E\mathrm{e}^{-E/(kT)}\mathrm{d}E$ is the probability to have translational energy E in the interval between E and $(E+\mathrm{d}E)$.

The sticking probability is described as a function of the normal energy $E_n = E_i\cos^2\theta$ of the incoming molecules with the empiric function (sometimes called the S-function) usually employed to describe activated adsorption

$$S_0(E_i,\theta,\nu,J) = \frac{A(\nu,J)}{2}\left[1+\mathrm{erf}\left(\frac{E_n - E_0(\nu,j)}{W(\nu,j)}\right)\right]. \tag{32.7}$$

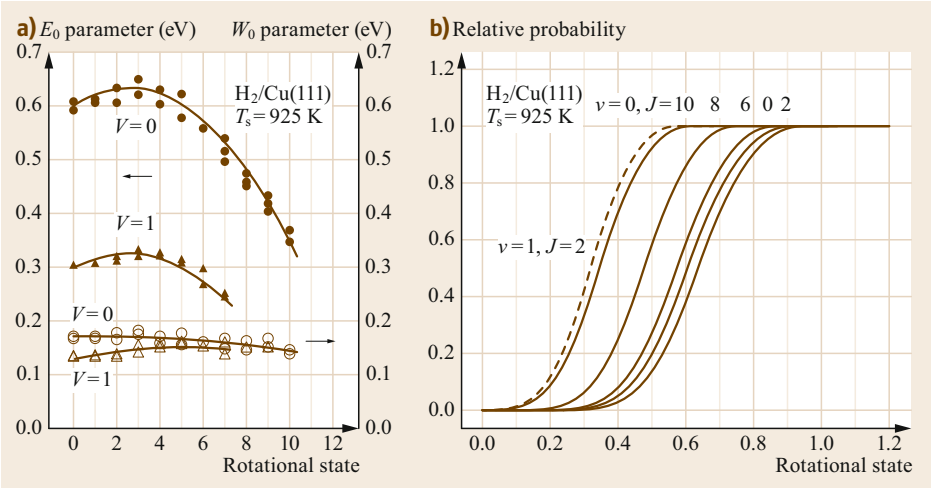

Fig. 32.2 **(a)** Dependence of the parameters E_0 and W on rotational quantum number for H_2 with $\nu = 0$ and $\nu = 1$ desorbed from Cu(111) at 925 K. The *lines* are quadratic fits to the points. **(b)** Quantum-state-specific adsorption probability functions for the same system. *Curves* are shown for $J = 0$, 2, 6, 8, and 10 for H_2 in the fundamental $\nu = 0$ state (*continuous lines*) and for $\nu = 1$ (*dashed line*) (Reprinted from [32.24], with the permission of AIP Publishing)

Here, $E_0(\nu, j)$ estimates the adsorption barrier, defined as the translational energy required for the adsorption probability of molecules in state (ν, j) to reach half its maximum value, $W(\nu, j)$ is a parameter that measures the steepness of the function (intuitively, the energy width of the adsorption barrier), and $A(\nu, J)$ is the saturation value of S_0 at high translational energy, again for molecules in state (ν, j).

The results of this experiment are summarized in Fig. 32.2. The adsorption barrier E_0 is significantly lower for $\nu = 1$ than for $\nu = 0$, indicating that vibrationally excited molecules require less kinetic energy to stick.

The dependence of E_0 on J is more complex: for H_2 in the fundamental vibrational state $\nu = 0$, E_0 rises with increasing J for J lower than 4 but falls steeply as J increases from 4 to 10. Quite similar results were obtained for D_2/Cu(111) [32.25]. These results indicate that the amount of translational energy needed to surmount the adsorption barrier increases with increasing J at low J but decreases with increasing J at high J. At low J, the molecules are very sensitive to the anisotropy of the potential energy surface, so that for $J \leq 4$ steric orientational effects dominate: the amount of time the reactants can remain in the preferred configuration during the reactive collision decreases with increasing J, thus inhibiting the occurrence of dissociative adsorption. For $J \geq 5$, on the contrary, the energy effect dominates: the increasingly effective conversion of rotational into translational energy during the reactive collision increases the sticking probability by effectively increasing the collision energy.

By using the same experimental setup, it was also possible to obtain information on the alignment of D_2 molecules desorbing off Cu(111). By rotating the polarization of the probe light so that it was either parallel or perpendicular to the surface normal vector z and by recording the intensities of the detected signal for these two polarizations as a function of arrival time at the detector, the degree of alignment of the desorbing molecules as a function of velocity was determined [32.26]. This result is shown in Fig. 32.3.

This figure shows that the probability for the formation of molecules with axis perpendicular and parallel to the surface are different and that this difference is large for large arrival times (corresponding to slow molecules) but approaches zero for short arrival times (fast molecules). The right panel shows a polar plot of the classical probability distribution of the angle θ between the angular momentum vector and the surface normal vector. Note that $\theta = 0, \pi$ corresponds to helicoptering motion, while $\theta = \pi/2$ corresponds to cartwheeling motion.

Thanks to detailed balance, such information about the preferred alignment in desorption provides information about the dependence of S_0 on alignment. At the lowest kinetic energy, only those molecules oriented close to the minimum-energy configuration in the transition state can dissociate. As the kinetic energy of the incident D_2 is increased, molecules with a wider range of alignments are able to dissociate, and the steric preference decreases, in agreement with these measurements. The observed *helicoptering* alignment of the recombinative desorption products observed here indicates that

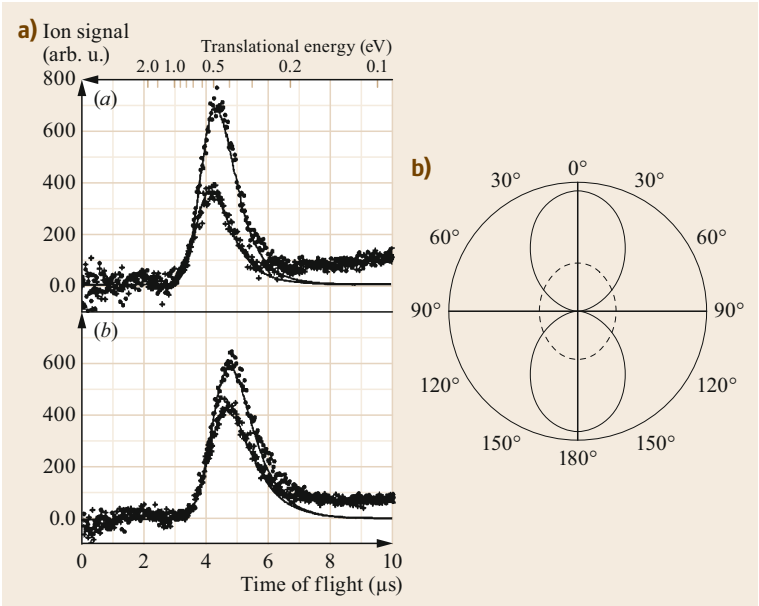

Fig. 32.3 **(a)** Alignment-sensitive time-of-flight spectra of specific quantum states of $D_2(v, J)$ formed by recombinative desorption from Cu(111) for (*a*) $D_2(v = 0, J = 11)$ and (*b*) $D_2(v = 1, J = 6)$. Measurements with the polarization of the probe laser perpendicular (•) and parallel (+) to the surface normal are shown. **(b)** Polar plot of $P(\theta)$, the classical probability distribution of the angle between the D_2 angular momentum unit vector $\boldsymbol{J}$ and the surface normal unit vector $\boldsymbol{z}$. The *dotted* and *solid curves* correspond to the minimum and maximum alignment observed at high and low kinetic energy, respectively (From [32.26]. Reprinted with permission from AAAS)

incident D_2 dissociatively adsorbs with the highest probability when it collides with its bond parallel to the surface. The dependence of the alignment on energy indicates that this steric preference is strong at low translational energies (0.3 eV) but decreases rapidly with increasing translational energy to nearly zero at 0.8 eV.

A similar *indirect* approach has also been employed to investigate larger molecules such as the interaction of N_2 with W(110) [32.27] and N_2 with Ag(111) [32.28, 29].

32.1.2 Effect of the Average *J* on the Sticking Probability

The first direct investigations of the effect of J on the adsorption probability were carried out by comparing its initial value S_0 for rotationally cold and hot molecules. Molecules at the end of the supersonic expansion are typically rotationally cold, especially when they are seeded in inert carriers and when the nozzle is operated at room temperature or below. Rotationally hotter molecules, i.e., molecules with a higher average J, can be obtained by operating the nozzle source at a sufficiently high temperature T_N. When using hydrogen, due to the large separation between subsequent rotational levels, it is possible to change T_N and distinguish between the sticking probability of molecules with close J values. On the contrary, when using larger molecules, for which the separation of rotational levels is much lower, only a semiquantitative result distinguishing between *low* and *high* J values is possible by such methods.

Comparing the existing literature, we conclude that there is not a general trend in the effect of rotational energy on the adsorption probability. As shown above for H_2/Cu(111), the rotational energy has a nonmonotonic effect on the adsorption barrier and thus on the resulting sticking probability; however, even for systems without any adsorption barrier, different behaviors have been reported.

As shown in Fig. 32.4, there exist systems (i.e., O_2/Ni(111), N_2/W(100), CO/FeSi(100) [32.30]) for which the sticking probability depends only on the translational energy but is independent of the amount of available rotation energy.

O_2/Ni(111) is a complex adsorption system. At low kinetic energy, the sticking probability is strongly temperature dependent and increases with *decreasing* kinetic energy at low temperature, indicating the existence of a precursor-mediated adsorption path. At high kinetic energy, S is nearly independent of temperature and increases with *increasing* kinetic energy, indicating the existence of a second, activated adsorption path. The sticking probability depends, however, only on the kinetic energy: it does not matter, for this system, whether its value has been attained by just increasing the nozzle temperature (and with it the average rotational quantum number) or, alternatively, by changing the seeding ratio (and thus without any significant change in the average rotational quantum number). In conclusion, the rotational energy does not seem to affect S_0 for O_2 on Ni(111) within experimental sensitivity.

A similar situation occurs for adsorption of N_2 on W(100): S decreases with increasing kinetic energy as

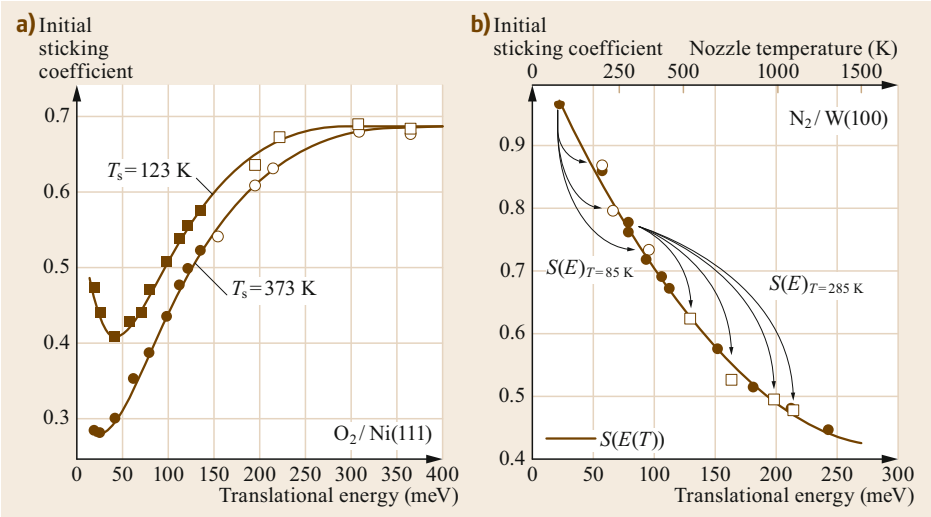

Fig. 32.4 **(a)** Sticking probability for O_2/Ni(111). **(b)** Sticking probability for N_2/W(100). *Filled symbols* correspond to different translational energies obtained by changing the nozzle temperature so that higher kinetic energy corresponds also to higher rotational states. *Open symbols* correspond to different translational energies obtained by different seeding mixtures at the same nozzle temperature. (Reprinted from [32.30], with permission from Elsevier)

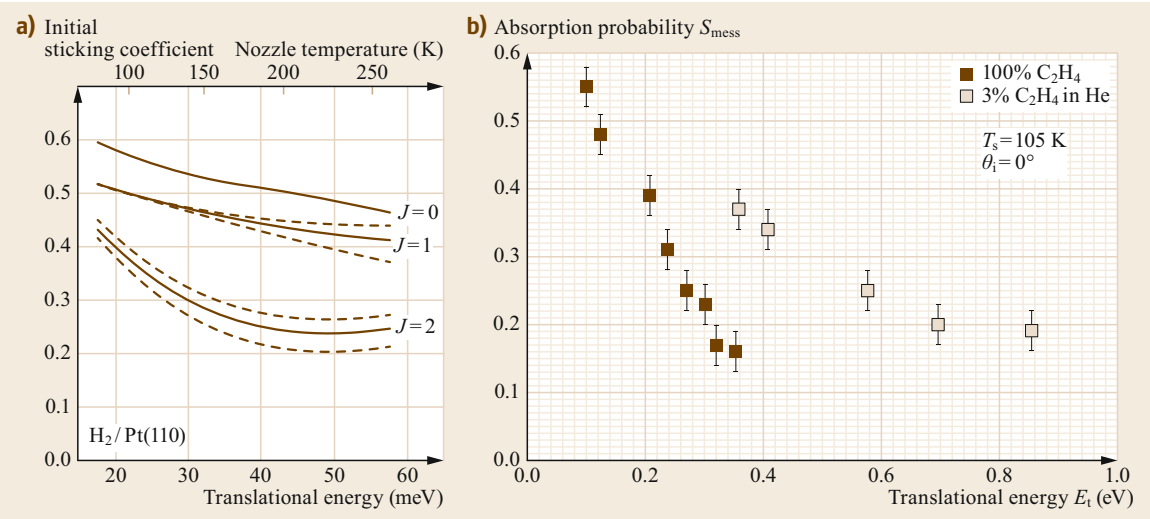

Fig. 32.5 **(a)** Sticking probability for H_2/Pt(110). **(b)** Sticking probability for C_2H_4/Ag(100) (**(a)** Reprinted from [32.31], with permission from Elsevier; **(b)** reprinted with permission from [32.2]. Copyright (1999) by the American Physical Society)

expected for a nonactivated adsorption system. As for O_2/Ni(111), the data points obtained at different nozzle temperatures (for which a different average J is expected) and the data obtained with different mixtures but at the same nozzle temperatures (for which the same or at least close J values are expected) fall on the same curve, thus again indicating a negligible effect of the rotational excitation on the adsorption probability [32.30].

However, there are also systems (i.e., H_2/Pt(110) [32.31], C_2H_4/Ag(100) [32.2]) for which the rotational energy has an adverse effect on adsorption and effectively suppresses the sticking probability.

As shown in Fig. 32.5, the sticking probability for H_2/Pt(110) decreases slowly with increasing kinetic energy and, more interestingly here, with increasing J. A similar result was obtained for a completely different system, viz. C_2H_4/Ag(100). The low adsorption energy indicates that most of the molecules are physisorbed. It is clear that, at the same kinetic energy (≈ 0.4 eV), S_0 is lower for rotationally hot molecules ($< J > \approx 8 \pm 4$,

obtained using a beam of C_2H_4 at $T_N = 900\,K$) than for rotationally cold molecules ($< J > \approx 1 \pm 1$, obtained by seeding ethene in He and keeping the nozzle at RT). In such cases, the presence of rotational energy effectively suppresses the sticking probability, favoring the backscattering of the molecule into the gas phase.

A similar result has been obtained for H_2 and D_2 on Pd(111) [32.32]. We can speculate that the key parameter is the efficiency of conversion of the existing rotational energy into translational energy. When this mechanism is effective, i.e., in the presence of a significantly corrugated interaction potential, the presence of rotational energy may favor adsorption in activated systems but disfavor it in nonactivated ones. When the conversion of rotational into translational energy is not effective, a sticking probability independent of the average rotational quantum number is found, independently of whether an adsorption barrier exists or not.

Such independence of S_0 from J can also occur as a consequence of strong steering: in the latter case, the molecule is attracted towards the adsorbed state, thus losing memory of its initial rotational state. Finally, we want to mention the intriguing results reported for the physisorption of hydrogen at very low temperature, where the adsorption probability is expected to be highest at low kinetic energy. Under such conditions, however, the rotational energy can be comparable to the kinetic energy, due to the larger separation between rotational levels for H_2 (and D_2), thus giving rise to a more complex phenomenology.

Due to the symmetry with respect to permutation of its nuclei, the rotational quantum number (J) of H_2 cannot be fixed independently of the total nuclear spin I. Because of this, molecules with even J must have $I = 0$ (i.e., so-called *para*-H_2), while when J is odd, $I = 1$ (so-called *ortho*-H_2). Such isomers appear in normal H_2 gas (n-H_2) in the proportion 1 : 3.

The reasons for the existence of a preferred orientation in such a weakly physisorbed system are still debated [32.33]. It is interesting to underline that molecular hydrogen physisorbed on smooth metal surfaces such as Ag(111) and Cu(100) behaves as a nearly free rotator [32.34].

Figure 32.6a shows measurements revealing the dependence of the initial sticking probability for n-H_2 and p-H_2. Resonances are clearly present in S_0 [32.35] for *para*-H_2, characterized by four times more molecules in even J states with respect to n-H_2. According to Andersson et al., three different kinds of resonances can occur: (i) rotation-mediated selective adsorption (RMSA) resonances, (ii) corrugation-mediated selective adsorption (CMSA) resonances, and (iii) combined resonances involving both rotation and corrugation, i.e., corrugation- and rotation-mediated selective adsorption (CRMSA).

RMSA involves rotational excitation but no diffraction ($g_{||} = 0$) and is indicated by

$$\begin{pmatrix} j \to j' \\ n \end{pmatrix} ,$$

where n is the bound state level involved; CMSA involves a specific lattice vector ($g_{||} \neq 0$) and is indicated by

$$\begin{pmatrix} hk \\ n \end{pmatrix} .$$

CRMSA involves both rotational excitation and diffraction and is specified by

$$\begin{pmatrix} hk, j \to j' \\ n \end{pmatrix} .$$

For the system shown in the figure, the resonances are of two kinds: RMSA, $j \to j'$, $0 \to 2$ (44.1 meV) and CRMSA, $j \to j'$, $0 \to 2$, and g(10). The peak at 24 meV appears to be dominated by CRMSA.

In Fig. 32.6b, the resonance-enhanced multiphoton ionization (REMPI)-temperature-programmed desorption (TPD) spectra for the two isomers are shown. It is apparent that the desorption temperatures are not the same, with *para*-H_2 starting to desorb first. The TPD spectra show the first-order desorption with $E_d = (28 \pm 2)$ meV for *ortho*-H_2 ($J = 1$) and (26 ± 2) meV for *para*-H_2 ($J = 0$). The difference in the desorption features can be ascribed to the anisotropic physisorption potential, where the perpendicular orientation is preferred over the parallel orientation.

This difference in adsorption energy is not peculiar to the H_2/Ag(111) system. Indeed, different desorption temperatures have also been observed for D_2/ice [32.36], where again molecules in the state $J = 1$ are more strongly bound. Note that, for D_2, the more strongly bound species, i.e., the one with rotational state $J = 1$, corresponds to *para*-D_2.

The inversion with respect to H_2 is due to the fact that the nuclei of this molecule consist of protons (with semiinteger spin) while D_2 consists of deuterons (with spin 1); the total wavefunction of H_2 must thus be antisymmetric with respect to permutation of the nuclei, while the wavefunction of D_2 must be symmetric under the same operation [32.37].

32.1.3 State-Selected Molecular Beam by Electrostatic Hexapole

The Stark effect was studied in the 1950s [32.6] for various kinds of molecules, and its application to obtain focusing and orientation started about 50 years ago [32.7–

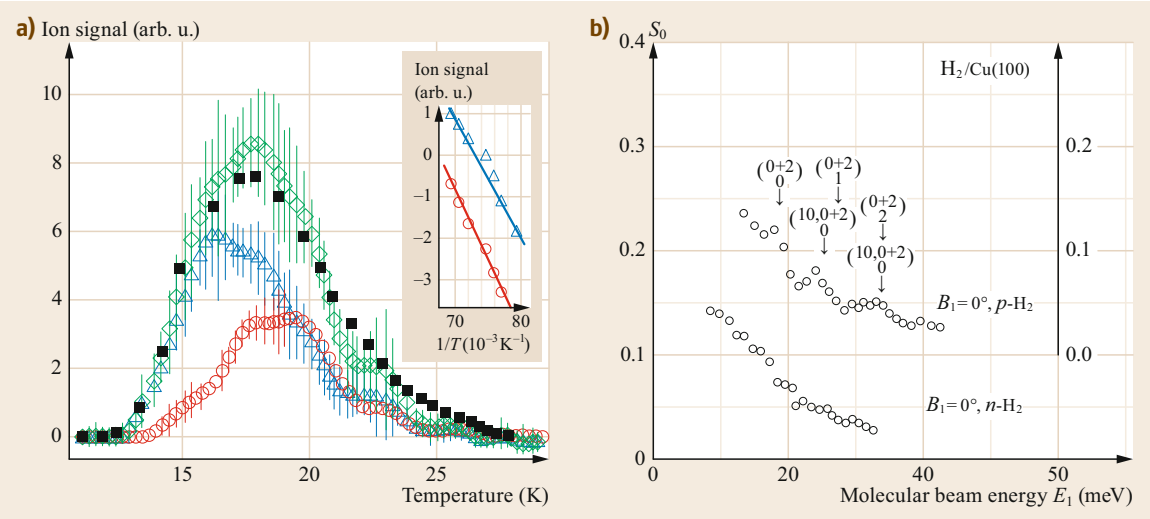

Fig. 32.6 **(a)** REMPI-TPD spectra for $J = 0$ of H_2 (*open triangles*) and $J = 1$ of H_2 (*open circles*) measured ≈ 30 s after 0.2 L dosage of H_2 on Ag(111) at 10 K with a heating rate of 2.5 K/s. The sum of the $J = 0$ and $J = 1$ REMPI-TPD spectra (*open diamonds*) and a QMS-TPD spectrum (*filled squares*) are shown for comparison. *Inset*: Arrhenius plots of the leading edge of the $J = 0$ and the $J = 1$ REMPI-TPD spectra. The *solid lines* are linear fits. **(b)** Initial sticking probability, S_0, versus molecular beam energy E_1, of *n*-H_2 and *p*-H_2 on Cu(100) at normal incidence. *p*-H_2 was produced via online conversion of the normal gases by use of a nickel-silicate catalyst kept at 25 K by a cool helium gas. The surface is kept at ≈ 10 K, such a low temperature is needed due to the very low adsorption energy for physisorbed H_2 (Reprinted with permission from [32.33, 35]. Copyright (2014) by the American Physical Society)

9]. Since then, molecular orientation effects have been studied in several chemical reactions [32.11, 13]. Recently, beam focusing and manipulation of a molecule using the Stark effect, the so-called hexapole technique, have been applied in a sophisticated way to excited CO molecules, OH radicals, NH_3, etc. [32.38–40]. Several groups have employed the hexapole technique in surface science studies.

NO is a simple molecule which has been studied most extensively regarding the stereodynamics of surface processes with and without a hexapole technique. Clear molecular orientation effects depending on the strength of the molecule–surface interaction were found in the scattering of NO from metal surfaces [32.12, 41–44]. The first demonstration of oriented NO scattering from a surface was carried out on NO/Ag(111), a weakly bound system [32.41].

The angular distribution of the scattered NO in Fig. 32.7 demonstrates that the adsorption probability is higher if the molecule approaches the Ag(111) surface with the O-end closer to the surface than the N-end. These results can be understood based on a strong anisotropic or orientation-dependent repulsion, resulting in preferential, rotationally mediated, adsorption for O-end incidence conditions [32.12].

While O-end incidence favors rotationally mediated adsorption for the weakly interacting system

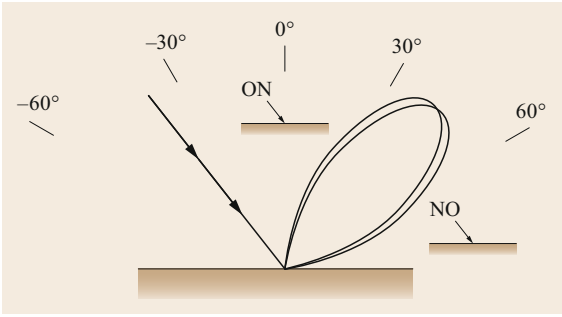

Fig. 32.7 Angular distributions for direct scattering of oriented NO from Ag(111) (after [32.41])

NO/Ag(111) [32.12, 41], the N-end approach is favored for the strongly interacting NO/Pt(111) system [32.43, 44]. The highly reactive preference for the N-end approach was also observed in other strongly adsorbed systems, such as NO/Al(111) [32.45], NO/Ni(100) [32.46], and NO/Pt(100) [32.47]. Even for a semiconductor surface such as Si(111), the N-end approach promotes the occurrence of surface reactions [32.48].

The hexapole technique can also be applied for orienting more complex polyatomic molecules such as N_2O [32.50] and CH_3Cl. Systematic studies of scattering of oriented alkyl halide molecules from highly

Table 32.1 Experimental results of steric effects in molecule–surface scattering ([32.49], © Elsevier 1989)

Molecule	Neat (low E_i)	He seeded (high E_i)	Steric effect sign and magnitude	Preferred orientation
CH_3F	×		+ M	$+H_3CF-\ldots Gr$
CH_3Cl	×	×	+ M	$+H_3CCl-\ldots Gr$
CHF_3	×	×	− S	$-F_3CH+\ldots Gr$
$CHCl_3$	×		− W	$-Cl_3CH+\ldots Gr$
$(CH_3)_3CCl$		×	+ M	$+(H_3C)_3CCl-\ldots Gr$
$(CH_3)CCl_3$		×	− W	$-Cl_3CCH_3+\ldots Gr$
$(CH_2)Cl_2$		×	− W*	$-Cl_2CH_2+\ldots Gr$
$CClF_3$	×		− W	$-F_3CCl+\ldots Gr$
$CFCl_3$	×		+ W	$+Cl_3CF-\ldots Gr$
CH_3NO_2		×	− M	$-O_2NCH_3+\ldots Gr$
CH_3OH	×		+ M	$+H_3COH-\ldots Gr$
CH_3CN		×	− W	$-NCCH_3+\ldots Gr$
$(CH_3)_3N$	×		− W	$+N(H_3C)_3+\ldots Gr$

Uncorrected raw data results: + indicates positive steric effect, − negative steric effect. W, M, and S indicate weak, medium, and strong effect, respectively. * very small effect

oriented pyrolytic graphite (HOPG) were performed in the early 1990s, and it was concluded that the steric effects depend on the alkyl chains and the halogens of the alkyl halide molecules [32.49, 51–53].

The obtained results are summarized in Table 32.1. They demonstrate the existence of steric effects for various polyatomic molecules having more degrees of freedom than NO. The alkyl halide molecules interact weakly with HOPG. The sign of the steric effect (with respect to the direction of the dipole vector relative to the surface normal) differs from one case to another. The negative end of the molecule sticks preferentially in some cases, while the positive end is preferred in others. Thus, the origins of the steric effects in the weak interaction of polyatomic molecules with surfaces have not been clarified yet.

The role of molecular orientation in the adsorption of CH_3Cl on strongly interactive Si(100) [32.54–56] and weakly interactive Si(111) [32.57] and HOPG [32.49, 52, 58, 59] has been intensively studied, revealing that the Cl-end collision is the favored one.

Here, we review the principles of focusing and orientation by using an electrostatic hexapole and a uniform field in front of the crystal surface. Since detailed reviews have already been published [32.12, 21, 60, 61], we briefly describe here the focusing of CH_3Cl, a typical symmetric-top molecule with a large dipole moment, 6.24×10^{-30} C m, which can be state selected and focused by a hexapole technique as explained below [32.62].

The experimental setup at Osaka University in Japan is shown schematically in Fig. 32.8. The apparatus consists mainly of three parts. The first part contains the nozzle and buffer chamber, generating a pulsed supersonic molecular beam (PSSMB). The second part contains the hexapole state selector with a beam stop and guiding electrodes. The third part hosts the ultrahigh-vacuum (UHV) chamber for analyzing surface-reaction processes. Detailed descriptions of such apparatuses are available elsewhere [32.62].

32.1.4 Rotational State Selection

The force exerted by the electric field $\boldsymbol{E}$ on molecules possessing a permanent dipole, $\boldsymbol{\mu}_{el}$, inside the electrostatic hexapole is radial and follows the derivatives of the Stark energy U_{Stark} [32.6]. The interaction energy U_{Stark} of a symmetric top molecule depends on the total angular momentum $\boldsymbol{J}$ and its projections onto the body-fixed molecular axis ($\boldsymbol{K}$) and onto the space-fixed axis defined by the electric field ($\boldsymbol{M}$). The force due to the inhomogeneous field of the state selector equals the derivative of the interaction energy U_{Stark} with respect to the radial distance r from the hexapole central axis

$$F_r = -\frac{dU_{Stark}}{dr} = \mu_{el}\frac{KM}{J(J+1)}\frac{dE}{dr}\,. \tag{32.8}$$

Here, J, K, and M are the quantum numbers corresponding to $\boldsymbol{J}$, $\boldsymbol{K}$, and $\boldsymbol{M}$, respectively; B, h, and c are the rotational and Planck constants, and the velocity of light, respectively; γ is the angle formed by $\boldsymbol{\mu}_{el}$ and $\boldsymbol{E}$. The values of μ_{el} and E stand for $|\boldsymbol{\mu}_{el}|$ and $|\boldsymbol{E}|$, respectively. The force remains radial because the azimuthal angular derivative $dU_{Stark}/d\phi$ vanishes for a linear Stark effect in a hexapole field.

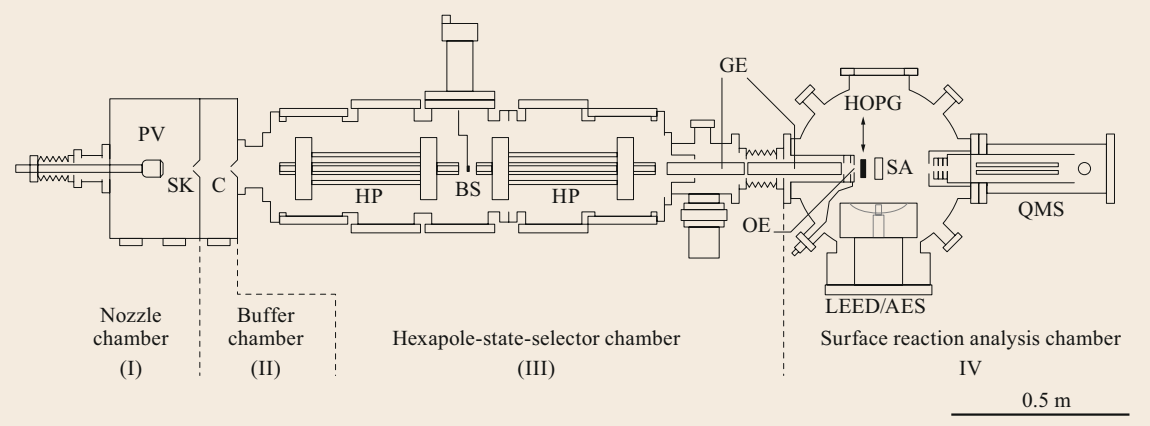

Fig. 32.8 Schematic top view of the oriented molecular beam line and surface-reaction analysis chamber (PV: pulsed valve, SK: skimmer, C: beam collimator, HP: hexapole device, BS: beam stop, GE: guiding electrode, OE: orientation electrode, HOPG: KW flag and SA: sample) (Reproduced from [32.62]. Copyright © 2005 The Japan Society of Applied Physics)

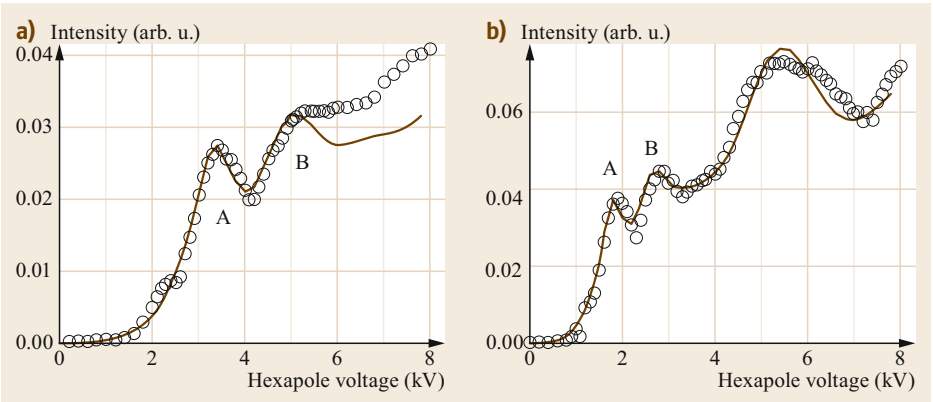

Fig. 32.9a,b Focusing curves for **(a)** CH_3Cl (25%)/Ar, and **(b)** CH_3Cl(25%)/Kr. The *open circles* and *full lines* indicate the measured and simulated focusing curves, respectively. Peak A and B in each panel correspond to the states $|JKM\rangle = |111\rangle$ and $|212\rangle$ (Reproduced from [32.54]. Copyright © 2005 The Japan Society of Applied Physics)

For a field $E = 3V_0r^2/R^2$ in the hexapole state selector, the force is

$$F_r = -\frac{dU_{Stark}}{dr} = \frac{6\mu_{el}V_0}{R^3}\frac{KM}{J(J+1)}r\,, \qquad (32.9)$$

where V_0 is the absolute value of the voltages applied to the hexapole. The negative and positive voltages are applied to every other pole of the hexapole; R is the radius of the circle inscribed within the surfaces of the rods. From 32.9 it follows that, for states with a positive Stark effect (i.e., $KM < 0$), $F_r < 0$ and the molecule will be deflected towards a region with low field strength on the axis of the PSSMB. This force shows a linear dependence on r, thus the motion of the CH_3Cl molecules focused using the hexapole deflector is sinusoidal. The molecule moves at a uniform velocity along the hexapole axis. Thus, by adjusting V_0, the focal length of the molecule can be controlled.

The state selection achieved using the hexapole is primarily verified by measuring the intensity I_B with the quadrupole mass spectrometer (QMS) as a function of voltage on the rods of the hexapole, obtaining the so-called focusing curve. By tuning the hexapole voltage, optimal focusing is easily achieved in the signal I_B on the detector.

Figure 32.9a,b shows the focusing curves for PSSMBs with $E_i = 120$ (CH_3Cl (25%)/Ar SSMB) and 65 meV (CH_3Cl (25%)/Kr SSMB) impinging directly upon the QMS, respectively. Here, the intensity I_B is plotted as a function of the absolute value of the voltages applied to the rods of the hexapole. There are several peaks in the focusing curves shown in Fig. 32.9.

To assign the peaks to the correct rotational states, trajectory simulations of CH_3Cl molecules were performed [32.62]. As a result of such simulations, peak A and B in Fig. 32.9 can be assigned to $|JKM\rangle = |111\rangle$ and $|212\rangle$ states, respectively.

32.1.5 Orientation

Molecules in a single KM state become oriented in a uniform electric field. Such a field is applied to obtain a beam of preferentially oriented CH_3Cl molecules. When a state-selected beam is introduced adiabatically into a uniform electric field, the orientation distribution for a molecule with the rotational state can be expanded into a series of Legendre polynomials $P_n(\cos\gamma)$ [32.63]

$$P_{JKM}(\cos\gamma) = \frac{2J+1}{2}\sum_{n=0}^{2J} C_n(JKM)P_n(\cos\gamma)\,. \tag{32.10}$$

Here, the coefficient C_n is given in the $3j$ symbolic description and γ is the angle between the orientation field and the permanent dipole of CH_3Cl. In real experiments, it is not feasible to select only a single state of molecules. Thus, the orientation distribution of the state-selected molecules can be described as the sum over the individual states weighted by the population of each state. As a result, the orientation distribution function $W_V(\cos\gamma)$ at a given hexapole voltage V_0 can be obtained once we know the distribution $W_V(JKM)$ of the $|JKM\rangle$ states at V_0 [32.64]

$$W_V(\cos\gamma) = \sum_{JKM} P_{JKM}(\cos\gamma)W_V(JKM)\,, \tag{32.11}$$

where $P_{JKM}(\cos\gamma)$ is given in (32.10).

Based on the simulation, we can obtain the state distribution function $W_V(JKM)$ of the $|JKM\rangle$ states at fixed V_0, and thus the orientation distribution function $W_V(\cos\gamma)$ in (32.11). The obtained $W_V(\cos\gamma)$ for the 120 meV CH_3Cl SSMB are shown in a polar plot for the Cl-end distribution, together with the random orientation distribution, in Fig. 32.10. $\bar{P}_1$ and $\bar{P}_2$ correspond to the average orientation and alignment, respectively. The Legendre moment $P_n = P_n(\cos\gamma)$ of $W(\cos\gamma)$ for the $|111\rangle$ state at 120 meV is determined as follows, taking the state purity into consideration: $\bar{P}_0 = 1$, $\bar{P}_1 = 0.47$, and $\bar{P}_2 = 0.06$, the higher terms being negligibly small.

For $|212\rangle$ at $E_i = 120$ meV, the moments $\bar{P}_n$ of $W(\cos\gamma)$ are $\bar{P}_1 = 0.33$ and $\bar{P}_2 = 0.11$, respectively. When we reverse the electric field, the distribution corresponds to the CH_3-end distribution. $W_V(\cos\gamma)$ for the 65 meV SSMB was reported in [32.55, 62].

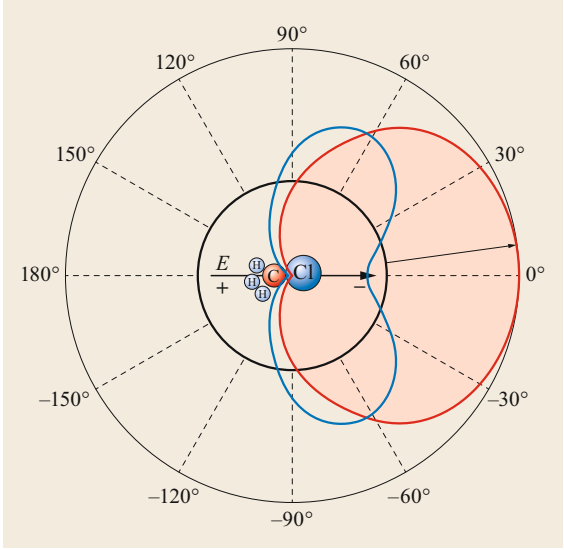

Fig. 32.10 Polar plots of orientation distribution for CH_3Cl $|111\rangle$ (*red*) and $|212\rangle$ (*blue*), estimated from the experimental focusing curve. The Cl-end distribution of CH_3Cl is shown in the case of the indicated electric field. The *black circle* around the center corresponds to the random orientation distribution (Reprinted with permission from [32.54]. Copyright (2005) by the American Physical Society)

32.1.6 Molecular Orientation Effects of CH_3Cl on Surfaces

By using such a state-selected and oriented beam, we can measure the rotational state dependence and molecular orientation dependence of the molecular sticking probability on surfaces [32.54, 56, 60, 61].

Figure 32.11 shows the T_s dependence of S_{Cl}/S_{random} and S_{Cl}/S_{CH_3} for the $|111\rangle$ incidence (black open and solid circles) at $E_i = 120$ meV. S_{Cl}, S_{random}, and S_{CH_3} are the initial sticking probabilities (S_0) for the Cl-end, the random orientation, and the CH_3-end incidence, respectively. Above 280 K, an obvious orientation effect appears and its onset agrees well with the decrease of S_{random}.

It is quite interesting that, when the surface is exposed to molecules in the $|212\rangle$ state (Fig. 32.10), no similar orientation effects are observed, as shown in Fig. 32.11. The steric effect observed for the $|111\rangle$ state strongly couples with the desorption off the potential well of the precursor state. Desorption occurs under nonequilibrium conditions before the molecule can thermalize in the precursor state, dissipating energy by phonon and/or electron–hole pair excitations.

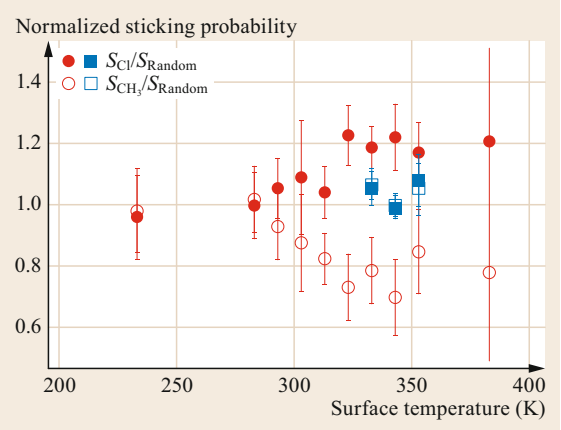

Fig. 32.11 T_s dependence of S_{Cl}/S_{random} and S_{CH_3}/S_{random} for CH_3Cl (*full* and *open circles*, respectively) and (*full* and *open squares*, respectively) incident at $E_i = 120$ meV (Reprinted with permission from [32.54]. Copyright (2005) by the American Physical Society)

For the $|212\rangle$ incidence, the first Legendre moment, corresponding to the orientation in the Legendre expansions of $W(\cos\gamma)$, is smaller than that for the $|111\rangle$ state. Moreover, as is apparent from the orientation distribution function shown in Fig. 32.10, the average orientation of the $|212\rangle$ state is closer to the stable precursor geometry and thus the steric effect is smeared out by the steering effect in the attractive well of the precursor state. We expect an effect of alignment for the $|212\rangle$ state due to the larger contribution of the second Legendre moment: this may account for the small offset of the data from 1 observed for the $|212\rangle$ state.

Figure 32.12 shows the T_s dependence of S_{Cl}/S_0 (full circles) and S_{CH_3}/S_0 (open circles) for the $|111\rangle$ (upper panel) and the $|212\rangle$ (lower panel) states at an incident energy of 65 meV. At variance with the results obtained at a kinetic energy of 120 meV for CH_3Cl incidence, when the kinetic energy is lowered to 65 meV, no clear orientation effects are observed for both the $|111\rangle$ and $|212\rangle$ states within experimental errors across the whole range of T_s. Steric effects thus disappear when lowering the kinetic energy, suggesting that strong steering effects reorient the slowly moving molecule into a more favorable orientation.

The steric effects in a shallow potential well (such as a precursor well) are confirmed in the scattering of CH_3Cl from HOPG [32.58, 59] and Si(111) [32.57]. Figure 32.13 shows the molecular orientation dependence of the TOF spectra for oriented 320 meV CH_3Cl incidence at $\theta_i = 45°$ (the detector being at $\theta_s = 45°$) on the Si surface at 300 K. Clearly, the scattering intensity for the CH_3-end collision is higher than that for the Cl-end collision at both temperatures. This result agrees well with the result obtained for HOPG.

In Fig. 32.13, the top panels also demonstrate that the molecular orientation effect appears in direct inelastic scattering. The profile of the difference spectrum between the CH_3-end and Cl-end collisions is in good agreement with the direct inelastic components obtained from the TOF spectra in an experiment performed for random incidence conditions. The higher trapping probability observed for the Cl-end collision on Si(111) is consistent with the molecular orientation dependence of the initial sticking probability reported for CH_3Cl on Si(100).

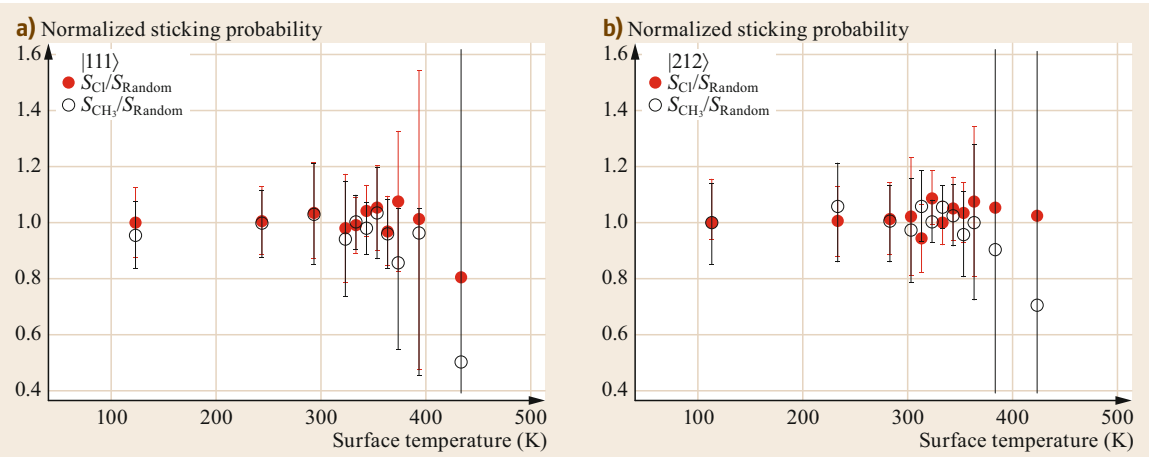

Fig. 32.12a,b T_s dependence of S_{Cl}/S_0 (*full circles*) and S_{CH_3}/S_0 (*open circles*) for the $|111\rangle$ **(a)** and $|212\rangle$ **(b)** states at an incident energy of 65 meV. The value of 1 corresponds to no steric effects (Reprinted with permission from [32.55]. Copyright (2008) American Chemical Society)

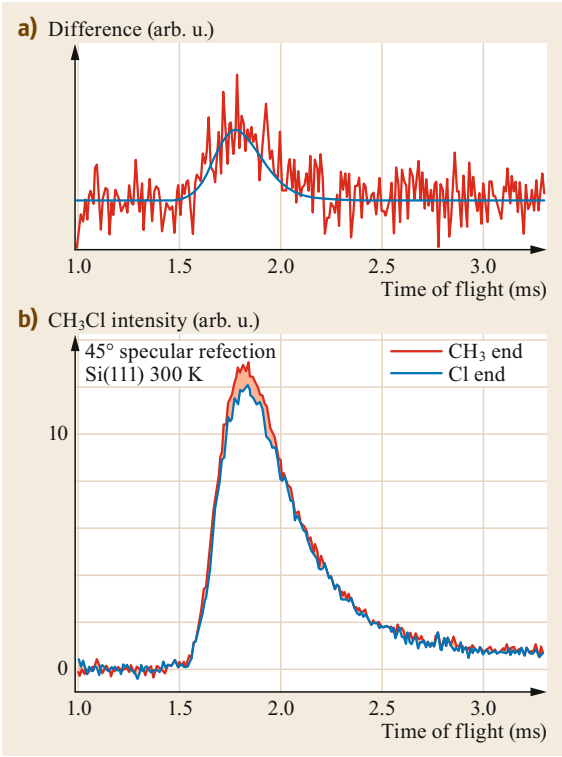

Fig. 32.13 **(a)** The difference (*red line*) of the TOF spectra in **(b)**. The *solid blue line* corresponds to direct inelastic scattering. **(b)** Molecular orientation dependence of the TOF spectra at $\theta_s = 45°$ for the CH_3-end (*red line*) and Cl-end (*blue line*) approaches for a kinetic energy of 320 meV and CH_3Cl incidence on Si(111) at $\theta_i = 45°$ and $T_s = 300$ K. (Reprinted with permission from [32.57]. Copyright (2010) American Chemical Society)

32.1.7 Alignment of O_2 by a Magnetic Hexapole

Kurahashi et al. developed a highly purified single spin-rotational state-selected ($(J, M) = (2, 2)$) O_2 beam by combining a supersonic oxygen beam with a magnetic hexapole field. The hexapole magnet is described in detail in previous reports [32.23, 65], so only a brief description is provided here. The strength of the inhomogeneous field $B(r)$ at a radial distance r in the gap between the poles of a hexapole magnet is given by

$$B(r) = B_0 \frac{r}{r_0} , \tag{32.12}$$

where r_0 is the Bohr radius and B_0 is the field strength at $r = r_0$. A molecule with an effective magnetic moment $\boldsymbol{\mu}_{\text{eff}}$ feels a deflection force towards the axis if $\mu_{\text{eff}} = |\boldsymbol{\mu}_{\text{eff}}| < 0$, but away from the axis if $\mu_{\text{eff}} > 0$. The force $F(r)$ can be expressed as follows if μ_{eff} is field independent

$$F(r) = 2\mu_{\text{eff}} \frac{B_0}{r_0^2} r . \tag{32.13}$$

This deflection force causes harmonic oscillation of a particle with $\mu_{\text{eff}} < 0$ and provides focusing of single rotational states of a molecule.

Figure 32.14 shows a schematic diagram of the apparatus used for the sticking probability measurements using state-resolved O_2. The beam line producing a state-selected O_2 consists of a beam source, a hexapole magnet, a spin flipper, and a Stern–Gerlach analyzer. The O_2 beam with $(J, M) = (2, 2)$ is generated by preparing a supersonic rotationally cold O_2

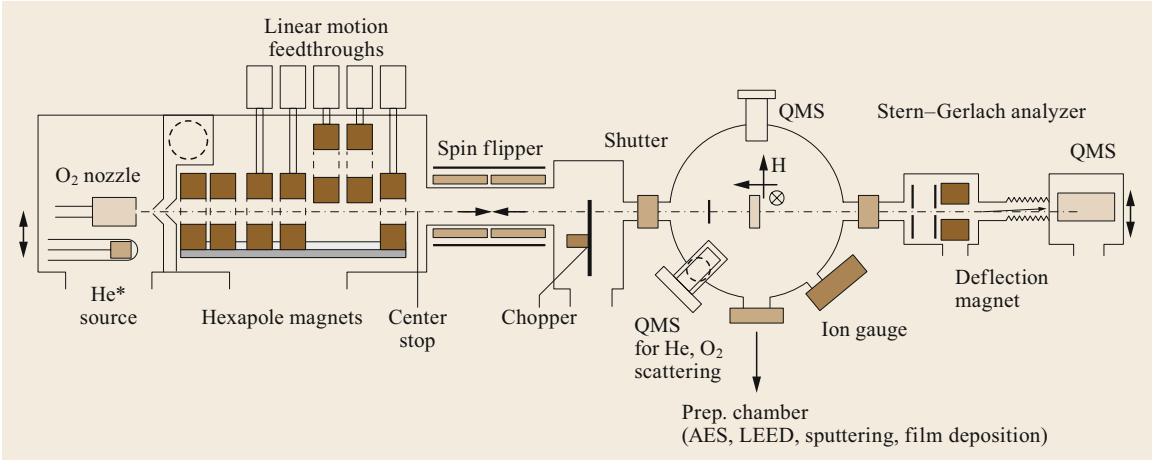

Fig. 32.14 Schematic diagram of experimental apparatus used for alignment- and spin-resolved O_2 sticking studies (Reprinted from [32.23], with permission from Elsevier)

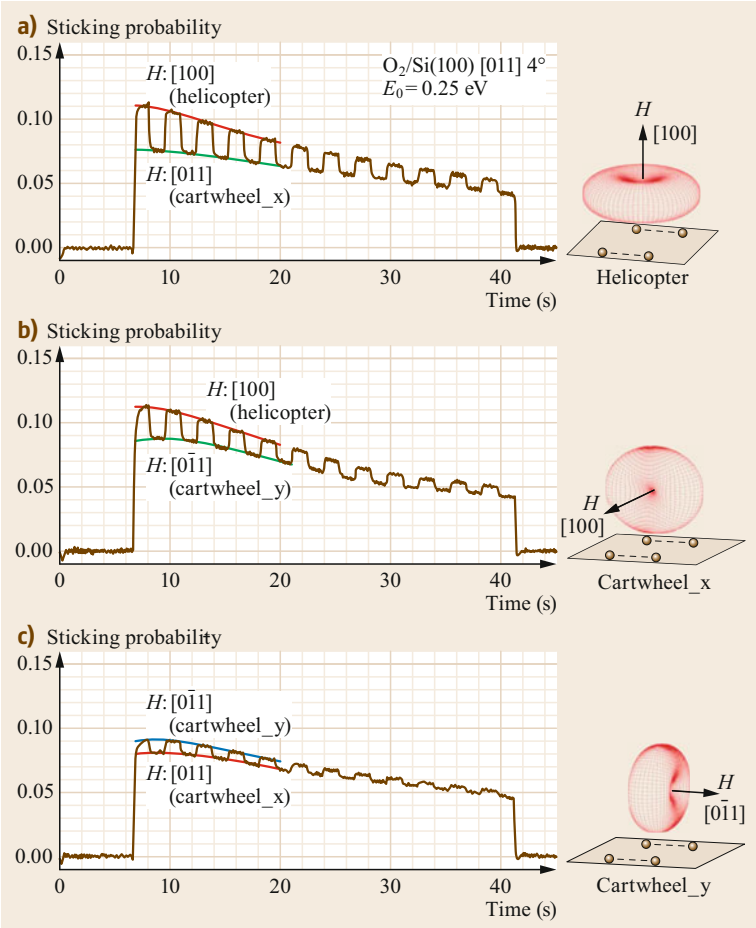

Fig. 32.15a–c Time evolution of sticking probability measured for a vicinal Si(100) surface at translational energy of 0.25 eV while alternating two of the three geometries shown in the *inset*. The dimers formed between two surface Si atoms are shown as short bars (Reprinted from [32.66], with the permission of AIP Publishing)

beam and selecting the (2,2) state of O_2 using the magnetic hexapole technique. Using this approach, control of both the molecular alignment and the spin direction relative to the magnetic field ($\boldsymbol{H}$) can be achieved [32.23, 65–69].

Since the O_2 molecular axis of $(J, M) = (2, 2)$ is dominantly perpendicular to the applied $\boldsymbol{H}$ direction, three different geometries can be realized by controlling the $\boldsymbol{H}$ direction at the sample, as shown in Fig. 32.15a–c.

By using such a state-selected molecular beam technique, the sticking probability for O_2 on Si(100)-(2×1) for different geometries of impingement was measured and a clear dependence of the sticking probability on the molecular alignment found [32.66]. The sticking probability is highest for the helicopter-like (HE) geometry (Fig. 32.15a), demonstrating the high preference for the side-on collision in dissociative adsorption. The two cartwheel-like (CW) geometries (Fig. 32.15b,c) reveal, on the other hand, the azimuthal dependence of the sticking probability, where O_2 is more reactive when its axis is perpendicular to the Si dimer [32.66].

Kurahashi and *Yamauchi* also measured the alignment dependence of the sticking probability of O_2 on Al(111) [32.68]. They clarified that O_2 reacts with its axis nearly parallel to the surface at kinetic energy < 0.2 eV and concluded that the abstraction process, which occurs when the O_2 axis is perpendicular to the surface, is a minor event at low kinetic energy.

The effect of spin in the dissociative adsorption of O_2 on a Ni(111) film was demonstrated by the same research group by using a state-selected molecular beam [32.69]. It was found that the sticking probability strongly depends on the relative spin directions of the Ni surface and the incoming O_2 in Fig. 32.16 and in particular that O_2 dissociates more efficiently when its spin is antiparallel to the majority spin direction of the Ni(111) film, a result relevant for spin-controlled surface chemical reactions.

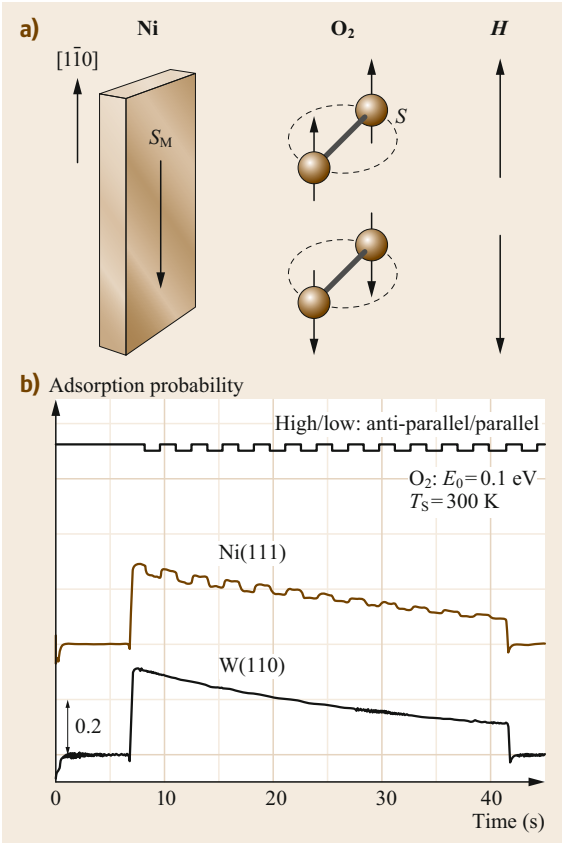

Fig. 32.16 (a) Control of the O_2 spin direction by the defining magnetic field. **(b)** Spin-dependent O_2 adsorption on a Ni(111) film surface. The adsorption probability is changed when the O_2 spin direction relative to the majority spin direction of the Ni film (S_M) is alternated. No spin-dependent effect is observed for O_2 adsorption on a nonmagnetic W(110) surface (Reprinted with permission from [32.69]. Copyright (2015) by the American Physical Society)

32.1.8 Collisional Alignment

Alignment and consequent molecular polarization can be induced by collisions in environments with anisotropic velocity distributions or temperature gradients. The occurrence of collisional alignment was firstly evidenced long ago in connection with the study of gaseous transport phenomena of paramagnetic molecules such as O_2 [32.70–72]. Subsequently, *Beenakker* et al. demonstrated that this phenomenon is common to nearly all diatomic gases, including diamagnetic molecules [32.73]. Collisional alignment in molecular beams, from supersonic nozzle sources, was anticipated by *Ramsey* [32.74] and first reported by *Steinfeld*, *Korving*, and coworkers [32.75, 76] in the 1970s.

The discovery of the dependence of the degree of alignment on the final speed for O_2 seeded in He [32.77], for N_2 [32.78], benzene [32.79], ethene [32.80], and acetylene [32.81], made it possible to perform experiments using aligned molecules both in the gas phase [32.82, 83] and at surfaces [32.84–90] by exploiting the velocity dependence of the collisional alignment [32.91, 92]. By seeding a few percent of such molecules in He (or Ne), hyperthermal beams are obtained.

Molecules in the beam are rotationally cold, due to the efficient energy transfer from the rotational degrees of freedom into translational energy made possible by the large number of collisions taking place in the nozzle region under the conditions of supersonic expansion. Notably, the low-speed tail of the velocity distribution has a statistical distribution of alignments, while the high-speed tail consists mainly of molecules in low-helicity states [32.93]. Molecules in orientations and rotational states that present a large collision cross section when viewed along the beam direction undergo a larger number of collisions during the supersonic expansion and thus end up with higher kinetic energy (fast tail), while the slowest molecules, which have undergone a smaller number of collisions, show no preferential alignment.

The strong dependence of the degree of alignment on velocity enables the use of a mechanical chopper (velocity selector) to select molecules in the slow or fast tail and to use them for gas-phase as well as adsorption experiments [32.94].

We have considered two different sets of systems:

a) Molecularly chemisorbed systems (such as $C_2H_4/O_2/Ag(001)$ [32.84, 87], $C_3H_6/Ag(001)$ [32.86], C_2H_4 on C-contaminated Cu(410) [32.21], $C_2H_4/Pd(100)$ [32.92])
b) Dissociative adsorption reactions (O_2 adsorption on bare and CO-precovered Pd(100) [32.85, 88–90], $O_2/Ag(001)$ [32.21].

A typical experiment is shown in Fig. 32.17. The slow tail (ST in the following) or the fast tail (FT in the following) is selected using an appropriately designed mechanical velocity selector. The degree of alignment for C_2H_4 as a function of velocity was obtained by scattering experiments with an inert gas target in Perugia using a high-resolution velocity selector. The selector used for adsorption studies has a lower resolution since a higher intensity is required to measure the sticking probability directly using the retarded reflector method of King and Wells. The concentration of CW estimated for the two-disk velocity selector operating in Genoa is 0.42 ± 0.03 for the ST

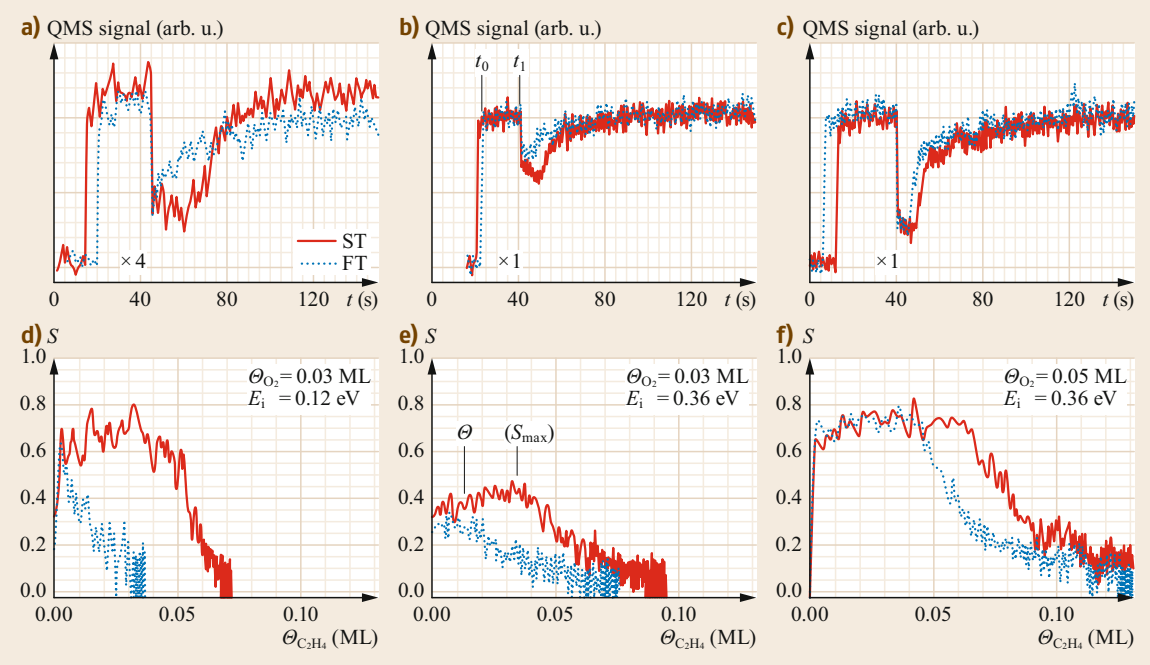

Fig. 32.17a–f KW traces **(a–c)** and $S(\Theta)$ curves **(d–f)** showing the results of ethene uptake experiments on O_2-precovered Ag(100). Different O_2 precoverages and C_2H_4 translational energies are reported (Reprinted from [32.21], with permission from Elsevier)

of the velocity distribution and 0.67 ± 0.05 for the FT.

Figure 32.17a–c shows the ethene partial pressure as a function of time for three different conditions. In all cases, the molecular beam enters the main chamber at $t \approx 20$ s, thus causing an increase in the quadrupole mass signal. As explained in the introductory paragraph, it is possible to obtain the coverage Θ by integrating $S(t)$ over time, thereby obtaining $S(\Theta)$. The result is shown in Fig. 32.17d–f. Inspection of the experimental data clearly shows that:

a) The initial sticking probability S_0 is independent of the polarization, being the same for ST and FT
b) With increasing surface coverage, a stereodynamical effect sets in above a certain coverage, which depends on the amount of preadsorbed oxygen molecules.

Above such ethene coverage, the sticking probability is higher for ST and FT, indicating that helicoptering molecules have a higher sticking probability than cartwheeling ones. We can thus safely conclude that, at the kinetic energies probed here, the interaction between ethene and the bare surface is not affected by the alignment of the impinging molecule. The same results have also been obtained for C_3H_6/Ag(001) and C_2H_4/C-Cu(410), thus indicating that the additional surface corrugation introduced by the presence of a preadsorbed species or by a regular array of steps is not sufficient to cause an observable effect of rotational alignment on the initial sticking probability. Possibly, despite the weakness of the bond, steering forces are still strong enough to suppress rotational effects in the low coverage limit, i.e., when only the interaction between the gas molecules and bare surface matters.

At higher coverage, a more complex scenario must be considered. Evidently, impinging helicopters have a higher chance to stick than cartwheels when they collide with preadsorbed species. Since the heat of adsorption decreases with increasing coverage, the onset of the stereodynamical anisotropy corresponds to the point at which steering is no longer strong enough to suppress the effect of the incoming alignment. The absence of any effect at all coverages for C_2H_4/Pd(100) [32.92], a more strongly bound chemisorption system with ethene molecules in a ff-bonded configuration, fits well with this picture.

Further consideration is needed regarding the relatively high magnitude of the steric effect at relatively low hydrocarbon coverage. If the anisotropy were to arise directly from the interaction between aligned gas-phase ethene and preadsorbed ethene molecule, it would not be possible to account for the huge difference in S of

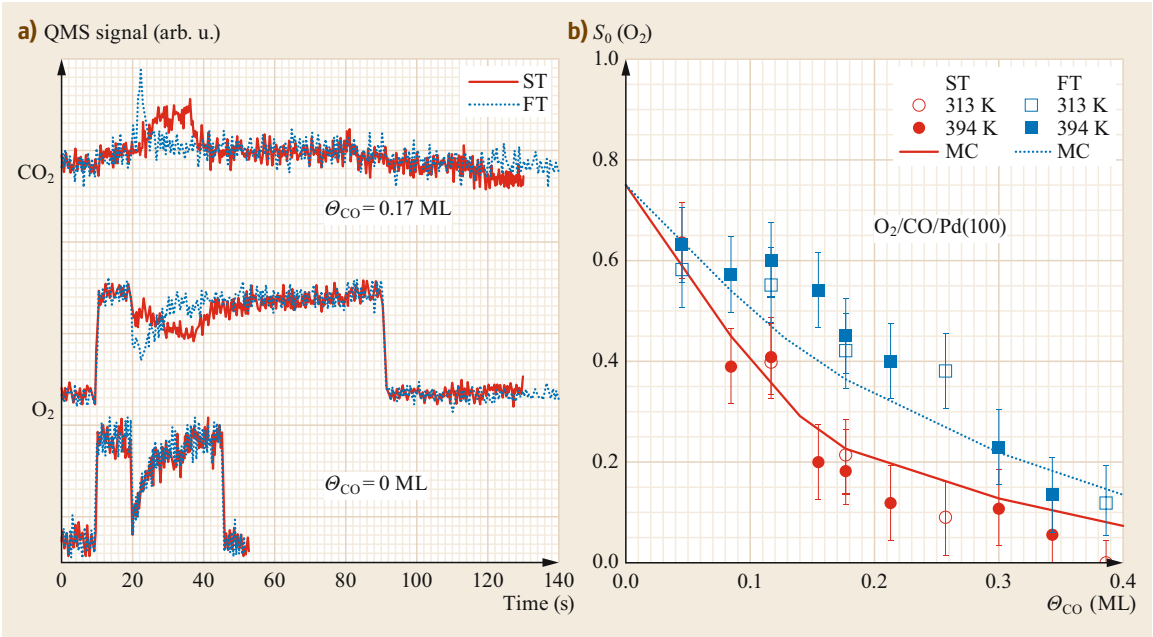

Fig. 32.18a,b O_2 partial pressure in the crystal chamber, measured by a QMS not in line of sight with the SMB, as a function of time for the ST and FT tails of oxygen SMBs interacting with the bare surface (*bottom traces*) and with Pd(100) precovered with 0.17 ML of CO (*middle traces*). The *top traces* show the signal due to CO_2 production during exposure (Reprinted from [32.21], with permission from Elsevier)

ST and FT observed for example at 0.05 ML at 0.12 eV and low O_2 precoverage. We must then conclude that C_2H_4 molecules that are not scattered immediately after the first hit with the surface must remain temporarily trapped as a mobile and nonthermalized precursor with a memory of its initial alignment so that, in this condition, CWs have a higher chance of being scattered back into the gas phase than HEs when colliding with already chemisorbed flat-lying C_2H_4 molecules.

No stereodynamical effects on the sticking probability S were observed for O_2/Ag(001) or O_2/Pd(001) (see Fig. 32.18 for $\Theta_{CO} = 0$): both its initial value and its coverage dependence resulted the same for ST and FT, within the attained experimental sensitivity [32.21].

When considering the interaction of O_2 with CO-precovered Pd(100), a more complex scenario is revealed. As is apparent from Fig. 32.18, the initial sticking probabilities S_0 for ST and FT are quite different in the presence of a significant CO precoverage ($\Theta_{CO} =$ 0.17 ML). In Fig. 32.18b, S_0 is plotted as a function of Θ_{CO} at two different temperatures for ST and FT. It is evident that:

a) S_0 decreases with increasing Θ_{CO} at both temperatures.
b) S_0 decreases more rapidly for ST than for FT. Since FT has a higher fraction of cartwheeling molecules (> 80%), this implies that cartwheeling molecules have a higher sticking probability in the presence of preadsorbed CO.

Point (a) is easily explained by the fact that, the higher Θ_{CO} is, the lower the number of free Pd sites available for the oxygen adatoms resulting from the dissociation of the incoming O_2. The fact that cartwheels have a higher sticking probability than helicopters at nonvanishing Θ_{CO} can be explained by considering in detail the array of empty sites needed for the landing and dissociation of helicoptering and cartwheeling O_2. A larger array is required for helicopters since, in a classical picture, their molecular axis is always parallel to the surface, thus explaining the more rapid decrease of S_0 for ST than FT. The reader is referred to the original papers for the details of the model; here we just underline that it can account in a quantitative way for the experimentally observed decrease (see lines in Fig. 32.18b).

A completely unexpected result was found for $\Theta_{CO} = 0.04$ ML (Fig. 32.19): despite the identical values of S_0 for ST and FT, a remarkably higher CO_2 yield was found for ST than for FT, both at 313 and at 393 K. It is clear that at least part of the oxygen atoms resulting from the dissociation of helicopters and cartwheels must end up at different sites to account for the observed large difference in reactivity.

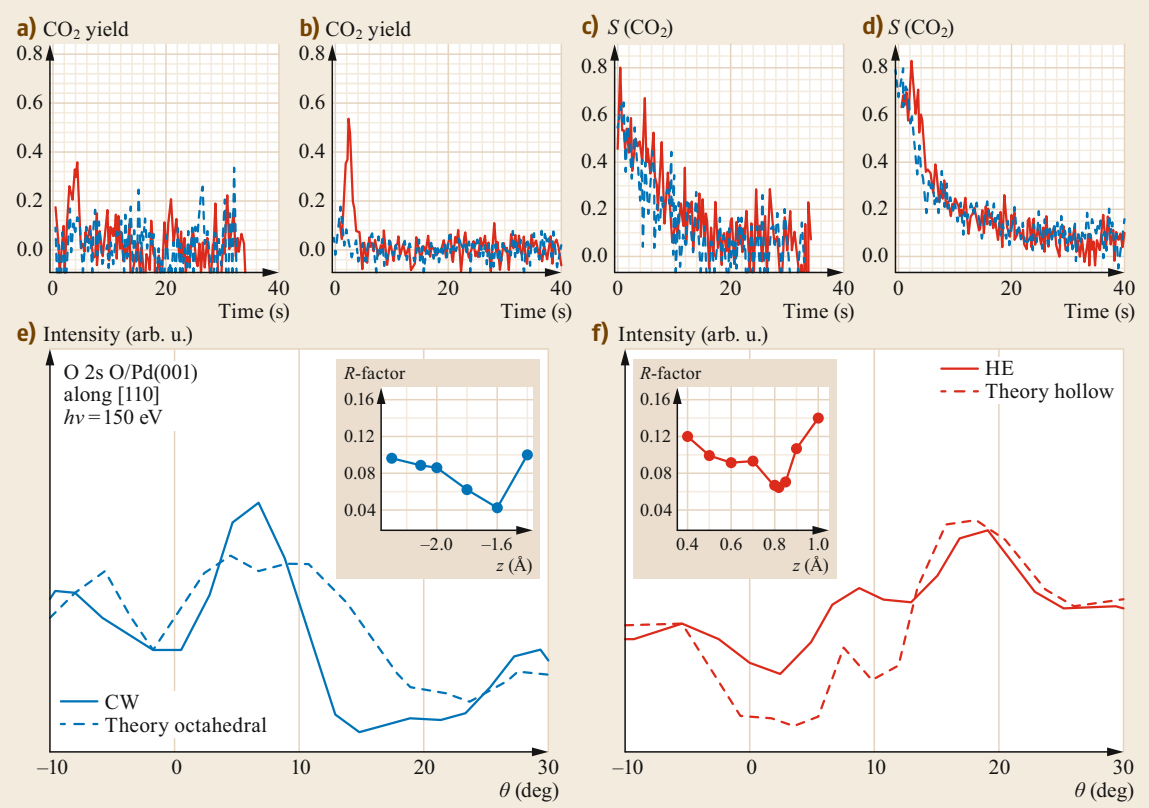

Fig. 32.19 **(a,b)** CO_2 yield and **(c,d)** O_2 sticking probability as functions of time for O_2 molecules from the ST (*red solid line*) and FT (*blue dashed line*) on Pd(001) precovered with 0.04 ML of CO at 313 K **(a,c)** and 394 K **(b,d)**. The traces for the CO_2 yield are corrected for the different ionization factor, so that the intensities can be directly compared. **(e,f)** Deconvoluted experimental XPD intensities of the O 2s level versus electron emission angle (*dot-dashed lines*) for HE **(f)** and CW **(e)**, compared with the theoretical fit using the model described in the text (*continuous line*). The photon energy is 150 eV, and the detection direction is along the ⟨110⟩ azimuth (Reprinted with permission from [32.88], © Wiley 2009)

X-ray photoelectron diffraction (XPD) experiments were then performed following adsorption of O_2 on Pd(100) in the absence of CO. Due to the proximity of the O 1s line to the Pd line, the photoelectron diffraction was performed for the O 2s line. The experimentally measured angle dependence of the diffracted intensity can be explained if the oxygen atoms resulting from the dissociation of the cartwheeling molecules occupy octahedral subsurface sites while the oxygen atoms resulting from the dissociation of helicopter-ing O_2 end up in fourfold hollow sites. Such assignments naturally account for the observed different CO_2 yield: since oxygen atoms occupying subsurface sites cannot react with adsorbed CO, the amount of CO_2 produced when the FT of the velocity distribution impinges onto a Pd(100) surface with 0.04 ML of CO is due to the fraction of helicopters present in FT.

A few experiments were also performed with higher nozzle temperatures [32.90]. While for $T_N = \mathrm{RT}$, almost all molecules populate the state with $K = 1$, at higher T_N a non-negligible fraction of O_2 populates higher rotational states with $K > 1$. Unfortunately, no experimental measurements of the degree of alignment have been performed for $T_N > \mathrm{RT}$. However, it is safe to assume that, with increasing T_N, higher rotational states start to be populated. Inspection of the O_2 uptake curves (Fig. 32.20) shows that molecules in higher rotational states behave differently with respect to rotationally cold ones with $K = 1$.

With increasing T_N, the amount of reactive O atoms produced with FT grows. This result indicates the propensity for rotationally hotter molecules in FT (i.e., for rotationally hotter cartwheels) to dissociate, yielding adatoms instead of oxygen atoms ending up at subsurface sites. Conversely, the lower amount of CO_2

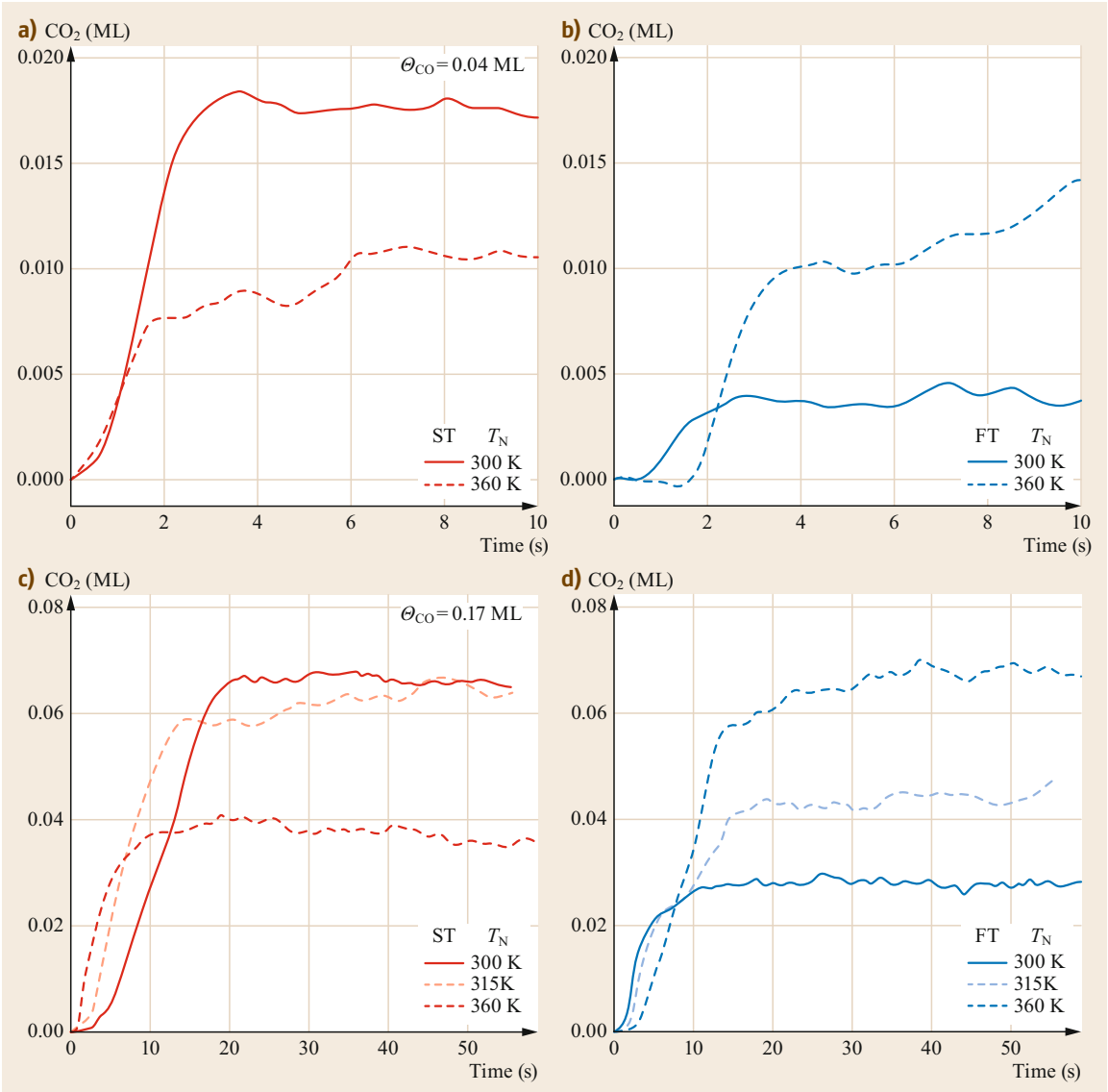

Fig. 32.20a–d Amount of CO_2 produced [in ML of the Pd(100) surface] versus time for a surface precoverage of $\Theta_{CO} = 0.04$ ML **(a,b)** and for $\Theta_{CO} = 0.17$ ML **(c,d)** for ST **(a,c)** and FT **(b,d)** while operating the source at different T_N (after [32.90])

produced by ST at higher T_N might indicate that non-reactive oxygen atoms are produced by the dissociation of the rotationally hotter molecules in ST (i.e., by rotationally hotter helicopters).

32.1.9 Laser-Based Methods

When using supersonic molecular beams, substantial rotational cooling occurs, so that molecules populate only low J states. Typical optical selection rules allow to change J only by 1 or 2 units, so that laser pumping of supersonic molecular beams cannot easily prepare molecules in states with predefined rotational quantum number [32.96]. Most results about rotationally hot molecules have indeed been obtained either by substantial annealing the nozzle so that a significant population of high rotational states may arise or by comparing the results of adsorption experiments using rotationally cold supersonic beams with effusive (i.e., rotationally hotter) beams.

As an example, we summarize here one of the few laser experiments reporting the effect of the rotational

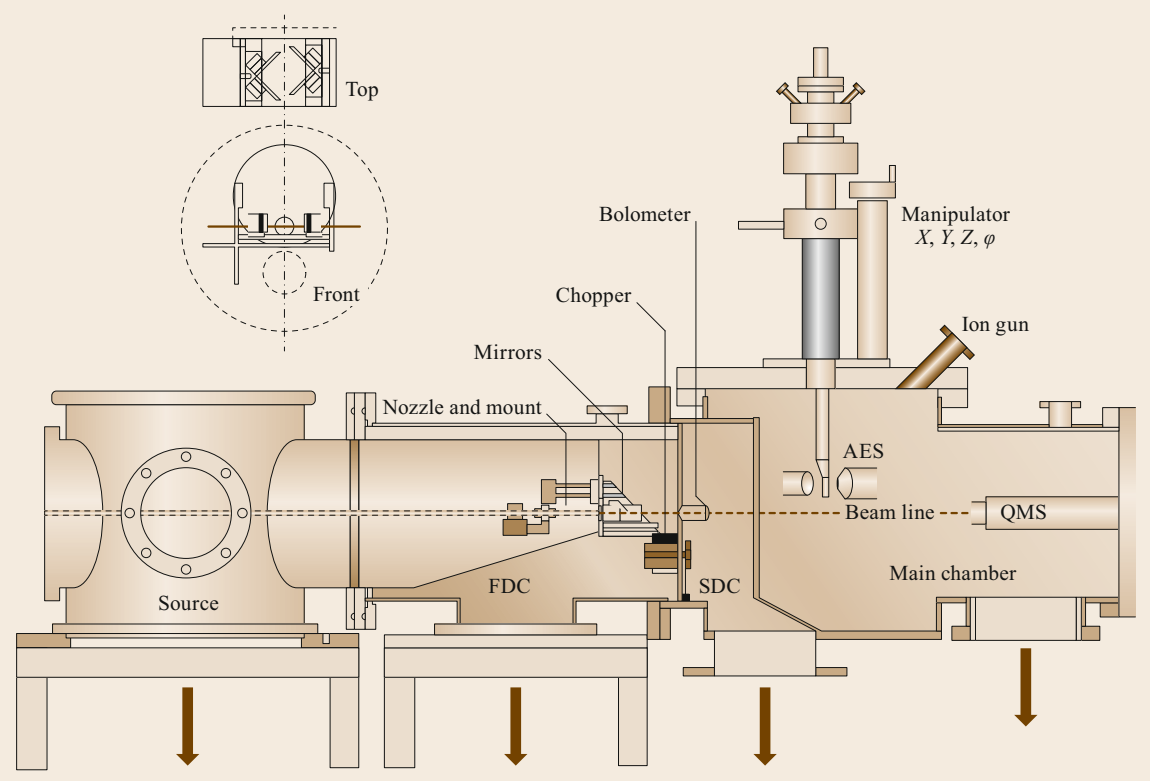

Fig. 32.21 Molecular beam–surface analysis chamber showing the four vacuum chambers, source, first differential pumping stage (FDC), second differential pumping stage SDC), and main surface analysis chamber (Reprinted from [32.95], with the permission of AIP Publishing)

state on the adsorption probability. The experimental setup is shown in Fig. 32.21.

Experimental results for methane excited from the ground state $\nu = 0$ to the first excited state $\nu = 1$ of the ν_3 antisymmetric CH stretching vibration are shown in Fig. 32.22. The total fraction of molecules excited in the beam is the product of the $\nu = 0, J''$ state population and the fractional excitation out of that state. Populations of levels ($\nu = 0$) in the molecular beam are calculated by scanning the infrared (IR) laser over $R(J'')$ transitions for all the J'' ($\nu = 0$) levels present in the beam, integrating the absorption signal, and normalizing for transition probability (see [32.95] for details).

The results for the initial sticking probability of vibrationally hot methane are shown in Fig. 32.22.

At first sight, rotational effects might be expected [32.18]; indeed, over the range of kinetic energy (from ≈ 0.1 to ≈ 0.5 eV) and of J values (up to $J = 3$) reported in that study, the timescale for rotation is comparable to the time the molecule spends in the effective range of the surface interaction potential. However, for this system, the initial sticking probability is independent of the rotational state, at least up to $J = 3$ and independently of the kinetic energy. On closer inspection, this result should not be surprising: adsorption of methane on Ni(100) occurs dissociatively, and vibrational excitation of the $\nu = 3$ mode is essential to obtain a high sticking probability, so that the dependence of the barrier on the rotational states (if present) becomes irrelevant.

32.2 Effect of Vibrational Energy on *S*

It is useful to address briefly also the relative role of kinetic and vibrational energy in determining the adsorption probability of a gas species at a surface. Polanyi suggested some simple rules to correlate the energy required for a chemical reaction and the shape of the potential energy surface (PES). For the reaction

$$\mathrm{A} + \mathrm{BC} \rightarrow \mathrm{AB} + \mathrm{C} \qquad (32.14)$$

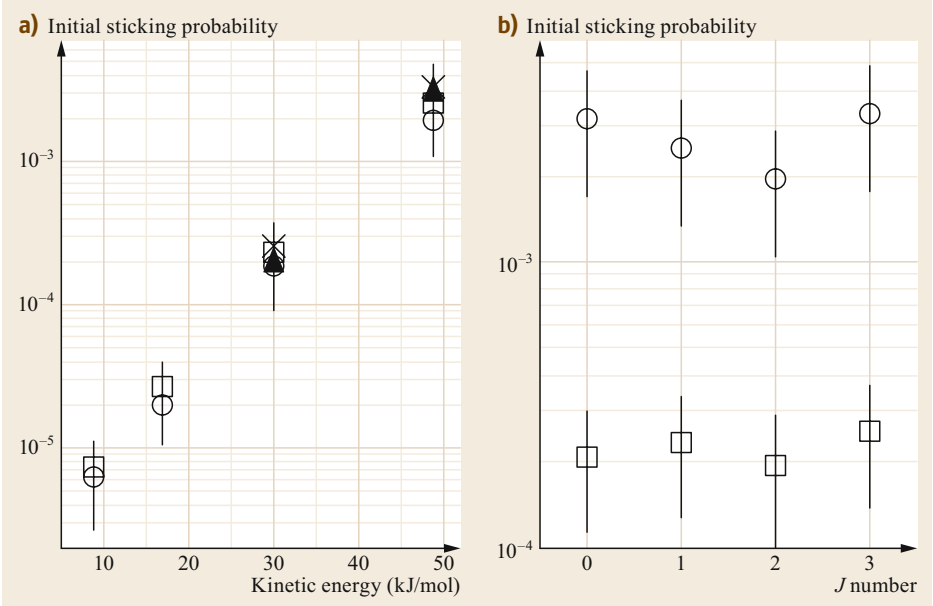

Fig. 32.22 **(a)** Initial sticking probability of methane on Ni(100) for $\nu = 1$ (ν_3) and different rotational states $J = 0$ (▲), $J = 1$ (□), $J = 2$ (◯), and $J = 3$ (×) as a function of kinetic energy. **(b)** Initial sticking probability for $\nu = 1$ (ν_3) as a function of J state for kinetic energy of 49 (◯) and 30 kJ mol^{-1} (□). Error bars show two standard deviations of convoluted uncertainties (Reproduced from [32.97] with permission of The Royal Society of Chemistry)

of an atom A with a diatomic molecule BC, basically two kinds of PES can be found (Fig. 32.23):

i) If the transition state separating the reactants from the products is located in the *entrance channel*, i.e., where the BC bond length has not yet increased, then a certain amount of kinetic energy is more effective than the same amount of vibrational energy in promoting adsorption.
ii) If, on the contrary, the transition state is located in the *exit channel*, then vibrational energy is more effective than kinetic energy.

These two ideal cases are often referred to as the early and late barrier cases, respectively. The validity of this idea was already confirmed in pioneering studies on gas–surface interactions [32.99].

Figure 32.24 shows experimental data for the initial sticking probability of D_2 on Cu(111) as a function of the kinetic energy associated with the motion in the direction normal to the surface, i.e., the so-called normal energy ($E\cos^2\theta$). Sets of data recorded for different nozzle temperatures T_N are shown. It is apparent that, at low normal kinetic energy, the sticking probability is remarkably higher for the data points obtained at the highest T_N, even if the kinetic energy is the same. This result indicates that both translational and internal energy play an important role in overcoming the barrier to adsorption. The difference is due unambiguously to the different internal energy content of the cold and hot beams. Even if the molecules are both rotationally and vibrationally excited, the enhancement of the adsorption probability was correctly ascribed to the vibrational energy.

The use of laser methods has allowed detailed investigation of the effect of vibrational excitation on the sticking probability. By experimentally studying the scattering probabilities of NO on clean and oxygen-covered copper (111) surfaces, it was found that highly excited ($\nu = 13$ and 15) NO molecules adsorb on clean copper (111) with a probability as high as 0.87, more than three orders of magnitude greater than the adsorption probability for ground-state NO [32.100].

It has even been shown [32.101] that highly vibrationally excited NO molecules can induce electron emission off Cs-covered Cu(111). This result has shown that, when the vibrational energy exceeds the surface work function, direct conversion of vibrational energy into electronic excitations can occur in surface scattering. Dedicated reviews have appeared [32.98, 102, 103] covering a relatively limited but growing literature [32.104–114].

Figure 32.26 shows the paradigmatic result obtained for the initial sticking probability of methane on Ni(100). By using lasers, molecules in defined vibra-

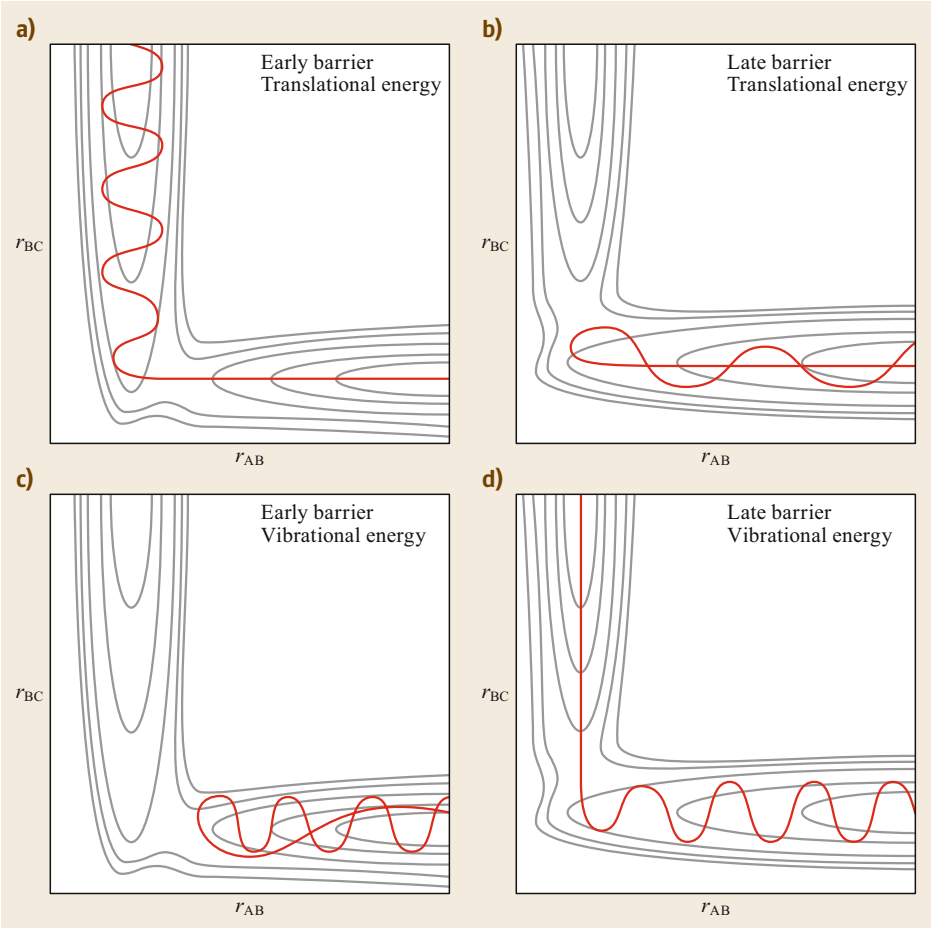

Fig. 32.23a–d Schematic potential energy surface for $A + BC \rightarrow AB + C$, showing the effect of adding translational energy **(a,b)** or vibrational energy **(c,d)** to the incident BC if the reaction has an early barrier **(a,c)** or late barrier **(b,d)** (Reproduced from [32.98] with permission of The Royal Society of Chemistry)

tional states are prepared (see the typical experimental setup in Fig. 32.25).

The amount of carbon (Fig. 32.26) produced by the cracking of methane is determined by inspection of the corresponding Auger signals after the exposure to beams of molecules in different vibrationally excited states and in the fundamental state (i.e., when the laser is turned off). By an appropriate calibration of the exposure, it is possible to obtain the sticking probability. The result of this experiment is shown in Fig. 32.26.

The data were fit using the equation for an S-shaped curve (32.7) applied to describe the energy dependence of S for activated systems. Independently of the exact mathematical definition of the barrier E_0, it is evident that the activation barrier decreases substantially when increasing vibrational excitation. It is thus apparent that CH_4 molecules in the second excited vibrational state ($2\nu_3$) have a sticking probability higher by more than one order of magnitude than molecules having the same kinetic energy in the fundamental vibrational state. The effectiveness of vibrational energy in promoting adsorption is moreover higher the lower the kinetic energy.

Similar results have been obtained for D_2O dissociation [32.110]. In order to determine the relative efficacy of translational and vibrational energy in overcoming the adsorption barrier it is instructive to compare the values of E_0 for $\nu_3 = 0$ and $\nu_3 = 1$. For methane dissociation, for example, the addition of 66 kJ mol^{-1} of translational energy increases S_0 for vibrationally cold molecule by the same amount as adding 72.1 kJ mol^{-1} of vibrational energy via the excitation of the $2\nu_3$ state.

It has also been shown that the reduction of the adsorption barrier $\Delta E_0 = E_0(\nu = 0) - E_0(\nu_i)$ produced by vibrational excitation depends on the identity of the reactant's quantum state. For methane dissociation on Pt(110), for example, ΔE_0 is 33.6 kJ mol^{-1} for the pure stretch ($2\nu_3$) but only 20.9 kJ mol^{-1} for the pure bend ($2\nu_2 + \nu_4$) modes [32.98]. This phenomenon is often referred to as vibrational state (or mode) specificity.

Utz and coworkers reported [32.103] a compilation of results showing the change in the adsorption barrier

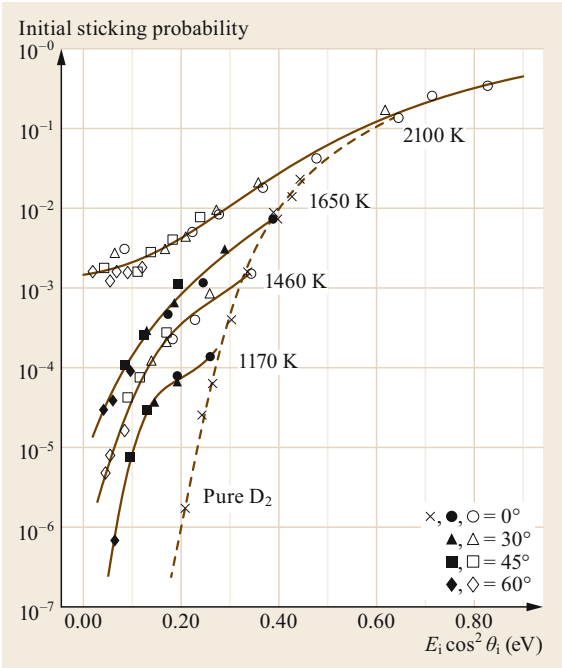

Fig. 32.24 Initial adsorption probability for D_2 on Cu(111) versus normal kinetic energy. Data obtained using seeded beams at four nozzle temperatures. The *solid line* is a guide to the eye through each set of data points recorded at the same nozzle temperature (Reprinted with permission from [32.99]. Copyright (1992) by the American Physical Society)

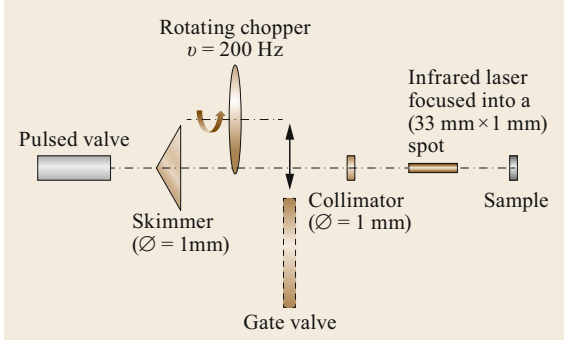

Fig. 32.25 Schematic of experimental setup. Methane seeded in H_2 is expanded, creating a pulsed supersonic molecular beam. The nozzle is opened by a valve operating at 20 Hz. The kinetic energy of the CH_4 molecules is controlled by the methane/H_2 ratio and by the temperature of the valve. A skimmer and a chopper control the profile of the beam and slice it into pulses. During its path to the sample (a single-crystal surface in these experiments), the molecular beam is irradiated by pulsed, tunable IR light to prepare a fraction (1–2%) in a specific rovibrationally excited quantum state. Sticking coefficients averaged over all vibrational states of methane populated in the beam were obtained from the ratio of the carbon coverage to the incident methane dose. Sticking coefficients for the state-selected CH_4 molecules were obtained from the difference between the coverages obtained with the laser on and off. (Data about the experimental setup taken from [32.105])

for different systems. These results are reported in Table 32.2.

Inspection of this table indicates that the excitation of the triply degenerate bending vibration $3\nu_4$ is much less effective than the excitation of the antisymmetric C–H ν_3, even though the amount of vibrational energy present in the former exceeds by 30% that available in the latter. These results contradict statistical theories of gas–surface reactivity and point to a central role for C–H stretching motion along the reaction path to dissociative chemisorption.

From this point of view, also the results shown for the adsorption of CH_4 on Ni(100) in Fig. 32.22 are not too surprising, since in this case the energy involved in the rotational motion is significantly lower than that provided by vibrational excitation.

The fundamentally nonstatistical nature of the phenomena is further proved by the experiment performed by *Killelea* et al. [32.115]. After exposing a clean Ni(111) surface to D atoms to preload the subsurface lattice sites with deuterium atoms, D adsorbed at the surface was removed (leaving only a residue of 0.03 ML) by recombinative desorption caused by the collision with Xe atoms. A surface prepared in this way is ready for testing with CHD_3 dissociation. The

Table 32.2 Compilation of experimental results about the efficacy of vibrational excitation of different quanta for CH_4 on different surfaces and for SiH_4 dissociation on Si(100) (1 × 2). The efficacy is defined here as the ratio between the change in the translational barrier ΔE_0 and the vibrational energy of the molecules (data taken from [32.103])

Molecule	State	E_{vib} (kJ mol^{-1})	Surface	ΔE_0 (kJ mol^{-1})	Efficacy
CH_4	ν_3	36	Ni(100)	34	0.94
CH_4	ν_3	71	Ni(100)	68	0.96
CH_4	ν_1	35	Ni(100)	50	1.4
CH_4	$3\nu_4$	45	Ni(100)	–	≤ 0.5
CH_4	ν_3	36	Ni(111)	45	1.25
CH_4	$2\nu_3$	71	Ni(111)	65	0.90
CH_4	$3\nu_4$	45	Ni(111)	34	0.72
CH_4	$2\nu_3$	71	Pt(111)	28	0.40
SiH_4	$\|2000\rangle$	53	Si(100) (1 × 2)	38	0.72
SiH_4	$\|1100\rangle$	55	Si(100) (1 × 2)	22	0.40

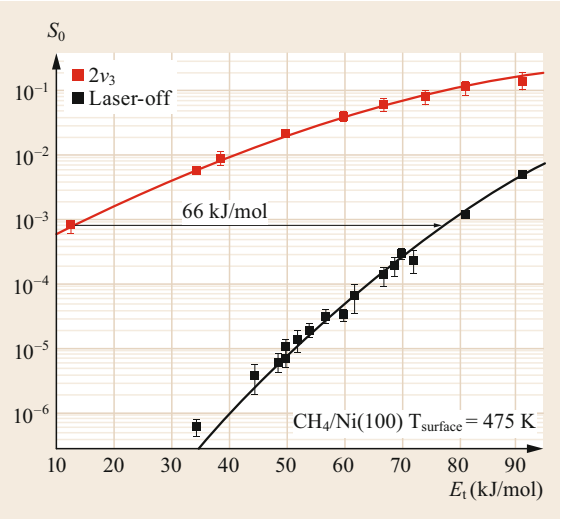

Fig. 32.26 The sticking coefficients measured for CH_4 molecules on a Ni(100) surface at a surface temperature of 475 K with two quanta of antisymmetric stretch ($2\nu_3$) vibration added through laser excitation and for vibrationally ground-state molecules at different kinetic energies. The *solid lines* show S-shape curve fits to the data (Reproduced from [32.98] with permission of The Royal Society of Chemistry)

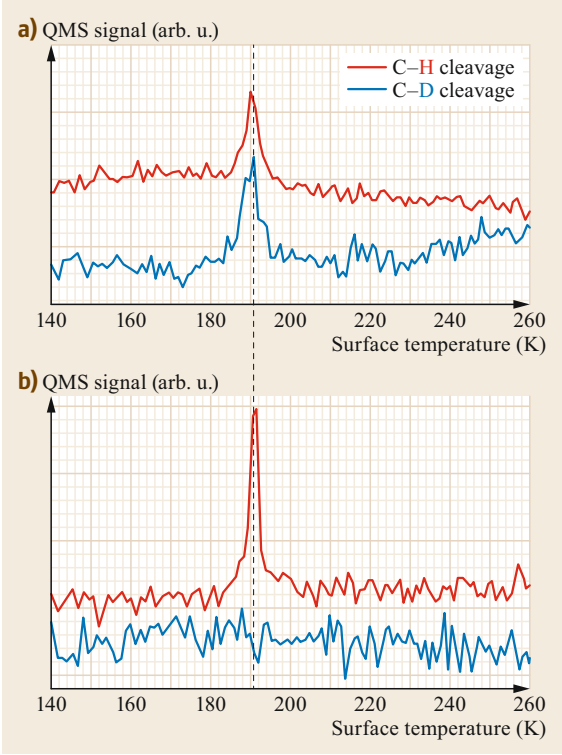

Fig. 32.27a,b Mass spectrometrically detected product yield for vibrationally mediated dissociative chemisorption of CHD_3 on Ni(111). **(a)** Yield of C–H and C–D cleavage products for a thermally populated ensemble of vibrational states. Approximately 40% of the molecules dissociated via C–H bond cleavage. In **(b)**, the product yield for CHD_3 molecules prepared in $\nu = 1$ of the ν_1 C–H stretching vibration is shown. At least 97% of the molecules dissociated via C–H bond cleavage (Reprinted from [32.103], with permission from Elsevier)

state-resolved experiments used a single-mode IR laser to excite CHD_3 to ν_1 ($\nu' = 1, J' = 2, K' = 0$) by the R(1)($\Delta K = 0$) transition at 3005.538 cm^{-1}. The vibrational energy (E_{vib}) is 36 kJ mol^{-1}, $\boldsymbol{J}'$ is the total angular momentum of the excited state, and $\boldsymbol{K}'$ is the projection of $\boldsymbol{J}'$ along the unique inertial axis.

The surface was exposed at 120 K, then temperature-programmed desorption was performed to check for the possible desorption products: D_2 (4 atomic mass units), CHD_3 (19 amu), and CD_4 (20 amu). During annealing, D atoms pre-embedded in the Ni lattice move to the surface, react with surface methyls, and form methane, which promptly desorbs. The integrated peak areas for 19 amu (CHD_3) and 20 amu (CD_4) provide a direct measure of C–D and C–H bond cleavage products, while Auger electron spectroscopy (AES) measurements were used to calibrate the coverage of desorbing species with respect to the surface coverage. The ratio of the two signals was used to quantify the branching ratio of C–D to C–H bond cleavage.

The product yields for C–H and C–D bond cleavage for thermal and state-resolved excitation of CHD_3 vibrations are compared in Fig. 32.27. In the upper panel (a), CHD_3 vibrations were thermally populated by keeping the source of the molecular beam at 600 K. The beam impinged on the surface with a kinetic energy of 57 kJ mol^{-1} and a vibrational energy of 5.9 kJ mol^{-1}. It was shown that about 40% of the reaction products were obtained from C–H bond cleavage while 60% were due to C–D bond cleavage. In the lower panel (b), the product yield for CHD_3 molecules prepared in $\nu = 1$ of the ν_1 C–H stretching vibration is shown. The vibrational energy is 36 kJ mol^{-1}, while the kinetic energy is still 57 kJ mol^{-1}, the total energy now being 93 kJ mol^{-1}. Since the yield of C–D bond cleavage products was below the detection limit (3%) of the total product yield, the authors could conclude that at least 97% of the molecules dissociated via C–H bond cleavage. The ratio between C–H and C–D bond cleavage was thus found to be higher than 30 : 1. In a complementary experiment, the authors compared this product ratio with that of another beam having the same total energy. By fixing the nozzle source at 830 K and using a 2% mixture of CHD_3 seeded in He, a beam with a ki-

netic energy of 80 kJ mol^{-1} and a vibrational energy of 14.4 kJ mol^{-1} for a total energy of 94 kJ mol^{-1} was obtained. Product yield measurements showed that 25% of the molecules dissociated via C–H bond cleavage. The corresponding C–H : C–D bond cleavage ratio was thus 1 : 3. Therefore, state-resolved excitation of the C–H stretching state altered the product ratio by nearly two orders of magnitude. This ensured that any differences in reactivity were not due to the total energy, but rather to the replacement of part of the incident kinetic energy with vibrational energy. The results of this experiment thus prove the nonstatistical nature of the underlying reaction mechanism.

A subsequent investigation using infrared spectroscopy extended this study to the chemisorption of all the partially deuterated methanes (CH_3D, CD_2H_2, and CHD_3) on Pt(111), reaching similar conclusions [32.116]. The results briefly reviewed here prove the relevant role played by vibrational energy in promoting methane dissociation and its nonstatistical nature. A key question now arises about the role of steric factors: does the orientation and or the alignment of the vibrationally excited molecule at impact influence its dissociation probability?

Circularly polarized light can be used to create an initially oriented sample where the population of the positive m levels is, for example, larger than that of the negative m levels, where m is the projection of $\boldsymbol{J}$ onto the quantization axis z. An aligned distribution can be prepared, on the other hand, by using linearly polarized light. Here, the population of the positive m level is the same as that of the negative m level while, for example, high $|m|$ levels are preferentially populated over low $|m|$ levels.

The possible transitions are classified into P, Q, and R branches according to the value of ΔJ (see top right panel in Fig. 32.28):

- $\Delta J = 0$ for the Q branch
- $\Delta J = -1$ for the P branch and
- $\Delta J = 1$ for the R branch.

We focus here on alignment, attainable by the adsorption of linearly polarized photons. Since a linearly polarized photon carries no angular momentum, the selection rule for the absorption of a linearly polarized photon is $\Delta m = 0$ and, for Q branch excitation only, $m \neq 0$.

Since the population of each m level in the excited state is the same, in the strong pumping limit (i.e., at high laser power) it is not possible to create an alignment using P branch excitation. On the contrary, both R and Q branch excitation are adequate to produce an initially aligned distribution, with $\boldsymbol{J}$ being aligned perpendicular to the laser polarization for R branch excitation and parallel to the laser polarization for Q branch excitation.

If weak pumping (i.e., a lower laser power) is used, the population transferred from the ground level to the excited level is proportional to the transition strength. Thus, it is possible to create alignment using P, Q, or R branch excitation.

The dependence of the initial chemisorption probability ($S_0(\theta)$) on the angle θ between the laser polarization and the plane of the surface is shown in Fig. 32.28. The aligned molecules were prepared through excitation of the ν_1 (C–H stretch) normal mode by linearly polarized IR light using rapid adiabatic passage. The alignment of the angular momentum causes also the alignment of the vibrational amplitude of the molecule, which for CHD_3 lies along the unique C–H bond.

When using Q branch excitation, both $\boldsymbol{J}$ and the C–H bond are aligned parallel to the polarization of the laser, while when using R branch excitation, the C–H bond is parallel and $\boldsymbol{J}$ is perpendicular to the polarization of the laser.

If the polarization of the laser is rotated, the alignment of the angular momentum $\boldsymbol{J}$ and of the C–H bond with respect to the plane of the surface are also modified. For R branch excitation, the sticking coefficient was found to decrease when the laser polarization was changed from parallel to perpendicular to the surface (Fig. 32.28a). The reactivity when the laser polarization is parallel to the surface (corresponding to $\theta = 0$) is up to 60% larger than when the laser polarization is aligned perpendicular to the surface ($\theta = 90°$).

The experiment was then repeated using Q branch excitation: the sticking probability was found to be larger when the laser polarization was parallel to the surface than perpendicular to it.

Since the direction of motion of the atoms due to the presence of the vibrational excitation is parallel to the laser polarization in both cases, while the direction of $\boldsymbol{J}$ is parallel to the polarization for Q branch excitation but perpendicular for R branch excitation, these experiments unambiguously demonstrate that the alignment effect is not due to the alignment of the angular momentum but to the alignment of the vibrational motion.

Yoder et al. also studied the alignment dependence of the dissociative chemisorption of CH_4 on Ni(100) when the ν_3 mode is excited. This mode corresponds to the antisymmetric C–H stretch normal mode, for which all four bonds vibrate with the same amplitude, although with different phases. Experiments show that the sticking probability is largest when the laser polarization is parallel to the surface, as shown in Fig. 32.28.

The Ni(100) surface was exposed to CH_4 molecules in a single rovibrationally excited state (one quantum of

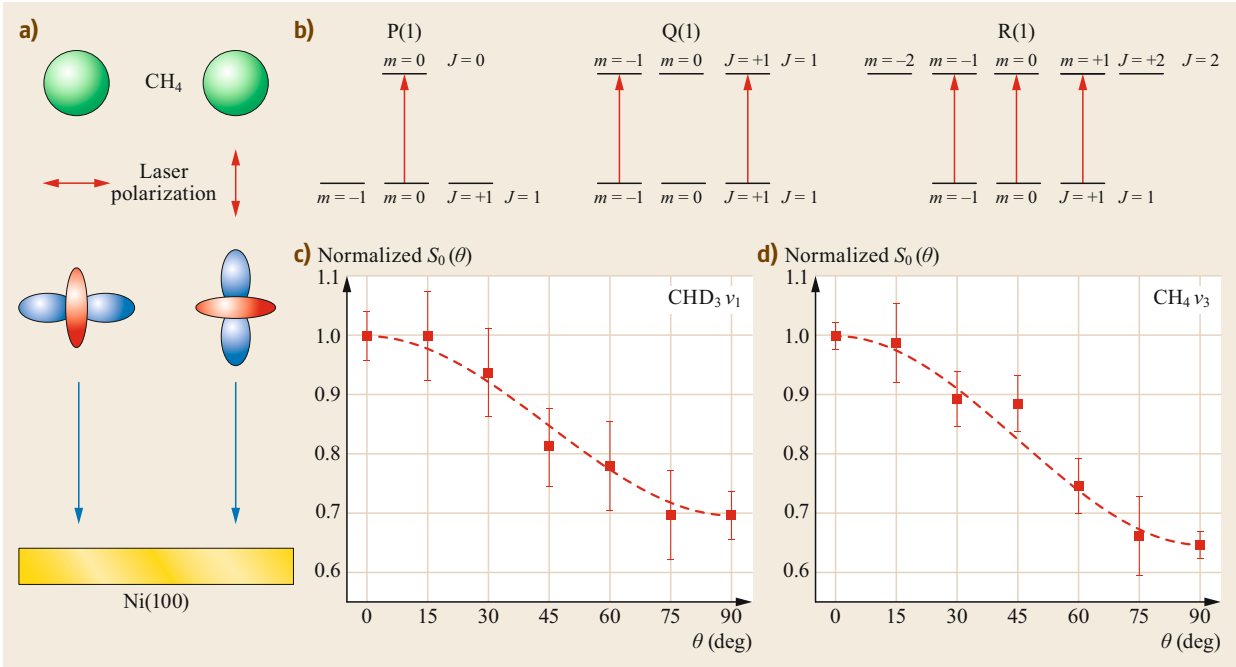

Fig. 32.28 **(a)** Schematic of the state-prepared and laser-aligned molecular beam deposition experiment. A molecular beam of CH_4 with initially isotropic spatial distribution of angular momentum $\boldsymbol{J}$ (*green spheres at top*) impinges on a Ni(100) surface at normal incidence (*yellow disc at bottom*). In their path towards the surface, the molecular beam is crossed by a continuous, linearly polarized laser beam focused in the direction of the molecular beam. Incident CH_4 molecules are prepared in a specific rovibrationally excited state by rapid adiabatic passage through the resonant laser beam. See [32.108] for details. The resulting probability distributions for $\boldsymbol{J}$ (*red*) and vibrational transition dipole moment $\boldsymbol{\mu}$ (*blue*) are shown for the case of R(0) excitation and two orthogonal polarization directions indicated by the *double-headed arrows*. **(b)** Scheme of the allowed transitions for P, Q, and R branch excitation for the absorption of a linearly polarized photon. **(c,d)** $S_0(\theta)$, normalized to the value measured when the laser polarization was parallel to the surface, as a function of the angle between the laser polarization and the surface (θ) for CHD_3 following ν_1 excitation **(c)** and CH_4 following ν_3 excitation **(d)**. The experimental data were obtained following R(0) excitation. The *line* is a guide to the eye (Reproduced from [32.98] with permission of The Royal Society of Chemistry)

the antisymmetric C–H stretch vibration ν_3 with aligned angular momentum $\boldsymbol{J}$ and with vibrational transition dipole moment in the laboratory frame) by using linearly polarized infrared radiation.

The preparation of the antisymmetric C–H stretch vibration ν_3 by using the R(0) transition at $3028.75\,\mathrm{cm}^{-1}$ ensures that alignment is attained by control of the laser polarization direction. Different laser polarization directions were employed, and the amount of C at the surface was then measured by Auger electron spectroscopy: the reactivity was found to be up to 60% higher with the laser polarization parallel to the plane of the surface than for perpendicular polarization.

If the preparation of the state is performed via the ν_3-P(1) transition, which produces no alignment of the excited molecules, no dependence of the reactivity on the direction of polarization is detected.

The dependence of the reactivity on the alignment of the vibrational motion demonstrates the absence of strong steering effects as the molecule approaches the surface: in the opposite case, the molecules would be turned when approaching the surface and S_0 would be independent of the angle of polarization of the laser.

Using similar experimental methods, the effect of vibrational energy on the physisorption of methane on Pt(111) has also been investigated [32.112]. It was found that vibrational excitation of the incident CH_4 with one quantum of ν_3 vibration does not produce any measurable effect on the trapping probability, in sharp contrast to the dissociative chemisorption process.

32.3 Conclusions

After briefly summarizing the main results obtained indirectly by use of detailed balance and by comparing experiments at different nozzle temperatures, we proceeded to highlight paradigmatic results obtained by preparing molecules in at least partially defined rotational and vibrationally excited states and measuring the sticking probability by the method of King and Wells.

We considered in particular:

a) Recent studies on chemical reactions of single-crystalline Si surfaces induced by oriented molecular beams prepared by the electrostatic hexapole technique. Steric effects were found in the dissociative adsorption of CH_3Cl on Si(100) surfaces. Trapping into a shallower precursor well plays an important role in the appearance of the observed steric effects. This conclusion is supported by the observation of steric effects in scattering processes in weakly bound systems of CH_3Cl on Si(111).
b) Recent studies on the adsorption of alignment-controlled molecular beams prepared by the magnetic hexapole technique. Precise control of the alignment (including spin) of a molecule is a new approach to the transition state for dissociative adsorption and for related chemical reactions.
c) Recent studies obtained by using collisional alignment of rotationally cold molecules in seeded beams. The latter method can be used for molecules having zero electric and magnetic moment, for which the former techniques cannot be applied. None of the systems investigated so far have shown steric anisotropy in the initial sticking probability on a bare surface, while large steric effects have been found at nonzero coverage. However, the possibility of tuning the final adsorption state by controlling the rotational alignment of the incoming molecule has been shown for O_2–Pd(100) as well as its effect on the reaction probability with preadsorbed CO.
d) State-of-the-art experiments in which molecules such as methane or water are prepared in well-defined vibrational states and their adsorption probability is measured as a function of kinetic energy. The dissociative adsorption probability turns out to be enhanced if appropriate vibrational modes are vibrationally excited, while the physisorption probability is not affected.
e) Dedicated experiments have shown the fundamentally nonstatistical nature of the role of vibrational energy in promoting dissociative adsorption (mode specificity).

Specific polarization (parallel to the surface) of the vibrational excitation is more effective than rotational alignment in promoting surface reactions when the vibrational excitation involves motion along the reaction coordinate.

We envisage two possible lines of development:

1) The use of oriented/aligned simple molecules to study and also control the selectivity of surface reactions and the synthesis of thin films.
2) The extension of these methods to more complex systems, such as model catalytic systems and biomolecular systems.

The coupling of such techniques with local probe microscopies [32.117] might in particular reveal new and still unexpected processes.

References

32.1 G. Scoles (Ed.): *Atomic and Molecular Beam Methods*, Vol. 1+2 (Oxford Univ. Press, New York Oxford 1988)
32.2 L. Vattuone, U. Valbusa, M. Rocca: Influence of rotational energy on adsorption probability for a physisorbed system: C_2H_4 on Ag(001), Phys. Rev. Lett. **82**, 4878–4881 (1999)
32.3 D.A. King, M.G. Wells: Molecular beam investigation of adsorption kinetics on bulk metal targets: nitrogen on tungsten, Surf. Sci. **29**, 454–482 (1972)
32.4 L. Vattuone, L. Savio, M. Rocca: Chemisorption dynamics in the presence of well defined surface defects. In: *Surface Dynamics*, ed. by D.P. Woodruff (Elsevier, Amsterdam 2003)
32.5 L. Savio, L. Vattuone, M. Rocca: Dynamics of the interaction of O_2 with stepped and damaged Ag surfaces, J. Phys. Condens. Matter. **14**, 6065–6079 (2002)
32.6 C.H. Townes, A.L. Schawlow: *Microwave Spectroscopy* (McGraw-Hill, New York 1955)
32.7 P.R. Brooks: Reactions of oriented molecules, Science **193**, 11–16 (1976)
32.8 K.H. Kramer, R.B. Bernstein: Focusing and orientation of symmetric-top molecules with the electric six-pole field, J. Chem. Phys. **42**, 767–770 (1965)
32.9 S. Stolte, J. Reuss, H.L. Schwartz: Orientational anisotropy in the total collision cross section of

state selected no molecules, Physica **66**, 211–216 (1973)
32.10 R. Zare: *Angular Momentum: Understanding Spatial Aspects in Chemistry and Physics*, 2nd edn. (Wiley, New York 1988)
32.11 D.H. Parker, R.B. Bernstein: Oriented molecule beams via the electrostatic hexapole: preparation, characterization, and reactive scattering, Annu. Rev. Phys. Chem. **40**, 561–595 (1989)
32.12 A.W. Kleyn: Non-reactive orientations of molecules at surfaces, Prog. Surf. Sci. **54**, 407–420 (1997)
32.13 T. Kasai, K. Kuwata: Chap. 19. In: *Steric Effects in Small Radical Formation in Advanced Series in Physical Chemistry*, Vol. 6, ed. by K. Liu, A. Wagner (World Scientific, Singapore 1995) p. 842
32.14 T. Seideman: Rotational excitation and molecular alignment in intense laser fields, J. Chem. Phys. **103**, 7887–7896 (1995)
32.15 A. Gross, M. Scheffler: Steering and ro-vibrational effects on dissociative adsorption and associative desorption of H_2 / Pd(100), Prog. Surf. Sci. **53**, 187–196 (1997)
32.16 G.J. Kroes: Six-dimensional quantum dynamics of dissociative chemisorption of H_2 on metal surfaces, Prog. Surf. Sci. **60**, 1–85 (1999)
32.17 A. Hodgson: State resolved desorption measurements as a probe of surface reactions, Prog. Surf. Sci. **63**, 1–61 (2000)
32.18 G.O. Sitz: Gas surface interactions studied with state-prepared molecules, Rep. Prog. Phys. **65**, 1165–1193 (2002)
32.19 H. Staplelfeldt, T. Seideman: Colloquium: Aligning molecules with strong laser pulses, Rev. Mod. Phys. **75**, 543–557 (2003)
32.20 D. Herschbach: Chemical stereodynamics: Retrospect and prospect, Eur. Phys. J. D **38**, 3–13 (2006)
32.21 L. Vattuone, L. Savio, F. Pirani, D. Cappeletti, M. Okada, M. Rocca: Interaction of rotationally aligned and of oriented molecules in gas phase and at surfaces, Prog. Surf. Sci. **85**, 92–160 (2010)
32.22 C. Vallance: Generation, characterisation, and applications of atomic and molecular alignment and orientation, Phys. Chem. Chem. Phys. **13**, 14427–14441 (2011)
32.23 M. Kurahashi: Oxygen adsorption on surfaces studied by a spin- and alignment-controlled O_2 beam, Prog. Surf. Sci. **91**, 29–55 (2016)
32.24 C.T. Rettner, H.A. Michelsen, D.J. Auerbach: Quantum-state-specific dynamics of the dissociative adsorption and associative desorption of H_2 at a Cu(111) surface, J. Chem. Phys. **102**, 4625–4641 (1995)
32.25 H.A. Michelsen, C.T. Rettner, D.J. Auerbach, R.N. Zare: Effect of rotation on the translational and vibrational energy dependence of the dissociative adsorption of D_2 on Cu(111), J. Chem. Phys **98**, 8294–8307 (1993)
32.26 H. Hou, S.J. Gulding, C.T. Rettner, A.M. Wodtke, D.J. Auerbach: The stereodynamics of a gas–surface reaction, Science **277**, 80–82 (1997)
32.27 T.F. Hanisco, A.C. Kummel: Rotationally inelastic scattering of N_2 from W(110), J. Vac. Sci. Technol. A **11**, 1907–1913 (1993)
32.28 G.O. Sitz, A.C. Kummel, R.N. Zare: Alignment and orientation of N_2 scattered from Ag(111), J. Chem. Phys. **87**, 3247–3248 (1987)
32.29 G.O. Sitz, A.C. Kummel, R.N. Zare: Direct inelastic scattering of N_2 from Ag(111). I. Rotational populations and alignment, J. Chem. Phys. **89**, 2558–2571 (1988)
32.30 M. Beutl, K.D. Rendulic, G.R. Castro: Does the rotational state of a molecule influence trapping in a precursor? An investigation of N_2/W(100), CO/FeSi(100) and O_2/Ni(111), Surf. Sci. **385**, 97–106 (1997)
32.31 M. Beutl, M. Riedler, K.D. Rendulic: Adsorption dynamics for para- and n-hydrogen on Pt(110), Chem. Phys. Lett. **256**, 33–36 (1996)
32.32 M. Beutl, M. Riedler, K.D. Rendulic: Strong rotational effects in the adsorption dynamics of H_2/Pd(111): Evidence for dynamical steering, Chem. Phys. Lett. **24**, 249–252 (1995)
32.33 T. Sugimoto, K. Fukutani: Effects of rotational-symmetry breaking on physisorption of ortho- and para-H_2 on Ag(111), Phys. Rev. Lett. **112**, 146101 (2014)
32.34 S. Andersson, J. Harris: Observation of rotational transitions for H_2, D_2, and HD adsorbed on Cu(100), Phys. Rev. Lett. **48**, 545–548 (1982)
32.35 S. Andersson, L. Wilzen, M. Persson, J. Harris: Sticking in the quantum regime: H_2 and D_2 on Cu(100), Phys. Rev. B **40**, 8146–8168 (1989)
32.36 L. Amiaud, A. Momeni, F. Dulieu, J.H. Fillion, E. Matar, J.L. Lemaire: Measurement of the adsorption energy difference between ortho- and para-D_2 on an amorphous ice surface, Phys. Rev. Lett **100**, 056101 (2008)
32.37 K. Fukutani, T. Sugimoto: Physisorption and ortho–para conversion of molecular hydrogen on solid surfaces, Prog. Surf. Sci. **88**, 279–348 (2013)
32.38 R.T. Jongma, G. Berden, D. van der Zande, T. Rasing, H. Zacharias, G. Meijer: State-to-state scattering of metastable CO molecules from a LiF(100) surface, Phys. Rev. Lett. **78**, 1375–1378 (1997)
32.39 K.M. Backstrand, M.A. Weibel, R.M. Moision, T.J. Curtiss: Temperature programmed desorption studies of OD coadsorbed with H_2 on Pt(111), J. Chem. Phys. **112**, 7209–7218 (2000)
32.40 H.L. Bethlem, G. Berden, F.M.H. Crompvoets, R.T. Jongma, A.J.A. van Roij, G. Meijer: Electrostatic trapping of ammonia molecules, Nature **406**, 491–494 (2000)
32.41 E.W. Kuipers, M.G. Tenner, A.W. Kleyn, S. Stolte: Observation of steric effects in gas-surface scattering, Nature **334**, 420–422 (1988)
32.42 F.H. Geuzebroek, A.E. Wiskerke, M.G. Tenner, A.W. Kleyn, S. Stolte, A. Namiki: Rotational excitation of oriented molecules as a probe of molecule-surface interaction, J. Phys. Chem. **95**, 8409–8421 (1991)

32.43 E.W. Kuipers, M.G. Tenner, A.W. Kleyn, S. Stolte: Steric effects for NO/Pt(111) adsorption and scattering, Phys. Rev. Lett. **62**, 2152–2155 (1989)

32.44 R.J.W.E. Lahaye, S. Stolte, S. Holloway, A.W. Kleyn: Orientation and energy dependence of NO scattering from Pt(111), J. Chem. Phys. **104**, 8301–8311 (1996)

32.45 A.J. Komorowski, H. Ternow, R. Razaznejad, B. Berenbak, J.Z. Sexton, I. Zoric, B. Kasemo, B.I. Lundqvist, S. Stolte, A.W. Kleyn, A.C. Kummel: Dissociative adsorption of NO upon Al(111): Orientation dependent charge transfer and chemisorption reaction dynamics, J. Chem. Phys. **117**, 8185–8189 (2002)

32.46 G.H. Fecher, N. Böwering, M. Volkmer, B. Pawlitzky, U. Heinzmann: Dependence of the sticking probability on initial molecular orientation: NO on Ni(100), Surf. Sci. **230**, L169–L172 (1990)

32.47 M. Brandt, H. Müller, G. Zagatta, O. Wehmeyer, N. Böwering, U. Heinzmann: Sticking and scattering of gas-phase oriented NO at Pt(100) as a function of the translational energy and of molecular orientation, Surf. Sci. **331–333**, 30–34 (1995)

32.48 M. Hashinokuchi, M. Okada, H. Ito, T. Kasai, K. Moritani, Y. Teraoka: Stereodynamics in dissociative adsorption of NO on Si(111), Phys. Rev. Lett. **100**, 256104 (2008)

32.49 R.S. Mackay, T.J. Curtiss, R.B. Bernstein: Determination of preferred orientation for sticking of polar molecules in beams incident on a graphite (0001) surface, Chem. Phys. Lett. **164**, 341–344 (1989)

32.50 M. Brandt, T. Gerber, N. Böwering, U. Heinzmann: The role of molecular state and orientation in harpooning reactions: N_2O on Cs/Pt(111), Phys. Rev. Lett. **81**, 2376–2379 (1998)

32.51 T.J. Curtiss, R.B. Bernstein: Steric effect in the scattering of oriented CH_3F molecules by graphite (0001), Chem. Phys. Lett. **161**, 212–218 (1989)

32.52 T.J. Curtiss, R.S. Mackay, R.B. Bernstein: Steric effect in the scattering of hexapole-oriented beams of symmetric-top molecules by graphite(0001), J. Chem. Phys. **93**, 7387–7405 (1990)

32.53 S.I. Ionov, M.E. Lavilla, R.S. Mackay, R.B. Bernstein: Surface temperature dependence of the steric effect in the scattering of oriented tert-butyl chloride and fluoroform molecules by graphite(0001), J. Chem. Phys. **93**, 7406–7415 (1990)

32.54 M. Okada, S. Goto, T. Kasai: Dynamical steric effect in the decomposition of methyl chloride on a silicon surface, Phys. Rev. Lett. **95**, 176103 (2005)

32.55 M. Okada, S. Goto, T. Kasai: Steric effects in dissociative adsorption of low-energy CH_3Cl on Si(100): orientation and steering effects, J. Phys. Chem. C **112**, 19612–19615 (2008)

32.56 M. Okada, S. Goto, T. Kasai: Reaction-path selection with molecular orientation of CH_3Cl on Si(100), J. Am. Chem. Soc. **129**, 10052–10053 (2007)

32.57 H. Ito, M. Okada, D. Yamazaki, T. Kasai: Steric effects in the scattering of oriented CH_3Cl molecular beam from a Si(111) surface, J. Phys. Chem. A **114**, 3080–3086 (2010)

32.58 T. Fukuyama, M. Okada, T. Kasai: Steric effects in the scattering of oriented CH_3Cl molecular beam from a graphite surface: weak interaction of physisorption, J. Phys. Chem. A **113**, 14749–14754 (2009)

32.59 M. Hashinokuchi, T. Fukuyama, M. Okada, T. Kasai: Kinetics and dynamics in physisorption of CH_3Cl on HOPG: Surface temperature and molecular orientation dependence, Phys. Chem. Chem. Phys. **13**, 6584–6589 (2011)

32.60 M. Okada: Surface chemical reactions induced by well-controlled molecular beams: Translational energy and molecular orientation control, J. Phys. Condens. Matter **22**, 263003 (2010)

32.61 M. Okada: Supersonic molecular beam experiments on surface chemical reactions, Chem. Rec. **14**, 775–790 (2014)

32.62 M. Okada, K. Moritani, S. Goto, T. Kasai: New development of ultrahigh-vacuum oriented-molecular-beam machine and its application to chemical reactions on silicon surface, Jpn. J. Appl. Phys. **44**, 8580–8589 (2005)

32.63 S.E. Choi, R.B. Bernstein: Theory of oriented symmetric-top molecule beams: precession, degree of orientation, and photofragmentation of rotationally state-selected molecules, J. Chem. Phys. **85**, 150–161 (1986)

32.64 S.E. Choi, R.B. Bernstein: Orientational opacity function for CH_3I+Rb reactive backscattering: the steric cone of nonreaction, J. Chem. Phys. **83**, 4463–4469 (1985)

32.65 M. Kurahashi, Y. Yamauchi: Production of a single spin-rotational state $[(J; M) = (2, 2)]$ selected molecular oxygen beam by a hexapole magnet, Rev. Sci. Instrum. **80**, 083103 (2009)

32.66 M. Kurahashi, Y. Yamauch: Fully alignment-specified O_2 chemisorption on vicinal Si(100), J. Chem. Phys. **140**, 031102 (2014)

32.67 M. Kurahashi, Y. Yamauchi: Huge steric effects in surface oxidation of Si(100), Phys. Rev. B **85**, 161302 (2012)

32.68 M. Kurahashi, Y. Yamauchi: Steric effect in O_2 sticking on Al(111): preference for parallel geometry, Phys. Rev. Lett. **110**, 246102 (2013)

32.69 M. Kurahashi, Y. Yamauchi: Spin correlation in O_2 chemisorption on Ni(111), Phys. Rev. Lett. **114**, 016101 (2015)

32.70 H. Senftleben: Effects of magnetic fields on paramagnetic gas heat conductivity, Phys. Z. **31**, 822 (1930)

32.71 H. Senftleben: Further studies concerning the effects of magnetic fields on paramagnetic gas heat conductivity, Phys. Z. **31**, 961–963 (1930)

32.72 C.J. Gorter: Interpretation of the Senftleben effect, Naturwissenschaften **26**, 140 (1938)

32.73 J.J.M. Beenakker, G. Scoles, H.F.P. Knaab, J.M. Jonkman: The influence of magnetic field on transport properties of diatomic molecules in gaseous state, Phys. Lett. **2**, 5–6 (1962)

32.74 N.F. Ramsey: Collision alignment of molecules, atoms, and nuclei, Phys. Rev. **98**, 1853–1854 (1955)

32.75 M.P. Sinha, C.D. Caldwell, R.N. Zare: Alignment of molecules in gaseous transport: alkali dimers in supersonic nozzle beams, J. Chem. Phys. **61**, 491–503 (1974)

32.76 A.G. Visser, J.P. Bekooy, L.K. van der Meij, C. de Vreugd, J. Korving: Angular momentum polarization in molecular beams of I_2 and Na_2, Chem. Phys. **20**, 391–408 (1977)

32.77 V. Aquilanti, D. Ascenzi, D. Cappelletti, F. Pirani: Velocity dependence of collisional alignment of oxygen molecules in gaseous expansions, Nature **371**, 399–401 (1994)

32.78 V. Aquilanti, D. Ascenzi, D. Cappelletti, R. Fedeli, F. Pirani: Molecular beam scattering of nitrogen molecules in supersonic seeded beams: a probe of rotational alignment, J. Phys. Chem. A **101**, 7648–7656 (1997)

32.79 F. Pirani, M. Bartolomei, V. Aquilanti, M. Scotoni, M. Vescovi, D. Ascenzi, D. Bassi, D. Cappelletti: Collisional orientation of benzene molecular plane in supersonic seeded expansions probed by infrared polarized laser absorption spectroscopy and by molecular beam scattering, J. Chem. Phys. **119**, 265–276 (2003)

32.80 D. Cappelletti, M. Bartolomei, V. Aquilanti, F. Pirani, G. De Marchi, D. Bassi, S. Iannotta, M. Scotoni: Alignment of ethene molecules in supersonic seeded expansions probed by infrared polarized laser absorption and by molecular beam scattering, Chem. Phys. Lett. **420**, 47–53 (2006)

32.81 F. Pirani, D. Cappelletti, M. Bartolomei, V. Aquilanti, G. De Marchi, P. Tosi, M. Scotoni: The collisional alignment of acetylene molecules in supersonic seeded expansions probed by infrared absorption and molecular beam scattering, Chem. Phys. Lett. **437**, 176–182 (2007)

32.82 V. Aquilanti, D. Ascenzi, M. Bartolomei, D. Cappelletti, S. Cavalli, M. De Castro-Vıtores, F. Pirani: Quantum interference scattering of aligned molecules: Bonding in O_4 and role of spin coupling, Phys. Rev. Lett. **82**, 69–72 (1999)

32.83 V. Aquilanti, D. Ascenzi, M. Bartolomei, D. Cappelletti, S. Cavalli, M. De Castro-Vıtores, F. Pirani: Molecular beam scattering of aligned oxygen molecules. the nature of the bond in the O_2–O_2 dimer, J. Am. Chem. Soc. **121**, 10794–10802 (1999)

32.84 L. Vattuone, A. Gerbi, M. Rocca, U. Valbusa, F. Pirani, F. Vecchiocattivi, D. Cappelletti: Stereodynamic effects in the adsorption of ethylene onto a metal surface, Angew. Chem. Int. Ed. **43**, 5200–5203 (2004)

32.85 A. Gerbi, L. Savio, L. Vattuone, F. Pirani, D. Cappelletti, M. Rocca: Role of rotational alignment in dissociative chemisorption and oxidation: O_2 on bare and CO-precovered Pd(100), Angew. Chem. Int. Ed. **45**, 6655–6658 (2006)

32.86 A. Gerbi, L. Vattuone, M. Rocca, F. Pirani, U. Valbusa, D. Cappelletti, F. Vecchiocattivi: Stereodynamic effects in the adsorption of propylene molecules on Ag(001), J. Phys. Chem. B. **109**, 22884–22889 (2005)

32.87 A. Gerbi, L. Vattuone, M. Rocca, U. Valbusa, F. Pirani, D. Cappelletti, F. Vecchiocattivi: New insights on the stereodynamics of ethylene adsorption on an oxygen-precovered silver surface, J. Chem. Phys. **123**, 224709 (2005)

32.88 L. Vattuone, A. Gerbi, D. Cappelletti, F. Pirani, R. Gunnella, L. Savio, M. Rocca: Selective production of reactive and nonreactive oxygen atoms on Pd(001) by rotationally aligned oxygen molecules, Angew. Chem. Int. Ed. **48**, 4845–4848 (2009)

32.89 L. Vattuone, A. Gerbi, L. Savio, D. Cappelletti, F. Pirani, M. Rocca: Stereoselectivity in catalytic reactions: CO oxidation on Pd (100) by rotationally aligned O_2 molecules, Eur. Phys. J. B **75**, 81–87 (2010)

32.90 L. Vattuone, L. Savio, F. Pirani, M. Rocca: Sticking probability and reactivity of hyperthermal O_2 molecules impinging on CO pre-covered Pd (100): effect of rotational states with $K > 1$, Top. Catal. **58**, 580–590 (2015)

32.91 D. Cappelletti, F. Pirani, M. Scotoni, G. De Marchi, L. Vattuone, A. Gerbi, M. Rocca: Cooling and alignment of ethene molecules in supersonic seeded expansions: diagnostic and application to gas phase and surface scattering experiments, Eur. Phys. J. D **38**, 121–127 (2006)

32.92 D. Cappelletti, A. Gerbi, F. Pirani, M. Rocca, M. Scotoni, L. Vattuone, U. Valbusa: Collisionally aligned molecular beams: a tool for stereodynamical studies in the gas phase and at surfaces, Phys. Scr. **73**, C20–C24 (2006)

32.93 V. Aquilanti, D. Ascenzi, M. de Castro Vıtores, F. Pirani, D. Cappelletti: A quantum mechanical view of molecular alignment and cooling in seeded supersonic expansions, J. Chem. Phys. **111**, 2620–2632 (1999)

32.94 F. Pirani, D. Cappelletti, F. Vecchiocattivi, L. Vattuone, A. Gerbi, M. Rocca, U. Valbusa: A simple and compact mechanical velocity selector of use to analyze and select molecular alignment in supersonic seeded beams, Rev. Sci. Instrum. **75**, 349–354 (2004)

32.95 P.R. McCabe, L.B.F. Juurlink, A.L. Utz: A molecular beam apparatus for eigenstate-resolved studies of gas–surface reactivity, Rev. Sci. Instrum. **71**, 42–53 (2000)

32.96 K. Navin, S.B. Donald, D.G. Tinney, G.W. Cushing, I. Harrison: Communication: angle-resolved thermal dissociative sticking of CH_4 on Pt(111): Further indication that rotation is a spectator to the gas-surface reaction dynamics, J. Chem. Phys. **136**, 061101 (2012)

32.97 L.B.F. Juurlink, R.R. Smith, A.L. Utz: The role of rotational excitation in the activated dissociative chemisorption of vibrationally excited methane on Ni(100), Faraday Discuss. **117**, 147–160 (2000)

32.98 H. Chadwick, R.D. Beck: Quantum state resolved gas–surface reaction dynamics experi-

ments: A tutorial review, Chem. Soc. Rev. **45**, 3567–3758 (2016)
32.99 C.T. Rettner, D.J. Auerbach, H.A. Michelsen: Role of vibrational and translational energy in the activated dissociative adsorption of D_2 on Cu(111), Phys. Rev. Lett. **68**, 1164–1167 (1992)
32.100 H. Hou, Y. Huang, S.J. Gulding, C.T. Rettner, D.J. Auerbach, A.M. Wodtke: Enhanced reactivity of highly vibrationally excited molecules on metal surfaces, Science **284**, 1647–1650 (1999)
32.101 J.D. White, J. Chen, D. Matsiev, D.J. Auerbach, A.M. Wodtke: Conversion of large-amplitude vibration to electron excitation at a metal surface, Nature **433**, 503–505 (2005)
32.102 L.B.F. Juurlink, D.R. Killelea, A.L. Utz: State-resolved probes of methane dissociation dynamics, Prog. Surf. Sci. **85**, 69–134 (2009)
32.103 A.L. Utz: Mode selective chemistry at surfaces, Curr. Opin. Solid State Mater. Sci. **13**, 4–12 (2009)
32.104 L.B.F. Juurlink, P.R. McCabe, R.R. Smith, C.L. DiCologero, A.L. Utz: Eigenstate-resolved studies of gas-surface reactivity: $CH_4(\nu_3)$ dissociation on Ni(100), Phys. Rev. Lett. **83**, 868–871 (1999)
32.105 R.D. Beck, P. Maroni, D.C. Papageorgopoulos, T.T. Dang, M.P. Schmid, T.R. Rizzo: Vibrational mode-specific reaction of methane on a nickel surface, Science **302**, 98–100 (2003)
32.106 P. Maroni, D.C. Papageorgopoulos, M. Sacchi, T.T. Dang, R.D. Beck, T.R. Rizzo: State-resolved gas-surface reactivity of methane in the symmetric C–H stretch vibration on Ni(100), Phys. Rev. Lett. **94**, 246104 (2005)
32.107 L.B.F. Juurlink, R.R. Smith, D.R. Killelea, A.L. Utz: Comparative study of C–H stretch and bend vibrations in methane activation on Ni(100) and Ni(111), Phys. Rev. Lett. **94**, 208303 (2005)
32.108 B.L. Yoder, R. Bisson, R.D. Beck: Steric effects in the chemisorption of vibrationally excited methane on Ni(100), Science **329**, 553–556 (2010)
32.109 J. Kim, G.O. Sitz: The sticking of $H_2(v = 1, J = 1)$ on Cu(100) measured using laser-induced thermal desorption, Mol. Phys. **108**, 1027–1032 (2010)
32.110 P.M. Hundt, B. Jiang, M.E. van Reijzen, H. Guo, R.D. Beck: Vibrationally promoted dissociation of water on Ni(111), Science **344**, 504–507 (2014)
32.111 P.M. Hundt, M.E. van Reijzen, H. Ueta, R.D. Beck: Vibrational activation of methane chemisorption: The role of symmetry, J. Phys. Chem. Lett. **5**, 1963–1967 (2014)
32.112 L. Chen, H. Ueta, H. Chadwick, R.D. Beck: The negligible role of C–H stretch excitation in the physisorption of CH_4 on Pt(111), J. Phys. Chem. C **119**, 14499–14505 (2015)
32.113 E. Dombrowski, E. Peterson, D. Del Sesto, A.L. Utz: Precursor-mediated reactivity of vibrationally hot molecules: Methane activation on Ir(111), Catal. Today **244**, 10–18 (2015)
32.114 V.L. Campbell, N. Chen, H. Guo, B. Jackson, A.L. Utz: Substrate vibrations as promoters of chemical reactivity on metal surfaces, J. Phys. Chem. A **119**, 12434–12441 (2015)
32.115 D.R. Killelea, V.L. Campbell, N.S. Shuman, A.L. Utz: Bond-selective control of a heterogeneously catalyzed reaction, Science **319**, 790–793 (2008)
32.116 L. Chen, H. Ueta, R. Bisson, R.D. Beck: An ultrahigh vacuum single crystal adsorption microcalorimeter, Faraday Discuss. **157**, 285–295 (2012)
32.117 M. Smerieri, R. Reichelt, L. Savio, L. Vattuone, M. Rocca: Coupling scanning tunneling microscope and supersonic molecular beams: a unique tool for in situ investigation of the morphology of activated systems, Rev. Sci. Instrum. **83**, 093703 (2012)

Luca Vattuone

Dipt. di Fisica
Università di Genova and IMEM-CNR Unità di Genova
Genova, Italy
vattuone@fisica.unige.it

Luca Vattuone received his PhD from the University of Genoa in 1994, worked as postdoc at Cambridge University (1995) and at Genoa University (1996–1999). In 1999 he became Staff Researcher and in 2012 Associate Professor of Condensed Matter Physics at Genoa University. His research activity focuses on the experimental investigation of gas–surface interactions and surface plasmons.

Michio Okada

Institute for Radiation Sciences and Department of Chemistry, Graduate School of Science
Osaka University
Osaka, Japan
okada@chem.sci.osaka-u.ac.jp

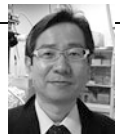

Michio Okada received his PhD from the University of Tokyo in 1993. He has worked at the University of Tennessee and Oak Ridge National Laboratory in the USA and at Osaka University in Japan, and is now a full professor at Osaka University. His research interests lie in the exploration of surface chemistry using molecular and ion beams.

Part H Chemical

Part H Chemical Reactions At Surfaces

Part H addresses the realm of surface reactions that occur under conditions similar to those present in catalytic industrial reactors. Surface reactions in the heterogenous phase can occur at either the gas–solid interface or the liquid–solid interface. The former case can be investigated under controlled ultrahigh-vacuum conditions; the latter by electrochemistry. The choice of catalyst for a particular product is dictated by not only thermodynamic and kinetic arguments but also—due to their impact in industrial processes—economic considerations, leading to a compromise between efficiency, selectivity, and costs.

It is necessary to underline that processes which can be investigated by surface science methods under controlled conditions are rather different from those that occur in industrial catalysis due to major differences in pressure and structure. The former arises because the typical pressure of an ultrahigh vacuum (UHV) is far lower than the atmospheric or higher pressures employed in reactors. The latter relates to the need to investigate single-crystal surfaces with very low defectivities to understand model systems and surfaces, even though these surfaces are quite different from those of the powders used in real catalysis. Studies performed at relatively high pressures (up to several mbar) and investigations of polycrystals have become feasible only very recently.

In electrochemistry, the application of a potential difference and the use of metallic electrodes introduces the possibility of adding energy to the system, thus facilitating endothermic reactions while exploiting the catalytic activity of the surface of the electrode. Experiments can be performed in highly controlled conditions, but additional variables are introduced since the nanoparticle morphology often depends on the external pressure, the concentrations of the reactants, and the pH of the environment.

Chapter 33 provides a synthetic overview of acidic, basic, oxidation, hydrogenation, and dehydrogenation catalysis utilizing metal, oxide, sulfide, and halide catalytic materials. The roles of promoters and stabilizers are explained. The catalytic system is often characterized by high complexity (it involves several components and different phases), which is difficult to address in fundamental surface science studies. As an example, the high-pressure steam reforming process for producing hydrogen from natural gas is described in detail. Attention is paid to the role of the Ni catalyst, as well as to the influence of the substrate that acts as a support. The roles of promoters and stabilizers are presented as well. These factors influence the choice of the reactor and the flow conditions to ensure the highest efficiency and selectivity.

Chapter 34 is devoted to electrocatalysis and focuses in particular on Pt and Au electrodes. Platinum (either pure or alloyed) is widely used in reactions relating to fuel cell technology, such as the hydrogen evolution reaction, hydrogen oxidation, oxygen reduction, and the oxidation of small organic molecules. Au electrodes are discussed for comparison. Starting from Faraday's law, the authors describe the correlation between the voltammetric behaviors of different solutions and the structure of the surface of the active electrode. The voltammetric signatures of several surface processes such as adsorption, surface reconstruction, faceting, and electrochemical reactivity are addressed, evidencing the roles of parameters such as the potential of zero charge and the maximum entropy.

33. From Surface Science to Industrial Heterogeneous Catalysis

Guido Busca

The different types of heterogeneous catalyst currently applied in the chemical industry are described. The catalytic activity is correlated to their main surface properties, which are the object of investigation based on surface science and theoretical calculations. Acidic, basic, oxidation, hydrogenation, and dehydrogenation catalysts are described. Metal, oxide, sulfide, and halide catalytic materials are considered. The practical need for promoters and stabilizers is underlined, frequently resulting in multicomponent and multiphasic catalytic systems. The complexity and multidisciplinarity of the field of heterogeneous catalysis research are emphasized, where collaboration among chemical engineers, material scientists, physical, inorganic, and organic chemists, and surface and material physicists is needed to fully understand phenomena and develop technologies. As a case study, the steam reforming process for producing hydrogen from natural gas is considered. The available data make it clear that knowledge on the molecular phenomena for most industrial processes is still largely incomplete and subject to debate. It is emphasized that surface science and surface chemistry, as well as computational studies, are needed to further improve existing technologies and to apply heterogeneous catalytic processes in the new era of industrial chemistry based on renewables.

M. Rocca, T.S. Rahman, L. Vattuone (Eds.), *Springer Handbook of Surface Science*, Springer Handbooks,
https://doi.org/10.1007/978-3-030-46906-1_33

33.1 Industrial Chemistry and Catalysis

Chemical technologies provide processes for the large-scale production of the materials (i.e., polymers, metals, semiconductors, etc.) and molecules (e.g., pharmaceuticals, cosmetics, detergents, etc.) that are essential for all other technologies (e.g., information and telecommunication technologies) and disciplines (e.g., medicine) as well as for household and personal life. In spite of the evident concerns associated with environment degradation, there is no doubt that industrial chemistry has been a major leading actor in the exponential technological development that has occurred over the last 150 years, allowing for the high level of wealth reached today by most of the population of developed countries. Unfortunately, this high level of wealth has not reached most of the population of less developed countries, as well as part of the inhabitants of industrialized countries. However, this is a matter of politics more than science and technology.

As first recognized by the Swedish chemist J. J. Berzelius in 1835 [33.1], catalysis is a phenomenon allowing a chemical reaction to occur faster when a nonreactant species is present. Catalysis gives rise to very relevant practical effects. In fact, such an increase in the rate of a reaction can in many cases result in practical feasibility. The acceleration of a desirable chemical conversion frequently allows it to be realized instead of other less desirable, competitive reactions, which become relatively slower. Thus, finding an appropriate catalyst to make the desired reaction faster than competing ones, as well as allowing it to be performed with high efficiency, is crucial to the development of industrial processes. For more than a century, heterogeneous catalysis has been a keystone of industrial chemistry [33.2].

33.2 Industrial Heterogeneous Catalysis and Catalysts

In practice, a large majority (likely $< 90\%$) of industrial chemical processes are catalyzed, and most of them are catalyzed by solids. World demand for catalysts is growing at a high rate, and the global market is expected to reach US $40B by 2022, up from US $28.6B in 2015, with a compounded average growth rate (CAGR) of 4.8% from 2016 to 2022 [33.3]. Refinery catalysts, environmental protection catalysts, polymerization catalysts, and chemical synthesis catalysts share the market.

The main reasons for using catalysts can be summarized as follows:

1. The use of a catalyst allows a desired reaction to become faster than competing reactions, thus allowing its practical realization.
2. For exothermic equilibrium reactions, the use of a catalyst also allows the reaction to be performed at a lower temperature at which it would be kinetically hindered otherwise. This allows the reaction to be realized in conditions where the thermodynamics is more favorable.
3. For endothermic equilibrium reactions, the use of a catalyst also allows the reaction to be performed at moderately high temperatures, where it would be kinetically hindered otherwise. This allows the reaction to be realized in conditions where the thermodynamics is already quite favorable with lower energy waste and using cheaper materials in the reactor.
4. For exothermic nonequilibrium reactions, the use of a catalyst allows reactions that are otherwise less favorable in terms of thermodynamics and kinetics to be realized instead of more favored and otherwise faster reactions.
5. The use of a better catalyst allows reactions to be performed in smaller flow reactors but with the same performance, or with better performance and fewer recycles of unconverted reactants in the same reactor, or even in shorter times in batch reactors.

In industry, solid catalysts are usually preferred over liquid catalysts because of their easier separation from the reaction fluid. Moreover, solid catalysts are

Table 33.1 Summary of some of the most relevant families of industrial catalysts and examples of their applications

Catalyst family	Reaction	Industrial catalyst	Catalyst functionality
Oxide catalysts			
Bulk single oxide	Alcohol dehydration to olefins and ethers	γ-Al_2O_3	Lewis acidic catalyst
Bulk mixed oxide	Aldol condensation	MgO-$MgAl_2O_4$ (calcined hydrotalcite)	Basic catalyst
Multicomponent oxide	Propane to acrylonitrile	V/Mo/Nb/Sb oxides	(Amm)oxidation
Oxide supported on oxide	*o*-Xylene to phthalic anhydride	V_2O_5/TiO_2	Selective oxidation
	Isobutane to isobutene	K_2O-Cr_2O_3/Al_2O_3	Dehydrogenation
Impregnated melt or liquid	SO_2 to SO_3	K_2SO_4-V_2O_5/SiO_2	Oxidation
	Olefin oligomerization	H_3PO_4/SiO_2 (*solid phosphoric acid*)	Protonic acid catalyst
Zeolite catalysts			
Protonic zeolite	Benzene + ethylene to ethylbenzene	H-BEA	Protonic acid catalyst
Cationic zeolite	N_2O decomposition/reduction	Fe-MFI (Mobil-5 zeolite)	Redox catalysts
Metal catalysts			
Bulk metals	Ammonia synthesis	Fe (CaO, K_2O, Al_2O_3, SiO_2 promoters)	Hydrogenation
Metal gauzes	Ammonia oxidation to NO	Pt (Rh stabilizer)	Selective oxidation
Supported metal	Acetylene hydrogenation in ethylene	Pd/Al_2O_3 (Ag promoter)	Preferential hydrogenation
	Car catalytic mufflers	Pt-Rh/Al_2O_3-CeO_2-ZrO_2	Combustion + NO red
	Alcohols to aldehydes	Pt/carbon	Liquid-phase oxidation
	Aromatization of paraffins	Pt/K-L zeolite	Dehydrog./aromatization
Sulfide catalysts			
Bulk sulfide	Bituminous sands to oil fractions	MoS_2	Deep hydrocracking
Supported sulfides	Gasoline treatment	NiS-MoS_2/γ-Al_2O_3	Hydrodesulfurization
Halide catalysts			
Bulk halides	Fluorination of chloroalkanes	CrF_3	Lewis acid catalyst
Supported halides	Ethylene and propene polymerizations	$TiCl_3/MgCl_2$	Stereospecific polymerization
	Aromatic alklylation	BF_3/γ-Al_2O_3	Lewis acidity
	Aldol-type condensations	KF/γ-Al_2O_3	Basic catalyst
	Ethylene to dichloroethane	$CuCl_2/\gamma$-Al_2O_3	Oxychlorination

frequently more environmentally friendly than liquid catalysts, and their manipulation is far safer. In practice, dangerous corrosive liquids characterized by unsafe manipulation procedures, difficult regeneration, and unsafe disposal (such as sulfuric acid, and $AlCl_3$-based Friedel–Crafts-type liquid acid, as well as concentrated soda solutions) and highly toxic and volatile compounds (such as hydrofluoric acid) have been replaced by environmentally friendly silicoaluminates and alkali-earth-containing solids. In parallel, the performance of such processes has also been remarkably improved.

Table 33.1 reports a summary of relevant industrial solid catalysts together with their applications. They mainly belong to four materials families: metals, metal oxides (including zeolites), metal sulfides, and metal halides. These categories refer to the main component, usually referred to as the *active phase*, whose presence is crucial for the catalytic effect.

33.3 On the Complexity of Industrial Catalytic Materials

A real industrial catalyst is frequently a very complex material, containing a number of components, whose functions are reported in Table 33.2. In fact, it has been found that inactive or almost inactive components can remarkably improve the catalytic activity or selectivity behavior of the main active phase(s). These components are generally referred to as *promoters* or *activators*. A promoting effect may frequently be observed for

Table 33.2 Components in industrial catalytic materials

Active phase(s)
Support
Activator(s) or promoter(s)
Stabilizer(s)
Cocatalyst(s)
Diffusion improver(s)
Binding matter

Table 33.3 Families of catalyst functionalities

1. Acid catalysis: Brønsted type
2. Acid catalysis: Lewis type (including halogenation catalysis)
3. Basic catalysis
4. Partial oxidation catalysis
5. Total oxidation catalysis
6. Hydrogenation/dehydrogenation catalysis
7. Polymerization catalysis (Ziegler–Natta type)

a particular carrier in the case of supported catalysts. Thus, the carrier is chosen also (but not only) with respect to its effect on the catalytic activity of the active phase. In the final composition, additional promoters may be added in trace amounts but sometimes prevalent with respect to the active phase. As an example, the active palladium/alumina catalyst for acetylene hydrogenation in treatment of the C2 steam cracking cut may contain 0.03 wt% Pd (active phase) and 0.18 wt% Ag (promoter) over a γ-Al_2O_3 support. Similarly, typical catalysts for denitrification of waste gases from power stations (selective catalytic reduction of NO_x by ammonia) may contain 1–3 wt% V_2O_5 (active phase) and 10 wt% WO_3 MoO_3 (the promoter) over an anatase TiO_2 support, which also has a promoting effect on vanadia.

The activity-promoting mechanism can have different origins: from electronic promotion due to a slight modification of the electronic state of the active phase by a promoter that must be in electronic contact, to structural promotion where the activator induces or stabilizes particular structures or morphologies of the active phase, e.g., favoring dispersion or surface roughness.

Activity promotion sometimes occurs in parallel with stabilization, as stabilizers reduce deactivation, allowing high catalytic activity to be retained during time in-stream. Stabilizers are components that inhibit sintering and solid-state reactivity (e.g., reactivity between the support and the supported phase or among different components, including their volatility). Also, species which act as inhibitors of poisoning and coking act as stabilizers.

Selectivity promoters may act electronically or as structural promoters, but are frequently specific poisons for the active sites of unwanted parallel/successive by-reactions. In some complex cases (e.g., Ziegler–Natta-type polymerization catalysts), a cocatalyst is needed to promote the active phase and act in some way as a reaction chain initiator. Additional components are needed to build extrudates (binding materials), in particular in the case of fluidized bed catalysts, and to favor diffusion in complex catalytic materials.

On the other hand, in several cases, multifunctional catalytic materials are needed for processes which involve treatment of complex feeds (e.g., broad hydrocarbon fractions or complex raw materials such as biomasses) and imply the occurrence of a number of different catalytic reactions simultaneously; this is the case, e.g., in fluid catalytic cracking of heavy oils and catalytic reforming of gasolines.

Table 33.3 reports the different categories of industrial catalyst applications in terms of chemical functionality.

33.4 Surface Science, Surface Chemistry, and Industrial Heterogeneous Catalysis

As is typical in the chemical industry, several relevant processes using catalysts, in particular heterogeneous catalysts, were industrially developed early on (Table 33.4 [33.4–6]), when knowledge of the phenomena occurring at the molecular level was still incomplete. Surface chemistry and surface science developed in more recent years, thanks to the introduction of sometimes very sophisticated experimental techniques, and even more recently with the application of high-level computational technologies enabled by modern fast electronics and computers. One of the main objectives of surface science consists in the identification of the *active site* of the catalytic reaction, and its working mechanism [33.7]. This is a very important achievement, but really represents only one of the various relevant aspects of the development of better catalysts. As mentioned above, real catalysts are very frequently complex and *multifunctional* materials, with a number of different functionalities working synergistically or in series. Their catalytic activity is frequently (although not always) associated with defect surface sites (edges, corners, and vacancies), contact points between phases,

Table 33.4 Starting year of industrial processes using heterogeneous catalysis

1880	SO_2 oxidation to SO_3 on platinum (Winkler in Freiberg, Germany, and Squire and Messel in England)
1880	Cl_2 from HCl oxidation on $ZnCl_2/CuCl_2$ (Deacon process)
1887	H_2S and SO_2 to S over bauxite (Claus process, Chance)
1889	Formaldehyde production by methanol oxidation on platinized asbestos (Trillat)
1902	Liquid-phase hydrogenation of fatty oils on Ni (Sabatier)
1906	Ammonia oxidation to NO over Pt (Ostwald nitric acid process, Bochum, Germany)
1911	Cottonseed oil hydrogenation over Ni (Procter & Gamble)
1913	Ammonia synthesis over Fe (Haber–Bosch process, BASF, Oppau, Germany)
1913	Water gas shift over Fe_2O_3-Cr_2O_3 (BASF, Oppau, Germany)
1913	Bioethanol dehydration to ethylene on alumina (Elektrochemische Werke, Bitterfeld, Germany)
1916	Naphthalene oxidation to phthalic anhydride on V_2O_5 (BASF)
1919	Coal liquefaction to liquid hydrocarbons by hydrogenation over Fe sulfide (Bergius process, Th. Goldschmidt AG, Germany)
1920	Oxidation of aromatics to aldehydes and anhydrides on V_2O_5
1923	Syngas conversion to methanol over ZnO-Cr_2O_3 (BASF, Leuna, Germany)
1930	Hydrogen cyanide by methane ammoxidation over Pt-Rh (Andrussow process)
1930s	Hydrocracking of gasoils over metals (Standard Oil, Baton Rouge, USA)
1931	Steam hydrocarbon reforming over Ni (Standard Oil, Baton Rouge, USA)
1932	Olefin oligomerization over *solid phosphoric acid* (UOP)
1933	Benzene oxidation to maleic anhydride on V_2O_5-MoO_3 (National Aniline and Chemical Co.)
1935	Syngas conversion to liquid hydrocarbons over Co/ThO_2-MgO catalyst (Fischer–Tropsch process, Ruhrchemie, Germany)
1937	Catalytic cracking on clays (Houdry process, Socony-Vacuum, Marcus Hook, PA, USA)
1937	Ethylene oxidation to ethylene oxide on Ag/Al_2O_3 (Lefort catalyst, Union Carbide)
1939	Vinylchloride from acetylene and HCl over $HgCl_2$/charcoal-based catalysts (I.G. Farben and Wacker, Germany)

and the dispersion of atoms from one phase into another.

The set of experimental techniques allowing information on real catalytic materials to be obtained is frequently called *surface chemistry*. It implies the application of a series of complementary techniques to real catalytic materials, most commonly in the form of fine powders. When possible, spectroscopic measurements are performed in the conditions of the catalytic reactions, i.e., in *operando* conditions, at high temperatures, sometimes high pressures, in contact with complex reactant mixtures while measuring the conversion, selectivities, and yields. The techniques most typically applied to real catalytic materials are summarized in Table 33.5 [33.8].

On the other hand, to obtain as detailed an understanding of the catalytic behavior of the reactant + catalyst system as possible, it is useful to simplify the picture by separating the phenomena and looking at the simplest materials (pure compounds, high crystallinity, or monocrystals), using focused and sophisticated techniques [33.9] applied in their own most appropriate conditions (sometimes very low temperature, high vacuum). This is the typical original approach of *surface science*.

It is evident that both a *material gap* and a *conditions gap* (mostly a *pressure gap*) may exist between surface science on one side and surface chemistry and catalysis on the other side. However, attempts have been made recently to reduce these gaps [33.10–15] by applying surface science techniques in more realistic conditions and by preparing materials with intermediate properties (stepped monocrystal surfaces, doped materials, and planar model catalysts). Although this approach has not always been successful, in many cases it has provided deeper knowledge of real catalysts.

In any case, surface science and surface chemistry have long offered fundamental support for the management and enhancement of early technologies as well as the development of new ones [33.16].

33.5 Surface Acido-basicity and Heterogeneous Acido-basic Catalysts

Acidity and basicity are, to some extent, two sides of the same coin. Acid catalysis is a main player in the fields of refinery and primary petrochemistry [33.17, 18]. Basic catalysts are largely used in the field of fine chemistry. Additionally, acido-basic materials have wide applications as supports for metal catalysts. Typ-

Table 33.5 Common characterization techniques applicable to real catalytic materials

1.	Determination of elemental composition	3.	Morphological characterization
1.1.	Atomic absorption and emission spectroscopies	3.1.	Measurement of surface area and analysis of porosity by Brunauer–Emmett–Teller (BET) method
1.2.	Inductively coupled plasma-mass spectrometry (ICP-MS)	3.2.	Crystal size measurements by XRD analysis
1.3.	X-ray fluorescence (XRF) spectroscopy	3.3.	Scanning electron microscopy (SEM)
1.4.	Energy-dispersive x-ray analysis (EDX)	3.4.	Field-emission scanning electron microscopy (FESEM)
2.	Determination of (bulk and surface) structural properties	3.5.	Transmission electron microscopy (TEM)
2.1.	X-ray diffraction (with Rietveld analysis)	3.6.	Scanning transmission electron microscopy (STEM)
2.2.	Electron diffraction	4.	Analysis of surface chemistry behavior
2.3.	Neutron diffraction	4.1.	Adsorption volumetry of adsorbed molecules
2.4.	Skeletal infrared spectroscopy	4.2.	Adsorption calorimetry of adsorbed molecules
2.5.	Skeletal Raman spectroscopy	4.2.	Infrared spectroscopy of adsorbed molecules
2.6.	X-ray absorption spectroscopy (XAS, EXAFS, XANES)	4.3.	Magic-angle spinning nuclear magnetic resonance (MAS NMR) of adsorbed molecules
2.7.	X-ray photoelectron spectroscopy (XPS)	4.3.	Temperature programmed desorption of adsorbed molecules
2.8.	Diffuse-reflectance ultraviolet–visible–near infrared (DR UV–Vis–NIR) spectroscopy	4.4.	Temperature programmed reduction (TPR)
2.9.	Magic-angle spinning nuclear magnetic resonance (MAS NMR) techniques	4.5.	Temperature programmed oxidation (TPO)
2.10.	Electron spin resonance (ESR)		

Table 33.6 Catalysts and conditions of industrial solid-acid-catalyzed reactions

Reaction	Catalyst	Reaction conditions	
Isobutane alkylation by isobutene	Ultra stable type Y (USY) zeolite	90 °C/10 bar	Liquid phase
Light paraffin isomerization	Chlorided alumina	150 °C	Gas phase
	Sulfated zirconia, tungstated zirconia	200 °C	Gas phase
	H-mordenite zeolite	250 °C	Gas phase
Light olefin oligomerization	Amberlite (sulfonated PS-PDV)	100 °C/40 bar	Liquid phase
	Solid phosphoric acid or zeolites	200 °C/30 bar	Gas phase
Benzene alkylations	H-BEA (beta)- or MCM-22 zeolites	200 °C/30–40 bar	Liquid phase
Diethyl ether and dimethyl ether syntheses	γ-Al_2O_3	300 °C	Gas phase
Light olefin isomerization	H-ferrierite zeolite	350 °C	Gas phase
	γ-Al_2O_3 (silicated or borated)	450 °C	Gas phase
Isomerization or transalkylation of xylenes	H-MFI zeolite	450 °C	Gas phase
Catalytic cracking	Rare-earth-containing H-faujasite zeolites	700 °C	Gas phase

ical acid catalytic materials are summarized in Table 33.6, with some of their most typical industrial applications.

33.5.1 Surface Acidity and Solid Acid Catalysts: Brønsted Type

According to the definitions of *Brønsted* [33.19] and *Lowry* [33.20], an acid is any hydrogen-containing species that is able to release protons, while a base is any species capable of combining with protons. In this view, acid–base interactions consist in the equilibrium exchange of a proton from an acid HA to a base B (which may be the solvent, e.g., water), generating the conjugated base of HA, i.e., A^-, plus the conjugated acid of B, i.e., HB^+ (e.g., the hydroxonium ion H_3O^+) thus

$$HA + B \rightleftharpoons A^- + HB^+$$

This theory, valid in dilute water solutions, was extended to concentrated and nonaqueous solutions by *Hemmett* in the 1930s [33.21].

Solid Brønsted acids are materials whose surface contains active protons that are able to protonate molecules that exhibit some basicity. They can be used in contact with water solutions but, even more commonly, in contact with nearly water-free liquid or vapor phases. Even weak Brønsted acids can protonate strong and medium-strength bases, such as n-bases, i.e., those having free electron pairs in nonbonding orbitals (such as oxygenated, nitrogenated, and sulfided organics).

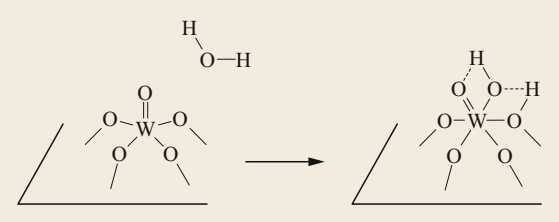

Fig. 33.1 Schematics of Brønsted acidic surface wolframate species on oxides

Strong to very strong acids and a nearly water-free environment are needed to protonate π-type bases (i.e., olefinic and aromatic hydrocarbons, whose bonding π-type orbitals are available for protonation) and also σ-type bases, i.e., paraffins.

Families of strong solid Brønsted acids contain surface species that are similar to homogeneous Brønsted acids; this is the case, e.g., of sulfated and tungstated zirconia, whose acidity is mainly due to the strong acidity of sulfuric and tungstic acids, although some properties (semiconducting character, slight reducibility) of zirconia also have an activating effect on protonic centers. Similarly, the medium-strong acidity of the so-called solid phosphoric acid (Kieselguhr silica impregnated by phosphoric acid) is due to the acidity of H_3PO_4. As in the case of homogeneous acids, the surface Brønsted acidity of sulfate-, tungstate-, and phosphate-containing solids is also associated with the presence of high-valency elements that are covalently bonded to a large number of oxygen atoms over which the anionic charge of the dissociated acid can be delocalized (Fig. 33.1). Another family of very strong solids acids is that of chlorided aluminas, i.e., γ-Al_2O_3 powders deliberately contaminated by chlorine, which actually contain $AlCl_3$ and adsorbed HCl [33.22].

Protonic zeolites today represent the most prominent family of solid strong Brønsted acids applied in refineries and petrochemistry [33.17, 23, 24]. Zeolites are natural and synthetic silicoaluminates characterized by a microporous crystal structure constituted by open channels and cages (Fig. 33.2). Substitution of aluminum for silicon in such a covalent silica network leads to a $[Si_{1-x}Al_xO_2]^{x-}$ negatively charged framework. This charge must be compensated by *extraframework* cations. In natural and *cationic* zeolites, alkali or alkali-earth metal cations located in the cavities play the role of compensating species. However, using different synthetic procedures, protons can substitute for metal cations, giving rise to protonic zeolites. In spite of the covalency of the resulting O–H bond of *bridging silanol groups*, the presence of the cavity and the structural features of the silicoaluminate framework make the protons of protonic zeolites exceptionally strong

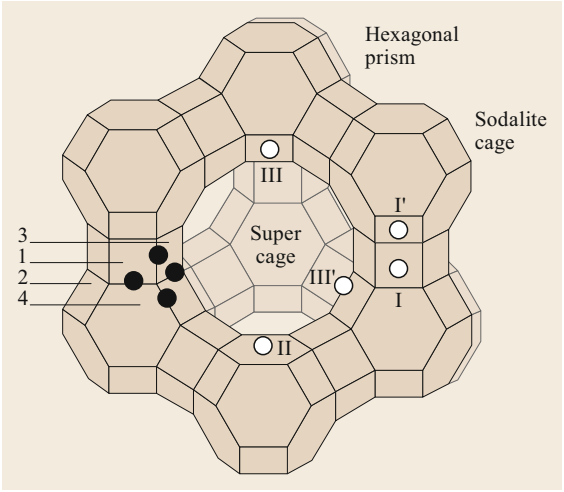

Fig. 33.2 Structure of faujasite zeolite. *Full circles*: position of the four crystallographic different oxygen positions. *Empty circles*: position of Na cations in dry Na-faujasites

Brønsted acids [33.25]. The spectra of adsorbed pyridine (a widely used basic probe molecule, Fig. 33.3) provides evidence of the formation of pyridinium ions (with ring stretching bands at 1633 and 1544 cm^{-1}). Looking at the OH stretching region, it is clear that protonation is related to the band at 3603 cm^{-1} due to OH stretching of *bridging* silanol groups.

The formation of this group (not found in non-microporous materials [33.26]), as well as its strong acidity, are certainly influenced by the cavities typical observed in zeolite structures. The hyperconjugation effect, i.e., the $n_O \rightarrow \sigma^*_{Si-O}$ (vicinal) interaction, a bonding interaction between an oxygen lone pair and the antibonding orbital of the vicinal Si–O bond, is very likely a key feature stabilizing the anionic charge of dissociated sites, thus justifying the strong Brønsted acidity [33.27, 28]. The delocalization of the negative charge of dissociated bridging silanols on the siloxane bridges, as well as the stabilization of the protonated species by interaction with the cavity wall, both contribute to the stabilization of the products of the proton transfer, thus increasing the Brønsted acidity (Fig. 33.4). In this case, it is evident that the surface is not flat, and such curvature may have an effect, as may also occur in the case of other porous systems.

33.5.2 Surface Acidity and Solid Acid Catalysts: Lewis Type

In 1923, the same year as the definitions of Brønsted and Lowry, *Lewis* [33.29] proposed a different approach to acidity and basicity. In his view, an acid is any species that, because of the presence of an incom-

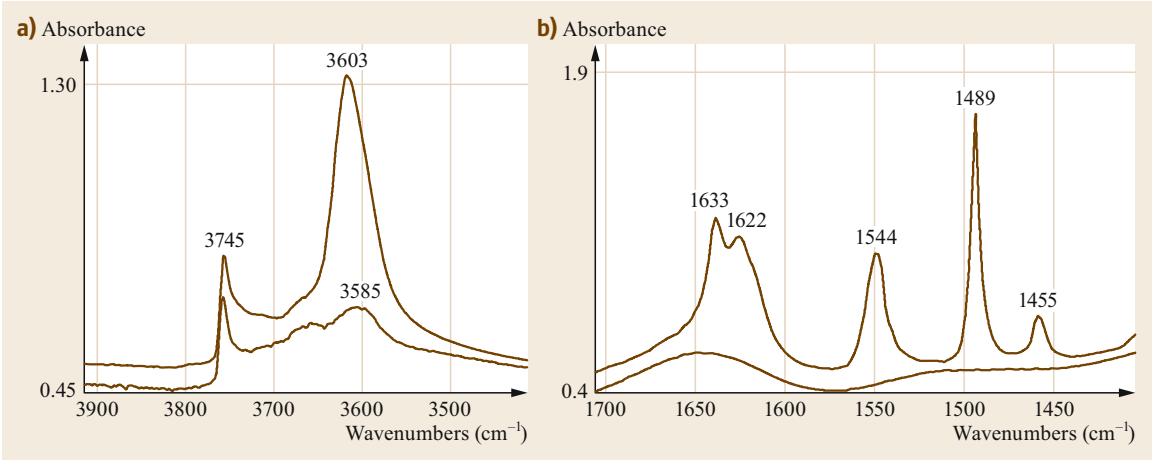

Fig. 33.3 **(a)** Infrared spectra of activated H-mordenite (lower spectra) and of the same material after adsorption of pyridine and outgassing at 100 °C. The band at 3745 cm^{-1} is due to weakly acidic external terminal OH, while the band near 3600 cm^{-1} is due to strongly acidic bridging silanols. **(b)** The bands at 1633 and 1544 cm^{-1} are due to pyridinium ions, those at 1622 and 1455 cm^{-1} are due to coordinated pyridine on Lewis acid sites, and the band at 1489 cm^{-1} to both species [33.23]

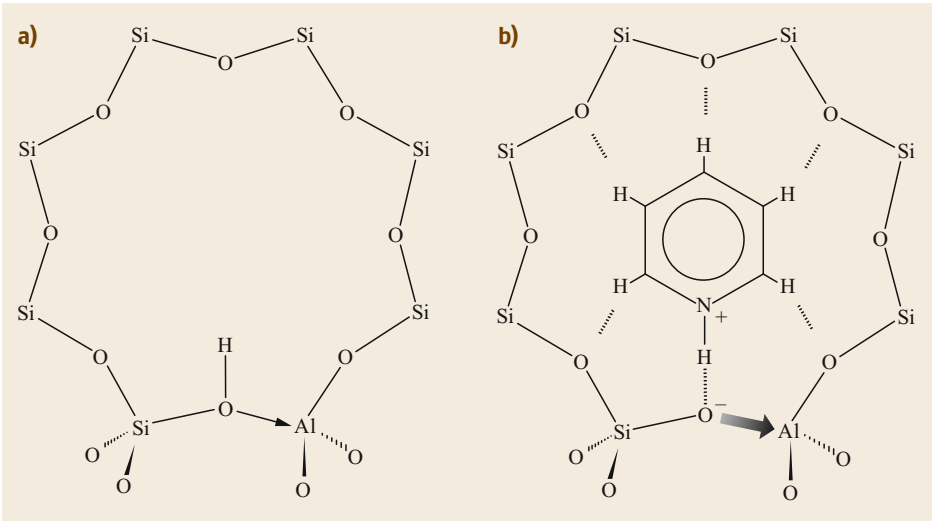

Fig. 33.4a,b Schematics of surface Brønsted sites in zeolites **(a)** and on pyridine protonation thereon **(b)**

plete electronic grouping, can accept an electron pair, thus forming a dative or coordination bond. Conversely, a base is any species possessing an electron pair which can be donated to form a dative or coordination bond. The Lewis-type acid–base interaction can thus be denoted as

$$B: + A_L \rightleftharpoons {}^{\delta+}B \rightarrow A_L^{\delta-}$$

In agreement with the Lewis definition, not only the proton H^+ but also metal cations ionically bonded to weakly basic anions are acidic. The most typical strong *Lewis acids* are metal compounds such as Al and B trihalides, as well as the halides of other cations such as $FeCl_3$, $ZnCl_2$, $TiCl_4$, $SnCl_4$, SbF_5, $BiCl_3$, etc. Several of these compounds, however, are liquid and volatile and easily hydrolyzed in mild conditions. They are also not environmentally friendly materials, giving rise to easy evolution of hydrogen halides and corrosion problems and being unsafe when disposed of.

As oxygen is the most electronegative element besides fluorine, the metal–oxygen bond is highly ionic. Thus, at the surfaces of metal oxides, the ionicity of the M–O bond results in coordinatively unsaturated cations

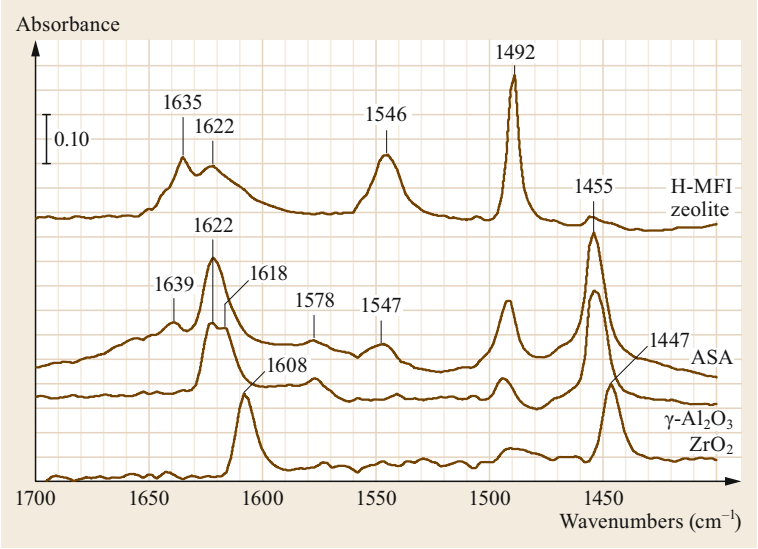

Fig. 33.5 Infrared spectra of pyridine adsorbed on catalysts. The bands at 1635 and 1546 cm^{-1} are due to pyridinium ions, those at 1625–1600 and 1455 cm^{-1} are due to coordinated pyridine on Lewis acid sites, and the band at around 1490 cm^{-1} to both species

and anions, with Lewis acidity of the cations and basicity of the anion. The balance between Lewis acidity and basicity depends on the size (radius, r) and charge (C) of the cation, i.e., its polarizing power (either C/r or C/r^2), as well as on its overall coordination. The smaller, the more charged, and the less coordinated the surface cation, the greater its Lewis acidity [33.17, 30].

The best Lewis acid solids in terms of activity, stability, and environmental friendliness are the so-called *transitional* aluminas [33.31], in particular γ-Al_2O_3, δ-Al_2O_3, η-Al_2O_3, θ-Al_2O_3, all containing the ionically bound and very small Al^{3+} species. These are metastable polymorphs with respect to the stable form, α-Al_2O_3 or *corundum*. Corundum is a very stable material whose surface is quite inert, likely due to the relatively high overall coordination of its ions also at the surface. In contrast, transitional aluminas are very active in adsorption and catalysis, due to the presence at the surface of low-coordination ions. While monocrystals of α-Al_2O_3 can be produced and their surface characterized by classical surface science techniques [33.32], this cannot be easily done with transitional aluminas, which have mostly been investigated using conventional surface chemistry techniques [33.31] as well as theory [33.33]. However, thin films of alumina have been prepared on the surface of selected single-crystal faces and are commonly used as a model for alumina to investigate its properties as a catalyst or support for catalysts [33.11, 34]. These materials can be analyzed using typical surface science techniques such as low-energy electron diffraction (LEED), high-resolution electron energy loss spectroscopy (HREELS), and infrared reflection absorption spectroscopy (IRAS), together with scanning tunneling microscopy (STM). Studies on these surfaces have essentially confirmed results coming from previous powder characterization.

The spectrum of pyridine adsorbed on transitional aluminas (Fig. 33.5) does not show the bands of pyridinium ion, indicating that the Brønsted acidity of alumina's OHs is weak. In contrast, the ring stretching bands of molecular pyridine at 1622 and 1614 cm^{-1} (well shifted up with respect to the value for free pyridine of 1588 cm^{-1}) and at 1455 cm^{-1} (shifted up from the 1440 cm^{-1} liquid-phase value) provide evidence of the presence of at least two families of strong Lewis acid sites. In the case of zirconia, the same bands are found at 1608 and 1447 cm^{-1}, indicating the presence of weaker Lewis acid sites with respect to transitional aluminas.

The Lewis acid sites of transitional aluminas have been characterized to be the strongest among binary metal oxides. However, in many cases, anion–cation couples work synergistically. To improve the thermal stability without losing acidity, aluminas may be additivated using small amounts of silica (silicated aluminas). The Lewis acido-basicity of γ-Al_2O_3 is associated with its *dispersing* ability for surface species, making it an excellent support for metallic catalysts as well as for sulfide catalysts.

Other very strong Lewis solid acids that are widely used in fluorine chemistry [33.35], i.e., for activating F_2 in the fluorination of chlorocarbons, are aluminum and chromium fluorides, which are high-melting-point solids.

33.5.3 Surface Basicity and Solid Basic Catalysts

According to both the Brønsted and Lewis definitions, bases are species that are characterized by their ability to bond with acids. Molecules having available electron pairs are both Brønsted and Lewis acidic, being at least in principle able to interact both with protons and with metallic cationic species. They are also nucleophilic, i.e., able to interact with electrophilic carbon atoms of organic molecules, and of CO_2 as well [33.30].

Basic solids have wide applications as catalysts and adsorbents in fine chemistry and environmental chemistry [33.36–38] (Table 33.7). As mentioned above, in the case of ionic oxides, the smaller and more charged the surface cation, and the lower its coordination, the stronger its polarizing power, i.e., its electron-withdrawing power and, consequently, its Lewis acidity. As a result, it bonds more strongly with basic oxide anions, thus decreasing their basicity. In contrast, the larger and less charged the cation, the weaker its Lewis acidity and, consequently, the stronger the basicity of the oxide anions. Thus, alkali and alkali-earth oxides, whose cations are large and low charge, are more basic, the larger and heavier the cation.

The surface basic reactivity of oxides of alkali metals is so high that they are essentially unstable in usual conditions, i.e., in the presence of water vapor, which is sufficient to convert them into the corresponding hydroxides, and of CO_2, which converts them into carbonates. Thus, bulk alkali-metal oxides cannot normally be used as basic catalytic materials. However, alkali-metal oxides can be supported or deposited on carriers, such as high-surface-area oxides (silica, alumina, titania, zirconia, magnesia, and zeolites) or activated carbons, by impregnation/calcination or vapor deposition procedures. They are also frequently introduced as dopants on the surface of transition-metal oxides and also of metal catalysts, to introduce basicity or reduce acidity. Potassium is frequently preferred over sodium, possibly because of its definitely larger ionic size that limits reactions with supports and formation of bulk salts. The basicity also tends to increase with cationic size, thus the Cs cation gives rise to extremely high basicity.

The alkaline-earth oxides (except BeO), whose cations are definitely large in size, are among the strongest solid bases that may be stable as such in practical conditions. They crystallize with rock-salt-type *periclase* structure, with octahedral coordination of both cation and anion. Increasing the size of the cation results in an increased unit cell size as well as decreasing Madelung potential, thus destabilizing the oxide anions.

Magnesium oxide is a stable material which can be prepared with different morphologies and crystal sizes. It has been the object of a large number of investigations from typical powder characterization to monocrystal studies and theoretical investigations. The presence of a number of different surface structures has been proposed as active sites, including differently coordinated oxide and hydroxide sites as well as combinations thereof [33.10, 39–41].

Actually, as for alkali oxides, alkaline-earth oxides are also so reactive that, when prepared as fine powders, they are largely converted into hydroxides and carbonates, at least at the surface, upon exposure to ambient air. Thus, high-temperature treatments are needed for their activation. On BaO, full desorption of carbonates is only obtained at 900 °C.

Mixed oxides containing alkali and alkali-earth cations may also exhibit strong basicity. Sr and Ba ions are involved in the formation of mixed oxides with less compact packing for oxide anions, such as perovskites and β-aluminas. Additionally, Sr and Ba ions may be supported on typical oxide carriers such as alumina and titania, forming quite stable basic materials. In fact, materials belonging to the $BaO\text{-}Al_2O_3$ and $K_2O\text{-}Al_2O_3$ systems find applications as traps for nitrogen oxides in lean NO_x trap-NO_x storage and reduction (LNT-NSR)

Table 33.7 Catalysts and conditions of industrial solid-base-catalyzed reactions

Reaction	Catalyst	Reaction conditions
$CH_3CHO + HCHO \rightarrow H_2C{=}CH{-}CHO + H_2O$	$NaOH\text{-}SiO_2$	300–320 °C
Butadiene from ethanol	$MgO\text{-}SiO_2$	370–390 °C
Crotonic condensation of 2-butanone	Na_2O/SiO_2, Cs_2O/SiO_2	325–400 °C
Acetone to methyl isobutyl ketone	(Pt)-$MgO\text{-}Al_2O_3$ (calcined hydrotalcite)	120–250 °C
Methyl methacrylate from methylpropionate + formaldehyde	Cs_2O/SiO_2	320–380 °C
Phenyl-1-propanone from benzoic acid with propionic acid	$CaO\text{-}Al_2O_3$	440–520 °C
2,4-Dimethyl-3-pentanone from isobutyric acid	ThO_2 or ZrO_2	430 °C
Biodiesel (FAME) by transesterification	$ZnAl_2O_4$	200–250 °C
Epoxide ring-opening/oxyethylation alcohol to polyethoxylates	$MgO\text{-}Al_2O_3$ (calcined hydrotalcite)	4–5 bar, 150–180 °C

technology for purification of waste gases from Diesel cars [33.42].

On the contrary, the size of Mg^{2+} is sufficiently small to enter close packing of oxygen ions. For this reason, Mg ions can participate in the formation, e.g., of mixed oxides such as spinels and ilmenites, whose oxygen packings are cubic close packed (ccp) and hexagonal close packed (hcp), respectively. In this regard, deposition of Mg ions at the surface of normal carriers such as alumina may give rise to poor stability due to the reaction producing Mg aluminate. Another way to provide stability for alkali-earth oxides is to mix them with more stable components. This is essentially what occurs when using hydrotalcite, a layered double hydroxide of magnesium and aluminum, with formula $Mg_6Al_2(OH)_{16}CO_3 \cdot 4H_2O$, available commercially [33.43]. It is a natural anionic clay having interesting basic properties. Its structure is formed by brucite-like $[Mg_6Al_2(OH)_{16}]^{2+}$ layers with carbonate ions and water molecules in the interlayer region. It is also a commercial synthesis product, used in medicine as a stomach antiacid, as well as an environmentally friendly, nontoxic, and heavy-metal-free filler for halogenated polymers (such as polyvinyl chloride (PVC)) to scavenge acid byproducts, and a heterogeneous catalyst. Hydrotalcite (HT) decomposes, releasing CO_2 and water, from 260 to 300 °C, thus acting as a flame-retardant and smoke suppressant. Thermal decomposition of hydrotalcite gives rise to a mixed oxide whose virtual composition is $5MgO \cdot MgAl_2O_4$, although these phases may give rise to mutual solid solubility, depending on the decomposition temperature. In fact, calcined HTs are intimate mixtures of rock-salt- and spinel-type solid solutions which retain the strong basicity of MgO with enhanced stability and high surface area due to the alumina or spinel.

33.6 Solid Catalysts for Oxidation Reactions

Three kinds of oxidation reaction are practiced commercially [33.44]:

i) Total oxidation to remove pollutants from waste gases [33.45, 46]
ii) Catalytic combustion of gaseous fuels for energy production [33.47]
iii) Partial (or *selective*) oxidation to produce chemicals [33.48, 49].

Total oxidation or combustion may be performed uncatalytically in air, but in this case high temperatures (> 1000 °C) are produced and, in parallel, nitrogen oxides will be formed, thus generating polluting waste gases. Catalytic combustion, i.e., total oxidation performed in the presence of solid catalysts, results in lower reaction temperatures (300–800 °C), thus avoiding the formation of substantial amounts of NO_x.

In the case of partial oxidation, catalysts are needed to make the desired reaction faster with respect to the total oxidation reaction and other possible partial oxidation reactions of the same substrate. To achieve this, the temperature of the catalytic bed must be controlled. Multitubular cooled reactors or cooled fluid bed reactors are mostly used.

Air is the cheapest oxidant in industrial processes. The use of pure oxygen as the oxidant is a second choice, when the presence of nitrogen generates drawbacks. When using both air and pure oxygen as the oxidant, O_2 is the stoichiometric oxidant molecule. In less favorable cases, other conditions (e.g., liquid phase and homogeneous catalysis) and/or other oxidants, such as hydrogen peroxide, ozone, or nitrous oxide (N_2O), must or can be applied.

33.6.1 Adsorption/Reaction/Activation of Oxygen

Upon catalysis, oxygen is supposed to adsorb and be *activated* over the catalyst surface, where it reacts with the substrate. According to early literature, a variety of different *adsorbed* or surface oxygen species can be obtained on solid surfaces, which have been identified mostly by vibrational spectroscopies (IR, Raman, or EELS) and electron spin resonance and are summarized in Table 33.8. Most of them have an intermediate redox state between dioxygen and the most reduced species, the oxide anion, O^{2-}. Thus they are, at least potentially, oxidizing species and are electrophilic. They are considered to be possibly involved in total oxidations. On the other hand, their formation from O_2 also implies the oxidation of a metal species, which can also act as an oxidizing species. The oxide anions, instead, are nucleophilic, and are assumed to be the main players in selective oxidations. When interacting with reducible cations, they act as oxygen insertion sites. In this case, the high-valency metal cations act as the oxidizing species, which reduce to a lower valency state by inserting oxide species into the reacting substrate.

Metals and other elements in very high oxidation states can give rise to element–oxygen *double*

Table 33.8 A summary of possible surface oxygen species

Formula	Oxidation state	Name	Properties	Possible structure
O^{2-}	–II	Oxide	Coordinatively unsaturated	
		Doubly bonded		
O^{-}	–I		Radical anion	
O_2^{2-}	–I	Peroxide	Side-on	
			Bridging	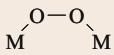
O_2^{-}	–0.5	Superoxide	Radical anion, end-on, bent	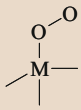
			Bridging	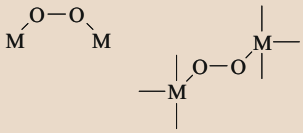
O_2	0	Neutral dioxygen		
O_2^{+}	+0.5	Dioxygen cation	Radical cation	

bonds in their oxides, i.e., very short bonds. This is the case of vanadyl(V), niobyl(V), molybdenyl(VI), chromyl(VI), and wolframyl(VI) groups, characterized by very high M=O oxygen stretching frequencies in vibrational spectroscopies (IR and Raman). Cations with short M=O double bonds are usually considered to be active in oxygen insertion into the substrates, even if it has been determined that the oxygen atom inserted is not that involved in the double bond. Among these elements, one can cite Mo^{6+}, Cr^{6+}, W^{6+}, and V^{5+}, which in fact are the key elements in important families of oxidation catalysts (molybdates, chromates, wolframates, and vanadates).

The mechanisms involving adsorbed oxygen species can be of Eley–Rideal type (adsorbed or surface oxygen reacting with a gas-phase substrate) or Langmuir–Hinshelwood type (both species react while adsorbed at the catalyst surface).

In a mechanism usually attributed to Mars and Van Krevelen, the catalyst acts between two oxidation states. In the higher oxidation state, the catalyst surface acts as the oxidant for the substrate, reducing itself to a lower oxidation state. Oxygen reoxidizes in situ the catalyst surface from its lower to higher oxidation state. The Mars–Van Krevelen mechanism (also referred to as the *redox* mechanism) actually implies that oxygen is adsorbed and activated in the form of oxide anions.

33.6.2 Metal Versus Metal Oxide Oxidation Catalysis

Transition metals and/or their oxides are typical catalysts used in heterogeneously catalyzed oxidations (Tables 33.9, 33.10). The question that arises is the actual state of the catalyst during the reaction.

According to thermodynamics, metal oxides are stable at low temperature while they tend to decompose to the corresponding metals at high temperature, depending on the oxygen pressure and the redox properties of the element. In most cases, however, melting of the oxide occurs in milder conditions than decomposition. Actually, base metals and most transition-metal elements are stable as oxides even under high vacuum up to their melting point, frequently occurring at high temperature. Thus, when these oxides are charged into an oxidation reactor, they are stable as oxides and act as catalytic oxides. Some high-oxidation-state transition-metal oxides may undergo partial decomposition to lower oxides, at moderate temperature, before melting (e.g., $Co_3O_4 \rightarrow CoO$ at $\approx 940\,^{\circ}C$, $CuO \rightarrow Cu_2O$ at $\approx 1000\,^{\circ}C$). Thus, different oxide phases may be active in oxidation catalysis.

A few transition-metal oxides, usually having high oxidation states, have quite low melting points. In a few cases, the catalyst can work in a partially melted state.

Table 33.9 Catalytic oxidations on noble-metal catalysts

Reaction	Catalyst	Reaction conditions
CO oxidation to CO_2	Au/ZrO_2	0 °C
	0.3% Pt–0.03% Fe/γ-Al_2O_3	100 °C
Vinyl acetate synthesis	Pd-Au/SiO_2	180 °C
Ethylene epoxidation	Ag/α-Al_2O_3	250 °C/20 bar
Methanol oxydehydrogenation to formaldehyde	Ag/α-Al_2O_3 or Ag gauzes	650 °C
Ammonia oxidation to NO (nitric acid synthesis)	Pt(Rh) gauzes	800–900 °C, 1–12 bar
Ammonia oxidation to N_2 (ASO, ammonia slip oxidation)	Promoted 0.5% Pt/γ-Al_2O_3	275 °C
Methane ammoxidation to HCN (Andrussow process)	Pt(Rh) gauzes	1100 °C
Methane partial oxidation to syngas (low-contact-time CPO)	Rh/α-Al_2O_3	1000 °C, $\tau^* = 5$ ms
Catalytic combustion of methane for energy production	5% PdO/α-Al_2O_3	650–850 °C
Catalytic combustion of VOCs	0.3% Pd/θ-Al_2O_3	500 °C
Gasoline engine aftertreatment	Pt-Rh(Pd)/CeO_2-ZrO_2-Al_2O_3/cordierite	400 °C

τ^* = contact time; CPO = catalytic partial oxidation; VOC = volatile organic compound

Table 33.10 Catalytic oxidations on transition-metal oxide catalysts

Reaction	Catalyst	Reaction conditions
SO_2 to SO_3	$V_2O_5/(Cs,K)_2SO_4/SiO_2$	400–500 °C
o-Xylene to phthalic anhydride	V_2O_5/TiO_2 (anatase)	400 °C
n-Butane to maleic anhydride	$(VO)_2P_2O_7$	350 °C
Methanol oxidation to formaldehyde (Formox)	$MoO_3/Fe_2(MoO_4)_3$	300 °C
Propene oxidation to acrolein	Bi-Mo (Fe,Co,Ni) multicomponent oxides	320 °C
Acrolein oxidation to acrylic acid	Mo-W-V-Fe oxides	280 °C
Propene ammoxidation to acrylonitrile	Bi-Mo (Fe,Cr,Ni,Co,Mg) multicomponent oxides	350 °C
Propane ammoxidation to acrylonitrile	U-Sb (Ti,Sn,Al,Fe,W,Te) multicomponent oxides	450 °C
Catalytic abatement of oxygenated VOCs	MnO_x/θ-Al_2O_3	400–500 °C
Catalytic abatement of chlorinated VOCs	CrO_x/θ-Al_2O_3	400–500 °C
Butene oxidative dehydrogenation to butadiene	$(Zn,Mg)Fe_2O_4$	550 °C
HCl oxidation to Cl_2	RuO_2/TiO_2 (rutile), RuO_2/SnO_2	300 °C

One of the most interesting case is $V_2O_5/K_2SO_4/SiO_2$ catalysts for SO_2 oxidation, where the V_2O_5/K_2SO_4 system with a low-melting eutectic forms and acts as a supported liquid catalyst.

For noble-metal oxides, decomposition to the metal may occur at quite low temperatures, also in an oxidizing atmosphere, frequently well below melting. On the other hand, noble metals are charged, sometimes, after a previous reducing pretreatment, thus being in metallic form. Metal oxidation to the oxide is kinetically hindered at low temperature, even when the oxide is the thermodynamically stable form. On metallic surfaces, adsorption of oxygen at low temperature produces superoxo (O_2^-) and peroxo (O_2^{2-}) molecular species. At higher temperature, atomic or dissociative adsorption occurs, producing surface and subsurface oxide species as an intermediate state towards the formation of the bulk oxide.

Gold and silver are the metal elements having the least stable oxides. Gold and silver oxides tend to decompose in the range of 100–250 °C and thus when heterogeneous catalysis most generally occurs.

For CO oxidation on supported gold nanoparticles, occurring at very low temperatures (down to 200 K), it is supposed that gold is indeed in the form of metallic clusters with low-coordination sites where CO and O_2 can adsorb cooperatively [33.50, 51], but with the possible participation of the support, at least in the case of Au/CeO_2 catalysts [33.52].

Silver catalysts are used in particular for the ethylene epoxidation reaction with oxygen or air, realized in the 200–300 °C temperature range. Today, authors agree that metallic silver with a high oxygen loading (a surface oxide layer) is needed for high selectivity to EO [33.53]. According to *Rocha* et al. [33.54], up to five different atomic oxygen species can exist over silver in conditions near those of real catalysis. A weakly bound electrophilic surface oxygen, $O^{\delta+}$, is suggested to enable selective epoxidation by directly attacking the C=C π-type electrons. In contrast, strongly bound nucleophilic surface oxygen, $O^{\delta-}$, is supposed to give rise to a oxometallacycle (OMC) surface intermediate, whose evolution can also produce EO but with lower selectivity, together with acetalde-

hyde and combustion to CO_2. Real catalysts contain a set of promoters, such as Cs, Re, and an oxo-ion, and work in the presence of some chloride hydrocarbon, which improves either the conversion or selectivity. The mechanism of such activation is still a matter of debate [33.55].

For Pd, in 1 mbar O_2, the $PdO \rightleftharpoons Pd + 1/2\,O_2$ transition is expected to occur at approximately 570 °C. Accordingly, PdO is known to decompose in practice into Pd metal in the range of 650–800 °C, depending on the O_2 partial pressure and reactive gas mixture composition. Combustion catalysts for methane are mostly supported on stabilized supports such as La-alumina, with loadings of a few wt% Pd. The transformation of PdO into Pd is reported to negatively affect the catalytic reaction by lowering the conversion, although the CH_4 combustion activity is reversibly restored upon reoxidation of Pd to PdO. The nature of the support is reported to influence strongly the reoxidation of Pd metal. The active catalyst is mostly considered to actually consist of a mixture of PdO and Pd or an intermediate species [33.56, 57].

33.6.3 Supporting Metal Catalysts

In most industrial applications, metal catalysts are supported over carriers. This is done for several reasons: it allows the production, in some cases, of very reactive nanoparticles, whose surface is rich in steps, edges, corners, kinks, and defects, thus being very reactive and active as catalysts. The interaction with the support may also stabilize strongly metal particles against sintering. Additionally, a very high surface-to-bulk ratio is obtained, thus allowing the amount of active metal to be limited sometimes to very low concentrations (sometimes even less than 0.1 wt% on the overall catalyst). This may be very important when precious metals are used.

The following materials are most commonly used industrially for supporting catalysts:

- *Aluminas*: When applications require a relatively low reaction temperature (< 500 °C), high-surface-area γ-, δ- or η-Al_2O_3 are common industrial catalyst supports ($S_{BET} > 150\,m^2/g$). These are typically highly ionic and highly dispersing catalyst carriers. These supports, however, are characterized by high acidity and reactivity and are thus not applicable when very reactive compounds are present in the reactant mixture. They are also unstable at temperatures > 500 °C, tending to convert into θ-Al_2O_3 or even α-Al_2O_3 with loss in surface area. For these reasons, less reactive and more stable lower-surface-area aluminas are used in several applications, such as θ-Al_2O_3 ($S_{BET} = 50–100\,m^2/g$) or α-Al_2O_3 ($S_{BET} < 10\,m^2/g$).
- *Metal aluminates*: Mg and Ca aluminates, with spinel and α-alumina structures, are also widely used as refractory, stable, and quite unreactive carriers for high-temperature applications such as steam reforming, partial oxidation, autothermal reforming, and catalytic total oxidations. The surface area of these materials may be low or very low, and the dispersion of their surface is frequently not high.
- *Silicas*: According to their ionic character, these are typically nondispersing carriers in spite of their high surface area. They have usually give rise to medium-sized supported metal particles. These supports have quite high thermal stability and high chemical inertness.
- *Titanias and zirconias*: These are supports with weak redox properties, medium acido-basicity, high dispersing ability, and high reactivities towards the metal, giving rise to strong metal–support interaction (SMSI) effects. Titania (anatase) and monoclinic zirconia (baddeleyite) have limited thermal stability, tending to convert to the more stable rutile and tetragonal/cubic zirconia phases.
- *Ceria*: Ceria is a typical support or support component characterized by redox properties and oxygen storage capacity, useful for redox reactions. This, however, also gives rise to some instability. However, ceria has a high dispersing ability for metal sites and some surface basicity.
- *Zinc oxide*: Zinc oxide has some hydrogenation/dehydrogenation activity. It is widely used as an activating support, in particular for copper and palladium hydrogenation catalysts. It gives rise to some kind of activating effect. Reduced Zn is supposed to have a synergy with copper metal for methanol synthesis and water gas shift, while the formation of Pd-Zn alloy is very likely in the case of the corresponding Pd-based catalysts.
- *Magnesia*: This strongly basic support is quite unstable in the presence of CO_2 and water. As a catalyst support, it suffers from quite low surface area and poor mechanical strength. In spite of this, it is reported to be an excellent support for some metal catalysts.
- *Zeolites*: Zeolites (Sect. 33.7) have high dispersing ability for cations. After reduction, the size of the metal particles may be limited by the size of the cavity. This may allow metal catalysis with shape selectivity. They also enable metal and strong protonic acid catalysis, or even metal and basic or neutral acid–basic catalysis when alkali-cationic zeolites are used (e.g., Pt-K-zeolite catalysts for aromatization reactions).

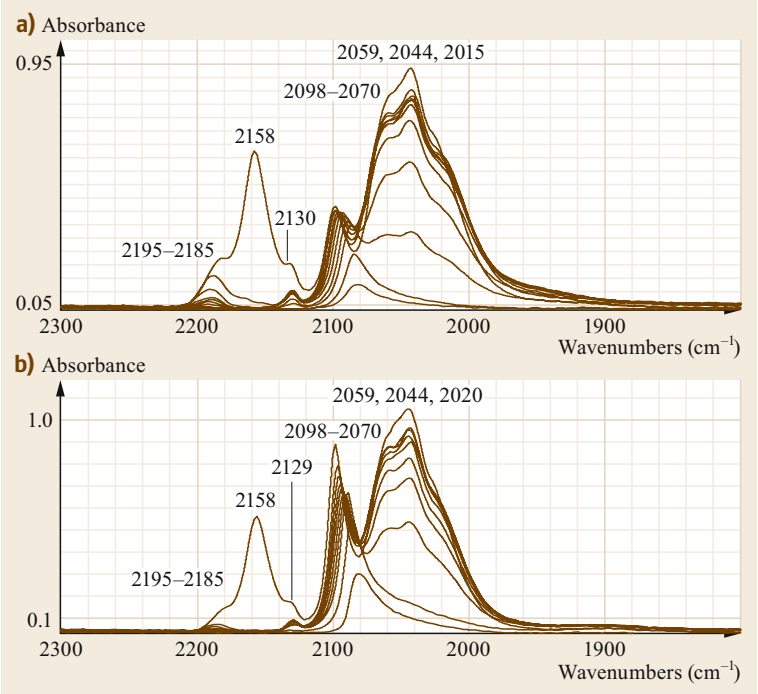

Fig. 33.6a,b IR spectra of CO adsorbed at low temperature on two Ni-alumina catalysts: **(a)** Ni 5%/Al_2O_3, **(b)** Ni 16%/Al_2O_3. While the band at 2098–2070 cm^{-1}, shifting down upon desorption, is due to CO on Ni particles, those at ca. 2130, 2060, 2045, and 2020 cm^{-1} are due to polycarbonyl species on isolated Ni metal centers

- *Carbons*: Different forms of carbon, such as activated carbons, graphite, etc., are used as supports mainly for noble-metal catalysts. They are used mainly for low-temperature liquid-phase applications, or gas-phase applications in reducing atmospheres. Their dispersing ability may be tuned, depending from the carbon pretreatment (oxidizing or reducing).
- *Calcium carbonate and barium sulfate*: These are supports for Pd in the so-called Lindlar catalysts Pd-Pb/$CaCO_3$ and Pd-Pb/$BaSO_4$, applied in organic chemistry for selective hydrogenations of C≡C bonds to C=C bonds.

Actually, in the case of most noble-metal-based industrial catalysts, the amount of metal is small or even very small. In this case, the dispersion of the metal may be very high and the size of the metal particles very small. Thus, supported metal particles cannot always be well characterized even by using transmission electron microscopy, and they are not always evident from x-ray diffraction analysis.

The presence of these particles justifies comparison with data obtained on monocrystal faces as well as theoretical calculations performed with periodic methods on metal crystal faces. The only limit, frequently somehow incorrectly neglected, is that, although these particles may expose the typical low-index faces well known to physicists and theoreticians, they have a very high density of defects, such as edges and corners between faces, whose behavior is more difficult to study.

Additionally, in the case of supported catalysts, isolated and very highly dispersed metal centers, such as small metal clusters, also usually strongly interacting with the supports, may form. This is evident from IR spectra, as shown in Fig. 33.6. In this case, the band of carbon monoxide adsorbed on top on flat nickel metal particles (2098–2070 cm^{-1}, typically shifting down with decreasing coverage) is observed together with a nonshifting multiplet (2130, 2059, 2044, and 2015 cm^{-1}), typically due to polycarbonyl species on isolated metal centers or small clusters. These highly dispersed centers, whose relative amount is greater on low-loading samples, may escape several characterization techniques (e.g., XRD and TEM) but have relevance in catalysis.

Theoretical studies reported on the stabilization of highly uncoordinated Pt and Pd metal centers by alumina reveal a relevant difference between alumina-supported catalysts and bulk metal surfaces [33.59]. The state of Pt and Pd is also dependent on the hydroxylation/dehydroxylation of the support: metal centers become positively charged when deposited on hydroxylated alumina faces, while they would be neutral or even negatively charged over dry surfaces. Other studies report on the existence of Pd particles decorated with a thin layer of an aluminate phase on Pd/Al_2O_3-supported catalysts [33.60]. The existence

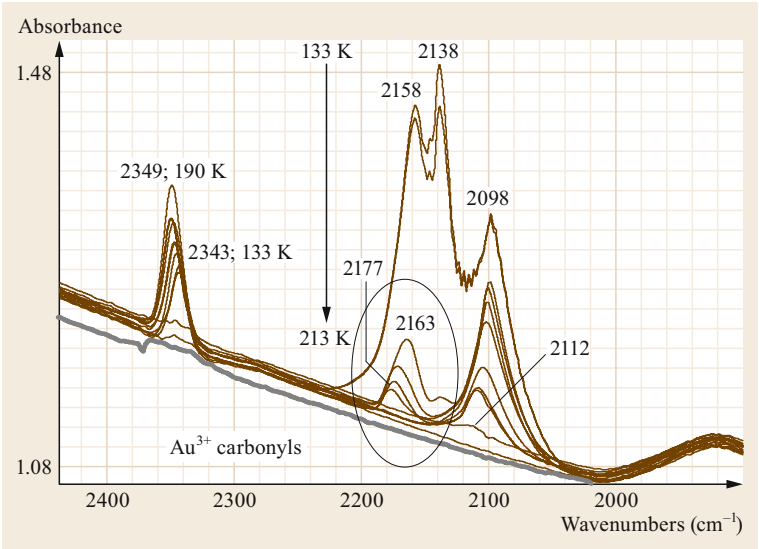

Fig. 33.7 IR spectra of CO adsorbed at low temperature on Au/Nb_2O_5 catalyst. While the band at 2098 cm^{-1}, shifting up upon desorption, is due to CO on Au particles, that at 2163 cm^{-1} is due to CO adsorbed on oxidized Au centers [33.58]

and likely catalytic activity of isolated centers have recently been proposed for CO oxidation and water gas shift on Pt/Al_2O_3-and different oxide-supported Pd catalysts [33.56, 61, 62] and also on gold catalysts [33.58]. Appropriate procedures indeed allow the preparation of atomically dispersed metal centers that exhibit catalytic activity and are even supposed to represent the real active sites in reactions such as CO oxidation and water gas shift [33.63, 64]. In Fig. 33.7, evidence is provided for the presence of isolated Au^{3+} centers on the surface of Au/Nb_2O_5 catalysts [33.58]. While the band shifting up from 2098 to 2112 cm^{-1} is typical of CO adsorbed on top of gold metal particles, the band at 2163 cm^{-1} is due to CO interacting with oxidized gold centers. As a result of this interaction, the band of CO_2 produced by CO oxidation on oxidized gold is observed growing at 2340–2350 cm^{-1}. In the case of Pd/CeO_2 catalysts, evidence for the possible introduction of palladium ions into the ceria lattice, producing a $Pd_xCe_{1-x}O_{2-x-\delta}$ solid solution, at the contact of palladium and cerium oxide nanoparticles, has been provided [33.65]. Indeed, the situation in the case of highly dispersed metals on oxide carriers may be even more similar to that of mixed oxides than of supported metal particles.

33.6.4 Activation of the Substrate upon Catalytic Oxidation

Oxidation catalysts are generally thought not only to activate oxygen but also to activate the substrate to be oxidized. Among hydrocarbons, the most reactive towards oxidation are functionalized molecules such as aromatics, with the activation of both ring positions as well as of benzylic positions. Also oxidation of olefins is very relevant industrially, with the possibility of oxidation at the C=C double bond or at the allylic position. The activation of unsaturated C=C bonds is frequently achieved by π-bonding over noble- or transition-metal centers. Alternatively, they can be activated by electrophilic attack. Activated saturated carbon atoms such as those at benzylic and allylic positions are activated by Lewis acid sites, which can abstract hydride species, or in a radical mode. Cations such as Sb^{3+}, Bi^{3+}, and Te^{4+}, i.e., having nonbonding electron pairs, are generally thought to be active in H abstraction from allylic positions [33.48, 49].

Heteroatom-containing molecules such as oxygenates, nitrogenated and halogenated compounds, which are in fact n-bases and more reactive to oxidation, are activated more easily. Activation likely involves the previous coordination of the molecules on Lewis acid sites using the lone pairs on heteroatoms. In Table 33.10, some relevant oxide oxidation catalysts are summarized.

33.6.5 Fixed Bed versus Fluidized Bed Catalytic Oxidations

Fixed bed multitubular reactors are mostly used for selective oxidations. Temperature is controlled by refrigeration fluids from the external surface of the catalytic tubes. These reactors have heavy drawbacks, in particular due to the difficult and long tube-charging operation, and possible preferential ways for the reactant mixtures when some tubes are not perfectly packed. Fluidized bed reactors allow much easier and faster charging and possibly also better temperature control. However, catalysts for fluid beds must be shaped as spheres that are resistant to abrasion. This is not always possible, depending on the catalyst composition.

33.7 Solid Catalysts for Hydrogenation and Dehydrogenation Reactions

33.7.1 Hydrogenations and Dehydrogenations

Hydrogenation reactions are exothermic equilibrium reactions, thus being performed at the lowest temperature allowed by the catalyst activity, and at medium to high pressure. Most of them are performed in the presence of solid metal-based catalysts, most frequently in multiple fixed beds with interbed cooling by heat exchange or quenching, in gas/solid or gas/liquid/solid conditions, or in slurry conditions, depending on the volatility of the reactants as well as the reaction temperature and pressure. In recent years, catalytic distillation processes have been developed, where the reaction occurs in distillation towers partly packed with a catalyst bed.

Catalytic activity in hydrogenation is associated with the ability of the catalytic material to adsorb hydrogen dissociatively, either heterolytically or homolytically, thus converting H_2 into atomic active forms.

Dehydrogenation reactions are endothermic equilibrium reactions, thus being performed at moderately high temperature and at low pressure, usually not far from ambient pressure. They are performed industrially in the presence of either metal-based catalysts or oxide catalysts, most frequently in single or multiple fixed beds with previous or interbed heating. Being reactions that occur at relatively high temperature and in the presence of organics and a reducing environment, catalyst coking may occur upon dehydrogenations. Reactor configurations must take this into account, allowing frequent or continuous regeneration. For this reason, several optional configurations have been developed: semi-regenerative processes, cyclic regenerative processes, and moving bed and continuous regenerative processes.

Most dehydrogenation catalysts are based on metals, mostly being the same as used also for hydrogenations, which are in fact the reverse reactions (Table 33.11). However, several oxides (such as chromia–aluminas and zinc oxide) also show catalytic behavior for some dehydrogenation reactions. Activity in dehydrogenation is driven by the ability of the catalyst to adsorb hydrogen as well as the unsaturated compound coming from dehydrogenation.

Catalysts that catalyze an equilibrium reaction also catalyze the reverse reactions. However, while hydrogenations are carried out at low temperature, dehydrogenations are carried out at high temperature. Thus, dehydrogenation catalysts may contain the same active phases as hydrogenation catalysts, but must be much more resistant to sintering and phase transformations than hydrogenation catalysts. As an example, catalysts for CO methanation work at 300–500 °C: they may be based on Ni on high-surface-area γ-Al_2O_3 [33.66]. The reverse reaction is methane steam reforming (see later). The latter reaction is realized at 800 °C: the catalysts are based on Ni supported on low-surface-area α-Al_2O_3 or metal aluminates (Sect. 33.8).

Table 33.11 Catalytic hydrogenations and dehydrogenations on metal catalysts

Reaction	Catalyst	Reaction conditions
Hydrogenation of nitrogen (ammonia synthesis)	Fe(K, Si, Al, Ca, Mg) Ru/graphite	400 °C, 200 bar, gas phase 300 °C, 100 bar, gas phase
Hydrogenation of CO, CO_2 (methanol synthesis)	55% Cu/ZnO/$ZnAl_2O_4$	250 °C, 100 bar, gas phase
Hydrogenation of CO, CO_2 (methanation)	25% Ni/γ-Al_2O_3 0.3% Ru/γ-Al_2O_3	250 °C, 20–50 bar, gas phase 170 °C, 20–50 bar, gas phase
Hydrogenation of CO, CO_2 (to hydrocarbons, LT Fischer Tropsch)	Co/γ-Al_2O_3	200 °C, 20–30 bar, slurry
Hydrogenation of CO, CO_2 (to hydrocarbons and oxygenates, HT Fischer Tropsch)	Fe-Fe_5C_2/SiO_2	300 °C, 20–40 bar, slurry
Hydrogenation of acetylene (C2 cut treatment)	0.03% Pd, 0.18% Ag/α-Al_2O_3	80 °C, 20 bar, gas phase
Hydrogenation of acetylenics	0.5% Pd/α-Al_2O_3	15 °C, 20 bar, liquid phase, fixed bed
Benzene saturation to cyclohexane	Ni Raney	200 °C, 50 bar, slurry
Hydrogenation of vegetable oils to margarine	Ni/SiO_2	200 °C, 5 bar, liquid phase
Light paraffin dehydrogenation to olefins	Pt/Li-Al_2O_3	550 °C
Heavy paraffin dehydrogenation	Pt/Li-Al_2O_3	475 °C, 2.5 bar
Aromatization	Pt/K-L zeolite	500 °C
Catalytic reforming of gasoline (aromizing)	Pt/K-L zeolite	500 °C
Dehydrogenation of alcohols to carbonyl compounds	Cu-ZnO-Al_2O_3 $CuCr_2O_4$	200–400 °C 200–400 °C

33.7.2 Hydrogenation Catalysts

Many metals, including platinum group metals, nickel, cobalt, iron, copper, etc., are active in hydrocarbon hydrogenation (Table 33.11). However, some noble metals are far more active, but quite easily deactivated, in particular by sulfur compounds. For these reasons, the catalyst composition for hydrocarbon hydrogenation is strongly dependent on the amount of sulfur impurities in the feed. Palladium, and to a lesser extent platinum, are the catalysts of choice for hydrogenation of clean feeds, while nickel is mostly used for hydrogenation of medium sulfur-containing feeds. Bimetallic noble-metal catalysts or other modified noble-metal catalysts may also have interesting resistance to medium/low concentrations of sulfur.

Metal sulfides are active in hydrogenations (Table 33.12) and are usually stable in sulfur-containing environments, needing sulfur in the feed to stay stable in a sulfided state. They are therefore the catalysts of choice for hydrodesulfurization and hydrocracking, and can be used for hydrogenation of hydrocarbons in sulfide-containing atmospheres.

Some metal oxides are also active in adsorbing hydrogen and can be used as catalysts for hydrogenation: in particular, some of them are used for hydrogenations of oxygenated compounds.

33.7.3 Adsorption of Hydrogen on Metals

There is general agreement that hydrogen adsorbs dissociatively and very quickly on almost all relevant metal surfaces, where the dissociation of hydrogen is only weakly activated or even barrierless [33.67]. As an example, it has been found that, when an H_2 molecule chemisorbs on a Pt surface, the antibonding σ^* orbital of H_2 is completely filled by electrons from platinum. Thus, nonactivated dissociative adsorption occurs; i.e., the adsorption step is not kinetically hindered. Only on group 11 metals (Cu, Ag, and Au) is hydrogen dissociation significantly activated [33.68] and may be endothermic. On-top, bridge or hollow sites can be occupied by atomic hydrogen species on metal surfaces. Such different coordinations for atomic hydrogen can be distinguished by vibrational spectroscopies, being surface metal hydride species (hydrogen on on-top sites) characterized by M–H stretchings in the $2000\,cm^{-1}$ region, while vibrations of hydrogen on bridge and hollow sites are detected at much lower frequencies [33.67, 69]. The formation of subsurface atomic hydrogen is also possible, usually via an endothermic and/or a slightly activated process. Tetrahedral and octahedral subsurface sites are occupied in this case. Only in the case of palladium is migration of hydrogen into the interior of the bulk apparently exothermic too, due to a very large binding energy ($-2.5\,eV$). This agrees with data showing that only in the case of Pd can a significant population of subsurface hydrogen occur and bulk hydrides also form.

33.7.4 Adsorption of Organic Substrates on Metals

Surface metal atoms, according to their coordinative unsaturation, present both Lewis acidity towards n-bases, as well as π-bonding activities towards unsaturated hydrocarbons. In fact, heteroatom-containing molecules such as saturated oxygenated compounds (including water), amines (including ammonia), sulfur compounds (including hydrogen sulfide), and halogens are supposed to interact by donation of their full n-type orbitals with empty d-type orbitals of transition-metal

Table 33.12 Catalytic hydrogenations and dehydrogenations on nonmetallic catalysts

Reaction	Catalyst	Reaction conditions
Hydrodesulfurization gasolines	Ni-MoS_2	300 °C, 20 bar, gas phase
Hydrodesulfurization gasoils	Ni-Co-MoS_2	350 °C, 50 bar, trickle bed
Hydrodenitrogenation of hydrocarbons	NiS-WS_2/Al_2O_3	350 °C, 50 bar, trickle bed
Hydrocracking heavy oils and residues	NiW-USY zeolite	400 °C, 150 bar, slurry
Deep hydrocracking (bottom of the barrel treatments)	MoS_2	450 °C, 200 bar, slurry
Hydro-deoxygenation of vegetable oils to green Diesel	CoS-MoS_2/Al_2O_3	250 °C, 50 bar, slurry
Hydrogenation of CO, CO_2 (HP methanol synthesis)	ZnO-$ZnCr_2O_4$	350 °C, 340 bar
Hydrodeoxygenation of carboxylic acids to aldehydes	Cr_2O_3-ZrO_2, CeO_2	310–400 °C, 1–30 bar
Hydrodealkylation of toluene	Cr_2O_3/Al_2O_3	600 °C, 50 bar
Dehydrogenation of light paraffins to olefins	K_2O-Cr_2O_3/Al_2O_3	550 °C
Dehydrogenation of ethylbenzene to styrene	K_2O-Fe_3O_4	600 °C, steam
Aromatization of light paraffins	Ga-ZSM5 zeolite	500 °C
Aromatization of light olefins	Zn-ZSM5 zeolite	500 °C

atoms, on-top. On the other hand, olefins, dienes, and aromatics are thought to adsorb on metal centers by electron donation from their full π-orbitals to empty d-type orbitals of transition metals with simultaneous electron back-donation from full d-type orbitals of transition metal to empty π^*-antibonding orbitals. This interaction with olefinic double bonds can be rapidly converted into di-σ-bonding and σ-alkyl groups [33.10, 70], while in the case of acetylene a tetra-σ-bonding or a threefold parallel-bridge configuration [33.71] is likely formed. In the case of aromatic rings, several σ-bondings are thought to form on the surface of active hydrogenation metals such as Pt(111) [33.72]. The picture for real catalysts is however possibly more complex due to the formation of carbonaceous matter on the metal surfaces, which can allow further adsorption mechanism to be active [33.10]. Sequential addition of single hydrogen atoms to the adsorbed hydrocarbon intermediate are thought to occur.

33.7.5 Metal Sulfides as Hydrogenation Catalysts

A number of metal sulfides act as hydrogenation catalysts [33.73, 74]. The most widely used sulfides for hydrogenations are based on MoS_2 and WS_2, pure or as solid solutions, with Co and/or Ni as activators. They are used either as bulk materials or supported, mainly on alumina [33.75, 76] (Table 33.12).

Molybdenum and tungsten sulfides, MoS_2 and WS_2, are isostructural layered phases. The tetravalent element forms a layer sandwiched between two two-dimensional hexagonal sulfide layers stacked over each other in an eclipsed fashion. Thus, the coordination around the metal is trigonal prismatic. Each sulfur center is pyramidal, being connected to three Mo centers.

Two main polymorphs of MoS_2 and WS_2 are reported to exist, due to the different relative position of the slabs. α-MoS_2 (molybdenite) hexagonal (space group $P63/mmc$), the most stable, is the most common and well-studied polymorph, and the natural form is isostructural with α-WS_2 tungstenite. β-MoS_2 and β-WS_2 are the rhombohedral modifications (space group $R3m$). Both sulfides may also be prepared in the form of fullerene-like particles as well as nanotubes, nanorods, nanostrips, nanowires, nanoflowers, nanoflakes, nanospheres, and nanohexagonal plates.

According to the most well-accepted theory, originally developed for supported MoS_2 catalysts, the catalytic chemistry of these materials should occur at the lateral termination (edges) of the MS_2 slabs. Two kinds of termination should exist for stoichiometric MoS_2, viz. the S edge ($\bar{1}010$ face), where coordinatively unsaturated sulfur is located for stoichiometric MoS_2, and the Mo edge ($10\bar{1}0$ face), where coordinatively unsaturated Mo species are expected in stoichiometric MoS_2.

The promoters Ni and Co introduce further defects and disorder into the structure, perturbing the stacking of the layered sulfides, introducing curvatures and non-stoichiometry. Additionally, or more importantly, they are mostly supposed to locate at the edges decorating them, increasing edge reactivity. In particular, most authors suggest that the promoters substitute for Mo or W at the edges of the $(Mo,W)S_2$ slabs, producing the most active sites for reaction.

For the Co-Mo-S system, other studies [33.77] have reported that the catalytic activity is directly proportional to the increase of the surface area of the two separate sulfide phases, Co_9S_8 and MoS_2. This suggests that the activity is directly connected with an increase of the contact surface area between the two sulfide phases. This approach has found further support, suggesting that the catalytic sites are located at the interface between cobalt sulfide crystallites and the stacks of MoS_2 slabs [33.78].

On the other hand, it has been underlined that, for fully saturated MoS_2, a metallic state extends over the slab basal (0001) plane, generating possible *brim* sites [33.79]. In fact, unsaturated molecules such as butadiene, thiophene, benzothiophene, pyridine, quinoline, benzene, and naphthalene may adsorb on the basal plane via van der Waals interactions. Additionally, it was recently shown that fully saturated MoS_{2+x} without any coordinative unsaturation can activate hydrogen and catalyze hydrogenation [33.80]. Thus, it seems that the details of the reaction mechanisms on unsupported sulfides remain to be completely defined.

Among other metal sulfides having relevant hydrogenation activities, much interest has been focused on ruthenium sulfides.

33.7.6 Adsorption of Hydrogen on Metal Sulfides

Two kinds of dissociation mechanism are supposed to exist, potentially, over sulfide surfaces: heterolytic dissociation, producing a molybdenum hydride species and a thionyl species, and homolytic *reducing* dissociation, producing two sulfidryl species and reduced molybdenum centers (Fig. 33.8).

To our knowledge, however, while the formation of thionyl SH groups has been directly detected by spectroscopic methods (e.g., bands at 2500 cm^{-1}, ν-SH, and 650 cm^{-1}, δ-SH, in inelastic neutron scattering spec-

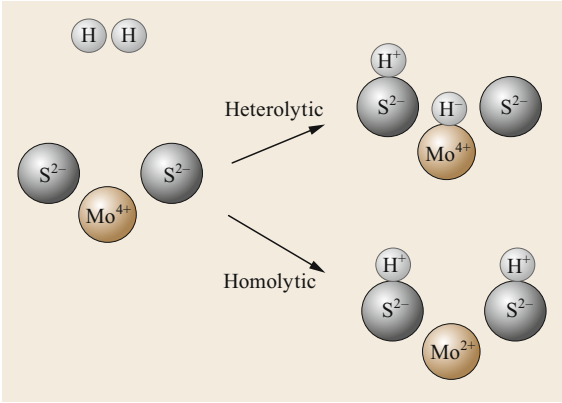

Fig. 33.8 Schematics of the mechanisms of dissociation of hydrogen on MoS_2

tra), no experimental evidence for molybdenum hydride species has been provided so far on MoS_2- or WS_2-based catalysts [33.81, 82].

Theoretical investigations suggest that heterolytic and homolytic dissociation of hydrogen may both occur, depending on the conditions and on the exposition of the Mo sites: heterolytic dissociation tends to occur on highly exposed Mo–S couples [33.83].

Interestingly, hydride species have been observed by inelastic neutron scattering on another catalytically active sulfide phase, RuS_2, thus providing evidence of a heterolytic dissociative adsorption mechanism there [33.84].

33.7.7 Supported Metal Sulfide Hydrogenation Catalysts

Transition-metal sulfide catalysts used in refineries for hydrotreatments are mostly molybdenum or tungsten sulfides supported on γ-Al_2O_3 and promoted by Co or Ni. The optimal promoter atomic ratio: $Co(Ni)/(Co(Ni) + Mo(W))$ is between 0.2 and 0.4. $CoMo/Al_2O_3$ catalysts are very efficient in the hydrodesulfurization (HDS) process [33.85] but are less active for hydrodenitrogenation (HDN) or aromatic hydrogenation. The degree of staking in MoS_2 and Co-Mo-S structures can be engineered by carefully controlling the properties and preparation parameters of the support. The formation of small stable single slabs of MoS_2 on alumina supports has been achieved. Conversely, NiMo phases are better HDN and hydrogenation catalysts and are preferred in order to treat feedstock with a high concentration of unsaturated compounds. NiW catalysts are highly effective for aromatic hydrogenation reactions but have higher cost. Other elements, such as phosphorus, boron, and titanium, are sometimes added to the alumina support, improving the catalytic activity. In particular, phosphorus improves the selectivity toward hydrogenolysis versus hydrogenation.

After sulfidation, crystallites of the MS_2 phase in the form of slabs form on the alumina surface. These crystallites may have different shapes, such as hexagonal, triangular, and truncated triangular, and may interact differently with the alumina surface. Promoter atoms (Co, Ni) are supposed to locate mainly in substitution of Mo (W) atoms at the edges of the slabs.

33.7.8 Metal Oxides in Hydrogenation and Dehydrogenation Reactions

A number of oxides significantly adsorb hydrogen and show useful activity as catalysts for hydrogenation and dehydrogenation reactions (Table 33.12). Adsorption of hydrogen on such materials is mostly reported to be heterolytic, occurring on exposed cation–oxide couples. Well-evident surface hydride species have been observed by vibrational spectroscopies (in particular infrared techniques) on ZnO [33.86–89], Cr_2O_3 and $ZnCr_2O_4$ [33.90], as well as on Ga_2O_3 [33.91] and ZrO_2 [33.92]. However, according to *Syzgantseva* et al. [33.93], on zirconia, hydrogen could dissociate via a different mechanism, adsorbing on two Zr^{3+} ions with a neighboring oxygen vacancy (νO), leading to formation of two Zr^{4+}–H hydride species.

On ZnO, surface hydride species cannot be observed in well-controlled single-crystal ultrahigh-vacuum (UHV) experiments, while they are detected on powders and at significant hydrogen pressure. At higher temperature, these species disappear, while contact with hydrogen can produce reduction of the surface.

A different mechanism, i.e., homolytic reductive adsorption, seems to occur in other cases, in particular on ceria [33.94]. The adsorption of hydrogen on ceria has been studied by density functional theory (DFT) calculations [33.95]. These studies have shown that H_2 may adsorb dissociatively on $CeO_2(111)$ with a relatively low activation barrier (0.2 eV) and strong exothermicity. Hydrogen homolytic dissociation is supposed to lead to two OH groups. Indeed, during the hydrogenation reaction, increased absorption in the OH stretching region of the IR spectra bands was observed [33.96]. Ceria is reported to be active in hydrodeoxygenation reactions, such as reduction of carboxylic acids to aldehydes, as well as in the hydrogenation of alkynes to alkenes.

It can be supposed that inverse mechanisms with the same intermediate states can be applied in the case of dehydrogenation reactions. These species will give rise to gaseous hydrogen after abstraction of a proton.

33.8 A Case Study: Steam Methane Reforming (SMR) for the Production of Hydrogen

33.8.1 Industrial Steam Reforming Processes: Some History

As summarized by *Rostrup-Nielsen* years ago [33.97], studies on the reaction of steam with hydrocarbons started in the last half of the nineteenth century [33.98]. The first patent on nickel catalysts for steam reforming was issued to BASF in 1913, while, apparently, the first detailed paper dealing with catalytic reforming of methane dates from 1924 [33.99]. Standard Oil started producing hydrogen by hydrocarbon steam reforming in the USA in 1931. As frequently occurs, chemical technology was fast to develop processes well before science was able to explain and describe in detail the phenomena at the molecular level. However, further technological improvements and plant management have taken much advantage of more recent scientific developments, allowing better understanding of the chemistry and physics of such systems, in particular through modeling [33.100]. Today, steam reforming of methane or natural gas is a very prominent technology for hydrogen and syngas production [33.101, 102].

33.8.2 Steam Methane Reforming: Thermodynamics

Steam reforming processes are endothermic equilibrium reactions performed to convert organics and water to syngases, i.e., hydrogen and CO_x mixtures. The most common application today is steam methane reforming (SMR) or reforming of natural gas. The main reaction is endothermic.

$$\mathrm{CH_4 + H_2O \rightarrow CO + 3\,H_2}$$
$$\Delta H^\circ_{298} = +206.63\,\mathrm{kJ/mol}$$
$$\Delta S^\circ_{298} = +214.63\,\mathrm{J/(K\,mol)}$$

The reaction, more favored at higher temperature and lower pressures, is practically performed at 700–900 °C, usually under 30–50 bar. This moderate pressure is used to reduce the reactor size and improve the efficiency of the overall process, despite the unfavorable thermodynamics of the reaction step.

In reaction conditions, also the so-called water gas shift equilibrium is established or approached

$$\mathrm{CO + H_2O \rightarrow CO_2 + H_2}$$
$$\Delta H^\circ_{298} = -41.16\,\mathrm{kJ/mol}$$
$$\Delta S^\circ_{298} = -42.08\,\mathrm{J/(K\,mol)}$$

Thus, the resulting product gas, denoted as syngas, is a mixture mainly containing H_2, CO, CO_2, and unreacted methane and water. In most cases, SMR processes are followed by one or more water gas shift steps, where CO is converted by reacting with water almost completely to CO_2, thus producing more hydrogen. Finally, hydrogen is separated from CO_2 and purified.

33.8.3 SMR: Metal Catalysts

Most transition metals are active in steam reforming. Platinum group metals, such as ruthenium, rhodium, iridium, and, possibly to a lower extent, palladium and platinum, are very active in SMR [33.103]. Nickel, if loaded at the same amount on the supports, is definitely less active than Ru and Rh, and more prone to deactivation. However, due to its much lower price, it can be charged on catalysts at much higher loadings (up to 50% instead of, e.g., $< 1\%$). Thus, nickel catalysts loaded at the level of 10–30 wt% are sufficiently active, cheap, stable, and robust to represent the best choice for SMR catalysis in practice.

33.8.4 SMR on Nickel: Surface Science and Computational Studies on the Reaction Mechanism

The mechanism of the SMR reaction over Ni metal surfaces was approached long ago by surface scientists [33.104] and, more recently, by theoreticians [33.105, 106], although full agreement has still not been reached.

Water activation on metallic nickel is supposed to produce hydroxyl and oxide species [33.107]. Most data suggest that methane is activated mostly on steps or edges of Ni particles, producing successively methyl (CH_3), methylene (CH_2), methine (CH), and carbide species by progressive dehydrogenation. A competition between methane and water adsorption has been reported [33.108].

However, methane can also be adsorbed and activated on oxide and/or hydroxyl sites, thus producing oxygenated intermediates. A further alternative consists in the reaction of water with CH_x adsorbed intermediates, producing oxygenated intermediates too. The final reaction step is the decomposition of such oxygenated intermediates, finally producing hydrogen and carbon monoxide.

33.8.5 SMR on Nickel: Kinetics

Kinetic modeling of SMR over Ni takes advantage of the above mechanistic considerations [33.109, 110]. The reaction order is close to one for methane and definitely negative for steam, with a weak positive effect of hydrogen [33.111–113]. The main data show that the rate-determining step in the overall process is most likely the first methane adsorption and dissociation step [33.108, 112], although some studies suggest that the decomposition of the surface oxygenated intermediates is rate determining [33.114]. Although scattered data are reported on activation energies, most authors [33.115] report a value of $\approx$ 100 kJ/mol, consistent with the values calculated for the C–H bond activation of CH_4 on Ni monocrystal surfaces [33.116].

33.8.6 SMR on Nickel: Managing the Problems

Sintering of Nickel Particles

As shown by surface chemistry studies, methane and water activation very likely occurs mostly at steps or kinks on Ni nanocrystals. On the other hand, the reaction conditions are certainly very demanding: high temperature, moderately high pressure, presence of large amounts of steam, and required lifecycles of several years. Taking into account that pure nickel melts at 1455 °C (1728 K), atomic mobility may already be active at such reaction conditions. In fact, the temperature for starting atom mobility in the solid state (the so-called Tammann temperature) is evaluated to be around half of the absolute melting temperature. For nickel, this temperature is consequently about 865 K. This means that sintering of Ni nanoparticles is possible. Sintering will obviously reduce the surface area of metallic nickel and the density of active step and corner sites. Thus, the catalyst composition (support and additives) must be chosen to reduce the sintering rate as much as possible. Ni–OH is assumed to dominate nickel transport at nickel surfaces in the presence of steam and hydrogen, as Ni–OH has the lowest combined energies of formation and diffusion compared with other potential nickel transport species [33.117].

Poisoning by Sulfur

Ni catalysts are rapidly deactivated by sulfur poisoning, due to the formation of inactive nickel sulfide [33.118, 119]. In practical SMR applications, this problem is solved by removing sulfur upstream. A hydrodesulfurization step with stoichiometric hydrogen over Ni-promoted MoS_2/Al_2O_3 catalysts at 350 °C is followed by an absorption step using ZnO at 400 °C [33.97, 101].

Formation of Carbon Deposits

Carbon matter forms at the reaction conditions on Ni catalysts [33.120], much more than for platinum group metal catalysts. A number of different forms of carbon are revealed by analysis of spent catalysts. The most evident one is represented by carbon whiskers [33.121], actually constituted by mulitiwalled carbon nanotubes whose formation is catalyzed by Ni surfaces (Fig. 33.9). It has been found that the (111) Ni faces are mostly responsible for the formation of this kind of carbon species. This carbonaceous matter tends to detach Ni crystals from the support. This form of carbon does not really deactivate the catalyst, at least during the first stages of formation. However, the whiskers occupy void spaces in the catalyst bed, causing pressure drops that worsen with time.

Other forms of carbon species can also be detected, such as gums and pyrolytic coke. In any case, all of these result in progressive catalyst deactivation. Most of the carbon species are formed by decomposition/dehydrogenation of higher hydrocarbons (butanes, propane) that are usually present in some amount in the feed. Pre-reforming beds allow specific reforming of higher hydrocarbons, whose reaction with water is

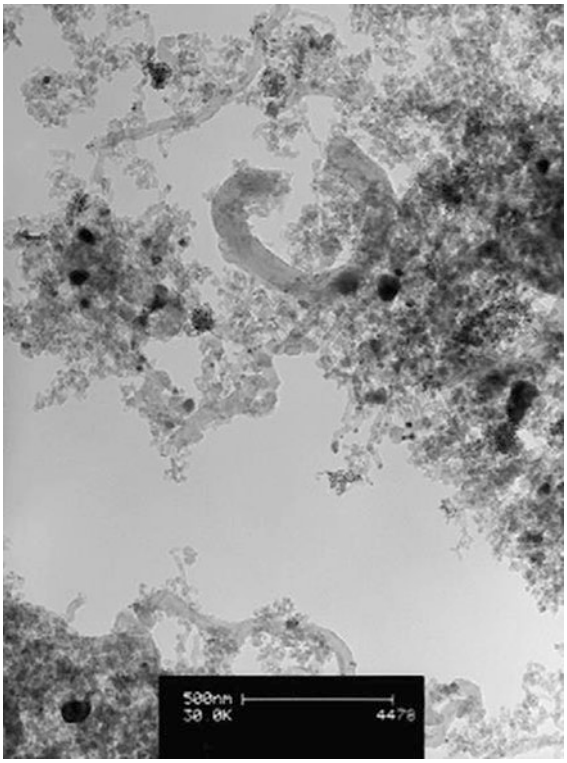

Fig. 33.9 TEM image of carbon whiskers formed on a Ni-Co/ZrO_2 steam reforming catalyst. From [33.122]. Reprinted with permission from AAAS

thermodynamically much more favorable than that of methane, at 500–600 °C. This limits the formation of carbon matter in the SMR tubes. Another way to reduce the formation of carbon matter consists in feeding a large excess amount of steam. In fact, the steam-to-carbon ratio typically applied in the SMR process is 3 : 6, compared with the S/C stoichiometric ratio of 1 for the main reaction. However, slow formation of C matter seems to be almost unavoidable and critical for the lifetime of the catalyst bed and also of the tubes. The formation of carbon matter can also be reduced by an appropriate choice of the support and of activators/stabilizers for Ni catalysts.

33.8.7 SMR on Nickel: The Choice of the Support

The SMR reaction is performed at high temperatures (700–900 °C) in the presence of a large amount of steam. The catalyst should be substantially stable for operation 24 h a day for several years. Thus, the catalysts must have an important refractory character. Typical methane steam reforming catalysts contain 10–25 wt% Ni, 70–85 wt% Al_2O_3, or aluminate supports and up to 5% K, Ba, Ca. The support phase is in fact a refractory oxide such as α-alumina (corundum), Mg aluminate spinel $MgAl_2O_4$, calcium aluminate $CaAl_{12}O_{19}$, and calcium-potassium aluminate $CaK_2Al_{22}O_{35}$. Metal aluminates, corundum, and Mg-, Ca- and K-aluminates, with spinel and β-alumina structures, are in fact refractory and high-melting-point materials. The surface area of these materials may be low (a few tens of m^2/g) or very low and dispersion of Ni on their surface is frequently not high, typically giving rise to Ni particles with sizes of 20–50 nm.

The presence of alkali and alkali-earth cations is associated with a significant basicity of these materials, which is needed to inhibit the formation of carbon matter on the support itself. These components can also act as activators or stabilizers of the nickel active phase.

The nature of the support, the amount of loaded metal, the nature and amount of promoters and stabilizers, and the preparation procedures are all factors that influence the crystal size and shape of the nickel nanoparticles on the catalyst. It seems that the best crystal size lies in the range of 20–50 nm (see Fig. 33.10 for a heavily charged Ni-Co/ZrO_2 catalyst). Actually, polycrystalline particles mainly form. Atoms at steps, edges, and defects are usually found to be the most reactive and probably represent the predominant active sites in the reaction.

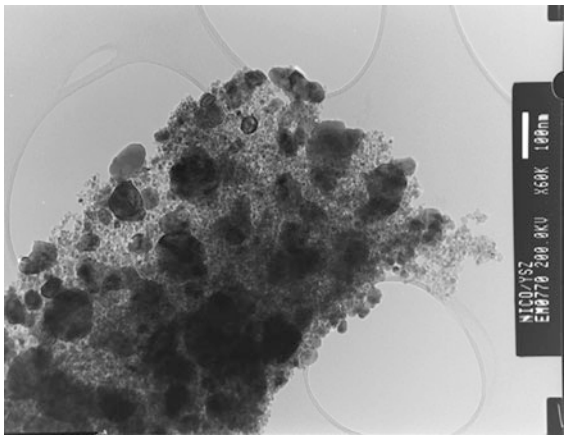

Fig. 33.10 TEM image of Ni-Co/ZrO_2 steam reforming catalyst. From [33.122]. Reprinted with permission from AAAS

33.8.8 SMR on Nickel: Promoters and/or Stabilizers

As mentioned above, catalyst components can influence the catalytic activity, poisoning, sintering, and carbon forming activity of nickel catalysts. According to the open literature, elemental analyses of industrial steam reforming catalysts indicate the presence, besides nickel and aluminum, of one or more alkali and alkali-earth elements, i.e., K, Mg, Ca, and Ba. These elements may be involved at least in part in the formation of aluminate phases, such as spinels and/or β-aluminas. They make the support stable at high temperature and under hydrothermal conditions. However, they also contribute by modifying the interaction between the nickel metal particles and the support itself. They may also modify the behavior of nickel and reduce the activity of the bare support surface. In particular, potassium has a very positive effect in reducing the formation rate of carbon species, with the drawback of slightly reducing the catalytic activity of the catalyst [33.120]. On the other hand, alkali-earth ions are reported to limit nickel dispersion, resulting in easier reducibility of nickel species [33.123, 124]. In the case of Ca, however, the behavior strongly depends [33.125] on the amount of Ca and the nature of the support. Other elements frequently cited as components of the catalysts are zirconium and rare earths, in particular lanthanum and cerium [33.126, 127]. La is reported to increase the catalytic activity [33.128] and aid in the removal of some of the carbon deposits more effectively by gasification [33.129].

The copresence of lanthanum and cobalt has been reported to be beneficial, at least for dry reforming activity [33.130]. Boron is also considered to act as an excellent structural promoter to obtain small Ni particles [33.129], but its behavior may depend on the impregnation procedure used [33.124].

The presence of small amounts of silica is also sometimes reported. Silica can stabilize the support as well as limit the dispersion of nickel, forming larger aggregates and reducing the amount of isolated nickel species [33.131].

Addition of Mo is also cited in literature: it is reported to decrease the surface metal area but increase the specific activity of the active sites [33.132].

Alloying of Ni with small amounts of other metals, in particular noble metals, is also considered to be useful [33.122], although it can also increase the cost of the catalyst. Ni-Au, Ni-Ag, Ni-Sn, Ni-Cu, and Ni-Co alloys are reported to exhibit superior catalytic performance in the methane steam reforming, i.e., high activity, high resistance to carbon formation and sintering of metal particles, and high selectivity to H_2 product [33.133]. In general, Co is reported to increase the catalytic activity of Ni in steam reforming reactions [33.134, 135]. Alloying Ni with Rh is reported to stabilize the metallic particles [33.129]. Alloying Ni with noble metals is reported to prevent sintering [33.136] and to display an *intelligent* behavior, with suppression of deactivation phenomena in case of daily start-up and shut-down operation, typical in case of hydrogen and fuel cells for domestic use [33.137].

33.8.9 SMR on Nickel: The Choice of Reactor and Reaction Conditions

The SMR process is usually realized today at 30–50 bar pressure, in spite of the negative effect of increasing the pressure on the reaction thermodynamics. In fact, although the hydrogen yield is slightly reduced by increasing the pressure, a great reduction of the reactor size is obtained. Medium/high pressures are convenient also because the other steps of the overall process are then conveniently performed. Finally, higher pressures may also allow higher flow rates, thus allowing higher productivities.

The reaction is usually performed in special steel tubes, 10–20 cm large and 10–15 m long, filled with the catalyst extrudates, mostly downflow, placed into fired furnaces. For large plants up to 1000 tubes may be present, while for small size plants 10–20 tubes are present. The small diameter of the tubes is due to the need to reduce temperature gradients in the section. The length is associated with the contact time needed to approach equilibrium and obtain the highest productivity. The space velocities typical for industrial reactors are on the order of 2000–4000 h^{-1}, being dictated predominantly by the heat transfer and tube design. The temperature profile along the tube is increasing, from $\approx 500\,^{\circ}C$ at the inlet to $\approx 800\,^{\circ}C$ at the outlet. The maximum temperature is a compromise between the need to improve the thermodynamics (the reaction is endothermic) and the needs to limit the catalyst sintering, fuel combustion, and tube metal costs and increase the lifetime of the tubes.

Steam is fed in excess, in spite of its reducing effect on the reaction rate: the steam-to-carbon ratio is usually > 3, to push the thermodynamics and reduce the formation of carbon species.

33.8.10 SMR on Nickel: Shaping the Catalyst

As cited above, shaping is necessary to reduce the pressure drops and improve the fluid dynamics and heat transfer effects. Cube extrudates were first used in commercial SMR plants by ICI (now Johnson Matthey) [33.138]. They were later substituted by cylinders with a single hole (Raschig rings), then by four-hole cylinders, and finally by quadralobes. Through this development, the relative activity was doubled while the pressure drop was more than halved. The most recent development in this field is the application of cylindrical foil-supported module structures (CATACEL JM SSRTM) that allow a further strong increase in the activity and decrease of the pressure drop.

33.9 Conclusions

The present review underlines the complexity and multidisciplinarity of the field of heterogeneous catalysis, where collaboration among chemical engineers, material scientists, physical, inorganic, and organic chemists, and surface and material physicists is needed to fully understand phenomena and develop technologies. Although several technologies were applied industrially very early on, knowledge on the molecular phenomena remains largely incomplete and subject to debate. Surface science and surface chemistry, as well as computational studies, are needed to further improve existing technologies. On the other hand, it is clear that a revolution is approaching, with the abandonment of the extensive use of fossil raw materials and the progres-

sive increasing application of renewable raw materials for production of chemicals and fuels. Heterogeneous catalysis will continue to play a fundamental role, and surface science and surface chemistry will help in developing such new technologies which will achieve sustainability for our high-technology civilization.

References

33.1 M.W. Roberts: Birth of the catalytic concept (1800–1900), Catal. Lett. **67**, 1–4 (2000)

33.2 A. Zecchina, S. Califano: *The Development of Catalysis: A History of Key Processes and Personas in Catalytic Science and Technology* (Wiley, New York 2017)

33.3 Anonymus: Catalysts market to reach $40 bn by 2022, globally, Focus Catal. **2**, 3 (2017), https://doi.org/10.1016/j.focat.2017.02.003

33.4 J.A. Moulijn, P.W.N.M. van Leeuwen, R.A. van Santen: Hystory of catalysis. In: *Catalysis: An Integrated Approach to Homogeneous, Heterogeneous and Industrial Catalysis*, ed. by A. Moulijn, P.W.N.M. van Leeuwen, R.A. van Santen (Elsevier, Amsterdam 1993) pp. 3–23

33.5 L. Loyd: *Handbook of Industrial Catalysis* (Springer, Berlin, Heidelberg 2011)

33.6 J.N. Armor: A history of industrial catalysis, Catal. Today **163**, 3–9 (2011)

33.7 J.K. Nørskov, T. Bligaard, B. Hvolbaek, F. Abild-Pedersen, I. Chorkendorff, C.H. Christensen: The nature of the active site in heterogeneous metal catalysis, Chem. Soc. Rev. **37**, 2163–2171 (2008)

33.8 G. Busca: *Heterogeneous Catalytic Materials: Solid State Chemistry, Surface Chemistry and Catalytic Behaviour* (Elsevier, Amsterdam 2014)

33.9 G. Bracco, B. Holst (Eds.): *Surface Science Techniques* (Springer, Berlin, Heidelberg 2013)

33.10 G. Spoto, E.N. Gribov, G. Ricchiardi, A. Damin, D. Scarano, S. Bordiga, C. Lamberti, A. Zecchina: Carbon monoxide MgO from dispersed solids to single crystals: A review and new advances, Progr. Surf. Sci. **76**, 71–146 (2004)

33.11 L. Vattuone, L. Savio, M. Rocca: Bridging the structure gap: Chemistry of nanostructured surfaces at well defined defects, Surf. Sci. Rep. **63**, 101–168 (2008)

33.12 F. Gao, D.W. Goodman: Model catalysts: Simulating the complexities of heterogeneous catalysts, Annu. Rev. Phys. Chem. **63**, 265–286 (2012)

33.13 K.W. Kolasinski: *Surface Science: Foundations of Catalysis and Nanoscience*, 3rd edn. (Wiley, New York 2012)

33.14 F. Zaera: Key unanswered questions about the mechanism of olefin hydrogenation catalysis by transition-metal surfaces: A surface-science perspective, Phys. Chem. Chem. Phys. **15**, 11988–12003 (2013)

33.15 J.Y. Park, G.A. Somorjai: Bridging materials and pressure gaps in surface science and heterogeneous catalysis. In: *Current Trends of Surface Science and Catalysis*, ed. by J.Y. Park (Springer, New York 2014) pp. 3–17

33.16 J.H. Sinfelt: Role of surface science in catalysis, Surf. Sci. **500**, 923–946 (2002)

33.17 G. Busca: Acid catalysts in the industrial hydrocarbon chemistry, Chem. Rev **107**, 5366–5410 (2007)

33.18 H. Hattori, Y. Ono: *Solid Acid Catalysis: From Fundamentals to Applications* (Taylor Francis, New York 2015)

33.19 J.N. Brønsted: Einige Bemerkungen über den Begriff der Säuren und Basen, Recl. Trav. Chim. Pays-Bas **42**, 718–728 (1923)

33.20 T.M. Lowry: The uniqueness of hydrogen, J. Chem. Tecnol. **42**, 43–47 (1923)

33.21 L.P. Hammett: *Physical Organic Chemistry* (McGraw-Hill, New York 1940)

33.22 G. Clet, J.-M. Goupil, G. Szabo, D. Cornet: Chlorinated alumina as an alkylation catalyst: Influence of superficial HCl, J. Mol. Catal. A Chem. **148**, 253–264 (1999)

33.23 W. Vermeiren, J.P. Gilson: Impact of zeolites on the petroleum and petrochemical industry, Top. Catal. **52**, 1131–1161 (2009)

33.24 A. Primo, H. Garcia: Zeolites as catalysts in oil refining, Chem. Soc. Rev. **43**, 7548–7561 (2014)

33.25 G. Busca: Acidity and basicity of zeolites: A fundamental approach, Microporous Mesoporous Mater. **254**, 3–16 (2017)

33.26 M. Bevilacqua, T. Montanari, E. Finocchio, G. Busca: Are the active sites of protonic zeolites generated by the cavities ?, Catal. Today **116**, 132–142 (2006)

33.27 J. Passmore, J.M. Rautiainen: On the lower Lewis basicity of siloxanes compared to ethers, Eur. J. Inorg. Chem. **2012**, 6001–6010 (2012)

33.28 F. Weinhold, R. West: Hyperconjugative interactions in permethylated siloxanes and ethers: The nature of the Si0 bond, J. Am. Chem. Soc. **135**, 5762–5767 (2013)

33.29 G.N. Lewis: *Valency and Structure of Atoms and Molecules* (The Chemical Catalog, New York 1923)

33.30 G. Busca: Bases and basic materials in industrial and environmental chemistry. Liquid versus solid basicity, Chem. Rev. **110**, 2217–2249 (2010)

33.31 G. Busca: Structural, surface and catalytic properties of aluminas, Adv. Catal. **57**, 319–404 (2014)

33.32 D.P. Woodruff: Quantitative structural studies of corundum and rocksalt oxide surfaces, Chem. Rev. **113**, 3863–3886 (2013)

33.33 R. Wischert, P. Florian, C. Copéret, D. Massiot, P. Sautet: Visibility of Al surface sites of γ-Alumina: A combined computational and experimental point of view, J. Phys. Chem. C **118**, 15292–15299 (2014)

33.34 M. Klimenkov, S. Nepijko, H. Kuhlenbeck, H.-J. Freund: Transmission electron microscopic investigation of an ordered Al_2O_3 film on NiAl(110), Surf. Sci. **385**, 66–76 (1997)

33.35 E. Kemnitz, J.M. Winfield: Fluoride catalysts: Their application in heterogeneous catalytic fluorination and related processes. In: *Advanced Inorganic Fluorides: Synthesis, Characterization and Applications*, ed. by T. Nakajima, B. Žemva, A. Tressaud (Elsevier, Amsterdam 2000) pp. 367–402

33.36 A. Corma, S. Iborra: Optimization of alkaline earth metal oxide and hydroxide catalysts for base-catalyzed reactions, Adv. Catal. **49**, 239–302 (2006)

33.37 G. Busca: Bases and basic materials in industrial and environmental chemistry: A review of commercial processes, Ind. Eng. Chem. Res. **48**, 6486–6511 (2009)

33.38 Y. Ono, H. Hattori: *Solid Base Catalysis* (Springer, Berlin 2011)

33.39 C. Chizallet, M.L. Bailly, G. Costentin, H. Lauron-Pernot, J.M. Krafft, P. Bazin, J. Saussey, M. Che: Thermodynamic Brønsted basicity of clean MgO surfaces determined by their deprotonation ability: Role of $Mg^{2+}-O^{2-}$ pairs, Catal. Today **116**, 196–205 (2006)

33.40 H. Petitjean, H. Guesmi, H. Lauron-Pernot, G. Costentin, D. Loffreda, P. Sautet, F. Delbecq: How surface hydroxyls enhance MgO reactivity in basic catalysis: The case of methylbutynol conversion, ACS Catalysis **4**, 4004–4014 (2014)

33.41 S. Tosoni, D. Spinnato, G. Pacchioni: DFT study of CO_2 activation on doped and ultrathin MgO films, J. Phys. Chem. C **119**, 27594–27602 (2015)

33.42 S. Roy, A. Baiker: NO_x storage-reduction catalysis: From mechanism and materials properties to storage–reduction performance, Chem. Rev. **109**, 4054–4091 (2009)

33.43 D.P. Debecker, E.M. Gaigneaux, G. Busca: Exploring, tuning and exploiting the basicity of hydrotalcites for applications in heterogeneous catalysis, Chem. Eur. J. **15**, 3920–3935 (2009)

33.44 F. Cavani, D. Duprez (Eds.): *Handbook on Advanced Methods and Processes in Oxidation Catalysis, From Laboratory to Industry* (Imperial College Press, London 2014)

33.45 M. Tomatis, H.-H. Xu, J. He, X.-D. Zhang: Recent development of catalysts for removal of volatile organic compounds in flue gas by combustion: A review, J. Chem. **2016**, 1–15 (2016)

33.46 M. Shahzad Kamal, S.A. Razzak, M.M. Hossain: Catalytic oxidation of volatile organic compounds (VOCs) – A review, Atm. Environ. **140**, 117–134 (2016)

33.47 W.R. Schwartz, D. Ciuparu, L.D. Pfefferle: Combustion of methane over palladium-based catalysts: Catalytic deactivation and role of the support, J. Phys. Chem. C **116**, 8587–8593 (2012)

33.48 G. Centi, F. Cavani, F. Trifirò: *Selective Oxidation by Heterogeneous Catalysis*, 2nd edn. (Springer, London 2012)

33.49 J.C. Védrine: Heterogeneous partial (amm)oxidation and oxidative dehydrogenation catalysis on mixed metal oxides, Catalysts **6**, 22 (2016)

33.50 I.N. Remediakis, N. Lopez, J.K. Nørskov: CO oxidation on gold nanoparticles: Theoretical studies, Appl. Catal. A Gen. **291**, 13–20 (2005)

33.51 V.P. Zhdanov: Kinetic models of CO oxidation on gold nanoparticles, Surf. Sci. **630**, 286–293 (2014)

33.52 H.Y. Kim, H.M. Lee, G. Henkelman: CO oxidation mechanism on CeO_2-supported Au nanoparticles, J. Am. Chem. Soc. **134**, 1560–1570 (2012)

33.53 M.O. Özbek, R.A. Van Santen: The mechanism of ethylene epoxidation catalysis, Catal. Lett. **143**, 131–141 (2013)

33.54 T.C.R. Rocha, A. Oestereich, D.V. Demidov, M. Hävecker, S. Zafeiratos, G. Weinberg, V.I. Bukhtiyarov, A. Knop-Gericke, R. Schlögl: The silver–oxygen system in catalysis: New insights by near ambient pressure X-ray photoelectron spectroscopy, Phys. Chem. Chem. Phys. **14**, 4554–4564 (2012)

33.55 W. Diao, C.D. DiGiulio, M.T. Schaal, S. Ma, J.R. Monnier: An investigation on the role of Re as a promoter in Ag-Cs-Re/α-Al_2O_3 high-selectivity, ethylene epoxidation catalysts, J. Catal. **322**, 14–23 (2015)

33.56 S. Specchia, E. Finocchio, G. Busca, P. Palmisano, V. Specchia: Surface chemistry and reactivity of ceria–zirconia-supported palladium oxide catalysts for natural gas combustion, J. Catal. **263**, 134–145 (2009)

33.57 H. Xiong, K. Lester, T. Ressler, R. Schlögl, L.F. Allard, A.K. Datye: Metastable Pd $\leftrightarrow$ PdO structures during high temperature methane oxidation, Catal. Lett. **147**, 1095–1103 (2017)

33.58 K. Musialska, E. Finocchio, I. Sobczak, G. Busca, R. Wojcieszak, E. Gaigneaux, M. Ziolek: Characterization of alumina- and niobia-supported gold catalysts used for oxidation of glycerol, Appl. Catal. A Gen. **384**, 70–77 (2010)

33.59 C.H. Hu, C. Chizallet, C. Mager-Maury, M. Corral-Valero, P. Sautet, H. Toulhoat, P. Raybaud: Modulation of catalyst particle structure upon support hydroxylation: Ab initio insights into Pd_{13} and Pt_{13}/γ-Al_2O_3, J. Catal. **274**, 99–110 (2010)

33.60 A.S. Ivanova, E.M. Slavinskaya, R.V. Gulyaev, V.I. Zaikovskii, O.A. Stonkus, I.G. Danilova, L.M. Plyasova, L.A. Polukhina, A.I. Boronin: Metal-support interactions in Pt/Al_2O_3 and Pd/Al_2O_3 catalysts for CO oxidation, Appl. Catal. B Environ. **97**, 57–71 (2010)

33.61 A.A. Vedyagin, A.M. Volodin, V.O. Stoyanovskii, I.V. Mishakov, D.A. Medvedev, A.S. Noskov: Characterization of active sites of Pd/Al_2O_3 model catalysts with low Pd content by luminescence, EPR and ethane hydrogenolysis, Appl. Catal. B Environ. **103**, 397–403 (2011)

33.62 G. Busca, E. Finocchio, V.S. Escribano: Infrared studies of CO oxidation by oxygen and by water over Pt/Al_2O_3 and Pd/Al_2O_3 catalysts, Appl. Catal. B Environ. **113/114**, 281–289 (2012)

33.63 M. Flytzani-Stephanopoulos, B.C. Gates: Atomically dispersed supported metal catalysts, Annu. Rev. Chem. Biomol. Eng. **3**, 545–574 (2012)

33.64 J.D. Kistler, N. Chotigkrai, P. Xu, B. Enderle, P. Praserthdam, C.-Y. Chen, N.D. Browning, B.C. Gates: A single-site platinum co oxidation catalyst in zeolite KLTL: Microscopic and spectroscopic determination of the locations of the platinum atoms, Angew. Chem. Int. Ed. **53**, 8904–8907 (2014)

33.65 E.M. Slavinskaya, T. Yu. Kardash, O.A. Stonkus, R.V. Gulyaev, I.N. Lapin, V.A. Svetlichnyi, A.I. Boronin: Metal–support interaction in Pd/CeO_2 model catalysts for CO oxidation: From pulsed laser ablated nanoparticles to highly active state of the catalyst, Catal. Sci. Technol. **6**, 6650–6666 (2016)

33.66 J. Gao, Q. Liu, F. Gu, B. Liu, Z. Zhong, F. Su: Recent advances in methanation catalysts for the production of synthetic natural gas, RSC Advances **5**, 22759–22776 (2015)

33.67 J. Greeley, M. Mavrikakis: Surface and subsurface hydrogen: Adsorption properties on transition metals and near-surface alloys, J. Phys. Chem. B **109**, 3460–3471 (2005)

33.68 L. Kristinsdóttir, E. Skúlason: A systematic DFT study of hydrogen diffusion on transition metal surfaces, Surf. Sci. **606**, 1400–1404 (2012)

33.69 G. Busca, A. Vaccari: Fourier transform i.r. detection of adsorbed hydrogen on a Cu–Zn–Cr low temperature methanol synthesis catalyst, J. Chem. Soc. Chem. Commun. **12**, 788–790 (1988)

33.70 C. Chizallet, G. Bonnard, E. Krebs, L. Bisson, C. Thomazeau, P. Raybaud: Thermodynamic stability of buta-1,3-diene and but-1-ene on Pd(111) and (100) surfaces under H_2 pressure: A DFT study, J. Phys. Chem. C **115**, 12135–12149 (2011)

33.71 X. Xie, X. Song, W. Dong, Z. Liang, C. Fan, P. Han: Adsorption mechanism of acetylene hydrogenation on the Pd (111) surface, Chin. J. Chem. **32**, 631–636 (2014)

33.72 H. Yildirim, T. Greber, A. Kara: Trends in adsorption characteristics of benzene on transition metal surfaces: Role of surface chemistry and van der Waals interactions, J. Phys. Chem. C **117**, 20572–20583 (2013)

33.73 P. Raybaud, G. Kressey, J. Hafnery, H. Toulhoat: Ab initio density functional studies of transition-metal sulphides: I. Crystal structure and cohesive properties, J. Phys. Condens. Matter **9**, 11085–11106 (1997)

33.74 R.R. Chianelli, G. Berhault, B. Torres: Unsupported transition metal sulfide catalysts: 100 years of science and application, Catal. Today **14**(7), 275–286 (2009)

33.75 P. Raybaud, H. Toulhoat (Eds.): *Catalysis by Transition Metal Sulphides. From Molecular Theory to Industrial Application* (Technip, Paris 2013)

33.76 A. Kanka, B. Kaglar: Hydrodesulphurization catalysis fundamentals. In: *Advances in Refining Catalysis*, ed. by D. Uner (CRC Press, Boca Raton 2017) pp. 113–146

33.77 M. Ramos, G. Berhault, D.A. Ferrer, B. Torres, R.R. Chianelli: Cobalt promotion in unsupported sulfide catalysts: HRTEM and molecular modeling of the MoS_2–Co_9S_8 interface, Catal. Sci. Technol. **2**, 164–178 (2012)

33.78 A. Hadj-Aïssa, F. Dassenoy, C. Geantet, P. Afanasiev: Solution synthesis of core–shell Co_9S_8@MoS_2 catalysts, Catal. Sci. Technol. **6**, 4901–4909 (2016)

33.79 P.G. Moses, B. Hinnemann, H. Topsøe, J.K. Nørskov: The effect of Co-promotion on MoS_2 catalysts for hydrodesulfurization of thiophene: A density functional study, J. Catal. **268**, 201–208 (2009)

33.80 T. Drescher, F. Niefind, W. Bensch, W. Grünert: Sulfide catalysis without coordinatively unsaturated sites: Hydrogenation, cis–trans isomerization, and H_2/D_2 scrambling over MoS_2 and WS_2, J. Am. Chem. Soc. **134**, 18896–18899 (2012)

33.81 M. Breysse, E. Furimsky, S. Kasztelan, M. Lacroix, G. Perot: Hydrogen activation by transition metal sulphides, Catal. Rev. **44**, 651–735 (2002)

33.82 M. Sun, A.E. Nelson, J. Adjaye: Ab initio DFT study of hydrogen dissociation on MoS_2, NiMoS, and CoMoS: Mechanism, kinetics, and vibrational frequencies, J. Catal. **233**, 411–421 (2005)

33.83 W. Wei, Z. Xiaoguang, L. Huifeng, Z. Han, L. Mingfeng: DFT study of H_2 dissociation on Mo_xS_y clusters, China Petrol. Process. Petrochem. Technol. **17**, 16–23 (2015)

33.84 C. Dumonteil, M. Lacroix, C. Geantet, H. Jobic, M. Breysse: Hydrogen activation and reactivity of ruthenium sulfide catalysts: Influence of the dispersion, J. Catal. **187**, 464–473 (1999)

33.85 B. Baubet, M. Girleanu, A.-S. Gay, A.-L. Taleb, M. Moreaud, F. Wahl, V. Delattre, E. Devers, A. Hugon, O. Ersen, P. Afanasiev, P. Raybaud: Quantitative two-dimensional (2D) morphology–selectivity relationship of CoMoS nanolayers: A combined high-resolution high-angle annular dark field scanning transmission electron microscopy (HR HAADF-STEM) and density functional theory (DFT) study, ACS Catal. **6**, 1081–1092 (2016)

33.86 G. Ghiotti, A. Chiorino, F. Boccuzzi: Surface chemistry and electronic effects of H_2 (D_2) on two different microcrystalline ZnO powders, Surf. Sci. **287/288**, 228–234 (1993)

33.87 S.A. French, A.A. Sokol, S.T. Bromley, C.R.A. Catlow, S.C. Rogers, P. Sherwood: Assignment of the complex vibrational spectra of the hydrogenated ZnO polar surfaces using QM/MM embedding, J. Chem. Phys. **118**, 317–320 (2003)

33.88 J. Kiss, A. Witt, B. Meyer, D. Marx: Methanol synthesis on ZnO (000-1) I. Hydrogen coverage, charge state of oxygen vacancies, and chemical reactivity, J. Chem. Phys. **130**, 184706 (2009)

33.89 H.F. Wilson, A.S. Barnard: Thermodynamics of hydrogen adsorption and incorporation at the ZnO($10\bar{1}0$) surface, J. Phys. Chem. C **119**, 26560–26565 (2015)

33.90 G. Busca: FT-IR study of the adsorption of hydrogen on chromia and on some metal chromites, J. Catal. **120**, 303–313 (1989)

33.91 S.E. Collins, M.A. Baltanás, A.L. Bonivardi: Hydrogen chemisorption on gallium oxide polymorphs, Langmuir **21**, 962–970 (2005)

33.92 J. Kondo, Y. Sakata, K. Domen, K. Maruya, T. Onishi: Infrared study of hydrogen adsorbed on ZrO_2, J. Chem. Soc. Faraday Trans., **86**, 397–401 (1990)

33.93 O. Syzgantseva, M. Calatayud, C. Minot: Hydrogen adsorption on monoclinic $(\bar{1}11)$ and $(\bar{1}01)$ ZrO_2 surfaces: A periodic ab initio study, J. Phys. Chem. C **114**, 11918–11923 (2010)

33.94 D.R. Mullins: The surface chemistry of cerium oxide, Surf. Sci. Rep. **70**, 42–85 (2015)

33.95 H.T. Chen, Y.M. Choi, M. Liu, M.C. Lin: A theoretical study of surface reduction mechanisms of CeO_2 (111) and (110) by H_2, ChemPhysChem **8**, 849–855 (2007)

33.96 G. Vilé, B. Bridier, J. Wichert, J. Pérez-Ramírez: Ceria in hydrogenation catalysis: High selectivity in the conversion of alkynes to olefins, Angew. Chem. Int. Ed. **51**, 8620–8623 (2012)

33.97 J.R. Rostrup Nielsen: Catalytic steam reforming. In: *Catalysis Science and Technology*, Vol. 5, ed. by M. Boudart, J.R. Anderson (Springer, Berlin, Heidelberg 1984) pp. 1–118

33.98 M. Tessie du Motay, M. Maréchal: Préparation industrielle de l'hydrogène, Bull. Soc. Chim. Fr. **9**, 334 (1868)

33.99 B. Neumann, K. Jacob: Die Gleichgewichtsverhältnisse bei der Methanbildung aus Kohlenoxyd und Wasserstoff, bzw. Kohlendioxyd und Wasserstoff, Z. Elektrochem. **30**, 557 (1924)

33.100 L.J. Christiansen: Use of modelling in scale-up of steam reforming technology, Catal. Today **272**, 14–18 (2016)

33.101 J.R. Rostrup Nielsen, J. Sehested, J.K. Nørskov: Hydrogen and synthesis gas by steam- and CO_2-reforming, Adv. Catal. **47**, 66–141 (2002)

33.102 K. Aasberg-Petersen, I. Dybkjær, C.V. Ovesen, N.C. Schjødt, J. Sehested, S.G. Thomsen: Natural gas to synthesis gas – Catalysts and catalytic processes, J. Nat. Gas Sci. Eng. **3**, 423–459 (2011)

33.103 J.R. Rostrup-Nielsen, J.-H. Bak Hansen: CO_2-reforming of methane over transition metals, J. Catal. **144**, 38–49 (1993)

33.104 T.V. Choudhary, D.W. Goodman: Methane activation on Ni and Ru model catalysts, J. Mol. Catal. A Chem. **163**, 9–18 (2000)

33.105 G. Jones, J. Jakobsen, S. Shim, J. Kleis, M. Andersson, J. Rossmeisl, F. Abild-Pedersen, T. Bligaard, S. Helveg, B. Hinnemann: First principles calculations and experimental insight into methane steam reforming over transition metal catalysts, J. Catal. **259**, 147–160 (2008)

33.106 C. Fan, Y.-A. Zhu, M.-L. Yang, Z.-J. Sui, X.-G. Zhou, D. Chen: Density functional theory-assisted microkinetic analysis of methane dry reforming on Ni catalyst, Ind. Eng. Chem. Res. **54**, 5901–5913 (2015)

33.107 A. Mohsenzadeh, K. Bolton, T. Richards: DFT study of the adsorption and dissociation of water on Ni(111), Ni(110) and Ni(100) surfaces, Surf. Sci. **627**, 1–10 (2014)

33.108 J.R.H. Ross, M.C.F. Steel: Mechanism of the steam reforming of methane over a coprecipitated nickel-alumina catalyst, J. Chem. Soc. Faraday Trans. **169**, 10–21 (1973)

33.109 J. Xu, G.F. Froment: Methane steam reforming, methanation and water-gas shift: I. Intrinsic kinetics, AIChE J. **35**, 88–96 (1989)

33.110 L. Maier, B. Schädel, K. Herrera Delgado, S. Tischer, O. Deutschmann: Steam reforming of methane over nickel: Development of a multi-step surface reaction mechanism, Top. Catal. **54**, 845–858 (2011)

33.111 K.-D. Ko, J.K. Lee, D. Park, S.H. Shin: Kinetics of steam reforming over a Ni/alumina catalyst, Kor. J. Chem. Eng. **12**, 478–480 (1995)

33.112 A.L. Dicks, K.D. Pointon, A. Siddle: Intrinsic reaction kinetics of methane steam reforming on a nickel zirconia anode, J. Power Sources **86**, 523–530 (2000)

33.113 M. Mbodji, J.M. Commenge, L. Falk, D. Di Marco, F. Rossignol, L. Prost, S. Valentin, R. Joly, P. Del-Gallo: Steam methane reforming reaction process intensification by using a millistructured reactor: Experimental setup and model validation for global kinetic reaction rate estimation, Chem. Eng. J. **207–208**, 871–884 (2012)

33.114 P. Van Beurden: On the catalytic aspects of steam-methane reforming, Rep. ECN-I **4**, 1–27 (2004)

33.115 M. Zeppieri, P.L. Villa, N. Verdone, M. Scarsella, P. De Filippis: Kinetics of methane steam reforming reaction over nickel- and rhodium-based catalysts, Appl. Catal. A Gen. **387**, 147–154 (2010)

33.116 B. Xing, X.-Y. Pang, G.-C. Wang: C–H bond activation of methane on clean and oxygen precovered metals: A systematic theoretical study, J. Catal. **282**, 74–82 (2011)

33.117 J. Sehested, N.W. Larsen, H. Falsig, B. Hinnemann: Sintering of nickel steam reforming catalysts: Effective mass diffusion constant for Ni-OH at nickel surfaces, Catal. Today **228**, 22–31 (2014)

33.118 Y. Chen, C. Xie, Y. Li, C. Song, T.B. Bolinc: Sulfur poisoning mechanism of steam reforming catalysts: An X-ray absorption near edge structure (XANES) spectroscopic study, Phys. Chem. Chem. Phys. **12**, 5707–5711 (2010)

33.119 G. Garbarino, A. Romero Perez, E. Finocchio, G. Busca: A study of the deactivation of low loading Ni/Al_2O_3 steam reforming catalyst by tetrahydrothiophene, Catal. Commun. **38**, 67–73 (2013)

33.120 M. Carlsson: Carbon formation in steam reforming and effect of potassium promotion, Johnson Matthey Technol. Rev. **59**, 313–318 (2015)

33.121 S. Helveg, J. Sehested, J.R. Rostrup-Nielsen: Whisker carbon in perspective, Catal. Today **178**, 42–46 (2011)

33.122 F. Besenbacher, I. Chorkendorff, B.S. Clausen, B. Hammer, A.M. Molnbroek, J.K. Norskøv,

I. Stensgaard: Design of surface alloy catalyst for steam reforming, Science **279**, 1913–1915 (1998)

33.123 J.S. Lisboa, D.C.R.M. Santos, F.B. Passos, F.B. Noronha: Influence of the addition of promoters to steam reforming catalysts, Catal. Today **101**, 15–21 (2005)

33.124 G. Garbarino, E. Finocchio, A. Lagazzo, I. Valsamakis, P. Riani, V. Sanchez Escribano, G. Busca: Steam reforming of ethanol–phenol mixture on Ni/Al_2O_3: Effect of magnesium and boron on catalytic activity in the presence and absence of sulphur, Appl. Catal. B Environ. **147**, 813–826 (2014)

33.125 Z. Hou, O. Yokota, T. Tanaka, T. Yashima: Characterization of Ca-promoted $Ni/-Al_2O_3$ catalyst for CH_4 reforming with CO_2, Appl. Catal. A Gen. **253**, 381–387 (2003)

33.126 T. de Freitas Silva, J.A. Costa Dias, C. Guimarães Maciela, J. Mansur Assafa: Ni/Al_2O_3 catalysts: Effects of the promoters Ce, La and Zr on the methane steam and oxidative reforming reactions, Catal. Sci. Technol. **3**, 635–643 (2013)

33.127 S. Sepehri, M. Rezaei, G. Garbarino, G. Busca: Preparation and characterization of mesoporous nanocrystalline La-, Ce-, Zr-, Sr-containing $Ni-Al_2O_3$ methane autothermal reforming catalysts, Int. J. Hydrogen Energy **41**, 8855–8862 (2016)

33.128 G. Garbarino, C. Wang, I. Valsamakis, S. Chitsazan, P. Riani, E. Finocchio, M. Flytzani-Stephanopoulos, G. Busca: A study of Ni/Al_2O_3 and $Ni–La/Al_2O_3$ catalysts for the steam reforming of ethanol and phenol, Appl. Catal. B Environ. **174–175**, 21–34 (2015)

33.129 D.A.J.M. Ligthart, J.A.Z. Pieterse, E.J.M. Hensen: The role of promoters for Ni catalysts in low temperature (membrane) steam methane reforming, Appl. Catal. A Gen. **405**, 108–119 (2011)

33.130 H.J. Ok, M.H. Park, D.J. Moon, J.H. Kim, N.C. Park, Y.C. Kim: The influence of promoter on Ni(15)/La(5)/γ-Al_2O_3 catalyst in CO_2-steam reforming of methane to syngas at high pressure, J. Nanosci. Nanotechnol. **15**, 449–453 (2015)

33.131 G. Garbarino, S. Chitsazan, T.K. Phung, P. Riani, G. Busca: Preparation of supported catalysts: A study of the effect of small amounts of silica on Ni/Al_2O_3 catalysts, Appl. Catal. A Gen. **505**, 86–97 (2015)

33.132 S.S. Maluf, E.M. Assaf: Ni catalysts with Mo promoter for methane steam reforming, Fuel **88**, 1547–1553 (2009)

33.133 H. Wu, V. La Parola, G. Pantaleo, F. Puleo, A.M. Venezia, L.F. Liotta: Ni-based catalysts for low temperature methane steam reforming: Recent results on Ni-Au and comparison with other bi-metallic systems, Catalysts **3**, 563–583 (2013)

33.134 C. Resini, M.C. Herrera Delgado, S. Presto, L.J. Alemany, P. Riani, R. Marazza, G. Ramis, G. Busca: Yttria-stabilized zirconia (YSZ) supported Ni–Co alloys (precursor of SOFC anodes) as catalysts for the steam reforming of ethanol, Int. J. Hydrogen Energy **33**, 3728–3735 (2008)

33.135 G. Busca, U. Costantino, T. Montanari, G. Ramis, C. Resini, M. Sisani: Nickel versus cobalt catalysts for hydrogen production by ethanol steam reforming: Ni–Co–Zn–Al catalysts from hydrotalcite-like precursors, Int. J. Hydrog. Energy **35**, 5356–5366 (2010)

33.136 F. Morales-Cano, L.F. Lundegaard, R.R. Tiruvalam, H. Falsig, M.S. Skjøth-Rasmussen: Improving the sintering resistance of Ni/Al_2O_3 steam-reforming catalysts by promotion with noble metals, Appl. Catal. A Gen. **498**, 117–125 (2015)

33.137 K. Takehira: Intelligent reforming catalysts: Trace noble metal-doped Ni/Mg(Al)0 derived from hydrotalcites, J. Nat. Gas Chem. **18**, 237–259 (2009)

33.138 C. Murkin, J. Brightling: Eighty years of steam reforming, Johnson Matthey Technol. Rev. **60**, 263–267 (2016)

Guido Busca

Università di Genova
Genova, Italy
guido.busca@unige.it

Guido Busca has been Full Professor of Industrial and Technological Chemistry at the University of Genoa since 2000. He is now the Director of the Civil, Chemical and Environmental Engineering Department of his University. He has authored one book, twelve books chapters, more than 430 papers, which collected more than 32 000 citations. His h-index in Scopus is 89.

34. Electrochemical Behavior of Single Crystal Electrodes on Model Processes

Victor Climent, Enrique Herrero

Platinum is among the most catalytic metals for many electrochemical reactions of applied interest. In particular, platinum or platinum-based alloys are the most active for the typical reactions related to fuel cell technology, such as hydrogen evolution, hydrogen oxidation, oxygen reduction and oxidation of small organic molecules. For this reason, there is great interest in understanding at a fundamental level the principles underlying the phenomena of electrocatalysis in relation to this metal. One aspect that has been revealed of particular interest is the sensitivity of most electrocatalytic reactions to the surface structure of the catalyst. To study this aspect of electrocatalysis, it is important to understand the techniques and methodologies to work with single-crystal electrodes. It is equally important to learn how to interpret the electrochemical behavior of well-defined surfaces from the perspective of their surface reactivity. In this chapter, we first review the techniques for the preparation of single-crystal electrodes with well-defined surfaces. Although gold is less important from an electrocatalytic point of view, its interfacial behavior is, precisely for this reason, easier to interpret. Therefore, the chapter focuses on and compares the behavior of two metals, platinum and gold. Some methodological details particular to the work of these electrodes in an electrochemical environment are described. The different surface structures obtained with the materials will be associated with the voltammetric behavior recorded in different supporting electrolytes, with the aim of characterizing processes such as adsorption, surface reconstruction and faceting, and basic electrochemical reactivity, using both in situ and ex situ techniques. Important parameters that describe the properties of the interphase are the potential of zero charge and the potential of maximum entropy. Techniques and methodologies for their determination and interpretation will be briefly reviewed. Finally, some practical examples of surface-sensitive reactions will be described, focusing on the underpotential deposition of metals and the oxidation of carbon monoxide and some small organic molecules.

M. Rocca, T.S. Rahman, L. Vattuone (Eds.), *Springer Handbook of Surface Science*, Springer Handbooks,
https://doi.org/10.1007/978-3-030-46906-1_34

The initial studies in the field of surface electrochemistry sought to gain the same level of knowledge previously achieved in the related but older fields of surface science and heterogeneous catalysis. In the first place, they aimed to establish relationships between surface structure and reactivity. Secondly, they tried to prove the effects of surface modification on electrocatalysis, to finally attain sufficient knowledge to attempt the rational design of optimal catalysts. When compared with the studies carried out in ultrahigh vacuum (UHV), the electrochemical media present some advantages. In the first place, the experimental procedures to attain comparable cleanliness conditions are easier in electrochemical environments (after you learn some basic precautions). Ultrapure water and high-quality chemicals, together with well-tested and defined cleaning procedures are the basic requirements to obtain a clean system. Also, the preparation (cleaning and ordering) of the single-crystal electrodes is easier and faster: a simple annealing (with a flame or induction oven) followed by cooling in an appropriate atmosphere is enough to attain high-quality surfaces. Second, the instrumentation involved in electrochemical studies is simpler and cheaper: a potentiostat with a signal generator, a signal recorder and a glass cell are the essential equipment in these studies. Finally, in electrochemical systems, there is an additional variable (alongside composition, temperature and pressure) that controls the reactivity of the surface: the electrode potential. When compared with temperature, the control and change of the electrode potential is straightforward and faster, which allows for greater versatility in the types of programs that can be used to modulate the change with time of this variable, providing a better understanding of the behavior of the systems. However, the presence of water (or any other solvent) in the electrochemical environment poses a major problem in the application of the techniques classically employed in UHV to probe the interfacial structure, particularly those based on electron spectroscopy. For this reason, in some of the first studies with single-crystal electrodes, the electrochemical system was coupled with a UHV chamber, so that the electrode, after its modification in the electrochemical system, was carefully transferred to the UHV chamber to analyze the surface and the possible adsorbates or intermediates. In this analysis, it was assumed that the loss of potential control and the modification of the environment (essentially the loss of the water layer and the supporting electrolyte in contact with the electrode) would not alter the system. This could be true in the case of strong adsorbing species, such as metal adatoms, but probably not in the case of other adsorbing molecules. The advent of synchrotron and scanning probe microscopy techniques enabled a comprehension of the surface modification processes similar to that reached previously in UHV, because they made possible the determination of the different surface structures and the composition of the topmost layer under in situ conditions. Multiple spectroscopic techniques have also been incorporated to the battery of methodologies used to interrogate in situ the electrochemical interphase. Fourier transform infrared reflection absorption spectroscopy (FTIRRAS) is one of the most common and available spectroscopic approaches. Other techniques like second-harmonic generation (SHG) and sum frequency generation (SFG) are also useful but require more complex and expensive instrumentation. Raman spectroscopy was largely limited to rough surfaces of coinage metals until the recent introduction of shell-isolated nanoparticle-enhanced Raman spectroscopy (SHINERS) [34.1, 2]. All these techniques provide information primarily about the composition of the interphase, although structural information is also provided indirectly. Thus, it was possible to establish, usually with a combination of methodologies, the key role of the solvent and supporting electrolyte in electrochemical systems, and to justify the differences with similar systems in UHV. In the following, some examples of the electrochemical systems studied with single-crystal electrodes will be reviewed. After a brief introduction of the experimental techniques typically employed in these studies, we summarize the voltammetric characterization of single-crystal surfaces of platinum and gold with increasing degrees of complexity. The initial stages of metal deposition (underpotential deposition of metals) are then described, ending with some examples of the electrocatalytic behavior of platinum.

34.1 Preparation of Single-Crystal Surfaces

The first step in the preparation of a well-defined single-crystal surface starts with the fabrication of a crystallographically well-defined single crystal. This is a piece of material composed of a single grain in which the positions of the atoms follow a coherent crystallographic network. There are many different methods to obtain a single crystal. They all have in common the slow formation of the solid phase in such a way that atoms

have time to adopt the right position in the crystallographic network. It can be solidification from the melted material, condensation from a vapor phase or even electrodeposition from a solution. The procedure described here, the so-called Clavilier method [34.3–5], is the one used in our laboratory, which is particularly interesting given its simplicity. It has been successfully applied to the fabrication of platinum, gold and rhodium single crystals. Fabrication of palladium crystals is more problematic with this method, given the ability of this metal to absorb gas, but it has also been reported in the literature [34.6]. The process consists of the formation of a small bead of the metal by melting the end of a high-purity wire with a torch. Butane/oxygen or hydrogen/oxygen flames are hot enough for this purpose. The rate of fusion/solidification can be controlled by slowly moving the flame up and down. It is better to move the torch and not the wire with the bead to avoid vibrations that would results in defects in the crystal structure. Alternatively, the temperature of the flame can be varied by regulating the flow of gases. The process of crystallization can be easily followed, since melt and solid phases have different brightness, resulting in an easy visualization of the front that separates the two phases. The size of the bead is limited by the surface tension that holds the drop of melted material hanging from the end of the wire. Typically, beads with diameters ranging from 2 to 4 mm can be obtained with a wire of 0.8 mm. By repeating the melting and solidification process several times, impurities in the metal tend to accumulate at the bottom of the bead (the last point to solidify), which have to be removed by treating the hot metal with aqua regia (a 3 : 1 mixture of HCl and HNO_3). The process is repeated several times until a single crystal bead of sufficient quality is obtained. The single-crystal nature of the bead can be checked by observing the facets formed on its surface. Typically, facets on the (111) directions are favored on the surface of the crystal and can easily be observed using a simple glass magnifier.

To accurately check the angle between the facets, which is a proof of the single-crystal nature of the bead, reflections of a laser beam on the facets can be used. When a laser beam is directed to the beam, reflections are formed pointing in the orientation of the facets. Usually, (111) and (100) facets give visible reflections. Then, to measure the angle between two facets, the angle between the two reflections is measured with great accuracy. For this purpose, the bead is mounted on a goniometer at the end of an optical bench, with the laser at the other end. The length of the bench gives the accuracy of the measurement. This procedure allows one not only to verify the single-crystal nature of the bead (comparing the obtained angles with the theoretical ones) but also to orient the crystallographic axis before cutting and polishing the piece to obtain a macroscopic surface with well-defined crystallographic orientation.

The orientation of the crystal prior to cutting is illustrated in Fig. 34.1 using stereographic projection. The crystal orientation process typically starts by locating two (111) facets and, after adequate rotations, placing their reflections in the horizontal plane. Starting from this position, we have access to the three basal planes and all stepped surfaces between (111) and (100) and between (111) and (110). To obtain stepped surfaces between (100) and (110) or other surfaces in the center of the stereographic triangle, two rotations are necessary, one to bring the surface to the horizontal plane and a second to bring it to the center [34.7]. Perpendicular to the center, the bench has a polishing disk that allows one to first cut and then polish the crystal in this orientation. Further details on the procedure are described in previous reviews [34.7, 8].

Prior to cutting and polishing, the crystal is protected with an epoxy resin to fix its position. Then the crystal is cut, typically until exposing a maximum diameter of the bead, using sandpaper of adequate grain size. The surface is then polished using either alumina or diamond paste of decreasing grain size, typically from 3 to 0.1 μm. Normally, a few hours of polishing at each grain size is necessary to obtain a high-quality mirror finished surface. The next step is to remove the epoxy resin to obtain a hemisphere-shaped electrode with an approximately circular flat surface with the desired crystallographic orientation.

The last step in the preparation of the crystal is the annealing of the bead at high temperature, close to the melting point of the material. At this temperature, the surface atoms have enough mobility to adopt positions that minimize the surface energy of the piece, usually following the nominal structure according to the angle in which the crystal was cut. For platinum, this can be easily achieved by holding the crystal in a Bunsen flame at red-hot temperature for ca. 20–30 min. The temperature of the Bunsen flame is sufficient to facilitate the ordering of the surface atoms but low enough to prevent melting of the platinum crystal. This is not the case for gold, which can be easily melted in a Bunsen flame, and therefore it has to be annealed with great care. Alternatively, annealing for several hours in a furnace at ca. 850 °C can be done without the danger of melting the crystal. The opposite situation holds for rhodium, which has a higher melting point and therefore requires a relatively oxygen-rich high temperature flame.

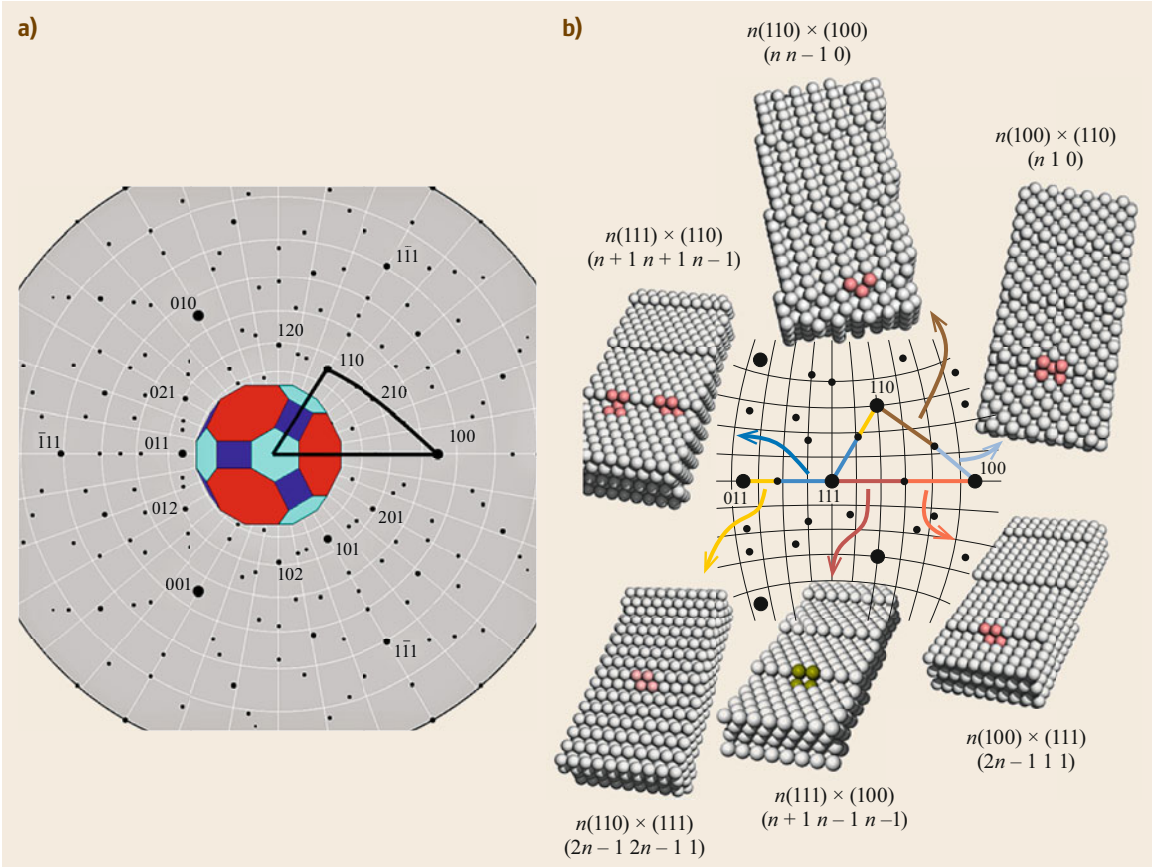

Fig. 34.1a,b Orientation of the crystal for the preparation of a well-defined electrode surface. **(a)** The crystal is oriented with two vertical (111) facets (*light blue*). One (110) facet (*dark blue*) is between the two (111) facets. One (100) facet (*red*) is also located vertical in the opposite direction. **(b)** Relation between the stepped surfaces, and their position in the stereographic projection. The *horizontal line* (011)-(111)-(100) indicates the stepped surfaces that can be prepared from the starting point represented in **(a)** by a single rotation. Other surfaces in the line (110)-(100) need two rotations. Labels in **(b)** give the relationship between the terrace length (n in the Lang, Joyner and Somorjai nomenclature, $n(hkl) \times (h'k'l')$) and the Miller indices (hkl) of the surface [34.9]

34.2 Some Remarks About the Experimental Procedures

Experiments in the investigation of surface electrochemical processes are particularly sensitive to the presence of small traces of contaminants. Organic contamination usually leads to the accumulation of molecular fragments irreversibly adsorbed on the surface of the electrode, deeply altering its electrocatalytic behavior. Inorganic contamination usually leads to specific adsorption of anions, which can be either reversible or irreversible, but in any case, also altering the electrochemical response of the material. Platinum and rhodium are usually more electroactive than gold, and therefore they are more sensitive to contaminants in solution. The sensitivity to contaminants also depends on the crystallographic orientation of the electrode surface: surfaces with a more open arrangement of atoms are usually more reactive.

We often encounter the following misconception: single-crystal surfaces are more sensitive to contamination than polycrystalline materials, and precautions can be relaxed to some extent when working with the latter. This is a dangerous misunderstanding. What really happens is that the response of a single-crystal electrode surface is better defined, and therefore, accumulation of contaminants is more easily detected. With polycrystalline materials, response is less defined and reproducible, and thus it is more difficult to discern whether differences in the electrochemical behavior are due to variations in the surface structure or to contam-

inants. However, this does not mean that, if there are impurities in the solutions, they will not affect the behavior of polycrystalline electrodes to the same extent as they do for single-crystal electrodes.

For the reasons outlined above, it is extremely important in surface electrochemistry to maintain the solution at a high level of purity. Deionized water of maximum quality should be used (18.2 MΩ cm). Also, all reactants must be of the maximum degree of purity. Glassware should be cleaned profusely before each experiment. Needless to say, detergents or surfactants are completely *forbidden* for this purpose. Cleaning is usually performed through a combination of strong oxidizing solutions, rinsing and boiling in water. Different oxidizing agents have been used for this purpose: chromic mixture (dichromate in concentrated H_2SO_4), Caro's acid (a 1 : 3 mixture of 30% H_2O_2 and concentrated H_2SO_4), peroxodisulfate solution (a 3 : 1 mixture of concentrated H_2SO_4 and HNO_3), a 10% HNO_3 solution or a potassium permanganate solution. Among them, the chromic mixture is not recommended because Cr(VI) is highly carcinogenic. Our favorite choice is the potassium permanganate solution ($\approx 2\,g\,L^{-1}$) in diluted H_2SO_4 (ca. 0.1 M). Glassware is left overnight in this solution. MnO_2 deposits formed on the surface of the glass can be easily removed by rinsing with 1% H_2O_2 in 0.1 M H_2SO_4 solution. Finally, the material is thoroughly rinsed with water and boiled in water (10−20 min) several times. The high temperature favors dissolution of contaminations that are later removed by rinsing. In cases where this mild treatment is not sufficient, boiling in 10% HNO_3 solution or even boiling in concentrated H_2SO_4 are more effective. However, the latter is particularly dangerous and detrimental to the different parts of the fume hood.

A stationary voltammogram with well-defined peaks, as shown later in Sects. 34.4 and 34.5, is a clear indication of good experimental conditions. Conversely, a continuous decrease in voltammetric current observed during potential cycling would be a clear symptom of surface fouling. Often, when the level of contamination is low but not negligible, the first voltammetric cycles are correct but the voltammogram later becomes increasingly distorted. Under these conditions, and depending on the time scale of the experiment, the results may range from slightly affected to completely wrong. As mentioned above, the same solution may appear *clean* for an electrode with a given crystallographic orientation but contaminated for a different electrode orientation. Low-coordinated atoms are usually more sensitive to contamination, since adsorption processes are favored on those atoms.

Another critical step in the electrochemical characterization of a surface is cleaning it while preserving the surface order. While the typical procedure for cleaning a (polycrystalline) electrode is to polish it, for instance with alumina, to renew the surface, such a procedure cannot be followed for a well-ordered surface, for obvious reasons. Repetitive cycles of surface oxidation and reduction have also often been used to clean the surface of platinum and gold single crystals. Again, this protocol cannot be followed with single crystals since, as will be shown below, oxide formation and subsequent reduction causes roughening of the surface.

Initial attempts to study well-ordered platinum surfaces used well-established procedures for surface preparation and characterization in UHV, followed by the transfer of the cleaned electrode to the electrochemical environment [34.10–17]. In this case, the problem was found in the transfer step, which turned out to be very difficult while preserving the cleanliness of the surface. Combination of UHV preparation followed by extensive surface oxidation and reduction was also attempted, but, as just mentioned, this process leads to defective surfaces [34.10, 12, 16, 17]. From a historical perspective, a key moment in the development of the field of surface electrochemistry was the introduction of the flame annealing technique for surface decontamination and reordering [34.3, 4, 18]. This includes the heating of the electrode in a flame (as described above for the reordering of the surface) followed by a rapid quenching of the electrode, while still hot, with water. In this way, the electrode is covered with a drop of water which protects the surface from possible contamination from the laboratory atmosphere (diffusion of contaminants is much slower in condensed media than in the gas phase). This gives enough time to transfer the electrode to the electrochemical cell while preserving the cleanliness of the surface. Following this methodology, completely new cyclic voltammograms were recorded for the three platinum basal planes [34.3, 4, 19, 20]. The voltammetry recorded for Pt(111) was particularly striking since it exhibited adsorption states at abnormally high potentials. Such adsorption states were called unusual adsorption states [34.21], although it was later demonstrated that there is nothing unusual about them (see full description of the voltammograms below). Although some controversy arose at the beginning about the validity of this methodology, it was soon demonstrated that surfaces prepared in UHV produce similar voltammograms when the transfer step is properly controlled [34.22]. This served as the definitive demonstration of the validity of the flame annealing procedure. Later, it was realized that the cooling atmosphere plays a crucial role in the ordering process and, for this reason, requires special control. In particular, it is important to avoid the oxidation of the surface during the quenching with water, since this process leads to its disordering. It was demonstrated that this point is less critical for Pt(111), because this highly packed

surface is more stable, but very important for the other, more open, surfaces [34.23]. To avoid oxidation of the surface during the quenching, the hot electrode can be cooled down in a reductive atmosphere (a 1 : 3 mixture of H_2 and Ar) and quenched with water in equilibrium with these gases. Other cooling atmospheres have also been tested. For instance, cooling the platinum electrodes in CO atmosphere results in the protection of the surface with this molecule, which is strongly adsorbed on platinum [34.24, 25]. In this case, the protection with the water drop is not necessary. The CO can be easily removed from the surface by electrooxidation (see below), resulting in a clean and ordered surface. Cooling in I_2 atmosphere has also been reported [34.26]. This molecule can be displaced with CO that can later be electrooxidized to give rise to a clean surface. However, CO and I_2 adsorption may produce faceted surfaces with structures that differ from the nominal one [34.27]. Flame annealing was initially proposed for platinum, but can also be used for other noble metals, such as gold and rhodium. While gold is not sensitive to the presence of O_2 in the cooling step, rhodium is very sensitive, and cooling in H_2/Ar is mandatory in this case.

The final point that deserves a comment is the way in which the electrode is contacted with the solution. Only the flat surface with the desired crystallographic orientation should be in contact with the solution, while the sides of the electrode, containing many other orientations, should not contact it. This is achieved with the so-called hanging meniscus configuration [34.28]. For this, the electrode is introduced in the solution and then raised above its level. The high surface tension characteristic of aqueous solutions facilitates the formation of a meniscus that wets only the flat surface. Sometimes formation of this meniscus is tricky, and a fraction of the sides of the electrode is also wet. This is usually noticed as a tilt in the voltammogram caused by the electrochemical contributions from the sides of the electrode taking place through a very thin layer of solution with a relatively high ohmic resistance. Also, oxygen (which is always present at trace level) can be reduced through the thin layer of solution at the sides of the electrode, resulting in additional tilt of the voltammogram at low potentials. The situation is particularly difficult when the electrode is hydrophilic (for instance, a gold electrode covered with a hydrophilic self-assembled monolayer (SAM)), when surface tension of the solution is decreased (for instance, in the presence of organic contaminants) or if the angle between the flat surface and the side of the electrode is $> 90°$.

34.3 Voltammetric Characterization

In cyclic voltammetry, the electrode potential is scanned linearly between two limits, at a given scan rate, while the current flowing through the potentiostat is recorded [34.29]. The graph of current as a function of potential is called a voltammogram. In the more general case, if an electroactive species is present in solution, current will flow when the electrode potential reaches a value sufficiently high (low) to produce its oxidation (reduction). For a simple process, current should keep increasing (in absolute value) as the difference between applied and equilibrium potentials increases. However, a maximum in the current is typically observed, beyond which the current starts to decrease, resulting in a peak in the voltammogram. The formation of this maximum can be due to two main reasons: (i) mass transport limitation or (ii) a decrease in the availability of surface sites for processes that involve adsorption. In this chapter, we are more concerned about adsorption processes, and hence the following discussion will explain the shape of the voltammetric peaks in this case. The reader is referred to the broad bibliography in the field to learn more about processes limited by mass transport [34.29–31].

For processes that involve electrosorption, the variation of the potential will drive a change in coverage of the electrosorbed species with current flowing in consequence. There is a direct relationship between coverage and charge, resulting from Faraday's law

$$q = -nF\Gamma_{\mathrm{ML}}\theta \,, \tag{34.1}$$

where n is the number of electrons exchanged in the adsorption process (positive for reductive adsorption of a cation and negative for the oxidative adsorption of an anion), F is the Faraday constant, Γ_{ML} is the maximum surface coverage and θ is the fractional coverage. For a reversible adsorption process, the coverage is directly determined by the electrode potential (at a given P, T and composition of the solution) according to a particular adsorption isotherm. In this case, we can write

$$\begin{aligned} j &= -nF\Gamma_{\mathrm{ML}}\left(\frac{\partial\theta}{\partial t}\right)_{P,T,\mu_i} \\ &= -nF\Gamma_{\mathrm{ML}}\left(\frac{\partial\theta}{\partial E}\right)_{P,T,\mu_i}\left(\frac{\partial E}{\partial t}\right) \\ &= -nF\Gamma_{\mathrm{ML}}v\left(\frac{\partial\theta}{\partial E}\right)_{P,T,\mu_i} \,, \end{aligned} \tag{34.2}$$

where $v = (\partial E/\partial t)$ is the scan rate and μ_i is the chemical potential of the specie i in the interphase. This equation demonstrates that the current is proportional to the scan rate for an adsorption process. This is a major difference with the voltammetric response for a process controlled by the diffusion of the reactants to the electrode surface, where the dependence of the peak current scales with the square root of the scan rate [34.29]. The exact shape of the voltammetric profile will depend on the nature of the adsorption isotherm, i.e., the functional relationship between the coverage and the electrode potential

$$\theta = f(E, P, T, \mu_i)\,. \tag{34.3}$$

For a Frumkin isotherm [34.31–33],

$$\frac{\theta}{1-\theta} = K\frac{c}{c^0}\exp\left(\frac{-nFE - r(\theta - 0.5)}{RT}\right), \tag{34.4}$$

where r is the lateral interaction parameter, K is the equilibrium constant, c the concentration in solution and c^0 is the concentration at the standard state. To obtain the current from such relationship, (34.4) should be differentiated with respect to the potential and the result introduced in (34.2). Figure 34.2 shows the voltammetric profile expected for an adsorption process that follows this isotherm for several values of the lateral interaction parameter. In this case, symmetrical peaks are obtained with the peak potential directly related to the energy of adsorption [34.31]

$$\Delta G^0_{\text{ads}} = -RT\ln(K) = -nFE_{\text{peak}} + RT\ln\left(\frac{c}{c^0}\right). \tag{34.5}$$

The width of the peak is controlled by the lateral interaction parameter. Positive values of r correspond to repulsion and result in broader peaks, while negative values indicate attractive interaction and result in narrower peaks [34.31–33]. Finally, the area under the peak gives a measure of the maximum coverage Γ_{ML}

$$\Gamma_{\text{ML}} = \frac{1}{nF}\int_{E_{\text{low}}}^{E_{\text{high}}}\frac{j}{v}\mathrm{d}E\,, \tag{34.6}$$

where E_{low} and E_{high} are the limit of the integration that should be chosen sufficiently below and above, respectively, to integrate the whole voltammetric peak. Equations (34.5) and (34.6) are general, and their validity is not limited to the Frumkin isotherm.

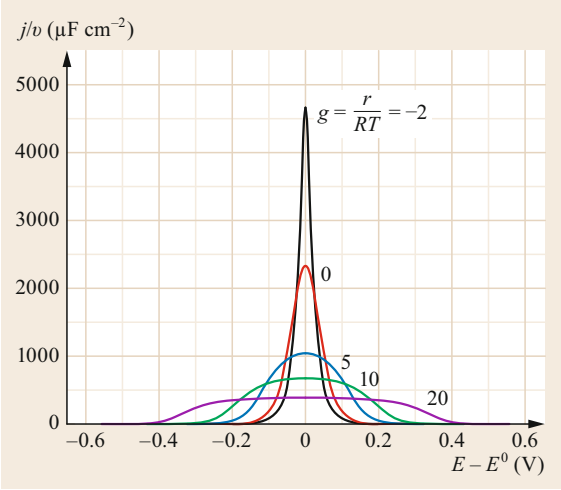

Fig. 34.2 Calculated voltammetric profiles expected for an electrosorption process following the Frumkin isotherm with different values of lateral interaction parameter, as indicated ($n = 1$, $c = 1\,\text{M}$ and $q_{\text{ML}} = 240\,\mu\text{C}\,\text{cm}^{-2}$)

In the case of a process with a limited reaction rate (the so-called irreversible or quasi-reversible processes), asymmetry appears in the peak that now depends on the scan rate. In this case, the peak separation between positive and negative sweeps is related to the rate constant. The latter can be obtained from a plot of peak potentials as a function of the logarithm of the scan rate [34.34].

The previous model applies to a homogeneous adlayer where local differences in the environment of adsorbates are not important. This is the mean-field approximation. In this case, the long-range order is not important. On the other hand, when strong lateral interactions lead to the formation of ordered adlayers, long-range order is very important, and the previous model does not apply. For this situation, Monte Carlo simulations are usually the way to analyze and predict the shape of the voltammetric profile [34.35].

Real voltammetric profiles recorded with platinum-group metals are usually composed of several peaks corresponding to different (most often competitive) adsorption process (hydrogen and anion adsorption) on different reactive sites on the surface (see later). In addition to electrosorption processes, the voltammetric profile also contains the capacitive response of the double layer. This usually has a smoother variation with potential, and in the scale of the other adsorption processes often appears as nearly constant. For gold electrodes, adsorption processes are less frequent, and variations in the differential capacity are more characteristic [34.36, 37].

34.4 Electrochemical Behavior of Gold Single-Crystal Surfaces

Figure 34.3 shows the cyclic voltammograms recorded with the three basal planes of gold in a perchloric acid solution. Perchloric acid is chosen as electrolyte because it is generally accepted that perchlorate anion adsorbs only weakly on metal surfaces. There are two regions in the voltammogram that can be clearly distinguished. Below 1.2 V, a relatively flat voltammetric profile signals the absence of adsorption processes. This is the so-called double-layer region. Above 1.2 V, the current sharply increases as a consequence of surface oxidation, resulting in a complex peak structure. Above 1.6 V, oxygen evolution takes place. Reduction of oxide takes place in the negative scan, resulting in a sharp peak, followed by one or more smaller peaks. The significant asymmetry between positive and negative scans is a clear indication of the irreversible nature of this process. In consequence, the voltammetric profile in the surface oxide region of gold is sensitive to the scan rate. The most important observation is that the voltammetric profile depends on the crystallographic structure, being like a fingerprint that enables the identification of the surface structure of the crystal. Enlargement of the double-layer regions reveals that current in this region also contains important features characteristic of the crystallographic structure of the surface [34.36–38].

According to the previous discussion, voltammetric characterization of gold single crystals can be done according to the profile obtained in the oxide region. Such characterization is often encountered in the literature. However, this method of characterization is not recommended since it is now well established that surface oxidation and subsequent reduction lead to formation of pits and islands resulting on a defective surface [34.39]. This conclusion was obtained from in situ scanning tunneling microscopy (STM) investigation of the surface [34.40]. With this technique, it is concluded that defects are formed during the desorption of the oxide. This observation is explained considering the existence of a place exchange mechanism in which oxygen atoms penetrate into subsurface positions. The subsequent extraction of such subsurface atoms drags gold atoms out of the equilibrium positions, resulting in the formation of pits and islands. The defective surface heals to some extent after prolonged potential cycling in the double-layer region, but it never recovers completely the initial state. For that reason, the voltammetric characterization should be limited to the double-layer region.

The electrochemical behavior of gold is dominated to some extend by the existence of surface reconstructions [34.41–43]. Such reconstructions are well known in UHV studies. For this environment, it is well established that the clean surface is terminated by a layer of atoms that occupy positions that are different from those corresponding to the normal truncation of the network in the bulk. The reason for this displacement of atoms is the existence of unbalanced bonds in the low-

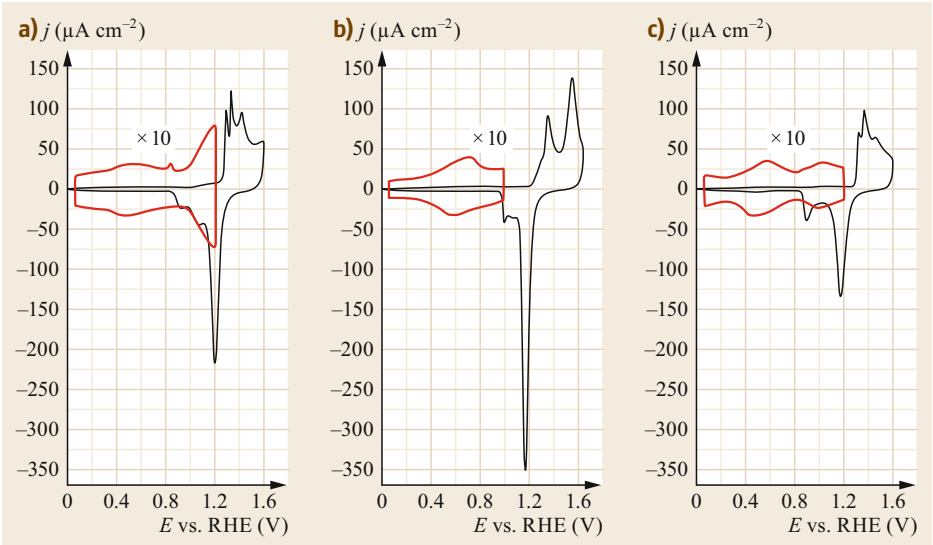

Fig. 34.3a–c Stationary cyclic voltammograms corresponding to the gold basal planes in 0.1 M $HClO_4$ solution: **(a)** Au(100), **(b)** Au(111), **(c)** Au(110). Scan rate: 50 mV s^{-1}. The *red curves* represent the magnification of the voltammetric profile measured in the so-called double-layer region and avoiding oxidation of the surface

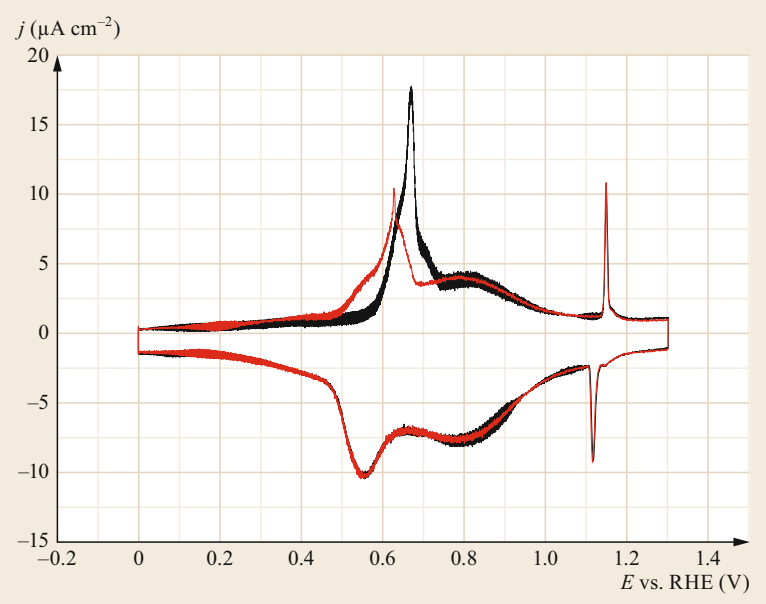

Fig. 34.4 Cyclic voltammograms of a Au(111) electrode in 0.1 M H_2SO_4. *Black curve*: first cycle after flame annealing and contacting the solution at 0.1 V; *red curve*: second cycle. Scan rate: 50 mV s^{-1}

coordinated atoms of the surface, as compared with atoms in the bulk. The surface reconstruction achieves a decrease in energy by increasing the atom density, thereby increasing the sharing of electron density in the low-coordinated atoms. Even the (111) surface of gold tends to reconstruct to form a higher-density $(\sqrt{3}\times 22)$ adlayer. Usually, adsorption eliminates reconstruction, since the adsorbate satisfies the necessity of surface atoms to share their electron density. In the electrochemical environment, the reconstructions are stabilized at lower potentials, where the higher electron density further destabilizes low-coordinated atoms at the surface in comparison with atoms in the bulk of the metal. The increased potential results in the disappearance of the reconstruction, usually linked to the onset of anion adsorption. The lifting of the reconstruction is usually coupled with a sudden change in the differential capacity, resulting in a relatively sharp peak in the voltammogram.

The voltammetric profile of Au(111) in 0.1 M H_2SO_4 shown in Fig. 34.4 is a good example to explain the phenomena described above. The electrode is contacted with the solution, after flame annealing, at low potentials, where the $(\sqrt{3}\times 22)$ reconstruction, formed during the annealing and cooling process, is stable. As the potential is increased, only a small capacitive current is recorded with a differential capacity of ca. 20 μF cm^{-2}. At ca. 0.54 V versus the reversible hydrogen electrode (RHE), sulfate adsorption starts to take place in a disordered way on the reconstructed surface. Immediately coupled with the onset of sulfate adsorption, reconstruction is suddenly lifted, resulting in a sharp voltammetric peak at ca. 0.6 V. Between 0.7 and 1.0 V, sulfate coverage keeps increasing. At ca. 1.15 V (RHE), sulfate coverage is large enough to trigger a disorder/order phase transition, which results in the formation of the $(\sqrt{3}\times\sqrt{7})$R19.1° sulfate adlayer [34.44, 45]. Such phase transition is signaled in the voltammogram by a very characteristic sharp spike. In the negative sweep, the order/disorder phase transition takes place at a slightly lower potential. This is followed by the slow desorption of sulfate that ends at ca. 0.45 V. Below this potential, the surface starts to reconstruct, driven by the increasing values of electron density. In this case, the reconstruction is not complete, because it is a slow process at room temperature. The fraction of the surface that is reconstructed depends on the time the electrode potential remains close to the lower end, which in turn depends on the scan rate. The red curve in Fig. 34.4 shows the second cycle. A strong difference can be observed in the peak corresponding to the lifting of the reconstruction between the first and second cycle, suggesting, as mentioned above, that the reconstruction was incomplete. Except for that, the first and second cycle are identical. The total charge integrated between 0.50 and 1.2 gives a measure of the amount of sulfate adsorbed.

On the other hand, the effects of surface oxidation on the structural integrity of the surface are shown in Fig. 34.5. In the first oxidation cycle, the oxidation of the surface is hindered by the rather compact sulfate adlayer formed after the sharp spike. This is why the

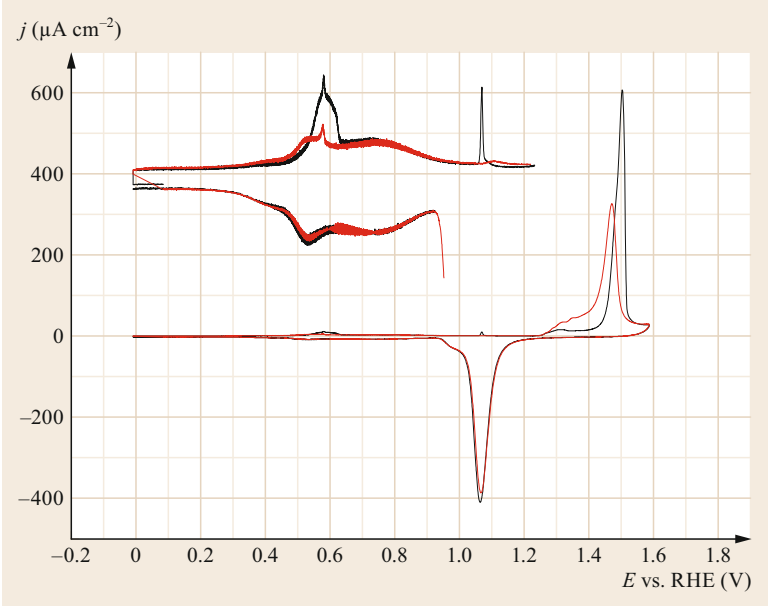

Fig. 34.5 Effect of surface oxidation on the voltammetric profile of Au(111) in 0.1 M H_2SO_4. *Black curves:* First cycle, before oxidation. *Red curves:* Second cycle, after oxidation. The *upper graphs* show an enlargement of the current in the double-layer region

peak corresponding to oxide formation is significantly shifted to higher potential values in comparison with the voltammogram in perchloric acid (see Fig. 34.3 for comparison). At some point, sufficient overvoltage is attained to replace the sulfate adlayer by oxide formation. As explained before, oxide formation is accompanied by the place exchange mechanism, resulting in subsurface oxygen. The subsequent reduction breaks the surface, resulting in the formation of pits and islands that disrupt the long-range order of the surface. This modification of the surface is reflected in the voltammetric profile of the second cycle. In this case, the amount of reconstructed surface significantly decreases, as deduced from the decreased magnitude of the peak at 0.63 V. However, the most significant effect is the almost complete disappearance of the sharp spike signaling the formation of the ordered $(\sqrt{3}\times\sqrt{7})$R19.1° sulfate adlayer. As explained above, formation of this ordered adlayer requires long-range order, and therefore the observation of the corresponding spike is a good indicator of the quality of the surface [34.46]. Another symptom of the disordering of the surface after the first oxidation/reduction cycle is the shift of the onset of the oxidation to lower potentials. This is a consequence of the formation of a defective sulfate adlayer, unable to prevent the surface oxidation as effectively as before. As mentioned above, there is a correlation between the onset of the lifting of the reconstruction and the strength of anion adsorption (Fig. 34.6). The voltammetric profile in the presence of bromide is very similar to that previously described for sulfate, but with all features shifted to lower potentials. Finally,

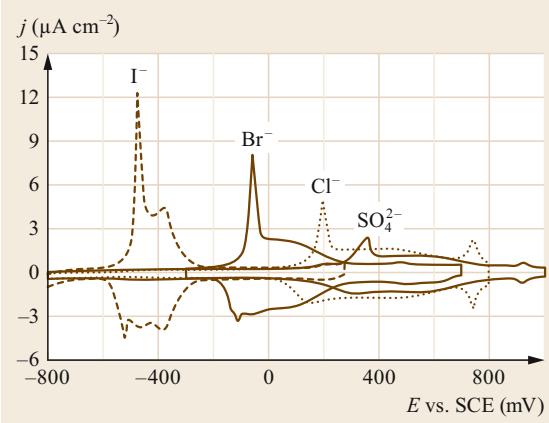

Fig. 34.6 Comparison of sulfate, chloride, bromide and iodide adsorption on the Au(111) electrode surface from 0.1 M $HClO_4 + 10^{-3}$ M K_2SO_4, KCl, KBr or KI solutions (SCE: saturated calomel electrode). Scan rate: 10 mV s^{-1}. Reprinted from [34.47], with permission from Elsevier

Fig. 34.7 shows the voltammetric profile for Au(100) in 0.01 M H_2SO_4. Similarly to what has been previously discussed for Au(111), this voltammogram is characterized by the observation of a very sharp peak signaling the lifting of a hexagonal reconstruction (also noted as (5×20)) that is observed for the clean surface in UHV and remains in an electrochemical environment at low enough potentials. As before, the magnitude of the peak is maximum after the flame annealing and, after a first scan, increases with the time spent at low potentials.

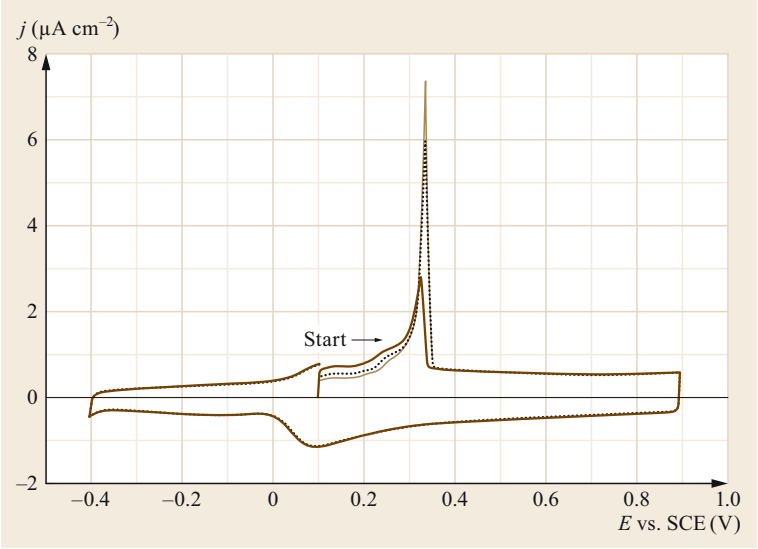

Fig. 34.7 Cyclic voltammograms for the unreconstructed, island-covered Au(100)-(1 × 1) surface in 10 mM H_2SO_4 after waiting at −350 mV for different lengths of time: 10 s (*thick line*), 60 s (*dotted line*) and 10 min (*thin line*) to allow potential-induced reconstruction. Scan rate: 10 mV s^{-1}; temperature: 20 °C. Reprinted from [34.48], with permission from Elsevier

34.5 Voltammetry of Platinum Single Crystals

Figure 34.8 shows a comparison of the voltammetric profiles recorded with the three basal planes of platinum in 0.1 M $HClO_4$ and 0.5 M H_2SO_4. As before, perchloric acid is chosen because perchlorate does not adsorb specifically on the surface of platinum (as will be demonstrated below). The potential scan is limited to the window between the onset of hydrogen evolution and the oxidation of the surface. In comparison with the voltammograms previously discussed for gold, current density is significantly higher for platinum, as a consequence of the existence of important adsorption processes. The first important observation is the significant sensitivity of the voltammetric profile to the crystallographic orientation of the electrode surface. Second, in the three cases, the effect of anion (sulfate) specific adsorption is to push adsorption states to lower potential values, resulting in sharper and higher peaks in sulfuric acid solution (red curves in Fig. 34.8). The key quantitative measure to analyze the voltammogram is the charge integrated according to

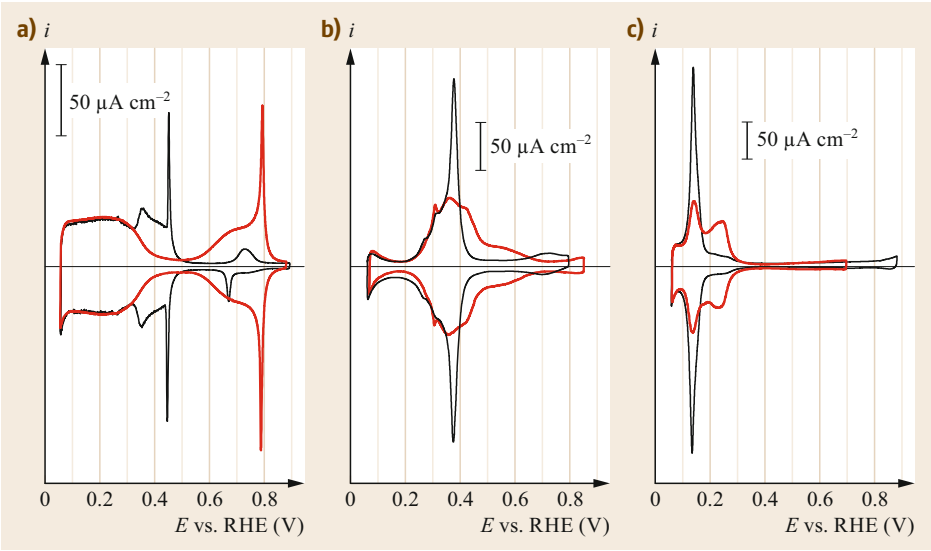

Fig. 34.8a–c Cyclic voltammograms of the three platinum basal planes in 0.1 M $HClO_4$ (*red curve*) and 0.5 M H_2SO_4 (*black curve*) for **(a)** Pt(111), **(b)** Pt(100) and **(c)** Pt(110) electrodes. Scan rate: 50 mV s^{-1}

Table 34.1 Values of the charge corresponding to a process exchanging one electron per surface atom (q) and atomic density (N) of the three basal planes of platinum and gold. Atomic diameters are calculated from the lattice parameter as $d = a/\sqrt{2}$: $a = 0.39236$ nm (for Pt) and $a = 0.40782$ nm (for Au) [34.49]

Miller index	S_{hkl}	Metal	q (μC cm^{-2})	N (cm^{-2})
(111)	$\sqrt{3}/2d^2$	Pt	240.3	1.50×10^{15}
		Au	222.5	1.39×10^{15}
(100)	d^2	Pt	208.1	1.30×10^{15}
		Au	192.7	1.20×10^{15}
(110)	$\sqrt{2}d^2$	Pt	147.2	9.19×10^{14}
		Au	136.2	8.50×10^{14}

$$q = \int_{E_1}^{E_2} \left(\frac{j}{v} - C_{\mathrm{dl}} \right) \mathrm{d}E \tag{34.7}$$

These charges have to be compared with the nominal values calculated for a reaction that involves one electron per surface atom, so that surface coverage can be determined. The nominal values can be calculated from the hard sphere model of the surface as

$$q_{hkl} = \frac{ne}{S_{hkl}}\,, \tag{34.8}$$

where n is the number of atoms in the unit cell, e is the unitary charge and S_{hkl} is the area of the unit cell of the surface with Miller indices (hkl). The values obtained for the three basal planes of platinum and gold, together with the expression for the surface of the unit cell as a function of the atomic diameter of both metals and the atomic density on the surface are given in Table 34.1.

For Pt(111) in 0.5 M H_2SO_4, the charge integrated between 0.06 and 0.6 V (after double-layer correction) amounts to ca 240 μC cm^{-2} (Table 34.2). This figure coincides outstandingly well with the value predicted by the hard sphere model for a one-electron process per platinum atom on this surface. This coincidence led to the initial hypothesis that the current in the whole potential range was due to a single process involving a single electron transfer and attaining a coverage close to 1. This process was thought to be hydrogen adsorption according to [34.21].

$$\mathrm{Pt} + \mathrm{H}^+ + \mathrm{e}^- \rightleftharpoons \mathrm{Pt{-}H} \tag{34.9}$$

However, there were several observations that soon casted doubts about this interpretation. First, the voltammogram in perchloric acid shows adsorption states at even higher potentials, above 0.5 V, too high to be due to hydrogen adsorption [34.55, 56]. Second, adsorption states below 0.3 V shift with pH of the solution, but they don't shift with (bi)sulfate concentration (using mixtures of $HClO_4$ and Na_2SO_4) [34.57]. Third, adsorption states above 0.3 V shift with (bi)sulfate concentration but not with pH [34.57]. The obvious conclusion from these observations is that there are two competitive processes in this case, hydrogen adsorption/desorption and (bi)sulfate adsorption/desorption. This latter process occurs according to

$$\mathrm{Pt} + \mathrm{HSO_4^-} \rightleftharpoons \mathrm{PtH_{1-}}_n\mathrm{SO_4^{z-}} + n\,\mathrm{H^+} + m\,\mathrm{e^-} \tag{34.10}$$

where m and n are the number of protons and electrons exchanged in the adsorption process, respectively. These processes partly overlap on Pt(111), although a minimum in the voltammetric current around 0.3 V

Table 34.2 Charges displaced by the potentiostatic adsorption of CO on the different platinum basal planes for different electrode potential and electrolyte composition. Total voltammetric charges (double-layer corrected) integrated in the voltammogram between the indicated potential limits are also given for comparison

Electrode	Electrolyte	Total charge (μC cm^{-2})	E vs. RHE (V)	Displaced charge (μC cm^{-2})	Reference
Pt(111)	0.1 M $HClO_4$	268 (0.06–0.90 V)	0.08	152	[34.50]
			0.40	−20	[34.50]
	0.5 M H_2SO_4	240 (0.06–0.55 V)	0.08	161	[34.51]
			0.50	−92	[34.51, 52]
Pt(100)	0.1 M $HClO_4$	256 (0.17–0.75 V)	0.10	196	[34.53, 54]
			0.50	−56	[34.53]
	0.5 M H_2SO_4	257 (0.18–0.80 V)	0.10	197	[34.51]
			0.45	−57	[34.51]
Pt(110)	0.1 M $HClO_4$	212 (0.06–0.40 V)	0.085	146	[34.50]
			0.34	−38	[34.50]
	0.5 M H_2SO_4	220 (0.06–0.50 V)	0.10	143	[34.51]
			0.34	−64	[34.51]

signals (at least formally) the transition from one process to the other. The situation is more complex on Pt(100) and Pt(110) where a single main peak is observed in the voltammogram, indicating that both processes are mainly coupled, i.e., sulfate adsorption pushes hydrogen desorption, and both processes take place as a single step.

$$\mathrm{Pt-H} + \mathrm{HSO_4^-} \rightleftharpoons \mathrm{PtH_{1-}}_n\mathrm{SO_4^{z-}} + (n+1)\,\mathrm{H^+} + m\,\mathrm{e^-} \qquad (34.11)$$

5 Therefore, additional information is required to separate and determine these contributions. This can be achieved with the charge displacement experiment discussed in the next section.

34.6 Charge Displacement Experiment

In this experiment, the current flowing during the potentiostatic adsorption of a neutral molecule is recorded as a measure of the interfacial charge at the potential of the experiment [34.58]. The adsorption of this molecule should be strong enough to displace all previously adsorbed species. It should also decrease the differential capacity of the interphase in such way that the charge at the end of the displacement can be considered negligible. The best displacing agent for platinum (and the one almost exclusively used for this purpose) is carbon monoxide. This molecule adsorbs very strongly on the platinum surface, displacing almost any other adsorbate. Besides, the interfacial charge on the CO-covered surface is very small, (although not always negligible; see below). Other advantages of this molecule are that the excess CO in solution can be easily removed just by argon bubbling, and that the free surface can be easily recovered by scanning the electrode potential to high values, which triggers the oxidation of the adsorbed molecules (see Sect. 34.10). This allows the experiment to be repeated several times without the need to exchange the solution or to clean the electrode surface again. Another displacing agent successfully used for platinum is iodine [34.59]. However, in this case, it is not possible to remove the iodine from the solution after the experiment is completed and requires changing the solution (and thoroughly cleaning the cell) in each repetition of the experiment. Moreover, the potential range where iodine is not electroactive is rather small, since it can be oxidized to iodate or reduced to iodide [34.59].

The advantage of using displacing agents in the gas state is that they can be easily introduced in the cell while avoiding the entrance of oxygen. In fact, the latter is the main experimental difficulty in the charge displacement technique. If a trace amount of oxygen accompanies the displacing agent, it will produce negative currents due to its reduction. This will interfere with the true displacement current, altering the measurement of the total charge. Thus, special care has to be taken to ensure the removal of any oxygen traces from the gas stream of the displacing agent.

Table 34.2 shows values of the displaced charge for the different platinum basal planes in different electrolytes. These values should be compared with the charges corresponding to the monolayer (one electron per platinum atom on the surface) in Table 34.1 and also with the charges integrated in the voltammogram. We observe that, at the onset of hydrogen evolution, nearly one monolayer of hydrogen is attained for Pt(100) and Pt(110) while only 2/3 of the monolayer are attained for Pt(111). Importantly, we observe that, in general, the maximum charge corresponding to hydrogen is always smaller than the total voltammetric charge, indicating that the latter includes some additional contribution, namely, anion adsorption. The definitive proof for this is the displacement of negative charges at higher potentials. In fact, there is no need to perform the displacement experiment at more than one potential since the difference between displaced charges at two potentials should always be equal to the integrated charge between these potential limits. In this way, from the charge displaced at one potential and the integration of the voltammogram, we can predict the charge that will be displaced at a second potential. This is further discussed in Sect. 34.8.

In the following, we describe in more detail the voltammetry of the different basal planes on the most typical media, under the light of the charge displacement results, but also considering complementary results of IR spectroscopy and STM microscopy.

34.6.1 Pt(111)

Let us discuss first the voltammetry of Pt(111) in 0.5 M H_2SO_4. Around 160 $\mu C\,cm^{-2}$ are displaced with CO at the onset of the hydrogen evolution (0.08 V), indicating that only 2/3 of the hydrogen monolayer are attained on this surface. Most likely, the maximum coverage is not attained in this case because hydrogen evolution starts before the monolayer is completed, limiting the effective potential range where the voltammogram can be recorded. Indeed, chronoamperommetric experiments

suggest that the monolayer is completed at lower potentials [34.60]. From the lower limit, if the potential is scanned positively, hydrogen will desorb oxidatively, resulting in positive currents. The voltammogram is rather flat in this region. In the framework of a Frumkin isotherm, the very broad peak can be understood as the consequence of rather strong repulsive interactions [34.31–33]. Small peaks at 0.12 and 0.26 V are sometimes observed. They signal the presence of (110) and (100) defects on the surface (see later) [34.61–64]. The absence of peaks in this region is an indication of a high-quality crystal (although it can also indicate a partial blockage of the surface by traces of contamination in the solution, because low-coordinated atoms at the defects are more susceptible to contamination). Around 0.3 V, the current starts to decrease as the surface concentration of hydrogen becomes very low. At this point, sulfate adsorption starts on the free surface that resulted from hydrogen desorption. Sulfate adsorption initially forms a disordered adlayer. At 0.44 V, a critical coverage is attained that triggers the transformation of the disordered adlayer into the $(\sqrt{3}\times\sqrt{7})$R19.1° ordered sulfate adlayer, as detected with STM [34.65–67]. As previously indicated, this adlayer has been observed for sulfate adsorbed on the (111) surface of gold [34.44, 45], platinum [34.65–67], palladium [34.68, 69], rhodium [34.70], iridium [34.71] and copper [34.72]. This seems to indicate that the structure of the adlayer is dominated by the matching interactions between the three oxygens in the tetrahedral structure of the sulfate ion with the trigonal arrangement characteristic of the (111) surface. The sharp spike that signals the disorder/order phase transition is very sensitive to the quality of the single crystal and to the purity of the solution. In this sense, a voltammogram like the one in Fig. 34.8 can be taken as a fingerprint of good experimental conditions.

One point that has aroused intense debate is the exact chemical nature of the adsorbed species, either sulfate or bisulfate. Spectroscopic investigation of the interphase should, in principle, be able to discern between those species since they have, in solution, easily distinguished vibrational spectra. The problem comes with the uncertainty about the effect of the chemical bond with the surface on the vibrational spectra. In this regards, the same spectral features have been interpreted by different research groups as clear indication of the presence of one or the other species on the surface [34.73–78]. Careful spectroscopic measurements using quantitative subtractively normalized interfacial Fourier transform IR spectroscopy (SNIFTIRS) [34.79] and a detailed thermodynamic analysis using solutions of different pH [34.80] seems to tip the balance in favor of sulfate as the adsorbed species. In this way, although the species that predominates in 0.5 M H_2SO_4 solution is bisulfate ($pK_a = 1.99$) [34.49], during the adsorption, the ion deprotonates. This trend is linked with the effect of the bond with the surface on the acid/base equilibrium of adsorbed acids. It seems that, in general, the bond with the metal surface has a withdrawing effect on the electron density that results in an increase in the acidity of adsorbed species [34.81–83].

Another controversial point is the nature of the small peak observed at ≈ 0.68 V. A thermodynamic analysis indicates a significant ($\approx 20\%$) increase in sulfate surface concentration associated with this process [34.84]. This led to the conclusion that this process could be associated with the restructuring of many different rotational domains present on the sulfate adlayer in the potential range between the spike and the small pair of peaks to form larger rotational domains [34.85]. The disappearance of domain boundaries would lead to this increase in sulfate coverage. However, STM observations have not corroborated this hypothesis. Different rotational domains are indeed observed at potentials lower than the pair of peaks [34.66, 67]. Nevertheless, at higher potentials, the ordered structure has not been observed [34.67]. Another interesting feature of this pair of peaks is its sensitivity to the nature of the alkaline cation present in solution, indicating that cations are coadsorbed with the sulfate adlayer in this potential region [34.85, 86].

Figure 34.9 shows the evolution of the voltammogram when the potential is scanned into the region of oxide formation. Similar to what happens with gold, the first cycle shows only capacitive currents up to a relatively high potential value. This behavior is associated with the protection of the surface by the ordered sulfate adlayer described above. A rather high potential is needed to trigger the substitution of sulfate by oxide. This oxidation implies place exchange, and when oxide is reduced, the surface becomes disordered, as can be deduced from the evolution of the voltammogram. The defective surface is oxidized at much lower potentials in the second cycle. After several cycles of oxidation and reduction, the resulting voltammogram is that characteristic of a disordered surface with mainly (110) defects, while the density of (100) defects is much lower. The onset for the replacement of sulfate by oxide depends on sulfate concentration and the pH of the solution [34.84].

When the voltammogram recorded in sulfuric acid is compared with the one recorded in perchloric acid, we observe that the two overlap perfectly below 0.30 V. This is also true in the presence of other anions: at low enough potentials, the anion is desorbed, and the current

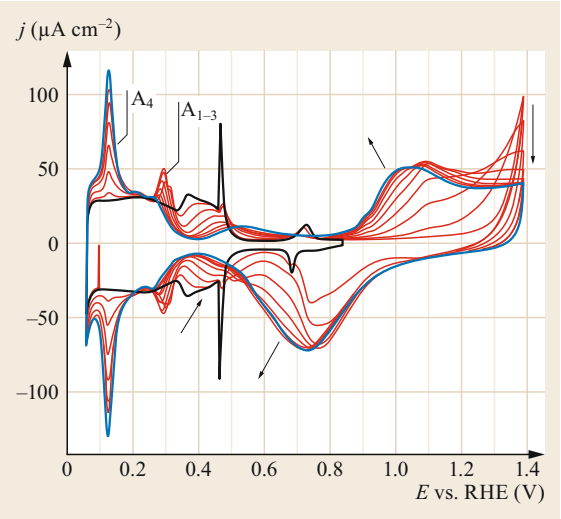

Fig. 34.9 Evolution of the voltammetric profile of the Pt(111) electrode in 0.5 M H_2SO_4 as the electrode potential is cycled at 50 mV s^{-1} between 0.06 and 1.40 V vs. RHE. The *black curve* indicates the initial voltammogram, the *red curves* indicate the evolution upon cycling and the *blue curve* corresponds to the profile attained after 12 cycles. *Arrows* indicate the evolution of the voltammogram. Reprinted from [34.87], with permission from Elsevier

becomes independent of the anion in solution [34.88, 89]. In accordance with this, the charge displaced at the onset of the hydrogen evolution is independent of the anion, since only hydrogen is displaced [34.90]. In perchloric acid, the hydrogen and anion adsorption regions are separated by a narrow double-layer region. In this region, current is mainly capacitive.

Regarding the adsorption process recorded above 0.55 V, it has been usually assumed that perchlorate is a poor Lewis base and therefore unable to adsorb specifically on the surface of platinum. This assumption was challenged based on spectroscopic observations [34.91, 92]. However, comparison of the voltammetry in the presence of other anions that do not adsorb specifically reveals that these adsorption states are not specific to the presence of perchlorate. Almost identical voltammetry is observed in HF/NaF mixtures [34.55, 77, 78] and in trifluoromethane sulfonic acid [34.93]. This supports the idea that these states correspond to the only common species in the three electrolytes: hydroxyl adsorption from water. These adsorption states are composed of a broad peak, which can be explained in terms of a Frumkin isotherm with rather large repulsive interactions, followed by a sharp peak at 0.8 V. The latter has been interpreted as indicative of phase transition in the hydroxyl adlayer [34.94]. However, the morphology of this peak is clearly different from the one observed in sulfuric acid, involving more charge. Besides, very low concentrations of different anions have interesting effects on the relative magnitude of the broad and sharp peak [34.95]. This led to a second interpretation of the two peaks, considering that they originate from two different kinds of water at the interphase: structured and unstructured water [34.95].

Increasing further the potential above 1.0 V reveals the existence of another peak that has been interpreted as the initial stages of the oxidation of the surface, i.e., transformation of OH into O [34.96, 97]. While for other surfaces of platinum, oxidation (and subsequent reduction) to this high potential value leads to the creation of defects, for Pt(111) in perchloric acid solution, scanning the potential up to 1.15 V does not induce changes in the surface, as deduced from the stability of the voltammetric profile [34.98]. Hence, it can be inferred that oxide formed in this initial peak does not involve place exchange.

We complete the picture of the electrochemical behavior of Pt(111) in different electrolytes with the examples shown in Fig. 34.10. Figure 34.10a shows the voltammograms recorded with this surface in solutions containing different anions, while Fig. 34.10b,c shows the voltammograms in solutions of different pH. To control the pH, an adequate buffer solution needs to be used. While phosphate adsorbs specifically on platinum (Fig. 34.10b), the mixtures of NaF/HF (Fig. 34.10c) are selected due to the absence of specific adsorption. Comparison of the voltammetry in halide-containing solution shows how the strength of adsorption increases in the order F < Cl < Br. Fluoride does not adsorb at all, as anticipated above, resulting in a voltammogram identical to that of perchloric acid (Fig. 34.10c). The increase in halide adsorption strength is signaled by a shift of adsorption states to lower potentials. Phosphate is another anion typically used to prepare electrolytes, especially for buffered solutions. At pH 2.2, the CV in phosphate-containing solution features a single, broad peak, similar to that of sulfate (at similar concentration) but without the characteristic spike. When the pH is increased, a rather complex voltammetric profile is obtained, featuring a number of peaks that varies with pH. These adsorption states involve the interconversion between phosphate species with different degrees of protonation [34.99, 100]. OH coadsorption is also likely to take place in this potential region at high pHs. It is worth pointing out the effect of the alkaline cation of the phosphate salt on the voltammetric profile [34.101]. While sharp peaks are measured with the sodium salt, more rounded features are measured when the potassium salt is employed.

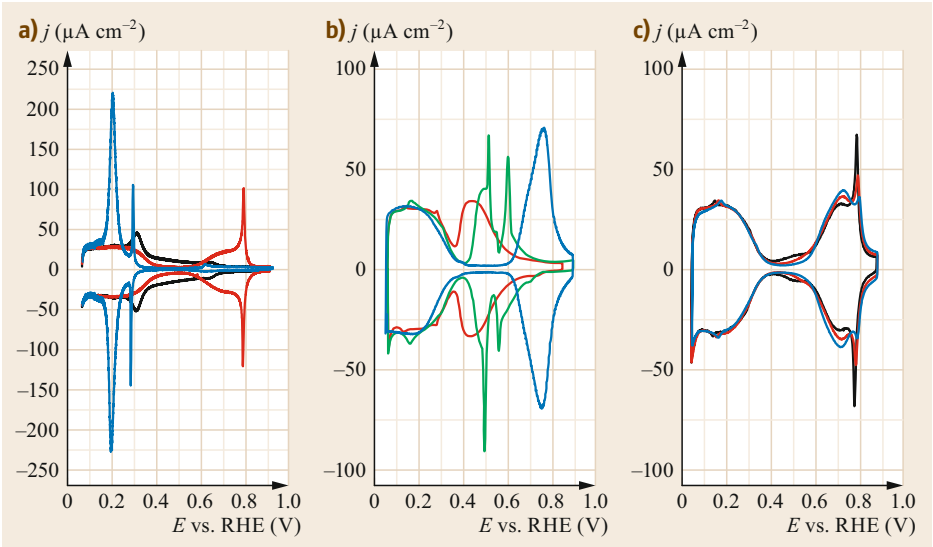

Fig. 34.10a–c Cyclic voltammograms of Pt(111). **(a)** 0.1 M $HClO_4$ (*red graph*), 0.1 M $HClO_4$ + 1.5 mM Cl^- (*black graph*), 0.1 M $HClO_4$ + 1.5 mM Br^- (*blue graph*); **(b)** 0.1 M NaH_2PO_4 + 0.047 M $HClO_4$, pH 2.2 (*red graph*), 0.094 M NaH_2PO_4 + 0.006 M Na_2HPO_4, pH 5.6 (*green graph*), 0.1 M NaOH (*blue graph*); **(c)** 0.1 M NaF + *x* M $HClO_4$ pH 3 (*black graph*), pH 4 (*red graph*), pH 5 (*blue graph*)

On the other hand, the voltammograms of Fig. 34.10c show the effect of increasing the pH on the different adsorption states. Both hydrogen and hydroxyl adsorption regions shift by nearly 59 mV per pH unit (that is, the potentials are constant in the RHE scale) [34.102–104]. Such shift is in accordance with Nernst's law, which would be another way to express the Frumkin isotherm. However, there are some subtle changes when the pH is increased. First a broad feature is observed in the double layer when the pH is between 2–4. This process is overlapped with the hydrogen adsorption at pH 1, but is decoupled from it when hydrogen shifts to lower potential with the increase in pH, whereas this process is unaffected by the pH. Further increasing of the pH above 4 makes this process move into the hydroxyl region. The charge associated to this process is around 1 $\mu C\,cm^{-2}$. This process has been associated with the reorientation of water dipoles as the potential is increased [34.105]. As this process is displaced from the hydrogen region to the hydroxyl region, hydrogen charge decreases and hydroxyl charge slightly increases as a consequence of pH increase. In addition, hydroxyl adsorption, that is divided into two peaks, one broad and one narrow, is redistributed when the pH increases. The broad peak increases, while the narrow peak decreases. This could be due to the different role of anions to modify the structure of water at the interphase. In alkaline solution (Fig. 34.10b), the voltammogram of Pt(111) still contains the same main features. Hydrogen adsorption is slightly lower, while the sharp peak in the hydroxyl adsorption has disappeared completely and shows a total charge of ca. 170 $\mu C\,cm^{-2}$.

34.6.2 Pt(100)

We come back now to the voltammogram of Pt(100) in Fig. 34.8b. As previously discussed, the total charge in the voltammogram is well above that corresponding to the monolayer of hydrogen, evidencing the competitive adsorption of hydrogen and anions. The voltammograms measured both in perchloric and sulfuric acid overlap at potentials below 0.3 V, indicating that the anion is not adsorbed in this potential range. Moreover, the charge displaced at 0.1 V is the same in both electrolytes (ca. 200 $\mu C\,cm^{-2}$), approaching the value of the monolayer on this surface.

The quality of the (100) surfaces is influenced in great extent by the existence of surface reconstructions. Similar to what has been described before for gold, the (100) surface of platinum also forms a hexagonal reconstruction (Pt(100)-hex-R0.7°) leading to a distribution of atoms with an atomic density ca. 20% higher than that of the (1×1) surface [34.106–108]. This reconstructed adlayer is stable in a wide range of temperatures between 77 and 1450 K [34.107]. UHV studies show that different adsorbates such as H_2, O_2, CO or NO swiftly cause the disappearance of the reconstruction [34.109–113]. The perseverance of the reconstruction in aqueous solutions has been

discussed in the past [34.114, 115], but there is now general consensus that the reconstruction is completely eliminated after the contact with the solution [34.40, 116–118]. The disappearance of the reconstruction involves significant movement of atoms that leads to the formation of surface defects [34.24–26]. Studies with stepped surfaces (see below) reveal that the small peak at 0.30 V can be ascribed to adsorption processes on such defects. A small peak or shoulder around 0.27 V is often observed, also related to surface defects. The quality of this surface is also very sensitive to the annealing and cooling conditions [34.21, 119]. Cooling in the presence of oxygen leads to the formation of a highly defective surface, with a voltammogram in sulfuric acid solutions characterized by a main peak at 0.26 V and only small contributions reminiscent of the peak at 0.38 V. On the other hand, cooling in H_2/Ar leads to the voltammogram shown in Fig. 34.8, with the main peak in sulfuric acid at 0.38 V corresponding to adsorption on ordered terraces. Other annealing conditions have been tried. In particular, cooling in CO seems to produce the best ordered surface [34.24, 25], although, in our experience, the difference between H_2/Ar and CO is important only if the quality of the electrode is not high. STM characterization enables relationships to be established between the voltammetric features and the morphology of the surface obtained by the different cooling conditions, corroborating the description given above [34.24, 25]. Finally, the small process at 0.71 V is usually ascribed to the replacement of adsorbed sulfate by adsorbed hydroxyl. Scanning the potential above 1.0 V produces the disordering of the surface, as discussed above [34.120].

The description of the voltammogram in perchloric acid solution follows the same lines as the case of sulfuric acid. Starting from a monolayer of hydrogen at 0.1 V, the increase of the potential causes the desorption of hydrogen, initially from defect sites, peaking at ca. 0.3 V, and then, at slightly higher potentials, from terrace sites. In the absence of specific anion adsorption, the desorption of hydrogen spans over a broader potential range, signaling the existence of repulsive lateral interactions in the hydrogen adlayer [34.121]. The inflection at 0.50 V is usually taken as a change in the main process from hydrogen desorption to hydroxyl adsorption. Around 0.50 V, the two processes overlap. From CO displacement, it can be inferred that the maximum hydroxyl charge attained at 0.70 V is around 77 $\mu C\,cm^{-2}$, equivalent to 0.37 species per surface platinum atom [34.121]. To conclude this description of the Pt(100) surface, Fig. 34.11 shows the voltammogram obtained in 0.1 M NaOH. The voltammetric profile is significantly more complicated, with important differences from those recorded in acid media. The peak

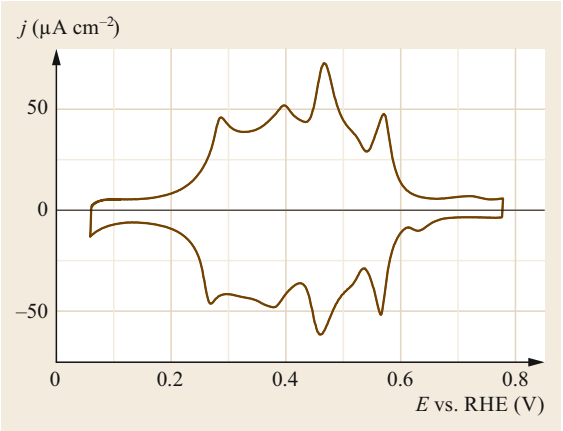

Fig. 34.11 Voltammetric profile for the Pt(100) electrode in 0.1 M NaOH. Scan rate: 50 mV s^{-1}

corresponding to surface defects now splits into two peaks at 0.28 and 0.38 V, while the peak corresponding to adsorption on the terraces shifts to 0.45 V [34.122]. Finally, a new peak at 0.56 V may be ascribed to hydroxyl adsorption. The charge displaced at 0.1 V is still close to that corresponding to the monolayer of hydrogen, and the total charge integrated in the whole potential range is close to the value obtained in acidic media (ca. 264 $\mu C\,cm^{-2}$).

34.6.3 Pt(110)

This is the most open surface among the three basal planes and therefore the most reactive and unstable. In UHV, the clean surface is reconstructed to form a (1×2) structure characterized by the disappearance of one every second row of atoms [34.43, 123]. Such structure minimizes the surface energy by creating (111) microfacets. This reconstruction has been studied extensively in UHV [34.123–125]. Similarly to what happens with the (100) surface, the adsorption of different adsorbates causes the lifting of the reconstruction [34.126–128]. It is also worth mentioning that other reconstructions with higher periodicity $(1\times n)$ have also been reported. Regarding the persistence of the reconstruction in an electrochemical ambient, it seems to depend very much on the preparation method and cooling conditions. Ex situ characterization of surfaces extracted from the electrochemical cell at different potentials indicated that the reconstruction may persist in the electrochemical environment [34.15, 129]. However, in situ measurements using STM cast some doubt on this result, since with this method, only (1×1) surface is observed [34.130–132]. In fact, the resulting topography, with a large number of small islands, is that expected after lifting of the reconstruction [34.24]. Finally, in situ surface x-ray

scattering (SXS) studies [34.133, 134] concluded that a fast cooling rate freezes the (1×1) structure obtained at high temperature (above 800 °C) in the flame, while slow cooling of the the electrode (in nitrogen) results in the (1×2) surface that persists in an electrochemical environment.

The voltammetric profile of this surface in different acidic solutions is shown in Fig. 34.8c. The voltammogram in H_2SO_4 shows a main peak at 0.145 V and a small shoulder at 0.16 V. The resolution of this shoulder seems linked to the quality of the crystal and it is better resolved when the electrode is cooled in CO after the flame annealing [34.24, 135]. This treatment gives wider (1×1) (110) terraces. In the absence of anion adsorption (0.1 M $HClO_4$), the peak and shoulder separate completely, giving rise to two peaks at 0.14 and 0.24 V. The surface cooled in CO gives rise to a complex number of peaks in the voltammogram recorded in 0.1 M $HClO_4$, which renders this surface particularly sensitive to the cooling conditions [34.135]. The charge displaced with CO at potentials close to the onset of hydrogen evolution is close to 150 $\mu C\,cm^{-2}$, therefore indicating that the monolayer of hydrogen is attained under these conditions [34.50, 51]. Also, displacement of negative charges at potentials higher than the voltammetric peak allows us to unambiguously assign this peak to the coupled desorption of hydrogen and the adsorption of anion, either sulfate or hydroxyl. Regarding the voltammogram in 0.1 M $HClO_4$, it is tempting to assign each of the two peaks observed in the voltammogram to each one of the processes taking place, namely, hydrogen and hydroxyl adsorption. However, the charge of the peaks does not match with the expected charges inferred from the CO displacement. Charge displaced at the onset of hydrogen evolution is close to 150 $\mu C\,cm^{-2}$, while the charge of the first peak is only around 110 $\mu C\,cm^{-2}$. Therefore, if the first peak (in the positive sweep) were hydrogen desorption, this process would extend 40 $\mu C\,cm^{-2}$ into the second peak. Most likely, both processes take place in a concerted way in each of the peaks, and the peak splitting seems to be related more to the existence of different atomic geometries on the surface than to the occurrence of different chemical processes [34.136].

34.7 Stepped Surfaces

Additional information about the relationship between the voltammetric profile and the surface structure can be obtained from the systematic study of stepped surfaces prepared by cutting the crystal at an angle between two basal planes. The different kinds of stepped surfaces that can be obtained and the relationship between surface structure and Miller indices has been summarized in Fig. 34.1. Figure 34.12 shows the corresponding voltammetric profiles of a selection of these surfaces. What turns out to be very interesting is that, in most cases, the voltammogram of a stepped surface can be understood as a combination of terrace and step

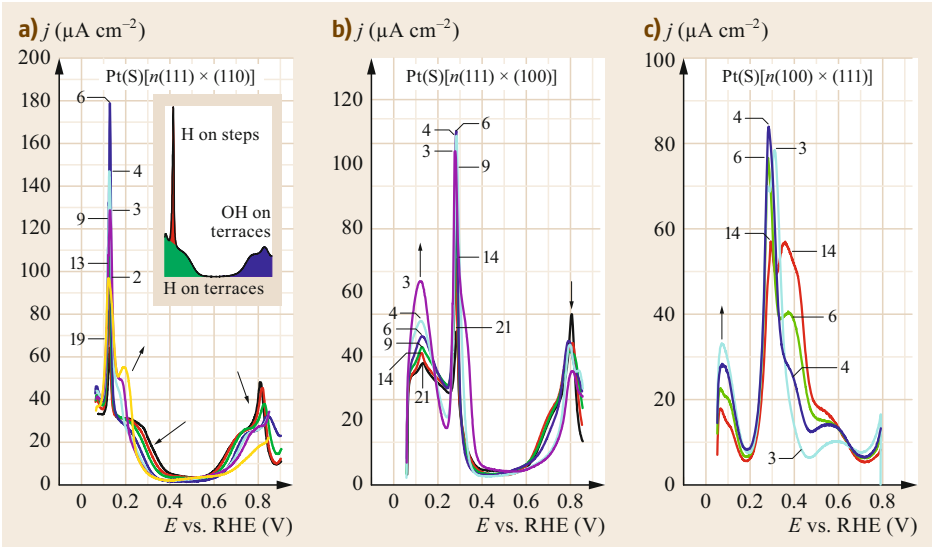

Fig. 34.12a–c Cyclic voltammograms for Pt stepped surfaces in 0.1 M $HClO_4$: **(a)** Pt(S)[$n(111) \times (111)$]; **(b)** Pt(S)[$n(111) \times (100)$] and **(c)** Pt(S)[$n(100) \times (111)$]. Numbers in each figure indicate the length of the terrace in atomic rows (n). *Inset* in **(a)** indicates the separation of different contribution to the charge. Scan rate: 50 $mV\,s^{-1}$

contributions [34.61, 62, 137, 138]. From the systematic variation of the step density, it is easy to infer which contribution corresponds to each kind of site. For instance, careful observation of the voltammograms in the $[1\bar{1}0]$ zone, i.e., Pt(S)$[n(111)\times(110)]$ surfaces, reveals that, as the length of the terrace (n) decreases, and therefore the step density increases, the voltammetric contribution assigned to hydrogen and anion adsorption on the (111) sites decreases, and a new contribution at 0.12 V builds up. According to this, contribution of step sites can be immediately associated with the new peak at 0.12 V. Moreover, the specific voltammetric profile obtained in this case allows us to separate terrace and step sites, taking a relatively unambiguous base line, as illustrated in the inset of Fig. 34.12a. The charge integrated in this way for different stepped surfaces can be compared with the hard sphere model to test the accuracy of the step/terrace description of the surface. It turns out that the measured charges fit quite well with the hard sphere model for Pt(S)$[n(111)\times(110)]$ and Pt(S)$[n(111)\times(100)]$. Deviations are observed in the latter case for the charge of the terrace, which can be attributed to the contribution from anion adsorption [34.139]. Also, deviations are observed for the step charge at large step densities. When steps are very close, the electronic perturbation from two adjacent steps overlaps, and the surface can no longer be considered a combination of terrace and step sites.

The previous analysis demonstrates that stepped surfaces can be prepared with a high degree of accuracy with a resulting structure close to the ideal one, at least for some corners of the stereographic triangle. STM studies also corroborate this [34.27, 54, 140]. In this way, the use of stepped surfaces in electrocatalytic studies has allowed us, in many different situations, to separate the contributions from the different geometric parts of the surface, resulting in a deeper understanding of the relation between surface structure and reactivity.

34.8 Potential of Zero Charge

The electrochemical interphase is, by definition, neutral, which does not imply that the electrode and the solution charge are zero. In fact, the charges of the electrode and solution have the same absolute value and opposite sign, that gives rise to a charge separation in the same way as in a capacitor. This charge is a function of the potential, pressure, temperature and solution composition. The existence of charge separations at the electrochemical interphase is one of its key distinctive characteristics in comparison with interphases in other contexts. The magnitude of the charge separation will have a great influence on the properties of the interphase and its reactivity under given conditions. The charge separation is responsible for the existence of the electric field, polarization of dipoles, inhomogeneous distribution of charges, etc. Despite its importance, charge is not the primary variable controlled in a standard electrochemical experiment, and the properties of the interphase are usually determined as a function of the electrode potential, measured with respect to a reference electrode. Therefore, for a deep understanding of the electrochemical reactivity, it is necessary to establish the relationship between electrode potential and interfacial charge.

The concept of the potential of zero charge (pzc), i.e., the potential at which the charge of the electrode is zero (and therefore the charge of the solution is also zero), was introduced in 1928 by Frumkin [34.141]. Knowledge of the pzc enables the determination of the electrode charge from the integration of the differential capacity or the voltammetric current. Without it, an integration constant is missing and only charge differences can be determined.

The dependence of the pzc on the crystallographic orientation of the electrode has been sufficiently demonstrated in those cases where this magnitude is easily accessible. This is the case of gold and silver electrodes, where the position of the pzc can be identified by locating the minimum in the differential capacity in diluted solutions, according to Gouy–Chapman–Stern theory of the double layer [34.142, 143]. It has been demonstrated that the dependence of the pzc on the crystallographic orientation follows the same trends as the work function in UHV, therefore demonstrating the intimate relationship between the two magnitudes [34.144–146]. For gold single-crystal electrodes, the effect of the selective introduction of steps on the surface has been studied extensively [34.38, 147–152]. In this case, the pzc decreases linearly with the density of steps, similarly to the work function. This decrease is rationalized in terms of the creation of surface dipoles due to the Smoluchowski effect [34.153] or the smearing of the electron density around the hard profile defined by the position of the atomic nuclei around the step. This results in an excess of electron density at the bottom of the step and a deficiency at the top, creating the surface dipole. From the slope of the decrease in either the work function or the pzc as a function of the step density, a value for such dipole can be estimated. The comparison of the dipole associated to the same step observed in UHV or in an electrochemical environment has relevant implications for the interaction of water with the surface [34.147].

Also, the effect of the temperature on the pzc provided interesting information on the entropy of formation of the interphase with important implication for the understanding of the interaction between water and the surface [34.38, 151, 152, 154–156]. These concepts are explained below in more detail for the case of platinum.

The unambiguous definition of the electrode charge requires the use of the concept of the ideally polarizable interphase. This implies the absence of charge transfer through the interface (Note: the interphase is the three-dimensional region of the space through which the properties change from those of the bulk metal to those of the bulk of the electrolyte; the interface is an imaginary two-dimensional plane that divides the interphase into two regions), which means that charged species can be unambiguously assigned to each side of it: electron density is assigned to the metal side, and ionic species are assigned to the electrolyte side. When charged species can circulate through the interface, the concept of charge is ill-defined. For such systems, the concept of the ideally nonpolarizable interface can be introduced [34.141]. In this case, the potential of the electrode cannot be changed without the simultaneous change in the composition of the solution. When charge transfer is limited to adsorption processes, the system shares properties between both situations, ideally polarizable and ideally nonpolarizable. It is ideally polarizable in the sense that the potential can be changed without changing the composition of the solution. However, it is nonpolarizable in the sense that the potential is fixed by the adsorption equilibrium and cannot be changed without changing the activity of the adsorbed species (at constant solution composition). Introduction of the concept of the total charge helps in adapting the thermodynamic equations to a situation with adsorption processes. The total charge can be defined as the charge that has to be supplied to the electrode when its surface is increased by one surface unit with the concentration of solution species remaining constant [34.141]. According to this definition, total charge also involves the charge flowing during the electrosorption process. For a platinum electrode that can adsorb hydrogen through (34.9) and an anion through equation

$$A^{z-} \rightleftharpoons A_{ads} + z\,e^- \,, \tag{34.12}$$

the relation between total charge, q and the true electronic charge density, σ_M (free charge in the following), is given by

$$q = \sigma_M - F\Gamma_H + z_A F\Gamma_A \tag{34.13}$$

where Γ_i is the amount of adsorbed species i. Total charge and not the free charge is what can be measured

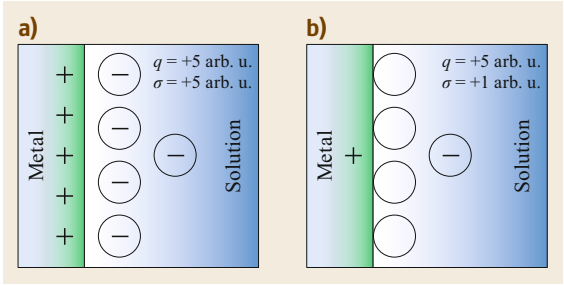

Fig. 34.13a,b Schematic representation of the interphase illustrating the relationship between total and free charge. **(a,b)** Two situations with equal total charge but different values of free charge

through the usual electrochemical experiment. It can be shown that the total charge is also the thermodynamic quantity that has to replace the charge density σ_M to adapt the electrocapillary equation to a situation that involves adsorption processes. The relationship between total and free charge is exemplified in the diagrams of Fig. 34.13. Both situations in Fig. 34.13 require the same supply of electricity from an external source for the creation of a new unit of surface. The difference between them requires only an internal reorganization of charge without external supply of electricity and therefore cannot be distinguished from the *external* observation of the system. The difference between both systems can also be explained by saying that, in the definition of total charge, the charge of the adsorbed species still counts as part of the solution, while in the definition of the free charge, it has been incorporated into the metal side, i.e., the definition of charge depends on the position of the interface.

The consequence of the previous definitions is that two different pzc should be distinguished in the presence of adsorption processes: the potential of zero total charge (pztc) and the potential of zero free charge (pzfc). Total charges, and therefore values for pztc, can be determined using the CO charge displacement experiment. The assumption implied in this is that no faradaic charge flows during CO adsorption, and therefore the charge integrated in the displacement process, $q_{dis}(E)$, can be equated with the difference between the charge present on the electrode before, $q_i(E)$, and after, $q_f^{CO}(E)$, the introduction of CO

$$q_{dis}(E) = q_f^{CO}(E) - q_i(E). \tag{34.14}$$

The desired quantity is $q_i(E)$. To calculate it from the measured value of $q_{dis}(E)$, the value of $q_f^{CO}(E)$ is required. The latter can be calculated from the integration of the differential capacity in the presence of CO if the value of the pzc of the surface covered with

CO is known. As a first approximation, $q_f^{CO}(E)$ can be neglected [34.63]. This assumption is based on the low magnitude of the differential capacity of the CO-covered electrode (ca. $14\,\mu F\,cm^{-2}$) when compared with the pseudocapacity of platinum (ca. $600\,\mu F\,cm^{-2}$ for Pt(111) in the hydrogen region). The estimation of $q_f^{CO}(E)$ can be improved if an approximate value of the pzc of the CO-covered electrode is known. Such estimation was given for Pt(111)-CO based on UHV measurements of work function values [34.157] and later determined experimentally for the same system by the immersion method [34.158]. The result obtained by both approaches coincides, within the experimental uncertainty, in a value around 1.0 V RHE. This gives a value for $q_f^{CO}(E)$ around $-13\,\mu C\,cm^{-2}$ at 0.1 V RHE. This remaining charge represents a correction of ca. 9%. Unfortunately, the value of $q_f^{CO}(E)$ is not known for surfaces different from Pt(111).

Once the charge at one potential is known, within the uncertainty explained in the previous paragraph, it can be calculated at any other potential from the integration of the voltammogram according to

$$q(E) = \left[q^{CO}(E^*) - q_{dis}(E^*)\right] + \int_{E^*}^{E} \frac{j}{v} dE \,, \qquad (34.15)$$

where E^* is the potential of the displacement experiment, j the voltammetric current and v the scan rate (with sign). When recording the voltammogram for the integration, a sufficiently low scan rate should be used to ensure a situation close enough to equilibrium. To ensure the consistency between displaced and voltammetric charges, the displacement experiment can be repeated at more than one potential. Then, a least squares method can be used to fit the voltammetric charge to the displaced charge values. The procedure is exemplified in Fig. 34.14.

The result of this analysis is a curve that relates total charge and potential. From this curve, the value of the pztc can be directly measured. Charge values at other potentials can be useful in coulometric analysis, when coverage of an adlayer is calculated from charge involved in its stripping. In this case, after the stripping of the adlayer, the bare surface should recover the charge that corresponds to the final potential, and this charge can be read from the charge–potential curve described here. This charge turned out to be very important in the calculation of CO coverage from its stripping (see later) [34.160].

The pztc of different platinum electrodes has been determined with this method, and the effect of crystallographic orientation, presence of specifically adsorbed anions, density of steps and pH has been analyzed.

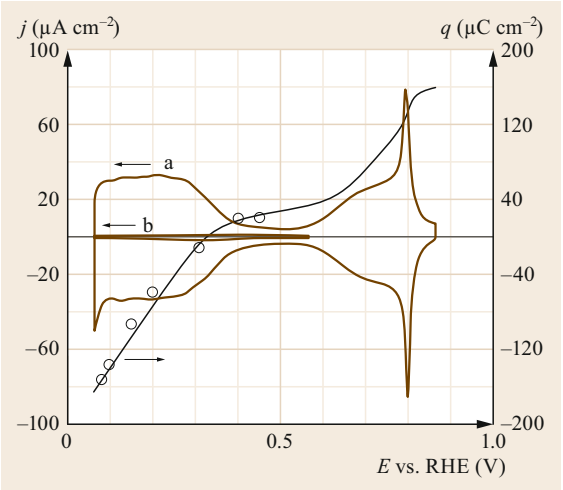

Fig. 34.14 *Right axis*: Comparison of integrated voltammetric charges (*full line*) with CO displaced charges (dots) for Pt(111) in 0.1 M $HClO_4$. *Left axis*: a and b represent the voltammetric profiles of the unmodified and CO covered Pt(111) electrode in this solution, respectively. Comparison of integrated voltammetric charges with CO displaced charges for Pt(111) in 0.1 M $HClO_4$. Scan rate: $50\,mV\,s^{-1}$. Reprinted with permission from [34.159]. Copyright (2019) American Chemical Society

Determination of free charge and pzfc for platinum electrodes is less straightforward. As mentioned above, usual charge measurements do not allow for separation of free charge from adsorption charge. One approach is to separate both contributions relying on their different time scale. Adsorption processes involving charge transfer are expected to be slower, while double-layer phenomena involving reorganization of ions at the interphase are likely to be faster. According to this, a fast perturbation of potentials would enable separation of both contributions. This has been achieved with impedance spectroscopy, although a very high-frequency modulation, above the normal range of common instrumentation, has to be used [34.161, 162]. The laser-induced potential temperature jump method mentioned below would also fall within the philosophy of this approach. Alternatively, one can measure a structural property of the interphase that is related to the electric field and therefore to the free charge. In this regard, the orientation of water dipoles can be inferred from their vibrational spectroscopic properties. The potential where dipoles change orientation is also related to the location of the pzfc [34.46, 163–165].

According to (34.13), at the pztc, adsorption charge compensates the free charge. If the pztc lies in the hydrogen region, $\Gamma_A = 0$, and therefore at the pztc

$$\sigma_M = F\Gamma_H \,. \qquad (34.16)$$

This means that free charge is positive at the pztc, and therefore the pzfc is located more negative than the pztc. The case of Pt(111) in $HClO_4$ is particularly interesting because, in this case, hydrogen and hydroxyl adsorption regions are separated. It is usually assumed that the region between them is purely capacitive. Therefore, in this potential region, free and total charge coincide; in consequence, the value of the free charge in this region is known. If the differential capacity of the electrode is also known, it can be combined with the known value of free charge in the capacitive region to calculate the free charge at any other potential. Two different approaches have been followed here. The more rigorous approach used a thermodynamic analysis based on the electrocapillary equation to separate total and free differential capacities from the dependence of the total charge with pH [34.104]. Such values of differential capacities can be combined with the known value of free charge at the double-layer region to locate the position of the pzfc [34.166]. However, the thermodynamic analysis that leads to the calculation of the differential capacity has only been performed in a narrow range of pH values. To extend the analysis to other pH values, an approximate approach has been followed consisting of the extrapolation of the charge in the double-layer region considering a constant double-layer differential capacity [34.102]. Interestingly, a constant value of the pzfc independent of pH was obtained with this approximate approach. Moreover, the study of Pt(111) in solutions of different pH demonstrated that, while in acid solution the pztc lies in the hydrogen region with the implication mentioned above, pzfc < pztc, for pH > 4 the pztc lies in the hydroxyl region and the pzfc > pztc. At pH 3, pzfc = pztc [34.103].

To conclude this section, we mention another approach that has proved very valuable in the investigation of the interfacial properties of single-crystal electrodes: the laser-induced temperature jump method. In this approach, pulsed laser irradiation is used to induce a sudden change in the temperature of the interphase. With the use of enough laser intensity, the temperature of the electrode surface can be increased by 10–20K in a few nanoseconds. By monitoring the change in the open-circuit potential during the decay of the temperature, information about the interphase can be obtained. Among the different contributions to the variation in the open-circuit potential with temperature, the most important is that due to the perturbation of the dipolar contribution from the orientation of the solvent. In this way, when free charge on the metal is positive, solvent dipoles will tend to orient with the negative end towards the metal, giving a negative contribution to the potential drop. Increasing the temperature will decrease the orientation of the dipoles, causing a decrease in this negative contribution, and therefore increasing the potential. The opposite is observed at negative charges. Thermodynamic arguments show that the thermal coefficient of the potential drop is related to the entropy of formation of the double layer [34.167–170]. A significant point is the potential where no net dipolar orientation is observed. This coincides with the potential of maximum entropy (pme) of double-layer formation and with a situation of zero change in the potential with the increase in temperature. This approach has been applied to study the interphase of mercury [34.171, 172], gold(111) [34.173], platinum basal planes [34.174], platinum stepped surfaces [34.175, 176], single-crystal electrodes modified with adatoms [34.177, 178] and single-crystal electrodes in ionic liquids [34.179, 180].

The resulting values of pme obtained for the three platinum basal planes are shown in comparison with the values of pztc in Fig. 34.15. For Pt(111), the pztc and pme nearly coincide. This is explained considering that, in this case, pztc lies in the double-layer region, and therefore pztc and pzfc are nearly identical. For Pt(100) and Pt(110), the pme is located at lower potentials than the pztc. This agrees with the argument that follows (34.16), and it shows that the pme can be taken as a good indicator of the position of the pzfc when this is located in a region where adsorption processes overlap with the purely capacitive charging of the double layer. Moreover, the pme of the three surfaces follows the order (111) > (100) > (110), which parallels the variation in the work function, again stressing the relationship between pme and pzfc.

34.9 Underpotential Deposition of Metals on Single-Crystal Electrodes

This was one of the first processes studied in detail on single-crystal electrodes. The general reaction for the deposition of a metal is given by

$$M^+ + e^- \rightleftharpoons M \qquad (34.17)$$

The equilibrium potential for this reaction is given by the thermodynamic Nernst equation, and at potentials more negative than this, bulk deposition of the metal occurs. However, it was found that the deposition of the first layer(s) of the metal onto a foreign substrate

$$S + M^+ + e^- \rightleftharpoons S{-}M \qquad (34.18)$$

can take place at potentials more positive than the equilibrium potential for the bulk deposition [34.181, 182].

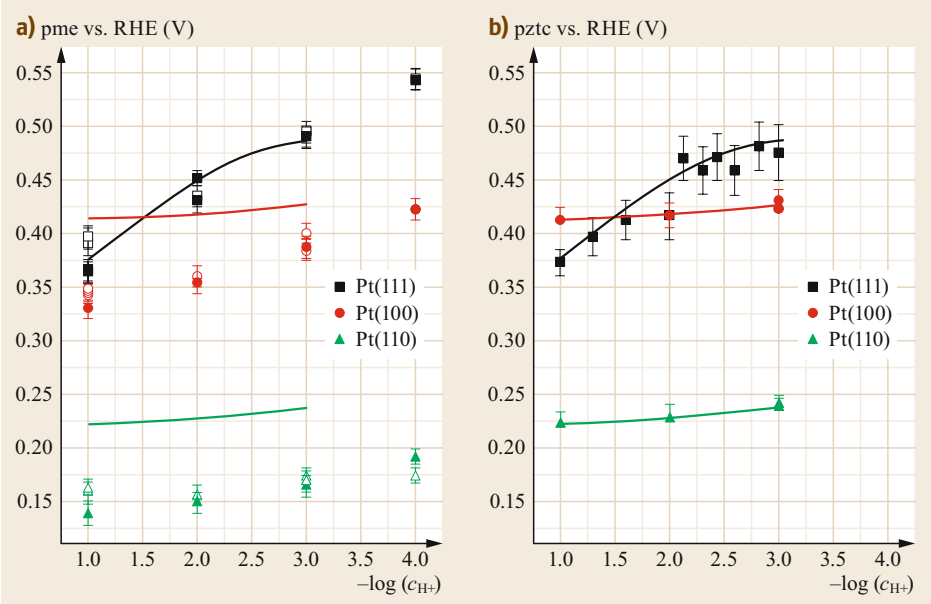

Fig. 34.15a,b Values of **(a)** uncorrected (*open symbols*) and corrected (*filled symbols*) pme values determined from the thermodiffusion potential, and **(b)** pztc values for Pt(111), Pt(100), and Pt(110) electrodes in $(0.1-x)$ M $KClO_4$ + x M $HClO_4$ solutions. *Lines* are drawn to indicate the tendencies of pztc values, and they are reproduced in **(a)** in order to facilitate the comparison with pme values. Reprinted with permission from [34.174]. Copyright (2019) American Chemical Society

For this reason, this phenomenon was then termed as underpotential deposition (UPD). The explanation for the *apparent violation* of the thermodynamic laws of the process lays in the different interaction of the metal with the substrate. The equilibrium potential for the bulk metal deposition corresponds to the deposition of new metal atoms onto a bulk material of the same chemical nature and therefore involves the formation of new metal–metal bonds. However, when the metal is deposited on a foreign substrate, the initial stages of the deposition are governed by the substrate–metal interactions [34.183]. If these interactions are stronger than the metal–metal interactions, the initial deposition stages will take place at potentials more positive than the bulk metal deposition, due to the favorable metal–substrate interaction. Thus, the UPD of metals is normally restricted to the deposition of the first (and sometime second) layer.

From the initial studies, it was found that the work function differences between the metal and the substrate could be used to rationalize this phenomenon [34.181]. Thus, the UPD occurs when the work function of the metal substrate is larger than that of the deposited metal. Moreover, the difference between the potential for the UPD process and the bulk deposition potential was essentially the same as the difference between work functions. Given that, the UPD process is clearly controlled by the surface properties and should be structure-sensitive, and for that reason, as soon as single-crystal electrodes were introduced in electrochemistry, many different systems were thoroughly studied. There are several reviews that cover the topic in detail [34.184–186]. To illustrate the behavior of this electrochemical process, the results of copper UPD on gold single-crystal electrodes will be reviewed. These results exemplify how the surface structure, electrode potential and electrolyte composition affect the deposition process.

The first studies with gold single-crystal electrodes revealed the important effect of the surface structure on the process. As shown in Fig. 34.16, the voltammetric profiles for the Cu UPD on Au(111), Au(100) and Au(110) electrodes in sulfuric acid solution are very different [34.187–189]. Although the onset potential for the process is similar for all three electrodes, the shape of the voltammogram is not the same. Moreover, for the Au(111) electrode, the process splits into two main peaks, whereas for Au(110) and Au(100) electrodes, only one broad peak (with several shoulders) is observed. The presence of sharp peaks in the Cu UPD process on Au(111) electrodes suggests the formation of ordered adlayers, since sharp peaks with narrow widths are normally associated to order-disorder phase transitions. For the three electrodes, the bulk deposition of Cu took place at potentials below 0.3 V, which agrees with the thermodynamic value for the onset of bulk Cu deposition.

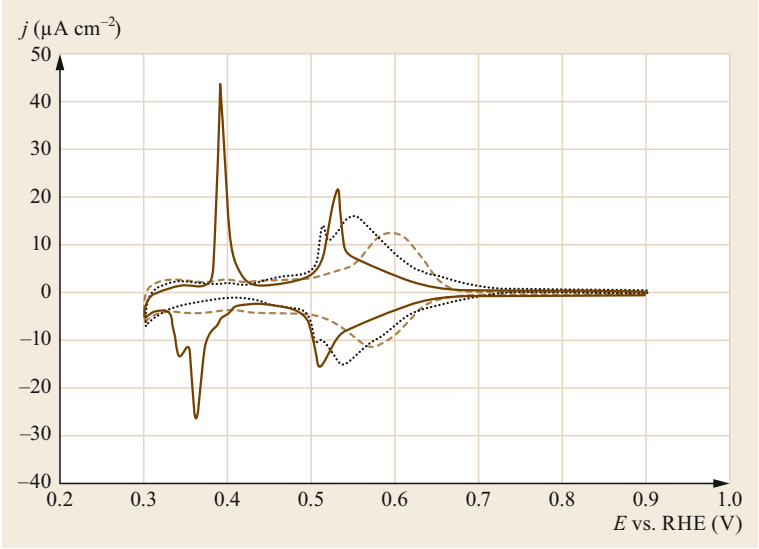

Fig. 34.16 Cu UPD on Au(111) (*solid line*), Au(110) (*dashed line*) and Au(100) (*dotted line*) in 0.05 M $H_2SO_4 + 10^{-3}$ M Cu^{2+}. Scan rate 5 mV s^{-1}

After the voltammetric profile for the process is recorded, normally, the first magnitude that is calculated is the charge associated to the deposition/dissolution process of Cu. Initially, it was supposed that charge processes that give rise to the voltammetric peaks correspond exclusively to the reduction of the Cu^{2+} ions. Thus, the charge measured in the deposition peak would give the Cu coverage. In the case of the Au(111) electrode, the charge measured was 450–460 μC cm^{-2} [34.190–194]. This value should be compared with the theoretical value for the deposition of a Cu atom per Au(111) surface atom in the unreconstructed surface (440 μC cm^{-2}) (see Table 34.1). The measured value is very close to the theoretical value, and thus it was supposed that the Cu layer formed a (1 × 1) isomorphic layer on the unreconstructed Au(111) surface. For the other two surfaces, the charge measurements also give values compatible with the formation of a (1 × 1) isomorphic layer.

It was soon confirmed that the UPD process was more complicated than this initial assignment of all measured charge to the Cu^{2+}/Cu redox process. It was already observed in the initial studies that there was an important dependence of the voltammetric profile on the anion present in solution (see Fig. 34.17 for the comparison when bromide is present in solution), a clear indication that the anion in solution plays a role in the whole deposition process. In the case of the sulfuric acid solution, the deposition process takes place on a surface which is partially covered by sulfate ions. Thus, Cu^{2+} ions, when deposited, should replace the sulfate ions and the sulfate coverage can change. The change in sulfate coverage on the surface also gives rise to a charge transfer, so that the measured charge in

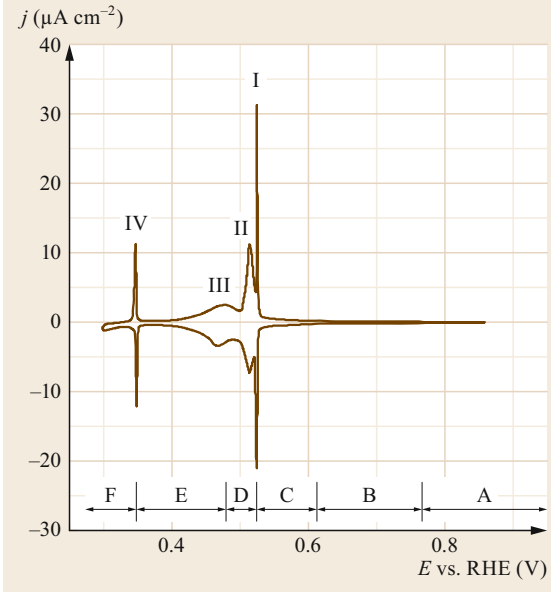

Fig. 34.17 Cu UPD on Au(111) in 0.1 M $HClO_4 + 1.0$ mM NaBr + 1.0 mM Cu^{2+}. Scan rate 1 mV s^{-1}

the voltammogram contains information not only from the Cu^{2+}/Cu redox process and on how the Cu coverage changes with electrode potential, but also on the change in the coverage of the surface-adsorbed anions. Two techniques were used to determine the coverage changes in sulfate anions and Cu with the potential during the UPD process: the electrochemical quartz crystal microbalance (EQCM) [34.190, 191] and chronoamperometry [34.192–194]. In the first one, mass changes during the deposition process are calculated using the

variation in the vibrational frequency of the quartz crystal on which the gold electrode is deposited. Those mass changes are then related to the measured charge, and Cu and sulfate coverage can be estimated. With the second technique, the effect of the anion and Cu^{2+} concentration on the measured charge for the process is evaluated using a thermodynamic approach, which allows the coverage of both species to be determined. Both techniques showed that the coverage of adsorbed sulfate on the electrode surface changed during the process. However, the final coverage of adsorbed sulfate at potentials close to the onset of bulk deposition was the same as that found on the bare Au(111) surface above 1.1 V (0.20) [34.192–194], which indicates that the net effect of the change in adsorbed sulfate coverage on the measured total charge was negligible, and a commensurate (1×1) Cu layer was formed on the electrode when the UPD process was completed. In fact, the surface structure for the adsorbed sulfate before and after the formation of the Cu adlayer was the same: the $(\sqrt{3} \times \sqrt{7})$R19.1° structure [34.195]. As mentioned above, the ordered adlayers formed by adsorbed sulfate on the (111) surfaces of Au [34.44, 45], Pd [34.69], Ir [34.71] and Pt [34.65, 66, 196] are identical. The only difference between the adlayers on the different metals is the potential at which this ordered adlayer is formed, which is related to the interaction of sulfate ions with the atoms on the surface. For Au, adsorption of sulfate starts at 0.5 V and the ordered adlayer is formed after the spike recorded at 1.1 V. Thus, the presence of the adsorbed sulfate adlayer on the Cu UPD layer indicates the large affinity of sulfate for the adsorption on Cu surfaces. Moreover, theoretical calculations indicate that the presence of adsorbed sulfate is the key element that stabilizes the (1×1) Cu adlayer [34.197].

The formation of a (1×1) Cu adlayer on the electrode prior to the bulk deposition (at 0.3 V) was first confirmed by UHV vacuum studies [34.198, 199]. If the electrode after the full deposition process was transferred to the UHV chamber, a (1×1) low-energy electron diffraction (LEED) pattern was found. Also, the presence of adsorbed sulfate was confirmed by Auger spectroscopy, although the coverage could not be accurately estimated due to the changes induced by the removal of the water layer, which is involved in the formation of the adlayer. The formation of the commensurate (1×1) layer was confirmed by in situ techniques, such as STM [34.200] and surface-extended x-ray absorption fine structure (SEXAFS) [34.201–203]. Moreover, the data obtained with SHG suggested that the Cu atoms were deposited on a 3-fold hollow site [34.204]. Additionally, detailed x-ray absorption near-edge structure (XANES) analysis revealed the polar character of the Cu–Au bond on the surface, in which Cu has charge deficiency [34.202, 205].

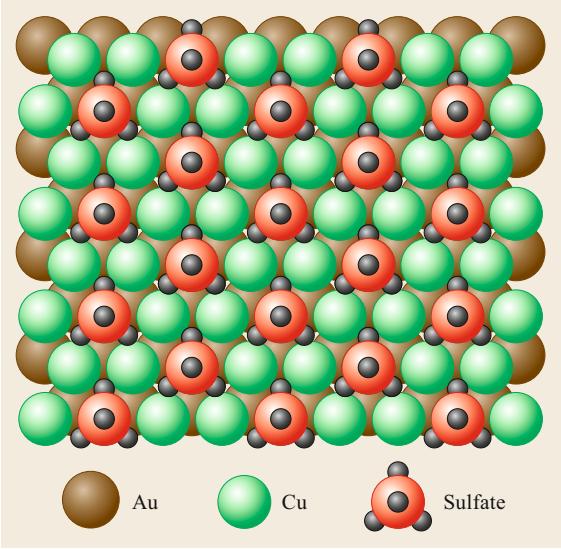

Fig. 34.18 Honeycomb structure formed for Cu UPD on Au(111) after the first deposition peak. Reprinted with permission from [34.206]. Copyright (2019) by the American Physical Society

For the adsorbed adlayer formed after the first UPD peak, that is at ca. 0.45 V, there was some initial controversy. Although charge measurements indicate that the Cu coverage was 2/3, the STM images revealed a $(\sqrt{3} \times \sqrt{3})$R30°, which is associated with a 1/3 coverage [34.190–194]. The detailed chronoamperometric analysis of the charge evolution with the concentration of sulfate and Cu^{2+} in solution also indicated that the Cu coverage was 2/3 and the sulfate coverage was 1/3 [34.192–194]. The correct interpretation of all this data was obtained after the in situ gracing incident X-ray analysis, which revealed a honeycomb structure (Fig. 34.18), in which the Cu coverage was 2/3, and that the sulfate was adsorbed in the center of the honeycomb structure [34.206, 207]. Thus, the structure observed with the STM images corresponds to the adsorbed sulfate on top of the Cu structure.

As mentioned above, the anion present in solution has a strong influence on the deposition process. This effect is clear, since the anion is adsorbed on top of the Cu layer, and therefore modifies the Cu–Au interaction. A clear example of this effect is the modification of the Cu UPD process on the Au(111) electrode in the presence of bromide anions [34.208, 209]. As can be seen in Fig. 34.17, the shape of the voltammogram is completely different from that observed in the presence of sulfate. Two sharp peaks can be easily distin-

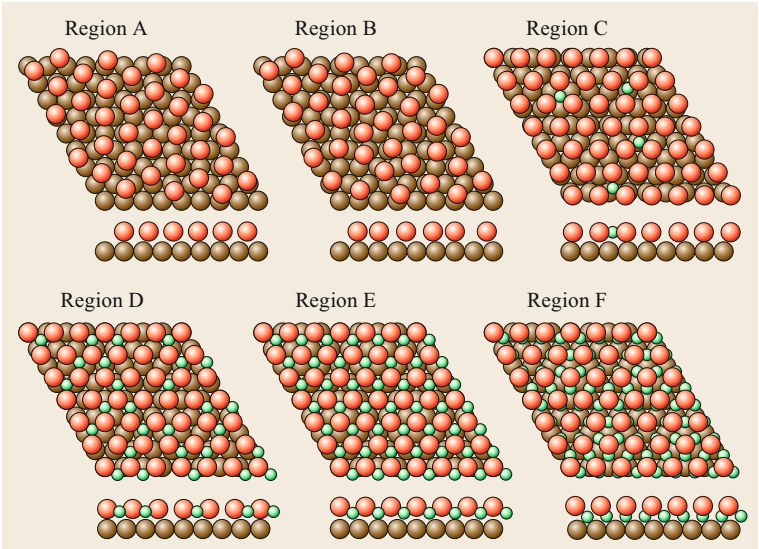

Fig. 34.19 Structures formed during the Cu UPD on Au(111) in 0.1 M $HClO_4$ + 1.0 mM NaBr + 1.0 mM Cu^{2+} in the different regions shown in Fig. 34.17 (Au atoms marked *brown*, Br atoms marked *red*, and Cu atoms marked *green*)

guished (peaks I and IV) and two additional shoulders (peaks II and III) appear around peak I. In situ detailed X-ray analysis of the process (both grazing incident X-ray diffraction and crystal truncation rods analysis) revealed changes in the structure as a function of potential and how bromide shaped the process [34.208, 209]. The analysis demonstrated that there were six different regions (as shown in Fig. 34.17) corresponding to six different adlayer structures (Fig. 34.19). At very positive potentials (region A), bromide is adsorbed on the electrode, forming a rotated and incommensurate hexagonal layer with a bromide coverage of 0.495 (defined as the number of bromide species per Pt surface atom). The structure of this adlayer is depicted in region A in Fig. 34.19 and is the same as the one observed in the absence of copper in solution [34.210, 211]. As the potential is decreased, bromide starts to desorb and the ordered adlayer disappears. However, as soon as the initial copper atoms are deposited at 0.56 V (onset of region C in Fig. 34.17), bromide anions are readsorbed, and a pseudo (4×4) incommensurate bromide structure with a coverage of 0.5 is observed (region C in Fig. 34.19). The fact that bromide is readsorbed as the potential is made more negative (which is an unexpected behavior) reveals the strong interaction between copper adatoms and bromide. As the deposition of Cu progresses, the bromide structure compresses until the commensurate (4×4) bromide structure is obtained (region D in Fig. 34.19) at the potential of peak I. The compression/relaxation and the changes in rotation angles with respect to the substrate orientation are processes that often occur in UPD reactions. From that point, the bromide adlayer does not change, but copper is progressively deposited between the Au(111) topmost layer and the bromide layer until the (1×1) Cu structure is formed after peak IV.

34.10 CO Adsorption and Oxidation on Platinum Single-Crystal Electrodes

CO is considered a model molecule to probe the properties of the surface. For this reason, it has been studied extensively in UHV. In electrochemical environments, it has also been used to determine the properties of the surface, as was shown previously in Sect. 34.6. In addition, its oxidative behavior is very important for practical purposes, especially in fuel cell technology. In this technology, hydrogen or other small molecules are oxidized in an electrochemical cell, generating electric energy. CO is present as a contaminant in the hydrogen sources coming from the reformate of organic molecules and, as will be shown in the next section, it also appears as an intermediate in the oxidation mechanism of small organic molecules such as formic acid, methanol or ethanol. For these reasons, its electrochemical behavior has also been widely studied in electrochemical environments.

The initial studies for adsorbed CO on platinum single-crystal electrodes attempted to determine the coverage, surface structure and adsorption modes of CO on the different surfaces. As expected, the CO adsorption/oxidation process was sensitive to the surface

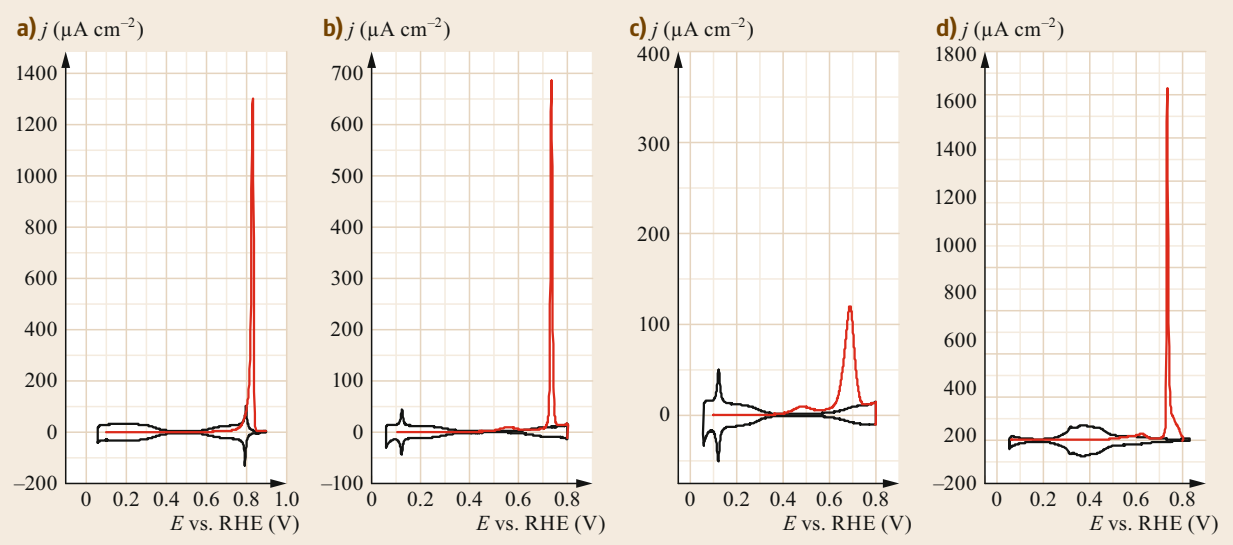

Fig. 34.20a–d Voltammetric profile for the oxidation of CO on the different Pt electrode surfaces in 0.1 M $HClO_4$: **(a)** Pt(111), **(b)** Pt(776), **(c)** Pt(554), and **(d)** Pt(100). Scan rate: 50 mV s^{-1}

structure of the electrode, as shown by the different peak position for the voltammetric profiles corresponding to the oxidation of an adsorbed CO layer on the different low-index electrodes (Fig. 34.20). From these profiles, the coverage could be easily determined by the charge integration of the oxidation peak obtained in the voltammetry [34.212, 213]. The major problem in this procedure was the determination of the correction to the charge to take into account the transferred charge in the processes taking place simultaneously with the CO oxidation process, that is, the changes in the surface charge and all the processes related to them [34.50]. Soon it was observed that there was a disagreement between the coverage determined depending on the corrections applied [34.214]. The discrepancies had arisen because there was still a lack of clarity regarding the nature of the so-called unusual adsorption states on the Pt(111). If the species responsible for these states was hydrogen adsorption on the surface, at 0.8 V, the potential at which CO is oxidized, hydrogen would be completely desorbed and thus no adsorption process would be contributing additional charge to the oxidation process. Thus, the only correction in the charge measurements would be that of the residual double-layer modification (which is a very minor correction). On the other hand, if anion adsorption processes give rise to these voltammetric features, anions should be readsorbed after CO adsorption, with the concomitant charge transfer. This would require a large correction of the measured charge. As mentioned in Sect. 34.6, the charge displacement measurements revealed that the unusual adsorption states correspond to an anion adsorption process with charge transfer involved in the process. Therefore, the calculation of coverage from CO oxidation should consider this value for a correct estimation of the coverage from the charge measurements. Following these arguments, the integrated charge for the whole oxidation process can be split into two contributions, the true faradaic charge for CO oxidation and the charge involved in the reorganization of the interphase

$$q_{\mathrm{raw}} = q_{\mathrm{far}} + q\left(E^{+}\right) - q^{\mathrm{CO}}\left(E^{-}\right), \qquad (34.19)$$

where q_{raw} is the total charge integrated in the voltammetric sweep, q_{far} is the true faradaic charge of CO oxidation, $q(E^{+})$ is the total charge at the higher limit of integration and $q^{\mathrm{CO}}(E^{-})$ is the charge present on the CO-covered surface at the lower limit of the sweep. The latter contribution is rather small, as discussed in Sect. 34.8; $q(E^{+})$ can be read in the curve relating total charge with potential, introduced in Sect. 34.8. This involves use of charge displacement data, as previously explained. It can be shown that, because the calculation of $q(E^{+})$ from CO displacement data also involves the term $q^{\mathrm{CO}}(E^{-})$ (34.14), both terms cancel, and the correction is sufficiently accurate without the need for any additional assumptions [34.215].

In parallel with the determination of the coverage, the surface structure of adsorbed CO was investigated. As in the case of the UPD, in the initial studies, the electrodes covered by CO were transferred from the electrochemical environment to the UHV chamber to examine the CO structure by LEED [34.216–218]. It

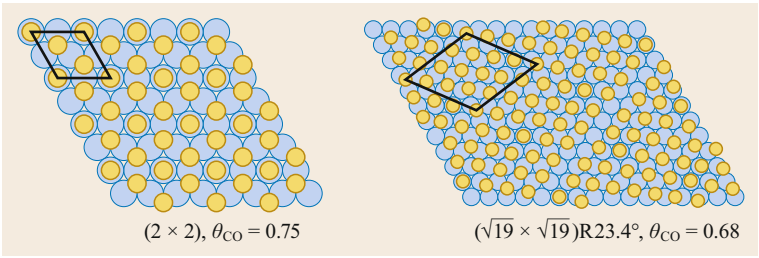

Fig. 34.21 CO structures on Pt(111) surfaces in acidic solutions

was revealed that the CO adlayers obtained in electrochemical environments have higher coverage than those obtained when CO was dosed under UHV conditions. This fact indicated the important role that water played in the adlayer formation process. As mentioned above, in the transfer process from the electrochemical environment to the UHV chamber, there is always the issue of the possible adlayer modification after the water removal process and the loss of potential control. To try to evaluate these possible modifications, the coverage values obtained from the measured structures and those obtained from the charge measurements were compared. Coverage values were in agreement after proper correction of the charge measurements [34.157, 214, 218, 219], which indicated that CO was not desorbed during the transfer process.

However, in situ STM measurements soon revealed the major effect of the electrode potential and water in the CO adlayer structure. STM images revealed three different adlayers formed on the Pt(111) surface, depending on the conditions [34.220, 221], which were later confirmed by grazing incidence x-ray diffraction (GIXD) measurements [34.47, 55–59]. These adlayers were different from those reported in the electrochemistry-UHV experiments, which, once more, highlighted the importance of the water on the adlayer. When CO was present in the solution, a (2×2)-3CO-$\theta_{CO} = 0.75$ structure was formed (Fig. 34.21A) [34.222–224]. This coverage value is significantly higher than that measured in UHV (0.5) [34.214]. The adlayer is only stable when CO is present in solution and requires long ordered domains, that is, the presence of steps reduces the stability of the adlayer [34.225]. A second structure was observed when CO was removed from solution after CO adsorption. In these conditions, the adlayer has a $(\sqrt{19}\times\sqrt{19})$R23.4°-$\theta_{CO} = 0.68$ structure (Fig. 34.21) [34.220, 226]. This coverage is in agreement with the values determined from the voltammetry [34.64, 214]. An additional structure is also formed at very mild dosing conditions: a $(\sqrt{7}\times\sqrt{7})$R19.1°-$\theta_{CO} = 0.56$ structure could also be detected [34.220].

The infrared spectra of the different electrode surfaces have also been studied in detail. In general, two peaks corresponding to the C–O stretching vibration appear on the spectra for the single-crystal electrodes, one at ca. 2030–2070 cm^{-1} for atop CO, and a second one at 1850–1870 cm^{-1} for bridge-bonded CO [34.227–229]. In the case of the (2×2)-3CO-$\theta_{CO} = 0.75$ structure on the Pt(111) electrode, the latter peak is replaced by one at ca. 1800 cm^{-1}, which corresponds to multicoordinated CO [34.220, 225, 230]. In all cases, the peak at 2030–2070 cm^{-1} is the dominant feature in the spectra. However, as shown in Fig. 34.21, atop CO is not the dominant species in the CO structures: for the (2×2)-3CO-$\theta_{CO} = 0.75$ adlayer, multicoordinated CO is more abundant than atop CO, whereas bridge-bonded CO predominates for the $(\sqrt{19}\times\sqrt{19})$R23.4°-$\theta_{CO} =$ 0.68 structure. Theoretical calculations demonstrate that there is a strong energy transfer from the band at low wave numbers to the band at high wave numbers, so that the atop CO band dominates in the spectra [34.220, 230].

In the case of the Fourier transform infrared (FTIR) spectra obtained in electrochemical conditions, the band position is dependent not only on the coverage and surface structure, but also on the electrode potential. Peak positions shift to higher wave number values as the potential is made more positive, in what is known as the Stark effect. The changes in the electronic populations of the metal or the electric field as the potential is made more positive have been postulated as the origin of the Stark effect. Detailed density functional theory (DFT) calculations have shown that field-dependent back-donation is the main contribution of the observed Stark effect on platinum metals [34.231–235].

The kinetics of the oxidation of CO has also been studied in detail, because of its technological relevance. CO oxidation follows a Langmuir–Hinselwood (L-H) mechanism in which adsorbed CO requires an adjacent adsorbed OH to produce CO_2 as a final product. Once the oxidation of the CO adlayer has started on specific sites, the progression of the oxidation can take place according to two different kinetic models. The first one is the nucleation and growth mechanism, in which the oxidation progresses from the initial points and extends over the whole surface, following the Bewick–Fleischmann–Thirsk model [34.236]. In the second kinetic model, the mobility of CO on the surface is fast, so that a random CO distribution is obtained through-

out the surface, following the mean-field L–H equation [34.237]. When the current transient at constant potential or the voltammetric peaks for CO oxidation in acidic media are analyzed, they are found to follow the mean-field equation [34.238–247], suggesting a large mobility of the adsorbed CO molecules on the surface.

On the other hand, in alkaline solutions, the situation is much more complex. Several differences between the behavior of the oxidation of CO adlayers in acidic and alkaline solutions are observed. In acidic solutions, the voltammetric oxidation shows only one peak for (111) stepped surfaces, whereas multiple peaks are observed in alkaline solutions [34.248–254]. The peaks are related to the presence of steps and kinks on the surface. Moreover, the transients do not follow the mean-field equation [34.249, 252]. Although other explanations have been proposed, the most probable justification of the differences is related to a change in the mobility of CO on the surface. In the case of alkaline solutions, the mobility of CO is negligible, explaining the peak multiplicity for stepped surfaces and the different kinetic equation for the current transients [34.252–254]. Additionally, the kinetic analysis of the transient has allowed us to calculate rates and to establish the role of steps and defects on the CO adlayer structure. It has been found that the presence of steps on the surface [34.245, 247] and of defects on the adlayer catalyze the oxidation [34.241, 254, 255]. The steps or defects in the adlayer are the initiation sites for the oxidation from where it propagates throughout the surface.

34.11 Oxidation of Small Organic Molecules on Platinum Single-Crystal Electrodes

The electrocatalysis of the oxidation of small organic molecules is a very relevant technological issue, since it is directly linked to the economic viability of fuel cell technology. Several molecules have been proposed for use in this technology, but the most studied are formic acid, methanol and ethanol. To reach the efficiency goals in the oxidation of these molecules for practical uses, the oxidation should take place at the lowest possible overpotential with the highest current, especially because the catalysis of these oxidation reactions requires the use of noble metals. In fact, platinum is the pure metal which shows the highest activity for these oxidation reactions. However, its activity is still low for practical uses, and thus, alloys and other modifications of platinum have been tested as electrocatalysts.

34.11.1 Formic Acid Oxidation Reaction

Formic acid oxidation reaction is the simplest reaction of these types of molecules. In the oxidation to CO_2, only two electrons are exchanged.

$$HCOOH \rightleftharpoons CO_2 + 2\,H^+ + 2\,e^- \qquad (34.20)$$

Apparently, the reaction is very straightforward, since only of two bonds, H–C and O–H bonds, need to be broken to form CO_2. The O–H bond breaking is involved in the acid base equilibria of formic acid, and thus, it is a facile reaction, whereas the cleavage of the H–C bond requires the use of a metal that has good dehydrogenation properties, such as platinum or palladium [34.256]. This reaction route would be the *natural* reaction mechanism for the oxidation. However, it was soon realized that the reaction was more complex than the simple mechanism proposed above. A blocking intermediate was soon detected when the reaction was studied on platinum [34.256], and identified using IR spectroscopy as adsorbed CO [34.257]. The formation of CO indicates that the reaction also proceeds with a different route in which H–C and C–OH bonds are broken. The formation of CO is also a major problem in the oxidation reaction, since it is strongly adsorbed, blocking the surface, and it is only oxidized at high potentials. Thus, the formic acid oxidation reaction involves a complex mechanism with two parallel pathways, one going through CO, which is regarded as a poisoning intermediate and the second one, going directly to CO_2 through an active intermediate, as shown in the following reaction scheme.

$$HCOOH \begin{cases} \nearrow \text{Active intermediate} \searrow \\ \searrow \text{CO} + H_2O \nearrow \end{cases} CO_2 + 2\,H^+ + 2\,e^- \qquad (34.21)$$

This parallel pathway mechanism was confirmed using isotopically labeled formic acid and differential electrochemical mass spectrometry (DEMS) [34.258]. In general, the electrocatalysis of this reaction seeks to increase the reaction rate through the active intermediate and the inhibition of CO formation.

In the initial studies of the reaction with single-crystal electrodes, it was soon realized that the reaction was very sensitive to the surface structure [34.259],

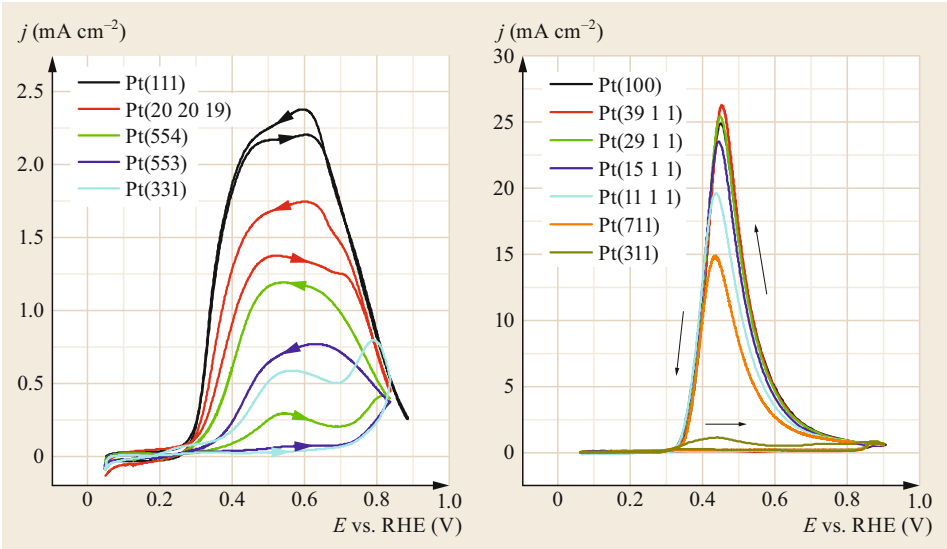

Fig. 34.22 Formic acid oxidation on different single-crystal electrodes in 0.1 M HCOOH + 0.5 M H_2SO_4. Scan rate: 50 mV s^{-1}

as shown in Fig. 34.22. Current densities and onset potentials for the oxidation depend on the surface structure. Moreover, the voltammetric profiles of the three basal planes show a distinct hysteresis between positive and negative scan directions. The formation of CO was responsible for this difference in the scan directions [34.260–262]. CO is formed at low potentials and partially blocks the electrode surface [34.261, 262]. The presence of CO leads to small currents in the positive scan direction. At 0.7 V, CO is oxidized, liberating surface sites, and when the scan is reversed, higher activity is recovered because no poison species are blocking the surface. Thus, CO formation rates can be qualitatively assessed by the difference in currents between the positive and negative scan directions, whereas the activity through the direct pathway can be estimated using the maximum currents in the negative scan direction. For both reaction paths, the activity order is Pt(100) > Pt(110) > Pt(111).

Once the qualitative behavior of the reaction was understood, the detailed mechanism for both reaction paths was studied. First, the variation in the solution composition allowed us to determine the active species in the reaction. For a fixed total formic acid/formate concentration, the maximum activity is proportional to the concentration of formate, indicating that solution formate is the active species in the reaction [34.263–265]. As any other anion, formate can be adsorbed on the surface, and in fact, it has been detected on polycrystalline electrodes [34.266–269] and on the Pt(111) electrode [34.270]. However, the actual role of this species has been subject to controversy. Recent studies suggest that this species is not the active intermediate, because, as DFT calculation indicates, the activation energy for the cleavage of the C–H bond in this configuration is very high [34.271]. However, the presence of adsorbed formate enables the adsorption of an additional formate species with a C–H bond directed toward the surface. In this configuration, the activation energy for the cleavage of the C–H bond is low [34.271], yielding CO_2 as final product. A kinetic model derived from this proposed mechanism was able to reproduce the voltammetric behavior, validating this reaction scheme [34.263, 270].

Reaction rates for both pathways were studied using pulsed voltammetry, which is a transient technique that allows one to determine the activity of the reaction in the absence of CO formation as well as the CO formation rate [34.272, 273]. When the different behavior of the electrodes was analyzed, it was clear that the Pt(111) surface has a very distinct behavior. First, it was shown that CO formation rate on this electrode was negligible [34.273–275]. In fact, the decoration of the Pt(111) and vicinal electrodes with adatoms indicated that the formation of CO on these surfaces was associated with the presence of steps or defects [34.261, 276–280]. Thus, on an ideal Pt(111) surface, the reaction would take place only through the active intermediate route and would produce no adsorbed CO, as happens in the UHV environment [34.281]. For the other surfaces, the formation of CO takes place in the potential region where the presence of adsorbed species on the surface is minimum, that is, in the vicinity of the potential of zero total charge [34.273–275]. The quantitative analysis of the data produced the following order in reactivity: (100) terraces ≈ steps on (100) terraces > (111) terraces > (110) steps on (111) terraces > (100) steps on (111) terraces.

34.11.2 Methanol and Ethanol Oxidation Reactions

Methanol and ethanol oxidation reactions have been widely studied for their possible use in fuel cells [34.282]. When compared with hydrogen or formic acid oxidation reactions, the other proposed fuels, their specific energies are significantly higher, which would favor their potential use. However, methanol and ethanol oxidation reactions are significantly more complex than the formic acid oxidation reaction, since 6 and 12 electrons are exchanged in the final oxidation to CO_2. The complexity of the reactions is due not only to the large number of electrons exchanged, but also to the type of bonds that have to be broken and formed in these reactions. For the methanol oxidation reaction, the mechanism involves dehydrogenation steps to gave rise to adsorbed CO. Although platinum is regarded as an excellent dehydrogenation catalyst, the oxidation of CO requires the transfer of an oxygen group (see Sect. 34.9), which is not favorable on platinum electrodes. For this reason, currents and onset potentials for the oxidation are higher. In the case of ethanol, the cleavage of the C–C bond should also take place in addition to the dehydrogenation processes, ending up with two adsorbed CO molecules, which should be oxidized to CO_2. If the C–C bond is not broken, acetic acid is formed, a molecule which is very difficult to oxidize. In general, the behavior of the different single-crystal electrodes for both reactions follows the same general scheme. Pt(111) is the less active electrode, but also has a lower onset potential for the reaction [34.283–286]. Moreover, this surface is inactive for the cleavage of the C–C bond [34.285, 286]. The addition of steps catalyzes the oxidation of these molecules, and higher currents are obtained, although at higher potentials due to the formation of CO [34.285–287]. In order to catalyze these reactions, Ru or Sn, which catalyze the oxidation of CO, or Rh for catalyzing the cleavage of the C–C bond, are generally used.

34.12 Concluding Remarks

Intense progress over the past few decades in the field of surface electrochemistry has brought it to the stage where attaining detailed control of surface structure at an atomic level becomes a reality. Such control enables the comprehension of catalytic processes with unprecedented detail. As already discussed, the electrocatalytic phenomena is intimately related to the existence of specific interaction between reactants and intermediates with the electrode surface. Attempting the study of such phenomena using complex polycrystalline surfaces would complicate enormously the interpretation of results. Conversely, the combination of methodologies that work with single-crystal electrodes with well-defined surfaces, and spectroscopic and microscopic techniques providing structural information, sometime at atomic-level resolution, has paved the way toward a situation where rational design of new catalytic materials can be based on deep comprehension of the processes taking place. In addition, the increasing power of computing capabilities experienced in recent years enables the rationalization of some experimental results from first-principles calculations. Future trends in this field should attempt exploiting even more the synergies between theory and experiments. In this regard, we stress how important it is for corroborating theoretical results to have access to high-quality experimental results under strictly controlled conditions.

Another question is how to bridge the gap between the knowledge acquired under such controlled conditions and the real situation under true applied conditions. Such distance can be decreased with the use of dispersed catalysts if the preparation of the catalysts is still done with careful control of experimental conditions. An example of this is the use of platinum and gold nanoparticles with preferential shapes, where the surface of the nanoparticles contains preferential surface sites similar to those of the different basal planes. While laboratory conditions in experiments with nanoparticles are still far from the real conditions of applied interest, particularly when it comes to purity of solutions employed, they can be taken as model systems closer to real applications.

In this review, we have given methodological clues to work with single-crystal electrodes of gold and platinum and to understand their electrochemical behavior. In particular, we showed how cyclic voltammetry can be used to characterize the structure of the single crystal with simple instrumentation. The importance of the charge separation to describe the interphase has been stressed, and the use of CO displacement has been described to obtain charge values for platinum electrodes. Finally, some important reactions in the field of surface electrochemistry and electrocatalysis have been reviewed, namely, underpotential deposition of metals, carbon monoxide oxidation and formic acid and methanol oxidation.

Future trends will most likely involve the use of increasingly complex surface composition involving al-

loys of several metals while maintaining comparable degree of control of the surface structure. Another trend in the field involves the use of nonaqueous solutions. In particular, in recent years, notable interest has arisen in the field of ionic liquids and their use in electrocatalysis. It is obvious that our comprehension of the interfacial properties in contact with such solvents is very far from the one achieved in water, so there is plenty of space for progress in this direction.

References

34.1 J.F. Li, Y.F. Huang, Y. Ding, Z.L. Yang, S.B. Li, X.S. Zhou, F.R. Fan, W. Zhang, Z.Y. Zhou, D.Y. Wu, B. Ren, Z.L. Wang, Z.Q. Tian: Shell-isolated nanoparticle-enhanced Raman spectroscopy, Nature **464**, 392–395 (2010)

34.2 J.F. Li, J.R. Anema, T. Wandlowski, Z.Q. Tian: Dielectric shell isolated and graphene shell isolated nanoparticle enhanced Raman spectroscopies and their applications, Chem. Soc. Rev. **44**, 8399–8409 (2015)

34.3 J. Clavilier, R. Faure, G. Guinet, R. Durand: Preparation of monocrystalline Pt microelectrodes and electrochemical study of the plane surfaces cut in the direction of the {111} and {110} planes, J. Electroanal. Chem. Interfacial Electrochem. **107**, 205–209 (1980)

34.4 J. Clavilier: The role of anion on the electrochemical behaviour of a {111} platinum surface; an unusual splitting of the voltammogram in the hydrogen region, J. Electroanal. Chem. Interfacial Electrochem. **107**, 211–216 (1980)

34.5 J. Clavilier, D. Armand, S.G. Sun, M. Petit: Electrochemical adsorption behaviour of platinum stepped surfaces in sulphuric acid solutions, J. Electroanal. Chem. Interfacial Electrochem. **205**, 267–277 (1986)

34.6 N. Hoshi, K. Kagaya, Y. Hori: Voltammograms of the single-crystal electrodes of palladium in aqueous sulfuric acid electrolyte: Pd(S)-[*n*(111) × (111)] and Pd(S)-[*n*(100)×(111)], J. Electroanal. Chem. **485**, 55–60 (2000)

34.7 V. Climent, J.M. Feliu: Surface electrochemistry with Pt single-crystal electrodes. In: *Nanopatterned and Nanoparticle-Modified Electrodes*, Advances in Electrochemical Science and Engineering, Vol. 17, ed. by R.C. Alkire, P.N. Bartlett, J. Lipkowski (Wiley, New York 2017) pp. 1–57

34.8 C. Korzeniewski, V. Climent, J.M. Feliu: Electrochemistry at platinum single crystal electrodes. In: *Electroanalytical Chemistry. A Series of Advances. Vol. 24*, ed. by A.J. Bard, C. Zoski (CRC, Boca Raton 2012) pp. 75–169

34.9 B. Lang, R.W. Joyner, G.A. Somorjai: Low energy electron diffraction studies of high index crystal surfaces of platinum, Surf. Sci. **30**, 440–453 (1972)

34.10 A.T. Hubbard, R.M. Ishikawa, J. Katekaru: Study of platinum electrodes by means of electrochemistry and low energy electron diffraction: Part II. Comparison of electrochemical activity of Pt(100) and Pt(111) surfaces, J. Electroanal. Chem. Interfacial Electrochem. **86**, 271–288 (1978)

34.11 P.N. Ross Jr.: Structure sensitivity in the electrocatalytic properties of Pt: I. Hydrogen adsorption on low index single crystal and the role of steps, J. Electrochem. Soc. **126**, 67–77 (1979)

34.12 P.N. Ross Jr.: Hydrogen chemisorption on Pt single crystal surfaces in acidic solutions, Surf. Sci. **102**, 463–485 (1981)

34.13 E. Yeager, W.E. O'Grady, M.Y.C. Woo, P. Hagans: Hydrogen adsorption on single-crystal platinum, J. Electrochem. Soc. **125**, 348–349 (1978)

34.14 W.E. O'Grady, M.Y.C. Woo, P.L. Hagans, E. Yeager: Electrode surface studies by Leed-Auger, J. Vac. Sci. Technol. **14**, 365–368 (1977)

34.15 E. Yeager, A. Homa, B.D. Cahan, D. Scherson: Spectroscopic techniques for the study of solid-liquid interfaces, J. Vac. Sci. Technol. **20**, 628–633 (1982)

34.16 A.S. Homa, E. Yeager, B.D. Cahan: LEED-AES thin layer electrochemical studies of hydrogen adsorption on platinum single crystals, J. Electroanal. Chem. Interfacial Electrochem. **150**, 181–192 (1983)

34.17 F.T. Wagner, P.N. Ross Jr.: LEED analysis of electrode surfaces: Structural effects of potentiodynamic cycling on Pt single crystals, J. Electroanal. Chem. Interfacial Electrochem. **150**, 141–164 (1983)

34.18 J. Clavilier: Flame-annealing and cleaning technique. In: *Interfacial Electrochemistry. Theory, Experiment, and Applications*, ed. by A. Wieckowski (Marcel Dekker, New York, Basel 1999) pp. 231–248

34.19 J. Clavilier, R. Durand, G. Guinet, R. Faure: Electrochemical adsorption behaviour of Pt(100) in sulphuric acid solution, J. Electroanal. Chem. Interfacial Electrochem. **127**, 281–287 (1981)

34.20 J. Clavilier, D. Armand, B.L. Wu: Electrochemical study of the initial surface condition of platinum surfaces with (100) and (111) orientations, J. Electroanal. Chem. Interfacial Electrochem. **135**, 159–166 (1982)

34.21 J. Clavilier, A. Rodes, K. El Achi, M.A. Zamakhchari: Electrochemistry at platinum single-crystal surfaces in acidic media: Hydrogen and oxygen-adsorption, J. Chim. Phys. Physicochim. Biol. **88**, 1291–1337 (1991)

34.22 D. Aberdam, R. Durand, R. Faure, F. El-Omar: Structural changes of a Pt(111) electrode induced by electrosorption of oxygen in acidic solutions: A coupled voltammetry, LEED and AES study, Surf. Sci. **171**, 303–330 (1986)

34.23 J. Clavilier, K. El Achi, M. Petit, A. Rodes, M.A. Zamakhchari: Electrochemical monitoring of the thermal reordering of platinum single-crystal surfaces after metallographic polishing from the

early stage to the equilibrium surfaces, J. Electroanal. Chem. **295**, 333–356 (1990)
34.24 L.A. Kibler, A. Cuesta, M. Kleinert, D.M. Kolb: In-situ stm characterisation of the surface morphology of platinum single crystal electrodes as a function of their preparation, J. Electroanal. Chem. **484**, 73–82 (2000)
34.25 A.V. Rudnev, T. Wandlowski: An influence of pretreatment conditions on surface structure and reactivity of Pt(100) towards CO oxidation reaction, Russ. J. Electrochem. **48**, 259–270 (2012)
34.26 J.M. Feliu, A. Rodes, J.M. Orts, J. Clavilier: The problem of surface order of Pt single-crystals in electrochemistry, Pol. J. Chem. **68**, 1575–1595 (1994)
34.27 E. Herrero, J.M. Orts, A. Aldaz, J.M. Feliu: Scanning tunneling microscopy and electrochemical study of the surface structure of Pt(10,10,9) and Pt(11,10,10) electrodes prepared under different cooling conditions, Surf. Sci. **440**, 259–270 (1999)
34.28 D. Dickertmann, F.D. Koppitz, J.W. Schultze: A method for elimination of side effects on electrochemical measurements of single crystals. Additional test of the adsorption systems silver-lead ion and gold-cupric ion, Electrochim. Acta **21**, 967–971 (1976)
34.29 A.J. Bard, L.R. Faulkner: *Electrochemical Methods. Fundamental and Applications* (Wiley, New York 2001)
34.30 R.G. Compton, C.E. Banks: *Understanding Voltammetry* (World Scientific, Singapore 2007)
34.31 V. Climent, J.M. Feliu: Cyclic voltammetry. In: *Reference Module in Chemistry, Molecular Sciences and Chemical Engineering*, ed. by K. Wandelt (Elsevier, Amsterdam 2015)
34.32 E. Gileadi, B.E. Conway: The behaviour of intermediates in electrochemical catalysis. In: *Modern Aspects of Electrochemistry, Vol. 3*, ed. by J. Bockris, B.E. Conway (Butterworth, London 1964) pp. 347–442
34.33 E. Gileadi: *Electrode Kinetics for Chemists* (Wiley-VCH, Weinheim 1993)
34.34 E. Laviron: General expression of the linear potential sweep voltammogram in the case of diffusionless electrochemical systems, J. Electroanal. Chem. Interfacial Electrochem. **101**, 19–28 (1979)
34.35 N. Garcia-Araez, J.J. Lukkien, M.T.M. Koper, J.M. Feliu: Competitive adsorption of hydrogen and bromide on Pt(100): Mean-field approximation vs. Monte Carlo simulations, J. Electroanal. Chem. **588**, 1–14 (2006)
34.36 A. Hamelin: Cyclic voltammetry at gold single-crystal surfaces. 2. Behaviour of high-index faces, J. Electroanal. Chem. Interfacial Electrochem. **407**, 13–21 (1996)
34.37 A. Hamelin: Cyclic voltammetry at gold single-crystal surfaces. 1. Behaviour at low-index faces, J. Electroanal. Chem. Interfacial Electrochem. **407**, 1–11 (1996)
34.38 A.F. Silva, A. Martins: Capacitive and voltammetric responses from stepped faces of gold. In: *Interfacial Electrochemistry*, ed. by A. Wieckowski (Marcel Dekker, New York 1999) pp. 449–461
34.39 X. Gao, M.J. Weaver: Nanoscale structural changes upon electro-oxidation of Au(111) as probed by potentiodynamic scanning tunneling microscopy, J. Electroanal. Chem. Interfacial Electrochem. **367**, 259–264 (1994)
34.40 I. Villegas, M.J. Weaver: Nature of the atomic-scale restructuring of Pt(100) electrode surfaces as evidenced by in-situ scanning-tunneling-microscopy, J. Electroanal. Chem. Interfacial Electrochem. **373**, 245–249 (1994)
34.41 D.M. Kolb, J. Schneider: Surface reconstuction in electrochemistry: Au(100)-(5×20), Au(111)-(1×23) and Au(110)-(1×2), Electrochim. Acta **31**, 929–936 (1986)
34.42 D.M. Kolb: *Surface Reconstruction at Metal-Electrolyte Interfaces* (Wiley-VCH, Weinheim 1993) pp. 65–102
34.43 D.M. Kolb: Reconstruction phenomena at metal-electrolyte interfaces, Prog. Surf. Sci. **51**, 109–173 (1996)
34.44 O.M. Magnussen, J. Hageböck, J. Hotlos, R.J. Behm: In situ scanning tunnelling microscopy observations of a disorder-order phase transition in hydrogensulfate adlayers on Au(111), Faraday Discuss. **94**, 329–338 (1992)
34.45 G.J. Edens, X. Gao, M.J. Weaver: The adsorption of sulfate on gold(111) in acidic aqueous media: Adlayer structural inferences from infrared spectroscopy and scanning tunneling microscopy, J. Electroanal. Chem. Interfacial Electrochem. **375**, 357–366 (1994)
34.46 T. Wandlowski, K. Ataka, S. Pronkin, D. Diesing: Surface enhanced infrared spectroscopy – Au(1 1 1-20 nm)/sulphuric acid – New aspects and challenges, Electrochim. Acta **49**, 1233–1247 (2004)
34.47 J. Lipkowski, Z.C. Shi, A.C. Chen, B. Pettinger, C. Bilger: Ionic adsorption at the Au(111) electrode, Electrochim. Acta **43**, 2875–2888 (1998)
34.48 H. Striegler, P. Skoluda, D.M. Kolb: On the stability of unreconstructed Au(100)-(1×1) at negative potentials in aqueous sulfate solution, J. Electroanal. Chem. **471**, 9–13 (1999)
34.49 D.R. Lide, H.P.R. Frederikse (Eds.): *CRC Handbook of Chemistry and Physics*, 79th edn. (CRC, Boca Raton 1998)
34.50 J. Clavilier, R. Albalat, R. Gómez, J.M. Orts, J.M. Feliu, A. Aldaz: Study of the charge displacement at constant potential during CO adsorption on Pt(110) and Pt(111) electrodes in contact with a perchloric acid solution, J. Electroanal. Chem. Interfacial Electrochem. **330**, 489–497 (1992)
34.51 J. Clavilier, J.M. Orts, R. Gómez, J.M. Feliu, A. Aldaz: On the nature of the charged species displaced by CO adsorption from platinum oriented electrodes in sulphuric acid solution. In: *Electrochemistry and Materials Science of Cathodic Hydrogen Absorption and Adsorption*, Physical Electrochemistry Division Proceedings, Vol. 94, ed. by B.E. Conway, G. Jerkiewicz (The Electrochemical Society, Pennington 1994) pp. 167–183

34.52 J.M. Feliu, J.M. Orts, R. Gómez, A. Aldaz, J. Clavilier: New information on the unusual adsorption states of Pt(111) in sulphuric acid solutions from potentiostatic adsorbate replacement by CO, J. Electroanal. Chem. Interfacial Electrochem. **372**, 265–268 (1994)

34.53 V. Climent, R. Gómez, J.M. Orts, A. Rodes, A. Aldaz, J.M. Feliu: Electrochemistry, spectroscopy and scanning tunneling microscopy images of small single-crystal electrodes. In: *Interfacial Electrochemistry*, ed. by A. Wieckowski (Marcel Dekker, New York 1999) pp. 463–475

34.54 K. Domke, E. Herrero, A. Rodes, J.M. Feliu: Determination of the potentials of zero total charge of Pt(100) stepped surfaces in the [01-1] zone. Effect of the step density and anion adsorption, J. Electroanal. Chem. **552**, 115–128 (2003)

34.55 F.T. Wagner, P.N. Ross: Long-range structural effects in the anomalous voltammetry on ultra-high vacuum prepared Pt(111), J. Electroanal. Chem. Interfacial Electrochem. **250**, 301–320 (1988)

34.56 P.N. Ross: The role of defects in the specific adsorption of anions on Pt(111), J. Chim. Phys. **88**, 1353–1380 (1991)

34.57 K.A. Jaaf-Golze, D.M. Kolb, D. Scherson: On the voltammetry of curves of Pt(111) in aqueous solutions, J. Electroanal. Chem. Interfacial Electrochem. **200**, 353–362 (1986)

34.58 J. Clavilier, R. Albalat, R. Gómez, J.M. Orts, J.M. Feliu: Displacement of adsorbed iodine on platinum single-crystal electrodes by irreversible adsorption of CO at controlled potential, J. Electroanal. Chem. Interfacial Electrochem. **360**, 325–335 (1993)

34.59 E. Herrero, J.M. Feliu, A. Wieckowski, J. Clavilier: The unusual adsorption states of Pt(111) electrodes studied by an iodine displacement method: Comparison with Au(111) electrodes, Surf. Sci. **325**, 131–138 (1995)

34.60 D. Strmcnik, D. Tripkovic, D. van der Vliet, V. Stamenkovic, N.M. Marković: Adsorption of hydrogen on Pt(111) and Pt(100) surfaces and its role in the HOR, Electrochem. Commun. **10**, 1602–1605 (2008)

34.61 J. Clavilier, K. El Achi, A. Rodes: In situ characterization of the Pt(S)-[n(111) × (111)] electrode surfaces using electrosorbed hydrogen for probing terrace an step sites, J. Electroanal. Chem. Interfacial Electrochem. **272**, 253–261 (1989)

34.62 A. Rodes, K. El Achi, M.A. Zamakhchari, J. Clavilier: Hydrogen probing of step and terrace sites on Pt(S)-[n(111) × (100)], J. Electroanal. Chem. Interfacial Electrochem. **284**, 245–253 (1990)

34.63 V. Climent, R. Gómez, J.M. Feliu: Effect of increasing amount of steps on the potential of zero total charge of Pt(111) electrodes, Electrochim. Acta **45**, 629–637 (1999)

34.64 R. Gómez, V. Climent, J.M. Feliu, M.J. Weaver: Dependence of the potential of zero charge of stepped platinum(111) electrodes on the oriented step-edge density: Electrochemical implications and comparison with work function behavior, J. Phys. Chem. B **104**, 597–605 (2000)

34.65 A.M. Funtikov, U. Linke, U. Stimming, R. Vogel: An in-situ STM study of anion adsorption on Pt(111) from sulfuric acid solutions, Surf. Sci. **324**, L343–L348 (1995)

34.66 A.M. Funtikov, U. Stimming, R. Vogel: Anion adsorption from sulfuric acid solutions on Pt(111) single crystal electrodes, J. Electroanal. Chem. **428**, 147–153 (1997)

34.67 B. Braunschweig, W. Daum: Superstructures and order/disorder transition of sulfate adlayers on Pt(111) in sulfuric acid solution, Langmuir **25**, 11112–11120 (2009)

34.68 Y.G. Kim, J.B. Soriaga, G. Vigh, M.P. Soriaga: Atom-resolved EC-STM studies of anion adsorption at well-defined surfaces: Pd(111) in sulfuric acid solution, J. Colloid Interface Sci. **227**, 505–509 (2000)

34.69 L.J. Wan, T. Suzuki, K. Sashikata, J. Okada, J. Inukai, K. Itaya: In situ scanning tunneling microscopy of adsorbed sulfate on well-defined Pd(111) in sulfuric acid solution, J. Electroanal. Chem. **484**, 189–193 (2000)

34.70 L.J. Wan, S.L. Yau, K. Itaya: Atomic-structure of adsorbed sulfate on Rh(111) in sulfuric-acid-solution, J. Phys. Chem. **99**, 9507–9513 (1995)

34.71 L.J. Wan, M. Hara, J. Inukai, K. Itaya: In-situ scanning tunneling microscopy of well-defined Ir(111) surface: High-resolution imaging of adsorbed sulfate, J. Phys. Chem. B **103**, 6978–6983 (1999)

34.72 M. Wilms, P. Broekmann, C. Stuhlmann, K. Wandelt: In-situ STM investigation of adsorbate structures on Cu(111) in sulfuric acid electrolyte, Surf. Sci. **416**, 121–140 (1998)

34.73 Y. Shingaya, M. Ito: Interconversion of a bisulfate anion into a sulfuric acid molecule on a Pt(111) electrode in a 0.5 M H_2SO_4 solution, Chem. Phys. Lett. **256**, 438–444 (1996)

34.74 Y. Shingaya, M. Ito: Simulation of the electric double layers on Pt(111), Surf. Sci. **386**, 34–47 (1997)

34.75 P.W. Faguy, N.S. Marinković, R.R. Adžić: An *in situ* infrared study on the effect of pH on anion adsorption at Pt(111) electrodes from acid sulfate-solutions, Langmuir **12**, 243–247 (1996)

34.76 P.W. Faguy, N.S. Marinković, R.R. Adžić: Infrared spectroscopic analysis of anions adsorbed from bisulfate-containing solutions on Pt(111) electrodes, J. Electroanal. Chem. Interfacial Electrochem. **407**, 209–218 (1996)

34.77 F.C. Nart, T. Iwasita, M. Weber: Vibrational spectroscopy of adsorbed sulfate on Pt(111), Electrochim. Acta **39**, 961–968 (1994)

34.78 A. Lachenwitzer, N. Li, J. Lipkowski: Determination of the acid dissociation constant for bisulfate adsorbed at the Pt(111) electrode by subtractively normalized interfacial Fourier transform infrared spectroscopy, J. Electroanal. Chem. **532**, 85–98 (2002)

34.79 Z.F. Su, V. Climent, J. Leitch, V. Zamlynny, J.M. Feliu, J. Lipkowski: Quantitative SNIFTIRS studies of (bi)sulfate adsorption at the Pt(111) electrode sur-

face, Phys. Chem. Chem. Phys. **12**, 15231–15239 (2010)
34.80 N. Garcia-Araez, V. Climent, P. Rodriguez, J.M. Feliu: Elucidation of the chemical nature of adsorbed species for Pt(111) in H_2SO_4 solutions by thermodynamic analysis, Langmuir **26**, 12408–12417 (2010)
34.81 A. Berná, A. Rodes, J.M. Feliu: Oxalic acid adsorption and oxidation at platinum single crystal electrodes, J. Electroanal. Chem. **563**, 49–62 (2004)
34.82 J.M. Delgado, A. Berná, J.M. Orts, A. Rodes, J.M. Feliu: In situ infrared study of the adsorption and surface acid-base properties of the anions of dicarboxylic acids at gold single crystal and thin-film electrodes, J. Phys. Chem. C **111**, 9943–9952 (2007)
34.83 R. Martínez-Hincapié, A. Berná, A. Rodes, V. Climent, J.M. Feliu: Surface acid-base properties of anion-adsorbed species at Pt(111) electrode surfaces in contact with CO_2-containing perchloric acid solutions, J. Phys. Chem. C **120**, 16191–16199 (2016)
34.84 N. Garcia-Araez, V. Climent, P. Rodriguez, J.M. Feliu: Thermodynamic analysis of (bi)sulphate adsorption on a Pt(111) electrode as a function of pH, Electrochim. Acta **53**, 6793–6806 (2008)
34.85 V. Climent, N. Garcia-Araez, J.M. Feliu: Influence of alkali cations on the infrared spectra of adsorbed (bi)sulphate on Pt(111) electrodes, Electrochem. Commun. **8**, 1577–1582 (2006)
34.86 N. Garcia-Araez, V. Climent, P. Rodriguez, J.M. Feliu: Thermodynamic evidence for K^+-SO_4^{2-}-ion pair formation on Pt(111). New insight into cation specific adsorption, Phys. Chem. Chem. Phys. **12**, 12146–12152 (2010)
34.87 A. Björling, E. Ahlberg, J.M. Feliu: Kinetics of surface modification induced by submonolayer electrochemical oxygen adsorption on Pt(111), Electrochem. Commun. **12**, 359–361 (2010)
34.88 N. Garcia-Araez, V. Climent, E. Herrero, J. Feliu, J. Lipkowski: Thermodynamic studies of chloride adsorption at the Pt(111) electrode surface from 0.1 M $HClO_4$ solution, J. Electroanal. Chem. **576**, 33–41 (2005)
34.89 N. Garcia-Araez, V. Climent, E. Herrero, J. Feliu, J. Lipkowski: Thermodynamic studies of bromide adsorption at the Pt(111) electrode surface perchloric acid solutions: Comparison with other anions, J. Electroanal. Chem. **591**, 149–158 (2006)
34.90 J.M. Orts, R. Gómez, J.M. Feliu, A. Aldaz, J. Clavilier: Potentiostatic charge displacement by exchanging adsorbed species on Pt(111) electrodes—Acidic electrolytes with specific anion adsorption, Electrochim. Acta **39**, 1519–1524 (1994)
34.91 Y. Shingaya, M. Ito: Anion adsorption on clean or copper-modified Pt(111) and Rh(111) electrode surfaces studied by in-situ infrared reflection absorption spectroscopy, J. Electroanal. Chem. Interfacial Electrochem. **372**, 283–288 (1992)
34.92 Y. Sawatari, J. Inukai, M. Ito: The structure of bisulfate and perchlorate on a Pt(111) electrode surface studied by infrared spectroscopy and ab-initio molecular orbital calculation, J. Electron Spectrosc. Relat. Phenom. **64/65**, 515–522 (1993)
34.93 A. Berná, J.M. Feliu, L. Gancs, S. Mukerjee: Voltammetric characterization of Pt single crystal electrodes with basal orientations in trifluoromethanesulphonic acid, Electrochem. Commun. **10**, 1695–1698 (2008)
34.94 M.T.M. Koper, J.J. Lukkien: Modeling the butterfly: The voltammetry of $(\sqrt{3} \times \sqrt{3})R30°$ and $p(2 \times 2)$ overlayers on (111) electrodes, J. Electroanal. Chem. **485**, 161–165 (2000)
34.95 A. Berná, V. Climent, J.M. Feliu: New understanding of the nature of OH adsorption on Pt(111) electrodes, Electrochem. Commun. **9**, 2789–2794 (2007)
34.96 M. Wakisaka, H. Suzuki, S. Mitsui, H. Uchida, M. Watanabe: Identification and quantification of oxygen species adsorbed on Pt(111) single-crystal and polycrystalline Pt electrodes by photoelectron spectroscopy, Langmuir **25**, 1897–1900 (2009)
34.97 M. Wakisaka, Y. Udagawa, H. Suzuki, H. Uchida, M. Watanabe: Structural effects on the surface oxidation processes at Pt single-crystal electrodes studied by x-ray photoelectron spectroscopy, Energy Environ. Sci. **4**, 1662–1666 (2011)
34.98 A.M. Gomez-Marin, J.M. Feliu: Pt(111) surface disorder kinetics in perchloric acid solutions and the influence of specific anion adsorption, Electrochim. Acta **82**, 558–569 (2012)
34.99 F.C. Nart, T. Iwasita, M. Weber: In-situ FTIR study on the adsorption of phosphate species on well-ordered Pt(111) single crystal surfaces, Ber. Bunsenges. Phys. Chem. **97**, 737–738 (1993)
34.100 M. Weber, F.C. Nart, I.R. de Moraes, T. Iwasita: Adsorption of phosphate species on Pt(111) and Pt(100) as studied by in situ FTIR spectroscopy, J. Phys. Chem. **100**, 19933–19938 (1996)
34.101 J.M. Feliu, M.J. Valls, A. Aldaz, M.A. Climent, J. Clavilier: Alkali-metal cations and pH effects on a splitting of the unusual adsorption states of Pt(111) voltammograms in phosphate buffered solutions, J. Electroanal. Chem. Interfacial Electrochem. **345**, 475–481 (1993)
34.102 R. Rizo, E. Sitta, E. Herrero, V. Climent, J.M. Feliu: Towards the understanding of the interfacial pH scale at Pt(111) electrodes, Electrochim. Acta **162**, 138–145 (2015)
34.103 R. Martínez-Hincapié, P. Sebastián-Pascual, V. Climent, J.M. Feliu: Exploring the interfacial neutral pH region of Pt(111) electrodes, Electrochem. Commun. **58**, 62–64 (2015)
34.104 N. Garcia-Araez, V. Climent, E. Herrero, J.M. Feliu, J. Lipkowski: Thermodynamic approach to the double layer capacity of a Pt(111) electrode in perchloric acid solutions, Electrochim. Acta **51**, 3787–3793 (2006)
34.105 T. Pajkossy, D.M. Kolb: On the origin of the double layer capacitance maximum of Pt(111) single crystal electrodes, Electrochem. Commun. **5**, 283–285 (2003)

34.106 S. Hagstrom, H.B. Lyon, G.A. Somorjai: Surface structures on the clean platinum (100) surface, Phys. Rev. Lett. **15**, 491–493 (1965)

34.107 P. Heilmann, K. Heinz, K. Müller: The superstructures of the clean Pt(100) and Ir(100) surfaces, Surf. Sci. **83**, 487–497 (1979)

34.108 M.A. Van Hove, R.J. Koestner, P.C. Stair, J.P. Bibérian, L.L. Kesmodel, I. Bartoš, G.A. Somorjai: The surface reconstructions of the (100) crystal faces of iridium, platinum, and gold: I. Experimental observations and possible structural models, Surf. Sci. **103**, 189–217 (1981)

34.109 H.B. Nielsen, D.L. Adams: The effect of hydrogen adsorption at low temperatures on the structure of the reconstructed phases of the Pt(100) surface, studied by LEED, Surf. Sci. **97**, L351–L356 (1980)

34.110 M.A. Barteau, E.I. Ko, R.J. Madix: The adsorption of CO, O_2 and H_2 on Pt(100)-(5 × 20), Surf. Sci. **102**, 99–117 (1981)

34.111 J. Radnik, F. Gitmans, B. Pennemann, K. Oster, K. Wandelt: Adsorbate-induced structure transitions at the reconstructed Pt(100) surface, Surf. Sci. **287/288**, 330–335 (1993)

34.112 H.P. Bonzel, G. Broden, G. Pirug: Structure sensitivity of NO adsorption on a smooth and stepped Pt(100) surface, J. Catal. **53**, 96–105 (1978)

34.113 P. Gardner, M. Tüshaus, A.M. Bradshaw: The lifting of the Pt(100) surface reconstruction by NO adsorption, Vacuum **41**, 304–306 (1990)

34.114 M.S. Zei, N. Batina, D.M. Kolb: On the stability of reconstructed Pt(100) in an electrochemical cell: An ex-situ LEED/RHEED and in-situ STM study, Surf. Sci. Lett. **306**, L519–L528 (1994)

34.115 K. Wu, M.S. Zei: Electrochemical behavior and structural changes of a reconstructed Pt(100) electrode in sulfuric acid: A comparison with Pt(100)-(1 × 1), Surf. Sci. **415**, 212–226 (1998)

34.116 I.M. Tidswell, N.M. Marković, P.N. Ross: Potential dependent surface relaxation of the Pt(100)/electrolyte interface, Phys. Rev. Lett. **71**, 1601–1604 (1993)

34.117 A. Al-Akl, G.A. Attard, R. Price, B. Timothy: Voltammetric and UHV characterization of the (1 × 1) and reconstructed hex-R0.7° phases of Pt(100), J. Electroanal. Chem. **467**, 60–66 (1999)

34.118 K. Sashikata, T. Sugata, M. Sugimasa, K. Itaya: In-situ scanning-tunneling-microscopy observation of a porphyrin adlayer on an iodine-modified Pt(100) electrode, Langmuir **14**, 2896–2902 (1998)

34.119 J. Clavilier, J.M. Feliu, A. Fernandez-Vega, A. Aldaz: Electrochemical-behavior of irreversibly adsorbed bismuth on Pt(100) with different degrees of crystalline surface order, J. Electroanal. Chem. Interfacial Electrochem. **269**, 175–189 (1989)

34.120 N. Furuya, M. Ichinose, M. Shibata: Structural changes at the Pt(100) surface with a great number of potential cycles, J. Electroanal. Chem. **460**, 251–253 (1999)

34.121 V. Climent, R. Gómez, J.M. Orts, J.M. Feliu: Thermodynamic analysis of the temperature dependence of OH adsorption on Pt(111) and Pt(100) electrodes in acidic media in the absence of specific anion adsorption, J. Phys. Chem. B **110**, 11344–11351 (2006)

34.122 R.M. Arán-Ais, M.C. Figueiredo, F.J. Vidal-Iglesias, V. Climent, E. Herrero, J.M. Feliu: On the behavior of the Pt(100) and vicinal surfaces in alkaline media, Electrochim. Acta **58**, 184–192 (2011)

34.123 S. Titmuss, D. Wander, D.A. King: Reconstruction of clean and adsorbate-covered metal surfaces, Chem. Rev. **96**, 1291–1305 (1996)

34.124 J. Kuntze, M. Huck, T. Rauch, J. Bomermann, S. Speller, W. Heiland: The Pt(110) surface studied by STM and RHEED, Surf. Sci. **355**, L300–L304 (1996)

34.125 S. Speller, J. Kuntze, T. Rauch, J. Bomermann, M. Huck, M. Aschoff, W. Heiland: The (1 × 2) and (1 × 4) structure on clean Pt(110) studied by STM, AES and LEED, Surf. Sci. **366**, 251–259 (1996)

34.126 T. Gritsch, D. Coulman, R.J. Behm, G. Ertl: Mechanism of the CO-induced 1 × 2->1 × 1 structural transformation of Pt(110), Phys. Rev. Lett. **63**, 1086–1089 (1989)

34.127 R.E. von Glan, U. Korte: The NO-induced (1 × 2)->(1 × 1) structural transition of Pt(110): A quantitative RHEED investigation, Surf. Sci. **375**, 353–366 (1997)

34.128 T. Gritsch, D. Coulman, R.J. Behm, G. Ertl: A scanning tunneling microscopy investigation of the 1 × 2<->1 × 1 structural transformation of the Pt(110) surface, Appl. Phys. A **49**, 403–406 (1989)

34.129 R. Michaelis, D.M. Kolb: Stability and electrochemical properties of reconstructed Pt(110), J. Electroanal. Chem. Interfacial Electrochem. **328**, 341–348 (1992)

34.130 G.A. Beitel, O.M. Magnussen, R.J. Behm: Atomic structure of clean and Cu covered Pt(110) electrodes, Surf. Sci. **336**, 19–26 (1995)

34.131 A.M. Bittner, J. Wintterlin, G. Ertl: Effects of iodine coating and desorption on the reconstruction of a Pt(110) electrode – A scanning-tunneling-microscopy study, J. Electroanal. Chem. Interfacial Electrochem. **388**, 225–231 (1995)

34.132 W.L. Desimone, J.J. Breen: Structures of iodine on Pt(110) single-crystal electrode surfaces, Langmuir **11**, 4428–4432 (1995)

34.133 C.A. Lucas, N.M. Marković, P.N. Ross: Surface structure and relaxation at the Pt(110)/electrolyte interface, Phys. Rev. Lett. **77**, 4922–4925 (1996)

34.134 N.M. Marković, B.N. Grgur, C.A. Lucas, P.N. Ross: Surface electrochemistry of CO on Pt(110)-(1 × 2) and Pt(110)-(1 × 1) surfaces, Surf. Sci. **384**, L805–L814 (1997)

34.135 G.A. Attard, A. Brew: Cyclic voltammetry and oxygen reduction activity of the Pt{1 1 0}-(1 × 1) surface, J. Electroanal. Chem. **747**, 123–129 (2015)

34.136 J. Souza-Garcia, V. Climent, J.M. Feliu: Voltammetric characterization of stepped platinum single crystal surfaces vicinal to the (110) pole, Electrochem. Commun. **11**, 1515–1518 (2009)

34.137 J. Clavilier, K. El Achi, A. Rodes: In situ probing of step and terrace sites on Pt(S)-*n*(111) × (111) electrodes, Chem. Phys. **141**, 1–14 (1990)

34.138 G.A. Attard, O. Hazzazi, P.B. Wells, V. Climent, E. Herrero, J.M. Feliu: On the global and local values of the potential of zero total charge at well-defined platinum surfaces: Stepped and adatom modified surfaces, J. Electroanal. Chem. **568**, 329–342 (2004)

34.139 J.M. Feliu, E. Herrero, V. Climent: Electrocatalytic properties of stepped surfaces. In: *Catalysis in Electrochemistry*, ed. by E. Santos, W. Schmickler (Wiley, Hoboken 2011) pp. 127–163

34.140 N. Garcia-Araez, V. Climent, E. Herrero, J.M. Feliu: On the electrochemical behavior of the Pt(100) vicinal surfaces in bromide solutions, Surf. Sci. **560**, 269–284 (2004)

34.141 A.N. Frumkin, O.A. Petrii, B.B. Damaskin: *Potential of Zero Charge*, Vol. 1 (Plenum, New York 1980) pp. 221–289

34.142 D.C. Grahame: The electrical double layer and the theory of electrocapillarity, Chem. Rev. **41**, 441–501 (1947)

34.143 A. Hamelin: Double layer properties at sp and sd metal single-crystal electrodes. In: *Modern Aspects of Electrochemistry, Vol. 16* (Plenum, New York 1985) pp. 1–101

34.144 S. Trasatti: The electrode potential. In: *Comprehensive Treatise of Electrochemistry*, Vol. 1 (Springer, Boston 1980) pp. 45–81

34.145 S. Trasatti, L.M. Doubova: Crystal-face specificity of electrical double-layer parameters at metal/solution interfaces, J. Chem. Soc. Faraday Trans. **91**, 3311–3325 (1995)

34.146 S. Trasatti, E. Lust: The potential of zero charge. In: *Modern Aspects of Electrochemistry, Vol. 33*, ed. by R.E. White, J. Bockris, B.E. Conway (Kluwer, Plenum, New York 1999) pp. 1–215

34.147 J. Lecoeur, J. Andro, R. Parsons: The behaviour of water at stepped surfaces of single crystal gold electrodes, Surf. Sci. **114**, 320–330 (1982)

34.148 J. Lecoeur, J.P. Bellier, C. Koehler: Comparison of crystallographic anisotropy effects on potential of zero charge and electronic work function for gold {111}, {311}, {110} and {210} orientations, Electrochim. Acta **35**, 1383–1392 (1990)

34.149 J. Lecoeur, J.P. Bellier, C. Koehler: Study of the electrochemical behaviour of gold(111) vicinal faces situated on the [011] zone in aqueous solutions, J. Electroanal. Chem. Interfacial Electrochem. **337**, 197–216 (1992)

34.150 J. Lecoeur, J.P. Bellier, C. Koehler: Dipole effects of (100) monoatomic steps of gold $n(111) \times (100)$ vicinal faces in contact with aqueous solutions and under ultrahigh vacuum, J. Electroanal. Chem. Interfacial Electrochem. **375**, 117–122 (1994)

34.151 F. Silva, M.J. Sottomayor, A. Martins: The temperature coefficient of the potential of zero charge of stepped faces of gold in contact with aqueous perchloric acid solutions, J. Electroanal. Chem. Interfacial Electrochem. **360**, 199–210 (1993)

34.152 F. Silva, M.J. Sottomayor, A. Martins: Temperature coefficient of the potential of zero charge and entropies of formation for the interface of stepped faces of gold in contact with aqueous perchloric acid solutions, J. Chem. Soc. Faraday Trans. **92**, 3693–3699 (1996)

34.153 R. Smoluchowski: Anisotropy of the electronic work function of metals, Phys. Rev. **60**, 661–674 (1941)

34.154 A. Hamelin, L. Stoicoviciu, F. Silva: The temperature dependence of the double-layer properties of gold faces in perchloric acid solutions. Part I. The (210) gold face, J. Electroanal. Chem. Interfacial Electrochem. **229**, 107–124 (1987)

34.155 A. Hamelin, L. Stoicoviciu, F. Silva: The temperature dependence of the double-layer properties of gold faces in perchloric acid solutions. Part II. The (110) gold face, J. Electroanal. Chem. Interfacial Electrochem. **236**, 283–294 (1987)

34.156 F. Silva, M.J. Sottomayor, A. Hamelin, L. Stoicoviciu: The temperature dependence of double layer properties of gold faces in perchloric acid. Part III. The gold (100) face, J. Electroanal. Chem. Interfacial Electrochem. **295**, 301–316 (1990)

34.157 M.J. Weaver: Potentials of zero charge for platinum(111)-aqueous interfaces: A combined assessment from in-situ and ultrahigh-vacuum measurements, Langmuir **14**, 3932–3936 (1998)

34.158 A. Cuesta: Measurement of the surface charge density of CO-saturated Pt(111) electrodes as a function of potential: The potential of zero charge of Pt(111), Surf. Sci. **572**, 11–22 (2004)

34.159 V. Climent, R. Gómez, J.M. Orts, A. Aldaz, J.M. Feliu: The potential of zero total charge of single-crystal electrodes of platinum group metals. In: *The Electrochemical Double Layer*, Physical Electrochemistry Division Proceedings, Vol. 97, ed. by C. Korzeniewski, B.E. Conway (The Electrochemical Society, Pennington 1997) pp. 222–237

34.160 R. Gómez, J.M. Feliu, A. Aldaz, M.J. Weaver: Validity of double-layer charge-corrected voltammetry for assaying carbon monoxide coverages on ordered transition metals: Comparisons with adlayer structures in electrochemical and ultrahigh vacuum environments, Surf. Sci. **410**, 48–61 (1998)

34.161 E. Sibert, R. Faure, R. Durand: High frequency impedance measurements on Pt(111) in sulphuric and perchloric acids, J. Electroanal. Chem. **515**, 71–81 (2001)

34.162 E. Sibert, R. Faure, R. Durand: Pt(111) electrosorption impedance in mixed electrolyte, J. Electroanal. Chem. **528**, 39–45 (2002)

34.163 T. Iwasita, X.H. Xia: Adsorption of water at Pt(111) electrode in $HClO_4$ solutions. The potential of zero charge, J. Electroanal. Chem. Interfacial Electrochem. **411**, 95–102 (1996)

34.164 K. Ataka, T. Yotsuyanagi, M. Osawa: Potential-dependent reorientation of water molecules at an electrode/electrolyte interface studied by surface-enhanced infrared absorption spectroscopy, J. Phys. Chem. **100**, 10664–10672 (1996)

34.165 K.I. Ataka, M. Osawa: In situ infrared study of water-sulfate coadsorption on gold(111) in sulfuric acid solutions, Langmuir **14**, 951–959 (1998)

34.166 V. Climent, N. Garcia-Araez, E. Herrero, J.M. Feliu: The potential of zero total charge of platinum

single crystals. A local approach to stepped surfaces vicinal to Pt(111), Russ. J. Electrochem. **42**, 1145–1160 (2006)

34.167 J.A. Harrison, J.E.B. Randles, D.J. Schiffrin: Entropy of formation of the mercury–aqueous solution interface and the structure of the inner layer, J. Electroanal. Chem. Interfacial Electrochem. **48**, 359–381 (1973)

34.168 N. Garcia-Araez, V. Climent, J.M. Feliu: Determination of the entropy of formation of the Pt(111)|perchloric acid solution interface. Estimation of the entropy of adsorbed hydrogen and OH species, J. Solid State Electrochem. **12**, 387–398 (2008)

34.169 N. Garcia-Araez, V. Climent, J. Feliu: Separation of temperature effects on double-layer and charge-transfer processes for platinum|solution interphases. Entropy of formation of the double layer and absolute molar entropy of adsorbed hydrogen and OH on Pt(111), J. Phys. Chem. C **113**, 19913–19925 (2009)

34.170 N. Garcia-Araez, V. Climent, J. Feliu: 1 temperature effects on platinum single-crystal/aqueous solution interphases. Combining Gibbs thermodynamics with laser-pulsed experiments. In: *Interfacial Phenomena in Electrocatalysis*, Modern Aspects of Electrochemistry, Vol. 51, ed. by C.G. Vayenas (Springer, New York 2011) pp. 1–105

34.171 V.A. Benderskii, S.D. Babenko, A.G. Krivenko: Investigation of the charge relaxation in the double layer by a thermal jump, J. Electroanal. Chem. Interfacial Electrochem. **86**, 223–225 (1978)

34.172 V.A. Benderskii, G.I. Velichko: Temperature jump in electric double-layer study. Part I. Method of measurements, J. Electroanal. Chem. Interfacial Electrochem. **140**, 1–22 (1982)

34.173 V. Climent, B.A. Coles, R.G. Compton: Laser-induced potential transients on a Au(111) single-crystal electrode. Determination of the potential of maximum entropy of double layer formation, J. Phys. Chem. B **106**, 5258–5265 (2002)

34.174 N. Garcia-Araez, V. Climent, J. Feliu: Potential-dependent water orientation on Pt(111), Pt(100), and Pt(110), as inferred from laser-pulsed experiments. Electrostatic and chemical effects, J. Phys. Chem. C **113**, 9290–9304 (2009)

34.175 V. Climent, B.A. Coles, R.G. Compton, J.M. Feliu: Coulostatic potential transients induced by laser heating of platinum stepped electrodes: Influence of steps on the entropy of double layer formation, J. Electroanal. Chem. **561**, 157–165 (2004)

34.176 N. Garcia-Araez, V. Climent, J.M. Feliu: Potential-dependent water orientation on Pt(111) stepped surfaces from laser-pulsed experiments, Electrochim. Acta **54**, 966–977 (2009)

34.177 V. Climent, N. Garcia-Araez, R.G. Compton, J.M. Feliu: Effect of deposited bismuth on the potential of maximum entropy of Pt(111) single-crystal electrodes, J. Phys. Chem. B **110**, 21092–21100 (2006)

34.178 N. Garcia-Araez, V. Climent, J.M. Feliu: Evidence of water reorientation on model electrocatalytic surfaces from nanosecond-laser-pulsed experiments, J. Am. Chem. Soc. **130**, 3824–3833 (2008)

34.179 P. Sebastián, V. Climent, J.M. Feliu: Characterization of the interfaces between Au(hkl) single crystal basal plane electrodes and [Emmim][Tf_2N] ionic liquid, Electrochem. Commun. **62**, 44–47 (2016)

34.180 P. Sebastián, A.P. Sandoval, V. Climent, J.M. Feliu: Study of the interface Pt(111)/[Emmim][Ntf_2] using laser-induced temperature jump experiments, Electrochem. Commun. **55**, 39–42 (2015)

34.181 D.M. Kolb: Physical and electrochemical properties of metal monolayers on metallic substrates. In: *Advances in Electrochemistry and Electrochemical Engineering, Vol. 11*, ed. by H. Gerischer, C.W. Tobias (Wiley, New York 1978) pp. 125–271

34.182 W.J. Lorenz, H.D. Hermann, N. Wüthrich, F. Hilbert: The formation of monolayer metal films on electrodes, J. Electrochem. Soc. **121**, 1167–1177 (1974)

34.183 V. Sudha, M.V. Sangaranarayanan: Underpotential deposition of metals: Structural and thermodynamic considerations, J. Phys. Chem. B **106**, 2699–2707 (2002)

34.184 S. Szabo: Underpotential depostion of metals on foreing metal substrates, Int. Rev. Phys. Chem. **10**, 207–248 (1991)

34.185 E. Herrero, L.J. Buller, H.D. Abruña: Underpotential deposition at single crystal surfaces of Au, Pt, Ag and other materials, Chem. Rev. **101**, 1897–1930 (2001)

34.186 O.A. Oviedo, L. Reinaudi, S.G. García, E.P.M. Leiva: *Underpotential Deposition: From Fundamentals and Theory to Applications at the Nanoscale*, Monographs in Electrochemistry (Springer, Cham 2016)

34.187 M. Cappadonia, U. Linke, K.M. Robinson, J. Schmidberger, U. Stimming: Anion effects on the cyclic voltammetry of copper underpotential deposition on Au(100), J. Electroanal. Chem. Interfacial Electrochem. **405**, 227–232 (1996)

34.188 M.H. Hölzle, V. Zwing, D.M. Kolb: The influence of steps on the deposition of Cu onto Au(111), Electrochim. Acta **40**, 1237–1247 (1995)

34.189 F. Möller, O.M. Magnussen, R.J. Behm: CuCl adlayer formation and Cl induced surface alloying: An *in situ* STM study on Cu underpotential deposition on Au(110) electrode surfaces, Electrochim. Acta **40**, 1259–1265 (1995)

34.190 G.L. Borges, K.K. Kanazawa, J.G. Gordon, K. Ashley, J. Richer: An in-situ electrochemical quartz crystal microbalance study of the underpotential deposition of copper on Au(111) electrodes, J. Electroanal. Chem. Interfacial Electrochem. **364**, 281–284 (1994)

34.191 M. Watanabe, H. Uchida, M. Miura, N. Ikeda: Electrochemical quartz crystal microbalance study of copper ad-atoms on highly ordered Au(111) electrodes in sulfuric acid, J. Electroanal. Chem. Interfacial Electrochem. **384**, 191–195 (1995)

34.192 Z. Shi, J. Lipkowski: Coadsorption of Cu^{2+} and SO_4^{2-} at the Au(111) electrode, J. Electroanal.

Chem. Interfacial Electrochem. **365**, 303–309 (1994)
34.193 Z. Shi, J. Lipkowski: Investigations of SO_4^{2-} adsorption at the Au(111) electrode in the presence of underpotentially deposited copper adatoms, J. Electroanal. Chem. Interfacial Electrochem. **364**, 289–294 (1994)
34.194 Z. Shi, J. Lipkowski, M. Gamboa, P. Zelenay, A. Wieckowski: Investigations of SO_4^{2-} adsorption at the Au(111) electrode by chronocoulometry and radiochemistry, J. Electroanal. Chem. Interfacial Electrochem. **366**, 317–326 (1994)
34.195 B. Madry, K. Wandelt, M. Nowicki: Sulfate structures on copper deposits on Au(111): In situ STM investigations, Electrochim. Acta **217**, 249–261 (2016)
34.196 K. Itaya: In-situ scanning-tunneling-microscopy in electrolyte-solutions, Prog. Surf. Sci. **58**, 121–247 (1998)
34.197 P. Vélez, A. Cuesta, E.P.M. Leiva, V.A. Macagno: The underpotential deposition that should not be: Cu(1×1) on Au(111), Electrochem. Commun. **25**, 54–57 (2012)
34.198 Y. Nakai, M.S. Zei, D.M. Kolb, G. Lehmpfuhl: A LEED and RHEED investigation of Cu on Au(111) in the underpotential region, Ber. Bunsenges. Phys. Chem. **88**, 340–345 (1984)
34.199 M.S. Zei, G. Qiao, G. Lehmpfuhl, D.M. Kolb: The influence of anions on the structure of underpotentially deposited Cu on Au(111): A LEED, RHEED and AES study, Ber. Bunsenges. Phys. Chem. **91**, 349–353 (1987)
34.200 M.P. Green, K.J. Hanson: Copper adlayer formation on Au(111) from sulfuric acid electrolyte, J. Vac. Sci. Technol. A **10**, 3012–3018 (1992)
34.201 L. Blum, H.D. Abruña, J. White, M.J. Albarelli, J.G. Gordon, G.L. Borges, M.G. Samant, O.R. Melroy: Erratum: Study of underpotentially deposited copper on gold by fluorescence detected surface EXAFS [J. Chem. Phys. **85**, 6732–6738 (1986)], J. Chem. Phys. **86**, 6568–6568 (1987)
34.202 L. Blum, H.D. Abruña, J. White, J.G. Gordon, G.L. Borges, M.G. Samant, O.R. Melroy: Study of underpotentially deposited copper on gold by fluorescence detected surface EXAFS, J. Chem. Phys. **85**, 6732–6738 (1986)
34.203 O.R. Melroy, M.G. Samant, G.L. Borges, J.G. Gordon, L. Blum, J.H. White, M.J. Albarelli, M. McMillan, H.D. Abruña: In-plane structure of underpotentially deposited copper on gold(111) determined by surface EXAFS, Langmuir **4**, 728–732 (1988)
34.204 D.A. Koos, G.L. Richmond: Structure and stability of underpotentially deposited layers on gold(111) studied by optical second harmonic generation, J. Phys. Chem. **96**, 3770–3775 (1992)
34.205 A. Tadjeddine, D. Guay, M. Ladouceur, G. Tourillon: Electronic and structural characterization of underpotentially deposited submonolayers and monolayer of copper on gold (111) studied by *in situ* x-ray-absorption spectroscopy, Phys. Rev. Lett. **66**, 2235–2238 (1991)
34.206 M.F. Toney, J.N. Howard, J. Richer, G.L. Borges, J.G. Gordon, O.R. Melroy, D. Yee, L.B. Sorensen: Electrochemical deposition of copper on a gold electrode in sulfuric acid: Resolution of the interfacial structure, Phys. Rev. Lett. **75**, 4472–4475 (1995)
34.207 M. Nakamura, O. Endo, T. Ohta, M. Ito, Y. Yoda: Surface x-ray diffraction study of Cu UPD on Au(111) electrode in 0.5 M H_2SO_4 solution: The coadsorption structure of UPD copper, hydration water molecule and bisulfate anion on Au(111), Surf. Sci. **514**, 227–233 (2002)
34.208 E. Herrero, S. Glazier, H.D. Abruña: X-ray and electrochemical studies of Cu UPD on Au(111) single-crystal electrodes in the presence of bromide, J. Phys. Chem. B **102**, 9825–9833 (1998)
34.209 E. Herrero, S. Glazier, L.J. Buller, H.D. Abruña: X-ray and electrochemical studies of Cu UPD on single crystal electrodes in the presence of bromide: Comparison between Au(111) and Pt(111) electrodes, J. Electroanal. Chem. **461**, 121–130 (1999)
34.210 O.M. Magnussen, B.M. Ocko, R.R. Adzic, J.X. Wang: X-ray diffraction studies of ordered chloride and bromide monolayers at the Au(111)-solution interface, Phys. Rev. B **51**, 5510–5513 (1995)
34.211 O.M. Magnussen, B.M. Ocko, J.X. Wang, R.R. Adzic: In-situ x-ray diffraction and STM studies of bromide adsorption on Au(111) electrodes, J. Phys. Chem. **100**, 5500–5508 (1996)
34.212 J.M. Feliu, J.M. Orts, A. Fernández-Vega, A. Aldaz, J. Clavilier: Electrochemical studies in sulphuric acid solutions of adsorbed CO on Pt(111) electrodes, J. Electroanal. Chem. Interfacial Electrochem. **296**, 191–201 (1990)
34.213 J.M. Orts, A. Fernández-Vega, J.M. Feliu, A. Aldaz, J. Clavilier: Electrochemical-behaviour of CO layers formed by solution dosing at open circuit on Pt(111). Voltammetric determination of CO coverages at full hydrogen adsorption blocking in various acid-media, J. Electroanal. Chem. Interfacial Electrochem. **327**, 261–278 (1992)
34.214 M.J. Weaver, S.C. Chang, L.W.H. Leung, X. Jiang, M. Rubel, M. Szklarczyk, D. Zurawski, A. Wieckowski: Evaluation of absolute saturation coverages of carbon monoxide on ordered low-index platinum and rhodium electrodes, J. Electroanal. Chem. Interfacial Electrochem. **327**, 247–260 (1992)
34.215 V. Climent, N. Garcia-Araez, E. Herrero, J. Feliu: Potential of zero total charge of platinum single crystals: A local approach to stepped surfaces vicinal to Pt(111), Russ. J. Electrochem. **42**, 1145–1160 (2006)
34.216 D. Zurawski, M. Wasberg, A. Wieckowski: LEED and voltammetry of carbon monoxide electrosorbed on platinum(111), J. Phys. Chem. **94**, 2076–2082 (1990)
34.217 D. Zurawski, A. Wieckowski: Lateral modification and the organization of carbon monoxide-iodine mixed adlattices on platinum(111), Langmuir **8**, 2317–2323 (1992)
34.218 C.K. Rhee, J.M. Feliu, E. Herrero, P. Mrozek, A. Wieckowski: Auger electron spectroscopy, low-

energy electron diffraction, and electrochemistry of carbon monoxide on a platinum(100) electrode, J. Phys. Chem. **97**, 9730–9735 (1993)

34.219 M.J. Weaver, X.P. Gao: In-situ electrochemical surface science, Annu. Rev. Phys. Chem. **44**, 459–494 (1993)

34.220 I. Villegas, M.J. Weaver: Carbon monoxide adlayer structures on platinum (111) electrodes: A synergy between in-situ scanning tunneling microscopy and infrared spectroscopy, J. Chem. Phys. **101**, 1648–1660 (1994)

34.221 I. Villegas, X.P. Gao, M.J. Weaver: Local-structure and phase-transitions within ordered electrochemical, adlayers: Some new insights from in-situ scanning-tunneling-microscopy, Electrochim. Acta **40**, 1267–1275 (1995)

34.222 C.A. Lucas, N.M. Marković, P.N. Ross: The adsorption and oxidation of carbon monoxide at the Pt(111)/electrolyte interface: Atomic structure and surface relaxation, Surf. Sci. **425**, L381–L386 (1999)

34.223 N.M. Marković, B.N. Grgur, C.A. Lucas, P.N. Ross: Electrooxidation of CO and H_2/CO mixtures on Pt(111) in acid solutions, J. Phys. Chem. B **103**, 487–495 (1999)

34.224 K.C. Chang, A. Menzel, V. Komanicky, H. You: Electrosorbed carbon monoxide monolayers on Pt(111), Electrochim. Acta **52**, 5749–5758 (2007)

34.225 A. Rodes, R. Gómez, J.M. Feliu, M.J. Weaver: Sensitivity of compressed carbon monoxide adlayers on platinum(111) electrodes to long-range substrate structure: Influence of monoatomic steps, Langmuir **16**, 811–816 (2000)

34.226 Y.V. Tolmachev, A. Menzel, A.V. Tkachuk, Y.S. Chu, H.D. You: In situ surface x-ray scattering observation of long-range ordered ($\sqrt{19} \times \sqrt{19}$)R23.4°-13CO structure on Pt(111) in aqueous electrolytes, Electrochem. Solid-State Lett. **7**, E23–E26 (2004)

34.227 S.C. Chang, L.-W.H. Leung, M.J. Weaver: Comparison between coverage dependent infrared frequencies for carbon monoxide adsorbed on ordered platinum(111), (100) and (110) in electrochemical and vacuum environments, J. Phys. Chem. **93**, 5341–5345 (1989)

34.228 S.C. Chang, M.J. Weaver: In situ infrared spectroscopy of CO adsorbed at ordered Pt(100)-aqueous interfaces: Double layer effects upon the adsorbate binding geometry, J. Phys. Chem. **94**, 5095–5102 (1990)

34.229 S.C. Chang, M.J. Weaver: Coverage dependent dipole coupling for carbon monoxide adsorbed at ordered Pt(111)-aqueous interfaces: Structural and electrochemical implications, J. Chem. Phys. **92**, 4582–4594 (1990)

34.230 M.W. Severson, C. Stuhlmann, I. Villegas, M.J. Weaver: Dipole–dipole coupling effects upon infrared-spectroscopy of compressed electrochemical adlayers: Application to the Pt(111)/CO system, J. Chem. Phys. **103**, 9832–9843 (1995)

34.231 M.T.M. Koper, R.A. van Santen, S.A. Wasileski, M.J. Weaver: Field-dependent chemisorption of carbon monoxide and nitric oxide on platinum-group (111) surfaces: Quantum chemical calculations compared with infrared spectroscopy at electrochemical and vacuum-based interfaces, J. Chem. Phys. **113**, 4392–4407 (2000)

34.232 S.A. Wasileski, M.J. Weaver, M.T.M. Koper: Potential-dependent chemisorption of carbon monoxide on platinum electrodes: New insight from quantum-chemical calculations combined with vibrational spectroscopy, J. Electroanal. Chem. **500**, 344–355 (2001)

34.233 S.A. Wasileski, M.T.M. Koper, M.J. Weaver: Metal electrode-chemisorbate bonding: General influence of surface bond polarization on field-dependent binding energetics and vibrational frequencies, J. Chem. Phys. **115**, 8193–8203 (2001)

34.234 S.A. Wasileski, M.T.M. Koper, M.J. Weaver: Field-dependent chemisorption of carbon monoxide on platinum-group (111) surfaces. Relationships between binding energetics, geometries, and vibrational properties as assessed by density functional theory, J. Phys. Chem. B **105**, 3518–3530 (2001)

34.235 S.A. Wasileski, M.T.M. Koper, M.J. Weaver: Field-dependent electrode-chemisorbate bonding: Sensitivity of vibrational Stark effect and binding energetics to nature of surface coordination, J. Am. Chem. Soc. **124**, 2796–2805 (2002)

34.236 A. Bewick, M. Fleischmann, H.R. Thirsk: Kinetics of the electrocrystallization of thin films of calomel, Trans. Faraday Soc. **58**, 2200–2216 (1962)

34.237 A.V. Petukhov, W. Akemann, K.A. Friedrich, U. Stimming: Kinetics of electrooxidation of a CO monolayer at the platinum/electrolyte interface, Surf. Sci. **402**, 182–186 (1998)

34.238 M. Bergelin, E. Herrero, J.M. Feliu, M. Wasberg: Oxidation of CO adlayers on Pt(111) at low potentials: An impinging jet study in H_2SO_4 electrolyte with mathematical modeling of the current transients, J. Electroanal. Chem. **467**, 74–84 (1999)

34.239 E. Herrero, J.M. Feliu, S. Blais, Z. Radovic-Hrapovic, G. Jerkiewicz: Temperature dependence of CO chemisorption and its oxidative desorption on the Pt(111) electrode, Langmuir **16**, 4779–4783 (2000)

34.240 E. Herrero, B. Alvarez, J.M. Feliu, S. Blais, Z. Radovic-Hrapovic, G. Jerkiewicz: Temperature dependence of the CO_{ads} oxidation process on Pt(111) Pt(100), and Pt(110) electrodes, J. Electroanal. Chem. **567**, 139–149 (2004)

34.241 C.A. Angelucci, E. Herrero, J.M. Feliu: Modeling CO oxidation on Pt(111) electrodes, J. Phys. Chem. C **114**, 14154–14163 (2010)

34.242 N.P. Lebedeva, M.T.M. Koper, E. Herrero, J.M. Feliu, R.A. van Santen: CO oxidation on stepped Pt [n(111) × (111)] electrodes, J. Electroanal. Chem. **487**, 37–44 (2000)

34.243 M.T.M. Koper, J.J. Lukkien, N.P. Lebedeva, J.M. Feliu, R.A. van Santen: Adsorbate interactions and phase transitions at the stepped platinum/-electrolyte interface: Experiment compared with Monte Carlo simulations, Surf. Sci. **478**, L339–L344 (2001)

34.244 B. Pozniak, Y. Mo, D.A. Scherson: The electrochemical oxidation of carbon monoxide adsorbed on Pt(111) in aqueous electrolytes as monitored by in situ potential step-second harmonic generation, Faraday Discuss. **121**, 313–322 (2002)

34.245 N.P. Lebedeva, M.T.M. Koper, J.M. Feliu, R.A. van Santen: Role of crystalline defects in electrocatalysis: Mechanism and kinetics of CO adlayer oxidation on stepped platinum electrodes, J. Phys. Chem. B **106**, 12938–12947 (2002)

34.246 N.P. Lebedeva, M.T.M. Koper, J.M. Feliu, R.A. van Santen: Mechanism and kinetics of the electrochemical CO adlayer oxidation on Pt(111), J. Electroanal. Chem. **524**, 242–251 (2002)

34.247 F.J. Vidal-Iglesias, J. Solla-Gullón, J.M. Campiña, E. Herrero, A. Aldaz, J.M. Feliu: CO monolayer oxidation on stepped Pt(S) [$(n-1)(100) \times (110)$] surfaces, Electrochim. Acta **54**, 4459–4466 (2009)

34.248 G. Garcia, M.T.M. Koper: Stripping voltammetry of carbon monoxide oxidation on stepped platinum single-crystal electrodes in alkaline solution, Phys. Chem. Chem. Phys. **10**, 3802–3811 (2008)

34.249 G. Garcia, M.T.M. Koper: Mechanism of electrooxidation of carbon monoxide on stepped platinum electrodes in alkaline media: A chronoamperometric and kinetic modeling study, Phys. Chem. Chem. Phys. **11**, 11437–11446 (2009)

34.250 G. Garcia, M.T.M. Koper: Dual reactivity of step-bound carbon monoxide during oxidation on a stepped platinum electrode in alkaline media, J. Am. Chem. Soc. **131**, 5384–5385 (2009)

34.251 G. Garcia, P. Rodriguez, V. Rosca, M.T.M. Koper: Fourier transform infrared spectroscopy study of CO electro-oxidation on Pt(111) in alkaline media, Langmuir **25**, 13661–13666 (2009)

34.252 E. Herrero, Q.-S. Chen, J. Hernandez, S.-G. Sun, J.M. Feliu: Effects of the surface mobility on the oxidation of adsorbed CO on platinum electrodes in alkaline media. The role of the adlayer and surface defects, Phys. Chem. Chem. Phys. **13**, 16762–16771 (2011)

34.253 M.J.S. Farias, E. Herrero, J.M. Feliu: Site selectivity for CO adsorption and stripping on stepped and kinked platinum surfaces in alkaline medium, J. Phys. Chem. C **117**, 2903–2913 (2013)

34.254 M.J.S. Farias, C. Buso-Rogero, R. Gisbert, E. Herrero, J.M. Feliu: Influence of the CO adsorption environment on its reactivity with (111) terrace sites in stepped Pt electrodes under alkaline media, J. Phys. Chem. C **118**, 1925–1934 (2014)

34.255 R.M. Arán-Ais, F.J. Vidal-Iglesias, M.J.S. Farias, J. Solla-Gullón, V. Montiel, E. Herrero, J.M. Feliu: Understanding CO oxidation reaction on platinum nanoparticles, J. Electroanal. Chem. **793**, 126–136 (2017)

34.256 R. Parsons, T. Vandernoot: The oxidation of small organic molecules: A survey of recent fuel cell related research, J. Electroanal. Chem. Interfacial Electrochem. **257**, 9–45 (1988)

34.257 S.G. Sun, J. Clavilier, A. Bewick: The mechanism of electrocatalytic oxidation of formic acid on Pt(100) and Pt(111) in sulphuric acid solution: An EMIRS Study, J. Electroanal. Chem. Interfacial Electrochem. **240**, 147–159 (1988)

34.258 J. Willsau, J. Heitbaum: Analysis of adsorbed intermediates and determination of surface potential shifts by DEMS, Electrochim. Acta **31**, 943–948 (1986)

34.259 J. Clavilier, R. Parsons, R. Durand, C. Lamy, J.M. Leger: Formic acid oxidation on single crystal platinum electrodes. Comparison with polycrystalline platinum, J. Electroanal. Chem. Interfacial Electrochem. **124**, 321–326 (1981)

34.260 J. Clavilier, S.G. Sun: Electrochemical study of the chemisorbed species formed from formic-acid dissociation at platinum single-crystal electrodes, J. Electroanal. Chem. Interfacial Electrochem. **199**, 471–480 (1986)

34.261 E. Herrero, A. Fernández-Vega, J.M. Feliu, A. Aldaz: Poison formation reaction from formic acid and methanol on Pt(111) electrodes modified by irreversibly adsorbed Bi and As, J. Electroanal. Chem. Interfacial Electrochem. **350**, 73–88 (1993)

34.262 E. Herrero, J.M. Feliu, A. Aldaz: Poison formation reaction from formic acid on Pt(100) electrodes modified by irreversibly adsorbed bismuth and antimony, J. Electroanal. Chem. Interfacial Electrochem. **368**, 101–108 (1994)

34.263 J.V. Perales-Rondón, E. Herrero, J.M. Feliu: Effects of the anion adsorption and pH on the formic acid oxidation reaction on Pt(111) electrodes, Electrochim. Acta **140**, 511–517 (2014)

34.264 J.V. Perales-Rondón, S. Brimaud, J. Solla-Gullón, E. Herrero, R.J. Behm, J.M. Feliu: Further insights into the formic acid oxidation mechanism on platinum: pH and anion adsorption effects, Electrochim. Acta **180**, 479–485 (2015)

34.265 J. Joo, T. Uchida, A. Cuesta, M.T.M. Koper, M. Osawa: Importance of acid-base equilibrium in electrocatalytic oxidation of formic acid on platinum, J. Am. Chem. Soc. **135**, 9991–9994 (2013)

34.266 G. Samjeske, A. Miki, S. Ye, M. Osawa: Mechanistic study of electrocatalytic oxidation of formic acid at platinum in acidic solution by time-resolved surface-enhanced infrared absorption spectroscopy, J. Phys. Chem. B **110**, 16559–16566 (2006)

34.267 G. Samjeske, M. Osawa: Current oscillations during formic acid oxidation on a Pt electrode: Insight into the mechanism by time-resolved IR spectroscopy, Angew. Chem. Int. Ed. **44**, 5694–5698 (2005)

34.268 Y.X. Chen, M. Heinen, Z. Jusys, R.J. Behm: Bridge-bonded formate: Active intermediate or spectator species in formic acid oxidation on a Pt film electrode?, Langmuir **22**, 10399–10408 (2006)

34.269 Y. Chen, M. Heinen, Z. Jusys, R. Behm: Kinetics and mechanism of the electrooxidation of formic acid—Spectroelectrochemical studies in a flow cell, Angew. Chem. Int. Ed. **45**, 981–985 (2006)

34.270 V. Grozovski, F.J. Vidal-Iglesias, E. Herrero, J.M. Feliu: Adsorption of formate and its role as intermediate in formic acid oxidation on plat-

inum electrodes, ChemPhysChem **12**, 1641–1644 (2011)
34.271 H.-F. Wang, Z.-P. Liu: Formic acid oxidation at Pt/H_2O interface from periodic DFT calculations integrated with a continuum solvation model, J. Phys. Chem. C **113**, 17502–17508 (2009)
34.272 J. Clavilier: Pulsed linear sweep voltammetry with pulses of constant level in a potential scale, a polarization demanding condition in the study of platinum single-crystal electrodes, J. Electroanal. Chem. Interfacial Electrochem. **236**, 87–94 (1987)
34.273 V. Grozovski, V. Climent, E. Herrero, J.M. Feliu: Intrinsic activity and poisoning rate for HCOOH oxidation on platinum stepped surfaces, Phys. Chem. Chem. Phys. **12**, 8822–8831 (2010)
34.274 V. Grozovski, V. Climent, E. Herrero, J.M. Feliu: Intrinsic activity and poisoning rate for HCOOH oxidation at Pt(100) and vicinal surfaces containing monoatomic (111) steps, ChemPhysChem **10**, 1922–1926 (2009)
34.275 V. Grozovski, J. Solla-Gullon, V. Climent, E. Herrero, J.M. Feliu: Formic acid oxidation on shape-controlled Pt nanoparticles studied by pulsed voltammetry, J. Phys. Chem. C **114**, 13802–13812 (2010)
34.276 E. Herrero, M.J. Llorca, J.M. Feliu, A. Aldaz: Oxidation of formic acid on Pt(111) electrodes modified by irreversibly adsorbed tellurium, J. Electroanal. Chem. Interfacial Electrochem. **394**, 161–167 (1995)
34.277 V. Climent, E. Herrero, J.M. Feliu: Electrocatalysis of formic acid and CO oxidation on antimony-modified Pt(111) electrodes, Electrochim. Acta **44**, 1403–1414 (1998)
34.278 M.D. Maciá, E. Herrero, J.M. Feliu, A. Aldaz: Formic acid self-poisoning on bismuth-modified Pt(755) and Pt(775) electrodes, Electrochem. Commun. **1**, 87–89 (1999)
34.279 M.D. Maciá, E. Herrero, J.M. Feliu, A. Aldaz: Formic acid self-poisoning on bismuth-modified stepped electrodes, J. Electroanal. Chem. **500**, 498–509 (2001)
34.280 M.D. Maciá, E. Herrero, J.M. Feliu: Formic acid self-poisoning on adatom-modified stepped electrodes, Electrochim. Acta **47**, 3653–3661 (2002)
34.281 M.R. Columbia, A.M. Crabtree, P.A. Thiel: The temperature and coverage dependences of adsorbed formic acid and its conversion to formate on platinum(111), J. Am. Chem. Soc. **114**, 1231–1237 (1992)
34.282 M.T.M. Koper, S.C.S. Lai, E. Herrero: Mechanisms of the oxidation of carbon monoxide and small organic molecules at metal electrodes. In: *Fuel Cell Catalysis: A Surface Science Approach*, ed. by M.T.M. Koper (Wiley, Hoboken 2009) pp. 159–207
34.283 K. Franaszczuk, E. Herrero, P. Zelenay, A. Wieckowski, J. Wang, R.I. Masel: A comparison of electrochemical and gas-phase decomposition of methanol on platinum surfaces, J. Phys. Chem. **96**, 8509–8516 (1992)
34.284 E. Herrero, K. Franaszczuk, A. Wieckowski: Electrochemistry of methanol at low index crystal planes of platinum: An integrated voltammetric and chronoamperometric study, J. Phys. Chem. **98**, 5074–5083 (1994)
34.285 F. Colmati, G. Tremiliosi-Filho, E.R. Gonzalez, A. Berná, E. Herrero, J.M. Feliu: Surface structure effects on the electrochemical oxidation of ethanol on platinum single crystal electrodes, Faraday Discuss. **140**, 379–397 (2008), discussion 417–437
34.286 F. Colmati, G. Tremiliosi, E.R. Gonzalez, A. Berná, E. Herrero, J.M. Feliu: The role of the steps in the cleavage of the C–C bond during ethanol oxidation on platinum electrodes, Phys. Chem. Chem. Phys. **11**, 9114–9123 (2009)
34.287 V. Grozovski, V. Climent, E. Herrero, J.M. Feliu: The role of the surface structure in the oxidation mechanism of methanol, J. Electroanal. Chem. **662**, 43–51 (2011)

Victor Climent

Instituto Universitario de Electroquímica
Universidad de Alicante
San Vicente del Raspeig, Alicante, Spain
victor.climent@ua.es

Victor Climent obtained his PhD at the University of Alicante (2000). After a postdoctoral period at the University of Oxford (UK), he returned to the University of Alicante in 2003 where he is currently professor. His main research interest is the investigation of the relationship between the structure of the electrode surface, its composition and its electrochemical reactivity.

Enrique Herrero

Instituto Universitario de Electroquímica
Universidad de Alicante
San Vicente del Raspeig, Alicante, Spain
herrero@ua.es

Enrique Herrero received his PhD from the University of Alicante in 1995. After a two years of postdoctoral stay at Cornell University, he returned to the University of Alicante, where he is currently professor. His research focusses on the understanding of fundamental aspects of electrochemistry, especially those associated with the effect of the interfacial structure on the reactivity.

Part I Current T

Part I Current Topics In Surface Science

Part I is devoted to topics which, in the opinion of the Editors, must be covered to ensure that this Handbook is comprehensive. These topics relate to the current frontiers of surface science research but do not fit easily into the other sections. So, instead of general surface properties, the present section focuses on some new low-dimensional materials (graphene, silicene, and carbon clusters) as well as nanotribology and nuclear investigation methods.

Chapter 35 considers contact mechanics and nanotribology. The chapter explores the theory of contact mechanics and stick-slip motion at the nanoscale. In the theoretical part, analytical predictions regarding contact mechanics for lengths spanning several orders of magnitude are attempted based on morphology and material properties. The ultimate limits of friction measurements are illustrated for the sliding of an atomically sharp tip over a crystal lattice.

The next two chapters focus on the properties of two-dimensional materials and complement the information given in Chap. 9.

Chapter 36 deals with graphene. It describes its structure, possible defects, methods of preparation, peculiar electronic properties, and chemical reactivity in detail. The properties of graphene may be influenced by the substrate on which it is deposited, as highlighted by a comparison of single layers grown on different materials. The chapter also addresses the role of doping and the possibility of using adsorption to tune the band gap.

Chapter 37 describes the structural, electronic, and vibronic properties of monolayer silicene as well as the growth and electronic properties of multilayer silicene. The chapter also reviews the fabrication procedures for the first field-effect transistors based on this material, and reports on exotic forms of silicon for zero-dimensional (benzene-like nanodots) and one-dimensional (pentasilicene-like nanoribbons) materials.

Chapter 38 describes the use of supersonic cluster beam deposition (SCBD) to grow carbon (nsC) thin films with controlled nanostructures. The growth conditions ensure that incoming particles land on the growing interface and do not diffuse significantly. Due to the absence of stress, it is possible to grow films with a wide range of thicknesses. Their low density and high surface roughness make them promising materials for the fabrication of several devices (electrolyte-gated transistors, supercapacitors, photocatalytic systems, etc.).

Chapter 39 reviews the use of nuclear methods in ion beam analysis at high energies. It covers Rutherford backscattering spectrometry (RBS), elastic recoil detection analysis (ERDA), and nuclear reaction analysis (NRA). Because of the very short interaction time involved, inelastic collisions can be neglected, so the cross-section is determined by nuclear properties alone. Hence, the intensity of the signal is not affected by environmental factors, meaning that these methods can be used to quantify the elemental compositions of samples, including hydrogen, which is often not possible with other techniques.

35. Selected Topics in Contact Mechanics and Nanotribology

Enrico Gnecco

Driven by recent developments in nanotechnology and materials modeling and simulations, our understanding of contact mechanics, and more specifically of solid friction down to the nanometer scale, is experiencing a period of exceptional growth. Since a dedicated handbook would be not enough to summarize the latest experimental and theoretical achievements, we focus on two selected topics, which will hopefully stimulate the reader to examine the specialized literature in the growing field of nanotribology. These topics are the contact mechanics theory, recently developed by B.N.J. Persson, and the stick–slip motion on the nanoscale. While the first theory, to the best of our knowledge, is the first one embracing the contact between rough surfaces over length scales of several orders of magnitude, and making analytical predictions based on the morphology and material properties of the constituent materials, the second topic concerns the ultimate limits of friction measurements, i.e., the sliding of an atomically sharp tip over a crystal lattice. The two topics are not yet well related, but the situation may change in the near future. For this reason, it is also of interest to mention basic attempts in modeling stick–slip of multi-asperity contacts, as done in an intermediate section of this chapter. Last but not least, the dissipation accompanying the motion of a nanoslider in close proximity to but not touching a solid surface, and oppositely, of a similar object penetrating and scraping the surface, is briefly discussed, as it can be investigated with the most important technique available for this kind of study, i.e., atomic force microscopy.

Friction is a very important subject in surface science, as well as in everyday life. On one hand, friction is not only beneficial, as one can easily realize when driving on an icy road, but even vital, since life would be very difficult on planet Earth if the friction forces between meteorites and atmospheric particles were not strong enough to pulverize the former. On the other hand, friction is usually an annoying phenomenon, as proven by uncountable examples in engineering applications. Beyond that, it is estimated that a consistent part of the GDP of industrialized countries is consistently eroded by our ignorance of basic friction mechanisms. Friction may lead to abrasive wear over the long term, and ultimately to failure of many mechanical components, with more damage than that caused by fracture and plastic deformation. The situation is even worse in contacts formed on small length scales. Let us consider an object with linear dimension L. Since the fraction of atoms at the surface increases as $1/L$ when the size of the body is reduced, it is not surprising that friction forces play a key role in the dynamics of tiny objects ranging from microelectromechanical systems (MEMS) to microorganisms.

A compact and exhaustive treatment of friction phenomena is clearly impossible. Rather than following this approach, the chapter will thus focus on two selected topics which, in the author's opinion, have experienced significant progress in recent years. These topics are (i) the contact mechanics of rough surfaces as modeled in the continuum theory by B.N.J. Persson and (ii) the stick–slip motion of an atomically sharp tip elastically driven on a crystal surface. Both of these should be relevant for anyone interested in modern tribology. The corresponding two sections are joined by an *interlude* introducing the multiscale concept of stick–slip. Finally, nanotribology experiments under extreme loading conditions are mentioned. Traditional lubrication techniques and many other topics in *classical* tribology are deliberately ignored.

M. Rocca, T.S. Rahman, L. Vattuone (Eds.), *Springer Handbook of Surface Science*, Springer Handbooks,
https://doi.org/10.1007/978-3-030-46906-1_35

35.1 Contact Between Rough Surfaces

Any surface of practical use is ultimately rough. Assuming that the surface height is described by a function $h(\boldsymbol{r})$, where $\boldsymbol{r} \equiv (x, y)$ defines the position on a reference plane, as a fundamental quantity describing the surface roughness we can introduce the standard deviation $h_{\mathrm{rms}} = \langle (h - \overline{h})^2 \rangle^{1/2}$, where $\langle \ldots \rangle$ denotes averaging on the plane, and $\overline{h}$ is the mean height of the surface, which in the following will be assumed equal to zero. Nevertheless, two surfaces may be characterized by the same value of h_{rms} and appear very different. This is due to the different degree of *correlation* between locations at a given distance on the surface. This concept can be made quantitative by introducing the *self-correlation function*

$$C(\Delta \boldsymbol{r}) = \overline{h(\boldsymbol{r} + \Delta \boldsymbol{r}) h(\boldsymbol{r})} \, .$$

Essentially, $C(\Delta \boldsymbol{r})$ measures the *memory* that the surface has of its own features over a distance $\Delta \boldsymbol{r}$. If the surface is isotropic, the function C depends only on the module of the vector $\Delta \boldsymbol{r}$. Without loss of generality, we will simply refer to this module also as r. Alternatively, a solid surface can be described by its *power spectrum*, which can be defined as the Fourier transform of the correlation function

$$S(k) = \frac{1}{(2\pi)^2} \int C(\boldsymbol{r}) \mathrm{e}^{-\mathrm{i}\boldsymbol{k}\boldsymbol{r}} \mathrm{d}^2 r \, .$$

In the context of modern contact theories, the use of $S(k)$ is often more practical than that of $C(r)$.

When two bodies are pressed against each other, their surface profiles are unavoidably changed according to the elastic and plastic properties of the contacting materials. Additionally, the contact response will vary with the rate by which stresses or strains are applied, if viscoelastic or viscoplastic processes are effective. We begin with the easiest case of pure elastic surfaces. For two contacting spheres with radii R_1 and R_2, the problem was brilliantly solved by *Hertz* in 1885 [35.1]. In this case, based on energy considerations, it can be proven that the contact circle has a radius

$$a_0 = \left(\frac{3 F_{\mathrm{N}} R}{4 E^*} \right)^{1/3} \, , \tag{35.1}$$

where F_{N} is the normal (loading) force, $R^{-1} = R_1^{-1} + R_2^{-1}$, and the effective elastic modulus E^* is defined by the relation

$$\frac{1}{E^*} = \frac{1 - \nu_1^2}{E_1} + \frac{1 - \nu_2^2}{E_2} \, , \tag{35.2}$$

with E_i and ν_i $(i = 1, 2)$ the Young's modulus and the Poisson ratio of each material, respectively. Furthermore, the penetration depth $\delta = a^2/R$. Thus, the contact area A is not proportional to F_{N}, but it scales as $F_{\mathrm{N}}^{2/3}$. If the (kinetic or static) friction f is supposed to be proportional to the contact area, we reach the conclusion that $f \propto F_{\mathrm{N}}^{2/3}$. This is in contrast to most experimental observations on real surfaces, which show that friction is proportional to the normal load (so-called *Amontons' law*).

The paradox is only apparent, since real surfaces, including spherical ones, are usually rough, but it was a long time before a convincing explanation was proposed. A key step was the model developed by *Greenwood* and *Williamson* (GW) in the 1960s [35.2]. In this model, the authors considered a distribution of independent spherical asperities with the same radius R in elastic contact with a rigid half-space. If the height distribution of the asperities decays exponentially as $\mathrm{e}^{-\lambda h}$, it is easy to see that

$$A(F_{\mathrm{N}}) = \frac{\sqrt{\pi R \lambda}}{E^*} F_{\mathrm{N}} \, , \tag{35.3}$$

consistently with the Amontons' law. The same conclusion approximately holds in the more realistic case of a Gaussian height distribution. However, in spite of its popularity, the GW model has severe limitations. First, assuming that a surface can be approximated as an ensemble of similar asperities is not realistic. Second, the model does not consider the interaction between two asperities, which is unavoidable if the asperities are not far from each other. It was *Persson* who proposed a solution to this problem in the first years of the new millennium [35.3]. Starting from the general description of the surface roughness introduced in Sect. 35.1, he was indeed able to conclude that, if the contact is elastic and the loading force is not too high, the Amontons' law is verified on almost *any* surface of practical interest.

The Persson theory is based on the concept of *magnification*. Suppose that, from the power spectrum $S(k)$ of a given surface, all components above a certain threshold value k are cut off. The surface corresponding to the new spectrum so obtained has features down to the wavelength $\lambda = 2\pi/k$. If L is the linear size of the original surface, the quantity $\zeta = L/\lambda$ may be called the magnification degree (Fig. 35.1). Without loss of generality, it can be proven that when the surface is pressed against a rigid half-space with a loading force F_{N}, the stress distribution $P(\sigma, \zeta)$ satisfies the diffusion-like equation

$$\frac{\partial P}{\partial \zeta} = D(\zeta) \frac{\partial^2 P}{\partial \sigma^2} \, , \tag{35.4}$$

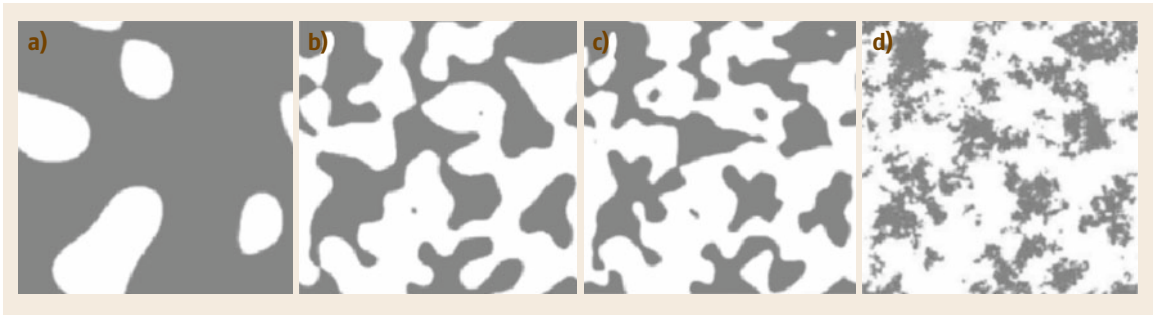

Fig. 35.1a–d Contact region between a rough rigid substrate and an elastic block at different magnifications **(a)** $\zeta = 3$, **(b)** $\zeta = 9$, **(c)** $\zeta = 12$ and **(d)** $\zeta = 648$. When $\zeta \approx 12$, the non-contact region percolates. (From [35.4] © IOP Publishing. Reproduced with permission. All rights reserved)

where ζ and σ take the roles of time and distance, respectively. In contrast to the well-known Fick's law, the *diffusion coefficient* in (35.4) is not constant, but depends on the magnification as $D(\zeta) = G'(\zeta)$, where the quantity

$$G(\zeta) = \frac{\pi}{4} E^{*2} \int_{k_0}^{2\pi\zeta/L} k^3 S(k) \mathrm{d}k \tag{35.5}$$

is defined by the surface power spectrum. Thus, all elastic and morphological properties of the undeformed surface are contained in (35.5). The boundary conditions of (35.4) are given by the simple fact that, in the absence of adhesion, the surfaces detach when $\sigma = 0$ and, on the other hand, that the stress cannot become anywhere infinite in a finite contact area. In this way, (35.4) can be solved. Since the contact area at the magnification ζ is $A(\zeta) = A_0 P(\zeta)$, where A_0 is the nominal contact area, the load dependence of the friction force (which is assumed to be proportional to A) can be estimated. The result is shown in Fig. 35.2a. If F_N is sufficiently low, the relation is a simple proportionality

$$A(F_\mathrm{N}) = \frac{F_\mathrm{N}}{\sqrt{\pi G_1}}\,, \tag{35.6}$$

where G_1 is the value of $G(\zeta)$ corresponding to $\zeta = 1$. Equation (35.6) generalizes (35.3) including all possible length scales.

Note that the Persson theory can also be applied to elastic-plastic and viscoelastic contacts. In the former case, the stress distribution P must be zero when σ equals the yield strength Y of the material. The latter case requires that the elastic constant is generalized according to the *correspondence principle* [35.7]

$$E^* \to \int E^*\left(t - t'\right) \frac{\mathrm{d}}{\mathrm{d}t'} \ldots \mathrm{d}t'\,; \tag{35.7}$$

(note that this principle is only applicable if the contact is growing with time). As a result, the area of contact is found to increase with time, as seen in Fig. 35.2b. Applications beyond contact mechanics are also possible, since the Persson theory can be used to study heat transfer and electrical conductivity through a contact formed by rough surfaces. Interestingly, it is found that in general, friction has a negligible influence on the thermal and electrical contact resistance. Very important for practical applications is also the influence of the contact structure on the flow of a liquid confined between two surfaces. The simple observation of Fig. 35.1 shows that a flow, let's say from the bottom edge to the top edge of the image, is only possible above a threshold value ζ_c, which can be numerically evaluated from the relation $A(\zeta_\mathrm{c}) \approx 0.4 A_0$ [35.4]. Depending on the loading force, the threshold is changed.

Adhesive effects were introduced in the Hertz theory by *Johnson* et al. [35.8]. In the *JKR model* so established, the contact radius is expected to increase, for a given normal load F_N, as

$$a^3 = a_0^3 \left[1 + \frac{3\Delta\gamma\pi R}{F_\mathrm{N}} + \sqrt{\frac{6\Delta\gamma\pi R}{F_\mathrm{N}} + \left(\frac{3\Delta\gamma\pi R}{F_\mathrm{N}}\right)^2} \right], \tag{35.8}$$

where $\Delta\gamma$ is the local change in surface tension when the contact is formed. The contact becomes unstable when a reaches a critical value given by

$$a_\mathrm{c} = \left(\frac{9\pi\Delta\gamma R^2}{8E^*}\right). \tag{35.9}$$

This value corresponds to a critical force

$$F_\mathrm{c} = -\frac{3\pi}{2}\Delta\gamma R, \tag{35.10}$$

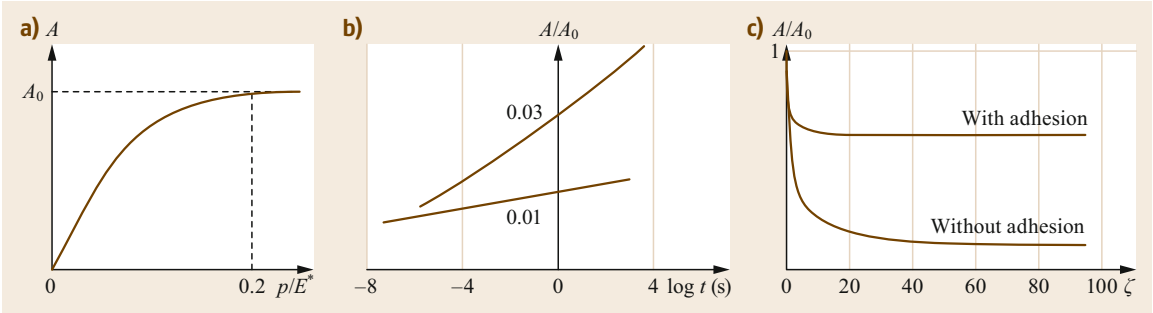

Fig. 35.2a–c Applications of the Persson contact mechanics theory. **(a)** Apparent contact area between an elastic rough surface and a rigid half-space as a function of the squeezing pressure. (Reprinted by permission from [35.3], © Elsevier 2006). **(b)** Relative contact area of two blocks of tread rubber (*upper curve*) and of rim rubber (*lower curve*) squeezed against a steel surface by a pressure $p = 0.1\,\mathrm{MPa}$. (Reprinted by permission from [35.5], © IOP Publishing 2005). **(c)** Typical dependence of the projected area of contact on the magnification ζ with and without adhesion. (After [35.6])

the opposite of which can be considered as the *adhesion force* F_{adh} of the contact. Note that the JKR model is applicable only to large compliant contacts. In the opposite case

$$a^3 = a_0^3\left(1 + \frac{2\pi\Delta\gamma R}{F_{\mathrm{N}}}\right) \tag{35.11}$$

is a more accurate approximation [35.9], whereas intermediate cases can be treated within the Maugis–Dugdale model [35.10]. Also in this case, an extension to rough contacts has been proposed by *Persson* [35.6]. The analysis occurs through a series of consecutive steps. For a given surface with power spectrum $S(k)$, an effective surface tension γ_{eff} is first defined. This quantity is related to the adhesion force F_{adh} that is experienced by a rigid sphere of radius R pressed against the surface (at the magnification ζ) as

$$\gamma_{\mathrm{eff}} = \frac{2F_{\mathrm{adh}}}{3\pi R}\,. \tag{35.12}$$

The largest stress at the magnification ζ is then obtained using the Griffith theory for crack propagation

$$\sigma_a(\zeta) = \sqrt{\frac{2\gamma_{\mathrm{eff}}(\zeta)E^*k}{\pi^2}}\,. \tag{35.13}$$

Finally, (35.4) is solved with the boundary condition $P(-\sigma_a(\zeta),\zeta) = 0$. As expected, the adhesion increases the contact area considerably, as shown in Fig. 35.2c.

35.2 Macroscopic Sliding Friction

Having described how the problem of determining the pressure distribution in the contact between two surfaces can be elegantly solved within the Persson theory, it makes sense to ask how the previous relations change, and the friction force evolves, when the surfaces start sliding past each other. However, a general solution for sliding friction based on the Persson theory does not yet exist. A satisfying analytical treatment exists only for simple geometries, with most results coming from the past century [35.11]. Suppose that, besides the normal loading force F_{N}, a tangential force F_{x} is applied at the contact between two elastic spheres. In this case the shear stress distribution in the contact circle is given by

$$\tau(r) = \frac{\tau_0}{\sqrt{a^2 - r^2}}\,, \tag{35.14}$$

where $\tau_0 = F_{\mathrm{x}}/2\pi a^2$. This stress becomes infinite, and therefore not bearable, at the perimeter of the circle. As a result, a ring-shaped part of the circle must be necessarily detached. The radius c of the remaining part is related to F_{x} by the formula

$$c = a\left(1 - \frac{F_{\mathrm{x}}}{\mu F_{\mathrm{N}}}\right)^{1/3}\,, \tag{35.15}$$

where μ is the coefficient of static friction. When F_{x} increases, c becomes progressively smaller, until the sphere is fully detached when $F_{\mathrm{x}} = \mu F_{\mathrm{N}}$. Similar results hold in the case of a cylindrical contact (with the detachment occurring on the trailing edge). What happens after the detachment? If the lateral force is large enough to overcome the kinetic friction, a shear stress with the same distribution of the Hertzian pressure is

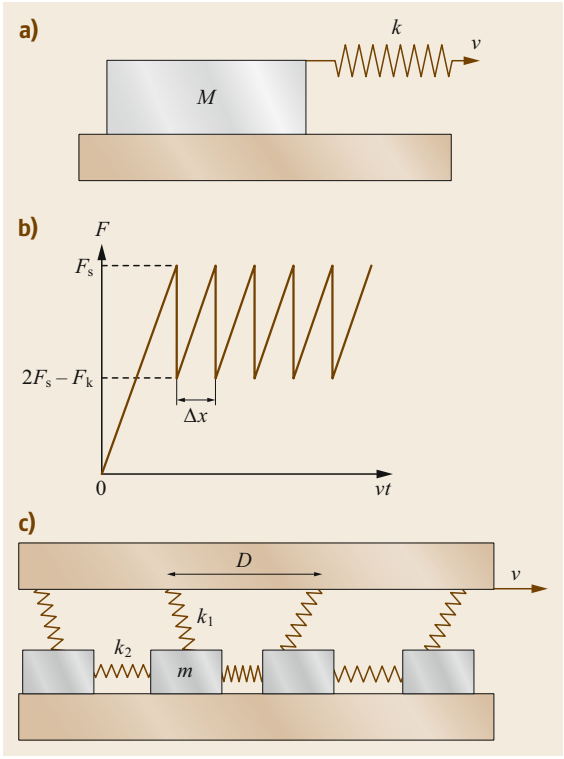

Fig. 35.3 **(a)** A block of mass m sliding on a flat substrate; **(b)** time dependence of the spring force in the quasi-static limit $v \to 0$; **(c)** schematics of the Burridge–Knopoff model

kept at the contact while sliding. Otherwise, the surfaces will *stick* again.

The *Stick-slip* process is a very general phenomenon, and can be better understood in the simple case of a block of mass M pulled by a spring (constant k), the free end of which moves with constant velocity v, as shown in Fig. 35.3a. If the static and kinetic friction have the constant values F_s and F_k, respectively, with $F_s > F_k$, it is not difficult to prove that the block will also move through alternate stick and slip phases, in which the block remains in contact with the surface or abruptly detaches and is quickly stopped again. When the stick time

$$t_{\text{stick}} = \frac{2(F_s - F_k)}{kv} , \tag{35.16}$$

the slip time is given by

$$t_{\text{slip}} = \frac{2}{\omega_0} \arctan\left(\frac{\omega(F_s - F_k)}{kv}\right) , \tag{35.17}$$

where $\omega_0 = \sqrt{k/m}$ is the resonance frequency of the linear oscillator. If v is very low and the oscillations immediately following the detachment are quickly damped (so-called *quasi-static* case), then $t_{\text{stick}} \gg t_{\text{slip}} \approx \pi/\omega_0$, and the spring force F essentially varies with time following the sawtooth profile in Fig. 35.3b. It is also interesting to study the same problem under the assumption that F_s increases with the time of contact (so-called *contact aging*). In this case, stick–slip can also be observed, but only if the initial rate of increase of the static friction is low enough

$$\left.\frac{dF_s}{dt}\right|_{t\to 0} > k . \tag{35.18}$$

If this is not the case, sliding occurs steadily.

The simple stick–slip model can be extended in several ways. As an example, Fig. 35.3b shows several similar blocks connected to one another by springs k. The blocks are driven altogether by a series of springs K that are connected to a much larger rigid block moving with a constant velocity v. The importance of the *Burridge–Knopoff* (BK) *model* so defined [35.12] is given by the fact that it can also be treated analytically, and its solution gives a good understanding of thermally activated effects that are also expected in real-life situations (e.g., in earthquakes). In the BK model, it can indeed be proven that the motion of each small block is prevented by an energy barrier $\Delta E \propto (F_s^2 - F^2)$, where F is the force acting on the large block, and the coefficient of proportionality is determined by the values of K and k. In the course of time, the value of F increases and ΔE decreases. Neglecting thermal fluctuation, a block detaches when $\Delta E = 0$, but at a finite temperature T, one can introduce the probability p that the block remains stuck and observe that, according to the Kramers rate theory, the time variation of this quantity is given by the *master equation*

$$\frac{dp}{dt} = -f_0 \exp\left(-\frac{\Delta E}{k_B T}\right) p(t) . \tag{35.19}$$

In (35.19), f_0 is a prefactor (depending on ω_0, the damping coefficient γ and the average distance between two consecutive blocks). As a result, the friction force is found to increase with the logarithmic sliding velocity. This is also the case if the contact area is as small as the junction formed by an atomically sharp tip driven on a crystal surface, which is discussed in the next section.

35.3 Sliding Friction on the Atomic Scale

The *Prandtl–Tomlinson* (PT) *model* [35.13] differs from the model in Fig. 35.3a for the fact that (i) the block is replaced by a point mass m, and (ii) the mass is driven on a periodic (crystal) surface. For sake of simplicity, we limit the discussion to the one-dimensional motion on a sinusoidal potential with period a and amplitude U_0 and, again, consider the quasi-static limit only. Introducing the parameter

$$\eta = \frac{4\pi^2 U_0}{ka^2} \tag{35.20}$$

it is easy to see that, if $\eta < 1$, the mass m follows the driving spring continuously in a *steady sliding* with negligible friction [35.14]. If $\eta > 1$, the motion consists in an alternation of long *stick* phases and rapid *slip* events between consecutive minima of the potential. In this case the static friction force is

$$F_s = \frac{ka}{2\pi}\sqrt{\eta^2 - 1}\,. \tag{35.21}$$

The kinetic friction force F_k can be estimated as the ratio between the potential drop ΔU observed in the slip phase and a. A simple analytical expression for F_k is not possible, but it is interesting to observe that in a first approximation, $F_k \propto (\eta - 1)$ when $\eta \to 1$, and $F_k \propto \eta$ when $\eta \gg 1$. These conclusions hold if the damping coefficient γ is so high that m is pinned in the first minimum encountered after slip. If this is not the case, *long jumps* (corresponding to integer multiples of a) are possible, the occurrence of which can be related numerically to the values of η, γ and the temperature T. Various extensions to two-dimensional energy landscapes, with the symmetries of natural or artificial crystal surfaces, are available in the literature. Their validity is confirmed from lattice-resolved lateral force maps, which nowadays can be routinely acquired using *atomic force microscopy* (AFM). In this technique, a sharp probing tip is scanned over a solid surface in a sequence of parallel scan lines. The tip is located at the end of a flexible microcantilever, the bending of which is determined by the normal force F_N on the tip, whereas its torsion corresponds to the lateral force F_L. In this way, the friction force acting on the tip can be recorded as a function of the normal loading and the sliding velocity v, and mapped over an entire selected scan area. Examples of molecular-scale resolution achieved across monatomic step edges [35.15], on Moiré patterns [35.16, 18] and on molecular thin films on mineral surfaces [35.17] are given in Fig. 35.4. Note that this resolution is usually only possible in ultrahigh vacuum (UHV) conditions or with the probing tip completely embedded in water (in ambient conditions high resolution being prevented by the formation of a water meniscus between tip and sample).

The PT model can also be used to estimate how atomic-scale sliding friction varies with the velocity and temperature. In order to do that, one has again to consider the energy barrier ΔE preventing a slip event. On a sinusoidal potential ΔE depends on the spring force F as $\Delta E \propto (\text{const} - F)^{3/2}$. The higher the velocity, the lower the number of attempts to overcome the barrier, and, again using the Kramers rate theory, it is found

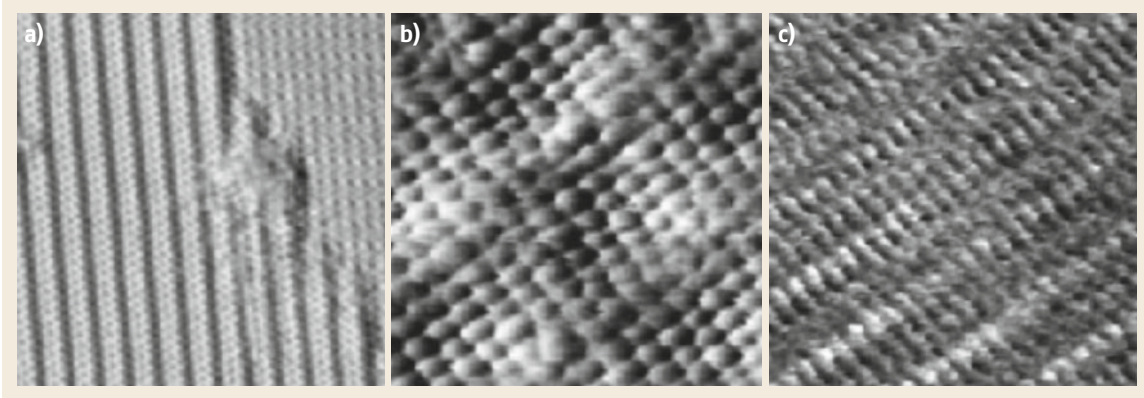

Fig. 35.4a–c Lateral force maps of **(a)** a (2×1) reconstructed Ge(001) surface. **(b)** A KBr monolayer grown on NaCl(001), **(c)** parallel stacks of perylene diimide derivative molecules on a dolomite cleavage surface. These results, corresponding to scan areas of a few nm^2, can be well reproduced with the PT model. (**(a)** Reprinted with permission from [35.15]. Copyright (2011) by the American Physical Society. **(b)** Reprinted with permission from [35.16]. Copyright (2011) by the American Physical Society. **(c)** Reprinted with permission from [35.17]. Copyright (2018) American Chemical Society)

that the friction should increase logarithmically with the sliding velocity [35.19]. However, this is only true if the contact area and the related contact stiffness do not change in the stick phase. If this is not the case, an opposite trend is expected, which has indeed been observed on SiO_2 and NaCl at cryogenic temperatures [35.20, 21]. The origin of the contact aging processes on the basis of this trend can be traced back to the formation and rupture of chemical bonds, and it obviously depends on the system. The rate theory combined with the PT model can also be used to prove that the friction force decreases if the temperature increases. This can be understood by simply observing that, the higher the temperature, the larger the number of attempts to overcome the energy barrier. This prediction has also been confirmed experimentally [35.22].

The motion of a point mass elastically driven on a crystal surface is the starting point for more complex friction models focusing on finite but still tiny contact areas. In some analogy with the BK model (Sect. 35.2), one can consider a chain of point masses connected by springs k_1 and driven by an external spring k on a periodic potential. Several combinations are possible. In the simplest case, corresponding to the so-called *edge-driven Frenkel–Kontorova* (FK) *model*, the external spring is connected to the point mass at the leading edge of the chain (a detailed review of the FK model is given in [35.23]). Recent nanomanipulation experiments performed by *Kawai* et al. on polyfluorene chains [35.24] and graphene nanoribbons [35.25] on a gold surface could indeed be reproduced using the edge-driven FK model. These experiments were performed in the so-called *noncontact mode*, with the probing tip oscillating in close proximity to the substrate but without *touching* it. From the variation in the resonance frequency of the cantilever, mechanical force gradients (in the normal direction) can be estimated and related to the friction forces through the potential energy landscape determined by integration. Stick-slip motion of single-stranded DNA chains on graphene [35.26] has also been investigated numerically by molecular dynamics combined with the FK model.

35.4 Ultimate Limits of Nanotribology: From Noncontact Friction to Abrasive Nanowear

How to reduce friction? Here we will try to give partial answers considering only *physical* methods applicable on the nanoscale. We begin by noting that the logarithmic velocity strengthening (without aging) does not occur at very low velocities, where *back-jumps* become efficient and cause that, in the limit $v \to 0$, the lateral force tends to zero [35.27]. Nevertheless, due to the very low velocity values where such effect (so-called *thermolubricity*) is expected, this is not a practical method for reducing friction. According to (35.21), the friction is also negligible when the PT parameter $\eta \to 1$. In this case the transition from stick–slip to steady sliding can be observed experimentally [35.28], but only with very low normal force values F_N in the order of 1 nN. Nevertheless, the energy barrier ΔE preventing slip can also be reduced (on average) if F_N oscillates. In this way, the transition to steady sliding can be easily observed if the excitation frequency f_{exc} is close to the resonance frequency of the tip in contact with the sample surface [35.29]. Note that in this case the average value $\overline{F}_N$ can be considerably higher than the (steady) value of F_N causing the transition without oscillations. Similar results are obtained if the tip oscillates parallel to the sample [35.30]. On finite contact areas, friction is significantly reduced if the two contacting surface lattices are *unmatched*, i.e., they are incommensurate or, if they are commensurate, their principal crystallographic directions are not parallel. Depending on the reciprocal orientation and/or the ratio between the lattice constants, stick–slip or *structural lubricity* [35.31] can be observed. Note that the last one is often called *superlubricity*, but this term is not universally accepted. Experimental verification of this effect also came from AFM measurements performed with a dedicated setup [35.32] and, more recently, from nanomanipulation experiments [35.33]. In this context, it should be pointed out that exceptionally low dissipative forces (in the order of 10−100 aN) can be measured when two surfaces move past each other in UHV without forming a real (repulsive) contact. Among the possible mechanisms leading to these effects, one has to distinguish between van der Waals, electrostatic and phononic *friction*. To detect *noncontact friction*, one of the two surfaces is usually oscillated, then the excitation is stopped and the time decay of the oscillations is measured. The resulting damping coefficients can be as small as 10^{-13} kg/s, although *giant* noncontact friction of 10^{-5} kg/s has been reported on charge density wave systems [35.34].

Last but not least, it is also worth mentioning what happens in the opposite limit of *high* loading forces (usually of a few tens of nN), where abrasive wear occurs. In contrast to friction, abrasive wear is still poorly explained in a satisfactory analytical way, but,

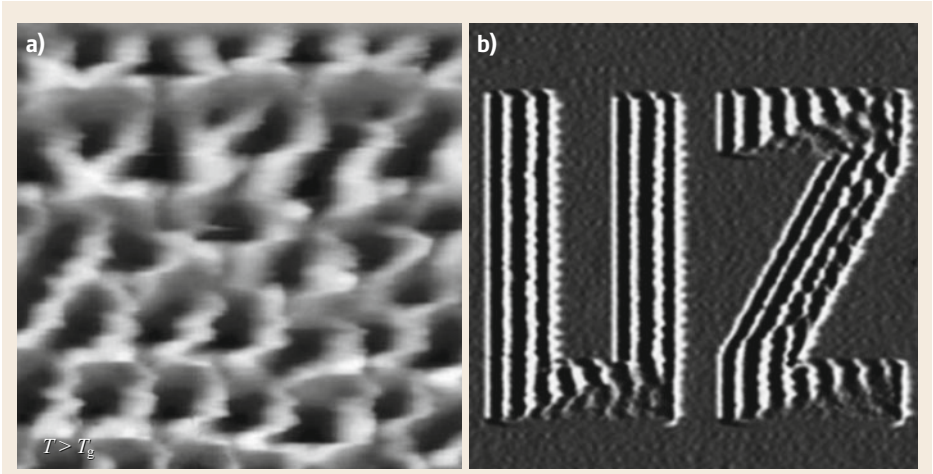

Fig. 35.5 **(a)** Abrasive wear patterns on polysulfone above T_g ($\approx 220\,^{\circ}\mathrm{C}$). AFM scan size: $1\,\mu\mathrm{m}$. (Reprinted by permission from [35.35]. Copyright 2009 by the American Physical Society). **(b)** Ripple patterns on solvent-enriched polystyrene at room T. The loading force was deliberately increased in two areas corresponding to the letters U and Z. (Reprinted by permission from [35.36]. Copyright (2019) by the American Physical Society)

similar to friction, AFM in UHV offers the possibility to investigate its time evolution in the *cleanest* possible conditions. As an example, in an early experiment of this kind it was found that when a groove is scraped by an AFM tip on a brittle KBr surface, the removed material recrystallizes in a periodic hilly pattern surrounding the groove [35.37, 38]. Interestingly, this result is not unique to alkali halides, but was also reported on semiconductors [35.39] and especially on polymer surfaces [35.40]. The regular *ripple* features formed in the abrasive process can also be modeled invoking the PT mechanism [35.41]. In this case, the surface profile plays the role of variable surface potential. The longer the tip sticks at a given place on the surface, the deeper is the potential well formed there. Assuming that at time $t = 0$ the surface is perfectly flat, a ripple pattern may develop or not depending on the values of the lateral stiffness k, indentation rate N, sliding velocity v and linear size of the tip a. The condition for ripple formation is

$$v < C\frac{N}{ak}\,, \tag{35.22}$$

where the parameter C is of the order of unity. Also, in this case, abrasive wear can be suppressed by mechanical oscillations applied during sliding, and the effect is more pronounced in the proximity of the contact resonance frequency [35.42]. In spite of its simplicity, surface rippling can develop in more complex *mogul* patterns (in polymers above the glass transition temperature T_g) or can be *tuned* by changing the scan conditions with dedicated scripts (Fig. 35.5).

35.5 Conclusions

To summarize, this short review has attempted to give a *flavor* on two topics of current research in macro- and nanotribology. Many questions are still open. What are the lower limits of continuum mechanics? How does the value of the friction coefficient depend on quantum effects involving the electron clouds of the contacting atoms? How reliable is molecular dynamics when used to understand phenomena extended over several length and time scales? The answers that the reader can find in the specialized literature are only partial, and they are often based on *guessing* rather than on rigorous mathematical proofs. This is not necessarily a negative conclusion, but should rather help to stimulate further experimental and theoretical research on this fascinating multidisciplinary subject.

References

35.1 H. Hertz: On the contact of elastic solids, Z. Reine Angew. Math. Mech. **92**, 156 (1882), in German

35.2 J.A. Greenwood, J.B. Williamson: Contact of nominally flat surfaces, Proc. R. Soc. A **295**, 300 (1966)

35.3 B.N.J. Persson: Contact mechanics for randomly rough surfaces, Surf. Sci. Rep. **61**, 201 (2006)

35.4 B.N.J. Persson, C. Yang: Theory of the leak-rate of seals, J. Phys. Condens. Matter **20**, 315011 (2008)

35.5 B.N.J. Persson, O. Albohr, U. Tartaglino, A.I. Volokitin, E. Tosatti: On the nature of surface roughness with application to contact mechanics, sealing, rubber friction and adhesion, J. Phys. Condens. Matter **17**, R1 (2005)

35.6 B.N.J. Persson: Adhesion between an elastic body and a randomly rough hard surface, Eur. Phys. J. E **8**, 385 (2002)

35.7 J.R.M. Radok: Viscoelastic stress analysis, Q. Appl. Math. **15**, 198 (1957)

35.8 K.L. Johnson, K. Kendall, A.D. Roberts: Surface energy and the contact of elastic solids, Proc. R. Soc. A **324**, 301 (1971)

35.9 B.V. Derjaguin, V.M. Müller, Y.P. Toporov: Effect of contact deformations on the adhesion of particles, J. Colloid Interface Sci. **53**, 314 (1975)

35.10 D. Maugis: Adhesion of spheres – the JKR-DMT transition using a Dugdale model, J. Colloid Interface Sci. **150**, 243 (1992)

35.11 K.L. Johnson: *Contact Mechanics* (Cambridge Univ. Press, Cambridge 1987)

35.12 R. Burridge, L. Knopoff: Model and theoretical seismicity, Bull. Seismol. Soc. Am. **57**, 341 (1967)

35.13 V.L. Popov, J.A.T. Gray: Prandtl-Tomlinson model: history and applications in friction, plasticity, and nanotechnologies, J. Appl. Math. Mech. **92**, 683 (2012)

35.14 E. Gnecco, R. Roth, A. Baratoff: Analytical expressions for the kinetic friction in the Prandtl-Tomlinson model, Phys. Rev. B **86**, 035443 (2012)

35.15 P. Steiner, E. Gnecco, F. Krok, J. Budzioch, L. Walczak, J. Konior, M. Szymonski, E. Meyer: Atomic-scale friction on stepped surfaces of ionic crystals, Phys. Rev. Lett. **106**, 186104 (2011)

35.16 S. Maier, E. Gnecco, A. Baratoff, E. Meyer: Atomic-scale friction modulated by a buried interface: combined atomic and friction force microscopy experiments, Phys. Rev. B **78**, 045432 (2008)

35.17 R. Buzio, A. Gerbi, M. Barra, F. Chiarella, E. Gnecco, A. Cassinese: Subnanometer resolution and enhanced friction contrast at the surface of perylene diimide PDI8-CN_2 thin films in ambient conditions, Langmuir **34**, 3207 (2018)

35.18 T. Filleter, R. Bennewitz: Structural and frictional properties of graphene films on SiC(0001) studied by atomic force microscopy, Phys. Rev. B **81**, 155412 (2010)

35.19 E. Gnecco, R. Bennewitz, T. Gyalog, C. Loppacher, M. Bammerlin, E. Meyer, H.J. Güntherodt: Velocity dependence of atomic friction, Phys. Rev. Lett. **84**, 1172 (2000)

35.20 I. Barel, M. Urbakh, L. Jansen, A. Schirmeisen: Multibond dynamics of nanoscale friction: the role of temperature, Phys. Rev. Lett. **104**, 066104 (2010)

35.21 I. Barel, M. Urbakh, L. Jansen, A. Schirmeisen: Unexpected temperature and velocity dependencies of atomic-scale stick-slip friction, Phys. Rev. B **84**, 115417 (2011)

35.22 L. Jansen, H. Hölscher, H. Fuchs, A. Schirmeisen: Temperature dependence of atomic-scale stick-slip friction, Phys. Rev. Lett. **104**, 256101 (2010)

35.23 O.M. Braun, Y.S. Kivshar: *The Frenkel-Kontorova Model: Concepts, Methods, and Applications* (Springer, Berlin, Heidelberg 2004)

35.24 S. Kawai, M. Koch, E. Gnecco, A. Sadeghi, R. Pawlak, T. Glatzel, J. Schwarz, S. Goedecker, S. Hecht, A. Baratoff, L. Grill, E. Meyer: Quantifying the atomic-level mechanics of single long physisorbed molecular chains, Proc. Natl. Acad. Sci. **111**, 3968 (2014)

35.25 S. Kawai, A. Benassi, E. Gnecco, H. Söde, R. Pawlak, X. Feng, K. Müllen, D. Passerone, C.A. Pignedoli, P. Ruffieux, R. Fasel, E. Meyer: Superlubricity of graphene nanoribbons on gold surfaces, Science **351**, 957 (2016)

35.26 J.G. Vilhena, E. Gnecco, R. Pawlak, F. Moreno-Herrero, E. Meyer, R. Perez: Stick-slip motion of ssDNA over graphene, J. Phys. Chem. B **122**(2), 840–846 (2017)

35.27 S.Y. Krylov, K.B. Jinesh, H. Valk, M. Dienwiebel, J.W.M. Frenken: Thermally induced suppression of friction at the atomic scale, Phys. Rev. E **71**, 65101 (2006)

35.28 A. Socoliuc, R. Bennewitz, E. Gnecco, E. Meyer: Transition from stick-slip to continuous sliding in atomic friction: entering a new regime of ultralow friction, Phys. Rev. Lett. **92**, 134301 (2004)

35.29 A. Socoliuc, E. Gnecco, S. Maier, O. Pfeiffer, A. Baratoff, E. Meyer: Atomic-scale control of friction by actuation of nanometer-sized contacts, Science **313**, 207 (2006)

35.30 R. Roth, O.Y. Fajardo, J.J. Mazo, E. Meyer, E. Gnecco: Lateral vibration effects in atomic-scale friction, Appl. Phys. Lett. **104**, 083103 (2014)

35.31 M.H. Müser: Structural lubricity: role of dimension and symmetry, Europhys. Lett. **66**, 97 (2004)

35.32 M. Dienwiebel, G.S. Verhoeven, N. Pradeep, J.W.M. Frenken, J.A. Heimberg, H.W. Zandbergen: Superlubricity of graphite, Phys. Rev. Lett. **92**, 126101 (2004)

35.33 D. Dietzel, U.D. Schwarz, A. Schirmeisen: Nanotribological studies using nanoparticle manipulation: principles and application to structural lubricity, Friction **2**, 114 (2014)

35.34 M. Langer, M. Kisiel, R. Pawlak, F. Pellegrini, G.E. Santoro, R. Buzio, A. Gerbi, G. Balakrishna, A. Baratoff, E. Tosatti, E. Meyer: Giant frictional dissipation peaks and charge-density wave slips at the $NbSe_2$ surface, Nat. Mater. **13**, 173 (2014)

35.35 E. Gnecco, E. Riedo, W.P. King, S.R. Marder, R. Szoszkiewicz: Linear ripples and traveling circular ripples produced on polymers by thermal AFM probes, Phys. Rev. B **79**, 235421 (2009)
35.36 J.J. Mazo, P.J. Martinez, P. Pedraz, J. Hennig, E. Gnecco: Plowing-induced structuring of compliant surfaces, Phys. Rev. Lett. **122**, 256101 (2019)
35.37 E. Gnecco, R. Bennewitz, E. Meyer: Abrasive wear on the atomic scale, Phys. Rev. Lett. **88**, 215501 (2002)
35.38 A. Socoliuc, E. Gnecco, R. Bennewitz, E. Meyer: Ripple formation induced in localized abrasion, Phys. Rev. B **68**, 115416 (2003)
35.39 B. Such, F. Krok, M. Szymonski: AFM tip-induced tripple pattern on AIII-BV semiconductor surfaces, Appl. Surf. Sci. **254**, 5431 (2008)
35.40 O.M. Leung, M.C. Goh: Orientational ordering of polymers by atomic force microscope tip-surface interaction, Science **255**, 64 (1992)
35.41 E. Gnecco, P. Pedraz, P. Nita, F. Dinelli, S. Napolitano, P. Pingue: Surface rippling induced by periodic instabilities on a polymer surface, New J. Phys. **17**, 032001 (2015)
35.42 P. Pedraz, R. Wannemacher, E. Gnecco: Controlled suppression of wear on the nanoscale by ultrasonic vibrations, ACS Nano **8**, 8859 (2015)

Enrico Gnecco

Otto Schott Institute of Materials Research
Friedrich Schiller University Jena
Jena, Germany
enrico.gnecco@uni-jena.de

Enrico Gnecco is Professor of Physics at Friedrich Schiller University Jena. He received his PhD from the University of Genova, and worked as Postdoctoral Researcher at the University of Basel and as independent Group Leader at IMDEA Nanoscience, Madrid. His research focuses on nanoscale friction, scanning-probe manipulation of metal clusters and nanocrystals, nanomechanics of abrasive wear in polymers and glasses, and the influence of ultrasonic vibrations on friction.

36. Graphene

Ado Jorio, Edmar Avellar Soares, Roberto Paniago, Mario Rocca, Luca Vattuone

This chapter presents a review on different aspects of graphene (Gr), the one-atom-thick two-dimensional sp^2 bonded carbon system. It starts by describing the pristine structure of graphene, including strain, layer stacking, and defects. Atomic and interlayer vibrations are also discussed. Next, the synthesis of graphene is addressed, including growth by segregation, using silicon carbide, molecular-beam epitaxy, and chemical vapor deposition, the latter depending on the substrate, including Ni(111), Ir(111), Rh(111), and Ru(0001). The substrate effects are considered, addressing graphene on metals, on Gr/Ni(111) (strongly n-doped), and on Gr/Rh(111) and Gr/Ru(0001) (strongly corrugated Moiré patterns). Finally, the chapter addresses metal intercalation and reactivity in graphene, ending with a summary and perspectives.

This chapter addresses the basic aspects of graphene. It is organized as follows: Section 36.1 describes the structure of graphene, considering the pristine lattice and the effect of strain (Sect. 36.1.1). Then defects are considered (Sect. 36.1.2), as well as vibrations (Sect. 36.1.3), both intra- and interlayer. Section 36.2 addresses graphene synthesis, considering growth by segregation (Sect. 36.2.1), from silicon carbide (Sect. 36.2.2), molecular-beam epitaxy (MBE) (Sect. 36.2.3), and chemical vapor deposition (CVD) (Sect. 36.2.4). Section 36.3 discusses the dependence of the CVD-grown structure on different substrates, namely Ni(111)—Sect. 36.3.1, Rh(111), and Ru(0001)—Sect. 36.3.2, Ir(111)—Sect. 36.3.3. Section 36.4 addresses metal atom intercalation under graphene. Section 36.5 deals with the reactive properties of graphene, and Sect. 36.6 provides a summary and perspectives.

The term graphene was coined in 1962 by *Boehm* et al. [36.2] to describe a one-atom-thick planar sheet of sp^2-bonded carbon atoms, densely packed in a two-dimensional (2-D) honeycomb crystal lattice, basically a single atomic layer of graphite. Graphene has been recognized as one of the most important materials for next-generation technology applications [36.3] due to its unique electronic (carrier mobility up to $200\,000\,\mathrm{cm^2\,V^{-1}\,s^{-1}}$, at electron densities of $\approx 2\times 10^{11}\,\mathrm{cm^{-2}}$ [36.4] 100 times better than silicon), mechanical (Young's modulus 1 TPa, i.e., 5× larger than stainless steel [36.5]), and optical (already some percentage absorption in the optical range for the monolayer) [36.6] properties. An isolated (single-layer) graphene, as first demonstrated in 2004 by *Noselov* et al. [36.7], can be obtained by peeling an already existing bulk graphite crystal. The fact that it could be produced by that surprisingly simple exfoliation

M. Rocca, T.S. Rahman, L. Vattuone (Eds.), *Springer Handbook of Surface Science*, Springer Handbooks,
https://doi.org/10.1007/978-3-030-46906-1_36

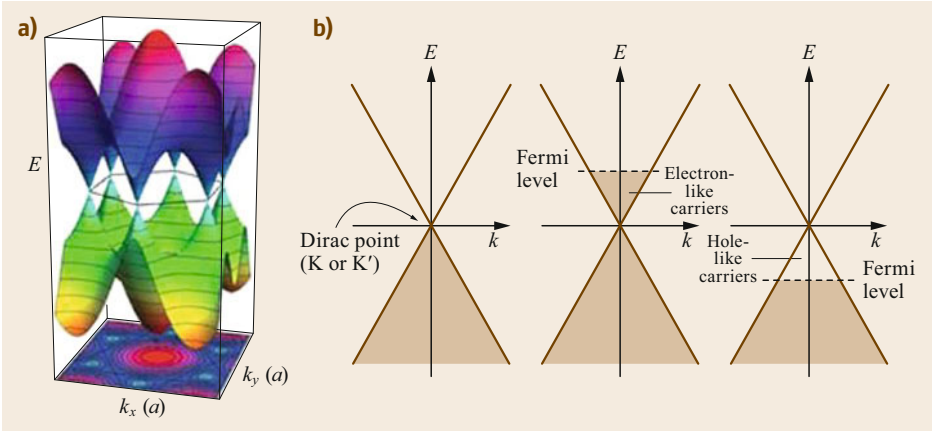

Fig. 36.1 **(a)** Calculated band structure of graphene showing the occupied (*yellow–green*) and unoccupied (*blue–red*) states, which touch each other without an energy gap at six K points in the first Brillouin zone; **(b)** simplified band structure near the K points and Fermi level-dependent charge carrier concentration. n- or p-type doping can create electron-like or hole-like charge carriers. (From [36.1] © IOP Publishing. Reproduced with permission. All rights reserved)

method has stimulated much research on this material, both fundamental and device-related.

One aspect that makes graphene so unique is that the out-of-plane p orbitals hybridize touching only at the Dirac points (K and K′ points of the two-dimensional Brillouin zone) and have a linear dispersion (Fig. 36.1). Thus the Fermi level falls at the Dirac point for freestanding pristine graphene, making it a gapless semiconductor. The carrier concentration may be easily modified, either by doping the layer with electron donors or acceptors, or applying electric fields or adsorbing gases.

36.1 Structure

Graphene is a one-atom-thick, perfectly two-dimensional system made of carbon atoms arranged in a honeycomb structure, where the atoms are bound to each other by sp^2 bonds. The strong $sp^2\sigma$ bonds allow unprecedented manipulation of this purely surface material [36.8]. This section describes the structure of the pure freestanding material, followed in the next sections by the study of its interactions with the surface of supports.

36.1.1 Pristine Graphene

In an isotropic environment, monolayer graphene exhibits a hexagonal symmetry belonging to the space group $P6/mmm$ (D^1_{6h}), with two inequivalent C atoms in the unit cell, sitting at sites usually named A and B [36.9]. The graphene unit cell, defined by the vectors $\boldsymbol{a}_1$ and $\boldsymbol{a}_2$, is illustrated in the left sketches of Fig. 36.2a,b. Small modifications in the graphene structure may lead to different symmetry groups, as indicated by the other schematics in Fig. 36.2a,b, sometimes related to other 2-D materials [36.10]. For example, starting from hexagonal graphene (left panel in Fig. 36.2a) and inducing a compressive strain along the $\hat{\boldsymbol{x}}$-direction leads to a symmetry change to the space group D^{19}_{2h} (middle panel in Fig. 36.2a), which is commonly observed for graphene under strain. Subsequently, stronger uniaxial compression may drive graphene into the space group D^7_{2h} (right panel in Fig. 36.2a), where the light and dark gray atoms are in different levels along the $\hat{\boldsymbol{z}}$-direction, a structure naturally observed in phosphorene (black P). A biaxial compressive homogeneous strain on hexagonal graphene (Fig. 36.2b) may lead to a phase transition to the D^3_{3d} space group (right panel in Fig. 36.2b). Again, light and dark gray atoms correspond to different levels along the $\hat{\boldsymbol{z}}$-direction. Such structure is also observed in phosphorene (blue P).

When stacking graphene to form many-layer systems, the most common is the so-called AB (Bernal) stacking, where one sheet is displaced with respect to the other, with corresponding carbon atoms moving from sites A and B when moving from one layer to the next. N-layer graphene (N = number of layers) has $2N$ atoms in the unit cell. Graphite ($N \to \infty$) has four atoms in the unit cell, usually in the AB stacking

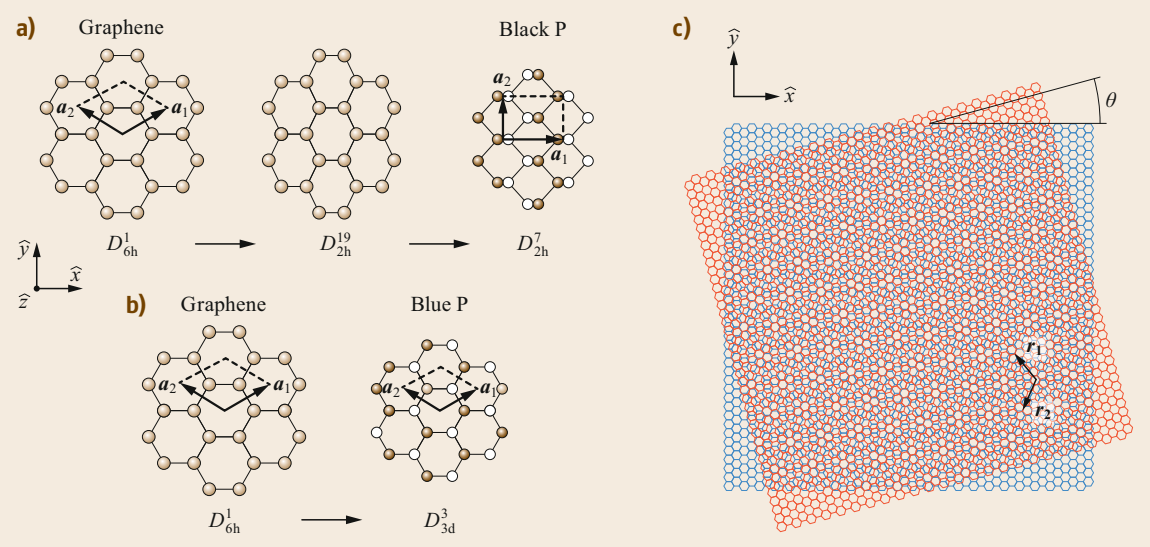

Fig. 36.2a–c Atomic structure of graphene and the effect of lattice distortions, uniaxial in (a) and hydrostatic in (b) [36.10]. Vectors $\boldsymbol{a}_1$ and $\boldsymbol{a}_2$ indicate the unit cell, where the two atoms are located on sites A (*left*) and B (*right*). The space group symmetries are given below the respective structures. When *light* and *dark gray* atoms are used, they indicate C atoms at different levels along the $\hat{z}$-direction. (c) Twisted bilayer graphene formed by two graphene sheets stacked with a mismatch angle θ between their crystallographic sheets. (Reprinted with permission from [36.11]. Copyright (2011) by the American Physical Society)

arrangement. The point group symmetries for N-layer graphene, with N even or odd, are the same as for bilayer and trilayer graphene, respectively, which are D_{3d} for N even and D_{3h} for N odd [36.9]. The main symmetry operations distinguishing these structures are (i) the horizontal mirror plane, absent for N even, and (ii) the inversion, absent for N odd.

Another interesting structure is generated by stacking two graphene layers with a mismatch rotation angle θ between the lattice structures in each layer, building the so-called twisted bilayer graphene (tBLG) [36.11–16]. The mismatch angle θ produces a superstructure that creates a Moiré pattern, which generates many other interesting phenomena. The superstructure exhibits a θ-dependent periodicity described by the two vectors

$$\boldsymbol{r}_1(\theta) = -\frac{a}{4}\left[\sqrt{3} + \cot\left(\frac{\theta}{2}\right)\hat{\boldsymbol{x}}\right] - \frac{a}{4}\left[1 - \sqrt{3}\cot\left(\frac{\theta}{2}\right)\hat{\boldsymbol{y}}\right]$$

and

$$\boldsymbol{r}_2(\theta) = \frac{a}{4}\left[\sqrt{3} - \cot\left(\frac{\theta}{2}\right)\hat{\boldsymbol{x}}\right] - \frac{a}{4}\left[1 + \sqrt{3}\cot\left(\frac{\theta}{2}\right)\hat{\boldsymbol{y}}\right].$$

36.1.2 Defective Graphene

From a topology standpoint, defects in two-dimensional (2-D) systems can be either one-dimensional (1-D, Fig. 36.3a–c; [36.17, 18]) or zero-dimensional (0-D, Fig. 36.3d; [36.19]). 0-D defects in the 2-D graphene lattice are vacancies, dopants, functional chemical groups, crystallographic variations, such as 7-5-7 Stone–Wales defects; 1-D defects in 2-D graphene are dislocations, sequence of 7-5-7-structures, and crystallite borders which appear during growth, thus enclosing a crystallite area, or simply the edge of a graphene flake [36.20–22]. This simple geometrical distinction changes defect functionality and their influence on graphene properties. Moreover, defects in the sp^2 honeycomb carbon lattice dictate structural amorphization from pristine graphene or three-dimensional (3-D) graphite down to more complex structures, such as amorphous carbon, carbon black, charcoal, biochar or, to a greater extent, organic molecules [36.23–25]. The example of sp^3 formation induced by strain in graphene will be discussed later.

36.1.3 Lattice Vibrations

The two unit-cell atoms in pristine monolayer graphene moving in three-dimensional space generate six phonon branches—three acoustic (A), with in-phase displace-

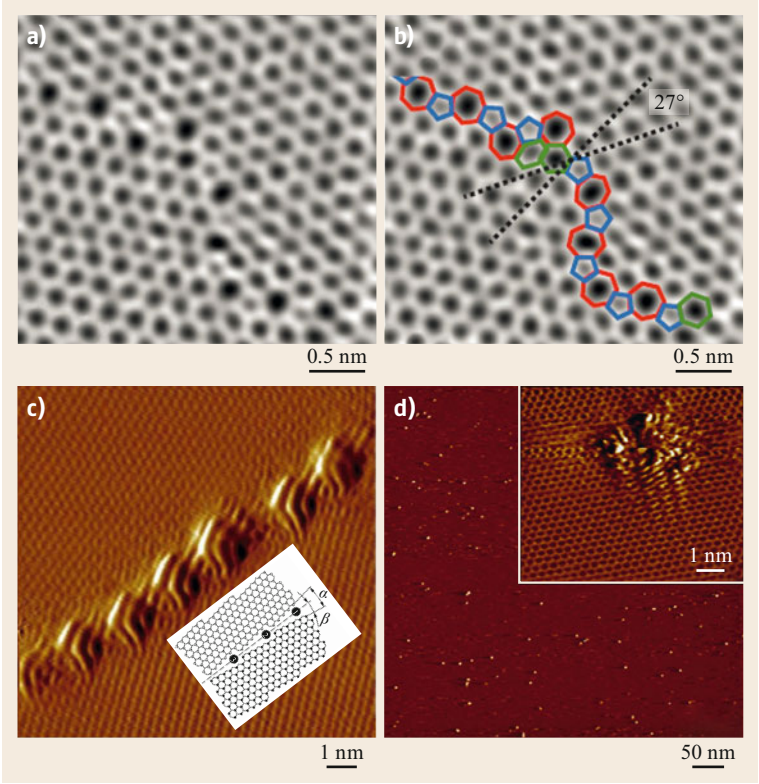

Fig. 36.3a–d Transmission electron microscopy (TEM **(a)** and **(b)**) and scanning tunneling microscopy (STM **(c)** and **(d)**) images of defects in graphene [36.17–19]. **(a–c)** are line defects [36.17]. The schematic in **(c)** shows the atomic structure responsible for the measured electronic disturbance [36.18]. **(d)** Point defects produced by Ar^+ ion bombardment on the top graphene layer in a highly oriented pyrolytic graphite (HOPG) [36.19]. The *inset* of **(d)** is a zoom of the electronic disturbance caused by a single ion impact. (**(a,b)** From [36.17]. **(c)** Reprinted with permission from [36.18]. Copyright (2009) by the American Physical Society. **(d)** Reprinted from [36.19], with permission from Elsevier)

ments of the two unit-cell atoms, and three optical (O), with out-of-phase displacements of the two unit-cell atoms. The atomic displacements in the graphene plane (i for in-plane) can be longitudinal (L) or transverse (T) with respect to the phonon wavevector direction. The atomic displacements perpendicular to the graphene plane (o for out-of-plane) are transverse (T) phonons, and they generally exhibit lower frequencies because the out-of-plane restoring forces are much weaker than the in-plane ones [36.26, 27].

Vibrations within the two-dimensional graphene plane are usually characterized by relatively large frequencies, and the stacking of multiple layers has minor importance. The in-plane longitudinal optical (iLO) and the in-plane transverse optical (iTO) phonons are degenerate, representing the only first-order Raman-active mode of graphene, called G band, belonging to the double-degenerate irreducible representation E_{2g}, appearing at $1584\,\mathrm{cm}^{-1}$ [36.26–29]. The relatively high frequency of this optical phonon ($\approx 0.2\,\mathrm{eV}$) allows the use of Raman spectroscopy to probe small environmental perturbations, including variations in strain [36.30], doping [36.31], and temperature [36.32]. The out-of-plane transverse optical (oTO) mode at the Γ point is active in infrared absorption spectroscopy [36.9]. However, the polar character of this vibration is very weak because graphene is monatomic, and infrared spectroscopy is mostly used to measure the vibrations from functionalization agents and other contaminants in graphene [36.33, 34], in addition to direct electronic effects near the K point [36.35, 36].

Interlayer vibrations exhibit much lower frequencies, because the interlayer coupling in two-dimensional materials is governed by van der Waals bonds, which are much weaker than the in-plane bonds [36.37, 38]. The physics of interlayer vibrations is independent of the specific in-plane symmetry, being general for two-dimensional materials with two layers or more, and can be used to monitor the number of layers and to study the evolution from the two-dimensional system to the bulk form [36.9]. There are two main types of interlayer vibrations, corresponding to shear (in-plane) and breathing (out-of-plane) motion of adjacent layers [36.39–45].

Experimentally, due to momentum conservation requirements necessary for achieving scattering by phonons in the interior of the Brillouin zone, most measurements rely on either neutron or x-ray inelastic scattering to probe phonon dispersion [36.37, 38, 46]. The so-obtained dispersion is shown in Fig. 36.4.

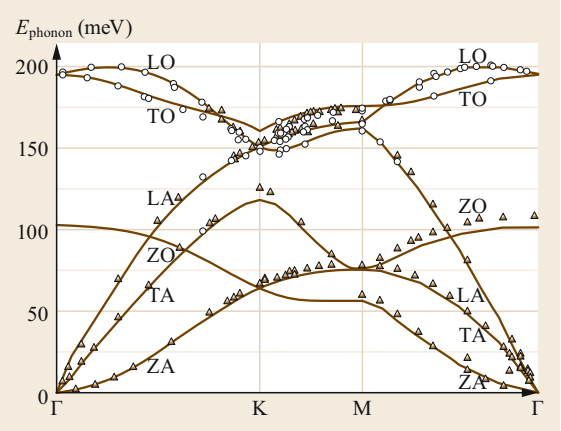

Fig. 36.4 Phonon dispersion for graphite as obtained from inelastic x-ray scattering. *Triangles* and *circles* correspond to two different sets of data, while the *continuous line* indicates density functional theory (DFT) calculations ([36.38] for details). (Reprinted with permission from [36.38]. Copyright (2007) by the American Physical Society)

Graphene, however, has a combination of factors that give rise to unique effects, making it possible to probe the phonon dispersion with inelastic light scattering in the visible range [36.11, 15, 16, 48–50].

Figure 36.5a shows a Raman spectrum obtained from an ion-bombarded graphene sample [36.19, 47]. This spectrum shows the first-order allowed G band ($\approx 1584\,\mathrm{cm}^{-1}$) and the second-order (or two-phonon) G′ ($\approx 2700\,\mathrm{cm}^{-1}$, also called 2-D band in the literature) and 2-D′ ($\approx 3120\,\mathrm{cm}^{-1}$) bands. The spectrum also shows three additional disorder-induced bands, namely the D band ($\approx 1350\,\mathrm{cm}^{-1}$), the D′ band ($\approx 1620\,\mathrm{cm}^{-1}$), and the combination D+D′ ($\approx 2970\,\mathrm{cm}^{-1}$) [36.19, 26–28, 47]. The origin of the unlabeled feature near $2450\,\mathrm{cm}^{-1}$ has been a matter of debate in the literature [36.51–53].

It has been shown [36.19] that the D to G peak area ratio (A_D/A_G) increases when increasing the number of defects, reaching a maximum value when there is defect coalescence. After this point, the A_D/A_G ratio decreases with the increasing number of defects, and the line widths increase even more significantly. The right panel of Fig. 36.5 shows a Raman-based diagram where the A_D/A_G ratio is plotted as a function of the G-band line width (Γ_G) [36.54]. Actually, A_D/A_G is normalized by multiplying the measured values by the fourth power of the excitation laser energy (E_L^4), which is known to turn the D to G area ratio independently of the excitation energy (E_L) utilized to generate the Raman scattering [36.55]. Since both A_D/A_G and Γ_G are known to depend differently on the amount of point versus line defects [36.19, 47, 56], the phase diagram was shown to span the possible amorphization trajectories for graphene, from pristine (left-hand side of the plot and $(A_D/A_G) = 0$) to highly amorphous (right-hand side of the plot). The solid line is the trajectory for purely one-dimensional defects, while the dashed line is the trajectory for purely zero-dimensional defects [36.54].

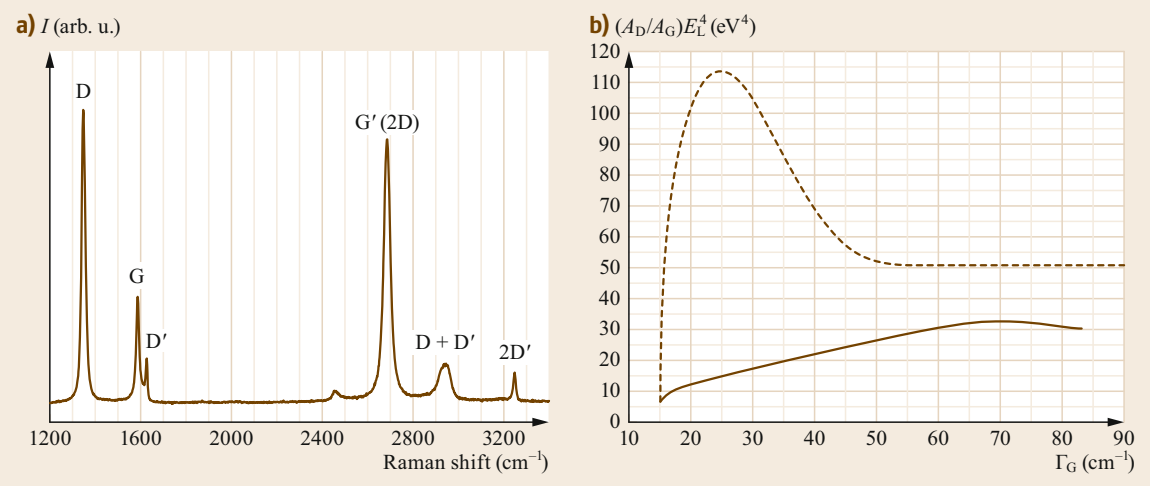

Fig. 36.5 **(a)** Raman spectrum obtained from an ion-bombarded graphene sample with average distance between point defects $L_D \approx 5\,\mathrm{nm}$ [36.47]. **(b)** Raman phase diagram for graphene amorphization. The *left-hand side* of the plot at $(A_D/A_G) = 0$, with A_D and A_G the areas of D and G peaks, respectively, corresponds to the pristine structure. Fully amorphous material appears on the *right-hand side* of the plot. The *solid/dashed lines* provide the amorphization trajectories for 1-D/0-D defects. (**(a)** Reprinted with permission from [36.47]. Copyright (2011) American Chemical Society)

36.2 Growth

Since mechanical exfoliation of graphite only produces micrometer-sized graphene flakes, great effort has been dedicated to producing graphene through different methods. Epitaxial growth is an attractive alternative, but achieving large graphene domains is still a challenge. One of the first observations of the epitaxial growth of graphene dates back to 1975 [36.57]. Heating silicon carbide in ultrahigh vacuum (UHV) causes silicon sublimation, and the nucleation of carbon atoms forming a graphene layer occurs. More recently, chemical vapor deposition (CVD), molecular-beam epitaxy (MBE), and surface segregation methods have been developed to synthesize graphene mostly on top of transition-metal surfaces. Optimization of those methods seeks high-quality graphene which should generally present large area and high crystallinity (few defects), and in most cases should also be transferable onto any substrate.

Here we focus on methods in which graphene is prepared (grown) directly on surfaces. That implies that either carbon already exists inside the substrate (diluted or a substrate constituent, as in SiC) or is added by deposition (CVD or MBE). Such methods have several advantages: they are reproducible, they do not depend on a pre-existing graphite crystal and, most importantly, they permit the production of large areas, not to mention the possibility of graphene functionalization, oxidation, doping, and intercalation, which can be done during or after the growth process. In the following section, we discuss the main methods for graphene growth on polycrystalline and on single-crystalline substrates, and also give some examples of metal–graphene intercalation to form interfaces.

36.2.1 Graphene Growth by Segregation

Traces of carbon are inevitably present in most bulk metals, and thermal annealing can drive carbon impurities to the surface, a phenomenon known as segregation. This carbon can be used to grow graphene without the need for any external carbon source, as demonstrated for Ni, Co, Fe, and Cu-Ni polycrystalline films [36.58]. The mechanism of graphene formation has been described as occurring in three steps: thermally induced diffusion of dissolved carbon to the surface; creation of growth nuclei by trapping of carbon atoms at grain boundaries (2-D-defects) and at step edges; and finally, graphene growth around those centers by lowering the temperature. The carbon segregation method also has the ability to produce multilayered graphene, in contrast to the single-layer limitation of the CVD method. Ni, Co, and Fe show very efficient growth by this method due to their high carbon solubility, while Cu, with very low maximum carbon solubility (0.04%), does not. In some experiments using single crystals, interstitial carbon enrichment is accomplished by hydrocarbon (mostly ethylene) exposure at very high temperatures. Eventually, the hydrocarbon source is closed, and the substrate is slowly cooled in order to promote graphene nucleation. Growth by carbon segregation has been obtained on single-crystalline Ru(0001) [36.59–61] (Fig. 36.6a,b) and Pt(111) [36.62], among others. For Ru(0001), it has been shown that at 850 °C, a graphene island starts its growth and, in a time scale of 90 s, achieves a length of ca. 30 μm. Two-layer-thick graphene has also been observed on ruthenium, the second layer showing weak electronic coupling to the metal.

36.2.2 Silicon Carbide

When a silicon carbide substrate is annealed at high temperature, Si atoms (or species) selectively desorb from the surface, causing its carbon enrichment, and under appropriate conditions, graphene is formed (Fig. 36.7a). Because SiC is a wide-bandgap semiconductor, graphene on commercial SiC substrates could in principle be used for electronics applications. Films grown in this way can be patterned using standard nanolithography, making them very promising for large-scale applications. This technique has been developed to grow epitaxial graphene monolayers on SiC(0001), the Si-face of silicon carbide, typically at 1200 °C and in a UHV environment [36.64, 65]. Mono-, bi-, tri-, etc., layers are formed, depending on growth parameters like temperature, heating rate, and pressure. Nevertheless,

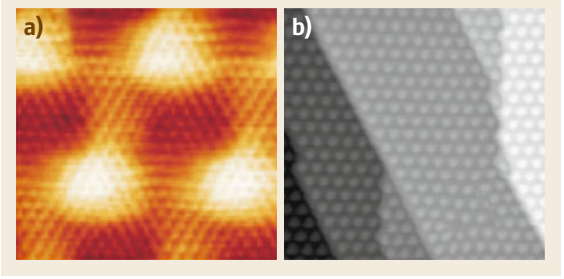

Fig. 36.6 **(a)** STM image of graphene/Ru(0001) (50 Å × 40 Å, $I_t = 1$ nA, $V_{sample} = -0.05$ V) showing different levels of apparent height, as well as atomic resolution. **(b)** Zoom-out showing the surface fully covered by graphene (500 Å × 400 Å). (Reprinted with permission from [36.59]. Copyright (2007) by the American Physical Society)

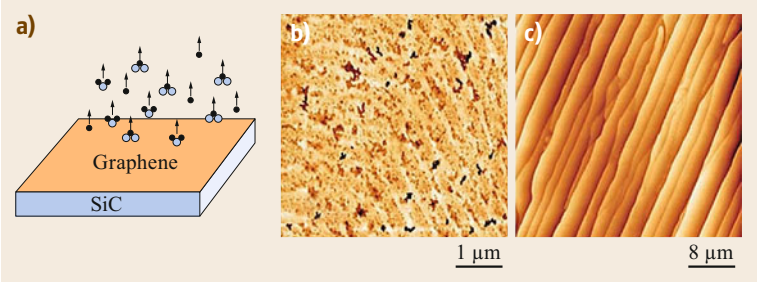

Fig. 36.7 **(a)** Growth of epitaxial graphene on SiC, via selective sublimation of Si species (Si atoms marked *blue*, C atoms marked *black*). Atomic force microscopy image of graphene grown on SiC(0001) by annealing **(b)** in UHV at 1280 °C and **(c)** in Ar environment at 1650 °C. (From [36.63])

as compared with exfoliated graphene, SiC graphene usually presents large numbers of defects, and consequently a much lower electron mobility. It is also possible to grow graphene at the Si(0001) face (so-called C-face), although in the literature, authors claim it is more difficult to control the number of layers. This aspect has to be further investigated. Even though the thermal decomposition of SiC in UHV appears promising for large-scale production, this method usually produces small grains (30–200 nm) with variable thickness. The high annealing temperature needed to provoke sublimation moreover causes drastic morphological changes at the surface. Some attempts have been made to obtain morphologically superior graphene layers, for example by using high-pressure argon (1 bar) and annealing SiC at 1650 °C [36.63]. Despite the higher temperature, this reduces the Si evaporation rate, because part of the silicon atoms are reflected back to the surface, delaying graphene formation, and allowing surface reconstruction by the enhanced surface diffusion. This method has enabled substantial surface quality improvement to be achieved (Fig. 36.7b,c).

36.2.3 Growth by MBE

Graphene formation has also been obtained on silicon carbide substrates by molecular-beam epitaxy using a solid carbon source on both SiC basal-plane surfaces [36.66, 67]. Because of the lower substrate temperatures used, this method has the advantage of not altering the SiC crystals, in contrast to the conventional graphitization method in UHV. Carbon can be generated by sublimation from a heated graphite filament [36.66] or from an effusion cell containing C_{60} [36.68], with the substrate held in the 850–1100 °C temperature range. It has been shown that by using vicinal SiC surfaces, well-ordered graphene nanoribbons (10 nm wide) are grown [36.69], in that case with carbon atoms supplied by heating resistive carbon plates at 2200 °C. Graphene growth was also successfully realized by MBE on h-BN [36.70], Al_2O_3(0001) [36.71], Pt(111), and Au(111) [36.72]. The growth of graphene from different solid carbon sources, such as polymeric films, has been demonstrated as well. By spin-coating poly(methyl methacrylate) (PMMA) thin films and heating the substrate (800–1000 °C) with a reductive gas flow (H_2/Ar), both pristine and N-doped graphene were grown [36.73].

36.2.4 Growth by CVD

A very promising way to produce large areas of high-quality graphene is the chemical vapor deposition (CVD) method, which relies on the catalytic decomposition of hydrocarbons on hot metal surfaces. The mechanism of graphene growth by CVD (Fig. 36.8) involves:

(i) Decomposition at the substrate surface
(ii) Graphene nucleation
(iii) Expansion.

However, the first step can be different for metals having high carbon solubility (such as Ni and Fe), since in that case it will diffuse into the hot substrate. As the substrate cools, the dissolved carbon will segregate to the surface, and grow graphene. Several transition-metal substrates catalyze the formation of graphene.

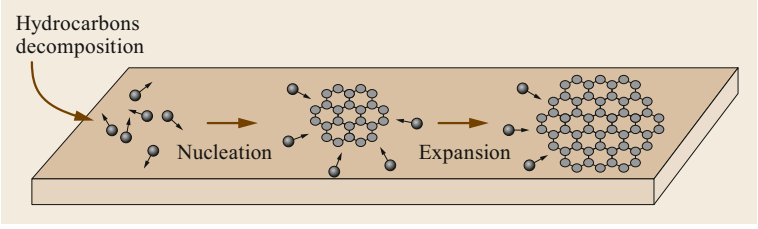

Fig. 36.8 CVD growth mechanics on transition-metal surfaces

Successful CVD growth has been reported, e.g., for Ni, Co, Ru, Ir, Pt, and Cu. The catalytic potential of transition metals is considered to be related to their partially filled d-orbitals and the formation of intermediate carbon compounds. Furthermore, growth mechanisms should be substrate-specific, and also dependent on several substrate characteristics, such as carbon solubility, tendency for carbide formation, grain boundaries, surface crystallography, and surface cleanliness. In fact, very little is established about the influence of all these factors, such as the role of transition-metal carbides in graphene formation. Nickel-carbide, which is metastable in bulk, can form an ordered surface carbide phase. It has been observed that on Ni(111), an atomic-layer-thick Ni_2C phase competes with graphene growth [36.74]. On the other hand, it has been argued that graphene growth by CVD on group IVB–VIB metals is facilitated by carbide formation [36.75]. Optimization of graphene growth is achieved by tuning several variables, including the flow of hydrocarbon gases, use of additional flow gases (e.g., Ar, H_2), substrate temperature, and cooling rate. Efforts have been made to obtain highly crystalline graphene on polycrystalline Ni and Cu. Because of the wide availability and low cost, the use of copper foils has been a standout in graphene synthesis by CVD, producing large-area and one-layer-thick graphene with excellent quality. Temperatures ranging from 800 to 1050 °C and hydrocarbons ethylene and methane are usually employed. Despite exhibiting very low reactivity with carbon, the copper surface can bind weakly to carbon atoms. Because of the low carbon solubility and because the graphene film acts as a diffusion barrier for other carbon atoms, graphene formation on Cu is regarded as predominantly a surface process. Not only is the thickness restricted to a single monolayer on polycrystalline copper, but annealing promotes larger grains. It has been observed that the highest-quality monolayer graphene is grown on the (111)-facets, with higher area coverage and short growth time in comparison with the (100)-facet or higher-index facets [36.76]. This has been attributed to the higher diffusion and improved adsorption of carbon-containing species on Cu(111). The state-of-the-art single-crystalline graphene obtained by CVD are grains with lateral size of about 1 mm and just 1 h of synthesis [36.77].

36.3 Graphene on Metal Surfaces

The epitaxial growth of large-area graphene sheets on metal surfaces is one of the most promising methods for technology applications. A thorough understanding of the atomic and electronic properties of the graphene–metal interface is therefore essential. The main driving forces of these properties are the strength of the carbon–metal interaction at the interface and the mismatch between the graphene and the metal surface lattice constants [36.78–80].

Several metal surfaces have been used as support for graphene growth, most of them having hexagonal symmetry. The local high-symmetry adsorption sites for an fcc(111) surface are presented in Fig. 36.9. In the atop geometry, the center of the graphene hexagon lies on top of the surface metal atoms, and the carbon atoms sit on the substrate fcc- and hcp-hollow sites. In the hcp configuration, the hexagon's center is on top of the second-layer metal atoms (hcp-hollow), and the carbon atoms are on atop and fcc-hollow sites, respectively. The center of the carbon–carbon bond lies on top of the topmost surface metal atom in the bridge geometry. Finally, the carbon atoms are respectively on atop and hcp-hollow sites in the fcc geometry. If there is no mismatch between the graphene and the underlying substrate, these sites define the (1×1) structures; otherwise they appear locally in the Moiré structure.

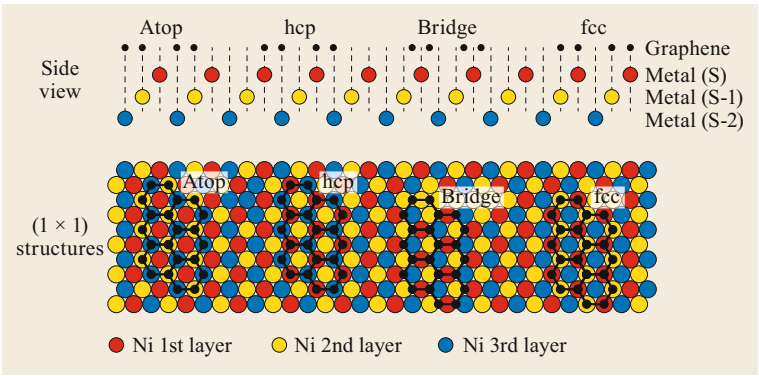

Fig. 36.9 Local adsorption sites of graphene on fcc(111) and hcp(0001) metallic surfaces

36.3.1 Graphene on Ni(111)—Strongly n-doped

Among the most commonly used single-crystalline substrates for graphene synthesis is Ni(111), with a surface lattice constant of 2.49 Å. Nickel therefore has the smallest lattice mismatch with graphene (2.46 Å). This enables a commensurate epitaxial relationship between graphene and the underlining substrate. Graphene growth by CVD on metallic single crystals usually requires previous in situ UHV surface preparation by cycles of ion sputtering (most commonly Ar^+) and annealing at high temperature. After an atomically clean and well-ordered Ni(111) is obtained, graphene can be prepared via thermal hydrocarbon decomposition at the surface. This is typically done by establishing a partial pressure (10^{-7}–10^{-6} mbar range) of propene (C_3H_6) in a UHV chamber for ca. 10 min with the crystal kept at 550 °C, resulting in a complete graphene monolayer [36.81]. It has been observed that epitaxial growth can be achieved up to 650 °C, with higher temperatures usually leading to the highest-quality graphene epitaxy, while at temperatures below 500 °C, undesired nickel carbide is formed. Growth at still higher temperatures (between 650–800 °C) is achieved only if the carbon content in the substrate is first enhanced. At these temperatures there is a significant increase in the number of rotated domains, as observed by low-energy electron diffraction (LEED) [36.82].

In the case where propene is deposited at room temperature and Ni(111) is post-annealed at temperatures between 350 and 550 °C, graphene islands are grown instead of complete coverage of that substrate [36.83]. Such graphene islands are observed to be commensurate (1×1) with Ni(111) and show either triangular or hexagonal shapes, depending on the reaction temperature. Some edges appear as zigzags, while others exhibit reconstructions, as demonstrated by atomically resolved STM images [36.84]. Evidence of a one-to-one relationship between edge type, graphene stacking, and orientation of the graphene islands has been noted.

As already pointed out, due to the small mismatch between the graphene and the Ni(111) lattice constants (about 1.3%), graphene grows assuming the substrate periodicity resulting in a (1×1) structure. Most experimental and theoretical investigations on the structure of Gr/Ni(111) have considered six possible structural models, which are presented in Fig. 36.10.

The first structural determination of the Gr(1×1)/Ni(111)(1×1) interface was performed by *Gamo* et al. [36.86] using LEED. In this work, the hcp model was the one that best fit the experimental LEED-IV curves. However, first-principles calculations based on the DFT approximation, including the van der Waals interactions, predicted that hcp and bridge models were energetically degenerate and that both structures could coexist on the surface [36.87]. The first experimental evidence of this coexistence came from a high-resolution x-ray photoemission spectroscopy (HR-XPS) study [36.88]. The graphene domains in the fcc structure were also observed on the surface in STM experiments [36.89] and in a subsequent XPS study [36.90], where the relative coverage of

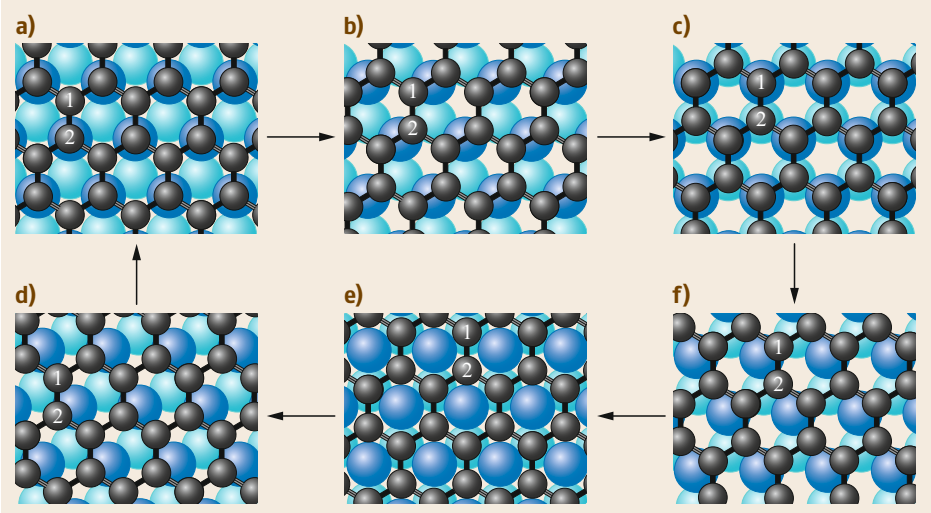

Fig. 36.10a–f Possible structural models for graphene on Ni(111): **(a)** top-fcc (hcp), **(b)** bridge-top (bridge), **(c)** top-hcp (fcc), **(d)** bridge-hcp (bridge-hcp), **(e)** hcp-fcc (atop), and **(f)** bridge-fcc (bridge-fcc). The models are obtained by shifting the graphene layer with respect to the Ni(111) surface in a direction along a C–C bond

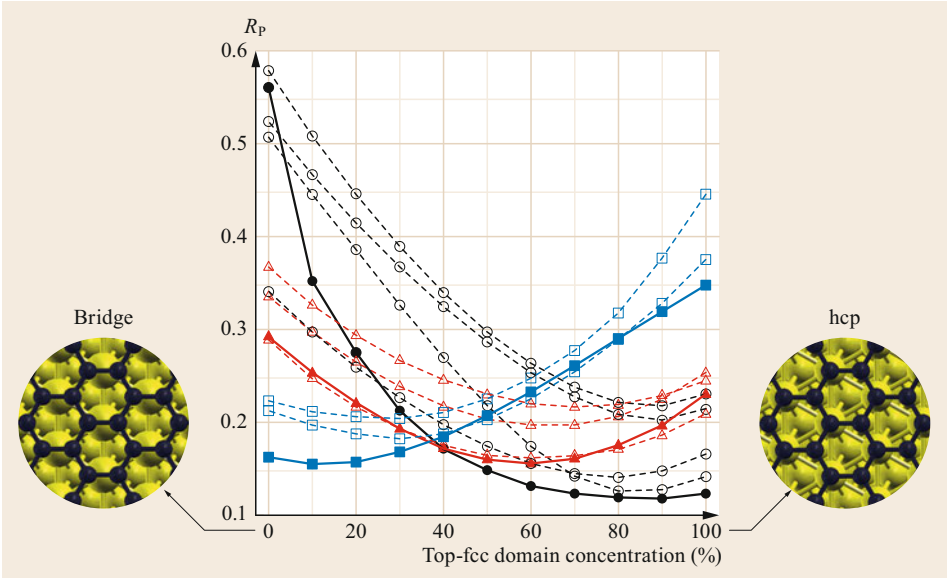

Fig. 36.11 Pendry R-factor R_P as a function of the hcp domain concentration for the 12 different LEED experiments. (Reprinted with permission from [36.85]. Copyright (2014) by the American Physical Society)

the different structures was shown to depend strongly on the details of the graphene preparation procedure. In a more recent structural determination combining LEED, photoelectron diffraction (PED), and DFT calculations, the hcp and bridge domains were found to coexist, and the structures of both were successfully determined [36.85]. The R_P-factor (a quantity defined to quantify the agreement between the experimental and theoretical LEED-IV curves) [36.91] as a function of the hcp domain concentration is presented in Fig. 36.11 for the 12 different LEED experiments. The best-fit models range from pure hcp domains (black lines) to pure bridge domains (blue lines). The experiments where a coexistence of both domains better reproduces the experimental LEED-IV curves are plotted in red. No evidence of the fcc structure was observed in this study.

A summary of the Gr(1×1)/Ni(111)(1×1) structural parameters is presented in Table 36.1 and Fig. 36.12. The main structural features are the interlayer distance between graphene and the topmost Ni layer of 2.11 Å, and the very small height difference (0.05 Å) between the two carbon atoms of the graphene sublattices. This small interlayer distance, compared with graphite interlayer distances, is a consequence of the strong interaction between C and Ni atoms at the interface. In particular, there is strong n-doping of graphene due to electron transfer from the Ni 4s to the Gr π states, and angle-resolved photoemission electron spectroscopy (ARPES) experiments performed on this interface clearly show a gap opening on the Gr π band [36.78].

36.3.2 Graphene on Rh(111) and Ru(0001)

Graphene growth on Rh(111) is also possible by CVD by exposing it to hydrocarbons (e.g., ethyne: C_2H_2) in UHV. However, for this system, the temperature window is much narrower (740–780 °C), with lower-temperature synthesis inducing rhodium carbide growth. STM images exhibit large graphene domains crossing several substrate steps without visible defects and also forming a Moiré structure caused by the lattice mismatch [36.92, 93]. The corrugation of graphene/Rh(111) measured by STM and AFM was between 0.5 and 1.5 Å, depending on the imaging conditions. The growth of high-quality single-layer

Table 36.1 The most relevant structural parameters for the Gr(1×1)/Ni(111)(1×1) interface (given in Å)

Distance	Old LEED (hcp) [36.84]	LEED (hcp) [36.89]	LEED (bridge) [36.89]	PED (hcp) [36.89]	DFT+vdW (hcp) [36.89]	DFT+vdW (bridge) [36.89]
d_{C-C}	0.05	0.05 ± 0.03	0.07 ± 0.05	0.04	0.01	0.00
d_{C-Ni1}	2.11 ± 0.07	2.11 ± 0.03	2.13 ± 0.05	2.12	2.11	2.05
$d_{Ni1-Ni2}$	1.96 ± 0.07	2.01 ± 0.01	1.98 ± 0.05	2.01	2.05	2.05
$d_{Ni2-Ni3}$	2.09 ± 0.07	2.04 ± 0.03	2.03 ± 0.04	2.04	2.04	2.04
$d_{Ni3-Bulk}$	2.03	2.03 ± 0.05	2.03 ± 0.04	2.04	2.04	2.05

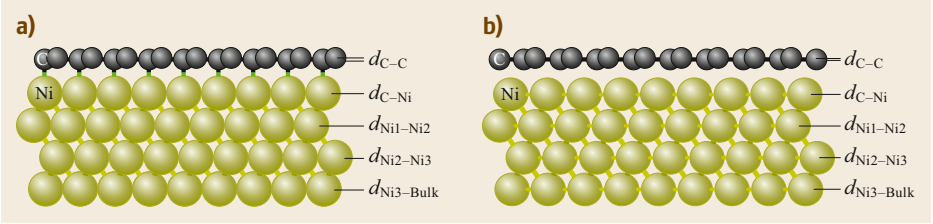

Fig. 36.12a–b Side view of the hcp **(a)** and bridge models **(b)** for the Gr(1×1)/Ni(111)(1×1) interface

graphene on rhodium has also been reported by low-pressure CVD (2×10^{-7} mbar, 90 L exposure) using 3-pentanone ($CH_3-CH_2-CO-CH_2-CH_3$) with the substrate at 790 °C [36.94].

Growth of graphene on Ru(0001) is usually performed by carbon segregation [36.60], firstly exposing a clean Ru(0001) surface to 10^{-7} mbar of ethylene or propylene at room temperature, followed by annealing to 1030 °C [36.95]. Due to the large misfit between the graphene and the surface lattice constants and the strong interaction of carbon and metal atoms at the high-symmetry adsorption sites, the growth of graphene on Ru(0001) always leads to the formation of strongly corrugated Moiré patterns [36.60, 78, 79, 96, 97]. For the Gr/Ru(0001) interface, the lattice mismatch is about 9.0%, and most of the structural details have been revealed by LEED, surface x-ray diffraction (SXRD), STM, and ab initio calculations [36.59, 98–105]. Nowadays, the widely accepted structure is the Gr(25×25)/Ru(0001)(23×23), which means that 25 graphene unit cells are contained in 23 Ru(0001) surface unit cells. All the structural studies agree that graphene has considerable corrugation of about 1.5 Å (from the LEED analysis), and the minimum graphene–metal distance is about 2.1 Å. A summary of the results reported in the literature for this complex system is presented in Fig. 36.13.

The large modulation exhibited by the Gr(25×25)/Ru(0001)(23×23) interface has been used as a template for self-organized growth of different types of nanostructures [36.106]. The regions in the Moiré structure at different heights with respect to the underlying substrate have different surface potentials and behave differently with regard to nucleation centers. A textbook case is the deposition, at room temperature, of C_{60} molecules on the Gr(25×25)/Ru(0001)(23×23) interface. In the low-coverage range of 0.04–0.4 ML, STM images reveal the successive occupation of the adsorption sites within the Moiré structure. First, individual molecules populate the hcp valley sites, followed by an additional six molecules in a close-packed arrangement. Next, the fcc valley sites are occupied, followed by the Moiré hill sites. Around 0.4 ML, six additional close-packed molecules are imaged around the hill sites [36.107]. A correlation between the site occupation and the variation in the absorption energies between the different sites in the Moiré structure can be established.

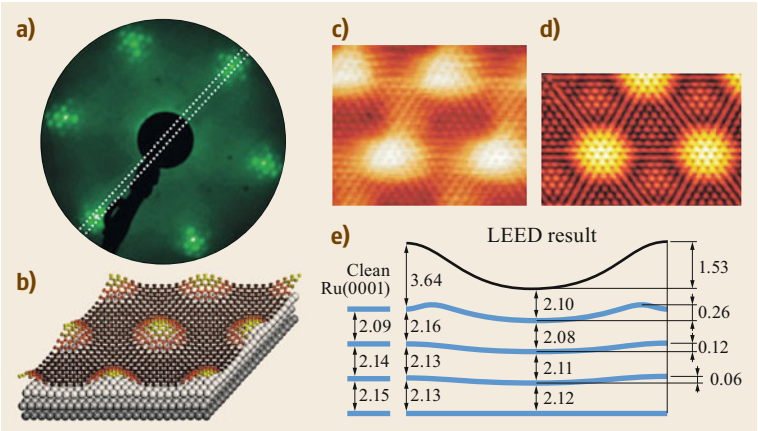

Fig. 36.13a–e Summary of results reported in the literature for the Gr(25×25)/Ru(0001)(23×23) interface. **(a)** LEED pattern at 112 eV showing single-domain graphene with superstructure spots due to Moiré pattern. **(b)** A three-dimensional surface structure model. **(c)** Experimental STM image acquired at 0.05 V bias voltage and 1 nA tunnel current. **(d)** Simulated STM image, and **(e)** schematic drawing of graphene and Ru-surface layers derived from LEED I(V) analysis, values are given in Å (Reprinted from [36.79], with permission from Elsevier)

Another good example of self-organized growth at the Gr/Ru(0001) interface is the deposition of iron phthalocyanine (Fe-Pc) molecules [36.108]. At lower coverage, the Fe-Pc molecules preferentially adsorb in the fcc valley sites. After saturation of the fcc sites, the molecules adsorb at the edge of the Moiré sites, avoiding the hcp valley hollows.

36.3.3 Graphene on Ir(111)

The growth of epitaxial graphene on Ir(111) was investigated extensively by *Coraux* et al. [36.109, 110] using STM, employing two preparation procedures: (i) room-temperature ethyne (C_2H_2) adsorption followed by thermal decomposition (600–1200 °C), and (ii) direct exposure of the hot substrate (600–1050 °C). The morphologies are distinct, the first route leading to graphene nanoislands with controllable size, depending on the growth temperature. The second route enables 100% coverage and very high structural quality above 930 °C. Because of the 9% surface lattice mismatch with Ir(111), both routes result in single-layer graphene with a Moiré superstructure, so that the positions of the C atoms relative to the underling metal atoms change periodically. The interaction between graphene and Ir(111) is very weak, which may cause the appearance of misoriented domains. In general, synthesis at lower temperatures leads to rotated domains, while higher growth temperature induces preferred orientation, forming the Moiré structure with periodicity of (10×10)/(9×9), as shown in Fig. 36.14. In comparison with other metal substrates, Ir(111) shows one of the highest graphene–substrate separations (3.4 Å), characterizing a weakly interacting system. For strongly interacting metals such as Ni(111), Rh(111), and Ru(0001), the graphene–metal separation is about 2.2 Å. That is also a reason why the graphene is shown crossing step edges on the Ir(111) substrate while maintaining structural coherency.

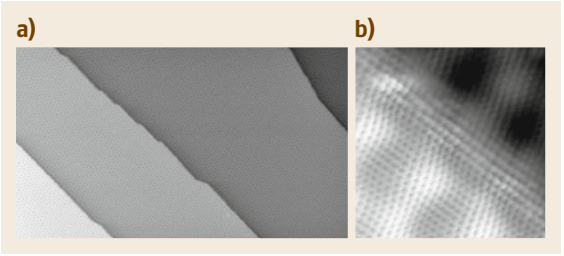

Fig. 36.14 **(a)** STM image (2500 Å × 1250 Å, 0.10 V, 30 nA) of graphene/Ir(111), showing Moiré superstructure crossing several Ir steps. **(b)** Atomically resolved STM (50 Å × 50 Å, 0.04 V, 30 nA) across a step edge. (Reprinted with permission from [36.109]. Copyright (2008) American Chemical Society)

36.4 Metal Intercalation

The intercalation of a different material layer between the graphene and substrate can lead to the fabrication of novel low-dimensional structures, in many cases significantly altering the interface interaction. That has been evidenced, for example, by interfacial reaction with oxygen, which decouples the graphene from Ru(0001) [36.111], originally exhibiting a strong interaction at the graphene–metal interface. Therefore, intercalation can in some cases result in quasi-freestanding graphene, which could potentially be transferred to another material.

An epitaxial interface with a certain metal, onto which graphene does not grow directly, can be produced by metal intercalation. It has been observed for the graphene/Ni(111) system intercalated by Au that the π bands recover the typical linear dispersion near the K point, resembling a nearly free layer [36.112]. Cs intercalation between graphene and Ni(111) has the effect of enlarging the distance between the graphene sheet and the substrate, achieving quasi-freestanding graphene as well [36.113, 114]. It was also shown that the intercalation of Al between the graphene layer and Ni(111) surface is able to detach the graphene from the substrate. After intercalation, the graphene/Al/Ni(111) interface shows a (2×2) reconstruction [36.115].

One of the obstacles to the effective use of graphene in electronics is the lack of an energy gap. It has been shown that bandgap opening can be obtained by epitaxial growth on a SiC substrate [36.116], or by the patterned adsorption of atomic hydrogen onto the Moiré superlattice positions of Gr/Ir(111) [36.117]. There are several examples of Gr/metal-intercalated systems showing substantial gap opening at the Dirac point of graphene, including Gr/Cu/Ir(111) [36.118], Gr/Pb/Pt(111) [36.119], Gr/Bi/Ir(111) [36.120], and Gr/Ag/Ni(111) [36.121]. Moreover, the graphene binding energy can be altered by means of alkali metal and halogen intercalation, which induces n-doping and p-doping of graphene, respectively. It has been shown that the Dirac point can be tuned almost continuously between strong n-type doping for Li, and strong p-type doping for F [36.122].

Protection of metal surfaces is another well-known property of graphene/metal systems. It has been

demonstrated both experimentally and theoretically that graphene layers on Cu, Ni, and Cu/Ni alloys protect the underling substrate from corrosion. The possibility of intercalating different metallic layers between graphene and an original substrate opens up a wide range of options in this matter and in interface magnetism as well. In general, metal intercalation produces modifications of the crystallographic and electronic structure of the system.

The intercalation of metal monolayers such as Au, Ag, Cu, Fe, and Sn underneath a graphene sheet grown on Ni(111) has been the object of several investigations. The intercalation of one or two Fe monolayers (ML) is accomplished by deposition of this nominal thickness on freshly prepared graphene/Ni(111), followed by annealing at 320 °C for 15 min [36.123]. At this temperature (and heating time), interfacial alloying effects are negligible, leading to a graphene/Fe/Ni(111) intercalated system. The mechanism of metal–atom intercalation is not completely understood, but it is believed to occur through grain boundaries and structural defects. For 1- and 2 ML films, iron atoms assume commensurate fcc stacking on the Ni layer, with graphene maintaining the same registry as for graphene/Ni(111). Moreover, the carbon distance to the last iron layer for graphene/Fe/Ni(111) is very similar (2.1 Å) to the graphene/Ni(111) system [36.123]. Fe-intercalation was also produced on graphene/Pt(111); in that case the iron strongly modified the graphene band structure by lifting its band spin degeneracy [36.124]. Co-intercalation has also been obtained for graphene on Ir(111) [36.125]. This graphene-covered system showed unconventional magnetic properties, much different from pristine cobalt films, suggesting magnetic interaction with graphene.

36.5 Chemical Reactivity of Graphene

The reactive properties of graphene were recently reviewed [36.1]. Adsorption of gases is important in fabricating highly sensitive sensors, removing undesired molecules in environmental applications, or inducing a gap opening for electronic applications. The importance of this topic is manifested in the growing number of papers in the literature each day.

36.5.1 Adsorption of Gases at Freestanding Graphene

Due to its electronic configuration, graphene is expected to be chemically inert. However, pioneering experiments [36.126] have demonstrated that it can be used as a very sensitive sensor for various simple gases, and that the latter can be regenerated by annealing to 423 K. The nature of the adsorption site on graphene may well be connected to defects or dopants rather than to adsorption at pristine sites, since the sensing activity was demonstrated to be suppressed after removing the contaminants introduced by the use of nanolithography [36.127].

Several theoretical papers have addressed the gas–graphene interaction, calculating for this purpose the adsorption energy of simple molecules such as CO, H_2O, NO, and NH_3 on freestanding graphene. While the actual result depends on the adsorption site, molecular orientation, and critically on the calculation method used (see [36.128] for H_2O), the values obtained are always quite low, at most 47 meV for H_2O, 31 meV for NH_3, 14 meV for CO, 67 meV for NO_2, and 29 meV for NO [36.129]. Nevertheless, the charge transfer for the different gases, albeit small, came out with the correct sign, whereby H_2O and NO_2 behave as electron acceptors, and NH_3, CO, and NO as donors. This small charge transfer causes significant n- or p-doping of graphene [36.1] because of the vanishingly low carrier concentration at the Dirac point. Doping therefore results in a measurable change in the resistivity.

The adsorption energy of the simple molecules mentioned above on unsupported graphene should be significantly larger at doped sites and at defects [36.130]. For example, for NO and NO_2 at N-doped sites, the adsorption energy is predicted to be 341 and 325 meV, respectively [36.131]. Similarly, doping with Al increases the latter values significantly for CO, CO_2, and O_2. In general, doping with heteroatoms such as Al, Cr, or Mn has a larger effect for O_2 than N- or B-doping [36.132].

The adsorption energy of simple gases is also predicted to be larger at di-vacancies: for example, it should be as high as −8.44, −4.53, −13.83, and −3.86 eV for O_2, N_2, B_2, and CO, respectively [36.133]. Another theoretical paper suggested that graphene vacancies could be healed by sequential exposure to CO and NO. The former gas would thereby adsorb at the vacancy, while NO would react with it to NO_2, leaving a C atom which could eventually repair the vacancy. Similarly, controllable N-doping should be achievable by vacancy creation (e.g., by an electron beam) and subsequent exposure to NO at room temperature [36.134].

As an example of an environmental application, we cite the use of graphene for the removal of bisphenol A (BPA), a monomer used for the production of epoxy resins and harmful to living organisms, from aqueous solutions, with the remarkable adsorption capacity of 182 mg/g [36.135]. The process is exothermic by 34 kJ/mol but, thanks to the entropic contribution to the free energy, adsorption can also take place spontaneously around room temperature. The large adsorption affinity of graphene for BPA was explained by the interaction of its single-layer planes with aromatic rings and the residual oxygen-containing groups, which can form π–π and hydrogen bonds with the benzene rings and the hydroxyl groups of BPA.

Graphene powders obtained from the reduction of graphene oxide have demonstrated a hydrogen adsorption capacity of the order of 0.1 wt% at 298 K. The latter is expected to increase up to 0.72 wt% at 100 bar given a measured isosteric heat of adsorption value between 4 and 5.9 kJ/mol [36.137].

At least one review paper has recently appeared that covers the topic of environmental application of graphene composites for water remediation and gas adsorption [36.138]. The material employed, however, is often not graphene, but graphene oxide, which is much more reactive than graphene itself and has very different electronic properties. For example, experiments have shown that NH_3 can be effectively removed by modifying graphene oxide with polycations or nanoparticles. These materials are undoubtedly promising for applications.

Adsorption of organic molecules on graphene flakes has also been investigated. In this case, low values of the chemisorption energy are found (Table 36.2).

In Fig. 36.15, the adsorption enthalpy versus increasing surface coverage is shown for three organic molecules. It was found to decrease with exposure and to become independent of coverage above ≈ 2% coverage. This process was modeled theoretically, simulating the graphene layer with a coronene molecule. About 60% of the adsorption energy was found to be provided by dispersive forces, while the second major contribution came from electrostatic interactions.

Table 36.2 Experimentally determined adsorption enthalpies for several organic molecules on graphene flakes [36.136]

Molecule	ΔH_{ads} (kcal/mol)
Acetone	-8.2 ± 0.3
Acetonitrile	-7.6 ± 0.3
Dichloromethane	-5.9 ± 0.5
Ethanol	-7.3 ± 0.7
Ethyl acetate	-11.5 ± 0.2
Hexane	-12.2 ± 0.2
Toluene	-13.5 ± 0.3

As long as freestanding graphene is considered, strong chemisorption at pristine graphene sites can be obtained only in solution for highly reactive radicals (e.g., aryl), in vacuum for atomic hydrogen or using plasmas.

36.5.2 Reactivity of Supported Graphene Layers

Most studies on graphene reactivity have been performed for layers grown on a reactive substrate or transferred on a support by different methods. Such layers may thus show effects associated with mechanical strain and are influenced by the possibly strong interaction with the support.

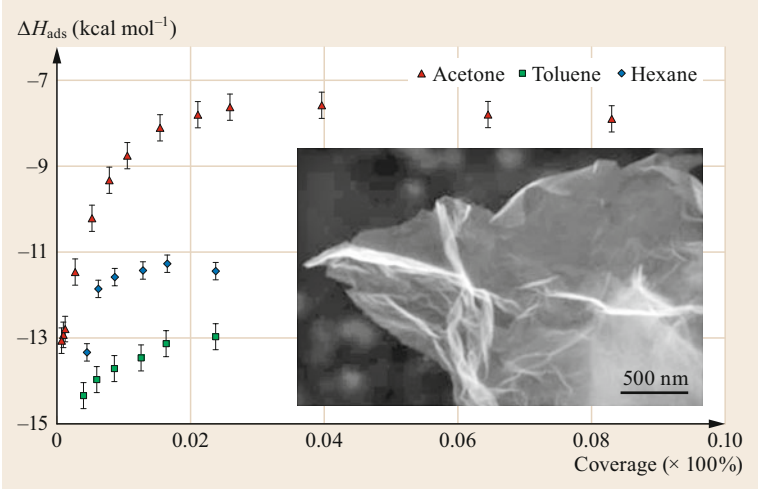

Fig. 36.15 Adsorption enthalpies (ΔH_{ads}) of acetone, toluene, and hexane on graphene flakes as a function of coverage. In the *inset* a SEM image of the graphene flake is shown. (Reprinted with permission from [36.136]. Copyright (2013) American Chemical Society)

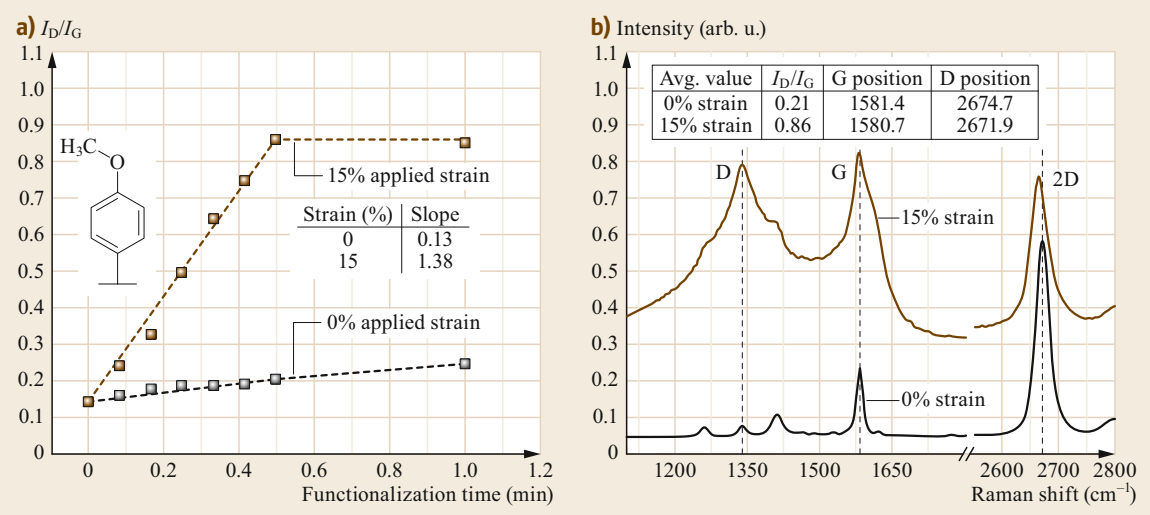

Fig. 36.16 **(a)** Ratio of the intensity of D and G bands as a function of the dose to 4-MBD for unstrained (*black*) and 15% strained graphene (*red*). **(b)** Comparison of the corresponding Raman spectra. (Reprinted with permission from [36.139]. Copyright (2013) American Chemical Society)

Effect of Mechanical Strain

Mechanical strain can be applied to graphene by stretching the supporting substrate. The effect on the reactivity was probed with three different aryl molecules: 4-nitrobenzenediazonium (4-NBD), 4-bromobenzenediazonium (4-BBD), and 4-methoxybenzenediazonium (4-MBD) [36.139]. The reaction occurs in two steps: first, a delocalized electron from an occupied level of graphene is transferred into an unoccupied level of the diazonium cation, giving rise to an aryl radical; the latter then binds to the graphene lattice, modifying the local hybridization state from sp^2 to sp^3. Such modification causes an increase in the defect-related D band in the Raman spectrum (Sect. 36.1.2). The ratio of the intensities of the D and G bands can thus be used to monitor the process. Since functionalization induces doping, the Raman spectrum also exhibits a shift of G and 2-D peaks (see table in the inset of Fig. 36.16b). We remind the reader here that p-type doping causes an upshift of the frequencies, while n-type doping has the opposite effect, for both G and 2-D modes (see Fig. 36.16). It is apparent that the increase in the ratio of the peak intensities I_D/I_G with functionalization dose occurs more rapidly for the strained sample, and also that the final concentration of the functionalized sites is then larger, thus proving that straining effectively modifies the reactivity of graphene with respect to covalent functionalization.

Mechanical strain can also be obtained by depositing nanoparticles on the substrate. For this purpose, monolayer graphene was deposited on a Si wafer decorated with SiO_2 nanoparticles (NPs) and then exposed to aryl radicals. Using micro-Raman mapping, the latter were found to selectively react with the regions of graphene strained by the underlying NPs [36.140].

Role of the Support in Determining the Chemical Reactivity of Graphene

Since in real systems graphene is rarely freestanding and is almost always supported on a substrate, the question that naturally arises is whether the interaction with the substrate can affect the reactivity of the graphene layer.

Burghaus and coworkers [36.141] investigated adsorption of water on graphene supported on Cu and on SiO_2 under controlled UHV conditions. In Fig. 36.17 we show the temperature desorption spectroscopy (TDS) rates recorded by these authors after different exposures to water for graphene on silica (Fig. 36.17a) and on a Cu foil (Fig. 36.17b).

The following are apparent: (a) For graphene/SiO_2, the only TDS feature shifts initially to lower temperatures with increasing exposure (see the red dashed line in Fig. 36.17a) and then remains constant. The leading edges at low temperature and low coverage are not aligned, yielding a straight line with positive slope in an Arrhenius plot (not shown), indicating deviation from zero-order kinetics. The latter is restored at higher exposures, since water then starts to condense. (b) Also, for graphene/Cu, only one TDS peak is evident. It shifts slightly to greater temperatures, however, with increasing exposure. The exponential rise of the peak at low temperature and the common leading edges are indicative of ice sublimation and zero-order kinetics.

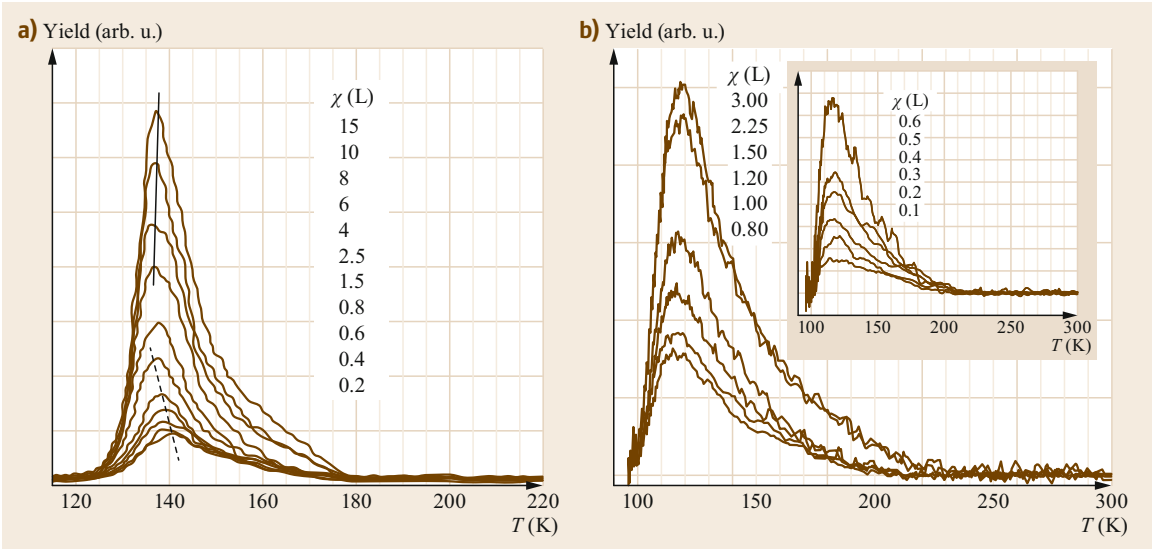

Fig. 36.17a,b TDS of water ($m/e = 18$) as a function of water exposure on hydrophilic graphene/SiO_2 **(a)** and on graphene/Cu **(b)**. Data for lower exposures are shown in the *inset*. (Reproduced from [36.141] with permission of The Royal Society of Chemistry)

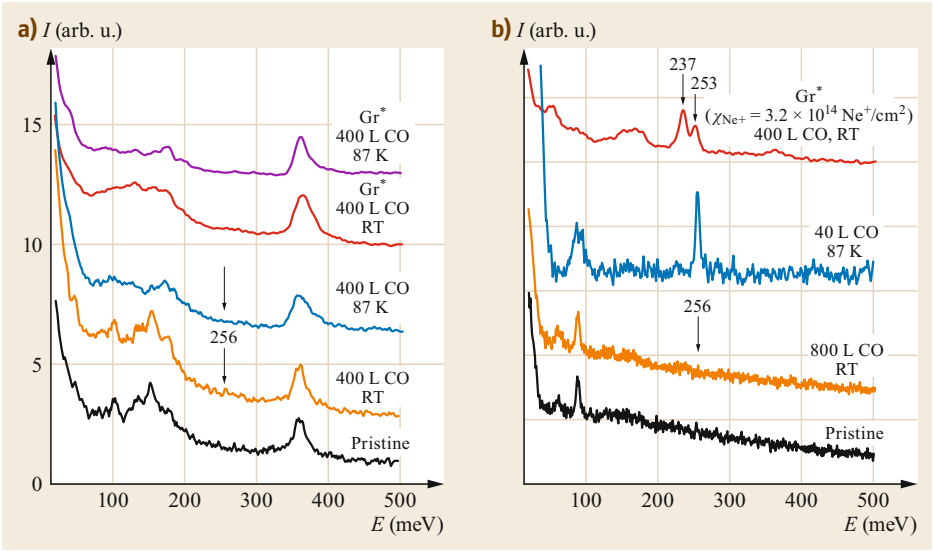

Fig. 36.18a,b High-resolution electron energy loss spectra recorded after exposure to CO graphene grown on **(a)** polycrystalline Cu and **(b)** Ni(111) under different conditions

The deviation from zero-order desorption kinetics for water adsorption on graphene/SiO_2 at lower exposures is indicative of a hydrophilic interaction and of surface wetting. On the contrary, water adsorption on graphene/Cu is consistent with hydrophobic interactions, similar to the case of water on graphene/Ru [36.142]. The authors concluded that graphene wettability is inversely correlated with the wettability of the support, i.e., if the support is hydrophobic, graphene shows wetting behavior, and if the support is hydrophilic, it shows nonwetting behavior.

The influence of the substrate on graphene reactivity was also investigated using CO as a probe under controlled UHV conditions [36.143]. The results are summarized in Fig. 36.18.

It is apparent that in the high-resolution energy loss (HREEL) spectra:

1. No signature of CO adsorption is observed upon exposure of pristine graphene at room temperature (RT).

2. On the contrary, at liquid nitrogen temperature, a loss at 256 meV forms, corresponding to the CO stretch mode, which is apparent upon exposure of graphene grown on Ni(111) but not on polycrystalline Cu. The additional losses present for the latter system are due to incomplete dehydrogenation of the molecules used to produce the graphene layer and are also present before CO exposure (see lowest trace).
3. If isolated defects are introduced in the graphene layer by a small ion bombardment dose with 100 eV Ne^+ ions (Gr^*), the subsequent exposure to CO at RT generates two electron energy losses for graphene grown on Ni(111), but not for graphene on Cu.

These results clearly indicate that graphene on Cu is inert with respect to CO adsorption, while graphene on Ni(111) is reactive.

If the sample is heated, the CO-related features disappear at quite different temperatures in the absence and in the presence of defects. In the former case, the heat of adsorption is estimated to be 0.35 eV/molecule at 1/3 ML, and 0.58 eV/molecule in the low-coverage limit. These values, the presence of the molecule-surface stretch, and the redshift of the CO stretch frequency with respect to the gas phase value provide evidence of weak molecular chemisorption. Out of the different configurations that Gr can take on Ni(111), the top-fcc (hcp) configuration (Sect. 36.3.1) was proven to have the highest reactivity to CO. The active site was identified with the carbon atom placed in the fcc position [36.144].

The reactivity of graphene on Ni(111) has also been investigated experimentally using water as probe gas. Following exposure at RT, decomposition and hydrogen production occur [36.145].

The interpretation of the results for CO adsorption on sputtered graphene is not straightforward. Two CO stretch features are present in the HREEL spectra, suggesting the existence of both single (loss at 253 meV) and doubly coordinated (loss at 237 meV) CO admolecules. If the vacancy itself were reactive, as suggested by several theoretical investigations for freestanding graphene [36.129], adsorption should also occur for sputtered graphene on Cu, contrary to experimental evidence.

Both energy losses of CO on Gr^*/Ni(111) disappear upon annealing between 350 and 400 K. Indeed, this temperature range and the observed vibrational frequencies compare well with those of CO/Ni(111). It was thus concluded that CO adsorption does not occur *at the vacancy* itself, but that, thanks to the presence of the vacancy, CO has intercalated between graphene and the Ni substrate. This straightforwardly explains the inertness of Gr^* on Cu, since the heat of adsorption of CO on this metal is too low to allow for stable adsorption.

Interestingly, if the Gr^*/Ni(111) system is annealed to induce CO desorption and then is exposed again at RT, the newly obtained CO coverage is smaller than for the first uptake. This indicates that part of the vacancies were repaired in the previous cycle and are therefore unreactive. For this reason, it was suggested that a Boudouard reaction between two adsorbed CO molecules takes place on the Ni substrate, producing CO_2 (which desorbs) and leaving one carbon atom that can repair the vacancy. This process is enabled with high efficiency thanks to the confinement of the CO admolecules in the space between the graphene layer and nickel surface, providing an example of a reaction under cover (see dedicated section below). The role of vacancies in the chemistry of graphene is thus not as straightforward as was suggested by pioneering theoretical studies for freestanding graphene. The substrate does indeed play a key role in determining the chemical reactivity of the graphene layer.

Other results indicate an active role of vacancies for functionalization. For example, enhanced reactivity toward selective oxidation of the amino group and the subsequent integration of the nitrogen atom within the graphene network was reported for graphene deposited on SiC [36.146]. The effect was ascribed to the excess charge at carbon dangling bonds at single-atomic vacancies. Graphene deposited on silicon carbide thus behaves differently from graphene on metals. The difference is presumably due to the formation of bonds between the C at the edge of the vacancy and the metallic substrate.

For water adsorption, theory predicts a different reactivity for vacancies drilled on graphene grown on Cu and Pt [36.147]. The C atoms close to the vacancy backbond to the metallic substrate in both cases, but since the Pt–C bond is stronger than the Cu–C bond, it is energetically convenient for H_2O to dissociate at the vacancy site of graphene on Cu, but not when the substrate is Pt.

The role of the substrate in graphene reactivity is also evident in the efficacy of covalent functionalization. The presence of large surface charge fluctuations induced by the substrate, for example, enhances the reactivity of aryl diazonium molecules with graphene supported on SiO_2 and Al_2O_3 [36.148], while adsorption is negligible on alkyl-terminated and hexagonal boron nitride (hBN) surfaces.

A review on the functionalization of graphene derivatives, including graphene oxide (GO), hydrogenated graphene (graphane), and graphene fluoride (fluorographene), was recently published [36.149].

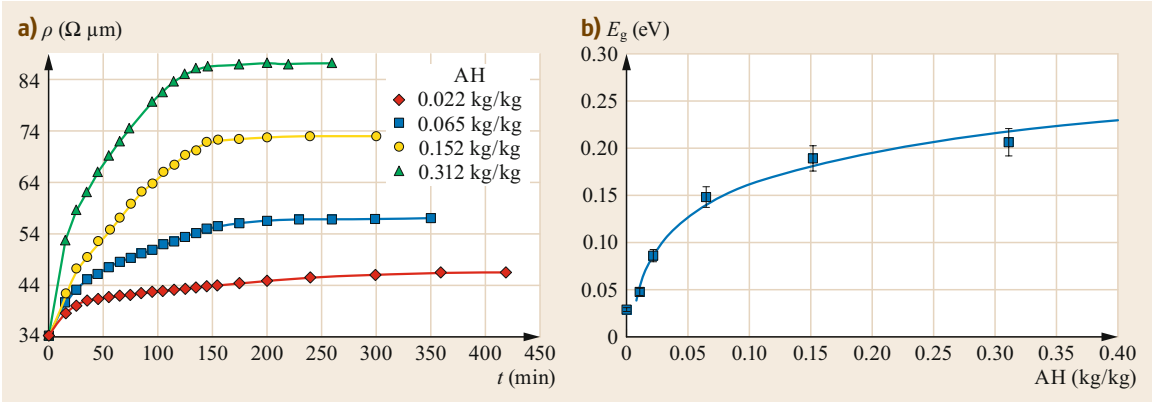

Fig. 36.19 **(a)** Change in resistivity ρ for a graphene film as a function of time for different absolute humidity. **(b)** Bandgap (E_g) as a function of absolute humidity (AH, given in kg water vapor in kg air). The bandgap increases sharply with humidity, saturating at a level of ≈ 0.206 eV. (Reprinted with permission from [36.150])

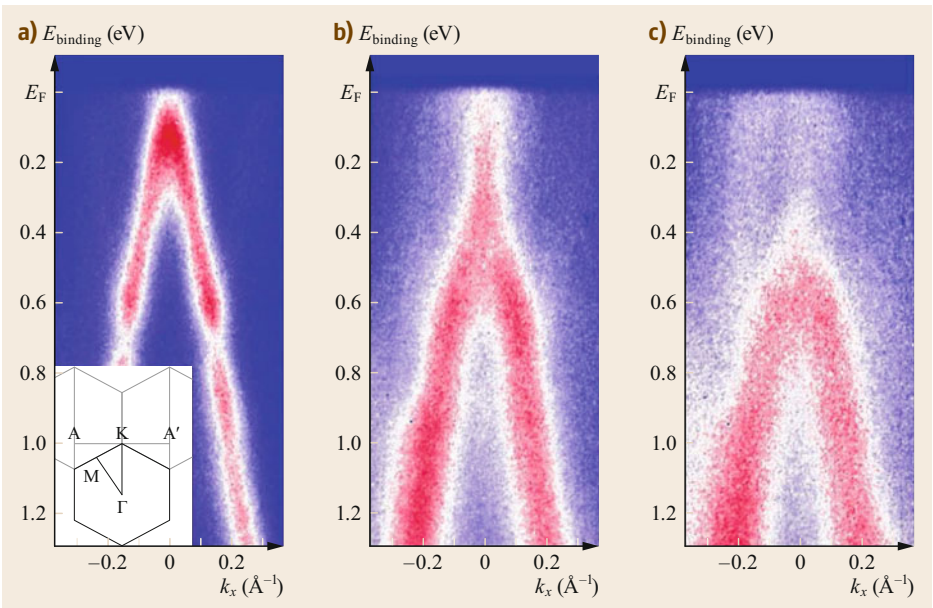

Fig. 36.20 **(a)** Photoemission intensity along the A-K-A′ direction of the Brillouin zone for clean graphene on Ir(111), **(b,c)** graphene exposed to 30 and 50 s of atomic hydrogen, respectively. The corresponding estimated coverage is of the order of some tenths of a monolayer. The *inset* shows the Brillouin zone of graphene. (From [36.117])

Controlling the Bandgap by Adsorption

It is well established that the absence of a bandgap is one of the major factors preventing the direct use of graphene in nanoelectronic devices. A bandgap can be artificially engineered through the introduction of defects [36.151], doping with adatoms [36.152], electrical gating [36.153–155], or the adsorption of gases [36.156].

The latter case was demonstrated using ambient humidity [36.150]. Graphene adlayers were grown by chemical vapor deposition (CVD) on copper (Cu) and coated with a thin poly(methyl methacrylate) (PMMA) film. The Cu substrate was eventually chemically dissolved and the graphene film transferred onto a Si substrate with an approximately 300 nm-thick insulating SiO_2 layer. Photolithography was then used to pattern four electrodes (Ti/Au, 3/30 nm) on the top surface of the transferred graphene film. The experimentally measured change in resistance with time for different absolute humidities (measured in weight of water content with respect to weight of air) is shown in Fig. 36.19. It is apparent that the resistance increases with time

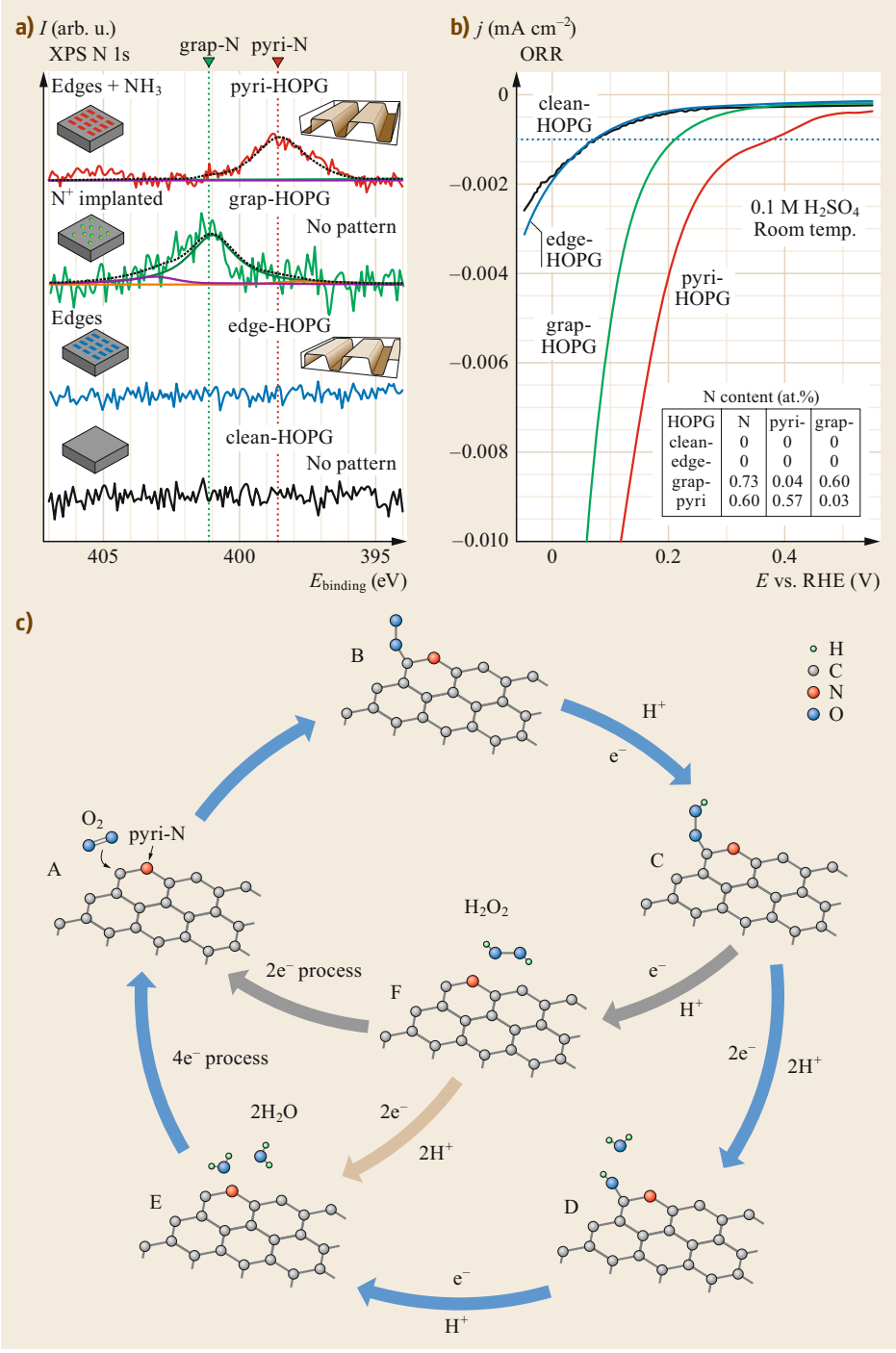

Fig. 36.21a–c N 1s XPS spectra of the different model catalysts **(a)** and the corresponding ORR results **(b)** obtained by cyclic voltammetry. **(c)** Schematic pathways for the ORR for the pyri-HOPG case. (From [36.157]. Reprinted with permission from AAAS)

and that the increase is greater the higher the humidity. Interestingly, water adsorption occurs reversibly. To prove the opening of a bandgap, the authors measured the conductivity at a fixed humidity level as a function of temperature, obtaining the gap values shown in the right panel of Fig. 36.19.

Theory also predicts the possibility of obtaining a tunable bandgap by introducing a periodic modula-

tion of the graphene lattice [36.159]. The feasibility of this approach was demonstrated [36.117] by exposing graphene on Ir(111) to atomic hydrogen. This system exhibits a Moiré pattern that survives H adsorption, as demonstrated by STM. Photoemission experiments have shown the opening of a bandgap upon H adsorption, as shown in Fig. 36.20.

36.5.3 Chemical Reactivity of Doped Graphene

Despite the presence of a large body of theoretical work suggesting the role of doping in promoting chemical reactivity, only a few experimental investigations have been performed. Two examples, addressing the role of n-doping for the oxygen reduction reaction (ORR) and for the stabilization of adsorbed CO, will be discussed.

For the former reaction, the electrochemical performance was investigated for pristine and N-doped highly oriented pyrolytic graphite (HOPG) and for graphene nanosheets (NGS). The results are shown in Fig. 36.21. Clean HOPG and edge HOPG indicate the undoped pristine and defect-rich surfaces, respectively, while grap-HOPG and pyri-HOPG correspond to substitutional and pyridinic N dopants. Cyclic voltammetry (CV) under oxygen saturation conditions shows that the pyri-HOPG sample provides the highest current density. The scheme in the lower part of the same figure shows that two alternative mechanisms are active for the reaction, involving four or $2+2$ electrons, respectively. O_2 initially adsorbs at the C site next to pyridinic N. In the four-electron mechanism, a proton attaches to the O_2, forming O−OH. Two further protons then react, leading to water formation by cleavage of the O–OH bond leaving OH groups at the surface, which are then reacted away by the fourth H. In the other reaction mechanism ($2+2$ electrons), an H_2O_2 intermediate forms due to the reaction of O−OH with a proton, which is then reduced to water by two further protons upon readsorption.

In another experimental investigation, the effect of N-doping in promoting adsorption was studied for CO chemisorption at graphene supported on Ni(111). N doping was attained by low-energy ion bombardment [36.161], and the so-obtained layer was exposed to CO in UHV conditions at low temperature. HREELS inspection demonstrated that in the presence of N, a further CO moiety, characterized by a CO stretch at 238 meV, forms in addition to the one vibrating at 256 meV also present for pristine graphene/Ni(111) [36.158] (Fig. 36.18). Such species is characterized by a higher desorption energy (0.85 eV/molecule) than that of CO adsorbed at pristine graphene sites (0.54 eV/molecule), as indicated by the temperature evolution of the spectra upon annealing, shown in Fig. 36.22. The stabilization of adsorption

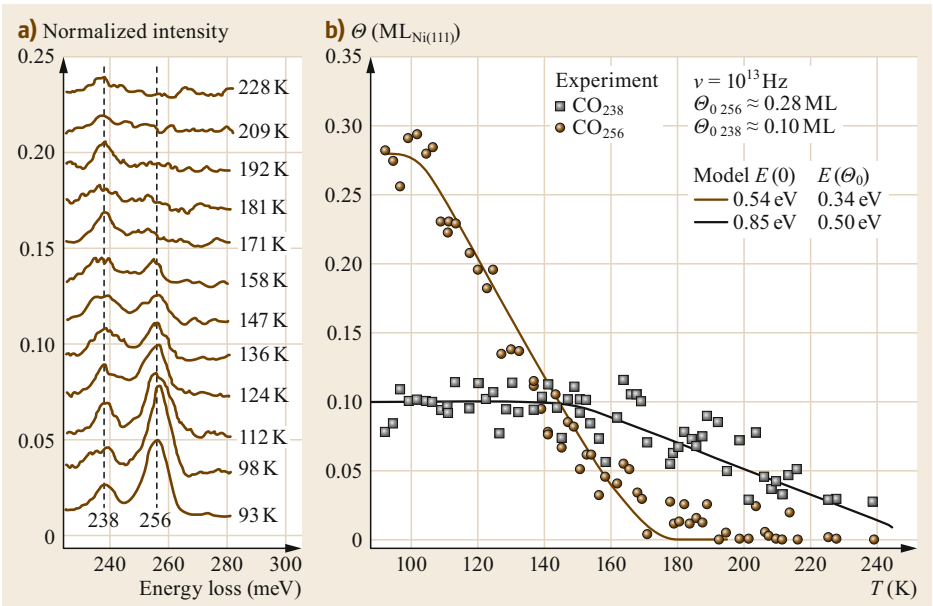

Fig. 36.22 (a) Evolution of HREEL spectra in the region of the CO stretch upon annealing after exposing N-doped graphene/Ni(111) to CO. Two losses are apparent: the one at 256 meV is also present for pristine graphene/Ni(111), while the one at 238 meV forms only for N-doped layers. (b) Coverage of the two CO species (CO_{238} and CO_{256}) as a function of annealing temperature. (Reprinted from [36.158], with permission from Elsevier)

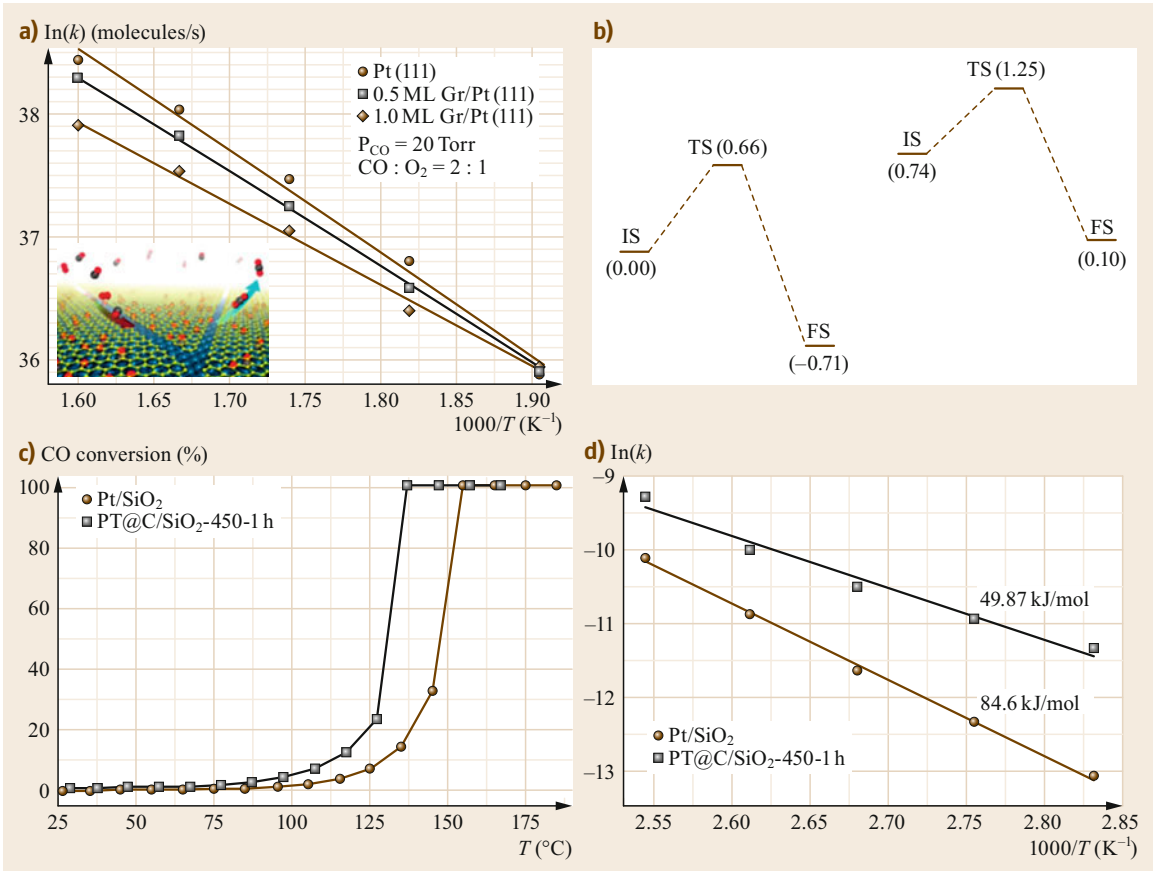

Fig. 36.23 **(a)** Arrhenius plots of the CO_2 formation rate k on the Pt(111) surface and graphene/Pt(111) from 525 to 625 K. The reaction gas mixture consists of 20 Torr CO and 10 Torr O_2. **(b)** Calculated reaction barriers for the oxidation of CO on Pt(111) (*left*) and Gr/Pt(111) (*right*), respectively. Values in brackets are in electron volts. **(c)** CO conversion as a function of reaction temperature over the Pt nanoparticles on SiO_2 and graphene-covered Pt nanoparticles at SiO_2 catalysts; **(d)** Arrhenius plots of the CO oxidation reaction rate (between 80 and 120 °C) over the Pt nanoparticles at SiO_2 and graphene-covered Pt nanoparticles at SiO_2. (Reproduced from [36.160] with permission of The Royal Society of Chemistry)

provided by N doping is effective not only at low coverage, but also at saturation. The adsorption energy at N sites is then 0.50 eV/molecule, i.e., 0.16 eV/molecule more than at pristine graphene sites.

36.5.4 Reactions Under a Graphene Cover

Reactions occurring *under cover* are particularly interesting, since the space between graphene and the catalytically active support acts like a *nanoreactor*, where chemistry takes place with a hindered ability for the reactants to desorb. The activation barriers of the reactions may be reduced as well. An example of a reaction under cover was mentioned above for defective graphene on Ni(111), where the Boudouard reaction was shown to proceed with much higher efficiency than for CO adsorption on bare Ni(111) [36.162].

In Fig. 36.23, the results for the CO oxidation reaction on bare Pt(111) and under graphene cover on Pt(111) are compared [36.160, 163–165]. It is apparent that, while the formation rate is always higher on Pt(111), the slope of the Arrhenius plot, i.e., the activation barrier, is lower for the monolayer graphene-covered Pt(111) surface (Fig. 36.23a). Theory confirms a reduction of the activation barrier from 0.66 to 0.51 eV (Fig. 36.23b). The comparison becomes even more interesting for bare and graphene-covered Pt nanoparticles (Fig. 36.23c,d), since the activation barrier is then reduced from 85 to 50 kJ/mol, and the reaction rates are always higher for Gr-covered nanoparticles.

36.6 Summary and Perspectives

The fascinating physical properties of graphene have established its reputation as the most famous two-dimensional crystalline structure. Given its only one-atomic-layer thickness and outstanding mechanical and electronic properties, one can only imagine how vast its use will be in the future, replacing existing technologies and materials. Considering applications in areas such as electronics, composites and coatings, sensors, spintronics, photovoltaics, and even biomedical devices, a good understanding not only of pristine graphene but also of defective and interactive graphene is indispensable. This need has stimulated the development of various preparation methods, growth on top of different substrates and in different forms, and functionalization and interfacing with various materials. In pursuit of a detailed characterization of its physical properties, continuous improvements in both experimental and theoretical surface science methods have taken place.

Very recently, the importance of twisted bilayer graphene with very low rotation angle (near 1 degree and below) has increased significantly. A low twist angle between the two stacked crystal networks in bilayer graphene enables self-organized lattice reconstruction with the formation of a periodic domain, the presence of strain solitons, topological points [36.166], and the eventual observation of strong correlation and superconductivity [36.167]. The control of the interlayer twist angle in two-dimensional van der Waals (vdW) heterostructures falls into a new reserach field baptized twistronics.

The ways that electronic, chemical, and magnetic properties are influenced by different substrates, dopants, and forms (nanoribbons, edge structures, etc.) are hot topics at the moment. In addition, graphene has generally served as a prototype material for the development of nanometrology. Thus it is used as a reference material for the detailed study of the the properties of nanotools. As the basics of graphene science are being established, engineers will continue to engage in expanding the development of graphene-based applied science and technology.

References

36.1 L. Kong, A. Enders, T.S. Rahman, P.A. Dowben: Molecular adsorption on graphene, J. Phys. Condens. Matter **26**, 443001 (2014)

36.2 H.P. Boehm, R. Setton, E. Stumpp: Nomenclature and terminology of graphite intercalation compounds, Pure Appl. Chem. **66**, 1893–1901 (1994)

36.3 P. Avouris, F. Xia: Graphene applications in electronics and photonics, MRS Bulletin **37**, 1225–1234 (2012)

36.4 S.V. Morozov, K.S. Novoselov, M.I. Katsnelson, F. Schedin, D.C. Elias, J.A. Jaszczak, A.K. Geim: Giant intrinsic carrier mobilities in graphene and its bilayer, Phys. Rev. Lett. **100**, 016602 (2008)

36.5 C. Lee, X.D. Wei, J.W. Kysar, J. Hone: The measurement of the elastic properties and intrinsic strength of graphene, Science **321**, 385–388 (2008)

36.6 F. Bonaccorso, Z. Sanna, T. Hasan, A.C. Ferrari: Graphene photonics and optoelectronics, Nat. Photonics **4**, 611–622 (2010)

36.7 K.S. Novoselov, A.K. Geim, S.V. Morozov, D. Jiang, Y. Zhang, S.V. Dubonos, I.V. Grigorieva, A.A. Firsov: Electric field effect in atomically thin carbon films, Science **306**, 666–669 (2004)

36.8 A. Jorio: Raman spectroscopy in graphene-based systems: Prototypes for nanoscience and nanometrology, ISRN Nanotechnology (2012), https://doi.org/10.5402/2012/234216

36.9 L.M. Malard, M.H.D. Guimarães, D.L. Mafra, M.S.C. Mazzoni, A. Jorio: Group-theory analysis of electrons and phonons in *N*-layer graphene systems, Phys. Rev. B **79**, 125426 (2009)

36.10 J. Ribeiro-Soares, R.M. Almeida, L.G. Cançado, M.S. Dresselhaus, A. Jorio: Group theory for structural analysis and lattice vibrations in phosphorene systems, Phys. Rev. B **91**, 205421 (2015)

36.11 V. Carozo, C.M. Almeida, E.H.M. Ferreira, L.G. Cançado, C.A. Achete, A. Jorio: Raman signature of graphene superlattices, Nano Lett. **11**, 4527–4534 (2011)

36.12 A. Jorio, L.G. Cançado: Raman spectroscopy of twisted bilayer graphene, Solid State Commun. **175/176**, 3–12 (2013)

36.13 O. Frank, M. Mohr, J. Maultzsch, C. Thomsen, I. Riaz, R. Jalil, K.S. Novoselov, G. Tsoukleri, J. Parthenios, K. Papagelis, L. Kavan, C. Galiotis: Raman 2D-band splitting in graphene: Theory and experiment, ACS Nano **5**, 2231–2239 (2011)

36.14 A. Righi, S.D. Costa, H. Chacham, C. Fantini, P. Venezuela, C. Magnuson, L. Colombo, W.S. Bacsa, R.S. Ruoff, M.A. Pimenta: Graphene Moiré patterns observed by umklapp double-resonance Raman scattering, Phys. Rev. B **84**, 241409(R) (2011)

36.15 J. Campos-Delgado, L.G. Cançado, C.A. Achete, A. Jorio, J.-P. Raskin: Raman scattering study of the phonon dispersion in twisted bilayer graphene, Nano Res. **6**, 269–274 (2013)

36.16 V. Carozo, C.M. Almeida, B. Fragneaud, P. Bedê, J. Moutinho, M.V.O. Ribeiro-Soares, N. Andrade, A.G. Souza Filho, M.J.S. Matos, B. Wang, M. Terrones, R.B. Capaz, A. Jorio, C.A. Achete, L.G. Cançado: Resonance effects on the Raman

spectra of graphene superlattices, Phys. Rev. B **88**, 085401 (2013)
36.17 P.Y. Huang, C.S. Ruiz-Vargas, A.M. van der Zande, W.S. Whitney, M.P. Levendorf, J.W. Kevek, S. Garg, J.S. Alden, C.J. Hustedt, Y. Zhu, J. Park, P.L. McEuen, D.A. Muller: Grains and grain boundaries in single-layer graphene atomic patchwork quilts, Nature **469**, 389–392 (2011)
36.18 J. Cervenka, C.F.J. Flipse: Structural and electronic properties of grain boundaries in graphite: Planes of periodically distributed point defects, Phys. Rev. B **79**, 195429 (2009)
36.19 M.M. Lucchese, F. Stavale, E.H. Martins Ferreira, C. Vilani, M.V.O. Moutinho, R.B. Capaz, C.A. Achete, A. Jorio: Quantifying ion-induced defects and Raman relaxation length in graphene, Carbon **48**, 1592–1597 (2010)
36.20 G.D. Lee, C.Z. Wang, E. Yoon, N.-M. Hwang, D.-Y. Kim, K.M. Ho: Diffusion, coalescence, and reconstruction of vacancy defects in graphene layers, Phys. Rev. Lett. **95**, 205501 (2005)
36.21 J. Ma, D. Alfè, A. Michaelides, E. Wang: Stone-Wales defects in graphene and other planar sp^2-bonded materials, Phys. Rev. B **80**, 033407 (2009)
36.22 O.V. Yazyev, S.G. Louie: Topological defects in graphene: Dislocations and grain boundaries, Phys. Rev. B **81**, 195420 (2010)
36.23 A.C. Ferrari, J. Robertson: Interpretation of Raman spectra of disordered and amorphous carbon, Phys. Rev. B **61**, 14095 (2000)
36.24 A. Jorio, L.G. Cançado: Perspectives on Raman spectroscopy of graphene-based systems: From the perfect two-dimensional surface to charcoal, Phys. Chem. Chem. Phys. **14**, 15246–15256 (2012)
36.25 A. Jorio, A.G. Souza Filho: Raman studies of carbon nanostructures, Annu. Rev. Mater. Res. **46**, 357–382 (2016)
36.26 S. Reich, C. Thomsen: Raman spectroscopy of graphite, Philos. Trans. A **362**, 2271–2288 (2004)
36.27 A. Jorio, M.S. Dresselhaus, R. Saito: *Raman Spectroscopy in Graphene Related Systems* (Wiley-VCH, Weinheim 2011)
36.28 A.C. Ferrari: Raman spectroscopy of graphene and graphite: Disorder, electron–phonon coupling, doping and nonadiabatic effects, Solid State Commun. **143**, 47–57 (2007)
36.29 A.C. Ferrari, D.M. Basko: Raman spectroscopy as a versatile tool for studying the properties of graphene, Nat. Nanotechnol. **8**, 235–246 (2013)
36.30 M. Huang, H. Yan, C. Chen, D. Song, T.F. Heinz, J. Hone: Phonon softening and crystallographic orientation of strained graphene studied by Raman spectroscopy, Proc. Natl. Acad. Sci. U. S. A. **106**, 7304–7308 (2009)
36.31 A. Das, S. Pisana, B. Chakraborty, S. Piscanec, S.K. Saha, U.V. Waghmare, K.S. Novoselov, H.R. Krishnamurthy, A.K. Geim, A.C. Ferrari, A.K. Sood: Monitoring dopants by Raman scattering in an electrochemically top-gated graphene transistor, Nat. Nanotechnol. **3**, 210–215 (2008)
36.32 A.A. Balandin, S. Ghosh, W. Bao, I. Calizo, D. Teweldebrhan, F. Miao, C.N. Lau: Superior thermal conductivity of single-layer graphene, Nano Lett. **8**, 902–907 (2008)
36.33 M. Acik, G. Lee, C. Mattevi, M. Chhowalla, K. Cho, Y.J. Chabal: Unusual infrared-absorption mechanism in thermally reduced graphene oxide, Nat. Mater. **9**, 840–845 (2010)
36.34 G. Dovbeshko, O. Gnatyuk, O. Fesenko, A. Rynder, O.Y. Posudievskii: Enhancement of infrared absorption of biomolecules absorbed on single-wall carbon nanotubes and graphene nanosheets, J. Nanophotonics **6**, 061711 (2012)
36.35 L.M. Zhang, Z.Q. Li, D.N. Basov, M.M. Fogler, Z. Hao, M.C. Martin: Determination of the electronic structure of bilayer graphene from infrared spectroscopy, Phys. Rev. B **78**, 235408 (2008)
36.36 Z.Q. Li, E.A. Henriksen, Z. Jiang, Z. Hao, M.C. Martin, P. Kim, D.N. Basov: Dirac charge dynamics in graphene by infrared spectroscopy, Nat. Phys. **4**, 532–535 (2008)
36.37 R. Nicklow, N. Wakabayashi, H.G. Smith: Lattice dynamics of pyrolytic graphite, Phys. Rev. B **5**, 4951–4962 (1972)
36.38 M. Mohr, J. Maultzsch, E. Dobardžić, S. Reich, I. Milošević, M. Damnjanović, A. Bosak, M. Krisch, C. Thomsen: Phonon dispersion of graphite by inelastic x-ray scattering, Phys. Rev. B **76**, 035439 (2007)
36.39 J.-W. Jiang, H. Tang, B.-S. Wang, Z.-B. Su: Raman and infrared properties and layer dependence of the phonon dispersions in multilayered graphene, Phys. Rev. B **77**, 235421 (2008)
36.40 T. Mishina, K. Nitta, Y. Masumoto: Coherent lattice vibration of interlayer shearing mode of graphite, Phys. Rev. B **62**, 2908 (2000)
36.41 K.H. Michel, B. Verberck: Theory of rigid-plane phonon modes in layered crystals, Phys. Rev. B **85**, 094303 (2012)
36.42 P.H. Tan, W.P. Han, W.J. Zhao, Z.H. Wu, K. Chang, H. Wang, Y.F. Wang, N. Bonini, N. Marzari, N. Pugno, G. Savini, A. Lombardo, A.C. Ferrari: The shear mode of multilayer graphene, Nat. Mater. **11**, 294–300 (2012)
36.43 C.H. Lui, L.M. Malard, S.-H. Kim, G. Lantz, F.E. Laverge, R. Saito, T.F. Heinz: Observation of layer-breathing mode vibrations in few-layer graphene through combination Raman scattering, Nano Lett. **12**, 5539–5544 (2012)
36.44 D. Boschetto, L. Malard, C.H. Lui, K.F. Mak, Z. Li, H. Yan, T.F. Heinz: Real-time observation of interlayer vibrations in bilayer and few-layer graphene, Nano Lett. **13**, 4620–4623 (2013)
36.45 V.N. Popov, C. Van Alsenoy: Low-frequency phonons of few-layer graphene within a tight-binding model, Phys. Rev. B **90**, 245429 (2014)
36.46 A. Grüneis, J. Serrano, A. Bosak, M. Lazzeri, S.L. Molodtsov, L. Wirtz, C. Attaccalite, M. Kritsch, A. Rubio, F. Mauri, T. Pichler: Phonon surface mapping of graphite: Disentangling quasi-degenerate phonon dispersions, Phys. Rev. B **80**, 085423 (2009)
36.47 L.G. Cançado, A. Jorio, E.H. Martins Ferreira, F. Stavale, C.A. Achete, R.B. Capaz,

M.V.O. Moutinho, A. Lombardo, T.S. Kulmala, A.C. Ferrari: Quantifying defects in graphene via Raman spectroscopy at different excitation energies, Nano Lett. **11**, 3190–3196 (2011)

36.48 C. Thomsen, S. Reich: Double resonant Raman scattering in graphite, Phys. Rev. Lett. **85**, 5214 (2000)

36.49 R. Saito, A. Jorio, A.G. Souza Filho, G. Dresselhaus, M.S. Dresselhaus, M.A. Pimenta: Probing phonon dispersion relations of graphite by double resonance Raman scattering, Phys. Rev. Lett. **88**, 027401 (2001)

36.50 D.L. Mafra, G. Samsonidze, L.M. Malard, D.C. Elias, J.C. Brant, F. Plentz, E.S. Alves, M.A. Pimenta: Determination of LA and TO phonon dispersion relations of graphene near the Dirac point by double resonance Raman scattering, Phys. Rev. B **76**, 233407 (2007)

36.51 P. Venezuela, M. Lazzeri, F. Mauri: Theory of double-resonant Raman spectra in graphene: Intensity and line shape of defect-induced and two-phonon bands, Phys. Rev. B **84**, 035433 (2011)

36.52 P.T. Araujo, D.L. Mafra, K. Sato, R. Saito, J. Kong, M.S. Dresselhaus: Phonon self-energy corrections to nonzero wave-vector phonon modes in single-layer graphene, Phys. Rev. Lett. **109**, 046801 (2012)

36.53 P. May, M. Lazzeri, P. Venezuela, F. Herziger, G. Callsen, J.S. Reparaz, A. Hoffmann, F. Mauri, J. Maultzsch: Signature of the two-dimensional phonon dispersion in graphene probed by double-resonant Raman scattering, Phys. Rev. B **87**, 075402 (2013)

36.54 L.G. Cançado, M.G. da Silva, E.H.M. Ferreira, F. Hof, K. Kampioti, K. Huang, A. Penicaud, C.A. Achete, R.B. Capaz, A. Jorio: Disentangling contributions of point and line defects in the Raman spectra of graphene-related materials, 2D Materials **4**, 025039 (2017)

36.55 L.G. Cançado, K. Takai, T. Enoki, M. Endo, Y.A. Kim, H. Mizusaki, A. Jorio, L.N. Coelho, R. Magalhães-Paniago, M.A. Pimenta: General equation for the determination of the crystallite size L_a of nanographite by Raman spectroscopy, Appl. Phys. Lett. **88**, 163106 (2006)

36.56 J. Ribeiro-Soares, M.E. Oliveros, C. Garin, M.V. David, L.G.P. Martins, C.A. Almeida, E.H. Martins-Ferreira, K. Takai, T. Enoki, R. Magalhaes-Paniago, A. Malachias, A. Jorio, B.S. Archanjo, C.A. Achete, L.G. Cançado: Structural analysis of polycrystalline graphene systems by Raman spectroscopy, Carbon **95**, 646–652 (2015)

36.57 A.J. Van Bommel, J.E. Crombeen, A. Van Tooren: LEED and Auger electron observations of the SiC(0001), Surf. Sci. **48**, 463–472 (1975)

36.58 N. Liu, L. Fu, B. Dai, K. Yan, X. Liu, R. Zhao, Y. Zhang, Z. Liu: Universal segregation growth approach to wafer-size graphene from non-noble metals, Nano Lett. **119**, 297–303 (2011)

36.59 S. Marchini, S. Günther, J. Wintterlin: Scanning tunneling microscopy of graphene on Ru(0001), Phys. Rev. B **76**, 075429 (2007)

36.60 P.W. Sutter, J.-I. Flege, E.A. Sutter: Epitaxial graphene on ruthenium, Nat. Mater. **7**, 406–411 (2008)

36.61 K.F. McCarty, P.J. Feibelman, E. Loginova, N.C. Bartelt: Kinetics and thermodynamics of carbon segregation and graphene growth on Ru(0001), Carbon **47**, 1806–1813 (2009)

36.62 P. Sutter, J.T. Sadowski, E. Sutter: Graphene on Pt(111): Growth and substrate interaction, Phys. Rev. B **80**, 245411 (2009)

36.63 K.V. Emtsev, A. Bostwick, K. Horn, J. Jobst, G.L. Kellogg, L. Ley, J.L. McChesney, T. Ohta, S.A. Reshanov, J. Rohr: Towards wafer-size graphene layers by atmospheric pressure graphitization of silicon carbide, Nat. Mater. **8**, 203–207 (2009)

36.64 C. Berger, Z. Song, T. Li, X. Li, A.Y. Ogbazghi, R. Feng, Z. Dai, A.N. Marchenkov, E.H. Conrad, P.N. First, W.A. de Heer: Ultrathin epitaxial graphite: 2D electron gas properties and a route toward graphene-based nanoelectronics, J. Phys. Chem. B **108**, 19912–19916 (2004)

36.65 C. Riedl, U. Starke, J. Bernhardt, M. Franke, K. Heinz: Structural properties of the graphene-SiC(0001) interface as a key for the preparation of homogeneous large-terrace graphene surfaces, Phys. Rev. B **76**, 245406 (2007)

36.66 E. Moreau, F.J. Ferrer, D. Vignaud, S. Godey, X. Wallart: Graphene growth by molecular beam epitaxy using a solid carbon source, Phys. Status Solidi (a) **207**, 300–303 (2010)

36.67 A. Al-Temimy, C. Riedl, U. Starke: Low temperature growth of epitaxial graphene on SiC induced by carbon evaporation, Appl. Phys. Lett. **95**, 231907 (2009)

36.68 J. Park, W.C. Mitchel, L. Grazulis, H.E. Smith, K.G. Eyink, J.J. Boeckl, D.H. Tomich, S.D. Pacley, J.E. Hoelscher: Epitaxial graphene growth by carbon molecular beam epitaxy (CMBE), Adv. Mater. **22**, 4140–4145 (2010)

36.69 T. Kajiwara, Y. Nakamori, A. Visikovskiy, T. Iimori, F. Komori, K. Nakatsuji, K. Mase, S. Tanaka: Graphene nanoribbons on vicinal SiC surfaces by molecular beam epitaxy, Phys. Rev. B **87**, 121407 (2013)

36.70 J.M. Garcia, U. Wurstbauer, A. Levy, L.N. Pfeiffer, A. Pinczuk, A.S. Plaut, L. Wang, C.R. Dean, R. Buizza, A.M. Van Der Zande, J. Hone, K. Watanabe, T. Taniguchi: Graphene growth on h-BN by molecular beam epitaxy, Solid State Commun. **152**, 975–978 (2012)

36.71 M.H. Oliveira Jr., T. Schumann, R. Gargallo-Caballero, F. Fromm, T. Seyller, M. Ramsteiner, A. Trampert, L. Geelhaar, J.M.J. Lopes, H. Riechert: Mono- and few-layer nanocrystalline graphene grown on Al_2O_3(0001) by molecular beam epitaxy, Carbon **56**, 339–350 (2013)

36.72 I. Hernández-Rodríguez, J.M. García, J.A. Martín-Gago, P.L. de Andrés, J. Méndez: Graphene growth on Pt(111) and Au(111) using a MBE carbon solid-source, Diam. Relat. Mater. **57**, 58–62 (2015)

36.73 Z. Sun, Z. Yan, J. Yao, E. Beitler, Y. Zhu, J.M. Tour: Growth of graphene from solid carbon sources, Nature **468**, 549–552 (2010)

36.74 J. Lahiri, T.S. Miller, A.J. Ross, L. Adamska, I.I. Oleynik, M. Batzill: Graphene growth and stability at nickel surfaces, New J. Phys. **13**, 25001 (2011)

36.75 Z. Zou, L. Fu, X. Song, Y. Zhang, Z. Liu: Carbide-forming groups IVB-VIB metals: A new territory in the periodic table for CVD growth of graphene, Nano Lett. **14**, 3832–3839 (2014)

36.76 J.D. Wood, S.W. Schmucker, A.S. Lyons, E. Pop, J.W. Lyding: Effects of polycrystalline Cu substrate on graphene growth by chemical vapor deposition, Nano Lett. **11**, 4547–4554 (2011)

36.77 L. Gao, W. Ren, H. Xu, L. Jin, Z. Wang, T. Ma, L.-P. Ma, Z. Zhang, Q. Fu, L.-M. Peng, X. Bao, H.-M. Cheng: Repeated growth and bubbling transfer of graphene with millimetre-size single-crystal grains using platinum, Nat. Commun. **3**, 699 (2012)

36.78 Y. Dedkov, E. Voloshina: Graphene growth and properties on metal substrates, J. Phys. Condens. Matter **27**, 303002 (2015)

36.79 M. Batzill: The surface science of graphene: Metal interfaces, CVD synthesis, nanoribbons, chemical modifications, and defects, Surf. Sci. Rep. **67**, 83–115 (2012)

36.80 J. Wintterlin, M.-L. Bocquet: Graphene on metal surfaces, Surf. Sci. **603**, 1841–1852 (2009)

36.81 Y.S. Dedkov, M. Fonin, C. Laubschat: A possible source of spin-polarized electrons: The inert graphene/Ni(111) system, Appl. Phys. Lett. **92**, 052506 (2008)

36.82 A. Dahal, M. Batzill: Graphene-nickel interfaces: A review, Nanoscale **6**, 2548–2562 (2014)

36.83 M. Olle, G. Ceballos, D. Serrate, P. Gambardella: Yield and shape selection of grapene nanoislands grown on Ni(111), Nano Lett. **12**, 4431–4436 (2012)

36.84 A. Garcia-Lekue, M. Olle, D. Sanchez-Portal, J.J. Palacios, A. Mugarza, G. Ceballos, P. Gambardella: Substrate-induced stabilization and reconstruction of zig-zag edges in graphene nanoislands on Ni(111), J. Phys. Chem. C **119**, 4072–4078 (2015)

36.85 D.E. Parreiras, E.A. Soares, G.J.P. Abreu, T.E.P. Bueno, W.P. Fernandes, V.E. de Carvalho, S.S. Carara, H. Chacham, R. Paniago: Graphene/Ni(111) surface structure probed by low-energy electron diffraction, photoelectron diffraction, and first-principles calculations, Phys. Rev. B **90**, 155454 (2014)

36.86 Y. Gamo, A. Nagashima, M. Wakabayashi, M. Terai, C. Oshima: Atomic structure of monolayer graphite formed on Ni(111), Surf. Sci. **374**, 61–64 (1997)

36.87 M. Fuentes-Cabrera, M.I. Baskes, A.V. Melechko, M.L. Simpson: Bridge structure for the graphene/Ni(111) system: A first principles study, Phys. Rev. B **77**, 035405 (2008)

36.88 W. Zhao, S.M. Kozlov, O. Höfert, K. Gotterbarm, M.P.A. Lorenz, F. Viñes, C. Papp, A. Görling, H.-P. Steinrück: Graphene on Ni(111): Coexistence of different surface structures, Phys. Chem. Lett. **2**, 759–764 (2011)

36.89 F. Bianchini, L.L. Patera, M. Peressi, C. Africh, G. Comelli: Atomic scale identification of coexisting graphene structures on Ni(111), Phys. Chem. Lett. **5**, 467–473 (2014)

36.90 L.L. Patera, C. Africh, R.S. Weatherup, R. Blume, S. Bhardwaj, C. Castellarin-Cudia, A. Knop-Gericke, R. Schloegl, G. Comelli, S. Hofmann, C. Cepek: In situ observations of the atomistic mechanisms of Ni catalyzed low temperature graphene growth, ACS Nano **7**, 7901–7912 (2013)

36.91 J.B. Pendry: Reliability factors for LEED calculations, J. Phys. C **13**, 937–944 (1980)

36.92 E.N. Voloshina, Y.S. Dedkov, S. Torbrügge, A. Thissen, M. Fonin: Graphene on Rh(111): Scanning tunneling and atomic force microscopies studies, Appl. Phys. Lett. **100**, 241606 (2012)

36.93 G. Dong, J.W.M. Frenken: Kinetics of graphene formation on Rh(111) investigated by in situ scanning tunneling microscopy, ACS Nano **7**, 7028–7033 (2013)

36.94 S. Roth, J. Osterwalder, T. Greber: Synthesis of epitaxial graphene on rhodium from 3-pentanone, Surf. Sci. **605**, L17–L19 (2011)

36.95 K. Katsiev, Y. Losovyj, Z. Zhou, E. Vescovo, L. Liu, P.A. Dowben, D.W. Goodman: Graphene on Ru(0001): Evidence for two graphene band structures, Phys. Rev. B **85**, 195405 (2012)

36.96 W. Moritz, B. Wang, M.-L. Bocquet, T. Brugger, T. Greber, J. Wintterlin, S. Günther: Structure determination of the coincidence phase of graphene on Ru(0001), Phys. Rev. Lett. **104**, 136102 (2010)

36.97 G. Li, L. Huang, W. Xu, Y. Que, Y. Zhang, J. Lu, S. Du, Y. Liu, H.-J. Gao: Constructing molecular structures on periodic superstructure of graphene/Ru(0001), Philos. Trans. A **372**, 20130015 (2014)

36.98 D. Martoccia, P.R. Willmott, T. Brugger, M. Björck, S. Günther, C.M. Schlepütz, A. Cervellino, S.A. Pauli, B.D. Patterson, S. Marchini, J. Wintterlin, W. Moritz, T. Greber: Graphene on Ru(0001): A 25×25 supercell, Phys. Rev. Lett. **101**, 126102 (2008)

36.99 D. Martoccia, M. Björck, C.M. Schlepütz, T. Brugger, S.A. Pauli, B.D. Patterson, T. Greber, P.R. Willmott: Graphene on Ru(0001): A corrugated and chiral structure, New J. Phys. **12**, 043028 (2010)

36.100 D. Stradi, S. Barja, C. Díaz, M. Garnica, B. Borca, J.J. Hinarejos, D. Sánchez-Portal, M. Alcamí, A. Arnau, A.L. Vázquez de Parga, R. Miranda, F. Martín: Role of dipersion forces in the structure of graphene monolayers on Ru surfaces, Phys. Rev. Lett. **106**, 186102 (2011)

36.101 D. Stradi, S. Barja, C. Díaz, M. Garnica, B. Borca, J.J. Hinarejos, D. Sánchez-Portal, M. Alcamí, A. Arnau, A.L. Vázquez de Parga, R. Miranda, F. Martín: Electron localization in epitaxial graphene on Ru(0001) determined by moiré corrugation, Phys. Rev. B **85**, 121404(R) (2012)

36.102 A.L. Vázquez de Parga, F. Calleja, B. Borca, M.C.G. Passeggi Jr., J.J. Hinarejos, F. Guinea, R. Miranda: Periodically rippled graphene: Growth and spatially resolved electronic structure, Phys. Rev. Lett. **100**, 056807 (2008)

36.103 B. Borca, F. Calleja, J.J. Hinarejos, A.L. Vázquez de Parga, R. Miranda: Reactivity of periodically rippled graphene grown on Ru(0001), J. Phys. Condens. Matter **21**, 134002 (2009)

36.104 E. Sutter, D.P. Acharya, J.T. Sadowski, P. Sutter: Intercalation of metal islands and films at the interface of epitaxially grown graphene and Ru(0001) surfaces, Appl. Phys. Lett. **94**, 133101 (2009)

36.105 B. Borca, S. Barja, M. Garnica, J.J. Hinarejos, A.L. Vázquez de Parga, R. Miranda, F. Guinea: Periodically modulated geometric and electronic structure of graphene on Ru(0001), Semicond. Sci. Technol. **25**, 034001 (2010)

36.106 J.M. MacLeod, F. Rosei: Molecular self-assembly on graphene, Small **10**, 1038–1049 (2014)

36.107 J. Lu, P.S.E. Yeo, Y. Zheng, Z. Yang, Q. Bao, C.K. Gan, K.P. Loh: Using the graphene Moiré pattern for the trapping of C_{60} and homoepitaxy of graphene, ACS Nano **6**, 944–950 (2012)

36.108 H.G. Zhang, J.T. Sun, T. Low, L.Z. Zhang, Y. Pan, Q. Liu, J.H. Mao, H.T. Zhou, H.M. Guo, S.X. Du, F. Guinea, H.-J. Gao: Assembly of iron phthalocyanine and pentacene molecules on a graphene monolayer grown on Ru(0001), Phys. Rev. B **85**, 245436 (2011)

36.109 J. Coraux, A.T. N'Diaye, C. Busse, T. Michely: Structural coherency of graphene on Ir(111), Nano Lett. **8**, 565–570 (2008)

36.110 J. Coraux, A.T. N'Diaye, M. Engler, C. Busse, D. Wall, N. Buckanie, F.-J. Meyer zu Heringdorf, R. van Gastel, B. Poelsema, T. Michely: Growth of graphene on Ir(111), New J. Phys. **11**, 0023006 (2009)

36.111 P. Sutter, P. Albrecht, X. Tong, E. Sutter: Mechanical decoupling of graphene from Ru(0001) by interfacial reaction with oxygen, J. Phys. Chem. C **117**, 6320–6324 (2013)

36.112 A. Varykhalov, J. Sánchez-Barriga, A.M. Shikin, C. Biswas, E. Vescovo, A. Rybkin, D. Marchenko, O. Rader: Electronic and magnetic properties of quasifreestanding graphene on Ni, Phys. Rev. Lett. **101**, 157601 (2008)

36.113 N. Ligato, A. Cupolillo, L.S. Caputi: Study of the intercalation of graphene on Ni(111) with Cs atoms: Towards the quasi-free graphene, Thin Solid Films **543**, 59–62 (2013)

36.114 M. Alattas, U. Schwingenschlögl: Quasi-freestanding graphene on Ni(111) by Cs intercalation, Sci. Rep. **6**, 26753 (2016)

36.115 E.N. Voloshina, A. Generalov, M. Weser, S. Böttcher, K. Horn, Y.S. Dedkov: Structural and electronic properties of the graphene/Al/Ni(111) intercalation system, New J. Phys. **13**, 113028 (2011)

36.116 S.Y. Zhou, G.-H. Gweon, A.V. Fedorov, P.N. First, W.A. de Heer, D.-H. Lee, F. Guinea, A.H. Castro Neto, A. Lanzara: Substrate-induced bandgap opening in epitaxial graphene, Nat. Mater. **6**, 770–775 (2007)

36.117 R. Balog, B. Jørgensen, L. Nilsson, M. Andersen, E. Rienks, M. Bianchi, M. Fanetti, E. Lægsgaard, A. Baraldi, S. Lizzit, Z. Sljivancanin, F. Besenbacher, B. Hammer, T.G. Pedersen, P. Hofmann, L. Hornekær: Bandgap opening in graphene induced by patterned hydrogen adsorption, Nat. Mater. **9**, 315–319 (2010)

36.118 H. Vita, S. Böttcher, K. Horn, E.N. Voloshina, R.E. Ovcharenko, T. Kampen, A. Thissen, Y.S. Dedkov: Understanding the origin of band gap formation in graphene on metals: Graphene on Cu/Ir(111), Sci. Rep. **4**, 5704 (2014)

36.119 I.I. Klimovskikh, M.M. Otrokov, V.Y. Voroshnin, D. Sostina, L. Petaccia, G. Di Santo, S. Thakur, E.V. Chulkov, A.M. Shikin: Spin–orbit coupling induced gap in graphene on Pt(111) with intercalated Pb monolayer, ACS Nano **11**, 368–374 (2017)

36.120 J. Warmuth, A. Bruix, M. Michiardi, T. Hänke, M. Bianchi, J. Wiebe, R. Wiesendanger, B. Hammer, P. Hofmann, A.A. Khajetoorians: Band-gap engineering by Bi intercalation of graphene on Ir(111), Phys. Rev. B **93**, 165437 (2016)

36.121 A. Varykhalov, M.R. Scholz, T.K. Kim, O. Rader: Effect of noble-metal contacts on doping and band gap of graphene, Phys. Rev. B **82**, 121101(R) (2010)

36.122 M. Andersen, L. Hornekær, B. Hammer: Understanding intercalation structures formed under graphene on Ir(111), Phys. Rev. B **90**, 155428 (2014)

36.123 E.A. Soares, G.J.P. Abreu, S.S. Carara, R. Paniago, V.E. de Carvalho, H. Chacham: Graphene-protected Fe layers atop Ni(111): Evidence for strong Fe-graphene interaction and structural bistability, Phys. Rev. B **88**, 165410 (2013)

36.124 M. Cattelan, G.W. Peng, E. Cavaliere, L. Artiglia, A. Barinov, L.T. Roling, M. Favaro, I. Píš, S. Nappini, E. Magnano, F. Bondino, L. Gavioli, S. Agnoli, M. Mavrikakis, G. Granozzi: Thee nature of the Fe-graphene interface at the nanometer level, Nanoscale **7**, 2450–2460 (2015)

36.125 A.D. Vu, J. Coraux, G. Chen, A.T. N'Diaye, A.K. Schmid, N. Rougemaille: Unconventional magnetization texture in graphene/cobalt hybrids, Sci. Rep. **6**, 24783 (2016)

36.126 F. Schedin, A.K. Geim, S.V. Morozov, E.W. Hill, P. Blake, M.I. Katsnelson, K.S. Novoselov: Detection of individual gas molecules adsorbed on graphene, Nat. Mater. **6**, 652–655 (2007)

36.127 Y. Dan, Y. Lu, N.J. Kybert, Z. Luo, A.T.C. Johnson: Intrinsic response of graphene vapor sensors, Nano Lett. **9**, 1472–1475 (2009)

36.128 J. Ma, A. Michaelides, D. Alfe, L. Schimka, G. Kresse, E. Wang: Adsorption and diffusion of water on graphene from first principles, Phys. Rev. B **84**, 033402 (2011)

36.129 O. Leenaerts, B. Partoens, F.M. Peeters: Adsorption of H_2O, NH_3, CO, NO_2, and NO on graphene: A first-principles study, Phys. Rev. B **77**, 125416 (2008)

36.130 Y.-H. Zhang, Y. Chen, K.-G. Zhou, C. Liu, J. Zeng, H. Zhang, Y. Peng: Improving gas sensing prop-

erties of graphene by introducing dopants and defects: A first-principles study, Nanotechnology **20**, 185504 (2009)
36.131 J. Dai, J. Yuan, P. Giannozzi: Gas adsorption on graphene doped with B, N, Al, and S: A theoretical study, Appl. Phys. Lett. **95**, 232105 (2009)
36.132 J. Dai, J. Yuan: Adsorption of molecular oxygen on doped graphene: Atomic, electronic, and magnetic properties, Phys. Rev. B **81**, 165414 (2010)
36.133 B. Sanyal, O. Eriksson, U. Jansson, H. Grennberg: Molecular adsorption in graphene with divacancy defects, Phys. Rev. B **79**, 113409 (2009)
36.134 B. Wang, S.T. Pantelides: Controllable healing of defects and nitrogen doping of graphene by CO and NO molecules, Phys. Rev. B **83**, 245403 (2011)
36.135 J. Xu, L. Wang, Y. Zhu: Decontamination of bisphenol A from aqueous solution by graphene adsorption, Langmuir **28**, 8418–8425 (2012)
36.136 P. Lazar, F. Karlicky, P. Jurecka, M. Kocman, E. Otyepkova, K. Safarova, M. Otyepka: Adsorption of small organic molecules on graphene, J. Am. Chem. Soc. **135**, 6372–6377 (2013)
36.137 G. Srinivas, Y. Zhu, R. Piner, N. Skipper, M. Ellerby, R. Ruoff: Synthesis of graphene-like nanosheets and their hydrogen adsorption capacity, Carbon **48**, 630–635 (2010)
36.138 K.C. Kemp, H. Seema, M. Saleh, N.H. Le, K. Mahesh, V. Chandra, K.S. Kim: Environmental applications using graphene composites: Water remediation and gas adsorption, Nanoscale **5**, 3149–3171 (2013)
36.139 M.A. Bissett, S. Konabe, S. Okada, M. Tsuji, H. Ago: Enhanced chemical reactivity of graphene induced by mechanical strain, ACS Nano **7**, 10335–10343 (2013)
36.140 Q. Wu, Y. Wu, Y. Hao, J. Geng, M. Charlton, S. Chen, Y. Ren, H. Ji, H. Li, D.W. Boukhvalov, R.D. Piner, C.W. Bielawski, R.S. Ruoff: Selective surface functionalization at regions of high local curvature in graphene, Chem. Commun. **49**, 677–679 (2013)
36.141 A. Chakradhar, N. Sivapragasam, M.T. Nayakasinghe, U. Burghaus: Support effects in the adsorption of water on CVD graphene: An ultrahigh vacuum adsorption study, Chem. Commun. **51**, 11463–11466 (2015)
36.142 A. Chakradhar, U. Burghaus: Adsorption of water on graphene/Ru(0001)—An experimental ultrahigh vacuum study, Chem. Commun. **50**, 7698–7701 (2014)
36.143 M. Smerieri, E. Celasco, G. Carraro, A. Lusuan, J. Pal, G. Bracco, M. Rocca, L. Savio, L. Vattuone: Enhanced chemical reactivity of pristine graphene interacting strongly with a substrate: Chemisorbed carbon monoxide on graphene/nickel(111), ChemCatChem **7**, 2328–2331 (2015)
36.144 E. Celasco, G. Carraro, M. Smerieri, L. Savio, M. Rocca, L. Vattuone: Influence of growing conditions on the reactivity or Ni supported graphene towards CO, J. Chem. Phys. **146**, 104704 (2017)
36.145 A. Politano, M. Cattelan, D.W. Boukhvalov, D. Campi, A. Cupolillo, S. Agnoli, N.G. Apostol, P. Lacovig, S. Lizzit, D. Farías, G. Chiarello, G. Granozzi, R. Larciprete: Unveiling the mechanisms leading to H_2 production promoted by water decomposition on epitaxial graphene at room temperature, ACS Nano **10**, 4543–4549 (2016)
36.146 R.A. Bueno, J. Martínez, R.F. Luccas, N. Ruiz del Árbol, C. Munuera, I. Palacio, F.J. Palomares, K. Lauwaet, S. Thakur, J.M. Baranowsk, W. Strupinski, M.F. López, F. Mompean, M. García-Hernández, J.A. Martín-Gago: Highly selective covalent organic functionalization of epitaxial graphene, Nat. Commun. **8**, 15306 (2017)
36.147 L. Ferrighi, D. Perilli, D. Selli, C. Di Valentin: Water at the interface between defective graphene and Cu or Pt(111) surfaces, ACS Appl. Mater. Interfaces **9**, 29932–29941 (2017)
36.148 Q.H. Wang, Z. Jin, K.K. Kim, A.J. Hilmer, G.L.C. Paulus, C.-J. Shih, M.-H. Ham, J.D. Sanchez-Yamagishi, K. Watanabe, T. Taniguchi, J. Kong, P. Jarillo-Herrero, M.S. Strano: Understanding and controlling the substrate effect on graphene electron-transfer chemistry via reactivity imprint lithography, Nat. Chem. **4**, 724–732 (2012)
36.149 V. Georgakilas, M. Otyepka, A.B. Bourlinos, V. Chandra, N. Kim, K.C. Kemp, P. Hobza, R. Zboril, K.S. Kim: Functionalization of graphene: Covalent and non-covalent approaches, derivatives and applications, Chem. Rev. **112**, 6156–6214 (2012)
36.150 F. Yavari, C. Kritzinger, C. Gaire, L. Song, H. Gullapalli, T. Borca-Tasciuc, P.M. Ajayan, N. Koratkar: Tunable bandgap in graphene by the controlled adsorption of water molecules, Small **6**, 2535–2538 (2010)
36.151 X.C. Dong, Y.M. Shi, Y. Zhao, D.M. Chen, J. Ye, Y.G. Yao, F. Gao, Z.H. Ni, T. Yu, Z.X. Shen, Y.X. Huang, P. Chen, L.J. Li: Symmetry breaking of graphene monolayers by molecular decoration, Phys. Rev. Lett. **102**, 135501 (2009)
36.152 T. Ohta, A. Bostwick, T. Seyller, K. Horn: Controlling the electronic structure of bilayer graphene, Science **313**, 951–954 (2006)
36.153 E. Rudberg, P. Sałek, Y. Luo: Nonlocal exchange interaction removes half-metallicity in graphene nanoribbons, Nano Lett. **7**, 2211–2213 (2007)
36.154 Y.W. Son, M.L. Cohen, S.G. Louie: Half-metallic graphene nanoribbons, Nature **444**, 347–349 (2006)
36.155 Y.B. Zhang, T.T. Yang, C. Girit, Z. Hao, M.C. Martin, A. Zettl, M.F. Crommie, Y.R. Shen, F. Wang: Direct observation of a widely tunable bandgap in bilayer graphene, Nature **459**, 820–823 (2009)
36.156 S.Y. Zhou, D.A. Siegel, A.V. Fedorov, A. Lanzara: Metal to insulator transition in epitaxial graphene induced by molecular doping, Phys. Rev. Lett. **101**, 086402 (2008)
36.157 D. Guo, R. Shibuya, C. Akiba, S. Saji, T. Kondo, J. Nakamura: Active sites of nitrogen-doped carbon materials for oxygen reduction reaction clarified using model catalysts, Science **351**, 361–365 (2016)

36.158 G. Carraro, E. Celasco, M. Smerieri, L. Savio, G. Bracco, M. Rocca, L. Vattuone: Chemisorption of CO on N-doped graphene on Ni(111), Appl. Surf. Sci. **428**, 775–780 (2018)

36.159 E.J. Duplock, M. Scheffler, P.J.D. Lindan: Hallmark of perfect graphene, Phys. Rev. Lett. **92**, 225502 (2004)

36.160 Q. Fu, X. Bao: Surface chemistry and catalysis confined under two-dimensional materials, Chem. Soc. Rev. **46**, 1842–1874 (2017)

36.161 W. Zhao, O. Höfert, K. Gotterbarm, J.F. Zhu, C. Papp, H.-P. Steinrück: Production of nitrogen-doped graphene by low-energy nitrogen implantation, J. Phys. Chem. C **116**, 5062–5066 (2012)

36.162 H. Nakano, J. Ogawa, J. Nakamura: Growth mode of carbide from C_2H_4 or CO on Ni(111), Surf. Sci. **514**, 256–260 (2002)

36.163 R. Mu, Q. Fu, L. Jin, L. Yu, G. Fang, D. Tan, X. Bao: Visualizing chemical reactions confined under graphene, Angew. Chem. Int. Ed. **51**, 4856–4859 (2012)

36.164 H. Li, J. Xiao, Q. Fu, X. Bao: Confined catalysis under two-dimensional materials, Proc. Natl. Acad. Sci. U. S. A. **114**, 5930–5934 (2017)

36.165 Y.X. Yao, Q. Fu, Y.Y. Zhang, X.F. Weng, H. Li, M.S. Chen, L. Jin, A.Y. Dong, R.T. Mu, P. Jiang, L. Liu, H. Bluhm, Z. Liu, S.B. Zhang, X.H. Bao: Graphene cover-promoted metal-catalyzed reactions, Proc. Natl. Acad. Sci. U. S. A. **111**, 17023–17028 (2014)

36.166 J.S. Alden, A.W. Tsen, P.Y. Huang, R. Hovden, L. Brown, J. Park, D.A. Muller, P.L. McEuen: Strain solitons and topological defects in bilayer graphene, Proc. Natl. Acad. Sci. U. S. A. **110**(28), 11256–11260 (2013)

36.167 Y. Cao, V. Fatemi, S. Fang, K. Watanabe, T. Taniguchi, E. Kaxiras, P. Jarillo-Herrero: Unconventional superconductivity in magic-angle graphene superlattices, Nature **556**(7699), 4350 (2018)

Ado Jorio

Departamento de Física
Universidade Federal de Minas Gerais
Belo Horizonte, Brazil
adojorio@gmail.com

Ado Jorio is a professor of Physics at the Federal University of Minas Gerais (UFMG), from where he earned a doctoral degree in 1999. He works with research and development of scientific instrumentation in optics for the study of nanostructures with applications in new materials and biomedicine. He was a postdoctoral fellowship at MIT (2000-2001), a visiting Professor at ETH Zurich (2013) and at Freie Universitat Berlin (2016).

Edmar Avellar Soares

Departamento de Física
Universidade Federal de Minas Gerais
Belo Horizonte, Brazil
edmar@fisica.ufmg.br

Edmar Soares is an associate professor at the Physics Department of Federal University of Minas Gerais (Brazil) where he received his PhD in 1998. He was a visiting researcher at University of Warwick-UK, LBNL-USA and CEA/ESRF Grenoble-France. His research has focused on the determination of atomic-scale structure and bonding at solid surfaces and in nanostructures, in order to better understand the atomistic basis of surface science, nanoscience and their many technological applications.

Roberto Paniago

Departamento de Física
Universidade Federal de Minas Gerais
Belo Horizonte, Brazil
paniago@fisica.ufmg.br

Roberto Paniago received his PhD in Physics at the University of Kassel (Germany) and is currently full professor of condensed matter physics at the Federal University of Minas Gerais (Brazil), with focus on Surface Science. His research activity aims at understanding the correlation of structural, electronic and magnetic properties of ultrathin-epitaxial films and nanostructures.

Mario Rocca

Dipt. di Fisica
Università di Genova
Genova, Italy
rocca@fisica.unige.it

Mario Rocca received his PhD in Physics at the University of Aachen (Germany) and is currently full professor of condensed matter physics at the University of Genova (Italy), where he leads a joint research group on Surface Science with CNR-IMEM. His major scientific achievements are on gas-surface interaction, ultrathin film growth, surface phonons and acoustic surface plasmons.

Luca Vattuone

Dipt. di Fisica
Università di Genova and IMEM-CNR Unità di Genova
Genova, Italy
vattuone@fisica.unige.it

Luca Vattuone received his PhD from the University of Genoa in 1994, worked as postdoc at Cambridge University (1995) and at Genoa University (1996–1999). In 1999 he became Staff Researcher and in 2012 Associate Professor of Condensed Matter Physics at Genoa University. His research activity focuses on the experimental investigation of gas–surface interactions and surface plasmons.

37. Silicene

Eric Salomon, Daniel Beato-Medina, Paola De Padova, Thierry Angot, Guy Le Lay

We introduce silicene, the Si-based analog of graphene, an emerging two-dimensional topological insulator, and its realization by epitaxial growth on the favored silver (111) substrate. We describe the structural, electronic and vibronic properties of monolayer silicene, and the growth and electronic properties of multilayer silicene. We next address the hydrogenation and oxidation of these new silicon allotropes. We further report the fabrication of the first field-effect transistors made with a silicene channel. Finally, we discuss exotic forms of silicon at zero and one dimension, namely benzene-like nanodots and pentasilicene-like nanoribbons, before drawing enticing perspectives.

The 2016 Nobel Prize in Physics was awarded to David J. Thouless, F. Duncan M. Haldane and J. Michael Kosterlitz "for theoretical discoveries of topological phase transitions and topological phases of matter" [37.1]. The subject of this chapter, *silicene*, is a hallmark of an emerging new two-dimensional (2-D) topological state of quantum matter, an atom-thin 2-D elemental topological insulator (TI) characterized by the quantum spin Hall effect (QSHE) [37.2, 3]. It is made solely of silicon atoms arranged in a low-buckled honeycomb structure, as shown in Fig. 37.1 for freestanding silicene [37.4–6], similar to but different from graphene, which is basically flat [37.7].

Topological insulators represent a fascinating recently discovered class of quantum states of matter with insulating bulk but helical conducting surface or edge states. *Topological* refers to a mathematical concept that describes the invariant property of objects during an adiabatic evolution process. Typically, as pedagogical classical examples, an orange cannot be deformed continuously into a donut (with, per se, a hole), but you can transform a donut into a mug. The topology of an object is characterized by an integer associated with the integral of its curvature. A trivial insulator (like vacuum) has an integer value of zero; a TI (equivalently, a quantum spin Hall insulator (QSHI)) has a value of one.

It turns out that the quantum mechanical wave functions in momentum space of crystals have properties similar to the curvature of a donut. Within a bulk energy gap, TIs possess gapless boundary states, spin-locked due to the protection of the time-reversal symmetry: the propagation direction of the surface electrons is robustly linked to their spin orientation, as illustrated in Fig. 37.2.

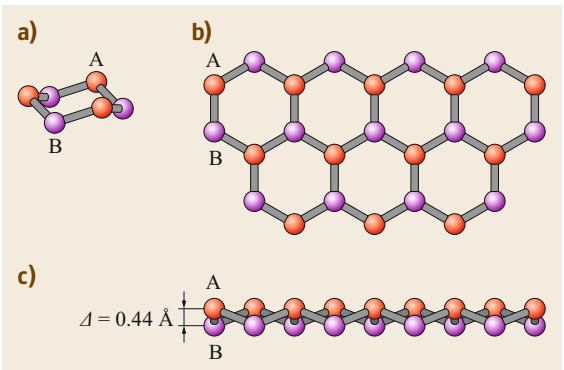

Fig. 37.1 (a) Perspective, (b) top and (c) side views of freestanding silicene. A and B represent the two sublattices, vertically displaced by $\Delta = 0.44$ Å, the buckling ►

M. Rocca, T.S. Rahman, L. Vattuone (Eds.), *Springer Handbook of Surface Science*, Springer Handbooks,
https://doi.org/10.1007/978-3-030-46906-1_37

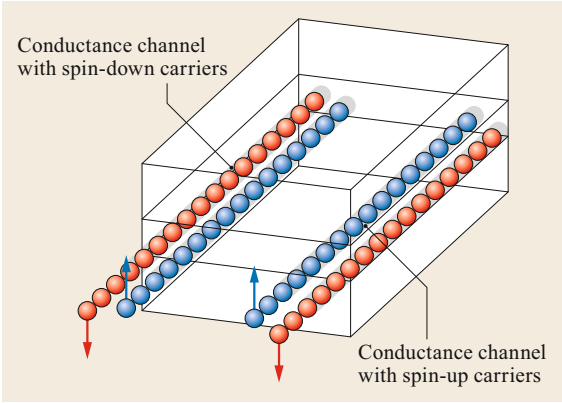

Fig. 37.2 Edge states in the quantum spin Hall insulator. Schemes of the spin-polarized edge channels (From [37.8]. Reprinted with permission from AAAS)

Graphene was the first material proposed to be such a QSHI governed by spin–orbit coupling (SOC) [37.10], opening a bandgap in such 2-D Dirac semimetals. It exemplified a theoretical toy model already proposed in 2-D honeycomb lattice systems by *Haldane* in 1988 [37.11]. However, the spin–orbit interaction in graphene is so weak ($\approx 10^{-3}$ meV) that the QSHE can only occur at unrealistically practical low temperatures, at variance with silicene, with a SOC gap value of 1.55 meV [37.3, 12], which makes it a robust TI up to ≈ 15 K.

As further stated by *Ma* and coworkers [37.13], 2-D TIs are immune to all the scattering of electrons in the presence of nonmagnetic impurities, leading to dissipation-less transport edge channels, while Majorana fermions, which besides their fundamental physical importance may play an important role in topological quantum computation schemes, should appear when the material comes in contact with a superconductor.

Moreover, as emphasized by *Persichetti* et al. [37.14], silicene, like graphene, is a Dirac material in which electrons near the K and K′ points of the Brillouin zone behave as relativistic massless particles because of the linear dispersion around the Fermi level. The velocity of the charge carriers, estimated to be of the order of 10^5–10^6 m/s [37.5], is also comparable to that in graphene. However, silicene (and germanene) shows peculiar physical properties that make it better suited than graphene in the race for ultimate thickness scaling of nanoelectronic devices [37.9]. Indeed, it offers perfect compatibility with the current Si-based technology of semiconductor processing, and more importantly, its buckled structure makes it more flexible than that of graphene because of the absence of strong π-bonds enforcing planarity. This buckling, along with the resulting much larger SOC, makes it easier to create a required energy bandgap in such a Si (and Ge) 2-D crystal without degrading its electronic properties.

As seen in Fig. 37.3, to pursue Moore's law, and to push scaling towards the 5 nm gate length in the fabrication of field-effect transistors (FETs), the use of low-dimensionality materials, especially channels based on *intrinsically* 2-D structures to mitigate so-called short channel effects and related power dissipation issues, could be imperative [37.9, 15].

Such reasons explain why, boosted by the first realizations of silicene in 2012 [37.16–18], the research on silicene has become the hottest front in physics after the Higgs boson, the neutrino and gravity ones, according to a Thomson Reuters citation-based study covering the years 2011 to 2014, as seen in Table 37.1.

In this chapter, we will present the basic concepts on silicene, its synthesis by epitaxial growth, the characterization of its structural, electronic and vibrational properties on the favored silver (111) template, and then the growth and electronic properties of multilayer silicene. Next, we will address the hydrogenation and oxidation of these Si-based nanostructures and the fabrication of the first FETs made with a silicene channel. Finally, novel exotic forms of low-dimensional silicon will be described, before drawing conclusions and offering intriguing perspectives.

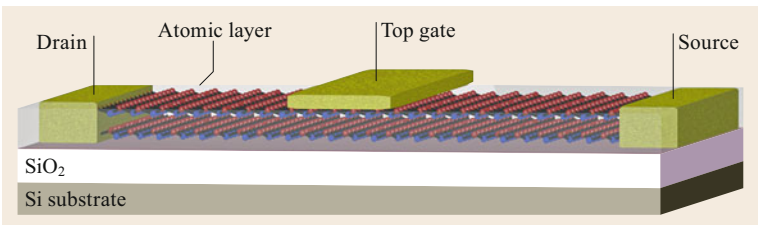

Fig. 37.3 The reduction of the channel thickness is at the center of the nanoelectronic device scaling scenario. Ultimate thickness downsizing with atomically thin layers could be one of the most important options for aggressive scaling beyond the 5 nm technology node, offering excellent electrostatic control (From [37.9] © IOP Publishing. Reproduced with permission. All rights reserved)

Table 37.1 Development trend of the top 10 research fronts in physics (Reprinted by permission from [37.19])

Rank	Research fronts	Core papers	Citations	Mean year of core papers
1	Observation of Higgs boson	2	1905	2012
2	Global neutrino data analysis	12	2350	2011.8
3	Nonlinear massive gravity	32	1814	2011.8
4	**The growth and properties of silicene**	**25**	**1859**	**2011.7**
5	MoS_2 and transistors	20	3147	2011.5
6	Spin–orbit-coupled Fermi gases	43	3246	2011.4
7	Alkali-doped iron selenide superconductors A_xFe_2-$_ySe_2$	35	2995	2011.2
8	Graphene plasmonics	15	1711	2011.1
9	Topological Mott insulators	33	2326	2011
10	Hydrodynamics of relativistic heavy ion collisions	29	2020	2011

37.1 The Concept: Freestanding Silicene

Ten years before the isolation of graphene, two pioneers had already shown, through density functional theory (DFT) calculations, the "possibility of stage corrugation in Si and Ge analogs of graphite" [37.4], in other words of freestanding silicene, so coined in 2007 [37.5], and germanene, the germanium counterpart. The stability of the low-buckled structure with respect to phonons was demonstrated in 2009 [37.6], together with the cone-like dispersion of the π and π^* states near the Fermi level at the corners of the 2-D Brillouin zone, as shown in Fig. 37.4. For silicene, the 0.44 Å buckling corresponds to a bond angle of $\theta = 116.2°$, which gives a sp^D degree of hybridization ($D = -1/\cos(\theta) = 2.27$) closer to sp^2, as in graphene, than to sp^3 in normal crystalline silicon [37.20].

For nearly two decades, until the very first synthesis of silicene on Ag(111) in 2012 [37.16], practically no one believed in the possibility of graphene-like silicon: a spectacular illustration is given in Fig. 37.5, which shows, according to the Web of Science (WOS), upon searching for silicene for the period from 2007, when the term silicene was introduced [37.5], to the end of November 2016, a sudden jump in the number of papers and citations in 2012/2013.

As underlined in the introduction, the SOC opens a bandgap at the Dirac point of silicene and its group 14 cousins, namely germanene and stanene (also sometimes called tinene), which exhibit SOC of respectively 1.55, 23 and 73 meV (compared with only 8 μeV for graphene), facilitating the 2-D material transition from semimetallic to a QSH insulator [37.21, 22]. Other properties are worth mentioning. We stress, to name a few, the electrically tunable bandgap [37.23], a possibility of phonon-mediated superconductivity [37.24], and the predicted very high mobility for both electrons and holes (μ_e and μ_h) at room temperature (RT), as shown in Table 37.2 [37.25].

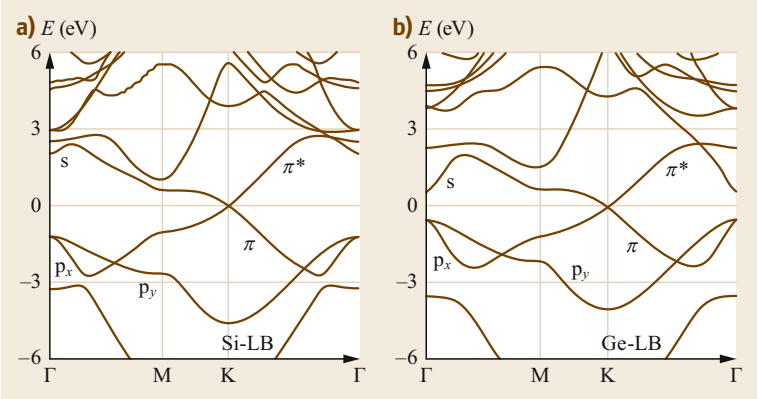

Fig. 37.4 Band structures of silicene and germanene in the low-buckled (LB) geometry (Reprinted with permission from [37.6]. Copyright (2012) by the American Physical Society)

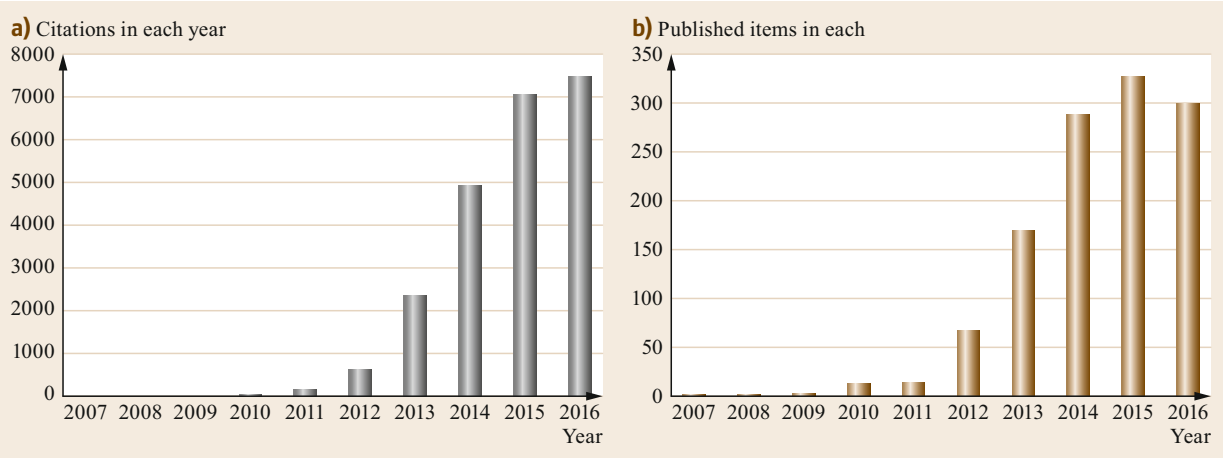

Fig. 37.5a,b Report reflecting citations **(a)** to source items **(b)** indexed within the Web of Science Core Collection with silicene as topic for the period 2007 to November 28th, 2016

37.2 Silicene Synthesis and Characterization

The first synthesis of silicene on a silver (111) single-crystal surface proceeds from earlier investigations of the inverse system, namely Ag/Si(111), during the study of the growth mechanisms of the noble metal/semiconductor heterostructures, i.e., Ag, Au/Si(111), Ge(111), as illustrated in Fig. 37.6. Ag/Si(111) is the most prototypical system, growing in the Stranski-Krastanov mode. The interface is atomically abrupt, and, past the formation of a Si(111)-$(\sqrt{3}\times\sqrt{3})$R30° 2-D superstructure, three-dimensional Ag(111) islands develop in parallel epitaxy with a *magic* relationship: four Ag–Ag nearest-neighbor distances in the Ag(111) contact plane matching nearly exactly three Si–Si nearest-neighbor distances within the Si(111) surface plane [37.26]. This inspired the idea to try to grow silicene the other way around.

Success came when depositing Si onto a Ag(111) surface held at about 200 °C. Such a process results in the observation of a highly ordered 2-D layer, with the aspect of a very nice *flower pattern* in scanning tunneling microscopy (STM) imaging, which did not appear directly at all as a graphene-like arrangement but which could be interpreted as revealing a hidden honeycomb structure (Fig. 37.7).

Table 37.2 Predicted mobility at 300 K (10^5 cm^2/V s) along the zigzag and armchair directions (Reprinted by permission from [37.25], © RSC 2014)

Material	Electron mobility	Hole mobility
Graphene	3.39	3.22
	3.20	3.51
Silicene	2.58	2.23
	2.57	2.22
Germanene	6.09	6.39
	6.24	6.54

Typically, three unit lattice vectors of silicene matched perfectly four unit lattice vectors of the Ag(111) surface, forming a Ag(111)-(4×4) reconstruction with respect to the silver substrate, but a puckered (3×3) superstructure in terms of silicene. In a seminal paper published in 2012, we name this archetype, most energetically favorable silicene phase, in short, $(3\times3)/(4\times4)$ [37.16]. A linearly dispersing band, with possibly a gap opening, was measured in angle-resolved photoelectron spectroscopy (ARPES) experiments at the K/K′ points of the surface Brillouin zone and thence eventually assigned to a branch of a Dirac cone. Later, however, it was shown to be a hybridized band resulting from a significant interaction of the monolayer silicene sheet with the Ag(111) surface [37.27–29].

The $(3\times3)/(4\times4)$ silicene phase on Ag(111) was soon confirmed [37.17]. Further diffraction studies by reflection high-energy positron diffraction (RHEPD) showing that 95% of the surface of the substrate was covered by this unique structure [37.30], by dynamical low-energy electron diffraction (LEED) [37.31], and lastly by grazing incidence x-ray diffraction [37.32], firmly established the proposed atomic geometry, initially proposed by Vogt et al., following DFT calculations [37.16].

Other superstructures are formed on the Ag(111) surface at higher temperatures. A $(\sqrt{7}\times\sqrt{7})/(\sqrt{13}\times$

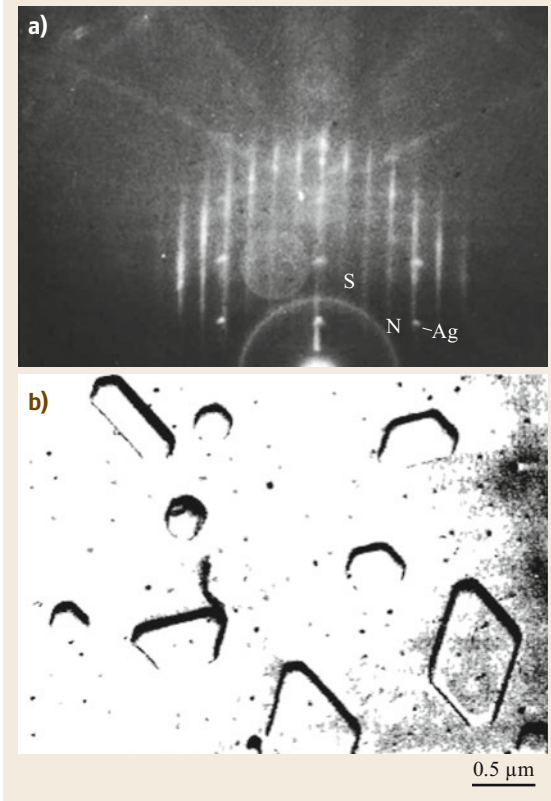

Fig. 37.6a,b Ag(111) crystallites in parallel orientation on the Ge (or, similarly, Si). **(a)** (111)-$(\sqrt{3}\times\sqrt{3})$R30°-Ag surface superstructure detected in situ by reflection high-energy electron diffraction (RHEED): pattern along the $\langle 11\bar{2}\rangle$ azimuth (*N*: normal substrate streaks, *S*: 1/3 order superstructure streaks). **(b)** In situ-prepared carbon replica observed ex situ after extraction in HF solution by transmission electron microscopy (TEM): one observes the imprints of (111) Ag crystallites, which have been attacked by HF, on the Si(111) substrate (Reprinted from [37.26], with permission from Elsevier)

$\sqrt{13}$) one, using the same notation convention as for the $(3\times3)/(4\times4)$ phase, is also a slightly expanded silicene phase, existing by symmetry in four equivalent domains as depicted by *Resta* et al. [37.33] and shown in Fig. 37.8.

Interestingly, at low temperatures, a vortex-like appearance is manifested in such domains upon STM imaging (Fig. 37.9) [37.34]. Still, the continuity of the honeycomb array is preserved, but with very different local buckling configurations [37.35]. We tentatively assign this spectacular behavior to the very different thermal expansion coefficients of the silver substrate, which behaves normally upon cooling from the growth temperature of ≈ 493 to ≈ 4 K, and that of the silicene overlayer, initially slightly stretched, which most probably possesses a negative thermal expansion coefficient at low temperatures [37.36], and consequently behaves like a synergetic combination of silicon atoms and graphene-like structure, both silicon and graphene having negative thermal expansion coefficients. Then, the vortex pattern would result from a complex buckling relaxation process of the strain accumulated upon cooling.

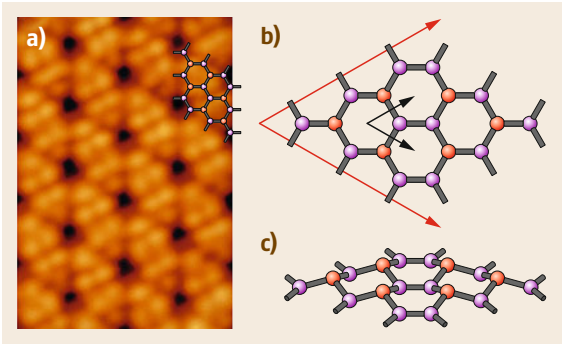

Fig. 37.7 **(a)** The *flower pattern* appearance of the archetype $(3\times3)/(4\times4)$ silicene phase formed on Ag(111) at $\approx 200\,^{\circ}$C. **(b)** Top and **(c)** perspective views of the atomic structure of the puckered silicene sheet

A distorted 2-D sheet forming a pseudo "$(2\sqrt{3}\times 2\sqrt{3})$" reconstruction with respect to the Ag(111) substrate, with local honeycomb appearance in STM imaging, is covering most of the surface at high temperatures [37.37]. It is at the verge of a dewetting process with formation of three-dimensional (3-D) silicon crystallites [37.38], and might possibly correspond to a surface alloy [37.39].

Just two months after the publication of the seminal paper on the archetype $(3\times3)/(4\times4)$ silicene phase on Ag(111), another important silicene phase, formed this time by segregation of Si atoms through a metallic ZrB2 thin film epitaxially grown on a Si(111) template, was reported [37.18]. This is a $(\sqrt{3}\times\sqrt{3})$ reconstructed silicene monolayer matching a (2×2) reconstructed ZrB2 (0001) surface; in our notation it is a $(\sqrt{3}\times\sqrt{3})/(2\times2)$ phase. Such a $(\sqrt{3}\times\sqrt{3})$ silicene reconstruction, now matching a $(\sqrt{7}\times\sqrt{7})$ supercell, i.e., a $(\sqrt{3}\times\sqrt{3})/(\sqrt{7}\times\sqrt{7})$, was also found on an iridium (111) surface [37.40]. Later, 2-D Si nanosheets with local hexagonal structure were reported on a MoS_2 surface [37.41]. However, the very high buckling, leading to a metallic nature, makes an assignment to silicene questionable. Instead, the formation of germanene on the same substrate appears more reliable [37.42]. Clearly, the growth of silicene (and germanene or stanene) on a semiconductor or an insulator is highly desirable for practical applications

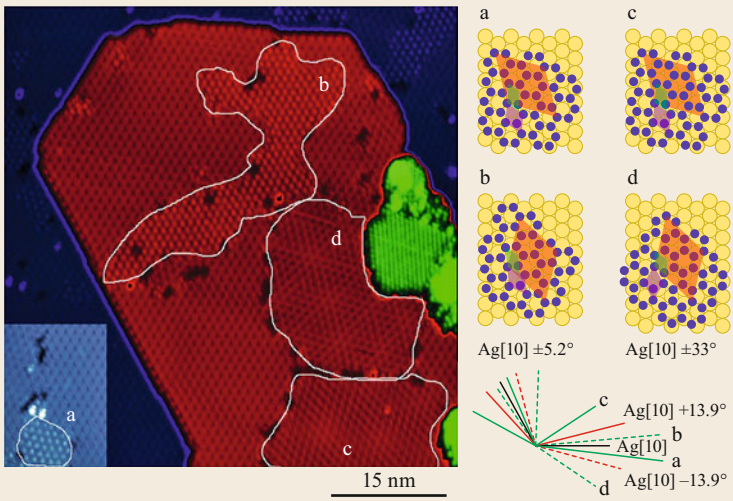

Fig. 37.8 The four domains (*encircled in red*) expected for the $(\sqrt{7}\times\sqrt{7})/(\sqrt{13}\times\sqrt{13})$ phase. *Left:* STM topography image acquired at room temperature; a second-layer $(\sqrt{3}\times\sqrt{3})$ domain appears in *green* (filled states, $U_{\text{bias}} = -1.18\,\text{V}, I = 0.33\,\text{nA}$). *Right:* Ball model (silicon atoms are in *blue*, silver atoms in *yellow*) of the four distinct domains. The silicene $(\sqrt{7}\times\sqrt{7})\text{R}\pm19.1°$ unit cells in coincidence with the Ag(111)-$(\sqrt{13}\times\sqrt{13})\text{R}\pm13.9°$ unit cells are in *orange*; the silicene-(1×1) unit cells are in *magenta* and the Ag(111)-(1×1) cells are in *green* (From [37.33])

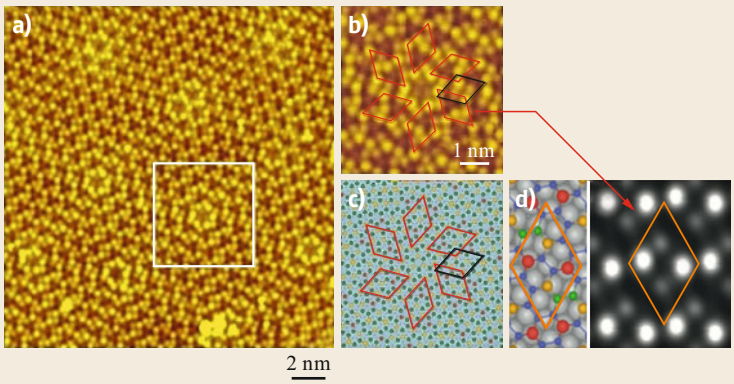

Fig. 37.9 **(a)** Vortex structure of the $(\sqrt{7}\times\sqrt{7})/(\sqrt{13}\times\sqrt{13})$ silicene phase at 4 K. **(b)** One vortex surrounded by six lozenges, which represent six different domains, as illustrated in **(c)**, where the black rhombus is analogous to the model in **(d)** (Reprinted with permission from [37.35]. Copyright (2013) by the American Physical Society)

in electronics. Yet, even though predictions have been made on the stability of van der Waals (vdW) heterostructures made of silicene, germanene or stanene with hexagonal boron nitride (h-BN) [37.43], such hybrid structures have not been convincingly realized until now.

37.3 Multilayer Silicene

Beyond the first $(3\times3)/(4\times4)$ monolayer (ML), at the same growth temperature of $\approx 200\,°\text{C}$, a layered arrangement in successive flat terraces is observed, as displayed in Fig. 37.10 [37.44]. All terraces possess the apparently same $(\sqrt{3}\times\sqrt{3})\text{R}30°$ reconstruction with respect to freestanding silicene seen in the corresponding LEED pattern. Topographic profiles recorded on the $(\sqrt{3}\times\sqrt{3})\text{R}30°$ reconstruction point to a periodic lattice constant of $0.64\pm0.01\,\text{nm}$, meaning that there is in reality a $\approx 4\%$ contraction of the reconstructed cell with respect to $(\sqrt{3}\times\sqrt{3})$ times that of the unit cell of freestanding silicene [37.44–46].

Profiles along the dashed white lines in the figure also indicate a step height between successive terraces, from the second to upper ones, of $\approx 0.3\,\text{nm}$. If growth is performed at slightly higher temperatures, where the first ML shows an admixture of $(3\times3)/(4\times4)$ and $(\sqrt{7}\times\sqrt{7})/(\sqrt{13}\times\sqrt{13})$ phases, the next layers still possess the $(\sqrt{3}\times\sqrt{3})$ reconstruction, but with different orientations, as seen in Fig. 37.11 [37.47]. These orientations follow those of the domains of the initial first ML already displayed in Fig. 37.8. It is thus likely that each first layer within each domain is reconstructed upon growth of the second and further layers on top of it.

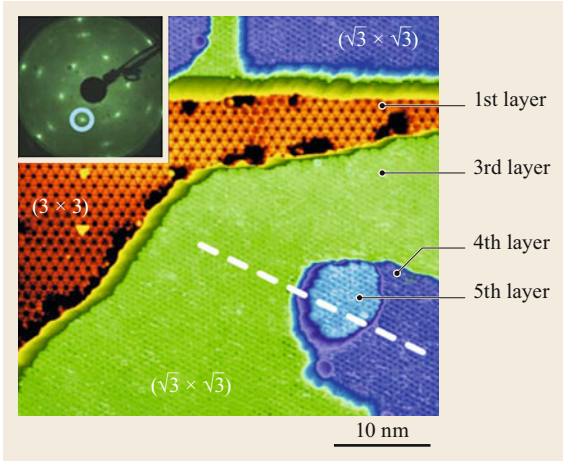

Fig. 37.10 STM topographic image ($44 \times 44\,\text{nm}^2$, $U_{\text{bias}} = -1.14\,\text{V}$, $I = 0.54\,\text{nA}$), after deposition of several MLs of Si onto the $(3\times3)/(4\times4)$ first-layer silicene sheet. Three well-ordered terraces can be seen showing the $(\sqrt{3}\times\sqrt{3})\text{R30}^\circ$ arrangement. The first $(3\times3)/(4\times4)$ silicene layer is still visible at the bottom. *Top-left inset*: corresponding LEED pattern clearly dominated by the $(\sqrt{3}\times\sqrt{3})\text{R30}^\circ$ spots (Reprinted from [37.44], with the permission of AIP Publishing)

The actual nature of the $(\sqrt{3}\times\sqrt{3})$ reconstruction of multilayer silicene has been, and still is, in strong debate. On the one hand, several groups state that the so-called multilayer silicene is just a Si(111) thin film grown with silver atoms at its very surface acting as a surfactant [37.48–51]. Then the $(\sqrt{3}\times\sqrt{3})$ structure would be just the well-known Si(111)-$(\sqrt{3}\times\sqrt{3})\text{R30}^\circ$-Ag surface reconstruction completed at 1 ML coverage, represented by the honeycomb-chained-triangle (HCT) model at room temperature (Fig. 37.12a,b), following dynamical fluctuations of the most energetically favorable inequivalent triangle (IET) configuration obtained at low temperatures [37.52].

On the other hand, the first ARPES measurements obtained by *De Padova* et al. on a multilayer silicene exhibit a cone-like band structure and a reported Fermi velocity of $0.3\times10^6\,\text{m s}^{-1}$, a value much lower than the $1.3\times10^6\,\text{m s}^{-1}$ measured in the case of Si(111)-$(\sqrt{3}\times\sqrt{3})\text{R30}^\circ$-Ag [37.54, 55]. Also, several STM measurements showed that the in-plane lattice parameter of multilayer silicene (around 6.4 Å) is a few percent smaller than the expected one for the Ag-terminated Si(111) surface reconstruction (6.65 Å) [37.47, 53, 56–59]. Furthermore, a very recent work performed by *Li* et al., and based on scanning tunneling microscopy and spectroscopy as well as Raman spectroscopy, demonstrates that a silicene multilayer can be grown with an atomically resolved buckled honeycomb structure (Fig. 37.12c,d), excluding the possibility of a Ag-terminated Si(111) surface [37.53]. Hence, the controversial sets of data raising the question about the possibility of growing a new layered silicon allotrope were clarified.

Finally, the issue was recently solved by *De Padova* et al. [37.46], who carried out energy-dispersive grazing incidence x-ray diffraction (ED-GIXRD) and Raman spectroscopy measurements comparing multilayer thin films to Si(111)-$(\sqrt{3}\times\sqrt{3})\text{R30}^\circ$-Ag samples used as a reference.

Figure 37.13 displays a summary of the ED-GIXRD data recorded for three different samples. In the case of the $(\sqrt{3}\times\sqrt{3})$ multilayer film grown at $\approx 200\,^\circ\text{C}$, the first-order in-plane reflection appears at $q_{xy} = 0.970 \pm 0.005\,\text{Å}^{-1}$, demonstrating a cell size of the multilayer film of 6.477 ± 0.015 Å, in fair agreement with the STM determination. Interestingly, in the case of both the film grown at 300 °C and the Si(111)-$(\sqrt{3}\times\sqrt{3})\text{R30}^\circ$-Ag sample, the in-plane first-

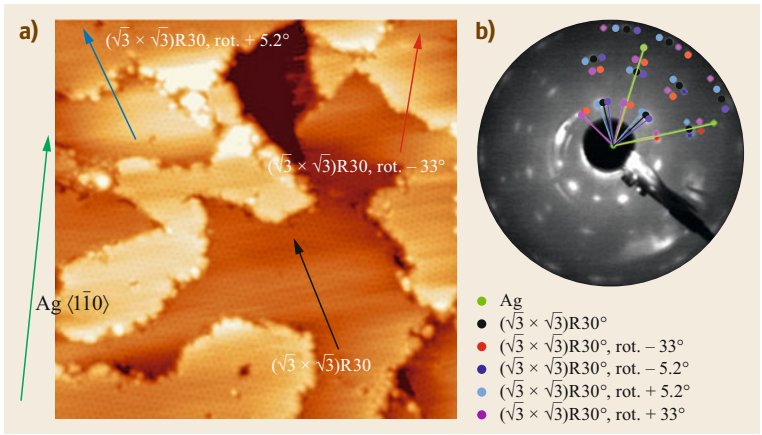

Fig. 37.11 **(a)** 42 nm × 42 nm STM micrograph of multilayer silicene in differently oriented domains, all showing the $(\sqrt{3}\times\sqrt{3})\text{R30}^\circ$ reconstruction. Tunneling parameters: $I_t = 0.27\,\text{nA}$, $U_{\text{bias}} = -1.12\,\text{mV}$ (occupied states). The *blue*, *black* and *red arrows* represent three, out of five, domains with different orientations. **(b)** Corresponding LEED pattern taken at 75 eV together with a simulation of a LEED pattern of $(\sqrt{3}\times\sqrt{3})$ reconstructed multilayer silicene in five different orientations

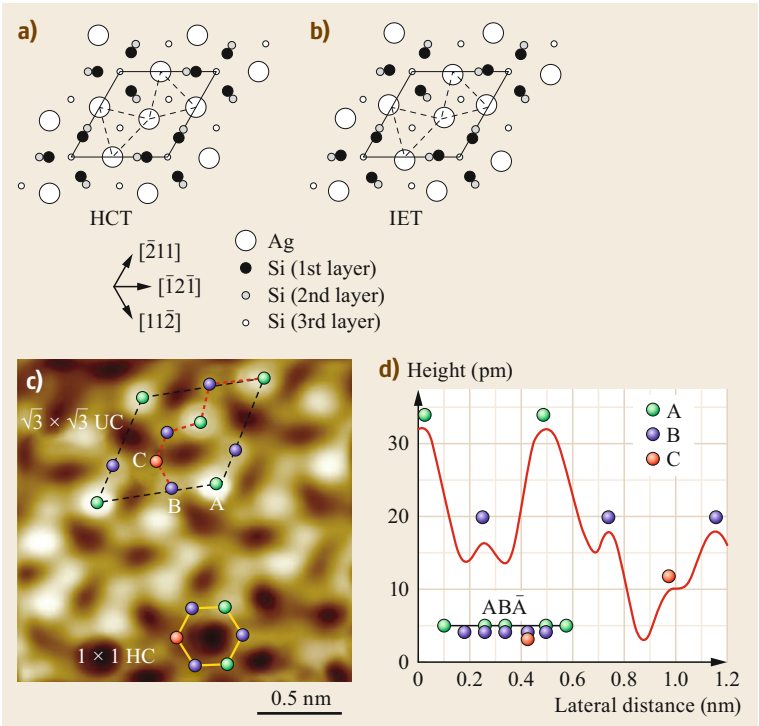

Fig. 37.12a–d Schematic illustrations of **(a)** the HCT structure and of **(b)** the inequivalent triangle (IET) model for the atomic structure of the Si(111)-($\sqrt{3} \times \sqrt{3}$)R30°-Ag surface. *Solid lines* indicate the unit cell, and *dashed lines* represent chained Ag triangles. The top layer of the surface is composed of Ag triangles that are chained to each other, whereas the next layer consists of Si trimers. (Reprinted by permission from [37.52], © Elsevier 1999) **(c)** High-resolution STM image revealing that the $\sqrt{3} \times \sqrt{3}$ multilayer silicene is constructed from a primitive 1×1 honeycomb structure (as indicated by the *yellow honeycomb*, 1×1 HC). The *black dashed line* represents the $\sqrt{3} \times \sqrt{3}$ unit cell ($\sqrt{3} \times \sqrt{3}$ UC). The ABĀ buckled structure is reflected by the brightness of the Si atoms. The *green*, *blue* and *red balls* labeled in the $\sqrt{3} \times \sqrt{3}$ silicene unit cell denote the top, middle and bottom silicon atoms, respectively (2 nm × 2 nm, $V = -3$ mV, $I = 4$ nA). (Reprinted by permission from [37.53], © ACS 2016) **(d)** Height profile corresponding to the *red dashed line* in **(c)**. The inset is a side view of the ABĀ buckled structure corresponding to the height profile. (Reprinted with permission from [37.53]. Copyright (2016) American Chemical Society)

order reflection appears at $q_{xy} = 0.944 \pm 0.005\,\text{Å}^{-1}$, i.e., a cell size of 6.655 ± 0.015 Å. All this demonstrates that the multilayer film grown at low temperature possesses an in-plane lattice parameter markedly different from and smaller than that of a usual diamond-type Si(111) arrangement, whether terminated by a Si(111)-($\sqrt{3} \times \sqrt{3}$)R30°-Ag superstructure or even by an intrinsic Si(111)-($\sqrt{3} \times \sqrt{3}$)R30° reconstruction ($a_{\text{Si(111)-}\sqrt{3}} = 6.655 \pm 0.015$ Å) [37.60, 61]. Hence, these measurements, along with a systematic shift of the main Raman peak with respect to Si(111)-($\sqrt{3} \times \sqrt{3}$)R30°-Ag, have demonstrated the existence, in this low-temperature growth regime, of a new layered metastable structure of silicon, which we call multilayer silicene [37.44, 46]. If, instead, growth is performed at higher temperatures approaching 300 °C, diamond-type Si(111) crystallites terminated by the Si(111)-($\sqrt{3} \times \sqrt{3}$)R30°-Ag superstructure are effectively formed [37.48, 62–65].

Hence, the conflicting issues described above are somehow reconciled: whether multilayer silicene is formed on Ag(111) substrates depends crucially on the actual growth temperature, a parameter which is, unfortunately, often not very well controlled. This is also observed during annealing experiments. An in situ Raman spectroscopy study clearly demonstrates that a structural phase transition from epitaxial $(3 \times 3)/(4 \times 4)$ silicene takes place at ≈ 300 °C (Fig. 37.14) [37.66], in agreement with earlier results [37.37, 67].

This is obvious from the disappearance of the A modes found at 175 and 216 cm^{-1}, as well as the E mode found at 514 cm^{-1} at RT described in [37.68] and

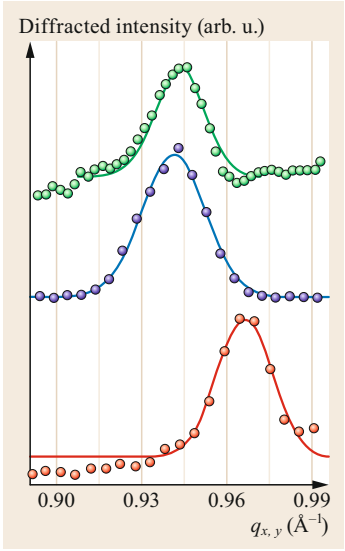

Fig. 37.13 ED-GIXRD pattern recorded from a $(\sqrt{3}\times\sqrt{3})$ multilayer film (10 ML in thickness) grown on Ag(111) at $\approx 200\,^{\circ}$C and Gaussian fits (*bottom*), $(\sqrt{3}\times\sqrt{3})$ multilayer film (10 ML in thickness) grown on Ag(111) at $\approx 300\,^{\circ}$C and Gaussian fits (*middle*) and Si(111)-$(\sqrt{3}\times\sqrt{3})$R30°-Ag and Gaussian fits (*top*)

its replacement by a dominant L(T)O bulk silicon mode at 520 cm^{-1}, due to the formation of Si 3-D crystallites observed by atomic force microscopy (AFM).

Here it is worth mentioning that a single-domain epitaxial monolayer silicene sheet with $(\sqrt{3}\times\sqrt{3})$ structure was recently obtained on $ZrB_2(0001)$ templates [37.69]. As could be anticipated, further growth on top generated pure $(\sqrt{3}\times\sqrt{3})$ layered films, indeed, without the issues raised with the Ag(111) substrates [37.70].

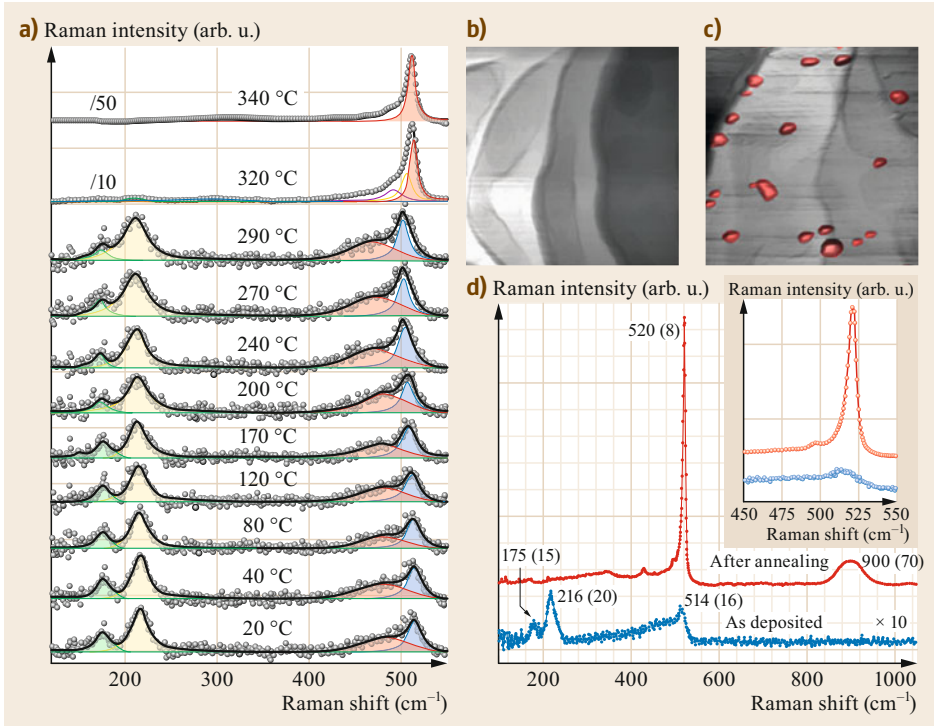

Fig. 37.14 **(a)** Series of Raman spectra of $(3\times3)/(4\times4)$ silicene measured at various temperatures. At about 300 °C, the spectral line shape fundamentally changes following a phase transition due to a dewetting process. **(b)** AFM image (2 µm × 2 µm) of the bare initial Ag(111) surface. **(c)** AFM image (2 µm × 2 µm) after annealing up to 500 °C of the $(3\times3)/(4\times4)$ silicene monolayer, resulting in small islands (in *red*) with an average size distribution of (10 ± 8) nm, distributed on the Ag(111) surface. **(d)** Raman spectra of the epitaxial silicene before and after annealing to 500 °C, both measured at room temperature (From [37.66])

37.4 Functionalization and Encapsulation

The intrinsic low buckling in freestanding silicene preserves the massless Dirac fermion character of the charge carriers and their extremely high mobility. Yet, SOC and symmetry breaking of the A and B sublattices (Fig. 37.1), as well as reconstructions, which are observed until now on all metallic substrates, can eventually open a bandgap. Indeed, the opening of a bandgap is further facilitated by the reactivity of silicene due to its buckled or puckered structures, with intermediate sp^2/sp^3 hybridizations. A striking example is given by the in situ hydrogenation of the $(3\times3)/(4\times4)$ monolayer phase on Ag(111). Figure 37.15 displays an STM image of monolayer silicene after atomic hydrogen exposure [37.71]. Interestingly, upon hydrogen adsorption, the $(3\times3)/(4\times4)$ periodicity is preserved, but the symmetry between the two rhombi halves is broken, as depicted in Fig. 37.15.

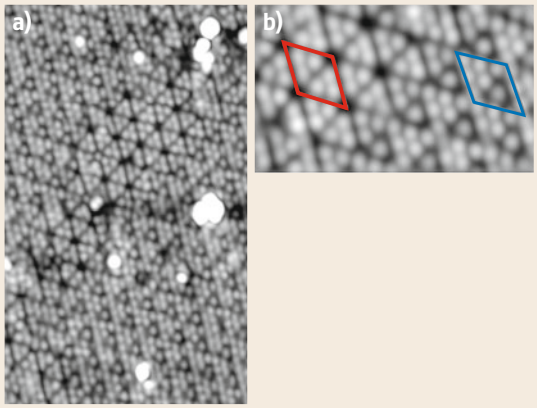

Fig. 37.15 **(a)** 11 nm × 18 nm STM image of $(3\times3)/(4\times4)$ silicene exposed to cracked molecular hydrogen at room temperature for 480 s; $I_{tunnel} = 0.55$ nA, $U_{bias} = -515$ mV (filled states). **(b)** 4 nm × 7 nm zoom-in; the asymmetric unit cell is enclosed in the *blue rhombus*, while the symmetric one is highlighted by the *red rhombus*

In effect, a new reconstruction, labeled γ-(3×3), formed by the repetition of asymmetric unit cells (see the blue rhombus in Fig. 37.15a) is visible. Their minor diagonals split those rhombi into two different triangles. One of them is entirely occupied by six bright protrusions, whereas the other one only displays one bright protrusion located at its center. The explanation behind the new structure probably relies on modified buckling and would be evidence of a structural phase transition from the silicene-(3×3)-α phase to the silicene-(3×3)-β phase, more stable after hydrogenation, as first demonstrated by *Qiu* et al. [37.72]. In addition, let us mention that upon adsorption, the surface corrugation increased by approximately 10 pm, reflecting a modification of the Si buckling [37.71].

Another stimulating point is that for relatively high hydrogen exposure doses, the surface can be fully passivated with respect to oxidation, as demonstrated by high-resolution electron energy-loss spectroscopy (HREELS) measurements. As exhibited in Fig. 37.16, the HREELS spectrum of silicene exposed to low doses of hydrogen (60 s) is dominated by peaks at 98 meV (790 cm^{-1}) and 249 meV (2009 cm^{-1}), which can be readily attributed to the Si–O and Si–H stretching, respectively. This demonstrates that the silicene-(3×3)

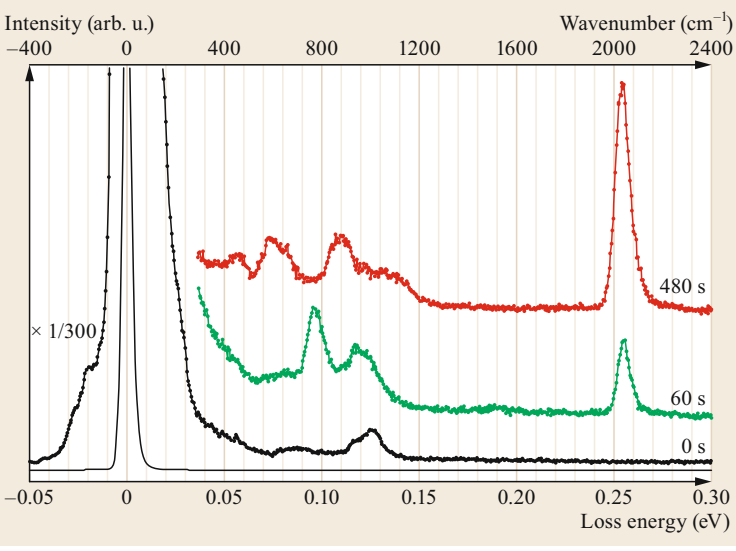

Fig. 37.16 HREELS spectra of hydrogenated monolayer $(3\times3)/(4\times4)$ silicene for different exposure times to atomic hydrogen

surface is reactive and could easily be contaminated during the experiment. On the other hand, after a longer exposure time (480 s) to hydrogen, the spectrum no longer exhibits peaks related to the Si–O, but only the Si–H modes [37.71]. This shows that the silicene-(3×3) can be fully passivated and that it is possible to protect it from contamination, or at least oxidation, through exposure to atomic hydrogen.

Controlled hydrogenation or halogenations should allow bandgap tuning and, furthermore, could lead to ferromagnetic properties [37.73–75]. Indeed, the tuning of a sizable energy gap is on the wish list to push Moore's law beyond the 5 nm node, where 2-D material channels most likely will become indispensable [37.9, 76].

Regarding oxidation, on the one hand, *Du* et al. reported a quasi-freestanding silicene layer that could be successfully obtained through oxidization of bilayer silicene on the Ag(111) surface, the oxygen atoms intercalating into the underlayer silicene, resulting in isolation of the top layer of silicene from the substrate [37.77]. On the other hand, thicker multilayer silicene films were shown by *De Padova* et al. to be resistant to ambient air exposure for at least 24 h: protected by an ultrathin native-oxidized skin, the rest of the body underneath is fully protected [37.78].

Although not as resistant, monolayer epitaxial silicene on Ag(111) can be efficiently preserved by Al- and Al_2O_3-based encapsulation [37.79].

37.5 Devices

The encapsulation of the first silicene layer has been crucial for the successful fabrication of the first-ever field-effect transistors with ambipolar characteristics based on a monolayer silicene channel and operating at room temperature [37.80]. This achievement was made possible by the smart fabrication process depicted in Fig. 37.17.

Remarkably, the derived mobility of the charge carriers for both electrons and holes was about $100\,cm^2\,V^{-1}\,s^{-1}$, which is quite low compared with estimated intrinsic values for freestanding silicene ($\approx 10^5\,cm^2\,V^{-1}\,s^{-1}$) [37.25]. However, it is of the same order of magnitude as the carrier mobility in single-layer MoS_2 [37.81], which suggests that the devices are promising candidates for 2-D transistors. The low mobility is attributed to strong scattering from acoustic phonons and to grain boundary scattering.

It was emphasized that plenty of room remained to achieve higher mobility and better device performance, for example by optimizing silicene growth, engineering and characterizing the interfaces, and tuning and enlarging the bandgap (e.g., by surface adsorption), fabricating and protecting the monolayer silicene gate (which is exposed to air in the present devices), and probably using multilayer instead of monolayer silicene [37.82]. It turns out that in the last case, mobility twice as large was obtained, $\approx 200\,cm^2\,V^{-1}\,s^{-1}$, but somewhat to the detriment of the I_{On}/I_{Off} ratio because of the semimetallic Dirac character of the material [37.83].

In spintronics, exciting possibilities have been proposed. One is the design for a silicene-based spin filter that should enable the spin-polarization of an output current to be switched electrically, without switching external magnetic fields [37.84]. Another one suggests very promising applications by edge-state manipulations, leading typically to a giant magnetoresistance and a perfect spin filter [37.85].

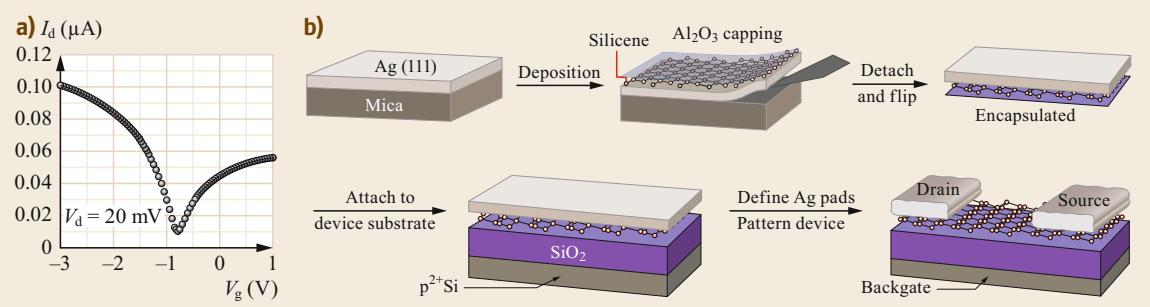

Fig. 37.17 **(a)** The transfer characteristics of a back-gated field-effect transistor with a silicene channel exhibiting ambipolar behavior. **(b)** Schematic of the fabrication process of the silicene device with source/drain contacts defined in the native silver film (From [37.80])

37.6 Exotic Forms of Silicon in Zero and One Dimension

When using a silver (110) substrate exposing a lower-symmetry surface with a rectangular 1×1 unit cell to deposit a submonolayer amount of silicon at room temperature, one obtains two types of perfectly defined novel Si nano-objects, whose atomic structures have remained elusive for more than a decade. As seen in Fig. 37.18, identical zero-dimensional Si nanodots (SiNDs) coexist with an ensemble of highly perfect, massively parallel one-dimensional Si nanoribbons (SiNRs) with the same width of just 0.8 nm, all aligned along the $[1\bar{1}0]$-direction of the surface. While the SiNDs possess the symmetry of the (110) surface, the SiNRs obviously break this symmetry, showing a $\times 2$ reconstruction along the $[1\bar{1}0]$-direction, but with a glide shift of their two rows of protrusions.

Recently, thorough DFT calculations have unveiled the hidden atomic structures [37.86]. The SiNDs sit on two Ag vacancies and consist of a hexasilabenzene-like molecule to which 4 Si atoms are symmetrically attached, as shown in Fig. 37.19. Here we stress that to the best of our knowledge, a hexasilabenzene molecule, i.e., the silicon analog of benzene, has never been synthesized up to now.

The presence of the two vacancies points to the propensity of the noble metal (110) surfaces to reconstruct. Typically, the Au(110) surface is spontaneously reconstructed with a 2×1 superstructure explained by a missing row model, while Ag(110) is unreconstructed, but just at the verge of a missing row reconstruction [37.87]. Each SiNR generates such a missing row by changing the silver surface free energy. It is lying over the missing row with a unique, striking arrangement of Si pentagonal tiles, creating an unprecedented strip of pentasilicene, which we named a single strand, as seen in Fig. 37.20. Again, to the best of our knowledge, this is the first time that a pentasilicene-like structure, i.e., of the Si counterpart of a strip of pentagraphene [37.88], has been synthesized. Remarkably, the amazing atomic arrangement theoretically proposed for the single-strand SiNRs was very rapidly confirmed by synchrotron radiation grazing incidence x-ray diffraction measurements on a highly perfect array of double-strand SiNRs, all 1.6 nm in width [37.89], obtained by lateral compaction of single-strand ones upon deposition (or annealing) at $\approx 200\,^{\circ}\mathrm{C}$, realizing a 5×2 grating with a pitch of just 2 nm [37.90].

Finally, let us quickly mention that several works have reported on the functionalization of SiNRs using atoms or molecules. While adsorption of atomic hydrogen results in an etching of the surface, adsorption of molecules appears to modify the electronic properties of the SiNRs by opening a bandgap depending on the molecular species [37.91–94]. These results, in different ways, appear to be potentially interesting from the perspective of future nanoelectronic devices.

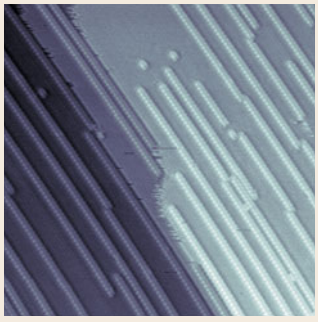

Fig. 37.18 40 nm × 40 nm STM image of a collection of Si nanoribbons with sparse Si nanodots upon deposition of Si onto the Ag(110) at room temperature. $I_{\mathrm{tunnel}} = 0.35$ nA, $U_{\mathrm{bias}} = -50$ mV (filled states)

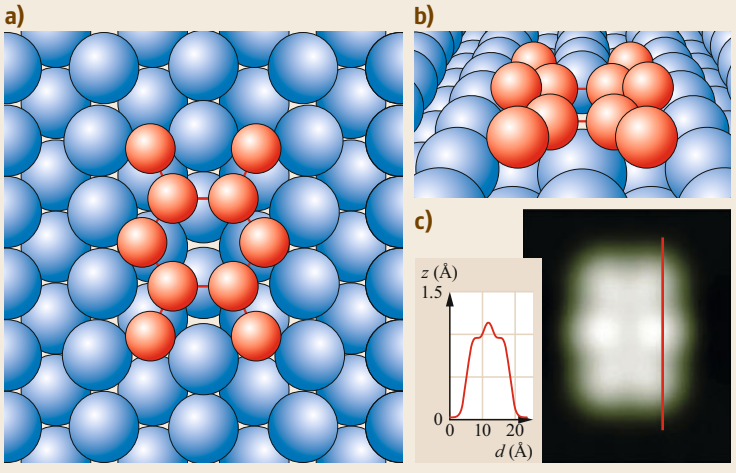

Fig. 37.19 (a,b) Top and perspective views of the nanodot structure with 2 Ag vacancies. (c) Simulated STM topographic image and line profile along the *solid line* (From [37.86])

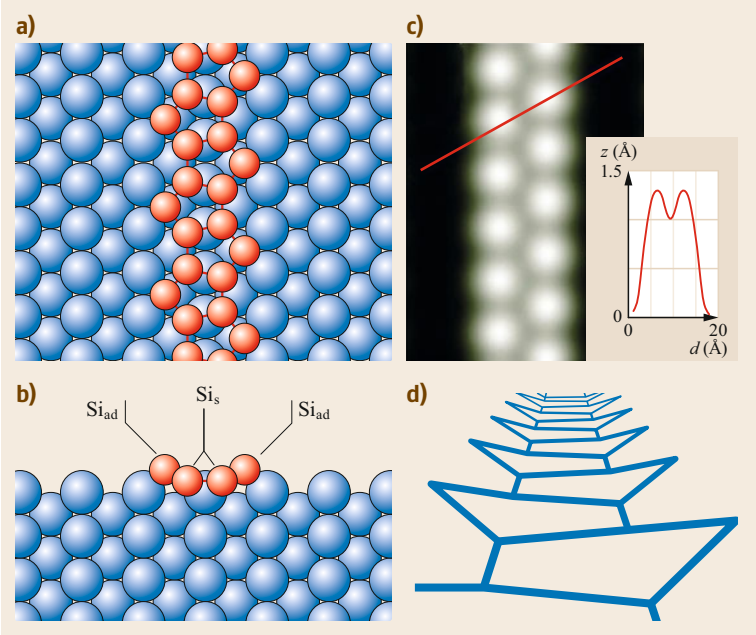

Fig. 37.20a–d Optimized geometry of the pentagonal missing row model. **(a–c)** Top, side and simulated topographic STM image for the SiNR phase prepared at room temperature. **(d)** Perspective view of a pentasilicene strand without the silver surface. (From [37.86])

37.7 Perspectives and Conclusion

Beyond graphene, which descends from graphite, researchers have initially looked for existing semiconductor lamellar crystals that could be peeled to the ultimate monolayer limit, typically transition metal dichalcogenides. The first fabrication of a transistor with a 2-D single-layer MoS_2 channel was realized in 2011 [37.81]. Next, black phosphorus, a layered elemental P allotrope, was rediscovered [37.95], leading to high-performance field-effect transistors based on few-layer crystals with thickness down to a few nanometers [37.96].

However, it was only in 2012 that the first artificial elemental analog of graphene, namely silicene, was synthesized [37.16–18]. Soon after, boosted by this discovery, a cornucopia of novel elemental synthetic 2-D materials including germanene, stanene, plumbene, borophene, blue phosphorene, arsenene, antimonene and bismuthene were shown to possibly exist, and have been eventually realized [37.97]. Strikingly, just three years after the advent of silicene, the first FETs with a monolayer silicene channel were fabricated [37.80].

All this opens exciting prospects, indeed, especially for silicene, and the group 14 novel synthetic 2-D materials, which are directly compatible with the Si-based electronics industry [37.98]. Because these emerging artificial elemental 2-D materials are so young, their properties and potential applications are barely explored [37.99]. Yet, we think that several of them are meant for a bright future, as they will offer fascinating prospects for future nanoelectronics, optoelectronics, spintronics, for quantum computing and flexible devices.

Will one of them be the next silicon? Silicene, the novel 2-D silicon allotrope, and its elemental cousins are clearly in the race.

References

37.1 L. Kou, Y. Ma, Z. Sun, T. Heine, C. Chen: Two-dimensional topological insulators: progress and prospects, Phys. Chem. Lett. **8**, 1905–1919 (2017)

37.2 M.Z. Hasan, C.L. Kane: Colloquium: topological insulators, Rev. Mod. Phys. **82**, 3045–3067 (2010)

37.3 C.C. Liu, W.X. Feng, Y.G. Yao: Quantum spin Hall effect in silicene and two-dimensional germanium, Phys. Rev. Lett. **107**, 076802–076806 (2011)

37.4 K. Takeda, K. Shiraishi: Theoretical possibility of stage corrugation in Si and Ge analogs of graphite, Phys. Rev. B **50**, 14916–14922 (1994)

37.5 G.G. Guzmán-Verri, L.C. Lew Yan Voon: Electronic structure of silicon-based nanostructures, Phys. Rev. B **76**, 075131 (2007)

37.6 S. Cahangirov, M. Topsakal, E. Aktürk, H. Sahin, S. Ciraci: Two- and one-dimensional honeycomb structures of silicon and germanium, Phys. Rev. Lett. **102**, 236804 (2009)

37.7 K.S. Novoselov, A.K. Geim, S.V. Morozov, D. Jiang, Y. Zhang, S.V. Dubonos, I.V. Grigorieva, A.A. Firsov: Electric field effect in atomically thin carbon films, Science **306**, 666–669 (2004)

37.8 M. Konig, S. Wiedmann, C. Brune, A. Roth, H. Buhmann, L.W. Molenkamp, X.-L. Qi, S.-C. Zhang: Quantum spin Hall insulator state in HgTe quantum wells, Science **318**(5851), 766–770 (2007)

37.9 A. Dimoulas: Silicene and germanene: silicon and germanium in the "flatland", Microelectron. Eng. **131**, 68–78 (2015)

37.10 C.L. Kane, E.J. Mele: Quantum spin Hall effect in graphene, Phys. Rev. Lett. **95**, 226801 (2005)

37.11 F.D.M. Haldane: Model for a quantum Hall effect without Landau levels: condensed matter realization of the "parity anomaly", Phys. Rev. Lett. **61**, 2015–2018 (1988)

37.12 Y. Yao, F. Ye, X.L. Qi, S.C. Zhang, Z. Fang: Spin-orbit gap of graphene: first-principles calculations, Phys. Rev. B **75**, 041401 (2007)

37.13 Y. Ma, Y. Dai, L. Kou, T. Frauenheim, T. Heine: Robust two-dimensional topological insulators in methyl-functionalized bismuth, antimony, and lead bilayer films, Nano Letters **15**, 1083–1089 (2015)

37.14 L. Persichetti, F. Jardali, H. Vach, A. Sgarlata, I. Berbezier, M. De Crescenzi, A. Balzarotti: van der Waals heteroepitaxy of germanene islands on graphite, J. Phys. Chem. Lett. **7**, 3246–3251 (2016)

37.15 M.V. Fischetti, B. Fu, W.G. Vandenberghe: Theoretical study of the gate leakage current in sub-10 nm field-effect transistors, IEEE Trans. Electron. Devices **60**, 3862–3869 (2013)

37.16 P. Vogt, P. De Padova, C. Quaresima, J. Avila, E. Frantzeskakis, M.C. Asensio, A. Resta, B. Ealet, G. Le Lay: Silicene: compelling experimental evidence for graphenelike two-dimensional silicon, Phys. Rev. Lett. **108**, 155501 (2012)

37.17 C.-L. Lin, R. Arafune, K. Kawahara, N. Tsukahara, E. Minamitani, Y. Kim, N. Takagi, M. Kawai: Structure of silicene grown on Ag(111), Appl. Phys. Express **5**, 045802 (2012)

37.18 A. Fleurence, R. Friedlein, T. Ozaki, H. Kawai, Y. Wang, Y. Yamada-Takamura: Experimental evidence for epitaxial silicene on diboride thin films, Phys. Rev. Lett. **108**, 245501 (2012)

37.19 C. Day: Hot physics, PhysicsToday (2015), https://doi.org/10.1063/PT.5.010331

37.20 S. Cahangirov, H. Sahin, G. Le Lay, A. Rubio: *Introduction to the Physics of Silicene and Other 2D Materials*, Springer Lect. Notes Phys., Vol. 930 (Springer, Cham 2017)

37.21 M. Ezawa: A topological insulator and helical zero mode in silicene under an inhomogeneous electric field, New J. Phys. **14**, 033003 (2012)

37.22 L. Matthes, O. Pulci, F. Bechstedt: Massive Dirac quasiparticles in the optical absorbance of graphene, silicene, germanene, and tinene, J. Phys. Condens. Matter **25**, 395305 (2013)

37.23 N.D. Drummond, V. Zólyomi, V.I. Fal'ko: Electrically tunable band gap in silicene, Phys. Rev. B **85**, 075423 (2012)

37.24 W. Wan, Y. Ge, F. Yang, Y. Yao: Phonon-mediated superconductivity in silicene predicted by first-principles density functional calculations, Europhys. Lett. **104**, 36001 (2013)

37.25 X.-S. Ye, Z.-G. Shao, H. Zhao, L. Yang, C.-L. Wang: Intrinsic carrier mobility of germanene is larger than graphene's: first-principle calculations, RSC Advances **4**, 21216–21220 (2014)

37.26 G. Le Lay, G. Quentel, J.P. Faurie, A. Masson: Epitaxy of noble metals and (111) surface superstructures of silicon and germanium II study after annealing, Thin Solid Films **35**, 289–303 (1976)

37.27 S. Cahangirov, M. Audiffred, P. Tang, A. Iacomino, W. Duan, G. Merino, A. Rubio: Electronic structure of silicene on Ag(111): strong hybridization effects, Phys. Rev. B **88**, 035432 (2013)

37.28 D. Tsoutsou, E. Xenogiannopoulou, E. Golias, P. Tsipas, A. Dimoulas: Evidence for hybrid surface metallic band in (4×4) silicene on Ag(111), Appl. Phys. Lett. **103**, 231604 (2013)

37.29 R. Stephan, M.-C. Hanf, P. Sonnet: Spatial analysis of interactions at the silicene/Ag interface: first principles study, J. Phys. Condens. Matter **27**, 015002 (2015)

37.30 Y. Fukaya, I. Mochizuki, M. Maekawa, K. Wada, T. Hyodo, I. Matsuda, A. Kawasuso: Structure of silicene on a Ag(111) surface studied by reflection high-energy positron diffraction, Phys. Rev. B **88**, 205414 (2013)

37.31 K. Kawahara, T. Shirasawa, R. Arafune, C.-L. Lin, T. Takahashi, M. Kawai, N. Takagi: Determination of atomic positions in silicene on Ag(111) by low-energy electron diffraction, Surf. Sci. **623**, 25–28 (2014)

37.32 A. Curcella, R. Bernard, Y. Borensztein, A. Resta, M. Lazzeri, G. Prévot: Determining the atomic structure of the (4×4) silicene layer on Ag(111) by combined grazing-incidence x-ray diffraction measurements and first-principles calculations, Phys. Rev. B **94**, 165438 (2016)

37.33 A. Resta, T. Leoni, C. Barth, A. Ranguis, C. Becker, T. Bruhn, P. Vogt, G. Le Lay: Atomic structures of silicene layers grown on Ag(111): scanning tunneling microscopy and noncontact atomic force microscopy observations, Sci. Rep. **3**, 2399 (2013)

37.34 Z.-L. Liu, M.-X. Wang, J.-P. Xu, J.-F. Ge, G. Le Lay, P. Vogt, D. Qian, C.-L. Gao, C. Liu, J.-F. Jia: Various atomic structures of monolayer silicene fabricated on Ag(111), New J. Phys. **16**, 075006 (2014)

37.35 Z.-X. Guo, S. Furuya, J.-I. Iwata, A. Oshiyama: Absence and presence of Dirac electrons in silicene on substrates, Phys. Rev. B **87**, 235435 (2013)

37.36 L.-F. Huang, P.-L. Gong, Z. Zeng: Phonon properties, thermal expansion, and thermomechanics of silicene and germanene, Phys. Rev. B **91**, 205433 (2015)

37.37 E. Cinquanta, E. Scalise, D. Chiappe, C. Grazianetti, B. van den Broek, M. Houssa, M. Fanciulli, A. Molle: Getting through the nature of silicene: an sp^2–sp^3 two-dimensional silicon nanosheet, J. Phys. Chem. C **117**, 16719–16724 (2013)

37.38 A. Acun, B. Poelsema, H.J.W. Zandvliet, R. van Gastel: The instability of silicene on Ag(111), Appl. Phys. Lett. **103**, 263119 (2013)

37.39 M.S. Rahman, T. Nakagawa, S. Mizuno: Growth of Si on Ag(111) and determination of large commensurate unit cell of high-temperature phase, Jpn. J. Appl. Phys. **54**, 015502 (2015)

37.40 L. Meng, Y. Wang, L. Zhang, S. Du, R. Wu, L. Li, Y. Zhang, G. Li, H. Zhou, W.A. Hofer, H.-J. Gao: Buckled silicene formation on Ir(111), Nano Letters **13**, 685–690 (2013)

37.41 D. Chiappe, E. Scalise, E. Cinquanta, C. Grazianetti, B. van den Broek, M. Fanciulli, M. Houssa, A. Molle: Two-dimensional Si nanosheets with local hexagonal structure on a MoS_2 surface, Adv. Mater. **26**, 2096–2101 (2014)

37.42 L. Zhang, P. Bampoulis, A.N. Rudenko, Q. Yao, A. van Houselt, B. Poelsema, M.I. Katsnelson, H.J.W. Zandvliet: Structural and electronic properties of germanene on MoS_2, Phys. Rev. Lett. **116**, 256804 (2016)

37.43 M. Wang, L. Liu, C.-C. Liu, Y. Yao: van der Waals heterostructures of germanene, stanene, and silicene with hexagonal boron nitride and their topological domain walls, Phys. Rev. B **93**, 155412 (2016)

37.44 P. Vogt, P. Capiod, M. Berthe, A. Resta, P. De Padova, T. Bruhn, G. Le Lay, B. Grandidier: Synthesis and electrical conductivity of multilayer silicene, Appl. Phys. Lett. **104**, 021602 (2014)

37.45 L. Chen, C.-C. Liu, B. Feng, X. He, P. Cheng, Z. Ding, S. Meng, Y. Yao, K. Wu: Evidence for Dirac fermions in a honeycomb lattice based on silicon, Phys. Rev. Lett. **110**, 085504 (2013)

37.46 P. De Padova, A. Generosi, B. Paci, C. Ottaviani, C. Quaresima, B. Olivieri, E. Salomon, T. Angot, G. Le Lay: Multilayer silicene: clear evidence, 2D Materials **3**, 03101 (2016)

37.47 E. Salomon, R. El Ajjouri, G. Le Lay, T. Angot: Growth and structural properties of silicene at multilayer coverage, J. Phys. Condens. Matter **26**, 185003 (2014)

37.48 Y. Borensztein, A. Curcella, S. Royer, G. Prévot: Silicene multilayers on Ag(111) display a cubic diamondlike structure and a $\sqrt{3}\times\sqrt{3}$ reconstruction induced by surfactant Ag atoms, Phys. Rev. B **92**, 155407 (2015)

37.49 S.K. Mahatha, P. Moras, P.M. Sheverdyaeva, R. Flammini, K. Horn, C. Carbone: Evidence for a diamondlike electronic band structure of Si multilayers on Ag(111), Phys. Rev. B **92**, 245127 (2015)

37.50 S.K. Mahatha, P. Moras, P.M. Sheverdyaeva, V. Bellini, T.O. Mentes, A. Locatelli, R. Flammini, K. Horn, C. Carbone: Absence of Dirac cones in monolayer silicene and multilayer Si films on Ag(111), J. Electron Spectrosc. Relat. Phenom. **219**, 2–8 (2017)

37.51 T. Shirai, T. Shirasawa, T. Hirahara, N. Fukui, T. Takahashi, S. Hasegawa: Structure determination of multilayer silicene grown on Ag(111) films by electron diffraction: evidence for Ag segregation at the surface, Phys. Rev. B **89**, 241403(R) (2014)

37.52 H. Aizawa, M. Tsukada, N. Sato, S. Hasegawa: Asymmetric structure of the Si(111)-$\sqrt{3}\times\sqrt{3}$-Ag surface, Surf. Sci. **429**, L509–L514 (1999)

37.53 Z. Li, J. Zhuang, L. Chen, Z. Ni, C. Liu, L. Wang, X. Xu, J. Wang, X. Pi, X. Wang, Y. Du, K. Wu, S.X. Dou: Observation of van Hove singularities in twisted silicene multilayers, ACS Cent. Sci. **2**, 517 (2016)

37.54 P. De Padova, P. Vogt, A. Resta, J. Avila, I. Razado-Colambo, C. Quaresima, C. Ottaviani, B. Olivieri, T. Bruhn, T. Hirahara, T. Shirai, S. Hasegawa, M.C. Asensio, G. Le Lay: Evidence of Dirac fermions in multilayer silicene, Appl. Phys. Lett. **102**, 163106 (2013)

37.55 J.N. Crain, K.N. Altmann, C. Bromberger, F.J. Himpsel: Fermi surfaces of surface states on Si(111)-Ag, Au, Phys. Rev. B **66**, 205302 (2002)

37.56 R. Arafune, C.-L. Lin, K. Kawahara, N. Tsukahara, E. Minamitani, Y. Kim, N. Takagi, M. Kawai: Structural transition of silicene on Ag(111), Surf. Sci. **608**, 297 (2013)

37.57 L. Chen, C.-C. Liu, B. Feng, X. He, P. Cheng, Z. Ding, S. Meng, Y. Yao, K. Wu: Evidence for Dirac fermions in a honeycomb lattice based on silicon, Phys. Rev. Lett. **109**, 056804 (2012)

37.58 B. Feng, Z. Ding, S. Meng, Y. Yao, X. He, P. Cheng, L. Chen, K. Wu: Evidence of silicene in honeycomb structures of silicon on Ag(111), Nano Letters **12**, 3507 (2012)

37.59 B. Feng, H. Li, C.-C. Liu, T.-N. Shao, P. Cheng, Y. Yao, S. Meng, L. Chen, K. Wu: Observation of Dirac cone warping and chirality effects in silicene, ACS Nano **7**, 9049 (2013)

37.60 W.C. Wang, A. Ignatiev, H. Huang, S.Y. Tong: Observation and structural determination of $(\sqrt{3}\times\sqrt{3})$R30° reconstruction of the Si(111) surface, Phys. Rev. Lett. **62**, 1516–1519 (1989)

37.61 J. Chen, Y. Du, Z. Li, W. Li, B. Feng, J. Qiu, P. Cheng, S.X. Dou, L. Chen, K. Wu: Delocalized surface state in epitaxial Si(111) film with spontaneous $(\sqrt{3}\times\sqrt{3})$ superstructure, Sci. Rep. **5**, 13590 (2015)

37.62 M. Hashimoto, F.-Z. Guo, M. Suzuki, M. Ueda, Y. Matsuoka, T. Kinoshita, K. Kobayashi, S. Shin, M. Oura, T. Takeuchi, Y. Saito, T. Matsushita, T. Yasuea, T. Koshikawa: Mapping of chemical bonding states of Ag/Si(111) with synchrotron radiation photoemission electron microscopy, Surf. Interface Anal. **40**, 1772–1776 (2008)

37.63 A.J. Mannix, B. Kiraly, B.L. Fisher, M.C. Hersam, N.P. Guisinger: Silicon growth at the two-dimensional limit on Ag(111), ACS Nano **8**, 75-38-7547 (2014)

37.64 T. Yamagami, J. Sone, K. Nakatsuji, H. Hirayama: Surfactant role of Ag atoms in the growth of Si layers on Si(111)$\sqrt{3}\times\sqrt{3}$, Appl. Phys. Lett. **105**, 151603 (2014)

37.65 H.-D. Chen, K.-H. Chien, C.-Y. Lin, T.-C. Chiang, D.-S. Lin: Few-layer silicon films on the Ag(111) surface, J. Phys. Chem. C **120**, 2698–2702 (2016)

37.66 D. Solonenko, O.D. Gordan, G. Le Lay, H. Sahin, S. Cahangirov, D.R.T. Zahn, P. Vogt: 2D vibrational properties of epitaxial silicene on Ag(111), 2D Materials **4**, 015008 (2017)

37.67 Z.-L. Liu, M.-X. Wang, C. Liu, J.-F. Jia, P. Vogt, C. Quaresima, C. Ottaviani, B. Olivieri, P. De Padova, G. Le Lay: The fate of the would-be $2\sqrt{3}\times2\sqrt{3}$R(30°) silicene phase on Ag(111), APL Materials **2**, 092513 (2014)

37.68 M. Ezawa, E. Salomon, P. De Padova, D. Solonenko, P. Vogt, M.E. Dávila, A. Molle, T. Angot, G. Le Lay: Fundamentals and functionalities of silicene, germanene, and stanene, Riv. Nuovo Cim. **41**, 175–224 (2018)

37.69 A. Fleurence, T.G. Gill, R. Friedlein, J.T. Sadowski, K. Aoyagi, M. Copel, R.M. Tromp, C.F. Hirjibehedin, Y. Yamada-Takamura: Single-domain epitaxial silicene on diboride thin films, Appl. Phys. Lett. **108**, 151902 (2016)

37.70 T.G. Gill, A. Fleurence, B. Warner, H. Prüser, R. Friedlein, J.T. Sadowski, C.F. Hirjibehedin, Y. Yamada-Takamura: Metallic atomically-thin layered silicon epitaxially grown on silicene/ZrB_2, 2D Materials **4**, 021015 (2017)

37.71 D. Beato Medina, E. Salomon, G. Le Lay, T. Angot: Hydrogenation of silicene films grown on Ag(111), J. Electron Spectrosc. Relat. Phenom. **219**, 57–62 (2017)

37.72 J. Qiu, H. Fu, Y. Xu, A.I. Oreshkin, T. Shao, H. Li, S. Meng, L. Chen, K. Wu: Ordered and reversible hydrogenation of silicene, Phys. Rev. Lett. **114**, 126101 (2015)

37.73 C.-W. Zhang, S.-S. Yan: First-principles study of ferromagnetism in two-dimensional silicene with hydrogenation, J. Phys. Chem. C **116**, 4163–4166 (2012)

37.74 F.-B. Zheng, C.-W. Zhang: The electronic and magnetic properties of functionalized silicene: a first-principles study, Nanoscale Res. Lett. **7**, 422 (2012)

37.75 W.-Z. Yu, J.-A. Yan, S.-P. Gao: Band gap characters and ferromagnetic/antiferromagnetic coupling in group-IV monolayers tuned by chemical species and hydrogen adsorption configurations, Nanoscale Res. Lett. **10**, 351 (2015)

37.76 F. Schwierz, J. Pezoldt, R. Granzer: Two-dimensional materials and their prospects in transistor electronics, Nanoscale **7**, 8261–8283 (2015)

37.77 Y. Du, J. Zhuang, J. Wang, Z. Li, H. Liu, J. Zhao, X. Xu, H. Feng, L. Chen, K. Wu, X. Wang, S.X. Dou: Quasi-freestanding epitaxial silicene on Ag(111) by oxygen intercalation, Sci. Adv. **2**, e1600067 (2016)

37.78 P. De Padova, C. Ottaviani, C. Quaresima, B. Olivieri, P. Imperatori, E. Salomon, T. Angot, L. Quagliano, C. Romano, A. Vona, M. Muniz-Miranda, A. Generosi, B. Paci, G. Le Lay: 24h stability of thick multilayer silicene in air, 2D Materials **1**, 021003 (2014)

37.79 A. Molle, C. Grazianetti, D. Chiappe, E. Cinquanta, E. Cianci, G. Tallarida, M. Fanciulli: Hindering the oxidation of silicene with non-reactive encapsulation, Adv. Funct. Mater. **23**, 4340–4344 (2013)

37.80 L. Tao, E. Cinquanta, D. Chiappe, C. Grazianetti, M. Fanciulli, M. Dubey, A. Molle, D. Akinwande: Silicene field-effect transistors operating at room temperature, Nat. Nanotechnol. **10**, 227–232 (2015)

37.81 B. Radisavljevic, A. Radenovic, J. Brivio, V. Giacometti, A. Kis: Single-layer MoS_2 transistors, Nat. Nanotechnol. **6**, 147–150 (2011)

37.82 G. Le Lay: 2D Materials: silicene transistors, Nat. Nanotechnol. **10**, 202–203 (2015)

37.83 C. Grazianetti, E. Cinquanta, L. Tao, P. De Padova, C. Quaresima, C. Ottaviani, D. Akinwande, A. Molle: Silicon nanosheets: crossover between multilayer silicene and diamond-like growth regime, ACS Nano **11**, 3376–3382 (2017)

37.84 W.-F. Tsai, C.-Y. Huang, T.-R. Chang, H. Lin, H.-T. Jeng, A. Bansil: Gated silicene as a tunable source of nearly 100% spin-polarized electrons, Nat. Commun. **4**, 1500 (2013)

37.85 S. Rachel, M. Ezawa: Giant magnetoresistance and perfect spin filter in silicene, germanene, and stanene, Phys. Rev. B **89**, 195303 (2014)

37.86 J.I. Cerdá, J. Sławińska, G. Le Lay, A.C. Marele, J.M. Gómez-Rodríguez, M.E. Dávila: Unveiling the pentagonal nature of perfectly aligned single-and double-strand Si nano-ribbons on Ag(110), Nat. Commun. **7**, 13076 (2016)

37.87 I. Vilfan, F. Lançon, E. Adam: Lattice vibrations and stability of reconstructed (110) noble metal surfaces, Surf. Sci. **440**, 279–289 (1999)

37.88 S. Zhang, J. Zhou, Q. Wang, X. Chen, Y. Kawazoe, P. Jena: Penta-graphene: a new carbon allotrope, Proc. Natl. Acad. Sci. **112**, 2372 (2015)

37.89 G. Prévot, C. Hogan, T. Leoni, R. Bernard, E. Moyen, L. Masson: Si nanoribbons on Ag(110) studied by grazing-incidence x-ray diffraction, scanning tunneling microscopy, and density-functional theory: evidence of a pentamer chain structure, Phys. Rev. Lett. **117**, 276102 (2016)

37.90 H. Sahaf, L. Masson, C. Léandri, B. Aufray, G. Le Lay, F. Ronci: Formation of a one-dimensional grating at the molecular scale by self-assembly of straight silicon nanowires, Appl. Phys. Lett. **90**, 263110 (2007)

37.91 E. Salomon, T. Angot, C. Thomas, J.-M. Layet, P. Palmgren, C.I. Nlebedim, M. Göthelid: Etching of silicon nanowires on Ag(110) by atomic hydrogen, Surf. Sci. **603**, 3350–3354 (2009)

37.92 E. Salomon, T. Angot: Modification of physical properties of silicon nanowires, grown onto Ag(110), by selective adsorption: from atomic hydrogen to molecules, Sci. Adv. Mater. **3**, 1–8 (2011)

37.93 P. De Padova, C. Leandri, S. Vizzini, C. Quaresima, P. Perfetti, B. Olivieri, H. Oughaddou, B. Aufray, G. Le Lay: Burning match oxidation process of silicon nanowires screened at the atomic scale, Nano Letters **8**, 2299–2304 (2008)

37.94 E. Salomon, A. Kahn: One-dimensional organic nanostructures: a novel approach based on the selective adsorption of organic molecules on silicon nanowires, Surf. Sci. **602**, L79–L83 (2008)

37.95 X. Ling, H. Wang, S. Huang, F. Xia, M.S. Dresselhaus: The renaissance of black phosphorus, Proc. Natl. Acad. Sci. **112**, 4523–4530 (2015)
37.96 L. Li, Y. Yu, G.J. Ye, Q. Ge, X. Ou, H. Wu, D. Feng, X.H. Chen, Y. Zhang: Black phosphorus field effect transistors, Nat. Nanotechnol. **9**, 372–377 (2014)
37.97 A. Molle, J. Goldberger, M. Houssa, Y. Xu, S.-C. Zhang, D. Akinwande: Buckled two-dimensional Xene sheets, Nat. Mater. **16**, 163 (2017)
37.98 G. Le Lay, E. Salomon, T. Angot: Silicene: silicon conquers the 2D world, EuroPhys. News **47**, 17–21 (2016)
37.99 M.E. Dávila, L.C. Lew Yan Voon, J. Zhao, G. Le Lay: Elemental group IV two-dimensional materials beyond graphene. In: *2D Materials*, Semiconductors and Semimetals, ed. by F. Iacopi, J.J. Boeckl, C. Jagadish (Elsevier, Amsterdam 2016) pp. 149–188

Eric Salomon

Physics Department, Campus de Saint-Jérôme
Aix-Marseille Université
Marseille, France
eric.salomon@univ-amu.fr

Dr. Eric Salomon is Associate Professor at the Physics Department of Aix-Marseille University since 2008. His research interests center on surface and materials sciences, and especially on the reactivity, electronic, structural and vibrational properties of hybrid organic/inorganic interfaces as well as low-dimensional structures based on silicon and germanium.

Daniel Beato-Medina

CNRS, PIIM, Campus de Saint-Jérôme
Aix-Marseille Université
Marseille, France

Daniel Beato Medina studied Physics at the Complutense University of Madrid in 2011. He later enrolled as a doctoral student at Aix-Marseille University, where he successfully defended his thesis, "Characterization of 2-D architectures on metallic substrates by electron spectroscopy and microscopy," in 2016. He is now Data and Algorithm Specialist at Santander Global Tech in Madrid, Spain.

Paola De Padova

Istituto di Struttura della Materia
Consiglio Nazionale delle Ricerche
Roma, Italy
paola.depadova@ism.cnr.it

Paola De Padova is Senior Scientist, with over 20 years of work experience, at the National Research Council, Institute of Structure of Matter, Rome, Italy. Well known and appreciated worldwide for her research in surface science physics, she is a pioneer in the synthesis of the new allotrope of silicon, namely silicene, contributing significantly to the development of 2-D elemental systems beyond graphene.

Thierry Angot

CNRS, PIIM, Campus de Saint-Jérôme
Aix-Marseille Université
Marseille, France
thierry.angot@univ-amu.fr

Thierry Angot is Professor at Aix-Marseille University. He has worked in the field of surface science for more than 25 years, with a particular interest in the interaction of hydrogen (atoms, ions and plasmas) with metal surfaces, semiconductors and 2-D materials.

Guy Le Lay

PIIM CNRS Campus de Saint-Jérôme
Aix-Marseille University
Marseille, France
guy.lelay@univ-amu.fr

Guy Le Lay, Professor, Aix-Marseille Université, PIIM-CNRS Laboratory, graduated as an Engineer from the School of Mines in Nancy (France) in 1968, and in Marseille (France) received two Doctorates, one in Engineering and one in Physics at the University of Provence, in 1972 and 1977, respectively. He was the French PI of the European Collaborative Project "Two-Dimensional Nanolattices", and in Marseille pioneered the first synthesis of silicene.

38. Cluster-Assembled Carbon Thin Films

Luca Giacomo Bettini, Massimiliano Galluzzi, Alessandro Podestà, Paolo Piseri, Paolo Milani

The supersonic cluster beam deposition (SCBD) of neutral carbon clusters produced in a pulsed microplasma cluster source (PMCS) is an effective technique for producing nanostructured carbon (nsC) thin films with controlled nanostructures. The use of carbon clusters as building blocks allows the synthesis of carbonaceous materials with structural properties that are determined not only by the characteristics of the clusters but also by their organization upon deposition. NsC films produced by SCBD/PMCS grow in a ballistic deposition regime where incoming particles land on the growing interface and do not diffuse significantly. This growth regime leads to remarkable statistical scale invariance of the evolving interface at which the carbon clusters aggregate in larger and larger superunits. Due to negligible stress accumulation during the low-energy deposition process, nsC films with thicknesses of between a few tens of nanometers and a few micrometers can be routinely deposited onto and will adhere to almost any kind of surface. This deposition approach enables the production of carbon thin films characterized by low density, high surface roughness, and high porosity, making them promising materials for use in the fabrication of devices such as electrolyte-gated transistors, supercapacitors, and photocatalytic systems for sustainable energy technologies.

Carbon is one of the most versatile elements. Its valence atomic orbitals can hybridize into alternative orbitals (commonly known as sp^1, sp^2, and sp^3 hybrid orbitals), and it can aggregate in many different allotropic forms exhibiting a variety of different physicochemical properties [38.1, 2]. Besides the bulk forms of sp^2- and sp^3-bonded carbon atoms, i.e., graphite and diamond, there are a vast number of intermediate forms of carbon in which sp^1-, sp^2-, and sp^3-hydridized carbon coexist, such as fullerenes, graphene, carbon nanotubes, and carbynes [38.1, 3].

Carbon-based materials fabricated by assembling carbon nanoobjects (nanostructured carbons) are considered among the most promising systems for a wide variety of applications, ranging from energy production and storage to catalysis and biomedicine [38.4, 5]. The increasing use of nanostructured carbons in real-world applications is due mainly to their high surface area, nanoscale porosity, chemical inertness, and low cost [38.6].

The need for nanostructured carbons with optimized characteristics integrated into complex devices calls for the development of synthesis technologies that enable not only the fabrication of materials with tailored nanostructures but also the deposition of nanostructured carbons in the form of thin films, as this allows nanostructured carbons to be integrated into platforms produced with planar fabrication methods.

Supersonic cluster beam deposition (SCBD) is a versatile bottom-up approach for the synthesis of cluster-assembled nanostructured carbon (nsC) thin films with controlled structural properties [38.3, 7, 8]. Depositing clusters from a supersonic beam makes it possible to grow nanostructured materials in which the physicochemical properties of the pristine clusters are preserved [38.9]. This *memory effect* is ob-

M. Rocca, T.S. Rahman, L. Vattuone (Eds.), *Springer Handbook of Surface Science*, Springer Handbooks,
https://doi.org/10.1007/978-3-030-46906-1_38

tained when the kinetic energy of the clusters in the supersonic molecular beam is low enough to avoid significant structural reorganization upon deposition but high enough to activate cluster bonding to the substrate and prevent cluster diffusion. In this low-energy cluster beam deposition regime, the growth of thin films can be viewed as the random stacking of particles (just as for ballistic deposition), leading to materials that exhibit granular and porous nanostructure and low density [38.10].

38.1 Supersonic Cluster Beam Deposition

The supersonic cluster beam deposition (SCBD) of carbon clusters produced in the gas phase is a well-established approach for the production of carbon thin films [38.3, 7, 11, 12]. Owing to the so-called memory effect, the meso- and nanostructure of the resulting thin films are reminiscent of those of the free clusters [38.3, 7, 11, 12]. Moreover, the ballistic deposition regime typical of the SCBD process enables the growth of nsC with high porosity and surface corrugation, low density, and well-controlled thickness [38.7, 11, 13, 14].

The growth of nsC thin films using SCBD is typically achieved using two differentially evacuated chambers operating in the high-vacuum regime, as depicted in the sketch shown in Fig. 38.1a. The deposition process involves four main steps: (i) carbon cluster formation, (ii) cluster extraction, (iii) cluster transport, and (iv) cluster deposition [38.7, 11, 12, 14, 15]. The carbon clusters are typically produced in a pulsed microplasma cluster source (PMCS) coupled to the SCBD apparatus, as shown in Fig. 38.1a [38.7, 15]. The PMCS, which is presented schematically in Fig. 38.1b, is a cluster source based on the pulsed vaporization of bulk electrodes. In order to form carbon clusters, a rod of the graphite to be vaporized is inserted into the small cavity inside the ceramic body of the PMCS. A pulsed valve injects an inert gas such as helium into the cavity to promote an electrical discharge between the cathode (i.e., the graphitic rod) and a copper anode placed inside the source. The discharge, driven by a high-voltage pulse (typically between 600 and 800 V), lasts 60–90 ms and results in the ablation of a very small region of the graphite target. The gas-phase carbon atoms from the sputtered target are then quenched by collisions with the helium gas, nucleate, and condense inside the cavity of the source, forming an aerosol of carbon clusters that is eventually transported out of the PMCS in a seeded supersonic expansion [38.11, 14]. The separation effects attainable in aerosol flow dynamics permit the cluster size distribution produced in the PMCS to be refined, and the particles are concentrated by a series of aerodynamic lenses [38.11, 12, 14]. After passing through the aerodynamic focusing system, the carbon cluster aerosol undergoes supersonic free-jet expansion and enters the expansion chamber, forming a molecular beam. Finally, the central part of the beam is selected by a skimmer and eventually reaches a substrate placed on the sample holder in the deposition chamber [38.11, 14].

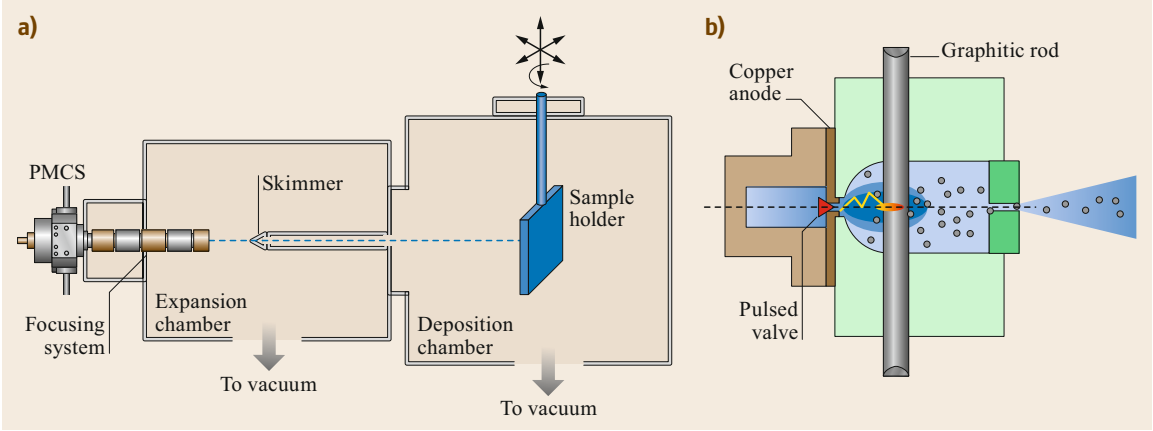

Fig. 38.1a,b Schematic representations of **(a)** a typical apparatus for supersonic cluster beam deposition and **(b)** a pulsed microplasma cluster source for carbon cluster deposition and generation

38.2 Surface Morphology of Cluster-Assembled Carbon Thin Films

Figure 38.2a shows a representative topographic map, acquired by atomic force microscopy (AFM), of a nsC film of thickness 220 nm (the thickness is measured with high precision by scanning the AFM tip across a sharp step on the film produced by masking the substrate during cluster deposition). The surface morphology of the nsC film is characterized by high specific area and roughness and by the presence of a fine raster of nanometer-sized grains, which are typical of cluster-assembled films deposited by SCBD [38.16–18]. The rough and granular nature of the film is a consequence of the deposition of the building blocks (the carbon clusters), which are typically nanosized according to their mass distribution [38.19]. Clusters impact with low kinetic energies per atom on the growing interface, thus avoiding substantial fragmentation [38.19]. Upon deposition, the more unstable and reactive carbon clusters may undergo aggregation and/or coalescence [38.10]. The resulting morphology is statistically scale invariant (self-affine) across several orders of magnitude in length: from the size of the pristine clusters produced by gas-phase aggregation inside the cluster source and the size of the surface grains formed after deposition and film growth right up to the size of the largest morphological features observed in Fig. 38.2a (which are micrometer-sized for the thickest films shown in Fig. 38.2b) [38.18, 20]. The rms roughness R_q, calculated as the standard deviation of the surface heights (typically measured from AFM scan traces extending over an area of $5\,\mu m \times 5\,\mu m$), generally increases with film thickness, as clearly shown in Fig. 38.2b (from bottom to top). The roughening of the growing interface is known to be regulated by scaling laws (the Family–Vicsek scaling relations) that are typical of a variety of growing interfaces [38.21–24] and result in a statistically scale-invariant topography. The scaling laws govern the evolution of morphological parameters such as the rms roughness and the lateral correlation length, i.e., in practical terms, half the maximum (average) size of the largest morphological features that develop during film growth, such as the supergrains visible in the AFM maps of Fig. 38.2b [38.21].

Despite the disordered surface morphologies of cluster-assembled carbons, as well as the randomness of the deposition process, the existence of a scaling law for roughness evolution allows precise control over the morphological properties of the nsC thin films. This is achieved by simply adjusting the deposition time, since the film thickness increases linearly with the deposition time at a constant deposition rate. Quantitative analysis of AFM topographies has shown that the evo-

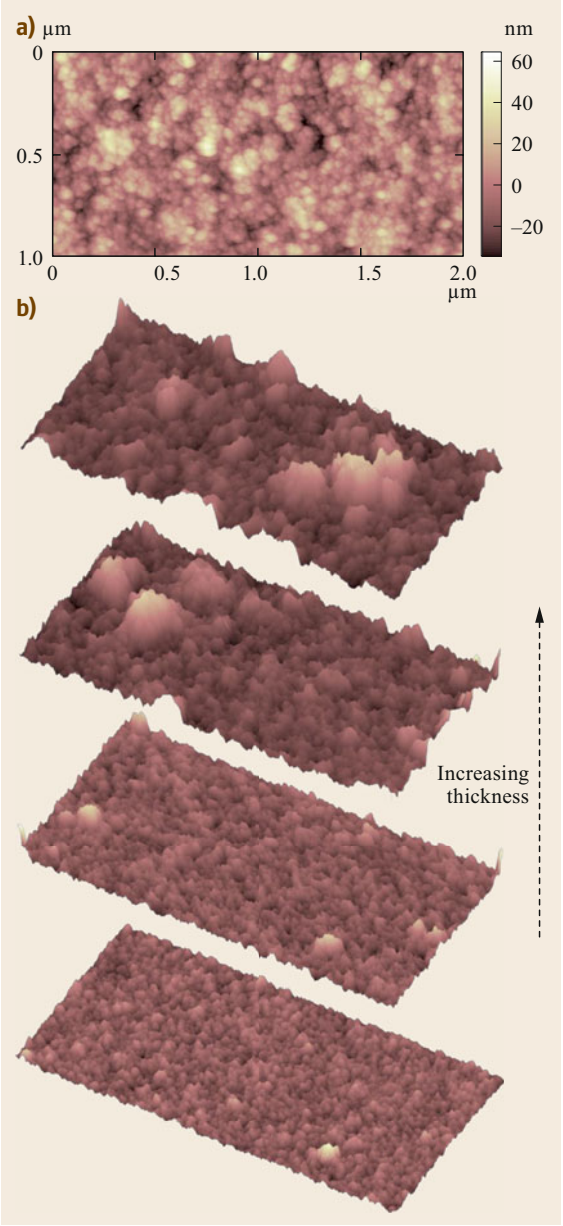

Fig. 38.2 **(a)** A representative 2-D view of the surface morphology of a nsC film of thickness 220 nm. A fine raster of surface nanometer-sized grains is visible. **(b)** Images depicting how the surface rms roughness of the nsC film varies as a function of increasing film thickness (the thickness varies from 36 to 500 nm and the rms roughness varies from 9 to 65 nm from the *bottom* to the *top* image; the scan area in each image is $2\,\mu m \times 1\,\mu m$, and the vertical range is 600 nm) ►

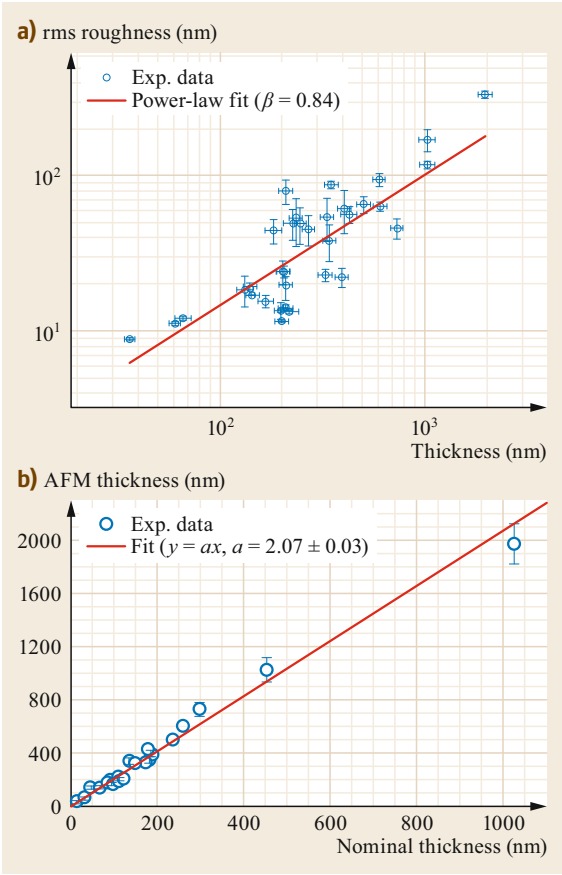

Fig. 38.3 **(a)** Scaling of the rms roughness of the surface of a nsC film deposited via SCBD. The linear fit obtained for the log–log plot highlights the power law character of the evolution of roughness with film thickness (deposition time). The evolution of the surface roughness conforms to a scaling law that is compatible with the ballistic deposition regime; **(b)** nsC film thickness as measured by AFM versus the film thickness measured by QCM assuming a material density of 1 g/cm^3 ◄

lution of the rms roughness R_q with the thickness h of the nsC film obeys the power law $R_q \approx h^\beta$, with $\beta = 0.84 \pm 0.19$ (Fig. 38.3a). The value of the growth exponent β is larger than expected for a purely ballistic deposition growth model (for which $\beta = 0.33$), which is typical of deposition processes in which the added particles land on and stick to the growing interface without diffusing significantly [38.21, 24]. Incidentally, the growth of cluster-assembled metal oxide films deposited by SCBD (either titania or zirconia) obeys the scaling laws of the ballistic deposition regime [38.16, 17]. Pinning and quenched noise mechanisms may be key to understanding the scaling of nsC film morphological properties, in contrast to nanostructured metal oxides [38.23]. It has indeed been observed that larger clusters can act as pinning locations, locally quenching the evolution of the growing interface [38.20].

The surface granularity revealed by the AFM maps shown in Fig. 38.2 reflects the structure of the bulk material, which exhibits a low density, is highly porous, and has a high surface area. The density of the nsC film was calculated by comparing the nominal film thickness measured by a quartz crystal microbalance (QCM, configured assuming a nominal material density of 1 g/cm^3 and that the acoustic impedance data of graphite are applicable) placed close to the sample during deposition with the film thickness measured ex situ by AFM (Fig. 38.3b). Assuming that the same mass of nsC per unit area is deposited on the QCM and the sample, and that the AFM provides an accurate measurement of the film thickness, the inverse of the slope of the curve shown in Fig. 38.3b was found to represent the correction factor to the nominal density assumed for the QCM measurement. A density of about 0.5 g/cm^3 was therefore estimated for nsC. This is about one-fourth of the density of graphite (≈ 2.2 g/cm^3), confirming the porous nature of the nsC deposited by SCBD. This explains why nsC is attracting considerable interest in the context of functional devices where high porosity at the nanoscale and a large specific surface area are beneficial.

38.3 Cluster-Assembled Carbon Nanocomposites

The preservation of cluster nanostructure when the clusters land on the growing interface during SCBD enables the deposition of a wide variety of carbon nanocomposites by the controlled introduction of heterospecies into the cluster-assembled carbon matrix. Cluster-assembled thin films of carbon nanocomposites have been effectively produced via different approaches based on the SCBD/PMCS method, including (i) the application of He-based gas mixtures as sputtering gases instead of pure He [38.25, 30], (ii) the utilization of a PMCS equipped with a multicomponent cathode [38.27, 31], and (iii) the use of multiple simultaneous SCBD processes to deposit clusters of different materials produced in separate sources [38.29]. The aforementioned strategies provide high versatility in terms of the variety and the concentrations of materials embeddable in the nsC, thus enabling the highly tunable introduction of nanoparticles, dopant atoms, and graphitization catalysts into the carbon matrix, which in turn allows the structural and electrical properties

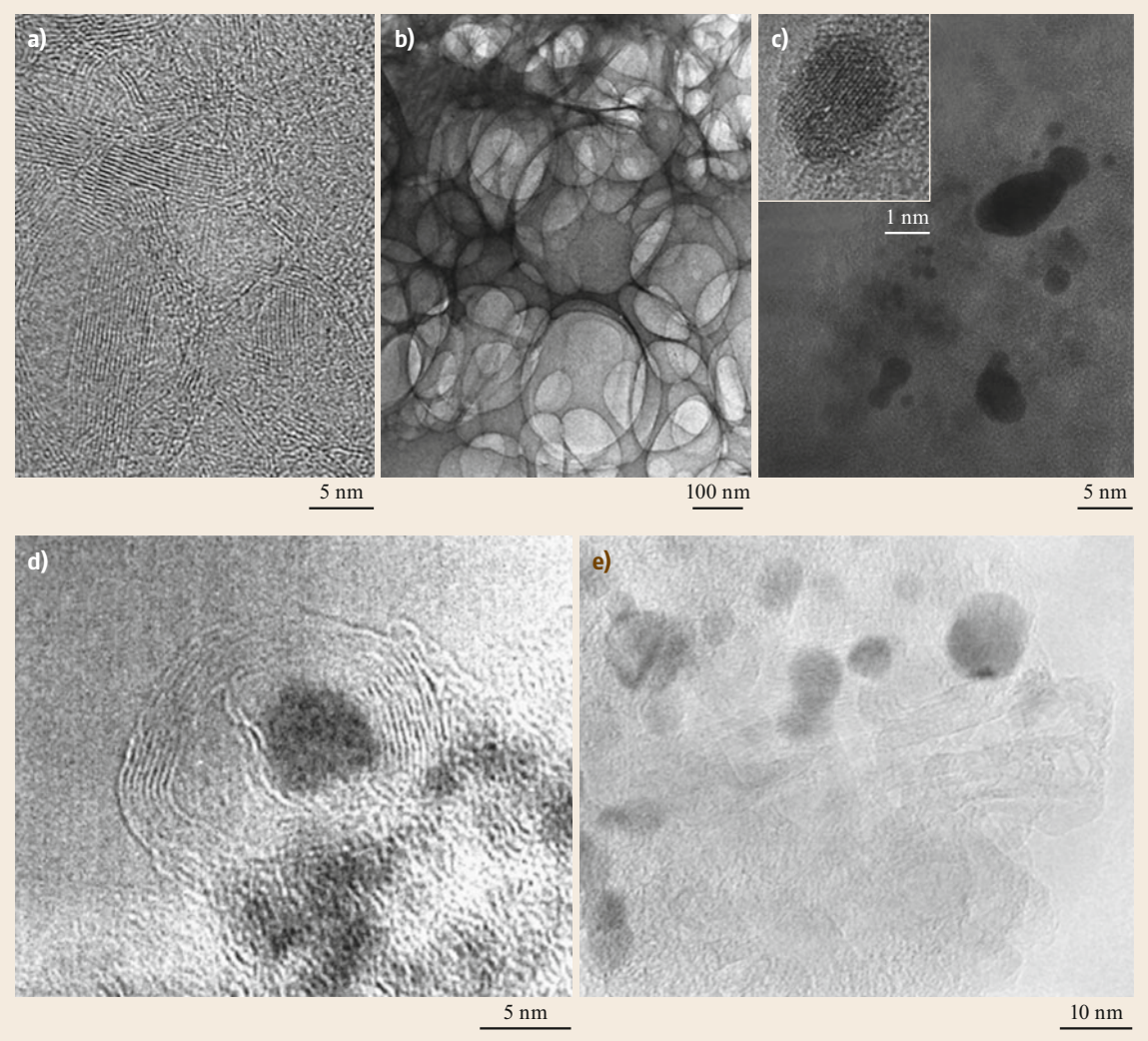

Fig. 38.4 **(a)** Densely packed graphitic planes and onion-like particles present in a nsCN_x film obtained by mixing NH_3 and He (reprinted from [38.25], with permission from Elsevier), **(b)** foam-like carbon obtained by adding metallorganic Mo to the He (from [38.26]), **(c)** TiO_x nanoinclusions dispersed in the nsC matrix (reprinted from [38.27], with the permission of AIP Publishing), **(d)** Ni nanoparticles embedded in nsC and surrounded by equally spaced graphitic shells (reprinted with permission from [38.28]. Copyright (2003) by the American Physical Society), and **(e)** tubular onion-like carbon structures consisting of concentric curved graphitic sheets that formed in Ni-containing nsC thin films upon mild thermal treatment (From [38.29]. © IOP Publishing. Reproduced with permission. All rights reserved)

of nsC thin films to be tailored according to requirements.

Dopant inclusion in nsC films has been achieved by operating the PMCS with nitrogen-containing gases, such as N_2 and a He-NH_3 mixture instead of pure He [38.25], and by mixing metallorganic compounds such as molybdenum(V) isopropoxide and cobalt(II) methoxyethoxide with the He carrier gas before it enters the source [38.30]. In this way, molecules in the buffer gas are cracked by the electric discharge and add N, Mo, and Co atoms to the condensing carbon vapor, favoring the growth of carbon clusters with a higher degree of organization than seen for undoped clusters. The availability of nitrogen atoms in the reaction chamber of a PMCS operated with a graphite target leads to the formation of a cluster-assembled CN_x film with a nanostructure characterized by the coexistence of interwoven graphitic planes, onion-like nanoparticles, and multiwalled nanotubes embedded in an amorphous carbon matrix (Fig. 38.4a; [38.25]), whereas supplying

a very low concentration of Mo or Co produces nsC thin films rich in spongy schwarzite structures consisting of fully connected 3-D sp^2 networks with a topology typical of negatively curved graphene layers (Fig. 38.4b) and with pore sizes that depend on the metallic precursor (e.g., narrower and larger pores were reported for Co and Mo doping, respectively) [38.30].

The loading of metal and metal oxide nanoparticles into nsC thin films has been obtained by either operating a PMCS with a carbon-metal composite cathode or using two cluster sources, one with a carbon and one with a metal cathode. In the former case, a mixed supersonic beam seeded with both carbon and metal clusters is produced; in the latter, two incident supersonic beams are formed, and the carbon and metal clusters are finally mixed on a substrate located at the intersection of the beam trajectories. Mixed cluster beams obtained using metal-graphite composite cathodes have been successfully used to uniformly disperse noble and transition metals into nsC in order to realize thin films with different metal abundances, particle sizes, and dilutions [38.31]. Nanocomposite nsC thin films containing noble metals such as Au, Pt, and Pd at concentrations of between 2 and 20 at.% and with metal nanoparticle diameters between 1 and 15 nm show very similar structures and carbon networks to those of of pure nsC thin films. Conversely, the inclusion of transition metals (e.g., Ti and Ni) drastically alters the nsC matrix as these metals catalyze the formation of crystalline sp^2 nanostructures. Titanium-containing nsC thin films show the presence of TiO_x nanoinclusions; the size of these nanoinclusions increases according to the Ti content in the film, ranging from a few nm for the lowest concentration (ca. 3 at.%) up to 10–15 nm for higher concentrations (9–11 at.%). Titanium-containing nsC thin films also exhibit more ordered carbon structures—open and defective graphitic cages—than pure nsC (Fig. 38.4c; [38.27, 31]). Interestingly, these thin films undergo significant metallization under exposure to a focused vacuum UV photon beam, enabling complex metallic patterns to be drawn with submicrometric resolution on the films [38.27, 32]. More of the ordered graphitic structures are formed when the carbon clusters are grown in the presence of <2 at.% Ni atoms, and the resulting nanocomposite Ni:nsC films contain sp^2-hybridized ribbon-like, onion-like, and cage nanostructures with small (2–7 nm) metal particles embedded (Fig. 38.4d; [38.28, 31]). Ni:nsC nanocomposites with different volumetric Ni concentrations (0–35%) have also been deposited by appropriately adjusting the relative intensities of nickel and carbon-cluster beams produced in different PMCSs [38.29]. Due to the low-energy deposition regime applied, the inclusion of preformed Ni nanoparticles in the nsC does not increase the graphitic order of the carbon matrix. Nevertheless, upon mild thermal treatment at 300 °C, the embedded metals promote the formation of curved graphitic sheets, and the Ni:nsC thin films become rich in tubular onion-like structures with lengths of up to several tens of nanometers (Fig. 38.4e; [38.29]).

38.4 Cluster-Assembled Carbon Thin Films for Energy Applications

Nanostructured materials with high surface-to-volume ratios have enhanced interfacial properties that are beneficial in a number of emerging energy storage and conversion technologies (e.g., photovoltaics, batteries, fuel cells, and photocatalytic systems) where the device performance is typically governed by surface-mediated physicochemical processes [38.33]. The synthesis of nanostructured materials with controlled structural and morphological properties is the key to understanding these processes, and paves the way for the development of efficient and green energy technologies [38.33, 34]. The need to transition to a sustainable energy scenario is currently being accelerated by the Internet of Things paradigm in which an enormous number of smart devices and sensors are linked together in communication networks; this requires efficient energy management, often including energy harvesting and storage functions [38.35]. The ability to produce and deposit functional materials with well-controlled nanostructures is crucial to the development of devices that integrate systems capable of harvesting energy from the environment, storing it, and delivering the power required to switch on functional units such as sensors and transceivers.

Electrochemical cells are important enabling technologies for renewable energy as well as energy management, conversion, and storage [38.36]. These technologies rely on interfacial processes that strongly depend on the morphological characteristics of the interfaces between electrodes and electrolytes. Electrochemical cell development would thus benefit from the fabrication of nanostructured electrodes with engineered interfacial properties.

Carbon thin films with high surface-to-volume ratios are used extensively as electrode materials in a number of emerging electrochemical systems due to their chemical inertness, high electrical conductivity, low density, and relatively low cost [38.6]. These

systems typically take advantage of the large specific surface area of the employed carbons to promote the storage and/or exchange of charge at the electrode–electrolyte interface. However, the techniques commonly used to fabricate porous carbons are not readily compatible with thin film deposition processes and/or micropatterning techniques, and are therefore unsuitable for the development of micro and on-chip integrated energy devices, as required by the rapidly growing market of autonomous miniaturized electronic systems. The use of aggressive chemical and thermal treatments to improve the carbon porosity is another issue that limits the integration of carbon electrodes into diverse substrates that would greatly increase their range of applications, such as polymers and paper.

The miniaturization and integration of carbon electrodes requires an ability to synthesize porous carbon thin films by high-throughput techniques that allow fine control over the physicochemical characteristics of the material and compatibility with standard microfabrication processes and substrates.

The assembly of carbon clusters via SCBD is a promising approach with demonstrated applicability to the production of carbon-based materials and electrodes with structural and morphological properties that are beneficial for electrochemical applications. Moreover, the deposition of nsC thin films at room temperature and under clean high-vacuum conditions, which is characteristic of the SCBD method, leads to novel opportunities in the context of integrating highly porous carbon electrodes into diverse platforms.

38.4.1 Microsupercapacitors

Electric double-layer capacitors, also known as supercapacitors (SCs), are energy storage devices that play an important role in encouraging the widespread adoption of renewable energy sources. SCs store energy in the electric double layer formed upon the electrostatic separation of charges at the interface between a polarizable (and typically carbon-based) porous electrode and an ion-conducting electrolyte [38.37]. Due to the reversibility and speed of the double-layer formation mechanism, SCs can be quickly and almost endlessly charged and discharged, offering a much higher power density and much longer cycle life than electrochemical batteries [38.38]. SCs are extensively used in a variety of applications, such as electric vehicles and grid storage, and have great potential to replace batteries or to be used in combination with energy harvesters to power microelectronic devices and develop self-sustaining miniaturized devices [38.39]. The integration of microsupercapacitors into more complex systems that include energy harvesters and functional devices is a valuable strategy for developing autonomous systems. However, the fabrication of porous carbon electrodes with controlled and optimized properties (e.g., shape, thickness, porosity, morphology, and structure) remains a challenge.

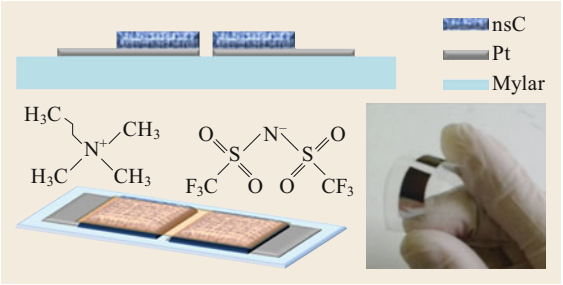

Fig. 38.5 Schematic of a planar microsupercapacitor fabricated by the SCBD of nsC electrodes on a flexible Mylar substrate (Reprinted from [38.41], with permission from Elsevier)

The deposition of nsC thin films by SCBD is an effective approach to the synthesis of carbon electrodes with promising electrochemical energy storage properties [38.29, 40–42]. NsC thin films with thicknesses in the range between 100 nm and 1 μm have been reported to exhibit an electric double-layer capacitance of about 80 F/g in the aqueous and organic electrolytes commonly employed in the production of SCs [38.42, 43], and similar capacitances have been measured upon soaking the nsC in ionic liquids featuring a bis(trifluoromethanesulfonyl)imide anion and imidiazolium- or ammonium-based cations [38.40, 41]. NsC thin films have been also successfully integrated into prototype microsupercapacitors fabricated by SCBD on glass and polymeric substrates [38.40, 41, 44]. As reported in Fig. 38.5, SCBD-generated microsupercapacitors consist of two coplanar nsC electrodes that are deposited using stencil masks and have areas of 0.2–1 cm^2 and thicknesses in the range between 100 and 500 nm. The electrodes are then soaked with a thin layer of ionic liquid serving as electrolyte. The resulting devices exhibit a specific capacitance of about 10 F/cm^3 and have been demonstrated to operate in a flat or bent configuration at 3 V with long cycling stability (over 2×10^4 cycles) even at temperatures up to 80 °C, as well as to have a volumetric specific power and energy of 10–14 W/cm^3 and 2.5–10 mWh/cm^3, respectively [38.40, 41].

Although they are nonoptimized prototypes, the energy storage performance of microsupercapacitors based on nsC thin films is of interest for different devices that, if properly designed and connected, could bring about miniaturized autonomous systems [38.45]. Moreover, compared to other forms of carbon that

have been employed as electrode materials in microsupercapacitors (e.g., carbide-derived carbons, onion-like carbons, and graphenes [38.39]), nsC thin films have the key advantage of being inherently porous and depositable in a single step, avoiding the need for complicated postdeposition processing, such as sintering, chemical activation, and binder mixing.

38.4.2 Electrolyte-Gated Transistor

In the race to produce autonomous electronic devices, electrolyte-gated transistors (EGTs) are attractive platforms owing to their very low voltage operation [38.46]. EGTs make use of electrolytes instead of conventional gate dielectrics and exploit electrolyte–channel interfaces with high electrical double-layer capacitance to modulate currents across several orders of magnitude at relatively low gate voltages. The use of porous carbon-based material with a high specific surface area as the gate electrode enables operation below 1 V and renders the presence of an external reference electrode to monitor the channel potential unnecessary, thus simplifying the structure of the device [38.47, 48]. Indeed, carbon gate electrodes with high capacitance can electrostatically store an amount of charge that can, if counterbalanced in the transistor channel, lead to channel doping and current modulation [38.47, 48]. Moreover, the integration of porous carbon gate electrodes into EGTs enables these systems to be used as energy storage structures, resulting in a class of devices known as transcaps, where the charge stored at the gate interface permits the transistor to be operated without an external power supply [38.49]. The coupling of a transistor with a capacitor within the same structure could therefore yield a very interesting energy device for autonomous electronic and bioelectronic systems, but this remains a challenging approach due to the lack of effective fabrication techniques that enable the deposition and integration of porous carbon thin films into EGTs [38.49].

Recently, cluster-assembled nsC thin films with a thickness of about 750 nm were successfully integrated as gate electrodes into planar and flexible poly(3,4-ethylenedioxythiophene) polystyrene sulfonate (PEDOT:PSS)-based organic electrochemical transistors patterned by orthogonal lithography on a Mylar substrate using poly(sodium 4-styrenesulfonate) (PSSNa) gel as an electrolyte [38.50]. The large specific surface area of a nsC thin film deposited by SCBD allows a considerable amount of charge to be stored in the electric double layer formed at the gate–electrolyte interface, enabling the doping/dedoping of the transistor channels by the counterbalanced charge at the channel–electrolyte interface. The electrical characteristics of the devices

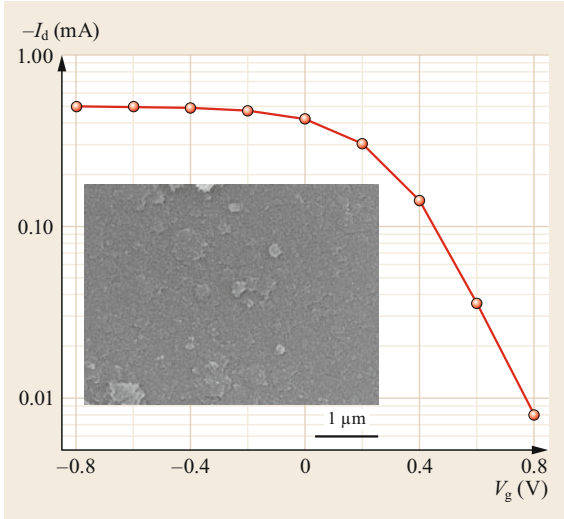

Fig. 38.6 Transfer curve of an electrolyte-gated transistor that is based on a PEDOT:PSS channel and employs a nsC thin-film gate electrode and a PSSNa-based gel electrolyte. The *inset* of the figure is a SEM image of the nsC gate electrode. (Reprinted by permission from [38.50])

present very good drain-source current modulation at low voltages (the gate voltage was varied between −0.8 and 0.8 V) with an on/off ratio of about 60 (Fig. 38.6). Moreover, due to the high electric double-layer capacitance of nsC thin films, the device can also act as a hybrid supercapacitor with efficient charge retention and satisfactory energy storage characteristics. The resulting system can maintain the applied voltage for a short period of time (ca. 10 s), allowing the operation of the transistor and the modulation of the current without an external power supply [38.50]. This demonstrates that the deposition of carbon clusters by SCBD is a suitable approach for the fabrication of flexible EGTs and transcaps featuring carbon-based gate electrodes.

38.4.3 Photocatalytic Systems

Photocatalytic processes are extensively used in a variety of applications, such as hazardous waste remediation, hydrogen production, and photoelectrochemical energy conversion [38.51]. Metal oxide semiconductors (e.g., TiO_2, WO_3, ZnO) are among the most thoroughly investigated photocatalysts due to their ability to use photogenerated charge to initiate redox reactions in adsorbed species, their high chemical stability, and their low cost [38.52]. Although the photocatalytic activity of these materials results from a synergistic effect of several physicochemical properties, considerable effort is being directed into enlarging their surface-to-volume

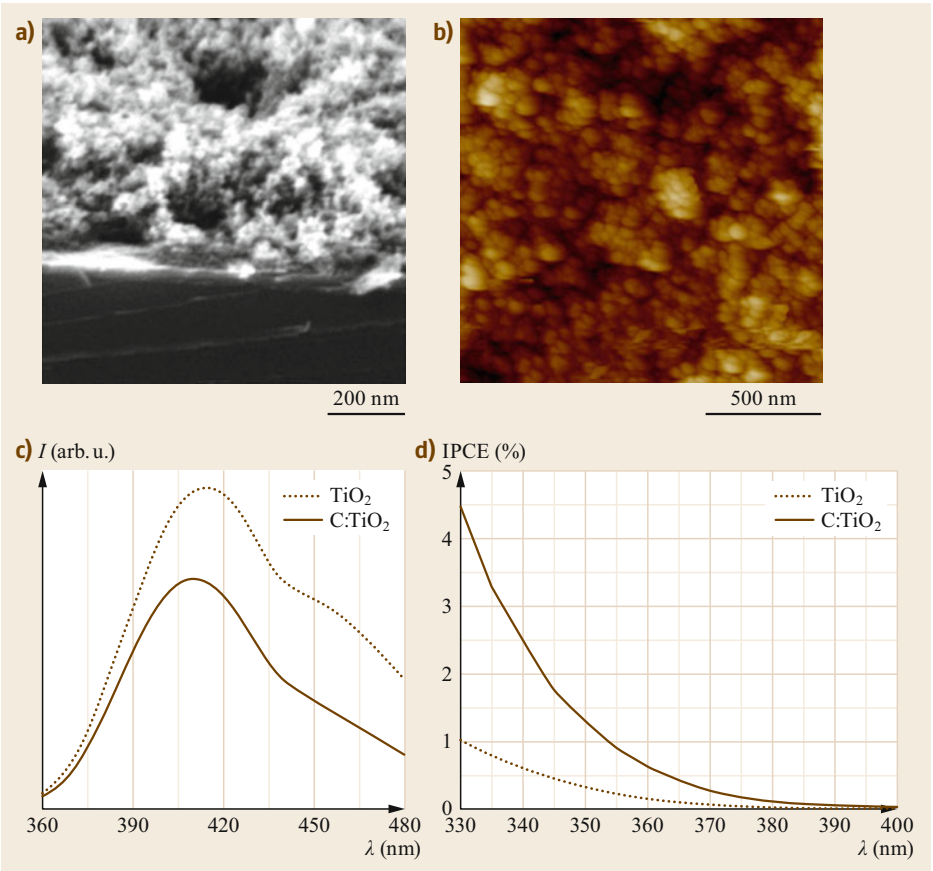

Fig. 38.7 **(a)** SEM and **(b)** AFM images of the cluster-assembled TiO_2:C nanocomposite formed using a nsC thin film as substrate for the deposition of TiO_2 nanoparticles, **(c)** fluorescence spectra of salicylic acid solution in contact with illuminated cluster-assembled TiO_2 and TiO_2:C films, and **(d)** incident photon-to-current efficiency spectra acquired under monochromatic illumination in 1 M KOH electrolyte and without external bias using cluster-assembled TiO_2 and TiO_2:C as photoanodes

ratio via nanostructuring to favor the adsorption of the compounds to be reduced and/or oxidized.

To use a nanosized photocatalyst practically, it must be embedded into an appropriate support material with a high surface area (e.g., a porous membrane): so to maximize the mass-transfer to the catalyst, to allow photons reach the active material, and to minimize the loss of catalyst into the environment [38.53]. Moreover, as nanoparticle-based metal oxide materials typically suffer from poor electronic connectivity due to the relatively high number of grain boundaries present in the system [38.54], conductive support materials are needed to facilitate the transport of the electric charge at the interface with the photocatalyst. Carbon thin films with high specific surface areas and electric double-layer capacitance are promising support materials for metal oxide photocatalysts [38.55].

The use of cluster-assembled nsC thin films of thickness 200 nm as substrate layers for the deposition of TiO_2 nanoparticles was recently reported to be an effective strategy for the fabrication of TiO_2-based materials with high photocatalytic activity. This approach yields TiO_2:C nanocomposite thin films with high surface corrugation (Fig. 38.7a,b) and greater surface roughness and electric double-layer capacitance than materials that consist of the same amount of TiO_2 nanoparticles only and are deposited using the same technique on flat substrates [38.56]. The beneficial effect of the structure of the nanocomposite on its photocatalytic activity was proven by the significantly increased activity of the TiO_2 nanoparticles embedded in the nsC in the oxidative photodegradation of salicylic acid (Fig. 38.7c) and the production of hydrogen via photoelectrochemical water splitting (Fig. 38.7d; [38.56]).

These improvements demonstrate that the SCBD-based fabrication of photocatalytic materials through the deposition of TiO_2 nanoparticles on nsC thin films not only allows the surface morphology and porosity of the nanoparticle-assembled TiO_2 to be adjusted to enhance mass transport to the surface of the photocatalyst, but it also improves the electrical properties of the photocatalyst, thus facilitating the transfer of the photogenerated charge from the TiO_2 nanoparticles to the adsorbed species.

38.5 Conclusions

The assembly of carbon clusters produced in a pulsed microplasma cluster source (PMCS) and deposited by supersonic cluster beam deposition (SCBD) has emerged as a very effective approach for growing carbon thin films. SCBD enables neutral carbon clusters to be manipulated through supersonic expansion and aerodynamic focusing, thus permitting the deposition of carbon thin films with controlled nanostructures. Precise control over the conditions applied during cluster production, extraction, and deposition is crucial not only in basic research but also to meet the requirements imposed by applications. Cluster-assembled carbon thin films produced via SCBD exhibit low density, high surface roughness, and high porosity—characteristics that potentially make these films useful in a wide range of devices, such as electrolyte-gated transistors, supercapacitors, and photocatalytic systems. These properties, together with the compatibility of SCBD with standard planar microfabrication processes, are key to the development of energy storage and conversion devices that require the integration of extremely thin films of nanostructured carbon.

References

38.1 V. Georgakilas, J.A. Perman, J. Tucek, R. Zboril: Broad family of carbon nanoallotropes: classification, chemistry, and applications of fullerenes, carbon dots, nanotubes, graphene, nanodiamonds, and combined superstructures, Chem. Rev. **115**, 4744–4822 (2015)

38.2 G. Benedek, P. Milani, V.G. Ralchenko: Nanostructured carbon for advanced applications. In: *Proc. NATO Advanced Study Institute on Nanostructured Carbon for Advanced Applications Erice* (Springer, Berlin 2001)

38.3 G. Bongiorno, A. Podestà, L. Ravagnan, P. Piseri, P. Milani, C. Lenardi, S. Miglio, M. Bruzzi, C. Ducati: Electronic properties and applications of cluster-assembled carbon films, J. Mater. Sci. Mater. Electron. **17**, 427–441 (2006)

38.4 P. Serp, B. Machado: *Nanostructured Carbon Materials for Catalysis* (R. Soc. Chem., London 2015)

38.5 Y. Gogotsi, V. Presser: *Carbon Nanomaterials*, 2nd edn. (CRC, Boca Raton 2013)

38.6 S.L. Candelaria, Y. Shao, W. Zhou, X. Li, J. Xiao, J.-G. Zhang, Y. Wang, J. Liu, J. Li, G. Cao: Nanostructured carbon for energy storage and conversion, Nano Energy **1**, 195–220 (2012)

38.7 P. Milani, P. Piseri, E. Barborini, A. Podesta, C. Lenardi: Cluster beam synthesis of nanostructured thin films, J. Vac. Sci. Technol. Vac. Surf. Films. **19**, 2025–2033 (2001)

38.8 L. Ravagnan, F. Siviero, C. Lenardi, P. Piseri, E. Barborini, P. Milani, C.S. Casari, A. Li Bassi, C.E. Bottani: Cluster-beam deposition and in situ characterization of carbyne-rich carbon films, Phys. Rev. Lett. **89**, 285506 (2002)

38.9 M. Bogana, L. Ravagnan, C.S. Casari, A. Zivelonghi, A. Baserga, A.L. Bassi, C.E. Bottani, S. Vinati, E. Salis, P. Piseri, E. Barborini, L. Colombo, P. Milani: Leaving the fullerene road: presence and stability of sp chains in sp^2 carbon clusters and cluster-assembled solids, New J. Phys. **7**, 81 (2005)

38.10 D. Donadio, L. Colombo, P. Milani, G. Benedek: Growth of nanostructured carbon films by cluster assembly, Phys. Rev. Lett. **83**, 776–779 (1999)

38.11 P. Piseri, A. Podestà, E. Barborini, P. Milani: Production and characterization of highly intense and collimated cluster beams by inertial focusing in supersonic expansions, Rev. Sci. Instrum. **72**, 2261–2267 (2001)

38.12 K. Wegner, P. Piseri, H.V. Tafreshi, P. Milani: Cluster beam deposition: a tool for nanoscale science and technology, J. Phys. Appl. Phys. **39**, R439 (2006)

38.13 E. Barborini, P. Piseri, A. Podesta', P. Milani: Cluster beam microfabrication of patterns of three-dimensional nanostructured objects, Appl. Phys. Lett. **77**, 1059–1061 (2000)

38.14 P. Piseri, H.V. Tafreshi, P. Milani: Manipulation of nanoparticles in supersonic beams for the production of nanostructured materials, Curr. Opin. Solid State Mater. Sci. **8**, 195–202 (2004)

38.15 E. Barborini, P. Piseri, P. Milani: A pulsed microplasma source of high intensity supersonic carbon cluster beams, J. Phys. Appl. Phys. **32**, L105 (1999)

38.16 A. Podestà, F. Borghi, M. Indrieri, S. Bovio, C. Piazzoni, P. Milani: Nanomanufacturing of titania interfaces with controlled structural and functional properties by supersonic cluster beam deposition, J. Appl. Phys. **118**, 234309 (2015)

38.17 F. Borghi, E. Sogne, C. Lenardi, A. Podestà, M. Merlini, C. Ducati, P. Milani: Cluster-assembled cubic zirconia films with tunable and stable nanoscale morphology against thermal annealing, J. Appl. Phys. **120**, 055302 (2016)

38.18 P. Milani, A. Podesta, P. Piseri, E. Barborini, C. Lenardi, C. Castelnovo: Cluster assembling of nanostructured carbon films, Diam. Relat. Mater. **10**, 240–247 (2001)

38.19 P. Milani, E. Barborini, P. Piseri, C.E. Bottani, A.C. Ferrari, A. Li Bassi: Nanostructured carbon films from supersonic cluster beam deposition: structure and morphology, Eur. Phys. J. D **9**, 63–68 (1999)

38.20 R. Buzio, E. Gnecco, C. Boragno, U. Valbusa, P. Piseri, E. Barborini, P. Milani: Self-affine properties of cluster-assembled carbon thin films, Surf. Sci. **444**, L1–L6 (2000)

38.21 A.-L. Barabási, H.E. Stanley: *Fractal Concepts in Surface Growth* (Cambridge Univ. Press, Cambridge 1995)

38.22 F. Family, T. Vicsek (Eds.): *Dynamics of Fractal Surfaces* (World Scientific, Singapore 1991)

38.23 M.O. Robbins, M. Cieplak, H. Ji, B. Koiller, N. Martys: Growth in systems with quenched disorder. In: *Growth Patterns in Physical Sciences and Biology*, ed. by J.M. Garcia-Ruiz, E. Louis, P. Meakin, L.M. Sander (Springer, Boston 1993) pp. 65–75

38.24 F. Family, T. Vicsek: Scaling of the active zone in the Eden process on percolation networks and the ballistic deposition model, J. Phys. Math. Gen. **18**, L75–L81 (1985)

38.25 G. Bongiorno, M. Blomqvist, P. Piseri, P. Milani, C. Lenardi, C. Ducati, T. Caruso, P. Rudolf, S. Wachtmeister, S. Csillag, E. Coronel: Nanostructured CN_x ($0 < x < 0.2$) films grown by supersonic cluster beam deposition, Carbon **43**, 1460–1469 (2005)

38.26 E. Barborini, C. Lenardi, P. Piseri, P. Milani, R.G. Agostino, T. Caruso, E. Colavita, S.L. Rosa, M. Bertolo, C. Ducati: Morphology and electronic structure of nanostructured carbon films embedding transition metal nanoparticles, Eur. Phys. J. **24**, 273–276 (2003)

38.27 M. Amati, C. Lenardi, R.G. Agostino, T. Caruso, C. Ducati, S. La Rosa, G. Bongiorno, V. Cassina, P. Podestà, L. Ravagnan, P. Piseri, P. Milani: Electrical conductivity of cluster-assembled carbon/titania nanocomposite films irradiated by highly focused vacuum ultraviolet photon beams, J. Appl. Phys. **101**, 064314 (2007)

38.28 R.G. Agostino, T. Caruso, G. Chiarello, A. Cupolillo, D. Pacilè, R. Filosa, V. Formoso, E. Colavita, L. Papagno, C. Ducati, E. Barborini, C. Lenardi, G. Bongiorno, P. Piseri, P. Milani: Thermal annealing and hydrogen exposure effects on cluster-assembled nanostructured carbon films embedded with transition metal nanoparticles, Phys. Rev. B **68**, 035413 (2003)

38.29 L.G. Bettini, G. Divitini, C. Ducati, P. Milani, P. Piseri: Nickel nanoparticles effect on the electrochemical energy storage properties of carbon nanocomposite films, Nanotechnology **25**, 435401 (2014)

38.30 E. Barborini, P. Piseri, P. Milani, G. Benedek, C. Ducati, J. Robertson: Negatively curved spongy carbon, Appl. Phys. Lett. **81**, 3359–3361 (2002)

38.31 G. Bongiorno, C. Lenardi, C. Ducati, R.G. Agostino, T. Caruso, M. Amati, M. Blomqvist, E. Barborini, P. Piseri, S. La Rosa, E. Colavita, P. Milani: Nanocrystalline metal/carbon composites produced by supersonic cluster beam deposition, J. Nanosci. Nanotechnol. **5**, 1072–1080 (2005)

38.32 T. Caruso, R.G. Agostino, G. Bongiorno, E. Barborini, P. Piseri, P. Milani, C. Lenardi, S. La Rosa, M. Bertolo: Writing submicrometric metallic patterns by ultraviolet synchrotron irradiation of nanostructured carbon and TiO_x–carbon films, Appl. Phys. Lett. **84**, 3412–3414 (2004)

38.33 A.S. Aricò, P. Bruce, B. Scrosati, J.-M. Tarascon, W. van Schalkwijk: Nanostructured materials for advanced energy conversion and storage devices, Nat. Mater. **4**, 366–377 (2005)

38.34 E. Serrano, G. Rus, J. García-Martínez: Nanotechnology for sustainable energy, Renew. Sustain. Energy Rev. **13**, 2373–2384 (2009)

38.35 Z.L. Wang: Self-powered nanosensors and nanosystems, Adv. Mater. **24**, 280–285 (2012)

38.36 S.P.S. Badwal, S.S. Giddey, C. Munnings, A.I. Bhatt, A.F. Hollenkamp: Emerging electrochemical energy conversion and storage technologies, Front. Chem. (2014), https://doi.org/10.3389/fchem.2014.00079

38.37 B.E. Conway: *Electrochemical Supercapacitors: Scientific Fundamentals and Technological Applications* (Springer, Berlin 2013)

38.38 R. Kötz, M. Carlen: Principles and applications of electrochemical capacitors, Electrochim. Acta **45**, 2483–2498 (2000)

38.39 M. Beidaghi, Y. Gogotsi: Capacitive energy storage in micro-scale devices: recent advances in design and fabrication of micro-supercapacitors, Energy Environ. Sci. **7**, 867–884 (2014)

38.40 L.G. Bettini, M. Galluzzi, A. Podestà, P. Milani, P. Piseri: Planar thin film supercapacitor based on cluster-assembled nanostructured carbon and ionic liquid electrolyte, Carbon **59**, 212–220 (2013)

38.41 L.G. Bettini, P. Piseri, F. De Giorgio, C. Arbizzani, P. Milani, F. Soavi: Flexible, ionic liquid-based micro-supercapacitor produced by supersonic cluster beam deposition, Electrochim. Acta **170**, 57–62 (2015)

38.42 L.G. Bettini, G. Bardizza, A. Podestà, P. Milani, P. Piseri: Electrochemical impedance spectroscopy on nanostructured carbon electrodes grown by supersonic cluster beam deposition, J. Nanopart. Res. **15**, 1429 (2013)

38.43 L. Diederich, E. Barborini, P. Piseri, A. Podestà, P. Milani, A. Schneuwly, R. Gallay: Supercapacitors based on nanostructured carbon electrodes grown by cluster-beam deposition, Appl. Phys. Lett. **75**, 2662–2664 (1999)

38.44 L.G. Bettini, A. Bellacicca, P. Piseri, P. Milani: Supersonic cluster beam printing of carbon microsupercapacitors on paper, Flex. Print. Electron. **2**, 025002 (2017)

38.45 F. Soavi, L.G. Bettini, P. Piseri, P. Milani, C. Santoro, P. Atanassov, C. Arbizzani: Miniaturized supercapacitors: key materials and structures towards autonomous and sustainable devices and systems, J. Power Sources **326**, 717–725 (2016)

38.46 S.H. Kim, K. Hong, W. Xie, K.H. Lee, S. Zhang, T.P. Lodge, C.D. Frisbie: Electrolyte-gated transistors for organic and printed electronics, Adv. Mater. **25**, 1822–1846 (2013)

38.47 J. Sayago, F. Soavi, Y. Sivalingam, F. Cicoira, C. Santato: Low voltage electrolyte-gated organic transistors making use of high surface area activated carbon gate electrodes, J. Mater. Chem. C **2**, 5690–5694 (2014)

38.48 H. Tang, P. Kumar, S. Zhang, Z. Yi, G.D. Crescenzo, C. Santato, F. Soavi, F. Cicoira: Conducting polymer transistors making use of activated carbon gate

electrodes, ACS Appl. Mater. Interfaces **7**, 969–973 (2015)
38.49 J. Sayago, U. Shafique, F. Soavi, F. Cicoira, C. Santato: TransCap: a monolithically integrated supercapacitor and electrolyte-gated transistor, J. Mater. Chem. C **2**, 10273–10276 (2014)
38.50 Z. Yi, L.G. Bettini, G. Tomasello, P. Kumar, P. Piseri, I. Valitova, P. Milani, F. Soavi, F. Cicoira: Flexible conducting polymer transistors with supercapacitor function, J. Polym. Sci. B **55**, 96–103 (2017)
38.51 M.R. Hoffmann, S.T. Martin, W. Choi, D.W. Bahnemann: Environmental applications of semiconductor photocatalysis, Chem. Rev. **95**, 69–96 (1995)
38.52 M. Miyauchi, A. Nakajima, T. Watanabe, K. Hashimoto: Photocatalysis and photoinduced hydrophilicity of various metal oxide thin films, Chem. Mater. **14**, 2812–2816 (2002)
38.53 M.N. Chong, B. Jin, C.W.K. Chow, C. Saint: Recent developments in photocatalytic water treatment technology: a review, Water Res. **44**, 2997–3027 (2010)
38.54 P. Hartmann, D.-K. Lee, B.M. Smarsly, J. Janek: Mesoporous TiO_2: comparison of classical sol–gel and nanoparticle based photoelectrodes for the water splitting reaction, ACS Nano **4**, 3147–3154 (2010)
38.55 A.Y. Shan, T.I.M. Ghazi, S.A. Rashid: Immobilisation of titanium dioxide onto supporting materials in heterogeneous photocatalysis: a review, Appl. Catal. Gen. **389**, 1–8 (2010)
38.56 L.G. Bettini, D.F. Foglia, P. Milani, P. Piseri: Nanostructured carbon substrate improves the photoelectrochemical water splitting activity of cluster-assembled Ti02 thin films, Int. J. Hydrog. Energy **40**, 6013–6020 (2015)

Luca Giacomo Bettini

CIMaINa and Dipartimento di Fisica "Aldo Pontremoli"
Università degli Studi di Milano
Milano, Italy
lucagiacomo.bettini@gmail.com

Luca Giacomo Bettini worked as a postdoc researcher at the University of Milan from 2013 to 2018, before joining STMicroelectronics. He received his PhD in Physics in 2013 from the University of Milano with a thesis focused on cluster-assembled carbon thin films. His research interests include the production and deposition of gas-phase nanostructured materials (e.g., carbon, metal oxides, and nanocomposites) for energy storage and conversion applications.

Massimiliano Galluzzi

Shenzhen Institutes of Advanced Technology, Chinese Academy of Sciences
Materials Interfaces Center
Shenzhen, China
galluzzi@siat.ac.cn

Massimiliano Galluzzi is a research scientist at the Shenzhen Institutes of Advanced Technology, Chinese Academy of Science, China. He received his MSc (2011) and PhD (2015) in physics from the University of Milan. His research mainly focuses on the AFM-based characterization of the morphological, mechanical, and electrical properties of polymeric soft matter, biological specimens (living cells and membranes), ionic liquids, and nanostructured interfaces.

Alessandro Podestà

CIMaINa and Dipartimento di Fisica "Aldo Pontremoli"
Università degli Studi di Milano
Milano, Italy
alessandro.podesta@mi.infn.it

Alessandro Podestà is an associate professor at the Department of Physics of the University of Milan. His research focuses on the investigation of systems and interfaces at the nanoscale using scanning probe techniques, and is supported by the development and implementation of AFM-based techniques and protocols.

Paolo Piseri

CIMaINa and Dipartimento di Fisica "Aldo Pontremoli"
Università degli Studi di Milano
Milano, Italy
paolo.piseri@fisica.unimi.it

Paolo Piseri is an associate professor at the Department of Physics of the University of Milan. He has contributed to the development of the supersonic cluster beam deposition technique for synthesizing nanostructured materials since it was first conceived. His research largely focuses on the development of advanced characterization techniques for free clusters, in particular the investigation of gas-phase clusters with short-wavelength probe radiation from synchrotron and FEL sources.

Paolo Milani

CIMaINa and Dipartimento di Fisica "Aldo Pontremoli"
Università degli Studi di Milano
Milano, Italy
paolo.milani@mi.infn.it

Paolo Milani is a full professor at the Department of Physics of the University of Milan and Director of the Interdisciplinary Centre for Nanostructured Materials and Interfaces (CIMAINA). His research focuses on cluster-assembled materials and their integration into microfabricated platforms via supersonic cluster beam deposition technology. He is active in the field of nanostructured systems and devices for stretchable electronics and optics, biotechnology and medicine, and energy production and storage.

39. Nuclear Methods in Surface Science

Daiichiro Sekiba

Some techniques in ion beam analysis (IBA), profoundly related to surface science, interfaces, and thin films, are introduced. In particular, this chapter details Rutherford backscattering spectrometry (RBS) and elastic recoil detection analysis (ERDA) as well as their high-resolution varieties, and nuclear reaction analysis (NRA), as well as recent progress that has allowed, e.g., the extension of the realm of applications to ambient conditions. These techniques have a long history that overlaps with the development of nuclear and elemental particle physics. Indeed, one could say that IBA is a byproduct of these branches of physics. Therefore, the principles of linear accelerators are also briefly mentioned in this chapter. The advantages of IBA derive from the *swiftness* of the probe ion beams produced by particle accelerators. The resulting very short interaction time ensures a precise description of differential cross section in RBS and ERDA while neglecting inelastic collisions since no chemical reactions can occur. Similarly, the cross section of NRA is well determined by nuclear physics and is not affected by environmental factors. These characteristics allow the *absolute* quantification of elemental compositions, including of hydrogen, on as well as under solid surfaces without the need to refer to any standard sample. Finally, it is noteworthy that IBA intrinsically offers nanoscale depth resolution because of the stopping power of the target material, which is an important concept defined in this chapter also in relation to the recent development of particle radiotherapy for oncological treatments.

39.1 Methods Employing Swift Ion Collisions

The most widely used ion beam analysis (IBA) techniques employing *swift* ions for solid-state physics are particle-induced x-ray emission (PIXE), particle-induced γ-ray emission (PIGE), Rutherford backscattering spectrometry (RBS), elastic recoil detection analysis (ERDA), and nuclear reaction analysis (NRA). Among these, RBS, ERDA, and NRA offer good depth resolution and can be easily applied to surface and interface studies, provided that the experiment is designed appropriately. In particular, RBS is sensitive to the relatively heavy elements present in the sample, while ERDA and NRA are suitable to detect light elements

M. Rocca, T.S. Rahman, L. Vattuone (Eds.), *Springer Handbook of Surface Science*, Springer Handbooks,
https://doi.org/10.1007/978-3-030-46906-1_39

including hydrogen. Therefore, ERDA and/or NRA investigations are usually performed simultaneously with RBS due to the complementary information that can be retrieved. These techniques are compatible, since the detector used for RBS does not affect ERDA and NRA measurements.

Despite their long history, such methods are still undergoing improvements in terms of their depth resolution and detection limits. The reason why these traditional methods remain important is that IBA offers the unique advantage of enabling *absolute* quantification of elemental composition without the need for calibration samples. These techniques thus enable the identification of novel compounds in solid chemistry samples and the derivation of information on their surface properties.

This chapter does not cover low-energy ion scattering (LEIS), also known as ion scattering spectroscopy (ISS), even though this technique plays an important role in surface science studies. The most distinct difference between ISS and the other above-mentioned IBA techniques is that it makes use of low-kinetic-energy ions (up to some keV), which makes the interaction time with the target atoms long enough to enable chemical interactions, inhibited for swift ions. For this reason, the scattering process in ISS is usually inelastic, and information can be retrieved only by comparison with trajectory simulations. ISS data interpretation is still being improved, e.g., by including the electronic interaction between probe ions and targets. From the experimental side, a recent development is the use of spin-polarized beams (SP-ISS) for surface investigation, which delivers valuable information on materials that exhibit a substantial spin–orbit interaction. ISS has been recently reviewed by *Brongersma* et al. [39.1]. For information on SP-ISS, the papers by *Suzuki* [39.2, 3] are recommended.

39.2 Accelerators

In IBA, an electrostatic accelerator, with a terminal voltage of 0.1−10 MV, is used. Synchrotrons or cyclotrons, which can accelerate charged particles up to ≈ 100 MeV, are rarely employed in IBA for materials science applications, while they are often used for medical purposes, such as oncological therapy [39.4]. The latter takes advantage of the knowledge and experience gathered in the long history of IBA. The study of particle radiotherapy from the physics viewpoint is therefore useful not only for medical doctors but also for IBA scientists.

Two types of accelerator are usually employed for IBA: the tandem type (Fig. 39.1a) and the single-end type (Fig. 39.1b) [39.5]. The former is suitable for high-energy beams, while the latter is used for relatively low energies when a high beam current is required. Most IBA apparatuses consist of an ion source, a terminal shell kept at a high positive voltage, and a measurement system (target and detectors). We first describe the tandem-type accelerator setup. Since the ion source creates negative ions and IBA users are interested in many different elements of the Periodic Table, the task of the ion source is to produce negative ions of each desired element; For example, in the case of oxygen (O) or chlorine (Cl) beams, one can use a sputtering-type ion source, which consists of an oven, employing usually cesium (Ce), an ionizer, and a target (Fig. 39.1c). Solid Ce is inserted into the oven, and Ce vapor is generated by sublimation when heating the oven. The hot ionizer creates Ce^+ ions that are attracted toward the target (often called the cathode) in which the desired element is included. When the Ce^+ ions sputter the cathode, negative ions of the desired element are produced and then accelerated by the repulsive force due to the negative electric voltage applied to the cathode. When the negative ions reach the external part of the ion source, they are further affected by the negative voltage applied on the ion source. Usually, this negative voltage lies in the range from −50 to ≈ −100 keV. Compared with photon sources used, e.g., in photoemission, the disadvantage of an ion source is its instability. The user must accurately control the heating power of the Ce oven and ionizer to stabilize the ion beam current.

If the user wants to employ inert gases such as He or Ne, other specific ion sources are used. The principles of operation of such ion sources for inert gases are completely different from those of the sputtering type. The ion source for the inert gas has a Li oven to generate Li vapor by sublimation, although sometimes alkali metals other than Li are used instead. Negative ions of inert gases are usually produced by direct collision of an electron beam with the Li vapor. After negative ions of the inert gas are generated, the acceleration mechanism is the same as for the solid cathodes used for other elements. At many facilities, the accelerators have several ion sources to enable various types of experiment.

The negative ions are guided by magnets toward the entrance of the accelerator. The accelerator is usually contained in a large tank of SF_6 gas at ≈ 0.8 MPa to avoid discharge. A part called the *terminal shell* is placed at a high (positive) voltage at the center of the accelerator and connected to its entrance and

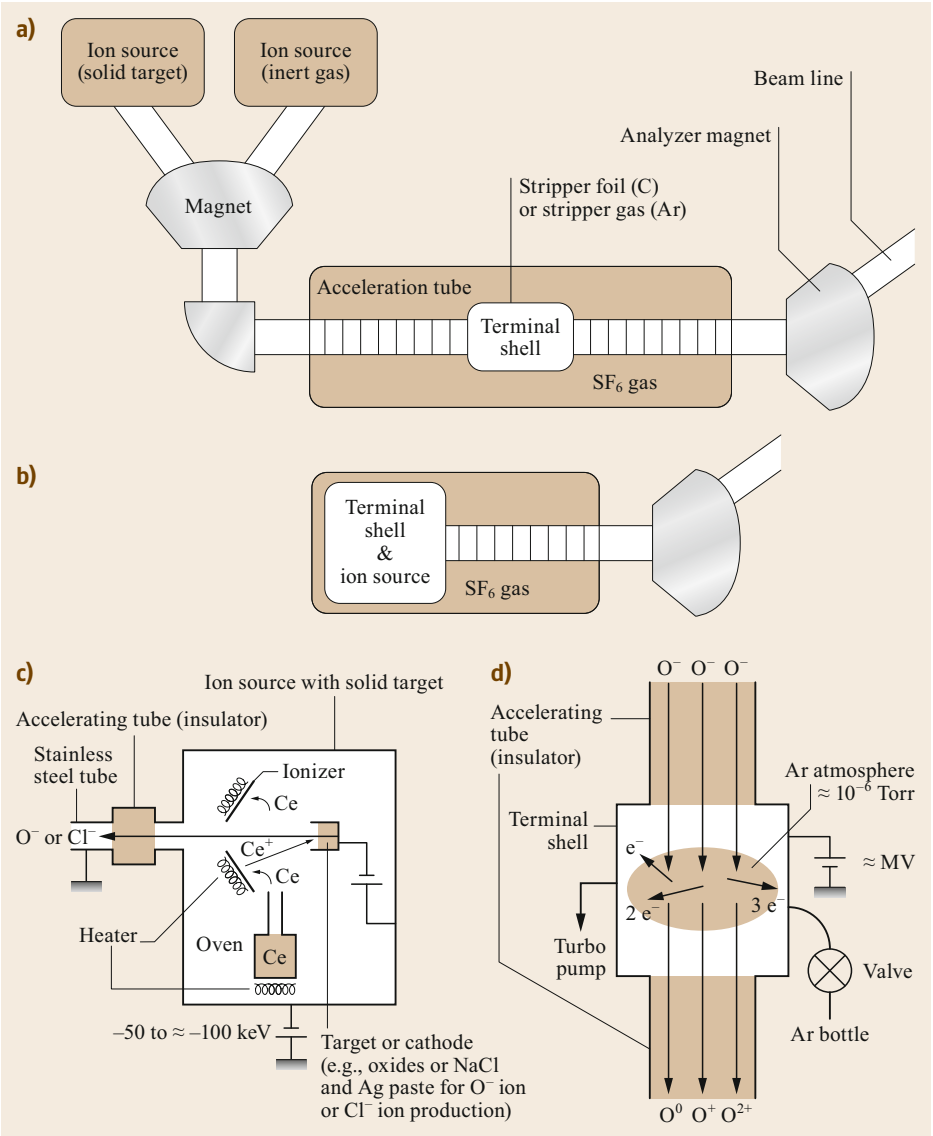

Fig. 39.1
(a) Tandem-type electrostatic accelerator, **(b)** single-end-type electrostatic accelerator. **(c)** Schematics of ion source with solid target, which generates the desired negative ions. **(d)** Schematics of charge conversion process in the terminal shell

exit by acceleration tubes, which are usually made of ceramic with resistor divider circuits. When the negative ions reach the entrance of the accelerator, they start being accelerated by the attraction to the positive voltage of the terminal shell. In the terminal shell, several electrons are removed from the negative ions by a stripper foil (carbon) or stripper gas (Ar) (Fig. 39.1d). The particles then become positive ions and are again accelerated by the repulsive force from the terminal shell. This process is called charge conversion. Thus, by using this trick of charge conversion, a tandem-type accelerator can provide a high-energy beam starting from a single terminal shell.

Any IBA technique usually requires monochromatic beams. The user must thus pay attention to the fact that ions with various valences can coexist after the occurrence of charge conversion. They have, of course, different energies. Therefore, an analyzer magnet (Fig. 39.1a,b) is inserted downstream of the accelerator so that users can select the desired energetic particles.

On the other hand, a single-end-type accelerator contains an ion source in a terminal shell. The ion source produces positive ions instead of the negative ones produced by a tandem-type accelerator. This represents a great advantage from the point of view of

the beam current, because in most cases, the creation of positive ions is much easier than that of negative ions.

There are two methods to obtain the high voltage applied to the terminal shell, viz. Van de Graaf and Cockcroft–Walton type accelerators [39.6–8]. Both methods are still in common use for a wide range of terminal voltages. Nowadays, in particular the Van de Graaf type is operated using a pellet chain [39.9] instead of a rubber band.

39.3 Stopping Power

The intrinsic high depth resolution of RBS, ERDA, and NRA is based on the stopping power of the target materials towards the probe ions. The typical value for common materials (semiconductors and/or metals) is several keV/nm. When selecting energies of ≈ 100 keV, referred to as medium energy in this field, the stopping power becomes an order of magnitude larger. In RBS and ERDA, the depth resolution is determined by the combination of the energy resolution of the detector, the stopping power, and the relative angle between the surface normal and the beam incidence direction. For NRA, the key factors are the resonance energy width and the energy straggling of the incident beam.

There is no established general theory to calculate the stopping power. It is a complicated function of the electronic stopping power and the nuclear stopping power. When the incident ions are swift enough, the electronic stopping power dominates. Usually, RBS, ERDA, and NRA are performed in this energy region, in which the electronic stopping power varies almost linearly and moderately, so that the user can easily convert an ion energy loss into a depth from the surface. If the target region is limited to a shallow subsurface region or to an interface below a thin film, the change of the stopping power is negligible and it can be treated as constant. The nuclear stopping power becomes important when the velocity of the incident beam is small; e.g., the sputtering process in secondary-ion mass spectroscopy (SIMS) [39.10] and/or the efficiency of radiotherapy are greatly affected by the nuclear stopping power. Practically, in RBS, ERDA, and NRA, one uses tabulated values of experimentally measured stopping powers. Today, such data are well known and users can easily extract the necessary stopping power using the Stopping and Range of Ions in Matter (SRIM) code [39.11].

When users need the stopping power of a new compound, it can be obtained by Bragg's rule to a good approximation [39.12] under the condition that the electronic stopping power is dominant. Briefly, the stopping power of a compound is calculated by the summation of each element included with a weight connected to the particle density. This calculation can also be performed by the SRIM code [39.11].

While measurements on devices with operation have been intensely developed in many fields, an accurate database of stopping powers for gas atmospheres and liquids is required for the field of IBA. Indeed, efforts are still being devoted to the measurement of the stopping power for various gas and liquid phases [39.13–15]. These data are also important for the medical field, e.g., for particle radiotherapy.

39.4 Principles of RBS and ERDA

Most nuclear methods in surface science employ an energetically monochromatic ion beam accelerated by an electrostatic accelerator. Usually ions with energies from several hundred keV up to MeV are used. One can choose the desired elements as accelerated ions, as mentioned above. RBS is one of the oldest methods using high-energy particles. When *Rutherford* and his collaborators found the nucleus of gold (Au) by the incidence of α particle, the principle of RBS was almost established [39.16]. As often used in kinematic explanations (Fig. 39.2), the parallel beam produced by a double-slit system is guided to a scattering chamber. Suppose that the masses and kinematic energies of the incident and target particles in the laboratory frame are M_1, E_0, and M_2, 0, respectively, before the collision.

After the collision, the kinematic energy of the scattered particle E_1 becomes as follows in the laboratory system, where the factor in front of E_0 is often called the k-factor. The scattering angle θ is measured with respect to the beam incident angle.

$$E_1 = \left(\frac{M_1 \cos\theta + \sqrt{M_2^2 - M_1^2 \sin^2\theta}}{M_1 + M_2} \right)^2 E_0 \equiv \mathrm{k}E_0$$

One of the most useful advantages of RBS is that the differential cross-section $\sigma(E, \theta)$ is almost independent

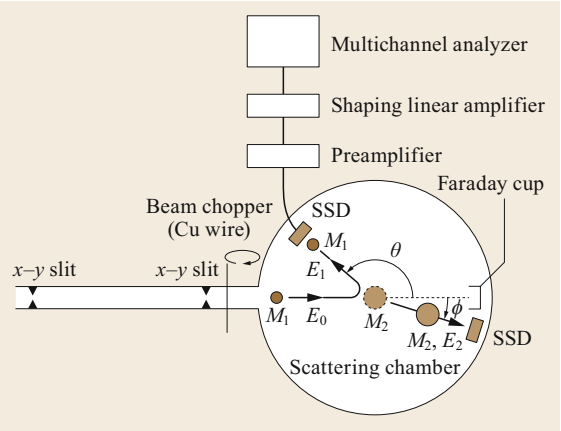

Fig. 39.2 Schematics of elastic collision with Coulomb potential and measurement of particle energies. The probe beam comes from the left through the double x–y slit system, which reduces its angular divergence. The beam current is monitored by a beam chopper to normalize the number of incident probe particles. In the case of the author's laboratory, a simple combination of a rotating Cu wire (3 Hz) and a digital current integrator is used. The current read on the Cu wire is calibrated using a Faraday cup placed at the end of the beam line. Both scattered and recoiled particles are usually detected by a solid-state detector (SSD) or surface barrier detector (SBD). The SSD measures the particles' energies from the electric current pulses that are proportional to the number of electron–hole pairs created inside the p–n junction of the SSD. The electric current pulses are treated in series by a preamplifier and shaping linear amplifier, then finally read by a computer through a multichannel analyzer (current digitizer). The principle of SSD is described in detail in [39.17]

of the chemical composition of the target. This is due to the swiftness of the incident particle, which does not have enough time to form chemical bonds with the target materials. In other words, RBS, ERDA, and other nuclear methods can be used to determine the absolute elemental compositions without any other information except the stopping power data table, which is well established. The differential cross-section can thus be written as a function of the atomic number of the incident (Z_1) and target (Z_2) particles as

$$\sigma(E,\theta) = \left(\frac{Z_1 Z_2 e^2}{2E}\right)^2 \frac{1}{\sin^4\theta} \times \frac{\left(\cos\theta + \sqrt{1-(M_1/M_2)^2\sin^2\theta}\right)^2}{\sqrt{1-(M_1/M_2)^2\sin^2\theta}} .$$

It is apparent that RBS is more sensitive to the heavier elements present in the sample. However, due to the increase of the cross section at low energy, it is necessary to pay attention to the beam energy: if the velocity of the incident particle is not large enough, the measurement could be destructive. Nondestructiveness is indeed one of the main advantages of RBS, ERDA, and NRA. While RBS is affected by small statistics errors if the mass of the target particles is heavier than the matrix, ERDA is more useful to quantify lighter elements in the matrix. The fundamental kinematics of ERDA is common to that of RBS (Fig. 39.2). The kinematic energy of the recoil particle with mass of M_2 is written as

$$E_2 = \frac{4M_1M_2\cos^2\phi}{(M_1+M_2)^2}E_0 \equiv k_{\text{recoil}}E_0 .$$

Here, the recoil angle ϕ is measured from the beam incident direction. The differential cross-section is also almost matrix independent and described as

$$\sigma(E,\phi) = \left(\frac{Z_1 Z_2 e^2\,(M_1+M_2)}{2M_2E}\right)^2 \frac{1}{\cos^3\phi} .$$

A difficulty in ERDA is the choice of an appropriate stopper foil to be placed in front of the SSD or SBD. As can be easily imagined, usually other, nonrelevant, particles enter the detector for ERDA, for example, forward scattered incident particles and recoils of other elements in the matrix. To remove such noninteresting particles, one uses a stopper foil, taking advantage of the different stopping powers of the different elements in the material of the stopper foil. As a typical case, to observe hydrogen on the surface and in subsurface regions, 2.5-MeV He ions are used. In this case, Al foil with $t = 10\,\mu\text{m}$ or Mylar foil with $t = 12\,\mu\text{m}$ are typically used as stoppers [39.18]. The author recommends Mylar foil, because Al thin foil sometimes has pinhole defects.

It is noteworthy that the differential cross-sections for RBS and ERDA described above are based on Rutherford scattering due to the Coulomb potential. When the atomic numbers of both the incident beam and target are small, the Coulomb barrier is overcome and the interaction occurs between the nuclei. In this limit, the non-Rutherford cross-section should be applied. Non-Rutherford cross-sections have been determined experimentally for the most widely used situations and are available on the Internet [39.19]. As an example, the author often uses the cross-sections determined experimentally by *Baglin* et al. [39.20] and *Besenbacher* et al. [39.21] to quantify the amount of H and D (deuterium), respectively, by ERDA with 2.5-MeV He^{2+} beam [39.22]. IBA users should thus make a simple estimate before performing an experiment to determine whether the Coulomb barrier can be overcome or not.

RBS and ERDA are usually performed simultaneously in the same measurement. By doing so, one can determine the ratio of heavy metals and light elements precisely after first determining the solid angle ratio between the two detectors for RBS and ERDA by using well-known materials.

39.5 Application of RBS and ERDA

Here, an example of RBS and ERDA from the author's experience is summarized. The metal compound formed by Mg and Ni is known to be a hydrogen-absorbing material. Apart from the high concentration of hydrogen, a metal–insulator transition also occurs due to hydrogen absorption and desorption [39.23–25]. However, after repeated absorption–desorption cycles, the ideal properties are lost. The change in the Mg-Ni thin film after repeated hydrogen absorption–desorption cycles was thus investigated by RBS and ERDA [39.26]. Figure 39.3a shows the RBS setup using 1.6-MeV $^4He^+$ ions as the probe beam. The results and schematics of the sample are shown in Fig. 39.4.

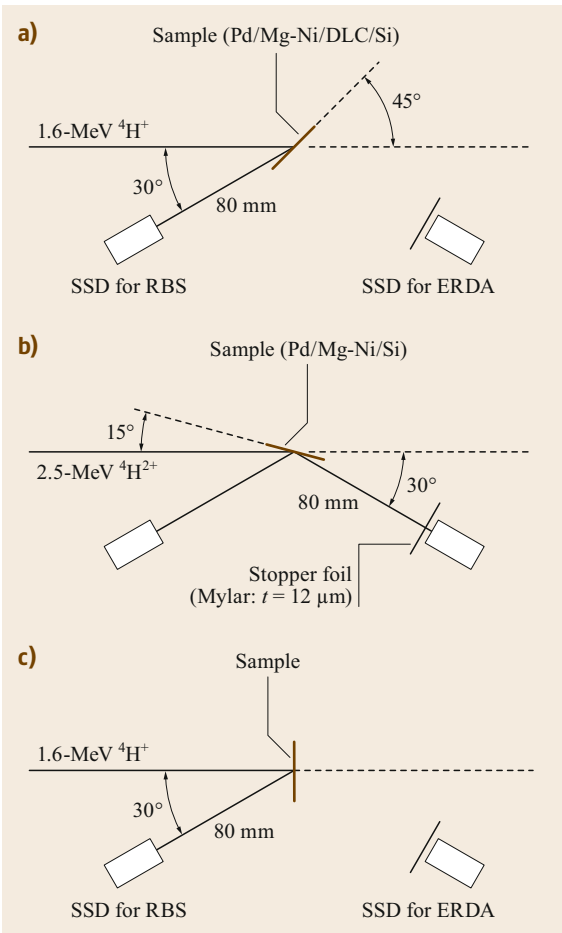

Even though the thin films deposited by the sputtering process are similar to each other, the well-separated depth profile and the change in each of the elements C, O, Si, Mg, Ni, and Pd can be observed. This sensitivity can be understood based on the k-factor in the kinematics equation, which implies that the heavier elements contribute in the higher energy region. After repeated hydrogen absorption–desorption cycles, mainly the width (or thickness) of the Mg depth profile is modified. Furthermore, a small amount of oxygen appears in the degraded sample. A simple analysis using simulations and ERDA measurements (mentioned below) demonstrates that these changes are induced by the formation of Mg hydride and Mg oxide under the Pd cap layer. For the analysis with simulations, the SIMNRA code may be useful for both RBS and ERDA as well as NRA [39.27].

The reader may wonder why the angle of incidence of the beam onto the sample is set at 45° (Fig. 39.3a): This technique is used to obtain higher depth resolution by increasing the track length of both the incident and scattered particle. In other words, grazing incidence and grazing emission are needed.

When investigating the elemental composition of a single-layer film, a simple arrangement such as that

Fig. 39.3a–c Setup of simultaneous RBS-ERDA measurements. **(a)** RBS setup for relatively high depth resolution, that is, with grazing incidence and grazing emission. Both the probe particle and the scattered particles pass the long track, so that the energy deposition per unit depth is increased. There is no special meaning for the value of the energy (1.6 MeV) of the incident beam, except that the accelerator of the author's laboratory is then stable. **(b)** Typical setup for RBS-ERDA simultaneous measurements. Although in this schematic the beam incident angle and the recoil emission angle with respect to the surface normal are identical, this is not a compulsory requirement. The beam energy (2.5 MeV) is rather critical when He ions are used as probe particles. This value is useful to avoid the detection of forward scattered He ions thanks to the stopper foil placed in front of the SSD for recoil (in this case, H ions). **(c)** The simplest setup for RBS. The advantages of this setup are that a probe beam with a large diameter (i.e., large beam current) can be used while the energy separation for each element in the sample is large ◄

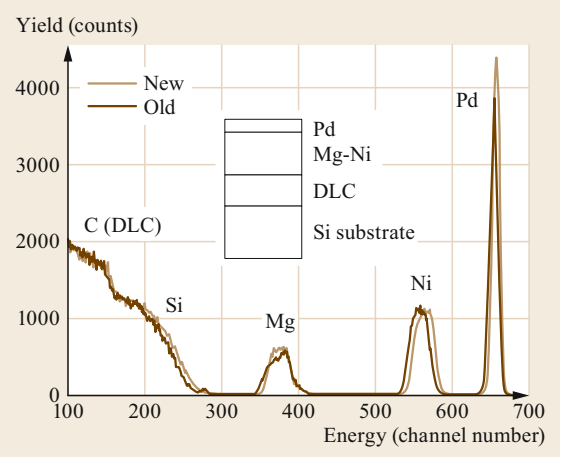

Fig. 39.4 RBS spectrum taken on the Mg-Ni metal compound before and after repeated hydrogen absorption–desorption cycles. The setup shown Fig. 39.3a was used, so that the grazing incidence (of the probe ion) and grazing emission (of the scattered ion) enable high depth resolution (see the caption of Fig. 39.3a). DLC indicates diamond-like carbon, corresponding to sp^3-rich amorphous carbon (Reprinted from [39.26], with the permission of AIP Publishing) ◄

shown in Fig. 39.3c is sufficient. When the thickness of the Mg-Ni film is relatively small (≈ 40 nm), the change of the depth profile after repeated hydrogen absorption–desorption cycles can be well distinguished using the setup shown in Fig. 39.3a.

Figure 39.5 shows the ERDA and RBS spectra simultaneously recorded for samples as shown in the inset in Fig. 39.4. The experimental setup is changed as shown in Fig. 39.3b. One can see that the depth resolution becomes worse when changing the setup, but hydrogen quantification is now attained. The results reveal that a lot of hydrogen is included in the degraded sample after repeated hydrogen absorption–desorption cycles. Comparison of the simultaneously recorded RBS and ERDA measurements enables a direct determination of the hydrogen concentration in the degraded film. More details can be found in [39.26].

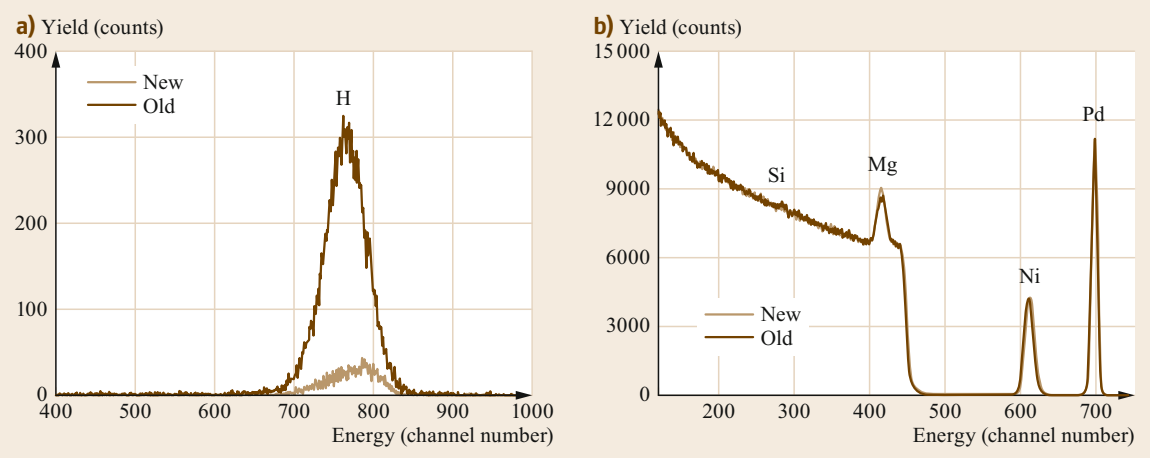

Fig. 39.5 (a) ERDA and (b) RBS spectra taken simultaneously on the Mg-Ni metal compound before and after repeated hydrogen absorption–desorption cycles using the setup shown in Fig. 39.4b (Reprinted from [39.26], with the permission of AIP Publishing)

39.6 Advanced ERDA

In conventional ERDA, various different operational modes may be implemented, known as dE–E telescope ERDA and ToF–E telescope ERDA, where *ToF* signifies *time of flight*, while E indicates the kinetic *energy* of the recoils. Both techniques are used mainly for the identification of light elements. In principle, ERDA (and also RBS) can distinguish the elements in the sample based on the energy deposited into the detector. However, such measurements are often carried out on samples containing several different light elements such as Li, B, C, N, O, and F. Because the energy of recoil depends on both the atomic number and the depth from

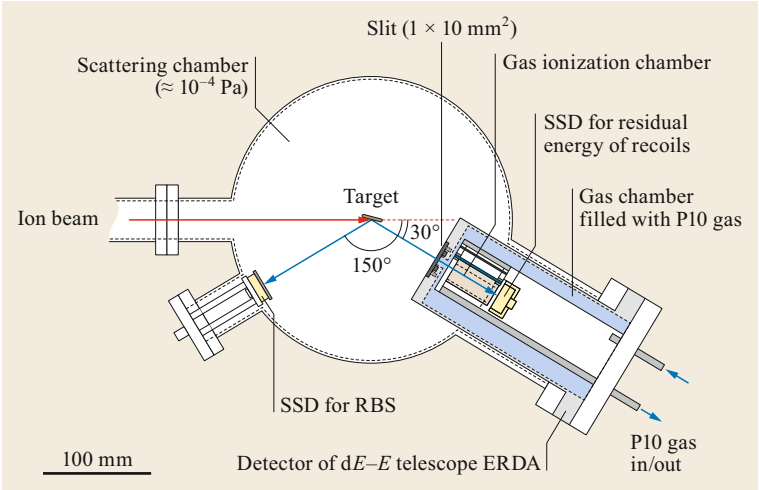

Fig. 39.6 Setup of a simultaneous RBS and dE–E telescope ERDA system with ≈ 40-MeV $^{35}Cl^{7+}$ beam. P10 gas is a mixture of 90% argon and 10% methane (Reprinted from [39.28], with permission from Elsevier)

the sample surface, it is difficult to identify the elements from the recoiling particle energy alone. Telescope-type ERDA determines the element and particle energies by using two detectors, so even if the recoils of different elements, for example, O and N, have the same kinetic energy, the element and kinetic energy can still be determined at the same time. In the case of dE–E telescope ERDA, the recoils penetrate a first detector (gas ionization chamber) and deposit about 5−10% of their kinetic energy, indicated by ΔE or dE. Then the particles that penetrate the gas ionization chamber are stopped by a second detector (an SSD in the case shown in Fig. 39.6), which determines the residual kinetic energy. Therefore, $\Delta E + E_{\mathrm{res}}$ is often also called the total energy (E_{total}). The point is that elemental identification now becomes possible based on the different interactions with the Ar gas. In other words, even though N and O have the same kinetic energy, they generate a different number of Ar^+ and e^- pairs during their penetration through the gas ionization chamber. For the first detector, usually ionization chambers filled with Ar gas are used. Sometimes, a thin SSD is used to separate H and D from relatively thick samples [39.29]. Because the interaction between the Ar gas and the recoil of each element is different, one can distinguish the elements from the ΔE values even when the E_{total} values are the same.

Figure 39.6 shows schematics of the author's setup for simultaneous RBS and dE–E telescope ERDA analysis [39.28]. This system was developed for measurements of metal oxynitride thin films on various substrates. The length of the gas ionization chamber is 50 mm. The energy resolution of a typical gas ionization chamber is 100−200 keV. Therefore, the energy loss difference between O and N during their penetration of the gas ionization chamber filled with 6000 Pa Ar should be greater than 500 keV. The length of the gas ionization chamber was determined to satisfy this condition. When using 40-MeV $^{35}Cl^{7+}$ as the incident beam, the typical kinetic energy of O and N recoils is ≈ 25 MeV. Thanks to the simulation, the length of the gas ionization chamber is determined unambiguously. Usually the multianion or multiligand system consists of a relatively heavy metal at the center of the unit cell and some surrounding light elements. As may be imagined, the ratios between the metal and light elements are determined by simultaneous RBS and dE–E telescope ERDA measurements. Figure 39.7 shows some example two-dimensional dE–E histograms taken on oxides and multianion systems [39.30–36].

On the other hand, while dE–E telescope ERDA can identify the difference between the interactions of the individual elements with the Ar gas, ToF–E telescope ERDA allows one to distinguish the light elements by the recoil. In general, if the mass (or element) of recoil is different, the velocity is also different, even though some recoils may have the same kinetic energy. Figure 39.8a shows a two-dimensional map of energy versus time of flight taken on a sample containing multiple light elements [39.37]. Improving the mass and depth resolution of such measurements has attracted much attention over the years. In Fig. 39.8a, the isotopes ^6Li and ^7Li show well-separated lines. By extracting the lines of each element, one can reproduce their depth profiles individually, as shown in Fig. 39.8b. In the same paper, readers can find a depth profile with depth resolution of ≈ 1 nm. Figure 39.8c, d shows a typical setup for ToF–E telescope ERDA, where the velocities of the recoils are acquired by measuring the time of flight between the two detectors.

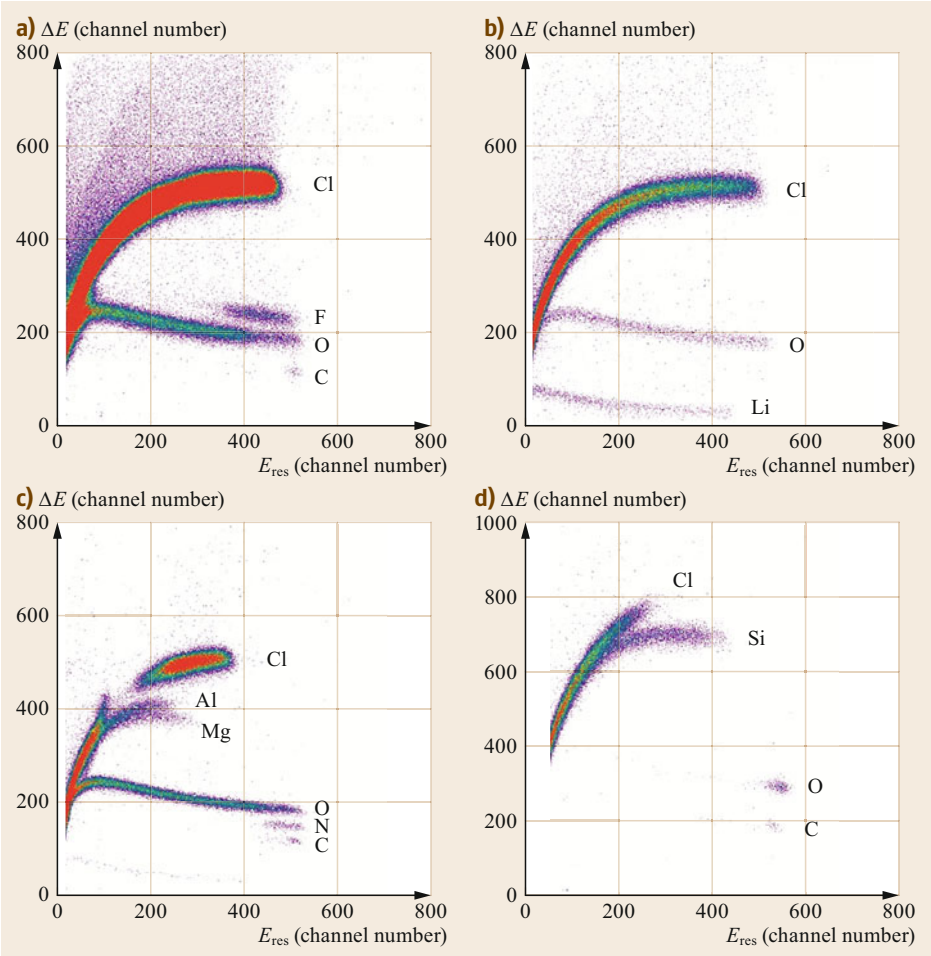

Fig. 39.7a–d dE–E histograms taken on **(a)** InO_xF_y film ($t = 125$ nm) deposited on Y:ZrO_2 substrate; **(b)** thick $LiTaO_3$ plate; **(c)** CoO_xN_y film ($t = 90$ nm) deposited on $MgAl_2O_4$ substrate, and **(d)** SiO_2 film ($t = 47$ nm) deposited on Si wafer. Here, E_{res} means ($E_{total} - dE$) and t indicates the film thickness (Reprinted from [39.28], with the permission of AIP Publishing)

The ToF detectors usually consist of a carbon foil, electrostatic mirror, and microchannel plate (MCP). Recently, very thin (50–100 nm) SiN membranes have been used instead of carbon foils. The SiN membranes usually have a coating of low-work-function material to enhance the secondary-electron emission. MCPs detect the secondary electrons emitted from the carbon foil due to the recoil penetration. The detections of the secondary electrons by the two detectors are used as the *start* and *stop* signals. Compared with dE–E telescope ERDA, ToF–E telescope ERDA measurements can be performed with lower-energy probe ions. It is noteworthy that, even though H is also well detected in Fig. 39.8a, the data obtained for H by ToF–E telescope ERDA are not suitable for accurate quantification. The detection efficiency of H in ToF–E telescope ERDA is not stable and depends on the condition of the carbon foil and/or SiN membrane surfaces [39.37, 38]. Recently, the combination of ToF–E and dE–E has also been suggested to achieve better mass and depth resolution near surfaces [39.39, 40].

39.7 Outline of HRBS, HERDA, and MEIS

Followingthe development of smaller transistors and thin insulator layers, ion beam analyzers equipped with higher depth resolution have been suggested. As mentioned above, the determination of the elemental depth profile in ion beam analysis, in general, is performed based on the stopping power. In this respect, the strategy to improve the depth resolution involves the flowing steps:

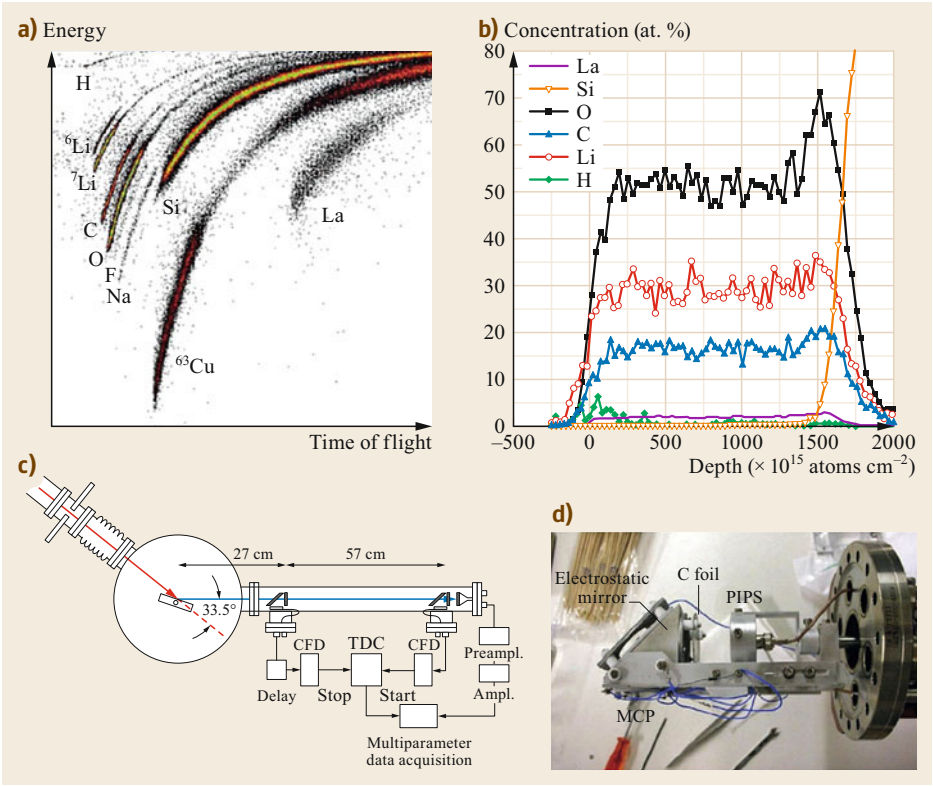

Fig. 39.8 **(a)** Two-dimensional map of energy versus time of flight taken on LiLaO by ToF–*E* telescope ERDA with 16-MeV ^{63}Cu beam. **(b)** Depth profile of each element extracted from data reported in panel **(a)**. **(c)** Overview of ToF–*E* telescope ERDA setup (CFD: constant fraction discriminator, TDC: time-to-digital converter). **(d)** Picture of second time detector and SSD, written as PIPS (passivated implanted planar silicon). This is a description of a product of Canberra Co. (present name MIRION Technology Co.) (Reprinted from [39.37], with permission from Elsevier)

1. Maximize the energy loss of the incident and/or emitted particles per unit depth. For this purpose, there are two possibilities: using grazing incidence of the primary ions or grazing emission of the scattered ions or recoils. Another practical solution is to make use of so-called medium-energy (100–500 keV) projectiles.
2. The detection of scattered ions (in RBS) and recoils (in ERDA) should be improved to ≈ 0.5 keV. The group of Mannami and Kimura have proposed the combination of a 90° sector magnetic spectrometer with a position-sensitive detector (PSD) for both RBS [39.41] and ERDA [39.42]. Usually a position-sensitive microchannel plate (MCP) is employed as the PSD. The setups for high-resolution RBS (HRBS) and high-resolution ERDA (HERDA) are quite similar. In the case of HRBS, scattering angles of 60°–90° are often used, while recoil angles of 25°–30° are suitable for HERDA, as shown in Fig. 39.9 [39.43]. The user can determine the appropriate detection angle mainly by increasing the cross-section while avoiding interference between the target elements in the spectra. In the case of HERDA, the degradation of the depth resolution due to kinematic broadening becomes crucial, so a small electrostatic quadrupole lens (singlet lens is enough) is placed in front of the 90° magnetic sector lens to compensate for the broadening [39.42, 43]. The group of Mannami and Kimura achieved monolayer depth resolution on the PbTe(001) surface by RBS (Fig. 39.10), and the author's group proved that nearly monolayer depth resolution can be attained for H on an amorphous carbon film by HERDA [39.43]. In the case of Mannami and Kimura, the exit angle of the scattered ion is set at 2° from the surface plane, and the 300-keV ^{4}He$^+$ beam is generated by a single-end accelerator. This study demonstrated unambiguously that the topmost layer of PdTe(001) is Te rich.

Medium-energy ion scattering (MEIS) is a method quite similar to HRBS, and the energy region of the

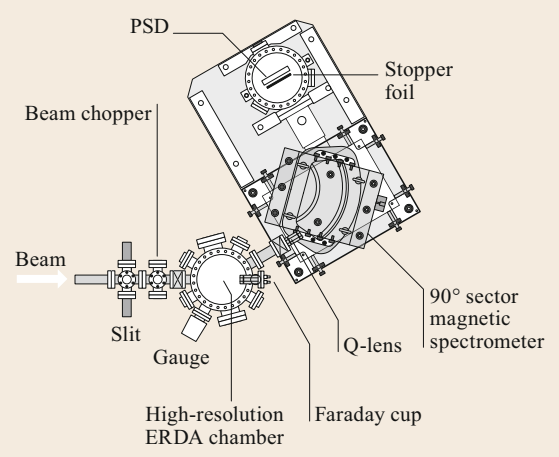

Fig. 39.9 Arrangement of HERDA system. The recoil angle is set at 30° from the beam incident angle (Reprinted from [39.43], with permission from Elsevier)

projectile is common to these techniques. Traditionally, the two methods are distinguished according to the detection type. One method employs a magnetic lens for the detector and is called HRBS, while the technique using an electrostatic lens is usually called MEIS. MEIS was developed first. In a sense, HRBS is a kind of variation of MEIS. The advantage of MEIS, in which an electrostatic lens is used, is that it can use a set of toroidal lenses and a two-dimensional PSD as shown in Fig. 39.11 [39.44], which enables the blocking condition to be found easily. MEIS was originally developed with the intention of surveying the crystallographic structure of surfaces by scanning the channeling and blocking patterns, as briefly explained in the next section. The reader can find details on the MEIS setup and principles in the good review by *van der Veen* [39.45]. Recently, MEIS has often been used as HRBS or HERDA to determine the depth profile of light elements at interfaces.

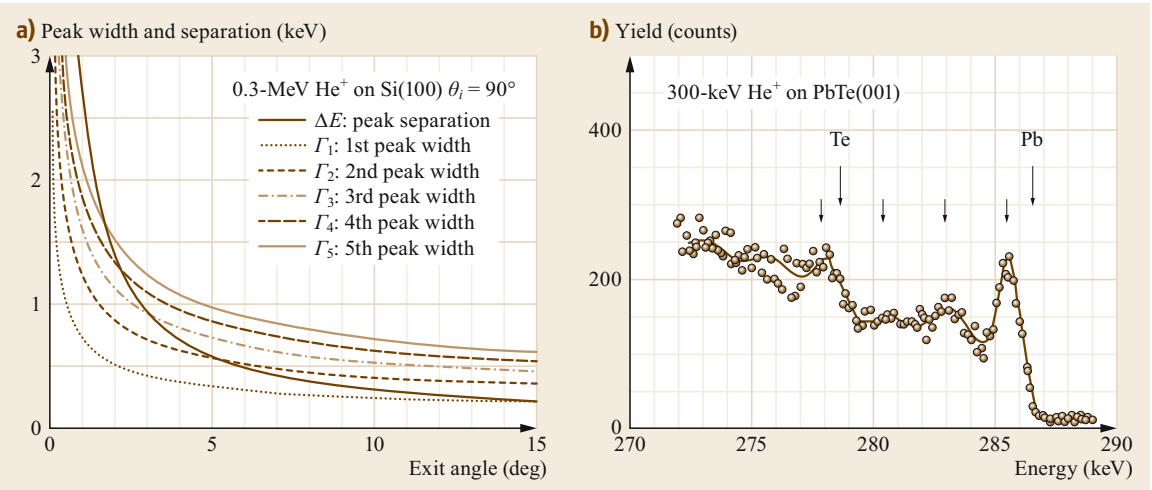

Fig. 39.10 **(a)** The relationship between the exit angle of the scattered ion and depth resolution. Γ_i indicates the ions obtained from the i-th layer atoms counted from the sample surface. **(b)** The obtained high-resolution RBS spectrum on PdTe(001) surface (Reprinted from [39.41], with permission from Elsevier)

39.8 Ion Channeling and Blocking in MEIS, HRBS, and RBS

The channeling effect is frequently used in the framework of RBS to determine the surface relaxation and/or strain of lattices, not only along the surface normal but also in the surface plane. Channeling is induced when the beam incident angle lies within the acceptance angle with respect to some crystallographic direction. In this case, the incident particle is guided by multiple forward scattering into the bulk. Therefore, the RBS yield is extremely reduced under channeling conditions [39.47].

Before discussing surface strain, it is worth introducing a simple but still impressive and famous example concerning channeling and blocking, i.e., the direct observation of surface melting by MEIS [39.46]. Figure 39.12a shows how to proceed. When the surface and subsurface region is a well-ordered crystalline lattice, a sharp scattering yield from the topmost layer, the so-called surface peak, is present. On the other hand, if some molten layer exists at the surface, the surface peak

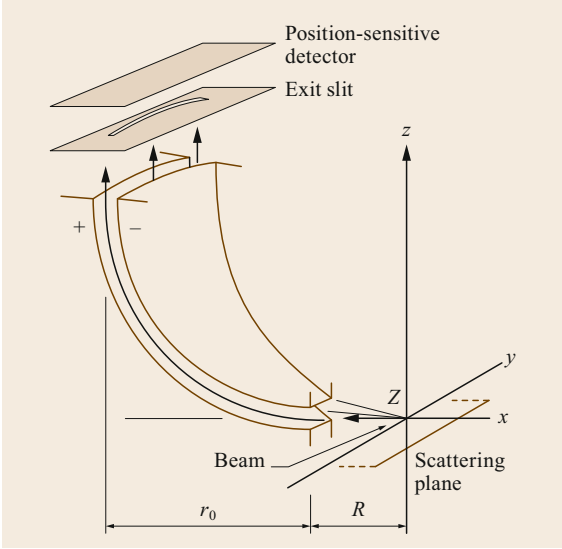

Fig. 39.11 Schematic view of toroidal analyzer and PSD (Reprinted from [39.44], with permission from Elsevier)

broadens to a width corresponding to the melted layer thickness. *Frenken* and *van der Veen* carried out MEIS experiments on the Pb(110) surface [39.46]: a significant and rather abrupt broadening of the surface peak at 600 K (Fig. 39.12c, 600.5-K curve) was observed, indicating the occurrence of surface melting. Since the line shape could not be adequately reproduced by a simple Monte Carlo simulation including more than 40 Pb layers (see the dashed line in Fig. 39.12c notated as M), the superposition of M and of the shifted 561-K curve, noted as I, was tested, revealing that such a superposition well reproduces the 600.5-K curve in Fig. 39.12c. This finding implies that the topmost and/or second layer start to melt already at 560 K (Fig. 39.12c, 561-K curve), and that such an intermediate or interface layer always exists between the solid region and the completely melted region. The melting layer constructing line M included ≈ 16.5 molten Pd layers. It was thus clearly revealed that the solid–liquid transition at the surface starts at ≈ 40 K below the bulk melting point of Pb.

Using MEIS and HRBS, it is also possible to observe strain. While scanning the beam incident angle around the channeling directions, one can find dips in the RBS yield for each channeling axis. Figure 39.13 shows the simple explanation for the relationship between the surface relaxation and/or strain and the shift of the channeling dip angle [39.48]. The same effect is caused also by blocking of the scattered ion in the framework of MEIS [39.47, 49]. This method thus qualifies as a powerful tool to investigate lattice strain in semiconductor devices and improve their development.

Figure 39.14a shows the role of the Si(001) surface oxidation method in determining the blocking around the [111] axis by comparing O_2^+ ion implantation and subsequent annealing with thermal oxidation [39.49]. It is apparent that the method employing ion implantation induces larger blocking dip shifts. From the energy loss observed in MEIS and HRBS spectra, it is possible to extract the dependence of strain on depth. Figure 39.14b

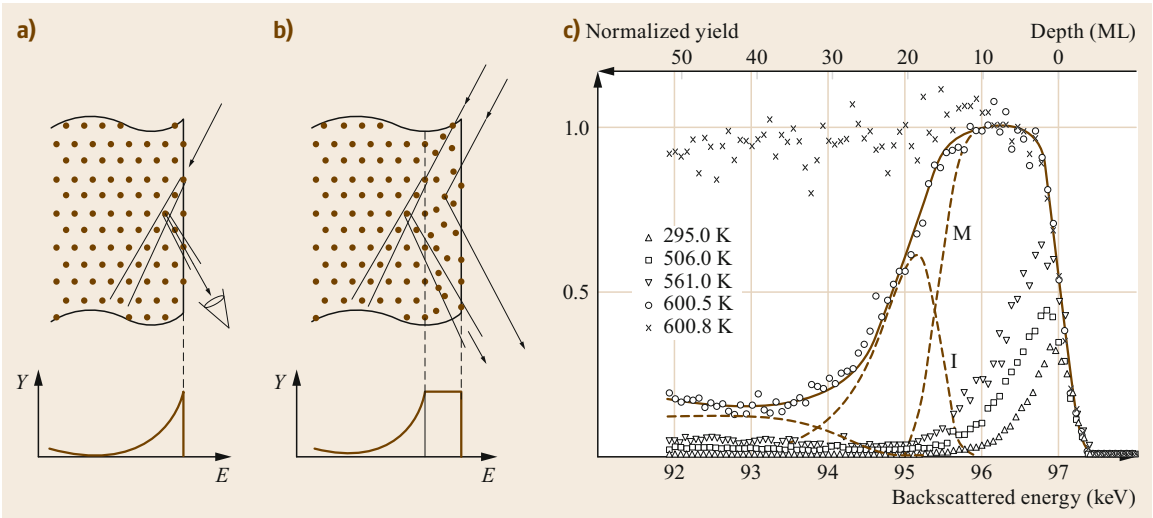

Fig. 39.12a–c Energy spectra obtained in shadowing, blocking geometry for **(a)** a well-ordered crystal surface and **(b)** a crystal covered by a liquid surface film. **(c)** Experimental energy spectra calibrated with respect to the yield of the plateau region in the random spectrum at different temperatures (Reprinted with permission from [39.46], © 1985 by the American Physical Society)

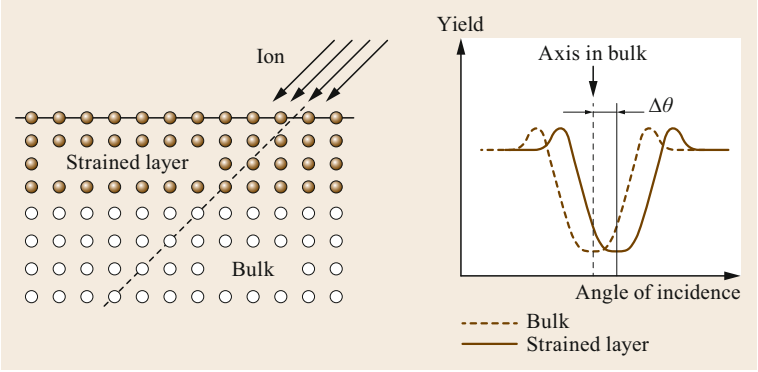

Fig. 39.13 Schematic explanation of relation between surface relaxation (or strain) and shift of channeling dip (reprinted by permission from [39.48], © The Vacuum Society of Japan 2006)

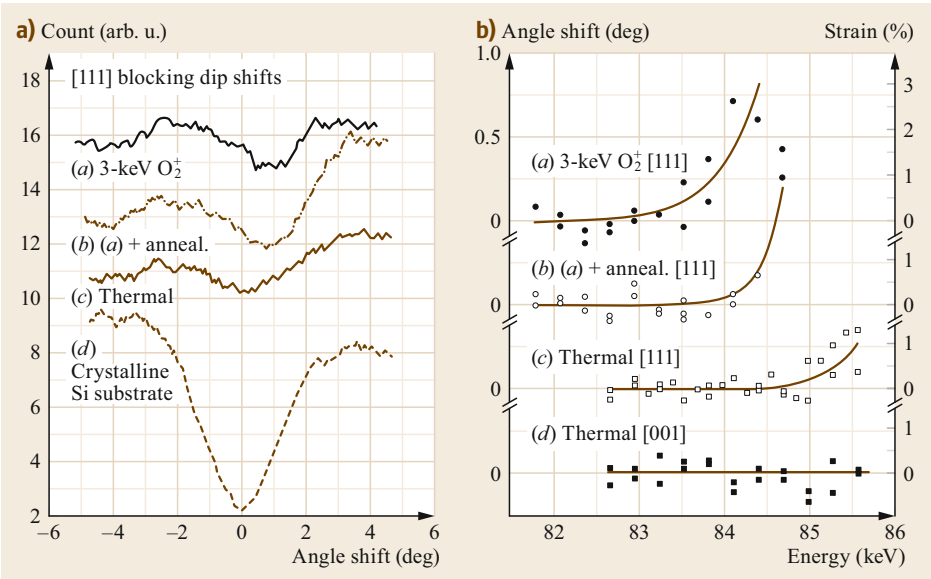

Fig. 39.14 **(a)** Shift of blocking dip at $Si_2/Si(001)$ interface observed by MEIS with various oxidation conditions. **(b)** The estimated strains in the bulk near the interfaces as a function of distance from the interfaces (Reprinted from [39.28], with the permission of AIP Publishing)

shows the lattice strain determined on the samples as a function of distance from the interface. One can see that the lattice strain near the interface obtained by ion implantation is larger by up to 3% and that it is not significantly removed by the subsequent annealing. The lattice strain present after thermal oxidation is, on the contrary, much less pronounced.

A similar experiment was performed by HRBS on the $HfO_2/Si(001)$ surface and interface [39.50]. Figure 39.15a shows the series of channeling dips, instead of the blocking dip seen in Fig. 39.14a, recorded when sweeping the beam incident angle around the [111] channeling axis. Each line shows the channeling dip corresponding to a different depth. As seen, the bottom position in angle shifts depending on the depth. The depth profile of the strain is summarized in Fig. 39.15b. There is strong compressive strain of up to $\approx 1\%$ in the vertical direction, and the strain is released and the lattice constant returns to the bulk value at a distance of $\approx$ 4 nm from the interface. It was thus shown that the strain distribution is rather larger than expected. In devices such as metal–oxide–semiconductor field-effect transistors (MOSFETs), the carrier (electron and/or hole) moves in the semiconductor side near the interface (at a distance of several nanometers from the interface). The results shown in Figs. 39.14 and 39.15 indicate that the region where the carriers move is strongly strained and the electronic band structure is also strongly modified. This information is valuable and should be taken into consideration in the design of such devices.

Related to the insulator–semiconductor system, an interesting case was presented by *Kido* et al., who reported the existence of the surface peak for an amorphous SiO_2 film deposited on the Si(001) substrate as shown in Fig. 39.16 [39.51]. In general, the charged state of a swift ion in a material is expressed as an equilibrium charge, which is a function of the velocity of the ion and does not strongly depend on the material.

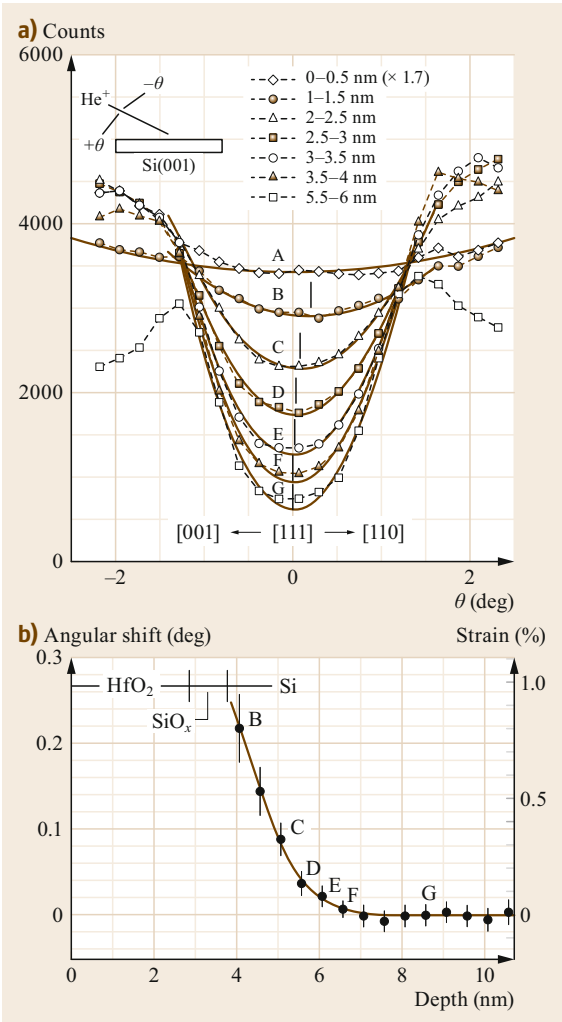

Fig. 39.15 **(a)** Series of channeling dips taken on $HfO_2/Si(001)$ interface as a function of the distance from the interface. **(b)** Depth profile of strain extracted from the series of channeling dips (Reprinted from [39.50], with the permission of AIP Publishing)

Furthermore, the charged state is usually not integer, because the incident ion may catch and release electrons from and to the target atoms, in processes such as $He^+ + e^- \rightarrow He^0$ and the reverse process $He^0 \rightarrow He^+ + e^-$. The process starts immediately. However, one could argue about the meaning of "immediately." The surface peak appearing in Fig. 39.16 can be assigned to the transient state of the charged state of the incident He ions. In other words, the He particles scattered from the topmost layer include both He^+ and He^0 at the moment of collision, and the stopping power of materials towards these two different charged states is different. As a result, the kinetic energies of scattered He^+ and He^0 can

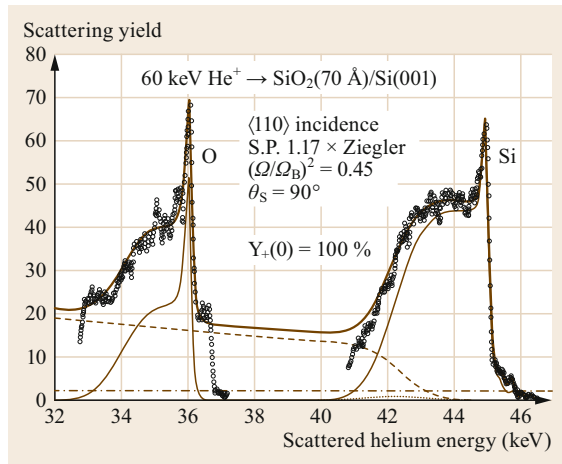

Fig. 39.16 Backscattering spectra in MEIS from Si and O of SiO_2 (70 Å) layer on Si(001) for 60-keV He^+ incident along [011] axis and backscattered at 90° (Reprinted with permission from [39.51], © 1999 by the American Physical Society)

be resolved when the energy resolution (corresponding to the depth resolution) is extremely high. Thus, the high resolution of MEIS enables observation of the nonequilibrium state of ion–surface interactions just at the moment when the ions collide with the solid surface.

Here, another impressive work on RBS channeling and blocking can be introduced. When N atoms are implanted in a shallow region of the Cu(100) surface and annealing is eventually performed, a two-dimensional array of square patches (Fig. 39.17a) spontaneously forms. RBS channeling and blocking measurements by *Cohen* et al. confirmed that this self-organized structure is induced by the lattice strain due to the adsorption of nitrogen at the topmost layer both in the plane and along the vertical direction, obtaining not only qualitative but also quantitative agreement between model and experiment [39.52]. Figure 39.17b shows the blocking dip around the 130° axis taken on stage 1 and stage 2, which correspond to a surface with a two-dimensional array of patches and the N-saturated surface, respectively. On both surfaces, the bottom positions of the blocking dips are significantly shifted from the 135° direction. The dashed and solid lines in Fig. 39.17b show the dip patterns simulated based on the Cu atom displacement shown in Fig. 39.17c. One can thus conclude that the lattice strain is induced not only at the topmost layer but also in the relatively deep subsurface region. Following this report, the authors undertook a detailed study of the electronic structure of the Cu(100)-N surface by photoemission and found a modification of the band structure both at the surface and in the subsurface region [39.53, 54].

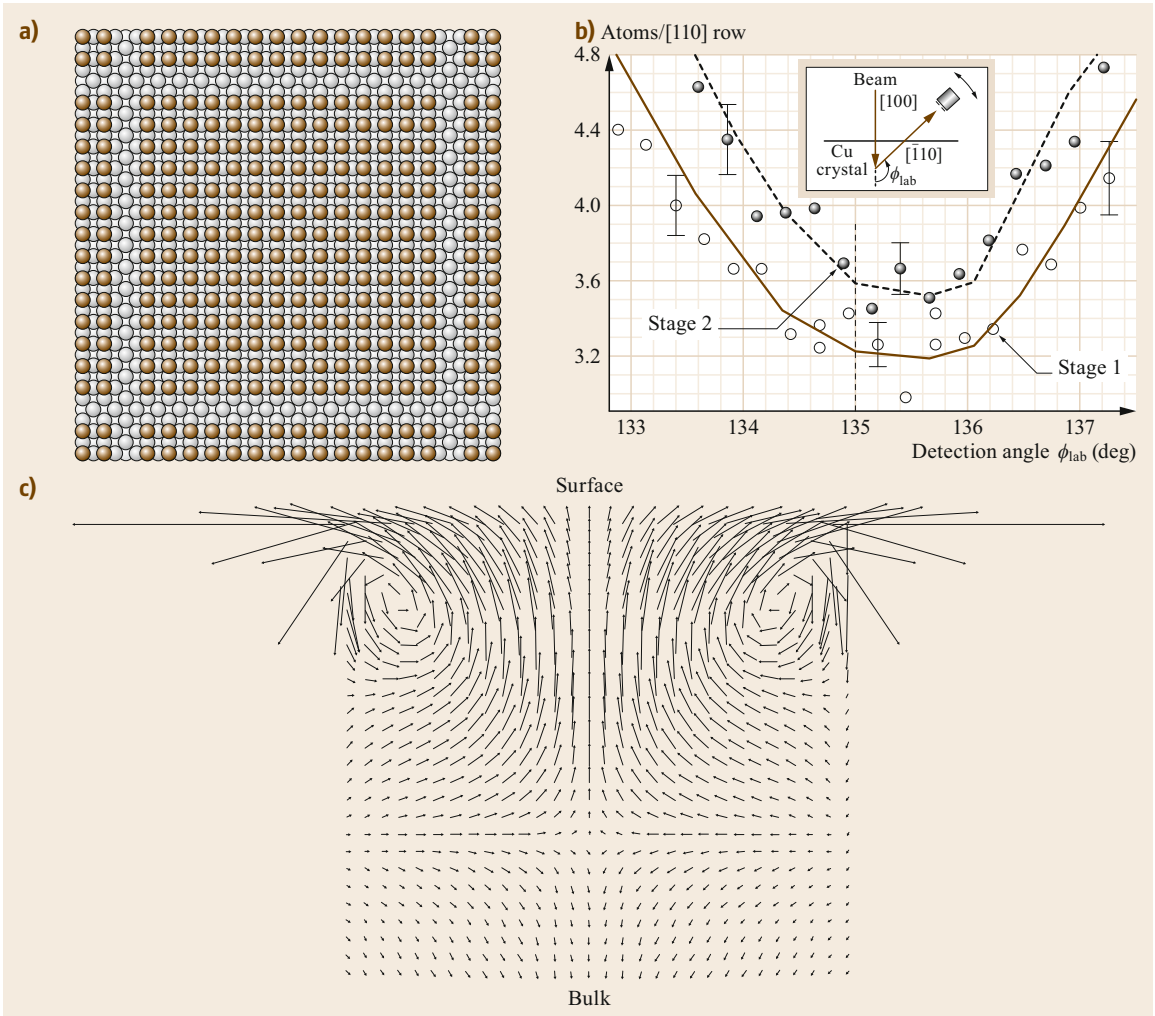

Fig. 39.17 **(a)** Schematics of Cu(100)c(2 × 2)N system, **(b)** RBS blocking dip taken around the 135° axis, **(c)** schematics of N-induced Cu atom displacement reproducing the experimental results (Reprinted from [39.52], with permission from Elsevier)

39.9 Introduction to NRA

One of the most useful aspects of the ion beam technique or ion beam analysis is that they are sensitive to protons at or in materials. Dissociatively adsorbed hydrogen always exists as a proton, because its only electron is involved in the chemical bond with neighbors. Therefore, techniques that use inner-shell electrons as probes, such as x-ray photoemission and/or Auger electron spectroscopy, are blind to the amount of hydrogen at surfaces or subsurface sites. Despite the existence of different nuclear reactions to observe the presence of hydrogen, the $^{1}H(^{15}N, \alpha\gamma)^{12}C$ reaction between 6.385-MeV ^{15}N and a proton is the most frequently used in surface science, because of its very high cross section (≈ 1.65 b) and very narrow (≈ 1.85 keV) resonant width. The latter property enables the investigation of the dynamics of hydrogen at surfaces and subsurface sites. This reaction emits an α-particle and a γ-ray. Usually, the characteristic 4.43-MeV γ-rays, which can easily penetrate through the vacuum chamber wall, are detected by scintillators outside the chamber. $Bi_4Ge_3O_{12}$ (BGO) scintillators are often used because, although they do not have very good energy resolution

for γ-rays, their detection efficiency is better for 4-MeV γ-rays than most other common crystals. Once the effective solid angle of the detector (usually a scintillator) has been determined, the γ-ray yield is proportional to the quantity of hydrogen (or proton) in the corresponding depth region. Of course, NRA is useful not only for observation of hydrogen but also to detect other light elements. A study using ^{16}O and ^{18}O detection is introduced below; regarding other reactions, with B etc., the reader is redirected to specific IBA textbooks [39.55].

39.10 Application of NRA for H at the Surface and in the Subsurface Region

The H absorption–desorption properties of Pd have attracted much attention for a long time and remain a hot topic. As for the bulk properties, the author lists some textbooks as references [39.56, 57]. During absorption and desorption of hydrogen, entrance and exit occur at the surface of Pd. The microscopic behavior of hydrogen atoms at the Pd surface and in the subsurface region, in particular at subsurface sites, is not yet completely understood. In thermal desorption spectroscopy (TDS), hydrogen at subsurface sites desorbs first, followed by hydrogen at on-surface sites. Figure 39.18a shows an NRA profile taken on the Pd(100) surface at 100 K. All the sample preparations and measurements were performed in ultrahigh vacuum (UHV) as for any other surface science study [39.58]. One can see a peak at a depth of 0 nm, corresponding to hydrogen adsorbed at the Pd(100) surface. There are also a shoulder and a tail up to depth of ≈ 8 nm, corresponding to subsurface hydrogen. The dark filled circles shown in Fig. 39.18b are the TDS spectra for this system. There are two peaks, seen just below 200 and at ≈ 320 K. These peaks can be clearly assigned based on the temperature dependence of the NRA yields. According to the NRA results, the subsurface (≈ 6 nm depth) hydrogen disappears just below 200 K, while the NRA yield at the surface (0 nm depth) does not change at this temperature. The hydrogen on the surface desorbs at the temperature at which the second TDS peak appears (≈ 320 K). In other words, the subsurface hydrogen desorbs first, followed by surface hydrogen at much higher temperature. This phenomenon is commonly seen also on other metal surfaces. It is still a great puzzle to explain how hydrogen atoms in the subsurface or at shallow bulk sites can find a partner and desorb as H_2 without visiting a surface adsorption site.

39.11 Application of NRA for H in Nanoclusters on the Surface

It is often said that the discrepancy between industrial catalysis and surface science studies may result from the nanosize of the metal particles used in industrial conditions. The hydrogen absorption properties of Pd nanoclusters seem to be different from those of well-defined Pd surfaces. *Wilde* et al. studied the hydrogen concentration on and in well-defined Pd nanoclusters self-organized on the Al_2O_3/NiAl(110) surface [39.59]. The typical dimensions of the Pd nanocluster are ≈ 10 nm width and ≈ 2 nm height. Figure 39.19a shows NRA profiles taken on Pd nanoclusters (0.59 nm)/Al_2O_3/NiAl(110) at 90 K in an H_2 atmosphere with pressure of 2×10^{-5}, 6×10^{-4}, and 2×10^{-3} Pa, respectively. With increasing H_2 pressure, the amount of absorbed hydrogen (blue line) increases while the concentration on the Pd nanoclusters (orange Gaussian) remains constant. These results are rather obvious and not very interesting. The problem is the stability of hydrogen in the Pd nanoclusters against temperature (or heat). Figure 39.19c shows the temperature dependence of the NRA yields taken at the surface (open circles) and inside (blue filled circles) of the Pd nanoclusters when keeping the H_2 pressure at ≈ 10^{-3} Pa. The amount of surface hydrogen becomes half as large at ≈ 350 K, while that of absorbed hydrogen decreases by a factor of two already at ≈ 250 K. This tendency for surface hydrogen to be more stable than absorbed hydrogen is similar to the tendency observed on the extended surface. However, the desorption temperature of absorbed hydrogen of ≈ 250 K is much higher than the value on the single-crystal Pd(100) surface, which is ≈ 180 K. This could be attributed to the scenario that the lattice relaxation of Pd due to the nanosize effect stabilizes α-phase hydrogen in the Pd nanoclusters.

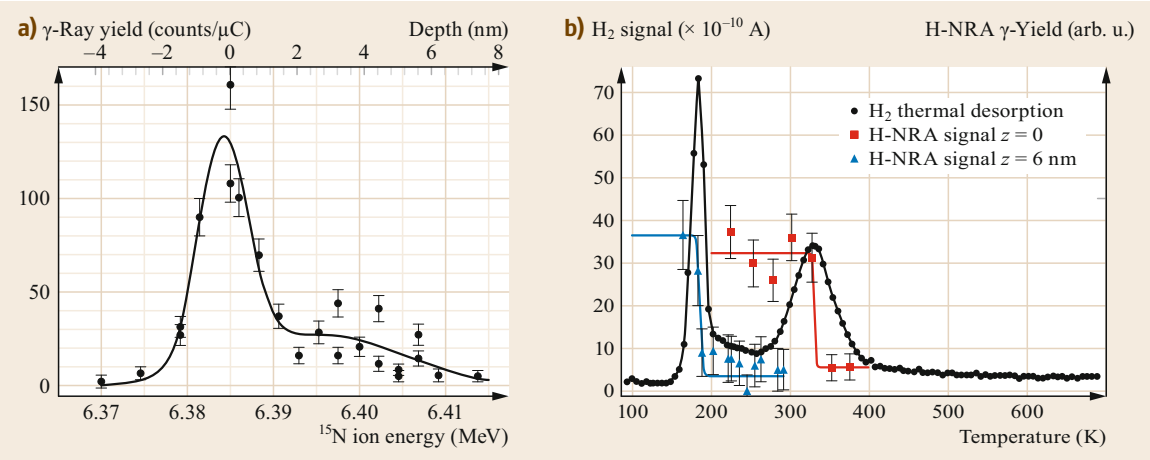

Fig. 39.18 **(a)** NRA profile taken on Pd(100) surface after exposure to hydrogen atmosphere at 100 K. **(b)** The H_2 TDS spectra taken on Pd(100) surface after exposure to hydrogen at 100 K, and temperature dependence of NRA yield at depth of 0 and 6 nm (Reprinted with permission from [39.58], © 2008 by the American Physical Society)

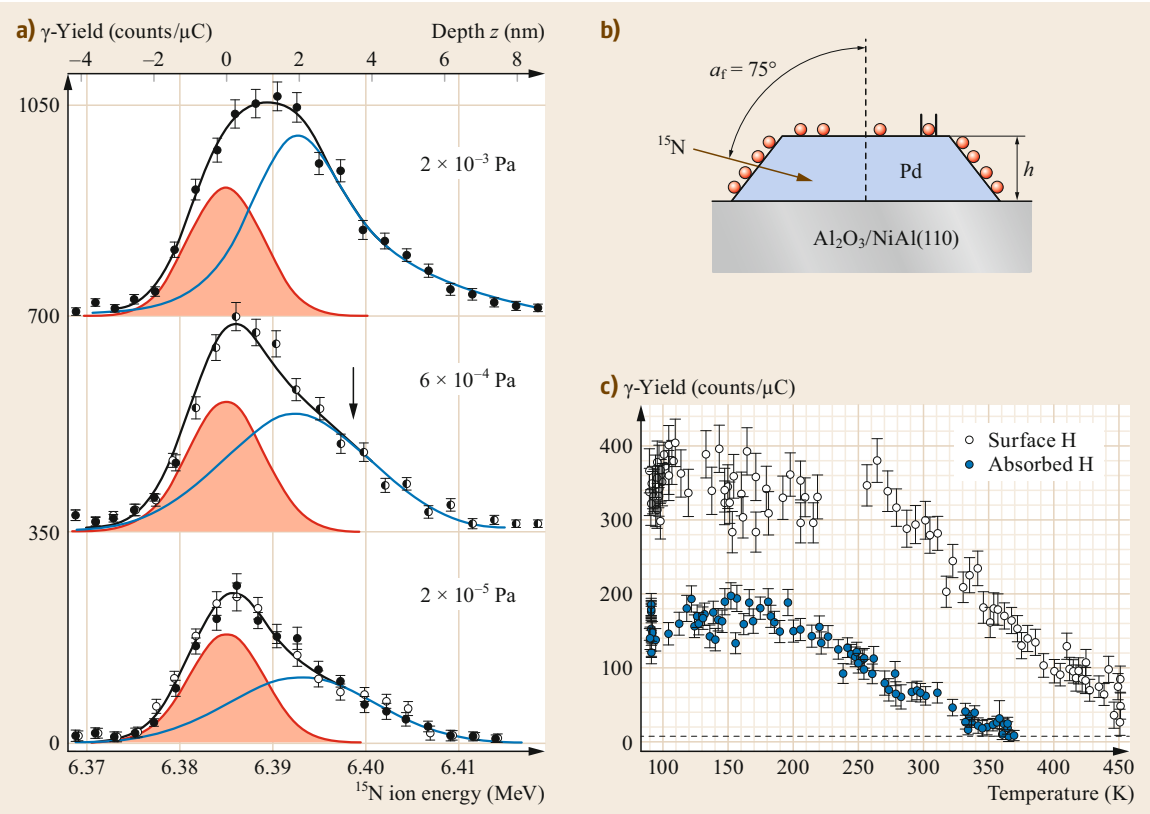

Fig. 39.19 **(a)** NRA profiles taken on Pd nanoclusters (0.59 nm)/Al_2O_3/NiAl(110) at 90 K with H_2 pressure of 2×10^{-5}, 6×10^{-4}, and 2×10^{-3} Pa. **(b)** Grazing ion incidence geometry and schematic Pd cluster morphology. **(c)** The temperature dependence of the NRA yield taken at the surface and inside of the Pd nanocluster (Reprinted with permission from [39.59], © 2008 by the American Physical Society)

39.12 Hydrogen Embrittlement Studied by Microbeam NRA

Hydrogen embrittlement of metal structures is a serious problem in architecture and civil engineering. While many macroscopic phenomenological models have been established, there are still open questions about the microscopic mechanism. IBA may not always be useful to study hydrogen embrittlement, because the diffusion coefficient of atomic hydrogen or protons in metals is very large. On the other hand, the typical time resolution of IBA is from several minutes to several tens of minutes. However, IBA techniques such as NRA can make some contributions by detecting clues regarding the hydrogen embrittlement process.

In this regard, fatigue-fractured surfaces of glassy alloys $Zr_{50}Cu_{37}Al_{10}Pd_3$ and $Zr_{50}Cu_{40}Al_{10}$ have been studied [39.60]. For both samples, the fracture started from the region surrounded by the white broken lines visible in Fig. 39.20a,e. The hydrogen accumulation or concentration was surveyed by NRA with a lateral resolution given by the beam diameter of 150 μm over a $3 \times 3\,mm^2$ area. NRA in-plane mapping was performed at three depths of ≈ 2.5, ≈ 8, and ≈ 20 nm (Fig. 39.20). Note that, in the shallow region, accumulations are seen just below the area where the fatigue fractures started (area A in Fig. 39.20b and D in Fig. 39.20f). Similar accumulations were also found in deeper regions on the $Zr_{50}Cu_{40}Al_{10}$ but not $Zr_{50}Cu_{37}Al_{10}Pd_3$ sample. This difference can be ascribed to the existence of a small amount of Pd in the $Zr_{50}Cu_{37}Al_{10}Pd_3$. Further studies are needed to obtain a more detailed interpretation.

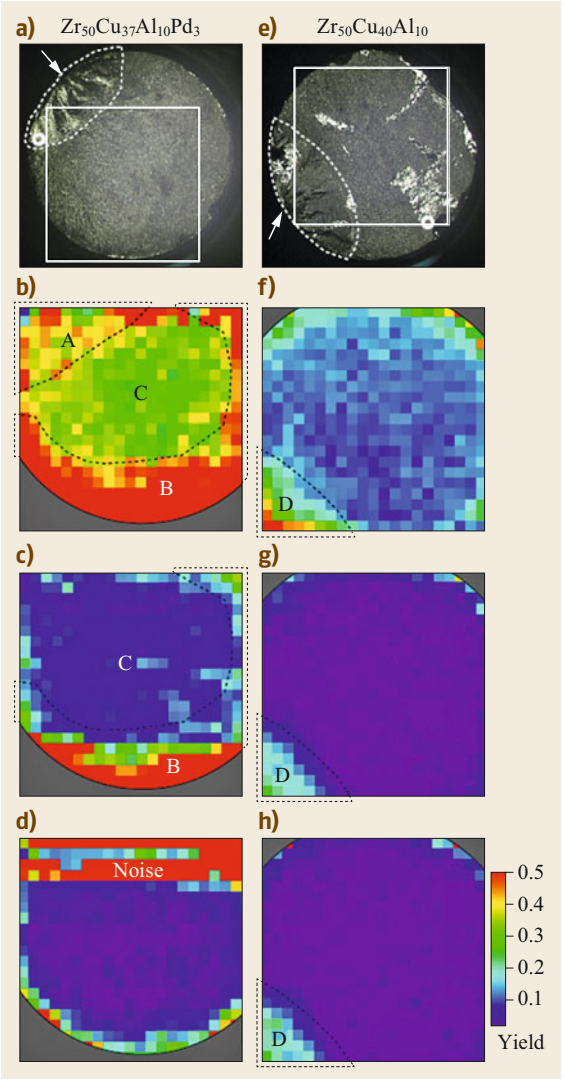

Fig. 39.20 **(a,e)** Optical microscopy images of the alloys $Zr_{50}Cu_{37}Al_{10}Pd_3$ and $Zr_{50}Cu_{40}Al_{10}$, The other panels show the in-plane distribution of the γ-ray relative yield taken at three different depths on $Zr_{50}Cu_{37}Al_{10}Pd_3$ **(b–d)** and $Zr_{50}Cu_{40}Al_{10}$ **(f–h)** at ≈ 2.5, ≈ 8, and ≈ 20 nm, respectively (Reprinted from [39.60], with permission from Elsevier) ►

39.13 NRA to Study Oxide Film Growth

As mentioned above, various NRA techniques can be used to quantify light elements. Here an isotope tracing method for ^{18}O with the 151-keV $^{18}O(p,\alpha\gamma)^{15}N$ resonance is introduced [39.61]. Sensitivity to only one specific isotope is a main advantage provided by IBA. $Hf^{16}O_2$ films were deposited first on Si(100) wafers using $HfCl_4$ and H_2O, then the films were exposed to an $^{18}O_2$ atmosphere at 100 mbar and 800 °C. The results revealed that the ^{16}O in the initial HfO_2 film was easily replaced by $^{18}O_2$ from the gas phase and that O defects were repaired. Figure 39.21a,b shows the ^{18}O depth profiles taken on HfO_2 films with different thicknesses of 3.5 and 7.5 nm, respectively. These two figures indicate that, after applying an annealing process in vacuum or N_2 atmosphere, the exchange process of oxygen between the gas and solid phases is considerably suppressed. The degree of suppression seems to depend on the HfO_2 film thickness. For the thinner film ($t = 3.5$ nm), the suppression was not so significant after N_2 annealing at 425 °C, while it was substantial

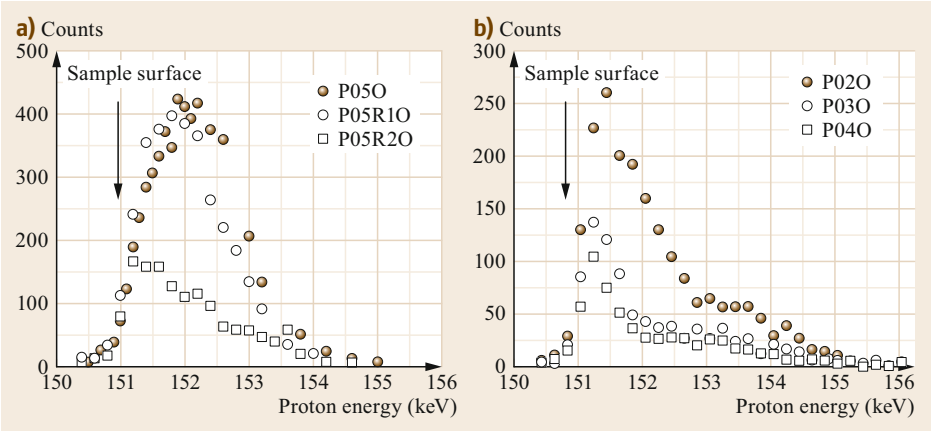

Fig. 39.21a,b NRA profiles of 151-keV $^{18}O(p,\alpha\gamma)^{15}N$ resonance taken on **(a)** 3.5-nm and **(b)** 7.5-nm HfO_2 thin films oxidized in $^{18}O_2$ atmosphere at 425 °C just after deposition (*filled circles*), postdeposition N_2 annealing at 425 °C (*open circles*), and postdeposition N_2 annealing at 800 °C (*open squares*). The details for each sample can be found in [39.61, Table 1]. (Reprinted from [39.61], with permission from Elsevier)

after N_2 annealing at 800 °C. On the other hand, on the thicker films ($t = 7.5$ nm), any type of N_2 annealing suppressed the oxygen exchange except for the surface and subsurface regions. This results implies that the crystallographic change or damage of HfO_2 film at the interface depends not only on the N_2 annealing condition but also on the thickness of the film. While the origin of this effect has not been understood yet, accumulation of lattice strain depending on the film thickness could be one of the possible causes. Thus, the isotope tracing method based on IBA is useful to assess the origin of elements in desired functional films.

39.14 Conclusions

IBA techniques with swift ions were reviewed in this chapter. Because of its intrinsic ≈ nm depth resolution, IBA is suitable to investigate surfaces, interfaces, and thin films. In particular, RBS, ERDA, and NRA allow the determination of the *absolute* elemental composition and yield a depth profile. Sufficient sensitivity to hydrogen or protons in materials is another distinctive property of IBA techniques. Although the basis of most IBA techniques was established almost 100 years ago, they are still developing fast. One of the reasons is the recent progress in MOSFETs using wide-gap semiconductors such as GaN, SiC, and diamond, for which IBA information has proved to be crucial. Accurate control of the interface content of light elements is indeed mandatory for such devices. Another reason is connected to the new strategy for functional materials synthesis, for which thin films without rare metals are required.

References

39.1 H.H. Brongersma, M. Draxler, M. de Ridder, P. Bauer: Surface composition analysis by low-energy ion scattering, Surf. Sci. Rep. **62**, 63–109 (2007)

39.2 T.T. Suzuki: Atomic arrangement and spin polarization at a Ge/Fe(100) surface studied by spin-polarized ion scattering spectroscopy, Surf. Sci. **663**, 1–6 (2019)

39.3 T.T. Suzuki: Electron-spin dependent surface scattering of a polarized $^4He^+$ ion beam, J. Surf. Sci. Soc. Jpn. **38**, 164–169 (2017), in Japanese

39.4 H. Paganetti (Ed.): *Proton Therapy Physics*, 2nd edn. (CRC Press, Boca Raton 2018)

39.5 A.W. Chao, K.H. Mess, M. Tigner, F. Zimmermann (Eds.): *Handbook of Accelerator Physics and Engineering*, 2nd edn. (World Scientific, Singapore 2013)

39.6 R.J. Van de Graaf, K.T. Compton, L.C. Van Atta: The electrostatic production of high voltage for nuclear investigations, Rhys. Rev. **43**, 149–157 (1933)

39.7 J.D. Cockcroft, E.T.S. Walton: Experiments with high velocity positive ions. (I) Further developments in

the method of obtained high velocity ions, Proc. R. Soc. A **136**, 619–630 (1932)
39.8 J.D. Cockcroft, E.T.S. Walton: Experiments with high velocity positive ions. (II). The disintegration of elements by high velocity protons, Proc. R. Soc. A **137**, 229–242 (1932)
39.9 D.B. Cline, D.J. Larson, W. Kells, F.E. Mills, J.R. Adney, J.A. Ferry, M.L. Sundquist: Intermediate energy electron cooling for antiproton sources using a Pelletron accelerator, IEEE Trans. Nucl. Sci. **30**, 2370–2372 (1983)
39.10 A. Benninghoven, J. Giber, J. Laszlo, M. Riedel, H.W. Wemer: *Secondary Ion Mass Spectrometry SIMS III*, Springer Series in Chemical Physics (Springer, Berlin, Heidelberg 1982)
39.11 J.F. Ziegler: Interactions of ions with matter, http://www.srim.org/
39.12 W.H. Bragg, R. Kleeman: On the α particle of radium, and their loss of range in passing through various atoms and molecules, Philos. Mag. **10**(57), 318–340 (1904)
39.13 J.L. Price, S.H. Stern, D.G. Simons, D.J. Land, J.G. Brennan: Stopping powers for 400 to 2400 keV N ions in He and Ar, Nucl. Instrum. Methods B **56/57**, 348–351 (1991)
39.14 J.L. Price, D.G. Simons, S.H. Stern, D.J. Land, N.A. Guardala, J.G. Brennan, M.F. Stumborg: Stopping powers of the noble gases for (0.3–10)-MeV nitrogen ions, Phys. Rev. A **47**, 2913 (1993)
39.15 A. Fukuda: Stopping powers of the rare gases for 50–200 keV N^+ ions, J. Phys. B **29**, 3717–3725 (1996)
39.16 E. Rutherford: The scattering of α and β particles by matter and the structure of the atom, Philos. Mag. **6**(21), 669–688 (1911)
39.17 G.K. Knoll: *Radiation Detection and Measurement*, 4th edn. (Wiley, New York 2010)
39.18 B.L. Doyle, P.S. Peercy: Technique for profiling ^{1}H with 2.5-MeV Van de Graaf accelerators, Appl. Phys. Lett. **34**, 811–813 (1979)
39.19 A. Gurbich: Ion beam analysis nuclear data library, http://www-nds.iaea.org/ibandl/ (2019)
39.20 J.E.E. Baglin, A.J. Kellock, M.A. Crokett, A.H. Shih: Absolute cross section for hydrogen forward scattering, Nucl. Instrum. Methods B **64**, 469 (1992)
39.21 F. Besenbacher, I. Stensgaard, P. Vase: Absolute cross section for recoil detection deuterium, Nucl. Instrum. Methods B **15**, 459 (1986)
39.22 D. Sekiba, N. Takemoto, M. Okada, S. Ishii, T. Sakurai, K. Akimoto: Hydrogen isotope tracer experiment in a-C:H film deposition: reactive RF magnetron sputtering with CH_4 and D_2, Diam. Relat. Mater. **60**, 27–28 (2012)
39.23 J.N. Huiberts, R. Griessen, J.H. Rector, R.J. Wijngaarden, J.P. Dekker, D.G. de Groot, N.J. Koeman: Yttrium and lanthanum hydride films with switchable optical properties, Nature **380**, 231 (1996)
39.24 R. Armitage, M. Rubin, T. Richardson, N. O'Brien, Y. Chen: Solid-state gadolinium-magnesium hydride optical switch, Appl. Phys. Lett. **75**, 1863 (1999)
39.25 M.J. van Setten, G.A. de Wijs: Ab initio study of the effects of transition metal doping of Mg_2NiH_4, Phys. Rev. B **76**, 075125 (2007)
39.26 D. Sekiba, M. Horikoshi, S. Abe, S. Ishii: Mg segregation in Mg-rich Mg-Ni switchable mirror studied by Rutherford backscattering, elastic recoil analysis, and nuclear reaction analysis, J. Appl. Phys. **106**, 114912 (2009)
39.27 M. Mayer: SIMNRA computer simulation https://home.mpcdf.mpg.de/ mam/ (2019)
39.28 I. Harayama, K. Nagashima, Y. Hirose, H. Matsuzaki, D. Sekiba: Development of ΔE–E telescope ERDA with 40 MeV $^{35}Cl^{7+}$ beam in MALT in the University of Tokyo optimized for analysis of metal oxynitride thin films, Nucl. Instrum. Methods B **384**, 61 (2016)
39.29 M. Wielunski, M. Mayer, R. Behrisch, J. Roth, B.M.U. Scherzer: Simultaneous profiling of hydrogen and deuterium by 2.6 MeV ^{4}He ERDA using ΔE–E telescope detector, Nucl. Instrum. Methods B **122**, 113 (1997)
39.30 A. Suzuki, Y. Hirose, T. Nakagawa, S. Fujiwara, S. Nakao, Y. Matsuo, I. Harayama, D. Sekiba, T. Hasegawa: Enhanced electrical conduction in anatase TaON via soft chemical lithium insertion toward electronis application, ACS Appl. Nano Mater. **1**, 3981–3985 (2018)
39.31 T. Katayama, A. Chikamatsu, Y. Hirose, M. Minohara, H. Kumigashira, I. Harayama, D. Sekiba, T. Hasegawa: Ferromagnetism with strong magnetocrystalline anisotropy in A-site ordered perovskite $YBaCo_2O_6$ epitaxial thin film prepared via wet-chemical topotactic oxidation, J. Mater. Chem. C **6**, 6 (2018)
39.32 V. Motaneeyachart, Y. Hirose, A. Suzuki, S. Nakao, I. Harayama, D. Sekiba, T. Hasegawa: Epitaxial growth of Baddeleyite NbON thin films on yttria-stabilized zirconia by pulsed laser deposition, Chem. Lett. **47**, 65–67 (2018)
39.33 K. Kawahara, A. Chikamatsu, T. Katayama, T. Onozuka, D. Ogawa, K. Morikawa, E. Ikenaga, Y. Hirose, I. Harayama, D. Sekiba, T. Fukumura, T. Hasegawa: Topotactic fluorination of perovskite strontium ruthenate thin films using polyvinylidene fluoride, CrystEngComm **19**, 313–317 (2017)
39.34 T. Onozuka, A. Chikamatsu, T. Katayama, Y. Hirose, I. Harayama, D. Sekiba, E. Ikenaga, M. Minohara, H. Kumigashira, T. Hasegawa: Reversible resistance modulation induced by fluorine substitution in perovskitenickelate $NdNiO_2$ thin films, ACS Appl. Mater. Interfaces **9**, 10882–10887 (2017)
39.35 T. Yamazaki, K. Shigematsu, Y. Hirose, S. Nakao, I. Harayama, D. Sekiba, T. Hasegawa: Amorphous ZnO_xN_y thin films with high electron Hall mobility exceeding 200 $cm^2 V^{-1} s^{-1}$, Appl. Phys. Lett. **109**, 262101 (2016)
39.36 J. Takahashi, Y. Hirose, D. Oka, S. Nakao, C. Yang, T. Fukumura, I. Harayama, D. Sekiba, T. Hasegawa: Composition-induced structural, electrical, and magnetic phase transitions in AX-type mixed-valence cobalt oxynitride epitaxial thin films, Appl. Phys. Lett. **107**, 231906 (2015)

39.37 S. Giangrandi, T. Sajavaara, B. Brijs, K. Arstila, A. Vantomme, W. Vandervorst: Low-energy heavy-ion TOF-ERDA setup for quantitative depth profiling of thin films, Nucl. Instrum. Methods B **266**, 5144 (2008)

39.38 Z. Siketić, I.B. Radović, M. Jakšić: Development of a time-of-flight spectrometer at the Rufter Bošković Institue in Zagreb, Nucl. Instrum. Methods B **266**, 1328–1332 (2008)

39.39 J. Julin, T. Sajavaara: Conceptual study of a heavy-ion-ERDA spectrometer for energies below 6 MeV, Nucl. Instrum. Methods B **406**, 61–65 (2017)

39.40 S. Eschbaumer, A. Bergmaier, D. Seiler, G. Dollinger: Time of flight assisted ΔE–E method for enhanced isotope separation capabilities in heavy ion elastic recoil detection analysis, Nucl. Instrum. Methods B **406**, 10–14 (2008)

39.41 K. Kimura, M. Mannami: RBS with monolayer resolution, Nucl. Instrum. Methods B **113**, 270 (1996)

39.42 K. Kimura, K. Nakajima, H. Imura: Hydrogen depth profiling with sub-nm resolution in high-resolution ERD, Nucl. Instrum. Methods B **140**, 397 (1998)

39.43 D. Sekiba, K. Chito, I. Harayama, Y. Watahiki, S. Ishii, K. Ozeki: Installation of high-resolution ERDA in UTTAC at the University of Tsukuba: Determination of the energy resolution and the detection limit for hydrogen, Nucl. Instrum. Methods B **401**, 29 (2017)

39.44 R.G. Smeenk, R.M. Tromp, H.H. Kersten, A.J.H. Boerboom, F.W. Saris: Angle resolved detection of charged particles with a novel type toroidal electrostatic analyzer, Nucl. Instrum. Methods **195**, 581 (1982)

39.45 J.F. van der Veen: Ion beam crystallography of surfaces and interfaces, Surf. Sci. Rep. **5**, 199 (1985)

39.46 J.W.M. Frenken, J.F. van der Veen: Observation of surface melting, Phys. Rev. Lett. **54**, 134 (1985)

39.47 L.C. Feldman, J.W. Mayer, S.T.A. Picraux: *Materials Analysis by Ion Channeling: Submicron Crystallography* (Academic Press, New York 2012)

39.48 K. Nakajima, M. Suzuki, K. Kimura: Observation of lattice strain near interface using high-resolution RBS, J. Vac. Soc. Jpn. **49**, 286 (2006), in Japanese

39.49 Y.P. Kim, S.K. Choi, H.K. Kim, D.W. Moon: Direct observation of Si lattice strain and its distribution in the Si(001)–SiO_2 interface transition layer, Appl. Phys. Lett. **71**, 3504 (1997)

39.50 K. Nakajima, S. Joumori, M. Suzuki, K. Kimura, T. Osipowick, K.L. Tok, J.Z. Zheng, A. See, B.C. Zhang: Strain profiling of HfO_2/Si(001) interface with high-resolution Rutherford backscattering spectroscopy, Appl. Phys. Lett. **83**, 296 (2003)

39.51 Y. Kido, T. Nishimura, F. Fukumura: Anomalous surface peaks observed in the backscattering spectra from amorphus Si and SiO_2 films for medium energy He ions, Phys. Rev. Lett. **82**, 3352 (1999)

39.52 C. Cohen, H. Ellmer, J.M. Guigner, A. L'Hoir, G. Prévot, D. Schmaus, M. Sotto: Surface relaxation and near-surface atomic displacements in the N/Cu(100) self-ordered system, Surf. Sci. **490**, 336 (2001)

39.53 D. Sekiba, K. Nakatsuji, Y. Yoshimoto, F. Komori: Direct observation of strain-induced change in surface electronic structure, Phys. Rev. Lett. **94**, 016808 (2005)

39.54 D. Sekiba, Y. Yoshimoto, K. Nakatsuji, Y. Takagi, T. Iimori, S. Doi, F. Komori: Strain-induced change in electronic structure of Cu(100), Phys. Rev. B **75**, 115404 (2007)

39.55 M. Nastasi, J.W. Mayer, Y. Wang: *Ion Beam Analysis: Fundamentals and Applications* (CRC Press, Boca Raton 2014)

39.56 F.A. Lewis: *The Palladium Hydrogen System* (Academic Press, New York 1967)

39.57 Y. Fukai: *The Metal–Hydrogen System, Basic Bulk Properties* (Springer, Berlin 2004)

39.58 M. Wilde, K. Fukutani: Penetration mechanisms of surface-adsorbed hydrogen atoms into bulk metals: experiment and model, Phys. Rev. B **78**, 115411 (2008)

39.59 M. Wilde, K. Fukutani, M. Naschitzki, H.J. Freund: Hydrogen absorption in oxide-supported palladium nanocrystals, Phys. Rev. B **77**, 113412 (2008)

39.60 D. Sekiba, H. Yonemura, S. Ogura, M. Matsumoto, Y. Kitaoka, Y. Yokoyama, H. Matsuzaki, T. Narusawa, K. Fukutani: Development of micro-beam NRA for hydrogen mapping: Observation of fatigue-fractured surface of glassy alloys, Nucl. Instrum. Methods B **269**, 627 (2011)

39.61 J.J. Ganem, I. Trimaille, I.C. Vickridge, D. Blin, F. Martin: Study of thin hafnium oxides deposited by atomic layer deposition, Nucl. Instrum. Methods B **856**, 219–220 (2004)

Daiichiro Sekiba

Institute of Applied Physics
The University of Tsukuba
Tsukuba, Japan
sekiba@tac.tsukuba.ac.jp

Daiichiro Sekiba received his PhD from the University of Tsukuba in 2001. He worked in the University of Genova (Italy), Institute of Solid State Physics in the University of Tokyo (Japan), and Institute of Industrial Science in the University of Tokyo (Japan). He now works at the Institute of Applied Physics in the University of Tsukuba, focusing on ion beam analysis.

Subject Index

A

B

M. Rocca, T.S. Rahman, L. Vattuone (Eds.), *Springer Handbook of Surface Science*, Springer Handbooks,
https://doi.org/10.1007/978-3-030-46906-1

C

D

E

F

G

H

I

J

K

L

M

N

O

P

Q

R

S

T

U

V

W

X

Z